UNIVERSITY TURBINE SYSTEMS RESEARCH PROGRAM

ANNUAL REPORT

Reporting Period Start Date: January 1, 2005
Reporting Period End Date: December 31, 2005

Principal Authors: Lawrence P. Golan
Nicholas Rigas
Richard A. Wenglarz
William H. Day

April, 2006

DOE Award: DE-FC26-02NT41431

Submitted by: Clemson University Research Foundation
South Carolina Institute for Energy Studies
P.O. Box 946, 386-2 College Avenue, Clemson, SC 29633-0946

DISCLAIMER

This report was prepared as an account of work sponsored by an agency of the United States Government. Neither the United States Government nor any agency thereof, nor any of their employees, makes any warranty, express or implied, or assumes any legal liability or responsibility for the accuracy, completeness, or usefulness of any information, apparatus, product, or process disclosed, or represents that its use would not infringe privately owned rights. Reference herein to any specific commercial product, process, or service by trade name, trademark, manufacturer, or otherwise does not necessarily constitute or imply its endorsement, recommendation, or favoring by the United States Government or any agency thereof. The views and opinions of authors expressed herein do not necessarily state or reflect those of the United States Government or any agency thereof.

ABSTRACT

The US Department of Energy (DOE) initiated a cooperative agreement in 1992 with the South Carolina Institute for Energy Studies (SCIES) for the Advanced Gas Turbine Systems Research (AGTSR) program. In 2002, the DOE established a follow-up cooperative agreement for a program now designated as the University Turbine Systems (UTSR) Program. As stated in the cooperative agreement, the objective of the program is to support and facilitate development of advanced energy systems incorporating turbines through a university research environment.

This document is the fourth annual, technical progress report for the UTSR Program. The Executive Summary describes activities for the year of the South Carolina Institute for Energy Studies (SCIES), which administers the UTSR Program. Included are descriptions of:

- Outline of program administrative activities
- Award of the first 5 university research projects resulting from the year 2004 RFP
- UTSR Peer Review Workshop
- Twenty UTSR Fellowships awarded to higher level university students
- Increased number of Performing Member Universities to 110 institutions in 42 states
- Summary of outreach activities
- Summary table describing the active UTSR research projects during 2005

The Attachment gives more detail on SCIES activities by providing the monthly exceptions reports sent to the DOE during most the year, until the DOE indicated monthly reports were no longer needed.

The remainder of this report describes in detail the technical approach, results, and conclusions to date for the UTSR university projects.

TABLE OF CONTENTS

Page

INTRODUCTION …… 5

EXECUTIVE SUMMARY …….. 6

UTSR Activities for 2005 ……. 6

UTSR University Project Summaries ……. 10

UTSR UNIVERSITY PROJECTS

Understanding and Control of Combustion Dynamics in Gas Turbine Combustors, Georgia Tech University

Aerothermal Effects of Interfacial Leakage and Film Cooling Schemes with Endwall and Leading Edge Contouring, University of Minnesota

Measurement of Three Critical Parameters as a Basis for a Simple Life Prediction Method, University of Connecticut

Experiments and Computations on Film-Cooled End Walls with Contouring, Louisiana State University

Modeling and Control of Ultra-Lean Premixed Combustion Dynamics for Gas Turbines, Virginia Polytechnic Institute

Enhanced Prediction Techniques Based on Time-Accurate Simulations for Turbine Blade Internal Cooling, Virginia Polytechnic Institute

Mechanism-Based Testing Methodology for Improving the Oxidation, Hot Corrosion and Impact Resistance of High-Temperature Coatings for Advanced Gas Turbines, University of Pittsburgh

Advanced Sensor Approaches for Monitoring and Control of Gas Turbine Combustors, Georgia Institute of Technology

Assessment of Failure Mechanisms for Thermal Barrier Coatings by Photoluminescence, Electrochemical Impedance and Focused Ion Beam, University of Central Florida

Turbine Surface Degradation With Service and Its Effects on Performance, Brigham Young University

Advanced Optical Sensor for Monitoring and Control of Multiple Gas and Turbine Blade Properties, University of Wisconsin, Madison

Spectroscopic In-Situ Non-Destructive Evaluation to Monitor the Health of Thermal Barrier Coatings, Cleveland State University

Superior Thermal Barrier Coatings for Industrial Gas turbines Using a Novel Solution Plasma Spray, University of Connecticut

An Advanced Diagnostic and Prognostic System for Gas Turbine Generator Sets with Experimental Validation, Clemson University

The Effects of Fuel Distribution, Velocity Distribution, and Fuel Composition on Static and Dynamic Instabilities and NOx, Penn State University

Improved Film Cooling Performance for Turbine Vanes and Endwalls with Realistic Surface Conditions, Virginia Tech

Combustion Instability and Blowout Characteristics of Fuel Flexible Combustors, Georgia Tech

Correlation of Ignition Delay with IGCC Type Fuels, University of California, Irvine

Heat Transfer from Rotating Blade Platforms With and Without Film Cooling, Texas A&M University

Combustion Characterization and Modeling of Fuel Blends for Power Generation Gas Turbines, University of Central Florida

Effects of Coating Blockage and Deposits on Film Cooling Effectiveness and Heat Transfer, University of Pittsburgh

Investigation of Materials Performance in High Moisture Environments Including Corrosive Contaminants Typical of Those Arising by Using Alternate Fuels in Gas Turbines, University of Pittsburgh

Autoignition Studies of Syngas and Hydrogen (SGH) Fuels, Penn State University

Degradation of Thermal Barrier Coatings with Syngas Combustion, University of Central Florida

Aero Losses, Heat Transfer, Discharge Coefficients for Different Vane Trailing Edge Configurations for Syn Gas Fired Turbines, University of North Dakota

Deposition of Alternative (Syngas) Fuels on Turbine Blades with Film Cooling, Brigham Young University

Fundamental Studies in Syngas Premixed Combustion Dynamics, Massachusetts Institute of Technology

ATTACHMENT – Monthly Exception Reports for 2005

INTRODUCTION

Cooperative agreement DE-FC26-02NT41431 for the Advanced Gas Turbine Systems Research (AGTSR) program was established on March 20, 2002 between the U.S. Department of Energy/National Energy Technology Laboratory and the Clemson University Research Foundation/South Carolina Institute for Energy Studies (SCIES). This cooperative agreement established a five-year basic and fundamental research program that is a conduit for university support of the DOE's Fossil Energy Turbine Program. To emphasize the university role, the program was renamed the University Turbine Systems Research Program (UTSR) in late 2002.

One of the requirements of the Cooperative Agreement is a yearly technical progress report. This document provides the technical progress report for the year 2005.

The major activities specified in the Scope of Work for the UTSR Program are related to the oversight of university research projects and outreach activities. The research is to be of high importance to long-term health of the U.S. energy (especially gas turbine) industry. The outreach is to aid in transfer of university research technology and entice growth of the number of industry and university participants in the program.

Major Program Plan elements identified in the Scope of Work implemented by SCIES for the UTSR Program are:

- Identification and selection of university research topics
- Request for proposals (RFP)
- Proposal selection
- Technology transfer
- Outreach

SCIES activities for 2005 in these areas are briefly described in the Executive Summary of this report and more detail is given in the Attachment –Exceptions Reports for Year 2005, which were submitted during the year to describe ongoing work. The remainder of this report describes the ongoing university research projects that are being administered by SCIES in the UTSR Program and recently completed projects.

EXECUTIVE SUMMARY

In the UTSR Program, the DOE and Industrial Review Board (IRB) provide input to define needed energy systems (particularly gas turbine systems) research and Performing Member universities conduct the research. Under DOE direction, new activities were added to the UTSR Program beyond those of the previous AGTSR Program. These include:

- Outreach activities
- Emphasis on coal derived syngas and hydrogen fuels for turbines, rather than natural gas
- Broadened university research areas (e.g., instrumentation, sensors and life)
- New and expanded reporting requirements for SCIES and the universities. In 2005, some of the expanded reporting requirements (e.g., monthly reports) were reduced.

UTSR ACTIVITIES FOR 2005

Research Related Activities

UNIVERSITY PROJECT ADMINISTRATION – SCIES administration activities for the UTSR university projects included:

- New project awards/subcontracts established
- Administrative and technical oversight
- Processing requested subcontract modifications
- Sending semi-annual reports with evaluation forms to the IRB for review
- Informing university principle investigators of most significant IRB comments from review of their semi-annual reports
- Coordinating IRB reviews for sensitive information in university technical papers submitted for publication by the ASME and other technical societies

UNIVERSITY PROJECT AWARDS - From proposals in response to the year 2004 RFP, five university projects were awarded in 2005. Two of these projects are in the area of Aero/Heat Transfer, one is in the area of Materials, and two are in the area of Combustion. Telephone debriefings on their proposal evaluations by the IRB were also provided upon request to faculty that had unsuccessful proposals from the year 2004 RFP. The five UTSR projects that were awarded in 2005 are described in further detail in this report.

YEAR 2005 REQUESTS FOR PROPOSALS - The available UTSR budget over the five-year cooperative agreement supports a fixed number of multi-year university project awards. The much higher than average yearly number of projects that were awarded in the first two years of the program (10 in the first year and 9 in the second year) resulted in fewer projects than average that can be awarded in later years. Budget evaluations in the first quarter of 2005 showed insufficient funding for new project awards in 2006 due to funding requirements for the UTSR projects awarded to date, five projects to be awarded in 2005, and a decrease in the UTSR budget. Consequently, in agreement with the DOE Contracting Officer's Representative, SCIES notified contact persons at the Performing Member Universities that a UTSR RFP would not be released in 2005.

WORKSHOP – SCIES organized UTSR Peer Review Workshop III which was conducted at the Clemson University Madren Conference Center and Inn on October 18-20, 2005. The workshop included twenty-one peer review presentations describing on-going UTSR university research projects, seven in areo/heat transfer, five in combustion, six in materials, and three in instrumentation, sensors and life. UTSR Industrial Review Board and Academic Advisory Board "Activities and Perspectives" presentations were given by their respective chair persons. Posters from five newly awarded UTSR projects, nine UTSR fellows, and three workshop travel grant recipients were presented at an evening reception, along with a display providing highlights of successes of ongoing and completed UTSR projects. Rich Dennis, the DOE Manager of Turbine Technology, described "R&D Opportunities for the UTSR Program" during an after dinner presentation. Four breakout sessions provided opportunities for workshop participants to give their input on "Managing UTSR Growth." Ninety-one persons from academia, industry, and government attended the workshop.

IRB MEETING – The annual UTSR IRB meeting was held on October 17, 2005, the day before the start of the Workshop. The meeting addressed a summary of UTSR current finances, future outlook on finances, IRB outreach support, a proposed Academic Advisory Board (AAB) short course, and included administrative items such as possible changes in IRB fees and the privileges for Associate Members. Neither of these administrative items was adopted by the IRB.

UTSR FELLOWSHIP PROGRAM – During 2005, 20 students from 12 US universities were placed at 13 IRB companies for periods of 10-12 weeks. SCIES also worked with Debbie Haught at EERE to obtain funding for three of the Fellows. Siemens funded three additional students from among those that applied for UTSR Fellowships. This benefited the UTSR Program, since more of the Fellowship applicants received placements.

TECHNOLOGY INTERACTIONS WITH OTHER ORGANIZATIONS – In order to determine beneficial university research, SCIES interacted with several organizations to identify and exchange information on research needs and experience for turbines operating with syngas and high hydrogen fuels:

EPRI: The CoalFleet activity organized by EPRI is identifying technology needs for advanced coal based power systems, including IGCC plants. SCIES responded to an internet CoalFleet survey on technology needs which led to a visit to SCIES by EPRI and a presentation by SCIES at the July, 2005 CoalFleet Workshop.

ORNL: SCIES interacted with Oak Ridge National Labs (ORNL) in areas mutually beneficial to their DOE materials project and the UTSR project. ORNL will be conducting thermo-chemical analyses to calculate the composition of species (including trace ash compounds) in the flow path of turbines operating with syngas and high hydrogen fuels. This information will be useful input to materials and aero/heat transfer projects. SCIES suggested analyses at ORNL that will be beneficial to both programs (effects of turbine inlet temperature and variations in syngas ash chemistry) and obtained input information (e.g., fuel, air and diluent flows into a turbine combustor along with trace impurity data for syngas) needed for ORNL to conduct the thermo-chemical analyses.

CINERGY: SCIES previously visited the CINERGY Wabash River IGCC plant and obtained deposits and spalled TBC from a turbine inspection. Samples of deposits and spalled TBC were provided to two UTSR projects (at BYU and University of Pittsburgh) and earlier to ORNL for analyses. Initial results from an ORNL analysis were sent by SCIES to BYU and the University of Pittsburgh. A third stage blade from the same Wabash River turbine row that had experienced a blade failure was previously obtained by SCIES during an earlier visit to that plant. SCIES facilitated the analyses of the blade by South West Research Institute to determine if operation with syngas contributed to the failure.

UK-US Collaboration: Resulting from a recommendation by SCIES, one of several US-UK collaborative projects being developed involves using an existing Cranfield University (UK) facility to simulate turbine flow path conditions for tests of materials and turbine protection approaches for syngas turbines. SCIES was assigned as the lead for the US portion of this collaborative project. Of particular importance will be tests at the higher gas temperatures being considered for next generation syngas turbines to meet the DOE IGCC efficiency objectives. Information and data on turbine flow path environments and materials degradation resulting from this test program should be useful as input to UTSR projects.

TECHNICAL PAPER - A paper, "Erosion and Deposition in Turbomachinery", with coauthors from the University of Cincinnati and SCIES was invited for publication in a special issue of the AIAA Journal of Propulsion and Power that reviews gas turbine technologies. The paper was completed for the early 2006 special issue and the authors were informed that the AIAA will also publish it in a book of articles on gas turbine technologies.

Outreach Activities

In summary, major outreach activities for 2005 were in the areas of:

- Outreach for the UTSR
- Support of the DOE Turbine Program
- Outreach publications

OUTREACH FOR THE UTSR

UTSR MEMBERSHIP – New university members for 2005 are Montana State and UNLV. There are now 110 Performing Member Universities in 42 states. Companies that joined the Industrial Review Board during 2005 are BP, Cinergy, Clean Energy Systems, Precision Combustion, Ramgen (rejoining), EPRI (rejoining), Capstone and Ingersoll-Rand. The latter two are the first microturbine manufacturers to join.

USEFULNESS OF UTSR TO INDUSTRY – Single slide project descriptions depicting the ways in which industry has used the results of UTSR projects were completed by SCIES and approved by NETL for the following universities and project numbers: Brigham Young University Project SR104, Cornell Project SR049, GA Tech Project SR031, UC Irvine Project SR062 and U. of North Dakota Project SR086.

WEBSITE – SCIES enhanced the UTSR website so that project descriptions, PI's and universities are easier to find. Graphics and links to publications were improved utilizing the work done to produce the Annual Reports for 2003 and 2004.

WORK WITH IGTI – A cooperative promotional agreement was developed, which included promoting the Fellowship Program on the IGTI website. IGTI provided a booth and posters for the UTSR for Turbo Expo '05. SCIES developed handouts on the UTSR Program (expanded Fact Sheet, UTSR Benefits Package, reprints of Gas Turbine World articles), distributed them at the booth and made a joint presentation with Karen Thole of the AAB on the UTSR Program. SCIES provided a session chair and reviewed ASME papers for the conference.

GAS TURBINE SHORT COURSES – SCIES presented part of the first short course for NETL and worked with Karen Thole, Chair of the Academic Advisory Board, to develop the process to produce more short courses for companies; the additional short courses were nearing completion at the end of 2005.

SUPPORT OF THE OVERALL TURBINE PROGRAM

PROGRAM JUSTIFICATION – SCIES worked with Karen Thole of the AAB to provide material for documents which help justify an enhanced budget for the UTSR Program and with Dick Tuthill of P&W to help justify the budget for the overall Turbine Program.

PROPOSAL REVIEWS – SCIES reviewed and commented on 19 proposals from the Turbine Program solicitation June '05 and also recommended four additional reviewers.

OUTSIDE PUBLICATIONS RELEVANT TO THE TURBINE PROGRAM – On a continuing basis, SCIES has provided to NETL management, copies of articles in publications such as The Wall Street Journal, Business Week and Power Engineering on IGCC, which can be helpful to NETL in program planning and program justification.

TURBINE HANDBOOK – In addition to writing the section on the UTSR Program (see "Publications"), SCIES reviewed a section of the handbook written by Dr. Ashok Rao of UCI. Comments and suggestions were made which were incorporated in his section.

OUTREACH PUBLICATIONS

The following publications were either authored by SCIES or had substantial SCIES input.

"University Turbine Systems Research Program: An Innovative Approach to Graduate Education", ASME Paper # MECE2005-82534

"University Turbine Systems Research Program", ASME Paper #GT2006-90060

"Targeting Turbine Research Needed to Burn Syngas and Hydrogen Fuels", Gas Turbine World, March-April 2005

"University Turbine Systems Research Program", a section of the DOE Turbine Handbook

SCIES provided input to Lee Langston, the Editor of the Journal of Engineering for Gas Turbines and Power, so he could include IGCC's in his article on the gas turbine industry, which covers both aircraft engines and land based gas turbines. Lee's "Gas Turbine Overview" is published annually by IGTI.

A press release was produced by SCIES which coverers the Academic Advisory Board (AAB) and the appointment of Richard Huntington as Liaison to the AAB from the IRB. The press release was displayed on the ClemsoNews web location.

UTSR UNIVERSITY PROJECT SUMMARIES

Table 1 summarizes the active 2005 projects and identifies the principal investigator, university, project title and project objectives. Experimental and analyses approaches, results to date, and conclusions to date from these projects are discussed in the next section. The five university research subcontracts for projects SR117 through SR121 were awarded in 2005 under the UTSR Program.

Table 1. Active UTSR Projects in 2005

Contract No ; Applicant; Award Date	**Principal Investigator**	**City/State & Business Contact**	**Area of Research (Materials, AHT: Aero-Heat Transfer, Combustion, ISL: Instrumentation, Sensors, and Life): Project Title, Goal-Accomplishment**
02-01-SR095; Georgia Institute of Technology; 5/1/02	Ben Zinn 404.894.3033 ben.zinn@aerospace.gatech.edu	Atlanta, GA	C: "*Understanding and Control of Combustion Dynamics in Gas Turbine Combustors*." Experimentally evaluate factors that cause and sustain combustion instabilities and develop models to analytically predict the occurrence and amplitude of oscillations.
02-01-SR096; University of Minnesota; 5/1/02	Terrence Simon 612.625.5831 tsimon@mc.umn.edu	Minneapolis, MN	AHT: "*Aerothermal Effects of Interfacial Leakage and Film Cooling Schemes with Endwall and Leading Edge Contouring*." Evaluate the use of cooling flows, cavity flows, and endwall contouring to reduce aerodynamic losses and improve heat transfer for turbine flow passages.
02-01-SR097; University of Connecticut; 5/1/02	Eric Jordan 860.486.2371 jordan@engr.uconn.edu	Storrs, CT	M: "*Measurement of Three Critical Parameters as a Basis for a Simple Life Prediction Method*." Develop a TBC life prediction method using measurements of i) bond coat surface defects/irregularities, ii) stress in the thermal grown oxide (TGO), and iii) TGO thickness.

02-01-SR098; Louisiana State University; 5/1/02	Sumanta Acharya 225.578.5809 acharya@alpha2.eng.LSU.edu	Baton Rouge, LA	AHT: "*Experiments and Computations on Film-Cooled End Walls with Contouring*." Evaluate a strategy of end-wall contouring and leading edge fillet design to suppress passage aerodynamic losses due to secondary flows and explore coolant injection upstream of blades for effective end-wall cooling.
02-01-SR099; Virginia Polytechnic Institute; 5/1/02	Uri Vandsburger 540.231.4459 uri@shakti.me.vt.edu	Blacksburg, VA	C: "*Modeling and Control of Ultra-Lean Premixed Combustion Dynamics for Gas Turbines*." Develop and use design-oriented modeling capabilities for determining passive energy absorption strategies or active control approaches that reduce the occurrence and level of instabilities and extend lean blowout limits for combustors.
02-01-SR100; Virginia Polytechnic Institute; 5/1/02	Danesh Tafti 540.231.9975 dtafti@vt.edu	Blacksburg, VA	AHT: "*Enhanced Prediction Techniques Based on Time-Accurate Simulations for Turbine Blade Internal Cooling*." Evaluate alternate techniques for predicting flows in internal cooling passages of turbine blades and then validate those techniques in an experimental facility.
02-01-SR101; University of Pittsburgh; 5/1/02	Gerald Meier 412.624.9741 ghmeier@engrng.pitt.edu	Pittsburgh, PA	M: "*Mechanism-Based Testing Methodology for Improving the Oxidation, Hot Corrosion and Impact Resistance of High-Temperature Coatings for Advanced Gas Turbines*." Develop a mechanism-based non-destructive testing methodology to assess metallic coating and TBC degradation resulting from cyclic oxidation, hot corrosion, and foreign object impact damage.
02-01-SR102; Georgia Institute of Technology; 5/1/02	Jerry Seitzman 404.894.0013 jerry.seitzman@ae.gatech.edu	Atlanta, GA	RAM: "*Advanced Sensor Approaches for Monitoring and Control of Gas Turbine Combustors*." Develop sensing strategies to monitor turbine combustor health and performance and also enable control systems to actively manage engine condition to compensate for changes in ambient conditions and system degradation (e.g., wear).
02-01-SR103; University of Central Florida; 5/1/02	Yong-ho Sohn 407.882.1181 ysohn@mail.ucf.edu	Orlando, FL	M: "*Assessment of Failure Mechanisms for Thermal Barrier Coatings by Photoluminescence, Electrochemical Impedance and Focused Ion Beam*." Use multiple types of measurement methods to determine causes of TBC failures and refine non-destructive evaluation techniques for TBC coatings.

02-01-SR104; Brigham Young University; 6/1/02	Jeffrey Bons 801.422.8036 jbons@byu.edu	Provo, UT	AHT: "*Turbine Surface Degradation With Service and Its Effects on Performance*." Establish the groundwork for a model to assess the effect of turbine service time on engine performance degradation due to factors such as erosion, deposition and coating spallation from airfoils.
03-01-SR105; University of Wisconsin; 7/1/03	Scott Sanders 608.262.3540 sanders@engr.wisc.edu	Madison, WI	ISL/SYN: "*Advanced Optical Sensor for Monitoring and Control of Multiple Gas and Turbine Blade Properties*", Evaluate the potential of fiber optic sensors for monitoring and active control input for gas turbines. Sensed parameters include strain and temperature of gas turbine components and gas temperature and composition. Directly contributes to the advancement of SGH turbines through monitoring capabilities for measuring water vapor and alkalis, in addition to gas and surface temperatures.
03-01-SR106; Cleveland State University; 7/1/03	Kang Lee 216.433.5634 kang.n.lee@lerc.nasa.gov	Cleveland, OH	M/SYN: "*Spectroscopic In-Situ Non-Destructive Evaluation to Monitor the Health of Thermal Barrier Coatings",* Evaluate an approach based on optically monitoring turbine exhaust composition for detection of thermal barrier coating degradation and impending failure. Directly contributes to the development of SGH turbines because premature spallation of TBC has been an issue in current coal IGCC plants.
03-01-SR107; University of Connecticut; 7/1/03	Nitin Padture 860.486.4206 nitin.padture@uconn.edu	Storrs, CT	M/SYN: "*Superior Thermal Barrier Coatings for Industrial Gas turbines Using a Novel Solution Plasma Spray",* Evaluate a new Solution Plasma Spray (SPS) process to produce improved thermal barrier coatings. At representative syngas turbine conditions, determine the hot corrosion performance of SPS TBCs compared to conventional TBCs. Directly contributes to the advancement of SGH turbines by producing thicker TBC to improve component protection for increased temperature SGH turbines and evaluating the corrosion resistance of the unique SPS microstructure.
03-01-SR108; Clemson University; 7/1/03	John Wagner 864.656.7376 jwagner@clemson.edu	Clemson, SC	ISL/SYN: "*An Advanced Diagnostic and Prognostic System for Gas Turbine Generator Sets with experimental Validation",* Develop a real-time conditioning monitoring and prediction program for gas turbine engines to diagnose and predict short term health and readiness. Use behavior models, sensor fusion strategies, neural networks, and extensive statistical

			analyses in the program along with a prognostic model to predict onset of faults, degraded operation, and to facilitate maintenance scheduling. Indirectly contributes to the advancement of SGH turbines by improving turbine system diagnostic and prognostic methods concerning systems degradations for operation with both conventional and SGH fuels.
03-01-SR109; Pennsylvania State University; 7/1/03	Domenic Santavicca 814.863.1863 das8@psu.edu	University Park, PA	C/SYN: "*The Effects of Fuel distribution, Velocity Distribution, and Fuel Composition on Static and Dynamic Instabilities and NOx",* Investigate the effects of fuel-air profile and velocity profile on lean blowout, combustion dynamics, and NOx emissions under conditions representative of lean premixed combustors operating with coal syngas and natural gas. Directly contributes to the advancement of SGH turbines by addressing SGH fuel effects on combustor performance.
03-01-SR110; Virginia Polytechnic Institute; 7/1/03	Karen Thole 540.231.7192 thole@vt.edu	Blacksburg, VA	AHT/SYN: "*Improved Film Cooling Performance for Turbine Vanes and Endwalls with Realistic Surface Conditions*", Investigate the effects on airfoil cooling performance of surface roughness and cooling hole partial blockage, such as caused by deposits in syngas turbines. Evaluate cooling hole traverse slots to improve cooling effectiveness and alleviate effects of partial blockage of cooling holes by deposits. Directly contributes to the development of SGH turbines by evaluating deposition effects on cooling related to SGH fuels.
03-01-SR111; Georgia Institute of Technology; 7/1/03	Timothy Lieuwen 404.894.3041 tim.lieuwen@aerospace.gatech.edu	Atlanta, GA	C/SYN: "*Combustion Instability and Blowout Characteristics of Fuel Flexible Combustors",* Use experiments and analyses to improve understanding and develop modeling capabilities for effects of fuel variability on a combustor's static (lean blowout) and dynamic stability characteristics. Tests and analyses are expected to use fuels and gas compositions representative of coal syngas. Directly contributes to the development of SGH turbines by considering SGH fuel composition effects on combustor stability.

03-01-SR112; University of California, Irvine; 7/1/03	Scott Samuelsen 949.824.5468 gss@uci.edu	Irvine, CA	C/SYN: "*Correlation of Ignition Delay with IGCC Type Fuels",* Using simulated coal synfuels, conduct ignition delay experiments to identify design rules for avoiding autoignition in lean premixed combustion systems. Directly contributes to the development of SGH turbines by evaluating SGH fuel effects on combustor flashback and autoignition.
03-01-SR113; Texas A&M University; 7/1/03	J. C. Han 979.845.3738 jchan@mengr.tamu.edu	College Station, TX	AHT: "*Heat Transfer from Rotating Blade Platforms With and Without Film Cooling",* Obtain experimental data and numerical predictions to enable turbine designers to improve the cooling efficiency of rotating blades and thereby increase turbine power and efficiency. Indirectly contributes to the development of SGH turbines by developing information for the cooling design of increased temperature turbines planned for SGH fuels.
04-01-SR114; University of Central Florida; 8/1/04	E. Petersen, 407.823.6123 Petersen@mail.ucf.edu	Orlando, FL	C: "*Combustion Characterization and Modeling of Fuel Blends for Power Generation Gas Turbines*", Measure combustion characteristics (flame speed, autoignition, kinetics, NOx) over a wide range of fuel compositions and conditions representative of syngas turbines. Directly contributes to the development of SGH turbines by exploring fuel variability effects related to SGH fuels.
04-01-SR115; University of Pittsburgh; 8/1/04	M. Chyu 412.624.9783 mkchyu@engr.pitt.edu	Pittsburgh, PA	AHT: "*Effects of Coating Blockage and Deposits on Film Cooling effectiveness and Heat Transfer*", Experiments and computations to explore transport processes and effects on cooling performance associated with film cooling hole blockage and surface deposits. Directly contributes to the development of SGH turbines by evaluating deposition effects on cooling related to SGH fuels.
04-01-SR116; University of Pittsburgh; 8/1/04	F. S. Pettit 412.624.9730 pettit@engrng.pitt.edu	Pittsburgh, PA	M: "*Investigation of Materials Performance in High Moisture Environments Including Corrosive Contaminants Typical of Those Arising by Using Alternate Fuels in Gas Turbines*", Experiments and data analyses to develop a fundamental understanding of corrosion of typical turbine alloys and coatings due to deposits and moisture environments under conditions representative of operation with alternate fuels. Directly contributes to development of SGH turbines by evaluating effects on

			materials from conditions associated with SGH turbines.
05-01-SR117; Penn State University; 8/1/05	Robert Santoro 814.863.1285 rjs2@psu.edu	University Park, PA	C: *"Autoignition Studies of Syngas and Hydrogen (SGH) Fuels",* Experiments to characterize the autoignition of syngas and hydrogen (SGH) fuels at high pressures and temperatures typical of lean premixed gas turbine engine conditions. Autoignition delay times determined in the first two years for CO/H2 mixtures representing syngas (CO+3H2) to pure hydrogen (H2). For the third year, autoignition characteristics of CO/H2/H20 mixtures are evaluated. Directly contributes to the development of SGH turbines by evaluating combustion characteristics for SGH compositions and conditions.
05-01-SR118; University of Central Florida; 8/1/05	Yongho Sohn 407.882.1181 ysohn@mail.ucf.edu	Orlando, FL	M: *"Degradation of Thermal Barrier Coatings with Syngas Combustion",* Advanced microstructural analyses techniques (such as advanced electron microscopy) used for the first time to evaluate degradation mechanisms of TBCs under SGH conditions. Directly contributes to the development of SGH turbines by evaluating turbine materials in realistic syngas combustion environments produced at test facility located at the Dakota Gasification Company site.
05-01-SR119; University of North Dakota; 8/1/05	Forrest Ames 701.777.2095 forrest_ames@mail.und.nodak.edu	Grand Forks, ND	AHT: "*Aero Losses, Heat Transfer, Discharge Coefficients for Different Vane Trailing Edge Configurations for Syn Gas Fired Turbines*", Performance characteristics of five different approaches for cooling trailing edges of turbine airfoils experimentally evaluated in this project. Directly contributes to the development of SGH turbines through experiments that include representation of the effects of airfoil surface roughness caused by deposition in syngas turbines.
05-01-SR120; Brigham Young University; 8/1/05	Jeffrey Bons 801.422.8036 jbons@byu.edu	Provo, UT	AHT: "*Deposition of Alternative (Syngas) Fuels on Turbine Blades with Film Cooling*", A natural gas combustion stream seeded with coal and biomass products of combustion particulate and accelerated to turbine flow velocities in a simulator where specimens of turbine materials are exposed. Phase 1 of the project explores the possibility of increased cooling of specimens (and turbine surfaces) to mitigate deposition. Phase 2 evaluates the influence of deposit formation on film cooling. Directly contributes

			to the development of SGH turbines by evaluating deposition issues for ash bearing fuels such as SGH fuels.
05-01-SR121; Massachusetts Institute of Technology; 8/1/05	Ahmed Ghoniem 617.253.2295 ghoniem@MIT.EDU	Cambridge, MA	C: "*Fundamental Studies in Syngas Premixed Combustion Dynamics*", Data on flammability limits, stability characteristics, laminar and turbulent flame propagation, flame anchoring mechanisms, burning conditions, and syngas composition are collected experimentally and synthesized into models. Directly contributes to the development of SGH turbines by experimentally evaluating the fundamental characteristics of syngas combustion over a wide range of conditions representative of SGH turbines.

UTSR UNIVERSITY PROJECTS

COPIES OF THE MOST RECENT REPORTS FROM UTSR UNIVERSITY PROJECTS ACTIVE IN 2005 ARE IN THIS SECTION

Understanding and Control of Combustion Dynamics in Gas Turbine Combustors

Final Report

Reporting Period Start Date: May 1, 2002

Reporting Period End Date: November 30, 2005

Principal Investigators: Ben Zinn, Yedidia Neumeier, Tim Lieuwen

Date Report was issued June 30, 2005

DOE Award Number DE-FC26-02NT41431

UTSR Project Number 02-01-SR095

School of Aerospace Engineering

Georgia Institute of Technology

Atlanta, GA 30332-0150

DISCLAIMER:

"This report was prepared as an account of work sponsored by an agency of the United States Government. Neither the United States Government nor any agency thereof, nor any of their employees, makes any warranty, express or implied, or assumes any legal liability or responsibility for the accuracy, completeness, or usefulness of any information, apparatus, product, or process disclosed, or represents that its use would not infringe privately owned rights. Reference herein to any specific commercial product, process, or service by trade name, trademark, manufacturer, or otherwise does not necessarily constitute or imply its endorsement, recommendation, or favoring by the United States Government or any agency thereof. The views and opinions of authors expressed herein do not necessarily state or reflect those of the United States Government or any agency thereof."

1. ABSTRACT

This program investigates the causes and active control of combustion driven oscillations in low emissions gas turbines. These oscillations are a critical problem encountered in the development of new systems and the availability and maintainability of fielded systems. This document is the final report under this contract . During the duration of the contract, substantial progress has been made in improving the understanding of the dynamics of unstable combustors. Both experimental and theoretical efforts have been pursued and completed over the period of the contract.

This report describes all of the experimental and theoretical work undertaken during the last 3-1/2 years. Specifically, this report describes experimental studies which investigated the mechanisms responsible for saturation of the flame transfer function and therefore control the limit cycle amplitude of unstable gas turbine combustors. In addition, theoretical studies were performed to investigate nonlinear flame response behavior. Significantly, these studies were able to capture and explain many phenomenon observed in experiments.

Furthermore, experiments on unstable combustors including open loop active control studies and nonlinear frequency interaction investigations were performed to improve the understanding of the underlying physics which control combustion instabilities.

2. TABLE OF CONTENTS

1. ABSTRACT 3

2. TABLE OF CONTENTS 4

3. LIST OF FIGURES 5

4. EXECUTIVE SUMMARY 12

5. PROJECT DESCRIPTION 13

6. NONLINEAR FLAME TRANSFER FUNCTION CHARACTERISTICS 14

Gas Turbine Combustor Simulator 17

Atmospheric Swirl Stabilized Burner 29

7. 43

CONCLUDING REMARKS ..... ERROR! BOOKMARK NOT DEFINED.

APPENDIX A 104

APPENDIX B 104

APPENDIX C 105

APPENDIX D 106

APPENDIX E 108

8. NONLINEAR INTERACTIONS IN GAS TURBINE COMBUSTORS 83

Nonlinear Heat-Release/Linear Acoustic Interactions 83

NONLINEAR FREQUENCY INTERACTIONS 87

9. ACTIVE CONTROL OF COMBUSTION INSTABILITIES 93

Facility and Instrumentation 94

Control Implementation 95

Results 95

10. CONCLUSIONS 100

11. REFERENCES 104

3. LIST OF FIGURES

Figure 1: Qualitative description of the dependence of acoustic driving, H(*A*), and damping, D(*A*), processes upon amplitude of oscillation, *A* 15

Figure 2: Schematic of Georgia Tech lean, premixed combustor facility 17

Figure 3: Detail of mixing and combustion section 18

Figure 4: Dependence of mean CH* and OH* signals upon velocity oscillation amplitude (f_{drive} = 280 Hz, ϕ = 0.95) 20

Figure 5: Dependence of (a) linear velocity-CH* transfer function and (b) velocity-CH* phase angle upon driving frequency 21

Figure 6: Dependence of CH* chemiluminescence and pressure oscillation amplitude on velocity fluctuation amplitude (f_{drive} = 280 Hz, ϕ= 0.95). 22

Figure 7: Dependence of CH* and OH* chemiluminescence (a) amplitude and (b) phase angle on velocity oscillation amplitude. Chemiluminescence saturation occurs in (a) at $u'/u_o > 0.25$. Uncertainty in phase angle for $u'/u_o < 0.05$, $\Delta\theta \sim 30°$; for $u'/u_o > 0.05$, $\Delta\theta \sim 2°$. (f_{drive} = 283 Hz) 23

Figure 8: Dependence of (a) CH* chemiluminescence amplitude and (b) velocity-CH* chemiluminescence phase angle on amplitude of velocity oscillations at several equivalence ratios. Uncertainty in phase angle for $u'/u_o < 0.05$, $\Delta\theta \sim 30°$; for $u'/u_o > 0.05$, $\Delta\theta \sim 2°$. (f_{drive} = 300 Hz) 24

Figure 9: Dependence of CH* chemiluminescence (a) amplitude and (b) phase upon velocity amplitude at several driving frequencies. Uncertainty in phase angle for $u'/u_o < 0.05$, $\Delta\theta \sim 30°$; for $u'/u_o > 0.05$, $\Delta\theta \sim 2°$. (ϕ = 0.95) 25

Figure 10: Dependence of CH* 1st harmonic on the square of CH* fundamental at two equivalence ratios (f_{drive} = 300 Hz) 26

Figure 11: Dependence of pressure harmonic amplitude on velocity oscillation amplitude (f_{drive} = 290 Hz, ϕ = 0.95). Quadratic trend indicated by the solid line, cubic trend indicated by dashed line. 26

Figure 12: Dependence of CH* chemiluminescence fundamental-1st harmonic phase angle on velocity oscillation amplitude at several driving frequencies (ϕ = 0.95). Uncertainty in phase angle for $u'/u_o < 0.05$, $\Delta\theta \sim 30°$; for $u'/u_o > 0.05$, $\Delta\theta \sim 3°$. 27

Figure 13: Dependence of CH* subharmonic and transfer function gain on velocity oscillation amplitude (f_{drive}=280 Hz, ϕ = 0.95) 27

Figure 14. Schematic of swirl-stabilized combustor 30

Figure 15. Schematic of burner premixer. All dimensions are in mm (not to scale). 30

Figure 16. Schematic of laser setup for OH PLIF imaging 31

Figure 17. Dependence of (a) CH* oscillation amplitude and (b) u'-CH*' phase angle upon velocity oscillation amplitude (f_{drive} = 210 Hz, ϕ=0.80, Re_D = 21000). CH* saturation amplitude = 0.45. Uncertainty in phase angle < 5°. 33

Figure 18: Dependence of (a) CH* oscillation amplitude and (b) u'-CH*' phase angle upon velocity oscillation amplitude, ϕ = 0.80, Re_D = 21000. CH* saturation amplitude ~ 0.98. Uncertainty in phase angle < 5°. 33

Figure 19. Dependence of CH* oscillation amplitude upon amplitude of velocity oscillations for two driving frequencies (Re_D = 21000, ϕ = 0.80) 34

Figure 20. (a) Dependence of CH* oscillation amplitude upon amplitude of velocity oscillations for f_{drive} = 160-180 Hz. (b) Dependence of u'-CH*' phase angle upon velocity oscillation amplitude for f_{drive} = 170 Hz. (Re_D = 30000, ϕ = 0.80). 34

Figure 21. Fourier transforms of (a) pressure and (b) CH* chemiluminescence signals at local maximum of transfer function (red) and local minimum of transfer function (green) for f_{drive} = 180 Hz (Re_D = 30000, ϕ = 0.80). 35

Figure 22. Dependence of CH* nonlinear amplitude on driving frequency as a function of Reynolds number (ϕ = 0.80). 36

Figure 23: Phase-locked instantaneous line-of-sight images of flame over 1 cycle of acoustic forcing for (a) low (linear) and (b) high (nonlinear) amplitude of oscillation (f_{drive} = 410 Hz, Re_D = 21000, ϕ = 0.80). 37

Figure 24. Instantaneous OH PLIF images showing evolution of flame response over 1 cycle of acoustic forcing for (a) low (linear) and (b) high (nonlinear) velocity oscillation amplitudes (f_{drive} = 130 Hz, Re_D = 21000, ϕ = 0.80) 38

Figure 25. Phase-averaged flame edges showing evolution of flame response over 1 cycle of acoustic forcing for (a) low (linear, u'/u_o = 0.3) and (b) high (nonlinear, u'/u_o = 0.9) velocity oscillation amplitudes (f_{drive} = 130 Hz) 39

Figure 26. Averaged flame edges at 65-110 degrees phase angle at four velocity oscillation amplitudes (f_{drive} = 130 Hz, u'/u_o = 0.3, 0.6, 0.83, 0.90). Dashed (- - -)/ solid (—) lines indicate peak flame response when transfer function is linear/saturated, respectively. 40

Figure 27. Instantaneous OH PLIF images showing evolution of flame response over 1 cycle of acoustic forcing for (a) low (linear, u'/u_o = 0.2) and (b) high (nonlinear, u'/u_o = 0.6) velocity oscillation amplitudes (f_{drive} = 410 Hz, Re_D = 21000, ϕ = 0.80) 41

Figure 28. Average flame edges at 180-225 degree phase angle at four velocity oscillation amplitudes (f_{drive} = 410 Hz, u'/u_o = 0.2, 0.3, 0.53, 0.6). Dashed (- - -)/ solid (—) lines indicate peak flame response when transfer function is linear/saturated, respectively. 42

Figure 29. Qualitative description of the dependence of acoustic driving, $H(\varepsilon)$ and damping, $D(\varepsilon)$, processes upon amplitude, ε 44

Figure 30. Vorticity field superposed with the flame front. Image reproduced with permission from Ref. [] 45

Figure 31. Coordinate system illustrating the perturbed flame shape 49

Figure 32. Sketch of a flame that is initially wrinkled (top), showing the destruction of flame area by kinematic restoration processes (bottom) 50

Figure 33. Dependence of shear wave convection velocity and growth rate in a jet flow upon Strouhal number and ratio of jet radius to momentum thickness. Figure reproduced from Michalke (1971). 52

Figure 34. Parametric stability limits of flat flame (unity Lewis and Prandlt number, no gravity). 54

Figure 35. Illustration of conical (left) and wedge shaped (right) flame geometries. 55

Figure 36. Instantaneous conical flame shape with X axis along the flame front. β=2, ε=0.01, St = 39, K=0 60

Figure 37. Strouhal number dependence of the magnitude of the ratio of the transfer functions due to the flow non-uniformity and boundary condition terms for different values of η, σ^*=0 62

Figure 38. Strouhal number dependence of the phase of the ratio of the transfer functions due to the flow non-uniformity and boundary condition terms for conical flames for different values of η, σ^*=0 63

Figure 39. Strouhal number dependence of the phase of the ratio of the transfer functions due to the flow forcing and boundary condition terms for wedge flames. Shaded regions indicate points where boundary condition and flow non-uniformity terms are in phase, σ^*=0 63

Figure 40. Effect of Stretch on the Strouhal number dependence of transfer functions due to flow non-uniformity and boundary condition terms for wedge flames, σ^*=0.0005 .. 65

Figure 41. Axisymmetric conical linear transfer function $G_c(St_2,\eta)$ magnitude dependence upon the reduced Strouhal number (St_2) for different values of η, σ^*=0.0005..... 66

Figure 42. Axisymmetric conical linear transfer function $G_c(St_2,\eta)$ phase dependence upon the reduced Strouhal number (St_2) for different values of η, σ*=0.0005..... 66

Figure 43. Axisymmetric wedge linear transfer function $G_w(St_2,\eta)$ amplitude dependence upon the reduced Strouhal number (St_2) for different values of η, σ^*=0.0005..... 67

Figure 44 Axisymmetric wedge linear transfer function $G_w(St_2,\eta)$ phase dependence upon the reduced Strouhal number (St_2) for different values of η, σ^*=0.0005 68

Figure 45. Strouhal number dependence of the parameter η at which the maximum possible linear response occurs for axisymmetric conical and wedge flames, σ*=0 69

Figure 46. Dependence of flame area fluctuations upon disturbance velocity amplitude for axisymmetric conical flames at η=1 71

Figure 47. Dependence of non-linear part of the transfer function for axisymmetric wedge flames at η=1 73

Figure 48. Strouhal number dependence of the ratio of the magnitude of the flame area-velocity transfer function to its linear value for the axisymmetric wedge flame, β=1, σ^*=0.005 74

Figure 49. Strouhal number dependence of the phase of the flame area-velocity transfer function for the axisymmetric conical flame, β=1, σ^*=0.005 74

Figure 50. Strouhal number dependence of the ratio of the magnitude of the flame area-velocity transfer function to its linear value for the axisymmetric wedge flame, β=1, σ^*=0.005 75

Figure 51. Strouhal number dependence of the phase of the flame area-velocity transfer function for the axisymmetric wedge flame, β=1 , σ^*=0.005 75

Figure 52. Strouhal number dependence of the magnitude of the flame area-velocity transfer function for the axisymmetric wedge flame, α=0.8,K=2.5, σ^*=0.005..... 76

Figure 53. Experimentally measured gain for an inverted conical flame for a mean velocity u_o= 2.05 m/s, ϕ = 0.92. Data reproduced from Durox *et al*..... 77

Figure 54. Dependence of non-linear part of the transfer function on the phase speed of the disturbances (K) for axisymmetric wedge flames, St=1, σ=0 78

Figure 55. Dependence of the magnitude of the flame area-velocity transfer function on η for the axisymmetric conical flame for different Strouhal numbers, β=8, σ=0. Arrow points towards increasing velocity amplitude ε. 78

Figure 56. Dependence of acoustic driving, H(ε) (where H(ε) is equated for this example to $A_w'/A_{w,o}$) and damping, D(ε), processes upon velocity amplitude ε, for wedge flames at St_2=6.25 with K=2, α =0.8, σ^*=0.005 79

Figure 57. Qualitative representation of regions where nonlinear flame transfer exceeds (shaded) or is less than (white) linear transfer function, α=0.8,ε=0.1, σ=0 79

Figure 58. Amplitude dependence of the magnitude of the flame area-velocity transfer function for an axisymmetric wedge flame: Comparison between models with and without Stretch effects. β=1, K=0 80

Figure 59. Dependence of flame area fluctuations upon disturbance velocity amplitude for axisymmetric conical flames at η=1 82

Figure 60. Contours of constant L_{avg} (average flame length) as a function of K and St_2 for different values of α. Arrows indicate regions of increasing flame length. 82

Figure 61: Frequency–response curves at several excitation amplitudes for a second order oscillator with nonlinearities in (a) stiffness and (b) damping 83

Figure 62: Dependence of pressure amplitude upon frequency at (a) a single disturbance amplitude, 2.8A and (b) several disturbance amplitudes, 1.8-3.0A (ϕ = 0.95) 84

Figure 63: Excitation–response curves for softening spring oscillator at several excitation frequencies. 85

Figure 64: Dependence of pressure oscillation amplitude on excitation amplitude for varying driving frequencies (ϕ = 0.95) 85

Figure 65: Amplitude-frequency ranges over which the chemiluminescence-pressure-velocity relationship exhibited single and multi-valued behavior 86

Figure 66: Dependence of pressure-CH* transfer function on driving frequency (excitation amplitude = 2.4 amperes (a), excitation amplitude = 3.0 amperes (b), ϕ = 0.95) 87

Figure 67: (a) Spectrum of combustor pressure at two driving amplitudes showing decrease in combustor instability mode as driving amplitude is increased (instability frequency = 461 Hz, driving frequency = 200 Hz). (b) Dependence of instability amplitude on driving velocity amplitude at 200 Hz driving frequency. 88

Figure 68: Dependence of instability amplitude on driving amplitude for driving frequency = 410 Hz (instability frequency = 461 Hz). 90

Figure 69: Dependence of (a) velocity entrainment amplitude, AE, and (b) corresponding pressure amplitude values upon driving frequency (instability frequency = 461 Hz).. 90

Figure 70: Dependence of instability rolloff, δp on driving frequency (instability frequency = 461 Hz) 91

Figure 71: Dependence of AL parameter (velocity oscillation amplitude range which is independent of forcing) on driving frequency (instability frequency = 461 Hz) 91

Figure 72: Dependence of maximum acoustic power reduction on driving frequency (instability frequency = 461 Hz). 92

Figure 73. Block diagram of gain/phase shifter between pressure transducer and air actuator used to generate self-excited oscillations. 94

Figure 74 Low pass filtered time dependence of oscillatory combustor pressure amplitude with and without control. 96

Figure 75. Dependence of mean and fluctuating instability amplitude upon desired level. 96

Figure 76. Fourier transform of combustor pressure at desired amplitude levels of 0-0.4 psi..... 97

Figure 77. Fourier transform of combustor pressure at desired amplitude levels of 0.4, 0.2, 0.16, 0.14, and 0.13 psi (nominal instability amplitude = 0.35 psi)..... 98

Figure 78 Instability driving characteristic visualized by plotting the dependence of the instantaneous air actuator driving signal upon pressure..... 99

Figure 79. Dependence of instantaneous pressure amplitude upon time as phase of control signal is swept relative to that of the instability. 99

4. EXECUTIVE SUMMARY

Under the High Efficiency Engines and Turbines-University Turbine Research (HEET-UTSR) program, Georgia Institute of Technology is investigating the mechanisms and control of detrimental oscillations in gas turbine combustors. This program consists of two main tasks. The first task is investigating the dynamics of uncontrolled combustors. These results are improving capabilities to predict the occurrence and amplitudes of instabilities. The second task is investigating active control of combustion dynamics. This work is developing methods for suppressing these instabilities in the highly turbulent, harsh combustor environment and improving understanding of the factors that effect active control authority. Currently, combustion dynamics severely reduce the reliability and availability of gas turbines by damaging parts and substantially reducing time between overhauls, both of which ultimately affect the consumer by increasing the cost of electricity.

This program investigates the causes and active control of combustion driven oscillations in low emissions gas turbines. These oscillations are a critical problem encountered in the development of new systems and the availability and maintainability of fielded systems. This document is the final report under this contract . During the duration of the contract, substantial progress has been made in improving the understanding of the dynamics of unstable combustors. Both experimental and theoretical efforts have been pursued and completed over the period of the contract.

This report describes all of the experimental and theoretical work undertaken during the last 3-1/2 years. Specifically, this report describes experimental studies which investigated the mechanisms responsible for saturation of the flame transfer function and therefore control the limit cycle amplitude of unstable gas turbine combustors. In addition, theoretical studies utilizing one possible mechanism were performed to investigate nonlinear flame response behavior.

Furthermore, experiments on unstable combustors including active control studies and nonlinear frequency interaction investigations were performed to improve the understanding of the underlying physics which control combustion instabilities.

Interactions with industrial partners was also a priority during this contract. We have initiated a program with an OEM to incorporate and validate the modeling work performed under this program into their in-house prediction codes. We also maintain regular discussions with combustion engineers at many of the OEM's.

5. PROJECT DESCRIPTION

Under the High Efficiency Engines and Turbines-University Turbine Research (HEET-UTSR) program, Georgia Institute of Technology is investigating the mechanisms and control of detrimental oscillations in gas turbine combustors. This program consists of two main tasks. The first task is investigating the dynamics of uncontrolled combustors. These results are improving capabilities to predict the occurrence and amplitudes of instabilities. The second task is investigating active control of combustion dynamics. This work is developing methods for suppressing these instabilities in the highly turbulent, harsh combustor environment and improving understanding of the factors that effect active control authority.

Currently, combustion dynamics severely reduces the reliability and availability of gas turbines by damaging parts and substantially reducing time between overhauls, both of which ultimately affect the consumer by increasing the cost of electricity. This work will result in improved understanding of the processes that cause these oscillations and strategies to eliminate them. Successful completion of this project will benefit the gas turbine and energy industry in several ways. First, through its improvement of turbine reliability and availability, it will reduce maintenance needs and costly downtime. In addition, it will broaden the operating envelope of gas turbines, so that they will be able to operate at higher power as well as at idle without worry of damaging oscillations. For example, many fielded turbines are not able to operate at full power because of the enormous dynamics problems encountered there. Elimination of the dynamics problem will allow them to increase their maximum power, thereby improving their capabilities to respond to peak power demands.

6. NONLINEAR FLAME TRANSFER FUNCTION CHARACTERISTICS

This section describes an experimental investigation of the relationship between flow disturbances and heat release oscillations in a lean, premixed combustor. This work is motivated by the fact that combustion instabilities continue to be one of the most serious issues hindering the development and operation of industrial gas turbines[1-4]. These instabilities generally occur when the unsteady combustion process couples with one or more of the natural acoustic modes of the combustion chamber, resulting in self-excited oscillations. These oscillations adversely affect engine performance and emissions, and can be destructive to engine hardware.

Our focus here is on the amplitude response of the heat release at some frequency, f, to a harmonic disturbance of amplitude, A, at that same frequency. The heat release response, H(A), generally exhibits a linear dependence upon the disturbance amplitude at small values of A. At high amplitudes, however, they are related nonlinearly. This is significant because the dynamics of an unstable combustor are controlled by both linear and nonlinear processes. This can be seen from Figure 1, which plots the amplitude dependence of hypothetical driving, H(A), and damping, D(A), processes. Note that the disturbance amplitude stays the same, decreases, or increases depending upon whether H(A)=D(A), H(A)<D(A), or H(A)>D(A), respectively. Linear combustor processes generally control the balance between driving and damping processes at low amplitudes of oscillation, H(A)-D(A), and, thus, determine the frequency and growth rate, $A \sim e^{\alpha t}$, of inherent disturbances in the combustor. Note that the initial growth rate of the instability, α, is proportional to the difference between the driving and damping processes in the linear regime. Nonlinear combustor processes control the finite amplitude dynamics of the oscillations. For example, predicting the limit cycle amplitude of self-excited oscillations requires an understanding of the nonlinear characteristics of H(A) and D(A). To illustrate, Figure 1 depicts a situation where H(A) saturates and D(A) remains linear, so that the two curves cross at the limit cycle amplitude, A_{LC}.

Understanding of a combustor's linear dynamics is needed to predict the frequency and conditions under which inherent disturbances in the combustor grow or decay. As a result of extensive work in this area, capabilities for modeling the acoustics of the combustor system are reasonably well developed (e.g., see Refs. [5,6]). Also, capabilities for modeling the interactions of flow and mixture disturbances with flames, needed to predict the conditions under which instabilities occur, are improving rapidly[7,8]. Much of this work is being transitioned to industry and being incorporated into dynamics predictions codes. In fact, most gas turbine manufacturers have reported model development efforts for predicting instability frequencies, mode shapes, and conditions of occurrence[9-11].

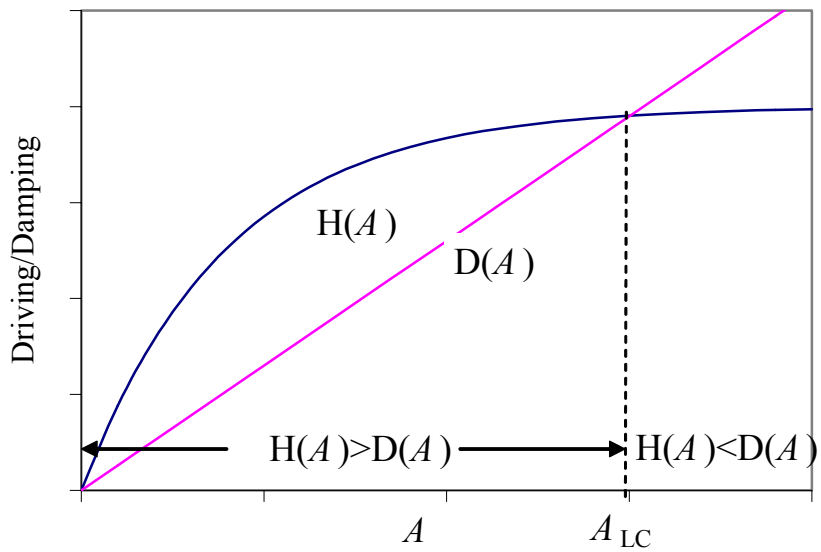

Figure 1: Qualitative description of the dependence of acoustic driving, H(*A*), and damping, D(*A*), processes upon amplitude of oscillation, *A*

As noted above, understanding of a combustor's linear dynamics is not sufficient to describe the finite amplitude dynamics of self-excited oscillations; e.g., for predicting the limit cycle amplitude. The need to predict instability amplitudes and observations of "triggered" instabilities in rockets that were linearly stable motivated past workers to consider these nonlinear effects; e.g., see Refs. [5, [12]-[14]]. Much of this work focuses on the role of nonlinear gas dynamics in combustors, however. As such, it is likely more relevant to instabilities in combustion systems where fluctuating pressure amplitudes achieve significant percentages of the mean (e.g., p'/p_o ~20-50%, such as is observed in rockets), than lean premixed gas turbine combustors where reported instability pressure amplitudes are typically on the order of 1-5% of the mean pressure[2, 15].

Recent studies[15-18] suggest that acoustic processes essentially remain in the linear regime, even under limit cycle operation, and that it is the nonlinear relationship between flow and heat release oscillations that causes saturation of the instability amplitude. As such, the flame's nonlinear response to harmonic disturbances may play a critical role in the overall dynamics of an unstable combustor. For example, Dowling[16] introduced a phenomenological model for the finite amplitude response of a flame to velocity perturbations. The model is dynamic in nature, but the essential nonlinearity consists of a quasi-steady relation between flow velocity and heat release rate. It assumes a linear relation between the heat release, Q, and velocity perturbation when the total velocity ($u(t) = u_o + u'(t)$) lies between 0 and $2u_o$. When $u(t)<0$, the heat release goes to zero and when it is greater than $2u_o$ it saturates at $2Q_o$. Thus, the essential mechanism of nonlinearity lies in the fact that the lowest amplitude of heat release oscillation cannot indefinitely decrease with perturbation amplitude because it cannot achieve negative values. A similar mechanism was proposed in an experimental study of Poinsot *et al.*[19]. In another study, Dowling[20] introduced a nonlinear boundary condition at the flame anchoring point. She assumed that the instantaneous flame anchoring point was fixed when the total gas velocity exceeded the flame speed. When the gas velocity fell below the flame speed, the former condition was replaced by one that allowed the flame to propagate upstream. Peracchio & Proscia[17] developed a quasi-steady nonlinear model to describe the response of the flame to

equivalence ratio perturbations. They assumed the following relationship for the response of the instantaneous mixture composition leaving the nozzle exit to velocity perturbations:

$$\phi(t) = \frac{\bar{\phi}}{1 + ku'(t)/\bar{u}} \tag{1}$$

where k is a constant with a value near unity. They also utilized a nonlinear relationship relating the heat release per unit mass of mixture to the instantaneous equivalence ratio. Wu *et al.*[18] developed a more general asymptotic analysis which focuses on the nonlinear interaction/coupling among acoustic, vortical, and Darrieus-Landau instability modes at the flame. This theory is found to agree well with the experimental work presented in Searby[21].

Several of the above analyses suggest that the ratio of fluctuating and mean velocity, u'/u_o, is an important non-dimensional parameter that controls the amplitude of the limit cycle oscillations through its effect upon the nonlinear relationship between flow disturbances and heat release oscillations. A similar conclusion was reached empirically in an experimental study of Lieuwen[15], who found that combustion instability amplitudes had a strong dependence upon a mean combustor velocity scale, u_o.

In an effort to understand the mechanisms controlling the growth rates and limit cycle amplitudes of combustion instabilities, the response of the flame under external forcing of the flow field has been analyzed by several researchers (e.g., see Refs.[[22]-[26]]). Külsheimer & Büchner[22] measured the effect of driving frequency and amplitude on premixed swirled and unswirled flames. They characterized the conditions under which large-scale coherent ring-vortex structure were evident, a key mechanism for self-excited oscillations, as well as the resulting flame response, on driving amplitude and frequency. They found that vortex formation occurred at lower driving amplitudes as the driving frequency was increased. Furthermore, the peak flame response in swirl flames shifted to higher frequencies for larger flow perturbations. No explicit characterization of the nonlinear interaction between the flame's heat release and the flow perturbations were reported, however.

The potentially significant nonlinear relationship between acoustic perturbations and heat release perturbations suggested by the theoretical studies above, are also supported by recent measurements of Lieuwen & Neumeier[23], Lee & Santavicca[24], and Balachandran *et al.*[26] who characterized the pressure-heat release relationship as a function of oscillation amplitude. The former study found that this relationship was linear for pressure amplitudes below about 1% of the mean pressure. At higher forcing levels, they found that the heat release oscillation amplitude began to saturate. In contrast to the assumed model of Dowling[16], however, Lieuwen & Neumeier found saturation to occur at $CH^{*\prime}/CH^{*}_{o}$ values of ~25%, in contrast to the 100% value assumed in her model. Data were only obtained at one operating condition and two driving frequencies, however, so the manner in which these saturation characteristics depend upon operating conditions and frequency is unclear.

Durox *et al.*[27] and Bourehla & Baillot[25] appear to have performed the only systematic study characterizing the response of a non-swirling flame to large amplitude perturbations. Their study was performed on a laminar Bunsen flame and primarily focused on its qualitative characteristics. No measurements of the dependence of unsteady heat release or chemiluminescence emissions were reported. They found that at low frequencies (f < 200 Hz) and velocity amplitudes (u'/u_o<0.3), the flame front wrinkles symmetrically about the burner axis due to a

convected wave traveling from the burner base to its tip. With increasing amplitude of low frequency velocity perturbations, they found that the flame exhibited a variety of transient flame holding behavior, such as flashback, asymmetric blowoff, and unsteady lifting and re-anchoring of the flame. In addition, they noted that its response was asymmetric and disordered. Finally, at high frequencies and forcing amplitudes (u'/u_o>1), they found that the flame tip collapses to a hemispherical shape.

As can be seen from the above review, there is a need for systematic measurements of the flame's nonlinear response to flow perturbations, i.e. saturation of the curve *H(A)* in Figure 1. Such characteristics must be understood in order to, for example, predict instability amplitudes or model the transient response of a combustor to active control. As such, we obtained measurements of the pressure/ velocity/ chemiluminescence amplitude and phase relationships in a swirling flame over a range of driving amplitudes. These results were obtained by externally driving oscillations in the combustor with varying amplitudes. Measurements were obtained at several driving frequencies and fuel/air ratio.

Gas Turbine Combustor Simulator

The data presented in this paper were measured in a lean, premixed gas turbine combustor simulator, shown in Figure 2, which has been previously described in Lieuwen *et al.*[28]. Tests were performed at a mean pressure of 1.7 atmospheres and mean equivalence ratios ranging from 0.83 to 1.0. All tests were performed at a total flow rate of 5.5 g/s which corresponds to a premixer velocity of 11.5 m/s. Inlet temperatures were kept constant at room temperature.

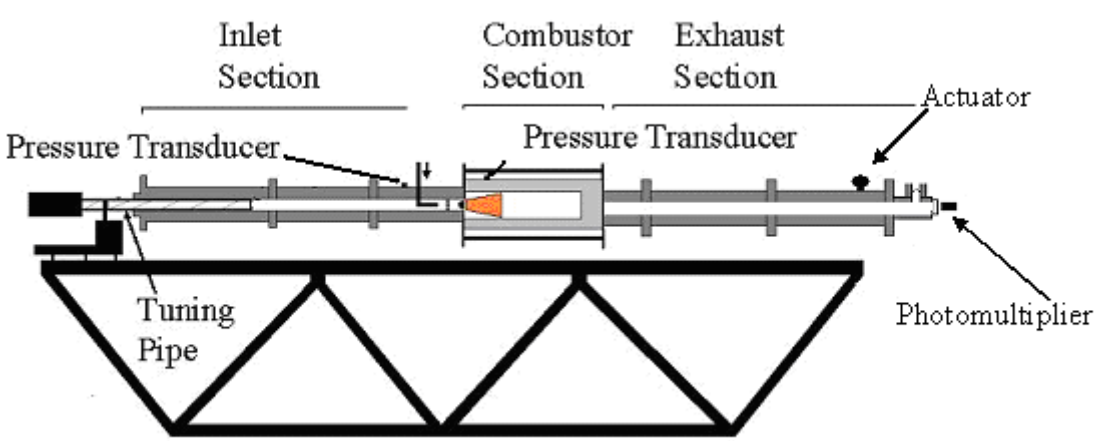

Figure 2: Schematic of Georgia Tech lean, premixed combustor facility

The facility consists of inlet, combustor and exhaust sections. High-pressure natural gas and air are supplied from building facilities, whose flow rates are measured with calibrated critical orifices. In order to ensure that acoustic oscillations do not affect fuel/air mixing processes, the air and fuel are introduced upstream of a second choke point, well upstream of the swirler. Thus, the equivalence ratio of the reactive mixture entering the flame is

essentially constant. This was done because of the sensitivity of the flame chemiluminescence levels to both heat release rate and equivalence ratio. If the equivalence ratio and heat release rate simultaneously vary, monitoring the flame chemiluminescence alone would not be sufficient to infer information about heat release fluctuations[24]. Note that the fuel/air mixing processes were not acoustically isolated in the previous study of Lieuwen & Neumeier[23].

The fuel-air mixture enters the circular 4.75cm diameter, 60cm long inlet section and passes through a 45° swirler prior to entering the combustor, see Figure 3. Combustion occurs in the 5x5x51cm square combustor downstream of the conical flame holder, and the combustion products then flow through a circular 7.6cm diameter, 195cm long exhaust section before leaving the system. A separate high-pressure air stream cools the combustor walls, and mixes with the combustion products in the exhaust section. The flow leaves the setup through an exhaust nozzle.

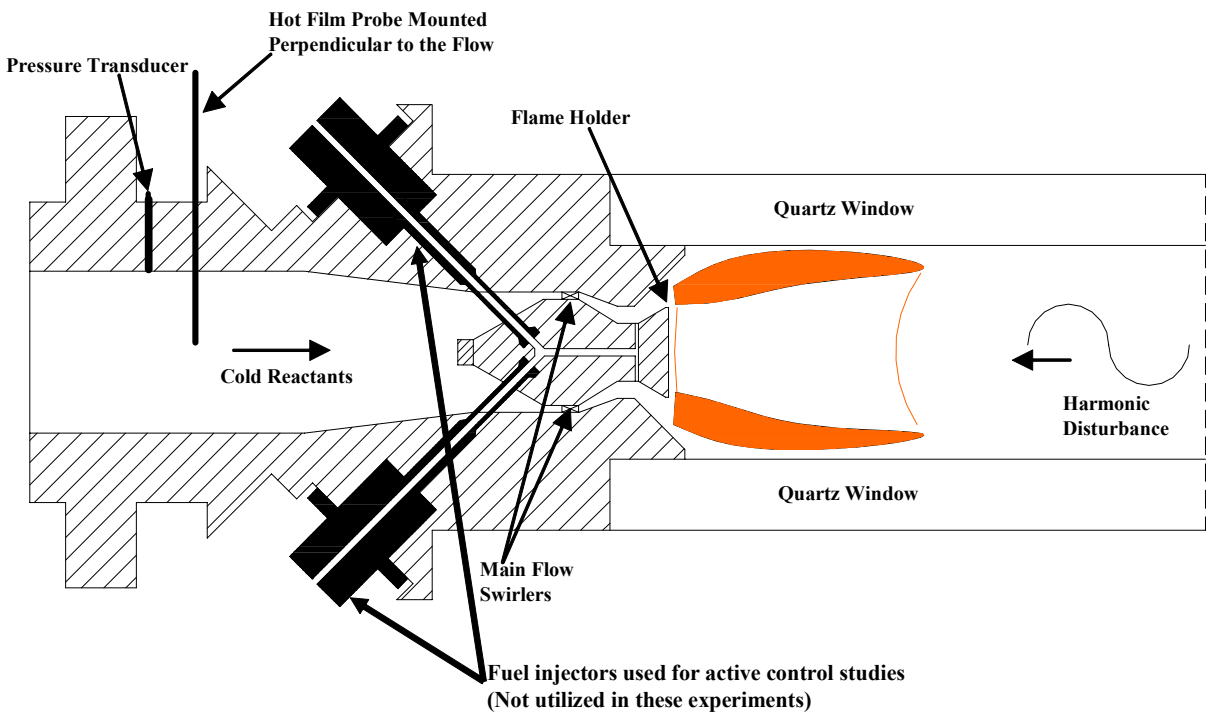

Figure 3: Detail of mixing and combustion section

Instrumentation

Pressure oscillations were measured with two Model 211B5 Kistler pressure transducers mounted in the inlet section and combustor. These transducers are mounted 33.2 cm upstream and 5.1 cm downstream of the conical flame holder, respectively. The latter transducer was flush mounted and water-cooled. The instantaneous velocity was measured with a TSI model hot-film probe mounted 23 cm upstream of the swirler and oriented perpendicular to the inlet flow in the radial center of the inlet pipe, as shown in Figure 3. The fluctuating velocity at the premixer exit, used to define the flame transfer function, was determined by measuring the transfer function between the velocity oscillations at the hot-wire location and the premixer exit in off-line experiments. This transfer function was also calculated with a quasi-one dimensional analysis by discretizing the premixer domain into a series

of regions characterized by their lengths and cross-sectional areas, and applying momentum and energy conservation at the interfaces (see Ref. [6]). The swirler was modeled as a resistance that was determined from the flow velocity and measured mean pressure drop. The model and measurements agreed very well over the 10-550 Hz frequency range, except in transfer function magnitude in the vicinity of 80 and 420 Hz. At these frequencies, the transfer function has large values (on the order of 5) and the model and measurements disagree by 100% in the peak magnitude; however, they agree quite well in predicting the frequencies at which these occur. At all other frequencies, the transfer function magnitude is essentially constant and equal to the cross sectional area ratio between the two points, as expected from quasi-steady considerations. Because of the sensitive frequency dependence of the velocity transfer function between the measurement location and premixer exit plane at 80 and 420 Hz, no nonlinear forced response studies were performed at these frequencies.

Global CH* and OH* chemiluminescence measurements were obtained with a photomultiplier tube (PMT) fitted with 10 nm bandwidth filters centered at 430 and 310 nm, respectively. The PMT was installed downstream of a quartz window at the rear end of the setup, see Figure 2. This arrangement permitted it to view the entire combustion zone. The linearity of the PMT output was verified over the entire range of instantaneous light intensity levels seen in these experiments. Data were obtained with a National Instruments DAQ controlled by Labview software at a sampling rate of 10 kHz. A total of 16,384 data points were taken during each test.

Oscillations were driven in the combustor with an actuator developed at Georgia Tech for active combustion control applications[29]. The actuator was mounted 5m downstream of the flame zone. It is capable of driving oscillations over a frequency range of approximately 0-1500Hz. The actuator modulates a constant secondary supply of air that is introduced near the combustor exit by periodically varying the degree of constriction of a valve. Maximum amplitude of driving occurs when the flow passage is completely blocked for a portion of the cycle and, thus, the actuator modulates 100% of the flow through the valve. The amplitude of forcing can be controlled via the supply pressure of air to the actuator.

Forced Flame Characteristics

The basic experimental procedure consists of externally driving oscillations in the combustor with varying amplitude at a fixed frequency or fixed amplitude at varying frequencies while obtaining simultaneous measurements of pressure, velocity, and chemiluminescence. For all cases, the combustor was quite stable in the absence of driving. The flame length ranged from 5-15cm between the equivalence ratios of 1.0-0.83, respectively.

Driving Effects on Average Flame and Coherence Characteristics

In addition to exciting oscillations, the imposed driving altered the mean flame characteristics, similar to prior observations (e.g., see Ref. [30]). With increased driving levels, the flame's time-averaged length increased by up to 100%. In addition, its global intensity generally decreased very slightly, but not always in a monotonic manner. Typical results are shown in Figure 4. In general, OH* and CH* levels were found to exhibit similar dependence upon disturbance amplitude.

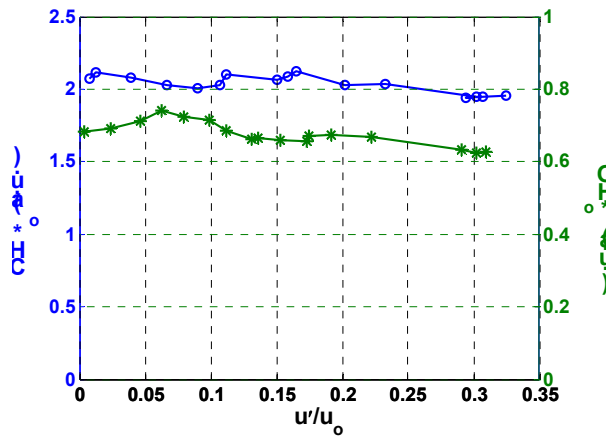

Figure 4: Dependence of mean CH* and OH* signals upon velocity oscillation amplitude (f_{drive} = 280 Hz, ϕ = 0.95)

In order to obtain accurate transfer function data, it is important to have good coherence between the pressure, velocity and chemiluminescence oscillations at the frequency of interest. This was always achieved except at the lowest driving amplitudes; typical coherence values were greater than 0.95. The effect of nonlinearities is to also decrease the coherence value, so we would not expect perfect coherence values, even if the input-output variables were perfectly correlated.

The amplitudes of the oscillations were determined by integrating the area under the power spectrum in the vicinity of the driving frequency. The RMS levels of the oscillations were determined from these values via Parseval's relation and then multiplied by $\sqrt{2}$ to obtain the fluctuating amplitude. This procedure is equivalent to determining the fluctuating amplitude after bandpass filtering the signal about the driving frequency. The phases of the fluctuating parameters were determined from their Fourier transforms at the driving frequency.

Linear Flame Response

Baseline measurements of the linear flame response were obtained by driving oscillations at low amplitudes over the 10-550 Hz frequency range. The amplitude of the velocity-CH* transfer function is plotted in Figure 5(a). The uncertainties were determined using formulae from Ref. [31].

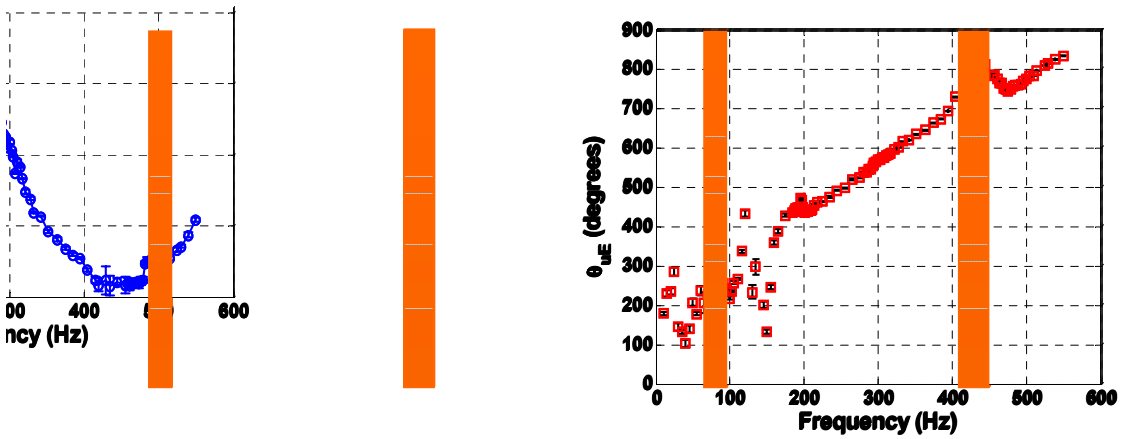

(a) (b)

Figure 5: Dependence of (a) linear velocity-CH* transfer function and (b) velocity-CH* phase angle upon driving frequency

This transfer function apparently has local maxima at 90 and 240 Hz and monotonically decays in the 250-400 Hz region. Similar peaks at intermediate frequencies were reported experimentally by Külsheimer and Büchner[22]. The corresponding phase of the transfer function is plotted in Figure 5(b). The phase results exhibit a linear increase with frequency up to approximately 400 Hz. This phase dependence suggests a roughly constant time delay relationship between the pressure/velocity and chemiluminescence; i.e., $CH^*(t) \sim u'(t-\tau)$. This time delay can be estimated from the slope of this phase dependence to yield a value of approximately 3.5 ms. For reference, the time required for a disturbance to convect the length of the approximately 8 cm flame at the premixer exit velocity is $\tau_{flame} \sim 7$ ms. This linear phase dependence ceases at frequencies above 400 Hz as the phase dips then rises again. Recall, however, that the transfer function between the velocity oscillations at the measurement point and flame base changes rapidly in the vicinity of 80 and 420 Hz. Thus the results at these frequencies should be interpreted with caution.

It is interesting to note the similarities between these gain and phase results and the measured and predicted transfer functions reported by Schuller *et al.*[32]. This is interesting because they obtained their results for a laminar flame while our data are obtained from a swirling, turbulent flame. Apparently, the average "V" shapes of the two flames are the primary thing they have in common. This observation indicates that the theoretical result used to describe laminar flame dynamics can be fit to our data very satisfactorily.

Nonlinear Flame Response

Next, we consider the amplitude dependence of this transfer function. For brevity, only velocity results are presented since the pressure-velocity relationship is linear over the entire driving amplitude range, e.g., see Figure 6. Therefore, the p'-CH* transfer function has an identical form (although the results are "cleaner" due to the larger p'-CH* coherence values). Figure 7(a) presents typical results showing the dependence of the normalized CH* and OH* chemiluminescence amplitudes upon the normalized velocity amplitudes over a range of driving amplitudes.

The departure of this transfer function from linearity is illustrated by comparing the data with the solid line that is drawn in (the reason for the gap in the data is discussed in the "Nonlinear Heat Release-Linear Acoustics Interaction" section). Note also in Figure 6 and Figure 7 that the normalized amplitudes of the pressure and velocity oscillations at the point where nonlinear effects become obvious are roughly 3% and 30% while the normalized chemiluminescence is approximately 40%. These relatively low pressure fluctuations and significant chemiluminescence oscillations are consistent with speculations that heat release nonlinearities, as opposed to gas dynamic ones, control the nonlinear dynamics of premixed combustion systems. It should be pointed out that these pressure amplitudes where nonlinearities in the p'-CH* relationship are observed (p'/p_o~2-3%) are of similar magnitude as typical instability amplitudes (p'/p_o~0.5-2%) which were measured in other tests on this combustor[28]. Also, the amplitude of the normalized CH* oscillations are on the order of 30-40% of the mean, consistent with previous experiments[23].

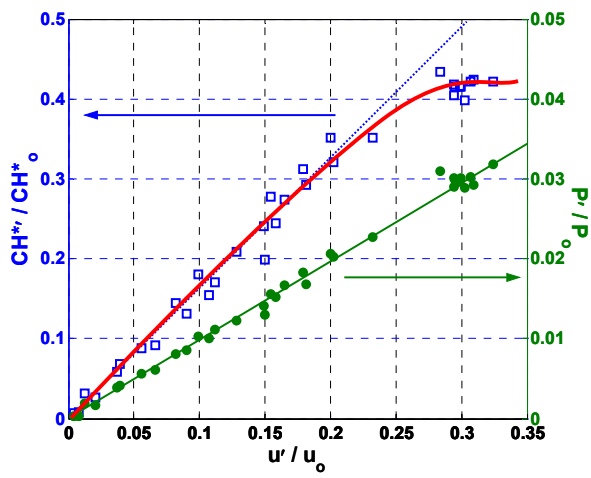

Figure 6: Dependence of CH* chemiluminescence and pressure oscillation amplitude on velocity fluctuation amplitude (f_{drive} = 280 Hz, ϕ= 0.95).

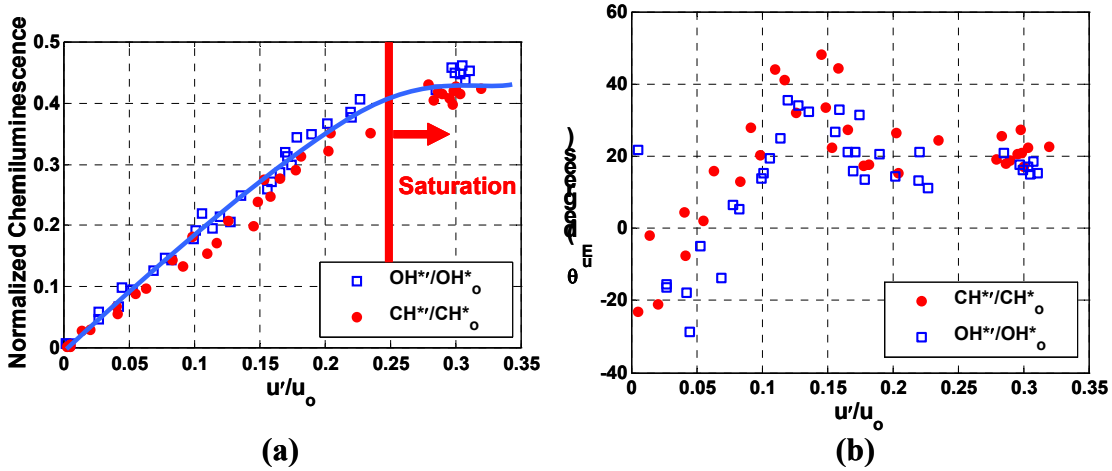

Figure 7: Dependence of CH* and OH* chemiluminescence (a) amplitude and (b) phase angle on velocity oscillation amplitude. Chemiluminescence saturation occurs in (a) at $u'/u_o > 0.25$. Uncertainty in phase angle for $u'/u_o < 0.05$, $\Delta\theta \sim 30°$; for $u'/u_o > 0.05$, $\Delta\theta \sim 2°$. ($f_{drive} = 283$ Hz)

Figure 7(b) presents the phase relationship between the velocity oscillations and the normalized chemiluminescence. The figures indicate that the phase angle has a complex dependence on the amplitude of oscillations. It increases monotonically by about 40 degrees from $0.05 < u'/u_o < 0.15$. At larger disturbance amplitude, the phase decreases somewhat, then levels off. Note that the phase exhibits amplitude dependence at disturbance levels significantly lower than the gain. It is likely that the monotonic phase increase in the $0.05 < u'/u_o < 0.15$ region is due to the lengthening of the flame with increased disturbance amplitudes. Due to the strong similarity in both the CH* and OH* results, only CH* results are presented in the remainder of the paper.

Equivalence Ratio Dependence

Figure 8(a) presents the dependence of CH*' upon u' for equivalence ratios ranging from 0.83 to 0.90. It is important to note that the maximum driving amplitude point is not due to actuator limitations, but flame blowoff. It is clearly seen that the slope in the linear regime as well as the CH* saturation amplitude decreases as the equivalence ratio is decreased. The results also show that the blowoff velocity oscillation amplitude for the majority of tests is approximately constant except for the leanest case investigated, $\phi = 0.83$. This result clearly shows that the saturation amplitude is a function of the equivalence ratio. For equivalence ratios between 0.87 and 0.9, the velocity-CH* relationship is highly nonlinear while the richest (ϕ=0.95, not shown) and leanest cases investigated show little nonlinearity, presumably because blowoff occurs before saturation. Figure 8(b) presents the corresponding phase relationship between u' and CH*'. In most cases, the phase angle initially increases to a maximum and then decreases or stays roughly constant with increase in velocity oscillation amplitude.

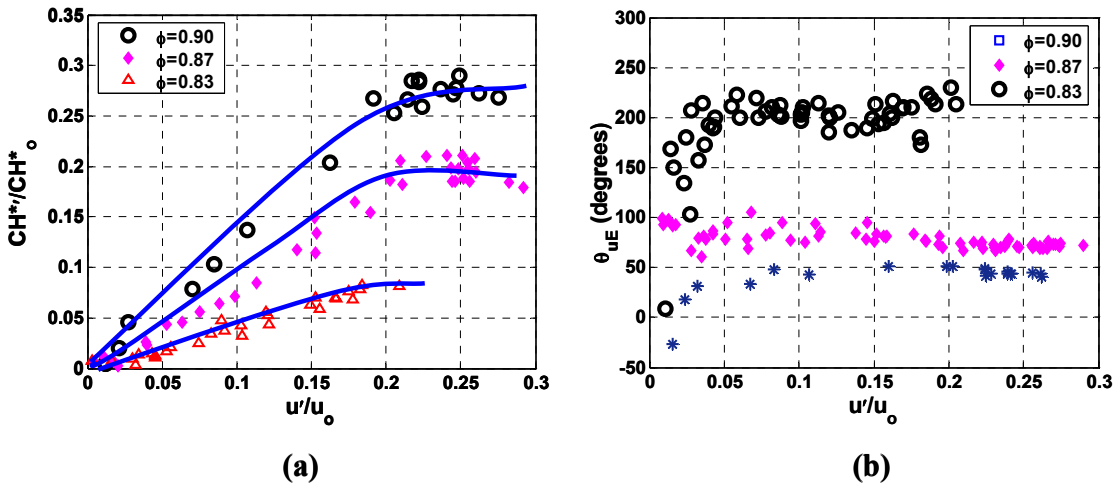

Figure 8: Dependence of (a) CH* chemiluminescence amplitude and (b) velocity-CH* chemiluminescence phase angle on amplitude of velocity oscillations at several equivalence ratios. Uncertainty in phase angle for $u'/u_o < 0.05$, $\Delta\theta \sim 30°$; for $u'/u_o > 0.05$, $\Delta\theta \sim 2°$. (f_{drive} = 300 Hz)

Driving Frequency Effects

In addition to varying the equivalence ratio, the effect of driving frequency between 260 and 320 Hz was extensively analyzed. This range was chosen because of the high quality data that could be obtained at these frequencies due to the large flame response, see Figure 5 and its proximity to a 310 Hz combustor resonance (discussed further below). Figure 9 presents the dependence of the CH* amplitude and phase upon u'/u_o over the 260 to 320 Hz frequency range. Note that the slopes of these curves in the linear region are equal to the transfer function values plotted in Figure 5. Nonlinearities in the CH*-u' gain relationship are prominent in the 280 and 290 Hz driving cases, while the transfer function is substantially more linear at the other frequencies. The near linearity of the transfer function in some cases all the way to flame blowoff strongly suggest that nonlinearity is not due to flame holding; if flame holding were a key nonlinear mechanism, one would expect the transfer function at all frequencies and equivalence ratios to become nonlinear near the blowoff point. The normalized CH* fluctuations at the point where nonlinearity is evident have similar values for 280 and 290 Hz, but the corresponding velocity amplitudes appear to vary slightly with driving frequency. Figure 9(b) shows that the phase exhibits similar amplitude dependence as in the equivalence ratio results. Again, note that nonlinearity is evident in the phase behavior at very low amplitudes, e.g., $u'/u_o \sim 0.05$, where the gain is still very linear.

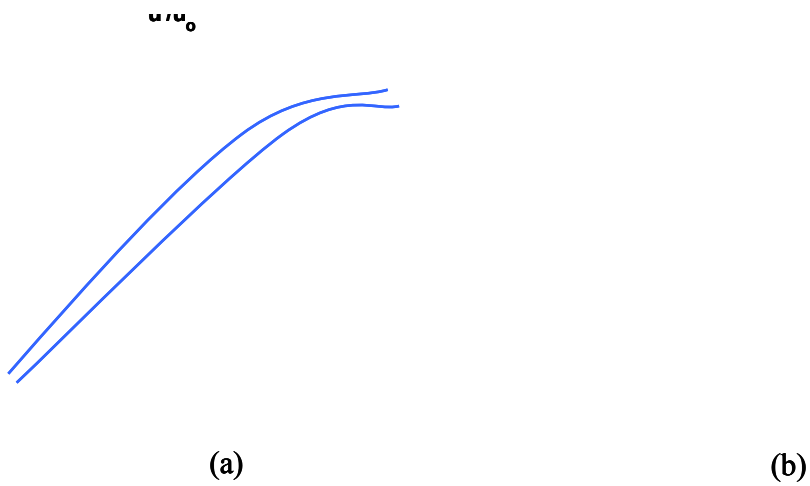

Figure 9: Dependence of CH* chemiluminescence (a) amplitude and (b) phase upon velocity amplitude at several driving frequencies. Uncertainty in phase angle for $u'/u_o < 0.05$, $\Delta\theta \sim 30°$; for $u'/u_o > 0.05$, $\Delta\theta \sim 2°$. ($\phi = 0.95$)

Harmonic and Subharmonic Characteristics

In addition to characterizing the dependence of the flame transfer function on the fundamental driving frequency, extensive analysis of the higher and sub-harmonics of the dynamic signals was performed. Prior studies suggest that such data are needed to obtain a comprehensive understanding of the nonlinear combustion process. For example, it is well established from forced response studies in various mixing layers, jets, and wakes that such understanding is key to the system's nonlinear dynamics (e.g., see Ref. [33]). These amplitudes are substantially smaller than those of the fundamental, however, resulting in reduced coherence between the fundamental and first harmonic, $\gamma_{i=f,j=2f}$. As such, only a single subharmonic and harmonic of the chemiluminescence signal ($CH^{*\prime}_{f=fdrive/2}$ and $CH^{*\prime}_{f=2fdrive}$) could be accurately quantified. The first subharmonic as well as the first and second harmonics of the pressure signal could be quantified due to much higher coherence values. While the presence of higher harmonics in the data could be either to actuator or combustion process nonlinearities, analysis of our data indicates that the dominant source of harmonic generation can be attributed to the nonlinear combustion process.

First harmonic characteristics of the CH* oscillations are presented in Figure 10 for two equivalence ratios, $\phi = 0.95$ and $\phi = 0.90$ at a driving frequency of 300 Hz. These two cases present examples where the flame transfer function remained linear throughout the range of disturbance amplitudes as well as where the flame transfer function saturated at large amplitudes of velocity oscillations. Figure 10 illustrates that the first harmonic behavior can change markedly between linear and nonlinear cases. For the linear case, $\phi = 0.95$, the first harmonic of the chemiluminescence exhibits a quadratic behavior on the fundamental throughout. This result is indicative of the other cases where the transfer function remains linear. For nonlinear cases, however, the functional relationship between the first harmonic and the fundamental changes. At low disturbance amplitudes, the general quadratic behavior is followed for $\phi = 0.90$. At forcing amplitudes above the saturation point of the fundamental, however, the first harmonic has been found to exhibit a variety of behaviors. For $\phi = 0.90$, the first harmonic deviates from the quadratic dependence, by increasing much more rapidly. In other cases, the first harmonic increases more

slowly than the quadratic dependence, such as can be seen in the pressure in Figure 11. The quadratic dependence between the fundamental and first harmonic is more clearly evident in the pressure data which has a much higher signal to noise ratio. We have also found that the amplitude of the second harmonic of the pressure (due to its higher coherence values) is essentially proportional to the third power of the fundamental, as might be expected, see Figure 11. Figure 12 presents the phase angle between the CH* chemiluminescence fundamental and first harmonic. While the overall phase dependence upon disturbance amplitude is approximately linear at each driving frequency, the amplitude dependence of the phase angle slope switches signs between 290 and 300 Hz. Furthermore, there is substantial amplitude dependence of this phase angle, as it changes by over 800 degrees.

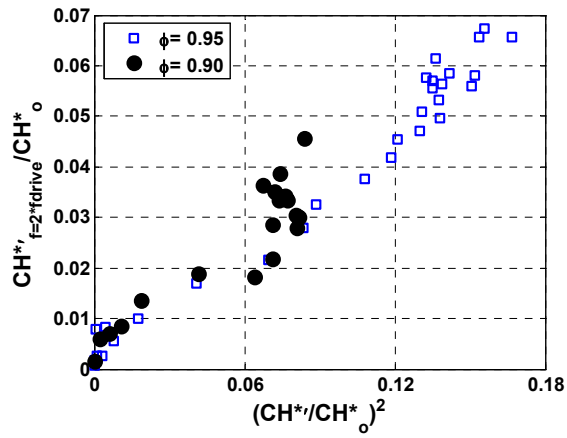

Figure 10: Dependence of CH* 1st harmonic on the square of CH* fundamental at two equivalence ratios (f_{drive} = 300 Hz)

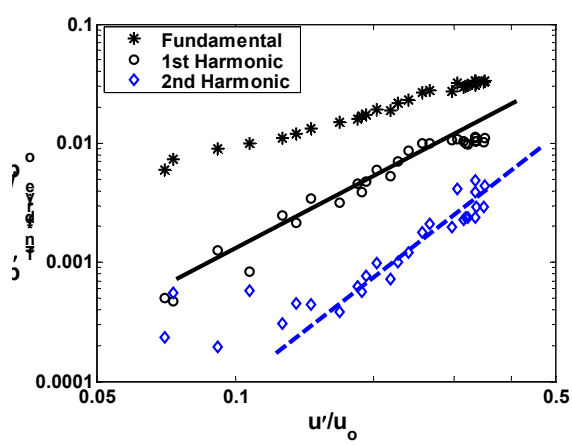

Figure 11: Dependence of pressure harmonic amplitude on velocity oscillation amplitude (f_{drive} = 290 Hz, ϕ = 0.95). Quadratic trend indicated by the solid line, cubic trend indicated by dashed line.

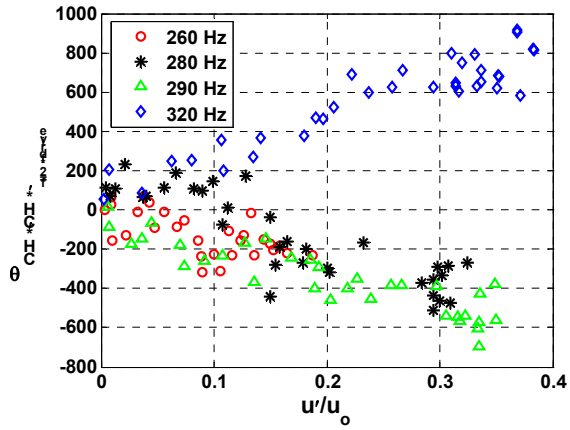

Figure 12: Dependence of CH* chemiluminescence fundamental-1st harmonic phase angle on velocity oscillation amplitude at several driving frequencies (ϕ = 0.95). Uncertainty in phase angle for u'/u_o < 0.05, $\Delta\theta \sim 30°$; for u'/u_o > 0.05, $\Delta\theta \sim 3°$.

Consider next the CH* subharmonic characteristics; i.e. $CH^*_{f=fdrive/2}$. In contrast to the higher harmonic characteristics, the subharmonic amplitudes do not exhibit a power law dependence upon the fundamental at low or high disturbance amplitudes. Its amplitude jumps up, however, in the vicinity of the point where the fundamental saturates, as shown in Figure 13. Figure 13 illustrates the dependence of the CH* chemiluminescence subharmonic on the amplitude of velocity oscillations for one case where the flame transfer function saturates, 280 Hz. In addition to the subharmonic, this figure also illustrates the gain of the flame transfer function over the entire range of disturbance amplitudes.

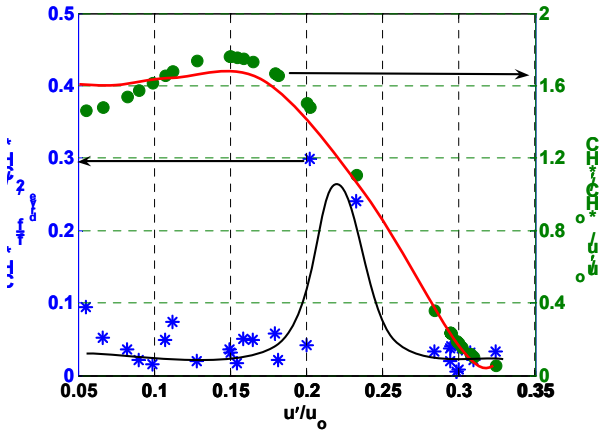

Figure 13: Dependence of CH* subharmonic and transfer function gain on velocity oscillation amplitude (f_{drive}=280 Hz, ϕ = 0.95)

For this case, the subharmonic amplitudes are very low and incoherent with respect to the fundamental when the corresponding transfer function is in the linear regime (u'/u_o < 0.2). Coherence values around 0.6-0.7 for these low values will create uncertainties which are as large as or larger than the values themselves. As the transfer function approaches the saturation point (approximately, $u'/u_o \sim 0.2$ for the case illustrated), the subharmonic

exhibits a sharp increase in amplitude. At this point, the coherence between the subharmonic and fundamental has values of ~ 0.99. Corresponding plots of the velocity and pressure subharmonics show no such increase and remain incoherent. After this sharp increase, the subharmonic amplitude decreases sharply and is again quite incoherent with the fundamental. This discontinuous dependence of the subharmonic on the fundamental is exhibited for all cases where saturation of the transfer function occurs. It should be noted, however, that the presence of subharmonic oscillations does not always accompany saturation. There were some cases where a peak in the CH* subharmonic occurred when the flame transfer function remained linear. This peak in the chemiluminescence subharmonic was accompanied by similar peaks in the velocity and pressure subharmonics, in contrast to the cases described above.

The subharmonic's dependence upon amplitude is very similar to the measurements of Bourehla and Baillot[25] in a laminar, Bunsen flame. At intermediate forcing amplitudes, they observed, in some cases, a subharmonic flame response. Analysis of this response showed that the subharmonic amplitude increased and the fundamental amplitude decreased as one went downstream from the burner lip. That is, the flame base responded more to the fundamental frequency and the flame tip responded more to the subharmonic. In all cases, the subharmonic response disappeared at the highest forcing amplitudes, and the flame exhibited the hemispherical behavior noted earlier. This phenomenon appears to be manifestation of the so-called "parametric instability", where pulsating cellular structures appear on the flame, which oscillate at half the instability frequency[34-37]. Analogous to Bourehla and Baillot's result, these studies in nominally flat flames found the subharmonic response only at intermediate amplitudes; at very high amplitudes the flame response was highly chaotic and disordered.

This instability is produced by the unsteady acceleration of the flame front by the velocity field, which separates two regions of differing densities, coupling with the three-dimensional flame dynamics. With increased amplitudes, the structures lose their well-defined nature and break up into disordered, turbulent wrinkles. This period doubling was recognized by Markstein[38] as indicative of a parametrically pumped oscillator that can be described by an equation of the form:

$$A\frac{d^2y(k,y)}{dt^2}+B\frac{dy(k,y)}{dt}+\left[C_o-C_1\cos(\omega t)\right]y(k,t)=0 \qquad (2)$$

where A, B, C are coefficients defined by Markstein, k is the wave number of the perturbation, and ω is the frequency of the imposed oscillations. The damping coefficient, B, is always positive, but the coefficient C_o is negative if the nominal planar flame front is unstable. Such an equation has the well known property that sub-harmonic oscillations (i.e., $\omega/2$) are excited for large enough disturbance amplitudes, C_1.

This is the first observation, to the authors' knowledge, of the presence of the parametric instability in a swirl-stabilized turbulent flame. Vaezi and Aldredge[37] have performed the only experimental work analyzing the parametric instability during turbulent flame propagation. They found substantial enhancement of axial and circumferential velocity fluctuations as a result of the parametric instability was found for all levels of pre-ignition turbulence. Also, the magnitude of amplification decreased with increasing Reynolds number. In our experiments,

the Reynolds number defined by the premixer exit diameter was substantially larger than those investigated by Vaezi & Aldredge[37]. Analogous to their results, no sudden visible changes in the flame position, length, or shape were noted before saturation of the transfer function occurred which indicate that turbulent flame speed enhancement was minimal. However, it appears highly probable that nonlinear interactions between the flow forcing and parametric instability (possibly through its impact on the fluctuating flame position) are responsible for saturation of the flame response. This is evidenced by the fact that 1) the jump in subharmonic amplitude occurs at essentially the same value as that at which saturation occurs, and 2) subharmonic oscillations are always present in cases where saturation of the fundamental occur.

Atmospheric Swirl Stabilized Burner

INSTRUMENTATION AND EXPERIMENTAL FACILITY

This section describes the continuation of the nonlinear flame response experiments described in the previous section. Instead of performing the experiments on the gas turbine combustor simulator (described in Figure 2), experiments were performed on an atmospheric, swirl-stabilized burner, schematically shown in Figure 14, which can be operated up to 100 KW. All tests were performed at a fixed equivalence ratio of 0.8. Unlike the previous test, we investigated more thoroughly the effect of driving frequency. In addition, we performed a parametric study on the effect of Reynolds number on the nonlinear flame response. The flow rate regime investigated ranged from Reynolds numbers of Re_D=21,000-43,000 (based on premixer exit diameter) corresponding to average premixer exit plane velocities of 22-44 m/s. Reactant inlet temperatures were kept constant at room temperature.

Natural gas and air are supplied from building facilities, whose flow rates are measured with rotameters. In order to ensure that acoustic oscillations do not affect fuel/air mixing processes, the air and fuel are introduced upstream of a choke point. Thus, the equivalence ratio of the reactive mixture entering the flame is essentially constant. This was done because of the sensitivity of the flame chemiluminescence levels to both heat release rate and equivalence ratio [24].

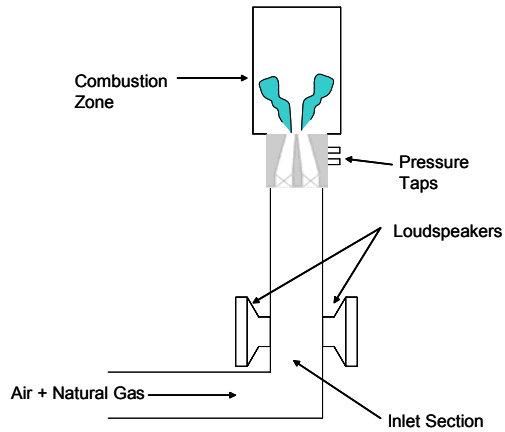

Figure 14. Schematic of swirl-stabilized combustor

The mixture goes through the premixer, consisting of a 40° swirler and an annular passage, see Figure 15. The flow expands into a cylindrical 70mm i.d. and 190 mm long quartz tube combustion chamber. Pressure oscillations are measured with Model 211B5 Kistler pressure transducers mounted downstream of the swirl vanes, located 5.85cm and 7cm upstream of the flame holder, respectively. Velocity oscillations are calculated using the two microphone method, outlined in, e.g. Ref. [39]. These results were checked with direct velocity measurements using a hot-wire anemometer in cold-flow conditions.

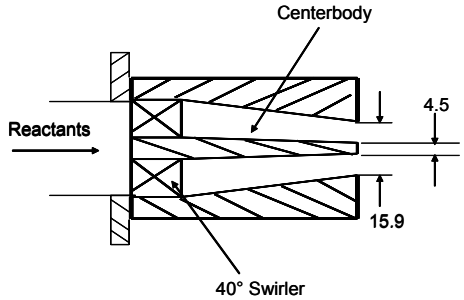

Figure 15. Schematic of burner premixer. All dimensions are in mm (not to scale).

The relative magnitude of the combustion heat release oscillations are obtained by measuring the global CH* and OH* chemiluminescence with photomultipliers fitted with a 10 nm bandwidth filter centered at 430 nm and 310 nm, respectively. The fiber optic is installed downstream of the flame zone at an angle such that it is allowed to "view" the entire combustion zone. For the results presented in this paper, the normalized chemiluminescence measured by the photomultipliers is nearly identical. Thus CH* chemiluminescence results will be shown for the remainder of the paper. Oscillations are driven in the combustor by two loudspeakers mounted into the 5.5 cm diameter inlet section.

In order to observe the flame, OH planar laser-induced fluorescence (PLIF) was utilized to obtain a two-dimensional image of the flame. Figure 16 shows the layout of the laser diagnostic facility used in the present study. The laser system consists of a cluster of an Nd:YAG laser, 1 dye laser, and high-resolution ICCD cameras. For OH

PLIF, the frequency-doubled output from the dye laser was tuned near 281.4 nm to pump the $R_1(9)$ transition of the $A^1\Sigma - X^2\Pi$ *(1, 0)* band. OH fluorescence integrated over a wavenumber range of 300-380 nm is captured by the ICCD camera through both a WG-305 and UG-11 Schott glass filter. The OH PLIF intensity images were corrected for background noise and also for beam profile inhomogeneities.

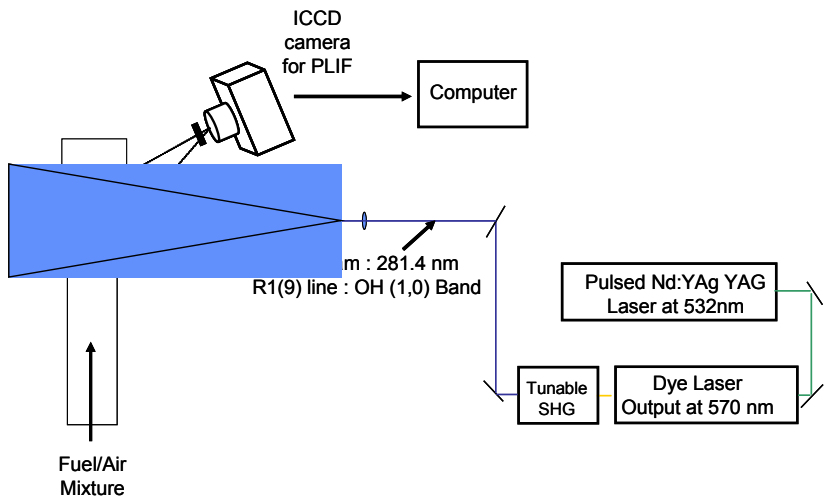

Figure 16. Schematic of laser setup for OH PLIF imaging

The laser imaging was phase locked with the driving signal input to the loudspeakers. The frequency of image acquisition is limited by the frequency of the Nd:YAG laser which operates at 10 Hz. Therefore, since the frequencies of interest in this study are much greater than this value, successive phase-locked images were actually obtained several cycles apart from each other. Then, the flame response over a sequence of phase angles is reconstructed over different phases and different cycles. The acoustic cycle was divided into 8 phases, with 200 images taken at each phase angle. The OH PLIF intensity images were corrected for background noise and also for beam profile inhomogeneities. These images were then filtered with a 3 pixel width Gaussian filter.

RESULTS AND DISCUSSION

PARAMETRIC CHARACTERIZATION OF NONLINEAR FLAME TRANSFER FUNCTION

Results were obtained by externally driving oscillations in the combustor with varying amplitude at a fixed frequency. Simultaneous measurements of pressure, velocity, and chemiluminescence were taken. For all cases, the combustor was quite stable in the absence of driving.

A typical transfer function between simultaneously measured CH* chemiluminescence and velocity oscillations is shown in Figure 17(a) at a Reynolds number of 21000 and equivalence ratio of 0.8. For low forcing amplitudes, Figure 17 shows that the CH* chemiluminescence increases with perturbation amplitude in a linear manner. At large velocity amplitudes, the CH* chemiluminescence saturates at values of $CH^{*\prime}/CH^{*}_{o}$ of ~0.45. These velocity and CH* values where saturation occurs are consistent with the results in the previous section. This result indicates that global extinction where oscillating heat release amplitudes reach 100% of the mean, proposed

theoretically by Dowling [16], is not an important mechanism at this condition. Figure 17(b) presents the corresponding u'-CH*' phase relationship. The phase relationship exhibits a complex amplitude dependence on the amplitude of velocity oscillations. The phase angle changes by nearly 50 degrees while the transfer function remains linear. The sharp decrease in phase angle at u'/u_o ~0.45 occurs after the $CH^{*\prime}/CH^{*}_{o}$ value saturates.

Figure 18(a) presents transfer function results for driving frequencies between 130-150 Hz at a Reynolds number of 21000. Figure 18 illustrates that the transfer function at 130 Hz and 140 Hz remains linear up to $CH^{*\prime}/CH^{*}_{o}$ values near 0.95 before saturating. Thus, the saturation amplitude here is substantially higher than that in Figure 17, illustrating the substantial dependence of saturation amplitude upon flow conditions and disturbance frequency. Note that the saturation amplitude here is quite close to 100%, suggesting a global extinction type mechanism as proposed by Dowling [16]. Figure 18(b) presents the corresponding u'-CH*' phase. Similar to the comparison between the saturation amplitudes between the cases at 210 and 130 Hz, the phase angle shapes for these two frequencies are also quite different. The phase angle at these frequencies exhibits significant amplitude dependence at velocity oscillation amplitudes where the gain of the transfer function remains in the linear regime. This effect is again consistent with the results in the previous section. The phase angle is seen to almost saturate as well and remain relatively constant around 85-90 degrees over nearly 50% of the velocity amplitude range.

Both Figure 17 and Figure 18 illustrate typical shapes of transfer functions that have been observed experimentally and proposed theoretically. For low velocity amplitudes, the corresponding heat release oscillations increase linearly. At the largest velocity amplitudes, the heat release fluctuations saturate. However, more complex amplitude dependencies were observed at other conditions. Figure 19 shows two such cases, obtained at 340 and 410 Hz, respectively. Both curves show that the CH* chemiluminescence increases linearly with increasing velocity oscillation amplitudes at low values of driving. At 340 Hz, the CH* oscillation amplitude begins to saturate at values around 0.65-0.7 of the mean value. However, instead of remaining nearly constant, with further increases in excitation amplitude the response increases again. In a similar manner, for 410 Hz, Figure 19 shows that the transfer function begins to saturate at a $CH^{*\prime}/CH^{*}_{o}$ value of 0.35. Similar to the 340 Hz case, the flame response begins to increase again before saturating again at $CH^{*\prime}/CH^{*}_{o}$ value of nearly 0.6. This trend is similar to the experimental results of Balachandran *et al.* for a bluff-body stabilized flame without swirl [26].

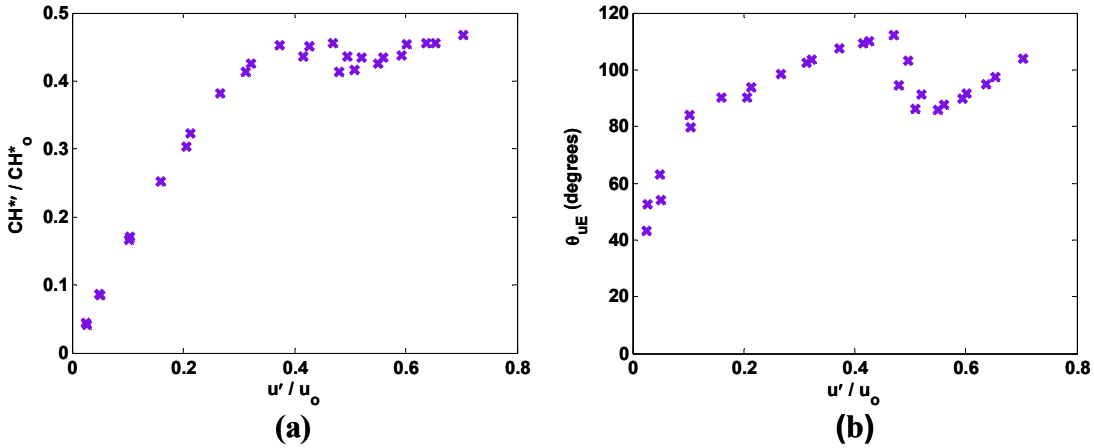

Figure 17. Dependence of (a) CH* oscillation amplitude and (b) u'-CH*' phase angle upon velocity oscillation amplitude (f_{drive} = 210 Hz, ϕ=0.80, Re_D = 21000). CH* saturation amplitude = 0.45. Uncertainty in phase angle < 5°.

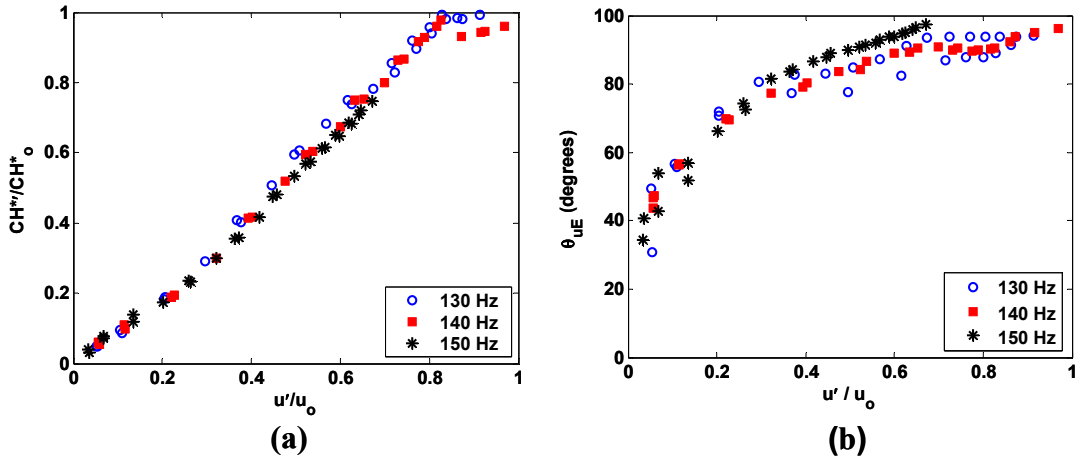

Figure 18: Dependence of (a) CH* oscillation amplitude and (b) u'-CH*' phase angle upon velocity oscillation amplitude, ϕ = 0.80, Re_D = 21000. CH* saturation amplitude ~ 0.98. Uncertainty in phase angle < 5°.

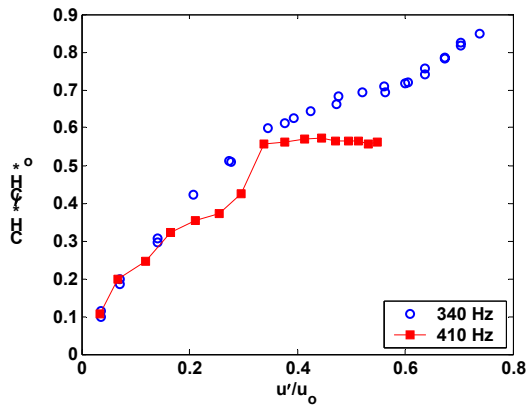

Figure 19. Dependence of CH* oscillation amplitude upon amplitude of velocity oscillations for two driving frequencies (Re_D = 21000, ϕ = 0.80)

Even more complex behavior was observed at other conditions. Figure 20 presents the u'-CH*' transfer function for 160-180 Hz at a Reynolds number of 30000 and equivalence ratio = 0.8. For these three cases, after an initial linear increase in heat release oscillations, there is a sharp decrease in these values, followed by an increase. This sharp decrease in the gain of the transfer function is also manifested in the corresponding phase between the velocity and chemiluminescence oscillations. Figure 20(b) shows the phase angle at f_{drive}= 170 Hz drops considerably (over 100 degrees) between normalized velocity oscillation amplitudes of 0.1 and 0.2. After this drop, the phase angle remains constant around 80 degrees, at similar values as the 130-150 Hz cases shown in Figure 18.

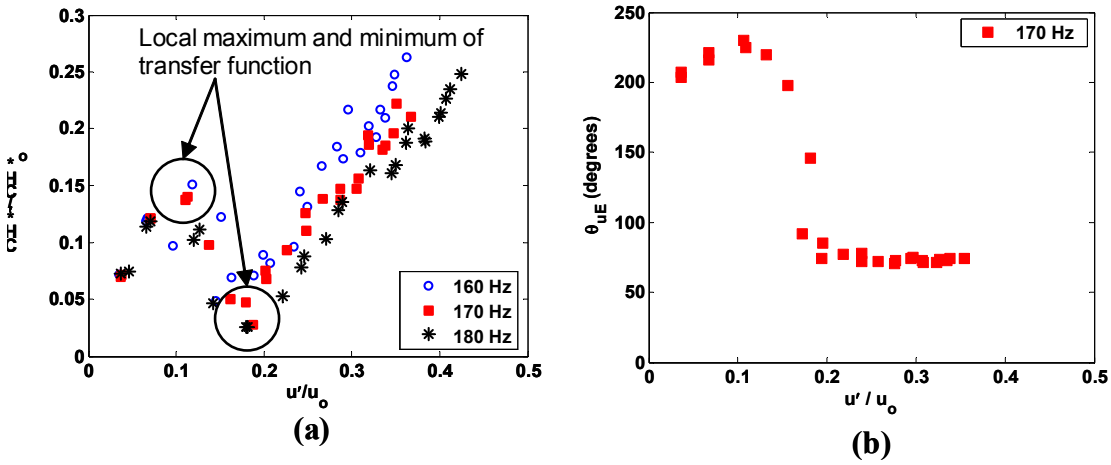

Figure 20. (a) Dependence of CH* oscillation amplitude upon amplitude of velocity oscillations for f_{drive} = 160-180 Hz. (b) Dependence of u'-CH*' phase angle upon velocity oscillation amplitude for f_{drive} = 170 Hz. (Re_D = 30000, ϕ = 0.80).

Figure 21 presents the Fourier transform of the chemiluminescence and one pressure transducer for two cases: at the local maximum in the transfer function and the local minimum in the transfer function (circled in Figure 20). Comparing the two chemiluminescence spectra, it is clear that the flame response shifts from the fundamental frequency to the 1st harmonic with an increase in driving from 10% velocity oscillation to 20% velocity oscillation.

The pressure FFT, on the other hand (and thus the velocity) always responds to the fundamental, however, and increases with increased driving. Similar behavior has also been reported in bluff-body flames by Balachandran *et al*.[26]. We are currently investigating the cause of this behavior to better understand the underlying mechanism.

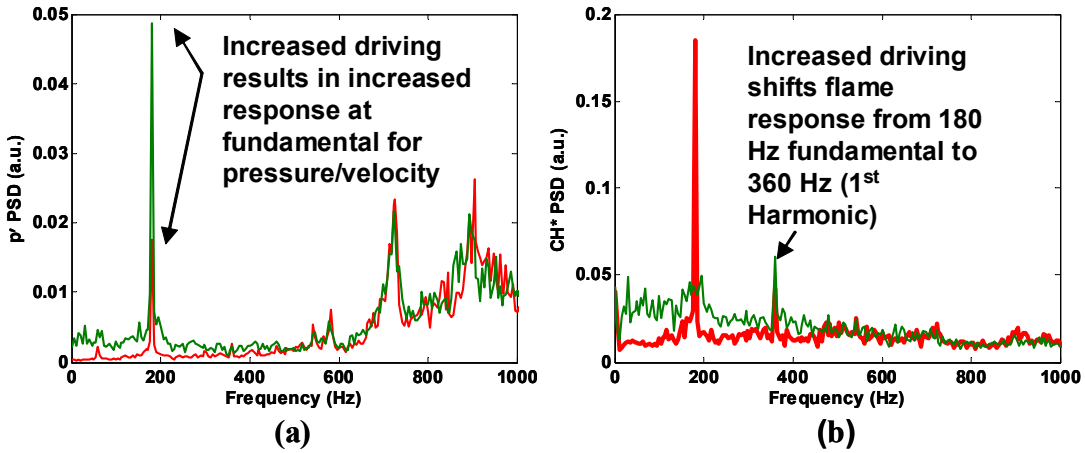

Figure 21. Fourier transforms of (a) pressure and (b) CH* chemiluminescence signals at local maximum of transfer function (red) and local minimum of transfer function (green) for f_{drive} = 180 Hz (Re_D = 30000, ϕ = 0.80).

One of the key conclusions we drew from this parametric study was that the flame response characteristics are more varied and complex than a simple linear response regime followed by a saturation regime. However, one of our goals for the study was to parameterize the dependence of saturation amplitude upon operating conditions, frequencies, etc. In order to compile all the results into one graph, we determined the chemiluminescence amplitude at which nonlinearity in the flame response becomes evident, see Figure 22. This amplitude was defined as the point where the transfer function deviates from its linear value by more than 10-20%. The lower limit is set for cases such as those in Figure 18, where saturation occurs at nearly 100% of the mean chemiluminescence value. The upper limit is set for saturation/nonlinear behaviors that occur at values much less than 100% of the mean, e.g., Figure 19 and Figure 20. At the lowest flow rate, Figure 22 indicates that the saturation amplitude varies with frequency by a factor of almost five. This frequency sensitivity is diminished at the higher flow rates. At the highest Reynolds number, the saturation amplitude is nearly constant over the frequency range investigated. Saturation at 100% chemiluminescence is only seen for the lowest flow rate. The results presented indicate that a variety of behaviors can exist in a single combustor. We should emphasize, however, that determination of the "amplitude at which nonlinearity becomes evident" is somewhat subjective. Thus, while these curves certainly have the form shown here, they could vary in detail somewhat based upon the method of parameterizing nonlinearity.

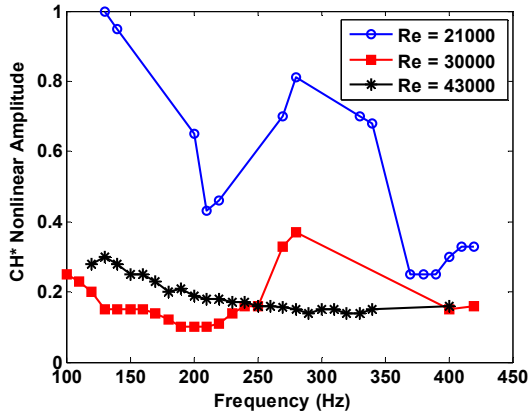

Figure 22. Dependence of CH* nonlinear amplitude on driving frequency as a function of Reynolds number (ϕ = 0.80).

IMAGING OF FLAME UNDER LARGE AMPLITUDE FORCING

During this parametric study it was observed that the flame visibly changed in structure at the point where the transfer function saturates when significant saturation occurred (e.g., f_{drive} = 210 Hz and 410 Hz); however, this was not necessarily the case in all situations (e.g., f_{drive} = 130 Hz). High speed line of sight images of the flame confirmed this observation as shown in Figure 23 which shows images of the flame at two different driving amplitudes at a driving frequency of 410 Hz. These sequences of images were obtained by phase locking an ICCD high speed camera to the input driving signal. A BG-38 Schott glass filter was placed in front of the ICCD camera to effectively eliminate wavelengths of light above ~700nm.

Figure 23(a) shows the line-of-sight view of the flame at low velocity amplitude where the transfer function remains linear in Figure 19. At this low amplitude of oscillation, the flame is easily observed to have a well-defined shape and stabilization point throughout the cycle. The flame responds to forcing by increasing and decreasing in length. No visible change in the shape is seen over the cycle. In contrast, Figure 23(b) shows the line-of-sight view of the flame at a velocity amplitude where the flame transfer function has saturated. From these images, it appears that the flame is not stabilized by the centerbody as shown in Figure 23(a). Instead the flame appears to have "lost" its structure and has become more chaotic in nature. This behavior begins to occur exactly at the point of saturation (e.g., $u'/u_o \sim 0.35$ in Figure 19).

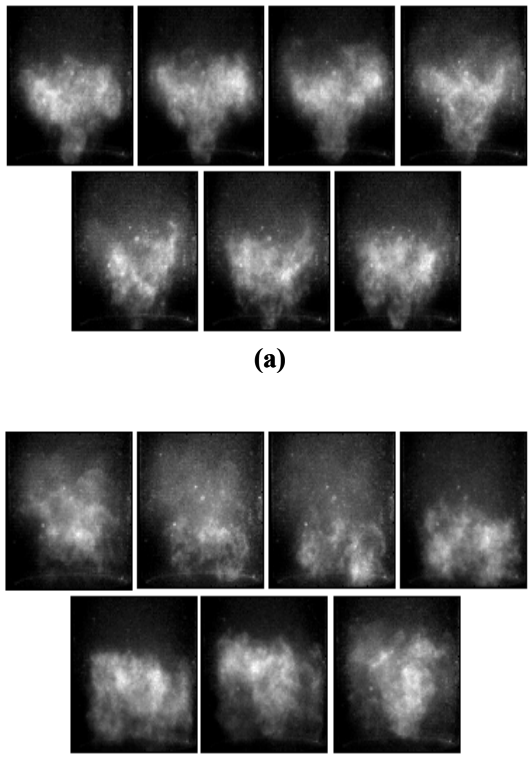

Figure 23: Phase-locked instantaneous line-of-sight images of flame over 1 cycle of acoustic forcing for (a) low (linear) and (b) high (nonlinear) amplitude of oscillation (f_{drive} = 410 Hz, Re_D = 21000, ϕ = 0.80).

Since similar flame behavior seen in Figure 23 for 410 Hz was not observed for 130 Hz, we will concentrate on these two results for the remainder of the paper. In an effort to further investigate some of the potential mechanisms controlling the nonlinear flame dynamics, we performed extensive OH-PLIF studies at these two driving frequencies. We should emphasize two key limitations of these images. First, the flow is highly three-dimensional, so that flame structures come in and out of the images. Thus, one cannot estimate the instantaneous flame area, of interest because of its relationship to heat release. Second, "consecutive" images are not truly consecutive, as they were taken several cycles apart – thus, one should only attempt to infer global flow features, and not try to track the evolution of a particular flow feature from image to image.

Figure 24(a) presents instantaneous OH PLIF images for the 130 Hz case at a low velocity oscillation amplitude. Here the heat release is in the linear response regime. The images obtained are phase-locked to the driving signal, but the phase angles presented in these figures are with respect to the velocity oscillations calculated from the two microphone method. These figures indicate that the flame is anchored on the centerbody throughout the cycle. The oscillating velocity is evident, as the flame moves back and forth throughout the cycle; in some images, the presence of convecting flow structures are perhaps evident. Figure 24(b) shows the corresponding flame response for high velocity oscillations; at this level of driving, the instantaneous flow velocity oscillates between 2-42 m/s through out the cycle. Thus it oscillates between nearly reversing itself to a very high speed jet. At the velocity minimum the turbulent flame speed is on the same order as the local velocity value and the flame is propagating towards the premixer. The flame, however, never flashes back into the premixer, but remains just at the

premixer exit. Thus there is a lower limit to the flame response. At the point of highest flow velocity and maximum flame length, the clear rollup of the flame into the central recirculation zone is evident, see 45 and 90 degrees.

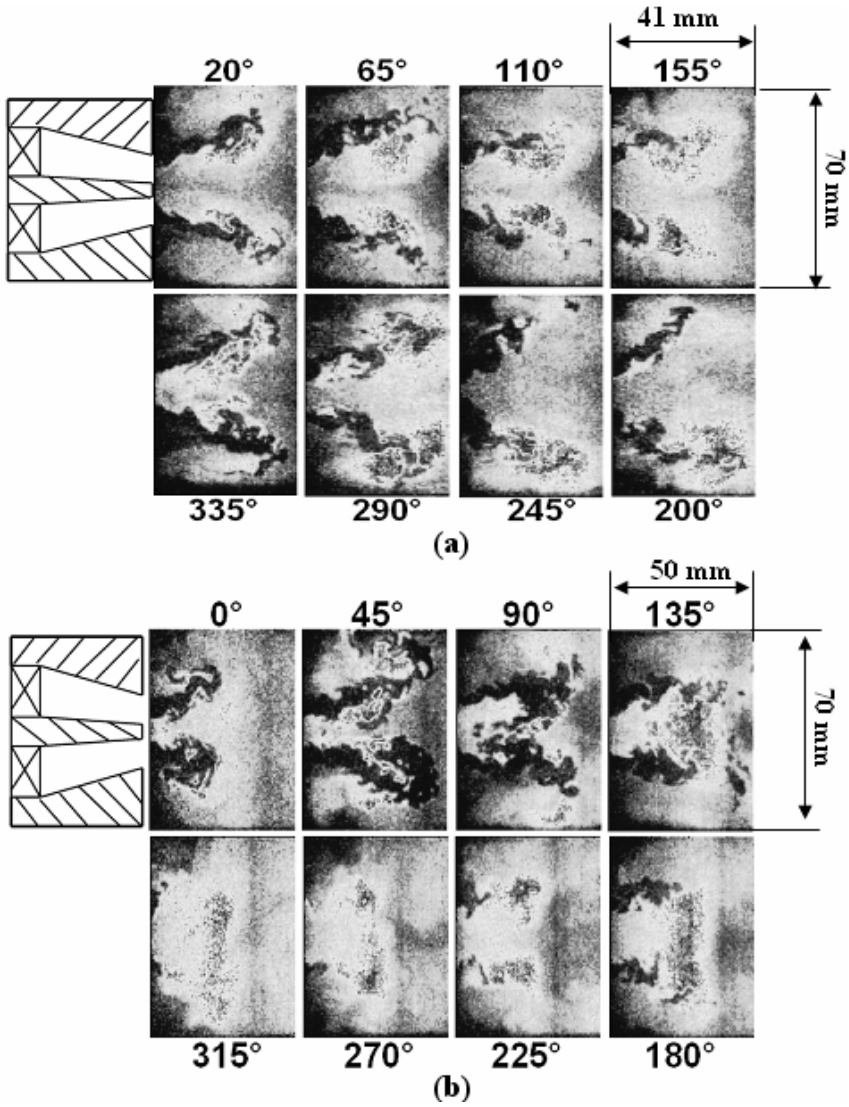

Figure 24. Instantaneous OH PLIF images showing evolution of flame response over 1 cycle of acoustic forcing for (a) low (linear) and (b) high (nonlinear) velocity oscillation amplitudes (f_{drive} = 130 Hz, Re_D = 21000, ϕ = 0.80)

This rollup of the flame into the central recirculation zone causes occasional merging of the two flamefronts. The rapid reduction in flame area associated with this rollup, and the subsequent flame propagation and rapid reduction in flame area, is believed to be the mechanism causing saturation of the flame response since this behavior is observed in most of the 200 images obtained at these phases. This assertion is also supported by the fact that rollup is first observed roughly at the point where the CH* chemiluminescence saturates at u'/u_o~0.8 in Figure 18. This is the same observation of Balachandran *et al.* in a non-swirling flame [26]. At this point, the flame area is very rapidly reduced, due to flame propagation normal to itself. Also, note that the flame remains attached throughout the cycle, even at the highest amplitudes, in contrast to the 410 Hz result shown next. Several other

features can also be noted. First, note the substantially more corrugated nature of the flame front at the point of highest jet velocity, 90 degrees, relative to lower velocity points. These images suggest that the turbulent flame speed is modulated through the cycle. .

At the point of highest flow velocity and maximum flame length, the clear rollup of the flame into the central recirculation zone is evident, see 45 and 90 degrees. In some images, this rollup of the flame into the central recirculation zone causes occasional merging of the two flame branches. As will be shown next, the rapid reduction in flame area associated with this rollup causes saturation of the flame response. This point can be seen from ensemble averages images of the flame, see Figure 25. The average flame edge shown in these images were obtained by averaging the PLIF images, and extracting the flame edge (roughly corresponding to a line of constant progress variable of 0.3) using a gradient method. In Figure 25(a), for low amplitude forcing, the flame is stabilized off of the bluff body at the exit of the premixer and confirms the observations made from the instantaneous images in Figure 24. Figure 25(b) shows the phase averaged flame fronts for high amplitude forcing, after the point where the *u'-CH*'* transfer function has saturated. This figure clearly shows the reactants on average are consistently rolled up towards the centerline of the burner at the point of peak response in the cycle, see 90 degrees. This roll-up of the flame causes a very rapid reduction in its certain area and, therefore, heat release rate. As such, the flame heat release response does not increase proportionately with the perturbation, and saturation occurs.

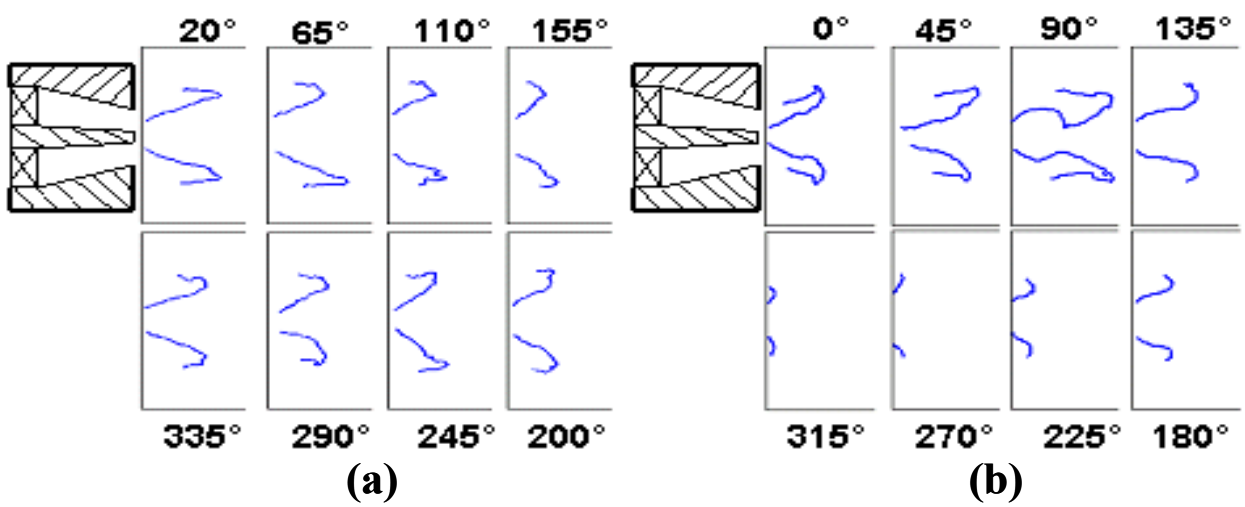

Figure 25. Phase-averaged flame edges showing evolution of flame response over 1 cycle of acoustic forcing for (a) low (linear, u'/u_o = 0.3) and (b) high (nonlinear, u'/u_o = 0.9) velocity oscillation amplitudes (f_{drive} = 130 Hz)

This flame rollup can be further seen in Figure 26 which illustrates the manner in which the flame response at the point of its maximum downstream displacement varies with disturbance amplitude. The dashed lines indicate the average flame front location (obtained by averaging all the images at this particular phase and using a gradient method to extract an edge) at excitation amplitudes where the transfer function remains linear, u'/u_o= 0.3 and 0.6. These curves show that the downstream flame displacement increases with perturbation amplitude, but with a

similar shape. In contrast, the solid lines show average flame front locations at excitation amplitudes near and beyond the point where saturation in flame response occurs, u'/u_o= 0.83, and 0.9. Here the downstream displacement of the flame position clearly stops growing with perturbation amplitude. Instead, the reactants roll up into the central recirculation zone, causing a more rapid reduction in flame surface area relative to the lower amplitude cases due to flame propagation normal to itself.

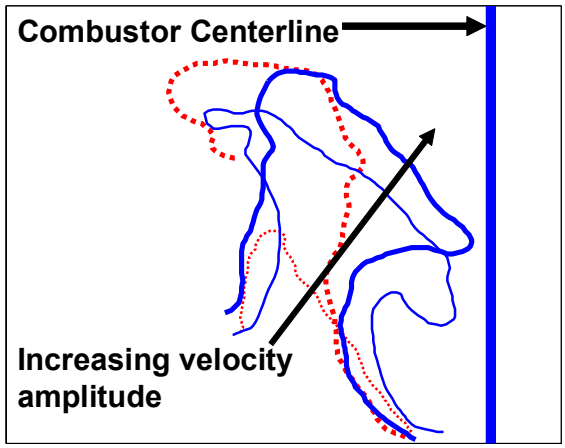

Figure 26. Averaged flame edges at 65-110 degrees phase angle at four velocity oscillation amplitudes (f_{drive} = 130 Hz, u'/u_o = 0.3, 0.6, 0.83, 0.90). Dashed (- - -)/ solid (—) lines indicate peak flame response when transfer function is linear/saturated, respectively.

Consider next the 410 Hz results. Recall from Figure 19 that saturation occurred well below 100% CH* chemiluminescence amplitude. Figure 27(a) shows the flame response at a low velocity amplitude (u'/u_o = 0.2) for 410 Hz. Similar to the 130 Hz in Figure 27(a) and inferred from Figure 23, the flame is stabilized at the centerbody of the premixer. The flame increases in length and shows increased wrinkling at the peak of the cycle. Figure 27(b) illustrates the flame response at a high velocity oscillation amplitude (u'/u_o = 0.6), where the flame exhibits a very different behavior from the 130 Hz results. First, at all 8 phases, the flame is clearly lifted off the centerbody and appears to be stabilized near the stagnation point in a low velocity region, as also shown in the direct flame images in Figure 23. Only at one small part of the cycle, 45-90 degrees, can the flame be seen attempting to stabilize itself on the centerbody.

The liftoff of the flame from the centerbody with increasing excitation amplitude can be seen from Figure 28. Similar to Figure 26, dashed lines indicate the flame front where the transfer function is linear (u'/u_o = 0.2, 0.3) and the solid lines indicates peak response flame edges near and beyond the saturation point of the transfer function (u'/u_o = 0.53, 0.6). The plot clearly shows the transition of the stabilization point of the flame from the centerbody to a point downstream with increasing disturbance amplitude. Since the flame is lifted off, the two flames that are present in the linear regime are merged together into one flame- it can be seen that the flame area is lower than it would be if the flame were attached. This unsteady liftoff, and consequent reduction in flame area, is the mechanism of nonlinearity for this case. It is first observed in the images at u'/u_o amplitudes around 0.35; i.e., where the transfer function begins to saturate

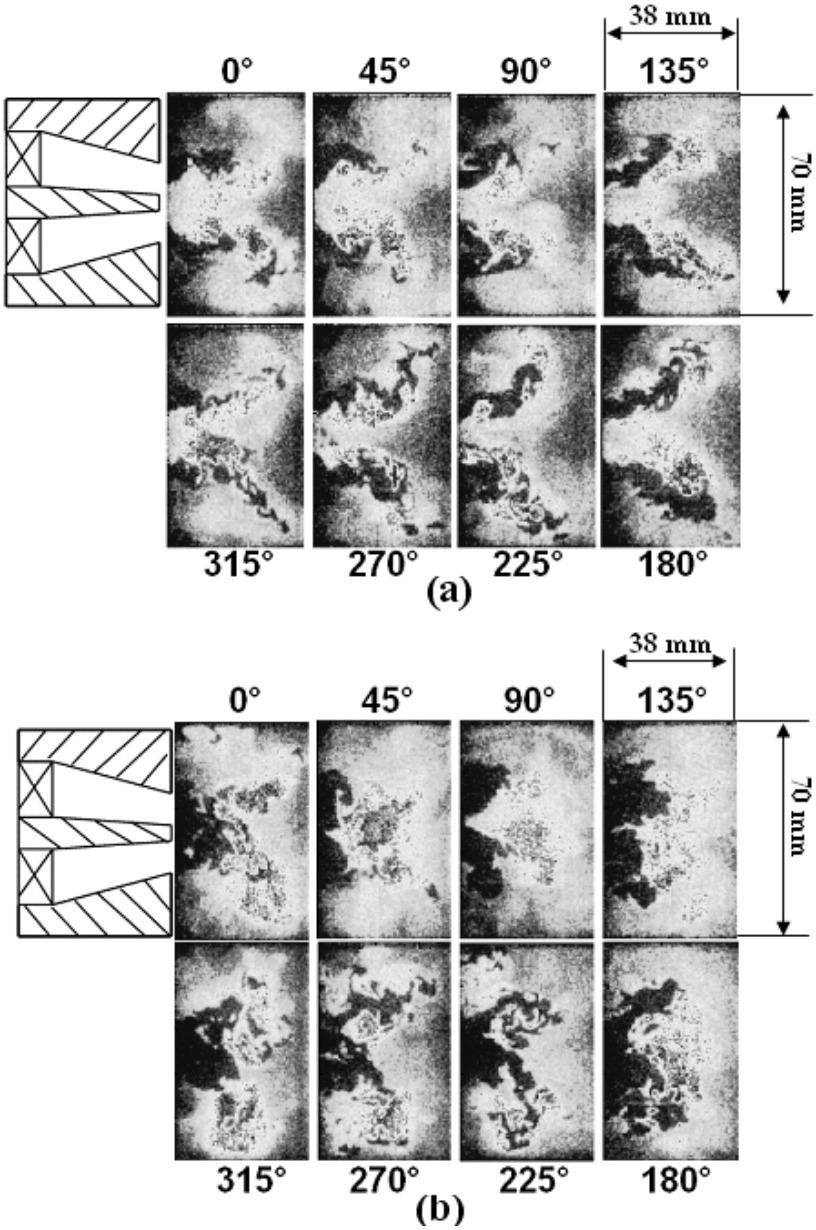

Figure 27. Instantaneous OH PLIF images showing evolution of flame response over 1 cycle of acoustic forcing for (a) low (linear, u'/u_o = 0.2) and (b) high (nonlinear, u'/u_o = 0.6) velocity oscillation amplitudes (f_{drive} = 410 Hz, Re_D = 21000, ϕ = 0.80)

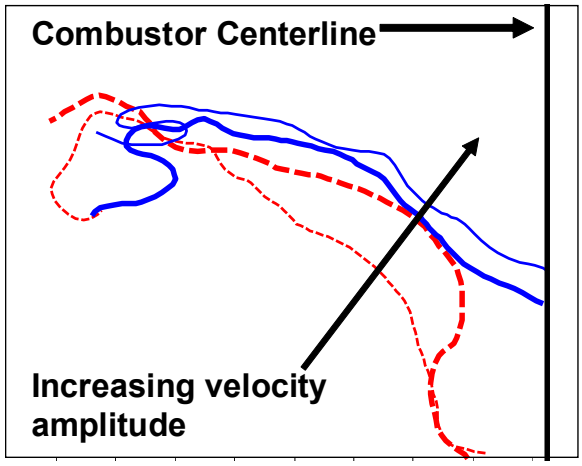

Figure 28. Average flame edges at 180-225 degree phase angle at four velocity oscillation amplitudes (f_{drive} = 410 Hz, u'/u_o = 0.2, 0.3, 0.53, 0.6). Dashed (- - -)/ solid (—) lines indicate peak flame response when transfer function is linear/saturated, respectively.

7. THEORETICAL NONLINEAR FLAME RESPONSE CHARACTERISTICS

This paper describes the dynamics of premixed flames responding to harmonic velocity disturbances. Results are derived from analytical and computational solutions of the nonlinear *G*-equation and used to interpret a number of experimental observations. It is shown that the linear and nonlinear characteristics of the flame dynamics are controlled by the superposition of two sources of flame disturbances: those originating at the flame anchoring point due to boundary conditions and from flow non-uniformities along the flame. These disturbances do not necessarily propagate along the flame at the same speed. Consequently, they may either constructively or destructively superpose with each other, so that the overall linear flame response depends upon two Strouhal numbers, St_2 and St_c, related to the amount of time taken for a flow (St_c) and flame front (St_2) disturbance to propagate the flame length, normalized by the acoustic period. Unsteady stretch effects, responsible for the reduction in the flame front wrinkle size in the flow direction (referred to as "filtering" by Bouehla & Baillot[25], become significant when $\sigma^* St_2 \sim O(1)$, where σ^* is a non-dimensionalized Markstein length. The nonlinear flame response is driven by flame propagation normal to itself ("kinematic restoration"), which smoothens out the wrinkles induced by the forcing. Because the overall flame response is a superposition of the two flame disturbance contributions, the flame's nonlinear response can exhibit two qualitatively different behaviors. For parameter values where these disturbances constructively interfere, the nonlinear flame transfer function gain saturates and is, therefore, always less than its linear value. When the flame disturbances destructively interfere, the nonlinear transfer function may actually exceed its linear value before saturating. This result explains Durox *et al's*[27] experimentally observed variation of the nonlinear flame response with frequency. One interesting prediction of this analysis concerns the impact of flow forcing on average flame length. We show that in most cases, the flame length decreases with increasing perturbation amplitude, as has been experimentally observed by Bourehla & Baillot[25] and Durox *et al*[40]. However, the analysis also predicts that the flame can lengthen under certain conditions, a result that has apparently not yet been experimentally observed.

This paper describes an analysis of the linear and nonlinear dynamics of laminar premixed flames responding to harmonic velocity disturbances. The key objective of this work is to predict the heat release response of the flame, and to isolate the key non-dimensional parameters which characterize these interactions. While this problem is of great interest from a fundamental standpoint, it is also motivated by pressing practical problems. This paper's focus on premixed flames is motivated by the fact that low emissions combustion systems for land-based gas turbines, future aircraft engines, industrial heaters and boilers rely on a premixed or partially premixed combustion process. Furthermore, its focus upon harmonically oscillating flow disturbances stems from the fact that these combustion systems are exceptionally prone to combustion instabilities[3,8, 41-44] which generally occur when the unsteady combustion process couples with the natural acoustic modes of the combustion chamber, resulting in self-excited oscillations. These oscillations are destructive to hardware and adversely affect performance and emissions.

While clearly the ultimate goal is to develop a general theory that describes the dynamics of harmonically perturbed, fully turbulent flames, our focus here upon laminar flames is motivated by the lack of understanding of their dynamics even in very simple situations.

An unstable combustor's dynamics are controlled by a complex interplay of linear and nonlinear processes. To illustrate, consider an acoustic disturbance with amplitude, ε. Referring to **Figure 29**, note that this disturbance amplitude stays the same, decreases, or increases depending upon the relative magnitudes of the driving, $H(\varepsilon)$, and damping, $D(\varepsilon)$, processes; i.e., whether $H(\varepsilon)=D(\varepsilon)$, $H(\varepsilon)<D(\varepsilon)$, or $H(\varepsilon)>D(\varepsilon)$, respectively. Linear combustor processes generally control the balance between driving and damping processes at low amplitudes of oscillation and, thus, determine the growth rate of inherent disturbances in the combustor. Nonlinear combustor processes control the finite amplitude dynamics of the oscillations. Predicting the limit cycle amplitude of self-excited oscillations requires an understanding of the nonlinear characteristics of $H(\varepsilon)$ and $D(\varepsilon)$. To illustrate, **Figure 29** depicts a situation where $H(\varepsilon)$ saturates and the two curves cross at the limit cycle amplitude, ε_{LC}.

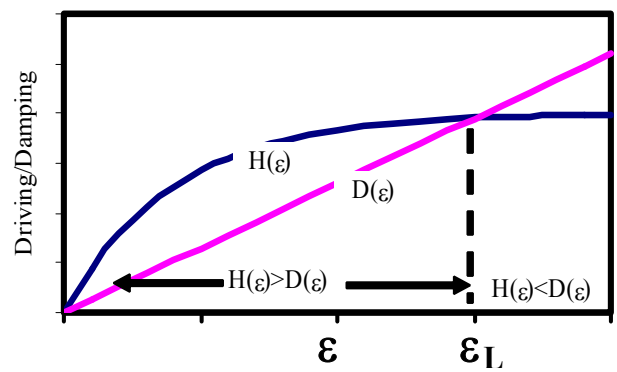

Figure 29. Qualitative description of the dependence of acoustic driving, H(ε) and damping, D(ε), processes upon amplitude, ε

The focus of this paper is on the heat release dynamics, i.e., to understand the characteristics of $H(\varepsilon)$ in both the linear and nonlinear regime. This focus on heat release dynamics is motivated by observations that the nonlinear gas dynamical processes are less significant in many premixed combustors. For example, Dowling[16] suggests that gas dynamic processes essentially remain in the linear regime, even under limit cycle operation, and that it is the relationship between flow and heat release oscillations that provides the dominant nonlinear dynamics in premixed combustors, i.e., $H(\varepsilon)$. The primary point of these observations have been confirmed by several experimental studies[45 - 47], which show that substantial nonlinearities in the heat release response to acoustic disturbances occur, even at amplitudes as low as $p'/p_o \sim 1\%$ and $u'/u_o \sim 20\%$.

A variety of mechanisms exist for causing nonlinearities in heat release dynamics; e.g., local or global flame extinction[16,19,48], pressure sensitivity of the mass burning rate[49-52], flame holding and/or nonlinear boundary

conditions[2,20] (e.g., the point where the flame anchors depending upon amplitude) equivalence ratio oscillations[15,17] and flame kinematics[53,54]. It is this latter kinematic mechanism, i.e., the response of the flame front position as it adjusts to perturbations in flow velocity that is the focus of this study. Because the flame's position and orientation depends upon the local burning rate and flow characteristics, velocity perturbations cause wrinkling and movement of the flame front. In turn, this modifies its local position and curvature, as well as its overall area or volume. These velocity disturbances can be acoustic or vortical in nature and, thus, propagate at the sound speed or with the flow, respectively. To illustrate the excitation of a flame by a velocity disturbance, Figure 30 shows a photograph from Durox *et al.* (2005)[40] of a Bunsen flame disturbed by flow oscillations generated by a loudspeaker placed upstream of the flame. The figure clearly shows the large distortion of the flame front. This flame disturbance is convected downstream by the mean flow, so that it varies spatially over a convective wavelength.

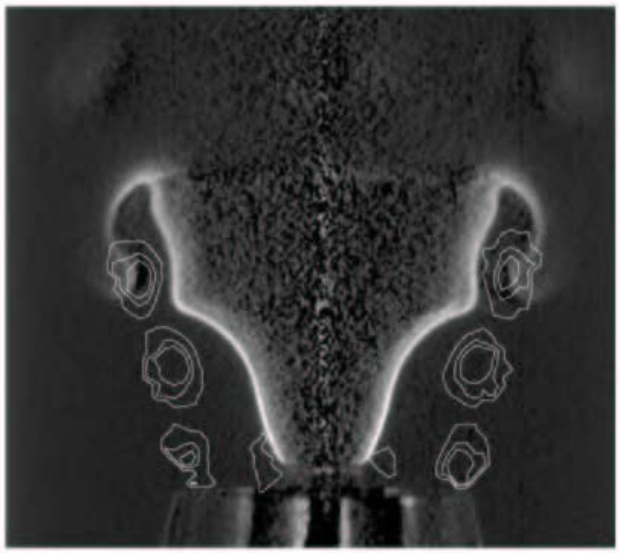

Figure 30. Vorticity field superposed with the flame front. Image reproduced with permission from Ref. [40].

A variety of experimental observations have been made of similar flames which will be reviewed next. Baillot and co-workers performed a systematic experimental and theoretical study of the response of laminar Bunsen flame to velocity perturbations of varying amplitude and frequency[25,27,55]. While their principal observations are quite similar to those previously observed by Blackshear[56], they appear to be the first systematic characterization of the flame response as a function of perturbation amplitude. Similar to the illustration in Figure 30, they found that at low frequencies (f<200 Hz) and velocity amplitudes (u'/u_o<0.3), the flame front wrinkles symmetrically about the burner axis due to a convected wave traveling from the burner base to its tip. At higher frequencies, but similar low amplitudes, they observed a phenomenon which they refer to as "filtering" wherein the flame wrinkles are only evident at the flame base and decay with axial location downstream. This high frequency behavior is due to the increased importance of the flame's curvature dependent burning velocity and the very short convective wavelengths of the imposed disturbances at these higher frequencies.

Bourehla & Baillot[25] also found that laminar, conical Bunsen flames subjected to high amplitude, low

frequency velocity perturbations exhibited a variety of transient flame holding behavior, such as flashback, asymmetric blowoff, unsteady lifting and re-anchoring of the flame. In addition, they note that its response is asymmetric and extremely disordered. However, at high frequencies and forcing amplitudes, the flame remains firmly attached, but its overall shape dramatically changes. They found that the flame becomes "collapsed" with a rounded off tip region, and for sufficiently high forcing intensities ($u'/u_o>1$), the flame's mean shape becomes hemispherical[25]. Baillot et al.[55] also reported a theoretical study, where they solved the *G*-equation and showed good agreement between predicted and measured flame shapes, even at larger amplitudes of forcing where the flame front becomes strongly cusped. The so-called *G*-equation is a front tracking equation for the flame position, given by:

$$\frac{\partial G}{\partial t} + \vec{u}\cdot\nabla G - S_L \left|\nabla G\right| = 0 \quad (1)$$

where $G(x,t)=0$ is an implicit expression defining the instantaneous flame position, $\vec{u}$ is the velocity field and S_L is the laminar burning velocity.

Recent work complements the studies of Baillot and co-workers discussed above, by quantifying the *global* heat release response, Q', of the flame[8,32,40]. These workers obtained high speed images and transfer functions, $(Q'/Q_o)/(u'/u_o)$, of acoustically forced Bunsen and inverted wedge flames. Significantly, they showed that most of the key flame response characteristics could be quantitatively predicted by assuming that the flame's heat release was directly proportional to its instantaneous area. The flame area was calculated using the *G*-equation, where measured velocity fields were used as inputs.

Solution of the *G*-equation is a key analytical approach used in this paper, as well as the above cited studies, for quantitative analysis of this problem. This approach for treating unsteady flame problems was apparently first introduced by Markstein[57] and, in the context of acoustically forced flames, by Marble & Candel[58]. It has subsequently been extensively developed[59] and is used in a variety of flame dynamic studies. The key assumption behind its application is the separation of acoustic/hydrodynamic scales of the flow field, and the flame thickness. Given the disparity between flame and acoustic length scales, the flame front essentially appears as a discontinuity to the flow. As such, the fluid dynamics of the flows up and downstream of the flame can often be treated separately from that of the flame structure. However, we should emphasize that there is not necessarily a *corresponding disparity in time scales*; e.g. forming a flame response time scale, τ_M, from the ratio of the laminar flame thickness and flame speed leads to values of τ_M~0.002 - .07 s for methane/air flames. These are of similar magnitude of perturbations with frequencies between 20-500 Hz. Thus, the interior flame structure and, consequently, quantities such as the flame speed, do not respond in a quasi-steady manner to flow perturbations.

Because of the mutual interaction between the flame position and the flow field, free boundary problems such as this are extremely difficult to handle analytically. Initial studies used an integral technique[58,60-63] to make it analytically tractable. Further progress has been made in more recent studies[7,8,53,60,] which circumvented the analytical difficulties encountered in the fully coupled flame-flow problem by neglecting the coupling of flow perturbations across the flame, as will also be done in this study. As such, they calculated the response of the flame from an imposed velocity disturbance of given amplitude and phase upstream of the flame. In essence, this

approximation neglects the density change across the flame front. Nonetheless, the substantially reduced complexity of the approach facilitates a much more transparent analysis; moreover, their results give excellent agreement with experiments in many instances. We will discuss the conditions under which this approximation is appropriate, and not appropriate, at length below.

In closing, we should draw the readers attention to several additional analyses which, though not directly aimed at the acoustic flame interaction problem, did analyze the kinematics of a nominally flat flame front in an unsteady and/or periodic, prescribed, flow field; e.g., see Refs. [64-67].

The key contribution of the present work is to provide a systematic treatment of linear and nonlinear flame dynamics – including unsteady stretch effects - in response to harmonically oscillating flow disturbances. The rest of the paper is organized in the following manner: Section 0 describes the key processes impacting the flame dynamics and the disturbance field. In particular, the principle assumptions of the analysis are identified and the phenomena which can and cannot be captured by the analysis are discussed. Section 0 presents the modeling approach and analysis procedure. Section 0 presents results that quantify the effects of flame geometry, disturbance field characteristics, perturbation frequency and stretch sensitivity upon the flames linear (Section 0) and nonlinear (Section 0) characteristics. The response of the flame at the perturbation frequency and its harmonics are discussed as well as changes in the mean flame length.

Basic Considerations

Flame Dynamics

The basic problem of interest is this: Given a disturbance velocity field, $u'\left(\vec{x},t\right)$, determine the response of the flame position, $\zeta\left(\vec{x},t\right)$, and in particular, the total heat release rate of the flame. The global heat release rate of the flame is given by:

$$Q(t) = \int_s \rho_l S_L \Delta h_R dA_{FL} \quad (2)$$

where the integral is performed over the flame surface, A_{FL}, and Δh_R is the heat release per unit mass of reactant. Equation (2) shows the three fundamentally different ways of generating heat release disturbances in a premixed flame: fluctuations in mass burning rate ($\rho_l S_L$), heat of reaction, or flame area. As noted by Clanet *et al.*[68], they can be classified based upon either their modification of the local internal structure of the flame (such as the local burning rate) or its global geometry (such as its area).

As we are focused upon the flame response to flow perturbations, we assume constant Δh_R and mixture density, ρ_l; analysis of the effects of these perturbations are given in Refs. [49,69]. Of course, if the flow perturbation is acoustic in origin, a density disturbance will accompany the velocity fluctuation. However, their relative impacts differ greatly, on the order of the flame speed Mach number. As such, our subsequent calculations focus upon the quantity:

$$\frac{Q'}{\overline{Q}} = \frac{\int S_L' d\overline{A}_{FL}}{\int \overline{S}_L d\overline{A}_{FL}} + \frac{A_{FL}'}{\overline{A}_{FL}} \quad (3)$$

Flame speed perturbations are generated by the oscillating stretch rate, proportional to $\nabla^2 G$, and are discussed in Section 0. Flame area fluctuations are directly related to perturbations in the flame position through the relation:

$$A_{FL}(t) = \int \delta\left(G - G_o\right)\left|\nabla G\right| dS \quad (4)$$

where G_o denotes the flame surface. This equation shows that the quantity of interest is not G itself, but its gradient ∇G - a very important observation. Another key observation is that only the velocity component normal to the flame, $\vec{u} \cdot \vec{n} = u_n$, a scalar quantity, impacts the flame dynamics. This can be seen by rewriting Eq. (1) as:

$$\frac{\partial G}{\partial t} + \left(u_n - S_L\right)\left|\nabla G\right| = 0 \quad (5)$$

This necessarily implies that the full three dimensional details of the velocity field are not significant; it is only the component that is normal to the flame. As such a detailed specification of the velocity field is not necessary for an understanding of the flame dynamics and, furthermore, a variety of different velocity fields can give an essentially identical flame response. This is the reason why we assume a relatively simple form of the disturbance velocity field, as will be detailed in Sec. 0. However, for large amplitude oscillations, this point must be conditioned with the fact that the flame normal exhibits large fluctuations, so the relative contribution of each vector component of the velocity field varies throughout the cycle.

Several general comments can be made regarding the dynamics of the flame position gradient, which is directly related to its surface area through Eq (4); these will provide a great deal of insight into the flame dynamics. From a mathematical point of view, the linear solution to the equation for flame surface area can be decomposed into two canonical components: the homogeneous solution and the particular solution. The linearized version of Eq. (1) can be written in a coordinate system aligned normal to the mean flame position as (see Figure 31)

$$\frac{\partial \xi}{\partial t} + U_o \frac{\partial \xi}{\partial X} = U'\left(X, t\right) \quad (6)$$

where X denotes the coordinate along the mean flame position, U_o is the mean velocity component along the X axis and $\xi\left(X,t\right)$ is the perturbed flame position normal to this coordinate. The dynamics of $\partial\xi / \partial X$, which is directly related to that of the flame area itself, is described by the following solution*:

* In Eq (7), after evaluating the velocity gradient $\partial U'/\partial X$, the integration has to be performed with respect to dx' after replacing the variable X by x' and t by $t-(X-x')/U_o$

$$\frac{\partial \xi(X,t)}{\partial X} = \underbrace{\frac{1}{U_o}\int_0^X \left(\frac{\partial U'(X,t)}{\partial X}\right)_{X\to x',\, t\to\left(t-\frac{X-x'}{U_o}\right)} dx'}_{\text{Flow non-uniformity (particular solution)}} + \underbrace{\frac{1}{U_o}\left(U'(X=0,t-\frac{X}{U_o}) - U'_{base}(t)\right)}_{\text{Boundary condition (homogeneous solution)}} \quad (7)$$

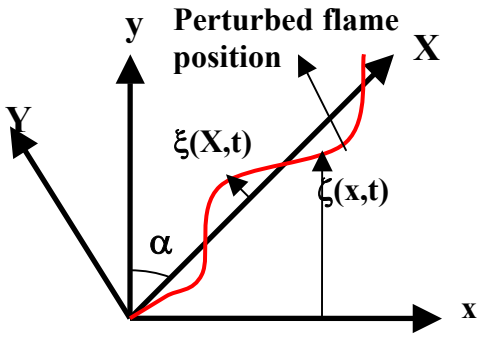

Figure 31. Coordinate system illustrating the perturbed flame shape

The homogeneous and particular solutions have a clear physical significance which can be understood as follows. A spatially uniform disturbance velocity disturbance only excites the homogeneous solution (second term in Eq (7)). This can be understood by first assuming that the flame edge moves exactly in step with the particle velocity, i.e., $U'_{base} = U'(X=0, t-\frac{X}{U_o})$. In this case, the entire flame simply moves up and down in a bulk motion without a change in shape or area[70]. However, if a flame anchoring boundary condition is imposed ($U'_{base} = 0$), such that the flame remains fixed, the flow disturbance excites a flame front disturbance that originates at the boundary and propagates along the flame front at a speed that is proportional to the mean flow velocity. These "homogeneous solution" flame dynamics were extensively analyzed by Fleifil *et al.*[7]. If the disturbance flow field is spatially non-uniform, i.e., $\partial U'/\partial X \neq 0$, the particular solution is excited (first term in Eq (7)). This results in waves originating at the spatial location(s) of flow non-uniformity that also propagate along the flame at roughly the mean flow velocity.

Because the *G*-equation is first order in time, the flame acts as a low pass filter to flow disturbances, so that the amplitude of the two canonical solutions individually decay with increases in frequency as *1/f*. As such, the transfer function relating the response of the flame area to a spatially uniform velocity disturbance (where only the homogeneous solution is excited), $(A'/A_o)/(u'/u_o)$ has a value of unity at zero frequency, decays monotonically with frequency, but generally is not identically zero[†]. In contrast, when the flame is perturbed by a spatially non-uniform disturbance (so that both the homogeneous and particular solution are excited), the flame area consists of a

[†]An exception occurs in two-dimensional flames at frequencies where the flame tip motion is zero. In this case, the flame's linear area response is also zero.

superposition of the two solutions. As such, though each solution decreases with frequency, their sum has oscillatory behavior and, in cases where they constructively interfere can even cause the transfer function, $(A'/A_o)/(u'/u_o)$ to exceed unity. This result was first predicted by Schuller *et al.*[32] and experimentally observed by Durox *et al.*[40]. In addition, the two solutions can destructively interfere, and in certain cases, exactly cancel each other so that the resulting transfer function $(A'/A_o)/(u'/u_o)$ identically equals zero.

Consider next several basic features of the nonlinear flame dynamics. The key mechanism of nonlinearity is illustrated in Figure 32. In this illustration, a flame is perturbed by a transient disturbance so that it has a corrugated shape, but then allowed to relax back to its steady state, planar position. Flame propagation normal to itself smoothens out the wrinkle, so that its area eventually returns to being constant in time. As such, kinematic processes work to destroy flame area, as shown by the dashed lines in the bottom sketch. The rate of these area destruction processes depends nonlinearly upon the amplitude and length scale of the flame front disturbance. Large amplitude corrugations are smoothed out at a relatively faster rate than small amplitude perturbations. In the same way, short length scale corrugations are smoothed out faster than long length scales of the same disturbance magnitude. As discussed further below, this is the reason that nonlinearity is enhanced at higher disturbance frequencies, which generate shorter length scale flame corrugations.

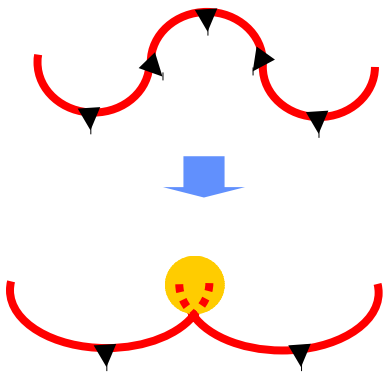

Figure 32. Sketch of a flame that is initially wrinkled (top), showing the destruction of flame area by kinematic restoration processes (bottom)

If the disturbance velocity field is spatially uniform (so that only the homogeneous solution is excited), nonlinear effects cause the nonlinear transfer function relating flame area and velocity perturbations, $(A'/A_o)/(u'/u_o)$, to monotonically decrease with disturbance amplitude[54]. In other words, the linear transfer function is larger than the nonlinear transfer function. Since the scale of flame wrinkling is inversely proportional to frequency (scaling roughly as u_o/f), this reduction in finite amplitude transfer function relative to its linear value grows with frequency. As such, the flame area response to a velocity disturbance exhibits saturation characteristics, quite similar to the $H(\varepsilon)$ curve plotted in **Figure 29**.

In the general nonlinear case, as in the linear case, the effect of the superposition of the homogeneous and particular solutions upon the overall flame response depends upon whether the two solutions lie in a region of constructive or destructive interference. In particular, it can be anticipated that if the two solutions lie in a region of destructive interference and are affected unequally by nonlinearity, their superposition may cause the nonlinear

transfer function to actually exceed its linear value. We will show that this occurs in some cases and, furthermore, has been experimentally observed.

Finally, the flame curvature introduced by the flow perturbations introduces perturbations in flame speed. In flames that are thermo-diffusively stable (as assumed in this analysis), these unsteady stretch effects act to smooth out the flame front corrugation. This causes the amplitude of the flame wrinkle to diminish as it propagates along the flame. As the radius of flame wrinkling is approximately proportional to the inverse of the squared frequency, it can be anticipated that this effect grows in significance with frequency. This axial decay in flame wrinkling amplitude has been observed by Bourhela & Baillot[25], which was referred to as "filtering".

Disturbance Field

The prior section touched upon the influence of the velocity field upon the flame dynamics. It showed that it is the normal component of the velocity, and not the velocity itself, that is significant in determining the flame response. Also implicit in Eq. (7) is that the detailed structure of these flow non-uniformities at each axial location is less significant than their integrated effect from the flame attachment point to that axial location. This section considers in more detail the character of the velocity field.

The velocity field can be decomposed into an irrotational, compressional component (the acoustic field) and a solenoidal, rotational component (vorticity field). Acoustic disturbances propagate with a characteristic velocity equal to the speed of sound. In a uniform flow, vorticity disturbances are convected at the bulk flow velocity, u_o. Acoustic properties vary over an acoustic length scale, given by $\lambda_a=c/f$, while vortical disturbances vary over a convective length scale, given by $\lambda_c=u_o/f$. Consequently, in low Mach number flows, these disturbances have substantially different length scales. The vortical mode "wavelength" is shorter than the acoustic wavelength by a factor equal to the mean flow Mach number, $\lambda_c/\lambda_a=u_o/c=M$.

Vorticity disturbances propagate with the mean flow and diffuse from regions of high to low concentration. In contrast, acoustic disturbances, being true waves, reflect off boundaries, are refracted at property changes, and diffract around obstacles. The reflection of acoustic waves from multi-dimensional flame fronts generally results in a complex, multi-dimensional acoustic field in the vicinity of the flame.

Experiments have highlighted the significance of both acoustic and vorticity wave interactions with the flame front. These vorticity oscillations are generally manifested as large scale, coherent structures that arise from the growth of intrinsic flow instabilities. The phase velocity and growth rate of the flow instabilities is strongly affected by the amplitude of forcing and the relationship between the acoustic forcing frequency and the intrinsic flow instability. Acoustic excitation often causes their shedding rate to "lock-in" to the forcing frequency or one of its harmonics. For example, visualizations from the study of Durox *et al.*[40], clearly indicate that these convected vortical disturbance are excited at the shear layer of the burner exit by the imposed acoustic oscillations. Figure 30 obtained from this study superposes an image of the instantaneous wrinkled flame front and the convected vorticity field. By incorporating the convective phase variation into the disturbance velocity field, they show that the modeled flame area response agrees quite well with their data.

The characteristics of the instability waves that grow and merge to form these large scale structures are a function of the specific characteristics of the burner exit shear layer, such as co-flow velocity, and specifically upon the receptivity of this shear layer to external disturbances. In addition, the phase speed of the convected vortical instability waves are not equal to the flow velocity, but vary with frequency and shear layer characteristics. The instability wave growth rate similarly varies with frequency and the shear layer characteristics. To illustrate, Figure 33 plots Michalke's[73] theoretical curves of the dependence of the phase speed, u_c, of shear layer instability waves in a jet flow upon Strouhal number, $S_\theta = f\theta/u_o$, for several values of the momentum thickness, θ, to jet radius, R, ratio, R/θ. The figure shows that, for all R/θ values, the ratio of u_c/u_o equals unity and 0.5 for low and high Strouhal numbers. For thin boundary layers, e.g., $R/\theta = 100$, the phase velocity actually exceeds the maximum axial flow velocity in a certain S_θ range. This ultra-fast phase velocity prediction has been experimentally verified by Bechert & Pfizenmaier[71] and may explain a similar measurement in a Bunsen flame by Ferguson *et al.*[72]. The dispersive character of the instability wave convection velocity has been confirmed by a variety of measurements in acoustically forced flames. For example, Baillot *et al.*[53] measured u_c/u_o values of 1.13 and 1.02 at 35 and 70 Hz, respectively, on a conical Bunsen flame. Durox *et al.*[40] measured $u_c/u_o = 0.5$ values at 150 Hz in an axisymmetric wedge flame.

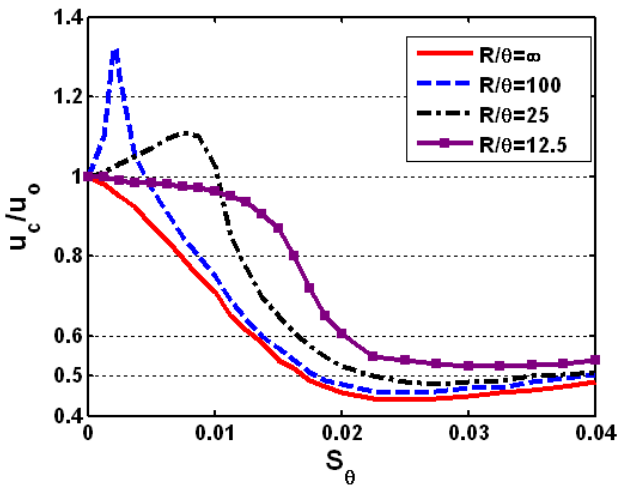

Figure 33. Dependence of shear wave convection velocity and growth rate in a jet flow upon Strouhal number and ratio of jet radius to momentum thickness. Figure reproduced from Michalke[73] (1971).

In general, the disturbance field may have both acoustic and vortical components, whose relative magnitude depends strongly upon the vortex shedding dynamics at the burner shear layer. For example, Ferguson *et al.*[72] found that the disturbance field transitioned from a convected character to one with an acoustic character at "low" and "high" frequencies, respectively. This behavior may be due to the corresponding dependence of vorticity wave growth rate upon frequency. These points show that the character of the disturbance field can vary significantly between its relative acoustic and vortical components, as well as their spatial structure (such as phase speed) – these characteristics will change with experimental configuration, frequency, and amplitude of

perturbation. This point is a key motivator for our development of a general theory for arbitrary phase speed velocity disturbances.

The amplitude dependence of the disturbance field characteristics should be noted. Even in the absence of convected vorticity waves, the impact of the fluctuating flame position upon the acoustic field should cause the acoustic disturbance field to have a "convected" character. This is due to the fact that the flame response to the acoustic field and the acoustic field disturbing the flame are coupled. For large amplitude disturbances, the flame develops large corrugations, such as can be seen in Figure 30, that convect with a phase speed proportional to the axial flow velocity. These convecting flame wrinkles impact the character of the interior acoustic field. It can be anticipated that this mechanism causes the acoustic field structure to revert from being nearly uniform (assuming a compact flame) to having some convected charactereristics at low and high amplitude disturbances, respectively. This issue requires further clarification, as the effects of amplitude and frequency on the acoustic field structure have not been measured or calculated in the large amplitude case.

In this analysis, we prescribe, rather than solve for, the velocity field as done in most recent studies of the problem. In general, it should be emphasized that the thermal expansion of gases at the flame front causes the flame to influence the velocity field upstream of it; this coupling is responsible for the Darrius-Landau flame instability. We next turn attention to the very important issue of the manner in which these mutual interactions impact the results, the conditions under which the present analysis is appropriate, and the conditions where additional physics qualitatively influences the flame dynamics.

First it should be noted that imposing the velocity field is a rigorously valid approximation in the limit of low dilatation flames; i.e., in the limit where $T_b/T_u \rightarrow 1$. This is also the limit considered by other authors for studies of the thermal-diffusive instability and is the basis of the Sivashinsky-Kuramoto equation[74,75]. Besides being of academic interest in allowing one to analytically handle the problem, this is actually a useful limit for many practical devices. It is often pointed out in the combustion literature that practical flames have temperature ratios on the order of 6-10. This is true for flame's consuming reactants at *room temperature* but not, however, for the conditions encountered in most practical devices. Due to the need for high efficiencies (e.g., devices utilizing regenerative heating or high compression ratios such as industrial boilers or gas turbines) or because the devices are using vitiated air (duct burners or jet engine augmentors), unburned gas temperatures are substantially higher. Correspondingly, the requirement for low NOx emissions implies lower burned gas temperatures. As such, typical temperature ratios for practical premixed combustion devices are in the range of 2-3, and even as low as 1.5 in certain industrial applications with large amounts of regenerative pre-heating.

Clearly, however, as T_b/T_u deviates from unity, there will be an impact upon the approach flow characteristics. It can readily be shown that the impact of the flame on the acoustic field scales as $(T_b/T_u)^{1/2}$, which is the ratio of the gas impedances across the flame. Based upon the discussion in the prior section it can be anticipated that, at least for low amplitude perturbations, the alteration of the local acoustic field by the flame does not introduce qualitative changes into the flame dynamics, although it may certainly exert quantitative impacts that increase as $(T_b/T_u)^{1/2}$. This assertion has been previously confirmed by Lee & Lieuwen[70], who computationally determined the

flame's acoustic nearfield for various T_b/T_u values, determined the flame area response, and compared the results to the constant density analyses of Fleifil *et al.*[7] and Ducruix *et al.*[8].

Similarly, it is known that the effect of a stable flame on the vortical approach flow velocity scales approximately as T_b/T_u[76] As in the acoustic case, there is clearly also a frequency-wavenumber dependence, as well as an inverse dependency upon proximity to flame stability boundaries.

The qualitative similarities between fully coupled flame dynamics and that determined using an imposed velocity field break down when both T_b/T_u and perturbation velocity amplitudes are large; i.e., new dynamics appear that cannot be captured with this analysis. This is due to the appearance of a parametric flame instability[35,36,77], manifested by cellular structures that oscillate at half the period of the disturbance. This parametric acoustic instability is due to the periodic acceleration of the flame front by the unsteady velocity field, which separates two regions of differing densities. With increased amplitudes, these organized cellular structures break down into a highly disordered, turbulent front. The regimes in T_b/T_u vs u'/S_L space where this instability occurs can be determined from from Eq. (1) in Bychkov's analysis for a given dimensionless frequency, defined as $w = \frac{\omega \delta_f}{S_L}$ where ω is the forcing frequency and δ_f is the flame thickness[35]. The results are plotted in Figure 34. This graph illustrates the regions (above the curve) where application of a prescribed velocity theory is inappropriate. As could be anticipated, it shows that the range of disturbance amplitudes diminishes with increasing temperature ratio across the flame.

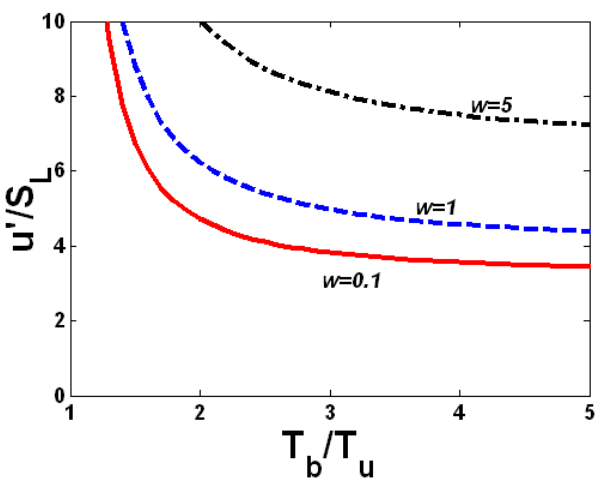

Figure 34. Parametric stability limits of flat flame (unity Lewis and Prandlt number, no gravity).

As such, we conclude that the qualitative linear dynamics of the flame are captured by this analysis for all T_b/T_u values, although the quantitative accuracy of the results deteriorates as T_b/T_u increases. Calculations that quantify these effects are given in Lee & Lieuwen[70]. In contrast, the nonlinear dynamics of the flame are only correctly described by this analysis for low T_b/T_u values. This is the reason for the restriction to low heat release flames indicated in the title of this paper.

Modeling Approach

Figure 35 illustrates the two basic geometries considered. On the left is a conical flame stabilized on a tube, such as a Bunsen flame. On the right is a wedge flame, stabilized on a bluff body. The flame's have axial and radial dimensions given by the flame length, L_f, and radius, R. The instantaneous flame sheet location at the radial location, r, is given by $\zeta(r,t)$, assumed to be a single-valued function of r. This assumption necessarily limits the range of amplitudes which can be treated with this formulation.

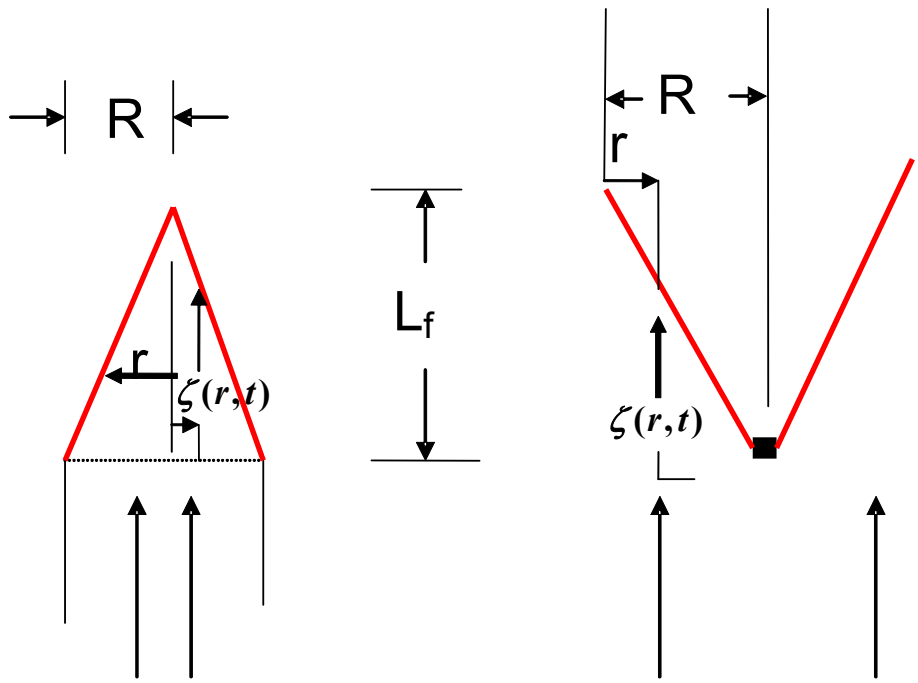

Figure 35. Illustration of conical (left) and wedge shaped (right) flame geometries.

Formulation

The analytical approach used here closely follows Refs. [7,8,53]. The flame's dynamics are modeled with the front tracking equation[59]:

$$\frac{\partial \zeta}{\partial t} = u - v\frac{\partial \zeta}{\partial r} - S_L\sqrt{\left(\frac{\partial \zeta}{\partial r}\right)^2 + 1} \quad (8)$$

where u and v denote the axial and radial velocity components, and S_L the flame speed.

Assuming that the flame speed is only a function of the local curvature of the flame front, it can be expressed as[57]:

$$S_L = S_{L,o}\left(1 - M_l\Phi\right) \quad (9)$$

where M_l is the Markstein length (a function of frequency) and the curvature Φ is given by:

$$\Phi = \frac{\frac{\partial^2 \zeta}{\partial r^2}}{\left(1+\left(\frac{\partial \zeta}{\partial r}\right)^2\right)^{\frac{3}{2}}} \quad (10)$$

The variables t, r, a, u and ζ are non-dimensionalized by u_o/L_f, R, R, u_o and L_f. (note that the value of L_f and R refer to their nominal values without imposed oscillations), where u_o is the mean axial velocity. They are related to the nominal flame speed and average flow velocity by:

$$\frac{u_o}{S_{L,o}} = \sqrt{\left(\frac{L_f}{R}\right)^2 + 1} \quad (11)$$

The ratio of the flame length to radius plays an important role in the flame's dynamics and is denoted by β.

$$\beta = \frac{L_f}{R} \quad (12)$$

Given these assumptions, the flame dynamics are given by (from this point on we use the same symbol for the dimensionless variable):

$$\frac{\partial \zeta}{\partial t} + \sqrt{\frac{1+\beta^2 \zeta_r^2}{1+\beta^2}}\left(1 - \frac{\sigma \beta \zeta_{rr}}{\left(1+\beta^2 \zeta_r^2\right)^{\frac{3}{2}}}\right) = u(\zeta,t) - \beta\, v(\zeta,t)\zeta_r \quad (13)$$

where $\sigma = M_l/R$ is the ratio of Markstein length to duct radius.

Following prior studies[7,53] we assume that the flame remains anchored at the base; i.e.,

$$\zeta(r=1,t) = 0 \quad (14)$$

For conical flames, the second boundary condition comes from the fact that the flame is symmetric about the axis (see Figure 35) i.e.

$$\frac{\partial \zeta(r=0,t)}{\partial r} = 0 \quad (15)$$

For wedge flames, the boundary condition is:

$$\frac{\partial^2 \zeta(r=0,t)}{\partial r^2} = 0 \quad (16)$$

It turns out that both of these boundary conditions introduce terms which are exponentially small functions of σ, terms which are neglected in the ensuing analytical treatments (but not in the computations). As such, although formally required to solve the problem, neither boundary condition exerts any influence on the leading order analytical solutions.

Specification of velocity field

The velocity field is specified as:

$$u(\zeta,t) = u_o + u' \, Cos[k\zeta - \omega_o t] \quad (17)$$

Here the convective wave number k is defined as:

$$k = \frac{\omega_o}{u_c} = \left(\frac{\omega_o}{u_o}\right)\left(\frac{u_o}{u_c}\right) = K\left(\frac{\omega_o}{u_o}\right) \qquad (18)$$

where u_c is defined as the phase velocity of the disturbance and ω_o denotes the angular frequency of the velocity disturbance. K is a parameter which denotes the ratio of the mean flow velocity to the phase velocity of the disturbances. The two key impacts of the flow field on the flame front given by the term $\partial u' / \partial X$ in Eq (7) are captured here by the perturbation amplitude ε and the velocity length scale, u_c/ω_o.

The non-dimensionalized velocity field is then given by:

$$u(\zeta,t) = 1 + \varepsilon Cos\left[St\left(K\zeta - t\right)\right] \quad (19)$$

where

Strouhal number, $St = \dfrac{\omega_o L_f}{u_o}$

Velocity perturbation: $\varepsilon = \dfrac{u'}{u_o}$

The velocity is assumed to be purely axial. It should be emphasized that our goal here is not to simulate the exact disturbance field of any particular experimental setup, but rather to elucidate the key physical processes and non-dimensional parameters that influence the flame's dynamics. However, assuming a two dimensional velocity field does not introduce substantial analytical difficulties, but does reduce the generality of the results, as its characteristics are strongly influenced by geometric details.

Note that the boundary condition given by Eq (14) cannot be used for disturbance velocity magnitudes where the instantaneous flow velocity is lower than the flame speed. In this case, the flame will flash back and Eq. (14) must be replaced by a different condition[20]. In this study, calculations are performed for velocity magnitudes up to this critical value, which will be referred to as ε_f, where:

$$\varepsilon_f = 1 - \frac{1}{\sqrt{1+\beta^2}} \quad (20)$$

Analysis Procedure

Two approaches were used to analyze the properties of Eqs (13) and (3). Analytical expressions for the linear and nonlinear flame response were obtained from a perturbation analysis carried out to third order in ε. Terms of $O(\varepsilon^3)$ are required to determine the leading order nonlinear correction to the flame transfer function at the forcing frequency. Nonlinear corrections to the average flame length and the flame response at the first harmonic, $2\omega_0$, are obtained at $O(\varepsilon^2)$. Exponentially small terms of σ, e.g., $\exp(-1/\sigma)$, are also neglected as these are smaller than all

powers of σ, i.e., $\lim_{\sigma \to 0} e^{-\frac{1}{\sigma}} < \sigma^n$, where n is any integer.

For the fully nonlinear case, Eq.(13) is solved numerically. A robust numerical scheme is necessary which can accurately capture the formation of sharp gradients and cusps in the distorted flame front. Spatial derivatives are discretized using a Weighted Essentially Non-Oscillatory (WENO) scheme designed specifically for Hamilton-Jacobi equations[79]. This scheme is uniformly fifth order accurate in regions wherein the spatial gradients are smooth and third order accurate in discontinuous regions. Derivatives at the boundary nodes are calculated using fifth order accurate upwind-differencing schemes so that only the nodes inside the computational domain are utilized. A Total Variation Diminishing (TVD) Runge-Kutta scheme[80], up to third order accurate, is used for time integration. The flame front perturbation is tracked and the corresponding change in the flame surface area is calculated as a function of time for a given upstream flow velocity perturbation. The transfer function relating the flame area to the convective velocity perturbation is then evaluated. The flame response at a given frequency was determined from the Fourier transform of the flame area at that frequency.

Results and Discussion

Linear Flame Dynamics

In this section, we derive expressions for the flame area-velocity transfer function that generalize the result of Schuller *et al.*[32], by determining the response of a flame to a disturbance with an arbitrary phase velocity and curvature dependent flame speed.

Flame shape

The flame position is expanded as[53]:

$$\zeta(r,t) = \zeta_o(r) + \zeta_1(r,t)\ \varepsilon\ +\ \zeta_2(r,t)\ \varepsilon^2 + \zeta_3(r,t)\ \varepsilon^3 + O(\varepsilon^4) \quad (21)$$

The evolution equation for $\zeta_1(r,t)$ is computed here and the $\zeta_2(r,t)$, $\zeta_3(r,t)$ terms are computed in Section 0. The mean flame shape in the absence of perturbations is given by

$$\zeta_o(r) = 1 - r + O\left(e^{-\frac{1}{\sigma}}\right) \quad (22)$$

Stretch effects at the flame tip provide an exponentially small correction to $\zeta_o(r)$. An exact expression for $\zeta_o(r)$ is given in Appendix A. Substituting Eqs (21) and (22) into Eq (13), the evolution equation for ζ_1 is:

$$\frac{\partial \zeta_1}{\partial t} - \frac{\beta^2}{1+\beta^2}\frac{\partial \zeta_1}{\partial r} - \frac{\sigma\beta}{\left(1+\beta^2\right)^{3/2}}\frac{\partial^2 \zeta_1}{\partial r^2} - Cos\left[St\left\{K(1-r)-t\right\}\right] = 0 \quad (23)$$

The solution of Eq. (23), given the boundary condition in Eq. (14) and Eq. (15) (for conical flames) or Eq. (16) (for wedge flames) (only terms of $O(\sigma^*)$ are shown below for brevity, full solutions are in Appendix B) is

$$\zeta_1 = \zeta_{1,BC} + \zeta_{1,Flow}$$

$$= \left(\frac{\left(\alpha^2 + (r-1)\sigma^* St^2\right) Sin\left[\left(\frac{St\ \ (r-1+\alpha t)}{\alpha}\right)\right]}{\alpha^2(\eta-1)\ \ St} - \frac{\sigma^*\eta^2 Cos\left[\left(\frac{St\ \ (r-1+\alpha t)}{\alpha}\right)\right]}{\alpha(\eta-1)^2} \right) \quad (24)$$

$$+ \left(\frac{\sigma^*\eta^2 Cos\left[St\left\{K(r-1)+t\right\}\right]}{\alpha(\eta-1)^2} - \frac{Sin\left[St\left\{K(r-1)+t\right\}\right]}{(\eta-1)\ \ St} \right)$$

where

$$\alpha = \frac{\beta^2}{\beta^2+1} \quad (25)$$

$$\sigma* = \frac{\sigma}{\beta\sqrt{\beta^2+1}} = \frac{\sigma(1-\alpha)}{\sqrt{\alpha}} \quad (26)$$

$$\eta = K\alpha \quad (27)$$

This equation explicitly decomposes the solution into contributions from boundary conditions and flow forcing non-uniformities. Note that this expression is valid for both conical and wedge flames (i.e. the second boundary condition is satisfied by the exponentially small terms which have been neglected in the above expressions.). The flame front position is controlled by the superposition of the flame disturbances created at each point due to flow non-uniformity and disturbances originating from the flame base that are convected along the flame front. The stretch contribution is controlled by the parameter σ^* and becomes prominent when $\sigma^* St$ ~O(1).

The limit where $\eta \to 1$ (corresponding to instances where the two disturbances propagate along the flame at the same speed), requires special care and is given by:

$$\lim_{\eta\to 1} \zeta_1 = (r-1)\left(\frac{\left(2\alpha^2 + \sigma^* St^2(r-1)\right) Cos[St\left\{\frac{(r-1)}{\alpha}+t\right\}] + 4\sigma^*\alpha St\ Sin[St\left\{\frac{(r-1)}{\alpha}+t\right\}]}{2\alpha^3} \right) \quad (28)$$

Note that for this case stretch effects have a stronger impact at high Strouhal numbers ($\sigma^* St^2$ ~O(1)).

In order to illustrate the effect of stretch on the flame shape, the deviation of the flame front from its average position is shown in Figure 36. The point X=0 in Figure 36corresponds to the point of attachment at the flame base. In the absence of stretch (σ^*=0), it is well known that the flame front exhibits sinusoidal wrinkling with a constant amplitude[60]. However, in the presence of stretch, the amplitude of the flame front perturbation decays continuously from the flame base to the tip, see Figure 36. This feature wherein the oscillations on the flame front are only evident at the flame base and become strongly damped at axial locations downstream has been experimentally observed and referred to as "filtering" by Bourhela & Baillot[25]. They observed this phenomenon for a conical flame under conditions corresponding to St>38, β=2 and σ^*~0.005, the same conditions simulated in the figure. The strong damping in the flame front oscillations away from the flame base at the same conditions is clearly

captured in Figure 36.

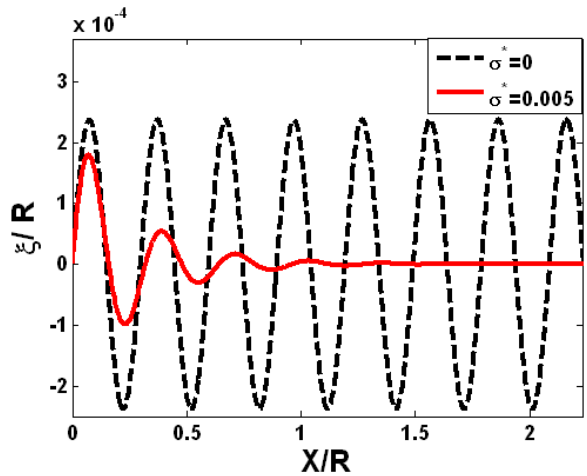

Figure 36. Instantaneous conical flame shape with X axis along the flame front. β=2, ε=0.01, St = 39, K=0

Flame area-velocity transfer function: relative contribution of different sources

Consider the total heat release of the flame, obtained using Eq (3). The first term is entirely due to stretch effects on the flame speed and for conical flames can be expressed as:

$$\frac{\int S_L' d\bar{A}_c}{\int \bar{S}_L d\bar{A}_c} = -2\varepsilon\sigma^* \alpha \int_0^1 r \frac{\partial^2 \zeta_1}{\partial r^2} dr = -2\varepsilon\sigma^* \alpha \left(\zeta_1(r=0,t) - \zeta_1(r=1,t) + \frac{\partial \zeta_1(r=1,t)}{\partial r} \right) \quad (29)$$

To evaluate the second term in Eq (3), note that the non-dimensionalized surface area for a conical flame is given by:

$$\frac{A_c(t)}{\bar{A}_c} = 2 \frac{\int_0^1 r \sqrt{1+\beta^2 \left(\frac{\partial \zeta}{\partial r} \right)^2} \, dr}{\sqrt{1+\beta^2}} \quad (30)$$

Substituting Eqs. (21), (22) and (24) in Eq. (30) and defining

$G_c = \dfrac{Q'/\bar{Q}}{u'/u_o}$ yields (only terms of O(σ^*) are shown below for brevity, full solutions are in Appendix B):

$$G_c(St_2, \eta, \sigma^*) = \overbrace{G_{c,S_L}}^{S_L \text{ Fluctuation}} + \overbrace{G_{c,Area}}^{\text{Area Fluctuation}} \quad (31)$$

where the contribution due to curvature induced S_L fluctuations is:

$$G_{c,S_L} = 2\sigma^* \left(1 + i \frac{e^{i\eta St_2} - e^{iSt_2}}{(\eta - 1)\ St_2} \right)$$

$G_{c,Area}$ can be written in the following form that explicitly separates the contributions from the boundary conditions and flow non-uniformity:

$$G_{c,Area} = G_{c,Area,BC} + G_{c,Area,Flow}$$

$$= \underbrace{2\left(\frac{e^{iSt_2} - 1 - iSt_2}{(\eta-1)\ St_2^2} + \sigma^* \frac{i(e^{iSt_2}-1)(1-\eta+\eta^2) + St_2\left(e^{iSt_2}(1-\eta)+\eta^2\right)}{(\eta-1)^2\ St_2}\right)}_{\text{Boundary Condition}} + \underbrace{2\left(\frac{1-e^{i\eta St_2} + i\eta St_2}{\eta(\eta-1)St_2^2} - \sigma^*\eta\frac{ie^{i\eta St_2} - i + \eta St_2}{(\eta-1)^2\ St_2}\right)}_{\text{Flow non-uniformity}}$$

Alternatively, it can be written in a form which separates out the stretch effects:

$$G_{c,Area} = 2\left(\frac{\eta\left(1-e^{iSt_2}\right) + e^{i\eta St_2} - 1}{\eta(1-\eta)St_2^2}\right) + \underbrace{2\sigma^*\left(i\frac{\left(e^{i\ St_2}\left(\eta^2-\eta+1\right) - \eta e^{i\ \eta St_2} - (\eta-1)^2\right)}{(\eta-1)^2\ St_2} + \frac{e^{i\ St_2}}{(1-\eta)}\right)}_{\text{Stretch Contribution to Area Fluctuation}}$$

where

$$St_2 = \frac{St}{\alpha} = \frac{St\left(1+\beta^2\right)}{\beta^2} \quad (32)$$

Following a similar procedure, the following result can be obtained for wedge flames:

$$\frac{A_w(t)}{\bar{A}_w} = 2\frac{\int_0^1 (1-r)\sqrt{1+\beta^2\left(\frac{\partial\zeta}{\partial r}\right)^2}\ dr}{\sqrt{1+\beta^2}} \quad (33)$$

$$G_w(St_2,\eta,\sigma^*) = \overbrace{G_{w,S_L}}^{S_L\ \text{Fluctuation}} + \overbrace{G_{w,Area}}^{\text{Area Fluctuation}}$$

$$G_{w,S_L} = 2\sigma^*\left(\frac{(i+St_2)e^{iSt_2} - (i+\eta St_2)e^{i\eta St_2}}{(\eta-1)\ St_2}\right)$$

$$G_{w,Area} = \underbrace{2\left(\frac{1+i(i+St_2)e^{iSt_2}}{(\eta-1)\ St_2^2} - \sigma^*\frac{\left(i(e^{iSt_2}-1) + St_2e^{iSt_2}\right)(1-\eta+\eta^2) + i(\eta-1)St_2^2e^{iSt_2}}{(\eta-1)^2\ St_2}\right)}_{\text{Boundary Condition}}$$

$$+ \underbrace{2\left(\frac{(1-i\eta St_2)e^{i\eta St_2} - 1}{\eta(\eta-1)St_2^2} + \sigma^*\eta\frac{e^{i\eta St_2}(i+\eta St_2) - i}{(\eta-1)^2\ St_2}\right)}_{\text{Flow non-uniformity}}$$

$$= 2\left(\frac{\eta - 1 + i(i+St_2)\eta e^{iSt_2} + (1-i\eta St_2)e^{i\eta St_2}}{\eta(\eta-1)St_2^2}\right)$$

$$- \underbrace{2\sigma^*\left(i\frac{\left(e^{i\ St_2}\left(\eta^2-\eta+1\right) - \eta e^{i\ \eta St_2} - (\eta-1)^2\right)}{(\eta-1)^2\ St_2} - \frac{(\eta^2-\eta+1)e^{i\ St_2} - \eta^2 e^{i\ \eta St_2}}{(\eta-1)^2} + \frac{iSt_2e^{i\ St_2}}{(\eta-1)}\right)}_{\text{Stretch Contribution to Area fluctuation}}$$

(34)

The above results reduce to those previously developed by Schuller *et al.*[32] when σ^*=0 and the phase speed of the disturbances is equal to that of the mean flow (i.e. K=1) (note that they refer to St_2 as ω_* and α as $\mathrm{Cos}^2\alpha$).

Thus, the linear flame transfer functions for both the conical and wedge flames, Eqs. (31) and (34), depend upon three parameters: St_2 ,η and σ^*. It is useful to define a Strouhal number based upon the convective velocity (u_c) of the flow disturbances, St_c, which naturally arises in the two transfer functions (Eqs. (31) and (34)) and equals ηSt_2:

$$\eta St_2 = KSt = \left(\frac{u_o}{u_c}\right)\left(\frac{\omega_o L_F}{u_o}\right) = \frac{\omega_o L_F}{u_c} = St_c \quad (35)$$

These two Strouhal numbers are related to the amount of time taken for a flow (St_c) and flame front (St_2) disturbance (which is ultimately created by a flow disturbance) to propagate the flame length, normalized by the acoustic period. Before looking at the total flame transfer functions, it is useful to understand the relative contributions of the two sources: Area fluctuations (G_{Area}) and flame speed fluctuations (G_{SL}). The contribution of the area fluctuations can in turn be broken down into contributions from the boundary condition and flow forcing non-uniformities. Their ratio is given by:

$$\frac{G_{c,Area,Flow}}{G_{c,Area,BC}} = \frac{1-e^{i\eta St_2}+i\eta St_2}{\eta\left(e^{iSt_2}-1-iSt_2\right)} + \sigma^* St_2 \frac{\left(1-e^{i\eta St_2}+i\eta St_2\right)\left(e^{iSt_2}(i+St_2)-i\right)}{\eta\left(e^{iSt_2}-1-iSt_2\right)^2}$$

$$\frac{G_{w,Area,Flow}}{G_{w,Area,BC}} = \frac{(1-i\,\eta\,St_2)e^{i\eta St_2}-1}{\eta\,\left(1-(1-i\,St_2)e^{iSt_2}\right)} - i\sigma^* St_2 \frac{\left((1-i\,\eta\,St_2)e^{i\eta St_2}-1\right)\left(1+e^{iSt_2}(-1+iSt_2+St_2^2)\right)}{\eta\left(-i+(i+St_2)e^{iSt_2}\right)^2}$$

When σ^*=0, the magnitude of this ratio is identical for both wedge and conical flames, see Figure 37. The phase of this ratio is different for conical and wedge flames and plotted in Figure 38 and Figure 39, respectively.

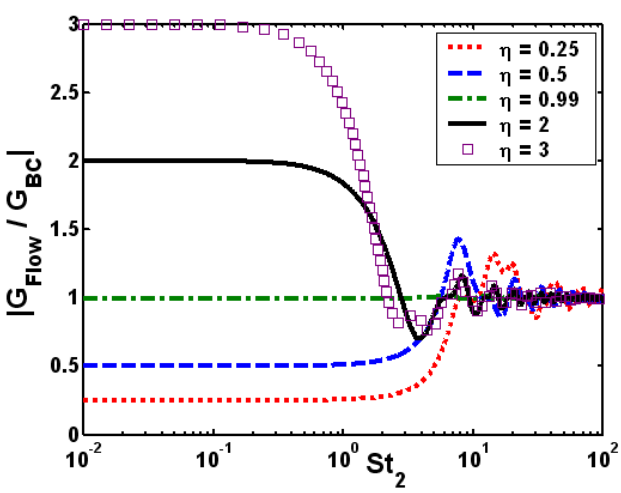

Figure 37. Strouhal number dependence of the magnitude of the ratio of the transfer functions due to the flow non-uniformity and boundary condition terms for different values of η, σ^*=0

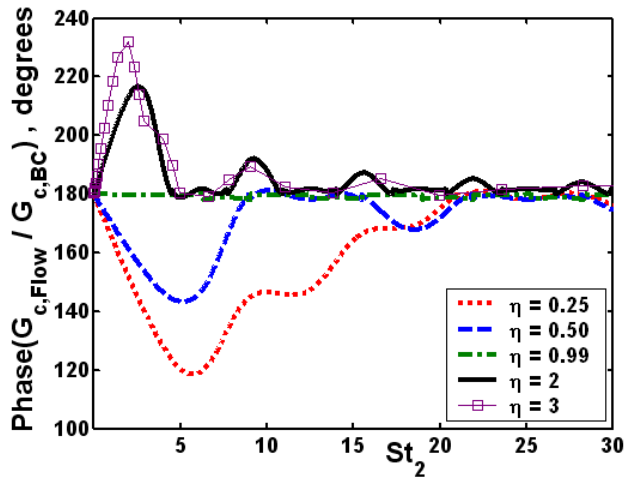

Figure 38. Strouhal number dependence of the phase of the ratio of the transfer functions due to the flow non-uniformity and boundary condition terms for conical flames for different values of η, σ^*=0

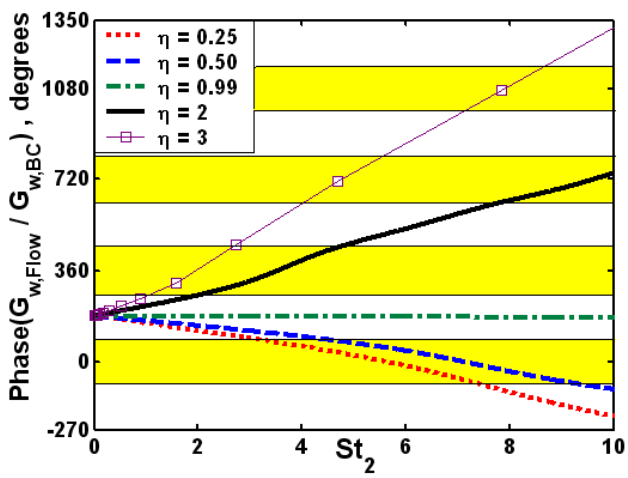

Figure 39. Strouhal number dependence of the phase of the ratio of the transfer functions due to the flow forcing and boundary condition terms for wedge flames. Shaded regions indicate points where boundary condition and flow non-uniformity terms are in phase, σ^*=0

It is instructive to analyze the characteristics of this ratio for limiting values of the parameters η and St_2. First, note that in the $\eta \to 0$ limit (i.e., a spatially uniform disturbance), the flame dynamics for both the wedge and conical flames is controlled exclusively by the boundary condition term, irrespective of the Strouhal number.

$$\lim_{\eta \to 0}\left(\frac{G_{c,Flow}}{G_{c,BC}}\right) = \lim_{\eta \to 0}\left(\frac{G_{w,Flow}}{G_{w,BC}}\right) = 0 \qquad (36)$$

This result can be anticipated from the discussion in the Introduction section and reflects the fact that only the homogeneous solution is excited when the flow disturbance is uniform.

In the $St_2 \to 0$ limit, the relative contribution of the two terms is determined by the value of the parameter η:

$$\lim_{St_2 \to 0}\left(\frac{G_{c,Flow}}{G_{c,BC}}\right)=\left(\frac{G_{w,Flow}}{G_{w,BC}}\right)=-\eta \quad (37)$$

The boundary condition and flow forcing terms dominate when η<1 and η>1, respectively. For long flames (β>>1), this physically corresponds to situations where the disturbance phase velocity is greater than and less than the mean flow velocity, respectively. The two terms tend toward equal magnitudes when $\eta = 1$[‡]. These points can be clearly observed in Figure 37. Note also that the flow disturbance and boundary condition terms are 180º out of phase for low St_2 values see Figure 38 and Figure 39. In the intermediate Strouhal number range, say $1<St_2<10$, either the flow forcing or the boundary condition may dominate depending upon η and St_2.

To understand the St_2>>1 limit, we need to consider stretch effects. The influence of stretch for wedge flames is illustrated quantitatively in Figure 40 wherein the transfer functions due to flow forcing and boundary conditions, normalized by their values in the absence of stretch (σ^*=0), are plotted as a function of the Strouhal number. As the Strouhal number increases, the length scale of wrinkling decreases, leading to curvature effects becoming prominent. The trends in Figure 40 indicate that contributions from the boundary condition term, $G_{w,Area,BC}$, are much more strongly affected than those due to flow non-uniformities, $G_{w,Area,Flow}$. Hence, stretch affects the flame response primarily through disturbances created at the anchoring point. This is also evident in Eq. (24) wherein the stretch effect on flame position is dominated by the term $\sigma^* St$ in $\zeta_{1,BC}$ whereas the contribution to the $\zeta_{1,Flow}$ is O~σ^*. A similar result holds for conical flames, although it should be noted that the conical flame transfer function is significantly less stretch sensitive than the wedge flame. This is due to the fact that stretch effects are more prominent at the flame tip, a region which contributes to the majority and negligible amount of the flame area for wedge and conical flames respectively.

In the limit of St_2>>1 (and σ^*=0), the contribution from both the boundary conditions and flow forcing term are equal, as shown in Figure 37:

$$\lim_{St_2 \to \infty}\left(\frac{G_{c,Area,Flow}}{G_{c,Area,BC}}\right)=-1-i\sigma^* St_2 e^{iSt_2}$$

$$\lim_{St_2 \to \infty}\left(\frac{G_{w,Area,Flow}}{G_{w,Area,BC}}\right)=-(1+\sigma^* St_2^2)e^{i(\eta-1)St_2} \quad (38)$$

‡ Some care is required in analyzing this η=1 result, as the two terms tend to have equal magnitudes and are 180 degrees out of phase. The overall response is not zero, however, as the common denominator (η-1) in Eqs. (31) and (34), which has been cancelled out when taking their ratio, causes their sum to have a non-zero value.

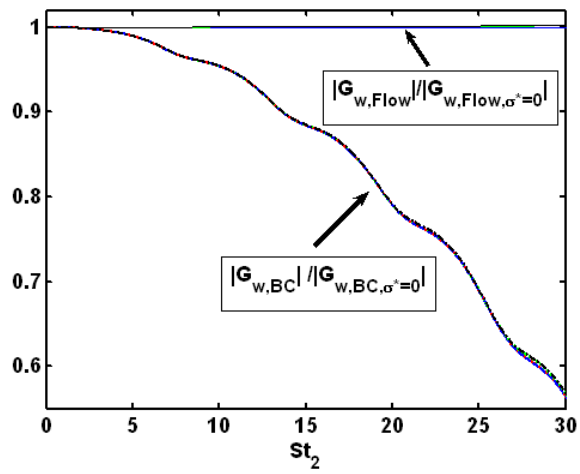

Figure 40. Effect of Stretch on the Strouhal number dependence of transfer functions due to flow non-uniformity and boundary condition terms for wedge flames, σ^*=0.0005

Equation (38) also shows that, in this limit, the relative magnitude contribution of these two terms is independent of η (assuming that the ηSt_2 product does not simultaneously go to zero). *Furthermore in the limit of* St_2>>1 and σ^*=0*, the two terms are always out of phase for conical flames irrespective of the Strouhal number and* η*,* as shown in Figure 38. In contrast, for wedge flames the phase difference between the two contributions monotonically increases with St_2, as shown in Figure 39 (the shaded bands in the figure indicate regions of constructive interference). Note that the above conclusion is modified in the presence of stretch. As discussed before in the case of wedge flames, stretch causes the contribution from the BC term to decrease with increasing Strouhal number. *Hence for wedge flames (which has an O~*$\sigma^* St_2^2$ *correction), in contrast to the* σ^**=0 case, the flow forcing term dominates over the contribution from the boundary condition at high Strouhal numbers*. Conical flames have a smaller stretch correction O~$\sigma^* St_2$ (see Eq (38)) and the response increases/decreases depending upon the Strouhal number.

To this point, the discussion has focused on contribution of the area fluctuations to the flame transfer function. Moving on to the contribution from the flame speed fluctuations (see Eqs. (31) and (34)), it can be shown that at low Strouhal numbers (where curvature effects are less), $G_{w,SL}$ and $G_{c,SL}$ tends to zero. The contribution reaches a maximum in the intermediate Strouhal number range (3<St_2<50) for a given η. Overall, the contribution from G_{SL} is insignificant in comparison to G_A for both conical and wedge flames for typical σ values (0.002-0.02), and is not considered further.

Flame area-velocity transfer function: overall features

The dependence of the magnitude and phase of the total conical flame transfer function $G_c(St_2,\eta,\sigma^*)$ upon St2 at several η values is plotted in Figure 41 and Figure 42, respectively. Consider the magnitude results first. As previously noted by Schuller et al.[32], at low Strouhal numbers the transfer function gain is identical in the cases

where η = 0 or 1 (this is not true at higher Strouhal numbers where stretch effects come into play). Physically, this corresponds to cases where the disturbance velocity is uniform, η=0 or its phase speed matches the flame front disturbance velocity, η=1. The gain transfer function differs for all other disturbance phase velocity cases. Note also that the gain value is always less than one and generally decreases monotonically with St_2, although there is some ripple at higher St_2 values due to constructive and destructive interference between $G_{c,Flow}$ and $G_{c,BC}$. The transfer function phase starts at zero degrees at low St_2 and initially increases monotonically with St_2. For the η=0 case, the phase tends to a limiting value of 90º for large St_2 (see Figure 42). In all other cases, the phase monotonically increases and for high values of η and St_2 the phase curves collapse into a single line.

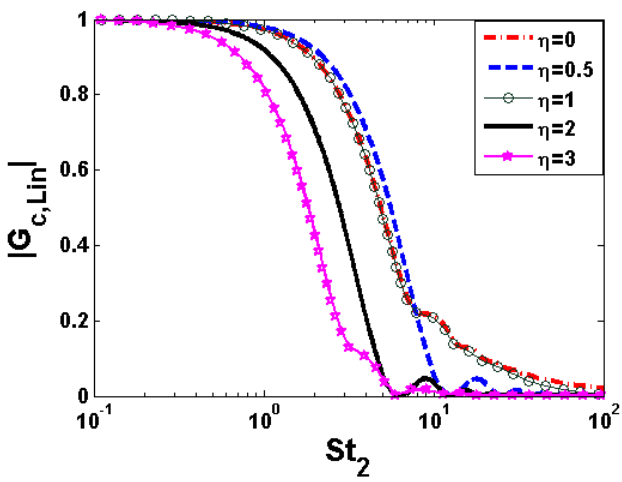

Figure 41. Axisymmetric conical linear transfer function $G_c(St_2,\eta)$ magnitude dependence upon the reduced Strouhal number (St_2) for different values of η, σ^*=0.0005

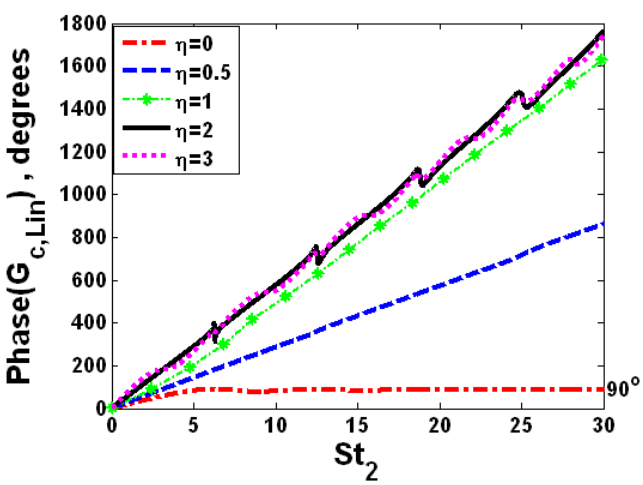

Figure 42. Axisymmetric conical linear transfer function $G_c(St_2,\eta)$ phase dependence upon the reduced Strouhal number (St_2) for different values of η, σ*=0.0005

For wedge flames, the gain and phase of the flame transfer function $G_w\left(St_2,\eta\right)$ are shown in Figure 43 and Figure 44 respectively. Note that, similar to conical flames, all gain values tend toward values of unity at low St_2. However, only in the uniform velocity case, η=0, does the gain then decrease with increases in St_2, as might be expected. In all other cases, the gain increases to values of greater than unity, due to the constructive superposition of $G_{w,Flow}$ and $G_{w,Bc}$. This amplification of the flame response over its quasi-steady value was previously predicted by Schuller *et al.*[32] and confirmed in measurements by Durox *et al.*[40]. The magnitude and St_2 value of the peak value of this amplification region is controlled by η. As shown in Figure 43, the magnitude of the peak value of G_w initially increases from unity as η increases with zero, reaches a maximum at η=1, and then decreases back to unity with further η increases. Note also from Figure 43 that the secondary maxima in the transfer functions appear at a lower St_2 values with increases in η. This behavior can be understood by noting that increases in η at a fixed St_2 is equivalent to an increase in the convective Strouhal number, $St_c=\eta St_2$. *In contrast to conical flames, stretch effects in wedge flames have a significant impact upon the high Strouhal number results,* $\lim_{St_2\to\infty} G_w = \frac{2i\sigma^* St_2 e^{iSt_2}}{1-\eta}$. Turning to the phase in Figure 44, note that the phase increases with St_2 with similar characteristics for all η values.

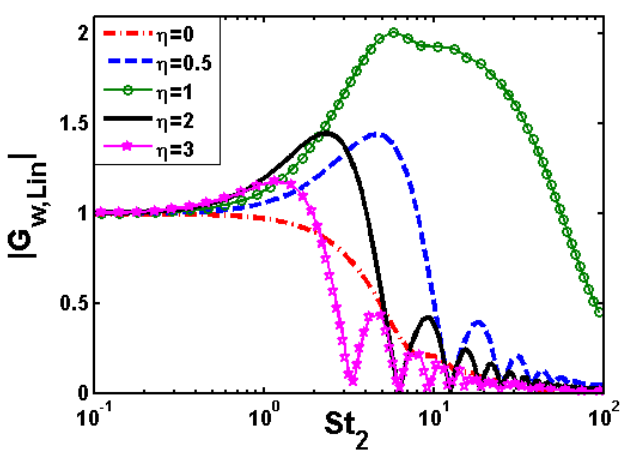

Figure 43. Axisymmetric wedge linear transfer function $G_w(St_2,\eta)$ amplitude dependence upon the reduced Strouhal number (St_2) for different values of η, σ^*=0.0005

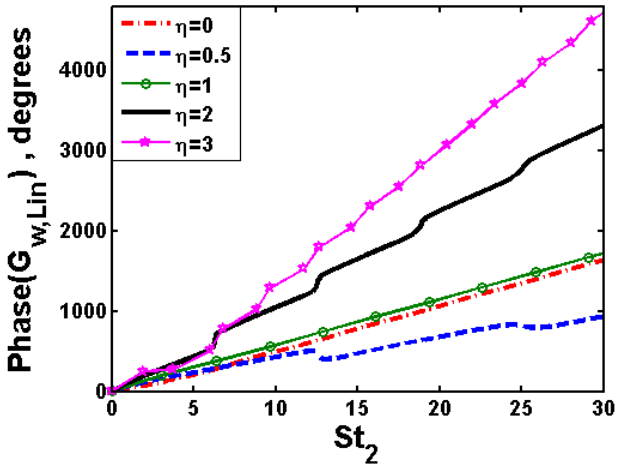

Figure 44 Axisymmetric wedge linear transfer function $G_w(St_2, \eta)$ phase dependence upon the reduced Strouhal number (St_2) for different values of η, σ^*=0.0005

As can be observed from Figure 41 and Figure 43, η (along with St_2) plays a significant role in determining the outcome of the competition between flow disturbance non-uniformity effects and boundary conditions. This fact is further highlighted in Figure 45 which shows, for a given Strouhal number, the value of the parameter η at which the maximum possible response occurs for conical and wedge flames. For conical flames in the range $0<St_2<8$, the maximum gain occurs at η=0.5 (see Figure 41 and Figure 45). For $St_2>8$, the maximum response occurs at two η values (η~0 and η~1) as shown in Figure 45. For wedge flames, the maximum possible gain for $St_2>5$ occurs at η=1 (see Figure 45). Note that for the η=1 case, the wedge flame acts as an amplifier for a wide range of St_2 values as shown in Figure 43. *It is interesting to note that, for any Strouhal number, the peak response for wedge flames always occurs for* $\eta\geq1$; i.e. for cases wherein the phase speed of the disturbances is less than the mean flow speed. In contrast the *maximum gain for conical flames, at any Strouhal number, always occurs for* $\eta\leq1$*;* i.e. for cases wherein the disturbances propagate faster than the mean flow speed.

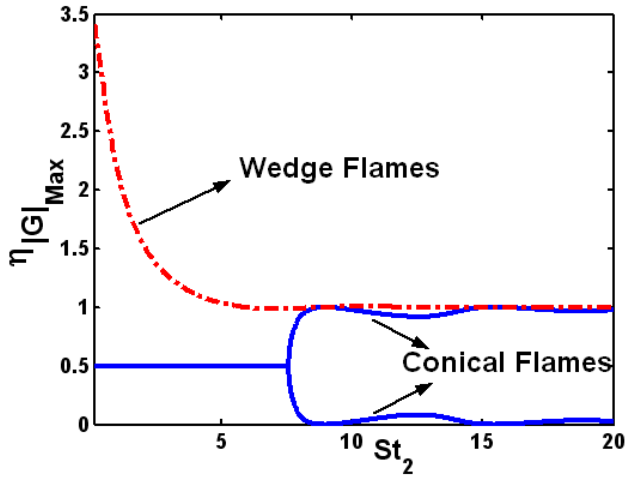

Figure 45. Strouhal number dependence of the parameter η at which the maximum possible linear response occurs for axisymmetric conical and wedge flames, σ*=0

Nonlinear Flame Dynamics

We turn our attention next to the large amplitude flame response. Before considering specific results in the nonlinear case, several general conclusions which can be obtained from analysis of the equations should be considered. Note that nonlinearities in the flame area response arise from three sources. The first is the nonlinear flame dynamics, through the term $\sqrt{1+\beta^2\left(\partial\zeta/\partial r\right)^2}$ in Eq. (13). The second is the static nonlinearity introduced through the dependence of the flame area upon flame position gradient through a term with the same form, $\sqrt{1+\beta^2\left(\partial\zeta/\partial r\right)^2}$, see Eqs. (30) and (33). In both of these cases, the nonlinearity is purely geometric in origin and is introduced by the relationship between the instantaneous flame front normal and flame position gradient. The third nonlinearity is due to the flow forcing itself, and is due to the dependence of the disturbance velocity at the flame front upon the flame position, $u(\zeta,t)$.

The fact that the first two sources of nonlinearity are identical can be used to write the final expressions for the flame area, Eqs. (30) and (33), in a revealing form. By substituting Eq. (13) into Eqs. (30) and (33), the term $\sqrt{\left(1+\beta^2\left(\partial\zeta/\partial r\right)^2\right)/\left(1+\beta^2\right)}$ which appears in both the area integrals can be written as:

$$\sqrt{\frac{1+\beta^2\left(\frac{\partial\zeta}{\partial r}\right)^2}{1+\beta^2}}=u(\zeta,t)-\frac{\partial\zeta}{\partial t} \qquad (39)$$

Thus, *the explicit form of the nonlinearity disappears*. Nonlinearities in flame front dynamics are included in the $\partial\zeta/\partial t$ term (note that the flow forcing nonlinearities also effect $\partial\zeta/\partial t$, as shown in Eq. (13)), while those due to the flow forcing nonlinearity noted above are included in the $u(\zeta,t)$ term. Based upon Eq. (39), the following

observations can be made regarding the effects of various parameters upon nonlinearity in the flame's response to flow perturbations.

Strouhal Number: At low Strouhal numbers, *St*, the unsteady term in Eq. (39) is negligible. Moreover, the ζ dependence of the velocity field, $u(\zeta,t)$, is weak, at least for the velocity fields considered here. Thus, the flame area's velocity response remains linear for low Strouhal numbers, as *St* is the dimensionless ratio of the flame response time to perturbation period. This point shows that the flame's *nonlinear area response is an intrinsically dynamic phenomenon; its quasi-steady response is linear*.

Flow Uniformity: Nonlinearities in the $u(\zeta,t)$ term are directly due to non-uniformity in flow disturbances. Thus, the contribution of this term to flame area nonlinearities is suppressed in the $\eta \to 0$ limit.

Boundary conditions: If the flame remains anchored at the attachment point, as it is in this study, then $\partial\zeta / \partial t$ is identically zero at this point for all time. As such, the flame area perturbations in the vicinity of the attachment point (where $\zeta \approx 0 \Rightarrow u \approx u(0,t)$) exhibit a linear dependence upon velocity amplitude. Nonlinearities only arise at points of the flame that are spatially removed from the attachment point. As such, the axisymmetric conical flame exhibits a more linear response than the axisymmetric wedge flame for comparable values of ε, since most and very little, respectively, of the flame area is concentrated near the attachment point. This discussion also shows the potential coupling between the flame kinematic and flame holding sources of nonlinearity.

Flame Aspect Ratio: The flame dynamics tend to linearity when $\beta >> 1$; i.e., when the flame is very long. This can be seen by noting that the left side of Eq. (13) becomes linear in this case: $\sqrt{1+\beta^2\left(\partial\zeta/\partial r\right)^2} = \pm\beta\,\partial\zeta/\partial r$. As such, the flame dynamics is approximately described by the equation $\frac{\partial\zeta}{\partial t} \pm \frac{\partial\zeta}{\partial r} = u(\zeta,t)$. In this case, the flame dynamics are linear, although the flow forcing term need not be. This discussion shows that β is an important nonlinearity parameter for this problem; i.e., the flame's area response can be anticipated to exhibit a linear dependence upon the perturbation velocity for much larger ε values at large β values.

Next, we derive an expression for the lowest order nonlinear correction to the flame area-velocity transfer function by determining the response of a flame to a disturbance with an arbitrary phase velocity. Stretch effects are not included here, but retained in the computations. Returning to the perturbation expansion for the flame position in Eq. (21), the following equations describe the dynamics of the second and third order correction terms, ζ_2 and ζ_3:

$$\frac{\partial\zeta_2}{\partial t} - \alpha\frac{\partial\zeta_2}{\partial r} + \frac{\alpha(1-\alpha)}{2}\left(\frac{\partial\zeta_1}{\partial r}\right)^2 + \zeta_1 KSt\ \ Sin[St\{K(1-r)-t\}] = 0$$

$$\frac{\partial\zeta_3}{\partial t} - \alpha\frac{\partial\zeta_3}{\partial r} + \frac{\alpha^2(1-\alpha)}{2}\left(\frac{\partial\zeta_1}{\partial r}\right)^3 + \alpha(1-\alpha)\left(\frac{\partial\zeta_1}{\partial r}\right)\left(\frac{\partial\zeta_2}{\partial r}\right) + \frac{\zeta_1^2 K^2 St^2}{2}\ \ Cos[St\{K(1-r)-t\}] + \zeta_2 KSt\ Sin[St\{K(1-r)-t\}] = 0 \qquad (40)$$

The solution of Eq. (40), subject to the boundary condition in Eq. (14), is given in Appendix C. In the ensuing discussion, we focus upon the total heat release response. Defining the conical flame area-velocity transfer

function at the fundamental frequency as $G_{c,\omega_o} = \dfrac{A_c'(\omega_o)/A_{c,o}}{u'(\omega_o)/u_o}$ yields:

$$G_{c,\omega_o} = G_{c,Lin} + \varepsilon^2 \left(\frac{\tilde{A}_{c,\omega_o}\ e^{i K\alpha St_2}}{8\ K\alpha^3\ (K\alpha-1)^5 St_2^2} + \frac{\tilde{B}_{c,\omega_o}\ e^{i St_2}}{8\ \alpha^2\ (K\alpha-1)^5 St_2^2} + \right.$$
$$\left. \frac{\tilde{C}_{c,\omega_o}\ K\ (\alpha-1)\ e^{i(2-K\alpha)St_2}}{8\ (K\alpha-2)^3\ (K\alpha-1)^5 St_2^2} + \frac{\tilde{D}_{c,\omega_o}\ K^2 e^{i(2K\alpha-1)St_2}}{8\ (2K\alpha-1)^2\ (K\alpha-1)^5 St_2^2} + \frac{\tilde{E}_{c,\omega_o}}{2K\alpha^3(K\alpha-2)^3(2K\alpha-1)^2\ St_2^2} \right)$$

(41)

where $G_{c,Lin}$ refers to the linear transfer function, Eq. (31) with σ^*=0. The coefficients $\tilde{A}_{c,\omega o}$ - $\tilde{E}_{c,\omega o}$ in this expression are defined in Appendix C.

Similarly, the wedge flame area transfer function is:

$$G_{w,\omega_o} = G_{w,Lin} + \varepsilon^2 \left(\frac{\tilde{A}_{w,\omega_o}\ e^{i K\alpha St_2}}{8\ K\alpha^3\ (K\alpha-1)^5 St_2^2} + \frac{\tilde{B}_{w,\omega_o}\ e^{i St_2}}{8\ \alpha^2\ (K\alpha-1)^5 St_2^2} + \right.$$
$$\left. \frac{\tilde{C}_{w,\omega_o}\ K\ (\alpha-1)\ e^{i(2-K\alpha)St_2}}{8\ (K\alpha-2)^3\ (K\alpha-1)^5 St_2^2} + \frac{\tilde{D}_{w,\omega_o}\ K^2 e^{i(2K\alpha-1)St_2}}{8\ (2K\alpha-1)^2\ (K\alpha-1)^5 St_2^2} + \frac{\tilde{E}_{w,\omega_o}}{2K\alpha^3(K\alpha-2)^3(2K\alpha-1)^2\ St_2^2} \right) \quad (42)$$

The coefficients $\tilde{A}_{w,\omega o}$ - $\tilde{E}_{w,\omega o}$ in Eq. (42) are defined in Appendix C.

The conical transfer functions evaluated using Eq. (41) are compared with numerical simulations (details of the numerical approach are given in Section 0) for a representative case in Figure 46. Although not shown, comparable results are obtained for wedge flames using Eq. (42). Non-linearity is enhanced as the velocity amplitude or the Strouhal number increases. As expected, the perturbation analysis is accurate at higher velocity amplitude when the Strouhal number is low.

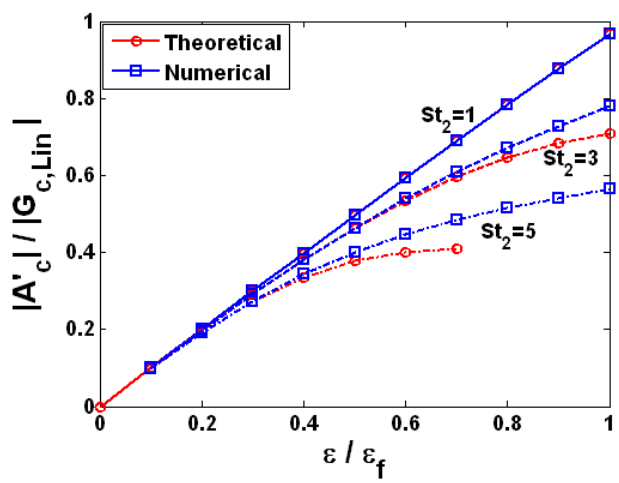

Figure 46. Dependence of flame area fluctuations upon disturbance velocity amplitude for axisymmetric conical flames at η=1

Note that, in the absence of stretch, the linear component of the transfer function in Eq. (41) and (42) is

described by only two parameters; i.e. $G_{Lin} = G(St_2, \eta)$. For the general nonlinear case, the gain G is also dependent on ε and β; i.e. , $G = G(St, K, \varepsilon, \beta)$. Also, as can be seen from the contribution of the non-linear terms to the transfer function in Eqs. (41) and (42), two new characteristic time scales arise which are represented by the non-dimensional terms: $(2-K\alpha)St_2 = 2St_2 - St_c$ and $(2K\alpha-1)St_2 = 2St_c - St_2$. As discussed in the previous section, the linear transfer function can be explicitly decomposed into contributions from boundary conditions and flow forcing non-uniformities. The boundary conditions and flow non-uniformities give rise to the characteristic times represented by the terms containing St_2 and St_c, respectively. When the analysis is extended to the non-linear regime, the same conclusions can be reached regarding the origin of the time scales represented by the terms St_2 and St_c (the terms with the coefficients $\tilde{B}_{\omega_o}$ and $\tilde{A}_{\omega_o}$ in Eqs. (41) and (42)). In addition, the time scale represented by the terms $(2K\alpha-1)St_2$ and $(2-K\alpha)St_2$ arises as a result of the nonlinear interaction between these two sources of flame disturbance. Hence, to the order of approximation considered here, the nonlinear characteristics of the flame dynamics are controlled by the superposition of the flame disturbances represented by the terms: St_2, St_c, $2St_2-St_c$ and $2St_c-St_2$.

It is worth considering two limits: $K\rightarrow 0$ and $\eta = K\alpha \rightarrow 1$. In both the limiting cases, albeit for different reasons, there is a single characteristic time scale represented by the term St_2. Recall from the prior discussion that the flame dynamics in the uniform velocity case (K=0) are exclusively controlled by the boundary condition. In this case, the transfer function expressions reduce to:

$$\lim_{K\rightarrow 0} G_{c,\omega_o} = \frac{2\left(1 - e^{i\,St_2} + iSt_2\right)}{St_2^{\,2}} - \varepsilon^2\left(1-\alpha\right)\left(\frac{6\alpha + iSt_2 + 2i\alpha St_2 + e^{i\,St_2}\left(-6\alpha - iSt_2 + 4i\alpha St_2 + \left(\alpha - 1\right)St_2^2\right)}{4St_2^2\alpha^2}\right)$$

(43)

$$\lim_{K\rightarrow 0} G_{w,\omega_o} = \frac{2\left(-1 + e^{i\,St_2}\left(1 - iSt_2\right)\right)}{St_2^2} - \varepsilon^2\left(1-\alpha\right)\left(\frac{6\alpha\left(-1 + e^{i\,St_2} - iSt_2 e^{i\,St_2}\right) - 3\alpha St_2^2 e^{i\,St_2} + i\left(\alpha - 1\right)St_2^3 e^{i\,St_2}}{4St_2^2\alpha^2}\right)$$

(44)

Note that in the limit of long flames ($\alpha\rightarrow 1$), the non-linear contribution to the transfer function disappears for both conical and wedge flames. This result was anticipated in the discussion in the beginning of this section.

The limit of $K\alpha\rightarrow 1$, corresponds to exact coincidence of flame front and flow disturbance velocity leading to a case wherein all the previously discussed dimensionless time scales, $(2-K\alpha)St_2$, $(2K\alpha-1)St_2$ and $K\alpha St_2$, reduce to a single one represented by the term St_2. Figure 47 shows the variation of the non-linear part of the transfer function for wedge flames as a function of the Strouhal number when $K\alpha\rightarrow 1$ for different values of α. Expectedly, for low Strouhal numbers ($St\rightarrow 0$), the contribution from the non-linearities goes to zero. The presence of a single characteristic frequency St_2 implies the absence of any destructive interference effect leading to a monotonic increase in the nonlinear contribution with increasing Strouhal number. Moreover, the contribution to the gain is substantially enhanced as the flame gets shorter (i.e. lower values of α) consistent with the *Flame Aspect Ratio* argument in the introduction of this section.

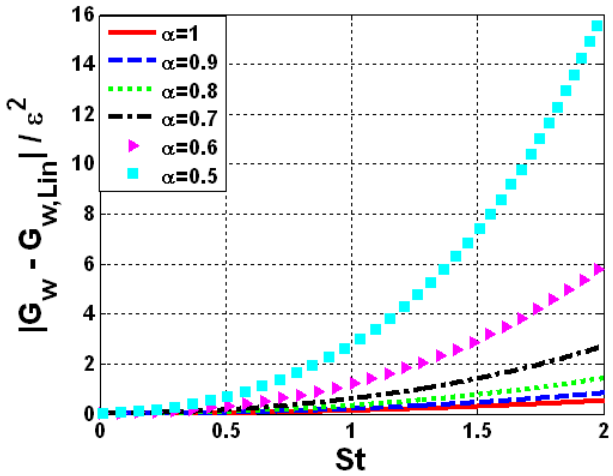

Figure 47. Dependence of non-linear part of the transfer function for axisymmetric wedge flames at η=1

Hence the presence of a single characteristic time scale, for the uniform velocity (K=0) and the $\eta=K\alpha\rightarrow 1$ case, causes the nonlinear contribution to monotonically increase with increasing Strouhal number and/or decreasing flame aspect ratio. As discussed further below, *it is only for these two cases that the non-linearities always lead to a reduction in the magnitude of the total transfer function*. These conclusions are valid even at higher velocity amplitudes as shown by numerical simulations in Figure 48-Figure 51 which plot the St_2 dependence of the gain and phase of the nonlinear transfer function upon St_2 at several η values. The gain transfer functions are normalized by their linear values, G/G_{Lin}. Results are shown for two convective wave speeds, η=0 and η=1, but the same β=1 value. Thus, these results allow for a convenient comparison of the effects of nonlinearities from boundary conditions alone, and the combined effect of boundary conditions and flow disturbance non-uniformity. Consider the gain curves first, Figure 48 and Figure 50. As predicted earlier, the response tends to its linear value in all cases at low St_2. In the η=0 case, nonlinear effects are more apparent at high St_2. For the wedge flame in Figure 50 the response is considerably nonlinear even at moderate values of Strouhal number. The enhanced nonlinear response of wedge over cone flames is explained by the *Boundary Conditions* argument discussed earlier.

Turning to the η=1 case, note the substantial reduction in flame area relative to its linear value; i.e., there is a substantial degree of gain saturation. Although plotted in a different form, the resulting gain curves look quite similar to the qualitative plot of $H_n(A)$ in **Figure 29**. In agreement with the *Strouhal Number* argument discussed earlier, the degree of nonlinearity increases with St_2. As shown in Figure 48 and Figure 50, the gain for the conical and wedge flames decreases by about 60% and 70% respectively (at $\varepsilon=\varepsilon_f$ in the St_2= 20 and η= 1 case). In contrast, the gain never drops below 5% of its linear value for conical flames and 35% of its linear value for wedge flames in the η=0 case. Moreover, unlike the η=0 case, the phase of the area response for both the conical and wedge flames exhibits a strong amplitude dependence, as shown in Figure 49 and Figure 51 respectively. These results indicate the extent to which flow non-uniformities can significantly modify the nonlinear flame response.

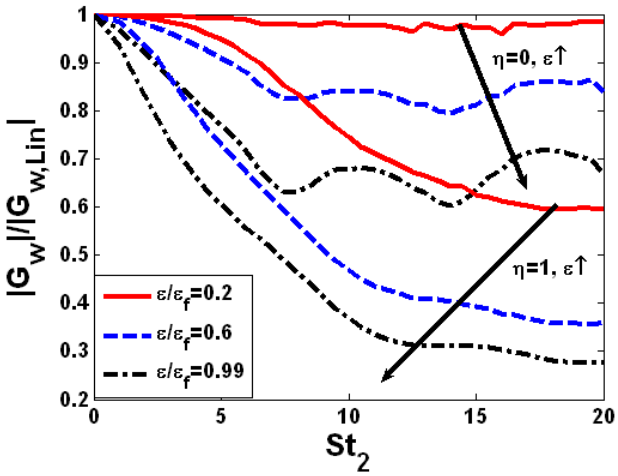

Figure 48. **Strouhal number dependence of the ratio of the magnitude of the flame area-velocity transfer function to its linear value for the axisymmetric wedge flame, β=1, σ^*=0.005**

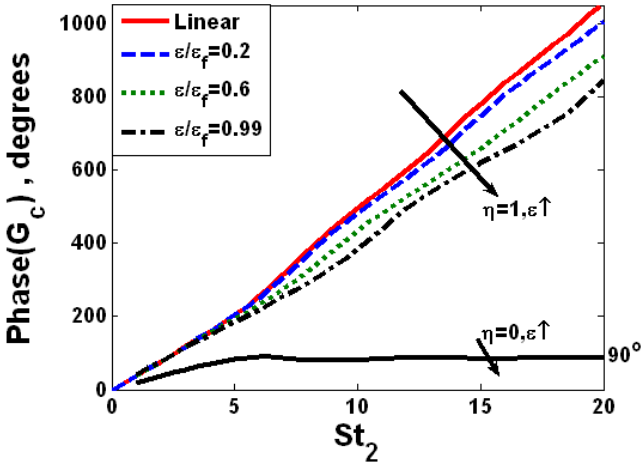

Figure 49. **Strouhal number dependence of the phase of the flame area-velocity transfer function for the axisymmetric conical flame, β=1, σ^*=0.005**

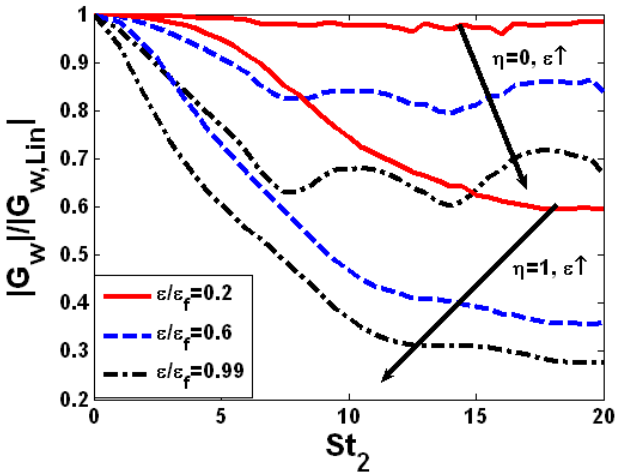

Figure 50. Strouhal number dependence of the ratio of the magnitude of the flame area-velocity transfer function to its linear value for the axisymmetric wedge flame, β=1, σ*=0.005

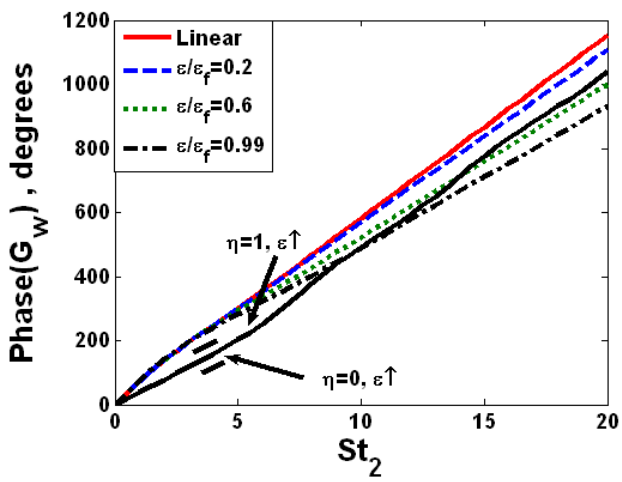

Figure 51. Strouhal number dependence of the phase of the flame area-velocity transfer function for the axisymmetric wedge flame, β=1 , σ*=0.005

In the more general case of $\eta \neq 0$, 1, the nonlinear flame dynamics is controlled by the superposition of flame disturbances with the four different characteristic time scales discussed earlier. In contrast to the above results, interactions between the boundary condition and flow forcing non-uniformity solutions causes a non-monotonic variation in the transfer function gain with disturbance amplitude. To illustrate, Figure 52 shows the flame response for a wedge flame when η=2 (i.e. α=0.8 and disturbances are traveling at $0.4u_o$). Note that the gain results are not normalized by their linear value here. The gain result indicates that in the $5<St_2<8$ range, the nonlinear transfer function actually *exceeds* its linear value. This result can be understood by noting that this behavior occurs in the vicinity of the regions where the linear transfer function achieves a minimum. At these St_2 values, the contributions from the boundary conditions and the flow forcing terms destructively interfere, leading to low linear gains. As the velocity amplitude is increased, nonlinearities cause the gain due to both the boundary conditions and the flow

forcing terms to decrease. However, since the relative "ages" of the two disturbances are unequal, the discussion in the context of Figure 32 shows that the magnitude of their gain reductions is different. Since the individual gain decreases by different amounts, the total gain does not go to zero at the St_2 value at which the linear gain is zero, but actually shifts to a higher St_2 value in the ε=0.2ε_f case. At higher disturbance levels, the two terms never exactly cancel and the gain does not go to zero. Rather, there is a monotonic decrease in the gain of the transfer function with increase in velocity amplitude. Analogous behavior also occurs in conical flames, although less dramatically.

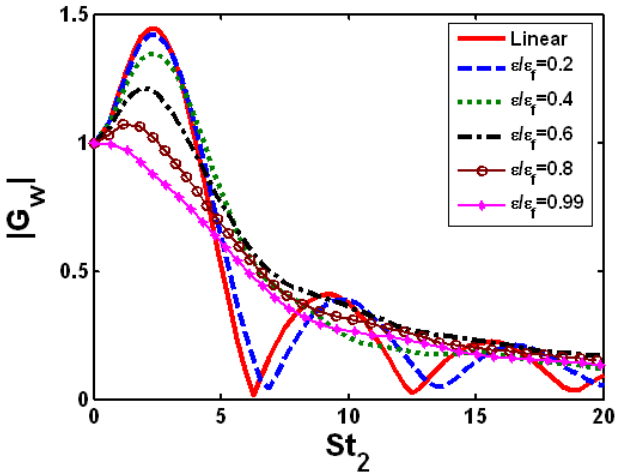

Figure 52. Strouhal number dependence of the magnitude of the flame area-velocity transfer function for the axisymmetric wedge flame, α=0.8,K=2.5, σ*=0.005

These predictions can be compared to related measurements on wedge flames, where the phase speed of the disturbances was half the mean flow speed40. They obtained measurements at four forcing amplitudes ε~0.05-0.2 and β~5.6. Interestingly, they found both increases and decreases in the transfer function gain with changes in disturbance amplitude, depending upon Strouhal number. Their results are reproduced in Figure 53. The transfer functions plotted here equals the ratio of the fluctuating CH^* emission intensity to the velocity disturbance amplitude slightly above the burner exit. Note the strong similarities between their measurement and the predictions from Figure 52. In the $2<St_2<5$ regions where the transfer function exceeds unity, the nonlinear gain monotonically decreases with disturbance amplitude. In the $5<St_2<8$ range, the nonlinear transfer function first increases with disturbance amplitude, then decreases. This trend is completely consistent with the predictions of this study.

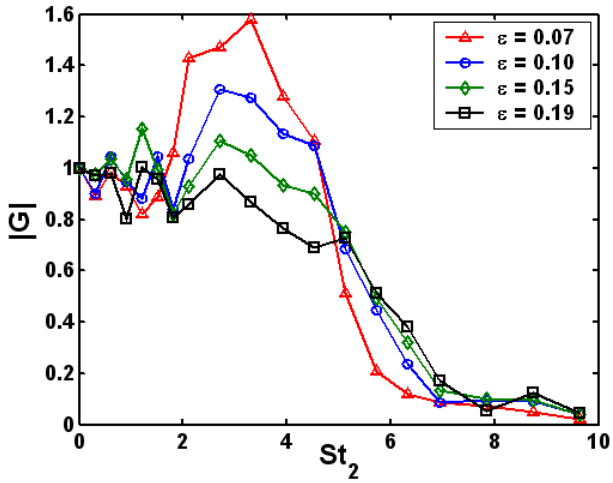

Figure 53. Experimentally measured gain for an inverted conical flame for a mean velocity u_o= 2.05 m/s, ϕ = 0.92. Data reproduced from Durox *et al.*[40].

Using the perturbation analysis, the non-linear contribution to the wedge flame transfer function is shown for varying phase speeds at unity Strouhal number in Figure 54. *It shows that the non-linear contribution is higher when the phase speed of the disturbances is less than the mean flow speed (i.e. K>1)* in comparison to the case wherein 0<*K*<1. This is a direct manifestation of the *Flow Uniformity* argument discussed earlier. As noted earlier, non-linearity decreases with increase in the flame aspect ratio (i.e. increasing α), consistent with the *Flame Aspect Ratio* argument. Note that this result is valid for a low Strouhal number case wherein the interaction between the disturbances of different characteristic time scales is weak. The results for a general case are shown in Figure 55 which plots the gain dependence upon η at different St_2 values for conical flames. For the St_2=1 case, the linear gain does not go to zero for both the conical and wedge flames (not shown here). Hence, the gain monotonically decreases with increasing disturbance amplitude. However in the St_2 = 5 and 10 cases, the linear gain goes to zero at certain η values. It is only in the vicinity of this η that we find the corresponding increase in nonlinear flame transfer function. This result prominently highlights the sensitivity of the flame response to the phase speed of the disturbances. Moreover, it demonstrates how the competition between boundary condition and flow nonuniformity terms can significantly impact the flame response behavior.

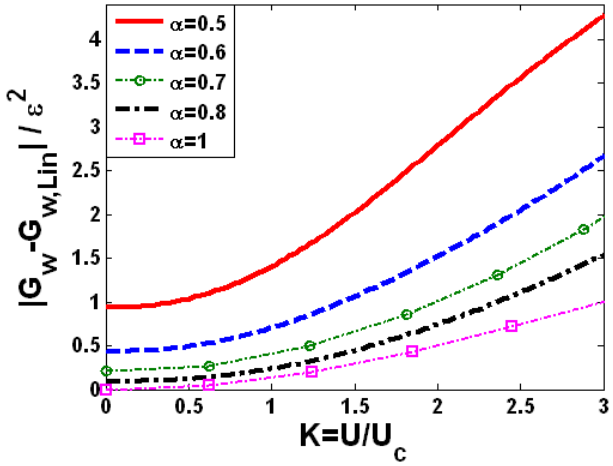

Figure 54. Dependence of non-linear part of the transfer function on the phase speed of the disturbances (K) for axisymmetric wedge flames, St=1, σ=0

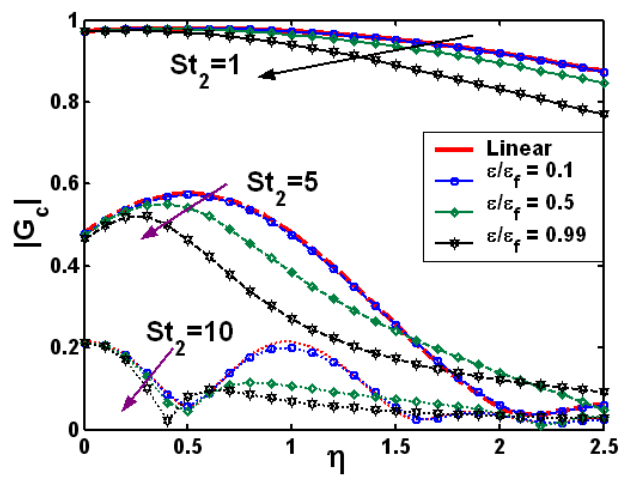

Figure 55. Dependence of the magnitude of the flame area-velocity transfer function on η for the axisymmetric conical flame for different Strouhal numbers, β=8, σ=0. Arrow points towards increasing velocity amplitude ε.

These results have important applications in the type of bifurcations which may be observed in unstable combustors. In situations where the gain curves resemble that qualitatively shown in **Figure 29**, only supercritical bifurcations will occur and a single stable limit cycle amplitude, ε_{LC} is possible. In situations where the gain exceeds, then is less than, the linear gain (see Figure 52); i.e., it exhibits an inflection point, multiple stable solutions for the instability amplitude may exist, and sub-critical bifurcations are possible. This can be seen from Figure 56, which plots the dependence of $A_w'/A_{w,o}$ vs ε for St_2=6.25, K=2.5, α=0.8. This curve represents $H(\varepsilon)$. A hypothetical damping curve, $D(\varepsilon)$ is also drawn in Figure 56. Note the 3 intersection points, two of which are stable, ε=0 and $\varepsilon=\varepsilon_{LC}$, and one of which is unstable, $\varepsilon=\varepsilon_T$. In this case two equally valid solutions are possible, ε=0 or $\varepsilon=\varepsilon_{LC}$, which one the system is actually at depends upon initial conditions. Such a system will manifest characteristics such as hysteresis and triggering (i.e., the destabilization of a linearly stable system by a sufficiently large disturbance[81]).

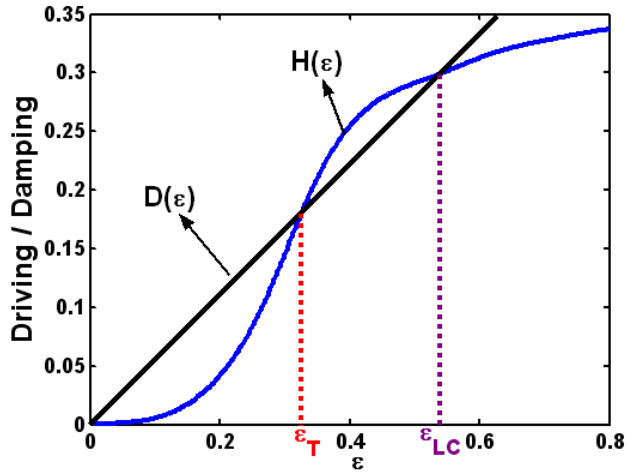

Figure 56. Dependence of acoustic driving, H(ε) (where H(ε) is equated for this example to $A_w'/A_{w,o}$) and damping, D(ε), processes upon velocity amplitude ε, for wedge flames at St_2=6.25 with K=2, α =0.8, σ^*=0.005

The regions in parameter space (defined by *K* and St_2), where the nonlinear transfer function has an inflection point can be determined from the analytical solutions and is shown in Figure 57. The plot shown is for a wedge flame with an aspect ratio α=0.8, ε=0.1. *Note that an inflection point is more likely to exist when the phase speed of the disturbances is less than the mean flow speed (K>1) in comparison to the case wherein 0<K<1.* This is in accordance with the earlier discussion which showed that non-linear effects were enhanced for *K*>1. *For the uniform velocity, K=0, and the Kα=1 case, the presence of a single characteristic time scale causes a monotonic decrease in the transfer function with increasing velocity amplitude, implying that it will always exhibit a supercritical type of bifurcation (see* Figure 57*).*

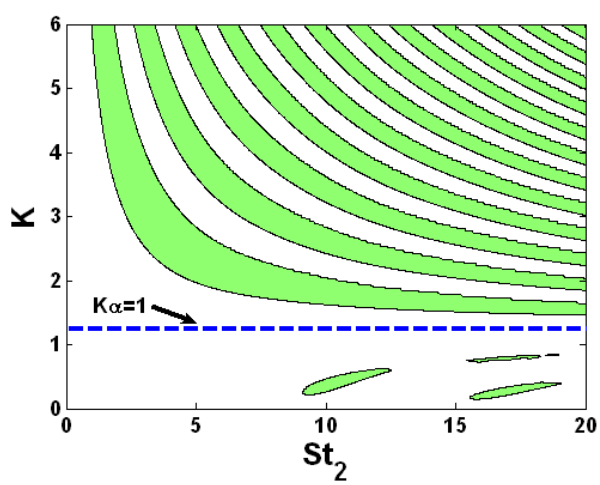

Figure 57. Qualitative representation of regions where nonlinear flame transfer exceeds (shaded) or is less than (white) linear transfer function, α=0.8,ε=0.1, σ=0

We next consider the combined effects of nonlinearity and stretch. Figure 58 plots the amplitude dependence of the wedge flame transfer function for cases with and without stretch. While the qualitative

dependence of the transfer function upon amplitude remains the same with or without stretch, note that the combined effects of stretch and nonlinearity draw the two curves closer together with increasing ε. Thus, stretch effects upon the *global* flame area dynamics become *less* significant with increasing amplitude. The reason for this is the following: stretch is most significant in the high curvature, concave regions of the flame with respect to the reactants. As the perturbation amplitudes increases, these regions become highly cusped, and have a progressively smaller influence upon the total flame area. Thus, while the effect of stretch becomes more significant in certain regions of the flame with increasing ε, these regions of the flame also occupy a progressively smaller fraction of its total flame area.

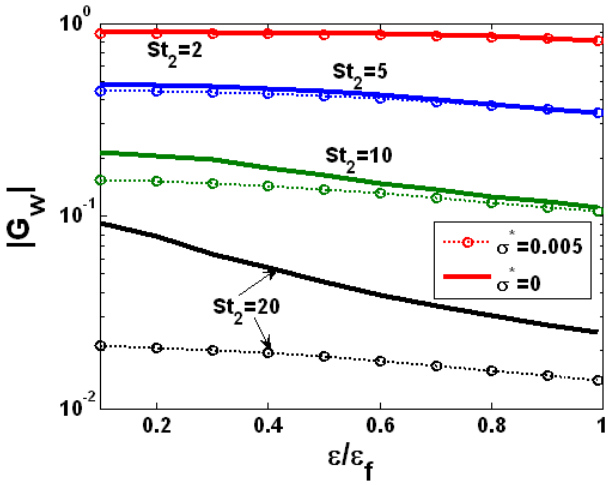

Figure 58. Amplitude dependence of the magnitude of the flame area-velocity transfer function for an axisymmetric wedge flame: Comparison between models with and without Stretch effects. β=1, K=0

Finally, a brief comment on the response of the flame at the first harmonic of the forcing frequency. The previous discussion about the role played by the phase speed of the disturbances, Strouhal number and the flame aspect ratio upon nonlinearity in flame response is directly applicable here as well, since excitation of harmonics is another manifestation of nonlinearity. These results are not discussed here, but analytical expressions for the flame response at $\omega = 2\omega_o$ are provided in Appendix E.

Flame Length

The changes in the average flame characteristics (such as its location and length) with increasing disturbance amplitude have been reported in many experimental studies[27,42,45]. These changes are indicative of non-linear effects and have potentially important effects upon the flame transfer function phase because they change the time delay between when a disturbance is created and when it encounters the flame. For example, Bellows *et al.*[45] observed a monotonic increase in the velocity-CH* chemiluminescence transfer function phase with disturbance amplitude and suggested it was due to the corresponding increase in flame length (however, note that this study was for a swirling flame).

Using the perturbation analysis, the average flame length normalized by its steady state value, L_f can be

expressed as:

$$L_{avg} = 1+\varepsilon^2 \frac{\left(\alpha\left(K\alpha-1\right)(-1+\alpha+2K\alpha+(\alpha-3)K^2\alpha^2)St_2+2\alpha^3K\left(K-1\right)Sin[\left(K\alpha-1\right)St_2]\right)}{4\alpha^3(K\alpha-1)^3St_2} \quad (45)$$

As shown in Eq. (45), the contribution of the non-linearities to the flame length is a function of the velocity amplitude, flame aspect ratio, Strouhal number and the phase speed of disturbances i.e. $L_{avg}=L_{avg}(\varepsilon,\alpha,St,K)$. In order to highlight the effect of each of these terms, we consider various limits. In the limit of $K\alpha\rightarrow1$, Eq. (45) reduces to:

$$\lim_{K\alpha->1} L_{avg} = 1-\varepsilon^2\frac{(1-\alpha)(3+St_2^{\,2})}{12\alpha^2} \quad (46)$$

Eq. (46) predicts that L_f decreases with increasing Strouhal number (note that α<1) and velocity amplitude. Moreover this effect is amplified with decreasing flame aspect ratio, α.

In the limit of low Strouhal numbers, the average flame length can be expressed as:

$$\lim_{St->0} L_{avg} = 1-\varepsilon^2\frac{(1-\alpha)}{4\alpha^2} \quad (47)$$

Equation (47) indicates that, at low Strouhal numbers, the average flame length is a function of only ε and flame aspect ratio and *is independent of the phase speed of the disturbances (K) and frequency (St)*. Moreover if the flame is long (i.e. $\alpha\rightarrow1$), the effect of non-linearities disappear (see Eq. (47)) and the average flame length remains constant.

Another interesting feature is that for uniform disturbance velocity (K=0), or when the phase speed and mean flow speed are equal (K=1), *the average flame length is independent of the Strouhal number*, i.e.:

$$\lim_{K->0} L_{avg} = \lim_{K->1} L_{avg} = \lim_{St->0} L_{avg} \quad (48)$$

Next we consider the case of long flames (i.e. $\alpha\rightarrow1$). For this case, the flame length expression can be simplified to:

$$\lim_{\alpha->1} L_{avg} = 1-\varepsilon^2 K\left(\frac{\left(K-1\right)St_2-Sin[\left(K-1\right)St_2]}{2(K-1)^2St_2}\right) \quad (49)$$

Figure 59 plots the normalized flame length (Lavg) as a function of the phase speeds at different Strouhal numbers when $\alpha\rightarrow1$. It can be inferred from Figure 59 that the flame length decreases with increased disturbance amplitudes when the phase speed of the disturbances is smaller than the mean flow speed (K>1). This conclusion is true in general (i.e. is not limited to long flames only) as shown in Figure 60, which plots the contours of constant Lavg as a function of St2 and K for a range of α. For a given flame aspect ratio α, the arrows in Figure 60 indicate regions in the parametric space (defined by St2 and K) wherein the average flame length increases. Note that it is only for fast phase speed disturbances (0<K<1) that the flame length actually increases for certain values of St2 (see Figure 60) and this effect is amplified at higher α. When the phase speed of the disturbances is smaller than the mean flow speed (K>1), the average flame length always decreases.

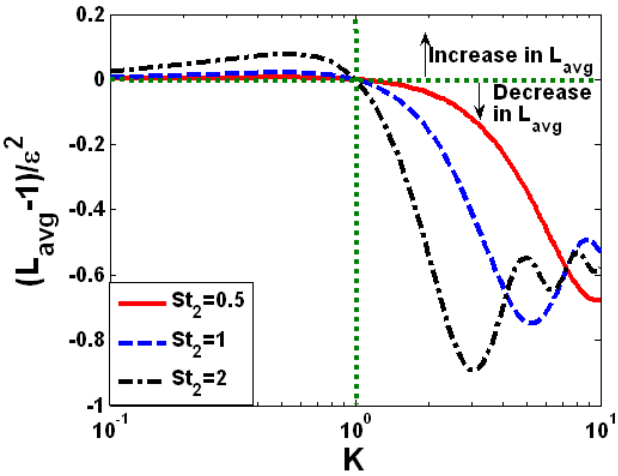

Figure 59. Dependence of flame area fluctuations upon disturbance velocity amplitude for axisymmetric conical flames at η=1

The discussion above is in conformity with experiments reported by Durox et al.[27], wherein a reduction in the average flame length was observed with increased velocity amplitudes. Their experiments were conducted at a frequency of 1000 Hz, α ~0.5 and a range of velocity amplitudes. The present analysis indicates (see Figure 60 which shows that α~0.57 is the lowest value for which the flame length may increase) that for α~0.5, the average flame length always decreases irrespective of the frequency and phase speed of the disturbances. Similar agreement is obtained with the results of Bourehla & Baillot[25] under conditions where their measured velocity profiles are similar to those considered here. These conditions correspond to K~1-2, St2~8-12 and K=0, St2>23.

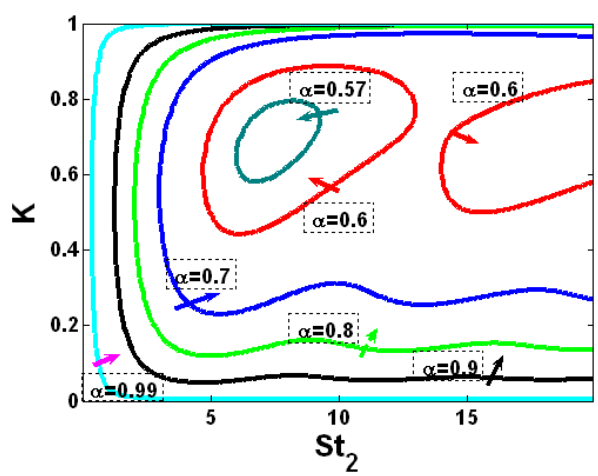

Figure 60. Contours of constant L_{avg} (average flame length) as a function of K and St_2 for different values of α. Arrows indicate regions of increasing flame length.

8. Nonlinear Interactions in Gas Turbine Combustors

Nonlinear Heat-Release/Linear Acoustic Interactions

It has been argued that the dynamics of an unstable combustor are dominated by heat release nonlinearities which interact with linear acoustic processes. Because the combustor is a reverberant acoustic environment, it possesses a number of acoustic modes. Many researchers (e.g., see Culick[14], Zinn & Powell[12], Culick & Yang[82]) have shown that the dynamics of each mode may be described by an oscillator equation of the form:

$$\ddot{\eta}_i + 2\zeta\omega_o\dot{\eta}_i + \omega_o^2\eta_i = F(\eta_i, \dot{\eta}_i) + E(t) \tag{1}$$

where ω_o is the linear natural frequency, ζ is the damping coefficient, $F(\eta_i, \dot{\eta}_i)$ refers to the system nonlinearities, and $E(t)$ is the external excitation.

Before presenting further data, we briefly summarize several classical results for a nonlinear system that is externally forced at a frequency near resonance, i.e. $E(t) = A\cos\omega t$, where $\omega \approx \omega_o$. Consider first nonlinearities in "stiffness", i.e. $F = F(\eta_i)$. It is well known that such a system exhibits "bending" in the frequency response curve, such as shown in Figure 61(a). As such, the frequency of the maximum oscillator response shifts with frequency; e.g., increases/decreases in the effective stiffness with increasing disturbance amplitude cause the curve to bend toward higher/lower frequencies. As the frequency of the large amplitude excitation is swept, the response of the nonlinear system follows one branch of the curves to a bifurcation point where the system jumps discontinuously to the other branch. This manifests itself in hysteresis in frequency and amplitude where this jump occurs.

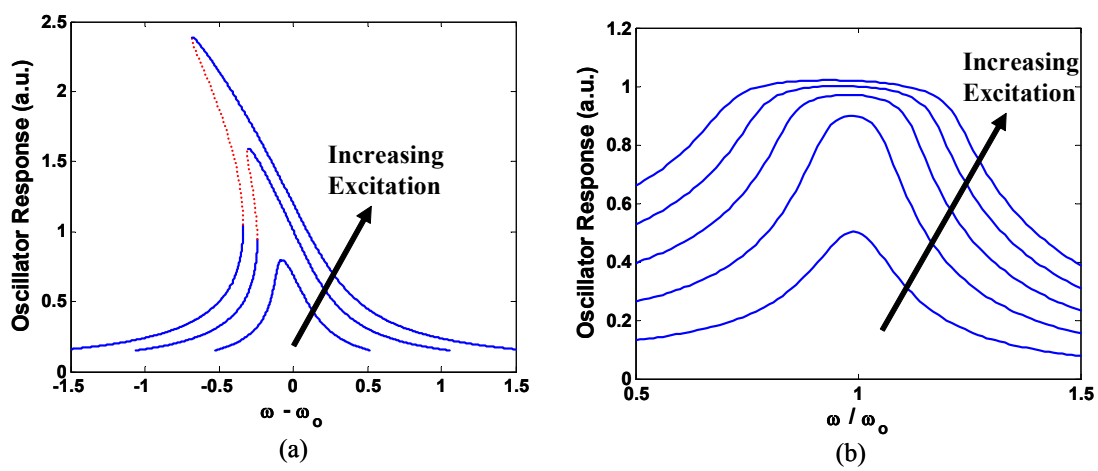

Figure 61: Frequency–response curves at several excitation amplitudes for a second order oscillator with nonlinearities in (a) stiffness and (b) damping

Consider next nonlinearities in damping, i.e., $F=F(\dot{\eta}_i)$. The peak amplitude of this type of nonlinear

system will not increase proportionally to the disturbance amplitude. If damping grows nonlinearly, amplitude saturation causes a flattening of the response curve around the resonant frequency. Therefore, the maximum response is distributed over a broader range of frequencies than a linear damped oscillator, e.g, see the example in Figure 61(b). Further details are in Nayfeh & Mook[83].

Both types of behavior illustrated in Figure 61 were observed in our data. These data were obtained in the gas turbine combustor simulator discussed previously and shown in Figure 2. A representative result is shown in Figure 62(a), which plots the frequency dependence of the pressure amplitude at a large disturbance amplitude. This data is obtained by keeping the driving amplitude constant and varying the driving frequency. Figure 62(a) shows that the pressure amplitude response bends over to the left indicative of a "softening" spring. Second, the pressure amplitude jumps in the 285-290 Hz range, with hysteresis in the frequency value where this jump occurs. Third, the peak response of the pressure remains relatively constant over a range of driving frequencies, indicating nonlinearity in damping. This behavior can be seen more clearly in Figure 62(b), which plots similar results at several driving amplitudes. The plot clearly shows the progressive trend away from a classical forced-resonant linear system at low disturbance amplitudes to a response that bends over toward lower frequencies and "flattens" in response.

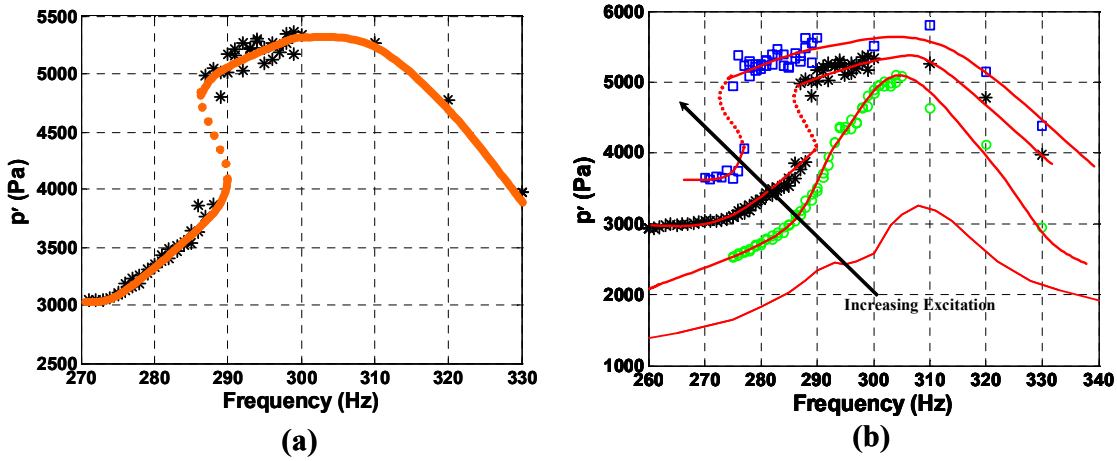

Figure 62: Dependence of pressure amplitude upon frequency at (a) a single disturbance amplitude, 2.8A and (b) several disturbance amplitudes, 1.8-3.0A (ϕ = 0.95).

If the forcing frequency is held constant, while the excitation amplitude is varied, a similar bifurcation occurs as shown in Figure 63. Figure 63 shows that the pressure oscillation data have a similar dependence on frequency. As noted above, the linear natural frequency is approximately 310 Hz. At 280 Hz there is a noticeable jump in the pressure response. At frequencies below and above 310 Hz, the pressure response exhibits a "quadratic" and "square root" dependence upon excitation amplitude.

Referring back to Figure 9(a), note the clear saturation of the CH*-velocity transfer function at 280 Hz. Referring to the specific data points, note that a clear "gap" in the velocity amplitude is observed at a point coinciding with that where saturation is observed. It should be noted that the driving levels were increased in a regular, stepwise fashion over the whole range of amplitudes. This jump in the velocity coincides with the jump in

pressure amplitude illustrated in Figure 64(a); i.e. the jump in pressure and velocity coincides with the point where the heat release response exhibits nonlinearity.

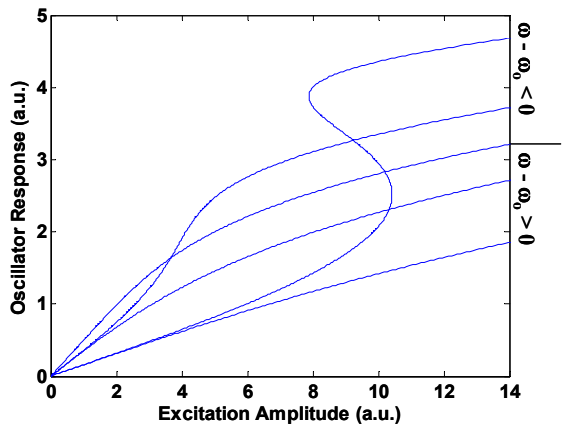

Figure 63: Excitation–response curves for softening spring oscillator at several excitation frequencies.

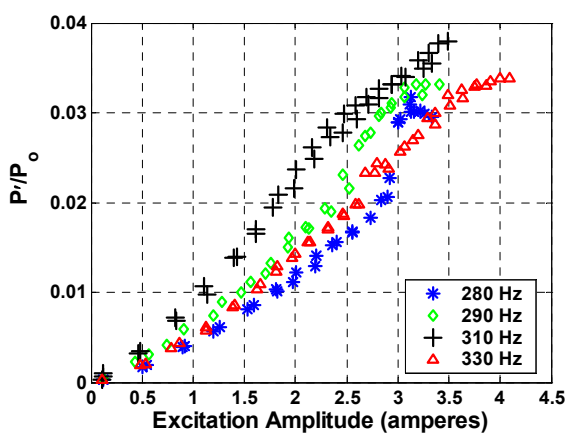

Figure 64: Dependence of pressure oscillation amplitude on excitation amplitude for varying driving frequencies (ϕ = 0.95)

A detailed study of this bifurcation and the associated hysteresis was performed in the 280-290 Hz frequency range. Figure 65 summarizes the amplitude-frequency parameter regions where single and multi-valued behaviors occur. Hysteresis occurs at driving amplitudes larger than about 2.6 Amperes (A) and extends all the way to 3.1A, where blowout occurred. The corresponding frequencies range from 292 to 276 Hz at the low and high amplitude driving ranges.

Figure 66 provides a further visualization of this bifurcation by quantifying the CH* - pressure transfer function as a function of frequency at fixed driving amplitudes (we illustrate the CH*-pressure relationship here due to the fact that the uncertainty values are smaller than those for the velocity measurements; the trends, however, are identical). The figure plots these dependencies at both a low and high driving amplitude of 2.4 and 3.0 Amperes.

For low driving amplitudes, the transfer function exhibits a smooth, monotonically decreasing dependence upon frequency, as would be anticipated by the results shown in Figure 5. However, when the driving amplitude is increased beyond the cutoff point of 2.6 amperes, the transfer function changes markedly. This result is illustrated in Figure 66(b) where a clear jump in the transfer function values occurs (~14% for the CH*-pressure transfer function value) for the 3.0 Amperes driving case. Note that the frequency dependence of the transfer function is much "flatter" in the high driving case. The frequency where the jump occurs depends upon the direction of frequency change (increasing/decreasing) with a total hysteresis of about 3 Hz. Note that the transfer function itself does not exhibit a discontinuous dependence upon amplitude; rather the pressure amplitude exhibits a discontinuity in the region where the transfer function changes. This transfer function change is responsible for the bifurcation in pressure amplitude. As such, it is not possible to measure a monotonic change in the transfer function at these frequencies because of the discontinuous jumps that occur in acoustic amplitude. A similar result is found in the corresponding phase relationships.

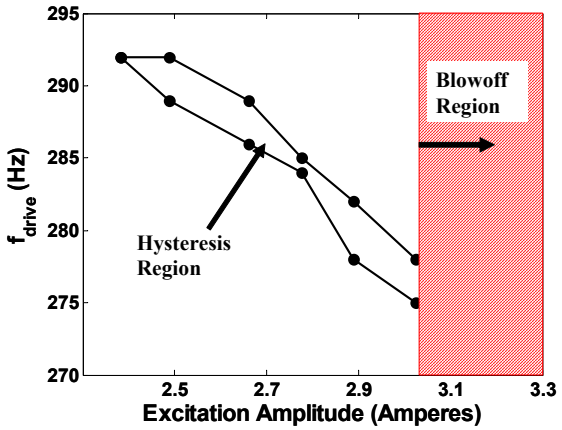

Figure 65: Amplitude-frequency ranges over which the chemiluminescence-pressure-velocity relationship exhibited single and multi-valued behavior

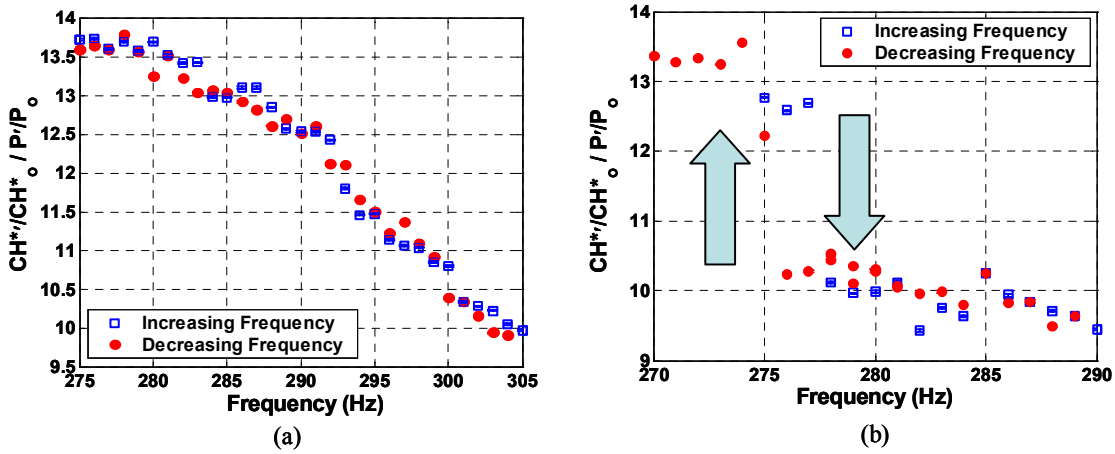

Figure 66: Dependence of pressure-CH* transfer function on driving frequency (excitation amplitude = 2.4 amperes (a), excitation amplitude = 3.0 amperes (b), ϕ = 0.95)

NONLINEAR FREQUENCY INTERACTIONS

This section describes an ongoing investigation into the nonlinear interactions between natural acoustic modes and driven oscillations in a lean, premixed swirl stabilized combustor. This work is motivated by the fact that combustion instabilities continue to hinder gas turbine combustor development and operation[84-88]. These instabilities occur when the unsteady combustion process couples with one or more of the combustor's acoustic modes, resulting in self-excited oscillations. The objective of this work is to improve the understanding of the nonlinear dynamics associated with these oscillations. Improved understanding of the nonlinear combustion process is needed to further development of methods to predict limit cycle amplitudes.

In addition to improved understanding of nonlinear combustor dynamics, this work also has implications on active instability control[89]. In many cases, active control is implemented by closed loop control of fuel flow oscillations that are out of phase with the instability. However, the use of open loop, non-resonant frequency, forcing has also been demonstrated by many researchers[90-94]. The present study provides some insight into the underlying combustor processes which impact the effectiveness of these open loop control strategies.

This work is motivated by a previous study focusing on the nonlinear flame transfer function between driven pressure oscillations and heat release fluctuations in a high-pressure, gas turbine combustor simulator**Error! Bookmark not defined.**. During these tests, nonlinear interactions between a natural combustor mode and those due to acoustic forcing were observed. Specifically, the amplitude of the unstable mode monotonically decreased, before it disappeared completely, with increases in amplitude of the driven mode. This behavior was attributed to frequency-locking, a well-known nonlinear oscillator phenomenon. Frequency locking is due to nonlinear interactions between oscillations that are closely spaced in frequency. It is manifested as a decrease in amplitude of the self-excited or natural mode oscillations as the amplitude of the driven oscillations increases.

Lieuwen & Neumeier[23] performed a limited investigation of the effect of forcing frequency upon this frequency locking phenomenon by considering two forcing frequencies. Their data did not indicate a significant change in the entrainment amplitude at the two driving frequencies. This was contrary to expectation, however, as we had anticipated the entrainment amplitude to be proportional to the frequency spacing between the forced and self-excited frequency. These considerations motivated this study, which more systematically investigates these frequency spacing effects on entrainment amplitude.

Experiments were performed on a 100 KW swirl stabilized burner, which was previously shown schematically in Figure 14. The reported tests were performed at a nominally unstable condition, with an instability frequency of 461 Hz. The forcing frequencies investigated ranged from 150 to 430 Hz and for all cases, the overall acoustic power was substantially reduced by the presence of acoustic forcing.

A typical result is shown in Figure 67. The nominal amplitude of the 461 Hz instability is about 1.5-2% of the mean pressure in the combustor. In this particular case, forced oscillations are excited at 200 Hz over a range of amplitudes. As shown in Figure 67, increased forcing levels cause the 461 Hz mode amplitude to monotonically decrease, and to nearly disappear when the driving amplitude reaches approximately 25% of the mean velocity. Thus, the entrainment amplitude for this case is u'/u_o=0.25. It is also seen that the harmonic associated with the instability at 922 Hz disappears. Also shown in the figure is the overall RMS amplitude in the 0-1000 Hz range, which has a minimum near the entrainment amplitude and then begins to rise with increased forcing levels, due to the growing amplitude of the imposed oscillations. The acoustic power in the spectra between 0 and 1000 Hz is reduced by 90% for this case.

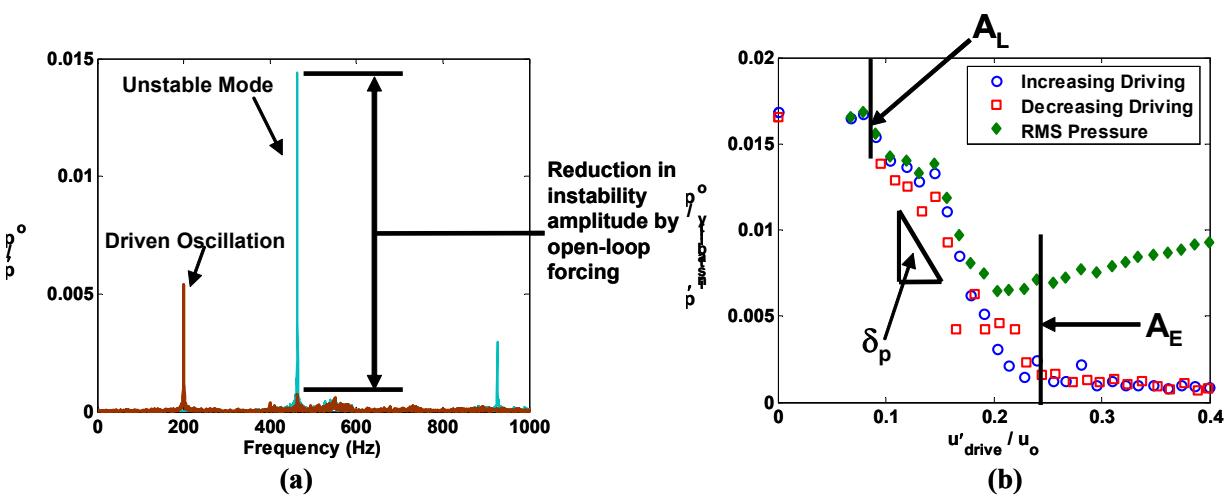

Figure 67: (a) Spectrum of combustor pressure at two driving amplitudes showing decrease in combustor instability mode as driving amplitude is increased (instability frequency = 461 Hz, driving frequency = 200 Hz). (b) Dependence of instability amplitude on driving velocity amplitude at 200 Hz driving frequency.

The typical dependence of the natural instability amplitude on the driving amplitude is shown in Figure

67(b). At the highest driving amplitudes, the instability has essentially disappeared at the cost of the increase in amplitude of the driven pressure. There are several basic features of the instability amplitude dependence upon driving amplitude that can be discerned from Figure 67(b). First, the instability amplitude is independent of the forcing amplitude for some amplitude range before decreasing; we have referred to the driving amplitude at which this decrease begins as A_L. Second, the instability amplitude decreases with some slope, δ_p, for further driving amplitude increases. Third, the instability amplitude essentially goes to zero, or to near zero values above some driving amplitude, referred to here as the entrainment amplitude, A_e. For example, in Figure 67(b) the entrainment amplitude is ~25% of the mean velocity at the premixer exit. Finally, the dependence of the unstable mode amplitude upon the driving amplitude exhibits some hysteresis. In this study, hysteresis occurred at only at select frequencies in the 150-430 range we have tested so far at this instability condition. No significant trend was found that was dependent on driving frequency. This hysteresis behavior is shown in Figure 68. Typical hysteresis levels are found to be between 3-5% of the mean velocity value.

These characteristics depend significantly upon driving frequency. We consider first the entrainment amplitude dependence upon driving frequency, which is plotted in Figure 69(a). The entrainment amplitude, A_E, grows as the forcing frequency is moved away from the instability frequency of 461 Hz, except very close to the instability (f_{drive} = 400-430 Hz). The trend in Figure 69 was expected although we do not have any specific theory our intuition was based upon. Figure 69 also reinforces the fact that the velocity oscillation amplitude in unstable combustors is a major controlling factor which affects the nonlinear combustion process. It should be noted that a different trend is observed if the perturbation pressure[§] (see Figure 69b), rather than velocity were used to quantify the forcing amplitude. This is due to the frequency dependence of the pressure-velocity relation. This result explains the confusion over this issue raised in our prior study, which used the perturbation pressure as a measure of disturbance amplitude.

[§] In this combustor, the entrainment pressure amplitude increases monotonically with decreasing frequency up to about 230 Hz. It then decreases for lower frequencies.

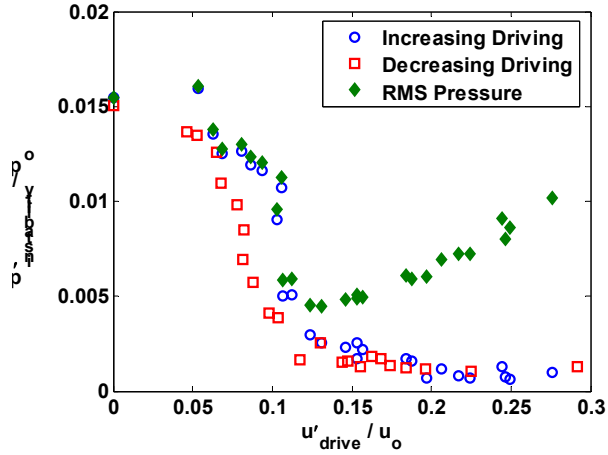

Figure 68: Dependence of instability amplitude on driving amplitude for driving frequency = 410 Hz (instability frequency = 461 Hz).

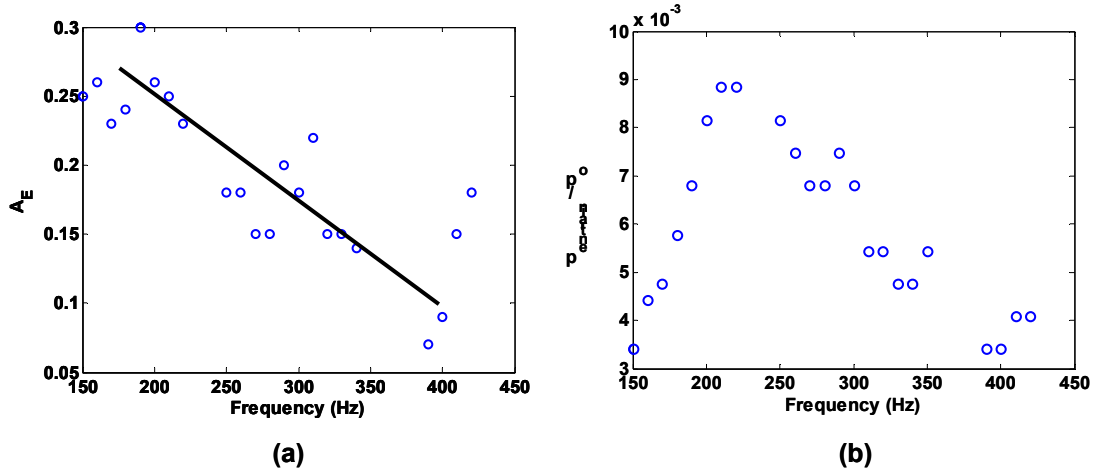

Figure 69: Dependence of (a) velocity entrainment amplitude, AE, and (b) corresponding pressure amplitude values upon driving frequency (instability frequency = 461 Hz).

We next consider the slope of the instability amplitude rolloff, δ_p, shown in Figure 70. In contrast to the entrainment amplitude, the instability rolloff has a complex dependence on frequency which is not understood. The highest slopes, and therefore the most rapid rolloff of the instability amplitude, occur at 250 and 400 Hz. Local minima are seen at 160 Hz and 310 Hz. Similarly, the parameter A_L's frequency dependence is shown in Figure 71. In general, A_L is found to be largest at frequencies which are far away from the instability and smallest at frequencies closer to the instability. The values of A_L range from u'/u_o= 0.02-0.10. At 240 Hz, this value decreases linearly from it maximum value, near where the instability rolloff hits its maximum, and flattens out after 310 Hz, where the instability rolloff hits a minimum. In general, the parameter A_L is seen to change values near local

minima and maxima in the instability rolloff value.

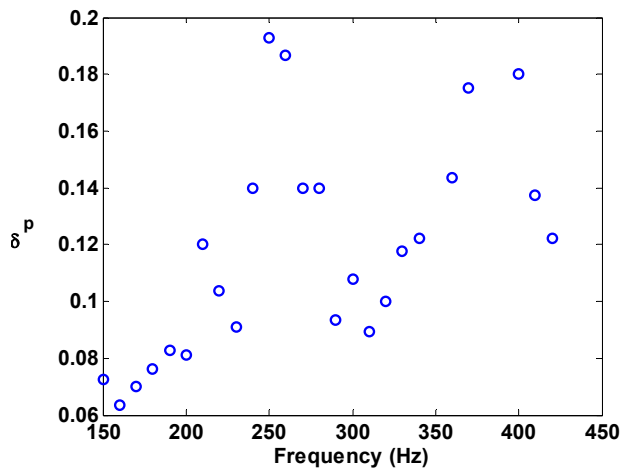

Figure 70: Dependence of instability rolloff, δp on driving frequency (instability frequency = 461 Hz)

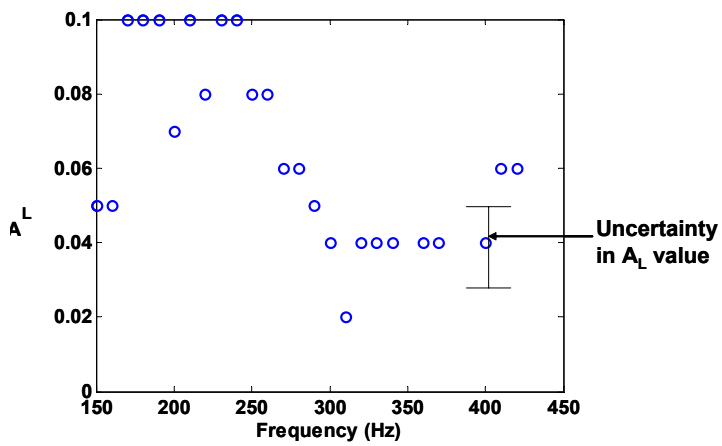

Figure 71: Dependence of AL parameter (velocity oscillation amplitude range which is independent of forcing) on driving frequency (instability frequency = 461 Hz)

As these results have direct implication on open loop forcing as an active control methodology, it is of interest to analyze the total acoustic power reduction in the 0-1000 Hz range where power is defined as:

$$Power = \int |p'|^2 df \qquad (1)$$

Figure 72 plots the frequency dependence of the maximum reduction in acoustic power due to open-loop forcing observed at each frequency over the whole forcing amplitude range. We have found that we can reduce the acoustic power by at least 70% of its original value at optimized driving amplitudes at this operating condition. The best results occur at frequencies where the entrainment *pressure* amplitude is smallest and the worst results are where the entrainment pressure amplitude is highest, as may be expected. For larger entrainment amplitudes, more

acoustic power is being added into the system at the point of entrainment. Therefore, the reduction in instability amplitude comes at the cost of larger driven amplitudes.

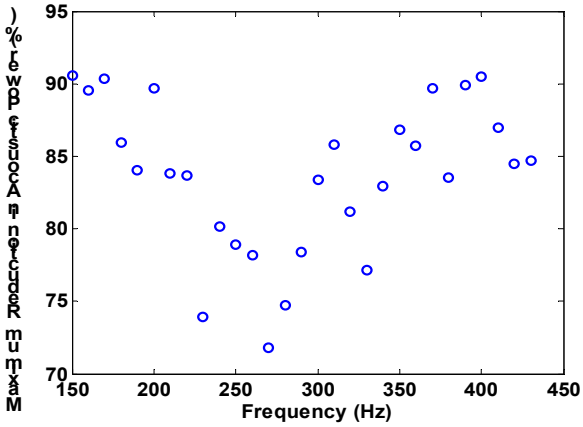

Figure 72: Dependence of maximum acoustic power reduction on driving frequency (instability frequency = 461 Hz).

9. Active Control of Combustion Instabilities

This note describes an experimental investigation of active control of instabilities in a high pressure, liquid fueled combustor. Active control has been widely demonstrated as a technically viable method for suppressing combustion instabilities (e.g., see Refs. [95, 96,97]). For example, it has been shown that instabilities can be suppressed by measuring the pressure or heat release in the combustor, suitably phase shifting and amplifying the measured signal, then driving a secondary fuel injector with this signal. While significant progress has been made, a number of problems are still in need of investigation. Active controllers are often found to work well at certain operating conditions, while their effectiveness is significantly reduced at others. Results in the literature quantifying the degree of suppression of the instability amplitude vary substantially, from factors of under 2 to over 50. Experiments have shown that the same methodology performs very differently on different combustors and at different operating conditions. Thus, although at this point it is well established that *some degree* of suppression of combustion instabilities is possible, more research is needed to understand the dynamics of actively controlled combustors and the factors that limit control effectiveness.

A variety of factors determine the impact of an active control system upon an instability. First, the uncontrolled combustor dynamics play a significant role on the effect active control has upon the oscillations. Control effectiveness will clearly depend upon such issues as instability amplitude, instability frequency and background noise levels. In addition, nonlinear characteristics of the combustor, such as hysteresis and saturation, play important roles in control effectiveness.

Next, the issues of observability and controllability are significant; i.e., the extent to which the state of the system can be sensed and affected by actuation, respectively. Observability does not appear to be a significant issue limiting control effectiveness, unless, for example, a pressure sensor is located in a node. Controllability issues are more significant due to the challenges of actuating coherent fuel pulses at high frequencies. In many cases, liquid fuel is actuated using on-off, pulse-width modulations which causes spectral broadening of the excited heat release oscillations about the carrier wave frequency. This broadening is partially responsible for the peak splitting phenomenon discussed by Cohen and Banaszuk [1]. Cohen and Banaszuk [1] and Lee and Santavicca [24] have also emphasized the importance of fuel placement and/or mixedness upon control effectiveness.

Turning to the controller itself, the poorly understood nonlinear and stochastic nature of crucial combustor processes renders classical model based approaches difficult for implementation on actual hardware. Prior experimental controllers have either filtered the pressure/ chemiluminescence signal about the instability frequency (which must be known *a priori*) or used observers to extract the amplitude and frequency of the instability. The optimal control phase is typically determined using either off-line testing or adaptive schemes.

Probably one of the most significant factors determining the effectiveness of the combined controller-actuation system is the overall controller time delay. As might be expected, several studies have shown that the combined effects of background noise and time delays substantially impair control effectiveness. For example, it has been observed that the combustor appears to “run away” from the control when sufficient control actuation is

applied; e.g., the phase of the oscillations rapidly moves around or even seems to jump [96]. In addition, time delays are partially responsible for the peak-splitting phenomenon encountered with high controller gains [1]. Many of these factors are reviewed in detail by Cohen and Banaszuk [1].

The above discussion emphasized a number of issues in need of investigation to better understand the factors determining control effectiveness. In this note, we focus on the effects of uncontrolled combustor dynamics and, in particular, the effect of the level to which the controller attempts to drive the instability amplitude toward. A systematic study of these effects requires capabilities to alter the nature of the investigated combustor. In order to accomplish this *in a known and controllable manner*, self-excited oscillations were created by feeding back the measured pressure through a phase-shifter to an air actuator mounted in the rear of the combustor. This air actuator drove oscillations by pulsing a high pressure air flow. The linear and nonlinear characteristics of the self-excited feedback loop were then varied by changing the gain and phase of the pressure signal that was used to drive the air actuator. Control of the induced oscillations was achieved by pulsing the combustor fuel flow rate with a second fuel actuator.

Facility and Instrumentation

Experiments were performed in the gas turbine combustor shown schematically in Figure 2 operating at 4.4 atm, 430 K inlet air temperature at an overall equivalence ratio of 0.9. The combustor operated under liquid fuel which was supplied through the fuel injectors outlined in Figure 3, which has not been used in our nonlinear flame response studies. As the facility has been described previously in Ref. [28] for gaseous operation and in Ref. [98] for liquid fueled operation, only its key features are summarized here. The fuel is injected into the swirling air stream at the end of a conical bluff body, where it is atomized by the shearing action of the high velocity, swirling air. Oscillations were driven in the combustor with a magneto-restrictive air actuator described earlier. The air actuator modulates a constant secondary supply of air that is introduced near the combustor exit by periodically varying the degree of constriction of a valve. In order to generate self-excited oscillations, whose linear and nonlinear characteristics could be varied in a *known and systematic manner*, the pressure signal was fed back to this air actuator through a gain and phase shifter; see Figure 73. Note that simply driving oscillations with a function generator does not emulate the critical features of combustion instabilities because the phase and amplitude of the oscillations remains fixed, regardless of the control action.

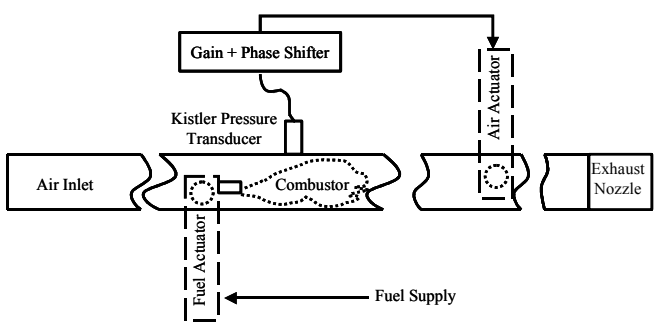

Figure 73. Block diagram of gain/phase shifter between pressure transducer and air actuator used to generate self-excited oscillations.

The combustor was operated under conditions under which it was nominally stable. By setting an appropriate gain and phase shift, the air actuator excited oscillations. The linear and nonlinear (e.g., saturation amplitude) characteristics of the oscillations could be systematically varied by changing the gain/saturation amplitude of this feedback loop. The amplitude dependence of the acoustic forcing provided by the air actuator closely resembles the saturating characteristic of heat release oscillations[16,99].

Fuel for active control is modulated using a second magnetostrictive fuel actuator. A controller is used to maintain the mean flow rate constant around the specified value, regardless of amplitude of the oscillating component.

Control Implementation

The details of the frequency observer and controller used here are described elsewhere [98], so only the key features are summarized here. The main components in the active controller are a pressure transducer, software comprising a real-time observer, a controller, and the magnetostrictive fuel actuator. During operation, the sensor continuously measures the combustor pressure which is bandpass filtered between 20 and 1000 Hz, digitized, and read in by the computer. The digitized signal is processed by the observer that extracts the amplitudes and frequencies of the largest amplitude combustor modes. The observed amplitude is compared to the desired amplitude and the difference between the two serves as the input to a PI type controller. The "desired" amplitude is the value which the controller attempts to drive the actual amplitude toward *and in general, is not zero*. It is important to note that if the desired amplitude is set to a level that the controller cannot satisfy, particularly zero, the integrator will increase until saturation. As shown in prior studies [1] and below, in such a case, the resulting large control signal that is applied to the fuel injector may result in reduced controller performance. However, if the desired amplitude is set to an attainable value, the integrator stabilizes at some non-saturated value and automatically set the control amplitude to the necessary value. The phase of the control signal relative to the measured pressure signal is set manually by determining the optimum value that maximizes instability amplitude suppression.

Results

As noted earlier, instabilities were generated by feeding back the pressure signal with a phase shift to the air actuator. A typical result showing the combustor pressure during a 0.31 psi, 92 Hz instability with and without control is shown in Figure 74. In these data, control was turned on at the indicated point, with the desired amplitude set to 0.18 psi. Once actuated, the control requires a little over one second to bring the amplitude to the desired level, due to integrator windup. Note that the control successfully brings the instability amplitude to the desired level; however, there is substantial "breathing" in amplitude of the oscillatory pressure both before and after control is implemented. At any instant in time, the actual instability amplitude varies about the indicated value by about 0.06 psi. The indicated fluctuating pressure amplitude was determined by low pass filtering the envelope of the pressure oscillations at 0.5 Hz.

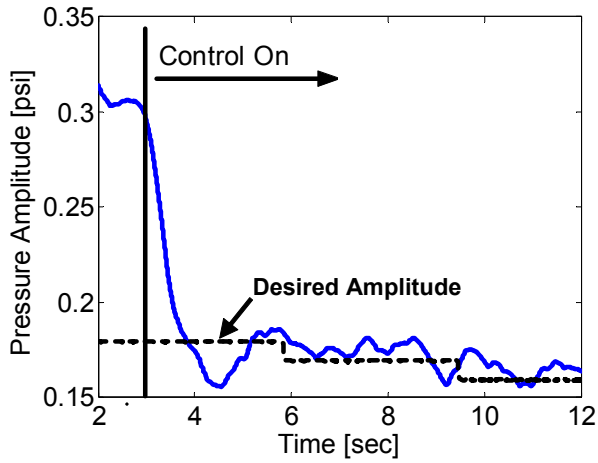

Figure 74 Low pass filtered time dependence of oscillatory combustor pressure amplitude with and without control.

Effect of Desired Amplitude

In order to elucidate the factors limiting control effectiveness, a series of experiments were performed where the "desired" instability amplitude was successively reduced. Recall that the "desired" amplitude refers to the amplitude the controller attempts to drive the oscillation level to, even if it is capable of reducing the instability amplitude further. Control performance was investigated as the desired amplitude level was monotonically decreased from 100 - 0% of its nominal value without control. Results quantifying the dependence of the actual oscillation amplitude upon the "desired" level are shown in Figure 75. The figure indicates that the nominal instability amplitude (without control) is 0.35 psi. Once the desired amplitude level drops below this value, the controller turns on to reduce the instability amplitude. The figure shows that the controller precisely drives the average instability amplitude to the desired levels down to about 0.14 psi, a 60% reduction in amplitude.

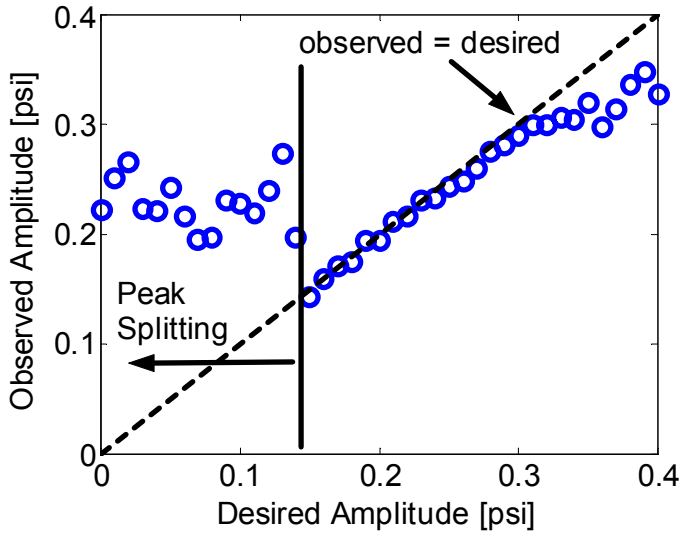

Figure 75. Dependence of mean and fluctuating instability amplitude upon desired level.

Returning to Figure 75, note the jump in instability amplitude for desired amplitude levels below 0.14 psi. This result clearly shows that *optimal control performance is not necessarily achieved by attempting to drive the instability amplitude to zero*. Rather, the best performance occurs at an intermediate value. This reduction in performance is due to imposing too large a gain on the system that introduces undesired dynamics in the combustor response. This can be seen from Figure 76 and Figure 77, which plot the Fourier transform of the combustor pressure at several desired amplitudes. Note the monotonic reduction in instability amplitudes at 92 Hz in Figure 75. Figure 76 and Figure 77 show that the 92 Hz oscillations are nearly absent and are replaced by two larger amplitude sidebands at 77 and 115 Hz. In this same region, the fuel injector command signal saturates.

This behavior is analogous to the "peak-splitting" phenomenon that has been previously explained by Cohen and Banaszuk [1]. The key processes responsible for this behavior is the fact that oscillations are excited over some spectral bandwidth centered about that of the instability frequency. If the controller phase is optimized to suppress oscillations at the center frequency, because of system time delays, they will necessarily not be optimized at higher and lower frequencies. In fact, the phase of the control at the excited sideband frequencies is 180º relative to the center frequency, resulting in the excitation of oscillations.

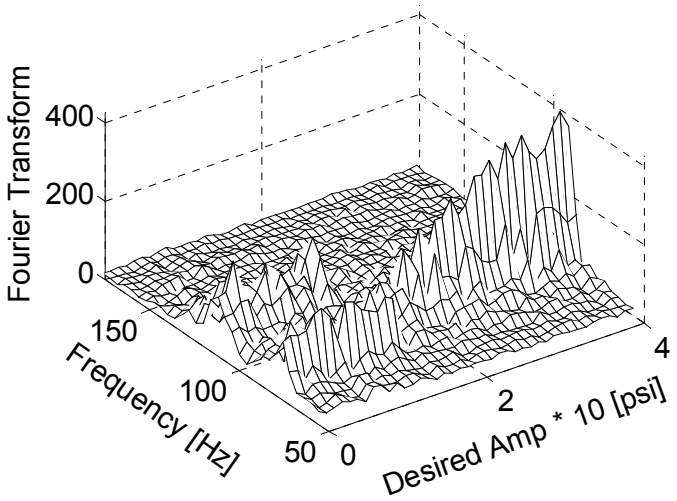

Figure 76. Fourier transform of combustor pressure at desired amplitude levels of 0-0.4 psi.

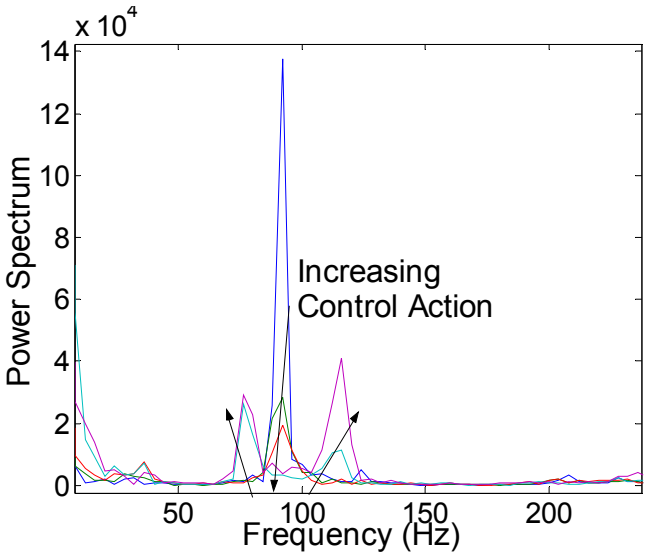

Figure 77. Fourier transform of combustor pressure at desired amplitude levels of 0.4, 0.2, 0.16, 0.14, and 0.13 psi (nominal instability amplitude = 0.35 psi).

Effect of Air Actuator Gain and Saturation

Control experiments were performed at two values of the gain between the unsteady pressure and the air actuator. The purpose of this experiment was to emulate the affects of different heat release dynamics (linear gain as well as saturation characteristics) and the resultant impact upon control effectiveness. As shown in Figure 78 the air actuator command signal and pressure amplitudes are linearly related at low amplitudes. At higher levels the air actuator amplitude driving signal is saturated, regardless of the pressure amplitude.

The effect of active control upon instability amplitude for these two air actuator gains is plotted in **Figure 79**. These data were taken by slowly sweeping the phase of the control signal relative to that of the pressure at a desired amplitude of zero. The horizontal line indicates the nominal instability amplitude. As expected, the instability amplitude is reinforced or damped, depending upon the phase. Comparing the two gain results, note the similarity and difference, respectively, in the amount the pressure amplitude is reinforced or damped. That is, the pressure amplitude is increased by nearly the same factor (two) in both gain results. The amplitude minima, however, are approximately 0.22 and 0.16 psi, a difference of 40% and a difference in reduction of 15%.

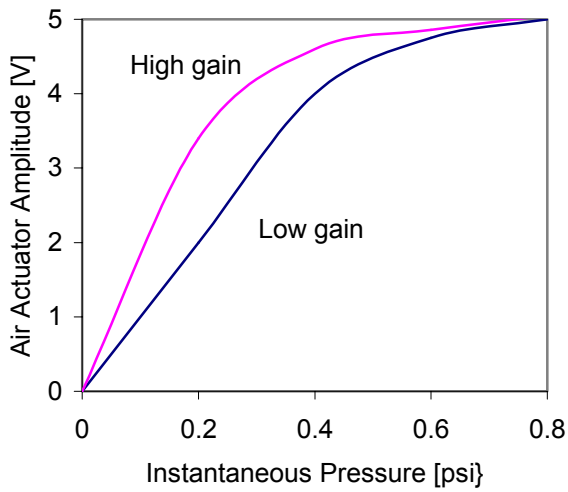

Figure 78 Instability driving characteristic visualized by plotting the dependence of the instantaneous air actuator driving signal upon pressure.

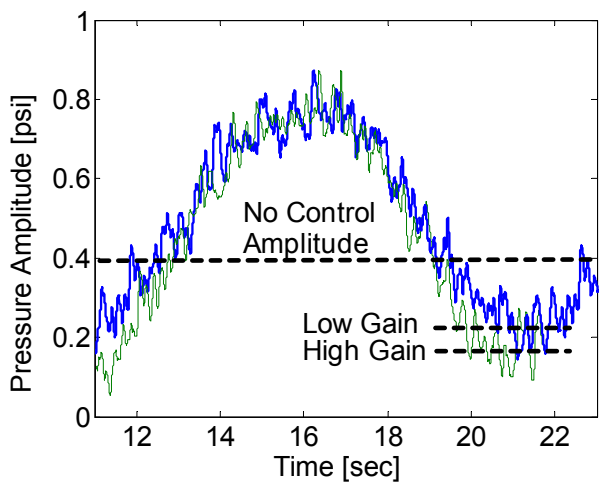

Figure 79. Dependence of instantaneous pressure amplitude upon time as phase of control signal is swept relative to that of the instability.

The same maximum amplitude is achieved because the air actuator driving command signal is saturated; i.e., there is no difference in driving characteristics above a pressure amplitude of about 0.6 psi. The difference in minima is apparently due to the effect that the combustor's nominal dynamics (i.e., without control) has upon its response to too large a gain of the fuel injector control signal, resulting in peak splitting. This over-gaining of the control signal is due to the fact that the desired amplitude was always set to zero. Analysis of the moving average of the Fourier transform shows the peak splitting phenomenon in the pressure over approximately 1/8 of the phase sweep cycle in the low gain case. In contrast, the peak splitting phenomenon just barely appears in the higher gain case, occurring only at the pressure minimum over about 1/32 of the phase sweep cycle.

10. CONCLUSIONS

This final report describes many important experimental and theoretical advances on the study of unstable gas turbine combustors. In particular, much emphasis was placed on the mechanisms which can control the limit cycle amplitudes of unstable combustors, as well as active control and interactions between natural and driven oscillations. The important conclusions from each aspect of this study are described below.

Nonlinear Flame Response – Gas Turbine Combustor Simulator

From these data, several conclusions can be drawn regarding the nonlinear response of the unsteady heat release to flow perturbations. The amplitude relationship between the pressure/velocity and heat release saturates at sufficiently high forcing levels at certain frequencies and equivalence ratios, but remains linear at others all the way to flame blowout. Also, substantial amplitude dependence of the CH* phase was found at all driving frequencies and equivalence ratios, clarifying the questions raised by Lieuwen & Neumeier[23]. These results suggest that heat release-acoustic nonlinearities in both gain and phase may play comparable roles in swirling, premixed combustors. While the measured flame transfer functions themselves are independent of the system's acoustics, a saddle-node bifurcation in pressure amplitude occurs around the natural frequency that is introduced by the nonlinear combustion process.

One of the key conclusions of this study is that nonlinear interactions between the flow forcing and parametric instability (possibly through its impact on the fluctuating flame position) may be responsible for saturation of the flame response. The presence of the parametric instability is manifested by the jump in amplitude of oscillations at half the driving frequency at certain disturbance amplitude values. This jump in subharmonic amplitude occurs at essentially the same value as that at which saturation occurs. Furthermore, subharmonic oscillations are always present in cases where saturation of the fundamental occurs. To our knowledge, this observation of the parametric instability is the first in a turbulent, swirl-stabilized flame.

In addition, however, there are other potential mechanisms which may also be present. These include local extinction of the flame and flame sheet kinematics. For example, increasing amplitudes of oscillation lead to increased flame strain which could cause local flame extinction events. Increased extinction could, in turn, result in decreased heat release response. This mechanism could be responsible for the decreasing mean chemiluminescence levels upon perturbation amplitude seen in some test cases. Additionally, flame sheet kinematics also may be important. While their significance was alluded to above in the context of the parametric flame instability (i.e., fluctuating flame position effects), they may play additional roles through nonlinear dependencies of flame area destruction with disturbance amplitude. For example, large amplitude corrugations of the flame may be consumed by flame propagation faster than small amplitude perturbations, as emphasized by Preetham and Lieuwen[100] based on theoretical considerations and very recently, by Balachandran *et al.*[26] , based on experimental imaging studies.

While it is not possible to conclusively determine the relative roles of all potential mechanisms of nonlinearity, we can eliminate some mechanisms which have been suggested as potentially significant:

Global" Extinction – This is the mechanism proposed by Dowling[16] and Poinsot *et al.*[19] which follows from the simple observation that the instantaneous heat release cannot go negative, thus limiting the chemiluminescence fluctuations to 100% of the mean value. Our data indicate saturation at substantially lower amplitudes, however, implying that this mechanism is not significant in this combustor.

Chemical Kinetics – Reaction rates depend upon pressure and temperature in a nonlinear manner. These nonlinearities will apparently become significant when the fluctuating pressure and temperature achieve amplitudes on the order of their mean values. This mechanism does not appear likely here, however, as nonlinearity occurs at p'/p_o values of ~2%.

Equivalence ratio oscillations – The nonlinear dependence of the equivalence ratio amplitude and heat release response discussed by Peracchio & Proscia[17] and Lieuwen[15] is not important here, as the fuel/air mixture had a constant composition. As such, though we cannot comment on the magnitude of these types of nonlinearities in situations where they are present, the data presented here indicate that other flame processes also cause nonlinearities in flame response.

Flame holding – The many data indicating a linear CH* response all the way to blowoff indicate that nonlinearities due to marginal flame holding are probably not important

Nonlinear Flame Response – Atmospheric Burner

From the results presented, we can make the following conclusions. First, substantial nonlinearities in the flame response to forced velocity oscillations have been shown. The phase between the flow oscillation and heat release is also seen to have substantial amplitude dependence. Various mechanisms appear to be important in different frequency and flowrate regimes. For instance, at low flow rates, the saturation amplitude of CH* can vary greatly with driving frequency and range from 25-100% of the mean value. In contrast, for higher flow rates, it is observed that the nonlinear amplitude of CH* is roughly independent of driving frequency. In addition, the shape of the transfer function can change markedly for different driving frequencies and flow rates. Therefore, there are a variety of behaviors which are present in a single combustor. Thus, one single theory is not adequate to describe the nonlinear dynamics of a forced or unstable combustor.

OH PLIF imaging of the flame was performed at two frequencies where two mechanisms potentially controlled the saturation amplitude of the global heat release from the flame. Two phenomena, vortex rollup and flame liftoff, are found to be the likely mechanisms which govern saturation of the flame transfer function from these images. The latter mechanism visibly changes the flame structure when comparing these results with line-of-sight images. Both mechanisms act to reduce the flame area.

No sub-harmonic flame response was observed in any of these studies, as opposed to the earlier study in the combustor simulator as mentioned above. This result is not understood, as it is well known that parametric flame instabilities occur at high forcing amplitudes, resulting in a subharmonic response. Future work will attempt to

reconcile these differing observations

Theoretical Nonlinear Flame Response

One of the key points made here is that the linear and nonlinear characteristics of the flame dynamics are controlled by the interaction between flame disturbances due to boundaries and flow non-uniformities. A constructive superposition of the two flame disturbance contributions can cause the flame to act as an "amplifier" at certain frequencies whereas a destructive superposition can cause the flame response to be identically zero. The theory also captures the effect of flame stretch and shows that it is responsible for the experimentally observed phenomenon of "filtering".

In the nonlinear regime, the flame response is critically dependent on whether the solution lies in a region of constructive or destructive interference of the flame disturbances. In regions of constructive interference, the nonlinear flame transfer function gain is always less than its linear value whereas in regions of destructive interference the nonlinear transfer function may exceed its linear value. These characteristics can cause the same combustor to exhibit sub-or supercritical type of bifurcation depending on the operating condition. The analysis shows that nonlinearity is enhanced and that there is a greater tendency for the nonlinear transfer function to have an inflection point when the phase speed of the disturbances is less than the mean flow speed. Moreover, the average flame length decreases with increasing perturbation amplitude for most conditions which is consistent with the available experimental data.

Several additional studies are motivated by this work. First is an analysis of the nonlinear flame response in cases where the flame is being simultaneously disturbed by deterministic harmonic fluctuations as well as random fluctuations. The latter fluctuations simulate the impact of background turbulent fluctuations. As such, the analysis would allow for a rudimentary comparison of the nonlinear dynamics of laminar and turbulent flames. Second there is a need to couple the flow field and flame dynamics so that the effect of gas expansion can be captured. This would introduce a new parameter into the results, the ratio T_b/T_u.

Nonlinear Interactions in Unstable Combustors

These results have implications of the type of bifurcations which may be observed in unstable combustors. This study clarifies a number of issues related to the nonlinear interactions between driven and natural unstable combustor modes but also raises new questions. It has been shown that the entrainment velocity amplitude monotonically grows with driving-instability frequency separation. We have found that the instability rolloff and velocity oscillation range which is independent of forcing amplitude both have complex dependencies on driving frequency. Changes in the parameter, A_L, are seen to accompany local minima and maxima in instability rolloff. Further work is being performed to analyze the effect on these parameters of driving frequencies greater than the instability frequency.

In addition, open loop forcing of the combustor, at frequencies different from the instability frequency, was

found to significantly reduce the acoustic power in the 0-1000 Hz range by as much as 90%. The performance of this open loop control scheme is dependent on the entrainment amplitude. The best results were obtained for frequencies which had the lowest entrainment pressure amplitudes, as might be expected.

The generality of this methodology is an open question, however, as we found some operating conditions where entrainment did not occur in the same fashion and the instability amplitude is marginally reduced. For example, in one situation, the addition of forcing caused a shift in instability frequency to a value 40 Hz higher than its unforced value (from 510 Hz to 550 Hz). For driving frequencies whose harmonics do not fall around this new frequency, this value is relatively constant. The acoustic power in the 0-1000 Hz range is only slight reduced (~20%) before increasing rapidly, unlike the conditions presented in this paper. An investigation on this behavior is also ongoing.

The theoretical study has further highlighted the importance of the interactions between the contributions from flame disturbances due to boundaries and flow non-uniformities. The present investigation extends the analytical solutions for the flame response from the linear to the non-linear regime.

Active Control Studies of Unstable Combustors

A variety of factors determine the impact of an active control system upon an instability. First, the uncontrolled combustor dynamics play a significant role on the effect active control has upon the oscillations. Control effectiveness will clearly depend upon such issues as instability amplitude, instability frequency and background noise levels. In addition, nonlinear characteristics of the combustor, such as hysteresis and saturation, play important roles in control effectiveness.

.

Appendix A

This section solves for the steady state flame shape $\zeta_o(r)$. The governing equation for the steady state case (see Eq (13)), is

$$\sqrt{\frac{1+\beta^2\zeta_{o,r}^2}{1+\beta^2}}\left(1-\frac{\sigma\beta\zeta_{o,rr}}{\left(1+\beta^2\zeta_{o,r}^2\right)^{\frac{3}{2}}}\right)=1 \quad (50)$$

Integrating Eq. (50) and applying the boundary condition for conical flames, Eq. (15), the exact implicit solution for $\zeta_o(r)$ can be expressed as:

$$\left(\frac{1+\zeta_{o,r}}{1-\zeta_{o,r}}\right)\left(\frac{\sqrt{1+\beta^2\zeta_{o,r}^2}+\sqrt{1+\beta^2}\ \zeta_{o,r}}{\sqrt{1+\beta^2\zeta_{o,r}^2}-\sqrt{1+\beta^2}\ \zeta_{o,r}}\right)=e^{\left(-\frac{2\beta\sqrt{1+\beta^2}}{\sigma}r-2\beta\, Tan^{-1}(\beta\zeta_{o,r})\right)} \quad (51)$$

The flame position gradient can be expanded in powers of exp($-r/\sigma^*$) as:

$$\zeta_{o,r}=-1+\frac{2}{\sqrt{1-\alpha}}e^{-\frac{1}{\sigma^*}r}+O[e^{-\frac{1}{\sigma^*}r}]^2$$

Hence the lowest order correction, for stretch effects, to the conical flame position gradient is an exponentially small function of σ^*.

Also note that for wedge flames, the solution given by $\zeta_{o,r}=-1$ satisfies the governing Eq (50) and the boundary conditions given by Eqs (14) and (16) .

Appendix B

Defining $\Lambda=\sqrt{1-4i\sigma^*\ St_2}$, the solution for $\zeta_1(r,t)$ in Eq (23) is:

$$\zeta_1(r,t)=Re\left(\frac{e^{-iSt\,t}\left(e^{i\eta St_2(1-r)}-e^{\frac{(1-r)(1-\Lambda)}{2\sigma^*}}\right)}{St\left(i(\eta-1)+\sigma^*\eta^2St_2\right)}\right)$$

The conical and wedge flame transfer functions in the linear regime can be expressed as:

$$G_c(St_2,\eta,\sigma^*) = 2\underbrace{\frac{\left((1+\Lambda)(\eta-1) - 2i\sigma^*\eta St_2 - 2\Lambda\eta e^{\frac{1-\Lambda}{2\sigma^*}} + e^{i\eta St_2}\left(1+\Lambda - i\sigma^*(1-\Lambda)\eta^2 St_2\right)\right)}{\eta St_2^2\left(1+\Lambda\right)\left(1-\eta+i\sigma^*\eta^2 St_2\right)}}_{\text{Area Fluctuation}}$$

$$+2\sigma^*\underbrace{\left(\frac{\left(\Lambda\eta+\eta-2\right)St_2 - 2i\Lambda e^{\frac{1-\Lambda}{2\sigma^*}} + ie^{i\eta St_2}\left(1+\Lambda-2i\sigma^*\eta St_2\right)}{St_2\left(1+\Lambda\right)\left(-1+\eta-i\sigma^*\eta^2 St_2\right)}\right)}_{S_L\text{Fluctuation}}$$

$$G_w(St_2,\eta,\sigma^*) = 2\underbrace{\frac{\left(\begin{array}{l} e^{i\eta St_2}\left((1+\Lambda)(1-i\eta St_2) - 2i\sigma^* St_2 + \sigma^*\eta St_2^2(-2+\sigma^*(1-\Lambda)\eta^2) - 2i\sigma^{*2}\eta^3 St_2^3\right) \\ + 2i\Lambda\eta e^{\frac{1-\Lambda}{2\sigma^*}}\left(\sigma^* St_2 + (i+St_2)\right) + \left((1+\Lambda)(\eta-1) - i\sigma^* St_2(\Lambda\eta-2+3\eta)\right)\end{array}\right)}{\eta St_2^2\left((\eta-1)-i\eta^2 St_2\sigma^*\right)\left(1+\Lambda-2iSt_2\sigma^*\right)}}_{\text{Area Fluctuation}}$$

$$+2\sigma^*\underbrace{\left(\frac{e^{\frac{1-\Lambda}{2\sigma^*}}2\Lambda(1-iSt_2) + e^{i\eta St_2}\left(-1+i\eta St_2 - 2\sigma^{*2}\eta^2 St_2^2 + \Lambda\left(-1+i\eta St_2+\sigma^*\eta^2 St_2^2\right) + \sigma^* St_2\left(2i+2\eta St_2+\eta^2 St_2\right)\right)}{St_2\left(i+i\Lambda+2\sigma^* St_2\right)\left(1-\eta+i\sigma^*\eta^2 St_2\right)}\right)}_{S_L\text{Fluctuation}}$$

Note that the term $\exp((1-\Lambda)/2\sigma^*)$ is not exponentially small and hence is retained in the analysis.

Appendix C

The solutions for the flame position are:

$$\zeta_o(r,t) = 1-r$$

$$\zeta_1(r,t) = \left(\frac{2Sin[\left(\frac{St(K\alpha-1)(1-r)}{2\alpha}\right)]}{(K\alpha-1)\ St}\right)Cos[St\left\{\frac{(K\alpha+1)(r-1)}{2\alpha}+t\right\}]$$

$$\zeta_2(r,t) = \left(\frac{r+\alpha-r\alpha-1}{4(K\alpha-1)^2\alpha^2}\right)Cos[2\ St\left\{\frac{r-1+\alpha t}{\alpha}\right\}] + \left(\frac{6K-4K\alpha-3K^2\alpha+K^2\alpha^2}{8\ St(K\alpha-1)^3}\right)Sin[2\ St\left\{\frac{r-1+\alpha t}{\alpha}\right\}] +$$

$$\left(\frac{K\alpha(K-1)}{2(K\alpha-1)^3 St}\right)Sin[St\ \frac{(1-r)(K\alpha-1)}{\alpha}] + \left(\frac{2K-K^2\alpha-K^2\alpha^2}{8\ St(K\alpha-1)^3}\right)Sin[2\ St(K(r-1)+t)] +$$

$$\left(\frac{-2K+K\alpha+K^2\alpha}{2(K\alpha-1)^3\ St}\right)Sin[St\left\{\frac{(K\alpha+1)(r-1)+2\alpha t}{\alpha}\right\}] + \left(\frac{(r-1)(-1+\alpha+2K\alpha-3K^2\alpha^2+K^2\alpha^3)}{4\alpha^2(K\alpha-1)^2}\right)$$

$$\zeta_3(r,t)=\left(\frac{(r-1)(1-\alpha)(-3+13K\alpha-4K\alpha^2-13K^2\alpha^2-3K^2\alpha^3+10K^3\alpha^3)}{8(K\alpha-1)^4\alpha^3}\right)Cos[St\left\{\frac{r-1+\alpha t}{\alpha}\right\}]\ -$$

$$\left(\frac{2(r-1)^2(1-\alpha)^2(K\alpha-1)^2St^2+K\alpha^4(4-4\alpha-8K-5K\alpha+9K\alpha^2+27K^2\alpha-15K^2\alpha^2-4K^2\alpha^3-18K^3\alpha^2+14K^3\alpha^3)}{16(K\alpha-1)^5\alpha^4\ St}\right)$$

$$\times Sin[St\left\{\frac{r-1+\alpha t}{\alpha}\right\}]-\left(\frac{K(r-1)(-1+\alpha+2\alpha K-3K^2\alpha^2+K^2\alpha^3)}{4\alpha^2(K\alpha-1)^3}\right)Cos[\ St(K(r-1)+t)]$$

$$-\left(\frac{K(\alpha-1)(-8+16K-21\alpha K^2-2K^2\alpha^2+15K^3\alpha^2)}{16(K\alpha-1)^5St}\right)Sin[\ St(K(r-1)+t)]$$

$$+\left(\frac{K(r-1)(1-\alpha)(1-2\alpha+K\alpha)}{8\alpha^2(K\alpha-1)^4}\right)Cos[St\frac{(1-r)(K\alpha-2)+\alpha t}{\alpha}]$$

$$+\left(\frac{K(\alpha-1)(4-8K+8K\alpha-3\alpha K^2-2K^2\alpha^2+K^3\alpha^2)}{16(K\alpha-1)^5St}\right)Sin[St\frac{(1-r)(K\alpha-2)+\alpha t}{\alpha}]+$$

$$\left(\frac{K^2\alpha(5-\alpha-3K-5K\alpha+2K^2\alpha+2K^2\alpha^2)}{16(K\alpha-1)^5St}\right)Sin[St\frac{(1-r)(2K\alpha-1)+\alpha t}{\alpha}]$$

$$+\left(\frac{(1-\alpha)(r-1)(-1+7K\alpha-4K\alpha^2-3K^2\alpha^2+K^2\alpha^3)}{8\alpha^3(K\alpha-1)^4}\right)Cos[3St\left\{\frac{r-1+\alpha t}{\alpha}\right\}]$$

$$+\left(\frac{K\alpha^4(-12+12\alpha+52K-57K\alpha+9K\alpha^2-45K^2\alpha+41K^2\alpha^2-4K^2\alpha^3+10K^3\alpha^2-6K^3\alpha^3)-6(r-1)^2(1-\alpha)^2(K\alpha-1)^2St^2}{48(K\alpha-1)^5\alpha^4\ St}\right)$$

$$\times Sin[3St\left\{\frac{r-1+\alpha t}{\alpha}\right\}]+\left(\frac{K(r-1)(1-\alpha)(-3+2\alpha+K\alpha)}{8\alpha^2(K\alpha-1)^4}\right)Cos[St\frac{(1-r)(K\alpha+2)-3\alpha t}{\alpha}]$$

$$+\left(\frac{K(\alpha-1)(-4+4\alpha+28K-32\alpha K+8K\alpha^2-23K^2\alpha+17K^2\alpha^2-2K^2\alpha^3+5K^3\alpha^2-K^3\alpha^3)}{16(K\alpha-1)^5St}\right)Sin[St\frac{(1-r)(K\alpha+2)-3\alpha t}{\alpha}]$$

$$-\left(\frac{K^2(4-3\alpha K-7\alpha^2K+2K\alpha^3+K^2\alpha^2+3K^2\alpha^3)}{48(K\alpha-1)^5St}\right)Sin[\ 3St(K(r-1)+t)]$$

$$+\left(\frac{K^2(12-13\alpha+5\alpha^2-9K\alpha+\alpha^2K+2\alpha^2K^2+2\alpha^3K^2)}{16(K\alpha-1)^5St}\right)Sin[St\frac{(r-1)(2K\alpha+1)+3\alpha t}{\alpha}]$$

Appendix D

The transfer function coefficients referred to in Eq. (41) are:

$$\mathcal{A}_{c,\omega_o} = -8\ (\alpha-1)^2 + 4K\alpha\left\{2 - i(\alpha-1)St_2\right\} - 2K^2\alpha^2\left\{10+\alpha+\alpha^2+i8St_2 - i4\alpha St_2\right\}$$
$$+K^3\alpha^3\left\{\ 27-\alpha(3+i8St_2)+i32St_2\right\} + K^4\alpha^4\left\{-17+9\alpha-i32St_2+i8St_2\alpha\right\} - i4K^5\alpha^5 St_2\left\{\alpha-3\ \right\}$$

$$\mathcal{B}_{c,\omega_o} = 2(\alpha-1)\left\{6\alpha+iSt_2-i4\alpha St-(\alpha-1)St^2\right\} + 4K\alpha(\alpha-1)\left\{-10+i4St_2-St_2^{\ 2}+\alpha(i+St_2)^2\right\}$$
$$+K^2\alpha^2\left\{-76+81\alpha-\alpha^2-i44(\alpha-1)St_2-i6(\alpha-1)St_2\alpha-2St_2^{\ 2}(\alpha-1)^2\right\}$$
$$+K^3\alpha^3\left\{-8\alpha^2+i(\alpha-1)(i49+46St_2+6\alpha St_2)\right\} + 2K^4\alpha^4\left\{-7+9\alpha-i10St_2(\alpha-1)\right\}$$

$$\mathcal{C}_{c,\omega_o} = \left\{8(iSt_2-2)\right\} + 4K\left\{5-\alpha-i3St_2(1+\alpha)\right\} + 2K^2\alpha\left\{2+6\alpha+i11St_2+i2St_2\alpha\right\}$$
$$-2K^3\alpha^2\left\{11+\alpha+i6St_2\right\} + K^4\alpha^3\left\{9+i2St_2\right\} - K^5\alpha^4$$

$$\mathcal{D}_{c,\omega_o} = 4-\alpha+\alpha^2-K\alpha(13+3\alpha)+2K^2\alpha^2(9+\alpha)-8K^3\alpha^3$$

$$\mathcal{E}_{c,\omega_o} = \quad 16(\alpha-1)^2 + 4K\alpha\left\{-6+10\alpha-8\alpha^2+iSt_2(3-5\alpha+2\alpha^2)\right\}$$
$$+2K^2\alpha^2\left\{2(-15+31\alpha-2\alpha^2)-iSt_2(19-28\alpha+9\alpha^2)\right\}$$
$$+3K^3\alpha^3\left\{29-44\alpha-5\alpha^2+i2St_2(12-13\alpha+\alpha^2)\right\}$$
$$+K^4\alpha^4\left\{-59+77\alpha+8\alpha^2+i2St_2\{-9+8\alpha+\alpha^2)\right\} + 2K^5\alpha^5\left\{7-9\alpha-i2St_2(\alpha-1)\right\}$$

The transfer function coefficients referred to in Eq. (42) are

$$\mathcal{A}_{w,\omega_o} = 8(\alpha-1)^2 - i8K\alpha\left\{-i+(\alpha-1)^2St_2\right\} + 2K^2\alpha^2\left\{10+\alpha+\alpha^2+i4St_2+2(\alpha-1)St_2^{\ 2}\right\}$$
$$+K^3\alpha^3\left\{\ -27-i20St_2-i2St_2\alpha^2+16\ \ St_2^{\ 2}+\ \alpha(3-i2St_2-8St_2^{\ 2})\right\}$$
$$+K^4\alpha^4\left\{17+i27St_2-32St_2^{\ 2}+\alpha(-9-i3St_2+8St_2^{\ 2})\right\} - K^5\alpha^5St_2\left\{i17-32St_2+\alpha(8St_2-i9)\ \right\}$$
$$+4\ \ K^6\alpha^6(\alpha-3)St_2^{\ 2}$$

$$\mathcal{B}_{w,\omega_o} = 2(\alpha-1)\left\{3\alpha St^2-6\alpha(1-iSt_2)-i(\alpha-1)St^3\ \right\} + i4K\alpha(\alpha-1)\left\{(\alpha+10)(1-iSt_2)-(5+\alpha)St_2^{\ 2}+i\ \ (\alpha-1)St_2^{\ 3})\right\}$$
$$+K^2\alpha^2\left\{(1-iSt_2)(76-81\alpha+\alpha^2)+2St_2^{\ 2}(\alpha-1)(23+2\alpha+iSt_2-i\alpha St_2)\right\}$$
$$+K^3\alpha^3\left\{8\alpha^2(1-iSt_2)-(\alpha-1)(-49+i49St_2+46St_2^{\ 2}+6\alpha St_2^{\ 2})\right\}$$

$$\mathcal{C}_{w,\omega_o} = \left\{-16(i+St_2)^2\right\} + 4K\left\{-5+\alpha+i10St_2+\ \ i2\alpha St_2\ \ +\ \ 6St_2^{\ 2}+8\alpha St_2^{\ 2}\right\} - 4K^2\alpha\left\{1+i3St_2+14St_2^{\ 2}\right.$$
$$\left.+\alpha(3-i7St_2+5St_2^{\ 2})\right\} + 2K^3\alpha^2\left\{11+\alpha-i24St_2-i8\alpha St_2+23St_2^{\ 2}+2\alpha St_2^{\ 2}\right\}$$
$$+K^4\alpha^3\left\{-9+i2(20+\alpha)St_2-16St_2^{\ 2}\right\} + K^5\alpha^4\left\{1-i11St_2+2St_2^{\ 2}\right\} + iK^6\alpha^5St_2$$

$$\mathcal{D}_{w,\omega_o} = \left\{\left(1+iSt_2(1-2K\alpha)\right)\ \left(-4+\alpha-\alpha^2+K\alpha(13+3\alpha)-2K^2\alpha^2(9+\alpha)+8K^3\alpha^3\right)\right\}$$

$$\mathcal{E}_{w,\omega_o} = -16(\alpha-1)^2 + 8K\alpha\left\{3-5\alpha+4\alpha^2\right\} + 4K^2\alpha^2\left\{15-31\alpha+2\alpha^2\right\} + 3K^3\alpha^3\left\{-29+44\alpha+5\alpha^2\right\}$$
$$+K^4\alpha^4\left\{59-77\alpha-8\alpha^2\right\} + 2K^5\alpha^5\left\{-7+9\alpha\right\}$$

The transfer function expressions in the limit of $K\alpha \to 1$ are given by:

$$\lim_{K\alpha\to 1} G_{c,\omega_o} = \frac{2\left(-1+e^{i\,St_2}(1-iSt_2)\right)}{St_2^{\,2}} + \varepsilon^2\left(\frac{26-59\alpha+31\alpha^2+iSt_2(\alpha-1)(5\alpha-4)}{2St_2^2\alpha^2} + \right.$$

$$\left. e^{i\,St_2}\frac{-30(26-59\alpha+31\alpha^2)+60iSt_2(11-25\alpha+13\alpha^2)+15St_2^2\left(3\alpha-2\right)(7\alpha-9)+5iSt_2^3\left(13-31\alpha+16\alpha^2\right)-(15St_2^4-2iSt_2^5)\left(\alpha-1\right)^2}{60St_2^2\alpha^2}\right)$$

$$\lim_{K\alpha\to 1} G_{w,\omega_o} = \frac{2\left(1+e^{i\,St_2}(-1+iSt_2+St_2^2)\right)}{St_2^{\,2}} + \varepsilon^2\left(\frac{-26+59\alpha-31\alpha^2}{2St_2^2\alpha^2} + \right.$$

$$\left. e^{i\,St_2}\frac{30(1-iSt_2-\frac{St_2^2}{2})(26-59\alpha+31\alpha^2)+5iSt_2^3\left(28-61\alpha+31\alpha^2\right)+5St_2^4\left(4-13\alpha+7\alpha^2\right)-(7iSt_2^5+2St_2^6)\left(\alpha-1\right)^2}{60St_2^2\alpha^2}\right)$$

Appendix E

The transfer function at the first harmonic, defined as $G_{2\omega_o} = \dfrac{A'\left(2\omega_o\right)/A_o}{u\left(\omega_o\right)'/u_o}$, is:

$$G_{2\omega_o} = \varepsilon\left(\frac{\tilde{A}_{2\omega_o}e^{i\,2K\alpha\,St_2}}{8\alpha(K\alpha-1)^3St_2^2} + \frac{\tilde{B}_{2\omega_o}e^{i\,2\,St_2}}{8\alpha(K\alpha-1)^3St_2^2} + \frac{\tilde{C}_{2\omega_o}\;K\,e^{i\,(K\alpha+1)\,St_2}}{(K\alpha+1)^2(K\alpha-1)^3St_2^2} + \frac{\tilde{D}_{2\omega_o}}{8\alpha(K\alpha+1)^2St_2^2}\right) \quad (52)$$

where the coefficients $\tilde{A}_{2\omega o}$ to $\tilde{D}_{2\omega_o}$ for conical flames are given as

$$\tilde{A}_{c,2\omega_o} = (3-\alpha-2K\alpha)$$
$$\tilde{B}_{c,2\omega_o} = (\alpha-3)\alpha^2K^2+(4-2\alpha(1+iSt_2)+2iSt_2)\alpha K+i2(\alpha-1)(i+St_2)$$
$$\tilde{C}_{c,2\omega_o} = (-3+2\alpha+\alpha^2K^2)$$
$$\tilde{D}_{c,2\omega_o} = 5-\alpha(3+i2St_2)+i2St_2+K\alpha(3-\alpha(1+i2St_2)+i2St_2)$$

The coefficients for wedge flames reduce to:

$$\tilde{A}_{w,\omega_o} = (-3+\alpha+2K\alpha)(1-i2\alpha KSt_2)$$
$$\tilde{B}_{w,\omega_o} = i(\alpha-3)(i+2St_2)\alpha^2K^2-2(\alpha-1)(-1+i2St_2+2St_2^2)+2\alpha K(-2+\alpha+i4St_2-i2\alpha St_2+2(\alpha-1)St_2^2)$$
$$\tilde{C}_{w,\omega_o} = i(-3+2\alpha+\alpha^2K^2)(i+St_2(1+\alpha K))$$
$$\tilde{D}_{w,\omega_o} = -5-3\alpha(K-1)+\alpha^2K$$

Note that the response at the first harmonic has three characteristic time scales represented by the terms $2St_2$, $2St_c$ and $(K\alpha+1)St_2 = St_2+St_c$. As discussed in the previous section, boundary conditions are solely responsible for St_2 while flow non-uniformities account for St_c. The new characteristic time scale represented by the term $(K\alpha+1)St_2$ arises from coupling between non-linearities due to boundary conditions and flow non-uniformities. Similar to the response at the fundamental frequency, there is a single characteristic time scale in the limit of $(K\alpha\to 1)$ represented by the term $2St_2$. In the limit of $(K\alpha\to 1)$, Eq. (52) reduces to:

$$\lim_{K\alpha\to 1} G_{c,2\omega_o} = \varepsilon\left(\frac{3(\alpha-2)(e^{i2St_2}-1)-3i(\alpha-1+(\alpha-3)e^{i2St_2})St_2+6e^{i2St_2}St_2^2+i2(\alpha-1)e^{i2St_2}St_2^3}{24\alpha St_2^2}\right)$$

$$\lim_{K\alpha\to 1} G_{w,2\omega_o} = \varepsilon\left(\frac{-3(\alpha-2)(e^{i2St_2}-1)+6(\alpha-2)(i+St_2)e^{i2St_2}St_2+4St_2^3e^{i2St_2}(i(\alpha+2)-(\alpha-1)St_2^4)}{24\alpha St_2^2}\right)$$

For the uniform velocity case (K=0), the transfer functions for conical and wedge flames can be simplified to:

$$\lim_{K\to 0} G_{c,2\omega_o} = \varepsilon(\alpha-1)\left(\frac{e^{2i\,St_2}(1-iSt_2)-1-iSt_2}{4St_2^2\alpha}\right) \quad (53)$$

$$\lim_{K\to 0} G_{w,2\omega_o} = \varepsilon(\alpha-1)\left(\frac{1+e^{2i\,St_2}(-1+2St_2(i+St_2))}{4St_2^2\alpha}\right) \quad (54)$$

As the flame becomes long (i.e. increase in α), the gain drops considerably.

11. REFERENCES

[1] Cohen, J., Banaszuk, A., *J. Prop. Power*, Vol. 19 (5), 2003.
[2] Straub, D.L., Richards, G.A., Effect of Fuel Nozzle Configuration on Premix Combustion Dynamics, *ASME paper # 98-GT-492*, 1998.
[3] Paschereit, C.O., Gutmark, E., Weisenstein, W., Control of Thermo-Acoustic Instabilities and Emissions in an Industrial Type Gas Turbine Combustor, *Proc. Comb. Inst.*, 1998.
[4] Hsiao, G.C., Pandalai, R.P., Hura, H.S., Mongia, H.C., Combustion Dynamic Modeling for Gas Turbine Engines, *AIAA paper # 98-3380*.
[5] Crocco, L., Cheng, S., *Theory of Combustion Instability in Liquid Propellant Rocket Motors*, Butterworths Scientific Publications, London, 1956.
[6] Munjal, M., *Acoustics of Ducts and Mufflers*, John Wiley & Sons: New York, 1987.
[7] Fleifil, M., Annaswamy, A.M., Ghoniem, Z.A., Ghoniem, A.F., Response of a Laminar Premixed Flame to Flow Oscillations: A Kinematic Model and Thermoacoustic Instability Results, *Comb. and Flame*, Vol. 106, 1996, pp. 487-510.
[8] Ducruix, S., Durox, D., Candel, S., Theoretical and Experimental Determinations of the Transfer Function of a Laminar Premixed Flame, *Proc. Comb. Inst*, Vol. 28, 2000.
[9] Kruger, U., Hüren, J., Hoffman, S., Krebs, W., Bohn, D., Prediction of Thermoacoustic Instabilities with Focus on the Dynamic Flame Behavior for the 3A-Series Gas Turbine of Siemens KWU, *ASME Paper #99-GT-111.*
[10] Walz, G., Krebs, W., Hoffman, S., Judith, H., Detailed Analysis of the Acoustic Mode Shapes of an Annular Combustion Chamber, *ASME Paper #99-GT-113*.
[11] Schuermans, B.H., Polifke, W., Paschereit, C.O., Modeling Transfer Matrices of Premixed Flames and Comparison with Experimental Results *ASME Paper #99-GT-132*.
[12] Zinn, B.T., Powell, E.A., Nonlinear Combustion Instability in Liquid- Propellant Rocket Engines, *Proc. Comb. Inst*, Vol. 13, 1970.
[13] Culick, F.E.C., Burnley, V., Swenson, G., Pulsed Instabilities in Solid-Propellant Rockets, *J. Prop. Power*, Vol. 11(4), 1995.
[14] Culick, F.E.C., Non-Linear Growth and Limiting Amplitude of Acoustic Oscillations in Combustion Chambers, *Comb. Sci. Tech.,* Vol. 3(1), 1971.
[15] Lieuwen, T., Experimental Investigation of Limit Cycle Oscillations in an Unstable Gas Turbine Combustor, *J. Prop. Power*, Vol. 18 (1), 2002.

[16] Dowling, A.P., Nonlinear Self-Excited Oscillations of a Ducted Flame, *J. Fluid Mech*. Vol. 346, pp. 271-290, 1997.
[17] Peracchio, A.A., Proscia, W.M., Nonlinear Heat Release/Acoustic Model for Thermo-Acoustic Instability in Lean Premixed Combustors, *Journal of Engineering for Gas Turbines and Power*, Vol. 121, 1999.
[18] Wu, X., Wang, M., Moin, P. Peters, N., Combustion Instability due to the Nonlinear Interaction Between Sound and Flame, *J. Fluid Mech.*, Vol. 497, 2003, pp.23-53.
[19] Poinsot, T., Veynante, D., Bourienne, F., Candel, S., Esposito, E., Surget, J., Initiation and Suppression of Combustion Instabilities by Active Control, *Proc. Comb. Inst*., Vol. 22, 1988.
[20] Dowling, A.P., A Kinematic Model of a Ducted Flame, *J. Fluid Mech*., Vol. 394, pp. 51-72, 1999.
[21] Searby, G., Acoustic Instability in Premixed Flames, *Comb. Sci. Tech.*, Vol. 81, 1992, pp.221-231
[22] Kulsheimer, C., Buchner, H. Combustion Dynamics of Turbulent, Swirling Flows, *Comb. and Flame*, Vol. 131, 2002, pp.70-84.
[23] Lieuwen, T., Neumeier, Y., Nonlinear Pressure-Heat Release Transfer Function Measurements in a Premixed Combustor, *Proc. Comb. Inst.*, Vol. 29, 2002.
[24] Lee, J.G., Santavicca, D. Experimental Diagnostics for the Study of Combustion Instabilities in Lean, Premixed Gas Turbine Combustors, *J. Prop. Power*, Sept. 2003.
[25] Bourehla, A., Baillot, F., Appearance and Stability of a Laminar Conical Premixed Flame Subjected to an Acoustic Perturbation, *Comb. and Flame*, Vol. 114, pp. 303-318, 1998.
[26] Balachandran, R., Ayoola, B.O., Kaminski, C.F., Dowling, A.P., Mastorakos, E., Experimental Investigation of the Nonlinear Response of Turbulent Premixed Flames to Imposed Velocity Oscillations, *Comb. And Flame*, Vol. 143, 2005, pp. 37-55.
[27] Durox, D., Baillot, F., Searby, G., Boyer, L., On the Shape of Flames Under Strong Acoustic Forcing: A Mean Flow Controlled by an Oscillating Flow, *J. Fluid Mech*., Vol. 350, pp. 295-310, 1997.
[28] Lieuwen, T., Torres, H., Johnson, C., Daniel, B.R., Zinn, B.T., A Mechanism for Combustion Instabilities in Premixed Gas Turbine Combustors, *Journal of Engineering for Gas Turbines and* Power, Vol. 123(1), 2001, pp. 182-190.
[29] Neumeier, Y., Nabi, A., Zinn, B.T., Investigation Of The Open Loop Performance Of An Active Control System Utilizing A Fuel Injector Actuator, *AIAA paper # 96-2757,* 1996
[30] Broda, J.C., Seo, S., Santoro, R.J., Shirhattikar, G., Yang, V., An Experimental Investigation of Combustion Dynamics of a Lean, Premixed Swirl Injector, *Proc. Comb. Inst.,* Vol. 27, 1998, pp. 1849-1856
[31] Bendat, J., Piersol, A., *Random Data: Analysis and Measurement Procedures*, John Wiley and Sons: New York, 1986
[32] Schuller, T., Durox, D., Candel, S., A Unified Model For The Prediction of Laminar Flame Transfer Functions: Comparisons Between Conical and V-Flame Dynamics, *Comb. Flame*, Vol. 134, pp. 21-34, 2003.
[33] Coats, C., Coherent Structures in Combustion, *Prog. Energy Combust. Sci*., Vol. 22, 1996, pp. 427-509
[34] Clavin, P., Pelce, P., He, L., One-Dimensional Vibratory Instability of Planar Flames Propagating in Tubes, *J. Fluid Mech.*, Vol. 216, 1990, pp. 299-322
[35] Searby, G., Rochwerger, D., A Parametric Acoustic Instability in Premixed Flames, *J. Fluid Mech.*, Vol. 231, 1991, pp. 529-543
[36] Vaezi, V., Aldredge, R.C., Laminar Flame Instabilities in a Taylor-Couette Combustor, *Comb. and Flame,* Vol. 121, 2000a, pp. 356-366
[37] Vaezi, V., Aldredge, R.C., Influences of Acoustic Instabilities on Turbulent-Flame Propagation, *Experimental Thermal and Fluid Science*, Vol. 20, 2000b, pp.162-169.
[38] Markstein, G., "Flames as Amplifiers of Fluid Mechanical Disturbances", *Proceedings of the Sixth National Congress on Applied Mechanics*, 1970, pp. 11-33.
[[39]] Abom, M., Boden H., Error Analysis of Two-Microphone Measurements in Ducts with Flow. *J. Acoust. Soc. Am.*, **83**(6), pp.2429–2438, 1988.
[40] Durox, D., Schuller, T. & Candel, S. 2005. *Proc. Comb. Inst* **30**: 1717-1724
[41] Candel, S. 2002. *Proc. Comb. Inst* **29**: 1-28
[42] Broda, J. C., Seo, S., Santoro, R. J., Shirhattikar, G. & Yang, V. 1998. *Proc. Comb. Inst.* **27**: 1849-1856
[43] Dowling, A. P. & Stow, S. R. 2003. *J. Prop. Power* **19**(5): 751-764
[44] Ducruix, S., Schuller, T., Durox, D. & Candel, S. M. 2003. *J. Prop. Power* **19**(5): 722-734
[45] Bellows, B., Zhang, Q., Neumeier, Y., Lieuwen, T. & Zinn, B. T. (2003-0824). AIAA

[46] Lee, J. G. & Santavicca, D. A. 2003. *J. Prop. Power* **19**(5): 735-750
[47] Lieuwen, T. & Neumeier, Y. 2002. *Proc. Comb. Inst.* **Vol. 29**(1): 99-105
[48] Poinsot, T., Veynante, D., Bourienne, F., Candel, S., Esposito, E. & Surget, J. 1988. *Proc. Comb. Inst.* **22**: 1363-1370
[49] McIntosh, A. C. 1999. *Phil. Trans. R. Soc. Lond. A.* **357**: 3523-3538
[50] Keller, D. & Peters, N. 1994. *Theoret. Comput. Fluid Dynamics* **6**: 141-159
[51] Peters, N. & Ludford, G. S. S. 1983. *Comb. Sci. Tech.* **34**: 331-344
[52] Van Harten, A., Kapila, A. & Matkowsky, B. J. 1984. *SIAM J. Appl. Math.* **44**(5): 982-995
[53] Baillot, F., Durox, D. & Prud'homme, R. 1992. *Comb. Flame* **88**(2): 149-168
[54] Lieuwen, T. 2005. *Proc. Comb. Inst.* **30**(2): 1725-1732
[55] Baillot, F., Bourehla, A. & Durox, D. 1996. *Comb. Sci Tech.* **112**: 327-350
[56] Blackshear, P. 1953. *Proc. Comb. Symp.* **4**: 553-566
[57] Markstein, G. H. (1964). Nonsteady flame Propagation, Pergamon
[58] Marble, F. E. & Candel, S. M. 1978. *Proc. Comb. Inst.* **17**: 761-769
[59] Matalon, M. & Matkowsky, B. 1982. *J. Fluid Mech.* **124**: 239-260
[60] Boyer, L. & Quinard, J. 1990. *Comb. Flame* **82**(1): 51-65
[61] Poinsot, T. & Candel, S. M. 1988. *Comb. Sci. Tech.* **61**
[62] Subbaiah, M. V. 1983. *AIAA* **21**(11): 1557-1564
[63] Yang, V. & Culick, F. E. C. 1986. *Comb. Sci. Tech.* **45**: 1-25
[64] Aldredge, R. 1992. *Comb. Flame* **90**(2): 121-133
[65] Ashurst, W. & Sivashinsky, G. 1991. *Comb. Sci Tech.* **80**(1-3): 159-164
[66] Ashurst, W., Sivashinsky, G. & Yakhot, V. 1988. *Comb. Sci Tech.* **62**(4-6): 273-284
[67] Joulin, G. & Sivashinsky, G. 1991. *Comb. Sci Tech.* **77**: 329-335
[68] Clanet, C., Searby, G. & Clavin, P. 1999. *J. Fluid Mech.* **385**: 157-197
[69] Cho, J. H. & Lieuwen, T. 2005. *Comb. Flame* **140**(1): 116-129
[70] Lee, D. H. & Lieuwen, T. 2003. *J. Prop. Power* **19**(5): 837-846
[71] Bechert, D. & Pfizenmaier, E. 1975. *J. Fluid Mech.* **72**: 341-352
[72] Ferguson, D., Richards, G., Woodruff, S., Bernal, S. & Gautam, M. 2001. *Proc. 2nd Joint Meeting U.S. Sections Comb. Inst.*
[73] Michalke, A. 1971. *Z. Flugwiss.(in German)* **19**
[74] Kuramoto, Y. & Tsuzuki, T. 1975. *Prog. Theo. Phys* **54**(3): 687-699
[75] Sivashinsky, G. I. 1983. *Ann. Rev. Fluid Mech* **15**: 179-199
[76] Searby, G. & Clavin, P. 1986. *Comb. Sci. Tech.* **46**(3-6): 167-193
[77] Bychkov, V. 1999. *Phys. Fluids* **11**(10): 3168-3173
[78] Searby, G. & Rochwerger, D. 1991. *J. Fluid Mech.* **231**: 529-543
[79] Jiang, G. & Peng, D. 2000. *SIAM J. Sci. Comput.* **21**: 2126-2143
[80] Gottlieb, S. & Shu, C. 1998. *Math. Comput.* **67**: 73-85
[81] Wicker, J. M., Greene, W. D., Kim, S. & Yang, V. J. 1996. *J. Prop. Power* **12**(6)
[82] Culick, F.E.C., Yang, V. "Overview of Combustion Instabilities in Liquid-Propellant Rocket Engines" *Liquid Rocket Engine Combustion Instability* Chapter 1, Progress in Astronautics and Aeronautics vol. 169, eds., V. Yang and W.E. Anderson, pp. 3-37, 1995.
[83] Nayfeh, A.H., Mook, D.T., *Nonlinear Oscillations*, John Wiley & Sons: New York, 1995.
[84] Cohen, J., Wake, B.E., Choi, D., Investigation of Instabilities in a Lean, Premixed Step Combustor*, J. Prop. Power*, Vol. 19(1), pp.81-88, 2003.
[85] Straub, D.L., Richards, G.A., Effect of Fuel Nozzle Configuration on Premix Combustion Dynamics, *ASME paper # 98-GT-492*, 1998..
[86] Paschereit, C.O., Gutmark, E., Weisenstein, W., Control of Thermo-Acoustic Instabilities and Emissions in an Industrial Type Gas Turbine Combustor, *Proc. Comb. Inst.*, 1998.
[87] Mongia, H.C., Held, T.J., Hsiao, G.C., Pandalai, R.P., Challenges and Progress in Controlling Combustion Dynamics in Gas Turbine Combustors, *J. Prop. Power*, Vol. 19(5), pp.822-829, 2003.
[88] Cowell, L.H., Experience at Solar Turbines with Combustion Oscillations in Lean Premixed Combustion, Proceedings of AGTSR Combustion Workshop, Penn. State, Sept. 10-11, 1995.

[89] McManus, K.R., Poinsot, T., Candel, S.M., Review of Active Control of Combustion Instabilities, *Prog. Energy Combust. Sci.*, **19**(1), 1993, pp.1-29.
[90] Neumeier, Y., Zinn, B.T., "Experimental Demonstration of Active Control of Combustion Instabilities Using Real Time Modes Observation and Secondary Fuel Injection", *Proc. Comb. Inst.,* **26**, 1996.
[91] Sattinger, S.S., Neumeier, Y., Nabi, A., Zinn, B.T., Amos, D.J., Darling, D.D., "Sub-scale Demonstration of Active Feedback Control of Gas-Turbine Combustion Instabilities", *Proc. Int. Gas Turbine and AeroEngine Congress and Exhibition,* 1998.
[92] Johnson, C.E., Neumeier, Y., Darling, D.D., Sattinger, D.D., Neumaier, M., Zinn, B.T., "Demonstration of Active Control of Combustion Instabilities on a Full Scale Gas Turbine Combustor", *36th AIAA/ASME/SAE/ASEE Joint Propulsion Conference,* 2000.
[93] Neumeier, Y., Cohen, J., Shcherbik, D., Lubarsky, E., Zinn, B.T., "Suppression of Combustion Instabilities in Gaseous Fuel Combustor Using Fast Adaptive Control, Part 1: Controllability Tests", *AIAA paper 2002-4076*, 2002.
[94] Lubarsky, E., Shcherbik, D., Zinn, B.T., "Active Control of Instabilities in High-Pressure Combustor by Non-Coherent Oscillatory Fuel Injection", *AIAA paper 2003-4519*, 2003
[95] McManus, K., Poinsot, T., Candel, S.M., *Prog. Energy Combust. Sci*., Vol. 19, pp. 1-29, 1993.
[96] Johnson, C., Neumeier, Y., Lubarsky, E., Lee, J., Zinn, B.T., *AIAA Paper # 2000-0476*.
[97] Sattinger, S.S., Neumeier, Y., Nabi, A., Zinn, B.T., Amos, D.J., Darling, D.D., *J. Engr. Gas Turbines Power*, Vol. 122, 2000, pp 262-268.
[98] Coker, A., Neumeier, Y., Lieuwen, T., Zinn, B.T., Menon, S., *AIAA Paper #2003-1009*.
99 Lieuwen, T., "Modeling Premixed Combustion-Acoustic Wave Interactions: A Review", Journal of Propulsion and Power., Vol. 19 (5), 2003, pp. 765-781.

[100] Preetham, Lieuwen, T., Nonlinear Flame-Flow Transfer Function Calculations: Flow Disturbance Celerity Effects Part 2, *AIAA paper 2005-0543*, 2005.

Aerothermal Effects of Interfacial Leakage and Film Cooling Schemes with Endwall and Leading Edge Contouring

Final Report
May 2002 -October 2005

by T.W. Simon (tsimon@me.umn.edu) and R.J. Goldstein (rjg@me.umn.edu), PIs
J.D. Piggush (jpiggush@me.umn.edu) and Marco Papa (marco.papa@me.umn.edu), RAs

Date Report was issued (December 2005)
DOE Award Number (Clemson U/02-01-SR096/DOE PR)
UTSR Project Number (02-01-SR096)

Heat Transfer Laboratory
Department of Mechanical Engineering
University of Minnesota
111 Church St. S.E.
Minneapolis, Minnesota
55455

Administrative Office: Sponsored Projects Administration, University of Minnesota
450 Gateway Building, 200 Oak Street S.E., Minneapolis, MN 55455-2070
c/o Shannon Lovelace <slovelac@umn.edu>

Disclaimer

This report was prepared as an account of work sponsored by an agency of the United States Government. Neither the United States Government nor any agency thereof, nor any of their employees, makes any warranty, express or implied, or assumes any legal liability or responsibility for the accuracy, completeness, or usefulness of any information, apparatus, product, or process disclosed, or represents that its use would not infringe privately owned rights. Reference herein to any specific commercial product, process, or service by trade name, trademark, manufacturer, or otherwise does not necessarily constitute or imply its endorsement, recommendation, or favoring by the United States Government or any agency thereof. The views and opinions of authors expressed herein do not necessarily state or reflect those of the United States Government or any agency thereof.

Abstract

In this report, significant results from the University of Minnesota endwall study conducted over a three-year contract period are presented. During this period, the test sections were modified and qualified then used to take detailed flow, heat (mass) transfer and adiabatic effectiveness measurements in both a vane cascade and a rotor cascade.

In the vane cascade, a series of experiments was completed where the effects on heat transfer coefficients and adiabatic effectiveness values were documented for various geometries and injection rates. The results show the effects of introducing gaps at the transition between the combustor and the first stage vane endwall or in the platform of the endwall. Shown is how the endwall convective heat transfer coefficients and adiabatic effectiveness values are changed by the gaps, gap leakage and steps at the gaps.

In the rotor cascade, direct comparisons of heat and mass transfer measurements on the blade and endwall surfaces show the validity of the heat and mass transfer analogy. The effects of leading edge modifications are investigated through heat and mass transfer measurements on the endwall of the cascade. The effects of simulated wheelspace coolant injection upstream of the cascade are quantified through mass transfer measurements, deriving maps of adiabatic cooling effectiveness on the blade and endwall surfaces. Finally, the use of mass transfer data to validate a numerical heat/mass transfer code is demonstrated, comparing mass transfer measurements on the blade and endwall surfaces to values predicted by a RANS simulation using the SST k-ω model for turbulence closure.

Table of Contents

Disclaimer 1
Abstract 2
Introduction 4
Executive Summary 6
Project Description 7
Experimental 8
Measurement Techniques in the Linear Vane Cascade 8
Measurement Techniques in the Linear Rotor Cascade 9
Results and Discussion 13
Measurements of Flow and Heat Transfer from a Linear First-Stage Vane Cascade 13
Measurements of Flow and Mass/Heat Transfer from a Linear First-Stage Rotor Cascade 15
Numerical Predictions 20
Conclusions 21
References 22

Introduction

The first stage turbine is directly downstream of the combustor and is thus subject to extremely high temperatures. Adding to the severity, recent combustor development in gas turbine engines has resulted in a more uniform temperature distribution across the first stage turbine inlet passage than in earlier designs. Thus, the endwall regions of the first stage turbine must support higher thermal loading than in earlier generations and efficient cooling schemes that focus on the endwall region must be developed. Cooling the endwall region of the turbine is made more difficult by complex secondary flows that result from interactions between passage and horseshoe vortices, leakage flows from component interfaces and emerging film-cooling flows. In support of the development of more efficient endwall cooling schemes, experiments are conducted to document the effectiveness of leakage through the combustor-to-turbine transition slot or through the endwall slashface gap within the turbine using various injection methods. To address real problems associated with assembly misalignment and in-use thermal growth, several flow path geometries that replicate less than ideal alignment of components are considered. Documentation is by way of endwall and airfoil heat or mass transfer rates and flow measurements within the passage, with focus on the near endwall regions. Heat transfer data are obtained under a nearly constant temperature boundary condition, which is equivalent to a constant mass concentration in the cases of mass transfer measurements. This is the best choice for thermal boundary condition of the traditional, well-defined, test-type boundary conditions for it is the best simulation of engine conditions. The measurements are taken at sufficiently high chord Reynolds number values that the test flows are similar to those in operating turbines.

The highest thermal loading is in the vane section. This region is studied experimentally via a vane cascade. Measurements focus on reduction of the effects of secondary flows in the endwall region via endwall contouring and on the effects of gaps in the endwall surface and leakage through those gaps. Aerodynamic measurements are with pitot and hotwire probes. The thermal measurement method uses a thermocouple probe to document the temperature field within the passage, including very near-wall temperature distributions that can be used to obtain local heat transfer coefficient values when the wall is heated. The same probe is employed to measure adiabatic effectiveness values when the wall is adiabatic. These boundary conditions are applied to the pressure surface, the suction surface and the endwall of the passage under study. Using near-wall temperature profiles, gradients in the thermal boundary layer are measured and used to calculate local heat flux values by Fourier's law. The near-wall temperature measurements are extrapolated to the wall to determine the wall temperature. Gaps either without steps or with forward- or backward-facing steps are introduced to the test geometry to allow measuring heat transfer coefficients and adiabatic effectiveness values on the endwall as affected by such non-ideal geometries. Also, aerodynamic losses within the passage are measured under such non-ideal passage geometries as described by the gaps and steps at the gaps. These gaps are ahead of the airfoil row and between airfoils on the endwall (gutters or slashfaces). The effects of leakage flow through the gaps are documented.

Though in a lower temperature region, the rotor has additional strength considerations associated with rotation. Thermal loading is, thus, equally as important as in the vane section. In the rotor study, local heat transfer coefficients are measured using a thermal boundary layer probe. A digital power supply is used to control heaters embedded in the

blade and endwall and maintain their surfaces at a constant set temperature. Concurrently, local mass transfer measurements are made in the same flow to provide higher resolution of the heat (mass) transfer coefficient distributions. This high resolution has been previously shown to be of great value toward describing how the complex near-endwall flow field affects the heat transfer. These data are used also to further describe the analogy between heat and mass transfer in complex flows. A better understanding of the analogy would allow a more complete utilization of the extensive mass transfer database that now resides in the literature. The effects of gaps and steps ahead of the airfoil row on heat (mass) transfer are documented, as well as the effects of leakage flow issuing out the gaps. In a gas turbine engine cooling air is generally bled from the compressor, fed to the wheelspace and then discharged into the mainstream through a `peripheral rim seal,' ideally preventing ingestion of hot gases into the wheelspace. While a number of studies have investigated the mechanisms that govern ingestion, very few have looked at the cooling potential of wheelspace coolant injection on the rotor blade and hubwall surfaces. In order to address this issue, the rotor cascade has been modified to include an injection system that simulates the wheelspace coolant injection upstream of the rotor blades.

Executive Summary

In the vane cascade, measurements of heat transfer performance with the various geometric changes quantify the effects of real passage geometry changes and real leakage flow injection rates on passage heat transfer. Once the thermal conditions are established, the measurements are taken by detailed surveys with a simple thermocouple probe. Computed are the wall heat flux, the wall temperature, the flow temperature distribution, the convective heat transfer coefficient distribution on the endwall and the adiabatic effectiveness of the leakage flow for endwall cooling. The vane cascade has on axially contoured endwall and one straight endwall. Sensitivities of heat transfer behavior to the presence of a gap in the contoured endwall, the amount of gap flow or the degree of misalignment at the gap are documented. One gap is at the junction between the turbine and the combustor-to-turbine transition section. Also presented are studies of the effects of having vane section gaps (slashface gaps). With the slashface gap are the slashface gap flow rate and the misalignment of vane sections on either side of the slashface. These results have been documented in five papers [1 though 5] which have been presented at gas turbine heat transfer sessions. The data indicate a large effect of the slashface gap.

In the rotor cascade study, heat and mass transfer measurements are taken on the blade and endwall surfaces and compared to verify the heat and mass transfer analogy, assessing sensitivity to Reynolds number, freestream turbulence and boundary layer thickness. The effects of a blade leading edge modification have been documented through heat and mass transfer measurements on the endwall surface. The effects of a simulated wheelspace coolant injection are documented through mass transfer measurements on the blade and endwall surfaces. The mass transfer data are reduced to derive maps of adiabatic cooling effectiveness.

I. Project Description

Thermal loading of the endwall region is of concern in the design of the first stage of a gas turbine engine for it is immediately downstream of the combustor and is therefore in a severe thermal environment. As a result, active cooling is needed. However, efficient cooling of the endwall region is difficult because of the complex secondary flows in that region, revealed as passage and horseshoe vortices, leakages from component interfaces and flow from film cooling jets. So far, designers' understanding of transport in this region is not complete and, as a result, cooling schemes are less than optimum. To achieve performance goals, the next generation of engines must have improved thermal management in this region.

The objective of this DOE AGTSR (Advanced Gas Turbine System Research) project is to use an experimental and computational approach to understand transport in the endwall region of a gas turbine and to use the understanding gained to support the design of cooling strategies for this region.

More specific objectives are to:

1. Describe the flow features more completely and document their effects on aerodynamic losses and heat transfer in the endwall region. This is done via detailed measurements of flow and surface heat transfer.

2. Investigate the effects of changes in design variables under simulated engine conditions. This is done via experiments. Variables include airfoil leading edge configurations near the endwall, endwall contouring shapes and degree of component (endwall segments and combustor–to-turbine transition duct joint) misalignment.

3. Document the performance of leakage flow in support of advanced cooling concepts which more efficiently utilize the available leakage flow as coolant.

4. Improve the analogy factor for converting mass transfer data to heat transfer values for flows such as turbine endwall flows.

5. Evaluate computational tools used for gas turbine thermal design.

II. The Experiments

2.1 Measurements in the Linear Vane Cascade

2.1.1 The Vane Cascade Test Facility

The test facility is designed to simulate the geometry and flow inside a first stage vane passage of a modern, mid-sized gas turbine engine. The test section, consisting of three airfoils with two passages, simulates the nozzle guide vanes and endwalls. A detailed description of the test facility is provided in references [1] through [6]. A schematic of the facility is shown in Figures 1 through 3. Contouring provides acceleration of the flow ahead of, and entirely through, the airfoil passage. This has a major influence on the strength of the secondary flow in the passage near each endwall. The freestream turbulence intensity for all cases in this facility is 12% at the vane row inlet plane.

2.1.2 Total Pressure Measurements

Total pressure measurements are made using a 0.7 mm (0.028in) diameter, square tipped total pressure probe. Diaphragm-type pressure transducers with carrier demodulators (Validyne DP-45 and Validyne CD15) produce voltages which are then digitized over a period of 20 seconds using an IOTech ADC488/8SA. These measurements are used to characterize the passage aerodynamic losses. Results were previously documented and are summarized in references [1] and [3]. An example is given in Figure 4.

2.1.3 Heat Transfer Measurements

Thermal measurements within the test section were made by thermocouples. The thermocouples used in this experiment were E-type formed from Constantan and Chromel wires. The wires used for measurement within uniform temperature flow and solids were made using thermocouples of 24 gage wires with junctions electrically welded. Traversing thermocouples used for in-flow measurement, including boundary layer traverses, were also E-type. However, they were formed of 76μm (3 mil) diameter wire and were butt-welded. A total of 117 temperature profiles are taken over the endwall surface for each test run. Measurements are more heavily clustered near the slashface gap and in the downstream portion of the passage (see Figure 5). The method produces accurate heat transfer coefficient distribution measurements over the passage endwall. The probe geometry prevents taking measurements very close to casting fillets at the junction of the vane and endwall and very close to the slashface gap. The heat transfer data were calculated from detailed and direct measurements of the thermal boundary layer at each of the measurement locations. Details can be found in [2], [4] and [6]. An example is shown in Figure 6. Dotted contour lines are included using intervals of 0.5 for Stanton numbers under 7×10^{-3}. Heat transfer measurements were taken in the upper passage (of the two passages of this test section). These data are replotted, without contour lines, in the adjacent passages. This method of obtaining heat transfer coefficients is particularly suitable for application to this vane passage experiment. First, it does not require the surface to be isothermal or of a uniform heat flux. With an aluminum wall and embedded heaters, the thermal boundary condition is nearer to a constant temperature condition, rather than to a constant heat flux condition. The constant temperature condition more

closely reproduces the passage thermal boundary conditions in the actual engine. For test cases similar to a turbine endwall, the calculated single-sample Stanton numbers were found to agree with those taken through traditional methods to within 11% [6]. To establish the repeatability of the method, the nominal case was repeated a total of four times. In order to more easily compare the cases, the passage is split into 6 regions and the heat transfer coefficients are averaged over each region. The standard deviation ranges from 2 to 7% of the average heat transfer coefficient, which is acceptable considering the difficulty in obtaining accurate heat transfer measurements in this geometry.

2.1.4 Adiabatic Wall Thermal Measurements

Adiabatic wall temperature measurements were made with the adiabatic contoured endwall and airfoil sections in place. For this series of runs, the leakage flow was heated to nominally10K above the freestream temperature. Extrapolation to the endwall of the data taken in the passage gives the surface temperature of the endwall and the adiabatic wall temperature. An example is shown in Figure 7. These data can be used to compute the adiabatic effectiveness. The flow passage data identify where the leakage fluid migrates and how it mixes. An example is shown in Figure 8. The same probe used in the heat transfer measurement is used for the adiabatic wall measurements, with a slight modification. A small detector switch is mounted on the stem of the probe so the switch is activated when the probe contacts the wall. The probe for the heated wall study could use an electrical continuity circuit to determine when the probe touches the wall.

2.1.5 Net Heat Flux Change

Calculation of the net heat flux reduction combines the information gathered from the heat transfer and adiabatic wall temperature studies to give an indication of how much area on the endwall is affected by a change in the blowing parameters. The comparison made in this study is designed to show the change between the heat flux at the nominal case and the heat flux found with some other set of parameters. This computed change distribution gives an indication of how changes in the leakage flow, or geometry of the endwall, may affect the heat flux into the vane endwall. An example is shown in Figure 9. A positive NHFC indicates a reduction of heat flux of the perturbation case over the nominal case.

2.2 Measurements in the Linear Rotor Cascade

2.2.1 The Rotor Cascade Test Facility

Investigations of the rotor flow field and heat/mass transfer are conducted in a blowing type wind tunnel with a five bladed linear cascade in a blade-centered configuration. The blades are large-scale models of a first stage rotor blade of a high-pressure turbine. Details of the facility can be found in Jin and Goldstein [7]. The test section, shown in Figures 10 and 11, has been modified to accommodate endwall plates for heat and mass transfer experiments (Figure 12). The main parameters of the turbine cascade are reported in Table 1.

Table 1. Turbine cascade parameters

Number of blades	5
Chord length of blade – C	18.4 cm
Axial chord length of blade – C_x	13.0 cm
Pitch of cascade – P	13.8 cm
Height of cascade – H	45.7 cm
Aspect ratio (Span/Chord) – H/C	2.48
Solidity (Pitch/Chord) – P/C	0.75
Blade inlet angle – β_1	35°
Blade outlet angle – β_2	-72.5^o
Inlet/Exit area ratio of the cascade (AR)	2.72
Area ratio of the contraction	6.25
Exit Reynolds number – $Re_{ex}x10_{-5}$ range	4.5-6.9

2.2.2 Mass Transfer Measurements

The heat transfer measurements are performed using an indirect technique that makes use of the analogy between heat and mass transfer [8]. The simulated blade and endwall surfaces are coated with naphthalene through a casting procedure and exposed to the wind tunnel flow. Photographs of the endwall and blade are reported in Figure 12b and 13b. The profiles of the two surfaces are measured with an LVDT (Linear Variable Differential Transformer) probe before and after the wind tunnel test to determine the sublimation of the naphthalene layer. Schematic diagrams of the measurement systems used for the naphthalene surface measurement are reported in Figure 11. The data are then reduced to derive non-dimensional mass transfer coefficients in the form of Sherwood numbers, *Sh*.

2.2.3 Heat Transfer Measurements

Direct heat transfer measurements are performed by measuring the temperature profiles within the conductive region of the thermal boundary layer. Three temperature probes with E-type thermocouples of a diameter of 76μm have been fabricated and calibrated for measurements on the bottom endwall and on the blade pressure and suction surfaces. Each probe consists of three parts: the bare thermocouple wire, the hypodermic needle holding the wire and the stem of the probe. A photograph is shown in Figure 15. The probes are traversed within the thermal boundary layer by a 5-axis measurement system, programmed to automatically find the wall position and move the probes normally to the surface.

A heat transfer endwall plate and a heat transfer blade have been designed to produce uniform surface temperature that would match the boundary conditions of the mass transfer experiments. The blade has fourteen holes for cartridge heaters and one slot near the trailing edge for a strip heater. Thermocouples are installed near the blade surface on both the suction and pressure. An insulating section made of ultra high molecular weight polypropylene with low conductivity (~ 0.4 W/mK) reduces heat conduction losses. This insulating section is hollow to facilitate passage of heater and thermocouple wires. The outputs of the fifteen heaters are individually adjusted to obtain uniform temperature. The heat transfer endwall plate consists of a balsa wood plate, an aluminum plate, a bottom

insulating plate, one hundred 25.4 mm x 25.4 mm strip heaters and thermocouples. Balsa wood is used to provide an unheated region in front of the aluminum plate. Thermocouples are installed close to the surface of the aluminum plate at the center of each heater. An insulating wall made of ultra high molecular weight polypropylene is placed underneath the heaters to reduce heat loss to the bottom wall. The heaters are individually controlled to obtain a uniform surface boundary condition. Photographs of the heat transfer endwall and blade are reported in Figures 12a and 12b, respectively.

A multiple-output digital power supply has been designed to control the 115 heaters (15 in the blade and 100 on the endwall). A PID control algorithm reads the temperatures measured by the thermocouples embedded in the blade and endwall and adjusts the power supplied to each heater to maintain uniform surface temperatures. A photograph of the power supply is reported in Figure 14. Its specifications are summarized in Table 2.

Table 2. Specification of multiple-output digital power supply

Total power	1200 watts
Power at each output	10 watts
Number of output	128
Voltage range	0-10, 20, 30 and 40 with 256 steps
Control method	Parallel port in Linux

2.2.4 Injection System

An injection system has been added to the facility to simulate the effects fo the wheelspace coolant injection upstream of the rotor blades. Compressed air taken from the building supply enters a plenum located below the wind tunnel test section before being injected into the mainstream. Schematic diagrams of the injections system are reported in Figure 16. The flow is injected at a 45º angle to the bottom endwall and has no component in the pitchwise direction of the cascade. This corresponds to an idealized situation in which the wheelspace coolant rotates with the disk onto which the rotor blades are mounted. This assumption allows the investigation of a limiting case and has the advantage of yielding the same injection direction for all blowing ratios.

Before entering the plenum, the injection air flows through a valve, a pressure regulator, a heat exchanger and a calibrated orifice meter. The heat exchanger, located in the wind tunnel upstream of the contraction, helps bring the temperature of the injection air close to the mainstream flow temperature. Finer adjustment of the temperature of the injection air is obtained using a tape heater controlled with a variable power supply, located shortly upstream of the plenum. The temperature of the injected flow is measured with an E-type thermocouple located in the upper portion of the plenum. Five E-type thermocouples embedded in the naphthalene with their beads close to the surface measure the naphthalene temperature at the interface with air. During the experiments, these two temperatures are kept to within 0.2 ºC of each other. Their variation in time during the run, which lasts for approximately one hour, does not exceed 0.2 ºC. Accurate measurement and control of the temperature is important, as the value of naphthalene vapor pressure is strongly dependent on temperature (roughly 10% variation per ºC).

In studying the effect of upstream component misalignment on fluid flow and mass transfer three configurations are used: a step up (forward facing step), a step down

(backward facing step) and no step. Schematic diagrams for the three configurations are reported in Figure 17. The step height and the slot width measure 3.1% of the axial chord, and the slot is located at a distance of 10% of the axial chord upstream of the cascade.

2.2.5 Adiabatic Cooling Effectiveness Measurements

Results of film cooling studies are usually presented in terms of the adiabatic cooling effectiveness, η_f, that can be calculated directly from temperature measurements on a nominally adiabatic surface. This parameter can also be derived from experiments with a constant wall temperature boundary condition [9], which can be conveniently performed using the heat/mass transfer analogy with naphthalene sublimation. The technique consists in coating the specimen with naphthalene and measuring the profiles before and after exposure to the flow to determine the local sublimation depth. The data are reduced to derive non-dimensional mass transfer coefficients in the form of Sherwood numbers, Sh. Two sets of experiments are needed to derive η_f. In the first case naphthalene-free air is injected upstream of the surface being studied, while naphthalene-saturated air is injected in the second set of experiments. In an equivalent heat transfer experiment these two conditions would correspond to injecting fluid at the freestream temperature and at the endwall temperature, respectively. The mass transfer coefficients obtained injecting naphthalene-saturated air are denoted using a prime in this report. The local adiabatic cooling effectiveness is calculated as $\eta_f = (Sh - Sh')/ Sh$.

III. Results and Discussion

3.1 Measurements of Flow and Heat Transfer from the Linear First-Stage-Vane Cascade Experiment

The cases studied may be generally grouped into eight configurations:

- Smooth passage: No steps, gaps or leakage flows
- Nominal configuration: No steps, 0.5% MFR through the slashface and transition section gaps
- Increased transition section gap leakage: No steps, 0.5% MFR through the slashface gap and 1.0% MFR through the transition section gap
- Increased slashface gap leakage: No steps, 1.0% MFR through the slashface gap and 0.5% MFR through the transition section gap
- Transition section forward facing step: 1.5% step at the transition section gap, 0.5% MFR through the slashface and transition section gaps
- Transition section backward facing step: -1.5% step at the transition section gap, 0.5% MFR through the slashface and transition section gaps
- Slashface forward facing step: 1.5% step at the slashface gap, 0.5% MFR through the slashface and transition section gaps
- Slashface backward facing step: -1.5% step at the slashface gap, 0.5% MFR through the slashface and transition section gaps

Five methods used to produce the data which document each of these configurations:

- Factorial study of experiment parameters on exit total pressure loss
- Single parameter perturbation study of exit total pressure loss
- Heat transfer coefficient study
- Adiabatic effectiveness distribution study
- Net heat flux change study

The conclusions for each of these cases based on the studies outline above are:

Smooth passage: No steps, gaps or leakage flows.

The smooth passage case has losses typical of other contoured vane passages studied in the literature. Contouring of one endwall (while keeping the second endwall straight) and the streamwise acceleration associated with contouring, was shown to strongly decrease endwall secondary flows on both the straight and the contoured endwalls. The effects of endwall curvature on the loss distribution are noted as added losses on the contoured endwall surface relative to the losses on the straight endwall surface. Heat transfer coefficients for this configuration are similar to those found in other studies with endwall contouring: inlet plane coefficients are characteristic of an inlet boundary layer development. Heat transfer coefficients increase as the flow accelerates in the passage and a zone of high heat transfer is observed in the vane wake. The substantial influence of the pressure side leg of the horseshoe vortex noted in cascades which had no endwall contouring was not observed in this case due to the contouring.

Nominal configuration: No steps, 0.5% MFR through the slashface and transition section gaps

The nominal configuration had a large increase in loss, as compared with the smooth passage case. This was due to the low-momentum leakage fluid being introduced at the slashface. Details of the flow measurements are in [1] and [3]. A comparison of pressure coefficient distributions is shown in Figure 18. Heat transfer coefficients are increased over those of the smooth case. This is mainly the result of the slashface gap which experiences a sink flow in the upstream portion of the gap. In the downstream portion of the passage, flow is ejected from the gap to the passage, pushing the thermal boundary layer off the endwall and creating blockage. This is shown in Figure 19. Details of the heat transfer measurements are in [2] and [4]. Adiabatic effectiveness values for the nominal case show good leakage coverage near the suction side of the transition section gap, but little coverage in downstream portions of the passage. This is shown in Figure 20. Details of the adiabatic effectiveness measurements are in [5].

Increased transition section gap leakage: No steps, 0.5% MFR through the slashface gap and 1.0% MFR through the transition section gap

The factorial study did not indicate a significant influence of the increased transition section flow on losses. However, the single parameter perturbation study indicates somewhat larger losses with high injection momentum flux ratios. Losses associated with transition section gap leakage appear to scale with momentum flux. The heat transfer is mainly affected by the higher mass of fluid in the boundary layer in the upstream portion of the cascade. Downstream portions of the endwall experience an increase in heat transfer coefficients due to the added turbulence. Adiabatic effectiveness measurements indicate much more uniformity with increased transition section leakage flow. The net heat flux is substantially reduced upstream of the throat. Downstream of the throat, some regions show a slight increase in heat flux with the increase in transition section gap leakage.

Increased slashface gap leakage: No steps, 1.0% MFR through the slashface gap an 0.5% MFR through the transition section gap

The factorial study indicates a large rise in loss with increased slashface blowing. Perturbation studies confirm that losses increase with increased slashface leakage. Heat transfer data indicate similar inlet plane heat transfer coefficients to those of the nominal case. Heat transfer coefficients downstream of the slot are depressed by the added mass of fluid in the boundary layer. Adiabatic effectiveness measurements indicate improved coverage downstream of the slashface gap; however, adiabatic effectiveness values remain small. The net heat flux is slightly reduced over much of the passage, with a greater reduction in the portion of the passage downstream of the slashface gap. This is shown in Figure 9.

Transition section forward facing step: 1.5% step at the transition section gap, 0.5% MFR through the slashface and transition section gaps

The forward facing step imposes acceleration on the flow just ahead of the inlet plane. This is shown by the factorial study to reduce losses. Heat transfer rates in the downstream portion of the passage are increased slightly. The leakage flow from the transition section gap is distributed more uniformly from the slot due to the imposed acceleration over the

gap. Heat flux is little changed over much of the endwall surface, except for the portion of the endwall between the suction side of the vane and the forward portion of the slashface gap. The heat flux is increased as a result of the forward-facing step at the transition section.

Transition section backward facing step: -1.5% step at the transition section gap, 0.5% MFR through the slashface and transition section gaps

The backward facing step is shown by the factorial study to increase losses. This may be due to the increase in boundary layer thickness produced by the low momentum fluid behind the step. Heat transfer data indicate lower heat transfer rates downstream of the slashface gap, as compared to values for the nominal case (Figure 21). This is the result of the thickened boundary layer. The value of adiabatic effectiveness over much of the passage is increased in this case and a corresponding reduction in the net heat flux is seen in some portions of the passage.

Slashface forward facing step: 1.5% step at the slashface gap, 0.5% MFR through the slashface and transition section gaps

The influence of the slashface step on passage losses is shown to not be significant in the factorial study; although a slight reduction in losses is observed in the single parameter perturbation study. Heat transfer rates are shown to be slightly decreased from those of the nominal study. The net heat flux in the forward of the passage is increased near the suction surface of the vane and decreased on the pressure side portion of the endwall. Heat flux rates in the portion of the passage downstream of the gap show a slight reduction, as compared to the nominal values.

Slashface backward facing step: -1.5% step at the slashface gap, 0.5% MFR through the slashface and transition section gaps

A slight reduction in losses is shown in the single-parameter perturbation study for this configuration. Heat transfer rates for this configuration are similar to those found in the nominal configuration. The net change in heat flux shows a slight reduction from nominal values over much of the endwall surface.

The study indicates that passage leakage flows have an impact on passage loss and heat transfer. The influence of misalignment appears to often change the distribution of heat flux. Some areas show an increase while others indicate a reduction. From an aerodynamic standpoint, the forward facing transition section step appears to be desirable. From a heat transfer perspective, the backward facing step is more beneficial. The slashface step appears to have an effect on passage heat flux, causing a slight reduction in the downstream portion for both the case of a forward facing step and a backward facing step. Similarly, a slight reduction in losses is observed for both of the slashface step heights.

3.2 Measurements of Flow and Mass/Heat Transfer from a Linear First-Stage-Rotor Cascade

3.2.1 Mass and Heat Transfer Measurements on the Endwall

Mass transfer experiments have been conducted for six different cases of varying

Reynolds numbers, turbulence intensity values and trip wire diameters. The conditions for each run are listed in Table 3.

Table 3. Mass transfer conditions on an endwall

No	Name	Trip wire diam. (mm)	Re_{ex}	U_{ex} (m/s)	Tu(%)
1	MT-B-Run1	0.5	4.5×10^5	39.2	0.2
2	MT-B-Run2	0.5	5.82×10^5	50.6	0.2
3	MT-B-Run3	1.0	4.38×10^5	38.5	0.2
4	MT-B-Run4	1.0	5.77×10^5	50.6	0.2
5	MT-B-Run5	1.0	4.27×10^5	37.4	8.5
6	MT-B-Run6	1.0	5.67×10^5	49.9	8.5

Some inferences can be made on the effects of the individual parameters. Results show that the boundary layer thickness does not play an important role. The larger diameter tip wire, which generates a thicker boundary layer, was therefore chosen for most of the runs. Sherwood number contours allow a clear identification of a number of secondary flow features associated with the complicated secondary flow system that exists in the near-wall region. The horseshoe vortices form close to the leading edge and merge with the leading edge corner vortices. The passage vortex develops from the pressure leg of the horseshoe vortex. The high turbulence intensity acts to suppress the passage vortex.

Heat transfer experiments have been conducted matching the experimental conditions used for the mass transfer tests. The boundary layer thickness was once again found to play a minor role. The 1*mm* diameter trip wire was used to trip the boundary layer for all three reported heat transfer runs. The Reynolds numbers were lower than those investigated in the mass transfer experiments, since higher Reynolds numbers were found to cause excessive vibration of the thermal probe. The detailed conditions for each run are listed in Table 4.

Table 4. Heat transfer conditions on an endwall

No	Name	Trip wire diam. (mm)	Re_{ex}	U_{ex} (m/s)	Tu(%)
1	HT-B-Run1	1.0	2.56×10^5	21.6	0.2
2	HT-B-Run2	1.0	1.95×10^5	16.2	0.2
3	HT-B-Run3	1.0	2.29×10^5	19.6	8.5

While the mass transfer experiment can measure more than 5000 points in an hour, the heat transfer experiment can only measure 140 points in six hours. The lower spatial resolution does not allow a detailed thermal field description as in the case of the local mass transfer measurements. A region of high heat transfer coefficients upstream of the leading edge is clearly identified but it is not possible to clearly distinguish the effects of the passage vortex, as was possible with the mass transfer measurements.

Comparison of the normalized Nusselt and Sherwood number distribution shows very good agreement when using an analogy factor, F, of 0.557 (corresponding to n=0.5, n being the exponent of the Pr (Sc) number dependency of the heat (mass) transfer coefficients).

3.2.2 Mass and Heat Transfer Measurements on the Blade

Mass transfer experiments are performed for one nominal set of experimental conditions. A single experiment provides data for both the pressure and suction sides at several spanwise locations. The detailed conditions for the reported run are described in Table 5.

Table 5. Mass transfer conditions on the blade

No	Name	Location	Re_{ex}	U_{ex} (m/s)	Tu(%)
1	MT-PS-Run1	3D	2.29×10^5	19.9	0.2

Mass transfer coefficients are measured on 53 locations on the suction side and 47 locations on the pressure side of the airfoil. In the spanwise direction, 55 locations are selected ranging from z/C=0.01 to 1.0.

Heat transfer experiments are conducted matching the experimental conditions used for the mass transfer tests. In this case, however, each run provides data for only one spanwise location. The data reported for different spanwise locations are therefore obtained from different experiments (e.g. cases 1 through 4). Table 6 describes the conditions used for each test.

Table 6. Heat transfer conditions on an endwall

No	Name	Location	Re_{ex}	U_{ex} (m/s)	Z/C	Tu (%)
1	HT-P-Run1	3-D-P	2.48×10^5	21.9	0.09	0.2
2	HT-P-Run2	3-D-P	2.49×10^5	21.9	0.18	0.2
3	HT-P-Run3	3-D-P	2.38×10^5	21.3	0.28	0.2
4	HT-P-Run4	3-D-P	2.38×10^5	21.2	0.66	0.2
5	HT-S-Run5	3-D-S	2.41×10^5	21.4	0.09	0.2
6	HT-S-Run6	3-D-S	2.41×10^5	21.4	0.18	0.2
7	HT-S-Run7	3-D-S	2.41×10^5	21.4	0.28	0.2
8	HT-S-Run8	3-D-S	2.42×10^5	21.4	0.66	0.2

Measurements are performed at 37 locations on the pressure side, ranging from S_p/C=0.0 to 1.0, and 43 locations on the suction side, ranging from S_s/C=0.07 to 1.26. Measurements on the suction side over the range from S_s/C=0.0 to 0.07 could not be performed due to physical restrictions imposed by the size of the access window.

The data at z/C=0.09 from MT-PS-Run1 and HT-P-Run1 are plotted for the pressure side in Figure 22. The data are normalized and compared to the normalized heat transfer results. The mass transfer coefficient is expressed as $Sh/(\mathrm{Re}^{1/2} Sc^n)$ and the heat transfer coefficient is expressed as $Nu/(\mathrm{Re}^{1/2} \mathrm{Pr}^n)$. The normalized Nusselt numbers agree well with the normalized Sherwood numbers on the pressure side when a value of n=0.5 is adopted.

The data at z/C=0.09 from MT-PS-Run1 and HT-S-Run1 are plotted for the suction side in Figure 23. Heat and mass transfer data are normalized in the same manner as described for Figure 22. On the suction side, normalized Nusselt numbers agree well with the normalized Sherwood numbers using n=0.5 up to S_s/C=0.6. Beyond S_s/C=0.6, the use

of n=0.7 allows better matching of the two data sets. The different behavior after the specified chord coordinate could be due to the different flow regimes. However, heat transfer measurements downstream of $S_s/C=0.6$ are extremely difficult to take due to the limited size of the linear conduction region near the wall compared to the probe size. Further investigations are needed to draw final conclusions on the interpretation of the results for this region.

3.2.3 Mass and Heat Transfer Measurements on the Endwall with a blade leading edge modification

A leading edge fillet was designed following the guidelines reported in Zess and Thole [10], having a height and length of seven times the boundary layer displacement thickness (~30 mm in the present apparatus). Mass transfer measurements were conducted with an active (mass transfer) endwall and an inactive blade. Two Reynolds numbers and two turbulence intensity values were used for the plain (no contouring) blade and for the modified leading edge blade to check the benefits of installing the fillet. Mass transfer measurements, which include 5000 points, are taken to show the development of secondary flows and the effects of these on endwall mass transfer.

In the case with 0.2% freestream turbulence, the fillet eliminates the horseshoes vortex and reduces the passage vortex significantly. However, the passage vortex still exists even though it is appears to be reduced and displaced downstream to x/C=0.4. With a higher turbulence intensity of 8.5%, the horseshoe vortex is not clearly observed, either with or without fillets.

For heat transfer measurements 130 positions on the endwall have been selected. Since the heat transfer measurement technique is sensitive to vibration, the Reynolds number was reduced to $Re=2.5 \times 10^5$. The heat transfer experiments do not show the fine detail given by the mass transfer technique, due to the smaller number of measurement locations.

Comparisons of heat and mass transfer measurements were made to validate the heat/mass transfer analogy in the cascade geometry on the endwall with the modified leading edge blades. Figure 24 compares the Nusselt and Sherwood number with n=0.5, Pr=0.707, and Sc=2.28. Each plot shows comparisons at different streamwise positions between blades. The rectangular bars represent the cross section of the blades and the numbers indicate the blade number. The letter 'P' indicates the blade pressure side and 'S' indicates the suction side. In the passage between blade 3 and blade 4, heat and mass transfer results with fillets show good agreement with n=0.5, as suggested by Eckert et al. [11].

3.2.4 Adiabatic cooling effectiveness on the blade and endwall surfaces

Measurements have been performed with no turbulence-generating grids at the exit Reynolds number of Re=600,000 based on true chord and cascade exit velocity. The injected flow is introduced at an effective blowing rate of unity, calculated as the ratio between the average velocity out of the slot and the freestream velocity. The density of the injected flow is equal to that of the freestream, yielding a density ratio of unity.

The boundary layer on the bottom wall of the tunnel is tripped with a 1*mm* wire placed 828*mm* upstream of the leading edge of the central blade of the cascade, producing a

turbulent boundary layer with close to zero freestream turbulence (<0.2%). Hot wire measurements performed at four locations upstream of the cascade show that the boundary layer profile follows a power law with exponent 1/6.45 and that the projected momentum thickness at the location of the central blade leading edge is 2.2*mm*.

Results show that the injection significantly alters the flow field and mass/heat transfer in the upstream portion of the passage. The coolant exiting from the slot is drawn to the suction side of the blade and climbs up the suction surface of the airfoil, being pushed up by the action of the passage vortex system and leaving a well defined streak of cooling effectiveness on the blade surface, as shown in Figures 25 and 26. For a blowing rate of unity, very little coolant reaches the pressure side of the blade.

For the step-up configuration, the coolant penetrates further downstream in the pressure side of the passage. When the endwall is brought down to create a step-down configuration, the coolant penetrates less on the pressure side of the passage and more on the suction side of the passage and on the airfoil suction surface, providing a higher overall cooling effectiveness.

IV. Numerical Predictions

4.1 Numerical Heat/Mass Transfer Predictions in the Linear Rotor Cascade

In recent years designers have been increasingly relying on numerical simulations to predict the temperature and flow fields within the turbine. While computationally intensive technique such as LES (Large Eddy Simulation) and DES (Detached Eddy simulation) are becoming more attractive, RANS (Reynolds Averaged Navier-Stokes) simulations still constitute the most common industrial practice as a result of the lower computational cost. In the development of codes, validation with experimental results remains a most important tasks.

Mass transfer measurements using naphthalene sublimation can be conveniently used for the validation of numerical codes. They can generally be performed with a high spatial resolution, they are free from conduction and radiation errors typical of heat transfer measurements and they allow the imposition of well-defined boundary conditions. In an equivalent heat transfer experiment, naphthalene coated surfaces would in fact correspond to isothermal boundaries while the non-coated surfaces would correspond to adiabatic boundaries.

The flow and heat/mass transfer in the rotor linear cascade in its baseline configuration (without injected flow and without leading edge modifications) are numerically predicted with a RANS code using the software "Fluent." The SST k-ω model is used for turbulence closure [12]. The flow and thermal boundary conditions are carefully matched to the ones measured in the experiments, providing guidelines for using mass transfer data for validation of numerical heat transfer codes.

Results show that the code generally performs well in predicting the main features of the secondary flows in the near-wall region. The numerical simulation captures the formation of the horseshoe vortex system upstream of the blade leading edge, and the migration of the pressure side leg of the horseshoe vortex towards the suction side of the neighboring blade, where it meets the suction side leg of neighboring horseshoe vortex system. The heat (mass) transfer rates on the endwall are very well predicted in the first portion of the passage, but downstream of the merge-point the code underpredicts the effect of the corner vortex and overpredicts the heat (mass) transfer rates associated with the cross-flow within the passage. On the airfoil surface, the simulation captures the enhancement of the heat transfer coefficients on the suction side of the blade due to the action of the passage vortex system. The agreement in the two-dimensional region of the airfoil is excellent, but the code predicts an early transition to turbulence on the blade suction side.

Figure 27 shows the predicted Sherwood number contour plots on the blade and endwall surfaces. Detailed results of the numerical simulation are reported in reference [13].

Conclusions

Test facilities have been constructed with the necessary features to carry out this experimental program with its various geometry changes and flow injection schemes. These facilities have been qualified, a major milestone in any test program. Measurements have been taken, as follows: 1). Aerodynamic losses have been measured within a passage with a contoured endwall. 2). Endwall heat and mass transfer measurements have been taken to document effects that the passage secondary flows have on the local transfer rates. 3). On-airfoil measurements of heat and mass transfer rates have been taken and the analogy between the two was described. Noted was the change in the analogy factor between upstream measurements and downstream measurements. This change is considered to be attributable to a change in flow regime.

In the vane cascade, the effects of gaps, gap flow and component misalignments on aerodynamic losses, heat transfer coefficients and adiabatic effectiveness values are presented.

In the rotor cascade, heat and mass transfer measurement are conducted with modified leading edge blades. The modified leading edge delays the development of the passage vortex and reduces the strength of the passage vortex in mass transfer measurements. The comparison between heat and mass transfer is in good agreement with the theory suggested by Eckert at el. [11]. The effect of the wheelspace coolant injection on the secondary flows and on the mass (heat) transfer in the wall and near-wall region has been documented. Misalignment between the endwall and the upstream platform was considered.

A numerical RANS code that uses the SST k-ω model has been developed to predict the flow and heat/mass transfer in the rotor cascade. Results are compared with mass transfer measurements taken on the blade and endwall surfaces with equivalent boundary conditions. The numerical simulation is able to capture most of the secondary flow features that have been experimentally observed.

References

[1] Piggush, J and Simon, T.W., 2005, :Flow Measurements in a First Stage Nozzle Cascade having Endwall Contouring, GT2005-68340, 2005 International Gas Turbine Conference, Reno, NV, Recommended for the J. of Turbomachinery.

[2] Piggush, J. D. and Simon, T. W., 2005. "Heat Transfer Measurements in a First Stage Nozzle Cascade having Endwall Contouring, Leakage and Assembly Features, HT2005-72573, 2005 National Heat Transfer Conference San Francisco, CA.

[3] Piggush, J. D. and Simon, T. W., 2005. "Flow Measurements in a First Stage Nozzle Cascade having Leakage and Assembly Features: Effects of Endwall Steps and Leakage on Aerodynamic Losses," IMECE2005-83032, 2005 IMECE, Orlando, FL.

[4] Piggush, J. D. and Simon, T. W., 2006. "Heat Transfer Measurements in a First Stage Nozzle Cascade having Endwall Contouring: Misalignment and Leakage Studies," GT2006-90575, 2006 International Gas Turbine Conference, Barcelona, Spain.

[5] Piggush, J. D. and Simon, T. W., 2006. "Adiabatic Effectiveness Measurements in a First Stage Nozzle Cascade having Endwall Contouring, Leakage and Assembly Features," GT2006-90576, 2006 International Gas Turbine Conference, Barcelona, Spain.

[6] Piggush, J., D., 2005. An experimental investigation of endwall leakage flows and misalignment in a gas turbine nozzle guide vane cascade. Master's thesis, Mechanical Engineering Department, University of Minnesota.

[7] Jin, P., and Goldstein, R. J., 2003. "Local mass/heat transfer on a turbine blade tip. international journal of rotating machinery," International Journal of Rotating Machinery, 9(2), pp. 81–95.

[8] Goldstein, R. J., and Cho, H. H., 1995. "A review of mass transfer measurements using naphthalene sublimation," Experimental Thermal and Fluid Science, 10, pp. 416–434.

[9] Eckert, E. R. G., 1984. "Analysis of film cooling and full coverage film cooling of gas turbine blades," Journal of Engineering for Power, 106, pp. 206–213.

[10] Zess G. A. and Thole K. A., "Computational Design and Experimental Evaluation of Using a Leading Edge Fillet on a Gas Turbine Vane," Journal of Turbomachinery, Vol. 124, 2002, p167-175.

[11] Eckert, E.R.G., Sakamoto, H., and Simon, T.W., "The Heat/Mass Transfer Analogy Factor, Nu/Sh, for Boundary Layers on Turbine Blade Profiles," International Journal of Heat and Mass Transfer, Vol. 44, 2001, p1223-1233.

[12] Menter, F. R., 1994. “Two-equation Eddy-Viscosity Turbulence Models for Engineering Applications.” AIAA Journal, vol. 32, pp. 1598–1605.

[13] Papa, M., Goldstein, R.J., Gori, F., 2006, “Numerical heat transfer predictions and mass/heat transfer measurements in a linear turbine cascade,” submitted to the 2006 ASME-ATI Conference, Milan, Italy.

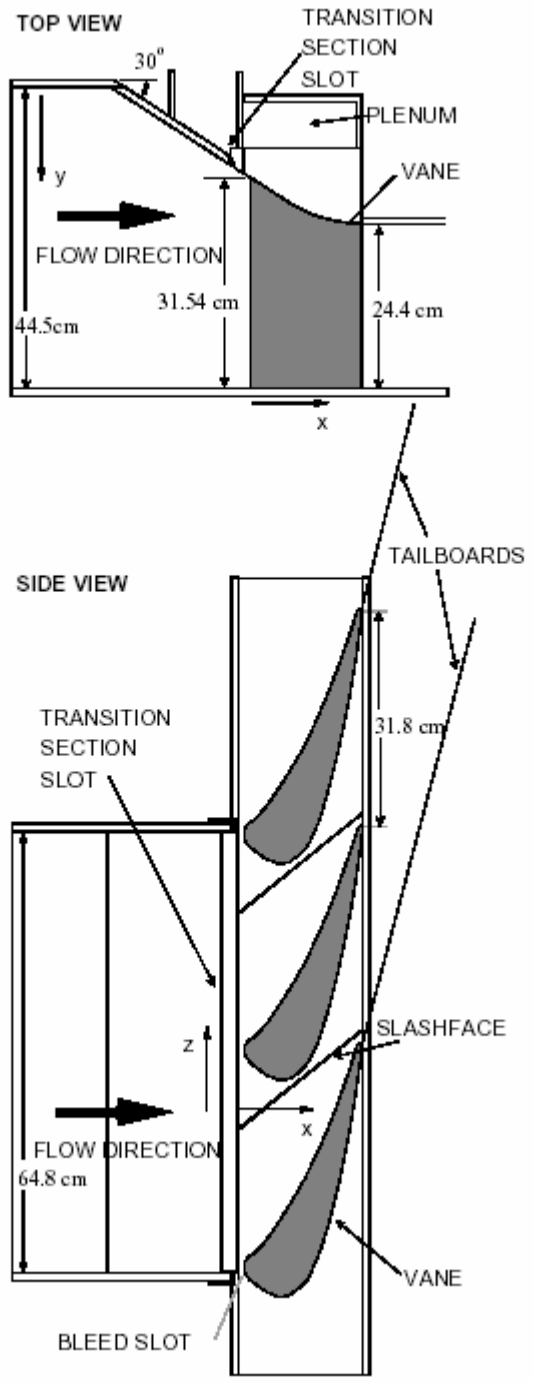

Figure 1: Schematic of the test facility.

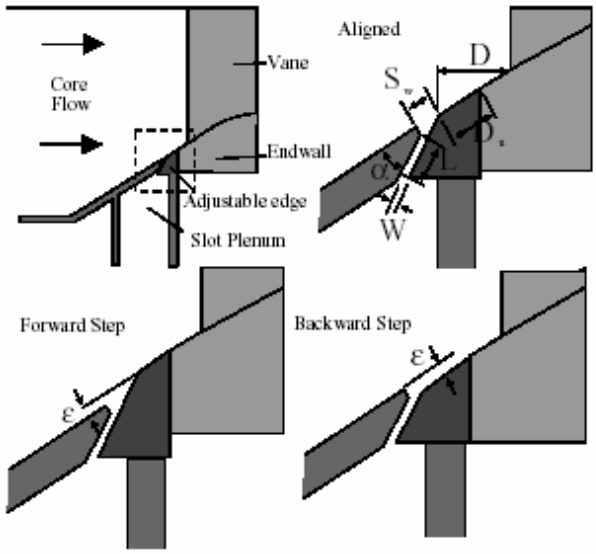

Figure 2: Schematic of the transition section slot geometry. Details are of the portion enclosed in the dashed square. Note that the light gray portion indicates the heated sections of the endwall and vane. The dark gray piece was moved to create steps at the transition section slot.

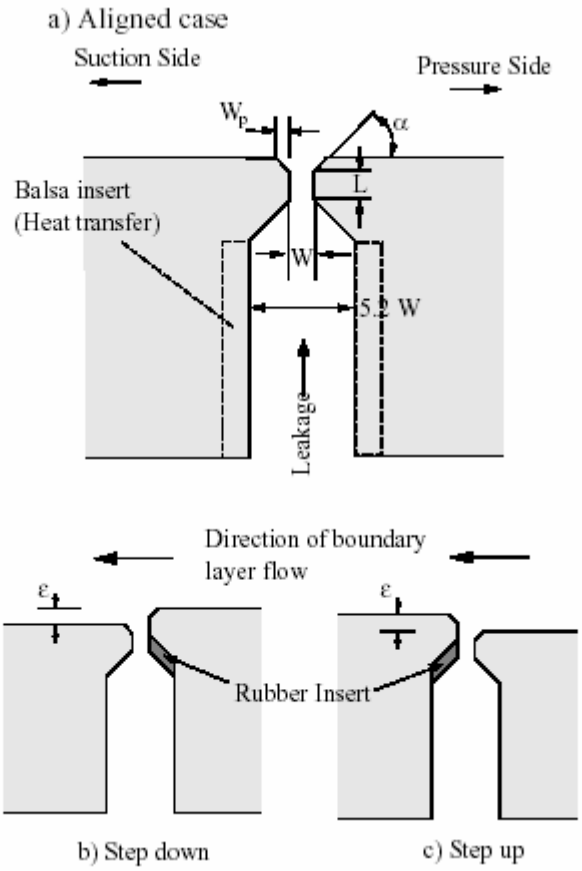

Figure 3: Schematic of the slashface slot geometry. The balsa and rubber insulation sections are included for the heat transfer studies.

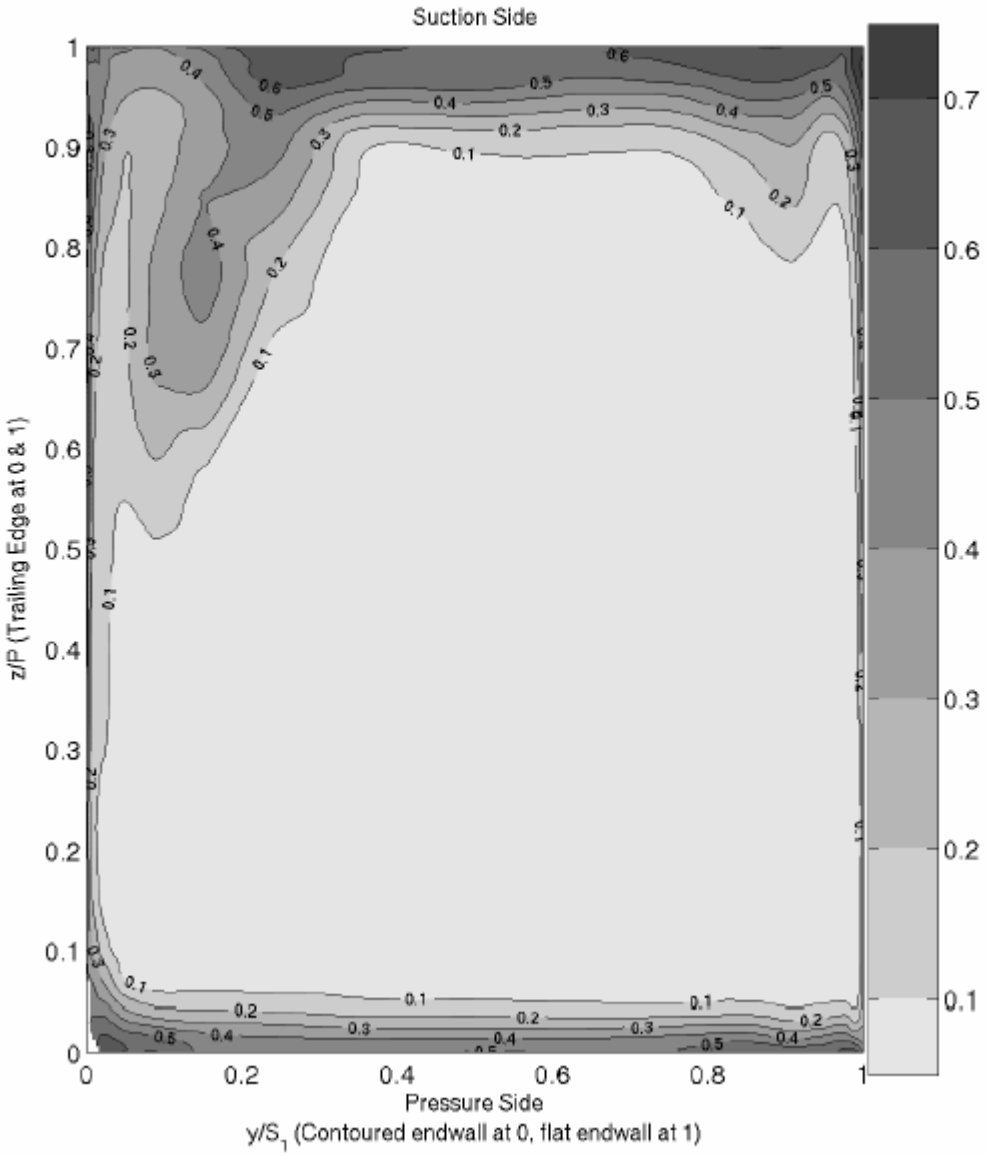

Figure 4: Exit pressure loss contours for the nominal case, where the gaps are open and are blowing at 5% of the passage mass flow rate. There are no steps.

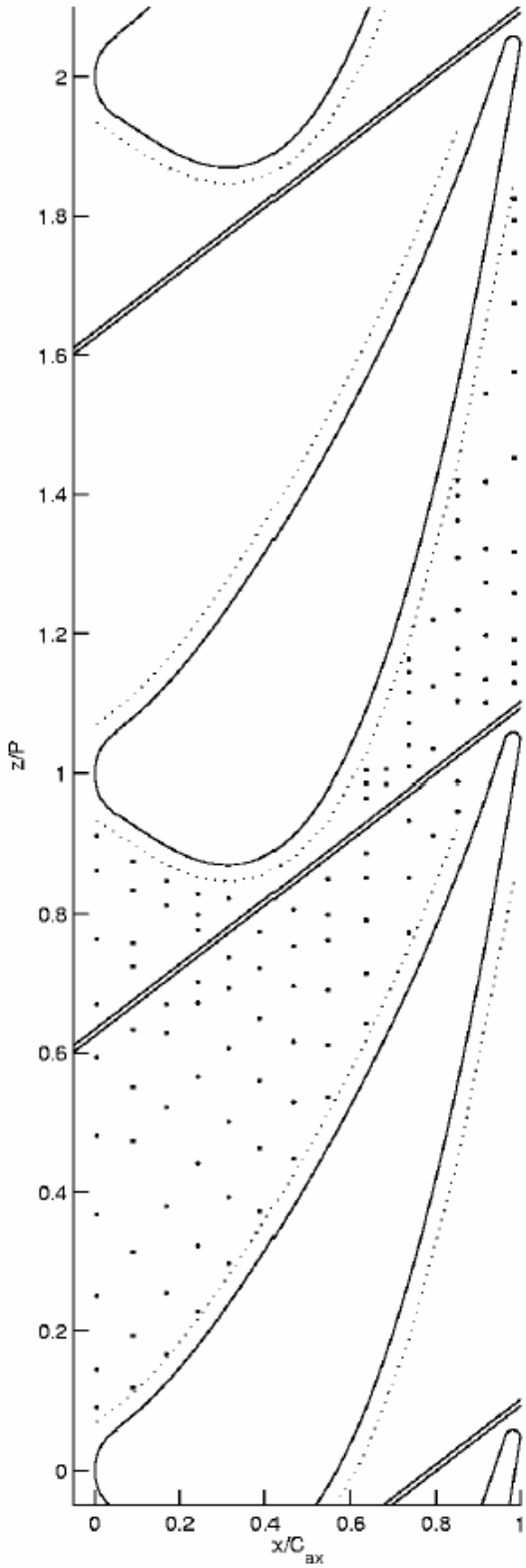

Figure 5: Locations of measurements points for temperature profile measurements.

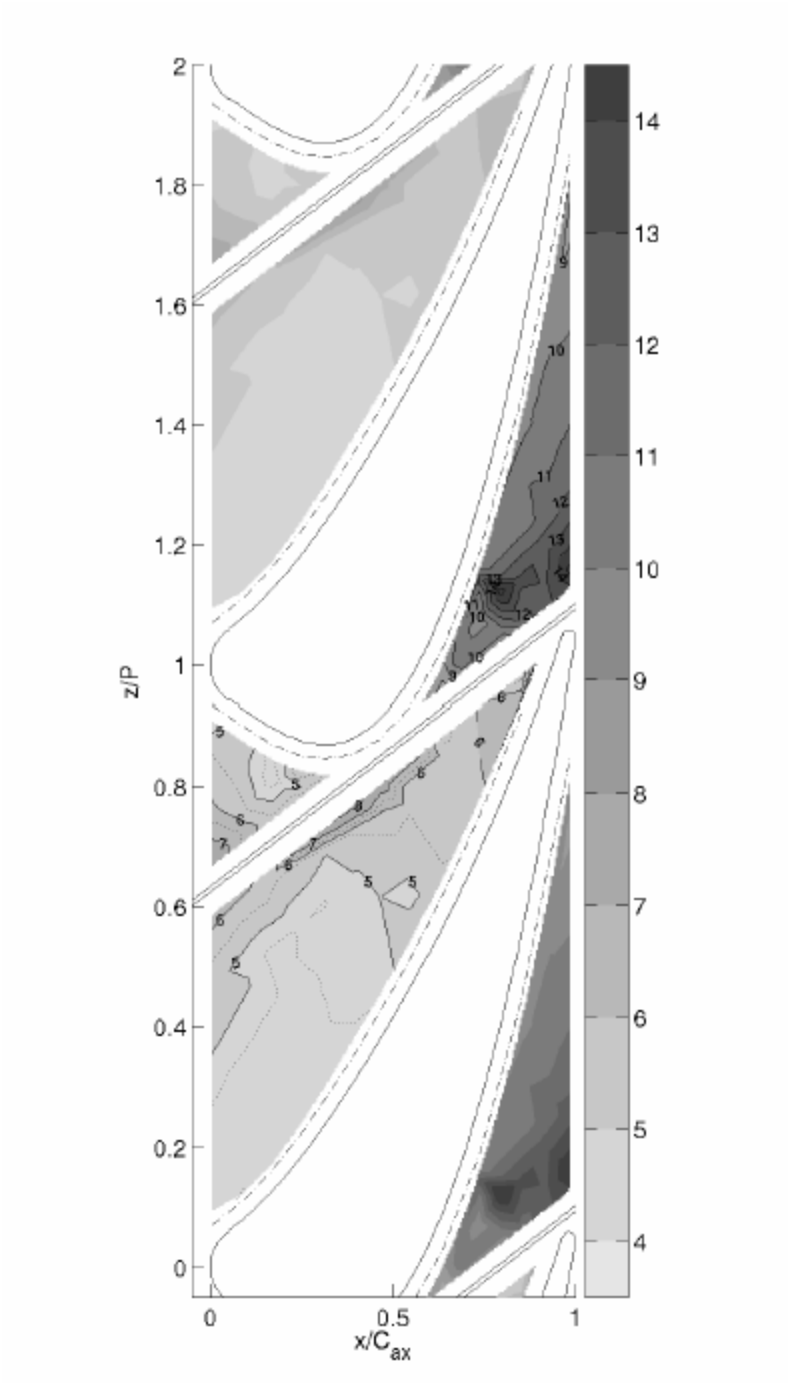

Figure 6: Stanton number (x1000). The nominal case, where the gaps are open and are blowing at 5% of the passage mass flow rate. There are no steps.

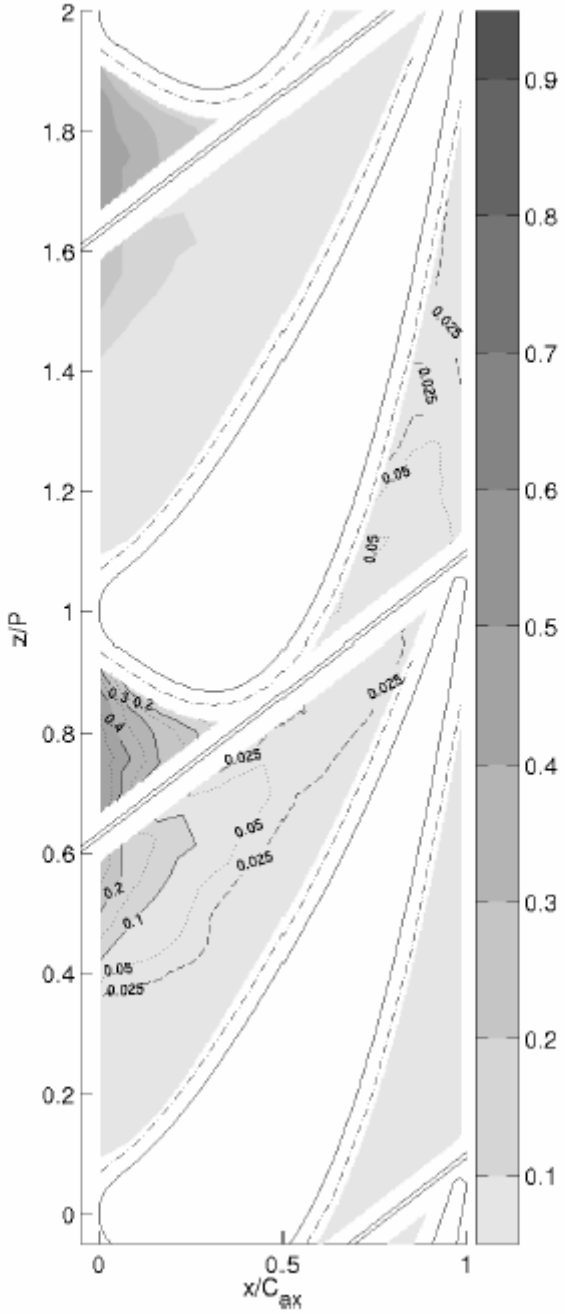

Figure 7: Adiabatic wall temperatures for the nominal case, where the gaps are open and are blowing at 5% of the passage mass flow rate. There are no steps.

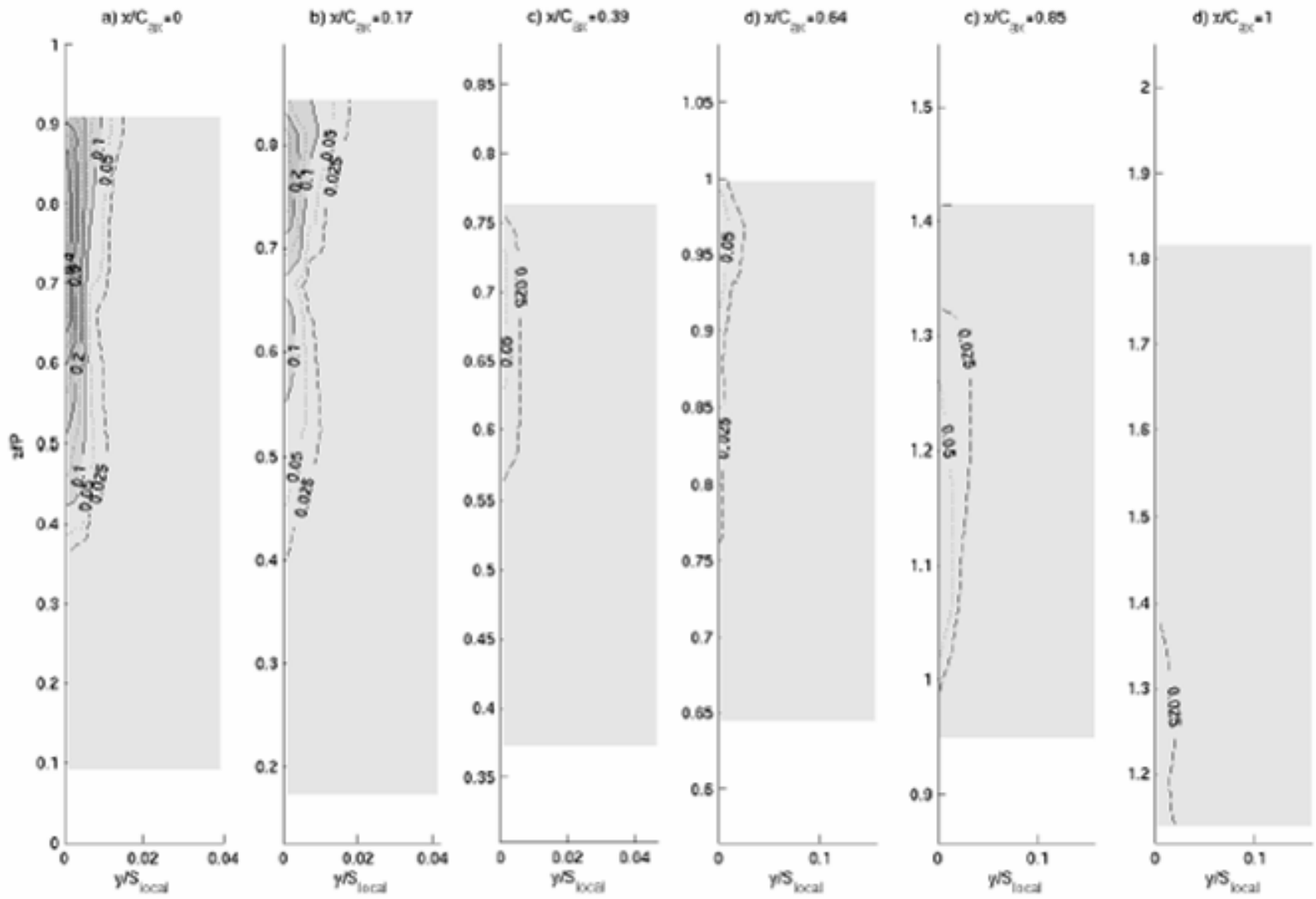

Figure 8: Adiabatic effectiveness distribution for the nominal case, where the gaps are open and are blowing at 5% of the passage mass flow rate. There are no steps.

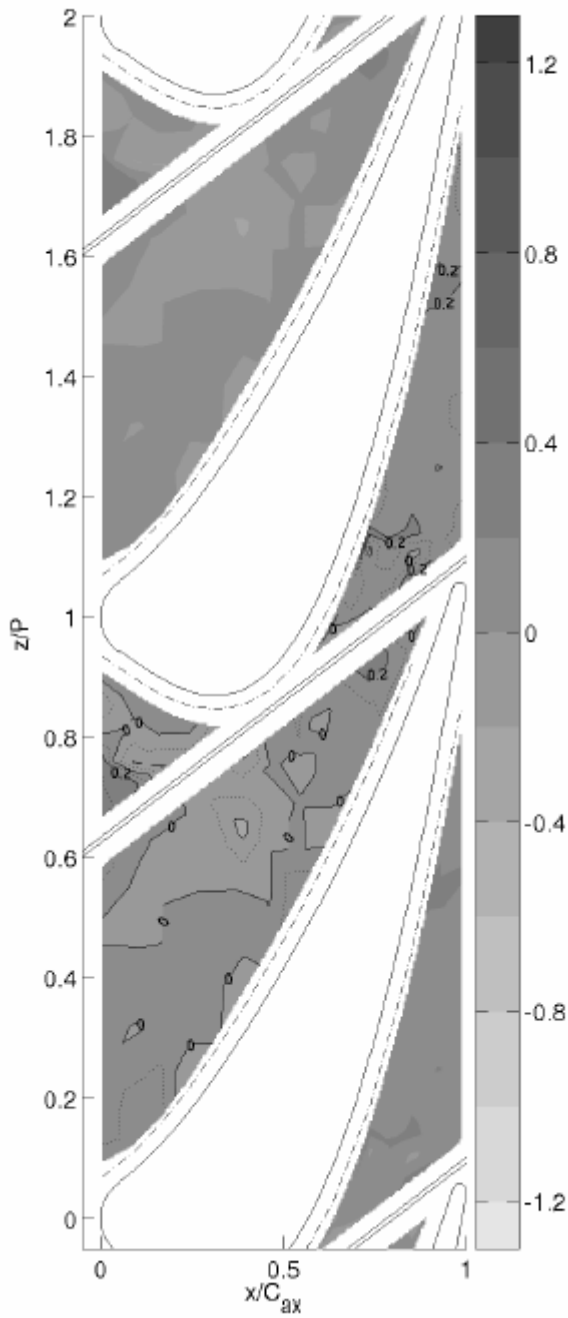

Figure 9: Net heat flux reduction, elevated slashface blowing of 1% of the passage mass flow rate vs. the nominal case, where the gaps are open and are blowing at 5% of the passage mass flow rate. There are no steps in either of the two comparison cases.

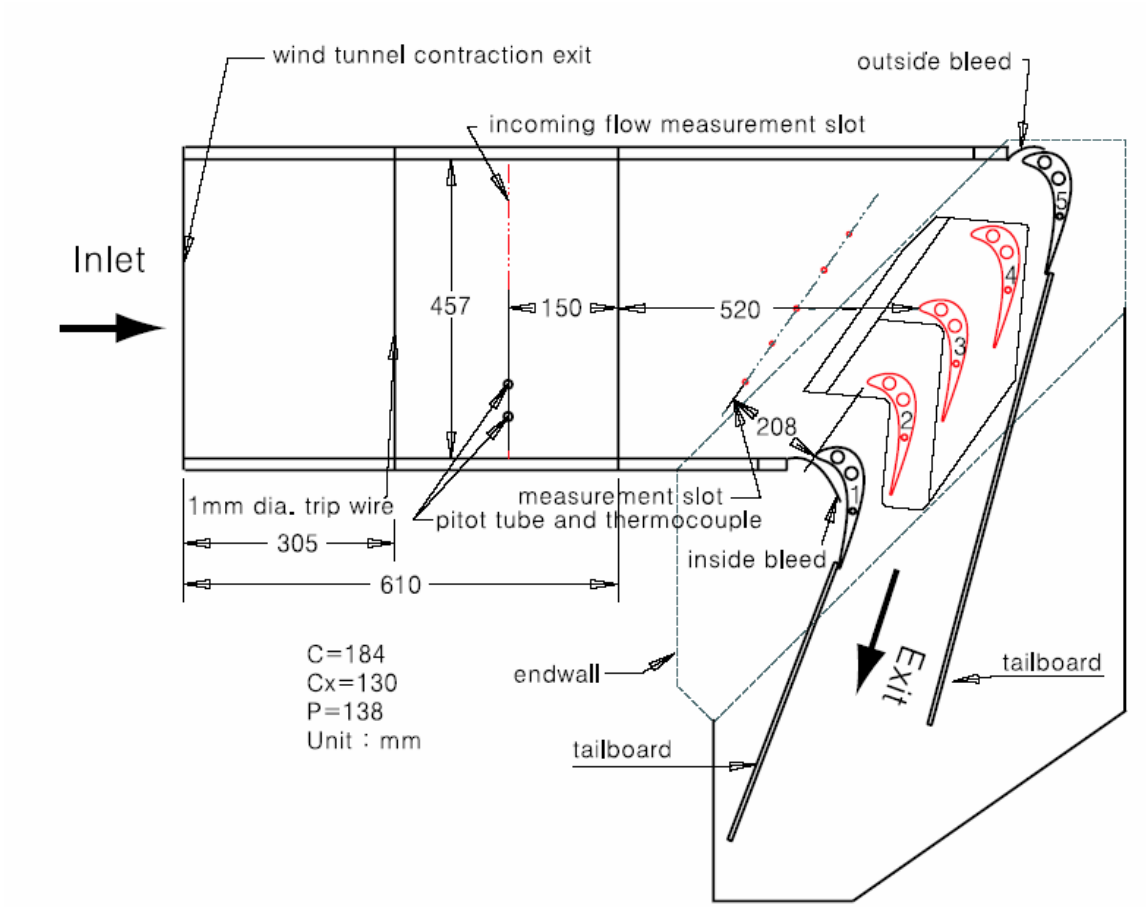

Figure 10: Linear rotor cascade facility

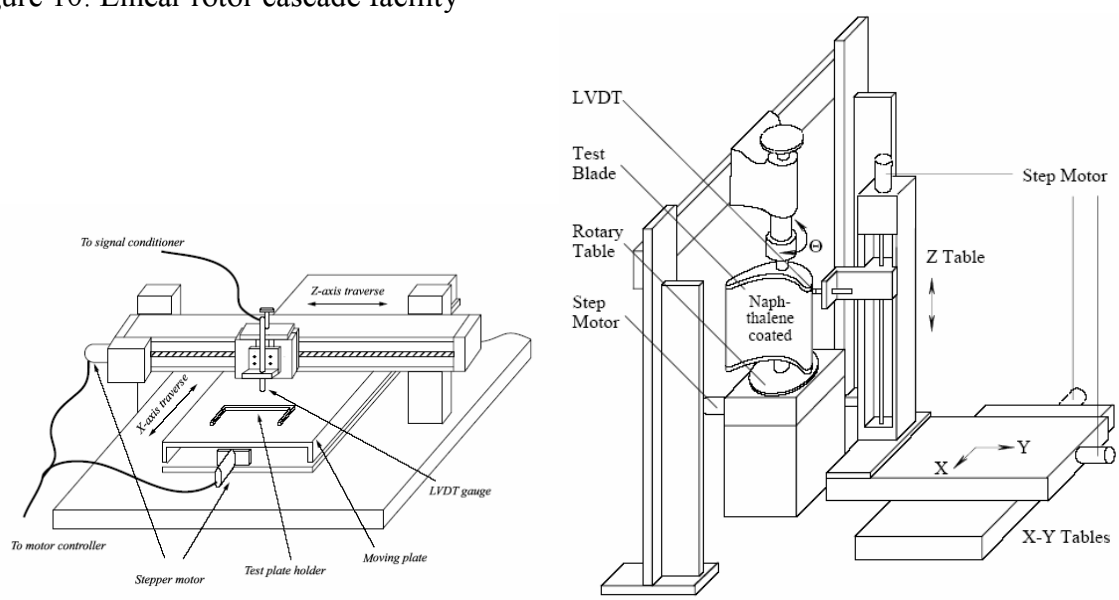

(a) 2-axis table (b) 4-axis table

Figure 11: Endwall and blade measurements systems for the acquisition of naphthalene surfaces profiles before and after exposure to the wind tunnel flow

(a) heat transfer plate

(b) mass transfer plate

Figure 12: Endwall plates for heat and mass transfer experiments

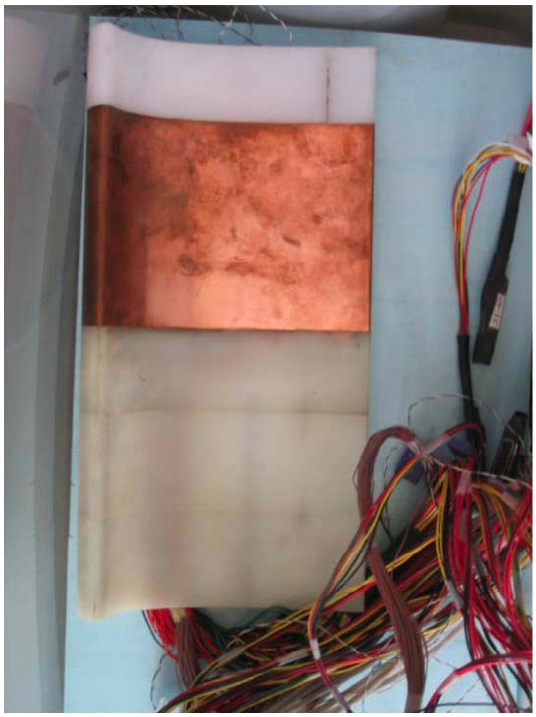

(a) heat transfer blade

(b) mass transfer blade

Figure 13: Blades for heat and mass transfer experiments

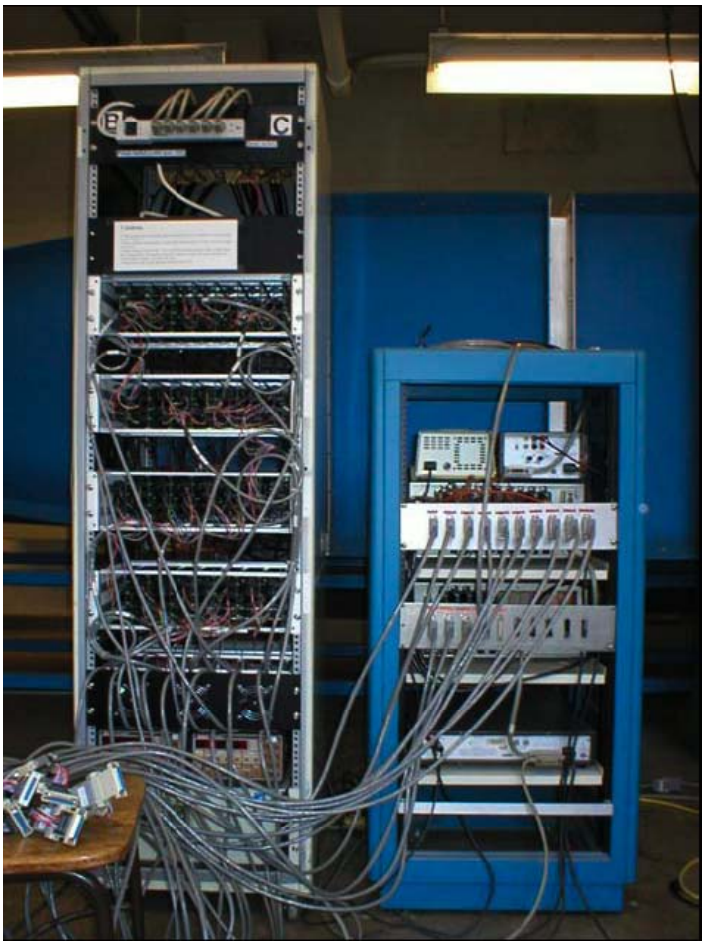

Figure 14 Digital power supply and measurement unit

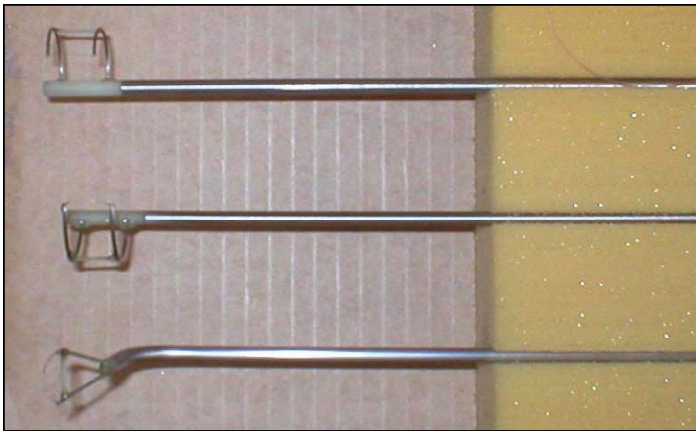

Figure 15 Photograph of temperature boundary layer probes used in the rotor cascade study

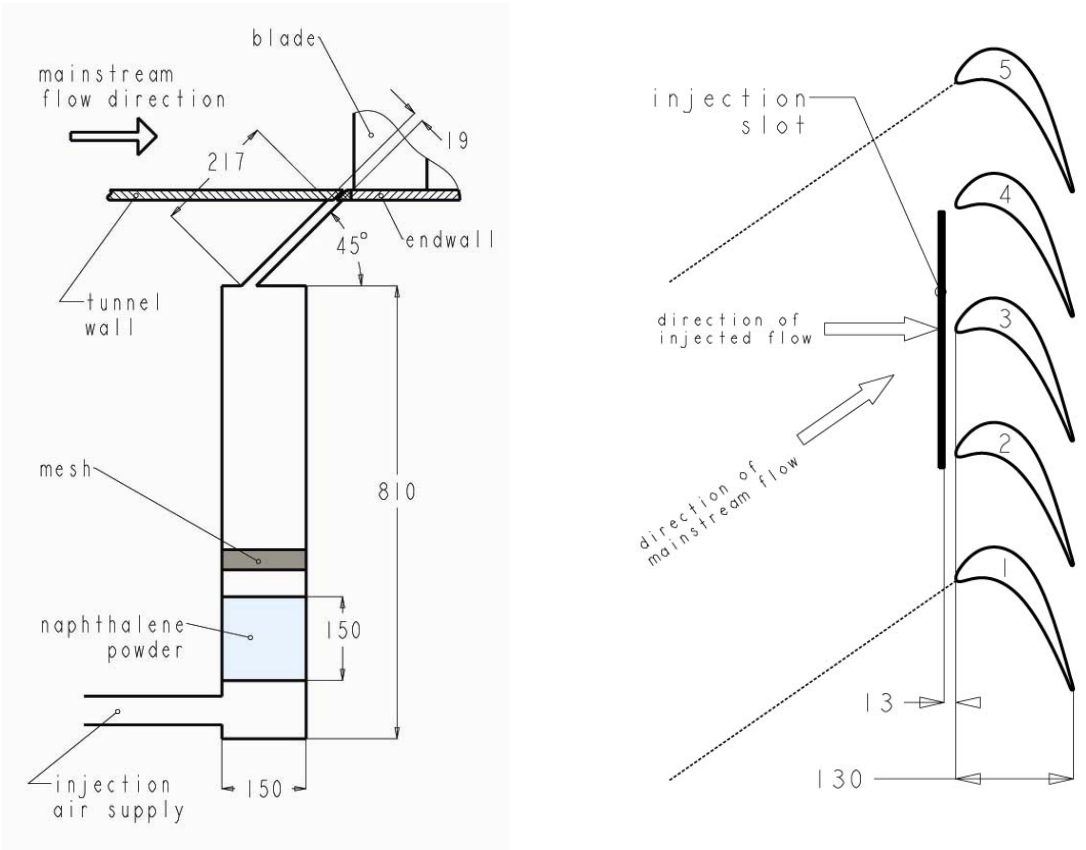

Figure 16: Schematic diagrams of injection system to simulate the wheelspace coolant injection upstream of the row of rotor blades

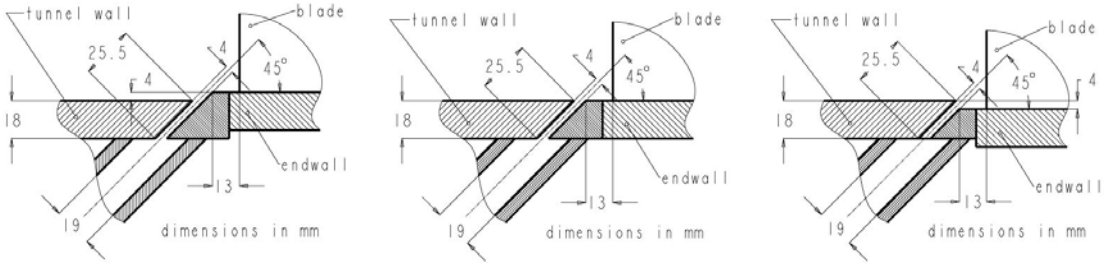

(a) step up (b) no step (c) step down

Figure 17: Gap configurations for the injection upstream of the rotor cascade

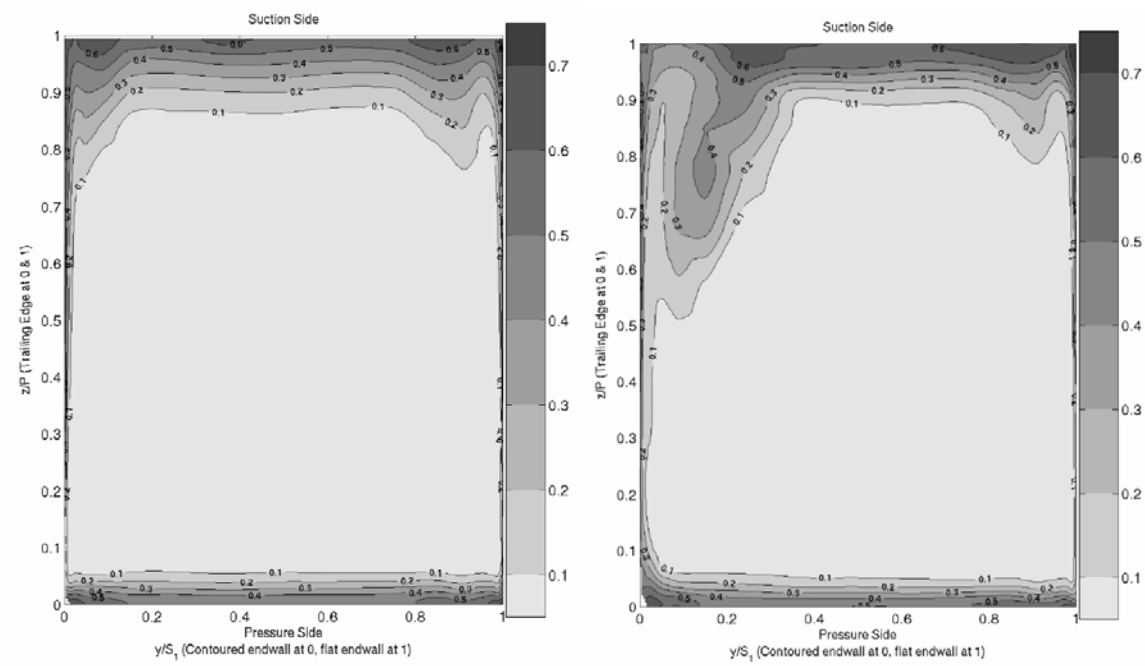

Figure 18. Exit pressure loss contours, $\frac{p_{0,1}(x,y) - p_{0,0}}{p_{0,0} - p_1}$. Smooth case (no steps, gaps or blowing), left, vs. nominal case (no steps, gaps open with 0.5% MFR through the transition section and slashface gaps), right. The main effect is due to flow into the upstream portions of the slashface gap, with ejection of that flow from the downstream portions of that gap.

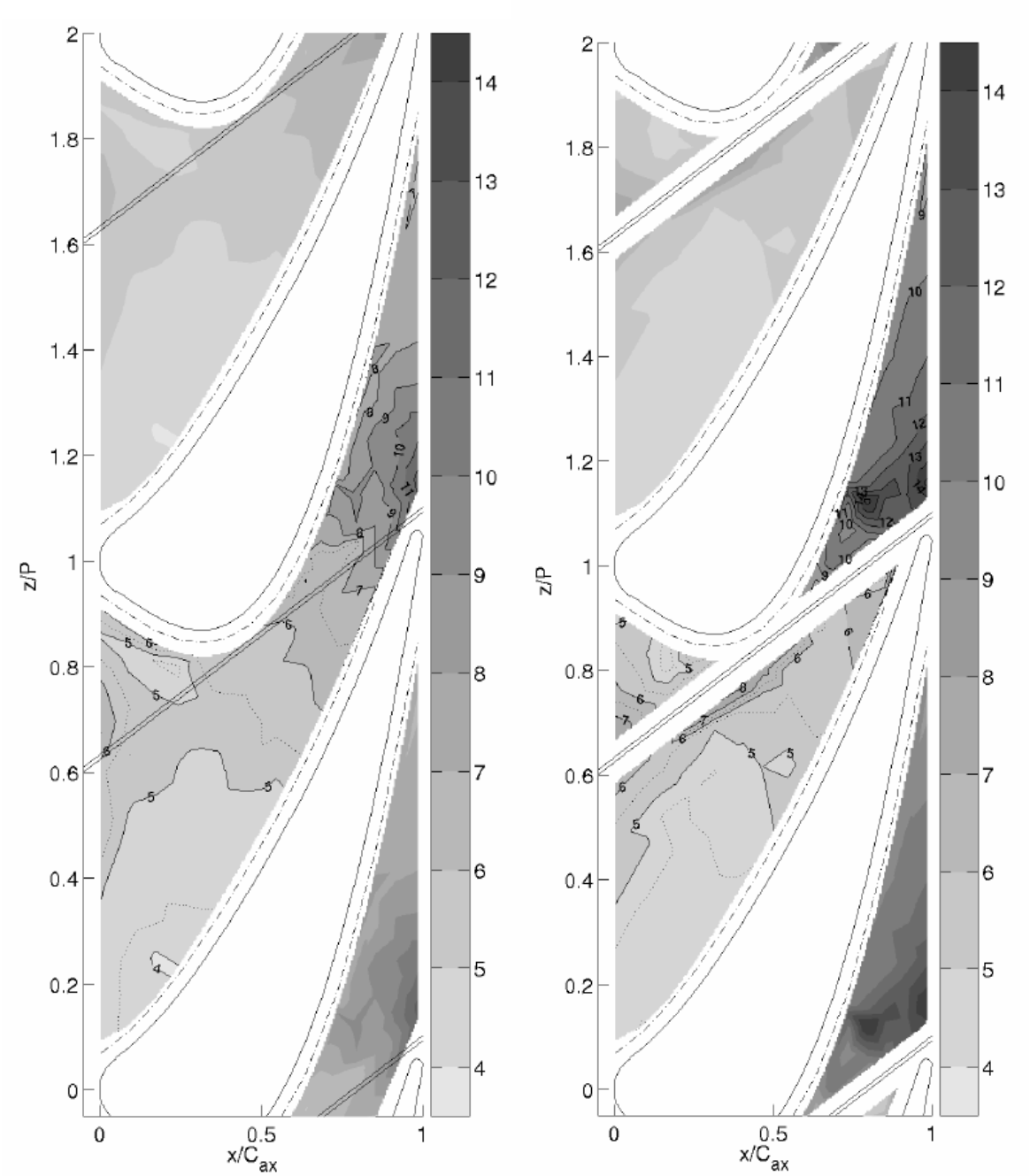

Figure 19 Endwall Stanton number distributions (x1000). Smooth case (no steps, gaps or blowing), left, vs. nominal case (no steps, gaps open with 0.5% MFR through the transition section and slashface gaps), right. The main effect on the heat transfer coefficient distribution is due to flow into the upstream portions of the slashface gap, with ejection of that flow from the downstream portions of that gap.

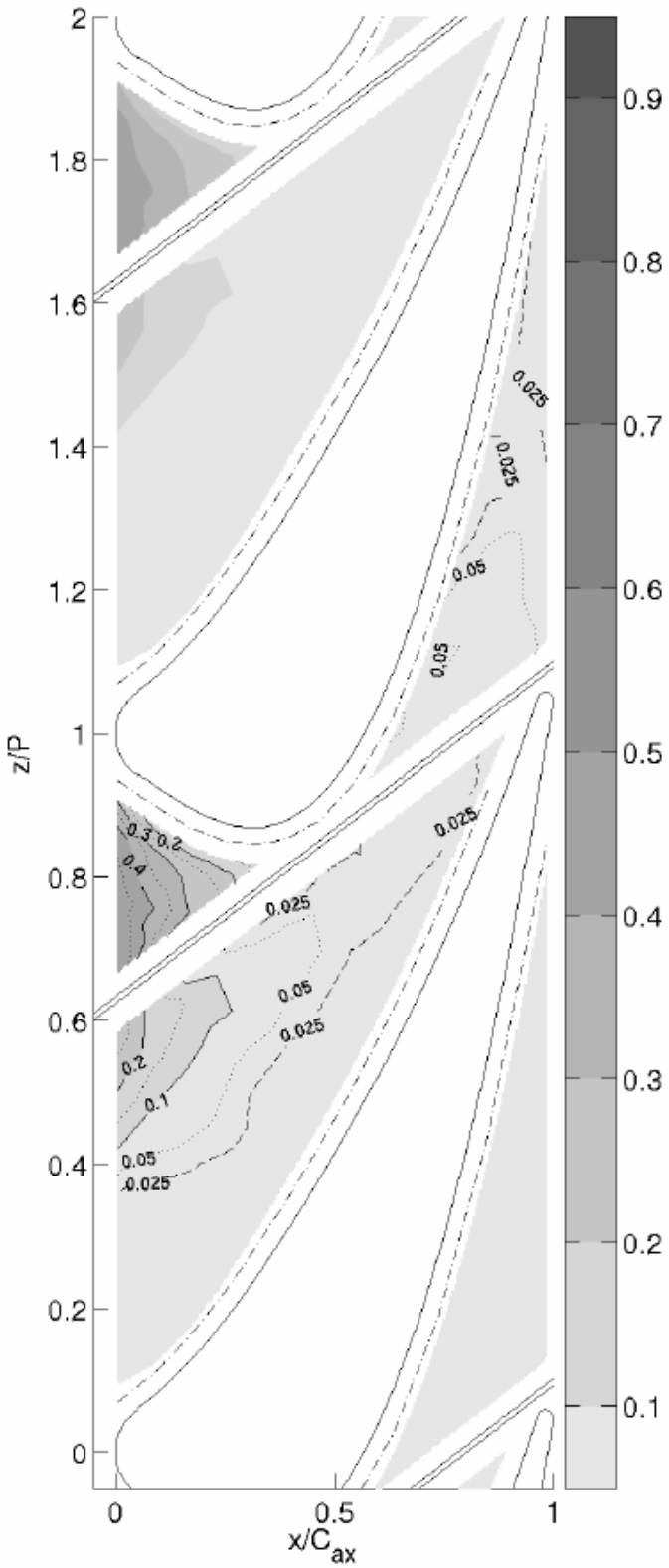

Figure 20 Adiabatic effectiveness value distribution for the nominal case (no steps, gaps open with 0.5% MFR through the transition section and slashface gaps).

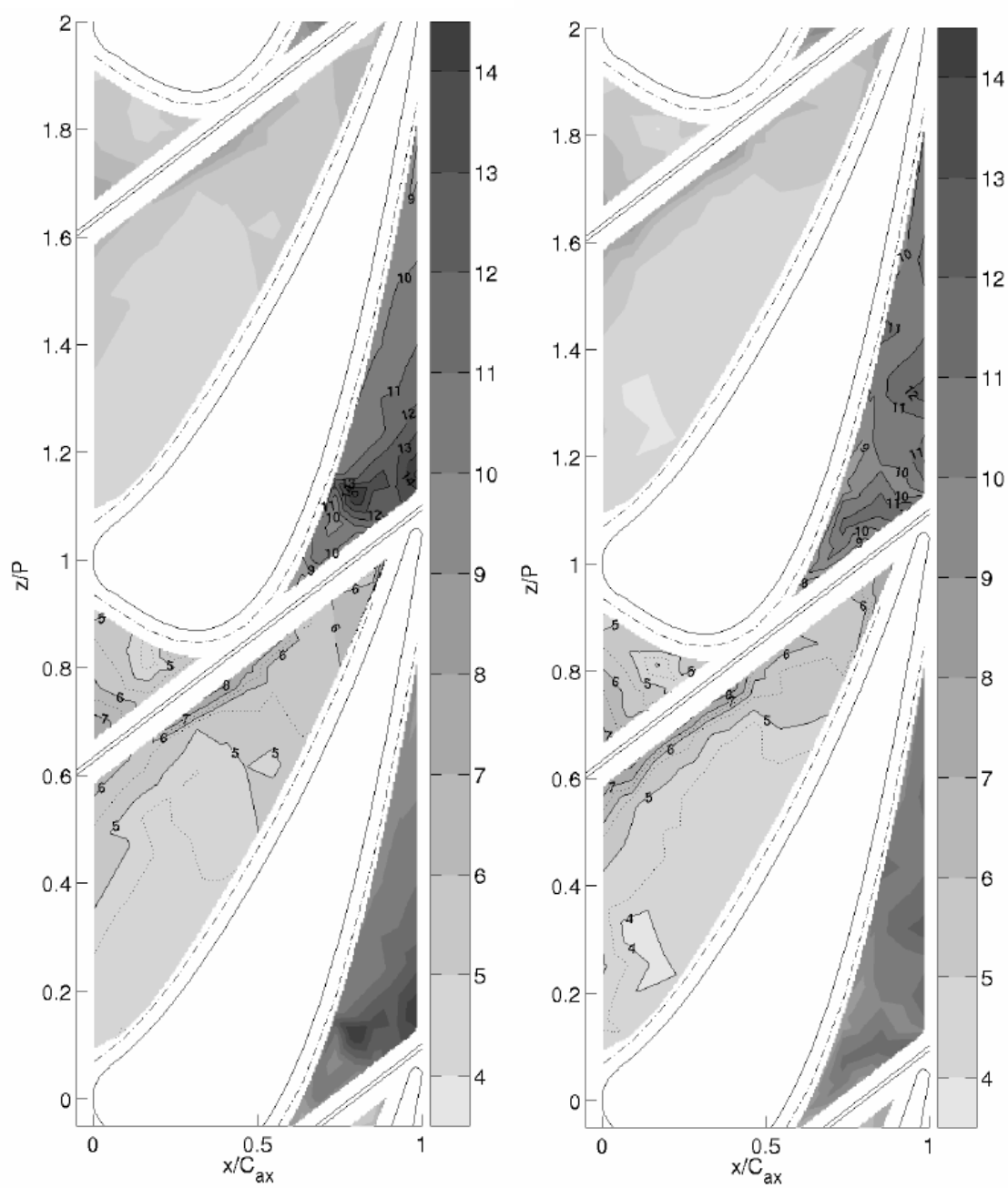

Figure 21 Stanton number (x1000) distributions for the nominal case (left) and the case with a backstep at the transition section gap (right).

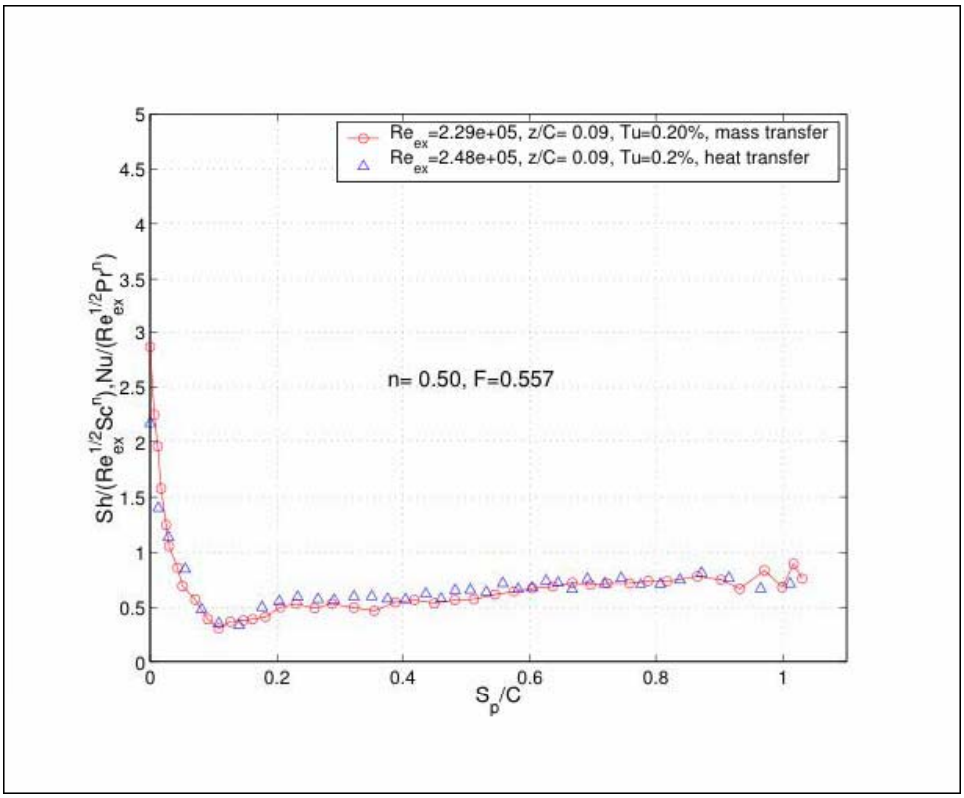

Figure 22 Heat and mass transfer comparison on the pressure side

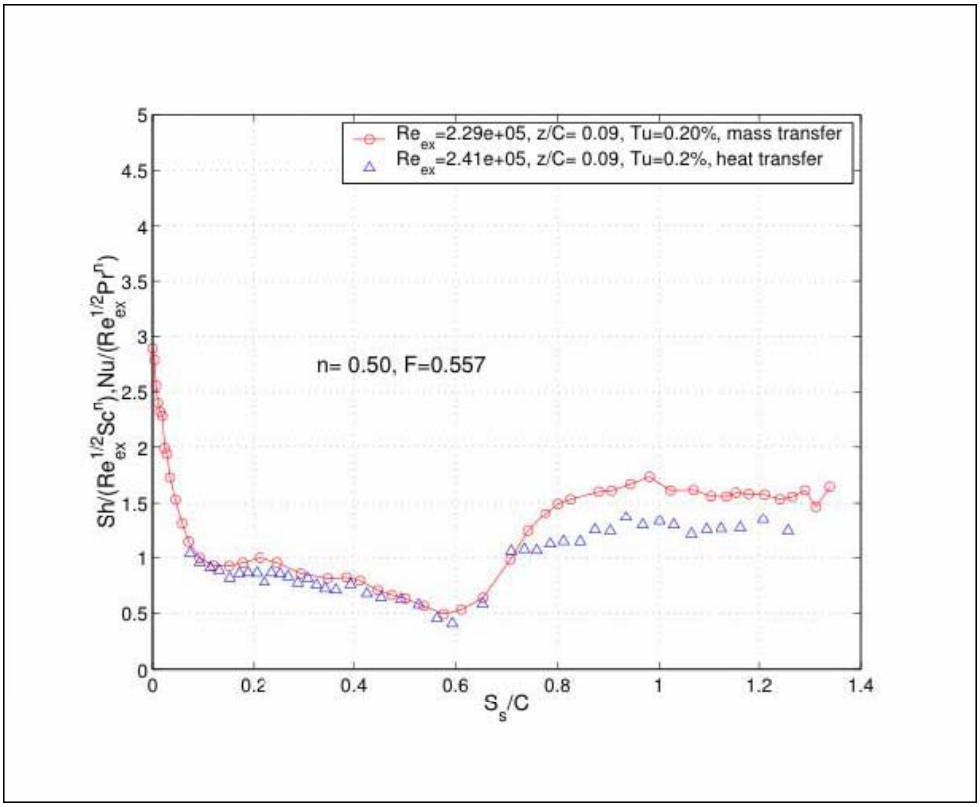

Figure 23 Heat and mass transfer comparison on the suction side

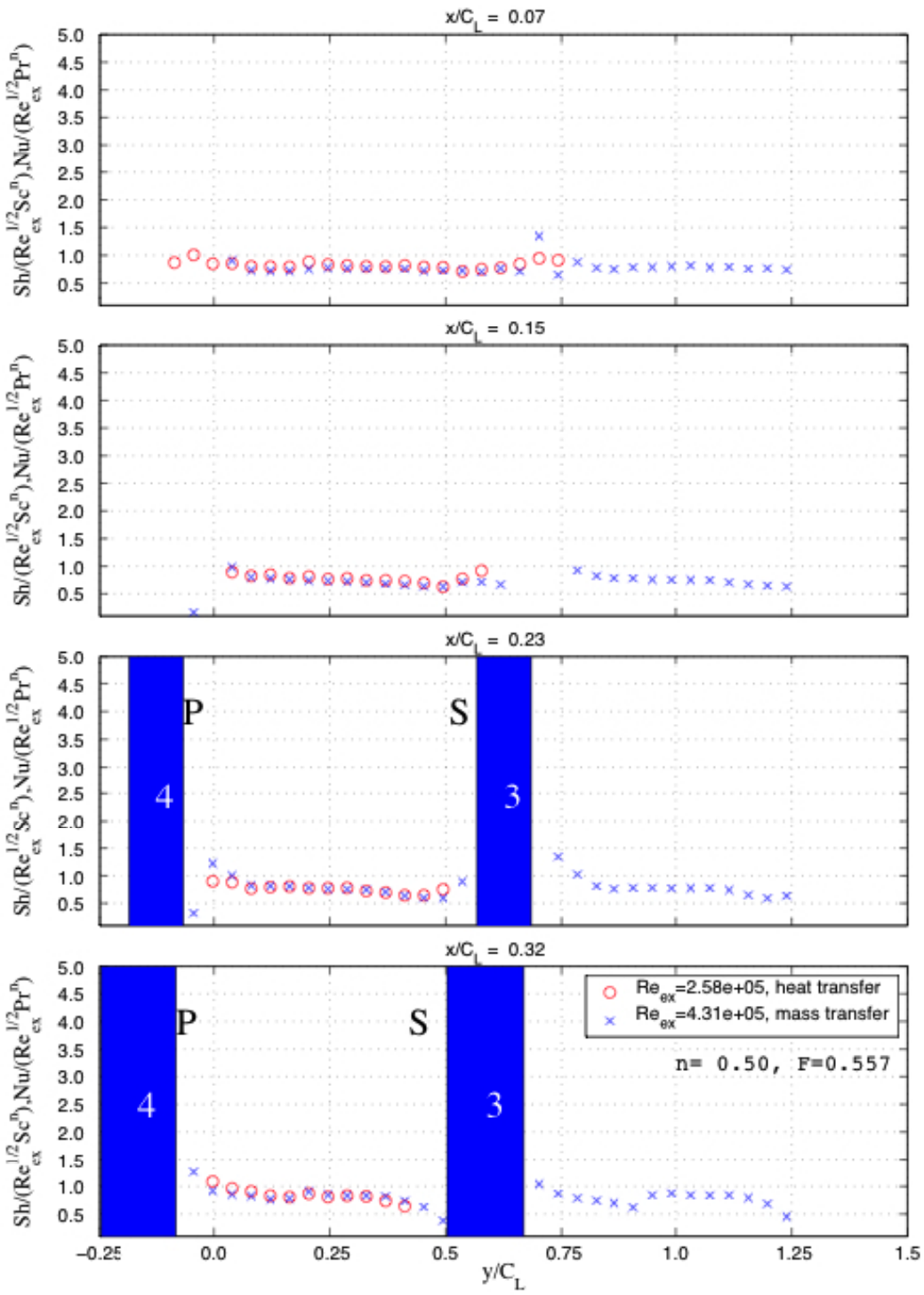

Figure 24 Nusselt and Sherwood number comparisons, with fillets

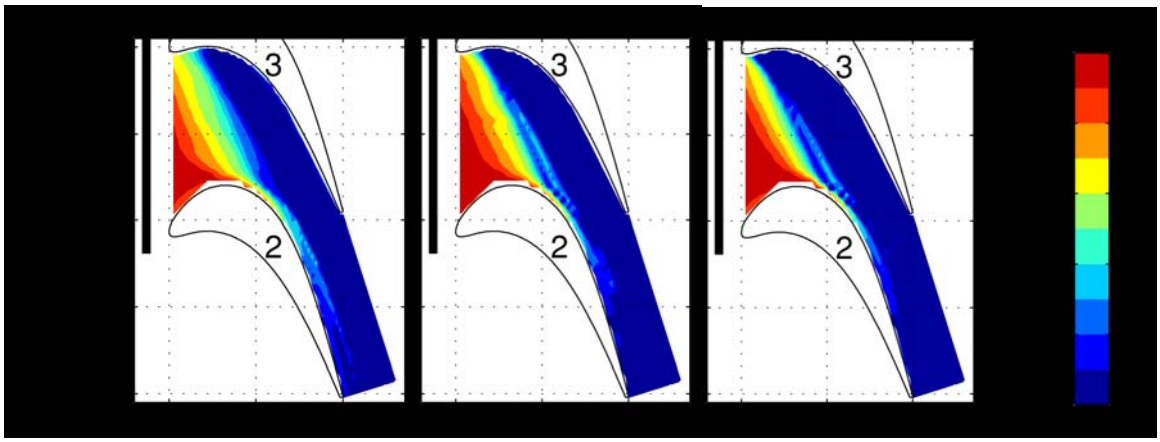

(a) step up (b) no step (c) step down

Figure 25 Adiabatic cooling effectiveness on bottom endwall in the rotor linear cascade with an effective blowing rate of unity

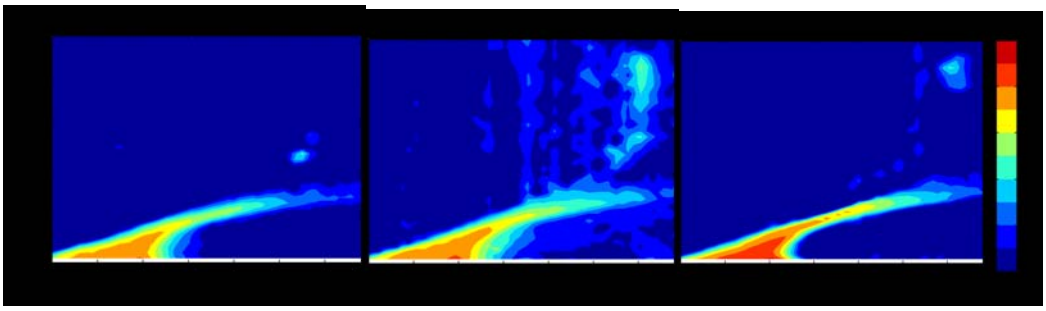

(a) step up (b) no step (c) step down

Figure 26 Adiabatic cooling effectiveness on blade suction side in the rotor linear cascade with an effective blowing rate of unity

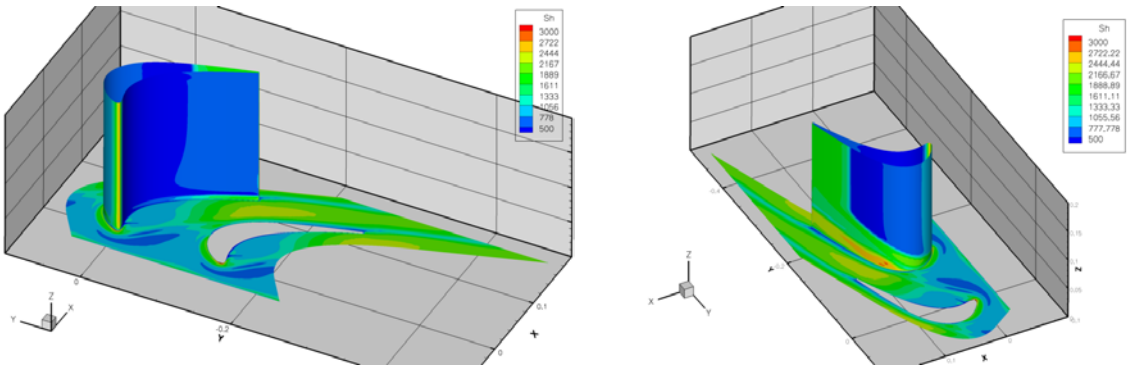

Figure 27 Sherwood number contour plots obtained from numerical simulations

MEASUREMENT OF THREE CRITICAL PARAMETERS AS A BASIS FOR A SIMPLE THERMAL BARRIER COATING LIFE PREDICTION METHODOLOGY

Semi-Annual Report
November 1, 2004 – April 30, 2005

Principal Investigators:
Dr. Eric Jordan and Dr. Maurice Gell

Student Researchers
Mei Wen, Swetha Sridharan
Nov 2004

Work Supported under DOE Contract
DE-FC26-02NT41431
UTSR 02-01-SR097

97 N Eagleville Road
Institute of Materials Science
University of Connecticut
Storrs, CT 06269

ABSTRACT

This report describes progress during the sixth 6-month period (November 1, 2004-April 30, 2005) of performance under a three-year program. The program is designed to develop a remaining life prediction system based on non-destructive measurement of three quantities, initial surface geometry, thermally grown oxide (TGO) stress and TGO thickness. In this reporting period, which is the final one in the original program schedule not including the no cost extension, emphasis was on comprehensive write up and interpretation of results. Accordingly this report includes complete summary of results obtained on 2 of the five systems studied. In addition it includes new results by which the cause of the observed bimodal spectra is shown to be oxide cracking and results for tests at 1100 º. During the no cost extension full write up of the other 2 systems along with the testing of the two phase bond coated system will be completed and put into a single comprehensive summary report.

The principal results to date include a life prediction method based on all three parameters needed for MCrAlY bond coated samples and a system which requires only non destructive measurement of oxide stress for Pt modified Ni Al bond coated samples. Using only measured stress remaining life predictions are made temperature blind and for EB-PVD/Pt-Al TBCs cycled at three temperatures (1100º ,C1151°C and 1121°C). The predictions for two temperature histories were made for the first time based on the thermally grown oxide stresses measured by the photoluminescence piezospectroscopy technique without knowing the test temperature. The predictions were compared using regression methods and neural network methods. It was found that both methods produce accurate life remaining predictions, but the neural network methods were superior. The lowest root mean square (RMS) error and maximum absolute error for the prediction was 6.1% and 8.2% respectively. For a data set with a 48.7% RMS spallation life variation about the mean, the prediction results obtained are highly encouraging. In addition, 1-hour thermal cycling tests are being carried out at 1100°C on EB-PVD Pt-Al TBCs. Photoluminescence piezo spectroscopy (PLPS) measurements are carried out throughout the thermal cycling. The evolution of PLPS spectral characteristics (average value of stress and its standard deviation, peak width, intensity ratio, number fraction of bimodal peak) is being studied.

1. Introduction

DISCLAIMER

This report was prepared as an account of work sponsored by an agency of the United States Government. Neither the United States Government nor any agency thereof, nor any of their employees, makes any warranty, express or implied, or assumes any legal liability or responsibility for the accuracy, completeness, or usefulness of any information, apparatus, product, or process disclosed, or represents that its use would not infringe privately owned rights. Reference herein to any specific commercial product, process, or service by trade name, trademark, manufacturer, or otherwise does not necessarily constitute or imply its endorsement, recommendation, or favoring by the United States Government or any agency thereof. The views and opinions of authors expressed herein do not necessarily state or reflect those of the United States Government or any agency thereof.

Thermal barrier coatings (TBCs) are widely used in gas turbine engines for propulsion and power generation to protect metallic components from the hot gas stream (*1-9*). The use of TBCs, along with improved structural design and internal cooling technology, increases the temperature capability and engine efficiency of gas turbine engines. Thermal barrier coatings comprise four layers: (1) a ceramic top coat which is usually 7 wt.% yttria-stabilized zirconia (7 YSZ); (2) a thermally grown oxide (TGO) layer, predominantly α-alumina, that forms between the ceramic top

coat and the bond coat; (3) an oxidation-resistant metallic bond coat; and (4) a superalloy substrate. All layers interact to determine the performance and durability of TBCs. Since spallation of TBCs can result in exposure of turbine component to high temperatures and lead to pre-mature component failure, the assessment of durability is one of the most important issues in the use of TBCs. In addition, non-destructive inspection techniques and accurate life prediction methods for TBCs are highly desirable, and would contribute to the more effective use of TBCs.

There are two commercial processes for the production of TBCs, i.e., air plasma spray and electron-beam physical vapor deposition (EB-PVD). Failure of EB-PVD TBCs typically originates at either the bond coat/TGO or the TGO/YSZ interfaces. The compressive stresses developed in the TGO layer due to the thermal expansion mismatch between the TGO and the underlying metal layers and due to TGO growth play important roles driving failure of the ceramic by spallation. Photoluminescence Piezospectroscopy (PLPS) has been used successfully to non-destructively measure the stress in the TGO based on the frequency shift of the R-line fluorescence from the chromium (Cr^{3+}) impurity in the TGO and has the potential to detect early TBC damage and assess the remaining life of TBCs.

The present study is designed to develop and experimentally validate methods for the life predictions of EB-PVD TBCs based on measurements of one or three critical properties: TGO stress, TGO thickness and bond coat surface geometry. Failure mechanisms are also studied to facilitate fundamental understanding of TBCs and to aid in the development of life prediction methodologies.

Different TBCs have different failure modes, thus life predictions must take the characteristic behavior of individual system into consideration. In this research, spallation failure in one TBC with a (Ni,Pt)Al bond coat was found to be associated with rumpling and the TGO stress was directly affected by the rumpling. The remaining life prediction was made successfully based on the systematic change of TGO stress during thermal cycling measured by photoluminescence. For another TBC with a NiCoCrAlY bond coat, spallation failure was associated with the out-of-plane tensile stress which is affected by bond coat surface geometry and strain energy in the oxide layer. The life prediction was made based on measurements of three critical TBC properties: TGO stress, thickness, and surface geometry of the bond coat and correlating these properties by fracture mechanics.

2. Background

The efficiency of gas turbine engines is improved with higher firing or turbine inlet temperature. The continuing quest for higher temperatures and improved component durability in gas turbine engines has been the fundamental driving force for the development of thermal barrier coatings (TBCs). To date thermal barrier coatings are widely used in turbine engines for propulsion and power generation to protect metallic components from the hot gas stream (*1-9*). The use of TBCs, along with improved structural design and internal cooling technology, provides reductions in the surface temperature of the superalloy and increases the temperature capability of gas turbine engines (Fig. 2.1). This enables engines to operate at temperatures that are 90-150°C (200-300°F) higher, thereby improving engine efficiency (*6*). In addition, lowering the temperature of the superalloy protects metal components from environmental attack, creep rupture, or fatigue and improves the durability of components (*6*).

2.1 Thermal Barrier Coating System

There are four primary constituents in a thermal barrier coating system (Fig. 2.2). They comprise (1) a ceramic top coat which is usually 7 wt.% yttria-stabilized zirconia (7 YSZ); (2) a thermally grown oxide (TGO) layer, predominantly α-alumina, that forms between the ceramic top coat and the bond coat; (3) a metallic bond coat; and (4) a superalloy substrate. All layers interact to determine the performance and durability of TBCs.

2.1.1 Ceramic Top Coat

The ceramic top coat provides thermal insulation and yttria stabilized zirconia (YSZ) has been found to be most suitable for thermal barrier coating applications. YSZ has low thermal conductivity (~1 $W/m^2 K$) with minimal temperature sensitivity (*8*). YSZ has high thermal expansion coefficient (~11×10^{-6} $°C^{-1}$, which helps alleviate stresses arising from the thermal expansion mismatch between the ceramic top coat and the underlying metal substrate (~14×10^{-6} $°C^{-1}$) (*9*). YSZ also meets other fundamental requirements of thermal barrier coating material: high melting point (~2700°C), relatively low density (~6.4mg•m^{-3}), high thermal shock resistance, and resistance to oxidation and chemical environmental attack (*6*).

YSZ exists as three different phases-monoclinic, tetragonal, and cubic-depending on the composition and temperature (Fig. 2.3). 7 to 8 weight% (~4 to 4.5 mol%) Y_2O_3 stabilized ZrO_2 has been found to be most successful in thermal barrier coatings and consist of the tetragonal t' phase. The t' phase is thought of being crystallographically similar (i.e. having the same unit cell arrangement) to t phase, but morphologically different (i.e. having different grain structure features such as antiphase boundaries, twins) (*10*). Unlike t phase with lower Y_2O_3 composition (~3 mol%), the t' phase does not undergo a martensitic transformation and has excellent strength and toughness.

2.1.1.1 Deposition Methods of Ceramic Top Coat

Two principal methods are currently used to deposit thermal barrier coatings. They are air plasma spray and electron beam physical vapor deposition (EB-PVD).

Each method produces characteristic microstructures with certain desirable attributes, as will be discussed below.

Plasma spray deposition is widely used in the coating industry. A schematic of plasma spray process is shown in Fig. 2.4. A DC electric arc between the cathode and anode in the plasma gun is used to ionize the carrier gas, which is usually a mixture of argon (Ar) and hydrogen (H_2) or nitrogen (N_2) and hydrogen (H_2) to generate aplasma. The temperature of the plasma gas at the anode nozzle may reach as high as 6000-12000°C, and the gas velocity may reach on the order of 200-600m/s (*6*). The YSZ ceramic powder, with particle size of 20-100 μm, is injected into the high temperature, high velocity plasma jet. The powder is entrained in the plasma gas, melted rapidly, and propelled toward the substrate by the carrier gas. Upon impact, the molten particles deform and are rapidly quenched to form "splats" or pancake structures which eventually result in formation of the desired coating (*7*). Based on the process, air plasma spray TBCs have characteristic microstructures shown in Fig. 2.5: (1) 15-25 vol% porosity which is introduced during deposition, (2) "splat" grain morphology with inter-"splat" boundaries and microcracks parallel to the metal/ceramic interface. These defective structures contribute to the low thermal conductivity of air plasma spray (APS) TBCs. On the other hand, these microstructural defects have low toughness and are preferential sites for crack initiation (*9, 11*). The bond coat surface required for plasma sprayed TBCs is relatively rough and the initial adhesion mechanism between the ceramic and metallic layer is complemented by mechanical interlocking.

Electron beam physical vapor deposition is a more advanced method of deposition and widely used in the gas turbine industry for applying both metallic and ceramic coatings. A schematic of an EB-PVD production facility is shown in Fig. 2.6. In a large vacuum chamber, an electron beam is directed onto the surface of YSZ ingot target within a crucible. YSZ in the crucible is heated, melted, and then evaporated. Oxygen is also provided within the chamber and bled into the YSZ vapor cloud to maintain the oxygen stoichiometry in the deposited ZrO_2 film (*5, 6*). The vapor deposits as a coating on the airfoils, which are held in rotatable and retractable fixtures above the vapor source. A typical microstructure of EB-PVD TBCs is shown in Fig. 2.7. The YSZ layer grows in columnar structure with small intercolumnar gaps separating the column grains. The columnar structure provides a coating with excellent strain tolerance because the strain within the coating can be accommodated by free expansion (or contraction) of the columns into the gaps (*5*). In contrast to the plasma sprayed TBCs, EB-PVD TBCs achieve maximum durability when applied to a smooth surface and the coatings depend on chemical bonding for adhesion between ceramic and metallic layer. Generally EB-PVD TBCs are more durable, but more expensive, and have higher thermal conductivity, compared to APS TBCs.

During high temperature service, YSZ layer degradation can occur. The contributing factors are sintering and grain growth, thermal decomposition of the t' phase, and the tetragonal-monoclinic phase transformation. Sintering at temperature as low as 1100°C has been found during service and it has been recognized that sintering is detrimental to coating performance (*12, 13*). Sintering will result in partial healing of the cracks and reduction in porosity, and therefore increases the

thermal conductivity and elastic modulus of the top coat (*14*). An increase of thermal conductivity will lead to reduced thermal insulation and a higher metal surface temperature which accelerates the bond coat oxidation and creep. Sintering can also increase the elastic modulus (*13*) of the top coat and induce higher thermal stresses. This leads to reduced strain tolerance of the top coat and accelerates TBC failure. Moreover, sintering can result in coating shrinkage and through-thickness cracking during cooling, thereby further accelerating the coating failure (*12*).

As shown in the ZrO_2-Y_2O_3 phase diagram (Fig. 2.3), the YSZ transforms from cubic to tetragonal, and monoclinic when cooled from high temperature. The tetragonal-monoclinic transformation is accompanied by a volume expansion of ~4%. This volume change will destroy the integrity of the ceramic coating and cause crack initiation. Therefore, use of YSZ requires that the YSZ be stabilized in its high temperature tetragonal (or cubic) phase down to ambient temperatures. 7 to 8 weight% (~4 to 4.5 mol%) Y_2O_3 stabilized ZrO_2 is stable in current TBC applications and the phase decomposition is not a concern. However, higher temperature applications may impose more strict requirements.

2.1.2 Bond Coat

The bond coat provides oxidation protection and enhances adherence between the top coat and the substrate. The bond coat is arguably the most crucial component of the TBC that affects durability. Its chemistry and microstructure influence durability through the structure and morphology of the TGO created as it oxidizes (*15*). The ideal bond coat is engineered to form a defect-free layer of α-Al_2O_3 with

slow and uniform growth. Such a TGO has a very low oxygen diffusivity and provides excellent diffusion barrier which decreases the oxidation of the bond coat. Significant bond coat characteristics that influence TBC reliability and durability include: composition (*16, 17*), deposition method (*1, 6*), post-processing (*18, 19*), surface roughness (*20, 21*), bond coat defects (*22, 23*). Moreover, system performance is related to its creep and yield characteristics (*8*). There are typically two types of bond coat, MCrAlYs and Platinum Aluminides. MCrAlYs such as NiCrAlY, NiCoCrAlY, and CoNiCrAlY, typically are deposited by low pressure plasma spray and high velocity oxygen-fuel methods. MCrAlYs usually consist of two phases (β-NiAl and either γ-Ni solid solution or γ'-Ni_3Al). The other type of bond coat is a Pt-modified diffusion aluminide, fabricated by electroplating a thin layer of Pt on the substrate and then diffusion-aluminizing by either chemical vapor deposition or pack cementation. These bond coats are usually single phase β, with Pt in solid solution (*15*). These two types of bond coats result in distinct TGO characteristics as well as differing tendencies for plastic deformation (*8*).

2.1.3 Thermally Grown Oxide

The bond coat oxidizes during coating processing and during service. A thin layer of thermally grown oxide (TGO; 1-10 μm in thickness) is formed between the bond coat and the ceramic top coat. Since the bond coat is designed as a local Al reservoir (Fig. 2.2), Al_2O_3 forms in preference to other oxides and is the most stable oxide product (Fig. 2.8). Whenever Al_2O_3 is stable, the oxygen activity at the interface is too low to form alternative oxides. Since alumina has very low oxygen

diffusivity, TGO provides an excellent diffusion barrier and retards further bond coat oxidation (*24*). The TGO also can provide adherence of the ceramic layer with the substrate. The TGO has a major influence on TBC durability (*15, 25-28*). This layer develops large residual compressive stresses due to thermal expansion mismatch with the substrate (Table 2.1) during cooling and TGO growth at high temperature. The high strain energy stored in this layer plays an important role in the failure mechanisms that will be discussed in section **2.2**.

2.1.3.1 TGO Perfection and Growth

The TGO layer is a reaction product that forms between the bond coat and the YSZ. Generally the growth rate is consistent with a parabolic law until spalling occurs:

$$h^2 = 2k_p t \qquad (2.1)$$

where h is the TGO thickness, t is time and k_p is the parabolic rate constant. The TGO growth is diffusion controlled rather than interface controlled (*8, 29-31*). The alumina grows predominantly by inward diffusion of anions (oxygen ion) along the TGO grain boundary, but in some cases TGO growth is controlled by outward diffusion of cations (Al ion). Although α-Al_2O_3 is the ideal and stable oxide product of bond coat oxidation, θ-Al_2O_3 forms first and then transforms to α-Al_2O_3 in some cases, especially on the Pt modified aluminide bond coat (*32-36*). The phase constituents of the TGO, especially during the early stages of oxidation, have been identified as critical factors influencing the adhesion at the TGO/coating interface (*18, 37, 38*). Specifically, the formation of transient θ-Al_2O_3 and its conversion to the

stable α-Al_2O_3 has been reported to have a profound effect on the structural integrity of TGO/coating interface. The transformation from θ- to α-Al_2O_3 is responsible for additional residual stress from the volumetric shrinkage in the TGO and nucleation of tensile cracking (*35, 36*). Therefore, the formation of a "perfect" oxide that consist only of stable α- Al_2O_3 prior to deposition of YSZ may lead to improved durability and reliability of both stand-alone metallic coatings and TBC bond coats. For MCrAlY bond coats, other non-Al_2O_3 oxides such as Cr_2O_3, Ni, Co-containing spinels can form during the transient oxidation stage and become the preferential location of crack initiation in the later stage of oxidation (*8, 9, 39*).

2.1.3.2 TGO Stress

The stresses in the TGO exert a central influence on TBC failure. There are two main sources of stress: one from thermal expansion mismatch upon cooling and the other from TGO growth at high temperature (*15, 40-44*). Ambient temperature measurements by X-ray diffraction (*45*) and photoluminescence piezospectroscopy (*40*) indicate that thermal expansion mismatch results in large compression (range between 2 and 6 GPa). High temprature X-ray peak shift measurements of growth stress (*45, 46*) show that growth stress is also compressive but much smaller than the thermal stress. Both stresses may be alleviated by TGO creep (*47, 48*) , TGO/bond coat interface rumpling (*49, 50*) and redistributed in the vicinity of imperfections (*51, 52*). Moreover, the stresses can be modified by thermal cycling conditions. The role of TGO stress and the high strain energy stored in this layer in the failure mechanisms will be discussed in section **2.2**.

2.1.3.3 TGO adhesion

The interface between the TGO and bond coat is critical since a weakly bonded scale can spall at the TGO/bond coat interface. Bond coat composition has a strong effect on TGO adherence. It is known that the segregation of S at the TGO/bond coat interface reduces the TGO adhesion dramatically (*53*). In addition, some other elements such as Y, Zr, Si, Hf have been added in the bond coat and show the improvement in TGO adherence and oxidation resistance of the bond coat (*16, 54-57*).

2.1.4 Substrate

The superalloy substrate sustains the structural and thermal loads. The substrates are usually Ni-based or Co-based superalloys with addition of various elements that are added for the enhancement of specific properties, such as high temperature strength, ductility, oxidation resistance, hot corrosion resistance and castability (*58*). The superalloy can be cast in single-crystal, directionally solidified-columnar grain, or poly-crystalline forms. It has been reported that substrate materials have an influence on cyclic TBC life (*59*). In addition, diffusion of the elements can occur between the substrate and the bond coat during engine service. These diffusing elements can occasionally be found in the TGO and the top coat, as well (*60, 61*). This interdiffusion also has profound influence on spallation failure of the TBC, making it necessary to build the right balance between components of the TBC.

2.2 TBC Failure Mechanisms

Thermal barrier coatings exhibit multiple failure mechanisms. The failure mechanisms of a specific TBC system depend on many factors, such as chemistry and processing of substrate (*59*), bond coat chemistry, morphology, and deposition method (*3, 62*), ceramic top coat microstructures and deposition method (*3, 8, 9*), and testing conditions (*63-65*). One general observation about TBC degradation is that the failure of APS TBCs usually occurs within the ceramic top coat, near the YSZ/TGO interface (*3, 66*), while the spallation of EB-PVD TBCs is predominantly located at the TGO/bond coat or TGO/ceramic interfaces (*22, 67*). Some of the most common failure mechanisms have been reported and are shown in Fig. 2.9.

2.2.1 Crack Initiation, Propagation and Coalescence within YSZ

This mechanism is usually observed in APS TBC systems (*3, 66*). The bond coat surface is usually rough prior to the deposition of YSZ in the APS process, so as to improve the bonding between the ceramic top coat and the bond coat. The out-of-plane stresses are tensile at the crests and compressive at the troughs (*68*). The tensile stresses and the pre-existing defects within YSZ will lead to cracking within the YSZ above the crests (*69*). As the TGO thickens, the sign of the out-of-plane stress within YSZ starts to switch at locations above the peaks and valleys of the bond coat, i.e., the stresses at the crests change from tensile to compressive, while those above the troughs change from compressive to tensile (*68, 70*). This sign transition of residual stress will cause cracking within YSZ above the troughs between the crests (*70*). The

cracks propagate and coalescence which eventually lead to the spallation failure of the coating (Fig. 2.10).

2.2.2 Separation at TGO Interfaces

This failure mechanism is usually observed in EB-PVD TBCs since the top coat is more "strain tolerant" than that in APS TBCs. When the TGO layer is perfectly flat, the TGO layer is under biaxial compression and there are no tensile stresses across the TGO/bond coat interface that can cause separation. However, in practice, the interface between the TGO/bond coat is not planar and always has some undulations or imperfections. The stress state of the TGO/bond coat interface has been analyzed by a number of authors (*8, 21, 71, 72*). Both analytical solutions (*71, 73*) and finite element calculations (*71, 74*) show that cooling of the oxide layer produces tensile stress across the TGO/bond coat interface at the ridges and corresponding compressive stress in the valley regions. When the oxide scale is thin with respect to the local radius of curvature of the asperity, the finite element results for the tensile stress across the interface can be represented with considerable accuracy by using a soap-film analogy (Fig. 2.11) in which the normal stress is given by the Laplace equation, namely the biaxial stress divided by the local curvature (*71*):

$$\sigma_N = -\left(\frac{1}{R_1} + \frac{1}{R_2}\right) \cdot h_{TGO} \cdot \sigma_0 \qquad (2.2)$$

where σ_N is normal (out-of-plane) stress in the TGO layer, σ_0 is the biaxial stress in the TGO layer, R_1 and R_2 are the principal radii of curvature at the asperities, h_{TGO} is the oxide thickness. As the TGO thickness increases, the normal stress increases.

Debonding occurs at the TGO/bond coat interface when the normal stress reaches a critical value (*75*). The debonding at the TGO/bond coat interface then produces a critical flaw with a strain energy release rate exceeding the interface toughness and leads to final failure driven by the strain energy stored in the TGO.

2.2.3 Cracking Nucleation in the TGO Imperfections

This failure mechanism is associated with imperfections located near the TGO layer, especially those that induce tensile stresses σ_{zz} normal to the TBC surface in the vicinity of the TGO (*8*). These stresses initiate cracks along trajectories having lowest toughness (*15, 76*). Undulations on the surface of bond coat are pervasive imperfections and failure is usually associated with progressive roughening of the bond coat surface (also referred to as rumpling and ratcheting) with thermal cycling (*8, 43, 49, 50, 64, 76-89*). When rumpling occurs, the TGO is displaced into the underlying bond coat. The amplitude of TGO displacement and undulations at the TGO/bond coat interface increase with increasing thermal cycles. The increase in the undulation amplitude induces out-of-plane tensile strains in the TBC. These strains can produce localized separation and cracking between the top coat and the substrate and eventually lead to large scale buckling and spallation failure of the TBC. The schematic process is shown in Fig. 2.12. To date, rumpling has been studied as a function of time during cyclic and isothermal oxidation. Rumpling does not occur during isothermal oxidation (*49, 79*). The effects of oxidation, initial surface roughness and coating thickness have also been studied (*49, 78, 79*). Rumpling does not occur and durability increases when the initial bond coat is smooth and when

imperfections are removed by polishing (*67*). In earlier thermal cycling experiments in an oxidizing atmosphere, rumpling was observed and lateral growth strain of oxide was assumed to be the prerequisite for rumpling (*76, 83, 88, 90*). Recently Tolpygo et al. (*79*) found that rumpling occurs as well during cyclic annealing in vacuum and it implies that TGO growth does not always play a major role in rumpling. Different rumpling mechanisms have been postulated after extensive research: (1) cyclic plastic strains in the bond coat driven by TGO growth and thermal expansion mismatch strains (*76, 83, 88, 90*), (2) bond coat martensitic transformation (*85*), (3) volume reduction in the bond coat due to β to γ' phase transformation (*49*), and (4) stress driven surface diffusion (*84*). In addition, rumpling may be driven by the combination of different mechanisms.

2.2.4 Spinels and Non α-Al_2O_3 Oxides Formation

This mechanism is observed in both EB-PVD and APS TBCs with MCrAlY bond coats (*15, 39, 87, 91-94*). Non α-Al_2O_3 oxides and spinels are thought to be the preferential path for crack initiation and propagation due to their brittle nature and the large volumetric change associated with their formation. The formation of these phases compromises the structural integrity of the TGO and accelerates localized oxidation by providing fast oxygen-diffusion paths (*8, 9*). These oxides, such as Cr_2O_3, NiO, Ni- and Co-containing spinels, $Y_3Al_5O_{12}$, or Y_2O_3 form mainly due to the Al depletion in the bond coat caused by oxidation and interdiffusion. When the Al content in the bond coat drops below a certain critical level, formation of Cr- or Ni-rich oxides or spinels will become thermodynamically possible and form below

the alumina scale. It is also possible that the formation occurs in breakaway oxidation of alloys (*92*). In this case, TGO cracking occurs on cooling due to high local surface curvatures and large thermal expansion mismatch. Such cracks would, on heating, create a direct transport path through alumina for oxygen to react with bond coat, and lead to the transient oxidation and formation of Cr- or Ni-rich oxides.

2.3 Non-destructive Inspection

Since the use of internal cooling and thermal barrier coatings enables gas turbine engines to operate at gas temperatures higher than their temperature capabilities, spallation of coatings can result in exposure of turbine component to high temperatures and lead to reduced component lifetimes. It is highly desirable to non-destructively evaluate the TBC condition and to assess its remaining life to determine whether engine components can be reliably used for another service interval. Current approaches involve using laboratory and/or engine part statistical data from groups of samples and determining minimum properties. One incentive for approaches based on non-destructive inspection is the prospect of using individual part behavior rather than statistical minimums. This may allow many parts with properties above the minimum to be more fully utilized. Therefore, remaining life predictions based on non-destructive inspection techniques would contribute to the more effective use of TBCs. Four NDI techniques are currently under development: Mid-Infrared Reflectance (MIR) (*95*), Thermal Wave Imaging (TWI) (*96, 97*), Electrochemical Impedance Spectroscopy (EIS) (*98, 99*), and Photoluminescence Piezospectroscopy (PLPS) (*23, 29, 30, 36, 38, 40, 100-106*).

Because of the translucent nature of YSZ TBCs particularly at MIR wavelength (3-5 μm), measured reflectance not only originates from the TBC surface, but also contains contributions from internal scattering within the coating and reflectance from the TBC/substrate interface. MIR technique monitors the changes in MIR reflectance and correlates the changes with the progress of the delamination near the TBC/substrate interface.

In the TWI technique, a pulse of heat is delivered to the specimen or component and the thermal signal amplitude distribution of the specimen is monitored as a function of time by an infrared camera. Non-destructive testing of materials is based on the fact that a defect region generally has a thermal conductivity difference from that of the reference region in the sample. Therefore, heat flows differently through the defect region than through the reference region. Differences in the heat flow result in differences in temperature distribution on the surface of the sample. A temperature distribution map can show hot spots and also elevated thermal wave amplitude signals.

In the EIS method, the electrochemical impedance response of TBCs to the applied voltage over a frequency range is examined and the obtained spectra are analyzed with an AC equivalent circuit consisting of elements (resistor, capacitor, inductor, etc). Since electrical conduction depends on the conductivity of electrolyte and micro-structural features of the multi-layers of TBCs (including the defect and damage through which electrolyte can penetrate), the characteristics of electrochemical process obtained from analyzing EIS spectra can be related to the

characteristics of materials system. However, the analysis and explanation of EIS spectra is not easy.

The PLPS technique, invented by Paton, Murphy and Clarke (*107*) for TBCs and further developed by Clarke et al. (*108-114*), Gell, Jordan, et al. (*29, 30, 36, 105, 106, 115*) , and Atkinson et al. (*116, 117*), has been used successfully in measuring the stress in the TGO non-destructively based on the frequency shift of the R-line fluorescence from the chromium (Cr^{3+}) impurity in the TGO. In addition to the frequency shift, other characteristics of the spectra such as peak width, peak shape and the peak area ratio can be extracted and provide information on the presence of damage (*112, 113, 118*).

The MIR and TWI techniques detect the partial debonding of the ceramic from the substrate and debonds larger than 1 mm can be detected. PLPS can detect debonds as small as several microns and can potentially assess coating quality and TGO damage prior to debonding by determining phase constituents of TGO and TGO stress. At present PLPS technique has been applied to both EB-PVD and APS coating. Since the columnar structure of EB-PVD coating acts as an optical waveguide for the lasers and the optical signals are not attenuated, PLPS can be used for full thickness EB-PVD coatings (≥300 μm) (*23, 29, 30, 105, 106*). In contrast to EB-PVD coatings, the microstructural defects in APS coating such as porosity and splat boundaries result in attenuation of the optical signal, making PLPS measurement viable for APS coatings of only ≤ 75 μm at present time (*103*).

2.3.1 Photoluminescence Piezospectroscopy

The basis of piezospectroscopy for measurement of stress is that an applied stress strains the lattice structure and alters the energy of electronic and vibrational states, which in turn alters the energy of any radiative transition such as photoluminescence. Thus, the applied stress can be determined by measurement of frequency shifts of luminescence lines. As shown in Fig. 2.13, the structure of α-Al_2O_3 is a hexagonal closed packed (hcp) structure with Al^{3+} ions occupying some of the octahedral sites. In α-Al_2O_3 a small fraction of Al^{3+} ions are always replaced by trace amounts of Cr^{3+} ions. The replacement will not produce undue strain in the crystal lattice due to their same ionic charges and similar radius (Cr^{3+} ion 0.69 Å, Al^{3+} ion 0.57 Å) (*119*). The electronic structure of α-Al_2O_3 with trace amounts of Cr^{3+} ion can be summarized in form of band diagram shown in Fig. 2.14 (*120*). The R_1 and R_2 fluorescence lines of Cr^{3+} ion in the α-Al_2O_3 are exceptionally sharp and occur at 14402 and 14432 cm^{-1} respectively. The frequency of R_1 and R_2 fluorescence lines is dependent on several factors. In addition to stress dependence, the fluorescence lines vary with temperature, applied electric or magnetic field, and dopant concentration. It has been experimentally verified (*121*) that the contributions to the fluorescence lines of Cr^{3+} ion in the α-Al_2O_3 from temperature, pressure, and concentration are essentially independent of one another in the range where measurements are practical. Therefore, the net frequency shift can be expressed as the superposition of each contribution:

$$\Delta\nu = \Delta\nu_{stress} + \Delta\nu_{temp} + \Delta\nu_{conc} \qquad (2.3)$$

2.3.1.1 Effect of Stress

The relationship between the observed line frequency shift in a fluorescence spectrum and the state of stress was first described by Grabner (*122*). The change in frequency Δν, can be expressed by the tensorial equation:

$$\prod_{ij} \sigma_{ij}^{c} = \prod_{ij} a_{ki} a_{lj} a_{kl} \qquad (2.4)$$

where $\prod_{ij}$ is the ij^{th} component of the piezospectroscopic coefficients and σ_{ij}^{c} is the stress state in the crystallographic basis of the crystal lattice. The mean line shift is obtained by averaging equation (2.4) over all possible crystallographic orientations (*110*). The line shift is only dependent on the trace of the stress tensor over the probed volume:

$$\overline{\Delta \nu_{stress}} = \frac{1}{3} \prod_{ii} \sigma_{jj} \qquad (2.5)$$

If assuming a flat alumina scale under biaxial stress $\sigma_{xx} = \sigma_{yy} = \sigma_0$ and $\sigma_{zz} = 0$, the frequency shift is:

$$\overline{\Delta \nu_{stress}} = \frac{2}{3} \prod_{ii} \sigma_0 \qquad (2.6)$$

The piezospectroscopic coefficients were determined experimentally and the values are 7.59 cm^{-1}/GPa for R_1 and 7.61 cm^{-1}/GPa for R_2 (*110*). The equation (2.6) can be used to determine the stress in the TGO from the frequency shift of R_2 line.

2.3.1.2 Effect of Temperature

Both R_1 and R_2 line shift to smaller wavenumbers with increasing temperature. The frequency dependence can be described as follows:

$$\Delta \nu_{temp} = \alpha (T - T_{ref}) \qquad (2.7)$$

where T_{ref} is the reference temperature, α is the linear fitting coefficients. It was found that α has a value of –0.144 and –0.134 $cm^{-1}/°C$ for the R_1 and R_2 lines respectively (*110*). Since all PLPS measurements are carried out at room temperature, the effect of temperature could be neglected if the variation of room temperature is minimal.

2.3.1.3 Effect of Chromium Concentration

The effect of chromium concentration of the frequency shift of R lines was investigated by systematic study on α-Al_2O_3 single crystal specimens at 77 K (*123*). Fig. 2.15 shows the linear relation of R_1 line frequency shift with respect to Cr concentration. It has been found that Cr concentration causes a linear variation on the R_2 line frequency shift as well. The linear relationship that is valid for Cr concentration of up to 1 wt% is shown as follows:

$$\begin{aligned} \Delta\nu_{R1} &= (0.96 \pm 0.05) \cdot C_{Cr}(wt\%) \\ \Delta\nu_{R2} &= (1.01 \pm 0.05) \cdot C_{Cr}(wt\%) \end{aligned} \qquad (2.8)$$

Schawlow et al. (*124*) analyzed the ruby spectra and investigated the effect of Cr concentration on the N-lines (Fig. 2.16). N-lines are the satellite peaks within a few hundred cm^{-1} away from the R-lines. It is shown that the N-lines intensities increase as the Cr/Al ratio increases. When the Cr concentration is below some level, the N-line intensity is too low to be detected.

2.3.2 PLPS Spectral Characteristics

In addition to the frequency shift, other characteristics of the spectra such as peak width, peak shape and the peak area ratio can be extracted and provide information on the material system (*36, 112, 113, 118*). Peng and Clarke (*112*) proposed that peak broadening is the result of stress variation within the probe volume. The observed spectrum is the superposition of several individual spectra, each corresponding to different stresses. Damage in the TGO would be expected to affect the localized stress and hence peak shape. To date such systematic shape changes with cycles have not been found in experiments, except as associated with bimodal peaks (Fig. 2.17), as now discussed.

One of the extreme cases of stress variation is that of a spectrum that contains two sets of R_1-R_2 peak pairs (also referred to as bimodal), exhibiting high and low (or stress free) stress components (*105, 112, 113, 116, 117*). It has been suggested that the low stress peak pairs are from the localized damage region (*105, 112, 113, 116, 117*). In such cases, the presence of low stress (or stress free) component is an indication of damage and it is potentially a means of quantifying local damage in the TGO. Selcuk and Atkinson (*116, 117*) mapped the low stress regions for an EB-PVD/Pt diffusion bond coat TBC and showed these regions were isolated at first and tended to coalesce into larger regions toward the end of life. It has also been suggested that the peak intensity ratio depends on the crystallographic orientation with respect to the polarization of the laser (*113, 118*). This can be a large effect for single crystal but not for polycrystalline alumina (*106*).

2.3.3 Determination of TGO Phase Constituents by PLPS

(Ni, Pt)Al bond coats can form metastable alumina phases, such as γ- and θ-Al_2O_3, in early oxidation and then transform to the stable α-Al_2O_3 phase (*32-36*). Besides stress measurement and damage detection, PLPS can also be used to determine the oxide type and its spatial distribution, which makes it a valuable tool to study alumina phase transformations (*32-36*) and control coating quality (*102*). Different phases of alumina (α, γ, θ-Al_2O_3) can be detected by the PLPS method due to the difference in the frequency of characteristic luminescence peaks. The difference of frequency is due to different crystal structure for alumina polymorphs. Fig. 2.18 shows example of luminescence spectra of different phases of alumina. From this figure, we can see that stress free α-Al_2O_3 has sharp peaks at around 14402 and 14432 cm^{-1}, stress free θ-Al_2O_3 has sharp peaks at around 14570 and 144620 cm^{-1}, and γ-Al_2O_3 has a broad band with a maximum around 14470 cm^{-1}.

2.4 Life Prediction

Spallation of TBC results in exposure of metallic components to hot gases and leads to components failure. This risk can be reduced if the spallation life can be reliably predicted. Therefore, life prediction is essential to take full advantage of TBCs.

Understanding of coating failure mechanisms is a prerequisite to the development of life models and, although understanding remains incomplete, there has been progress in this area in the past years. An oxidation-based model for TBC life was described in refs.(*1, 125, 126*). This model assumed that the complex states of stress and strain imposed on the coating system by the thermal loads could be

adequately expressed in terms of ε_r, the tensile, radial component of the thermal expansion mismatch strain. Next it was assumed that time-at-temperature effects could be described in terms of oxidation alone and that oxidation could be expressed in terms of the specific weight gain ω_N. The weight gain and strain were related in a Manson-Coffin type relationship and the model was used to calculate cycles-to-failure for plasma sprayed TBCs. Following this approach, a refined life prediction model was proposed by Cruse et al. (*27*) for plasma sprayed TBC. The cyclic strain was calculated using a modified form of the Walker viscoplastic material model which directly counts for both plasticity and creep effects. The correlation between the actual and predicted spallation lives was within a factor of 3.

Life prediction model was also developed for EB-PVD TBC based on the constitutive properties of the different TBC layers and fracture mechanics approaches (*28*). Specific activities included measurement of EB-PVD ceramic physical and mechanical properties and adherence strength, measurement of TGO growth kinetics, generation of quantitative cyclic thermal spallation life data, and development of a life prediction model based on maximum in-plane TGO tensile mechanical strain and TGO thickness. The model correlated the spallation lives within a factor of about ±2X (*28*).

Recently, the PLPS spectral characteristics have been evaluated as a function of 1-hour thermal cycles at a single temperature (*105, 106*). The preliminary results of using the systematic changes in stress levels and other spectral characteristics to make remaining life prediction was discussed in ref. (*127*). The remaining life

prediction was within ±7%. Therefore, PLPS is one of particularly promising technique in non-destructive inspection and life prediction of TBCs.

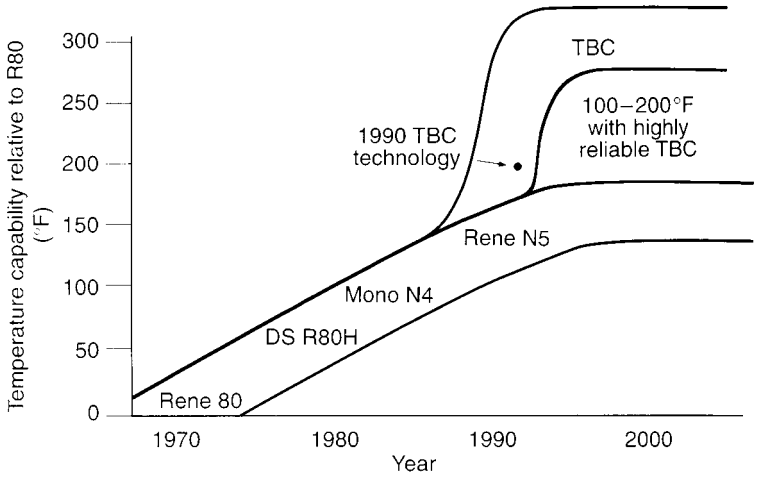

Fig. 2.1. Benefit of TBC applications (*6*)

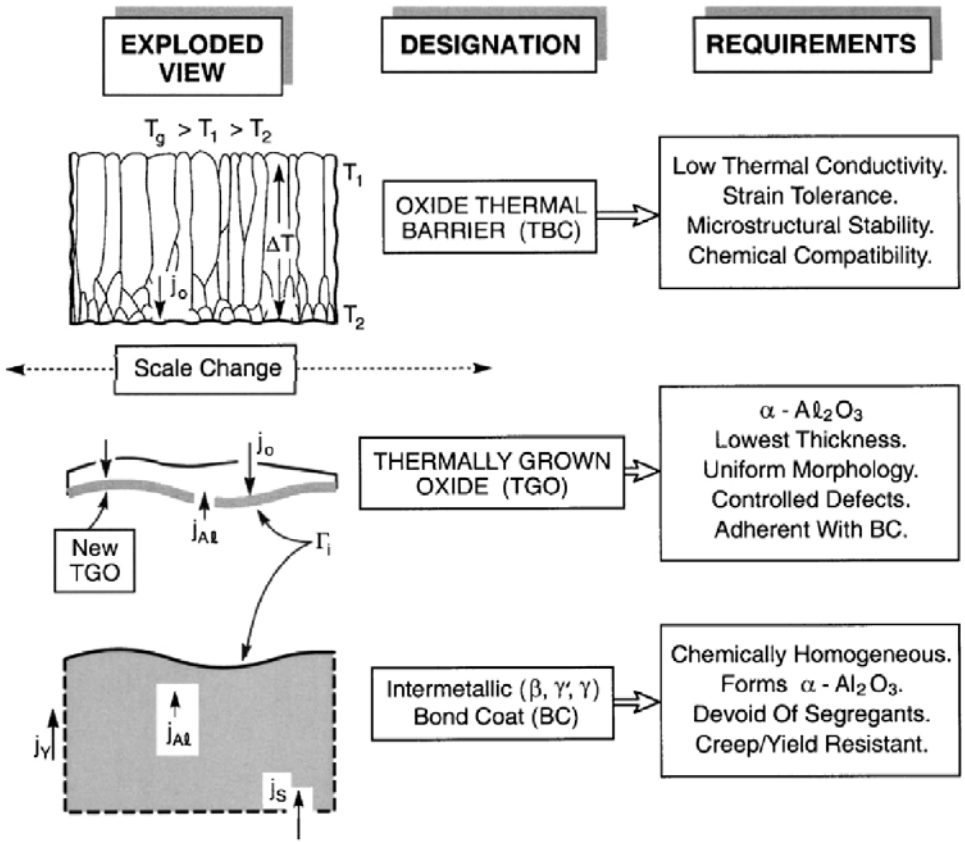

Fig. 2.2. Components of a thermal barrier system (*8*)

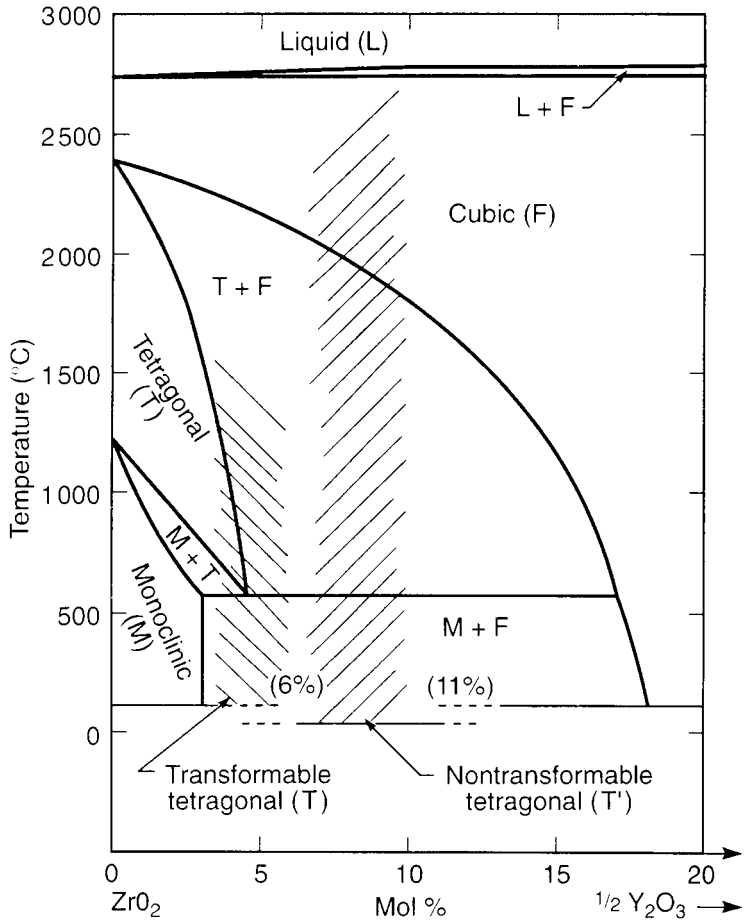

Fig. 2.3. Phase diagram of the ZrO_2-Y_2O_3 system (*6*)

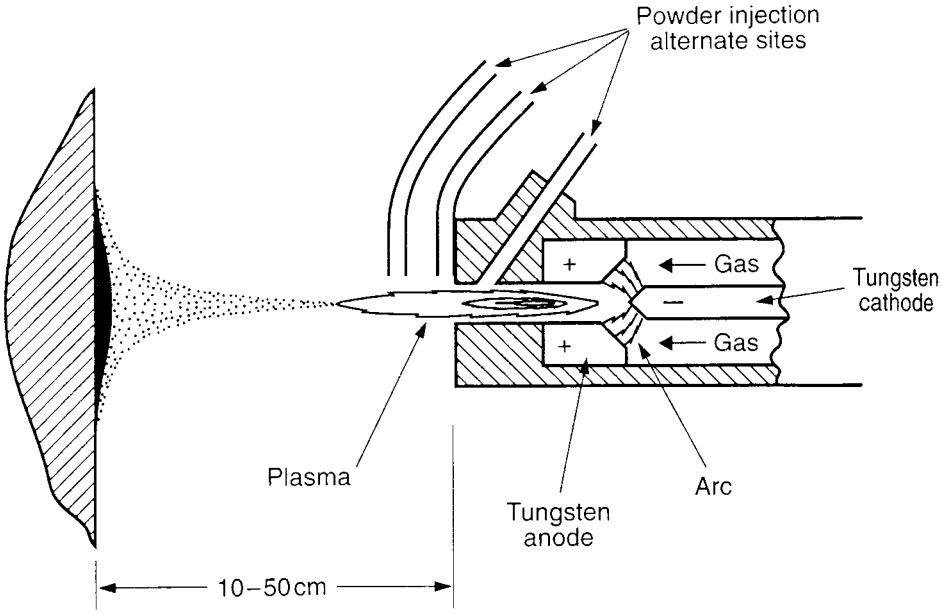

Fig. 2.4. Schematic illustration of plasma spray process (*6*)

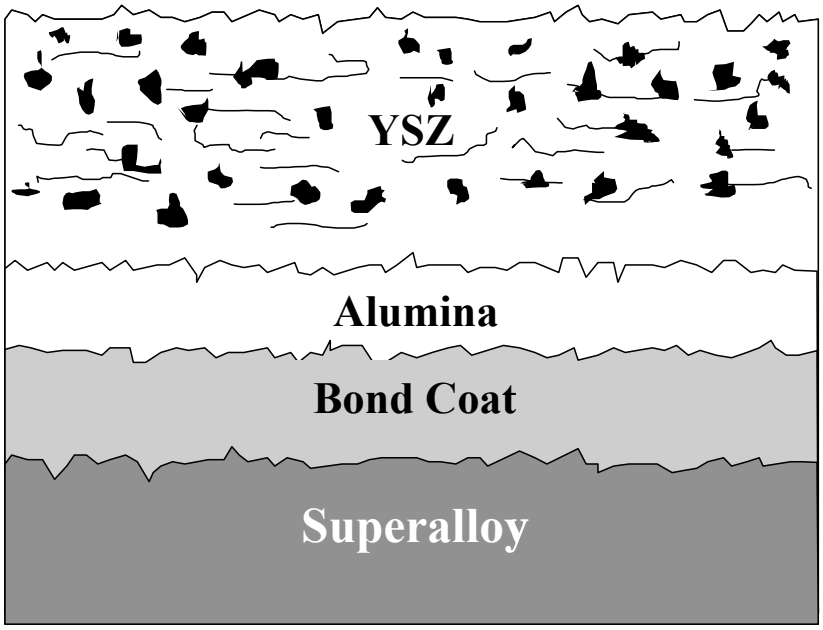

Fig. 2.5. Schematic of typical microstructure of plasma spray TBCs

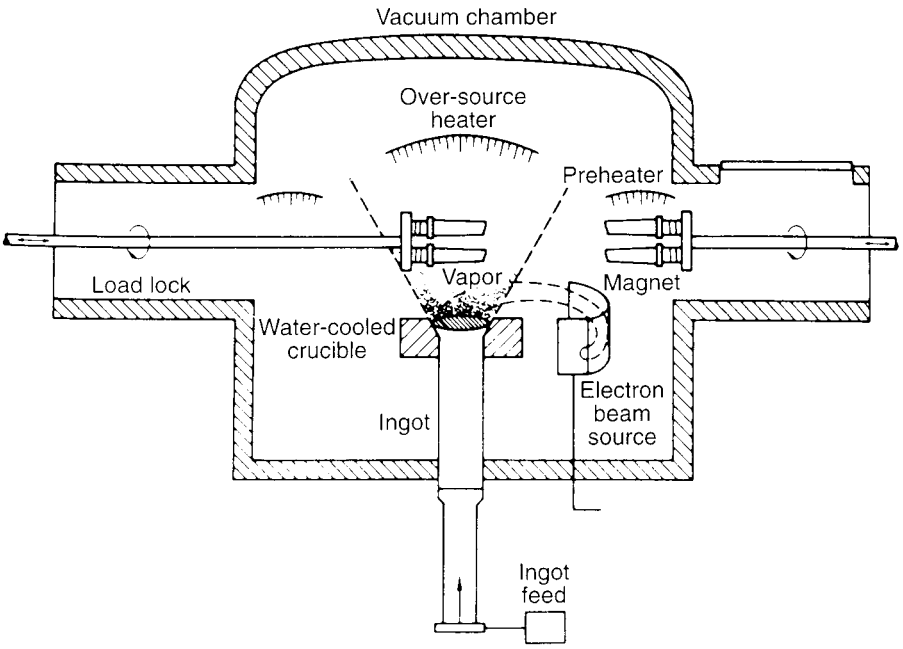

Fig. 2.6. Schematic of electron beam physical vapor deposition process (*6*)

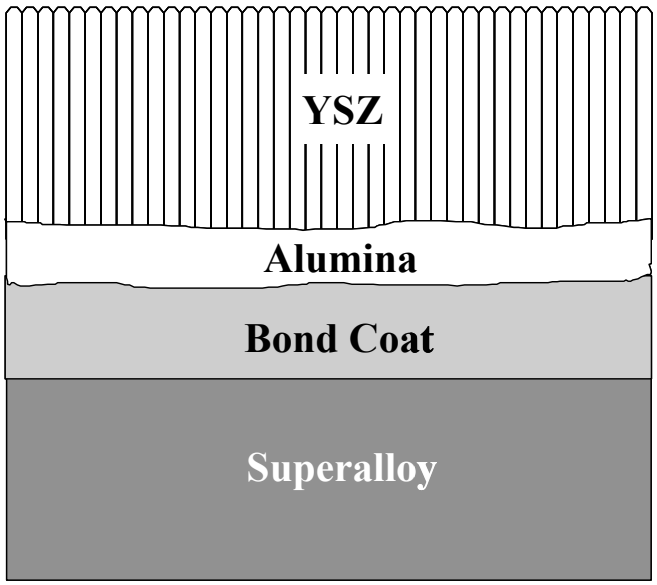

Fig. 2.7. Schematic of typical microstructure of EB-PVD TBCs

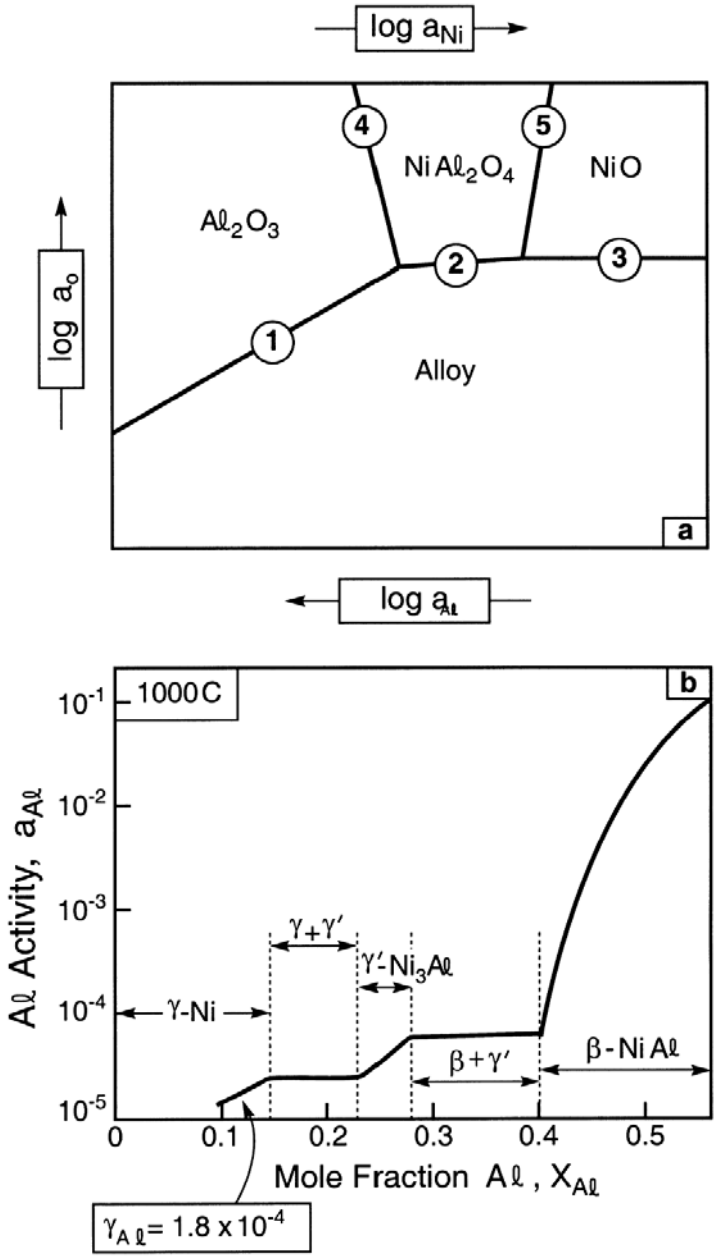

Fig. 2.8. (a) Thermodynamic diagram of Ni-Al-O system; (b) The activity coefficient for Al as a function of concentration for the Ni-Al binary (*8*).

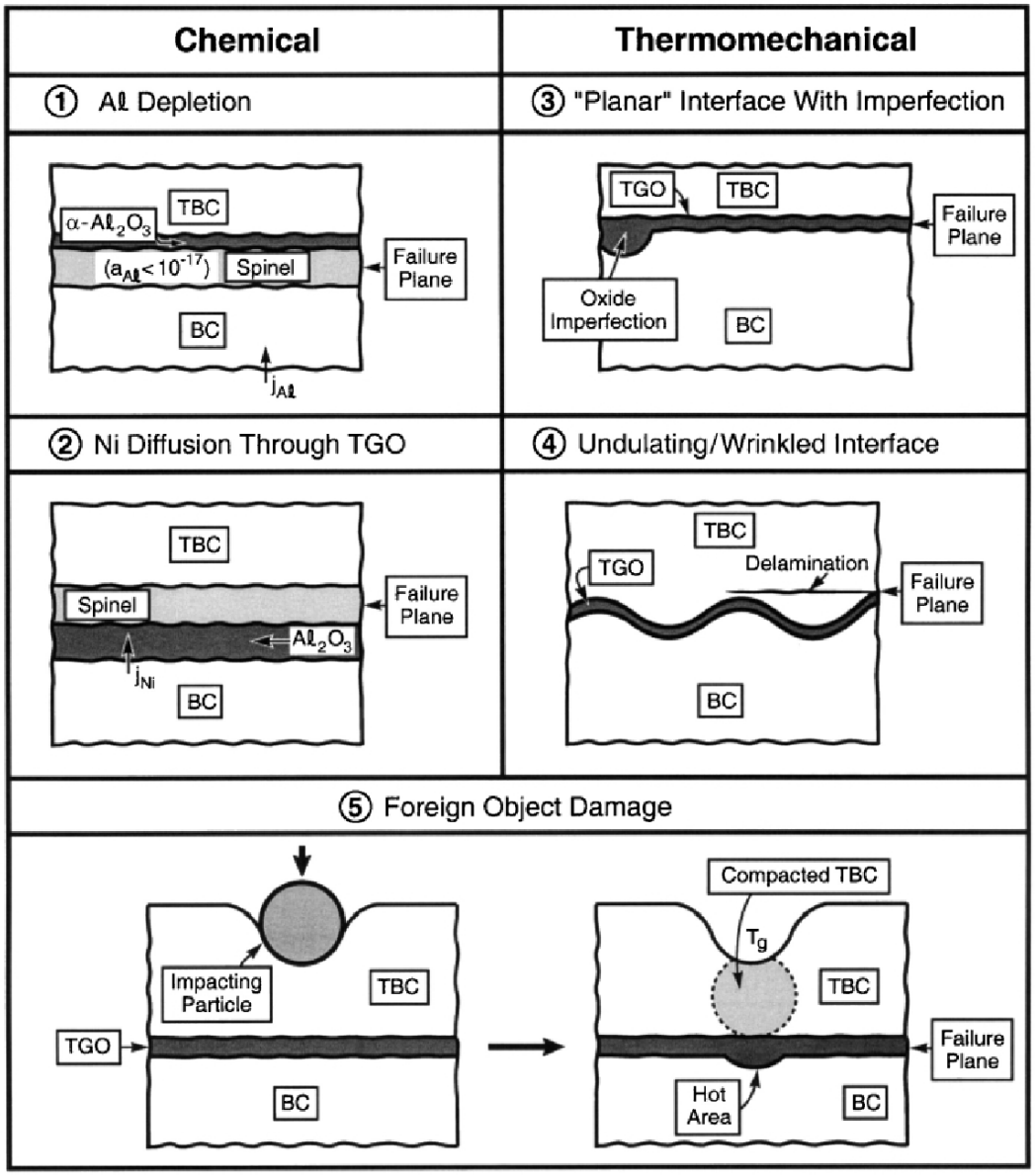

Fig. 2.9. Major failure categories for TBCs (*8*).

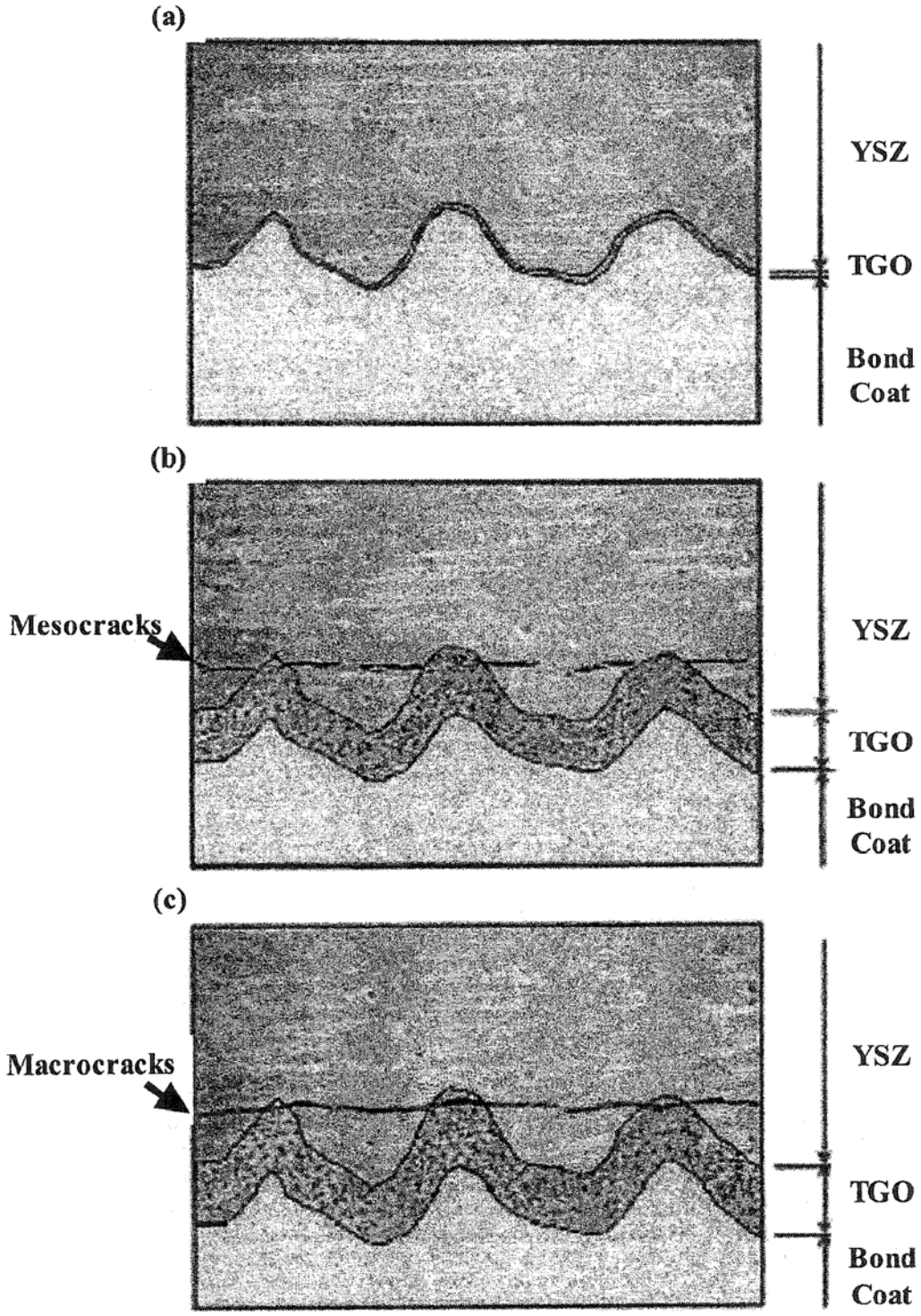

Fig. 2.10. Failure mode of plasma spray TBCs (*68*)

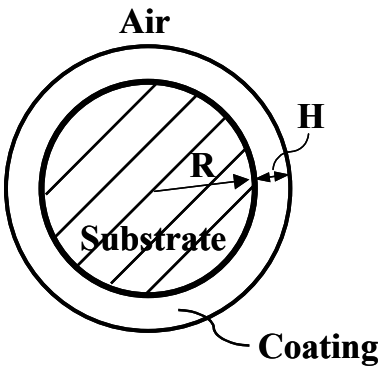

Fig. 2.11. Geometry used for analytic model of TGO/bond coat interface along bond coat ridges (*71*)

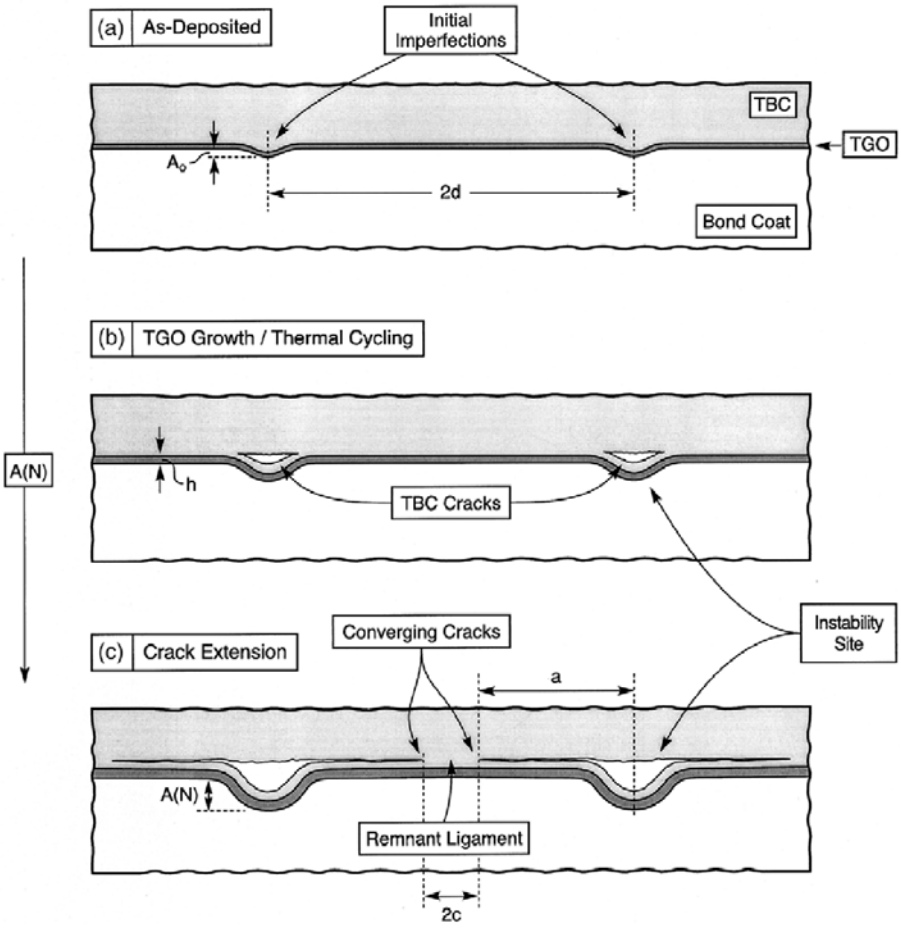

Fig. 2.12. Schematic indicating thermo-mechanical response of (Ni,Pt)Al TBCs (*88*)

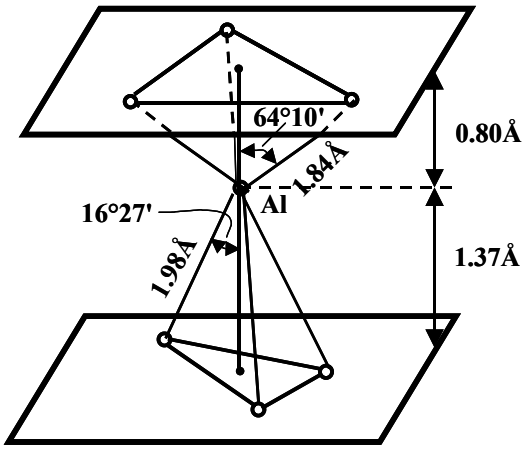

Fig. 2.13. Coordination of Al atoms in α-Al_2O_3 (*119*)

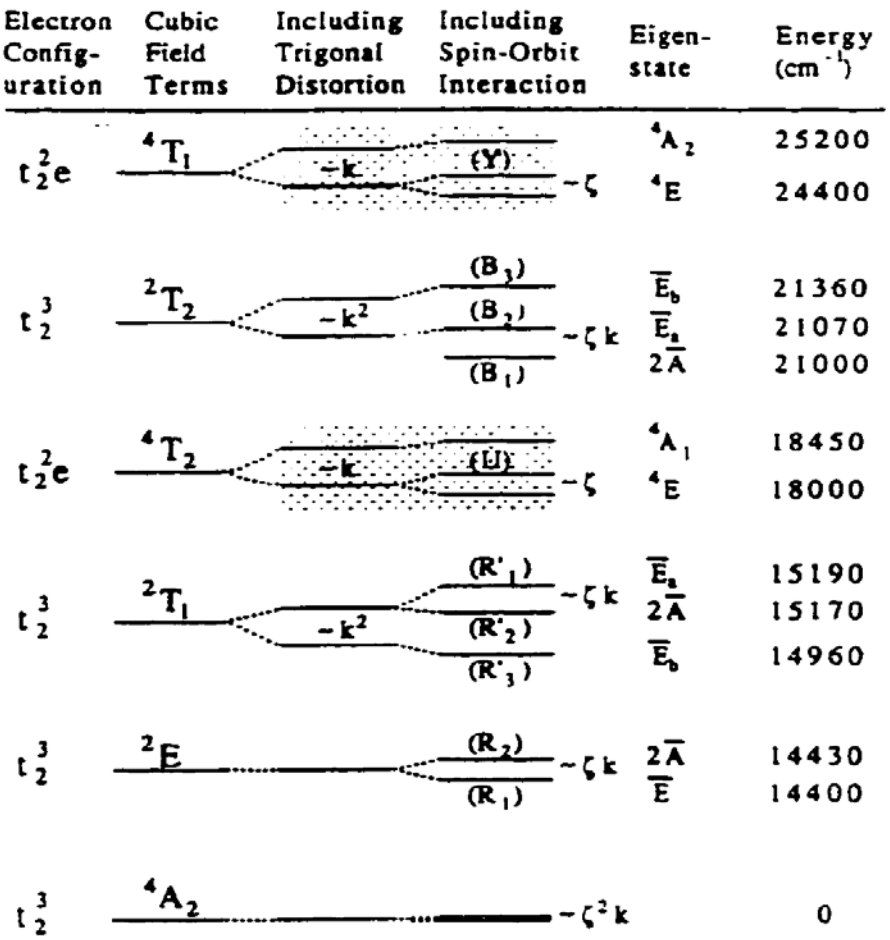

Fig. 2.14. Summary of electronic transitions in α-Al_2O_3 in the visible region (*120*)

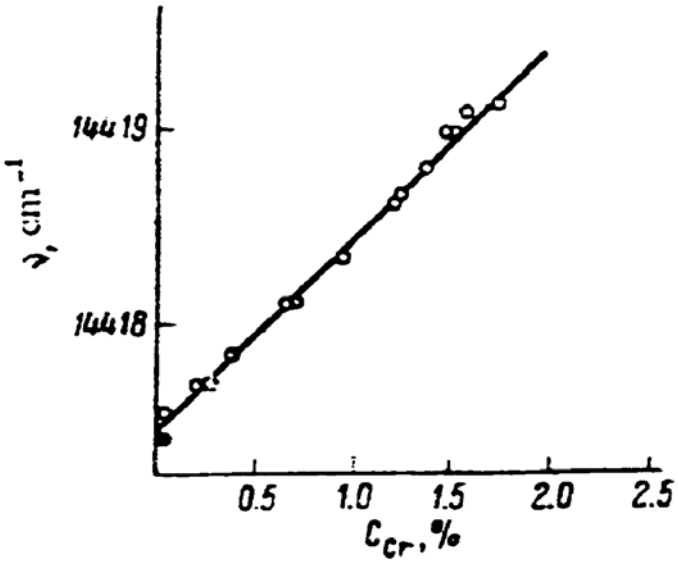

Fig. 2.15. Effects of chromium concentration on the frequency shift of R_1 peak (*123*)

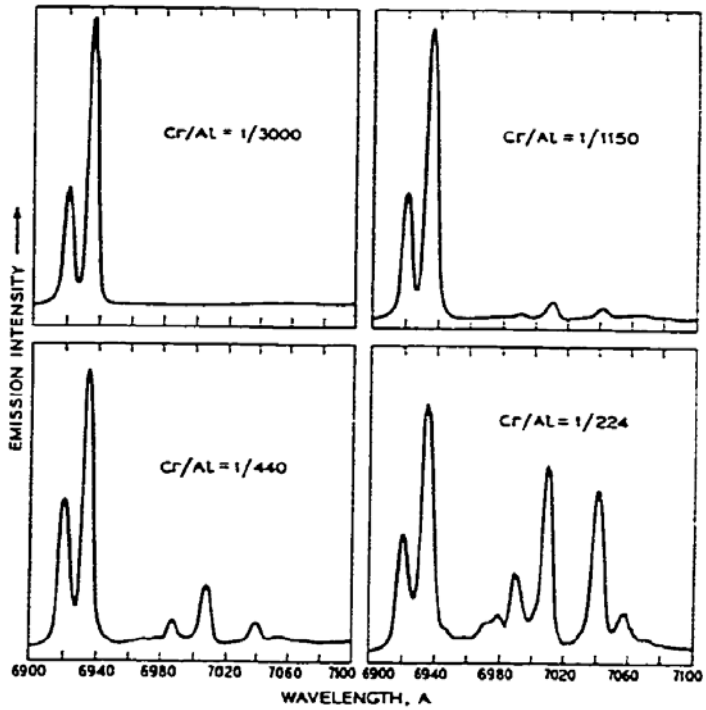

Fig. 2.16. Photoluminscence spectra of α-Al_2O_3 with different Cr concentration (*124*).

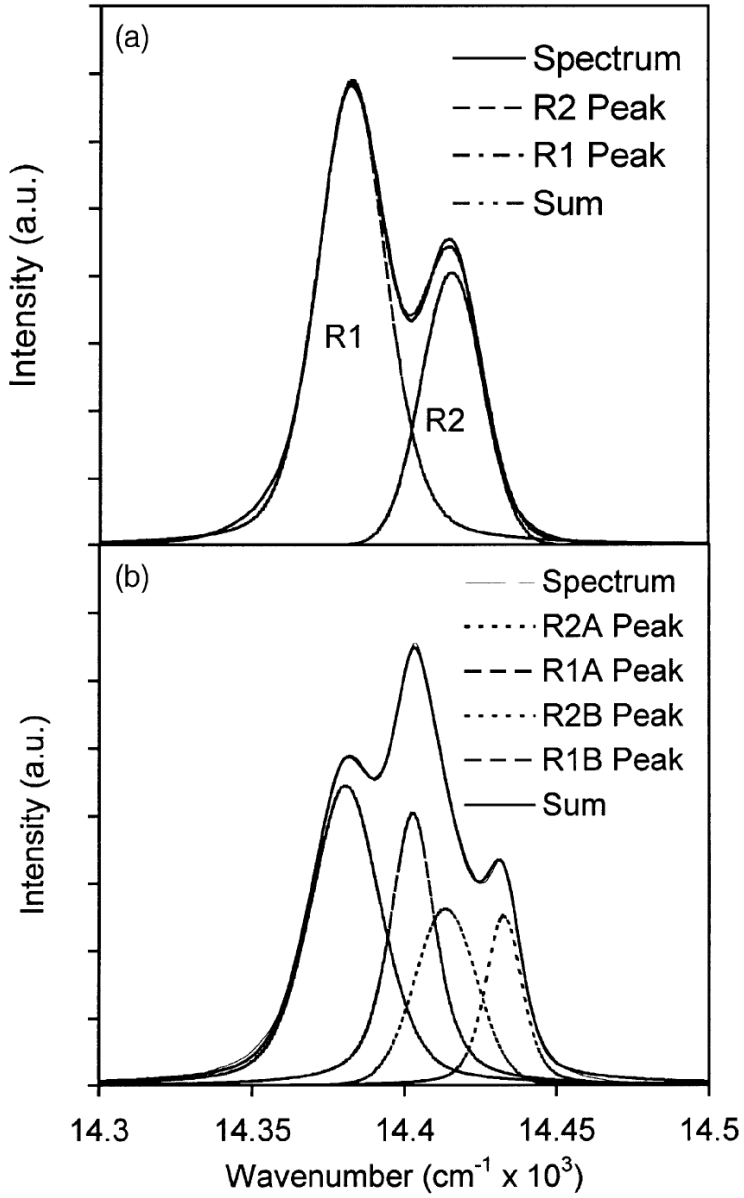

Fig.2.17. Examples of luminescence spectra and the fitted peaks, showing (a) unimodal containing one stress component and (b) bimodal containing two stress components (*117*)

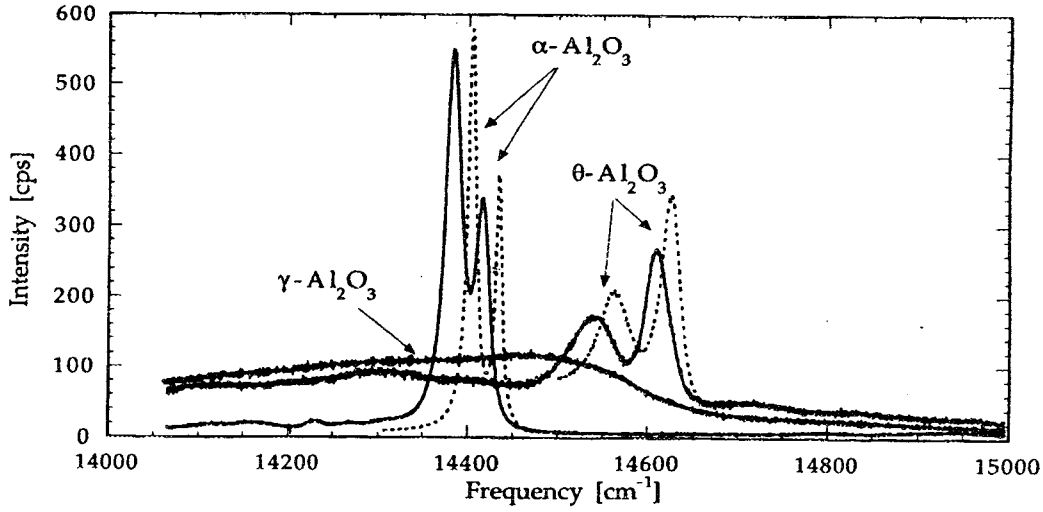

Fig. 2.18. Cr^{3+} luminescence spectra from α, θ, and γ alumina. The dashed lines for α, θ correspond to the stress-free state while the solid lines correspond to the stressed state (*35*).

Table 2.1. Summary of material properties (adopted from ref. (*8*))

TGO (α-Al_2O_3)	
Young's modulus, E_o (GPa)	350-400
Growth stress, σ_{xx} (GPa)	0-1
Misfit compression, σ_0 (GPa)	3-4
Mode I fracture toughness, Γ_0 (J m^{-2})	20
Thermal expansion coefficient, αo (C^{-1} ppm)	8-9
Bond Coat	
Young's modulus, *Es* (GPa)	200
Yield strength (ambient temperature) σ_Y (GPa)	300-900
Thermal expansion coefficient, αs (C^{-1} ppm)	13-16
Interface (α-Al_2O_3/bond coat)	
Mode I adhesion energy, Γ_1 (J m^{-2})	
Segregated	5-20
Clean	>100
TBC (ZrO_2/Y_2O_3)	
Thermal expansion coefficient, α_{tbc} (C^{-1} ppm)	11-13
Young's modulus, E_{tbc} (GPa)	0-100
Delamination toughness Γ_{tbc} (J m^{-2})	1-100

3. Experimental Procedure

3.1 Description of the TBCs

3.1.1 TBC with (Ni,Pt)Al Bond Coat

Disk-shaped (2.54 cm in diameter and 0.32 cm in thickness) TBC specimens investigated in this study were supplied by engine and coatings manufacturers. The configuration of the specimens is shown in Fig. 3.1. The specimens consist of a nominal thickness 140 μm electron beam physical vapor deposited (EB-PVD) 7 wt.% Y_2O_3 stabilized ZrO_2 (YSZ) coating, a nominally 50 μm thick platinum-modified nickel-aluminide bond coat (Ni, Pt)Al and a single crystal CMSX-4 superalloy substrate. The typical compositions of the coating and the superalloy used in this study are shown in Table 3.1. The specimens were bond coated on both sides to allow study of the oxidation behavior of the bare bond coat using the back side of specimens. Consistent with standard industry practice, the bond coats were grit blasted prior to TBC deposition by the EB-PVD process.

3.1.2 TBC with NiCoCrAlY Bond Coat

Disk-shaped specimens (2.54 cm in diameter and 0.32 cm in thickness) with the same configurations in Fig. 3.1 were used. The substrate was a nickel based single crystal superalloy CMSX-4. The bond coat was the vacuum plasma sprayed (VPS) MCrAlY (NiCoCrAlY with additions of Si and Hf) consolidated by a shot-peening process. Different surface finishing processes were carried out before TBC

deposition in order to study the effects of surface roughness on the durability of the TBCs.

Two surface finishing processes include: (1) as-received (vacuum plasma sprayed bond coat followed by shot-peening); (2) 90 minutes' centrifugal barrel finishing. The barrel finishing was done by USF Surface Preparation Group and is suitable for industrial processing of gas turbine blades. The centrifugal barrel finishing process is identical to conventional barrel finishing except the device is rotated in such away to create a force approximately 20 times that of gravity. Relatively coarse media (nuggets) were used in this study, but much smoother finishes are possible using multistage finishing. The surface morphology and roughness of the specimens were evaluated using scanning electron microscopy and ZYGO™ surface interferometry (see section **3.4**). After bond coat surface processing, the bond coat was pre-oxidized in Ar-H_2 ($P_{O2} \sim 10^{-8}$) at 1100°C for 2 hours. Then the coupons were sent to our industry partner for EB-PVD deposition of the 7 YSZ coating. The TBC consists of a nominally 145 μm thick electron beam physical vapor deposited (EB-PVD) 7 wt.% Y_2O_3 stabilized ZrO_2 (YSZ) coating, a nominally 100 μm thick NiCoCrAlY bond coat and a single crystal CMSX-4 superalloy substrate. The typical compositions of the coating and the superalloy used in this study are shown in Table 3.2.

3.2 Thermal Cycling Tests

Cyclic oxidation tests were performed in air at 1151°C, 1121°C and 1100°C for (Ni,Pt)Al bond coated TBCs in a CM™ rapid temperature cycle furnace (CM Inc.,

Bloomfield, NJ.) (*39*). The schematic of the furnace is shown in Fig. 3.2. The thermal cycles consisted of a 10-min heat-up to peak temperature, a 40-min hold at peak temperature, followed by a 10-min forced air quench (Fig. 3.3). The thermal couple was connected directly to the sample to ensure the accuracy of temperature measurement. Failure of the specimen was defined by spallation over more than 50% of the total area. Cyclic oxidation tests were performed in air at 1121°C for MCrAlY bond coated TBCs.

3.3 Specimen Preparation

Specimens were removed at specified intervals to investigate microstructure. The procedure of sample preparation used for microstructural investigation is described below. All specimens were sectioned using ISOMET™ low speed saw (Buehler). In order to minimize the mechanical damage caused by sectioning and avoid separation between the substrate and coatings during sectioning, specimens that had more than 30% of life were first mounted with epoxy prior to sectioning. After sectioning, the specimens were cold mounted with low-viscosity epoxy (EPO-THIN, Buehler). Because in some cases the shrinkage encountered upon curing of resins induces stresses that can delaminate the TGO/bond coat interface, the mounting conditions should be carefully controlled to minimize the curing rate. Then, the specimens were ground with 320, 600, 800, 1200 grit SiC papers and then polished using 1 μm diamond suspension on a semi-automatic polisher (Struers RotoPolish). Prior to microstructural observations, the specimens were coated with gold or carbon to minimize charging.

3.4 Characterization Methods

3.4.1 Surface Interferometry

Surface geometry and surface roughness of the bond coat were characterized using surface interferometry (Zygo™ NewView 5000, Zygo Corporation, Middlefield, CT). NewView 5000 is a precision microscope which uses Scanning White Light Interferometry (SWLI) to generate quantitative three-dimensional images. Scanning White Light Interferometry (SWLI) is a traditional technique in which a pattern of bright and dark lines (fringes) result from an optical path difference between a reference and a sample beam. Incoming light is split inside an interferometer, one beam going to an internal reference surface and the other to the sample. After reflection, the beams recombine inside the interferometer, undergoing constructive and destructive interference and producing light and dark fringe patterns.

The instrument schematic is shown in Fig. 3.4. In the NewView 5000, an interferometer objective is mounted in a precision closed loop piezo-scanning device that moves vertically (in the Z direction) over the sample. Data is collected from a precision vertical scanning transducer and CCD camera and is processed in a computer. The phase relationships of individual components of the white light spectrum in the interferogram are analyzed by Frequency Domain Analysis. Aquantitative 3-D image (surface map) with ultra high Z resolution is generated. Available data includes 3D plots, filled plots, multiple 2D profiles of 3D data, and a wide range of surface roughness parameters: PV, Ra, rms (see Fig. 3.5). PV is the height between the lowest and highest point on the test part surface. Ra (average roughness) is the average deviation of all points from a plane fit to the test part

surface. rms is the root-mean-square deviation of all points from a plane fit to the test part surface. Measurements have up to 1-angstrom vertical resolution. Measurements can be made over long vertical distances up to 5 mm and large fields of view up to 17.3 mm. All specimens were measured using a Scanning White Light Microscope with a 20X objective, which provides an imaging area of 320 μm × 240 μm. Surface roughness data were recorded and quantitative information about surface geometry was extracted.

3.4.2 Photoluminescence Piezospectroscopy (PLPS)

PLPS measurements were made using a Renishaw™ Ramascope™ 2000 (Renishaw, Glouchestershire, UK) in conjunction with a Leica™ DM/LM light microscope. The instrument schematic is shown in Fig. 3.6. The set-up utilizes an Ar-ion 514 nm wavelength laser beam for exciting the chromium impurity in the TGO layer. At specified intervals, a series of spectra were collected on each sample. The laser beam was focused on the surface of the YSZ and the spot was scanned over the specimen by moving the computer-controlled stage in a specified step size. The spot size on the TBC surface depends on lens magnification. The diameter of the spatial region from which spectra are collected through the TBC layer is estimated to be around 70 μm due to scattering by the columnar structure of the EB-PVD TBC (*114*). At each step position, a luminescence spectrum was acquired. The minimum step size can reach 1 μm. In coarse mapping, a total of 121 spectra were acquired in a 12 mm×12 mm grid area, with a step size of 1.2 mm. Thus, the spectral

characteristics obtained allow the average stress and standard deviation to be determined and give the variability over the area of each specimen.

In fine mapping, a total of 2601 spectra were acquired in a 2 mm×2 mm grid area with a step size of 40 μm. In both coarse and fine mapping, the center of the mapping region corresponded to the center of the disk specimen. In addition, for each specimen, the origin of the mapping grid is fixed at the same position and intentionally marked to ensure that the same general region of the specimen surface was inspected when the measurements were made at the specific cycling intervals. Finally the spectra were analyzed to extract multiple characteristics (frequency shift, peak with, peak area ratio, Lorentz/Gaussian fractions, fraction of bimodal spectra). The detailed procedure of spectra deconvolution will be described in section Appendix I.

The fraction of bimodal spectra were calculated according to the equation:

$$\text{Number fraction of bimodal} = N_{bimodal} / (N_{unimodal} + N_{bimodal}) \qquad (3.1)$$

Where: $N_{unimodal}$ = the number of spectra that show only one stress component;

$N_{bimodal}$ = the number of spectra that show two stress components.

3.4.3 Macro Photographic Characterization

Macro photography of TBC specimens was taken using a Nikon MacroPhot™, Tokyo, Japan. The observations were useful identifying large-scale spallation modes.

3.4.4 Optical Microscopy

A Nikon Microphot™ photographic unit (Nikon, Japan) was used to examine the cross sections during sample preparation and record the general appearance of the samples.

3.4.5 Scanning Electron Microscopy (SEM)

After sectioning, specimen microstructure and its evolution with thermal cycling were observed using one of three SEMs: (i) an environmental scanning electron microscopy ESEM 2020 (Philips Electron Optics, The Netherlands), (ii) an AMRAY 1000A equipped with EDAX 9100/60 energy dispersive x-ray spectrometer (JEOL, Tokyo, Japan), (iii) a JSM6335F equipped with a field-emission electron source for high resolution imaging (JEOL, Tokyo, Japan).

3.4.6 Energy Dispersive Spectroscopy (EDS)

Localized chemical analyses of specimens were performed using an AMRAY 1000A equipped with EDAX 9100/60 energy dispersive x-ray spectrometer (JEOL, Tokyo, Japan) that is capable of analyzing elements of atomic number down to sodium. Carbon coating is preferred over a gold coating in the EDS analysis since it provides minimum interference. Point analysis and area mapping (X-ray elemental maps) were performed.

3.4.7 X-ray Diffraction (XRD)

XRD was carried out to determine the phase structure of the TBC specimens, and the types of oxide found on spalled surfaces. All XRD analysis was done in the

Bruker AXS, D5005 X-ray diffractometer (Bruker Analytical X-ray Systems, Inc., Madison, WI) with Cu K_α radiation (λ=0.154 nm). The determination of phases was performed by comparison of obtained spectral patterns with the standard PDF data base.

3.5 Image Analysis

The image analysis in this study was performed using a UNIX-based application software (microGOP 2000, ContextVision, Linkoping, Sweden). Different image processing and analyzing procedures were used for different purposes; the detailed procedures will be described below.

3.5.1 Characterization of Rumpling

To study the morphological evolution of the metal-oxide interface during thermal cycling, a series of cross-sectional SEM micrographs were first taken at the same magnification for about 800 μm along the interface. Then, the morphological evolution of interface was characterized using image analysis of cross-sectional SEM micrographs. For roughness analysis, the coordinates of the metal-oxide interface were extracted from a series of SEM micrographs. The root mean square roughness parameter (RMS) was calculated from the resulting interface profiles.

$$RMS = \sqrt{\frac{1}{n}\sum_{i=1}^{n} y_i^2} \qquad (3.2)$$

where n is the number of data points along the interface and y_i is the current coordinate (height) of the interface relative to the mid-section (the height of mid-

section is defined equal to 0). Tortuosity was determined by the ratio of the interface length to the lateral straight-line length L/L_0. The spacing between inward displacements was characterized using a power spectrum plot and the Fast Fourier Transform (FFT) method.

3.5.2 Measurement of TGO Thickness

TGO thickness was studied as a function of thermal cycles at three temperatures. Cross-sectional SEM micrographs were taken and fifty measurements of TGO thickness were performed along each cross section. The average TGO thickness and its standard deviation were calculated.

3.5.3 Measurement of Crack Density

SEM micrographs were converted into binary images in which black represents cracks and white represents uncracked regions. The length for every crack was measured from each image. The crack density was calculated as the total length of cracks divided by the total image area.

3.5.4 Measurement of Area Fraction of Fracture Surface

SEM micrographs were input into the image analysis software. By choosing suitable threshold values, the gray image can be converted into a binary image in which the black represents the exposed bond coat surface and the white represents the rest of the fracture surface. The area fraction was calculated as the area of the exposed bond coat surface divided by the total area of surface.

Table 3.1. Typical composition of various layers of TBC 1

Layer	Material	Composition (wt.%)
Substrate	Single crystal superalloy CMSX-4	9 Co, 6.5 Cr, 6.5 Ta, 5.6 Al, 6.0 W, 3.0 Re, 0.6 Mo, 0.1 Hf, 1.0 Ti, balance Ni
Bond Coat	Ni-rich Pt-Al	20 Pt, 21 Al, balance Ni
Ceramic TBC	Yttria stabilized Zirconia	7 Y_2O_3 in ZrO_2

Table 3.2. Typical composition of various layers of TBC 2

Layer	Material	Composition (wt.%)
Substrate	Single crystal superalloy CMSX-4	9 Co, 6.5 Cr, 6.5 Ta, 5.6 Al, 6.0 W, 3.0 Re, 0.6 Mo, 0.1 Hf, 1.0 Ti, balance Ni
Bond Coat	NiCoCrAlY with addition of Si, Hf	20 Co, 18 Cr, 12.5Al, 0.6 Y, 0.4 Si , 0.25 Hf, balance Ni
Ceramic TBC	Yttria stabilized Zirconia	7 Y_2O_3 in ZrO_2

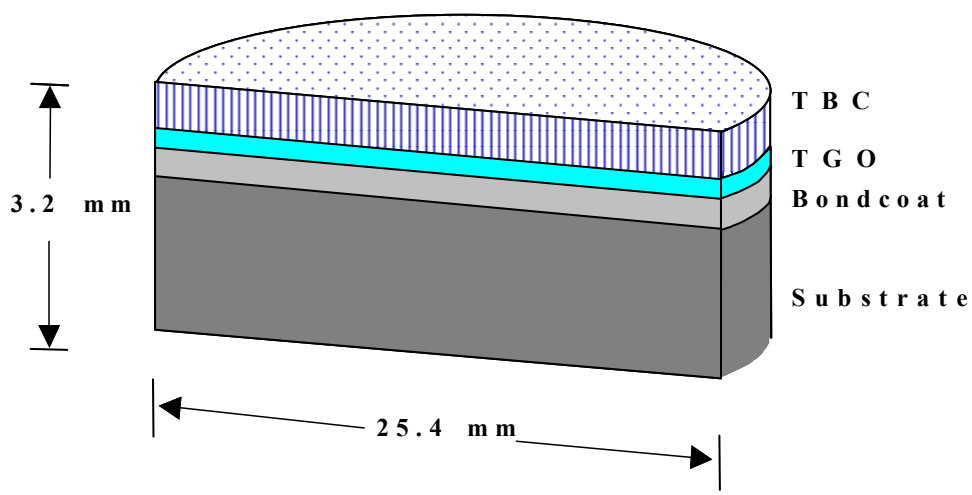

Fig. 3.1. Specimen configuration

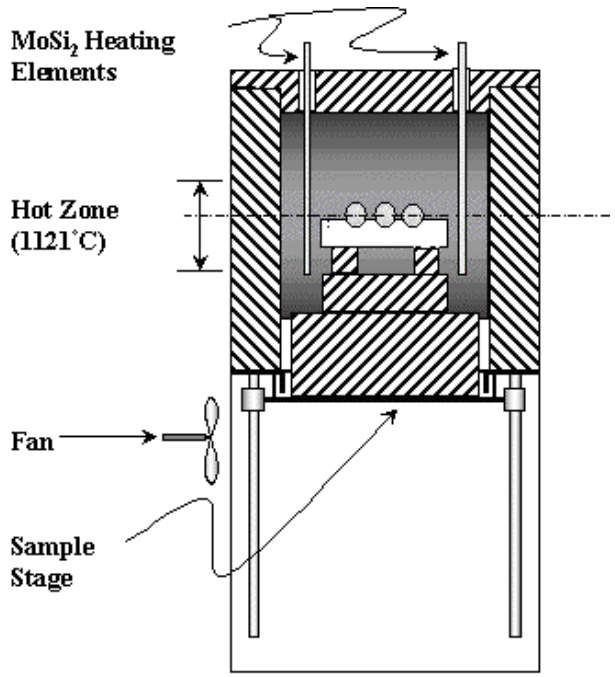

Fig. 3.2. Schematic of cyclic furnace

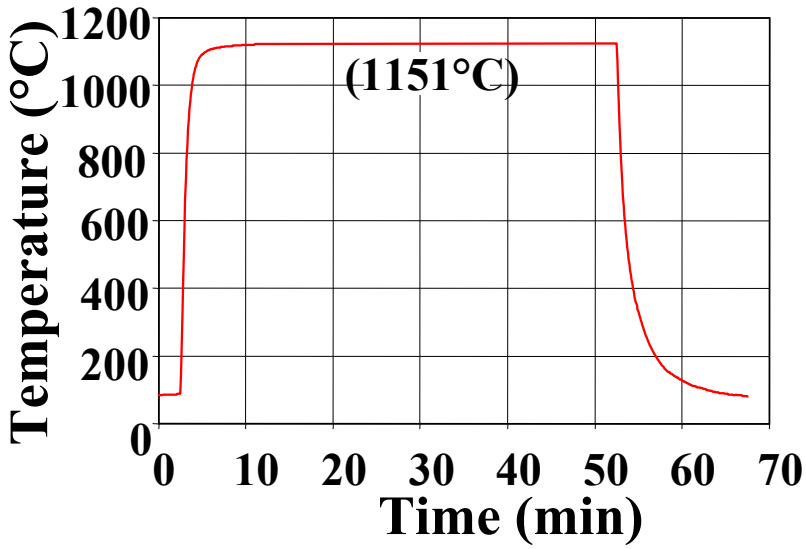

Fig. 3.3. Temperature profile for one-hour cycle test

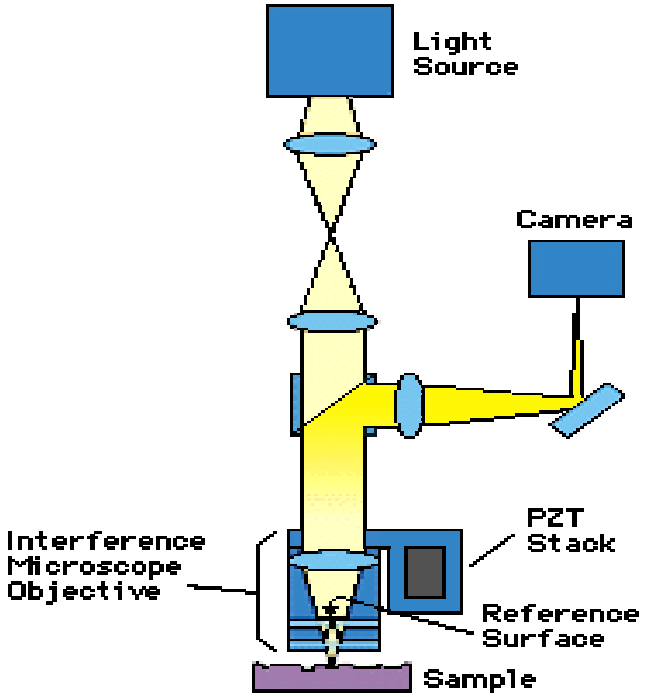

Fig. 3.4. Schematic of surface interferometry instrument set up (from www.zygo.com)

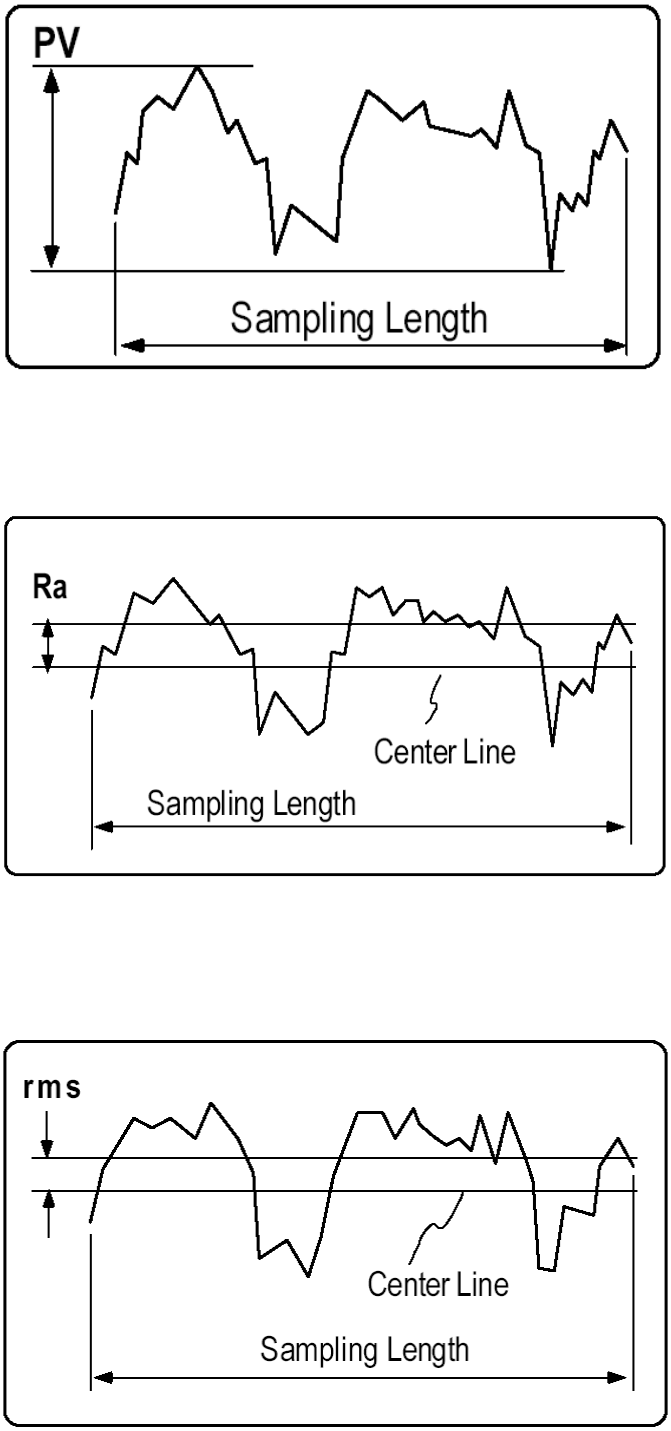

Fig. 3.5. Different expression of surface roughness value (from www.zygo.com)

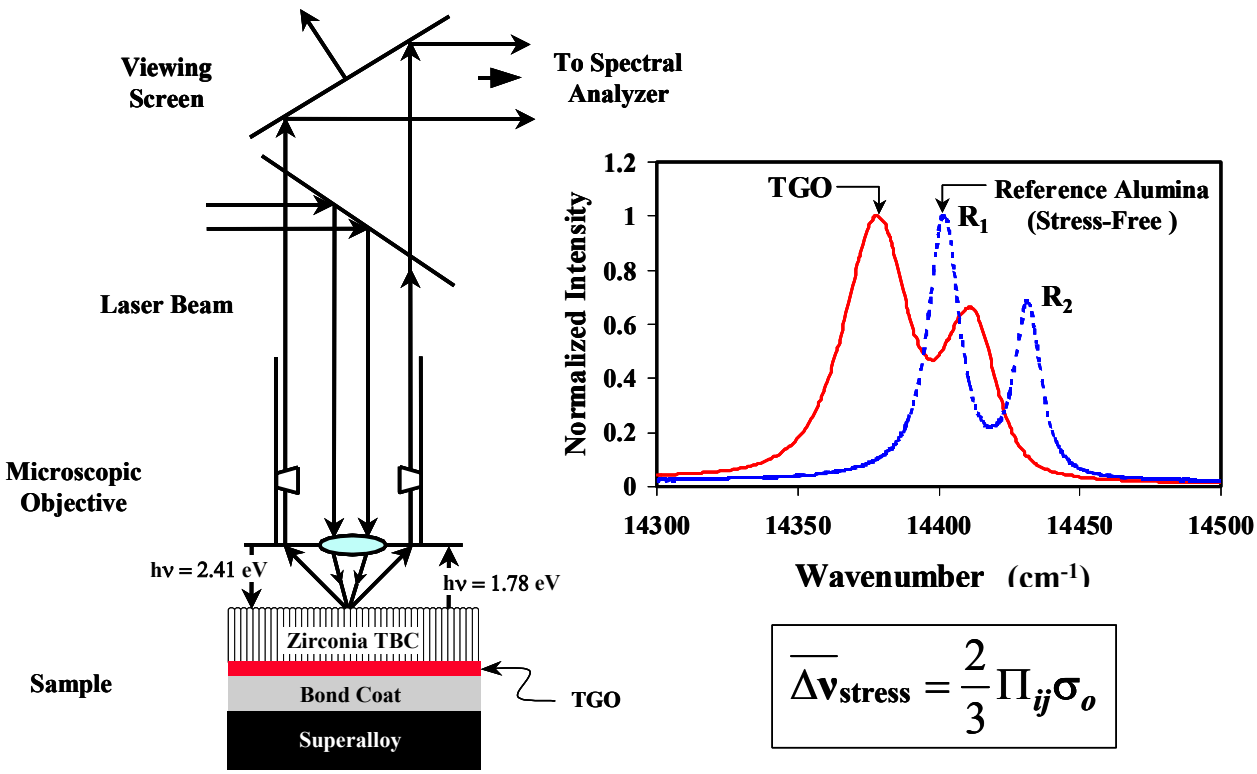

(a) (b)

Fig. 3.6. (a) Schematic illustration of the photo-stimulated luminescence piezospectroscopy technique; (b) Typical R_1/R_2 fluorescence spectra for chromium-containing stress-free and stressed α-Al_2O_3

4. Experimental Results

4.1 Results of (Ni,Pt)Al Bond Coated TBCs

4.1.1 Microstructure and Failure Analysis

4.1.1.1 Microstructure of As-Coated TBCs

X-ray diffraction of the as-coated YSZ shows the coating is made of the desirable, non-equilibrium tetragonal (t') phase (Fig. 4.1). It was observed that only parts of the peaks (400 and 200) were visible, indicating that the coating has a preferred orientation, which probably is due to its columnar structure. The top surface morphology of the as-coated YSZ coating is shown in Fig. 4.2 and the "cauliflower" like morphology is clear with a grain diameter about 2-3 μm.

The cross-sectional micrograph of the as-coated TBC is shown in Fig.4.3. The YSZ topcoat has a nominal thickness of 140 μm with a columnar structure. The platinum-modified nickel-aluminide bond coat (Ni, Pt)Al is nominally 50 μm thick. The bond coat closest to the TGO is single phase β-(Ni, Pt)Al, confirmed by XRD (Fig. 4.4). Further from the TGO and near the substrate, there is an inter-diffusion zone with the substrate. Alumina inclusions entrapped from the grit blasting procedure are present in the bond coat. A thin, continuous TGO layer (~ 0.5 μm) was observed and undulations of the interface between the ceramic top coat and bond coat were present. These undulations come from grit blasting of the bond coat before depositing the TBC.

Higher magnification micrographs (Fig. 4.5) show the imperfections where the bond coat surface is locally concave and the TBC near the TGO layer above this

concave region has some defects or voids. These imperfections have been observed previously in EB-PVD TBC systems with Pt modified aluminide bond coats (*88*). It has been proposed that these imperfections localize the thermal expansion mismatch stress, causing nucleation of cracks and separations driven by the strain energy stored in the TGO (*74*).

4.1.1.2 Microstructural Evolution of TBCs During Thermal Cycling

One-hour thermal cycling tests were conducted at 1151°C, 1121°C and 1100°C. It was found that the microstructural evolution was similar for specimens tested at all three temperatures. One typical example, well represented by Fig. 4.6, will be used to illustrate the microstructural evolution of TBCs during thermal cycling. Figs. 4.6 shows a cyclic sequence of cross-sectional micrographs for tests at 1151°C. The following major changes in the microstructure of specimens were observed with thermal cycling: (1) the interface between the top coat and the bond coat becomes rougher (referred to as either rumpling or ratcheting) and both the amplitude and the number of sites of downward displacement increase with cycles; (2) the TGO thickness increases; (3) β-(Ni, Pt)Al → γ'-Ni_3Al transformation occurs in the bond coat led by aluminum depletion due to oxidation and inter-diffusion with the substrate (*85*); and (4) cracking occurs. The cracks initiate at about 30% of the cyclic life.

A higher magnification image in Fig. 4.7 shows a typical example of crack initiation. As the TGO penetrates into the underlying bond coat, cracking initiates near the TGO/TBC interface above the rumpling-induced valley in the bond coat. This image also shows that a defective region in the TBC; a "pinched-off" region

characterized by columnar grains that converge a small distance from the interface. These regions, also observed by Mumm et al. (*88*), are often associated with as-fabricated depressions in the bond coat surface. After initiation, cracks extend laterally from these defects with increasing cyclic exposure as shown in Fig. 4.6c.

4.1.1.2.1 Interface Rumpling During Thermal Cycling

The bond coat/oxide interface profiles at various stages of thermal cycling were extracted from the cross-sectional micrographs and the results are shown in Fig. 4.8a (1151°C) and b (1100°C). It is apparent that the roughness of the interface, or the amplitude of rumpling, increases with thermal cycles at both temperatures. The amplitude of largest downward displacements is about 10 μm at both temperatures.

Quantitative analyses of the rumpling were carried out by calculating the RMS parameter and tortuosity from the interface profiles. The values of the interface RMS parameter and the tortuosity as a function of thermal cycles at different temperatures are shown in Fig. 4.9 and Fig. 4.10, respectively. The RMS parameter and the tortuosity increase almost linearly with thermal cycles at different temperatures, although there is some scatter of data. The slopes of the fitting lines represent the rate change of the roughness (characterized by the RMS parameter or tortuosity). The larger the slope the faster the roughness increases. It is clearly shown that the rumpling rate increases with temperature and the specimens with shorter lives have larger rumpling rate. Moreover, the values of the RMS parameter at failure are similar (~3.0 μm), despite the different test temperatures. This suggests that a critical rumpling value drives spallation for this TBC.

Power spectrum plots were obtained to characterize the spacing of downward displacements as a function of cycles using the Fast Fourier Transform (FFT) method (Only one example of a power spectrum plot for the profile of the specimen after 125 cycles at 1151°C is shown in Fig. 4.11). A broad range of frequencies was produced and no dominant wavelength could be determined. However, the most probable wavelength (indicated by the asterisk in Fig. 4.11) seems to decrease with thermal cycles (Fig.4.12), consistent with observations that the number of imperfection sites increases with cycles.

Rumpling was also studied on the backside of specimens (bond coated only without ceramic topcoat) using surface interferometry. It is clearly shown that the surface roughness increases with thermal cycles (Fig. 4.13 and 4.14). Compared to the metal/oxide interface, the rumpling amplitude of the bare bond coat side was found to increase faster, indicating the ceramic top coat partially constrains the roughening of the bond coat surface (Fig. 4.14).

4.1.1.2.2 TGO Thickness

The TGO thickness increases with thermal exposure and the thickness as a function of hot time is shown in Fig. 4.15. The TGO growth is consistent with parabolic growth kinetics. The TGO growth rate increases as the cycling temperature increases. Fig. 4.16 shows the logarithm of the parabolic growth coefficient at three temperatures as a function of the reciprocal of the temperature (1/T). It was found that the growth coefficient is governed by an Arrhenius equation

$$k = k_0 e^{\frac{-Ea}{RT}} \qquad (4.1)$$

where k is parabolic growth coefficient, Ea is the activation energy, T is the temperature. The activation energy for TGO growth was calculated from the slope of the fit line and found to be 282 kJ/mol. This activation energy is close to the value obtained by Sridharan et al. (*30*) on a similar system, and in the same range for the activation energy for oxygen transport in alumina (238 kJ/mol) (*128*). The activation energy values for TGO growth on (Ni, Pt)Al bond coat here and in ref. (*30*) are also comparable to that on NiCoCrAlY bond coat in ref. (*31*) after using the consistent parabolic law equation

$$h = k \cdot t^{1/2} \qquad (4.2)$$

where h is the TGO thickness, t is the time and k is the rate constant. This indicates that TGO growth is controlled by oxygen transport. The average TGO thickness at failure is 4.6-5.3 μm and it is approximately constant at the three temperatures.

Fig. 4.17 shows interface roughness as a function of TGO thickness. It was found that both the RMS parameter and tortuosity increase as TGO thickness increases, relatively independent of temperature and with surprisingly small data scatter.

4.1.1.3 Microstructural Analysis Near and After Spallation

The spallation life at the three temperature tests is shown in Table. 4.1. One specimen showed abnormally short life (202 cycles) at 1121°C, otherwise the samples showed relatively consistent spallation lives. The average spallation life and its standard deviation for tests at various temperatures are shown in Fig. 4.18. The average life of specimens are 928 cycles at 1100°C, 458 cycles at 1121°C, 178 cycles

at 1151°C, respectively. The average spallation life decreases by a factor of five on increasing the cycling temperature from 1100°C to 1151°C. These results are consistent with the results obtained by Kim et al. (*129*) and Sridharan et al. (*30*) on similar systems, where a temperature increase of 100°C decreases the hot time to failure by a factor of 10.

Fig. 4.19 shows macrophotographs taken at various stages of TBC life. The general observations are that the top surface of specimens showed no signs of damage until final spallation and only limited spallation occurs at the free edge of specimens during cycling (Fig. 4.19a). The final spallation was catastrophic and large scale buckling occurred with fracture propagation across the entire specimen surface (Fig. 4.19b and Fig. 4.20). Spallation failure of the ceramic is into many small pieces.

The spalled surface of the bond coat side is shown in Fig. 4.21. The spallation surface of the bond coat side of specimens consists of exposed regions of bond coat, TGO and TBC. Fig. 4.21b shows a typical higher magnification image of spalled surfaces and associated EDS spectra at different regions. It was found that the bond coat forms a continuous region containing islands of TGO and TBC. The TBC that remains on the spalled surface is almost always at the center of these TGO islands. The exposed bond coat surface shows the imprinted TGO grain morphology. The oxide contains cleavage facets indicating that they were mechanically detached from the TGO. The bond coat comprises 52 to 68% of the spalled surface.

Fig. 4.22 shows the spallation surface of the bottom side of the ceramic top coat. It consists of regions of TGO and TBC. The exposed TGO surface has the granular

morphology that mirrors the imprint in the bond coat side. The root of the exposed TBC columns is porous and equiaxed.

It is apparent that specimens exhibit a mixed failure pathway, with cracking occurring at the TGO/TBC and TGO/BC interfaces and even through the TGO. Fig. 4.23 shows the cross-sectional images near the failure in which cracks go through the TGO and along the TGO/BC interface. The fracture surfaces and the failure pathways are similar for specimens tested at all three temperatures. This indicates that, for this TBC, although the cracks initiate near the TGO/TBC interface (Fig. 4.7) and may extend laterally along this interface (Fig. 4.6c), they can also divert into the TGO and extend along the TGO/BC interface when the specimen is close to failure. Similar results have been reported by Spitsberg et al. (*89*).

In some cases, structural imperfections such as cavities form as shown in Fig. 4.24. Almost all cavities occur at locations having depressions due to rumpling, indicating that these cavities are strongly associated with rumpling induced depressions.

Fig. 4.25 shows the XRD patterns of the spalled surface on the bond coat side. The phase constituents include the β-NiAl, γ′- Ni_3Al and α-Al_2O_3. γ′- Ni_3Al comes from the phase transformation of β-NiAl and α-Al_2O_3 is the residual TGO on the spalled surface. Chen et al. (*85*) reported that a reversible β-M martensitic transformation accompanies thermal cycling in a platinum modified diffusion aluminide bond coated TBC and the strains caused by the martensitic transformation contributes to the rumpling. In contrast, no L10 martensite phase is detectable, indicating there is no martensitic transformation in this TBC.

4.1.1.4 Phase Stability and Sintering of YSZ Coating

Fig. 4.26 shows the comparison of the XRD patterns of as-coated and failed YSZ coatings. No significant phase changes were observed during thermal cycling.

The sintering behavior of the YSZ coating was examined using SEM. The top surface morphologies of the as-coated and failed coatings are shown in Fig. 4.27. "Mud-flat cracking" of the coating is seen in the failed specimens. A comparison of images at higher magnification, for both the as-coated and failed specimens, shows that the columns have sintered during thermal cycling. In addition, the surface of the failed specimen is smoother and the crystallographic facet structure of the individual columns becomes much less distinctive compared to the as-coated specimens.

Fig. 4.28 shows that the comparison of cross-sectional images for as-coated and failed specimens. Consistent with the surface morphologies, the serrations on the column edges become smoother with thermal cycling. In some cases, a neck is formed between adjacent columns (see Fig. 4.28e).

Raman spectroscopy was also used to detect coating phases with thermal cycling. As shown in Fig. 4.29, the coating remains t' phase during thermal cycling. Although there is no phase change, the peak width changes and the characteristic peaks become sharper with thermal cycling. The reason for this change is not clear; it may be due to the decrease in site disorder resulting from yttrium and oxygen vacancy ordering *(130)*.

4.1.2 TGO Stress Evolution

4.1.2.1 Typical Luminescence Spectra during Thermal Cycling

PLPS measurements were carried out for as-coated TBC specimens and for thermally cycled specimens at specified life-fractions at three temperatures (1151°C, 1121°C and 1100°C). All spectra were analyzed using the automated deconvolution procedure. This procedure was developed for the first time under this research and the details are described in Appendix I. The spectral characteristics (frequency shift, peak area ratio, peak width, and Lorenztian fraction) were extracted and analyzed as a function of thermal cycling. Typically, two types of spectra were observed in the specimens during thermal cycling. The first type is the spectra showing only one set of R_1-R_2 luminescence peaks and, correspondingly, exhibiting one major stress level (i.e. unimodal luminescence). The second type is the spectra showing two sets of R_1 and R_2 luminescence peaks exhibiting two stress components, with one of them being close to zero (i.e. bimodal luminescence). Examples of each type of spectra and the corresponding fitted peaks are shown in Fig. 4.30.

4.1.2.2 TGO Stress and Its Standard Deviation

The evolution of the residual stress in the TGO under the YSZ coating as a function of thermal cycles at 1151°C, 1121°C and 1100°C is shown in Fig. 4.31. In these and subsequent figures, the data points and error bars are the average values and associated standard deviations of multiple measurements on a single sample, respectively. At all three temperatures, the compressive stress increases to its maximum in the first few cycles and then decreases monotonically with thermal cycles until failure. The average compressive stress in the TGO increases from approximately 1.5 GPa to about 2.3 GPa in 5 cycles at 1151°C; whereas the

maximum stress value is reached in 50 cycles at 1121°C and 1100°C. In contrast, the specimen showing abnormally short life (202 cycles) at 1121°C starts with a higher stress and fails at an abnormally high stress (~2.4 GPa). This specimen is being studied in detail now and the explanation about its abnormal behavior needs further investigation. Since this specimen is the only specimen having such abnormal behavior, for the sake of clarity, this specimen will be eliminated from the following discussions.

The figures of average stress vs. thermal cycling are re-plotted after removing data points from the initial, transient stage (Fig. 4.32). As shown, the change of average stress vs. thermal cycles can be fit as a linear function. The slope of the linear function can be obtained and represents the rate of change of stress with cycling. There is a consistent relationship between the slope and the actual lives of specimens; the shallower the slope, the longer the spallation life.

Fig. 4.33 shows the standard deviation of the TGO stress as a function of thermal cycles. The standard deviation increases from the as-received condition to about 0.16 GPa and then decreases a little within a very short time. After the first 15% of cyclic life at all three temperatures, the standard deviation increases continuously until failure.

The average TGO stress values have also been plotted as a function of life fraction of the specimens, as shown in Fig. 4.34. The TGO stress decreases monotonically with life fraction after the initial stage (about 10% of the cyclic life). This result also shows that the TGO stress evolution with life fraction is quite

insensitive to the cycling temperature, consistent with the result obtained by Sridharan et al. (*30*) on another 7YSZ EB-PVD/ (Ni, Pt)Al/CMSX-4 TBC.

4.1.3 Relationships among Rumpling, TGO Stress Evolution and Specimen Life

As shown in section **4.1.2.2**, after an initial transient period, the TGO stress decreases monotonically with thermal cycles until failure at all three temperatures. Fig. 4.35 shows the TGO stress as a function of thermal cycles for one specimen at each temperature after removing the data points for the transient period. The stress decreases faster with increasing cycling temperature. The stress relaxation rates (GPa/cycle) of specimens were found to be 0.0053 at 1151°C, 0.0025 at 1121°C and 0.0011 at 1100°C. Comparisons of quantitative results of rumpling rate and TGO stress relaxation rate at various temperatures show that TGO stress relaxation rate increases with increasing rumpling rate. If we further combine TGO stress relaxation rate and rumpling rate with specimen life, it is found that both rumpling rate and TGO stress relaxation rate increase, while spallation life decreases as the cyclic temperature increases (Fig. 4.36).

4.1.4 PLPS Spectral Characteristics Evolution

PLPS data consists of the fluorescence spectra coming from the thermally grown oxide layer (TGO). For a homogeneous stress state, two peaks designated R_1 and R_2 are recorded and these peaks shift linearly with the magnitude of the hydrostatic stress in the TGO (Fig. 3.6). Because damage to the oxide can result in a

non-uniform stress, various features of the spectra can change, including: the peak position related to stress, the standard deviation of the stress from multiple measurements at different locations on a given sample, peak width related to stress homogeneity, the R_1/R_2 peak area ratio and the Gaussian/Lorentzian fraction used to fit the peaks. For this TBC, in addition to the TGO stress, all spectral characteristics changed in a similar manner with thermal cycling, independent of temperature. For the sake of brevity, spectral characteristics with cycling will be only described at two temperatures (1151°C and 1121°C) below.

4.1.4.1 Change of R_2 and R_1 Peak Area Ratio with Thermal Cycling

Fig. 4.37 shows the ratio of the integrated area of peak R_2 divided by the area of peak R_1 as a function of thermal cycles. Similar to the relationship of stress vs. thermal cycling, the area ratio increases initially and then decreases monotonically until failure. The change of area ratio vs. thermal cycles can also be fit using a linear function, excluding the initial transient stage, as shown in Fig. 4.38. Again, the rate of change can be related to specimen life, the shallower the slope, the higher the spallation life. This is the first time that a systematic change of area ratio with thermal cycling has been reported. The magnitude of area ratio for samples falls in the range of 0.35-0.45 which is close to the value of stress–free, randomly oriented polycrystalline α-Al_2O_3 (reference disk). This indicates that the TGO layer is randomly oriented and does not have preferential orientation.

4.1.4.2 Change of Peak Width and Shape with Thermal Cycling

Peak broadening is a measure of the TGO stress variation within a probed volume (*112, 118*). Fig. 4.39 shows the peak broadening (full width at half maximum (FWHM) height for the R_2 and R_1 peak) as a function of thermal cycles at 1151°C and 1121°C. No significant change in peak width was observed with thermal cycling.

There was no significant change of peak shape (as measured by Gaussian or Lorentzian fractions) with thermal cycling. The Lorentzian fractions were found to remain relatively unchanged with thermal cycling and have values of about 0.11 for the R_2 peak and 0.58 for the R_1 peak.

4.1.4.3 Change of Bimodal Spectra With Thermal Cycling

Bimodal luminescence spectra were observed during thermal cycling. For the bimodal spectra, the low stress component was usually close to zero (below 0.5 GPa in compression), but occasionally the low stress component reached a maximum tension level of 0.8 GPa. The high stress component ranged from 1.6 to 3.0 GPa in compression. The evolution of the fraction of bimodal spectra with thermal cycling at 1151°C for the TGO under the ceramic top coat, using the fine mapping technique, is shown in Fig. 4.40. The fraction of bimodal spectra shows systematic changes with thermal cycling. The fraction increases initially up to 5 cycles, gradually decreases and then increases again when close to failure. The evolution from coarse mapping shows the same trend as fine mapping.

4.1.4.4 Stress Distribution

Stress mapping was carried out with thermal cycling at both 1151°C and 1121°C. Stress distribution maps based on the bimodal luminescence contribution were obtained. Fig. 4.41 shows one example of a stress distribution map for a specimen cycled at 1121°C. The black regions represent the regions exhibiting bimodal spectra; whereas, the white regions represent the regions showing unimodal spectra. The maps show that the number and size of regions having bimodal spectra increase with thermal cycling. The increase is more pronounced when the sample is close to failure. It is noted that the fraction of bimodal spectra extracted from these maps does not decrease after the initial increase, which is different from the evolution of the fraction of bimodal spectra at 1151°C shown before. The possible reason is that we did not catch the correct time in the early stage to make measurements and missed the data points showing the initial increase and then decrease. However, we did observe that the number and size of regions having bimodal spectra increased when the sample was close to failure for tests at both 1151°C and 1121°C.

4.1.4.5 Relationship of TGO Cracking and Bimodal Luminescence

The back-sides of specimens which were bond coated but not ceramic coated were polished to remove the original thin oxide layer and then heated at 1151°C to form a new alumina scale.

Fig. 4.42 shows an optical image of the alumina morphology after 10 minutes oxidation and the corresponding PLPS spectra. Both unimodal spectra (one set of peak pairs) (Fig. 4.42b) and bimodal spectra (two set of peak pairs) (Fig. 4.42c and d) of α-Al_2O_3 were observed. The stress value for the low stress component of bimodal

spectra was close to zero. The regions producing bimodal spectra corresponded consistently to microcracked regions (Fig. 4.42a, point 2 and 3); whereas, all regions without visible cracks gave unimodal spectra (Fig. 4.42a, point 1). The fraction of bimodal spectra for the oxide layer without a ceramic top coat as a function of cyclic oxidation time is shown in Fig. 4.43. The fraction increases sharply up to 10 minutes (point a), gradually decreases (points a to c), and then increases (points c to d) again after 100 hours until spallation. The fraction of bimodal spectra for the oxide layer without a ceramic top coat shows the same trend with cyclic oxidation as that for TGO under the ceramic top coat with the initial increase, a subsequent decrease and a final increase before failure.

Fig. 4.44 shows the microstructure of the aluminum oxide surface after different exposure times. The alumina layer, formed on the surface of the bond coat after oxidation for 10 minutes at 1151°C, has a large number of microcracks. With increasing oxidation time, the microcracks start to heal and this result in a decrease in the number of microcracks. In some places, microcracks form outward protrusions (see arrows in the Fig. 4.44b). The density of microcracks reaches a minimum at 100 hours and the grain structure becomes evident. With increasing oxidation time, the alumina scale spalls, accompanied by the appearance of large cracks (Fig. 4.44d). The crack density as a function of time is shown in Fig. 4.45. The density of cracks as a function of oxidation time increases initially, decreases and then increases again after 100 hours. The change of the fraction of bimodal spectra as function of oxidation time is consistent with the change of the density of cracks (compare Figs

4.43 and 4.45). The fraction of bimodal spectra and the density of cracks exhibit a qualitative relationship and change in a similar manner with thermal cycling.

θ-Al_2O_3 can be detected by the PLPS method due to the fact that θ-Al_2O_3 has characteristic luminescence peaks easily distinguished from those of α-Al_2O_3 (*35*). Quite fortuitously, two small regions in which α-Al_2O_3 and θ-Al_2O_3 coexisted were observed to confirm the transformation after the initial oxidation stage. Fig. 4.46a shows an optical image of one region in which α-Al_2O_3 and θ-Al_2O_3 coexist after oxidation of 10 minutes at 1151°C. The small island of θ-Al_2O_3 was surrounded by the α-Al_2O_3 matrix. The existence of α-Al_2O_3 (R_2 = 14420 cm^{-1}) and θ-Al_2O_3 (R_2 = 14613 cm^{-1}) was identified by the different frequencies of the characteristic peaks in PLPS (Fig. 4.46b). Similar results were also obtained after oxidation for 2 minutes. With increasing oxidation time, the relative amount of α-alumina increases by the transformation of θ to α alumina. Fig. 4.46c is an oxide-type distribution area map indicating the distribution of alumina (alpha and non-alpha). The figure shows the initial presence of an island of θ-alumina surrounded by α-alumina. The island is reduced in size, by the transformation of θ to α alumina, after 1-hour exposure, and then disappears after 5 hours.

The aluminum oxide layer formed on the bare bond coat surface starts to become wavy or rumpled after oxidation for 5 hours. The amplitude of rumpling increases with increasing oxidation time (Fig.4.47). Measurements of the local residual stress in the oxide scale were made using PLPS. Since the oxide rumpling wavelength (the distance between the ridges and the valleys) is sufficiently large, the local stress in the vicinity of the ridges and the valleys can be resolved with a probe

whose size, (about 2 μm), is smaller than the rumpling wavelength. Figs. 4.48a and b show a typical morphology of rumpled α-Al_2O_3 scale after oxidation for 100 hr and the frequency shift of this oxide layer from a series of PLPS measurements, respectively. It is clear that the frequency shift is smaller at the ridges than at the valleys. Although the exact stress value cannot be obtained due to the wavy surface, the corresponding hydrostatic compressive stress is smaller at the ridges than at the valleys. This is consistent with finite element calculations (*21, 71, 74*) and from the expectation that a wrinkled scale produces tensile stress across the coating-metal interface at ridges and compressive stress in the valleys.

The oxide stress measured by PLPS is the overall stress in the small probed volume. The in-plane stress for the oxide is in compression at both the ridges and valleys; whereas, the out-of-plane stress is tensile at the ridges and compressive at the valleys. Thus, the overall hydrostatic compressive stress for the oxide scale at the ridges should be smaller than that at the valleys due to the normal stress contribution. The experimental results which were obtained from PLPS (Fig. 4.48) show the frequency shift is indeed smaller at ridges than at valleys.

4.1.5 TBC Life Prediction

Before describing the detailed procedure of remaining life prediction, we want to point out that, different approaches were used to make temperature-blind remaining life predictions based on the TGO stress for specimens tested at two temperatures (1151°C and 1121°C). Here, "temperature-blind" means that all data was placed together and the methodology did not know which specimen was tested at which

temperature. After the prediction accuracy of different approaches were compared, then the best approaches were applied and the predictions were extended for specimens tested at three temperatures.

4.1.5.1 Analysis Procedure

4.1.5.1.1 Description of Data Set and Prediction Methods

The data set consists of 7 samples tested to failure: 5 samples were tested at 1151°C and 2 samples were tested at 1121°C. The lifespan of each sample is known (Table 4.2).

For this TBC, the measured stress and its standard deviation and the R_1/R_2 peak area ratio are the only spectral characteristics that change systematically with cycles. By dividing the corresponding cycles at which measurements were made by the lifespan of each sample, the corresponding life fraction at which the measurements were taken was obtained. Thus, the original data set has several features: TGO stress, standard deviation of stress, R_1 and R_2 peak area ratio and the corresponding life fraction at which measurements were taken. In addition, we can extract other features from the original data set such as the first derivative and second derivative of stress with respect to life fraction.

There are, in principle, many ways in which the features can be combined or used separately to make predictions. Two methods were used to estimate the remaining life. First, a straightforward regression approach was used. Second, a method based on training a neural network was examined. The basic information about neural networks can be found in Appendix II.

4.1.5.1.2 Leave-one-out cross-validation

Leave-one-out cross-validation (*131*) was adopted as a means of assessing the predictive capabilities of the neural network approaches. In this approach, all data sets except one are used to train the neural network, and the predictive capacity of the network is tested by making a prediction of the data set left out. By repeating the procedure, leaving out each data set in turn, prediction accuracy measures such as average error, root mean square (RMS) error and maximum error of prediction can be determined in an unbiased way. The hypothetical prediction task provides a basis for making a decision whether to re-use or replace a given part during a regular inspection. The PLPS measurements are used to make the life prediction. Accordingly, the data for each test sample must be based on the PLPS measurements up to but not after the chosen inspection time.

4.1.5.2 Remaining Life Predictions Based on Regression

4.1.5.2.1 Prediction Using Stress vs. Life Fraction

The assessment of the predictive ability of the simple regression approach was based on a retirement for cause task in which a part replacement opportunity is available at half the expected life. We will use life prediction at an inspection around half life as an example to illustrate the proposed prediction method in the following. The data set has a total 7 samples at two temperatures 1151°C and 1121°C. For each sample, there is stress vs. life fraction data, as shown in Fig. 4.49. The whole data set was fit using a quadratic polynomial function to get the master curve (solid line in Fig. 4.49). To make a prediction for an individual sample, the sample's stress vs.

cycle data up to the last inspection at roughly half-life is fit to a quadratic function. The intersection of the quadratic line with the stress from the master curve corresponding to 50% life fraction (S=1.79 GPa) yields the number of cycles corresponding to half life for the individual sample and its predicted life is exactly twice the life at the point where the extrapolated stress curve reaches the stress on the master curve corresponding to half life. The prediction accuracy can be calculated from the difference between the actual and predicted lives.

The prediction results are shown in Table 4.2. The average value of absolute error is 11.2%. The root mean square (RMS) error of prediction is 12.4% and the maximum absolute error is 19.4%. It is worth noting that the above results are only an example showing the prediction at around half-life. In fact, depending on the stress level obtained from inspection (one stress measurement is the extreme case), corresponding life fractions predicted from the master curve can be obtained and the total life can be calculated from this life fraction and the number of cycles at which the sample is inspected.

There is inevitably uncertainty in prediction using the regression mean curve. In an engineering context, one is interested in how much reduction in expected usable life is required to achieve reduced probability of an unexpected failure. Statistical methods were used to study this uncertainty on the limited specimens available. It was found that two-parameter Weibull distribution represented life data pretty well (Fig. 4.50). The resulting cumulative distribution from this Weibull distribution is shown in Fig. 4.51. Using this distribution function, it is possible to estimate the reduction in expected remaining life fraction that is required to have various levels of

increased reliability against having a failure before the end of the expected remaining life fraction. This for example could be used to determine when the next inspection should be done or in making a decision to remove a part or continue running it. Table 4.3 shows results for PLPS inspections running at life fraction 25%, 50% and 75 % from the master curve. The values in the table show the allowable remaining life if the chance for a part reaching that life is to be 50%, 90% or 95% according to the Weibull analysis. For example, at the measurement at 50% of life, there is 50% of reliability that the remaining life is equal to or more than 49.6% while the reliability that the remaining life is equal to or more than 31.4% is 90%. We note that for a sample set as small as the present one, these are just engineering estimation that will be increasing questionable for tail ends of the distributions such as for prediction of very high reliabilities.

4.1.5.2.2 Prediction Using Peak Area Ratio and Standard Deviation of Stress vs. Life Fraction

Figures 4.52 and 4.53 show the peak area ratio and standard deviation of stress, respectively, as a function of life fraction for all samples. Following the same procedure of section *4.1.5.2.1*, life predictions can be separately made using R_1 and R_2 peak area ratio vs. life fraction and standard deviation of stress vs. life fraction. The corresponding results are shown in Tables 4.4 and 4.5. It is shown that the predictions using the peak area ratio (RMS error 23.9%), and standard deviation of stress (RMS error 30.3%), vs. life fraction were worse than those using the stress vs. life fraction (RMS error 12.4%). This is probably due to the fact that the change of

area ratio and standard deviation of stress as a function of life fraction are relatively temperature sensitive, which makes the data more scattered. In contrast, the change of stress as a function of life fraction is nearly temperature independent, which leads to a master curve representing all sample behavior fairly well; thus, the predicted results are better.

4.1.5.2.3 Prediction Using The Weighted Average of Three Features

The regression approach was used to make remaining life predictions based on all three features: TGO stress, peak area ratio, and standard deviation of stress vs. life fraction. A simple weighted average method was used to combine the three features and the results are shown in Table 4.6. The weighting factors for a given data feature were selected to be inversely proportional to the root mean square error found in regression predictions using that particular feature alone. As would be expected, the results were better than those based on the area ratio and standard deviation of stress vs. life fraction, but worse than those based on the stress vs. life fraction. The RMS error of the prediction was 19.3%. Therefore, predictions based on combination of multiple features by simple weighted average were inferior to those made using stress alone.

4.1.5.3 Remaining Life Predictions Based on Neural Network

4.1.5.3.1 First Neural Network Method

The input features into the training network are:

– Stress (smoothed, Fig. 4.54a)

- First derivatives of stresses (smoothed, Fig. 4.54b)
- Standard deviation of stresses
- R_1 and R_2 peak area ratio
- Second derivatives of stresses (smoothed, Fig. 4.54c)

The output is the predicted remaining life fraction at certain time points of measurements.

The results are shown in Table 4.7. It was found that the prediction is better for reduced measurements (three measurements) than for full measurements (five measurements). One possible reason for this is that the measurements prior to failure are noisier than those at the beginning of test. The comparison of the radial basis function network and generalized regression neural network (GRNN) did not show a significant difference in performance. Compared with the simple regression method or weighted average method, some accuracy has been gained by using neural networks, which allow simultaneously use of multiple features. For the data containing three measurements, the RMS error is 10.0% for the radial basis function network and 8.2% for the GRNN, respectively. However, the benefit of using neural network with this method is modest. As mentioned before, we think it is probably due to the fact that the change of area ratio and standard deviation of stress as a function of life fraction is relatively temperature sensitive, which makes the data more scattered. This increases the difficulty of pattern recognition by neural network and decreases the accuracy of prediction.

4.1.5.3.2 Second Neural Network Method

Recognizing that there is temperature sensitivity for the area ratio and standard deviation of stress, a second neural network method was developed. First, the stress vs. life fraction data was fit with a quadratic polynomial function to get the master curve (dashed line in Fig. 4.55), as was done before in the regression method. Second, the stress and the pseudo life fraction (pseudo LF) derived from the master curve were used in training neural networks and fit to the actual life fraction of samples at various times of measurement. So the input features used in training the network are:

- TGO Stress
- Pseudo life fraction (pseudo LF) at which the stress was measured that we derived from the master curve

The output is the predicted remaining life fraction at certain points in time.

The results are shown in Table 4.8. The prediction again is better for reduced measurements (three measurements) than for the full measurements (five measurements). Compared to the first method, it is shown that the accuracy of prediction is significantly better. We conclude that with the reduced measurements of current data, the radial basis function network combined with the master curve gives the best prediction results. The RMS error is 6.1% and the maximum absolute error is 8.2%, both of which are encouraging.

4.1.5.4 Remaining Life Predictions for Specimens Tested at Three Temperatures

Based on the above results, two approaches were chosen to predict remaining life for specimens tested at the three temperatures. One is the regression method

based on stress alone (Fig. 4.56), the other is the radial basis function network combined with the master curve. The prediction accuracy is shown in Table 4.9 and 4.10. Finally, the performance of predictions was compared with the inherent variation in spallation lives of all samples tested at three temperatures and the results are shown in Fig. 4.57. The standard deviations of predictions using training neural network and regression method are 6.6% and 14.7%, respectively, which are much improved compared to the inherent variation of spallation lives of 34.6%.

4.2 Results of NiCoCrAlY Bond Coated TBCs

4.2.1 Characterization of Bond Coat Surface Before YSZ Deposition

As described in section **3.1.2**, different surface finishing processes were carried out before TBC deposition in order to study the effect of surface roughness on the durability of NiCoCrAlY bond coated TBCs. Two surface finishing processes include: (1) as-received; (2) 90 minutes' centrifugal barrel finishing. Figure 4.58 shows one example of as received bond coat surface. It is shown that the surface of this specimen is very rough and has very large ridges. The height between peaks and valleys within sample (PV) is 18.6 μm.

Figure 4.59 shows one example of barrel finished bond coat surface. The surface roughness of specimen after centrifugal barrel finishing decreases significantly compare to the as-received specimen. The PV value is 5.6 μm. The change of surface roughness proves that centrifugal barrel finishing is very successful in removing large ridges.

The summary of surface roughness data after various surface finishing treatments is shown in Fig. 4.60. It is apparent that surface roughness of specimens decreases dramatically after barrel finishing. The average surface roughness (Ra) of as-received specimens is 2.6 μm. The surface of specimens after barrel finishing is smoother and the average surface roughness (Ra) of specimens after barrel finishing is 0.4 μm.

As described in section **2.2.2,** a parameter more directly related to the failure mechanism is the localized radius of curvature of the bond coat surface, rather than Ra or Pv. The surface geometry of specimens is characterized using a surface curvature map, a novel method developed in this study. The detailed procedure of developing the surface curvature mapping software is described in Appendix III. Fig. 4.61 shows one example of the original surface and the corresponding curvature maps for as-received and barrel finish bond coat surfaces. As shown in Fig. 4.61, the average roughness of the bond coat surface before barrel finishing is higher than that after finishing by a factor of three, but the curvature before finishing is smaller than that after finishing, which indicates that the asperity of the barrel finished surface is sharper and more severe.

Fig. 4.62 shows the surface morphology of a bond coat. Cavities were found on the as-received bond coat surface. After barrel finishing for 90 minutes, there is bond coat loss and the size and depth of both ridges and cavities decreases. On the other hand, some scratches were introduced.

The TGO layer formed after pre-oxidation and before YSZ deposition was studied using PLPS. From observation of PLPS, no θ-Al_2O_3 is shown (Fig. 4.63) in

any of the specimens regardless of surface conditions. All specimens contain stable α-Al_2O_3.

4.2.2 Microstructure of As-Coated TBCs

After bond coat processing and characterization, all specimens were sent for deposition of YSZ coating. The as-coated EB-PVD YSZ coating consists of a non-equilibrium tetragonal (t') phase. The cross-sectional micrograph of the as-coated TBC is shown in Fig.4.64. The YSZ topcoat has a nominal thickness of 145 μm with a columnar structure. The NiCoCrAlY bond coat is nominally 100 μm thick. The bond coat has a characteristic two-phase structure. The dark region is β-NiAl phase, and the light region is γ-Ni solid solution. A thin, continuous TGO layer (~ 0.5 μm) was observed for the as-coated TBCs. Below the relatively uniform TGO layer, TGO protrusions or embedded oxides were also found (see arrows in Fig. 4.64b and c). These imperfections originate from the shot-peening and heating treatment of the NiCoCrAlY bond coat prior to the deposition of the YSZ coating.

4.2.3 Spallation Life and Microstructural Evolution

One-hour thermal cycling tests were conducted at 1121°C and the spallation lifetime for specimens is shown in Fig. 4.65. The average spallation life for specimens with the as-received bond coat surface is 102 cycles and the average spallation life for specimens after barrel finishing is 98 cycles. Both types of specimens show fairly short lives compared to the typical lifetime for EB-PVD MCrAlY TBCs, which is around 500-700 cycles (*39*). The reasons why all the

specimens have short spallation lives have been studied and the detailed explanation can be found in ref. (*132*).

No significant changes in the surface morphology or the phase constituents of the YSZ coating were observed during thermal cycling. Microstructural evolution of TBCs is shown in Fig. 4.66. During thermal cycling, TGO thickness increases and recession of the two-phase ($\beta + \gamma$) region occurs. β- to γ- phase transformation occurs in the bond coat and the γ-phase grows at the expense of the β-phase. The quantitative results of TGO growth and recession of the two-phase region will be described in section **4.2.5**. Formation of oxide-filled cavities containing non-α-Al_2O_3 oxide was found in the embedded oxides as shown in Fig.4.67. The non-α-Al_2O_3 oxide in the cavities contained Cr-rich oxide and Y-rich oxide identified by EDS analysis (Figs. 4.68 and 4.69). The XRD pattern of the bond coat surface after spallation indicates that the phase constituent of the Y-rich oxide is $Al_5Y_3O_{12}$ (Fig. 4.70). Fig. 4.71 shows example of the TGO/bond coat interface rumpling during thermal cycling. TGO penetrates into the underlying NiCoCrAlY bond coat, similar to that in (Ni,Pt)Al bond coated TBC. However, contrast to (Ni,Pt)Al bond coated TBC, the rumpling is more limited and the amplitude of the largest displacement is only about 2 μm. No cracking or apparent damage were observed at TGO/TBC interface due to rumpling, even after separation of the TGO/BC interface due to increased strain energy.

Fig. 4.72 shows the macrographs of the failed specimens. The specimens spalled catastrophically into many small pieces. Prior to failure, limited spallation was observed originating from specimen edges (Fig. 4.72b). The top view of the

spalled surface on the bond coat side is shown in Fig. 4.73. The spalled surface consists primarily of bond coat, indicating that the failure occurs predominantly at the TGO/bond coat interface. The cross-sectional SEM image of the failed specimen is shown in Fig. 4.74. Consistent with the top view, the failure interface is predominantly at the TGO/bond coat interface. The area fraction of exposed bond coat surface is around 90%.

4.2.4 TGO Stress Evolution

The TGO stress was measured as a function of thermal cycles using PLPS. One typical example of PLPS spectra during thermal cycling is shown in Fig. 4.75. No evidence for θ-Al_2O_3 was found at any point of cyclic life. The TGO stress evolution is shown in Fig. 4.76. The average TGO stress in the as-coated condition ranges from 2.8 to 3.5 GPa. The compressive stress increases to the maximum stress (about 4.0 GPa) in the first 25 cycles and then remains relatively unchanged until failure. The fact that the TGO stress remains constant until failure makes it impossible to use this PLPS spectral characteristic to predict the TBC life.

Fig. 4.77 shows the standard deviation of stress as a function of thermal cycles. The standard deviation in stress has a tendency to increase with thermal cycles, which indicates that progressive TGO damage is occurring. However, the large data scatter within different samples precludes the possible use of the standard deviation of stress in life prediction. In previous study (*39*) on another EB-PVD MCrAlY bond coated TBC with life around 500-700 cycles, the TGO stress increases initially, remains relatively unchanged, and then sharply decreases prior to the final

spallation failure. In addition, the final decrease in the stress is accompanied by a sharp increase in the standard deviation of the stress. The systematic change of the TGO stress and its standard deviation has been used in life predictions (*127*). We think that the specimens in the present study did not show such behavior in stress, probably because the specimens failed prematurely.

4.2.5 TGO Thickness and β-depletion

The TGO grows with thermal cycling as shown in Fig. 4.78. TGO growth satisfies parabolic growth kinetics. The average TGO thickness at failure was around 4 μm. Along with the growth of the TGO, the β- to γ- phase transformation occurs in the bond coat and the γ-phase grows at the expense of the β-phase.

The thicknesses of both the lower and upper β-depletion zones were measured as a function of thermal cycles (Fig. 4.79). The recession of the two-phase (β + γ) region satisfies the parabolic growth law and the recession coefficient for the lower depletion zone was larger than for the upper depletion zone. The rates of TGO growth and two-phase recession were both parabolic, suggesting that both processes are controlled by diffusion.

As an attempt to non-destructively measure TGO thickness, TGO thickness was also measured using AC impedance by Jentek Sensors Inc.. The information about AC impedance measurement is described in Appendix IV. The thickness measured by AC impedance was compared to that measured by metallography. As shown in Fig. 4.80, the lift-off change measured by AC impedance matched the TGO thickness measured by metallography fairly well, except for specimen 1 at high cycles.

4.2.6 Life Prediction Based on TGO Stress, TGO Thickness and Curvature of Bond Coat Surface

The failure of this NiCoCrAlY bond coated TBC is predominantly at the TGO/bond coat interface. The high strain energy stored in the TGO layer plays an important role in driving the failure. Based on microstructural observations and the results of a previous study (*75*), the proposed failure scenario is as follows: first debonding occurs at ridge tops at a critical value of the tensile normal stress ($\sigma_{n\ (critical)}$) at the bond coat/TGO interface (Fig. 4.81) and then several ridge top debonds of sufficient size results in unstable fracture driven by the strain energy in the TGO. Therefore, a preliminary life prediction approach was proposed based on the measurement of initial bond coat surface geometry, TGO stress and TGO thickness, and correlating these properties by fracture mechanics as described below.

As described in section **2.2.2**, the tensile normal stress at the ridge tops can be expressed as

$$\sigma_N = -\left(\frac{1}{R_1} + \frac{1}{R_2}\right) \cdot h_{TGO} \cdot \sigma_0 \qquad (2.2)$$

where σ_N is normal (out-of-plane) stress in the TGO/bond coat interface, σ_0 is the biaxial stress in the TGO layer, R_1 and R_2 are the principal radii of curvature at the asperities, h_{TGO} is the oxide thickness. TBC failure occurs at a critical value of σ_N (*75*). Thus for specimens with the ridges with smallest radii of curvature, the TGO is relatively thin at spallation; whereas for the ridges with largest radii of curvature, the TGO has to grow considerably thicker before the same $\sigma_{N\ (critical)}$ is reached.

Conversely, for a given h_{TGO}, the regions having smaller radii of curvature than a minimum will debond according to equation (2.2) and size of the local debonding regions can be obtained if σ_N, σ_0 and $(1/R_1+1/R_2)$ are known. As shown in the above sections, σ_0 was measured by PLPS, $(1/R_1+1/R_2)$ was extracted from the surface curvature map. For an EB-PVD/(Ni,Pt)Al TBC in the previous study, $\sigma_{N\ (critical)}$ was found to be 0.3 GPa (*75*). However, it is reasonable to say that this critical value is different for different TBC. In the present approach, the critical stress value for debonding was derived from the known life data for specien with barrel finish. Then we used this critical stress value as a known input value to predict the life of specimen with as-received surface condition. The critical normal stress value was found to be 2.0 GPa for this TBC.

With thermal cycling, TGO thickness, TGO strain energy and the size of debonded regions increase. When the debonded regions reach sufficient size and the strain energy release rate exceeds the interface toughness, final failure will occur. The TGO thickness required for final failure at this sufficient large debond region can be calculated based on fracture mechanics. Finally, the spallation life is predicted according to this thickness value at failure and the oxide growth rate which can be extracted from the measured data of TGO thickness vs. exposure time.

Based on the above analysis, the flowchart of the life prediction procedure is shown in the Fig. 4.82. First, the surface curvature map is obtained. Second, a specific TGO thickness is proposed as an initial starting point. The continuous debond region at this thickness will be determined based on the equation (2.2). The size of every continuous debond region will be obtained using image analysis. In the

third step, whether the largest continuous debond region size reaches the critical size for bulk spallation or not is determined by fracture mechanics. If it is, then the proposed thickness is the minimum thickness to spallation. If not, then TGO thickness will be increased and then the steps 2 and 3 will be iterated until the minimum TGO thickness to spallation will be found. Finally, the spallation life is predicted based on this minimum thickness to spallation and the TGO growth rate.

Fig. 4.83 shows one example of surface curvature and the corresponding debond region at different TGO thickness. Table 4.11 shows the largest continuous debond region size at different TGO thickness. If we assume this debonded region has the shape as idealized in Fig. 4.84 (*133*) and near or parallel to the free edge of the specimen, the flaw at TGO thickness h = 4 μm has the shape with W = 8.45 μm and d = 3.45 μm. According to the result from Ambrico and Begley (*133*) done for such flaw shape (Fig. 4.85), in the present case, d/W = 0.41 and d/h = 0.86 gives a normalized strain energy release rate of G/G_0 = 0.37. The available strain energy G_0 ($G_0 = \frac{(1-\nu_{TGO}^2)\cdot h_{TGO}\cdot\sigma_0^2}{2\cdot E_{TGO}}$) is calculated using the TGO thickness and stress measured from PLPS and found to be 65 J/m^2. Thus the strain energy release to drive the crack is 24 J/m^2, which is greater than 10 J/m^2, the fracture toughness of TGO/bond coat interface (*134*). So the debond region when TGO thickness reaches 4 μm is sufficient to cause unstable fracture of the entire interface.

Fig. 4.86 shows that the prediction results for specimens with two surface conditions: as-received and barrel finish. The predicted and actual lives agree within 15%. It is worth noting that the spallation lives for as-received and barrel finished

specimens are comparable, although there are large differences in surface roughness. As shown before, the surface curvature does not vary much although the average roughness (Ra) does, which indicates that surface curvature is more directly related to TBC life than average roughness.

Table 4.1. Sample lives at three temperature tests.

Temperature (°C)	1151	1121	1100
Sample Life (Cycles)	190,200,200,150,150	610,550,470,202	1122,830,920,842

Table 4.2. Remaining life prediction based on average stress vs. life fraction

Temperature (°C)	Sample	Life (Cycles)	Actual Life Fraction at Stress S=1.79GPa[a]	Actual Remaining Life Fraction[b]	Error In Remaining Life Prediction
1151	1	190	0.648	0.352	-0.148
	2	200	0.694	0.306	-0.194
	3	200	0.469	0.531	+0.031
	4	150	0.361	0.639	+0.139
	5	150	0.378	0.622	+0.122
1121	1	610	0.404	0.596	+0.096
	2	550	0.556	0.444	-0.056
Average					0.112
RMS					0.124
Maximum					0.194

[a] Life fraction from master curve at S=1.79GPa, LF=0.50.
[b] Predicted remaining life fraction from master curve, RLF=0.50.

Table 4.3. Remaining life fraction at different reliability levels for PLPS inspections at life fraction 25%, 50% and 75% from master curve

Life Fraction from Master Curve	Remaining Life Fraction from Master Curve	Reliability		
		50%	90%	95%
0.25	0.75	0.817	0.536	0.416
0.50	0.50	0.496	0.314	0.260
0.75	0.25	0.131	0	0

Table 4.4. Remaining life prediction based on peak area ratio vs. life fraction

Temperature (°C)	Sample	Actual Life Fraction at Area Ratio A2/A1=37.7%[a]	Actual Remaining Life Fraction[b]	Error In Remaining Life Prediction
1151	1	0.341	0.659	0.159
	2	0.445	0.555	0.055
	3	0.411	0.589	0.089
	4	0.156	0.844	0.344
	5	0.013	0.987	0.487
1121	1	0.477	0.523	0.023
	2	0.584	0.416	-0.084
Average				0.177
RMS				0.239
Maximum				0.487

[a] Life fraction from master curve at peak area ratio A2/A1=37.7%, LF=0.50.
[b] Predicted remaining life fraction from master curve, RLF=0.50.

Table 4.5. Remaining life prediction based on standard deviation of stress vs. life fraction

Temperature (°C)	Sample	Actual Life Fraction at Deviation in Stress DS=0.171GPa[a]	Actual Remaining Life Fraction[b]	Error In Remaining Life Prediction
1151	1	0.669	0.331	-0.169
	2	0.985	0.015	-0.485
	3	0.142	0.858	0.358
	4	0.426	0.574	0.074
	5	0.878	0.122	-0.378
1121	1	0.214	0.786	0.286
	2	0.354	0.646	0.146
Average				0.271
RMS				0.303
Maximum				0.485

[a] Life fraction from master curve at deviation in stress DS=0.171GPa, LF=0.50.

[b] Predicted remaining life fraction from master curve, RLF=0.50.

Table 4.6. Remaining life fraction using weighted average method

Error (%)	Stress vs. Life Fraction	Peak Area Ratio vs. Life Fraction	Deviation in Stress vs. Life Fraction	Weighted Average of 3 Attributes
Average	11.2	17.7	27.1	16.3
RMS	12.4	23.9	30.3	19.3
Maximum	19.4	48.7	48.5	33.4

Table 4.7. Prediction results using neural network method 1

Error (%)	Using Three Measurements		Using Five Measurements	
	Radial Basis Network	Generalized Regression Neural Network	Radial Basis Network	Generalized Regression Neural Network
Average	7.2	7.2	14.3	13.1
RMS	10.0	8.2	16.0	15.1
Maximum	22.1	13.3	22.7	21.4

Table 4.8. Prediction results using neural network method 2

Error (%)	Using Three Measurements		Using Five Measurements	
	Radial Basis Network	Generalized Regression Neural Network	Radial Basis Network	Generalized Regression Neural Network
Average	5.5	7.2	6.5	12.2
RMS	6.1	8.8	7.4	13.1
Maximum	8.2	18.6	10.9	20.5

Table 4.9. Remaining life prediction based on average stress vs. life fraction for specimens tested at three temperatures

Temperature (°C)	Sample	Life (Cycles)	Actual Life Fraction at Stress S=1.76GPa[a]	Actual Remaining Life Fraction[b]	Error In Remaining Life Prediction
1151	1	190	0.672	0.328	-0.172
	2	200	0.722	0.278	-0.222
	3	200	0.521	0.479	-0.021
	4	150	0.376	0.624	0.124
	5	150	0.434	0.566	0.066
1121	1	610	0.462	0.538	0.038
	2	550	0.56	0.44	-0.060
1100	1	1122	0.302	0.698	0.198
	2	830	0.352	0.648	0.148
	3	920	0.276	0.724	0.224
Average					0.127
RMS					0.147
Maximum					0.224

[a] Life fraction from master curve at S=1.76GPa, LF=0.50.
[b] Predicted remaining life fraction from master curve, RLF=0.50.

Table. 4.10. Prediction accuracy made by regression and neural network for specimens tested at three temperatures

Error (%)	Radial Basis Network	Regression
Average	5.3	12.7
RMS	6.6	14.7
Maximum	13.4	22.4

Table 4.11. Size of debonding region at different TGO thickness

TGO Thickness (μm)	Size of Largest Debonding Region (μm)	Spallation
2	0	No
3	Length = 1.3; Width =1	No
4	Length = 16.9; Width =6.9	Yes

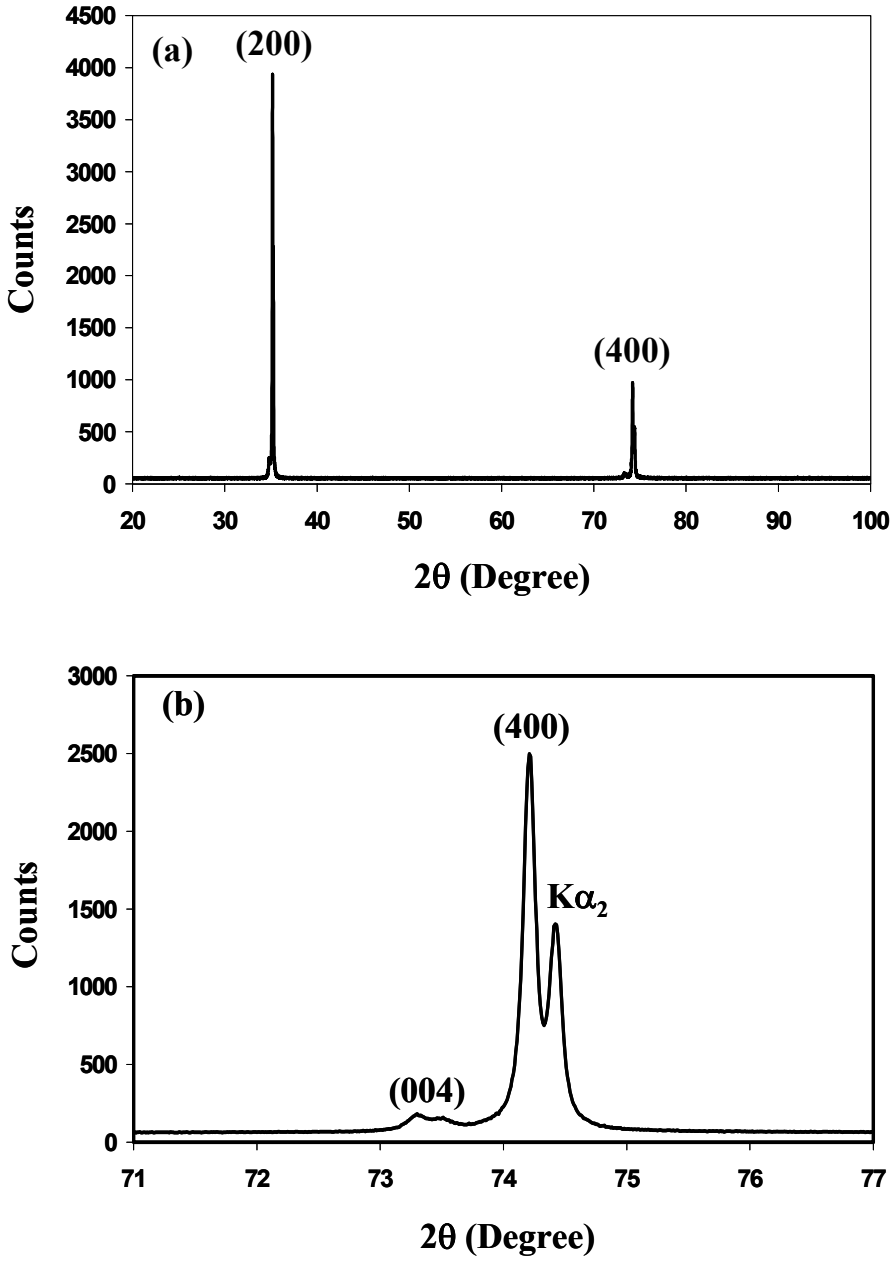

Fig. 4.1. XRD patterns of As-coated (Ni,Pt)Al bond coated TBC

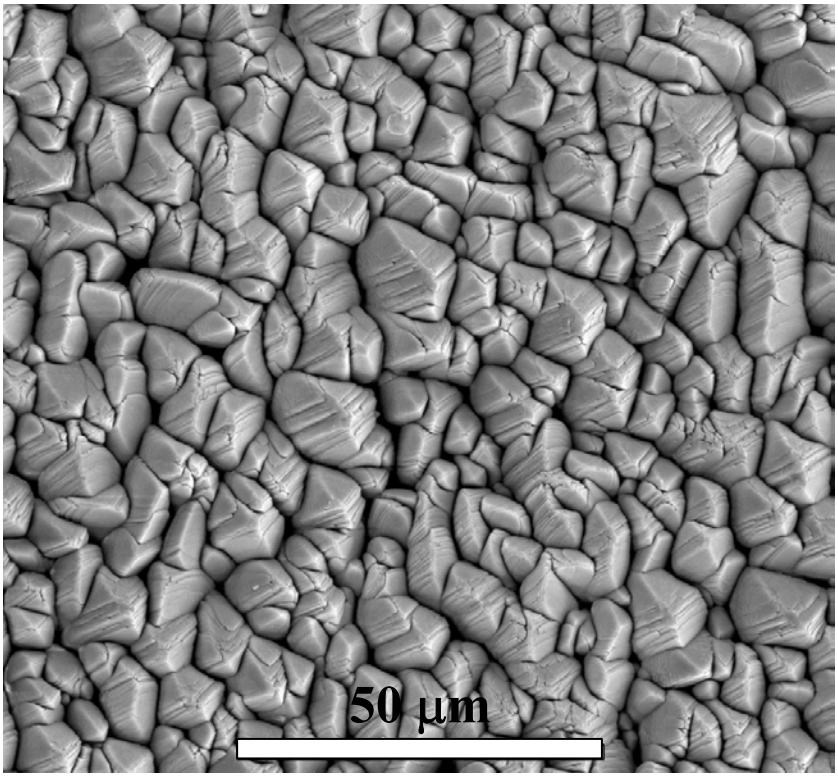

Fig. 4.2. Top surface morphology of as-coated TBC specimen with (Ni,Pt)Al bond coat

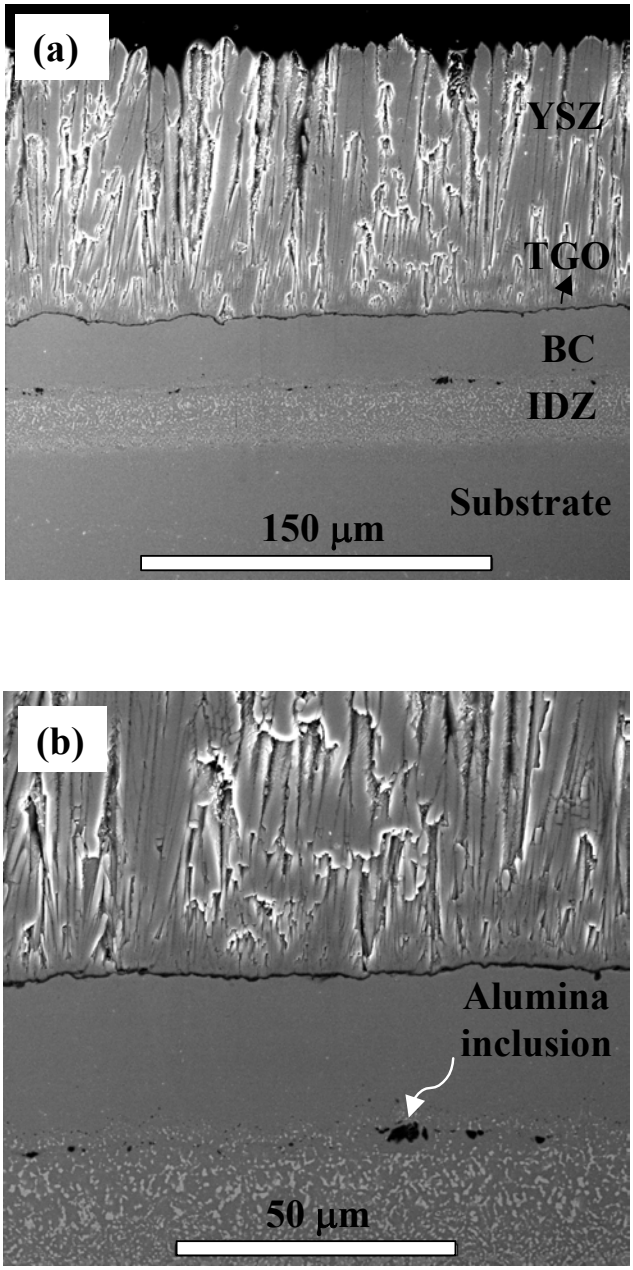

Fig. 4.3. As coated microstructure of (Ni,Pt)Al bond coated TBC

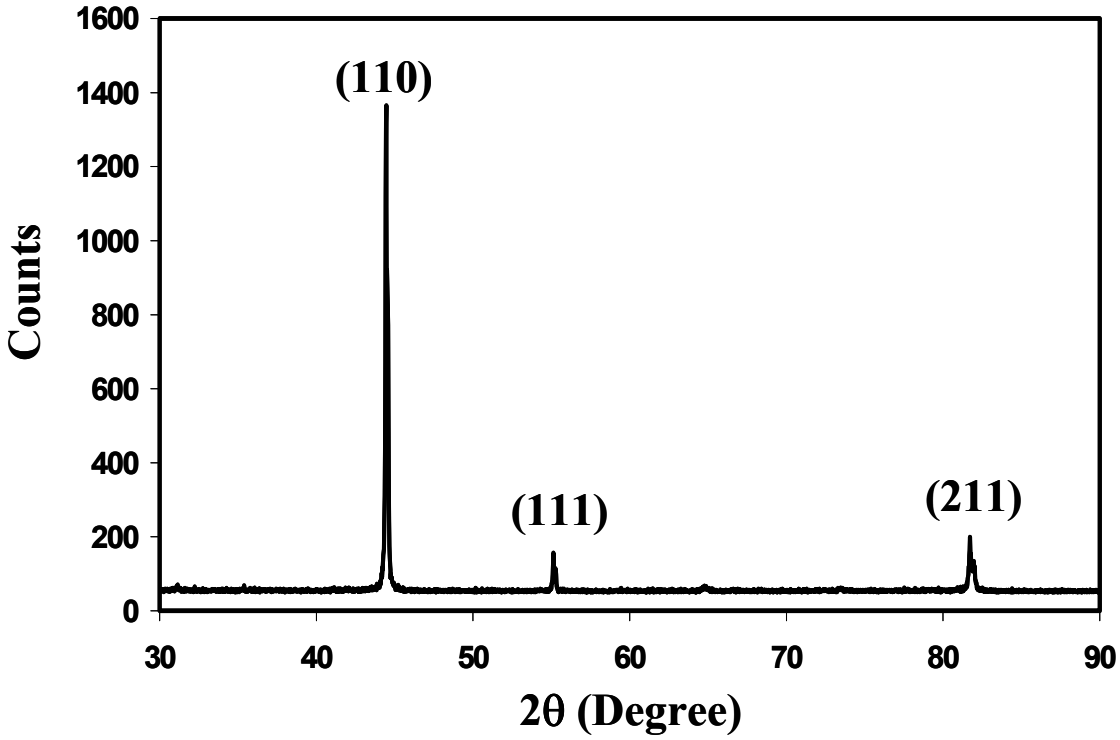

Fig. 4.4. XRD pattern of bond coat for as-coated (Ni,Pt)Al bond coated TBC

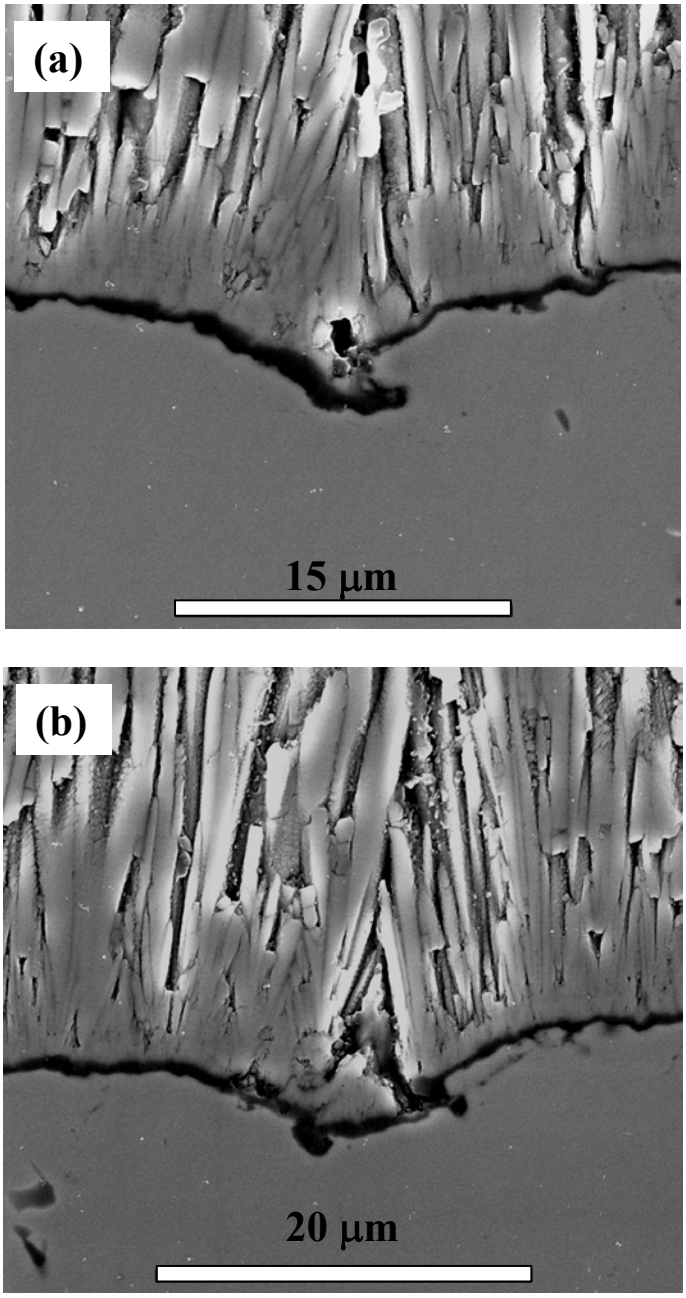

Fig. 4.5. Imperfections in the vicinity of TGO in the as-coated microstructure

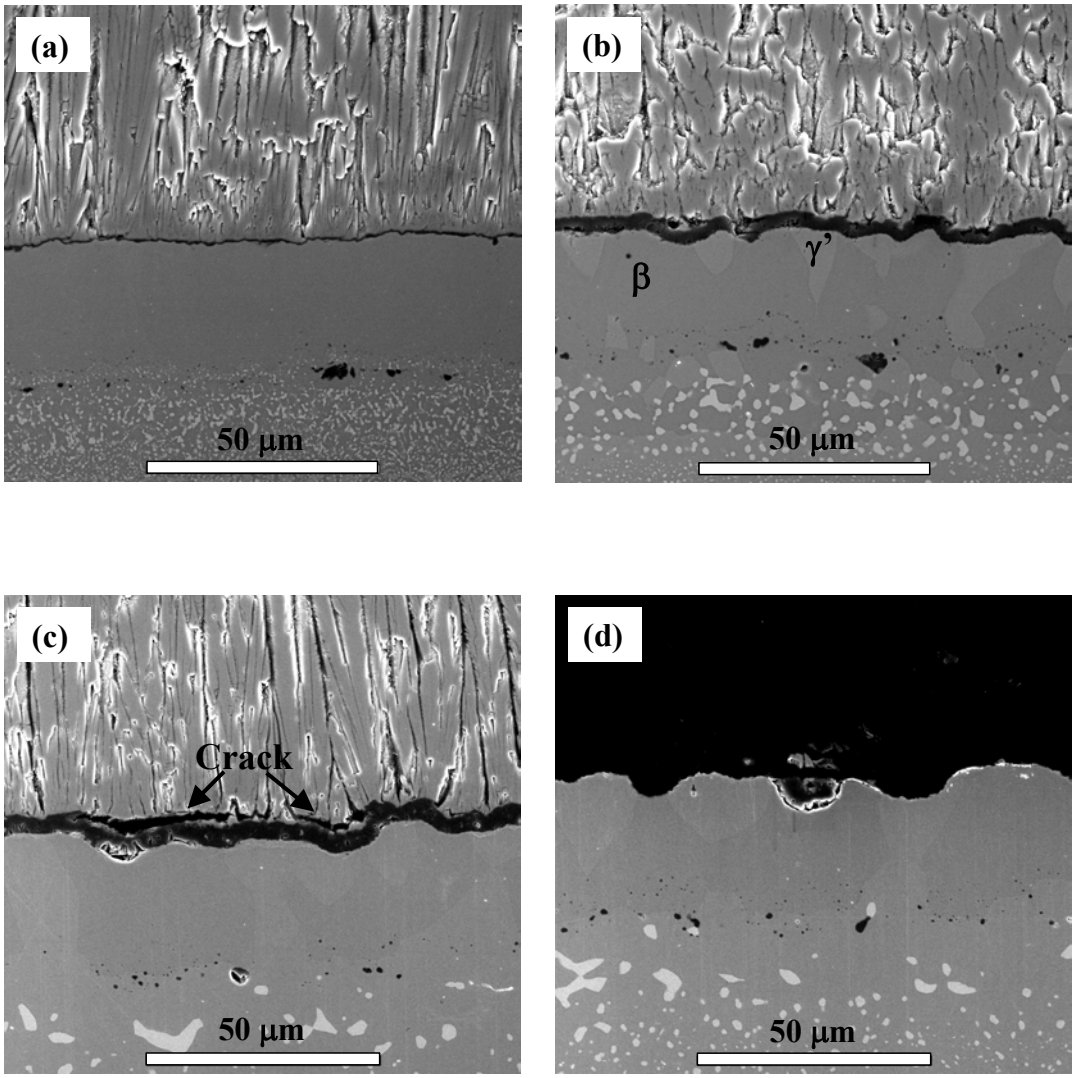

Fig. 4.6. Microstructural evolution at (a) 0 cycles, (b) 60 cycles, (c) 125 cycles and (d) 190 cycles at 1151°C

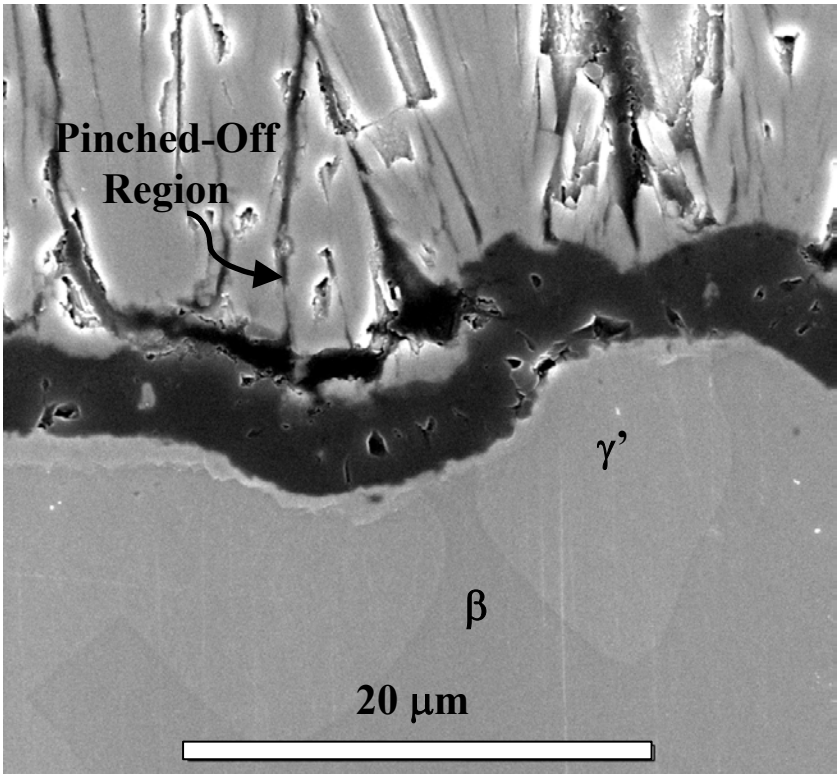

Fig. 4.7. Higher magnification image showing a typical example of crack initiation

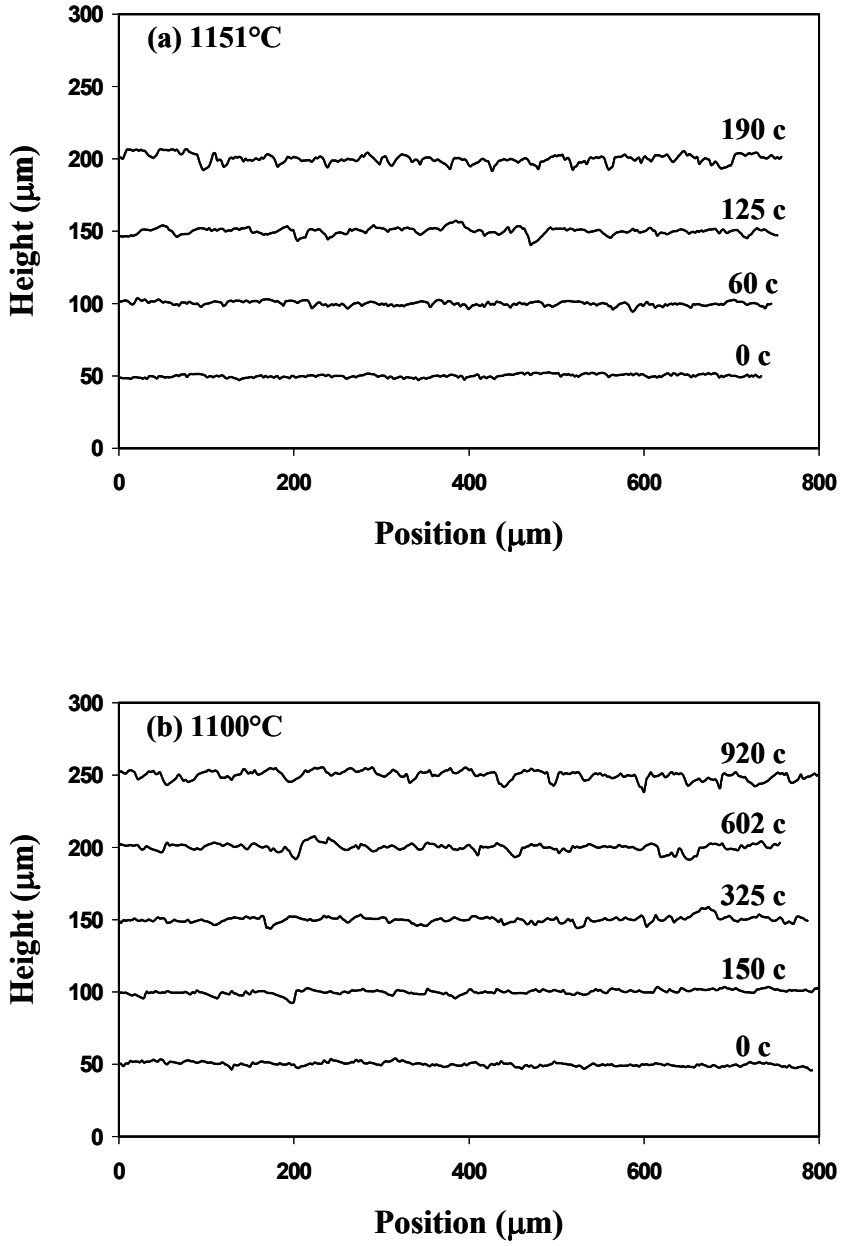

Fig. 4.8. Profiles of metal/oxide interface at various stages of thermal cycling at (a) 1151°C and (b) 1100°C

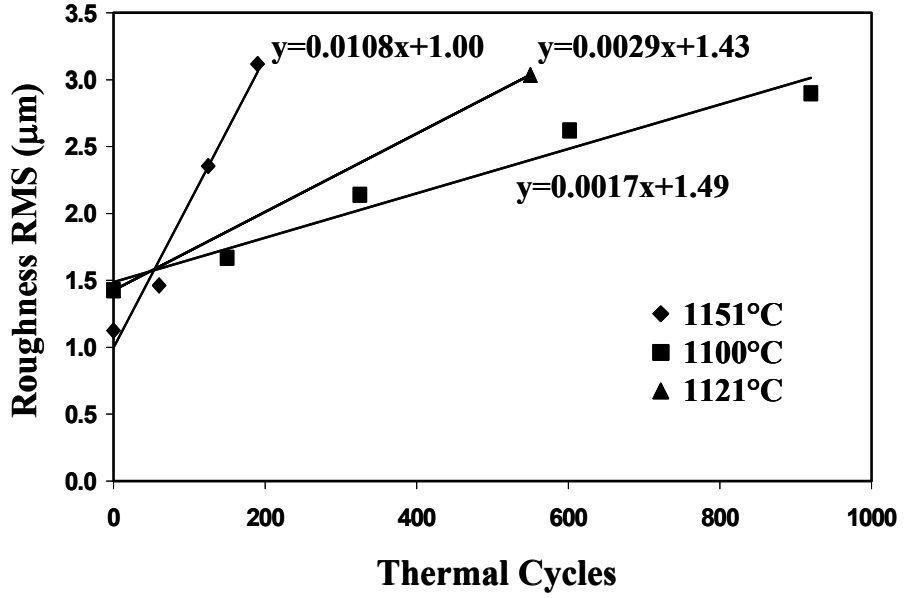

Fig. 4.9. Root-mean-square roughness (RMS) of metal/oxide interface as a function of thermal cycles at various temperatures

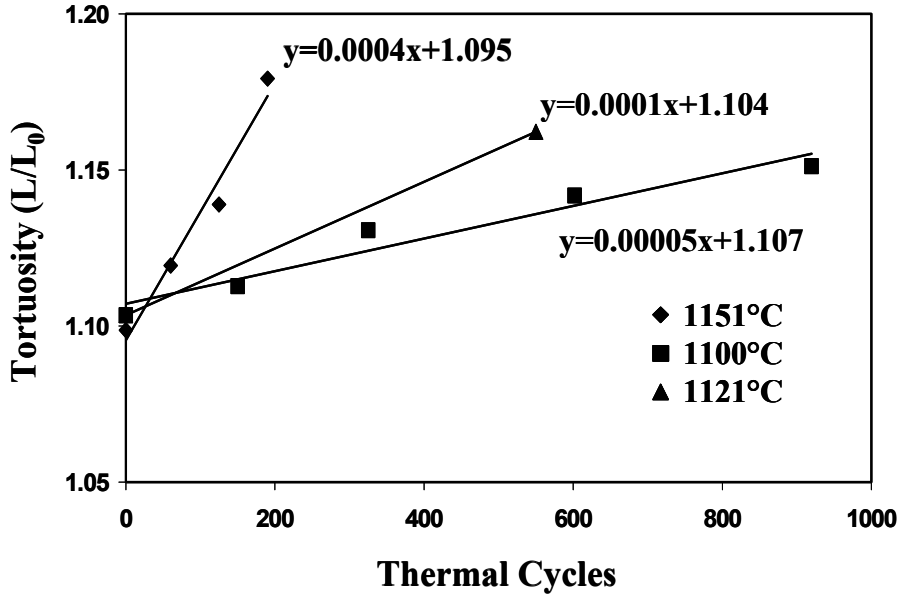

Fig. 4.10. Tortuosity of metal/oxide interface as a function of thermal cycles at various temperatures

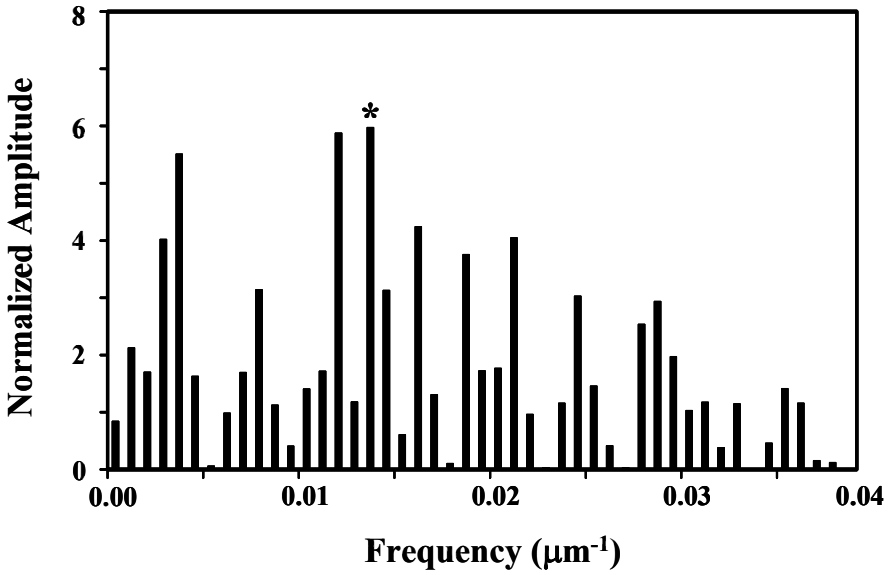

Fig. 4.11. Power spectrum plot for profile of specimen after 125 cycles at 1151°C in Fig. 4.8

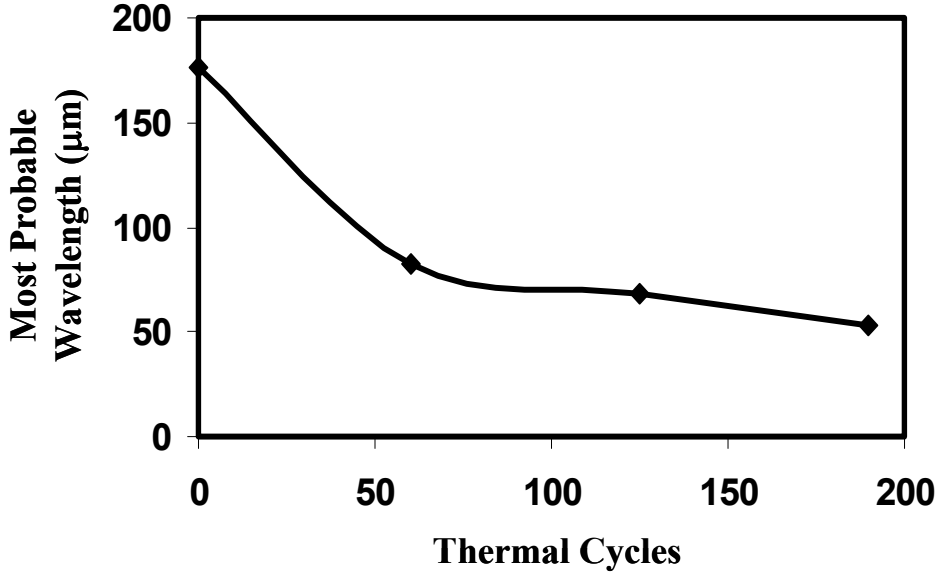

Fig. 4.12. Probable wavelength as a function of thermal cycles for specimens tested at 1151°C

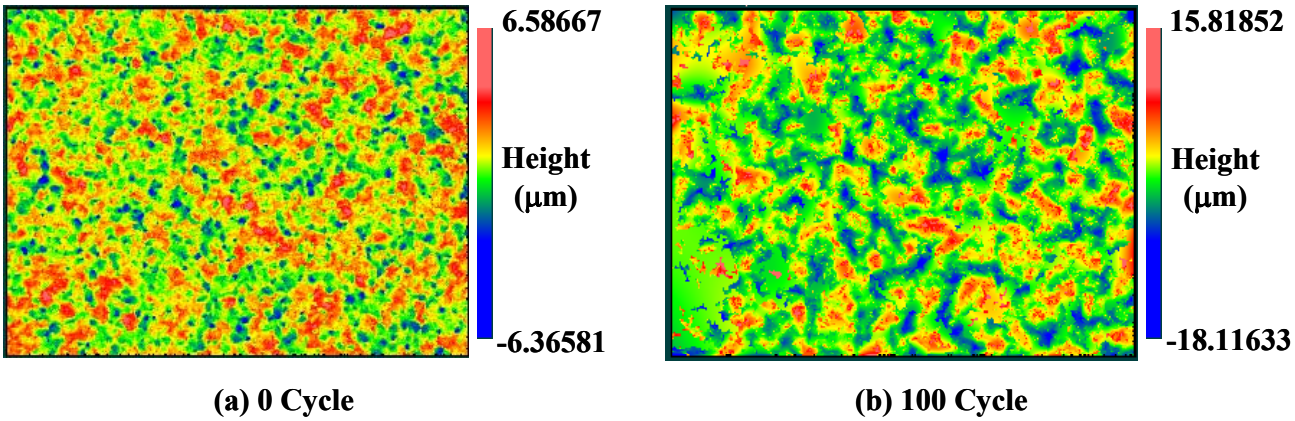

Fig. 4.13. Filled plot of back side of TBC specimen after (a) 0 and (b) 100 cycles at 1151°C

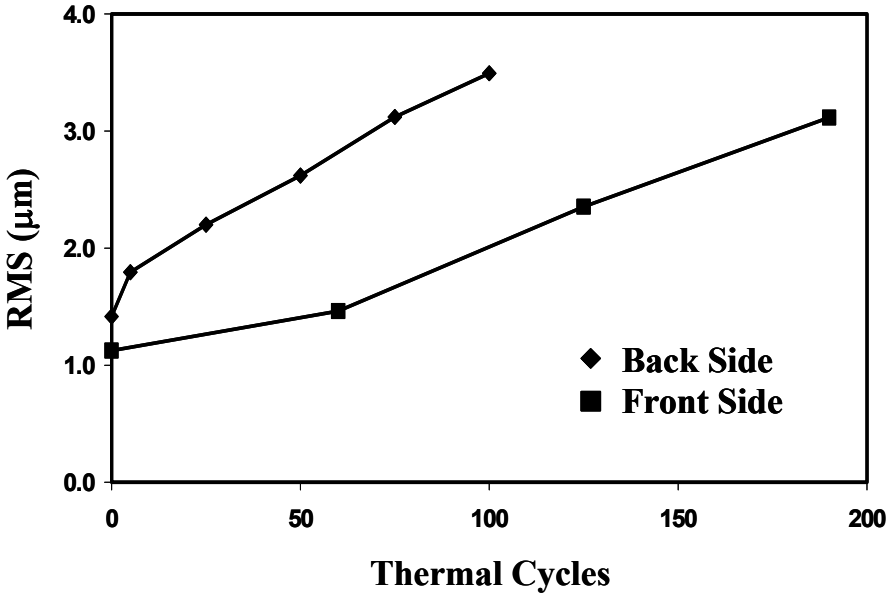

Fig. 4.14. RMS value of back side (bare bond coat) and front side (under ceramic top coat) of bond coat surface as a function of thermal cycles at 1151°C.

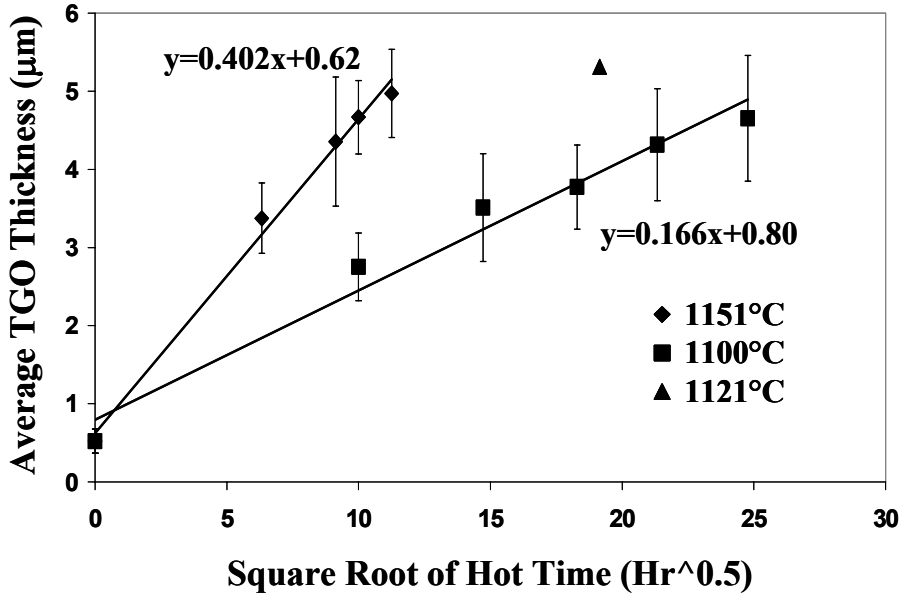

Fig. 4.15. TGO Thickness as a function of square root of hot time at various temperatures

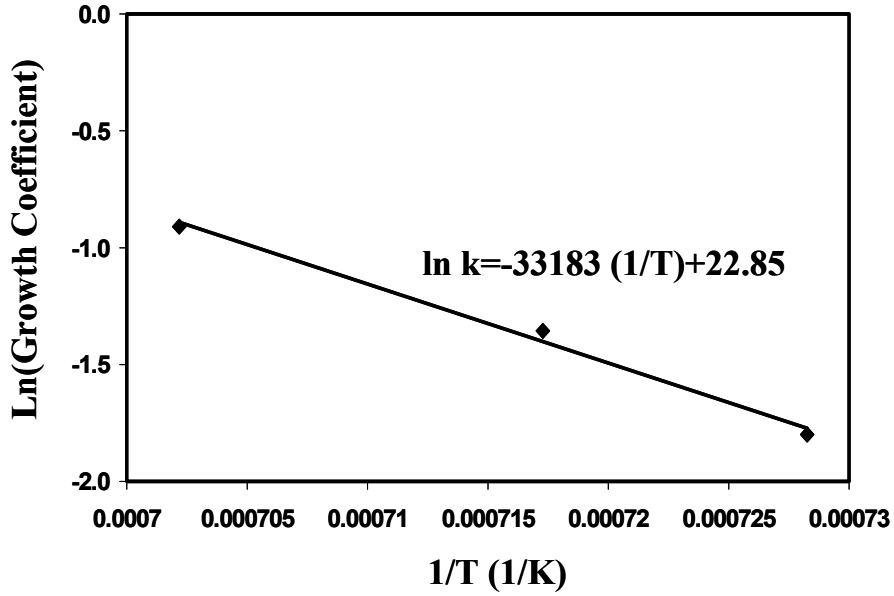

Fig. 4.16. Logarithm of parabolic growth coefficient (ln k) as a function of the reciprocal of the temperature (1/T)

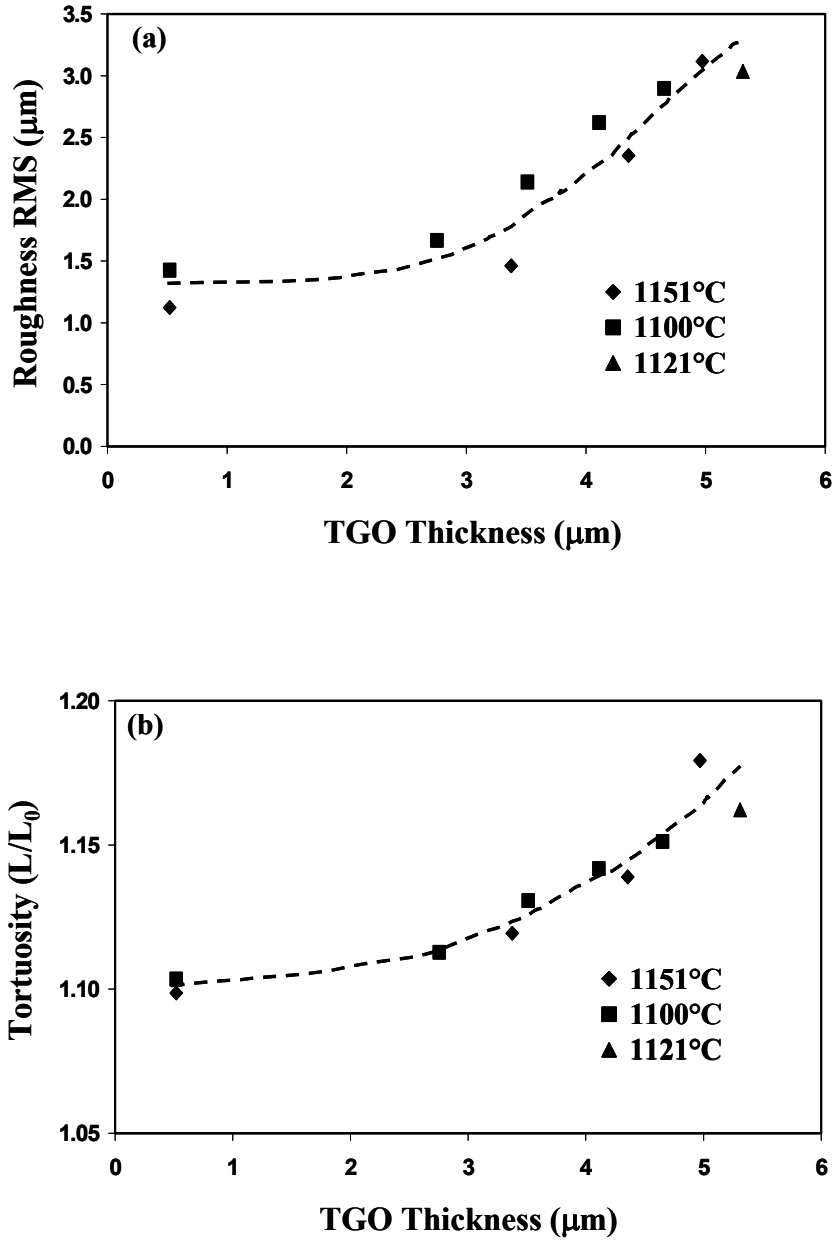

Fig. 4.17. (a) RMS roughness and (b) tortuosity as a function of TGO thickness

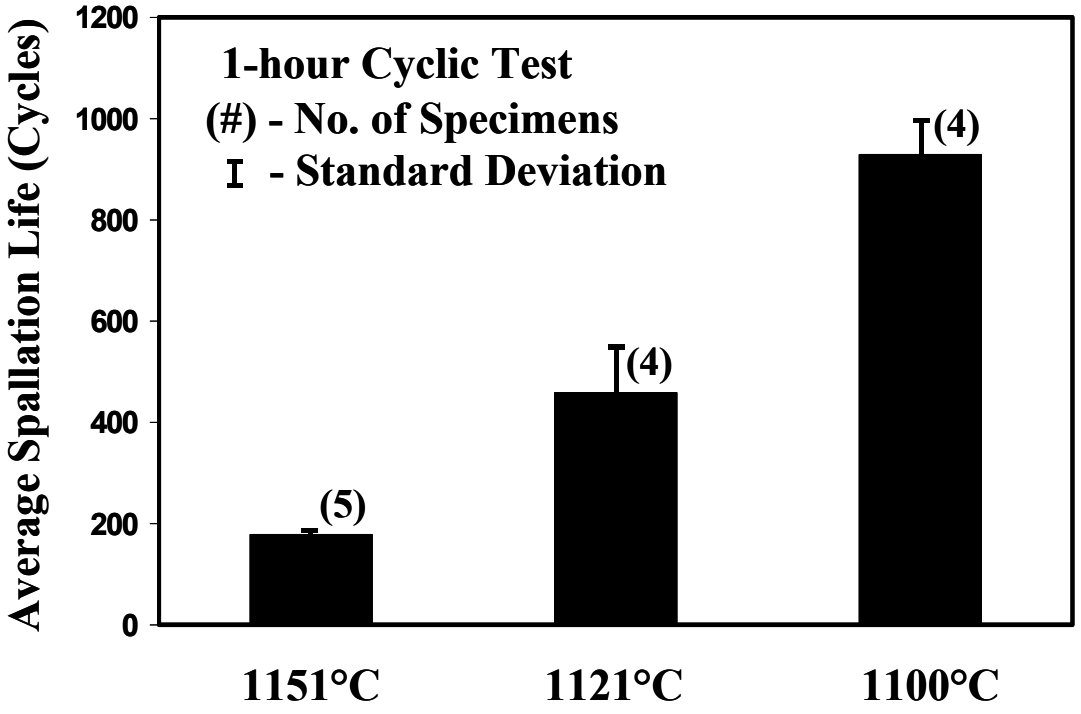

Fig. 4.18. Spallation lives of TBC specimens at various temperatures

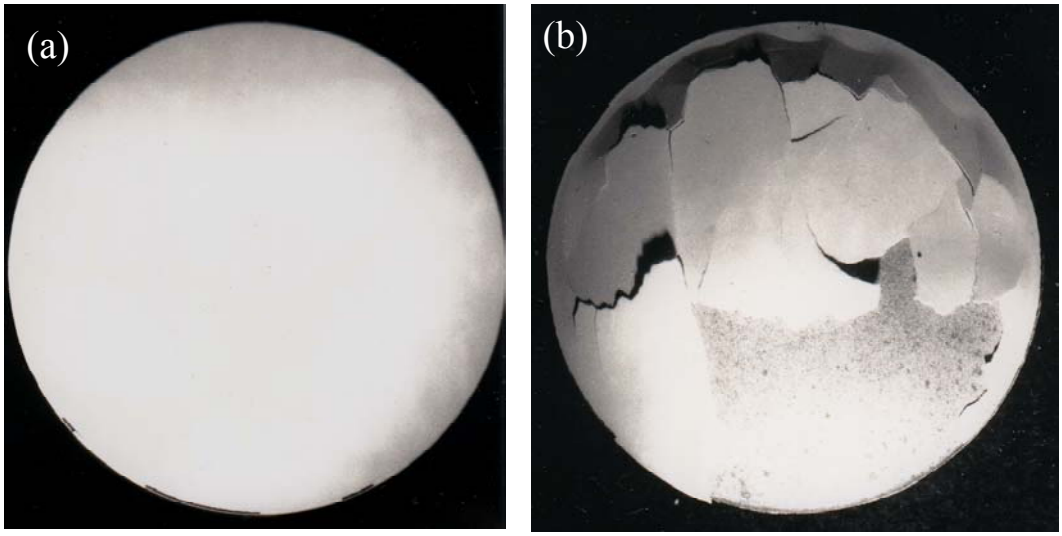

Fig. 4.19. Macrographs of specimens at (a) about 20% and (b) 100% of life

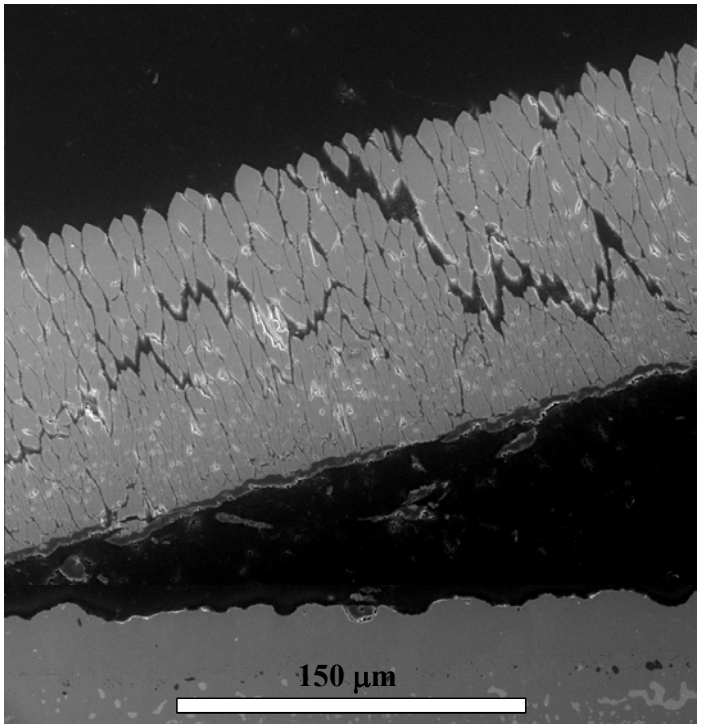

Fig. 4.20. Cross-sectional Micrograph of failed specimen showing buckling

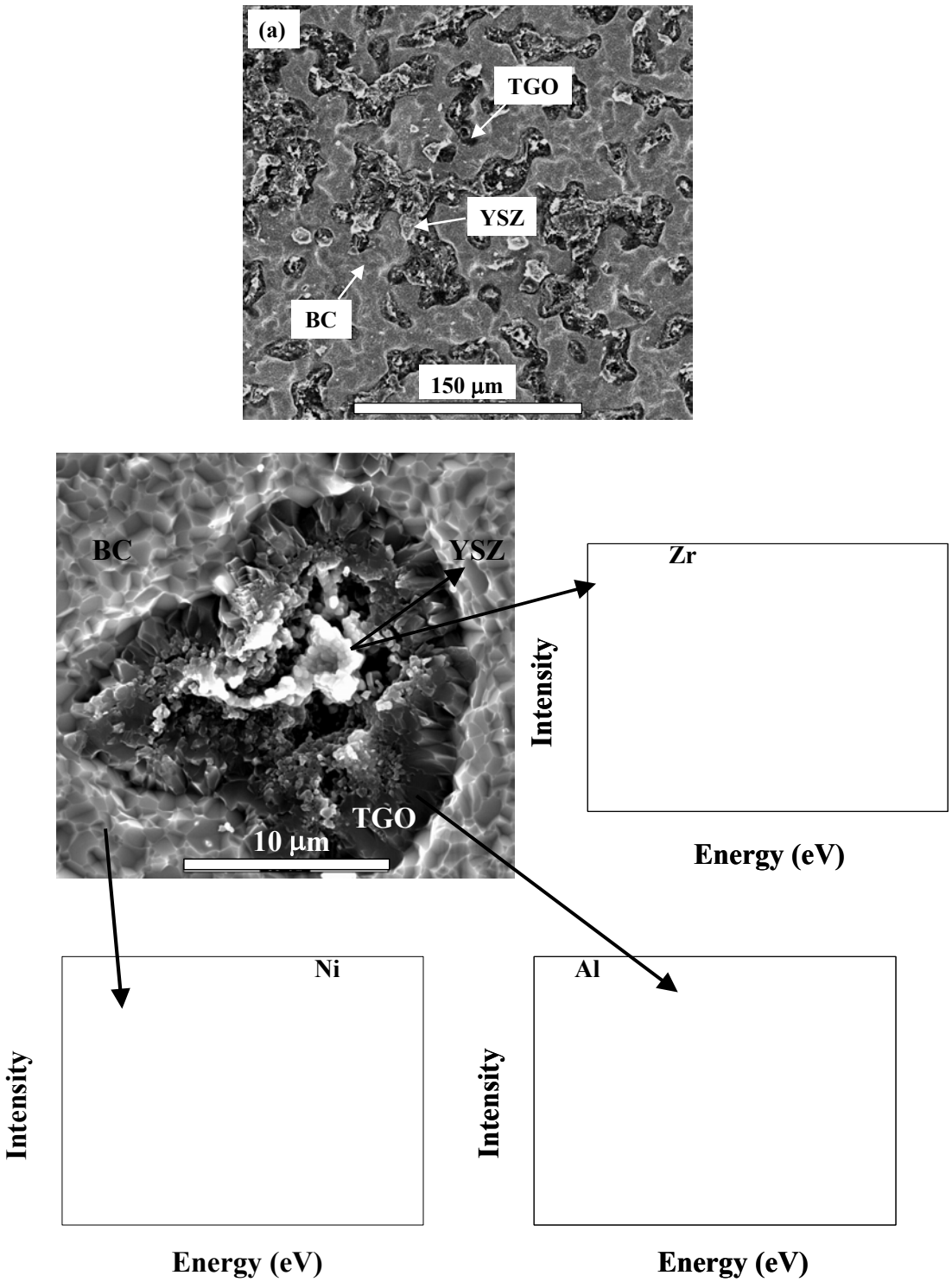

(b)

Fig. 4.21. Images of spalled surface of substrate side at (a) lower magnification and (b) higher magnification and associated EDS spectra after 190 cycles at 1151°C

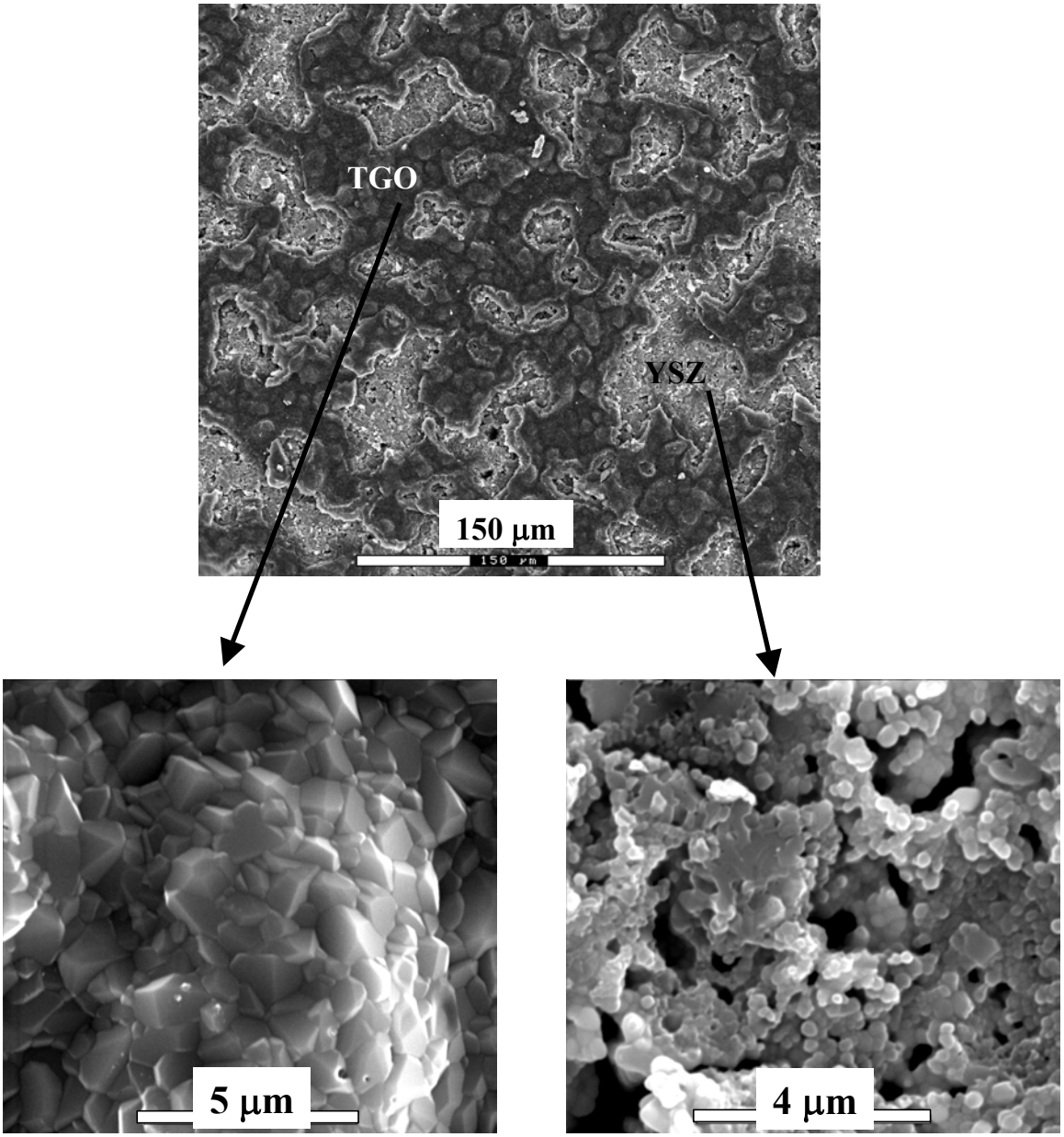

Fig. 4.22. Spalled surface of bottom side of YSZ after 190 cycles at 1151°C

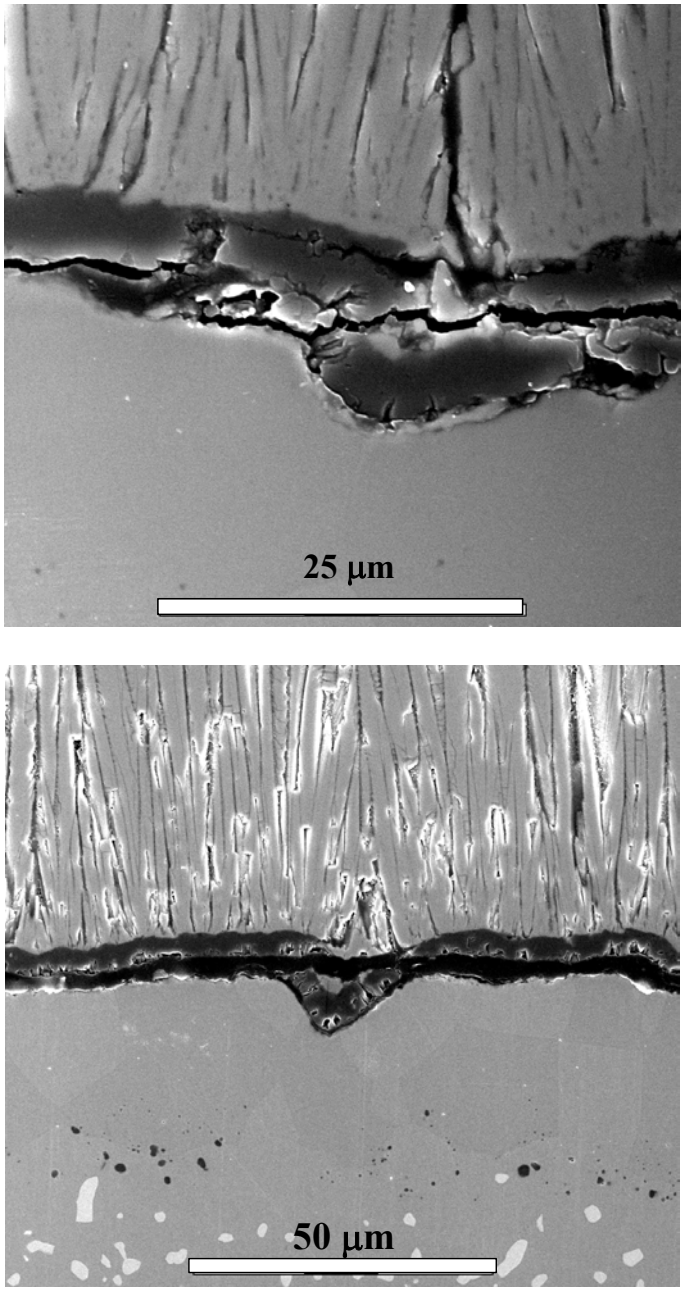

Fig. 4.23. Cross section images showing crack go through TGO and along TGO/BC interface

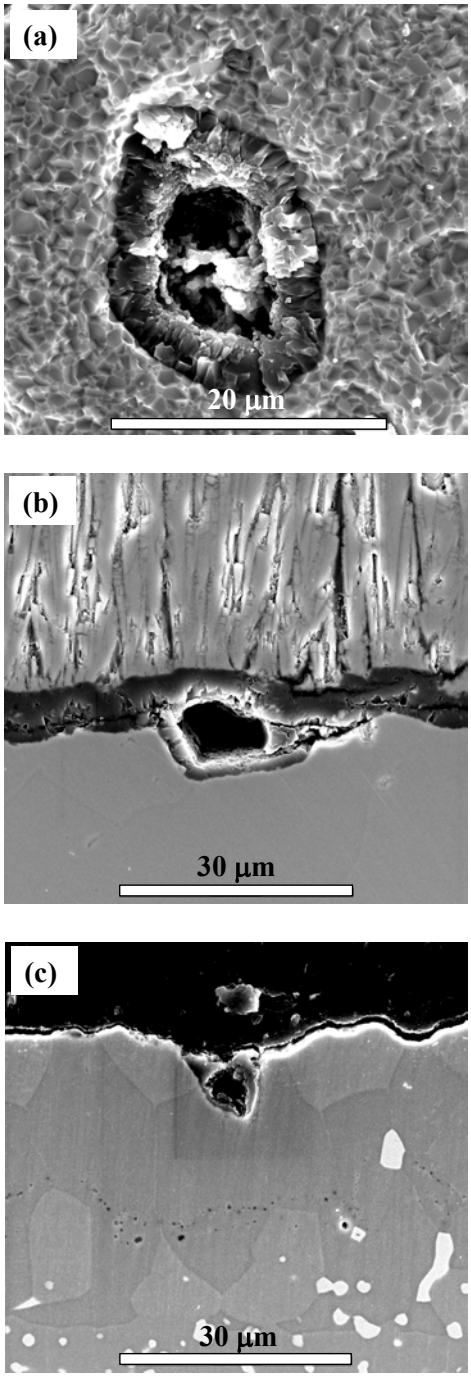

Fig. 4.24. Higher magnification images of spalled surface on substrate side (a) and cross-sectional images (b, c) showing cavity

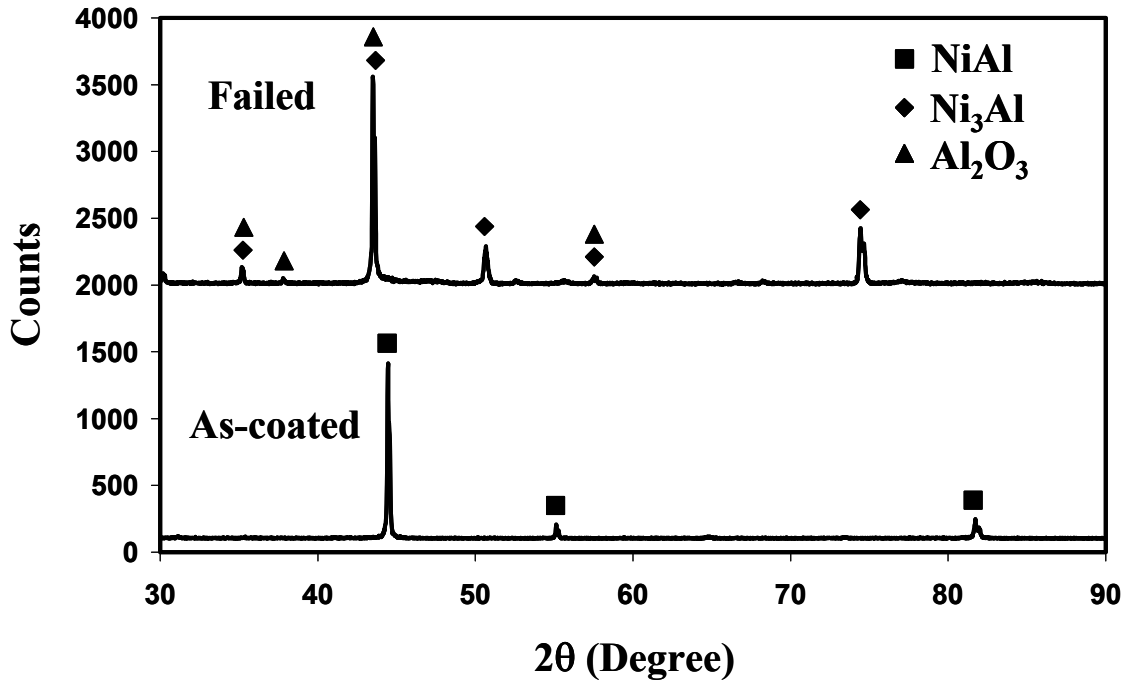

Fig. 4.25. XRD patterns of bond coat for as-coated and failed specimens

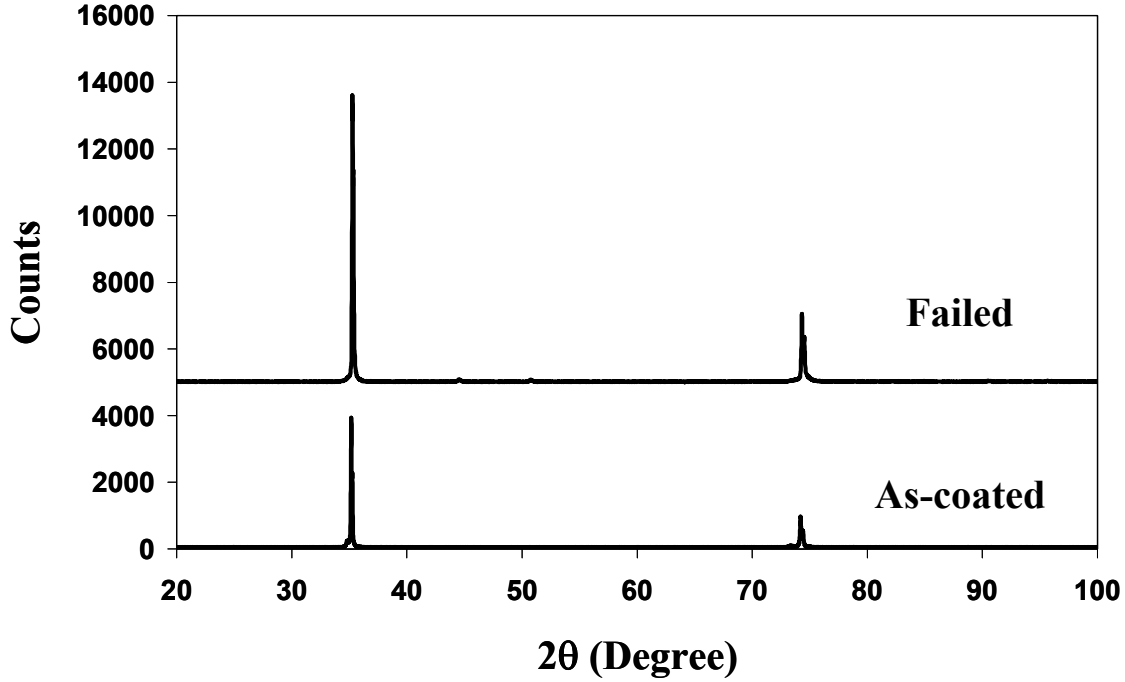

Fig. 4.26. XRD patterns of YSZ top surface for as-coated and failed specimens

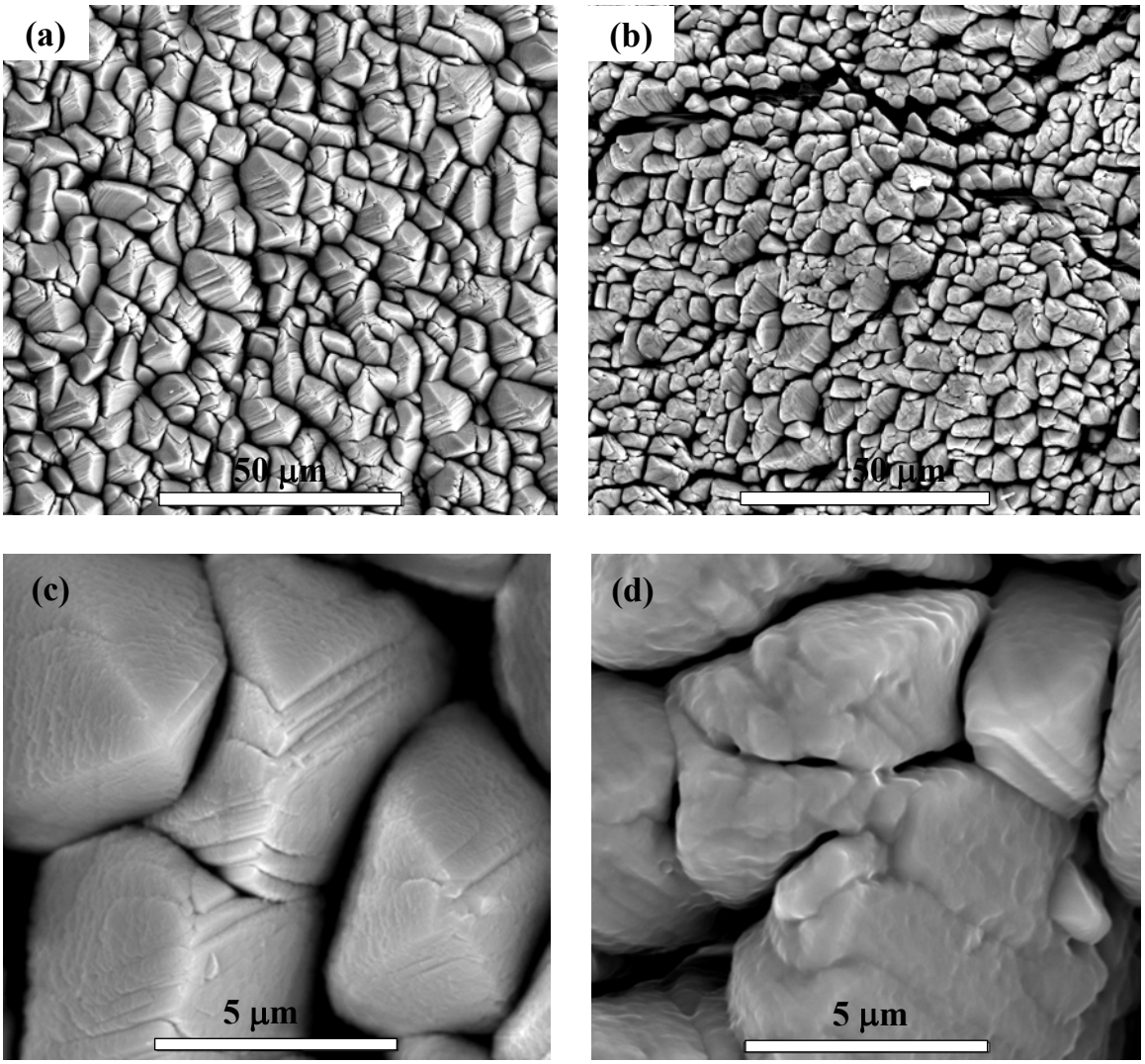

Fig. 4.27. Top surface morphology of as-coated (a, c) and failed (b, d) specimens

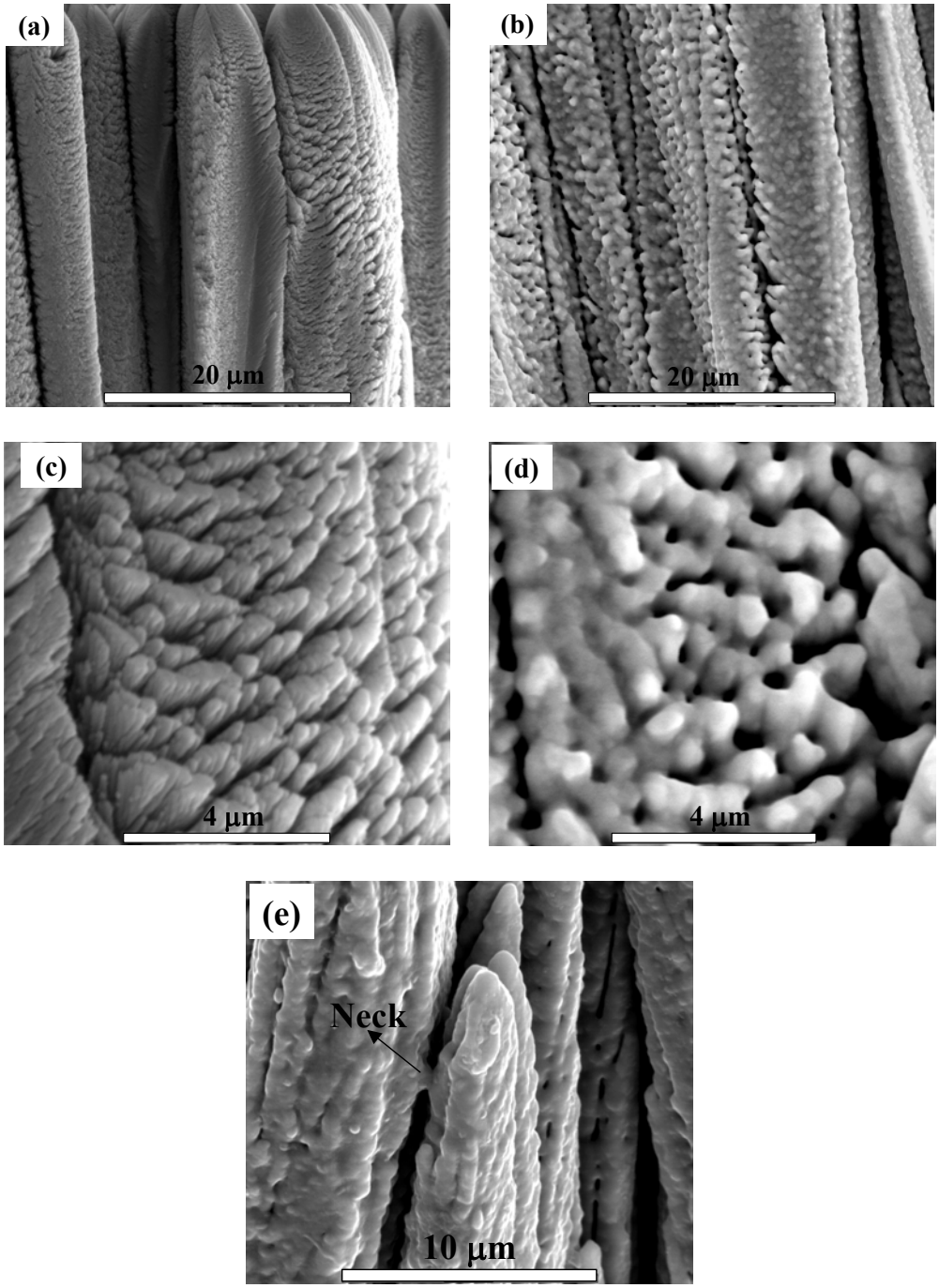

Fig. 4.28. Cross section images of YSZ columns of as-coated (a, c) and failed (b, d, e) specimens

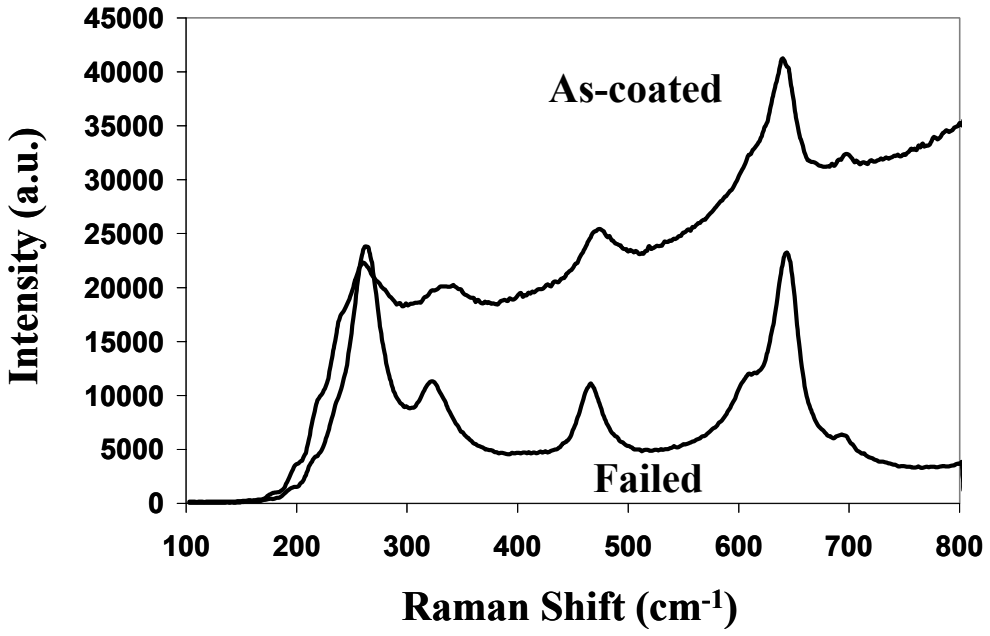

Fig. 4.29. Raman spectra of YSZ coating for as-coated and failed specimens both showing t' phase characteristic peaks

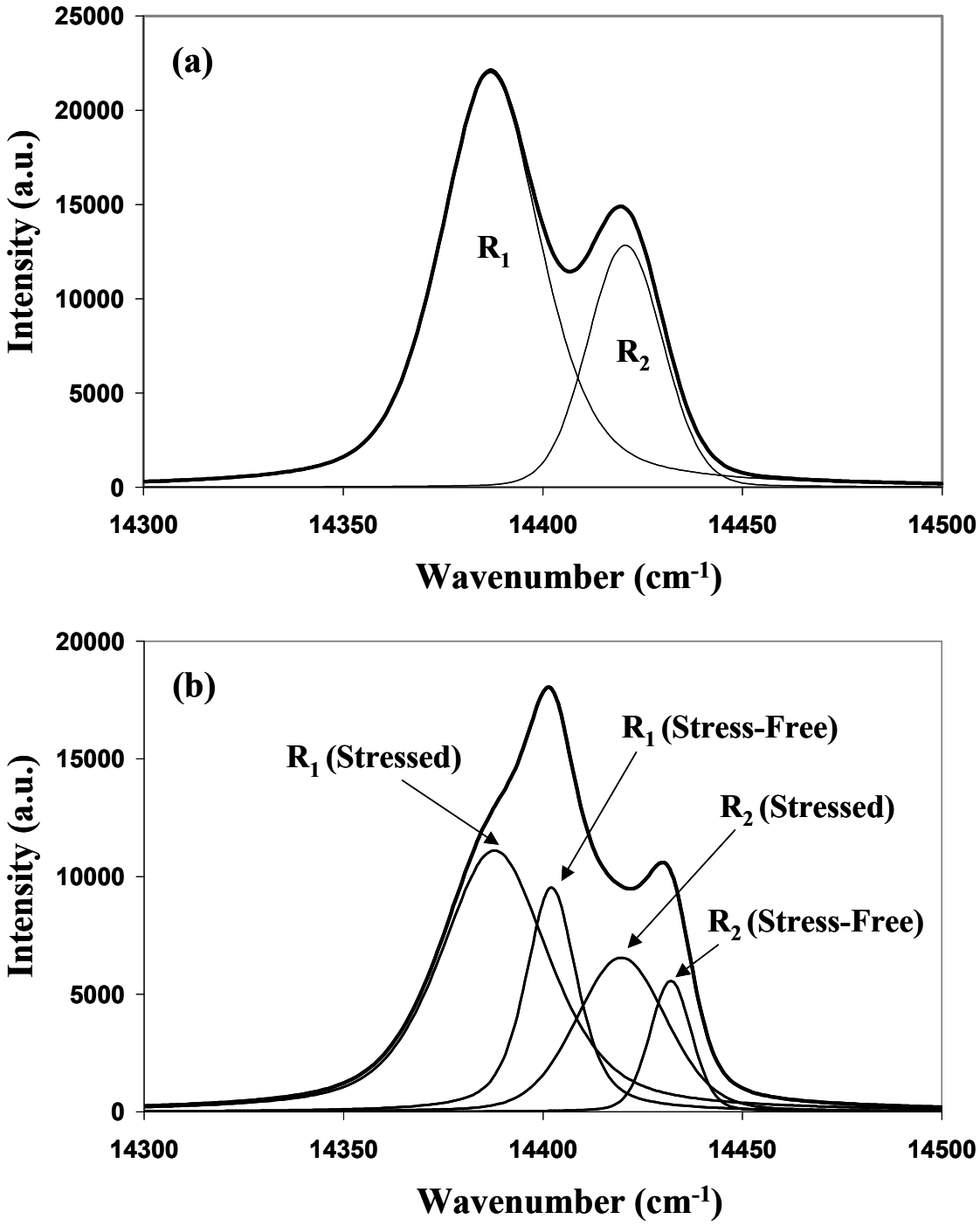

Fig. 4.30. Typical photoluminescence spectra showing (a) one set of peak pairs and (b) two sets of peak pairs

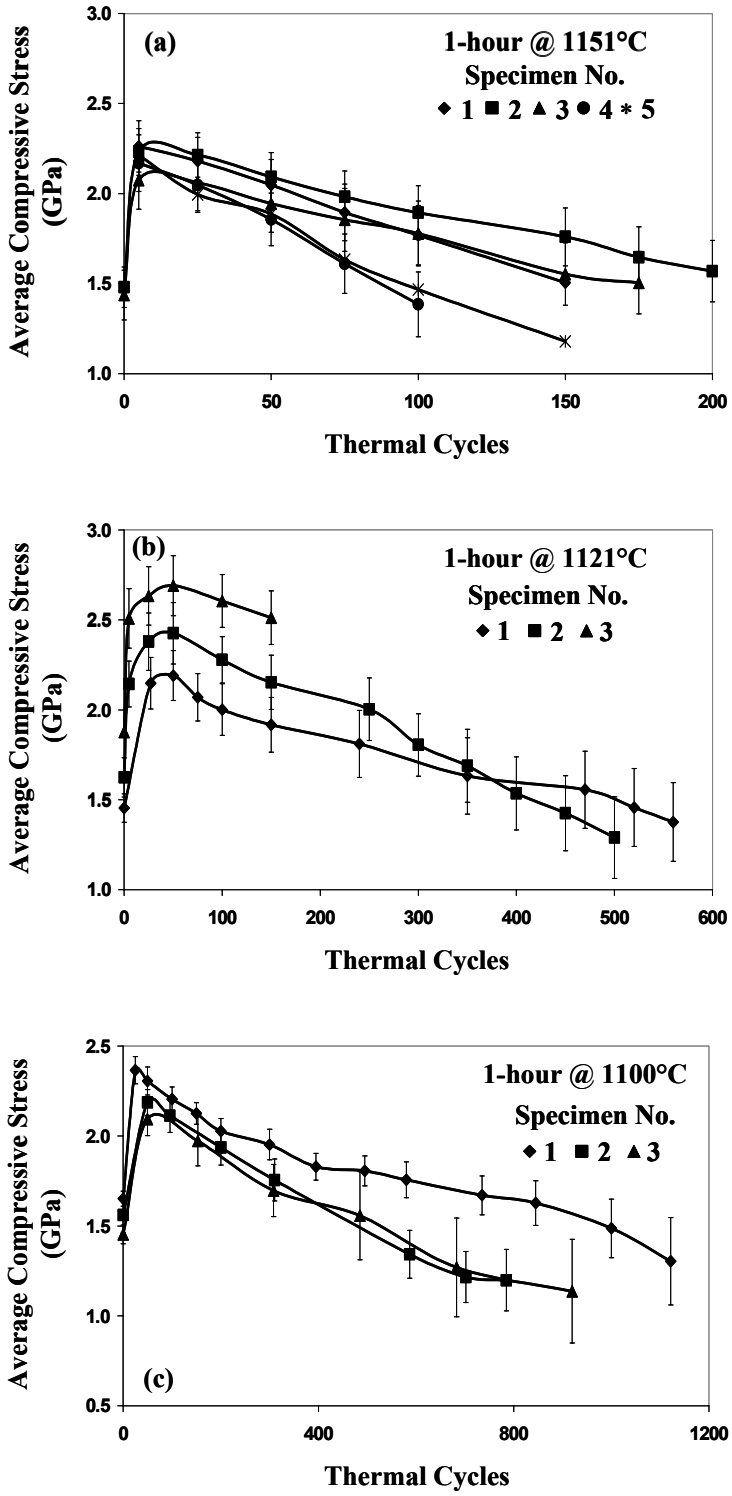

Fig. 4.31. Evolution of TGO stress as a function of thermal cycles at (a) 1151°C, (b) 1121°C and (c) 1100°C

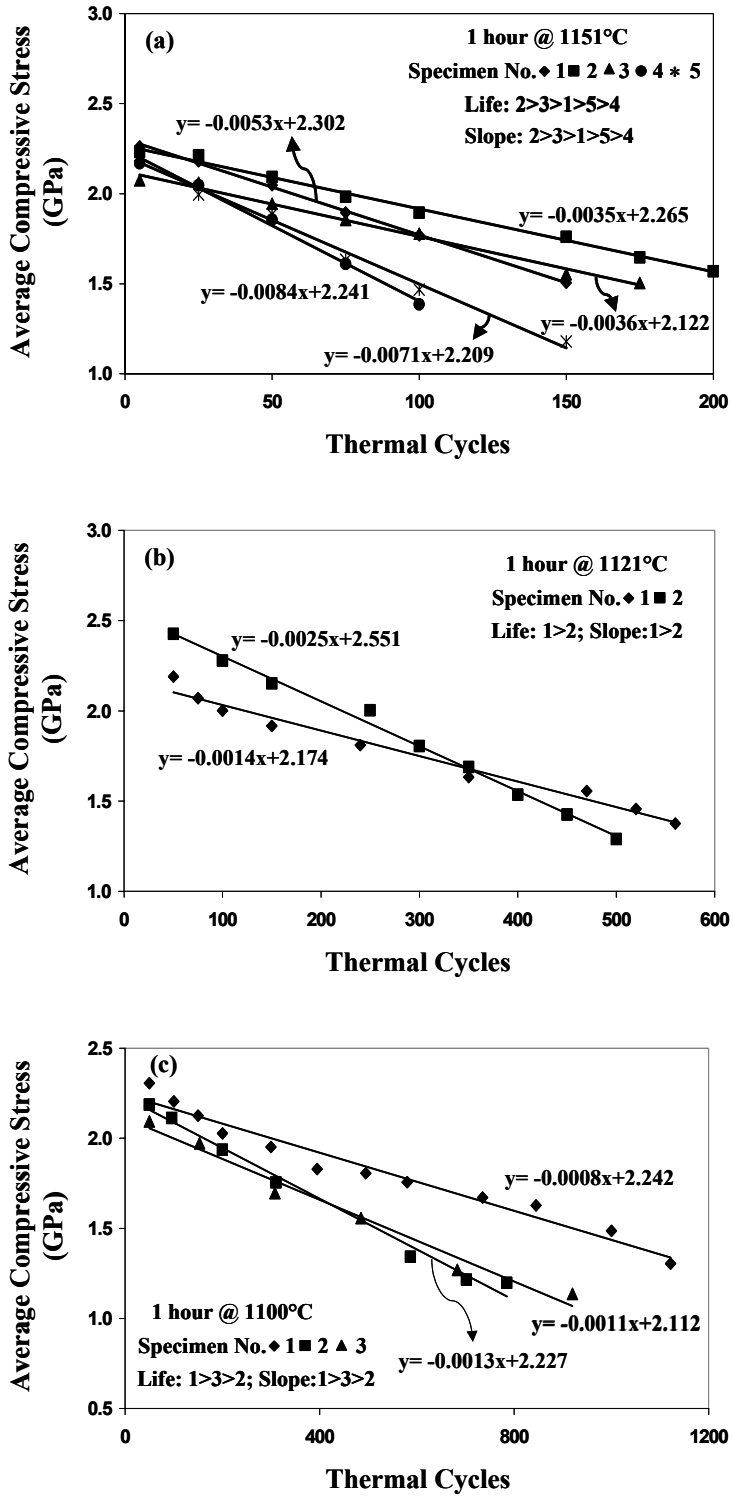

Fig. 4.32. Average stress vs. thermal cycles showing the relationship of slope and lives

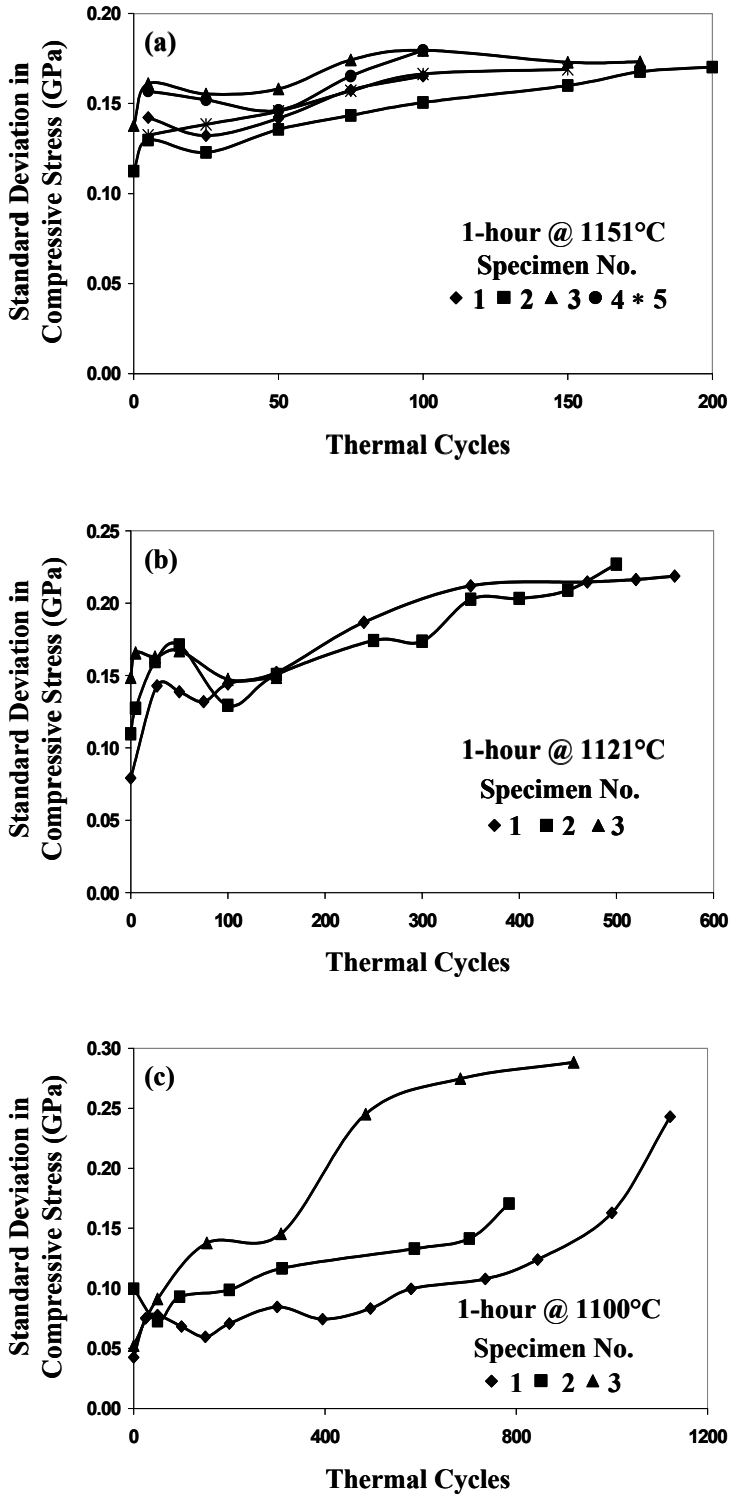

Fig. 4.33. Standard deviation in TGO stress as a function of thermal cycles at (a) 1151°C, (b) 1121°C and (c) 1100°C

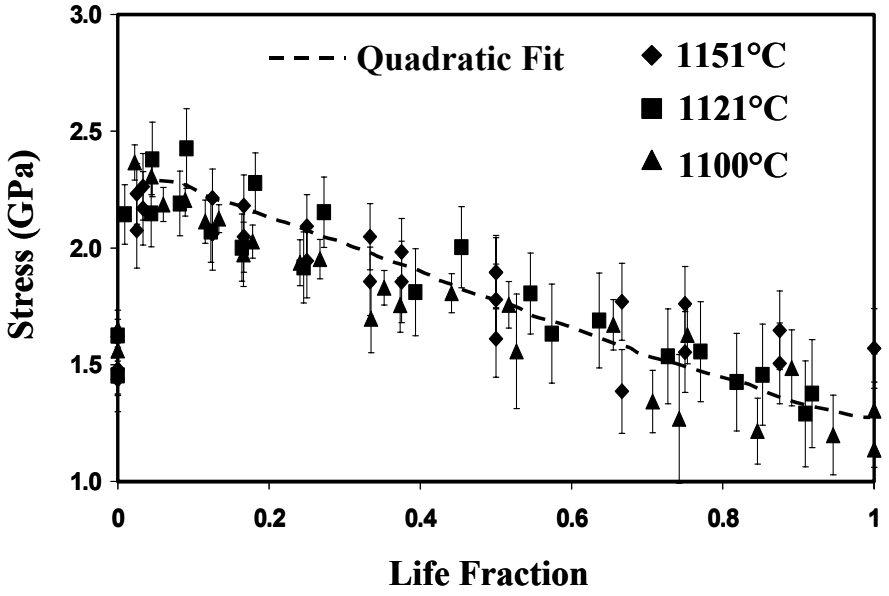

Fig. 4.34. Evolution of TGO stress as a function of life fraction at 1151°C and 1121°C

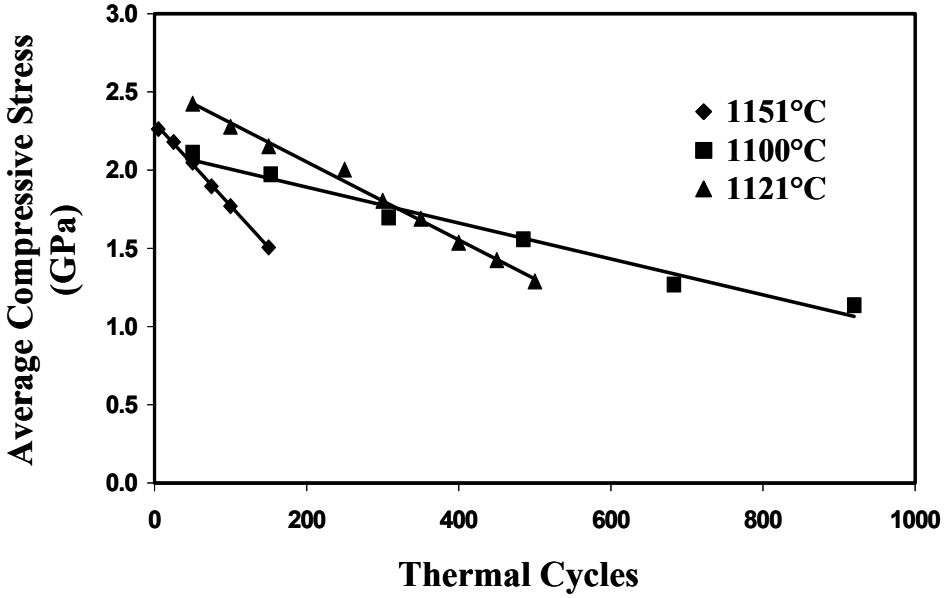

Fig. 4.35. Average TGO stress as a function of thermal cycles at various temperatures

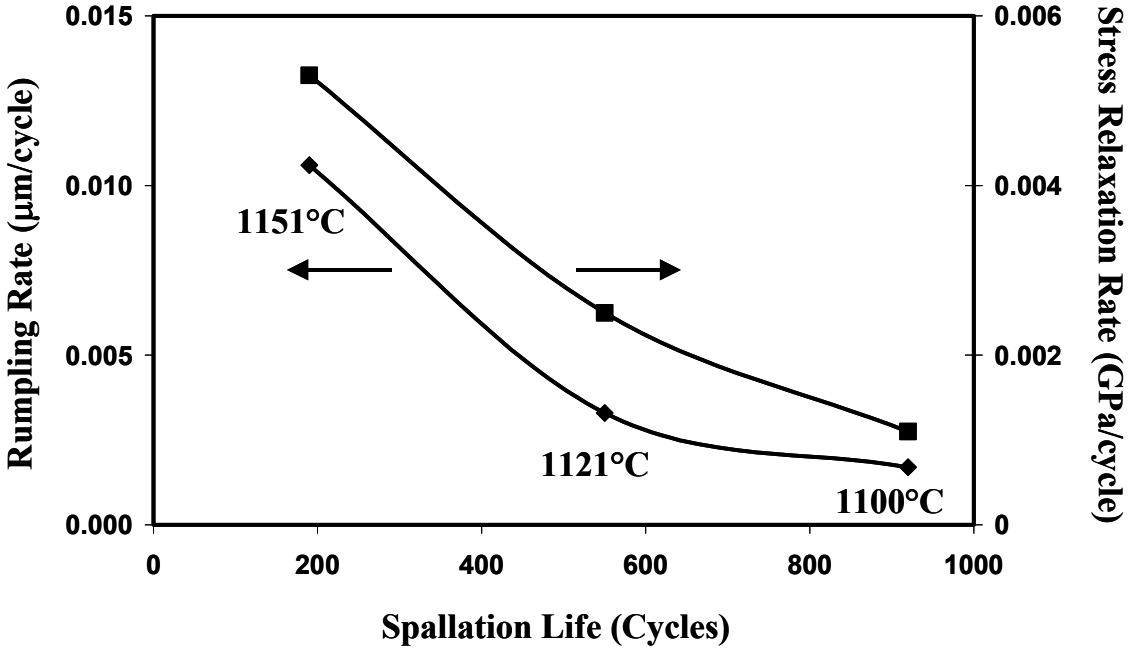

Fig. 4.36. Relationships among rumpling, TGO stress relaxation and specimen life

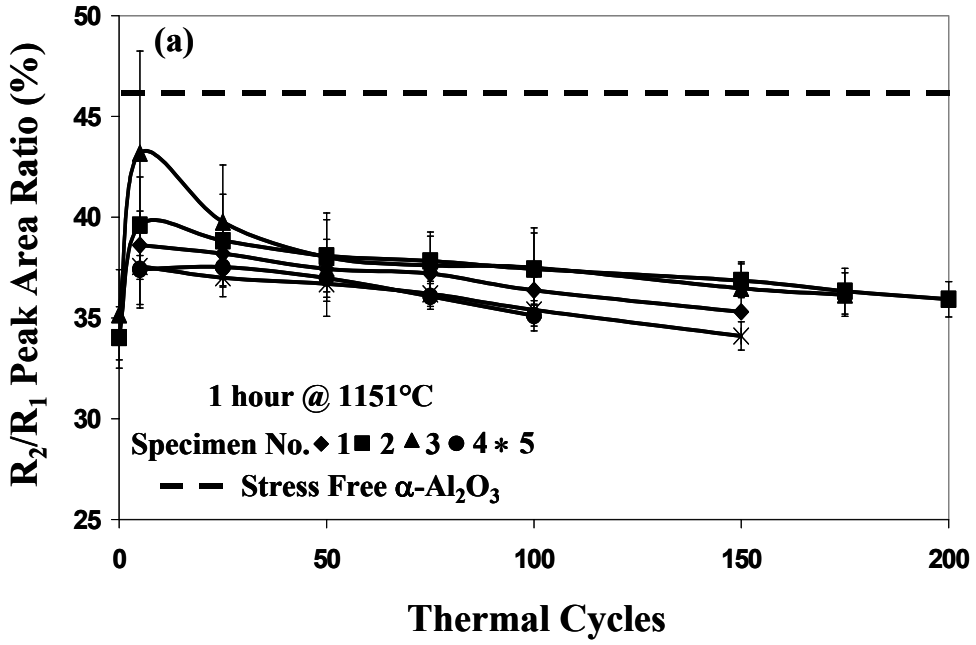

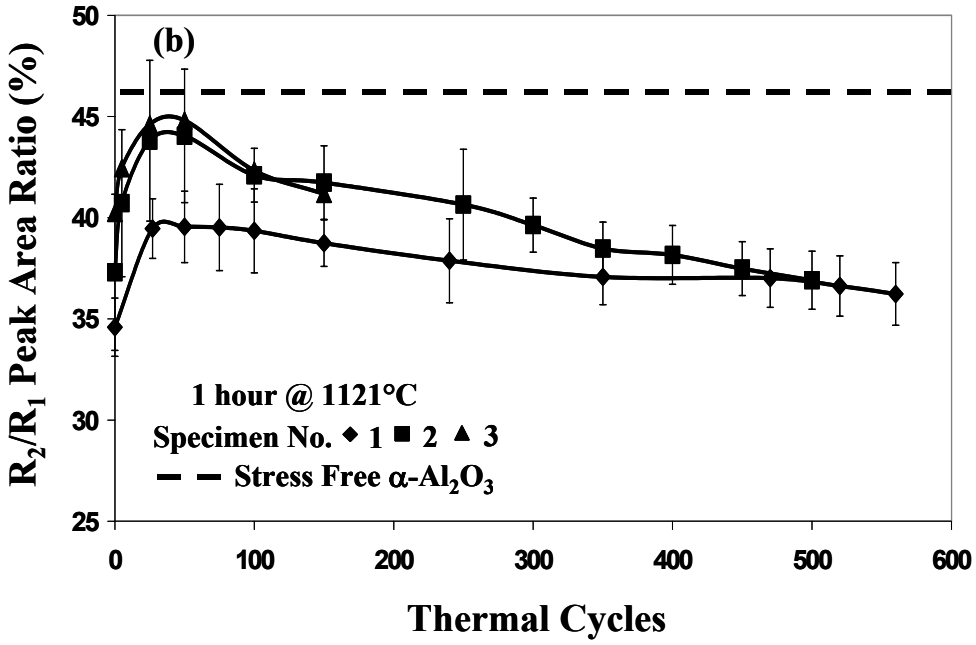

Fig. 4.37. Change of area ratio of R_1 and R_2 peak with thermal cycling at (a) 1151°C and (b) 1121°C

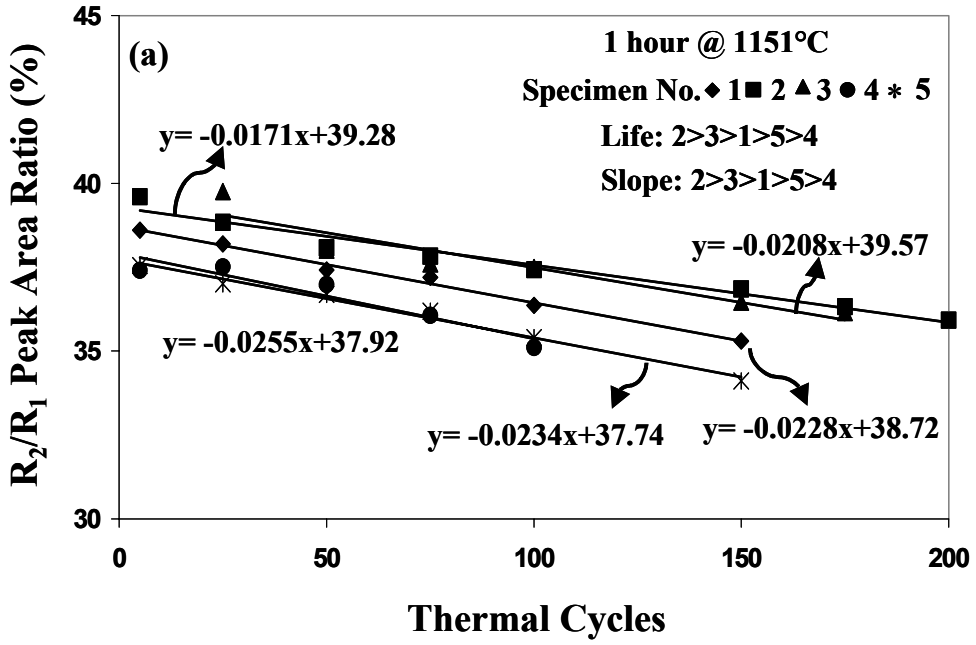

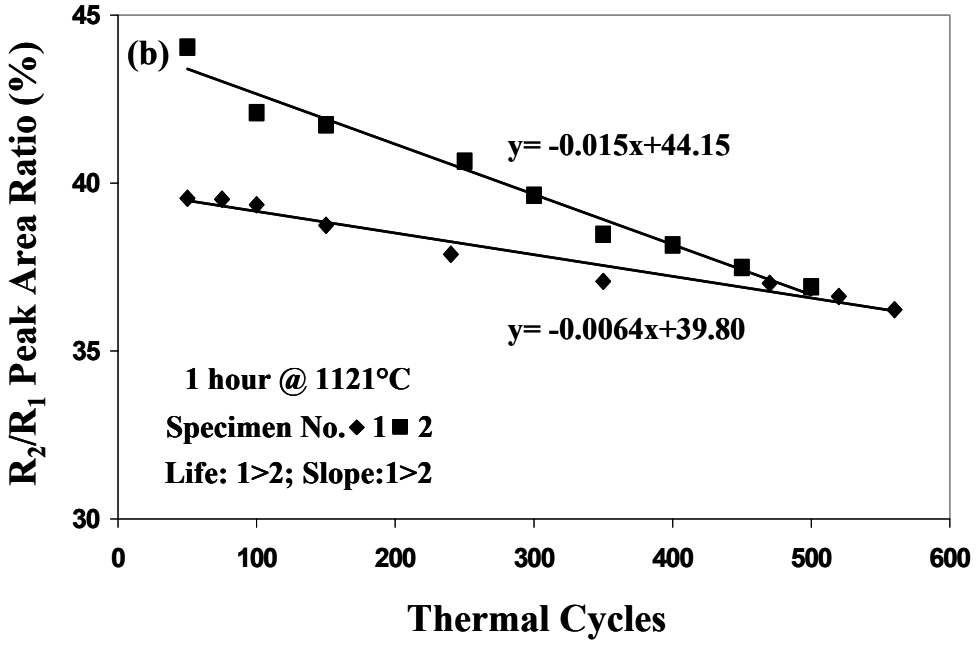

Fig. 4.38. Change of peak area ratio showing the relationship of slope and lives

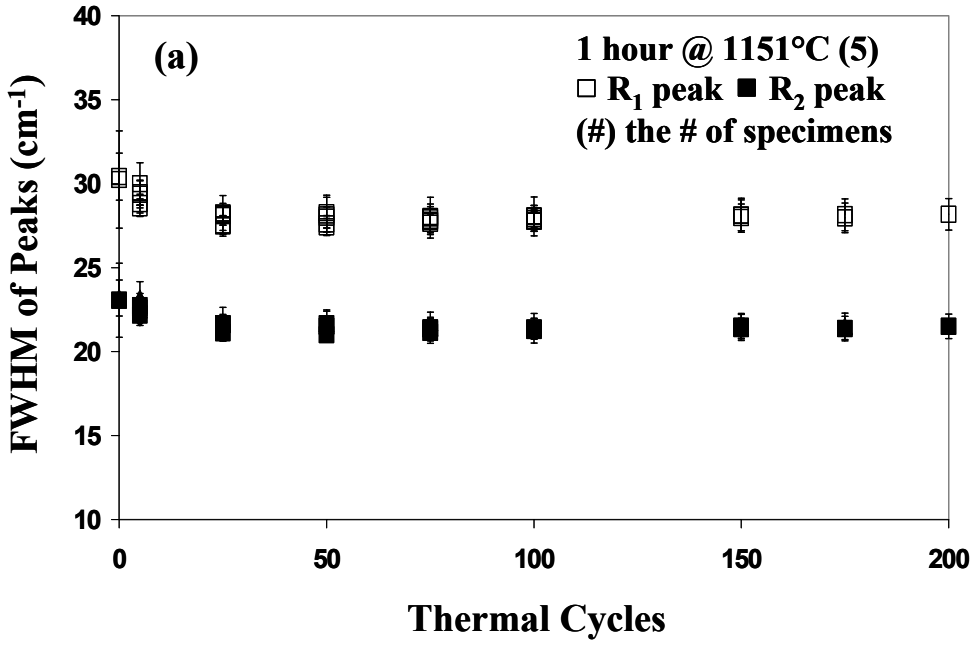

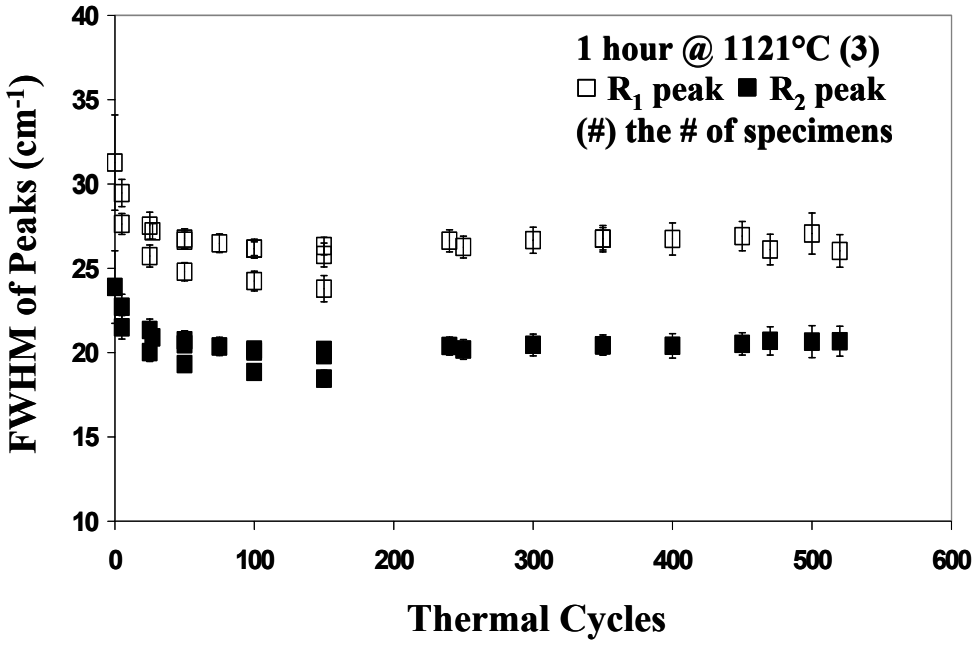

Fig. 4.39. Change of R_1 and R_2 peak width with thermal cycling at (a) 1151°C and (b) 1121°C

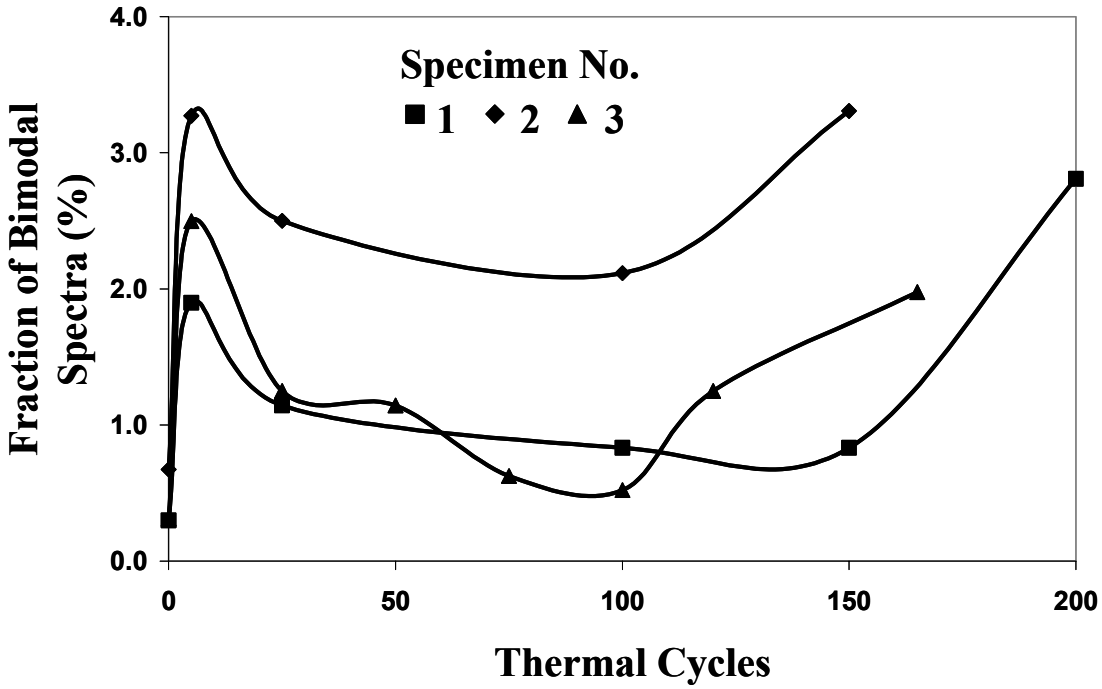

Fig. 4.40. Fraction of bimodal spectra of TBC specimens as a function of thermal cycles at 1151°C

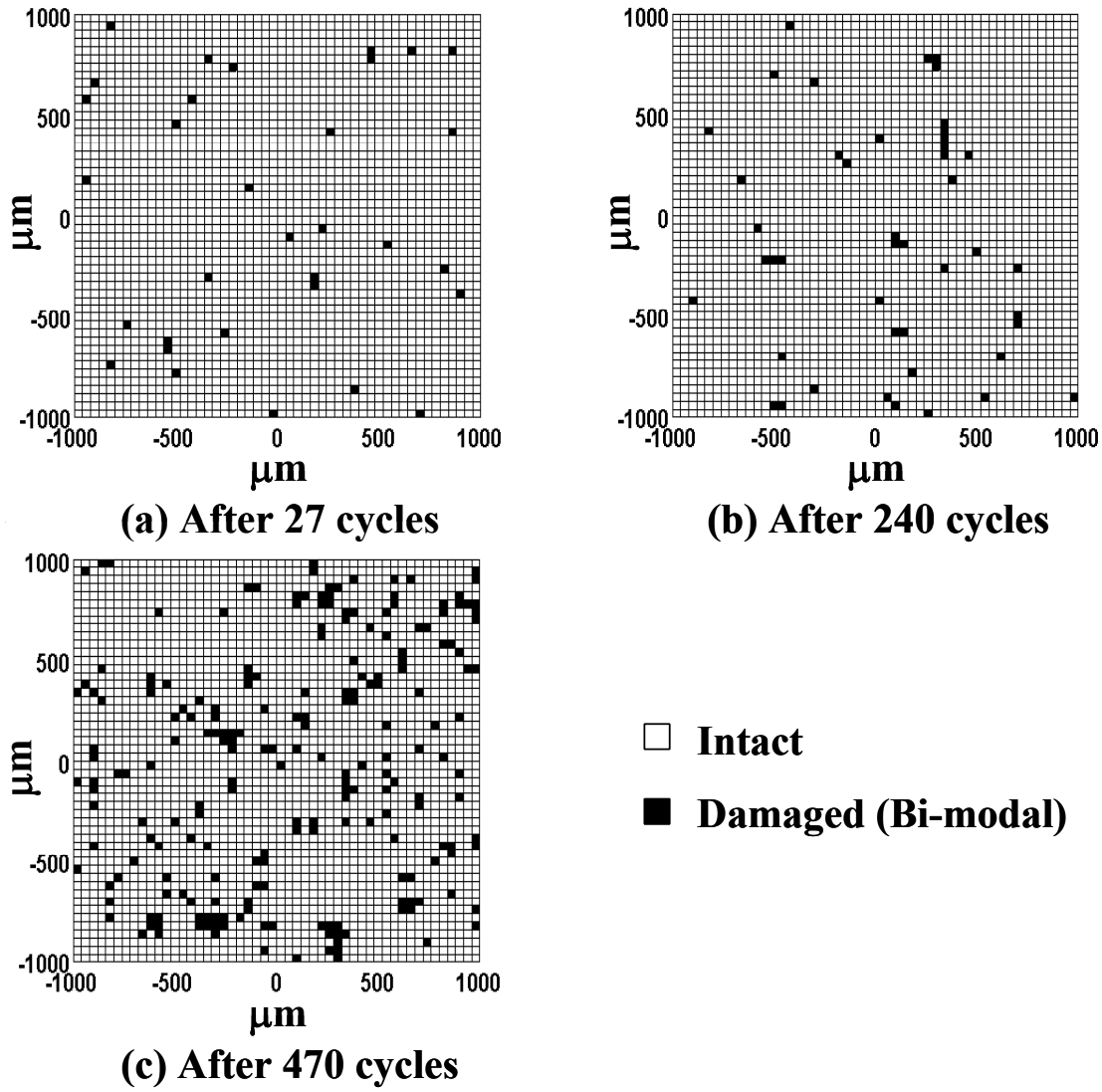

Fig. 4.41. TGO stress mapping distribution of TBC specimens after (a) 27 cycles, (b) 240 cycles and (c) 470 cycles at 1121°C

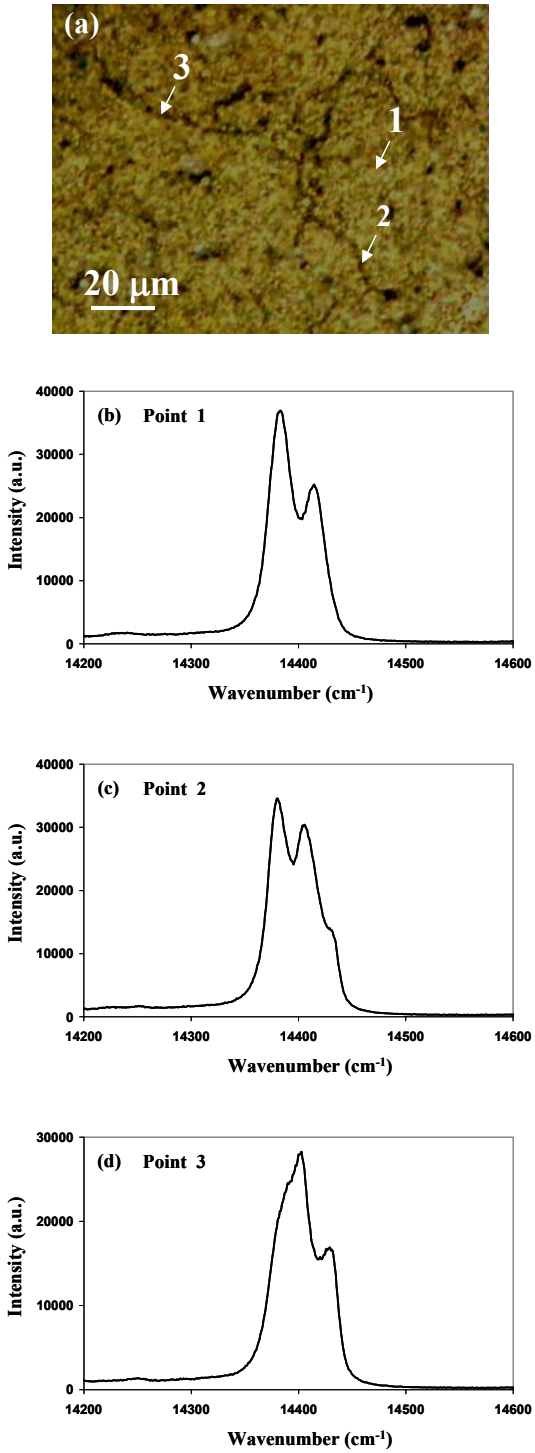

Fig. 4.42. Optical image (a) and corresponding luminescence spectra of alumina scale formed on different location of bare bond coat after oxidation 10 minutes at 1151°C showing: (b) unimodal, (c) bimodal, and (d) bimodal

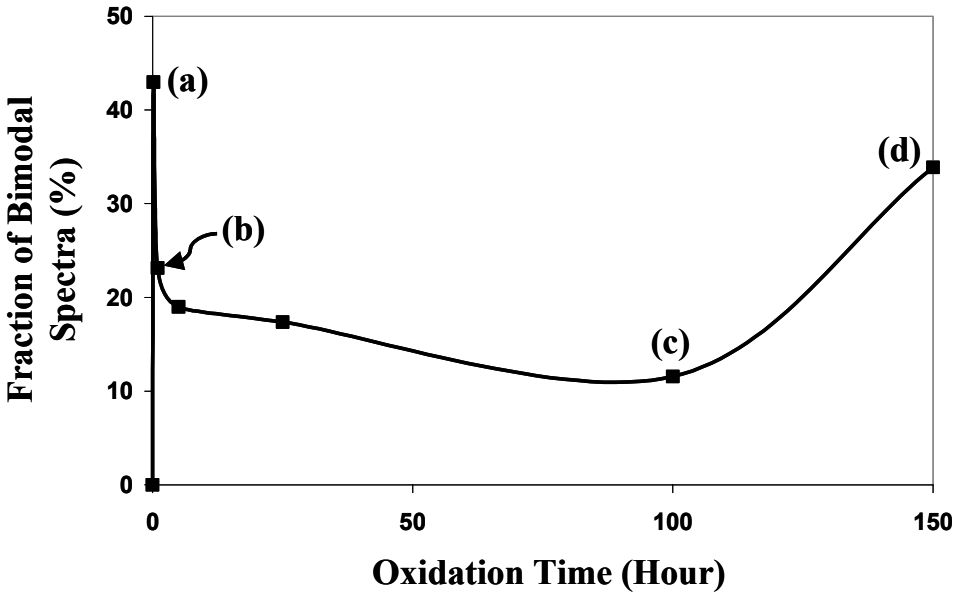

Fig. 4.43. Evolution of fraction of bimodal spectra on bare bond coated sample after oxidation at 1151°C for (a) 10 minutes, (b) 1 hour, (c) 100 hours, and (d) 150 hours

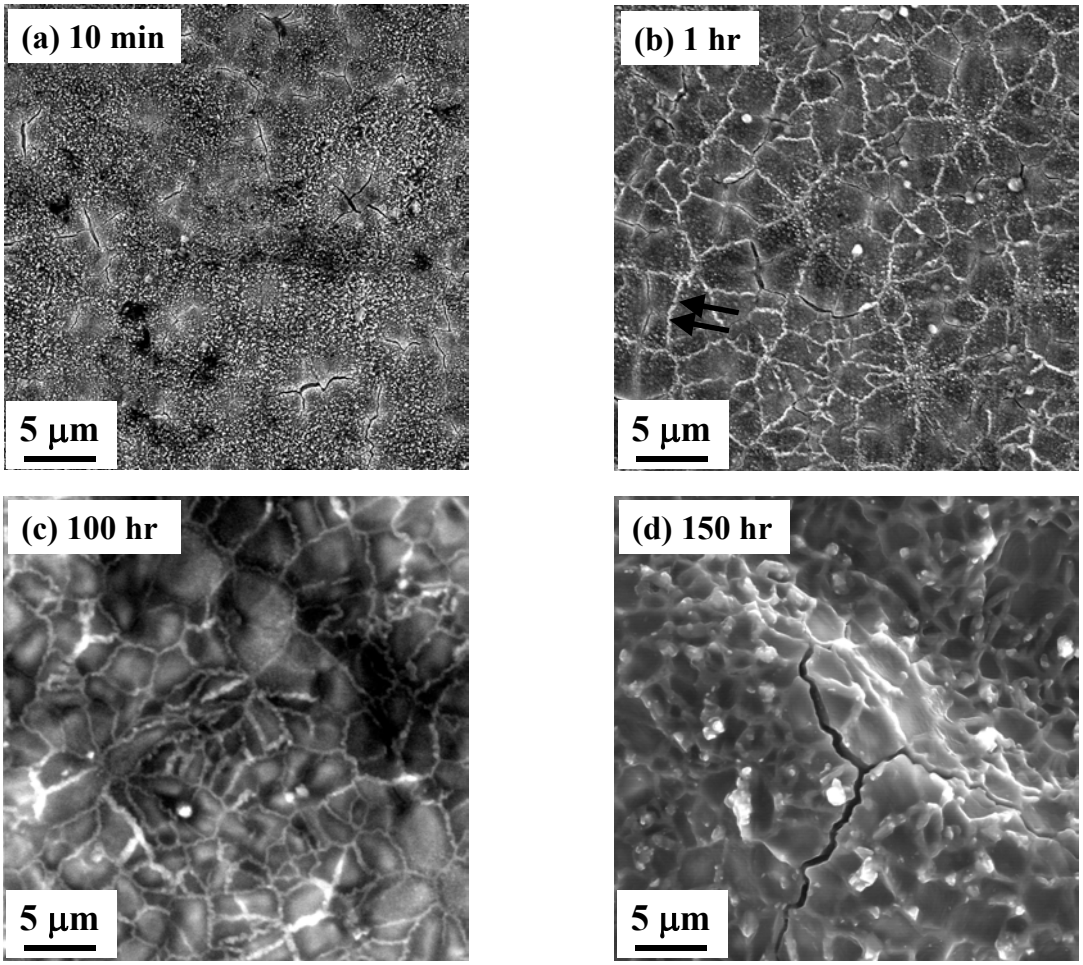

Fig. 4.44. Oxide morphology on bare bond coated sample after oxidation at 1151°C for (a) 10 minutes, (b) 1 hour, (c) 100 hours, and (d) 150 hours

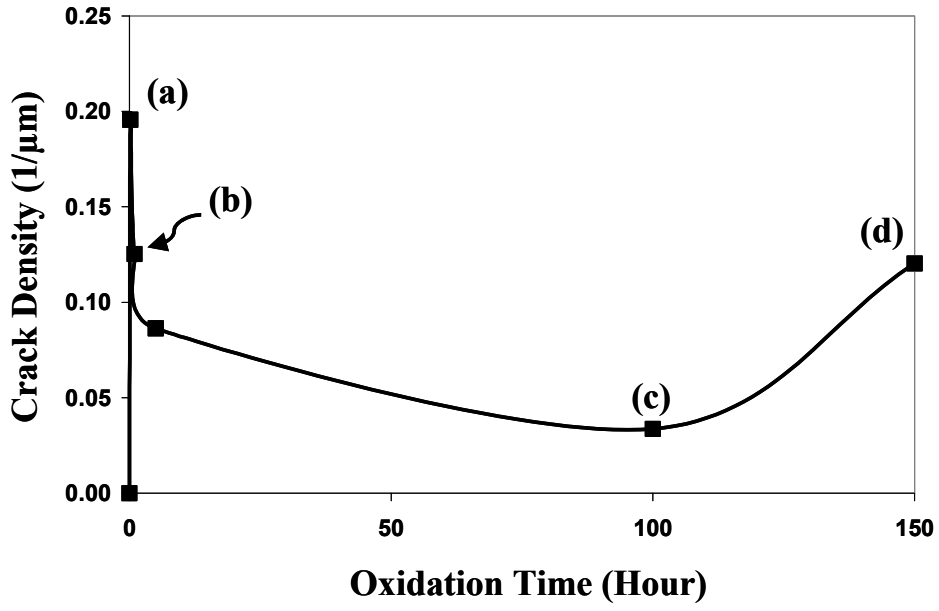

Fig. 4.45. Evolution of crack density on bare bond coated sample after oxidation at 1151°C for (a) 10 minutes, (b) 1 hour, (c) 100 hours, and (d) 150 hours

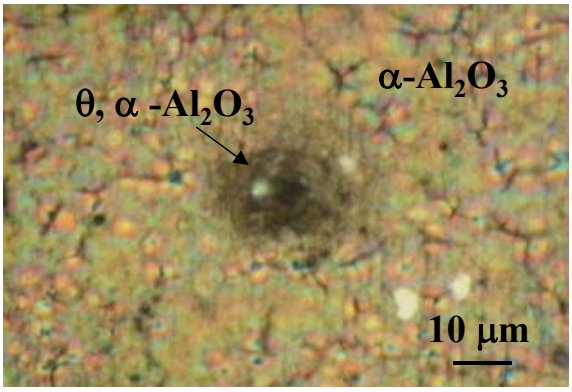

(a)

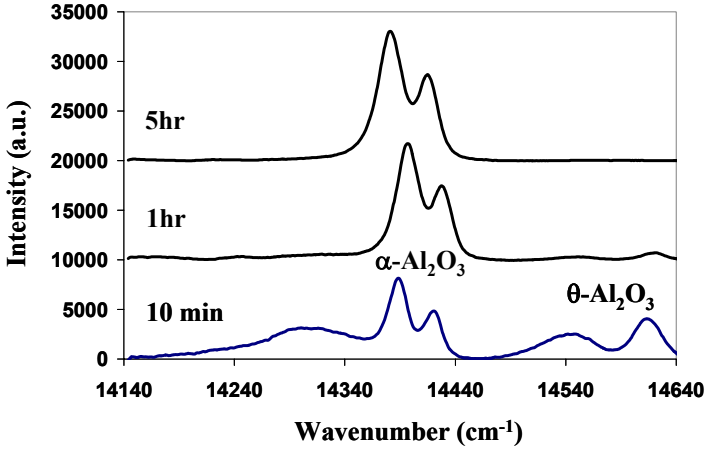

(b)

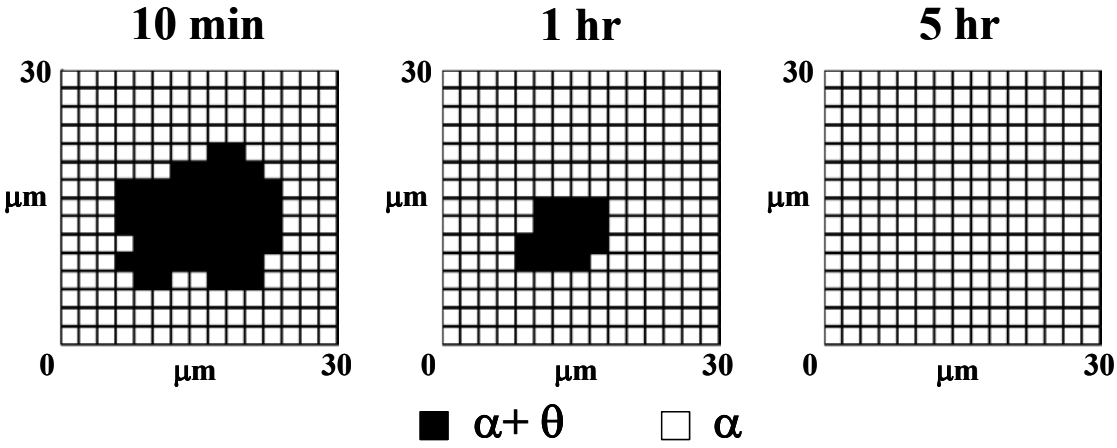

(c)

Fig. 4.46. Optical image (a), PLPS spectra (b) and oxide type distribution maps (c) of alumina scale on bare bond coated sample showing the distribution of α and θ alumina after oxidation different time at 1151°C

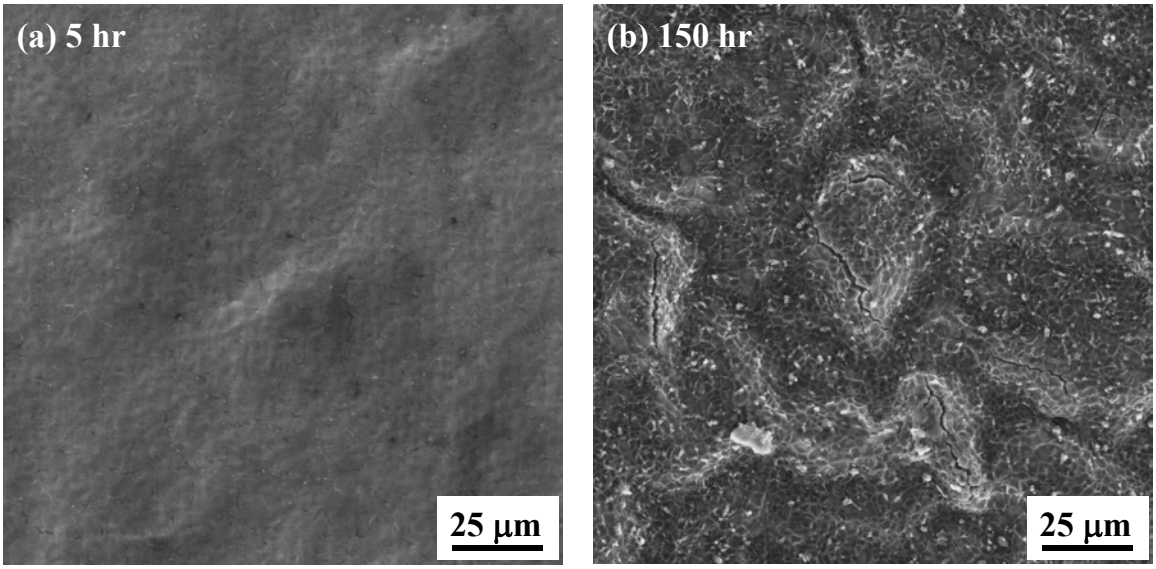

Fig. 4.47. Top surface of bare bond coated sample showing rumpling after oxidation

(a) 5 hours and (b) 150 hours at 1151°C

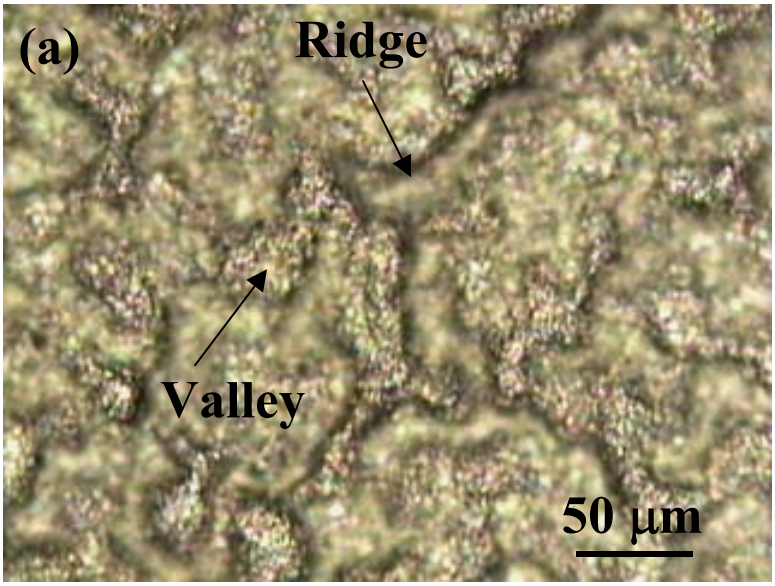

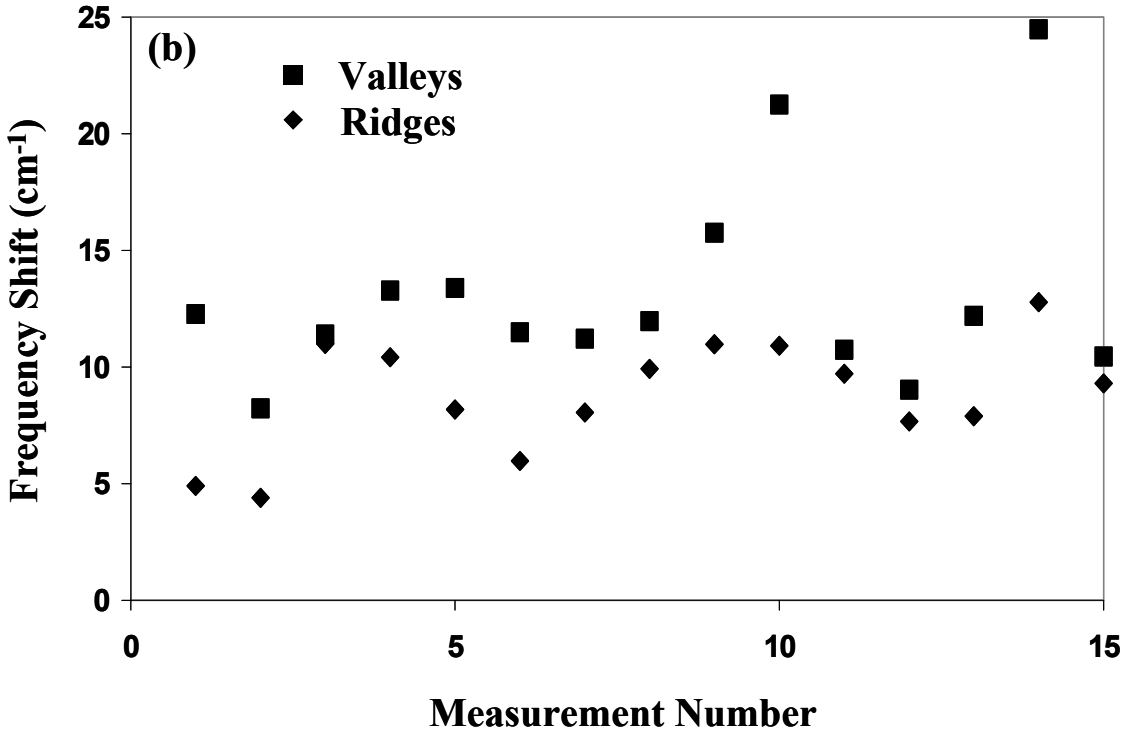

Fig. 4.48. Optical image (a) and luminescence results (b) of a series of measurements of the rumpled alumina scale after oxidation 100 hours at 1151°C

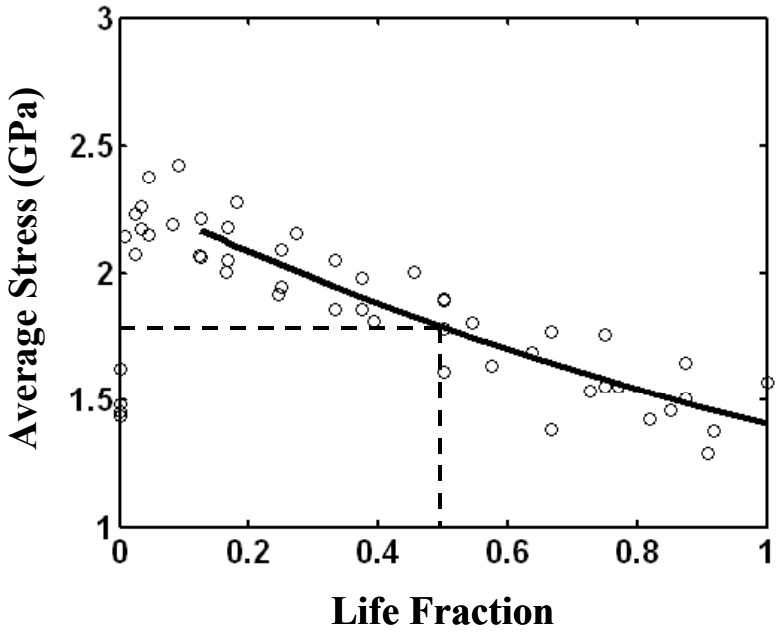

Fig. 4.49. Quadratic fit for stress vs. life fraction for samples tested at 2 temperatures

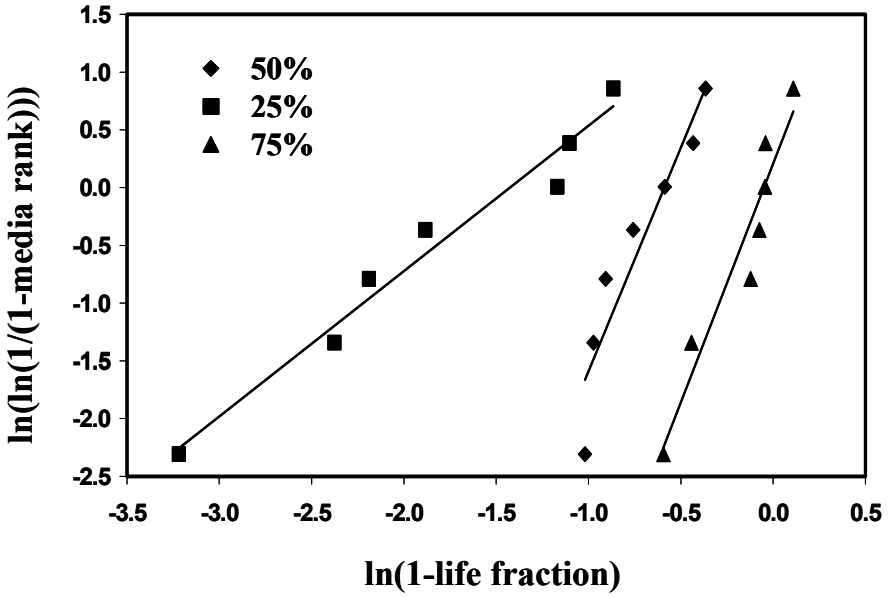

Fig. 4.50. Weibull plot of life fraction data for PLPS inspections at life fraction 25%, 50% and 75% from master curve.

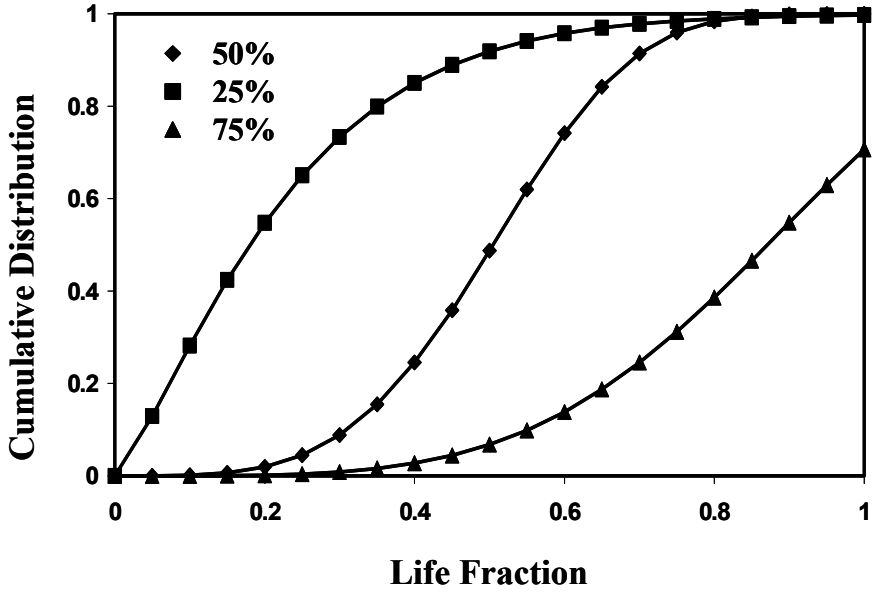

Fig. 4.51. Cumulative distribution of life fraction data for PLPS inspections at life fraction 25%, 50% and 75% from master curve

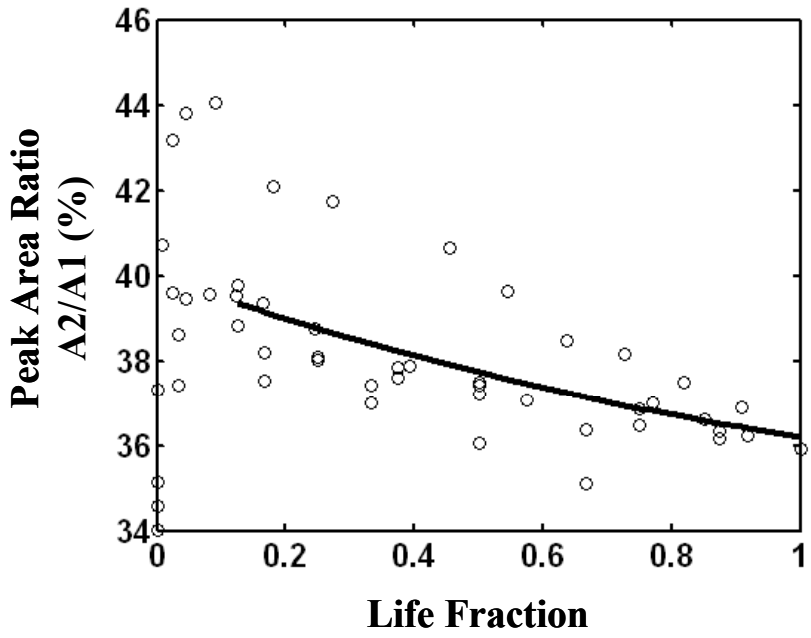

Fig. 4.52. Quadratic fit for peak area ratio vs. life fraction for samples tested at 2 temperatures

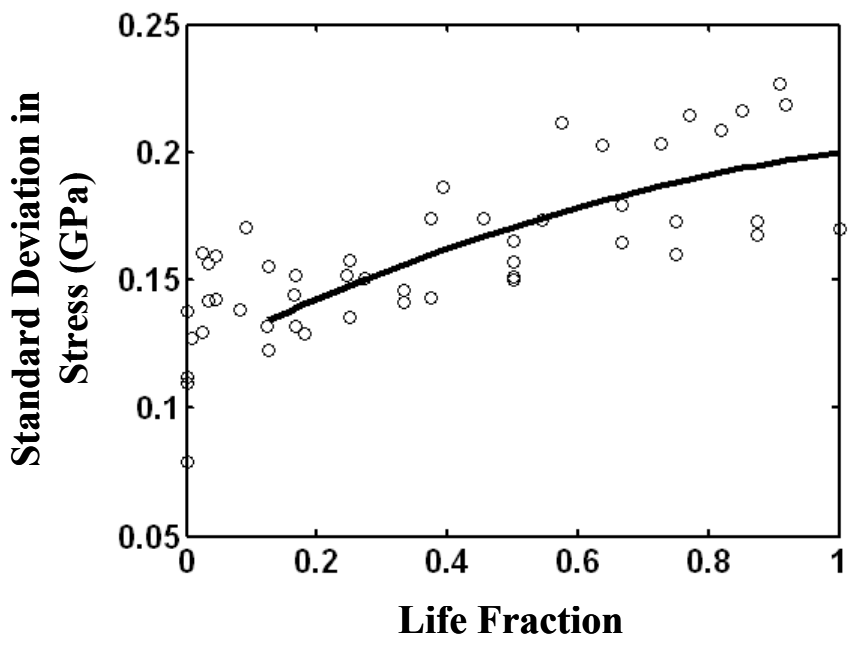

Fig. 4.53. Quadratic fit for standard deviation of stress vs. life fraction for samples tested at 2 temperatures

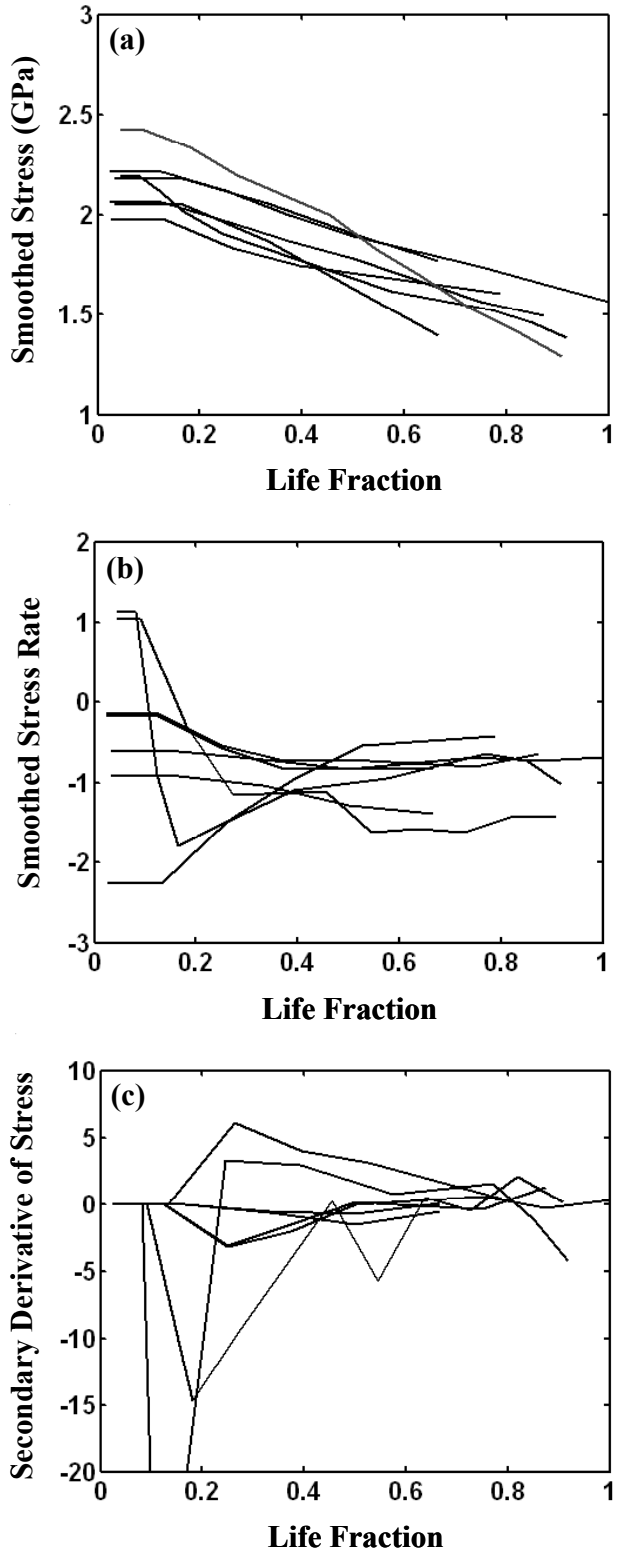

Fig. 4.54. (a) Smoothed stress, (b) first derivative and (c) second derivative of stress

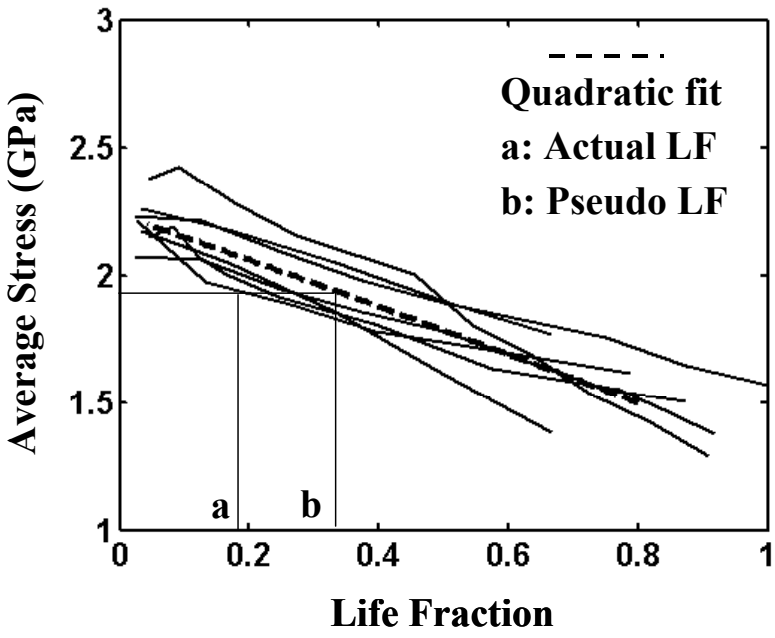

Fig. 4.55. Stress vs. life fraction for neural network method 2

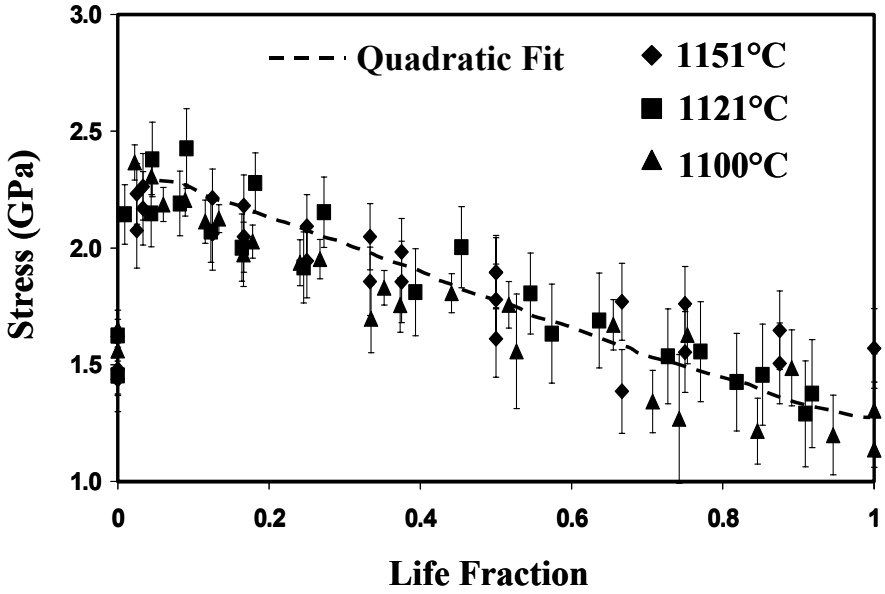

Fig. 4.56. Quadratic fit for specimens at three temperatures

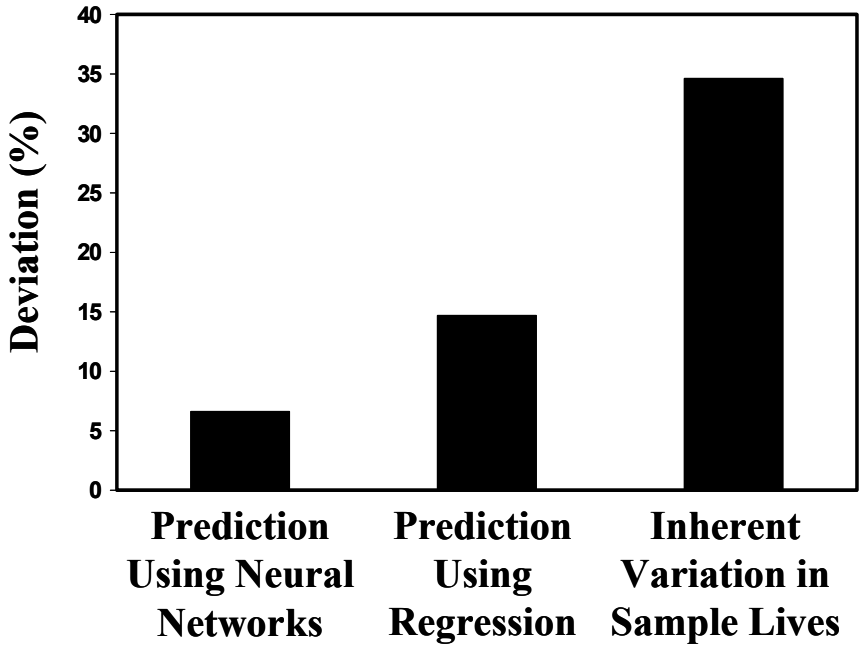

Fig. 4.57. Comparison of prediction accuracy and inherent variation of lives

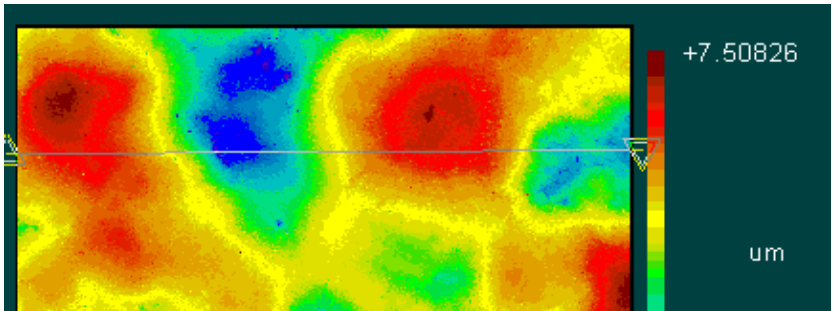

Fig. 4.58: Surface geometry of as-received specimen

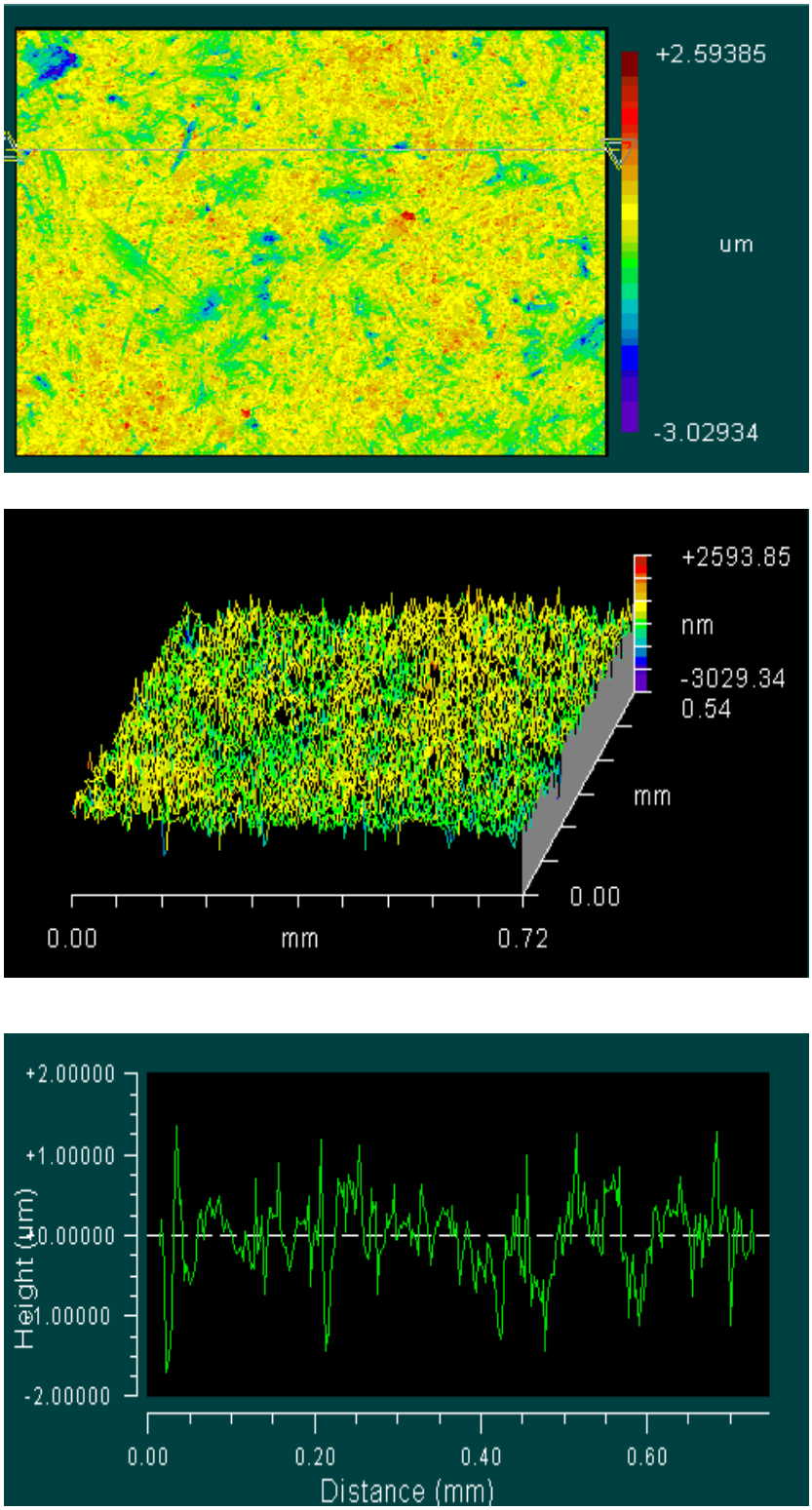

Fig. 4.59: Surface geometry of barrel finished specimen

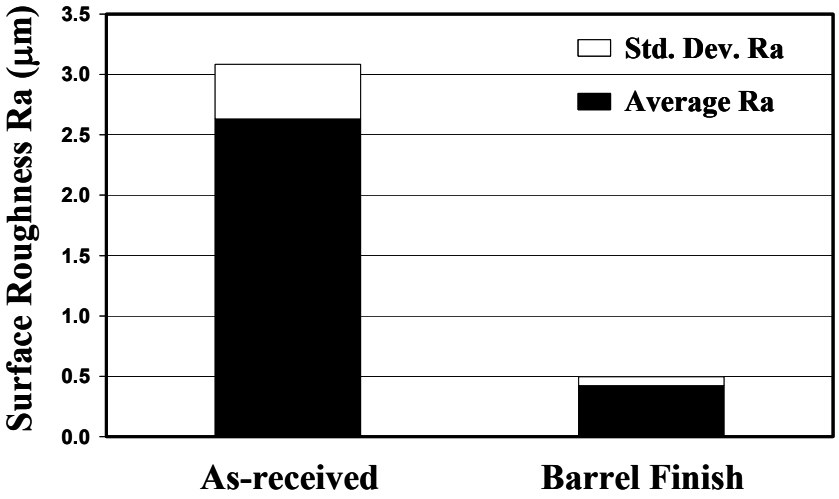

Fig. 4.60. Summary of surface roughness for specimens after different finishing

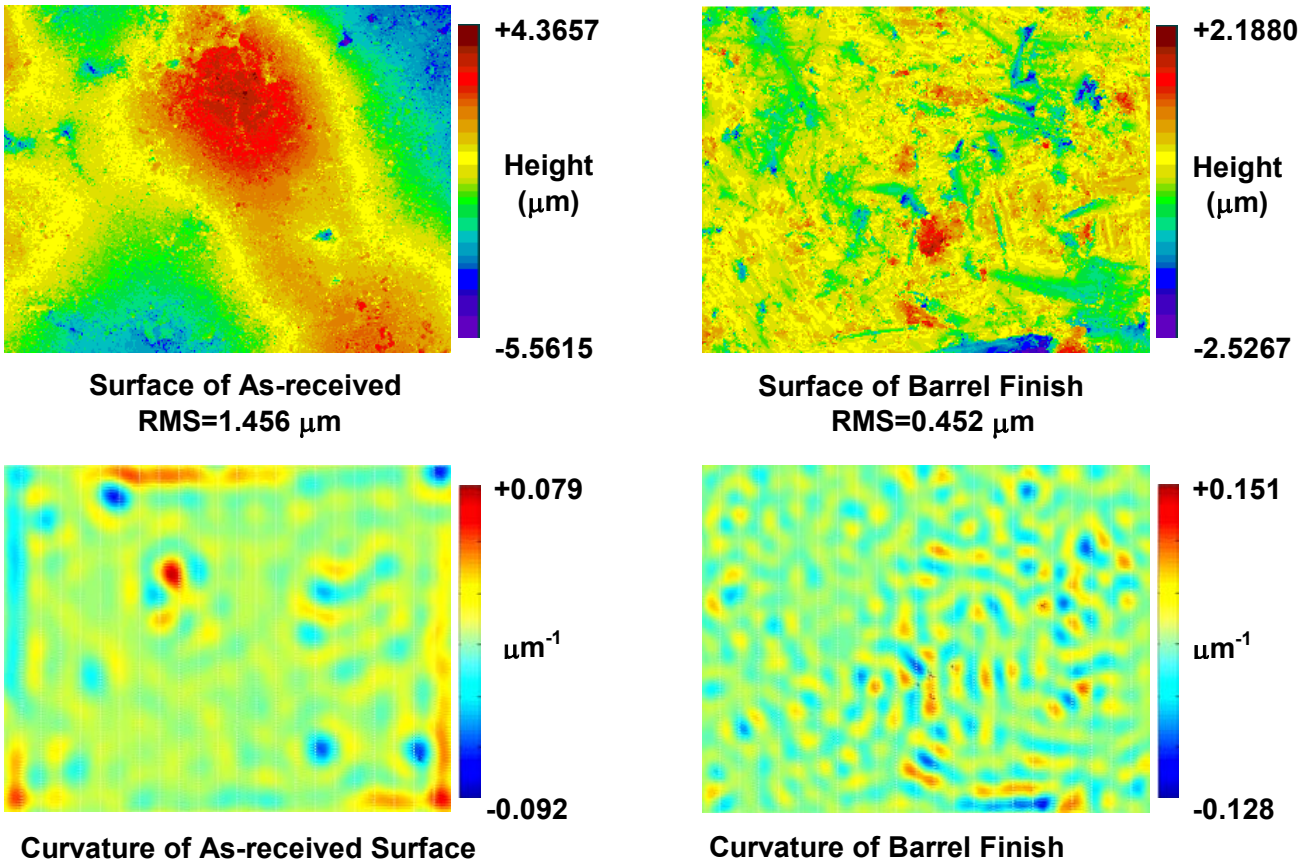

Fig. 4.61. Bond coat surface geometry and curvature map before and after barrel finishing

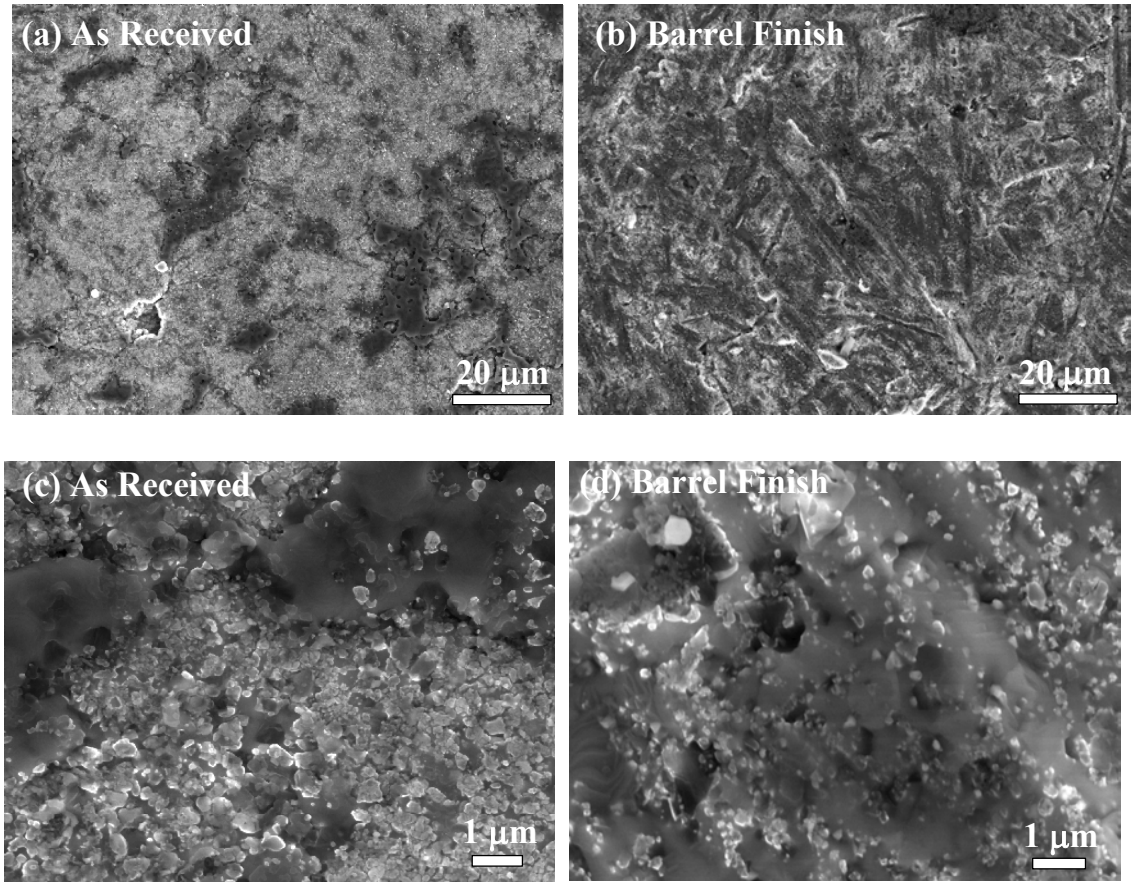

Fig. 4.62. SEM of as-received and barrel finished bond coat surface

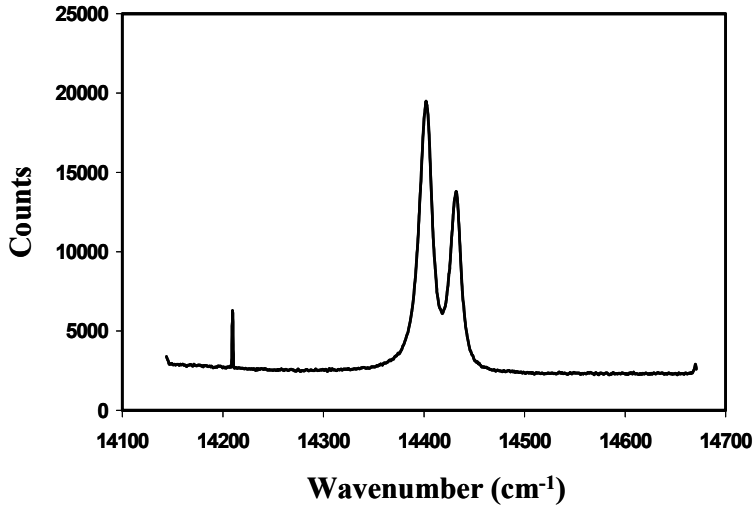

Fig. 4.63. PLPS spectra of bond coat surface showing α-Al_2O_3

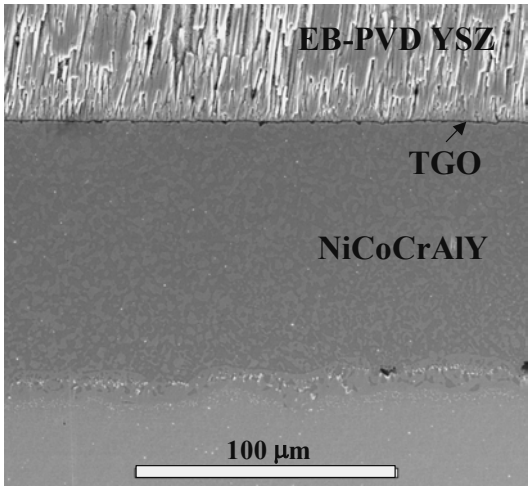

(a)

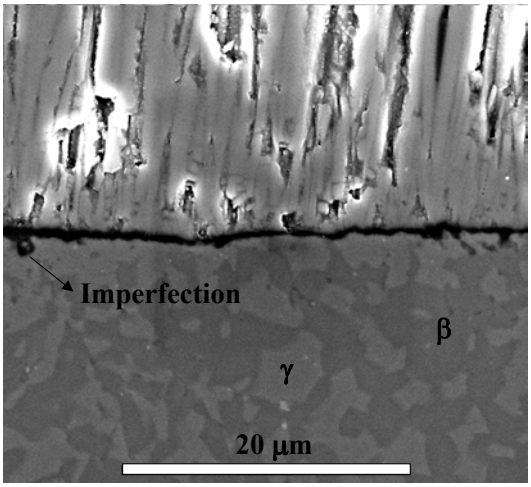

(b)

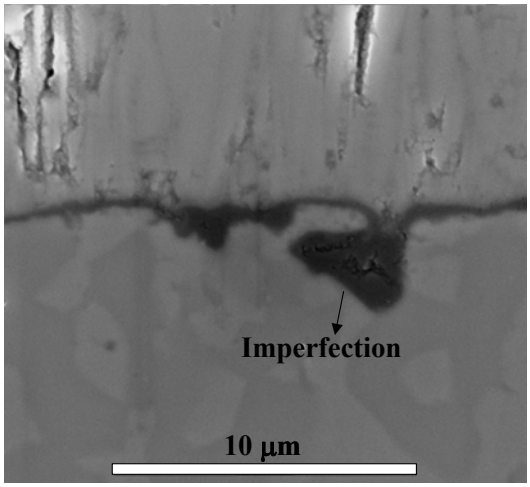

(c)

Fig. 4.64. SEM micrographs of as-coated TBC

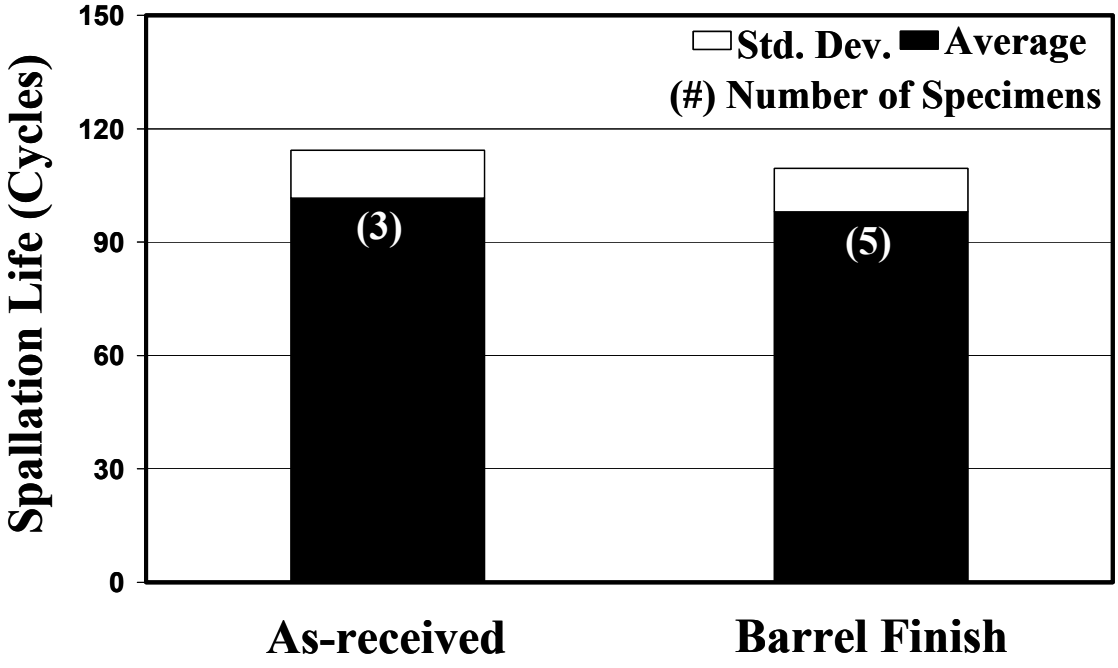

Fig. 4.65. Spallation life of specimens

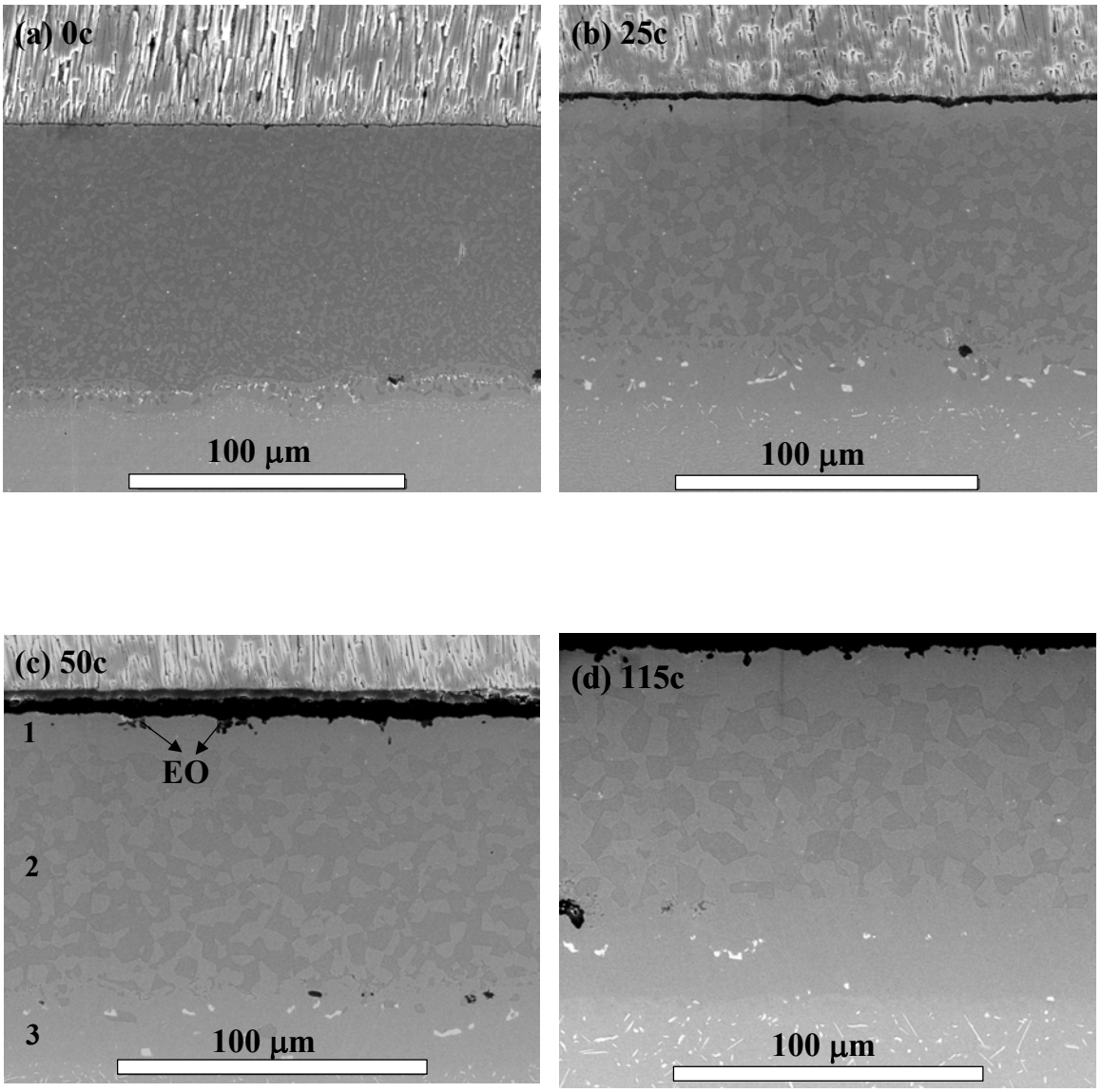

Fig. 4.66. SEM micrographs of specimens at various stages of thermal cycling showing: 1. upper depletion zone; 2. two-phase (β + γ) region; 3. lower depletion zone; and embedded oxides (EO).

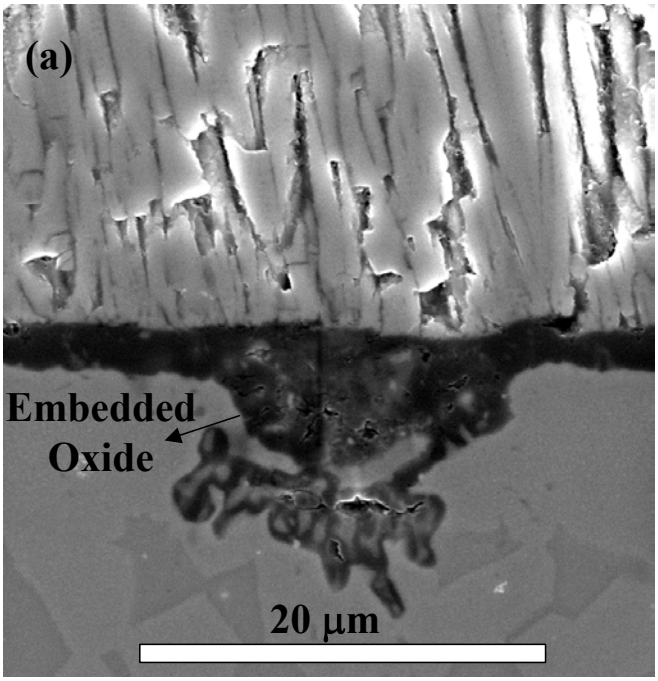

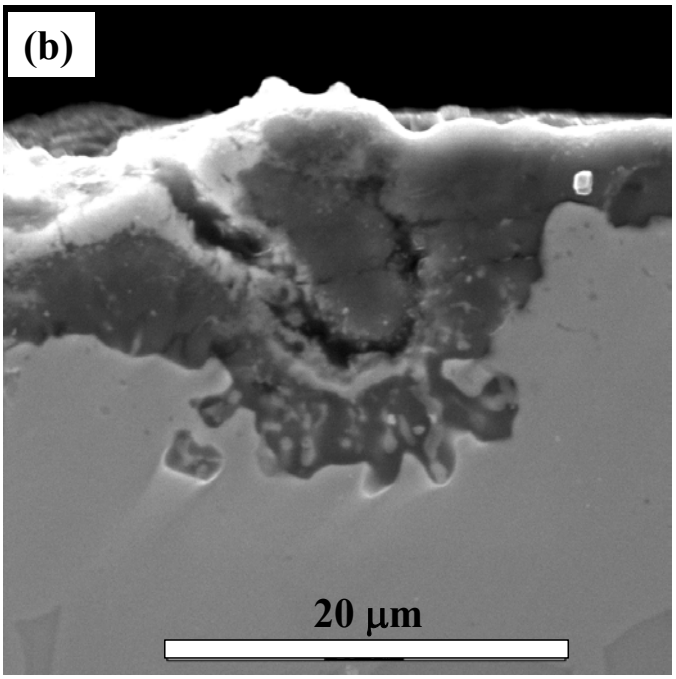

Fig. 4.67. SEM micrographs showing embedded oxides

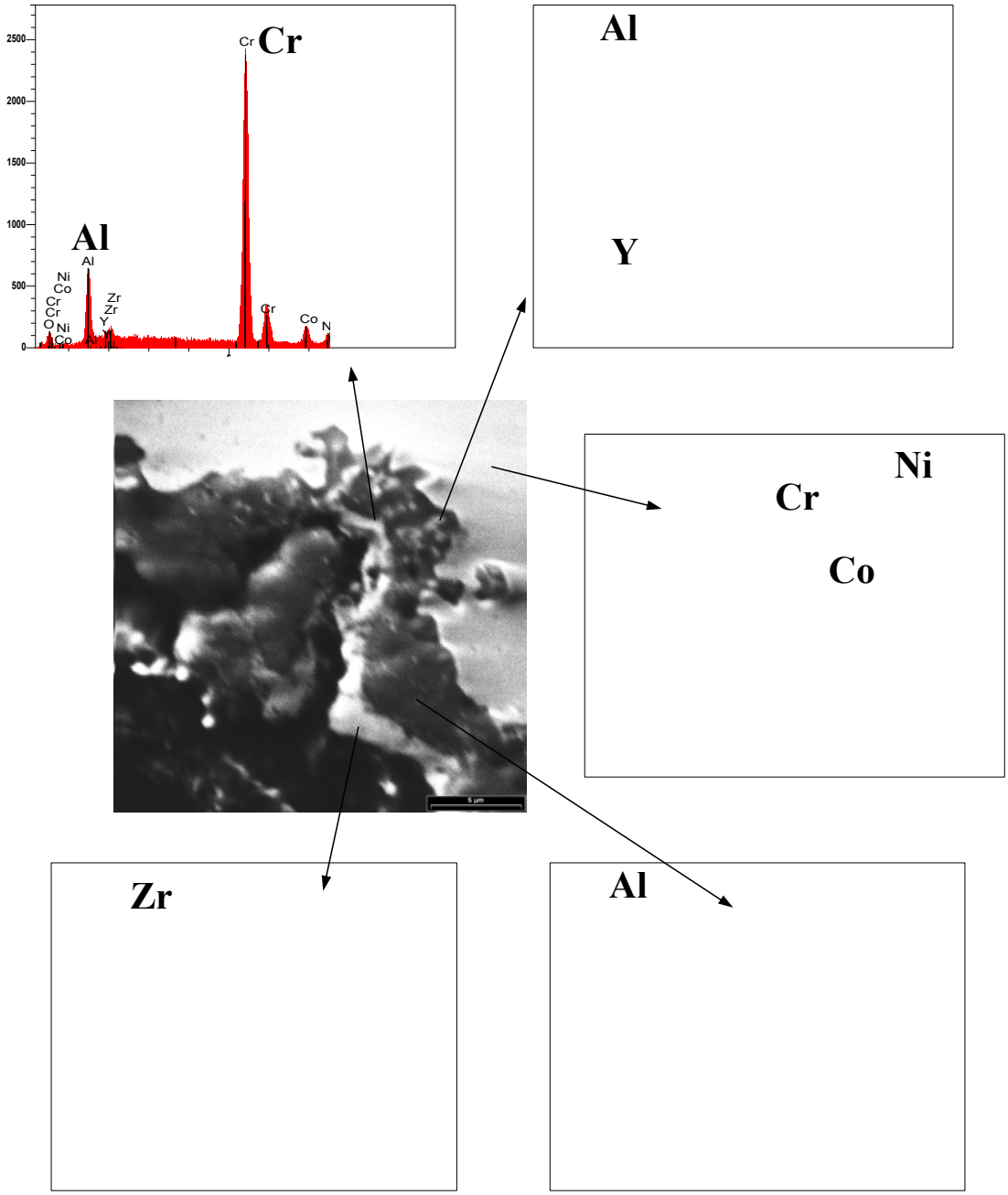

Fig. 4.68. Back scattered image of embedded oxide and EDS spectra at different regions

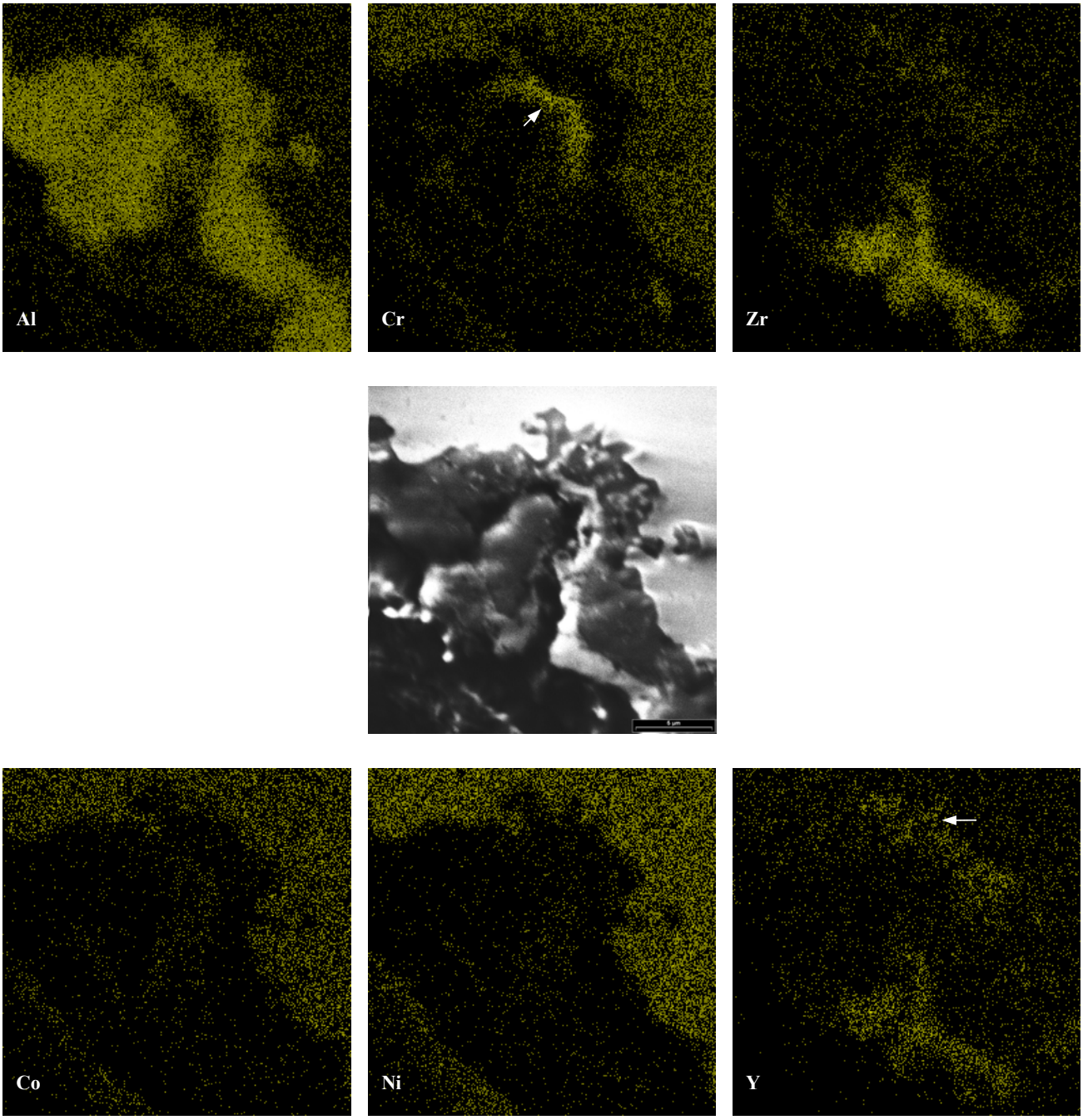

Fig. 4.69. Back scattered image of embedded oxide and x-ray mapping

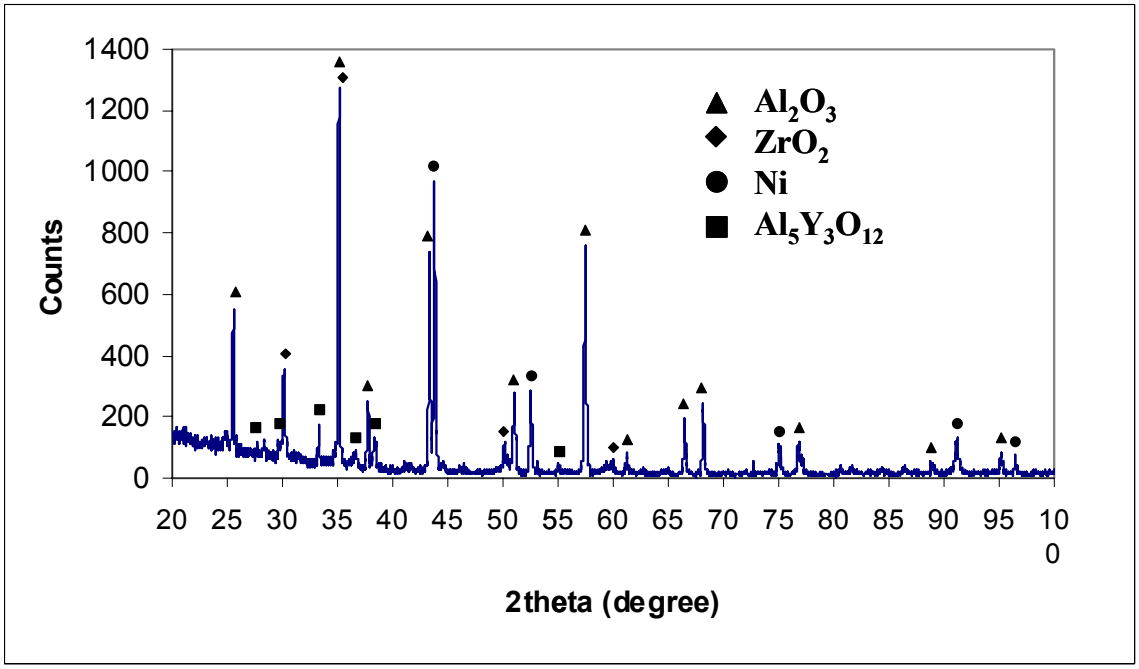

Fig. 4.70. XRD pattern of bond coat surface after spallation

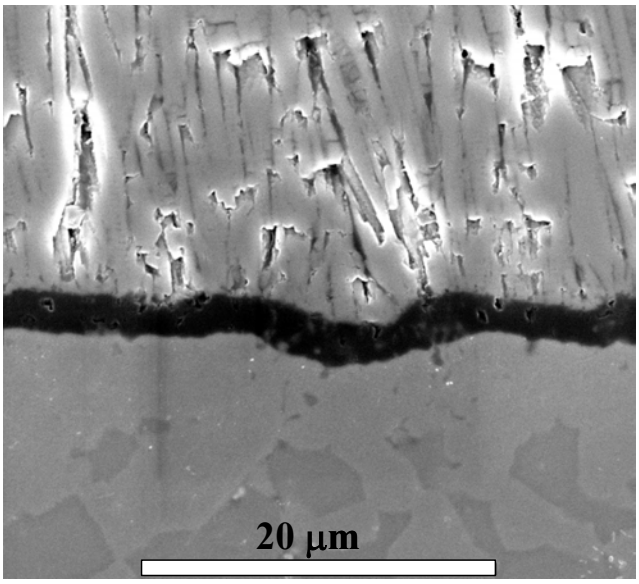

Fig. 4.71. SEM micrograph showing rumpling without damage

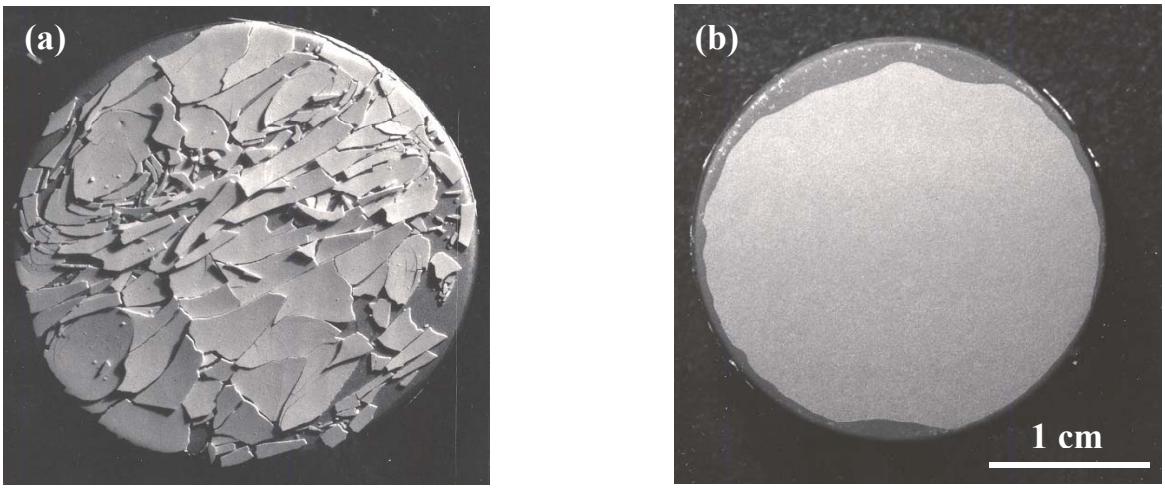

Fig. 4.72. Macrographs of failed specimens

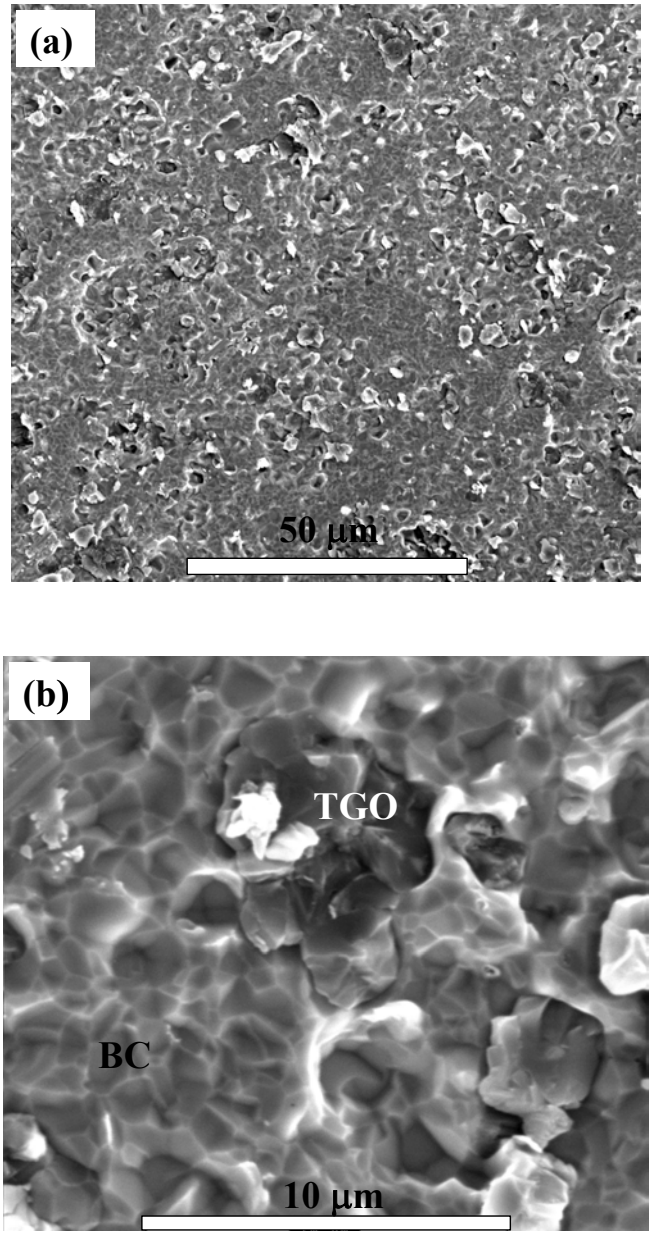

Fig. 4.73. SEM micrographs of spalled surface on the bond coat side

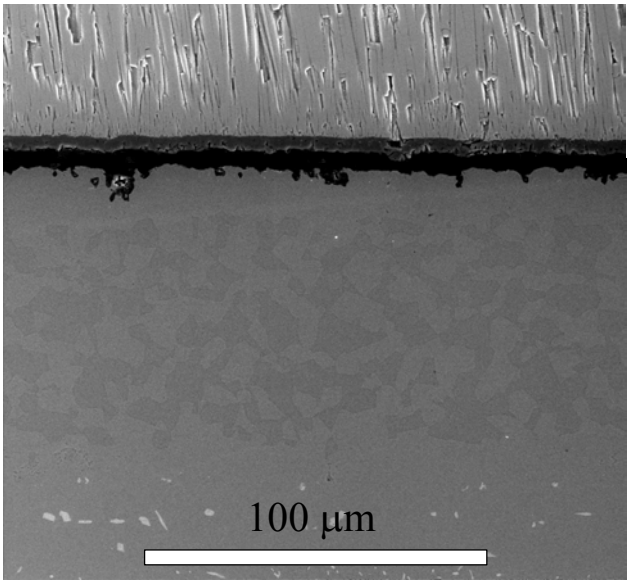

Fig. 4.74. Cross-section of failed specimen

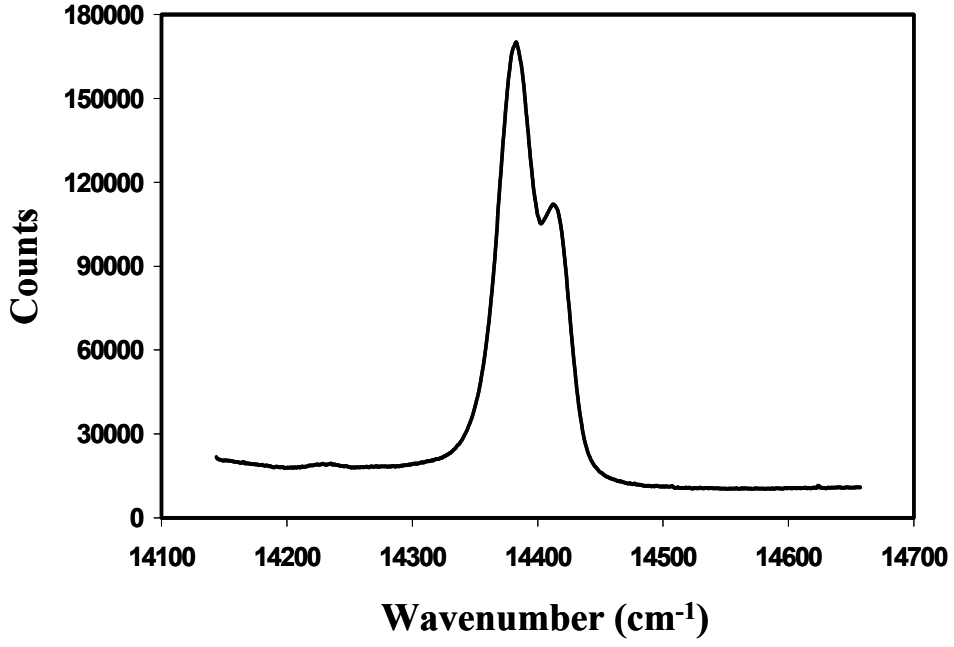

Fig. 4.75. Typical example of PLPS spectra during thermal cycling

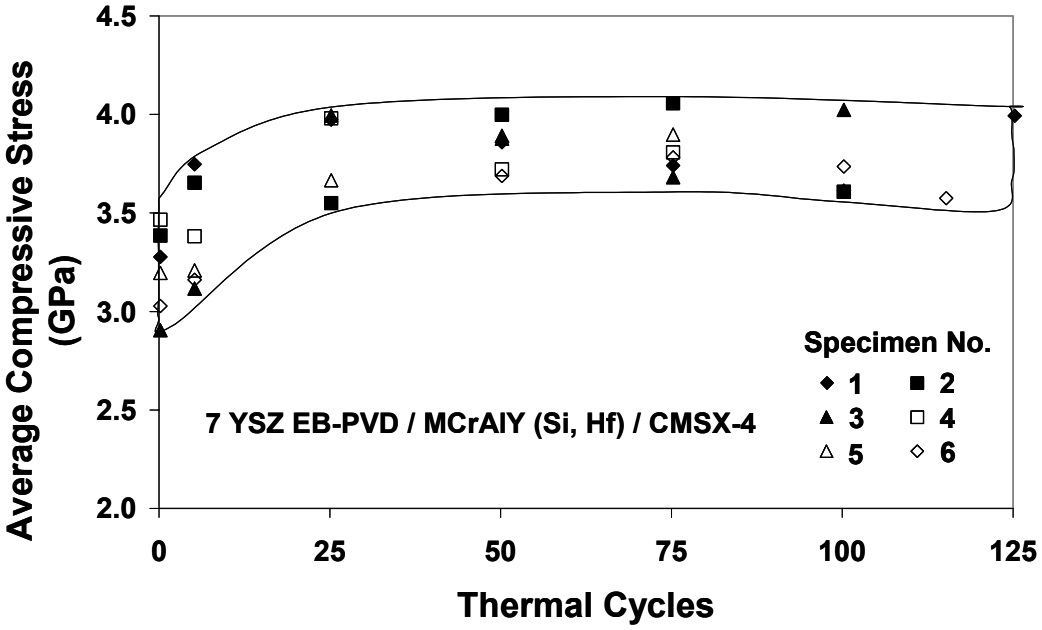

Fig. 4.76. Evolution of TGO compressive stress as a function of thermal cycling

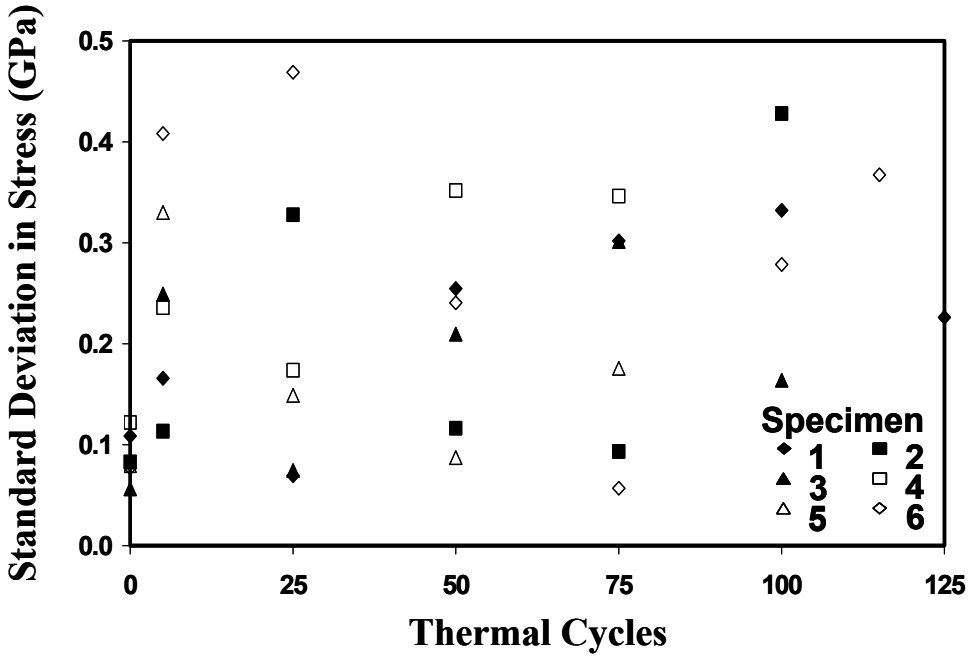

Fig. 4.77. Standard deviation in stress as a function of thermal cycles

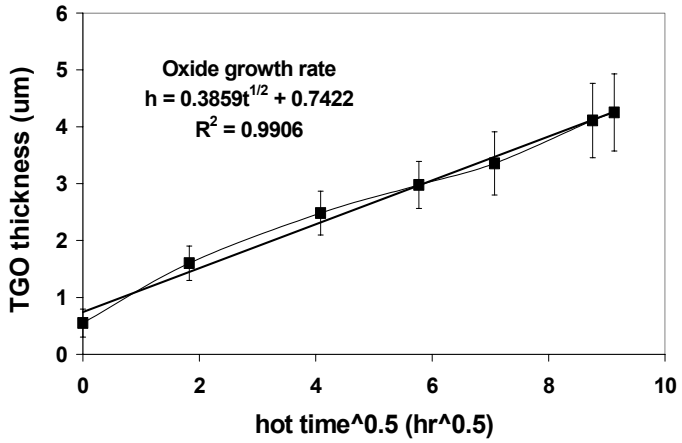

Fig. 4.78. TGO thickness as a function of square root of hot time

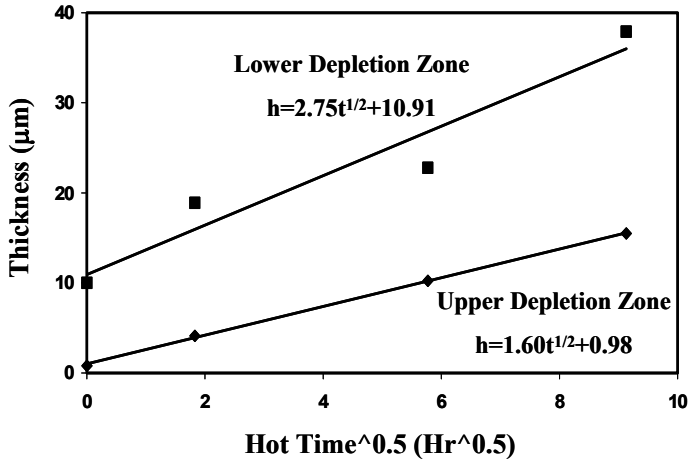

Fig. 4.79. Thickness of depletion zones as a function of square root of hot time

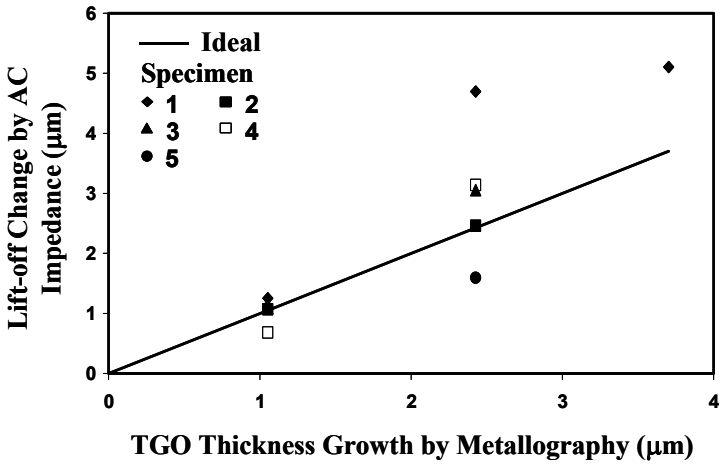

Fig. 4.80. Comparison of TGO thickness measured by metallography and AC impedance

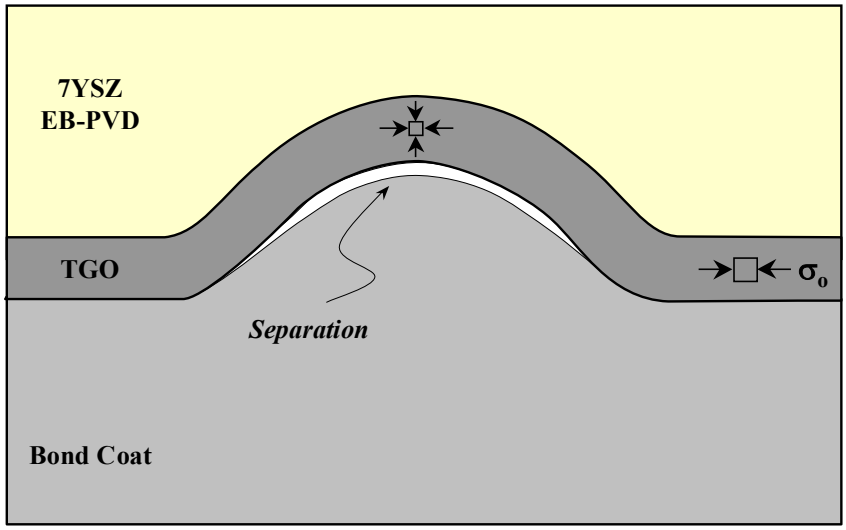

Fig. 4.81. Failure governed by debonding at ridge tops due to normal tensile stress that increase with TGO thickness (*75*).

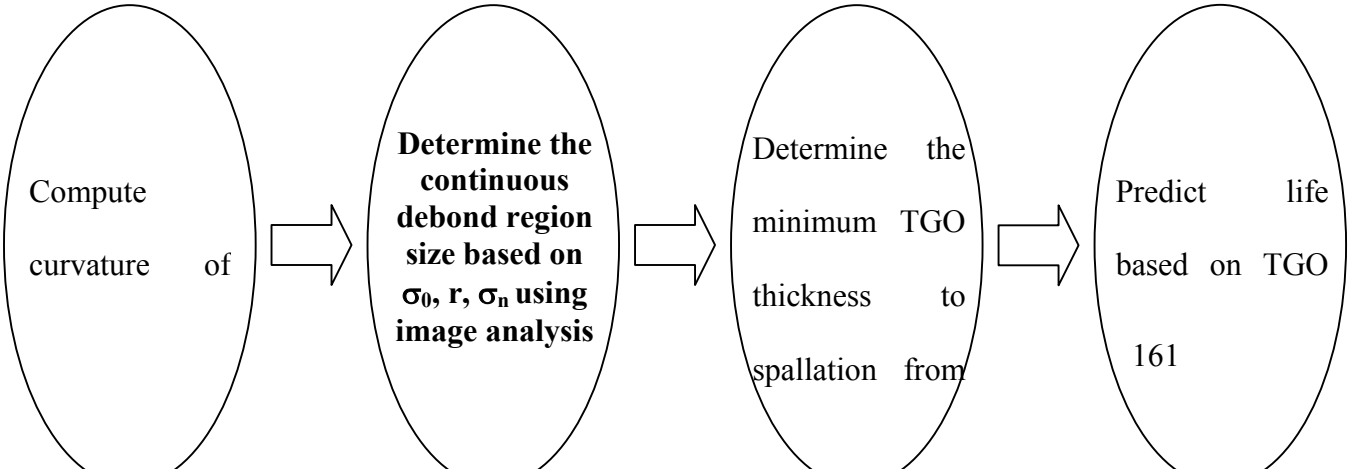

Fig. 4.82. Flow chart showing the procedure of life prediction

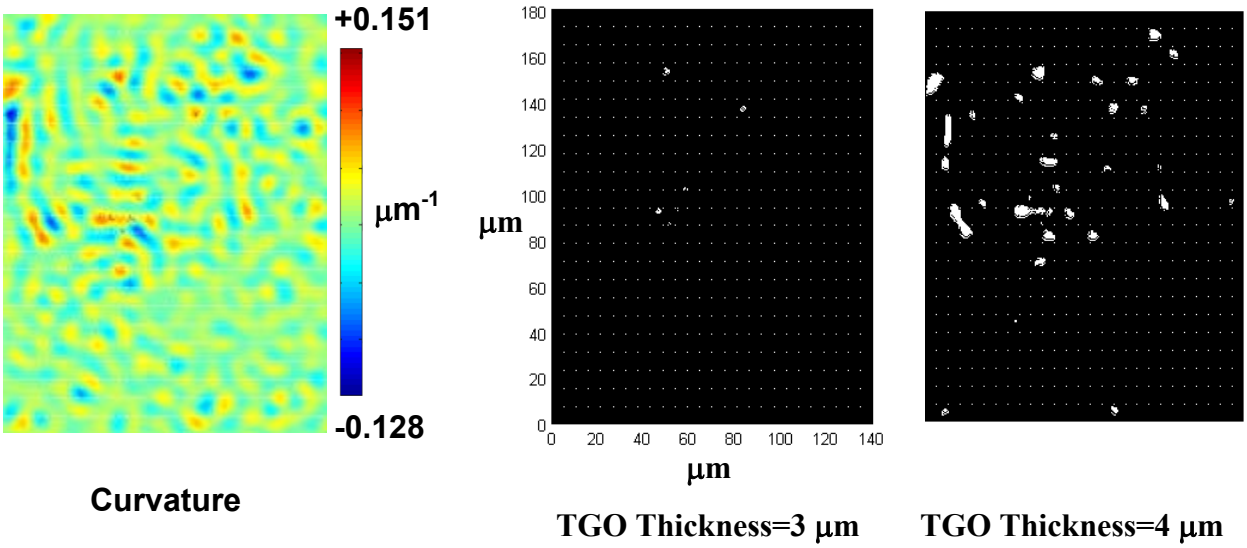

Fig. 4.83. Example showing the debonding region based on curvature map

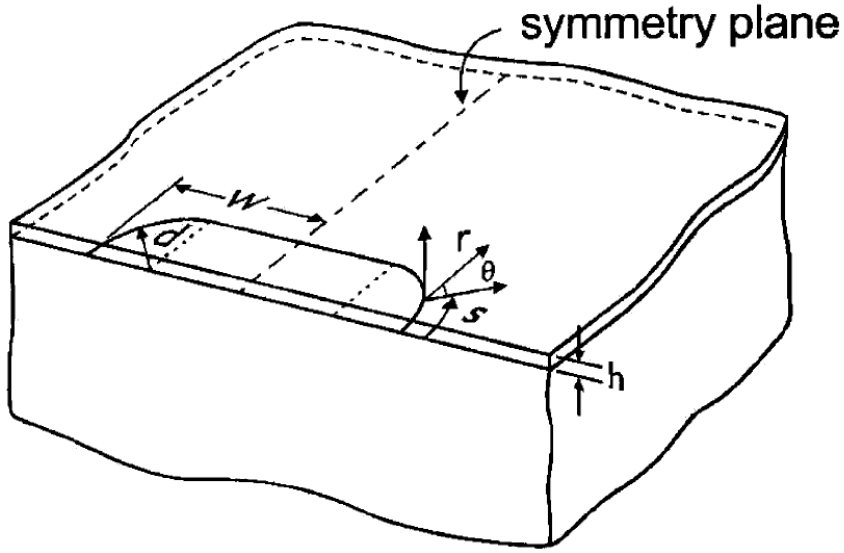

Fig. 4.84. General configuration of a flaw existing at the TGO/bond coat interface, along the free edge of the specimen (*133*)

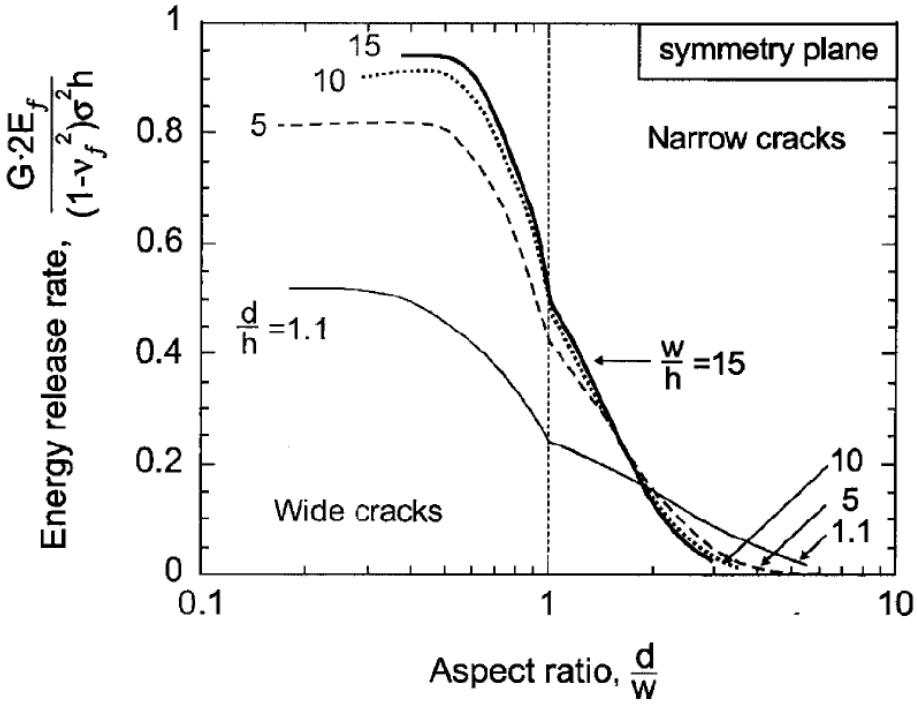

Fig. 4.85. Stored strain energy release rate (G_0) for different geometries of debonds (*133*)

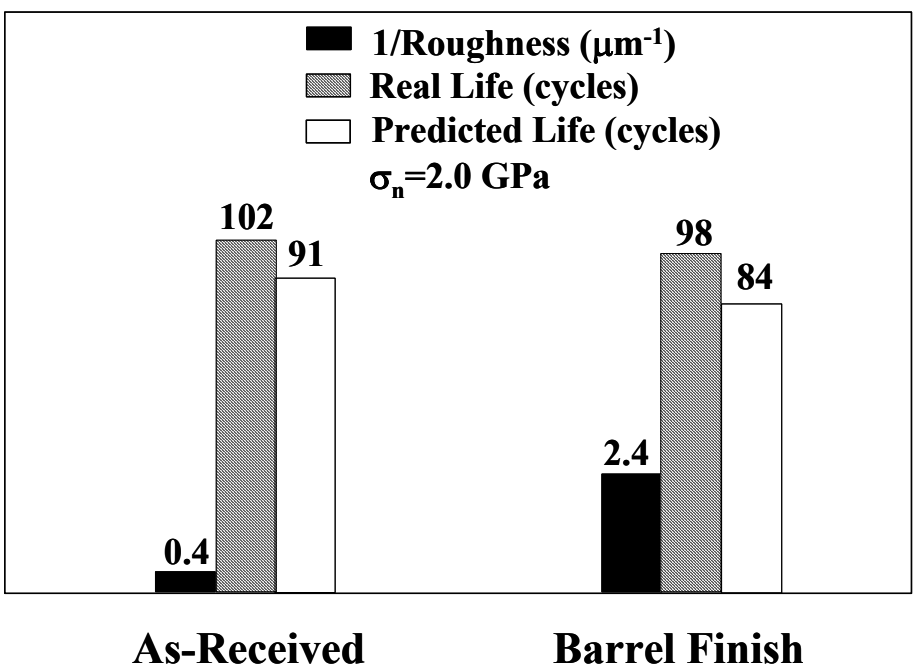

Fig. 4.86. Comparison of predicted and real lives

5. Discussion

Two different TBCs were studied in this research. One has a (Ni,Pt)Al bond coat , the other has a NiCoCrAlY bond coat. TBCs, in general, show a wide range of damage accumulation and spallation mechanisms. This general behavior is certainly exhibited by the two TBCs of this study, as described in the Experimental Results section. As will be described in this Discussion section, it is important to define the mechanisms of damage accumulation and spallation for each TBC to properly interpret and use PLPS data and other information for purpose of non-destructive inspection, assessment of life remaining, and life prediction.

5.1 (Ni,Pt)Al Bond Coated TBCs

4.2.1. Rumpling-TGO Stress-Spallation Life Analysis

4.2.1.1 Effect of Rumpling on Spallation Life

Rumpling has been frequently observed in Pt-modified aluminide bond coated TBCs (*8, 43, 49, 50, 64, 76-89*). The observations (Fig. 4.7) in the present study clearly show that rumpling can initiate the separation and cracking near the TGO/TBC interface above rumpling sites. As the TGO penetrates into the underlying bond coat, the displacement can induce the out-of-plane tensile strains in the TBC. The strains initiate localized cracking near the TGO/TBC interface. After initiation, cracks may extend laterally along the TGO/TBC interface (Fig. 4.6c), or they may go through the TGO or along the TGO/BC interface (Fig. 4.23). Eventually, these mixed mode cracks lead to spallation of the TBC (Fig. 4.21-23). In addition to cracking

initiation, formation of other structural imperfections (cavities) is also associated with rumpling.

An intriguing result is that the roughness values at failure are similar (~3.0 μm) at the three test temperatures with lives variation of 5X. A critical rumpling value seems to exist beyond which the coating will fail. TBC durability would be dominated by the rate of rumpling if there is a critical rumpling value. The spallation life would be shorter if the rate of rumpling is faster. It was found that the rate of rumpling increases as cycling temperature increases, whereas the spallation life decreases at same time (Figs. 4.9 and 4.10). This fact is consistent with the critical rumpling value observations. Based on the observations that cracks initiate at rumpling sites and there is a critical rumpling value at failure, rumpling is responsible for failure. The RMS parameter and tortuosity as a function of life fraction are shown in Fig. 5.1. The roughness increases monotonically as a function of life fraction relatively independent of temperature, consistent with the idea that rumpling is responsible for the failure and TBC durability is determined by rumpling.

Since rumpling is responsible for failure, decreasing the rate of rumpling will enhance TBC durability. It has been reported that rumpling did not occur and durability was increased for smooth bond coats and when surface imperfections were removed by polishing (*67*).

4.2.1.2 Oxide Growth and Its Relation to Rumpling

Tolpygo and Clarke (*135*) argue that there is a critical oxide thickness for failure. Kim et al. (*129*) support this concept and suggest that the TGO growth rate is

a key factor in determining TBC failure. Although a critical TGO thickness at failure was not observed in all cases (*26, 64*), it seems to be valid for the present TBC, where an approximately constant TGO thickness of 4.6 to 5.3 microns was observed at failure. The strong effect of temperature on TGO growth rate and the existence of a critical oxide thickness at failure indicate TGO growth kinetics plays an important role in determining failure. The strong effect of temperature on rumpling rate and a critical rumpling value at failure were also observed in this TBC, suggesting there is causal effect between rumpling and oxide growth.

As shown in Fig. 4.17, both the RMS parameter and tortuosity increase as TGO thickness increase relatively independent of temperature. The fact that rumpling is a single value function of TGO thickness is an indication that rumpling depends on oxide growth. Evans et al. (*76, 83, 88*) proposed that rumpling is related to the cyclic strains in the bond coat driven by growth strains in the oxide and the lateral growth of the TGO plays critical role in rumpling. Because lateral oxide growth is generally believed to be correlated to thickness growth, these results are consistent with the critical role of the in-plane growth strain (*76, 83, 88*) in rumpling, and are consistent with the behavior reported in Ref. (*64*) for a similar system. This relationship of oxide growth to rumpling is only true if the entire TGO lateral growth shows up as increased interface length as opposed to being absorbed by TGO yielding. Simulations (*83*) show that for low in-plane growth rates, TGO yielding will not occur and the resulting TGO rumpling tortuosity change is equal to that needed to accommodate the growth strain. The in-plane growth strain, calculated from the

tortuosity change, in the present study is in the range of low strain ($1 \times 10^{-3} \sim 5 \times 10^{-3}$) without TGO yielding obtained from simulations (*83*).

5.1.1.3 Relationship of Rumpling, TGO Stress and Spallation Life and Its Significance in TBC Life Prediction

The evolution of the TGO stress with thermal cycling for the (Ni,Pt)Al TBC can be separated into two stages. At all three temperatures, the compressive stress increases with cycling to its maximum in the first stage and then decreases monotonically in the second stage. The increase in the stress may be due to the growth stress in the TGO (*41, 43, 111*), which may be attributed, in part, to the θ to α phase transformation during the early stages of TBC deposition and oxidation (*111*). The transformation was observed in our studies from the occasional appearance of θ-Al_2O_3 spectra (R_2 = 14613 cm^{-1}), which co-existed with α-Al_2O_3 (R_2 = 14420 cm^{-1}) at very short oxidation time. It was observed that the end of the first stage coincided with the completion of the transformation.

After the initial transient stage, the TGO stress decreases monotonically until failure. The observed stress relaxation can be due to various mechanisms, such as rumpling (*88*) and the effect of oxide induced geometry changes on the stress with increasing TGO thickness on rough surfaces (*71*) and creep of the bond coat and the oxide (*47*). In the present study, rumpling of the bond coat surface occurs. The bond coat/TGO interface gets rougher and the amplitude of rumpling increases with thermal cycling (Fig. 4.9). Both the compressive growth stress and the compressive stress resulting from the thermal expansion mismatch in the TGO would provide a

strain energy driving force for deformation. Conversely, rumpling is certainly a mechanism of strain energy relaxation (*71*), although there may be other mechanisms. Associated with the observation of progressive rumpling of the oxide and the bond coat interface, the TGO stress was found to decrease monotonically until failure after the initial transient period. More convincing, the rate of stress relaxation increases with increasing rate of rumpling (Fig. 4.36). In addition, a previous study (*106*) shows that the TGO stress decreases very slowly and remains almost constant with cycling for specimens that do not exhibit rumpling behavior. Based on these observations, and the relationship between rumpling and stress relaxation, it is proposed that the oxide stress relaxation of this TBC is mainly due to rumpling.

Since the durability of this TBC is dominated by rumpling, the TGO stress relaxation and specimen life can be connected using rumpling as a bridge. The rate of stress relaxation relates to the severity of rumpling, and ultimately to spallation life. As the temperature increases, rumpling rate and TGO stress relaxation rate increase, while specimen life decreases (Fig. 4.36). This connection provides a physical basis for use of TGO stress measurements as a non-destructive method for TBC life prediction. In fact, as part of this thesis, successful life predictions have been made for specimens tested at different temperatures based on the measurement of TGO stress as a function of life fraction by PLPS. Most significantly, since the TGO stress can be monitored non-destructively during thermal cycling, TGO stress based TBC life predictions can be made. Thus, PLPS is an extremely powerful technique compared to other NDI techniques, for detecting early damage initiation, the progression of damage, and use in a mechanisms-based life prediction system.

5.1.2 Remaining Life Prediction of (Ni,Pt)Al TBC

The present study is the first attempt at remaining life predictions for TBC samples at three different temperatures, without using knowledge of the temperatures. We note the temperatures at critical locations in service components can vary within a component and from component to component within a given engine. Component temperature variation is one of the most important features leading to variations in component lives. It is, thus, important to have a life prediction method that doesn't require precise knowledge of temperatures.

The ability to make predictions in a temperature blind manner, over the limited ranges of temperatures that were practical to test in the current work, is promising. Even though test lives of specimens vary by a factor of 5, remaining life predictions (the radial basis network prediction with the RMS error of 6.6%) are still successful. The successful predictions are based on the fact that the TGO stress decreases systematically with life fraction relatively independent of temperature in the studied temperature range. If the temperature independence proves true over a wider range of temperatures, then knowledge of local temperatures will not be needed for good life prediction. To make life predictions of components in service, it is necessary to construct a data base for the exact coating/substrate system to be used and to select component relevant temperature ranges and cycle times. With such a data base and a few stress measurements (one in the extreme case) over time for the engine parts, life predictions can be made.

It is worth noting that the TGO stress based remaining life predictions are based on the experimentally determined failure mechanism of this TBC. In the present

predictions, the samples fail due to rumpling that directly influences the stress measured and the present results are expected to be applicable primarily to systems failing in this way. The failure modes of TBCs depend on the specifics of the alloy-bond coat- TBC being tested. Other failure modes can and do occur (*8*). In such cases, additional information may be needed to make life predictions. For example, for the NiCrCoAlY bond coated TBC, the prediction method was developed based on bond coat surface curvature maps, the TGO stress and thickness measurements (section **4.2.6**). In addition, for this and other TBCs, the occurrence of bimodal stress distributions may be predictive (*116,117*). It is worth noting that a commercial engine manufacturer has issued a contract to UConn to perform remaining life predictions on engine parts based on the results shown in this and a related UConn thesis (*136*).

5.1.3 Bimodal Luminescence and TGO Cracking

4.2.3.2 Bimodal Spectra Associated with TGO Cracking and Its Implication in NDI Use

In the present work, the bimodal spectra have for the fist time been clearly connected with TGO cracking (localized damage). First, there was a perfect one to one correspondence between the measured bimodal spectra and observed cracks in the bare TGO formed on the bond coat. That is, bimodal spectra were observed only from regions of the TGO in the immediate vicinity of cracks and never detected

where cracks were not seen (Fig. 4.42). Second, the crack density and fraction of bimodal spectra changed in the same manner with thermal cycling.

When the probed regions in the PLPS contain both intact and damaged regions, the probed regions will have stress variations and will produce two sets of peak pairs with the high stress component corresponding to intact regions and the low stress component corresponding to damaged regions. It would be reasonable to assume that the likelihood of getting bimodal spectra increases with increasing localized damage. In fact, there were consistent trends in the fraction of bimodal spectra and the crack density as a function of cycles. The fraction of bimodal spectra increases when the density of cracks increases (compare Fig. 4.43 and 4.45). The correspondence of the trends in the crack density and the fractional presence of bimodal spectra are consistent with the idea that bimodal spectra are caused by small regions of stress free TGO associated with cracking.

Tolpygo and Clarke (*35*) studied the theta-alpha transformation in alumina scales on platinum-modified nickel aluminides and found that bimodal spectra can originate from the alumina scales containing whiskers. The TGO consisting of continuous and whiskers morphologies is constrained and unconstrained, respectively, under in-plane compression with the underlying metal. The luminescence from regions containing both constrained and unconstrained TGO would give rise to bimodal spectra (*35*). In the present work, bare alumina scales were also observed containing whiskers (Fig. 5.2) and the whiskers disappeared after oxidation for 25 hours. In contrast with the Tolpygo's study, the bimodal spectra were not observed from the scales containing whiskers, but only from the regions of

the TGO in the immediate vicinity of observed cracks. The possible reason for the differing results in the two studies is that, in this study, the volume of whiskers is too small compared to the continuous and constrained TGO layer, making the low stress peaks from whiskers difficult to detect.

Because the association of bimodal spectra and cracking was directly observed on the bare TGO layer, the fraction of bimodal spectra measured through the ceramic layer also gives an indication of the extent of damage. In the case of measurements made through the ceramic layer, the diameter of the spatial region from which spectra are collected is estimated to be around 70 μm, due to scattering by the columnar structure of the EB-PVD TBC (*114*). As a result, the presence of bimodal spectra through the TBC has a statistical aspect representing the degree of cracking for a relatively large area of the TGO. The change in the fraction of bimodal spectra seen through the TBC parallels the change observed in the occurrence of bimodal spectra in the bare oxide and also for the crack density observed on the bare oxide (Fig. 4.40, 4.43 and 4.45).

In addition, the stress distribution mapping based on bimodal spectra contribution can provide a visual record of the number and size of the damage sites. The stress distribution maps (Fig. 4.41) show clearly that damage accumulation occurs with thermal cycling. Both the number and the size of continuous damage sites increase with thermal cycling. Therefore, the fraction of bimodal spectra is another powerful tool in assessing damage initiation, damage progression, and assessing remaining life. This is a recommended item for future research.

5.1.3.2 Mechanisms of Crack Formation During Thermal Cycling on the Bare Bond Coat

The early increase in bimodal spectra and associated observed cracking in this work is attributed to the effect of volume change associated with the transformation of θ-Al_2O_3 to α-Al_2O_3 (*35*). Numerous studies of nickel aluminides (*32-36,118*) have shown that metastable alumina phases such as θ-Al_2O_3 may form and then transform into stable phase α-Al_2O_3 in the very early stage of oxidation, which results in a volumetric shrinkage due to the phase change. The present experimental observations are consistent with the idea that transformation of θ-Al_2O_3 to α-Al_2O_3 is responsible for the early increase in crack density and associated increase in bimodal spectra. First, the transformation occurs early in oxidation, as confirmed by the occasionally observed regions in which α-Al_2O_3 and θ-Al_2O_3 coexist (Fig. 4.46). Second, the appearance of maximum peak crack density occurred just prior the time at which θ-Al_2O_3 disappeared based on the PLPS spectra. Finally, the θ-Al_2O_3 island was observed to be surrounded by an α-Al_2O_3 matrix, as would lead to isolated cracks (Fig. 4.46).

The subsequent decrease in the occurrence of bimodal spectra is associated with crack healing. This crack healing is directly observed as decreasing crack density seen on the bare oxide and indicated by the decrease in the fraction of bimodal spectra for both bare and ceramic coated specimens.

By direct observation, the final increase in the fraction of bimodal spectra is associated with TGO cracking, which occurs almost exclusively near the highest parts of protruding regions of the TGO as shown in Fig. 4.44d and 4.47b. It is worth

noting that these cracks are quite open and of the type expected if in-plane tension exists in the TGO. These cracks are therefore different from delamination cracks that result from out-of-plane tensile stresses (*21, 71, 74*). Local tensile stresses associated with rumpling and with elemental transport (aluminum depletion from oxide growth and Ni influx from the substrate (*85*)) seems to be the best candidate explanations for cracking at this time.

5.1.4 Combination of Multiple PLPS Characteristics for NDI Use

In previous studies on EB-PVD TBCs on platinum aluminide bond coats (*30, 106*), only the peak frequency shift (i.e. stress) has a systematic change with cycles and it seems that the stress level is the single most promising feature for possible use in NDI. In the EB-PVD TBCs on platinum aluminide bond coats studied in this thesis, the most striking result is that (a) the average TGO stress, (b) its standard deviation, and (c) the R_1 and R_2 peak area ratio all show systematic changes with thermal cycling. Both the average stress and R_1 and R_2 peak area ratio decrease monotonically with thermal cycling. It is surprising that this system showed a systematic change in R_1 and R_2 peak area ratio and standard deviation of stress while a highly similar system (*30*) from a different manufacturer did not show a systematic variation of these two quantities. Since both systems were tested in the same furnace and spectra analyzed using the same apparatus and procedure, the experimental details don't provide an explanation for such a difference. These results also highlight the importance of characterizing each individual TBC before using PLPS as a tool for detecting damage and assessing life remaining.

The intensity ratio of the R_1 and R_2 peaks is weakly dependent on temperature and pressure. Munro et al. (*137*) found the intensity ratio of the Ruby R lines (R_2/R_1) varied by $-0.00047°C^{-1}$ and -0.013 GPa^{-1}, with temperature and pressure, respectively. In this study, the temperature dependence can be ignored since all the measurements were taken at room temperature. According to the pressure dependence factor found by Munro et al. (*137*), the calculated area ratio change attributed to the stress change is about 20% of the observed area ratio change and is in the opposite direction. Therefore, the effect of pressure variation on peak area ratio is not an explanation for the observed changes. It has also been suggested that the peak intensity ratio depends on the crystallographic orientation with respect to the polarization of the laser in Refs. (*113, 118*). This can be a large effect for a single crystal but not for polycrystalline alumina. The ratio obtained in the present study falls in the range of 0.35-0.45. This is close to the value of an α-Al_2O_3 reference disk (stress free and randomly oriented polycrystalline) and in good agreement with the value (~0.5) for polycrystalline α-Al_2O_3 reported in Ref. (*118*). Also, the sample was randomly rotated and tilted and no change was observed for the area ratio. Therefore, it is reasonable to say that Al_2O_3 has no preferential orientation and it is un-textured or weakly textured. Thus, crystallographic orientation can be excluded from the cause for the systematic change of area ratio with cycles. At the present time, the cause of the systematic change of the area ratio with cycles is unknown.

The standard deviation of stress is a measure of the stress heterogeneity in the measured volume. In the present case, as damage increases, stress heterogeneity and the standard deviation increase. However if the characteristic dimension of the

heterogeneity is much smaller than the probe characteristic dimension (around 70 μm in this case (*114*)), then averaging would obscure this variation and may be the reason for not seeing this in the other TBC (*30*). Although the cause of the systematic change of the area ratio and standard deviation in the stress with cycles is unknown, as an engineering approach they can be used in an attempt to predict life due to a systematic change with cycles (section **4.1.5**).

Most importantly, it is clear that behavior of PLPS spectral characteristics with thermal cycling is sensitive to not only composition but also processing. Therefore, all the spectral characteristics need to be studied on a system-by-system basis for possible use in NDI. These complexities make it necessary to construct a PLPS database and continue to study the physical basis for spectral characteristics. For this particular TBC, because of the observed systematic variation with cycles of the three spectral characteristics, they are candidates for use in non-destructive inspection and making remaining life predictions.

5.2 NiCoCrAlY Bond Coated TBC

During thermal cycling, several changes in the microstructure related to the failure of the TBC were observed: TGO growth, depletion of β phase in the bond coat, the TGO/BC interface rumpling, and formation of non-α-Al_2O_3 oxide in the embedded oxide. TGO growth increases the strain energy available for crack propagation. The formation of a non-α-Al_2O_3 oxide decreases the toughness of the TGO/bond coat interface. Although rumpling has been found to be responsible for the failure of (Ni,Pt)Al bond coated TBC in this study, no apparent damage was

observed in the MCrAlY bond coated TBC due to rumpling even though some rumpling occurred. We believe that these samples prevented from failing by rumpling because another failure mode occurred first. This result is consistent with a previous study on MCrAlY bond coated TBCs (*39*). Based on the observations that the failure interface is predominantly at the TGO/bond coat interface and the embedded oxides only account for a small fraction of the total failure area, the failure is initiated by debonding at ridge tops and followed by unstable fracture driven by the strain energy in the TGO.

The most surprising feature of this experiment is that the spallation lives for as-received and barrel finished specimens are comparable despite their surface roughnesses (Ra) differing by a factor of about 6. However, the curvature before and after finishing does not vary much, although the average roughness (Ra) does (Fig. 4.61). Therefore, based on equation (2.2), the critical TGO thickness for failure for as-received and barrel finished specimens should not vary much. This is what leads to the equivalent lives for the as-received and barrel finished specimens.

From this experiment, we can clearly see the significance of surface curvature in evaluating TBC life. Compared to Ra values based on averaging height information from the sample surface, the curvature map can give the localized curvature at every location of the sample surface. Curvature is better in evaluating TBC life since the failure of the TBC is not determined by average information from the whole specimen surface but by the size and geometry of localized flaws. Specifically, though as-received specimens contain large ridges and deep cavities, the feature size is large and the surface height changes slowly. Thus, the localized

curvature is relatively small. On the other hand, for barrel finished specimens, the height between peaks and valleys is less than that of as-received specimens, but, the feature size is small and the localized surface height changes rapidly. Thus the curvature is comparable to or even larger than in as-received specimens.

The reason that barrel finishing produces this kind of surface is that barrel finishing removes the high ridges, however, at the same time it increases small features such as sharp corners or sharp scratches. At these localized sharp corners or scratches with large localized curvature, the tensile normal stress increases rapidly and debonding occurs preferentially. Thus the standard surface roughness analysis, which uses a single number, such as average surface roughness (Ra) or peak to valley (Pv) to characterize the surface, can give misleading information in evaluating TBC life. Surface curvature maps, developed in this research, appear to be a superior tool in characterizing surface geometry and determining TBC life.

5.3 Comparison of (Ni,Pt)Al and NiCoCrAlY Bond Coated TBCs

(Ni,Pt)Al and NiCoCrAlY bond coats have individually characteristic compositions and microstructures. These differences result in distinct different TGO growth characteristics, as well as differing tendencies for plastic deformation (*8*). Accordingly, the failure mechanisms are often different. Specifically, the similarities and differences of the two TBCs studied in this research are summarized in Table 5.1. The oxide growth in both TBCs satisfies parabolic growth kinetics, suggesting that

oxide growth is diffusion controlled. Aluminum depletion occurs in both bond coats due to oxide formation and interdiffusion.

Most importantly, there are some distinct behaviors between the two TBCs. Failure mechanisms and associated failure modes of the two TBCs are different. In the (Ni,Pt)Al bond coated TBC, rumpling is responsible for the failure and the durability of TBC is determined by rumpling. In the NiCoCrAlY bond coated TBC, limited rumpling occurs and no apparent damage occurs due to rumpling. Failure is determined by strain energy stored in the TGO layer. In addition, non-α- aluminum oxide forms in the NiCoCrAlY bond coated TBCs, consistent with other studies (*31, 39*). Formation of non-α-Aluminum oxide is usually observed in the NiCoCrAlY bond coated TBCs, mainly due to aluminum depletion in the bond coat (see section **4.2.3**) and exhibits poor adherence to the bond coat (*15, 91-94*).

In addition to failure mechanisms, the PLPS behavior for the two TBCs is also different. Consistent with other studies, the TGO stress for the EB-PVD TBC on platinum-aluminide bond coats shows a consistent and monotonic decline (*30, 106*) after the initial transient period. The peak area ratio and standard deviation in the stress also show systematic changes with cycles. These spectral characteristics can be used for NDI and remaining life prediction.

In contrast for the EB-PVD NiCoCrAlY bond coated TBC, the TGO stress remains constant with cycling after the initial period. This is probably associated with the relative absence of bond coat rumpling and other forms of damage progression that the PLPS technique can detect.

Since failure mechanisms and PLPS behavior are different for the two TBCs, the life prediction method selected will also be different. The life prediction for (Ni,Pt)Al bond coated TBC is based on the measurement of the TGO stress. The life prediction for NiCoCrAlY bond coated TBC is based on the measurement of initial bond coat surface geometry, TGO stress and TGO thickness, and correlating these properties by fracture mechanics.

5.4 Use of PLPS For TBC Quality Control, Non-Destructive Inspection and Life Prediction

5.4.1 PLPS for Quality Control

As described in section **4.1.4.5**, θ-Al_2O_3 and α-Al_2O_3 can be detected by the PLPS method due to the fact that they have characteristic luminescence peaks easily distinguished in the spectra and the oxide distribution can be obtained from the area mapping. It has been proposed that the transformation from θ- to α-Al_2O_3 is responsible for additional residual stress from the volumetric shrinkage in the TGO and nucleation of tensile cracking (*35*). The oxidation study of bare (Ni,Pt)Al bond coated TBC in this thesis also shows that the phase transformation of oxide produces microcracks (see section **4.1.4.5**). In a previous study (*132*) of the effects of bond coat surface finish and heat treatment on TBC performance, the presence of a thin layer of continuous TGO comprising α-alumina prior to YSZ deposition was found to be favorable for producing durable TBCs. In addition, some PLPS measurements on as-coated vanes showed that the long-life vanes had a TGO consisting only of α-

alumina, while the short life vanes had a TGO consisting of both α- and θ-alumina (*102*). Based on these results, the formation of a "perfect" oxide that consist only of stable α-Al_2O_3 prior to deposition of YSZ may lead to improved durability and reliability of both stand-alone metallic coatings and TBC bond coats. Therefore, the ability of PLPS to non-destructively determine the oxide type and its uniformity makes it a very valuable quality control tool.

5.4.2 PLPS for Non-destructive Inspection

For the (Ni,Pt)Al bond coated TBC, the TGO stress and R_1 and R_2 peak area ratio show a monotonic decline (Fig. 4.31), and the standard deviation in the TGO stress shows a systematic increase (Fig. 4.33) with thermal cycles. These systematic changes of specific spectral characteristics can be used in NDI to detect early damage and damage progression. The most significant result is that TGO stress evolution is relatively independent of temperature as a function of life fraction in the studied temperature range (Fig. 4.34). Thus knowledge of local temperatures is not needed and this greatly simplifies the use of PLPS as a NDI tool for turbine coatings since the temperature can vary with a component and from component to component in engine service.

Bimodal spectra were observed during thermal cycling in the (Ni,Pt)Al bond coated TBC. The occurrence of bimodal spectra has been found to be directly associated with TGO cracking in this research. Early TGO damage such as cracks as small as microns can be detected using PLPS. The fraction of bimodal spectra initially increases sharply, then gradually decreases and increases again close to TBC

failure (Fig.4.40). The area maps of stress distribution based on bimodal spectra contribution give the visual record of the number and size of damage sites. Damage progression is apparent with thermal cycles, as shown in Fig. 4.41. Thus both the fraction of bimodal spectra and stress maps can detect damage progression and have the potential to assess TBC life remaining.

5.4.3 PLPS for Remaining Life Prediction

When TBC coated components are examined following field service, it is desirable to evaluate the condition of the coating to determine whether it can be reliably used until the next planned inspection. For (Ni,Pt)Al bond coated TBCs, remaining life predictions cycled at three temperatures were made for the first time based on the PLPS data without knowledge of the test temperature. The predictions using regression methods and neural network methods were compared. It was found that both methods produce accurate life remaining predictions, but the neural network methods were superior. The lowest RMS error for the oxide-based predictions using regression method and neural network method was 14.7% and 6.6% respectively. For a data set with a 34.6% RMS spallation life variation about the mean, the prediction results obtained are highly encouraging. Therefore, satisfactory remaining life predictions in a temperature blind manner are promising for this TBC.

5.4.4 PLPS for Life Prediction

The fact that there was no systematic change of spectral characteristics with thermal cycling for the NiCoCrAlY bond coated TBC makes it impossible to solely

use spectral characteristics to predict TBC life. However, the failure of this TBC was shown to relate to the strain energy in the TGO layer which is associated with the TGO stress, thickness and curvature of the bond coat surface. A life prediction method was developed based on the measurement of initial bond coat surface geometry, TGO stress and TGO thickness, and the correlation of these characteristics by fracture mechanics. The predicted lives correlated with experimental results within 15%. PLPS measurements of the TGO stress were used as input in this prediction approach. Since the TGO stress is highly dependent on specific the TBC system and its thermal history, non-destructive measurement of the TGO stress allows a more accurate calculation of the TGO strain energy than using approximate value calculated from thermal expansion mismatch.

5.4.5 Overall Assessment of The PLPS Technique

This research has shown that PLPS is an extremely powerful technique for TBC quality control, non-destructive inspection, assessment of remaining life and for use in life prediction. The spectral characteristics (frequency shift, i.e. the TGO stress and its standard deviation, peak area ratio, peak width and peak shape, and bimodal spectra fraction) and their change with thermal cycling can give information about damage initiation, progression and can be used in quality control, NDI, assessment of remaining life and life prediction.

A systematic methodology should be employed in using PLPS for a new TBC because it is clear that PLPS spectral characteristics are dependent on both composition and processing. Different spectral characteristics and their change with

thermal cycling can be used for different TBCs. The combined use of multiple characteristics may give improved results in some applications. So all spectral characteristics need to be studied for each new TBC for possible use in NDI and life prediction. In addition, determination of TGO spallation mechanisms will aid in the application of the PLPS spectral data.

Table 5.1. Comparison of (Ni,Pt)Al and NiCoCrAlY bond coated TBCs

	(Ni,Pt)Al TBC	NiCoCrAlY TBC
Similarities	Oxide growth satisfies parabolic kinetics	
	Aluminum depletion occurs in the bond coat due to oxide growth and interdiffusion	
Differences	Rumpling is responsible for failure	Rumpling is more limited and no apparent damage occurs due to rumpling
	No non-α-Aluminum oxide; No embedded oxides	Non-α-Aluminum oxide forms; Embedded oxides exists
	Failure at TGO/bond coat and TGO/TBC interfaces or within TGO	Failure primarily at TGO/bond coat interface
	Failure is determined by rumpling	Failure is determined by strain energy in TGO
	TGO stress decreases monotonically after initial transient period	TGO stress is constant after initial transient period
	Peak area ratio, standard deviation in stress, and fraction of bimodal spectra show systematic change with thermal cycles	No spectral characteristics show systematic change with thermal cycles

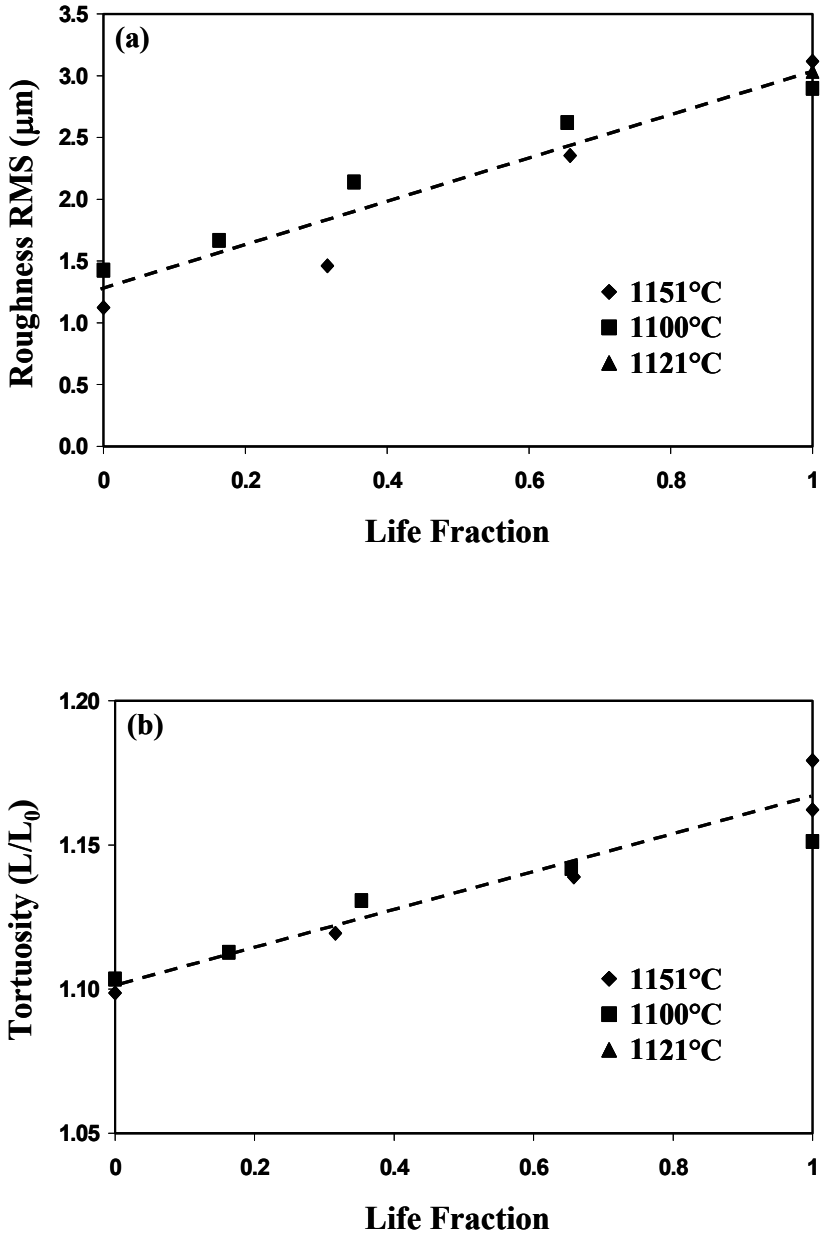

Fig. 5.1. (a) RMS roughness and (b) tortuosity as a function of life fraction

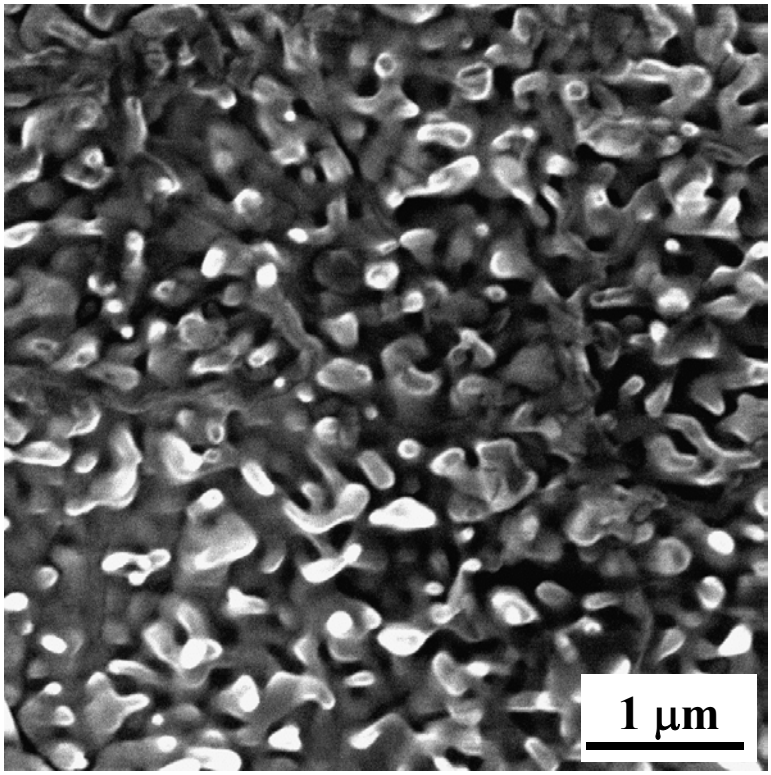

Fig. 5.2. Top view of alumina scale morphology after oxidation 10 minutes at 1151 °C showing whiskers

6. Summary and Conclusions

The major objectives of this research are to define failure mechanisms and to develop mechanism-based non-destructive life prediction methodologies for EB-PVD thermal barrier coatings. Moreover, the capabilities of Photoluminescence Piezospectroscopy (PLPS) in TBC quality control, non-destructive inspection for early damage, assessment of life remaining and for life prediction have been assessed in this research. It is shown that the two TBCs of this study exhibit different failure mechanisms, and therefore, different PLPS behavior. The selected life prediction methodologies are accordingly different. The life prediction for the (Ni,Pt)Al bond coated TBC is based on the systematic change of TGO stress with thermal cycles. The life prediction for the NiCoCrAlY bond coated TBC is based on measurements

of three properities: TGO stress, TGO thickness and bond coat surface geometry and the use of fracture mechanics. Specific conclusions of this research are as follows:

6.1 (Ni,Pt)Al Bond Coated TBC

1. The average spallation life decreases by a factor of five by increasing the cycling temperature from 1100°C to 1151°C.
2. Progressive rumpling initiates cracking and leads to spallation failure of TBCs. The durability of specimens is dominated by rumpling.
3. The rumpling amplitude increases with thermal cycles and rumpling rate increases with cyclic temperature. The rumpling amplitude at failure is almost the same at all three temperatures, suggesting a critical rumpling value drives spallation.
4. TGO growth satisfies parabolic growth kinetics at all three temperatures. The TGO growth rate increases with increasing cyclic temperature. The TGO thickness at failure is approximately constant at all three temperatures.
5. Rumpling is a single value function of TGO thickness, suggesting that TGO growth strains are critical to rumpling, and the TGO growth controls rumpling rate, which in turn controls spallation life.
6. The TGO stress decreases linearly with thermal cycles at all three temperatures. Longer life specimens show shallower slopes. Stress relaxation is mainly due to rumpling.
7. The TGO stress as a function of life fraction is relatively independent of temperature.

8. The relationships among rumpling rate, stress relaxation rate and spallation life are defined: as temperature increases, rumpling and stress relaxation rates increase, and spallation life decreases. The connection between TGO stress relaxation and specimen life provides a physical basis for use of TGO stress measurements as a non-destructive method for TBC damage initiation, damage progression, and life prediction.
9. The R_1 and R_2 peak area ratio decreases and the standard deviation of the TGO stress increases with thermal cycles. Peak width and Gaussian/Lorentzian fractions do not show systematic changes with thermal cycles. The spectral characteristics showing systematic change with thermal cycling can be used for NDI and determination of life remaining.
10. Bimodal luminescence originates from stress relaxation caused by TGO cracking. The degree of cracking increases initially as θ- transforms to α-Al_2O_3, then decreases as the cracks heal, and then increases again prior to spallation. Area stress maps, based on the bimodal luminescence and the average fraction of bimodal spectra with cycles, show damage progression and have the potential for non-destructive prediction of failure.
11. Temperature- blind remaining life predictions were made successfully based on TGO stress measurements at the three temperatures. The predictions were compared using regression and neural network methods. Both methods produce accurate life remaining predictions, but the neural network methods are superior.

12. The lowest root mean square error for life prediction using neural networks and regression methods was 6.6% and 14.7%, respectively. For a data set with a 34.6% RMS spallation life variation about the mean, the prediction results obtained are highly encouraging.

6.2 NiCoCrAlY Bond Coated TBC

1. Surface curvature mapping was developed for the first time to characterize surface geometry.
2. TGO stress increases initially and then remains constant until failure.
3. Initial damage occurs at localized debonds at the TGO/Bond Coat interface due to increasing out-of-plane tensile stresses. The spallation of the coating is driven by the strain energy stored in the TGO layer.
4. A life prediction methodology was developed based on the non-destructive measurement of three TBC parameters: bond coat surface geometry, TGO stress, and TGO thickness. A fracture mechanics methodology was used to correlate these three parameters. The predicted and actual lives agree within 15%.
5. Curvature maps are superior to Ra values in determining the life of thermal barrier coatings.

6.3 Use of PLPS for TBC Quality Control, Non-Destructive Inspection, and Life Prediction

1. It has been demonstrated that PLPS is an extremely powerful technique for TBC quality control, non-destructive inspection for early detection of damage, assessment of remaining life and for life prediction.
2. The behavior of PLPS spectral characteristics with thermal cycling is sensitive to both the composition and the processing of TBCs. All spectral characteristics need to be studied for each individual TBC for possible use in NDI and life prediction.
3. (Ni,Pt)Al and NiCoCrAlY bond coated TBCs exhibit different PLPS behaviors and failure mechanisms. Life prediction methods were developed for the specific observed failure mechanisms.

REFERENCES

1. R. A. Miller, *Surface and Coatings Technology* **30**, 1-11 (1987/1, 1987).

2. W. J. Brindley, R. A. Miller, *Advanced Materials and Processes* **136**, 29 (1989).

3. J. T. DeMasi-Marcin, K. D. Sheffler, S. Bose, *Journal of Engineering for Gas Turbines and Power* **112**, 521-526 (1990).

4. J. T. DeMasi-Marcin, D. K. Gupta, *Surface and Coatings Technology* **68/69**, 1-9 (1994).

5. T. E. Strangman, *Thin Solid Films* **127**, 93-105 (1985).

6. R. L. Jones, in *Metallurgical and Ceramic Protective Coatings* K. H. Stern, Ed. (Chapman & Hall, London, 1996) pp. 194-235.

7. S. M. Meier, D. K. Gupta, *Journal of Engineering for Gas Turbines and Power* **116**, 250-257 (January 1994, 1994).

8. A. G. Evans, D. R. Mumm, J. W. Hutchinson, G. H. Meier, F. S. Pettit, *Progress in Materials Science* **46**, 505-553 (2001).

9. N. P. Padture, M. Gell, E. H. Jordan, *Science* **296**, 280-284 (12 April 2002, 2002).

10. S. Bhattacharjee, U. Syamaprasad, R. K. Galgali, B. C. Mohanty, *Mater. Lett.* **15**, 281-284 (1992).

11. N. P. Padture *et al.*, *Acta Materialia* **49**, 2251-2257 (2001/7/17, 2001).

12. D. Zhu, R. A. Miller, *Surface and Coatings Technology* **108-109**, 114-120 (1998/10/10, 1998).

13. D.-M. Zhu, R. A. Miller, *MRS bulletin* **25**, 43-47 (2000).

14. H. E. Eaton, J. R. Linsey, R. B. Dinwiddie, in *Thermal conductivity 22* T. W. Tong, Ed. (Technomic, Lancaster, PA, 1994) pp. 289.

15. M. J. Stiger, N. M. Yanar, M. G. Topping, F. S. Pettit, G. H. Meier, *Z. Metallk* **90**, 1069-1078 (1999).

16. B. A. Pint *et al.*, *Materials Science and Engineering A* **245**, 201-211 (1998/5/1, 1998).

17. W. J. Brindley, R. A. Miller, *Surface and Coatings Technology* **43-44**, 446-457 (1990).

18. W. Lih, E. Chang, B. C. Wu, C. H. Chao, *Oxidation of Metals* **36**, 221 (1991).

19. W. Lih, E. Chang, C. H. Chao, M. L. Tsai, *Oxidation of Metals* **38**, 99 (1992).

20. A. G. Evans, M. Y. He, J. W. Hutchinson, *Acta Materialia* **45**, 3543-3554 (1997/9, 1997).

21. J. Cheng, E. H. Jordan, B. Barber, M. Gell, *Acta Materialia* **46**, 5839-5850 (1998/10/9, 1998).

22. M. Gell, K. Vaidyanathan, B. Barber, J. Cheng, E. Jordan, *Metallurgical and Materials Transactions A* **30A**, 427-435 (February 1999, 1999).

23. M. Gell *et al.*, *Surface and Coatings Technology* **120-121**, 53-60 (1999/11, 1999).

24. P. Kofstad, *High temperature corrosion* (Elsevier Applied Science, New York, 1988).

25. P. K. Wright, A. G. Evans, *Current Opinion in Solid State and Materials Science* **4**, 255-265 (1999/6, 1999).

26. P. K. Wright, *Materials Science and Engineering A* **245**, 191-200 (1998).

27. T. A. Cruse, S. E. Stewart, M. Ortiz, *Journal of Engineering for Gas Turbines and Power* **110**, 610-616 (October 1988, 1988).

28. S. M. Meier, D. M. Nissley, K. D. Sheffler, T. A. Cruse, *Journal of Engineering for Gas Turbines and Power* **114**, 258-263 (April 1992, 1992).

29. M. Wen, E. Jordan, M. Gell, *Materials Science and Engineering A* (2005).

30. S. Sridharan, L. Xie, E. H. Jordan, M. Gell, *Surface and Coatings Technology* **179**, 286-296 (2004/2/23, 2004).

31. M. Madhwal, E. H. Jordan, M. Gell, *Materials Science and Engineering A* **384**, 151-161 (2004/10/25, 2004).

32. D. Strauss *et al.*, *Surface and Coatings Technology* **135**, 196 (2001).

33. M. R. Brickey, J. L. Lee, *Oxidation of Metals* **54**, 237 (2000).

34. D. Toma, W. Brandl, U. Koster, *Surface and Coatings Technology* **120-121**, 8 (1999).

35. V. Tolpygo, D. R. Clarke, *Materials at High Temperatures* **17**, 59-70 (2000).

36. M. Wen, E. Jordan, M. Gell, *Surface and Coatings Technology* (2005).

37. C. Mennicke, D. R. Mumm, D. R. Clarke, *Z. Metallk* **90**, 1079-1085 (1999).

38. D. R. Clarke, R. J. Christensen, V. Tolpygo, *Surface and Coatings Technology* **94-95**, 89-93 (1997/10, 1997).

39. Y. H. Sohn, J. H. Kim, E. H. Jordan, M. Gell, *Surface and Coatings Technology* **146-147**, 70-78 (2001/0, 2001).

40. D. M. Lipkin, D. R. Clarke, *Oxidation of Metals* **45**, 267-280 (1996).

41. V. K. Tolpygo, J. R. Dryden, D. R. Clarke, *Acta Materialia* **46**, 927-937 (1998/1/23, 1998).

42. V. Sergo, D. R. Clarke, *Journal of the American Ceramic Society* **81**, 3237-3242 (1998).

43. V. K. Tolpygo, D. R. Clarke, *Acta Materialia* **46**, 5153-5166 (1998/9/1, 1998).

44. R. J. Christensen, D. M. Lipkin, D. R. Clarke, *Acta Materialia* **44**, 3813-3821 (1996/9, 1996).

45. C. Sarioglu, J. R. Blachere, F. S. Pettit, G. H. Meier, 1997.

46. E. Schumann, C. Sarioglu, J. R. Blachere, F. S. Pettit, G. H. Meier, *Oxidation of Metals* **53**, 259 (2000).

47. J. Rosler, M. Baker, M. Volgmann, *Acta Materialia* **49**, 3659-3670 (2001/10/26, 2001).

48. J. Cho, M. P. Harmer, H. M. Chan, J. M. Rickman, A. M. Tompson, *Journal of American Ceramic Society* **80**, 1013 (1997).

49. V. K. Tolpygo, D. R. Clarke, *Acta Materialia* **48**, 3283-3293 (2000/8/1, 2000).

50. M. Wen, E. Jordan, M. Gell, *Surface and Coatings Technology* (2005).

51. A. Evans, M. Y. He, J. W. Hutchinson, *Progress in Materials Science* **46**, 249-271 (2001).

52. A. Evans, J. W. Hutchinson, M. Y. He, *Acta Materialia* **47**, 1513-1522 (1999).

53. J. G. Smeggil, *Materials Science and Engineering A* **87**, 261 (1987).

54. D. K. Gupta, D. S. Duvall, *Superalloy 1982*.

55. B. A. Pint, *Oxidation of Metals* **48**, 303 (1997).

56. B. A. Pint, *Surface and Coatings Technology* **188-189**, 71-78 (2004/0, 2004).

57. J. L. Smialek, D. T. Jayne, J. C. Schaffer, W. H. Murphy, *Thin Solid Films* **253**, 285 (1994).

58. M. Gell, D. N. Duhl, D. K. Gupta, K. D. Sheffler, *journal of metals* **39**, 11 (1987).

59. U. Schulz, M. Menzebach, C. Leyens, Y. Q. Yang, *Surface and Coatings Technology* **146-147**, 117-123 (2001/0, 2001).

60. J. E. Schilbe, *Surface and Coatings Technology* **133-134**, 35-39 (2000).

61. U. Kaden, C. Leyens, M. Peters, W. A. Kaysser, paper presented at the TMS, Warrendale, OH 1999.

62. H. Lau, C. Leyens, U. Schulz, C. Friedrich, *Surface and Coatings Technology* **165**, 217-223 (2003/2/17, 2003).

63. D. Zhu, R. A. Miller, *Materials Science and Engineering A* **245**, 212-223 (1998/5/1, 1998).

64. S. Sridharan, L. Xie, E. Jordan, M. Gell, *Materials Science and Engineering A* **393**, 51-62 (2005).

65. D. R. Mumm, M. Watanabe, A. G. Evans, J. A. Pfaendtner, *Acta Materialia* **52**, 1123-1131 (2004).

66. R. A. Miller, C. E. Lowell, *Thin Solid Films* **95**, 265 (1982).

67. K. Vaidyanathan, M. Gell, E. Jordan, *Surface and Coatings Technology* **133-134**, 28-34 (2000/11, 2000).

68. E. P. Busso, J. Lin, S. Sakurai, M. Nakayama, *Acta Materialia* **49**, 1515 (2001).

69. A. Rabiei, A. Evans, *Acta Materialia* **48**, 3963 (2000).

70. K. W. Schlichting, N. P. Padture, E. H. Jordan, M. Gell, *Materials Science and Engineering A* **342**, 120-130 (2003/2/15, 2003).

71. X.-Y. Gong, D. R. Clarke, *Oxidation of Metals* **50**, 355-376 (1998).

72. C.-H. Hsueh, E. R. FullerJr., *Materials Science and Engineering A* **283**, 46-55 (2000/5/15, 2000).

73. A. G. Evans, G. B. Crumley, R. E. Demaray, *Oxidation of Metals* **20**, 193 (1983).

74. M. Y. He, A. G. Evans, J. W. Hutchinson, *Materials Science and Engineering A* **245**, 168-181 (1998).

75. K. Vaidyanathan, E. Jordan, M. Gell, *Acta Materialia* **52**, 1107-1115 (2004).

76. M. Y. He, A. G. Evans, J. W. Hutchinson, *Acta Materialia* **48**, 2593-2601 (2000/6/14, 2000).

77. V. K. Tolpygo, D. R. Clarke, *Acta Materialia* **46**, 5167-5174 (1998/9/1, 1998).

78. V. K. Tolpygo, D. R. Clarke, *Acta Materialia* **52**, 615-621 (2004/2/9, 2004).

79. V. K. Tolpygo, D. R. Clarke, *Acta Materialia* **52**, 5115-5127 (2004/10/4, 2004).

80. V. K. Tolpygo, D. R. Clarke, *Acta Materialia* **52**, 5129-5141 (2004/10/4, 2004).

81. A. M. Karlsson, A. G. Evans, *Acta Materialia* **49**, 1793-1804 (2001/6/13, 2001).

82. A. M. Karlsson, T. Xu, A. G. Evans, *Acta Materialia* **50**, 1211-1218 (2002/3/14, 2002).

83. A. M. Karlsson, J. W. Hutchinson, A. G. Evans, *Materials Science and Engineering A* **351**, 244-257 (2003/6/25, 2003).

84. R. Panat, S. Zhang, K. J. Hsia, *Acta Materialia* **51**, 239-249 (2003/1/8, 2003).

85. M. W. Chen, M. L. Glynn, R. T. Ott, T. C. Hufnagel, K. J. Hemker, *Acta Materialia* **51**, 4279-4294 (2003/8/15, 2003).

86. R. C. Pennefather, D. H. Boone, *Surface and Coatings Technology* **76-77**, 47-52 (1995/11, 1995).

87. D. R. Mumm, A. Evans, *Acta Materialia* **48**, 1815-1827 (2000).

88. D. R. Mumm, A. G. Evans, I. T. Spitsberg, *Acta Materialia* **49**, 2329-2340 (2001/7/17, 2001).

89. I. T. Spitsberg, D. R. Mumm, A. Evans, *Materials Science and Engineering A* **394**, 176-191 (2005).

90. M. Y. He, J. W. Hutchinson, A. Evans, *Acta Materialia* **50**, 1063-1073 (2002).

91. H. E. Evans, M. P. Taylor, *Oxidation of Metals* **55**, 17 (2001).

92. E. A. G. Shillington, D. R. Clarke, *Acta Materialia* **47**, 1297-1305 (1999/3/10, 1999).

93. B. C. Wu, E. Chang, S. F. Chang, D. Tu, *Journal of American Ceramic Society* **72**, 212 (1989).

94. E. Y. Lee, R. R. Biederman, R. D. Sisson, *Materials Science and Engineering A* **121**, 467-473 (1989).

95. J. I. Eldridge, C. M. Spuckler, J. A. Nesbitt, K. W. Street, *Ceramic Eng. Sc. Proc.* **24**, 511-516 (2003).

96. X. Chen, G. Newaz, X. Han, paper presented at the 2001 ASME Int. Mech. Eng. Congress, New York, NY 2001.

97. G. Newaz, X. Chen, *Surface and Coatings Technology* **190**, 7-14 (2005/1/3, 2005).

98. B. Jayaraj, V. H. Desai, C. K. Lee, Y. H. Sohn, *Materials Science and Engineering A* **372**, 278-286 (2004/5/15, 2004).

99. B. Jayaraj, S. Vishweswaraiah, V. H. Desai, Y. H. Sohn, *Surface and Coatings Technology* **177-178**, 140-151 (2004/1/30, 2004).

100. D. R. Clarke, *Current Opinion in Solid State and Materials Science* **6**, 237-244 (2002/6, 2002).

101. Q. Ma, D. R. Clarke, *Journal of the American Ceramic Society* **76**, 1433-1440 (1993).

102. M. Gell, S. Sridharan, M. Wen, E. Jordan, *International Journal of applied ceramic technology* **1**, 316-329 (2004).

103. K. W. Schlichting *et al.*, *Materials Science and Engineering A* **291**, 68-77 (2000/10/31, 2000).

104. R. J. Christensen, D. M. Lipkin, D. R. Clarke, *Applied Physics Letters* **69**, 3754-3756 (9 December 1996, 1996).

105. Y. H. Sohn, K. Vaidyanathan, M. Ronski, E. H. Jordan, M. Gell, *Surface and Coatings Technology* **146-147**, 102-109 (2001/0, 2001).

106. L. Xie, Y. Sohn, E. H. Jordan, M. Gell, *Surface and Coatings Technology* **176**, 57-66 (2003/0, 2003).

107. N. E. Paton, K. S. Murphy, D. R. Clarke, in *United States Patent*. (2000).

108. D. M. Lipkin, D. R. Clarke, *Journal of Applied Physics* **77**, 1855-1863 (1 March 1995, 1995).

109. J. He, D. R. Clarke, *Journal of the American Ceramic Society* **80**, 69-78 (1997).

110. J. He, D. R. Clarke, *Journal of the American Ceramic Society* **78**, 1347-1353 (1995).

111. D. M. Lipkin, H. Schaffer, F. Adar, D. R. Clarke, *Applied Physics Letters* **70**, 2550-2552 (12 May 1997, 1997).

112. X. Peng, D. R. Clarke, *Journal of the American Ceramic Society* **83**, 1165-1170 (2000).

113. J. A. Nychka, D. R. Clarke, *Surface and Coatings Technology* **146-147**, 110-116 (2001/0, 2001).

114. J. A. Nychka *et al.*, *Surface and Coatings Technology* **163-164**, 87-94 (2003/1/30, 2003).

115. Y. H. Sohn, K. Schlichting, K. Vaidyanathan, E. Jordan, M. Gell, *Metallurgical and Materials Transactions A* **31A**, 2388-2391 (September 2000, 2000).

116. A. Selcuk, A. Atkinson, *Materials Science and Engineering A* **335**, 147-156 (2002/9/25, 2002).

117. A. Selcuk, A. Atkinson, *Acta Materialia* **51**, 535-549 (2003/1/22, 2003).

118. D. M. Lipkin, D. R. Clarke, M. Hollatz, M. Bobeth, W. Pompe, *Corrosion Science* **39**, 231-242 (1997).

119. W. J. Moore, *Seven solid states* (W.A.Benjamin, Inc., New York, 1967).

120. J. H. Eggert, K. A. Goettel, I. F. Silvers, *Physical Review B* **40**, 5724-5732 (1989).

121. S. L. Wunder, P. E. Schoen, *Journal of Applied Physics* **52**, 3772-3775 (1981).

122. L. Grabner, *Journal of Applied Physics* **49**, 580-583 (1978).

123. A. A. Kaplayanskii, A. K. Przhevuskii, R. B. Rozenbaum, *Sov. Phys. Sol. State* **10**, 1864 (1969).

124. A. L. Schawlow, D. L. Wood, A. M. Clogston, *Physical Review Letter* **3**, 271-273 (1959).

125. R. A. Miller, *Journal of the American Ceramic Society* **67**, 517-521 (1984).

126. R. A. Miller, *Journal of Engineering for Gas Turbines and Power* **109**, 448-451 (October 1987, 1987).

127. E. H. Jordan *et al.*, paper presented at the Autotestcon, Valley Forge, PA 2001.

128. E.Dorre, H.Hubner, *Alumina-Processing, Properties and Applications,* (Springer-Verlag, New York, 1984)

129. G.M. Kim, N.M. Yanar, E.N. Hewitt, F.S. Pettit, G.H. Meier, *Scripta Mater.* **46,** 489-495 (2002)

130. V. Lughi, V.K. Tolpygo, D.R. Clarke, *Materials Science and Engineering A* **368,** 212-221 (2004)

131. D. Michie, D.J. Spiegelhalter, C.C. Taylor, *Machine Learning, Neural and Statistical Classification*, (Ellis Horwood, 1994), Chap. 7

132. J. Shen, *Thermal Barrier Coatings and Metallic Coatings with Improved Durability*, M.S. Thesis, University of Connecticut, Storrs, CT 2005

133. J.M. Ambrico, M.R. Begley, *Eng. Frac. Mech.* **70**, 1721, (2003)

134. J. W. Hutchinson, Z. Suo, in *Advanced Apply Mechanics,* J. W. Hutchinson, Y.Y. Wu Ed., (1992) pp. 63-191.

135. V.K. Tolpygo, D.R. Clarke, in: *Elevated Temperature Coatings: Science and Technology IV ,* N.B. Dahotre, J.M. Hampikian, J.E. Morral (Eds.), (TMS; 2001) pp.93-108

136. S. Sridharan, thesis to be finished

137. R.G. Munro, G.J. Piermarini, S. Block, W.B. Holzapfel, *J. Appl. Phys*. **57**, 165-169, (1985)

138. L.H. Tsoukalas, R.E. Uhrig, *Fuzzy and Neural Approaches in Engineering*, (John Wiley & Sons Inc., New York, 1997)

139. www.mathworks.com

140. Y. Bar-Shalom, X.R. Li, *Estimation and Tracking: Principles, Techniques and Software*, (Artech house, Dedham, MA, 1993)

141. N. Goldfine, D. Schlicker, Y. Sheiretov, in *Monitoring and Diagnostics Applications: ASME Turbo Expo Land, Sea & Air,* pp.1-9, (2001)

ENDWALL COOLING WITH ENDWALL CONTOURING AND LEADING EDGE FILLET

DOE Award Number: DE-FC26-02NT41431

UTSR Project Number: 02-01-SR098

Annual Report
June 2004-June 2005

Principal Investigator
Sumanta Acharya, Professor
acharya@me.lsu.edu

Collaborators
Gazi Mahmood, Ph.D., Research Associate
Arun Saha, Ph. D., Research Associate
Ross Gustafson, M. S student

Turbine Innovation and Energy Research (TIER) Center
Louisiana State University
Baton Rouge
Louisiana 70803

Administrative Office
James Bates, Director
Office of Sponsored Research
Louisiana State University
Baton Rouge, LA 70803

DISCLAIMER

This report was prepared as an account of work sponsored by an agency of the United States Government. Neither the United States Government nor any agency thereof, nor any of their employees, makes any warranty, express or implied, or assumes any legal liability or responsibility for the accuracy, completeness, or usefulness of any information, apparatus, product, or process disclosed, or represents that its use would not infringe privately owned rights. Reference herein to any specific commercial product, process, or service by trade name, trademark, manufacturer, or otherwise does not necessarily constitute or imply its endorsement, recommendation, or favoring by the United States Government or any agency thereof. The views and opinions of authors expressed herein do not necessarily state or reflect those of the United States Government or any agency thereof.

ABSTRACT

The potential of contouring the end wall and/or using a leading edge fillet to control secondary flows and heat transfer in blade passages is being investigated. Secondary vortical flows in blade passages enhance heat transfer to the end wall, and interfere with the film coolant jet. The goal of the ongoing project is to explore specific strategies of reducing in-passage secondary flows (contouring the end wall, placing a leading edge fillet, and strategically locating coolant injection) so that aerodynamic losses and thermal loading on the end wall is minimized.

The results here being reported are the work accomplished from June 2004 to June 2005 in continuation of the first two year's of activity. In the first two year's, attention had been focused primarily on: (1) setting up the atmospheric pressure cascade rig, (2) measurements and computations with leading edge fillets, and optimization of the leading edge fillet geometry and (3) computations with axi-symmetric contoured endwall profile. Results of these measurements and computations had been reported earlier. The present results include detail measurements and simulations in the linear blade passage employing a ***3-Dimensional non-axisymmetric contoured endwall with and without the full-coverage film cooling***. The data are obtained from: (i) experimental measurements with no film cooling, (ii) experimental measurements with film cooling, and (iii) computational simulations with no film cooling. Also, included are the numerical results showing optimization of the non-axisymmetric contoured endwall profile. The data with the film cooling reported here are measured with different inlet blowing ratios ranging from 1.0 to 2.4. None of the results have been reported in the previous annual reports, except the results with the flat endwall used here for comparison purposes only. The ongoing efforts are focused on experimental measurements and numerical simulations with film injections through the flat and axi-symmetric 2-Dimensional contoured endwall in vane and blade passages, and setting up a hot-cascade facility for measurements under more realistic conditions.

TABLE OF CONTENTS

Abstract……..3

Table of Contents……..4

List of Graphical Materials……..5

Introduction……...8

Executive Summary……..9

Project Description……..…11

Experiments & Results…..……13

Computations & Results……..……..27

Concluding Remarks……..29

References……...31

LIST OF GRAPHICAL MATERIALS

Fig. 1(a): Schematic of the cascade test facility and blade orientation in the test section.
Figure 1(b): Coordinate systems and flow analysis plane in the blade passage.
Figure 2(a): Curves employed to vary the pitchwise and streamwise heights of the experimental non-axisymmetric endwall profile.
Figure 2(b): Non-axisymmetric endwall profile height obtained from the curves in Fig. 2(a).
Figure 3: Blade wall static pressure coefficient at spanwise location Y/S=0.333 for the baseline and contoured endwall.
Figure 4: Endwall static pressure coefficient $C_{p,e}$ for baseline and contoured endwall.
Figure 5. Instantaneous flow visualization images in the plane PS1 for baseline and contoured endwall.
Figure 6. Instantaneous flow visualization images in the plane PS4 for baseline and contoured endwall.
Figure 7: Streamwise turbulence intensity in pitchwise plane at X_G/C_{ax}=0.085 for baseline and contoured endwall.
Figure 8: Streamwise turbulence intensity in pitchwise plane at X_G/C_{ax}=0.916 for baseline and contoured endwall.
Figure 9: Normalized axial vorticity, $\Omega_x C/U_{ref}$ in pitchwise plane at X_G/C_{ax}=0.085 for baseline and contoured endwall.
Figure 10: Normalized axial vorticity, $\Omega_x C/U_{ref}$ in pitchwise plane at X_G/C_{ax}=0.916 for baseline and contoured endwall.
Figure 11: Normalized pitchwise velocity, W/U_{ref} in pitchwise plane at X_G/C_{ax}=0.424 for baseline and contoured endwall.
Figure 12: Normalized pitchwise velocity, W/U_{ref} in pitchwise plane at X_G/C_{ax}=0.916 for baseline and contoured endwall.
Figure 13: Flow Yaw angle (degree) in pitchwise plane at X_G/C_{ax}=0.424 for baseline and contoured endwall.
Figure 14: Flow Yaw angle (degree) in pitchwise plane at X_G/C_{ax}=0.916 for baseline and contoured endwall.
Figure 15: Total pressure loss coefficient, $C_{pt,loss}$ in pitchwise plane at X_G/C_{ax}=0.085 for baseline and contoured endwall.
Figure 16: Total pressure loss coefficient $C_{pt,loss}$ in pitchwise plane at X_G/C_{ax}=0.916 for baseline and contoured endwall.
Figure 17: Normalized axial vorticity, $\Omega_x C/U_{ref}$ in pitchwise plane at X_G/C_{ax}=1.214 for baseline and contoured endwall.
Figure 18: Streamwise turbulence intensity in pitchwise plane at X_G/C_{ax}=1.214 for the contoured endwall.
Figure 19: Non-dimensional fluid temperature, θ in pitchwise planes near endwall at different axial locations for the contoured endwall with endwall heating at constant flux.
Figure 20: Nusselt number distributions on endwall along blade passage for baseline and 3D non-axisymmetric endwall.
Figure 21: Configuration of film cooling holes in contoured endwall and traverse locations of flow measuring probes relative to cooling holes.
Figure 22: Streamwise turbulence intensity in pitchwise plane at X_G/C_{ax}=0.085 for contoured endwall without and with film injection at inlet blowing ratios M_{in}=1.0 to 2.0.

Figure 23: Streamwise turbulence intensity in pitchwise plane at X_G/C_{ax}=0.424 for contoured endwall without and with film injection at inlet blowing ratios M_{in}=1.0 to 2.0.
Figure 24: Streamwise turbulence intensity in pitchwise plane at X_G/C_{ax}=0.916 for contoured endwall without and with film injection at inlet blowing ratios M_{in}=1.0 to 2.0.
Figure 25: Pitchwise mass-averaged streamwise turbulence intensity at X_G/C_{ax}=0.916 for contoured endwall without and with film injection at inlet blowing ratios M_{in}=1.0 to 2.4.
Figure 26: Overall mass-averaged streamwise and axial turbulence intensities as dependent upon inlet blowing ratio, M_{in} at X_G/C_{ax}=0.916 for contoured endwall with film injection.
Figure 27: Normalized axial vorticity, Ω_x*C/U_{ref} in pitchwise plane at X_G/C_{ax}=0.085 for contoured endwall without and with film injection at inlet blowing ratios M_{in}=1.0 to 2.0.
Figure 28: Normalized axial vorticity, Ω_x*C/U_{ref} in pitchwise plane at X_G/C_{ax}=0.424 for contoured endwall without and with film injection at inlet blowing ratios M_{in}=1.0 to 2.0.
Figure 29: Normalized axial vorticity, Ω_x*C/U_{ref} in pitchwise plane at X_G/C_{ax}=0.916 for contoured endwall without and with film injection at inlet blowing ratios M_{in}=1.0 to 2.0.
Figure 30: Normalized pitchwise velocity, W/U_{ref} in pitchwise plane at X_G/C_{ax}=0.424 for contoured endwall without and with film injection at inlet blowing ratios M_{in}=1.0 to 2.0.
Figure 31: Normalized pitchwise velocity, W/U_{ref} in pitchwise plane at X_G/C_{ax}=0.916 for contoured endwall without and with film injection at inlet blowing ratios M_{in}=1.0 to 2.0.
Figure 32: Total pressure loss coefficient, $C_{pt,loss}$ in pitchwise plane at X_G/C_{ax}=0.424 for contoured endwall without and with film injection at inlet blowing ratios M_{in}=1.0 to 2.0.
Figure 33: Total pressure loss coefficient, $C_{pt,loss}$ in pitchwise plane at X_G/C_{ax}=0.916 for contoured endwall without and with film injection at inlet blowing ratios M_{in}=1.0 to 2.4.
Figure 34: Pitchwise mass-averaged and overall mass averaged total pressure loss coefficient, $C_{pt,loss}$ at X_G/C_{ax}=0.916 for contoured endwall with and without film injection.
Figure 35: Non-dimensional fluid temperature, θ_f near endwall at X_G/C_{ax}=0.152 for contoured endwall with film injection at inlet blowing ratios M_{in}=1.0 to 2.0.
Figure 36: Non-dimensional fluid temperature, θ_f near endwall at X_G/C_{ax}=0.493 for contoured endwall with film injection at inlet blowing ratios M_{in}=1.0 to 2.0.
Figure 37: Non-dimensional fluid temperature, θ_f near endwall at X_G/C_{ax}=0.954 for contoured endwall with film injection at inlet blowing ratios M_{in}=1.0 to 2.0.
Figure 38: Computational domain and endwall grid geometry for baseline and contoured endwall
Figure 39: Endwall static pressure coeffis. for baseline and contoured endwall (computations)
Figure 40: Streamlines in pitchwise plane at X_G/C_{ax}=0.036 for baseline and contoured endwall.

Figure 41: Normalized axial vorticity $\Omega_x C/U_{ref}$ in pitchwise plane at X_G/C_{ax}=0.036 for baseline and contoured endwall.
Figure 42: Streamlines superimposed on normalized axial vorticity in pitchwise plane at X_G/C_{ax}=0.20 for baseline and contoured endwall (computations).
Figure 43: Streamlines superimposed on normalized axial vorticity $\Omega_x C/U_{ref}$ in pitchwise plane at X/C_{ax}=0.80 for baseline and contoured endwall (computations).
Figure 44: Total pressure loss coefficient $C_{pt,loss}$ in pitchwise plane at X_G/C_{ax}=0.80 for baseline and contoured endwall (computations).
Figure 45: Non-dimensional turbulent kinetic energy in pitchwise plane at X_G/C_{ax}=1.20 for baseline and contoured endwall (computations).

Figure 46: Streamlines and normalized axial vorticity $\Omega_x C/U_{ref}$ in pitchwise plane at X_G/C_{ax}=1.20 for baseline and contoured endwall (computations).
Figure 47: Total pressure loss coefficient $C_{pt,loss}$ in pitchwise plane at X_G/C_{ax}=1.20 for baseline and contoured endwall (computations).
Figure 48: Surface streamlines on the endwall for baseline and contoured endwall (computations).
Figure 49: Endwall Nusselt number Nu for baseline and contoured endwall (computations).

INTRODUCTION

Lean premixed combustors used in modern industrial gas turbine systems have relatively flat temperature profiles at the combustor exit. Thus, effective cooling strategy for the end walls has become increasingly important. Film cooling of the end walls is commonly employed. However, strong secondary flows in the vane/blade passage interfere with the injected coolant, and make effective cooling of the endwall a difficult problem. The secondary flows in the passage are driven by the development of the horseshoe vortex at the leading edge and the strong pressure gradients in the vane/blade passage. Therefore, for effective cooling of the endwall region, strategies for reducing or eliminating the passage secondary flows must be explored. *The ongoing work aims to investigate the strategies of endwall contouring and using leading edge fillets to suppress passage secondary flows. The work explores both uncooled and film-cooled end walls. Majority of the work for uncooled endwalls (flat end wall, filleted leading edge, and contoured end wall) and partial work for film cooled endwalls (non-axisymmetric endwall) have been completed. Experiments are currently underway for measuring the endwall film cooling effectiveness in a vane passage with axisymmetric endwall contouring and the film cooling effectiveness in a blade passage with flat endwall and non-axisymmetric end wall contouring.*

The end-goal of the project is to provide the turbine designer improved strategies for reducing the heat load to the endwall, and lowering aerodynamic losses. The results from the work will provide guidance for improved endwall designs leading to the lower utilization of coolant air, greater aerodynamic efficiency, and greater reliability. Results obtained indicate the potential of realizing the benefits in reducing losses and end wall thermal load.

EXECUTIVE SUMMARY

The potential of contouring the end wall and/or using a leading edge fillet to control secondary flows and heat transfer in vane/blade passages is being investigated. Secondary vortical flows in vane/blade passages enhance heat transfer to the end wall and interfere with the film coolant jet. The goals of the ongoing project are to explore specific strategies (contouring the end wall, placing a leading edge fillet, strategically locating coolant injection) so that secondary flows are minimized. Specific tasks include:

- Utilization of validated CFD to explore detailed flow physics, and to optimize leading edge fillet and end wall contouring parameters. The results of these parametric investigations are utilized in defining the experimental test matrix.
- Investigation of the effects of end-wall contouring on reducing secondary flows and thermal loading in the blade passage without end-wall cooling.
- Investigation of the effects of full coverage film cooling with strategically located film holes in the flat endwall in the blade passage.
- Investigation of the effects of end-wall contouring on reducing secondary flows in the vane/blade passage with film cooling. For the blade, non-axi-symmetric contouring is being explored, while for the vane, axi-symmetric contouring is being explored.
- To validate selected leading-edge contouring (fillet) configurations in a hot-cascade facility with realistic conditions for temperature ratios, turbulence conditions and pressure ratios.

Measurements and computations made so far have been in an atmospheric cascade facility with a blade geometry in the passage, and in a pressurized cascade facility with vane geometry in the passage. The measurements completed and reported here are on the blade passage with non-axisymmetric endwall contouring. Testing and measurements in the vane passage are underway. Present experimental results include qualitative and quantitative flow structures in the blade passage as well as flow temperature and endwall Nusselt number measurements in the blade passage. Results with leading edge fillets were reported earlier, and are not presented here. The present results include data with no film cooling flow and with full coverage film cooling flow at the non-axisymmetric endwall. The endwall geometry employed is contoured in both the axial and the pitchwise direction forming the non-axisymmetric profile. Numerical results have been obtained for several configurations of the non-axisymmetric contoured endwall. The optimum configuration based on the computational results is selected to be investigated experimentally.

The flow structure with the contoured endwall in the blade passage is determined with smoke flow visualization, and is quantified with five-hole pressure probe, and cross-wire anemometer measurements. Heat transfer coefficients are measured from infrared images in conjunction with thermocouples. Work done so far indicates that the contoured endwall reduces total pressure loss and end wall heat transfer coefficients across the passage compared to the baseline case. Through flow visualization and flow measurements one can conclude that the pressure and suction side leg of the horseshoe vortex and consequently the passage vortex reduce in size and strength with the contoured endwall. The total pressure losses are also reduced significantly compared to the baseline flat endwall case when the full coverage film cooling flow is introduced at the contoured endwall. Also, compared to the

case of the contoured endwall without any film flow, the total pressure losses are lower when the inlet blowing ratios are greater than 1.60 at the film cooled contoured endwall.

Numerical simulations show that heat transfer coefficients decrease significantly in the leading edge area and in the throat area with the optimized non-axisymmetric endwall contouring compared to the heat transfer at the flat endwall profile. Computations with contoured endwall are consistent with the measurements. Current efforts are aimed at measuring the cooling effectiveness of the full coverage film cooling in the contoured endwall and in flat endwall in conjunction with the leading edge fillets that area already tested. At the same time, numerical simulations are being performed to further optimize the present configuration of the film cooling holes. The projected benefits are the higher film cooling effectiveness and lower aerodynamic losses.

PROJECT DESCRIPTION

Gas Turbine Research Need

Secondary flows in blade passages contribute to increased aerodynamic losses, and increased heat transfer coefficients. These contribute to reduced efficiencies and increased cooling requirements. Therefore there is a clear need in the gas turbine community to reduce secondary flows. The ongoing research addresses this need through strategies aimed at reducing the formation and development of the horseshoe and passage vortices in the flow.

Experimental and Analytical Approach

The ongoing research includes both the experimental and computational effort. Both approaches are described in detail later. The experimental effort will be performed on three cascade facilities:

- An atmospheric cascade facility, with scaled up E^3 blades, which will permit detailed flow measurements and relatively easier modifications to accommodate a variety of end wall and leading edge contours. The detailed flow measurements are necessary for model validation in the computational effort. Measurements made include velocity measurements (using hot-wire anemometry, and five-hole pressure probe), heat transfer measurements (using Infra-red Imaging), flow temperature measurements (using a thermocouple probe), and surface static pressure measurements.
- A pressurized cascade facility, with E^3 vanes, which will permit heat transfer and flow measurements for a variety of contoured end wall sections with end wall film cooling. End wall heat transfer data will be collected with liquid-crystal or IR based techniques.
- A pressurized hot-cascade facility that will allow the simulation of realistic Mach numbers, Reynolds number, turbulence levels and length scales, and density ratios. The results from the atmospheric cascade tests and computations will define a more limited test matrix for this phase of study. Primarily surface heat transfer coefficient, cooling effectiveness, and pressures will be measured in this phase.

The computational work will primarily involve validated RANS approaches for predicting the in-passage flow and heat transfer. The goal of the computational effort is to make a detailed parametric study with different endwall and leading edge contours that will enable a more limited set of cases to be studied experimentally. Further, the simulations would provide additional information to help assess the flow and heat transfer behavior.

Expected Benefits

The goal of the project is to provide the turbine designer improved strategies for reducing the heat load to the end wall, and lowering aerodynamic losses. The strategies to be explored include contouring the end wall, placing a fillet along the leading edge of the blade, and strategically locating film cooling injection holes in the endwall. The results from the work will provide guidance for improved endwall designs leading to the lower utilization of coolant air, greater aerodynamic efficiency, and greater reliability.

Accomplishments

This report documents the results from the work accomplished during the period of June 2004 to June 2005. The following major activities were pursued during this time period:

Three Dimensional Non-axisymmetric Endwall Geometry-Atmospheric Cascade

Completed

- Flow-visualization of the passage vortex.
- Five hole probe measurements and hot-wire anemometer measurements at different axial chord planes for mapping the flow field with and without film cooling flow.
- Infrared thermal images of the heated endwall to obtain heat transfer coefficients.
- Validation of CFD results that provide optimization of the contoured endwall configuration.
- Preparation of two manuscripts for journal submission-one documents the computational flow structure and heat transfer results with contoured endwall and the other documents the flow and heat transfer measurements with film cooled contoured endwall. These manuscripts will be submitted to the ASME Tran. Journal of Turbomachinery, 2005. Two manuscripts on the work on the Leading Edge Fillets in the previous years have already been accepted in the ASME J. Transactions- one in the J. Heat Transfer (2005) and the other in the J. Fluid Engineering (2005). In addition, another manuscript on the work on Leading Edge Fillet comparing experiments and simulation is being prepared.

Ongoing

- Setting and modifications of the blade cascade test section to measure the film cooling effectiveness with film injections at the contoured endwall and at the flat endwall with leading edge fillets in blade passage.

Vane Cascade Geometry-Pressurized Cascade

Completed

- Construction of the vane cascade test facility with the E^3 first stage vane (scale 1:1) in a blow down high speed flow channel of cross section 8.93 cm by 3.81 cm. The cascade includes two passages with three vanes and is designed for the inlet to exit pressure ratio of about 2:1. The two-dimensional axi-symmetric contour endwall shape from the E^3 design and from computations is located upstream of the cascade inlet.
- A coolant loop that will supply coolant air to the vane test section has been completed. The loop is designed for providing the range of inlet blowing ratios from 1.0 to 2.0 and the coolant to main stream density ratio greater than 1.0.
- Necessary instrumentation (pressure taps, thermocouples, IR window, etc.) have been installed.
- The two passages in the cascade are aerodynamically balanced to simulate a periodic condition of the flow.

Ongoing

- Film cooling effectiveness measurements in a high speed vane cascade facility with axi-symmetric contoured endwall.

Hot Vane-Cascade Facility-Pressurized, Hot Cascade

Completed

- Lab renovation and installation of the required air handling capability needed for the hot cascade facility has been completed. The renovated labs have capability of 2600 SCFM and 150 psig pressure. In addition, a 200 psig natural gas line, and a 200 psig compressed water line has been installed for the pressurized cascade.
- The various components of the hot cascade facility and associated instrumentation have all been delivered by General Electric.

Ongoing

- The hot cascade test facility is being assembled.

Computations

Completed

- Numerical gridding and calculations of the selected vane/blade profile with the three dimensional endwall contours using GridPro and Fluent have been completed.
- Parametric explorations were performed with the numerical code for different three-dimensional endwall contours in the GE-E^3 blade passage. Eight different endwall contour cases were completed with incompressible flows.
- A final recommendation of a three-dimensional endwall contour was made for the experimental test program.

Ongoing

- Large Eddy Simulation of the blade-cascade flow geometry.

EXPERIMENTS & RESULTS

Atmospheric Cascade Facility

The experimental data presented here are obtained in a closed loop cascade facility that operates in a suction mode under atmospheric conditions. A schematic of the test facility is shown in Fig. 1(a). The construction of the facility allows air to flow through a two-dimensional nozzle of contraction ratio 3.4: 1, then through a smooth developing inlet channel of rectangular cross-section of aspect ratio 1.36:1 before entering the test section. The test section accommodates three two dimensional blades forming two blade passages. The two passages are made aerodynamically periodical by balancing the mass flow rate in the two passages by suitably positioning the two tailboards on the side blades with a traverse mechanism. The blade profiles are based on the hub side section of the GE-E^3 cascade geometry. The blade profile and passage configuration used in the study are scaled up ten times the actual blade geometry. The blades are oriented such that their stagnation planes are parallel to the mean flow stream in the inlet channel. Table 1 provides the geometry of the present cascade section and the flow conditions employed for the measurements. In the present arrangement, the data are measured with a flat smooth endwall at the tip side and a non-axisymmetric contoured endwall at the hub side of the blade cascade in the test section.

As shown in Figs.1 (a) and (b), the top wall of the test section has slots parallel to the passage inlet at different axial locations to allow access of the hot-wire probe and five-hole subminiature probe. During the heat transfer measurements on the bottom end-wall, this top wall is replaced

by another top wall of the same geometry with cut out sections for infrared image viewing. The bottom end-wall and the blade profiles are instrumented with thermocouples, foil heaters, and static pressures taps. The 0.30 mm diameter pressure taps are drilled in 1.65 mm diameter stainless steel tubes that are mounted flush in the grooves on the blade profile. The boundary layer suction bleeds in the top, bottom, and side walls of the inlet channel are adjusted to provide uniform flow conditions in the channel. A passive turbulence grid system made of cylindrical rods of diameter 1.22 cm is located 0.61 hydraulic diameter downstream of the nozzle exit or 4.12 chord upstream from the center blade stagnation point.

Pressure signals from the tubes and five-hole pressure probe are obtained in a HP3497A and in an Agilent 34970A data acquisition control unit through Validyne and Omega differential transducers. The five-hole subminiature probe, that has a tip diameter of 2.40 mm, is custom fabricated. Data acquisition rate with the five-hole probe is 240 Hz over a period of 60 sec through an Agilent 34970A^{TM} data acquisition control unit. The hot-wire sensors employed in the measurements are TSI^{TM} model constant cross-film anemometers. Signals from the hot-wire probes are obtained in a IFA-300^{TM} acquisition control unit. The data are acquired at the rate of 5.0 kHz over 13.1 sec and processed through the manufacturer supplied software.

Fig. 1(b) shows the locations of the flow measurement planes along with the coordinate systems employed in the cascade facility. The right hand (X_G,Y_G,Z_G) corresponds to the global coordinate system originated at the furthest upstream point on the center blade. The (X,Y,Z) then corresponds to the local coordinate systems inside the blade passages. The local velocity components (U,V,W) follow the local coordinate system (X,Y,Z). The measurement planes inside the passages are normal to the X_G- or X-direction.

Non-axisymmetric 3-Dimensional Contour Endwall

The non-axisymmetric contoured wall profile employed at the bottom endwall for the present measurements and computations in the blade passage is shown in Fig. 2. The top endwall remains always flat without any contouring as mentioned. The profile height varies in the pitchwise direction as well as in the axial direction. The design of the profile is based on the concept proposed in Ref. [1-5]. Several endwall profiles with the pitchwise profile-height and the axial profile-height varied by independent sinusoidal profiles were simulated numerically. The final profile chosen for the experimental study was based on the best numerical results that provide the lowest total pressure loss and endwall heat transfer along the passage.

Fig. 2(a) shows the independent sinusoidal curves chosen separately for the pitchwise and axial variations of the selected endwall profile employed for the experimental measurements. Height=0.0 mm refers to the location of the baseline flat endwall. Pitchwise height in Fig. 2(a) is flattened near the pressure side (for manufacturing ease) and is the lowest near the suction side where the two sine curves coincide. The two profile variations are then simply multiplied to obtain the non-axisymmetric profile heights shown in Fig. 2(b). The maximum height of the complete profile is located slightly downstream of the leading edge. The lowest trough in the profile is located across the maximum height in the pitchwise direction and near the suction side. The entire endwall was fabricated on a stereo-lithography printer in the Mechanical Engineering Department at LSU.

Upstream Flow Conditions of the Test Section

The reference properties for normalizing the measured quantities in the passage are measured across a plane parallel to the passage inlet. Computational data at the same location are used to normalize the numerical results. This reference plane is located 0.33C upstream of the passage inlet. The reference properties are then obtained from the arithmetic mean of the local data in the reference plane and shown in Table 2. In the table, conditions below atmospheric pressure refer to negative gage values.

Surface Static Pressure Coefficeint

Surface static pressures are measured on the blade surface and on the contoured endwall itself. Figure 3 presents the surface static pressure coefficients on the blade surface. The baseline data are included for comparison. Blade surface static pressure coefficients are determined from the equation as follow.

$$C_p = \frac{P_{stat} - P_{stat,o}}{0.5 * \rho_{air} * U_{ref}^2} \tag{1}$$

In the equation, P_{stat} is the measured wall static pressure at Y/S=0.333, $P_{stat,o}$ is the measured wall static pressure on the leading edge at Y/S=0.333, ρ_{air} is air density, and U_{ref} is reference velocity from Table 2. The surface coordinate s/C originates from the blade trailing edge at the suction side and the stagnation point is located at s/C∼1.50. Note, that the Y/S=0.0 for the endwall contour data refers to the location of the baseline endwall. The peak and trough locations on the contour endwall are located at Y/S=0.096 and -0.101 relative to the baseline endwall location. The C_p values in Fig. 3 are about the same for the endwall contour case and the baseline case on the pressure data. The C_p values further downstream on the suction side at s/C<0.90 for the contoured endwall are nearly identical or only slightly higher than for the baseline. This illustrates that the effects of the endwall profile on the flow in the free stream inviscid regions are very weak.

Endwall static pressure coefficients $C_{p,e}$ are presented in Fig. 4 and are determined from the following equation.

$$C_{p,e} = \frac{P_{s,w} - P_{stat,r}}{0.5 * \rho_{air} * U_{ref}^2} \tag{2}$$

Here, $P_{s,w}$ is endwall static pressure and $P_{stat,r}$ is the reference static pressure from Table 2. The difference in $C_{p,e}$ from the pressure side to suction side reduces significantly for the contoured endwall as compared to the baseline. For example, the maximum differences in $C_{p,e}$ at X_G/C_{ax}=0.20 and 0.70 between the pressure side and suction side are 1.60 and 1.40, respectively, for the baseline. At the same locations, the differences are 0.90 and 1.20, respectively, for the contoured endwall. Such differences in $C_{p,e}$ in the pitchwise direction for the contoured endwall significantly decrease upstream of the throat at X_G/C_{ax}<0.70. This can be considered a significant achievement toward weakening the secondary flows near the endwall. The cross-pitch pressure gradient is one of the primary sources for the development and energizing of the passage vortex near the endwall upstream of the throat [6-8].

Instantaneous Flow Visualization

Qualitative comparison of the secondary flow structure i.e., vortex location, size, and shape for the baseline and contoured endwall case are provided in the instantaneous images of flow visualization with smoke in Figs 5 and 6. The smoke in the channel is generated by applying coats of toy train liquid smoke on Nichrome wires (diameter 24 gage, 0.051 cm), which are then heated by passing controlled dc current through them. The wires are located about 1.5C upstream of the passage inlet and span across the width of the inlet channel. When air flows through the channel, plane sheets of white smoke are generated from nine wires that are placed both inside and outside the boundary layer upstream of the blade passage. As the sheets of smoke approach the passage, they contour according to the shape and size of the secondary flows. A plane sheet of light generated with a 2000 watts theatrical lamp shinning through a thin slot over the channel top wall illuminates the smoke patterns inside the passage. The images are captured and recorded by a SONY DFW-V500 digital video camera and image capturing software provided by the camera manufacturer. Images are captured at a frame rate of 60 Hz with 640x480 lines of resolution. The images are then further enhanced in Adobe Photoshop™ v8.10. The relative positions of the camera and light plane where the smoke flow pattern is illuminated are shown in Fig. 5. The camera focuses approximately normal to the light planes. The relative position of the camera changes as the location of the light plane changes. In Figs. 5 and 6, the endwall is located at the bottom, the pressure side is on the right, and the suction side is on the left of the image. Images in the two light planes PS1 and PS4 are presented here. More flow visualization instant images in other light plane locations were presented in the Semi-Annual Report for May 2004-December 2004 of the same project.

Figure 5 shows the secondary vortex patterns in the pitchwise plane PS1 which is located at X_G/C_{ax}=0.167 and slightly downstream the blade stagnation line. In the baseline image, two large vortex structures originating from the pressure side leg of the leading edge horseshoe vortex can be seen midway between the pressure side and suction side. This vortex pair rotates in the clockwise sense and periodically merge together to form one large vortex with the same sense of rotation. For the contoured endwall, the clockwise rotating vortex structures, also identified as originating from the pressure side leg vortex pair, are located just above the endwall but the individual vortices are separated far apart-one appears near the pressure side and the other is seen near the suction side. Their size is reduced significantly compared to the baseline vortex pair. Unlike the baseline case, this pair remains separated at relatively the same location. The pressure side leg vortex pair for the contour endwall case is smaller because the endwall structure along the leading edge plane displaces the boundary layer fluid reducing the boundary layer thickness and leading edge horseshoe vortex size. This occurs as the flow accelerates along the leading edge plane as the endwall height increases toward the leading edge (refer to Fig. 2(b)) forcing the incompressible fluid to be removed from the boundary layer due to the continuity. The clockwise rotating vortex pair of the pressure side leg remains separated on the contoured endwall in Fig. 5 as one horseshoe vortex forms at the leading edge of the contour endwall and the second one forms far apart at the junction of the blade leading edge and endwall. The smaller pitchwise pressure gradient and consequently the weaker pitchwise cross flow for the contour endwall case than the baseline are not strong enough to bring the vortex pair close together as the vortices advect inside passage along with the cross flow. Also note in

Fig. 5, the presence of a small counter-clockwise rotating vortex on the left and adjacent to the large vortex pair for the baseline case. The size of this single vortex is nearly one-third of the large vortex pair for the baseline. This is the suction side leg of the leading edge horseshoe vortex. The suction side leg vortex also appears above the contoured endwall but is located just above pressure side leg vortex near the suction side. The suction side leg vortex is comparable in size for both the endwall cases.

The visualization plane PS4 (nearly perpendicular to both the pressure and suction side) is located near the passage throat region. The baseline case shows two large structures of the passage vortex system rotating clockwise which again periodically merge into one large vortex having the same sense of rotation. Both the vortices are located near the suction side of the passage and little evidence of any smoke is present near the pressure side. This occurs as the strong cross flow and high pressure gradient at the flat endwall region sweep the pressure and suction side leg vortices toward the passage suction side as they travel inside the blade passage [6, 8]. Even at such a far downstream location as PS4, the contoured endwall in the left image of Fig. 6 shows the two pressure side leg vortex structures rotating clockwise are still far apart. One of the legs is situated on the endwall where the flat profile starts to dip down near the pressure side while other is situated just above the lowest location of the endwall near the suction side. This further illustrates that the contoured endwall reduces the pressure gradient and cross flow from the pressure side to suction side. Near the suction surface for the contoured endwall case of Fig. 6, the curling smoke pattern located above the pressure side leg vortex is the suction side leg vortex that rotates counter-clockwise. In comparing the sizes of the clockwise rotating vortices, the vortices above the contour endwall are nearly half of those above the flat baseline endwall.

Time-averaged Secondary Flow Field (No Coolant Flow)

The Time-averaged secondary flow field is measured for the contoured endwall case at four pitchwise planes (Plane 2, 3, 4, 5) located at four axial distances as shown in Fig. 1(b). The planes are parallel to the inlet and exit planes of the passage. Flow field measurements in the four planes are obtained at a reference velocity of 10.10 m/s. The measured quantities provide axial development of the total pressure loss, axial vorticity, pitchwise cross flow velocity, and streamwise turbulence intensity along the passage. These data are presented in the non-dimensional forms in this section along with the data for the baseline case. Total pressure loss coefficient $C_{pt,loss}$ is determined from the following equation. In this equation, P_t is the measured local total pressure and $P_{tot,r}$ is the reference pressure from Table 2.

$$C_{pt,loss} = \frac{P_{tot,r} - P_t}{0.5 * \rho_{air} * U_{ref}^2} \tag{3}$$

The axial vorticity Ω_x is determined from the derivatives of the spline fits on the local velocity data and from the following equation. V is velocity in spanwise direction and W is velocity in pitchwise direction.

$$\Omega_x = \frac{\partial W}{\partial Y} - \frac{\partial V}{\partial Z} \tag{4}$$

Figure 7 shows streamwise turbulence intensity in the plane at X_G/C_{ax}=0.085 for the baseline and contour endwall. The turbulence intensity values are much higher just above the baseline endwall for Z/P>-0.40 compared to the values at the same location for the contoured endwall. The high turbulence intensity just above the endwall is caused by the pressure and suction side leg vortices at this location. The data in Fig. 7 suggest that the vortices are much weaker and smaller for the contoured endwall. The streamwise turbulence intensity at X_G/C_{ax}=0.916 near the exit plane in Fig. 8 shows that it decreases significantly at 0.10<Y/S<0.22 and -0.65<Z/P<-0.55 with the contoured endwall as compared to the baseline case. The passage vortex at this location near the suction side (Fig. 8) causes the high turbulence intensity. Clearly, the passage vortex is weaker for the contoured endwall as indicated by the smaller magnitudes of the turbulence intensity.

Normalized axial vorticity $\Omega_x C/U_{ref}$ for the baseline and contoured endwall at X_G/C_{ax}=0.085 is compared in Fig. 9. The high negative $\Omega_x C/U_{ref}$ between -0.70<Z/P<-0.55 and positive $\Omega_x C/U_{ref}$ between -0.45<Z/P<-0.33 above the baseline endwall indicate strong suction side leg and pressure side leg vortex regions. Such high negative or positive $\Omega_x C/U_{ref}$ region is absent or much smaller above the contoured endwall in Fig. 9 indicating weaker and smaller vortex structures. Normalized axial vorticity near the trailing edge shown in Fig. 10 indicates that a much larger region and higher magnitude of $+\Omega_x C/U_{ref}$ is present above the baseline endwall than above the contoured endwall near the suction side. The high $\Omega_x C/U_{ref}$>6 region refers to the passage vortex location (contour level arbitrarily selected), and clearly, the contour endwall reduces the size and strength of this vortex significantly. However it should be noted that because of the three dimensional nature of the passage vortex, the center location and magnitude of axial vorticity are dependent upon the axis of rotation of the passage vortex. Thus, a quantitative conclusion on the vortex center or core location based on the results in Fig. 10 should be done with caution. A small negative $\Omega_x C/U_{ref}$ region exists above the passage vortex region near the suction side and represents the suction side leg of the horseshoe vortex. This negative region for the contoured endwall is about half the size of that for the baseline.

Pitchwise velocities indicating the cross flow from the pressure side to suction side are compared in Figs. 11 and 12 with negative magnitudes of W/U_{ref} velocity directed toward the suction side. Near the endwall at X_G/C_{ax}=0.424 in Fig. 11, the baseline case has a larger and stronger cross flow region with W/U_{ref} of lower negative magnitudes compared to the contoured endwall case. Near the contoured endwall in Fig. 11 the cross flow reduces because of the smaller surface pressure gradient as shown in Fig. 4. Normalized pitchwise velocities at X_G/C_{ax}=0.916, shown in Fig. 12, are much larger in magnitude for the contoured endwall case than for the baseline near the suction side. Pitchwise velocity reduces near the suction side when it encounters the clockwise rotating passage vortex. Stronger pitchwise velocities exists near the suction surface up to Y/S = 0.10. This indicates a larger region of cross-flow. As this cross-flow region approaches the suction surface its spanwise component becomes stronger in the positive Y/S direction, pushing the passage vortex up. The contoured endwall in Fig. 12 also shows a smaller cross flow region with W/U_{ref}<-1.30 between -0.82<Z/P<-0.30 compared to the baseline case. This causes the passage vortex for the contoured endwall to be located lower than that for the baseline case.

Flow yaw angles in Figs. 13 and 14 show the turning of the cross-flow relative to the axial direction. Positive and negative yaw angles indicate the flow turning counter-clockwise and clockwise, respectively, from the +X direction as shown in Fig. 1(b). Thus, the higher yaw angles indicate a stronger cross-flow component in the pitchwise direction. The yaw angles at

X_G/C_{ax}=0.424 in Fig. 13 decrease by about 15 deg, and at X_G/C_{ax}=0.916 in Fig. 14 the yaw angles decrease by about 20 deg near the contoured endwall relative to those near the baseline endwall. The pitchwise component of the cross-flow in the endwall boundary layer region funnels fluids into the passage vortex and strengthens it (refer to Figs. 10 to 12). Thus, the results in Figs. 13 and 14 signify that the secondary flows for the contoured endwall must have weakened. Also, note that the yaw angle magnitudes in the inviscid regions of Figs. 13 and 14 are more uniform in the pitch-direction for the contoured endwall than for the baseline. Particularly, the results at X_G/C_{ax}=0.916 in Fig. 14 show a significant improvement with the contoured endwall with more uniform exit flow angles.

Figure 15 compares the total pressure loss coefficients at X_G/C_{ax} = 0.085 for the baseline and contoured endwall. The left side of the figure is the suction side and the right side for the baseline case is located roughly at the pitchwise middle position in the plane. A higher $C_{pt,loss}$ region exists just above the endwall near the suction side between -0.65<Z/P<-0.45 for the baseline than for the contoured endwall. This region indicates the presence of a strong suction side leg of the horseshoe vortex for the baseline. $C_{pt,loss}$ for the contoured endwall are about 29.0% smaller in the region corresponding to the suction side leg vortex. The total pressure loss coefficient $C_{pt,loss}$ contours in Fig. 16 show that the high loss magnitudes representing the passage vortex are elevated from the endwall and shift closer to the suction side. This occurs as the passage vortex is driven by the cross flow. Here also, the contoured endwall reduces the size and magnitudes of the high $C_{pt,loss}$ in the passage vortex. The $C_{pt,loss}$ values are about 37% less in the core of the passage vortex region for the contoured endwall than for the baseline.

Measured flow field downstream of the cascade in the pitchwise plane at X_G/C_{ax}=1.214 is presented in Figs.17 and 18. The plane extends one complete pitch in the pitchwise direction. The complete structure of the passage vortex can be seen in the $\Omega_x C/U_{ref}$ and turbulence intensity contours in the figures between Y/S=0.10 and 0.30. The magnitudes of $\Omega_x C/U_{ref}$ >0.0 region in Fig. 17, which is caused by the passage vortex, is considerably reduced by the contoured endwall. The negative $\Omega_x C/U_{ref}$ regions above the passage vortex and about Z/P=-0.37 above the endwall represent the suction side leg/induced vortex and corner vortex[6]. These vortex structures are also reduced by the contoured endwall. In Fig. 17, the contour region of $-6<\Omega_x C/U_{ref}<-2$ is caused by the trailing edge wake. In Fig. 18, the streamwise turbulence intensity greater than 9% about Z/P=-0.37 is caused by the passage vortex and wake for the contoured endwall case. The high turbulence intensity just above the endwall is located at the same location where the high axial vorticity for the corner vortex occurs. The highest turbulence intensity between Y/S=0.15 and 0.30 is located at the core of the passage vortex where the total pressure losses are found to be the highest for the contoured endwall.

Non-dimensional Flow Temperature (No Coolant Flow)

Non-dimensional temperature profile of the air stream along the contoured endwall passage is shown in Fig.19. The contour values θ are determined from the following equation where $T_{o,in}$

$$\theta = \frac{T - T_{o,in}}{0.5 * U_{ref}^2 / C_p} \tag{5}$$

is the reference temperature from Table 2, T is local air stream temperature, and C_p is specific heat of air at constant pressure. The air stream in the passage is heated by heating the bottom endwall both upstream and inside the passage with a constant heat flux boundary condition of

magnitude 1600 W/m^2. Copper strips of width 5.0 mm soldered in a serpentine pattern are laid on the contoured endwall at 1.0 mm spacing and then are heated by passing controlled DC current. The upstream endwall is heated using commercially available Kapton^{TM} encapsulated air heater. A Chromel-Constant thermocouple (type-E) probe of tip diameter of 0.50 mm is traversed along the pitchwise plane to measure the air stream temperature.

The θ value at X_G/C_{ax}=0.152 in Fig. 19 is high above the endwall at -0.60<Z/P<-0.40 because of the presence of suction side leg vortex. The vortex flow mixes the near wall hot fluid with the cold main stream fluid and raises the mainstream air temperature. As the vortex structures grow downstream of the passage, the region of the heated air stream or high θ values also grow larger which is evidenced at X_G/C_{ax}=0.493. The region of high θ values is about the same size as the passage vortex region near the suction side and endwall junction. The region of high θ grows further at X_G/C_{ax}=0.954 in Fig. 19, and is elevated from the endwall as the passage vortex lifts upwards.

Heat Transfer Coefficient on the Endwall (No Coolant Flow)

Heat transfer measurements on the contoured endwall are obtained with the same heater arrangement as is used for air stream temperature measurements. Nusselt numbers on the endwall are computed from the time averaged infrared images and thermocouple data. Temperature from the thermocouples embedded in the endwall is used for the insitu calibration of the infrared images. One-dimensional energy balances are used to compute the conduction heat loss from the endwall. Infrared images are captured by a Raytheon Radiance HS 2012 camera at a frame rate of 33.3 Hz through a Zinc-Selenide window placed on the channel top wall. The images are recorded in the gray scale form of 12 bit/pixel in 256x256 pixel resolution. The pixel gray scale values then converted to local Nusselt numbers applying the insitu calibration data obtained during the infrared image data acquisition. Nusselt number is computed from the following equation where C is blade actual chord length, T_{wall} is end-wall temperature measured from the infrared images, $T_{o,in}$ is reference temperature from Table 2, and k_{air} is thermal conductivity of air at the temperature $T_{o,in}$.

$$Nu = \frac{q''_{conv} * C}{\left(T_{wall} - T_{o,in}\right) * k_{air}} \tag{6}$$

The convective heat flux q''_{conv} from the strip heaters is given by $q''_{conv} = \left(V * I - Q_{cond}\right) / A_{heater}$. Here, V is voltage drop across heater, I is current through heater, A_{heater} is heater area, Q_{cond} is one dimensional conduction loss through the end-wall. Radiation losses to the surrounding are assumed to be negligible as the wall temperature varies between 35 ^{o}C and 55 ^{o}C, and hence, is not accounted for in the Nu computation. Measured one dimensional conduction loss is small, 1.5% of the total power input for the baseline endwall and 7.0% of the total power input for the contoured endwall case. Thus, a constant heat flux boundary condition is assumed for the Nu calculation. A_{heater} in the above equation is based on the actual area of the contoured endwall. The input heater power level for the contoured endwall case is about twice of that for the baseline case. The convective heat flux q''_{conv} is 900 W/m^2 for the baseline and 1650 W/m^2 for the contoured endwall.

Figure 20 presents Nusselt number distribution along the contoured endwall. For the comparison, the baseline measurement is also included. The effects of the contoured profile of endwall on Nu are clearly distinguishable as the Nu are smaller everywhere upstream of the

throat region for the contoured endwall than for the baseline. Nu are significantly smaller at $X_G/C_{ax}<0.50$ for the contoured endwall. This occurs as the suction side leg vortex and passage vortex are considerably reduced in size and strength in this region of the contoured endwall. As evidenced, the legs of high Nu contours starting at the leading edge regions of both pressure and suction side of the baseline endwall are reduced considerably on the contoured endwall. Nusselt numbers are also much smaller at $0.60<X_G/C_{ax}<0.85$, which is the throat region, for the contoured endwall than for the baseline.

Film Cooling Hole Configuration (Contoured Endwall) and Coolant Supply Circuit

The geometric configuration of the film cooling holes is shown in Fig. 21(a) and is adopted based on input from the gas turbine industry. The same configuration is used for the baseline flat endwall and non-axisymmetric contoured endwall. The cylindrical coolant holes are oriented at 30 deg relative to the tangent on the surface profile. The orientation of the hole at the coolant ejection side is directed approximately along the inviscid local streamwise direction. The holes are 5.0 mm in diameter and machined in a 19.0 mm thick acrylic plate for the flat baseline endwall. The non-axisymmetric contoured endwall are fabricated with a stereo-lithography printer at LSU. The coolant holes are integrally fabricated during the lithography process. The same end-wall contour profile as in Fig. 2 is employed for the film cooling measurements. The thickness of the contoured endwall is 19.0 mm in the vertical direction. Therefore, the hole length-to-diameter ratio for baseline endwall is constant and 7.6, while it varies for the contoured endwall depending on the location of the a hole in the endwall. The coolant to the test section is supplied from a plenum located below the end wall.

Results presented in Figs. 22 to 37 include flow field and air stream temperature measurements. Figure 21(a) shows the axial location of the pitchwise planes where the measurements are obtained with the five-hole pressure probe, hot-wire probe, and thermocouple probe. Six inlet blowing ratios between Min=1.0 and 2.4 are employed for the measurements. The following table shows the test matrix which was completed for the film cooling measurements on the contoured endwall. Presently, the infra-red measurements of the film cooling effectiveness on the contoured endwall are underway. The inlet blowing ratio, M_{in} in the table below is determined based on the definition in [9].

$$M_{in} = \sqrt{\frac{P_{o,plenum} - P_{stat,r}}{P_{tot,r} - P_{stat,r}}} \tag{7}$$

In Eq. (7), $P_{stat,r}$ and $P_{tot,r}$ are the reference quantities from Table 2, and $P_{o,plenum}$ is the measured total pressure in plenum box for film cooling. The temperature difference between the main air stream and the coolant is maintained at about 0.0 ^oC and 20.0 ^oC during flow structure measurements and air stream temperature measurements, respectively. The endwall is unheated and maintained at the adiabatic condition as the thermal conductivity of the endwall material (which has a commercial name ABS plastic) is very low. The same ambient air as the main channel flow is used for the film cooling flow. As shown in Fig. 21(b), the ambient air is blown with a small blower of capacity 3.0 m^3/min in a secondary supply circuit where the air passes over two heat exchangers cooled by the chiller water. The cold air is then blown in the plenum box and then throug the film cooling holes. Mass flux of the film cooling flow and

consequently, the plenum pressure can be controlled by adjusting the blower speed with a dc power supply. The minimum temperature of the coolant flow thus achieved is 10.0 ^{o}C, but the coolant air density ρ_c is nearly the same as the main air stream density ρ_{air} for all the blowing ratios.

Measurement Test Matrix for Contoured Endwall with Film Cooling (Accomplished)

Measurement location	Five-hole probe measurement (I)	Hot-wire probe measurement (II)	Thermocouple probe measurement (III)
X_G/C_{ax}=0.085 (I, II) X_G/C_{ax}=0.152 (III)	M_{in}=1.0, 1.6, 2.0, 2.4 $T_c/T_{o,in}$=1.0 ρ_c/ρ_{air}=1.0	M_{in}=1.0, 1.6, 2.0 $T_c/T_{o,in}$=1.0 ρ_c/ρ_{air}=1.0	M_{in}=1.0, 1.6, 2.0 $T_c/T_{o,in}$=0.93 ρ_c/ρ_{air}=1.0
X_G/C_{ax}=0.424 (I, II) X_G/C_{ax}=0.493 (III)	M_{in}=1.0, 1.6, 2.0 $T_c/T_{o,in}$=1.0 ρ_c/ρ_{air}=1.0	M_{in}=1.0, 1.6, 2.0 $T_c/T_{o,in}$=1.0 ρ_c/ρ_{air}=1.0	M_{in}=1.0, 1.6, 2.0 $T_c/T_{o,in}$=0.93 ρ_c/ρ_{air}=1.0
X_G/C_{ax}=0.916 (I, II) X_G/C_{ax}=0.954 (III)	M_{in}=1.0, 1.3, 1.6, 1.8, 2.0, 2.4 $T_c/T_{o,in}$=1.0 ρ_c/ρ_{air}=1.0	M_{in}=1.0, 1.3, 1.6, 1.8, 2.0, 2.4 $T_c/T_{o,in}$=1.0 ρ_c/ρ_{air}=1.0	M_{in}=1.0, 1.6, 2.0 $T_c/T_{o,in}$=0.93 ρ_c/ρ_{air}=1.0

Time-averaged Secondary Flow Field (With Film Cooling Flow)

Time-averaged flow structure on the contour endwall with film cooling flow is measured for the same upstream conditions and in the same passage as those for the baseline case and the contoured endwall without film cooling case. Also, the same flow measuring probes and measurement techniques are used for all the cases. The film cooling holes are located in the passage between the center blade and the blade on the pressure side of the center blade (see Fig. 21). However, the same contour profile is employed in the two passages of the cascade in Fig. 1. Therefore, flow measurements downstream of the cascade where different fields from the two passages are mixing with each other are not obtained. The contoured endwall has already shown significant improvement in the flow field. Hence, the results with film cooling flow presented here are compared with those for the contoured endwall without coolant flow to report any further improvements in the flow field.

Figure 22 shows the streamwise turbulence intensity for three blowing ratios, M_{in}=1.0, 1.6, and 2.0 at X_G/C_{ax}=0.085. Compared to the no-coolant flow case on the left of the figure, the turbulence intensity near the endwall increases with the coolant flow. At the same location, turbulence intensity also increases with the blowing ratio. Most of the coolant jets upstream of this measurement plane are ejected at an angle to the approaching boundary layer and increase the turbulence intensity of the boundary layer. At Z/P>-0.30 near the pressure side, distinct traces of the coolant jets become clearly identifiable by the turbulence intensity contours of magnitudes greater than 9% as M_{in} increases. These jets are issued from the four holes located just upstream of this location near the pressure side. Similar pattern of turbulence intensity associated with the coolant jets near the leading edge pressure side are observed by [10]. Also, note the high turbulence intensity adjacent to junction of the suction side and contoured endwall especially for M_{in}=1.6 and 2.0. This is caused by the jets from holes located near the suction side at the leading edge. The momentum of these jets increases with the blowing ratio and the endwall profile dips down at this location near the suction side. Therefore, the coolant jets from

the holes located upstream of X_G/C_{ax}=0.085 near the suction side lift above the endwall causing high turbulence intensities adjacent to the suction side.

Figure 23 compares the streamwise turbulence intensity at X_G/C_{ax}=0.424 between the film cooled contoured endwall cases and baseline contoured endwall with no coolant jet flow. Film cooling data are presented for M_{in}=1.0, 1.6, and 2.0. The turbulence intensity contours of magnitudes greater than 10% at the junction of the suction side and baseline contour endwall indicate the passage vortex core. At the same location for the film cooling case in Fig. 23, the turbulence intensity in the passage vortex core decreases for all M_{in}. The turbulence intensity in the passage vortex core is the lowest for M_{in}=1.6. This suggests that the coolant flow jets weaken the passage vortex by opposing the turning of the cross flow near the endwall toward the suction side. However, the turbulence intensities above the endwall and adjacent to the suction side are higher for M_{in}=2.0 than for M_{in}=1.0 and 1.6. This is caused by the higher momentum of the coolant jets located upstream of X_G/C_{ax}=0.424 for the blowing ratio M_{in}=2.0.

The effects of the full coverage film cooling on the flow field are realized when the combined effects from all the coolant jets are measured at a downstream location of the holes. The streamwise turbulence intensities near the passage exit at X_G/C_{ax}=0.916 are presented in Fig. 24 for M_{in}=1.0, 1.6, and 2.0. The turbulence intensity of 11% and higher near the suction side at 0.05<Y/S<0.30 for the baseline contour endwall in the figure is caused by the passage vortex core which is elevated from the endwall at this axial position. Here also, it is clearly evident that the film cooling jets reduce the turbulence intensity in the passage vortex core significantly and thus, weaken the passage vortex. The area of high turbulence intensity in the vortex core is also reduced significantly in the film cooling case compared to the baseline contoured endwall case. The area of high turbulence intensity of 8% and higher at 0.05<Y/S<0.30 appears to be the smallest for M_{in}=2.0. The high magnitudes near the endwall-suction side corner for M_{in}=1.6 and 2.0 are caused by the high momentum coolant jets located near the suction side in the passage.

Figure 25 shows the mass-averaged streamwise turbulence intensities computed along constant pitchlines and plotted in the spanwise direction at X_G/C_{ax}=0.916. Data are presented for all six inlet blowing ratios. M_{in}=0 indicates the data for the baseline contoured endwall case with no coolant flow. The averaged turbulence intensities decrease from the location Y/S=-0.03 near the dip of the endwall profile to the location Y/S=0.03 near the hump of the endwall profile at X_G/C_{ax}=0.916. This occurs as most of the boundary layer fluid is swept toward the suction side, where the endwall dip is located, by the endwall cross-flow. Turbulence intensity then increase between Y/S=0.03 and Y/S=0.10 because of the passage vortex. Further above the endwall, average turbulence intensity decreases as Y/S increases. Little differences are observed in the data between Y/S=0.05 and Y/S=0.40 in Fig. 25. The pitchwise-averaged data at Y/S<0.05 are slightly higher for M_{in}=1.0, 1.3, and 2.4 than for the rest of the cases. The differences in the data at Y/S>0.40 are caused the coarse resolution of the measurement grids.

Figure 26 shows the overall mass-averaged streamwise turbulence intensity and axial turbulence intensity as varied with M_{in} at X_G/C_{ax}=0.916. The overall average is computed over the area extended from the endwall to the mid-span. Here also, M_{in}=0 is the case for the baseline contoured endwall. Both the streamwise turbulence intensity and axial turbulence intensity in Fig. 26 change little with M_{in}. This is a desirable result for the film cooling jet configuration as the overall turbulence intensity changes little for the film cooled endwall compared to the case for the baseline contoured endwall near the passage exit.

Normalized axial vorticity Ω_x*C/U_{ref} at X_G/C_{ax}=0.085 for blowing ratio M_{in}=1.0 to 2.0 is presented in Fig. 27. The vorticity magnitudes of -6 and lower at the corner of the baseline contour endwall and suction side are caused by the suction side leg vortex. The negative vorticity at the same location is almost absent in the data at X_G/C_{ax}=0.085 with the film cooling. The strong positive vorticity of the coolant jets near the leading edge suction side must have consumed the counter-clockwise rotating suction side leg vortex. The tiny region of positive vorticity with Ω_x*C/U_{ref}>2 near Z/P=-0.4 for the baseline contoured endwall indicates the trace of a very weak and small pressure side leg vortex. However, the Ω_x*C/U_{ref}>5 across entire pitchline above the endwall with the film cooling flow is mostly caused by the coolant jets. As the momentum of the jets increases with M_{in}, the area and magnitudes of these positive vorticity regions also increase.

Figure 28 shows normalized axial vorticity Ω_x*C/U_{ref} at X_G/C_{ax}=0.424 for M_{in}=1.0 to 2.0 and compares the data with the baseline contoured endwall case with no film cooling flow. For the baseline case, the positive vorticity region and the negative vorticity region above it near the suction side-endwall corner indicate the passage vortex and suction side led vortex, respectively. At the same corner for the film cooling case, the area and magnitudes of the positive vorticity are reduced significantly indicating the weakened structure of the passage vortex. The location of the positive vorticity region is also slightly elevated at the corner as the coolant films are injected under the boundary layer. The small region of high vorticity Ω_x*C/U_{ref}>10 adjacent to the suction side for M_{in}=1.6 and 2.0 is caused by the jets ejected near leading edge suction side. The signature of these jets adjacent to the suction side (Ω_x*C/U_{ref}>10) is also evident in Fig. 27. The signature of the suction side vortex (Ω_x*C/U_{ref} <0) above the positive vorticity region near the suction side is completely eliminated for the film cooling case. This is expected as the suction side vortex is also not evident in the film cooling data upstream at X_G/C_{ax}=0.085. However, the negative magnitudes of Ω_x*C/U_{ref} adjacent to the endwall across the pitchline in Fig. 28 indicates the signatures of the cooling jets. These Ω_x*C/U_{ref}<0 contours decrease in magnitudes and increase in area as M_{in} increases. Most of jets located upstream of X_G/C_{ax}=0.424 are ejected in the positive yaw angle direction (see Figs. 1(b) and 21(a)). As the boundary layer cross-flow travels toward the suction side, it tries to rotate the jet fluids counter-clockwise creating the negative vorticities in the coolant jets near X_G/C_{ax}=0.424. This is opposite to the mechanism observed at X_G/C_{ax}=0.085 where the jets have positive axial vorticities as shown in Fig. 27.

The combined effects of all the coolant jets on the axial vorticity are shown in the results of Fig. 29 for M_{in}=1.0 to 2.0. The contour size of the normalized axial vorticity Ω_x*C/U_{ref}>6 near the suction side at X_G/C_{ax}=0.916 indicating the passage vortex core is much smaller for the film cooling cases than for the baseline contoured endwall. The positive vorticity magnitudes in the passage vortex region at Z/P<-0.60 also reduce slightly as M_{in} increases. Also, note that the location of the Ω_x*C/U_{ref}>6 contour is higher in Y/S direction for the film cooling case than for the baseline contoured endwall case. The small regions of Ω_x*C/U_{ref}>6 near the pressure side for M_{in}=2.0 are the signature of the coolant jets located near the pressure side. At M_{in}=2.0, the momentum of these jets are high enough to remain attached to the endwall down to the location X_G/C_{ax}=0.916. The negative vorticity region about Y/S=0.30 near the suction side for the baseline contoured endwall is the signature of the suction side leg vortex and induced wall vortex [6]. But, the negative vorticity region at the same location and at bottom the corner of the suction side for the film cooling case are caused primarily either by the remnants of the film jets or by the induce vortex structures.

The normalized pitchwise velocity, W/U_{ref} at X_G/C_{ax}=0.424 shown in Fig. 30 near the endwall is increased in magnitudes for the film cooling cases compared that for the baseline contoured endwall case. The magnitudes near the endwall are also increased as the blowing ratio M_{in} increases from 1.0 to 2.0. This suggests that the strength of the cross flow along the pitchline is reduced with the film cooling and is reduced further as M_{in} increases. As a consequence, less amount of boundary layer fluid is funneled into the passage vortex and the secondary flow is weakened and reduced in size as M_{in} increases, which is also observed in Fig. 28. Figure 31 also shows W/U_{ref} at X_G/C_{ax}=0.916 for the M_{in}=1.0 to 2.0. Hers, the negative W/U_{ref} magnitudes in the passage vortex region between Y/S=0.17 and Y/S=0.30 near the suction side increases with the film cooling flow compared to that with the no coolant flow case. However, the negative W/U_{ref} magnitudes near the endwall region at Z/P<-0.40 decreases with the film cooling flow and as M_{in} increases compared to that with the no coolant flow case in Fig. 31. This occurs as the cross-pitch flow is strengthened by the film jets located downstream of X_G/C_{ax}=0.424 which are ejected along the cross flow direction.

Figure 32 shows the total pressure loss coefficients, $C_{pt,loss}$>0.40 at X_G/C_{ax}=0.424 due to the passage vortex is affected little when compared between no coolant flow case and coolant flow case up to M_{in}=1.6. The region of $C_{pt,loss}$>0.40 near the suction side-endwall corner becomes smaller for the higher blowing ratio at M_{in}=2.0. The distinct small region of $C_{pt,loss}$>0.50 adjacent to the suction side for M_{in}=1.6 and 2.0 is caused by the high vorticity of the lifted jet from the holes near the leading edge suction side.

The $C_{pt,loss}$ at X_G/C_{ax}=0.916 for the blowing ratios, M_{in}=1.0 to 2.4 are shown in Fig. 33. The local $C_{pt,loss}$, in fact, increases in the passage vortex region between Y/S=0.17 and Y/S=0.30 near the suction side with the film cooling flows compared to that with no coolant flow case. Since the passage vortex is weakened with the film cooling as evident earlier, the higher $C_{pt,loss}$ must have been caused by the coolant jets as they are lifted from the endwall and mixed with low energy boundary layer flow. However, the higher momentum of the coolant jets at M_{in}>1.6 decreases the $C_{pt,loss}$ above the endwall in Z/P>-0.60 which will be further evident in Fig. 34.

Figure 34 shows the pitchwise mass-averaged $C_{pt,loss}$ plot and overall mass-averaged $C_{pt,loss}$ plot at X_G/C_{ax}=0.916 for the blowing ratio ranging from 1.0 to 2.4. The baseline contoured endwall case is also included as M_{in}=0. The dotted line in the plots refers to the baseline flat endwall case. The pitchwise mass-averaged data computed the measured data along constant pitchline are plotted against the spanwise Y/S direction. The pitch-averaged $C_{pt,loss}$ data for the baseline flat endwall higher for most of the Y/S than for all the contour endwall cases (with and without film cooling). In comparing pitch-averaged data for the film cooled contour endwall with the baseline contoured endwall (M_{in}=0), the film cooled $C_{pt,loss}$ are higher at location Y/S<0.0. This is probably caused by the losses in the corner vortex which is strengthened by the film jets. At 0.0<Y/S<0.1, the averaged $C_{pt,loss}$ are lower for M_{in}>1.6 than for the other cases. This is caused by the small magnitudes of local $C_{pt,loss}$. Note that the averaged $C_{pt,loss}\leq 0.0$ for the cases of M_{in}=2.0 and 2.4 occurs because the high momentum film jets near the pressure side increase the local magnitudes of total pressure P_{tot}.

The overall mass-averaged $C_{pt,loss}$ in Fig. 34 are computed from the local data between the endwall and mid-span. Here, the averaged $C_{pt,loss}$ for all the contoured endwall cases are nearly half of that for the baseline flat endwall case. For contoured endwall cases, the overall-averaged $C_{pt,loss}$ are higher for M_{in}=1.0 to M_{in}=1.6 than for M_{in}=0.0. However, the overall-averaged data decreases as M_{in} increases from 1.0 to 2.4. Note that in defining the $C_{pt,loss}$ the coolant plenum pressure has not been used, and therefore for the film cooling cases, the $C_{pt,loss}$ values represent

a dimensionless pressure rather than a total loss coefficient. The $C_{pt,loss}$ values with coolant plenum pressures included will be presented in a later report.

Non-dimensional Flow Temperature (With Film Cooling Flow)

The non-dimensional flow temperature θ_f of the measured air stream temperature for the film cooling case is redefined in Eq. (8) below. The reference temperature in this definition is chosen

$$\theta_f = \frac{T - T_c}{0.5 * U_{ref}^2 / C_p} \tag{8}$$

to be the coolant temperature T_c which is the lowest temperature in the cascade. In Eq. (5), the reference temperature is $T_{o,in}$ as the inlet temperature of the flow is the lowest temperature. In Eq. (8) above, T is the local air temperature measured with the same thermocouple probe that is used for the data measurements on the heated contoured endwall. Thus, higher magnitudes of θ_f indicate the air stream higher above the endwall and lower magnitudes of θ_f indicate the air stream infected by the cold film jets. As mentioned earlier, the endwall is not heated and is maintained at the adiabatic condition for T measurements with the cold film jets. The results are presented in Figs. 35 to 37. The pitchwise Z resolution of the measurement grid is 2.0 mm near the blade surfaces and 4.0 mm at the mid-pitch locations. The spanwise Y resolution is 1.0 near the endwall and 5.0 mm at the mid-span locations.

Figure 35 shows θ_f at X_G/C_{ax}=0.152 for M_{in}=1.0, 1.6, and 2.0. The magnitudes of θ_f <325 are the signature of the cold jet stream above the endwall. The mass flux or volumetric flow rate of the coolant jet increases with M_{in}. Therefore, the region with θ_f <325 near the endwall increases with M_{in}. Note that the cold temperature region is bound well within the velocity boundary layer along most of the pitchline in Fig. 35. The lower θ_f higher above the endwall at the suction side is caused by the lifted jets at this location.

The θ_f contours for the same blowing ratios M_{in}=1.0 to 2.0 at X_G/C_{ax}=0.493 are shown in Fig. 36. Here also, the region of θ_f <325 identifying the coolant jets increases with M_{in}. The magnitudes of θ_f also decrease with increasing M_{in}. Nine distinct regions of θ_f <175 for M_{in}=1.6 and 2.0 identify nine coolant jets located upstream of X_G/C_{ax}=0.493. The θ_f contours near the endwall change little for M_{in}=1.6 and 2.0. The data in Fig. 36 also show that the low temperature fluid remain close to the endwall across the entire pitchline for $M_{in}\geq$1.6.

The θ_f contours at X_G/C_{ax}=0.954 in Fig. 37 show that θ_f magnitudes decrease significantly above the endwall across the pitchline as M_{in} increase from 1.0 to 2.0. Near the suction side, θ_f<325 extends up to Y/S=0.22 as the cross-flow and passage vortex lifts the cold boundary layer fluid and coolant jets higher above the endwall. The low temperature blanket above the endwall with θ_f<275 at Z/P>-0.40 are the thickest for M_{in}=2.0 because of the higher mass flux in the coolant jets ejected from the locations near the pressure side.

COMPUTATIONS & RESULTS

Calculations are performed with the commercial code FLUENT. Grid generation is done using GRIDPRO. The number of grid points used is generally over one million with near-wall stretching of the grid points toward the bottom end-wall. Realizable k-ε with two-layer near wall turbulent model is employed to simulate the flow. The grids are made fine enough near the walls so that the y+ values are below unity. The computations are performed for the same GE-E^3 first stage blade passage as in the experiments.

Several endwall contour configurations are simulated. The results presented here are only for the same contoured endwall as in the measurements since this configuration was shown to be the best in the numerical optimization studies. The summary results for the other contour configurations are presented in Table 3 of this report. Inlet flow conditions and cascade geometric parameters employed for the blade passage domain are obtained from Tables 1 and 2.

The results presented here are obtained in the computational domain and pitchwise planes as shown in Fig. 38. The domain spans one pitch distance in the pitchwise direction and $1.361C_{ax}$ upstream of the leading edge and $1.103C_{ax}$ downstream of the trailing edge. The baseline computation results are also included for the comparison. Figure 39 shows the static pressure coefficients $C_{p,e}$ on the endwall. The coefficients are computed from Eq. (2). The $C_{p,e}$ values increase on the suction side at $X/C_{ax}<0.50$ for the contoured endwall compared to baseline case. At this location, the elevation differences from the pressure side to suction side are significantly high on the contoured profile. This reduces the pressure gradient in the pitchwise direction in this location with the contoured endwall. However, $C_{p,e}$ values downstream of $X_G/C_{ax}=0.50$ near the suction side, where passage throat is located, decrease slightly for the contoured endwall compared to the baseline case.

The effects of pressure gradients in the pitchwise direction directly affect the pressure and suction side leg of the leading edge horseshoe vortex as illustrated in Figs. 40 and 41. These results are presented in the pitchwise plane at $X/C_{ax}=0.036$ that is located close to the blade leading edge. In these figures, the blade surface on the right hand side is the pressure side and on the left hand side is the suction side. Streamlines for the baseline case in Fig. 40 show the counter-clockwise rotating pressure side leg vortex structure between $0.0<Z/S<0.025$ and $0.05<Y/P<0.35$. A clear structure of the suction side leg vortex for the baseline case is not evident. The streamlines above the contoured endwall between $0.07<Z/S<0.15$ and $0.05<Y/P<0.35$ complete only half turn of a vortex structure and indicate weak formation of the pressure side leg vortex. The streamlines on the contoured endwall suction side are curled downwards in contrast to the baseline case. The strength of these vortex structures are shown in the normalized axial vorticity in Fig. 41. The values of $\Omega_x C/U_{ref}>35$ located very close to the endwall are associated with the near-wall boundary layer flow. The normalized vorticity in the pressure side leg vortex region is significantly smaller for the contoured endwall than for the baseline indicating again a very weak pressure side vortex structure. This is consistent with the measured data presented earlier. However, the $\Omega_x C/U_{ref}$ magnitudes on the suction side are higher for the contoured endwall case. As mentioned earlier, the two-dimensional vorticity does not provide a complete structure of the three-dimensional vortex system in the passage.

Figure 42 presents the streamlines superimposed on normalized axial vorticity $\Omega_x C/U_{ref}$ at $X/C_{ax}=0.20$. In the plots, the presence of cross flow from suction to pressure side of the blade is clearly seen for both the baseline case and contoured endwall case. Additionally, the formation of a roll up vortex (counter-clockwise rotation) near the pressure side is due to the pressure side

leg vortex in both cases. Comparison of the vortex roll up and the magnitude of the vorticity of the both cases reveal that the contoured endwall reduces the strength and size of the secondary flow significantly near the pressure side. Note that the contoured endwall shows the boundary layer separation at Y/P~0.20 near the wall; this is clear from the zoomed-out view of the streamlines. This particular phenomenon is absent for the flat endwall.

The streamlines superimposed on normalized axial vorticity contours at X/C_{ax}=0.80 are presented in Fig. 43. The magnitude and the size of the secondary vortices indicated by $\Omega_x C/U_{ref}$>4.0 near the suction side decrease in case of the contoured endwall compared with the baseline case. Though the vorticity contours reveal the strong generation of secondary vortices i.e. the passage vortex, the streamlines in the 2-D plane do not clearly exhibit the vortex roll-up as seen at an upstream location (see Fig. 42). This suggests a more 3-dimensional and diffused structure of the vortex. The streamline curvature seen near the baseline endwall-suction side corner is reduced for the contoured endwall case.

The total pressure loss coefficient $C_{pt,loss}$ at X/C_{ax}=0.80 plane for the baseline and the contoured endwall is compared in Fig. 44. The region of high $C_{pt,loss}$ at the suction side indicates the location of the passage vortex. The distribution of peak region of the loss coefficient is seen to be altered due to the contoured endwall and its location moves towards the bottom endwall. The magnitude of the peak coefficient is seen to be lower for contoured endwall. However, the overall (area averaged) total pressure loss coefficient for baseline and contoured endwall are computed to be about the same, 0.2164 and 0.2176, respectively. The decrease in the spatial pressure gradient for the contoured case, however, indicates the effectiveness of the three-dimensional endwall in reducing the cross flow locally.

Figure 45 illustrates the non-dimensional turbulent kinetic energy distribution in the pitchwise plane at X/C_{ax}=1.20 located downstream of the blade trailing edge. As evident, the drop in turbulent kinetic energy is distinct everywhere for the contoured endwall compared to the baseline case. The kinetic energy about Y/P=0.0 near the contoured endwall also decreases relative to the baseline case.

The normalized axial vorticity contours along with the streamlines are plotted at X/C_{ax}=1.20 plane in Fig. 46. The vorticity contours show the presence of high vorticity region ($\Omega_x C/U_{ref}$ >2.0) at 0.02<Z/S<0.23 for baseline and at 0.02<Z/S<0.15 for contoured endwall. The vorticities in the passage vortex for the two cases are further compared in the line plot at Y/P=–0.1 in Fig. 46. In this plot, the higher $\Omega_x C/U_{ref}$ between Z/S=0.10 and 0.25 for the baseline indicates that the size of the passage vortex for the contoured case is still smaller far downstream in the blade passage.

The contours of the total pressure loss coefficient at X/C_{ax}=1.20 for the baseline and contoured endwall are compared in Fig. 47. The closed contour lines represent the passage vortex here. Both the cases show almost identical magnitudes of the pressure loss. However, the center of the peak $C_{pt,loss}$ for the contour endwall moves towards the endwall. The magnitude of peak is also lower for the contoured case. The area-averaged $C_{pt,loss}$ are 0.2528 and 0.2474 for the baseline and contoured endwall, respectively, at this plane. It is seen that at the upstream location X/C_{ax}=0.80 the total pressure loss is less for the flat endwall. With the increase in the axial distance, the cross flow weakens by the action of imposed pressure field created by the contouring of the endwall and this results in lower $C_{pt,loss}$.

To get a clear idea about the near wall flow structures, surface streamlines are generated using the two components of shear stresses and shown in Fig. 48 for the baseline and contoured endwall. Because of the formation of horse-shoe vortex ahead of the blade leading edge, the

streamlines near the surface shows the separation line and saddle point. However, the position of the saddle moves farther inside the passage and the separating line pattern is different for the contoured endwall. Also, the distinctive separation line along the suction side of the baseline case is not clearly evident on the contoured endwall. Further note that the streamlines inside the passage are directed more toward the axial direction for the contoured endwall case than for the baseline case. This is a clear evidence of the weakened cross flow in the near wall region and is caused by the smaller pitchwise pressure gradient on the endwall for the contoured endwall case (refer to Fig. 39).

Figure 49 compares the endwall Nusselt numbers between the baseline and contoured endwall case. It is clearly seen that the flat endwall has larger region of high Nu around the blade leading edge region, particularly on the suction side. The leading edge horse-shoe vortex system is advected by the strong cross flow in the blade passage and forms three-dimensional pressure-side leg vortex and suction-side leg vortex systems. The contour endwall profile weakens the horse-shoe vortex and results in lower Nu at the leading edge region. As the flow accelerates towards the throat area because of the narrowing passage area, the heat transfer is enhanced. However, the region of high Nu found along the baseline throat area is reduced significantly for the contoured endwall. In the throat area itself, the peak Nu value is higher on the contoured endwall than on the baseline endwall. This is due to the fact that the flow accelerates locally in the throat area more for the contoured endwall because of the additional reduction in the flow area. The overall (area-averaged) Nusselt number is calculated to be 736 and 678 for the baseline and contoured endwall, respectively, thus giving a reduction of 8% in the average Nu for the contoured endwall.

Table 3 provides the summary of computed area-averaged Nusselt number and total pressure loss coefficient $C_{pt,loss}$ across the blade passage for several contoured endwall profile. The pitchwise variation for all the contoured profiles is the same as that given in Fig. 2(a). The table shows the axial variation of the contoured profile in each case. X_u is the distance of the peak height in the axial curve from the blade leading edge. X_d is the distance between the peak height in the axial curve and the end of the profile. Z is the height of the final non-axisymmetric endwall profile which is generated by combining the pitchwise profile and the axial profile. As shown in Table 3, case 9 provides the optimum results in terms of average Nu and $C_{pt,loss}$. All the results presented earlier are obtained with this profile.

CONCLUDING REMARKS

A three-dimensional non-axisymmetric endwall has been designed and tested both numerically and experimentally in the atmospheric cascade facility. Measurements are also obtained with the full coverage film cooling with the coolant holes located and oriented strategically in the contoured endwall. The performance of the endwall is compared first with that of a flat endwall with respect to heat transfer and secondary flow structure. The performance of the film cooling-hole configuration is then compared with that of the contoured endwall without film cooling. The following are the main conclusions drawn from the present work.

Contoured endwall without film cooling:

1. The three-dimensional endwall is found to be effective in bringing down the total pressure loss across the blade passage.

2. The strength and size of the secondary vortex flow reduces with the contoured endwall.
3. The heat transfer along the contoured endwall is lower compared with the flat endwall. The reduction in both the total pressure loss and heat transfer is a consequence of the decrease in the near-wall pitchwise pressure gradient.

Contoured endwall with film cooling:

1. The suction side leg vortex is completely eliminated and the passage vortex strength is reduced with the film cooling compared to that with the baseline contoured endwall.
2. Mass averaged total pressure loss is decreased with film cooling when the inlet blowing ratio is greater than 1.60 compared to that with the baseline contoured endwall.
3. Overall total pressure loss at the passage exit for the contoured endwall with and without film cooling is nearly half of that measured for the baseline flat endwall.
4. The cold film cooling jets can blanket the contoured endwall across the entire pitchline better at the higher inlet blowing ratios, $M_{in} \geq 1.60$.

Presently, experiments are underway to measure the film cooling effectiveness on the contoured endwall in the atmospheric blade cascade facility. Measurements are being obtained at different blowing ratios but at a constant coolant to main stream temperature ratio of 0.93. Soon, the contoured endwall will be replaced by a flat endwall with the film cooling holes. The same configuration of the cooling-hole geometry as in the contoured endwall is employed in the flat endwall. Measurements will be also obtained with the leading edge fillets placed on the film cooled flat endwall. The same fillets that were employed in the earlier measurements will be employed.

Also, a high speed blow down facility has been completed where two-dimensional section of the GE-E^3 first stage vane is undergoing tests. The vanes, with a scaling factor of 1:1, have been fabricated in the stereo-lithography printer at LSU. The experiments being conducted include the axial contouring of upstream bottom endwall and in-passage bottom endwall of the vane cascade test section. In addition, the film cooling effectiveness with film holes located upstream of the vane passage inlet is being measured with and without contouring of the endwall. The upstream contour has already been installed and measurements are in progress. The computational results in the vane passage with axially contoured endwall have already been reported in the previous reports. These results were used in selecting the test profile for the present measurements

In addition, a hot cascade facility built by General Electric (designed by Dr. Ron Bunker), is being set up. A no-cost extension request has been filed with SCIES to enable the hot cascade tests to be completed.

REFERENCES

[1] Hartland, J.C., Gregory-Smith, D.G., and Rose, M.G., 1998, "Non-axisymmetric endwall profiling in a turbine rotor blade," ASME 98-GT-525.
[2] Yan, J., Gregory-Smith, D.G., and Walker, P.J., 1999, "Secondary flow reduction in a nozzle guide vane cascade by non-axisymmetric end-wall profiling," ASME 99-GT-339.
[3] Harvey, N.W., Rose, M.G., Taylor, M.D., Shahpar, S., Hartland, J., and Gregory-Smith, D.G., 2000, "Nonaxisymmetric turbine end wall design: Part I- three-dimensional linear design system," ASME Tran., J. Turbomachinery, Vol. 122, pp.278-285.
[4] Hartlland, J.C., Gregory-Smith, D.G., Harvey, N.W., and Rose, M.G., 2000, "Nonaxisymmetric turbine end wall design: Part II- experimental validation," ASME Tran., J. Turbomachinery, Vol. 122, pp.286-293.
[5] Ingram, G., and Gregory-Smith, D., 2002, "The effect of end-wall profiling on secondary flow and loss development in a turbine cascade," ASME GT-2002-30339.
[6] Wang, H.P., Olson, S.J., Goldstein, R.J., and Eckert, E.R.G., 1997, "Flow Visualization in a Linear Turbine Cascade of High Performance Turbine Blades," ASME Tran. J. Turbomachinery, Vol. 119, pp. 1-8.
[7] Mahmood, G.I., Gustafson, R., and Acharya, S., 2005, "Experimental Investigation of Flow Structure and Nusselt Number in a Low Speed Linear Blade Passage With and Without Leading Edge Fillets," ASME Tran. J. Heat Transfer, Vol. 127, pp. 499-512.
[8] Mahmood, G.I. and Acharya, S., 2005, "Experimental Investigation of Secondary Flow Structure in a Blade Passage With and Without Leading Edge Fillets", accepted, ASME Trans. J. Fluids Engineering.
[9] Friedrichs, S., Hodson, H.P., and Dawes, W.N., 1997, "Aerodynamic Aspects of Endwall Film-Cooling," ASME Tran., J. Turbomachinery, Vol. 119, pp.786-793.
[10] Kost, F. and Nicklas, F., 2001, "Film-Cooled Turbine Endwall in a Transonic Flow Field: Part I- Aerodynamic Measurements," ASME Proc. Turbo Expo, 2001-GT-0145.

Table1: Cascade Geometric Parameters

Actual chord length, C (cm)	35.86
Axial chord length, Cax (cm)	30.36
Aspect ratio (true chord length to blade span), C/S	0.77
Solidity ratio (true chord length to blade pitch), C/P	1.23
Flow inlet angle (degrees)	0

Table 2: Upstream reference properties for measurements and computations

Average upstream reference velocity, U_{ref} (m/s)	10.10 (measurements) 10.26 (computations)
Inlet Reynolds number, Re_{in}	2.30×10^6 (measurements) 2.33×10^6 (computations)
Average reference static pressure, $P_{stat,r}$ (Pa, gage)	-138.0 (measurements) -40.0 (computations)
Average reference total pressure, $P_{tot,r}$ (Pa, gage)	-78.0 (measurements) 25.0 (computations)
BL thickness, δ (mm)	44.0 (measurements) 29.0 (computations)
Disp. thichness, $\delta 1$ (mm)	5.5 (measurements)
Mom. Thickness, $\delta 2$ (mm)	4.3 (measurements)
Thermal boundary layer thickness (mm)	28.0 (measurements) 18.0 (computations)
Stagnation temperature, $T_{o,in}$ (K)	302
Stagnation pressure, $P_{o,in}$ (Pa)	1.013×10^3 (measurements)
Upstream streamwise turbulence intensity	4.0%

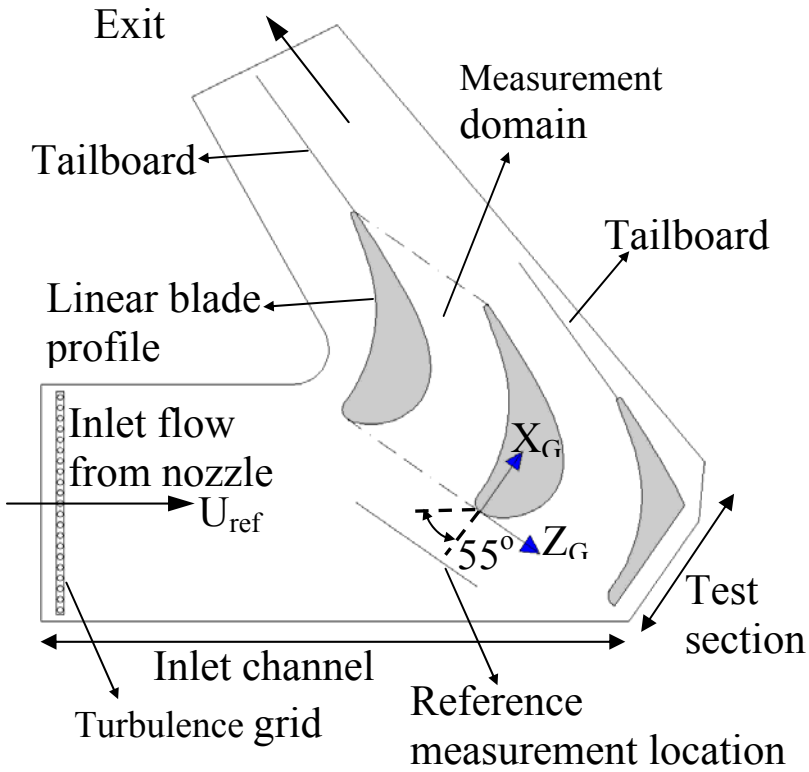

Fig. 1(a): Schematic of the cascade test facility and blade orientation in the test section.

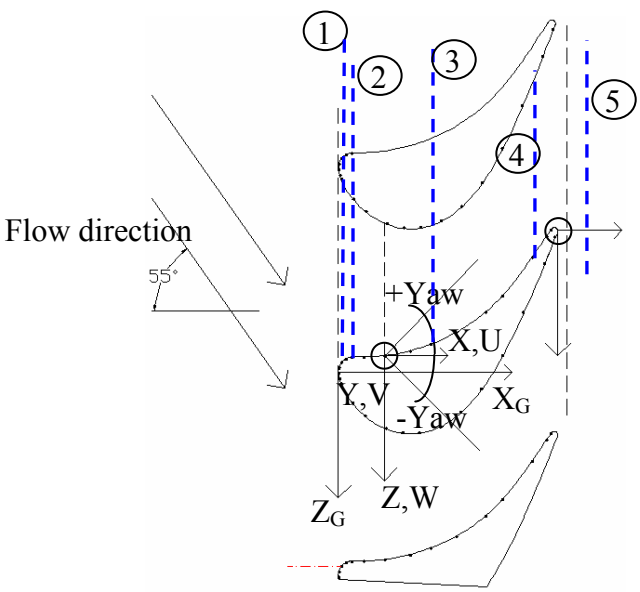

Flow analysis plane	Location, X_G/C_{ax}
1	0.036
2	0.085
3	0.424
4	0.916
5	1.241

Figure 1(b): Coordinate systems and flow analysis plane in the blade passage.

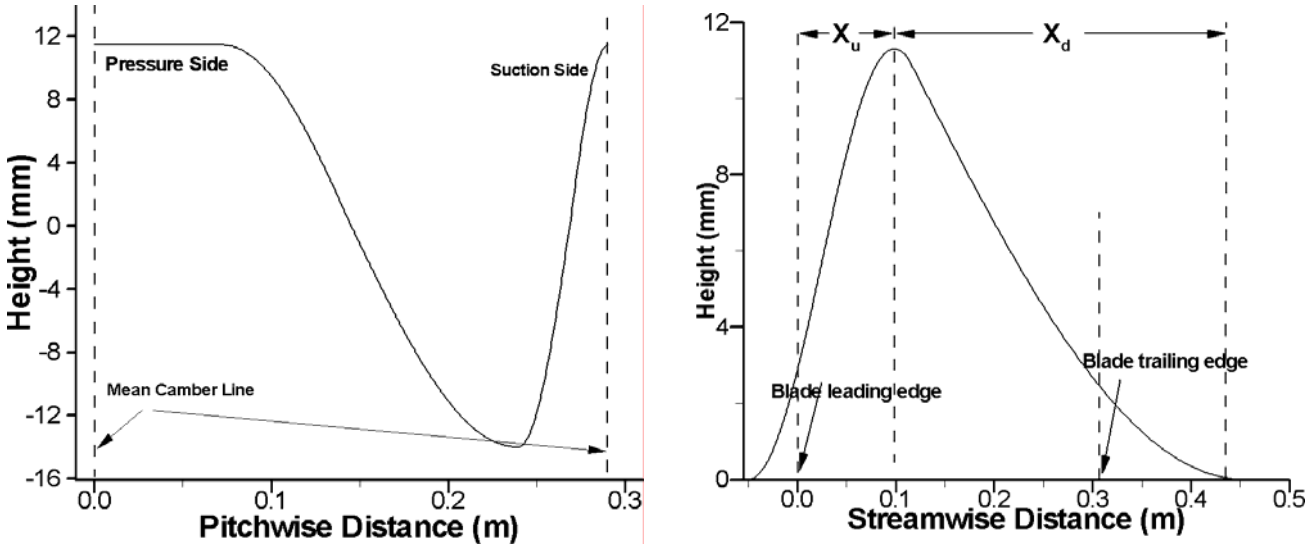

Figure 2(a): Curves employed to vary the pitchwise and streamwise heights of the experimental non-axisymmetric endwall profile.

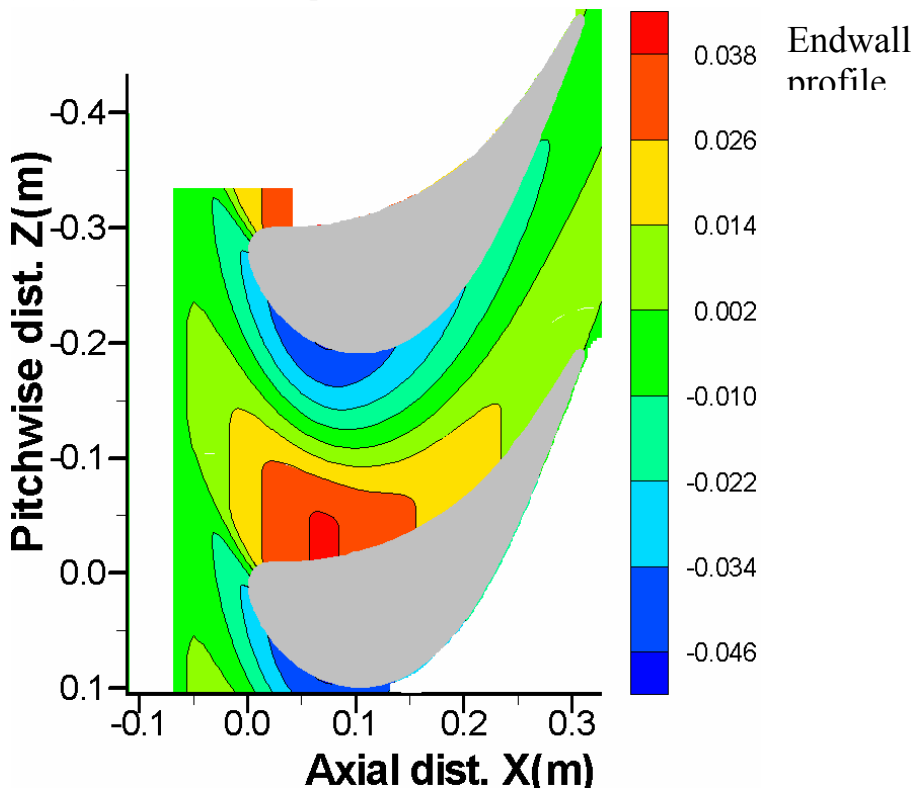

Figure 2(b): Non-axisymmetric endwall profile height obtained from the curves in Fig. 2(a).

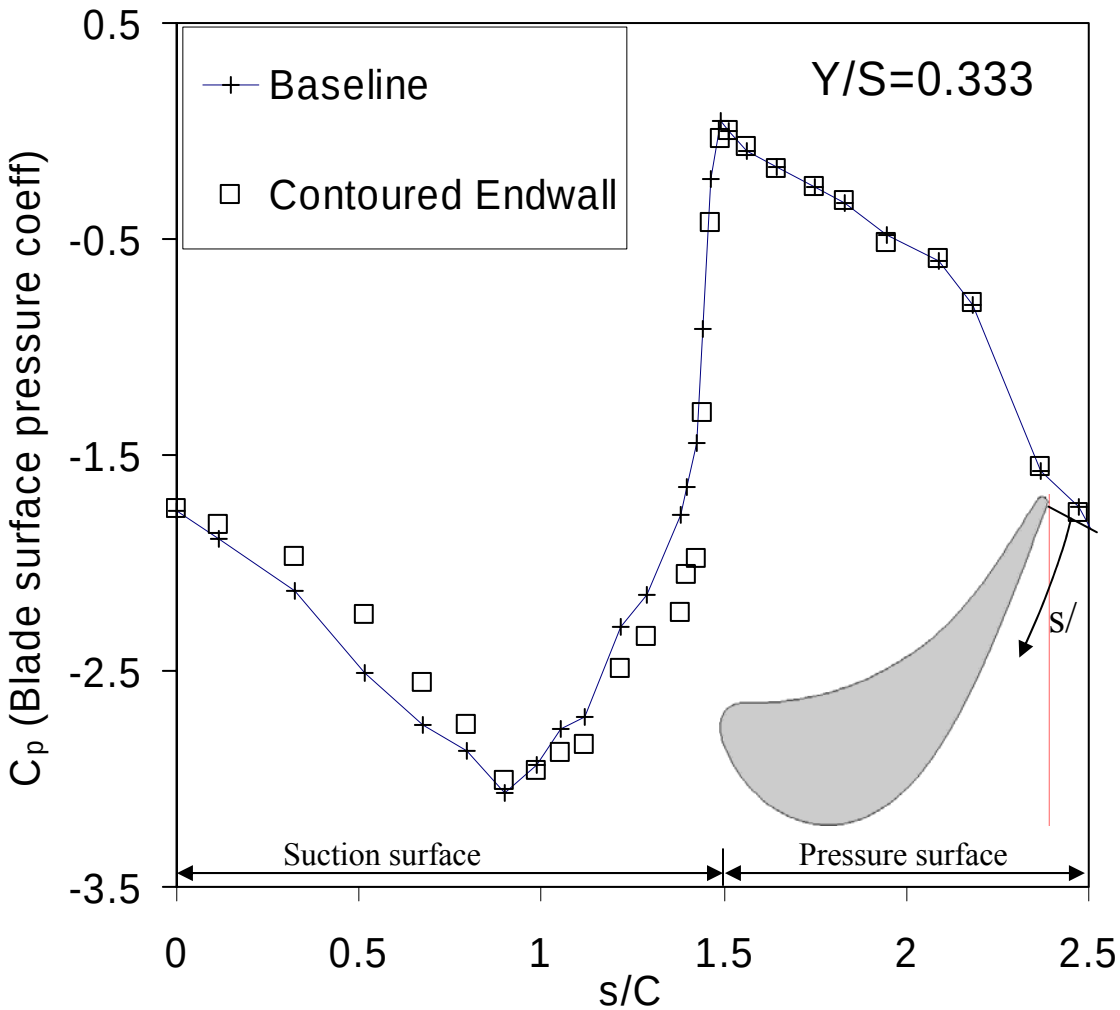

Figure 3: Blade wall static pressure coefficient at spanwise location Y/S=0.333 for the baseline and contoured endwall.

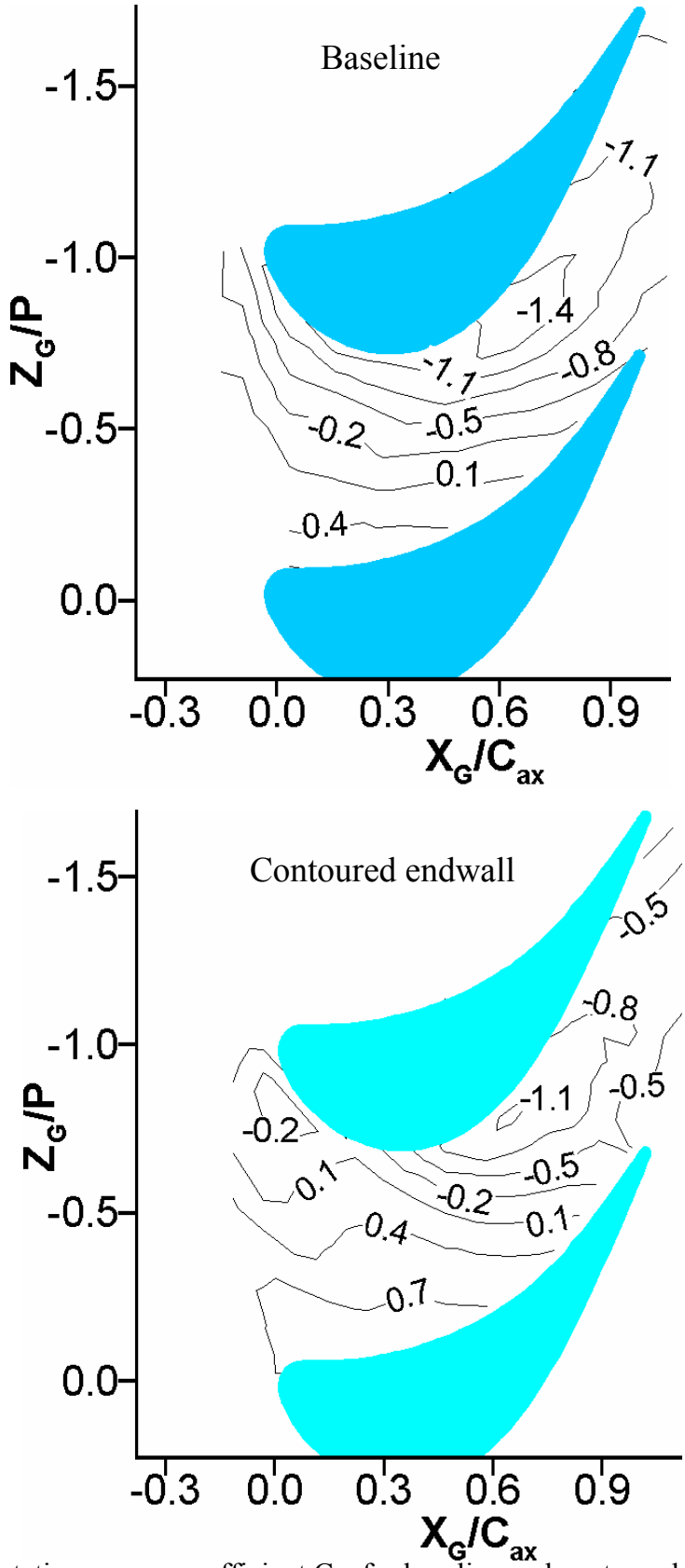

Figure 4: Endwall static pressure coefficient $C_{p,e}$ for baseline and contoured endwall.

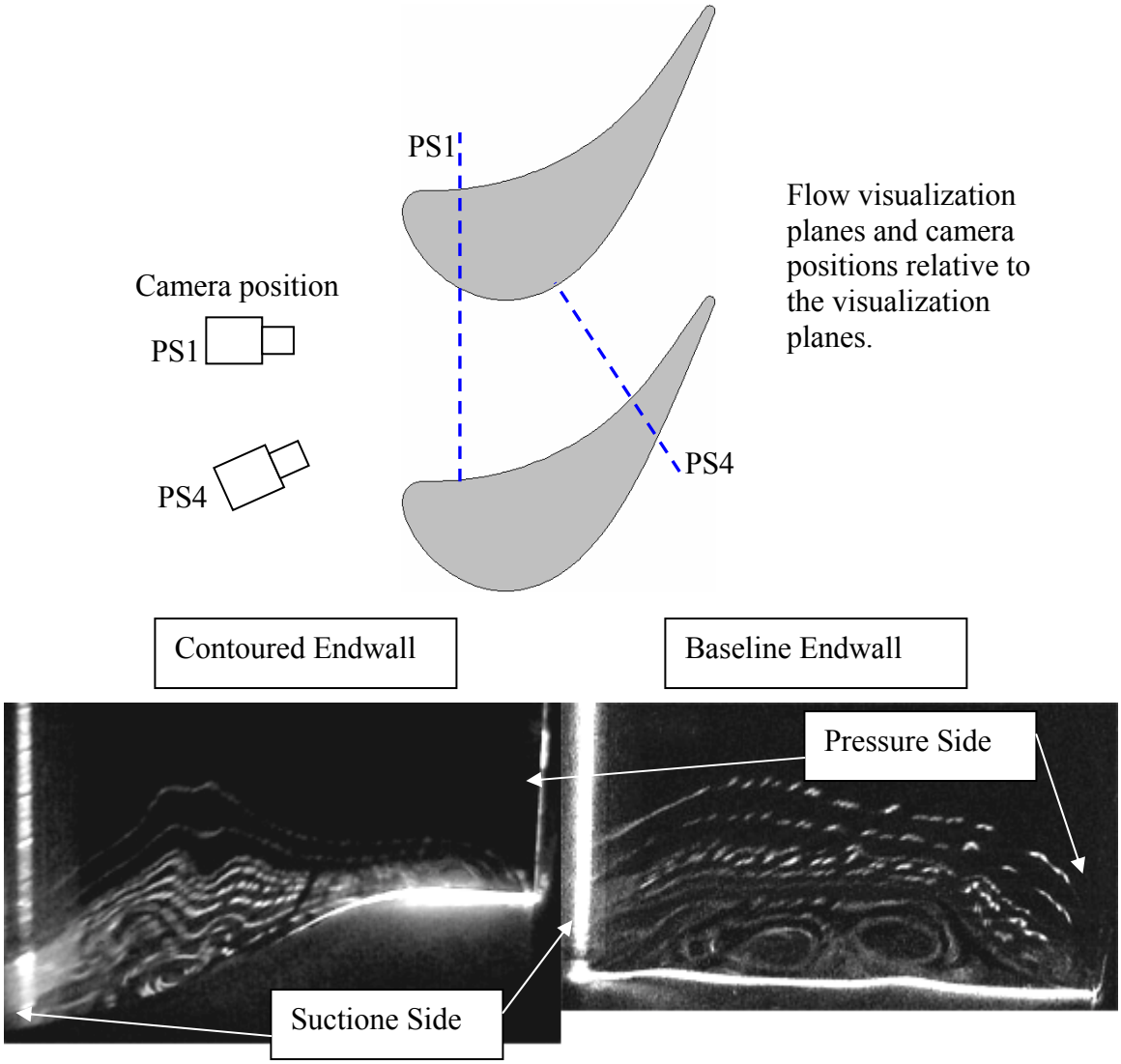

Figure 5. Instantaneous flow visualization images in the plane PS1 for baseline and contoured endwall.

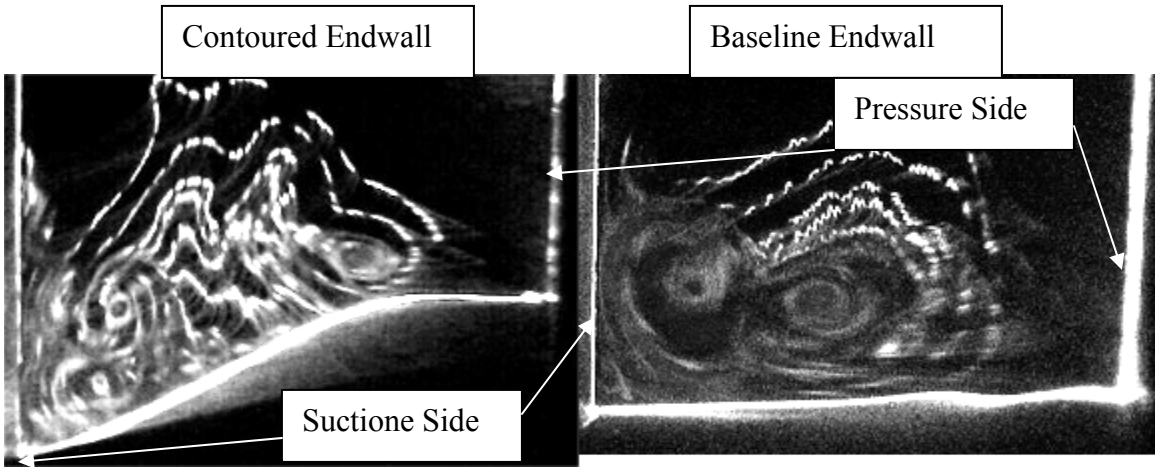

Figure 6. Instantaneous flow visualization images in the plane PS4 for baseline and contoured endwall.

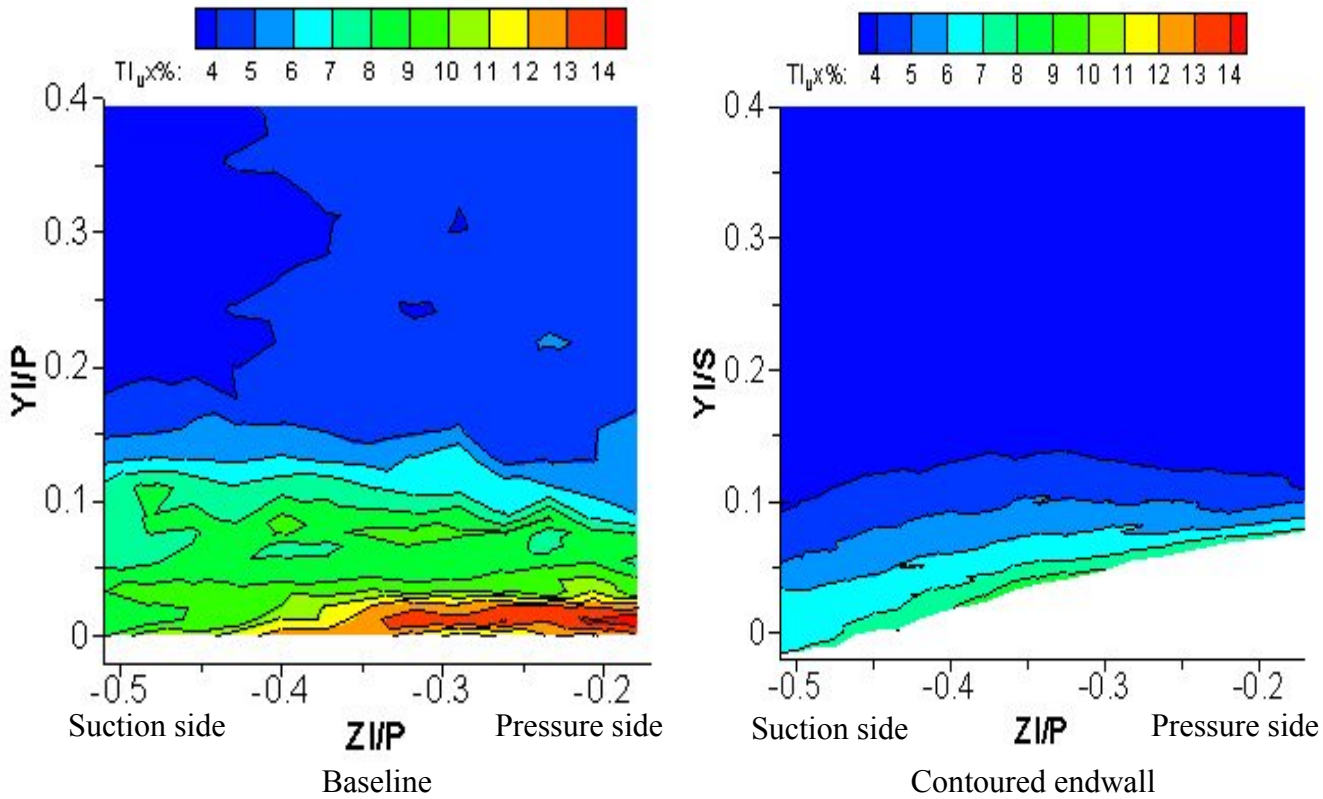

Figure 7: Streamwise turbulence intensity (%) in pitchwise plane at X_G/C_{ax}=0.085 for baseline and contoured endwall.

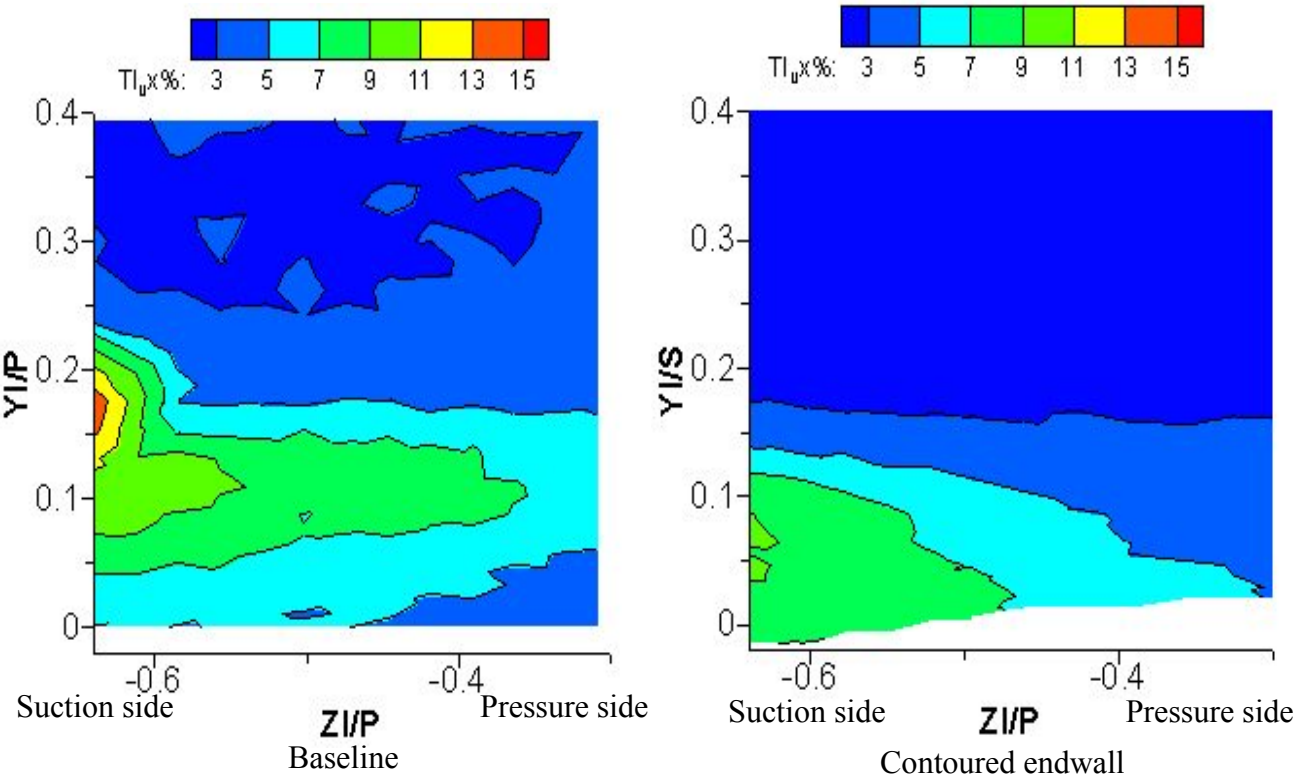

Figure 8: Streamwise turbulence intensity (%) in pitchwise plane at X_G/C_{ax}=0.916 for baseline and contoured endwall.

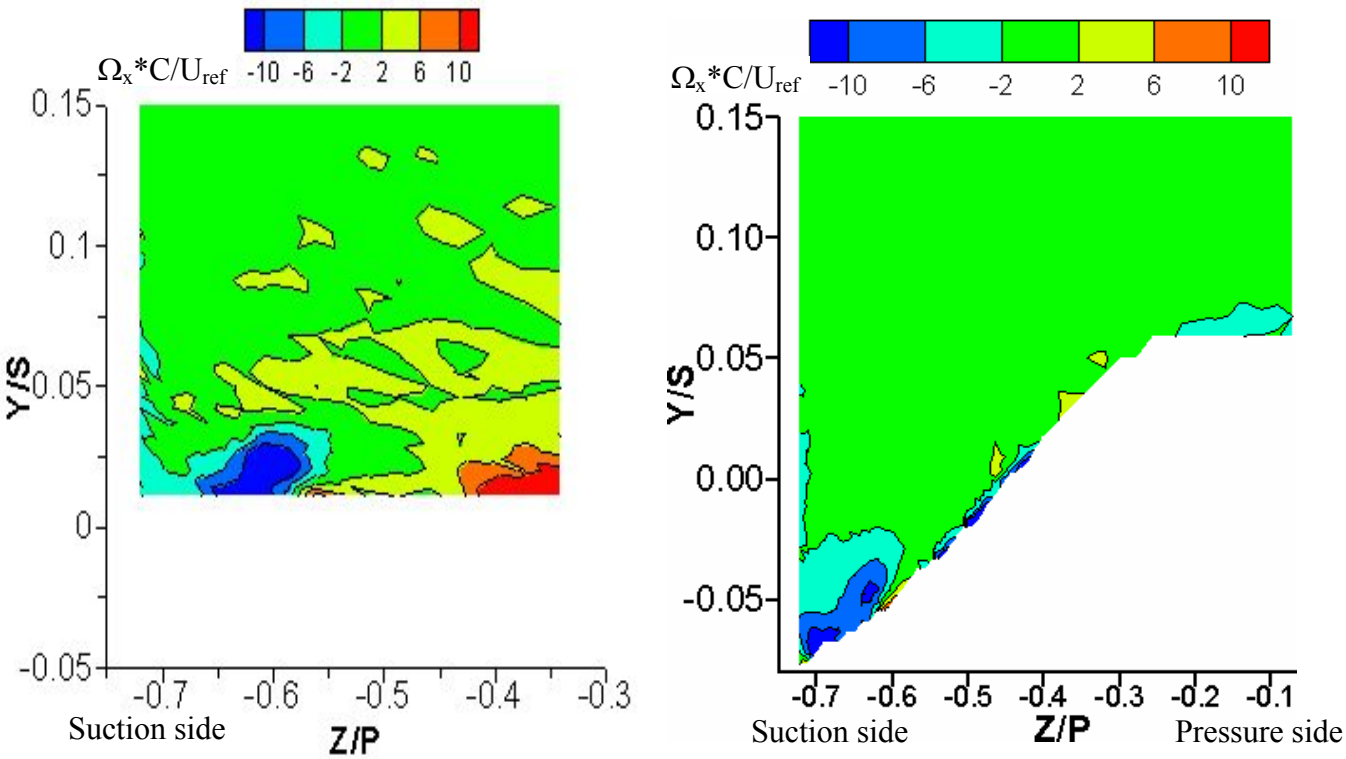

Baseline Contoured endwall

Figure 9: Normalized axial vorticity, $\Omega_x C/U_{ref}$ in pitchwise plane at X_G/C_{ax}=0.085 for baseline and contoured endwall.

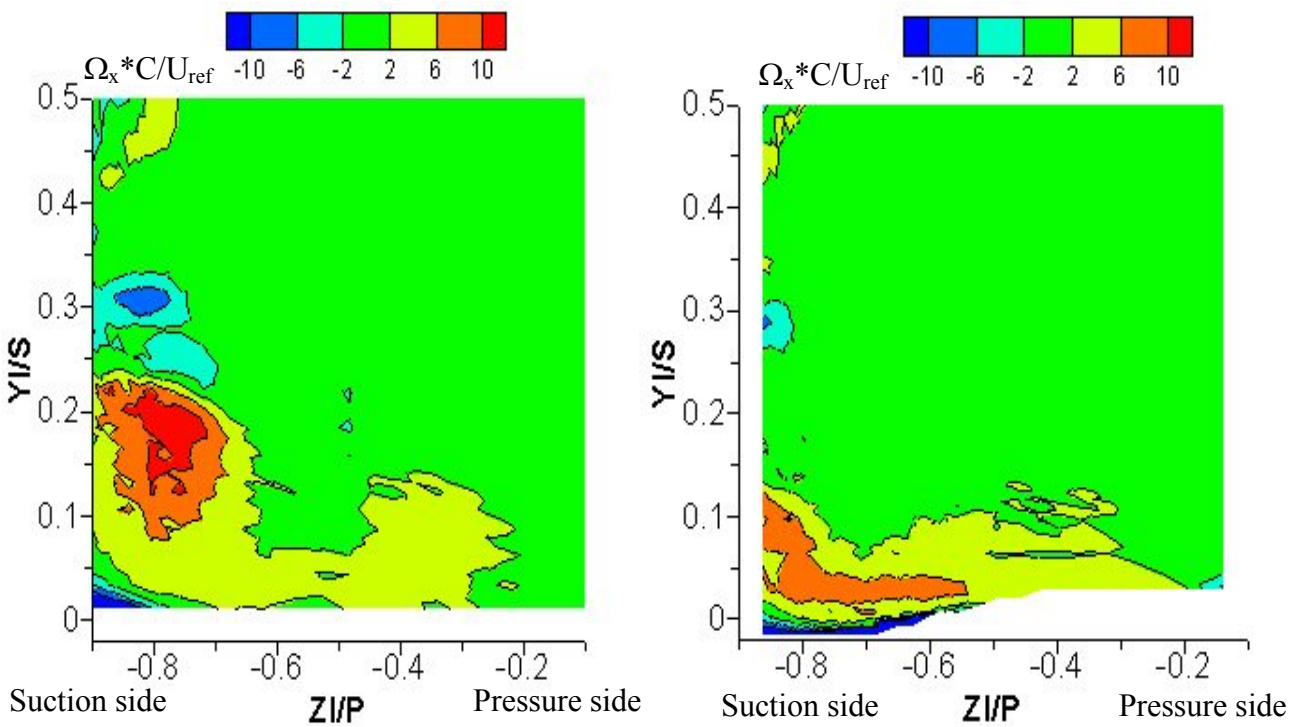

Baseline Contoured endwall

Figure 10: Normalized axial vorticity, $\Omega_x C/U_{ref}$ in pitchwise plane at X_G/C_{ax}=0.916 for baseline and contoured endwall.

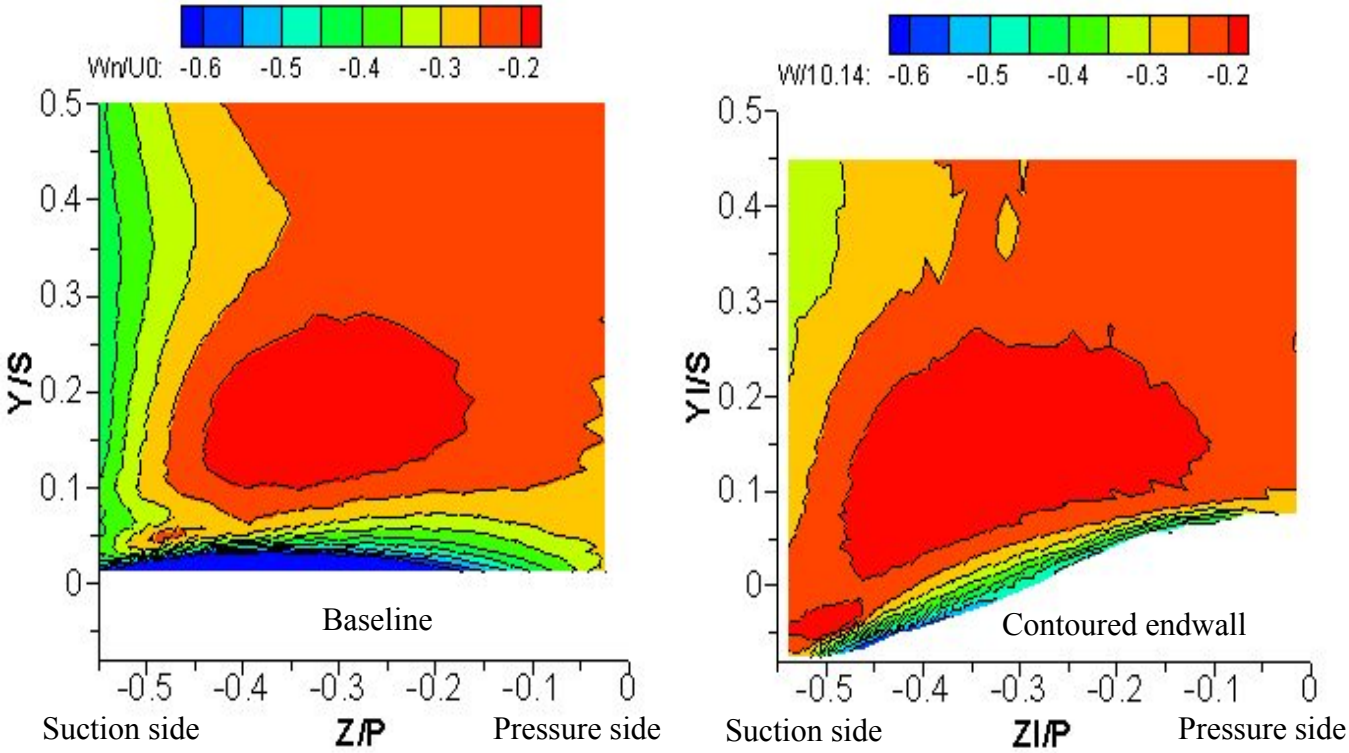

Figure 11: Normalized pitchwise velocity, W/U_{ref} in pitchwise plane at X_G/C_{ax}=0.424 for baseline and contoured endwall.

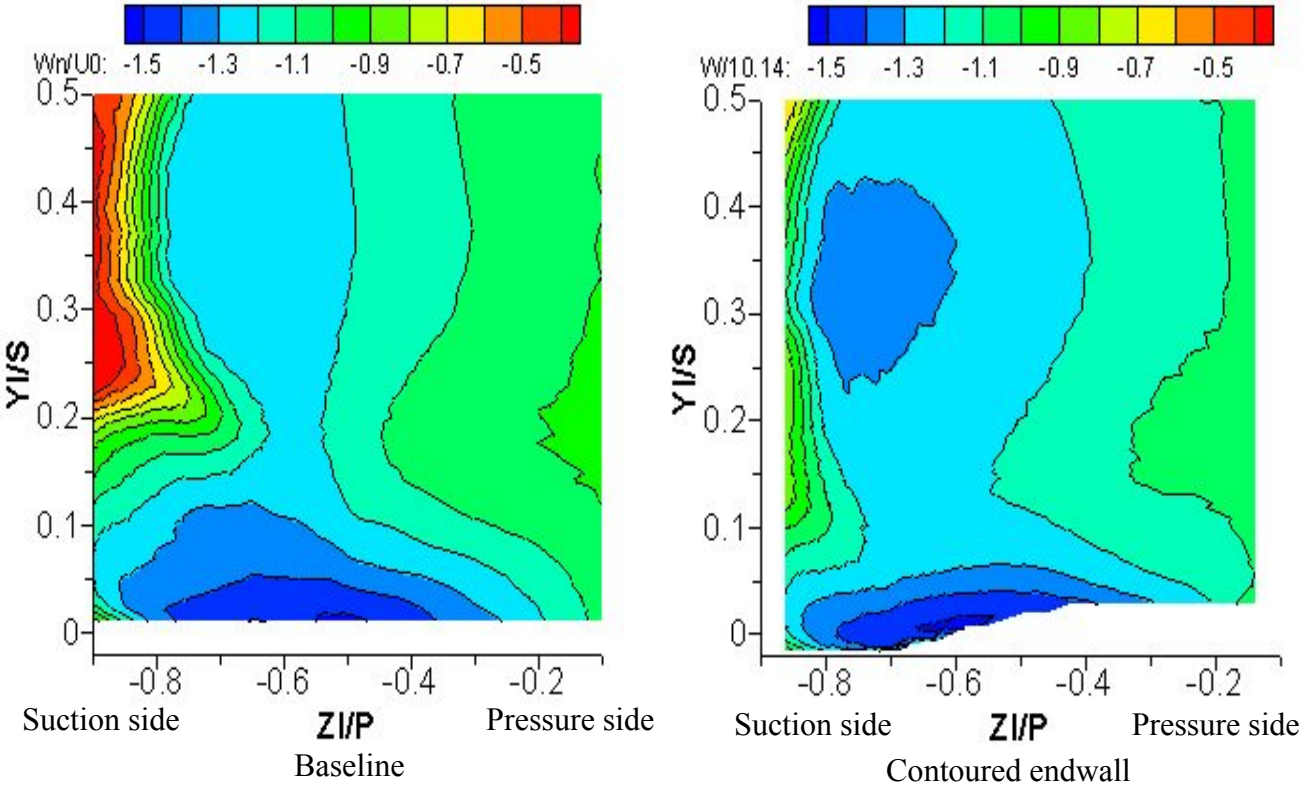

Figure 12: Normalized pitchwise velocity, W/U_{ref} in pitchwise plane at X_G/C_{ax}=0.916 for baseline and contoured endwall.

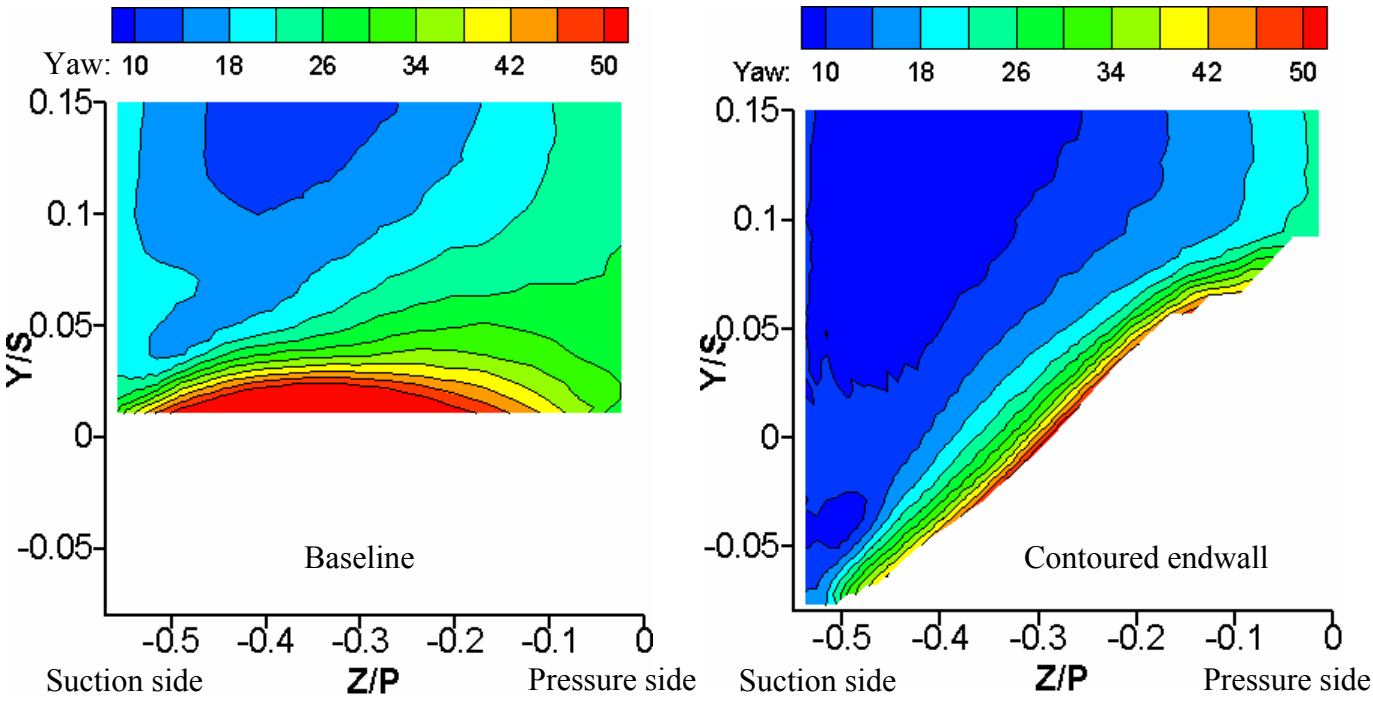

Figure 13: Flow Yaw angle (degree) in pitchwise plane at X_G/C_{ax}=0.424 for baseline and contoured endwall.

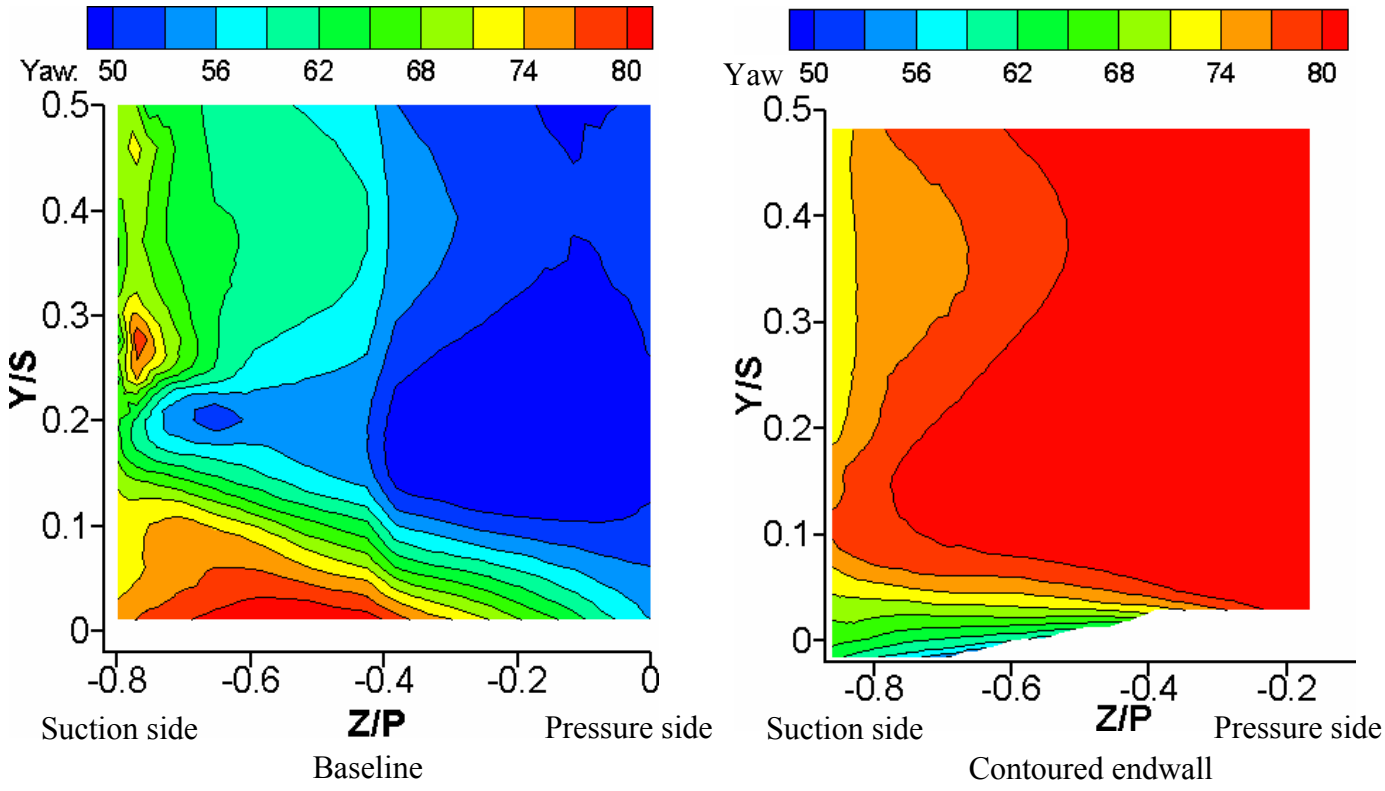

Figure 14: Flow Yaw angle (degree) in pitchwise plane at X_G/C_{ax}=0.916 for baseline and contoured endwall.

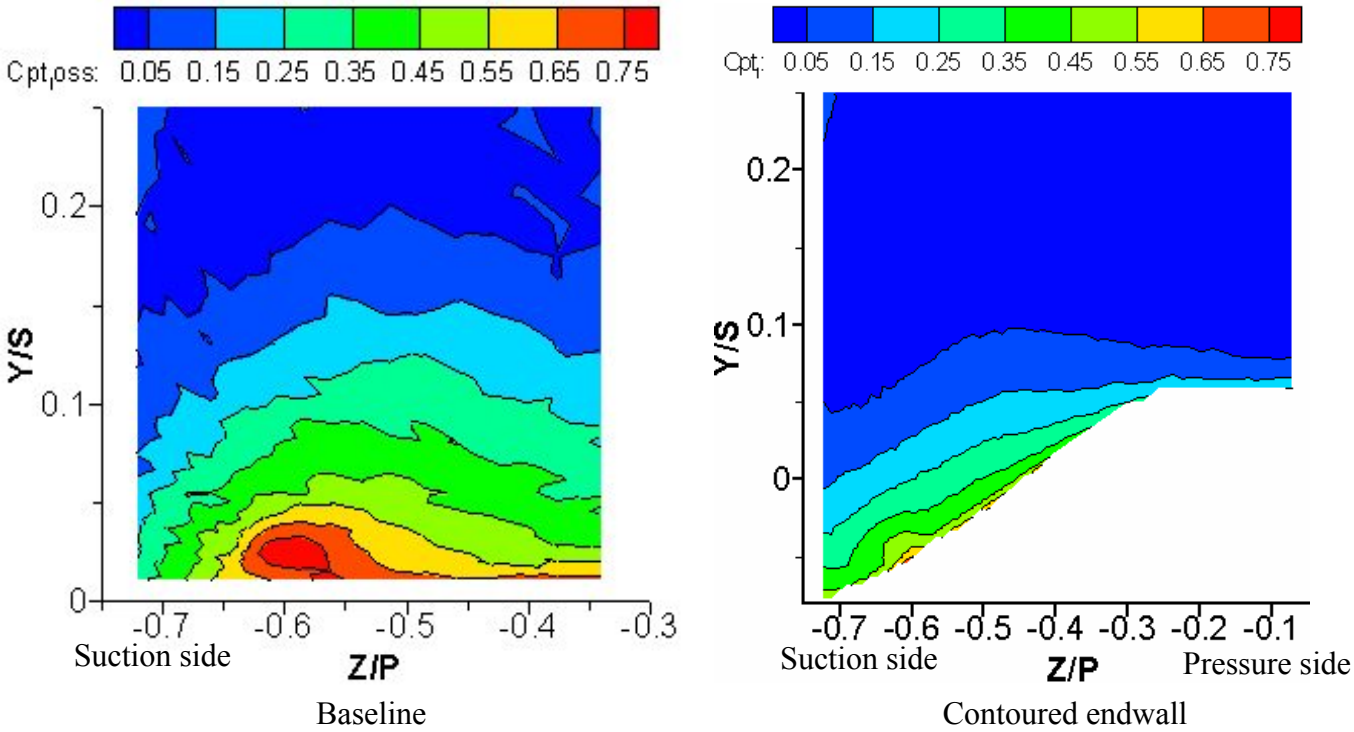

Figure 15: Total pressure loss coefficient, $C_{pt,loss}$ in pitchwise plane at X_G/C_{ax}=0.085 for baseline and contoured endwall.

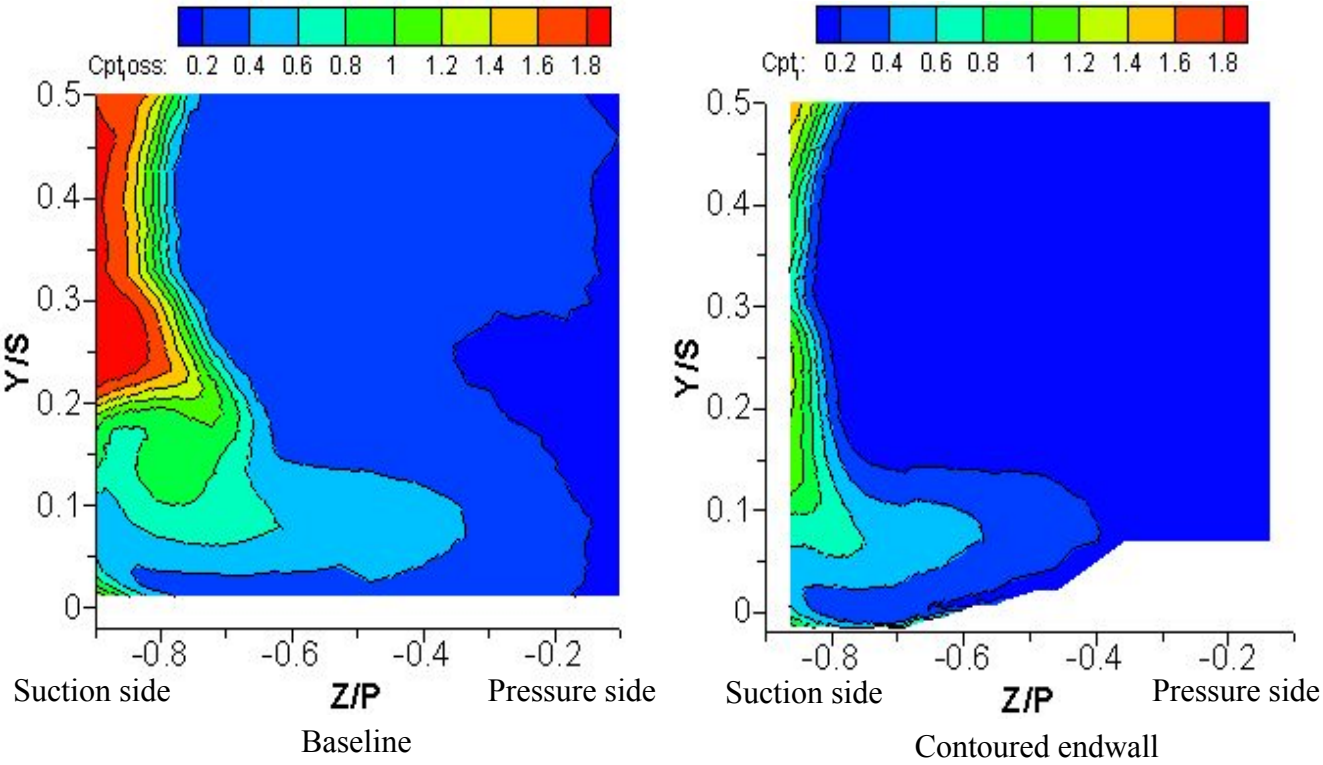

Figure 16: Total pressure loss coefficient $C_{pt,loss}$ in pitchwise plane at X_G/C_{ax}=0.916 for baseline and contoured endwall.

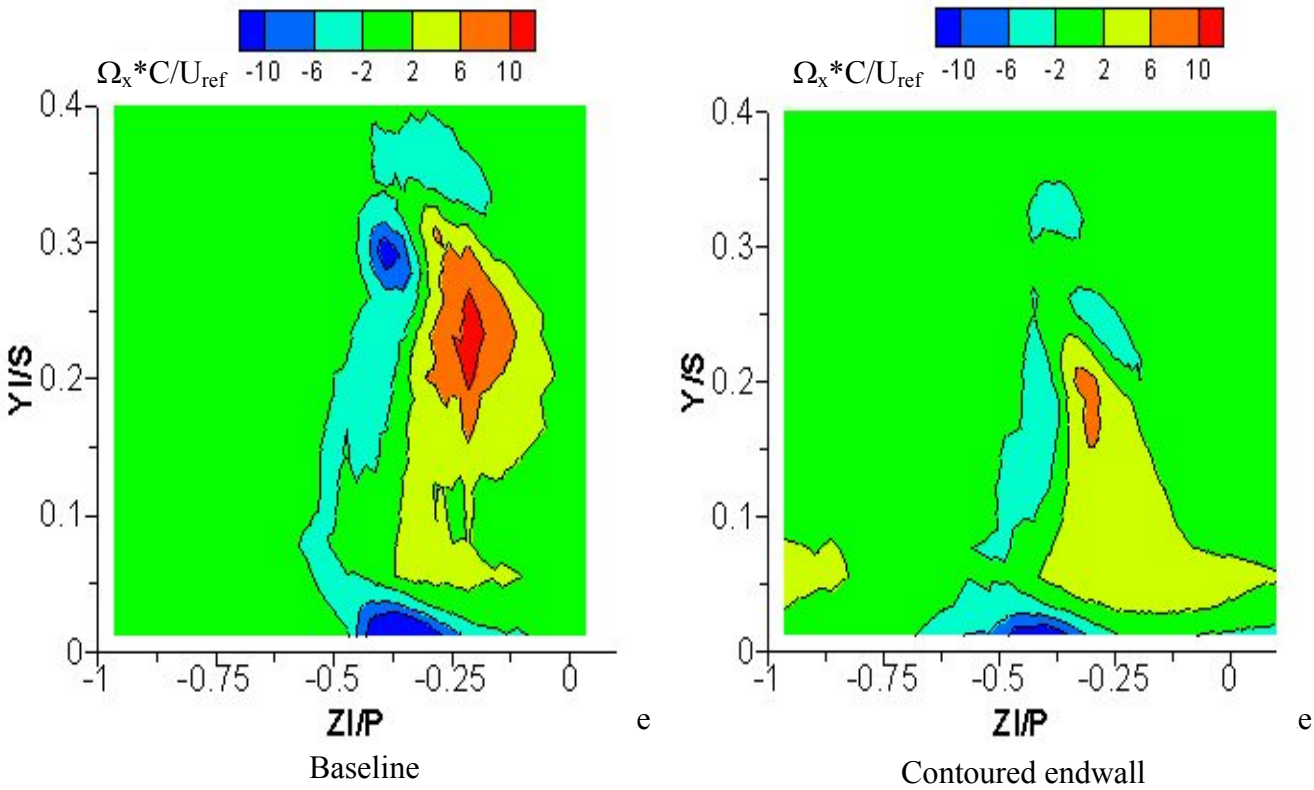

Figure 17: Normalized axial vorticity, $\Omega_x C/U_{ref}$ in pitchwise plane at X_G/C_{ax}=1.214 for baseline and contoured endwall.

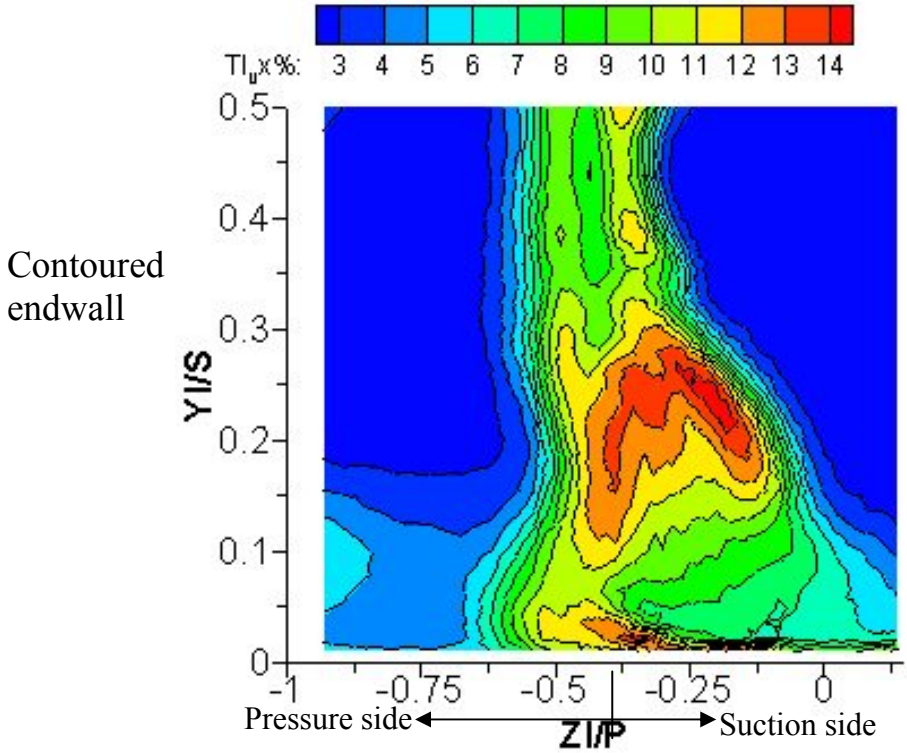

Figure 18: Streamwise turbulence intensity (%) in pitchwise plane at X_G/C_{ax}=1.214 for the contoured endwall.

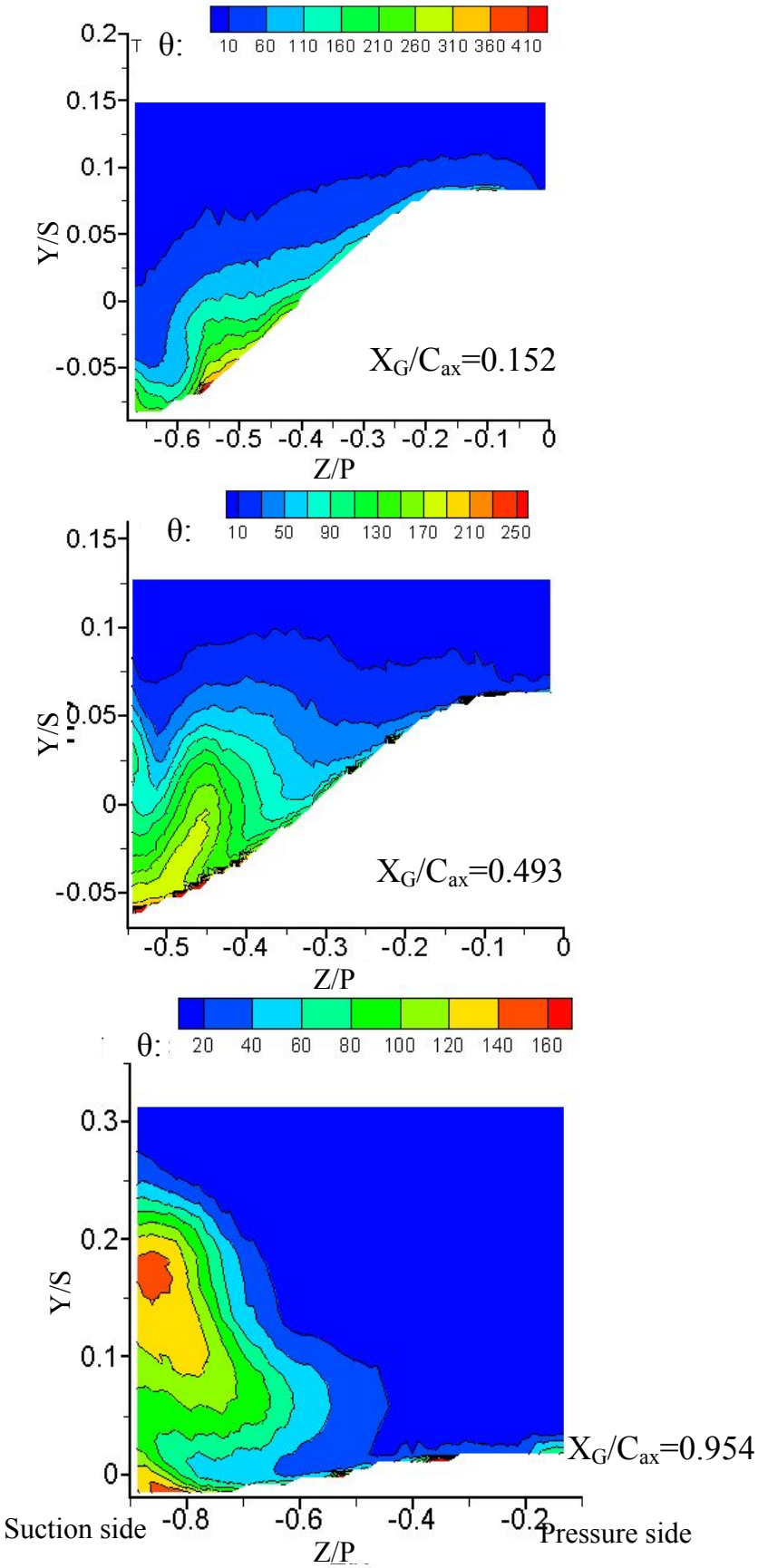

Figure 19: Non-dimensional fluid temperature, θ in pitchwise planes near endwall at different axial locations for the contoured endwall with endwall heating at constant flux.

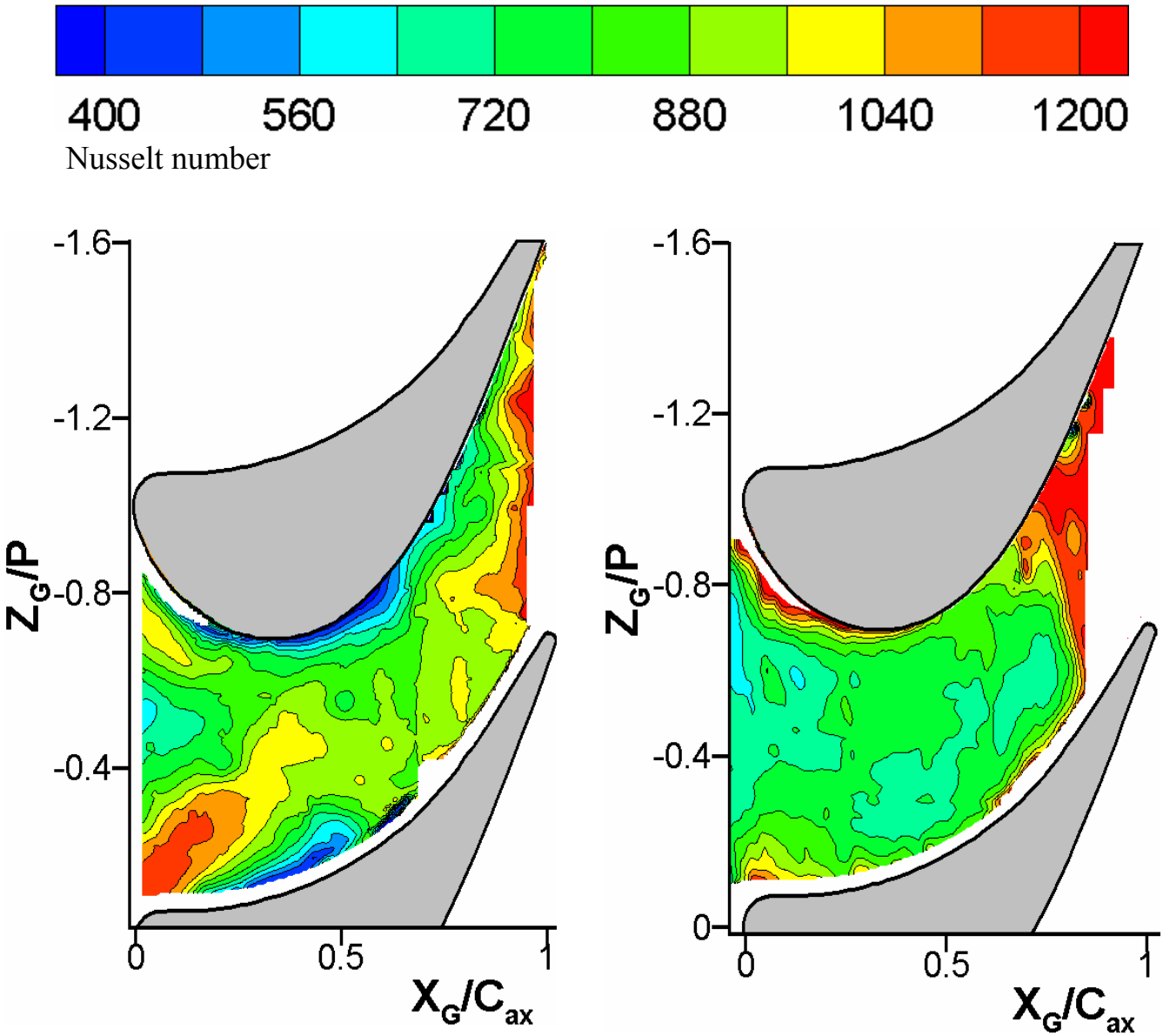

Baseline (flat endwall)

3D non-axisymmetric endwall

Figure 20: Nusselt number distributions on endwall along blade passage for baseline and 3D non-axisymmetric endwall.

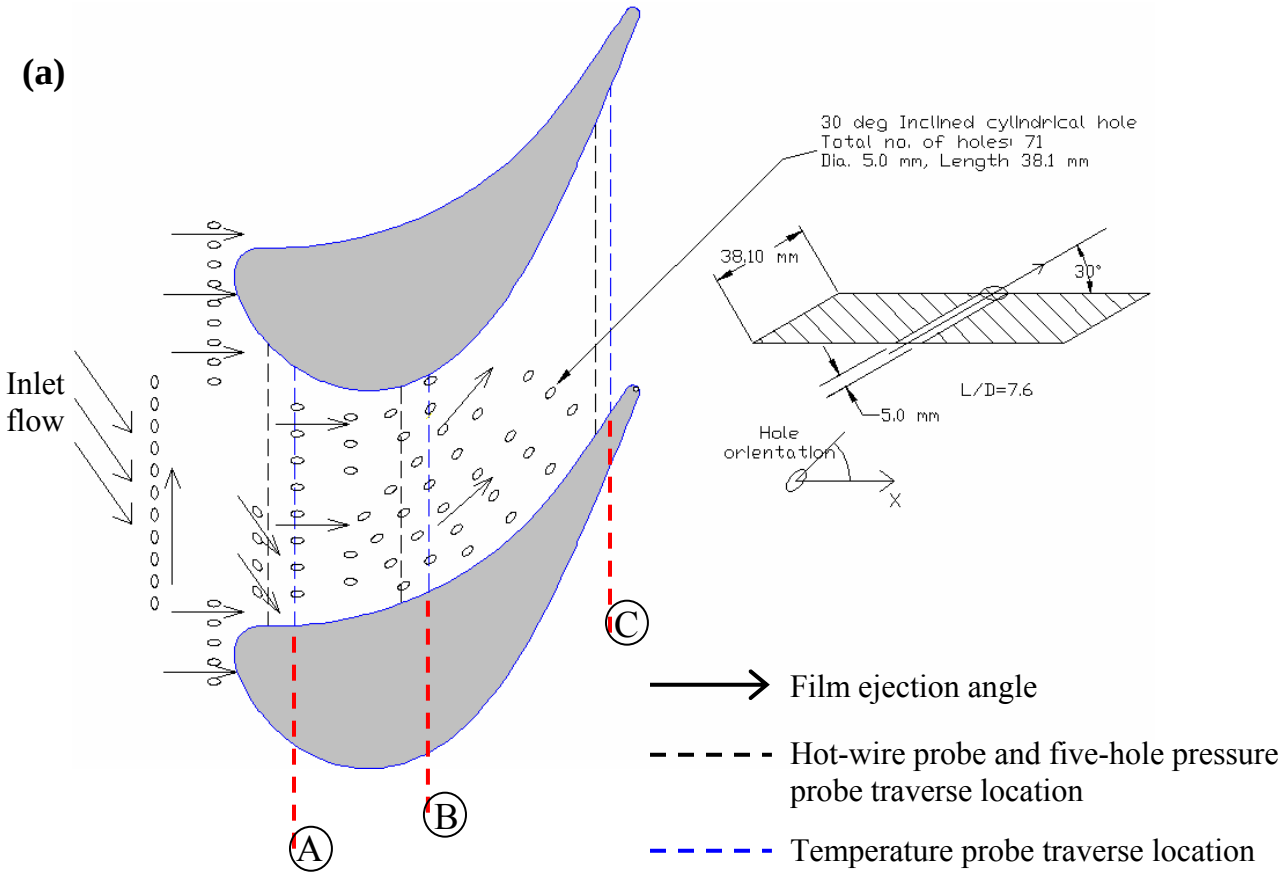

Temperature meas. plane	Location, X_G/C_{ax}
A	0.152
B	0.493
C	0.954

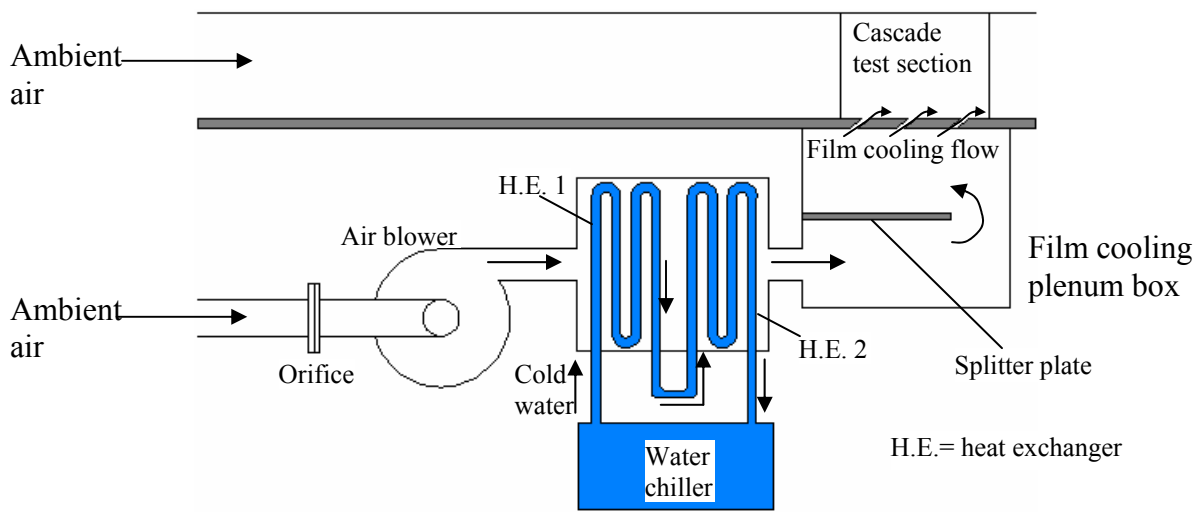

Figure 21: (a) Configuration of film cooling holes in contoured endwall and locations of flow measurement and temperature measurement planes relative to cooling holes.
(b) Schematic of coolant supply circuit to film cooled endwall.

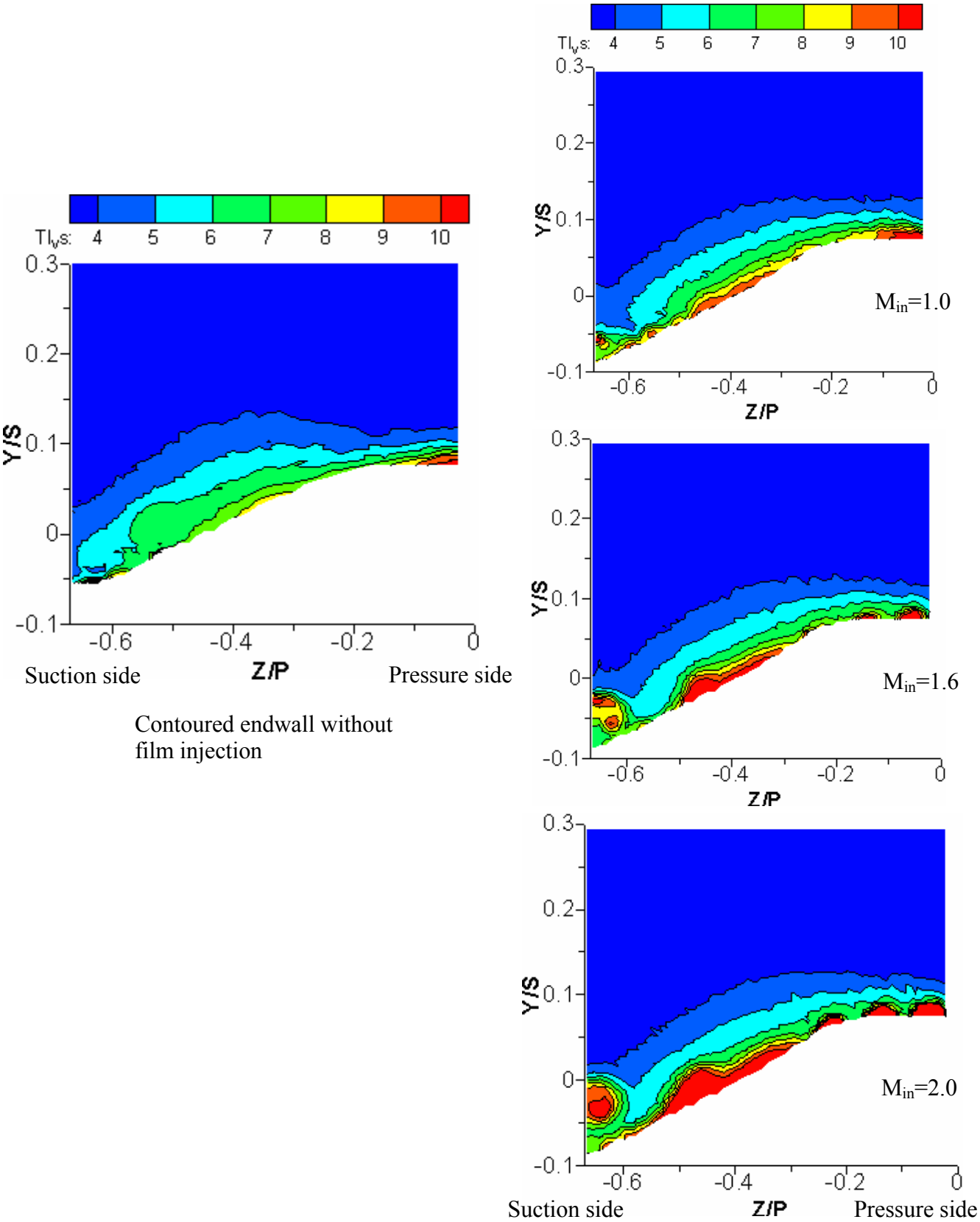

Figure 22: Streamwise turbulence intensity (%) in pitchwise plane at X_G/C_{ax}=0.085 for contoured endwall without and with film injection at inlet blowing ratios M_{in}=1.0 to 2.0.

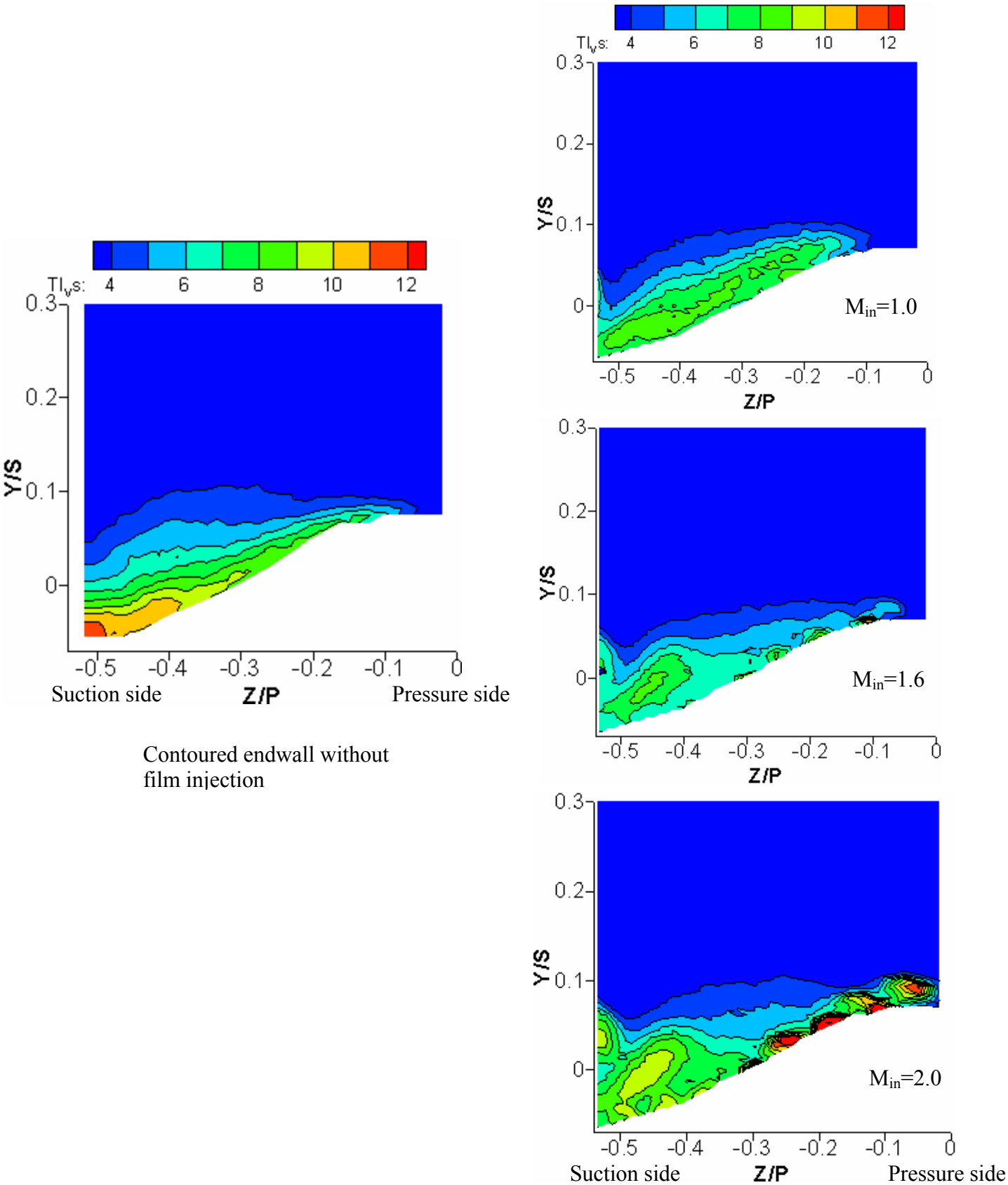

Figure 23: Streamwise turbulence intensity (%) in pitchwise plane at X_G/C_{ax}=0.424 for contoured endwall without and with film injection at inlet blowing ratios M_{in}=1.0 to 2.0.

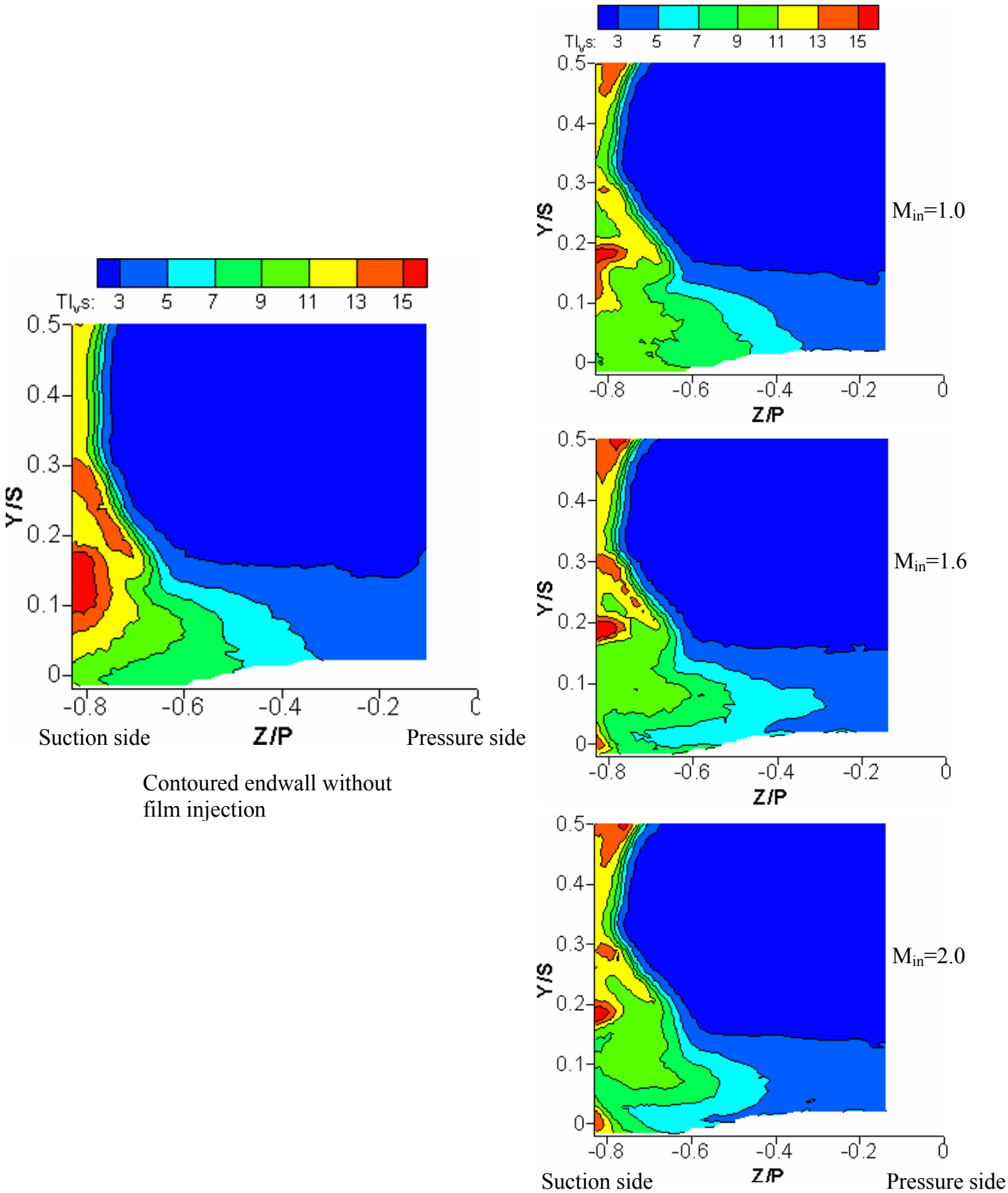

Figure 24: Streamwise turbulence intensity (%) in pitchwise plane at X_G/C_{ax}=0.916 for contoured endwall without and with film injection at inlet blowing ratios M_{in}=1.0 to 2.0.

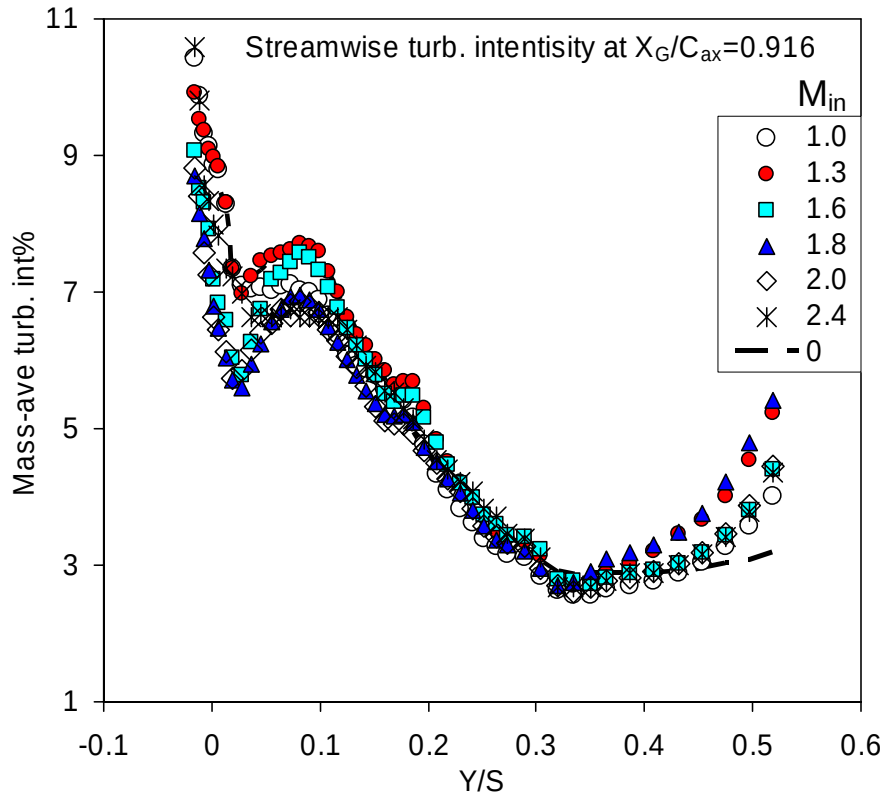

Figure 25: Pitchwise mass-averaged streamwise turbulence intensity at X_G/C_{ax}=0.916 for contoured endwall without and with film injection at inlet blowing ratios M_{in}=1.0 to 2.4.

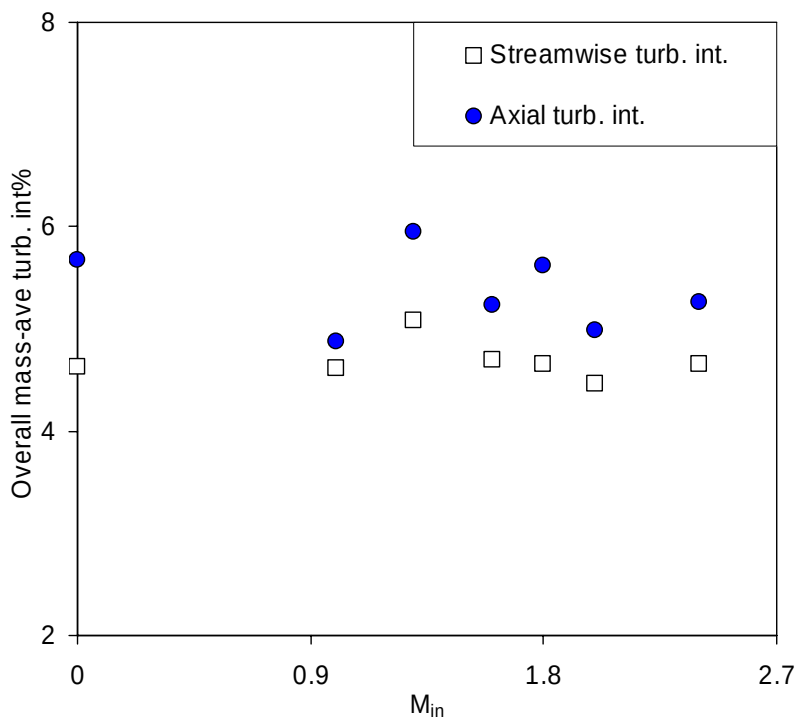

Figure 26: Overall mass-averaged streamwise and axial turbulence intensities as dependent upon inlet blowing ratio, M_{in} at X_G/C_{ax}=0.916 for contoured endwall with film injection.

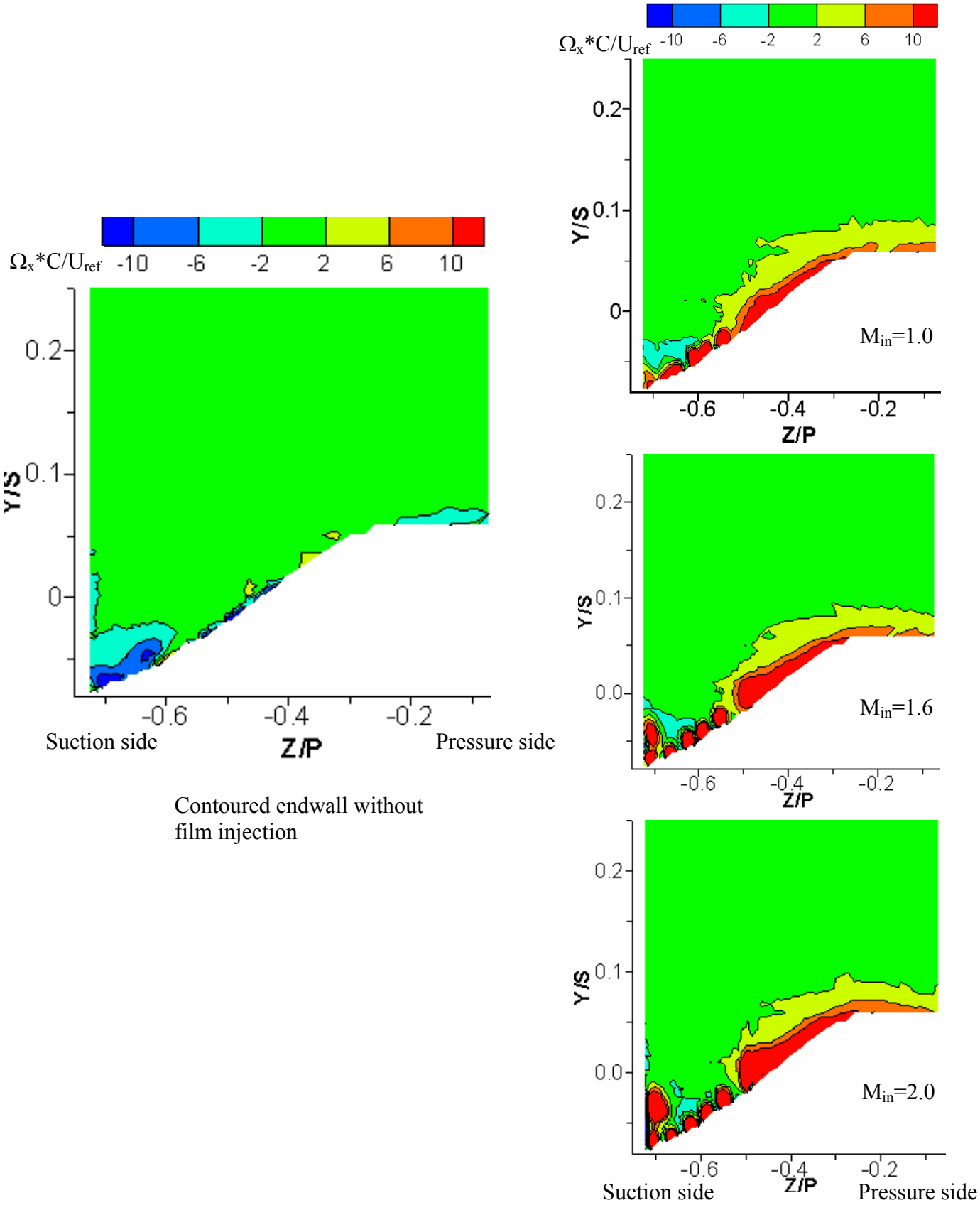

Figure 27: Normalized axial vorticity, Ω_x*C/U_{ref} in pitchwise plane at X_G/C_{ax}=0.085 for contoured endwall without and with film injection at inlet blowing ratios M_{in}=1.0 to 2.0.

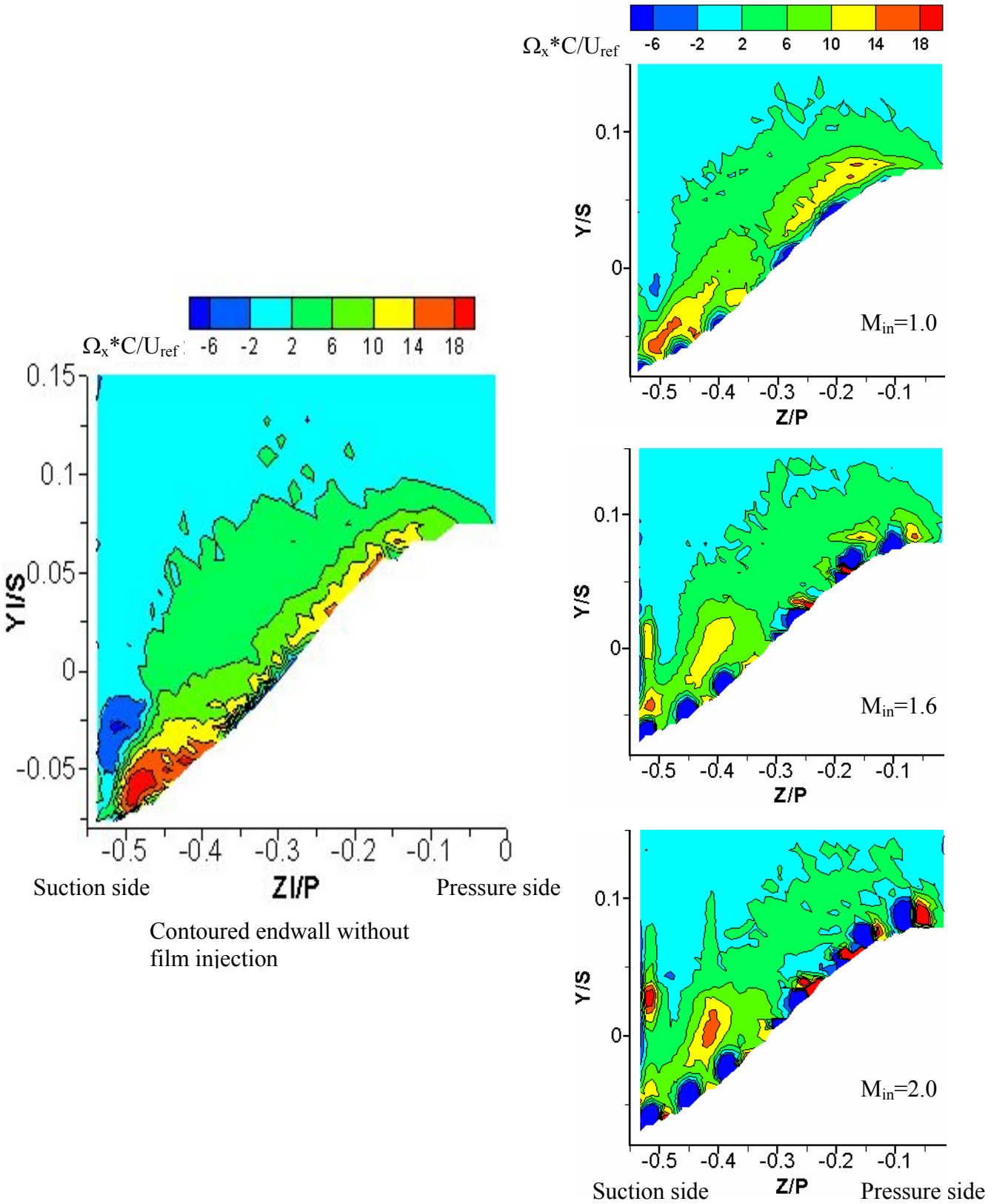

Figure 28: Normalized axial vorticity, Ω_x*C/U_{ref} in pitchwise plane at X_G/C_{ax}=0.424 for contoured endwall without and with film injection at inlet blowing ratios M_{in}=1.0 to 2.0.

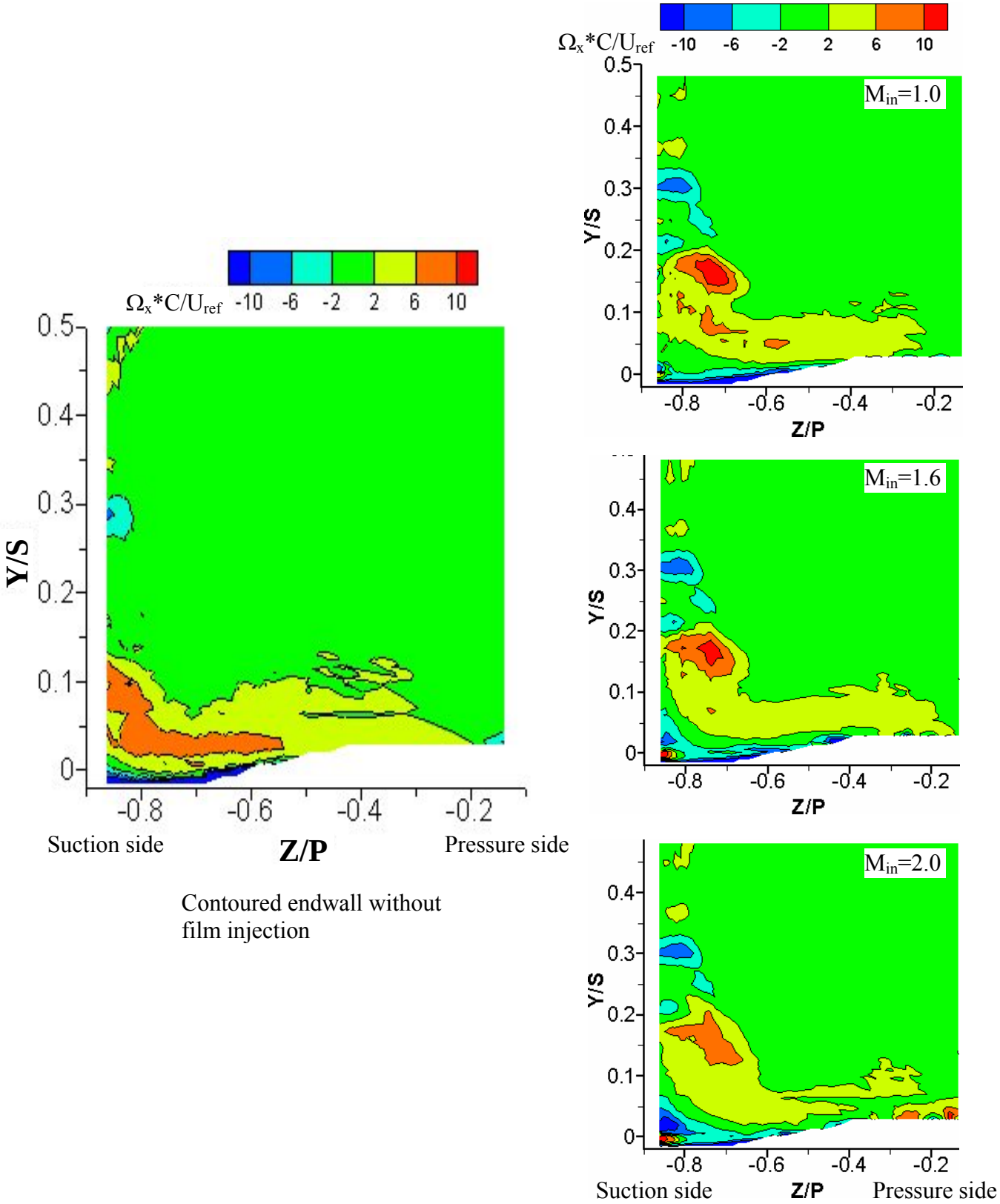

Figure 29: Normalized axial vorticity, Ω_x*C/U_{ref} in pitchwise plane at X_G/C_{ax}=0.916 for contoured endwall without and with film injection at inlet blowing ratios M_{in}=1.0 to 2.0.

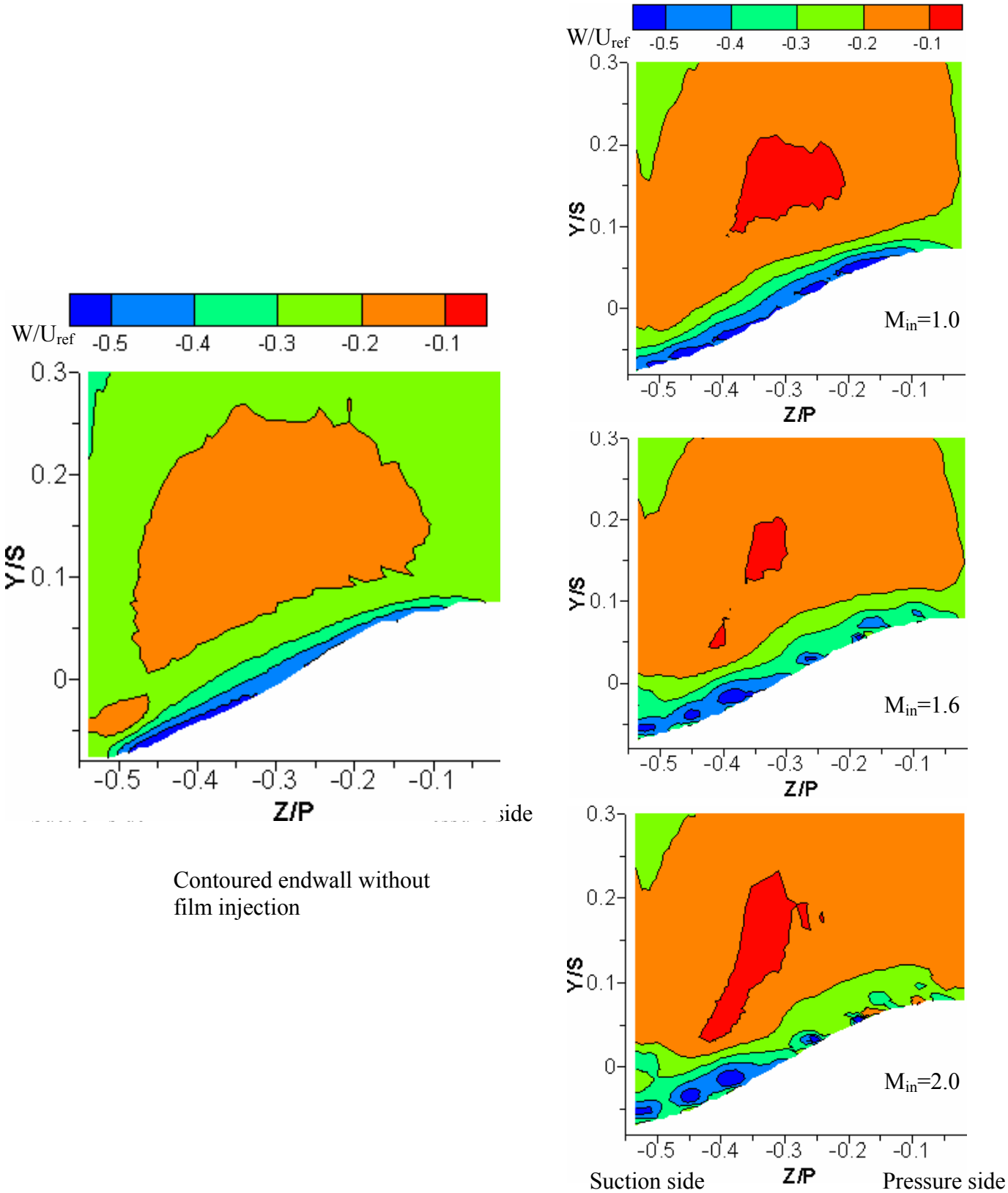

Figure 30: Normalized pitchwise velocity, W/U_{ref} in pitchwise plane at X_G/C_{ax}=0.424 for contoured endwall without and with film injection at inlet blowing ratios M_{in}=1.0 to 2.0.

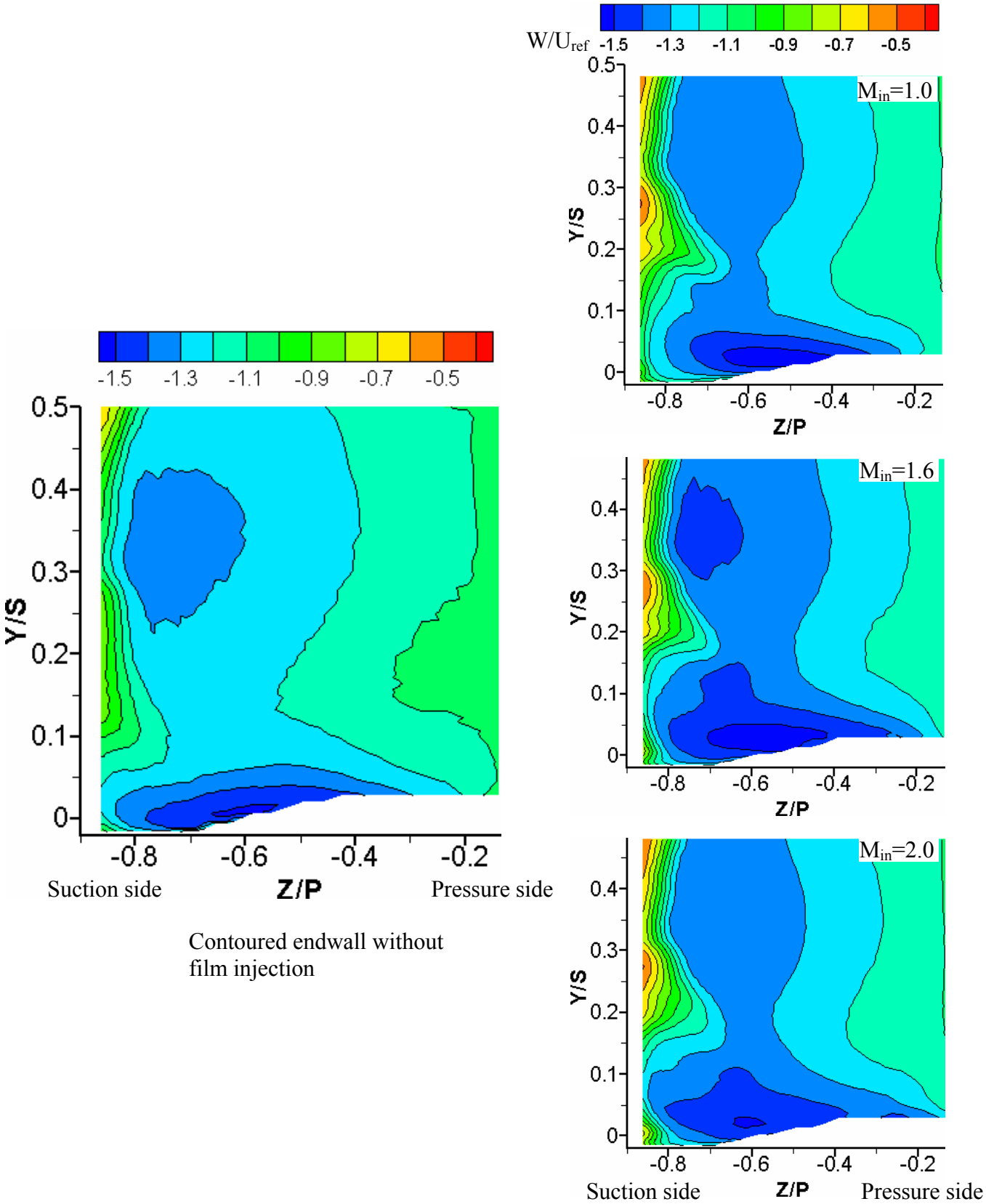

Contoured endwall without film injection

Figure 31: Normalized pitchwise velocity, W/U_{ref} in pitchwise plane at X_G/C_{ax}=0.916 for contoured endwall without and with film injection at inlet blowing ratios M_{in}=1.0 to 2.0.

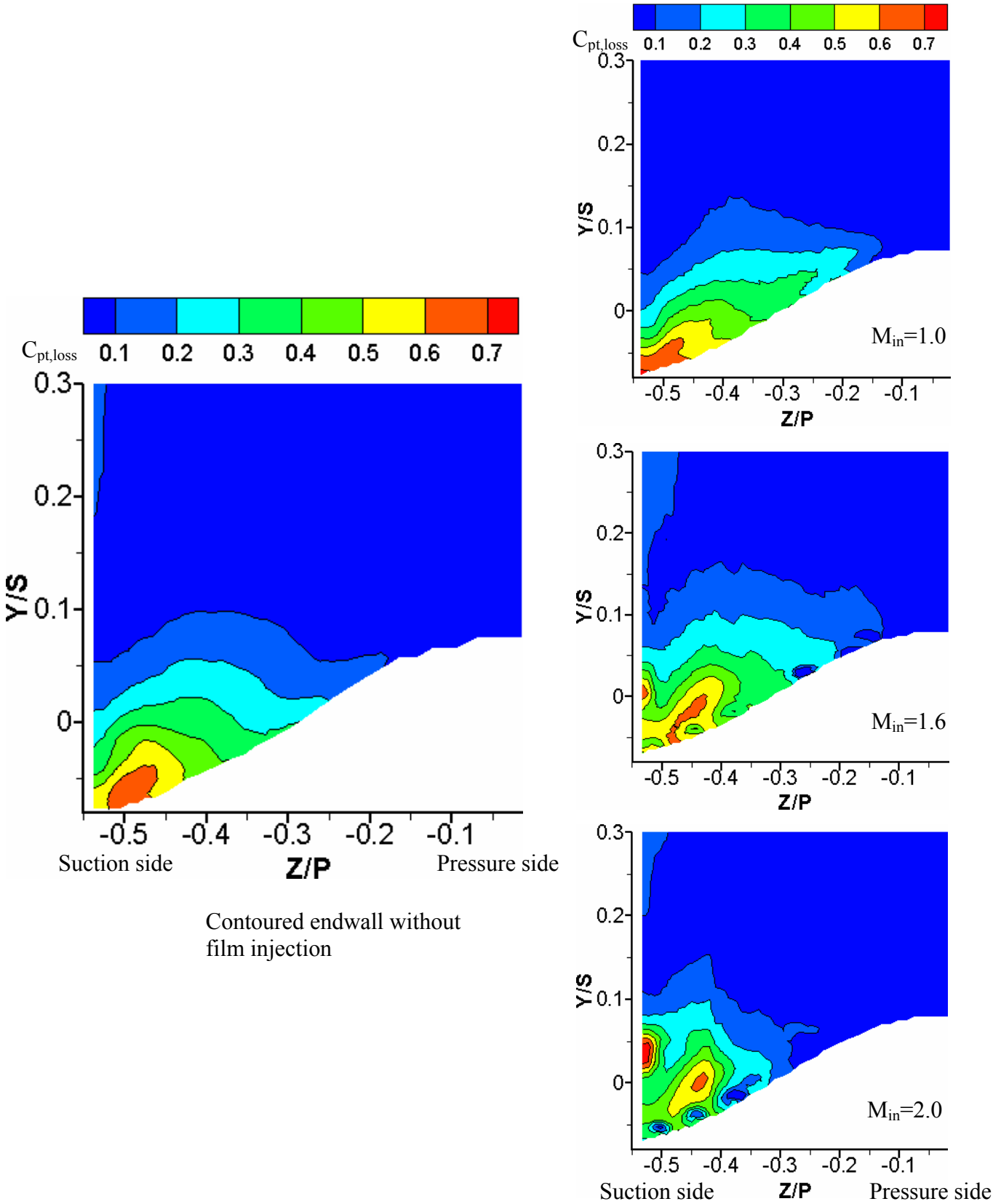

Contoured endwall without film injection

Figure 32: Total pressure loss coefficient, $C_{pt,loss}$ in pitchwise plane at X_G/C_{ax}=0.424 for contoured endwall without and with film injection at inlet blowing ratios M_{in}=1.0 to 2.0.

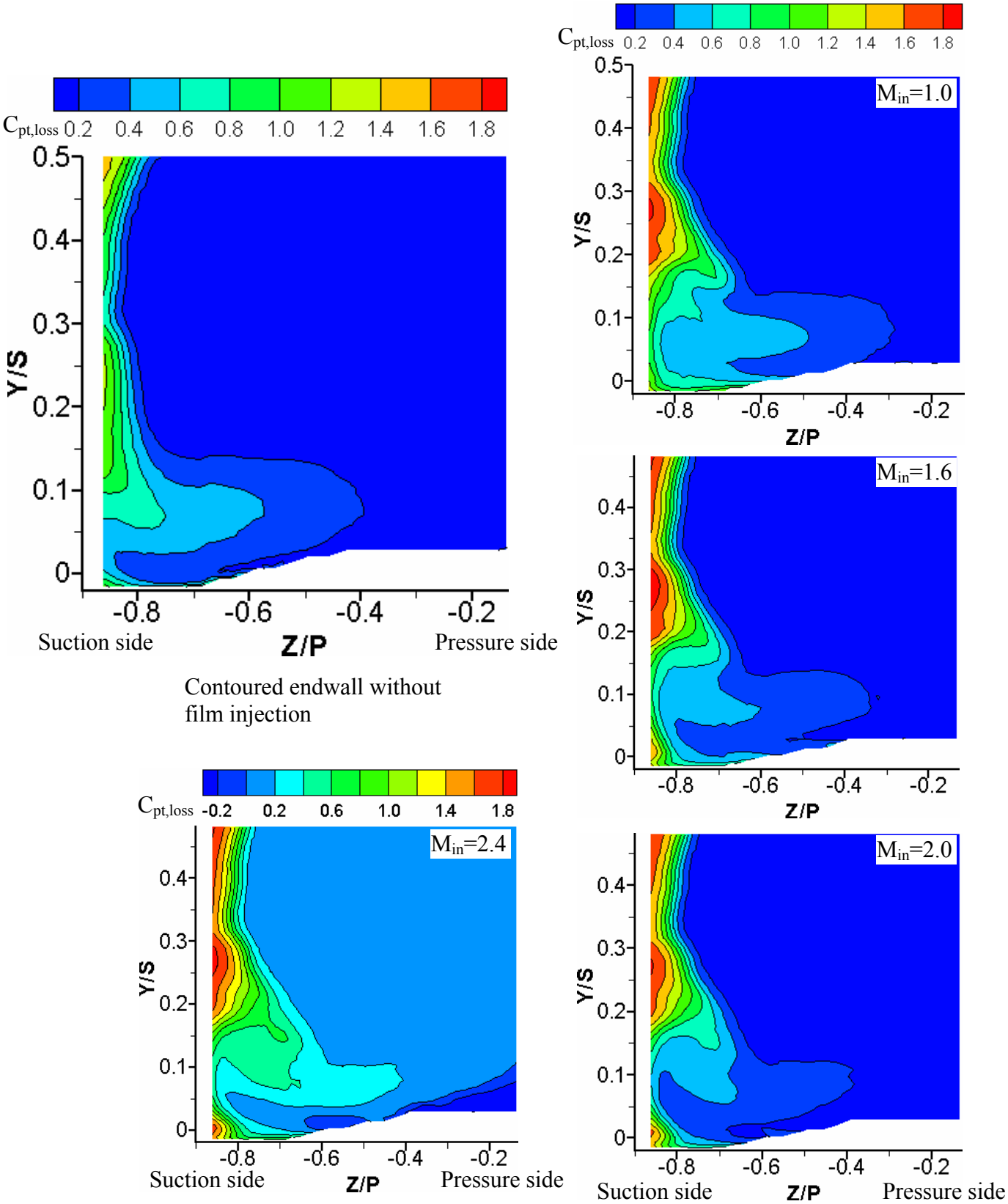

Figure 33: Total pressure loss coefficient, $C_{pt,loss}$ in pitchwise plane at X_G/C_{ax}=0.916 for contoured endwall without and with film injection at inlet blowing ratios M_{in}=1.0 to 2.4.

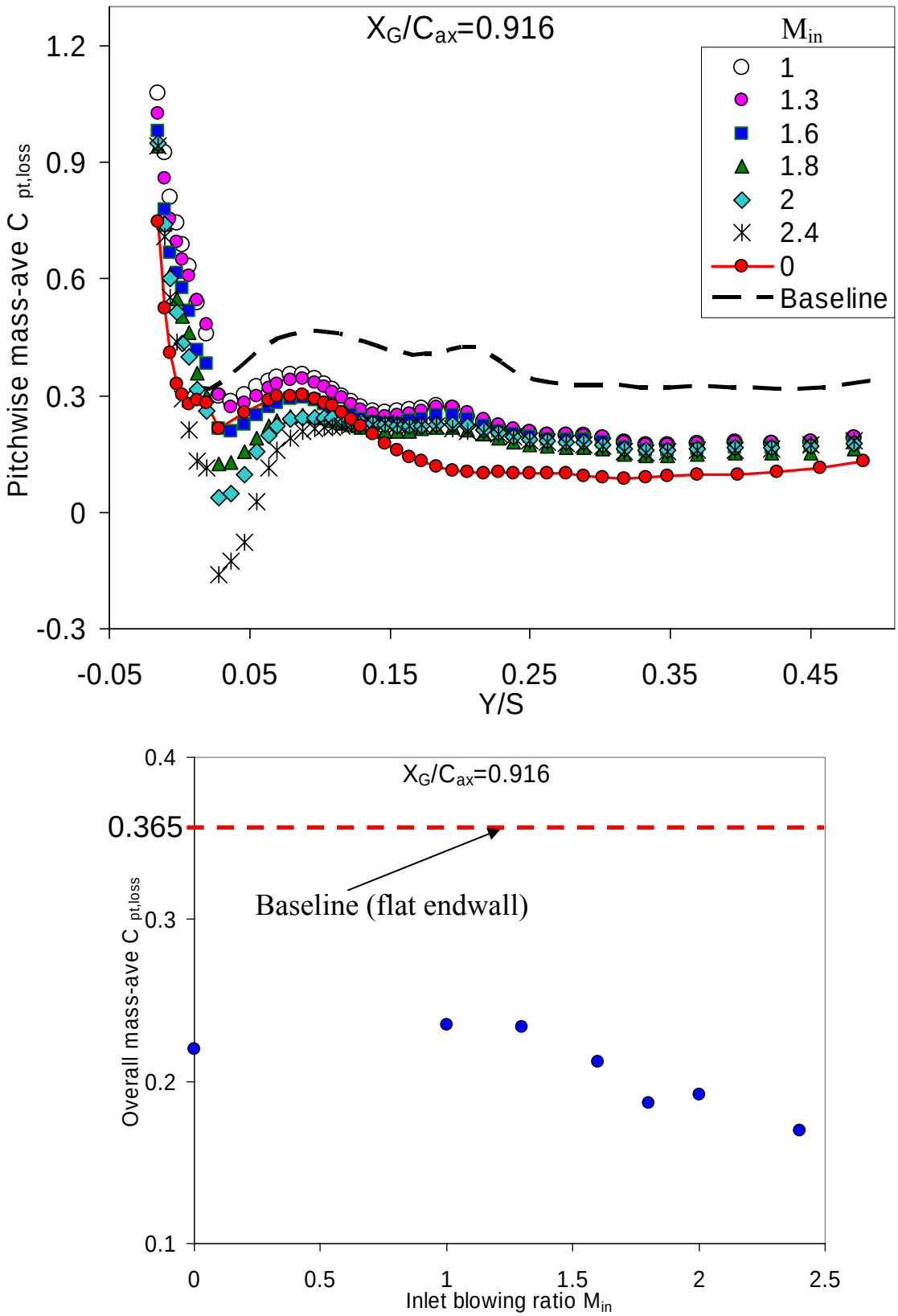

Figure 34: Pitchwise mass-averaged and overall mass averaged total pressure loss coefficient, $C_{pt,loss}$ at X_G/C_{ax}=0.916 for contoured endwall with and without film injection.

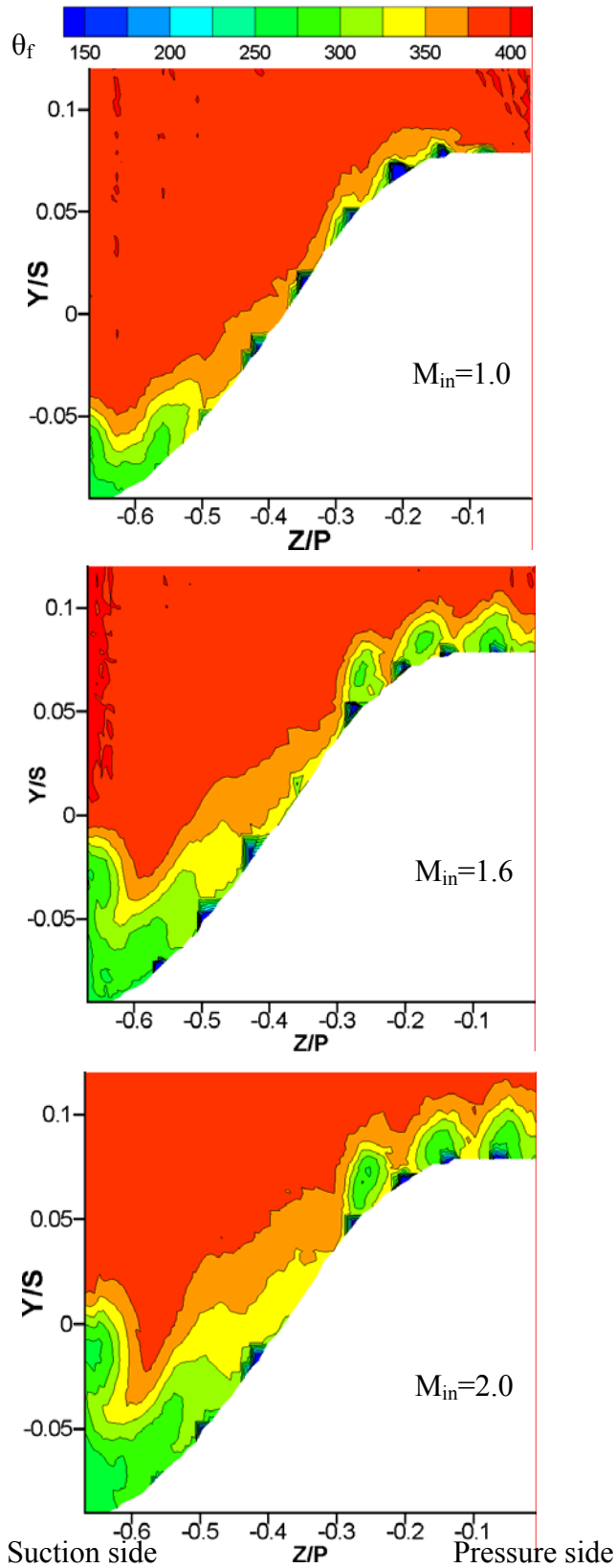

Figure 35: Non-dimensional fluid temperature, θ_f near endwall at X_G/C_{ax}=0.152 for contoured endwall with film injection at inlet blowing ratios M_{in}=1.0 to 2.0.

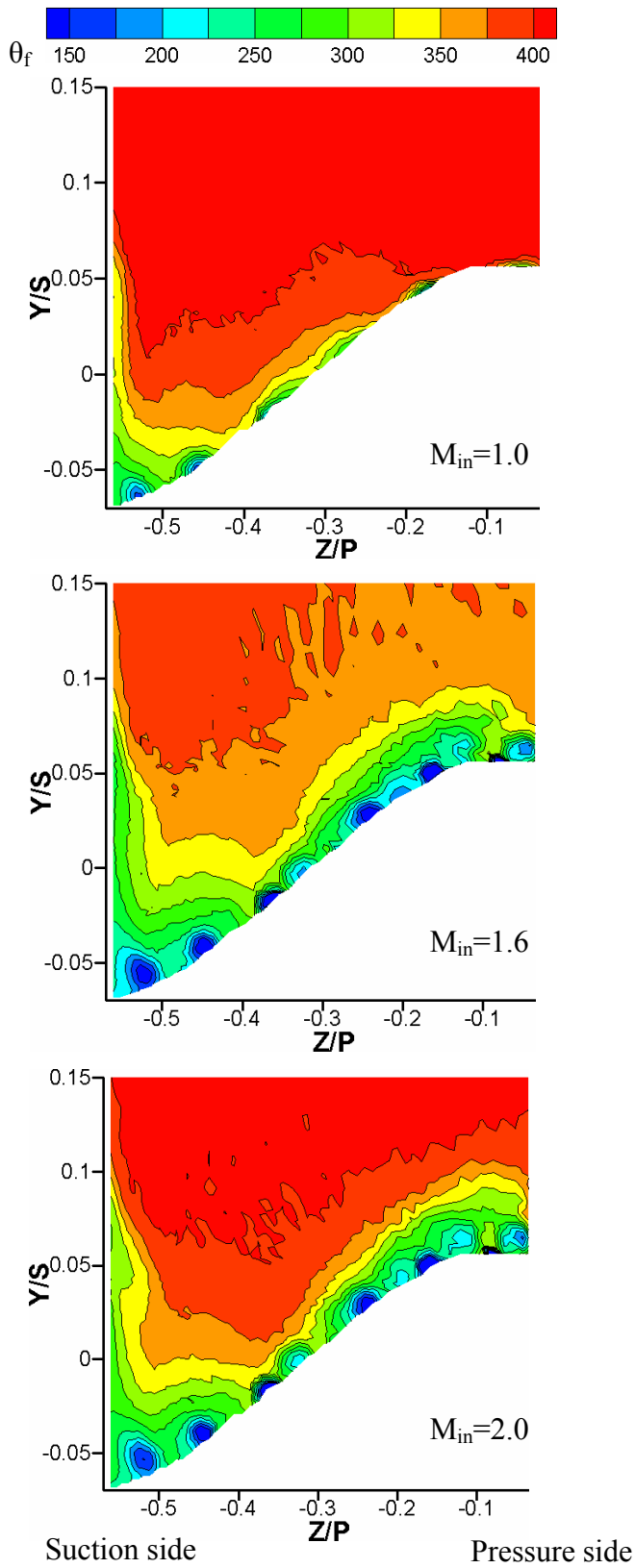

Figure 36: Non-dimensional fluid temperature, θ_f near endwall at X_G/C_{ax}=0.493 for contoured endwall with film injection at inlet blowing ratios M_{in}=1.0 to 2.0.

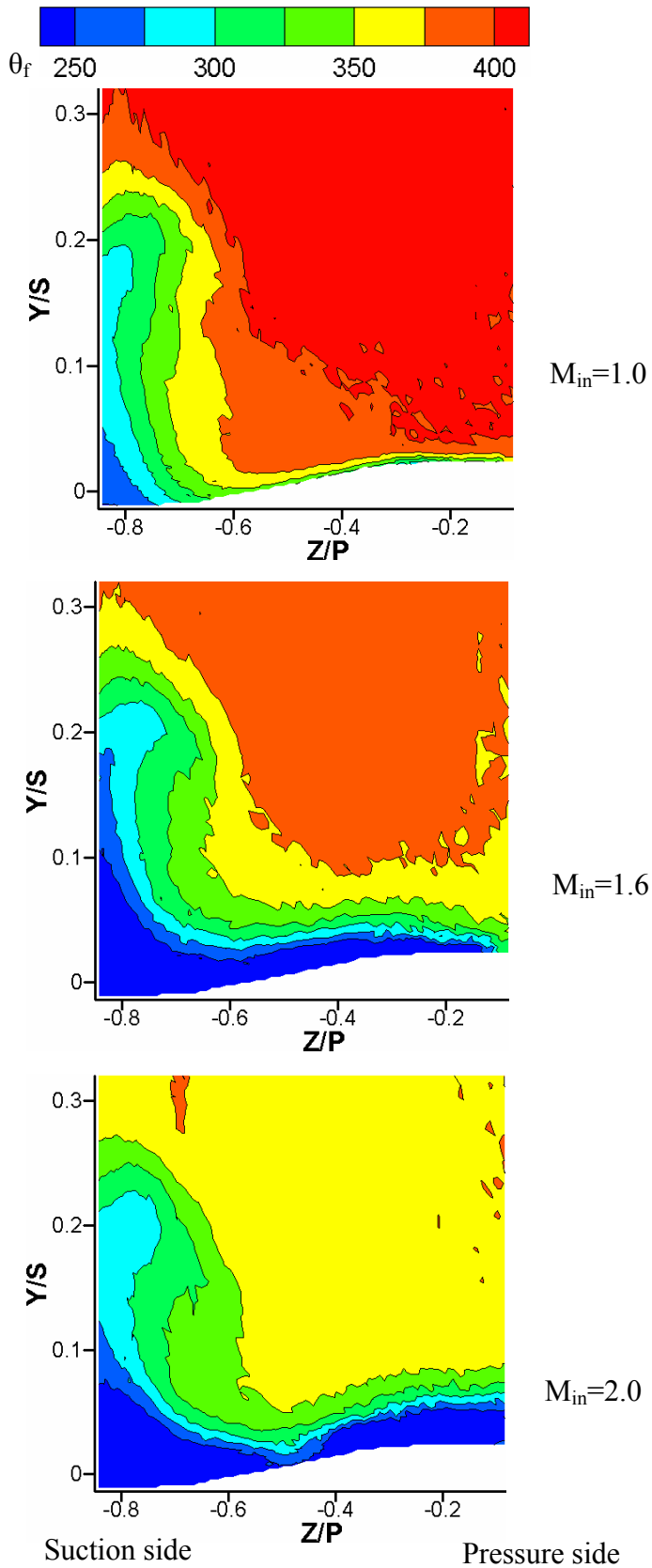

Figure 37: Non-dimensional fluid temperature, θ_f near endwall at X_G/C_{ax}=0.954 for contoured endwall with film injection at inlet blowing ratios M_{in}=1.0 to 2.0.

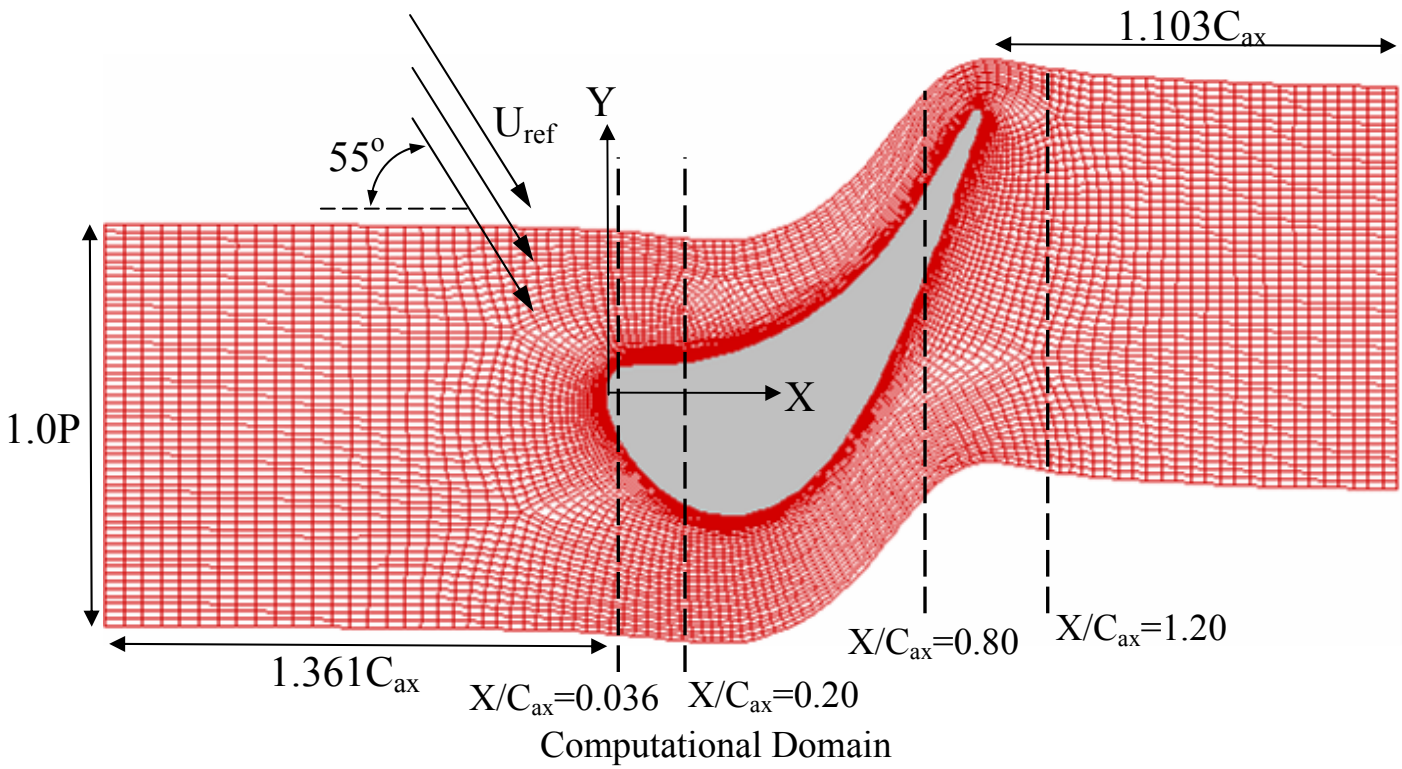

Figure 38: Computational domain and endwall grid geometry for baseline and contoured endwall.

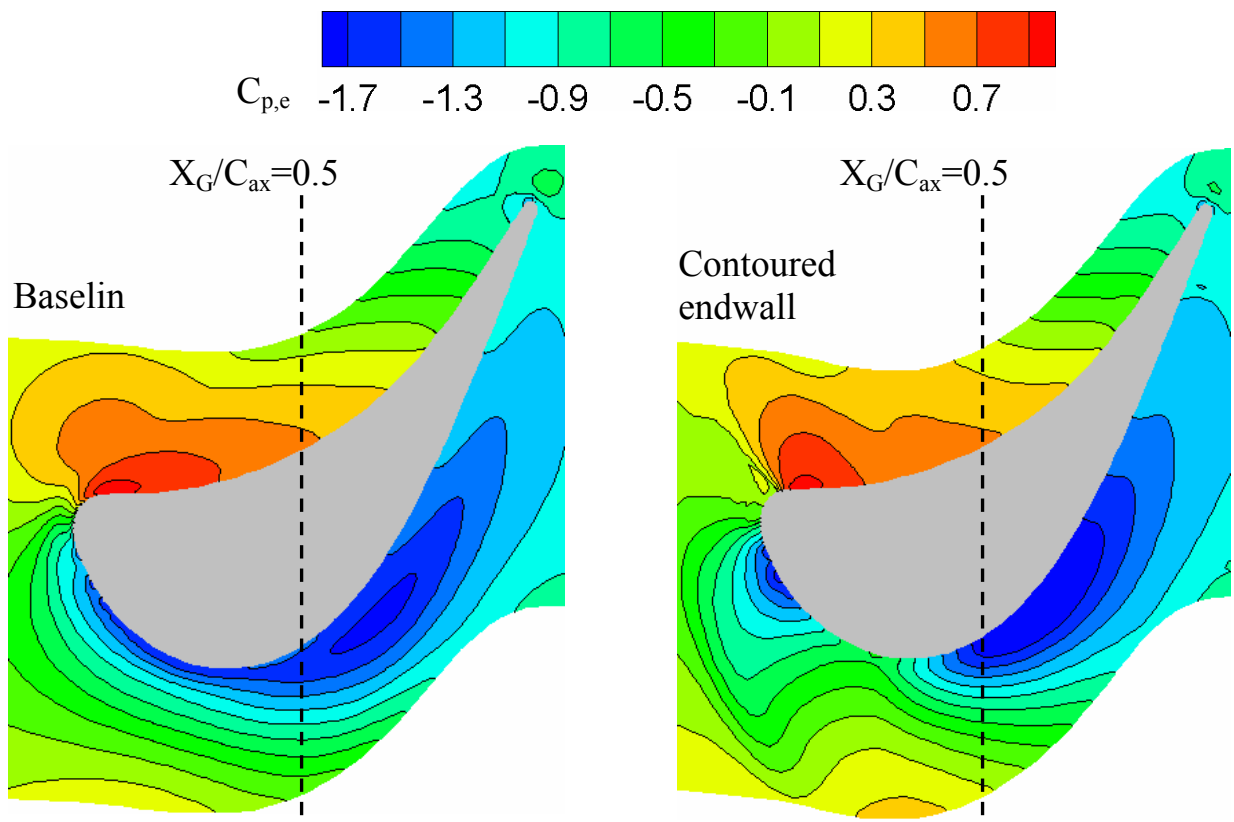

Figure 39: Endwall static pressure coeffis. for baseline and contoured endwall (computations).

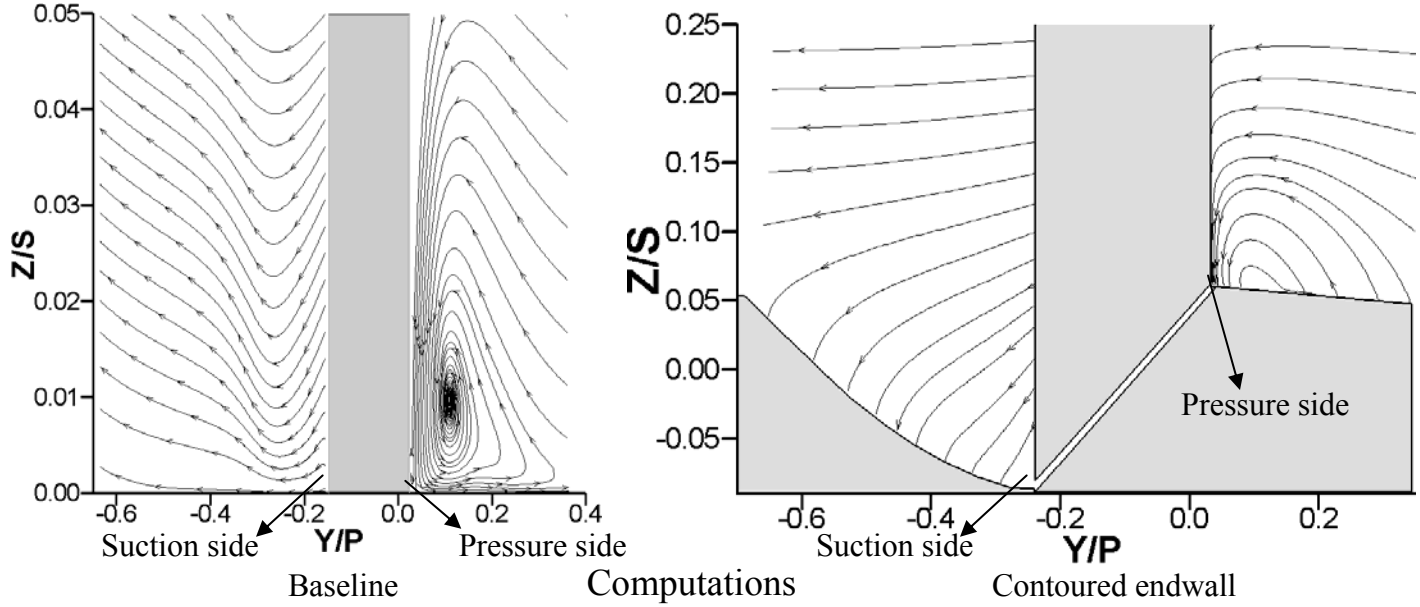

Figure 40: Streamlines in pitchwise plane at X_G/C_{ax}=0.036 for baseline and contoured endwall.

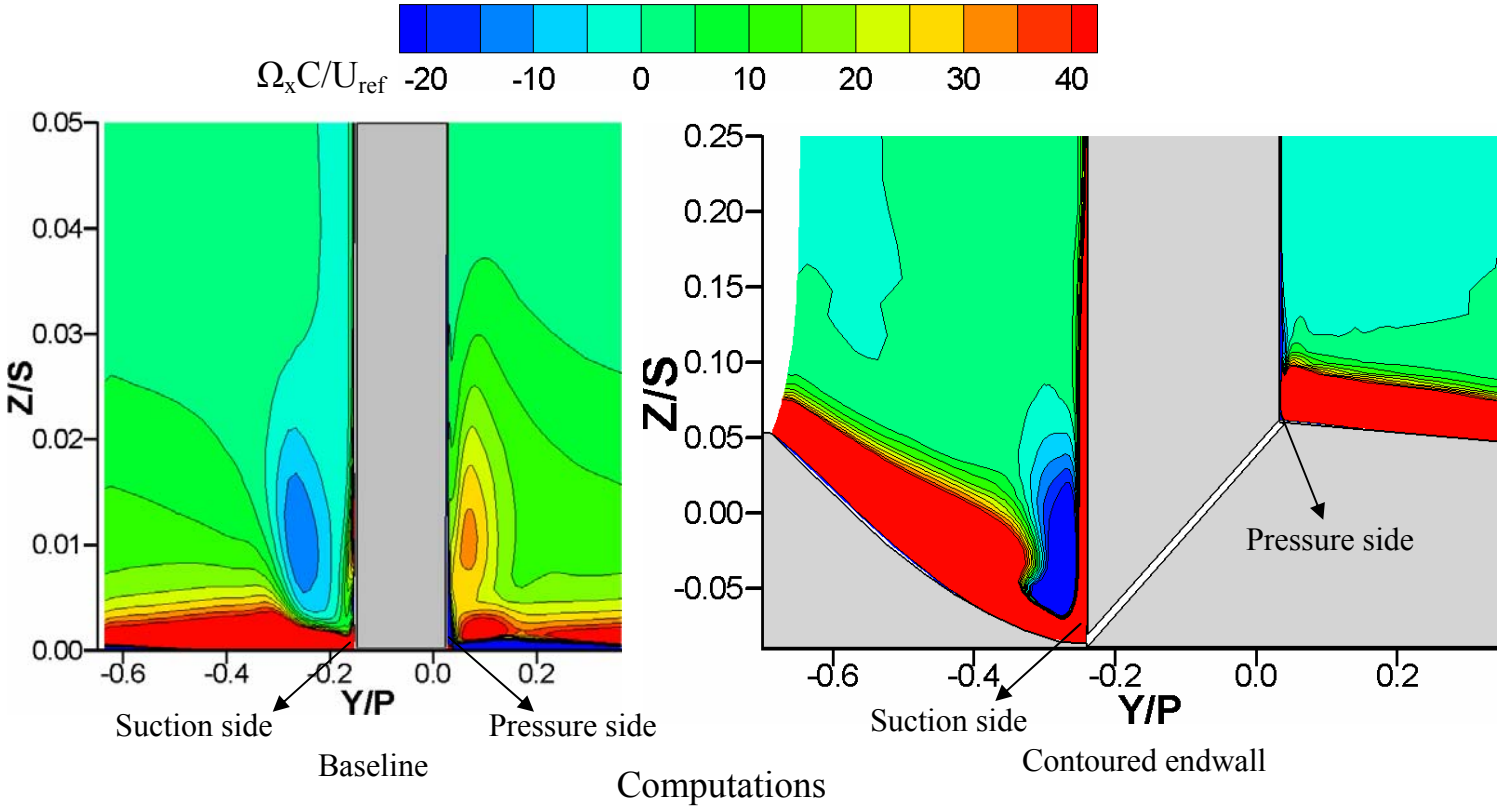

Figure 41: Normalized axial vorticity $\Omega_x C/U_{ref}$ in pitchwise plane at X_G/C_{ax}=0.036 for baseline and contoured endwall.

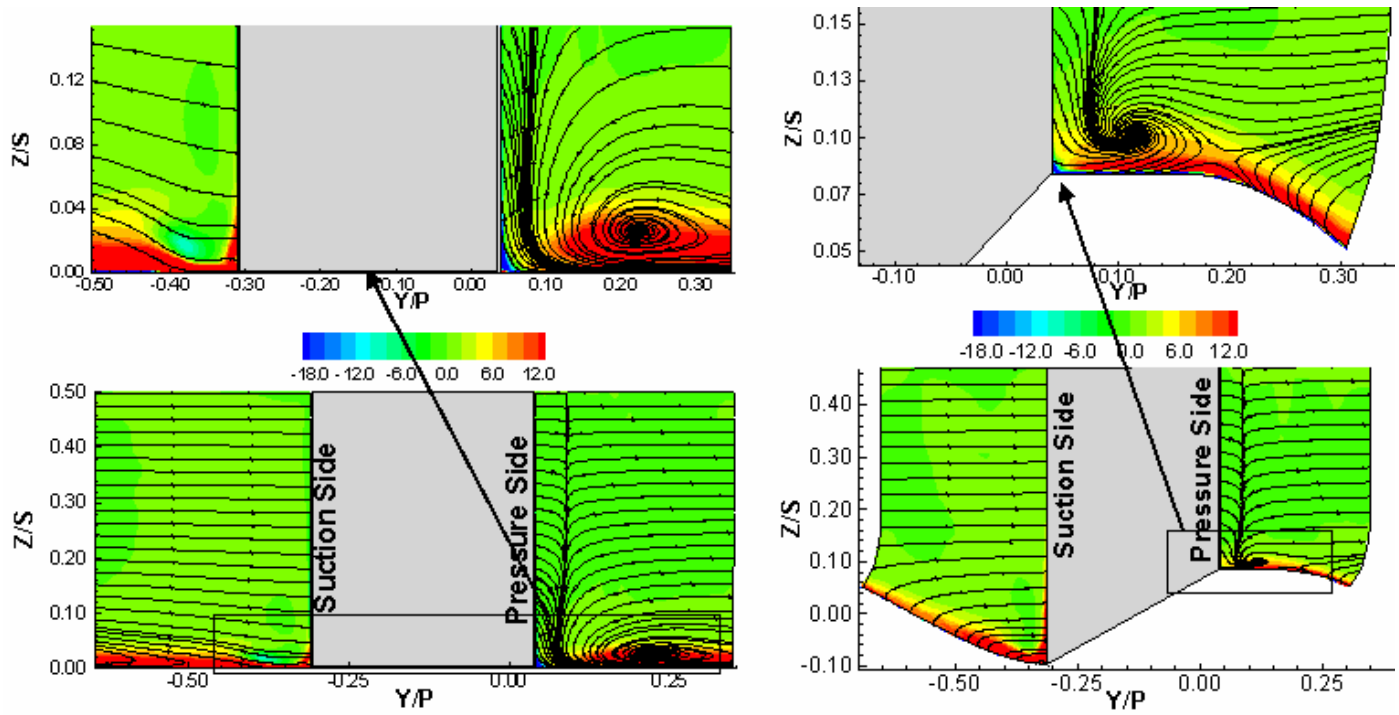

Baseline Contoured endwall

Computations

Figure 42: Streamlines superimposed on normalized axial vorticity in pitchwise plane at X_G/C_{ax}=0.20 for baseline and contoured endwall (computations).

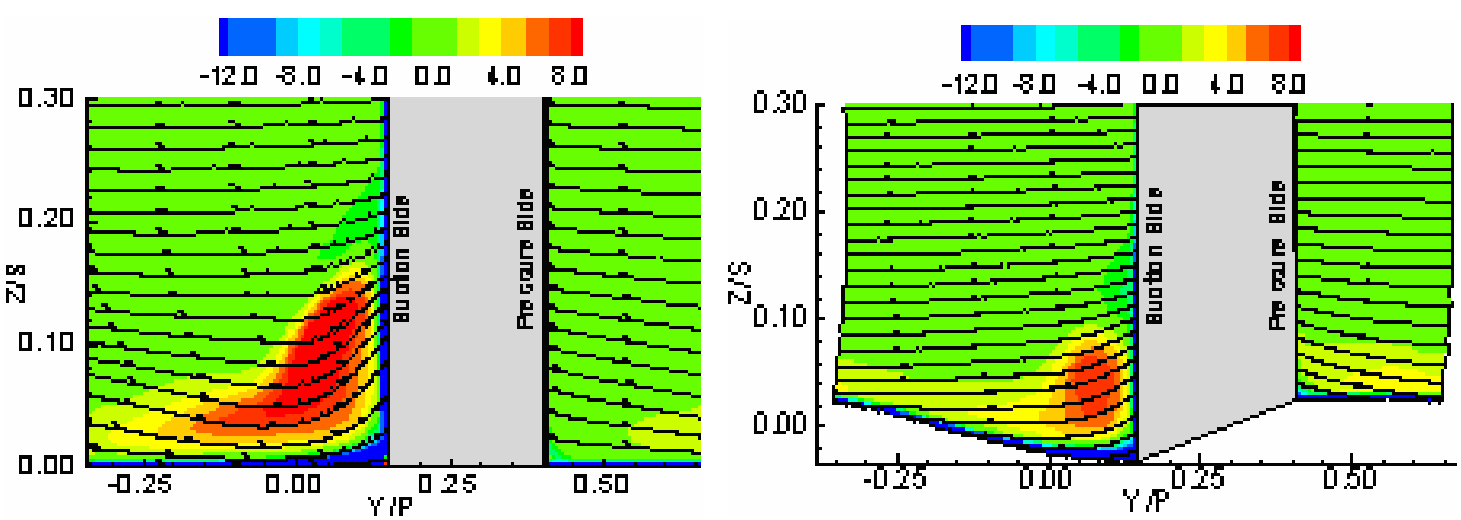

Baseline Contoured endwall

Computations

Figure 43: Streamlines superimposed on normalized axial vorticity $\Omega_x C/U_{ref}$ in pitchwise plane at X/C_{ax}=0.80 for baseline and contoured endwall (computations).

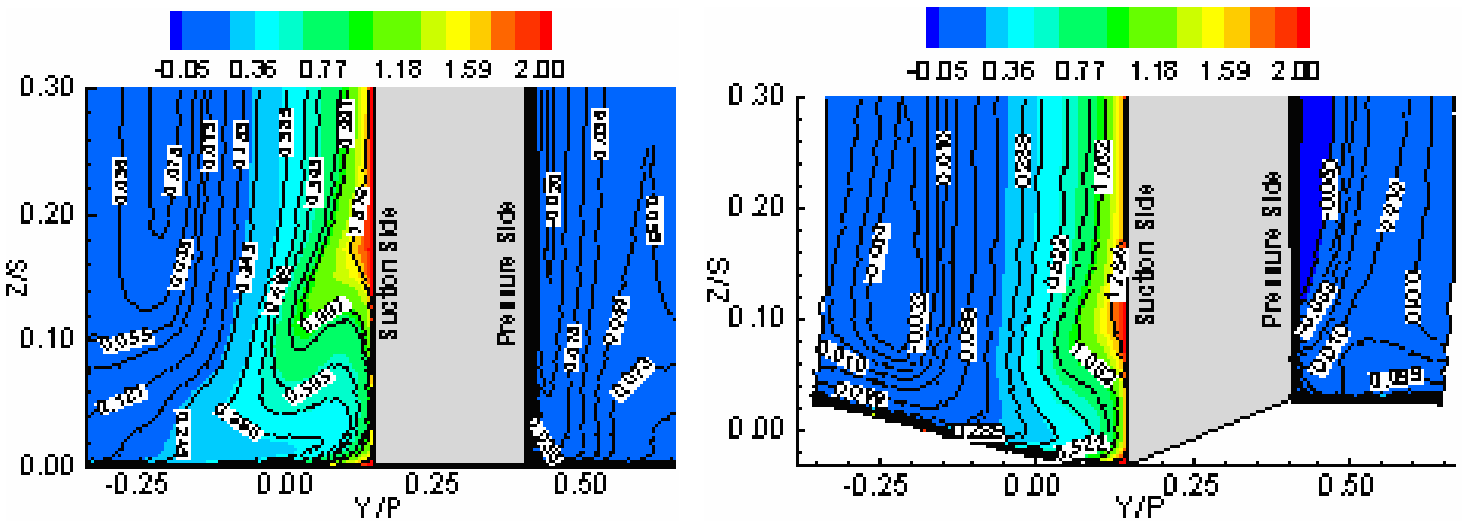

Baseline Contoured endwall

Computations

Figure 44: Total pressure loss coefficient $C_{pt,loss}$ in pitchwise plane at X_G/C_{ax}=0.80 for baseline and contoured endwall (computations).

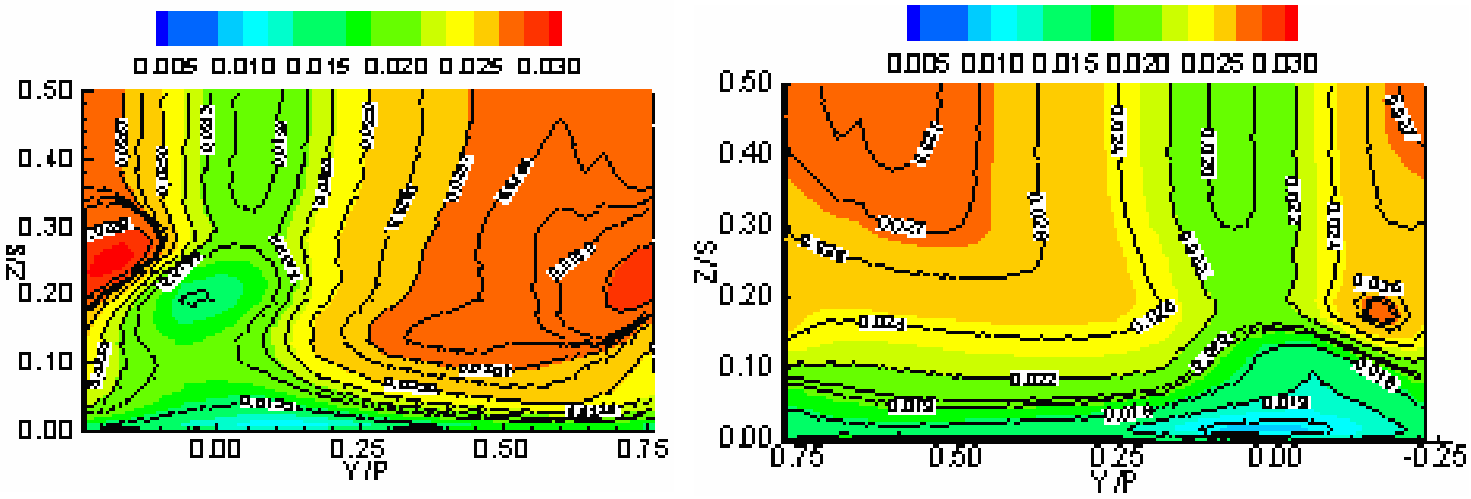

Baseline Contoured endwall

Computations

Figure 45: Non-dimensional turbulent kinetic energy in pitchwise plane at X_G/C_{ax}=1.20 for baseline and contoured endwall (computations).

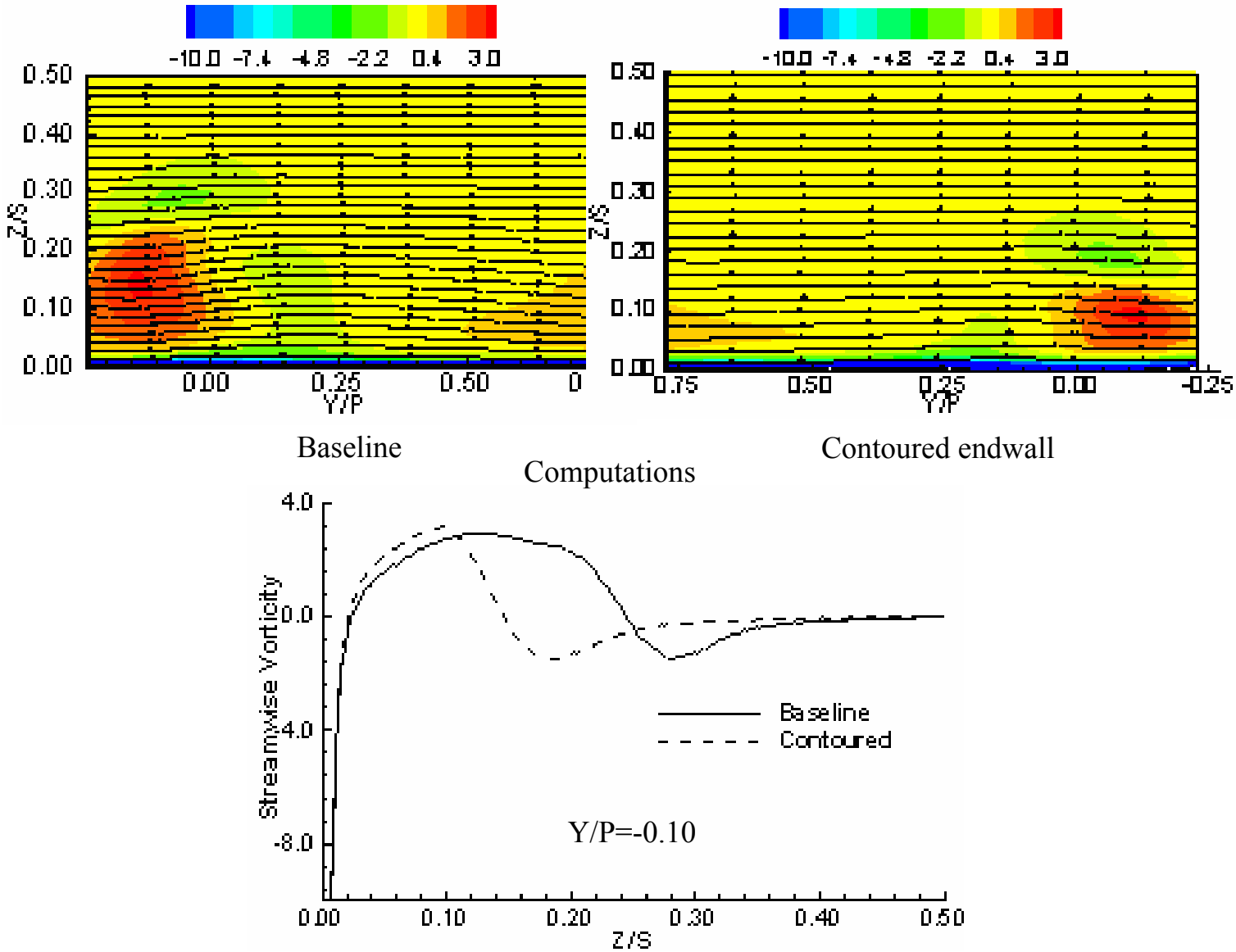

Figure 46: Streamlines and normalized axial vorticity $\Omega_x C/U_{ref}$ in pitchwise plane at X_G/C_{ax}=1.20 for baseline and contoured endwall (computations).

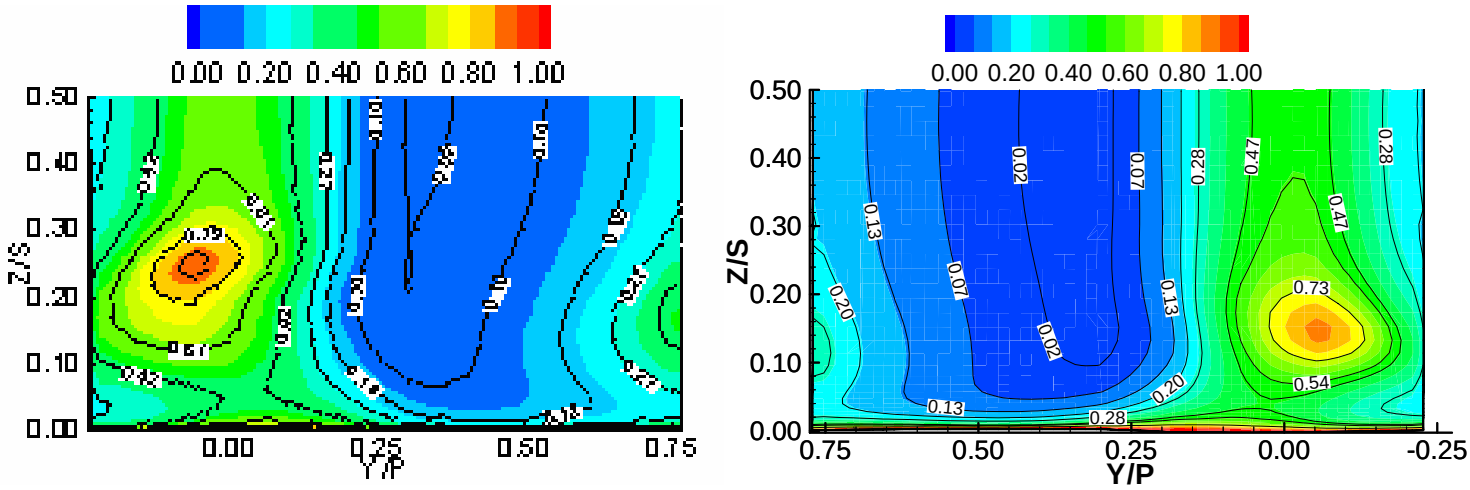

Baseline Contoured endwall

Computations

Figure 47: Total pressure loss coefficient $C_{pt,loss}$ in pitchwise plane at X_G/C_{ax}=1.20 for baseline and contoured endwall (computations).

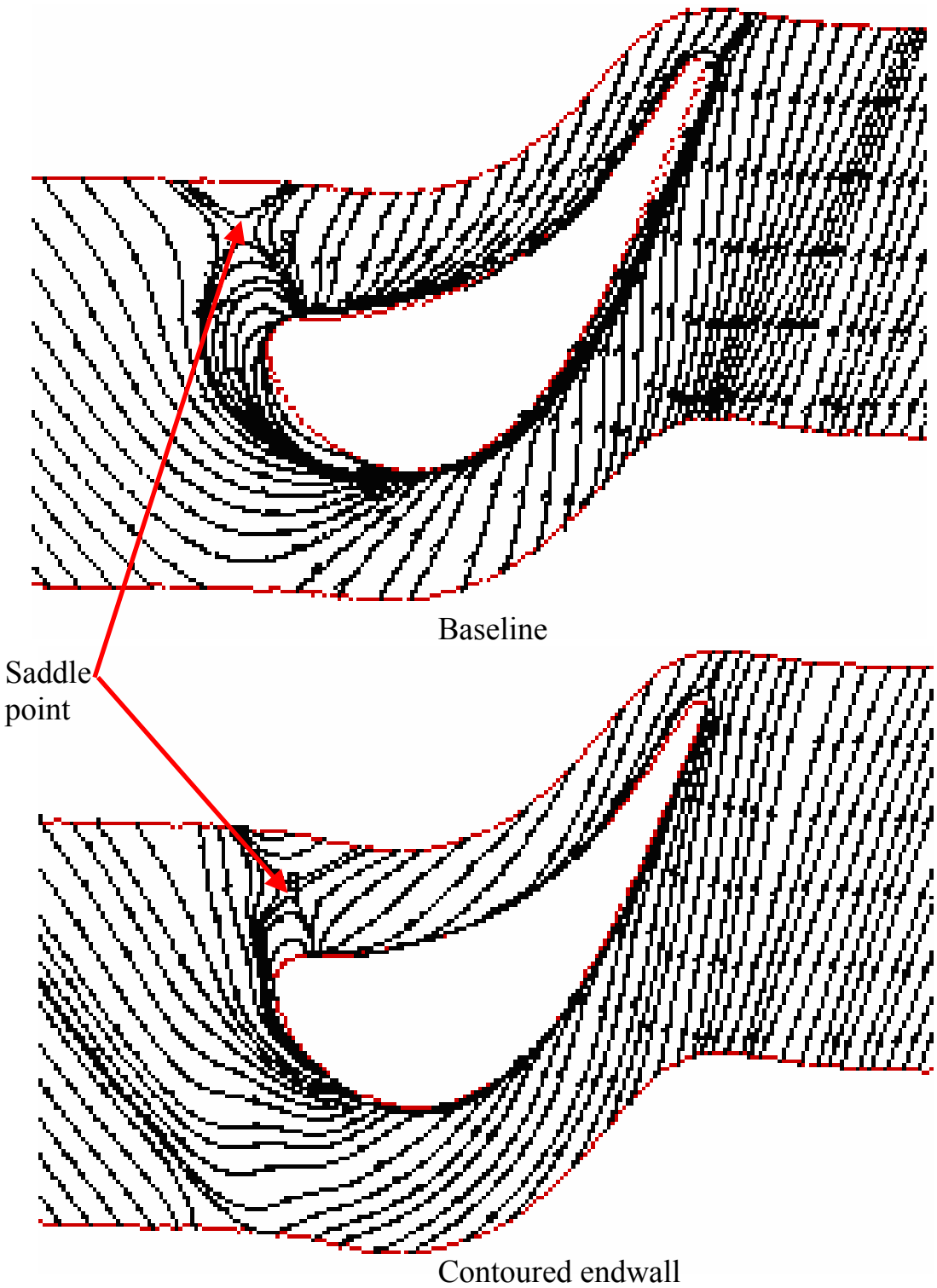

Figure 48: Surface streamlines on the endwall for baseline and contoured endwall (computations).

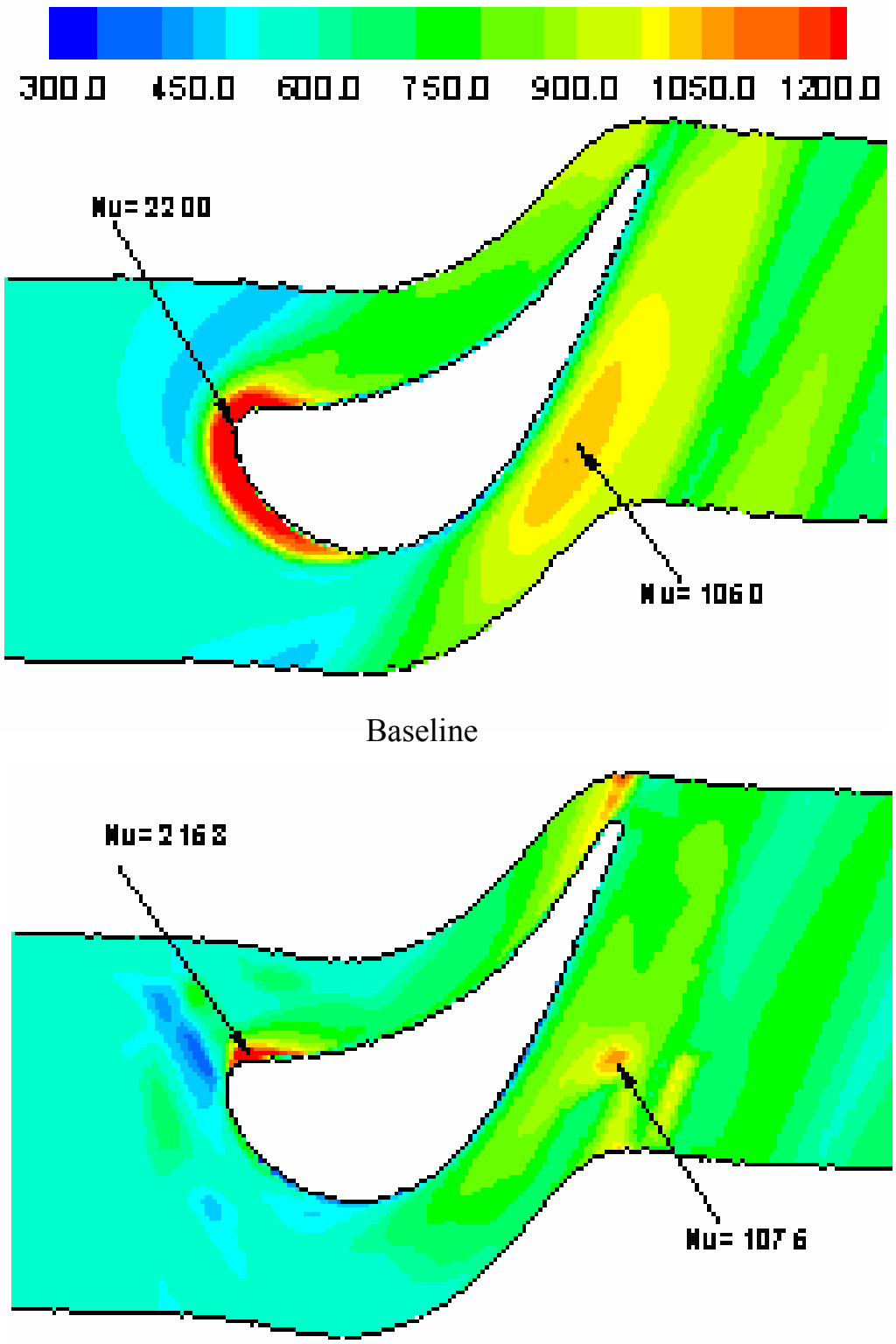

Figure 49: Endwall Nusselt number Nu for baseline and contoured endwall (computations).

Table 3: Summary Results (Computational) for Several Contoured Endwall Profile

Cases	Axial variation of contoured endwall	Geometric parameters(m) and Average Results
1	Flat Endwall (Baseline)	Nu= 736, $C_{pt,loss}$ = 0.2592 (exit plane)
2	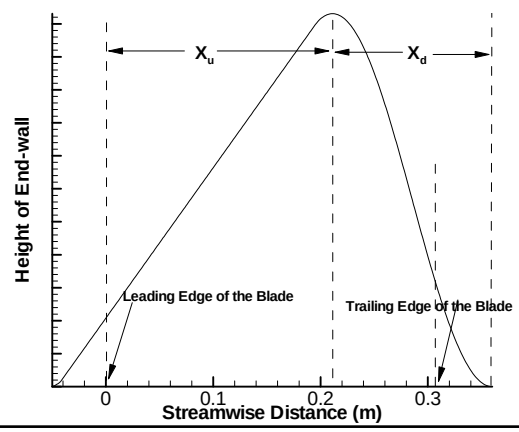	X_u=0.21, X_d=0.15 Endwall height, Z_{max}=0.039m , Z_{min}=-0.047m Nu= 710, $C_{pt,loss}$ = 0.2674 (exit plane)
3		X_u=0.18, X_d= 0.18, Z_{ma}=0.039, Z_{min}=-0.046 Nu= 709, $C_{pt,loss}$ = 0.2641 (exit plane)
4		X_u=0.16, X_d=0.2, Z_{max}=0.039, Z_{min}=-0.045 Nu= 704, $C_{pt,loss}$ = 0.2599 (exit plane)
5		X_u=0.13, X_d=0.23, Z_{max}=0.039, Z_{min}=-0.045 Nu= 697, $C_{pt,loss}$ = 0.2603 (exit plane)
6	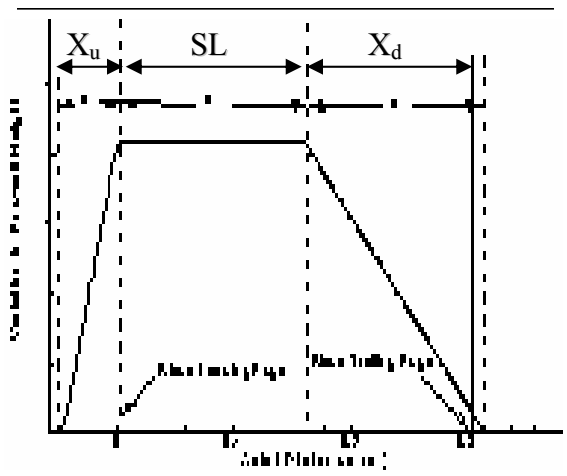	X_u=0.16, X_d=0.16, SL=0.07, Z_{max}=0.019, Z_{min}=-0.023 Nu= 691, $C_{pt,loss}$ = 0.2585 (exit plane)
7		X_u=0.16, X_d=0.16, SL=0.07, Z_{max}=0.029, Z_{min}=-0.035 Nu= 678, $C_{pt,loss}$ = 0.2589 (exit plane)
8	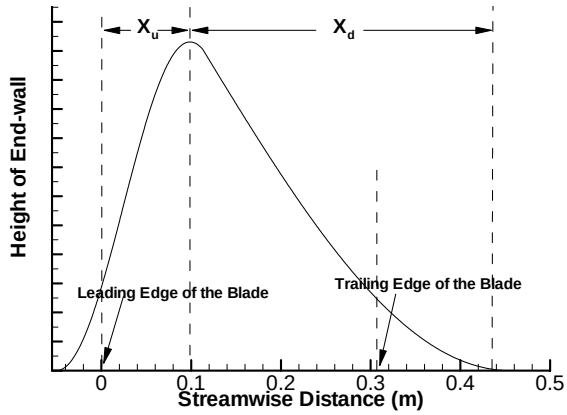	X_u=0.15, X_d=0.21, Z_{max}=0.039, Z_{min}=-0.046 Nu= 689, $C_{pt,loss}$ = 0.2596 (exit plane)
9		X_u=0.10, X_d=0.34, Z_{max}=0.039, Z_{min}=-0.046 Nu= 678, $C_{pt,loss}$ = 0.2548 (exit plane)

Modeling and Control of Ultra-Lean Premixed Combustion Dynamics for Gas Turbines

Semi-Annual Activity Report

Period: May 2005 - November 2005

Dr. William T. Baumann
Dr. William R. Saunders
Dr. Uri Vandsburger
Dr. Robert L. West

DOE Award Number DE-FC26-02NT41431
UTSR Project Number 02-01-SR099

P.O.C: Uri Vandsburger
Department of Mechanical Engineering
Email: uri@vt.edu
Phone: (540) 231-5882/4585

Virginia Active Combustion Control Group
College of Engineering
Mechanical Engineering Department MC0238
Virginia Polytechnic Institute and State University
Blacksburg, VA 24061

Submitted 10 February 2006

This report was prepared as an account of work sponsored by an agency of the United States Government. Neither the United States Government nor any agency thereof, nor any of their employees, makes any warranty, express or implied, or assumes any legal liability or responsibility for the accuracy, completeness, or usefulness of any information, apparatus, product, or process disclosed, or represents that its use would not infringe privately owned rights. Reference herein to any specific commercial product, process, or service by trade name, trademark, manufacturer, or otherwise does not necessarily constitute or imply its endorsement, recommendation, or favoring by the United States Government or any agency thereof. The views and opinions of authors expressed herein do not necessarily state or reflect those of the United States Government or any agency thereof.

Abstract

Under the Advanced Gas Turbine Systems Research – High Efficiency Engines and Turbines (AGTSR-HEET) program, Virginia Tech is developing reduced order models and control methodologies for ultra-lean premixed combustion dynamics. Specifically, the study includes the measurement and modeling of heat release dynamics, equivalence ratio fluctuations, high temperature acoustics, and lean blowout dynamics. Methodologies to control flame stabilization and thermoacoustic instabilities are also being investigated.

This report contains a detailed description of the activities which were executed in May-November 2005. The emphasis of the work was on advancing reduced order models of the various parts of the system, i.e., the combustor/flame, the acoustics, and the mixing process.

The activities follow the original plan as outlined in the proposal. The report also includes a work plan for each task for the period December 2005 through May 2006.

Table of Contents

Abstract ii
Table of Contents iii
List of Graphical Material iv
1 Introduction 1
2 Executive Summary 2
3 Project Description 3
3.1 Quantifying Heat Release Dynamics for Turbulent Swirled, Premixed, Lean Flames (Task 1). 3
3.2 Modeling Time Lag and Dispersion of Equivalence Ratio Variations (Task 2) 3
3.3 High Temperature Acoustics Validation (Task 3) 3
3.4 Premixed Flame Stabilization and Lean Blowoff Limits (Task 4) 4
3.5 Prediction of Combustor Instabilities and Dynamic LBO (Task 5). 4
3.6 Control of Unsteady Combustor Operation (Task 6) 4
4 Experimental 4
4.1 Experimental Apparatus 4
4.2 Data Acquisition and Observed Results 5
4.3 Planned Activities for Next Six Months 7
5 Turbulent Mixing and Convective Time Delay (Task 2) 7
5.1 Motivation 7
5.2 An Analytical Model 7
5.3 Experimental Measurements 9
5.4 Analysis 12
6 Combustor Acoustics 17
6.1 Introduction 17
6.2 Overview 17
6.3 One Dimensional Finite Element Modeling 18
6.3.1 One Dimensional Model 18
6.3.2 Finite Element Modeling Techniques 18
6.4 Experimental Comparison 19
6.5 Summary of Finite Element Modeling 22
6.6 Mode Visualization 23
6.7 Experimental Validation 24
6.8 Velocity/Impedance Measurements 25
6.9 Hot Combustor Acoustics Modeling 27
6.10 Status and Work Plan 28
7 Prediction of Combustion Instabilities 28
7.1 Introduction 28
7.2 Declaration of the Governing Equations 29
7.3 Methods for Constraining the Flame Size 30
7.4 Linearization of the Dynamic Equations 31
7.5 Constant Mass WSR Dynamics 32
7.6 Conclusions and Future Work 37
8 Conclusions (Summary) 38
9 Bibliography 39
10 List of Acronyms and Abbreviations 40

List of Graphical Material

Figure 4.1. Frequency response function to velocity perturbations for varying equivalence ratio

Figure 4.2. Frequency response function to velocity perturbations for varying equivalence ratio

Figure 4.3. Frequency response function to equivalence ratio perturbations for varying mean equivalence ratio.

Figure 5.1. Diagram of combustor cross section showing injection and measurement ports.

Figure 5.2. Frequency Response for Position 1.

Figure 5.3. Frequency Response for Position 2.

Figure 5.4. Definitions of Different Time Delays.

Figure 5.5. Frequency Response Fit for Position 1.

Figure 5.6. Impulse Response from Position 1.

Figure 5.7. Frequency Response Fit for Position 2.

Figure 5.8. Impulse Response from Position 2.

Figure 5.9. Comparison of Turbulent Mixing Model and Measured Frequency Response for Positions 1 and 2.

Figure 5.10. Comparison of Impulse Responses from Model and Reconstructed from the Measured Frequency Responses .

Figure 6.1. Block diagram for combustor model.

Figure 6.2. Schematic of combustor rig.

Figure 6.3. Frequency response function between pressure at location 1 and the pressure at the idealized flame location.

Figure 6.4 FRF between pressure at location 2 and the pressure at the idealized flame location.

Figure 6.5 FRF between pressure at location 4 and the pressure at the idealized flame location.

Figure 6.6. The VACCG Laboratory-Scale Combustor.

Figure 6.7. Particle velocity frequency response function between the pressure at the flame and the particle velocity directly upstream of the flame.

Figure 6.8. Particle velocity frequency response function between the pressure at the flame and the particle velocity at the fuel lines.

Figure 6.9. Approximate temperature distribution for combustion rig.

Figure 6.10. Flow diagram for acoustic Finite Element modeling for hot combustors.

Figure 7.5.1. Dynamic WSR reaction rate frequency response to mass-flow perturbations. The output is reaction rate, normalized by the mass-slow perturbation.

Figure 7.5.2. Dynamic WSR reaction rate frequency response to upstream Φ perturbations. The output is reaction rate, normalized by the Φ perturbation.

Figure 7.5.3. Φ excitation response change due to changes in *m* as it appears in Equation 3 while simultaneously varying *A* such that the blow-off limits are preserved.

Figure 7.5.4. The convective residence time was iteratively computed in order to produce a consistent exit fuel mass fraction for equivalence ratios of 0.50, 0.54, 0.58, 0.63, 0.66, and 0.70. The resulting frequency response plots are displayed in order starting from the upper left. The calculated dynamics (red) quite accurately predict the physical behavior (blue dots) for low frequencies.

Figure 7.5.5. Predicted convective pole frequency as a function of mean equivalence ratio. This is the frequency corresponding to a system with the time constant expressed in Equation 5.

1 Introduction

For the HEET program, ultra-low emissions (defined in this proposal as single digit NO_x and CO) are one of the strongest driving forces. Under the prior ATS program, this led to the choice of LP combustion, with ever increasing attempts to push the lean limit of operability. Lean operation has in turn led to the occasional occurrence of combustion oscillations. In this situation, a burner that has been designed for "static" operational conditions is being used under dynamic conditions, as manifested by velocity fluctuations, equivalence ratio fluctuations, and unsteady heat and mass transfer. Therefore, reduced order models development for ultra-lean combustion must address both static and dynamic flame stability, as well as combustion oscillations.

There is currently a debate in the combustion community about the efficacy of reduced-order models versus CFD models for combustor design. It is believed that highly complex CFD models will ultimately deliver the most accurate predictions of dynamic behavior in combustors. However, even if one assumes that available transient, reacting CFD codes are accurate; such models are unwieldy and extremely time-consuming when used as an iterative design tool. The proposed project, therefore, focuses on so-called "reduced-order models." The two key reasons for this focus are the natural link between achievable experimental measurements and reduced order models, as well as the easy transformation of reduced order models into linear stability models. Stability prediction is urgently needed by virtually all gas turbine designers, particularly for ultra-lean combustor designs.

Although it is relatively easy to qualitatively "explain" why instabilities might tend to occur under certain conditions and at certain frequencies, the problem of accurate prediction is much more difficult. Our approach to combustor stability predictive tools is based on systems theory and models the instability feedback loop as an interconnected set of subsystems, each corresponding to a relevant physical mechanism. For accurate stability prediction, it is absolutely necessary that all subsystem (dynamic) models accurately characterize the gain and phase versus frequency behavior of the actual subsystem in physical units. For example, it is not enough to show that a model predicts the trends of a voltage observed at the output of a transducer responding to heat release rate – it is necessary to accurately predict the total heat release rate in J/sec. It is obvious, therefore, that the current knowledge in this area needs to be advanced and the work tasks outlined in the following sections describe how this will be accomplished.

Ultra-lean premixed combustor operation is significantly more susceptible to lean-blowout of the flame. Thus, this project seeks to understand better the critical parameters that define both static and dynamic flame stability, with particular emphasis on the dynamic coupling between combustion oscillations and dynamic stability of the flame and the effects of fuel variability on these phenomena. Through a series of experiments dynamic models will be progressively defined in order to predict critical dynamic velocities that must be maintained in the combustors to ensure stable operation.

Several control strategies, including passive, active, and a blend of both, will then be considered in order to demonstrate the feasibility of extending the limits of flame stabilization while simultaneously minimizing the occurrence or severity of combustion oscillations during ultra-lean combustor operations.

The payoff from successful development of the types of models proposed here is enormous for the gas turbine community since such models will lead to predictive capabilities that can rapidly discern whether a specific combustor design is susceptible to unstable operation at any operating conditions. The great attraction of these tools is the potential significant shortening of the development cycle.

2 Executive Summary

The central goal of the proposed project is to develop dynamic models for ultra-lean combustion in gas turbine engines. Ultra-lean combustion is intended to satisfy single-digit NO_x emission goals without degrading CO emissions across a range of operating conditions. The primary obstacles to achieving successful ultra-lean operation for HEET platforms are static and dynamic flame stabilization (i.e. lean blowout), as well as thermoacoustic instabilities. To answer this need, this project will develop design-oriented modeling techniques that describe the flame-holding and thermoacoustic combustion subsystems based on aerodynamic, geometric, and various operating condition data. These models will then be utilized to develop passive energy absorption strategies or active control systems that reduce occurrence and level of instabilities and enhance the lean blowout limits. The proposed effort will encompass a broad range of HEET interests including: flame stabilization, LBO, reduced-order modeling, dynamic effects of fuel variability, and control system design. The project will be executed in combination and with active participation of willing IRB members. A university-sponsored workshop will be held at the conclusion of the project to facilitate the transition of the modeling tools to industry engineers working on ultra-lean combustor design.

As was stated earlier, we promised that the goals of the project will lead to marked improvements in reduced-order modeling capabilities via new investigations of: 1) three-dimensional finite element acoustic models versus duct acoustic models; 2) effects of fuel variability on ultra-lean combustion stability; and 3) system models that illuminate passive and active stabilization strategies for ultra-lean combustor operation.

The specific activities undertaken during the reporting period included:

1. Acquired all data for equivalence ratio fluctuations effect on flame dynamic heat release rate for natural gas.
2. Acquired FRFs for velocity (mass flow rate) fluctuations and equivalence ratio fluctuations for propane.
3. Developed a ROM for flame dynamics using an unsteady WRS (Well stirred reactor) modeling approach.
4. Developed a model for turbulent mixing and time lag of dispersion of f' pulse.
5. Assembled a finite element acoustic code with real boundary conditions for the turbulent, swirl-stabilized laboratory combustor.

   Executed code and compared with measurements.

The work plan for the period Nov 2005-May 2006 includes the following items:

1. Completion of a 3-D finite element model for the hot combustor acoustics.
2. Develop model of coupled combustion – acoustics, i.e., closed loop, based on FRF's obtained for the combustor acoustics and flame dynamics.
3. Acquire dynamics data for fuel variations, hydrocarbons and bydrogen.
4. Based on ROM of combustion dynamics develop control algorithm.

3 Project Description

3.1 Quantifying Heat Release Dynamics for Turbulent Swirled, Premixed, Lean Flames (Task 1).

Objectives: This task focuses on obtaining the frequency-resolved response of the heat release rate, in physical units, to perturbations in mass flow rate and equivalence ratio. Using the experimental frequency response, physics-based, reduced-order models will be derived. The models will then be validated on self-excited combustors in the Virginia Active Combustion Control Group laboratory, the National Energy Technology Laboratory, and in industry.

Methodology: To accurately measure heat release rate, Tunable Diode Laser Absorption Spectroscopy (TDLAS) and chemiluminescence will be used simultaneously. TDLAS methods will be used to measure the unsteady temperature of the products in the immediate post-flame zone. The temperature measurement is based on the ratio of the absorption of water lines at 1392 nm and 1343 nm. In this manner, the sensible part of the change in enthalpy can be obtained. Hydroxyl radical (OH*) chemiluminescence has been shown to be an excellent indicator of chemical heat release rate in premixed flames. Thus, it will be used to determine the chemical reaction contribution to changes in enthalpy. Both measurements will enable true characterization of the acoustic driving source term for thermo-acoustic instabilities.

In practical LP gas turbine combustors the onset of TA instabilities/oscillations involves fluctuations in both mass flow rate $\dot{m}'$ and the equivalence ratio, ϕ'. Therefore the dynamic response of the flame to $\dot{m}'$ and ϕ must be captured. Fluctuations in both will be imparted on the flow. $\dot{m}'$ fluctuations via a large speaker, and ϕ' with a high frequency on/off meso value. The fluctuations are quantified with an acoustic intensity meter and 3.39 μm absorption.

3.2 Modeling Time Lag and Dispersion of Equivalence Ratio Variations (Task 2).

Objectives: This task focuses on investigating the effect of time lag on flame stability and dynamics. The time lag is defined as the time for a perturbation in equivalence ratio to result in a perturbation in heat release rate. The effect of diffusion and turbulent mixing on equivalence ratio variations will also be studied.

Methodology: Methane absorption of an infrared Helium-Neon laser will be used to measure variations in equivalence ratio. The equivalence ratio will be modulated through a system employing high-frequency solenoid valves, rotating valves, voice coils, or loudspeakers. The effect of equivalence ratio variations on heat release rate will be measured via chemiluminescence and TDLAS methods, as described previously. The time lag will be measured as the time from when a perturbation is given to the equivalence ratio to the time a response is observed in heat release rate. Computational Fluid Dynamics (CFD) will be used to model the velocities and flame location in the combustor. This information can then be used to solve for the convective time lag and compare to the experimental values. Using this data, observations can be made on the effects of time lag on flame dynamics and stability. These observations will then be incorporated into reduced-order models. As in other tasks, the experimental methods will be verified on the laminar burner before beginning work on the turbulent burner.

3.3 High Temperature Acoustics Validation (Task 3).

Objectives: Using experimental data acquired from actuator excitations and flow noise, 3D FEA acoustical models for both cold, no-flow and actual operating conditions will be verified.

Methodology: FEA models of combustor acoustics, with ability to handle complex boundary conditions, and combustor CAD models as inputs will be developed. Recent experience in formulating FEA models of industrial combustors will serve as a baseline. Goals include

developing a neutral file format for sharing geometric data, integration with CFD models, and developing guidelines for partitioning models.

3.4 Premixed Flame Stabilization and Lean Blowoff Limits (Task 4).

Objectives: This task will focus on the measurement and modeling of static and dynamic lean blowoff limits over a range of operating conditions.

Methodology: The flame dynamics measurements will be extended to the lean blowoff limits. In addition, a system will be implemented to force fluctuations in equivalence ratio. The impact of equivalence ratio perturbations on flame stability will be investigated.

3.5 Prediction of Combustor Instabilities and Dynamic LBO (Task 5).

Objectives: The entire modeling methodology will be validated through prediction of combustion instabilities and lean blowoff limits on various combustors. Reduced-order models will be applied to VACCG test combustors, the NETL rig, and the Solar Turbines test rig.

Methodology: Using models for combustion system components developed in the preceding tasks, a model of the combustion instability feedback loop will be built for the target combustors. Stability predictions will be compared to experimental data over a wide range of operating conditions.

3.6 Control of Unsteady Combustor Operation (Task 6).

Objectives: Control unsteady combustor performance, i.e., TA instabilities and flame stabilization

Methodology: use developed ROM to design a control methodology for combustor stabilization over the whole equivalence ratio range. Pulsed pilots an main fuel, and staged premixed flames, will be considered.

4 Experimental

4.1 Experimental Apparatus

The experimental apparatus employed in continuing pursuit of quantifying heat release dynamics in turbulent, swirled, premixed, lean flames (task 1) is detailed in the Semi-Annual Activity Report for the period of May 2003-November 2003. A description of this apparatus in brief follows, with a schematic available in Figure 4.1. For the studies of flame dynamic response to velocity perturbations, an acoustic driver is used to generate a perturbation at a single frequency. The perturbation in velocity is measured with a two-microphone probe located around five inches below the flame. The pressure fluctuations measured by this probe are converted into velocity fluctuations according to the one dimensional form of Euler's equation written in the direction of the flow. The response of the flame heat release rate to this excitation is obtained through Hydroxyl radical chemiluminescence, measured via emission from the flame by a photomultiplier tube.

While fuel flow fluctuations were still measured using the methane laser absorption setup, a Matrix solenoid valve was added to the system to provide actuation for two radically opposed fuel injectors which introduced a fuel jet, creating equivalence ratio perturbations. The injectors were located at the same axial location as the two microphone probe, directly upstream of the swirler. The perturbations were introduced with the valve operating at a fixed frequency and a 50% duty cycle. The magnitude of the fuel pulses was approximately 10% of the premixed fuel flow.

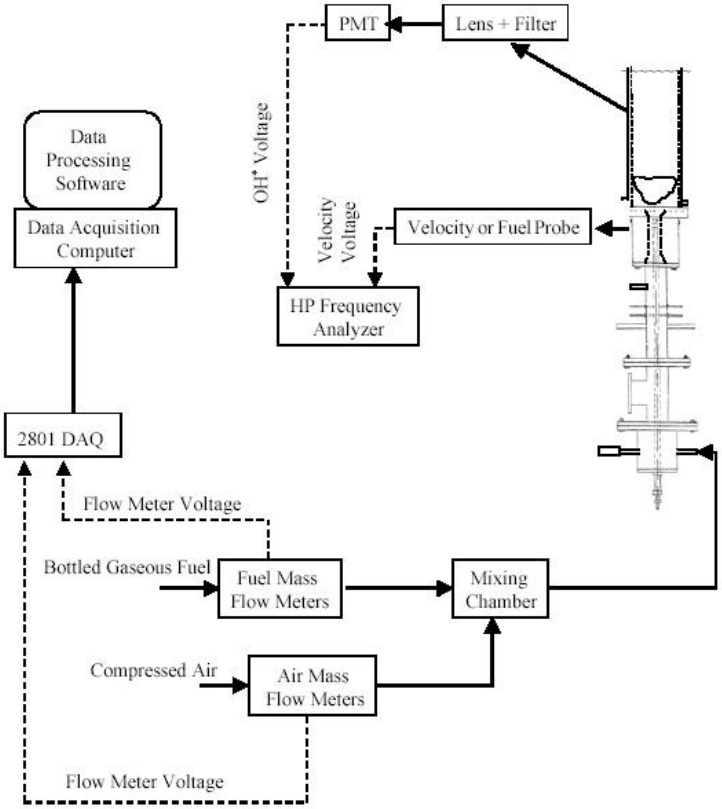

Figure 4.1 - Frequency response function to velocity perturbations for varying equivalence ratio

4.2 Data Acquisition and Observed Results

Tests were performed using LabView data acquisition software to control the speaker and fuel supply valve, which provided the fluctuations. Measurements were taken at several equivalence ratios for each of the perturbation types. Perturbations were introduced at a single frequency, while time-traces were stored for measurement of the perturbation and the flame heat release. The frequency of perturbation was varied from 10 to 400 Hz at a 10 Hz interval and data from the input and output signals experiencing this perturbation were stored. A time trace of 180000 data points on each channel at a sampling frequency of 3600 Hz was taken at each excitation frequency. When the frequency of perturbation was varied, 15 seconds were allowed prior to taking more data to allow transients to die out. The data was then processed at each frequency of excitation, calculating the transfer function by determining individual Fourier coefficients. The Fourier coefficients were then combined to form the full band transfer function.

The trends in this data with changes in frequency were validated through comparison to data obtained from the raw voltage signals by a Hewlett Packard spectrum analyzer. In the case of equivalence ratio perturbation, the HP measured signal had some uncertainty due to the inability to account for changes in the reference intensity, but trends still showed good agreement. Further, tests were carried out to validate the trends across mean equivalence ratio by fixing the frequency of excitation and varying the equivalence ratio. This helped to ensure there was no corruption in the data due to day-to-day variations in ambient environment or other factors. As before, in the case of equivalence ratio fluctuations, the inability to account for variations in reference intensity introduced some uncertainty, but still allowed for an overall increase in measurement confidence.

In the case of velocity perturbations, full transfer functions including coherence were found over the equivalence ratio range of 0.48 through 0.63. The leanest case was the stabilization limit for the flame in this experimental setup. Results for ultra lean conditions showed higher scatter and

lower coherence due to the reduced overall flame heat release and intrinsic fluctuations present as the flame began to flicker. All of the test conditions were checked for repeatability.

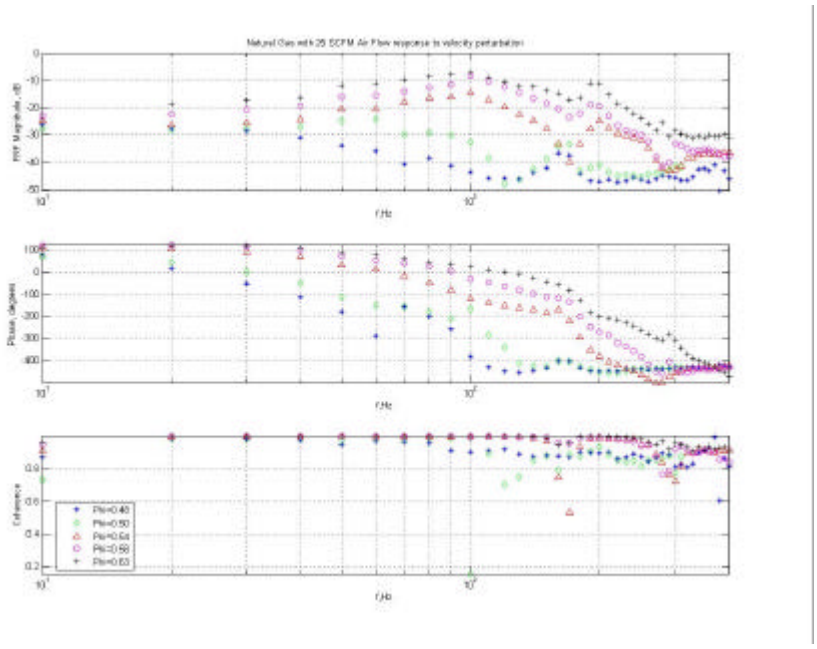

Figure 4.2 Frequency response function to velocity perturbations for varying equivalence ratio

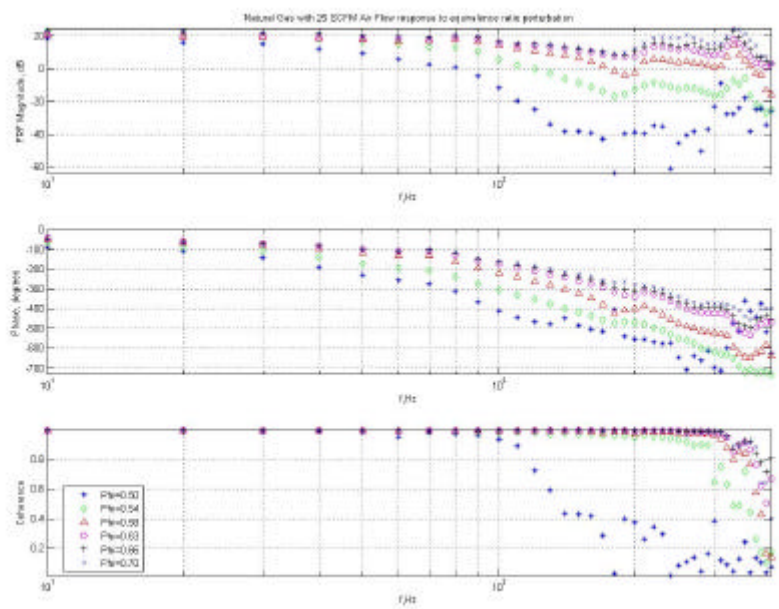

4.3 Frequency response function to equivalence ratio perturbations for varying mean equivalence ratio

The FRF data for the flame has a low pass characteristic. The data for richer equivalence ratios exhibit a slight peak immediately before rolling off around 100 Hz. This peak remains stationary until very lean equivalence ratios are reached. The break frequency and the low frequency magnitude decrease with decreasing equivalence ratio and the falloff becomes steeper. An acoustic

resonance is present in the system around 180 Hz and accounts for the dip in coherence at this point. Higher order dynamics are evidenced near 200 Hz and 300 Hz, especially in the richer cases.

Phi perturbations were introduced with equivalence ratio varying from 0.50 to 0.70. Again, low pass filter behavior was evidenced. In this case the initial band and roll off around 100 Hz appeared to be first order, though as with the velocity data, some higher order dynamics were present, especially at higher frequencies. A very small magnitude drop was observed with the decrease in equivalence ratio, particularly toward the leanest cases. A shortening bandwidth with decreasing equivalence ratio is also clearly evidenced by the data at lean equivalence ratios. The maximum drop for the richest cases was around 20 dB while the drop for leaner cases was significantly greater.

4.3 Planned Activities for Next Six Months

Further work in the direction of this task lies in the quantification of flame dynamics for varying fuels. This has important applications in the area of robust combustor design, with particular interest as a result of attempts to design combustors for medium BTU fuels. While varying blends of hydrocarbons yield one potential experimental area, application of similar techniques to measure dynamics of hydrogen combustion provide another direction of interest.

The most immediate work to be carried out is the investigation of the dynamic response of turbulent, premixed, swirl stabilized propane flames to perturbations in equivalence ratio and velocity. The experimental setup required for this study is identical to that required for natural gas. Blends of natural gas and propane will also be considered to evaluate the effect of fuel variability on the flame dynamics, yielding a beginning at understanding of the generalized effect of fuel composition on flame dynamics.

For reasons of expediency, the tasks dealing with LBO, 4 and 5, will be folded into the present both experimentally and in model development.

5 Turbulent Mixing and Convective Time Delay (Task 2)

5.1 Motivation

Dynamic variations in the fuel-air ratio and the transport delay associated with these variations are important characteristics of the overall combustion system model. In this section we investigate a simple model for turbulent mixing and transport, discuss the experimental measurements of these effects on a test combustor, and show that the model can be used to match the experimental observations.

5.2 An Analytical Model

A simple model of turbulent mixing and transport was proposed by Scarinci and Freeman based on concepts from the atmospheric dispersion of pollutants from a smokestack. The basic idea is that the concentration at a point x at time t is a function of the source concentration and the transition probability density — the probability that a particle at point x' at time t' ends up at point x at time t. For simplicity, only mixing in the axial direction will be considered, although the results can be easily extended to three dimensions. Assuming stationary, homogeneous turbulence, and a constant flow velocity, U, the transition probability Q has the Gaussian form

$$Q(x,t \mid x',t') = \frac{1}{\sqrt{2p}\,s_x(t)} \exp\left(-\frac{(x - x' - U(t-t'))^2}{2s_x^2} \right) \tag{5.2-1}$$

The fuel concentration at point x and time t can be written as

$$C(x,t) = \int_{-\infty}^{\infty}\int_{0}^{t} Q(x,t \mid x',t')S(x',t')dt'dx' \tag{5.2-2}$$

If the fuel is injected a distance x_o upstream of the point of interest, $x = 0$, then the response to a unit impulse of fuel injection, $S(x,t) = d(x + x_o)d(t)$, is given by

$$h(0,t) = \frac{1}{\sqrt{2p}\, s_x(t)} e^{-\frac{(x_o - Ut)^2}{2 s_x^2(t)}} \tag{5.2-3}$$

By taking the Fourier transform of this impulse response we can obtain the frequency response of the mixing process and by using the convolution integral

$$C(0,t) = \int_0^t h(0,t)S(x_o,t)\, dt \tag{5.2-4}$$

the time response of the concentration at $x = 0$ can be found due to a time-varying source concentration at $x = -x_o$.

To find $s_x(t)$, note that

$$s_x^2(t) = \left\langle X^2(t) \right\rangle = \int_0^t\int_0^t \left\langle v(t')v(t'') \right\rangle dt'dt'' \tag{5.2-5}$$

where v is the unsteady part of the x velocity and

$$R(t' - t'') = \left\langle v(t')v(t'') \right\rangle \tag{5.2-6}$$

is known as the Lagrangian correlation function. For turbulent diffusion problems, this function has been approximated by the simple exponential function

$$R(t - t') = \overline{v^2} e^{-b|t-t'|} \tag{5.2-7}$$

where *1/b* is the correlation time and $\overline{v^2}$ is proportional to the total turbulent kinetic energy of the flow. Plugging into the previous equations and making a change of variable results in

$$s_x^2(t) = 2\int_0^t (t-x)R(x)\,dx = \frac{2\overline{v^2}}{b^2}[bt-(1-e^{-bt})]$$

(5.2-8)

If the correlation time is much less than the convection time, then $bt >> 1$, and the previous expression reduces to

$$s_x^2(t) = \frac{2\overline{v^2}}{b}t$$

(5.2-9)

leaving only one unknown parameter.

We should note at this point that the above analysis is for a varying fuel input in a fixed mean velocity flow field. The actual problem in a combustor is for a fixed fuel input in a varying mean velocity flow field. This latter problem is significantly more complicated to set up analytically as it involves a variable time delay. We make the assumption that for small velocity perturbations the two problems will behave similarly.

5.3 Experimental Measurements

Experimental measurements were performed on a premixed, turbulent combustor that is shown diagrammatically in Figure 5.1. The main fuel and air enter the bottom of the combustion section shown already well mixed. A fast solenoid valve was used to inject fuel pulses at a 50% duty cycle into one of two ports below the swirler: position 1 is located slightly below the swirler and position 2 is located significantly below the swirler, as indicated in the figure. The fuel concentration was measured by laser absorption at a port slightly above the swirler position.

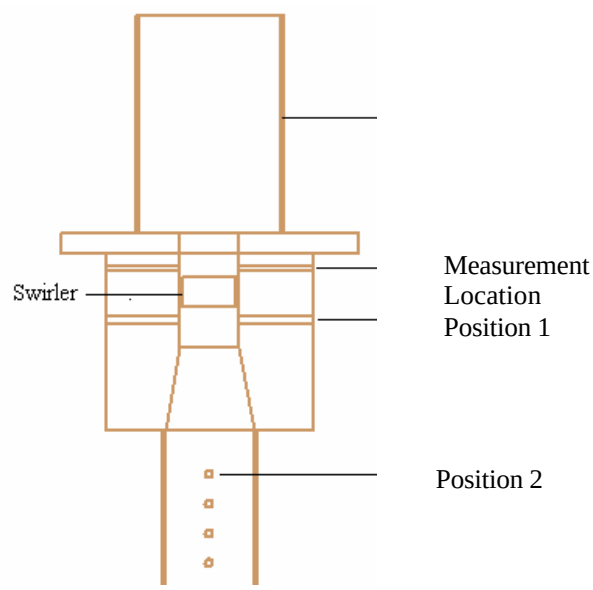

Figure 5.1: Diagram of combustor cross section showing injection and measurement ports.

The transfer functions between the input voltage to the solenoid valve and the fuel concentration fluctuations at the downstream measurement location were measured. The results for

Position 1 are given in Table 5.1 and plotted in Figure 5.2. The convection time delay, estimated based on the flow rate and distance traveled, is given by

$$T_{delay} = \frac{L}{U_{avg}} = \frac{4.445cm}{713.42cm/\sec} = 6.2m\sec$$

Table 5. 1: Frequency Response Data for Position 1

Frequency	Magnitude (dB)	Phase (degrees)
20.	-8.9	-56.8
40.	-10.9	-104.4
60.	-10.6	-149.7
80.	-14.6	-215.1
100.	-11.9	-233.2
120.	-17.9	-274.2
140.	-15.8	-314.2
160.	-18.2	-354.2
180.	-20.9	-419.3
200.	-23.4	-490.8
220.	-30.7	-612.2
240.	-33.9	-669.2
260.	-32.6	-643.0
280.	-30.8	-651.8
300.	-35.6	-637.0
320.	-31.6	-639.8
340.	-30.2	-588.6
360.	-30.1	-590.1

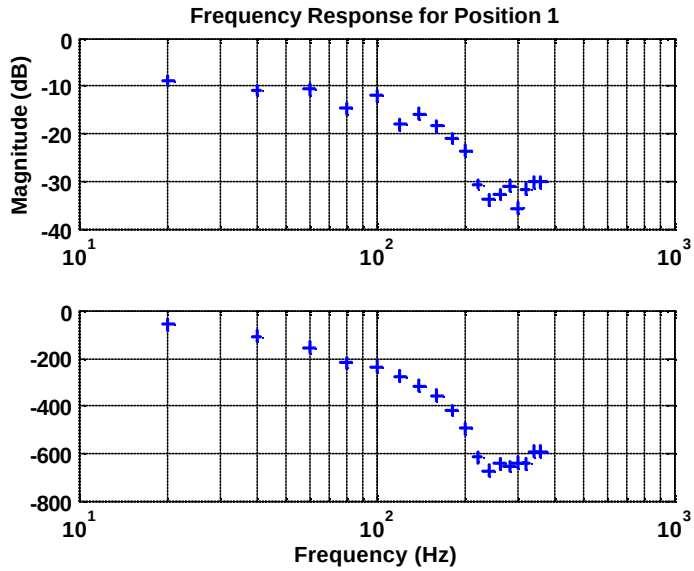

Figure 5.2.: Frequency Response for Position 1

Similarly, the results for Port 2 are given in Table 5.2. and plotted in Figure 5.3. The convection time delay estimated based on the flow rate and distance traveled is given by

$$T_{delay} = \left(\frac{L_1}{U_{avg_1}} + \frac{L_2}{U_{avg_2}} + \frac{L_2}{U_{avg_3}} \right) = \left(\frac{3.98}{253.4} + \frac{6.98}{483.41} + \frac{6.98}{713.42} \right) = 39.94 m\sec$$

where the three distances correspond to lengths having different cross sectional areas, and hence different mean velocities, as shown in the combustor schematic.

Table 5.2.: Frequency Response Data for Position 2

Frequency	Magnitude (dB)	Phase (degrees)
20	-17.9	-282
40	-18.0	-557
60	-20.5	-837
80	-23.7	-1107
100	-28.4	-1401
120	-35.1	-1668
140	-38.3	-1927
160	-46.0	-2243
180	-41.3	-2839
200	-39.1	-3106
220	-51.6	-3421

240	-53.1	-3506
260	-57.8	-3658
280	-47.5	-3838

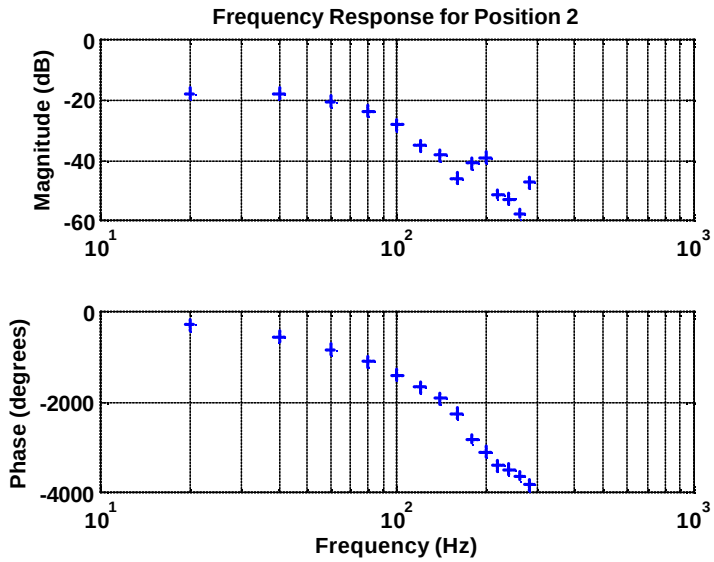

Figure 5.3: Frequency Response for Position 2

5.4 Analysis

The frequency response measurements detailed above are easier to make reliably than pulse measurements because of the higher signal to noise ratio. But our main interest is in how a pulse of fuel is delayed and mixed as it propagates through the mixer. Two different time delays must be distinguished, as shown in Figure 5.2.4: pure time delay and convective time delay. The pure time delay is the delay between when a pulse of fuel is applied and when it is first observed at the measurement location. The convective time delay is the time between when a pulse is applied and when the maximum change is observed at the measurement location. These two delays would be the same for a very narrow pulse if there were no mixing, but turbulent mixing causes the delays to be different.

From a modeling point of view, we are interested in pure time delay so that our overall model consists of the cascade of a delay followed by a causal dynamical system. If we use the convection time for the delay, then our dynamical system model would have to be acausal, which makes the modeling situation more complicated. On the other hand, convection time is easily estimated from the mean velocity and so is the more natural delay to discuss. For our present purposes, we will consider delay to mean convective delay.

To estimate the delay and diffusion of a fuel pulse from our frequency response data, we will fit this data as accurately as possible with a model consisting of a time delay and an a causal dynamical system. This will yield an estimate of the convection delay embodied in the frequency response data and the impulse response of the dynamical system will show how an impulse of fuel at the input position spreads out by the time it reaches the measurement position. This is a very effective way of getting the pulse shape due to a very narrow pulse of fuel. In addition, it is an effective way of estimating delay. Trying to estimate delay from looking at the phase of the system

is problematic since the phase has components from both the time delay and the dynamics, which can be difficult to separate.

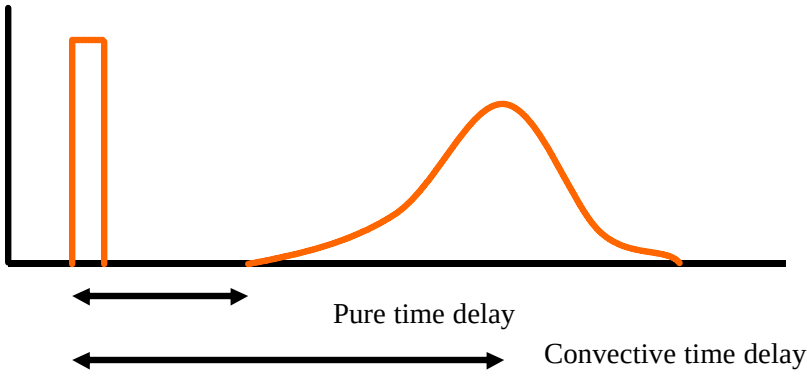

Figure 5.4: Definitions of Different Time Delays.

For position 1, the time delay was estimated to be 6.8msec and the frequency response fit and resulting impulse response are shown in Figures 5.5 and 5.6.

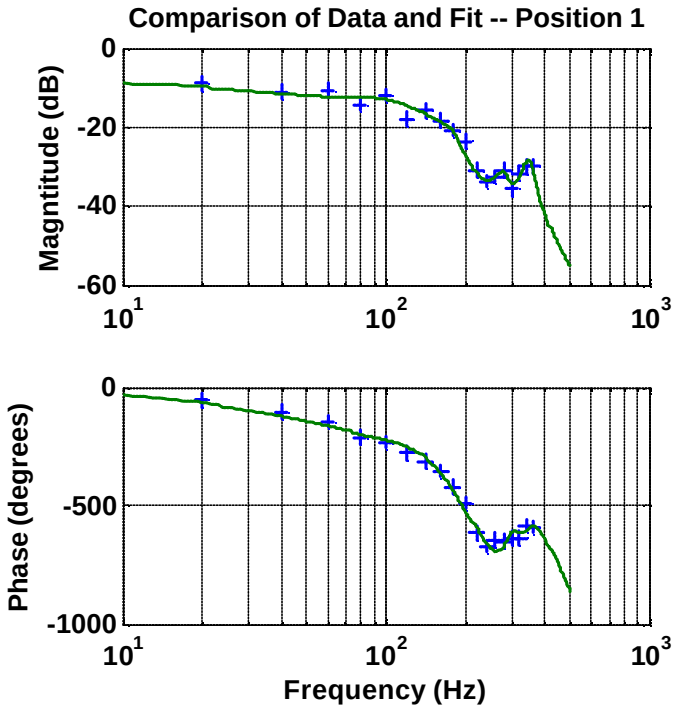

Figure 5.5: Frequency Response Fit for Position 1

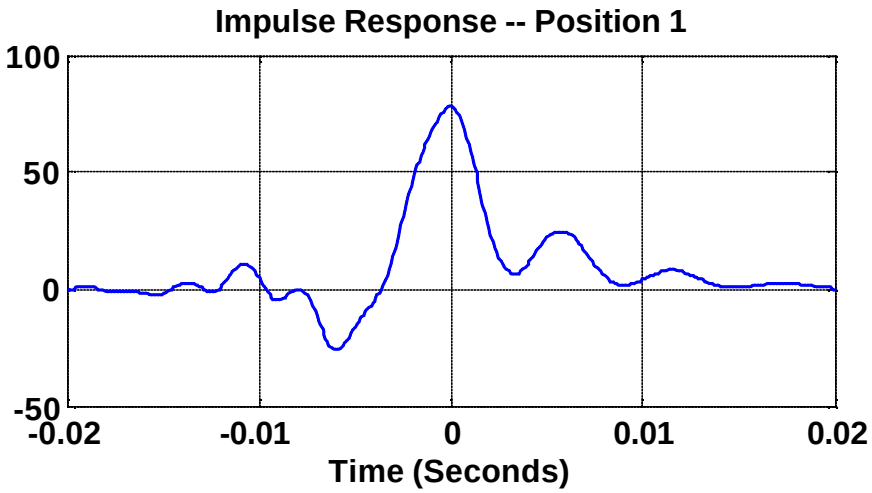

Figure 5.6: Impulse Response from Position 1.

For position 2, the time delay was estimated to be 38.8msec and the frequency response fit and impulse response are shown in Figures 5.7 and 5.8.

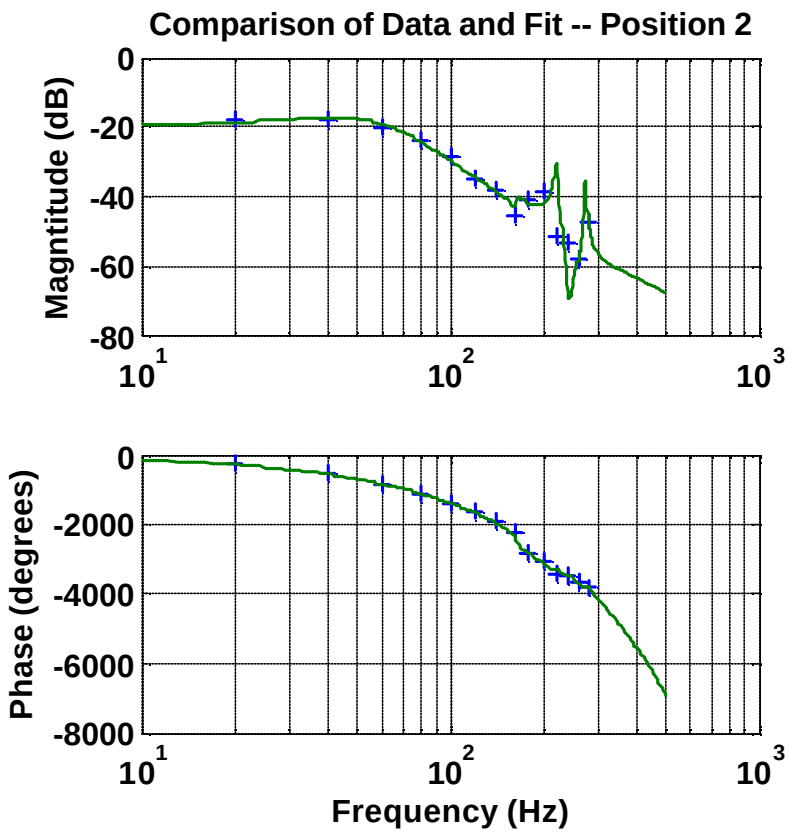

Figure 5.7: Frequency Response Fit for Position 2.

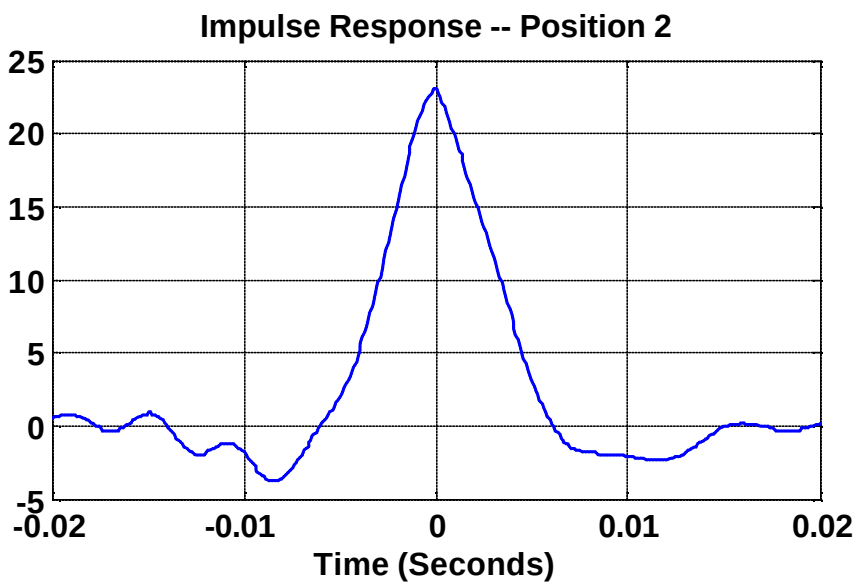

Figure 5.8: Impulse Response from Position 2.

As can be seen from the following table, the convection delay times determined by the frequency response fits compare very well with the simple distance over mean velocity calculations.

Table 5.3: Delay Times

Position	Convection	FRF
1	6.2msec	6.8msec
2	39.9	38.6

In addition, the delay times are different by a factor of about 6 while the pulse widths differ by a factor of about 2. From our analysis, we would expect the widths to be roughly proportional to the standard deviation (5.1.2) evaluated at the convection time. Since the standard deviation goes as $\sqrt{t}$, we would expect the pulse widths to vary as $\sqrt{6} = 2.4$, which is in reasonable agreement with the results of the frequency response analysis.

In its simplest form, the mixing model (5.1.1-2) requires the specification of only one parameter, the mean square turbulent velocity times the correlation time. If we take this to be $50cm^2$/sec and compare the model to the actual data we get the results shown in Figures 5.9-10. The impulse response can be computed directly from (5.1.1), while the frequency response can be computed from the Fourier transform of the impulse response. The frequency responses compare relatively well with the measured responses. At the higher frequencies, the measured data does not keep falling off as predicted by the model but exhibits additional dynamics. This discrepancy might be due to the reduced signal to noise ratio at these points, acoustic or fluid mechanical dynamics excited by the pulsed injection, or dynamics in the solenoid valve at high frequencies. But since these variations occur at a level 20dB below the low frequency response, they will probably be insignificant with regard to the overall loop stability.

The impulse responses for position 2 compare quite favorably, but the reconstructed and model responses for position 1 differ significantly in height, even after normalizing the measured frequency responses, which have arbitrary units, to have a dc gain of $1/U_{avg}$. (At very low frequencies, the amount of fuel injected per unit time at the injection point must pass the measurement point without attenuation). Since narrow pulse reconstruction will depend critically on the high frequency portion of the measured frequency response, the measurements and fit in this region are most critical while at the same time most likely to be in error.

On the whole, this simple model appears to give very reasonable results, especially considering that the flow goes through area/velocity changes and a swirler prior to measurement.

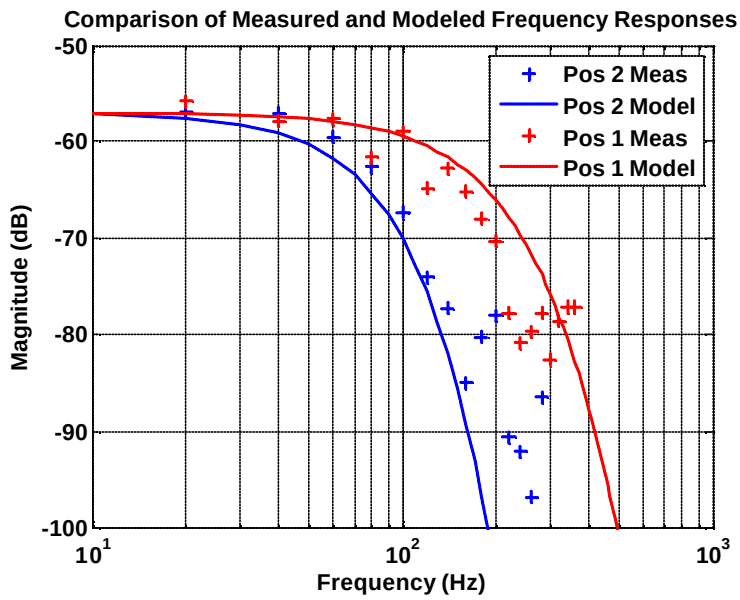

Figure 5. 9: Comparison of Turbulent Mixing Model and Measured Frequency Response for positions 1 and 2.

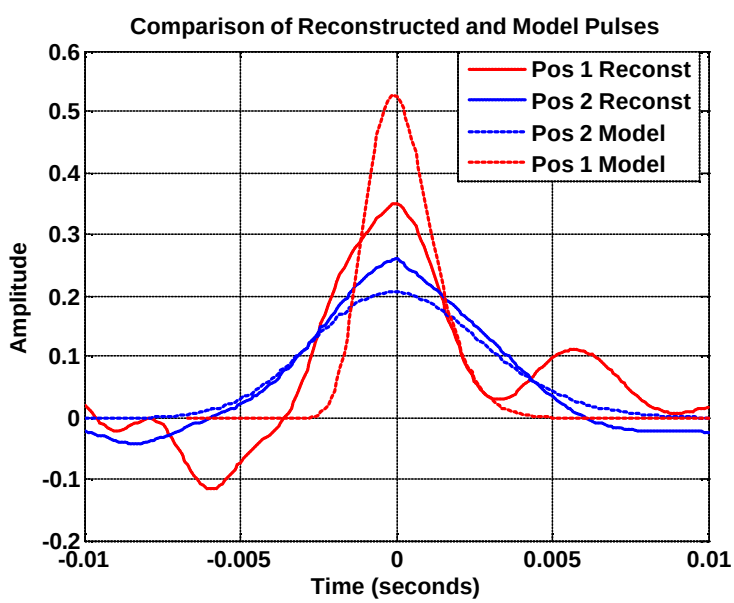

Figure 5.10: Comparison of Impulse Responses from Model and Reconstructed from the Measured Frequency Responses.

6 Combustor Acoustics

6.1 Introduction

Thermoacoustic combustion instabilities are often associated with large pressure amplitudes leading to serious performance degradation and severe structural damage. This problem has been studied for a long time; however, due to the complexity of this phenomenon, it is still not well understood.

The motivation for this project is to develop a process or methodology that industry can use to predict thermoacoustic instabilities for gas turbine combustor design purposes. In previous studies (Bloxsidge, 1988), it has been postulated that instabilities can be understood and predicted from a knowledge of the transfer function of the flame and the acoustic impedance on either side of the flame. This research is taking a similar approach. The flame transfer function is derived from first principles using a reduced order model and is discussed in a different section of this report. The acoustic impedance is discussed in this section and is described with a frequency response function (FRF) between the pressure at the flame to the particle velocity at desired locations.

Since currently the combustor is open at the top, the FRF downstream of the flame is disregarded. Upstream of the flame, two FRFs are required to account for the unsteady velocity approaching the flame and the equivalence ratio fluctuations at the fuel lines. Figure 6.1 shows a simple block diagram of the system. The diagram demonstrates the two ways in which the acoustics couple with the flame model to produce instabilities.

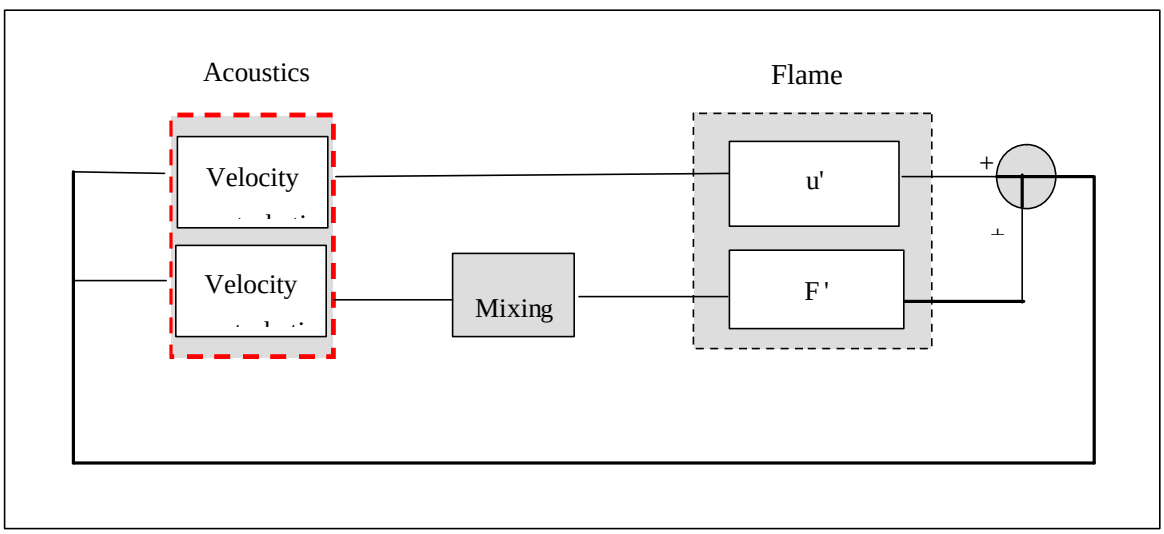

Figure 6.1: Block diagram for combustor model

6.2 Overview

Acquiring the frequency response functions mentioned above is accomplished by using a one dimensional acoustic finite element model. The focus of this section of the report will be devoted to discussing research progress, results, and issues of the acoustic finite element modeling task for this project period. Specifically, the following sections of the report focus on the motives for using "one dimensional" acoustic finite element models, modeling techniques, and a comparison with experimental results. Acoustic mode visualization is discussed and the experimental procedure is described. The frequency response functions for the "cold" combustor are shown and discussed.

Future work in temperature mapping and "hot" combustor modeling is also explained. Lastly, future goals and issues on hot combustor modeling and testing will be discussed.

6.3 One Dimensional Finite Element Modeling

6.3.1 One Dimensional Model

Originally, it was believed that a three dimensional finite element model was requisite to accurately predict the acoustic behavior of combustors. However, due to the decreased degrees of freedom inherent in reduced order modeling, it has become apparent that a one-dimensional acoustic model would be more appropriate.

The basis for a one-dimensional model is the fact that the frequency range of interest is typically very low. The reason for the low frequency range is due to the flame's low pass filter characteristics. In general, frequencies above about 250 Hz do not excite the flame and therefore do not produce significant enough dynamics to be considered important for reduced order modeling.

In the low frequency range of interest, plane wave behavior will be the dominant acoustic response. A plane wave is an acoustic wave that propagates in only one direction, longitudinally along the axis of the combustor and has no variation in properties over its cross-section. The plane wave assumption is valid until the frequency range exceeds the cut off frequency of the first cross mode. The equation for the cutoff frequency for a combustor of circular cross section is given below.

$$f_c = \frac{1.84c}{p\,d} \tag{0.1}$$

Where c is the speed of sound in the medium and d is the largest diameter in the combustor. For the laboratory gaseous combustor under study in this project, the cutoff frequency is about 1,364 Hz. In general, the plane wave assumption works well when the cutoff frequency for the first cross mode is less than the cutoff frequency of the flame (about 250 Hz).

6.3.2 Finite Element Modeling Techniques

As discussed above, the acoustic response of the combustor consists of plane wave interactions. In order to capture these interactions accurately, two parameters are required: the equivalent cross-sectional area, and the corresponding length of each section.

Once the equivalent geometry is known, it is used to create the structure for the finite element model. The ABAQUS finite element package is used in this research; however, other commercial codes may also be adequate.

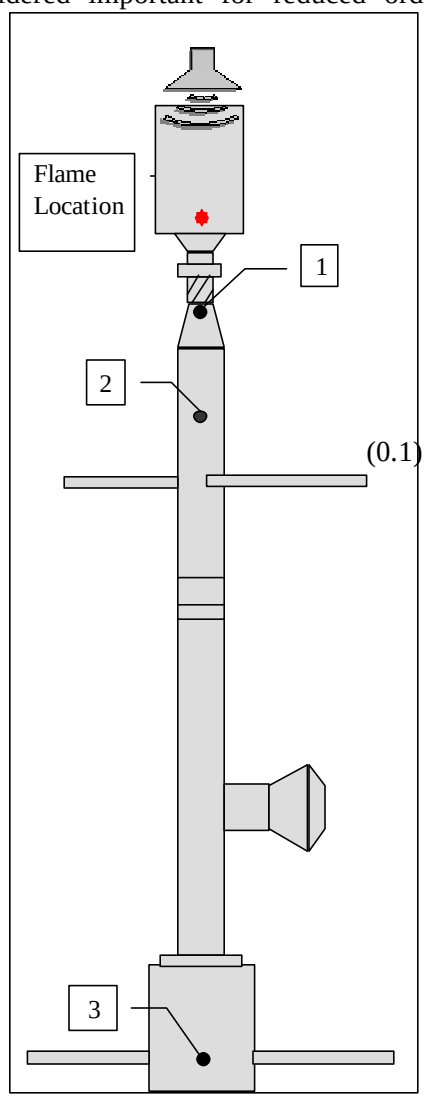

Figure 6.2: Schematic of combustor rig

In ABAQUS, a one dimensional deformable fluid structure of variable cross-sectional area was utilized. This structure was meshed with one-dimensional quadratic acoustic elements. There are a total of 1,097 elements in the finite element mesh. A higher number of elements produce no change in the results. In fact, it is likely that fewer elements are needed for the finite element solution to converge.

Rigid boundary conditions were enforced everywhere except at the top of the combustor where an open duct impedance condition was specified. Lastly, a constant volumetric drag of $50\ \mathrm{N \cdot s/m^4}$ was specified as material property of the air to make the finite element model lightly damped.

6.4 Experimental Comparison

Figure 6.2 shows a simple schematic of the combustor rig used for experimental validation. The three places numbered on the schematic represent three different locations where the finite element model was compared with experimental results. The results were compared using frequency response functions formed by dividing the pressures at the four different locations in the rig by the pressure at the idealized location of the flame.

Figures 6.3, 6.4, and 6.5 on the following pages show the FRF's predicted by the acoustic finite element model vs. the experimental FRF's at the same locations. It should be noted that the data being compared in the following graphs is only used as a means for validating the accuracy of the finite element model. It is not the actual data that will be input into the reduced order model; that data will be discussed in detail later in the "Velocity/Impedance Measurements" section of the report.

The frequency range displayed in the figures below goes from 25 to 650 Hz. Notice that in all three figures, the peaks in the FRF are approximately at the same frequencies. These frequencies are the first five natural or resonance frequencies of the combustor and each one has a corresponding mode shape that will be discussed in further detail in the "Mode Visualization" section.

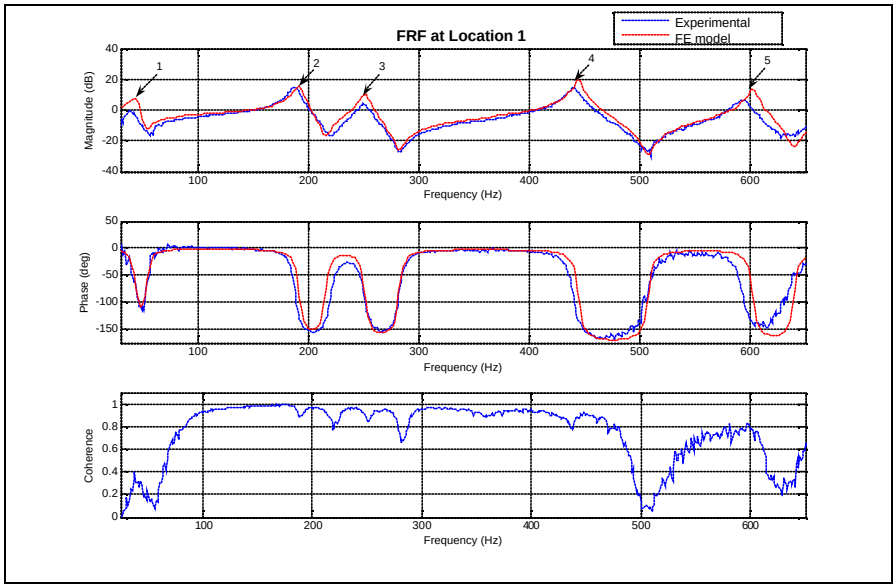

Figure 6.3: Frequency response function between pressure at location 1 and the pressure at the idealized flame location.

The frequency response function shown in Figure 6.3 is taken at location one (referenced in Figure 6.2), about 3.5 inches upstream from the flame. It can be seen from the figure above that both magnitude and phase of the FRF are very accurately predicted from the one-dimensional finite element model. It should also be noted that at the anti-resonance frequencies, the coherence is poor. This occurs because the FRF magnitude is so low at these locations that the inherent noise in the signal shows up and drives the coherence down.

The resonance frequencies are the most critical things to capture in the FRF's. These frequencies have been numbered in Figure 6.3 for convenience and will be referred to by the numbers in the future. Table 1 below compares the experimental and finite element resonance frequencies listing the frequencies, the difference between experimental and finite element, and the percent error. The percent error is calculated from the following equation.

$$\text{Percent Error} = \left| \frac{\text{Measured-Predicted}}{\text{Measured}} \right| \times 100$$

Table 6.1: Resonance Frequency comparison between experimental and finite element model

Number	Measured resonance Frequency (Hz)	Predicted resonance Frequency (Hz)	$\lvert$**Measured - Predicted**$\rvert$ (Hz)	Error (%)
1	39	42	3	7.7
2	190	192	2	1
3	250	250	0	0
4	440	444	4	.9
5	594	602	8	1.3

The table above shows that the first resonance frequency has the largest percent error with a value of 7.7%. However, it should be realized that the percent error calculation is more sensitive to differences at lower frequencies. The other resonance frequencies all have errors of less than two percent. These errors are very low, and fall within the acceptable range error established at the start of the project.

Figures 6.4 and 6.5 below are comparisons made at two other locations in the combustor and have essentially identical resonance frequencies and consequently the same small amount of error.

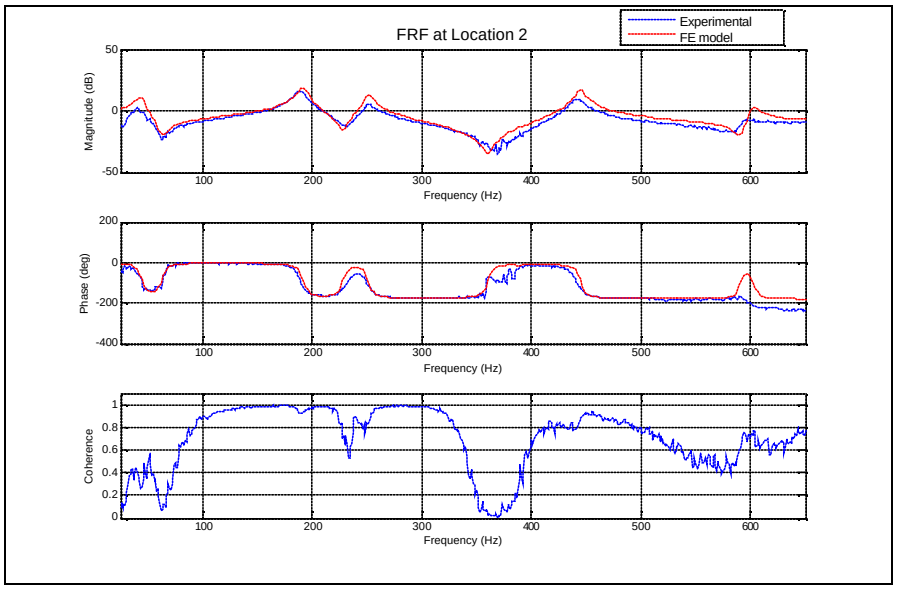

Figure 6.4: FRF between pressure at location 2 and the pressure at the idealized flame location.

The frequency response function shown in Figure 6.4 is taken at location two (refer to Figure 6.2), about 11 inches upstream from the flame. Once again, the finite element model does an accurate job in predicting the magnitude and phase of the FRF. It should be noted that there is some extra noise in the experimental magnitude and phase plots around 360 Hz, as well as a drop in coherence in this region. These affects are attributed to the resonance of a thin aluminum plate used to cap off the middle side branch where a speaker is sometimes placed (see Figure 6.2). To eliminate these affects the thin plate should be replaced with a significantly stiffer plate.

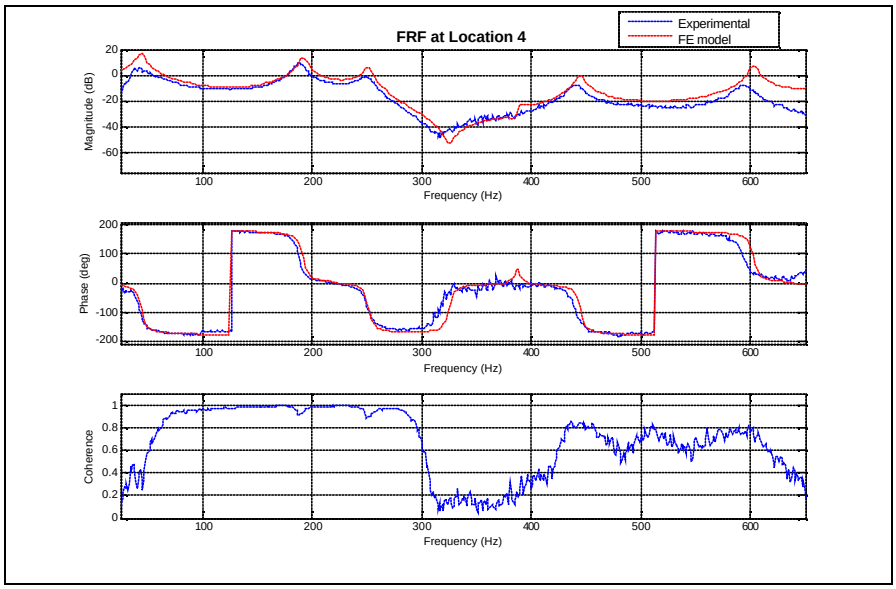

Figure 6.5: FRF between pressure at location 4 and the pressure at the idealized flame location.

The frequency response function shown in Figure 6.5 is taken at location 6.3 in Figure 6.2, about 40 inches upstream from the flame. The finite element model still does an excellent job at predicting magnitude and phase of the FRF. The overall magnitude of the FRF has been significantly reduced compared to the magnitudes in Figures 6.3 and 6.4. A large part of this magnitude reduction is due to a honeycomb and perforated plate section placed in the lower end of the combustor for flow straitening purposes. The result is that only a fraction of the acoustic wave is transmitted through. In the finite element model the honeycomb and perforated plate were modeled simply as an equivalent cross-sectional area reduction. It is evident from the high accuracy in the predicted FRF in Figure 6.5 that the equivalent area reduction works very well when modeling this type of obstruction.

As mentioned previously, there appears to be extra noise in the experimental data near 360 Hz due to the vibration of the thin aluminum plate. This again results in low coherence at these locations.

6.5 Summary of Finite Element Modeling

The accuracy of the one-dimensional finite element model is remarkable. This is especially evident when one looks at some of the geometric complexities in the feed lines, swirler, perforated plate, and cross sectional area changes shown in Figure 6, a picture of the actual combustor. In addition to the one dimensional model having excellent accuracy, it is also substantially easier to create than a three-dimensional model. For example, once the equivalent geometry and boundary conditions are known, it would take an experienced user of ABAQUS roughly two or three hours to create the finite element model. The one dimensional model also requires significantly less computational time to solve. For a three-dimensional finite element model of the combustor, it takes several hours on a super computer to solve. In comparison, it takes about one minute on a desktop computer to solve the one-dimensional combustor finite element model. Because of the very good accuracy and efficiency of the one-dimensional finite element model it is recommended that it be used in place of the three-dimensional model when ever possible.

6.6 Mode Visualization

The five resonance frequencies shown in Figures 6.3 through 6.5 correspond to the first five modes or dominant standing wave patterns of the combustor. These modes can be visualized by spatially plotting the real part of the acoustic pressure at the resonance frequency. The ability to visualize each acoustic mode aids in understanding the contribution and coupling of each geometric subsystem and how it affects the overall acoustics of the combustor. The visualization of modes can also be beneficial for both designing the geometry of the combustor, as well as, for creating passive control devices for controlling the thermoacoustic oscillations. The first three acoustic modes of the laboratory combustor are shown in the figures below.

1) **142 Hz ?** **First axial mode**, only the overall length of the combustor affects this mode. This mode is approximately a quarter wave, $\lambda/4$, mode.

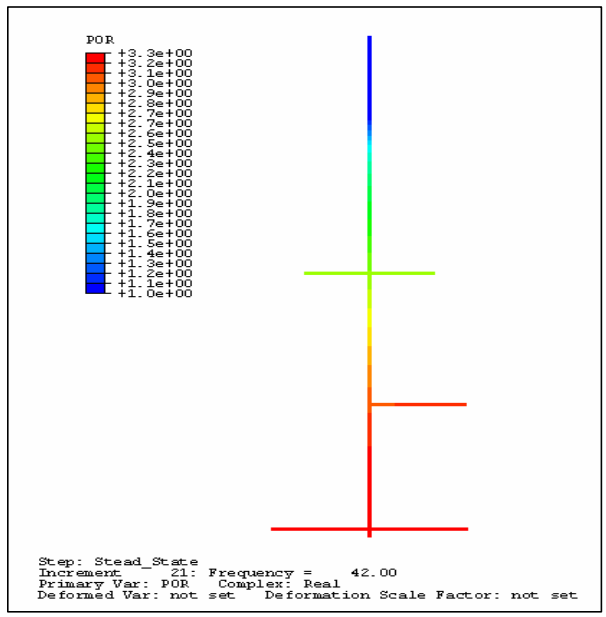

2) **192 Hz ?** **Second axial mode**, this mode is once again a function of the overall length slightly coupled with the lower side branch. This mode is approximated as a $3\lambda/4$ mode.

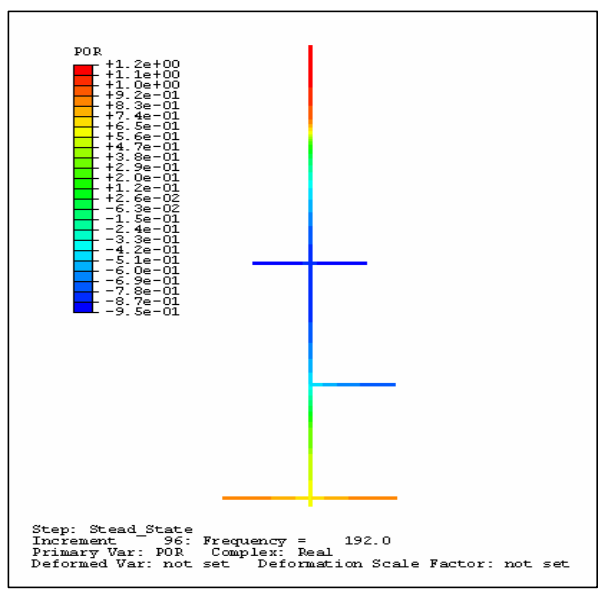

3) **250 Hz ?** **Third axial mode**, this mode is also a function of the overall length and is strongly affected by the dimension of the middle side branch. This mode is approximated as a 5λ/4 mode.

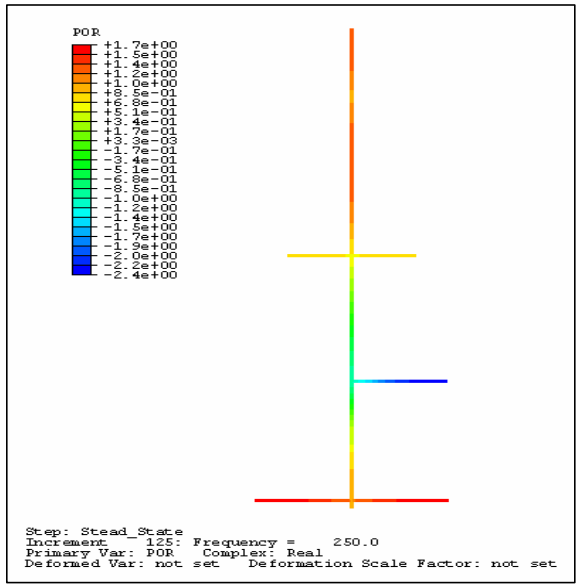

The mode visualization technique shown in the plots above is particularly useful in designing the geometry of the combustor. One can simply modify the geometry that a given acoustic mode is most sensitive to, and consequently modify the resonance frequency and amplitude of the mode. One example of this was observed with the resonance frequency associated with the third axial mode. When the length of the middle side branch was shortened by 1 inch, the third resonant frequency shifted from about 250 Hz to about 260 Hz. Similar results would occur from changing other dimensions in the combustor. As mentioned above, this process can be used as an important tool in the design of combustors.

6.7 Experimental Validation

Figures 6.3 through 6.5 show experimental results that were acquired on the gaseous laboratory combustor at Virginia Tech's Active Combustion and Control laboratory. A picture of the test apparatus has been attached below along with its specifications.

Table 6.2: Specifications for VACCG Laboratory-Scale Combustor

Combustor Type	Swirl and dump & enables turbulent flame stabilization
Air Flow rate	200 SCFM
Power	400 KW
Reynolds Number	100,000 max
Swirl Number	0.4-1.8
Pressure	Atmosphere to 10 bar

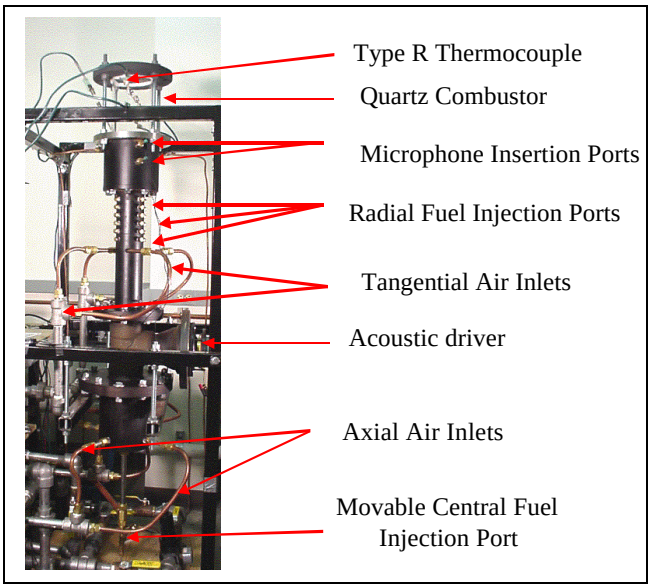

Figure 6.6: The VACCG Laboratory-Scale Combustor.

The purpose of the experiments was to determine the "cold" acoustic behavior of the combustor. A speaker was used to excite the acoustics with white noise at the top of the combustor. The speaker was placed in a location spatially consistent with the flame and can be considered as an acoustic source representing the flame. High precision microphones were used to measure the acoustic pressure at the several spatial locations in the combustor rig including the three locations referred to in Figures 6.3 through 6.6. The data from these experiments was used to reconcile the "cold" acoustic model, explore additional acoustic properties in the combustor, and provide frequency response functions used in the closed-loop reduced-order model.

Plans are currently being made to develop experimental procedures to verify the "hot" acoustic response of the combustor. The main challenge is to find ways to mount microphones so that they will not be damaged by heat.

6.8 Velocity/Impedance Measurements

As mentioned in the introduction, the desired outputs of the finite element model are the frequency response functions between the pressure at the flame to the particle velocity at desired locations. These FRF's are input into the reduced order flame model and play a significant role in predicting the thermoacoustic instabilities.

Two figures are shown below. Figure 6.7 shows the FRF immediately upstream of the flame. Figure 6.8 represents the FRF at the fuel lines.

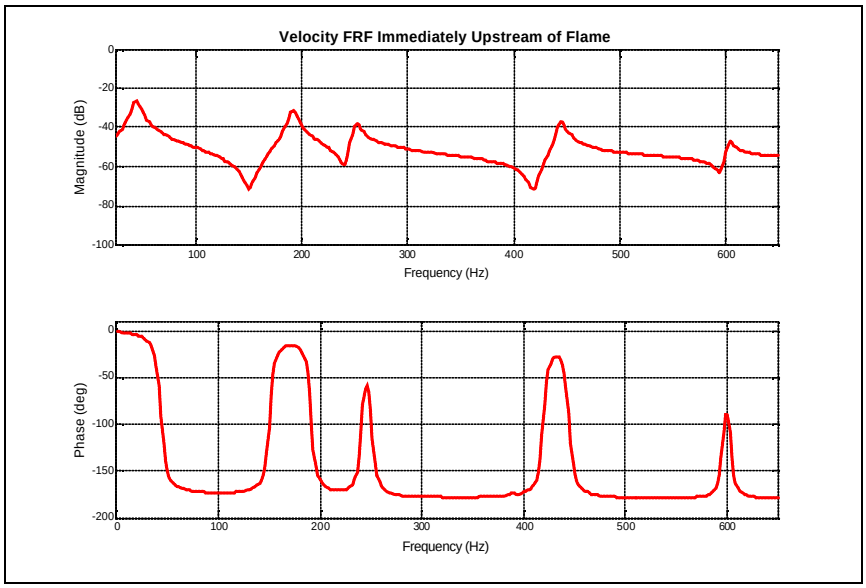

Figure 6.7: Particle velocity frequency response function between the pressure at the flame and the particle velocity directly upstream of the flame.

The above frequency response function describes the relationship between the pressure when the flame acts as an acoustic source and velocity fluctuations that occur in the air fuel mixture being fed to the flame. These velocity fluctuations essentially give the flame an unsteady air-fuel mixture which in turn causes heat release fluctuations. The unsteady heat release becomes the main cause of the thermoacoustic instabilities.

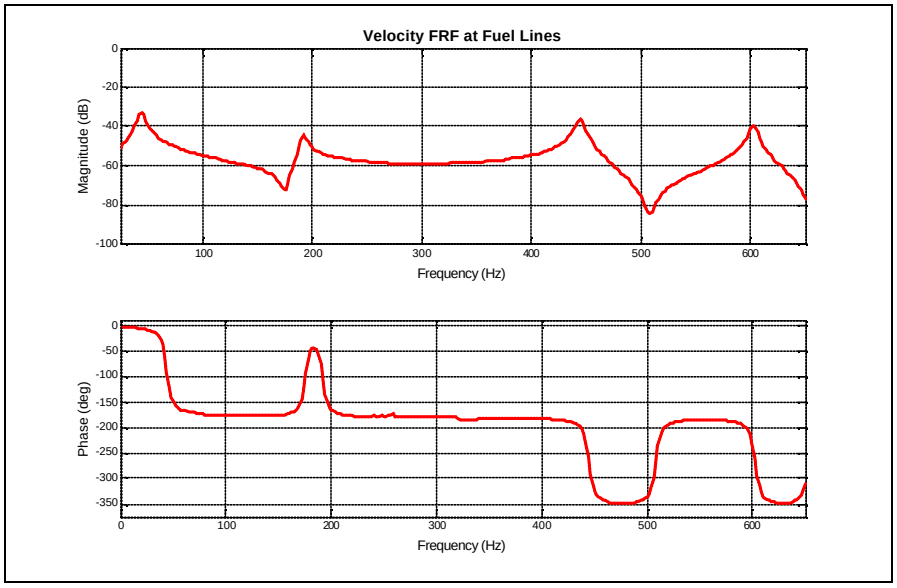

Figure 6. 8: Particle velocity frequency response function between the pressure at the flame and the particle velocity at the fuel lines.

The frequency response function shown above represents the relationship between the pressure when the flame acts as an acoustic source and velocity fluctuations that occur at the fuel lines. These fluctuations cause the equivalence ratio to vary and consequently variations in the heat release rate. Once again the heat release fluctuations are the main cause of thermoacoustic

instabilities. It is also interesting to note that the third resonance frequency at 250 Hz does not show up in this velocity FRF.

As mentioned previously, the FRF's shown in Figures 6.7 and 6.8 are the outputs from the finite element model which are input into the reduced order model.

6.9 Hot Combustor Acoustics Modeling

The current acoustic finite element model of the combustor has been validated to accurately predict the "cold" acoustic response of the combustor. Additionally, the impact of coupling different subsystems attached to the combustor on the overall acoustic behavior has also been explained. The last phase of the study is to incorporate temperature gradients into the acoustic model. Steep temperature gradients associated with combustion can cause both reflection and refraction of incident sound waves. These effects can cause the resonance frequencies to move. To account for this in the finite element model, temperature changes can be represented by changes in the bulk modulus and density of the medium. Both of these quantities are temperature dependent and can be spatially mapped to the finite element model once the spatial temperature distribution is known.

An approximation to the temperature distribution of the gaseous laboratory combustor is shown in Figure 6.9. The temperature distribution is based on experimental data taken on the combustor and from other combustors in the VT Combustion Systems Dynamics Laboratory.

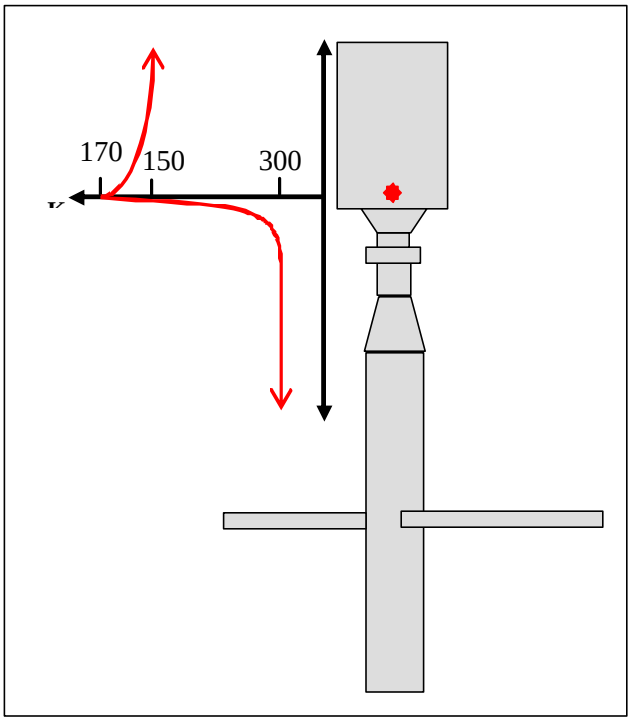

Figure 6.9: Approximate temperature distribution for combustion rig

The temperature profile above is an approximation of the actual temperature profile in the combustor under study. A more accurate distribution will be obtained in this phase of the study through the use of either computational fluid dynamics or actual experimental measurements on the

rig. As mentioned above there will also be a need to validate the "hot" acoustics experimentally. There is still a significant amount of work to be done on characterizing "hot" acoustics. This will become the focus of research in the upcoming months.

6.10 Status and Work Plan

The entire focus of this project is to develop a design-based methodology or process whereby industry can predict instabilities at the design level itself. Developing this process will help in predicting instabilities in both large scale and industrial scale combustors.

Figure 6.10, shown below, indicates the state of the acoustics tasks in the overall project. All the green tasks have been completed which refer to the development of the "cold" finite element model. Currently, work is being done to complete the yellow and red tasks. The task associated with mapping temperatures from either CFD code or experiments is well underway. Code has already been developed and the first significant revision has been made to that code for mapping temperatures onto the nodes of the acoustic finite element model; however, further refinement is planned.

The "hot" acoustic model is to be completed and coupled with the acoustic flame model by the end of April.

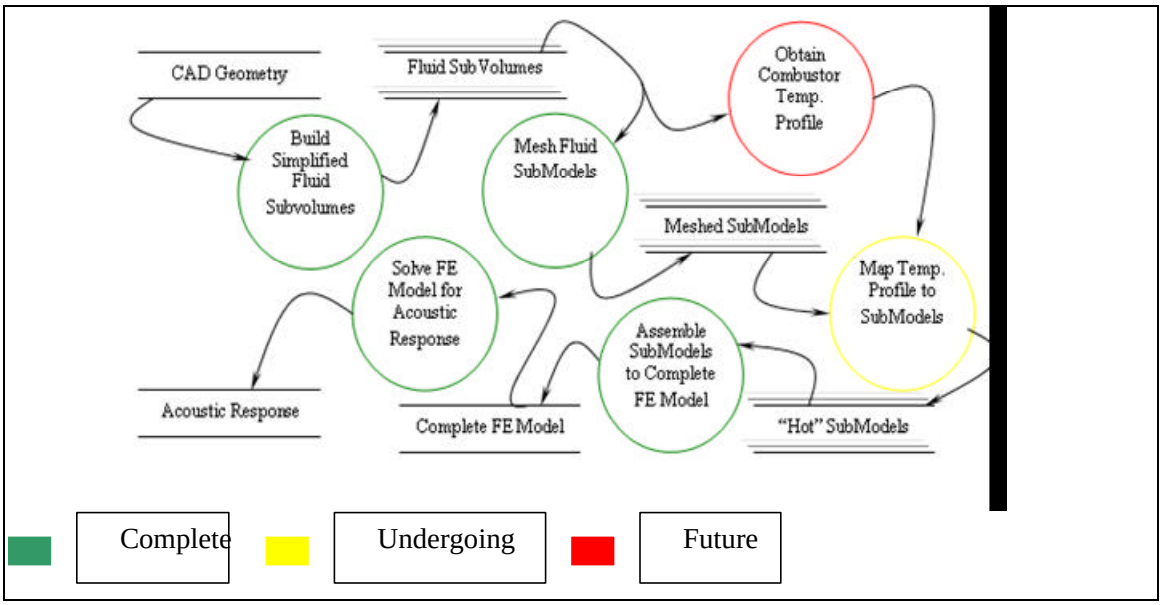

Figure 6.10: Flow diagram for acoustic Finite Element modeling for hot combustors

7 Prediction of Combustion Instabilities

7.1 Introduction

Thermo-acoustic combustion instabilities occur due to a dynamic coupling between a flame and the acoustic response inside the combustion chamber such that the two inherently stable phenomena produce an unstable system. To add to the complexities that are inherent to a reacting flow problem, the manner in which these couplings occur varies with a number of parameters. It is the unfortunate result that much of the work on modeling combustion instabilities in gas turbine engines is either combustor specific or utterly non-physical and only good for qualitative analysis.

This work is targeted to developing simplified equations that capture the significant physical elements of thermo-acoustic instability in a gas turbine combustor such that they may be applied to

numerous geometries in order to predict instability. Such models are of interest to academic and industrial communities since not only do predictive models provide invaluable influence in the design of new products and the modification of existing ones, but, as this discussion will show, can also provide unique insights into the physical phenomena that cause these instabilities.

Dissection of the System into Physical Components

The system can be modeled with general equations, treating spatial variations in species, pressure, temperature, density, etc… with partial differential equations. In additional to being far too cumbersome to hope for any sort of analytical solution, it would be difficult to even extract any meaningful, non-combustor-specific information from the model. It has become a common practice, therefore, to conceptualize thermo-acoustic combustion phenomena as consisting of two separate but interacting physical components – the *flame* and the *acoustics.*

Though this may seem so intuitive as to be obvious, the ability to decouple the two physical dynamic events and model them independently is an important step that presents some unique challenges of its own. The manner in which these components interact is dependent on a number of factors, including but not limited to fuel type (gaseous or liquid), injection method (direct or premixed), flow regime (turbulent or laminar), and numerous complications that can be brought on by the combustor geometry itself.

Works of Note

Works bearing resemblance to this are not uncommon in the literature. Lieuwen[1] et. al. of Georgia Tech have published multiple papers using models similar to ones presented in this document to model a dynamic combustor. Similarly, Gohniem[2] et. al. of MIT have even gone so far as to develop a closed-loop analysis with exactly the flame-acoustic decoupling mentioned above. Despite novel suggestions as to the potential causes for combustion instabilities, the simplified flame models often have difficulty matching the observed frequency response characteristics for physical flames. The MIT group has released papers using more advanced chemical kinetics that demonstrate reasonable bandwidths and that serve as a potential retort to the alleged limitations on the work.

This document treats the detailed development of one particular type of flame model, targeted specifically to the reasonably accurate prediction of dynamic phenomena. First, general governing integral equations are developed for the dynamic flame and later applied specifically to a Well-Stirred Reactor. These equations are developed, however, with the strict intent that they be general enough to be applied to other reactors as well. An appropriate chemical kinetic model is developed for the model. Lastly, various means for constraining the flame geometrically and the potential impacts on the model's dynamic response are investigated and compared with physical measurements.

7.2 Declaration of the Governing Equations

The Well Stirred Reactor's (WSR) governing equations are obtained by neglecting spatial variations in the flame region and integrating the full reacting flow equations to obtain the equations below. Since the only spatial change in properties that is permitted occurs at the inlet, the properties at the outlet are assumed to be identical to those throughout the reactor, leaving only two states that need to be considered – the inlet and the outlet. For ease of notation, any parameter evaluated at the inlet is designated with a zero subscript and all others are taken to be at the outlet. Equations 1 and 2 govern the conservation of species and energy respectively. Conservation of mass is absent since it is implicitly included in both the species and energy equations.

$$\frac{dY_i}{dt} + \frac{\dot{m}_0}{M}\left(Y_i - Y_{i,0}\right) = \frac{\dot{w}_i}{r}$$

(7.2-1)

$$\frac{dh}{dt} + \frac{\dot{m}_0}{M}\left(h_i - h_{i,0}\right) = \frac{1}{r}\frac{\partial p}{\partial t}$$

(7.2-2)

The mass source per unit mass due to chemical reaction for the ith species in Equation 1 as predicted by global, single-step, Arrhenius chemical kinetics is defined in Equation 3.

$$\dot{w}_i \equiv \left(n_i'' - n_i'\right) MW_i A \exp\left(-\frac{E_a}{R_u \bar{T}}\right)\left(\frac{Y_F}{MW_F}\right)^m \left(\frac{Y_F}{MW_F}\right)^n$$

(7.2-3)

Equation 2 is the WSR energy equation for inviscid, adiabatic flow. This can be manipulated to yield Equation 3, which is similar in form to those that typically appear in combustion texts. The reaction rate term naturally appears by substituting Equation 1, leaving us with a term that can intuitively be dubbed the heat release of the flame since it appears as a source term in the energy equation. In addition, with the perfect gas assumption the terms in the summation on the left could be reduced to sensible enthalpy convection. Since enthalpy cannot be assumed to be linear with temperature, however, it is necessary to keep the equation in this form.

$$c_p \frac{dT}{dt} + \frac{\dot{m}_0}{M}\sum_i Y_{i,0}\left(\frac{\partial h}{\partial Y_i} - \frac{\partial h_0}{\partial Y_i}\right) = \frac{1}{r}\frac{\partial p}{\partial t} - \sum_i \frac{\partial h}{\partial Y_i}\frac{\dot{w}_i}{r}$$

(7.2-4)

This model includes four species – fuel, oxidizer, products, and diluent. Since diluent does not participate in the chemical reaction and is therefore neither formed nor depleted, nor do changes in diluent mass fraction significantly influence the reaction rate apart from implicit changes in fuel or oxidizer mass fractions, it is sufficient to consider diluent mass fraction constant. Furthermore, at any given time at any given location in space, the sum of the mass fractions must be unity, so one of the remaining three mass fractions may be written explicitly in terms of the other two. Since fuel and oxidizer appear explicitly in the reaction rate equations, it is convenient to eliminate the product mass fraction from the equations.

Varying inlet mass flow, which appears as a coefficient in both Equations 1 and 2, parametrically excites the system, while inlet mass fractions appear as a source term in Equation 1. Since the variations in upstream mass fractions can be expressed explicitly as variations in upstream equivalence ratio, the system can be described as being excited by two inputs – equivalence ratio and mass flow.

7.3 Methods for Constraining the Flame Size

Traditional, steady WSR models assume a constant volume process. This is particularly appropriate for steady reaction processes where the reaction volume is well defined. However, the above equations are written in terms of the mass of materials inside the flame region, *M*. If this parameter is allowed to vary in time, it is necessary to establish a law that governs its change. It can be shown that regardless of how the flame mass changes in time, these same governing equations still apply, so it is only necessary to add a fourth equation to the system. If the equation is differential, it will simply increase the order of the system. If the equation is an algebraic

relationship, it can be solved for mass and directly substituted into the original equation. In the literature, this has typically been done by arbitrarily obeying the original constraints on WSR models by fixing the flame volume such that

$$M = \forall r \ . \tag{7.3-1}$$

Since the flame is known to pulsate in time with the various perturbations, this is a non-physical assumption. To specify the mass of materials in the reaction region to be constant in time is equally arbitrary, but affords a study on more intuitive physical parameters. Observe that if M is constant, the ratio of inlet mass flow to flame mass as it appears in Equations 1, 2, and 3 is also constant. Therefore, these equations take on a form that appears identical to typical convective control volumes with a well-documented first-order response, possessing a time constant of

$$t = \frac{M}{\dot{m}_0} \ . \tag{7.3-2}$$

7.4 Linearization of the Dynamic Equations

It is, therefore, possible to write a state equation on the state variable, x, and an input vector, u, where

$$x_1 = T \, , x_2 = Y_F \, , x_3 = Y_{Ox} \tag{7.4-1}$$

and

$$u_1 = \Phi, u_2 = \dot{m}_0 \tag{7.4-2}$$

such that

$$\dot{x}_i = G_i\left(x_j, u_k\right) \tag{7.4-3}$$

where G represents the dynamic WSR equations. In order to compute a frequency response using linear system theory, the system must be linearized. By considering a small perturbation from the steady operating conditions, a Taylor expansion of Equation 4 yields the desired linearized model. The steady state operating conditions may be computed by forcing Equation 4 to zero for some steady input vector. Therefore, the inverse of Equation 5 yields the steady operating condition.

$$0 = G_i\left(\bar{x}_j, \bar{u}_k\right) \tag{7.4-4}$$

Using the Einstein index summation convention for ease of notation, the Taylor expansion of a small perturbation about the steady state is given by

$$\dot{\tilde{x}}_i = G_i\Big|_{\bar{x},\bar{u}} + \left.\frac{\partial G_i}{\partial x_m}\right|_{\bar{x},\bar{u}} \tilde{x}_m + \left.\frac{\partial G_i}{\partial u_n}\right|_{\bar{x},\bar{u}} \tilde{u}_n + \mathrm{K} \tag{7.4-5}$$

Since G evaluated at the steady conditions has already been said to be zero, and since higher order terms may be neglected due to the small perturbation assumption, this expression can be reduced to Equation 6.

$$\dot{\tilde{x}}_i \approx \left.\frac{\partial G_i}{\partial x_m}\right|_{\bar{x},\bar{u}} \tilde{x}_m + \left.\frac{\partial G_i}{\partial u_n}\right|_{\bar{x},\bar{u}} \tilde{u}_n \tag{7.4-6}$$

Once in this realization, it is possible to find pole and zero locations and frequency response plots using traditional linear state space analysis.

7.5 Constant Mass WSR Dynamics

The first logical means of testing the validity of the model is to compare the frequency response plot generated from the linear theory of the previous section to the data collected from the physical system. Figures 1 and 2 show the frequency response plots for mass and phi perturbations respectively for various mean phi values. Though the bandwidth trends agree with the physical behaviors, the actual bandwidths are an order of magnitude or more higher than physical data has indicated. This is consistent with the work of Gohniem et al, who used more heavily simplified dynamic WSR models to examine possible explanations for combustion instability.

There is the appearance of low-frequency dynamics in the Φ-response that are absent in the mass-flow-response. These are characterized by a low frequency zero that causes a rising phase and rising amplitude, halted by a pole at a slightly higher frequency that causes a plateau in the amplitude and restores the phase to zero. The low-frequency pole is of great interest since it appears precisely in the frequency range (80 – 200Hz) at which the flame seems to consistently seems to lose response. These dynamics appear absent from the mass perturbations since the zero appears extremely close to the pole, almost exactly canceling the dynamics.

Because there are high frequency dynamics that seem to match crude trends, but that differ vividly in bandwidth and low frequency dynamics that have failed to even appear in most other works, the discussion of these results is divided into the high and low frequency dynamics.

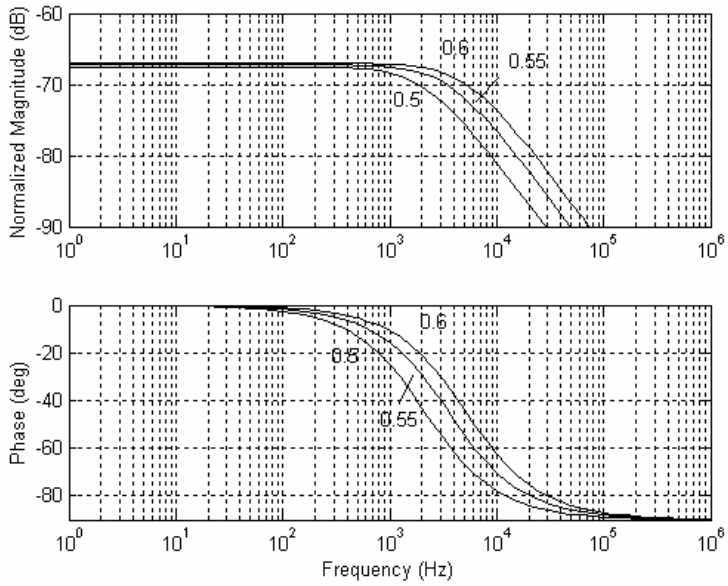

Figure 7.5.1 – Dynamic WSR reaction rate frequency response to mass-flow perturbations. The output is reaction rate, normalized by the mass-flow perturbation.

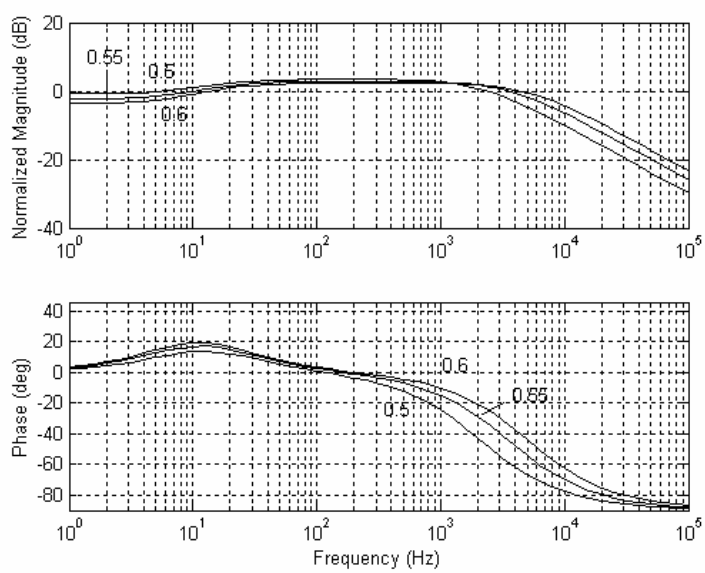

Figure 7.5.2 – Dynamic WSR reaction rate frequency response to upstream Φ perturbations. The output is reaction rate, normalized by the Φ perturbation.

High Frequency Dynamics

The high frequency dynamics are the only part of the results that seem to agree with other published works. The cutoff frequency decreases with falling equivalence ratio, similar to the physical data, but the pole is a full order of magnitude higher in frequency that the cutoffs observed in the physical system.

An investigation into the significant determining factors in the placement of the high frequency pole demonstrated sensitivity to a number of parameters, perhaps the most remarkable being the exponential constant on the fuel mass fraction appearing in Equation 3. Figure 3 shows three

frequency response plots overplotted for various values of *m*. As *m* was varied, a new value for *A* (also appearing in Equation 3) was selected such that the mass-flow limits for blow-off were conserved.

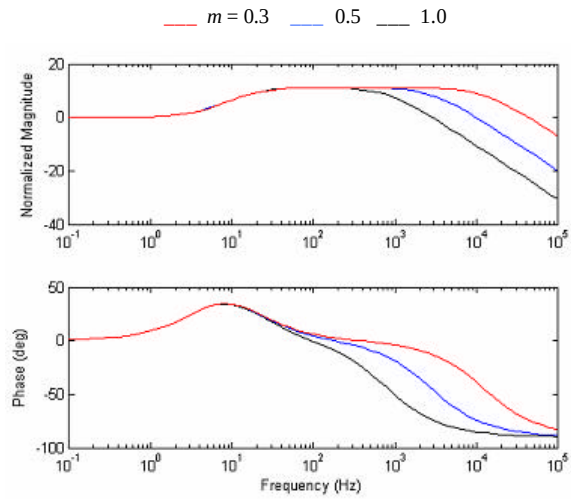

Figure 7.5.3 - Φ excitation response change due to changes in *m* as it appears in Equation 3 while simultaneously varying *A* such that the blow-off limits are preserved.

While the low-frequency dynamics showed no change whatsoever, the high frequency pole was clearly heavily influenced by changes in the chemical kinetic properties. Changes that affect the flame temperature had similar effects, though none were as significant as variations in *m*. This tends to indicate that the high-frequency pole is largely influenced by chemical kinetics. This is the school of thought most commonly found in the literature <Lieuwen, Gohniem>, though when using such a simplified chemical kinetic model designed to predict static events such as flammability limits, it is unlikely that accurate frequency response predictions could be reasonably expected.

Low Frequency Dynamics

The only dynamics that agree in bandwidth; the low frequency dynamics appear to differ completely in behavior from the physical system. Figures 1, 2, and 3 all demonstrate that despite changes in the equivalence ratio and chemical kinetics, the low-frequency pole and zero remained utterly unchanged. It is only as the mass flow or reactor mass is varied that the low frequency dynamics change at all. Furthermore the time constant corresponding to that pole is exactly that described as the convective residence time in Equation 5.

The low-frequency zero appears to be non-physical. Despite some hints of rising amplitude in the velocity perturbation data, none of the physical data seems to exhibit such a drastic plateau extending to high frequencies as the model predicts. Worst of all, the model predicts a positive and completely non-physical low frequency phase.

These points are motivation to reinvestigate the constant mass reactor assumption. It has been well documented that as the steady equivalence ratio is changed, the flame size should vary as well <Turns>. Leaner flames have lower flame temperatures, which result in slower reaction rates, requiring more burning time in order to exhaust the fuel. It stands to reason that at the very least the reactor mass should be a function of the steady equivalence ratio. That function may be defined by the reactor size necessary to completely consume the fuel.

If a WSR is forced to react all of its fuel, however, the WSR must also be of infinite size. This can easily be verified by observing that in the limit as fuel mass fraction goes to zero, the reaction rate also goes to zero, forcing *M* in the fuel species equation to infinity for any finite mass flow.

This problem can be solved by arbitrating that the fuel will combust until the fuel mass fraction drops below some critical value, below which the mixture can no longer support a reaction.

Using this scheme, some critical fuel mass fraction was selected and the reactor size was iteratively computed for a variety of steady equivalence ratios while mass flow remained fixed. Once the reactor sizes were computed, the dynamics were recomputed for each operating condition and compared with the physical data. Since the data is quite difficult to visually interpret, any attempt to obtain an empirical transfer function for comparison by curve fitting would be disappointingly arbitrary and could be massaged to demonstrate almost anything. Instead, in order to simply compare movements in the low-frequency dynamics, a simple, first order transfer function of the form

$$\frac{b}{s+a} \tag{7.5-1}$$

was overplotted with the physical data where a was determined by the iteratively computed low-frequency pole. Since the measured frequency response data is not in physical units with an unknown scaling factor, b had to be chosen to match the measured dc-gain rather than relying on the computed gain in order for the results to be directly compared.

The critical mass fraction was iteratively selected such that one of the frequency responses agreed in bandwidth with the equivalence ratio data. Then, the same critical value was used to generate all the other cases. Figure 4 shows the results for six different steady equivalence ratios. Figure 5 shows the predicted pole frequency as a function of equivalence ratio for the six cases.

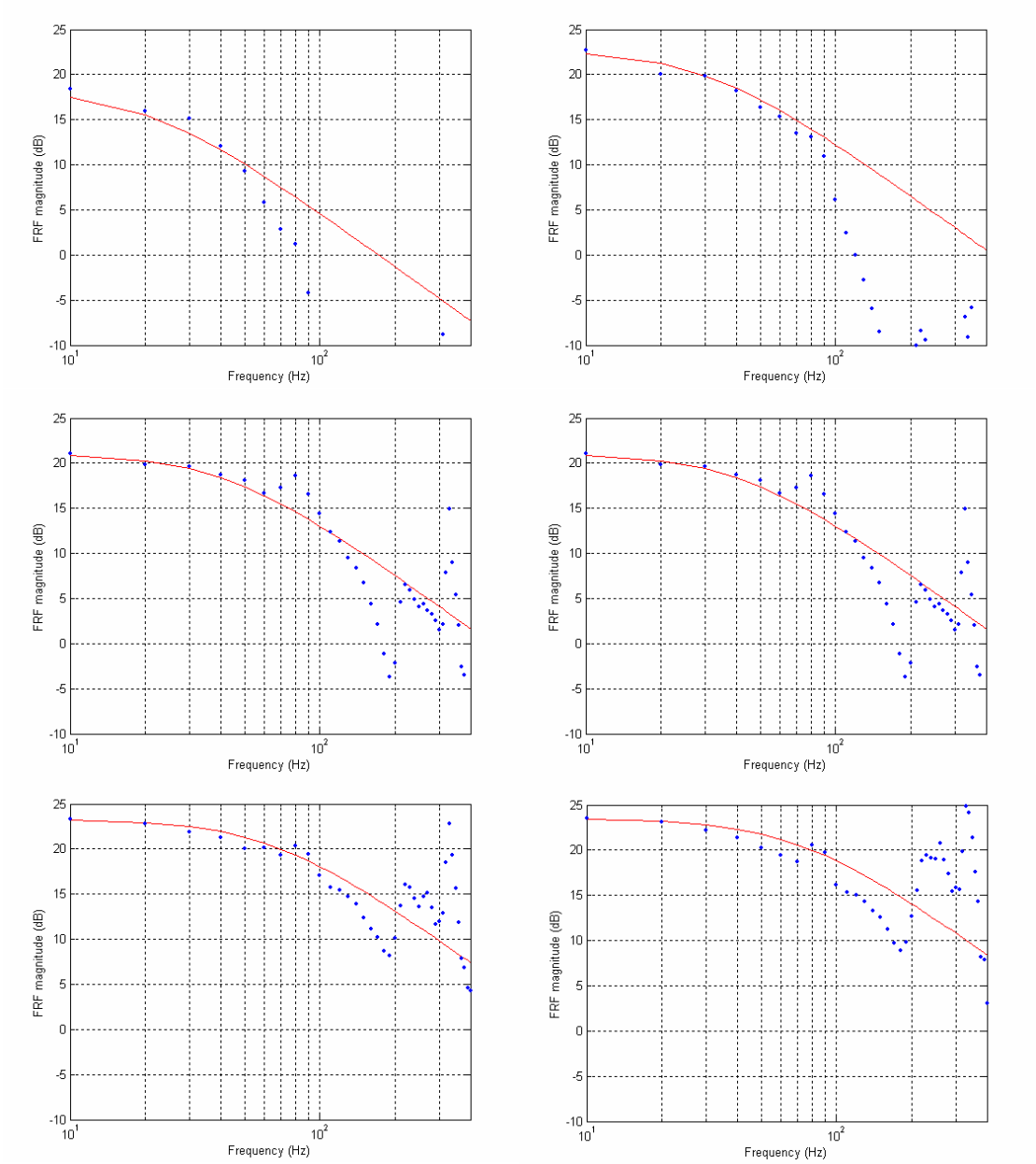

Figure 7.5.4 – The convective residence time was iteratively computed in order to produce a consistent exit fuel mass fraction for equivalence ratios of 0.50, 0.54, 0.58, 0.63, 0.66, and 0.70. The resulting frequency response plots are displayed in order starting from the upper left. The calculated dynamics (red) quite accurately predict the physical behavior (blue dots) for low frequencies.

In all cases, the pole prediction seems to be very accurate. Ultra-lean cases appear to encounter either a second pole or a resonant zero pair, which causes a sharper decline in the amplitude at higher frequencies before reaching a very low-magnitude plateau. At higher equivalence ratios, the magnitude only appears to deviate from the predicted curves with a resonant peak at 80Hz and a resonant zero at 200Hz. Since these phenomena are predicted at precisely these frequencies by the 1-dimensional acoustic model and have been measured in the physical rig, it is safe to suggest that these are small acoustic affects that normalization failed to remove.

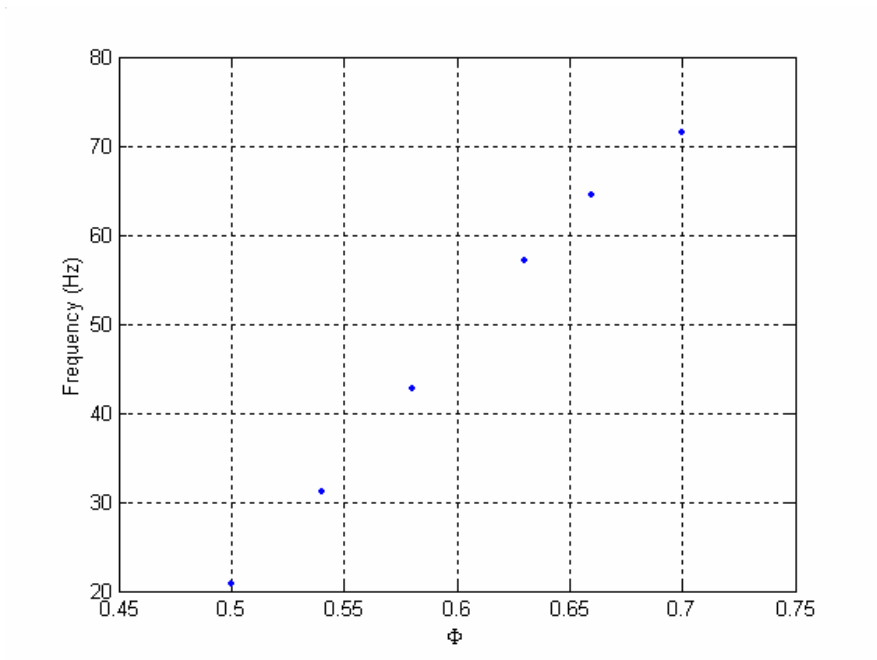

Figure 7.5.5 – Predicted convective pole frequency as a function of mean equivalence ratio. This is the frequency corresponding to a system with the time constant expressed in Equation 5.

7.6 Conclusions and Future Work

The precision to which the low frequency pole predictions match the measurements present a strong argument that it is simple convection and not chemical kinetics that decide the dominant dynamics of the turbulent flame. This conclusion, combined with the marked disagreement between the zeros predicted by the constant-mass reactor and physical data infers that arbitrary constraint of the reactor size is not only statically erroneous, but results in inaccurate dynamic predictions as well. Given the initial success of the work, there are three natural proceeding courses of actions.

1) If chemical kinetics rather than convection decided the dominant dynamics, an arbitrary assumption regarding the flame's size might not have affected the model significantly, but since convection is predominant mechanism limiting the flame's response, it is vital to accurately capture how the flame region oscillates in time. The next step is to derive governing equations for a WSR with new control volume constraints. Given the empirical evidence, it seems likely that the new constraints would follow the data far more closely.
2) The presence of the acoustic peaks in the data must be investigated so that they can be eliminated, ensuring an accurate flame transfer function measurement.
3) Once an accurate flame transfer function can be predicted a closed bop analysis will be used to predict conditions for thermo-acoustic instability. These conditions will be verified by modifying the existing combustor with a chimney to induce instability.

<u>Work Plan for January to May, 2006</u>

These are the goals for the remainder of the project:

January – resolve inconsistencies between these results and results observed in the literature. Investigate other geometric constraints on the flame.

February – Generate coupling equations between the flame and the acoustic transfer function. Is it adequate to model heat release rate as a pressure input to the acoustic equation? Are additional

dynamics present? Reconcile any differences between new conclusions and previous conclusions in the literature.

March – Code and analyze the resulting closed-loop model. Investigate different flame models and the effect of various assumptions on the stability of the model.

April – Conclude the analysis and generate a write-up summarizing the results.

8 Conclusions (Summary)

During the reporting period, May-November 2005 activities were conducted addressing tasks 1, 5, 2, 3, and 4. For tasks 1 and 4, measurements of the flame dynamic response to sine-dwell excitation were done for equivalence ratios from the lean-blowout (LBO) up to $f \approx 0.75$. Flame response was examined for $\dot{m}(m')$ fluctuations, as well as equivalence ratio fluctuation, f'. Flame response was measured via OH* Chemiluminescence. Very generally the turbulent, swirl stabilized flames behaved as first order systems, after it was suspected that higher frequency peaks may have been related to yet uncoupled rig acoustics, in spite of efforts done to that effect. This issue will be investigated with a hot wire probe, placed upstream of the swirler, to measure m' directly instead of using the two-microphone probe.

Follow-up work on task 1, will include, in addition to clarifying and achieving complete decoupling of the rig acoustics from the flame/combustion transfer function, an investigation of various fuels. Specifically dynamics of mixtures of HE fuels, and hydrogen-HC and hydrogen-HC-CO mixtures will be examined, i.e., the flame response to $m'(\dot{m})$ and f'.
A model for the dispersion and axial diffusion of a f' probe was constructed under Task 2. The model which incorporates turbulence characteristics was related to observed f' characteristics.

A model for the prediction of combustion instabilities, and blowout was constructed. The model will have to address the two key phenomena of the acoustics field in the combustor and attached cavities, and the flame/heat source. Initially the two models are developed separately, and after their verification, they are coupled.

Under Task 5a particular type of flame model targeted to provide a reasonably accurate prediction of dynamics. The uses the conservation equations applied to an unsteady Well Stirred Reactor (WSR). The equations were developed strictly so that they can be applied to other reactors too. Appropriate chemical kinetic model was also developed. Various means for constraining flame geometry and the potential impact on the model's dynamic response were investigated and compared with measurements.

The model resulted in good agreement with measured data at low frequencies, however, any acoustic peeks must be uncoupled. The low frequency agreement suggests that it is convection and not chemical kinetics that decide the dominant dynamics. Disagreement between a fixed mass reactor and measured zeros, indicate that size constraints on a reactor (V=const) lead to inaccurate dynamics, on top of erroneous statics.

The work plan for Nov 2005-May 2006 includes, resolution of disagreements with measurements, resolution of conflicts with literature, construct flame- acoustics coupled model to predict closed loop thermoacoustics.

Under Task 3 a very detailed model for the acoustics of the turbulent swirl stabilized combustor is being constructed. The activities, results and work plan are outlined below.

The work tasks for finite element modeling over the last project period were associated with updating cold combustor acoustics models of the laboratory-scale turbulent combustor and reconciling the models with experimental acoustic data. Experimental acoustic work was conducted on the turbulent combustor resulting in the acoustic natural frequencies and frequency response functions for the combustor. A plane-wave or one-dimensional finite element model was developed for the combustor justified on the fact that the frequency range of interest is low due to the flame's low pass filter characteristics and that acoustics above 250 Hz do not appear to excite the flame to produce significant dynamics for reduced order modeling. The accuracy of the one-dimensional finite element model is remarkable. This is especially evident when one looks at s the geometric complexities of the actual combustor. In addition to the one dimensional model having excellent accuracy, it is significantly easier to develop, solve and postprocess results than a three-dimensional model. The plane-wave FE model solves in less than one minute vs. the three-dimensional model which solves in several hours. The significant savings in model development, solution and postprocessing time allow engineering time to be spent on model exploration and design tasks. Because of the very good accuracy and efficiency of the one-dimensional finite element model it is recommended in place of the three-dimensional model when ever possible.

The last phase of this study is to incorporate temperature gradients into the acoustic model. Steep temperature gradients associated with combustion can cause both reflection and refraction of incident sound waves. These effects can cause the resonance frequencies to move. To account for this in the finite element model, temperature changes can be represented by changes in the bulk modulus and density of the medium. Both of these quantities are temperature dependent and can be spatially mapped over the finite element model once the spatial temperature distribution is known. An approximation to the temperature distribution of the gaseous laboratory combustor is based on experimental data taken on the combustor and from other combustors in the VT Combustion Dynamics Laboratory**.** A more accurate distribution will be obtained in this phase of the study through the use of either computational fluid dynamics or additional experimental measurements on the rig. As mentioned above there will also be a need to validate the "hot" acoustics experimentally. This task will become the focus of research in the upcoming months.

9 Bibliography

Bloxsidge, G.J., Dowling, A.P, Langhorne, P.J., "An acoustically coupled combustion instability. II – Theory" Journal of Fluid Mechanics 193, 445-473 (1988).

Park, S., Annasway, A., Ghoniem, A., "Heat release dynamics modeling of kinetically controlled burning," Combustion and Flame 1228:217-231 (2002).

Lieuwen, T. and B.T. Zinn, "The role of equivalence ratio oscillation sin driving combustion instabilities in low Nox turbines," In Proc. of the 27th International Symp. On Combustion, pp. 1809-1816, 1998a.

Liewen, T.Y., Neumeier, and B.T. Zinn, "The role of unmixedness and chemical kinetics in driving combustion instabilities in lean premixed combustors," Combustion Science and Technology, Vol. 135, pp. 193-211, 1998a.

Turns, S., *An Introduction to Combustion*, McGraw-Hill Co., New York, 2000.

10 List of Acronyms and Abbreviations

CAD	Computer-Aided Design
CFD	Computational Fluid Dynamics
FEA	Finite Element Analysis
He-Ne	Helium-Neon
IR	Infra-red
LBO	Lean Blow-Off
NETL	National Energy Technology Laboratory
p’	pressure perturbation
TEC	Thermo-Electric Cooler
TDLAS	Tunable Diode Laser Absorption Spectroscopy
u’	Velocity Perturbation
VACCG	Virginia Action Combustion Control Group
f'	Equivalence Ratio Fluctuation

Enhanced Prediction Techniques Based on Time-Accurate Simulations for Turbine Blade Internal Cooling

Semi-Annual Report
May 2005 – Nov. 2005

D. K. Tafti
A. Viswanathan
Mechanical Engineering Department

November 2005

DOE Award Number
DE-FC26-02NT41431

UTSR Project Number
02-01-SR100

Virginia Polytechnic Institute and State University
Blacksburg, VA 24061

Disclaimer

This report was prepared as an account of work sponsored by an agency of the United States Government. Neither the United States Government nor any agency thereof, nor any of their employees, makes any warranty, express or implied, or assumes any legal liability or responsibility for the accuracy, completeness, or usefulness of any information, apparatus, product, or process disclosed, or represents that its use would not infringe privately owned rights. Reference herein to any specific commercial product, process, or service by trade name, trademark, manufacturer, or otherwise does not necessarily constitute or imply its endorsement, recommendation, or favoring by the United States Government or any agency thereof. The views and opinions of authors expressed herein do not necessarily state or reflect those of the United States Government or any agency thereof.

Abstract

Numerical predictions of a hydrodynamic and thermally developed turbulent flow are presented for a rotating duct with square ribs aligned normal to the main flow direction. Three rotation numbers Ro=0.18, 0.35 and 0.67 are investigated. The rib height to channel hydraulic diameter (e/D_h) is 0.1, the rib pitch to rib height (P/e) is 10 and the calculations have been carried out for a bulk Reynolds number of 20,000. The capability of the Detached Eddy Simulation (DES) in predicting the turbulent flow field and the heat transfer under the effects of rotation has been evaluated against Unsteady Reynolds-Averaged Navier Stokes (URANS), Large-Eddy Simulations (LES), and experimental data. It is shown that DES by capturing a large portion of the turbulent energy in the resolved scales is much more capable than URANS in transcending the underlying shortcomings of the RANS model. DES shows much better fidelity in calculating critical components of the turbulent flow field and heat transfer than URANS.

The effect of rotation on flow and heat transfer in a 45° ribbed square duct is also investigated. Large-Eddy Simulations (LES) are used to investigate why rotation does not have any effect on heat transfer augmentation unlike 90 degree ribs, in which considerable changes are observed in augmentation at the trailing and leading walls of the duct. It is found that unlike 90 degree ribbed ducts, in which the heat transfer augmentation is strongly dependent on streamwise momentum, spanwise momentum dominates heat transfer in skewed ribs. Since Coriolis forces under orthogonal rotation about the z-axis do not directly contribute to spanwise momentum, they do not have as much of an effect on heat transfer at the ribbed walls at the trailing and leading sides. However, because of the augmentation of turbulence at the trailing side, the vortices which are produced in the separated shear layer of the rib and which move from the inside to the outside of the duct, break down and diffuse before they can impinge on the outer wall. Turbulence attenuation at the leading wall has the opposite effect which allows the vortices to maintain their coherence and impinge on the outer wall. This effect taken together with the streamwise flow being pushed to the leading side, produces an extended region of high heat transfer at the outer wall near the leading side. This is countered by lower heat transfer at the trailing side of the outer wall. Hence, although local variations are present due to rotation, the overall augmentation remains the same.

Table of Contents

Disclaimer ……2

Abstract ……3

Executive Summary ……5

Project Description ……7

Computational and Experimental Method 10

Results and Discussion ……20

Summary and Conclusions ……..... .. 39

References ……42

Executive Summary

Our objective is to evaluate and develop prediction techniques for the internal cooling of turbine blades based on time-accurate methods. The project plan calls for a systematic evaluation of these methods in different flow regimes encountered in the cooling passages, namely fully-developed conditions, developing flow conditions, and flow and heat transfer in 180º bends. The initial geometry chosen for evaluation of different techniques is a square duct with normal ribs of e/D_h=0.1 and P/e = 10 at a nominal bulk Reynolds number of 20,000. This geometry, together with the action of Coriolis and buoyancy forces, contains all the essential elements for testing and evaluation. Other angled ribbed configurations are also being studied.

Progress has been made in the application of Detached Eddy Simulation (DES). In previous work, it was shown that DES is able to capture the flow physics and predict heat transfer at a much lower cost in stationary ribbed channels. Current work is focusing on extending DES to include the effect of Coriolis and centrifugal buoyancy effects in the base turbulence model; In this report, a comparison between DES and URANS is presented in a rotating duct with Coriolis forces. It is shown that DES is more capable of capturing the effects of rotation than URANS. An additional calculation investigates the effect of rotation on a 45 degree ribbed duct. It is shown that since the flow and heat transfer are dominated by spanwise momentum transfer, unlike 90 degree ribs, orthogonal rotation of the duct does not have a large influence on the heat transfer at the leading and trailing walls .

Three graduate students, Samer Abdel-Wahab (M.S.), Evan Sewall (Ph.D) and Aroon Viswanathan (Ph.D) have been supported on this project. Samer Abdel-Wahab graduated with a M.S. degree and is employed at Florida Turbine Technologies. Evan Sewall graduated this semester and will be starting his new position at GE Corporate Research in January. Aroon Viswanathan will graduate in Summer 2006.

The project has been particularly successful in disseminating technical results via conference and journal publications and also in collaborating with industry. Since its inception, fourteen conference papers [1-14] and six journal publications [13-18] have resulted. Andy Smith at GE Global research is using our LES simulations to benchmark some of his reduced-order calculations.

Overall the project has accomplished all of its technical objectives to-date.

Project Description

The internal cooling of turbine blades is a critical problem for the gas turbine industry. Prediction of these flows has been complicated by the presence of turbulence generators for heat transfer augmentation, rotational Coriolis and buoyancy forces. The Reynolds number ranges from moderate $O(10^4)$ to very high $O(10^5)$, depending on the application. Rotation numbers can be of O(1), and centrifugal buoyancy driven Rayleigh numbers can be of $O(10^8)$. The turbulent flow is highly anisotropic, and all attempts at predicting the flow and heat transfer have focused on the solution of steady Reynolds–Averaged Navier-Stokes (RANS) and energy equations. Different turbulence closure models have been used with varying degrees of success. Eddy-viscosity-type models, which assume isotropy, do not perform very well, while more complicated models based on the solution of the turbulent stress equations have been found to perform reasonably well. However, in all cases the quality of the solution is dependent on empirical tuning of the models. Furthermore, steady RANS modeling provides minimal insight into the dynamic processes that enhance heat transfer. The validation of these models has been further plagued by the lack of velocity and turbulence data in internal cooling geometries under rotating conditions.

In this study we propose to look at alternative prediction techniques based on solving the time-dependent Navier-Stokes and energy equations. The objectives are two-fold: a) Use high resolution Large-Eddy Simulations (LES) for predicting and understanding the myriad of physical effects which affect heat transfer, and b) Develop and evaluate the prediction capabilities of hybrid unsteady RANS and LES methods via Detached Eddy Simulations (DES). The combined approach will be integrated with experiments from the literature as well as results from previously funded projects through this program for validation. To support the validation of the flow field predictions, three-component mean and turbulence measurements will be made in a large-scale, stationary flow channel with ribs using a laser Doppler velocimeter.

The work plan proposes to systematically apply these techniques to different flow regimes in internal cooling geometries with ribs: a) fully-developed flow regime, b) U-bend or sharp 180º bend, and c) developing flow regime. We will validate our procedures with experimental data from the literature and with experiments in which mean and turbulence velocities will be measured in a ribbed channel with a U-bend or sharp 180º bend. The validated calculations will then be extended to high rotation and buoyancy numbers, data for which is scarce in the literature.

Issues pertaining to subgrid modeling, numerics, and resolution will also be studied. The DES procedure will also be validated against LES calculations. In the final year of the project, we will apply a combined LES/DES procedure to a full two-pass channel with roughness elements.

The computational tools to be used in this research already exist and have been extensively validated in the past in unsteady flow simulations for air-side heat transfer enhancement in compact heat exchangers and other turbulent flows. Hence, code development will be minimal.

Because of the lack of literature documenting the mean and turbulent flow fields in a ribbed channel, the proposed work includes performing these measurements. The channel will be designed to insure that adequate spatial resolution is achieved while maintaining a velocity range that can be accurately measured. The channel will be constructed using plexiglass to allow for optical access since the primary measurement tool will be a three-component laser Doppler velocimeter.

The results of this project will add a large measure of repeatability and reliability in predicting the internal heat transfer coefficient under extreme operating conditions and will eventually lead to better blade designs.

The research tasks and their status as of April 2003 are summarized below:

1. <u>LES</u>

a. Fully-developed regime with ribs
    1. Stationary ribbed duct **(complete)**
    2. Rotating ribbed duct with Coriolis Forces **(complete)**
    3. Rotating ribbed duct with Coriolis forces and centrifugal buoyancy **(complete)**

b. Developing Flow regime with ribs

The calculations will start a sufficient distance upstream of the first rib in the passage and continue into the passageway until the flow is fully developed.

    1. Auxiliary calculations in smooth fully developed duct to generate time-dependent velocity inlet boundary conditions **(complete)**
    2. Stationary ribbed duct **(complete)**
    3. Rotating ribbed duct with Coriolis forces **(complete)**
    4. Rotating ribbed duct with Coriolis and centrifugal Buoyancy **(complete)**.

c. U-bend with ribs

These calculations will start upstream of the U-bend such that the inlet plane is outside the domain of influence of the U-bend and will extend downstream of the U-bend into the second-pass including the first few ribs.

    1. Stationary U-bend **(complete)**
    2. Rotating U-bend with Coriolis forces **(complete)**
    3. Rotating U-bend with Coriolis and centrifugal Buoyancy **(ongoing)**

2. <u>DES</u>

a. Implement suitable RANS model into computer code GenIDLEST under DES framework. **(complete).**

b. Smooth duct, fully developed. Test model for different mesh resolutions and evaluate accuracy against LES and experiments.

1. Stationary duct **(complete)**
2. Rotating duct with Coriolis forces **(NA)**
3. Rotating duct with Coriolis and centrifugal buoyancy **(NA)**

c. Ribbed duct, fully developed. Test model for different mesh resolutions and evaluate accuracy against LES and experiments.

1. Stationary duct **(complete)**
2. Rotating duct with Coriolis forces **(complete)**
3. Rotating duct with Coriolis and centrifugal buoyancy **(complete).**

3. <u>LES/DES in full two-pass channel with ribs.</u>

1. Effects of Coriolis forces **(complete)**
2. Effect of buoyancy **(ongoing)**

4. <u>Experimental Measurements</u> **(complete)**

d. Spatial maps of all the mean and turbulent quantities of all three components in the ribbed duct

1. Developing region
2. Fully-developed region
3. In the 180° bend region

Computational and Experimental Method

Computational Method

GenIDLEST (Generalized Incompressible Direct and Large-Eddy Simulations of Turbulence) is a computer program developed for application to turbulent flows in complex geometries. It utilizes a non-staggered finite-volume mesh with Cartesian velocities and temperature as the primary dependent variables. A fractional-step algorithm, with explicit as well as semi-implicit time advancement, is used. It uses both Message Passing Interface (MPI) and OpenMP for parallel execution. Full details about GenIDLEST are described in Tafti [19]. Here we give a brief overview.

GenIDLEST solves the incompressible Navier-Stokes and energy or temperature equations. The transformed *non-dimensional*, time-dependent, incompressible Navier-Stokes and energy equations are written in conservative form as[1]:

Continuity:

$$\frac{\partial}{\partial \xi_j}\left(\sqrt{g}U^j\right) = 0 \tag{1}$$

Momentum:

$$\begin{aligned}\frac{\partial}{\partial t}\left(\sqrt{g}u_i\right) + \frac{\partial}{\partial \xi_j}\left(\sqrt{g}U^j u_i\right) = -\frac{\partial}{\partial \xi_j}\left(\sqrt{g}(\vec{a}^j)_i P\right) + \frac{\partial}{\partial \xi_j}\left(\left(\frac{1}{\mathrm{Re}} + \frac{1}{\mathrm{Re}_t}\right)\sqrt{g}g^{jk}\frac{\partial u_i}{\partial \xi_k}\right) \\ -2\sqrt{g}\mathrm{Ro_k}\bar{u}_m \in_{ikm} + \sqrt{g}\cdot \in_{ilm} \cdot \in_{jlk} \cdot Ro_j \cdot Ro_m \cdot r_k \frac{(T - T_{ref})}{T_{ref}} + \sqrt{g}S_{u_i}\end{aligned} \tag{2}$$

Energy:

$$\frac{\partial}{\partial t}\left(\sqrt{g}T\right) + \frac{\partial}{\partial \xi_j}\left(\sqrt{g}U^j T\right) = \frac{\partial}{\partial \xi_j}\left(\left(\frac{1}{\mathrm{Pr}\,\mathrm{Re}} + \frac{1}{\mathrm{Pr}_t\,\mathrm{Re}_t}\right)\sqrt{g}g^{jk}\frac{\partial T}{\partial \xi_k}\right) + \sqrt{g}S_T \tag{3}$$

where $\vec{a}^i$ are the contravariant basis vectors[2], $\sqrt{g}$ is the Jacobian of the transformation, g^{ij} are the elements of the contravariant metric tensor, $\sqrt{g}U^j = \sqrt{g}(\vec{a}^j)_i u_i$ is the contravariant flux vector, u_i is the Cartesian velocity vector, T is the temperature, and S_{u_i} and S_T are the source terms in the momentum and energy equations, respectively. Re_t is the turbulent Reynolds number, and Pr_t is the

[1] Henceforth, all usage is in terms of non-dimensionalized values.

[2] The notation $\left(\vec{a}^j\right)_i$ is used to denote the *i-th* component of vector $\vec{a}^j$. $(\vec{a}^j)_i = \partial \xi_j / \partial x_i$

turbulent Prandtl number Ro is the rotation number, and r is the radial component from the axis of rotation. Re_t is calculated based on a subgrid scale stress model in the case of LES and by a RANS model in the case of RANS or DES calculations, the details of which are given in later sections.

In equation (2), both the rotational Coriolis forces and the centrifugal buoyancy forces are included in the formulation when relevant. In a developing flow, the effect of centrifugal buoyancy is strongest at the inlet to the duct and gets weaker as the temperature approaches the wall temperature in the streamwise direction, but is augmented as r, the distance from the axis of rotation increases. The centrifugal buoyancy term uses the Boussinesq approximation to approximate the effect of density differences from the bulk reference density. The mean centrifugal force term (centrifugal pumping) is implicitly included with the pressure gradient term.

Eqns. (1-3) are solved using an overlapping multi-block structured mesh topology. In each block the equations are mapped from physical $(\vec{x})$ to logical/computational space $(\vec{\xi})$ by a boundary conforming transformation $\vec{x} = \vec{x}(\vec{\xi})$, where $\vec{x} = (x, y, z)$ and $\vec{\xi} = (\xi, \eta, \zeta)$. Inter-block connectivity can be structured (ξ+ face adjoining a ξ- face) or unstructured. In an unstructured inter-block topology a ξ- face boundary can adjoin a η or ζ face with arbitrary axes orientations.

GenIDLEST can handle non-matching or non-conformal boundary interfaces, i.e. there does not have to be a one-to-one correspondence between meshes of adjoining block faces. This allows additional flexibility in meshing complex domains and can also be used for local refinement. In such cases dependent variables have to be interpolated between faces. For this purpose, bilinear interpolation functions are used together with integral conservation of mass, momentum, and energy fluxes. The fluxes are conserved globally (over face) versus locally, which would constrain the generality of the non-matching interfaces. Since the gradient of pressure is the driving force, it, instead of pressure, is conserved across non-matching interfaces.

The multiblock framework provides a natural framework for parallelization. Depending on the total number of blocks and processors, each processor is assigned multiple blocks. Further, within each block "virtual cache blocks" are used. The "virtual" blocks are not explicitly reflected in the data structure but are used only in the solution of linear systems. The motivation to construct much smaller "cache" blocks is to extract performance on cache-based hierarchical memory systems. These small "cache" blocks form the basic computing units for preconditioning linear systems. Hence, underneath the coarse grained parallelism of MPI processes, there exists additional

parallelism across multiple blocks, or across the mesh nodes in each block, and across the multiple cache blocks. Hence, GenIDLEST is instrumented for coarse-grained parallelism with MPI and for embedded or fine-grained parallelism with OpenMP.

The governing equations are discretized with a conservative finite-volume formulation. In non-orthogonal coordinate systems, there are a number of choices in the selection of the grid topology and the dependent variable in the momentum equations. In GenIDLEST, we adopt a non-staggered grid topology with Cartesian velocities as dependent variables. The Cartesian velocities, pressure, and temperature are calculated and stored at the cell center, whereas contravariant volume fluxes are stored and calculated at the cell faces. The convection term can be approximated in a number of different ways. Presently, there are two basic approximations, second-order central difference and the third-order upwind biased approximation, to calculate the cell face values. These two approximations can either be used in their basic form or combined with TVD criteria to preserve monotonicity of the convected variable. In addition to the TVD limiter, a multi-dimensional flux limiter [20] is also implemented. The flux limiter is based on the less restrictive universal limiter proposed by Leonard [21]. In this scheme, the intermediate velocities are first calculated with the base approximations and then checked for monotonicity in a multidimensional framework. Two subgrid-scale stress models are available at this time, the Smagorinsky [22] and the dynamic Smagorinsky model [23]. Additionally, several high and low *Re*-number RANS models, based on the k-ω model [24-26] and Menter's [27-29] models are also available.

A variety of boundary conditions are available in GenIDLEST, and they are specified individually for each computational block. With the exception of periodic or inter-block boundaries, each boundary face can have multiple boundary conditions assigned to it.

(a) Periodic or inter-block boundaries: Both of these boundaries precipitate the same action, which involves exchanging boundary information between adjacent faces. For unstructured block connectivity and/or non-conformal interfaces, the boundary information is filtered by coordinate rotations and interpolations as required. Coordinate rotations and interpolation factors are calculated at the beginning of each run.

(b) Wall boundary: When the velocity normal to the boundary is zero or there is no influx (outflux) of mass, the boundary is specified as a wall. Wall boundaries can have slip velocities imposed on them and temperature or heat flux (gradients) specified.

(c) Inlet boundary: When there is a known net influx (outflux) of mass from the boundary, it is specified as an inlet. Only temperature can be specified at this boundary.

(d) Outflow boundary: Outflow boundaries use a convective boundary condition in which the dependent variable is allowed to convect out of the domain. Both temperature and heat flux can be specified.

(e) Symmetry boundary: At this boundary, the normal velocity and gradients of tangential velocities and temperature are set to zero.

(f) Pressure boundary: Pressure, and not velocity, is specified at this boundary. The velocities are derived from the flow generated by the pressure.

For increased flexibility in meshing, internal blanked zones or solid obstacles can also be specified in each computational block. Boundary conditions on these regions use Dirichlet conditions on velocities, including suction or blowing. Temperature or heat flux can be specified.

The discretized continuity and momentum equations are integrated in time using a projection method. The temporal advancement is performed in two steps, a predictor step, which calculates an intermediate velocity field, and a corrector step, which calculates the updated divergence free velocity at the new time step. The predictor step can be fully explicit in time or semi-implicit, in which the viscous terms are treated implicitly. Both methods are incorporated in GenIDLEST. The semi-implicit method is useful for low Reynolds number flows and in flows with large effective viscosities by allowing larger time steps than what would be allowed by the viscous stability condition. The corrector step uses the continuity equation to formulate the pressure equation. The computed pressure is then used to update the intermediate velocity field.

The linear system generated in the solution of the pressure equation and the implicit treatment of viscous terms is non-symmetric on non-orthogonal meshes. Further, the presence of non-conformal or non-matching boundaries creates additional strong non-symmetries. In GenIDLEST we use Krylov methods based on the method of Conjugate Gradients (CG) for symmetric systems and BiCGSTAB or GMRES(m) for non-symmetric systems. These are coupled with preconditioners based on a two-level Additive Schwarz domain decomposition (DD) method [30,31,32].

GenIDLEST is very portable between different computer architectures and compilers. It has a front-end Java AWT/SWING interface for the creation of input files. A number of post-processing utilities are present, including the ability to obtain mean and turbulent statistics in a distributed

computing environment, time-dependent data dumps for analysis and visualization, and vortex identification techniques based on the $\nabla\vec{u}$ [33] and λ_2 method [34].

Fully-Developed Flow and Heat Transfer Assumption

In a fully-developed flow and heat transfer model, a periodically repeating spatial unit consisting of two ribs (one on either side of the duct) is simulated. An example configuration with normal ribs is shown in Figure 1. The duct walls as well as all six faces of the two ribs exposed to the main flow are heated by imposing a constant heat flux (q'') boundary condition. The governing flow and energy equations are non-dimensionalized by a characteristic length scale, which is chosen to be the hydraulic diameter of the channel (D_h), a characteristic velocity scale, given by the friction velocity $u_\tau = \sqrt{\Delta\bar{P}_x / \rho}$, and a characteristic temperature scale, given by $q'' D_h / k$. The assumed periodicity of the domain in the streamwise or x-direction requires that the mean gradients of pressure and temperature be isolated from the fluctuating periodic component as follows:

$$\begin{aligned} P(\vec{x},t) &= P_{in} - \beta x + p(\vec{x},t) \\ T(\vec{x},t) &= T_{in} + \gamma x + \theta(\vec{x},t) \end{aligned} \tag{4}$$

On substitution, Eqns. (2-3) take the following form:

Momentum:

$$\begin{aligned} &\frac{\partial}{\partial t}\left(\sqrt{g}u_i\right) + \frac{\partial}{\partial \xi_j}\left(\sqrt{g}U^j u_i\right) = -\frac{\partial}{\partial \xi_j}\left(\sqrt{g}(\vec{a}^j)_i\, p\right) + \frac{\partial}{\partial \xi_j}\left(\left(\frac{1}{\mathrm{Re}_\tau} + \frac{1}{\mathrm{Re}_t}\right)\sqrt{g}\, g^{jk}\frac{\partial u_i}{\partial \xi_k}\right) + \sqrt{g}\beta\delta_{i1} \\ &- 2\sqrt{g}(Ro_{\tau_k})\bar{u}_m \in_{ikm} + \sqrt{g}\cdot \in_{ilm} \cdot \in_{jlk} \cdot Ro_{\tau_j} \cdot Ro_{\tau_m} \cdot r_k \frac{(\theta - \theta_{ref})}{\theta_{ref}} + \sqrt{g}S_{u_i} \end{aligned} \tag{5}$$

Energy:

$$\frac{\partial}{\partial t}\left(\sqrt{g}\theta\right) + \frac{\partial}{\partial \xi_j}\left(\sqrt{g}U^j\theta\right) = \frac{\partial}{\partial \xi_j}\left(\left(\frac{1}{\mathrm{Pr}\,\mathrm{Re}_\tau} + \frac{1}{\mathrm{Pr}_t\,\mathrm{Re}_t}\right)\sqrt{g}\, g^{jk}\frac{\partial \theta}{\partial \xi_k}\right) - \sqrt{g}\gamma u_1 + \sqrt{g}S_T \tag{6}$$

In equation (5), both the rotational Coriolis forces and the centrifugal buoyancy forces are included in the formulation when needed. In the context of a periodic fully-developed flow, buoyancy parameter does not change with the radial or streamwise location ($\vec{r}$ is assumed fixed). The fully-developed calculations assume that the same buoyancy parameter is acting over the periodic pitch and represents one x- location (or a pitch surrounding one x- location) in a corresponding developing flow. In effect, a fixed Richardson number is defined as:

$$Ri_{\tau i} = \frac{\in_{ilm} \cdot \in_{jlk} \cdot Ro_{\tau j} \cdot Ro_{\tau m} \cdot r_k}{\theta_{ref}}$$

and the buoyancy term in eqn. (5) is represented as:

$$\sqrt{g} \cdot Ri_{\tau_i} \cdot (\theta - \theta_{ref})$$

The Buoyancy number (*Bo*) is commonly used to quantify the effect of centrifugal buoyancy. In the present context, the Buoyancy number (*Bo*) is related to the Richardson number (Ri_τ) by the following expression:

$$Bo = \frac{\Delta\rho}{\rho_o}\frac{r}{D_h}Ro^2 \approx \frac{Ri_\tau.\overline{(\theta_s - \theta_{ref})}}{\bar{u}_b{}^2}$$

where the quantity under the bar is area averaged over all heat transfer surfaces in the duct.

In the calculations, β is assumed to be unity, whereas γ is calculated from a global energy balance as: $\gamma = q''\Omega / \mathrm{Re}_\tau \Pr Q_X L_x$. The boundary conditions imposed on the duct walls and ribs are as follows:

$$\begin{aligned} &\vec{u} = 0 \\ &\nabla p \cdot \vec{n} = 0 \\ &\nabla \theta \cdot \vec{n} = 1 - \gamma \vec{e}_x \cdot \vec{n} \end{aligned} \tag{7}$$

and in the streamwise direction as:

$$\phi(x + L_x) = \phi(x), \ \phi = \vec{u}, p, \text{ and } \theta. \tag{8}$$

Subgrid-Scale Stress Modeling for LES

The subgrid-stresses are given by $\tau_{ij} = \left(\overline{u_i u_j} - \bar{u}_i \bar{u}_j\right)$, where $\bar{\phi}$ denotes a grid filtered quantity and $\phi = \bar{\phi} + \phi'$, where ϕ' is the subgrid quantity. In GenIDLEST, a top-hat grid filter implicit to the mesh resolution in physical space given by:

$$\begin{aligned} \bar{G}(x_i - x'_i) &= \frac{1}{\bar{\Delta}_i}; \qquad \left|x_i - x'_i\right| \le \frac{\bar{\Delta}_i}{2} \\ &= 0; \qquad \textit{otherwise} \end{aligned} \tag{9}$$

is used as the grid filter.

Two models are available in GenIDLEST, both of which utilize the Smagorinsky eddy-viscosity model to model the subgrid stresses in LES mode. The subgrid-stress tensor is modeled as:

$$\tau_{ij}^{a} = \tau_{ij} - \frac{1}{3}\delta_{ij}\tau_{kk} = -\frac{2}{\mathrm{Re}_t}\overline{S}_{ij}\,. \tag{10}$$

Re_t is the inverse of the non-dimensional eddy-viscosity modeled as

$$\frac{1}{\mathrm{Re}_t} = C_s{}^2(\sqrt{g})^{2/3}\left|\overline{S}\right|, \tag{11}$$

where $\left|\overline{S}\right|$ is the magnitude of the strain rate tensor given by $\left|\overline{S}\right| = \sqrt{2\overline{S_{ik}}\,\overline{S_{ik}}}$.

The strain rate tensor is given by

$$\overline{S}_{ik} = \frac{1}{2}\left((\vec{a}^{\,m})_k \frac{\partial\overline{u_i}}{\partial\xi_m} + (\vec{a}^{\,m})_i \frac{\partial\overline{u_k}}{\partial\xi_m}\right) \tag{12}$$

and the Smagorinsky constant takes on a constant value, $C_s = 0.1$, in the Smagorinsky model.

In the dynamic Smagorinsky model (DSM), C_s is not assumed to be a constant but is calculated from the local characteristics of the turbulence in the flow field. To this end, a second test filter, denoted by $\hat{G}$, is applied to the filtered governing equations with the characteristic length scale of $\hat{G}$ being larger than that of the grid filter, $\overline{G}$. The test filtered quantity is obtained from the grid filtered quantity by a second-order trapezoidal filter which is given by $\hat{\phi} = \frac{1}{4}\left(\overline{\phi}_{i-1} + 2\overline{\phi}_i + \overline{\phi}_{i+1}\right)$ in one dimension.

The resolved turbulent stresses, representing the energy scales between the test and the grid filters, $L_{ij} = \widehat{\overline{u}_i\overline{u}_j} - \hat{\overline{u}}_i\hat{\overline{u}}_j$, are then related to the subtest, $T_{ij} = \widehat{\overline{u_i u_j}} - \hat{\overline{u}}_i\hat{\overline{u}}_j$, and subgrid-scale ($\tau_{ij}$) stresses through the identity $L_{ij} = T_{ij} - \hat{\tau}_{ij}$.

The anisotropic subgrid and subtest-scale stresses are then formulated in terms of the Smagorinsky eddy viscosity model as:

$$\hat{\tau}_{ij}^{a} = -2C_s^2(\sqrt{g})^{2/3}\widehat{\left|\overline{S}\right|\overline{S}_{ij}} = -2C_s^2\beta_{ij} \tag{13a}$$

$$T_{ij}^{a} = -2C_s^2\alpha(\sqrt{g})^{2/3}\left|\hat{\overline{S}}\right|\hat{\overline{S}}_{ij} = -2C_s^2\alpha_{ij} \tag{13b}$$

where now

$$L_{ij}^{a} = L_{ij} - \frac{1}{3}\delta_{ij}L_{kk} = -2C_s^2(\sqrt{g})^{2/3}\left(\alpha\left|\hat{\overline{S}}\right|\hat{\overline{S}}_{ij} - \widehat{\left|\overline{S}\right|\overline{S}_{ij}}\right) = -2C_s^2(\sqrt{g})^{2/3}M_{ij} \tag{14}$$

Here α is the square of the ratio of the characteristic length scale associated with the test filter to that of the grid filter and is taken to be (6) $\left[\hat{\bar{\Delta}}_i / \bar{\Delta}_i = \sqrt{6}\right]$ for a three-dimensional test filtering operation [35]. Using a least-squares minimization procedure of Lilly [36] a final expression for C_s^2 is obtained as:

$$C_s^2 = -\frac{1}{2}\frac{1}{(\sqrt{g})^{2/3}}\frac{L_{ij}^a \cdot M_{ij}}{M_{ij} \cdot M_{ij}}, \tag{15}$$

where C_s^2 is constrained to positive values to maintain numerical stability.

RANS Modeling for RANS and DES Calculations

The Reynolds stresses are given by $\tau_{ij} = -\overline{u_i' u_j'}$ where $\bar{\phi}$ denotes an ensemble averaged quantity and $\phi = \bar{\phi} + \phi'$, where ϕ' is the fluctuating quantity. Several high and low *Re*-number models based on the *k*-ω model are available and used in GenIDLEST. Here only the basic *k*-ω model of Wilcox [26] is shown. In addition, the Wilcox [24] and Wilcox [25] low-*Re*-number models are also used. Two other models developed by Menter [27-29], the Baseline model (MBSL) and shear stress model (MSST), are also implemented and used. In the basic *k*-ω model, the turbulent Reynolds stresses are modeled by using an eddy viscosity such that

$$\tau_{ij}^a = \tau_{ij} + \frac{2}{3}\delta_{ij}k = \frac{2}{\mathrm{Re}_t}\bar{S}_{ij}, \tag{16}$$

where

$$\frac{1}{\mathrm{Re}_t} = \frac{k}{\omega}. \tag{17}$$

The *k*-ω equations are written as:

$$\frac{\partial}{\partial t}\left(\sqrt{g}k\right) + \frac{\partial}{\partial \xi_j}\left(\sqrt{g}U^j k\right) = \tau_{ij}^a\left((\vec{a}^m)_j \frac{\partial u_i}{\partial \xi_m}\right) - \beta^* k\omega + \frac{\partial}{\partial \xi_j}\left(\left(\frac{1}{\mathrm{Re}} + \frac{\sigma_k}{\mathrm{Re}_t}\right)\sqrt{g}g^{jk}\frac{\partial k}{\partial \xi_k}\right) + \sqrt{g}S_k \text{ and} \tag{18}$$

$$\frac{\partial}{\partial t}\left(\sqrt{g}\omega\right) + \frac{\partial}{\partial \xi_j}\left(\sqrt{g}U^j \omega\right) = \gamma\frac{\omega}{k}\tau_{ij}^a\left((\vec{a}^m)_j \frac{\partial u_i}{\partial \xi_m}\right) - \beta\omega^2 + \frac{\partial}{\partial \xi_j}\left(\left(\frac{1}{\mathrm{Re}} + \frac{\sigma_\omega}{\mathrm{Re}_t}\right)\sqrt{g}g^{jk}\frac{\partial \omega}{\partial \xi_k}\right) + \sqrt{g}S_\omega, \tag{19}$$

where σ_κ=0.5, σ_ω=0.5, β*=0.09, β=0.075, and γ=0.55.

In DES mode, the base model not only functions as a RANS model in the near wall region but also as the LES model in regions where the eddies are resolved by the underlying mesh. The switch

from RANS to LES is made by choosing a minimum of the RANS length scale and the length scale associated with the large eddies resolved on the underlying mesh: $l_{DES} = \min(l_{RANS}, l_{LES})$, where $l_{RANS} = \frac{\sqrt{k}}{\beta^* \omega}$ and $l_{LES} = C_{DES} \max(\Delta_x, \Delta_y, \Delta_z)$. For two equation models based on *k*, the dissipation term in Eqn. (18) is written in terms of the DES length scale as $k^{3/2} / l_{DES}$. The constant C_{DES} can assume values anywhere from 0.5 to 1.0. Previous studies have shown that the solution accuracy is not sensitive to $C_{DES.}$

Experimental Method (K. Thole)

A test rig designed for validation of the computations in this project was designed and built by a group of six undergraduate students as part of a senior-level design course. A photograph of the completed test rig is shown in Figure 2. The large-scale, two-pass channel was designed to simulate the developing and fully-developed regions of a two-pass channel as well as the upstream and downstream sides of a 180º bend. Two measurement techniques will be employed in the testing: Laser Doppler Velocimetry (LDV) for producing measurements of the turbulence quantities of the flow, and infrared thermography to provide heat transfer data on the heated surfaces.

The final design consists of a closed-loop, two-pass rig with a 180º bend. The channel includes a ribbed entrance region, a test section designed for studying the thermal development within a hydrodynamically fully-developed flow, and a 180º bend. Figure 3 shows a schematic indicating the entry length, test section and return section. A 2 hp fan, donated by Cincinnati Fan, is capable of producing Reynolds numbers ranging from 10,000 to 100,000. A heat exchanger, donated by Super Radiator Coils, is used initial flow conditioning, and a venturi tube is used for flow measurement through the return loop.

A one-to-one geometric comparison to the computations performed in this project was a primary goal of the rig construction, so the non-dimensional parameters describing the rib size and locations matches the same parameters simulated in the calculations. The duct has a square cross section with square ribs on two walls of size e/D_h = 0.1 spaced at a streamwise pitch P/e = 10. The hydraulic diameter of the channel is approximately 6 inches.

To study the heat transfer characteristics a separate test section was built. A constant heat flux is imposed on the bottom wall, ribs, and side wall with a series of Inconel strips. A heated rib, with

Inconel covering three sides, is compared to an unheated rib, used in the LDV measurements, in Figure 4. A full ANSYS model was created for the rib to insure uniform heating for this heated rib design.

Initial benchmark testing closely matches the fully-developed flow characteristics found in the literature. Figure 5 shows a comparison of local friction factors near the channel entrance for a Reynolds number of 20,000. This graph shows a comparison with experiments reported by Rau, et al. [37] for a fully developed internal turbine channel flow with a similar geometry. The close comparison seen in the figure suggests hydrodynamically fully-developed flow soon after the third rib with a flat velocity profile at the inlet.

RESULTS AND DISCUSSION

1. Detached Eddy Simulation of Turbulent Flow and Heat Transfer in the Fully Developed region of an internal cooling duct subjected to rotation

Objective of the study

The objective of the current study is to assess the capability of DES in capturing the effects of rotation on the flow and heat transfer in a fully developed ribbed channel. To the best of our knowledge this is the first application of DES to an internal non-canonical flow with heat transfer and follows an earlier study in stationary ribbed ducts (Viswanathan and Tafti, 2004; 2005d). Unlike the study by Nikitin *et al.,* (2000) in turbulent channel flows in which the Spalart-Allmaras model was used as a wall model, in the current study the two-equation model behaves as a hybrid RANS-LES model throughout the calculation domain. This paper aims to test the hypothesis as to whether DES can overcome known shortcomings of the underlying RANS model to increase the accuracy of the computation. In this case, it is the inability of eddy-viscosity RANS models to accurately predict the effects of rotation and Coriolis forces on flow structure and heat transfer.

A fully developed flow in a duct with normal ribs of rib pitch-to-height ratio P/e = 10 and a rib height to hydraulic diameter ratio e/D_h = 0.1, has been considered. The Reynolds number based on bulk velocity is 20,000. Three rotation numbers Ro = 0.18, 0.35 and 0.67 are considered. Since detailed experimental measurements are not available in the literature for rotating ducts, the DES and URANS results are compared with the LES results of Abdel-Wahab *et al.,* (2004a, 2004b). However the overall surface averaged heat transfer data is available from the experiments of Wagner *et al.,* (1992), Parsons *et al.,* (1994) and Liou *et al.,* (2001), and hence these are used for comparing the average heat transfer on the ribbed and the side walls.

Results and Discussion

Grid Sensitivity

DES is sensitive to grid resolution as shown by earlier DES calculations (Viswanathan *et al.,* 2004, 2005a, 2005d). DES, like any other scheme which resolves turbulent eddies, depends on the grid design and resolution for the overall success of the simulation. The grid dependency is not similar to LES where

an increase in resolution of the grid improves the solution. A fine grid might trigger an LES solution in the boundary layer, which might be detrimental if the resolution is not fine enough to resolve all the energy containing eddies. On the other hand, a coarse grid may eliminate the LES regions in the grid altogether, and in the limit the calculation would be a URANS calculation. Therefore, the grid should facilitate resolving a wide range of scales in the 'detached' regions (LES regions) while the regions near the wall are computed in the URANS mode. Computations were carried out for a stationary duct for a fully developed case on three grids: 48^3, 64^3 and 96^3. Figure 7 shows the comparison of the streamwise velocities for a stationary duct at a plane (Y/e = 0.25) passing through the rib, as predicted by the different grids used in comparison with the LES results on a 128^3 grid. The coarse grid (48^3) failed to capture the secondary reverse flow behind the rib, owing to the dominance of RANS in the solution. The 64^3 and the 96^3 grids predicted the trends accurately. The 96^3 grid did not show any added value, and so the 64^3 grid was considered to be sufficiently accurate for the rotating cases. Using the same argument, DES computations (Viswanathan and Tafti 2004, 2005d) were carried out for a stationary fully developed ribbed duct on the 64^3 grid. The results showed good agreement with the LES computations and the experiments. Hence the DES and the URANS calculations for the rotation cases are also carried out on the 64^3 grid.

While the 64^3 grid is observed to be appropriate for DES, the resolution is not sufficient for LES. A comparison of the reattachment lengths downstream of the rib for a stationary duct shows that the LES on a 128^3 grid and DES on the 64^3 grid predict a reattachment length of around 4.1 times the rib height, which is in good agreement with the experimental measurements on 4.1 – 4.25 by Rau *et al*., (1988). On the other hand, LES on the 64^3 grid predicts a reattachment length of 3.7. Figure 8 shows the comparison of the heat transfer augmentation at the ribbed and the side walls of a stationary duct with ribs normal to the flow direction. A comparison of the ribbed wall heat transfer augmentation shows that while the 128^3 LES, 96^3 LES and 64^3 DES predict heat transfer augmentation consistent with the heat transfer measured by Rau *et al.* (1988), 64^3 LES over-predicts the heat transfer in the separated region. A comparison of the side wall heat transfer also shows that the heat transfer in the vicinity of the rib ($y < 0.1$) is over-predicted

by 64^3 LES. The predictions by 64^3 DES and 128^3, 96^3 LES in this region are in good agreement with the values measured by the experiments. The under-prediction of the reattachment length and the over-prediction of the heat transfer in the region is a result of the coarser grid resolution in the 64^3 grid. Similar trends were observed for the rotation cases, where the reattachment lengths at the trailing and the leading sides were under-predicted and the heat transfer augmentations were over-predicted at the ribbed walls. In general the quality of the results is observed to deteriorate with LES as the grid is coarsened to 64^3. Thus it is inferred that the 64^3 grid used is not sufficient for an accurate LES computation, while the grid when used for DES is capable of yielding results comparable in accuracy to the LES computations.

DES Regions

The underlying idea of DES is to compute regions closer to the wall using a RANS model and solve the regions of separation, or the region of detached eddies, in LES mode. Figure 9(a) shows the fraction of time (during the whole computation) when the calculation is solved in the LES mode. DES with Menter's SST model uses a turbulent length scale which is computed from the turbulence equations solved (k and ω). So the turbulent (RANS) length scale is a function of time as well as space. This feature facilitates the computation to be cognizant of the eddy length scales and hence behave as RANS or LES depending on the instantaneous local conditions, unlike in the case of a Spalart-Allmaras based DES, where DES acts just like a wall model. Another prominent feature of the DES version of the SST model is that although an instantaneous discontinuity may exist between the RANS region and the LES region, in the mean however a smooth transition takes place from RANS to LES and vice versa. It can be observed from Figure 9 that the RANS regions transition into LES smoothly. In a DES Spalart-Allmaras model, the distance from the wall determines the switch from RANS to LES, which is not as receptive to instantaneous flow features.

The near wall region is always resolved in the RANS mode which transitions to the LES mode as the distance from the wall increases. The flow in the vicinity of the ribs is mostly resolved in LES mode all the way to the channel center. This includes the unsteady large-scale dynamics of the separated shear

layer as shown in Figure 9(b). In the inter-rib spacing, LES is only active near the ribbed wall and transitions to a full RANS mode at the center of the channel. The spatial distribution of the two methods (LES and RANS) of resolving turbulence are consistent with the underlying principles of DES and to a large degree is facilitated by some *a-priori* knowledge of the flow and judicious grid selection.

The grid facilitates the computation of the region in RANS and/or LES depending on the instantaneous conditions existing in the region. Downstream of the rib in the region of separation (Figure 9 (b)) it is observed that the computation is mostly carried out in the LES mode which ensures that the unsteady physics in the separated region is captured accurately. Regions of low turbulence in between the ribs are completely solved in RANS mode**.**

Mean Flow field

Early studies in turbulent channel flow (Halleen & Johnston, 1967; Lezius & Johnston, 1976) have established two important effects of rotation. When the rotational axis is perpendicular to the plane of mean shear, Coriolis forces have a considerable effect on the mean flow as well as on turbulent fluctuations. These effects are manifested as stabilization/destabilization of turbulence at leading/trailing walls and the generation of spanwise roll cells or secondary flow patterns. The secondary flow patterns are a direct result of the action of Coriolis forces on mean shear and are also observed in laminar flows subjected to system rotation.

It is well established that the production of turbulence in the near wall region and in shear layers is caused by the exchange of momentum through intense interactions between the fluctuating streamwise and cross-stream velocities. When Coriolis forces act in tandem with these events, turbulence is augmented, whereas it is attenuated when the two act in opposition. In the ribbed duct flow in this study, both the turbulent shear layer and near wall turbulence on the trailing surface are augmented by the direct effect of Coriolis forces, while the opposite effect

comes into play at the leading wall. The results for all three rotation numbers follow the general trends outlined above.

The flow at the center (z=0.5) of the duct is characterized by a large recirculation region behind the rib, a small region of recirculation in front of the rib, a small eddy on top of the rib and an eddy trapped behind the rib, between the large recirculation region and the rib. For a non-rotating case all these features are similar on both the ribbed walls. The reattachment of the rib separated shear layer was observed to be in the range 4.0 – 4.25*e* for the non-rotating case (Rau *et al*., 1988). The reattachment length predicted by DES was 4.1*e* which matched quite well with the experiments and LES predictions.

Figure 10 shows the streamlines at the center of the duct (z = 0.5) for the three rotation cases. Rotational Coriolis forces affect the size of the recirculation zones and so the flow is asymmetric about the center *y*-plane of the duct. The reattachment length increases at the leading wall and decreases at the trailing wall with rotation number. The reattachment is observed at around 4.0*e* for Ro = 0.18 at the trailing side. The size of the separation bubble decreases to a value close to 3.6*e* when the rotation increases to 0.35. On increasing the rotation further to 0.67 the reattachment length remains almost the same as the 0.35 case. On the other hand, the reattachment length at the leading wall increases from a value of 4.0 – 4.25*e* for the stationary case (Ro = 0.0) to a value of 4.5*e* at Ro = 0.18. No significant change is observed as the Ro is increased to 0.36, but on increasing the rotation further to 0.67, the recirculation region is observed to increase to a value of around 6.7*e*, and as a result it merges with the recirculation region in front of the next rib.

The reattachment lengths for the rotating cases are consistent with the LES predictions (Abdel-Wahab *et al.,* 2004a, 2004b). Figure 11 shows the comparison of the flowfield as predicted by LES, DES and URANS. The separation and reattachment downstream of the rib is predicted accurately by DES and the reattachment length is in agreement with LES both at the leading and the trailing walls. However URANS overpredicts the reattachment lengths both at the leading as well as the trailing wall. Overprediction of the

reattachment lengths is a result of the inability of the SST model to account for the effects of Coriolis forces, whereas in DES, the effect of Coriolis forces is captured in the resolved scales.

The secondary flow in between the two ribs (Figure 12) shows the presence of a pair of corner vortices in each quadrant when the ribbed duct is stationary. Similar vortices were observed by Liou *et al.* (2001) in their experiments. As the rotation increases to Ro = 0.18, the vortices on the leading side disappear, while the vortices at the trailing wall grow and move towards the center of the duct. As the rotation increases further the two vortices merge and grow bigger. At Ro = 0.67, the vortices occupy almost 80% of the channel height as observed in Figure 12(d).

While Figure 12 shows the structure of the secondary flow, Figure 13 shows the magnitude of the secondary flows (*v, w* velocities) for the stationary and the three rotation cases in the cross-section of the duct on top of the rib. The *v*- and *w*- velocities are plotted individually in each half of the span. For the stationary duct, (v,w) are symmetric about the center of the duct in the *y*- and *z*-directions (*v* is antisymmetric in the y-direction). Above the rib, the constriction posed by the rib results in flow being pushed towards the channel center, both at the center of the span and near the side wall. In addition to this effect, a spanwise flow is setup toward the center and toward the side wall which is represented by the high positive impingement w- velocities at the side wall. As rotation increases, the strength of the secondary impingement flow at the trailing side increases while it decreases at the leading side, which is evident from the intrusion of the high *v*-velocities towards the leading side near the side wall. The asymmetry in the *w*-velocity also increases as the rotation increases.

Turbulent Flow Characteristics

A comparison of the turbulent kinetic energies (TKE) predicted by the DES, LES and the URANS schemes are shown in Figure 14. It is observed that the resolved component of TKE is significantly larger than the modeled component in the DES computation almost in the entire flow field. So the resolved component of TKE is considered for comparison for the DES and the LES cases, while the sum of the resolved and modeled components are considered for the URANS case. A comparison of the TKEs on top

of the rib shows that the values resolved by DES compare well with that resolved by LES for all the three rotation cases. Localized peaks are observed at the trailing wall and the leading wall corresponding to the shear layer on top of the rib. The peak TKE at the trailing wall is around 0.28 for Ro = 0.18. The value is almost constant as the rotation increases to a value of 0.35 but shows a dramatic increase as the Ro increases further to 0.67 where the peak is around 0.38. At the leading wall the peak TKE reduces from a value of about 0.2 for the lowest rotation case to about 0.15 for the highest rotation case. The trend predicted by URANS at low rotation partly agrees with the LES computations towards the center of the channel, but the peaks in the shear layer are underpredicted by nearly 50%. At higher rotation cases the TKE are underpredicted through the complete height of the duct.

TKE values in between the ribs show similar trends. The location is just downstream of the reattachment point at the trailing wall and so represents the region of boundary layer redevelopment in all the three rotation cases. It is observed that DES underpredicts the TKE values in the boundary layer as compared to LES, but shear layer turbulence away from the immediate vicinity of the wall is represented accurately in all the cases. On the other hand, URANS drastically underpredicts the TKE values in all three rotation cases. The low turbulence levels in URANS results in larger recirculation regions as compared to DES and LES.

A comparison of the instantaneous coherent vorticity (Jeong and Hussein, 1995) as predicted by 128^3 LES, 64^3 DES and 64^3 URANS is shown in Figure 15. These plots give an idea of the flow structures resolved by the three schemes. It is observed that the magnitude of coherent vorticity and the characteristics predicted by DES is consistent with the magnitudes predicted by LES on a much finer grid. Predictions by URANS show lower vorticity levels as compared to LES and DES, both in the center of the duct as well as the inter-rib region. Thus the small modification in the URANS model to convert it into the equivalent DES model substantially improves the resolution of the simulation.

Figure 16 shows the power spectral density of the instantaneous streamwise velocity, obtained using a Fast Fourier Transform in the frequency domain for Ro = 0.35 at the leading wall of the duct. The most energetic mode is found at a non-dimensional frequency of approximately 11. The spectral density plot

also indicates that the resolved scales extend beyond the inertial range at this location. The insert in the figure shows the spectral density obtained using Welch's averaged, modified periodogram method using MATLAB's *psd* function (MATLAB, 2005). Welch's method is a modified periodogram which divides the time signal into windows or blocks, computes the FFT for each individual window and averages to obtain the discrete Fourier transforms for the whole time signal considered. Welch's method tends to average out the peaks observed in a plain FFT and gives a single characteristic non-dimensional frequency of 35. In the following figures, the smoothed spectral density is used to compare the energy carried by the resolved scales.

Figure 17 and Figure 18 show the turbulent spectrum and the sampled signal at the leading and trailing walls. Data was collected by placing probes in the shear layer near the reattachment region. Three probes were placed at the leading and the trailing walls in regions where the computation is completely RANS (DES = 0.0), partially RANS and partially LES (DES = 0.5) and completely LES (DES = 1.0). From the signals it is observed that the DES computation shows more unsteadiness, hence more resolved energy, as compared to the URANS computation. A one to one comparison can be made at the location at which DES=0 (full URANS in DES approach) versus the same location in the URANS calculation in Figure 17 and Figure 18. At the leading wall the resolved peak energy between the two cases varies by nearly two orders of magnitude, whereas at the trailing wall the ratio is about 5. Larger differences between DES and URANS is found at locations where DES operates in full LES mode (DES=1). Comparison of LES with DES at locations where DES=1 (full LES mode) shows that the peak resolved energy is of comparable magnitude – at the trailing wall, the LES peak is at 4 whereas the DES peaks at 4.5. At the leading wall, the DES peak energy is higher at 1.5 than the corresponding LES, which is at 0.6, indicating that the level of turbulent fluctuations is higher at this location in the DES calculation. This is suspected to be caused by a slight shift in the shear layer trajectory.

Figure 11 and 12 bring out an important observation, that for the same resolution, the DES framework allows a much larger part of the energy spectrum or scales to be resolved on the grid. URANS on the other hand, in spite of a relatively fine grid, models a large fraction of the turbulent fluctuations. While it

picks up the most energetic modes, only a fraction of the energy is present in the grid scales. This would not be a problem if the models were true to the physics, which for rotating ducts is not the case. The SST model does not include the effect of Coriolis forces on turbulence, but the consequence of that shortcoming is felt much more in the URANS model than in DES because a large fraction of the modal energy is resolved on the grid by DES and the effect of Coriolis forces is included directly through the momentum equations.

Mean Heat Transfer

The heat transfer trends at the leading and trailing walls are similar to the trends observed at the ribbed walls for the stationary case. The augmentation ratio is high in front of the rib as a result of the unsteady vortices in this region. These secondary vortices continuously transport cooler fluid from the mainstream to the ribbed wall increasing the heat transfer coefficient. Immediately behind the rib, a secondary recirculation is trapped between the wall and the primary recirculation zone. Although the action of the secondary eddy causes some localized augmentation in this region, the overall augmentation is low and similar to that in a smooth duct. Further downstream, the heat transfer coefficient increases steadily as the vortices from the separated shear layer impinge on the wall.

Figure 19 shows the heat transfer at the leading (upper half) and the trailing walls (lower half) for the three rotation cases. As the rotation number is increased, an increase in the heat transfer is observed at the trailing wall, especially in regions immediately upstream of the rib and near the reattachment point. This is countered by a decrease at the leading wall in the corresponding regions. The heat transfer augmentation in the region upstream of the reattachment point at the trailing wall increases from 4.4 for Ro = 0.18 to 4.8 for Ro = 0.35 and 5.6-6.0 for Ro = 0.67. At the trailing wall the heat transfer upstream of the reattachment point is observed to decrease from 2.8 for Ro = 0.18 to 1.6 for Ro = 0.35 and 0.67 respectively.

Figure 20 shows a comparison of the DES and the URANS with LES results at Ro=0.35. This shows that the URANS under-predicts the heat transfer at the trailing side, where the turbulence is enhanced by

rotation. The heat transfer augmentation predicted by DES agrees quite well with the LES computations. The peak heat transfer on the trailing wall in the region of shear layer reattachment is shifted away from the center of the duct due to the effect of secondary flows and is captured by all three methods. However, the URANS predicts this region further downstream because of the larger reattachment length. Heat transfer augmentations at the trailing wall reach values close to 5.2 immediately upstream of the rib where the unsteady vortices enhance the heat transfer. Both DES and URANS tend to over-predict the spatial extent of this region.

The flow at the leading wall is more stable than the flow at the trailing wall and so the overall heat transfer at the leading wall is almost half the heat transfer at the trailing wall. Upstream of the rib, heat transfer levels are almost 2.8 times that observed in a smooth duct case. Once again, both DES and URANS overpredict the extent and augmentation in this region. The heat transfer levels drop to values close to the smooth channel heat transfer values immediately behind the rib, but the augmentation increases to values close to 1.6 downstream of the reattachment point.

The trends predicted by DES are consistent with the LES results (Abdel-Wahab *et al.,* 2004a-b), with the exception of the region immediately upstream of the rib where higher levels of heat transfer are predicted. Similar results were observed by Viswanathan *et al.,* (2004, 2005d) in a stationary duct where a larger heat transfer augmentation was observed immediately upstream of the rib. On the other hand URANS results show a lot of discrepancy. The most prominent deviation from LES is the under-prediction of the heat transfer at the trailing wall of the duct. The heat transfer distributions at the ribbed walls are also much smoother than LES and DES predictions.

The secondary flows in the stationary and the rotation cases play a major role in the heat transfer at the side walls. Along the smooth (side) walls the heat transfer increases on moving from the trailing wall and reaches a maximum at the top front corner of the rib as a result of the secondary flow impingement on the wall. The heat transfer decreases on the side walls towards the center of the channel. Though the heat transfer patterns are the same for the stationary and the rotation cases the magnitudes of heat transfer are a function of the rotation.

For Ro = 0.18 (Figure 21) the secondary flow impingement results in levels of heat transfer as high as seven times that in a smooth channel at the trailing wall, at the corner of the rib and the side wall. The heat transfer decreases to values close to 2.0 towards the center of the duct. On moving towards the leading wall the heat transfer decreases further and drops to values lower than unity near the leading wall of the side wall. However secondary flow impingement near the corner of the ribs locally results in higher heat transfer. As the rotation increases higher heat transfer is observed near trailing wall and lower hear transfer regions move closer to the leading wall. This behavior is consistent with the secondary flow features observed, *i.e.*, stronger the impingement more is the heat transfer at the side walls.

Figure 22 compares the side wall heat transfer predicted by DES and URANS with LES for Ro = 0.35. The DES predictions compare well with LES. URANS predicts comparable trends except that a noticeably larger augmentation region is predicted near the rib at the trailing wall and the augmentation ratio is also underpredicted at the center of the duct and in the vicinity of the trailing wall.

Figure 23 shows a gradual increase in the average heat transfer augmentation at the side walls as the rotation number increases from 0 to 0.67. DES predicts these trends accurately but slightly underpredicts the augmentation compared to LES. URANS severely underpredicts the side wall heat transfer at Ro = 0.18 and 0.35, while the agreement is comparatively better at the highest rotation number.

The effect of rotation is more prominent at the leading and the trailing walls. Results for averaged Nusselt numbers on the leading and trailing faces for the three rotation numbers are compared with the experiments of Liou et al. (2001), Parsons et al. (1994), and Wagner et al. (1992). The experimental data of Liou *et al.* (2001) is at Re = 10,000 for e/D_h = 0.136 and P/e = 10 and Parsons *et al.* (1994) data is obtained at Re=5,000 for e/D_h = 0.125 and P/e = 10. The data of Wagner *et al.* (1992) includes the effects of buoyancy with a density ratio = 0.13 for a staggered rib arrangement with e/D_h = 0.1 and P/e = 10 at Re=25,000. Wagner's data includes the effects of centrifugal buoyancy effect which increase trailing wall heat transfer as the rotation number increases. In all cases, fully-developed data is extracted for comparison. Figure 24 compares the overall heat transfer augmentations at the leading and trailing walls predicted by DES and URANS cases, with the LES computations and experimental results. DES

predictions agree well with experiments and LES except for the trailing side at Ro=0.18, where the augmentation is underpredicted by 11% compared to Parson's data and about 15% compared to LES. On the other hand, URANS substantially underpredicts the trailing wall augmentation, by as much as 30% compared to LES, at the high rotation numbers of 0.35 and 0.67. Prediction accuracy of URANS is similar to that of DES at the leading wall which is within 10% of LES.

2. Large Eddy Simulation of fully developed flow and heat transfer in a rotating duct with 45° ribs

Objective

In 45 degree ribbed ducts, the overall heat transfer augmentation has been observed to be unaffected by rotation, as pointed out in the earlier studies by Iacovides *et al.* [85] and Rathjen *et al*.[87]. However, there is no detailed analysis of the flow and turbulent fields available to give some insight as to why this is the case. LES computations [1] on stationary ducts with 45 degree ribs showed good agreement of the flow features and heat transfer characteristics. Similar computations using an unsteady RANS model [11] showed the inability of URANS in capturing the flow features and heat transfer trends accurately. Hence the objective of this study is to use detailed LES calculations to investigate this phenomenon. In the process the physics of flow and heat transfer is compared to that in a stationary duct. For validating the calculations, results are compared with experimental results by Rathjen *et al*.[87] and Johnson *et al*.[82]. To the best of our knowledge, this is the first LES study under the conditions of high Reynolds number with rotation effects which elucidates on the physics of rotational effects.

Results and Discussion

Stationary Case (Ro = 0.0)

The most prominent feature of skewed ribs is the presence of strong secondary flows. Earlier experiments [98] and computational studies [99] on stationary ducts with skewed ribs describe in detail the flow. LES by Abdel-Wahab and Tafti [1] in Figure 25 show that the separated shear

layer from the rib has a strong rib-induced transverse component of momentum, which together with the rotational component in the shear layer form helical vortices which move from the inner to the outer wall of the duct. This strong secondary motion results in a mean helical vortex, which grows in size as it moves from the inner wall to the outer wall as shown in Figure 25. The vortex impinges at the outer wall and is deflected towards the center of the duct.

The helical vortices present downstream of the rib feed into a cross-sectional secondary flow. A cross-sectional view of velocity streamlines of v and w between two ribs (Figure 26) shows the mean secondary flow. Though physically distinct, the secondary flow and the mean helical vortex complement each other. Two counter-rotating cells of equal size are observed in the stationary case as reported in earlier studies. [98].

The heat transfer distribution in ducts with skewed ribs is strongly influenced by the secondary flow. Figure 27 shows the heat transfer at the ribbed and the smooth walls in a stationary duct. At the junction of the inner wall and the rib, where the helical vortex is closest to the wall, the heat transfer augmentation reaches values up to 4.5 times that in a smooth channel. The heat transfer decreases diagonally on moving towards the outer wall as the helical vortex moves away from the ribbed surface, and in the vicinity of the outer wall, values close to 2.5-3.0 are observed. Upstream of the rib heat transfer values are about 2.0 times that observed in a smooth channel.

At the inner wall, high levels of heat transfer are observed immediately downstream of the rib. The presence of the helical vortex results in heat transfer as high as 3.0-3.5 times that in a smooth channel. Lower heat transfer levels ($Nu/Nu_0 = 2.0$) are observed further downstream on moving towards the center of the inter-rib region. High heat transfer is also observed on top of the ribs. Towards the center of the duct the heat transfer augmentation is of the order of 1.5-2.0.

Heat transfer at the outer wall is higher than that at the inner wall due to the impingement of the vortices at the outer wall. For the stationary case the heat transfer in the inter-rib region is around 4.0-4.5 times that in a smooth duct. Regions of high heat transfer ($Nu/Nu_0 > 2.0$) are

observed up to around 3 times the rib height. Towards the center of the duct the average heat transfer is around twice that in a smooth duct.

Rotating Case (Ro = 0.1)

Mean Flow Characteristics

Figure 28 shows the resulting vortex structure at a rotation number of Ro = 0.1. While the helical vortex at the leading side of the duct is observed to be almost of the same size and structure as in the stationary case (Figure 28 a), at the trailing side the vortex breaks down as it passes half of the span (Figure 28 b) and disintegrates before it reaches the outer wall. This will be shown later to result from the increased turbulence intensities at the trailing side

A comparison of the streamwise velocities at the center span (z = 0.5) is shown in Figure 29. Though only minor differences are observed in the regions downstream of the ribs (in the region of the helical vortex), the region of high velocity (>1.4 times the bulk velocity) shifts towards the leading side. This behavior is also observed in ducts with normal ribs at high Reynolds number flow, where rotation results in a shift of the maximum velocity towards the leading side. The velocities at the trailing side decrease to values as low as 0.8 times the bulk velocity with rotation. Streamwise velocities of the helical vortices are observed to be just around 0.2-0.4 times the bulk velocity. In these same regions the magnitude of the spanwise velocities (w-velocity) is almost equal to the bulk velocity, pointing to the dominance of spanwise momentum transfer.

While the secondary cells in the stationary case are almost equal in size, the cell near the trailing wall decreases in size in the rotating case. This is compensated by the increase in size of the other cell which grows bigger to occupy the rest of the channel cross-section. The v- and w-velocity components are as high as 1.3 times the bulk velocity near the walls and at the junction of the two cells. Apart from the two primary cells, four corner cells are observed in both the rotating and the stationary cases.

A comparison of the overall friction factors for the stationary and the rotating cases show that both in the rotating as well as the stationary case the friction factor is augmented by around 13.1-13.8 times, showing that in spite of the differences in the localized flow features, rotation does not have a major impact on the overall friction factor.

Turbulent Flow Characteristics

The effect of the helical vortex and rotation on the turbulent kinetic energy along the span of the duct is shown in Figure 31. The *tke* values for the Ro = 0.0 case, at z = 0.25, 0.5 and 0.75 show that on moving from the inner wall to the outer wall the region of high *tke* becomes larger in size. The vortex core, which corresponds to the *tke* values of around 20%, is observed to be small near the inner wall (z = 0.25). On moving away from the inner wall, the core of the vortex increases in size by entraining more fluid and near the outer wall (z = 0.75) almost occupies half the rib pitch. At the center of the duct the *tke* values of around 6-10% are observed and a slight increase in these values is observed on moving from the inner wall to the outer wall. It is also observed that the region of high *tke* shifts slightly away from the rib on moving from the inner wall to the outer wall, and lifts off the ribbed wall as it approaches the outer wall.

In general, rotation tends to augment the turbulence level in the core of the duct near the trailing side where the *tke* values increase from around 8-10% to around 12%, and reduce *tke* at the leading side. An important observation relates to the *tke* values in the core of the helical vortex as it travels from the inner to the outer wall. At the first two planes examined (z = 0.25, 0.5) it is observed that in the vicinity of the rib at the trailing wall of the duct the *tke* values (~20%) are almost similar to the contours observed in the stationary case. However on moving towards the outer wall the vortex loses intensity, becomes diffuse, resulting in a drop of *tke* values to around 15%. This is consistent with what is observed in the mean flow in Figure 28. Contrary to the effect of rotation on the trailing wall, the helical vortex core at the leading wall remains intact but turbulent kinetic energy is attenuated as the vortex moves from the inside to the outside wall. This can be seen more clearly in Figure 32, which plots the *tke* distribution in a plane parallel (at a distance of $0.25D_h$ downstream of the rib) to the rib.

In the stationary duct, the region of high *tke* (17-20%) grows in size from the inner wall to the outer wall, as the helical vortex originates and grows in size downstream of the rib. At the outer wall, as the flow is deflected towards the core of the duct the *tke* values decrease to around 9-12%. Towards the core of the channel and near opposite wall the *tke* value is around 4%. For the rotating case it is observed that the helical vortex at the trailing side is stronger than the vortex at the leading side as shown in Figure 32 (b,c). However it is observed that at the trailing side the high *tke* value is not sustained by the vortex as it reaches the outer wall. At the leading wall, the helical vortex is observed to be less turbulent than the vortex in the stationary case, with the maximum *tke* values reaching values not larger than 12-15%.

In summary, it is observed that rotation increases the turbulence at the trailing side and decreases it on the leading side. Because of the increased turbulence intensity, the unsteady helical vortices which are formed at the trailing side of the duct become unstable and diffuse out before they impinge on the outer wall. On the other hand, the stabilizing effect of turbulence on the leading side of the duct, reduces the turbulent intensity in the helical vortices, but allows them to maintain their coherence till they impinge on the outer wall

In earlier studies on ducts with normal ribs [11,9], it has also been observed that the level of turbulence is augmented at the trailing side and attenuated at the leading side. However, while the peak *tke* at the trailing side increases by about 15% of the value in a stationary duct, the peak *tke* at the leading side drops by around 40%, even for the lowest rotation considered. In contrast the peak *tke* values observed in the current study (skewed ribs) do not show such large differences. While the overall *tke* value at the trailing side does increase, the corresponding decrease is around 15-20% at the leading side. The relative insensitivity of turbulence structure to rotation in ducts with skewed ribs is attributed to the dominance of transverse momentum transfer caused by the strong secondary flows and the fact that for orthogonal rotation (about z-axis), Coriolis forces do not have a direct effect on the transfer of momentum in the z-direction.

Heat Transfer Augmentation

A comparison of the heat transfer augmentation contours at the ribbed walls (Figure 33a-c) shows that rotation has little effect on the heat transfer at the ribbed wall. The separation

downstream of the rib near the inner wall results in a localized high heat transfer region where the heat transfer, as in the stationary case, is close to 4.5 times the heat transfer in a smooth duct. The diagonal variation of the heat transfer augmentation shows little deviation from the behavior observed in the stationary duct. Therefore it can be inferred that the heat transfer augmentation at the ribbed wall is largely influenced by the secondary flow. The bias in the turbulence levels at the leading and the trailing side of the duct is not as large as that in the duct with normal ribs and so the heat transfer is similar at the two sides. Figure 33d-e show the mass transfer augmentation distribution $12D_h$ downstream of the inlet for both the leading and the trailing sides as measured by Rathjen *.et al* [87]. It is observed that the heat transfer distributions predicted by LES are consistent with the measured distribution.

It is also established by comparing (Figure 27(b), Figure 34) that rotation does not have a significant effect on the heat transfer distribution at the inner wall of the duct. However, at the outer wall, it is observed that at the leading side the region of high heat transfer grows to around half the channel height (5 times the rib height). At the trailing side, because the mean helical vortex breaks down before it approaches the outer wall, heat transfer augmentation is substantially lower than in a stationary duct. This is shown in Figure 35.

To validate the LES computations, heat transfer augmentation at the inner and the outer walls are compared to experimental data by Rathjen *et al.* [87] as shown in Figure 36. The measurements were in between the ribs at the outer wall and on top of the ribs at the inner wall. It is observed from these measurements that the heat transfer reaches a peak value of around 4.5 times that in a smooth channel at the outer wall along the leading side, but values only as high as 2.6 are observed at the trailing side. Towards the center of the duct the heat transfer is around 1.5 times the smooth channel value. At the inner wall the heat transfer augmentation is observed to peak to a value of around 3.0 on top of the rib at the leading side. LES shows very good agreement with the experiments both at the outer wall and the inner wall.

In spite of the local differences in augmentation at the outer wall, the surface averaged level of augmentation does not change substantially over a stationary duct. This is due to the broader high heat transfer in regions near the leading side compensating for narrower high heat transfer

regions near the trailing wall. The heat transfer augmentation for the rotating case is observed to be around 2.44 times that in a smooth channel, as compared to the value of 2.55 observed in the stationary case. Both the stationary and the rotating cases have an average heat transfer augmentation of around 1.89 at the inner wall. A comparison of the heat transfer at the smooth and the rib roughened walls are shown in Table 1. The heat transfer augmentation at the rib roughened walls is around 2.39 and 2.43 at the leading and the trailing walls as compared to the value of 2.37 for the stationary case.

Studies on ducts with normal ribs [11,9] show a large difference in the heat transfer values predicted at the leading and the trailing sides as a result of rotation. The heat transfer observed at the trailing side is amplified by a factor of 1.5 while the heat transfer at the leading side decreases to a value of around 66% of that in a stationary duct. This large difference in ducts with normal ribs and minor difference in the skewed ribs is a result of the effect rotation has on the turbulence in the flow. While heat transfer augmentation with normal ribs is driven by streamwise momentum transfer on which Coriolis forces have a large effect, the augmentation in ducts with skewed ribs is driven by transverse momentum transfer on which Coriolis forces do not have a large effect.

Table 2 shows the comparison of the heat transfer at the various walls as predicted by LES and the experimental measurements by Rathjen *et al* [87]., and Johnson *et al* [82]. Rathjen's measurements have been carried out in a similar staggered rib arrangement in a complete two pass duct. The data presented is obtained $12D_h$ downstream of the inlet, where the rib-pitch averaged heat transfer characteristics are almost constant. Johnson's data were taken using rounded cross-section ribs, but the rib height and rib pitch was consistent with the current configuration studied. The data presented is obtained from the measurements $12D_h$ downstream of the inlet. Johnson's measurement show a difference in the heat transfer measured at the leading and the trailing walls, which may be due to the effects of buoyancy in the duct. Rathjen's data and the computations show little difference in the heat transfer augmentation ratios at the leading and the trailing walls. LES computations predict the heat transfer at all the wall with good accuracy. LES predictions match well with Rathjen's data and are within 6% of Johnson's measured values, which is within the experimental uncertainty.

Table 1: Comparison of the computed overall heat transfer and friction augmentations for stationary and rotating cases

	Ro = 0.0	Ro = 0.1
Heat Transfer Aug. Nu/Nu_0		
Leading Wall	2.37	2.39
Trailing Wall	2.37	2.43
Inner Wall	1.88	1.89
Outer Wall	2.55	2.44
Friction factor f/f_0	13.8	13.1

Table 2: Comparison of the overall heat transfer and friction augmentations with experiments

	LES	Rathjen *et al.*, (2002)	Johnson *et al.*, (1994)
Heat Transfer Aug. Nu/Nu_0			
Leading Wall	2.39	2.40	2.25
Trailing Wall	2.43	2.40	2.5
Inner Wall	1.89	1.76	-
Outer Wall	2.44	2.40	-
Friction factor f/f_0	13.1	-	-

SUMMARY AND CONCLUSIONS

1. Detached Eddy Simulation of Flow and Heat Transfer in Fully Developed Rotating Internal Cooling Channel with Normal Ribs

Conclusions

Results from DES and URANS of a fully developed flow in a 90° ribbed duct are presented for three rotation cases – Ro = 0.18, 0.35 and 0.67 at a Reynolds number of 20,000. The computations were performed on a 64^3 mesh tested earlier for a stationary case which is almost an order of magnitude less expensive than the analogous LES computation (Abdel-Wahab *et al.,* 2004a-b).

The effect of rotation is observed by the increase in the unsteadiness at the trailing wall due to which the reattachment length decreases. Secondary flow impingement is observed to become stronger as rotation increases. These flow features result in an increase in the heat transfer at the trailing wall. The peak heat transfer level increases from a value of about 3.0 for the stationary duct to a value of about 6.0 for the largest rotation. The overall heat transfer at the trailing wall increases by almost a factor of 1.5 as the system is rotated from rest to Ro = 0.67.

At the leading wall the opposite effect is observed. Rotation damps turbulence at the leading wall resulting in larger recirculation regions. It is observed that the recirculation region downstream of the rib almost overlaps the recirculation region upstream of the next rib. This results in low levels of heat transfer at the leading wall. The heat transfer distribution drops to values close to that in a smooth duct for the highest rotation considered.

The heat transfer at the side walls show distributions similar to a stationary duct. The heat transfer is high at the corner of the rib, which is due to the impingement of the secondary flows on the side walls. The heat transfer decreases on moving from the trailing wall to the leading wall. Rotation increases the magnitude of the secondary flows and increases the heat transfer augmentation on the side walls.

The flow and heat transfer distribution predicted by the SST DES case is consistent with the LES predictions. Though higher heat transfer is predicted immediately upstream of the rib, the distribution in the other regions are accurate. The overall heat transfer predicted also match well with the LES predictions and the experimental observations. URANS fails to capture the effects of the Coriolis forces at the trailing walls and underpredicts the heat transfer.

In summary, it is concluded that DES accurately predicts the physics of the rotation dominated flow, in addition to accurately predicting separation and reattachment and unsteady vortex induced secondary motions. The main contribution of this paper is in establishing that DES, like LES, can produce quality results at a cost which is an order of magnitude less than an equivalent LES. The payoffs are expected to be larger at Higher Reynolds numbers.

2. Large Eddy Simulation of fully developed flow and heat transfer in a rotating duct with 45° ribs

Conclusions

Computations have been carried out for a 45 degree ribbed duct, with a P/e = 10 and e/D_h = 0.1 to investigate the effect of orthogonal rotation on the flow and heat transfer. The flow features and the heat transfer has been compared and contrasted with 45 degree ribs in a stationary duct to determine why rotation does not have a large effect on heat transfer augmentation unlike ducts with 90 degree ribs.

The skewed geometry of the rib results in a massive transfer of momentum in the spanwise direction. This results in helical vortices downstream of the ribs which move from the inner to the outer wall. These vortices feed into the secondary flow in the cross-section of the duct, both of which together dominate the heat transfer augmentation patterns.

Rotation skews the streamwise velocity profile toward the leading side of the duct, augments turbulence level at the trailing side while attenuating turbulence at the leading side. The degree of augmentation and attenuation is not as well defined and strong as with normal ribs. However, because of the augmentation of turbulence at the trailing side, the helical vortices which are produced in the separated shear layer and which move from the inside to the outside of the duct,

break down and diffuse before they can impinge on the outer wall. Turbulence attenuation at the leading wall has the opposite effect which allows the helical vortices to maintain their coherence and impinge on the outer wall. This effect taken together with the streamwise flow being pushed to the leading side, produces an extended region of high heat transfer at the outer wall near the leading side. This is countered by lower heat transfer at the trailing side of the outer wall, giving little or no change in the overall augmentation.

Unlike 90 degree ribbed ducts, in which the augmentation is strongly dependent on the streamwise momentum, in skewed ribs it is the spanwise momentum which dominates heat transfer. Since the Coriolis forces under orthogonal rotation about the z-axis do not directly contribute to spanwise momentum, they do not have as much of an effect on heat transfer at the ribbed walls at the trailing and leading sides, which exhibit the same patterns and levels of augmentation as a stationary duct.

References

1. Abdel-Wahab, S. and Tafti, D. K., 2004a, Large Eddy Simulation of Flow and Heat Transfer in a Staggered 45º Ribbed Duct, GT2004-53800, ASME Turbo Expo: 2004, Vienna, Austria.
2. Abdel-Wahab, S. and Tafti, D. K., 2004b, Large Eddy Simulations of Flow and Heat Transfer in a 90º Ribbed Duct with Rotation – Effect of Coriolis Forces, GT2004-53796, ASME Turbo Expo: 2004, Vienna, Austria.
3. Graham, E, Sewall, E. and Thole, K. A., 2004, Flowfield Measurements in a Ribbed Channel Relevant to Internal Turbine Blade Cooling, GT2004-53361, ASME Turbo Expo: 2004, Vienna, Austria.
4. Sewall, E, and Tafti, D. K., 2005, Large Eddy Simulation of Flow and Heat Transfer in the Developing Flow Region of a Rotating Gas Turbine Internal Cooling Duct with Coriolis and Buoyancy Forces, GT2005-68519, ASME Turbo Expo 2005, June 6-9, Reno-Tahoe, Nevada, USA.
5. Sewall, E, and Tafti, D. K., 2004, Large Eddy Simulation of the Developing Region of a Rotating Ribbed Internal Turbine Blade Cooling Channel, GT2004-53833, ASME Turbo Expo: 2004, Vienna, Austria.
6. Sewall, E, and Tafti, D. K., 2004a, Large Eddy Simulation of the Developing Region of a Stationary Ribbed Internal Turbine Blade Cooling Channel, GT2004-53832, ASME Turbo Expo: 2004, Vienna, Austria.
7. Sewall, E, and Tafti, D. K., 2005a, Large Eddy Simulation of Flow and Heat Transfer in the 180° Bend Region of a Stationary Ribbed Gas Turbine Internal Cooling Duct, GT2005-68518, ASME Turbo Expo 2005, June 6-9, Reno-Tahoe, Nevada, USA.
8. Sewall, E.A., Tafti, D.K., 2004b. Large Eddy Simulations of the Developing Region of a Rotating Ribbed Internal Turbine Blade Cooling Channel, ASME Turbo Expo: 2004, Vienna, Austria. GT2004-53833.
9. Tafti D. K., 2003, Large Eddy Simulations of Heat Transfer in A Ribbed Channel for Internal Cooling of Turbine Blades, Paper No. GT2003-38122, Proceedings of ASME/IGTI Turbo Expo., Atlanta, Georgia, June 16-19, 2003.

10. Viswanathan, A. and Tafti, D. K., 2005a, Large Eddy Simulation of Flow and Heat Transfer in a Ribbed Duct with Skewed Ribs of Rounded Cross-Section, GT2005-68117, ASME Turbo Expo 2005, June 6-9, Reno-Tahoe, Nevada, USA.
11. Viswanathan, A. and Tafti, D. K., 2005b, Detached Eddy Simulation of Flow and Heat Transfer in a Stationary Internal Cooling Duct with Skewed Ribs, GT2005-68118, ASME Turbo Expo 2005, June 6-9, Reno-Tahoe, Nevada, USA.
12. Viswanathan, A. and Tafti, D. K., 2005c, Large Eddy Simulation of Flow and Heat Transfer in an Internal Cooling Duct with High Blockage Ratio 45° Staggered Ribs, GT2005-68086, ASME Turbo Expo 2005, June 6-9, Reno-Tahoe, Nevada, USA.
13. Abdel-Wahab, S. and Tafti, D. K., 2004c, Large Eddy Simulations of Flow and Heat Transfer in a 90º Ribbed Duct with Rotation - Effect of Coriolis and Centrifugal Buoyancy Forces, GT2004-53799, ASME Turbo Expo: 2004, Vienna, Austria. Accepted for publication in *J. Turbomachinery*, in press.
14. Viswanathan A. and Tafti, D. K., 2004, Detached Eddy Simulation of Turbulent Flow and Heat Transfer in a Duct, HT-FED2004-56152, ASME Heat Transfer/Fluids Engineering Summer Conference, July 11-15, Charlotte. Accepted for publication in *J. Fluids Engineering*.
15. Sewall, E.A., Tafti, D.K., Graham, A., Thole, K.A., 2005a. Experimental Validation of Large Eddy Simulation of flow and heat transfer in a Stationary Ribbed Duct. Submitted *Int. J. Heat and Fluid Flow*, 2005.
16. Tafti, D.K., 2005. Evaluating the Role of Subgrid Stress Modelling in a Ribbed Duct for the Internal Cooling of Turbine Blades, *Int. J Heat and Fluid Flow* 26(1), pp. 92-104, 2005., January 2004.
17. Viswanathan A.K., Tafti, D. K., 2005c, Detached Eddy Simulation of Flow and Heat Transfer in Fully Developed Rotating Internal Cooling Channel with Normal Ribs, Submitted to *Int. J. of Heat Fluid Flow*.
18. Viswanathan A.K., Tafti, D. K., 2005d, Detached Eddy Simulation of Turbulent Flow and Heat Transfer in a Two-Pass Internal Cooling Duct, Accepted for publication *Int. J. of Heat Fluid Flow*.

19. Tafti, D. K., 2001, GenIDLEST - A Scalable Parallel Computational Tool for Simulating Complex Turbulent Flows, Proceedings of the ASME Fluids Engineering Division, FED - vol. 256, pp. 347-356, ASME-IMECE, Nov. 2001, New York.
20. Thuburn, J., 1996, Multidimensional Flux-Limited Advection Schemes, *J. Comput. Phys.*, vol. 123, pp. 74-83.
21. Leonard, B. P., 1991, The ULTIMATE conservative difference scheme applied to unsteady one-dimensional advection, *Comp. Methods in App. Mech, and Engineering* 88, pp. 17-74.
22. Smagorinksy, J., 1963, General Circulation Experiments with the Primitive Equations. I. The Basic Experiment, *Monthly Weather Review,* vol. 91, pp. 99-164.
23. Germano, M., Piomelli, U., Moin, P., and Cabot, W. H., 1991, A dynamic subgrid-scale eddy viscosity model, *Physics of Fluids* A. vol. 3, pp. 1760-1765.
24. Wilcox David C. 1994, Simulation of Transition with a Two-Equation Turbulence model, *AIAA Journal*, vol. 32, No. 2, pp. 247-225.
25. Wilcox David C. 1998, Turbulence modeling for CFD, DCW Industries, Inc.
26. Wilcox, D.C., 1988. Reassessment of the Scale-Determining Equation for Advanced Turbulence Models, *AIAA Journal*, Vol 26 (11), pp 1299-1310. Nov 1988.
27. Menter Florian R., 1993, Zonal Two Equation $k-\omega$ Turbulence Models for Aerodynamic Flows, 24th Fluid Dynamics Conference, AIAA paper 93-2906, July 6 – 9, Orlando, Florida.
28. Menter, F.R., 1992. Improved Two-Equation k-ω Turbulence Models for Aerodynamic Flows, NASA Technical Memorandum 103975, Oct 1992.
29. Menter, F.R., 1993. Zonal Two Equation k-ω Turbulence Models for Aerodynamic Flows, AIAA Paper 93-2906.
30. Wang G., Tafti, D. K., 1998b, Parallel performance of Additive Schwarz preconditioners on Origin 2000. *Advances in Engineering Software*, vol. 29, no. 3-6, pp. 433.
31. Wang, G. and Tafti, D. K., 1999, Performance Enhancement on Microprocessors with Hierarchical Memory Systems for Solving Large Sparse Linear Systems. *The International Journal of Supercomputing Applications and High Performance Computing*, vol. 13, no. 1, pp. 63.
32. Wang, G., Tafti, D. K., 1998a, Uniprocessor performance enhancement by Additive Schwarz preconditioners on Origin 2000. *Advances in Engineering Software*, vol. 29, no. 3-6, pp. 425.

33. Chong, M. S., Perry, A. E., and Cantwell, B. J., 1990, A general classification of three-dimensional flow fields, *Physics of Fluids* A. vol. 2, pp. 765-777.
34. Jeong, J. and Hussain, F., 1995, On the identification of a vortex, *J. Fluid Mech*., vol. 285, pp 69-94.
35. Najjar, F. M. and Tafti, D. K., 1996a, Study of Discrete Test Filters and Finite Difference Approximations for the Dynamic Subgrid-Scale Stress Model, *Phys. Fluids*, vol. 8, pp. 1076-1088.
36. Lilly, D. K., 1992, A proposed modification of the Germano subgrid-scale closure method, *Phys. Fluids A* 4, 633.
37. Rau, G., Çakan, M., Moeller, D. and Arts, T., 1998, The Effect of Periodic Ribs on the Local Aerodynamic and Heat Transfer Performance of a Straight Cooling Channel, *ASME J. Turbomachinery*, 120, pp. 368-375.
38. Amano, R.S., Goel, P., 1995, Computation of Turbulent Flow beyond Backward Steps using Reynolds Stress Closure, *AIAA J,* 23, pp 1356.
39. Bradshaw, P., 1969, The Analogy Between Streamline Curvature and Buoyancy in Turbulent Shear Flow, *J. Fluid Mech*, 36, Part 1, pp 177-191.
40. Bradshaw, P., 1988, Effects of Extra Strain – Review, Near Wall Turbulence, Zoran Zaric Memorial Conference Ed. S J Kline, N.H. Afghan, Hemisphere Publishing Corporation, pp 106 - 122.
41. Bo, T., Iacovides, H., Launder, B.E., 1995, Developing Buoyancy-Modified Turbulent Flow in Ducts Rotating in Orthogonal Mode, Transactions of ASME 177, pp.474-484.
42. Chima, R.V., 1996, A k-ω turbulence model for quasi-three dimensional turbo machinery flows, *AIAA 96-0258.*
43. Driver. D., Seegmiller, H.L., 1985, Features of reattaching turbulent shear layer in divergent channel flow, *AIAA J.*, 23, 162-171.
44. Forsythe. J.R, Squires. K.D, Wurtzler. K.E., Spalart. P.R, 2002, Detached-Eddy Simulation of Fighter Aircraft at High Alpha, AIAA Paper 2002-0591..
45. Halleen, R.M., and Johnston, J.P., 1967, The Influence of Rotation of Flow in a Long Rectangular Channel – An Experimental Study, Report MD-18, Thermosciences Division, Dept. of Mech. Eng., Stanford University.
46. Hanjalic, K., Launder, B.E., 1980, Sensitizing the Dissipation Equation to Irrotational Strains, *ASME J. Fluids Eng.*, 102: 34.
47. Hellsten, A., 1998, Some improvements in Menter's k-ω SST turbulence model, *AIAA 98-2554.*

48. Hellsten, A., 2004, New advanced *k-ω* turbulence model for high-lift aerodynamics, *AIAA 2004-1120.*
49. Howard, J.H.G., Patankar, S.V., Bordynuik, R.M., 1980, Flow prediction in rotating ducts using Coriolis-modified turbulence models, *ASME Journal of Fluids Engg,* 102, pp 456-461.
50. Iacovides, H., Launder, B.E., 1991, Parametric and Numerical Study of Fully Developed Flow and Heat Transfer in Rotating Rectangular Ducts, *J. Turbomachinery* 133, pp.331-338.
51. Incropera, F.P., Dewitt, D.P., 2002, Fundamentals of Heat and Mass Transfer, fifth edition, John Wiley and Sons, New York.
52. Ishigaki, H., 1996, Analogy between turbulence flows in curved pipes and orthogonally rotating pipes, *Journal of Fluid Mechanics,* 307, pp 1 – 10.
53. Joeng, J., Hussain, F., 1995, On the Identification of a Vortex, *Journal of Fluid Mechanics*, 285, pp 69 – 94.
54. Kapadia, S., Roy, S., Wurtlzer, K., 2003, Detached Eddy Simulation Over a Reference Ahmed Car Model - AIAA 2003-0857.
55. Launder, B.E., Priddin, C.H., Sharma, B.I., 1977, The calculation of turbulent boundary layers on spinning and curved surfaces, *ASME Journal of Fluids Engg,* pp 231-239, March.
56. Lezius, D.K., and Johnston, J.P., Roll-Cell Instabilities in Rotating Laminar and Turbulent Channel Flows, *J. Fluid Mech.* Vol. 77, Part 1, pp. 153-175, 1976.
57. Lin, Y.L., Shih, T,I-P, Stephens, M.A., Chyu, M.K., 2001, A numerical study of flow and heat transfer in a smooth and a ribbed U-duct with and without rotation, ASME *Journal of Heat Transfer*, 123, pp 219-232.
58. Liou, T.M., Chen, M.Y., Tsai, M.H., 2001, Fluid Flow and Heat Transfer in a Rotating Two-Pass Square Duct with In-Line 90° Ribs, ASME Turbo Expo: 2001-GT-0185.
59. Liou, T.M., Wu, Y.Y., Chang, Y., 1993, LDV Measurements of Periodic Fully Developed Main and Secondary Flows in a Channel with Rib-disturbed Walls, *ASME Journal of Fluids Engineering,* Vol 115, pp 109-114.
60. MATLAB, 2005, Release Notes for Release 14 with Service Pack 3.
61. Menter, F.R., 1992, Improved Two-Equation *k-ω* Turbulence Models for Aerodynamic Flows, NASA Technical Memorandum 103975.
62. Menter, F.R., 1993, Zonal Two Equation *k-ω* Turbulence Models for Aerodynamic Flows, AIAA Paper 93-2906.
63. Murata, A., Mochizuki, S., 1999, Effect of cross-sectional aspect ratio on turbulent heat transfer in an orthogonally rotating rectangular smooth duct, *Int. J. Heat Mass Transfer* 42, pp. 3803-3814. *Int. J. Heat Mass Transfer* 43, pp. 1243-1259

64. Nikitin, N.V., Nicoud, F., Wasistho, B., Squires, K.D., Spalart, P.R., 2000, An Approach to Wall Modeling in Large-Eddy Simulations, *Physics of Fluids*, 12(7), 1629-1632.
65. Parsons, J.A., Han, J.C., Zang, Y.M., 1994, Wall Heating Effect on Local Heat Transfer in a Rotating Two-Pass Square Channel with 90º Rib Turbulators, *Int. J. Heat Mass Transfer* 37, 1411-1420.
66. Prakash, C., Zerkle, R., 1995, Prediction of Turbulent Flow and Heat Transfer in a Ribbed Rectangular Duct with and without Rotation, *J. Turbomachinery*, 117, pp.255-264.
67. Rau, G., Cakan, M., Moeller, D., Arts, T., 1988, The Effect of Periodic Ribs on Local Aerodynamic and Heat Transfer Performance of a Straight Cooling Channel, *ASME J. Turbomachinery,* 120, pp 368-375.
68. Rigby, D.L., 1998, Prediction of Heat and Mass Transfer in a Rotating Ribbed Coolant Passage with a 180 Degree Turn, 98-GT-329, International Gas Turbine and Aeroengine Congress and Exhibition, Stockholm, Sweden, June 2-5.
69. Rodi, W., Scheuerer, G., 1983, Calculation of curved shear layers with two-equation turbulence models, *Physics of Fluids,* 26(6).
70. Schweighofer, J., Hellsten, A., 1999, Computations of viscous flow around the HSVA-1 tanker using two versions of k-ω turbulence model, *Helsinki University of Technology, Laboratory of Aerodynamics, Report B-51.*
71. Spalart, P.R., 2001, Young Person's Guide to Detached-Eddy Simulation Grids, NASA Contractor Report 2001-211032.
72. Spalart, P.R., Jou, W.H., Streletes. M., Allmaras. S.R., 1997, Comments on the feasibility of LES for wings and a hybrid RANS/LES approach, First AFSOR Int. Conf. on DNS/LES, Aug 4-8, 1997, In Advances in DNS/LES, C.Liu and Z.Liu Eds, Greyden Press, Columbus, OH.
73. Speziale, G., Ngo, T., 1988, Numerical solution of turbulent flow past a backward-facing step using a nonlinear k - ε model. *Int. J. Engg Sci.,* 26:pp 1099-1112.
74. Squires. K.D, Forsythe. J.R, Morton. S.A, Blake.D.C, Serrano.M, Wurtzler. K.E, Strang. W.Z, Tomaro. R.F., Spalart. P.R, 2002, Analysis of full aircraft with massive separation using Detached-Eddy Simulation, Proceedings of the High Performance Computing Modernization Program 2002 Users Group Conference, Austin, Texas.
75. Stephens, M.A., Shih, T,I-P., Civinskous, K.C., 1996, Computations of flow and heat transfer in a rotating U-shaped square duct with smooth walls, *AIAA 96-3161.*
76. Strelets, M., 2001, Detached Eddy Simulation of Massively Separated Flows, AIAA 2001-0879.
77. Wagner, J.H., Johnson, B. V., Graziani, R.A., Yeh, F.C., 1992, Heat Transfer in Rotating Serpentine Passages with Trips Normal to the Flow, *J. Turbomachinery* 114, pp. 847-857.

78. Watanabe, K., Takahashi, T., 2002, LES Simulation and Experimental Measurement of Fully Developed Ribbed Channel Flow and Heat Transfer, Proc. ASME Turbo Expo: 2002-GT-30203.
79. Wilcox, D.C., Chambers, T.L., 1977, Streamline curvature effects on turbulent boundary layers, *AIAA Journal*, Vol 15, No.4.
80. Chanteloup, D., Juaneda, Y., Bolcs, A., Combined 3D Flow and Heat Transfer Measurements in a 2-pass Internal Coolant Passage of Gas Turbine Airfoils, Proc. ASME Turbo Expo:2002-GT-30214.
81. Tse, G.N., Steuber, G.D., Flow in a rotating Square Serpentine Coolant Passage with Skewed Trips, ASME Paper No. 97-GT-529, International Gas Turbine and Aeroengine Congress and Exhibition.
82. Johnson, B.V., Wagner, J.H., Steuber, G.D., Yeh, F.C., Heat Transfer in Rotating Serpentine Passages with Trips Skewed to the Flow, J. Turbomachinery 116, pp. 113-123, 1994..
83. Al-Hadhrami, L., Han, J.C., Effect of Rotation on Heat Transfer in Two-pass Square Channels with Five Different Orientations of 45 degree Angled Rib Turbulators, International Journal of Heat and Mass Transfer, Vol 46, pp 653-669,
84. Fu, W-L., Wright, L.M., Han, J-C., Buoyancy Effects on Heat Trasnfer in Five Difference Aspect-Ratio Rectangular Channels with Smooth Walls and 45-degree Ribbed Walls, GT2005-68493, Proceedings of ASME Turbo Expo 2005, Reno-Tahoe, June 2005.
85. Iacovides, H., Jackson, D.C., Kelemenis,G., Launder. B.E., Yuan, Y.M., Flow and heat transfer in a rotating U-bend with 45° ribs. International Journal of Heat and Fluid Flow, Vol 22, pp 308-314., 2001.
86. Azad, S., Uddin, M.J., Han, J.C., Moon, H.K., Glezer, B., Heat Transfer in a Two-Pass Rectangular Rotating Channel With 45-deg Angled Rib Turbulators, J. Turbomachinery 124, pp. 251-259, 2002.
87. Rathjen, L., Hennecke, D.K., Sivade, C., Semmler, K., Detailed Experimental and Numerical Heat/Mass Transfer Investigations in a Rotating Two-Pass Coolant Channel with Staggered 45º Ribs, *9th Int'l Symposium on Transport Phenomena and Dynamics of Rotating Machinery*, 2002.
88. Prakash, C., Zerkle, R., Prediction of Turbulent Flow and Heat Transfer in a Radially Rotating Square Duct: J. Turbomachinery 114, pp. 835-846, 1992.
89. Iacovides, H., Launder, B.E., Li, H.Y., The Computation of Flow Development Through Stationary and Rotating U-Ducts of Strong Curvature, Int. J. Heat Fluid Flow, 17, pp 22 – 33.
90. Chen, H.C., Jang, Y.J., Han, J.C., Computation of Flow and Heat Transfer in a Rotating Two-pass Square Channel by a Reynolds Stress Model, ASME Paper No. 99-GT-174.
91. Liou, T.M., Hwang, J.J., Chen, S.H., Turbulent Transport Phenomena in a Channel with Periodic Rib Turbulators, *J. of Thermophysics and Heat Transfer,* Vol. 6 (3), pp 513-521, 1992.

92. Liou, T.M., Wu, Y.Y., Chang, Y., LDV Measurements of Periodic Fully Developed Main and Secondary Flows in a Channel with Rib-disturbed Walls, *ASME Journal of Fluids Engineering,* Vol 115, pp 109-114, Mar 1993.
93. Iacovides, H., Raisee, M., Recent Progress in the Computation of Flow and Heat Transfer in Internal Cooling Passages of Turbine Blades *Int. J. Heat Fluid Flow,* 20. pp 320-328, 1999.
94. Saidi, A., Sunden, B., On Prediction of Thermal-Hydraulic Characteristics of Square-Sectioned Ribbed Cooling Ducts, *ASME J. of Turbomachinery,* Vol 123, 2001.
95. Ooi, A., Iaccarino, G., Durbin, P.A., Behnia, M., Reynolds Averaged Simulation of Flow and Heat Transfer in Ribbed Ducts, *Int. J. Heat and Fluid Flow,* 23, pp 750-757, 2002.
96. Al-Qahtani, M., Chen, H.C., Han, J.C., Prediction of Flow and Heat Transfer in Rotating Two-Pass Rectangular Channels With 45º Rib Turbulators, IGTI, No. 2001-GT-187.
97. Al-Qahtani, M., Chen, H.C., Han, J.C., A Numerical Study of Flow and Heat Transfer in Rotating Rectangular Channels with 45º Rib Turbulators by Reynolds Stress Turbulence Model, Proc. ASME Turbo Expo: 2002-GT-30216.
98. Bonhoff, B., Parneix, S., Leusch, J., Johnson, B.V., Schabacker, J., Bolcs, A., Experimental and numerical study of developed flow and heat transfer in coolant channels with 45 degree ribs, Int. *J. Heat Fluid Flow* 20, pp.311-319, 1999.
99. Jang, Y.J., Chen, H.C., Han, J.C., Flow and Heat Transfer in a Rotating Square Channel with 45 deg Angled Ribs by Reynolds Stress Turbulence Model, Transactions of ASME 123, pp.124-132, 2001
100. Germano, M., Piomelli, U., Moin, P., and Cabot, W.H., A dynamic subgrid-scale eddy viscosity model, Phys. Fluids, vol. 3, pp. 1760-1765, 1991.
101. Moin, P. Squires, K., Cabot, W., Lee, S., A Dynamic Sub-Grid-Scale Model for Compressibly Turbulence and Scalar Transport, Phys. Fluids A, 3-11 pp. 2746-2757, 1991.
102. Incropera, F.P. and Dewitt, D.P., Fundamentals of Heat and Mass Transfer, fifth edition, John Wiley and Sons, New York, 2002.

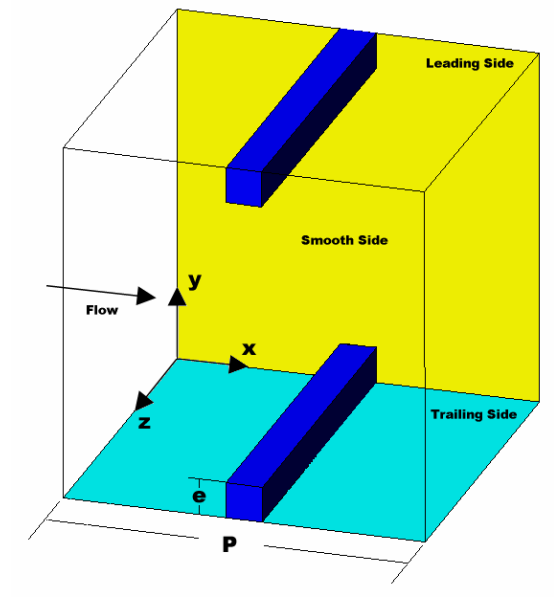

Figure 1: Computational domain for fully-developed flow and heat transfer in ribbed duct with and without rotation. Periodic boundary conditions are applied in the streamwise *x*-direction.

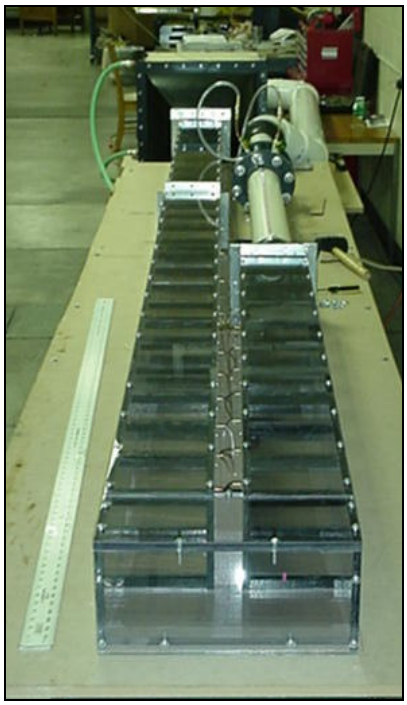

Figure 2: Photograph of the completed test rig. The ruler in the foreground is 6 feet long. The test rig was constructed of Lexan walls and equipped with pressure taps at 6-in. increments.

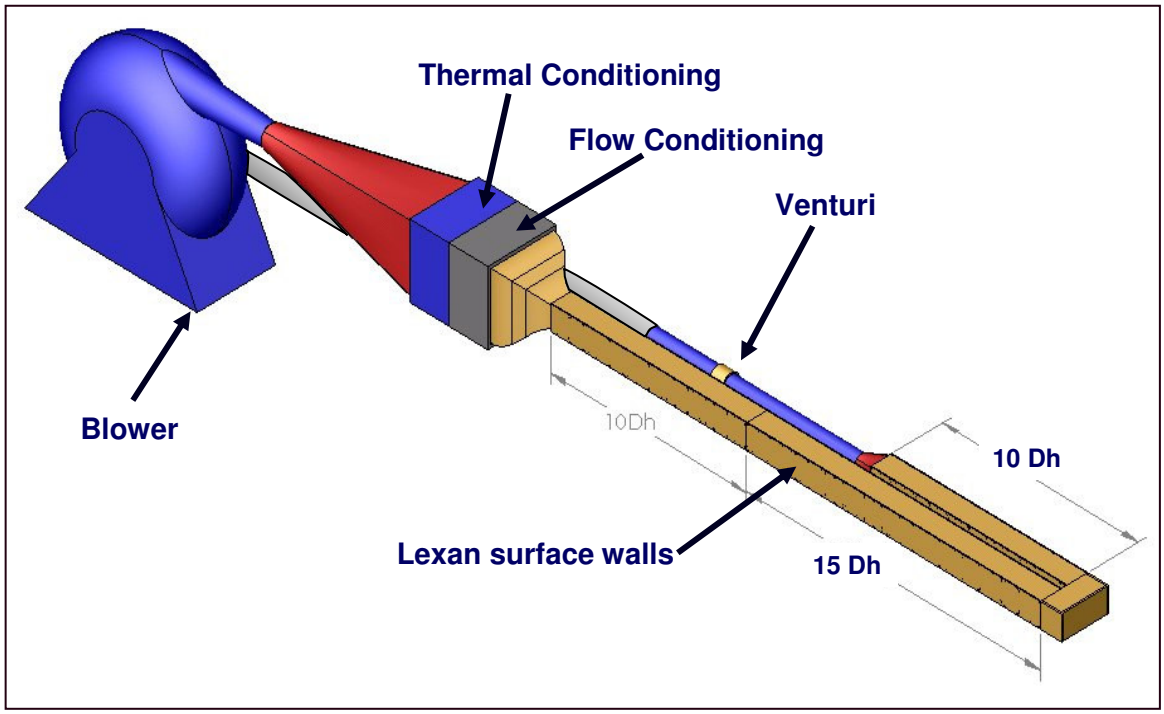

Figure 3: Three dimensional CAD rendering of testing facility for ribbed channel studies.

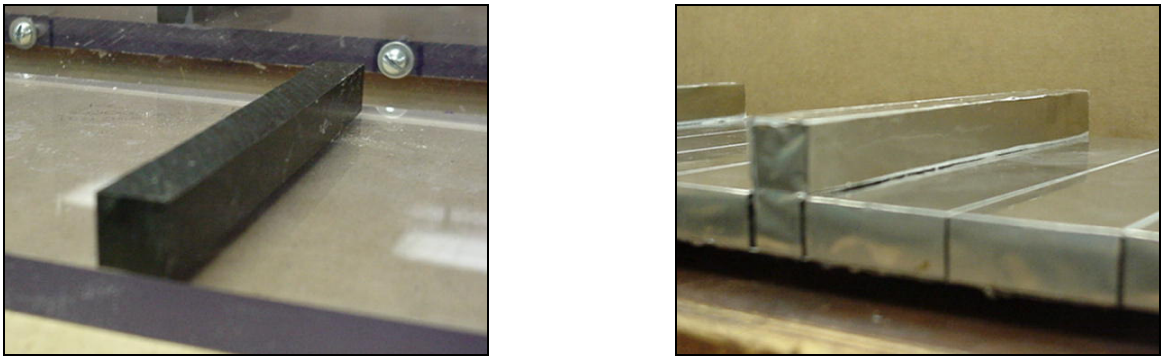

(a) (b)

Figure 4: Detailed photograph of Delrin rib for (a) heated and (b) unheated studies.

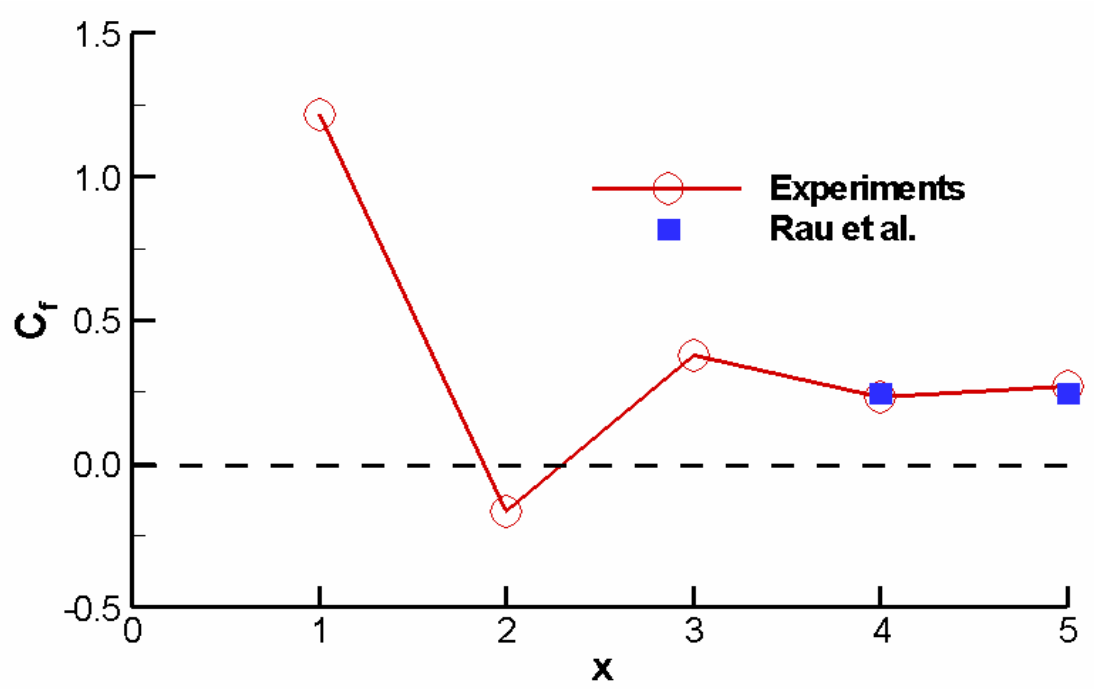

Figure 5: Comparison of experimental friction factors with data from Rau et al. [67].

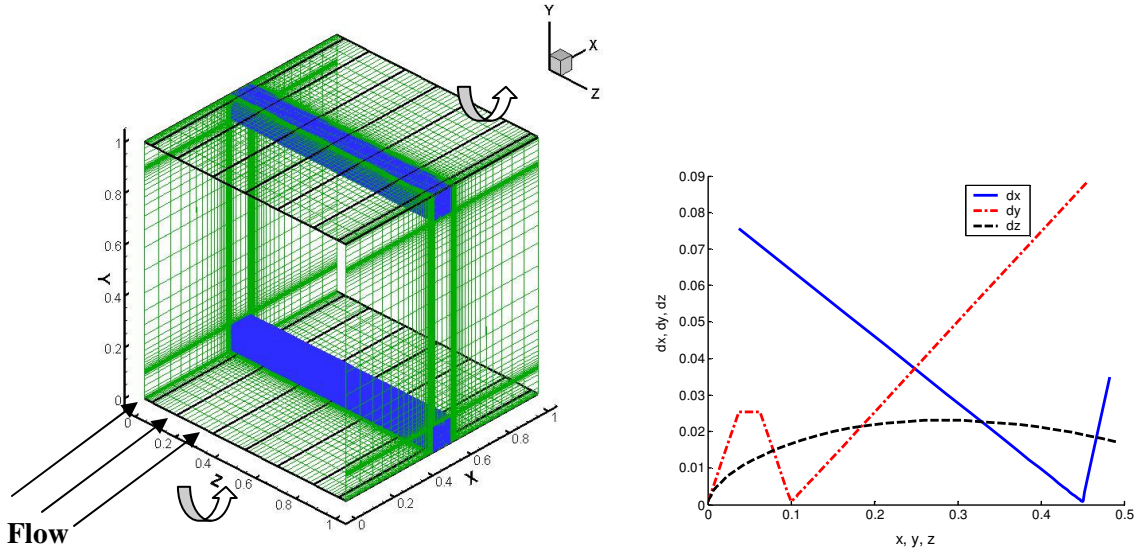

(a) (b)

Figure 6: (a) Schematic diagram representing the grid in the periodic ribbed duct. The system is rotated about the *z*-axis (b) Grid distribution in the three directions.

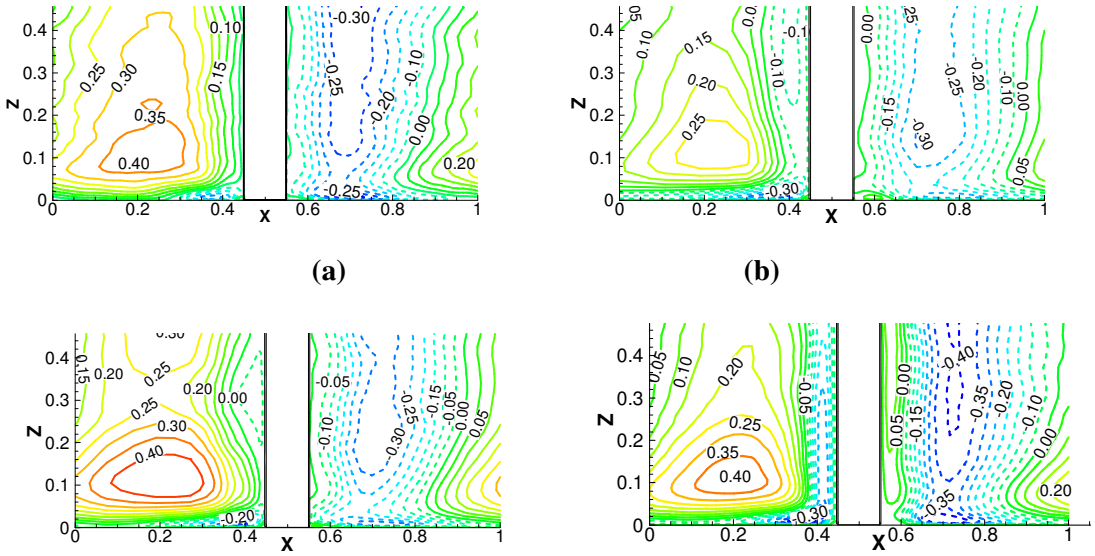

(a) (b)

(c) (d)

Figure 7: Comparison of the streamwise velocity contours at Y/e = 0.25 plane. (a) LES 128^3 (b) DES 48^3 (c) DES 64^3 (d) DES 96^3. Flow direction is from left to right.

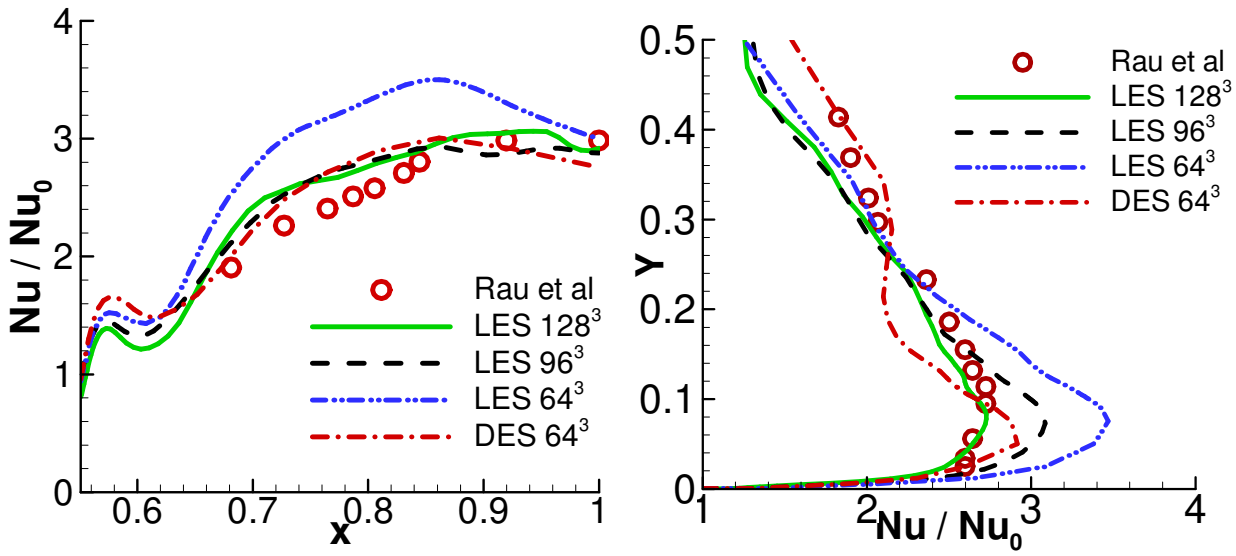

(a) **(b)**

Figure 8: Comparison of the heat transfer predictions (a) Ribbed Wall heat transfer downstream of the rib (z = 0.5) (b) Side Wall heat transfer comparison (x = 0.45)

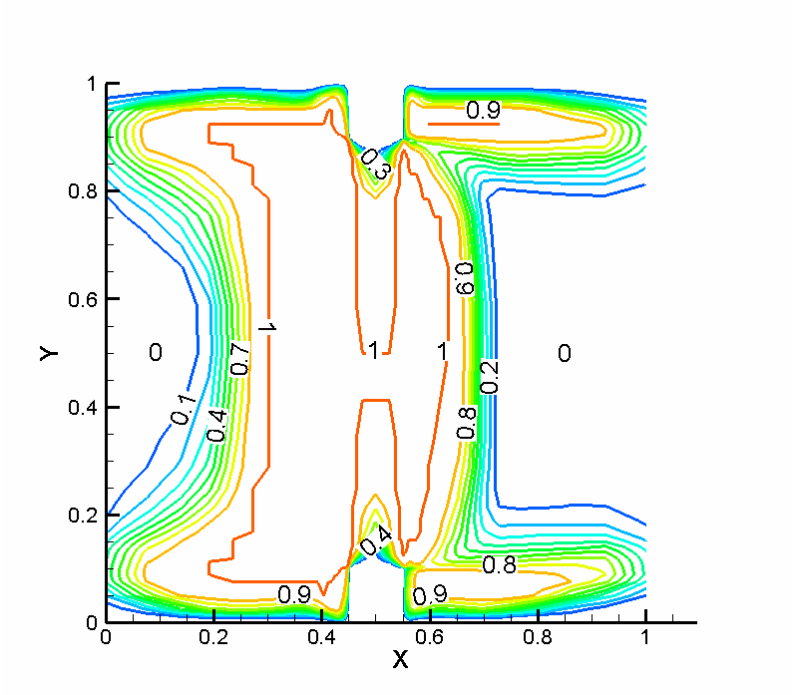

(a)

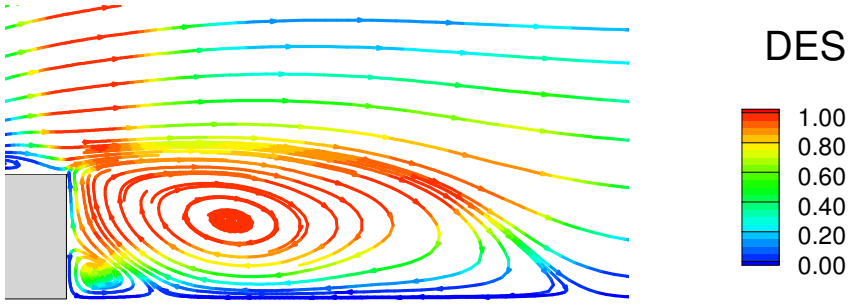

(b)

Figure 9: (a) Plot of the DES regions in the center plane ($Y/D_h = 0.5$) of the duct. A value of 0 denotes a region completely solved in URANS mode while 1 denotes a complete LES mode. (b) Streamlines showing the DES regions in the recirculation region. A major part of the recirculation region is solved in the LES mode.

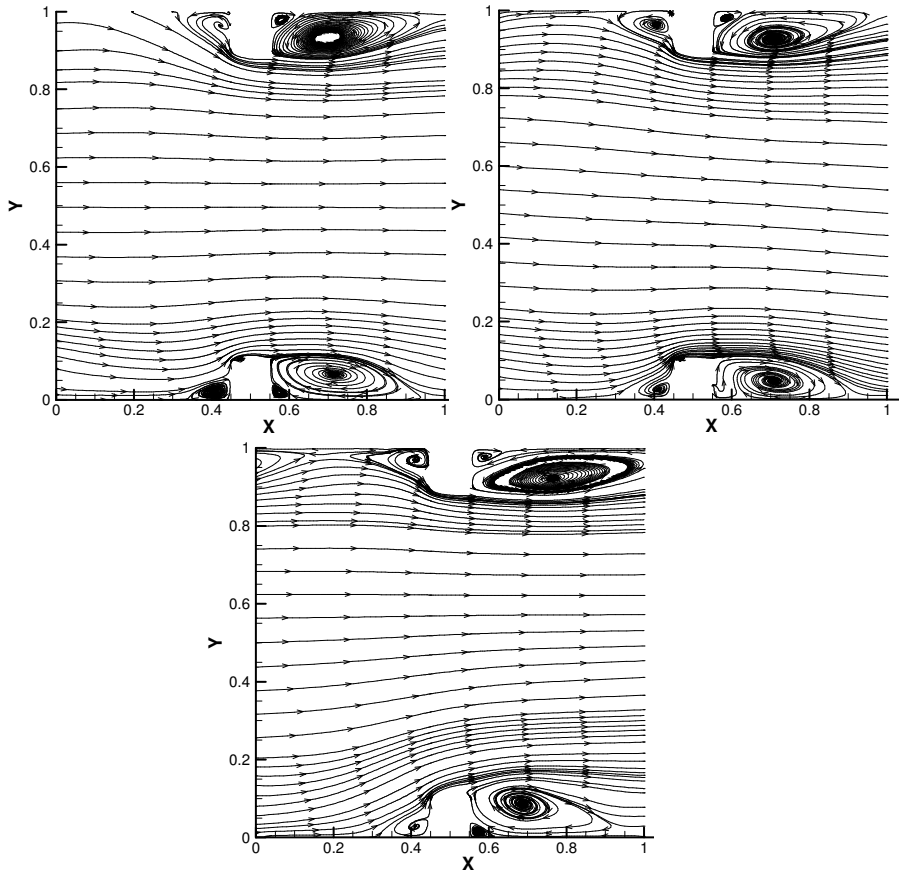

(a) **(b)** **(c)**

Figure 10: Streamlines showing the flow in a fully developed duct as predicted by DES SST at Z = 0.5 (a) Ro = 0.18 (b) Ro = 0.35 (c) Ro = 0.67. Y = 0 represents the trailing wall, while Y = 1 represents the leading wall. Flow direction is from left to right.

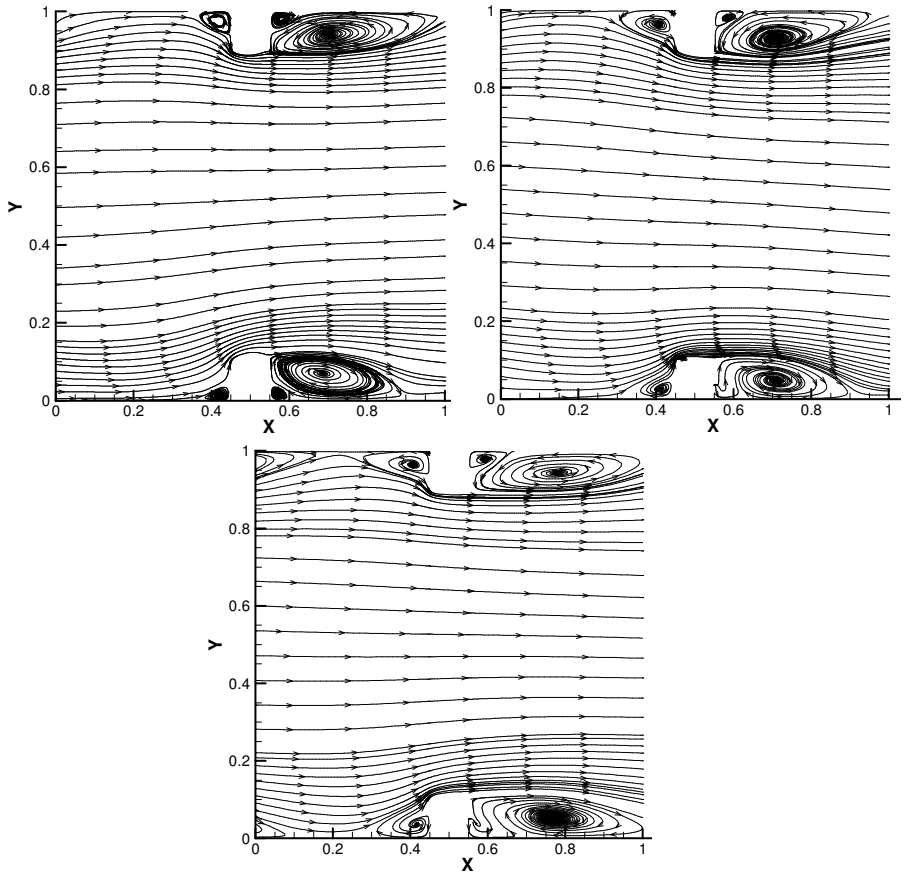

(a) **(b)** **(c)**

Figure 11: Streamlines showing the flow in a fully developed duct rotating at Ro = 0.35 at Z = 0.5 as predicted by (a) LES (b) DES SST (c) URANS SST. Y = 0 represents the trailing wall, while Y = 1 represents the leading wall. Flow direction is from left to right.

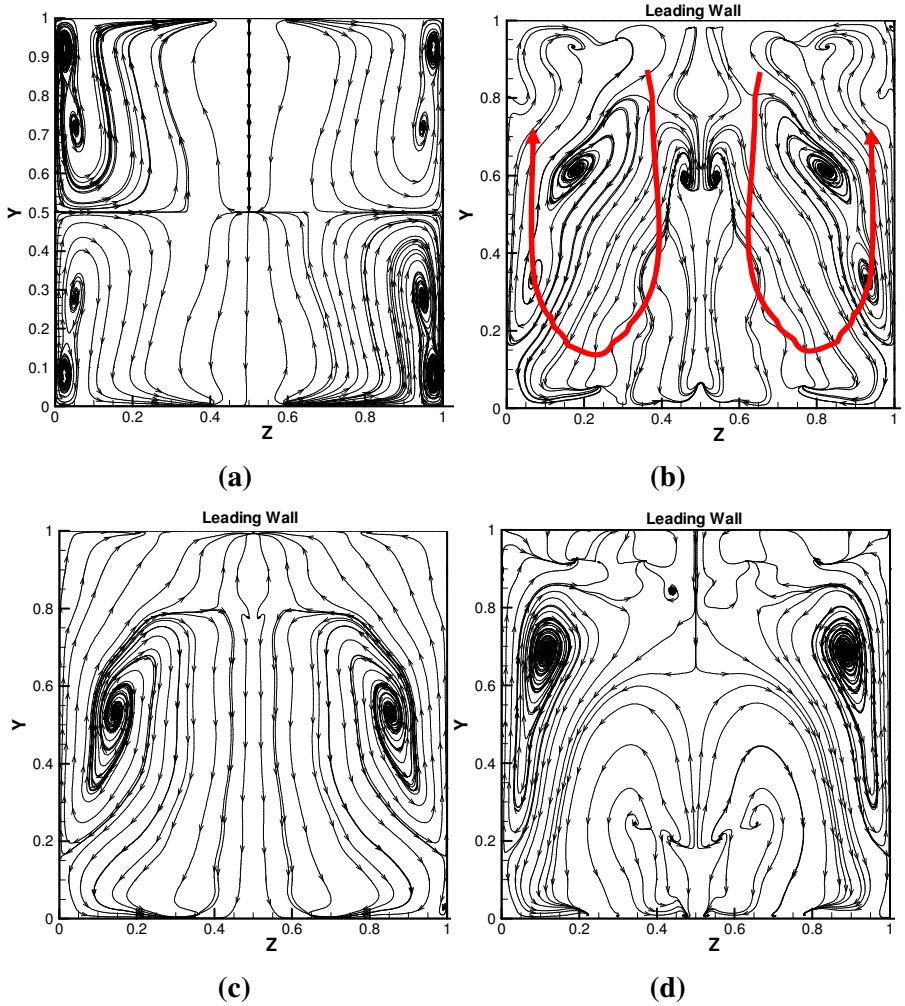

Figure 12: Streamlines showing the secondary flow in the center of the inter-rib space for (a) Ro = 0.0 (b) Ro = 0.18 (c) Ro = 0.35 (d) Ro = 0.67 as predicted by DES SST: Arrows show the effect of rotation on the flow

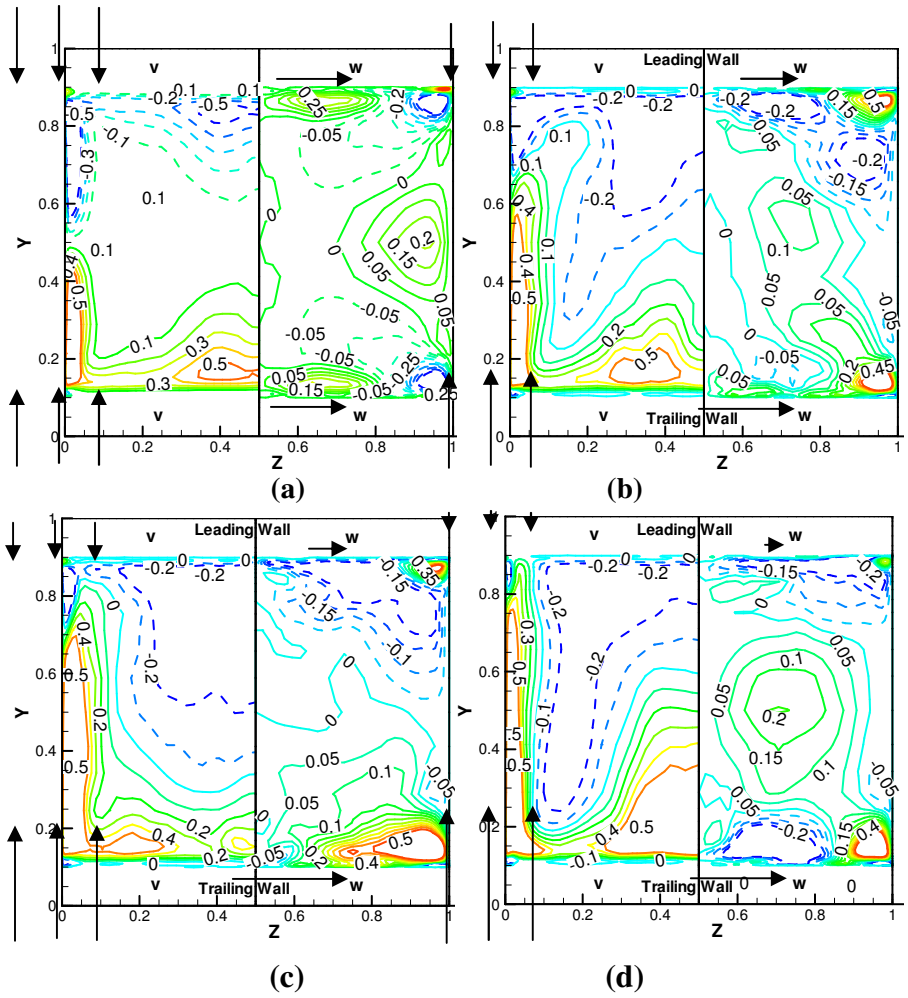

Figure 13: Secondary flow contours on the rib for (a) Ro = 0.0 (b) Ro = 0.18 (c) Ro = 0.35 (d) Ro = 0.67 as predicted by DES SST. The contours show the effect of rotation on the secondary flow in the cross-section. The arrows qualitatively represent the effect of rotation on the magnitude of the *v*- and *w*- velocities.

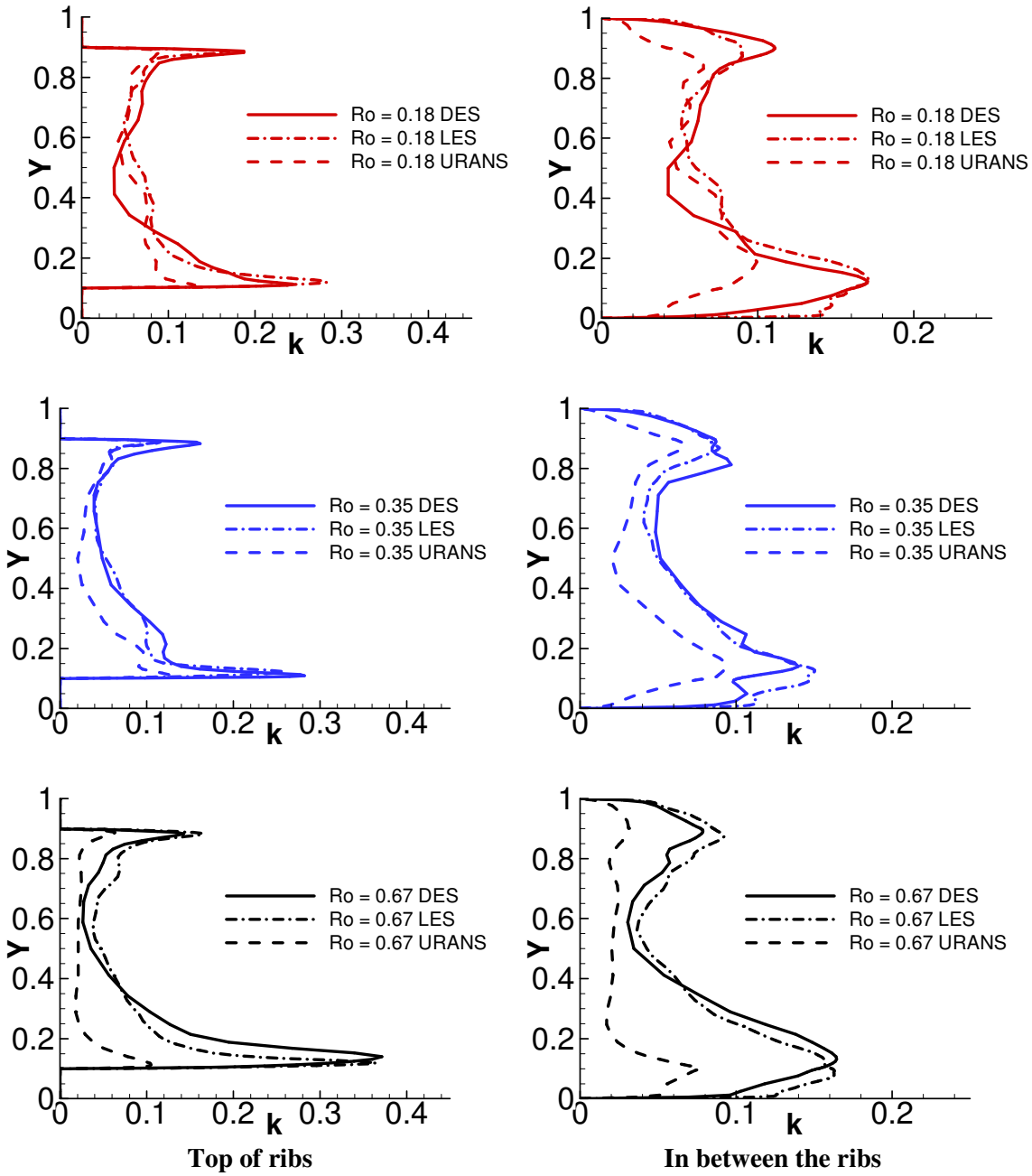

Figure 14: TKE values as predicted by the DES, LES and the URANS cases for the three rotation cases on top of the ribs and in between the ribs

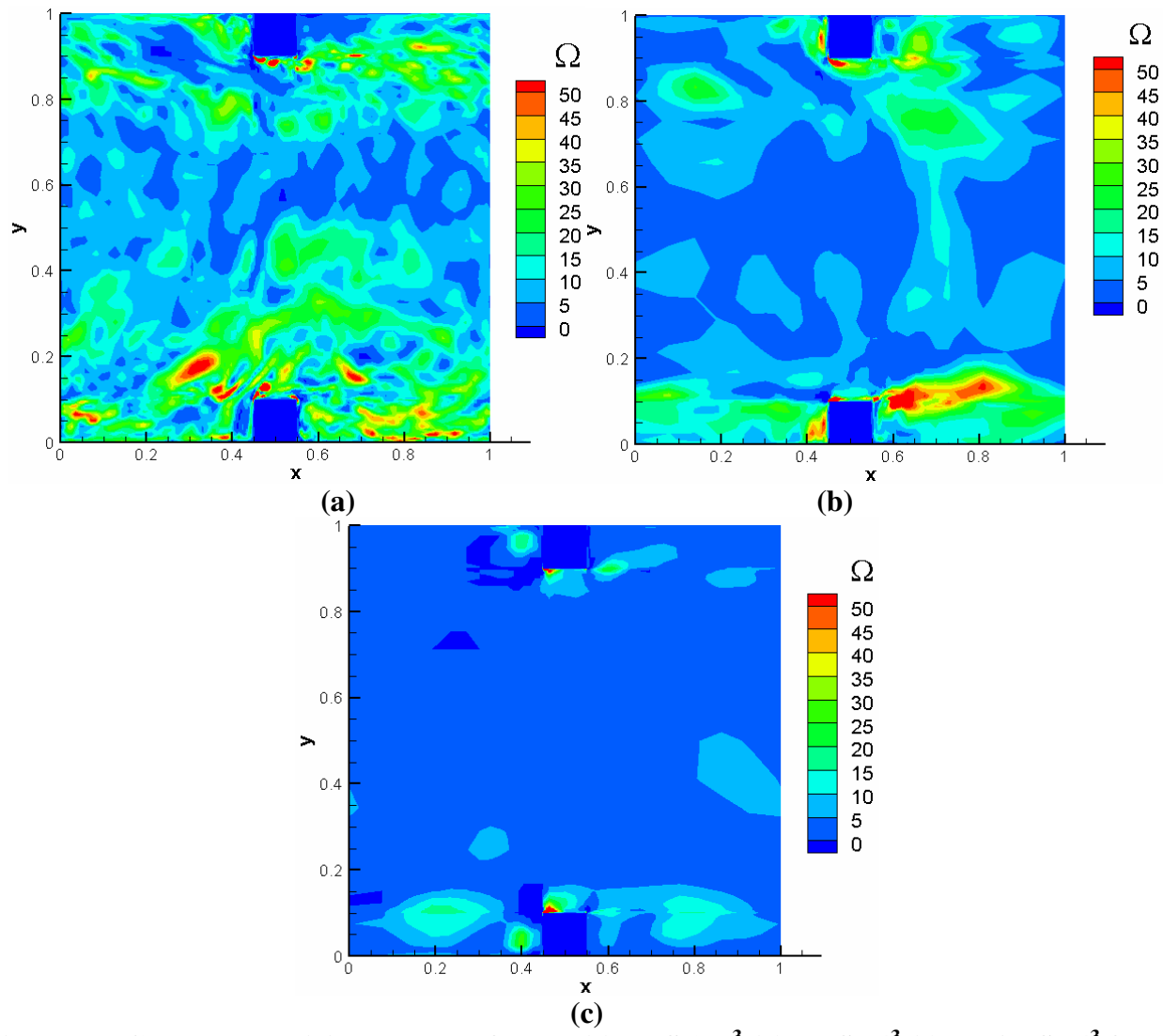

Figure 15: Coherent vorticity contours for the (a) LES 128^3 (b) DES 64^3 (c) URANS 64^3 for Ro = 0.35 show the scales resolved of the three schemes.

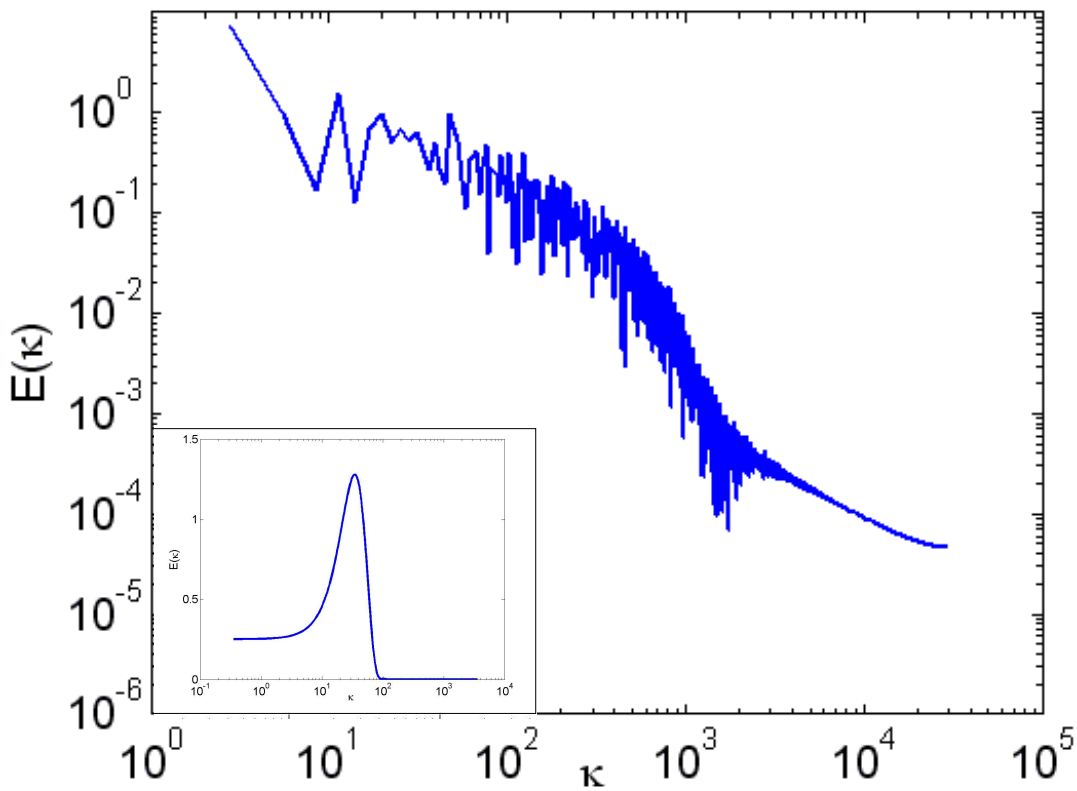

Figure 16: Power spectral density at the leading wall for Ro = 0.35. The insert shows the equivalent semi-log scale representation, which is used to compare the relative magnitudes of the first mode of dominant frequency for the LES, DES and URANS cases.

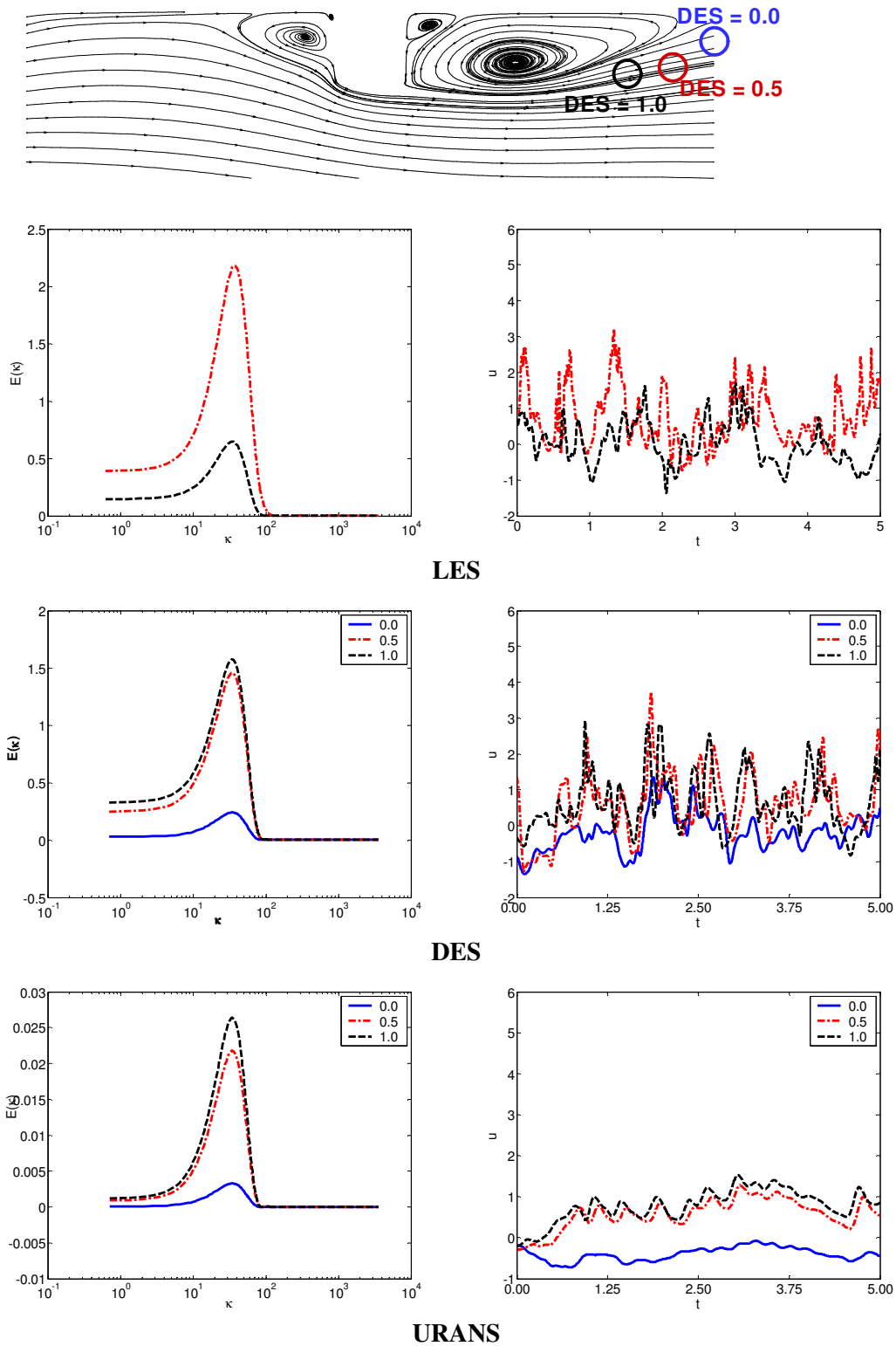

Figure 17: Turbulence spectrum and the signal sampled for 5.0 non-dimensional time units at the leading wall for Ro = 0.35

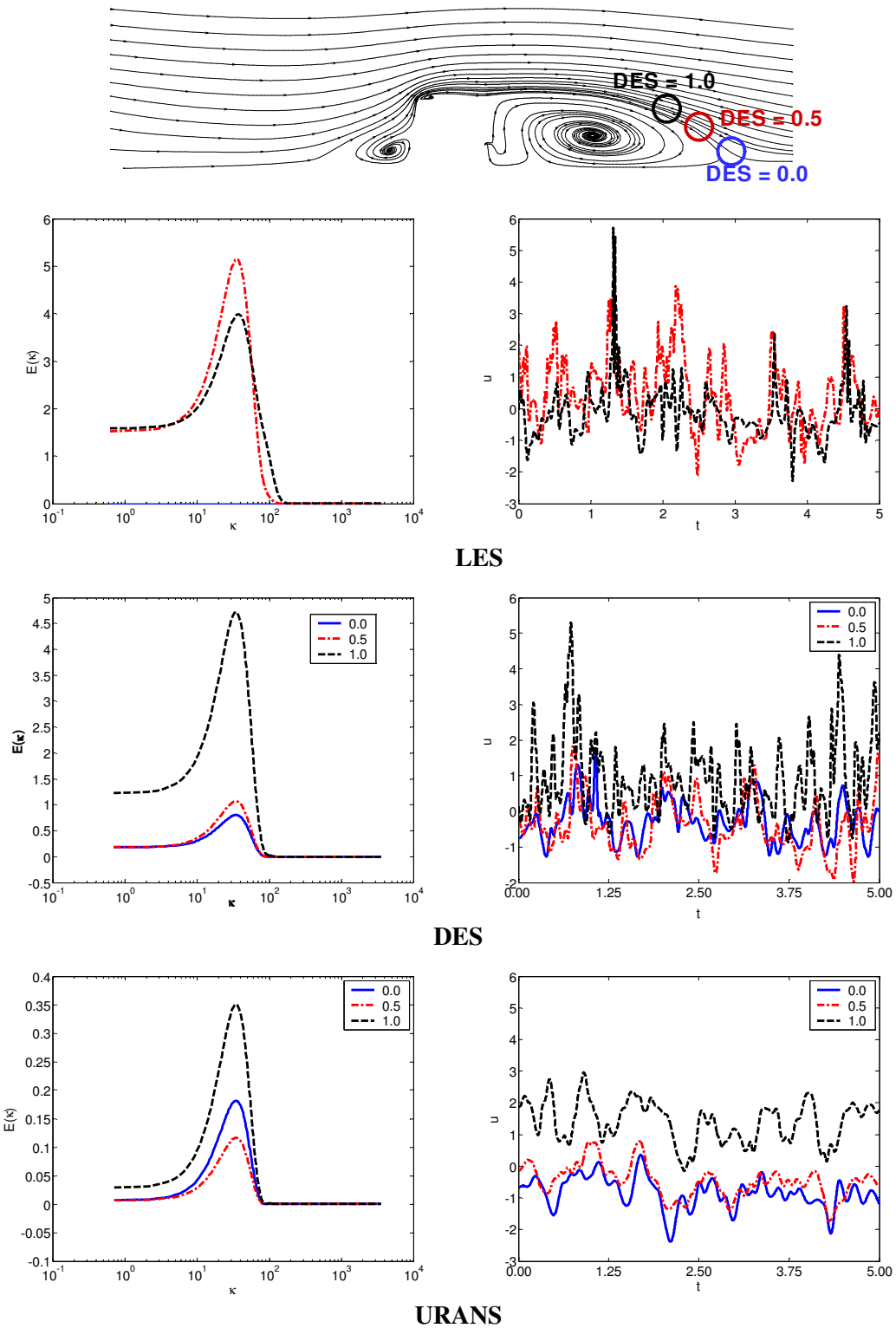

Figure 18: Turbulence spectrum and the signal sampled for 5.0 non-dimensional time units at the trailing wall for Ro = 0.35.

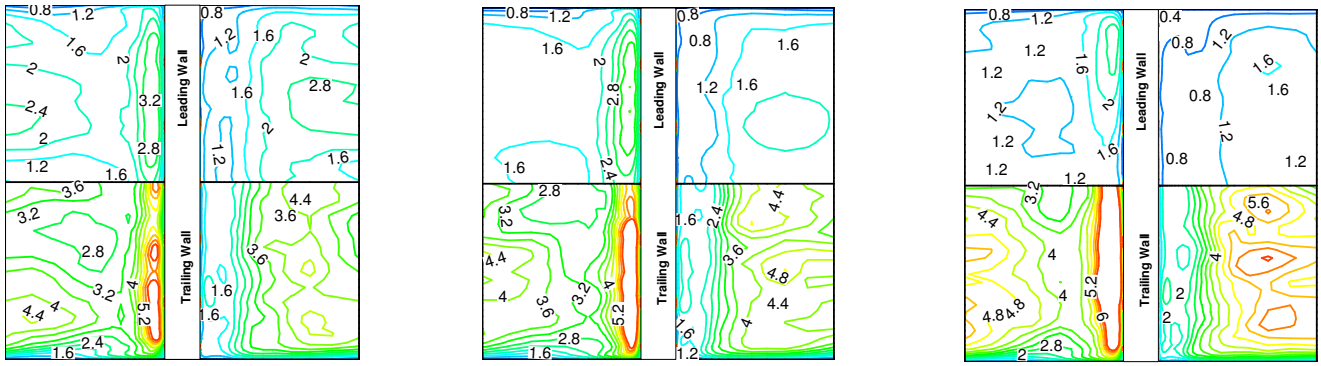

(a) (b) (c)

Figure 19: Heat transfer augmentation (Nu/Nu_0) predicted at the leading and the trailing walls by DES SST for (a) Ro = 0.18 (b) Ro = 0.35 (c) Ro = 0.67. Flow direction is from left to right.

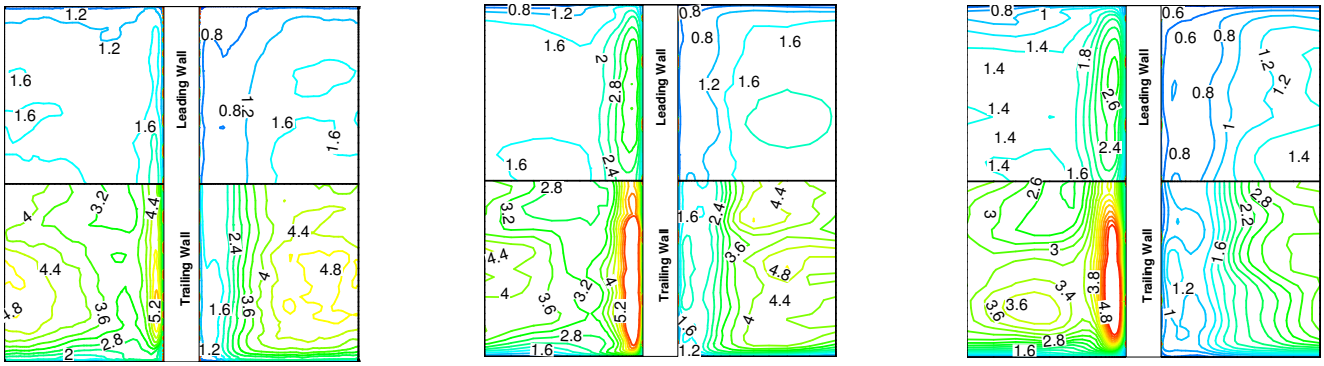

(a) (b) (c)

Figure 20: Heat transfer augmentation (Nu/Nu_0) predicted at the leading and the trailing walls for the Ro = 0.35 case by (a) LES (b) DES SST(c) URANS SST. Flow direction is from left to right.

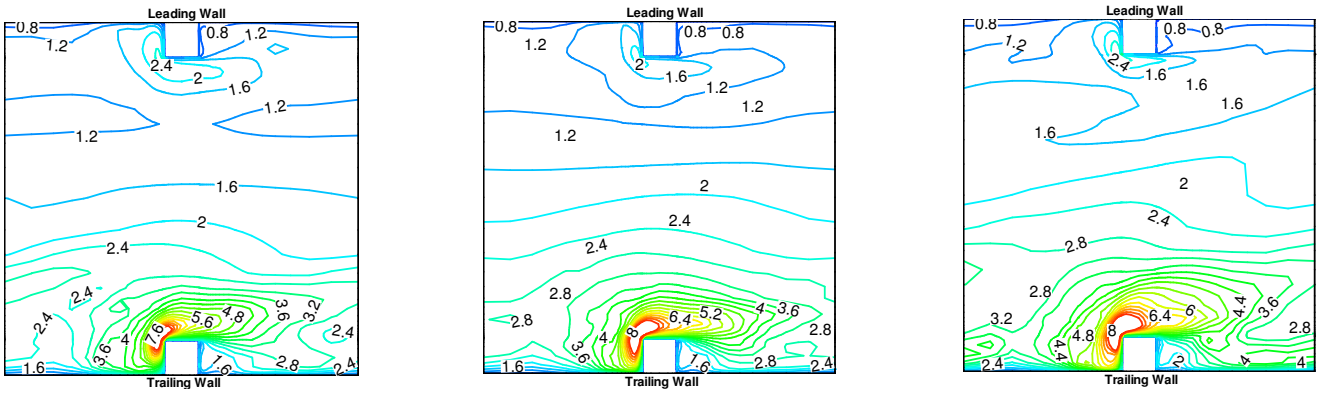

(a) (b) (c)

Figure 21: Heat transfer augmentation (Nu/Nu_0) predicted at the side wall by DES SST for the (a) Ro = 0.18 (b) Ro = 0.35 (c) Ro = 0.67. Flow direction is from left to right.

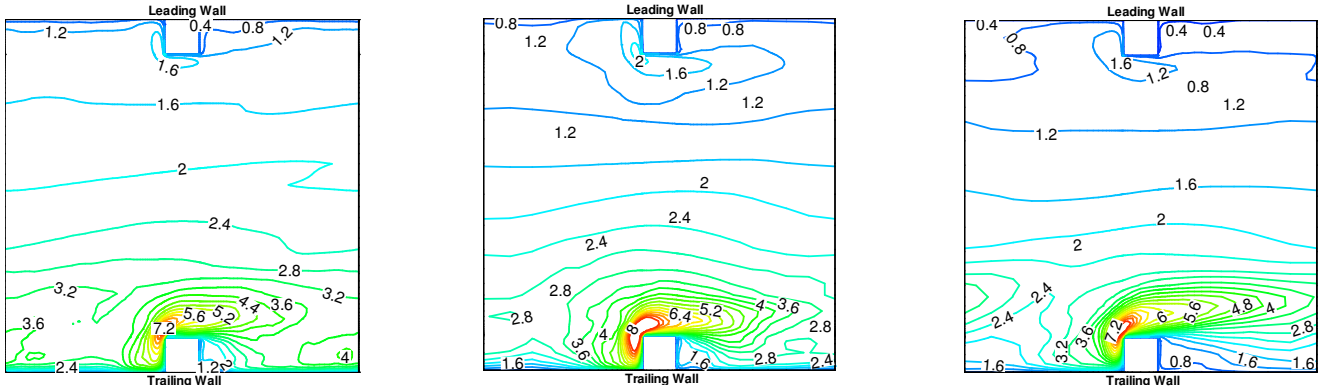

(a) (b) (c)

Figure 22: Heat transfer augmentation (Nu/Nu_0) predicted at the side wall for the Ro = 0.35 case by (a) LES (b) DES SST(c) URANS SST. Flow direction is from left to right.

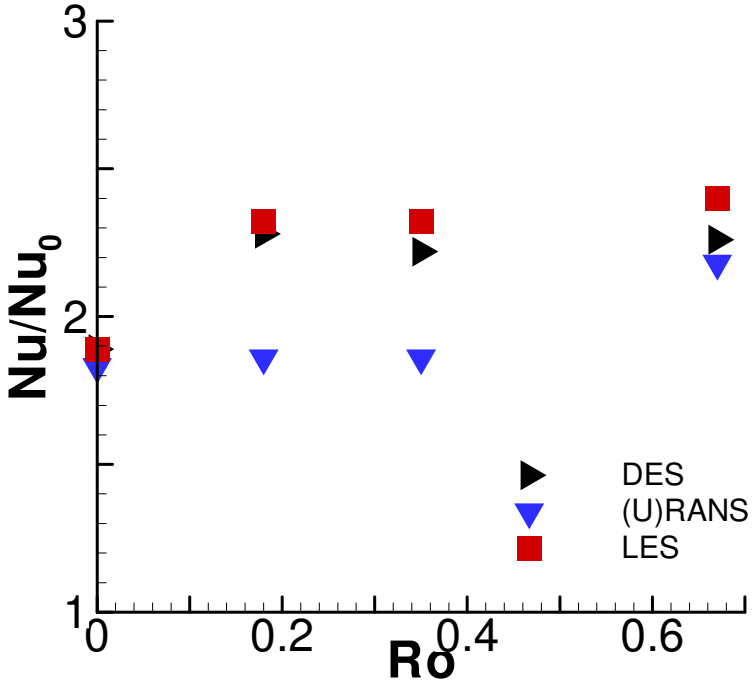

Figure 23: Side wall heat transfer predicted by LES, DES and URANS for the various rotation cases.

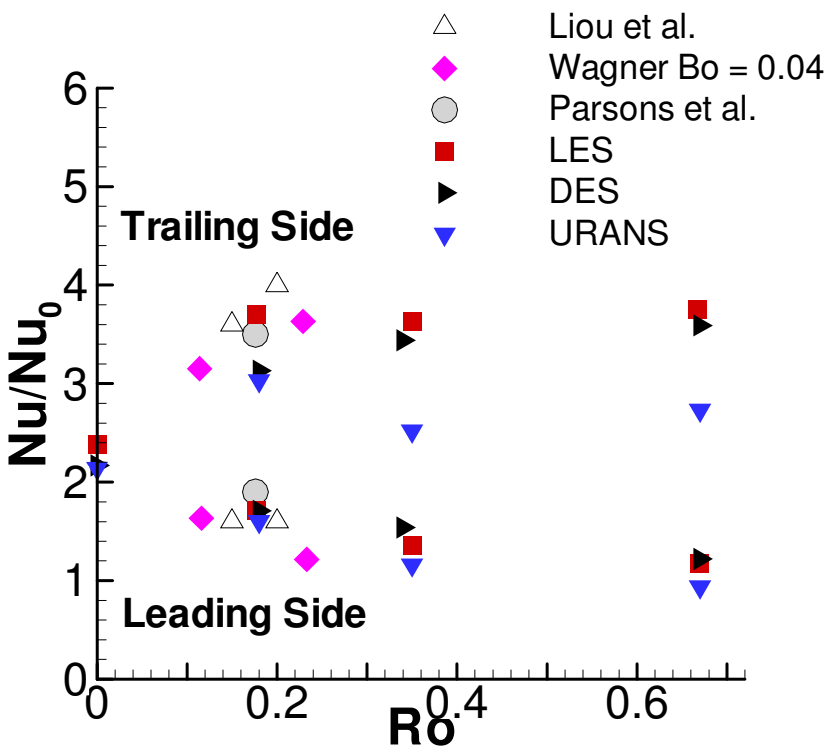

Figure 24: Comparison of average Nusselt number augmentation ratios at the leading and trailing sides with experiments.

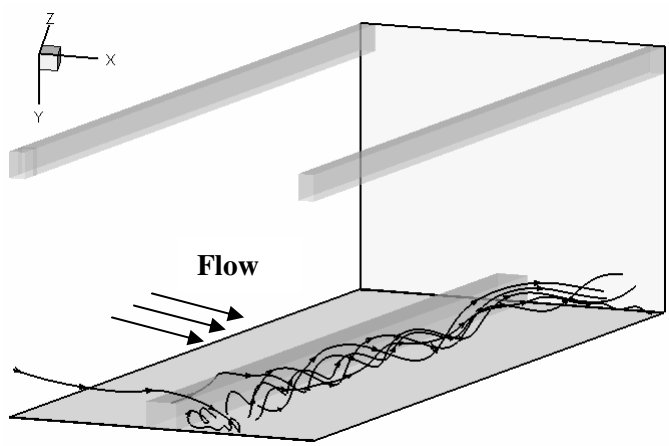

Figure 25: Flow predicted by LES on a 160 x 128 x 128 grid for the stationary duct

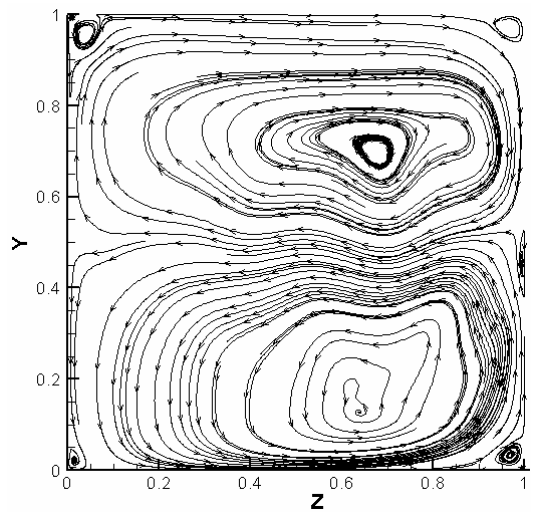

Figure 26: Comparison of the secondary flow in the duct for Ro = 0.0.

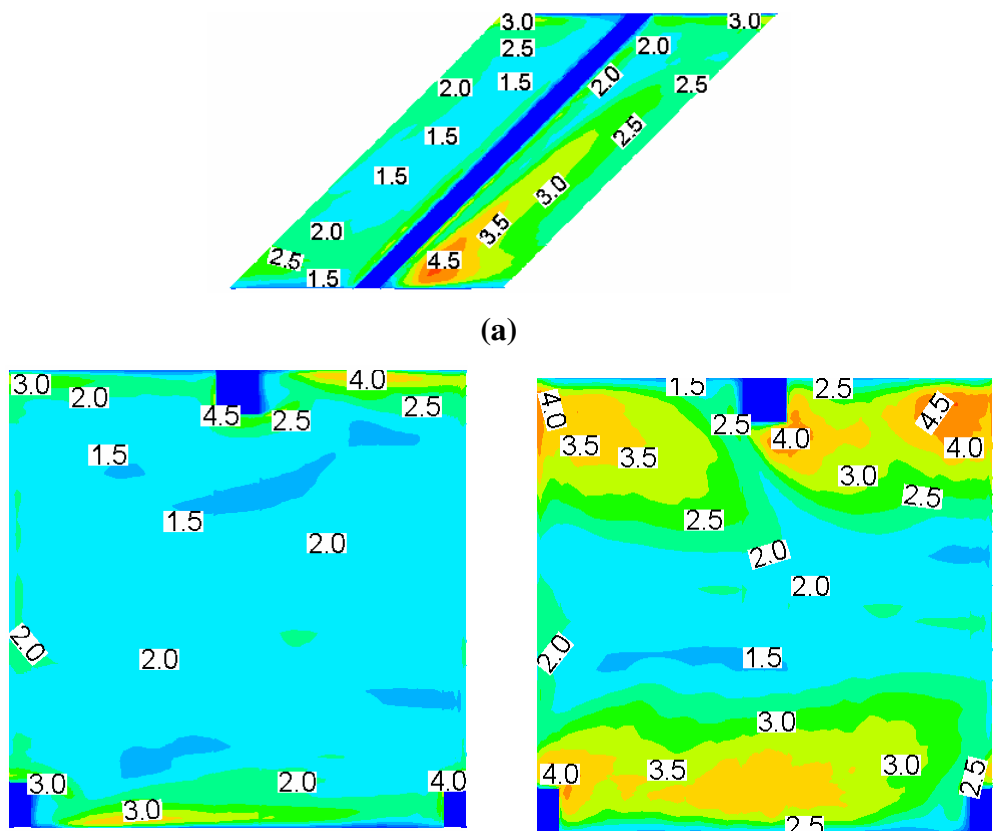

Figure 27: Heat transfer augmentation at (a) Ribbed Wall (b) Inner Wall (c) Outer Wall

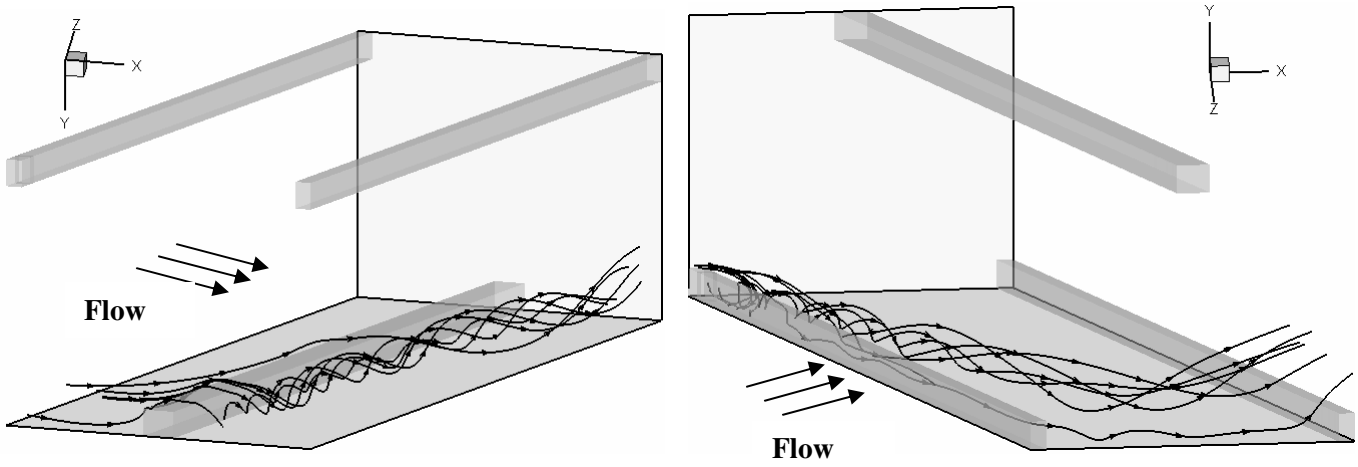

(a) **(b)**

Figure 28: Flow as predicted by LES on a 160 x 128 x 128 grid. (a) Leading and outer walls (b) Trailing and inner walls.

Leading side

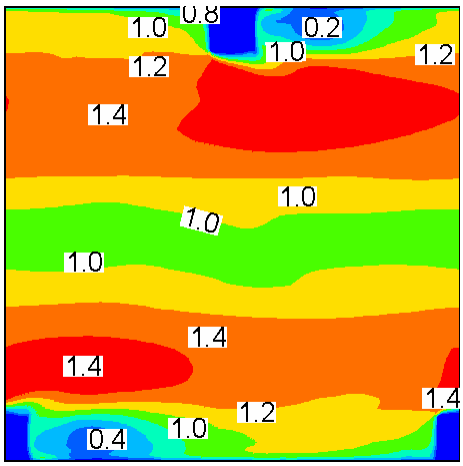

Trailing side

STATIONARY

Leading side

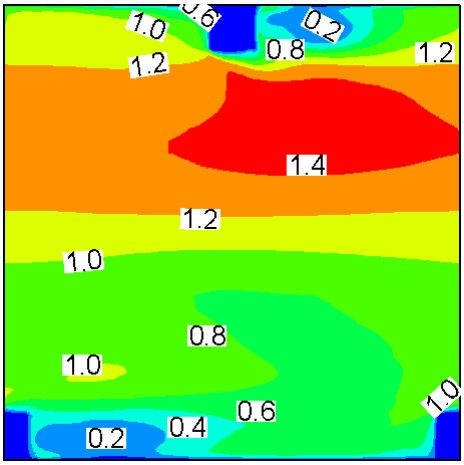

Trailing side

ROTATING

Figure 29: Comparison of the *u*-velocities for the stationary and the rotating cases. The single full rib is on the leading side while the two half ribs are on the trailing side.

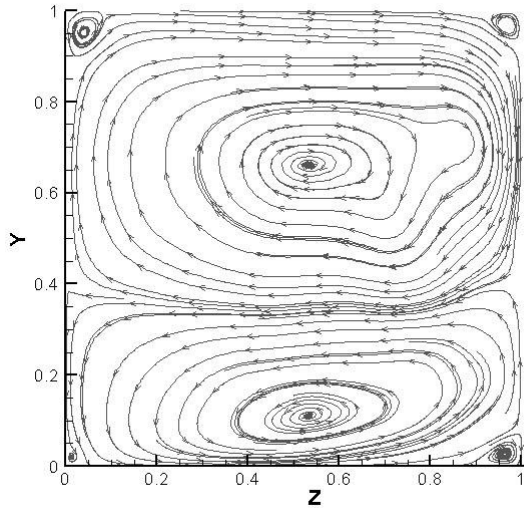

Figure 30: Comparison of the secondary flow in the duct, Ro = 0.1. Y = 0.0 corresponds to the trailing wall and Y = 1.0 corresponds to the leading wall.

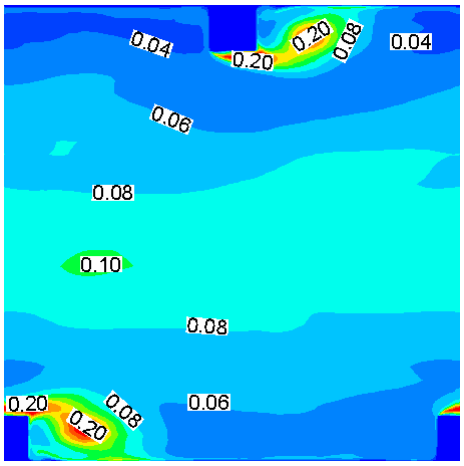

z = 0.25, Ro = 0.0

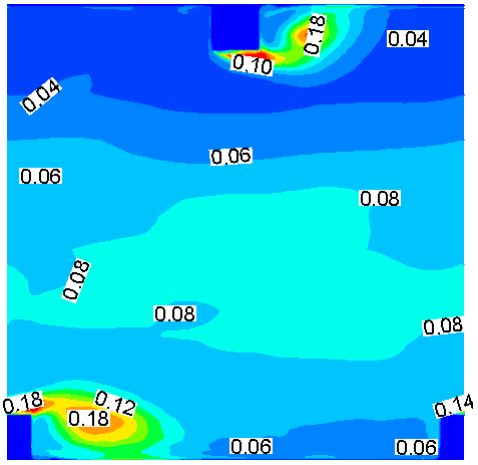

z = 0.25, Ro = 0.1

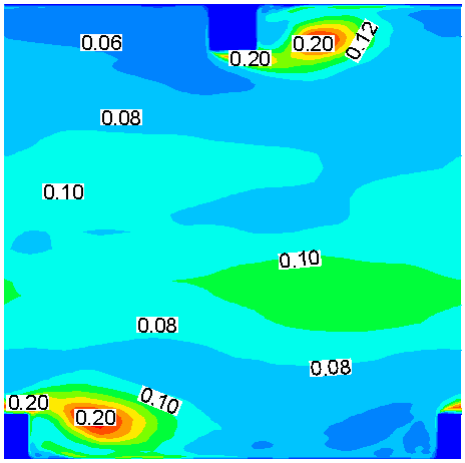

z = 0.50, Ro = 0.0

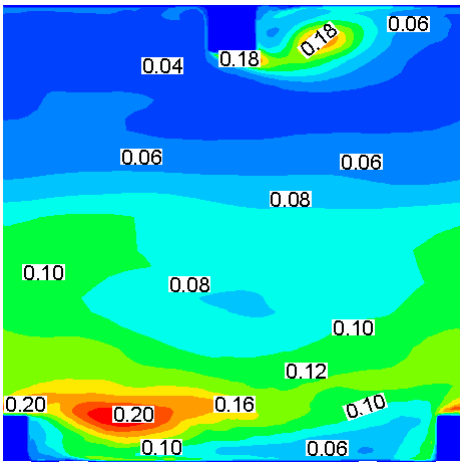

z = 0.50, Ro = 0.1

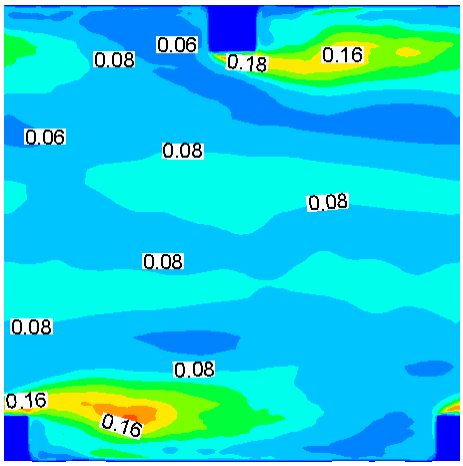

z = 0.75, Ro = 0.0

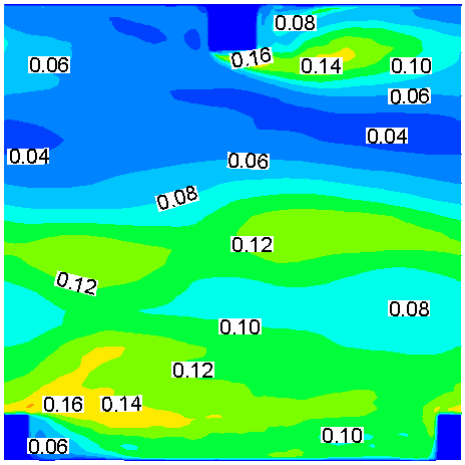

z = 0.75, Ro = 0.1

Figure 31: Comparison of the turbulent kinetic energies at three different planes along the span of the duct for the stationary and the rotating cases. The two half ribs are on the trailing wall and the full rib is on the leading wall.

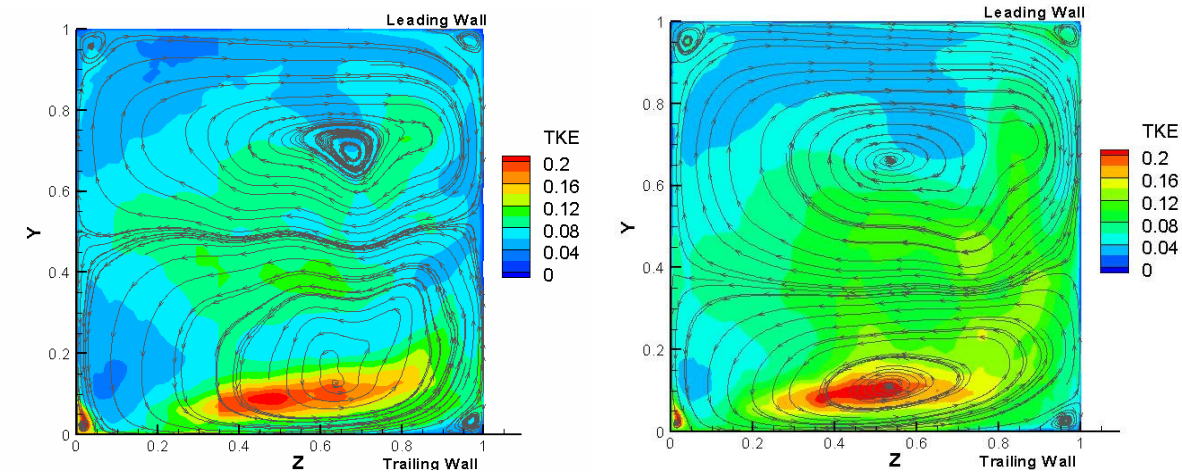

(a) **(b)**

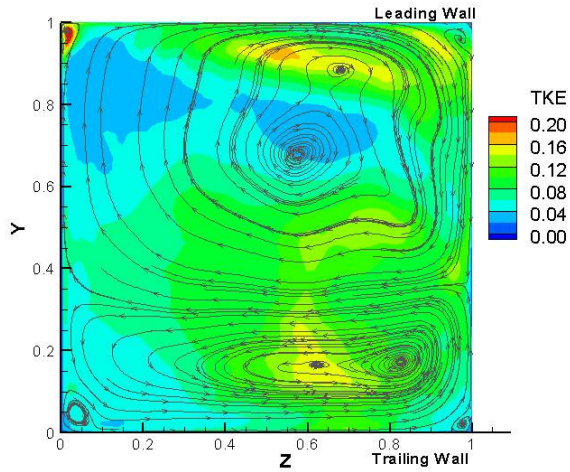

(c)

Figure 32: Comparison of the turbulent kinetic energies for (a) Ro = 0.0, 0.25D_h from the rib (b) Ro = 0.1, 0.25D_h downstream of the rib on trailing side (c) Ro = 0.1, 0.25D_h downstream of the rib on leading side.

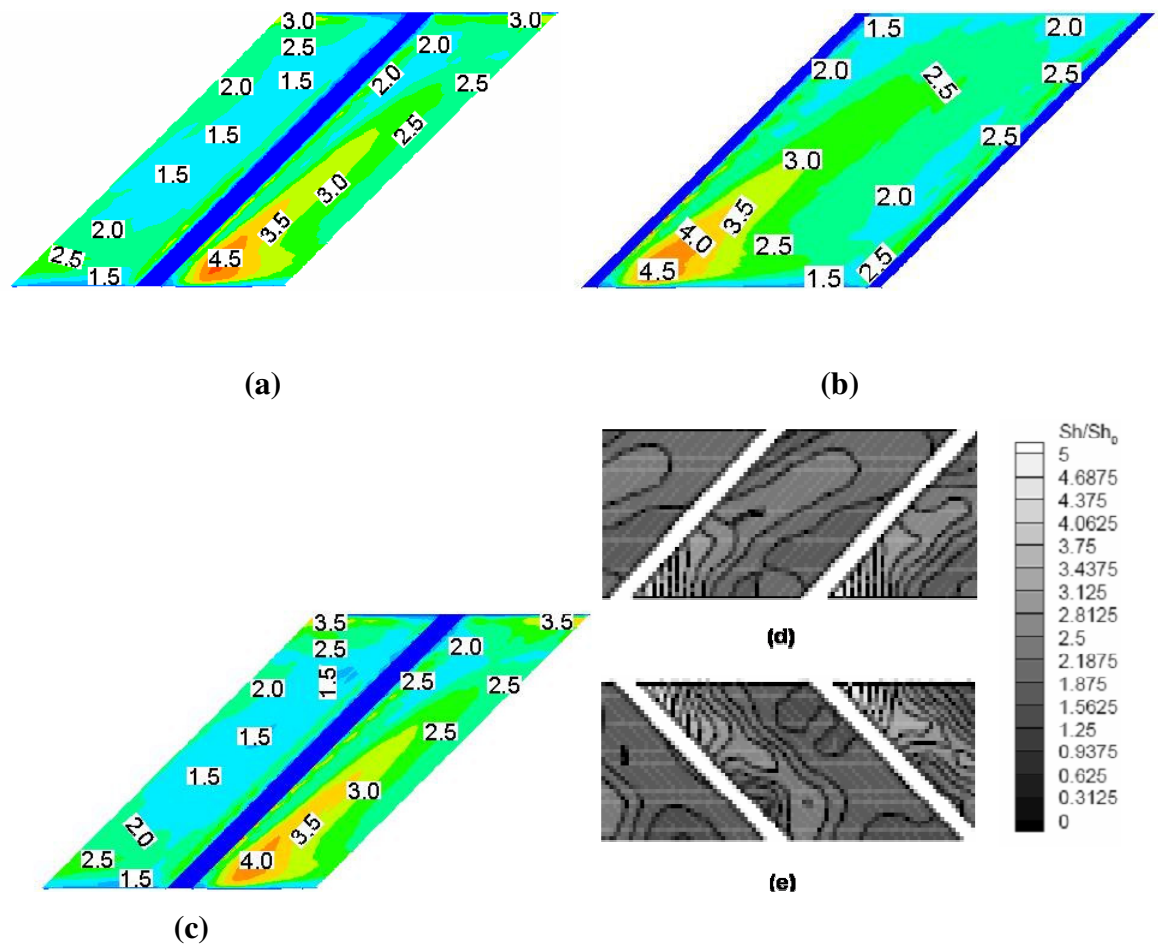

Figure 33: Comparison of the heat transfer augmentations at the ribbed walls (a) Ro = 0.0 (b) Ro = 0.1, Trailing Wall (c) Ro = 0.1, Leading Wall (d) Mass transfer augmentation Rathjen *et al.,* [87], Ro = 0.1, Trailing side (e) Rathjen *et al.,* [87], Leading side.

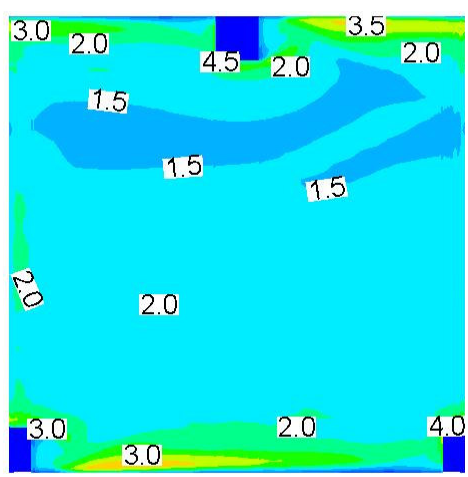

Figure 34: Heat transfer augmentation ratios at the inner wall for the rotating case

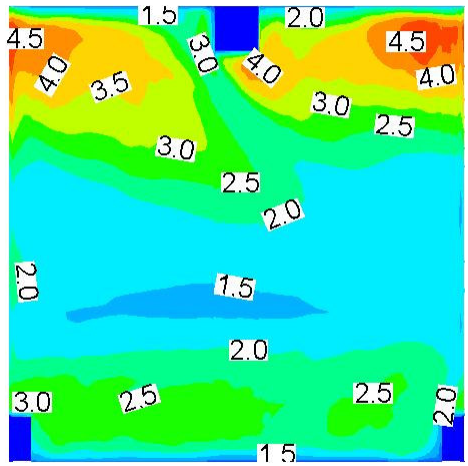

Figure 35: Comparison of the heat transfer augmentation ratios at the outer wall for the rotating case

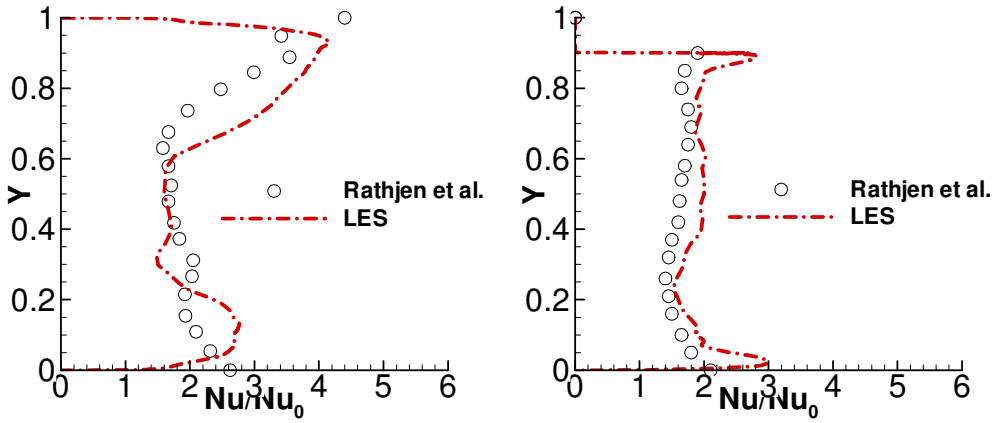

Figure 36: Comparison of the heat transfer augmentation predicted by LES with the mass transfer augmentation measured by the experiments (a) Outer Wall (b) Inner Wall

Mechanism-Based Testing Methodology For Improving the Oxidation, Hot Corrosion and Impact Resistance of High-Temperature Coatings for Advanced Gas Turbines

Final Report
30 November, 2005

Principal Investigators:
Frederick S. Pettit (pettit@engr.pitt.edu)
Gerald H. Meier (ghmeier@engr.pitt.edu)

Report Date: 31 May, 2005

DOE Award: DE-FC26-02NT41431
UTSR Project: 02-01-SR101

Submitted by:
Department of Materials Science & Engineering
848 Benedum Hall
University of Pittsburgh
Pittsburgh, PA 15261

Subcontract Information:
Department of Mechanical Engineering
Carnegie Mellon University
5000 Forbes Avenue
Pittsburgh, PA 15213-3890
Jack L. Beuth (beuth@andrew.cmu.edu)

DISCLAIMER This report was prepared as an account of work sponsored by an agency of the United States Government. Neither the United States Government nor any agency thereof, nor any of their employees, makes any warranty, express or implied, or assumes any legal liability or responsibility for the accuracy, completeness, or usefulness of any information, apparatus, product, or process disclosed, or represents that its use would not infringe privately owned rights. Reference herein to any specific commercial product, process, or service by trade name, trademark, manufacturer, or otherwise does not necessarily constitute or imply its endorsement, recommendation, or favoring by the United States Government or any agency thereof. The views and opinions of authors expressed herein do not necessarily state or reflect those of the United States Government or any agency thereof.

ABSTRACT
This project comprises a collaborative University/National Laboratory/Industry effort to develop a mechanism-based testing methodology for improving the oxidation resistance of high temperature metallic coatings and TBCs. This testing methodology involves a significant number of nondestructive tests directed at assessing coatings degradation and damage accumulation. The test results are being used in an attempt to develop a life prediction protocol. The work on the project has been detailed in six semi-annual reports. This document is the final report of this effort.

TABLE OF CONTENTS

	Page
Title Page	1
Disclaimer	2
Abstract	3
Table of Contents	4
List of Graphical Materials	5
Introduction	6
Executive Summary	11
Project Description	13
Experimental	15
Results and Discussion	22
References	23

LIST OF GRAPHICAL MATERIALS

Figure 1. Schematic diagram of oxide only and TBC systems.

Figure 2. Effect of Temperature on the Failure Time of Two TBC types.

Figure 3. Optical Micrograph of the Debonded Portions of an Indented TBC Specimen, as Viewed from Above.

Figure 4. Plot of Apparent Toughness Loss (Assuming no Changes in TBC System Properties) vs. Isothermal Exposure Time.

Figure 5 Arrhenius plot for various levels of apparent toughness.

Figure 6. Schematic diagram of the indentation test.

Figure 7. Acoustic Emission Testing Apparatus.

Figure 8. Graphical representation of important parameters in the COSP model.

INTRODUCTION

The primary goal of this research is to advance accelerated testing methods for cyclic oxidation and hot corrosion tests of interest to the gas turbine and coating manufacturing industries. Emphasis is on the study of fundamental mechanisms controlling coating degradation and correlating these mechanisms with standard and accelerated tests. The mechanisms of cyclic oxidation are being systematically studied via imaging of oxide and interface structures, mechanics models of interface decohesion, and stress and toughness measurements of coating systems as a function of exposure. The PIs are working closely with National Laboratories in conducting the research and with industrial collaborators to transition their findings to the coating and gas turbine industries, where the current standard is to perform time and cost-intensive burner rig tests to quantify coating durability.

The focus of this project has been on developing techniques for accelerated cyclic oxidation testing and measuring the fundamental properties of coatings systems that control oxide adherence. The systems studied consist of alumina scales grown on nickel-base superalloy substrates, coated superalloys, and analogous thermal barrier coating (TBC) systems that contain an alumina scale. Both types of coating systems typically include an oxidation-resistant bond coat, which is deposited onto the superalloy substrate.

The adherence of protective oxides to the coatings considered in this project is governed by the stored elastic energy in the oxide, which drives delamination, and the fracture resistance of the alloy/oxide interface as illustrated schematically in Figure 1.

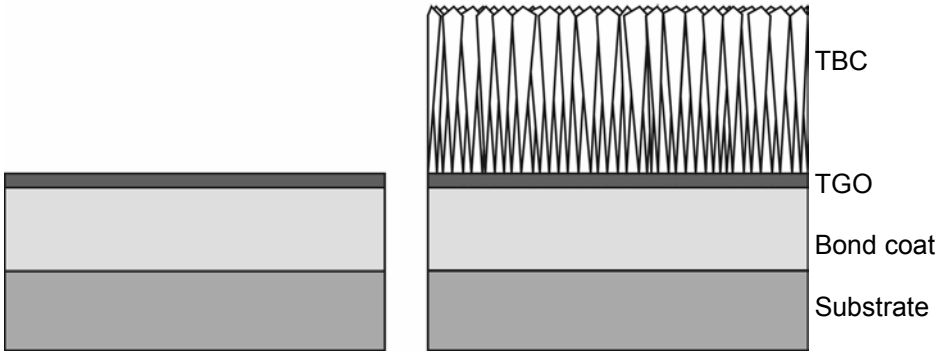

Figure 1. Schematic diagram of oxide only and TBC systems.

Clearly, any modifications to the alloy substrate or the exposure environment which decreases the former or increases the latter will improve the durability of a given system. The stored elastic energy is determined by the stress level in the oxide and the oxide thickness. The stress state in an oxide scale is determined by stresses which arise during the oxide formation (*Growth Stresses*), stresses produced during temperature changes as the result of thermal expansion mismatch between the oxide and the alloy (*Thermal Stresses*), and any stress relaxation which occurs as the result of creep of the scale or alloy. In systems that include a TBC, elastic energy is also stored in the TBC layer. Stresses in the TBC are purely thermal stresses, but their magnitude can be a strong function of the density of the TBC, which can change with high temperature exposure.

The fracture energy of the interface (i.e. TGO/bond coat or TBC/TGO interfaces) is a function of the composition at the interface, the microstructure in the interfacial region, and the composition of the exposure environment.

Previous research by the PIs has included

a. Measurement of Times to Failure of Oxidation-resistant Coatings and Thermal Barrier Coatings as a Function of Temperature

b. Measurement of Interface Fracture Toughness Using an Indentation Test and Arrhenius Analysis of Indent Test Results

This research is described in more detail in the following:

a. <u>Measurement of Times to Failure of Thermal Barrier Coatings as a Function of Temperature</u>

The study of measured times to failure of thermal barrier coatings (TBCs) in cyclic oxidation tests has indicated that the rate of failure follows an exponential dependence on the exposure temperature. Typical results are shown in Figure 2 for TBCs

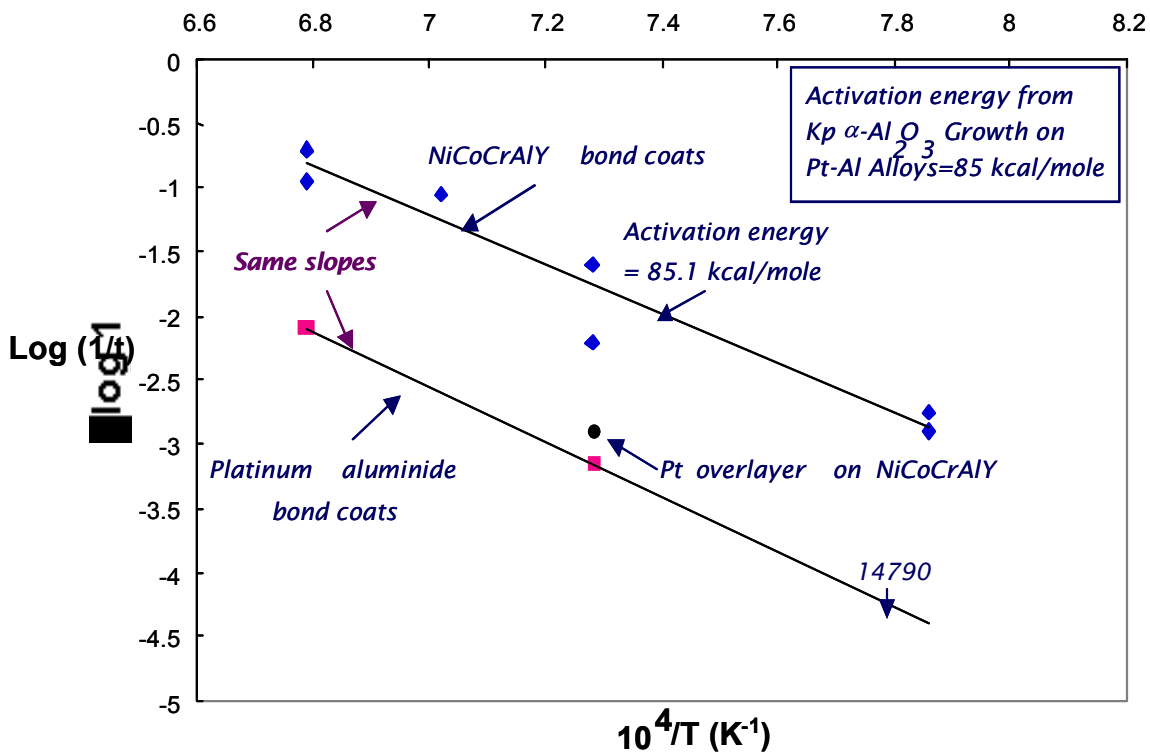

Figure 2. Effect of Temperature on the Failure Time of Two TBC types.

with two different bond coats. This Arrhenius behavior can form the basis for using relatively high temperature tests and extrapolating the results to lower temperatures where the failure times might be too long to reasonably study in the laboratory.

The exponential relationship between failure time and exposure temperature observed by the PIs also suggests that a single set of thermally activated mechanisms may govern TBC failure over a wide range of exposure temperatures. Fracture toughness testing (an indentation test described below), imaging of oxide and interface structures, oxide stress measurements and acoustic emission measurements are being used to search for additional evidence of a dominant failure mechanism for these systems.

b. Measurement of Interface Fracture Toughness using an Indentation Test: Accelerated Testing via Mechanical Loading

In a previous project, the PIs have developed indentation testing methods for quantifying changes in interfacial toughness in TBC systems as a function of thermal exposures. The indentation test produces spallation in oxide and TBC systems at times much shorter than those required for spontaneous failure. *Thus inducing spallation at early times (via indentation) has emerged as one means for accelerating the evaluation of coating system durability due to high temperature exposures.*

The test consists of indenting the TBC system with a Brale type conical indenter (a Rockwell hardness tester or mechanical testing machine can be used for this purpose). The indenter penetrates the TBC and oxide layers and plastically deforms the metallic bond coat and substrate below. As illustrated in Figure 3(as viewed from above), this induces an axisymmetric debond of the TBC and oxide layers. Systems with poor adhesion between the oxide and bond coat show large debond radii. Systems with good adhesion will show small debond radii or no debonding at all.

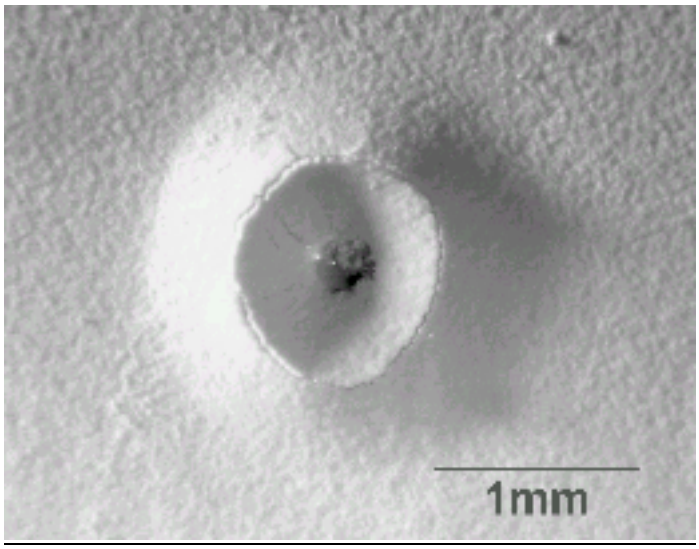

Figure 3. Optical Micrograph of the Debonded Portions of an Indented TBC Specimen, as Viewed from Above.

Fracture mechanics analyses of the indentation test have been performed to allow determination of an interfacial toughness (a value of critical stress intensity factor, K_c, or

critical energy release rate, G_c) for the interface between the oxide and bond coat layers, based on a measured debond radius.

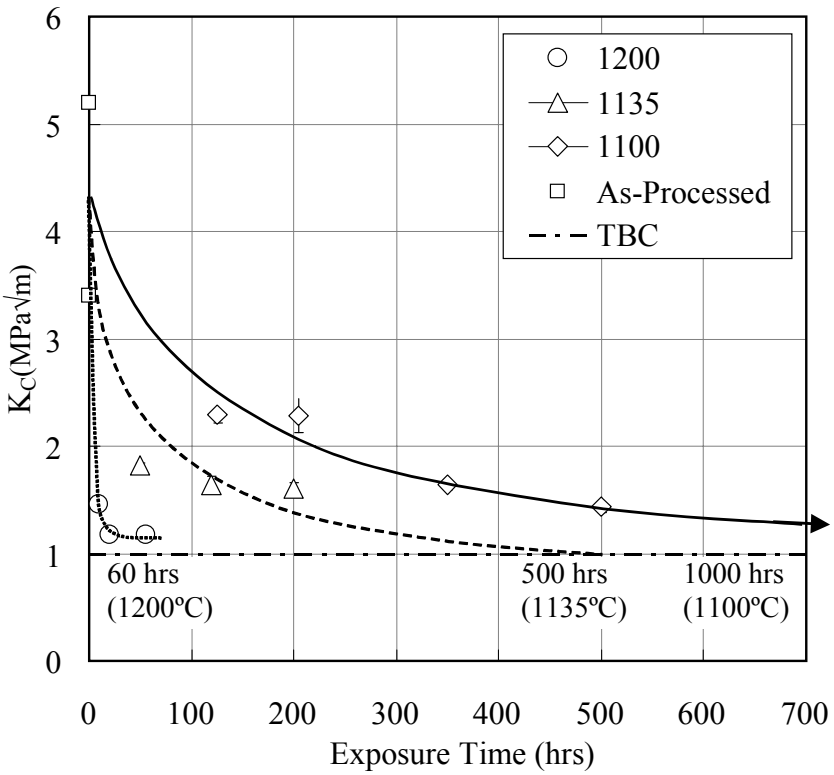

Figure 4. Plot of Apparent Toughness Loss (Assuming no Changes in TBC System Properties) vs. Isothermal Exposure Time.

This test allows tracking of toughness changes in TBC systems as a function of thermal exposures, including the ability to perform many indentations on a single specimen, as its exposure times are increased. For example, Figure 4 shows a plot of "apparent" losses of interfacial toughness for EBPVD TBC/PtAl bond coat systems exposed to 1200°C, 1135°C and 1100°C isothermal exposures in lab air, as determined by room temperature indent tests. (Note that there is some variability in the toughness for as-processed specimens.) The times of 60, 500 and 1000 hrs are approximate times to spontaneous spallation at temperatures of 1200°C, 1135°C and 1100°C, respectively. At such times, the interfacial fracture toughness matches the applied stress intensity factor due to thermal strains alone, which is approximately equal to 1 $MPam^{1/2}$. This is the first data of this type available for TBC systems and it indicates that substantial toughness loss occurs at a fraction of the time needed for spontaneous failure to occur. Because early toughness losses are correlated with TBC system life, measurement of toughness losses for short exposure times can be the basis of accelerated durability tests.

The data plotted in Figure. 4 assumes constant, as-processed properties of the TBC, system, not accounting for the effects of oxide growth, TBC density increases due to sintering or any other adhesion-reducing changes in the TBC system that may be independent of a true degradation of the oxide/bond coat interface. Because non-interfacial changes in the TBC system can result in a measured reduction in toughness, these are referred to as "apparent" losses of toughness.

Arrhenius Analysis of Indent Test Results: Accelerated Testing via Higher Temperatures

To gain further insight into the mechanisms leading to TBC system oxide/bond coat interfacial adhesion loss, the results presented in Figure 4 have been re-cast in the form of an Arrhenius plot. Figure 5 gives a plot of ln(1/time) vs. 1/Temperature, where the "time" variable is the time to reach a specified value of apparent interfacial toughness. In other words, a single line in Figure 5 is determined by drawing a horizontal line across the plot of Figure 4, at values of K_c = 2.5, 2.0, 1.5 or 1.0 $MPam^{1/2}$, and determining intersection points with test data at 1200°C, 1135°C and 1100°C. Data plotted for a K_c value of 1.0 $MPam^{1/2}$ denote times required to experience spontaneous spallation.

It is clear from Figure 5 that the slopes of the plotted lines for each K_c value are approximately the same (the slopes for K_c = 2.5, 2.0, and 1.5 are equal and the slope for K_c = 1.0 is a factor of 0.81 of the slopes for the other K_cs). Thus, the thermally activated mechanisms that lead to apparent toughness loss appear to be the same as those leading to spontaneous spallation (final failure). As a result, as suggested in the previous section, use of an indentation test to obtain measured toughness losses at early exposure times appears to be a valid means of gaining information on TBC system durability without having to perform long-term tests to failure.

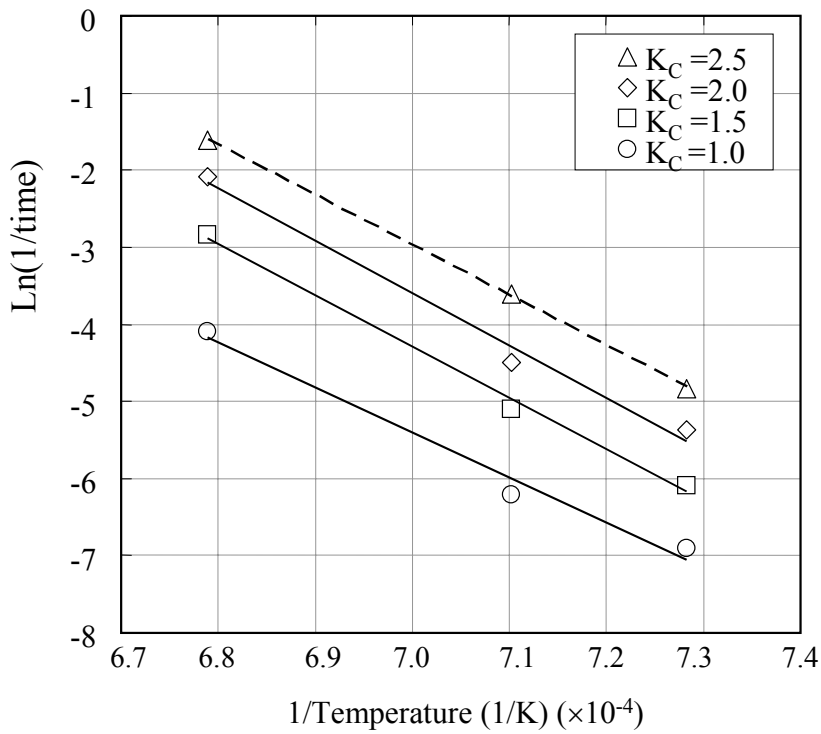

Figure 5 Arrhenius plot for various levels of apparent toughness.

EXECUTIVE SUMMARY

This project comprises a collaborative University/National Laboratory/Industry effort to develop a mechanism-based testing methodology for improving the oxidation resistance of high temperature metallic coatings and TBCs. This testing methodology involves a number of nondestructive tests directed at assessing coating degradation and damage accumulation. The ultimate goal is to use such tests as part of newly developed life prediction protocols.

The project team members and their areas of responsibility were as follows. Professors Pettit and Meier of the University of Pittsburgh led the effort and performed corrosion studies and acoustic emission and x-ray diffraction experiments. Professor Beuth of CMU performed indentation tests of spallation resistance and fracture mechanics analyses. Dr. Michael Lance of ORNL performed piezospectroscopic stress measurements and Dr. William Ellingson of ANL perform optical backscatter experiments. Specimens were prepared by Praxair and Howmet. GE provid input on testing conditions for the various degradation modes.

The specific tasks are summarized in the following.

Task I: Processing Comparisons and Modifications
This Task was concerned with processing comparisons and modifications using state-of-the art-coatings. Specimens of bare René N5, René N5 coated with a straight aluminide and platinum-modified aluminide, and René N5 with an EBPVD TBC over a platinum-modified aluminide bond coat were studied. Specimens with NiCoCrAlY coatings were fabricated by low pressure plasma spraying and Argon-shrouded plasma spraying.

Task II: Compositional Modifications
This Task involveed compositional modifications of state of the-art coatings. Growth of a very pure and adherent alumina scale on these alloys was attempted.

Task III: TBC Selection and Fabrication
This Task consists of selection and preparation of one or more TBC systems for study in this project. Thermal barrier coatings with platinum aluminide and NiCoCrAlY bond coats were studied.

Task IV: Specimen Testing
This Task was concerned with cyclic oxidation and hot corrosion testing of the prepared specimens.

Cyclic oxidation experiments involved testing of a variety of alumina-forming alloys and coatings with and without EBPVD TBCs for times up to that causing failure. Apparatus for hot corrosion testing was constructed but the actual testing is being included as a part of a separate UTSR project begun at the University of Pittsburgh in August, 2004.

Task V: Nondestructive Evaluation of Coating Systems
This Task involved using a number of nondestructive techniques to attempt to determine the amount of degradation of exposed systems. Specimens of René N5 with platinum aluminide coatings were exposed and examined by x-ray diffraction (XRD) and piezospectroscopic measurements of the stress in the alumina scale and by optical backscatter measurements to detect scale damage. Specimens of René N5 with a platinum aluminde coating and a TBC were exposed over a range of cycles and have undergone piezospectroscopic and optical backscatter measurements. Substantial improvements were made in the XRD stress measurement technique . Recent information regarding an error in the published elastic constants for alumina have necessitated recalculation of previously-determined stresses.

Task VI: Destructive Evaluation of Coating Systems
This Task was directed at documenting the amount of degradation present in specimens using destructive techniques. The main technique employed was an indentation test for TBC system interfacial toughness developed under a previous DOE ATS grant. This technique was used to track the toughness of as-received TBCs and TBCs exposed to a wide range of thermal cycles. The use of the nondestructive techniques of SEM charging and optical backscatter to image the debond produced by indentation improved the accuracy of the toughness measurements.

Task VII: Definition of Effective Nondestructive Evaluation Procedures
This Task consisted of selecting those nondestructive techniques, which are most effective in describing degradation. As documented in previous semi-annual reports, for coating systems without TBCs, acoustic emission has proven to be an effective nondestructive test. For coating systems with TBCs subjected to cyclic loading, piezospectroscopy has emerged as an effective nondestructive test for tracking the evolution of mechanical damage below the TBC (leading to loss of TBC adhesion).

Task VIII: Modeling and Prediction of Failures
This Task involved using the data from the nondestructive and destructive tests to develop models of the degradation processes and to attempt to predict coating lives. This effort involved using the COSP Model, developed at NASA, as the basis for the prediction. Acoustic emission measurements were used to obtain critical parameters in the model from short time experiments. As noted in previous semi-annual reports, substantial progress has been made in improving this modeling.

Task IX: Definition of Optimized Coatings for Specific Applications
This Task was directed at specifying coating compositions and processing procedures to optimize performance for specific applications. This task was performed using data from the other tasks.

This project offers the following benefits to the gas turbine industry: a) development and definition of metallic coatings and TBCs for use under specific gas turbine conditions, b) description of nondestructive tests to assess damage in coatings and TBCs, c) development of lifetime prediction models, d) close collaboration between

universities, national laboratories, and industrial coatings manufacturers and users, and e) a strong educational component contributing to the education of two Ph. D students. Two Ph. D degrees have been awarded during this project: Dr. Matthew J. Stiger (UPitt) and Dr. Qin Ma (CMU).

PROJECT DESCRIPTION

In the next generation gas turbine, resistance to thermal cycling damage may be as important as resistance to long isothermal exposures. Moreover, metallic coatings and Thermal Barrier Coatings (TBCs) may encounter attack by deposits arising from combustion of low-grade fuel and air borne impurities. Finally, there is currently a need for nondestructive techniques to assess metallic coating and TBC degradation and damage as a result of exposure to cyclic oxidation and hot corrosion.

The focus of the project is:

- Development of a mechanism-based testing methodology for improving the oxidation and hot corrosion resistance of high temperature metallic coatings and TBCs.
- Incorporation of a significant number of nondestructive tests in this methodology directed at assessing coatings degradation and damage accumulation.

The overall objectives of this program were to establish a mechanistic understanding of how the durability of oxidation resistant coatings and TBCs is affected by exposures to degradation conditions likely to be encountered in the operation of advanced gas turbines and develop approaches for minimizing detrimental effects on component lifetimes and predicting remaining lives of exposed coatings.

More specifically the goals were to use existing testing techniques and develop new techniques, particularly nondestructive ones, to

1.Evaluate the adhesion of alumina to MCrAlY and aluminide coatings.
2.Understand the degradation mechanisms of TBCs under thermal cycling conditions.
3.Evaluate the hot corrosion mechanisms of the coatings and the effect of intermittent exposure to hot corrosion conditions on cyclic oxidation resistance. (The bulk of this work will be completed under a UTSR grant that began at the University of Pittsburgh in August 2004).
4.Use the test data to model the degradation mechanisms of the coatings and extend the experimental results in a predictive manner.
5.Propose a limited number of improvements to existing coatings (compositions and processing) and evaluate their performance.

The University Turbine Systems Research (UTSR) program, the University of Pittsburgh and Carnegie Mellon University partnered with industry and several national laboratories in the development of a mechanism-based testing methodology for improving the oxidation, resistance of high temperature metallic coatings and TBCs. This testing methodology involved a significant number of nondestructive tests directed at assessing coatings degradation and damage accumulation. Metallic coatings on

superalloys were prepared by Praxair Surface Technologies and Howmet Inc. The coatings were tested and microstructurally characterized at the University of Pittsburgh and Carnegie Mellon University. Nondestructive testing of exposed specimens were performed at Oak Ridge National Laboratory (ORNL) and Argonne National Laboratory (ANL) as well as the University of Pittsburgh.

The project involved the following specific tasks. Task I was concerned with processing comparisons and modifications using state-of-the art-coatings. Task II involved compositional modifications of the state of the-art coatings. Task III consisted of selection and preparation of a TBC system. Task IV was concerned with oxidation and hot corrosion testing of the prepared specimens. Task V involved using a number of nondestructive techniques to attempt to determine the amount of degradation of exposed systems. Task VI was directed at documenting the amount of degradation present in specimens using destructive techniques. Task VII consisted of selecting those nondestructive techniques, which are most effective in describing degradation. Task VIII involved using the data from the nondestructive and destructive tests to develop models of the degradation processes and to attempt to predict coating lives. Task IX was directed at specifying coatings compositions and processing procedures to optimize performance for specific applications.

The project team members and their areas of responsibility were as follows. Professors Pettit and Meier of the University of Pittsburgh led the effort and performed corrosion studies and acoustic emission and x-ray diffraction experiments. Professor Beuth of CMU performed indentation and impact tests and fracture mechanics analysis. Dr. Michael Lance of ORNL performed piezospectroscopic stress measurements and Dr. William Ellingson of ANL performed optical backscatter experiments. Specimens were prepared by Praxair and Howmet. GE provided input on testing conditions for the various degradation modes.

This project offers the following benefits to the gas turbine industry: a) development and definition of metallic coatings and TBCs for use under specific gas turbine conditions, b) description of nondestructive tests to assess damage in coatings and TBCs, c) development of lifetime prediction models, d) close collaboration between universities, industrial coatings manufacturers, and e) a strong educational component contributing to the education of graduate and undergraduate students in areas important to gas turbine technology.

EXPERIMENTAL

Materials

A nickel-base single-crystal superalloy substrate, René N5, was studied.

Four coatings on this substrate were studied. These were:

- A NiCoCrAlY Overlay Coating
- Diffusion Aluminide and Platinum-modified Aluminide Coatings
- A TBC with NiCoCrAlY Bond Coat
- A TBC with Platinum-modified Aluminide Bond Coat

Evaluation Techniques

Destructive

Cyclic Oxidation Experiments

Cyclic oxidation exposures were performed in two furnaces, a bottom-loading furnace and a vertical tube furnace, in laboratory air. The initial exposures involved one-hour cycles between 1100°C and approximately 35°C. Failure of the TBC-coated specimens was taken as the time at which a significant amount of the TBC has separated from the substrate. Failure of the specimens without TBC coatings was taken as the time at which the mass change of the specimen reaches negative values.

Indentation Tests

Indentation tests [1, 2] were also performed on the specimens. The test, shown schematically in Figure 6, consists of indenting the TBC system with a Brale type conical indenter (a Rockwell hardness tester or mechanical testing machine can be used for this purpose). The indenter penetrates the TBC and oxide layers and plastically deforms the metallic bond coat and substrate below. As illustrated in Figure 3 (as viewed from above), this induces an axisymmetric debond of the TBC and oxide layers.

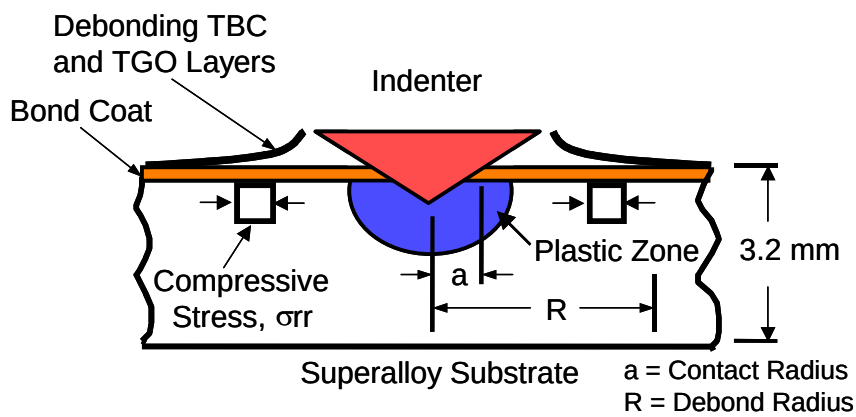

Figure 6. Schematic diagram of the indentation test.

Nondestructive

Stress Measurement by X-ray Diffraction

The stresses in the oxide films grown on specimens without TBCs were measured by x-ray diffraction (XRD). The stress normal to the free surface of a film is usually assumed to be zero. Neglecting shear stresses, the resulting biaxial stress can be expressed quite simply for an isotropic elastic medium, as described by Noyan and Cohen [3]. The quantities measured are strains, which can be measured by XRD as a change in lattice spacing with inclination with respect to the surface of a sample. This strain is usually expressed as:

$$\varepsilon_{\phi\psi} = \frac{d_{\phi\psi} - d_o}{d_o} \tag{1}$$

in which d_o is the stress-free lattice spacing of the selected (hkl) planes and $d_{\phi\psi}$ is the lattice spacing of these (hkl) planes for a given tilt ψ. It can be shown that this strain is expected to be proportional to $\sin^2\psi$. For an equal biaxial stress in the irradiated layer, equation 1 can be expressed as [3]:

$$\frac{d_{\phi\psi} - d_o}{d_o} = \tfrac{1}{2} s_2(hkl)\sigma_o \sin^2\psi + 2s_1(hkl)\sigma_o, \tag{2}$$

where $\frac{1}{2}s_2$ and s_1 are the x-ray elastic constants and σ_o is the biaxial stress in the oxide scale. A number of $d_{\phi\psi}$ are measured over a range of ψs to establish the classical d vs. $\sin^2\psi$ relation. This multipoint relation reduces the error of d_o compared to a single point method. If the $\sin^2\psi$ curve is linear, as is expected from an isotropic surface layer which is polycrystalline and not textured, the stress in any direction ϕ can be calculated from the slope of the measured d vs. $\sin^2\psi$ relation.

Another benefit of using the multipoint method is only one of the x-ray elastic constants is required. Two models have been proposed to average the response of the alumina grains to the average stress. Both models assume a random distribution of crystal orientations. The Voigt model assumes that the all grains are subjected to identical strains and the following relation exists[4] for hexagonal crystals

$$\tfrac{1}{2}s_2 = \frac{15}{7C_{11} + 2C_{33} - 5C_{12} - 4C_{13} + 12C_{44}} \tag{3}$$

where the C_{ij} are the single crystal elastic constants of stiffness for alumina. The other, the Reuss model, assumes a uniform stress in all grains and the $1/2s_2$ is determined from

$$\begin{aligned}\tfrac{1}{2}s_2(hkl) = {} & \tfrac{1}{2}(2S_{11} - S_{12} - S_{13}) - \tfrac{1}{2}(5S_{11} + S_{33} - 3S_{44} - S_{12} - 5S_{13})a_{33}^2 \\ & + \tfrac{3}{2}(S_{11} + S_{33} - S_{44} - 2S_{13})a_{33}^4 + 3S_{14}a_{22}a_{33}(3a_{11}^2 - a_{22}^2)\end{aligned} \tag{4}$$

where S_{ij} are the compliance constants for single crystal alumina. Previous work on this project was used to evaluate the relative accuracy of the Voigt and Reuss models for calculating the x-ray elastic constants. However, we have recently been alerted by colleagues [5] that a recent study [6] has detected a sign error in one of the elastic constants for alumina in the data used in every laboratory [7]. This has necessitated recalculation of all the stress values determined in this study. This work is proceeding.

Capabilities were developed at the University of Pittsburgh in four XRD stress measurement methods. These methods are the classical tilting and rocking techniques, which are equivalent and are based on the determination of the $\sin^2\psi$ curves. In the third method, the tilting method has been extended to thinner films by the use of fixed low incidence techniques. An XRD machine with an open Eulerian cradle provides the tilting of the specimen in symmetrical diffraction ("classical" method) or asymmetric diffraction with fixed low incidence. The rocking technique is performed on a powder machine. The powder machine and the dual arm are also used with a hot stage.

The design of the powder machine and the hot stage make it desirable that the specimen be nearly horizontal during high temperature experiments. For this purpose a new fixed (low) incidence XRD technique, the fixed incidence multiplane method (FIM), using more than one set of (hkl) planes has been developed. Usually for residual stress measurements, one (hkl) plane is tilted (or rocked) in order to measure the strain at various angles to the surface. With fixed incidence and a fixed specimen, diffraction occurs for different sets of (hkl) planes with different inclinations with respect to the surface thus providing the equivalent of the tilting or rocking in other methods.

The four methods were tested at room temperature and shown to give equivalent results. They have already been used for the measurement of residual stresses in chromia and alumina scales. The room temperature data are well behaved i.e. the $\sin^2\psi$ plots are good straight lines with no splitting or oscillation [8-10]. Results for alumina scales on

FeCrAl alloys are in close agreement for the calculated residual stresses with data obtained by piezospectroscopy [9]. The FIM method has been shown capable of application to the measurement of growth stresses at temperatures to 1100°C while still maintaining the advantages of the $\sin^2\psi$ analyses of the diffraction data [9].

Stress Measurement by Piezospectroscopy

Stresses in the alumina scales formed on specimens with and without TBCs were measured by piezospectroscopy by Dr. Michael Lance at ORNL. Aluminum oxide formed by high temperature oxidation invariably contains a minor concentration of chromium, either as a result of it being an alloying addition or as an impurity in the alloy. On oxidation, chromium is incorporated as Cr^{3+} into the aluminum oxide crystal structure, substituting for Al^{3+} and occupying an octahedral site. When appropriately stimulated, for instance with a laser beam or an electron beam, the chromium ion luminesces, emitting two particularly intense, narrow lines, the R_1 and R_2 lines. In the absence of any strain, the R_1 and R_2 lines have energies of 1.790 and 1.794 eV at room temperature.

When aluminum oxide is strained, the oxygen octahedra around the Cr^{3+} are distorted which, in turn, alters the crystal field of the d^3 electrons in the Cr^{3+} ions and thereby the energies of the R_1 and R_2 lines. The shift in energy of the luminescence spectrum with strain is termed the piezospectroscopic effect. For small strains, the shift in the R lines can be written phenomenologically in terms of the stress as:

$$\Delta\nu_{stress} = \Pi_{ijkl}\sigma_{ij}^{c} \tag{5}$$

where $\Delta\nu$ is the shift, expressed as a frequency, σ_{ij}^{c} is the stress and Π_{ijkl} is the piezospectroscopic tensor. When the stress is a hydrostatic pressure, the frequency shift is linearly related to the pressure and the equation reduces to the well-known equation used in the high pressure community to monitor the pressure in high pressure, diamond anvil cells. Since the frequency shift is related through equation 5 to the stress, equation 3 can be inverted so as to determine the stress from a measurement of the frequency shift. This is the basis of the piezospectroscopic measurement of stresses in alumina films proposed in this work.

In the technique pioneered by Prof. D. R. Clarke at UCSB [11], an optical probe is used to excite the R-line luminescence and the luminescence is recorded from all the Cr^{3+} ions within the probed volume. Thus, the measured frequency shift is the integration of the frequency shifts from the individual Cr^{3+} ions and the local stress within the probed volume. In addition, for polycrystalline materials, the probed volume, if it is larger than the grain size, also includes different orientations of the Cr-O octahedra. As a result, it can be shown that the measured frequency shift is related to the average stress within the probed volume as:

$$\overline{\Delta\nu} = \Pi_{ii}\langle\sigma_{ii}\rangle \tag{6}$$

An important feature of equation 6 is that the frequency shift is related to the trace of the stress tensor not simply the hydrostatic pressure. Thus, if the orientation of the stress field is known, for instance, for a thin film on a substrate well away from the edge, the stress field is biaxial, and so equation 6 can be used directly to measure the biaxial stress.

The precision of measurement depends on the accuracy to which the piezospectroscopic coefficients can be determined and the precision to which the frequency shift can be measured. The piezospectroscopic coefficients, including nonlinear terms, have been determined [12]. The accuracy of the frequency measurements depends on the spectral resolution of the spectrometer used as well as the temperature dependence of the spectrometer. It was found that the stress in single crystals of sapphire can be measured to ± 20 MPa and in polycrystalline films to ± 40 MPa. By using a focused optical probe, for instance, using an optical microscope or fiber optic, measurements can be made down to regions a few microns across.

A number of comparisons have been made between measurements of the stress in alumina films, grown by high temperature oxidation, made by X-ray diffraction and piezospectroscopy with good agreement [9].

Optical Backscatter Experiments

Experiments to evaluate thermal cycling damage or as-fabricated damage at the interfaces between the thermally grown oxide, the underlying metallic coating and/or the overlying TBC were performed by Dr. William Ellingson and Mr. Robert Visher at Argonne National Laboratory using an optical backscatter technique.

In this technique, polarized light from a laser is focused on the specimen. Because the materials under study are optically translucent, light from the laser can penetrate below the surface and back scatter out through the surface to a high sensitivity light detector. The backscattered radiation is acquired as the specimen is moved in the x and y directions, which gives the effect of the laser being rastered across the specimen surface. The backscattering process seems to be sensitive to variations in the topography at the interface between the TGO and the substrate, including debonds at the TGO-substrate interface. Now by analyzing the data from the high sensitivity detectors, primarily by looking at the x-y scan data as a two-dimensional statistical array, ANL computes the statistical parameter, C_v, the coefficient of variation , for each data set. By looking at the coefficient of variation as a function of the number of thermal cycles, a relationship can be established between the Cv and number of thermal cycles. Thus, in principle, with a reasonably strong experimental data base, one can predict damage that has been produced by thermal cycling well before specimen failure.

Acoustic Emission Measurements

Cracking caused by cyclic oxidation can be detected in-situ using acoustic emission measurements. The AE equipment used was the commercially available Physical Acoustic Group AEDSP-32/16B acquisition and processing hardware with the

Mistras-2000 data acquisition software. A R15 transducer with the frequency range from 100 to 1000Hz was attached to a stainless steel cone. The cone acts as a transition from the transducer diameter to the Pt-wave guide diameter of 1mm. This 80cm wave-guide was necessary for this application because of the incompatibility of the transducer and the high temperatures in the furnace. The apparatus used is shown schematically in Figure 7.

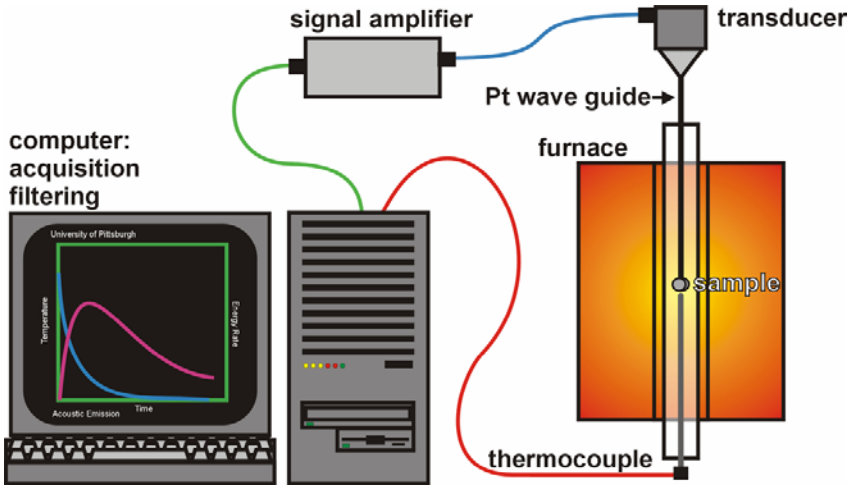

Figure 7. Acoustic Emission Testing Apparatus.

Modeling

A number of models have been created to describe the isothermal growth kinetics of oxide scales, but to describe the cyclic oxidation behavior, Lowell et. al. [13] have developed COSP (Cyclic Oxidation Spall Program). COSP is a statistical model that deals with each cycle as a step in an iterative process of growth and spallation of the scale. Two versions of this model exist as the uniform layer and Monte Carlo versions. The uniform layer version treats spallation of the oxide during cooling as fracture within the oxide and followed by loss of continuous top layer of oxide. The Monte Carlo version effectively divides the surface of the oxide into discrete elements and spallation occurs independently for each element. Although the uniform layer version is mathematically simple, the Monte Carlo version is a better representation of observed oxide spallation as independent areas.

Both versions of the COSP model follow similar steps but a description of the uniform layer method will be described in the following. Oxide growth behavior follows the isothermal growth kinetics to determine the weight of the oxide after the heating portion of the cycle prior to cooling, W'r. During the subsequent cooling step of the cycle, a portion of the oxide will spall with a mass of Ws. After the cycle is complete, the total mass of the oxide retained, Wr, is the starting point for the next cycle as graphically shown in Figure 8a.

In the COSP model, the fraction, F, of the oxide that spalls is proportional the amount of oxide that is present where

$$F = Qo \cdot W'r. \tag{7}$$

Here Qo is introduced as the spall constant and the expression for the weight of the spalled oxide is

$$Ws = F \cdot W'r. \tag{8}$$

With the W'r and Ws for this cycle, the Wr can then be calculated by

$$Wr = W'r - Ws. \tag{9}$$

Monitoring the amount of retained and spalled oxide through the duration of the calculations, mass change curves can then be calculated and the effect of Qo on these curves is shown Figure 8b.

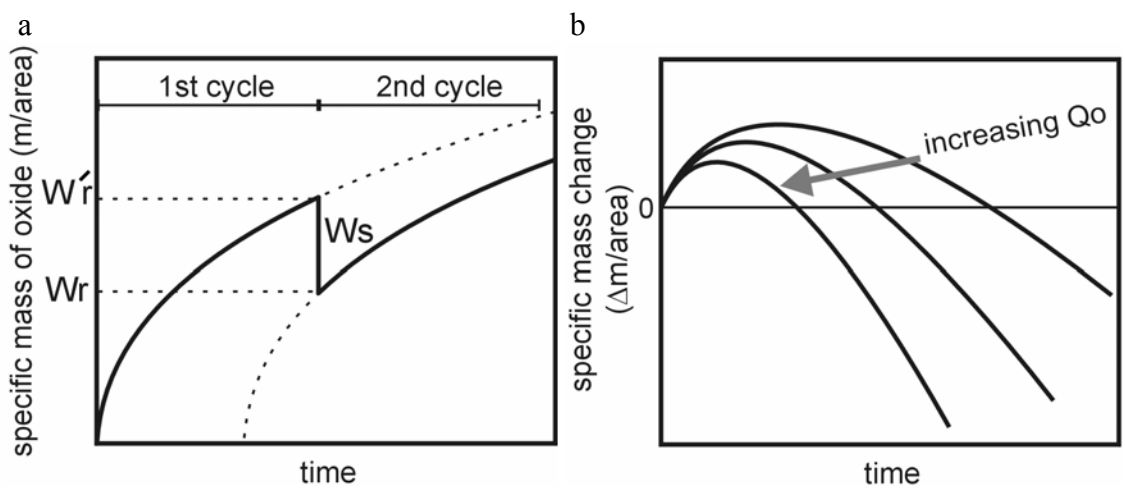

Figure 8. Graphical representation of important parameters in the COSP model.

In the Monte Carlo version, the surface of the sample is divided into separate areas and the growth and spallation of the oxide is treated independently for each area. This treatment allows complete oxide loss to expose the metallic substrate over discrete areas on the specimen. The amount of surface are that exhibits spallation is handled in a probabilistic manner. On a per surface unit basis, Wr' is similar to the UL version, yet the fraction of the spalled oxide will be one only when complete spallation occurs. The probability for complete spallation to the metal-oxide interface to occur is determined by

$$P = Qo \cdot W'r. \tag{10}$$

If the condition is met for complete spallation, Ws would equal Wr' and an oxide free surface would be ready for exposure on the next cycle. If no spallation, the oxide would continue to grow on the following cycle according to isothermal kinetics. Behavior of several area units are averaged to determine the behavior of the complete surface and a plot similar to Fig. 8b can be constructed.

RESULTS AND DISCUSSION

The earlier results from this program were presented in the six semi-annual reports [14-19]. These include:

1. Significant advances in the use of x-ray diffraction (XRD) to measure stresses in oxides grown on superalloys and coatings and correlation between stresses measured by XRD and luminescence (at ORNL).
2. Improvement of an indentation technique for measuring the fracture toughness of interfaces in TBC systems. This has been accomplished, in part, by developing SEM charging and optical backscatter techniques (at ANL) for imaging the debond produced by the indentation and measuring the debond radius. Also, the use of different indenter shapes to optimize the measurements for different types of systems has been accomplished.
3. Use of the indentation technique, coupled with stress measurements to characterize the mechanisms leading to toughness loss in TBC systems during thermal cycling. Results show a strong correlation between toughness loss caused by mechanical damage above, below and within the TGO layer and reductions in stress measured by piezospectroscopy.
4. The indentation test has been used to elucidate the effects of bond coat surface preparation on TBC degradation
5. Use of acoustic emission measurements to detect damage occurring in superalloys and coated superalloys at short times during thermal cycling and combining these measurements with modification of a spalling life model COSP (developed at NASA) to form the basis for a life prediction protocol.
6. For coating systems without TBCs, acoustic emission (coupled with TGA measurements and COSP modeling) has emerged as an effective nondestructive testing technique. For coating systems with TBCs subjected to cyclic loading, piezospectroscopy has emerged as a potentially effective nondestructive test for tracking the evolution of mechanical damage below the TBC (leading to loss of TBC adhesion).

The following section updates results obtained since the previous report.

1. Previous work on this project was used to evaluate the relative accuracy of the Voigt and Reuss models for calculating the x-ray elastic constants. However, we have recently been alerted by colleagues [5] that a recent study [6] has detected a sign error in one of the elastic constants for alumina in the data used in every laboratory [7]. This has necessitated recalculation of all the stress values determined in this study. This work is proceeding and will be submitted as a journal publication.

2. One of the objectives of the present study was to develop improved methods for hot corrosion testing. Hot corrosion testing apparatus has been constructed. However, a UTSR project focusing on hot corrosion degradation was begun at the University of Pittsburgh in August 2004 (UTSR Project 04 01 SR116) and the hot corrosion testing is being performed under the new project.

Technology Transfer

The results of this program have been disseminated in a variety of ways. This includes six Semi-annual UTSR Reports, two journal article articles:

Q. Ma, J. L. Beuth, F. S. Pettit, G. H. Meier, and M. J. Stiger, "Use of Indentation Fracture Tests to Investigate Toughness Loss Mechanisms in Thermal Barrier Coating Systems", Coatings 2005 (Nitin Padture, Lorraine Francis, Janet Hampikian and Narendra Dahotre, eds.) Proc. Materials Science and Technology 2005, Pittsburgh, September 2005, pp. 3-6.

M. J. Stiger, G. H. Meier, F. S. Pettit, Q. Ma, J. L. Beuth, and M. J. Lance "Accelerated Cyclic Oxidation Testing Protocols for Thermal Barrier Coatings and Alumina-Forming Alloys and Coatings" Materials and Corrosion, 27, 1-13 (2006).

and two Ph D theses:

Qin Ma, "Indentation Methods for Adhesion Measurement in Thermal Barrier Coating Systems", Ph D Thesis, Department of Mechanical Engineering, Carnegie Mellon University, 2004.

Mathew J. Stiger, "Correlation of Short-Term to Long-term Oxidation testing for Alumina Forming Alloys and Coatings", Ph D Thesis, Department of Materials Science and Engineering, University of Pittsburgh, 2004.

The results have also been described in over twenty oral presentations. These include UTSR Workshops, Professional Society Meetings and seminars at the laboratories of gas turbine manufacturers and coating vendors.

REFERENCES

1. A. Vasinonta, and J. L. Beuth, Engineering Fracture Mechanics, 68, 843 (2001).
2. R. A. Handoko, J. L. Beuth, G. H. Meier, F. S. Pettit, and M. J. Stiger, "Mechanisms for Interfacial Toughness Loss in Thermal Barrier Coating Systems," Durable Surfaces, D.R. Mumm, M. Walter, O. Popoola and W.O. Soboyejo, eds., Proceedings of the Materials Division Symposium on Durable Surfaces, 2000 ASME International

Mechanical Engineering Congress and Exposition, Orlando, November, 2000, Trans Tech Publications, Switzerland, pp.165-183.
3. I. C. Noyan and J. B. Cohen, Residual Stresses, Springer-Verlag, (1987).
4. P. D. Evenshor, W. Frohlich and V. Hauk, Z. Metallde., 62, 38 (1971).
5. Private Communication, D. Hovis and A. Heuer, Case Western Reserve University, 2005.
6. J. R. Gladden, J. H. So, J. D. Maynard, P. W. Saxe, and Y. LePage, Appl. Phys. Letters, 85, 392 (2004).
7. J. Wachtman, Jr., W. Tefft, D. Lam, and R. Stinchfield, J. Res. Natl. Bur. Stand., Section A, 64, 213 (1960).
8. E. Schumann, C. Sarioglu, J. R. Blachere, F. S. Pettit, and G. H. Meier, Oxid. Metals, 53, 259 (2000).
9. C. Sarioglu, G. H. Meier, F. S. Pettit, J. L. Smialek, J. R. Blachere, and C. Mennicke. "The Effects of Reactive Element Additions, Sulfur Removal, and Specimen Thickness, on the Oxidation Behavior Of Alumina-forming Ni- and Fe-base Alloys", Materials Science Forum, 251-254, 405 (1997).
10. C. Sarioglu, J. R. Blachere, F. S. Pettit, and G. H. Meier, "Room Temperature and In-Situ High Temperature Strain (or Stress) Measurements by XRD Techniques", Microscopy of Oxidation 3 , B. Newcomb and J. A. Little, eds., The Institute of Materials. London, 1997, p. 41.
11. D. M. Lipkin and D. R. Clarke, Oxid. Metals, 45, 267 (1996).
12. J. He and D. R. Clarke, J. Am. Ceram. Soc. 78, 1347 (1995).
13. C. E. Lowell, C. A. Barrett, R. W. Palmer, J. V. Auping, and H. B. Probst, Oxid. Metals, 36, 81 (1991).
14. F. S. Pettit, G. H. Meier, and J. L. Beuth, "Mechanism-Based Testing Methodology For Improving the Oxidation, Hot Corrosion and Impact Resistance of High-Temperature Coatings for Advanced Gas Turbines", First Semi-Annual Report on UTSR Project 02-01-SR101, November, (2002).
15. F. S. Pettit, G. H. Meier, and J. L. Beuth, "Mechanism-Based Testing Methodology For Improving the Oxidation, Hot Corrosion and Impact Resistance of High-Temperature Coatings for Advanced Gas Turbines", Second Semi-Annual Report on UTSR Project 02-01-SR101, May, (2003).
16. F. S. Pettit, G. H. Meier, and J. L. Beuth, "Mechanism-Based Testing Methodology For Improving the Oxidation, Hot Corrosion and Impact Resistance of High-Temperature Coatings for Advanced Gas Turbines", Third Semi-Annual Report on UTSR Project 02-01-SR101, November, (2003).
17. F. S. Pettit, G. H. Meier, and J. L. Beuth, "Mechanism-Based Testing Methodology For Improving the Oxidation, Hot Corrosion and Impact Resistance of High-Temperature Coatings for Advanced Gas Turbines", Fourth Semi-Annual Report on UTSR Project 02-01-SR101, May, (2004).
18. F. S. Pettit, G. H. Meier, and J. L. Beuth, "Mechanism-Based Testing Methodology For Improving the Oxidation, Hot Corrosion and Impact Resistance of High-Temperature Coatings for Advanced Gas Turbines", Fifth Semi-Annual Report on UTSR Project 02-01-SR101, February, (2005).
19. F. S. Pettit, G. H. Meier, and J. L. Beuth, "Mechanism-Based Testing Methodology For Improving the Oxidation, Hot Corrosion and Impact Resistance of High-

Temperature Coatings for Advanced Gas Turbines", Sixth Semi-Annual Report on UTSR Project 02-01-SR101, May, (2005).

ADVANCED SENSOR APPROACHES FOR MONITORING AND CONTROL OF GAS TURBINE COMBUSTORS

FINAL REPORT
FOR THE PERIOD 1 MAY 2002 – 31 OCT 2005

PIS: JERRY SEITZMAN AND TIM LIEUWEN

DEC 2005

DOE AWARD: DE-FC26-02NT41431

UTSR PROJECT: 02-01-SR102

GEORGIA INSTITUTE OF TECHNOLOGY

SCHOOL OF AEROSPACE ENGINEERING

ATLANTA, GA. 30332 – 0150

jerry.seitzman@aerospace.gatech.edu

tim.lieuwen@aerospace.gatech.edu

Disclaimer:

"This report was prepared as an account of work sponsored by an agency of the United States Government. Neither the United States Government nor any agency thereof, nor any of their employees, makes any warranty, express or implied, or assumes any legal liability or responsibility for the accuracy, completeness, or usefulness of any information, apparatus, product, or process disclosed, or represents that its use would not infringe privately owned rights. Reference herein to any specific commercial product, process, or service by trade name, trademark, manufacturer, or otherwise does not necessarily constitute or imply its endorsement, recommendation, or favoring by the United States Government or any agency thereof. The views and opinions of authors expressed herein do not necessarily state or reflect those of the United States Government or any agency thereof."

ABSTRACT

This report describes sensing strategies that were developed for monitoring the health and performance of gas turbine combustors. Sensor systems based on these approaches enable control and monitoring systems that improve combustor reliability and operability, achieve optimal performance (e.g., lower NO_x emissions) over extended periods of time, reduce maintenance, prevent forced outages, and increase engine life. Specifically, we developed methods to: 1) sense imminent loss of static combustor stability, e.g., precursors to flame loss or lean blow out; 2) determine local fuel-air ratio and heat release variations that can arise from mixedness variations; and 3) sense the proximity of the combustor to its dynamic stability margin, i.e., detecting how close the system is to the point where detrimental combustion instabilities would occur. The approaches involve a combination of nonintrusive optical and acoustic sensing, as well as ion concentration probes. The methods were evaluated for their applicability in natural gas and syngas fueled combustors. In addition to tests in our laboratory, field tests of the stability margin sensing were pursued with industrial partners.

TABLE OF CONTENTS

Abstract ..... **i**

Table of contents ..... **ii**

I. Executive Summary **1**

II. Project Description **2**

II.A. Overall Needs and Benefits 2
II.B. General Approach 2
II.C. Specific Sensing Issues and Approaches 3
Task 1. Transient Flame Holding Event Sensors *3*
Task 2. Flame Zone Sensors *3*
Task 3. Combustor Dynamics Stability Margin Sensors *4*

III. Experimental **4**

III.A. Combustors Overview 4
III.B. Measurement Approaches 6

IV. Results And Discussion **7**

IV.A. Transient Flame Holding (Blowout) Event Sensors 7
IV.A.1 Signal Analysis *8*
IV.A.1 Results *10*
IV.B. Flame Zone Sensors 12
IV.B.1 Natural Gas Combustion *12*
IV.B.2 Syngas Combustion and Modeling *15*
IV.C. Combustor Dynamics Stability Margin Sensors 18
IV.C.1 Stable Operation *19*
IV.C.2 Field Testing of Stability Margin Algorithm *20*
IV.C.3 Stability Margin in Unstable Operation *22*

V. Summary **25**

VI. References **25**

I. EXECUTIVE SUMMARY

This report covers the development of sensing strategies for monitoring gas turbine combustor health and performance. These new sensing capabilities will enable the development of control systems that actively manage engine condition and compensate for changes in ambient conditions or system degradation. Used for monitoring purposes, they will help gas turbine operators more quickly identify potential system problems, before they become serious, and allow them to vary conditions to remove the problem. Used as long term monitors of system operation, they can be used to help schedule required maintenance. Thus the development of these advanced sensor capabilities will improve combustor reliability and operability, achieve optimal performance, lower NOx emissions, reduce maintenance costs, prevent forced outages and increase system life.

Our approach was to develop methods to extract relevant combustor performance and status information from the light and sound naturally produced by the combustion processes. For example, some of the chemical reactions involved in combustion produce molecules in electronically excited states that give off light as they decay to their ground state. This is called chemiluminescence, and one example is the blue light produced by most hydrocarbon flames. Similarly, the turbulence and fluctuations in the heat released by the combustion processes are sources of sound (acoustics) in a gas turbine combustor. These optical and acoustic emissions can easily be monitored without requiring the placement of sensors directly into the most hostile regions of the flow. Furthermore, acoustic and optical sensors are already employed to some extent in currently fielded industrial gas turbines. We also explored ion current sensing that could be added to combustor igniters. We measured the sensor signatures of a number of different types of combustors as a function of operating conditions, such as fuel-air ratio, pressure, temperature, flow velocity, and system stability. We then used physics-based analysis methods to relate these system parameters to changes we observed in the sensor outputs.

Sensor methods were developed and tested for three specific applications: 1) sensing proximity static combustor stability loss (lean blow out); 2) determining local flame zone variables such as fuel-air ratio variations that can arise from unmixedness; and 3) sensing combustor dynamic stability margin, i.e., detecting how close the system is to the point where detrimental combustion instabilities would occur. The static stability sensing was successfully demonstrated for optical, acoustic and ion sensing in various combustors and for both natural gas and syngas fueled systems. The approach relies on capturing precursor events using a simple and robust thresholding method. Flame zone sensors for local fuel-air ratio monitoring were demonstrated for lean natural gas fueled combustors based on properly corrected ratios of CH and OH chemiluminescence. For lean ($\phi<0.7$) syngas systems, similar results can be obtained with the ratio of CO_2 and OH chemiluminescence. In addition, physics-based modeling of the combustion process was used to predict the chemiluminescence, which should allow further improvements in this sensing approach. Finally, dynamic stability margin sensing, based on dynamic pressure measurements, was demonstrated in various combustors by monitoring the decay of the autocorrelation at the known combustor instability frequencies. This method has been field tested in cooperation with industrial partners. The method was also extended to unstable operation conditions to help operators or control systems rapidly recover stable operation should instabilities occur.

II. PROJECT DESCRIPTION

II.A. Overall Needs and Benefits

This project involves the development of sensing strategies for monitoring gas turbine combustor health and performance. These sensing capabilities will enable control systems that actively manage engine condition and compensate for changes in ambient conditions or system degradation. Such monitoring systems will also be useful for isolating system problems and for scheduling engine maintenance. Thus the development of advanced sensor capabilities is expected to lead to: improvements in combustor reliability and operability, optimal performance (e.g., lower NO_x emissions) over extended periods of time, reduced maintenance downtown or forced outages, and increased combustor life.

II.B. General Approach

Combustor health and performance monitoring requires strategies that involve sensing conditions in the combustor, rather than downstream, especially when injector-to-injector variations are important. Given the harsh combustor environment, non-intrusive sensors are the most viable candidates. Since a combustor naturally produces light and sound, both can be monitored without requiring the placement of sensors directly into the most hostile regions of the flow.

While there are a number of sources for electromagnetic radiation from a combustor, the source most directly connected to the combustion reactions is chemiluminescence. This radiation is from (electronically) excited molecules that are produced by the oxidation reactions and which can relax to lower energy states by emitting light. Since the intensity of emission is proportional to the chemical production rate of the particular molecule, the chemiluminescence intensity can be related to chemical reaction rates.[1] For this reason, chemiluminescence has been used previously as a rough measure of reaction rate and heat release rate.[2-5] Chemiluminescence can provide information on the presence and strength of the combustion process in a specific region of the combustor. Also, it inherently has a fast time response providing fast detection of flame instability events. Acoustic radiation can be produced by combustion through temporal fluctuations in volume expansion in the flame zone due to changes in heat release rates. It has been shown by previous researchers that acoustic emissions from turbulent combustion processes are dominated by unsteady heat release processes as opposed to flow noise.[5, 6,7] Thus acoustic sensing can detect events associated with changes in the overall heat release rate and some details of dynamics of combustion at several time scales.

Since the combustor naturally produces light and sound, and they can be monitored without requiring the placement of sensors directly into the most hostile regions of the flow, this program is focused on developing the capability for interpreting the electromagnetic and acoustic waves radiated by the combustion processes. Furthermore, acoustic and optical sensors are already employed to some extent in some currently fielded industrial gas turbines. For example, a number of gas turbines are equipped with ports for measurements of acoustic pressure.

Ion concentration measurements can also provide useful diagnostics into (unsteady) combustion reaction characteristics.[8,9] It is widely accepted that during combustion, radicals from the fuel and oxidizer undergo chemi-ionization reactions[10] (e.g., CH + O =

$HCO^+ + e^-$) to produce ions (like HCO^+) and free electrons e^-, enabling the flow of electrical current through hydrocarbon flames. A typical flame ionization sensing technique consists of at least two electrodes arranged such that a voltage potential can be applied across the flame, or a part of the flame, and the induced current through the flame is measured. The probe therefore responds to the ion emission intensity, which is related to (specific) chemical reaction rates and is a rough measure of the heat release rate in the combustor.[11] Thus, ion probes can provide information on the presence and strength of the combustion process in a specific region of the combustor, making them suited for health monitoring and diagnostics.

II.C. Specific Sensing Issues and Approaches

This research program consists of three main tasks, involving both experimental and analytic efforts.

Task 1. Transient Flame Holding Event Sensors

The first task was development of methods for sensing transient flame holding events, such as imminent blowout. This will allow turbine engines to operate closer to the lean limit and hence, with lower NO_x emissions. The current, standard approach is passive control through combustor design or load scheduling. In this approach, one must ensure that the turbine operates within a conservatively *estimated* safety margin from the lean blowout point because of system uncertainties, fuel composition variability, system wear, or ambient condition changes. With an active control system that employs blowoff precursor detection, the system's operating point can be adjusted to prevent flame blowoff and loss of operability while achieving optimal performance. The approach in this case was to measure acoustic, optical emissions from the flame, and electrical signals from an ion sensor, under various operating conditions (and in multiple combustors), and analyze the results using a physical model of blowout.

This work was motivated by observations that the combustion process exhibits enhanced unsteadiness while transitioning between the static stability and blowout.[12-14] However, the primary focus of the pre-existing literature on the subject was devoted to predicting the blowout limits of a given system as a function of such parameters as equivalence ratio, air temperature, or pressure.[15-19] Little work had been done to characterize the combustion processes as it transitions from static stability to blowout.

Task 2. Flame Zone Sensors

The second task involved development of sensor approaches for monitoring local *reaction zone* equivalence ratio and heat release rate. Because key performance metrics, such as NO_x emissions and pattern factor, are directly related to locally richer packets of fuel or non-uniformity in heat release, the development of these sensing capabilities, combined with a control system, will provide increased hot section life and reduced pollutant emissions. Our approach is to use the light produced by the chemical reactions in the flame (chemiluminescence). First, we characterized the chemiluminescence of high-pressure, preheated natural gas combustion systems as a function of operating conditions. Then, we determined the dependence of the chemiluminescence signature on various combustor conditions, such as equivalence ratio and heat release.

<u>Task 3.</u> Combustor Dynamics Stability Margin Sensors

The third task involved sensing the proximity of the combustor to its dynamic stability margin, i.e., detecting how close the system is to the point where detrimental combustion instabilities would occur. Generally when turbines are being commissioned or during routine operation, the operator has no real-time information on how the relative stability of the system is affected by changes to fuel splits or other operating conditions (unless, of course, the system actually becomes unstable – leading to possible damage or shutdown). Dynamic stability margin sensors provide an online measure of the turbine stability. This diagnostic is achieved by measurement and advanced signal processing of the flame's acoustic signatures. The basic approach is to compute the autocorrelation function (i.e., the inverse Fourier transform of the power spectral density), and determine (primarily) the decay of its envelope.

III. EXPERIMENTAL

III.A.Combustors Overview

A number of combustors were employed in this effort. By studying multiple combustor geometries we increased the likelihood that the sensor methodologies developed here are robust. The first system is an atmospheric pressure, open burner, shown in Figure 1. The burner is supplied with air from compressed air tanks. The supply air passes through a plenum containing lined baffles for reducing flow noise. The duct transitions to a diverging/converging section to change the duct diameter from its supply value to the desired burner diameter. This section is followed by a straight section for flow conditioning. Fuel is introduced either after the baffle section, or near the exit in order to vary the amount of premixing. The figure shows a pilot stabilized configuration, where an array of closely spaced external pilot flames are placed around the burner exit. Besides this current circumferential piloting, several additional flameholding schemes can be examined, including swirl and bluff body approaches.

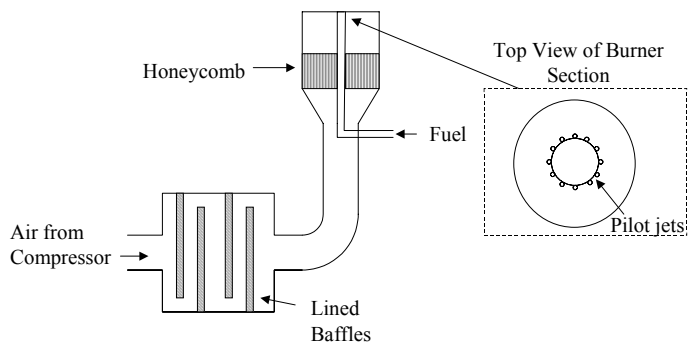

Figure 1. Simplified schematic of open burner assembly.

A confined, atmospheric pressure combustion is also being used (see Figure 2). It includes many of the attributes of a lean,

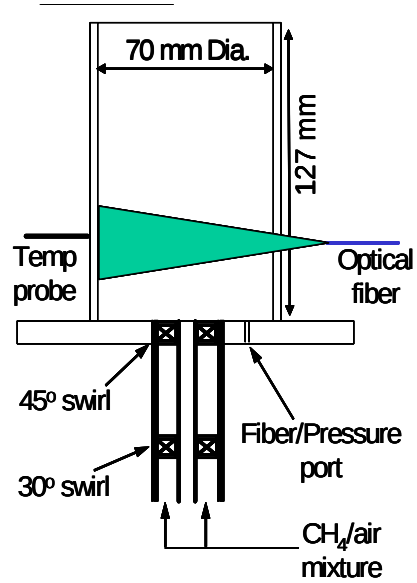

Figure 2. Atmospheric-pressure, swirl-stabilized gas turbine model combustor.

premixed gas turbine combustor, including a swirl inlet and a dump plane. In this design, a combustible mixture of fuel (methane or natural gas) and air flow passes through swirl vanes housed in a 22 mm i.d. tube, producing a swirl number of ~0.4. Upon leaving the swirler, the flow expands into a cylindrical, quartz combustor of 70 mm i.d.. The combustor typically operates with an average (post-combustion) gas velocity of 6-9 m/s.

The third combustor is a small scale, high pressure gas turbine combustor simulator (see Figure 3). This facility is designed to simulate conditions in typical gas turbine combustors, i.e., the air is preheated, the fuel is injected, the two are premixed and pass through a swirler. It can operate at pressures up to 30.4 kPa (30 atm) with air preheated up to 540 °C (1000 °F). The swirlers can be readily swapped out to determine the effect of different design parameters such as blade angle on the flow characteristics. The centerbody can be changed from a single outlet piloting type nozzle to one with multiple radial holes on its surface for active combustion control experiments. Also, the flow area can be varied in order to have different expansion ratios. The combustor is also optically accessible through the two side windows (one of which can be seen in the figure) as well as from the exhaust; i.e., both side and "end on" imaging of the flame is possible. This combustor was operated on both natural gas and synthetic fuel gas.

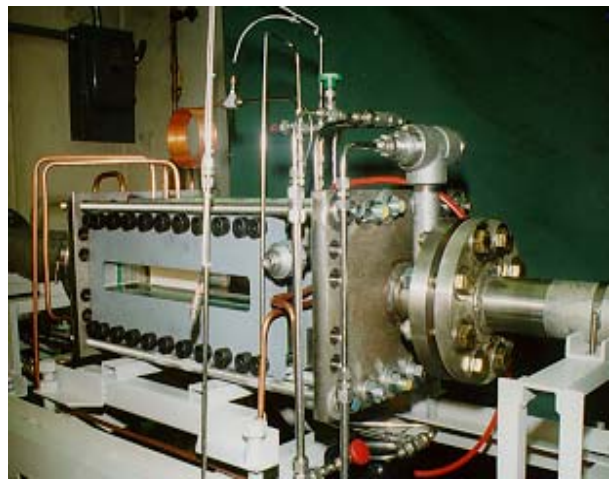

Figure 3. Georgia Tech high pressure gas turbine combustor simulator.

A simpler jet flame apparatus was also used for studying synthetic gas fuels (see Figure 4). The desired fuel composition is first prepared using a bank of calibrated rotameters, one for each gas. After mixing thoroughly, the fuel is split into two flows: the desired flowrate of fuel passes through another rotameter (calibrated for the particular fuel composition), while the remainder is flared in a diffusion flame. Finally, the required quantity of air is added, and the mixture goes to the burner. This arrangement allows simple control over the equivalence ratio (ϕ) and the average velocity through the burner. All the rotameters are calibrated with a bubble flow meter to $\pm$ 1% accuracy, with fuel flows in the range of 0.1 to 5 slpm. The reactants are preheated by electrical resistance tape wrapped around the burner. Once the desired reactant temperature is achieved (as

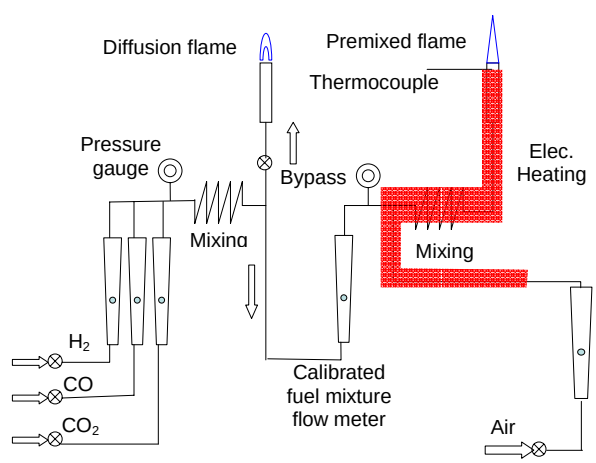

Figure 4. Apparatus for fundamental synthetic gas fuel measurements.

determined by a type-K thermocouple temporarily placed at the burner exit), the surface temperature of the burner is monitored by a second thermocouple and held constant by a temperature controller.

Some experiments were also performed on an atmospheric pressure, single cup swirl combustor (Figure 5). Non-vitiated, preheated air is supplied to the swirl cup from a plenum chamber. Air enters the combustor through counter-rotating swirlers, while the fuel is injected through a centrally located fuel nozzle. This is followed by a small annular passage leading to the test section. Liquid fuel was used for all tests.

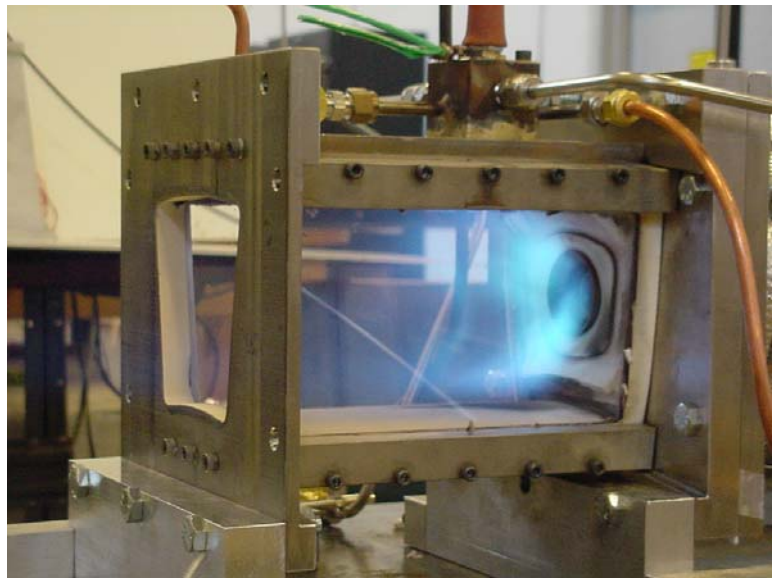

Figure 5. Single swirl-cup combustor.

III.B. Measurement Approaches

As noted above, the sensing approaches are based on measurement of the optical and acoustic radiation from the combustors. The optical signatures were measured using a variety of techniques. For measurement of "complete" optical spectra, we employed an imaging spectrometer. The spectrometer, with a 300 groove per mm grating, is coupled to a 1024×256 multi-element detector (intensified CCD). The system can simultaneously capture emission spectra from ~280–550 nm. The light is captured from the combustors using fiber optic inputs, to resemble more closely the behavior of a practical sensor. With this sensor, flame spectra can be acquired at a range of pressures, inlet air temperatures and equivalence ratios, but with relatively low temporal resolution (~10 Hz). Temporal variations in the spectral signature are measured using a group of miniature photomultipliers, with built-in amplifiers (bandwidth of 20 kHz) to convert the detector current to voltage. In this case, the optical collection also occurs through a fused silica optical fiber. The radiation passes through different interference filters to isolate specific spectral bands, e.g., a filter centered at 308 nm with a full-width-half-maximum of ~10 nm collects ultraviolet emissions from the OH $A^2\Sigma$-$X^2\Pi$ transition.

The acoustic radiation is measured by monitoring the acoustic pressure oscillations. Pressure oscillations are measured with Kistler pressure transducers (Model 211B5). For the flame holding measurements, a single transducer is used. For the dynamic stability sensing, two transducers are used, one in the inlet section and one in the combustor. The transducers are mounted 33.2 cm upstream and 5.1 cm downstream of the conical flame holder, respectively. The latter transducer is flush mounted and water-cooled. More recently, acoustic oscillations for sensing flame stability were measured with calibrated,

Bruel and Kjaer type 4939 condenser microphones that have a flat frequency response up to 40 kHz.

The ion measurement work reported here was performed in a collaborative program with Woodward Industrial Controls, which was partially funded by Woodward.

IV. Results And Discussion

IV.A. Transient Flame Holding (Blowout) Event Sensors

In previous work, we had shown that either optical (chemiluminescence) or pressure signals could be used to detect blowout precursors in swirl combustors. In this work, we first measured simultaneous optical and acoustic signals, or simultaneous acoustic and ion sensor signals from the two atmospheric-pressure, swirl-stabilized combustors. The combustor's proximity to blowout was controlled by varying the fuel and air flowrates (equivalence ratio). A well-defined combustion region was visible for the stable flames. Close to blowout, near flame loss events are occasionally observed.

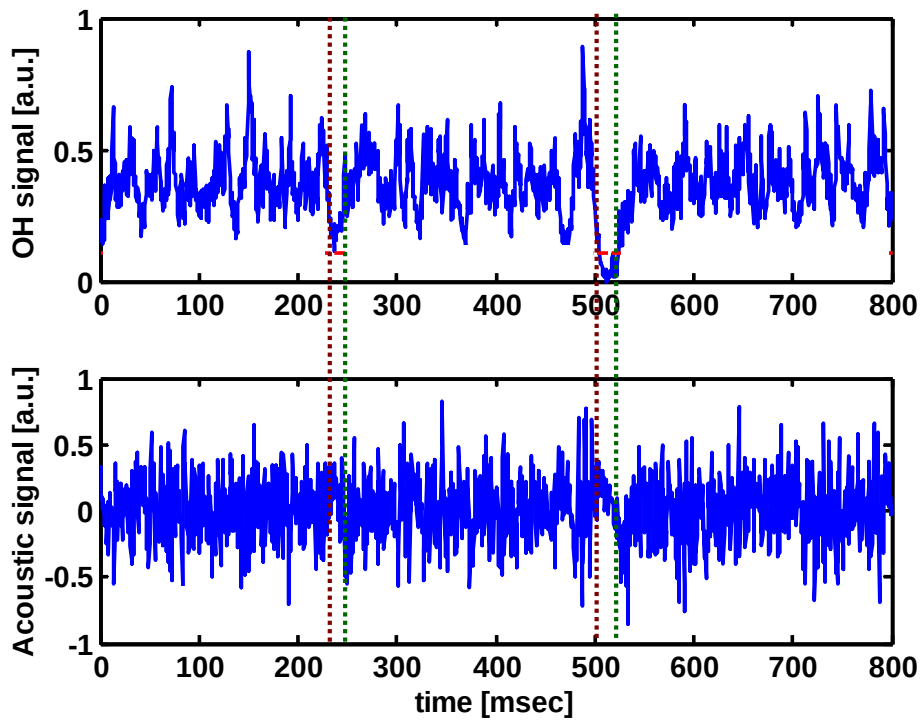

Figure 6. Comparison of optical and acoustic signals near lean blowout in a swirl stabilized combustor operating at atmospheric pressure.

As indicated in Figure 6, strong precursor events are simultaneously can be detected by multiple types of sensors (optical and acoustic in this case). During the precursor events, the flame disappears from part of the combustor. Then, the radiation signal re-appears, suggesting re-ignition of the unburned fuel. These extinction and re-ignition events span a period of several to tens of milliseconds, depending on the combustor and operating conditions. The events are nonperiodic and occur prior to blowout. As the lean blowout limit is approached, the frequency and duration of these events increase.

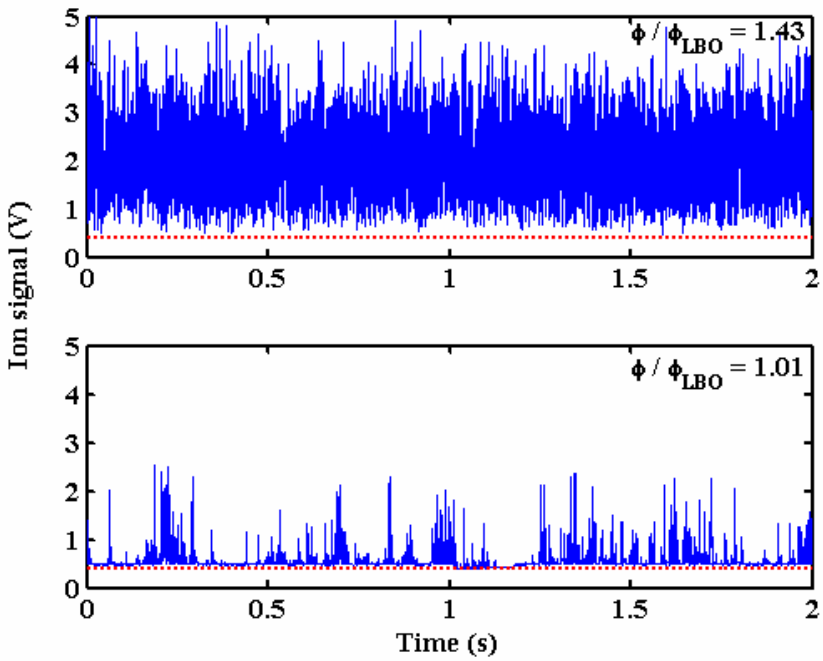

Figure 7. Ion signal from the burner for ϕ/ϕ_{LBO} = 1.43 (stable case) and 1.01 (close to blowout).

This work represents the first use an ion sensor to capture the events previously sensed using optical and acoustic approaches. Figure 7 shows ion signals obtained at two conditions, ϕ/ϕ_{LBO}=1.43 and 1.01, where ϕ_{LBO} is the equivalence ratio at lean blowout. The mean ion concentration decreases with equivalence ratio in this case, as the fuel flow rate is reduced here and therefore decreases heat release. As the combustor was brought closer to its blowout limit, the ion emissions occasionally dropped to its "near" zero value (which corresponded to ~0.4V), indicating the occurrence of the short duration, extinction events. These events increased in duration and number as blowout was approached.

IV.A.1 Signal Analysis

In this work, we evaluated various methods for identifying the precursors in the various sensor signals. The most straightforward approach explored to detect these time-localized surges in the signal is thresholding. The basic idea is to count the number of times the instantaneous signal level crosses a threshold value, usually defined as some multiple of the signal's recent mean or standard deviation. Thresholding the data provides a convenient way of converting a data stream into a quantitative blowout indicator; e.g. an LBO avoidance logic can be invoked when the data exceeds a threshold level a certain number of times.

Thresholding worked quite well when applied to the raw optical and ion sensor outputs. Because the acoustic signal is a spatially integrated measure of the unsteady heat release over the entire flame, very pronounced changes in the heat release in a localized region of the flame may not be very evident in the overall signal. As such, we found thresholding techniques to be most useful when performed after wavelet-based filtering of the acoustic data.[20] The advantage of identifying a "customized" wavelet lies in its ability to accentuate the amplitude of time-localized events whose shape resembles that

of the wavelet. An example is shown in Figure 8; the dashed lines correspond to a threshold of 1.02σ (σ is the variance of the wavelet coefficient for the stable combustion case). Near blowout, many more events (threshold crossings) occur. The effect of threshold upon level crossing frequency of the wavelet filtered acoustic signal can be understood from Figure 9, which plots the PDF of the wavelet coefficients for ϕ/ϕ_{LBO} = 1.8, 1.1 and 1.01 at a wavelet scale of 18.5 Hz. The increased presence of high amplitude outliers close to blowout results in the long tail in the PDF. The figure indicates that the signal from the stable flames rarely exceeds ~1σ.

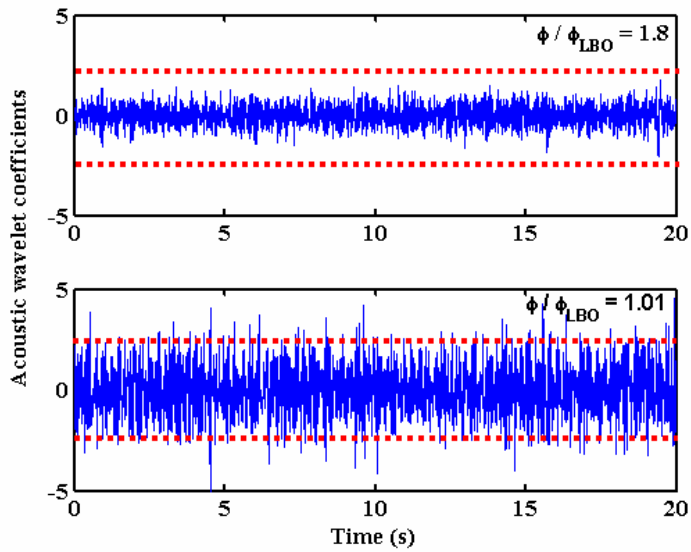

Figure 8. Time dependence of computed $W_2(t)$ wavelet coefficients of acoustic signal at a scale of 18.5 Hz for ϕ/ϕ_{LBO} = 1.8 and 1.01.

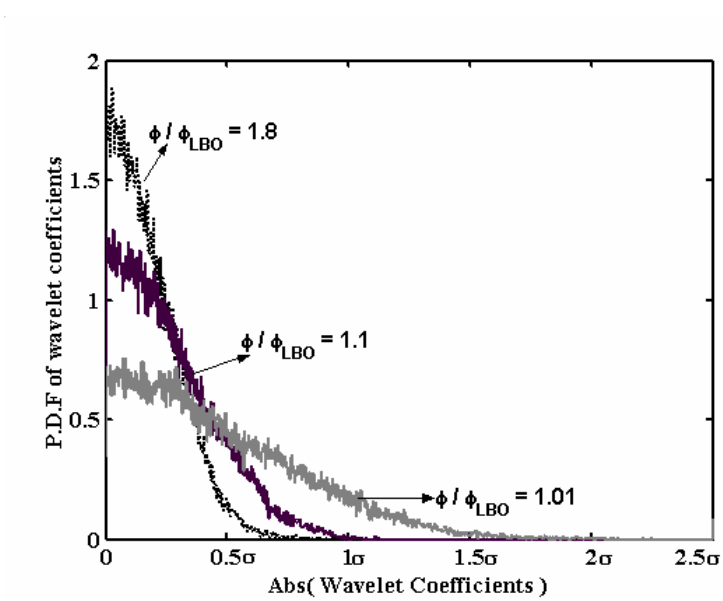

Figure 9. P.D.F of acoustic wavelet coefficients at a scale of 18.5 Hz for of ϕ/ϕ_{LBO} = 1.8, 1.1 and 1.01.

IV.A.1 Results

The ability to determine proximity to LBO is illustrated in Figure 10, which shows the dependence of the number of acoustic events upon ϕ/ϕ_{LBO} at three thresholds: 0.86σ, 1.02σ and 1.21σ. There are two influences of the threshold level: number of events detected and the ϕ/ϕ_{LBO} value where events are first detected. With increasing threshold level, there are fewer events detected. Furthermore, no events are detected until the system is very close to blowout. In contrast, at low thresholding levels, the frequency and duration of the alarms close to blowout is much higher, however, events are detected at equivalence ratios much farther from blowout.

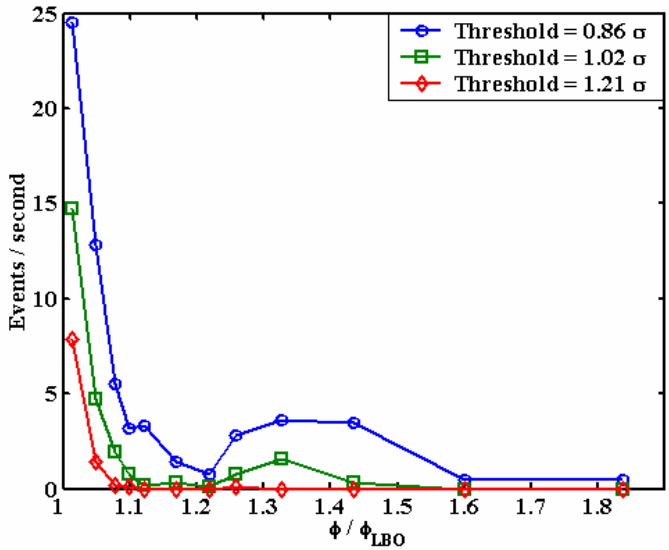

Figure 10. Dependence of the number of acoustic events upon ϕ/ϕ_{LBO} for three thresholding levels of 0.86σ, 1.02σ and 1.21σ.

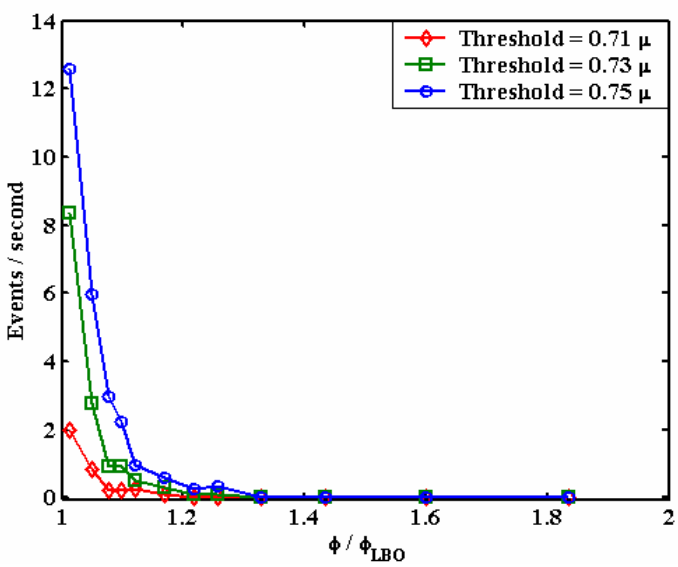

Figure 11. Dependence of the number of ion events upon ϕ/ϕ_{LBO} for three thresholding levels of 0.71μ , 0.73μ and 0.75μ.

Results for thresholding of the raw ion signal are shown in Figure 11 for three (lower) thresholds of 0.71μ, 0.73μ and 0.75μ (where μ is the time-localized mean of the ion signal). The number of events detected clearly increases as LBO is approached. Similar results and tradeoffs as illustrated in the case of the acoustic signal are observed for the ion signal as well.

During the latter part of this effort, our efforts were refocused on extending the blowout precursor sensing to hydrogen-enhanced natural gas combustors and syngas fueled combustors. Experiments were performed in the high pressure, swirl-stabilized gas turbine model combustor with acoustic and optical sensing. Figure 12 shows results obtained for a hydrogen-doped natural gas case. As in the earlier tests, the occurrence of the LBO precursors increases dramatically as the combustor approaches its blowout limit. Figure 13 shows similar result for a syngas mixture. What is dramatically different in the results is the way the precursor rate increase near LBO. For the natural gas case, the rise is relatively gradual, with precursors beginning around $\Delta\phi$=0.02 before the LBO limit. For the syngas case, the rise is much more rapid, with $\Delta\phi$=0.005. While the syngas fuel does produce a more stable combustion, the change in the precursor behavior is primarily limited to the way in which the threshold was chosen for the optical sensor.

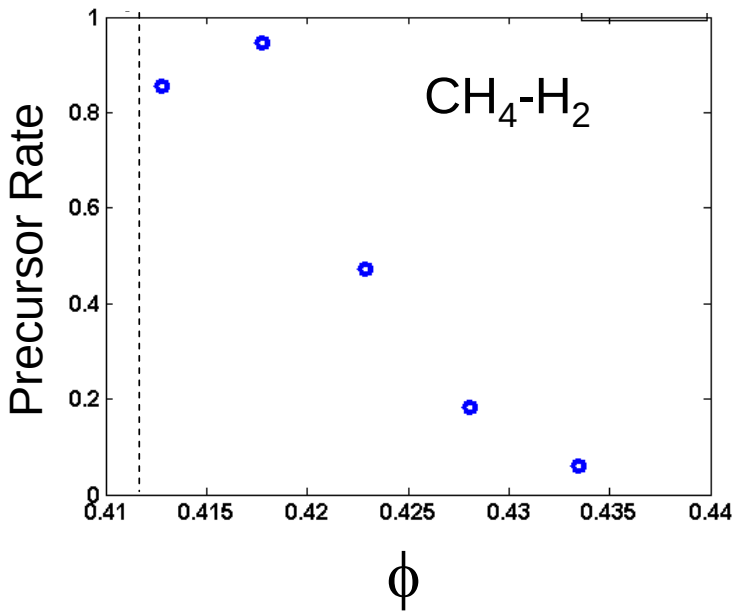

Figure 12. LBO sensor output as a function of operating fuel-air ratio for a natural gas fuel with a small amount of hydrogen added. The combustor was run preheated at a pressure of 1.5 atm. LBO occurs just before an equivalence ratio of 0.41 (as indicated by the dashed line).

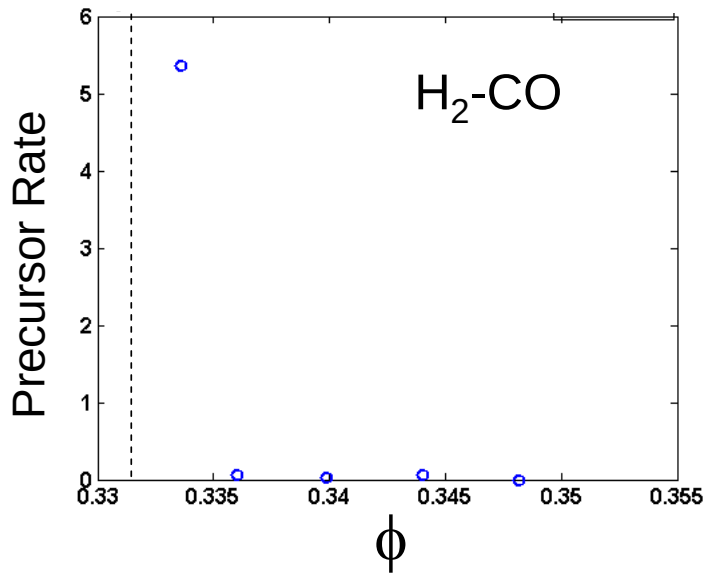

Figure 13. LBO sensor output as a function of operating fuel-air ratio for a syngas mixture. The combustor was run preheated at a pressure of 1.6 atm. LBO occurs just before an equivalence ratio of 0.33 (as indicated by the dashed line).

As part of this effort, we have worked with Alta Solutions, a turbine monitoring company, to code up and test an acoustic technique for monitoring blowout margin. We have shared our code with Alta and several test data sets. They are working to bring this technique to turbine field testing.

IV.B. Flame Zone Sensors

IV.B.1 Natural Gas Combustion

In the initial phase of this work, the flame zone sensing effort focused on examining the ratio of chemiluminescence from different species to monitor equivalence ratio (ϕ). We examined the chemiluminescence signals from the open tube burner (Figure 1), the confined, swirling combustor (Figure 2) and the high pressure, gas turbine combustor (Figure 3). Over most equivalence ratios of interest to modern gas turbines (ϕ<1.1) , CH and OH radiation are the dominant sources in natural gas combustion.

We examined the relative slope sensitivity, *S,* of the chemiluminescence signal, defined as,

$$S = \frac{d\left(CH^*/OH^*\right)}{d\phi}\frac{1}{\left(CH^*/OH^*\right)}$$

where CH^* is the chemiluminescence signal from the CH radical, and OH^* represents the OH chemiluminescence. Figure 14 shows results for methane (99.99% purity) and natural gas in the three combustor. Within the accuracy of the measurements, the difference between methane and natural gas is negligible. Thus small variations in the composition of natural gas should not effect this sensing approach. The good agreement in the various systems also shows that *S* is not a strong function of combustor geometry or overall flow velocity. This apparently universal behavior of the CH^*/OH^* signal was achieved only

when the data are properly corrected for broadband background emission due to CO_2^* chemiluminescence and blackbody (wall) radiation.

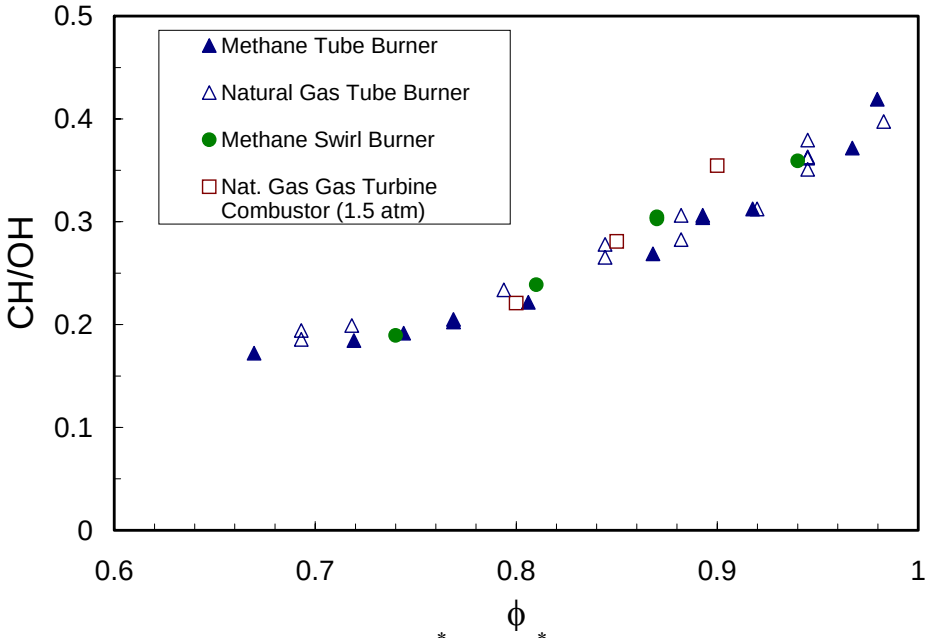

Figure 14. Comparison of the CH^* to OH^* chemiluminescence ratio in the three combustors studied.

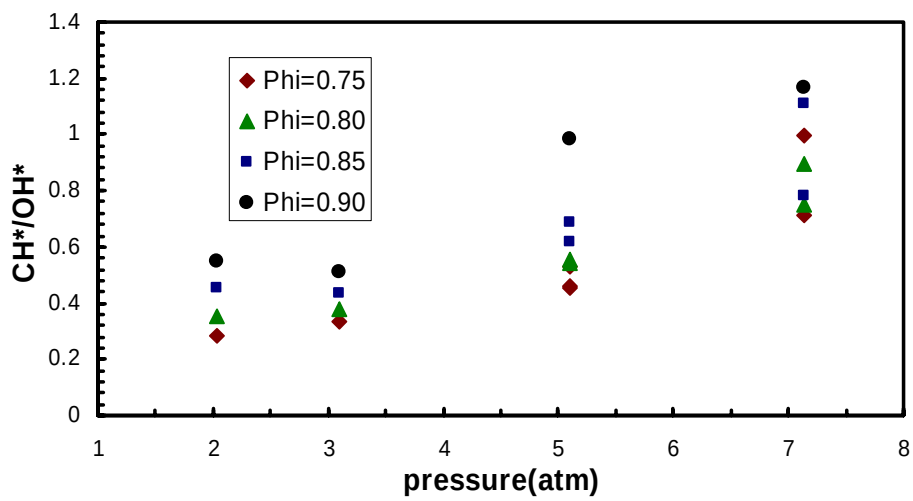

Figure 15. CH to OH chemiluminescence ratio measured in the high pressure, gas turbine combustor simulator at various pressures (absolute) for fixed mass flow rate (30g/s).

We also examined the effect of pressure on CH^*/OH^*. Results were obtained in the Georgia Tech high pressure gas turbine combustor simulator. As indicated in Figure 15, increases in fuel-air ratio still increase CH^*/OH^*. However, increasing the pressure at a fixed fuel/air ratio also generally increases CH^*/OH^*. Thus, use of this approach to monitor equivalence ratio (or fuel-air mixing variations) may also require measurement of the combustor pressure. This requirement is not severe, however, since combustor pressures are normally monitored, and because the sensitivity to pressure is not dramatic.

Figure 16 shows the separate OH^* and CH^* radiation. For lean cases, both signals increase with equivalence ratio (ϕ) and pressure. At higher ϕ, however, the signals drop with pressure. Part of this is likely due to the relative increase in the quenching collision rate of the excited state at high pressures, as compared to the production rates of OH and CH from chemical reactions. However, these results are also influenced by background radiation from the flameholder. At higher pressures, the flame sits on the flameholder, whose temperature therefore increases. This makes the background radiation underlying the (visible) CH* emission much greater than the CH^* signal (Figure 17). Thus, we conclude that some of the pressure dependence observed is due to difficulties in determining the true CH* signal at high pressures, where the flame in the current combustor sits close to the flameholder.

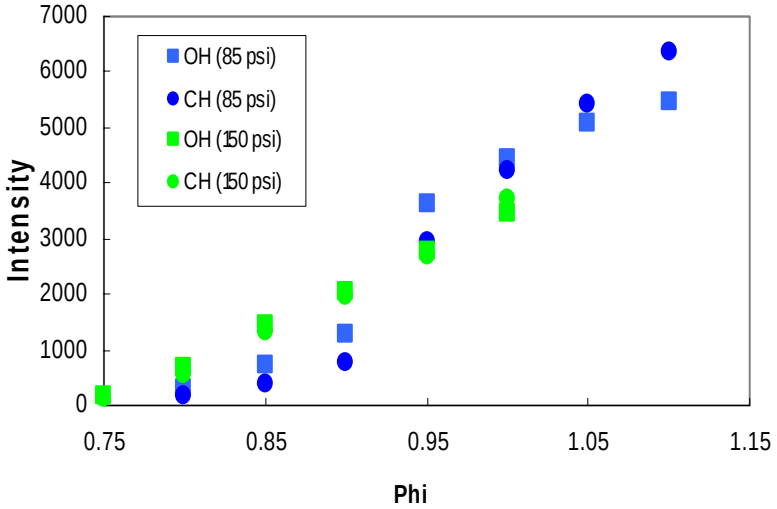

Figure 16. Chemiluminescence from OH* and CH* for a flowrate of 50 g/s at two pressures.

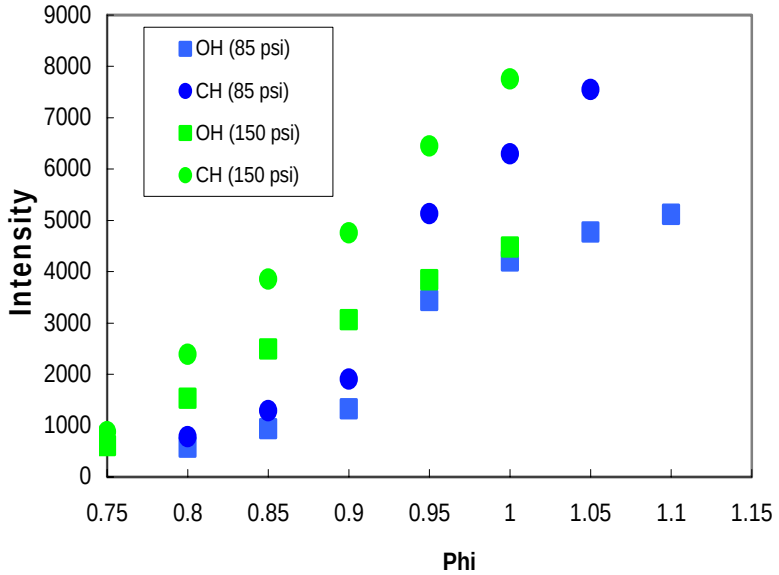

Figure 17. Background signals underlying the OH* and CH* for the same conditions of Figure 16.

IV.B.2 Syngas Combustion and Modeling

During the latter portion of this program, we focused on characterizing chemiluminescence from syngas fueled combustors. Such fuels are usually composed of varying amounts of H_2, CO, CO_2, H_2O and N_2, as well as other trace or minor species. The fuel species in these mixtures are H_2 and CO, while the other gases act primarily as diluents. The primary chemiluminescence species in these flames were found to be OH*, produced primarily through hydrogen oxidation reactions and CO_2*, produced primarily by the combination reaction of CO with O. The OH* emission is the narrow peak at ~310 nm, while CO_2* gives broadband emission centered in the blue part of the spectrum. For the results here, the CO_2^* emission is recorded at 375 nm.

It was found that the ratio, CO^*_2/OH^*, was only a weak function of equivalence ratio. In order to understand this better, we decided to attempt to model the chemiluminescence in this relatively simple chemical mixture. According to Ref. [21], chemiluminescence from CO_2^* can be modeled as a multistep mechanism, written in its simplest form as,

$CO + O + M \leftrightarrow CO_2^* + M$

$CO_2^* \rightarrow CO_2 + h\nu$

$CO_2^* + M \leftrightarrow CO_2 + M$

Assuming the first step proceeds slowly compared to the last step, the volumetric chemiluminescence rate can be modeled as

$$R_{CO_2^*} = k_{CO_2^*}[CO][O]$$

where $k_{CO_2^*}$ is 4.1×10^{29} $e^{-2300K/T}$ (photon/s)(cm^3/mol^2). Similarly, Petersen *et al.*[22] have proposed that OH* emission in hydrogen fueled systems is dominated by the reactions

$H + O + M \leftrightarrow OH^* + M$

$OH^* \rightarrow OH + h\nu$

$OH^* + Q \leftrightarrow OH + Q$

where Q is a third body quencher, e.g., water has a high efficiency as a quencher. Again making the assumption that the chemical formation step proceeds slowly, and the quenching is fast (typical rates would be 10^8-10^9 s), one can write the volumetric chemiluminescence rate as

$$R_{OH^*} = \frac{k_{OH*}}{\sum_i \eta_i T^n e^{-T_i/T}[Q_i]}[H][O]$$

where k_{OH*} is 2.5×10^{39} $e^{-3600K/T}$ (photon/s)(cm^3/mol^2) and η_i, n and T_i depend on the specific quenching species.

We used a laminar flame model (Chemkin PREMIX with GRIMech 3.0) to calculate the variation of T and composition across various syngas flames. Then the chemiluminescence was calculated from the two rate given above. Figure 18 shows results for a specific composition, with the reactants at room pressure and temperature. As expected, most of the chemiluminescence is produced in the reaction zone where most of the heat release occurs.

Figure 19 shows comparisons of our modeling and experiments (also in a laminar flame) for the OH^* and CO_2^* ratio for four fuel compositions and over a range of fuel-air

ratios. Similarly, Figure 20 shows results for preheated and diluted 50:50 $CO:H_2$ fuel compositions. The agreement between the modeling and experiments is quite remarkable, suggesting that the modeling can be used to better understand and predict the behavior of chemiluminescence sensors in syngas combustors. Both experiments and modeling show little dependence of the chemiluminescence ratio on equivalence ratio for $\phi>0.7$. There is a more significant dependence for leaner mixtures, which may be important for undiluted H_2/CO syngas compositions, which would likely be burned in lean mixtures due to the high flame temperatures.

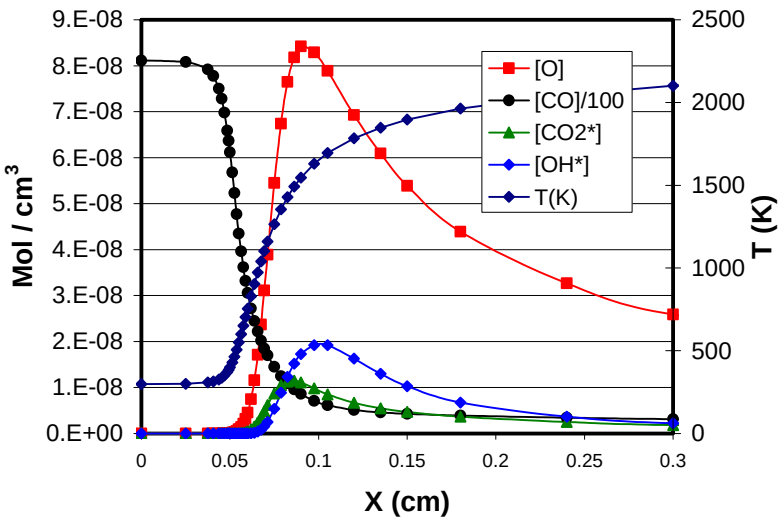

Figure 18. Laminar flame model results for composition, temperature and OH^* and CO_2^* variation across a syngas flame.

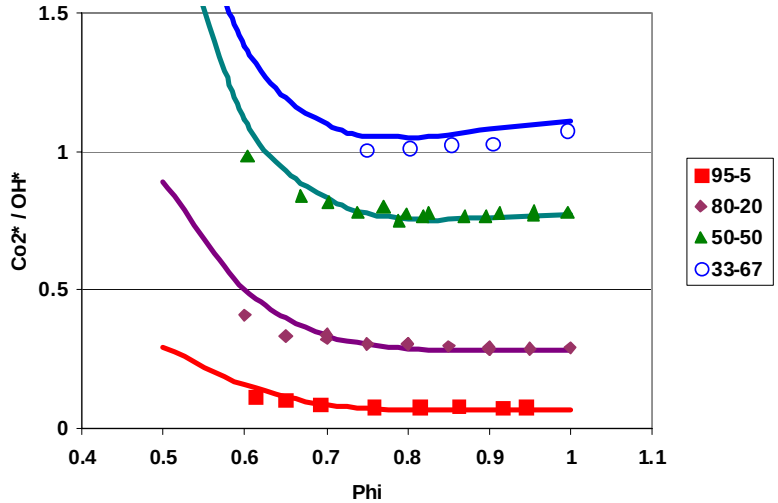

Figure 19. Comparison of model and experimental results for the chemiluminescence ratio CO_2^*/OH^* for various H_2:CO compositions and equivalence ratios (symbols=exper., lines=model).

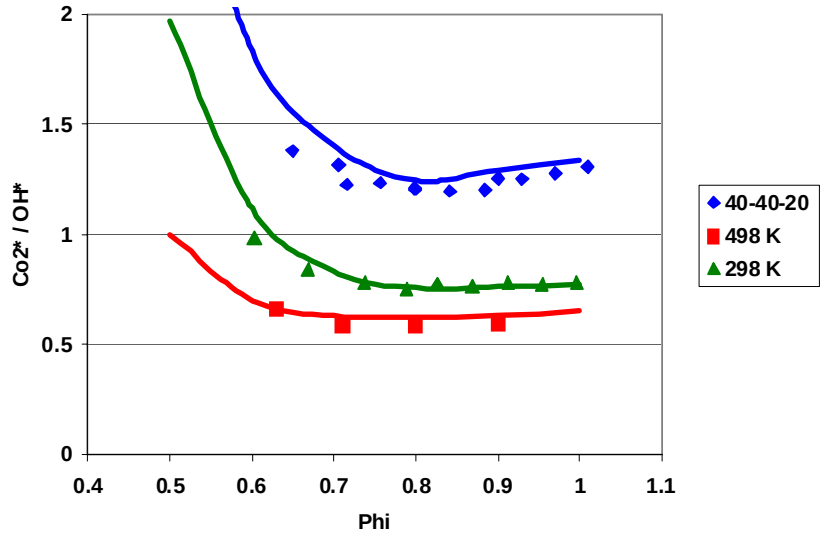

Figure 20. Comparison of model and experimental results for the chemiluminescence ratio CO_2^*/OH^* for a 50:50 H_2:CO composition at two initial temperatures (298 and 498 K), and for 298 K and 20% CO_2 dilution (symbols=exper., lines=model).

The results are also able to predict the absolute CO_2^* and OH^* signals. The results showed that both scale linearly with fuel flow rate for a fixed equivalence ratio, but both increase with increasing fuel-air ratio. Thus, the modeling is able to predict the response of the sensors to heat release rate variations.

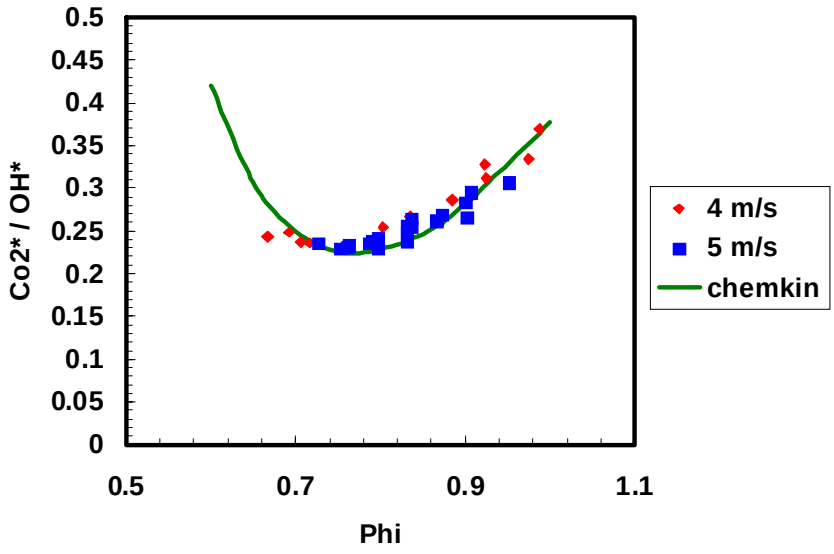

Figure 21. Comparison of model and experimental results for the chemiluminescence ratio CO_2^*/OH^* for methane-air combustion in the swirl-stabilized, atmospheric pressure combustor.

This ability to predict chemiluminescence signals via modeling is a new contribution of this work. The robustness of the method is indicated in Figure 21. We employed the

same modeling approach, except with one step added to the OH* mechanism due to a reaction with CH^{23} to model CO_2^*/OH^* for the earlier methane/natural gas results. As in the syngas studies, the modeling results are able to accurately predict the measurements.

IV.C. Combustor Dynamics Stability Margin Sensors

Currently, when turbines are being commissioned or simply going through day to day operation, the operator has no idea how the stability of the system is affected by changes to fuel splits/operating conditions unless, of course, the system actually becomes unstable (which could result in, for example, flame blowoff and complete system shutdown). This point is illustrated in Figure 22 below, which plots combustor pressure amplitude data obtained from Georgia Tech's gas turbine combustor simulator. This figure shows that the combustor was stable and unstable at inlet velocities above and below, respectively, about 23.5 m/s. Suppose now that this system is operated under a stable condition, say at an inlet velocity of 22 m/s. Although the turbine operator will know that the system is stable, they will not, in general, know how close the system is to instability.

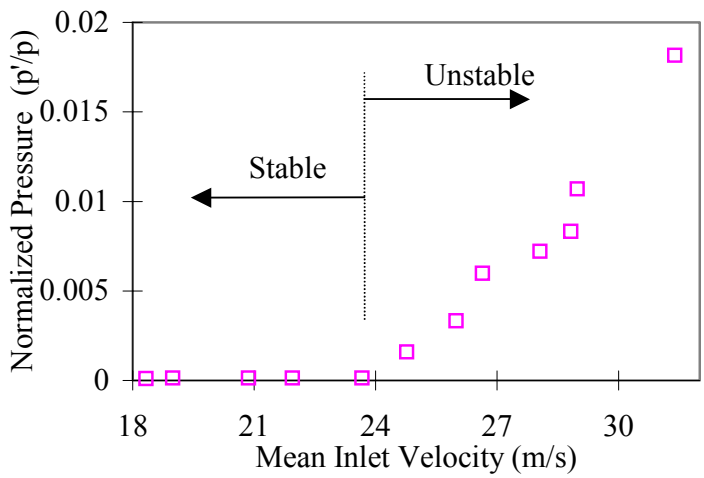

Figure 22. Variation of 630 Hz dynamic pressure amplitude in combustor with inlet velocity. Data obtained from Georgia Tech's gas turbine combustor simulator.

As part of the reported effort, we developed and tested an autocorrelation analysis of pressure data as a methodology for ascertaining stability margin. The autocorrelation of a signal is defined as:

$$C(\tau) = \frac{\int_0^T p'(t)p'(t+\tau)dt}{\int_0^T p'^2(t)dt} \qquad [2]$$

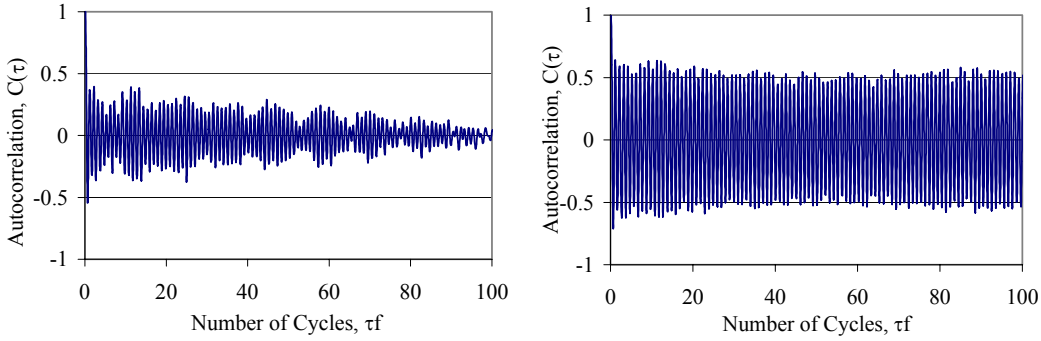

(a) (b)

Figure 23. Dependence of autocorrelation of acoustic pressure measured under stable (Figure 23-a, at inlet velocity of 21 m/s, see Figure 22) and unstable (Figure 23-b, at inlet velocity of 27 m/s) conditions.

IV.C.1 Stable Operation

Figure 23 plots two autocorrelations of the same data shown in Figure 22 measured under stable and unstable conditions. It is important to note the qualitatively different characteristics of these autocorrelations with increasing delay, τ. Under stable conditions, the amplitude of the autocorrelation steadily decays, while it remains relatively constant under unstable conditions. It is this behavior under stable conditions that is of interest here. Under these conditions the oscillations are driven by ambient background noise, but are damped. The decay in autocorrelation is physically due to the fact that this damping causes a loss of "memory" in the system, which causes oscillations at separate time instants to become increasingly uncorrelated. These points are illustrated by referring to the following equation:

$$\frac{d^2p'}{dt^2} + 2\varsigma\omega_o \frac{dp'}{dt} + \omega_o{}^2 p' = \xi(t) \qquad [3]$$

Such a second order oscillator equation resembles that typically used to model small amplitude oscillations in combustion chambers.[24] The variables p', ζ, ω_o, and ξ denote the unsteady pressure, damping, natural frequency, and background noise excitation, respectively. This is a linear equation and is suitable for describing combustor dynamics under *unstable* conditions, because inclusion of nonlinearities is necessary. The Fourier transform of the unsteady pressure described by this equation can be determined using standard techniques in spectral analysis. In turn, once the Fourier transform of the unsteady pressure is known, the autocorrelation, $C(\tau)$ can be determined from the inverse transform of the power spectrum using the Wiener-Khinchin theorem. It can be shown that the autocorrelation of Eq. [3] is given by:

$$C(\tau) = e^{-\omega_o\varsigma\tau}(\cos(\omega_o\tau\sqrt{1-\varsigma^2}) + \varsigma/\sqrt{1-\varsigma^2}\,\sin(\omega_o\tau\sqrt{1-\varsigma^2})) \qquad [4]$$

The result is an *expression that relates the autocorrelation to the system damping*.

It was found that the autocorrelation decays at a rate that can be modeled as

$$C = e^{-cycles*a} \qquad [5]$$

where C is the autocorrelation coefficient, *cycles* is the instability frequency multiplied by time, and a is the **slope of the autocorrelation curve**. Because C is already calculated by the autocorrelation relationship [4], and the number of cycles is known (for a *known* instability frequency), a can be found using simple linear regression between cycles and the logarithm of C.

Figure 24 shows the slope trends for the entire range of inlet velocities. In order to see how well the autocorrelation predicts the onset of instabilities, the slope data (circles) is plotted with pressure amplitudes (crosses). It is readily apparent that as instability is approached, the slope data gradually decreases. The pressure data in conjunction with the slope data shows that the autocorrelation analysis not only determines whether or not a combustor is operating stably, it can be used as a method to determine the margin of that stability.

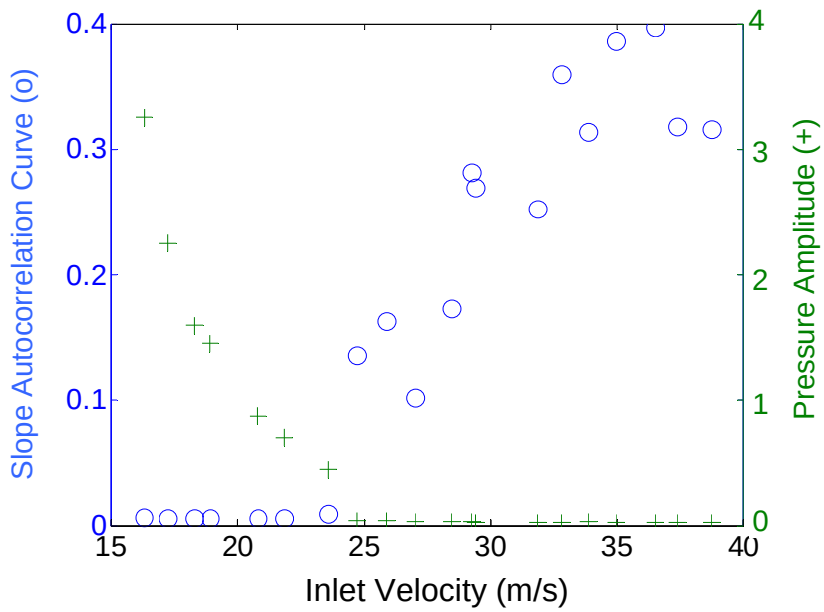

Figure 24. Slope of autocorrelation curve for varying inlet velocities, plotted with pressure amplitudes (Data filtered about 430 Hz)

IV.C.2 Field Testing of Stability Margin Algorithm

This algorithm was licensed to Alta Solutions, a well known turbine monitoring company whose software has been installed on a large number of Westinghouse and GE engines. Alta incorporated our algorithm into a software package compatible with their diagnostics, developed a graphical user interface that the turbine operator could use to adjust algorithm parameters, and implemented it at two beta sites, in cooperation with Calpine Corporation. A screen shot of this software module is illustrated in Figure 25.

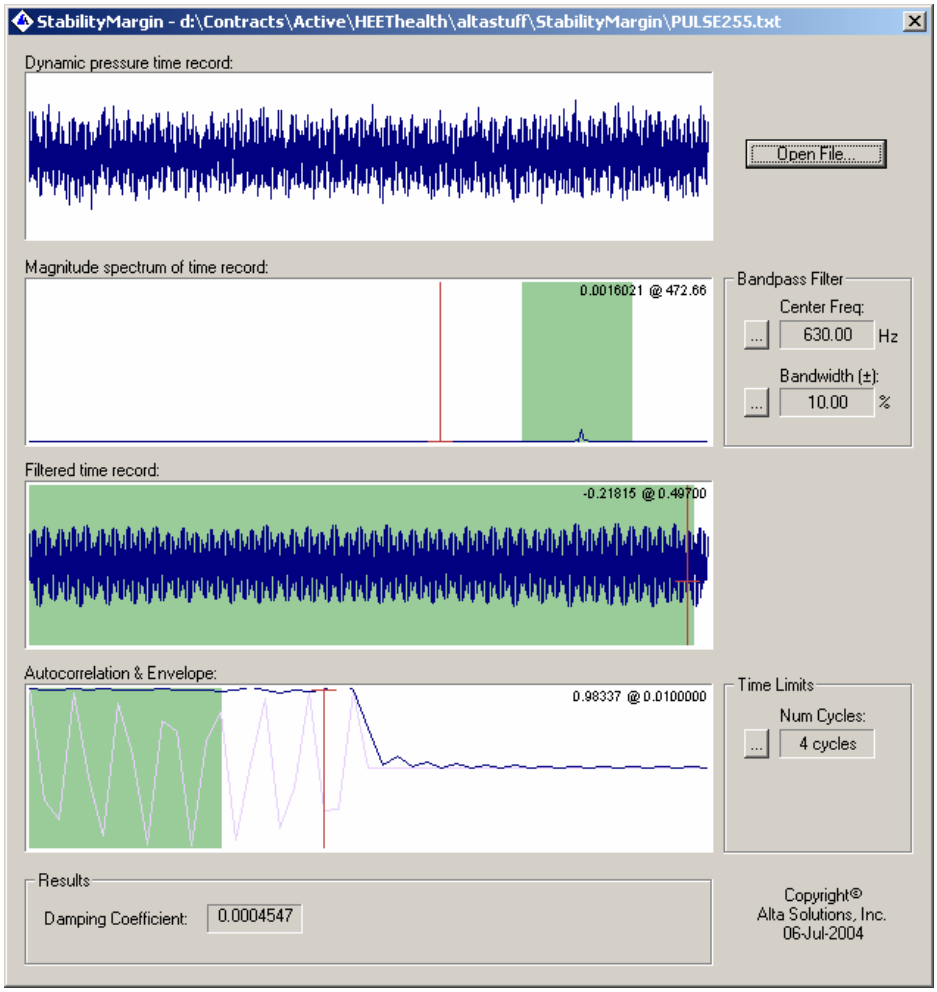

Figure 25. Relation between combustor damping parameter and observed pressure amplitude oscillations.

The Calpine installation data were evaluated, with a key question being the extent to which the algorithm could be used to discern relative differences in stability margin from one combustor can to another. Since combustor cans can acoustically interact, the measurements in each can are somewhat contaminated by others. To address this question, we determined the cross correlation between pressure oscillations measured in different combustor baskets, see Figure 26. This figure shows the correlation between one basket and another spaced a distance apart given by the number on the x axis. For example at a "Distance from Basket" of four, we evaluated the correlation between each combustor and the one 4 cans away from it. The data shows cross correlation values of about 0.35 between baskets next to each other, but that the value drops below 0.15 at larger separations. This data implies that the stability margin from each can is corrupted only by the baskets on either side; baskets farther away make a negligible contribution.

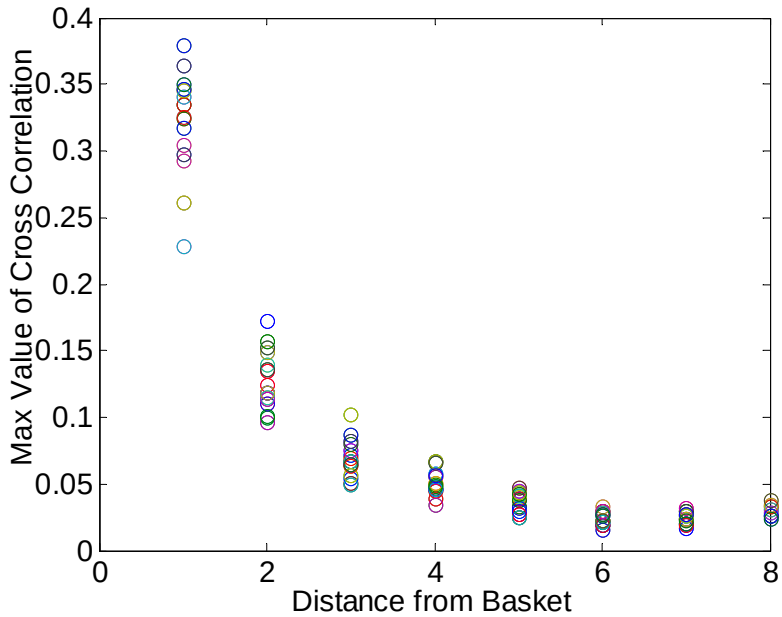

Figure 26. Dependence of cross correlation between oscillations in different combustor baskets.

In addition, data from Solar Turbines and KEMA show that the algorithm is effective over a wide range of conditions.

IV.C.3 Stability Margin in Unstable Operation

The stability margin technique described previously is applicable only to situations where the combustor is stable. The latter portion of this effort focused on developing techniques to evaluate stability margin when the combustor is unstable. This is a substantially more complicated problem as the analysis is no longer linear, but requires analysis of nonlinear, stochastic differential equations. However, the basic idea is similar – to determine the value of the instability growth or damping rate.

The basic analytical approach follows from prior work on statistically characterizing pressure oscillations in unstable combustors.[25] Acoustic oscillations in combustion chambers can be modeled as the superposition of nonlinearly interacting oscillators, where each oscillator typically represents a natural acoustic mode of the combustor. Accordingly, by retaining the contributions of the first *m* modes of oscillation, the pressure at a single point in the combustor can be written as:

$$p'(t) = \sum_{i=1}^{m} \eta_i(t) \qquad [6]$$

$$\frac{d^2\eta_i(t)}{dt^2} + \omega_i^2\eta_i(t) = \frac{\alpha_i}{\omega_i}\frac{d\eta_i(t)}{dt} + \theta_i\eta_i(t) - \hat{f}(\eta_j(t), \frac{d\eta_j(t)}{dt}, \ldots)\ i, j = 1, 2, \ldots m \qquad [7]$$

where the function $\hat{f}$ describes the nonlinearities in the system (specific expressions for $\hat{f}$ are introduced by gas dynamical or combustion processes). Here, we investigated a slightly modified form of Eq. (7) that incorporates the effects of temporal perturbations of

the system parameters and external forcing of the oscillators by "background noise" (e.g., by turbulent fluctuations) in the combustor:

$$\frac{d^2\eta_i(t)}{dt^2} + \omega_i^2\eta_i(t) = (\frac{\alpha_i + \tilde{\alpha}_i(t)}{\omega_i})\frac{d\eta_i(t)}{dt} + (\theta_i + \tilde{\theta}_i(t))\eta_i(t) - ((\hat{f} + \tilde{f})(\eta_j(t), \frac{d\eta_j(t)}{dt}, ...)) + \xi_i(t) \qquad i, j = 1, 2, \ldots m \qquad [8]$$

where $\tilde{\alpha}_i(t)$, $\tilde{\theta}_i(t)$, and $\tilde{f}$ denote parametric disturbances of the instability growth rate, frequency, and system nonlinearities, respectively, and $\xi_i(t)$ denotes an external excitation.

To reduce the complexity of this system of equations while retaining most of the important physical features of the investigated problem we assumed that: 1) the unsteady pressure is dominated by the oscillations of a single mode that interacts nonlinearly with itself, 2) the parametric excitation terms are negligible, 3) the correlation time of the external excitation is small relative to the other pertinent time scales of the problem and, thus, $\xi(t)$ is idealized as a random, white noise source, and 4) the terms on the right hand side of Eq. (3) are "small".

With these assumptions, Eqs. (6) and (8) are combined to yield:

$$\frac{d^2p'(t)}{dt^2} + \omega^2 p'(t) = \frac{\alpha}{\omega}\frac{dp'(t)}{dt} + \theta p'(t) - \hat{f}(p'(t), \frac{dp'(t)}{dt}) + \xi(t) = - f(p'(t), \frac{dp'(t)}{dt}) + \xi(t) \qquad [9]$$

Since the pressure oscillations are nearly harmonic, it is convenient to decompose $p'(t)$ and $dp'(t)/dt$ in the following manner:

$$p'(t) = A(t)\cos(\omega t + \sigma(t)) \qquad [10]$$

$$dp'(t)/dt = -A(t)\,\omega\sin(\omega t + \sigma(t)) \qquad [11]$$

where $A(t)$ and $\sigma(t)$ denote the fluctuating amplitude and phase of the oscillations. Using Eqs. (10-11), Eq. (9) can be rewritten as the following set of first order differential equations for the instability amplitude and phase:

$$\frac{dA(t)}{dt} = \frac{\sin\Phi}{\omega}(f(A\cos\Phi, -A\omega\sin\Phi) - \xi(t)) \qquad [12]$$

$$\frac{d\sigma(t)}{dt} = \frac{\cos\Phi}{A\omega}(f(A\cos\Phi, -A\omega\sin\Phi) - \xi(t)) \qquad [13]$$

where $\Phi = \omega t + \sigma(t)$.

Equations (12-13) describe the dynamics of the oscillatory amplitude, $A(t)$, and phase, $\sigma(t)$. Rather than analyzing the temporal evolution of $A(t)$ and $\sigma(t)$, however, the objective of this analysis is to determine their statistical characteristics. The Fokker-Planck equations for the PDF's of A and σ are:

$$W(A) = CAe^{-\frac{2\omega}{\pi S(\omega)}\int_0^A F(\psi)d\psi} \qquad [14]$$

$$W(\sigma) = 1/2\pi \qquad [15]$$

where C is a normalizing constant, $S(\omega)$ is the power spectral density of the noise $\xi(t)$ at the frequency ω, and:

$$F(A) = -\frac{1}{2\pi}\int_0^{2\pi} f(A\cos\Phi, -A\omega\sin\Phi)\sin\Phi d\Phi \qquad [16]$$

No additional assumptions on the function f are required. Examination of these expressions shows that the amplitude PDF, W(A), depends upon the system nonlinearities and instability growth rate through the function F(A). The phase PDF, $W(\sigma)$, is uniform; i.e., *there is equal probability that* $\sigma(t)$ *will equal any value*, $-\pi<\sigma<\pi$ and, in contrast to the amplitude PDF, no value of $\sigma(t)$ has maximum probability. Furthermore, this result is true regardless of the system parameters and nonlinearities. Thus, phase analysis provides no information for us on system parameters.

In order to complete the analytical description of W(A) in Eq. (14), it is necessary to derive an expression for the function F(A). This can be accomplished in a general fashion by expanding the function f(p', dp'/dt) in the following Taylor series:

$$\begin{aligned} f(p', dp'/dt) = {} & -\theta p' - \frac{\alpha}{\omega}\frac{dp'}{dt} + b_{20}p'^2 + \frac{b_{02}}{\omega^2}(\frac{dp'}{dt})^2 + \frac{b_{11}}{\omega}p'\frac{dp'}{dt} + b_{30}p'^3 + \frac{b_{21}}{\omega}p'^2\frac{dp'}{dt} + \frac{b_{12}}{\omega^2}p'(\frac{dp'}{dt})^2 + \frac{b_{03}}{\omega^3}(\frac{dp'}{dt})^3 \\ & + b_{40}p'^4 + \frac{b_{31}}{\omega}p'^3\frac{dp'}{dt} + \frac{b_{22}}{\omega^2}p'^2(\frac{dp'}{dt})^2 + \frac{b_{13}}{\omega^3}p'(\frac{dp'}{dt})^3 + \frac{b_{04}}{\omega^4}(\frac{dp'}{dt})^4 \end{aligned} \qquad [17]$$

where the b_{ij}'s are constants. Although f(p', dp'/dt) is truncated at fourth order in Eq. (17), it can be expanded to an arbitrary order in a straightforward manner. Substituting Eq. (17) into Eq. (16) yields:

$$F(A) = -\frac{\alpha A}{2} + (\frac{3b_{03} + b_{21}}{8})A^3 + \ldots = -\frac{\alpha A}{2} + \frac{k^2}{2}A^3 + \ldots \qquad [18]$$

Equation (13) shows that only three out of the fourteen terms in Eq. (12) contribute to F(A). Furthermore, two out of the three nonlinearities combine into a single cubic term. Inserting Eq. (13) into Eq. (9) yields the final result for the PDF of the mode's amplitude:

$$W(A) = \frac{4}{\sqrt{\pi}}\frac{\sqrt{\frac{k^2\omega}{\pi S(\omega)}}e^{-\frac{\alpha^2\omega}{4\pi k^2 S(\omega)}}}{1+\mathrm{erf}\sqrt{\frac{\alpha^2\omega}{4\pi k^2 S(\omega)}}}Ae^{\frac{\omega A^2}{\pi S(\omega)}(\alpha - k^2A^2)} \qquad [19]$$

Introducing the dimensionless amplitude $\tilde{A} = \sqrt[4]{\frac{\omega k^2}{\pi S(\omega)}}A$ yields:

$$W(\tilde{A}) = \frac{4}{\sqrt{\pi}}\frac{e^{-\Omega^2/4}}{1+\mathrm{erf}(\Omega/2)}\tilde{A}e^{\tilde{A}^2(\Omega-\tilde{A}^2)} \qquad [20]$$

where $\Omega = \frac{\alpha}{|k|}\sqrt{\frac{\omega}{\pi S(\omega)}}$. Significantly, Eq. (20) shows that $W(\tilde{A})$ only depends upon the parameter Ω, which in turn is directly proportional to the instability damping or growth rate, α. As opposed to our prior analysis, this result is applicable to situations where the combustor is either stable or unstable.

V. SUMMARY

Sensor methods were developed and tested for three specific applications: 1) sensing proximity static combustor stability loss (lean blow out); 2) determining local flame zone variables such as fuel-air ratio variations that can arise from unmixedness; and 3) sensing combustor dynamic stability margin, i.e., detecting how close the system is to the point where detrimental combustion instabilities would occur. Our work focused on physics-based analysis methods to extract relevant combustor performance and status information primarily from the light and sound naturally produced by the combustion processes. These optical and acoustic emissions can easily be monitored without requiring the placement of sensors directly into the most hostile regions of the combustor. Furthermore, acoustic and optical sensors are already employed to some extent in currently fielded industrial gas turbines. We also explored ion current sensing that could be added to combustor igniters.

Static stability sensing was successfully demonstrated for optical, acoustic and ion sensing in various combustors and for both natural gas and syngas fueled systems. The approach relies on capturing precursor events using a simple and robust thresholding method. Flame zone sensors for local fuel-air ratio monitoring were demonstrated for lean natural gas fueled combustors based on properly corrected ratios of CH and OH chemiluminescence. For lean ($\phi<0.7$) syngas systems, similar results can be obtained with the ratio of CO_2 and OH chemiluminescence. In addition, physics-based modeling of the combustion process was used to predict the chemiluminescence, which should allow further improvements in this sensing approach. Finally, dynamic stability margin sensing, based on dynamic pressure measurements, was demonstrated in various combustors by monitoring the decay of the autocorrelation at the known combustor instability frequencies. This method has been field tested in cooperation with industrial partners. The method was also extended to unstable operation conditions to help operators or control systems rapidly recover stable operation should instabilities occur.

These new sensing capabilities should enable the development of control systems that actively manage engine condition and compensate for changes in ambient conditions or system degradation. Used for monitoring purposes, they should help gas turbine operators more quickly identify potential system problems, before they become serious, and allow them to vary conditions to remove the problem. Used as long term monitors of system operation, they can be used to help schedule required maintenance.

VI. REFERENCES

[1]Gaydon, A.G. and Wolfhard, H.G., "Flames: Their Structure, Radiation, and Temperature", Fourth edition, Chapman and Hall, 1978.

[2]Keller, J.O. and Saito, K., "Measurements of the Combusting Flow in a Pulse Combustor", *Combustion Science and Technology*, Vol. 53, 1987, pp. 137-163.

[3]Lawn, C.J., "Distributions of Instantaneous Heat Release by the Cross-Correlation of Chemiluminescent Emissions," *Combustion and Flame*, Vol. 132, 2000, pp. 227-240.

[4]Roby, R.J., Hamer, A.J., Johnsson, E.L., Tilstra, S.A., and Burt, T.J., "Improved Method for Flame Detection in Combustion Turbines", *Transactions of the ASME*, Vol. 117, 1995, pp. 332 –340.

[5]Mehta, G.K., Ramachandra, M.K., and Strahle, W.C., "Correlations between Light Emission, Acoustic Emission and Ion Density in Premixed Turbulent Flames", *Eighteenth Symposium (International) on Combustion,* 1981, pp 1051-1059.

[6]Bragg, S., "Combustion Noise", *J. Inst. Fuel*, Vol. 36(1), 1963.

[7]Strahle, W.C., "On Combustion Generated Noise", *J. Fluid Mech.*, Vol. 49(2), 1971.

[8] Calcote, H. F., "Mechanism for the Formation of Ions in Flames", *Combustion and Flame*, Vo1.6, 1957,pp. 385-403.

[9] Fialkov, A.B., "Investigations on Ions in Flames", *Prog. Energy Comb. Sci*., Vol. 23, 1997, pp. 399-528.

[10] J.M. Goodings, D.K. Bohme and C.W. Ng., "Detailed ion chemistry in methane-oxygen flames", *Combustion and Flame*, Vol. *36*, 1979, pp. 27-43.

[11] Keller, J.O. and Saito, K., "Measurements of the Combusting Flow in a Pulse Combustor", *Combustion Science and Technology*, Vol. 53, 1987, pp. 137-163.

[12] Nicholson, H., Field, J., "Some Experimental Techniques for the Investigation of the Mechanism of Flame Stabilization in the Wake of Bluff Bodies", *Proc. Comb. Inst*., Vol.3, 1951, pp. 44-68.

[13] Chao, Y.C., Chang, Y.L., Wu, C.Y., Cheng, T.S., "An Experimental Investigation of the Blowout Process of a Jet Flame," *Proc. Comb. Inst*., Vol.28, 2000, pp. 335-342.

[14] Hedman, P.O., Fletcher, T.H., Graham, S.G., Timothy, G.W., Flores, D.V., and Haslam, J.K., "Observations of Flame Behavior in a Laboratory-Scale Pre-mixed Natural Gas/Air Gas Turbine Combustor from PLIF measurements of OH", *Proceedings of ASME Turbo Expo*, ASME Paper GT-2002-30052, Amsterdam, Netherlands, June, 2002.

[15] Wohl, K., Kapp, N.M., and Gazley, C., "Flame Stabilization and Quenching", *Proc. Comb. Inst.*, Vol.3, 1951, pp. 3-21.

[16] Longwell, J.P., Chenevey, J., Clark, W., and Frost, E., "Flame Stabilization by Baffles in a High Velocity Gas Stream", *Proc. Comb. Inst*., Vol.3, 1951, pp. 40-44.

[17] Williams, G., Hottel, H., Scurlock, A., "Flame Stabilization and Propagation in High Velocity Gas Streams", *Proc. Comb. Inst*., Vol.3, 1951, pp. 21-40.

[18] Jensen, W.P., Shipman, C.W., "Stabilization of Flames in High Speed Flows By Pilot Flames", *Proc. Comb. Inst*., Vol.7, 1951, pp. 674-680.

[19] Williams, G.C., Shipman, C.W., "Some Properties of Rod Stabilized Flames of Homogeneous Gas Mixtures", *Proc. Comb. Inst*., Vol.4, 1953, pp. 733-742.

[20] Nair, S., Muruganandam, T. M, Meyers, A., Lieuwen, T.C., Seitzman, J.M., "Lean Blowout Detection in a Single Nozzle CFM56 Swirl Cup", *42nd AIAA Aerospace Sciences Meeting and Exhibit,* AIAA Paper 2003-5084, Reno, NV, January, 2004.

[21]Slack, M. and Grillo, A., "High-Temperature Rate Coefficient Measurements of CO + O Chemiluminescence," *Combustion and Flame*, 59 (2), 1985, pp. 189-196.

[22] Peterson, E, L., Kalitan, D, M. and Rickard, M. J. A., "Calibration and Chemical Kinetics Modeling of an OH Chemiluminescence Diagnostic," 39th AIAA/ASME/SAE/ASEE Joint Propulsion Conference and Exhibit, Huntsville, Alabama, July 20-23, 2003

[23] Petersen, E. Private Communication.

[24]Peracchio, A.A., Proscia, W.M., Nonlinear Heat Release/Acoustic Model for Thermo-Acoustic Instability in Lean Premixed ombustors, *ASME Paper # 98-GT-269*.

[25] Lieuwen, T., "Statistical Characteristics of Pressure Oscillations in a Premixed Combustor", *Journal of Sound and Vibration*, Vol. 260, 2003, pp. 3-17.

Assessment of Failure Mechanisms for Thermal Barrier Coatings by Photoluminescence, Electrochemical Impedance and Focused Ion Beam

Report Type:	Final Report
Reporting Period Start Date:	May 1, 2002
Reporting Period End Date:	November 1, 2005

Principal Investigators:	Y.H. Sohn and V.H. Desai
Affiliation:	Advanced Materials Processing & Analysis Center and Mechanical, Materials and Aerospace Engineering University of Central Florida Orlando, FL 32816-2455

Date Issued:	December 30, 2005
DOE Award Number:	DE-FC26-02NT41431
UTSR Project Number:	02-01-SR103

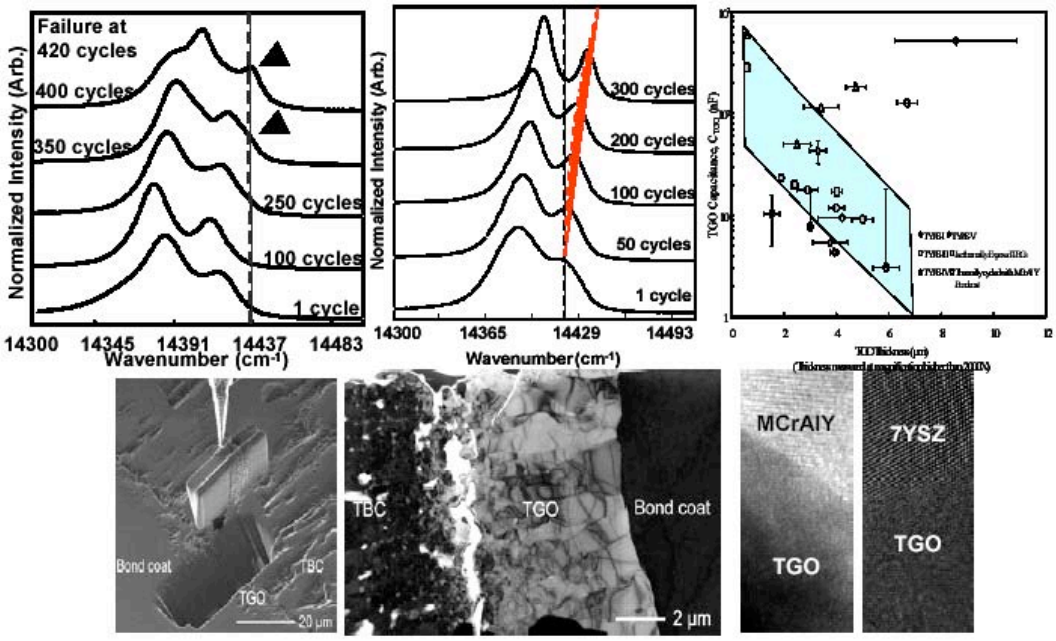

From upper left: TGO stress relief detected by photostimulated luminescence: TGO stress relaxation detected by photo luminescence: TGO thickness measurement by electrochemical impedance: From lower left: in-situ focused ion beam lift out: bright field image of thermally cycled TBC with 9mm-thick: lattice image of intact MCrAlY-TGO interface: and lattice image of intact TGO-YSZ interface.

DISCLAIMER

This report was prepared as an account of work sponsored by an agency of the United States Government. Neither the United States Government nor any agency thereof, nor any of their employees, makes any warranty, express or implied, or assumes any legal liability or responsibility for the accuracy, completeness, or usefulness of any information, apparatus, product, or process disclosed, or represents that its use would not infringe privately owned rights. Reference herein to any specific commercial product, process, or service by trade name, trademark, manufacturer, or otherwise does not necessarily constitute or imply its endorsement, recommendation, or favoring by the United States Government or any agency thereof. The views and opinions of authors expressed herein do not necessarily state or reflect those of the United States Government or any agency thereof.

ABSTRACT

Development and applications of thermal barrier coatings (TBCs) based on a clearer understanding of failure mechanisms can help increase performance efficiency and reduce the emission of advanced gas turbine engines. In addition, development and refinement of robust non-destructive evaluation (NDE) techniques can enhance the reliability, availability and maintainability (RAM) of advanced gas turbines engines. Two complimentary non-destructive evaluation (NDE) techniques, namely photostimulated luminescence spectroscopy (PSLS) and electrochemical impedance spectroscopy (EIS) along with advanced characterization techniques, including focused ion beam (FIB) in-situ lift-out (INLO) and transmission electron microscopy (TEM) and scanning TEM (STEM), were employed in this investigation to provide a better understanding of TBC failure as well as to develop and refine PSLS and EIS. This report summarizes all results obtained from this study. Data acquisition and analysis of NDE was completed by PSLS and EIS for 1-, 10- and 50-hour thermal cycling. Relevant microstructural characterization for TBCs after 1-, 10- and 50-hour thermal cycling was carried out at specified lifetime using SEM and TEM/STEM via FIB-INLO. Results from PSLS and EIS as a function of thermal cycling demonstrated outstanding assessment of TBC degradation observed via microscopy, including sub-critical damage detection.

From PSLS NDE results for two types (III and IV) we can qualitative detect the damages in the TGO scale before the actual TBC failure. These sub-critical damages were related to stress relief/relaxation from the TGO scale. Also for type-IV TBCs, the damage detection was confirmed with another technique namely EIS, in which the TGO, represented as the capacitance (C_{TGO}), increased before the actual failure. These damages are further confirmed using microscopic techniques namely OM, SEM and TEM/STEM.

This report has been independently prepared by graduate and undergraduate students and has been approved by the principal investigators of this research program.

TABLE OF CONTENTS

	Page
DISCLAIMER	**ii**
ABSTRACT	**iii**
TABLE OF CONTENTS	**iv**
LIST OF FIGURES	**vi**
LIST OF TABLES	**xx**
I. INTRODUCTION	**1**
II. EXECUTIVE SUMMARY	**6**
III. PROJECT DESCRIPTION	**8**
IV. EXPERIMENTAL	**9**
IV.1. Description and Thermal Cycling of Thermal Barrier Coatings	**9**
IV.2. Photostimulated Luminescence Spectroscopy	**10**
IV.3. Electrochemical Impedance Spectroscopy	**12**
IV.4. Microstructural Characterization	**14**
V. RESULTS AND DISCUSSION	**15**
V.1. Lifetime Assessment and Visual Observation of TBC Spallation	
V.1.1. Thermal Cycling Lifetime	**15**
V.1.2. Visual Observation of TBC Spallation for 1-hour thermal cycling-APS TBCs	**18**
V.1.3. Visual Observation of TBC Spallation for 1-hour thermal cycling-EB-PVD TBCs	**19**
V.1.4. Visual Observation of TBC Spallation for 10-hour thermal cycling-APS TBCs	**20**
V.1.5. Visual Observation of TBC Spallation for 10-hour thermal cycling-EB-PVD TBCs	**21**
V.1.6. Visual Observation of TBC Spallation for 50-hour thermal cycling-APS TBCs	**23**
V.1.7. Visual Observation of TBC Spallation for 50-hour thermal cycling-EB-PVD TBCs	**23**
V.2. Photostimulated Luminescence Spectroscopy of As-coated EB-PVD TBCs	**25**
V.2.1. As-Coated EB-PVD Thermal Barrier Coatings	**25**
V.2.2. PSLS of EB-PVD TBCs as a Function of 1-hour Thermal Cycling	**31**
V.2.3. PSLS of EB-PVD TBCs as a Function of 10-hour Thermal Cycling	**41**
V.2.4. PSLS of EB-PVD TBCs as a Function of 50-hour Thermal Cycling	**48**
V.3. Electrochemical Impedance Spectroscopy of Thermal Barrier Coatings	**51**
V.3.1. NDE of Thermally Cycled Type I APS TBCs by EIS	**51**
V.3.2. NDE of Thermally Cycled Type V APS TBCs by EIS	**56**
V.3.3. NDE of Thermally Cycled Type II, III and IV Thermal Barrier Coatings by	**61**

EIS
V.3.4. Sub-critical damage detection before actual TBC failure **70**
V.3.5.NDE of Type I APS TBCs by EIS 10 and 50-hour thermal cycling **70**
V.3.6. Selected EIS Observations for TBC Applications **76**
V.4. Microstructural Analysis of Thermal Barrier Coatings **84**
V.4.1. As-coated Type I and V Air Plasma Sprayed Thermal Barrier Coatings **84**
V.4.2. Thermally Cycled Type I and V Air Plasma Sprayed Thermal Barrier Coatings **90**
V.4.3. As-coated Electron Beam Physical Vapor Deposited Thermal Barrier Coatings **104**
V.4.4. Thermally Cycled Electron Beam Physical Vapor Deposited Thermal Barrier Coatings **111**
V.4.5. Characterization of Failure for Air Plasma Sprayed Thermal Barrier Coatings for 1-hour Thermal cycling **128**
V.4.6. Characterization of Failure for EB-PVD Thermal Barrier Coatings for 1-hour Thermal cycling **132**
V.4.7. Characterization of Failure for Air Plasma Sprayed Thermal Barrier Coatings for 10-hour Thermal cycling **140**
V.4.8. Characterization of Failure for Electron Beam Physical Vapor Deposited Thermal Barrier Coatings for 10-hour thermal cycling **143**
V.4.9. Characterization of Failure for APS Thermal Barrier Coatings for 50-hour Thermal cycling **147**
V.4.10. Characterization of Failure for Electron Beam Physical Vapor Deposited Thermal Barrier Coatings for 50-hour thermal cycling **148**

VI. CONCULSION **152**

REFERENCES **153**

LIST OF ACRONYMS AND ABBREVIATIONS **155**

APPENDIX

A. RE-PRINTS AND PRE-PRINTS OF RELATED PUBLICATIONS

LIST OF FIGURES

No.	Title	Page
1.	Backscatter electron micrographs of as-coated TBC: (a) APS YSZ on MCrAlY bond coat; (b) EB-PVD YSZ on MCrAlY bond coat; and (c) EB-PVD YSZ on (Ni,Pt)Al bond coat.	1
2.	Task-based program flow chart.	4
3.	Program schedule according to specific tasks.	5
4.	Specimen geometry for thermal barrier coatings employed in this program.	9
5.	A schematic diagram of the CM™ Rapid Temperature cyclic oxidation furnace during (a) high temperature oxidation and (b) cooling.	10
6.	A schematic diagram of photostimulated luminescence spectroscopy, and R_1-R_2 luminescence doublets from stressed and stress-free α-Al_2O_3.	11
7.	(a) N-type luminescence arising from the presence of Cr_2O_3 in α-Al_2O_3 scale, (b) luminescence from γ, α and θ-Al_2O_3 labeled G, R_1-R_2 and Q_1-Q_2, respectively.	12
8.	A schematic diagram of a typical set-up for electrochemical impedance spectroscopy.	13
9.	A model of an EIS ac equivalent circuit for TBCs with and without TGO.	14
10.	Lifetime during thermal cycling at 1121°C for five-types of TBCs. Values in parenthesis represent the number of specimen employed to determine the lifetime (a) 1- and 10-hour thermal cycling	16
11.	Lifetime during thermal cycling at 1121°C for five-types of TBCs. Values in parenthesis represent the number of specimen employed to determine the lifetime 1, 10 and 50 –hour thermal cycling.	16
12.	Dwell time life during thermal cycling at 1121°C for five-types of TBCs at 1, 10 and 50 –hour thermal cycling.	17
13.	Macro photographs illustrating failure mode of type I APS TBCs with NiCoCrAlY bondcoat with average lifetime of 527 cycles: (a) bottom surface of spalled YSZ coating and (b) top surface of bondcoat after YSZ spallation.	18
14.	Macro photographs illustrating failure mode of type V APS TBCs with NiCoCrAlY bond coat with average lifetime of 286 cycles: (a) top surface of bond coat after YSZ spallation that (b) occurred with initial damage at the edge of the button.	18

LIST OF FIGURES (Continued)

No.	Title	Page
15.	(a,b) Macro photographs illustrating failure mode of type II EB-PVD TBCs with NiCoCrALY bondcoat with average lifetime of 280 cycles.	19
16.	(a,b) Macro photographs illustrating failure mode of type III EB-PVD TBCs with as-coated (Ni,Pt)Al bondcoat with average lifetime of 418 cycles.	19
17.	Macro photographs illustrating failure mode of type IV EB-PVD TBCs with grit-blasted bondcoat with average lifetime of 362 cycles: (a) top surface of buckled YSZ and (b) disintegration of the YSZ coating afterwards.	20
18.	Macro photographs illustrating failure mode of type I APS TBCs with NiCoCrAlY bondcoat with average lifetime of 113 cycles: (a) bottom surface of spalled YSZ coating and (b) top surface of bondcoat after YSZ spallation.	20
19.	Macro photographs illustrating failure mode of type V APS TBCs with NiCoCrAlY bondcoat with average lifetime of 18 cycles: (a) bottom surface of the YSZ after spallation of the coating from the bondcoat (b) top surface of bondcoat after YSZ spallation.	21
20.	(a,b) Macro photographs illustrating failure mode of type II EB-PVD TBCs with NiCoCrAlY bondcoat with average lifetime of 25 cycles.	21
21.	(a,b) Macro photographs illustrating failure mode of type III EB-PVD TBCs with as-coated (Ni,Pt)Al bondcoat with average lifetime of 55 cycles.	22
22.	Macro photographs illustrating failure mode of type IV EB-PVD TBCs with grit-blasted bondcoat with average lifetime of 42 cycles: (a, b) top surface of buckled YSZ and (c) A magnified view of the buckling of YSZ coating.	22
23.	Macro photographs illustrating failure mode of type I APS TBCs with NiCoCrAlY bondcoat with average lifetime of 39 cycles: (a) top surface of bondcoat after YSZ spallation and (b) bottom surface of YSZ after spallation.	23
24.	Macro photographs illustrating failure mode of type V APS TBCs with VPS NiCoCrAlY bondcoat with average lifetime of 8 cycles: (a, b) top surface of delaminated YSZ and (c) A front view of the delamination of YSZ coating.	23
25.	Macro photographs illustrating failure mode of type II EB-PVD TBCs with shot-peened NiCoCrAlY bondcoat with average lifetime of 3.5 cycles: (a) top surface of buckled YSZ after 6 cycles and (b) A top surface view of buckled YSZ after 1 cycle.	24

LIST OF FIGURES (Continued)

No.	Title	Page
26.	Macro photographs illustrating failure mode of type III EB-PVD TBCs with as-coated (Ni,Pt)Al bondcoat with average lifetime of 12cycles, Large scale buckling observed in both the samples after 50-hour thermal cycling.	24
27.	Macro photographs illustrating failure mode of type IV EB-PVD TBCs with grit-blasted (Ni,Pt)Al bondcoat with average lifetime of 9 cycles, Large scale buckling observed in both the samples after 50-hour thermal cycling.	25
28.	Typical photostimulated luminescence spectrum from as-received type II EB-PVD TBCs with NiCoCrAlY bond coat.	26
29.	Typical photostimulated luminescence spectrum from as-received type III EB-PVD TBCs with as-coated (Ni,Pt)Al bond coat.	27
30.	Relative luminescence intensity from α-, γ- and θ-Al_2O_3 in TGO for as-coated type III TBCs with as-coated (Ni,Pt)Al bond coat.	27
31.	Higher average compressive residual stress of α-Al_2O_3 TGO determined from bimodal luminescence for as-coated type III TBCs.	28
32.	Lower average compressive residual stress of α-Al_2O_3 TGO determined from bimodal luminescence for as-coated type III TBCs.	28
33.	Typical photostimulated luminescence spectrum from as-received type IV EB-PVD TBCs with grit-blasted (Ni,Pt)Al bond coat: (a) 16 specimens with strong luminescence and (4) the remaining 4 specimens with low signal-to-noise ratio.	29
34.	Relative luminescence intensity from α-, γ- and θ-Al_2O_3 in TGO for as-coated type IV TBCs with grit-blasted (Ni,Pt)Al bond coat.	29
35.	Higher average compressive residual stress of α-Al_2O_3 TGO determined from bimodal luminescence for as-coated type IV TBCs.	30
36.	Lower average compressive residual stress of α-Al_2O_3 TGO determined from bimodal luminescence for as-coated type IV TBCs.	30
37.	Compressive residual stress within TGO as a function of 1-hour thermal cycling for type II EB-PVD TBCs with NiCoCrAlY bondcoat. Values of compressive residual stress were calculated from bimodal luminescence corresponding to (a) higher and (b) lower shifts in luminescence.	32

LIST OF FIGURES (Continued)

No.	Title	Page
38.	Typical photostimulated luminescence spectra as a function of 1-hour thermal cycling for type III EB-PVD TBCs with as-coated (Ni,Pt)Al bond coats. TBC spallation has occurred after 420 cycles and luminescence from stress-relieved TGO scale (marked by dotted vertical line and arrows) was observed starting 350 cycles by examining the derivatives of the spectra.	34
39.	(a) Typical derivatives of luminescence spectrum associated with stress-relieved luminescence frequency at $\upsilon \cong 14432 \pm 3$ for R_2 for 1-hour thermal cycling. (b) Number of photostimulated luminescence spectra that exhibits variation in derivative at stress-relief luminescence as a function of 1-hour thermal cycling for type III EB-PVD TBCs with as-coated (Ni,Pt)Al bond coats.	35
40.	Type-III TBCs cycled until 50% thermal cyclic life time, Relative Luminescence Intensity from θ and α (R2, R'2 & R"2) in TGO with as-coated (Ni,Pt)Al bond coat.	36
41.	Type-III TBCs cycled until 70% thermal cyclic life time, Relative Luminescence Intensity from q and a (R2, R’2 & R’’2) in TGO with as-coated (Ni,Pt)Al bond coat.	36
42.	Compressive residual stress within TGO as a function of 1-hour thermal cycling for type III EB-PVD TBCs with as-coated (Ni,Pt)Al bond coats. Values of compressive residual stress were calculated from tri-modal luminescence corresponding to tri-modal lower shifts in luminescence.	37
43.	Compressive residual stress within TGO as a function of 1-hour thermal cycling for type III EB-PVD TBCs with as-coated (Ni,Pt)Al bond coats. Values of compressive residual stress were calculated from (a) higher shift in luminescence and (b) lower shift in luminescence from bimodal and tri-modal luminescence.	38
44.	Typical photostimulated luminescence spectra as a function of 1-hour thermal cycling for type IV EB-PVD TBCs with as-coated (Ni,Pt)Al bond coats. TBC spallation has occurred after 420 cycles and luminescence from stress-relieved TGO scale (marked by dotted vertical line) was observed starting 350 cycles by examining the derivatives of the spectra.	39
45.	Compressive residual stress within TGO as a function of 1-hour thermal cycling for type IV EB-PVD TBCs with grit-blasted (Ni,Pt)Al bondcoat. Values of compressive residual stress were calculated from bimodal luminescence corresponding to (a) higher and (b) lower shifts in luminescence.	40

LIST OF FIGURES (Continued)

No.	Title	Page
46.	Compressive residual stress within TGO as a function of 10-hour thermal cycling for type II EB-PVD TBCs with NiCoCrAlY bondcoat. Values of compressive residual stress ere calculated from bimodal luminescence corresponding to (a) higher and (b) lower shifts in luminescence.	42
47.	Typical photostimulated luminescence spectra from stress-relieved TGO scale (marked by dotted vertical line and arrows) was observed as a function of 10-hour thermal cycling for type III EB-PVD TBCs with as-coated (Ni,Pt)Al bond coats. TBC spallation has occurred at 54 cycles.	44
48.	Typical derivatives of luminescence spectrum associated with stress-relieved luminescence frequency at $\upsilon \cong 14432 \pm 3$ for R_2 for 10-hour thermal cycling.	44
49.	Compressive residual stress within TGO as a function of 10-hour thermal cycling for type-III TBCs with as-coated (Ni,Pt)Al bondcoat. Values of compressive residual stress were calculated from bimodal and tri-mode luminescence.	45
50.	Typical luminescence spectrum observed as a function of 10-hour thermal cycling observed for type-IV TBCs with grit blasted (Ni, Pt)Al bondcoat. TBC spallation occurred at 44 cycles and there is no changes in the luminescence shifting towards stress free as observed in 1-hour thermal cycling.	46
51.	Compressive residual stress within TGO as a function of 10-hour thermal cycling for type-IV TBCs with grit-blasted (Ni, Pt)Al bondcoat. The values of compressive residual stress were calculated from bi-modal luminescence corresponding to higher and lower shift in luminescence (a) as a function of 10-hour thermal cycles (b) as a function of 10-hour thermal cyclic life time.	47
52.	Compressive residual stress within TGO as a function of 50-hour thermal cycling for type II EB-PVD TBCs with NiCoCrAlY bondcoat. Values of compressive residual stress ere calculated from bimodal luminescence corresponding to higher and lower shifts in luminescence.	48
53.	Compressive residual stress within TGO as a function of 50-hour thermal cycling for type-III TBCs with as-coated (Ni,Pt)Al bondcoat. Values of compressive residual stress were calculated from bimodal luminescence.	49
54.	Type-III TBCs cycled until thermal cyclic life time, Relative Luminescence Intensity from R2, R'2 in TGO with as-coated (Ni,Pt)Al bond coat.	50
55.	Compressive residual stress within TGO as a function of 50-hour thermal cycling for type-IV TBCs with Grit blasted (Ni,Pt)Al bondcoat. Values of compressive residual stress were calculated from bimodal luminescence.	50

LIST OF FIGURES (Continued)

No.	Title	Page
56.	Typical Impedance plots from as-coated and as a function of thermal cyclic life time for type-I APS TBCs	52
57.	Typical Phase plots from as-coated and as a function of thermal cyclic life time for type-I APS TBCs.	52
58.	Evolution of ceramic topcoat resistance (R_{YSZ}) for type I APS TBCs as a function of thermal cycling at 1121°C.	54
59.	Evolution of ceramic topcoat capacitance (C_{YSZ}) for type I APS TBCs as a function of thermal cycling at 1121°C.	54
60.	Evolution of TGO resistance (R_{TGO}) for type I APS TBCs as a function of thermal cycling at 1121°C.	55
61.	Evolution of TGO capacitance (C_{TGO}) for type I APS TBCs as a function of thermal cycling at 1121°C.	55
62.	Typical Impedance plots from as-coated and as a function of thermal cyclic life time for type-V APS TBCs.	56
63.	Typical Phase angle plots from as-coated and as a function of thermal cyclic life time for type-V APS TBCs	57
64.	Evolution of ceramic top coat resistance (R_{YSZ}) for type V APS TBCs as a function of thermal cycling at 1121°C.	58
65.	Evolution of ceramic top coat capacitance (C_{YSZ}) for type V APS TBCs as a function of thermal cycling at 1121°C.	59
66.	Evolution of TGO resistance (R_{TGO}) for type V APS TBCs as a function of thermal cycling at 1121°C.	59
67.	Evolution of TGO capacitance (C_{TGO}) for type V APS TBCs as a function of thermal cycling at 1121°C.	60
68.	Evolution of ceramic top coat resistance (R_{YSZ}) for type V APS TBCs as a function of thermal cycling at 1121°C.	60
69.	Evolution of ceramic TGO resistance (R_{TGO}) for type V APS TBCs as a function of thermal cycling at 1121°C.	61

LIST OF FIGURES (Continued)

No.	Title	Page
70.	Evolution of ceramic TGO capacitance (C_{TGO}) for type V APS TBCs as a function of thermal cycling at 1121°C.	61
71.	Typical Impedance plots from as-coated and as a function of thermal cyclic life time for type-III EB-PVD TBCs.	62
72.	Typical Phase angle plots from as-coated and as a function of thermal cyclic life time for type-III EB-PVD TBCs.	63
73.	Evolution of Ceramic topcoat resistance (R_{YSZ}) for type III EB-PVD TBCs as a function of thermal cycling at 1121°C.	64
74.	Evolution of Ceramic topcoat capacitance (C_{YSZ}) for type III EB-PVD TBCs as a function of thermal cycling at 1121°C.	64
75.	Evolution of TGO resistance (R_{TGO}) for type III EB-PVD TBCs as a function of thermal cycling at 1121°C.	65
76.	Evolution of TGO capacitance (C_{TGO}) for type III EB-PVD TBCs as a function of thermal cycling at 1121°C.	65
77.	Typical Impedance plots from as-coated and as a function of thermal cyclic life time for type-IV EB-PVD TBCs.	66
78.	Typical phase angle plots from as-coated and as a function of thermal cyclic life time for type-IV EB-PVD TBCs.	67
79.	Evolution of Ceramic topcoat resistance (R_{YSZ}) for type IV EB-PVD TBCs as a function of thermal cycling at 1121°C.	68
80.	Evolution of Ceramic topcoat capacitance (C_{YSZ}) for type IV EB-PVD TBCs as a function of thermal cycling at 1121°C.	68
81.	Evolution of TGO resistance (R_{TGO}) for type IV EB-PVD TBCs as a function of thermal cycling at 1121°C.	69
82.	Evolution of TGO capacitance (C_{TGO}) for type IV EB-PVD TBCs as a function of thermal cycling at 1121°C.	69
83.	Master plot showing the linear relation between the C_{TGO} and thickness of TGO prior to spallation and change in the linear relation with sub-critical damages.	70

LIST OF FIGURES (Continued)

No.	Title	Page
84.	Typical Impedance plots from type-I APS TBCs as a function of 10-hour thermal cycling	72
85.	Typical Impedance plots from type-I APS TBCs as a function of 1, 10 and 50-hour thermal cycling	72
86.	Evolution of ceramic topcoat resistance (R_{YSZ}) for type I APS TBCs as a function of dwell time at 1121°C.	74
87.	Evolution of ceramic topcoat capacitance (C_{YSZ}) for type I APS TBCs as a function of dwell time at 1121°C.	74
88.	Evolution of TGO resistance (C_{YSZ}) for type I APS TBCs as a function of dwell time at 1121°C.	75
89.	Evolution of TGO capacitance (C_{YSZ}) for type I APS TBCs as a function of dwell time at 1121°C.	75
90.	Ceramic resistance R_C and capacitance C_C of 7YSZ monoliths (open-pores) as a function of thickness and density non-destructively determined by EIS [25].	76
91.	An increase in the ceramic top coat resistance R_C and the corresponding Nyquist plots as a function of thickness for as-coated EB-PVD TBCs.	77
92.	Evolution of TGO resistance and capacitance as a function of thermal cycling at 1121°C.	77
93.	Evolution of TGO capacitance and resistance as a function of isothermal oxidation at various time and temperature.	78
94.	Spallation of TGO scale (Al_2O_3) from the NiAl surface after 5 and 10 hours of isothermal exposure at 1300°C.	79
95.	Evolution in (a,c) resistance and (b,d) capacitance of (a,b) EB-PVD 7YSZ and (c,d) TGO during thermal cycling at 1121˚C.	80
96.	Ceramic top coat resistance R_C and capacitance C_C of APS 7YSZ and $CaTiO_3$ as a function of thickness.	81
97.	Evolution of YSZ capacitance and resistance as a function of time and temperature of isothermal sintering.	82

LIST OF FIGURES (Continued)

No.	Title	Page
98.	Macroscopic photographs of specimens after air-quenching from sintering at 1300°C for (a) 5 and (b) 10 hours. These specimens developed a large-scale crack upon air quenching to a room temperature.	82
99.	Secondary electron micrographs of YSZ monoliths with open pores: (a) as-received; (b) sintered at 1200°C for 5 hours, (c) sintered at 1300°C for 10 hours.	83
100.	Typical backscatter electron micrographs of (a,b) type I and (c,d) type V APS TBCs specimens.	85
101.	High magnification backscatter electron micrographs of (a) type I and (b) type V APS TBCs specimens.	86
102.	Secondary electron micrograph generated during FIB-INLO technique.	86
103.	(a) Bright field and (b) HAADF micrograph of as-received type I APS TBC exhibiting extensive presence of voids, and TGO that consists of agglomerated α-Al_2O_3 particles (~100nm in size). (c,d) APS 7YSZ consisted of non-equilibrium tetragonal (t') and retained cubic (f') phase. (e) The agglomerated Al_2O_3 particles (~100nm in size) in TGO indexed to equilibrium α phase.	87
104.	Bright-field lattice images showing intimate bonding at (a) TGO/bond coat and (b) YSZ/TGO interfaces. This atomic-level bonding was *not* frequently observed due to extensive presence of voids as presented in Figure 103(a).	88
105.	(a) Bright field and (b) HAADF image of as-coated type V APS TBC exhibiting extensive presence of carbon-filled voids, absence of TGO, and conventional columnar YSZ grains within splats. (c) SADP demonstrated that the APS 7YSZ consisted of non-equilibrium tetragonal (t') and/or retained cubic (f') phase.	89
106.	Typical backscatter electron micrographs of type I APS TBCs specimens with progressive 1-hour thermal cycles.	92
107.	Typical backscatter electron micrographs of type I APS TBCs specimens with progressive 10-hour thermal cycles.	93
108.	(a) Typical backscatter electron micrographs of type I APS TBCs specimens at 20-cycles (50-hour thermal cycles) (b) BSE image of YSZ.	92
109.	Secondary electron micrographs of type-I APS TBCs YSZ showing sintering/micro cracking behavior with progressive 1-hour thermal cycling.	94

LIST OF FIGURES (Continued)

No.	Title	Page
110.	(a,b,c) Secondary electron micrographs of type-I APS TBCs YSZ showing sintering/micro cracking behavior with progressive 10-hour thermal cycling (d) back scatter electron micrograph of the cross section of bondcoat after YSZ spallation.	95
111.	TBC specimen type I after thermal cycling (a) BF TEM and (b) HAADF STEM images after 10% lifetime (c) HAADF STEM images and (d) BF TEM after 70% lifetime.	96
112.	Higher magnification HAADF STEM images of type-I APS TBCs after 70% 1-hour thermal cyclic lifetime.	97
113.	Typical backscatter electron micrograph of type-V APS TBCs with progressive thermal cycling	98
114.	Typical backscatter electron micrographs for type-V showing the TGO scale cracking with thermal cycling but the TBC remained intact.	99
115.	Typical backscatter electron micrograph of type-V APS TBCs with progressive 10-hour thermal cycling.	100
116.	Secondary electron micrographs of type-V APS TBCs showing the sintering/micro cracking behavior within the YSZ with progressive 1-hour thermal cycling.	101
117.	Bright field TEM image of type-V TBCs after 10% thermal cycling lifetime (a) presence of MOZ with cracks and voids near the YSZ/TGO interface and a dense-columnar-continuous Al_2O_3 TGO near the bond coat. (b) MOZ with cracks and voids near the YSZ/TGO interface, and (c) HAADF STEM image showing Y and Al rich oxides and a MOZ near to YSZ topcoat (d) Convergent Beam Electron Diffraction (CBED) pattern from the Y rich oxide (d) SAD pattern from the same Y rich oxide showing a lattice parameter > 18 Å and (f,g) EELS spectra from the same Y rich oxide.	102
118.	TEM images from type-V TBCs after 50% thermal cyclic lifetime (a) HAADF STEM image showing splat YSZ and voids at YSZ/TGO interface (b) Bright Field TEM image showing the same.	103
119.	Typical backscatter electron micrographs of (a,b) type II, (c,d) type III, and (e,f) type IV EB-PVD TBCs specimens.	105
120.	High magnification backscatter electron micrographs of (a,b) type II, (c) type III and (d) type IV EB-PVD TBCs specimens.	106

LIST OF FIGURES (Continued)

No.	Title	Page
121.	(a) Bright field and (b) HAADF image of as-coated type II EB-PVD TBC exhibiting columnar microstructure of 7YSZ coating and continuous TGO layer without presence of "mixed-oxide" layer. SADP (inset) demonstrated that the EB-PVD 7YSZ consisted of non-equilibrium tetragonal (t') and/or retained cubic (f') phase.	107
122.	(a) Bright field and (b) HAADF image of as-coated type III EB-PVD TBC exhibiting columnar microstructure of 7YSZ coating and continuous TGO layer with a significant presence of "mixed-oxide" layer. (c) SADP demonstrated that the EB-PVD 7YSZ consisted of non-equilibrium tetragonal (t') and/or retained cubic (f') phase. (d) SADP of α-Al_2O_3 in TGO.	108
123.	HAADF image of the "mixed-oxide" layer in TGO in as-coated type III EB-PVD TBC.	109
124.	(a) Bright field and (b) HAADF images of as-received type IV EB-PVD TBCs with grit-blasted (Ni,Pt)Al bond coat. (c) SADP demonstrates that SADP demonstrated that the EB-PVD 7YSZ consisted of non-equilibrium tetragonal (t') and/or retained cubic (f') phase.	109
125.	(a) High resolution image and (b) corresponding FFT diffractogram from TGO in re-recieved type IV EB-PVD TBCs with grit-blasted (Ni,Pt)Al bond coat.	110
126.	(a) Bright field and (b) HAADF images of as-received type IV EB-PVD TBCs with grit-blasted (Ni,Pt)Al bond coat. Presence of large residual α-Al_2O_3 particles from grit blasting was frequently observed.	110
127.	Typical backscatter electron micrographs of type II, EB-PVD TBCs specimens with NiCoCrAlY bondcoat after thermal cycling that corresponds to their lifetimes.	113
128.	Typical back scatter electron micrographs of type-II TBCs showing the depletion of β-NiAl and also internal oxidation of the NiCoCrAlY bondcoat shown in arrows.	114
129.	For type-II TBCs after thermal cycling (10% of lifetime): (a) BF TEM image showing presence of MOZ with cracks and voids near to the YSZ / TGO interface and a dense columnar Al_2O_3 TGO (b) HAADF STEM image showing presence of Ni/Co rich oxides near to the TGO/YSZ interface, MOZ with cracks and voids . The observed Y rich particle is identified as Y_2O_3 by diffraction analysis (SAD pattern as inset).	115

LIST OF FIGURES (Continued)

No.	Title	Page
130.	For type-II TBCs after thermal cycling (50% of lifetime): (a) HAADF STEM image showing presence of MOZ with cracks and voids near to the YSZ / TGO interface, a dense Al_2O_3 TGO and Ni/Co/Al rich oxides near the TGO/YSZ interface (b) BF TEM image showing MOZ with cracks and voids near to the YSZ / TGO interface and a dense columnar Al_2O_3 TGO near the TGO/bondcoat interface.	116
131.	After 50% thermal cyclic lifetime for type-II TBCs (a) L_{10} martensitic twin structure (b) Ordered L_{12} super structure and (d) γ solid solution structure were observed in the (Ni,Pt)Al bondcoat and (c) the TGO identified was $\propto$-Al_2O_3.	117
132.	Typical back scatter electron micrograph of type-III EBPVD TBCs with as-coated (Ni,Pt)Al bondcoat with progressive 1-hour thermal cycling.	118
133.	Typical back scatter electron micrograph of type-III EBPVD TBCs with as-coated (Ni,Pt)Al bondcoat with progressive 10-hour thermal cycling.	119
134.	Typical back scatter electron micrograph of type-III EBPVD TBCs with as-coated (Ni,Pt)Al bondcoat after 6 cycles(50-hour thermal cycling).	119
135.	HAADF STEM image for type-III TBCs after thermal cycling (10% lifetime) showing distinct two zone TGO microstructure with presence of voids in the MOZ/Columnar TGO interface (MOZ: Mixed Oxide Zone).	120
136.	BF TEM images of type III EB-PVD TBCs after thermal cycling that corresponds to 10% of its lifetime: (a) presence of MOZ with voids near the YSZ/TGO interface and a dense-columnar-continuous Al2O3 TGO; (b) a distinctive two-zone TGO microstructure.	120
137.	For type-III TBCs after 10% of thermal cyclic life time HRTEM image corresponding FFT diffractogram (inset) showing matrix near to the dispersed Zr rich particle consists of metastable θ-Al2O3 and the embedded Zr rich particle is in the tetragonal ZrO_2 form.	121
138.	TEM image of type-III EBPVD with as-coated (Ni,Pt)Al bondcoat TBCs after 70% thermal cyclic life time (a) HAADF STEM image showing well defined two zone TGO microstructure (b) BF TEM image showing the as-coated (Ni,Pt)Al bondcoat having B_2 structure near to the TGO.	122
139.	Typical back scatter electron micrograph of type-IV EB-PVD TBCs with grit blasted (Ni,Pt)Al bondcoat with progressive 1-hour thermal cycling.	123

LIST OF FIGURES (Continued)

No.	Title	Page
140.	Typical back scatter electron micrograph of type-IV EB-PVD TBCs with grit blasted (Ni,Pt)Al bondcoat with progressive 10-hour thermal cycling.	124
141.	Typical back scatter electron micrograph of type-IV EB-PVD TBCs with grit blasted (Ni,Pt)Al bondcoat after 4 cycles (50-hour thermal cycling).	124
142.	For type-IV TBCs after thermal cycling that corresponds to 10% of its lifetime: (a) HAADF STEM image showing the presence of MOZ traces near the YSZ/TGO interface and a dense Al2O3 TGO near the (Ni,Pt)Al bond coat; (b) BF TEM image showing presence of equiaxed Al2O3 grains near to the YSZ/TGO interface, and (c) a dense columnar continuous Al_2O_3 TGO.	125
143.	TEM images for type-IV EBPVD TBCs with grit blasted (Ni,Pt)Al bondcoat after 50% thermal cyclic lifetime (a) BF TEM image showing two zone microstructure in TGO and also voids present in the MOZ (b) HAADF STEM image showing through crack in the TGO scale with TBC still intact.	126
144.	TEM images for type-IV EBPVD TBCs with grit blasted (Ni,Pt)Al bondcoat after 70% thermal cyclic lifetime (a) HAADF STEM image showing voids near the ratcheted TGO (b)BF TEM image showing the same (c) SAD pattern from the bondcoat showing L_{10} martensitic structure.	127
145.	Backscatter electron micrographs of fracture surfaces in type I TBCs: (a,b) bottom of the spalled-YSZ coating and (c,d) top of the bond coat where YSZ coating has spalled off. Exposure of NiCoCrAlY surface was extremely rare.	129
146.	Cross-sectional backscatter electron micrographs of type I TBCs after spallation: (a,b) spalled-YSZ coating and (c,d) bond coat after YSZ spallation.	130
147.	Backscatter electron micrographs of fracture surfaces in type V TBCs: (a,b) bottom of the spalled-YSZ coating and (c,d) top of the bond coat where YSZ coating has spalled off. Exposure of NiCoCrAlY surface was extremely rare.	131
148.	Cross-sectional secondary and backscatter electron micrographs of type V TBCs after spallation: (a,b) spalled-YSZ coating and (c,d) bond coat after YSZ spallation.	132
149.	Backscatter electron micrographs of fracture surfaces in type II TBCs: (a,b) bottom of the spalled-YSZ coating and (c,d) top of the bond coat where YSZ coating has spalled off.	133
150.	Cross-sectional secondary electron micrographs of type II TBCs after spallation showing the internal oxidation of NiCoCrAlY bond coat.	133

LIST OF FIGURES (Continued)

No.	Title	Page
151.	Cross-sectional bright field transmission electron micrographs of TGO scale on type II TBCs after failure.	134
152.	Backscatter electron micrographs of fracture surfaces in type III TBCs: (a,b) bottom of the spalled-YSZ coating and (c,d,e) top of the bond coat where YSZ coating has spalled off.	135
153.	Cross-sectional backscatter electron micrographs of type III TBCs after spallation showing the preferential oxidation of (Ni,Pt)Al bond coat along the grain boundaries associated with ridges.	135
154.	Cross-sectional bright field and high angle annular dark field transmission electron micrographs of TGO scale on type III TBCs after failure.	136
155.	Backscatter electron micrographs of fracture surfaces in type IV TBCs: (a,b) bottom of the spalled-YSZ coating and (c,d) top of the bond coat where YSZ coating has spalled off.	137
156.	Cross-sectional backscatter electron micrographs of type IV TBCs after spallation showing the undulation of TGO/bond coat interface.	138
157.	Cross-sectional bright field and HAADF transmission electron micrographs of TGO scale on type IV TBCs after failure.	139
158.	Backscatter electron micrographs of fracture surfaces in type-I TBCs from 10-hour thermal cycling (a,b) bottom of the spalled-YSZ coating and (c,d) top of the bondcoat where YSZ coating has spalled off. Exposure of NiCoCrAlY surface was extremely rare.	140
159.	Cross-sectional backscatter electron micrograph of type I TBCs after spallation (a, c) bondcoat after YSZ spallation and (b) delamination at YSZ/TGO within the coating.	141
160.	Backscatter electron micrographs of fracture surfaces in type-V APS TBCs from 10-hour thermal cycles (a,b) bottom of spalled YSZ coating and (c,d) top of the bondcoat where YSZ coating has spalled off. Exposure of NiCoCrAlY was extremely rare.	142
161.	Cross-sectional backscatter electron micrographs of type V TBCs after spallation: (a,b) bondcoat after YSZ spallation.	142
162.	Backscatter electron micrographs of fracture surfaces in type II TBCs with NiCoCrAlY bondcoat (a,b) bottom of the spalled-YSZ coating and (c,d) top of the bondcoat where YSZ coating has spalled off.	143

LIST OF FIGURES (Continued)

No.	Title	Page
163.	Backscatter electron micrographs of fracture surfaces in type III TBCs with (Ni,Pt)Al bondcoat (a,b) bottom of the spalled-YSZ coating and (c,d) top of the bondcoat where YSZ coating has spalled off.	144
164.	Cross-sectional backscatter electron micrographs of type-III TBCs after spallation showing less preferential oxidation of (Ni,Pt)Al bondcoat along grain boundaries associated with ridges.	145
165.	Backscatter electron micrographs of fracture surfaces in type IV TBCs with grit-blasted (Ni,Pt)Al bondcoat (a,b) top of the bondcoat where YSZ coating has spalled off (c) Cross section of the spalled-YSZ coating and (d) cross section of the bondcoat.	146
166.	Backscatter electron micrographs of fracture surfaces in type-I TBCs from 50-hour thermal cycling (a,b) bottom of the spalled-YSZ coating and (c,d) top of the bondcoat where YSZ coating has spalled off. Exposure of NiCoCrAlY surface was extremely rare.	147
167.	Backscatter electron micrographs of fracture surfaces in type-II TBCs from 50-hour thermal cycling (a,b) bottom of the spalled-YSZ coating and (c,d) top of the bondcoat where YSZ coating has spalled off.	148
168.	Backscatter electron micrographs of fracture surfaces in type III TBCs with (Ni,Pt)Al bondcoat (a,b) top of the bondcoat where YSZ coating has spalled off (c,d) delamination at TGO/bondcoat interface shown in arrows.	149
169.	Cross-sectional backscatter electron micrographs of type-III TBCs after spallation showing less preferential oxidation of (Ni,Pt)Al bondcoat along grain boundaries associated with ridges.	150
170.	Backscatter electron micrographs of fracture surfaces in type IV TBCs with grit-blasted (Ni,Pt)Al bondcoat (a) top of the bondcoat where YSZ coating has spalled off (b) Cross section of the spalled-YSZ coating and (c) cross section of the bondcoat.	151

LIST OF TABLES

No.	Title	Page
I.	Primary NDE and microstructural analysis techniques employed in this program to examine the critical materials phenomena associated with TBC failure.	3
II.	Specifications for five types of commercial production thermal barrier coating systems employed in this program.	9
III.	Matrix of the thermal cyclic oxidation test for each TBC type.	10
IV.	Specifications and thermal cycling lifetime for five types of commercial production TBCs employed in this program.	15
V.	Thermal cyclic lifetime for commercial production TBCs and specimens employed for microstructural analysis.	17
VI.	Resistance and capacitance of Type-I APS TBCs constituents as a function of thermal cycling.	53
VII.	Resistance and capacitance of type-V APS TBCs constituents as a function of thermal cycling.	58
VIII.	Resistance and capacitance of type-III EB-PVD TBC constituents as a function of thermal cycling.	63
IX.	Resistance and capacitance of type-IV EB-PVD TBC constituents as a function of thermal cycling.	67
X.	Resistance and capacitance of type-I APS TBC constituents as a function of 10-hour thermal cycling.	73
XI.	Resistance and capacitance of type-I APS TBC constituents as a function of 50-hour thermal cycling.	73

I. INTRODUCTION

Thermal barrier coatings (TBCs) are widely used for thermal protection of hot section components in turbines for power generations. TBCs, in general consist, of a thermally-insulating outer ceramic (ZrO_2-7wt.%Y_2O_3; YSZ) coating, a thermally grown oxide (TGO) scale, an oxidation resistant metallic bond coat, and a superalloy substrate. Commonly, YSZ coatings are deposited either by air plasma spray (APS) or electron beam physical vapor deposition (EB-PVD). Bond coats are deposited by low-pressure/vacuum plasma spray (LPPS/VPS) for a MCrAlY (M=Ni and/or Co) bond coat and a combination of plating and chemical vapor deposition (CVD) in the case of a (Ni,Pt)Al bond coat [1-5]. Reliable and durable TBCs can significantly improve the operating efficiency while reducing the harmful emission of turbine engines through an increased operating temperature and an increased durability of engine components. Figure 1 shows the typical microstructure of three types of commercial-production TBCs.

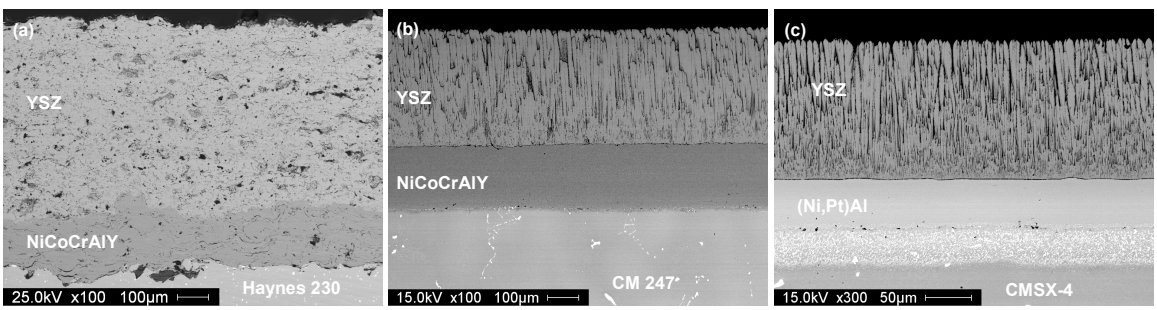

Figure 1. Backscatter electron micrographs of as-coated TBC: (a) APS YSZ on MCrAlY bond coat; (b) EB-PVD YSZ on MCrAlY bond coat; and (c) EB-PVD YSZ on (Ni,Pt)Al bond coat.

Generally, failure of TBCs occurs at the interface between bond coat and TGO, or TGO and YSZ, or within TGO [1-5]. Failure of TBCs can be attributed to time-dependent interplay between (1) chemical (i.e., thermo-kinetics) and (2) mechanical (i.e., thermo-mechanical) evolution associated with the growth of TGO via high temperature oxidation of metallic bond coat and thermal expansion mismatch between TGO and underlying metallic bond coat. Growth of TGO increases the strain energy stored within the TGO scale. Growth rate of TGO is essentially parabolic (i.e., diffusion-controlled) at high temperatures:

$$y^2 = 2k_p t \qquad \text{and} \qquad k_p = \tilde{D}_i \left(\delta_{YSZ/TGO} - \delta_{TGO/Bondcoat}\right) \qquad [1]$$

where y refers to the thickness of TGO, t, the time, k_p, the oxide growth constant, $\tilde{D}_i$, the interdiffusion coefficient of rate-controlling specie *i*, and δ, the stoichiometric deviation of TGO at the interfaces. In general, TGO primarily consists of α-Al_2O_3, whose growth rate is controlled by $\tilde{D}_i$ of oxygen (i.e., inward growth). Presence of metastable θ- and γ-Al_2O_3 can significantly alter the interfacial morphology and increase the TGO growth rate by altering the growth mechanism to outward, since $\tilde{D}_{Al} > \tilde{D}_O$ [6].

Compositional change and phase transformation in the metallic bond coat occur as a function of time due to high temperature oxidation and interdiffusion between bond coat and

the superalloy substrate. These changes and transformations are governed by the activity coefficient γ_i of component *i*, and other constituents *j*, which can be related by Gibbs-Duhem transformation:

$$\gamma_i = \frac{a_i}{X_i} \qquad \text{and} \qquad \log(\gamma_j) = -\int_1^{X_j} \left(\frac{X_i}{X_j}\right) d\log\gamma_i \Big|_{\gamma_{k..n-1}} \qquad [2]$$

where a_i is the activity of specie *i* and X_i is the mole fraction of *i* in the bond coat. The thermodynamic description of elemental constituents in the bond coat changes dynamically due to interdiffusion between the bond coat and the superalloy substrate and can be described by Onsager's formalism [7] of interdiffusion flux for component *i*, $\tilde{J}_i$:

$$\tilde{J}_i = -\sum_{j=1}^{n-1} \tilde{D}_{ij}^{n} \frac{\partial C_j}{\partial x} \quad (i = 1,2,3,...,n-1) \qquad [3]$$

where $\tilde{D}_{ij}^{n}$ refers to the interdiffusion coefficients and $\frac{\partial C_j}{\partial x}$ is the (n-1) independent concentration gradient. With compositional (or thermodynamic activity coefficient) changes, various types of oxidation can take place:

$$2(Al,Cr) + 3O = (Al,Cr)_2O_3 \qquad [4]$$
$$(Ni,Co)+O=(Ni,Co)O \qquad [5]$$
$$(Ni,Co)+2(Al,Cr)+4O=(Ni,Co)(Al,Cr)_2O_4 \qquad [6]$$
$$(Al,Cr)_2O_3+ (Ni,Co)O=(Ni,Co)(Al,Cr)_2O_4 \qquad [7]$$

In particular, formation of $(Ni,Co)(Al,Cr)_2O_4$ spinels after the depletion of Al in the bond coat has been documented to be detrimental to the integrity of TBCs due to their low fracture toughness [8]. Thus characterization of compositional change and phase transformation is critical in understanding the failure of TBCs.

Two main sources of stresses in the TGO exert additional influence on TBC failure: one from thermal expansion misfit upon cooling and the other from TGO growth [9]. Since TGO is thin, the stress in the TGO, denoted σ_{ij} from thermal expansion misfit is given by:

$$\frac{\sigma_{ij}}{\sigma_o} = H_{ij}\alpha_D \frac{A}{L} \text{ and } \sigma_o = \frac{E_o \Delta\alpha_o \Delta T}{1-\upsilon} \text{ and } \alpha_D = \frac{\bar{\varepsilon}_{TGO} - \bar{\varepsilon}_{bondcoat}}{\bar{\varepsilon}_{TGO} + \bar{\varepsilon}_{bondcoat}} \qquad [8]$$

where α_D is the Dundurs' parameter defined by plane strain $\bar{\varepsilon}_i$, Young's modulus of TGO, E_o, the temperature difference during thermal cycling, ΔT, Poisson ratio, υ, the thermal expansion coefficient difference, $\Delta\alpha_o$, and geometrical descriptors A and L. Also, oxidation (i.e., a process of converting metal to oxide) is accompanied by strain ε that is associated with growth stress σ^g:

$$\varepsilon = \varepsilon_{zz}\sigma_{xx}^{g} + 2\varepsilon_{xx}\sigma_{xx}^{g} \qquad [9]$$

where subscripts xx and zz refers to in-plane and out-of-plane (orthogonal to TGO/metal interface) directions, respectively. Additional factors that influence durability and reliability of TBCs include (1) creep of metallic bond coat and TGO, (2) imperfections and impurity segregation at the TGO/bond coat interface, and (3) phase transformation or sintering of YSZ coatings. Table I lists several critical materials phenomena associated with TBC failure.

Table I. Primary NDE and microstructural analysis techniques employed in this program to examine the critical materials phenomena associated with TBC failure.

Main factors Associated with TBC Failure	Potential NDE Technique	Microstructural Analysis
Thickness/Growth of TGO	EIS	SEM, TEM
Polymorphic Transformation of Al_2O_3 in TGO	PSLS	XRD, TEM
Residual Stress in α-Al_2O_3 TGO	PSLS	-
Formation of Ni/Co Rich TGO	PSLS (?)	SEM, TEM, n-EDS
Sintering of YSZ	EIS	SEM
Phase Transformation of YSZ	XRD, RS	
Adhesion Integrity of TGO/Bond Coat Interface	PSLS, EIS	SEM, TEM
Adhesion Integrity of YSZ/TGO Interface	EIS	SEM, TEM
Sulfur Segregation	AES, XPS, SIMS	

Given the wide applications and complexity of TBCs, detailed high resolution microstructural analysis via novel specimen preparation technique is essential to elucidate the failure mechanisms of TBCs. Concurrently, development of non-destructive evaluation (NDE) techniques for TBCs in commercial applications is needed for enhanced reliability, availability and maintainability (RAM) of advanced turbine engines. Development of NDE techniques must be based on a robust correlation to the mechanisms of TBC degradation and failure.

The overall objective of this program was to provide a clearer understanding of TBC failure by concurrently utilizing two NDE techniques, namely photostimulated luminescence spectroscopy (PSLS) and electrochemical impedance spectroscopy (EIS), and state-of-the-art characterization techniques including focused ion beam (FIB) in-situ lift out (INLO) [10], transmission electron microscopy (TEM) and scanning TEM (STEM). The PSLS and EIS were selected for this program since these two techniques can provide non-destructive methods to examine the critical materials phenomena associated with TBC failure as listed in Table I. Results of NDE were correlated with systematic microstructural analysis using FIB-INLO and TEM/STEM. Site-specific preparation of specimens that are thin enough for TEM/STEM analysis is now feasible through FIB-INLO for traditionally difficult-to-prepare specimens such as TBCs, especially after thermal cycling [11]. Upon FIB-INLO preparation, detailed microstructural analysis was carried out using TEM/STEM equipped with bright/dark field imaging, nano-spot energy dispersive spectroscopy (n-EDS), convergent beam electron diffraction (CBED), high angle annular dark field (HAADF) imaging, and electron energy loss spectroscopy (EELS). The main objective of this program was achieved by accomplishing the following goals:

1. Evaluate and examine five different types of commercial production TBCs during thermal cyclic oxidation concurrently by PSLS and EIS, the two complimentary NDE techniques.
2. Evaluate five types of commercial production TBCs after specified thermal cyclic oxidation and after failure by the state-of-the-art characterization techniques including SEM, EDS, FIB-INLO and TEM/STEM equipped with n-EDS, CBED, HAADF and EELS.
3. Define clearer failure mechanisms for five types of commercial production TBCs.
4. Demonstrate the relationship between the results of NDE techniques, microstructural analysis and failure mechanisms for five types of commercial production TBCs.
5. Transfer to industrial partners the attained knowledge on TBC failure, refinement of NDE techniques, feasible approaches to improve TBC durability and to develop/refine lifetime prediction models for TBCs.
6. Provide collaborative/competitive team-based research activities for student research teams with active interaction from industrial partners.

To achieve these goals, six tasks were defined, structured, and scheduled as presented in Figures 2 and 3. In this program, the University of Central Florida is privileged to have a strong and supportive partnership with four industrial gas turbine manufacturers and a coating manufacturer. The industrial partners will contribute to this program by supplying commercial production TBCs, providing non-proprietary experience to the program and interacting (technically, educationally and professionally) with student research teams.

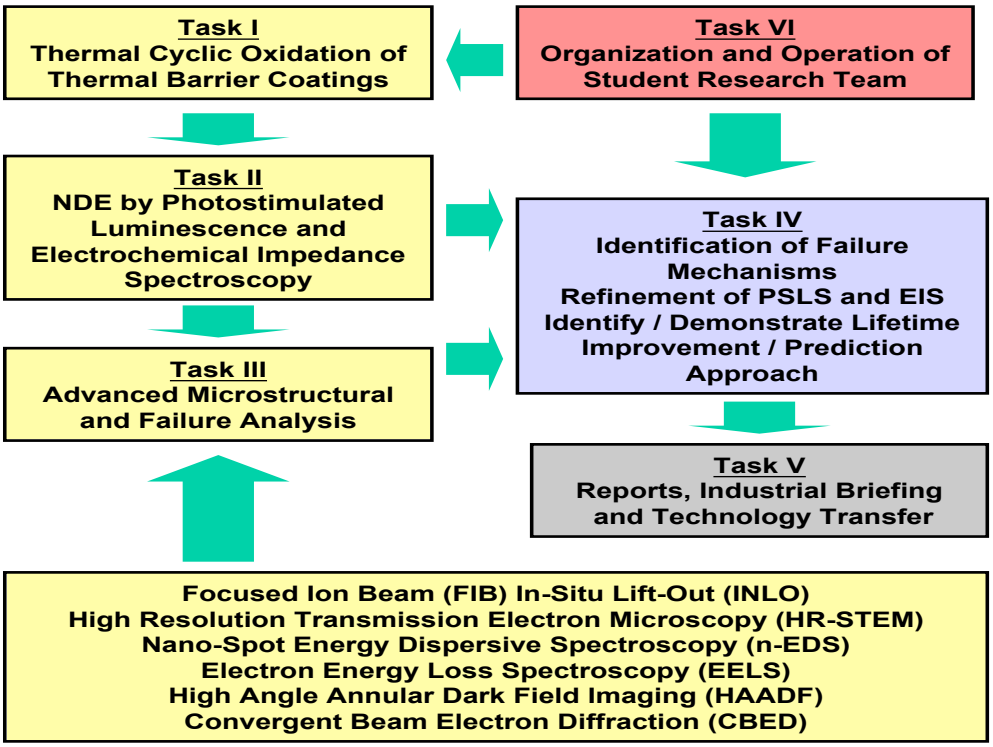

Figure 2. Task-based program flow chart.

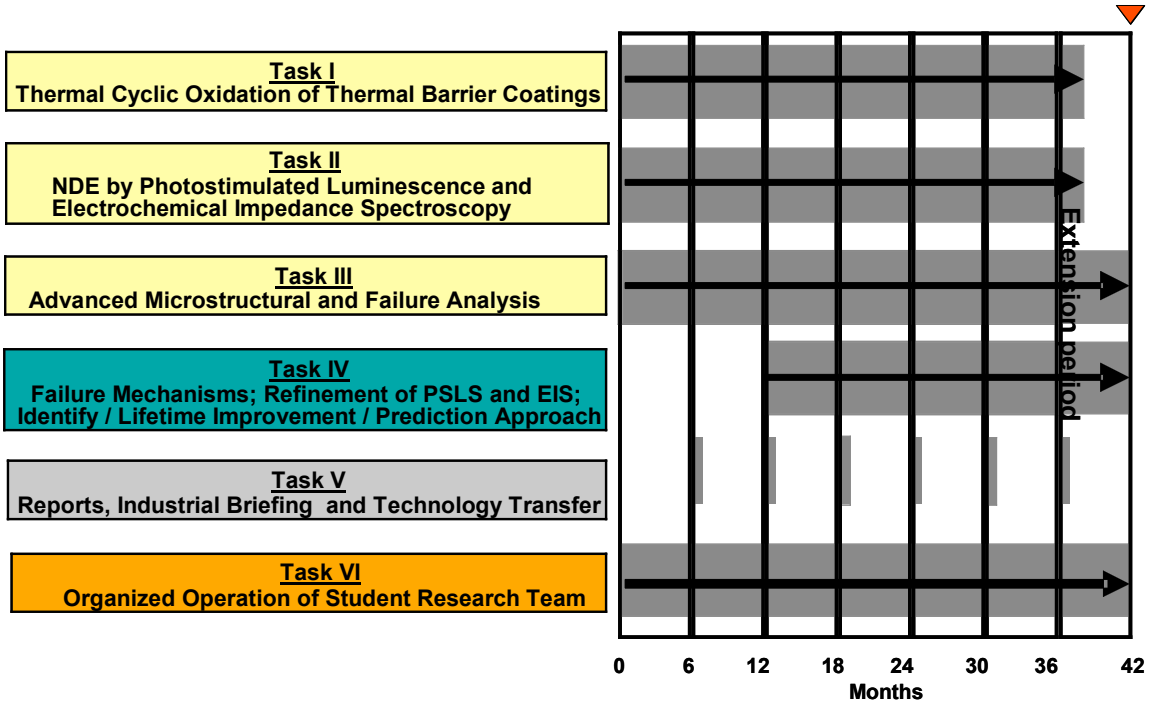

Figure 3. Program schedule according to specific tasks.

II. EXECUTIVE SUMMARY

Project Title: **Assessment of Failure Mechanisms for Thermal Barrier Coatings by Photoluminescence, Electrochemical Impedance and Focused Ion Beam**

Identifiers: **DOE DE-FC26-02NT41431 and UTSR No. 02-01-SR103**

PIs: **Yongho Sohn and Vimal H. Desai**
Affiliation: **Advanced Materials Processing and Analysis Center and Mechanical, Materials and Aerospace Engineering**
University of Central Florida
Orlando, FL 32816-2455

Reporting Period: **May 1, 2002 ~ January 30, 2006**
Date Issued: **December 30, 2005**

Durable and reliable service of thermal barrier coatings (TBCs) can increase the performance efficiency and reduce the harmful emission during the operation of advanced gas turbine engines. Enhanced reliability, availability and maintainability (RAM) of advanced turbine engines require robust non-destructive evaluation (NDE) techniques for TBCs. There is a need for a clearer scientific understanding for TBC failure mechanisms based on the fundamental foundation of thermo-kinetics and thermo-mechanics. There is even a greater need for NDE techniques that can monitor the degradation in TBCs, and can be correlated to the fundamental materials phenomena associated with mechanisms of TBC failure.

Faculty and students of Advanced Materials Processing and Analysis Center (AMPAC) at the University of Central Florida have elucidated the failure mechanisms for five types of commercial production TBCs during thermal cyclic oxidation under University Turbine Systems Research (UTSR) program. Failure characteristics and mechanisms have been examined by using two complimentary NDE techniques: photostimulated luminescence spectroscopy (PSLS) and electrochemical impedance spectroscopy (EIS). Concurrently, microstructural analysis of TBCs was carried out at atomic-micro-macro levels using a variety of characterization techniques including transmission electron microscopy (TEM) and scanning TEM (STEM). This program was specifically designed to correlate the results of NDE and microstructural analysis in order to better understand failure mechanisms of TBCs and to develop/refine NDE techniques.

During this study, the following tasks were successfully completed:

- **Completed lifetime evaluation of all five TBC types using 1, 10 and 50-hour thermal cycling at 1121°C (2050°F), and non-destructive evaluation of all TBCs as a function of thermal cycling by PSLS and EIS.**

- **Detected pre-spallation event by PSLS including TGO stress-relief (i.e., sub-critical cracking) and TGO stress-relaxation (i.e., racheting) for EB-PVD TBCs during 1- and 10-hour thermal cycling.**
- **Completed the microstructural analysis for each type of TBCs as a function of 1, 10 and 50- hour thermal cycling by SEM with EDS.**
- **Completed detailed site-specific microstructural analysis for TBCs with 1-hour thermal cycling using TEM/STEM via FIB-INLO with several analytical/imaging modes/detectors such as high angle annular dark field (HAADF), selected area diffraction (SAD), nano-spot energy dispersive spectroscopy (n-EDS) and electron energy loss spectroscopy (EELS).**

While this document reports the technical results and discussion of this program, some highlights can be found is refereed journal articles (complete list in Appendix A):

1. **B. Jayaraj et al., "Changes in Electrochemical Impedance with Microstructural Development in Thermal Barrier Coatings," *JOM*, vol. 57 (2006) pp. 61-64.**
2. **J. Byeon, et al., "Non-Destructive Evaluation of Degradation in Multi-Layered Thermal Barrier Coatings by Electrochemical Impedance Spectroscopy," *Mater. Sci. Eng. A,* Vol. 407 (2005) pp. 213-225.**
3. **J.W. Byeon, et al., "Transmission Electron Microscopy of Isothermally Oxidized EB-PVD Thermal Barrier Coatings on (Ni,Pt)Al Bondcoat," *Mater. Sci. Forum*, Vol. 486-487 (2005) pp. 149-152.**
4. **J.W. Byeon, et al., "Characterization of Isothermally Oxidized ZrO_2-8wt.%Y_2O_3 Thermal Barrier Coatings by Electrochemical Impedance Spectroscopy," *Mater. Sci. Forum*, Vol. 486-487 (2005) pp. 145-148.**
5. **Y.H. Sohn, et al., "Non-Destructive and Microstructural Characterization of Thermal Barrier Coatings," *JOM*, Vol. 56 (2004) 53-56.**
6. **B.W. Kempshall, et al., "An Observation of Nearly Failed Electron Beam Physical Vapor Deposited Thermal Barrier Coating with Grit Blasted (Ni,Pt)Al Bond Coat: Photostimulated Luminescence and Transmission Electron Microscopy," *Thin Solid Films*, Vol. 466 (2004) pp. 128-136.**
7. **B. Jayaraj, et al., "Electrochemical Impedance Spectroscopy of Porous ZrO_2 – 8 wt.% Y_2O_3 and Thermally Grown Oxide on Nickel Aluminide," *Mater. Sci. Eng. A*, Vol. A372 (2004) pp. 278-286.**
8. **B. Jayaraj, et al., "Electrochemical Impedance Spectroscopy of Thermal Barrier Coatings as a Function of Isothermal and Cyclic Thermal Exposure," *Surf. Coat. Technol.*, Vol. 177-178 (2004) pp. 140-151.**
9. **S. Laxman, et al., "Phase Transformation of Thermally Grown Oxide on (Ni,Pt)Al Bond Coat During Electron Beam Physical Vapor Deposition and Subsequent Oxidation," *Surf. Coat. Technol.*, Vol. 177-178 (2004) pp. 121-130.**
10. **Y.H. Sohn, B. Jayaraj, "Evolution in Photoluminescence and Electrochemical Impedance with Microstructural Changes in Thermal Barrier Coatings," *Surf. Coat. Technol.*, Submitted, March, 2006.**
11. **B. Jayaraj, Y.H. Sohn, "Thermal Cycling Lifetime and Microstructural Development of Thermal Barrier Coatings with Air Plasma Sprayed NiCoCrAlY Bond Coats," *Surf. Coat. Technol.*, Submitted, March, 2006.**

Findings and technical achievements of this program fertilized direct research interaction with UTSR-IRB members (Siemens, Solar and GE) with contract value of over $480,000, and formed a basis for a patent (U.S. Patent 6,979,991 B2, December 27, 2005) from one of the UTSR IRB members (P&W). Finally and most importantly, this program was carried out by two student research teams, each consisting of one graduate and one undergraduate student for collaborative and competitive development of PSLS and EIS. This program supported Mr. Balaji Jayaraj, who was a recipient of "UCF's Most Outstanding M.S. Thesis of 2003." Mr. Jayaraj expect to complete his doctoral dissertation in early 2005 and join Mitsubishi Power Systems, Orland, FL. Ms. Barbara Franke, now with Solar Turbines earned her M.S., and was a recipient of Recipient of Honeywell Leadership Scholarship, and 2003 and 2004 UTSR Fellow. Overall this program has support 1 Ph.D., 4 M.S. and 4 undergraduate students. A complete list of achievements and placement of students supported by this program are listed in Appendix B.

III. PROJECT DESCRIPTION

Development of durable and reliable thermal barrier coatings (TBCs) for blades and vanes can increase the performance efficiency and reduce the harmful emission during the operation of advanced turbine engines. In addition, development of robust non-destructive evaluation (NDE) techniques to detect a sub-critical, yet significant TBC damage prior to a complete failure can substantially enhance the reliability, availability and maintainability (RAM) of advanced turbine engines. To fulfill these industrial needs, a robust scientific foundation for TBC failure mechanisms must be established through understanding of materials thermo-kinetics and thermo-mechanics. In addition, novel NDE techniques must be developed on the premises that NDE data can monitor and be correlated to the fundamental materials phenomena related to TBC degradation and failure mechanisms.

Under the University Turbine Systems Research (UTSR) program, the University of Central Florida have elucidated the failure mechanisms for five types of commercial production TBCs during thermal cyclic oxidation. Failure characteristics and mechanisms were examined by using two complimentary NDE techniques, photostimulated luminescence spectroscopy (PSLS) and electrochemical impedance spectroscopy (EIS). Concurrent microstructural analysis of TBCs was carried out at atomic-micro-macro level. Site-specific and routine (<3 hours) preparation of TBC specimens for transmission electron microscopy (TEM) and scanning TEM (STEM) has been achieved through this program using focused ion beam (FIB) in-situ lift out (INLO) technique. This achievement now allows a systematic TEM/STEM investigation of TBCs as a function of thermal exposure, and will give a detailed understanding of microstructural evolution, and ultimately how TBCs fail when correlated with NDE.

IV. EXPERIMENTAL

IV.1. Description and Thermal Cycling of Thermal Barrier Coatings

Five TBC systems, identified in Table II as type I through V, were selected for this program. The industrial partners of this program have supplies 20 specimens of each TBC type with geometrical specification schematically illustrated in Figure 4 (25.4 mm in diameter and 3.2 mm in thickness).

Table II. Specifications for five types of commercial production thermal barrier coating systems employed in this program.

TBC System	7YSZ Deposition and Thickness	Bond Coat Type and Thickness	Superalloy Substrate	Notes
I	APS; 600 μm	NiCoCrAlY; 175 μm	Haynes 230	-
II	EB-PVD; 350 μm	NiCoCrAlY; 200 μm	CM247	-
III	EB-PVD; 145 μm	(Ni,Pt)Al; 50 μm	CMSX-4	As-Coated Bond Coat
IV	EB-PVD; 140 μm	(Ni,Pt)Al; 35 μm	Rene'N5	Grit-Blasted Bond Coat
V	APS; 200 μm	NiCoCrAlY; 100 μm	MAR-M-509	-

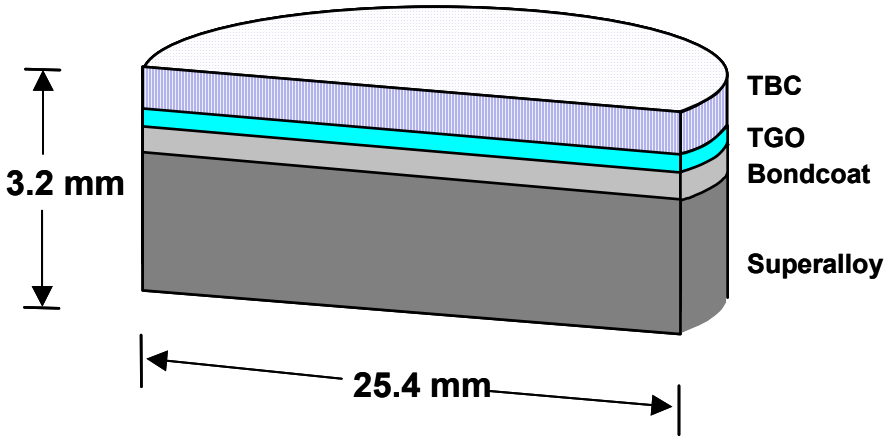

Figure 4. Specimen geometry for thermal barrier coatings employed in this program.

Thermal cyclic oxidation for each type of TBC has been carried out using CM™ Rapid Temperature furnace with vertical cycling package. Each cycle consists of 10-minute heat-up to 1121°C (2050°F), 0.67, 10 or 50-hour hold at 1121°C, and 10-minute forced-air quench. A schematic illustration of thermal cycling is presented in Figure 5. Temperature of the specimen stage (20 cm by 20 cm) has been monitored by S-type thermocouples attached to YSZ disk (25.4 mm in diameter and 3 mm in thickness). For 20 specimens of each TBC type, thermal cyclic oxidation testing has been carried out using the matrix given in Table III. At specified thermal cycles, TBCs have been visually inspected, photographed and examined by PSLS and EIS. Selected TBC specimens after specific thermal cycles have been also employed for microstructural analysis according to Table III.

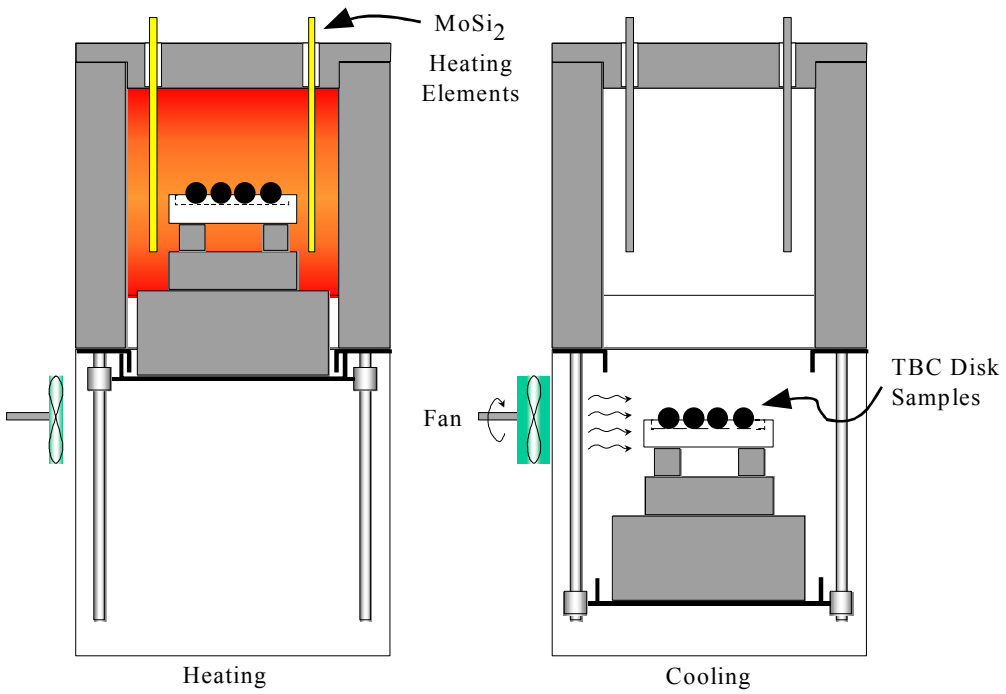

Figure 5. A schematic diagram of the CM™ Rapid Temperature cyclic oxidation furnace during (a) high temperature oxidation and (b) cooling.

Table III. Matrix of the thermal cyclic oxidation test for each TBC type.

Number of TBCs*	Type of Oxidation Test	NDE by PSLS and EIS (cycles)	Microstructural Analysis (% lifetime∇)
1	N.A.	0	0
9	1 hour	0,1,5,10-Failure#	10, 50, 80, 90, Failure (5 spc.)
5	10 hour	0,1,2,3,4,…Failure	30, 80, Failure (3 specimens)
5	50 hour	0,1,2,3,4,…Failure	30, 80, Failure (3 specimens)

* Total number of TBC specimens required for each type: 20.
# Every 10 cycles until failure.
∇ Approximate values; will be adjusted to equivalent time-at-1121°C.

IV.2. Photostimulated Luminescence Spectroscopy

Photo-Stimulated Luminescence Spectroscopy (PSLS), pioneered by Clarke et al. [12-16] and refined by Sohn, Gell, Jordan et al. [17-19] has demonstrated its capability as a NDE technique for TBCs. Specifically, PSLS can provide information regarding the following factors associated with TBC failures:

- Residual stress of α-Al_2O_3 (i.e., TGO structural integrity).
- Polymorphic transformation of Al_2O_3.
- Formation of other oxides (containing Ni, Co, Y, etc.) in TGO [20].

In PSLS technique, schematically illustrated in Figure 6, a systematic shift in the position of R_1 and R_2 luminescence doublets can be phenomenologically translated into residual stress in α-Al_2O_3, assuming that the TGO consists of randomly oriented polycrystals. The average biaxial residual stress $\overline{\sigma}$ in the α-Al_2O_3 scale is generally calculated from the average shift in the position of R_2 luminescence $\overline{\Delta\upsilon}$ using the relation [12-15]:

$$\overline{\Delta\upsilon} = \frac{2}{3}\Pi\overline{\sigma} \qquad [10]$$

where Π is the piezospectroscopic coefficients. Clarke et al. [15,16] as well as Sohn, Gell, Jordan et al. [17,18] have demonstrated that the damage of TGO by cracking during thermal cyclic oxidation results in relief of TGO residual stress. In addition, Figure 7 shows the N, Q and G-luminescences arising from, respectively, a significant Cr_2O_3 concentration in the TGO [21], the presence of metastable θ, and γ-Al_2O_3 in TGO. Intensity of these luminescence's can be determined relatively using the relation:

$$\frac{I_R}{I_T} + \frac{I_N}{I_T} + \frac{I_Q}{I_T} + \frac{I_G}{I_T} = 1 \qquad [11]$$

where I_R, I_N, I_Q, I_G and I_T refer to the integrated luminescence intensities of α-Al_2O_3, N-luminescence, θ-Al_2O_3, γ-Al_2O_3 and total luminescence, respectively. Formation of other constituents in TGO such as Y-rich oxide (e.g., YAl_5O_{12}, Y_2O_3), and Ni/Co-rich oxide (e.g., NiO, CoO, $(Ni,Co)(Cr,Al)_2O_4$-spinel) may be detected by the PSLS technique based on theory of photoluminescence [20]. Thus, NDE of these TGO characteristics by PSLS as a function of thermal cyclic oxidation can provide insight into the failure mechanisms of TBCs specifically associated with the factors listed in Table I.

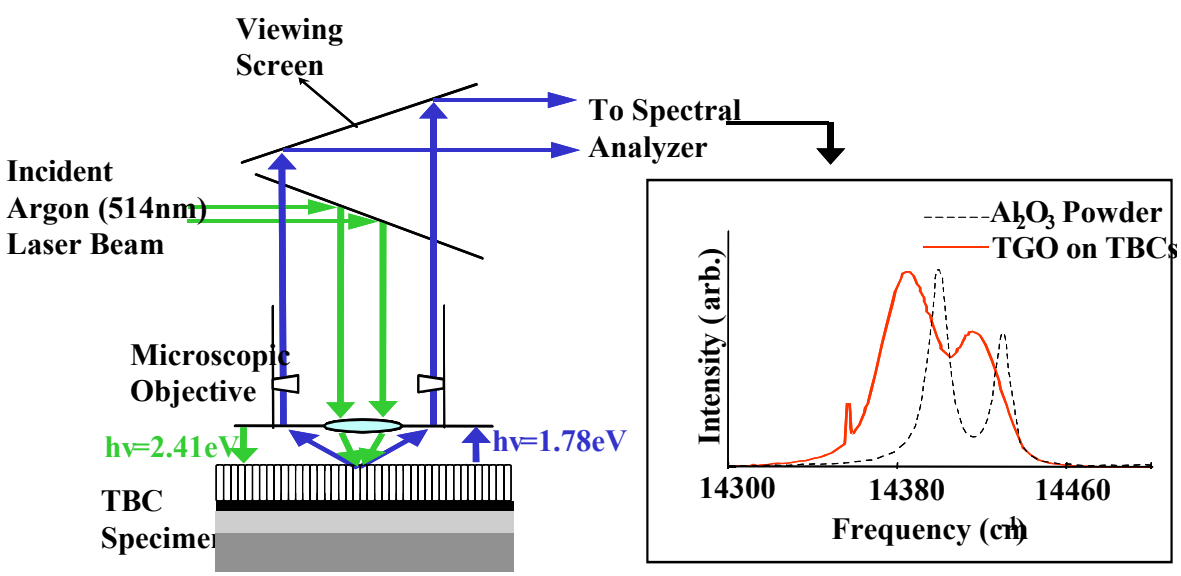

Figure 6. A schematic diagram of photostimulated luminescence spectroscopy, and R_1-R_2 luminescence doublets from stressed and stress-free α-Al_2O_3.

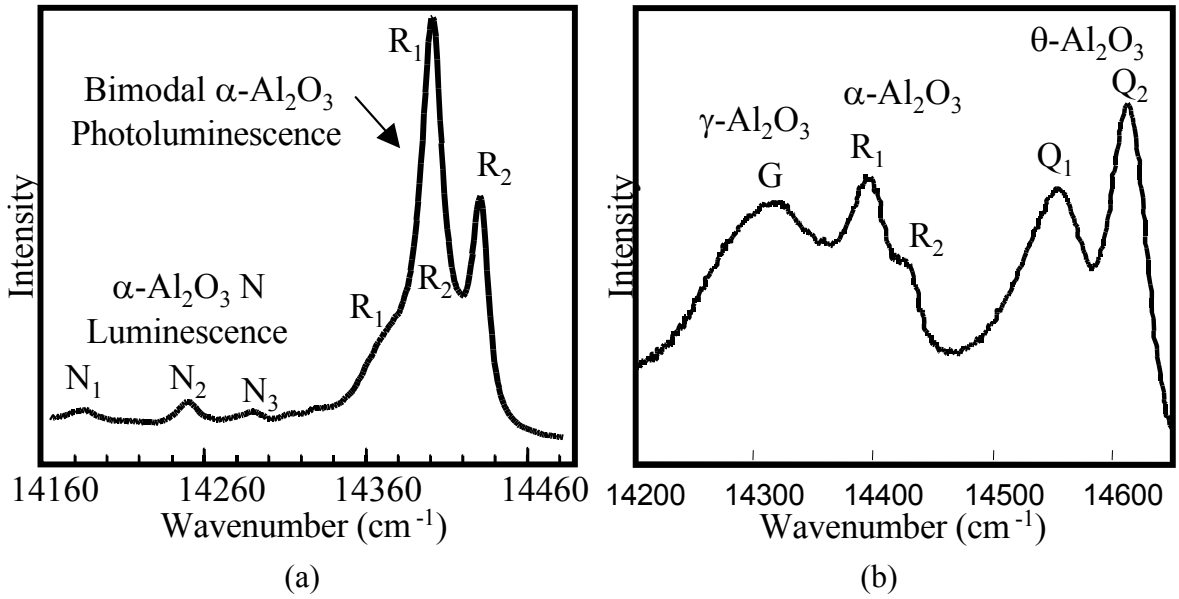

Figure 7. (a) N-type luminescence arising from the presence of Cr_2O_3 in α-Al_2O_3 scale, (b) luminescence from γ, α and θ-Al_2O_3 labeled G, R_1-R_2 and Q_1-Q_2, respectively.

In this study, after specified thermal cycles reported in Table III, TBC specimens have been carefully removed from the CM furnace for NDE by PSLS. NDE by PSLS has been restricted to EB-PVD TBCs, since PSLS cannot be applied to APS TBCs without impregnating APS YSZ coatings with other medium [22] whose effect on TBC lifetime has not been investigated. TGO residual stress, polymorphic transformation of Al_2O_3, formation of Ni/Co rich TGO, and development of sub-critical TGO damage have been carefully monitored using PSLS. Minimum of 20 measurements, randomly over the surface of the specimen coupon are carried out for each specimen. Spectra are collected using Renishaw™ 1000B μ-Raman spectrometer and analyzed using GRAMS™ software.

IV.3. Electrochemical Impedance Spectroscopy

Electrochemical impedance spectroscopy (EIS) is a well-established technique in materials engineering related to corrosion. This technique was first employed to examine TBCs by V.H. Desai through a previous AGTSR program (No. 98-01-SR067) [23]. Results from this program indicated that the EIS technique has a good potential to provide information regarding the following factors associated with TBC failure [23,24]:

- Thickness of TGO.
- Adhesion integrity of TGO/bond coat and YSZ/TGO interfaces.
- Microstructure, thickness, sintering and cracking in YSZ.

EIS technique, schematically shown in Figure 8, involves measurement of the multi-layer system response subjected to a small ac signal at various frequencies, and representing it

with Nyquist and Bode plots, which represents the changes in impedance and phase angle. With concurrent simulation of equivalent ac circuits, various aspects of TBCs including YSZ microstructure, TGO thickness and TBC structural integrity can be evaluated non-destructively. An EIS ac equivalent circuit employed in this study is presented in Figure 9 for (a) as-coated APS TBCs without continuous/significant TGO scale and (b) as-coated EB-PVD TBCs with TGO and thermally cycled TBCs deposited either by APS or EB-PVD. For APS TBCs, constant phase elements are employed instead of pure capacitance to accommodate any non-uniform charge distribution that may arise due to surface/interface roughness. NDE of TBCs by EIS as a function of thermal cyclic oxidation can provide insight to the failure mechanisms, specifically associated with the factors listed in Table I.

Similar to PSLS, after specified thermal cycles reported in Table III, TBC specimens have been carefully removed from the CM furnace for NDE by EIS. TGO thickness, interfacial adhesion and damage, and microstructural evolution of YSZ coatings have been carefully monitored using EIS. Minimum of 3 measurements are carried out by applying 10mV over a frequency range of 1MHz to 10mHz. EIS set-up employed in this study consist of IM6E BAS Zahner frequency response analyzer and a three-electrode system, namely counter electrode (Pt-mesh), reference electrode (standard calomel) and working electrode (TBC) in contact with $K_3Fe(CN)_6/K_4Fe(CN)_6\text{-}3H_2O$ electrolyte solution. The center of the TBC coupons has been examined by EIS with a measurement diameter of 1 cm.

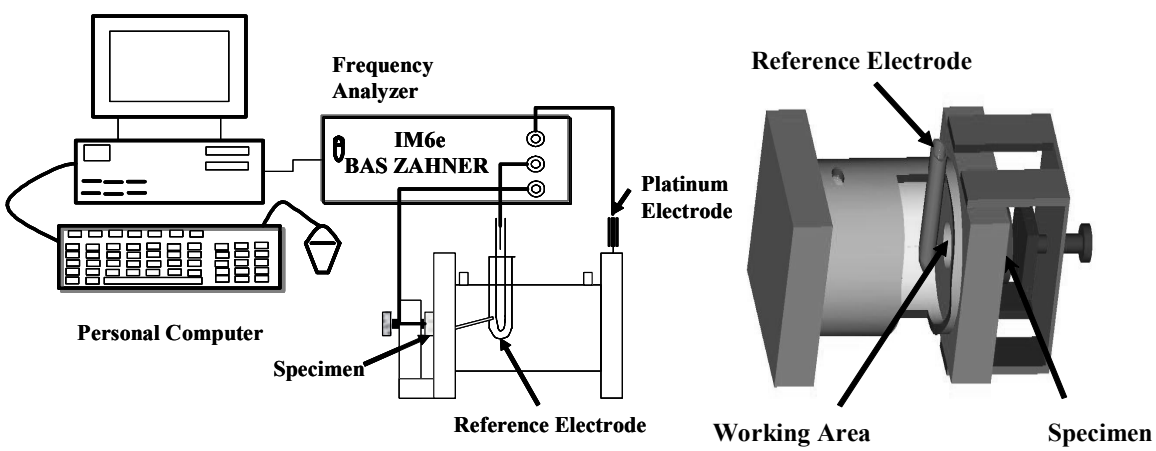

Figure 8. A schematic diagram of a typical set-up for electrochemical impedance spectroscopy.

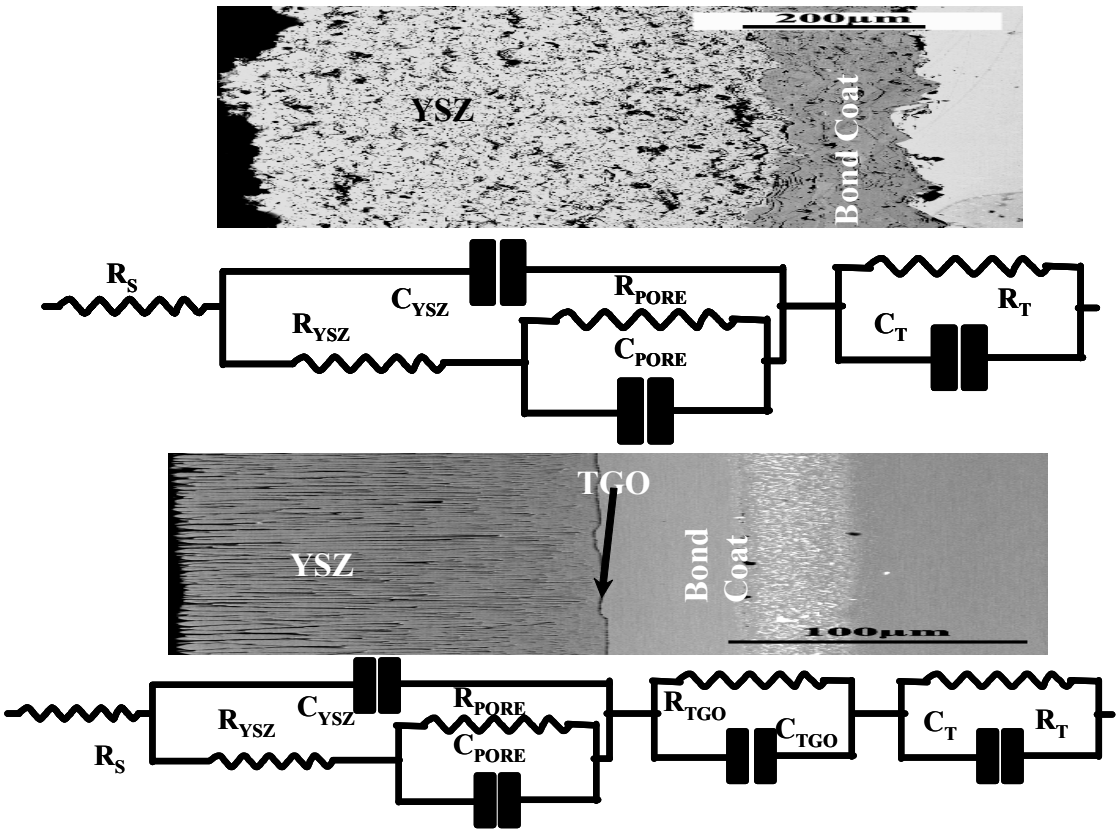

R_S: Solution Resistance
R_{YSZ}: Ceramic topcoat Resistance
R_{PORE}: Pore Resistance
R_{TGO}: Oxide Scale Resistance
R_T: Interface Transmission Resistance

C_{YSZ}: Ceramic topcoat Capacitance
C_{PORE}: Pore Capacitance
C_{TGO}: Oxide Scale Capacitance
C_T: Interface Transmission Capacitance

Figure 9. A model of an EIS ac-equivalent circuit for TBCs with and without TGO.

IV.4. Microstructural Characterization

During and after thermal cyclic oxidation testing as presented in Table III, selected specimens of TBCs have been employed for the microstructural and failure analysis as presented in Table III. Development of microstructural features and failure characteristics of TBCs have been examined as a function of thermal cycles. Aforementioned, this task employs state-of-the-art characterization techniques with emphasis on field emission scanning electron microscopy (FE-SEM), energy dispersive spectroscopy (EDS), focused ion beam (FIB) in-situ lift out (INLO), Philips™/Tecnai™ F30 300KeV transmission electron microscopy (TEM) and scanning TEM (STEM) equipped with nano-spot-EDS (n-EDS), convergent beam electron diffraction (CEBD), high angle annular dark field (HAADF) imaging and electron energy loss spectroscopy (EELS). In addition, facilities at the Advanced Materials Processing and Analysis Center (AMPAC) at UCF such as X-ray diffraction (XRD), auger electron spectroscopy (AES) with depth profiling, X-ray photoluminescence spectroscopy (XPS), Rutherford backscattering spectroscopy (RBS), and secondary ion mass spectroscopy (SIMS) with depth profiling can be employed if necessary.

V. RESULTS AND DISCUSSION

V.1. Lifetime Assessment and Visual Observation of TBC Spallation

V.1.1. Thermal Cycling Lifetime

The TBC lifetime for 1, 10 and 50- hour thermal cycling at 1121°C (2050°F) was determined with 5, 3 and 2 specimens, respectively. The furnace cycling consisted of 10-minute heat-up, 40-minute, 9.8 hours and 49.8 hours dwell at 1121°C and 10-minute forced air-quench. The TBC lifetimes are presented in Table IV and Figures 10 and 11. Independent of the dwell time at 1121°C (2050°F) the lifetime of type I TBCs remained the highest followed by types III, IV, II and V as shown in Figure 11. The cyclic dwell time life for the five different types of TBCs is also shown in Figure 12.

From the lifetime from all five types of TBCs, 10%, 50% and 70% lifetime was calculated as presented in Table V. Similar calculation of lifetime at 30% and 80% for the five types of TBCs was carried out for 10-hour and 50% for 50-hour thermal cycling as reported in Table V. Furnace thermal cycling was carried out up to these cycles to examine the microstructural evolution of TBC specimens as functions of thermal cycling.

Table IV. Specifications and thermal cycling lifetime for five types of commercial production TBCs employed in this program.

TBC System	7YSZ Deposition and Thickness	Bond Coat and Thickness	Superalloy Substrate	Dwell Time (Hrs) at 1121°C (2050°F)	Number of Specimens Tested	TBC Lifetime and Standard Deviation (#)
I	APS 600 μm	NiCoCrAlY 175 μm	Haynes 230	0.67 9.8 49.8	5 3 2	527 (20) 113 (1) 39 (0.7)
II	EB-PVD 350 μm	NiCoCrAlY 200 μm	CM247	0.67 9.8 49.8	5 3 2	280 (35) 25 (5) 3.5 (3.5)
III	EB-PVD 145 μm	As-Coated (Ni,Pt)Al 50 μm	CMSX-4	0.67 9.8 49.8	6 4 2	406 (22) 55 (3) 12 (1.5)
IV	EB-PVD 140 μm	Grit-Blasted (Ni,Pt)Al 35 μm	Rene'N5	0.67 9.8 49.8	6 3 2	360 (39) 42 (2) 9.5 (0.7)
V	APS 200 μm	NiCoCrAlY 100 μm	MAR-M-509	0.67 9.8 49.8	8 1 1	286 (76) 18 (0) 8 (0)

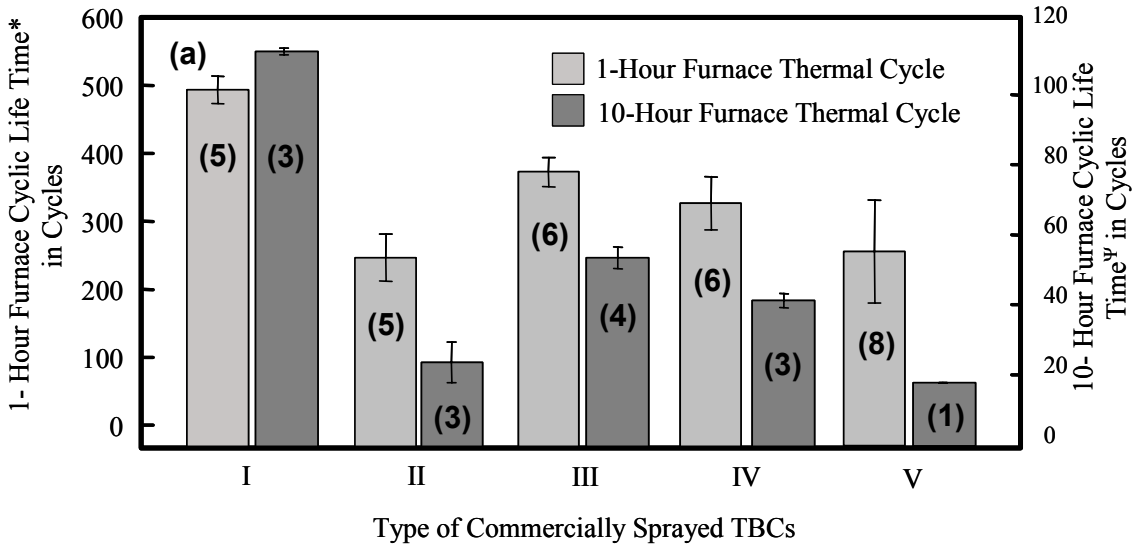

*1- Hour Cycle Consist of 10-minute ramp, 40- minute hold at 1121°C (2050 °F) and 10 –minute forced air quench

$^{\Psi}$10-Hour Cycle consist of 10-minute ramp, 9.8 hours hold at 1121°C (2050 °F) and 10 –minute forced air quench

Figure 10. Lifetime during thermal cycling at 1121°C for five-types of TBCs. Values in parenthesis represent the number of specimen employed to determine the lifetime (a) 1- and 10-hour thermal cycling.

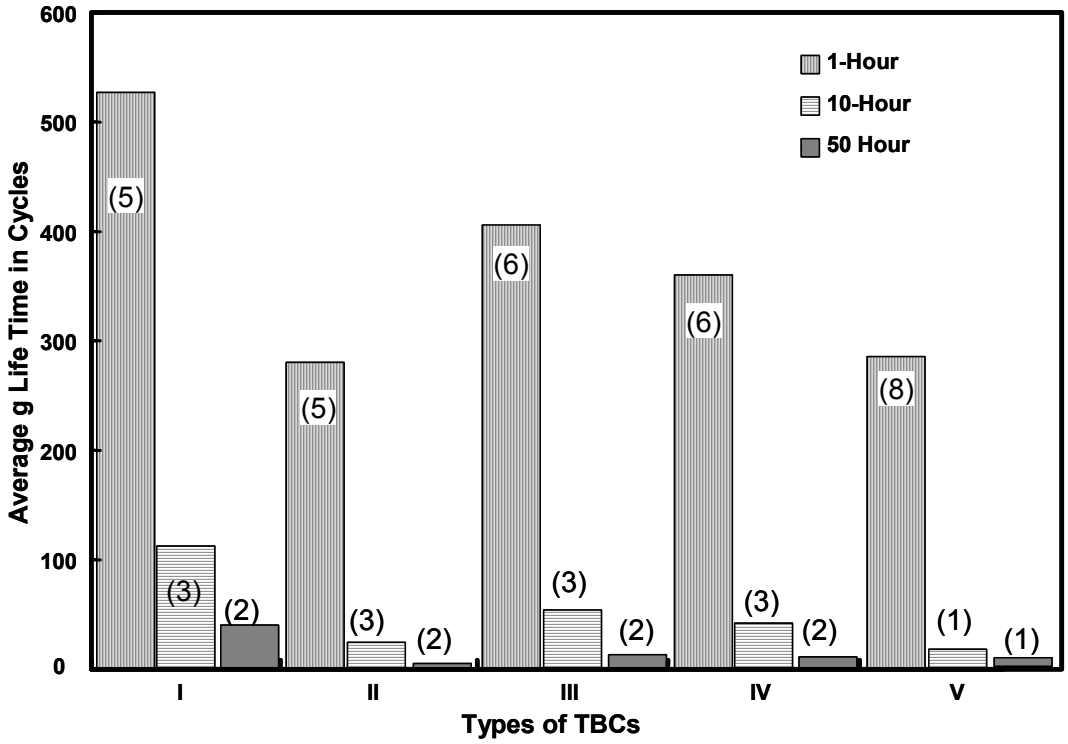

Figure 11. Lifetime during thermal cycling at 1121°C for five-types of TBCs. Values in parenthesis represent the number of specimen employed to determine the lifetime 1, 10 and 50 –hour thermal cycling.

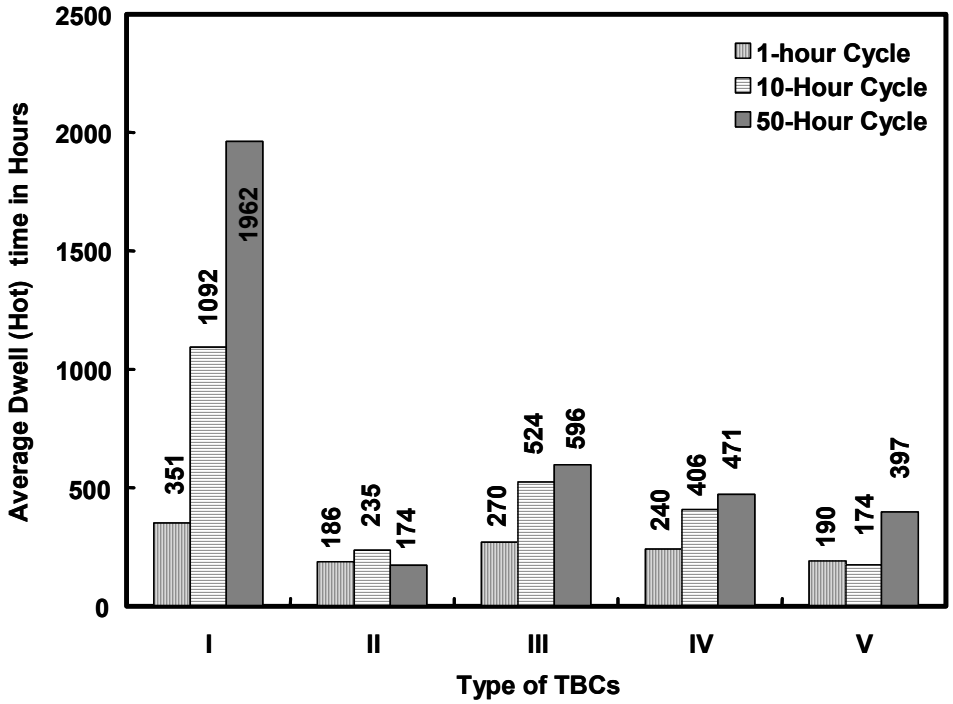

Figure 12. Dwell time life during thermal cycling at 1121°C for five-types of TBCs at 1, 10 and 50 –hour thermal cycling.

Table V. Thermal cyclic lifetime for commercial production TBCs and specimens employed for microstructural analysis.

TBC System	TBC Lifetime and Standard Deviation (#)	1-Hour Thermal Cycling			10-Hour Thermal Cycling		50-Hour Thermal Cycling
		10% Lifetime	50% Lifetime	70% Lifetime	30% Lifetime	80% Lifetime	50% Lifetime
I	527 (20) 113 (1) 39 (0.7)	50	260	360	35	90	20
II	280 (35) 25 (5) 3.5 (3.5)	30	140	200	8	20	2
III	406 (22) 55 (3) 12 (1.5)	45	200	280	20	45	6
IV	360 (39) 42 (2) 9.5 (0.7)	35	180	250	15	35	4
V	286 (76) 18 (0) 8 (0)	30	140	200	5	15	4

V.1.2. Visual Observation of TBC Spallation for 1-Hour Thermal Cycling-APS TBCs

Figure 13 shows the fractographic surface of the type-I APS TBCs with APS NiCoCrAlY bondcoat. Form the YSZ bottom surface we can observe two contrasts namely the black and the white. The black is supposedly the TGO and the white region is YSZ. A similar inference can be made on the bondcoat surface after spallation shown in Figure 11a. This leads to a conclusion that the fracture path was between the YSZ/TGO interfaces. A similar observation and explanation can be given to the type-V APS TBCs with VPS NiCoCrAlY bondcoat shown in Figure 14. A detailed analysis was carried out in section V.4.

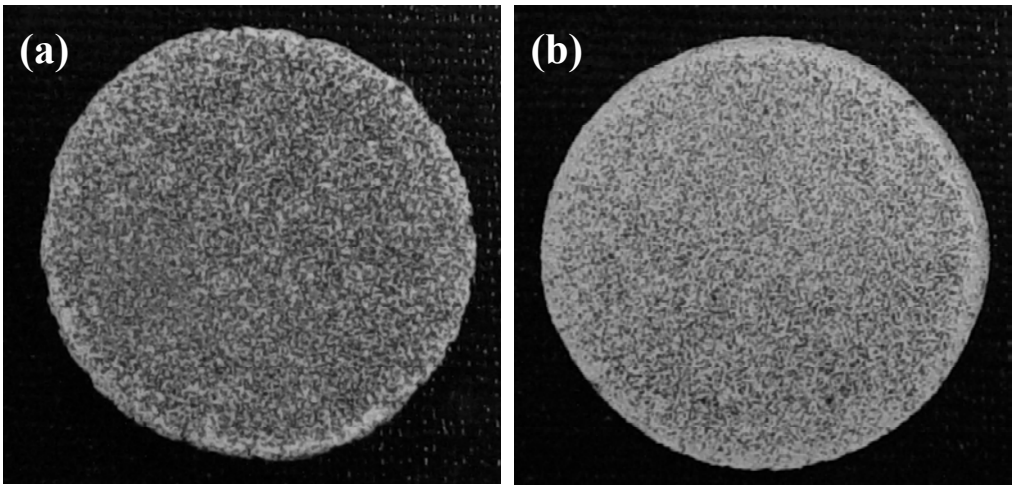

Figure 13. Macro photographs illustrating failure mode of type I APS TBCs with NiCoCrAlY bondcoat with average lifetime of 527 cycles: (a) bottom surface of spalled YSZ coating and (b) top surface of bondcoat after YSZ spallation.

Figure 14. Macro photographs illustrating failure mode of type V APS TBCs with NiCoCrAlY bondcoat with average lifetime of 286 cycles: (a) top surface of bondcoat after YSZ spallation that (b) occurred with initial damage at the edge of the button.

V.1.3. Visual Observation of TBC Spallation for 1-Hour Thermal Cycling-EB-PVD TBCs

Figure 15 shows the macro fractographic surface of the fractured type-II EB-PVD with NiCoCrAlY bondcoat. From these figures we can observe that the YSZ is cracked into pieces with cracks observed on the YSZ surface. This cracking of the YSZ may be due to the sintering and surface irregularities at the interface between the YSZ/TGO. This cracking of the YSZ may be related to the flat and large scale buckling failure of this particular type of TBCs. A detailed study was done this fracture surface and discussed in the section V.4.

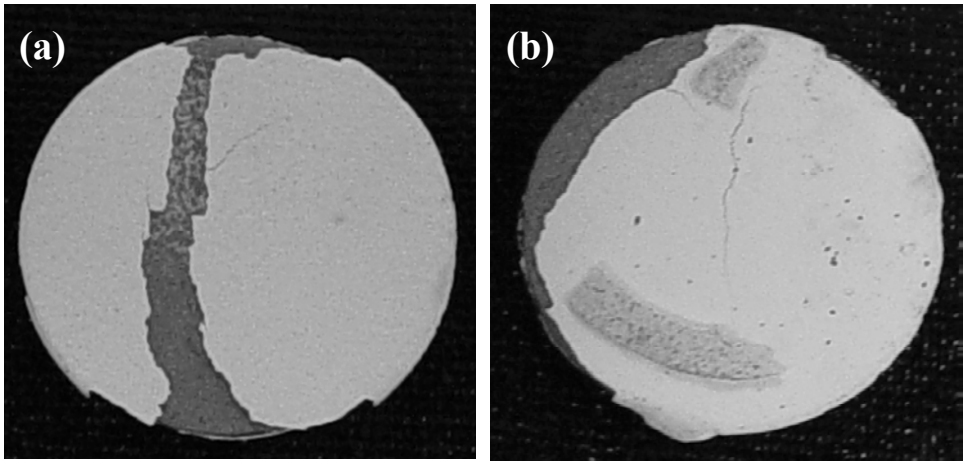

Figure 15. (a,b) Macro photographs illustrating failure mode of type II EB-PVD TBCs with NiCoCrALY bondcoat with average lifetime of 280 cycles.

Figure 16 shows the fracture surface of type-III EB-PVD TBCs with (Ni,Pt)Al bondcoat. This type showed the fracture of the entire YSZ coating. This type of fracture is related to the buckling of the YSZ coating due to the bondcoat ridges (discussed in section V.4). A similar observation type of observation is made for the type-IV coating with grit-blasted (Ni,Pt)Al bondcoat as shown in Figure 17. Here in this type the large scale buckling of the YSZ is due to another phenomena quiet frequently observed for this type of oxidation called racheting (see section V.4).

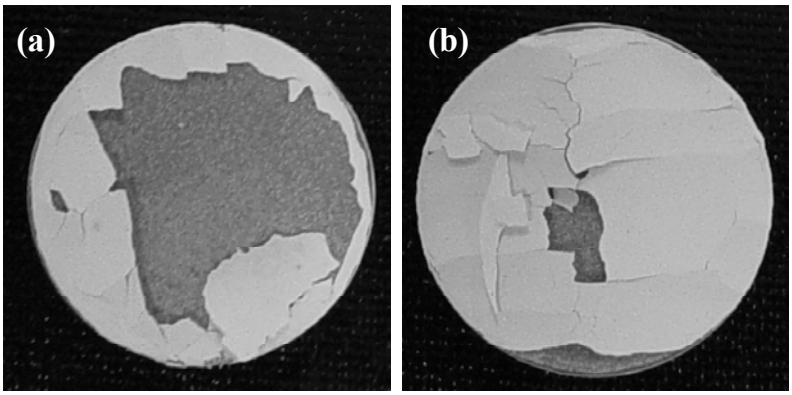

Figure 16. (a,b) Macro photographs illustrating failure mode of type III EB-PVD TBCs with as-coated (Ni,Pt)Al bondcoat with average lifetime of 418 cycles.

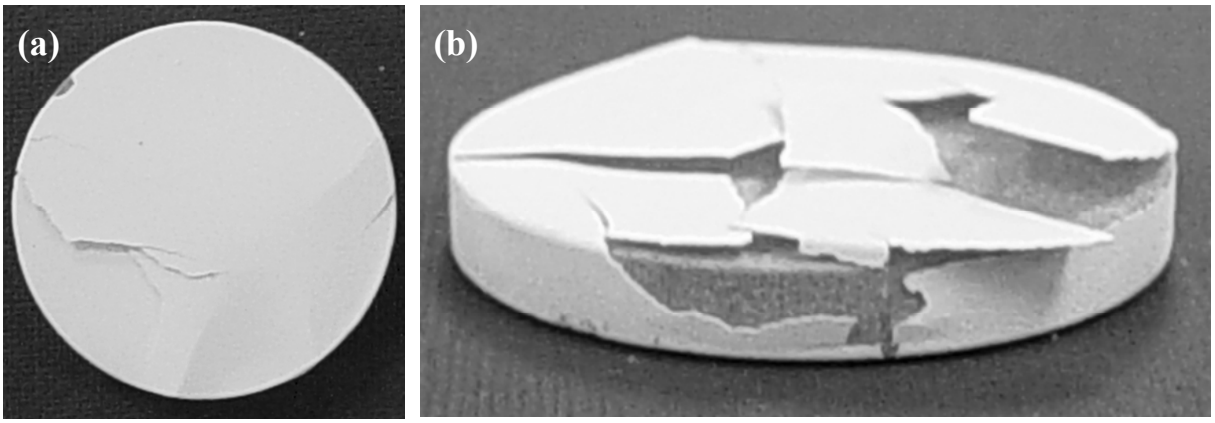

Figure 17. Macro photographs illustrating failure mode of type IV EB-PVD TBCs with grit-blasted bondcoat with average lifetime of 362 cycles: (a) top surface of buckled YSZ and (b) disintegration of the YSZ coating afterwards.

V.1.4. Visual Observation of TBC Spallation for 10-Hour Thermal Cycling for APS TBCs

Figures 18 and 19 show the fracture surface of type-I and type-V APS TBCs for 10-hour thermal cycling. The fracture surface remained the same macroscopically when compared to the 1-hour thermal cycling.

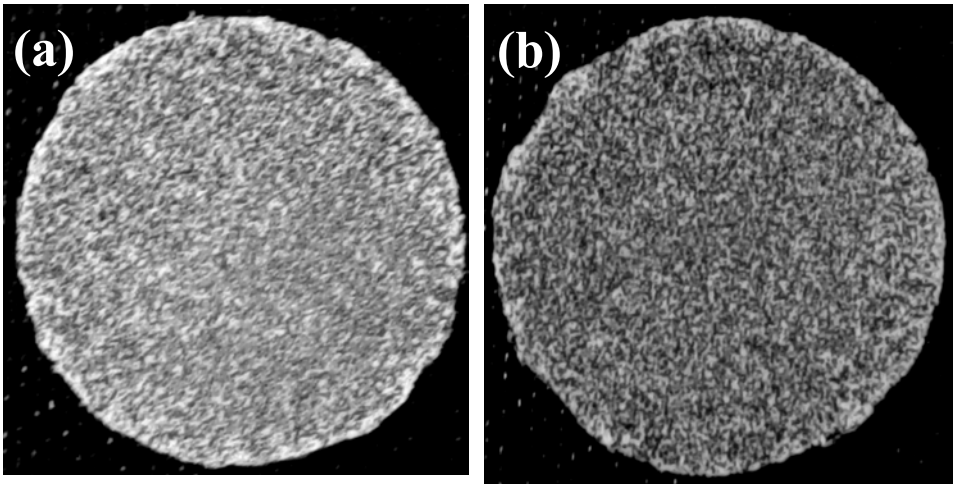

Figure 18. Macro photographs illustrating failure mode of type I APS TBCs with NiCoCrAlY bondcoat with average lifetime of 113 cycles: (a) bottom surface of spalled YSZ coating and (b) top surface of bondcoat after YSZ spallation.

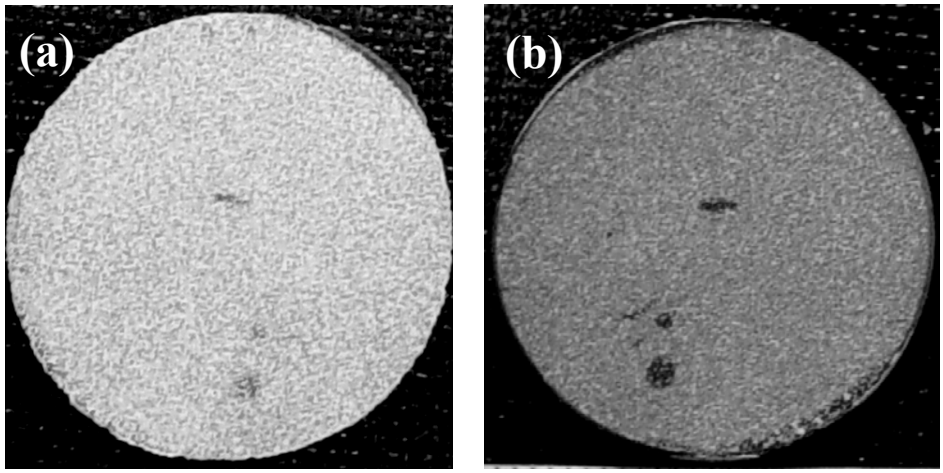

Figure 19. Macro photographs illustrating failure mode of type V APS TBCs with NiCoCrAlY bondcoat with average lifetime of 18 cycles: (a) bottom surface of the YSZ after spallation of the coating from the bondcoat (b) top surface of bondcoat after YSZ spallation.

V.1.5. Visual Observation of TBC Spallation for 10-Hour Thermal Cycling-EBPVD TBCs

Figure 20 shows the fracture of the type-II EB-PVD TBCs with NiCoCrAlY bondcoat. A similar fracture trend was observed when compared to 1-hour thermal cycling macroscopically. A detailed study was done and discussed comparing the 1-hour and 10-hour thermal cycling for this type in section V.4.

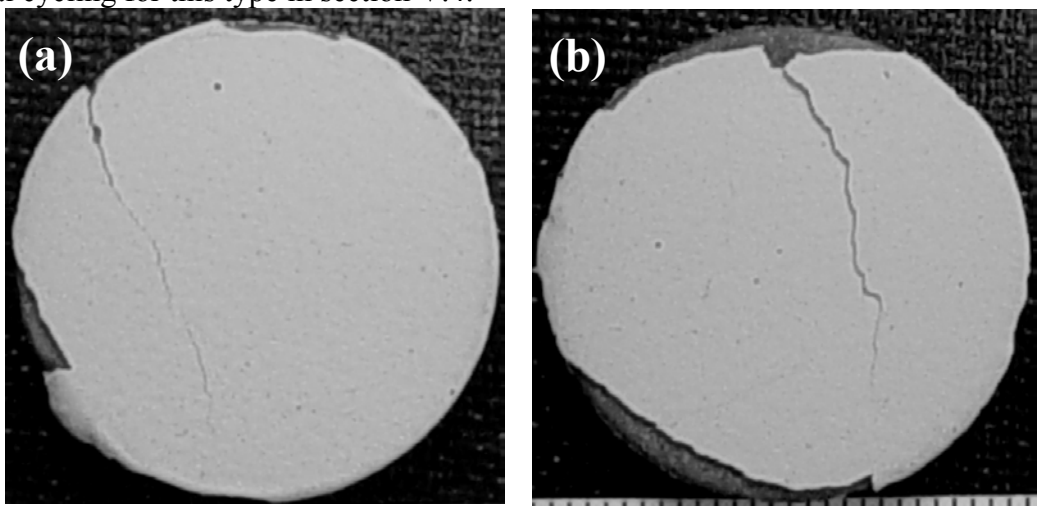

Figure 20. (a,b) Macro photographs illustrating failure mode of type II EB-PVD TBCs with NiCoCrALY bondcoat with average lifetime of 25 cycles.

Figure 21 shows the fractured surface type-III EB-PVD with as-coated (Ni,Pt)Al bondcoat. Macroscopically we can observe that this type of TBCs compared to the 1-hour thermal cycling did differ from 10-hour thermal cycling. This type of failure is related to the large scale buckling for this type of TBCs.

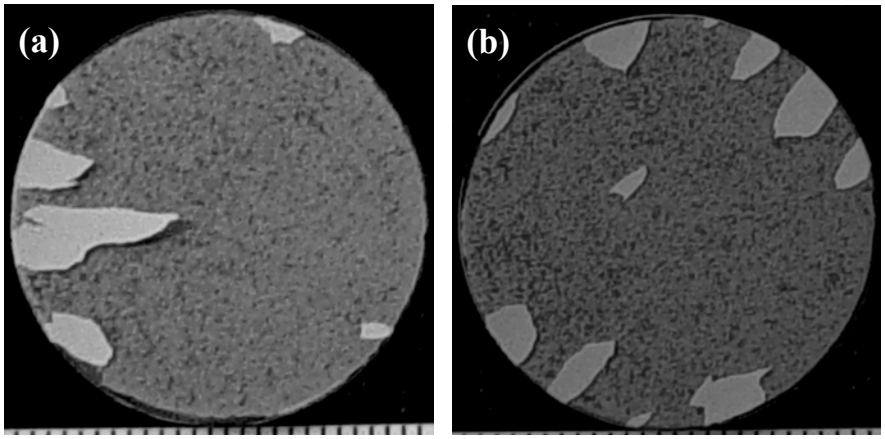

Figure 21. (a,b) Macro photographs illustrating failure mode of type III EB-PVD TBCs with as-coated (Ni,Pt)Al bondcoat with average lifetime of 55 cycles.

Figure 22 shows macroscopically the fracture surface of type-IV EB-PVD TBCs from 10-hour thermal cycling. Significantly this particular type did differ from 1-hour thermal cycling where we can observe that the buckling is localized to a particular region and also we can observe intact TBCs. A higher magnification on the buckled region shows cracks running through the YSZ. A detailed microstructural characterization was carried on this type and discussed in section V.4.

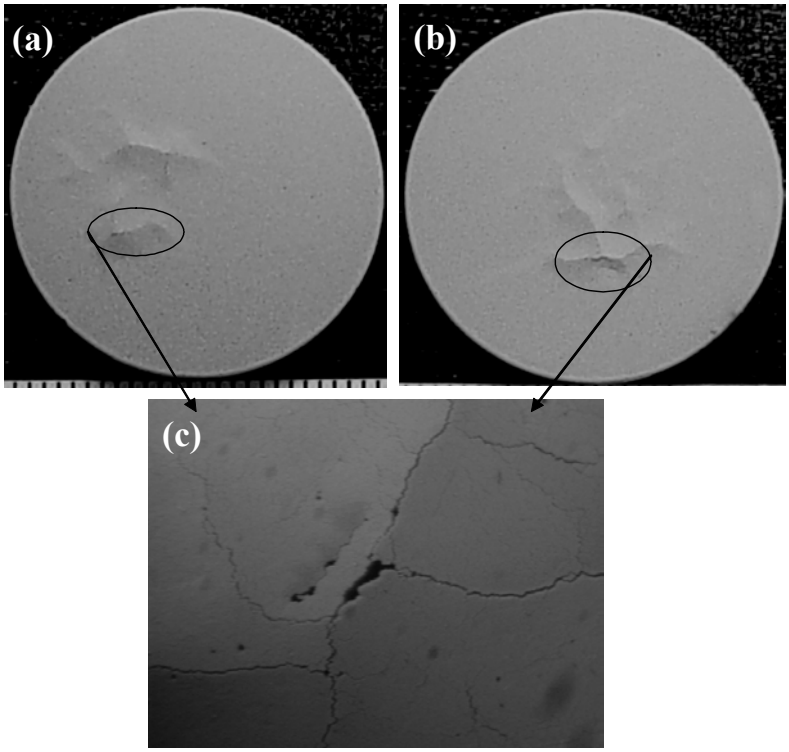

Figure 22. Macro photographs illustrating failure mode of type IV EB-PVD TBCs with grit-blasted bondcoat with average lifetime of 42 cycles: (a, b) top surface of buckled YSZ and (c) A magnified view of the buckling of YSZ coating.

V.1.6. Visual Observation of TBC Spallation for 50-Hour Thermal Cycling for APS TBCs

Figures 23 and 24 shows macroscopic fracture of type-I APS coatings for 50-hour thermal cycling. The fracture surfaces look similar to that of the 1 and 10- hour thermal cycling. The micro constituents of the fracture surface will be reported in the next report during the extension period.

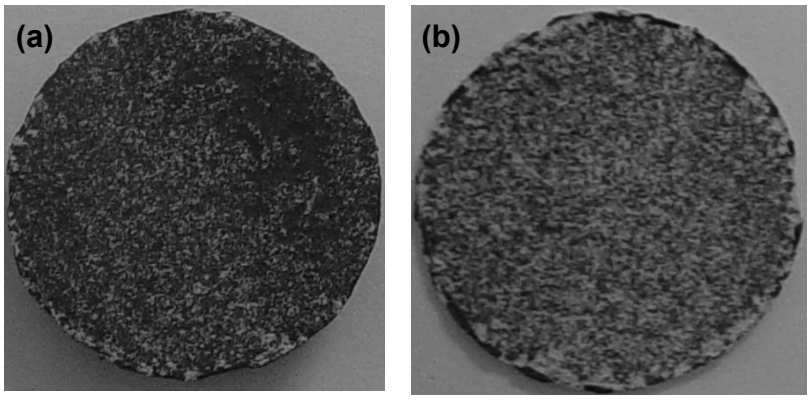

Figure 23. Macro photographs illustrating failure mode of type I APS TBCs with NiCoCrAlY bondcoat with average lifetime of 39 cycles: (a) top surface of bondcoat after YSZ spallation and (b) bottom surface of YSZ after spallation.

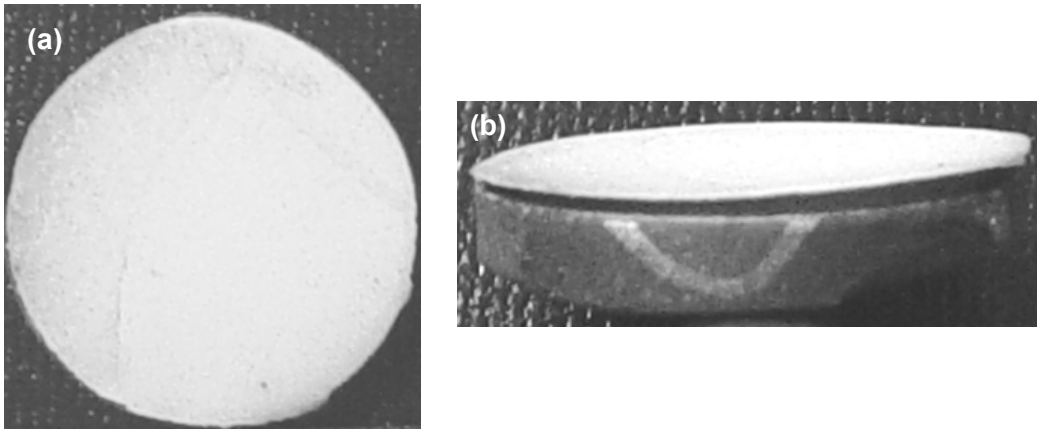

Figure 24. Macro photographs illustrating failure mode of type V APS TBCs with VPS NiCoCrAlY bondcoat with average lifetime of 8 cycles: (a, b) top surface of delaminated YSZ and (c) A front view of the delamination of YSZ coating.

V.1.7. Visual Observation of TBC Spallation for 50-Hour Thermal Cycling for EB-PVD TBCs

Figure 25 shows the fracture for type-II EB-PVD TBCs with shot-peened NiCoCrAlY bondcoat. The fracture was similar to that of the 1 and 10-hour thermal cycling. Both specimens shown in Figure 25 failed by buckling but one of the specimens shown in Figure 25 (b) failed after one cycle. A detailed microstructure analysis on these two types will be done in the following report.

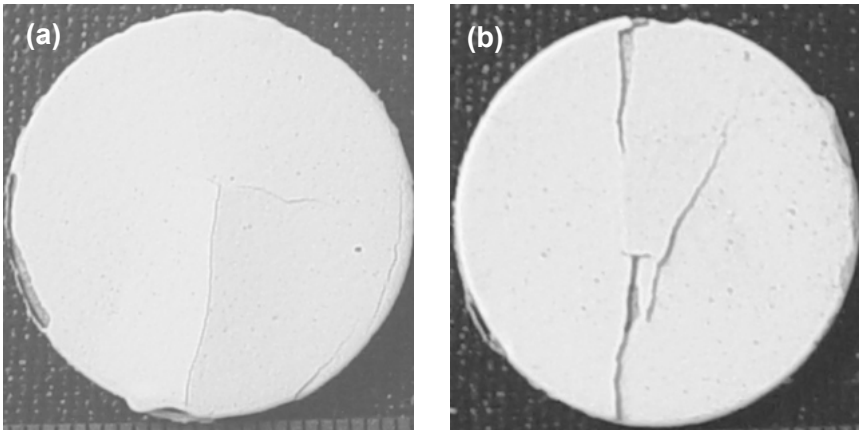

Figure 25. Macro photographs illustrating failure mode of type II EB-PVD TBCs with shot-peened NiCoCrAlY bondcoat with average lifetime of 3.5 cycles: (a) top surface of buckled YSZ after 6 cycles and (b) A top surface view of buckled YSZ after 1 cycle.

Figure 26 shows the macroscopic failure of type-III EB-PVD TBCs with as-coated (Ni,Pt)Al bondcoat after 50-hour thermal cycling. The fracture surface appeared different from those observed after 1 and 10-hour thermal cycling. A detailed investigation will be presented in the final report. This type of observation is related to large scale buckling that is observed for this type of TBCs.

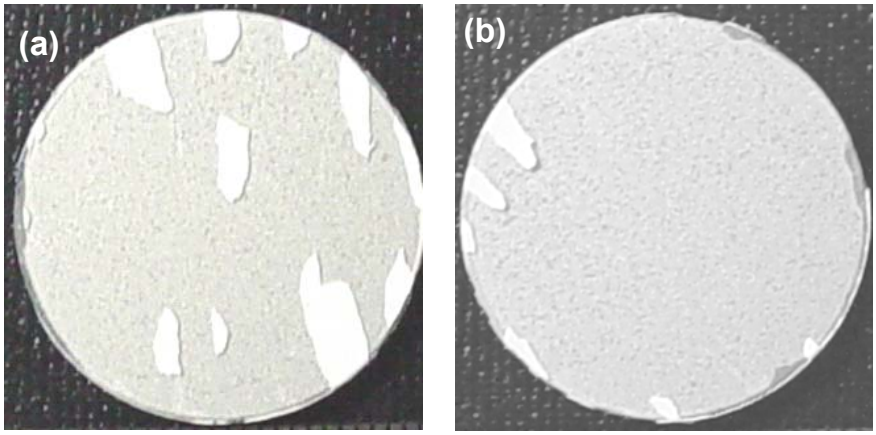

Figure 26. Macro photographs illustrating failure mode of type III EB-PVD TBCs with as-coated (Ni,Pt)Al bondcoat with average lifetime of 12cycles, Large scale buckling observed in both the samples after 50-hour thermal cycling.

Figure 27 shows the macrograph of type-IV EB-PVD TBCs with grit-blasted (Ni,Pt)Al bondcoat. From the macrograph it's observed that these samples did also fail by large scale buckling comparing to the 10-hour thermal cycling. The micro-constituents and any difference microscopically of the fracture surface will be presented in the final report.

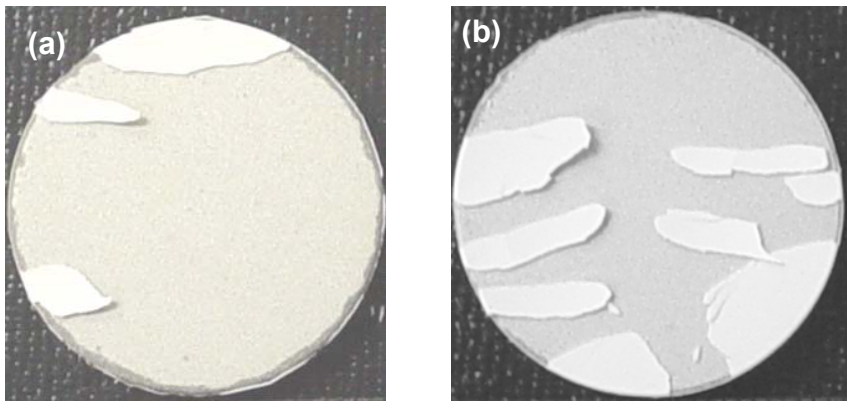

Figure 27. Macro photographs illustrating failure mode of type IV EB-PVD TBCs with grit-blasted (Ni,Pt)Al bondcoat with average lifetime of 9 cycles, Large scale buckling observed in both the samples after 50-hour thermal cycling.

V.2. Photostimulated Luminescence Spectroscopy of Thermal Barrier Coatings

V.2.1. As-Coated Electron Beam Physical Vapor Deposited Thermal Barrier Coatings

NDE by PSLS has been restricted to EB-PVD TBCs (type II, III and IV), since PSLS cannot be applied to APS TBCs (type I and V) without impregnating APS YSZ coatings with other medium [22], whose effect on TBC lifetime may be harmful.

For type II as-coated EB-PVD TBCs with NiCoCrAlY bond coat, PSLS was collected for all 20 specimens. For each specimen, 30 random-spot measurements were carried out. Typical luminescence observed from type II TBCs are presented in Figure 28. Due to the nature of the spectra, relative luminescence intensity and luminescence frequency for type II TBCs could not be analyzed properly in the as-received condition. This unclear and indistinguishable luminescence can be due to under-developed TGO scale, potentially consisting of θ-Al_2O_3. However, luminescence from type II TBCs has been carried out with ease after initial thermal cycling since a clearer and distinguishable luminescence from better-developed TGO was observed.

Luminescence from α-, γ- and θ-Al_2O_3 was observed in all spectra for all type III EB-PVD specimens with as-coated (Ni,Pt)Al bond coat in the as-received condition. Figure 29 represents typical luminescence observed from type III EB-PVD TBCs. Relative luminescence intensity from α-, γ- and θ-Al_2O_3 polymorphs is presented in Figure 30. In general, 70~80% of luminescence was from α-Al_2O_3 while 20~30% luminescence was from γ- and θ-Al_2O_3 for as-coated type III TBCs. These values *do not* correspond to the actual volume fraction of Al_2O_3 polymorphs.

Figures 31 and 32 present the shift in the position of R_2 luminescence $\overline{\Delta\upsilon}$ based on 30 random-spot measurements for type III TBCs. In all cases, bimodal (i.e., two sets of R_1 and R_2) luminescence corresponding to higher (~5 GPa) and lower (~3.5 GPa) compressive residual stress in α-Al_2O_3 was observed.

PSLS was collected for 20 specimens of type IV as-coated EB-PVD TBCs with grit-blasted (i.e., removal of grain boundary ridges) (Ni,Pt)Al bond coat. For all 20 specimens with luminescence, 30 random-spot measurements were carried out. Clear and distinguishable luminescence from α-, γ- and θ-Al_2O_3 was observed in all spectra for 16 specimens as presented in Figure 33(a). *Extremely weak luminescence with much noise was obtained from the remaining 4 specimens; possibly a result of under-developed TGO.* The remaining four specimens exhibited luminescence with low signal-to-noise ratio as presented in Figure 33(b). Relative luminescence intensity from α-, γ- and θ-Al_2O_3 polymorphs is presented in Figure 34. In general, 60~70% of luminescence was from α-Al_2O_3 while 30~40% luminescence was from γ- and θ-Al_2O_3 for as-coated type IV TBCs. These values *do not* correspond to the actual volume fraction of Al_2O_3 polymorphs. Relative to type III TBCs with as-coated (Ni,Pt)Al bond coat, a slightly stronger γ-Al_2O_3 luminescence than θ-Al_2O_3 was observed.

Figures 35 and 36 represent the shift in the position of R_2 luminescence $\overline{\Delta\upsilon}$ determined based on 30 random-spot measurements for type IV TBCs. In all cases, bimodal (i.e., two sets of R_1 and R_2) luminescence corresponding to higher (~6 GPa) and lower (~1 GPa) compressive residual stress in α-Al_2O_3 was observed.

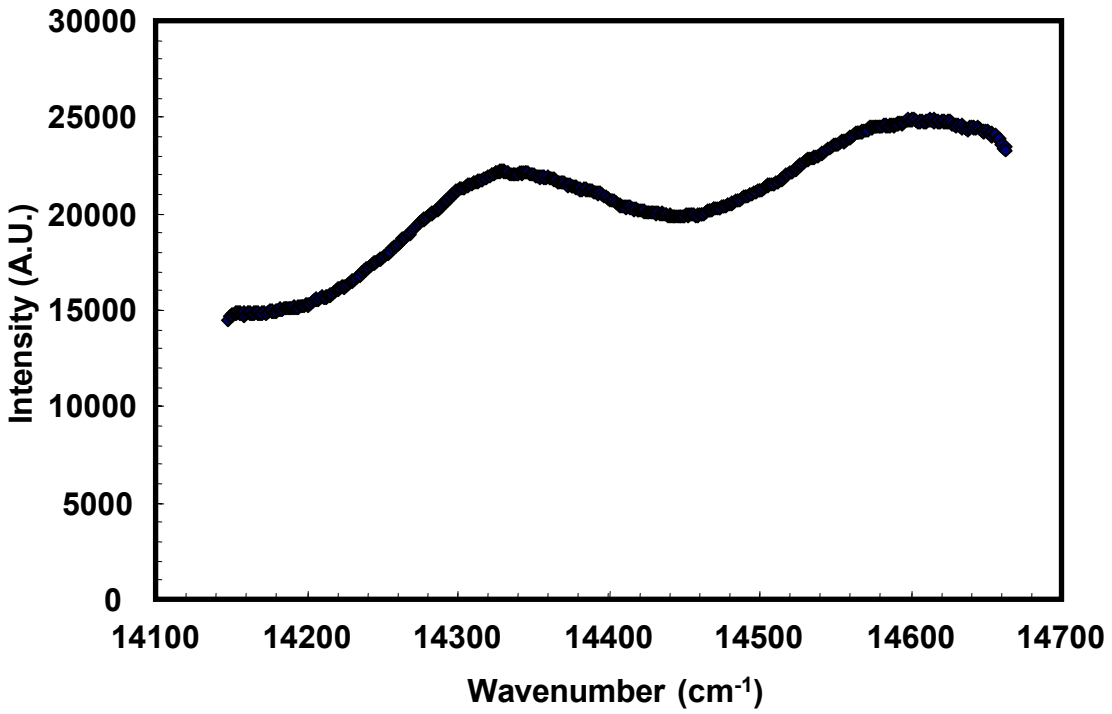

Figure 28. Typical photostimulated luminescence spectrum from as-received type II EB-PVD TBCs with NiCoCrAlY bond coat.

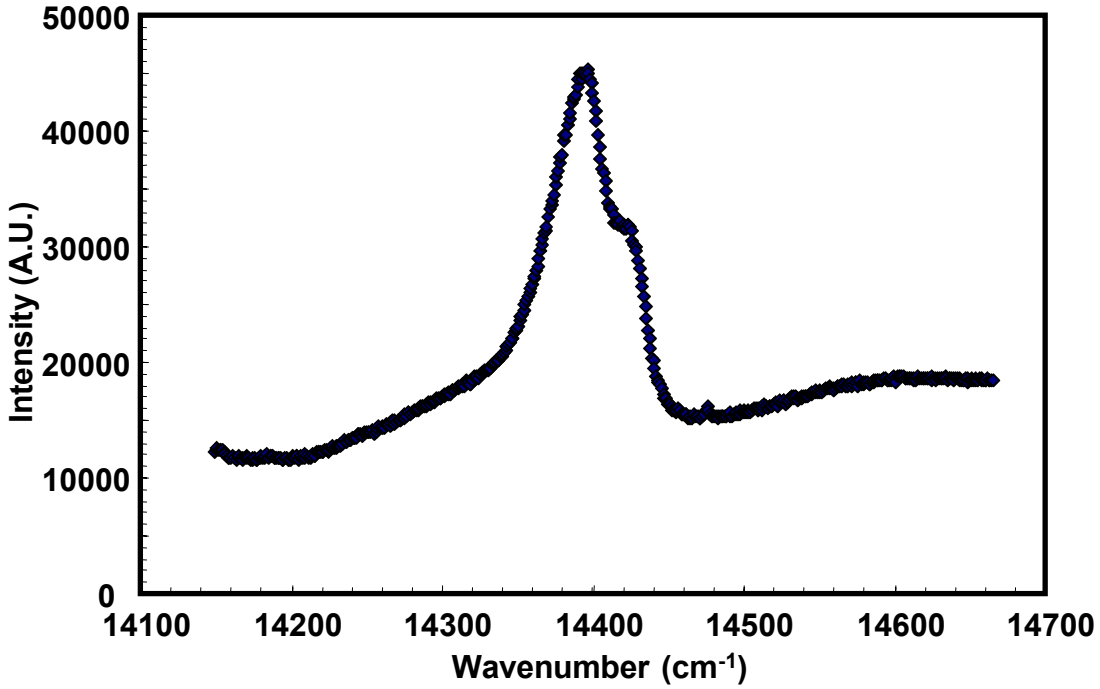

Figure 29. Typical photostimulated luminescence spectrum from as-received type III EB-PVD TBCs with as-coated (Ni,Pt)Al bond coat.

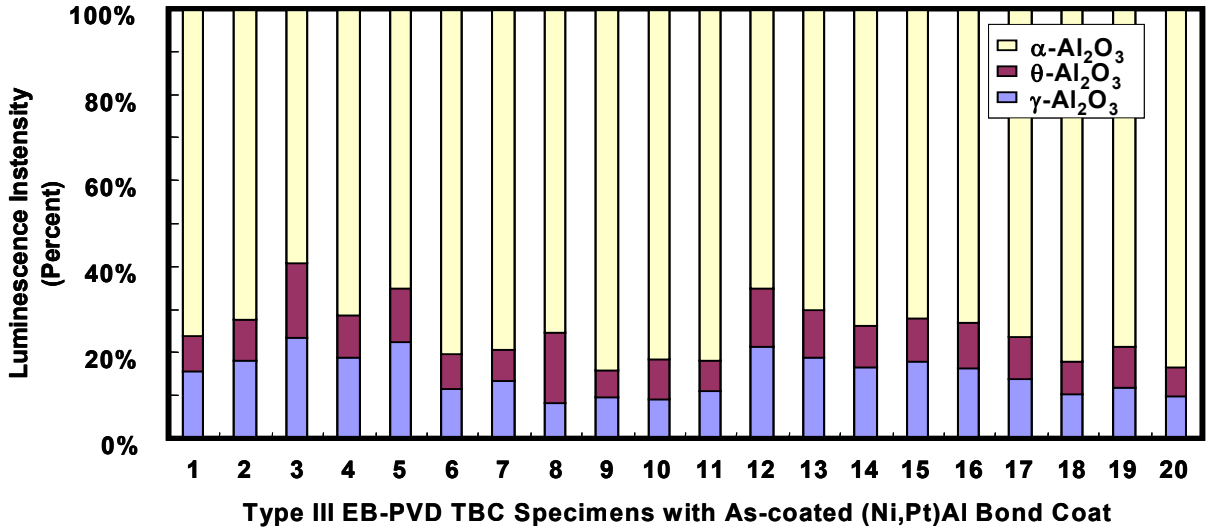

Figure 30. Relative luminescence intensity from α-, γ- and θ-Al_2O_3 in TGO for as-coated type III TBCs with as-coated (Ni,Pt)Al bond coat.

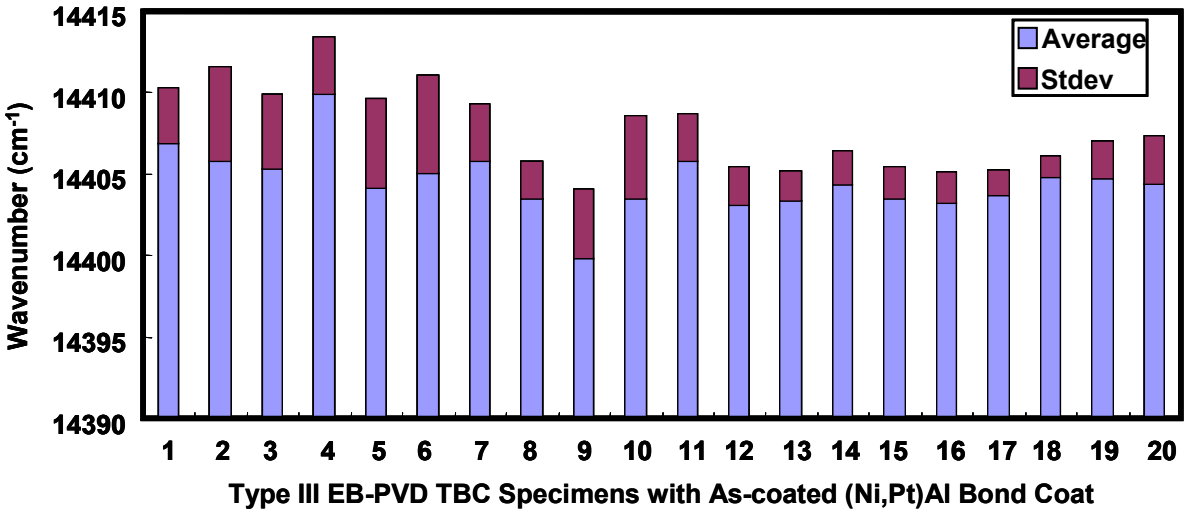

Figure 31. Higher average compressive residual stress of α-Al_2O_3 TGO determined from bimodal luminescence for as-coated type III TBCs.

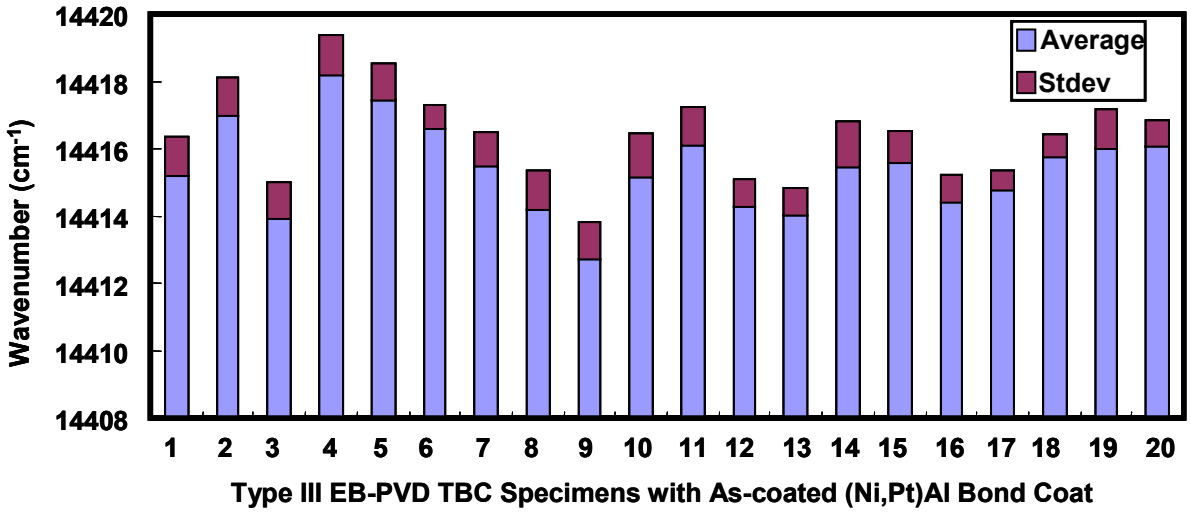

Figure 32. Lower average compressive residual stress of α-Al_2O_3 TGO determined from bimodal luminescence for as-coated type III TBCs.

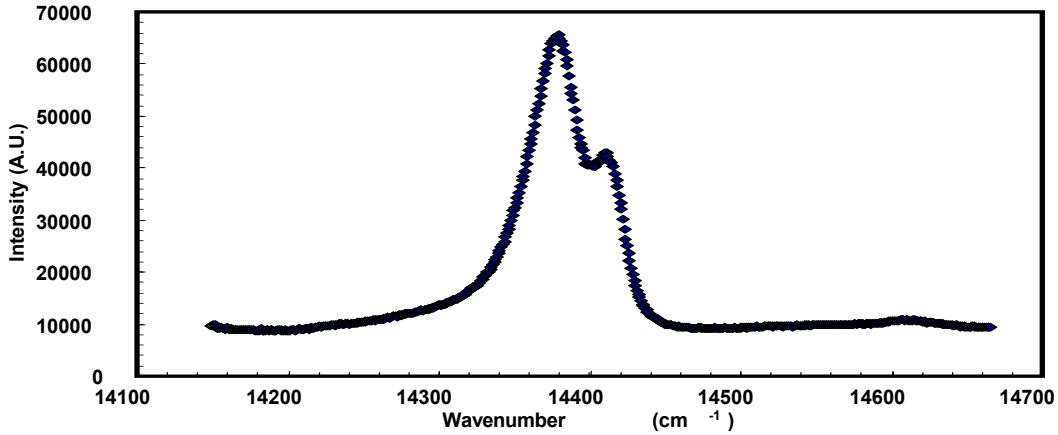

(a)

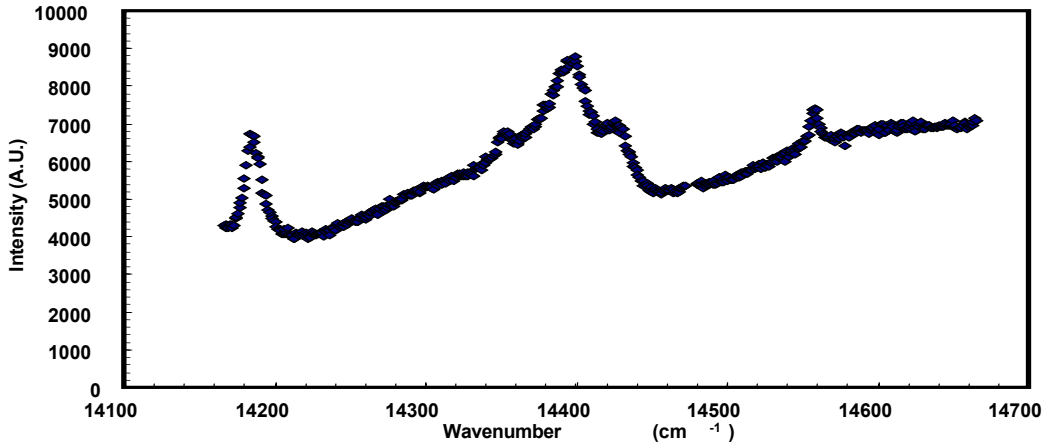

(b)

Figure 33. Typical photostimulated luminescence spectrum from as-received type IV EB-PVD TBCs with grit-blasted (Ni,Pt)Al bond coat: (a) 16 specimens with strong luminescence and (4) the remaining 4 specimens with low signal-to-noise ratio.

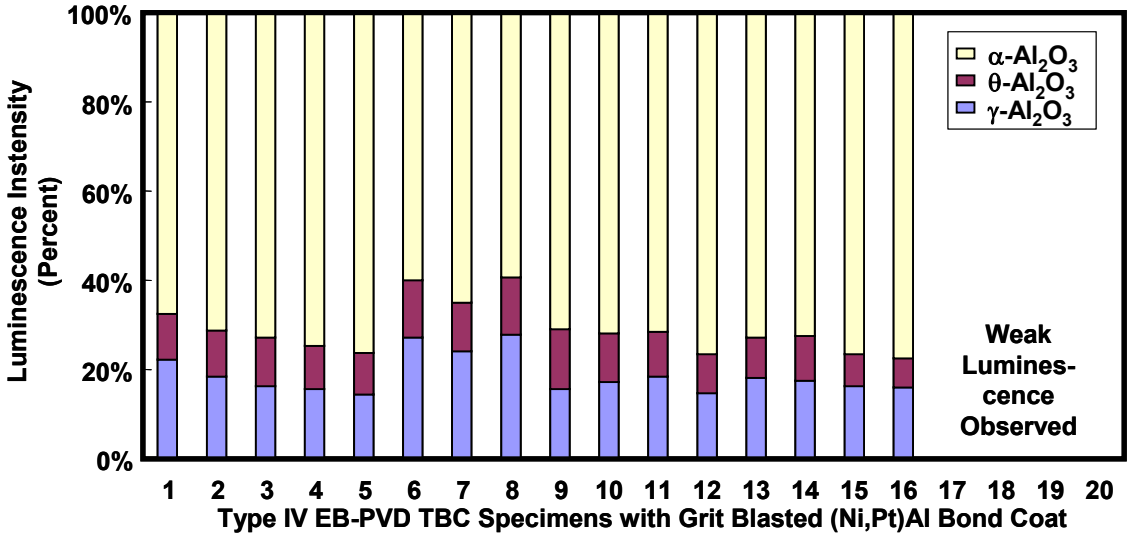

Figure 34. Relative luminescence intensity from α-, γ- and θ-Al_2O_3 in TGO for as-coated type IV TBCs with grit-blasted (Ni,Pt)Al bond coat.

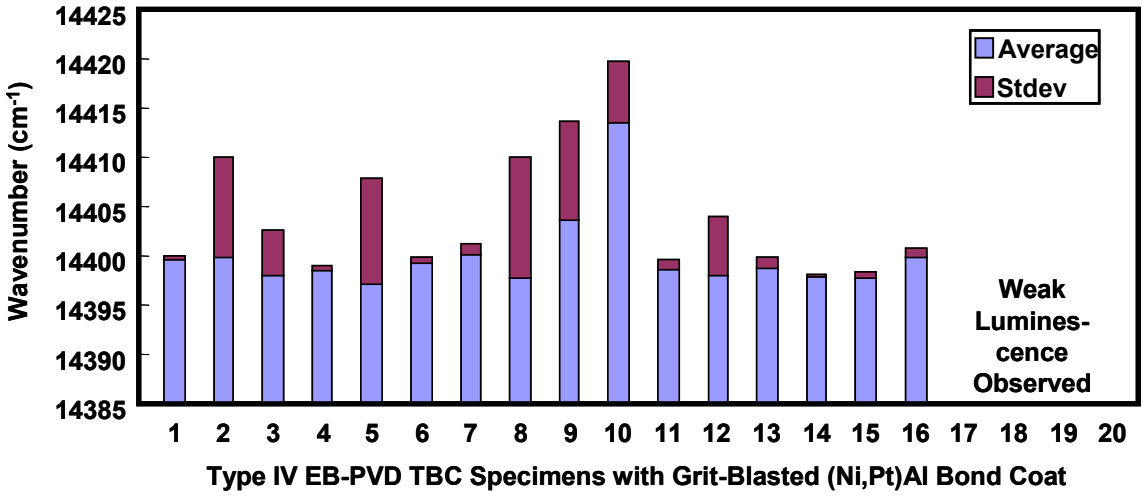

Figure 35. Higher average compressive residual stress of α-Al_2O_3 TGO determined from bimodal luminescence for as-coated type IV TBCs.

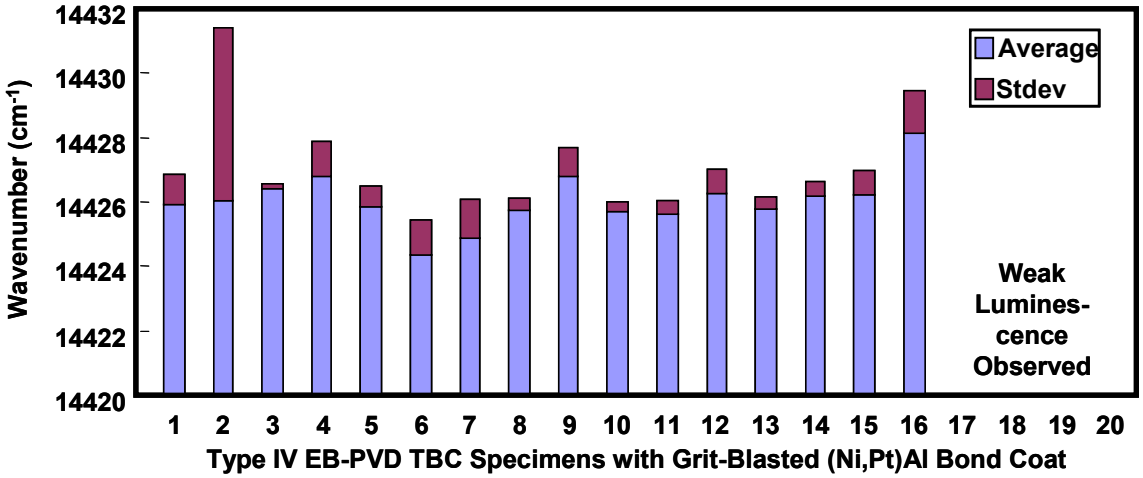

Figure 36. Lower average compressive residual stress of α-Al_2O_3 TGO determined from bimodal luminescence for as-coated type IV TBCs.

V.2.2. PSLS of EB-PVD TBCs as a Function of 1-Hour Thermal Cycling

The compressive residual stress within the TGO as a function of 1-hour thermal cycling for type II EB-PVD TBCs with NiCoCrAlY bond coats is presented in Figure 37. The value of stress is calculated based on shift of photostimulated luminescence via piezospectroscopic coefficients. Bimodal luminescence (i.e., two sets of R_1-R_2 luminescence) was observed for type II TBCs after thermal cycling. After the initial increase (i.e., starting 1st thermal cycle) in the compressive residual stress (for both higher and lower compressive residual stress arising from bimodal luminescence), the magnitude of the TGO stress remained quite constant throughout the entire thermal cycling (i.e., 5.5 and 3.5 GPa in compression). Luminescence from metastable Al_2O_3 phases disappeared after the 1st cycle.

No significant changes in the value of stress or standard deviation were observed prior to spallation as presented in Figure 37. While the initial increase may be due to development of the TGO scale, it is somewhat discouraging that no detectable changes in the luminescence was observed prior to failure of type II TBCs. Microstructural and failure investigation of type II TBCs indicate that the fracture primarily occurred at the YSZ/TGO interface and a significant internal oxidation of NiCoCrAlY bond coat has occurred (see section V.4.4). This is somewhat abnormal. Constant values of compressive residual stress can be correlated to lack of interfacial undulation at the NiCoCrAlY/TGO interface.

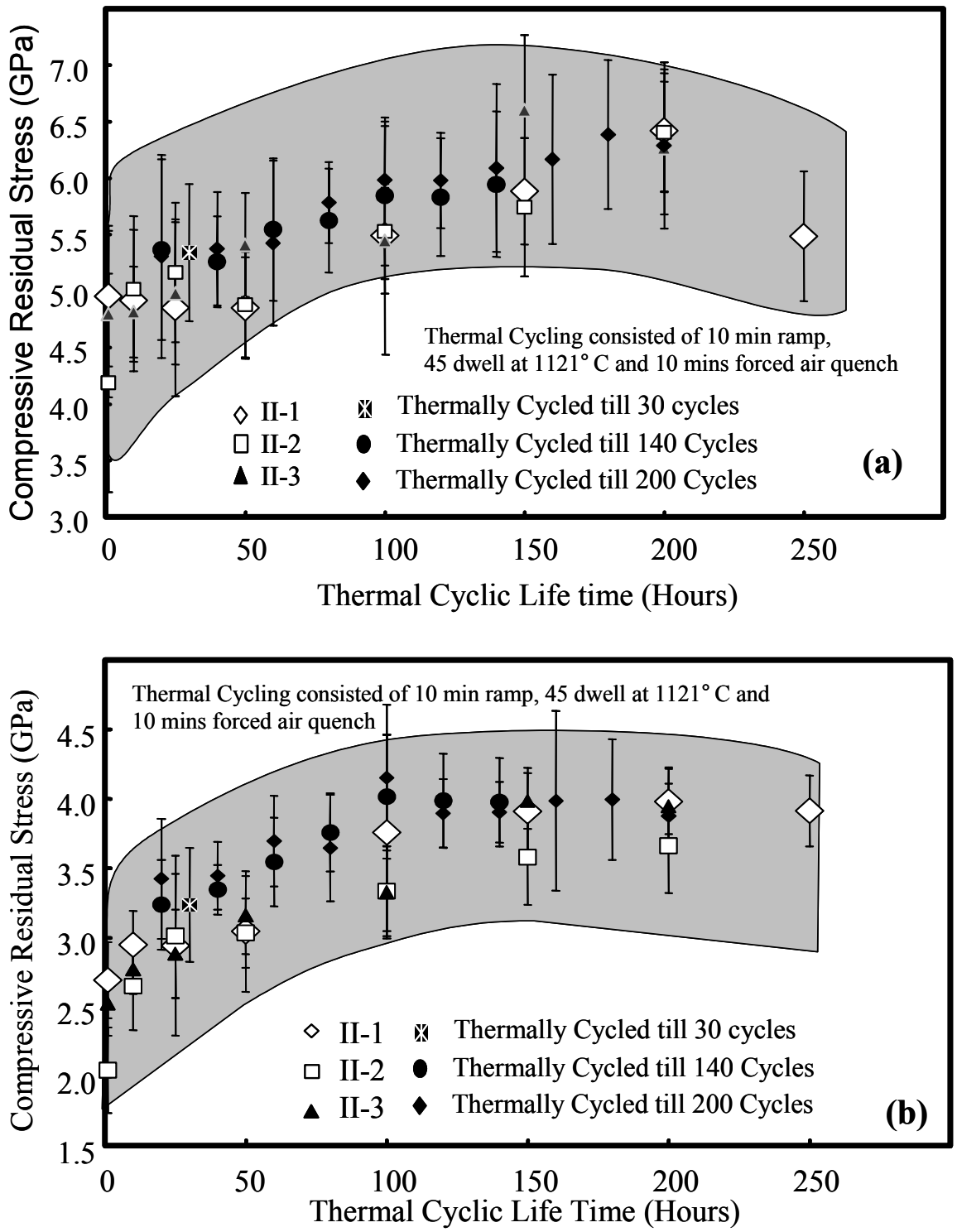

Figure 37. Compressive residual stress within TGO as a function of 1-hour thermal cycling for type II EB-PVD TBCs with NiCoCrAlY bondcoats. Values of compressive residual stress ere calculated from bimodal luminescence corresponding to (a) higher and (b) lower shifts in luminescence.

Figure 38 represents typical luminescence observed for type III TBCs as a function of 1-hour thermal cycling. While the failure of TBCs occurred at 420 1-hour cycles, detectable increase in the luminescence associated with stress-relief of the TGO emerged starting 350 cycles as shown in Figure 38. After 400 cycles, more than half of 20-randomly-selected measurement indicated localized stress-relief associated with damage in the TGO scale. The evolution and detection of stress-relief in the TGO for type III TBCs can be quantified by examining the first $(dc/d\upsilon)$ and second $(d^2c/d\upsilon^2)$ derivatives of luminescence spectrum associated with stress-relieved luminescence frequency at $\upsilon \cong 14432$ for R_2. As show in Figure 39(a), the luminescence spectrum with $(dc/d\upsilon) = 0$ at $\upsilon = 14432 \pm 3$ and $(d^2c/d\upsilon^2) = 0$ at $\upsilon = 14432 \pm 3$ was observed, starting 350 cycles, and thereafter gradually increased in terms of population out of 20 random-spot measurements with thermal cycling shown in Figure 39(b).

Similar to type II TBCs, bimodal luminescence (i.e., two sets of R_1-R_2 luminescence) was observed for type III TBCs throughout thermal cycling. However, for type III TBCs, a tri-mode luminescence emerged starting from approximately 50% lifetime, and the emerging third set of R_1-R_2 luminescence were clearly associated with stress-relief of the α-Al_2O_3 scale. The evolution of relative luminescence intensity obtained up to 50% and 70% of lifetime for the type III TBCs is presented in Figures 40 and 41, respectively. In these Figures, R_2, R_2', and R_2" refer to tri-mode luminescence of higher, lower and no shift, respectively, where the emergence of "no-shift" luminescence may be related to the stress-relief associated with damage within the TGO. The compressive residual stress within TGO as a function of 1-hour thermal cycling for type III EB-PVD TBCs with (Ni,Pt)Al bond coats is presented in Figures 42 and 46.

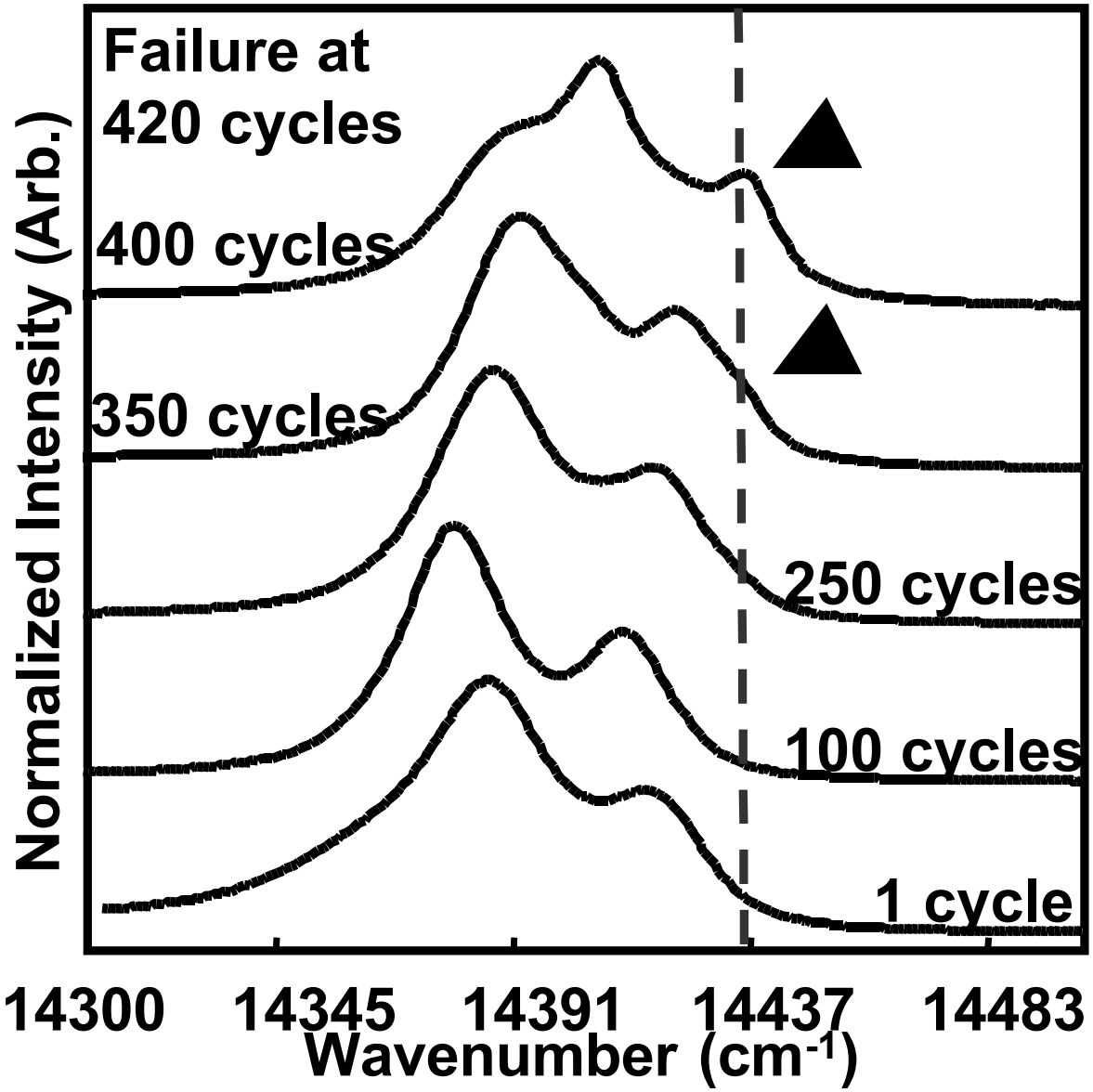

Figure 38. Typical photostimulated luminescence spectra as a function of 1-hour thermal cycling for type III EB-PVD TBCs with as-coated (Ni,Pt)Al bond coats. TBC spallation has occurred after 420 cycles and luminescence from stress-relieved TGO scale (marked by dotted vertical line and arrows) was observed starting 350 cycles by examining the derivatives of the spectra.

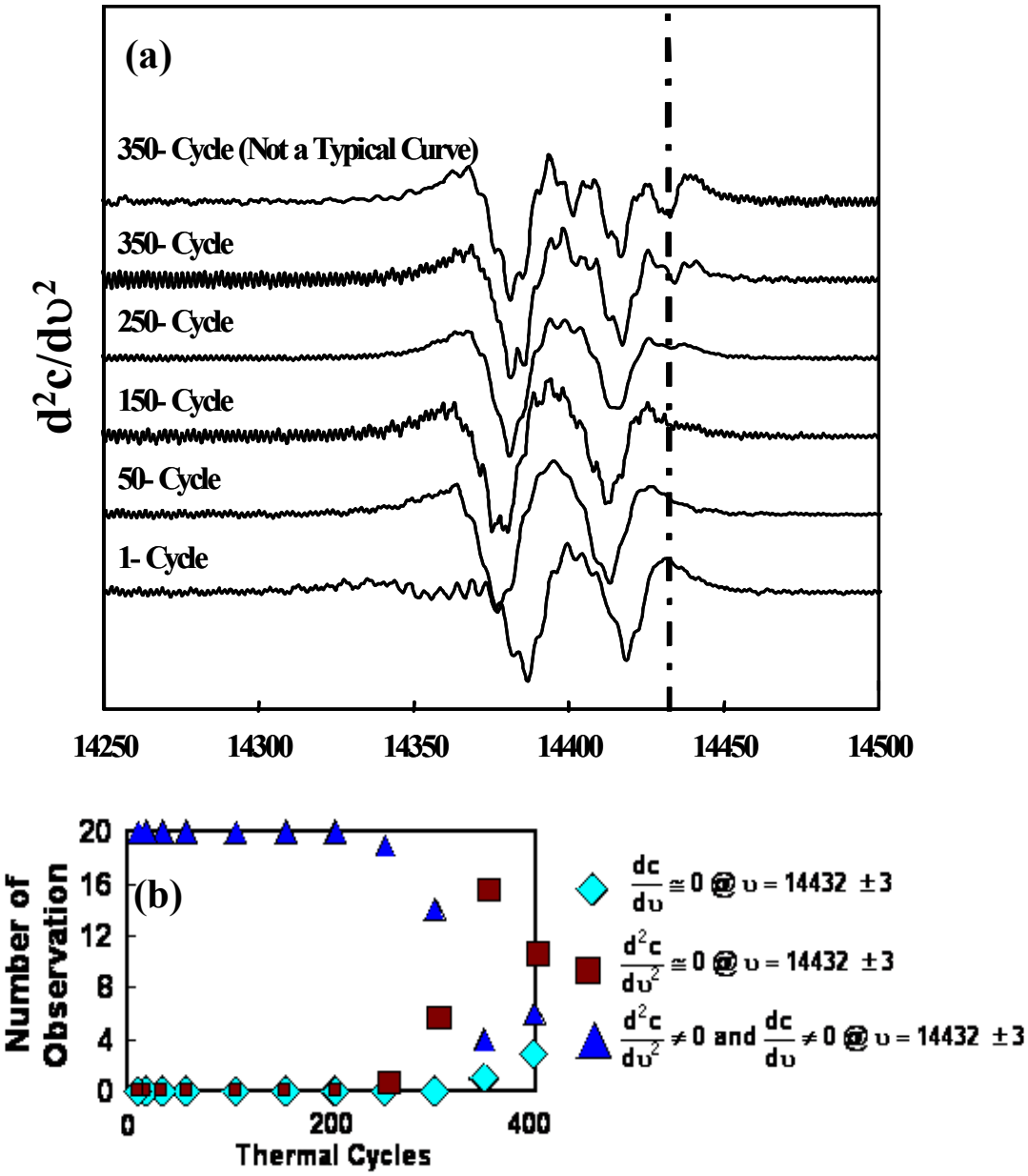

Figure 39. (a) Typical derivatives of luminescence spectrum associated with stress-relieved luminescence frequency at $\upsilon \cong 14432 \pm 3$ for R_2 for 1-hour thermal cycling. (b) Number of photostimulated luminescence spectra that exhibits variation in derivative at stress-relief luminescence as a function of 1-hour thermal cycling for type III EB-PVD TBCs with as-coated (Ni,Pt)Al bond coats.

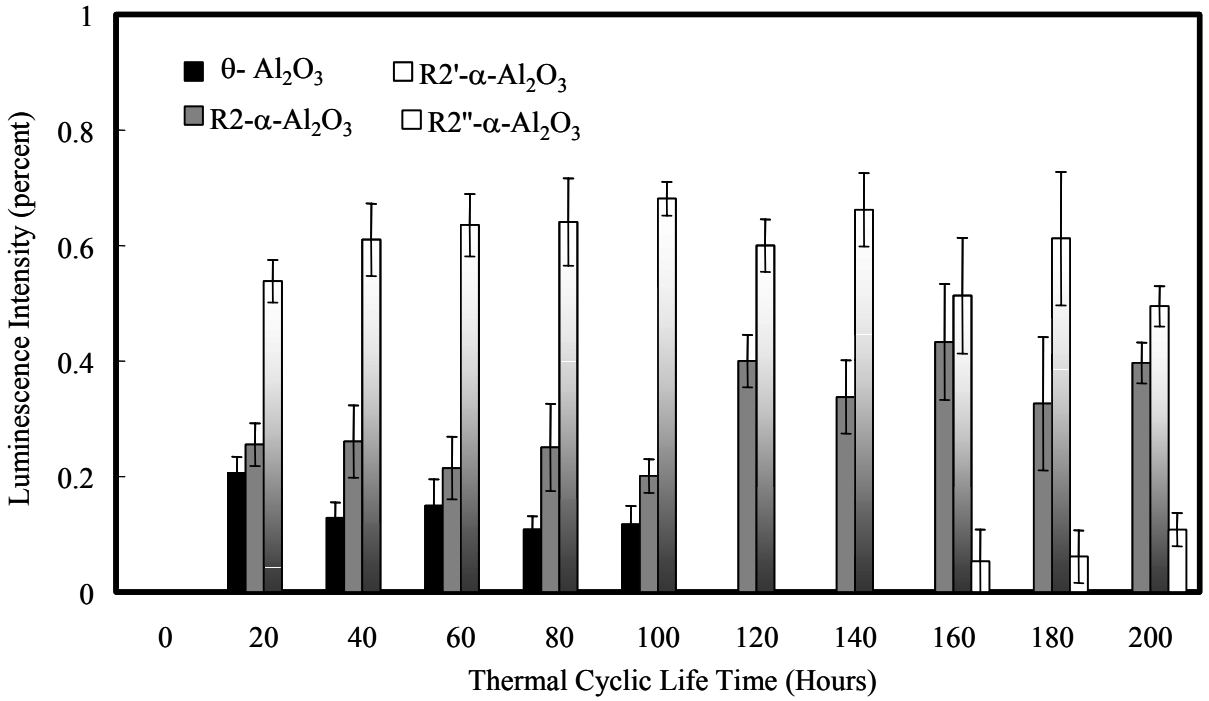

Figure 40. Type-III TBCs cycled until 50% thermal cyclic life time, Relative Luminescence Intensity from θ and α (R2, R'2 & R"2) in TGO with as-coated (Ni,Pt)Al bond coat.

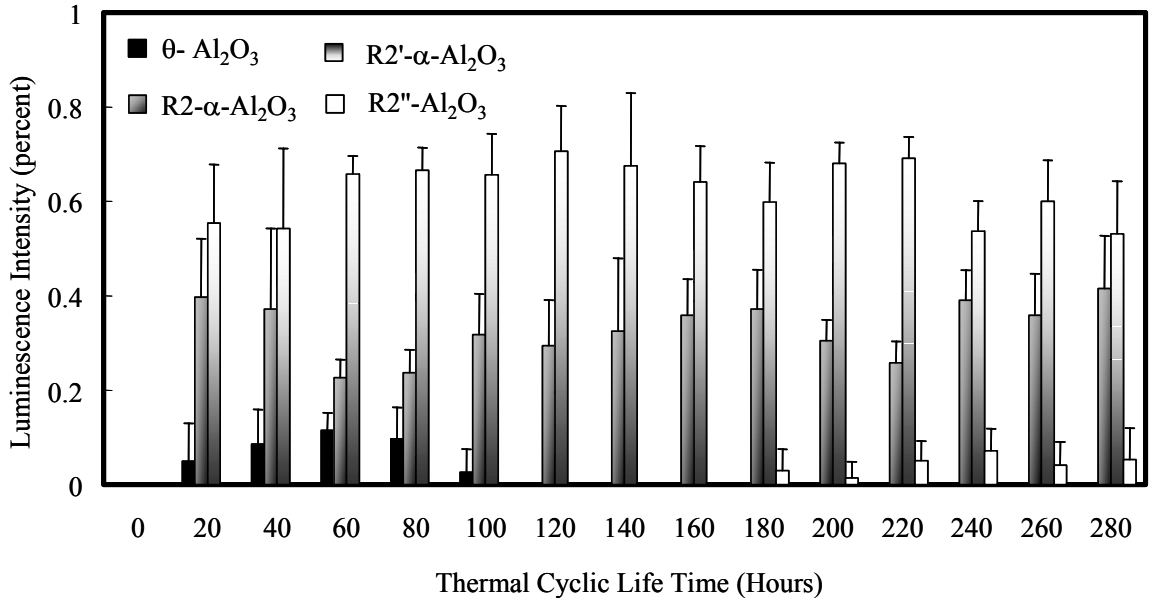

Figure 41. Type-III TBCs cycled until 70% thermal cyclic life time, Relative Luminescence Intensity from θ and α (R2, R'2 & R"2) in TGO with as-coated (Ni,Pt)Al bond coat.

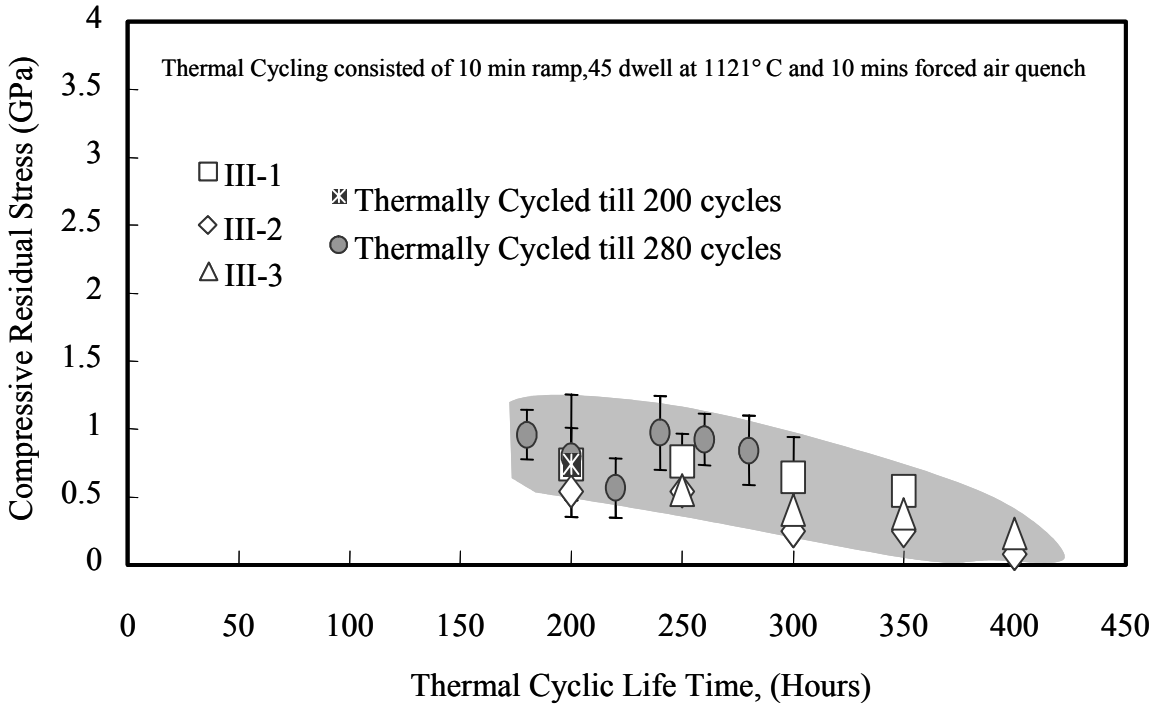

Figure 42. Compressive residual stress within TGO as a function of 1-hour thermal cycling for type III EB-PVD TBCs with (Ni,Pt)Al bondcoats. Values of compressive residual stress were calculated from the emerging luminescence with minimum shift in the tri-modal luminescence.

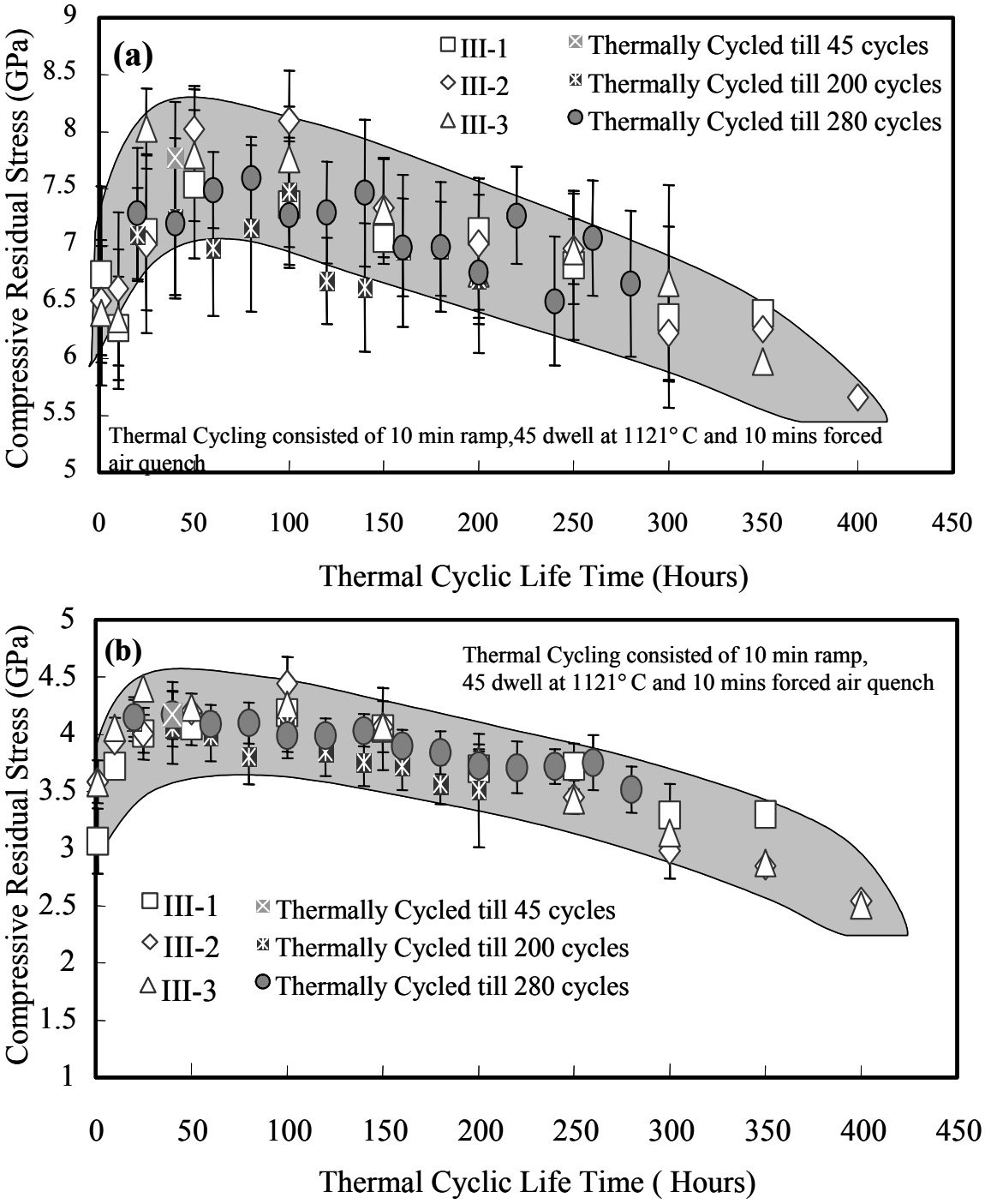

Figure 43. Compressive residual stress within TGO as a function of 1-hour thermal cycling for type III EB-PVD TBCs with as-coated (Ni,Pt)Al bond coats. Values of compressive residual stress were calculated from the (a) higher shift luminescence and (b) lower shift luminescence from the bimodal/trimodal luminescence.

Typical photostimulated luminescence spectra from type IV EB-PVD TBCs with grit-blasted bond coat are presented in Figure 44 as a function of 1-hour thermal cycling. Overall, a gradual decrease in the compressive residual stress was observed nearing complete stress-relief at 300 cycles as shown in Figure 45. This particular specimen failed after 350 cycles. Both higher and lower stressed luminescence arising from the bimodal luminescence exhibited an initial increase and a gradual and significant decrease before the final spallation. While the initial increase may be due to initially under-developed TGO scale, gradual changes in the luminescence frequency are significant and can serve to assess life-remain for type IV TBCs. This decrease may be related to undulation of TGO-bond coat interface and related damages (see section V.4.4) that occurred during the 1-hour thermal cycling.

The evolution in the magnitude of compressive residual stress within TGO, σ_{TGO} may be examined with respect to thermal cycling, c, quantitatively by using the relation:

$$\sigma_{TGO} = \sigma^{o}_{TGO} + K_1 c^{(l/n)} - K_2 c^{(l/m)} \qquad [10]$$

where σ^{o}_{TGO} is the initial value of the compressive residual stress, K_1 and n are the constants related to initial development of TGO scale and K_2 and m are the constants related to relaxation or relief of residual stress within the TGO scale. This type of quantitative analysis regarding life-remain assessment are being examined.

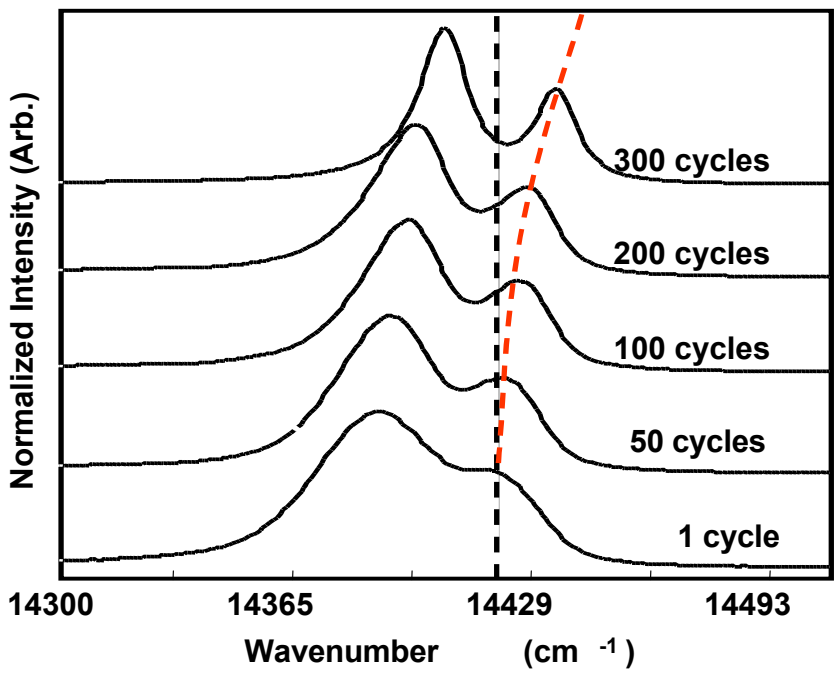

Figure 44. Typical photostimulated luminescence spectra as a function of 1-hour thermal cycling for type IV EB-PVD TBCs with grit blasted (Ni,Pt)Al bond coats. TBC spallation has occurred after 420 cycles and luminescence from stress-relieved TGO scale (marked by dotted vertical line) was observed starting 350 cycles by examining the derivatives of the spectra.

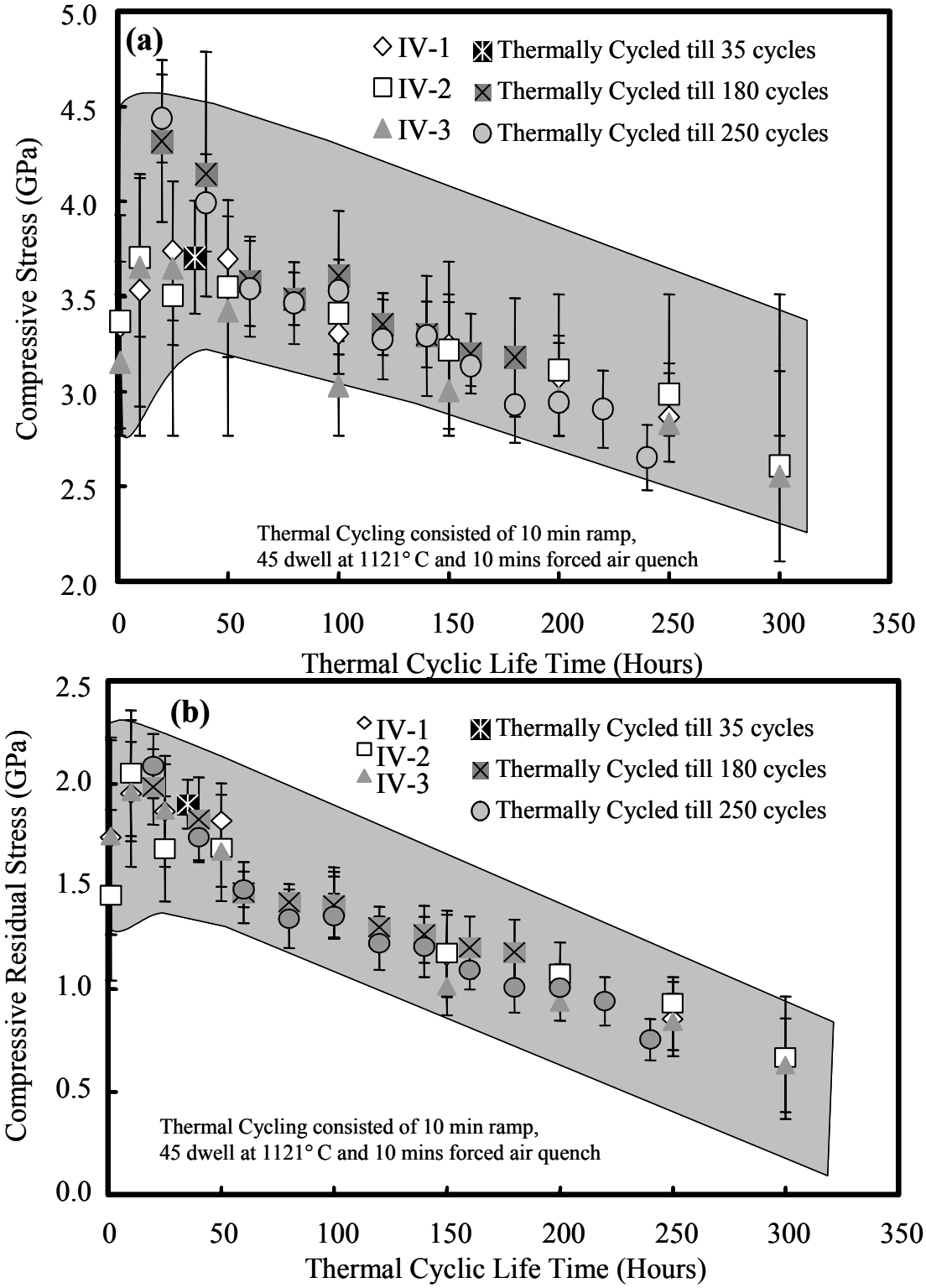

Figure 45. Compressive residual stress within TGO as a function of 1-hour thermal cycling for type IV EB-PVD TBCs with grit-blasted (Ni,Pt)Al bondcoats. Values of compressive residual stress were calculated from bimodal luminescence corresponding to (a) higher and (b) lower shifts in luminescence.

V.2.3. PSLS of EB-PVD TBCs as a Function of 10-Hour Thermal Cycling

The compressive residual stress within the TGO as function of 10-hour thermal cycling for type-II TBCs with NiCoCrAlY bondcoat is presented in the Figure 46. The value of the stress is calculated similar to the 1-hour thermal cycling based on shift of photostimulated luminescence via piezospectroscopic coefficients. The evolution of the compressive residual stress in the TGO scale was similar to that of TBCs with 1-hour thermal cycling: an initial increase (i.e., starting at 1st 10-hour thermal cycle) for both higher and lower compressive residual stress arising from bimodal luminescence. The magnitude of the compressive residual stress within the TGO remained constant throughout the entire thermal cycling as seen in Figure 46.

There was no significant or observable change in the magnitude and standard deviation of the TGO stress before the TBC spallation. Microstructural and failure investigation of type-II TBCs indicated that the failure occurred primarily at the YSZ/TGO interface and a significant internal oxidation of the NiCoCrAlY bondcoat occurred. This internal oxidation of the bondcoat was much more severe than type II TBCs tested with 1-hour thermal cycling.

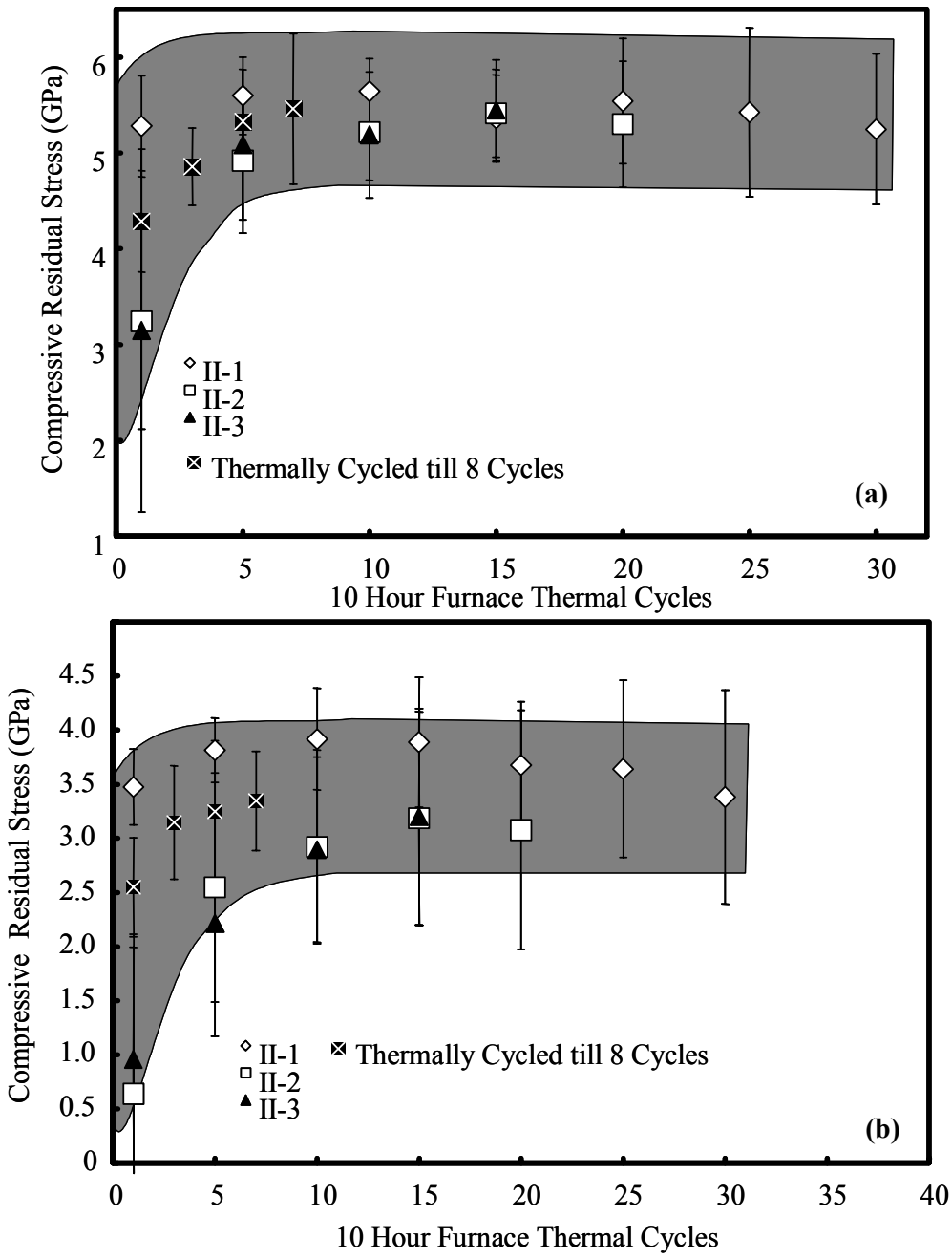

Figure 46. Compressive residual stress within TGO as a function of 10-hour thermal cycling for type II EB-PVD TBCs with NiCoCrAlY bondcoat. Values of compressive residual stress ere calculated from bimodal luminescence corresponding to (a) higher and (b) lower shifts in luminescence.

Figure 47 represents typical luminescence observed for type-III TBCs as a function of 10-hour thermal cycling. The TBC spallation occurred at 54 cycles. This trend is similar to type-III TBCs examined with 1-hour thermal cycling: stress relief associated with the damage in the TGO scale. The evolution and detection of stress-relief in the TGO scale for type-III TBCs can be quantified by taking the second derivatives ($d^2c/d\upsilon^2$) of luminescence spectrum at υ=14432 for R_2 luminescence. As shown in Figure 48, the luminescence spectrum with $d^2c/d\upsilon^2 = 0$ at $\upsilon \cong 14432 \pm 3$ were observed.

For type-III TBCs with as-coated (Ni,Pt)Al bondcoat the luminescence shift associated with the stress relief of the TGO scale was observed even for 10-hour cycle as function of thermal cycling as shown in Figure 40. These spectrums were deconvoluted based on the bimodal luminescence (i.e., two sets of R_1-R_2 luminescence) until 60% lifetime. After 60% lifetime, a third set of R_1-R_2 luminescence emerged, which was clearly related to the stress free luminescence of α-Al_2O_3 that arises due to the stress-relief within the TGO scale. This stress-relief can be associated with the sub-critical damages within the TGO aforementioned. The compressive residual stress within the TGO scale for 10-hour thermal cycling and 30% lifetime of type-III TBCs is shown in Figure 49.

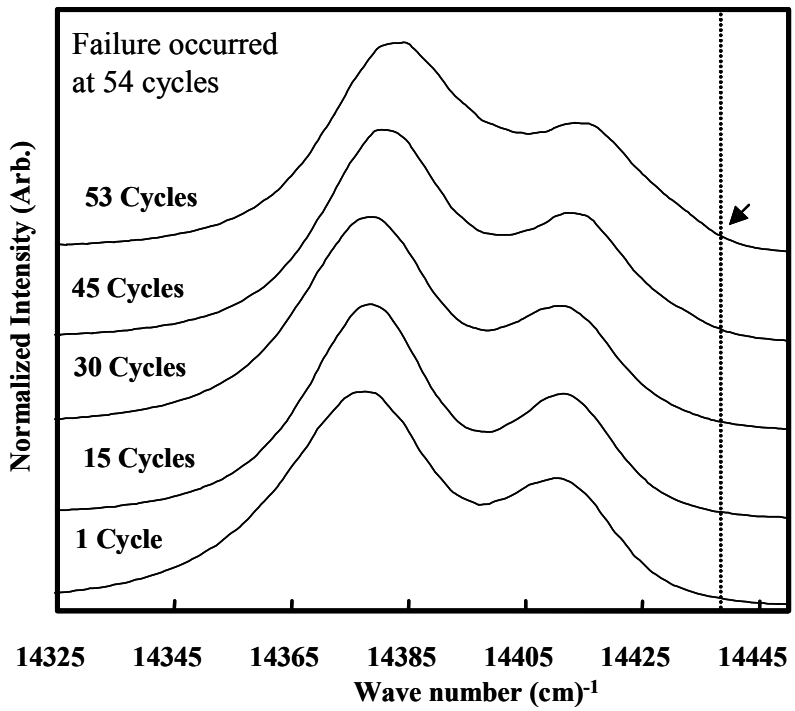

Figure 47. Typical photostimulated luminescence spectra from stress-relieved TGO scale (marked by dotted vertical line and arrows) was observed as a function of 10-hour thermal cycling for type III EB-PVD TBCs with as-coated (Ni,Pt)Al bond coats. TBC spallation has occurred at 54 cycles.

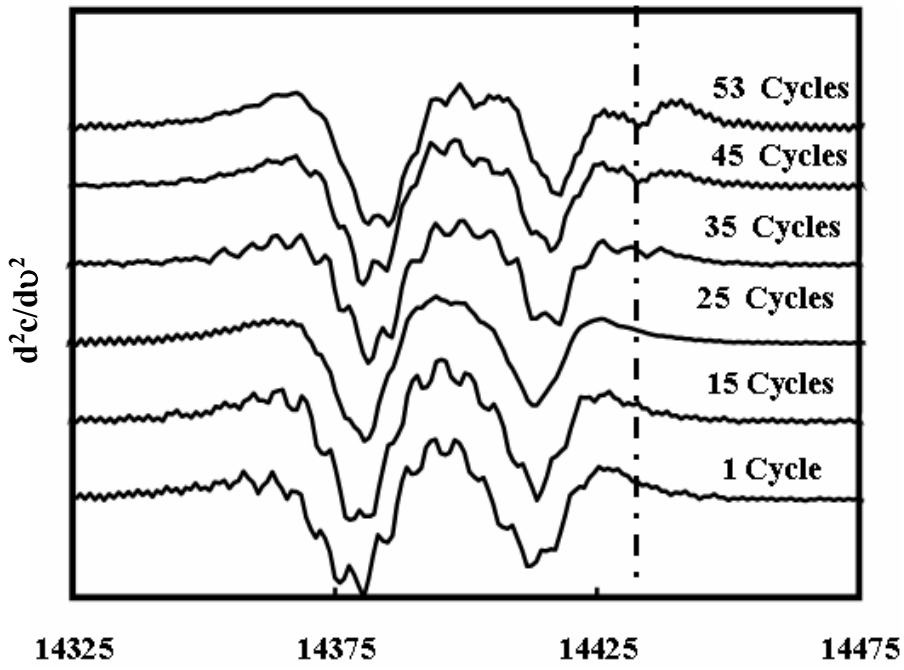

Figure 48. Typical derivatives of luminescence spectrum associated with stress-relieved luminescence frequency at $\upsilon \cong 14432 \pm 3$ for R_2 for 10-hour thermal cycling.

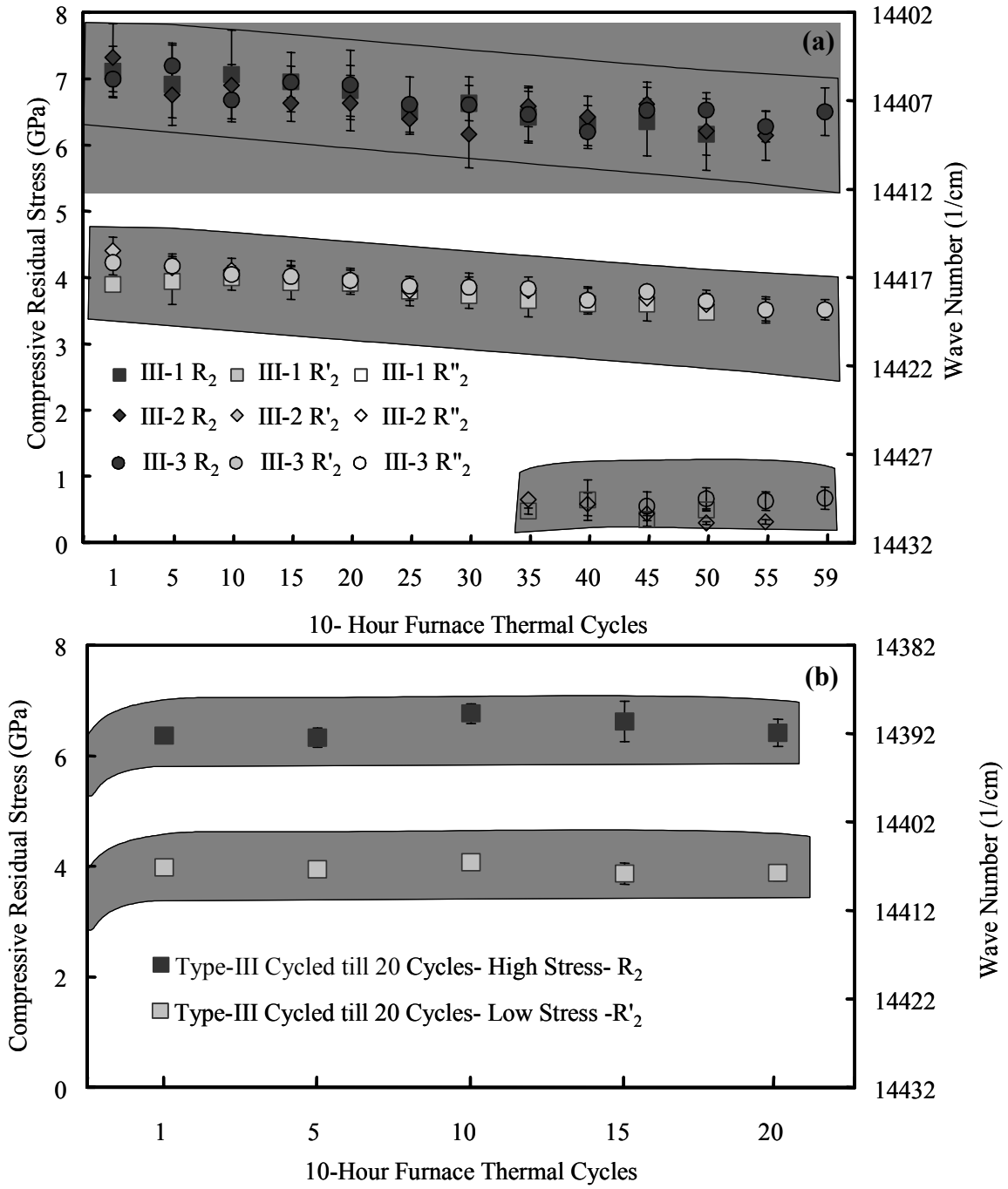

Figure 49. Compressive residual stress within TGO as a function of 10-hour thermal cycling for type-III TBCs with as-coated (Ni,Pt)Al bondcoat. Values of compressive residual stress were calculated from bimodal and tri-mode luminescence.

Typical luminescence spectra from type-IV TBCs with grit-blasted (Ni,Pt)Al bondcoat are presented in Figure 50. Unlike type-IV TBCs examined with 1-hour thermal cycling, a gradual shift towards stress free luminescence was not observed for these TBCs during 10-hour thermal cycling. The compressive residual stress within the TGO scale as a function of 10-hour thermal cycling, including up to 30% and 80% is presented in Figure 51. There was an initial increase in the magnitude of the compressive residual stress arising from under-developed TGO. However, the magnitude of the compressive residual stress in the TGO scale remained quite constant as a function of 10-hour thermal cycling. This type of behavior may be specific for TBC type, and in particular, type of thermal cycling (e.g., dwell time at high temperature).

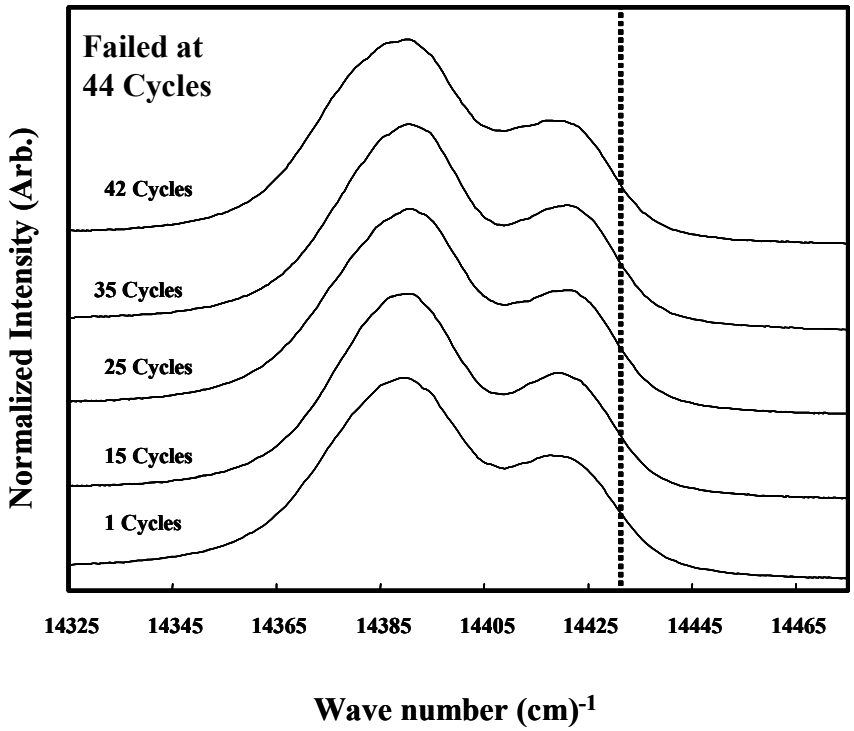

Figure 50. Typical luminescence spectrum observed as a function of 10-hour thermal cycling observed for type-IV TBCs with grit blasted (Ni, Pt)Al bondcoat. TBC spallation occurred at 44 cycles and there is no changes in the luminescence shifting towards stress free as observed in 1-hour thermal cycling.

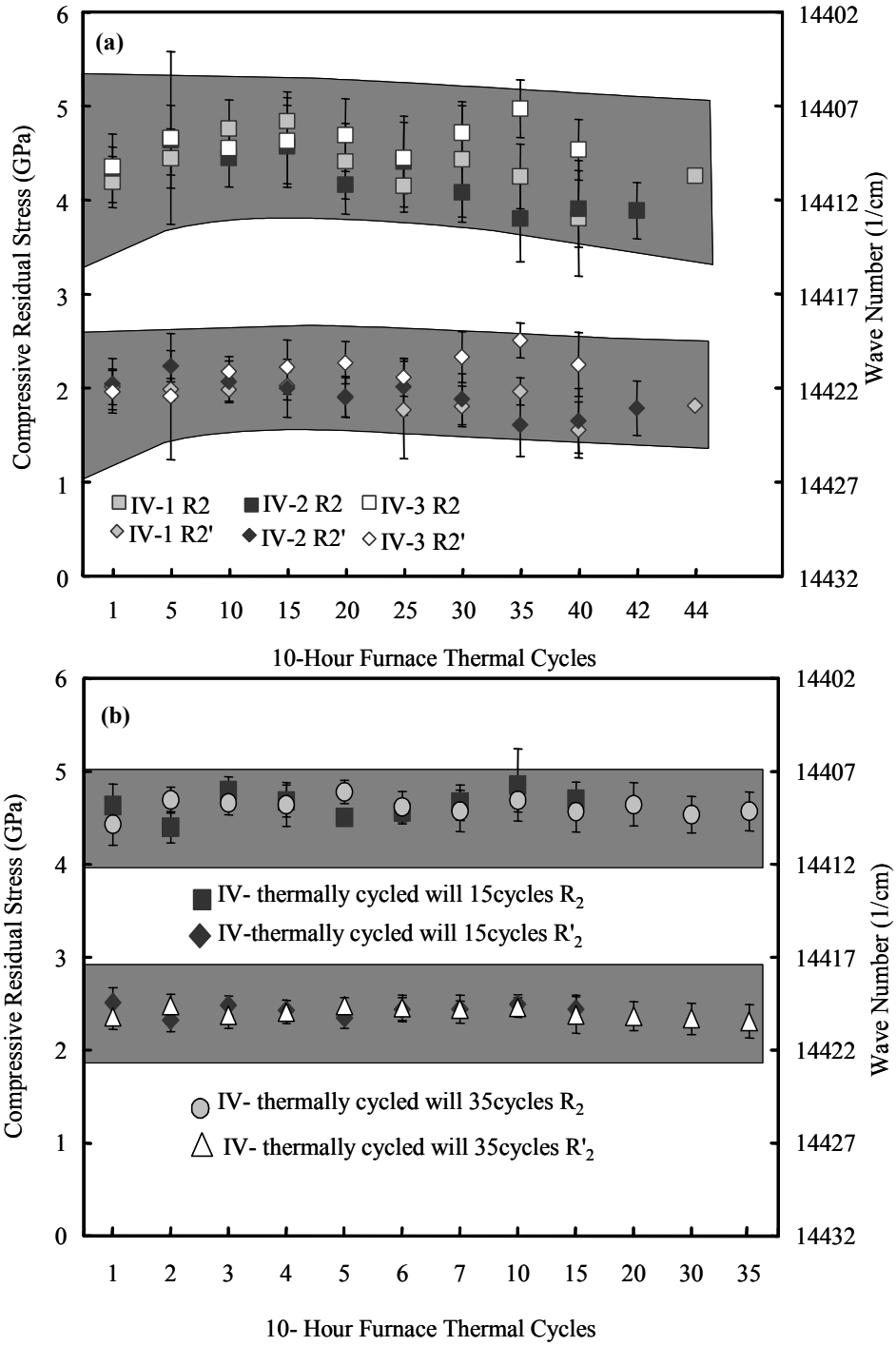

Figure 51. Compressive residual stress within TGO as a function of 10-hour thermal cycling for type-IV TBCs with grit-blasted (Ni, Pt)Al bondcoat. The values of compressive residual stress were calculated from bi-modal luminescence corresponding to higher and lower shift in luminescence (a) as a function of 10-hour thermal cycles (b) as a function of 10-hour thermal cyclic life time.

V.2.4. PSLS of EB-PVD TBCs as a Function of 50-Hour Thermal Cycling

The magnitude of compressive residual stresses within the TGO scale as a function of 50-hour thermal cycle is shown in Figure 52. The compressive residual stress magnitude calculated based on the systematic shift in PSLS luminescence via piezospectroscopic coefficient is quite similar to those observed previously for 1 and 10-hour cycles. The magnitude of stresses remained between 3-4.5 GPa on the higher side and around 2GPa from the lower shift in luminescence. The initial increase in the stress is because of the growth of TGO for both higher and lower compressive residual stresses arising from bimodal luminescence. There were no significant changes in the magnitude of the stress before the actual spallation of TBCs as reported earlier for this particular type.

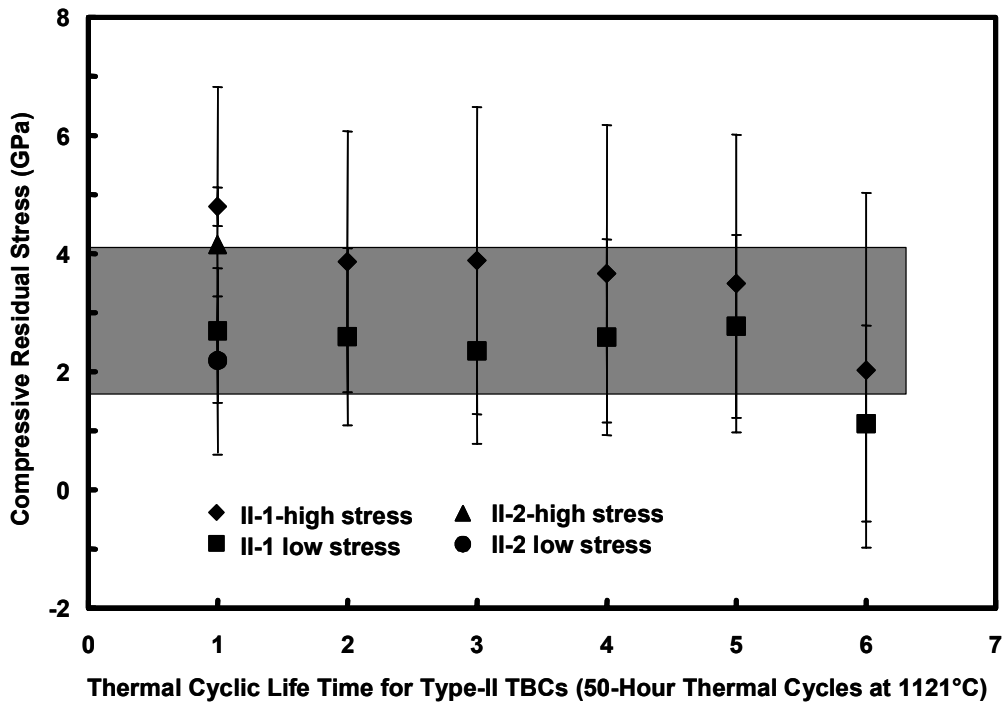

Figure 52. Compressive residual stress within TGO as a function of 50-hour thermal cycling for type II EB-PVD TBCs with NiCoCrAlY bondcoat. Values of compressive residual stress ere calculated from bimodal luminescence corresponding to higher and lower shifts in luminescence.

The value of compressive residual stress for type-III TBCs with as-coated (Ni,Pt)Al is shown in the Figure 53. The evolution of relative intensities obtained up to failure for type-III TBCs is presented in Figure 54. From the Figure R_2 and R_2' refer to bi-modal luminescence of the higher and lower shift in luminescence. In this particular type there was no emergence of stress free luminescence that was detected previously in 1 and 10 hour thermal cycles. The compressive residual stress reported in Figure 53 both high and low stresses continued to decrease till failure.

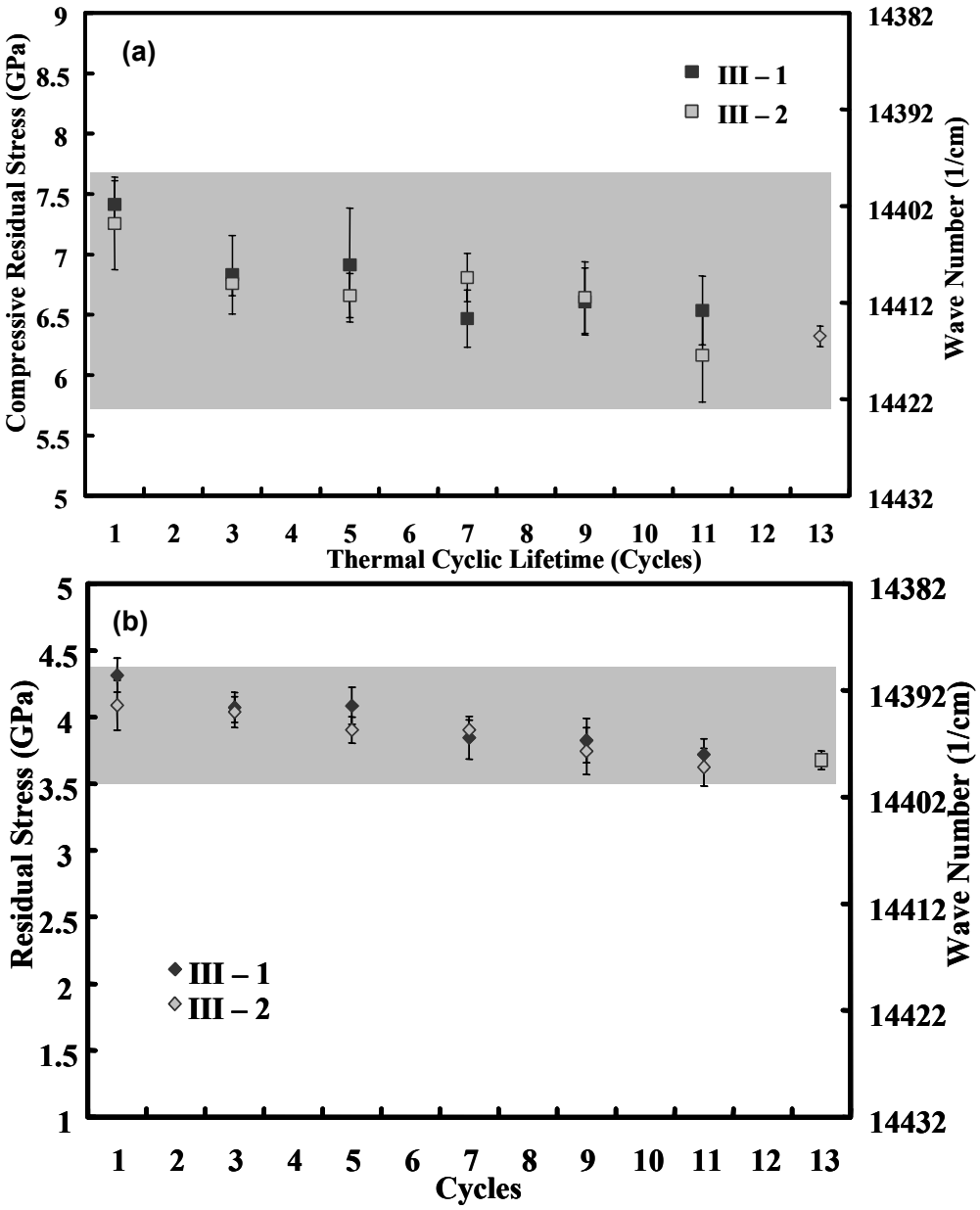

Figure 53. Compressive residual stress within TGO as a function of 50-hour thermal cycling for type-III TBCs with as-coated (Ni,Pt)Al bondcoat. Values of compressive residual stress were calculated from bimodal luminescence.

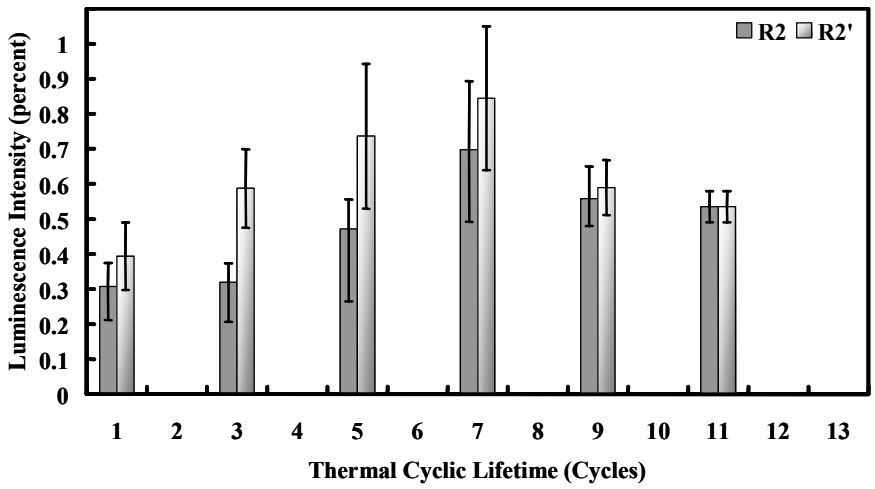

Figure 54. Type-III TBCs cycled until thermal cyclic life time, Relative Luminescence Intensity from R2, R'2 in TGO with as-coated (Ni,Pt)Al bond coat.

The values of compressive residual stress as function of 50-hour thermal cycles are shown in Figure 55. The compressive residual stress remained constant with an initial increase in the early stages due to the development of TGO. This trend was similar to 10-hour thermal cycles that were reported earlier for this particular type which is dependent on the type of thermal cycling.

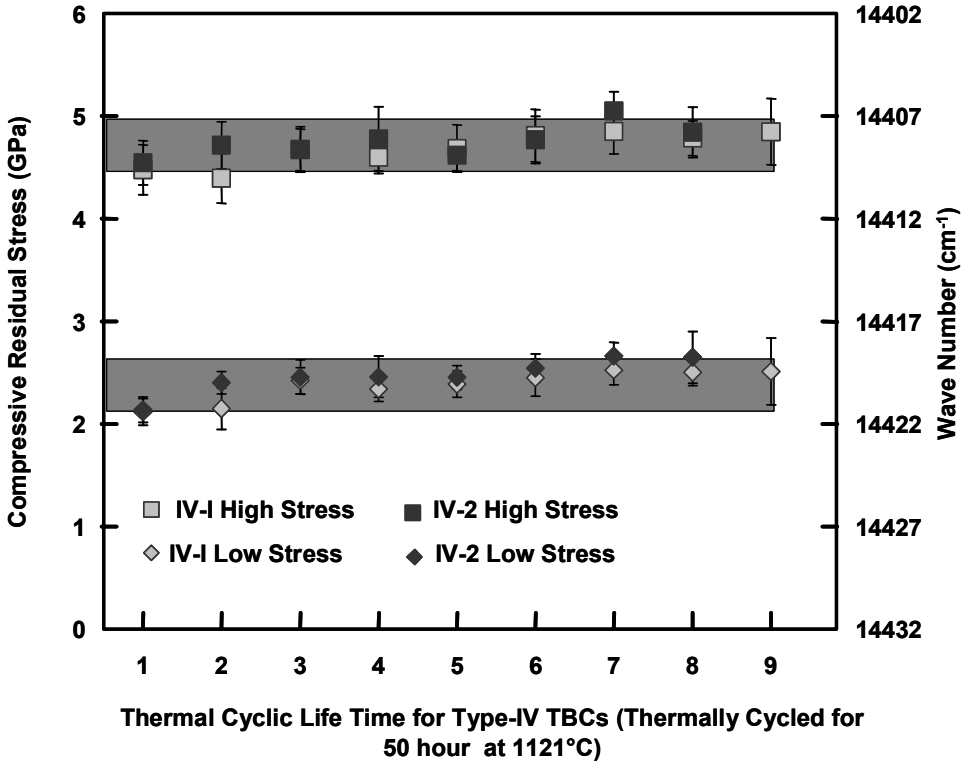

Figure 55. Compressive residual stress within TGO as a function of 50-hour thermal cycling for type-IV TBCs with Grit blasted (Ni,Pt)Al bondcoat. Values of compressive residual stress were calculated from bimodal luminescence.

V. 3. Electrochemical Impedance Spectroscopy of Thermal Barrier Coatings

V.3.1. NDE of Type I APS TBCs by EIS

For type I APS TBCs, EIS measurement was carried out 3 times on specimens before thermal cycling and after thermal cycling that corresponds to 10%, 50% and 70% of its lifetime. The variation in the impedance and phase angle plot with respect to the thermal cycling is presented in Figures 56 and 57, respectively. Table VI also reports the values of resistance and capacitance of the various TBC constituents, which were calculated based on the ac-equivalent circuit presented in Figure 9. For the as-coated APS TBCs, there is no significant presence of the TGO. Hence the TGO is not represented in terms of the electrical parameters. The ac equivalent circuit for APS TBCs, after exposure is different from that of the as-coated ones because of the bond coat oxidation and the formation of uniform and continuous TGO. The impedance of TGO cannot be neglected in the EIS measurement system. Thus, an ac equivalent circuit for the thermally cycled TBC consists of the electrical parameters that represent the TGO.

Resistance and capacitance of TBC constituents reported in Table VI is presented as a function of thermal cycles as presented in Figures 58 through 61. The impedance plot presented in Figure 45 shows that the impedance response of the TBCs increases initially during thermal cycling and then decreases after thermal cycling corresponding to 50% of its lifetime. This increase in the impedance response may be attributed to the sintering of the YSZ topcoat and growth of TGO with high temperature exposure. The decrease in the impedance response may correspond to the sub-critical damages that initiate in the topcoat and TGO with thermal cycling. These sub-critical damages prior to the final failure have been documented by microstructural analysis (see section V.4.1).

With an increase in the impedance, the resistance of the topcoat and the TGO increased. With further prolonged thermal cycling the resistance of the topcoat and the TGO decreased. The capacitance of the topcoat increased at failure because of the large scale damage in the topcoat. The capacitance of the TGO did not increase abruptly at failure because the fracture path of the APS TBCs observed for type-I TBCs primarily occur at the YSZ\TGO interface as shown in Figure 94 (see section V.4.4) and rarely exposes the conductive surface of the metallic bondcoat.

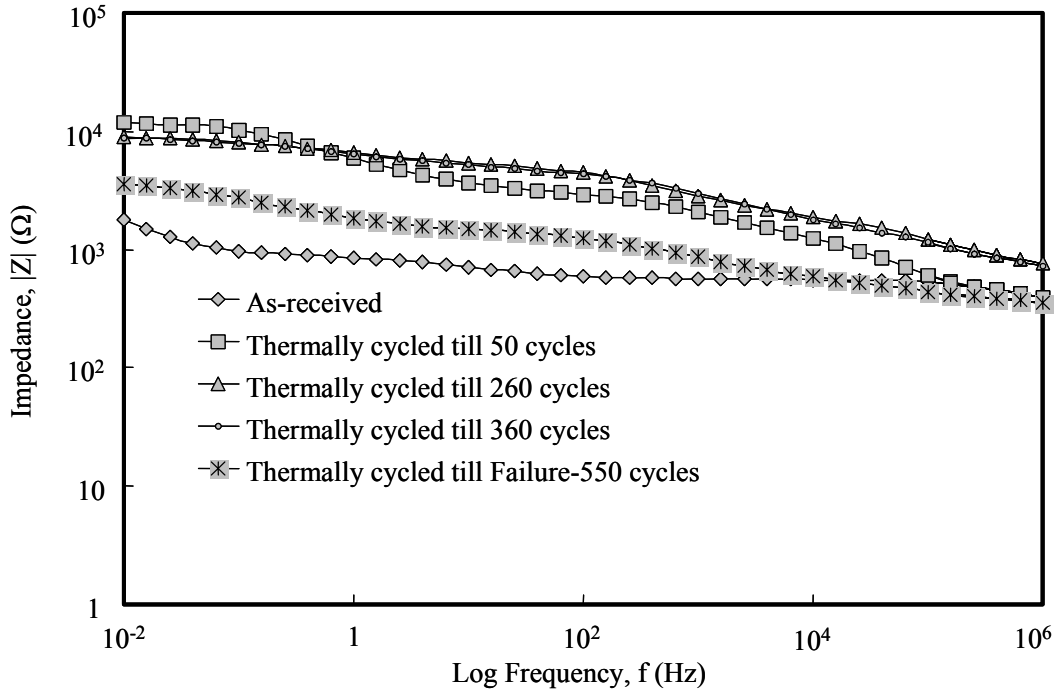

Figure 56. Typical Impedance plots from as-coated and as a function of thermal cyclic life time for type-I APS TBCs

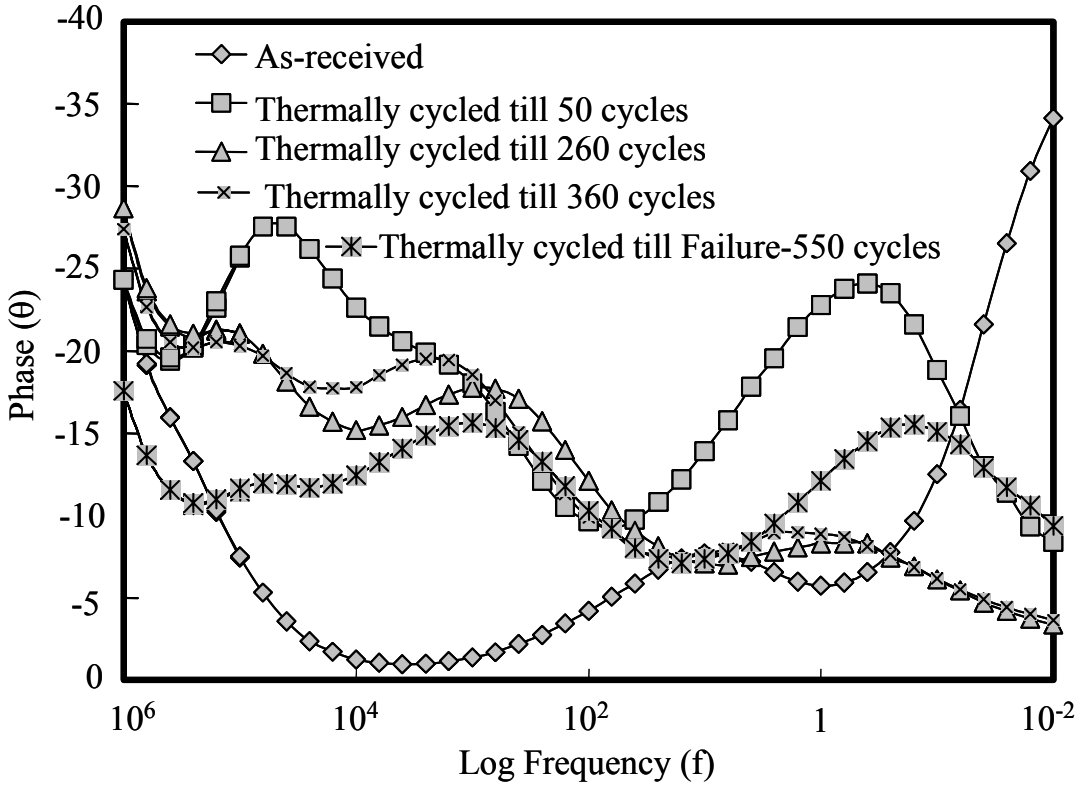

Figure 57. Typical Phase plots from as-coated and as a function of thermal cyclic life time for type-I APS TBCs.

Table VI. Resistance and capacitance of Type I APS TBC constituents as a function of thermal cycling.

Thermal cycles	R_C (kΩ)	C_C (nF)	R_P (kΩ)	C_P (νF)	R_O (kΩ)	C_O (nF)	R_T (kΩ)	C_T (νF)
As-received	0.50 ± 0.4	2.2 ± 0.4	10.6 ± 4.2	377700 ± 21959	0	0	0.3 ± 0.1	16486 ± 2747
50 (10% lifetime)	2.72 ± 0.7	60.7 ± 21.9	13.55 ± 1.38	1574.3 ± 502.3	0.58 ± 0.4	42.9 ± 10.9	1.22 ±0.86	1347.3 ±192
260 (50% lifetime)	3.31 ± 0.09	49.6 ± 0.8	4.40 ± 0.03	1505 ± 18	1.05 ± 0.02	5.38 ± 0.2	1.06 ±0.05	571.9 ±2.8
360 (70% lifetime)	3.25 ± 0.10	45.8 ± 0.4	4.64 ± 0.07	1449 ± 45.7	0.96 ± 0.03	4.32 ± 0.3	0.80 ±0.03	33.6.3 ±1.9
550 (Failure)	0.59 ± 0.03	191.4 ± 5.9	2.96 ± 0.18	10789 ± 983.2	0.40 ± 0.01	3.5 ± 0.3	0.35 ±0.02	1321.6 ±40.2

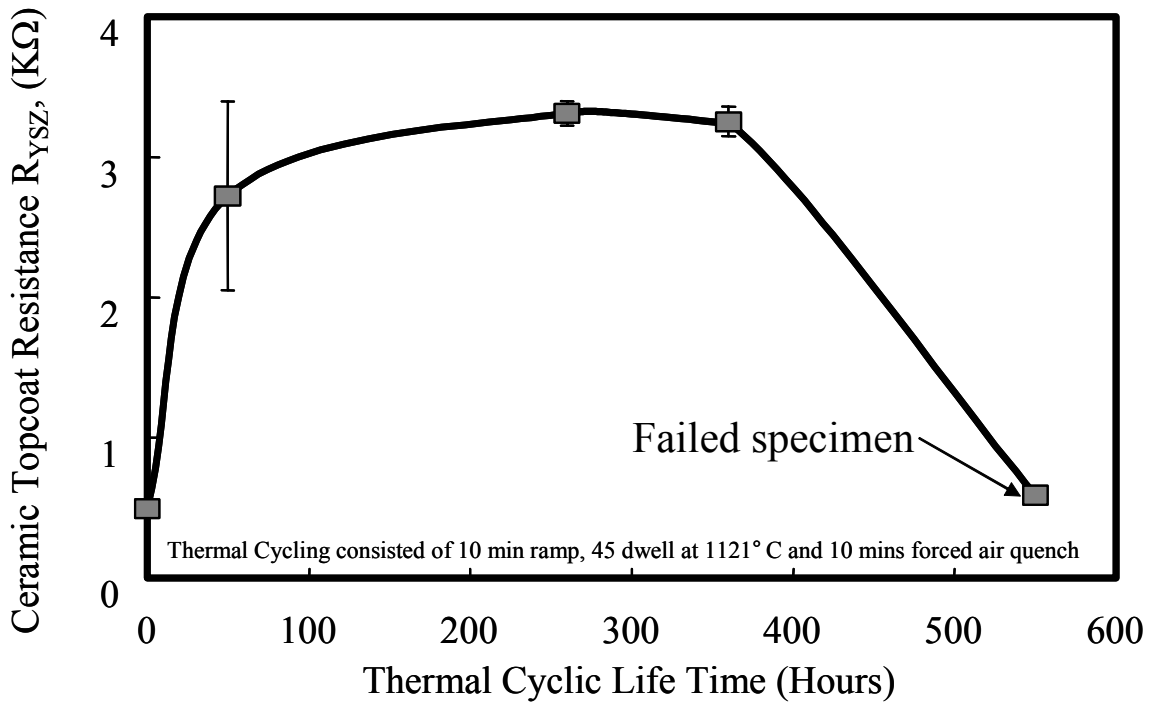

Figure 58.Evolution of ceramic topcoat resistance (R_{YSZ}) for type I APS TBCs as a function of thermal cycling at 1121°C.

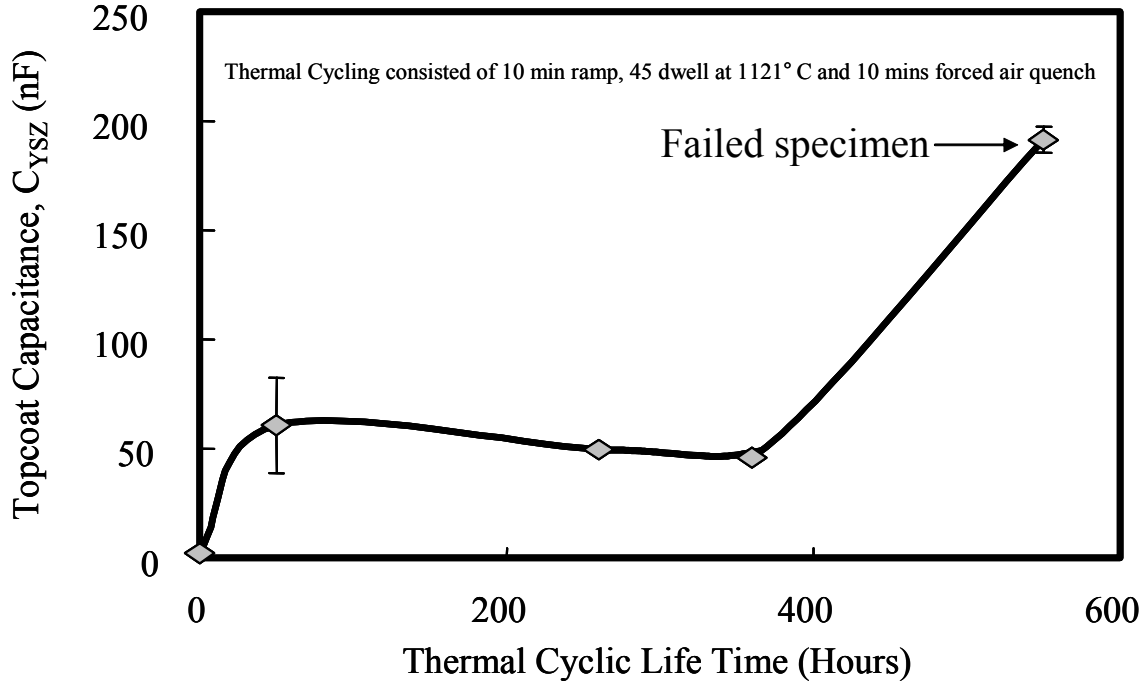

Figure 59.Evolution of ceramic topcoat capacitance (C_{YSZ}) for type I APS TBCs as a function of thermal cycling at 1121°C.

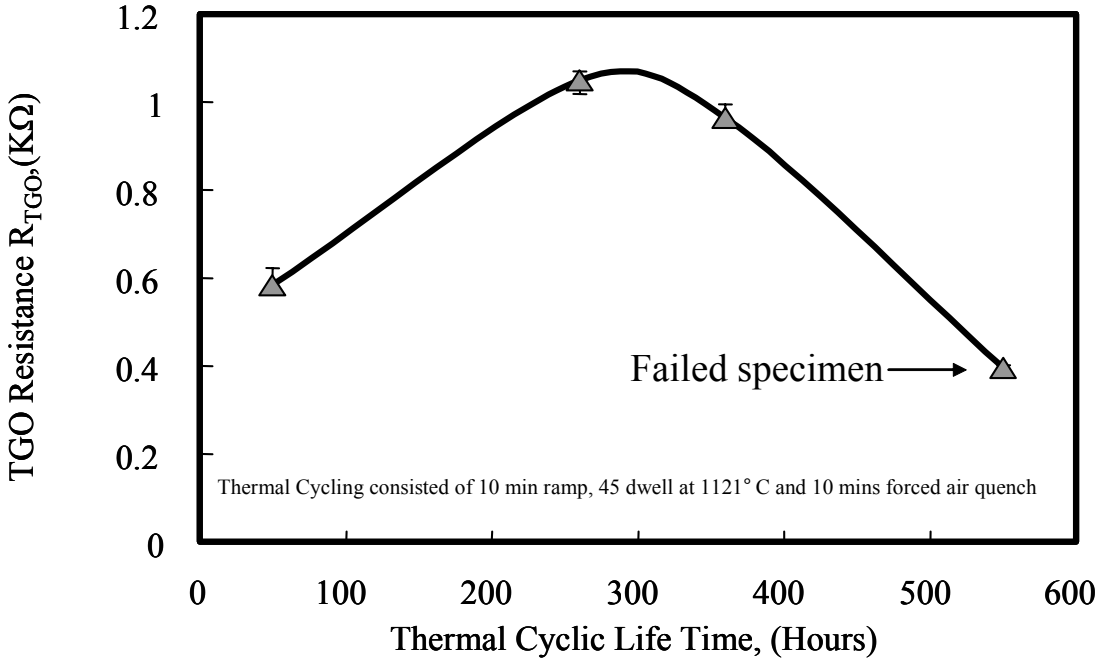

Figure 60. Evolution of TGO resistance R_{TGO} in type I APS TBCs as a function of thermal cycling at 1121°C.

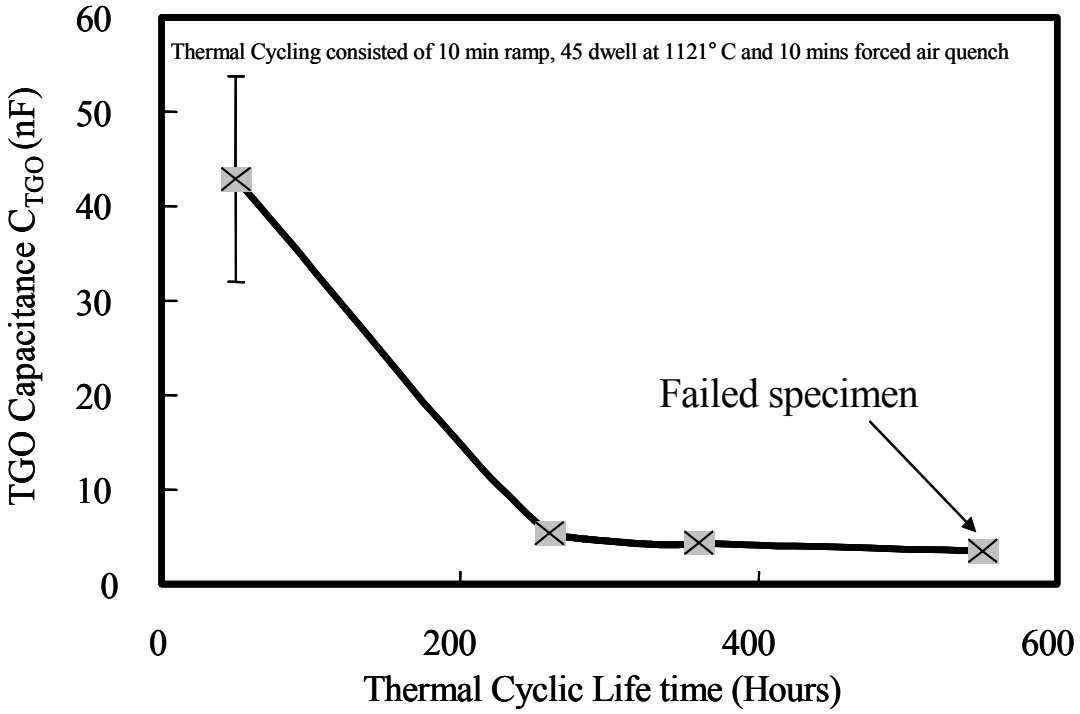

Figure 61. Evolution of TGO capacitance C_{TGO} in type I APS TBCs as a function of thermal cycling at 1121°C.

V.3.2. NDE of Type V APS TBCs by EIS

For type V APS TBCs, EIS measurement was carried out 3 times on specimens before thermal cycling and after thermal cycling that corresponds to 10%, 50% and 70% of its lifetime. The variation in the impedance and phase angle plot with respect to the thermal cycling is presented in Figures 62 and 63, respectively. Table VII also reports values of resistance and capacitance of the various TBC constituents, which were calculated based on the ac-equivalent circuit in Figure 9.

Resistance and capacitance of TBC constituents was determined as a function of thermal cycles as presented in Figures 64 through 67. Ceramic top coat resistance R_C initially increased then decreased and stabilized till failure with thermal cycling; this perhaps reflects two important microstructural changes, namely sintering and micro-cracking. While the growth of the TGO should intuitively increase the resistance and decrease the capacitance, the opposite results were observed for capacitance of the TGO as presented in Figures 66 and 67. As seen in Figure 66, the TGO resistance, R_{TGO} (not defined for as-coated condition) continuously decreases and the TGO capacitance, C_{TGO} continuously increases with thermal cycling. In addition, a sharp 2~5X increase in the C_{TGO} was observed as presented in Figure 67 for failed specimens. These trends have been consistently observed and may reflect early initiation and growth of sub-critical damage in the TGO through which electrolyte can penetrate. Similar trends were observed earlier for these types of TBCs and are reported in the Figures 68 through 70.

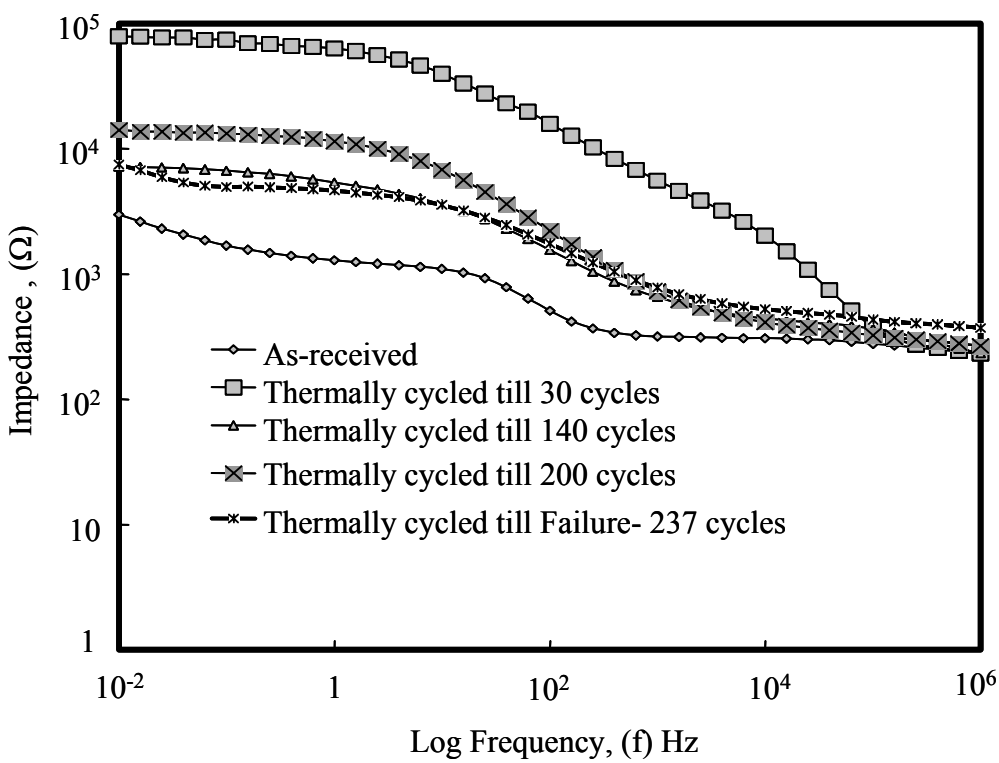

Figure 62. Typical Impedance plots from as-coated and as a function of thermal cyclic life time for type-VAPS TBCs.

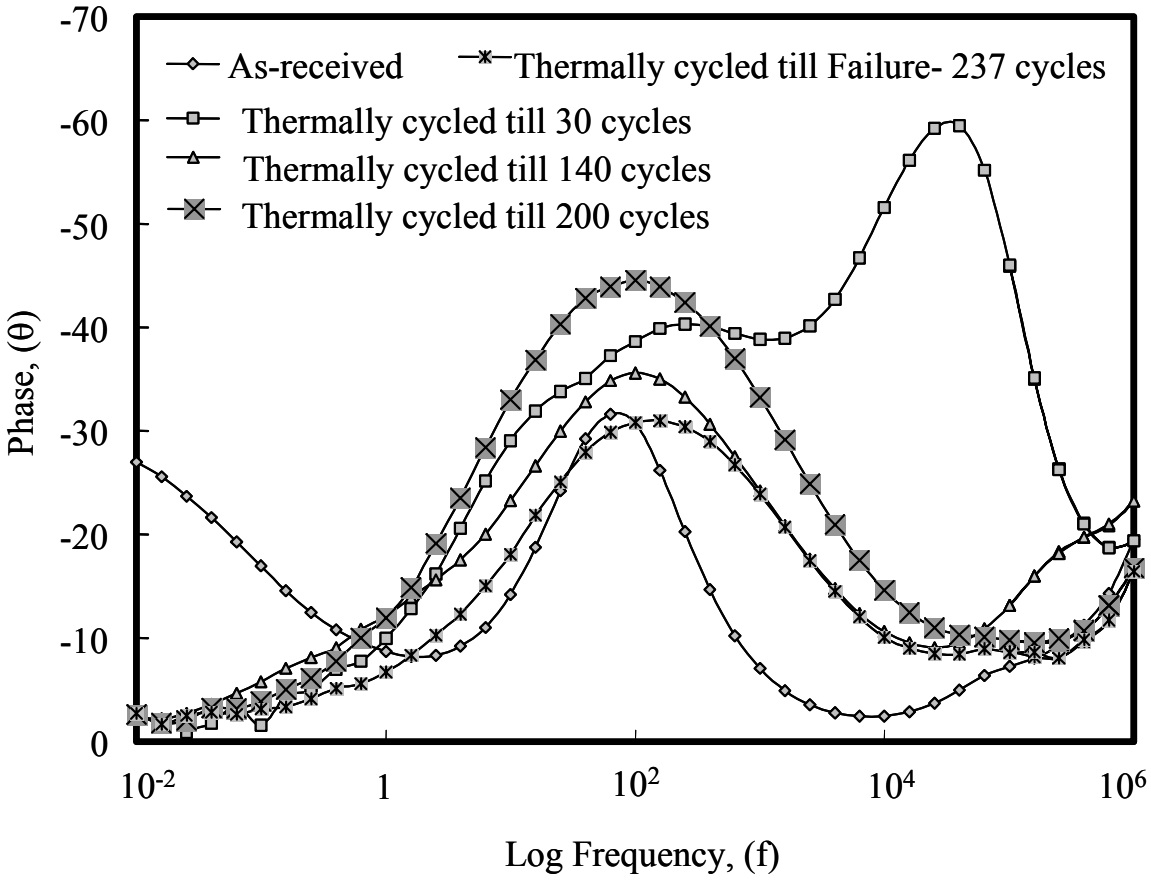

Figure 63.Typical Phase angle plots from as-coated and with respect to thermal cyclic life time for type-I APS TBCs

Table VII. Resistance and capacitance of type-V APS TBC constituents as a function of thermal cycling.

Thermal cycles	R_C (kΩ)	C_C (nF)	R_P (kΩ)	C_P (nF)	R_O (kΩ)	C_O (nF)	R_T (kΩ)	C_T (nF)
As-received	0.29 ± 0.02	4.8 ± 0.5	11.8 ± 1.4	38016.6 ± 9317	0	0	0.9 ± 0.1	3883 ± 219.2
35 (10% lifetime)	1 ± 0.06	13.9 ± 21.9	103.7 ± 3.3	33980 ± 1513	3.72 ± 0.2	9.42 ± 0.01	0.71 ±0.01	1228 ±39.6
140 (50% lifetime)	0.63 ± 0.03	4.6 ± 0.8	0.88 ± 0.8	351.3 ± 48.7	4.8 ± 0.1	517 ± 17.1	6.2 ±1.2	1534.7 ±131.4
200 (70% lifetime)	0.27 ± 0.01	3.3 ± 0.4	3.79 ± 0.3	941.1 ± 62.2	1.3 ± 0.07	32386.67 ± 644.7	9.7 ±0.6	454 ±3.3
Failure 237	0.37 ± 0.01	2.6 ± 5.9	1.04 ± 0.6	864.6 ± 182.1	1.3 ± 0.4	35635 ± 10981.4	5.2 ±1.8	623 ±164.1

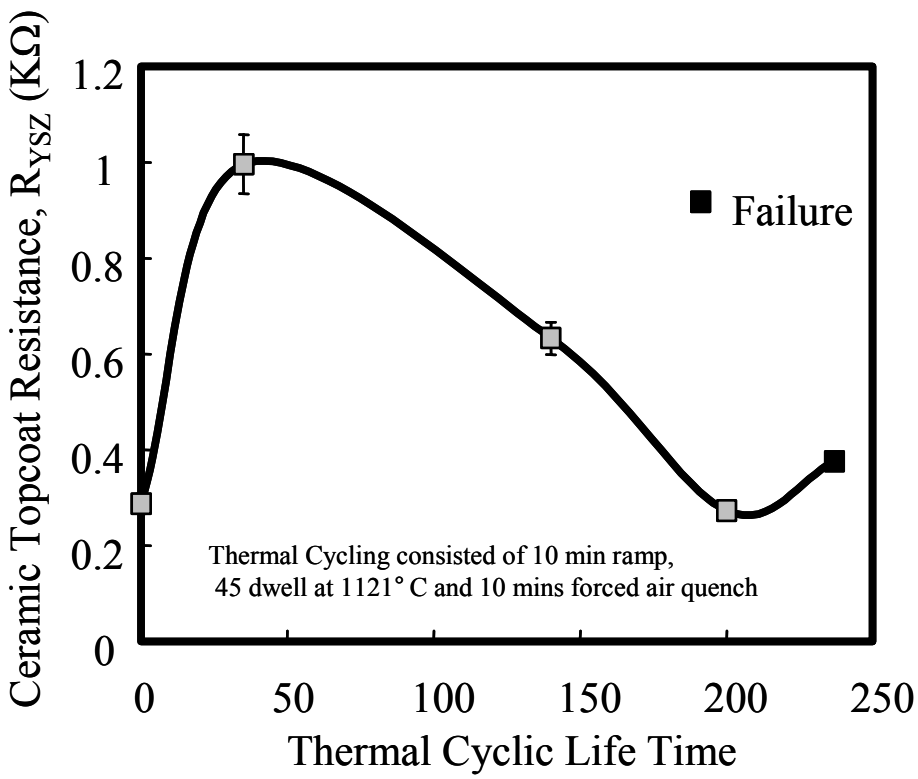

Figure 64. Evolution of ceramic top coat resistance (R_{YSZ}) for type V APS TBCs as a function of thermal cycling at 1121°C.

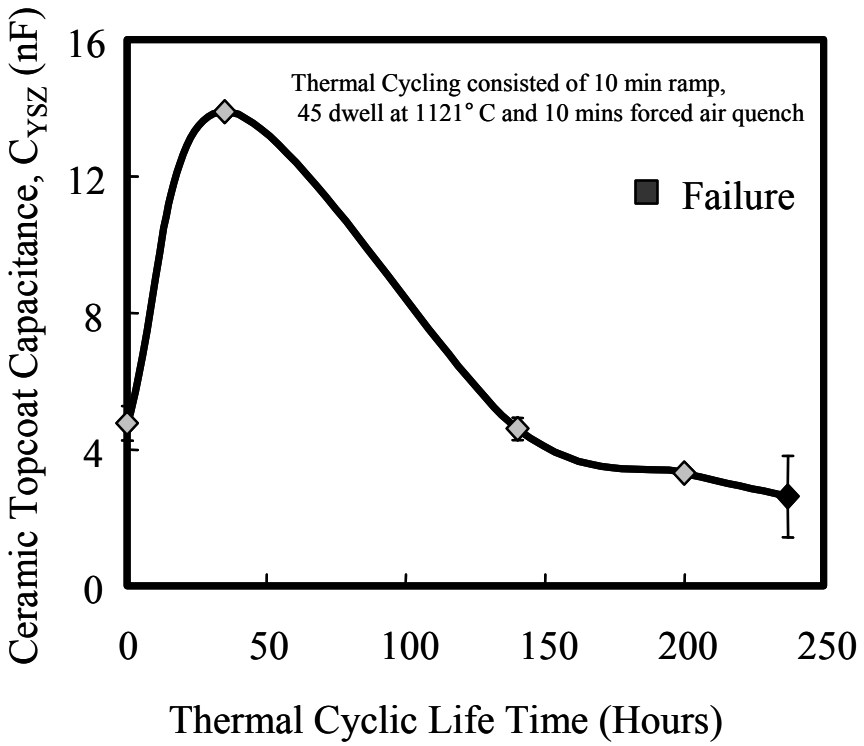

Figure 65.Evolution of ceramic top coat capacitance (C_{YSZ}) for type V APS TBCs as a function of thermal cycling at 1121°C.

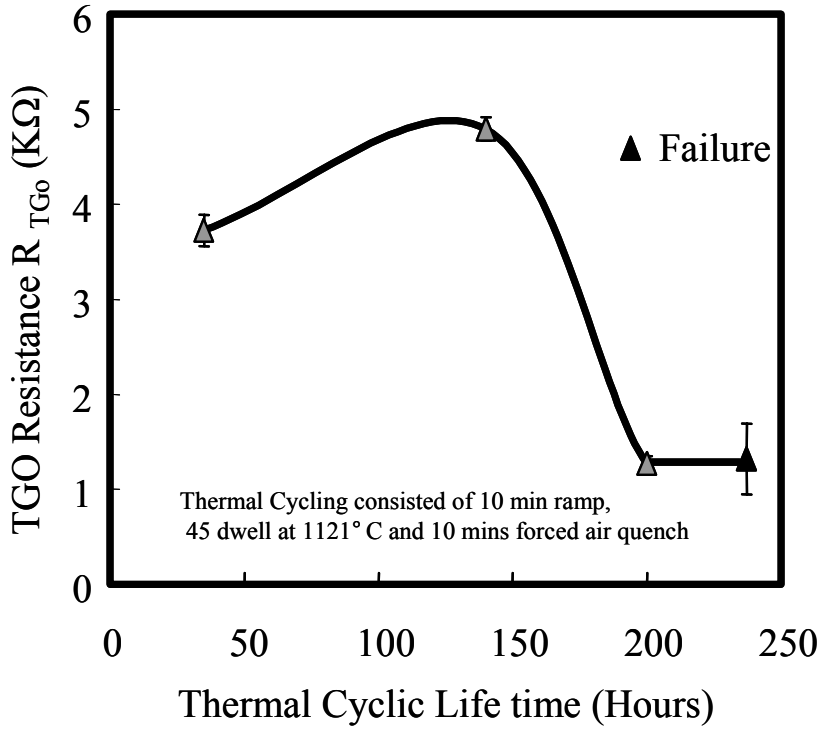

Figure 66.Evolution of TGO resistance (R_{TGO}) in type V APS TBCs as a function of thermal cycling at 1121°C.

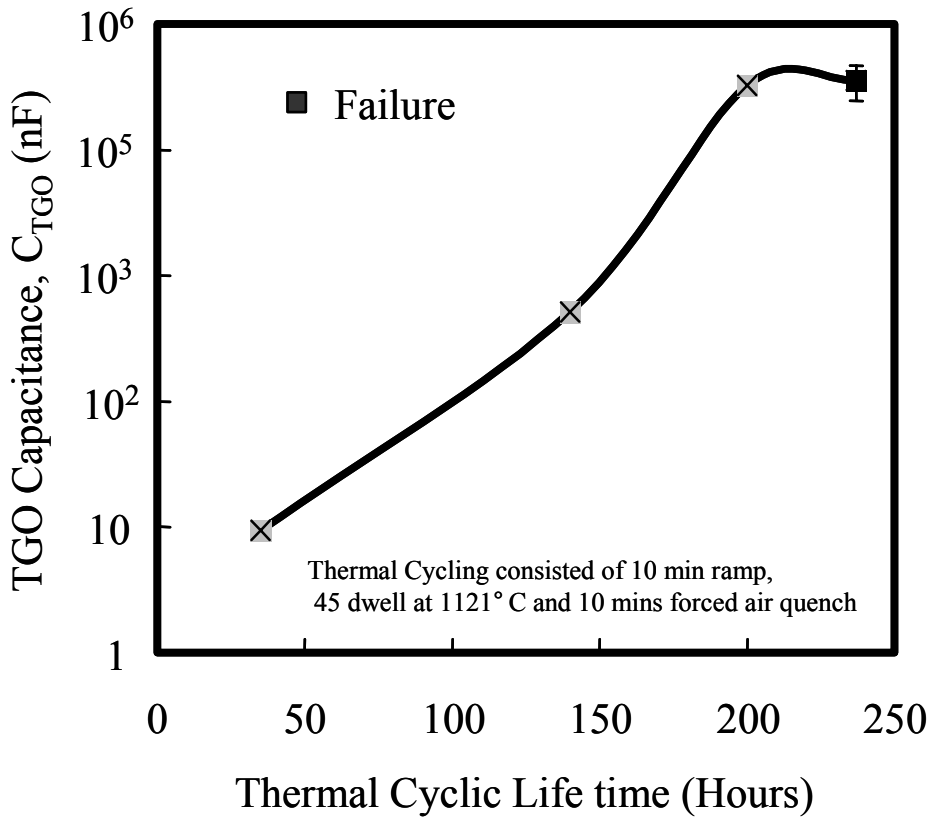

Figure 67. Evolution of TGO capacitance (C_{TGO}) in type V APS TBCs as a function of thermal cycling at 1121°C.

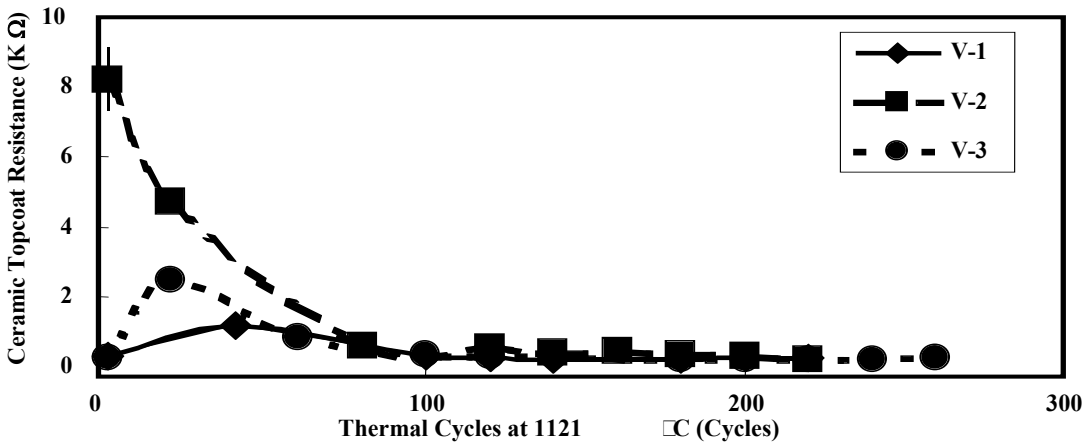

Figure 68. Evolution of ceramic top coat resistance (R_{YSZ}) in type V APS TBCs as a function of thermal cycling at 1121°C.

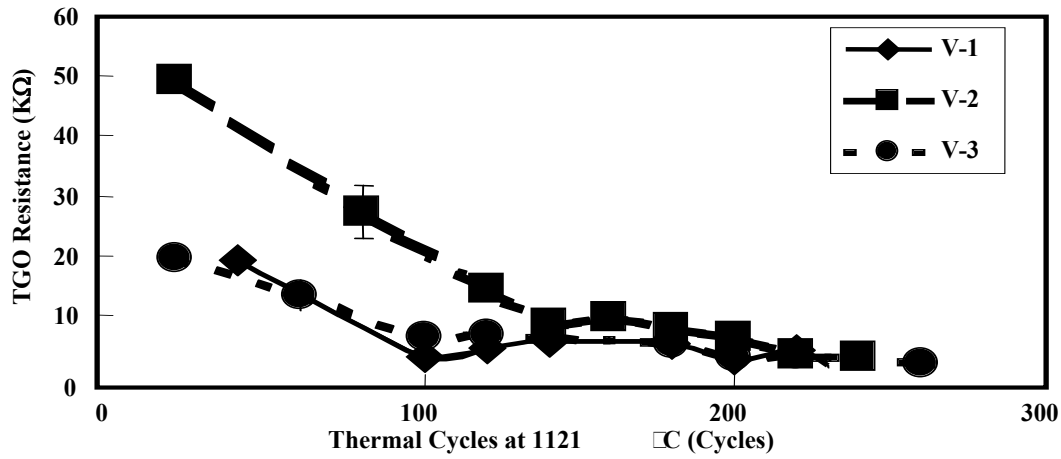

Figure 69. Evolution of TGO resistance (R_{TGO}) in type V APS TBCs as a function of thermal cycling at 1121°C.

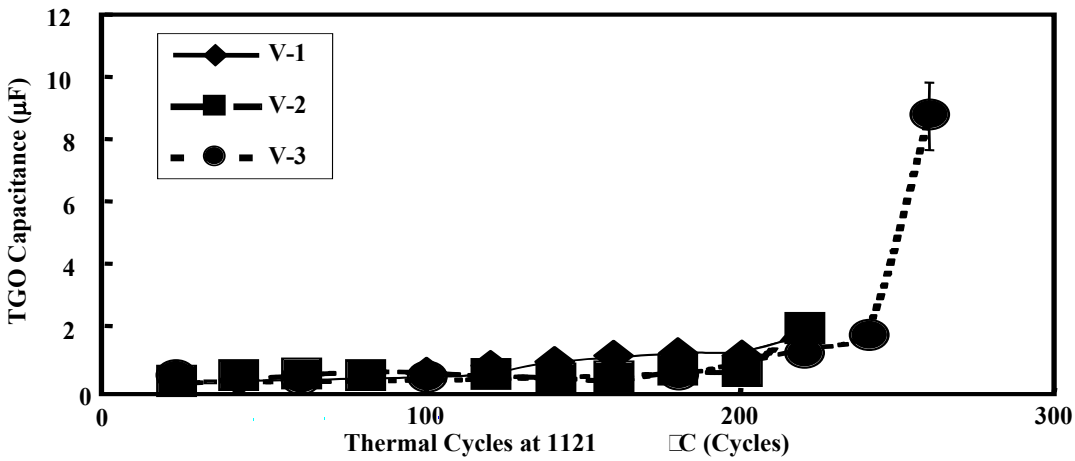

Figure 70. Evolution of TGO capacitance (C_{TGO}) in type V APS TBCs as a function of thermal cycling at 1121°C.

V.3.3. NDE of Thermally Cycled Type II, III and IV Thermal Barrier Coatings by EIS

For type II EB-PVD TBCs, frequent desktop failure was observed along the fragile interface between the YSZ/TGO. Early formation of non-protective spinels were observed for type II TBCs, and EIS could not be carried out.

For type III TBCs EIS measurement was carried out 3 times for as-received, thermally cycled and failed specimen. Typical impedance and phase angle plots for these specimens are presented in Figures 71 and 72, respectively. Table VIII reports values of resistance and capacitance of the various TBC constituents that were determined based on the ac-equivalent circuit presented in Figure 9. Evolution in the resistance and capacitance of TBC constituents as a function of thermal cycling is presented in Table VIII and Figures 73 through 76. The

initial increase in the resistance of the YSZ and the TGO, shown in Figures 73 and 75, may be due to the sintering of the YSZ and growth of the TGO with thermal exposure. After prolonged exposure corresponding to the 70% of thermal cyclic lifetime, the resistance of the YSZ and TGO started to decrease, indicating the penetration of electrolyte through damages (e.g., cracks and voids) in the YSZ and the TGO. At failure there is a sharp increase in the capacitance of the YSZ and the TGO, because of the large-scale cracks through which the electrolyte penetrates down to the exposed and conductive bond coat surface (see section V.4.4).

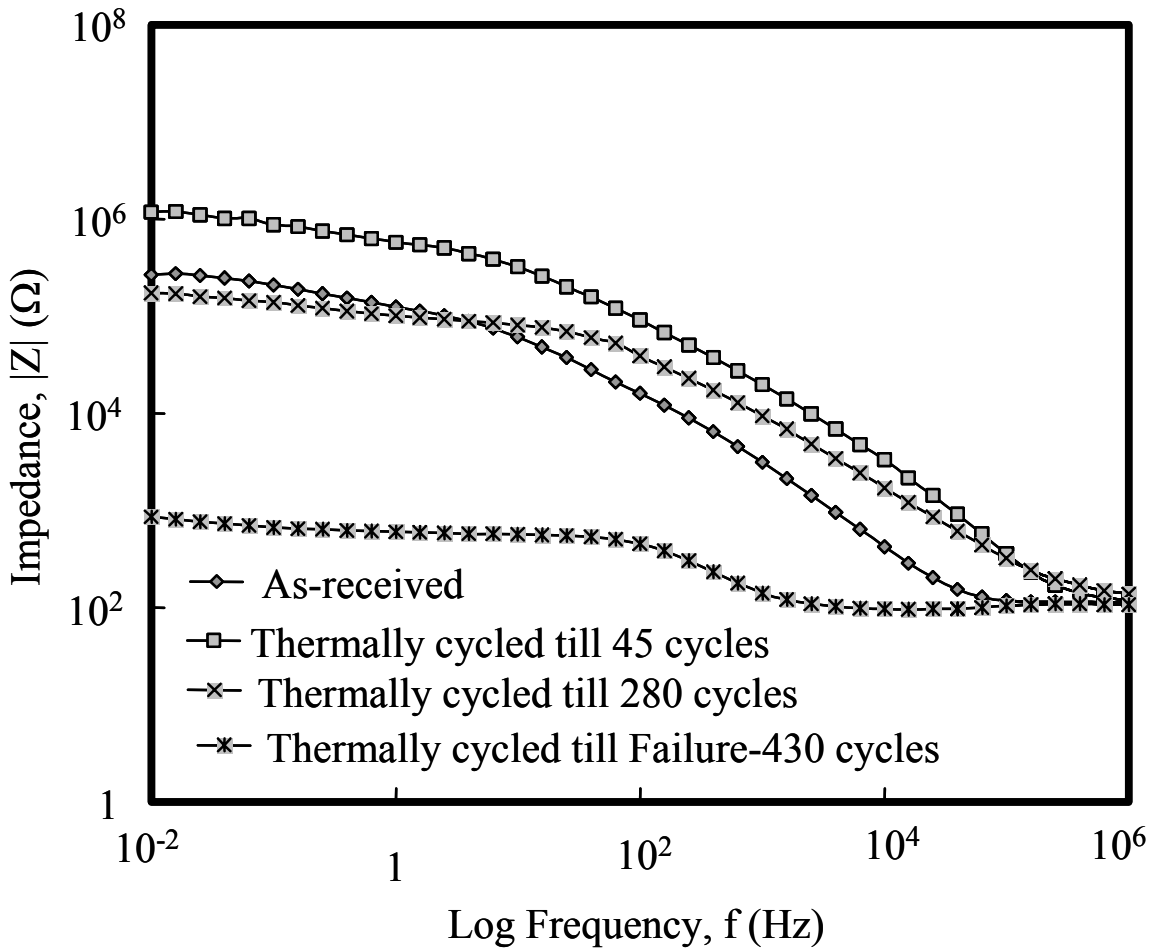

Figure 71.Typical Impedance plots from as-coated and as a function of thermal cyclic life time for type-III EB-PVD TBCs.

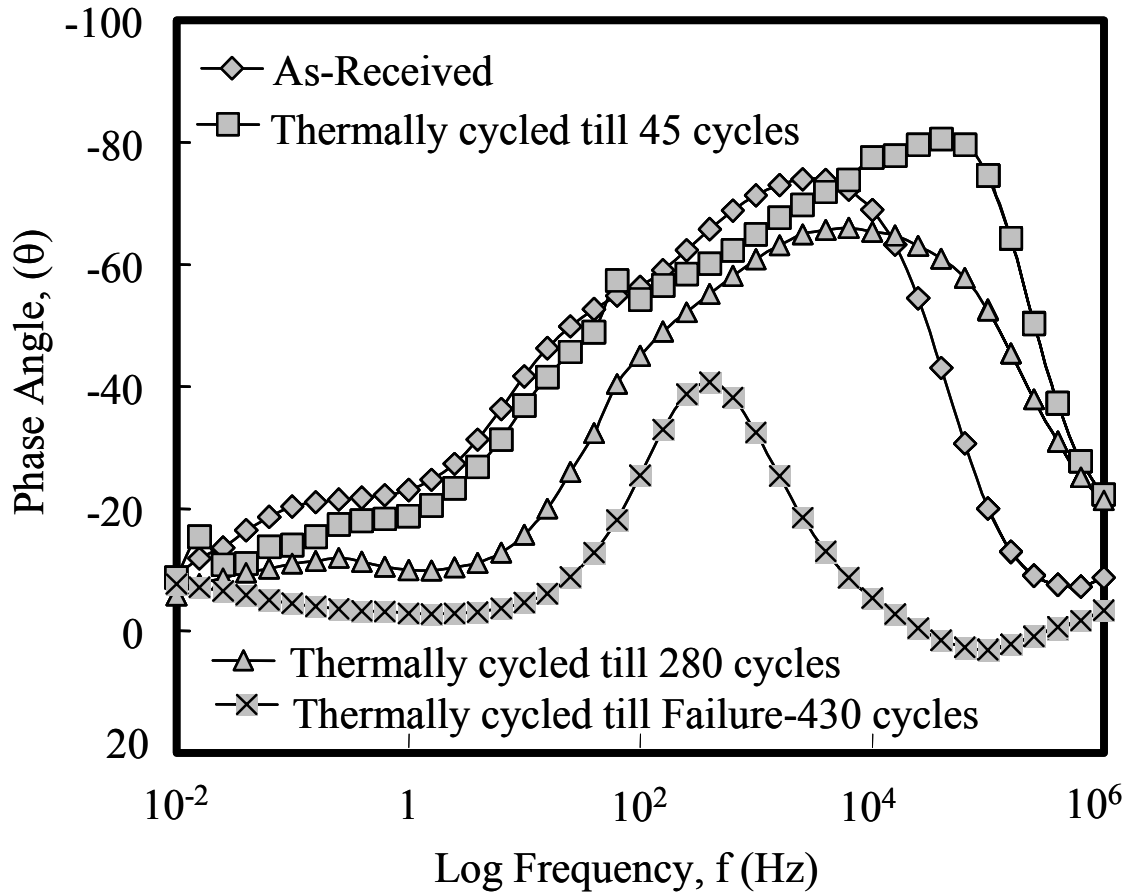

Figure 72.Typical Phase angle plots from as-coated and as a function of thermal cyclic life time for type-III EB-PVD TBCs

Table VIII. Resistance and capacitance of type-III EBPVD TBC constituents as a function of thermal cycling.

Thermal Cycles	R_C (kΩ)	C_C (nF)	R_P (kΩ)	C_P (nF)	R_O (kΩ)	C_O (nF)	R_T (kΩ)	C_T (μF)
As-received	1.90 ± 0.45	46.9 ±2.3	309.8 ±81.7	24.46 ±0.03	0.05 ±0.01	283 ±19.4	28.3 ±4.9	447 ±135
45 (10% lifetime)	38.0 ±1.3	9.8 ±0.3	163.7 ±5.2	7.4 ±0.8	7.5 ±4.7	20 ±1.5	1.6 ±0.02	14.7 ±0.1
280 (70% lifetime)	22.8 ±7.2	26.6 ±0.6	262.4 ±74.2	7 ±1.9	4.8 ±0.2	17.03 ±0.07	0.28 ±0.01	8.9 ±0.12
430 (After Failure)	0.25 ±0.01	5015 ±61.5	0.75 ±0.1	63813 ±6542	0.17 ±0.01	9999 ±70.3	0.07 ±0.01	4193 ±145.5

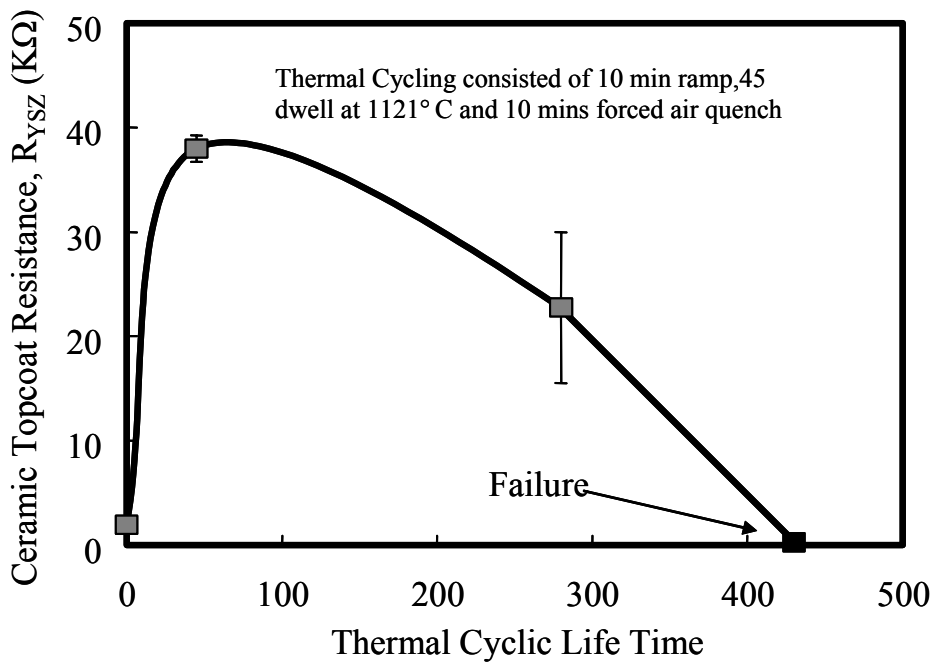

Figure 73.Evolution of Ceramic topcoat resistance (R_{YSZ}) for type III EB-PVD TBCs as a function of thermal cycling at 1121°C.

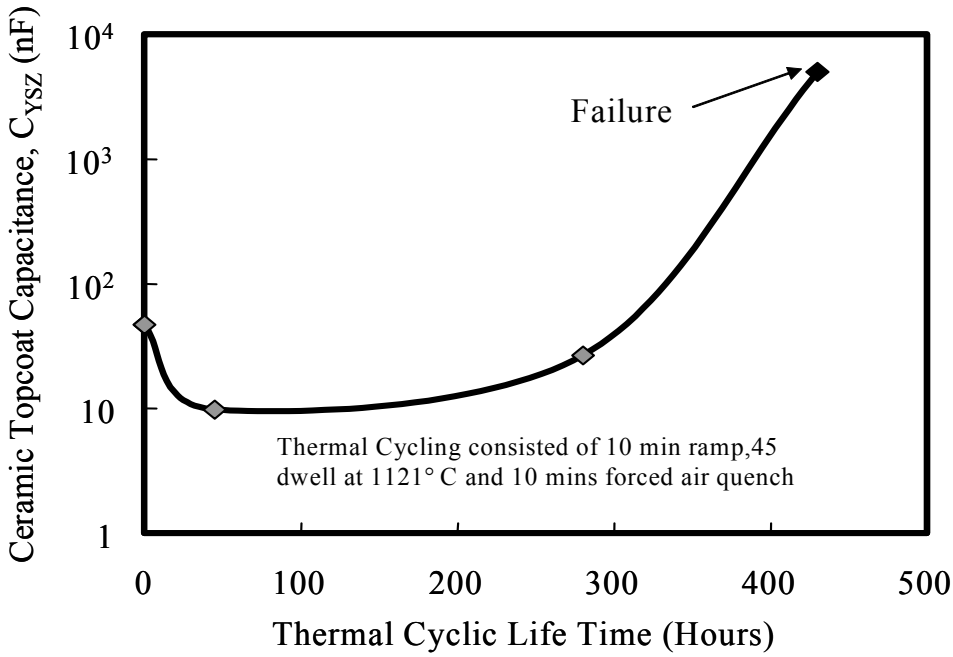

Figure 74.Evolution of Ceramic topcoat capacitance (C_{YSZ}) for type III EB-PVD TBCs as a function of thermal cycling at 1121°C.

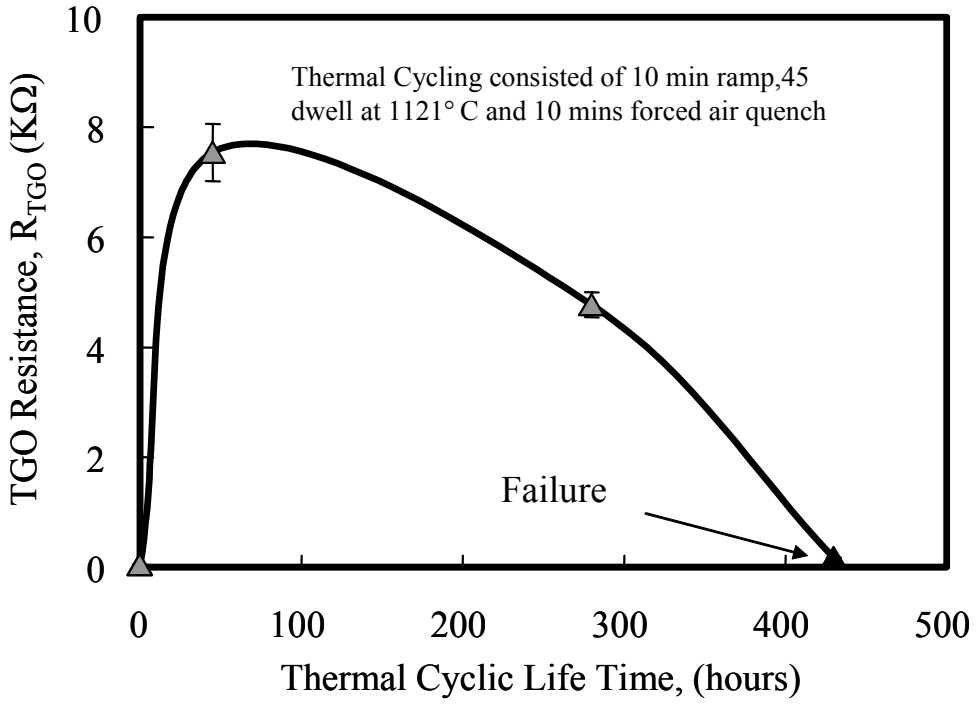

Figure 75.Evolution of TGO resistance (R_{TGO}) for type III EB-PVD TBCs as a function of thermal cycling at 1121°C.

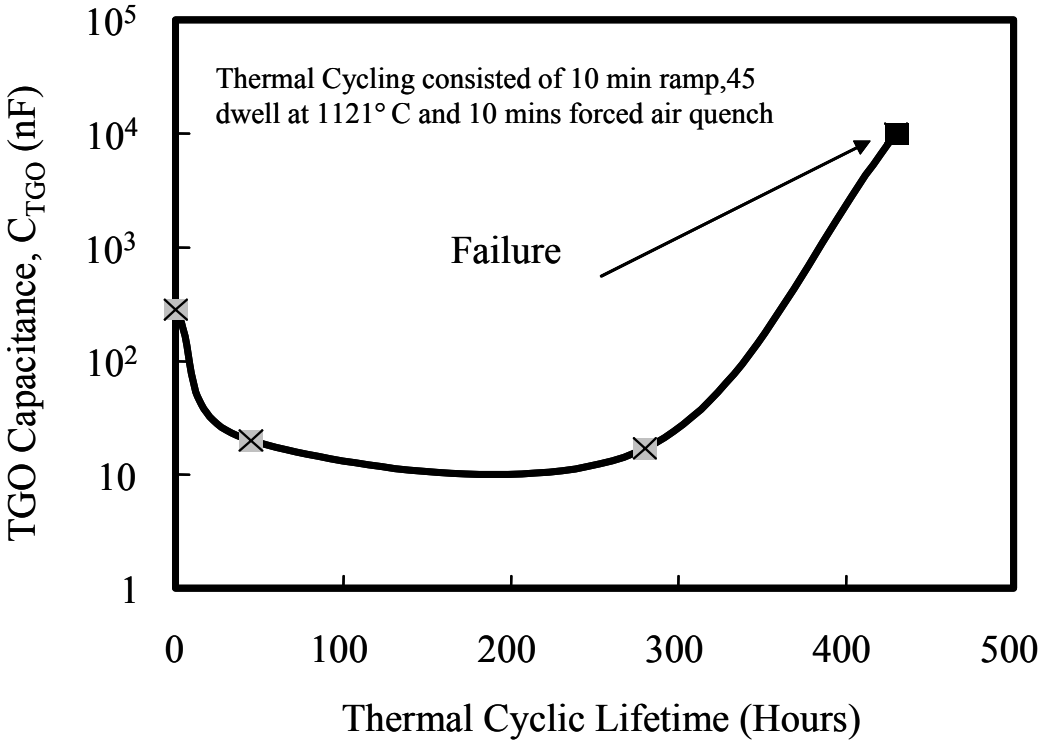

Figure 76.Evolution of TGO capacitance C_{TGO} for type III EB-PVD TBCs as a function of thermal cycling at 1121°C.

For type IV TBCs EIS measurement was carried out 3 times for as-received, thermally cycled and failed specimen. Typical impedance and phase angle plots for these specimens are presented in Figures 77 and 78, respectively. Table IX also reports the values of resistance and capacitance of the various TBC constituents that were calculated based on the ac-equivalent circuit in Figure 9. Evolution of resistance and capacitance of TBC constituents as a function of thermal cycling is presented in Table IX and Figures 79 through 82. Figure 77 shows that the impedance of the type-IV TBCs increased with thermal cycling and decreased after prolonged exposure. This increase in the impedance is attributed to the growth of the TGO and the high temperature sintering of the YSZ. Aforementioned, this microstructural changes can be related to the electrical parameters such as the resistance and capacitance of the YSZ and the TGO. The resistance of the YSZ and TGO increased initially and decreased after prolonged exposure as shown in Figures 79 and 80. Whereas the capacitance of the YSZ shown in the Figure 80, decreased initially and remained constant until failure when a sharp increase was observed. This is because the impedance of the failed specimen is lower than that of the as-received specimen due to the exposure of the bond coat surface observed on the fracture surface (see section V.4.4). On the other hand the capacitance of the TGO shown in Figure 71, decreased initially and increased with further thermal cycling.

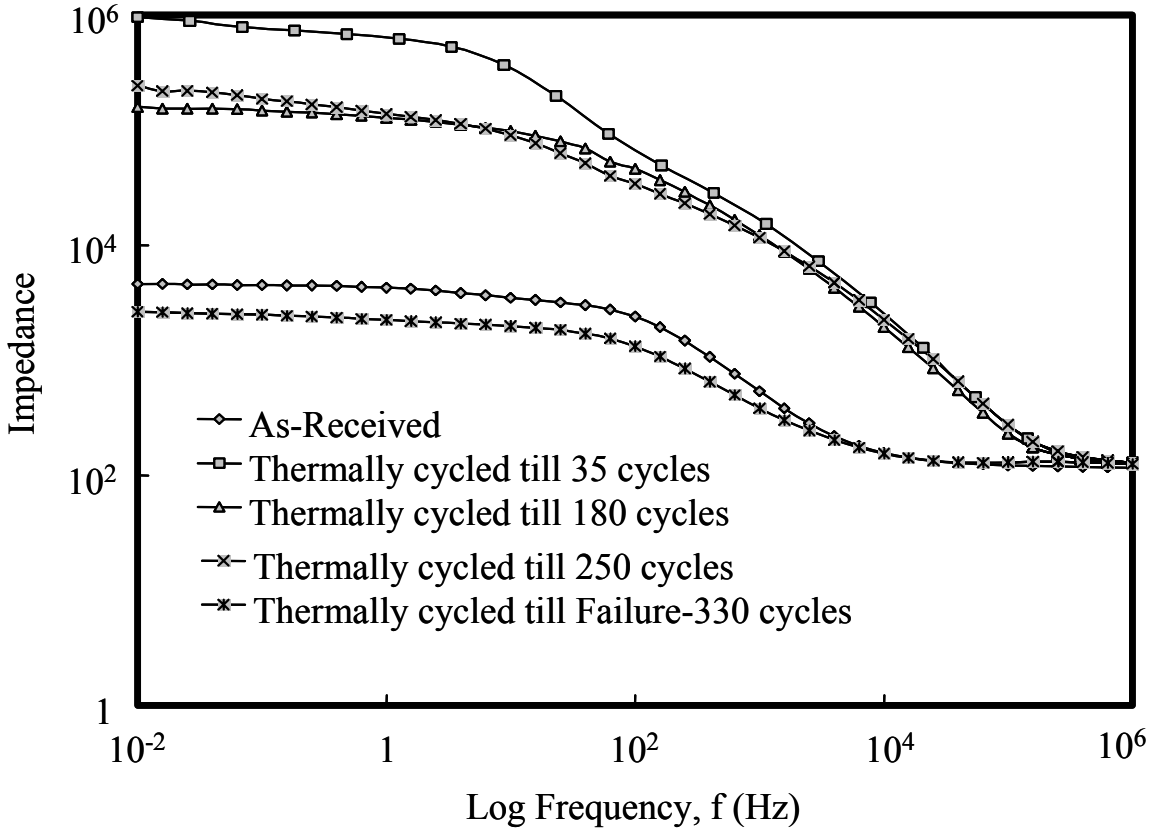

Figure 77. Typical Impedance plots from as-coated and as a function of thermal cyclic life time for type-IV EB-PVD TBCs

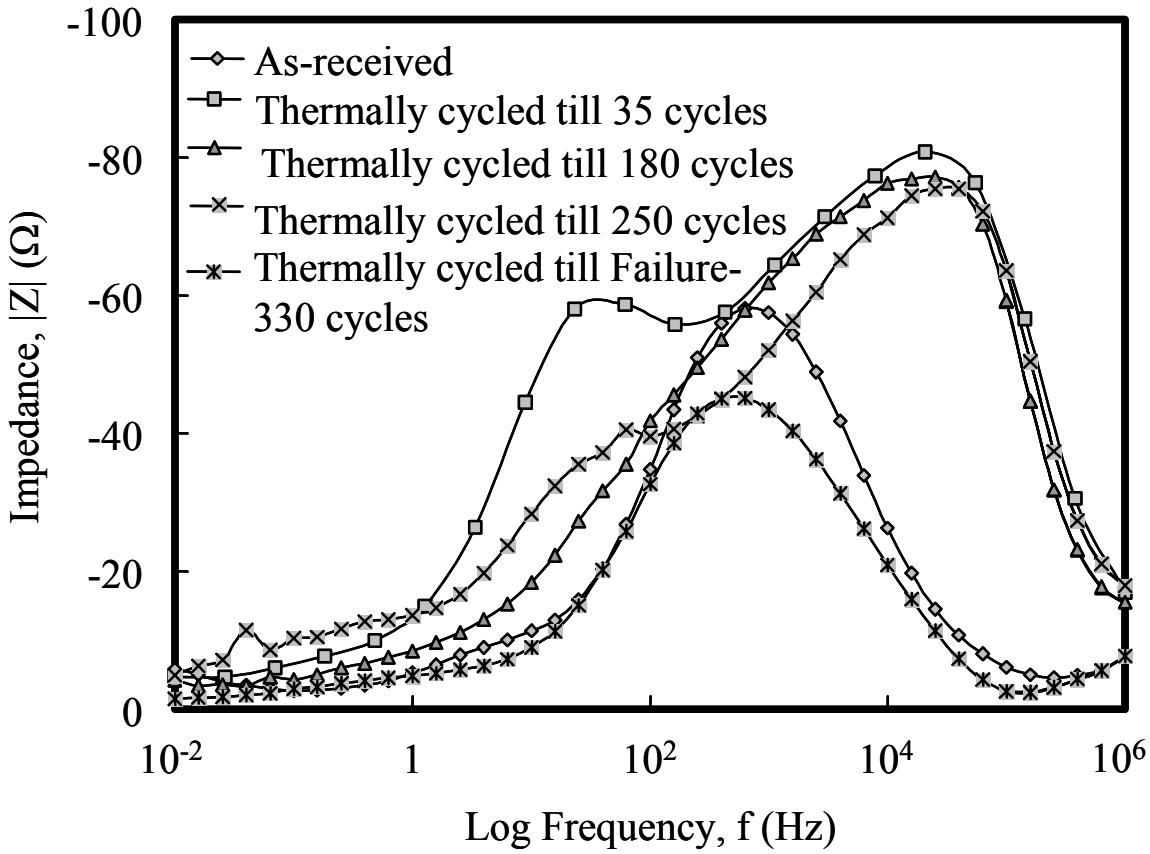

Figure 78. Typical phase angle plots from as-coated and as a function of thermal cyclic life time for type-IV EB-PVD TBCs

Table IX. Resistance and capacitance of type-IV EB-PVD TBC constituents as a function of thermal cycling.

Thermal Cycles	R_C (kΩ)	C_C (nF)	R_P (kΩ)	C_P (nF)	R_O (kΩ)	C_O (nF)	R_T (kΩ)	C_T (nF)
As-received	.01 ± 0	224 ±16.3	2.17 ±0.3	523.7 ±26.2	2.1 ±0.3	600 ±14.5	37.2 ±0.7	2 ±0.1
45 (10% lifetime)	6.2 ±2.2	6.8 ±0.2	735.5 ±175.6	8.6 ±0.8	431 ±6.6	50.1 ±2.3	23.8 ±0.9	2.4 ±0.3
180 (50% lifetime)	2.6 ±0.05	8.2 ±0.05	134.8 ±2.8	8.7 ±0.05	27.6 ±0.10	115 ±1.6	31.1 ±0.2	2.3 ±0.04
280 (70% lifetime)	0.44 ±0.05	6.5 ±0.04	140.2 ±26.8	9.72 ±0.15	31.43 ±0.8	182 ±15.8	35 ±0.3	1.9 ±0.01
330 (After) Failure	0.02 ±0	250 ±48.8	1.7 ±0.2	450.3 ±99.6	0.96 ±0.06	1203.2 ±365.4	40.8 ±0.9	1.7 ±0.1

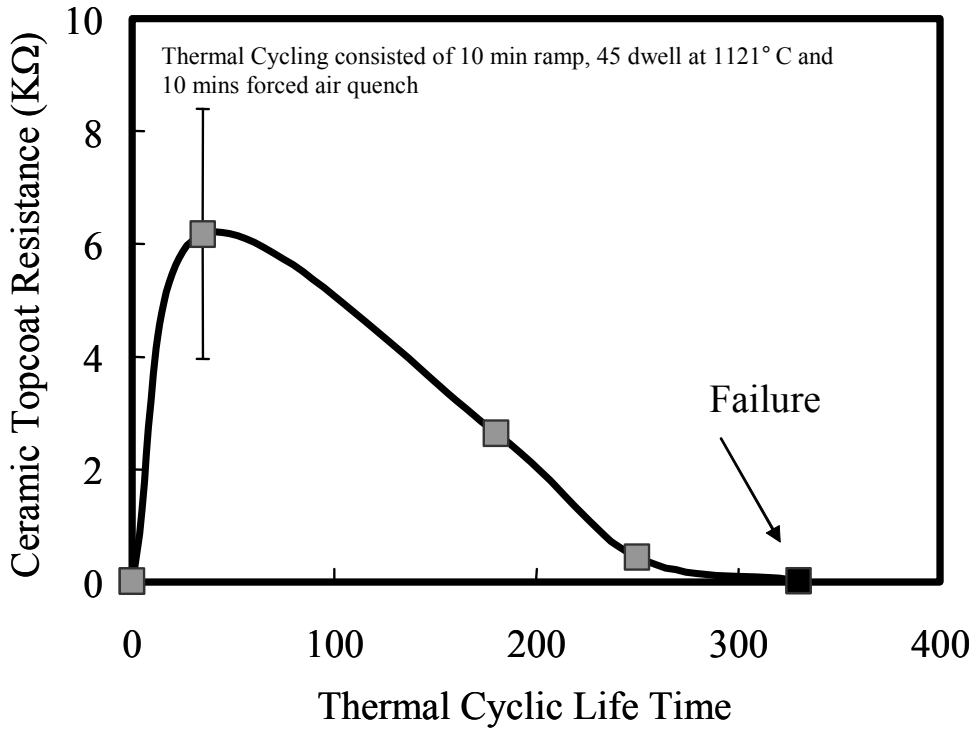

Figure 79. Evolution of Ceramic topcoat resistance (R_{YSZ}) for type IV EB-PVD TBCs as a function of thermal cycling at 1121°C.

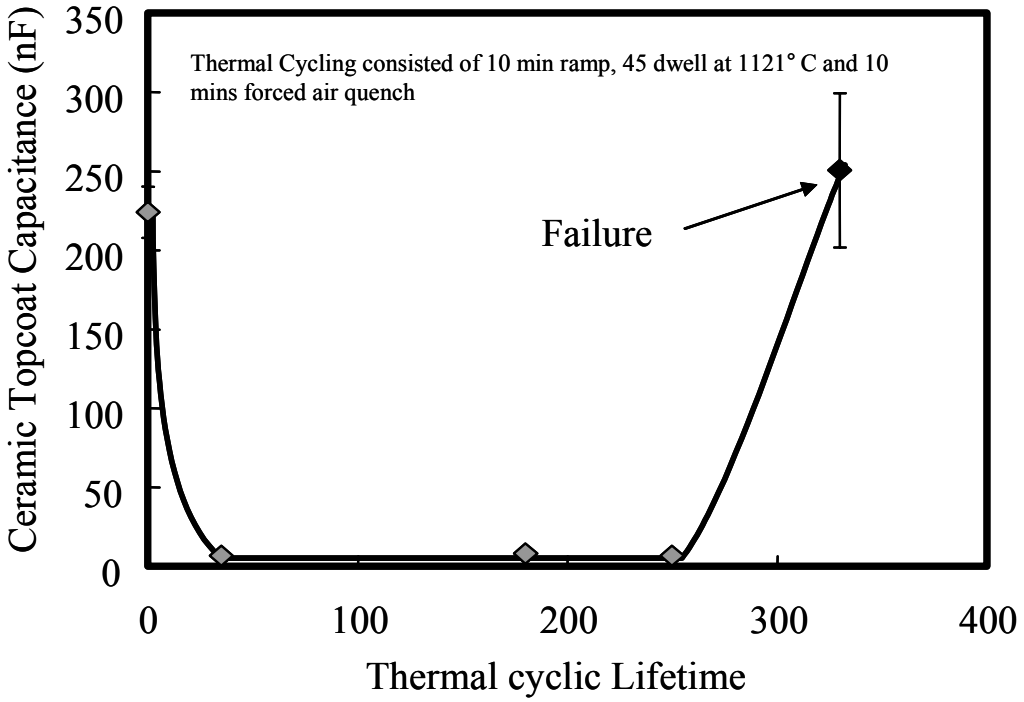

Figure 80. Evolution of Ceramic topcoat capacitance (C_{YSZ}) for type IV EB-PVD TBCs as a function of thermal cycling at 1121°C.

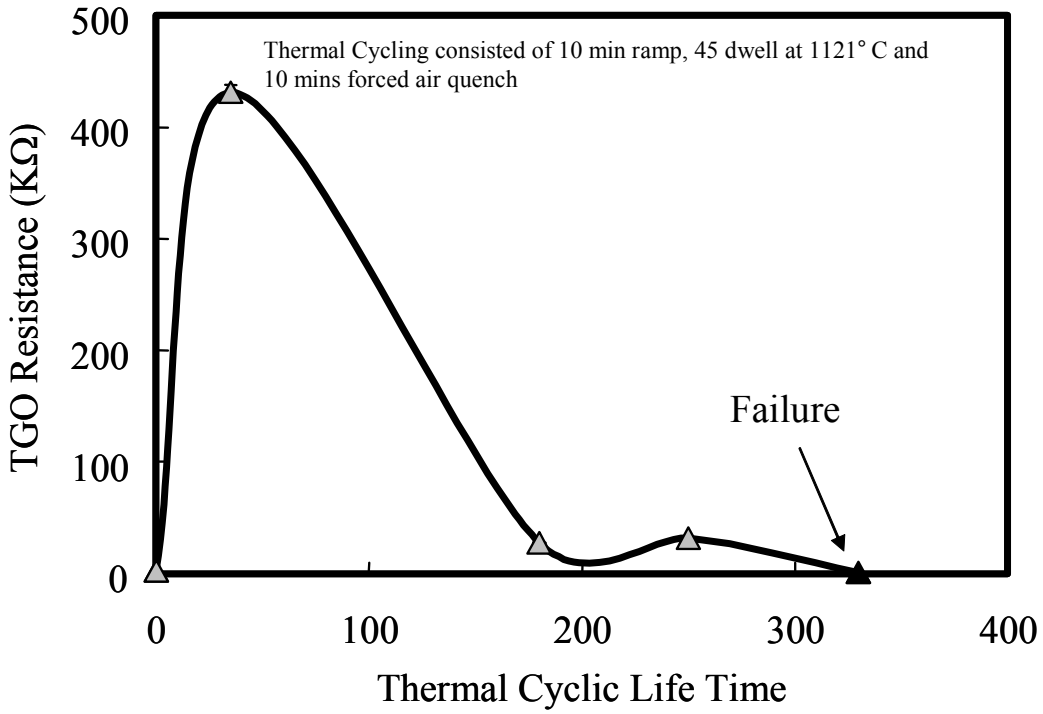

Figure 81. Evolution of TGO resistance (R_{TGO}) for type IV EB-PVD TBCs as a function of thermal cycling at 1121°C.

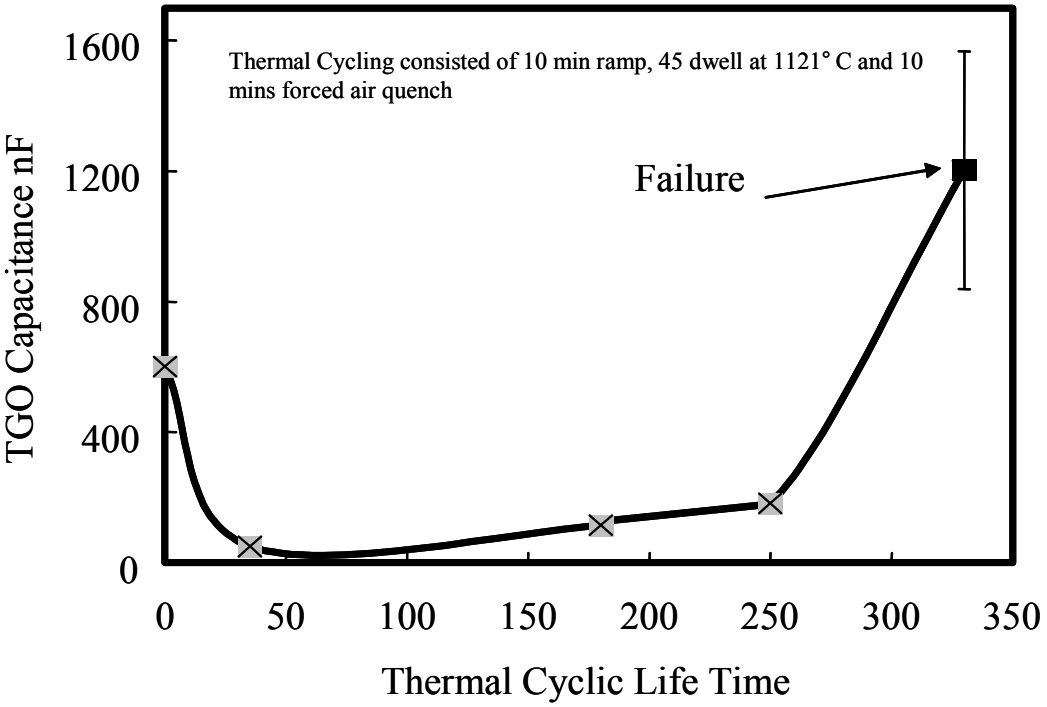

Figure 82. Evolution of TGO capacitance (C_{TGO}) for type IV EB-PVD TBCs as a function of thermal cycling at 1121°C.

V.3.4. Sub-critical damage detection before actual TBC failure

From the EIS results discussed in the previous section a master plot is generated for the C_{TGO} and thickness of the TGO and is shown in Figure 83. Without any damages there is an inverse linear trend between the C_{TGO} and the thickness of TGO. Since capacitance does vary inversely to the thickness [26]. A deviation from this trend was observed for one particular type-IV TBCs with grit-blasted (Ni, Pt)Al bondcoat. This may be due to the sub-critical damages in TGO that can expose the metallic surface or the effective thickness of the TGO scale reduces with this damage. These sub-critical damages are shown in the section v.4.

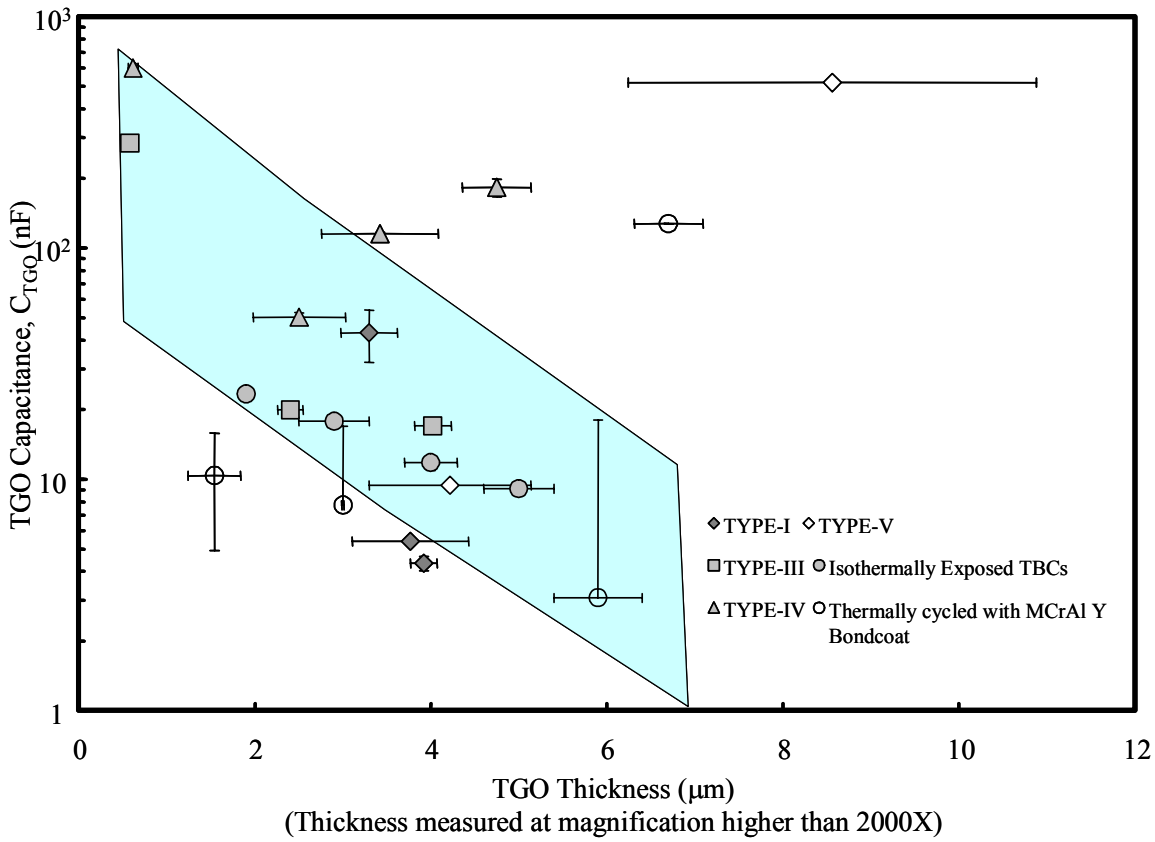

Figure 83. Master plot showing the linear relation between the CTGO and thickness of TGO prior to spallation and change in the linear relation with sub-critical damages.

V.3.5. NDE of Type I APS TBCs by EIS- 10 and 50- hour thermal cycling

For type I APS TBCs, EIS measurement was carried out 3 times on specimens before thermal cycling and after 10- hour thermal cycling that corresponds to 30% and 80% of its lifetime. The variation in impedance with respect to the 10 – hour thermal cycling is presented in Figures 56 and 57, respectively. Table X also reports the values of resistance and capacitance of the various TBC constituents, which were calculated based on the ac-equivalent circuit presented in Figure 9. For the as-coated APS TBCs, there is no significant presence of the TGO. Hence the TGO is not represented in terms of the electrical parameters. The ac equivalent circuit for APS TBCs, after exposure is different from that of the as-coated

ones because of the bond coat oxidation and the formation of uniform and continuous TGO. The impedance of TGO cannot be neglected in the EIS measurement system. Thus, an ac equivalent circuit for the thermally cycled TBC consists of the electrical parameters that represent the TGO.

The impedance plot presented in Figure 84 shows that the impedance response of the TBCs did not vary significantly with 10-hour thermal cycling however there are subtle changes in the values resistance and capacitance of YSZ and TGO these are reported in table X. This initial increase in the impedance response may be attributed to the sintering of the YSZ topcoat and growth of TGO with high temperature exposure from as received condition. After continuous 10-hour thermal cycling the impedance did not vary significantly this may be because of the micro-cracks that develop in the YSZ topcoat and also the sub-critical damages associated with topcoat sintering at the interface between YSZ/TGO. These sub-critical damages prior to the final failure have been documented by microstructural analysis (see section V.4.2, 4.7 and 4.9).

A further comparison of impedance response with 1-hour thermal cycling is shown in Figure 85. From Figure 85 we can see the increase in the impedance for 1-hour thermal cycling is because of prolonged exposure and formation of well developed TGO as well as topcoat sintering. Whereas in case of 10-hour and 50-hour thermal cycling the impedance response is lower in that frequency range which depends on TGO scale development and YSZ sintering this is because of the sub-critical damages that are seen in topcoat and YSZ/TGO interface (see section V.4.2, 4.7 and 4.9).

The resistance and capacitance of YSZ and TGO reported for type APS TBCs are presented as function of dwell time in Figures 86 through 89. With an increase in the impedance, the resistance of the topcoat and the TGO increased. With further prolonged dwell time the resistance of the topcoat and the TGO decreased. The capacitance of the topcoat increased at failure because of the large scale damage in the topcoat. The capacitance of the TGO did not increase abruptly at failure because the fracture path of the APS TBCs observed for type-I TBCs primarily occur at the YSZ\TGO interface as shown in Figures 146 and 159 (see section V.4.2, 4.7 and 4.9) and rarely exposes the conductive surface of the metallic bondcoat.

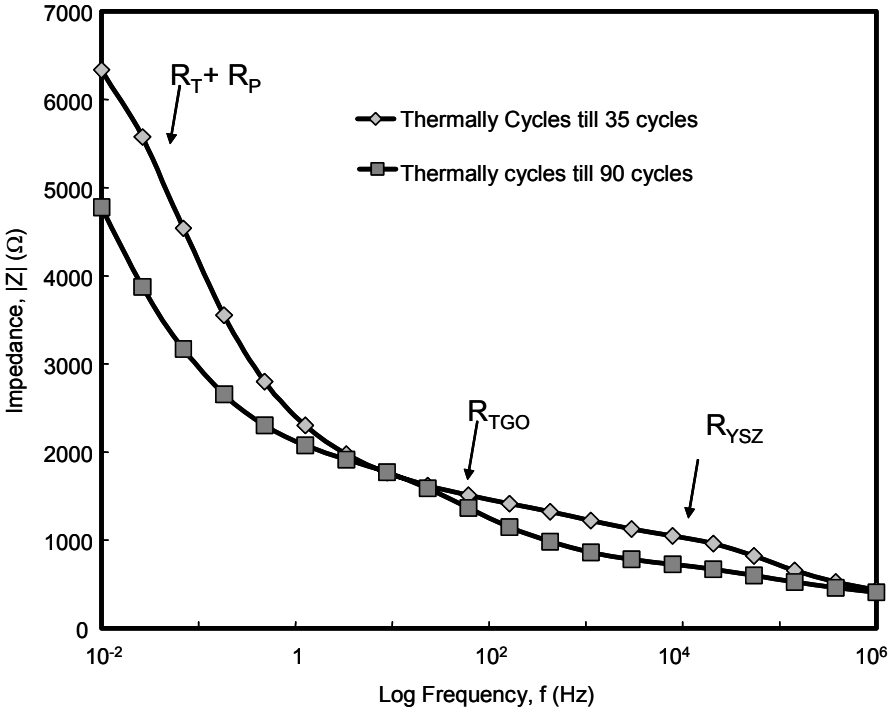

Figure 84. Typical Impedance plots from type-I APS TBCs as a function of 10-hour thermal cycling

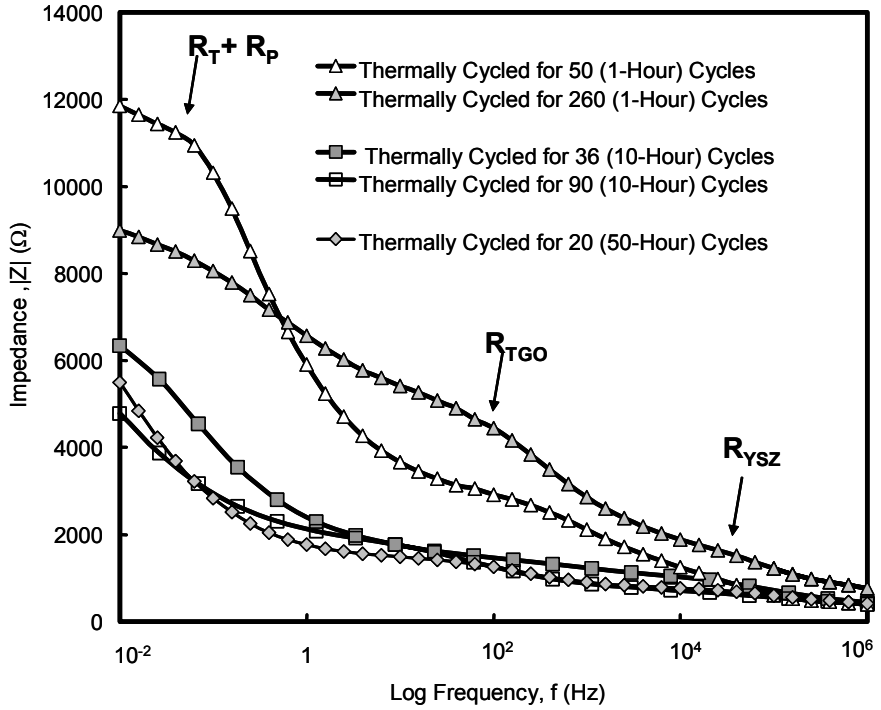

Figure 85. Typical Impedance plots from type-I APS TBCs as a function of 1, 10 and 50- hour thermal cycling

Table X. Resistance and capacitance of type- I APS TBCs constituents as a function of 10-hour thermal cycling.

Thermal Cycles	R_C (kΩ)	C_C (nF)	R_P (kΩ)	C_P (uF)	R_O (kΩ)	C_O (nF)	R_T (kΩ)	C_T (nF)
As-received	0.50 ± 0.4	2.2 ± 0.4	10.6 ± 4.2	377700 ± 21959	0	0	0.3 ± 0.1	16486 ± 2747
36 cycles (30% lifetime)	.64 ±0.002	374.6 ±82.1	5.6 ±0.18	18.48 ±0.22	0.98 ±0.02	9.94 ±0.72	0.55 ±0.02	10531 ±996
90 cycles (80% lifetime)	0.88 ±0.09	431.95 ±0.0	6.58 ±4.87	11.34 ±0.02	0.58 ±0.10	6.14 ±0.01	0.51 ±0.13	3262 ±15.5

Table XI. Resistance and capacitance of type- I APS TBCs constituents as a function of 50-hour thermal cycling.

Thermal Cycles	R_C (kΩ)	C_C (nF)	R_P (kΩ)	C_P (uF)	R_O (kΩ)	C_O (nF)	R_T (kΩ)	C_T (nF)
As-received	0.50 ± 0.4	2.2 ± 0.4	10.6 ± 4.2	377700 ± 21959	0	0	0.3 ± 0.1	16486 ± 2747
20 cycles (50% lifetime)	.60 ±0.01	892.3 ±21.7	4.03 ±0.08	7.3 ±0.32	0.78 ±0.02	8.5 ±0.16	9.6 ±0. 10	16085 ±148

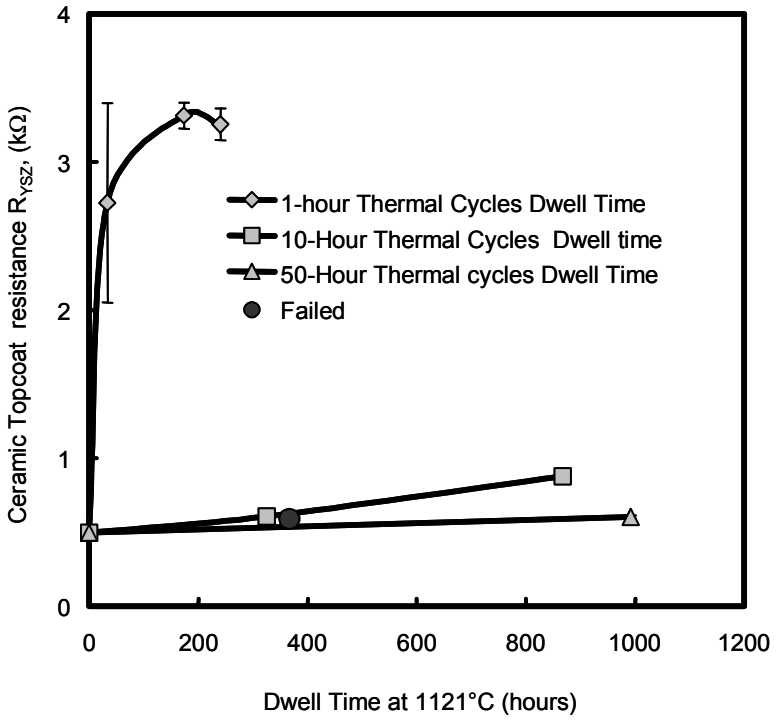

Figure 86. Evolution of ceramic topcoat resistance (R_{YSZ}) for type I APS TBCs as a function of dwell time at 1121°C.

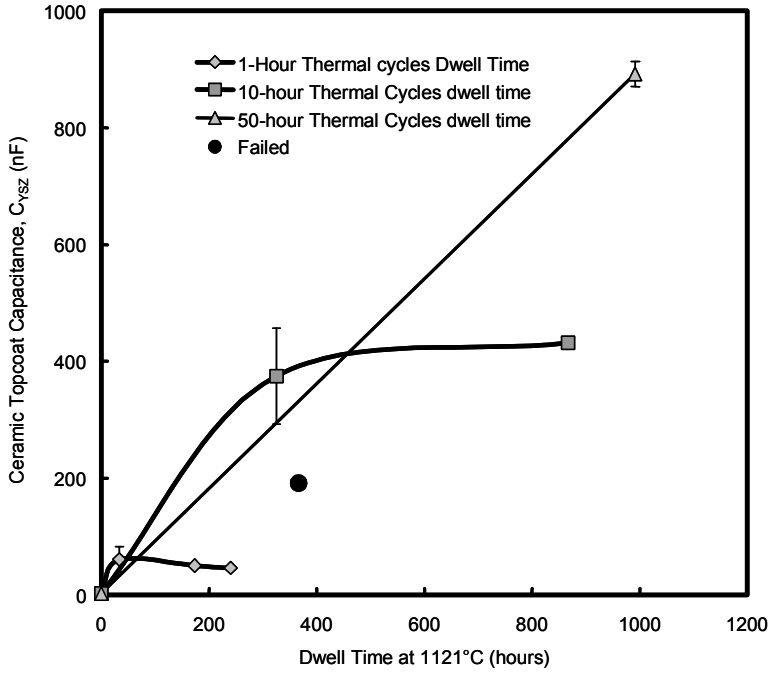

Figure 87. Evolution of ceramic topcoat capacitance (C_{YSZ}) for type I APS TBCs as a function of dwell time at 1121°C.

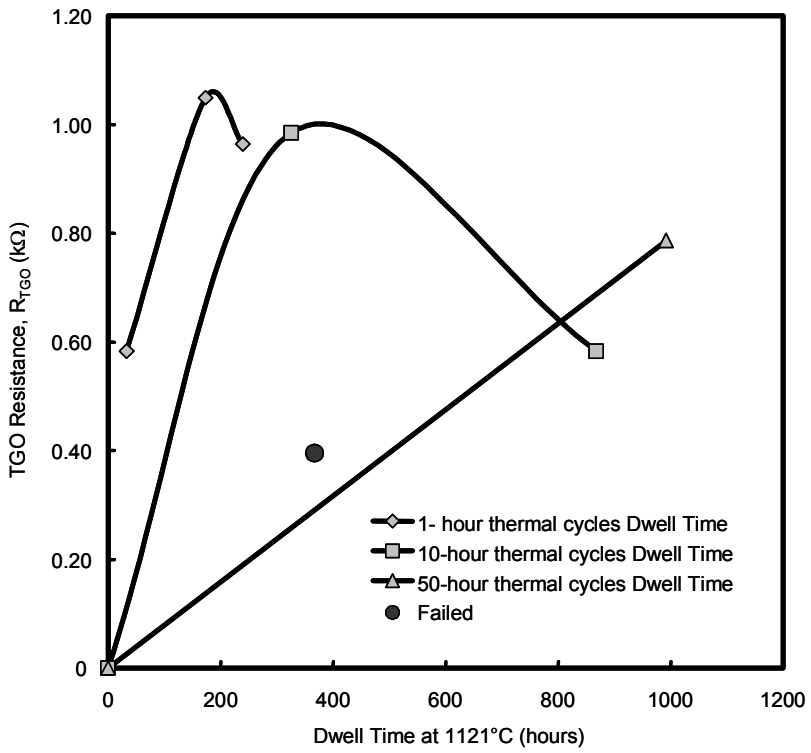

Figure 88. Evolution of TGO resistance (C_{YSZ}) for type I APS TBCs as a function of dwell time at 1121°C.

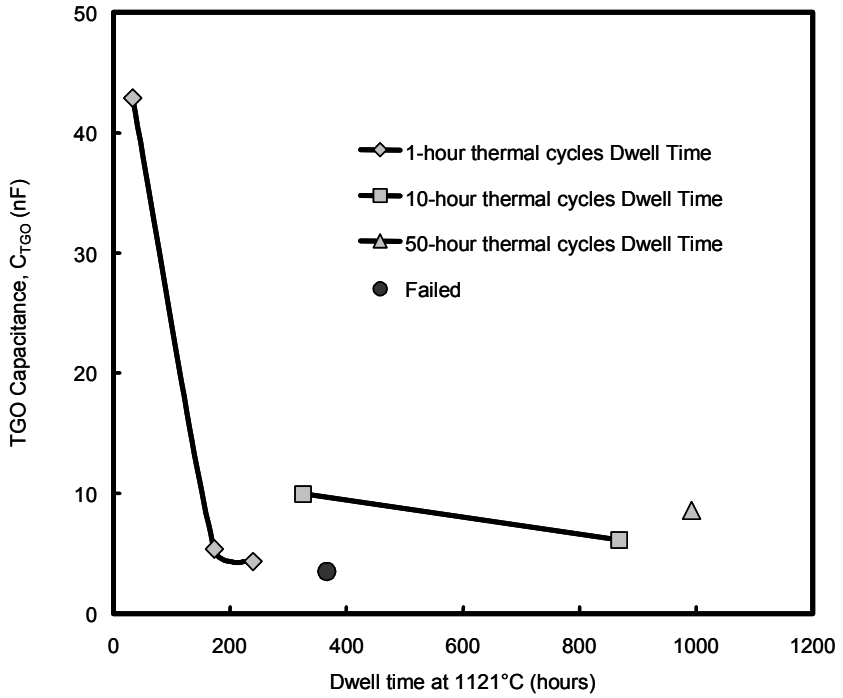

Figure 89. Evolution of TGO capacitance (C_{YSZ}) for type I APS TBCs as a function of dwell time at 1121°C.

V.3.6. Selected EIS Observations for TBC Applications

Along with NDE of five types of TBCs by EIS, selected experiments were carried out for EIS independently at UCF and in collaboration with industrial partners. The following summarizes the results from these additional specimens.

Monolithic 7YSZ with Varying Thickness and Density

Monolithic 7YSZ with varying thickness and density, received from Trans-Tech, Adamstown, PA, was examined by EIS. Figure 90 shows an increase in resistance (and a corresponding decrease in capacitance) with increasing thickness. In addition, lower resistance was observed for more porous 7YSZ as seen in Figure 90, reflecting greater conduction via electrolyte penetration through 7YSZ [25].

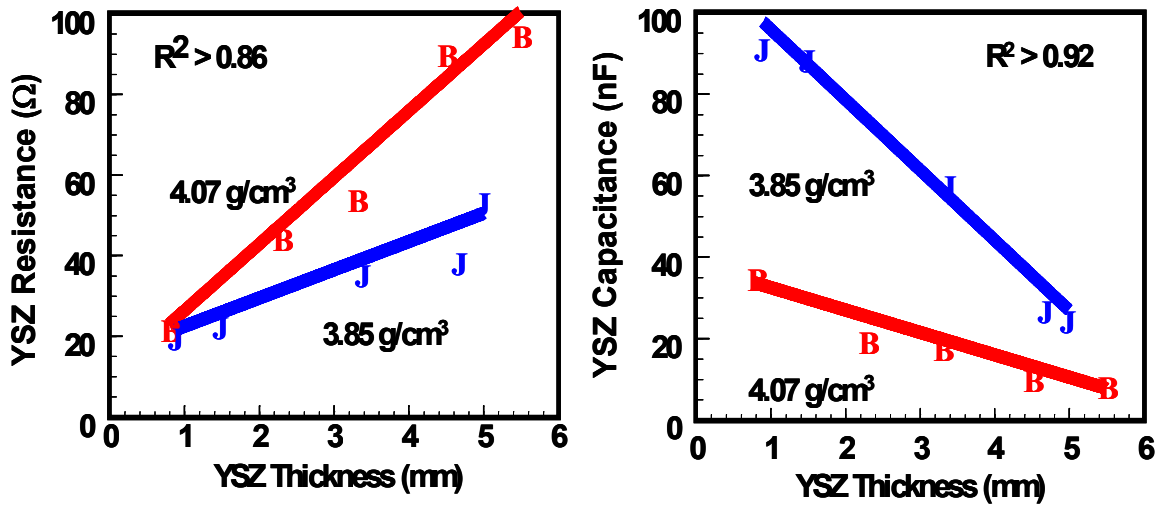

Figure 90. Ceramic resistance R_C and capacitance C_C of 7YSZ monoliths (open-pores) as a function of thickness and density non-destructively determined by EIS [25].

Electron Beam Physical Vapor Deposited 7YSZ with Varying Thickness

A series of as-coated EB-PVD 7YSZ TBCs with varying thickness, which is controlled by deposition time, was examined by EIS. Specimens were provided by one of the industrial partners. An increase in the ceramic resistance was observed with increasing thickness as presented in Figure 91 [25].

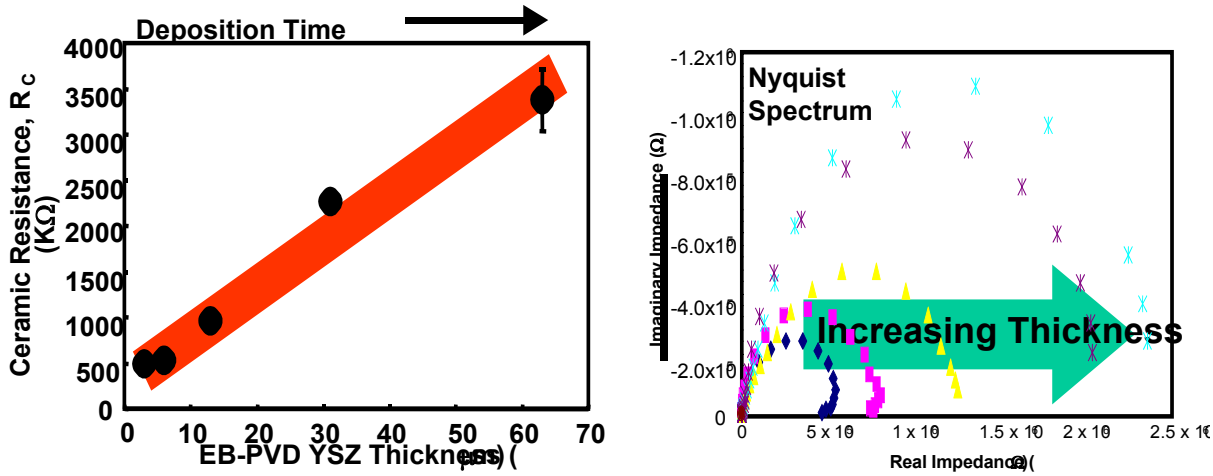

Figure 91. An increase in the ceramic top coat resistance R_C and the corresponding Nyquist plots as a function of thickness for as-coated EB-PVD TBCs.

NiAl Disk Specimens as a Function of Thermal Cycling

Hot-extruded NiAl disk specimens, received from NASA-GRC, were thermally cycled at 1121°C using a 10-minute heat-up, a 40-minute hot-time and a 10-minute forced-air-quench. Resistance and capacitance of TGO, R_O and C_O were monitored as a function of thermal cycles as presented in Figure 92. Initial increase and decrease, in the resistance and capacitance, respectively, of TGO correspond to the parabolic growth (thickening) of TGO scale [25]. This trend in the resistance and capacitance of the TGO, changes between 20 and 50 cycles, at which, the spallation of TGO was observed using optical microscopy [25]. Upon spallation of TGO, localized exposure of NiAl surface to the electrolyte will decrease the resistance, and increase the capacitance.

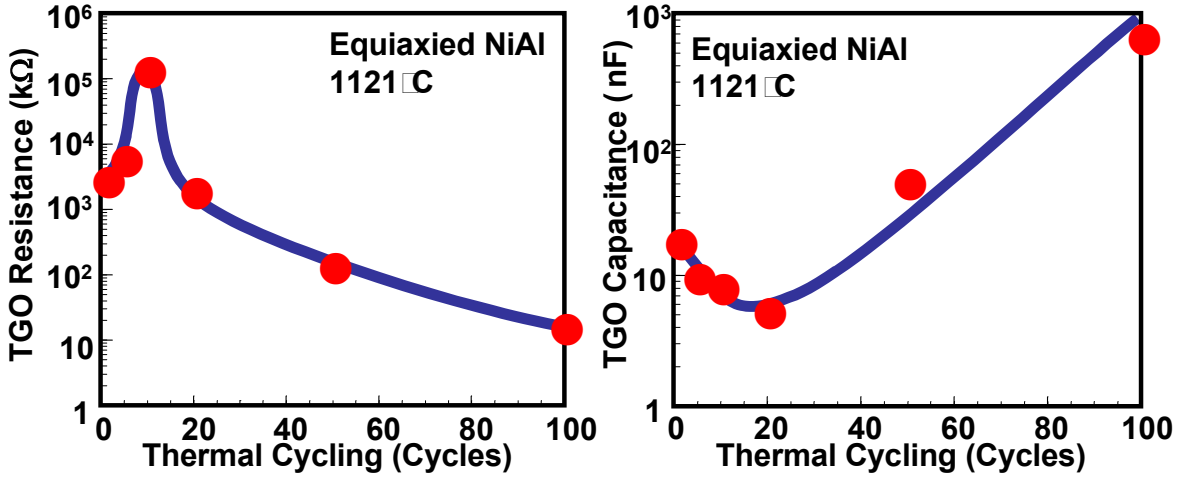

Figure 92. Evolution of TGO resistance and capacitance as a function of thermal cycling at 1121°C.

NiAl Disk Specimens as a Function of Isothermal Oxidation

Similar results were obtained for NiAl disk specimens, which were isothermally oxidized at various time (2, 5 and 10 hours) and temperature (1100°, 1200° and 1300°C). Figure 93 shows a decrease in capacitance (C_{TGO}) and corresponding increase in resistance (R_{TGO}) with increasing time and temperature. However, reverse trend was observed in resistance and capacitance for specimens oxidized at 1300°C with varying time. This trend is related to the spallation of the oxide scale on the NiAl substrate which leads to the contact of the electrolyte directly to the metal. Figure 94 shows the spallation of the oxide scale from the substrate. Upon spallation of TGO, localized exposure of NiAl surface to the electrolyte will decrease the resistance, and increase the capacitance.

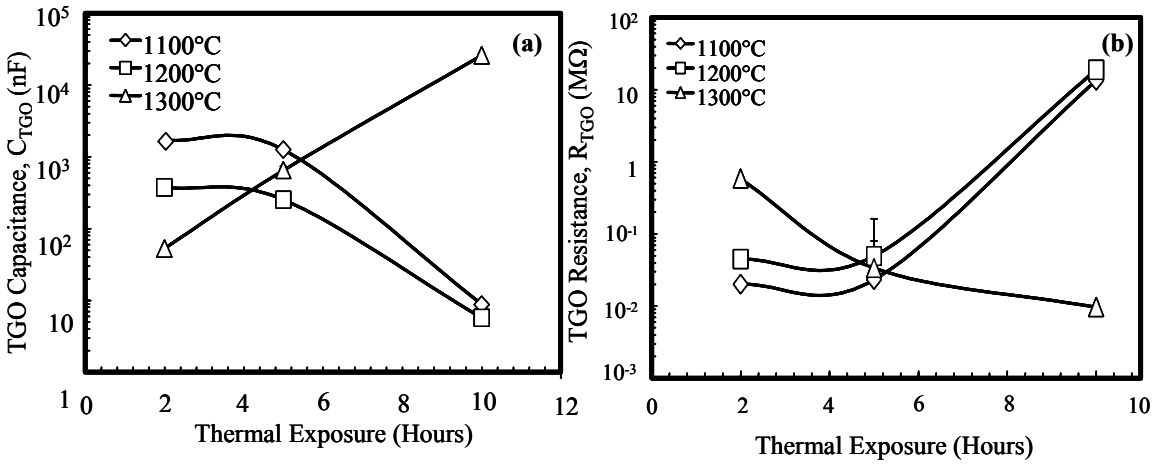

Figure 93. Evolution of TGO capacitance and resistance as a function of isothermal oxidation at various time and temperature.

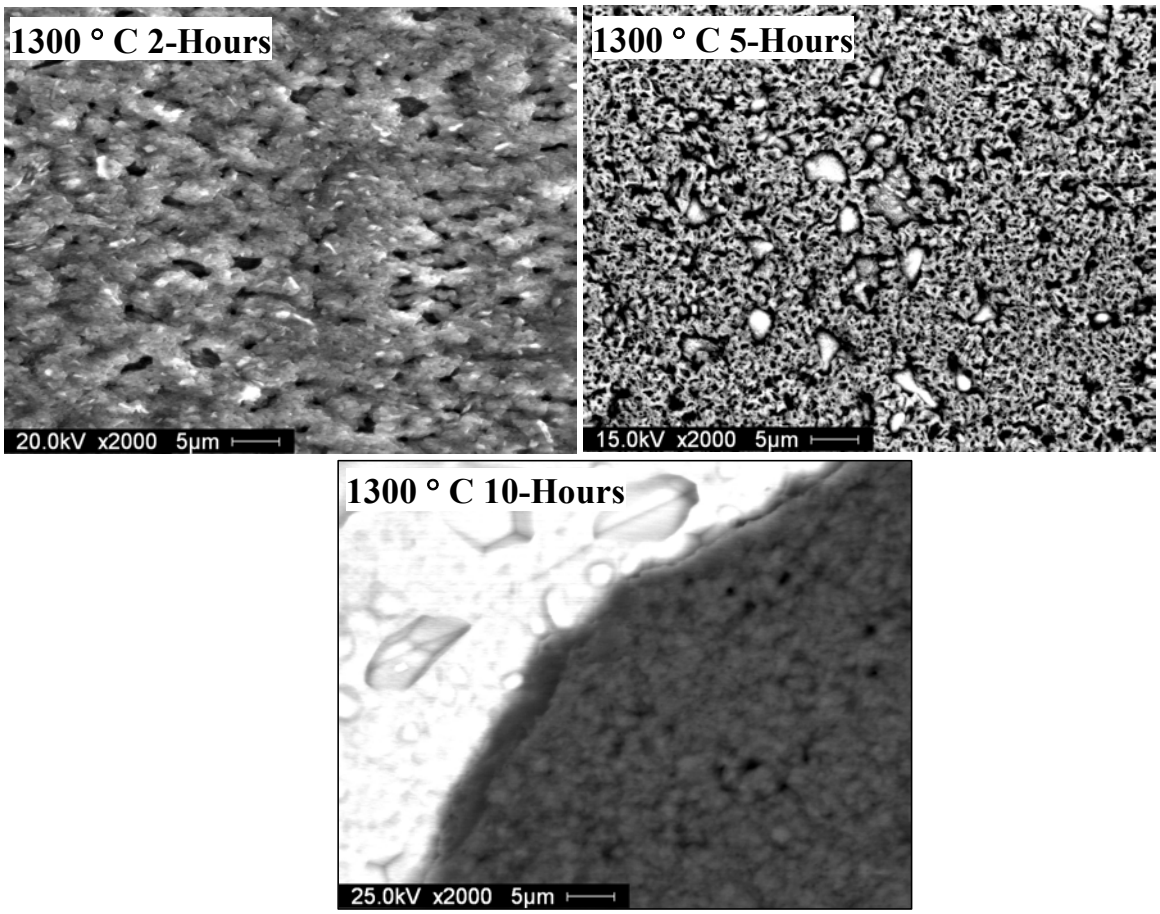

Figure 94.Spallation of TGO scale (Al_2O_3) from the NiAl surface after 5 and 10 hours of isothermal exposure at 1300° C.

Electron Beam Physical Vapor Deposited TBCs as a Function of Thermal Cycling

EB-PVD TBCs with various thermal cycling at 1121°C (40-minute hot-time) were examined by EIS with specimens provided by the University of Connecticut/industrial partner. Resistance and capacitance of YSZ and TGO were monitored as a function of thermal cycles as presented in Figure 95. After prolonged thermal cycling, a sharp decrease and an increase in the resistance and capacitance, respectively, of YSZ was observed [26]. Initial increase and decrease in the resistance and capacitance of TGO, respectively, correspond to the parabolic growth (thickening) of TGO scale [26]. Abrupt changes in the resistance and capacitance of TGO, by orders of magnitude, occurred with the failure [26]. A decrease in the resistance of TGO occurred prior to failure [26]. This observation is consistent with that from the oxidation of NiAl (Figures 92 & 93) and for the types of TBC specimens reported above.

A decrease in the resistance and the corresponding increase in the capacitance of insulating oxide (YSZ and TGO) reflect the conduction via penetration of electrolyte. This

penetration of electrolyte can occur through porosity, and more importantly, through damages/cracks that develop within YSZ and TGO during thermal cycling.

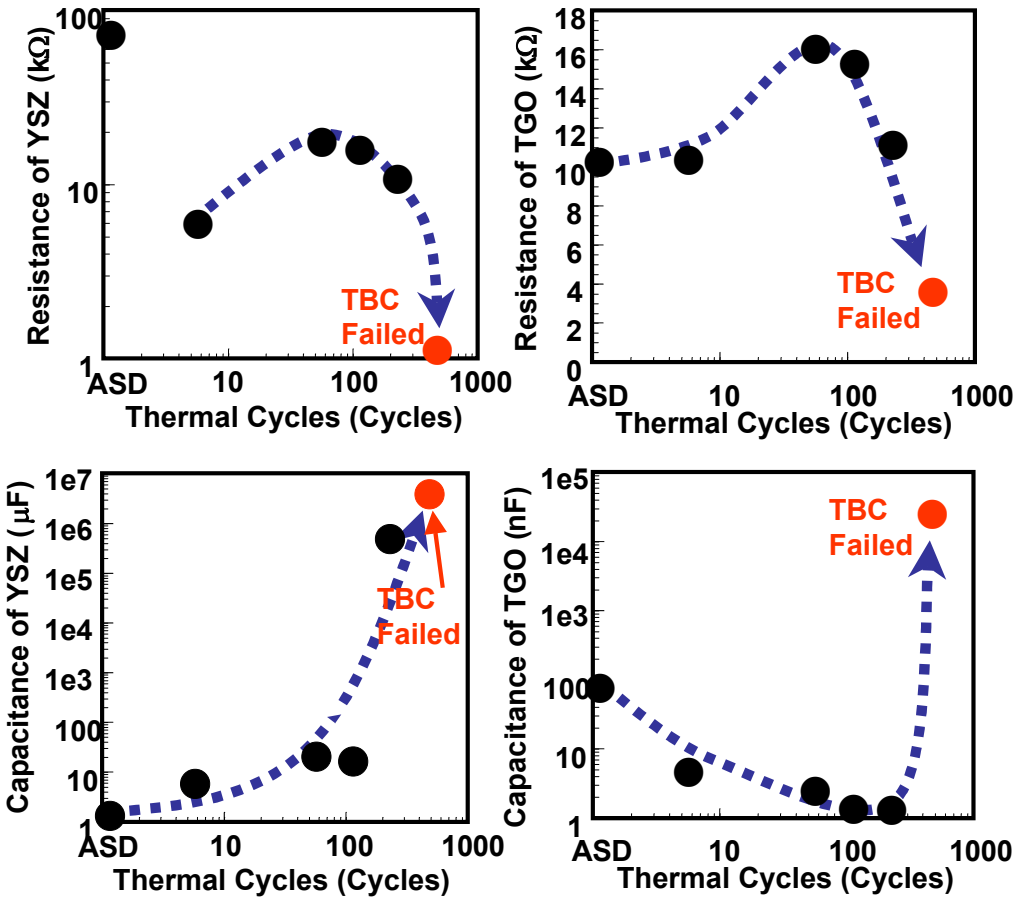

Figure 95. Evolution in (a,c) resistance and (b,d) capacitance of (a,b) EB-PVD 7YSZ and (c,d) TGO during thermal cycling at 1121C.

<u>7YSZ and $CaTiO_3$ Air Plasma Sprayed Thermal Barrier Coatings</u>

YSZ and $CaTiO_3$ TBCs with varying thickness, provided by one of the industrial partners, were examined by EIS. There is a decrease in the capacitance of ceramic top coat with increasing thickness as presented in Figure 96 [27]. A decrease in capacitance also corresponds to an increase in resistance as presented in Figure 96 [27]. Variation in thickness was measured on these specimens using scanning electron microscopy. The dielectric constant of $CaTiO_3$ is around 160 while that for YSZ is in the range of 40-60. The resistivity of $CaTiO_3$ is in the order of 10^{14} Ω-cm and that of YSZ is approximately 10^9 Ω-cm. From these values of dielectric constant and resistivity, the resistance and the capacitance of the $CaTiO_3$ must be higher than that of YSZ at similar thickness as presented in Figure 96.

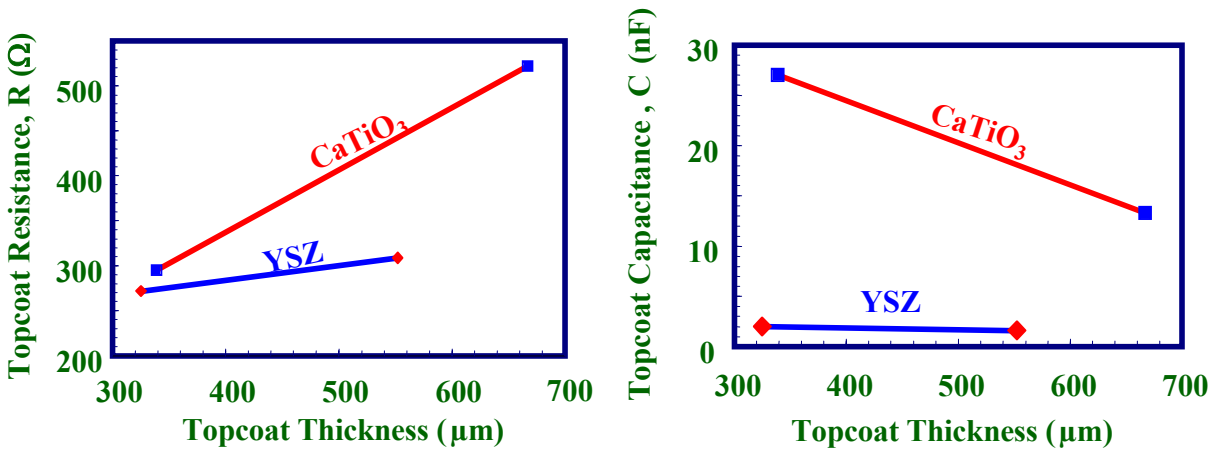

Figure 96. Ceramic top coat resistance R_C and capacitance C_C of APS 7YSZ and $CaTiO_3$ as a function of thickness.

Monolithic 7YSZ as a Function of Sintering

Monolithic 7YSZ with open pores, received from Trans-Tech, Adamstown, PA, was examined by EIS as a function of sintering time (2, 5 and 10 hours) and temperature (1100°, 1200° and 1300°C). Figure 97 shows a decrease in capacitance (and a corresponding increase in resistance) with increasing time and temperature of sintering after furnace cooling. However, air quenching after sintering at 1300°C for 5 and 10 hours produced a opposite trend in capacitance (i.e., an increase) and resistance (i.e., a decrease), which indicates that the penetration of electrolyte through sintered YSZ was easier for these specimens. In accordance with these EIS results, macro-scale cracks were observed for the specimens, which were air quenched after sintering at 1300°C for 5 and 10 hours as presented in Figure 98. The increase in capacitance and the decrease in the resistance due to electrolyte penetration through damage are consistent with observation made for TBCs presented in this report. Secondary electron micrographs of sintered specimens are presented in Figure 99.

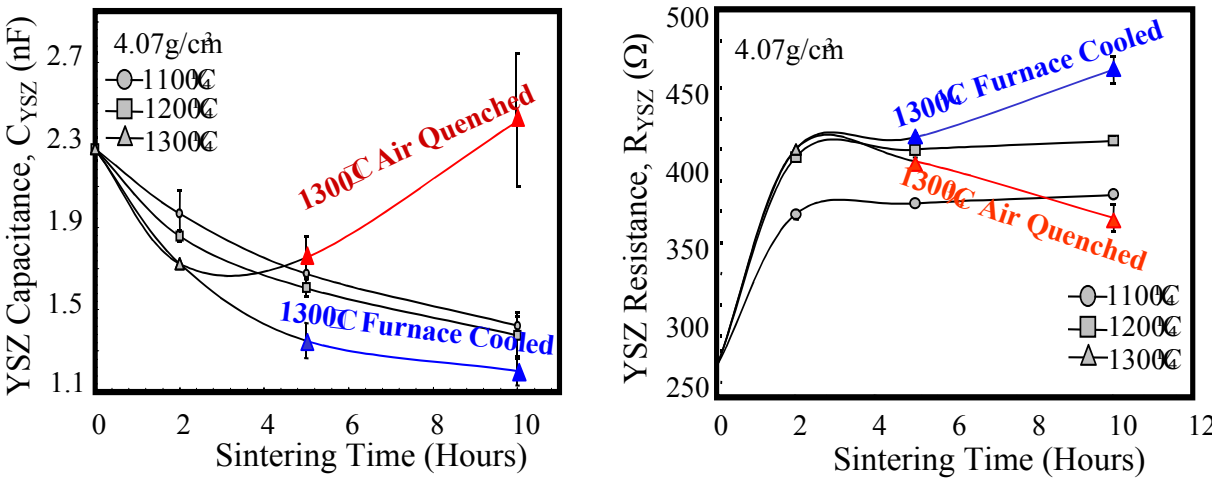

Figure 97. Evolution of YSZ capacitance and resistance as a function of time and temperature of isothermal sintering.

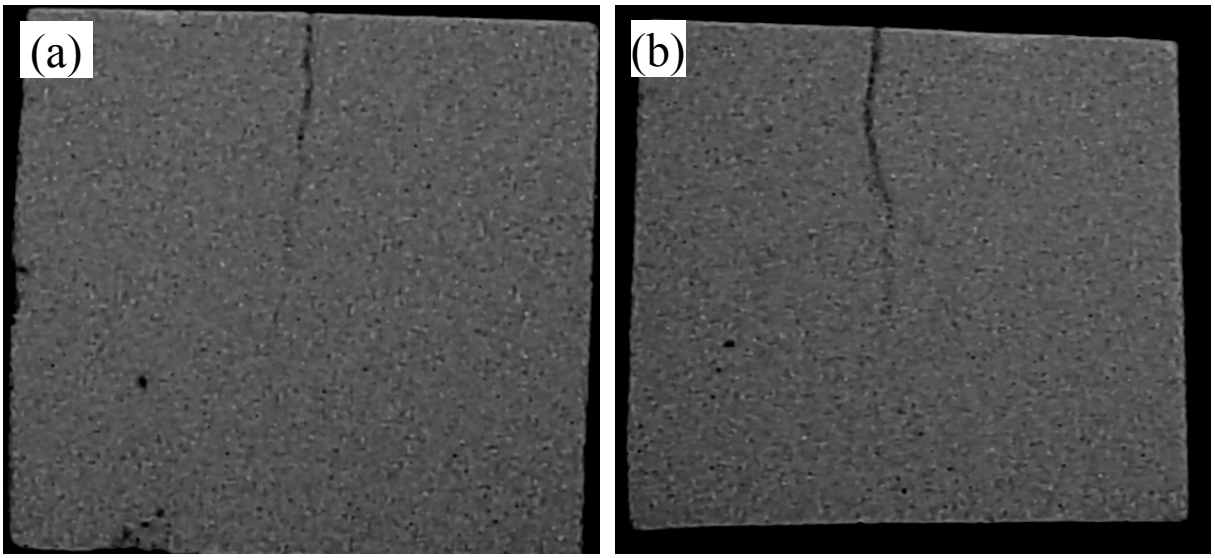

Figure 98. Macroscopic photographs of specimens after air-quenching from sintering at 1300°C for (a) 5 and (b) 10 hours. These specimens developed a large-scale crack upon air quenching to a room temperature.

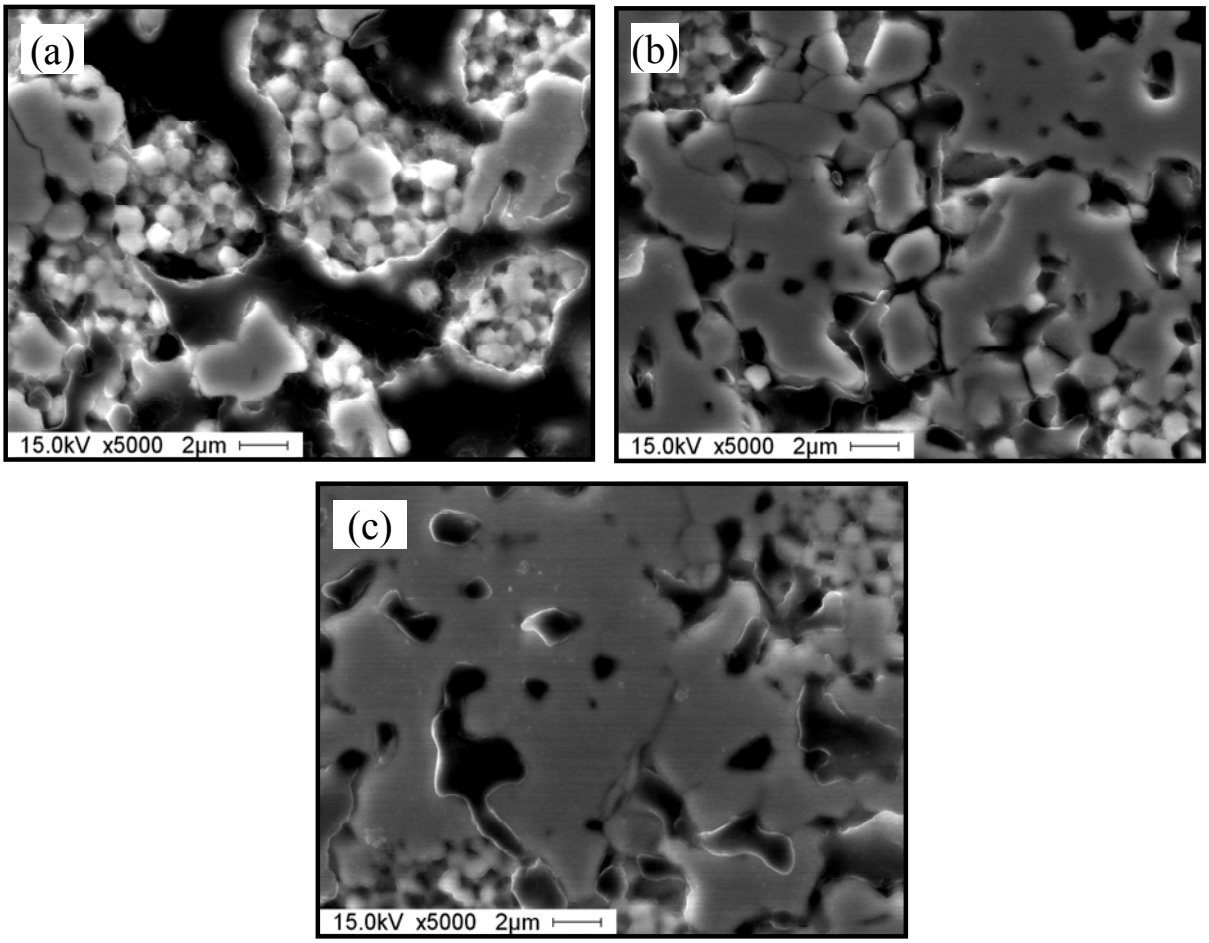

Figure 99. Secondary electron micrographs of YSZ monoliths with open pores: (a) as-received; (b) sintered at 1200°C for 5 hours, (c) sintered at 1300°C for 10 hours.

V.4. Microstructural Analysis of Thermal Barrier Coatings

V.4.1. As-coated Type I and V Air Plasma Sprayed Thermal Barrier Coatings

Figure 100 represents typical backscatter electron micrograph of as-received type I (600μm-thick) and type V (200μm-thick) APS TBCs. Specimens conformed to the specification described in Table II. Using SEM, no significant TGO scale was observed in the as-received APS TBCs as shown in Figure 100. However, a difference in the microstructure of APS YSZ was observed. Type I APS TBC did not exhibit splat morphology while type V TBC did as seen in Figure 100. This difference may be correlated to the NDE results by EIS (section V.3.1): a distinctive difference in pore capacitance C_P for these two specimens is reported in Table VI and Table VII. This difference in microstructure of the APS 7YSZ coatings is presented in Figure 101 with higher magnification backscatter electron micrographs. After OM and SEM, a site-specific specimen for TEM/STEM was prepared using FIB-INLO. Figure 102 shows an ion beam generated secondary electron images from the TEM specimen preparation of APS TBCs by FIB-INLO technique: the specimen has been welded to a micromanipulator and lifted out.

In the as-coated type I TBC specimen, extensive presence of voids between YSZ and MCrAlY bond coat was observed as presented in Figure 103(a). The TGO consisted of agglomerated α-Al_2O_3 particles ~100 nm in size. Figure 102 also shows that the microstructure of type I APS YSZ coating does not have the typical columnar grains within splats and splat boundaries. No other types of oxide (e.g., Ni, Cr, Co containing oxides) were found as presented by HAADF image in Figure 103(b). In general, APS 7YSZ coatings consisted of non-equilibrium tetragonal (t') phase as presented in Figure 103(c) by the SADP, however SADP from retained cubic (f') phase was also observed as presented in Figure 97(d). SADP from agglomerated α-Al_2O_3 particles is presented in Figure 103(e). At localized regions where TGO has fully developed, atomic level bonding was observed at YSZ/TGO and TGO/bond coat interfaces as presented in Figure 104. These microstructural observations indicate that the integrity of type I APS TBCs, at least in as-coated condition, may be maintained significantly by "mechanical interlocking" with some adhesion by "atomic bonding."

In the as-coated type V TBC sample, interfacial void between YSZ and MCrAlY bond coat was largely filled with carbon (presumably from mounting epoxy) as seen in Figure 105(a). Also, TGO was completely absent. Figures 105(a) and (b) also show that the microstructure of type V APS YSZ coating consists of typical columnar grains within splats, and splat boundaries. APS 7YSZ consisted of non-equilibrium tetragonal (t') and/or retained cubic (f') phase as presented by the SADP in Figure 105(c).

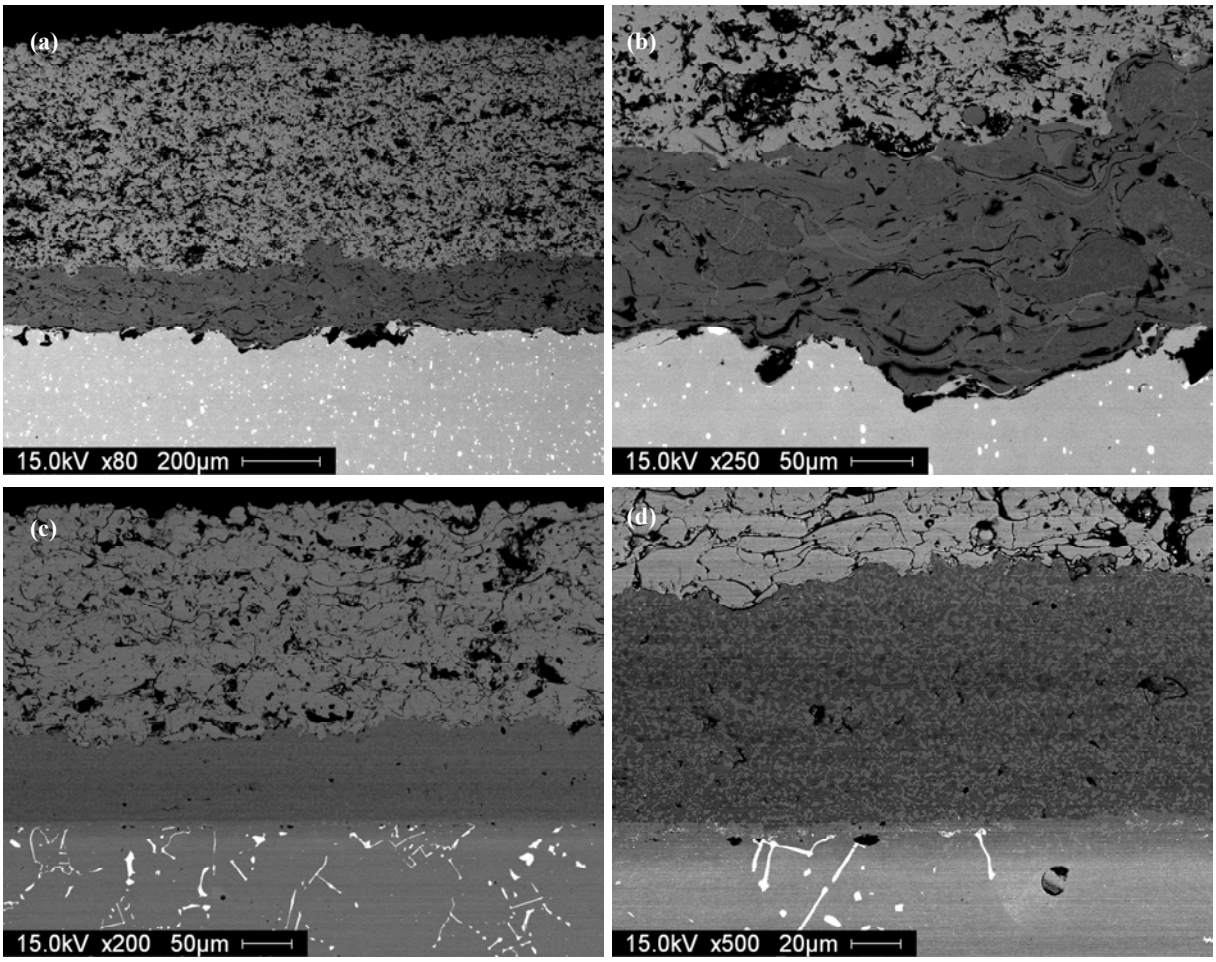

Figure 100. Typical backscatter electron micrographs of (a,b) type I and (c,d) type V APS TBCs specimens.

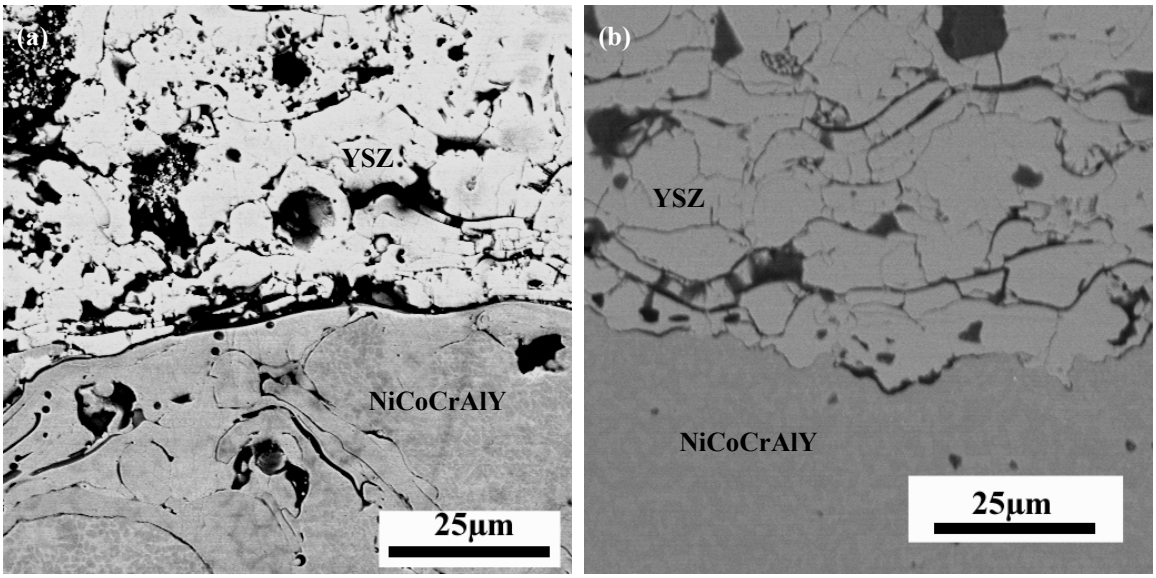

Figure 101. High magnification backscatter electron micrographs of (a) type I and (b) type V APS TBCs specimens.

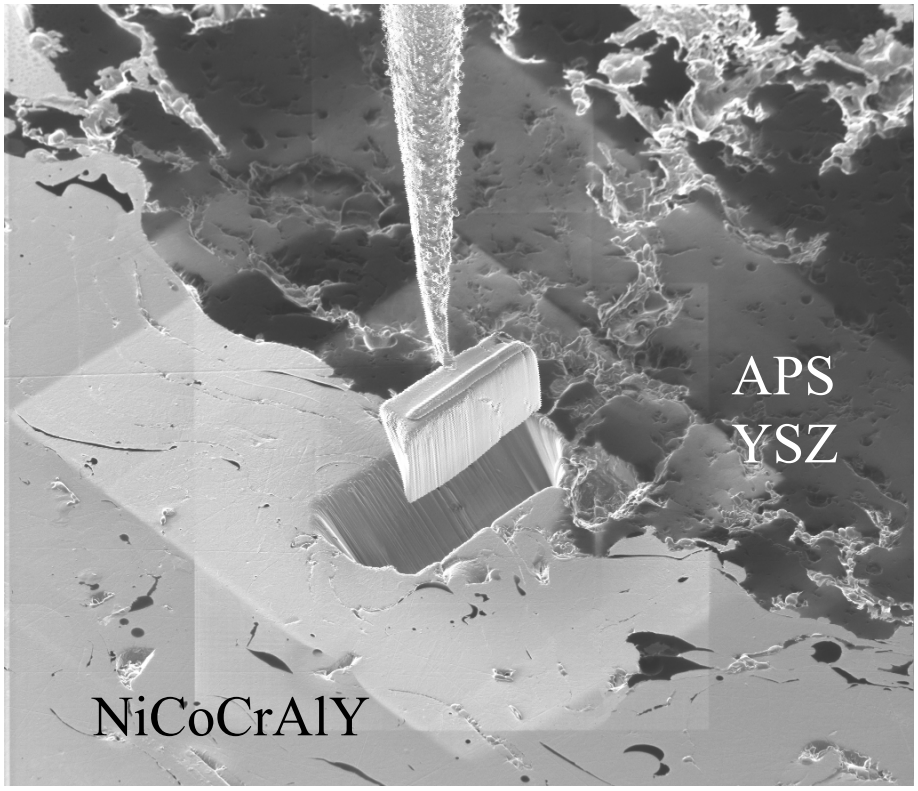

Figure 102. Secondary electron micrograph generated during FIB-INLO technique.

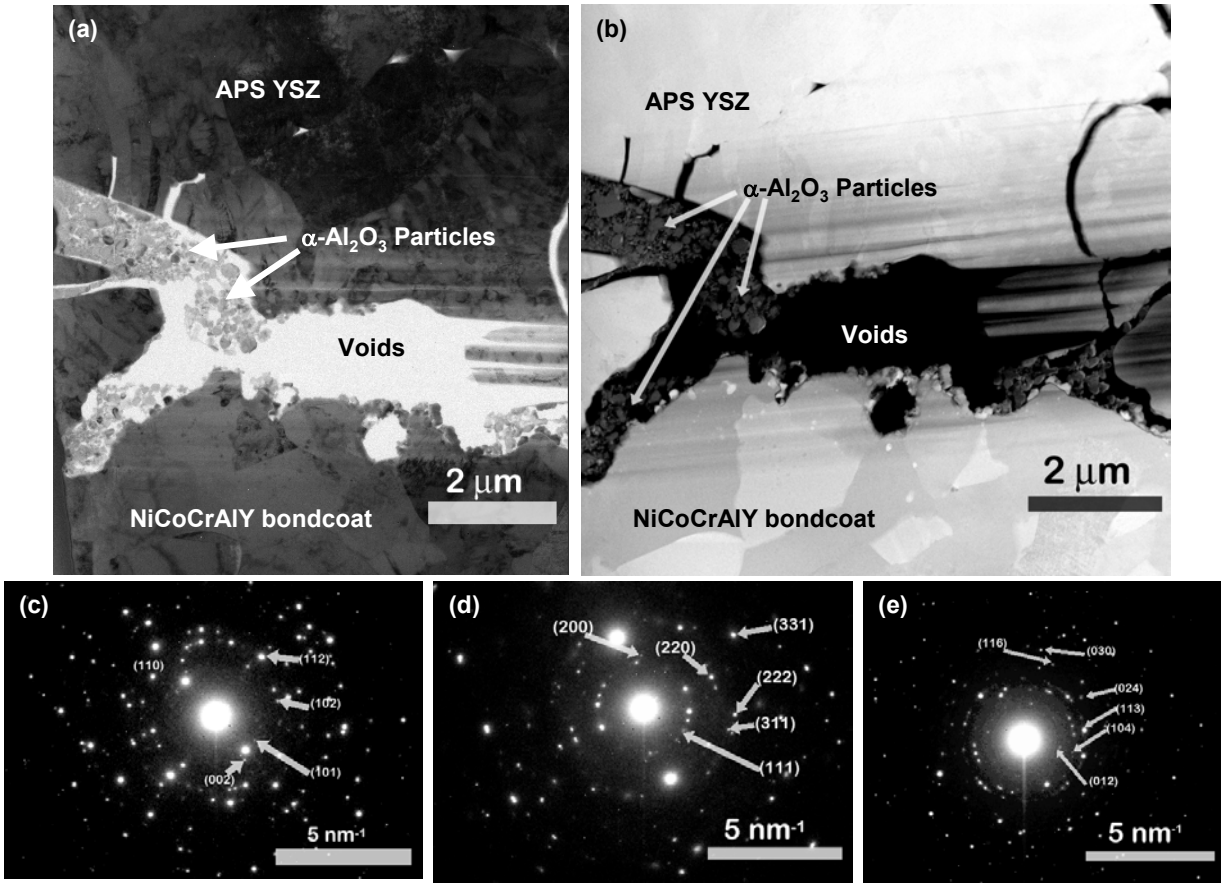

Figure 103.(a) Bright field and (b) HAADF micrograph of as-received type I APS TBC exhibiting extensive presence of voids, and TGO that consists of agglomerated α-Al_2O_3 particles (~100nm in size). (c,d) APS 7YSZ consisted of non-equilibrium tetragonal (t') and retained cubic (f') phase. (e) The agglomerated Al_2O_3 particles (~100nm in size) in TGO indexed to equilibrium α phase.

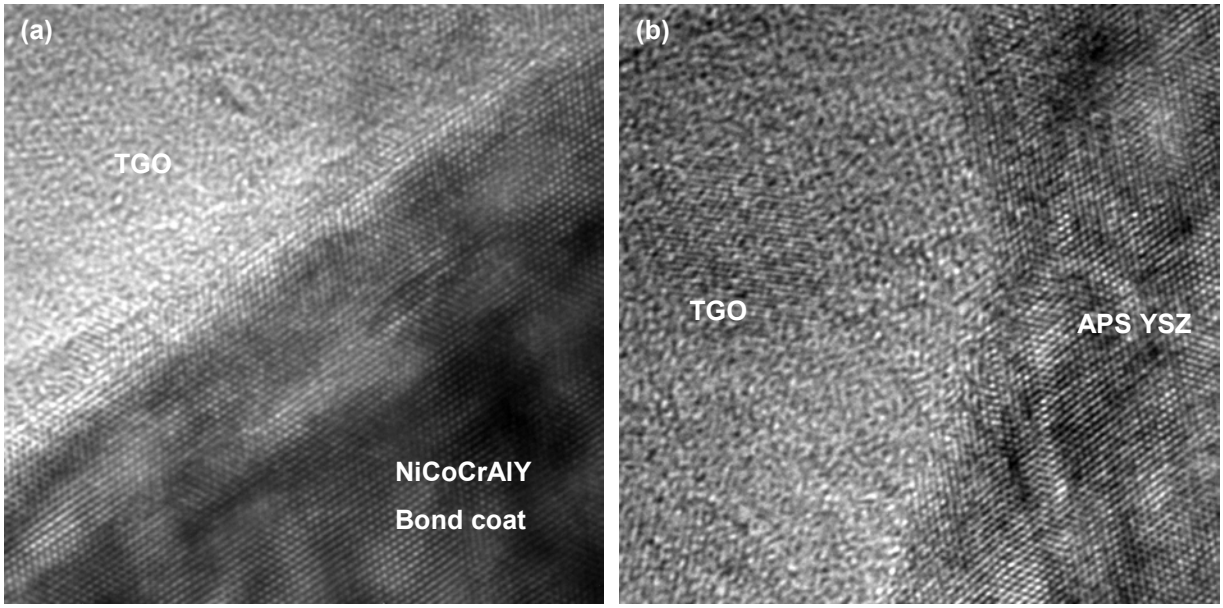

Figure 104. Bright-field lattice images showing intimate bonding at (a) TGO/bond coat and (b) YSZ/TGO interfaces. This atomic-level bonding was *not* frequently observed due to extensive presence of voids as presented in Figure 97(a).

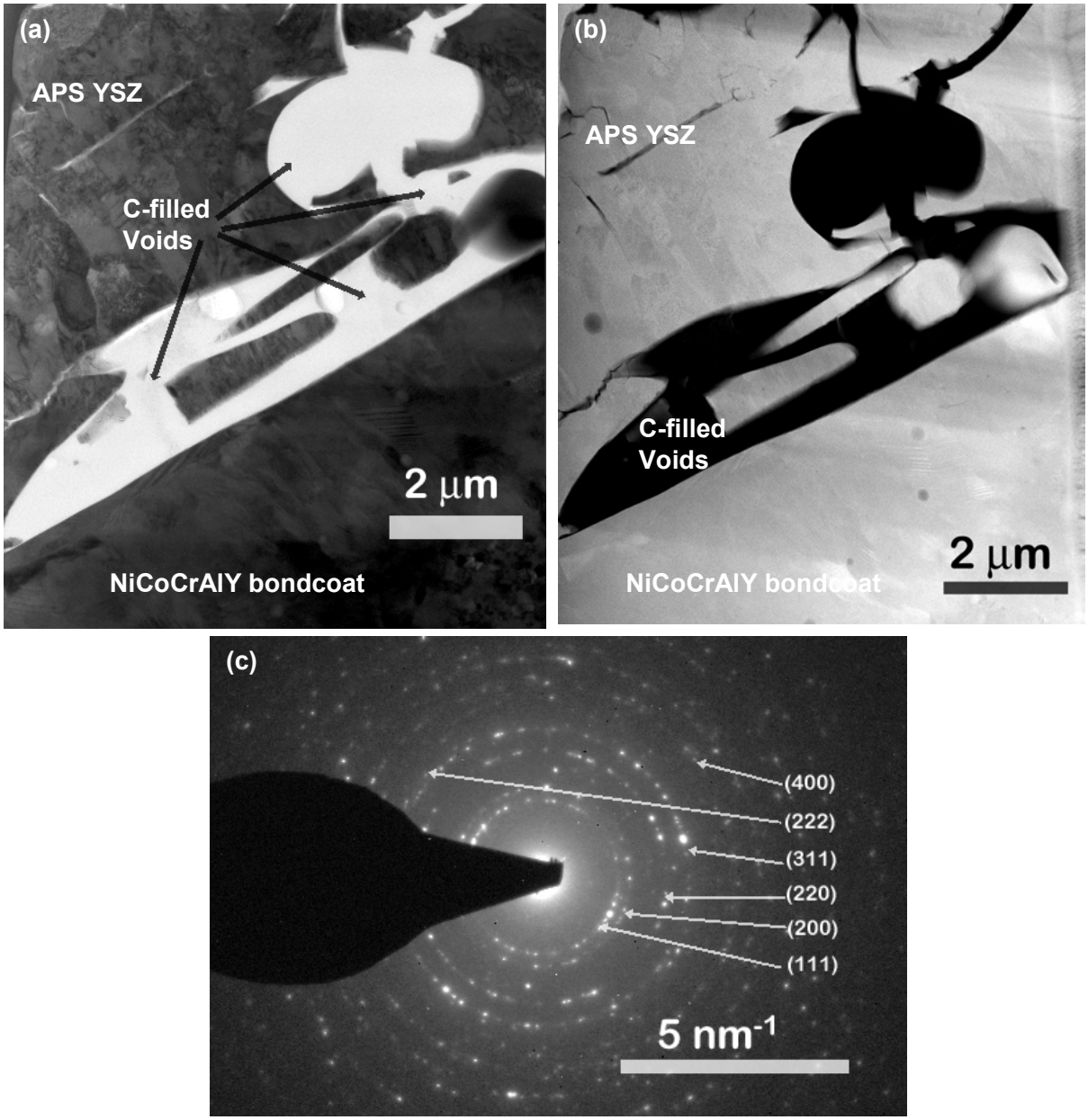

Figure 105. (a) Bright field and (b) HAADF image of as-coated type V APS TBC exhibiting extensive presence of carbon-filled voids, absence of TGO, and conventional columnar YSZ grains within splats. (c) SADP demonstrated that the APS 7YSZ consisted of non-equilibrium tetragonal (t') and/or retained cubic (f') phase.

V.4.2. Thermally Cycled Type I and V Air Plasma Sprayed Thermal Barrier Coatings

Figures 106, 107 and 108 represents typical backscatter electron images of type I APS TBCs as a function of 1-10 and 50-hours thermal cycling. Clearly there is a growth of the TGO scale with thermal cycling. In addition, there is an extensive internal oxidation of bond coats for this type I TBCs. The internal oxidation observed are parallel to the YSZ/bond coat interface, presumably following the splat boundaries of the NiCoCrAlY bondcoat, and mainly consists of Al-rich oxides (presumably α-Al_2O_3). A similar trend is also observed for 10 and 50 hour thermal cycles as reported in Tables X through XI. Abrupt changes [26] associated with C_{TGO} are not observed since the failure of type-I APS TBC occurs within the YSZ near the YSZ/TGO interface as shown in Figure 106(e) and 107(c). With progressive thermal cycling for various dwell the R_{YSZ} and C_{YSZ} increased and decreased as shown in Figures 86 and 89. This is because of YSZ sintering that take place at high temperature, and can be observed with progressive thermal cycling dwell time as shown in Figures 109 and 110. Also in Figure 86 the magnitude of R_{YSZ} for 1-hour thermal cycling is higher compared to that of 10 and 50-hour thermal cycles this is because of the effect of sub-critical damages that are seen as micro cracks in Figure 110 for 10 and 50-hour thermal cycles.

With the growth of TGO the R_{TGO} and C_{TGO} as shown in Figure 88 and 89 increased and decreased for 1, 10 and 50-hour thermal cycling. With progressive thermal cycling in case of 10 and 50-hour thermal cycles there is significant amount of damages at the YSZ/TGO interface as shown in Figures 107 and 108. These damages are observed around oxides rich in (Ni,Co)Cr commonly referred as spinals. Because of these damages the impedance response from 10-hour and 50-hour thermal cycles samples was less compared to that of 1-hour thermal cycles as shown in Figure 85.

Extensive presence of voids and cracks in the mixed oxide zone (MOZ) between the continuous TGO and the YSZ topcoat was observed for type I TBCs after 10% of its lifetime thermal cycling as shown in Figure 110 (a) and (b). In the BF and HAADF TEM images shown in Figure 110(a) and (b), the TGO on the type I TBC specimen contained Ni/Co-rich oxides at the interface between the YSZ/TGO. This Ni/Co rich oxides continued to grow with further thermal cycling which can be seen in Figure 110 (c) and (d). In general, the topcoat and the MOZ, and the MOZ within the TGO scale contained Y rich particles dispersed throughout the TGO. It is further observed at 70% thermal cycling life time there were extensive cracks/voids at YSZ/TGO interface, cracks within the TGO and voids at near the TGO/bondcoat interface.

As shown in Figure 111, extensive void formation in the interface between the TGO and Ni/Co oxides were observed. Further it is observed that Ca segregated in the phase interfaces and chromium oxide segregated in the regions near to the bondcoat in the TGO. In addition several Zr rich islands were observed dispersed on a Ti rich oxide matrix near to the carbon filled void in the type 1 APS TBC.

Figure 112 represents typical backscatter electron micrographs of thermally cycled type-V APS TBCs. Clearly there is a growth of TGO with thermal cycling. These

microstructural changes can related to the EIS NDE results presented in Figures 88 through 89.

EIS response for this type-V TBCs compared to the other types of TBCs was distinctively different. The R_{TGO} increased initially corresponding to the growth of the TGO that can be seen in Figure 112. However, the C_{TGO} increased continuously with thermal cycling. This can be related to the TGO scale cracking with thermal cycling that was observed as shown in Figure 113. The EIS results for R_{YSZ} and C_{YSZ} presented in Figures 64 and 65 can be related to the sintering behavior of the YSZ as shown in Figure 116. Figure 115 shows the microstructural evolution with respect to 10-hour thermal cycling. EIS measurements were not carried on these samples because of premature failure observed after thermal cycling.

In the thermally cycled type-V TBC specimen, development of a mixed oxide zone was observed after the thermal cycling that corresponds to the 10% of its lifetime as presented in Figure 117. It is further observed that the MOZ consisted of numerous voids and micro-cracks; however the TGO beneath the MOZ is dense, columnar and continuous as presented in BF TEM image in Figures 117(b) and (c). The MOZ consisted of Zr and Al oxide particles as observed in the HAADF image in Figure 113(b). Furthermore, large islands of oxides very rich in Y/Al were observed within the TGO scale as shown in Figure 117 (c). The diffraction phase analyses of these Y/Al rich oxides revealed that the lattice parameter is greater than 18 angstroms. The phase identification of these particles is currently in progress.

Development of microstructure for type V APS TBCs, after 50% thermal cycling lifetime is shown in Figure 118. This shows a splat YSZ morphology that is different from the YSZ morphology as discussed earlier with type-I APS TBCs.

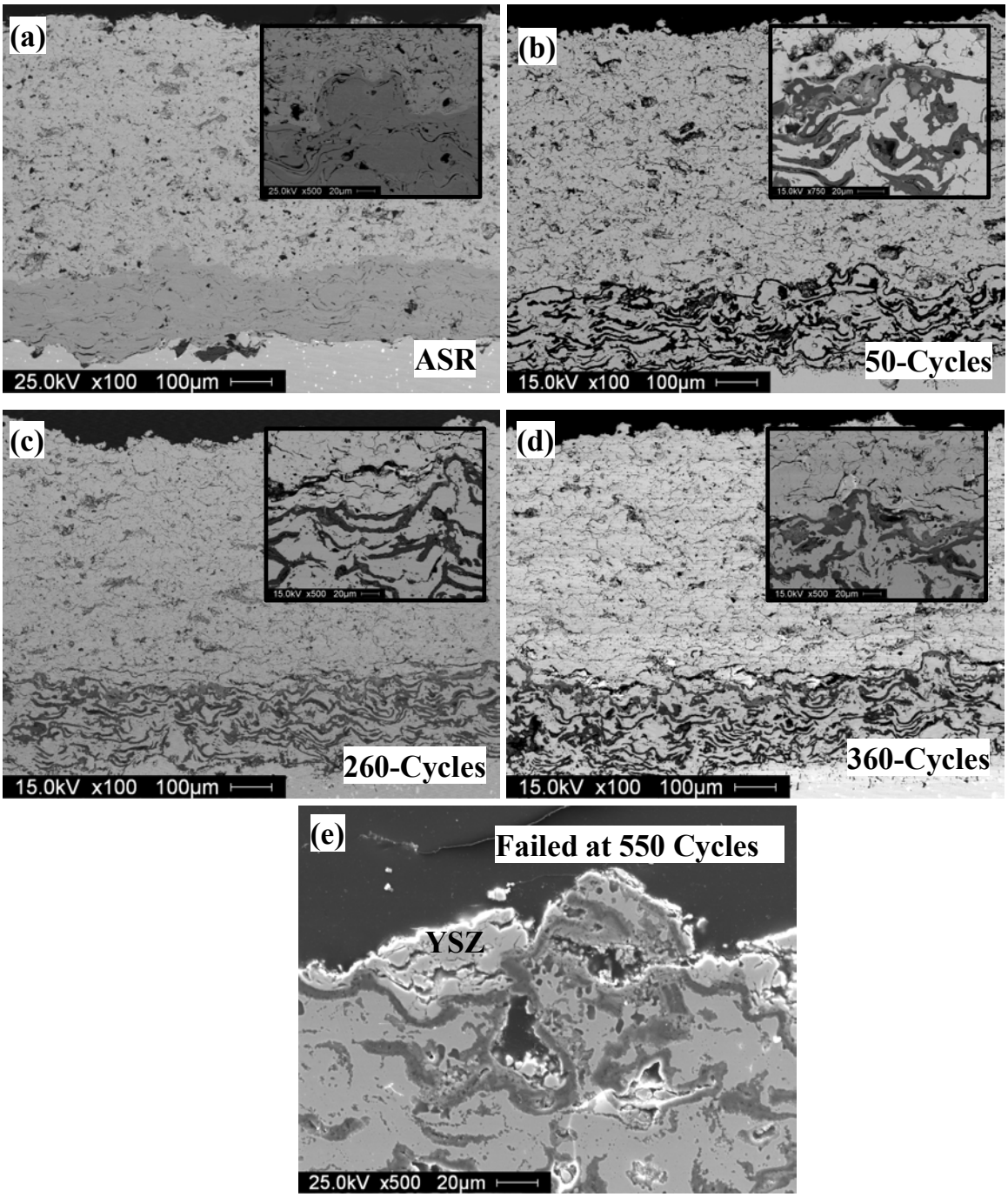

Figure 106. Typical backscatter electron micrographs of type I APS TBCs specimens with progressive 1-hour thermal cycles.

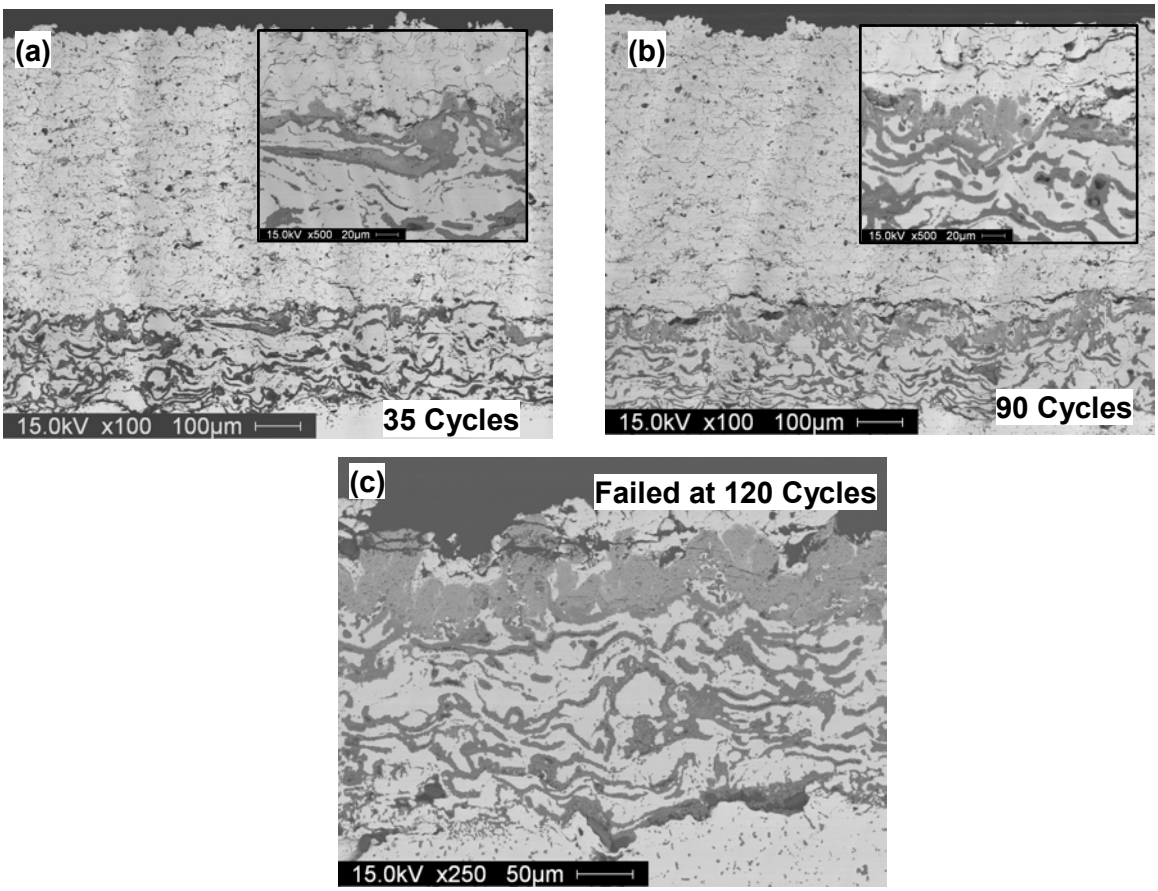

Figure 107. Typical backscatter electron micrographs of type I APS TBCs specimens with progressive 10-hour thermal cycles.

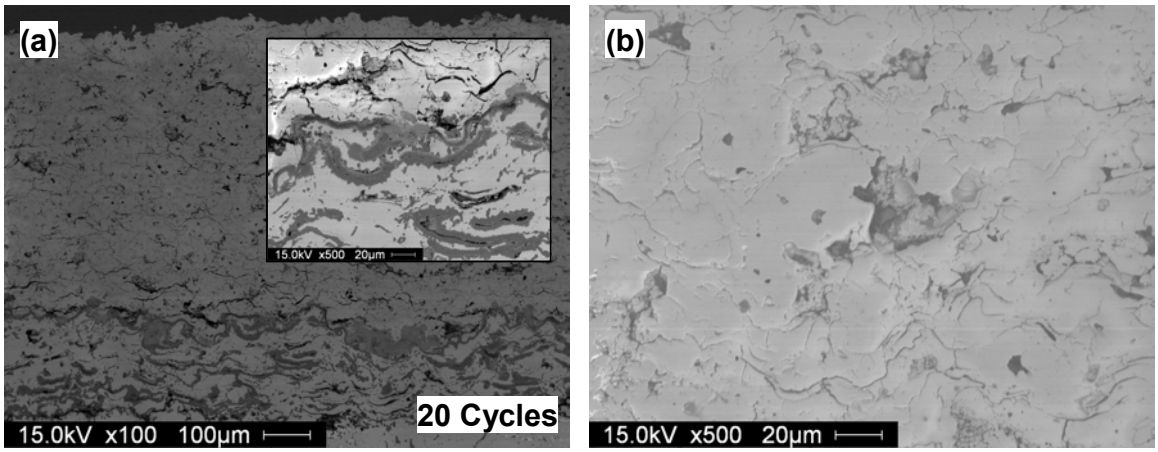

Figure 108. (a) Typical backscatter electron micrographs of type I APS TBCs specimens at 20 cycles (50-hour thermal Cycles) (b) BSE image of YSZ.

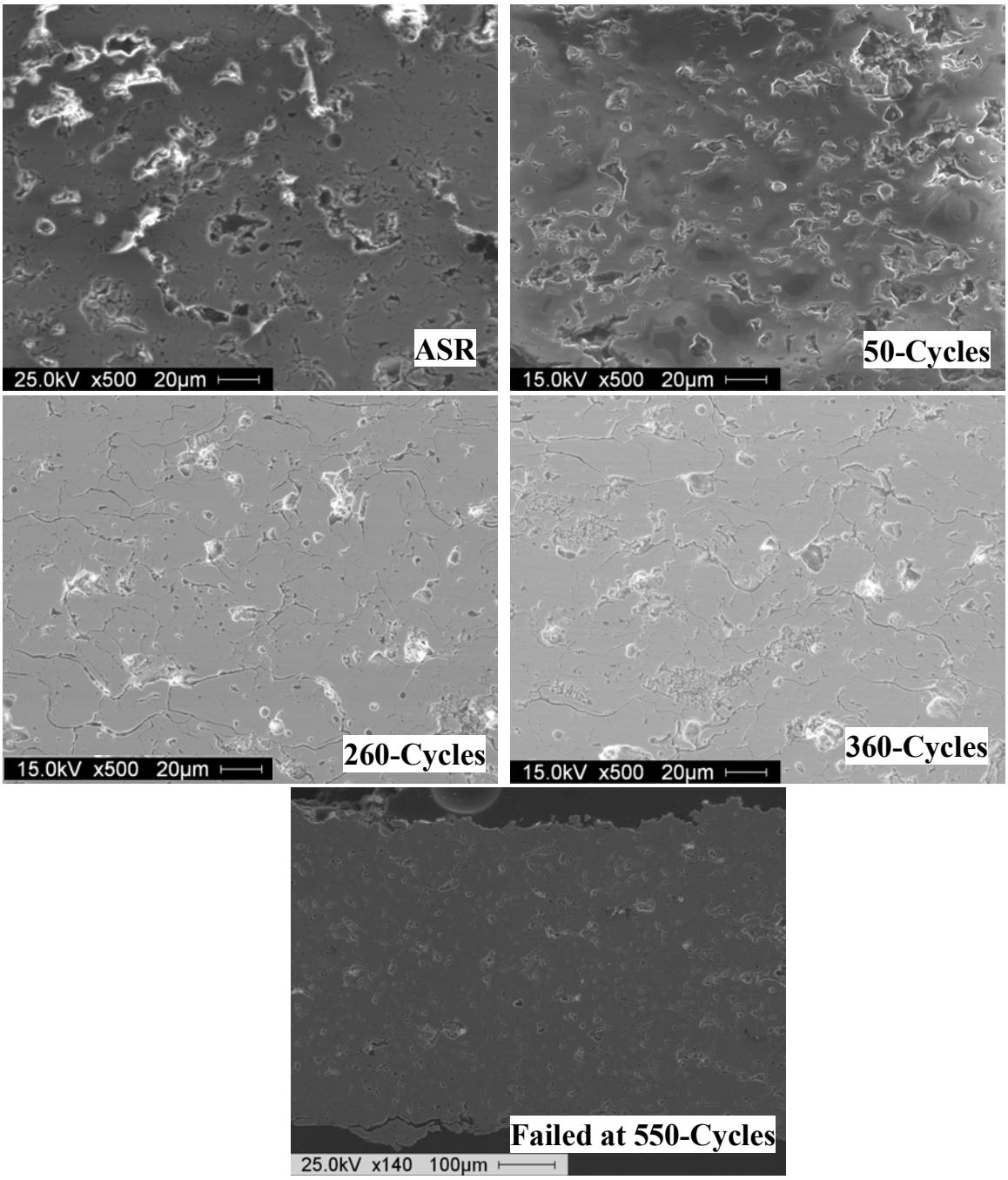

Figure 109. Secondary electron micrographs of type-I APS TBCs YSZ showing sintering/micro cracking behavior with progressive 1-hour thermal cycling.

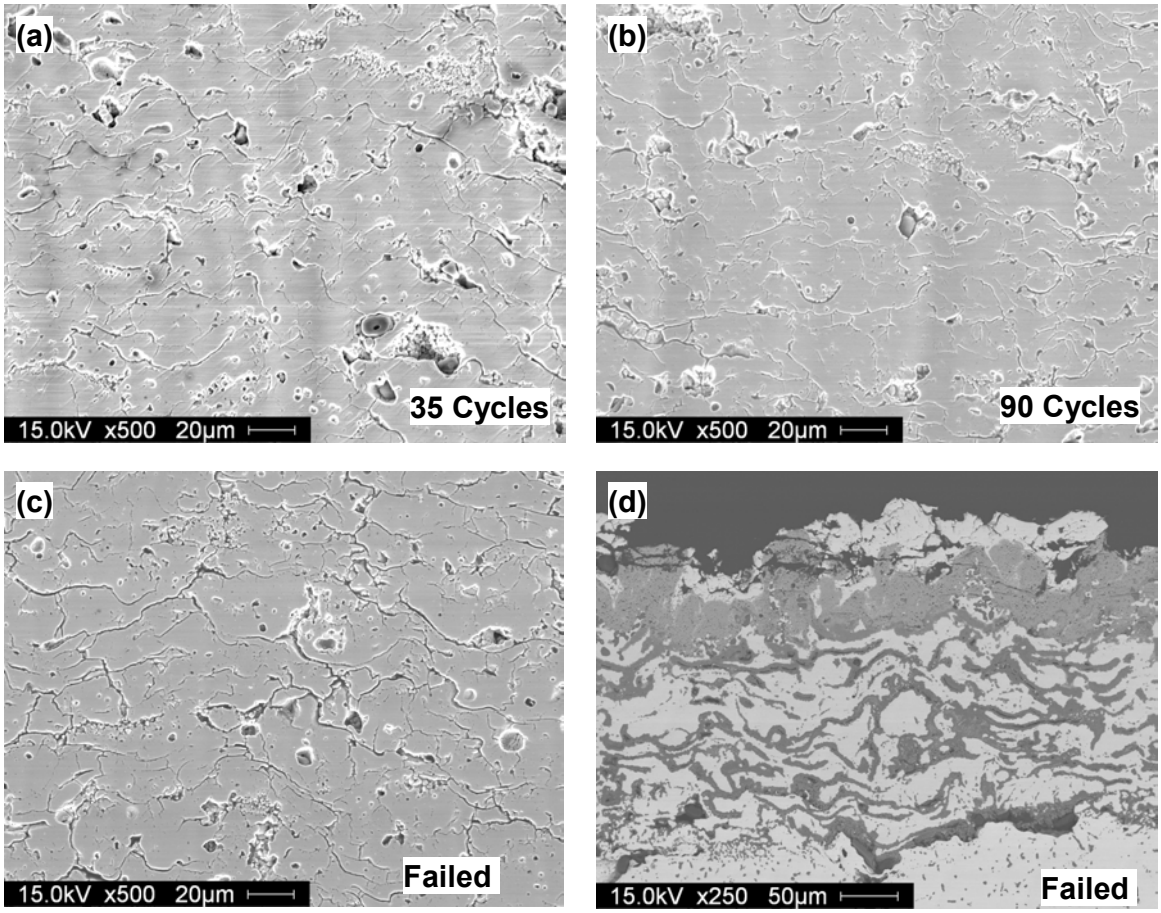

Figure 110. (a,b,c) Secondary electron micrographs of type-I APS TBCs YSZ showing sintering/micro cracking behavior with progressive 10-hour thermal cycling (d) back scatter electron micrograph of the cross section of bondcoat after YSZ spallation.

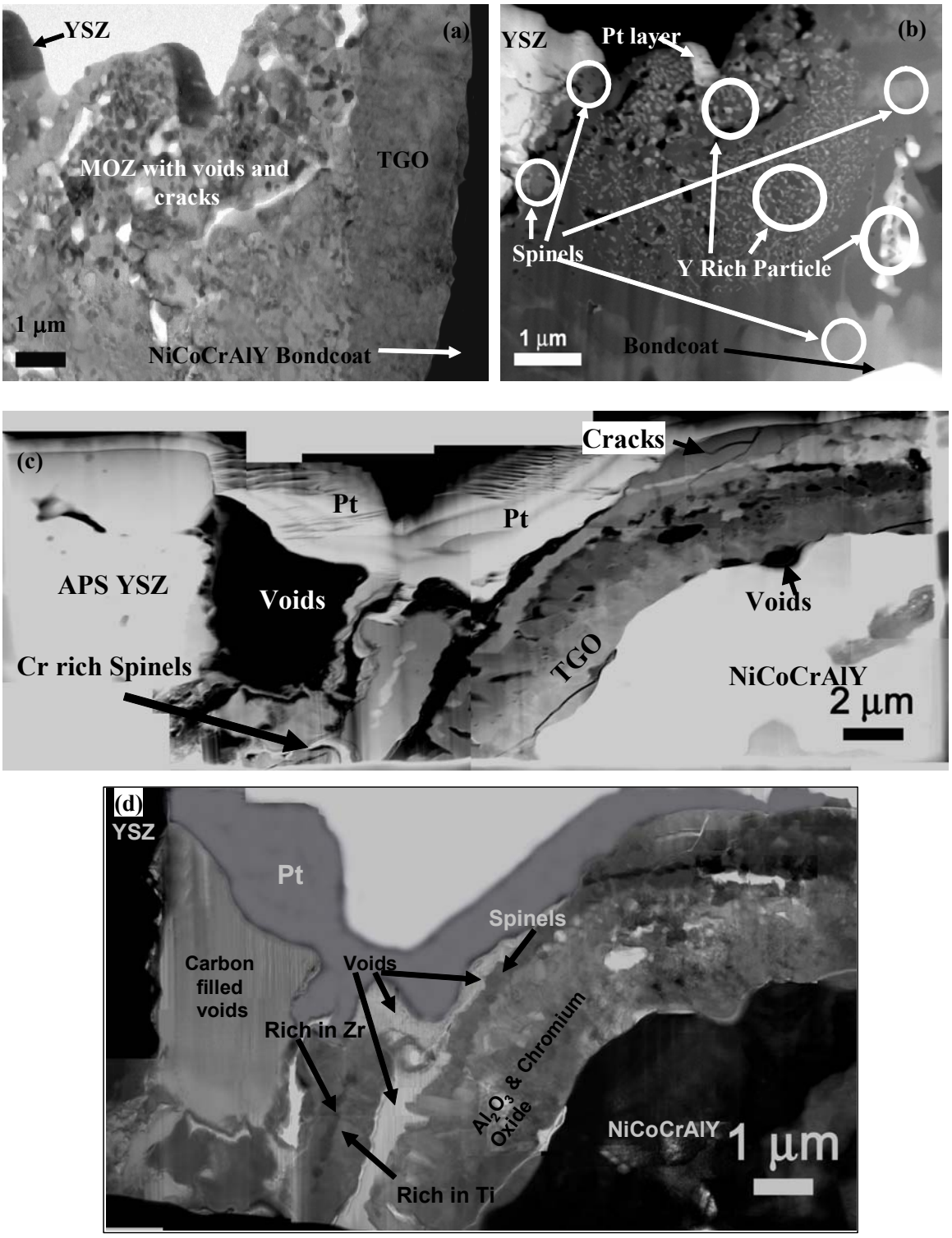

Figure 111. TBC specimen type I after thermal cycling (a) BF TEM and (b) HAADF STEM images after 10% lifetime (c) HAADF STEM images and (d) BF TEM after 70% lifetime.

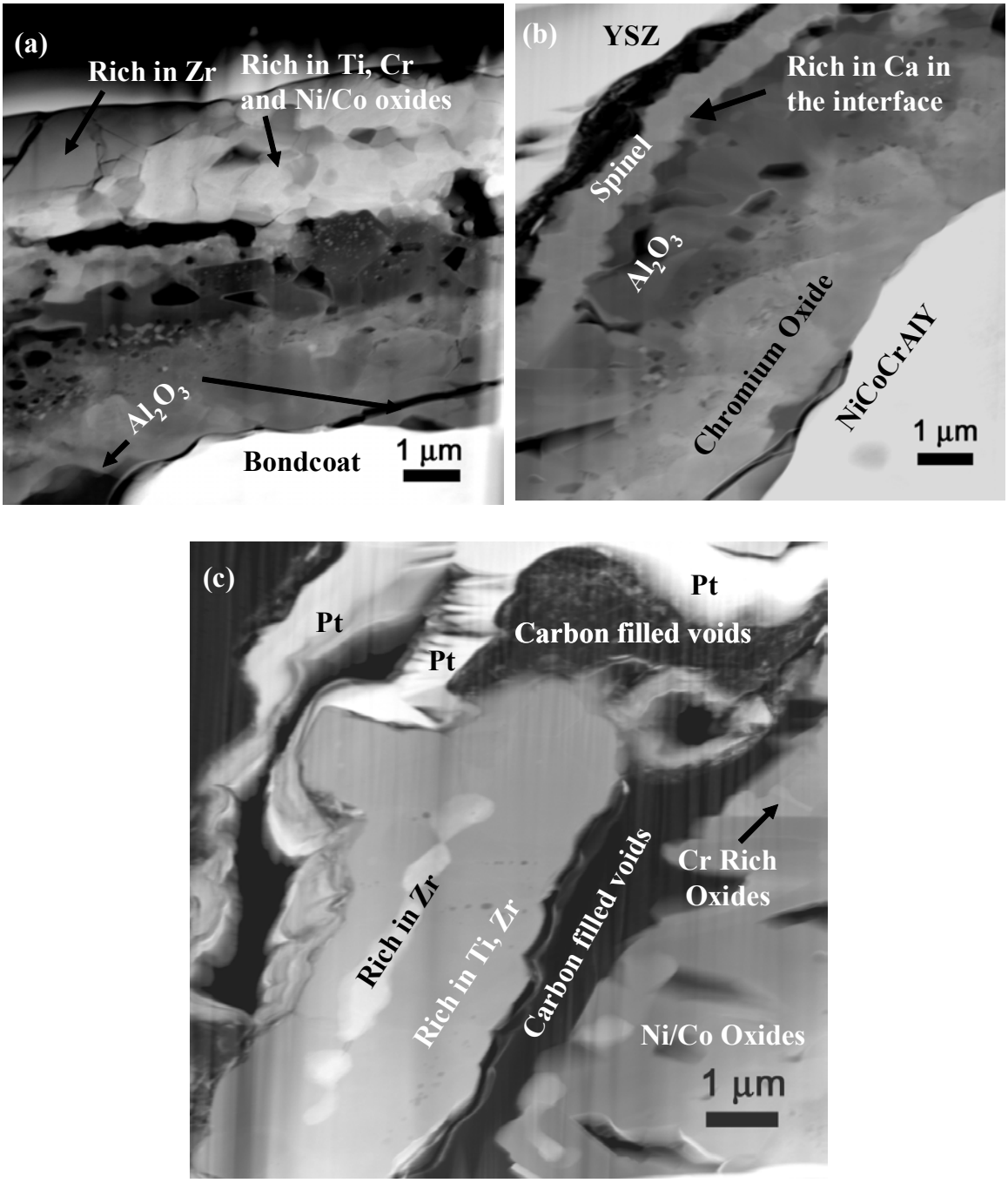

Figure 112. Higher magnification HAADF STEM images of type-I APS TBCs after 70% 1-hour thermal cyclic lifetime.

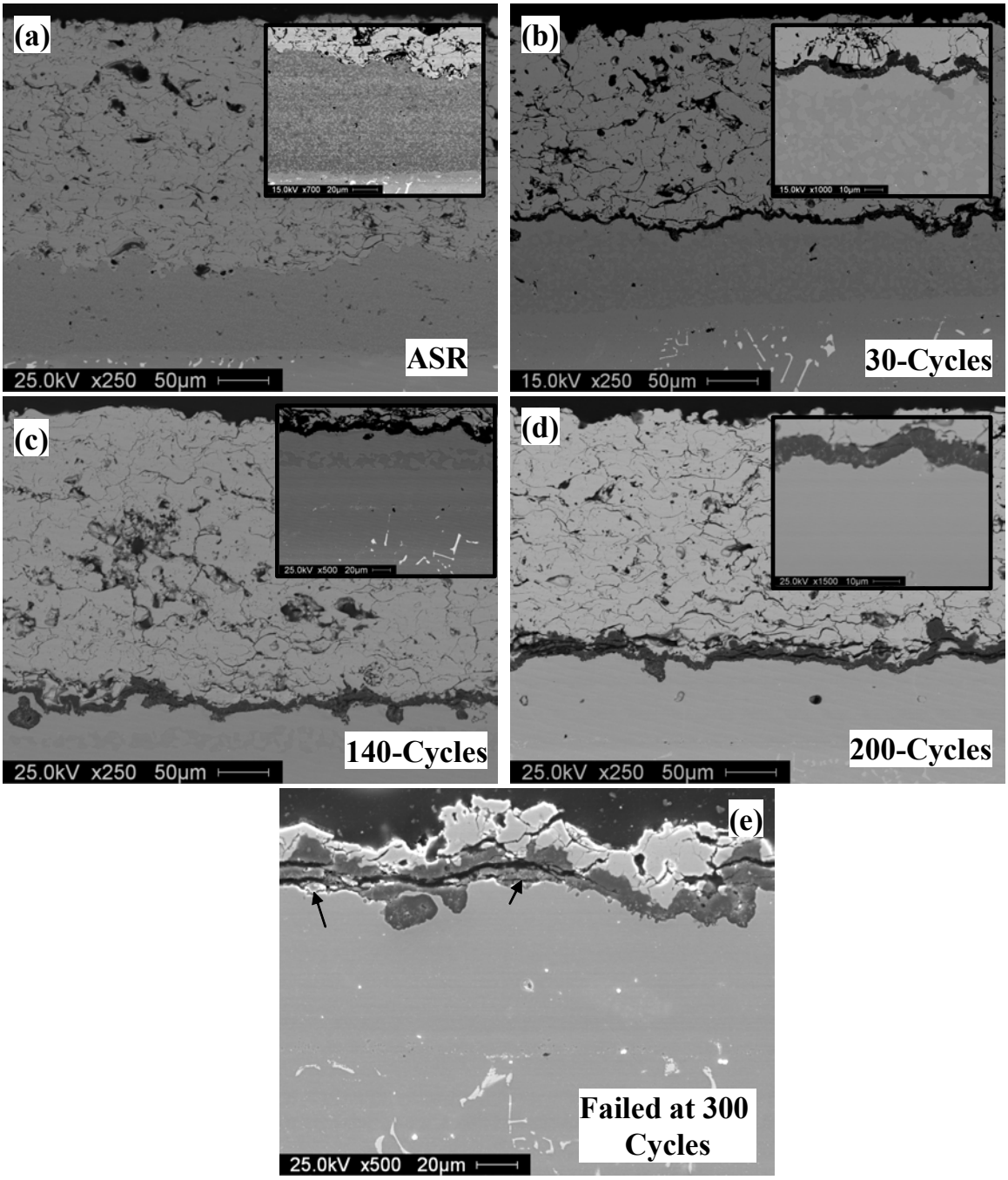

Figure 113. Typical backscatter electron micrograph of type-V APS TBCs with progressive thermal cycling.

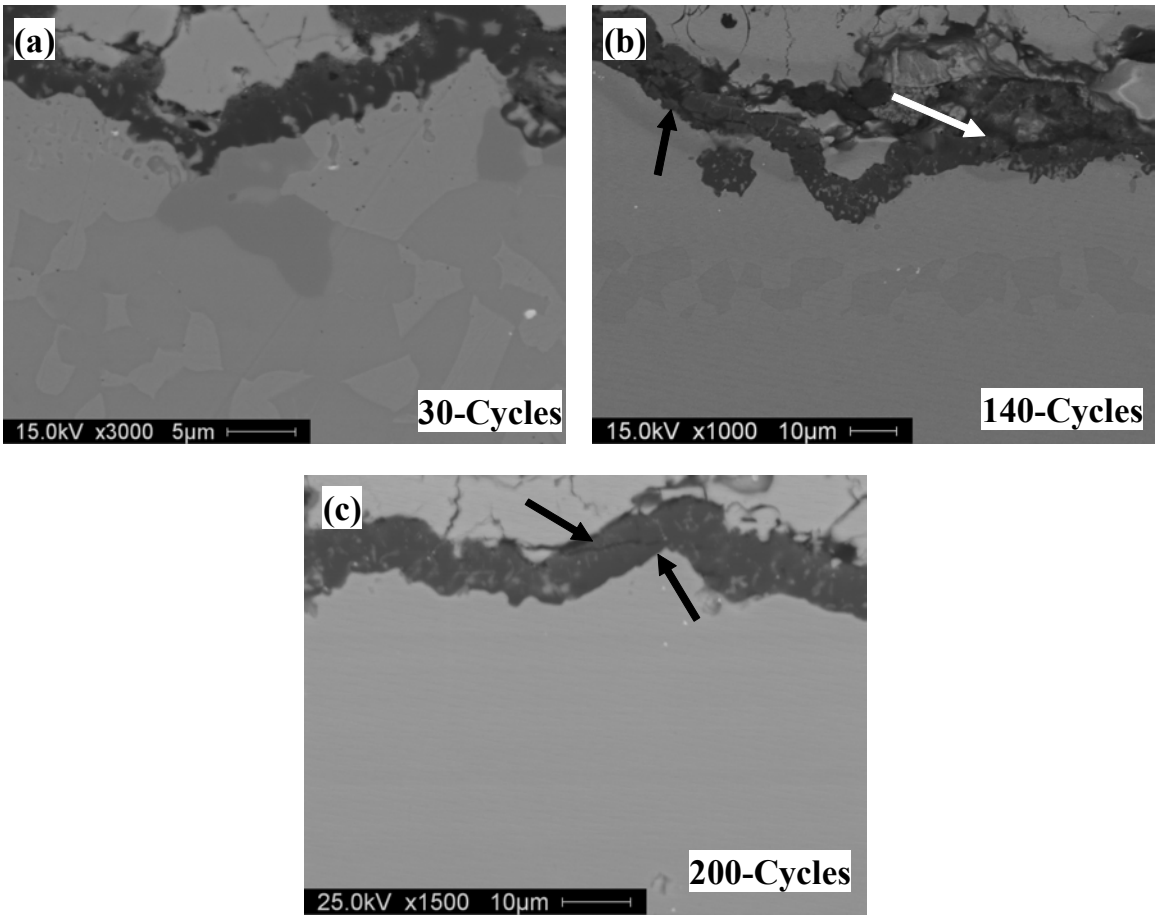

Figure 114. Typical backscatter electron micrographs for type-V showing the TGO scale cracking with 1-hour thermal cycling but the TBC remained intact.

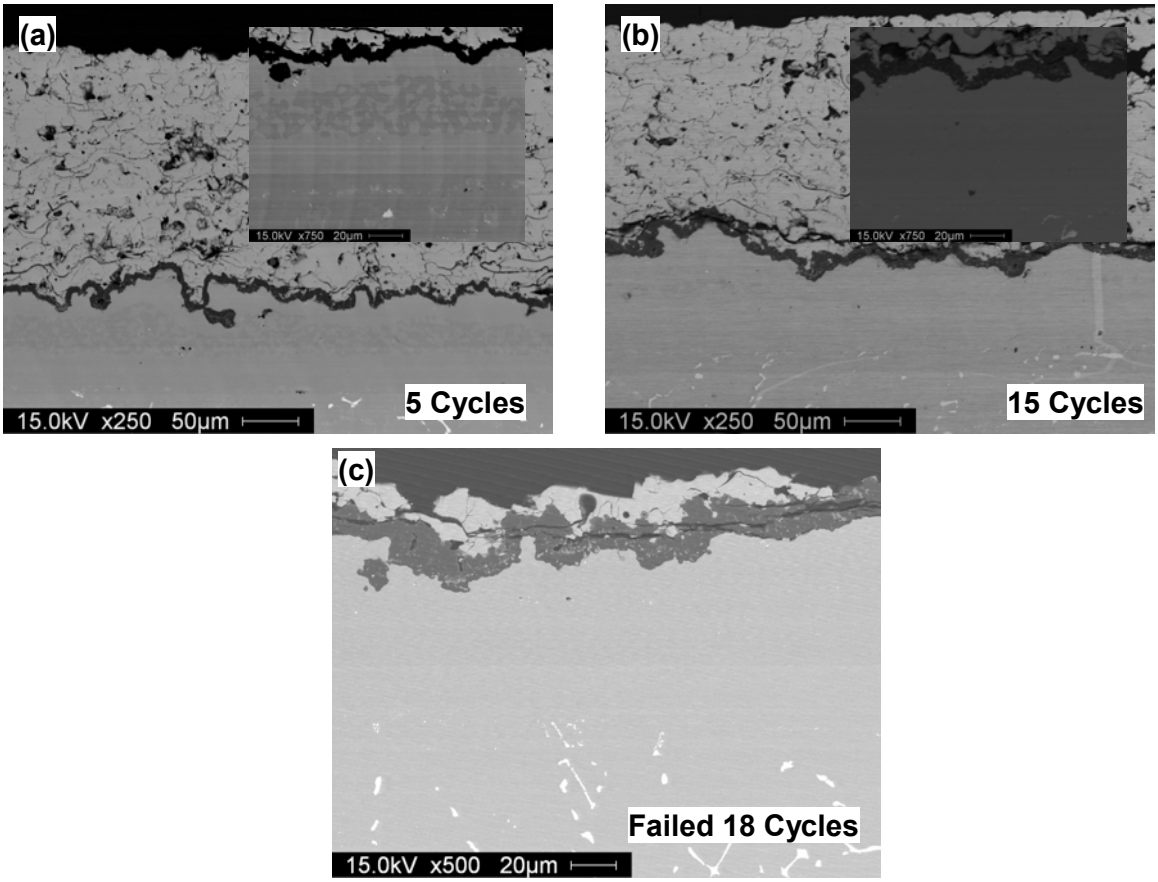

Figure 115. Typical backscatter electron micrograph of type-V APS TBCs with progressive 10-hour thermal cycling.

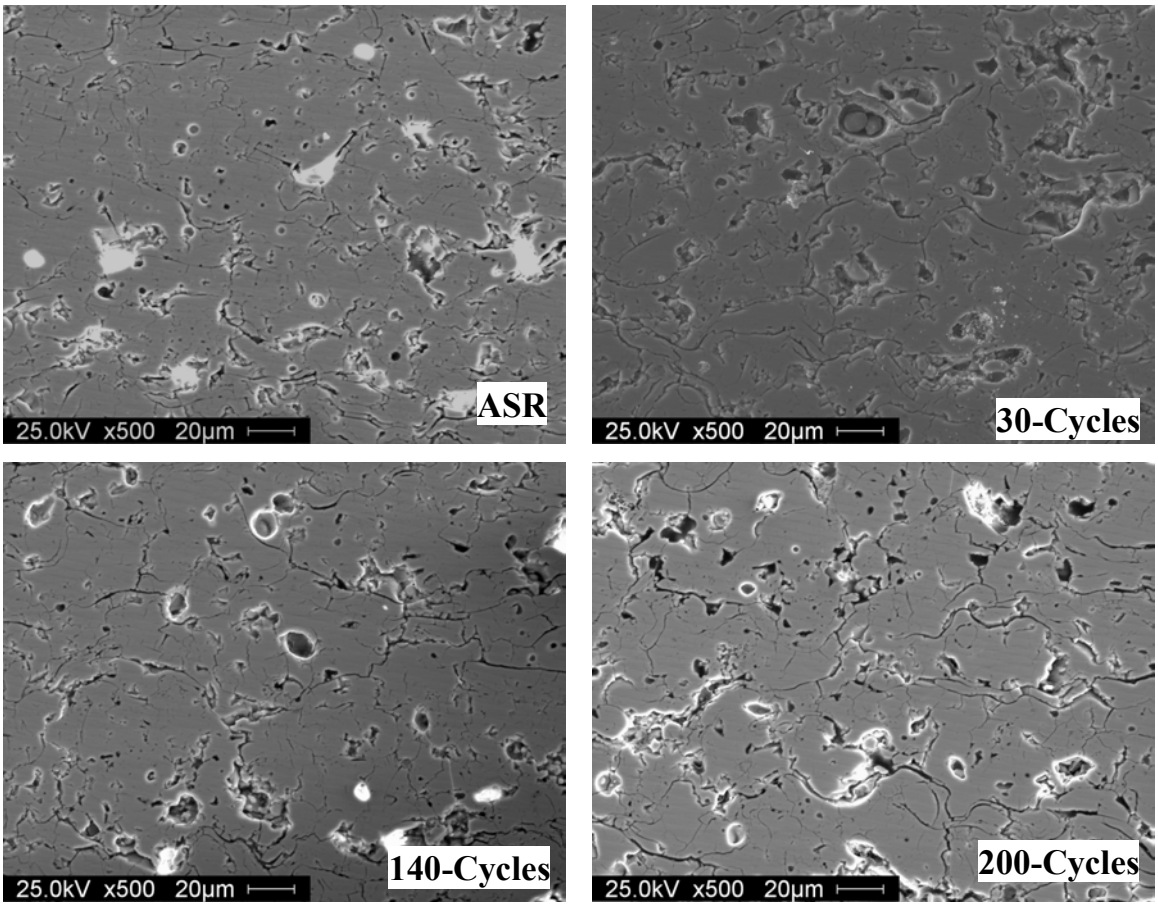

Figure 116. Secondary electron micrographs of type-V APS TBCs showing the sintering/micro cracking behavior within the YSZ with progressive 1-hour thermal cycling.

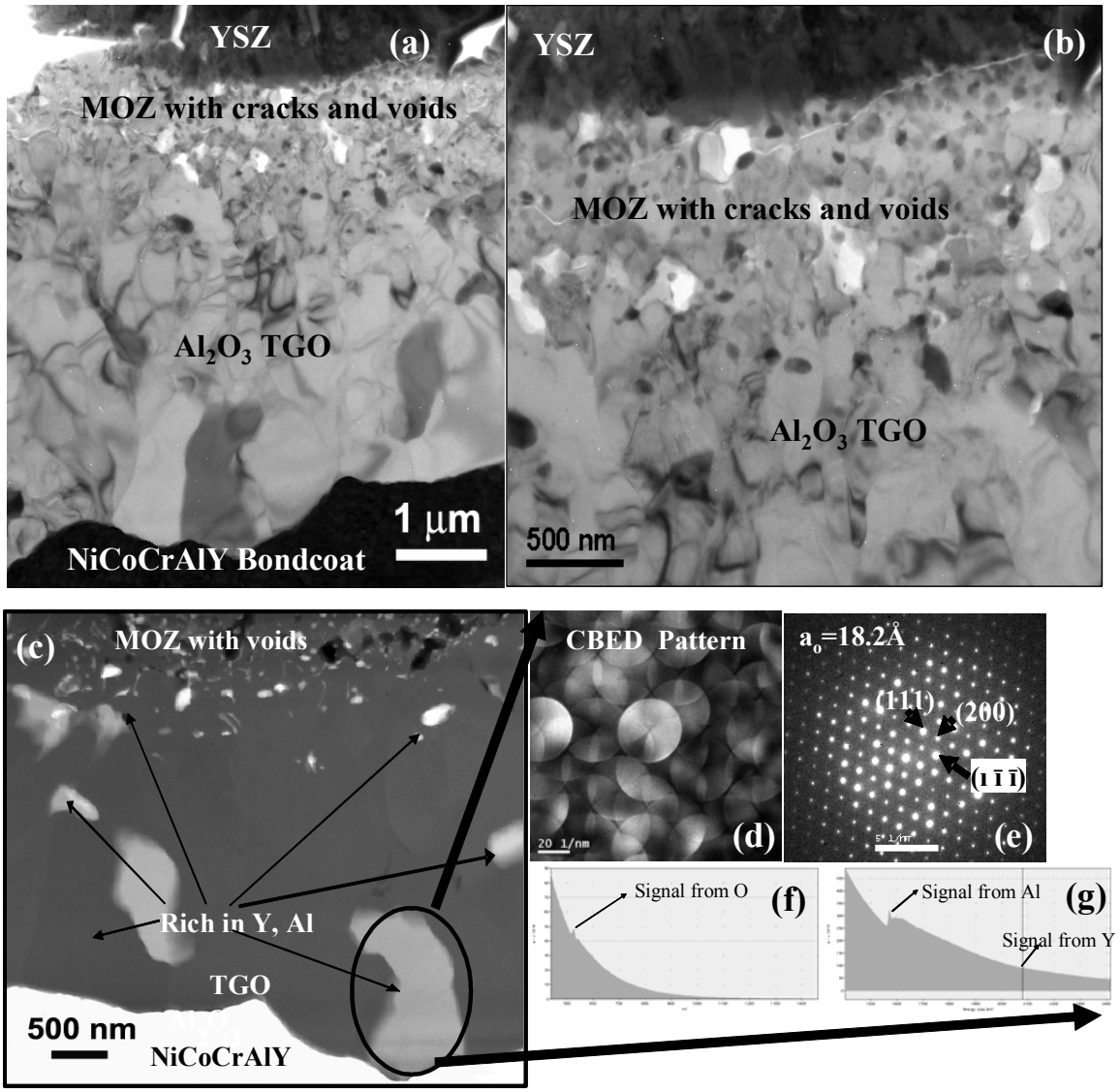

Figure 117. Bright field TEM image of type-V TBCs after 10% thermal cycling lifetime (a) presence of MOZ with cracks and voids near the YSZ/TGO interface and a dense-columnar-continuous Al_2O_3 TGO near the bond coat. (b) MOZ with cracks and voids near the YSZ/TGO interface, and (c) HAADF STEM image showing Y and Al rich oxides and a MOZ near to YSZ topcoat (d) Convergent Beam Electron Diffraction (CBED) pattern from the Y rich oxide (d) SAD pattern from the same Y rich oxide showing a lattice parameter > 18 Å and (f,g) EELS spectra from the same Y rich oxide.

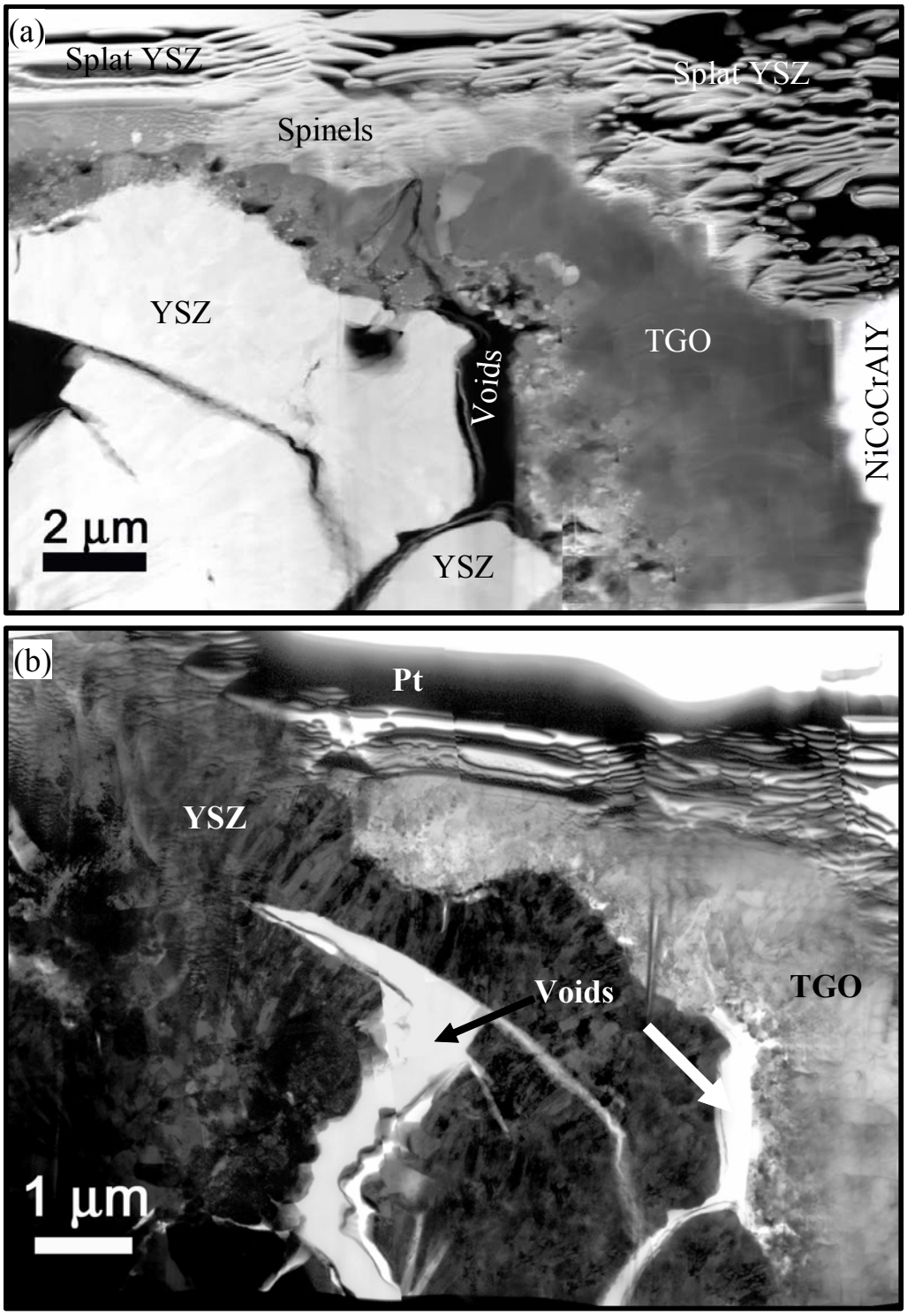

Figure 118. TEM images from type-V TBCs after 50% thermal cyclic lifetime (a) HAADF STEM image showing splat YSZ and voids at YSZ/TGO interface (b) Bright Field TEM image showing the same.

V.4.3. As-coated Electron Beam Physical Vapor Deposited Thermal Barrier Coatings

Figure 119 presents backscatter electron micrographs of the as-coated type II, III and IV EB-PVD TBCs. The specimens conformed to the specification described in Table II. All three types of EB-PVD YSZ coatings exhibited strain-tolerant columnar microstructure.

For all TBCs, a thin TGO layer was observed in the as-received condition as presented in Figures 119 and 120. Morphology of interface between YSZ and bond coat, where a thin TGO exists, was slightly different presumably due to the surface-finish treatment of bond coats. For type II TBC, a shot-peened NiCoCrAlY surface exhibited roughness and irregularity (ranging from ~5μm to less than 1μm) including sharp peaks and troughs as presented in Figures 120(a) and (b). The as-coated (Ni,Pt)Al bond coat for type III TBCs exhibited smooth interface except for the ridges associated with the bond coat grain boundaries as shown in Figure 120(c). The grit-blasted (Ni,Pt)Al bond coat for type IV TBCs exhibited rough and irregular interface where ridges associated with the bond coat grain boundaries have been removed as presented in Figure 120(d). For all TBCs, no significant amount of embedded oxide was observed.

After OM and SEM, the site-specific specimen was prepared for HR-STEM using FIB-INLO. In as-coated type II TBC, a continuous TGO layer was observed without a significant presence of "mixed-oxide" layer as seen in Figure 121. The SADP, inset of Figure 121(a) demonstrated that the EB-PVD 7YSZ consisted of non-equilibrium tetragonal (t') and/or retained cubic (f') phase.

In the as-coated type III TBC, a continuous TGO layer was observed along with patches of "mixed-oxide" layer as seen in Figure 112. Regions in the TGO with "mixed-oxide" were always thicker (~0.5μm) than those consisting of continuous α-Al_2O_3 layer (~0.1μm) as presented by Figure 122(b). Based on n-EDS and EELS, the "mixed-oxide" layer consisted of oxides containing primarily Al, Zr, Y and Ni with traces of Cr, Co and Mo. SADP presented in Figure 122(c) demonstrate that the EB-PVD 7YSZ consisted of non-equilibrium tetragonal (t') and/or retained cubic (f') phase. SADP in Figure 112(d) from TGO indexes to α-Al_2O_3. High magnification HAADF image of the "mixed oxide" layer is presented in Figure 123.

Relative to type III TBCs, the microstructure of type IV EB-PVD TBC specimen presented in Figure 124 exhibited many distinctive features including (1) larger intercolumnar voids, (2) more feathery YSZ columns, (3) thinner Al_2O_3 TGO without a "mixed-oxide" layer, (4) large residual α-Al_2O_3 particles from grit blasting, and (5) smaller β-(Ni,Pt)Al grains. The as-deposited YSZ consisted of non-equilibrium tetragonal (t') and/or retained cubic (f') phase as presented in Figure 124(c). The TGO scale primarily consisted of α-Al_2O_3 as presented by FFT diffractogram in Figure 125. A secondary and backscatter electron micrographs showing the residuals from grit-blasting are presented in Figure 126.

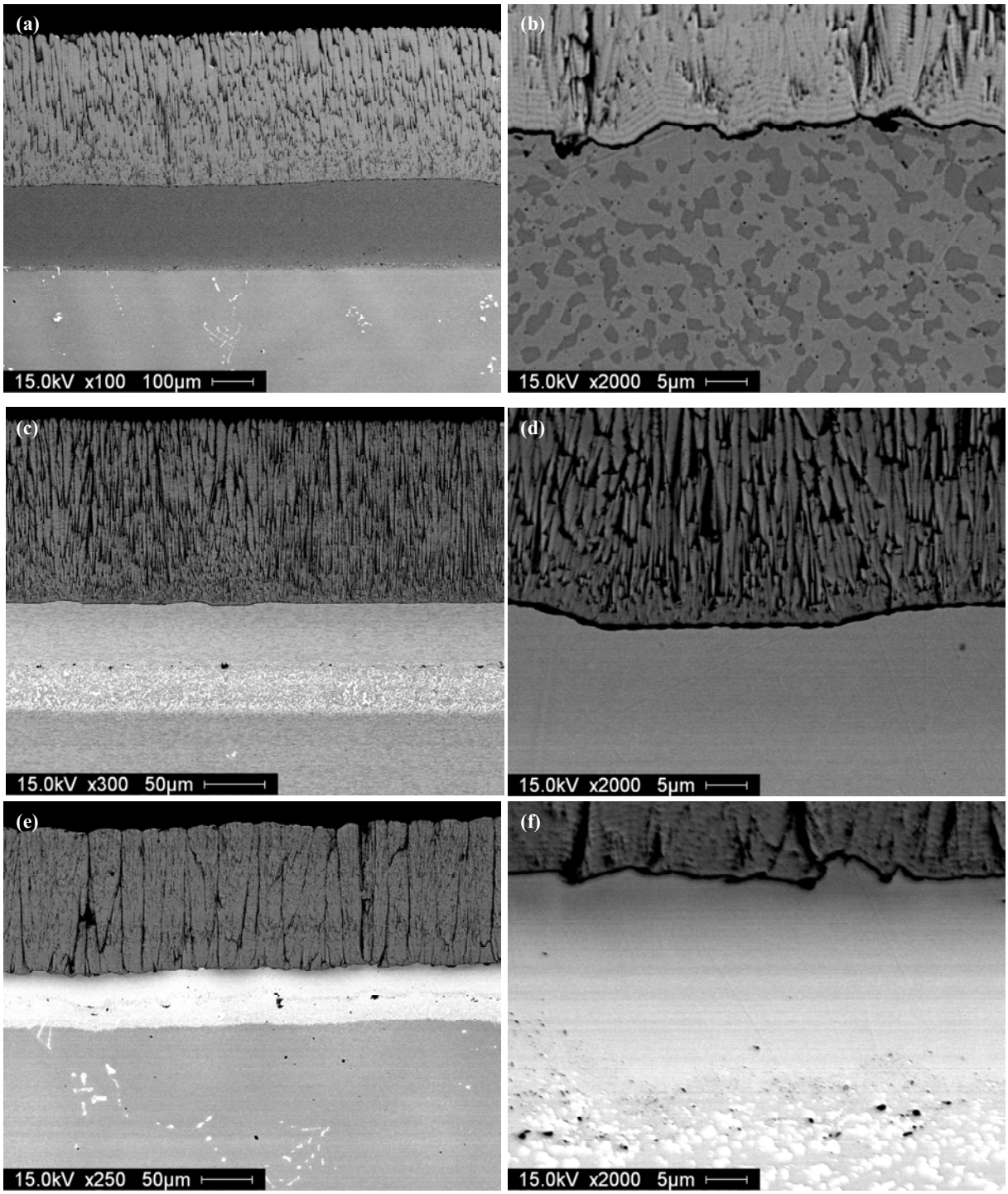

Figure 119. Typical backscatter electron micrographs of (a,b) type II, (c,d) type III, and (e,f) type IV EB-PVD TBCs specimens.

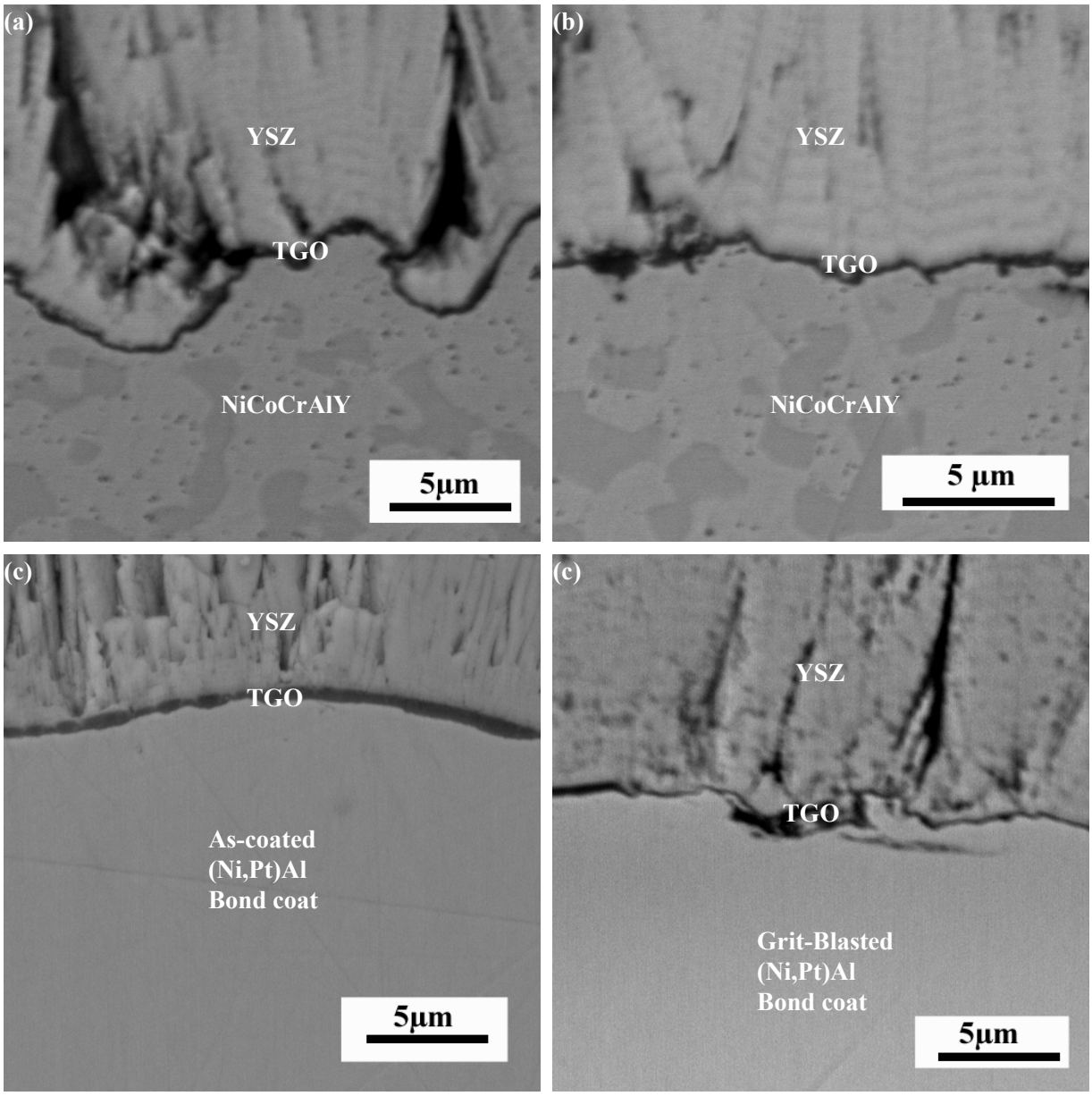

Figure 120. High magnification backscatter electron micrographs of (a,b) type II, (c) type III and (d) type IV EB-PVD TBCs specimens.

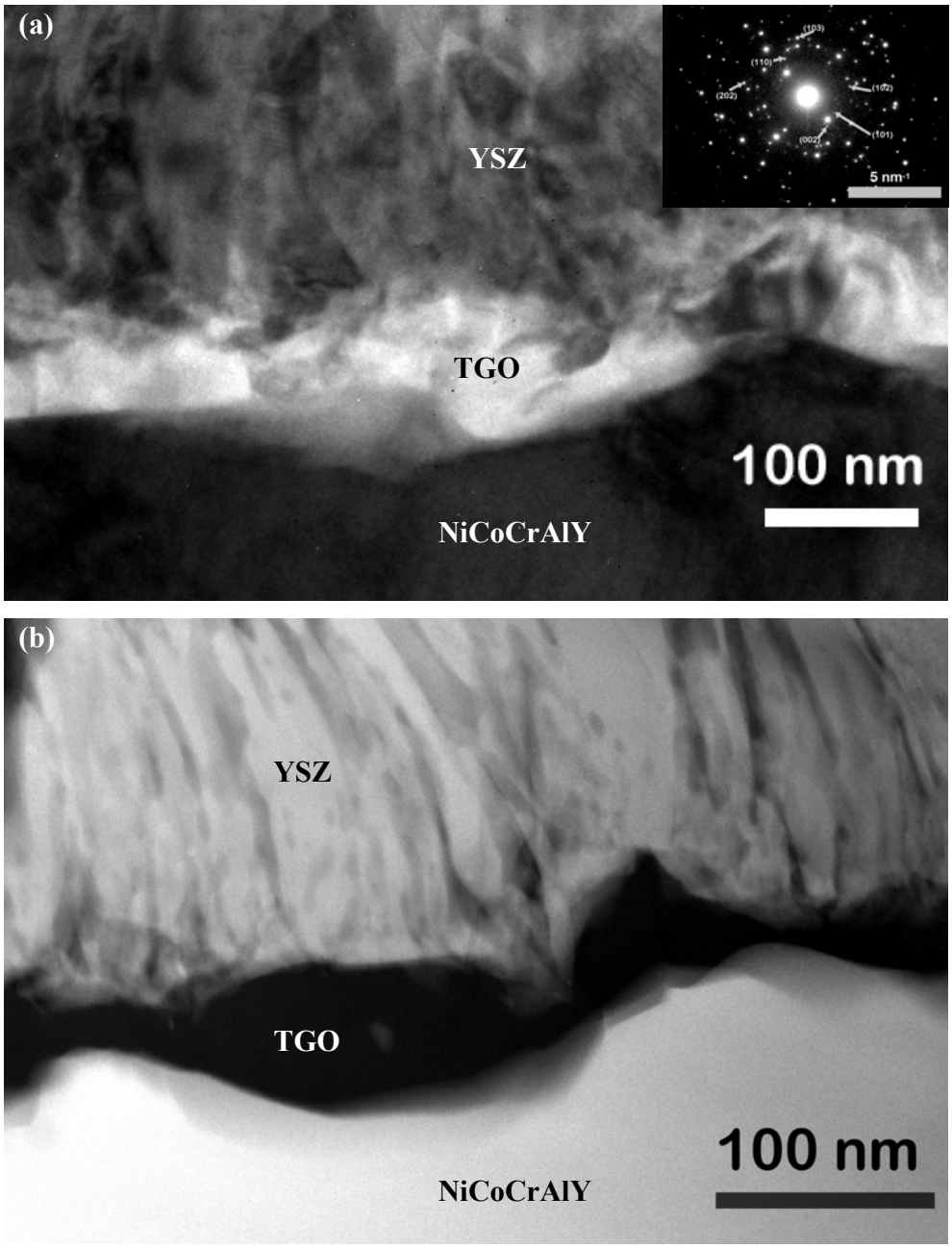

Figure 121.(a) Bright field and (b) HAADF image of as-coated type II EB-PVD TBC exhibiting columnar microstructure of 7YSZ coating and continuous TGO layer without presence of "mixed-oxide" layer. SADP (inset) demonstrated that the EB-PVD 7YSZ consisted of non-equilibrium tetragonal (t') and/or retained cubic (f') phase.

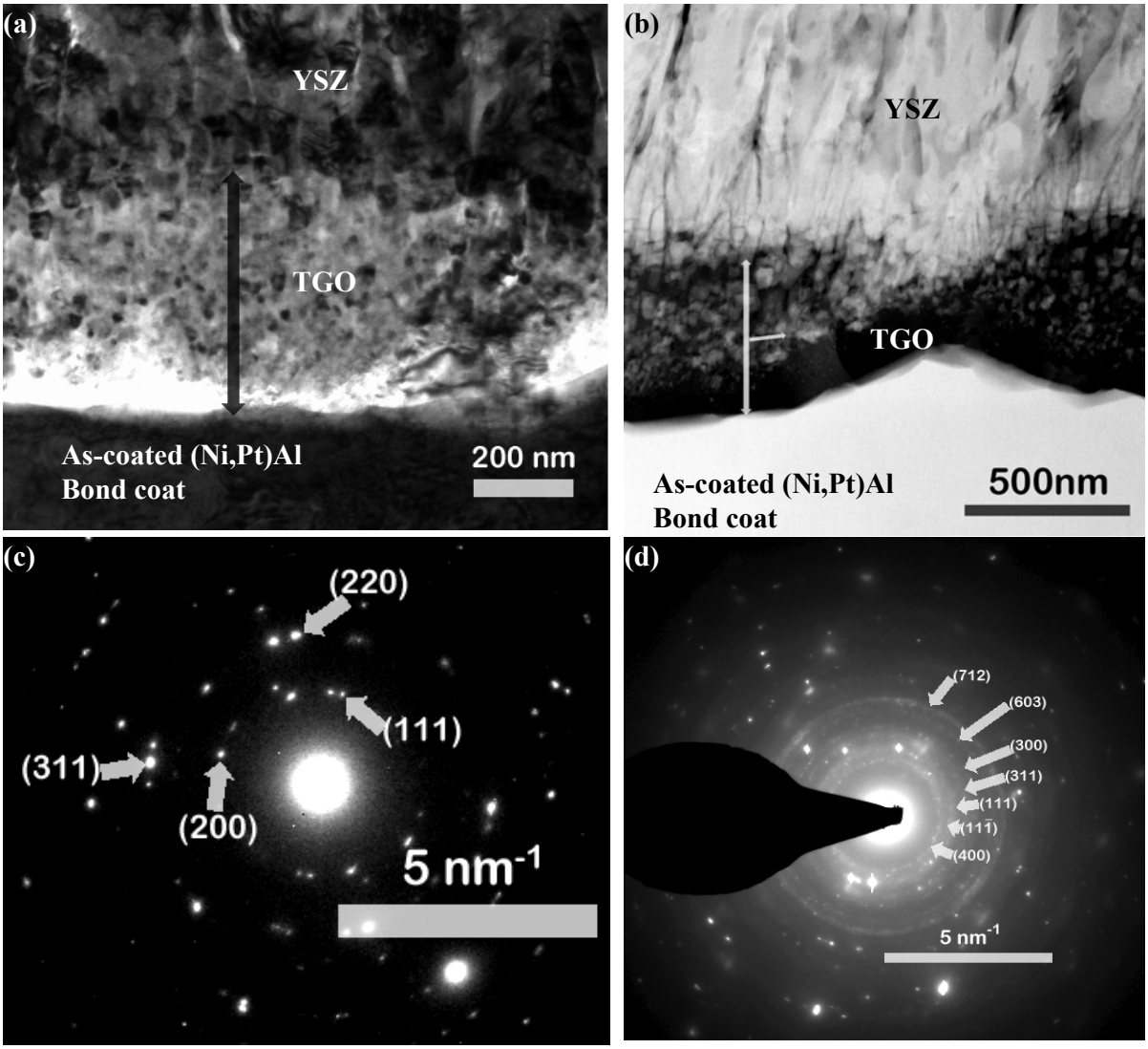

Figure 122.(a) Bright field and (b) HAADF image of as-coated type III EB-PVD TBC exhibiting columnar microstructure of 7YSZ coating and continuous TGO layer with a significant presence of "mixed-oxide" layer. (c) SADP demonstrated that the EB-PVD 7YSZ consisted of non-equilibrium tetragonal (t') and/or retained cubic (f') phase. (d) SADP of α-Al_2O_3 in TGO.

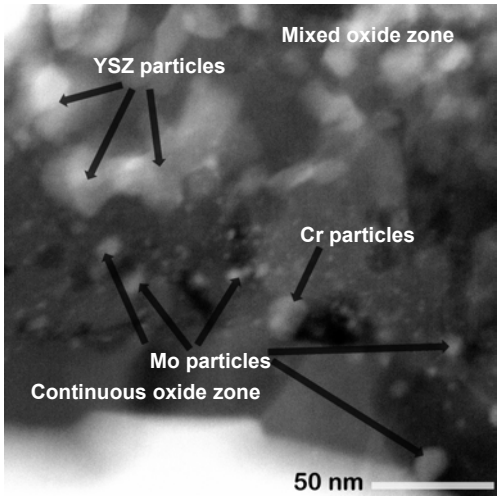

Figure 123. HAADF image of the "mixed-oxide" layer in TGO in as-coated type III EB-PVD TBC.

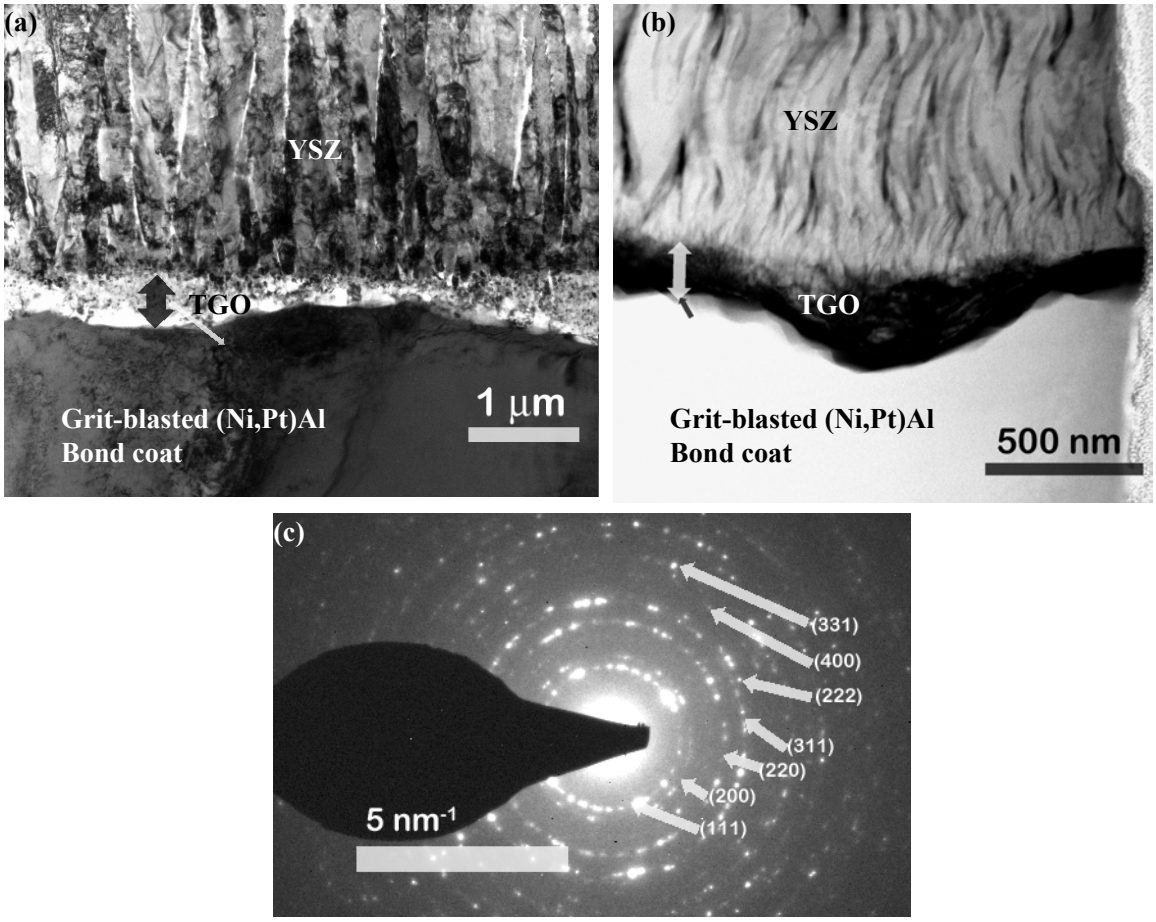

Figure 124. (a) Bright field and (b) HAADF images of as-received type IV EB-PVD TBCs with grit-blasted (Ni,Pt)Al bond coat. (c) SADP demonstrates that SADP demonstrated that the EB-PVD 7YSZ consisted of non-equilibrium tetragonal (t') and/or retained cubic (f') phase.

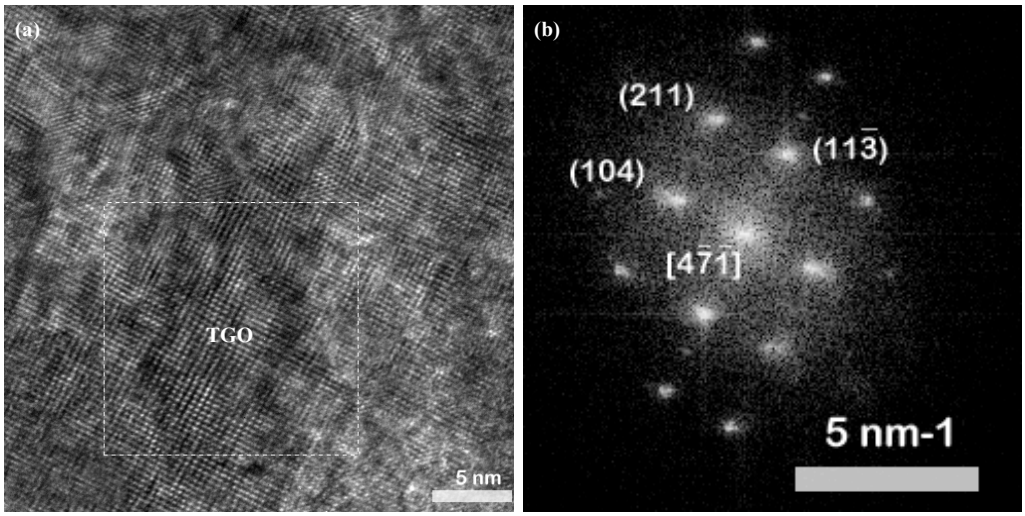

Figure 125. (a) High resolution image and (b) corresponding FFT diffractogram from TGO in re-received type IV EB-PVD TBCs with grit-blasted (Ni,Pt)Al bond coat.

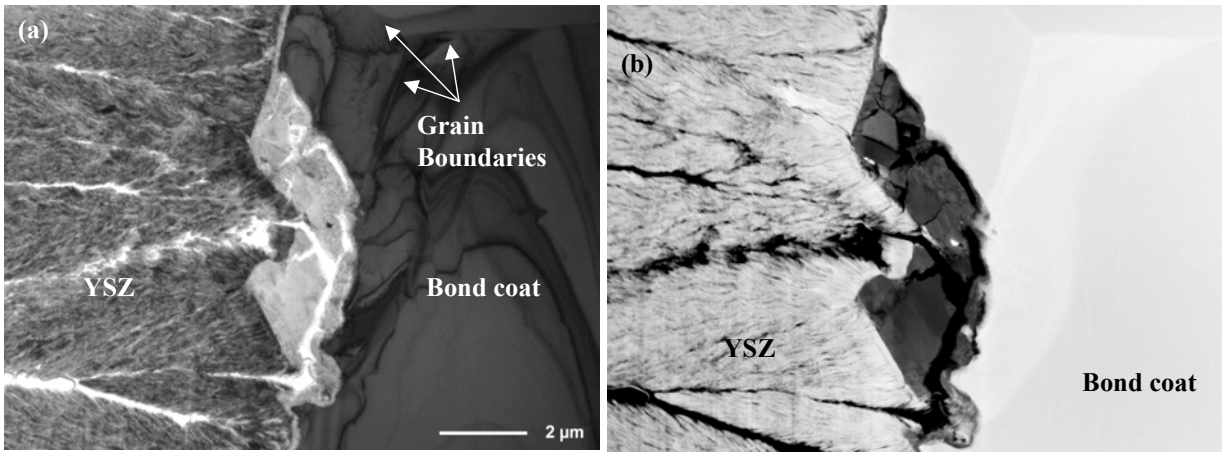

Figure 126. (a) Bright field and (b) HAADF images of as-received type IV EB-PVD TBCs with grit-blasted (Ni,Pt)Al bond coat. Presence of large residual α-Al_2O_3 particles from grit blasting was frequently observed.

V.4.4. Thermally Cycled Electron Beam Physical Vapor Deposited Thermal Barrier Coatings

Figure 127 represents backscatter electron micrographs of the type II EB-PVD TBCs as a function of 1-hour thermal cycling. From these figures we can observe the growth of the TGO with thermal cycles. For this type-II EBPVD TBCs we can clearly observe the depletion of the β-NiAl from the NiCoCrAlY bondcoat after the 10% thermal cyclic lifetime of the TBCs as shown in Figure 128. These TBCs had the lowest lifetime compared to the other EBPVD TBCs studied in this work. This may be due to the formation of the Ni/Co rich oxides that formed as early as 10% of its thermal cyclic lifetime of the TBCs with β-NiAl still present in the NiCoCrAlY bondcoat. Moreover with progressive thermal cycling, we observe damages within the TGO which is not detected by the NDE methods used in this study which is discouraging for this type of TBCs with NiCoCrAlY bondcoat.

Irrespective of the specification described in Table II for bond coat surface preparation, a "mixed-oxide" layer (MOZ) was observed for all types of EB-PVD TBCs. This MOZ consisted of spheroids of zirconia particles dispersed in the alumina matrix. With thermal cycling the growth of columnar $\propto$-Al_2O_3 was observed as shown in Figures 129 and 130 for type II TBCs. The interface between the YSZ and columnar TGO had a mixed oxide zone with voids and cracks. The yttrium rich particles that were dispersed in the TGO as shown in Figures 131(b) and 130(a) were identified as Y_2O_3 by diffraction analysis as seen in Figure 129(b). Another important observation that was made in 50% thermal cyclic life time is the identification of marternsitic structure (L_{10}) as shown in Figure 131(a). Further an ordered L_{12} super lattice structure was observed in 50% thermal cyclic life time as shown in Figure 131(b).

Figure 132 represents backscatter electron micrographs of type-III EBPVD TBCs with as-coated (Ni,Pt)Al bondcoat as a function of 1-hour thermal cycling from as-coated condition. With thermal cycling there is growth of TGO which can be correlated to the initial increase in the compressive residual stress within the TGO scale as shown in Figure 43. This growth in TGO is also correlated to the R_{TGO} and C_{TGO} as shown in Figures 75 and 76. With progressive 1-hour thermal cycles we observe damages in the TGO scale indicated by arrows in Figure 132. This sub-critical damage is manifested as stress-relief within the TGO, identified by PSLS as presented in Figure 39. Also these damages may be related to an increase in the C_{TGO} as shown in Figure 76.

Figure 133 represents backscatter electron micrographs of type-III EBPVD TBCs with as-coated (Ni,Pt)Al bondcoat as a function of 10-hour thermal cycling from as-coated condition. With thermal cycling damages were seen in TGO scale indicated by arrows in Figure 133 are related to the stress-relief within TGO scale as identified by PSLS and shown in Figure 47. These damages are not seen for 50-hour thermal cycling as shown in Figure 134.

For the type III TBC specimen with as-coated (Ni,Pt)Al bond coat, the TGO scale consisted of two distinctive microstructural zones as presented in the HAADF image in Figure 135: a mixed oxide zone containing Zr rich particles dispersed on a Al_2O_3 matrix near to the YSZ topcoat and a dense-continuous-columnar α-Al_2O_3 TGO near to the (Ni,Pt)Al bond coat. The thickness of the TGO, both the MOZ and the COZ (continuous oxide zone), grew with

thermal cycling. The MOZ consisted of numerous voids as observed in the BF TEM image in Figure 136 (a). The COZ near to the bond coat had a columnar structure as presented by the BF TEM image in Figure 136 (b). Fast Fourier Transformed diffractograms in Figure 137 indexes to γ-Al_2O_3 and t-ZrO_2 and demonstrate that the Al_2O_3 in the MOZ near the ZrO_2 particles is metastable. This observation explains the growth of the MOZ since the growth rate of metastable Al_2O_3 phases is much faster in comparison to the equilibrium α-Al_2O_3 phase. The volume contraction associated with the metastable-to-equilibrium Al_2O_3 transformation can be attributed to the formation of voids in the MOZ. The rate of phase transformations in the presence of γ-Al_2O_3 stabilizer such as ZrO_2 is being examined currently.

Figure 138 represents microstructure of the type-III EB-PVD TBCs with as-coated (Ni,Pt)Al bondcoat after 70% thermal cyclic lifetime. Aforementioned, the TGO was observed with two-zone microstructure consisting of the MOZ and COZ. With progressive thermal cycling the voids were more frequently observed. Further a diffraction analysis in the as-coated bondcoat near the TGO revealed B2 NiAl and martensitic twins as shown in Figure 138.

Typical backscatter electron micrographs of type IV TBCs with the grit-blasted (Ni,Pt)Al bond coat as a function of thermal cycling is shown in Figure 139. With thermal cycling there is a growth of TGO which can be related to NDE results of PSLS and EIS: an initial increase in the compressive residual stress as shown in Figure 45; an initial increase and a decrease in the R_{TGO} and C_{TGO} as shown in Figures 81 and 82. With progressive thermal cycles, "racheting" was observed during 1-hour thermal cycles as shown in Figure 139. Figure 139 also shows vertical cracks in the TGO scale due to "racheting" which is further confirmed by TEM micrographs in Figure 143. This "racheting" phenomena can lead to stress relaxation which was observed for type-IV EB-PVD TBCs with grit-blasted (Ni,Pt)Al bondcoat. For the type-IV TBCs, luminescence from PSLS shifted gradually towards stress-free luminescence with thermal cycling as presented in Figures 44 and 45. This type of sub-critical damages may be related to the evolution of the C_{TGO} that increased significantly before the final failure of TBCs as shown in Figures 82 and 83.

Figures 140 and 141 represents back scatter electron micrographs of type-IV TBCs with grit-blasted (Ni,Pt)Al bondcoat as a function of 10 and 50-hour thermal cycling. For this particular type of TBCs, racheting is dependent on thermal cyclic dwell time because in case of 10 and 50-hour thermal cycles "rumpling" of the bondcoat is observed more significantly than racheting. With rumpling of the bondcoat the damages are seen frequently at the TGO/bondcoat interface which is shown in Figures 165 and 170. Also there is no evidence of stress relaxation as observed for 1-hour thermal cycles.

Type IV TBC specimen with the grit-blasted (Ni, Pt)Al bondcoat had traces of mixed oxide zone even after progressive thermal cycling as shown in Figures 142 through 144. Further it is observed that the TGO near the YSZ topcoat had an equiaxed structure as seen in Figures 142 (b) and (c). After 50% thermal cyclic lifetime, cracks through the TGO near the ratcheted regions were observed as seen in Figure 143(b). This further confirms the stress-relaxation that was observed by PSLS. After 70% thermal cyclic lifetime, extensive voids

were present near to the ratcheted TGO as shown in Figure 144(a) and (b). A SAD pattern on the bondcoat confirmed that there is a L_{10} martensitic twin microstructure near to the TGO.

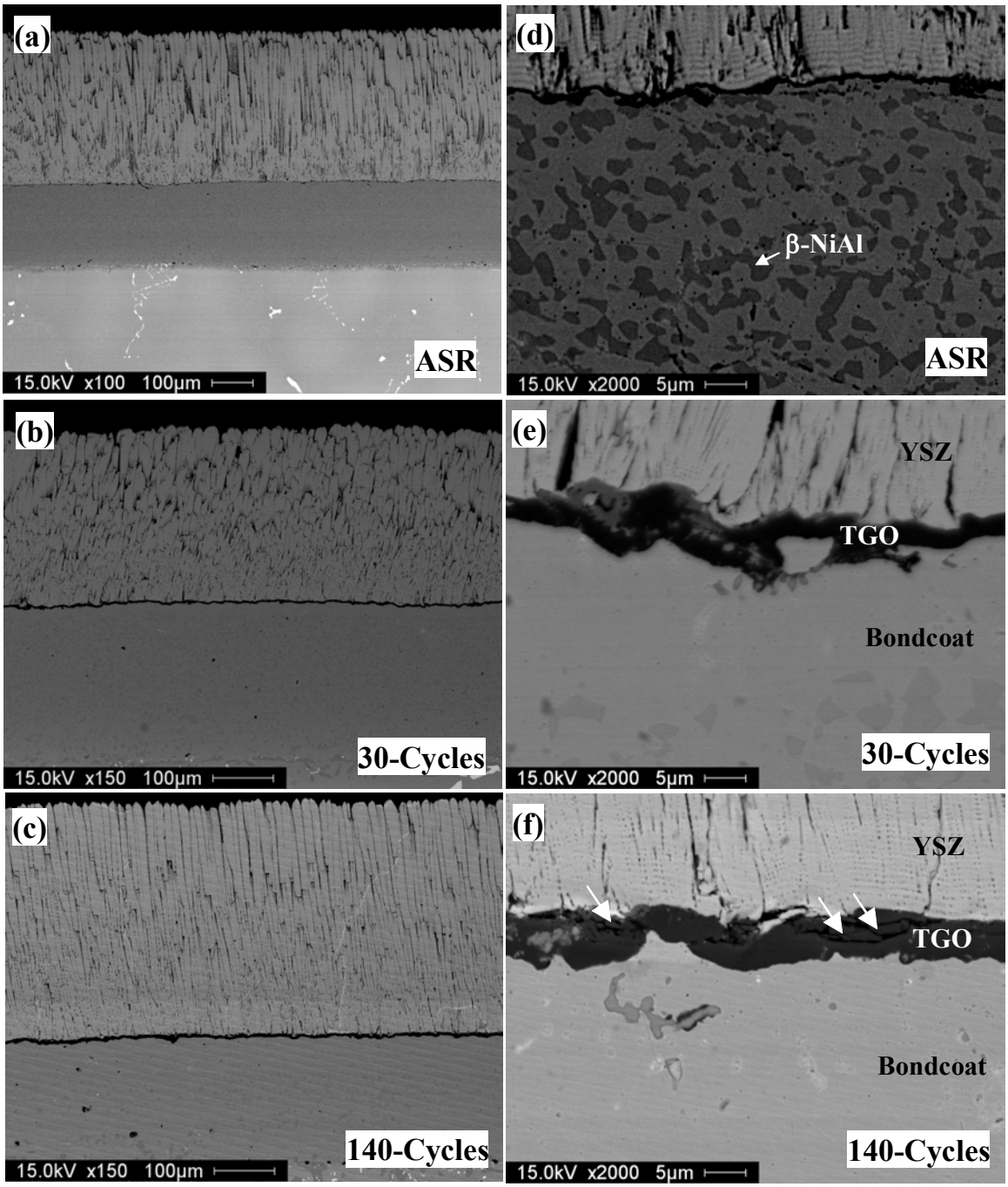

Figure 127. Typical backscatter electron micrographs of type II, EB-PVD TBCs specimens with NiCoCrAlY bondcoat after thermal cycling that corresponds to their lifetimes.

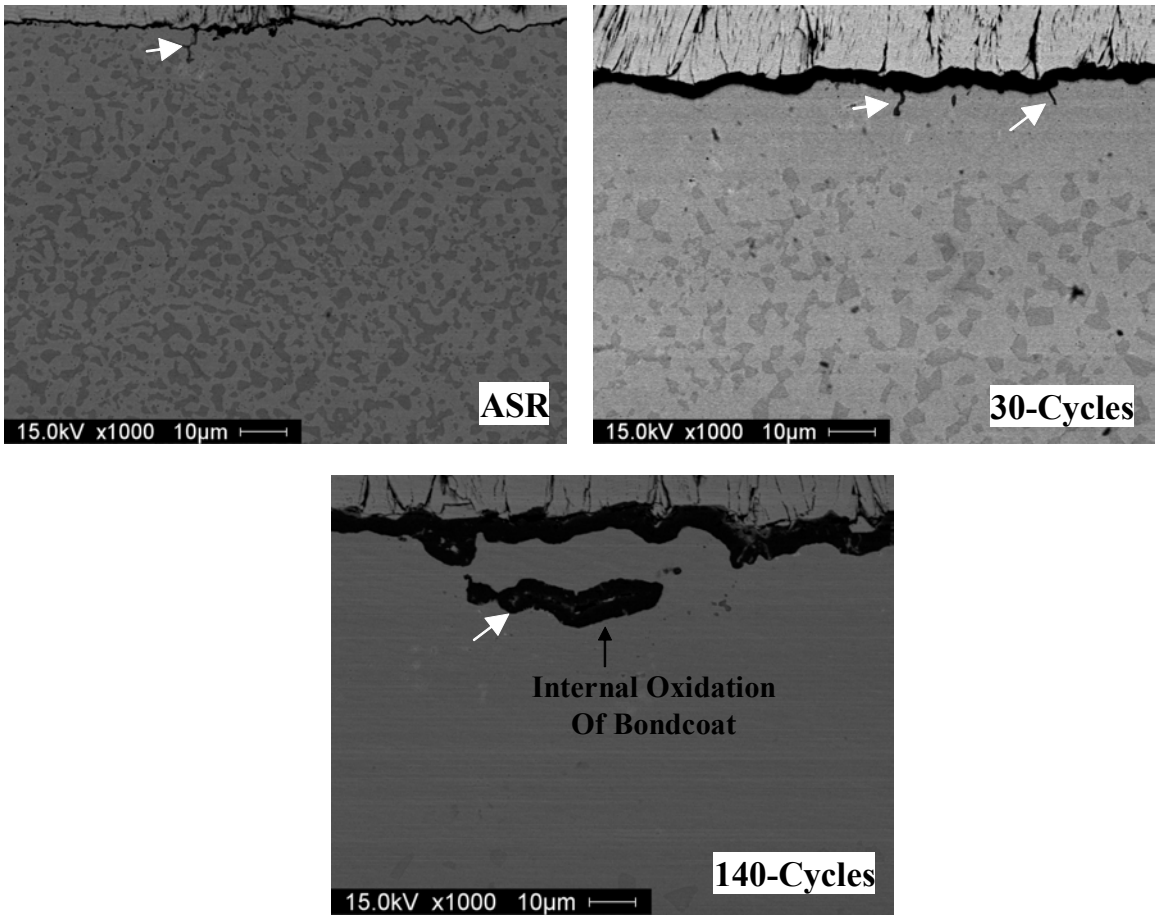

Figure 128. Typical back scatter electron micrographs of type-II TBCs showing the depletion of β-NiAl and also internal oxidation of the NiCoCrAlY bondcoat shown in arrows.

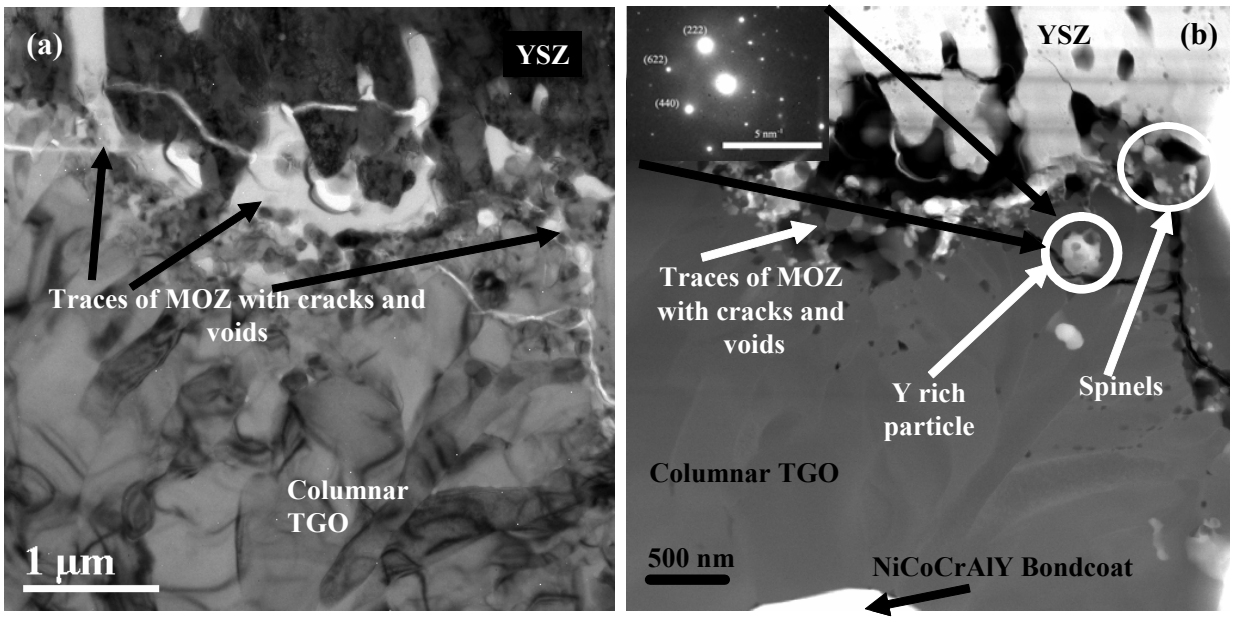

Figure 129. For type-II TBCs after thermal cycling (10% of lifetime): (a) BF TEM image showing presence of MOZ with cracks and voids near to the YSZ / TGO interface and a dense columnar Al_2O_3 TGO (b) HAADF STEM image showing presence of Ni/Co rich oxides near to the TGO/YSZ interface, MOZ with cracks and voids . The observed Y rich particle is identified as Y_2O_3 by diffraction analysis (SAD pattern as inset).

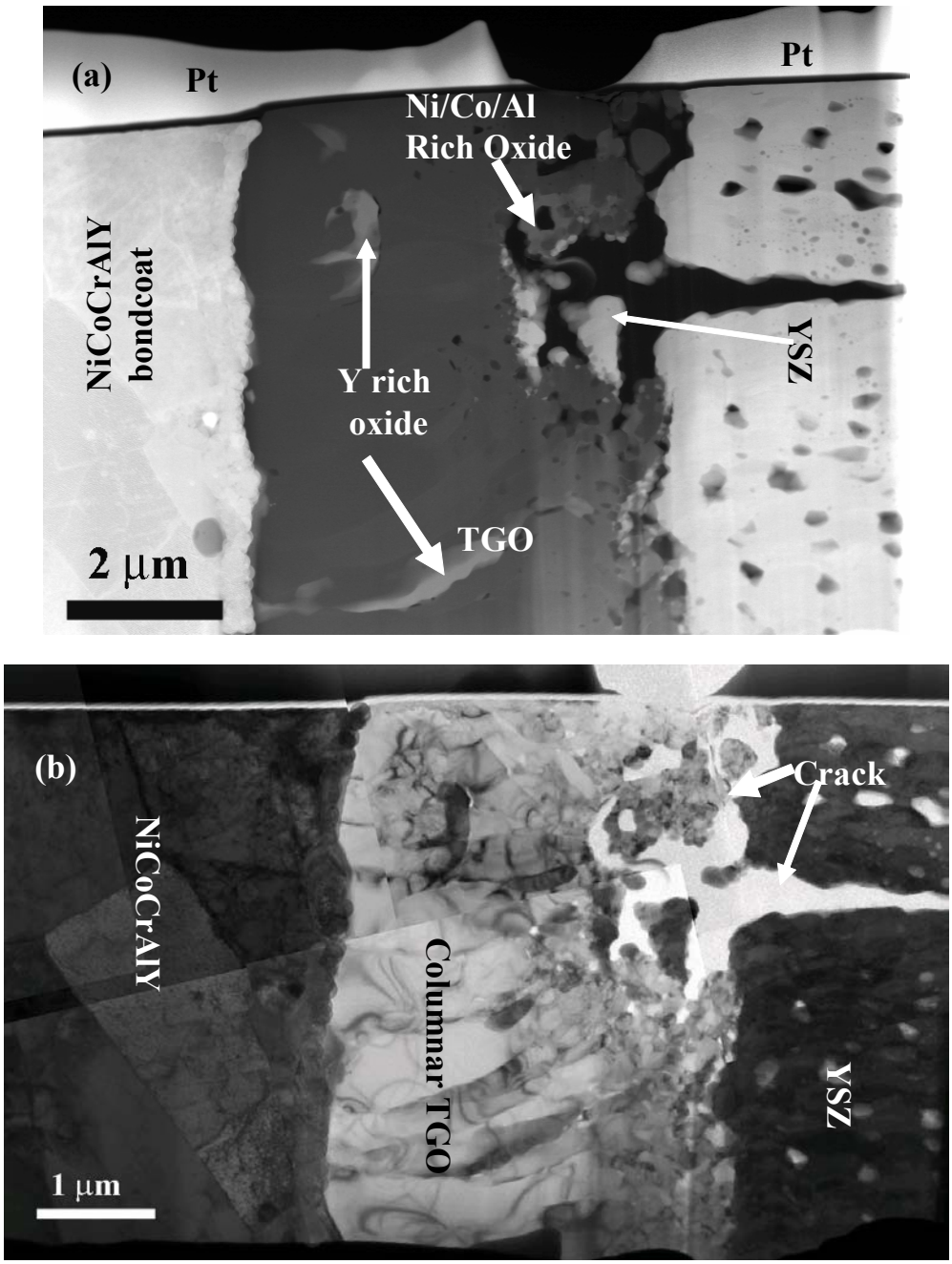

Figure 130. For type-II TBCs after thermal cycling (50% of lifetime): (a) HAADF STEM image showing presence of MOZ with cracks and voids near to the YSZ / TGO interface, a dense Al_2O_3 TGO and Ni/Co/Al rich oxides near the TGO/YSZ interface (b) BF TEM image showing MOZ with cracks and voids near to the YSZ / TGO interface and a dense columnar Al_2O_3 TGO near the TGO/bondcoat interface.

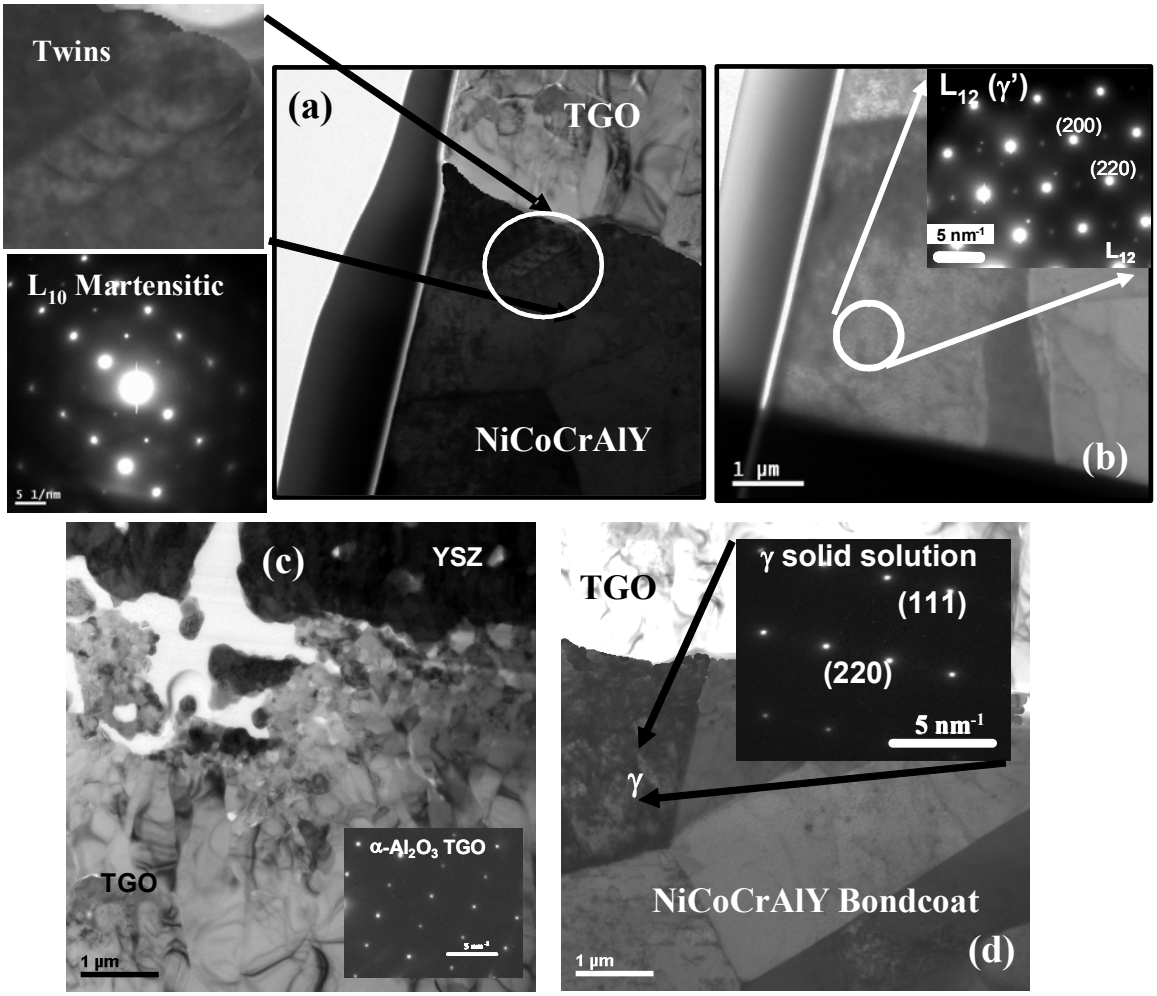

Figure 131. After 50% thermal cyclic lifetime for type-II TBCs (a) L_{10} martensitic twin structure (b) Ordered L_{12} super structure and (d) γ solid solution structure were observed in the (Ni,Pt)Al bondcoat and (c) the TGO identified was α-Al_2O_3.

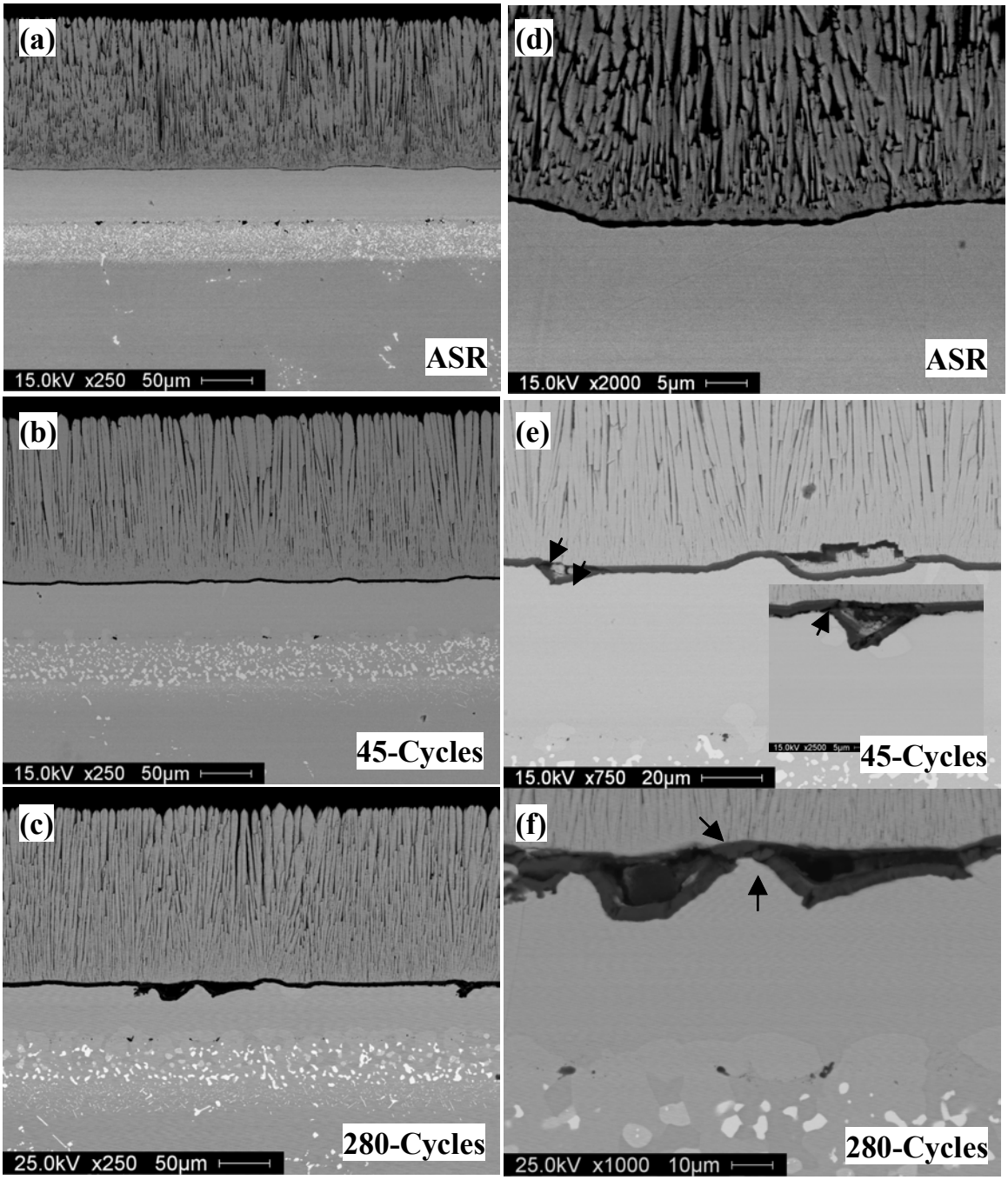

Figure 132. Typical back scatter electron micrograph of type-III EBPVD TBCs with as-coated (Ni,Pt)Al bondcoat with progressive 1-hour thermal cycling.

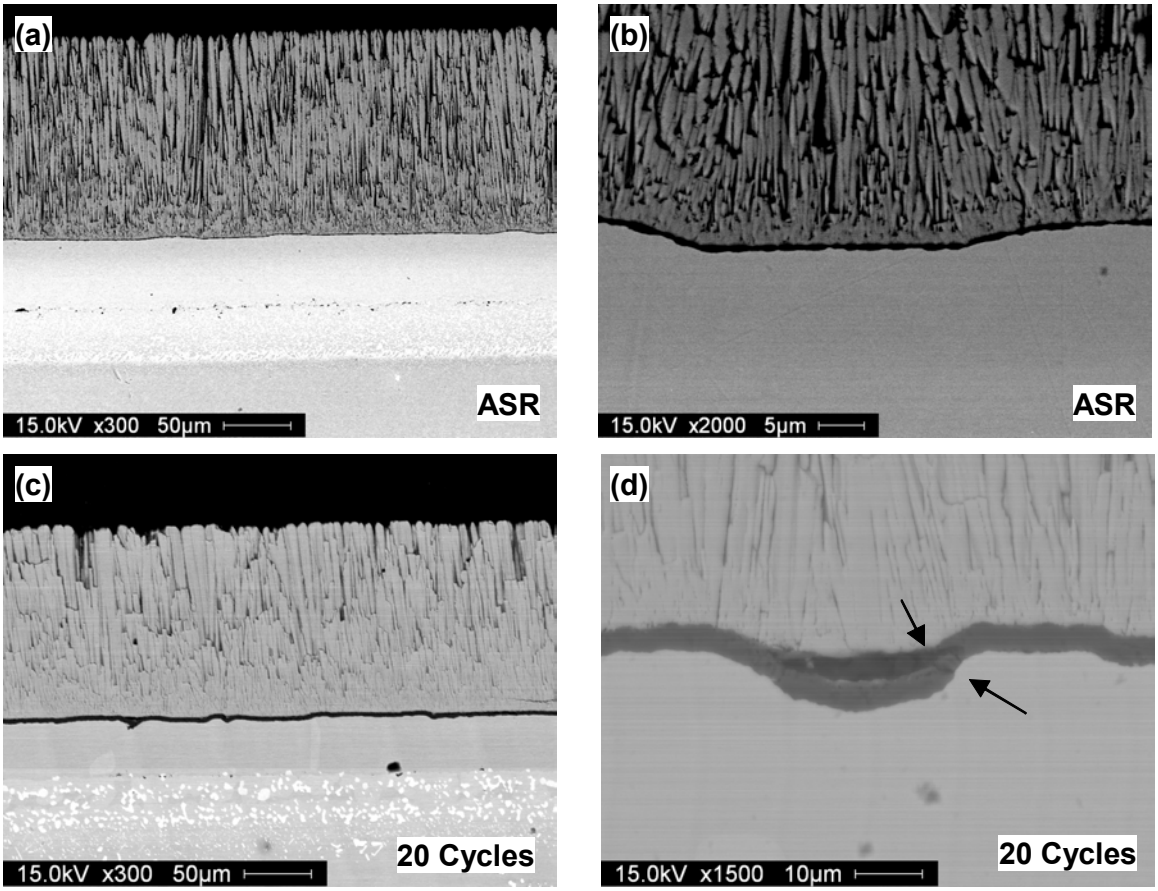

Figure 133. Typical back scatter electron micrograph of type-III EBPVD TBCs with as-coated (Ni,Pt)Al bondcoat with progressive 10-hour thermal cycling.

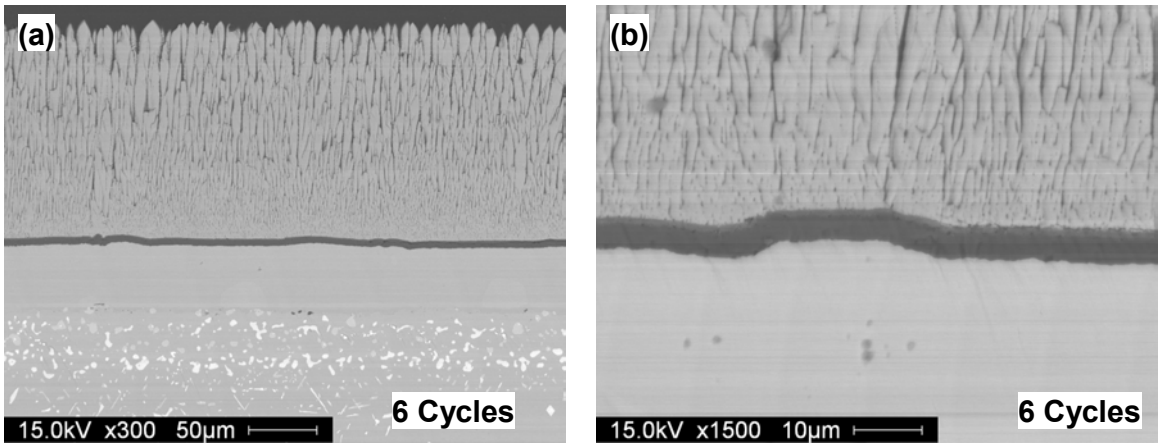

Figure 134. Typical back scatter electron micrograph of type-III EBPVD TBCs with as-coated (Ni,Pt)Al bondcoat after 6 cycles(50 hour thermal cycling).

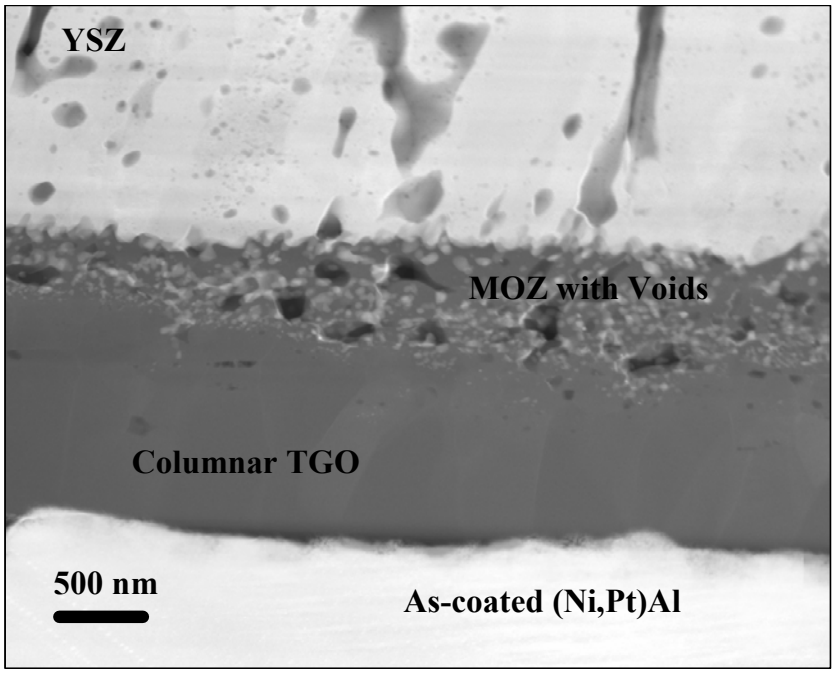

Figure 135. HAADF STEM image for type-III TBCs after thermal cycling (10% lifetime) showing distinct two zone TGO microstructure with presence of voids in the MOZ/Columnar TGO interface (MOZ: Mixed Oxide Zone).

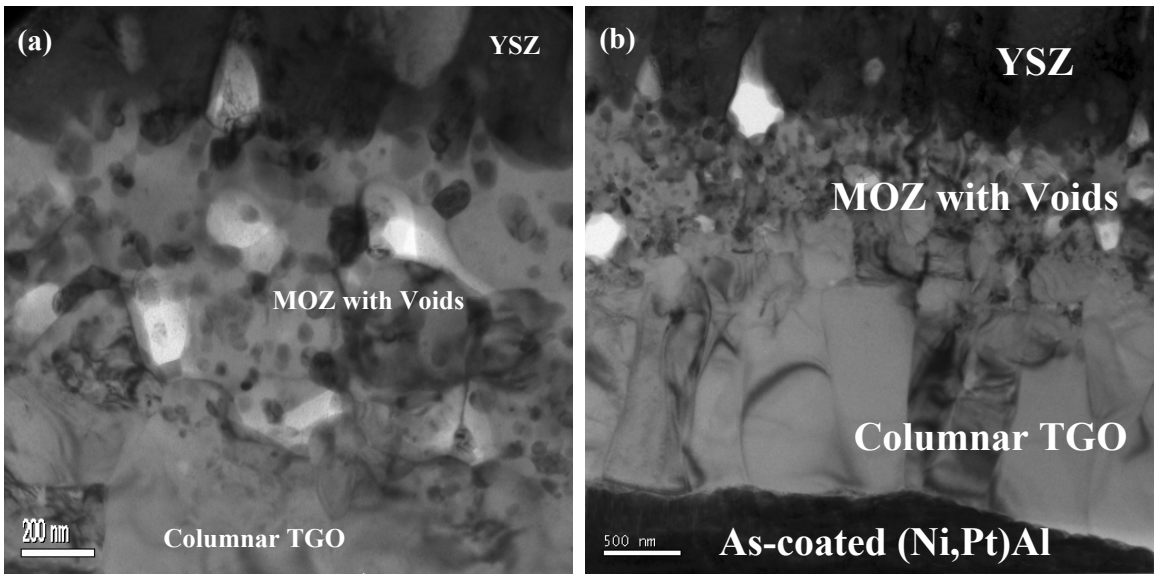

Figure 136. BF TEM images of type III EB-PVD TBCs after thermal cycling that corresponds to 10% of its lifetime: (a) presence of MOZ with voids near the YSZ/TGO interface and a dense-columnar-continuous Al_2O_3 TGO; (b) a distinctive two-zone TGO microstructure.

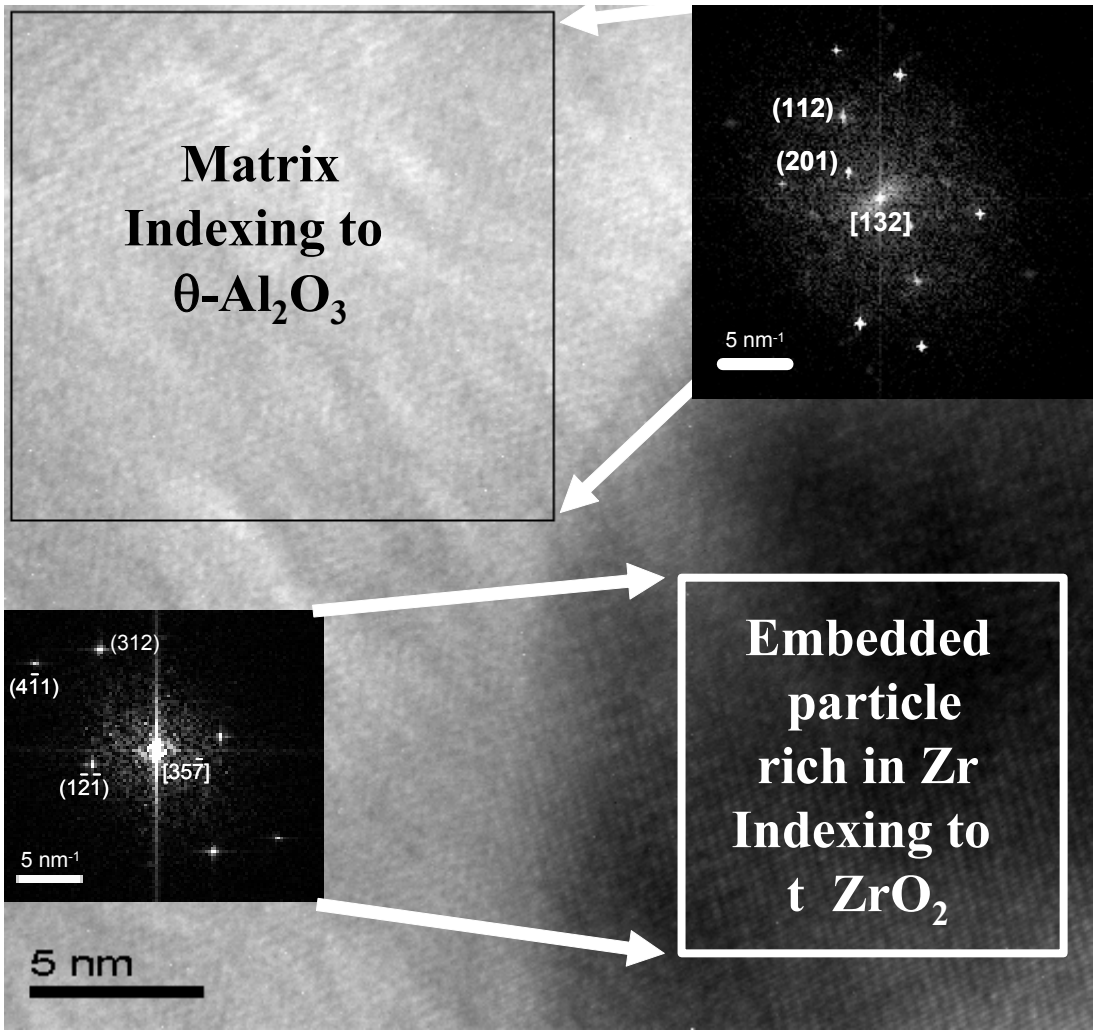

Figure 137. Type-III TBCs after thermal cycling (10% of lifetime): HRTEM image and the corresponding FFT diffractograms (inset) demonstrate MOZ matrix near the dispersed Zr-rich oxide consists of metastable θ-Al_2O_3, and the embedded Zr-rich oxide is t-ZrO_2.

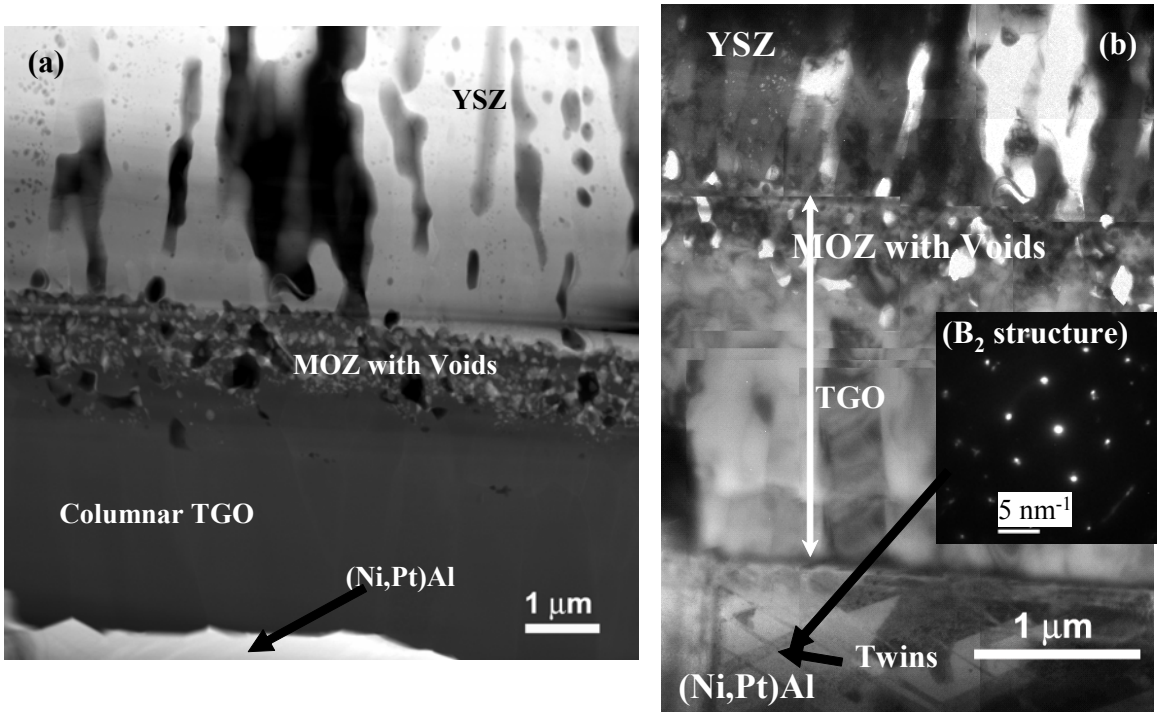

Figure 138. TEM image of type-III EBPVD with as-coated (Ni,Pt)Al bondcoat TBCs after 70% thermal cyclic life time (a) HAADF STEM image showing well defined two zone TGO microstructure (b) BF TEM image showing the as-coated (Ni,Pt)Al bondcoat having B_2 structure near to the TGO.

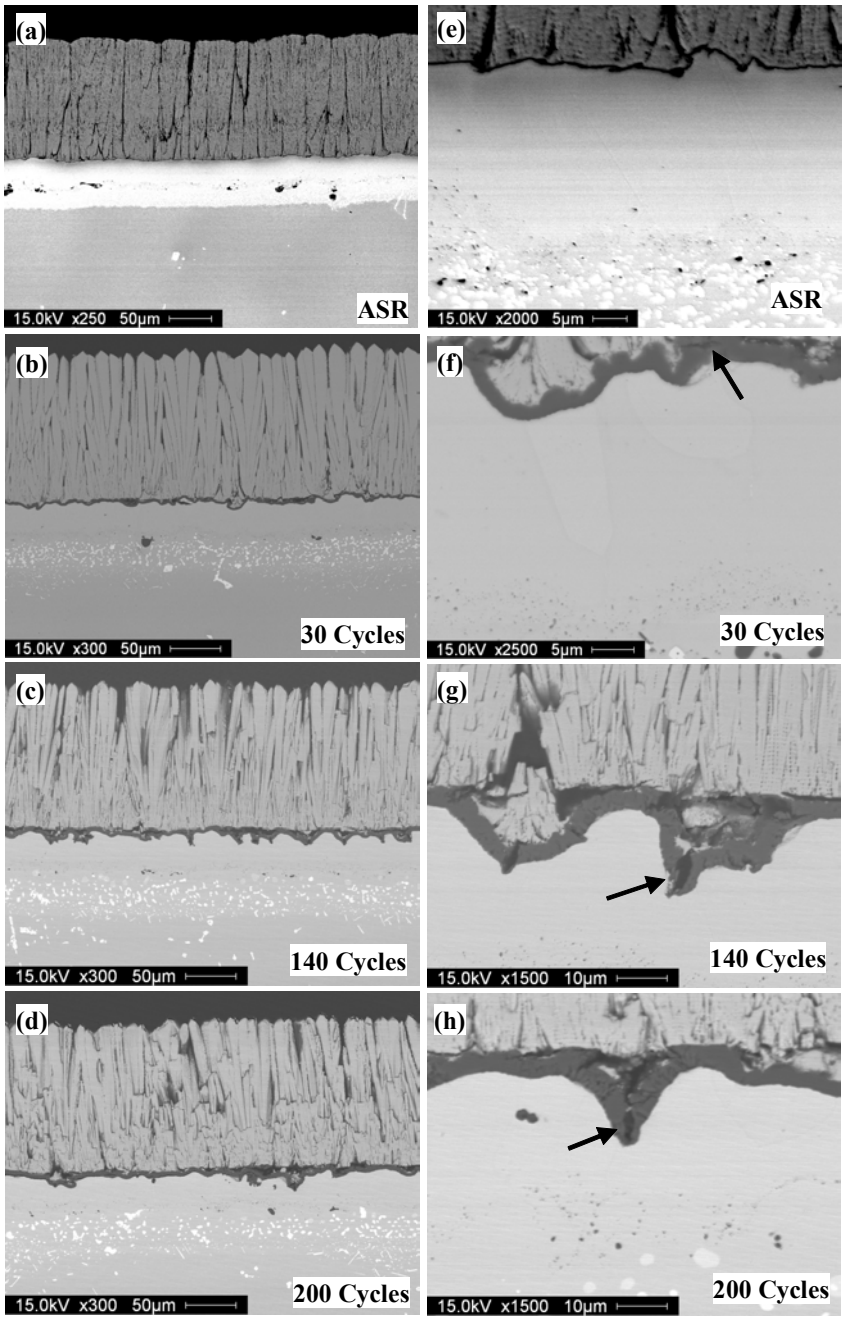

Figure 139. Typical back scatter electron micrograph of type-IV EB-PVD TBCs with grit blasted (Ni,Pt)Al bondcoat with progressive 1-hour thermal cycling.

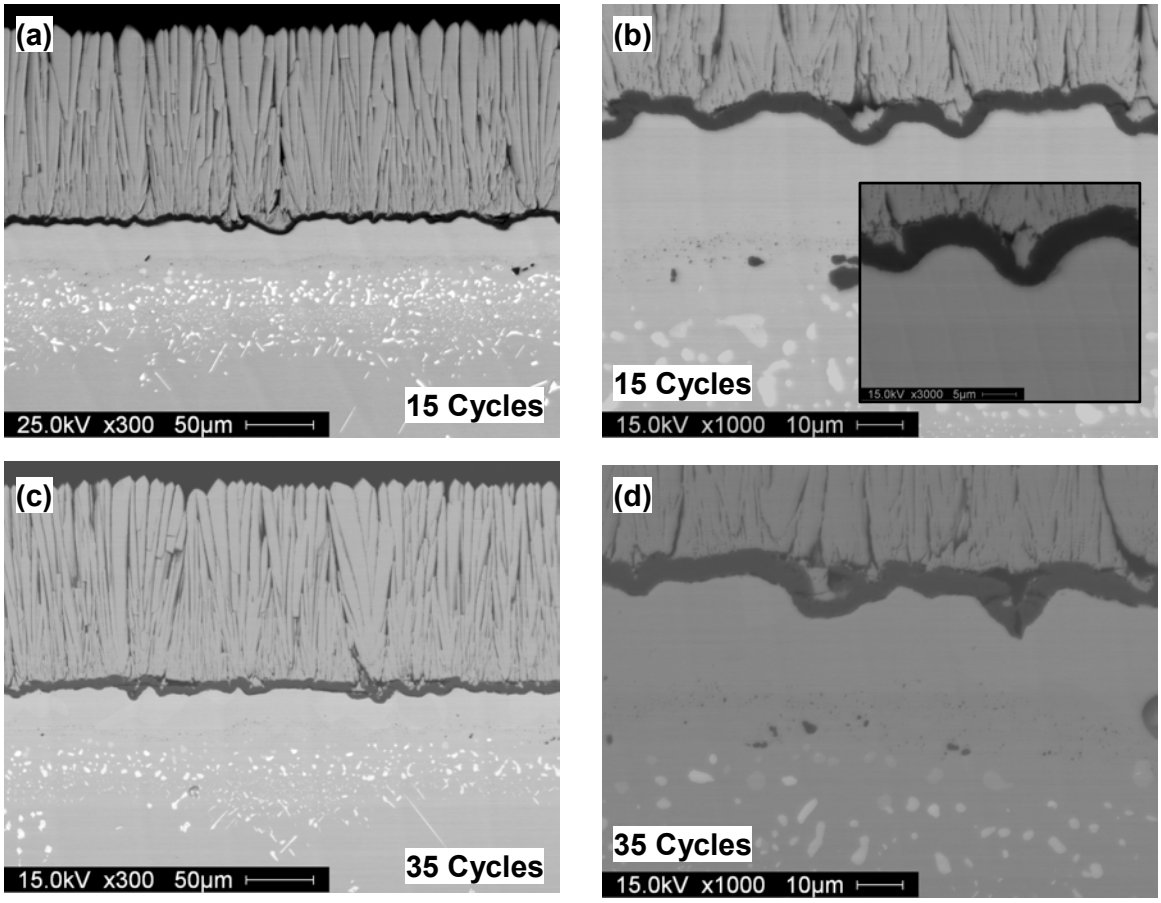

Figure 140. Typical back scatter electron micrograph of type-IV EB-PVD TBCs with grit blasted (Ni,Pt)Al bondcoat with progressive 10-hour thermal cycling.

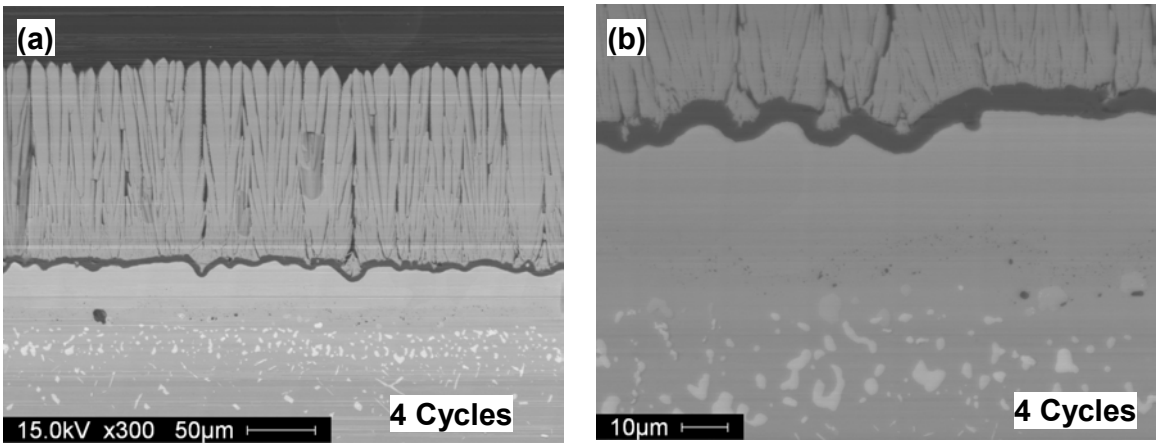

Figure 141. Typical back scatter electron micrograph of type-IV EB-PVD TBCs with grit blasted (Ni,Pt)Al bondcoat after 4 cycles (50-hour thermal cycling).

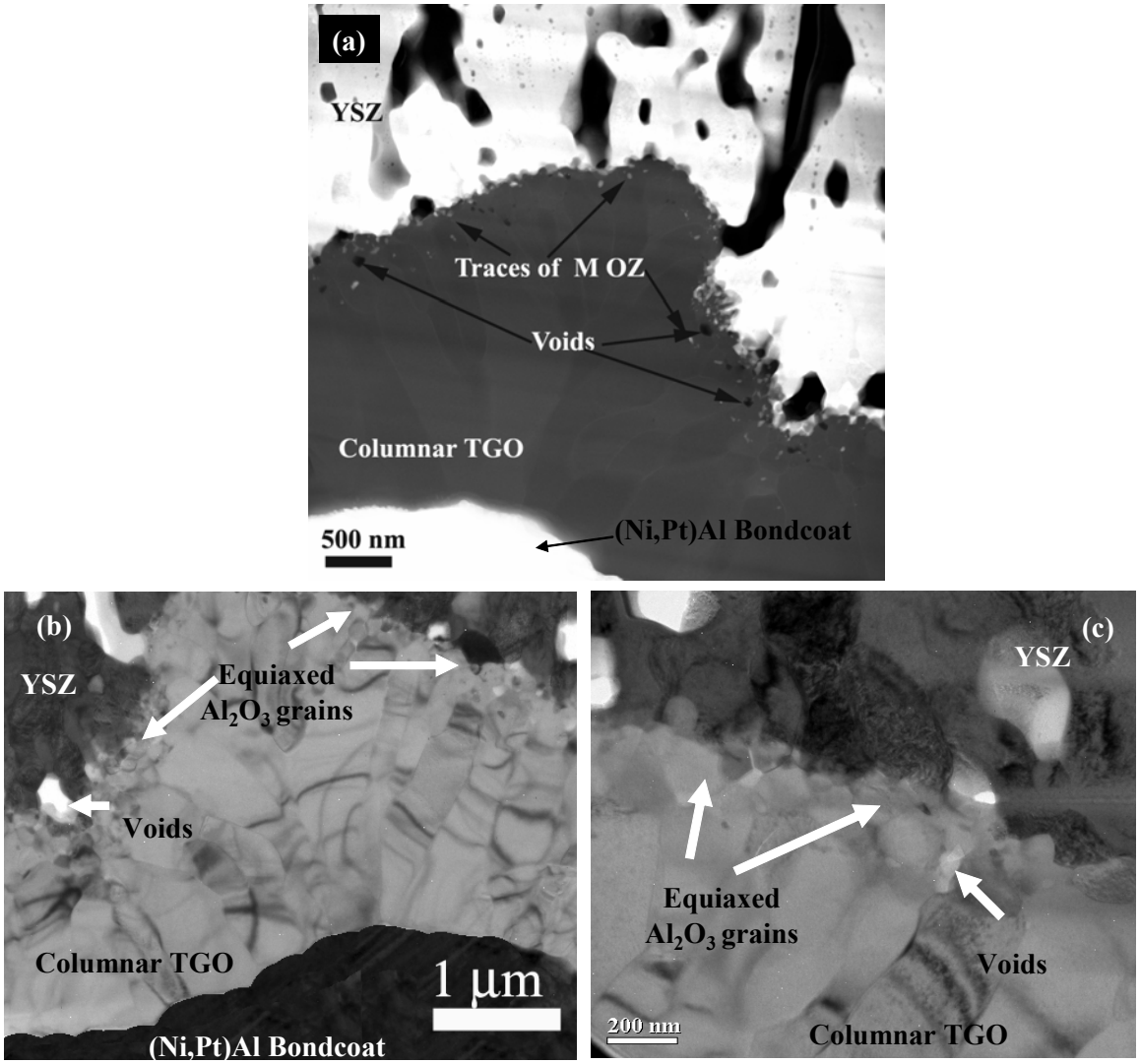

Figure 142. For type-IV TBCs after thermal cycling that corresponds to 10% of its lifetime: (a) HAADF STEM image showing the presence of MOZ traces near the YSZ/TGO interface and a dense Al_2O_3 TGO near the (Ni,Pt)Al bond coat; (b) BF TEM image showing presence of equiaxed Al_2O_3 grains near to the YSZ/TGO interface, and (c) a dense columnar continuous Al_2O_3 TGO.

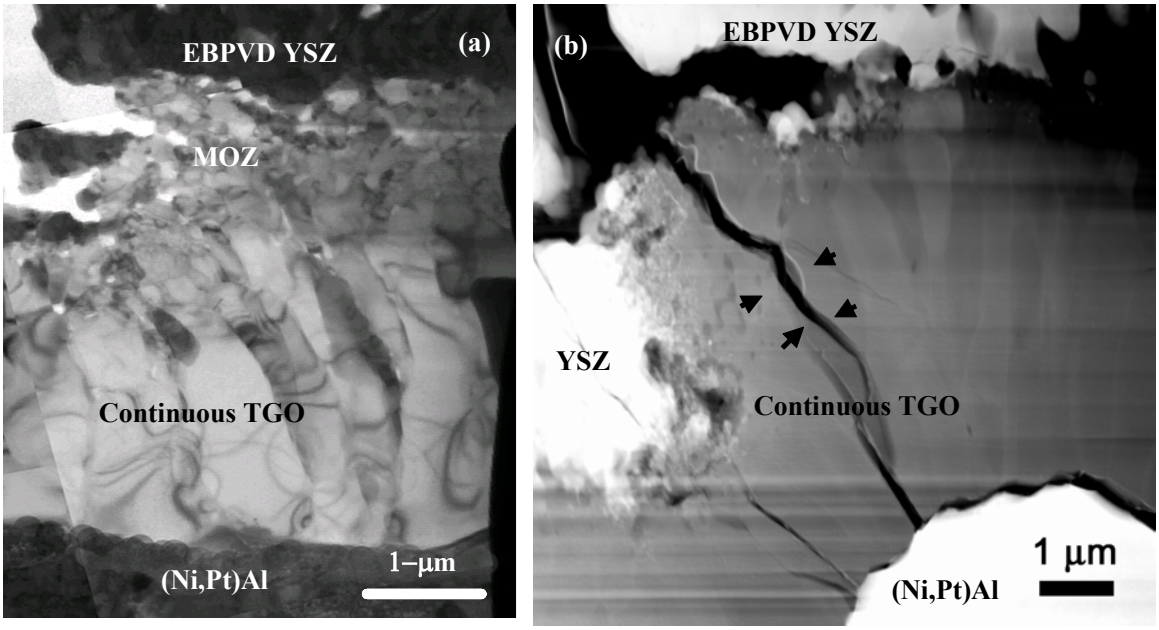

Figure 143. TEM images for type-IV EBPVD TBCs with grit blasted (Ni,Pt)Al bondcoat after 50% thermal cyclic lifetime (a) BF TEM image showing two zone microstructure in TGO and also voids present in the MOZ (b) HAADF STEM image showing through crack in the TGO scale with TBC still intact.

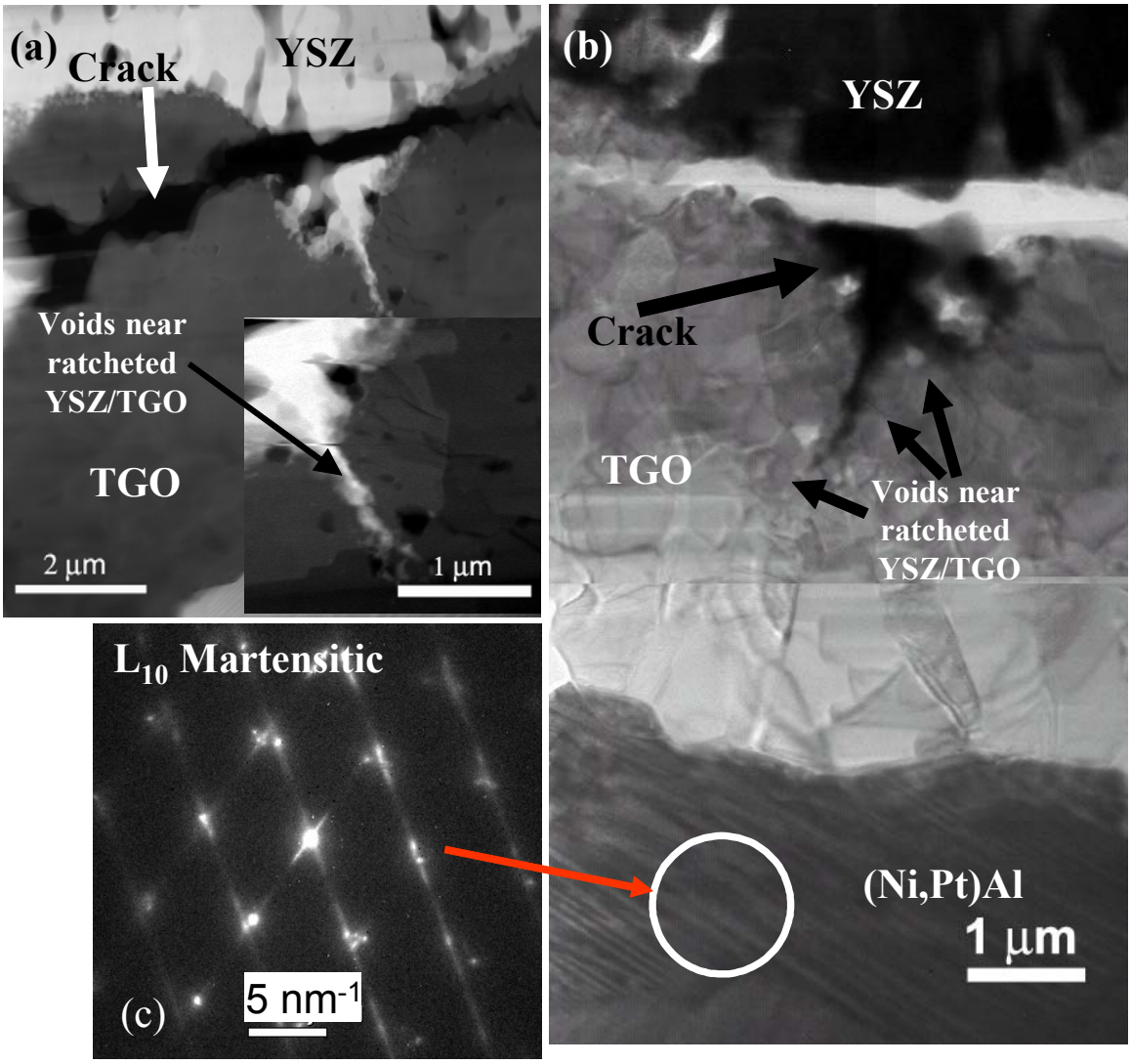

Figure 144. TEM images for type-IV EBPVD TBCs with grit blasted (Ni,Pt)Al bondcoat after 70% thermal cyclic lifetime (a) HAADF STEM image showing voids near the ratcheted TGO (b)BF TEM image showing the same (c) SAD pattern from the bondcoat showing L_{10} martensitic structure.

V.4.5. Characterization of Failure for Air Plasma Sprayed Thermal Barrier Coatings for 1-hour thermal cycling

Figure 145 represents backscatter electron micrograph of spallation surfaces in type I (600μm-thick) APS TBCs with NiCoCrAlY bond coat. This TBC type had an average lifetime of 527 1-hour cycles. Microscopic constituents of YSZ and TGO were observed on both bottom of the spalled-YSZ in Figure 145(a,b) and top of the bond coat surface where YSZ coating has spalled off in Figure 145(c,d). These micrographs indicate that the fracture for the spallation of type I TBCs occurred within the YSZ, within the TGO and at the YSZ/TGO interface. Most of the TGO were observed as islands, and contained Al, Ni, Co and Cr. The exposure of bond coat surface was extremely rare. Because of this kind of fracture the C_{TGO} does not change significantly as reported in the Figure 61.

Cross-sectional backscatter electron micrographs also demonstrated similar fracture paths as presented in Figure 146. A few residual TGO was observed on the spalled-YSZ as shown in Figure 146(b) while a few residual YSZ was observed on the top of the bond coat as shown in Figure 146(d). A significant internal oxidation of the bond coat was also observed as presented in Figure 146(c) following the splat boundaries of NiCoCrAlY bond coat. The TGO, both external and internal scale, primarily consisting of Al_2O_3 (dark gray) as well as those rich in Ni, Co and Cr (light gray) were also observed.

Similar fracture was observed for type V (200 μm-thick) APS TBCs with NiCoCrAlY bond coat as presented in Figures 147 and 148. This TBC type had an average lifetime of 286 1-hour cycles. Microscopic constituents of YSZ and TGO were observed on the bottom of the spalled-YSZ in Figure 147(a,b) and top of the bond coat surface where YSZ coating has spalled off in Figure 148(c,d). These micrographs indicate that the fracture for the spallation of type V TBCs occurred within the YSZ, within the TGO and at the YSZ/TGO interface. More of TGO on the fracture surface was observed for type V when compared to type I TBCs. Most of the TGO were observed as islands and contained Al only. The exposure of bond coat surface was extremely rare. But for one failed specimen, the C_{TGO} increased abruptly as reported in Figure 67, due to the bond coat surface exposure.

Cross-sectional secondary and backscatter electron micrographs also demonstrated similar fracture paths as presented in Figure 148. A few residual TGO was observed on the spalled-YSZ as shown in Figure 148(a) while a few residual YSZ was observed on the top of the bond coat as shown in Figure 148(d). No internal oxidation of the bond coat or TGO rich in Ni, Co, and Cr was observed for type V TBCs.

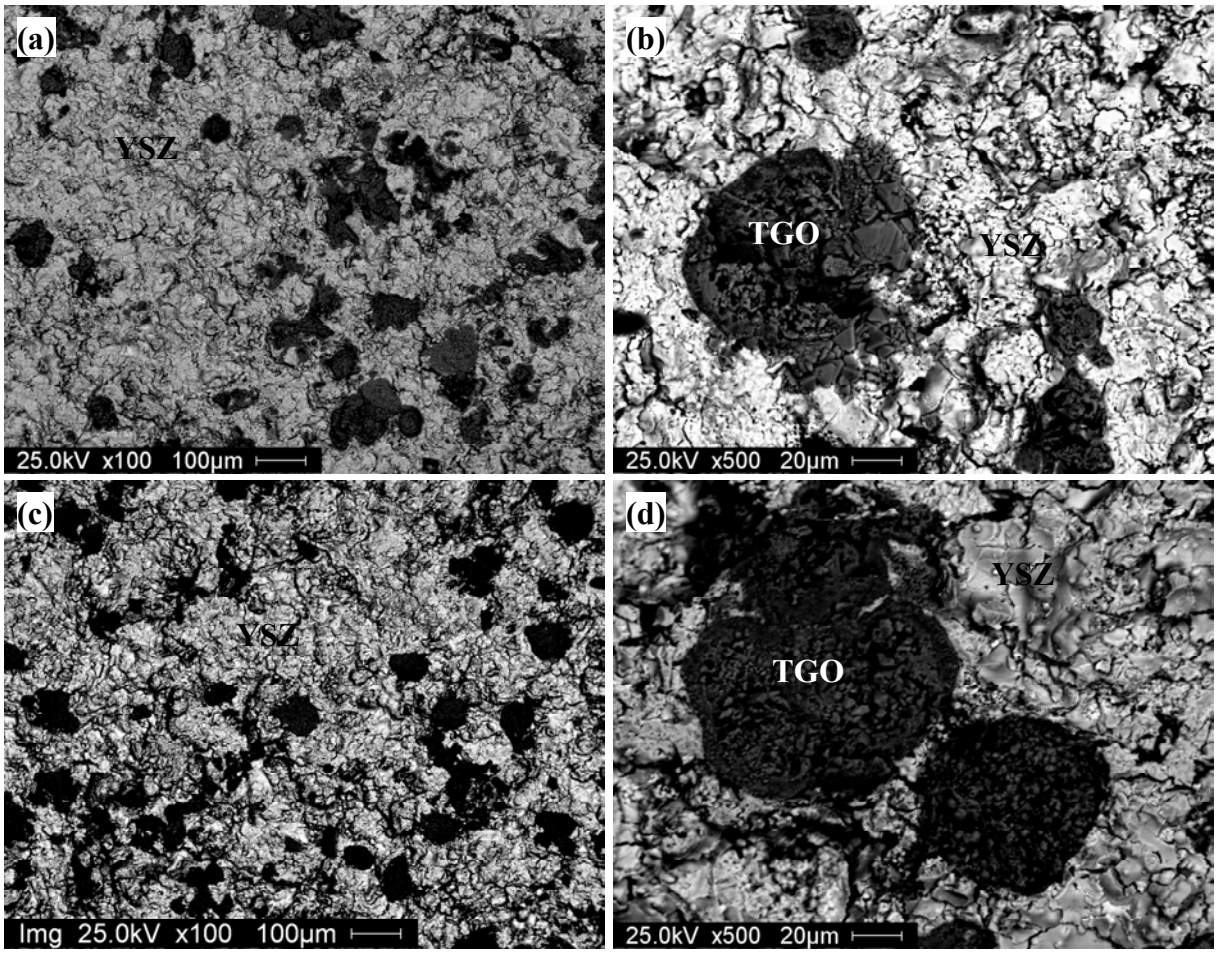

Figure 145. Backscatter electron micrographs of fracture surfaces in type I TBCs: (a,b) bottom of the spalled-YSZ coating and (c,d) top of the bond coat where YSZ coating has spalled off. Exposure of NiCoCrAlY surface was extremely rare.

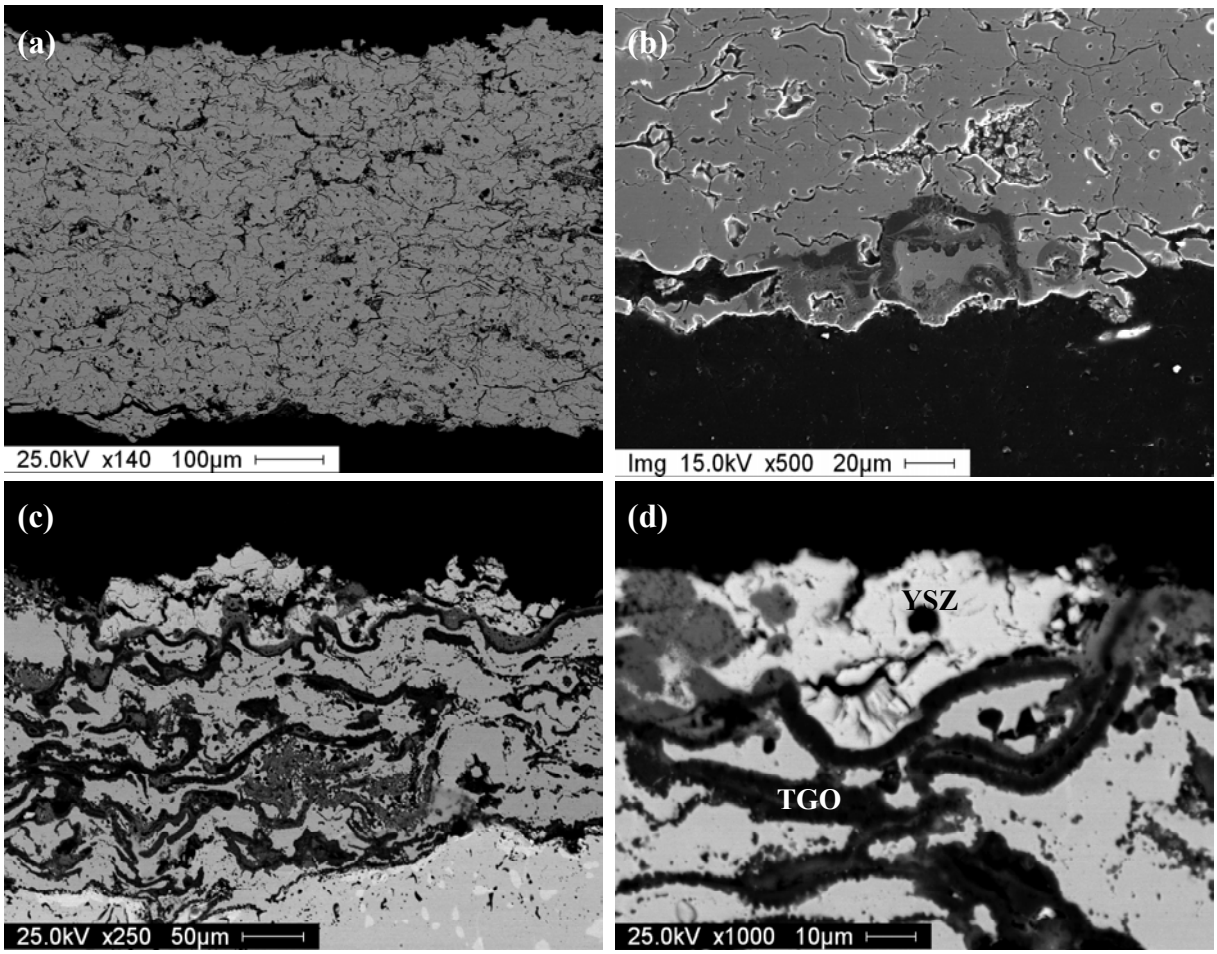

Figure 146. Cross-sectional backscatter electron micrographs of type I TBCs after spallation: (a,b) spalled-YSZ coating and (c,d) bond coat after YSZ spallation.

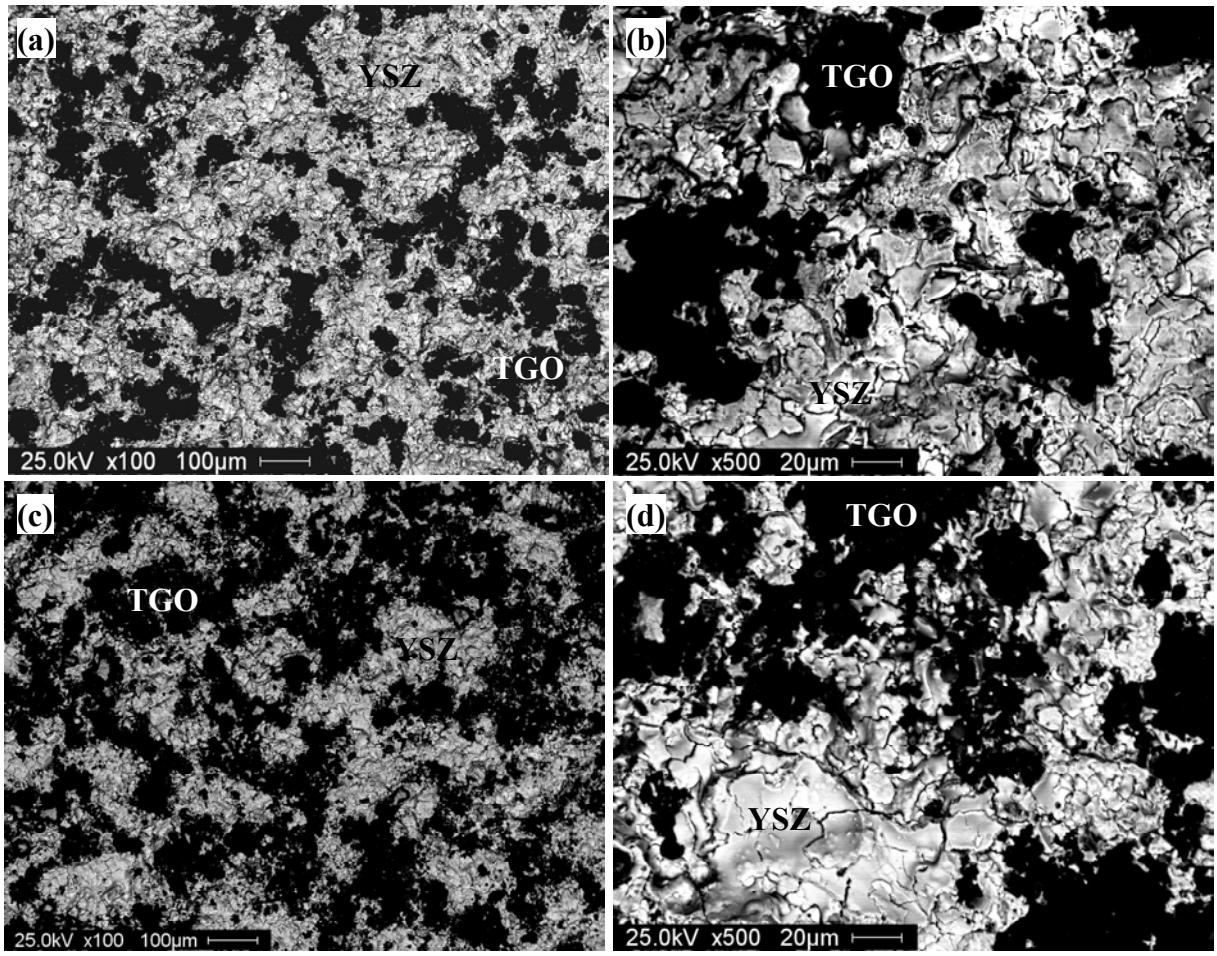

Figure 147. Backscatter electron micrographs of fracture surfaces in type V TBCs: (a,b) bottom of the spalled-YSZ coating and (c,d) top of the bond coat where YSZ coating has spalled off. Exposure of NiCoCrAlY surface was extremely rare.

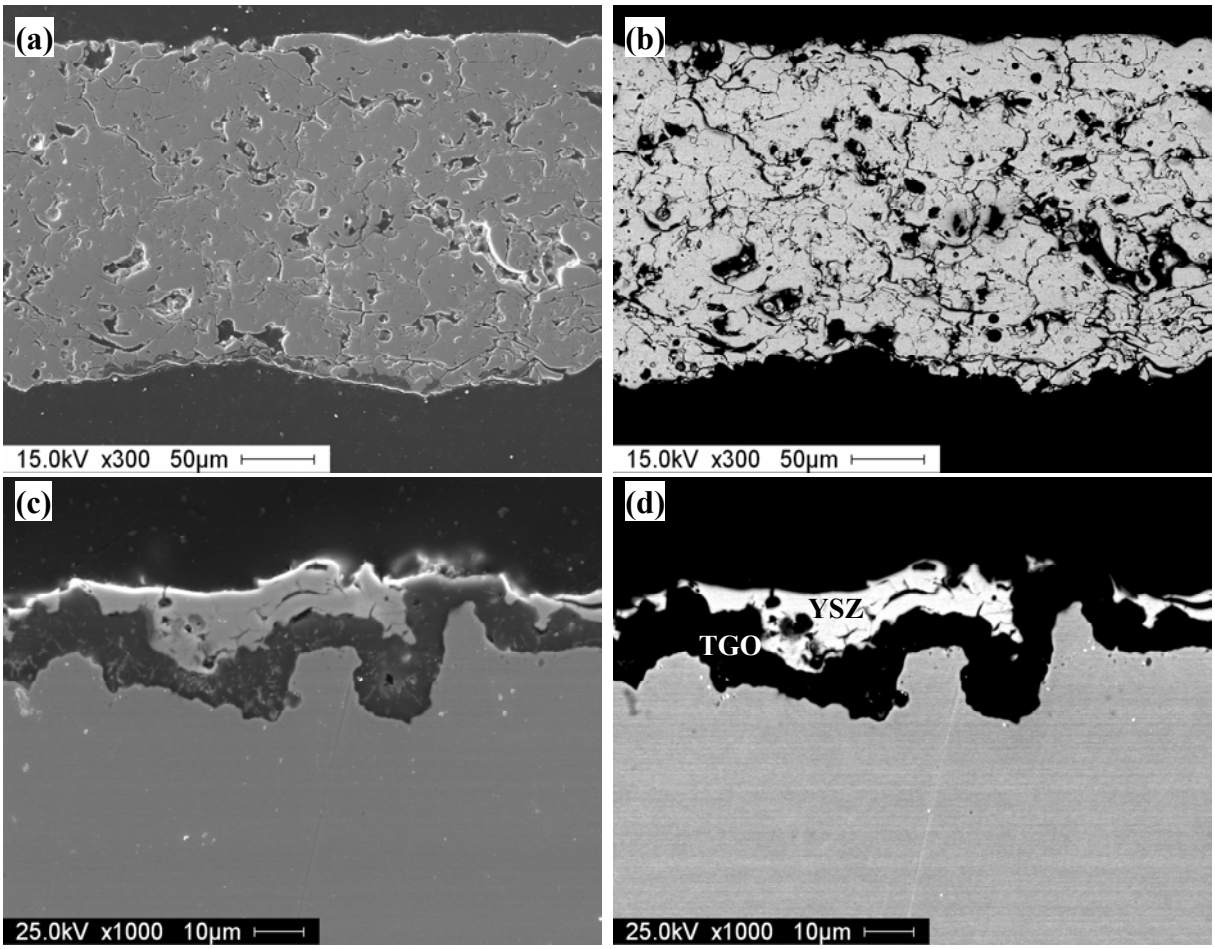

Figure 148. Cross-sectional secondary and backscatter electron micrographs of type V TBCs after spallation: (a,b) spalled-YSZ coating and (c,d) bond coat after YSZ spallation.

V.4.6. Characterization of Failure for Electron Beam Physical Vapor Deposited Thermal Barrier Coatings for 1-hour thermal cycling

Figure 149 represents backscatter electron micrographs of spallation surfaces for type II (350µm-thick) EB-PVD TBCs with NiCoCrAlY bond coat. This TBC type had an average lifetime of 280 1-hour cycles. Microscopic constituents of YSZ and TGO were observed on both bottom of the spalled-YSZ in Figure 149(a,b) and top of the bond coat surface where YSZ coating has spalled off in Figure 149(c,d). Small amount of metallic surface of NiCoCrAlY bond coats was observed. These micrographs indicate that the spallation of type II TBCs occurred within the YSZ, at the interface between YSZ and TGO, within the TGO and at the interface between TGO and bond coat. Most of the TGO were observed as islands and contained Al, Ni, Co and Cr. Cross-sectional secondary electron micrographs demonstrate that an internal oxidation of the bond coat occurred as presented in Figure 150. Cross-sectional bright-field images from TEM presented in Figure 151 also indicated that the TGO was still in-tact with NiCoCrAlY bond coat, and oxides containing Y_2O_3 were also observed.

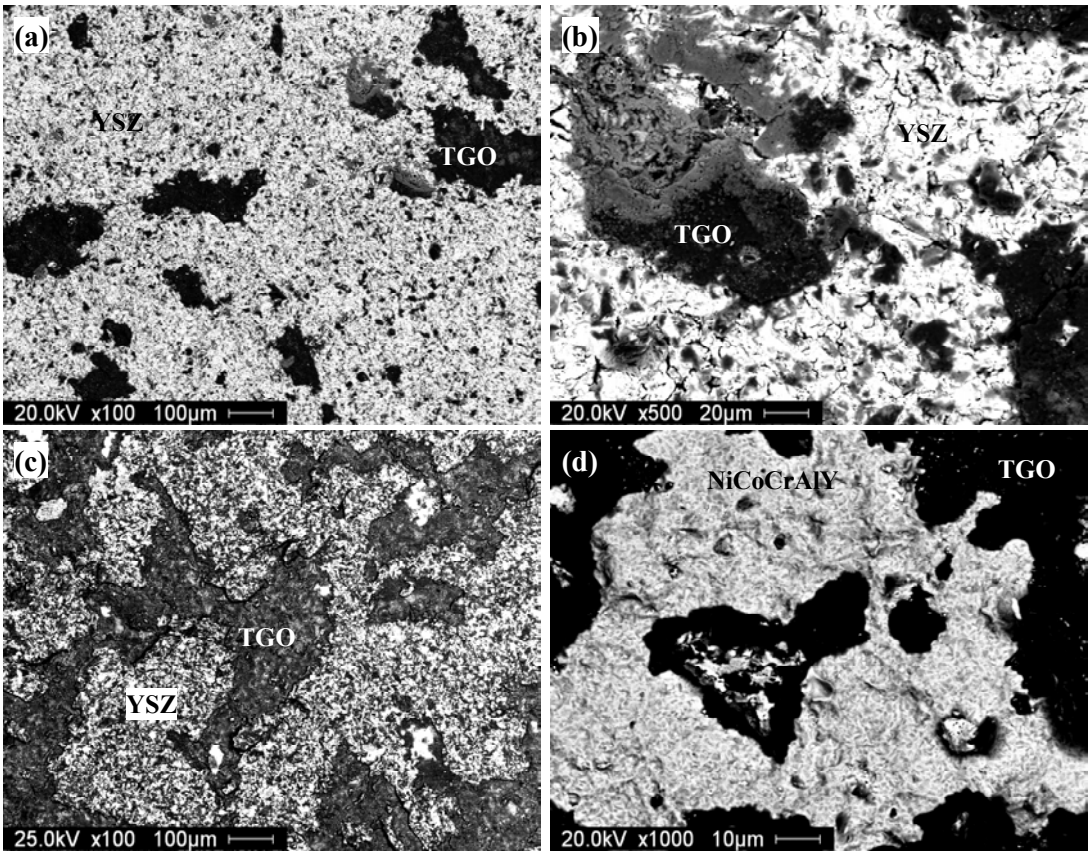

Figure 149. Backscatter electron micrographs of fracture surfaces in type II TBCs: (a,b) bottom of the spalled-YSZ coating and (c,d) top of the bond coat where YSZ coating has spalled off.

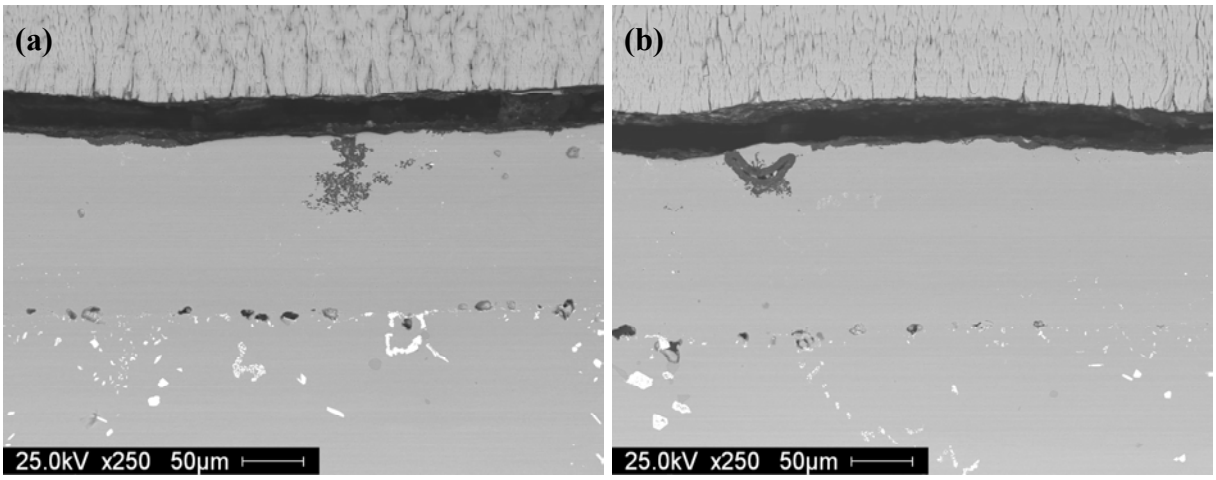

Figure 150. Cross-sectional secondary electron micrographs of type II TBCs after spallation showing the internal oxidation of NiCoCrAlY bond coat.

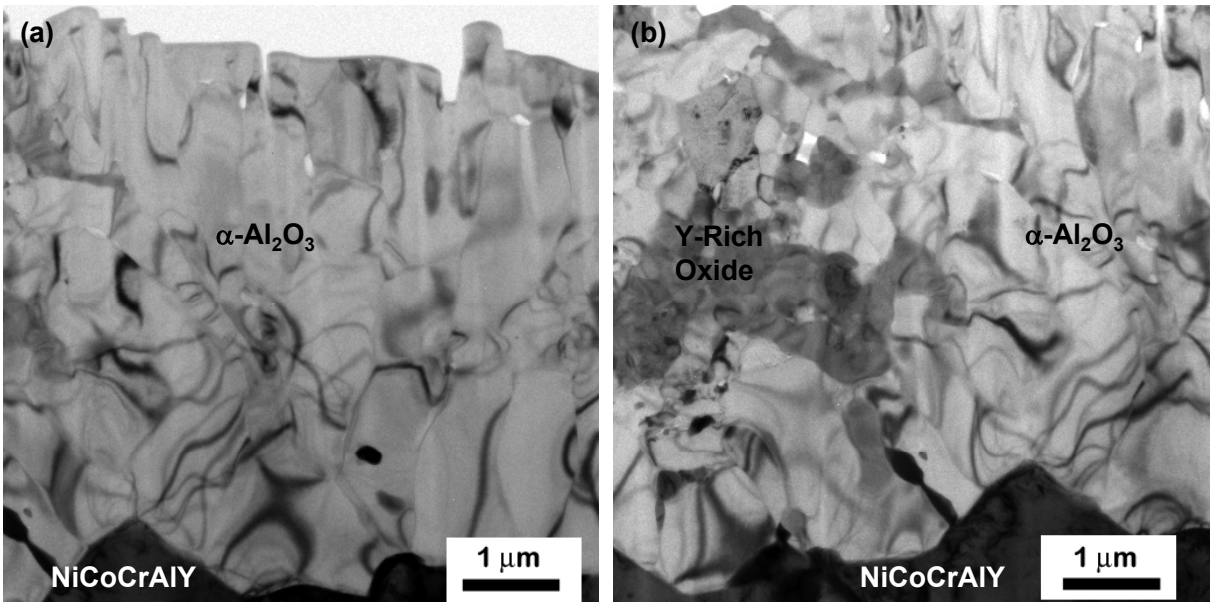

Figure 151. Cross-sectional bright field transmission electron micrographs of TGO scale on type II TBCs after failure.

Figure 152 represents backscatter electron micrograph of spallation surfaces in type III (145μm-thick) EB-PVD TBCs with as-coated (Ni,Pt)Al bond coat. This TBC type had an average lifetime of 418 1-hour cycles. Microscopic constituents of YSZ and TGO were observed on both bottom of the spalled-YSZ in Figure 152(a,b) and top of the bond coat surface where the YSZ coating has spalled off in Figure 152(c,d,e). Presence of mixed oxide zone (MOZ) and metallic surface of (Ni,Pt)Al bond coats were observed on the top surface of the bond coat. These micrographs indicate that the spallation of type III TBCs occurred within YSZ, at the interface between the YSZ and TGO including MOZ, within the TGO including MOZ and at the interface between the TGO and bond coat. With the exposure of the bond coat surface, the impedance response of the TBC specimen, shown in the Figure 60, decreased which in-turn is related to the decrease in the resistance (R_{TGO}) and a sharp increase in the capacitance (C_{TGO}) reported in Figure 75 and Figure 76. Most of the TGO observed on the fracture surface indicates the intimate relationship between grain boundary ridges of (Ni,Pt)Al bond coat.

Cross-sectional secondary electron micrographs demonstrate that a preferential oxidation of the bond coat below the ridges associated with the grain boundaries has occurred as presented in Figure 153. However, it should be noted that the crack at the asperity tip of the grain boundary ridges are not necessarily observed with the preferential oxidation of grain boundaries. Cross-sectional bright-field images from TEM presented in Figure 154 also indicated that TGO was still in-tact with (Ni,Pt)Al bond coat. Presence of MOZ was observed on the top of the TGO scale along with some voids.

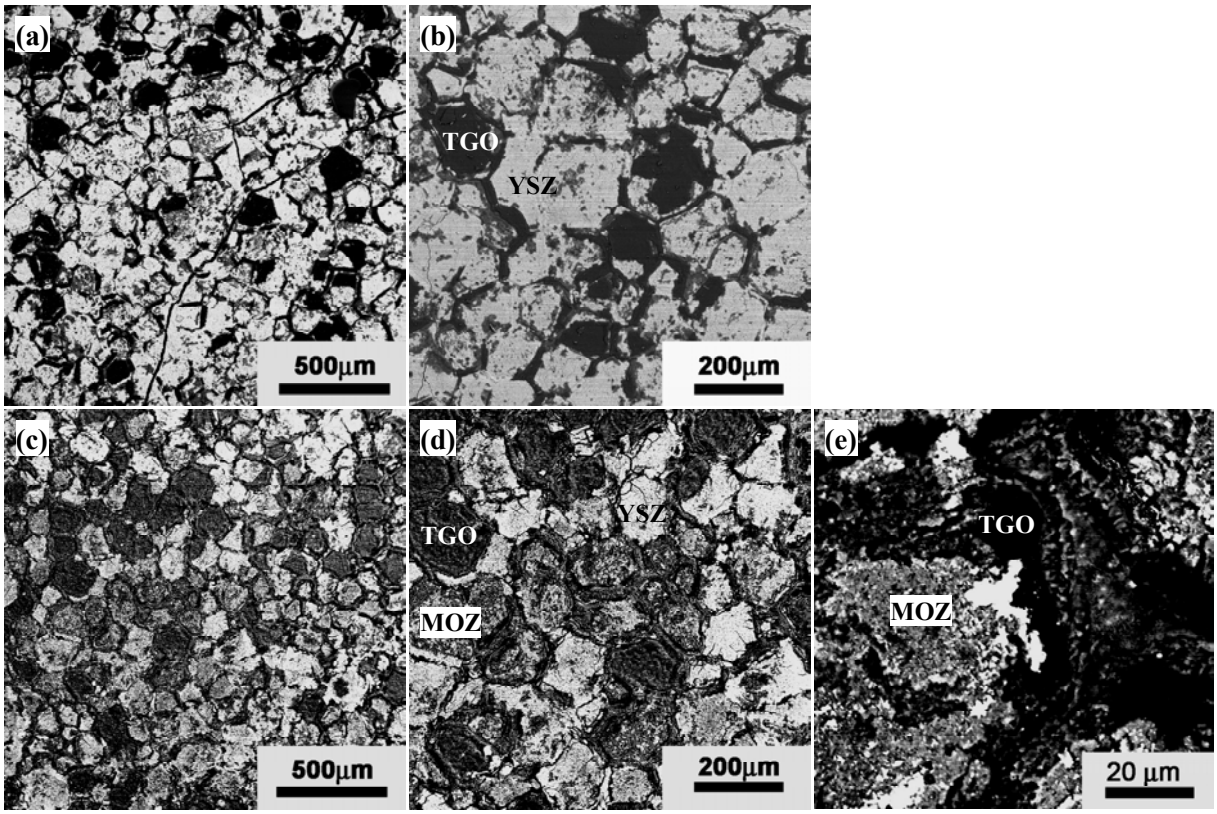

Figure 152. Backscatter electron micrographs of fracture surfaces in type III TBCs: (a,b) bottom of the spalled-YSZ coating and (c,d,e) top of the bond coat where YSZ coating has spalled off.

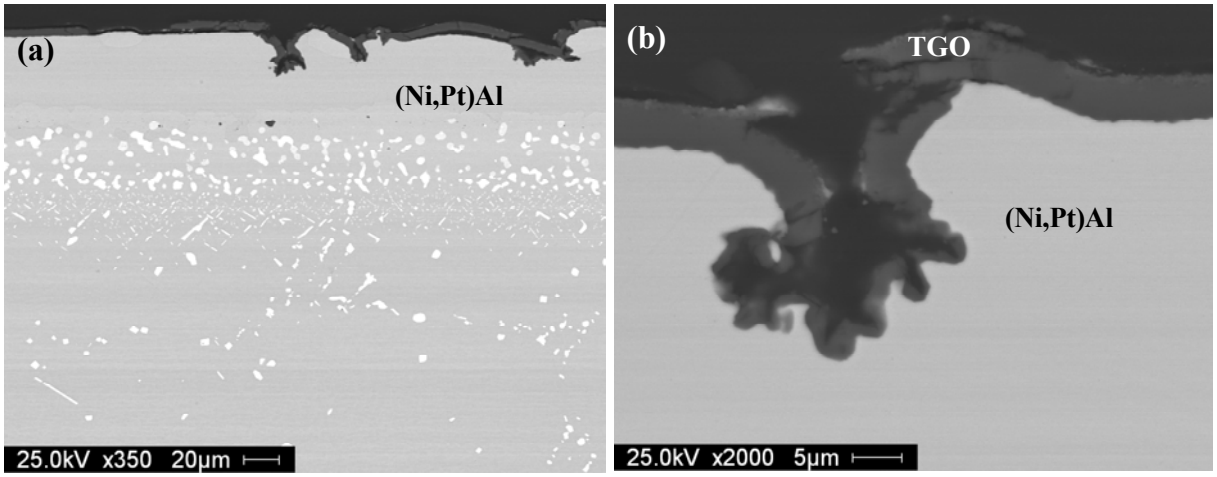

Figure 153. Cross-sectional backscatter electron micrographs of type III TBCs after spallation showing the preferential oxidation of (Ni,Pt)Al bond coat along the grain boundaries associated with ridges.

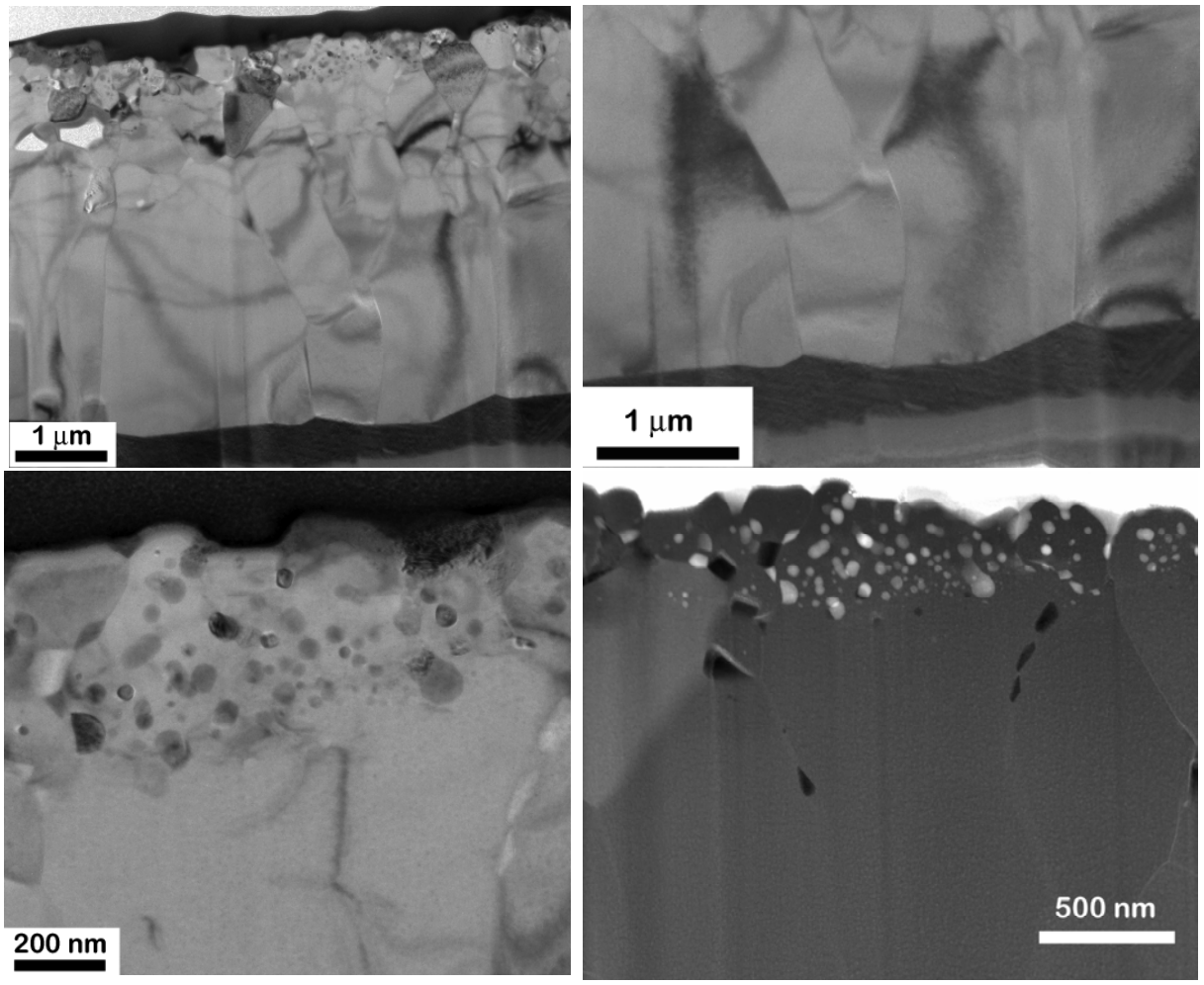

Figure 154. Cross-sectional bright field and high angle annular dark field transmission electron micrographs of TGO scale on type III TBCs after failure.

Figure 155 represents backscatter electron micrographs of spallation surfaces for type IV (140μm-thick) EB-PVD TBCs with grit-blasted (Ni,Pt)Al bond coat. This TBC type had an average lifetime of 362 1-hour cycles. Microscopic constituents of YSZ and TGO were observed on both bottom of the spalled-YSZ in Figure 155 (a,b) and top of the bond coat surface where YSZ coating has spalled off in Figure 155 (c,d). Presence of mixed oxide zone (MOZ) and metallic surface of (Ni,Pt)Al bond coats were also observed on the top surface of the bond coat. These micrographs indicate that the fracture for the spallation of type IV TBCs occurred within YSZ, at the interface between YSZ and TGO including MOZ, within TGO including MOZ and at the interface between TGO and bond coat. With the exposure of the metallic surface (bond coat) the impedance response as shown in the Figure 77 for failed specimen decreased compared to the as-coated condition. This decrease can be correlated to the electrical parameters representing the TGO namely, R_{TGO} and C_{TGO} reported in Figure 81 and 82. The resistance decreased and capacitance increased sharply at failure.

Cross-sectional secondary electron micrographs demonstrated a significant undulation of the TGO/bond coat interface (e.g., racheting) as presented in Figure 156. Cross-sectional bright-field images from TEM presented in Figure 157 also indicated that TGO was still intact with (Ni,Pt)Al bond coat. Presence of MOZ was observed on the top of the TGO scale along with some voids.

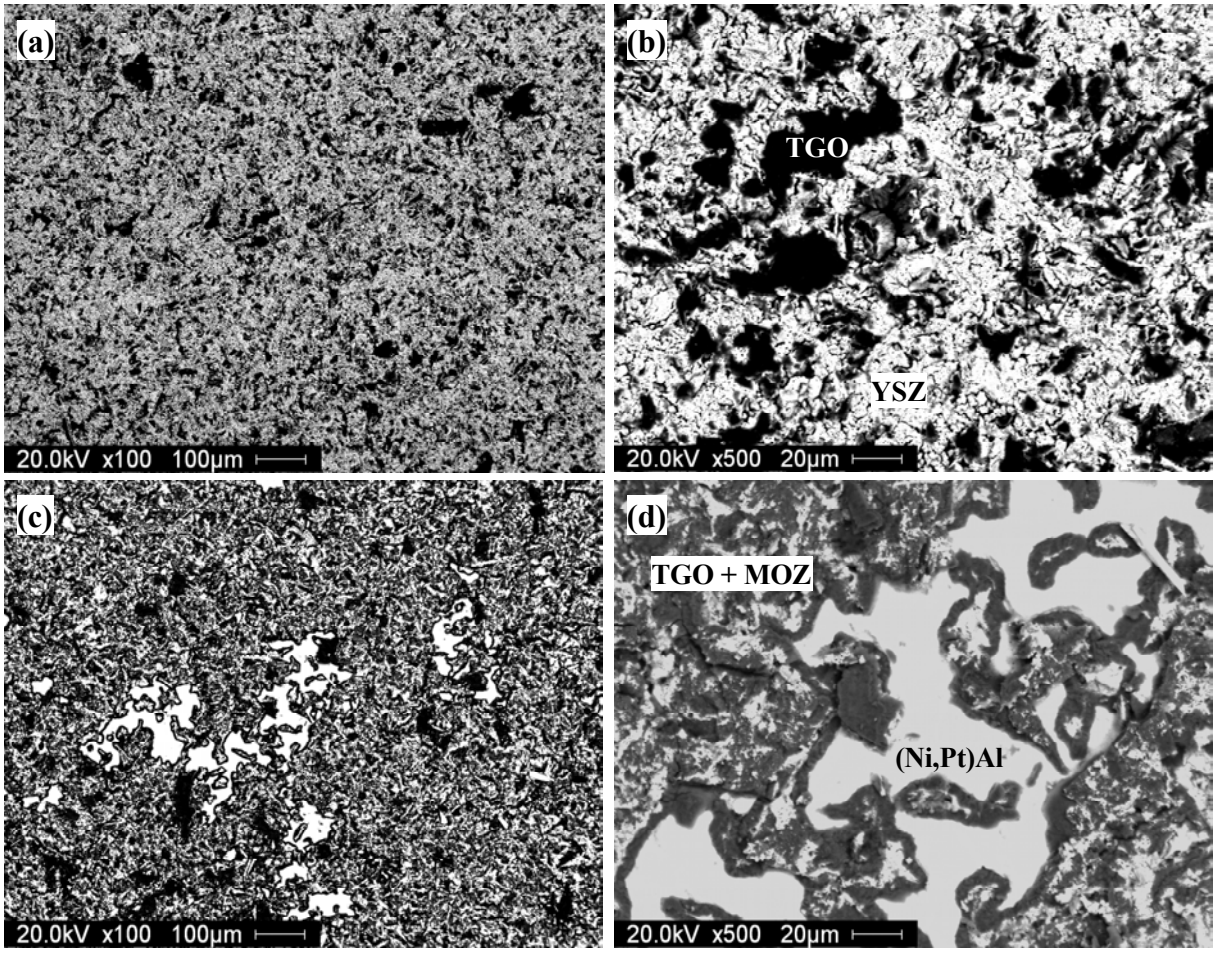

Figure 155. Backscatter electron micrographs of fracture surfaces in type IV TBCs: (a,b) bottom of the spalled-YSZ coating and (c,d) top of the bond coat where YSZ coating has spalled off.

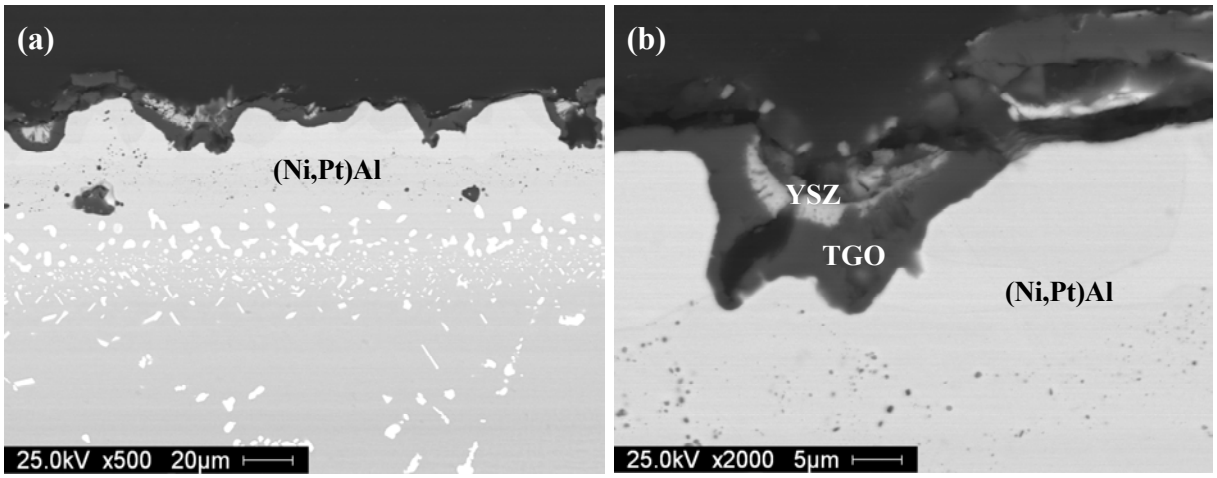

Figure 156. Cross-sectional backscatter electron micrographs of type IV TBCs after spallation showing the undulation of TGO/bond coat interface.

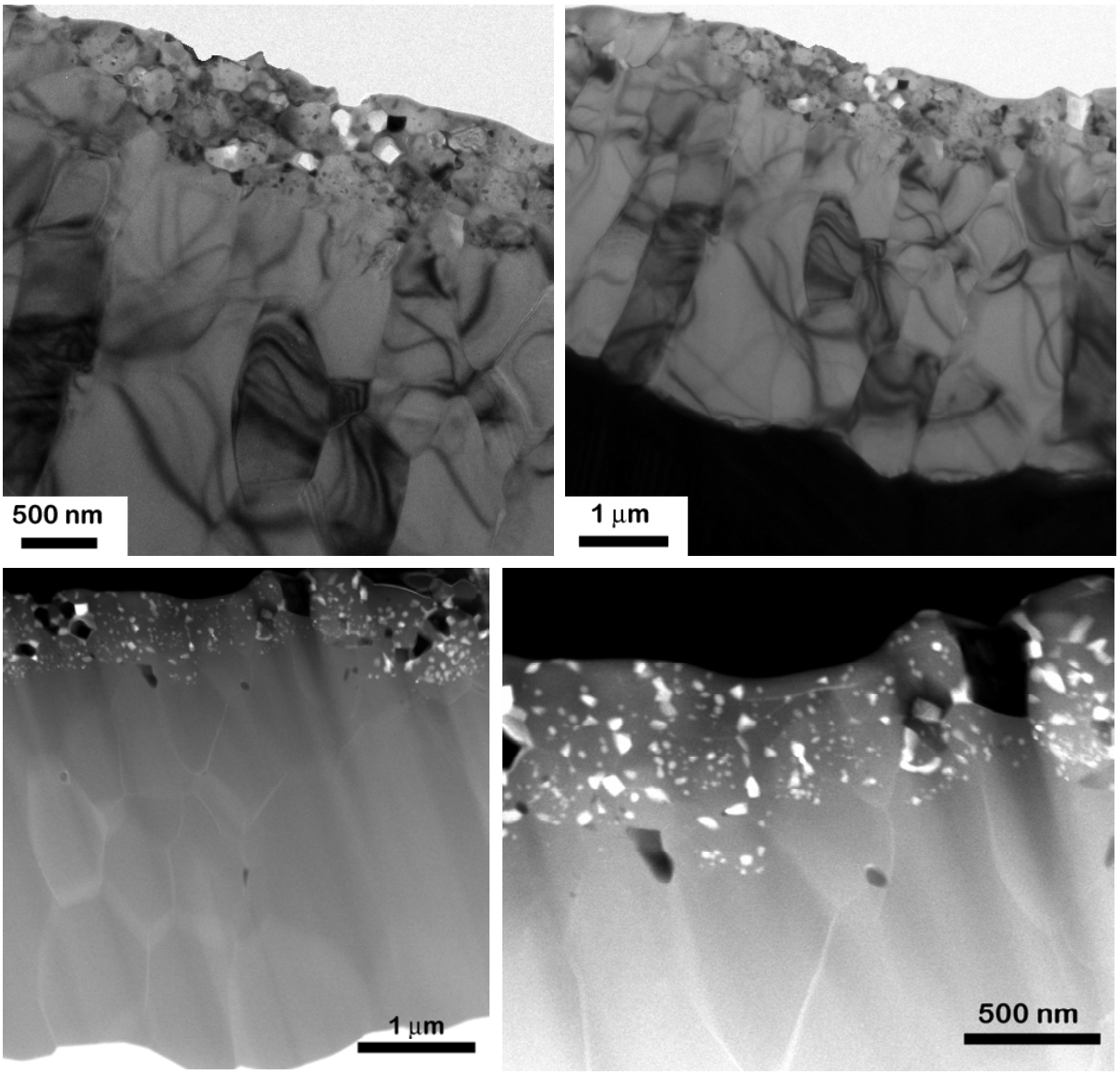

Figure 157. Cross-sectional bright field and HAADF transmission electron micrographs of TGO scale on type IV TBCs after failure.

V.4.7. Characterization of Failure for Air Plasma Sprayed Thermal Barrier Coatings for 10-hour thermal Cycling

Figure 158 represents backscatter electron micrographs of spallation of type-I APS TBCs with NiCoCrAlY bondcoat from 10-hour thermal cycling. This type of TBC had an average lifetime 113 10-hour cycles. The microscopic constituents were similar to the 1-hour thermal cycles as discussed earlier for this type of APS TBCs. Also the fracture path was similar to 1-hour thermal cycling and it occurred within YSZ near the YSZ/TGO interface. Further the cross-sectional micrographs from these coatings shown in Figure 159 showed that the micro constituents of the fracture are same as 1-hour thermal cycling.

Similar fracture was observed for type-V APS TBCs with 10-hour thermal cycling as shown in Figure 160. The average lifetime of these coatings is 18 10-hour thermal cycles. This fracture surface and path are similar to that observed for 1-hour thermal cycling as mentioned earlier in section V.4.5 and this is shown in Figure 161.

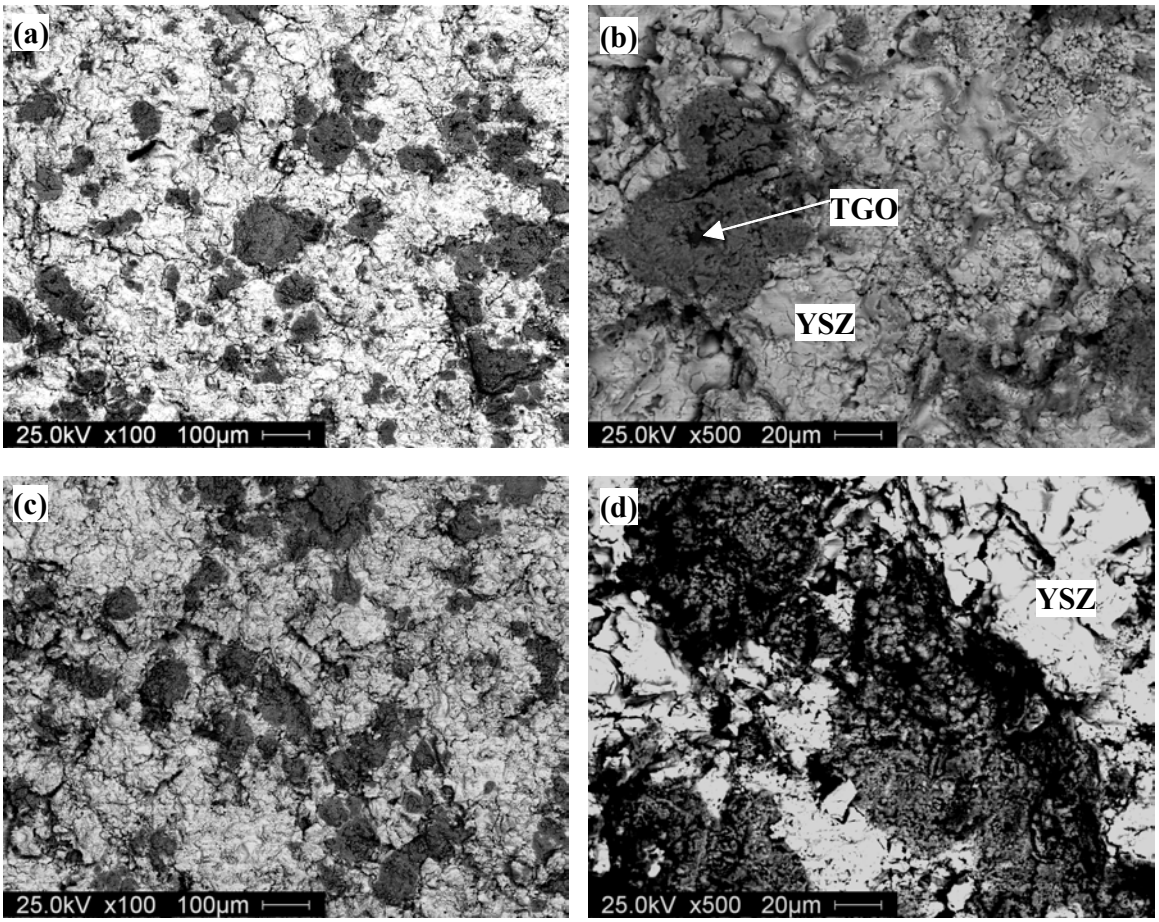

Figure 158. Backscatter electron micrographs of fracture surfaces in type-I TBCs from 10-hour thermal cycling (a,b) bottom of the spalled-YSZ coating and (c,d) top of the bondcoat where YSZ coating has spalled off. Exposure of NiCoCrAlY surface was extremely rare.

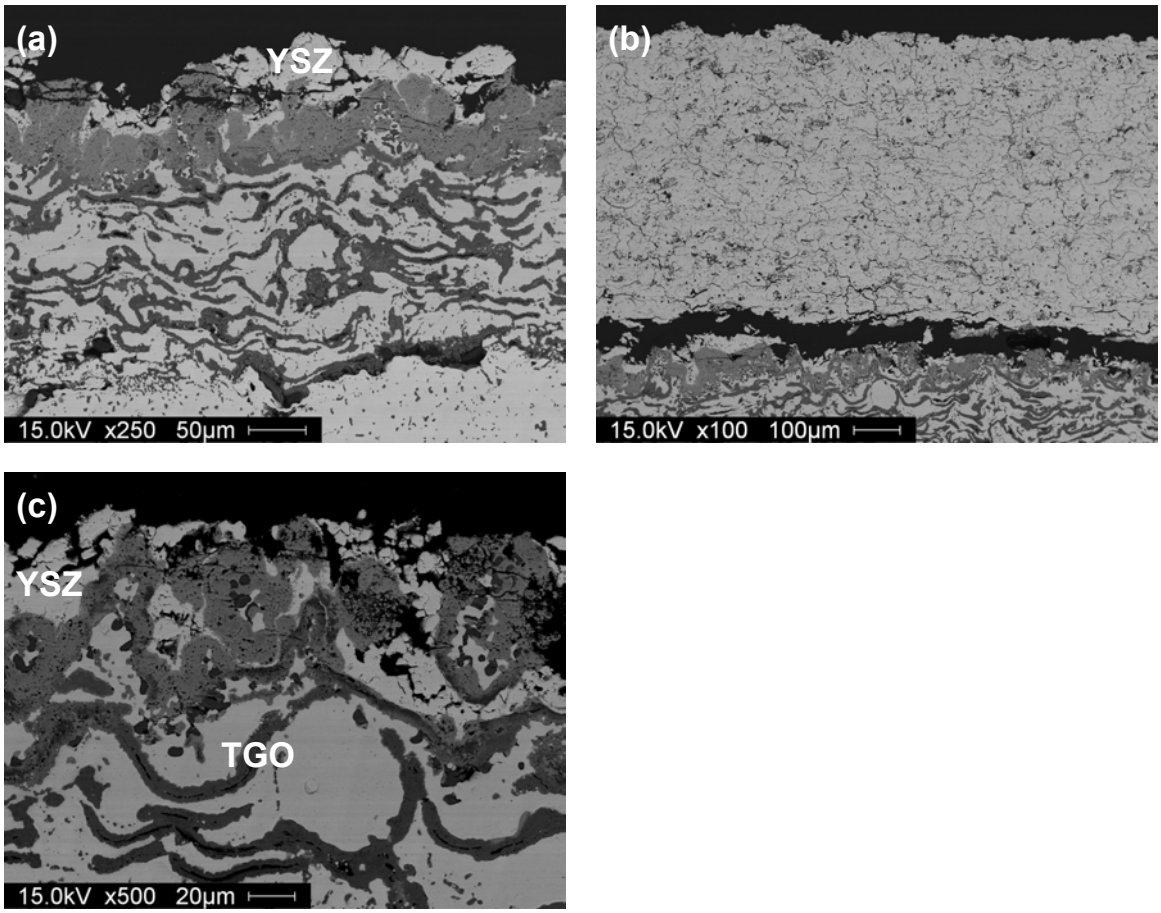

Figure 159. Cross-sectional backscatter electron micrograph of type I TBCs after spallation (a, c) bondcoat after YSZ spallation and (b) delamination at YSZ/TGO within the coating.

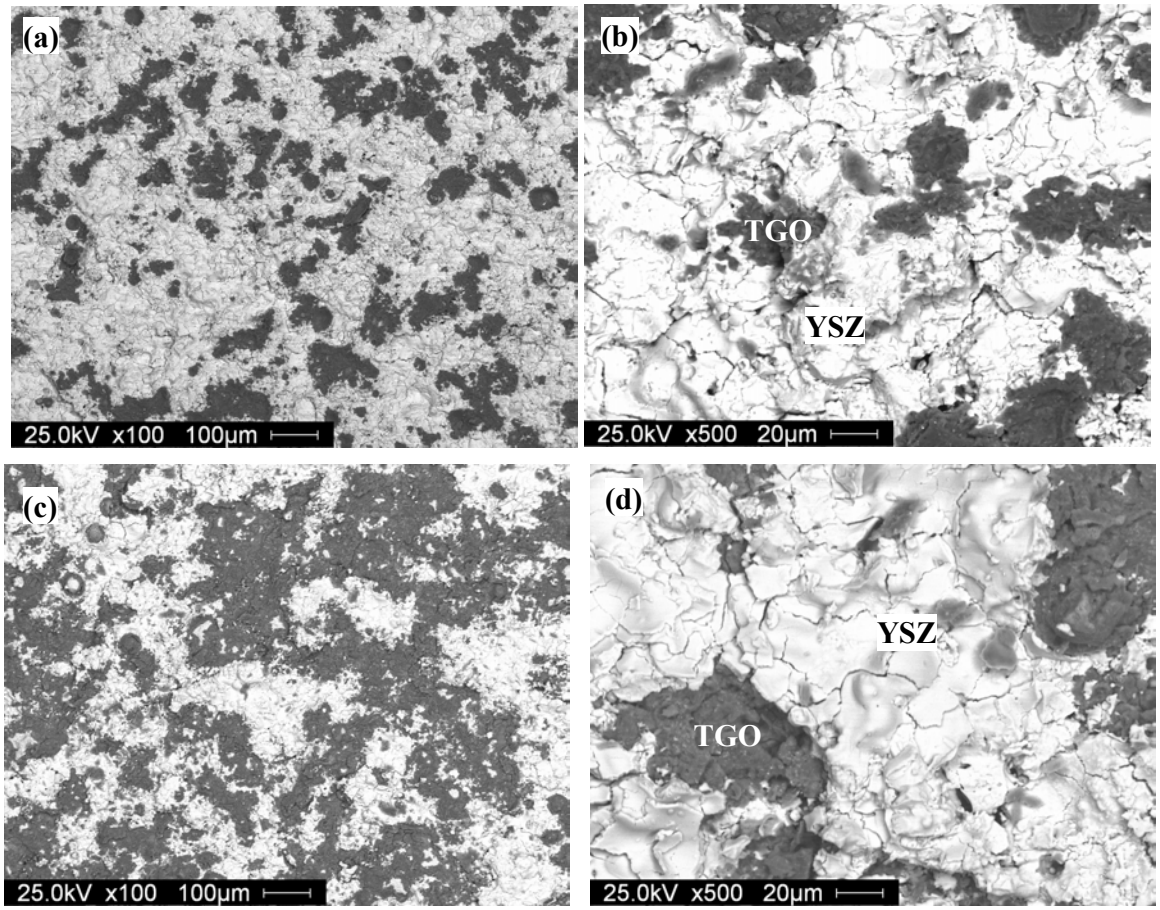

Figure 160. Backscatter electron micrographs of fracture surfaces in type-V APS TBCs from 10-hour thermal cycles (a,b) bottom of spalled YSZ coating and (c,d) top of the bondcoat where YSZ coating has spalled off. Exposure of NiCoCrAlY was extremely rare.

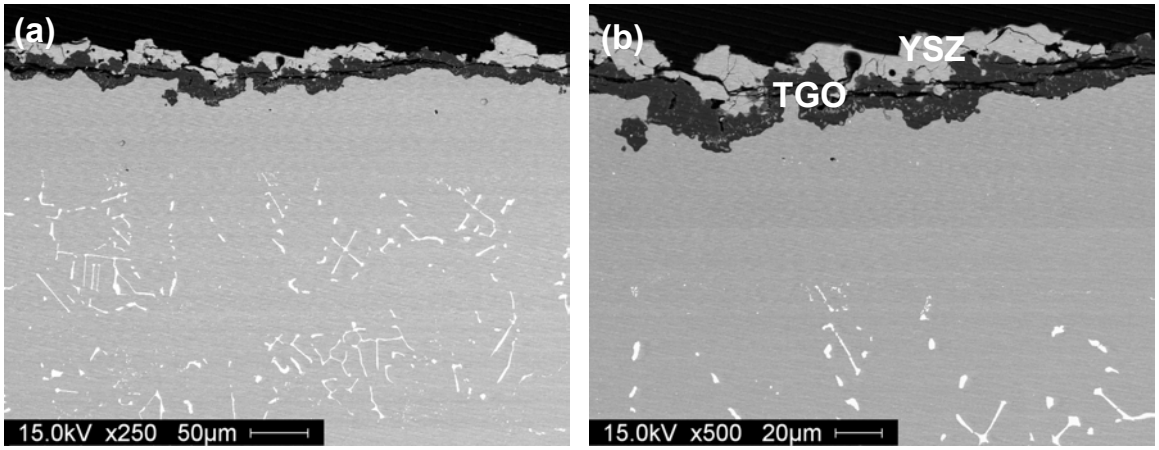

Figure 161 . Cross-sectional backscatter electron micrographs of type V TBCs after spallation: (a,b) bondcoat after YSZ spallation.

V.4.8. Characterization of Failure for EB-PVD Thermal Barrier Coatings for 10-hour thermal Cycling

Figure 162 represents backscatter electron micrographs of the spallation surfaces for type-II EB-PVD TBCs with NiCoCrAlY bondcoat from 10-hour thermal cycles. This TBC type had an average life time of 25 10-hour thermal cycles. Microscopic constituents of YSZ and TGO were observed on both bottom of the spalled-YSZ in Figure 162(a,b) and top of the bondcoat surface where YSZ coating has spalled off in Figure 162(c,d). One distinctive difference from that of TBCs failed by 1-hour thermal cycling shown in Figure 35 is that there was no exposure of the metallic NiCoCrAlY surface after spallation.

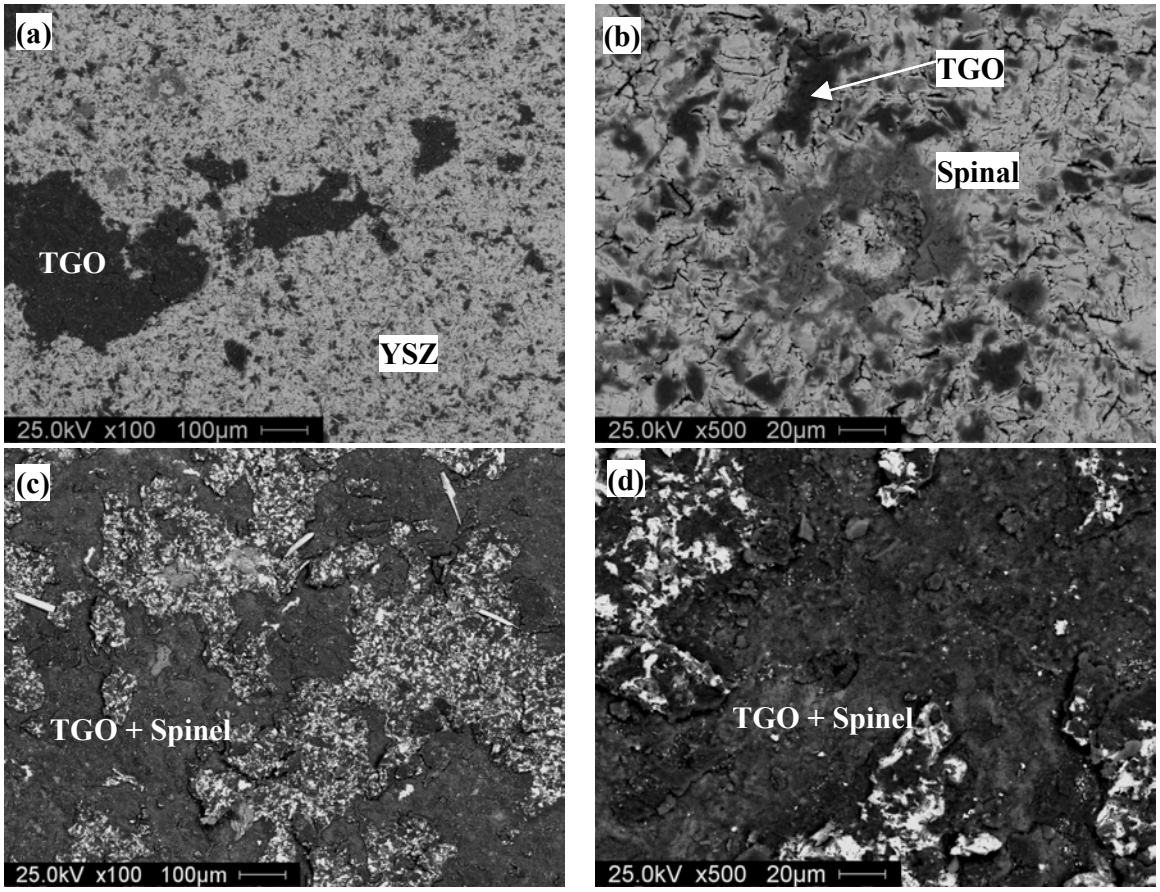

Figure 162. Backscatter electron micrographs of fracture surfaces in type II TBCs with NiCoCrAlY bondcoat (a,b) bottom of the spalled-YSZ coating and (c,d) top of the bondcoat where YSZ coating has spalled off.

Figure 163 represents backscatter electron micrographs of spallation surface of type-III EB-PVD TBCs with as-coated (Ni,Pt)Al bondcoat. This type of TBC had an average lifetime of 55 10-hour thermal cycles. Presence of extensive MOZ and metallic surface of (Ni,Pt)Al bondcoat were observed on the top surface of the bondcoat shown in 163(c,d). These micrographs indicate that the fracture for spallation of type-III TBCs occurred within

TGO including MOZ and also at the interface between TGO/bondcoat. This was different in case of 1-hour thermal cycles, were significant remains of YSZ was found on the top surface of the bondcoat. Also the cross-sectional images showed in Figure 164 shows less preferential oxidation along grain boundary associated ridges.

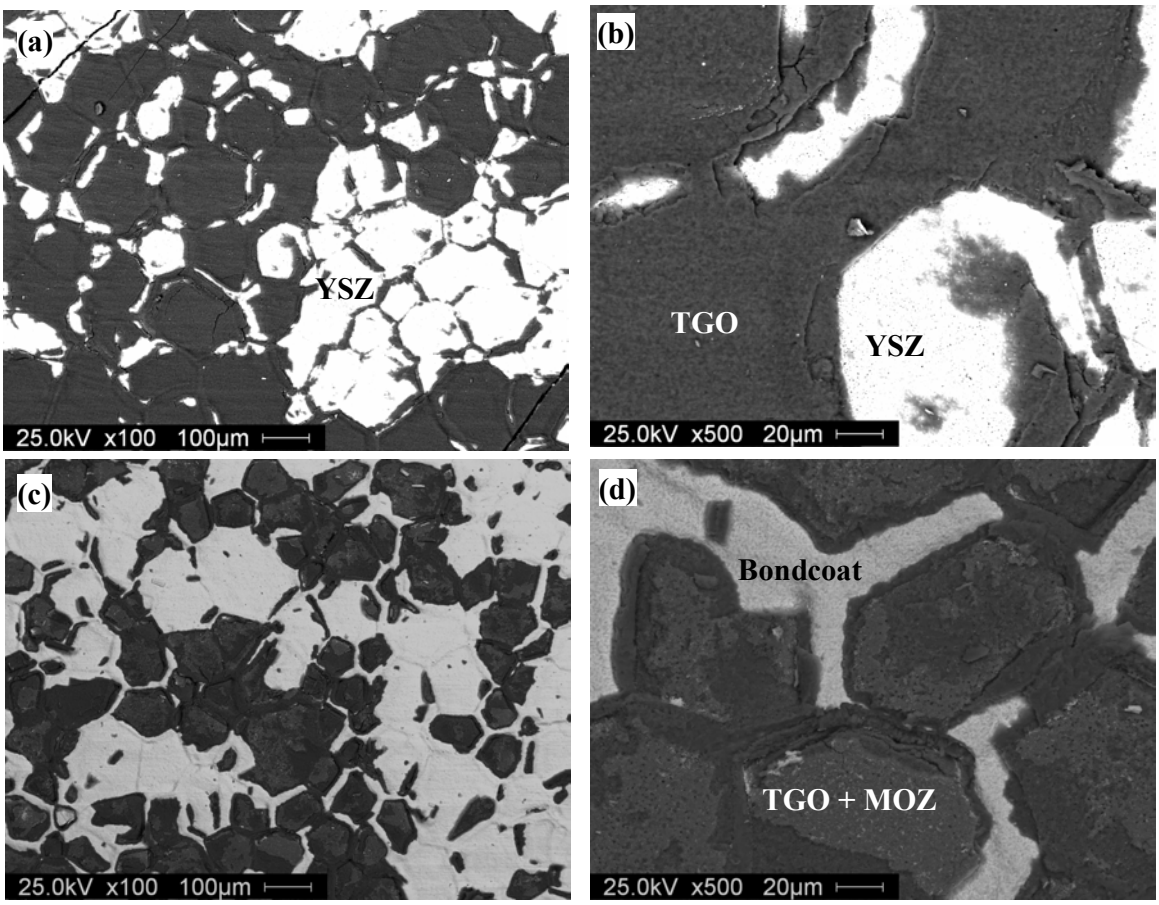

Figure 163. Backscatter electron micrographs of fracture surfaces in type III TBCs with (Ni,Pt)Al bondcoat (a,b) bottom of the spalled-YSZ coating and (c,d) top of the bondcoat where YSZ coating has spalled off.

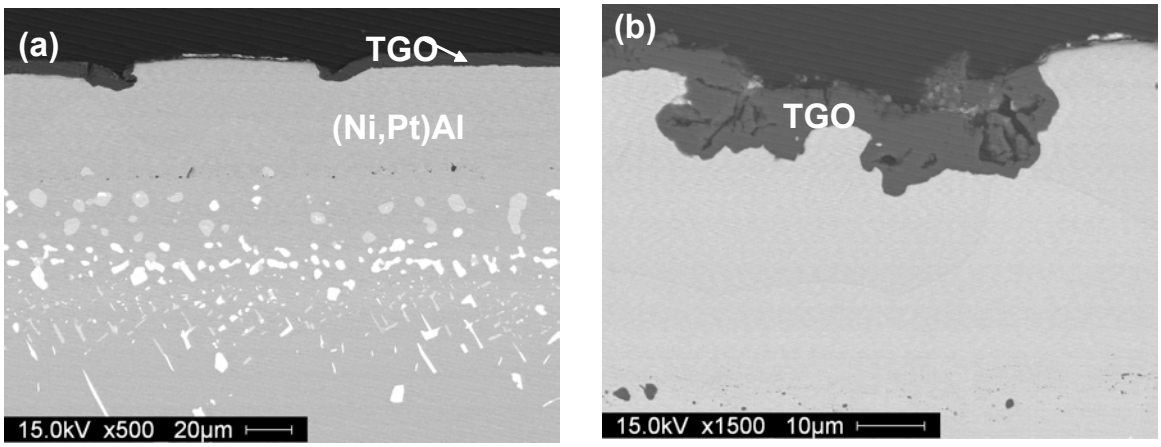

Figure 164. Cross-sectional backscatter electron micrographs of type-III TBCs after spallation showing less preferential oxidation of (Ni,Pt)Al bondcoat along grain boundaries associated with ridges.

Figure 165 represents backscatter electron micrographs of spallation surface of type-IV EB-PVD TBCs with grit-blasted (Ni,Pt)Al bondcoat. This type of TBC had an average lifetime of 42 10-hour thermal cycles. These micrographs indicate that the spallation of type IV EB-PVD TBCs with grit-blasted (Ni,Pt)Al bondcoat occurred predominantly at the TGO/bondcoat interface because the cross sectional backscatter micrograph of YSZ shown in Figure 165(c) shows that the TGO is still intact with the YSZ. Cross-sectional backscatter electron micrograph shown in Figure 165(d) demonstrates that there is minimum undulation of the TGO/bondcoat interface when compared to the racheting failure of TBCs after 1-hour thermal cycling. This mainly is due to the difference in dwell time for type IV TBCs.

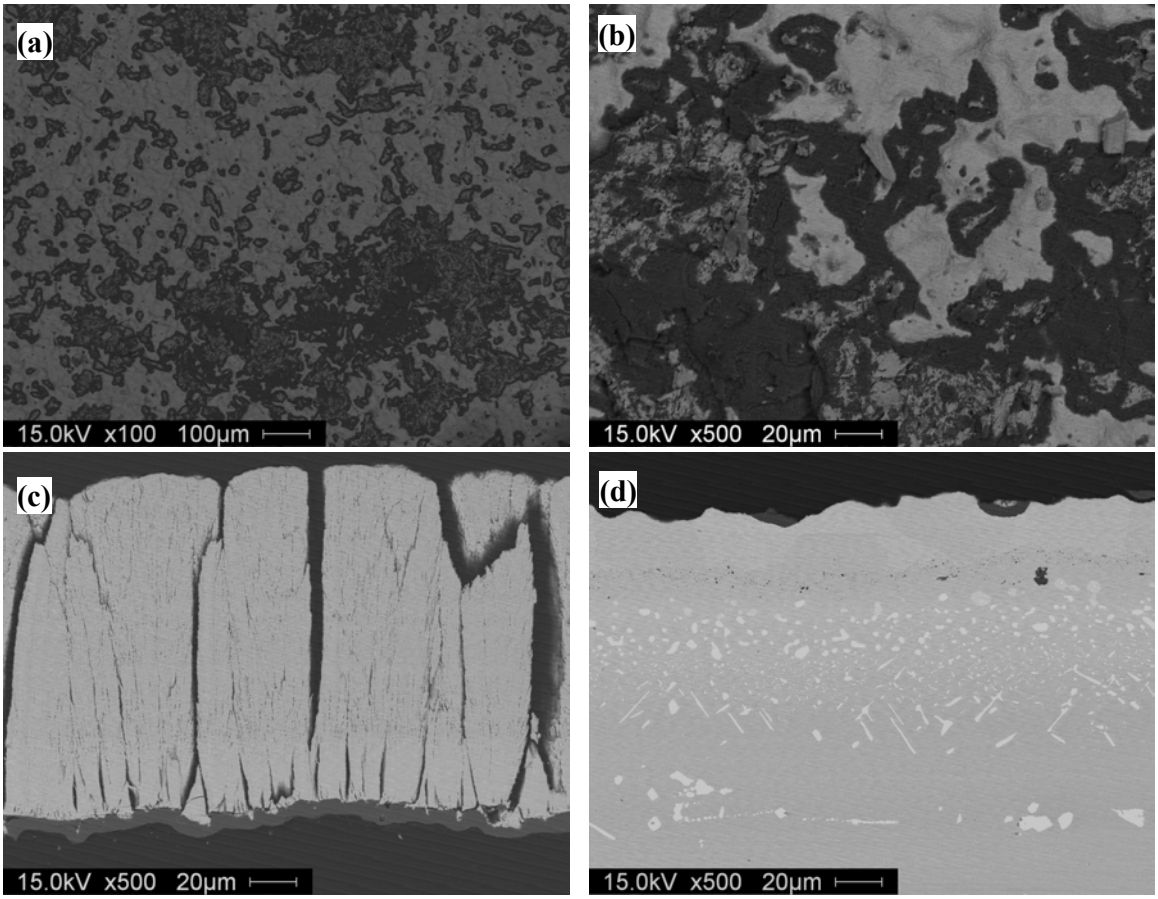

Figure 165. Backscatter electron micrographs of fracture surfaces in type IV TBCs with grit-blasted (Ni,Pt)Al bondcoat (a,b) top of the bondcoat where YSZ coating has spalled off (c) Cross section of the spalled-YSZ coating and (d) cross section of the bondcoat.

V.4.9. Characterization of Failure for APS Thermal Barrier Coatings for 50-hour thermal Cycling

Figure 166 represents backscatter electron micrographs of spallation of type-I APS TBCs with NiCoCrAlY bondcoat from 50-hour thermal cycling. This type of TBC had an average lifetime 39 50-hour cycles. The microscopic constituents were similar to the 1 and 10-hour thermal cycles as discussed earlier for this type of APS TBCs. Also the fracture path was similar to 1 and 10-hour thermal cycling and it occurred within YSZ near the YSZ/TGO interface.

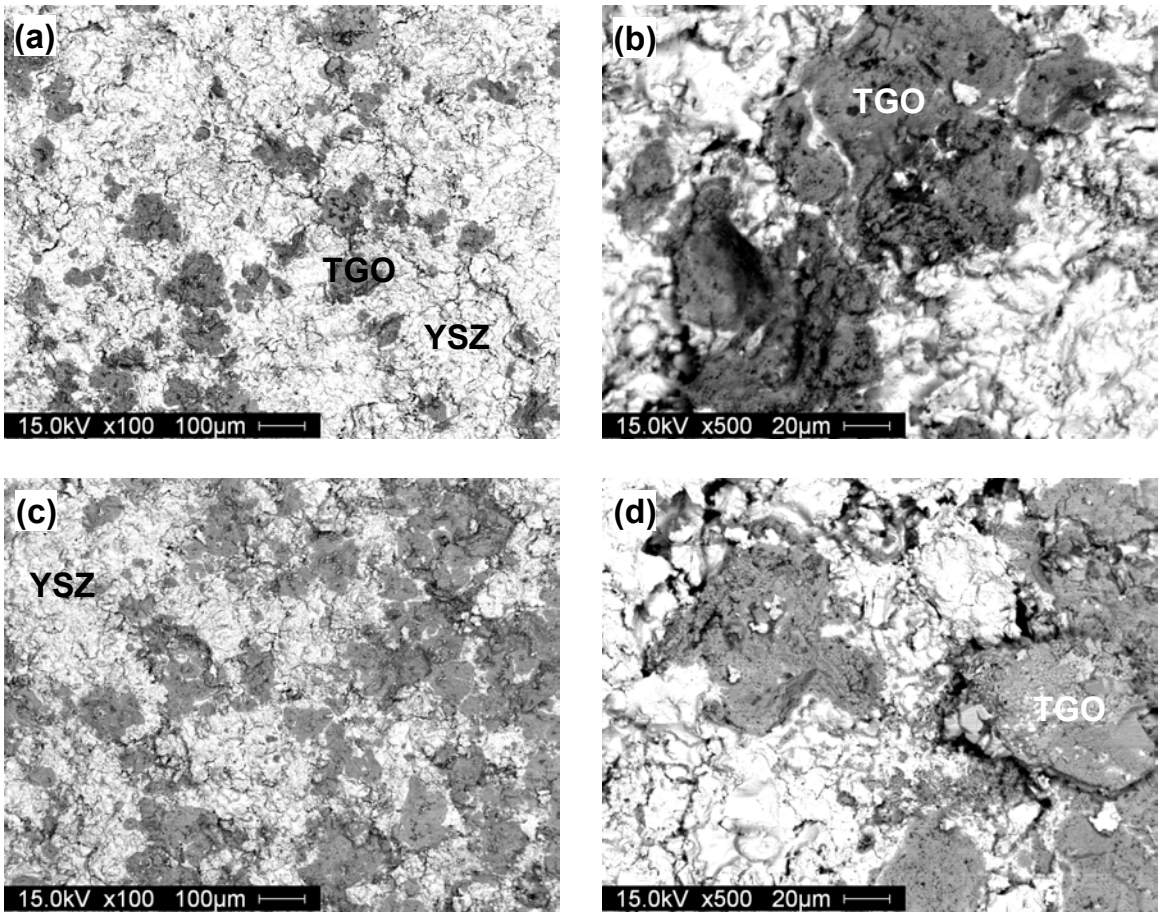

Figure 166. Backscatter electron micrographs of fracture surfaces in type-I TBCs from 50-hour thermal cycling (a,b) bottom of the spalled-YSZ coating and (c,d) top of the bondcoat where YSZ coating has spalled off. Exposure of NiCoCrAlY surface was extremely rare.

V.4.10. Characterization of Failure for EB-PVD Thermal Barrier Coatings for 50-hour thermal Cycling

Figure 167 represents backscatter electron micrographs of the spallation surfaces for type-II EB-PVD TBCs with NiCoCrAlY bondcoat from 50-hour thermal cycles. This TBC type had an average life time of 3.5 50-hour thermal cycles. Microscopic constituents of YSZ and TGO were observed on both bottom of the spalled-YSZ in Figure 167(a,b) and top of the bondcoat surface where YSZ coating has spalled off in Figure 167(c,d). One distinctive difference from that of TBCs failed from other thermal cycling is that exposure of the metallic NiCoCrAlY surface after spallation. The fracture predominantly occurred at the TGO/bondcoat interface.

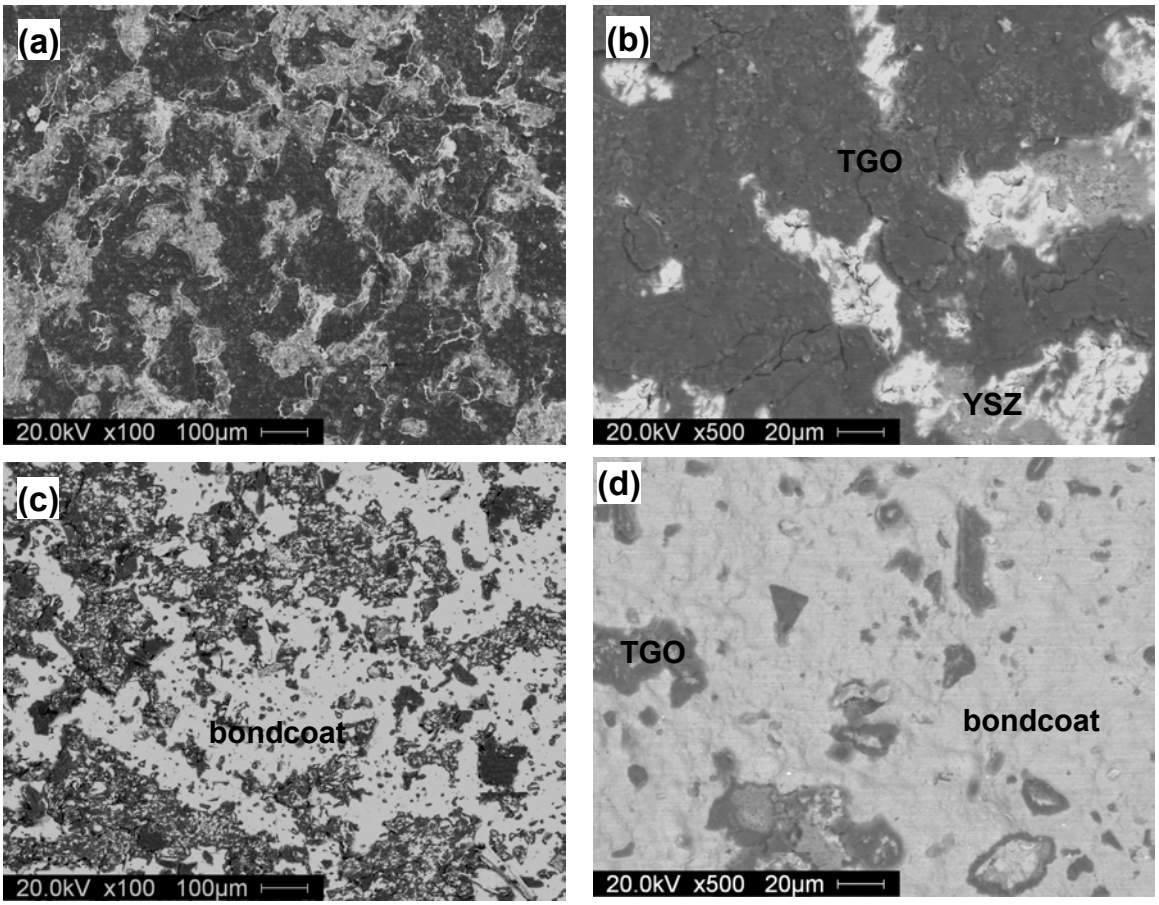

Figure 167. Backscatter electron micrographs of fracture surfaces in type-II TBCs from 50-hour thermal cycling (a,b) bottom of the spalled-YSZ coating and (c,d) top of the bondcoat where YSZ coating has spalled off.

Figure 168 represents backscatter electron micrographs of spallation surface of type-III EB-PVD TBCs with as-coated (Ni,Pt)Al bondcoat. This type of TBC had an average lifetime of 12 50-hour thermal cycles. Presence of MOZ and metallic surface of (Ni,Pt)Al bondcoat were observed on the top surface of the bondcoat shown in 168(a,b). These micrographs indicate that the fracture for spallation of type-III TBCs occurred at TGO/bondcoat interface including MOZ. This was different in case of 1-hour thermal cycles, were significant remains of YSZ was found on the top surface of the bondcoat. Also the cross-sectional images showed in Figure 169 shows less preferential oxidation along grain boundary associated ridges.

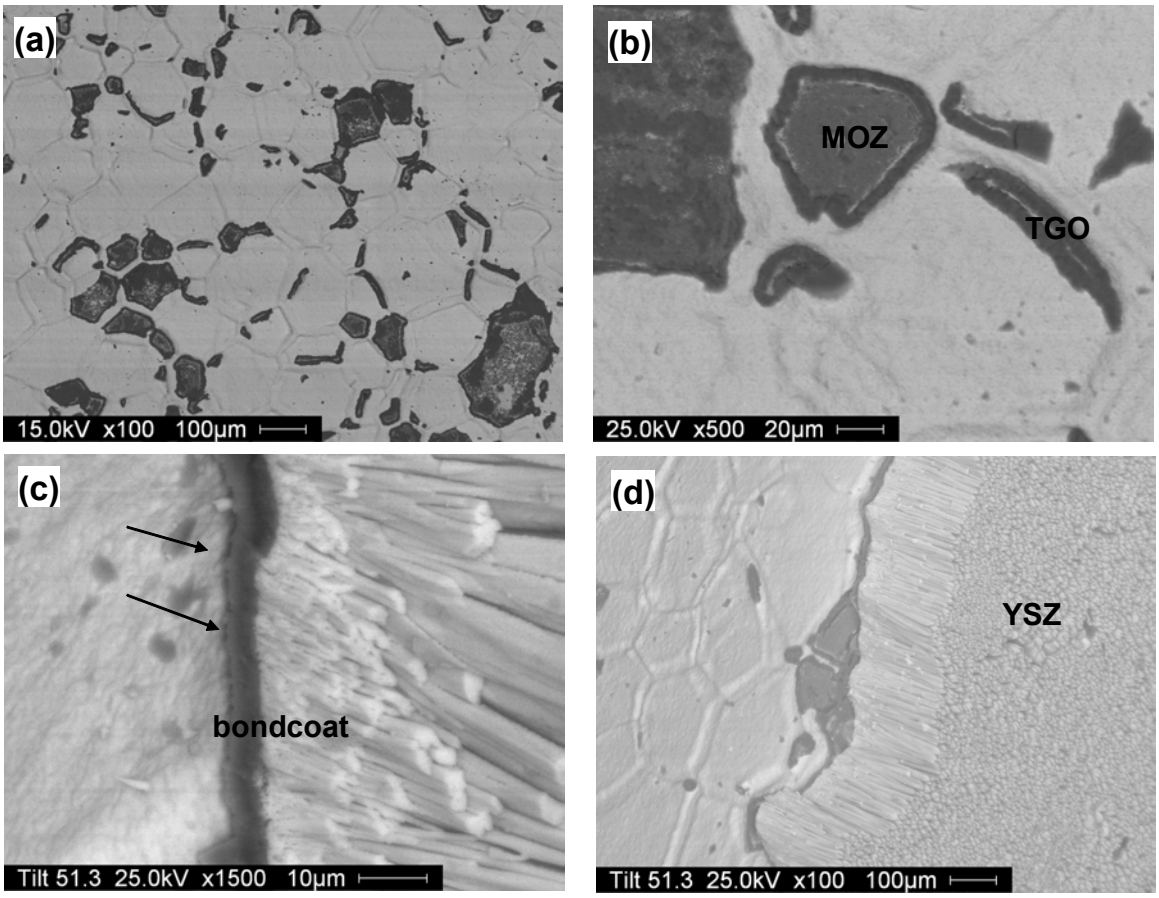

Figure 168. Backscatter electron micrographs of fracture surfaces in type III TBCs with (Ni,Pt)Al bondcoat (a,b) top of the bondcoat where YSZ coating has spalled off (c,d) delamination at TGO/bondcoat interface shown in arrows.

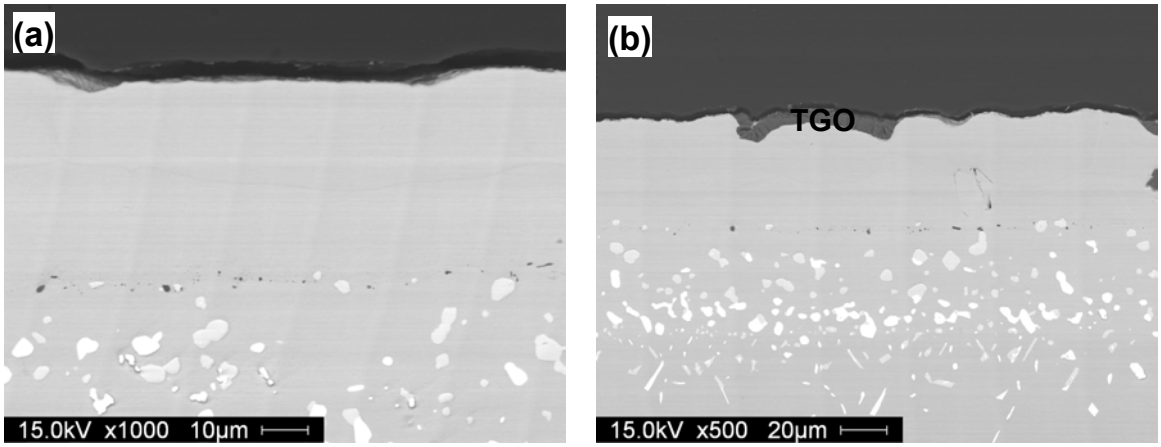

Figure 169. Cross-sectional backscatter electron micrographs of type-III TBCs after spallation showing less preferential oxidation of (Ni,Pt)Al bondcoat along grain boundaries associated with ridges.

Figure 170 represents backscatter electron micrographs of spallation surface of type-IV EB-PVD TBCs with grit-blasted (Ni,Pt)Al bondcoat. This type of TBC had an average lifetime of 9.5 50-hour thermal cycles. These micrographs indicate that the spallation of type IV EB-PVD TBCs with grit-blasted (Ni,Pt)Al bondcoat occurred predominantly at the TGO/bondcoat interface because the cross sectional backscatter micrograph of YSZ shown in Figure 170(b) shows that the TGO is still intact with the YSZ. Cross-sectional backscatter electron micrograph shown in Figure 170(c) demonstrates that there is minimum undulation of the TGO/bondcoat interface when compared to the racheting failure of TBCs after 1-hour thermal cycling. This mainly is due to the difference in dwell time for type IV TBCs.

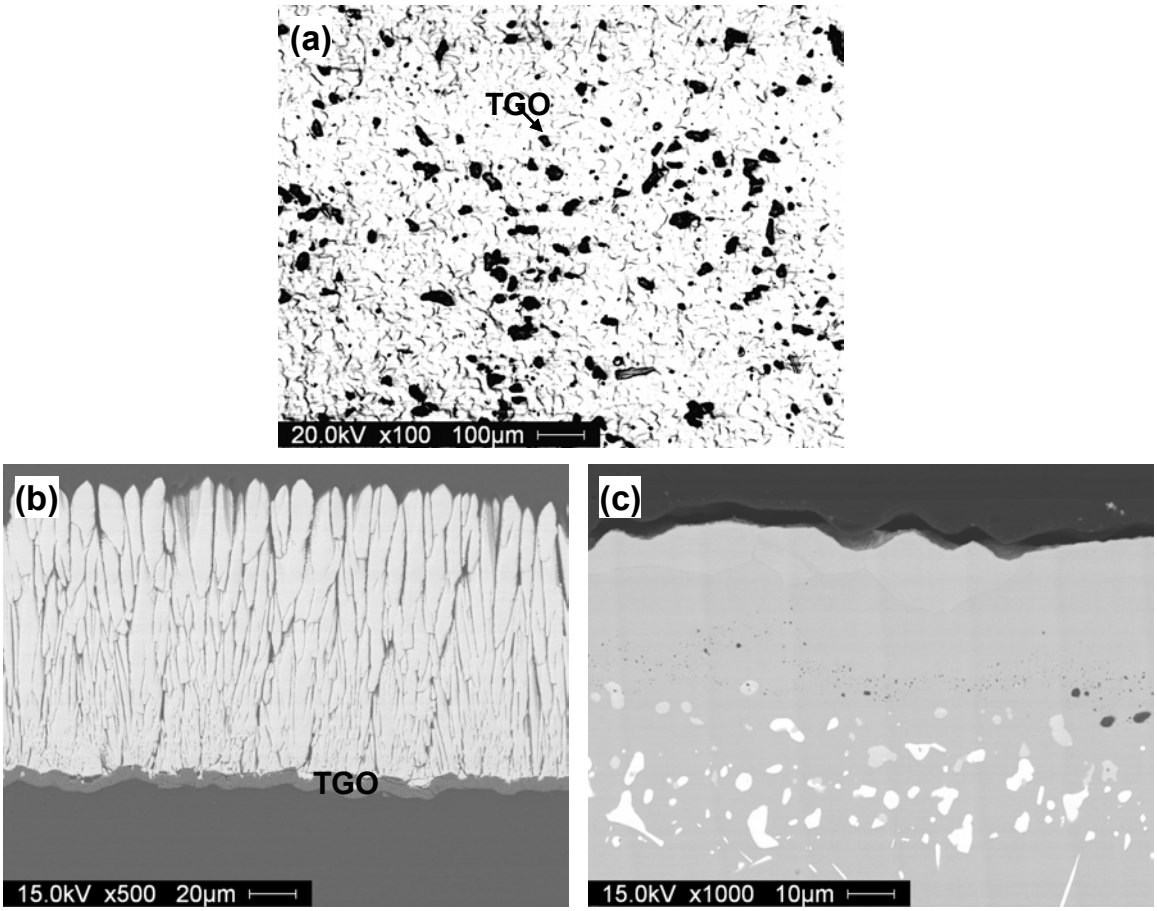

Figure 170. Backscatter electron micrographs of fracture surfaces in type IV TBCs with grit-blasted (Ni,Pt)Al bondcoat (a) top of the bondcoat where YSZ coating has spalled off (b) Cross section of the spalled-YSZ coating and (c) cross section of the bondcoat.

VI. CONCLUSION

Failure characteristics and mechanisms for five types of commercial production TBCs were investigated by using two complimentary NDE techniques PSLS and EIS. In addition, microstructural analysis of TBCs is carried out at atomic-micro-macro levels using a variety of characterization techniques including TEM/STEM with site-specific specimen preparation by FIB-INLO. The results of NDE and microstructural analysis were correlated to provide a clearer understanding of the failure mechanisms in TBCs, and further development/refinement of NDE techniques.

During thermal cycling, TBC specimens are being non-destructively examined by PSLS and EIS. For type III EB-PVD TBCs, a photostimulated luminescence associated with stress-relief of the TGO scale was observed prior to the final spallation. Correspondingly, micro-cracking associated with ridges on the (Ni,Pt)Al bond coat was observed via microscopy. For type IV TBCs, a stress-relaxation associated with racheting of the TGO/bondcoat interface towards complete relief was observed as a function of 1-hour thermal cycling. However, this observation related to racheting was not observed during 10- and 50-hour thermal cycling. Analyzing EIS results with TBCs and other selected experiments has demonstrated potentials to monitor several microstructural changes that occur in TBCs during thermal cycling. These include sintering of YSZ, growth of TGO scale, sub-critical damage in TBCs prior to failure.

Findings of this program have been published in 9 refereed journal publications (additional 3 in preparation/submitted) and 8 refereed conference proceedings, as well as 4 invited presentations (additional 3 invited), 25 presentations (additional 3 to be presented). This program fully and partially supported following graduate and undergraduate as research assistants. Mr. Balaji Jayaraj earned his M.S. and will be granted his Ph.D. in materials science and engineering. He is a recipient of UCF's Most Outstanding M.S. Thesis of 2003, and will be employeed at (March, 2006) Mitsubishi Power Systems, Orlando, FL. Ms. Barbara Franke, Now with Solar Turbines Incorporated, San Diego, CA, earned her B.S. and M.S. in materials science and engineering with honors such as Honeywell Leadership Scholarship, 2003 and 2004 UTSR Fellow, UTSR undergraduate research assistant prior to her graduate work. Through undergraduate research assitantship, Mr. Christopher Petorak earned his B.S. in mechanical engineering and is now at Purdue University for Ph.D. in materials science and engineering working on doctoral dissertation involving stress relaxation of APS TBCs. Mr. Travis Patterson was another undergraduate research assistant who just received his B.S. in mechanical engineering with 2005 UTSR Fellowship. Mr. Patterson will pursue his Ph.D. in materials science and engineering at University of Central Florida starting Fall, 2006.

REFERENCES

1. R.A. Miller, *J. Am. Ceram. Soc*., 67 (1984) 517.
2. A.G. Evans, D.R. Mumm, J.W. Hutchison, G.H. Meier, F.S. Pettit, *Prog. Mater. Sci.*, 46 (2000) 505.
3. N.P. Padture, E.H. Jordan, M. Gell, *Science*, 296 (2002) 280.
4. P.K. Wright, *Current Opinions in Solid State Mater. Sci*., 4 (1999) 255.
5. R.D. Sisson, Jr., E.Y. Lee and Y.H. Sohn, Proc. PRICM-II, (1995) 1203.
6. M.J. Graham, J.I. Eldridge, D.F. Mitchell, R.J. Hussey, *Mater. Sci. Forum*, 43 (1989) 207.
7. L. Onsager, *Ann. NY Acad. Sci*., 46 (1965) 241.
8. E.Y. Lee, R.R. Biederman, R.D. Sisson, Jr., *Micro. Sci*., 7 (1991) 505.
9. D.M. Lipkin, D.R. Clarke, *Oxi. Met*., 45 (1996) 267.
10. L.A. Giannuzzi, F.A. Stevie, *Micron*, 30 (1999) 197.
11. Y.H. Sohn, B.W. Kempshall, S.K. Jha, R.R. Vanfleet, J. Kimmel, *Thin Solid Films*., Submitted, 2003.
12. Q. Ma, D.R. Clarke, *J. Am. Ceram. Soc*., 76 (1993) 1433.
13. Q. Ma, D.R. Clarke, *J. Am. Ceram. Soc*., 77 (1994) 298.
14. J.R. Christensen, D.M. Lipkin, D.R. Clarke, K. Murphy, *Appl. Phys. Lett*., 69 (1996) 3745.
15. V. Sergo, D.R. Clarke, *J. Am. Ceram. Soc*., 81 (1998) 3237.
16. D.R. Clarke, J.R. Christensen, V. Tolpygo, *Surf. Coat. Technol*., 94/95 (1997) 89.
17. Y.H. Sohn, K. Vaidyanathan, M. Ronski, E.H. Jordan, M. Gell, *Surf. Coat. Technol.*, 146/147 (2001) 102.
18. Y.H. Sohn, K. Schlichting, K. Vaidyanathan, E.H. Jordan, M. Gell, *Metall. Mater. Trans. A*, 31A (2000) 2388.
19. M. Gell, E. Jordan, K. Vaidyanathan, *Surf. Coat. Technol*., 120/121 (1999) 53.
20. Q. Wen, D.M. Lipkin, D.R. Clarke, *J. Am. Ceram. Soc*., 81 (1998) 3345.
21. A.L. Schawlow, D.L. Wood, A.M. Clogston, *Phys. Rev. Lett*., 3 (1959) 271.
22. K.W. Schlitchting, K. Vaidyanathan, Y.H. Sohn, E.H. Jordan, M. Gell, N.P. Padture, *Mater. Sci. Eng. A*, A291 (2000) 68.
23. V.H. Desai, "Development of Electrochemical Impedance Spectroscopy for Non-Destructive Evaluation of Thermal Barrier Coatings," Final Report for AGTSR No. 98-01-SR067, 2001.
24. J. Zhang, "Development of Electrochemical Impedance Spectroscopy for Non-Destructive Evaluation of Thermal Barrier Coatings," Ph.D. Dissertation, The University of Central Florida, 2001.
25. B. Jayaraj, V.H. Desai, C.K. Lee, Y.H. Sohn, *Materi. Sci. Eng. A*., 372 (2004) 278.
26. B. Jayaraj, S. Vishweswaraiah, V.H. Desai, Y.H. Sohn, *Surf. Coat. Technol*., 177 (2004) 140.
27. S. Vishweswaraiah, B. Jayaraj, Y.H. Sohn, T. Du, V.H. Desai, Proc. 2003 International Thermal Spray Conferences, Proc. 2003 International Thermal Spray Conference and Exposition (2003) 1487.
28. L.A. Giannuzzi, J.L. Brown, S.R. Brown, R.B. Irwin, F.A. Stevie, *Mat. Res. Soc. Symp. Proc.*, 480 (1997) 19.
29. H.C. Chen, J. Heberlein, E. Pfender, *Thin Solid Films*, 301 (1997) 105.

30. A.H. Carim, T.A. Dobbins, L.A. Giannuzzi, D.R. Arenas, D.A. Koss, M.J. Mayo, *Mater. Sci. Eng. A*, A334 (2002) 65.
31. O. Unal, T.E. Mitchell, A.H. Heuer, *J. Am. Ceram. Soc*., 77 (1994) 984.
32. K.S. Murphy, K.L. More, M.J. Lance, *Surf. Coat. Technol*., 146/147 (2001) 152.
33. K. Fritscher, M. Schumuecker, C. Leyens, U. Schulz, *Mater. Sci. Forum*, 251/254 (1997) 965.
34. U. Schulz, M. Menzebach, C. Leyens, Y.Q. Yang, *Surf. Coat. Technol*., 146/147 (2001) 117.

LIST OF IMPORTANT ACRONYMS AND SYMBOLS

Acronyms	Description
(Ni,Pt)Al	Pt-modified nickel aluminide
7YSZ	7wt.% yttria stabilized zirconia
AES	Auger electron spectroscopy (or spectroscope)
AMPAC	Advanced materials processing and analysis center
APS	Air plasma spray (or sprayed)
CBED	Convergent beam electron diffraction
CVD	Chemical vapor deposition (or deposited)
CE	Counter electrode
EB-PVD	Electron beam physical vapor deposition (or deposited)
EDS	Energy dispersive spectroscopy (or spectroscope)
EELS	Electron energy loss spectroscopy (or spectroscope)
eFIB	Ex-situ focused ion beam
EIS	Electrochemical impedance spectroscopy (or spectroscope)
FE-EDS	Field emission scanning electron microscopy (or microscope)
FFT	Fast Fourier transformation (or transformed)
FIB	Focused ion beam
HAADF	High angle annular dark field
HEET	High efficiency engines and turbines
HR-STEM	High resolution scanning transmission electron microscopy (or microscope)
iFIB	In-situ focused ion beam
LPPS	Low pressure plasma spray (or sprayed)
NDE	Non-destructive evaluation
n-EDS	Nano-spot energy dispersive spectroscopy (or spectroscope)
NiAl	Nickel aluminide
OM	Optical microscopy (or microscope)
PSLS	Photostimulated luminescence spectroscopy (or spectroscope)
RAM	Reliability, availability and maintainability
RBS	Rutherford backscatter spectroscopy (or spectroscope)
SAD	Selected area diffraction
STEM	Scanning transmission electron microscopy (or microscope)
TBC	Thermal barrier coating
TGO	Thermally grown oxide
UCF	University of central Florida
UTSR	University turbine systems research
WE	Working electrode
XPS	X-ray photoluminescence spectroscopy (or spectroscope)
XRD	X-ray diffraction
YSZ	Yttria stabilized zirconia

LIST OF IMPORTANT ACRONYMS AND SYMBOLS (Continued)

Symbols	Description
α-Al_2O_3	Equilibrium Al_2O_3 with monoclinic structure
α_D	Dundur's parameter
a_i	Thermodynamic activity of component *i*
a_o	Linear thermal expansion coefficient
β	Nickel aluminde solid solution with B_2 crystal structure
C_{YSZ}	Electrochemical capacitance of ceramic top coat
C_{TGO}	Electrochemical capacitance of thermally grown oxide
C_{PORE}	Electrochemical pore capacitance
C_T	Electrochemical capacitance of interface transmittance
Δ	Change in; Difference in
$\widetilde{D}_i$	Interdiffusion coefficient in binary system
$\widetilde{D}_{ij}^{n}$	Multicomponent interdiffusion coefficient
$\partial C_i / \partial x$	Concentration gradient of component *i*
δ_i	Stoichiometric deviation at interface *i*
ε	strain
E_o	Young's modulus
G	Luminescence from γ-Al_2O_3
γ-Al_2O_3	Metastable Al_2O_3 with complex cubic structure
γ_i	Thermodynamic activity coefficient of component *i*
I_i	Integrated intensity of luminescence
$\widetilde{J}_i$	Interdiffusion flux of component *i*
k_p	Parabolic oxide growth constant
%LT	Percent thermal cyclic life time
N	Luminescence from α-Al_2O_3 with a significant amount of chromia
Π	Piezospectroscopic coefficients
Q	Luminescence from θ-Al_2O_3
θ-Al_2O_3	Equilibrium Al_2O_3 with hexagonal structure
R	Luminescence from α-Al_2O_3; Ruby fluorescence doublet
R_{YSZ}	Electrochemical resistance of ceramic top coat
R_{TGO}	Electrochemical resistance of thermally grown oxide
R_{PORE}	Electrochemical pore resistance
R_S	Electrolyte solution resistance
R_T	Electrochemical resistance of interface transmittance
σ	stress
σ^g	Growth stress of thermally grown oxide
t	Time
T	Temperature
υ	Luminescence frequency
X_i	Mole fraction of component *i*
y	Thickness of thermally grown oxide
$\lvert Z \rvert$	Modulus of electrochemical Impedance

Turbine Surface Degradation with Service and Its Effects on Performance

1 June2002 to 30 November 2005
Final Report

Principal Investigator: Dr. Jeffrey Bons
Report Issue Date: 15 November 2005
DOE Award Number: DE-FC26-02NT41431
UTSR Project Number: 02-01-SR104

Submitting Organization: Brigham Young University
435 CTB, PO Box 24201, Provo, UT 84602-4201

Co-Investigators
Drs. Richard Rivir and Rolf Sondergaard, Air Force Research Laboratory
Drs. Tom Shih and Z.J. Wang, Iowa State University
Drs. Awatef Hamed & Widen Tabakoff University of Cincinnati

DISCLAIMER

This report was prepared as an account of work sponsored by an agency of the United States Government. Neither the United States Government nor any agency thereof, nor any of their employees, makes any warranty, express or implied, or assumes any legal liability or responsibility for the accuracy, completeness, or usefulness of any information, apparatus, product, or process disclosed, or represents that its use would not infringe privately owned rights. Reference herein to any specific commercial product, process, or service by trade name, trademark, manufacturer, or otherwise does not necessarily constitute or imply its endorsement, recommendation, or favoring by the United States Government or any agency thereof. The views and opinions of authors expressed herein do not necessarily state or reflect those of the United States Government or any agency thereof.

ABSTRACT

This report summarizes work completed over the full three and a half year research effort into turbine roughness. In order to reduce the length of this report the activity from each of the entities represented has been summarized in brief. Thus, the reader is referred previous reports and conference/journal papers referenced in this document that will contain more details concerning this research effort. The objective of this effort is to document the service-related surface degradation of turbine hardware and evaluate the associated losses in performance. During the period of this grant, significant progress was achieved by all of the parties involved. BYU developed a facility capable of producing engine-like deposits in an accelerated format. This has allowed the evaluation of various material systems and synfuels with regard to their rate of deposition and degradation. It also permitted the study of evolving deposits which were then evaluated in a wind tunnel facility using scaled models of the evolved deposits. AFRL has analyzed aircraft engine components from several engine companies and from within the Air Force. A partial summary of their findings is included in this report. UC conducted a series of material system evaluations using a wind tunnel that simulates erosion in a gas turbine. They subsequently correlated erosion to roughness evolution and included this empirical model in their particle-tracking CFD simulations of erosion. Finally, ISU made significant progress with the use of 2D and 3D simulations over turbine roughness structures. The limitations of current 3-D time accurate simulations of roughness were evaluated and new roughness correlations were developed from a series of 2D simulations over rough surfaces.

TABLE OF CONTENTS

Page	Section
1	Title Page
3	Abstract
4	Table of Contents
5	Executive Summary
7	Full Progress Report
7	Project Description
8	Experimental Method
12	Results and Discussion - BYU
26	Results and Discussion - BYU
30	Results and Discussion - BYU
33	Results and Discussion - BYU
40	Conclusion
40	References

EXECUTIVE SUMMARY

The ultimate objective of this 3-year research effort is the development of a model that will allow the direct assessment of the effect of service time on turbine aerothermodynamics. To achieve this objective will require four essential building blocks: acquisition of relevant data from serviced hardware, experimental and computational modeling of deposition and erosion (the two primary degradation mechanisms), experimental measurement of performance degradation for surfaces with service-related roughness, and finally detailed computational modeling of these performance effects. The following is a brief summary for each task:

Roughness Measurement on Serviced Hardware: Measurements of serviced hardware were conducted at AFRL and BYU with blades from Oklahoma City (USAF engine maintenance facility), Pratt-Whitney, Siemens, Solar, GE, and Standard-Aero.

Deposition Laboratory Simulations: A new accelerated testing facility was developed at BYU for the study of foreign deposit layers typical to the operation of land-based gas turbines. This facility was designed to produce turbine deposits in a 4-hour test that would simulate 10,000 hours of turbine operation. This is accomplished by matching the net foreign particulate throughput of an actual gas turbine. Flow Mach number, temperature and particulate impingement angle are also matched. Validation tests were conducted to model the ingestion of foreign particulate typically found in the urban environment. The majority of this particulate is ceramic in nature and smaller than 10 microns in size, but varies up to 80 microns. Deposits were formed for flow Mach number and temperature of 0.4 and 1150degC respectively, using air plasma sprayed (APS) TBC material coupons donated from industry. Investigations over a range of impingement angles yielded samples with deposit thicknesses from 20 to 100 microns in 4-hour, accelerated-service simulations. Test validation was achieved using direct comparison with deposits from service hardware. Deposit characteristics affecting blade heat transfer via convection and conduction were assessed. Surface topography analysis indicated that the surface structure of the generated deposits were similar to those found on actual turbine blades. Scanning electron microscope (SEM) and x-ray spectroscopy analyses indicated that the deposit microstructures and chemical compositions were comparable to turbine blade deposit samples obtained from industry. Multiple tests were also conducted to study foreign deposit layers typical to the operation of land-based gas turbines. Tests were conducted to model the use of syngas fuels such as coal, petcoke, sawdust, and straw. Deposits were formed for flow Mach number and temperature of 0.4 and 1150degC respectively, using TBC-coated material coupons donated from Praxair. Experiments show substantial variations in deposition with fuel type. Finally, successive deposits were formed for flow Mach number and temperature of 0.4 and 1150degC respectively, using TBC-coated material coupons donated from Praxair. Each 2-hour test was conducted to simulate 3 months of gas turbine operation in typical atmospheric conditions. The evolved deposits were used in subsequent wind tunnel testing to measure heat transfer coefficient change over time.

Erosion Laboratory Simulations: Testing was completed in UC's erosion tunnels under the direction of Dr. Tabakoff. Coated and uncoated samples of typical turbine materials were subjected to hot and cold erosion simulations at various particulate loadings, impingement angles, and velocities. The eroded specimens were then evaluated at AFRL. The erosion

produced is fairly isotropic with scales depending primarily on particulate size and impingement angle. These data were helpful in characterizing particle restitution and rebound models for later study.

Experimental Measurement of Roughness Effects on Performance: Scaled models of evolved deposits were used for wind tunnel testing during this phase of the project. Heat transfer measurements were initiated at representative flow Reynolds numbers (750,000). Roughness measurements show an initial rapid growth of roughness followed by a lull in growth as valleys between deposit peaks are filled with subsequent deposits. Not surprisingly, St measurements showed a similar lull in their trend upwards with time.

Computational Modeling: Three parallel efforts were conducted in the computational arena.
i) Dr. Hamed (UC) made progress in erosion simulation using the GE E^3 first stage LP turbine as a test platform. Particle-tracking software was used to predict the trajectories of various sizes of particles released in the flowfield. Erosion and particle restitution data were then used to model the impact of the particles on the blade surface. This led to a prediction of the surface erosion for a given particle loading. These simulations provide insight into the variation of component erosion with various engine operating parameters.
ii) Dr. Shih (ISU) explored the use of 2D simulations over representative roughness panels. Parametric studies included the variation of the boundary layer thickness to roughness height ratio as well as stretching and compressing the roughness signature for a fixed boundary layer height. Dr. Shih has also initiated simulations of film cooling flows with and without roughness.
iii) Dr. Wang (ISU) pursued two parallel computational studies to model the effects of surface roughness on shear stress and heat transfer. He successfully integrated the industry standard Spalart-Allmaras turbulence model into his detached-eddy simulation (DES) solver for arbitrary unstructured grids (MUSIC). At the same time, a standard RANS solver with the Spalart-Allmaras turbulence model was used for comparison. Both solvers are being used with a dense 3D grid generated by Dr. Wang's adaptive griding routines. This unstructured adaptive grid generation method is very efficient in resolving disparate length scales. It is estimated that the number of cells generated is over an order of magnitude less than that with a structured grid. Results showed the RANS model to be accurate to within 3% on c_f and 13% on St. Due to convergence failure of the DES simulation, further investigations continued with the RANS solver for additional roughness panels, including one representative of TBC spallation.

Summary: In summary, results from this roughness study are very promising. Industrial participation was very strong. The study included both the measurement of actual hardware and the laboratory simulation of degradation mechanisms (erosion and deposition). By performing the two components in parallel, we hope to have insured the relevancy of the laboratory simulations. Because they are performed in a controlled environment, these erosion and deposition studies should provide the framework for semi-empirical roughness evolution models. As these models are incorporated into computational codes, this will in turn provide the engine community with powerful roughness predictive capabilities.

FULL PROGRESS REPORT

PROJECT DESCRIPTION:

Gas Turbine Research Need: Modern turbine airfoils operate in severe environments with high temperatures and near critical stresses. As design tools of ever increasing sophistication (CFD) are employed to reduce design uncertainty, manufacturing specifications and tolerances are tightened and factors of safety reduced. At the same time, it is well recognized that due to their harsh operating environment, turbine surfaces experience significant degradation with service. Measurements indicate an order of magnitude increase in rms roughness is typical (Bons et al., 2001). To allow user confidence in gas turbine reliability and maintainability, engine companies must be able to accurately predict the effect of such surface roughness on engine performance as a function of operational life. Traditional loss correlations based on the "equivalent sandgrain roughness" concept pioneered by Schlichting are becoming increasingly suspect as the true nature of surface degradation and its effects are uncovered (Bons, 2002).

Recent surveys of engine hardware (Bons et al., 2001) establish that turbine surface roughness is generally not uniform over the entire blade surface. In addition, different degradation mechanisms (erosion, deposition, and coating spallation) have distinctive roughness signatures. Laboratory measurements indicate that these distinctive features can have considerable influence on the Reynolds analogy, often used to relate skin friction to heat transfer effects. These recent insights into spatial and character variations of rough surfaces are helpful, but they don't directly address the real issue facing the turbine user. Specifically, the gas turbine user needs an accurate method to estimate the variation of turbine surface condition with service time so that the associated decreases in stage efficiency and increases in heat transfer can be accounted for. To our knowledge, there is no model or information available in the open literature that would provide this link between service life and performance loss due to surface condition. This research effort lays the groundwork for the development of such a complete model that will allow the direct assessment of the effect of service time on turbine aerothermodynamics.

Project Experimental and Analytical Approach: To meet the need stated above will require four essential tasks: the acquisition of surface data from serviced hardware as a function of service time, the experimental and computational modeling of the effects of deposition and erosion (the two primary degradation mechanisms) on surface roughness as a function of time, experimental measurement of performance degradation for surfaces at different times in their roughness evolution, and finally detailed computational modeling of these performance effects. To accomplish these tasks, we assembled a highly qualified research team with expertise in the required disciplines: BYU/AFRL in the surface measurement and wind tunnel testing of rough surfaces, Iowa State University in CFD and grid generation, and University of Cincinnati in erosion experimental and computational studies.

This effort began with the characterization of in-service turbine hardware arranged through industry contacts. 2D and 3D surface traces were taken on hardware from different engines and operating environments at various service intervals. These data provided the baseline surface trends for subsequent laboratory testing and computational modeling.

At the same time, UC researchers conducted experimental studies into the effects of erosion on typical turbine metals as part of Task 2. These experiments were accomplished in UC's erosion tunnels (with surface measurements made at AFRL) over a wide range of operating parameters.

In addition, experimental studies were conducted on particle rebound and restitution in order to develop adequate empirically-based models for numerical simulation of erosion and deposition. Also, deposition studies were conducted in a newly constructed combustor simulator at BYU. Evolution of deposits and surface character were measured for typical engine conditions. Following this, fundamental flat-plate measurements were made by BYU in a low speed wind tunnel. Heat transfer (Stanton number, St) was evaluated at appropriate Reynolds numbers and relative boundary layer dimensions.
The final step was the modeling and simulation of skin friction and heat transfer on rough surfaces. Both high accuracy/high resolution (DES) and lower-order modeling approaches (RANS) were pursued.

Expected Results/Benefits: This BYU-led roughness study will hopefully provide the power generation community with tools to aid in the predicting of surface degradation history of hot section components and their associated performance decrements. This critical information will eventually allow the engine user to establish more economical maintenance schedules and procedures. Operators will have a better idea of the cycle penalties associated with accumulated surface roughness and be able to make informed decisions about when to take power plants off line for maintenance. At the same time, engine designers will have the ability to estimate the expected performance history of their product for a given operating environment. The combination of these added capabilities will reduce operating costs for the energy producer and prevent possible emergency shut-downs due to unanticipated surface degradation or part failure.

EXPERIMENTAL METHOD

Airborne Deposit Simulation at BYU: A natural gas burner in the Advanced Combustion Engineering Research Center (ACERC) at BYU was used to conduct accelerated turbine deposition studies. Figure 1 shows a schematic of the facility. The combustor burns natural gas in a facility capable of mass flow rates up to 1000 slpm. With an exit contraction from 30.5cm to 1.6cm diameter, the exit flow from the combustor can exceed 350m/s at temperature. A number of tests were conducted with the following parametric ranges: exit Mach number from 0.3 – 0.4, exit temperature from 900°C to 1150°C, and impingement angles from 30° – 90° (stagnation). Sample turbine materials donated by General Electric, Siemens-Westinghouse, Praxair, and Solar Turbines were used as the target coupons in tests conducted to simulate 10,000hrs of 1st stage HP airfoil exposure to airborne particulate (particularly the stagnation zone).

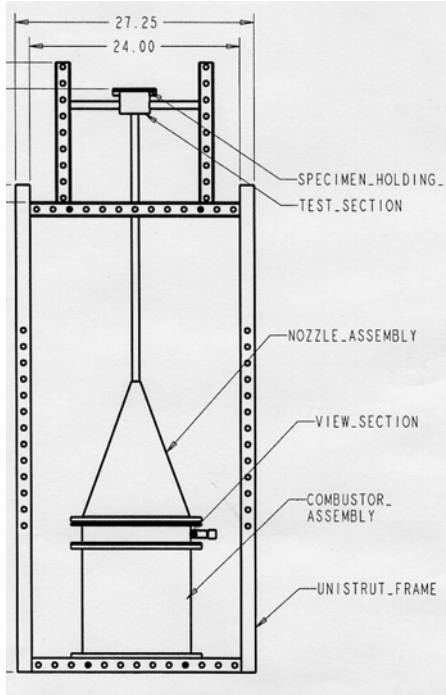

Figure 1: BYU Turbine Deposition Facility schematic.

Since the combustor fuel is methane mixed with filtered high pressure air, deposits are created by seeding with selected particulates using a particle feeder. The feeder allows controlled rates of fine, dry particulates (powders) to be added to the hot section and accelerated in the combustor exit. A 1.2m long exhaust pipe is provided to insure thermal and velocity equilibrium of the particulate with the gas stream. To study the effect of airborne particulates, experiments were conducted with varying concentrations (parts per million weight or ppmw)of a particle test mixture used in the characterization of GT inlet filter performance by the Air Filter Testing Laboratories, Inc. The dust selected conforms to the ASHRAE (American Society of Heating, Refrigeration, and Air Conditioning Engineers) test standards for size and is representative of real chemical compositions as it is collected from the atmosphere rather than artificially mixed. Tests with various synfuel ashes were also conducted with the following operating conditions: flow Mach number 0.3, gas temperature 1150°C, and 45° impingement angles. Turbine coupons donated by Siemens-Westinghouse and Praxair were used as the target coupons in these tests. Tests were also conducted to model deposit evolution. Specific test findings are presented in the Results section.

Turbine Component Measurements at AFRL and BYU: Turbine components donated from General Electric, Pratt-Whitney, Solar Turbines, Standard Aero Inc., Oklahoma City (USAF engine maintenance facility), and Siemens-Westinghouse were evaluated. The precise features of the various articles were not divulged in order to respect proprietary concerns of the industry participants. Surface measurements were made with a Taylor-Hobson Form Talysurf Series 2 contact stylus measurement system at AFRL and a Hommel contact stylus measurement system at BYU. Results from these measurement surveys are discussed in the Results section of this document.

Erosion Simulation at UC: The specific characteristics of the erosion tunnel employed in UC's testing are presented in Tabakoff and Wakeman (1979). A schematic of the facility is provided in Figure 2. The facility matches operating turbine temperatures and particle impact velocities over a full range of impingement angles with various target materials and particulates. Testing results are discussed in the Results section of this document.

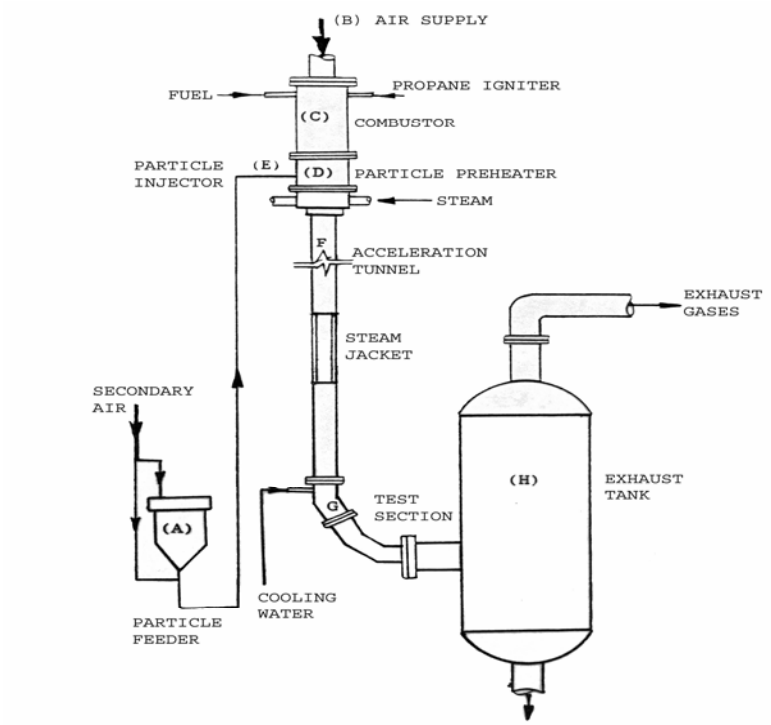

Figure 2: University of Cincinnati erosion tunnel schematic.

Computational Modeling at UC: Using erosion data from Dr. Tabakoff's experimental testing combined with particle trajectory predictions from CFD, erosion rate predictions were made for the GE E^3 first stage LP turbine. Details are summarized in the Results section.

Computational Modeling at ISU: At Iowa State University (ISU), two parallel computational efforts were conducted to study the effects of surface roughness on shear stress and heat transfer.
i) Direct numerical simulation (DNS) of real 3D rough surfaces by using detached-eddy simulation vs. RANS (Z.J. Wang): In this approach, every detail of the irregularities in surface geometry is simulated. With DES, the near wall region is simulated by using the Reynolds-averaged Navier-Stokes (RANS) approach. But, away from walls, large-eddy simulation is used, which enables the unsteady, three-dimensional flow structures induced by roughness to be captured by essentially first principles. This approach, though expensive, has the potential to reveal understanding that cannot be obtained by RANS. Also, DES results can be used to guide the modeling of more accurate RANS models.
ii) RANS computations over 2D surfaces taken from real 3D turbine surfaces using Spalart-Allmaras turbulence modeling (Tom Shih): In this approach, 2D traces are taken from 3D turbine roughness surfaces generated by Bons et al. Fluent calculations are performed over various profiles with particular attention given to flow structures and engineering properties. 2D

is used because it is considerably cheaper than 3D. The research plan is to use these simulations to guide further modeling of rough surfaces.

Results with these two complementary approaches are discussed in the Results section of this document.

RESULTS AND DISCUSSION - BYU

ORGANIZATION: This section is organized by school rather than by task.

Validation of Turbine Accelerated Deposition Facility: During the second year of this program a new deposition facility (TADF) was successful validated at BYU. A paper documenting the test facility validation was presented at the 2004 IGTI in Vienna, Austria (Paper # GT2004-53324: "Simulated Land-Based Turbine Deposits Generated In An Accelerated Deposition Facility" by Jensen, Squire, Bons, and Fletcher) in June, 2004. The paper has since been published in the ASME *Journal of Turbomachinery* (Vol. 127, pp. 462-470, July 2005) and was awarded the 2005 Heat Transfer Committee award for best paper.

Figures 3a&b show surface maps of two surfaces. Surface 3a is from a first stage turbine blade with 25,000 hrs of service. The topology map was taken at roughly 60% chord and 30% span on the blade suction surface, a region with obvious brownish deposits. Surface 3b is an accelerated deposition coupon that was tested for 4hrs at 60ppmw (T = 1150C and M = 0.4). The coupon was oriented for stagnation flow (impingement angle = 90), but the surface map shown was taken at the edge of the coupon where the flow was more tangential to the surface of the coupon as the impinging jet stream turned about the edges of the target. The strong similarities between the two images are reinforced by a review of their surface statistics.

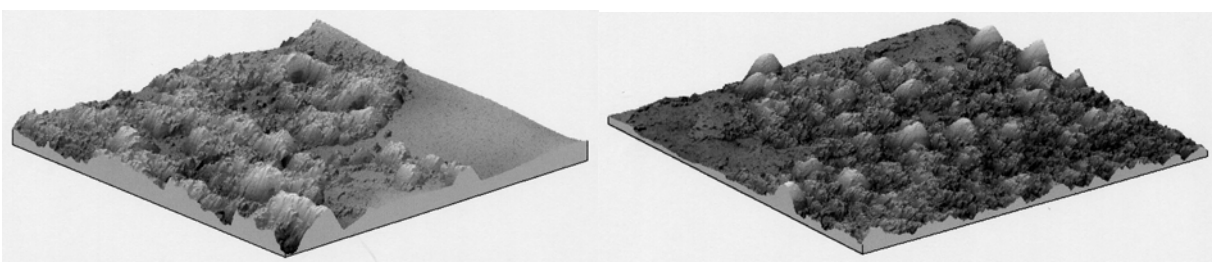

3(a) 3(b)

Figures 3: Surface map of deposits from (a) 1st stage turbine with 25,000 hours and (b) accelerated deposit surface after 4hrs at 60ppmw. Both maps are 4mm x 4mm with approximately the same vertical scale.

Table 1: Roughness statistics for surfaces in Figure 3a&b.

Surface	Ra [μm]	Rt [μm]	Surface Angle rms	Wetted Surface Fraction	Λ_s Form Parameter
Fig 3a	32	240	27	1.36	22
Fig 3b	28	257	29	1.43	13

Scanning electron microscopy (SEM) and x-ray spectroscopy were also used with both the deposits formed in this accelerated facility and actual turbine samples obtained from Standard Aero Inc. to evaluate the internal structure of the deposits. The deposit samples were potted in epoxy to prevent disruption of the structure during cross-section. Figure 4 shows SEM images of two different samples. Elongated structures oriented parallel to the blade surfaces are evident in

both images. Deposit chemistry evaluations also indicated similar types and concentrations of elemental constituents.

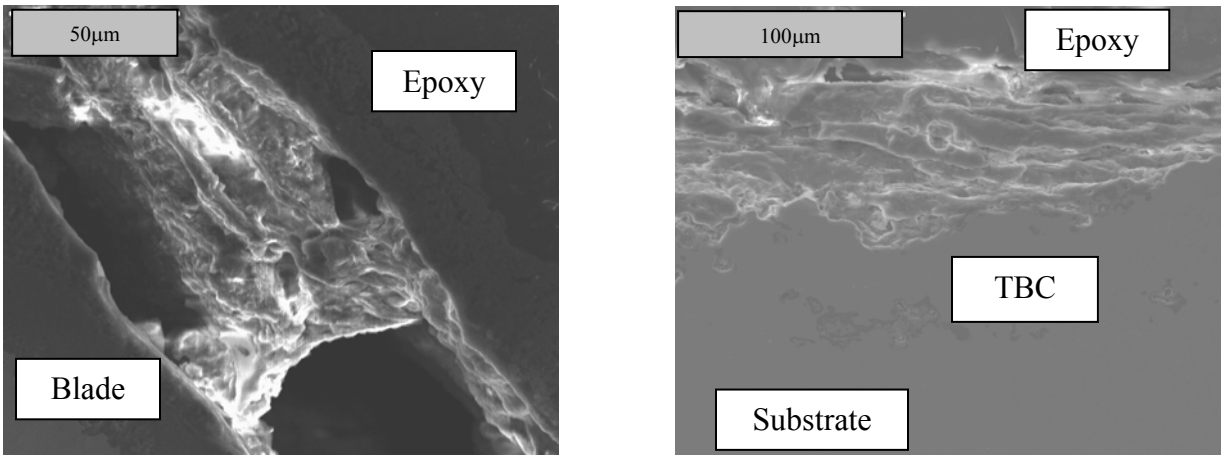

4(a) 4(b)

Figure 4: SEM cross-section of (a) a 16000-hour service blade with 50-μm metering bar at top left and (b) an accelerated deposit specimen with 100-μm metering bar at top left

Deposition Simulation with Synfuels at BYU: Subsequent to this, a study was conducted simulating syngas deposits with particulate from straw, sawdust, coal, and petroleum coke. These results were presented at the 2005 IGTI in Reno (Paper # GT2005-68479: "High Pressure Turbine Deposition in Land Based Gas Turbines from Various Synfuels" by Bons, Crosby, Wammack, Bentley, and Fletcher) in June, 2005. The paper has since been accepted for archival journal publication in the ASME *Journal of Turbomachinery*.

The combustor was seeded with finely-ground fuel ash particulate from four different fuels: straw, sawdust, coal, and petroleum coke. The four ash samples used in this study were collected from various sources. Coal and petcoke samples were obtained externally, while the biomass samples were prepared locally using facilities in BYU's Advanced Combustion Engineering Research Center (ACERC). Subbituminous coal fly ash was obtained from an operating power plant, while the petcoke ash is boiler slag obtained from a combined cycle gas turbine power plant operating with a blend of 55% petcoke and 45% coal. Straw ash was produced in a two-step process. First, raw material was partially burned to eliminate volatiles. Second, the partially burned ash was placed in a programmable furnace and cycled through a standard ashing process. This same two step process was repeated to generate sawdust ash. A standard kitchen wheat grinder set on the finest setting was used to grind the ash particles to the size needed for testing. Figure 5 show typical ESEM images from two of the ash samples. The coal ash particles appeared mostly spherical in shape while the straw ash particles were more uniform in size but more irregular in shape. A Coulter counter was used to measure particle size and spectroscopy yielded the elemental composition. Both of these are shown in Table 2.

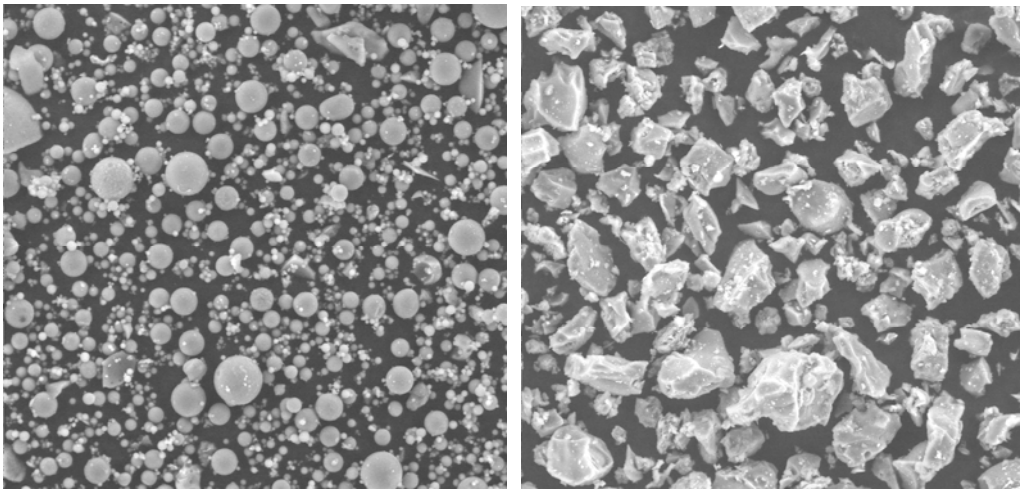

(a) Coal (b) Straw

Figure 5: ESEM images of (a) coal and (b) straw ash after processing. Images are approximately 150μm x 150μm.

Table 2: Ash particle summary statistics: size, density, and elemental composition.

	Coal	Petcoke	Straw	Sawdust
Mass mean diameter (μm)	13.3	33.0	17.6	19.7
Median diameter (μm)	10.6	28.5	15.1	11.8
Bulk density (g/cc)	0.99	1.45	0.84	0.48
Apparent density (g/cc)	1.98	2.90	1.68	0.96
Elements in order of atomic number	Weight %	Weigh t %	Weight %	Weigh t %
Na	6.9	4.3	1.7	5.9
Mg	3.6	2.2	2.54	12.4
Al	17.8	14.5	1.8	5.1
Si	47.4	38.3	48.4	11.6
P	1.6	0.0	3.4	2.2
S	1.8	1.0	3.0	1.3
Cl	0.0	0.0	2.8	0.0
K	2.6	2.5	23.4	10.7
Ca	8.7	7.5	7.8	42.9
Ti	1.6	0.8	0.0	1.3
V	0.0	3.4	0.0	0.0
Cr	0.0	0.0	0.0	0.0
Mn	0.0	0.0	0.0	4.5
Fe	6.4	22.9	5.0	1.0
Ni	0.0	0.9	0.0	0.0

The entrained ash particles were accelerated to a combustor exit flow Mach number of 0.31 before impinging on a thermal barrier coating (TBC) target coupon at 1150°C. Figure 6 shows typical post-test deposition patterns using coal and straw.

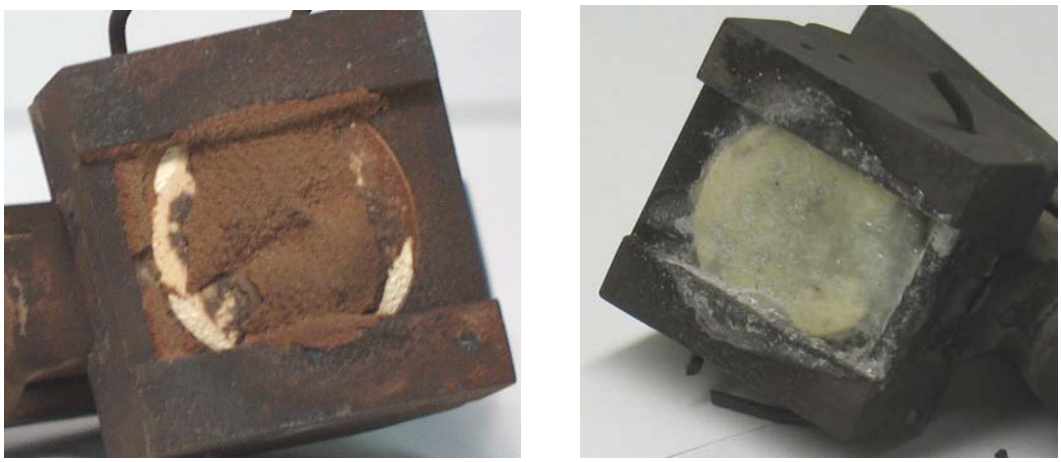

a) Coal b) Straw

Figure 6: Digital images of post-test coupons with deposit before removal from coupon holder. Coupon diameters are approximately 2.41cm.

Post exposure analyses included surface topography, scanning electron microscopy, and x-ray spectroscopy. After completing the tests each sample was weighed and compared to its pre-burn weight. The samples were then placed on a Hommel profilometer to measure the surface topography and roughness of the deposits. Multiple steps were required to prepare the sample for analysis in the ESEM. Each sample was potted in epoxy to preserve the deposit. Using a water-cooled, diamond tipped saw, each sample was cut in half perpendicular to the flow direction. The cut sample was then encased in bakelite and polished. Finally, because deposit layers and TBC are not electrically conductive, the sample was coated with a fine layer of carbon to prevent charge buildup from distorting the ESEM images.

Due to significant differences in the chemical composition of the various fuel ash samples, deposit thickness and structure vary considerably for each fuel. These data are summarized in Table 3. Using the pre-test and post-test weight measurements, the net specimen weight gain during exposure was assessed. Dividing this deposit weight by the exposed coupon surface area and the test duration yielded deposition rate measurements of 143 mg/cm^{2}hr and 76 mg/cm^{2}hr for the highest particle loading coal and petcoke cases, respectively (Table 3). This coal deposition rate is comparable to those witnessed in the coal water fuel study of Wenglarz and Fox [1990] where deposition rates from 200-400 mg/cm^{2}hr were recorded at comparable gas temperatures. The petcoke deposit is a factor of 4 less dense than the coal deposit. It has twice the average thickness but only half the weight. This is indicative of the porous nature of the petcoke deposit as will be seen in the ESEM images. This finding is particularly surprising since the petcoke ash apparent density is roughly 50% higher than that for coal ash (Table 2). One final deposition metric that is tabulated in Table 2 is the net particle capture efficiency (mg/hr of deposit divided by mg/hr of particulate in the flow). Coal has the highest capture efficiency (17%), which drops to 12% as particle loading (ppmw) is increased. The petcoke and biomass net capture efficiencies are less than half of the lowest value calculated for coal. Biomass products (e.g. sawdust and straw) are significantly less prone to deposition than coal and petcoke for the same particle loading conditions. In a test simulating one turbine operating year at a

moderate particulate loading of 0.02 parts per million by weight, deposit thickness from coal and petcoke ash exceeded 1 mm and 2 mm respectively. These large deposits from coal and petcoke were found to detach readily from the turbine material with thermal cycling and handling. The smaller biomass deposit samples showed greater tenacity in adhering to the TBC surface.

Table 3: Particle loading test conditions.

Ash Type	Test Duration [hrs]	Particle concentration [ppmw]	Net particle loading [ppmw-hr]	Net deposit weight [mg]	Deposition rate [mg/cm^{2}hr]	Net particle capture efficiency [%]
Coal	3	55	165	1.1	72	17%
Petcoke	2	70	140	Not measured	N/A	N/A
Straw	2	77	154	<0.1	N/A	N/A
Sawdust	3	37	111	0.2	13	5%
Coal	4	150	600	2.9	143	12%
Petcoke	3	165	495	1.15	76	6%

Scanning electron microscope (ESEM) cross-section images of the four different fuel deposits reveal significant differences in the deposit structure as well. The previous study with airborne dust particles showed layering in the deposit (Jensen et al.), with structures predominantly oriented parallel to the surface. By comparison, the fuel deposits in this study are fairly isotropic in structure and composition. Figure 7a is an ESEM cross-section image of the coal deposit. The coal deposit is riddled with 30-80 μm diameter inclusions. Further interrogation using x-ray spectroscopy indicated that while the majority are solid (metal) particles that were trapped in the molten deposit at temperature, some are porous cavities. The second coal ESEM image (Figure 7b) was taken at high magnification near the deposit/TBC interface. At this location, a crack in the TBC has been penetrated by the coal deposit. In all 4 cases, corrosive elements (e.g. Na, K, V, Cl, S) were found to penetrate the TBC layer during the accelerated deposition test.

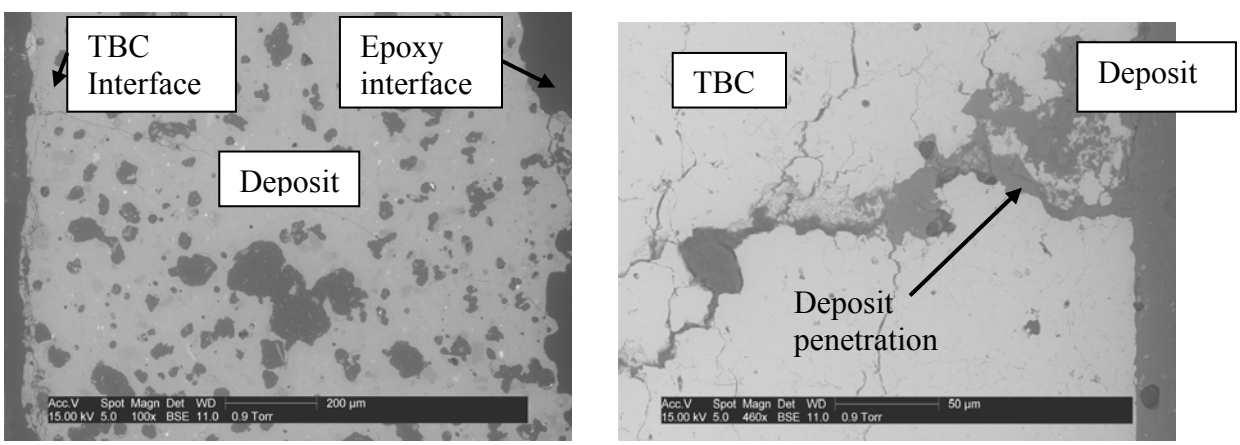

a) Coal surface deposit structure b) Coal deposit penetration into TBC

Figure 7: ESEM cross-section of coal surface deposit and coal/TBC interface.

While mounted in the ESEM, the deposits were interrogated using x-ray spectroscopy. The ESEM registers regions of different structure with distinctively different hues (e.g. the inclusions in Figures 7). Some of these regions exhibited significantly different elemental composition as well. In all cases, at least three measurements were made in each region of the deposit. The composition values are reported as area-weighted averages of the various measurements. In general, the relative concentration of elements detected in the deposits are similar to those detected in the ash. A side-by-side comparison of these data can be used to determine if there are specific preferences for deposition at the given operating conditions (Figure 8). For example, the petcoke and sawdust deposits show significant increases in the concentration of Si in the deposit (relative to the ash) at the expense of Fe (in the case of petcoke) and Ca, K, Mg (in the case of sawdust). Since silicon is non-corrosive and essentially insulates the TBC surface, this rend is favorable for blade life. On the other hand, sharp increases in Na, P, and Cl (e.g. the straw deposit) are undesirable for blade life.

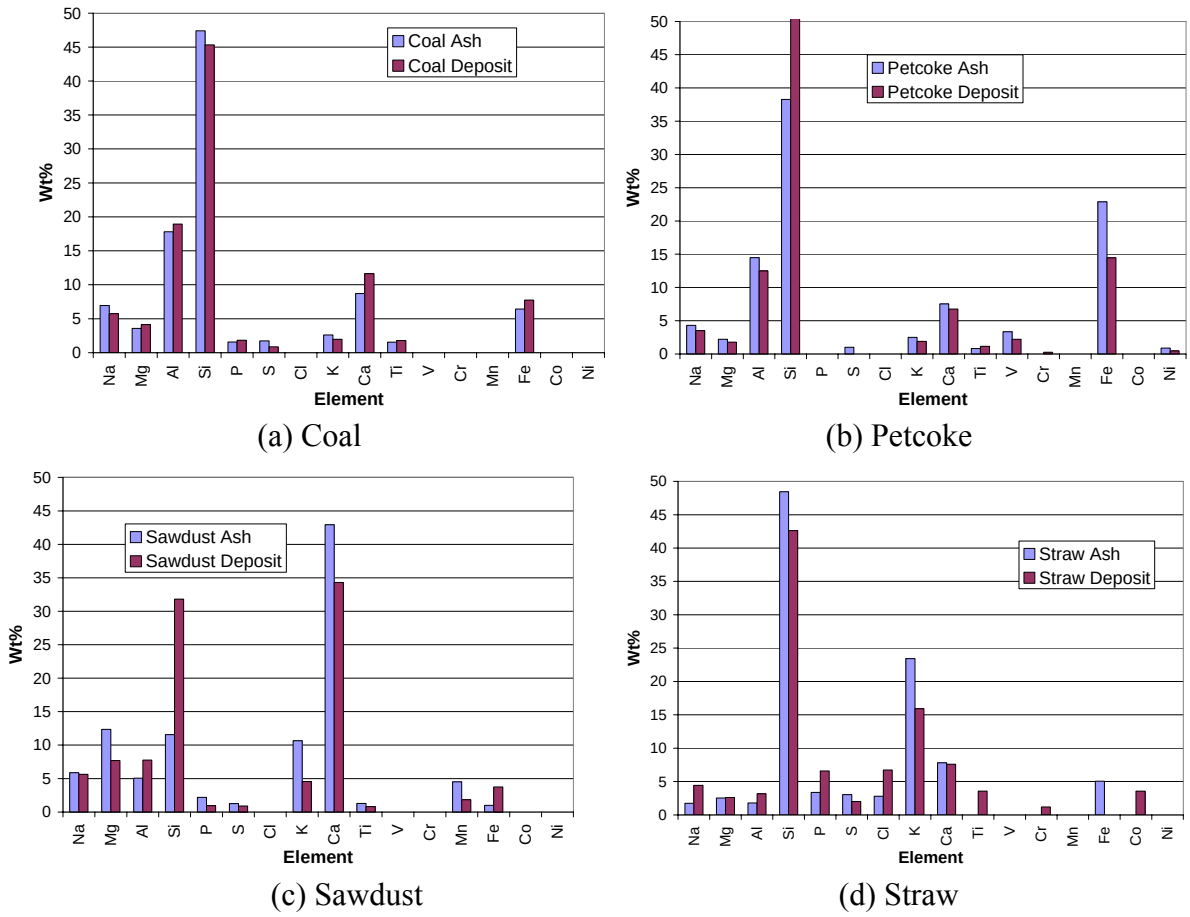

Figure 8: Comparison of element weight percent for fuel ash vs. deposit: (a) coal (b) petoke (c) sawdust (d) straw.

Perhaps even more worrisome for the health of the turbine blade material system is the observed penetration of deposit materials into cracks in the TBC (Figures 7). These vertical segmentation cracks are deliberately formed in the air plasma sprayed (APS) TBC to improve erosion and

thermal shock resistance. It is possible that these fissures present paths for premature contamination of the TBC. Further study is necessary to more rigorously examine these internal deposits and determine whether this deposit penetration leads to accelerated corrosion in the base metal alloy.

Evolutionary Deposits and Wind Tunnel Testing: During the third year, turbine blade coupons with three different surface treatments were exposed to deposition conditions in the accelerated deposition facility. Each of the coupons underwent four consecutive experiments in the TADF. Each burn was intended to simulate approximately one quarter of an operational cycle between maintenance periods. Following each test, the surface topography was measured with a Hommel profilometer. Scaled models were the placed in a low speed wind tunnel where St measurements were made using a transient IR technique. The results have been accepted for presentation at the 2006 IGTI in Barcelona, Spain in the form of two papers: "Evolution of Surface Deposits on a High Pressure Turbine Blade, Part 1: Physical Characteristics," by J.E. Wammack, J. Crosby, D.H. Fletcher, J.P. Bons, and T.H. Fletcher, and "Evolution of Surface Deposits on a High Pressure Turbine Blade, Part 2: Convective Heat Transfer," by J.P. Bons, J.E. Wammack, J. Crosby, D.H. Fletcher, and T.H. Fletcher. Both papers were also accepted for eventual publication in the *ASME Journal of Turbomachinery*.

In this experiment, the combustor exit flow was seeded with dust particulate that would typically be ingested by a large utility power plant. The particulate used in this study is identical to that used by Jensen et al. [2005], and is primarily composed of silicon and aluminum oxides (80%) with smaller concentrations of Na, K, Mg, Ca, and Fe. The mass mean diameter is 15 μm. The turbine blade coupons donated from the gas turbine industry for this study were flat, circular disks with a diameter of approximately 2.54 cm. Like actual turbine blades, the coupons consisted of a nickel-cobalt superalloy substrate with various surface treatments. Three types of surface treatment were studied: (1) bare polished metal, (2) polished thermal barrier coating with bondcoat, and (3) unpolished, 310 μm thick oxidation resistant bondcoat. The TBC was approximately 1 mm thick air plasma-sprayed (APS), yttria stabilized zirconia (YSZ). The polished bare metal and TBC coupons both had initial roughness levels (Ra) less than 0.6 μm, while the "as-applied" oxidation resistant bondcoat had a roughness level of 16 μm. This initial level of surface roughness had a significant effect on deposition evolution as will be shown.

Each of the coupons used in this study underwent four consecutive experiments (hereafter referred to as "Burns") in the TADF. Each burn was intended to simulate approximately one quarter of an operational cycle between maintenance periods. During a burn, each coupon experienced approximately 45 minutes of warm-up time, during which the TADF was brought to an operational freestream temperature of 1150ºC and a flow Mach number of approximately 0.31. Once steady state had been reached, particulate was introduced into the facility. This particulate flow was maintained for a period of two hours. During each two hour burn, an average of 25 ppmw of particulate was introduced into the TADF for a total of 50 ppmw-hrs. This is intended to simulate approximately 2500 hours of operation with a particulate concentration of 0.02 ppmw, for a total of 10,000 simulated hours during a standard series of four experiments per coupon. Figure 9 shows digital photographs of a coupon subjected to successive 2-hr periods of deposition (images are only shown at 0, 2, and 8 hrs). Uncertainty in the particle concentration measurement was <6 ppmw for typical flow conditions.

a) 0 hrs b) 2 hrs c) 8 hrs

Figure 9: Digital photographs of test coupons after successive deposition tests.

Following an experiment, the coupon was allowed to cool for several hours, after which it was removed from its fixture. Upon removal, the coupon was placed in a profilometer fixture while topological measurements were taken. Following this process, the coupon was stored until the subsequent burn. Three-dimensional maps of the deposit-roughened surfaces were created between each test, representing a total of four measurements evenly spaced through the lifecycle of a turbine blade surface. From these measurements the surface topology and roughness statistics were determined. Figure 10 shows the evolution of deposition on the bare metal coupon.

(a) Before

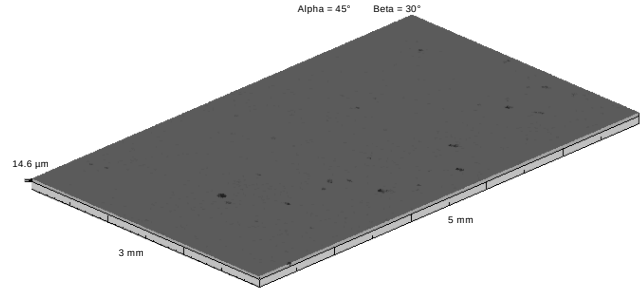

(b) After Burn 1

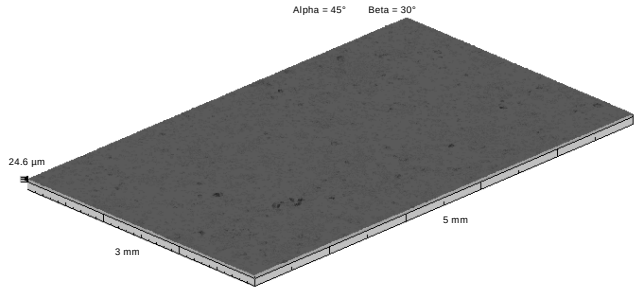

(c) After Burn 2

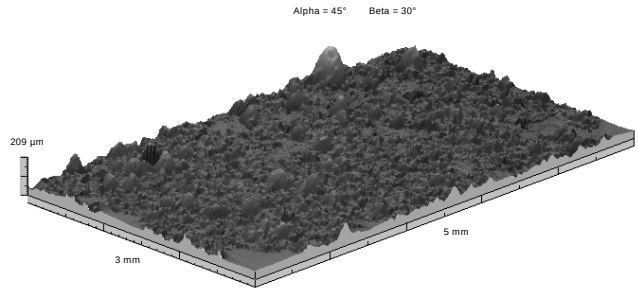

(d) After Burn 3

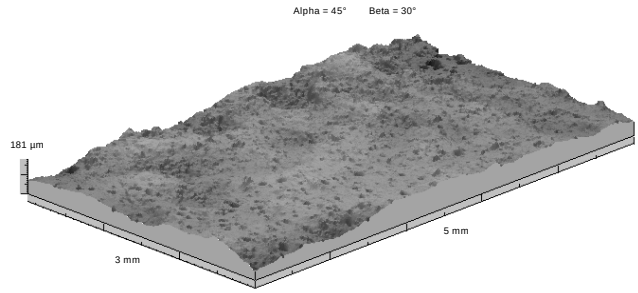

(e) After Burn 4

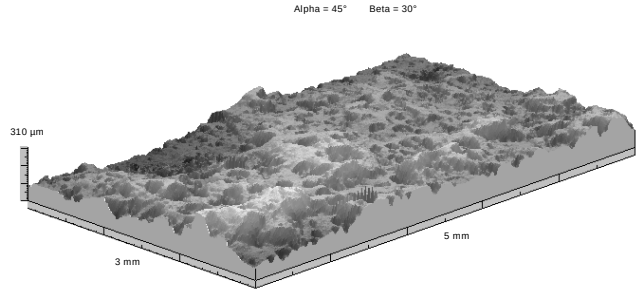

Figure 10: Surface topologies of 3 mm x 5 mm section of deposit on bare metal coupon after each burn.

The deposit structure changes substantially from Burn 2 to Burn 4. Figure 10 contains a series of 3D topologies showing the deposit evolution on a 3mm x 5mm area near the coupon center. The most dramatic changes occur during Burn 2, after the residue beneath the flaked off deposit from Burn 1 has altered the virgin surface by roughening it slightly (Ra = 0.5 µm after Burn 1). The deposit structures become noticeably less peaked after Burn 3, as the subsequent deposit fills in valleys in the irregular surface. Finally, Burn 4 again shows the reemergence of new deposit peaks.

This evolution can be summarized quantitatively by plotting the trend of roughness height (as represented by Ra and Rz) and the roughness shape (as represented by $\overline{\alpha_f}$). These data are plotted in Fig. 11 for the same 3 mm x 5 mm region of the coupon shown in Fig. 10. If the surface left behind after Burn 1—in which nearly all deposits had flaked off—were taken as a starting point for deposit evolution, then an interesting trend is revealed. Roughness height (Ra and Rz) initially increases substantially (Burn 1 to Burn 2). This is followed by a phase in which the rate of increase slows (Burn 2 to Burn 3). Finally, the roughness increases again (Burn 3 to Burn 4). At the same time, the peakedness of the deposit structures varies also, as shown both by a visual examination of the three-dimensional surface representations (Fig. 10) as well as by the average forward facing angle (Fig. 11). After Burn 1 and the subsequent flaking of the local deposits, the zoomed surface showed a relatively low value of $\overline{\alpha_f}$. This value increased

dramatically after Burn 2, resulting in the peak-dominated surface seen in Fig. 10c. With Burn 3, a 'wavier' surface was produced with an attendant 40% drop in average forward facing angle. Finally, Burn 4's surface returned to a more peaked state.

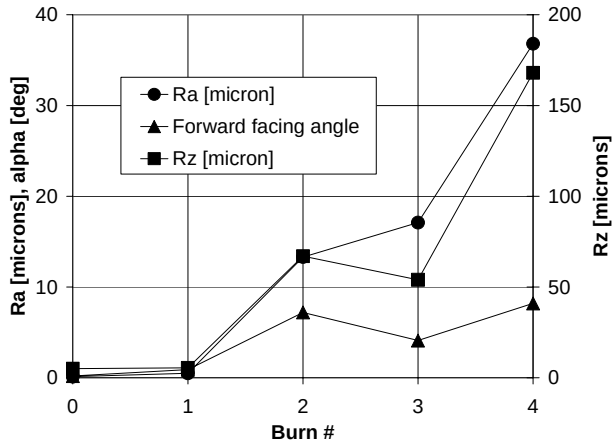

Figure 11: Roughness statistics for the bare metal coupon deposit.

Despite the different surface treatments, all three surfaces (bare metal, TBC, an unpolished coating) exhibited similar non-monotonic increases in roughness with repeated exposure. In each case, an initial build-up of isolated roughness peaks was followed by a period when valleys between peaks were filled with subsequent deposition. This trend is well documented using the average forward facing roughness angle in combination with the average roughness height as characteristic roughness metrics.

For the TBC coupons, there was also significant evidence of deposition-related mechanisms leading to spallation. Both TBC coupons began to show signs of spallation after the second burn. For the TBC1 coupon, this initially consisted of shallow 1-2mm patches of TBC that became dislocated from the surface leaving small 50-100 μm deep valleys in the TBC layer. This process came to a head after Burn 3 when a 6 mm long crack formed near the left edge of the coupon. The TBC on the side of the crack nearest the coupon edge was raised up 100 μm from the central portion of the coupon. This prevented the contact stylus of the Hommel profilometer from traversing this section of the coupon. Accordingly, the crack was manually enlarged until the entire edge of TBC spalled away from the coupon. The spalled piece of TBC was retained for later evaluation. The remaining coupon was then exposed to deposition in Burn 4. For the TBC2 coupon, the spallation process was much more rapid. Nearly 30% of the coupon surface showed TBC loss after Burn 2, increasing to over 60% after Burn 4. Some of the coupon edges experienced TBC loss down to the metal substrate.

To better understand the role of deposition in TBC spallation and crack development, the broken off piece from TBC1 as well as the entire coupon were prepared for cross-section analysis with the ESEM. Figures 12(a) and (b) show the cracked region and the spalled chip of TBC. Regions where deposit compounds were identified using x-ray spectroscopy are indicated on the figure. The top right corner of the chip shows significant penetration of deposit through cracks in the TBC. This is the portion of the chip nearest the exposed coupon surface that lifted away from the surface during Burn 3. The lower portions of the TBC chip show no signs of deposition penetration, which is understandable since this is the region where the crack was manually forced to propogate after Burn 3. The exposed TBC surface in the spalled crater does show signs of significant deposit, due to the subsequent burn (Burn 4) after the chip was

removed. Thus, it seems likely that spallation was initiated by the penetration of deposits into the upper corner of the TBC chip. Whether the crack would have naturally propogated to the coupon edge during the ensuing burn is difficult to speculate. It is clear, however, that deposition played a role in the development of the spalled region. To ascertain if the spallation was merely a result of thermal cycling, a third TBC coupon (TBC3) was subjected to the identical 4 x 2 hour testing sequence in the TADF, but without injecting particulate into the combustor. The surface showed no signs of spallation during the testing cycle, though the mean Rz roughness increased by a factor of three.

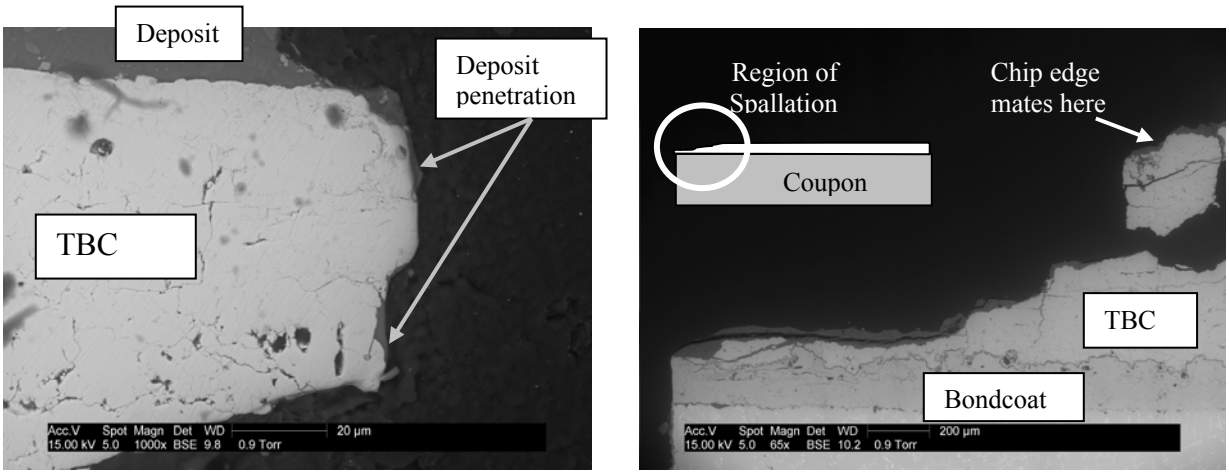

(a) enlarged view of TBC chip **(b) spalled corner of coupon**

Figure 12: ESEM cross-section of spalled region of the TBC1 coupon and spalled chip.

Three-dimensional maps of the deposit-roughened surfaces were created between each test, representing a total of four measurements evenly spaced through the lifecycle of a turbine blade surface. From these measurements, scaled models were produced for testing in a low-speed wind tunnel with a turbulent, zero pressure gradient boundary layer at Re = 750,000 (Fig. 13).

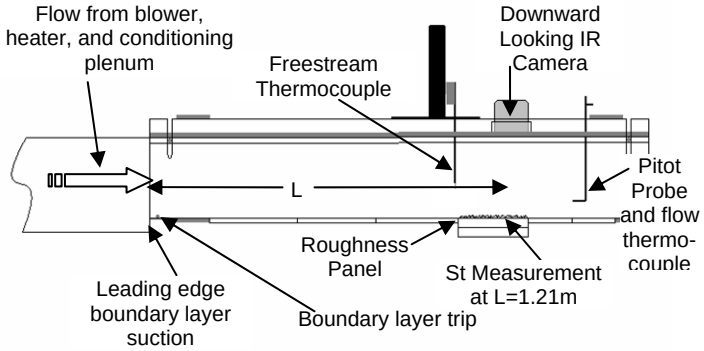

Figure 13: Wind Tunnel Facility

The average surface heat transfer coefficient was measured using a transient surface temperature measurement technique described in Bons [2002]. Heat transfer measurements were made at constant flow velocity for each of the four deposit models and a smooth baseline panel. Figure 14 shows the Stanton number computed using the area-averaged surface temperature as obtained from the IR camera measurement described above. Each data point in Fig. 14

represents the average of at least three separate transient tests, usually conducted on different days. Error bars show the range of measurements for each data point. The Stanton number values are presented as a percent difference between the rough surface value (St_R) and the smooth surface reference value (St_o).

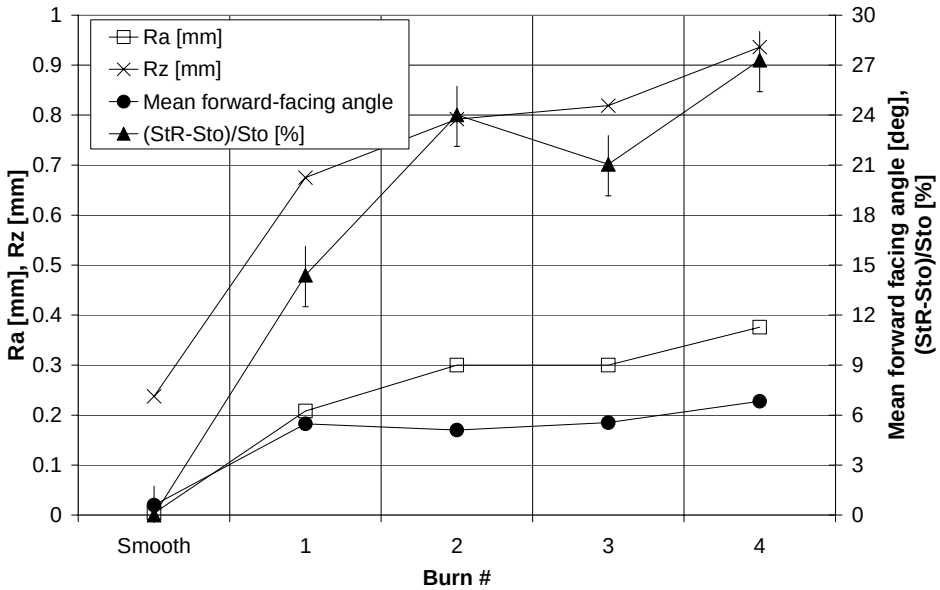

Figure 14: Stanton number augmentation and roughness statistics for the scaled roughness models

The trend in Stanton number follows closely the trend in roughness statistics. The St augmentation levels off between Burns 2 and 3 followed by a marked rise with Burn 4 as the roughness height and mean angle experience a resurgence. Data accumulated by Bons [2005] using roughness characterizations obtained from serviced turbine components indicate that the effect of roughness on c_f and St is reduced as the average forward facing angle decreases for the same mean roughness height (Rz). A comparison of Bons' correlation and that of Dipprey and Sabersky with the experimental data in Fig. 14 is shown in Fig. 15.

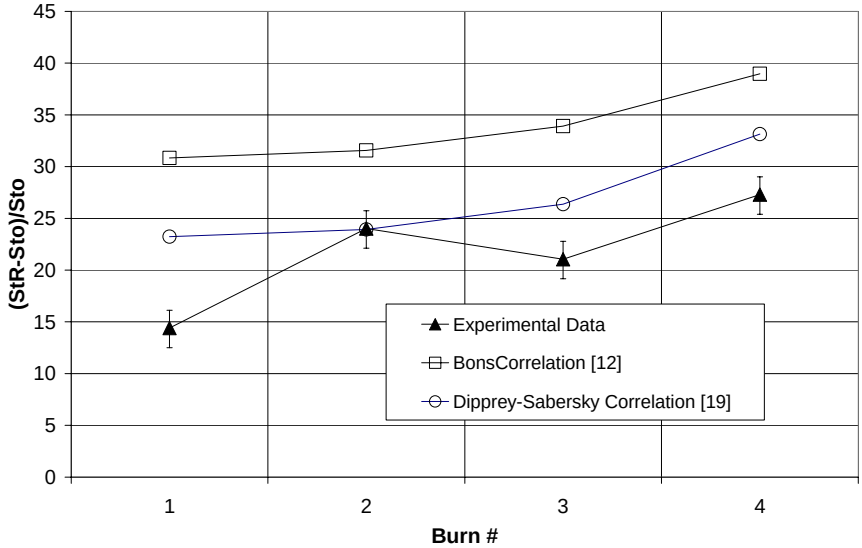

Figure 15: Comparison of experimental St augmentation with empirical prediction.

Both models capture the correct trend of increasing roughness with subsequent burns but appear to lack the sensitivity to capture the changes noted in the St data and the roughness statistics.

The spatial resolution of the infrared camera permits a detailed evaluation of the heat transfer around specific roughness features in addition to the area-averaged measurements presented above. Successive 240 x 320 pixel IR images were processed pixel by pixel using the same Eq. (3) methodology to obtain surface maps of Stanton number. This methodology makes no correction for lateral conduction within the three-dimensional roughness features on the scaled model. For instance, an isothermal roughness peak subjected to instantaneous heated flow will exhibit a more rapid temperature response partly because of the increased convective heat transfer of a roughened surface, but also partly due to its extremity from the base surface. Convection to the sides of the peak will increase the temperature in the 1-D path directly beneath the roughness crest. Thus, the assumption of 1-D transient thermal propogation into an isothermal, semi-infinite solid is jeopardized. Since this effect was not accounted for in the present analysis, the St values will be overestimates of the actual local convective heat transfer. Because the deposit roughness features studied are typically of relatively low aspect ratio (peak height to base diameter ratio ≤ 0.2), this is expected to have only a second order effect on the results presented. Table 4 contains the minimum, average, maximum, and standard deviation of St for each of the roughness surfaces.

Table 4: Spatial statistics for heat transfer coefficient.

	Min St	Avg St	Max St	Std Dev St
Burn 1	**0.00192**	**0.00264**	**0.00427**	**8.3%**
Burn 2	**0.00215**	**0.00284**	**0.00383**	**9.5%**
Burn 3	**0.00209**	**0.00282**	**0.00399**	**9.9%**
Burn 4	**0.00136**	**0.00291**	**0.00397**	**11.7%**

In all four cases, there is a substantial variation in heat transfer over the rough surfaces. In general, roughness peaks can experience nearly 100% higher heat transfer than adjacent valleys. This is partially due to the energetic interaction between the flow and the roughness peak as the flow accelerates to navigate around the obstruction. In addition, the peak reaches further from the wall into the thermal boundary layer where higher temperature fluid (on average) is present; thus, the elevated measurements in these regions. This is actually welcome news for turbine thermal load management. Since a substantial portion of the heat transfer augmentation occurs at these elevated peaks of the deposit, the path to the metal substrate (through the deposit peak) is longer, resulting in a greater thermal resistance. Thus, the increase in local metal temperature beneath the deposit (and TBC) will be less severe. Unfortunately, flow separation behind the deposit roughness peaks generates highly turbulent flow in the wake of the protuberances. This is shown in Fig. 6 which contains side-by-side surface height and St contour plots for the region near roughness peaks on the Burn 1 & 2 models. Though not as high as the heat transfer at the roughness peak, the wake regions [indicated by dashed circles in Fig. 16 (b)] still experience heat transfer augmentation that is 25% higher than the surrounding surface when compared to the smooth surface heat transfer. And if the deposit is thinner in this wake-affected region, the lack of added insulation from the deposit could result in a local hot spot penetrating deep into the TBC layer.

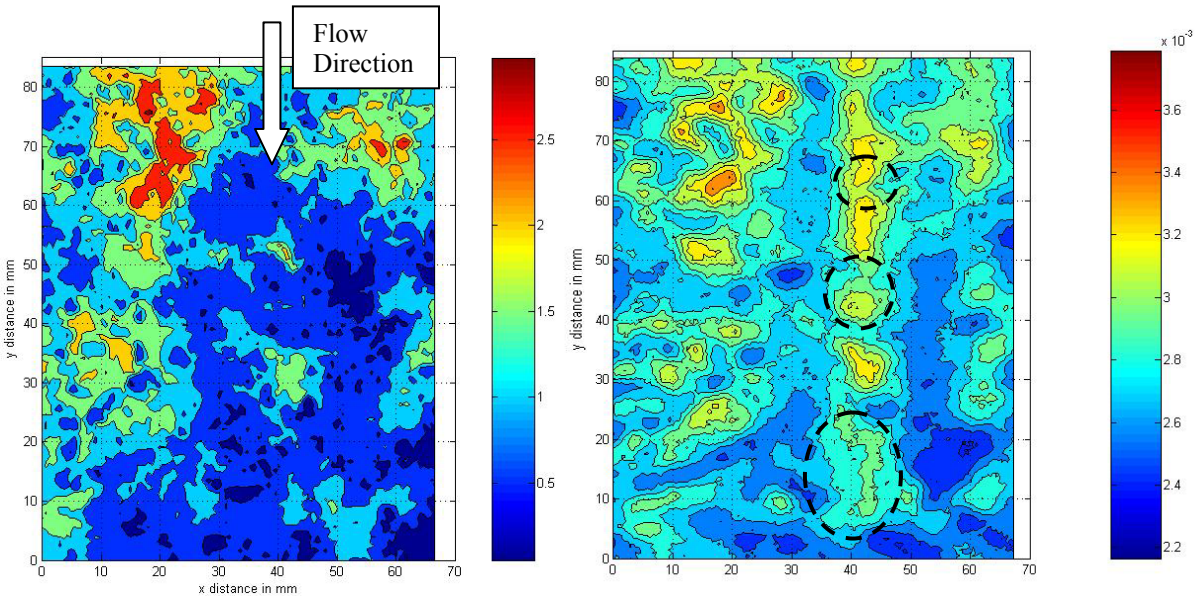

(a) Burn 2 surface height contour plot [mm] **(b) Burn 2 St contour map**

x distance in mm

Figure 16: Heat transfer coefficient and surface height plots for a 67 mm x 83 mm region on the Burn 2 roughness model. (Flow direction is from top to bottom as indicated.) Wake regions with elevated St values are circled.

RESULTS AND DISCUSSION - AFRL

Turbine Component Measurements at AFRL: Sample blades and vanes were contributed from General Electric, Siemens-Westinghouse, and Pratt-Whitney. The majority of the test articles are from aircraft turbines with only a handful being from land-based turbines. The land-based articles generally have larger surface roughness, but are physically larger as well. Generally, the roughness appears to scale approximately with geometry. The aircraft vanes and rotor blades had operating times from 10,000 to 15,000 hours (3,000 to 9,000 cycles) while the land-based components were at 9,000 and 20,000 hours.

The aircraft turbine blades were film cooled and TBC coated. Nominally fourteen 2D traverses equally distributed on the stagnation, suction, pressure surfaces and two 3D traverses were taken on each blade. About 375 traverses were performed in all. Measurements were made using a Taylor Hobson profilometer. All relevant roughness parameters were calculated (e.g. Ra, Rq, Rz, correlation length, etc…). On the leading edge of each turbine blade, Ra ranged from 0.9 to 2.4 microns. There was no apparent correlation between Ra and service time in this region. A sample set of pressure surface data (near the leading edge) is illustrated in Figure 1 for 20 HPT blades. The centerline average roughness, Ra, is plotted vs. operating hours.

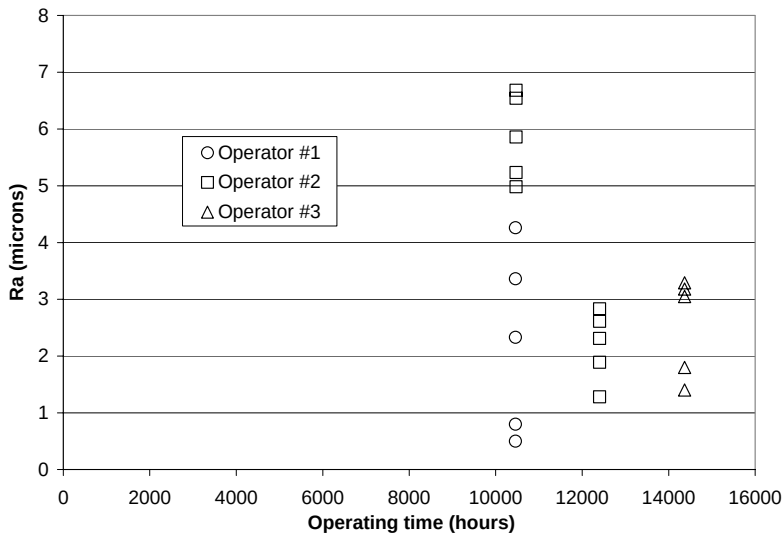

Figure 1: Ra vs. operating hours for sample of 20 HP turbine blades from 3 different operators. Data traces on pressure surface near leading edge.

The lack of correlation with service hours evidenced in Figure 5 is similar to data previously presented in Bons et al. (2001) and Tarada and Suzuki (1993). The same data plotted vs. number of cycles shows a similar lack of dependency. However, when the data is divided into blades originating from different aircraft operators, the results can be grouped as shown in the Figure. This correlation with operator suggests a dependency on operation and maintenance procedures that are specific to each engine operator. Data from the suction surfaces (not shown) evinces a similar trend - a correlation between roughness and operator rather than operating hours or cycles. This correlation appears on the suction and pressure surfaces but not on the leading edge, where values tend to remain consistent regardless of operator or cycles.

Measurements on a second set of LP and HP turbine hardware are still underway. Typical LPT roughness values are on the order of 6 to 9 microns and fairly uniform. The HPT

blades show signs of severe combustor exit temperature profiles with increases in roughness around the stagnation area near mid-span.

To supplement the data acquired from these industrial sources, contact was made with 2 engine service facilities: the Air Force's turbine maintenance facility at Oklahoma City (OC-ALC/LP) and Standard-Aero Inc. (an independent turbine overhaul facility located in Canada). Standard-Aero contributed over 20 small (3 cm chord) land-based turbine blades for the study. These test articles were taken from similar turbine designs which had operated for varying periods in different environments. A detailed analysis of the surface degradation exhibited from these specimens does indicate some evolution with time. Figure 2 shows pressure surface deposits from 3 different blades.

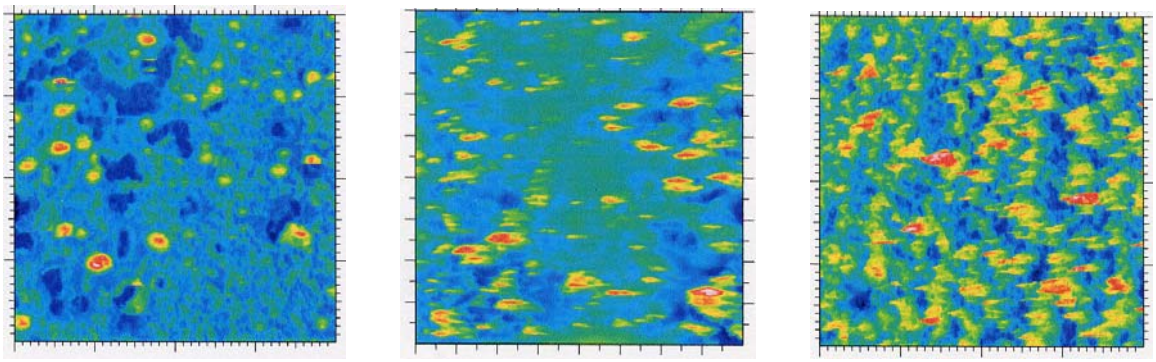

(a) (b) (c)

Figure 2: Pressure surface maps show increased deposition with service hours. Each map is 4mm x 4mm colored by height. Hours are: (a) 2,700 (b) 15,700 and (c) 25,200.

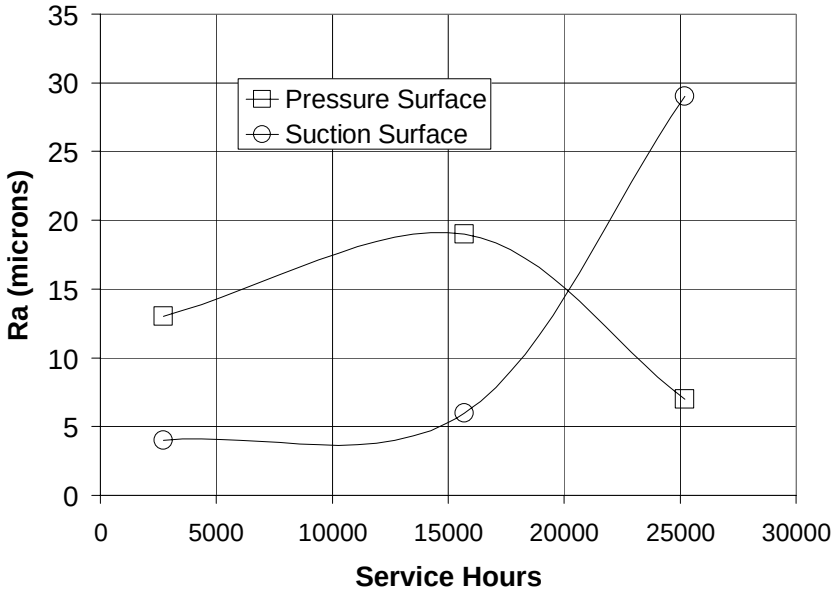

Figure 3: Trends in centerline averaged roughness (Ra) with service hours for Standard Aero turbine specimens.

Figure 3 quantifies the observed variation in Figure 2 by plotting the centerline averaged roughness (Ra) for the pressure surface measurements. The monotonic increase with service hours noted on the pressure surface is not repeated on the suction surface data. This is probably because the blades (though from similar turbines) were not operated in the same environment. As noted in the previous semi-annual report, operating conditions (including environment) appear to have a greater correlation with surface degradation than service hours alone. This explains the need for the laboratory simulation facilities being employed at BYU and UC.

Dr. Rivir also received 4 large boxes of serviced 119 blades from the Air Force's turbine maintenance facility at Oklahoma City (OC-ALC/LP).

Roughness measurements made by Dr. Rivir using eroded specimens from UC were instrumental in the development of a joint paper by UC and AFRL that was presented at the 2004 IGTI in Vienna, Austria (Paper # GT 2004-54328 "Turbine Blade Surface Deterioration by Erosion") in June, 2004. The paper has since been published in the ASME *Journal of Gas Turbines for Power and Propulsion* and was awarded the 2005 Aircraft Engine Committee award for best paper.

Previous surface roughness measurements in AFRL's 2D tunnel were extended with detailed surface static pressure measurements on one of the simulated turbine roughness surfaces. Results suggest the use of the ratio Ra/Rt (Ra, centerline-average, and Rt, peak to valley) to characterize the rough surface in the vicinity of the static pressure measurement, instead of just Ra or Rq. Data show a rate of increase in the local streamwise pressure gradient with roughness length and roughness height (Rt). Detailed BL measurements made with 2-component X wires show that all turbulence quantities increased, with normal stresses increased by factors of 2-3 over the smooth wall case. Figure 4 shows typical turbulent shear stress profiles over a scaled erosion roughness panel. Severe spanwise variations exist due to the highly irregular roughness character. Roughness was observed to cause a non-constant wall normal pressure gradient, invalidating the thin BL approximation, with wall pressures higher than free stream. It can be shown that this pressure variation is directly related to the generation of wall-normal velocity fluctuations. Inner layer recovery downstream of the roughness is slower than common sand paper roughness. The velocity profiles over these large roughness elements appear to scale with the pressure gradient velocity, u_p [$u_p^3 = (\nu/\rho)dP/dx$], rather than the traditional shear velocity, u_τ. These insights are critical to proper simulations of roughness in turbulence modeling. The paper "Effects of Strong Irregular Roughness on the Turbulent Boundary Layer" to Flow, Turbulence and Combustion Journal has been accepted for publication.

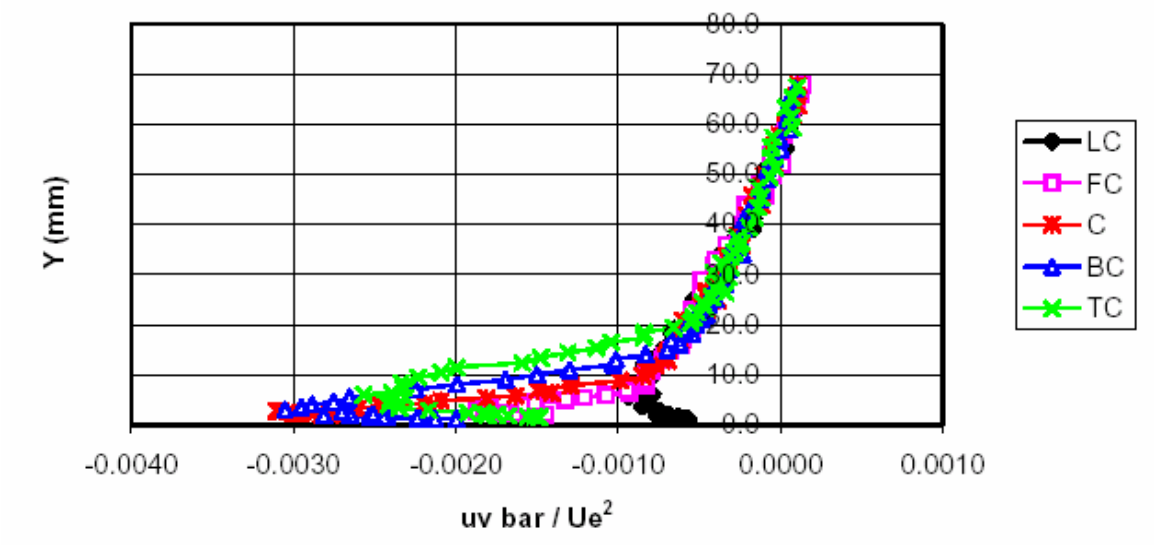

Figure 4: uv profiles vs. spanwise position for roughened surface from X-wire measurements near static pressure taps.

RESULTS AND DISCUSSION - UC

Erosion Simulation at UC: Dr. Tabakoff performed erosion testing of various coated and uncoated samples of typical turbine materials in his 2 erosion tunnels. Part of the focus during the 1st year was hot-erosion tests, conducted at 1000°F and 1500°F. Erosion rate data for 4 different materials are shown in Figure 1. Trends with impingement angle vary substantially with different coated and uncoated specimens. Though the particles used are more typical in size to those seen in aircraft turbine operation, land-based turbines can also see large particulate if operated with improper filtering.

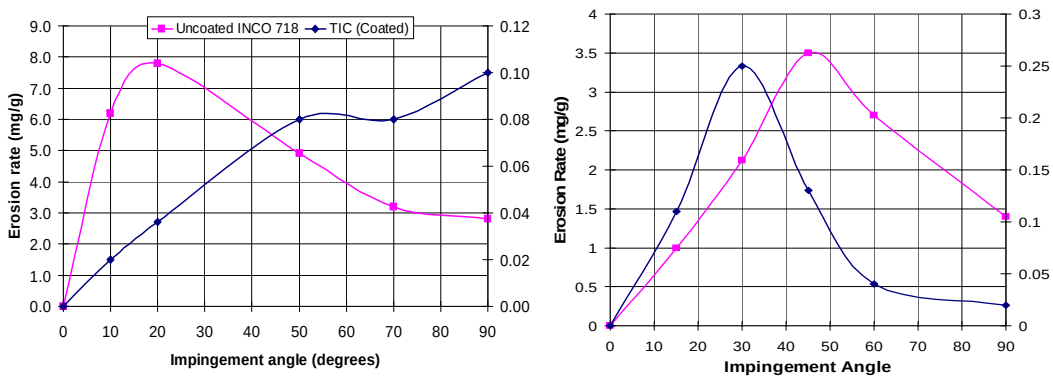

(a) (b)

Figure 1: Erosion rate data for (a) 1550 ft/sec, 1000°F with chromite particles and (b) 1850ft/sec, 1500°F, with fly ash particles.

Computational Modeling at UC: Dr. Hamed first completed a preliminary flow calculation validating 2D code accuracy for the 1st Stage GE E^3 LP Turbine. The stage configuration is shown in Figure 2 with pertinent operating conditions.

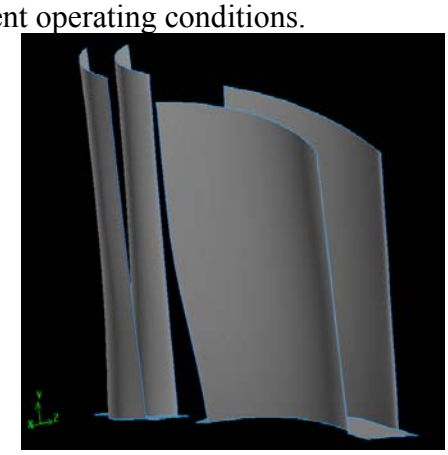

Figure 2: 1st Stage GE E^3 LP Turbine configuration for UC flow simulation (Inlet stagnation temperature = 2000°R, inlet stagnation pressure=37 psia, stage pressure ratio = 1.3, at 3450 rpm).

Numerical simulations were next conducted to determine the three-dimensional flow field and the associated solid particle trajectories through the GE E^3 first stage LP turbine. The compressible viscous flow simulations were based on the implicit solution of the Reynolds-

averaged Navier-Stokes equations in conservation law form, and the RNG κ–ε turbulence mode. The Lagrangian particle dynamics simulations were performed in the relative reference frame of each blade row and included models for the momentum exchanges with the flow field and blade passage surfaces. Particle-gas interaction models represent the momentum exchange between the two phases through the aerodynamic forces due to the motion of particles relative the gas flow field. Experimentally based particle-surface interaction models are used in the trajectory simulations to determine the particle restitution characteristics after they impact the vane and blade surfaces.

Figure 3 presents the discretizational grid used in the flow field, particle trajectories, and blade erosion rate computations. Sample results from the 3-D trajectory simulations for 30-micron particles through the vanes and rotor are presented in **Figure 4**. One can see that the particles impact the vane pressure surface and rebound with reduced absolute velocities. Because of their lower velocities relative to the gas they first impact the rotor blade suction surface and gain sufficient momentum to continue their trajectory and impact the rotor blade pressure surface. The experimentally measured erosion rate data previously acquired in Dr. Tabakoff's erosion tunnel testing was then used along with the vane surface impact data (e.g. Figure 4) to compute the vane erosion rate per unit surface area per unit mass of ingested particles in the turbine. **Figure 5** shows increasing erosion rates over the vane's pressure surface towards the trailing edge and a narrow high-erosion band at the vane's leading edge.

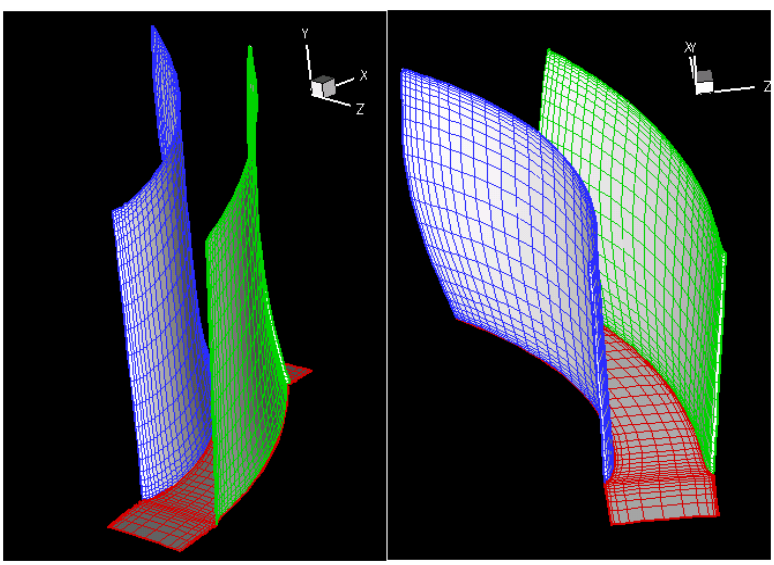

Figure 3. Computational grid for UC Erosion Simulation

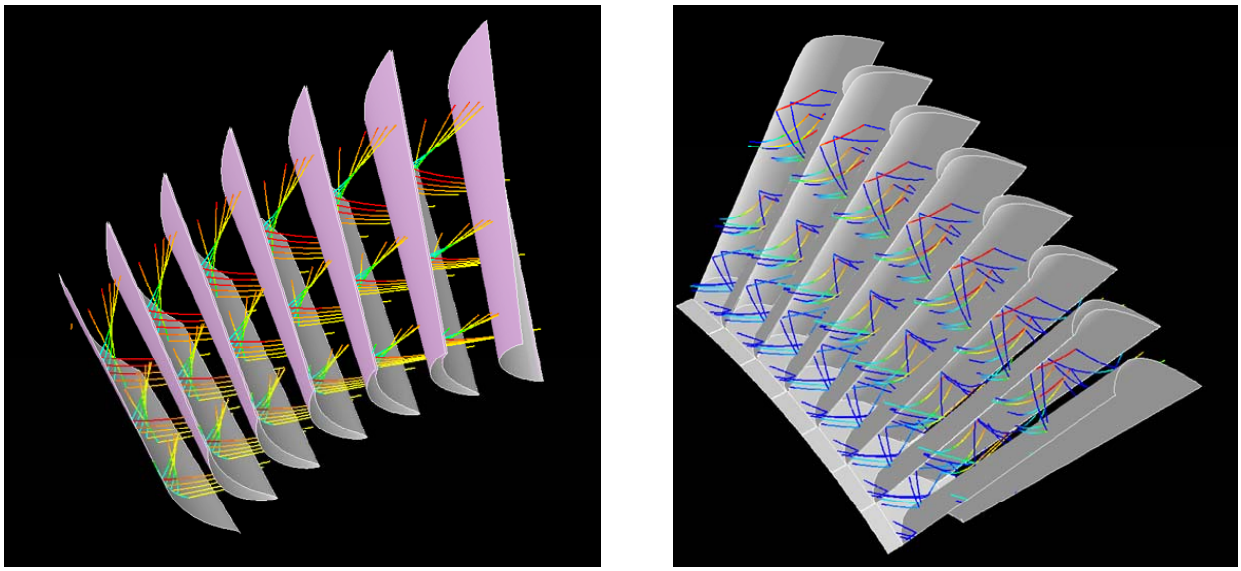

a. Rear view of the stator b. Front view of the rotor

Figure 4. Sample 30 micron particle trajectories

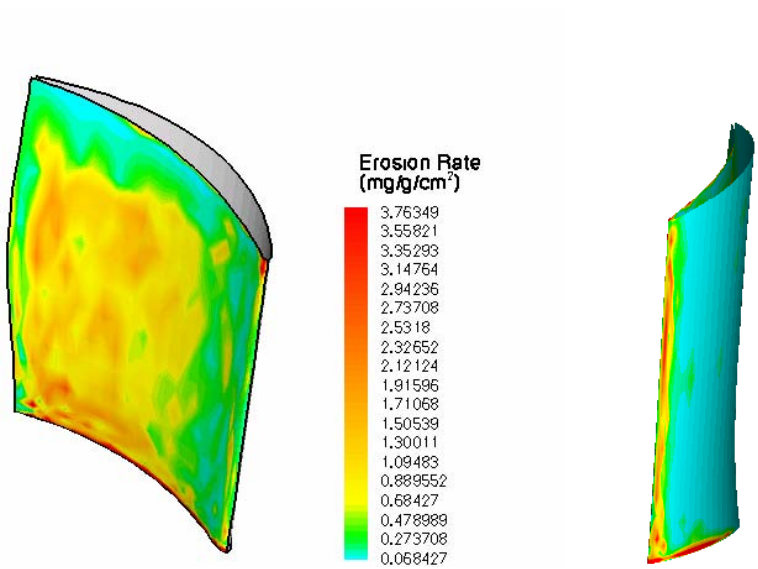

a: Vane pressure surface b: Vane leading edge

Figure 5. Vane Surface Erosion rate

These results were presented in a joint paper with AFRL at the 2004 IGTI in Vienna, Austria (Paper # GT 2004-54328 "Turbine Blade Surface Deterioration by Erosion") in June, 2004. The paper has since been published in the ASME *Journal of Gas Turbines for Power and Propulsion* and was awarded the 2005 Aircraft Engine Committee award for best paper.

RESULTS AND DISCUSSION - ISU

3D Computational Roughness Modeling at ISU: The following summarizes efforts conducted by Drs. Wang and Shih to produce accurate 3D roughness simulations.

Direct Simulation of Surface Roughness Effects with a RANS Approach on Viscous Adaptive Cartesian Grids

Z.J. Wang, X.K. Chi and Tom Shih
Department of Aerospace Engineering, Iowa State University, Ames, IA 50011-2271

Summary

The main objective of this research is to directly compute the skin friction (c_f) and heat transfer (St) coefficients on real rough surfaces using a state-of-the-art unstructured adaptive grid-based finite volume method. Recent experiments with real roughness panels by Bons are computationally simulated in this study. Computational results are compared with experimental data to assess the simulation accuracy. A RANS (Reynolds-Averaged Navier-Stokes) approach based on the Spalart-Allmaras turbulence model was employed for the computations, and grid refinement studies were conducted to assess the effects of grid resolution. In two cases with rough surfaces, the RANS approach is capable of accurately predicting c_f (within 3.5%) while under-predicting S_t by 13%.

Technical Approach and Results

Viscous Cartesian Grid Generation

The viscous Cartesian grid generation method is a recently developed automatic grid generation approach for very complex, and possibly "dirty" geometries. The three major steps in the method are described as follows.

Adaptive Cartesian Grid Generation: The grid generation method is initiated by specifying the minimum and maximum sizes of Cartesian grid cells to be generated. The adaptive Cartesian grid is generated by recursively subdividing a single coarse root Cartesian cell. Since the root grid cell must cover the entire computational domain, the surface geometry is contained in the root cell. The size of the Cartesian cells intersecting the geometry is controlled by constraining the cell size in the geometry normal and tangential directions. The recursive sub-division process stops when all the Cartesian cells intersecting the geometry satisfy the length scale requirements. To insure solution accuracy, the maximum cell aspect ratio and grid smoothness were also monitored. In the present study, the sizes of any two neighboring cells in any coordinate direction cannot differ by a factor exceeding two.

Cartesian Grid Front Generation and Smoothing: In order to "insert" a viscous layer grid between the Cartesian grid and the body surface, Cartesian cells intersected by the geometry must be removed, leaving an empty space between the Cartesian grid and the body surface. All the Cartesian cells intersected by the geometry are determined using a tree-based search algorithm. Once the Cartesian cells intersected by the geometry, and cells outside the computational domain are removed, a Cartesian grid "volume" remains. The boundary faces of this volume form the Cartesian front. Before this front is "projected" to the geometry, it is smoothed with a Laplacian smoother.

Projection of the Cartesian Front to the Body Surface: After the smoothed Cartesian front is obtained, each node in the front needs to be connected to the body surface to form the viscous grid needed to resolve the turbulent boundary layer. After the front is projected to the boundary geometric entities, a "water-tight" surface grid is generated on the boundary. The “foot prints” of the layer grids on the body surface have the same topology (or connectivity) as the Cartesian front. By connecting each point on the Cartesian front with the corresponding projected point on the boundary, a single layer of prism grids is obtained. This single layer can be sub-divided into multiple layers with proper grid clustering near the geometry to resolve a viscous boundary layer.

Example viscous adaptive Cartesian grids for both the fuel deposit and the erosion surface geometries are displayed in Fig. 1. The surface grid generated from the Cartesian front projection is displayed in Fig. 2 (for the erosion surface only). The grid cells near the roughness panels are adaptively refined to resolve the roughness elements.

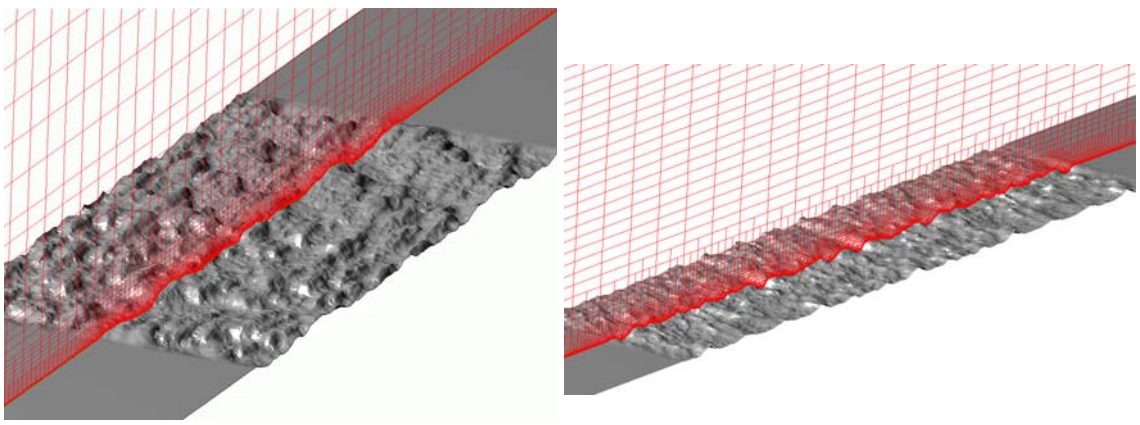

(a) (b)

Figure 1. Cutting planes showing the viscous adaptive Cartesian grids for the (a) fuel deposit and (b) erosion surfaces. Roughness regions are 240mm x 120mm and 240mm x 60mm respectively.

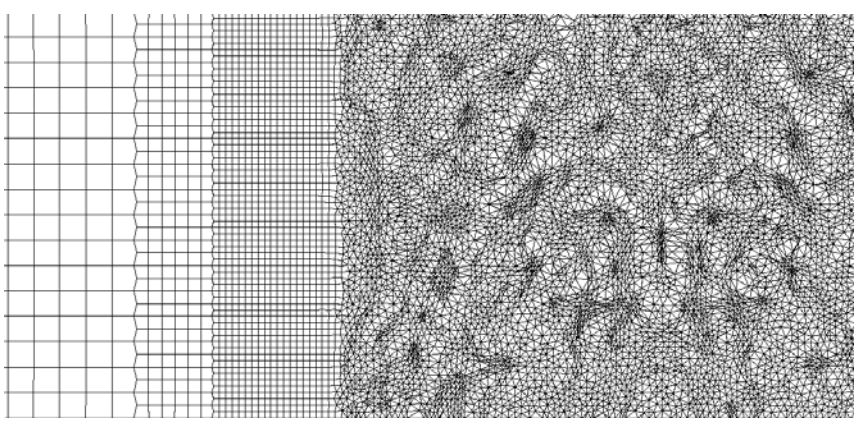

Figure 2. Surface grid on the erosion surface showing grid refinement near leading edge.

Numerical Method

A flow solver capable of handling arbitrary polyhedrons has been developed to uniformly handle the adaptive Cartesian and the viscous layer grids. The Reynolds-averaged Navier-Stokes equations can be written in the following integral form:

$$\int_V \frac{\partial Q}{\partial t} dV + \oint_S (F - F_v) dS = 0 \tag{1}$$

where Q is the vector of conserved variables, F and F_v are inviscid and viscous flux vectors, respectively. The integration of Eq. (2) in an arbitrary control volume, V_i, gives:

$$\frac{d\overline{Q}_i}{dt} V_i + \sum_f F_f S_f = \sum_f F_{v,f} S_f \tag{2}$$

where $\overline{Q}_i$ is the vector of cell-averaged conserved variables, F_f and $F_{v,f}$ are the numerical inviscid and viscous flux vectors through face f, and S_f is the face area. To compute the inviscid and viscous fluxes through any given face, the standard Godunov-type finite volume approach is employed. Using a linear least-squares reconstruction algorithm, a cell-wise linear distribution can be built for each solution variable (in the present study the primitive variables). To compute the inviscid flux, an approximate Riemann solver such as Roe flux difference splitting is used given the reconstructed solutions at both sides of a face. To handle steep gradients or discontinuities, a limiter due to Venkatakrishna is used. The viscous flux is computed using a simple and robust approach presented by Wang without a separate viscous reconstruction.

Although explicit schemes are easy to implement, and are often useful for steady-state, inviscid flow problems, implicit schemes are found to be much more effective for viscous flow problems with highly clustered computational grids. An efficient block LU-SGS (Lower-Upper Symmetric Gauss-Seidel) implicit scheme has been developed for time integration on arbitrary grids. This block LU-SGS (BLU-SGS) scheme takes much less memory than a fully (linearized) implicit scheme, while having essentially the same or better convergence rate. The BLU-SGS scheme can be used to integrate Eq. (2) with first or second order accuracy. For steady flow computations, the backward Euler approach is employed, i.e.,

$$\frac{Q_i^{n+1} - Q_i^n}{\Delta t} V_i + \sum_f F_f^{n+1} S_f = \sum_f F_{v,f}^{n+1} S_f . \tag{3}$$

To simulate flow turbulence, a RANS Spalart-Allmaras (S-A) model was employed without modifications. The computational domain extends from x = 0 to 2.04 m in the wind tunnel. To further reduce the computational cost, only 1/3 of the 0.36 m transverse span of the tunnel is included in the computational domain for the fuel deposit surface, while only 1/6 is included for the erosion surface. Symmetry or slip wall boundary conditions are used on the two end walls in the span-wise direction.

Two viscous adaptive Cartesian meshes were generated for each of three cases: smooth wall, fuel deposit surface, and erosion surface. The cell count and average y+ for the first layer grids next to the wall are shown in Table 1.

Table 1: Grid sizes for 3D RANS model.

	Number of Cells	Average y+
Smooth Wall – coarse	37,888	0.8
Smooth Wall – fine	58,368	0.3
Fuel Deposit Surface – coarse	1,260,051	~1
Fuel Deposit Surface – fine	3,999,040	~1
Erosion Surface – coarse	873,221	~1
Erosion Surface - fine	1,601,430	~1

For the rough surfaces, the fine grid essentially doubles the grid resolution near the roughness panels while maintaining an average y+ of 1 in the wall normal direction. The coarse mesh has about 64 cells in the span-wise direction with a grid resolution of about 1 mm along the tangential direction, while the fine mesh has a grid resolution of about 0.5 mm. The fine grids have about 50-80 layers in the tunnel height direction. If structured grids were used for this configuration, the fine grid would have about 10-25 million cells. Thus, by using the viscous adaptive Cartesian grid approach, the number of grid cells is reduced by over an order of magnitude.

To further speed convergence, local time steps are used in Eq. (3). The flow convergence is monitored by the history of the average c_f and St over the roughness panels, with the solution typically converging after a few thousands of iterations. Grid generation was executed on a Pentium 4 Linux workstation (2.8GHz), requiring 2-4 hrs per rough surface. Due to the size and complexity of the surfaces, even the finer computational grids required that the surface data matrix be sampled by every 4th data point in the streamwise (x) and spanwise (z) directions. The surface resolution was thereby reduced from the printed experimental model, with approximately 14% less wetted surface area (i.e. $S_w/S = 1.06$ vs. 1.2). The RANS solver required 24 hrs to reach a converged solution on a Linux cluster with 8 processors.

To simulate the transient method used for the experimental St measurement, both models start the thermal and velocity boundary layers simultaneously at x=0 (without an unheated starting length). Also, since the thermal boundary condition at the wall is neither constant wall temperature nor constant wall heat flux, the models employed an exponential $T_w(x)$ boundary condition derived empirically, i.e… $[T_e-T_w(x)]/\Delta T_{TS} = (x/x_{TS})^{0.1}$. This distribution accounts for the increased thermal resistance of the thermal boundary layer from the leading edge to the measurement location. The experimental freestream velocity and temperature were used as inflow conditions.

Results and Discussion

Table 2 contains the predicted and experimental values of area-averaged c_f and St for the smooth and rough panels. The 3D RANS data are for the fine and coarse grid models. Also shown in the table are smooth and rough-wall correlation values which are provided as a reference. The various rough wall correlations were all derived using a sandgrain roughness height (k_s) based on the experimentally measured Sigal-Danberg (Λ_s) parameter from Table 1.

Table 2: Comparison of c_f and St data from experiment, computation, and correlations.

Skin Friction, c_f	Smooth	Fuel Deposit	Erosion Surface
Experimental	0.00349	0.00937	0.0103
3D RANS Model - fine	0.00345	0.00970	0.0100
3D RANS Model - coarse	0.00333	0.0128	0.0113
Empirical Correlations	0.00367	0.0083-0.0112	0.0087-0.0119
Stanton Number, St	Smooth	Fuel Deposit	Erosion 2
Experimental	0.00215	0.00308	0.00308
3D RANS Model - fine	0.00204	0.00274	0.00304
3D RANS Model - coarse	0.00199	0.00268	0.00268
Empirical Correlations	0.00219	0.0034-0.0037	0.00345-0.0038

The skin friction predictions for the 3D RANS fine-grid models are within 3.5% of the experimental values in all 3 cases. This is a marked improvement over the k_s-based empirical correlations for c_f which ranged from 16% below to 20% above the measured values. The agreement in St is not as good, with the RANS predictions falling within ±13% of the experimental data (compared to ±23% for the empirical correlations).

Conclusions

In the present study, the skin friction (c_f) and heat transfer (St) coefficient on real rough surfaces are directly computed using a state-of-the-art unstructured adaptive grid-based finite volume flow solver. Computational results are compared with experimental data to assess the simulation accuracy. Based on the present study, the following conclusions can be drawn:

1. The unstructured adaptive grid generation method is very efficient in resolving disparate length scales. It is estimated that the number of cells generated is over an order of magnitude less than that with a structured grid. The rough surfaces can be handled by the grid generator with minimum user interference;
2. On the flat panel case, the RANS approach is capable of predicting c_f and St, thus validating the implementation;
3. With proper grid resolution, the S-A model was able to accurately predict c_f for both rough surfaces (within 3.5% of experimental data). The computational predictions for St showed 13% differences from the experimental data.

This work has been presented in the following venues:

1) "A Comparison of Approximate vs. Exact Geometrical Representations of Roughness for CFD Calculations of cf and St," by J.P. Bons, S.T. McClain, Z.J. Wang, X. Chi, and T.I. Shih. Presented at IMECE 2005 in Orlando, FL, Nov. 2005. Submitted for publication in *ASME Journal of Turbomachinery* June 2005. Accepted for publication – Jan. 06.
2) "Direct Simulation of Surface Roughness Effects with a RANS and DES Approach on Viscous Adaptive Cartesian Grids," by Z. Wang, X. Chi, T. Shih, and J.P. Bons. Presented at the 2nd AIAA Flow Control Conference in Portland, OR, 28 June – 1 July (paper #AIAA 2004-2420)

2D Computational Modeling at ISU: Dr Tom Shih at Iowa State University is pursuing efficient models for roughness simulations. Since 3-D unsteady DNS calculations for a rough turbine blade are still prohibitive due to computational requirements, it is necessary to evaluate more efficient alternatives using 2D simulations and lower order turbulence models. During the past six months, Dr. Shih's team has focused on analyzing the statistical properties of the roughness surfaces provided by Jeffrey Bons. 2D slices were then selected from each 3D surface ensuring that they had similar statistics to the full 3D rough surface. Table 3 shows a typical result of this process.

	Ra	**Rq**	**Sk**	**Ku**	**Rt**	
3D surface	1.239274	1.503101	0.154	2.64	7.19	
2D sample	1.239954	1.507079	-0.0305	2.247641	6.16	X = **23.12782**

Table 3: 3D and 2D data for Ra, Rq, Rt, Sk, Ku

Using these 2D models, CFD simulations were performed of boundary-layer flow over the 2D slice. This was followed by a detailed parametric study of the effects of boundary-layer thickness and various roughness geometric parameters. Basically, Dr. Shih's team is doing a series of 2D CFD simulations in which the 2D slice is kept the same, but the approaching boundary layer has different thicknesses. The above is being repeated for several different 2D slices that represent typical and extreme roughness shapes. This study will be completed by the DOE workshop meeting in September 2004. In addition to the above, Dr. Shih is also performing 2D simulations of roughness after film cooling from a slot.

Some results from ISU's roughness study are shown below. Figure 3 shows a typical grid for a 2D slice of the 3D rough surface. Please note the high resolution of the roughness geometry. Figure 4 shows typical results for the velocity magnitude about the roughness. The predictions are made using Fluent with a Spallart-Almaras turbulence model. Figure 5 shows the separated region behind a roughness element via velocity vectors. Results from these studies can be compared to higher-order 3D calculations for validation. Also, c_f and St predictions from 2D simulations can be used to gage the relative importance of various roughness and boundary layer parameters.

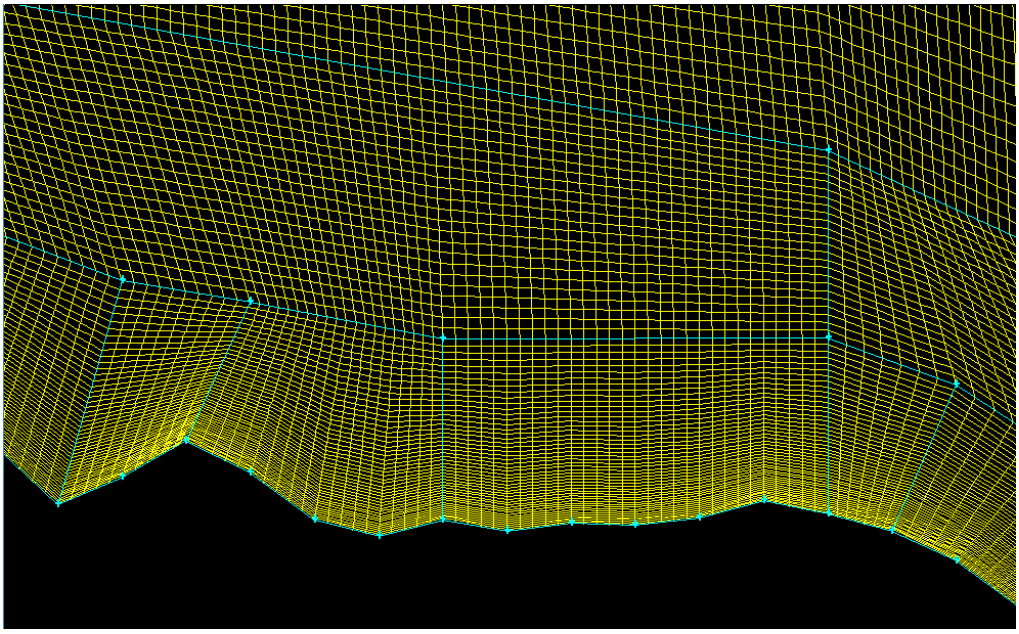

Fig. 3. Grid system for a 2D slice of the 3D rough surface.

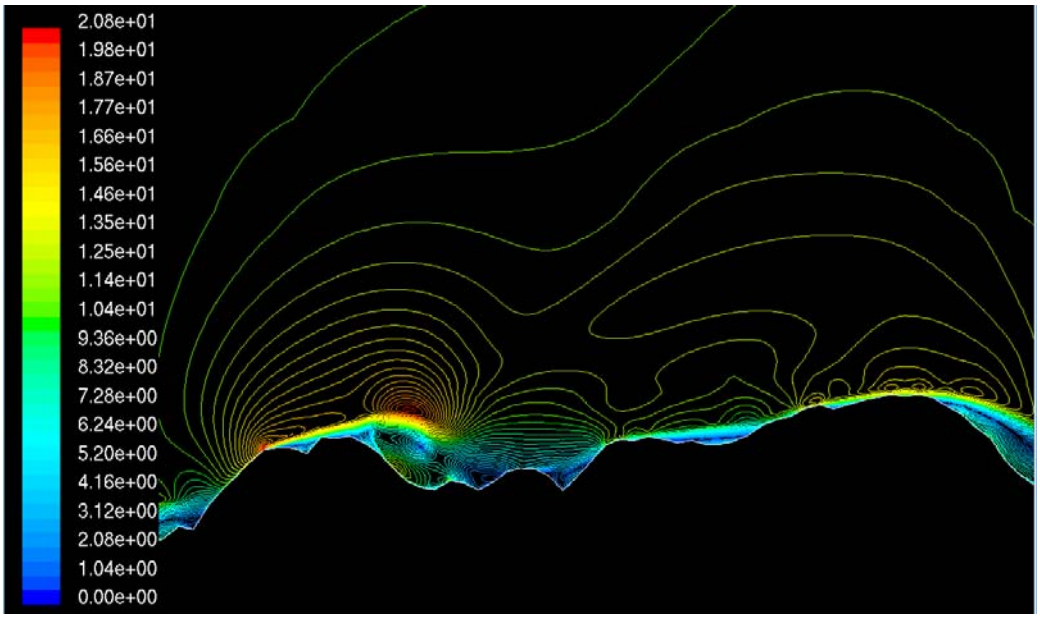

Fig. 4. CFD results for the velocity magnitude. Freestream velocity is 10 m/s.

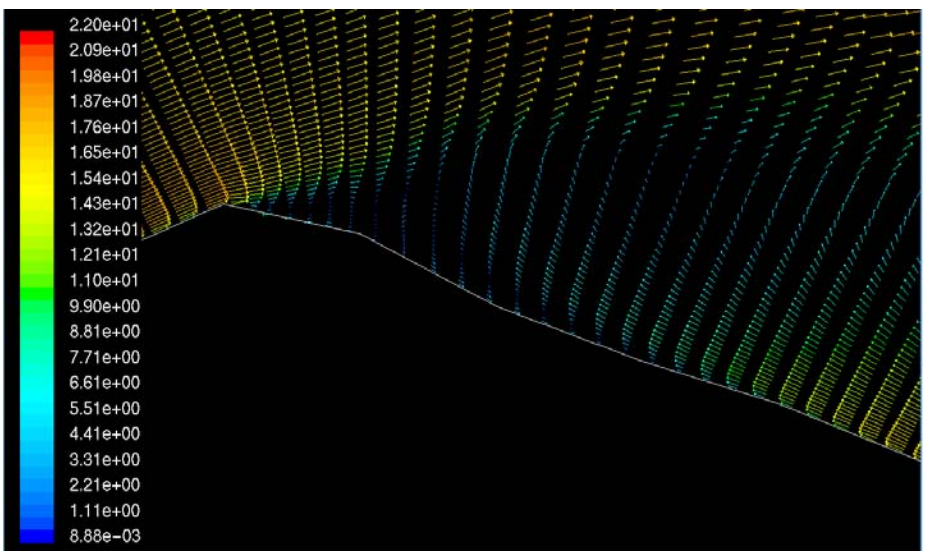

Fig, 5. Separated region downstream of a roughness element.

This work has been presented in "Flow and Heat Transfer over Rough Surfaces: Usefulness of 2-D Roughness-Resolved Simulations," by S. Yoon, S. Na, Z.J. Wang, J. P. Bons, and T.I-P. Shih. Presented at the AIAA 44th Aerospace Sciences Meeting and Exhibit in Reno, NV, 9-12 Jan 2006 (paper #AIAA 2006-0025).

CONCLUSIONS:

In conclusion, results from this three year roughness study are very promising. Industrial participation was excellent and synergy between the four groups on the team was healthy. The study included both the measurement of actual hardware and the laboratory simulation of degradation mechanisms (erosion and deposition). By performing the two components in parallel, we hope to have insured the relevancy of the laboratory simulations. Because they are performed in a controlled environment, these erosion and deposition studies should provide the framework for semi-empirical roughness evolution models. As these models are incorporated into computational codes, this will in turn provide the engine community with powerful roughness predictive capabilities.

REFERENCES:

Bons, J.P., Taylor, R., McClain, S., and Rivir, R.B., "The Many Faces of Turbine Surface Roughness," *Journal of Turbomachinery*, Vol. 123, No. 4, October 2001, pp. 739-748.

Bons, J.P., "St And c_f Augmentation For Real Turbine Roughness With Elevated Freestream Turbulence", *Transactions of the ASME J. Turbomachinery*, *Journal of Turbomachinery*, Vol. 124, No. 4, October 2002, pp. 632-644.

Bons, J.P, "A Critical Assessment of Reynolds Analogy for Turbine Flows," *ASME Journal of Heat Transfer – Special Issue on Gas Turbines* Vol. 127, May, 2005, pp. 472-485.

Borom, Marcus P., Johnson, Curtis A., and Peluso, Louis A., 1996, "Role of environmental deposits and operating surface temperature in spallation of air plasma sprayed thermal barrier coatings," Surface and Coatings Technology 86-87, pp116-126.

Hamed, A., Tabakoff, W., Rivir, R.B., Das, K., and Arora, P., "Turbine Blade Surface Deterioration by Erosion," presented at IGTI04 in Vienna, June 2004 and accepted for publication. Paper # GT-2004-54328.

Jensen, J.W., Squire, S.W., Bons, J.P., and Fletcher, T.H., "Simulated Land-Based Turbine Deposits Generated In An Accelerated Deposition Facility". To be presented at IGTI 2004 in Vienna, June 2004. Paper # GT2004-53324.

Kim, J., Dunn, M.G., and Baran, A.J. et al, 1993, "Deposition of Volcanic Materials in the Hot Sections of Two Gas Turbine Engines," J. Engr. Gas Turbines & Power vol. 115, Jul 1993, pp 641-651.

McClain, S.T., Hodge, H.T., and Bons, J.P., 2004, "Predicting Skin Friction and Heat Transfer for Turbulent Flow over Real Gas-Turbine Surface Roughness Using the Discrete-Element Method," *ASME Journal of Turbomachinery*. Vol. 126, pp. 259-267, Apr. 2004.

Subramanian, C.S., King, P.I., Reeder, M.F., Ou, S., and Rivir, R.B., "Effects of Strong Irregular Roughness on the Turbulent Boundary Layer," 2003, accepted for publication in the *International Journal of Flow, Turbulence and Combustion*.

Tabakoff, W., and Wakeman, T., 1979, "Test Facility for Material Erosion at High Temperature," ASTM Special Publication 664, pp. 123-135.

Tarada, F. and Suzuki, M., 1993, "External Heat Transfer Enhancement to Turbine Blading due to Surface Roughness," presented at ASME IGTI in Cincinnati OH, May 1993, ASME Paper 93-GT-74.

Wang, Z.J., Chi, X.K., Shih, T., and Bons, J., 2004, "Direct Simulation of Surface Roughness Effects with RANS and DES Approaches in Viscous Adaptive Cartesian Grids," presented at AIAA Flow Conference in Portland OR, June 2004, #AIAA-2004-2420.

Wenglarz, R. A., and Fox, R. G., "Physical Aspects of Deposition from Coal Water Fuels under Gas Turbine Conditions", ASME Journal of Engineering for Gas Turbines and Power, vol. 112, January, 1990, pp. 9-14.

Wenglarz, R.A., and Wright, I.G., "Alternate Fuels for Land-Based Turbines," published in proceedings of the "Workshop on Materials and Practices to Improve Resistance to Fuel Derived Environmental Damage in Land- and Sea-Based Turbines", October 22-24, 2002, Colorado School of Mines, Golden, Colorado.

Advanced optical sensor for monitoring and control of multiple gas and turbine-blade properties

Semi-annual report

Reporting period: 7/1/04 – 12/31/04

Principal investigator: Scott T. Sanders

Report date: January 2005

DOE award number: DE-FC26-02NT41431

UTSR project number: 03-01-SR105

Submitted by:
Scott T. Sanders
University of Wisconsin-Madison
1500 Engineering Dr.
Madison, WI 53706

DISCLAIMER

"This report was prepared as an account of work sponsored by an agency of the United States Government. Neither the United States Government nor any agency thereof, nor any of their employees, makes any warranty, express or implied, or assumes any legal liability or responsibility for the accuracy, completeness, or usefulness of any information, apparatus, product, or process disclosed, or represents that its use would not infringe privately owned rights. Reference herein to any specific commercial product, process, or service by trade name, trademark, manufacturer, or otherwise does not necessarily constitute or imply its endorsement, recommendation, or favoring by the United States Government or any agency thereof. The views and opinions of authors expressed herein do not necessarily state or reflect those of the United States Government or any agency thereof."

ABSTRACT

The goal of this project is to develop a fiber-optic sensor for monitoring gas properties in turbine engines. The sensor is designed to measure the temperature profile of combustion gases at the turbine inlet. We will also attempt to incorporate into the sensor the ability to monitor temperatures in the turbine blades themselves. Turbine blade monitoring is not possible with thermocouples or similar instrumentation, because of difficulties associated with transferring electrical signals from parts moving at high speed. We regularly visit gas turbine test facilities to demonstrate our sensing technology and to remain abreast of challenges to practical optical sensors. By the conclusion of the project we hope to investigate the possibility of using the sensors for real-time control of gas turbine performance, with the goals of reduced emissions, increased efficiency, and increased component life.

TABLE OF CONTENTS

INTRODUCTION 5
EXECUTIVE SUMMARY 5
Fiber-optic access 6
Wavelength-agile lasers.....6
Data reduction.....6
PROJECT DESCRIPTION.....7
EXPERIMENTAL.....7
FDML Laser 8
Optical Design 8
Averaging.....9
Emission.....10
Thermal Boundaries.....10
Results.....11
CONCLUSIONS 14
REFERENCES 15

INTRODUCTION

We have demonstrated the capability to fiber-couple light to and from optically harsh turbine environments, such as the research main burner test rig shown in Figure 1. This project aims to maximize the amount of useful information that can be obtained from such optical access. Key considerations include: tailoring fiber-optic access for gas turbine environments, using wavelength-tunable lasers to acquire spectral information from the test environment, and reducing measured optical data to quantitative properties. The "research-grade" sensors developed in this project are expected to be directly useful to gas turbine engine researchers; in addition, the sensing methodologies should ultimately contribute to the design of "production-grade" sensors.

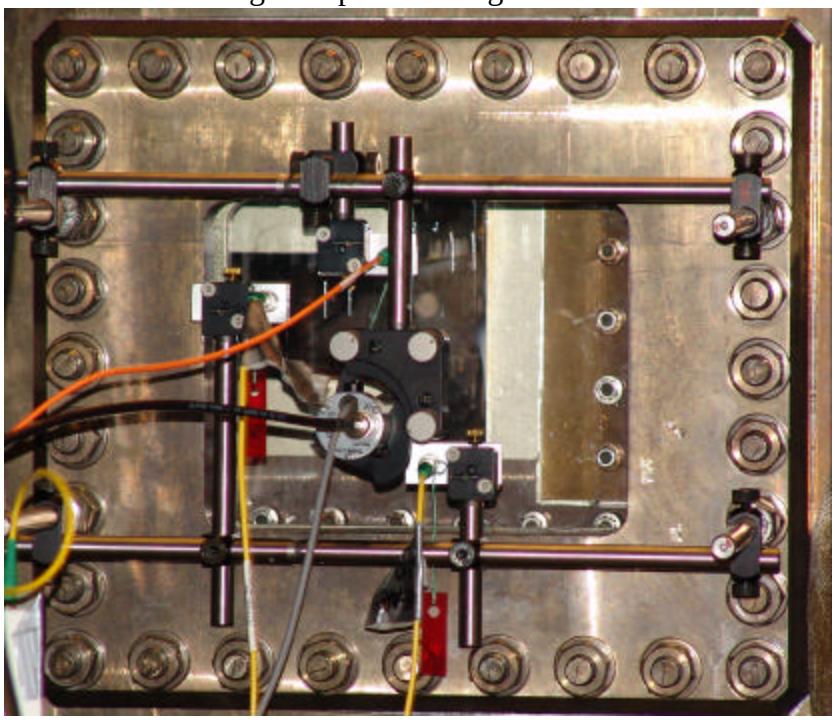

Figure 1. Gas turbine combustor test facility at Wright-Patterson Air Force Base with fiber-optic probes installed

EXECUTIVE SUMMARY

We are developing fiber-optic sensors for measuring gas and turbine blade properties in gas turbine engines. Toward that end, we have made many important accomplishments this reporting period. We categorize our accomplishments into three categories: fiber optic access, wavelength-agile lasers, and optical data reduction.

Fiber-optic access

Aided by discussions with Pratt & Whitney, General Electric, and Woodward Industrial Controls, we have refined our strategy for maintaining fiber-optic access to the mainburner/turbine area. We use a single fiber to deliver and receive laser light at each measurement station. This simplification is made possible by using a co-axial dual-clad fiber (DCF)[1]. Signal light is transmitted to the engine down the axis or core of the DCF, and received from the engine in the cladding surrounding the core. Various reflective surface options for returning light efficiently to the DCF have been discussed with manufacturers; one candidate is a thermal barrier coating (TBC) containing sapphire spheres. We have carefully considered "beamsteering" this reporting period[2]; "beamsteering" refers to the non-ideal light propagation that occurs in materials of inhomogeneous refractive index, such as combustion gases. We have developed a computer code that optimizes optical designs in beamsteering environments, and used it to make a three-fold improvement in collection efficiency. We have solved similar optical access problems relative to communicating optical signals with fiber Bragg gratings embedded in moving metal components[1]. Finally, we have refined our strategy for distributing light to many locations (up to 64) using fiber-optic components; our design incorporates a single laser, a single detector, and no moving parts.

Wavelength-agile lasers

A key to obtaining quantitative information in harsh environments is the ability to acquire optical spectra, rather than optical information at one or two discrete wavelengths. We have demonstrated the value of lasers that scan quickly through a broad range of wavelengths, such as 1374 nm – 1472 nm every 85 μs[3]. This reporting period, we have developed a new type of laser known as a "modeless" wavelength-agile laser[4]. Highlighting the success of our program from an educational perspective, the modeless laser was designed and constructed by an undergraduate research fellow (Ms. Renata Bartula) in our laboratories. In addition to the new modeless laser, we have continued to refine our supercontinuum-based sources[5] which provide scans such as 1330 – 1670 nm every 5 μs. Both the modeless laser and the supercontinuum laser produce continuous average output powers in excess of 10 mW; such high powers are critical for practical engine applications.

Data reduction

We have enhanced our computer algorithm used to infer gas properties from measured spectra. Our automated, LabVIEW-based system is now able to reduce H_2O vapor spectra recorded in gas turbine burners to temperature in near-real time, with an absolute accuracy of ± 2% or better.

The accomplishments in each of these three categories bring our sensing strategy much closer to the goal of revealing temperature information in the main burner and turbine. By providing this new information, the sensor will be useful in a number of ways, all of which ultimately increase efficiency, reduce emissions, and increase component lifetime.

First, the sensor can be used in engine test facilities for optimization of the temperature profile entering the turbine. The most desirable operating conditions can be mapped out in this way. Second, the sensor can be used to diagnose new engine designs. By rapidly providing insight into the combustion process, new designs can be evaluated more effectively. The direct effects of operating an engine on syngas, for example, could be evaluated in this manner. Another related application would be using this sensor, with its time constant of ~ 5 μs, to more fully characterize combustion driven oscillations. Finally, once the sensor has established more widespread use as a testing aid in the turbine industry, the sensor could be integrated into production engines to enable active, real-time control of temperature distributions. This strategy would likely have the most dramatic effect on engine performance, by allowing robust optimization under dynamic conditions.

In addition to the uses listed above, the sensor could also have broader impacts in the turbine industry. The sensor is designed to measure gas temperature and water vapor mole fraction in combustion gases. However, the same strategy (and in some cases the same equipment) could also be used to measure temperature or other gas species concentrations at a variety of locations in turbine systems.

PROJECT DESCRIPTION

Gas turbine engine designers have expressed a desire to accurately monitor and / or control the temperature distribution of gases entering the turbine. This is because of the important role temperature plays in determining engine efficiency, emissions levels, and component lifetime. Careful optimization of the temperature distribution at the turbine inlet would enhance engine efficiency and reduce emissions. The optical sensor developed in this project will address this need by enabling measurements of gas temperature distributions at the turbine inlet as well as actual turbine blade temperatures. We envision laser light distributed by fiber-optics and pitched through the combustion gases as well as routed through turbine blade material to support these measurements. The primary goals of this project are demonstrations of the sensor in large-scale test facilities. These demonstrations will pave the way for more widespread sensor use in the gas turbine industry.

At the conclusion of the project, it is hoped that the sensor will become a ready tool for optimizing the gas temperature distribution entering the turbine, possibly by active closed-loop control. In addition, they can potentially be used for “plug-and-play” attachment to prototype engines under test, thus providing critical information at the design stage and thereby reducing the cost of evaluating engine designs.

EXPERIMENTAL

Initial gas temperature measurements in the combustion zone of a gas turbine sector rig were made using wavelength-agile absorption spectroscopy. The wavelength-agile laser

that was used is a Fourier-domain mode-locking (FDML) laser. These measurements are among the first of their kind and demonstrate promise for simple and reliable gas turbine engine sensors. The FDML laser is a rugged all-fiber system, amendable to distributed multi-line-of-sight measurements that could be coupled with tomographic reconstruction algorithms [6]. Significant related work has been performed on a piston engine at the University of Wisconsin's Engine Research Center, which has lead to an overall improvement of the experimental process [7]. Limited experimental time at the turbine at Wright-Patterson Air Force Base was obtained for this experiment. Although off site measurements are generally more difficult due to transportation issues, unfamiliar set-up conditions, and the inevitable unknowns, the overall experiment went well and worked in the limited time provided.

This paper presents an overview of the laser and the method for obtaining H_2O absorption spectra. The inference of gas temperature from the spectra is then discussed, and the results are compared to flame temperature calculations based on emission gas analysis.

FDML Laser

In traditional swept laser sources, like external-cavity diode lasers, the center wavelength of the light is swept by an external means, like a diffraction grating, and the light at each wavelength is built up from spontaneous emission of the laser medium [4]. The maximum scanning speed is thus limited by the amount it takes to build up laser action from spontaneous emission at each frequency [8, 9]. If one tries to scan the laser faster than this limit, broader spectral linewidth output generally results. One approach for circumventing the build-up time limitation is Fourier-domain mode-locking (FDML).

The laser is capable of producing a complete spectrum every 5 μs (200 kHz). This speed is essentially fixed by the total length of the light path within the laser (or, the total fiber length). The spectral range depended on the SOA; for this experiment, we used an SOA that resulted in a 1330-1380 nm bandwidth. Successful spectra using a different SOA have been produced with a 1390-1460 nm bandwidth. Other bandwidths could also be achieved, the requirement being a fiber coupled broad source in the desired range. For the tests reported here, the spectral resolution of the FDML laser was measured to be 0.1 nm using a low pressure cell (~50 kPa) containing water vapor. This represents roughly two times better resolution than other wavelength-agile lasers we have developed [3, 4]. The average output power of the laser was measured to be 5 mW. Further details of laser operation and capabilities can be found in the literature [7, 9, 10].

Optical Design

The design of the absorption spectroscopy experiment, as well as a description of the tested gas turbine conditions are described in this section. Particular detail concerning differences between this experiment and previous successful measurements are emphasized.

Previous absorption spectroscopy experiments using the FDML laser have been successfully performed in a piston/cylinder engine run under homogenous charge compression ignition (HCCI) and a shock tube [7]. There are several differences between those environments and the gas turbine which will be discussed here, specifically averaging capabilities, emission, and distinct thermal boundaries. Figure 2 diagrams the overall setup used to obtain water absorption spectra. The pitching and collecting lenses were chosen to reduce the amount of light that was lost due to beam steering (light deviating from the intended path due to index of refraction gradients, generally caused by turbulent boundaries) [2]. The neutral density (ND) filter (optical density = 0.9) and iris were used to limit collection of thermal emission. For simplicity, we chose not to include spectral filtering to further limit thermal emission. Part of the motivation for this choice is as follows. In a typical combustion measurement, we find that hot H_2O vapor is the dominant source of thermal emission. In this case, reduction of the detected emission by spectral filtering offers improvement by approximately a factor of two only; the P-branch emission can be rejected but our detector must view the entire R-branch of the water band monitored. The photo detector was chosen to balance effects of beam steering (larger collection area), thermal emissions (smaller collection area), and bandwidth considerations (sufficiently fast). The required bandwidth to measure water lines at atmospheric pressure with the 200kHz scanning frequency FDML laser has been found to be at least 100MHz. The photo detector that was chosen was a Thorlabs (PDB150C), 350 MHz, 0.3 mm diameter InGaAs detector.

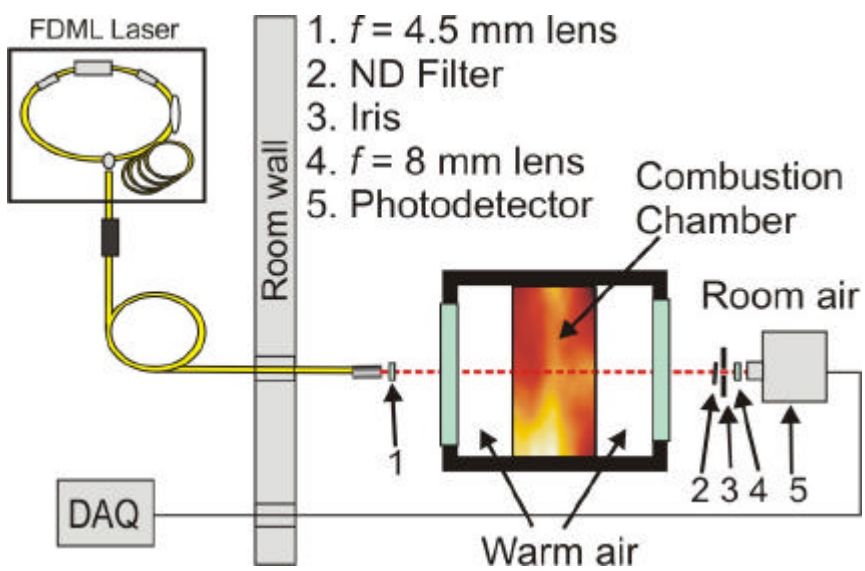

Figure 2: Experimental configuration - the laser and data acquisition system were located in an adjacent room.

Averaging

It has been shown that the results from single shot measurements using the FDML laser suffer from the intensity noise of our current FDML laser [7], however averaging multiple spectra significantly improves precision. The engine and shock tube applications are unsteady, making direct averaging difficult. To gain the advantages of

averaging in the engine, cycle-by-cycle averaging can be implemented (because the engine is repeatable, although unsteady). Opportunities for averaging in the shock tube environment are severely limited because the event is short and singular (test conditions last ~ 1 ms and the next shock takes several hours to prepare).

The gas turbine, on the other hand, is relatively steady and continuous, allowing for straightforward averaging. In this paper, 1000 averages were used throughout. Each measurement therefore required a total time of 10 ms (5 μs single scans skipping every other scan), although this time could be reduced. For example, the shock tube measurements have demonstrated 2% accuracy over a cumulative time of 150 μs [7]. With future laser intensity noise reductions, single-shot measurements (5 μs) are possible.

Emission

Another difference in the testing environments was the amount of emission. The amount of emission in both the engine and shock tube was low enough that the photo detector never saturated. Emission correction simply involved turning off the laser for ~ 1 μs preceding each scan and subtracting the associated detector output voltage from the remainder of the scan.

The emission observed in the gas turbine test case was significantly higher than levels observed in piston engines and shock tubes, even at similar values of measured gas temperature. More soot created during combustion, particulate deposits accumulated on the windows, and the hot windows themselves can all contribute to high emission. While collecting water absorption spectra, we simultaneously recorded emission spectra on an optical spectral analyzer (OSA). These spectra showed significant broad emission, completely overpowering any water emission lines, implying emission from solid sources (hot windows, and hot dirt on the windows).

To deal with the emission, both a ND filter and an iris were used to reject emission while retaining sufficient signal even in the presence of beam steering. A detector with a small area (diameter = 0.3 mm) was also chosen to reduce the collection of emission. The optical set up was placed 6 cm downstream from the hottest section (and therefore highest emitting section). As with the engine and shock tube, a constant value obtained when the laser was briefly turned off was subtracted from the measured signal.

Thermal Boundaries

The final significant difference between this experimental environment and previously successful experiments is the existence of absorbing H_2O outside the combustion region of interest (as can be seen in Figure 1, see “Combustion Zone”, “Warm Air”, and “Room Air”). Both the engine and the shock tube experiments had all room air purged of water (using either nitrogen or dry air). The combustion zones for these experiments were also roughly homogeneous; therefore the spectrum measured from the line of sight was thought to be meaningful. The warm and room air sections could, in the future, be purged of water. For the simplicity of this initial test however, that was not done.

The conditions of the gas turbine are such that there are 3 distinct conditions in the laser's line of sight: the room air, the warm air, and the combustion zone. In addition to these primary sections, thermal boundary layers at each window surface contributed to uncertainties in the measurements. The warm air (on either side of the combustion area) was expected to have a sufficiently low H_2O mole fraction to be negligible in our final results. Therefore we ignored this section, but we did not verify that it was sufficiently dry to do so. The room air was corrected as explained below. In future measurements, one would hope to bring fiber coupling directly to the combustion gas to avoid such concerns.

Results

1000 signals were first averaged, then converted to absorbance using the Beer-Lambert law ($I/I_o = \exp(-k_\lambda L)$), where I is the transmitted light intensity, I_o the incident light intensity, L is path length, k_λ is the absorbance coefficient at wavelength λ, and the product '$k_\lambda L$' is termed absorbance. The wavelength axis for the spectrum was determined by finding the maximum and minimum wavelengths using the OSA. These wavelength extremes were used to generate the wavelength axis assuming sinusoidal motion within the tunable etalon in the FDML laser. For a simple sensor, this process could be automated by aligning water absorption peaks from spectra created using the HITEMP database (or improved databases) with the measured peaks.

The top panel of figure 3 shows the raw measured spectrum for the $\Phi = 0.220$, P = 696 kPa case. The middle panel shows the spectra that result when the raw spectrum was corrected by subtracting out the room water spectrum. The bottom panel shows the HITEMP spectrum [11]for the corresponding flame temperature (1277 K, 696 kPa).

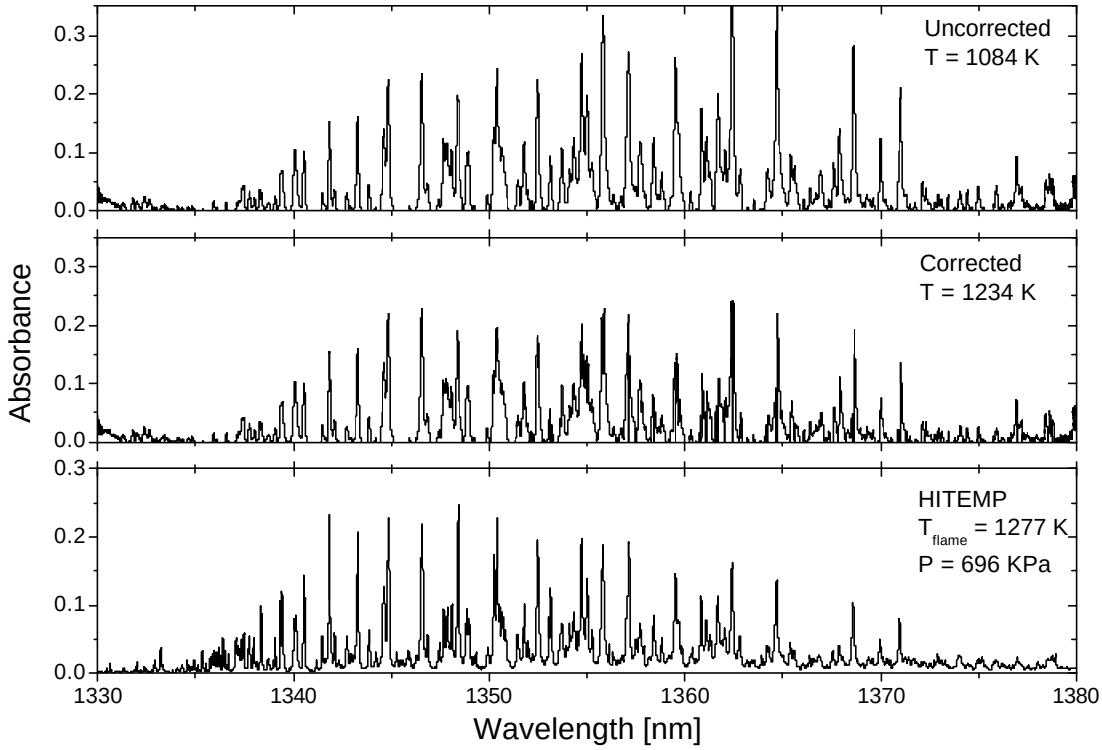

Figure 3: Raw measured spectrum (top panel), corrected spectrum (middle panel), and corresponding HITEMP spectrum (bottom panel) at the theoretical flame temperature for the F = 0.220, P = 696 kPa case.

The method for calculating temperature and water mole fraction has been described previously in detail [3], therefore only a brief summary and specific details to this experiment will be repeated here. First, both the measured and theoretical spectra are smoothed and differentiated. Next, they are interpolated such that there is exactly one data point every 0.25 cm^{-1}. The absorbance of the measured spectrum is then plotted against the absorbance of a theoretical spectrum at the measured pressure, and a line is fit to these data points using a standard least-squares scheme. This smoothing and differentiation strategy has been previously shown to be effective under similar conditions [3, 7]. Sensitivities to noise in the measured data, broadband offsets caused by either unknown absorbers or beam steering (due to refractive index gradients caused by turbulence), and discrepancies between simulated and measured spectra are all dramatically reduced with this smooth and differentiate method.

Figure 4 shows the temperatures from the raw data calculated as described above (in grey) as a function of the measured equivalence ratio. The black points are the calculated flame temperature based on the conditions. It is expected that the measurements would be slightly lower than the flame temperature since the laser was mounted downstream from the hottest part of the combustion chamber. The measurements in Figure 3 however are unacceptably low, due to the fact that they include the room air.

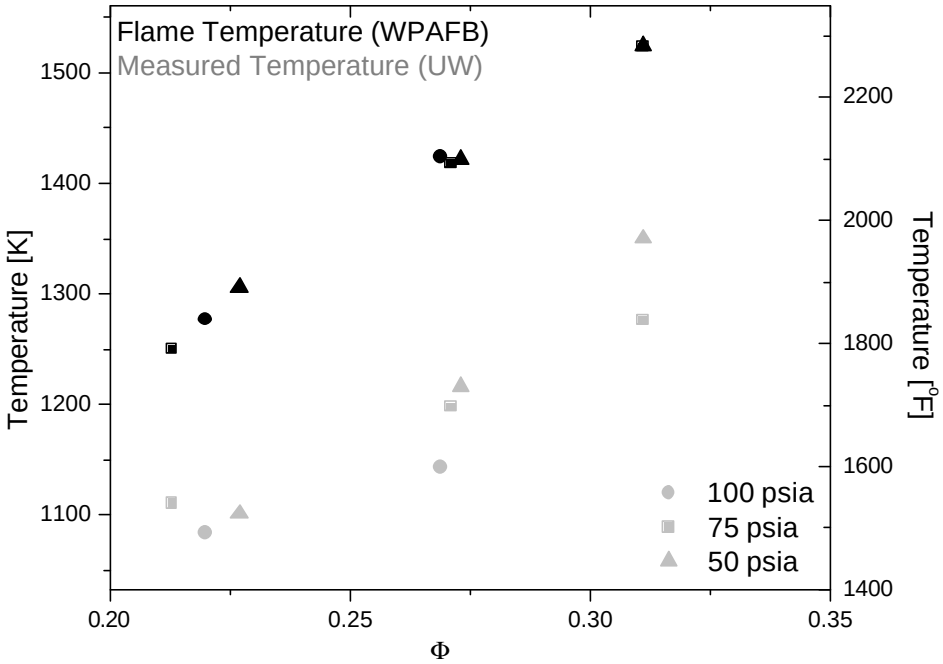

Figure 4: Uncorrected results which include room and warm air.

The path for the room air totaled 25 cm. A water spectrum at 322 K (120°F), 25 cm long, and 0.014 water mole fraction (corresponding to 54% relative humidity at room temperature, measured that day) was subtracted from the measured spectra. This temperature is higher than regular room temperature because the turbine warmed up the surroundings. Future measurements should purge all room air from the line of sight measurement. Figure 4 shows the results when the room water was subtracted out.

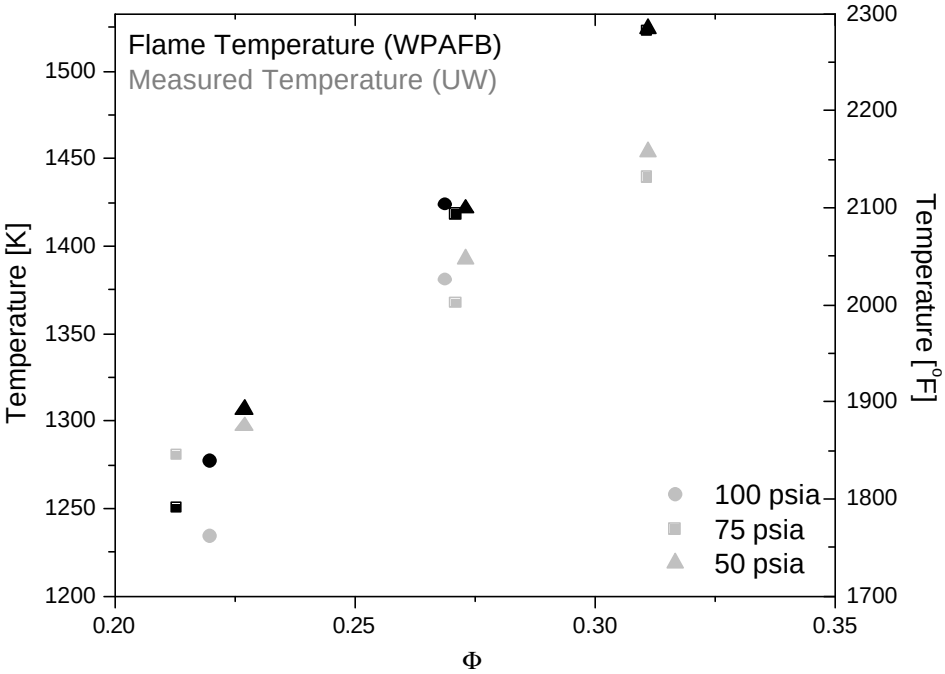

Figure 5: Corrected results where room air spectrum was subtracted out of measured spectrum.

As a proof of concept, the experiment has shown that this method of measuring water spectra in a gas turbine can be successful. Compared to previous successful combustion measurements, the gas turbine environment has an advantage in that it is relatively steady, however increased emission and thermal boundary layers add to the overall complexity of the experiment. Figure 5 shows how close the temperature measurements were to the flame temperature; generally the results were biased low, however the correct trends were observed in the measured results. This low bias could be due to any of at least three factors: the warm air path contained non-negligible H_2O, the measurements were taken 6 cm downstream from the hottest part of the chamber, and thermal boundary layers were present near the windows. In order to make the results more meaningful, future experiments should fiber-couple the light directly into the combustion gas (which would avoid having to deal with humidity in the room air), and measure the trace amounts of water in the warm air path. There is also potential to deal with emission better by getting a stronger filter, smaller iris, and smaller surface area detector. This would allow measurements to be made directly in the flame region. Future experiments could also include either multiple laser paths or traversing the entire set-up to create a temperature tomography of the flame.

CONCLUSIONS

We have presented our designs for an optical system for monitoring gas and turbine-blade properties at multiple stations in turbine engine systems. By enabling measurements at many different locations, the spatial distribution of gas and turbine-blade properties will ultimately be revealed. The capability to measure such information will be invaluable to gas turbine engine researchers.

We have organized our effort into the categories of fiber-optic access, wavelength-agile lasers, and data reduction. These three components of the project are now coming together, and we have already begun testing our strategies at off-site facilities. A protograph from a recent visit to the Wright Patterson Air Force Base (WPAFB) in Dayton, OHis shown in Figure . We are scheduled to travel to WPAFB again this summer and also hope to visit other facilities, possibly including General Electric in Schnectady, NY. We look forward to these off-site measurement opportunities. If the reader has suggestions for other off-site measurement possibilities, please feel free to email Scott Sanders (ssanders@engr.wisc.edu) directly.

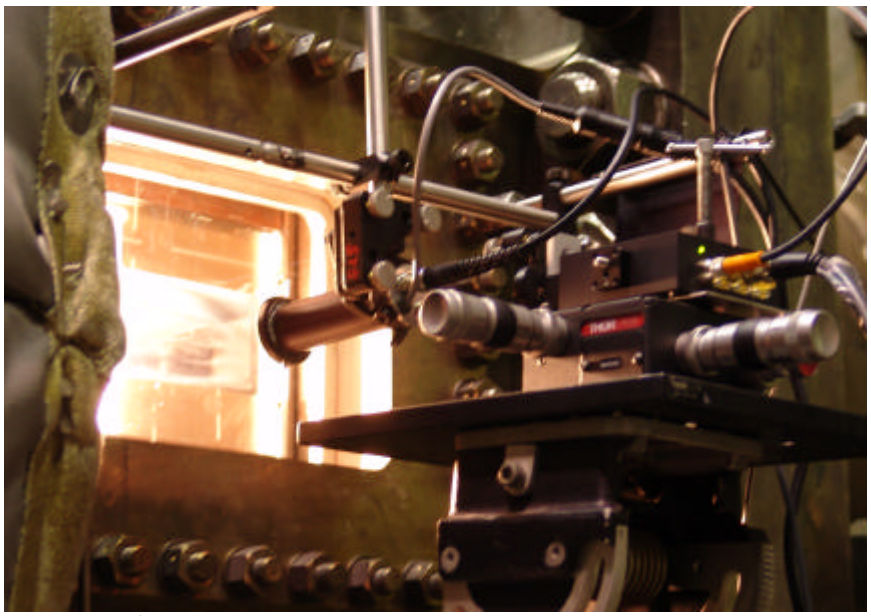

Figure 6. Photograph of the tested wavelength-agile sensor strategies under test at Wright-Patterson Air Force Base in Dayton, OH.

REFERENCES

[1] Hagen,Christopher L., Schmidt,Jason R., and Sanders,Scott T., 2005, "Spectroscopic Sensing Via Dual-Clad Optical Fiber," IEEE Sensors Journal**, accepted**.

[2] Kranendonk,L. A., and Sanders,S. T., 2005, "Optical Design in Beam Steering Environments with Emphasis on Laser Transmission Measurements," Appl. Opt.**, 44**(31), pp. 6762-6772.

[3] Kranendonk,L. A., Walewski,J. W., Kim,T., and Sanders,S. T., 2005, "Wavelength-Agile Sensor Applied for HCCI Engine Measurements," Proc. Comb. Inst.**, 30**, pp. 1619-1627.

[4] Kranendonk,L. A., Bartula,R. J., and Sanders,S. T., 2005, "Modeless Operation of a Wavelength-Agile Laser by High-Speed Cavity Length Changes," Opt. Express**,** **13**(5), pp. 1498-1507.

[5] Walewski,J., Filipa,J., Hagen,C., and Sanders,S., 2005, "Standard Single-Mode Fibers as Convenient Means for the Generation of Ultrafast High-Pulse-Energy Super-Continua," Applied Physics B(Submitted.).

[6] Caswell,Andrew W., Sanders,Scott T., and Chiaverini,Martin J., 2005, "Swept-Wavelength Laser Absorption Tomography for Imaging Rocket Plume Gas Properties,", *41st AIAA/ASME/SAE/ASEE Joint Propulsion Conference and Exhibit*, Anonymous eds.

[7] Kranendonk,L. A., Walewski,J. W., Sanders,S. T., Huber,J., and Fujimoto,J. G., 2006, "Measurements of Gas Temperature in a HCCI Engine using a Fourier Domain Mode Locking Laser," SAE(2006-01-1366).

[8] Huber,R., Wojtkowski,M., Taira,K., Fujimoto,J. G., and Hsu,K., 2005, "Amplified, Frequency Swept Lasers for Frequency Domain Reflectometry and OCT Imaging: Design and Scaling Principles," Opt. Express**, 13**(9), pp. 3513-3528.

[9] Huber,R., Taira,K., and Fujimoto,J. G., 2005, "Fourier Domain Mode Locking: Overcoming Limitations of Frequency Swept Light Sources and Pulsed Lasers," CLEO/Europe - EQEC 2005**, CP3-5-THU**.

[10] Huber,R., Taira,K., Wojtkowski,M., and Fujimoto,J. G., 2005, "Fourier Domain Mode Locked Lasers for OCT Imaging at Up to 290kHz Sweep Rates," Proc OSA-SPIE Biomed Opt**, 5861**(58611B).

[11] Rothman,L. S., Barbe,A., and Benner,D. C., et al, 2003, "The HITRAN Molecular Spectroscopic Database: Edition of 2000 Including Updates through 2001," J.Quant.Spectrosc.Radiat.Transf.**, 82**, pp. 5-44.

Spectroscopic In-Situ Non Destructive Evaluation to monitor the Health of Thermal Barrier Coatings

Semi-annual Report
1 July 2005 to 31 December 2005

Surendra Tewari, Co-principal Investigator
Kang Lee, Co-Principal Investigator
Guofeng Chen, Postdoctoral Fellow

February 2006

DOE Award number:

UTSR Project Number: 03-01-SR106

Department of Chemical and Biomedical Engineering
Cleveland State University
Cleveland, OH 44115

DISCLAIMER:

"This report was prepared as an account of work sponsored by an agency of the United States Government. Neither the United States Government nor any agency thereof, nor any of their employees, makes any warranty, express or implied, or assumes any legal liability or responsibility for the accuracy, completeness, or usefulness of any information, apparatus, product, or process disclosed, or represents that its use would not infringe privately owned rights. Reference herein to any specific commercial product, process, or service by trade name, trademark, manufacturer, or otherwise does not necessarily constitute or imply its endorsement, recommendation, or favoring by the United States Government or any agency thereof. The views and opinions of authors expressed herein do not necessarily state or reflect those of the United States Government or any agency thereof."

ABSTRACT

In the previous report, Li_2O doped TBCs applied by plasma spraying process was investigated by exposing coated coupons to thermal cycling. Twenty hour thermal cycling test at 1115^oC and 1150^oC indicated that double-layered TBC structure with a thinner inner layer of YSZ, doped with relatively low lithium oxide concentrations, is preferable. Spectral response of the plasma sprayed 1 wt% Li_2O doped TBCs was also examined using oxy-acetylene welding torch as the flame source. Activation energy for the transition causing lithium emission was also calculated. It was also reported that the emission detection system has been miniaturized so that it can be transported to the test site for future burner-rig simulations. In addition some initial data from the flat-flame burner test were also reported.

During this reporting period,

(1) Work with the flat-flame burner to generate emission spectrum data has continued. Unfortunately the burner got damaged because of cooling water flow problem, and had to be repaired. However, the burner is now fully functional and is being utilized for this research.

(2) More data have been generated to examine the one hour thermal cycling response of the coating architecture for the 1100 ^oC as the hot temperature. Tests have been conducted for the 1, 2 and 3 wt% Li_2O doped plasma sprayed TBC superalloy coupons with 1/9, 2/8 and 3/7 configurations (The values to the left of the slash correspond to thickness in mils of the inner Li_2O doped YSZ layer, and the values on the right indicate thickness of the outer YSZ layer). These tests indicated that in general, thinner doped layer is beneficial for TBC life. With 1/9 configuration 1 wt% Li_2O dopant concentration gave lives comparable with that of standard YSZ. The 1/9 configuration even with the high 3 wt% Li_2O content has good response. For the 2/8 configuration only the 1 wt% Li_2O dopant concentration gave thermal fatigue lives comparable with that of standard YSZ. It is however, important to examine these results in the burner-rig set up, because the thermal stresses on flat super alloy coupons coated only on one side and the cylindrical samples coated on all sides that are used in the burner rig will be different.

(3) Superalloy 0.5-inch diameter cylindrical samples have been procured and given to our colleagues at NASA-Glenn Research Center for Li_2O doped YSZ TBC coating.

TABLE OF CONTENTS

EXECUTIVE SUMMARY……..……..5

PROJECT DESCRIPTION……..6

EXPERIMENTAL…….6

RESULTS AND DISCUSSION……7

FUTURE WORK …… 9

EXECUTIVE SUMMARY

Due to the extreme environment it experiences, one gas turbine engine component most often associated with failure is the thermal barrier coating (TBC) on turbine blades. Early detection of TBC degradation and failure is critical to prevent catastrophic engine failure as more advanced gas turbine engines depend on TBCs for their high temperature operation. Thermal barrier coatings on turbine hot section components, therefore, require regular maintenance. A typical maintenance is a visual inspection of the TBC for cracks, erosion or other damages that will indicate the remaining TBC life. These visual inspections require the engine to be taken out of service and to be partially disassembled to provide access to the TBC by boroscope. This type of maintenance is costly because it requires skilled labor and the interruption of service. Substantial savings in engine maintenance could be obtained if the TBC materials could be made to emit signals that contain information about their deterioration (cracking/spalling) and instrumentation could be developed to detect these signals *in-situ* during engine operation.

An exciting development in rocket engine health monitoring shows great promise for application in in-situ, real-time TBC health monitoring. The technique consists of optical detection of species in the vapor phase inside the chemically reacting or expanding flow. Species originating from the deteriorating TBC would appear as atomic vapor, oxides, and/or hydroxide species in the engine flow path. During flow expansion through the turbine and nozzle, these species equilibrate, typically by collisional de-excitation or emission of radiation. This radiation can be monitored anywhere in the engine where optical access can be designed into the engine components. The use of fiber optics as light guides facilitates the optical access and could allow the design of low cost, in-situ TBC health monitoring equipment.

An ideal engine monitoring system would correctly identify the engine part before it fails. Our idea is to detect and track the TBC failure throughout the life of the component. We plan to dope the TBC with signature marker materials that can be monitored optically in the combustion gas or the exhaust. Marker materials can be incorporated in the area where the failure is generally initiated, which is the inner yittria-stabilized zirconia (YSZ) at the thermally grown oxide (TGO)/YSZ interface in the case of plasma-sprayed thermal barrier coatings. From the presence of the marker species in the combustion gas or the exhaust, determined by a spectroscopic interpretation of the observed optical emission, the mechanical condition and deterioration of TBC can be inferred.

Our preliminary research demonstrated the feasibility of spectroscopic in-situ NDE to monitor the deterioration of mullite/BSAS environment barrier coatings (EBC) on SiC/SiC composites. Lithium oxide (Li_2O) was identified as the most promising marker material for EBCs. A significant lithium emission spectra peak was detected when the mullite bond coat was doped with as low as 0.025 wt% Li_2O in the absence of BSAS topcoat, while no lithium peak was detected in the presence of the BSAS topcoat. The lithium peak was detected again when simulated cracks were machined through the BSAS topcoat, indicating that lithium vapors escaped through the cracks. The lithium spectral intensity increased linearly with the increasing number of cracks. These results

suggest that the lithium spectral intensity can be correlated with the extent of cracking and/or spallation of the EBC.

Literature survey indicates that Li_2O is also compatible with the key TBC components (ZrO_2, Y_2O_3, Al_2O_3), suggesting the feasibility of using emission spectroscopy of lithium as an NDE tool to monitor the cracking/spalling of Li_2O-doped TBC. In this period, further thermal cycling tests were performed on the 1, 2 and 3 wt% Li_2O doped plasma sprayed TBC with two-layered ceramic top coat (1/9, 2/8 and 3/7) (The values to the left of the slash indicate inner Li_2O doped YSZ layer thickness in mils, and the values to the right indicate the thickness of the outer YSZ layer).

Thermal cycling tests carried out on coated superalloy coupons indicate that in general, thinner doped layer is beneficial for TBC life. The higher Li2O concentration and thicker inner doped layer are detrimental to the thermal fatigue response. With 1/9 configuration 1 wt% Li_2O dopant concentration gave lives comparable with that of standard YSZ, whereas with 2/8 configuration only 1 wt% Li_2O dopant concentration gave lives comparable with that of standard YSZ.

Ten cylindrical superalloy samples are being coated by plasma spray with the varying TBC coating architecture: (a) the Li_2O layer varying from 1 to 3 mil while keeping the overall coating thickness as 10 mil, (b) Li_2O content varying from 1 to 3 wt% in the doped YSZ layer at the bond-coat.

PROJECT DESCRIPTION

Developing self-sensing smart high-temperature coating for critical gas turbine engine components that can allow in-situ monitoring of its own mechanical health during operation of the engine will result in significant cost saving, as compared with the present invasive inspection techniques that require the engine to be shut down and partially disassembled for inspection. This research will not only benefit the land based power turbines but will also be useful for aircraft engine applications

EXPERIMENTAL

(1) Flat flame burner: A flat flame burner, shown in Figure 1, that uses an air and methane mixture set-up for this study is currently being used. It yields more stable flame temperatures between 1000-1500 K as compared with the welding torch used before.

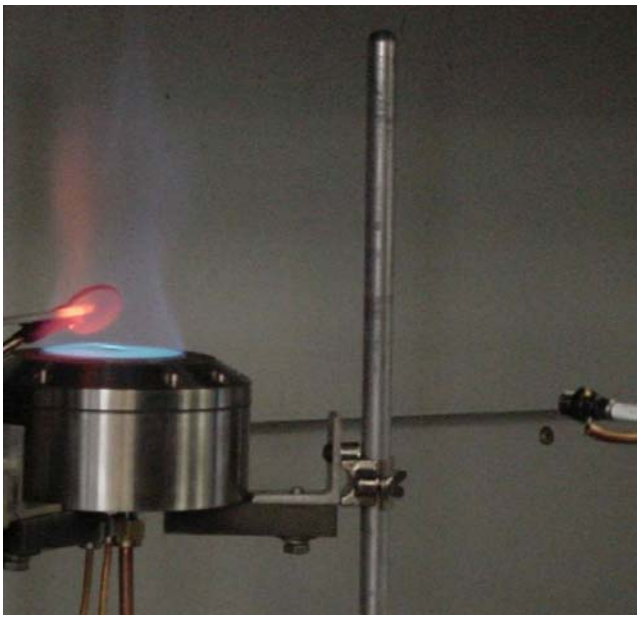

Figure 1 Flat-flame burner in use

(2) Optical set-up: A miniature spectrometer (Model HR2000, Ocean Optics Inc., Dunedin, FL) centered at 670 nm has been installed and configured to cover the emission wavelengths from 320 to 800 nm. The light emitted from the Lithium emission source in the flame is collected by using a lense and fiber-optics cable that feeds the signal into the spectrometer. Spectrometer out-put is fed into a PC for data acquisition.

(3) Lithium oxide as a marker material in plasma sprayed YSZ coating: Yttria stabilized zirconia ($ZrO_2$8-wt% Y_2O_3) powders doped with Li_2O of 1, 2 and 3 wt % obtained from a commercial vendor (Praxair Specialty Ceramics, Woodinville, WA) are being used. Plasma spraying was used to deposit the lithium oxide doped, and undoped YSZ ceramic layers on the CMSX-4 superalloy substrate coupons having a NiCoCrAlY bond coat. The coupons are about 1-inch in diameter and 3-mm thick. Following different types of configurations, presented in Table 1, have been examined. Samples without Li_2O dopant were also prepared for comparison.

Table 1: Configuration of the plasma sprayed TBCs

Configuration	Li_2O concentration, wt%
Substrate / **B**ondcoat / Li_2O doped YSZ / YSZ (value indicating the thickness of YSZ in mil):	
S / B / 1 / 9	1, 3
S / B / 2 / 8	1, 3
S / B / 3 / 7	1, 3
Substrate / **B**ondcoat / YSZ	
S / B / 10	N/A

(4) Thermal cycling of plasma-sprayed TBC in air: All the as-processed samples were subjected to an annealing treatment at 1100°C in Ar-5H_2 atmosphere for 4 hours before

thermal cycling test. Thermal cycling test was performed at 1100-1150°C in air. Each cycle includes heating up to the temperature, at a rate of 20°C/min, 1 or 20 h at the temperature, cooling down to room temperature, at 20°C/min.

RESULTS AND DISCUSSION

(1) Flat-flame burner set-up:

The flat flame burner yields a more stable flame compared to that from the welding torch. Fig 2 plots the typical in-situ measured temperature and luminescence intensity as a function of time for a sintered 1 wt% Li_2O doped YSZ pellet. The steps correspond to the times when adjustments in the gas-mixture were made to achieve higher temperatures. It was earlier observed that for similar thermocouple out-puts the flat-flame burner arrangement yields higher emission intensity as compared with the welding torch. It has been seen that the difference is because of the more uniform flame-coverage of the sample when using the flat-flame burner and concentrated-localized heating of the sample surface in the case of welding torch. This temperature difference of about 260-270°C to yield nearly identical emission intensities was observed to be constant in the temperature range examined, 800 to 1200°C, Fig 3; the flat-flame arrangement consistently yields the same intensity at temperatures that are less than those with the welding-torch arrangement.

(3) Thermal cycling

Tables 2, 3 and 4 show all the data compiled so far for the thermal cycling life of doped and undoped (standard) YSZ TBCs at various temperatures and cycling frequencies. In general, thinner doped layer is beneficial for TBC life. With 1/9 configuration 1 – 3 wt% Li_2O dopant concentration gave lives comparable with that of standard YSZ, whereas with 2/8 configuration only 1 wt% Li_2O dopant concentration gave lives comparable with that of standard YSZ. The higher temperature hold during thermal cycling is significantly more detrimental (compare the results from Table-2 and 3 below). The short duration cycles give large number of cycles. Considering all the data examined so far the 1/9 coating texture with 1wt % Li_2O appears to be optimum.

Table 2. Thermal cycling life (20-h cycle test at 1150°C)

Configuration	1 wt% Li_2O	3 wt% Li_2O
1/9	16, 22	24
2/8	18, 20	19
3/7	13, 20	3
Standard YSZ	22	

Table 3. Thermal cycling life (20-h cycle test at 1115°C)

Configuration	1 wt% Li_2O	2 wt% Li_2O	3 wt% Li_2O
1/9	25, 35	30	40, 103
Standard YSZ	25, 75		

Table 4. Thermal cycling life (1-h cycle test at 1100°C)

Configuration	1 wt% Li_2O	2 wt% Li_2O	3 wt% Li2O
1/9	790, 840	900	790, 910
2/8	900	-	20,15
3/7	-	2	1
Standard YSZ	483,750		

FUTURE WORK

The cylindrical superalloy samples, about 0.5-inch in diameter and 5-inch long, have been procured and have been given to NASA-Glenn Research Center Plasma Spray facility for coating. The following samples should become available for future Burner Rig evaluation of coatings, their emission characteristics and their failure.

1 wt% Li_2O: 1/9 mil, 2/8 mil, 3/7 mil and 5/5 mil
3 wt% Li_2O: 1/9 mil, 2/8 mil, 3/7 mil
YSZ only: 10 mil
1 wt% Li_2O only: 1mil
3 wt% Li_2O only: 1 mil

The miniaturized emission spectrum measuring set-up will be taken to NASA-Glen Research Center for burner-rig testing.

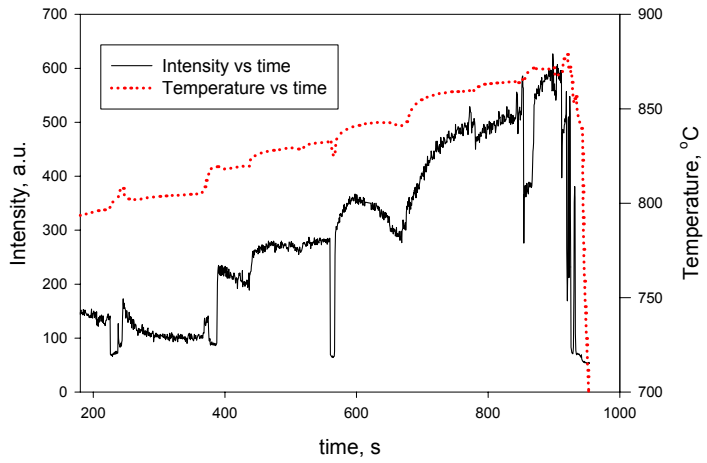

Figure 2. In-situ measured temperature and luminescence intensity for a 1 wt% Li_2O doped YSZ pellet by using flat burner arrangement.

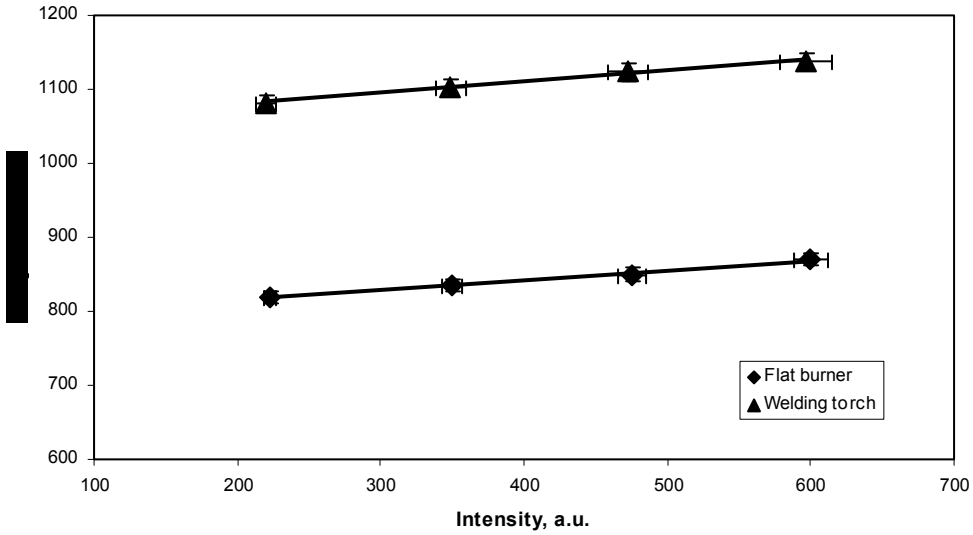

Figure 3. The flat-flame burner appears to yield the same emission intensity as the welding torch samples at 260-270 °C lower temperatures.

Superior Thermal Barrier Coatings for Industrial Gas-Turbine Engines Using a Novel Solution Plasma Spray Process

UTSR Semi-Annual Report

July 1, 2005 to December 31, 2005

Principal Investigators:

Profs. Maurice Gell, Eric H. Jordan

Institute of Materials Science
University of Connecticut

Prof. Nitin P. Padture

Department of Materials Science and Engineering
The Ohio State University

January 13, 2006

Prime Agreement Contract No. DE-FC26-02NT41431
US Department of Energy

UTSR Subcontract No. 03-01-SR107

Principal Investigators: Eric H. Jordan, Professor
Department of Mechanical Engineering
The University of Connecticut
Storrs, CT 06269-3139
Phone: (860) 486-2371 Fax: (860) 486-5088
E-mail: jordan@engr.uconn.edu

Maurice Gell, Professor-in-Residence
Department of Materials Sci & Engr,
Institute of Materials Science
University of Connecticut
Storrs, CT 06269-3136
Phone: (860)486-3514 Fax: (860)486-4745
Email: mgell@mail.ims.uconn.edu

Research Students/Post-Doc: Mr. Amol Jadhav
Mr. Dianying Chen
Dr. Fang Wu

Subcontractors: The Ohio State University (Prof. N.P. Padture)
2041 N. College Road
Columbus, OH 43210
Phone: (614)247-8114 Fax: (614)292-1537

Inframat Corporation (Dr. X. Ma)
74 Batterson Park Road, Farmington, CT 06032
Phone: (860)678-7561 Fax: (860)678-7569

DISCLAIMER

This report was prepared as an account of work sponsored by an agency of the United States Government. Neither the United States Government nor any agency thereof, nor any of their employees, makes any warranty, express or implied, or assumes any legal liability or responsibility for the accuracy, completeness, or usefulness of any information, apparatus, product, or process disclosed, or represents that its use would not infringe privately owned rights. Reference herein to any specific commercial product, process, or service by trade name, trademark, manufacturer, or otherwise does not necessarily constitute or imply its endorsement, recommendation, or favoring by the United States Government or any agency thereof. The views and opinions of authors expressed herein do not necessarily state or reflect those of the United States Government or any agency thereof.

ABSTRACT

In order to protect metallic components in gas turbine engines against the high temperatures, which they experience during their operational cycle, thermal barrier coatings (TBCs) of yttria-stabilized zirconia (YSZ) are applied to metallic parts. Applying thicker TBCs than the ones which are currently state-of-art may result in lower thermal diffusivities and thus lower cooling requirements or increased operating temperatures of gas turbine engines and thus improved efficiency. Conventional air-plasma-sprayed (APS) coatings are limited to less than 0.6 mm thickness to prevent spontaneous premature spallation. Using the solution-precursor plasma-spray (SPPS) process, we have already demonstrated the ability to produce durable ultra-thick (~4mm thick) TBCs. Previously, microstructural tailoring of SPPS coatings was shown to reduce its thermal conductivity significantly. In this semi-annual report, we report estimation of thermal conductivity of TBCs using object oriented finite element analysis (OOF). Deposition, thermal cyclic performance, and failure mechanisms of 1.5 mm thick SPPS TBCs, and their comparison with APS TBCs of the same thickness has also been done during this semi-annual period. Based on the experimental observations, a mechanism for chemical failure of SPPS coatings has been proposed.

TABLE OF CONTENTS

Disclaimer iii

Abstract iv

1. Executive Summary 2

2. Project Description 2

3. Experimental 3
   - 3.1. Specimen Fabrication 3
   - 3.2. Characterization 3
   - 3.3. Thermal Cycling 3

4. Results and Discussion 4
   - 4.1 Thermal Conductivity Prediction Using Object Oriented Finite Element Analysis 4
   - 4.2 Thermal Cycling of SPPS and APS Coatings 5
   - 4.3 Failure Mechanisms of SPPS Coatings 5

5. Conclusions 10

REFERENCES 10

1. EXECUTIVE SUMMARY

In the semiannual period of this 3-year project, we have focused on the following three tasks.

First, we have used object oriented finite element analysis method (OOF) to evaluate thermal conductivity of solution precursor plasma spray (SPPS), layered SPPS and air plasma-sprayed (APS) coatings.

Second, we have evaluated the thermal cycling lives of 1.5 mm thick SPPS and reference APS TBCs deposited on optimized bond-coated superalloy substrates. We have found that, while the APS TBCs lasted 536 thermal cycles (1-hour each cycle with peak temperature 1121 ˚C), the average life of SPPS TBCs is 633 cycles (average of 3 failed specimens is used for both APS and SPPS TBCs).

Third, we have characterized the failed SPPS and APS samples along with interrupted thermal cycling study of SPPS TBCs using various materials characterization methods. Based on the results, a possible mechanism for chemical failure of SPPS TBCs has been suggested.

Next phases of the project will entail further Microstructural analysis of thermally cycled thick SPPS and APS coatings using focused ion beam (FIB) and transmission electron microscopy (TEM) techniques. Additionally, effect of coating thickness on failure of thick SPPS coatings will be studied in details using both, interface microstructure and stress analysis. Finally, outcomes of the studies will be used to deposit improved thick TBCs.

2. PROJECT DESCRIPTION

For the next generation of combustion engines used for aerospace applications and in energy production, higher operating temperatures (>1300 ºC) are desirable. Thus, stricter environmental requirements can be fulfilled, and the efficiency of the gas turbine can be increased. Current state-of-art plasma-sprayed thermal barrier coatings (TBCs) on MCrAlY bond coats with top-coat thickness of about 0.35 mm permit a temperature of the inner air-cooled combustion chamber walls of about 900 ºC [1]. The use of thicker TBCs allows for higher operating temperatures and lower temperatures at the bond coat. The latter reduces the oxidation of the bond coat.

One of the major hurdles with the development and application of thick TBCs on engine components is its reduced lifetime due to spallation under typical gas-turbine engine operating conditions. This is caused by faster degradation of the thick TBC due to higher volume under stresses, and steep thermal gradients present in the system [2]. These residual stresses in a TBC system can be reduced by introduction of through-thickness cracks in the ceramic top-coat [3]. In addition to improved spallation resistance, thermal insulation, thermal stability, and hot-corrosion resistance are also required in a modern TBC system to meet the ever-increasing demands for durability and performance in industrial engines. Previously, it has been successfully demonstrated that a novel process — Solution Precursor Plasma Spray (SPPS) — has the potential to satisfy all of these requirements [4, 5]. The SPPS process is ideally suited for the deposition of thick TBC, which is being explored in this project.

3. EXPERIMENTAL

3.1. Specimen Fabrication

The SPPS and APS coatings required for testing were fabricated by using the direct current (dc) plasma torch (Sulzer Metco, Westbury, NY), which was attached to a 6-axis robotic arm. For SPPS coatings the plasma precursor used was an aqueous solution containing zirconium and yttrium salts, to result in a solid solution of 93-wt % ZrO_2 and 7-wt % Y_2O_3 (7YSZ) in the coating. Coatings reported here were deposited under standard spray conditions [4] on plasma preheated (preheating temperature ~ 200°C) bond-coated superalloy circular substrates (diameter = 25.4 mm; thickness = 3.18mm). The APS coatings were deposited using (ZrO_2-8 wt % Y_2O_3) powder (Metco 204NS, 104 mesh+10 μm). 10 SPPS and three APS coatings were deposited with the coatings thickness in each case ~ 1.5 mm.

3.2. Characterization

Cross-sections of coatings were cut and polished to 1 μm final finish using routine metallographic techniques. The cross-sectional coating microstructures were observed in an optical microscope and a scanning electron microscope (SEM; Quanta, FEI, Hillsboro, OR). EDX spot analysis and x-ray elemental mapping of cross-section specimens has been performed by using SEM. Quantitative image analysis was performed on the SEM images (at least 25 micrographs per coating) using a image-analysis software (Clemex Vision, Clemex Technologies Inc., Longueil, Canada).

PAD-V x-ray diffractometer was used to identify phases present in top-coat and failed samples.

3.3. Thermal Cycling

The usual practice for the thermal cycling experiments adopted as University of Connecticut is as follows: A specially designed bottom-loading box furnace is preheated to a temperature of 1121°C. The following steps constitute one thermal cycle: (i) the furnace is opened by lowering the floor of the furnace (using an elevator) and the samples are placed on the floor. The samples are leaned against a refractory holder such that the TBCcoated circular face, which is almost normal to the floor, does not make contact with the refractory holder. (ii) The floor is raised and the furnace is closed; the time is set to zero. (iii) After 50 min, the floor is lowered and the samples are convectionally cooled using a fan for 10 min. Steps (ii) and (iii) are repeated. Each red-hot sample was observed visually during the cooling cycle. The occurrence of spallation, where the TBC falls off the metal substrate, is easy to discern. Complete spallation of TBC was considered was the failure criterion here. Note that in this test both the substrate and the coating are at the same temperature in the furnace. In an actual TBC application, the substrate is at a relatively lower temperature due to internal cooling, resulting in a thermal gradient across the TBC and relatively longer thermal cyclic lives. Three each of SPPS and APS TBCs were thermally cycled to failure to get the average life. SPPS coatings were also thermally cycled for intermediate thermal cycling to study their failure mechanisms. The samples were taken out of the thermal cycling furnace after 1, 10, 40, 140, 400, 500 and 600 thermal cycles.

4. RESULTS AND DISCUSSION

4.1. Thermal Conductivity Prediction Using Object Oriented Finite Element Analysis

Microstructures of SPPS, layered SPPS and APS coatings along with their experimental thermal conductivities in the temperature range of 100-1000ºC have been described in previous annual report. Analytical model of thermal conductivities was also used to study microstructural effects on the thermal conductivities of the TBCs studied.

Object oriented finite element analysis (OOF) is a relatively new finite-element based approach that combines data in the form of microstructures with fundamental material data (such as elastic modulus or thermal conductivity of the constitutive phases) as a basis for understanding behavior of complex materials [6]. The 7YSZ phase was assigned dense-7YSZ thermal conductivity for a given temperature, and the pore phase was assigned thermal conductivity of gaseous.

The thermal conductivity results for three different types of TBC microstructures obtained using OOF analysis are plotted in Fig.1. In the cases of the APS, SPPS, and layered-SPPS coatings the agreements between the experimental data and the OOF results are within 7.5%, 6.2%, and 10.9%, respectively. These agreements are better than those obtained using analytical modeling, reported previously. This can be attributed to fact that "real" microstructures are used as input in OOF, instead of the approximated, ideal microstructures used in the analytical modeling.

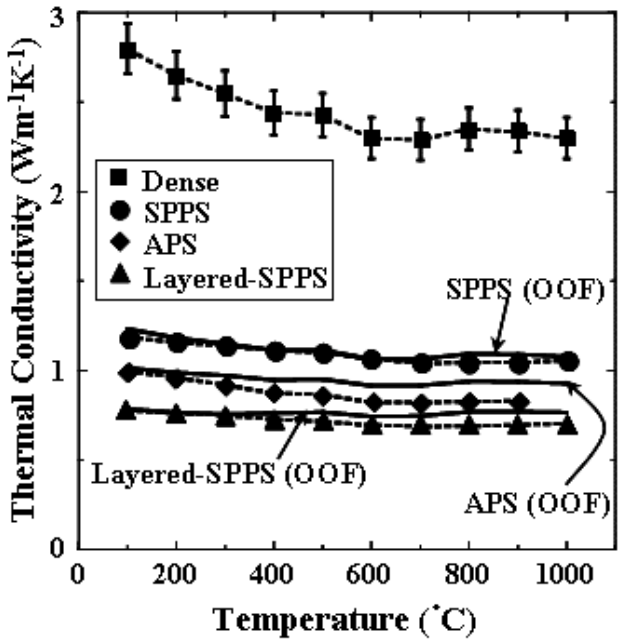

Figure 1. Comparison of thermal conductivity of SPPS, APS and layered SPPS coatings by obtained by experimental techniques and OOF.

4.2. Thermal Cycling of SPPS and APS Coatings

Fig. 2 shows a comparison of thermal-cycling lives of SPPS TBCs and reference APS TBCs. Although not very significant, some life improvement has been observed for the SPPS coatings over APS coatings.

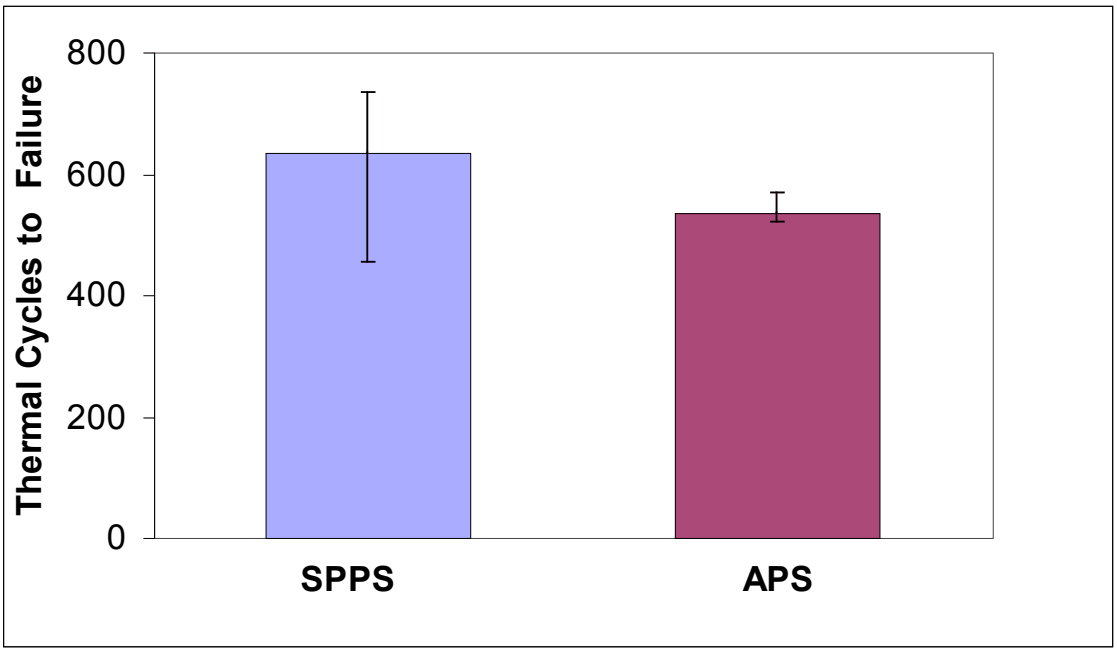

Figure 2. Thermal cycling durability of 1.5 mm thick SPPS and APS TBCs deposited on bond-coated superalloy.

4.3. Failure Mechanisms of SPPS Coatings

Cross-sectional view in the as-sprayed coating shows good bonding between the top-coat and the bond-coat (Fig. 3a). Just after one thermal cycle, development of dark and grey phases of thermally grown oxide (TGO) was detected as shown in the Fig. 2b. The TGO thickness was observed to increase further with increase in thermal cycling of SPPS samples. Fig. 4 shows the relationship between TGO thickness and thermal cycles. Oxidation of bond-coat was also investigated (Fig. 5) using x-ray diffractometer. 7YSZ peaks along with NiAl2O4, NiO, and □-alumina were found to be present. Combining the outcomes of the EDS spot analysis and x-ray diffraction patterns, the grey phase is associated with mixture of Ni and Cr oxides along with their spinels. The dark phase is □-alumina. Similar type of failure interface can be seen for APS TBC failed after 536 thermal cycles. The average thickness of dark phase (alumina) for the failed APS sample is found to be very similar to that of the failed SPPS coating after 735 thermal cycles (Fig. 4).

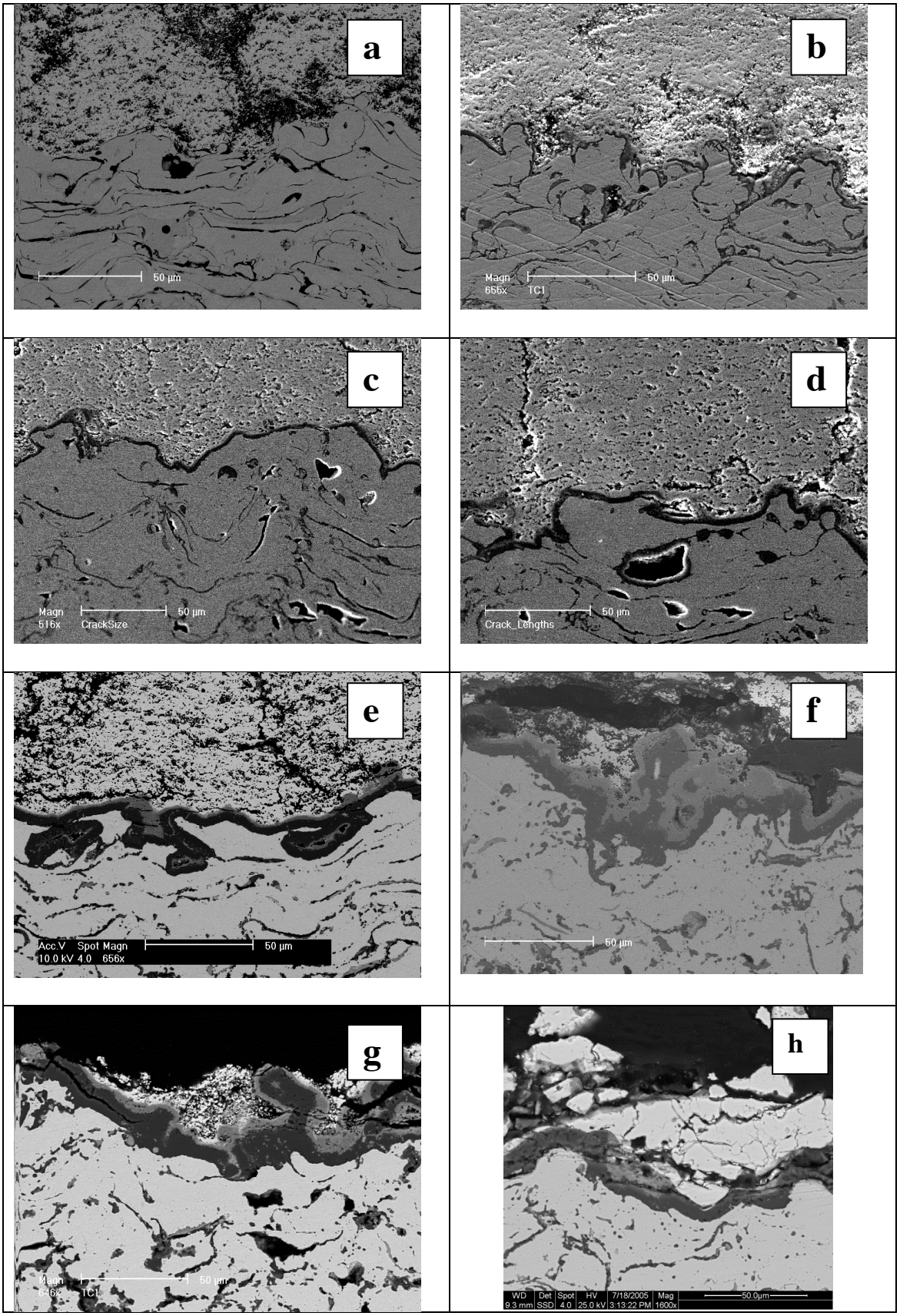

Figure 3. Change of coating microstructure with thermal cycling. (a)-(g):SPPS coating; (h) Failed APS coating.

During early stages of thermal cycling, long cracks were seen to be developed at the edges of the sample near the interface inside the top-coat. Cracks in the regions away from the edges were primarily formed inside top-coat in the regions of bond-coat asperities. After 140 cycles, horizontal cracks are observed at the grey TGO phase. These cracks propagate and coalesce with thermal cycling (Fig. 2e–g). Development of crack pattern during thermal cycling has been shown in the Fig. 6 for total length of measured cross section of 6000 microns. It can be observed that most of the cracking occurs inside the top-coat and through TGO. Failed sample shows sudden increase in the contribution of TGO cracks suggesting that final failure is mostly dominated by crack propagation through TGO.

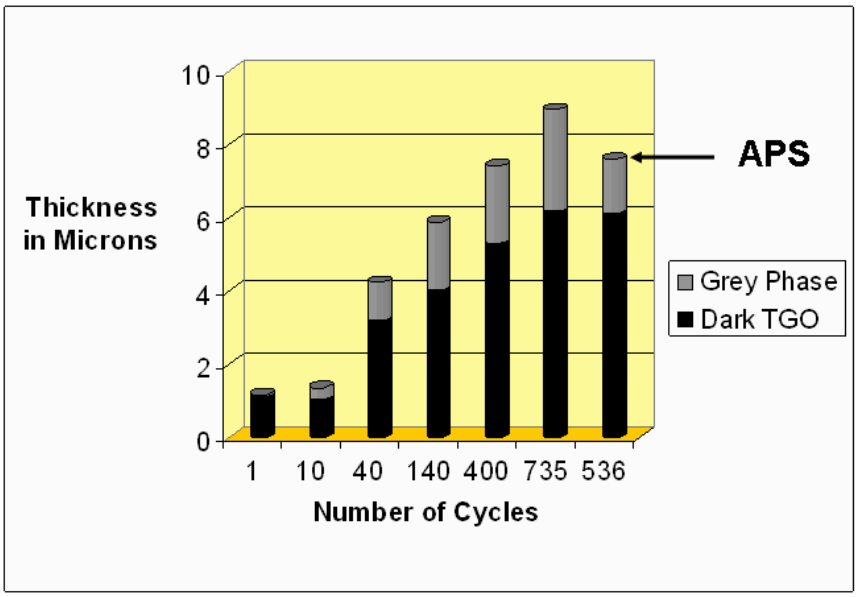

Figure 4. Thickness of alumina (dark region of bar) and non-alumina oxides (grey region) as function of thermal cycles for SPPS coatings and APS coating.

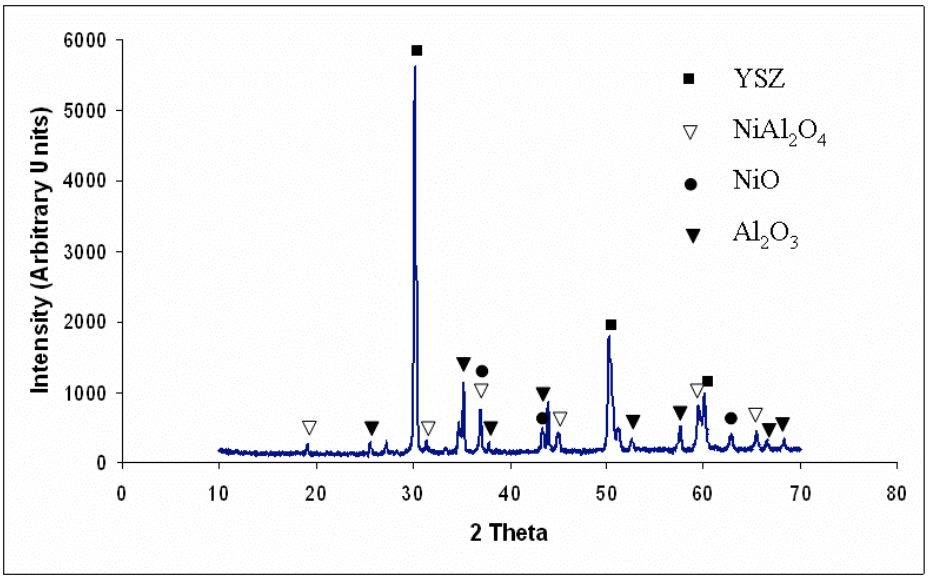

Figure 5. X-ray diffraction pattern for bond-coat top-surface after coating spallation.

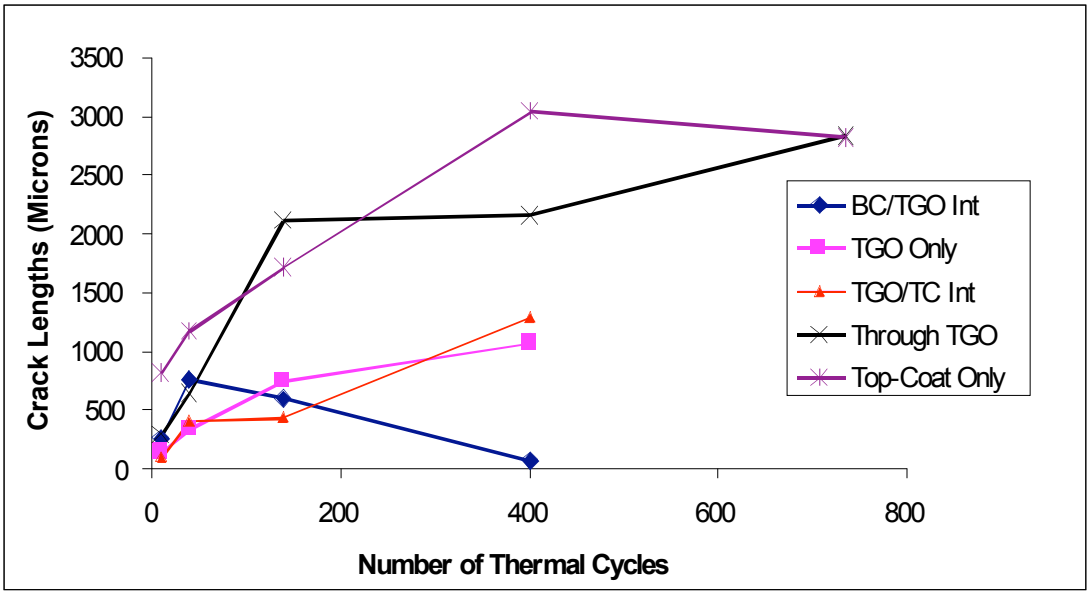

Figure 6. Crack lengths in bond-coat/top-coat interface region of 1.5 mm thick SPPS TBCs after various thermal cycles. Total cross-section scanned in each case ~ 6000 µm.

Based on the observation of SEM micrographs and chemical analysis of the interrupted thermally cycled SPPS samples, following mechanism of chemical failure of SPPS coatings has been suggested.

Early transient oxidation of bond-coat during the very first cycle results in the formation of spinel layer ($NiAl_2O_4$ and $NiCr_2O_4$) along with islands of NiO [7]. Typically, the mixed oxide and spinel layer appears to be less a micron thick from SEM micrographs. Oxygen diffusion through relatively less protective mixed oxide layer results selective oxidation of aluminum within the alloy and has been observed during first few cycles (Fig.7). The non-alumina layer at the top offers some protection and reduced oxygen partial pressure at the bond-coat surface. Under these conditions, as enough Cr and Al concentrations are available in the BC, alumina layer starts forming in the subscale region during further oxidation and keeps growing with time. Early evidence of non-uniform alumina layer formation can be seen in the Fig. 7. A solid state reaction between NiO and newly formed Al_2O_3 is possible at the thermal cycling temperature which can convert NiO into $NiAl_2O_4$ spinel with continued cycling. It can be given as

$$NiO_{(s)} + Al_2O_{3(s)} = NiAl_2O_{4(s)}$$

Once a complete impervious layer of alumina is obtained, the spinel growth stops. Alumina layer experiences steady-state growth as oxygen can penetrate through both spinel and alumina. After a relatively continuous alumina layer formation, anion transport becomes relatively more important and forms columnar layer of alumina beneath the fine grained layer of alumina and mixed oxides (Fig. 8).

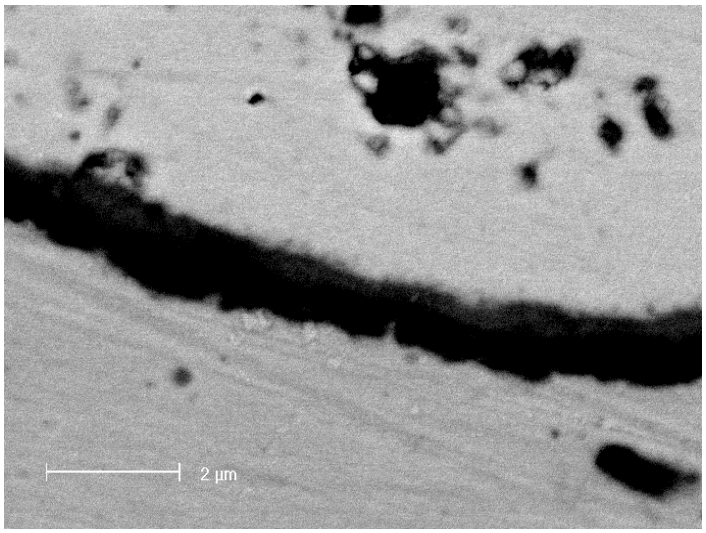

Figure 7. Formation of discontinuous alumina layer (dark) after one thermal cycle.

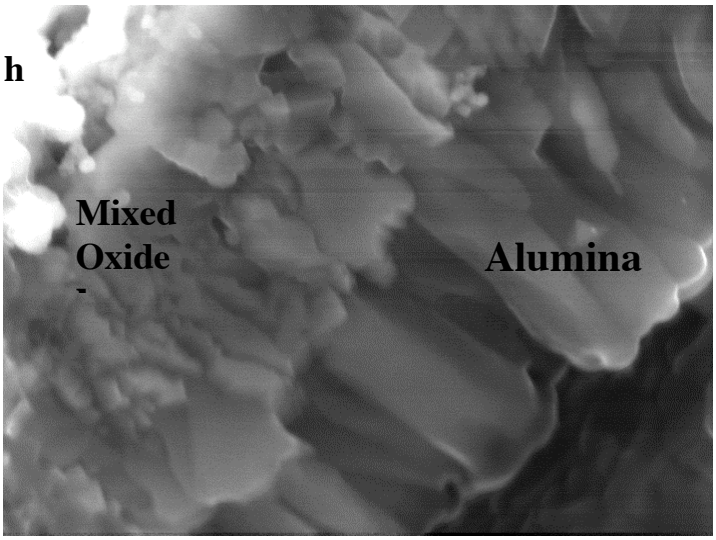

Figure 8. Cross-section image of TGO layer separated from the bond coat. Columnar alumina layer beneath fine grained mixed oxide layer can be observed.

Alumina layer formed in the regions of bond coat asperities is susceptible to through-thickness cracking due to high stresses under thermal cycling conditions. Once cracked, the bare bond-coat is exposed to oxygen for further oxidation. If the amount of Al is insufficient to heal the crack, other oxides (such as NiO) can be formed, which rapidly converts into $NiAl_2O_4$ spinel. This new path can further enhance the diffusivity of Ni^{+2} through the alumina film and increase thicknesses of the pre-exiting mixed oxides. If enough Al is present at BC-TGO interface beneath the cracked region, alumina TGO will be healed.

With increase in heat treatment, alumina layer protected under spinel layer becomes more and more dense and defect free (free from cracks and internal porosity). Yttrium rich regions with peg-like shapes have been observed during later stages of the thermal cycling. It has been suggested that these pegs conduct oxygen rapidly along the alumina grain boundaries. They also cause the cation transport inhibition in those regions.

5. CONCLUSIONS

From these studies it can be concluded that

i. the thermal conductivity of SPPS and APS TBCs can be predicted reliably using OOF technique.

ii. transient oxidation of bond-coat and thermal cycling stresses play important role in the determining amount of non-alumina oxides for rough and smoother bond coat surface regions, respectively.

6. REFERENCES

1. Padture, N.P., Gell, M., and Jordan, E.H., *Science*, 2002, 296, 280.
2. Rejda, E.F., Socie, D.F., and Beardsley, B., *Fatigue Fract. Engng. Mater. Struct.*, 1997, 20, 1043.
3. Steffens, H.D., Babiak, Z., and Gramlich, M., *J. Ther m. Spray Technol.*, 1998, 8, 517.
4. Padture, N. P., Schlichting, K. W. , Bhatia, T., Ozturk, A., Cetegen, B., Jordan, E. H., Gell, M., Jiang, S., Xiao, T. D., Strutt, P. R., Gracia, E., Miranzo, P., and Osendi, M. I., *Acta. Mater.*, 2001, 49, 2251.
5. Bhatia, T., Ozturk, A., Xie, L., Jordan, E. H., Cetegen, B., Gell, M., Ma, X., and Padture, N. P., *J. Mater. Res.*, 2002, 17, 2363.
6. Langer SA, E.R. Fuller J and Carter WC. *Comp. Sci. Engr.* 2001; 3: 15.
7. Giggins C.S. and Pettit F.S. J. Electrochem. Soc. 1971, 118, 1782.

An Advanced Diagnostic and Prognostic System for Gas Turbine Generator Sets with Experimental Validation

June 30, 2005 to January 1, 2006

John R. Wagner , Ph.D., P.E., Principal Investigator
J. Leo Gaddis, Ph.D., Co-Investigator
H. Bassily, Rajat Sekhon, Trey Bolcoz, Student Researchers
Department of Mechanical Engineering
Clemson University
Clemson, South Carolina 29634-0921

DOE Award Number: DE-FC26-02NT41431
UTSR Project Number: 03-01-SR108

DISCLAIMER

"This report was prepared as an account of work sponsored by an agency of the United States Government. Neither the United States Government nor any agency thereof, nor any of their employees, makes any warranty, express or implied, or assumes any legal liability or responsibility for the accuracy, completeness, or usefulness of any information, apparatus, product, or process disclosed, or represents that its use would not infringe privately owned rights. Reference herein to any specific commercial product, process, or service by trade name, trademark, manufacturer, or otherwise does not necessarily constitute or imply its endorsement, recommendation, or favoring by the United States Government or any agency thereof. The views and opinions of authors expressed herein do not necessarily state or reflect those of the United States Government or any agency thereof."

ABSTRACT

On a global basis, the demand for electric power continues to rise for both industrial and consumer needs. Stationary gas turbines offer size effective reliable power generation capabilities using multiple fuels. Gas turbines experience short and long term transient operating conditions due to changing shaft loads, environmental effects, and system disturbances, and component deteriorations which can lead to performance degradations. An effective health management strategy can enhance overall plant Reliability, Availability and Maintainability (RAM) through the continual monitoring of system operation. An efficient health management system is based on the integration of sensors and real-time diagnostic/prognostic monitoring strategies which can warn of impending problems within the gas turbine and its subsystems. Diagnostics, in conjunction with prognostics, detect and predict the likelihood of component faults. This report presents the past six month effort by the Clemson University research team to develop a real-time diagnostic/prognostic algorithm for gas turbines. A dynamic mathematical model representing a Mercury 50 gas turbine system has been developed and initially validated. Experimental data acquisition has been performed for the Mercury 50 4.5 MW gas turbine located at the Clemson University campus. A model based diagnostic strategy including the implementation of a Kalman observer and a statistical decision rule for the resulting estimation innovations has been achieved and experimentally validated. A prognostic methodology using real-time statistical manipulation of the system data has been studied. The report presents the results of the culmination of two years of research.

TABLE OF CONTENTS

Page

ABSTRACT..... 3

1. INTRODUCTION 7

2. EXECUTIVE SUMMARY.....7

3. PROJECT DESCRIPTION 9

3.1 Gas Turbine Research Need..... 9

3.2 Project Approach..... .9

3.2.1 Analytical Model..... 9

3.2.2 Diagnostic Module…….. 10

3.2.3 Prognostic Module……..……..……..……20

4. EXPERIMENTAL WORK..... 28

4.1 Mercury 50 gas turbine 28

4.2 Data Acquisition..... 28

4.3 Experimental Data..... 28

4.4 Simulation Results..... 32

4.5 Model Validation..... 32

5. RESULTS AND DISCUSSIONS……..35

6. CONCLUSIONS..... 35

REFERENCES..... 36

APPENDIX A - Nomenclature List..... 37

APPENDIX B – System State Equations..... 38

TABLE OF FIGURES

Page

Figure 1. Recursive state and observation estimation using Kalman recursion equation……...12

Figure 2. Autocorrelation function of a White Noise…….....14

Figure 3. Actual autocorrelation function of the resulting innovations exhibiting high correlation between values at different time lags……..…….....15

Figure 4. Kalman estimation error at recursion algorithm start exhibiting fast error decay decay (about 5 time steps) to the steady state value for three signals (ω, T_{03}, P_{02}) ...….17

Figure 5. Lube oil header temperature indicating the effect of the cooler blockage on a Solar Mercury 50 stationary gas turbine: Fault introduced at t = 8,000 seconds…….....…17

Figure 6. Original innovations error (3 states) sampled at one second rate and containing a long memory (low frequency component)…….....……...….18

Figure 7. Filtered innovations (differenced at lag = 1 second) to extract the stationary high frequency component ……..……...….18

Figure 8. Squared and normalized innovations corresponding to the "failure" and the "no failure" conditions of the system versus the 95 percentile threshold ……...……..19

Figure 9. Normal Distribution with standard deviations ……...……...…..22

Figure 10. Fuel flow and power generated for a Mercury 50 gas turbine run at steady state conditions…….……...…....22

Figure 11. Regression curve ($\vec{Z}$) based on second order polynomial trend (r=2) using minimized least squares method for fuel flow and power versus time at t=9270 seconds…….....…… ……...….24

Figure 12. Regression curve ($\vec{Z}$) based on second order polynomial trend (r=2) using minimized least squares method for fuel flow and power versus time at t=9360 seconds…….....…24

Figure 13. Tuples centered on second order polynomial trend using minimized least squares method for coefficients and two standard deviations envelope at t=9270 seconds…….……...……...…...…..26

Figure 14. Tuples centered on second order polynomial trend using minimized least squares method for coefficients and two standard deviations envelope at t=9360 seconds……26

Figure 15. Forecast of power and fule flow versus time plotted at 1) 9090, 2) 9180, 3)9360 seconds.....27

Figure 16. Gas turbine primary sensor location points along with the signalsrecorded.....29

Figure 17. Shaft speed for the Mercury 50 gas turbine during a start up sequence for four runs.....29

Figure 18. Power generated for the Mercury 50 gas turbine during a start up sequence for four runs.....30

Figure 19. Fuel flow for the Mercury 50 gas turbine during a start up sequence for four runs.....30

Figure 20. Compressor outlet pressure for the Mercury 50 gas turbine during a start up sequence for four runs.....31

Figure 21. Turbine inlet temperature for the Mercury 50 gas turbine during a start up sequence for four runs.....31

Figure 22. Model validation effort - estimated and actual shaft speed comparison (02-02-05).....32

Figure 23. Model validation effort - estimated and actual power generated comparison (02-02-05).....33

Figure 24. Model validation effort - estimated and actual fuel flow comparison (02-02-05).....33

Figure 25. Model validation - estimated and actual compressor outlet pressure comparisons.....34

Figure 26. Model validation effort - estimated and actual turbine rotor inlet temperature comparison (02-02-05).....34

1. INTRODUCTION

Gas turbine systems have become an integral part of the industrial and electric power generation sectors throughout the world. These systems operate under varying conditions which makes them susceptible to degradation and breakdowns. The objective for this research project is to develop a real-time monitoring and prediction program for stationary gas turbines to diagnose and predict short and long-term system health and readiness using behavior models, sensor fusion strategies, hidden Markov models, and extensive statistical analysis.

To monitor and control these machines as part of the desired health management system, the formulation and introduction of online diagnostics and prognostics modules is a necessity. The combination of these modules complements the plant sensors and controllers on a real time basis in a parallel manner. The implementation of these modules allows the detection and prediction of abnormal behavior. Diagnostic strategies utilize hardware and software to detect, isolate, and identify a deviation from the normal plant behavior. Prognostic algorithms focus on the estimation of the current health and prediction of the life of a critical component. A unified diagnostics and prognostics strategy is being investigated by the Clemson University research team for condition monitoring and fault diagnosis.

2. EXECUTIVE SUMMARY

This project will develop a real-time health management system for stationary gas turbines to improve turbine reliability and allow higher availability levels. The formulation and implementation of real-time diagnostic and prognostic strategies, which detect and predict the onset of system degradation and maintenance needs, will constantly monitor the overall system performance to reduce operation and maintenance costs.

The project encompasses seven tasks. During the last six months, considerable gains have been made.

Task 1. Analytical Modeling of the Turbine System

A model based diagnostics approach requires the existence of a real time mathematical model that describes the turbine system using differential and algebraic equations. The model should depict the "normal" turbine system behavior. The Clemson research team has developed a transient gas turbine model. The major components have been modeled as subsystems and linked together to create a simulation tool. The model simulates a Mercury 50 gas turbine located at Clemson University. The model has undergone encouraging validation activities

Task 2. Real-Time Turbine Sensor Data Streaming

Real-time experimental data is being collected and recorded from the Mercury 50 gas turbine located at the Clemson University main campus. The present computer code initializes the recording of twenty eight different signals at the sampling rate of one second. This one way link permits data reading only to prevent interference with the plant operation. The data is stored

in the form of arrays, using the MATLAB/SIMULINK software package on the Energy Systems Laboratory computer workstation. Efforts are undergoing to allow real-time data analysis. The performance of the Mercury 50 can be evaluated using this streamed data. The benefit of such a data collection connection is that it can be used by turbine engineers to formulate a data base for turbine health management systems.

Task 3. Sensor Fusion for Data Analysis

The Clemson University research team has selected a set of twenty eight plant signals to be monitored and recorded. The total available number of signals is 180. This smaller subset of signals is being recorded in real time and can be fused to monitor the system. These signals include key temperature and pressure measurements which will be used for model validation and in the diagnostic/prognostic module.

Task 4. Diagnostic Module Design

Model-free and model-based diagnostics are under development. For the model-free diagnostic module, a limit and trend checking strategy to directly monitor the signals' for departures from acceptable operating ranges has been developed. The model-based strategy is based on statistical and stochastic techniques. This strategy consists of three tools: (i) innovations generation, (ii) fault detection and (iii) fault isolation algorithms. The application of innovations generation algorithm has been accomplished

Task 5. Prognostic Module Design

The Clemson research team has developed an initial method to statistically analyze a given population of experimental data points. The method visually presents the data in three-dimensional views and incorporates statistics to predict. Furthermore the method gives a clear visual presentation of the variability of the data. Further work will be completed using the concept of wavelets for development of gas turbine health prognostic tools..

Task 6. Experimental Work

The periodic experimental data recorded from the Mercury 50 gas turbine runs, has been used by the Clemson University research team to initially validate the mathematical model, (described in Task 1).The results from the mathematical model were compared with this experimental data and relevant model parameters were adjusted. The initial results are encouraging. The experimental data has also been used in diagnostic/prognostic algorithms

Task 7. Industry Interactions

Industrial interaction has been maintained with Solar Turbines (San Diego, California), through data sharing and technical conversations with field engineers.

3. PROJECT DESCRIPTION

3.1 Gas Turbine Research Need

The Reliability, Availability, and Maintainability (RAM) technical area of the High Efficiency Engines and Turbines (HEET) program encompasses the design of gas turbine health management systems. The introduction of real-time diagnostic and prognostic capabilities on gas turbines can provide increased reliability, safety, and efficiency. The diagnostic module is responsible for the prompt detection of system degradations followed by the isolation, or classification, of the failure, and determination of the magnitude. Prognostic activities are focused on the prediction of anomalous plant behavior such that maintenance measures may be performed to permit continued operation.

3.2 Project Approach

The objective of the project is to develop an integrated diagnostic and prognostic health management system. The approach to achieve this objective is described in the following sections.

3.2.1 Analytic Model

The two primary monitoring approaches for dynamic systems (including stationary gas turbines) can be classified as model-based and model-free diagnostics. The Clemson University research team is investigating both methods. For the model based approach, a real time mathematical model must exist to estimate "normal" system operation. The reliability of a model based diagnostics strategy is dependent on the model's accuracy. The quantitative modeling of a physical system requires knowledge of the process, mathematical representation in the form of differential and algebraic equations, and availability of system parameters. However system uncertainty, noise, and nonlinearities often introduce discrepancies and deviations from ideal behavior. Consequently, a mathematical model's estimates often differ from the experimental measurements. The various gas turbine subsystems have been modeled and analyzed with the explicit presentation of the governing differential and algebraic equations. The analytical model as described in the previous report has been used to simulate the behavior of a Mercury 50 gas turbine. During the last six months some model enhancements were made which would be described in the following section

A. Model Enhancement (Turbine Map)

The turbine mass flow rate has been approximated using variable inlet guide vane angles (VIGV) and flow velocity inside the turbine as compressor maps are not available for the Mercury 50. The derived mass flow rate is a function of pressure ratio for different rotational speeds. A single stage analysis was performed to obtain the mass flow and compressor outlet temperature.

3.2.2 Diagnostic Module

Diagnostic strategies generally attempt to detect, isolate, and identify a deviation from "normal" behavior in dynamic systems through on-line health monitoring. Two methods are under investigation: model free (limit checking) and model based (innovation testing). In the next section the model based diagnostic strategy being investigated by the Clemson University research team will be discussed in detail along with the experimental results.

A. Model Based Diagnostics

The model based diagnostics strategies compare the actual behavior of the system versus the model estimates under the same operating conditions. A useful quantity for this comparison is the innovation (or residual) which is the difference between the actual model behavior and the model estimates. A deviation from the “normal” behavior of the residuals may be an indication of system departing from the normal or “no fault” condition. The main task is generating the residuals and setting the acceptable level of normal system operation. A full state Kalman observer is used to generate the model estimates. Since the analytical mathematical model state equations are nonlinear, a linearization of the system equations is first performed at a system operating point determined by the selected steady condition (e.g. load and speed). The subsequent sections detail the methodology pursued by the research team to achieve a robust model based fault detection algorithm. This algorithm includes two novel features which are: [i] an estimation technique of the disturbance covariance matrices from the actual observations leading to faster error decay, and [ii] an adaptation of the classical technique to the case of non-white noise residuals resulting from slow system dynamics.

A.1 System Equations and Kalman estimation

The previously developed mathematical model features three state equations (Refer to Appendix A) that may be defined as

$$\left[\dot{\omega}(t), \dot{T}_{03}(t), \dot{P}_{r02}(t)\right]^T = f_i\left(\omega, T_{03}, P_{r02}, W, T_{01}\right) \text{ for } i \in (1,2,3)$$

(1)

where ω denotes the rotating shaft speed, T_{03} denotes the TRIT (Turbine Rotor Inlet Temperature), P_{r02} denotes the PCD (Pressure at Compressor Delivery). The symbols W, T_{01}, and f_i denote the power, the ambient temperature, and the ith component of the nonlinear multivariate state function $\bar{f}(.)$, respectively. A linearized form of those equations can be obtained using a Taylor series expansion and neglecting higher order so that

$$\dot{\bar{x}}(t) = A\bar{x}(t) + B\bar{u}(t), \quad \bar{y}(t) = C\bar{x}(t) \tag{2}$$

where $\bar{x}(t) = \left[\omega(t), T_{03}(t), P_{r02}(t)\right]^T$ and $\bar{u}(t) = \left[W(t), T_{01}(t)\right]^T$ are the state and input vectors at time *t*. The system matrices *A* and *B* are obtained by differentiating the multivariate state function $\bar{f}(.) = \left[f_1(.), f_2(.), f_3(.)\right]^T$ as follows

$$A=\begin{bmatrix} \frac{\partial f_1}{\partial \omega} & \frac{\partial f_1}{\partial \omega} & \frac{\partial f_1}{\partial \omega} \\ \frac{\partial f_2}{\partial T_{03}} & \frac{\partial f_2}{\partial T_{03}} & \frac{\partial f_2}{\partial T_{03}} \\ \frac{\partial f_3}{\partial P_{r02}} & \frac{\partial f_3}{\partial P_{r02}} & \frac{\partial f_3}{\partial P_{r02}} \end{bmatrix}, B=\begin{bmatrix} \frac{\partial f_1}{\partial W} & \frac{\partial f_1}{\partial T_{01}} \\ \frac{\partial f_2}{\partial W} & \frac{\partial f_2}{\partial T_{01}} \\ \frac{\partial f_3}{\partial W} & \frac{\partial f_3}{\partial T_{01}} \end{bmatrix} \tag{3}$$

and evaluating those derivatives at the given operating point. Since all given states are directly measured from their signals, the observation matrix, *C*, can be taken close to the unity matrix. By considering the Euler approximation $\dot{\bar{x}}(t)=\frac{\bar{x}(t+\Delta t)-\bar{x}(t)}{\Delta t}=\frac{\Delta \bar{x}}{\Delta t}$, the discrete time form of equations (2) can be written as

$$\bar{x}(k+1)=A\bar{x}(k)+B\bar{u}(k), \quad \bar{y}(k)=C\bar{x}(k) \tag{4}$$

where *k* denotes the time step defined by the discrete time increment Δt. The experimental section includes the selection details of the Δt value.

A.2 Kalman Estimation

The main purpose of Kalman estimation is to predict the system states and subsequently, generate estimated plant observations based on the model parameters embodied in the system matrices. A modified form of the system state equations (4) is

$$\bar{x}(k+1)=A\bar{x}(k)+B\bar{u}(k)+\bar{w}(k), \; \bar{y}(k)=C\bar{x}(k)+\bar{v}(k) \tag{5}$$

where the vectors $\bar{w}(k)=\left[w_1(k),w_2(k),w_3(k)\right]^T$ and $\bar{v}(k)=\left[v_1(k),v_2(k),v_3(k)\right]^T$ denote the state transition error and the state observation error, respectively. A popular fashion is to represent these disturbance terms as independent and identically distributed (IID) multivariate Gaussian random variables (white noise) having the distributions $\bar{w}(k)\sim N(0,\Sigma w)$ and $\bar{v}(k)\sim N(0,\Sigma v)$, respectively. Accordingly, based on the derived system matrices *A*,*B*, and *C*, the Kalman recursion equations at time step *k* can be stated as

$$K(k)=P(k)^{-}C^T\left[CP(k)^{-}C^T+R\right]^{-1} \tag{6a}$$

$$\hat{\bar{x}}(k)=\hat{\bar{x}}(k)^{-}+K(k)\left[\bar{y}(k)-C\bar{x}(k)^{-}\right] \tag{6b}$$

$$\hat{\bar{y}}(k)=C\hat{\bar{x}}(k) \tag{6c}$$

$$P(k)=A\left[I-K(k)C\right]P(k)^{-}A^T+Q \tag{6d}$$

$$\hat{\bar{x}}(k+1)^{-}=A\hat{\bar{x}}(k)+B\bar{u}(k) \tag{6e}$$

where $K(k)$ is the Kalman gain matrix evaluated at time step *k*. $P(k)^{-}$ and $P(k)$ are the *a priori* and the *posteriori* estimations of the state prediction error *P* at time step *k*. In this case, the term "*a priori*" refers to the initial estimate and one time step delay update while "posteriori" refers to the update obtained in the time step calculation. The vectors $\hat{\bar{x}}(k)^{-}$, $\hat{\bar{x}}(k)$ and $\hat{\bar{y}}(k)$ denote the *a priori* state, *posteriori* state and observation estimation at time step *k*, respectively. The matrices

R and Q denote the covariance matrices Σv and Σw of the disturbance vectors $\bar{v}(k)$ and $\bar{w}(k)$, respectively. Starting with an initial guess of the matrices $P(1)^{-}$ and $\hat{\bar{x}}(1)^{-}$, the recursion equations (6) are implemented to calculate subsequent estimations of the state and observation vectors as detailed in Figure 1.

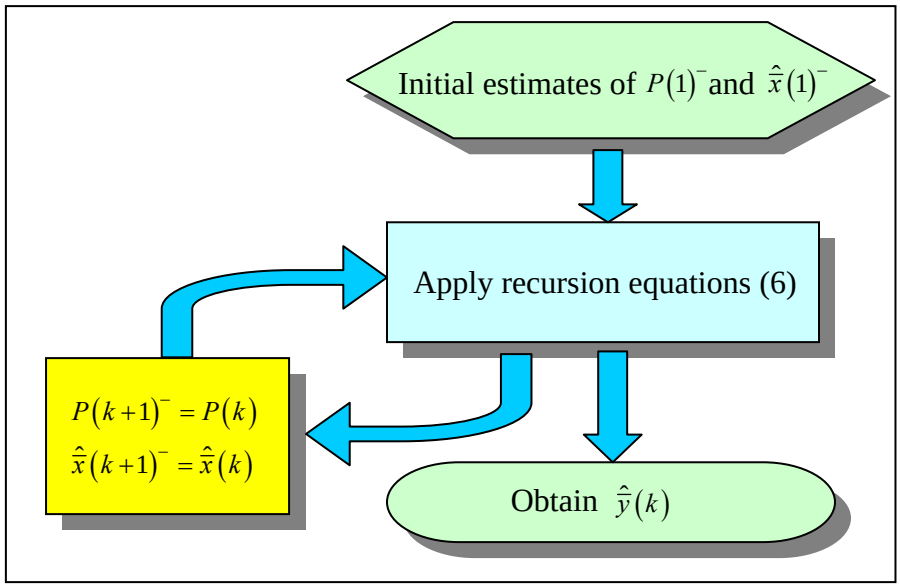

Figure 1. Recursive state and observation estimation using Kalman recursion equations

A.3 Estimation of the Disturbance Covariance Matrices

The proper estimation of the parameters of the disturbance vectors $\bar{v}(k)$ and $\bar{w}(k)$ in the system equations (5) ensures a fast convergence of the filter estimates to the actual observations. Since those vectors are assumed to be IID multivariate Gaussian variables, it is therefore required to estimate the covariance matrices Σv and Σw. Several techniques (e.g. optimization techniques, likelihood maximization technique and direct measurement) are presented in the literature to estimate those matrices. An empirical technique based on the actual system observations and on time series analysis is proposed, hereafter, to evaluate the covariance matrices Σv and Σw.

Considering that for large samples, the sample parameters are the best estimates of the population parameters, the system state equations at the sample time t can be written as

$$\bar{x}(t+k) = A\bar{x}(t) + B\bar{u}(t) + \bar{w}(t), \quad \bar{y}(t) = C\bar{x}(t) + \bar{v}(t) \tag{7}$$

From equation (7), we can express the sample system states at time t and time $t+k$ as

$$\bar{x}(t+k) = C^{-1}\bar{y}(t+k) - C^{-1}\bar{v}(t+k), \quad \bar{x}(t) = C^{-1}\bar{y}(t) - C^{-1}\bar{v}(t) \tag{8}$$

By substituting from equations (8) into equation (7) and re-arranging, we get the expression

$$C^{-1}\bar{y}(t+k) - AC^{-1}\bar{y}(t) - B\bar{u}(t) = C^{-1}\bar{v}(t+k) - AC^{-1}\bar{v}(t) + \bar{w}(t) \tag{9}$$

Interpolating the values of $\bar{y}(t)$ and $\bar{y}(t+1)$, an approximation of $\bar{y}(t+k)$ can be reached. Accordingly, the LHS vector represents an observable variable which is completely determinable from the actual measurement and expressed as

$$\bar{\Upsilon}(t) = C^{-1}\bar{y}(t+k) - AC^{-1}\bar{y}(t) - B\bar{u}(t) \tag{10}$$

Therefore, equation (9) can be re-written as

$$\bar{\Upsilon}(t) = C^{-1}\bar{v}(t+k) - AC^{-1}\bar{v}(t) + \bar{w}(t) \tag{11}$$

Considering the auto-covariance (covariance of a random variable at a certain time *t* and the same variable at a different time $t \pm h$) of both sides of equation (11) at time lags $h = 0$ and $h = -k$, we have

$$Cov\left[\bar{\Upsilon}(t), \bar{\Upsilon}(t)\right] = Cov\left\{\left[C^{-1}\bar{v}(t+k) - AC^{-1}\bar{v}(t) + \bar{w}(t)\right], \left[C^{-1}\bar{v}(t+k) - AC^{-1}\bar{v}(t) + \bar{w}(t)\right]\right\} \tag{12a}$$

$$Cov\left[\bar{\Upsilon}(t), \bar{\Upsilon}(t-1)\right] = Cov\left\{\left[C^{-1}\bar{v}(t+k) - AC^{-1}\bar{v}(t) + \bar{w}(t)\right], \left[C^{-1}\bar{v}(t) - AC^{-1}\bar{v}(t-k) + \bar{w}(t-k)\right]\right\} \tag{12b}$$

in which by denoting $Cov\left[\bar{\Upsilon}(t), \bar{\Upsilon}(t)\right]$ by $\Gamma_{\Upsilon}(0)$ and $Cov\left[\bar{\Upsilon}(t), \bar{\Upsilon}(t-k)\right]$ by $\Gamma_{\Upsilon}(1)$ and considering the independence property of the terms in the RHS, we can reach the expression

$$\Gamma_{\Upsilon}(0) = \left[I + A^2\right]C^{-2}\Sigma v + \Sigma w \tag{13a}$$

$$\Gamma_{\Upsilon}(1) = -AC^{-2}\Sigma v \tag{13b}$$

Providing that the vector $\bar{\Upsilon}(t)$ is completely known for all sample times *t*, the auto-covariance functions $\Gamma_{\Upsilon}(0)$ and $\Gamma_{\Upsilon}(1)$ can be directley calculated from

$$\Gamma_{\Upsilon}(0) = E\left[\bar{\Upsilon}(t)\bar{\Upsilon}(t)^T\right] - \left\{E\left[\bar{\Upsilon}(t)\right]\right\}\left\{E\left[\bar{\Upsilon}(t)\right]\right\}^T \tag{14a}$$

$$\Gamma_{\Upsilon}(1) = E\left[\bar{\Upsilon}(t)\bar{\Upsilon}(t-1)^T\right] - \left\{E\left[\bar{\Upsilon}(t)\right]\right\}\left\{E\left[\bar{\Upsilon}(t-1)\right]\right\}^T \tag{14b}$$

where $E[.]$ denotes the expected value which is the mean of the designated variable. Accordingly, equations (13) reduce to a system of two equations of the two unknown matrices Σv and Σw.

A.4 Innovations Analysis

Based on a sampling time *t*, the innovations can be expressed as

$$\bar{\Omega}(t) = \bar{y}(t) - \hat{\bar{y}}(t) \tag{15}$$

A powerful statistical quantity for subsequent statistical tests is the sum of normalized square innovations, $L_w(t)$, which may be expressed as

$$L_w(t) = \sum_{j=t-W+1}^{t} \bar{\Omega}(j)^T \Gamma_{\Omega}^{-1}(t)\bar{\Omega}(j) \tag{16}$$

where *W* is a specified window length for accumulation, and $\Gamma^{-1}{}_{\Omega}(t)$ denotes the innovations covariance matrix for each window sample. The window size, *W*, should be selected large enough to avoid excessive sensitivity to noise, yet small enough to remain sensitive to system failures. Following the assumption of white noise and a null hypothesis of "no failure", the quantity $L_w(t)$ should follow a Chi-square distribution with a degree of freedom ($W * p$) where *p*

represents the dimension of the innovation vector. based on the IID property of the white noise, the autocorrelation function of the innovations should exhibit a behavior similar to that of Figure 2. It is clear that the autocorrelation value at any time lag other than zero is practically negligible.

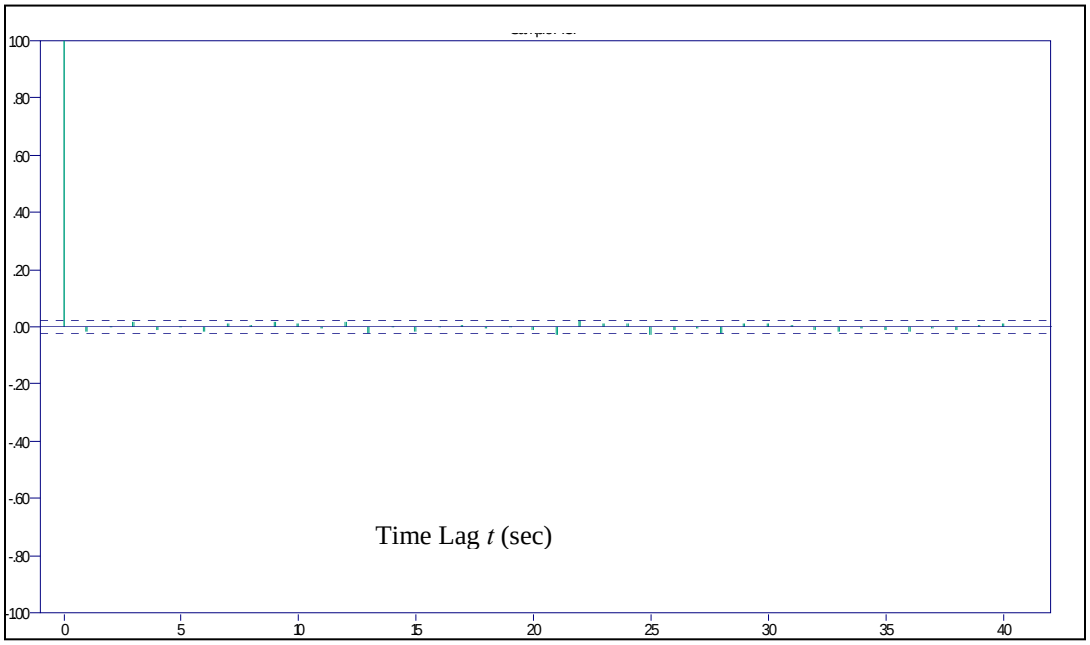

Figure 2. Autocorrelation function of a White Noise

Actually, the resulting innovation for the "no failure" case shows a long memory (i.e. dependence on value at big time lags) behavior, demonstrated in Figure 3, which drives the innovations away from being white noise. Accordingly, a difference filter is proposed to reduce the memory effect and obtain stationary innovations. This lag difference filter can be expressed as

$$\bar{\eta}(t) = \bar{\Omega}(t) - \bar{\Omega}(t-1) \tag{17}$$

where $\bar{\eta}(t)$ denotes the filtered innovations. The long memory behavior of the innovation is a result of slow system dynamics characterized by the presence of a system pole near the origin. Since the filtered innovations still carry a dependence on previous values, an ARMA (Auto Regressive Moving Average) model would be more suitable to represent the innovations instead of the white noise assumption. Accordingly, the chi-square distribution would not be appropriate to represent the innovation and an adaptation should be implemented.

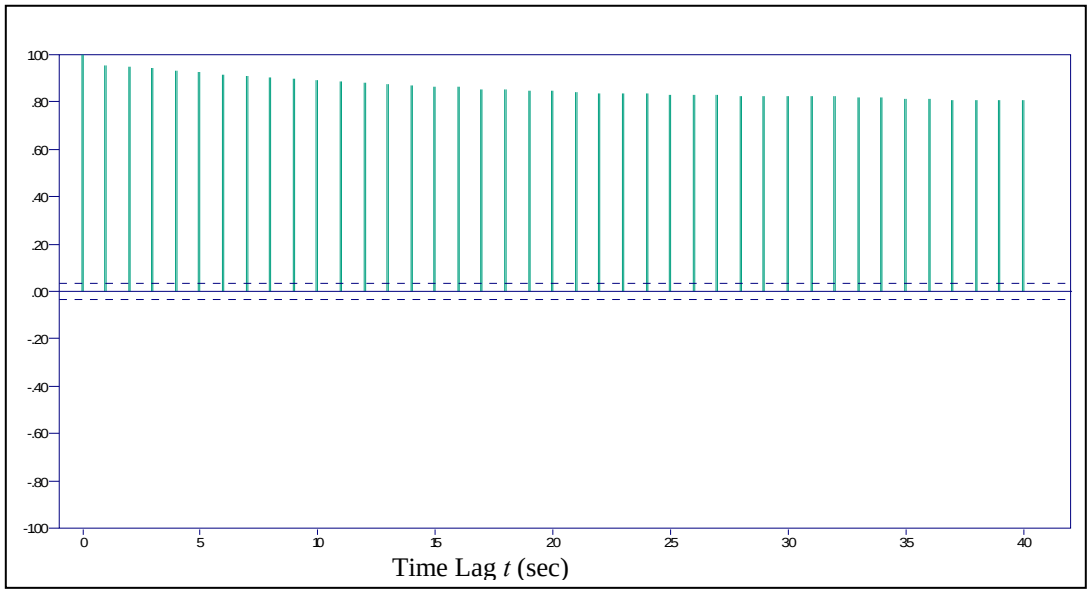

Figure 3. Actual autocorrelation function of the resulting innovations exhibiting high correlation between values at different time lags

An experimental procedure based on a counting technique (e.g. data binning histograms) is proposed to obtain a percentile distribution of the squared and normalized filtered innovations. The standardized and filtered innovations sequence is analyzed to accept or reject the null hypothesis of normal system operation. In this case, L_{w_t} should be corrected to be

$$L_w(t) = \sum_{j=t-W+1}^{t} \bar{\eta}(j)^T \Gamma_\eta^{-1}(t) \bar{\eta}(j) \tag{18}$$

The derived statistical properties of $L_w(.)$ (i.e., the percentile distribution) permit the application of a threshold test. The decision rule becomes

$$\left\{ \bigcup_{j=0}^{t} \left[L_w(t) \geq \xi_{cr}^2 \right] \Big/ \sum_{j=0}^{t} W_j \right\} \leq \text{ False alarm percentile } \rightarrow No - Failure \tag{19a}$$

$$\left\{ \bigcup_{j=0}^{t} \left[L_w(t) \geq \xi_{cr}^2 \right] \Big/ \sum_{j=0}^{t} W_j \right\} > \text{False alarm percentile } \rightarrow Failure \tag{19b}$$

which is determined by counting innovations exceeding ξ_{cr}^2 over windows and normalizing by total number of windows up to time *t*. The parameter ξ_{cr}^2 is the selected critical value of $L_w(t)$ at the desired confidence percentile (false alarm percentile). The selected ξ_{cr}^2 can be chosen according to a suite of "no failure" operating runs of the turbine as the derived percentile distribution approaches the actual distribution of $L_w(t)$ as the number of runs grows to infinity. Initially a confidence percentile of 95 has been selected.

A.5 Implementation and Experimental Results

To implement the Kalman estimation algorithm, linearization of the system state equations (refer to Appendix A) is performed. A steady state operating point defined as steady state nominal rotational speed of 14,191 rpm or 1486.1 rad/sec and steady state generated power of 3842.2 KW is selected. Applying the Taylor series expansion, the system matrices of equation (2) were found to be

$$A=\begin{bmatrix} -0.0425 & 0.01223 & 0.00645 \\ 6.66927 & -16.21922 & -1.63667 \\ -1.29289 & 8.32227 & -12.21839 \end{bmatrix}, B=\begin{bmatrix} -0.00187 & 0.12311 \\ 4.81475 & 51.40946 \\ 0 & -40.41598 \end{bmatrix}, C=\begin{bmatrix} 1 & 0 & 0 \\ 0 & 1.03 & 0 \\ 0 & 0 & 1 \end{bmatrix} \tag{20}$$

based on measured steady state values of 1405.2 °K for the TRIT, 950.1 KPa for the PCD, 150 m/s for the axial flow velocity, and 272 °K for the ambient temperature. These values correspond to an experimental run of the Solar Mercury 50 turbine performed on 12/22/2005, starting at 6:10 am and ending at 11:45 am, during which the turbine was maintained at steady state conditions for 15,000 seconds. The error between the actual turbine data and the model simulation output was minimized by adapting the observation matrix *C*. An observability assessment of the system was performed and the system was found to be fully observable (i.e. rank *O*=3, O is the observability matrix). The poles of the linearized dynamic system were calculated and found to be $\lambda_1 = -0.0367$, $\lambda_2 = -14.2218 + 3.1031i$, and $\lambda_3 = -14.2218 - 3.1031i$ which correspond to natural frequencies of $f_1 = 0.0058$ Hz and $f_2 = 2.3167$ Hz. Accordingly, a time step, *k*, of 0.01 sec was adequately set for the Kalman estimation while maintaining a data acquisition rate of one second. A zero order hold for the input signals and an interpolation of the output signal were performed to up-sample the acquired input and observation data to the Kalman filter rate. An initial estimate of ones for the state prediction error matrix and the mean of the observations for the initial state estimates were selected to start the Kalman recursion equations (6). Figure 4 illustrates the fast observation error decay consistent to the filter robustness and the proper selection of the covariance matrices Σv and Σw.

A.6 Experimental Fault and Results

To assess the derived fault detection technique an experimental fault was introduced to the system. A manual blockage of the oil cooler passages was performed starting after 8,000 seconds of normal steady state operation. Consequently, the oil temperature rose from 47°C to 66.4°C in 4,500 seconds. Figure 5 shows the oil header temperature during this experiment. The residuals (innovations) were calculated according to equation (15) at a sampling rate of one second. Due to the slow system dynamics ($f_1 = 0.0058$ Hz), and subsequently the long memory behavior (manifested by the presence of a low frequency component) they were filtered to obtain the stationary high frequency component as previously demonstrated in equation (17). Figures 6 and 7 demonstrate the residuals (innovations) before and after removing the low frequency non-stationary component.

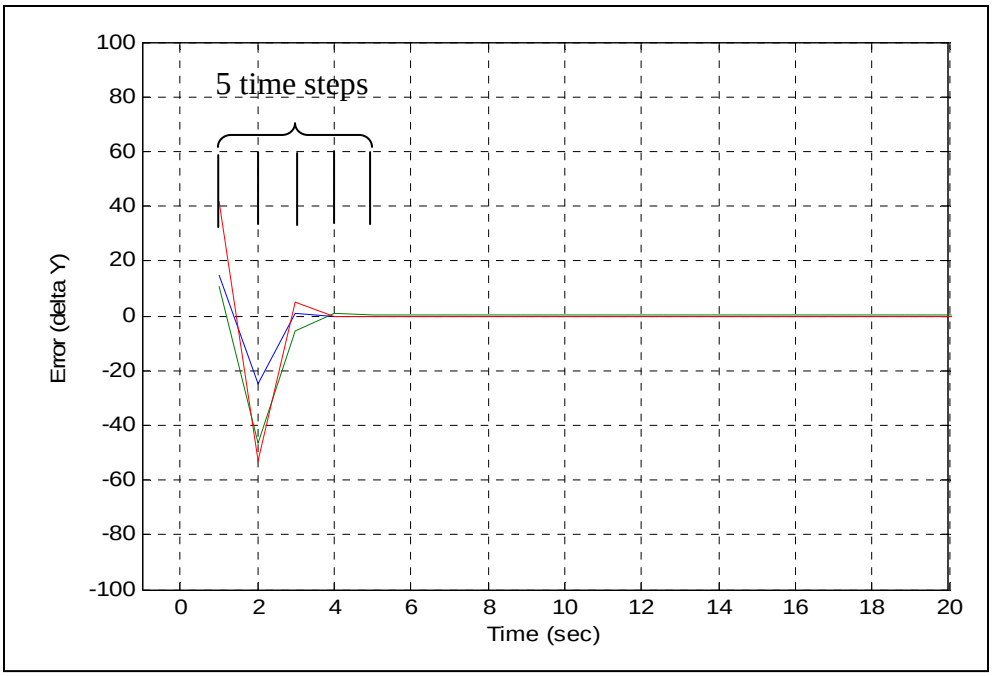

Figure 4. Kalman estimation error at recursion algorithm start exhibiting fast error decay (about 5 time steps) to the steady state value for three signals (ω, T_{03}, P_{02})

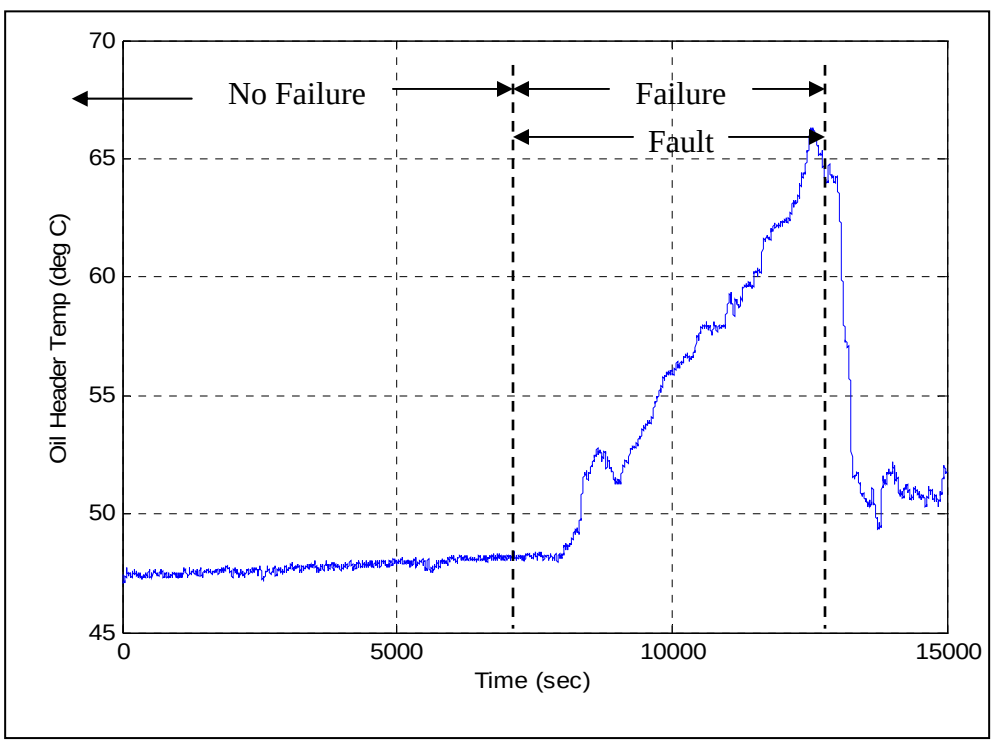

Figure 5. Lube oil header temperature indicating the effect of the cooler blockage on a Solar Mercury 50 stationary gas turbine: Fault introduced at t = 8,000 seconds

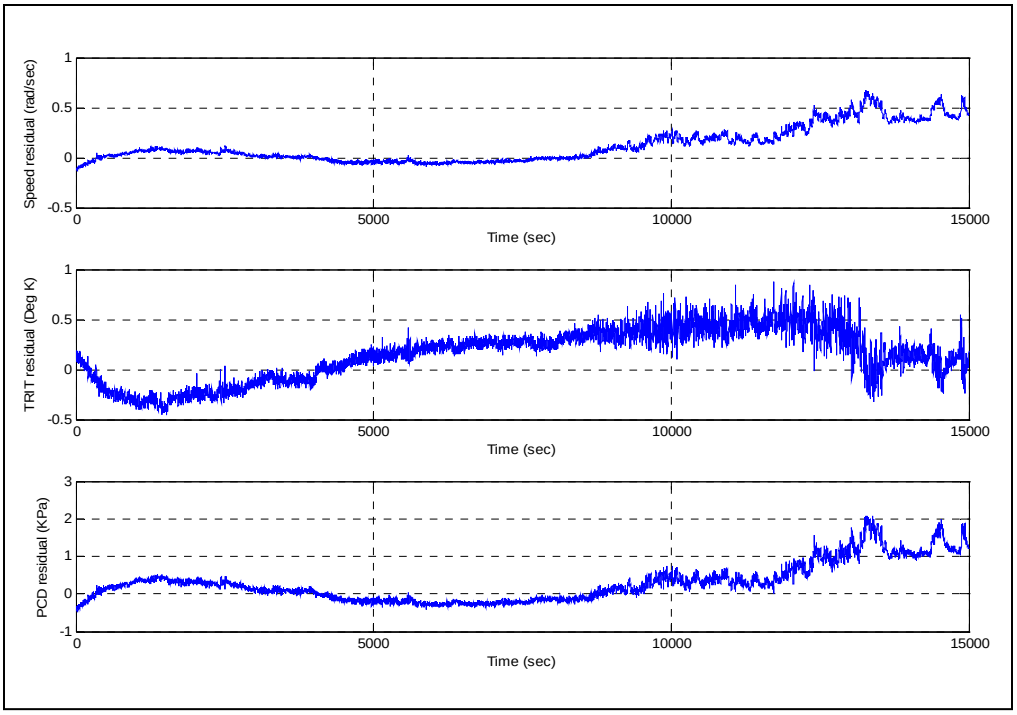

Figure 6. Original innovations error (3 states) sampled at one second rate and containing a long memory (low frequency component)

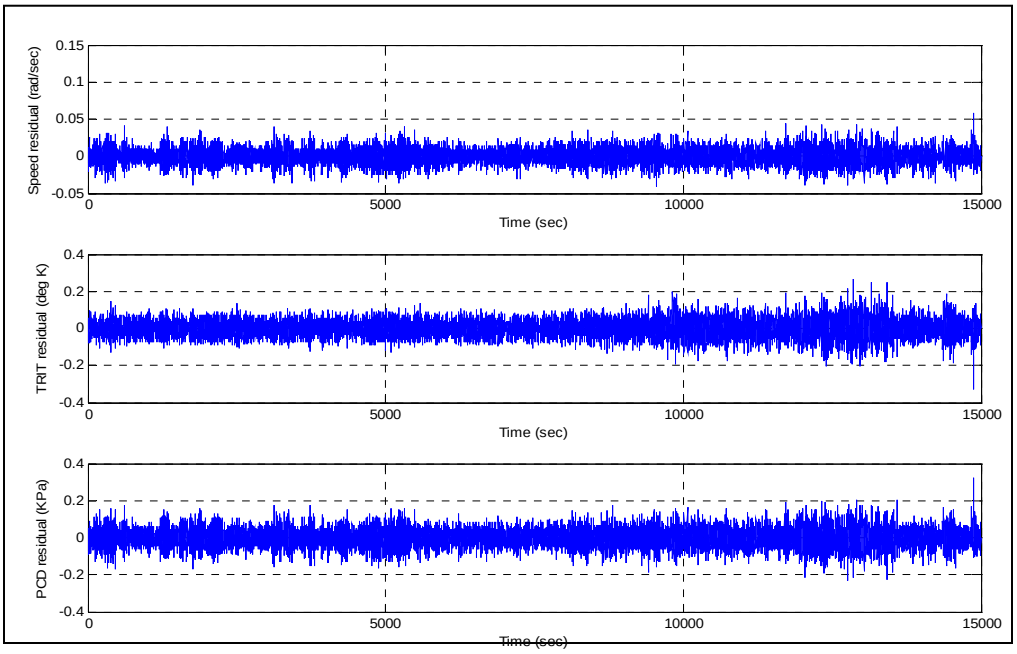

Figure 7. Filtered innovations (differenced at lag = 1 second) to extract the stationary high frequency component

A time window, W, of 40 seconds (40 samples) was selected as a statistically reasonable sample size. The innovations were normalized and squared according to equation (18). For the "no failure" portion of the data, a data binning process was executed and an accumulative 95 percentile of the data frequency was selected. The 95% accumulative value is selected to make

the decision algorithm unaffected by the chance of false alarm yet sensitive enough to detect abnormal increase in the squared and normalized innovations. Accordingly, ξ_{cr}^{2} was found to be 118.03. Consequently, a statistical decision threshold, consistent with equation (18), was set at this value. The normalized and squared innovations were subsequently plotted for the whole experiment period and compared to the selected threshold as illustrated in Figure 8 in which an obvious threshold violation concomitant to the fault occurrence is clearly present.

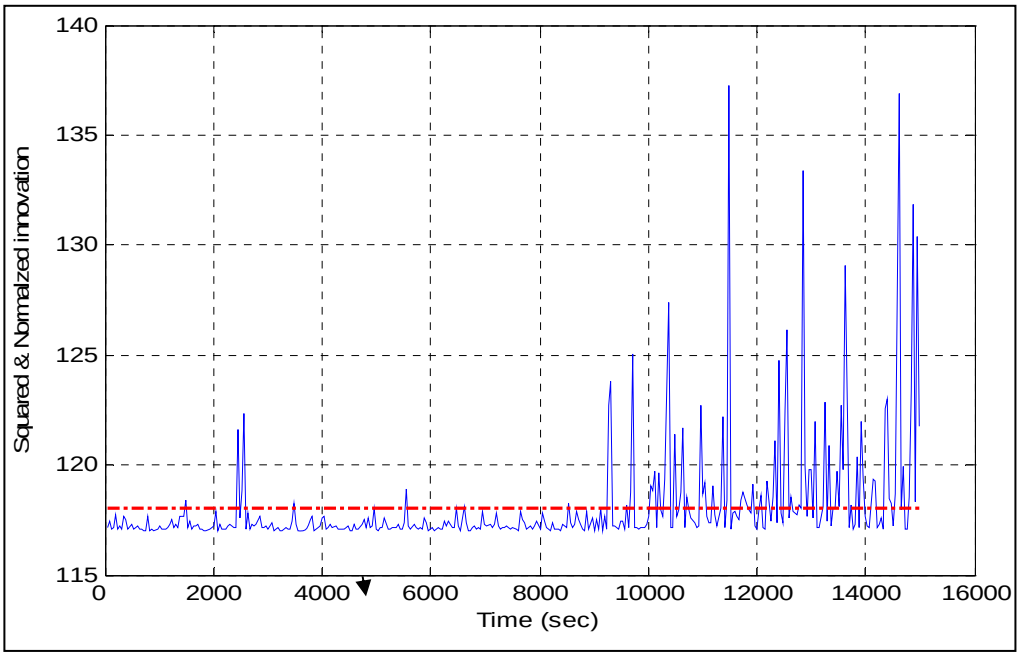

Figure 8. Squared and normalized innovations corresponding to the "failure" and the "no failure" conditions of the system versus the 95 percentile threshold

A.7 Discusion and Conclusion

From Figure 8, it is clear that a persistent violation of the selected threshold starts at time t=9200 seconds corresponding to an oil temperature of 52 °C (about 10% deviation from the normal value) which contribute to the sensitivity of the fault detection algorithm. Although better detection resolution can be achieved by either increasing the sample rate or decreasing the window size, a compromise should always be considered between the algorithm sensitivity and the calculation speed, especially when real time application is considered.

Another point of interest is present in this analysis. Although a direct impact of the introduced fault was expected on the vibration level with minor effects on the observed signals (Speed, TRIT and PCD). The results demonstrate that this fault propagates in a way that these later parameters were considerably affected by it. The only justification of this phenomenon could be that as a secondary effect of the oil temperature and the vibration level increase, the clearances inside the compressor stages have temporarily been altered, leading by this mean to an adversary effect on the compressor efficiency noted by the inconsistent behavior of the PCD, TRIT and hence the shaft speed consequently. This later results could be significant from the turbine manufacturer perspective.

3.2.3 Prognostic Module

Prognostics predict the future health state of a system component from the present operating conditions and historical data. The health monitoring system can incorporate a prognostic algorithm to effectively interpret and determine the plant's healthy working span. The application of prognostics to a system can be based on different approaches including physical/analytical models, "rules" databases, and statistical models. In the physical model based approach, mathematical models predict the system behavior depending on the varying inputs. For the development of "rules" based on experience, design and maintenance experts are required to compare the past and present system behavior to estimate and predict its health. Finally, statistical models use extensive input/output data to analyze trends.

The Clemson University research team has formulated an initial prognostic approach for stationary gas turbine health management systems. The model free prognostic strategy uses statistics to determine trends and predict future parameter values for Mercury 50 gas turbine. A unique three-dimensional representation of the data has been developed to aid the visualization of data. The next step in the gas turbine prognostics will be a wavelet approach.

A. Statistical Foundations

Statistics are a valuable tool for gas turbine prognostics by analyzing historical data to predict future behavior. Currently, twenty eight signals are recorded at regular intervals from the Mercury 50 gas turbine at Clemson University. The data is stored in the array *y(t)*

$$y(t) = \begin{bmatrix} y_1(t_1) & y_1(t_2) & \cdots & y_1(t_n) \\ y_2(t_1) & y_2(t_2) & \cdots & y_2(t_n) \\ \vdots & \vdots & \ddots & \vdots \\ y_j(t_1) & y_j(t_2) & \cdots & y_j(t_n) \end{bmatrix} \tag{21}$$

where j and *n* represent the total number of signals collected and the final time recorded, respectively. The signals are observed measurements such as vibration amplitudes, temperatures, pressures, and flow rates (refer to Table 1). Statistics can be used to evaluate these signals individually, or collectively, in an attempt to recognize patterns in behavior that might precede turbine degradations. If a signal is assumed to be a random variable, there are two important ways to describe it. First, the mean value of the signal, $\bar{y}_j$, can be expressed as

$$\bar{y}_j = \frac{\sum_{i=1}^{n} y_j(t_i)}{n} \qquad \text{for } j = (1,2,\ldots,28) \tag{22}$$

y_j	Measured Variable	Description of Measured Parameters	Units
1	Temp1	NGP – Turbine Speed	%
2	Temp32	Lube Oil Header Temperature	˚K
3	Temp34	Air Inlet Temperature	˚K
4	Temp43	Gas Fuel Supply Pressure	Pa
5	Temp46	Fuel Flow	kg/sec
6	Temp51	Compressor Inlet Acceleration Env.	gE
7	Temp54	Center Frame Axial Acceleration Env.	gE
8	Temp57	Compressor Diffuser Acceleration Env.	gE
9	Temp60	Generator Driven End Acceleration Env.	gE
10	ge64	Gearbox Acceleration Env.	gE
11	Temp89	Combustor Oscillation	Pa
12	Temp73	Lube Oil Header Pressure, TP380	Pa
13	Temp79	PCD, TP349	Pa
14	Temp80	Gas Producer Brg1 Y-Axis	mil pp
15	Temp81	Gas Producer Brg1 X-Axis	mil pp
16	Temp82	Gas Producer Brg2 Y-Axis	mil pp
17	Temp87	Gas Producer Brg2 X-Axis	mil pp
18	Temp88	Gas Producer Brg3 Y-Axis	mil pp
19	Temp103	Gas Producer Brg3 X-Axis	mil pp
20	Temp104	Relief Valve #2 Position	%
21	Temp107	Air Diverter Valve Position	%
22	Temp189	Alt Average L-L Volts	V
23	Temp199	Power in kW Total	kW
24	Temp18	Enclosure Temperature	˚K
25	Temp291	T7.1 Average	˚K
26	Temp292	T7.0 Average	˚K
27	Temp293	T2.45 Average	˚K
28	Temp295	Calculated TRIT	˚K

Table 1. Signals recorded from the Mercury 50 gas turbine run

where j represents the signal number recorded by the data acquisition system. Second, the variance, s_j^2, which is the sum of the difference between the actual values of a signal at given instances in time and the signal mean

$$s_j^{\ 2} = \frac{\sum_{i=1}^{n} [y_j(t_i) - \bar{y}_j]^2}{n-1} \qquad \text{for j= (1,2,…,28)} \qquad (23)$$

The square root of the variance is known as standard deviation, s_j. Figure 9 displays a normal distribution with three standard deviations plotted on either side of the mean and the corresponding percent of the sample contained within each range. For a normally distributed sample, 95% of all signal data collected should lie within two standard deviations of the sample mean. This information can be valuable in evaluating signals with the purpose of predicting the future health of a system.

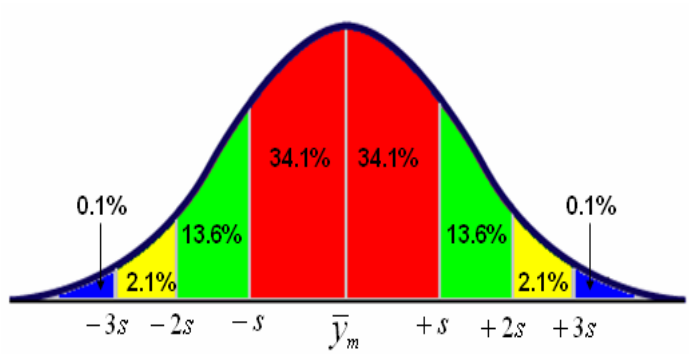

Figure 9. Normal distribution with standard deviations

B. Linear Regression to Describe Behavior

Ideally, a dynamic system such as a stationary gas turbine will behave in a consistent manner. In fact, the gas turbine is characterized by steady-state operation (i.e., power production) with occasional start up and shut down sequences. A uniform set of system input conditions should result in similar outputs each time the turbine is operated. Unfortunately, this is rarely the case due to system faults and noise disturbances. However, this general idea can be used in a prognostic system. Figure 10 shows a sample of two signals, fuel flow rate and power, plotted versus time for recorded data.

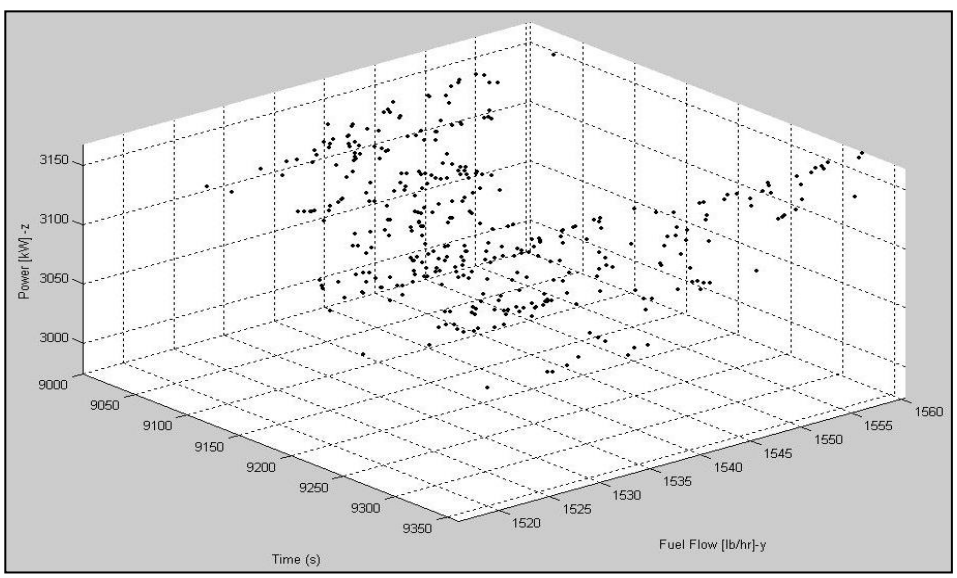

Figure 10. Fuel flow and power generated for a Mercury 50 gas turbine run at steady state conditions versus time

The research team has experimented with several techniques to characterize the data including moving mean and least-squares methods. However, the latter method seems to be the most successful. This method weighs large errors more than small errors and positive errors equally with negative errors. Typically, the least-squares method uses polynomial curves to

describe the data. To obtain the mathematical description of the dominant data trend, a minimized least square fit has been initially selected for the regression curve equation, Z,

$$\vec{Z} = \sum_{j=1}^{n} \sum_{i=0}^{r} a_{ij} t^{i} \qquad \text{for } 1 \le n \le 28 \qquad (24)$$

where t is the time and the sum of squares of the deviations between N points in the sample data and the regression curve, $\vec{D}$, is given as

$$\vec{D} = \sum_{i=1}^{N} \left[\vec{y}_j(t) - \vec{Z} \right]^2 = \sum_{i=1}^{N} \left[\sqrt{\sum_{j=1}^{n} y_j(t)^2} - \sum_{j=1}^{n} \sum_{i=0}^{r} a_{ij} t^{i} \right]^2 \qquad \text{for } 1 \le n \le 28 \qquad (25)$$

which is minimized to get a regression curve as $\frac{\partial \vec{D}}{\partial a_i} = 0$ for i= (0,1,…,r), where r is the polynomial order. The polynomial coefficients, $a_{0j}, a_{1j}, \ldots\ldots a_{rj}$, can be obtained by solving the (r+1) equations numerically

$$\frac{\partial}{\partial a_{i \in [0,r],j}} \left\{ \sum_{i=1}^{N} \left[\sqrt{\sum_{j=1}^{n} y_j(t)^2} - \sum_{j=1}^{n} \sum_{i=0}^{r} a_{ij} t^{i} \right]^2 \right\} = 0 \qquad \text{for j= } 1 \le n \le 28 \qquad (26)$$

In this initial study, two signals were related to time using the least-squares method and a second-order polynomial line fit. As new data is collected, the algorithm updates and redraws the line fit according to the data already collected and the data being added. Figures 11, and 12 show the regression line which depicts the fuel flow rate and the generated power relationship versus time.

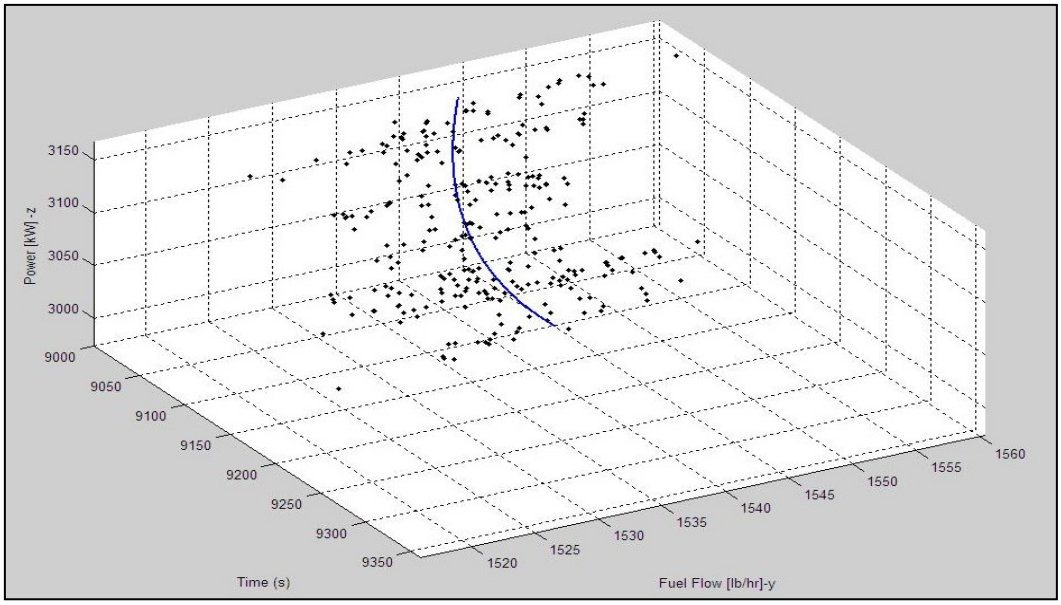

Figure 11. Regression curve ($\vec{Z}$) based on a second order polynomial trend using a minimized least squares method for fuel flow and power versus time at t=9270 seconds

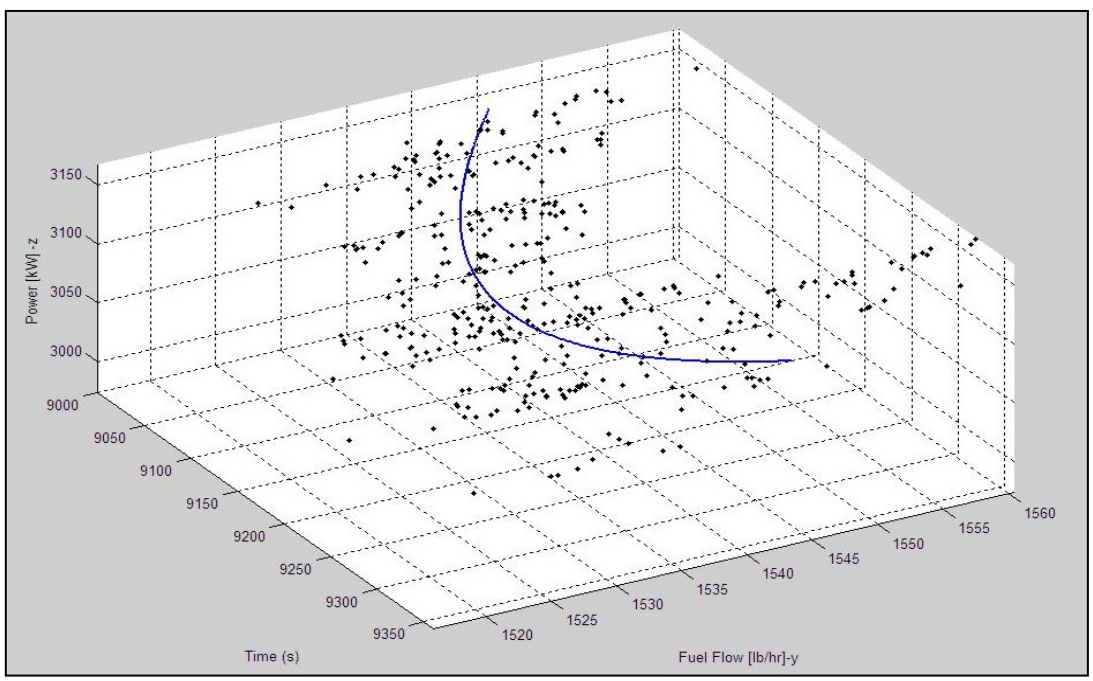

Figure 12. Regression curve ($\vec{Z}$) based on second order polynomial trend using minimized least squares method for fuel flow and power versus time at t=9360 seconds

C. Enclosing the Data

As shown in Figures 11 and 12, the data points are scattered around the regression line. Ideally, a method may be created to visually represent the data and its variability. To accomplish this, ellipses were used. An ellipse is a closed plane curve consisting of all points for which the sum of the distances between a point on the curve and two fixed points (i.e., foci) is the same. The center of an ellipse is the point halfway between its foci. The major axis is the chord that passes through the foci; the minor axis is the chord that passes through the center perpendicular to the major axis. 2*a* and 2*b* are the lengths of these axes; the larger axis receives the major designation, and the smaller axis receives the minor designation. A circle is also a form of an ellipse of eccentricity zero, (i.e., one in which the center and the two foci all coincide).

Since an ellipse can have two axes of differing lengths, it is an excellent way to depict the variation in two data signals. One axis can represent the variation in one signal while the other axis represents the variation in the other. Using standard deviation to determine the size of each axis, a certain percentage of data can then be enclosed within an ellipse. Or in this case, a certain percentage of data can be enclosed within a series of ellipses or *tuples* (set of ordered elements). Using the equation of the ellipse $\left\{\frac{p^2}{f^2}+\frac{q^2}{h^2}=1\right\}$, which is used to plot tuples in the form

$$p^2 = \frac{f^2h^2 - q^2f^2}{h^2} \tag{27}$$

where u and v are the coordinates of the two independent variables, and f and h represent the length of the semi-major and semi-minor axis. As mentioned previously, a range that lies two standard deviations on either side of the mean of a normally distributed sample encloses 95% of the points in that sample. The standard deviations of the two signals being analyzed were calculated based on the same set of data used to predict the regression curve. The length of the semi-major and semi-minor axis were obtained as

$$f = 2\sqrt{\frac{\sum_{i=1}^{n}[y_j(t_i)-\bar{y}_j]^2}{n-1}} \quad \text{and} \quad h = 2\sqrt{\frac{\sum_{i=1}^{n}[y_m(t_i)-\bar{y}_m]^2}{n-1}} \tag{28}$$

where *m* and *j* denote two different turbine signals and *p* and *q* should be $p \in (-f, f)$ and $q \in (-h, h)$. Accordingly, a selection of *q* can be made and the corresponding value of *p* can be reached with knowledge of *f* and *h* as per equations (27) and (28). The center of each ellipse is set onto the regression line $O\left[\vec{Z}(t)\right]$, so that the ellipse signifies two standard deviations of the fuel flow signal and two standard deviations of the power signal on either side of the regression line in the y- and z-directions, respectively. By picking a value of *p*, *q* can be calculated accordingly. Figures 13 and 14 show tuples plotted with major and minor axes sized according to the signal that they represent and centered on the regression curve for selected times in the turbine run.

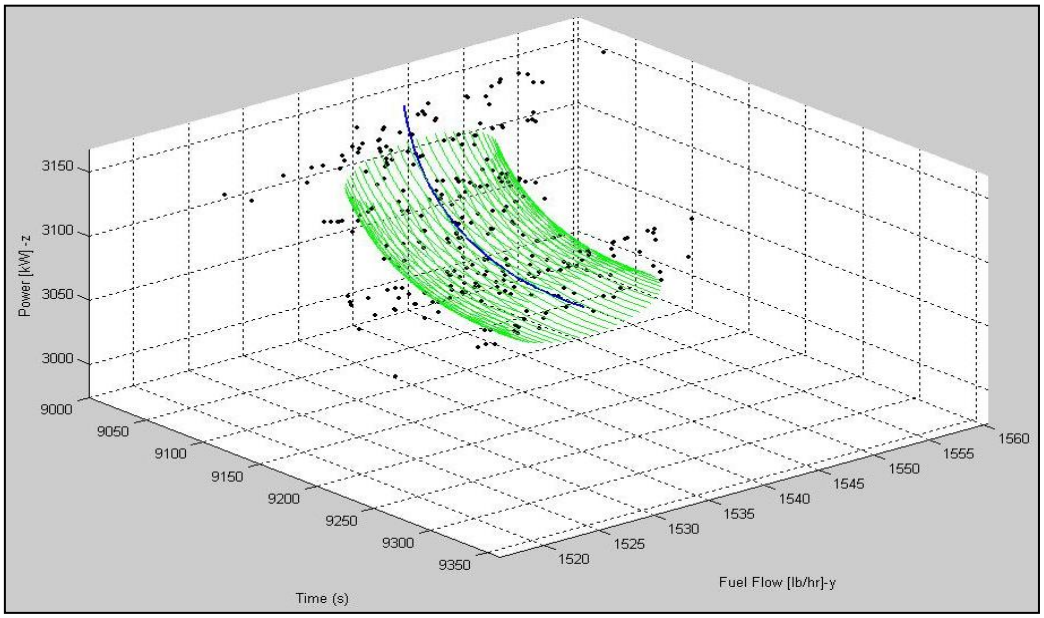

Figure 13. Tuples centered on a second order polynomial trend using a minimized least squares method for coefficients and a two standard deviation envelope at t=9180 seconds

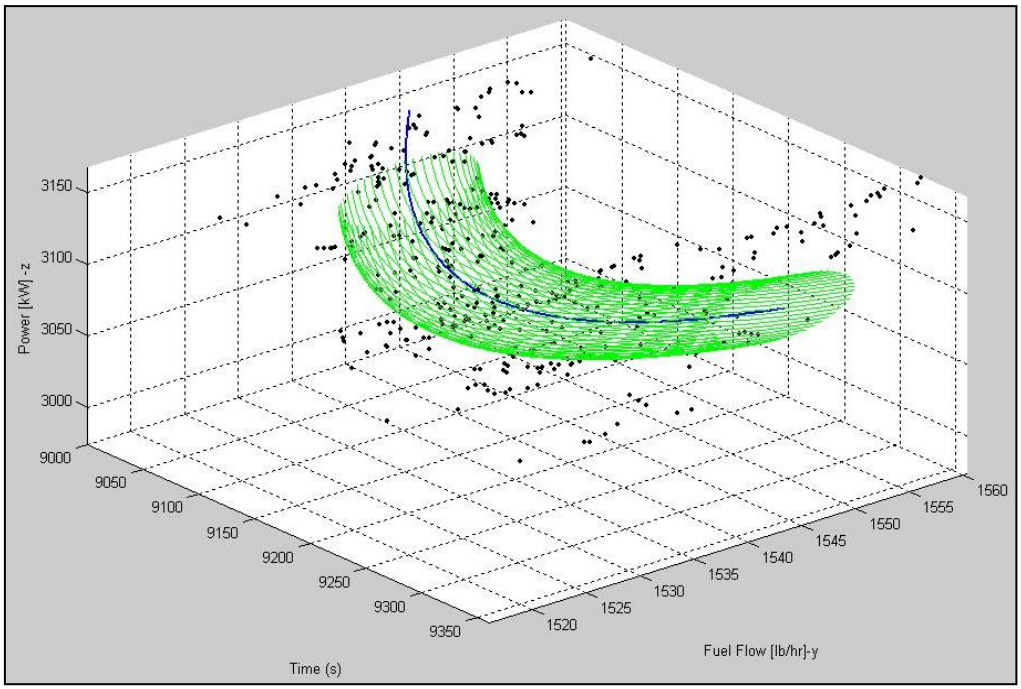

Figure 14. Tuples centered on a second order polynomial trend using a minimized least squares method for coefficients and a two standard deviation envelope at t=9360 seconds

These tuples allow one to visualize the behavior of the turbine. The points outside of the tuples represent points occurring during operation that are greater than two standard deviations of the recorded data away from the trend line.

D. Forecasting

The idea behind a prognostic system is to be able to predict turbine behavior in the future based on current behavior. After developing a method to analyze current behavior, a method was developed to forecast system performance. The regression lines may be extended past the recorded data range into the future to predict turbine behavior. Tuples were plotted around the extended regression line with the same major and minor axes as the recorded data. Figure 15 gives an illustration of the forecast shown in red; the forecast predicts turbine behavior sixty seconds into the future. This method involves a "learning curve" for the algorithm.

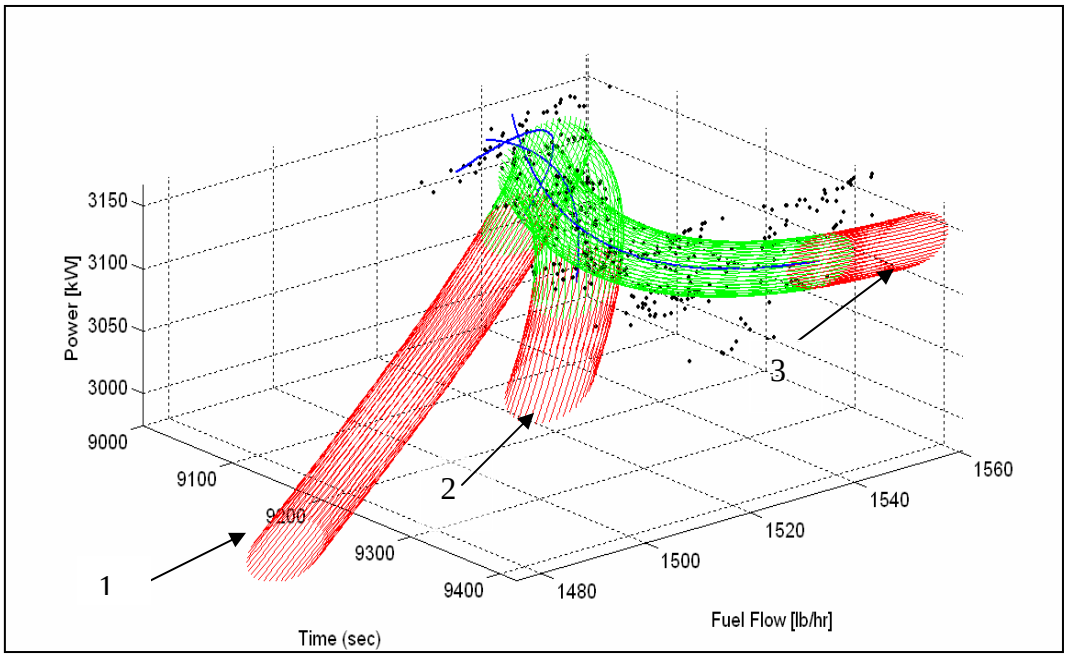

Figure 15. Forecast of power and fuel flow rate versus time displayed at
1) 9090, 2) 9180, 3)9360 seconds

This "learning curve" means that the forecast is very volatile at the start of data collection because it is based on a small amount of time; however, as more data is collected, the forecast behaves more predictably and more closely reflects the actual behavior The first two sets, 1 and 2, show the forecast heading away from the actual turbine behavior, but the third set, 3 shows the forecast moving in the proper direction. This forecasting method is very basic, but it does give a general idea of what the turbine will be doing at short time into the future. In the figure above, the data collected is only a six-minute window of time; larger sets of data will allow longer, more accurate forecasts.

The next logical steps for the team will be to first develop a method for handling points that fall outside of the tuples for the recorded data range. The second step will be to determine a way to compare the forecast to the actual behavior. The team will also investigate other signals and their relationships to determine which combinations of signal behavior might indicate faults.

4. EXPERIMENTAL WORK

4.1 Mercury 50 Gas Turbine

The Mercury 50 gas turbine is used by the Clemson University facilities to provide supplemental electrical power to the campus. It consists of a single shaft recuperated cycle turbine engine, a generator with accessories, and auxiliary systems. The Mercury 50 has a power production capacity of 4.5 MW with a maximum rotational speed of approximately 14,800 RPM. It contains a ten stage compressor and a two stage turbine. The Mercury50 turbine's operation can be recorded at the Clemson University research facility computer workstations to determine the status of the gas turbine's operation including system temperatures, pressures, vibration levels, and power output. This real time output data is available for observation and use with diagnostic and prognostic modules.

4.2 Data Acquistion

The experimental data from the Mercury 50 gas turbine is recorded using a RSLINX OPC server connection which links the Mercury 50 with the computer workstations in Energy Systems Laboratory at Clemson University. At present, twenty eight signals are recorded and transmitted to the MATLAB software in real time. This data is stored in the form of arrays. The data transmission from the Allen Bradley PLC is one way so that the turbine operation is not affected. The data acquisition is started by running the initializing code through the workstation at the Energy System Laboratory which includes specifying the signals to be recorded and the time for which the data has to be acquired.

The present data acquisition rate is one second. Once initialized the algorithm records and stores the desired data signals. The data is acquired from a set of 180 sensors located at the various points in the Mercury 50 gas turbine. In Figure 16, the main sensor locations are displayed in addition to the signals detected at those points. The logged signals from the turbine sensors are compared to the model generated simulated values for the diagnostic strategy. These signals have been also used to validate and verify the current gas turbine model. Efforts are being made to install a flow meter for recording the air mass flow through the Mercury 50 gas turbine.

4.3 Experimental Data

The experimental data has been recorded from the Mercury 50 gas turbine, during the past year twenty data sets have been recorded in collaboration with the Clemson University Facilities staff. Figure 17 shows the turbine shaft speed variation during the start up phase of the Mercury 50 gas turbine operation for four different experimental runs. It can be seen that the shaft speed ramps up to a speed of approximately 14,200 RPM in each case. At this point, steady state behavior is attained. From this point, the speed remains constant until the turbine shutdown.

Load applications to the turbine system cause the variations in the shaft speed during the start up phase.

The power generated during the start up phase of the Mercury 50 gas turbine for four different operational sessions may be observed from the Figure 18. The power generation begins at 400 seconds after the turbine has started. The power generated increases with time, until when the generator reaches the desired value of power to be generated. The generated power attains a steady state value ranging from 2.2 MW to approximately 4 MW which it continues to generate till shutdown of the turbine. The power generated and the duration of the turbine run both vary depending on the requirements of the Clemson University campus.

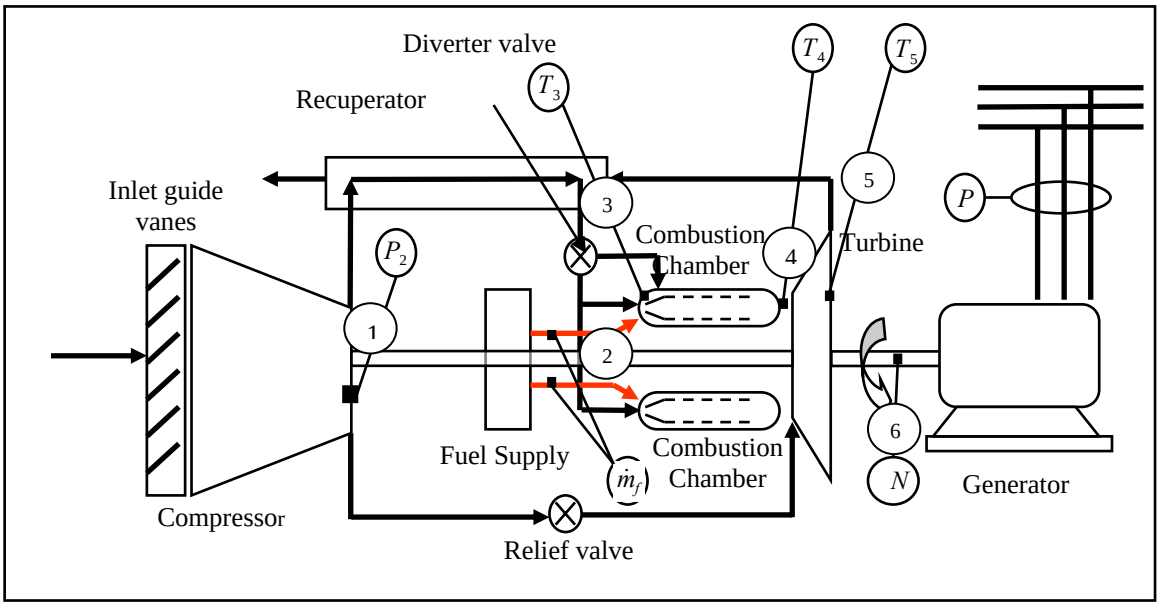

Figure 16. Gas turbine primary sensor location points along with the signals recorded

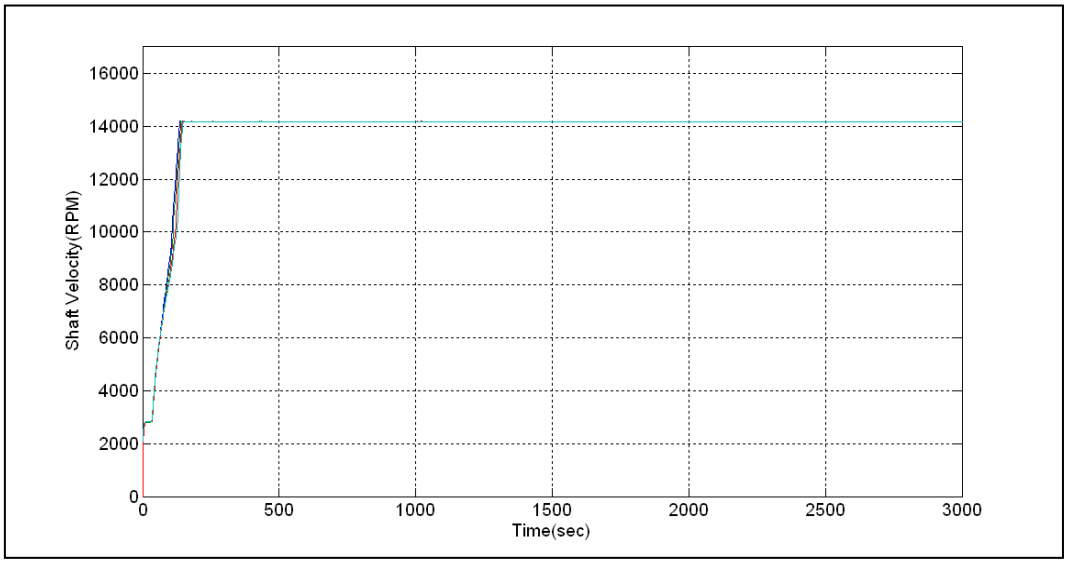

Figure 17. Shaft speed for the Mercury 50 gas turbine during start up sequence for 4 runs

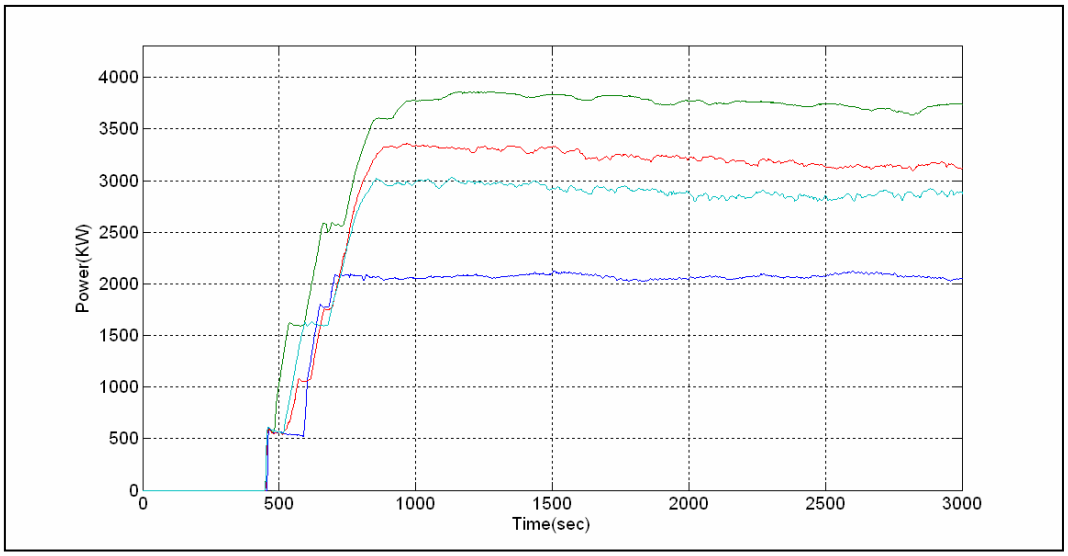

Figure 18. Power generated for the Mercury 50 gas turbine during start up sequence for 4 runs

Figure 19 displays the fuel flow signal for four different operational turbine runs. It can be observed from this figure that, there is a high degree of variations in the fuel flow during the start up phase of the turbine. These variations may be attributed to the loading phase of the turbine; every time the load is increased during the start up sequence, the fuel flow has to be increased to maintain a constant shaft speed. The maximum fuel flow rate depends on the power to be generated as can be seen from figures 19 that more the load higher is the fuel flow rate.

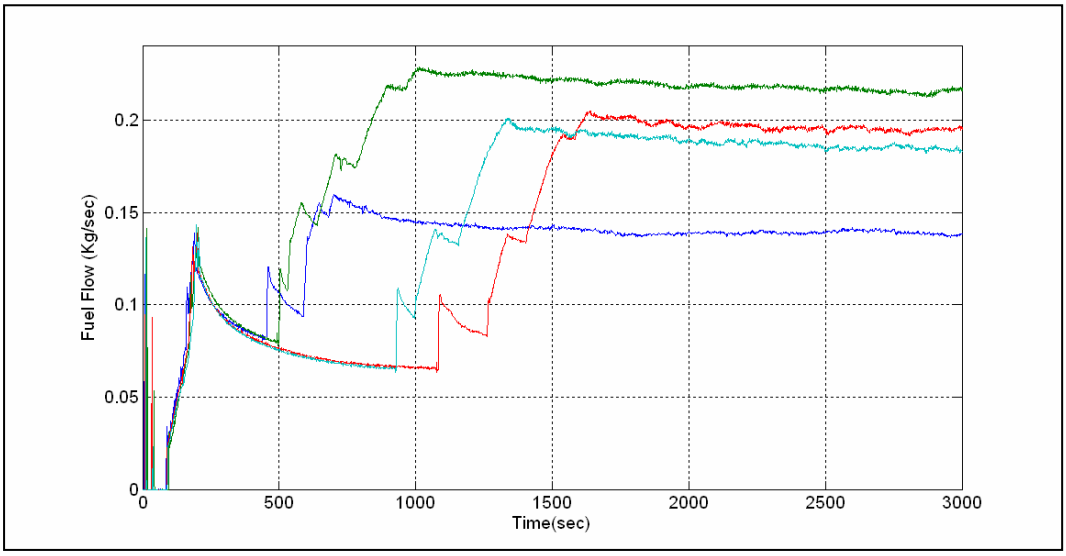

Figure 19. Fuel flow for the Mercury 50 gas turbine during start up sequence for 4 runs

Figure 20 presents the variation in the compressor outlet pressure for the Mercury 50 turbine during the start up phase for four runs. The compressor pressure gradually ramps up to the steady state value ranging from about 685 kPa to 920 kPa depending on the load applied for the various

runs. The transients in the start up phase occur due to the application of the power generation load. Note that the compressor pressure signal graph follows the same general pattern as the previously discussed turbine signals.

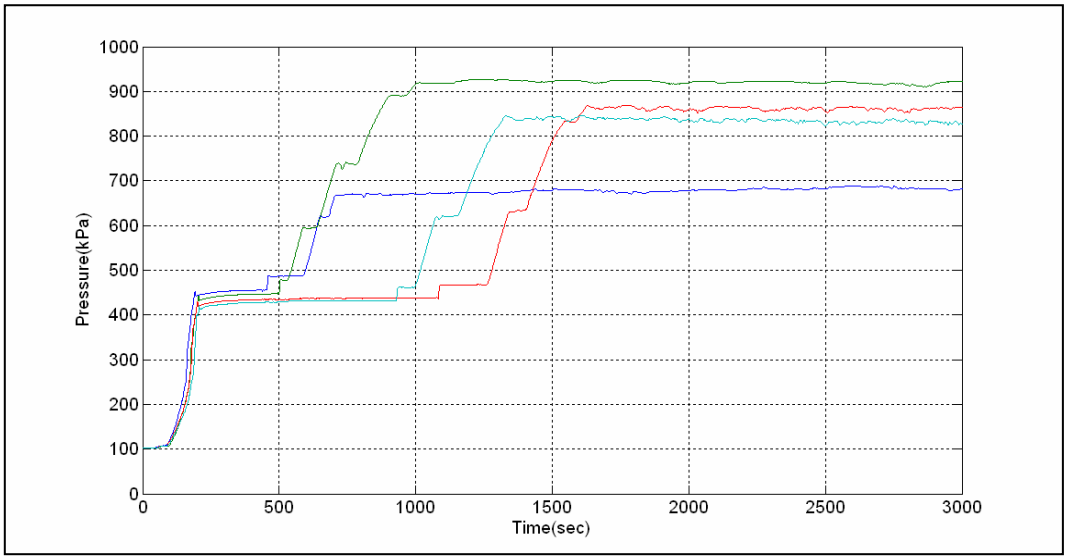

Figure 20. Compressor outlet pressure for the Mercury 50 gas turbine during start up sequence for 4 runs

In Figure 21, the turbine inlet temperature during the start up phase. This signal also varies in a similar manner during the start up process, and attains a maximum steady state value of approximately 2000 F in each of the four turbine runs, the range of variation for the turbine rotor inlet temperature is narrow as compared to the other turbine signals discussed previously as both the maximum and minimum temperatures are constrained by material properties.

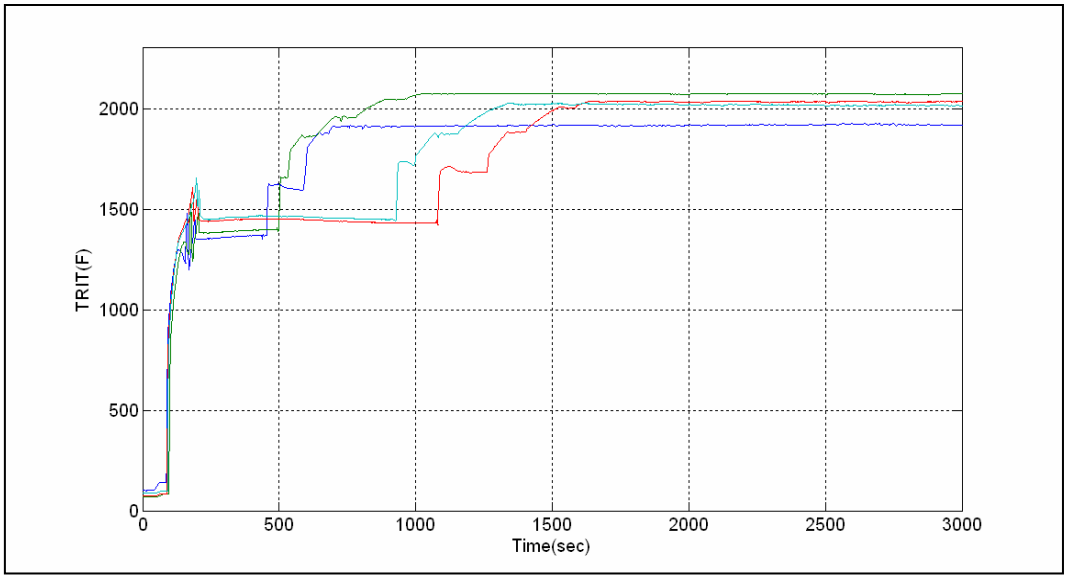

Figure 21. Turbine inlet temperature for the Mercury 50 gas turbine during start up sequence for 4 runs

4.4 Simulation Results

The dynamic simulation model consists of the differential and algebraic equations listed in the previous report. The subsystems have been linked with one another in Matlab/Simulink to create a simulation tool set that uses the ODE (Dormand-Prince) variable step solver. A variety of model input/output signals have been considered including the generator power, shaft speed, fuel flow, compressor outlet pressure, and combustion chamber outlet temperature.

As the turbine maps are not readily available, the input values were determined empirically and by observation. The Mercury 50 gas turbine component dimensions were also identified in a similar manner. The loading sequence was varied based on the available data. These simulation results were then compared to the experimental runs for the Mercury 50 gas turbine.

4.5 Model Validation

To validate the mathematical model, comparisons between the analytical model and the experimental results from the Mercury 50 gas turbine have been studied. Overall, the model behavior is similar to the experimental results. Each of the signals (e.g., shaft speed, power fuel flow, turbine rotor inlet temperature, and compressor outlet pressure) were superimposed on their corresponding experimental results graphs. The model validation results presented in this paper as based on the Mercury 50 gas turbine run for February 2, 2005.

The model validation of the turbine shaft speed shaft speed is shown in Figure 22. Due to fuel flow variations before steady state behavior is obtained, there is some deviation of the model results from the experimental shaft speed. This deviation between 100<t<650 is under investigation. Apart from this discrepancy, the model shows close resemblance to the experimentally determined speed for the steady state profile.

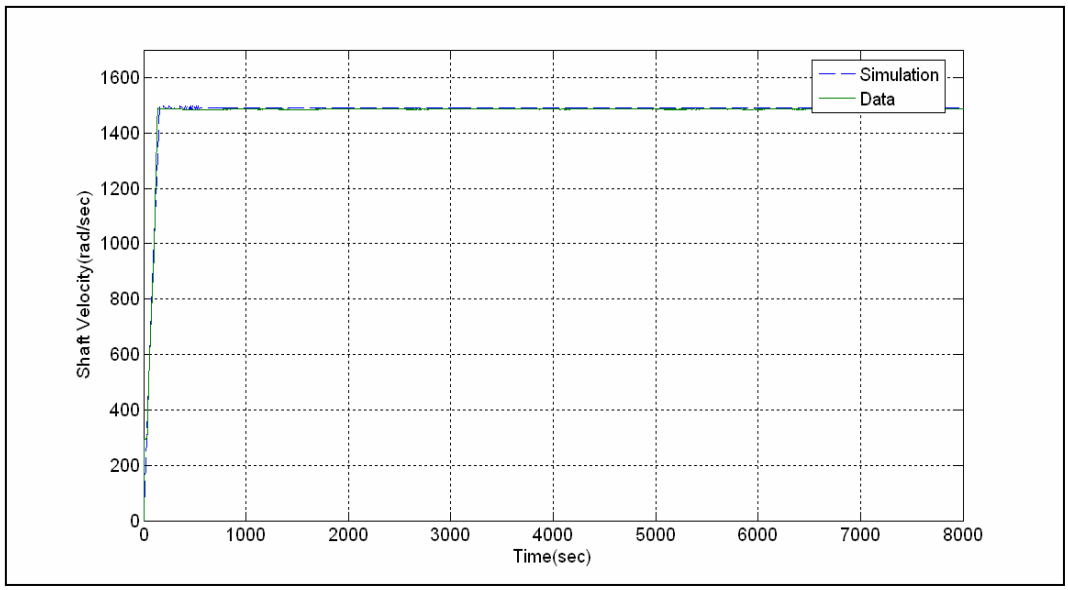

Figure 22. Model validation effort - estimated and actual shaft speed comparison (02-02-05)

In Figure 23, the model validation of the power generated is presented. The model results show good correlation to the experimental results for the start up, the transient and the steady state operation. A good match has been obtained (i.e., within 2% of the experimental data). It can be observed that the model simulates the start of power generation: (400 seconds after the initial start up), and sequential loading at various times during start up, and the attainment of steady state at approximately 650 seconds after start up.

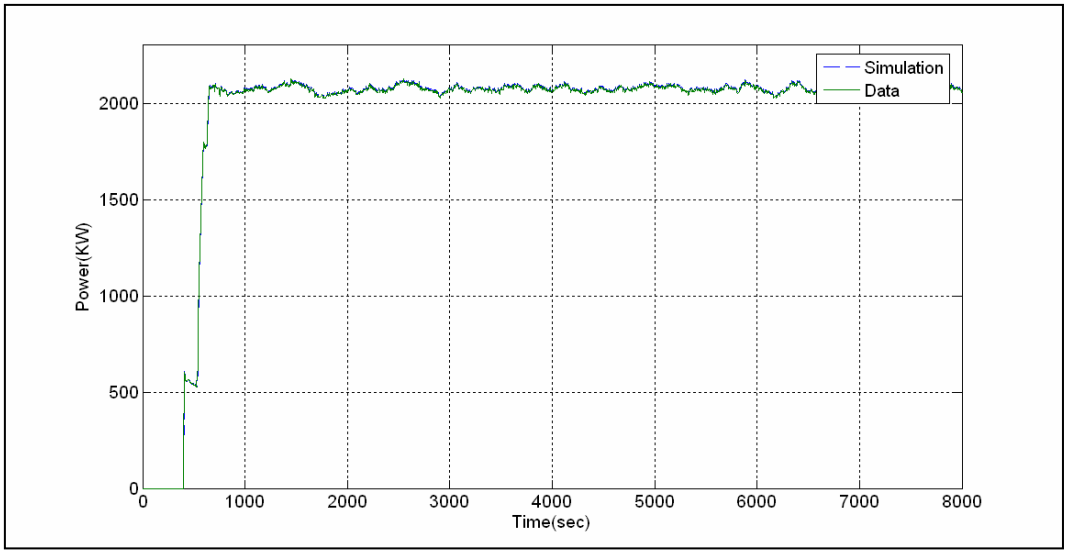

Figure 23. Model validation effort - estimated and actual power generated comparison (02-02-05)

The model validation for fuel flow rate is presented in Figure 24. Since no fuel control information is available, fuel flow map has been generated empirically. The flow of fuel into the combustion chamber varies according to the applied load. The model closely predicts the actual fuel flow during the loading sequence between 200 and 700 seconds.

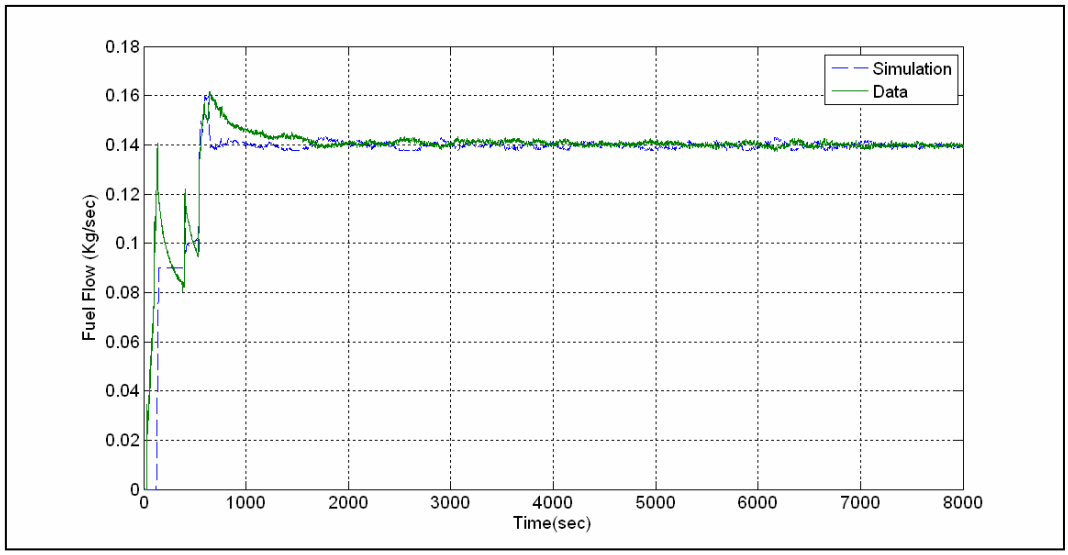

Figure 24. Model validation effort - estimated and actual fuel flow comparison (02-02-05)

Figure 25 displays the model validation for compressor outlet pressure (PCD). Although there are some deviations between the analytical and experimental results during the start up phase, the steady state results agree closely. Further improvements are under investigation.

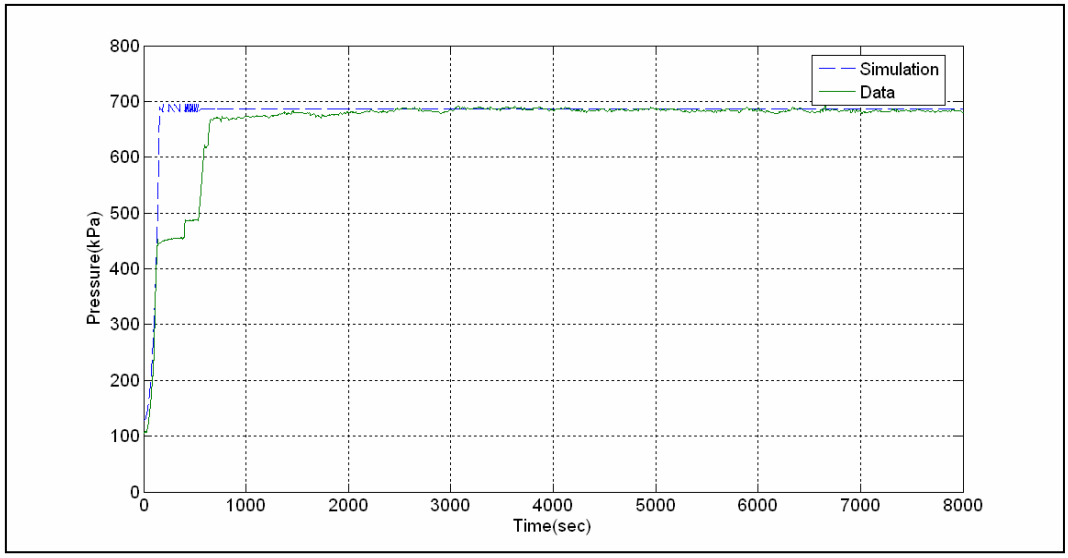

Figure 25. Model validation - estimated and actual compressor outlet pressure comparison (02-02-05)

Finally, Figure 26 presents the comparison between experimentally determined and analytically estimated temperature, turbine rotor inlet temperature. Due to extremely high temperatures at the turbine inlet it is not possible to install a temperature sensor that can measure the temperature of the hot gases at the turbine inlet. This problem is overcome by empirically calculating the turbine rotor inlet temperature. Overall a good match has been achieved.

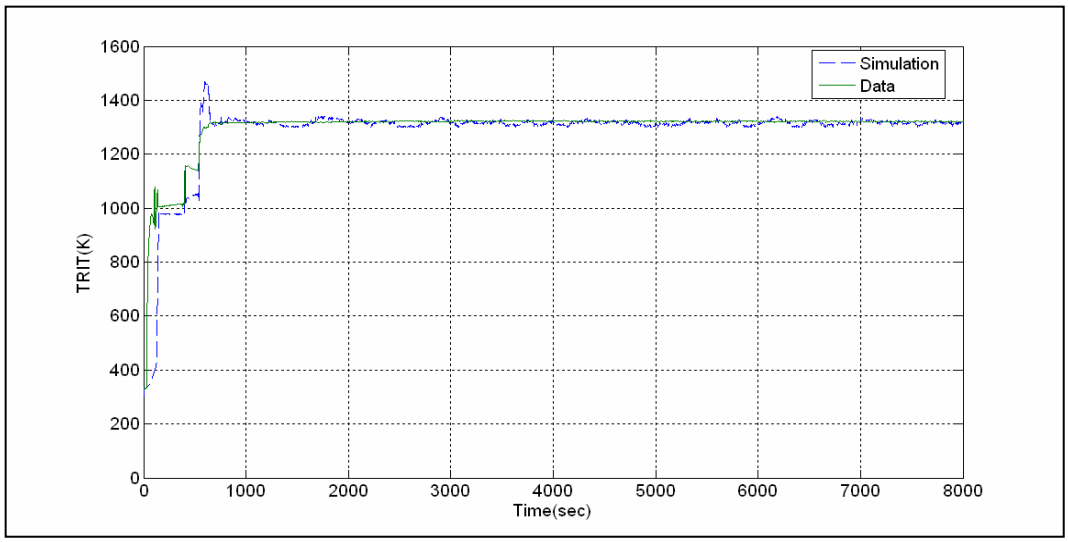

Figure 26. Model validation effort - estimated and actual turbine rotor inlet temperature comparison (02-02-05)

5. RESULTS AND DISCUSSIONS

A dynamic mathematical model has been formulated and initially validated. Both model-free and model-based strategies have been formulated and implemented with the results presented in Section 3. The results of a prognostic model-free strategy are also presented in Section 3. Experimental data has been collected and used for: (i) the model validation, (ii) the model based diagnostic strategy validation and (iii) the prognostic strategy implementation.

6. CONCLUSIONS

This report presents the work performed by the Clemson University research team during the past six months on stationary gas turbine diagnostic strategy. A dynamic mathematical turbine model has been presented and initially validated using experimental data. A model free and model based diagnostic strategy have been presented with accompanying discussion regarding its implementation. For the prognostic strategy a model free method for trend analysis framework for turbine signals has been developed and presented. A Mercury 50 gas turbine located at Clemson University Facilities has been operated and several data sets are gathered for analysis and used in the modeling, diagnostic, and prognostic activities. Overall, the project results are promising and significant progress is anticipated in the next reporting period.

REFERENCES

Ailer, P., Santa, I., Szederkenyi, G., and Hangos, K.M., "Non Linear Model-Building Of A Low-Power Gas Turbine", *Periodica Polytechnica Ser. Transp. Eng*., vol. 29, no. 1-2, pp. 117-135, October 2001.

Cooper, G., and McGillen, C., *"Probabilistic Methods of Signal and System Analysis"*, CBC College Publishing, 1986.

Frank, P. M., "Fault Diagnosis in Dynamic Systems Using Analytical and Knowledge Based Redundancy-A Survey and Some New Results", proceedings of IFAC Symposium on Advanced Information Processing in Automatic Control, pp. 457-459, Nancy, France, May 1990.

Howell, J. R., and Buckius, R. O., *"Fundamentals of Engineering Thermodynamics",* McGraw-Hill, 1987.

Krikelis, J., and Papadakis, F., "Gas Turbine Modelling Using Pseudo-Bond Graphs", *International Journal of System Science*, vol. 19, no. 4, pp. 537-550, 1998.

Krishnaswami, V., Luh, G. C., and Rizzoni, G., "Nonlinear Parity Equation-Based Residual Generation for Diagnosis of Automotive Engine Faults", *Journal of Control Engineering Practice*, vol. 3, no. 10, pp. 1385-1392, October 1995.

Kwan, C., Zhang, X., Xu, R., and Haynes, L., "A Novel Approach to Fault Diagnostics and Prognostics", proceedings of IEEE International Conference on Robotics and Automation, vol. 1, pp. 604-609, Taipei, Taiwan, September 2003.

Roemer, M. J., and Kacprzynski, G. J., "Advanced Diagnostics and Prognostics for Gas Turbine Engine Risk Assessment", proceedings of the IEEE aerospace Conference, vol. 6, pp 345-354, Big Sky, MT, March 2000.

Roemer, M. J., Kacprzynski, G. J., and Orsagh, R. F., "Assessment of Data and Knowledge Fusion Strategies for Prognostics and Health management", proceedings of the IEEE Aerospace Conference, vol. 6, pp. 2979-2988, Big Sky, MT, March 2001.

Sarvanamuttoo, H. I. H., Rogers, G. F. C., and Cohen, H., *"Gas Turbine Theory",* Pearson Education, 2001.

Walsh, P., and Fletcher, P., *"Gas Turbine Performance",* Blackwell Publishing, 2004.

APPENDIX A: Nomenclature List

A	System matrix
a	Polynomial coefficient
B	System input matrix
C	System observation matrix
f	Tuple ellipse major axis half length
h	Tuple ellipse minor axis half length
K	Kalman filter gain matrix
k	Time step (sec)
L_w	Squared and normalized residuals
N	Sample size
P	State estimation error matrix
P_r	Pressure (Kpa)
p	Dummy variable for ellipse construction
Q	State transition error covariance matrix
q	Dummy variable for ellipse construction
R	Observation error covariance matrix
r	Regression polynomial order
s	Standard deviation
T	Temperature (°K)
t	Time (sec)
u	System input vector
v	Observation error vector
W	Generated power (KW)
w	State transition vector
x	System state vector
y	System observed signal
Z	Best fit regression polynomial
Γ	Auto covariance function
η	Filtered residuals vector
ξ_{cr}	Critical value of normalized residuals
Σ	Covariance matrix
Υ	Observed variables vector
Ω	Residuals vector
ω	Shaft rotation speed (rad/sec)

Subscripts:

0	Stagnation
$1,2,3,\ldots$	Thermodynamic cycle state point

All units used for this project are SI (“Le Systeme International d’Unites”)

APPENDIX B: SYSTEM STATE EQUATIONS

From the derived model equations presented in the last annual report, the three state equations can be obtained from:

$$\frac{d\omega}{dt} = \frac{1}{(J_{eq})}(\tau_T - \tau_C - \tau_{FRIC} - \tau_L) \tag{A.1}$$

$$\frac{dT_{03}}{dt} = \frac{\dot{m}_f\left(\eta_{cc}LHV + 0.95T_{03}C_{pg1}\right) + \dot{m}_a T_{05}C_{pa} - \left(\dot{m}_a + \dot{m}_f\right)T_{03}C_{pg}}{\left(\dot{m}_a + \dot{m}_f\right)C_{pg}\left[0.95/k_1\dot{m}_a\right]} \tag{A.2}$$

$$\frac{dP_{02}}{dt} = \frac{kRT_{02}}{V_p}(\dot{m}_c - \dot{m}_t) \tag{A.3}$$

By substitution the different terms in the RHS of the above equations with their appropriate expressions in terms of $\omega, T_{03}, P_{02}, W$ and T_{01}, we can get the three state equations. Table A.1 includes the designation of each term in the three state equations.

J_{eq}	Equivalent lumped moment of inertia
τ_T	Torque produced by the turbine
τ_C	Torque consumed by the compressor
τ_{FRIC}	Friction torque
τ_L	Torque introduced by the electric load
$\dot{m}_f$	Fuel mass flow rate
η_{cc}	Combustion efficiency
LHV	Lower heat calorific value of the fuel
C_{pg1}	Gas specific heat at combustion chamber exit
$\dot{m}_a$	Air mass flow rate
T_{05}	Air stagnation temperature at recuperator outlet
C_{pa}	Air specific heat
C_{pg}	Gas specific heat at combustion chamber inlet
k_1	Average adiabatic index of the gas mixture inside the combustion chamber
k	Adiabatic index of air
R	Universal gas constant
V_p	Plenum volume
$\dot{m}_c$	Mass flow rate inside the compressor
$\dot{m}_t$	Mass flow rate inside the turbine

Table A.1 Nomenclature of the terms of the three state equations

The Effects of Fuel Distribution, Velocity Distribution, and Fuel Composition on Static and Dynamic Instabilities and NO_x Emissions in Lean Premixed Combustors

Semi-Annual Report

Reporting Period: July 1, 2005 to Dec 31, 2005

Prepared by:
Domenic A. Santavicca (Principal Investigator)
Jong Guen Lee (Co-Principal Investigator)

March 2006

DOE Award DE-FC26-02NT41431

UTSR Project No. 03-01-SR109

Submitted by:
The Pennsylvania State University
University Park, PA 16802

Disclaimer

"This report was prepared as an account of work sponsored by an agency of the United States Government. Neither the United States Government nor any agency thereof, nor any of their employees, makes any warranty, express or implied, or assumes any legal liability or responsibility for the accuracy, completeness, or usefulness of any information, apparatus, product, or process disclosed, or represents that its use would not infringe privately owned rights. Reference herein to any specific commercial product, process, or service by trade name, trademark, manufacturer, or otherwise does not necessarily constitute or imply its endorsement, recommendation, or favoring by the United States Government or any agency thereof. The views and opinions of authors expressed herein do not necessarily state or reflect those of the United States Government or any agency thereof."

Abstract

An experimental study is being conducted to determine of the effects of combustor operating conditions on the static and dynamic stability characteristics and NO_x emissions of lean premixed combustors operating on natural gas and coal-derived syngas fuels. The results of this study will be used to gain new insights and understanding of the causes of unstable combustion and to support the development of advanced numerical models and phenomenological-based models of unstable combustion. Results are presented in this semi-annual report from the first half of the third year of this three-year program. These results are from continuing studies of the effects of the dump plane recirculation zone on lean blow out and of the role of flame-vortex interactions during unstable combustion

In the lean blowout study, previously reported results have indicated that combustion in the dump plane recirculation zone plays an important role in determining the lean blowout limit. During the current reporting period the use of an angled dump plane to alter the dump plane recirculation zone and thereby lean blowout was investigated. In the instability study, previously reported results have shown that a vortex time-lag model can be used to predict the preferred instability frequency as a function of operating conditions from measurements of the stable flame location. During the current reporting period, preliminary testing has demonstrated that this method of predicting the preferred instability frequency can be extended to predicting the effects of fuel composition changes on stability characteristics. Work has also been initiated using FLUENT to predict the stable flame location as a function of operating conditions. This will make it possible to predict stability characteristics without measuring the flame location.

Table of Contents

	page
Title Page	1
Disclaimer	2
Abstract	3
Table of Contents	4
Executive Summary	5
Project Description	6
Experimental	7
Results and Discussion	8
The Effect of the Dump Plane Recirculation Zone on Lean Blowout	8
Predicting the Preferred Instability Frequency as a Function of Operating Conditions	13
Conclusion	16
Appendix A: Test Matrix for Lean Blowout Experiments	18

Executive Summary

Static and dynamic instabilities continue to be limiting factors in the development and use of lean premixed gas turbine combustors for achieving the NO_x levels required by current and future emissions regulations. These issues assume even greater significance with current interest in the effects of fuel variability, which includes variations in the composition of natural gas, the use syngas fuels, and the use of 100% hydrogen fuel, as well as recent interest in the use of "oxygen-combustion". To date, the only successful strategy for addressing static and dynamic stability problems is through the application of passive and, in a few cases, active control systems after instabilities have been encountered. Such solutions are not always successful, can be expensive to implement and usually do not work over a broad range of operating conditions. What is needed is an understanding of the factors affecting static and dynamic stability, an ability to predict the occurrence of lean blowout and unstable combustion, and models that can be used as the basis of a methodology for designing stable lean premixed combustors. This research program is intended to provide the detailed data and phenomenological understanding that is necessary for the development of such model-based design tools.

The goals of this research are (1) to determine the effect of combustor operating conditions on the static and dynamic stability characteristics of lean premixed combustors operating on natural gas and coal-derived syngas fuels, (2) to use this information to gain new insights and understanding of the causes of unstable combustion, and (3) to use this information to support the development of advanced numerical models and phenomenological models of unstable combustion.

During this reporting period, on-going research on the role of the dump plane recirculation zone on lean blowout and on the development of a methodology of predicting the preferred instability characteristics of flame-vortex driven instabilities was continued.

Project Description

Gas Turbine Research Need: Static and dynamic instabilities continue to be limiting factors in the development and use of lean premixed gas turbine combustors for achieving the NO_x emission levels required by current and future emissions regulations. These issues assume even greater significance with current interest in the effects of fuel variability, which includes variations in the composition of natural gas, the use syngas fuels, and the use of 100% hydrogen fuel, as well as recent interest in the use of "oxygen-combustion". To date, the only successful strategy for addressing these problems is through the application of passive and, in a few cases, active control systems after instabilities have been encountered. Such solutions are not always successful, can be expensive to implement and usually do not work over a broad range of operating conditions. What is needed is an understanding of the factors affecting static and dynamic stability, an ability to predict the occurrence of lean blow-out and unstable combustion, and models that can be used as the basis of a methodology for designing stable lean premixed combustors. This research program is intended to provide the detailed data and phenomenological understanding that is necessary for the development of such model-based design tools.

Approach and Expected Benefits: The objective of this project is to conduct experiments in an optically-accessible, laboratory-scale combustor to determine the effect of combustor operating conditions on the static and dynamic stability characteristics of lean premixed combustors. Of interest are both natural gas and coal-derived syngas fuels. These experiments involve a number of measurements aimed at characterizing the overall and detailed behavior, and at identifying the instability mechanism(s), of any observed instabilities. These include simultaneous measurements of the pressure, overall heat release and equivalence ratio fluctuations, as well as, phase-synchronized measurements of the two-dimensional structure of the flame. A unique feature of the combustor which is used in this study is the capability of varying the length of the combustor while the combustor is operating. This allows for the identification of the preferred instability frequency as a function of operating conditions from which the relationship between the combustor's stability characteristics and operating conditions is revealed. It also allows for the study of stable and unstable operation at the same operating condition. Information obtained with this unique facility is expected to provide valuable new insights regarding the mechanisms of unstable combustion.

Experimental

A schematic drawing and a photograph of the variable-length, optically-accessible, lean premixed combustor facility used in this research is shown in Fig. 1. Details on this combustor were given in previous reports.

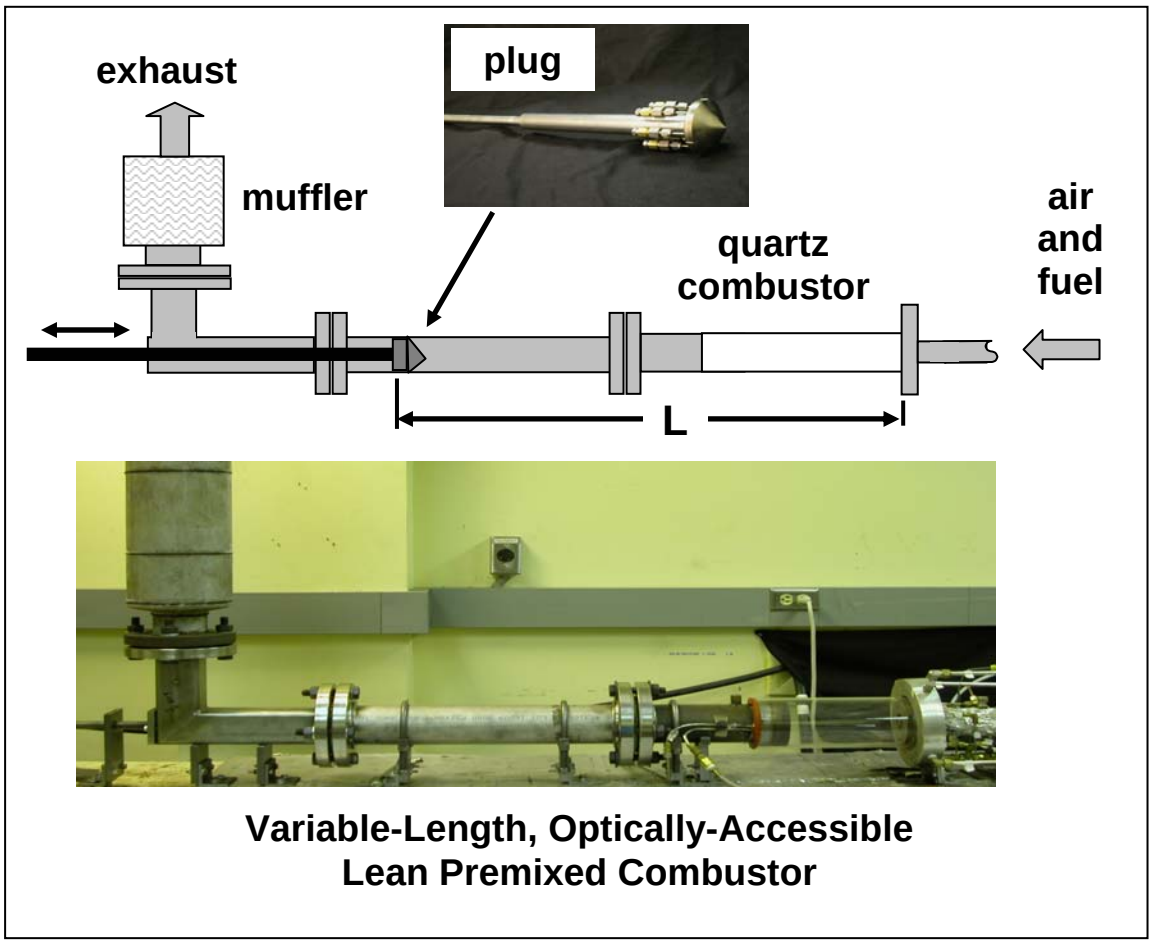

Figure 1. Variable length, optically accessible lean premixed combustor.

Results and Discussion

In the lean blowout study, previously reported results have indicated that combustion in the dump plane recirculation zone plays an important role in determining the lean blowout limit. During the current reporting period the use of an angled dump plane to alter the dump plane recirculation zone and thereby lean blowout was investigated. In the instability study, previously reported results have shown that a vortex time-lag model can be used to predict the preferred instability frequency as a function of operating conditions from measurements of the stable flame location. During the current reporting period, preliminary testing has demonstrated that this method of predicting the preferred instability frequency can be extended to predicting the effects of fuel composition changes on stability characteristics. Work has also been initiated using FLUENT to predict the stable flame location as a function of operating conditions. This will make it possible to predict stability characteristics without measuring the flame location. The status and the results obtained to date from each of these activities are discussed below.

The Effect of the Dump Plane Recirculation Zone on Lean Blowout

In order to study the role that the dump plane recirculation zone plays at lean blowout an angled insert was attached to the dump plane to reduce the volume available for the dump plane recirculation zone. This is illustrated in Fig. 1, where α is the dump plane angle. Two inserts were fabricated for testing, one with an angle of 30° and a second with and an angle of 45°.

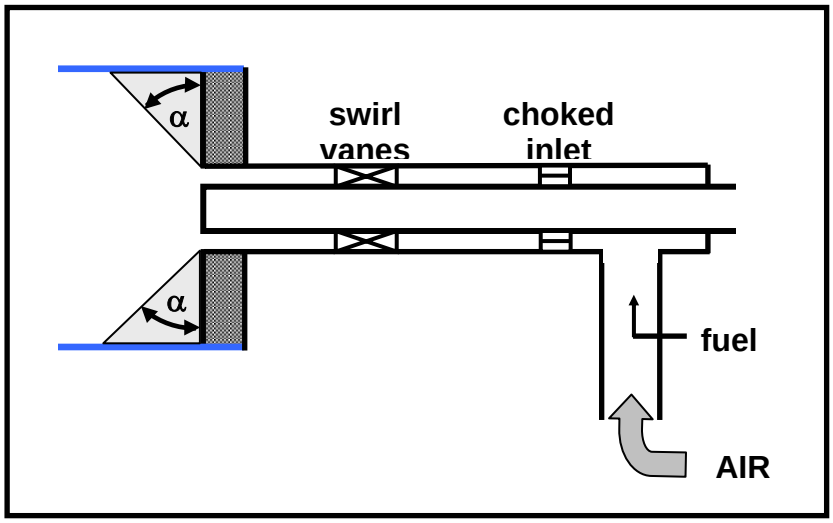

Figure 1. Schematic drawing of premixer and dump plane showing angled dump plane insert.

Lean blowout tests will be conducted at the same operating conditions that the previously reported lean blowout tests were conducted. These test conditions encompass three inlet temperatures (200°C, 300°C, and 375°C) and for each a matrix of sixteen hydrogen-carbon monoxide-natural gas fuel mixtures, for a total of 48 cases. The detailed test matrix is given in Appendix A of this report.

To date lean blowout tests have been conducted at 8 of the 48 test cases using the 30° angled insert. The behavior observed at lean blowout with the 30° angled insert is very similar to that observed previously with no insert; i.e., as lean blowout is approached combustion is observed in the dump plane recirculation zone and stays there until the flame becomes detached from the dump plane and shortly thereafter blows out. The lean blowout results for the 8 cases tested to date with the 30° angled insert are shown in Figures 2 – 9, along with the previous results with no insert. These results indicate that the 30° insert might improve the lean blowout limit, particularly for fuels containing hydrogen. These results, however, are preliminary and additional measurements and analysis are necessary to substantiate this possibility. That work is in progress.

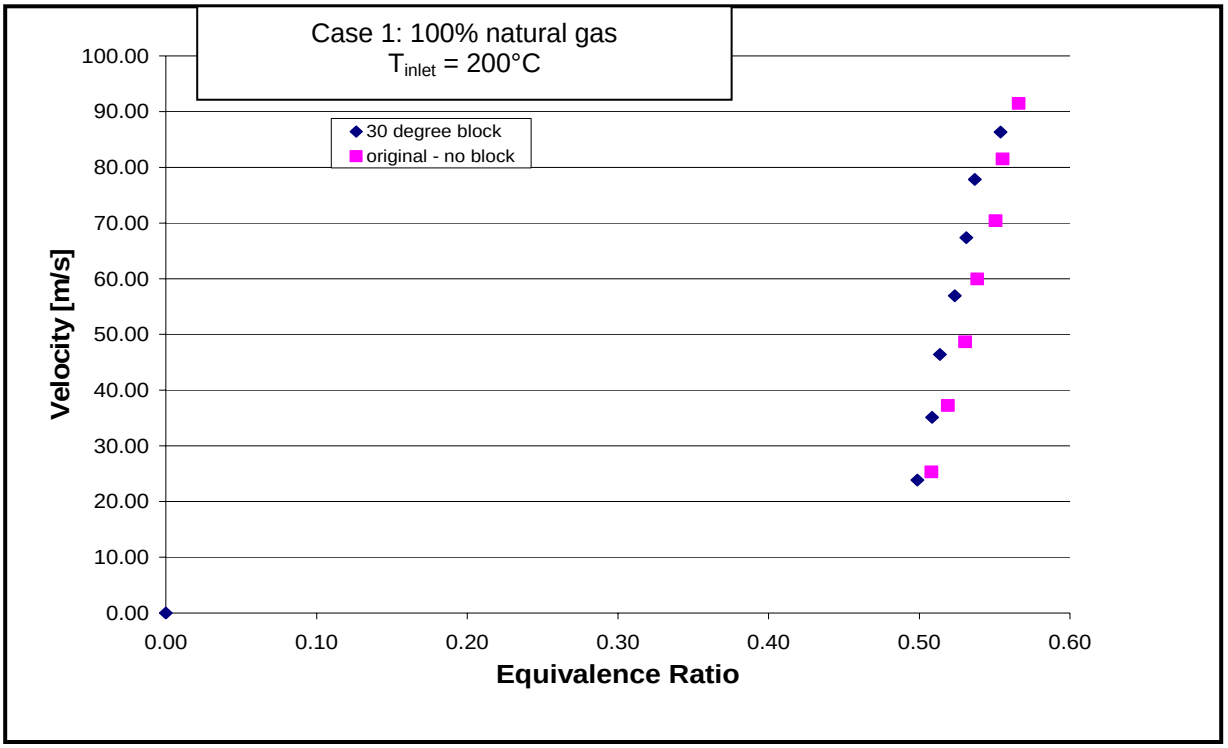

Figure 2. A comparison of the velocity at lean blowout versus equivalence ratio for the case 1 operating condition with and without a 30° angled dump plane insert.

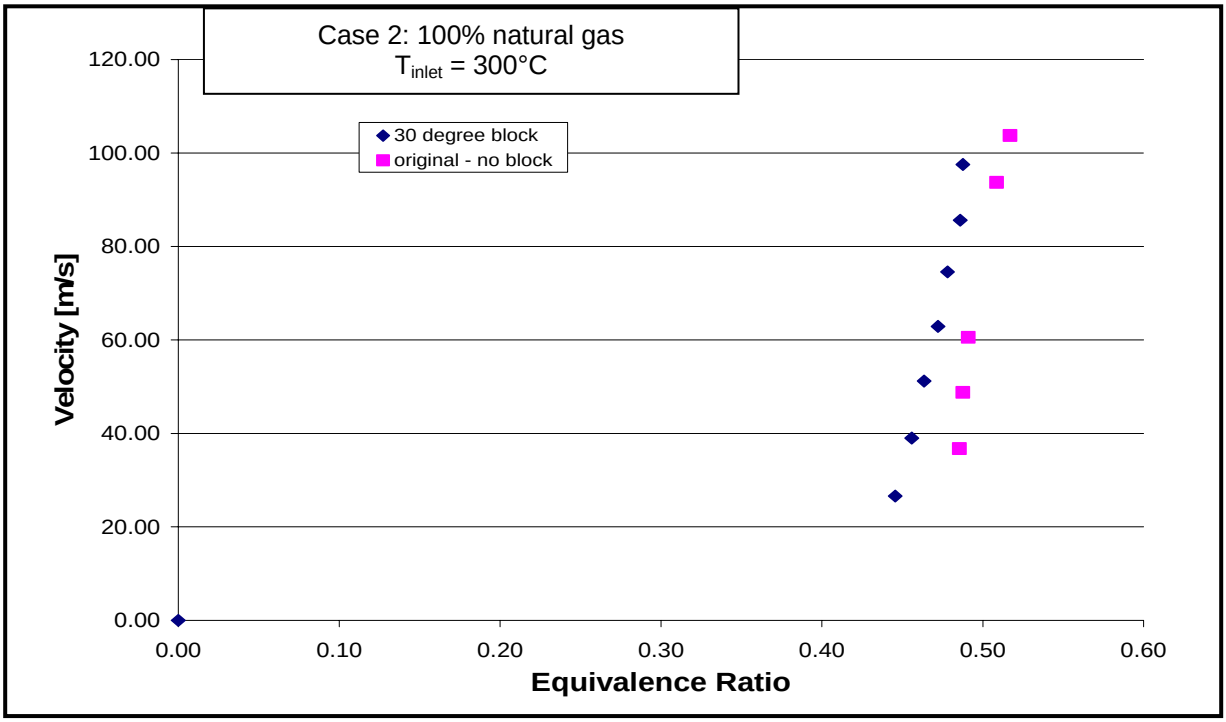

Figure 3. A comparison of the velocity at lean blowout versus equivalence ratio for the case 2 operating condition with and without a 30° angled dump plane insert.

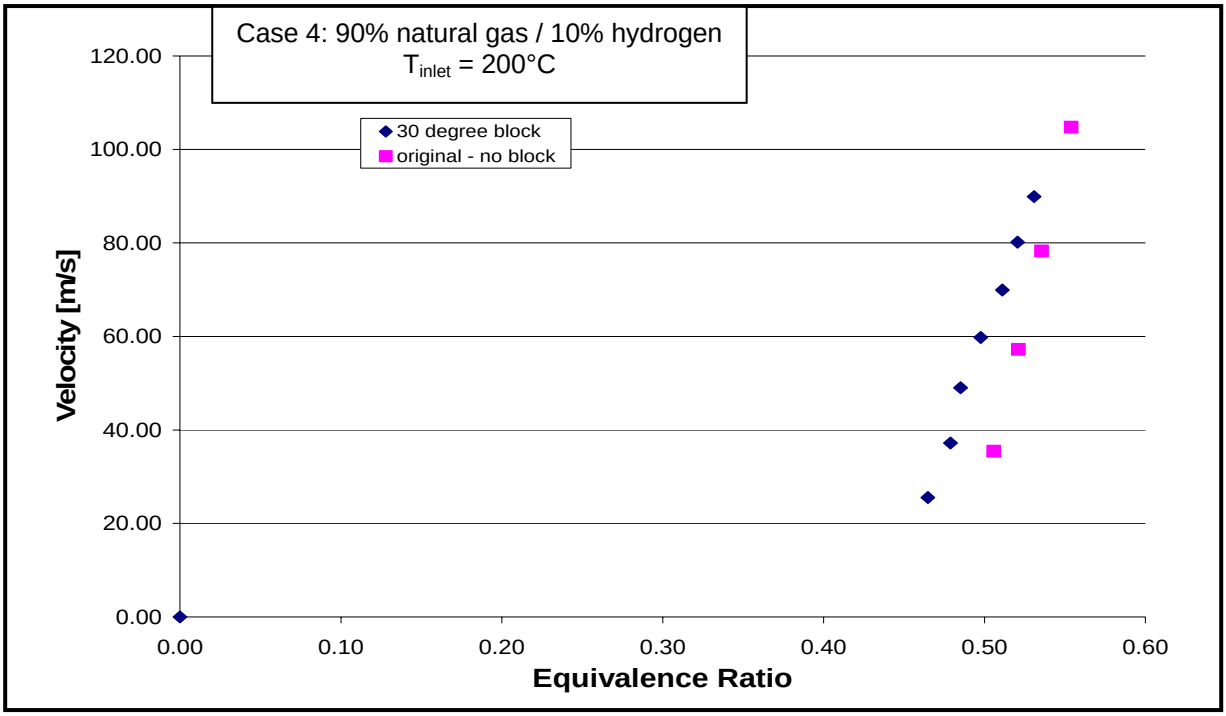

Figure 4. A comparison of the velocity at lean blowout versus equivalence ratio for the case 4 operating condition with and without a 30° angled dump plane insert.

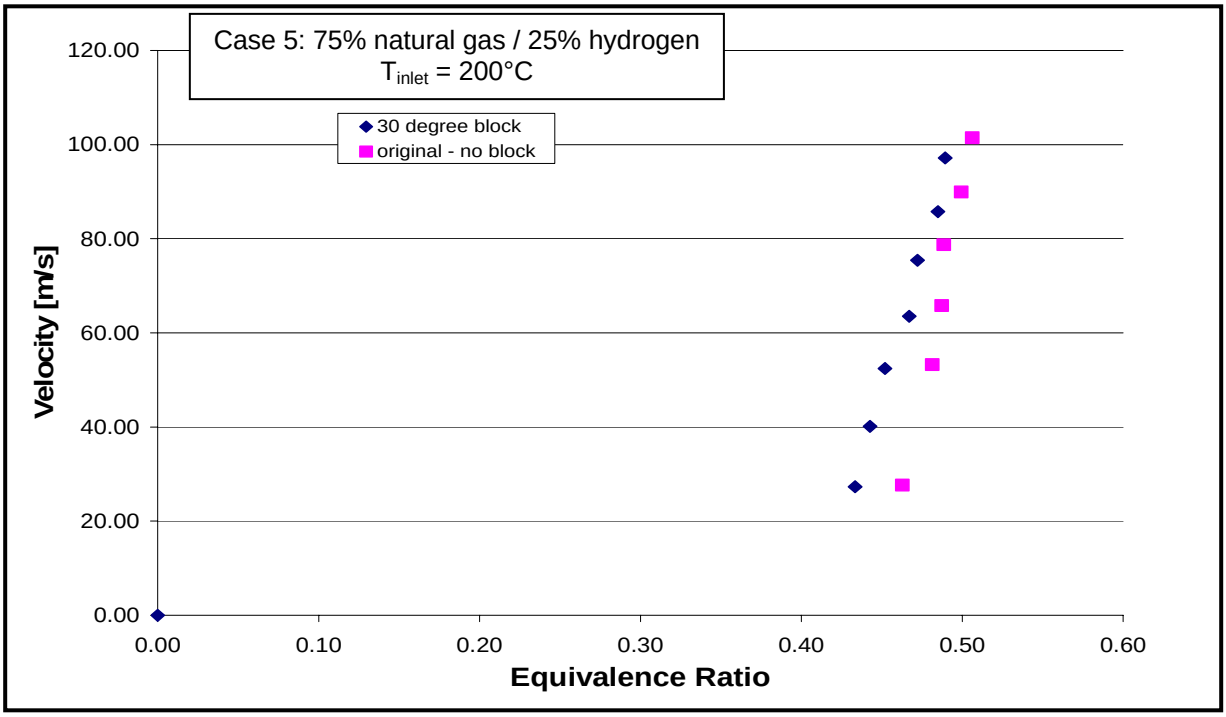

Figure 5. A comparison of the velocity at lean blowout versus equivalence ratio for the case 5 operating condition with and without a 30° angled dump plane insert.

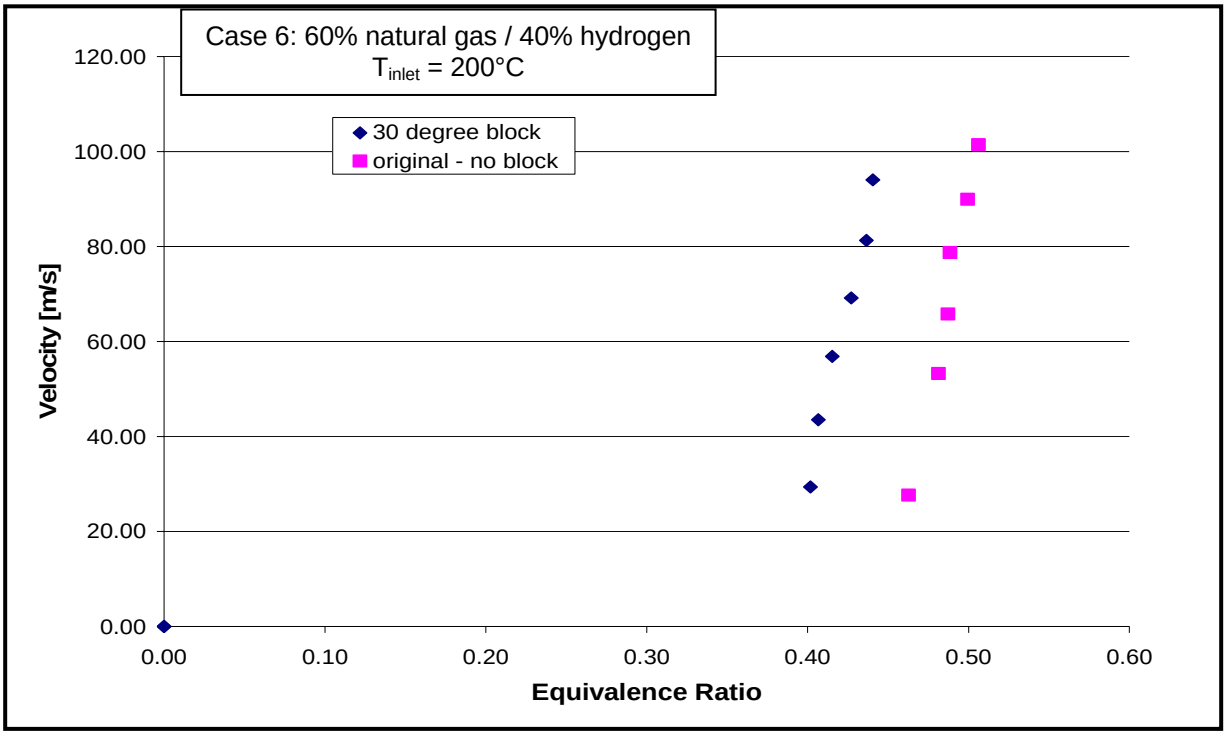

Figure 6. A comparison of the velocity at lean blowout versus equivalence ratio for the case 6 operating condition with and without a 30° angled dump plane insert.

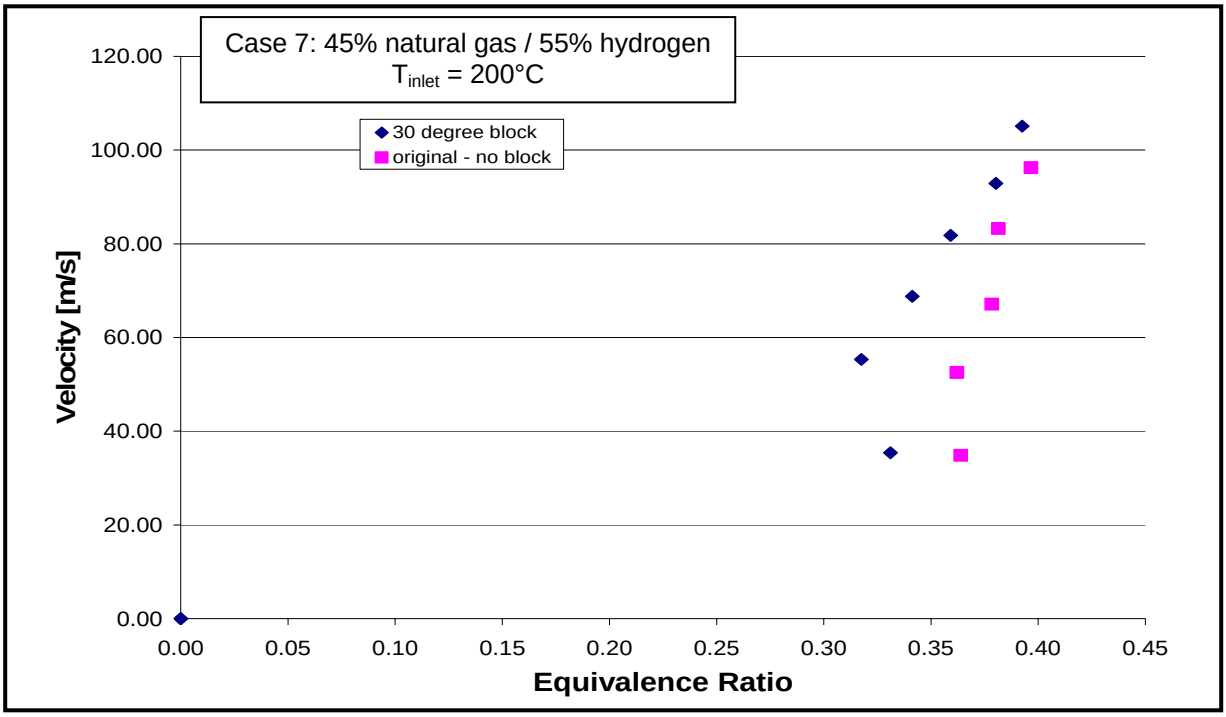

Figure 7. A comparison of the velocity at lean blowout versus equivalence ratio for the case 7 operating condition with and without a 30° angled dump plane insert.

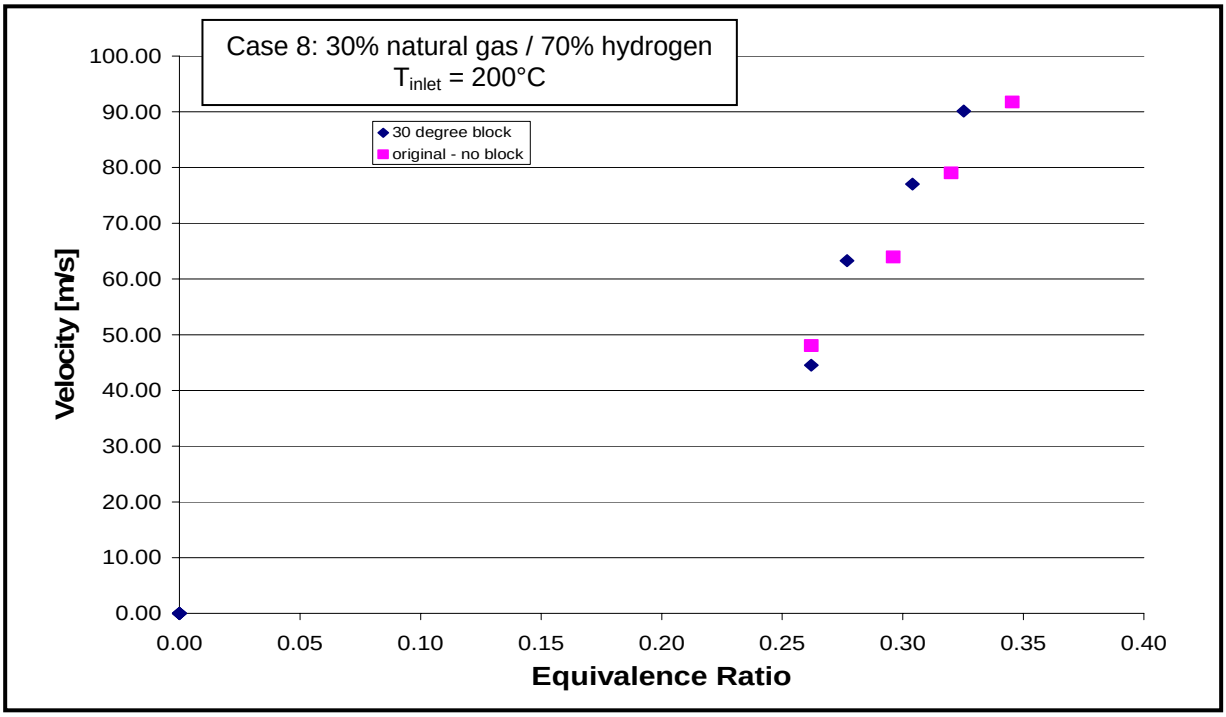

Figure 8. A comparison of the velocity at lean blowout versus equivalence ratio for the case 8 operating condition with and without a 30° angled dump plane insert.

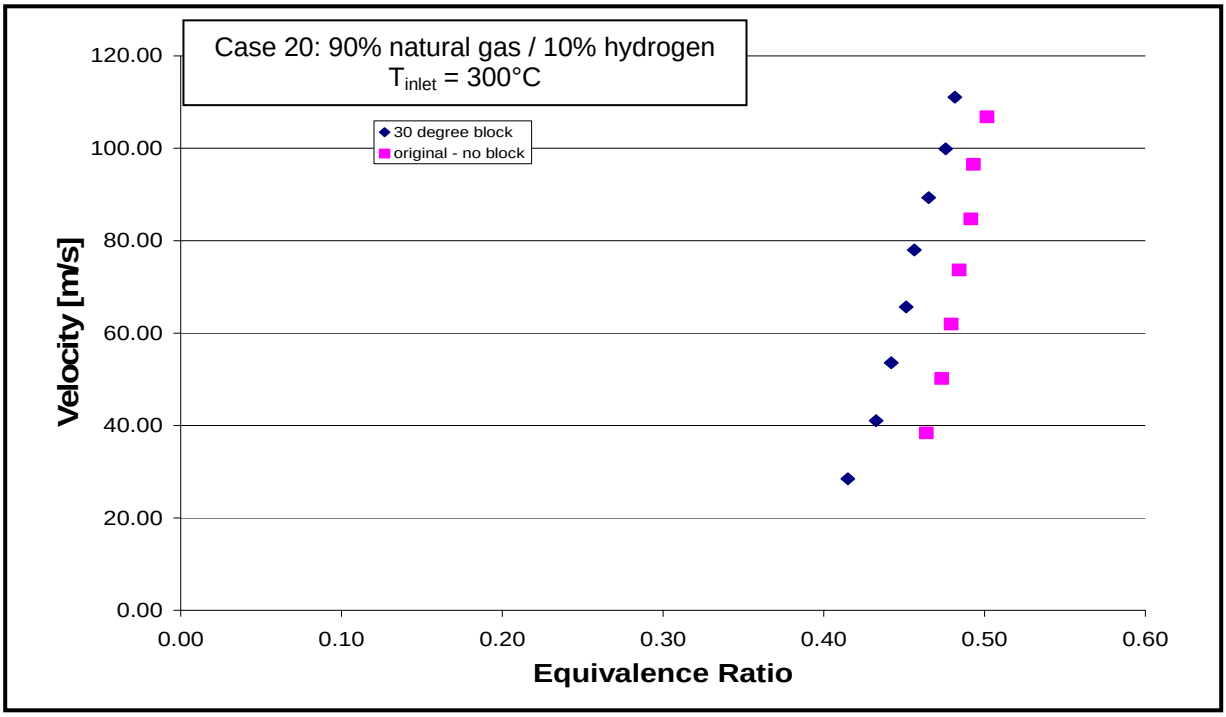

Figure 9. A comparison of the velocity at lean blowout versus equivalence ratio for the case 20 operating condition with and without a 30° angled dump plane insert.

Predicting the Preferred Instability Frequency as a Function of Operating Conditions

In the progress report that was submitted one year ago, results from a study of the role of flame-vortex interactions on the stability characteristics of a lean premixed combustor were presented. This study was conducted using a unique variable length combustor which allows for the determination of the preferred instability frequency due to flame-vortex interactions as a function of operating conditions. Using measurements of the stable flame geometry as a function of operating conditions obtained using chemiluminescence imaging and an empirically estimated vortex convection time, it was demonstrated that a vortex time-lag analysis could predict the preferred instability frequency of the combustor as a function of operating conditions, and that the predicted and measured preferred instability frequencies were in good agreement. This is evidenced by the time-lag plot shown in Fig. 10. These results were presented at the 41st AIAA/ ASME/SAE/ASEE Joint Propulsion Conference in July 2005 as AIAA Paper No. 2005-4330. This work has been continued during the current reporting period through the following two efforts.

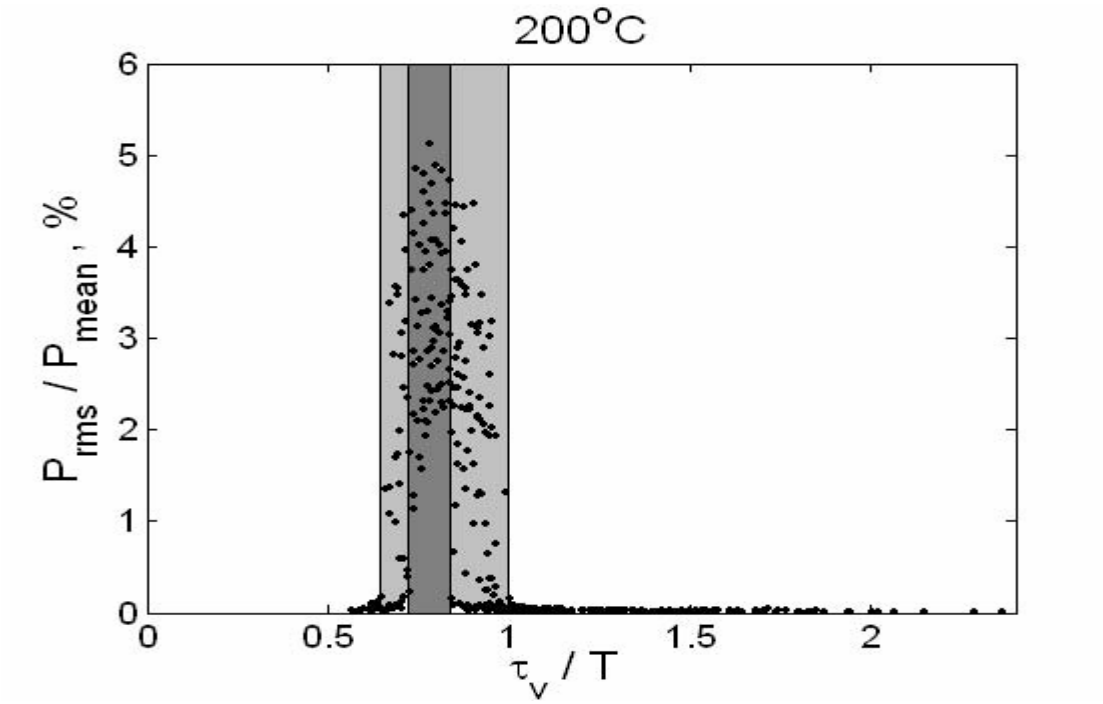

Figure 10. Time-lag analysis of flame-vortex driven instabilities.

One of the main goals of this research is to develop an understanding of the effects of fuel composition on the stability characteristics of lean premixed combustors and to use that understanding to support the development of phenomenological and reduced-order models for predicting the occurrence of unstable combustion as fuel composition changes. Of particular interest are syngas fuels and hydrogen. The methodology described in the previous paragraph was used to identify the preferred instability frequency of our lean premixed combustor operating on a 50% natural gas / 50% hydrogen fuel mixture. This was done by first selecting an operating condition (200°, 84m/s, ϕ = 0.7) at which the stable flame location for a 100% natural gas flame had been measured (for this case the stable flame's "center of mass" was located 71 mm from the dump plane). Then the combustor was run at the same inlet temperature and inlet velocity with a 50% natural gas / 50% hydrogen fuel and the equivalence ratio was varied until the flame location was the same as that of the 100% natural gas flame. This occurred at an equivalence ratio of 0.525. As expected the equivalence ratio required to give the same location was less with 50% natural gas / 50% hydrogen than with 100% natural gas because of the greater laminar flame speed of hydrogen. The variable length combustor was then run at this operating condition with the 50% natural gas / 50% hydrogen fuel at an equivalence ratio of 0.525. The results are plotted in Fig. 11,

for both the 50% natural gas / 50% hydrogen fuel and the 100% natural gas fuel. As shown, the preferred instability is the same for both fuels at there respective operating conditions.

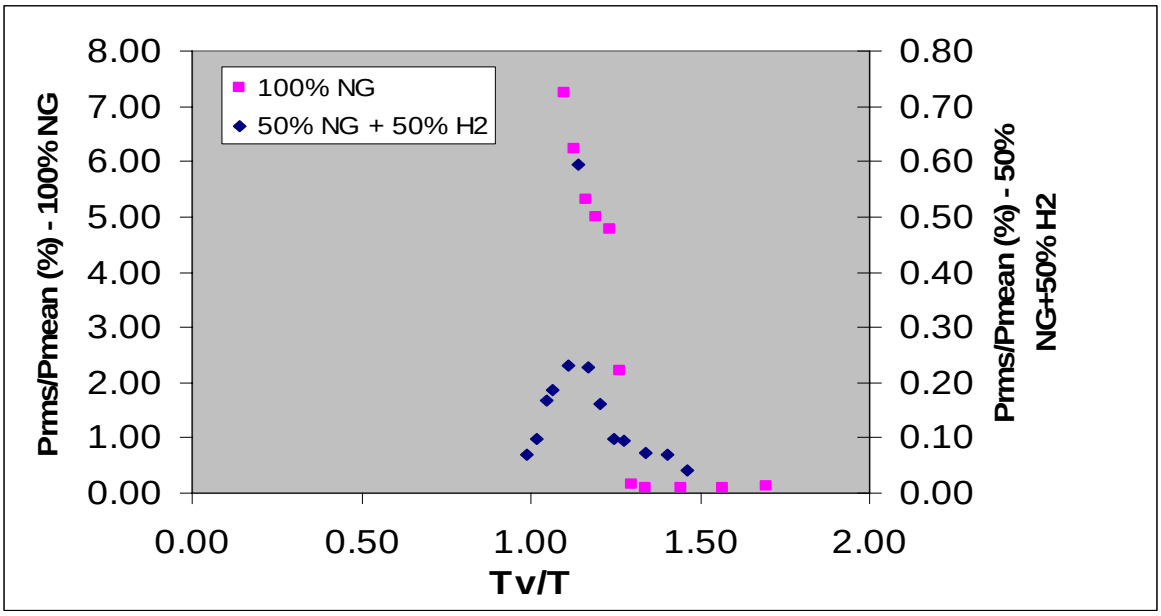

Figure 11. Preferred instability frequency measurements for natural gas and 50%natural gas/50% hydrogen flames having the same flame location.

The results presented in Fig. 11 show that the preferred instability frequency at different operating conditions and with different fuels can be predicted if the flame location and the vortex convection time are known (in this particular case the vortex convection time was kept constant by keeping the inlet velocity constant). Obtaining this information experimentally is very time consuming and is extremely difficult to do in real combustors. An alternative and simpler approach is to calculate the flame location and vortex convection velocity. Because these calculations are for stable flames, they are well within the capabilities of a number of commercially available codes. An effort has been initiated during this reporting period to use FLUENT to obtain this information. Preliminary results are show in Fig. 12 which is a two-dimension plot of the reaction rate, which is shown in pseudo-color (red is high and blue is low). Since this is an axisymmetric calculation, only the upper half of the combustor is shown. The results shown in Fig. 12 are for an inlet temperature of 500K, and an equivalence ratio of 0.7. The upper figure is for an inlet velocity of 84 m/s and the lower is for an inlet velocity of 21 m/s. Although these results are qualitatively similar to those

obtained experimentally using two-dimensional chemiluminescence imaging, there are significant quantitative differences. This work will continue through the remaining six months of this project.

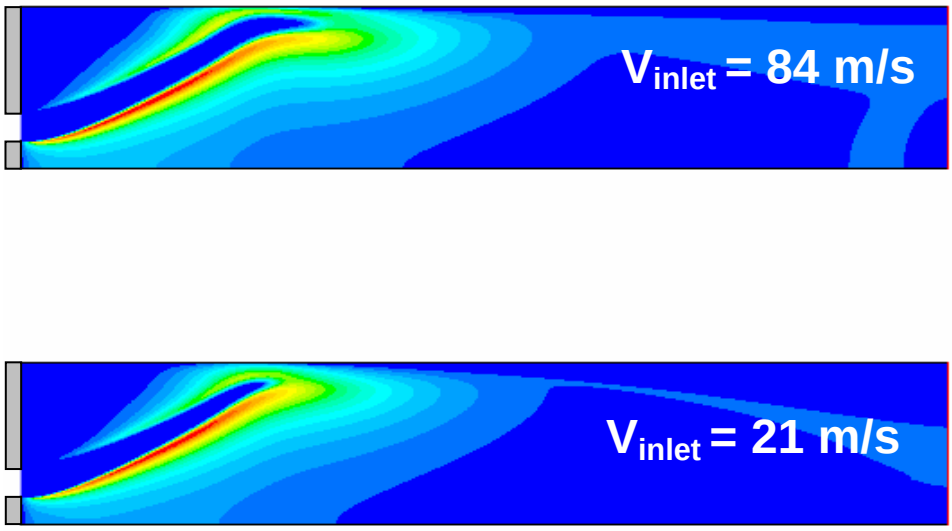

Figure 12. Fluent calculations of the reaction rate.

Conclusions

Results are presented in this semi-annual report from the first half of the third year of this three-year program. These results are from continuing studies of the effects of the dump plane recirculation zone on lean blow out and of the role of flame-vortex interactions during unstable combustion

In the lean blowout study, previously reported results have indicated that combustion in the dump plane recirculation zone plays an important role in determining the lean blowout limit. During the current reporting period the use of an angled dump plane to alter the dump plane recirculation zone and thereby lean blowout was investigated. Preliminary results with a 30° angled dump plane insert suggest that the lean blowout limit might be improved with the insert,

particularly with hydrogen/natural gas fuels. In the instability study, previously reported results have shown that a vortex time-lag model can be used to predict the preferred instability frequency as a function of operating conditions from measurements of the stable flame location. During the current reporting period, preliminary testing has demonstrated that this method of predicting the preferred instability frequency can be extended to predicting the effects of fuel composition changes on stability characteristics. Work has also been initiated using FLUENT to predict the stable flame location as a function of operating conditions. This will make it possible to predict stability characteristics without measuring the flame location.

References

None

Appendix A: Test matrix for lean blowout experiments.

Case	Swirl	Inlet Temp	% Nat Gas	% H_2	% CO
1	30°	200°C	100	0	0
2	30°	300°C	100	0	0
3	30°	400°C	100	0	0
4	30°	200°C	90	10	0
5	30°	200°C	75	25	0
6	30°	200°C	60	40	0
7	30°	200°C	45	55	0
8	30°	200°C	30	70	0
9	30°	200°C	15	85	0
10	30°	200°C	0	100	0
11	30°	200°C	45	45	10
12	30°	200°C	45	35	20
13	30°	200°C	45	25	30
14	30°	200°C	30	60	10
15	30°	200°C	30	50	20
16	30°	200°C	30	40	30
17	30°	200°C	15	75	10
18	30°	200°C	15	65	20
19	30°	200°C	15	55	30
20	30°	300°C	90	10	0
21	30°	300°C	75	25	0
22	30°	300°C	60	40	0
23	30°	300°C	45	55	0
24	30°	300°C	30	70	0
25	30°	300°C	15	85	0
26	30°	300°C	0	100	0
27	30°	300°C	45	45	10
28	30°	300°C	45	35	20
29	30°	300°C	45	25	30
30	30°	300°C	30	60	10
31	30°	300°C	30	50	20
32	30°	300°C	30	40	30
33	30°	300°C	15	75	10
34	30°	300°C	15	65	20
35	30°	300°C	15	55	30
36	30°	375°C	90	10	0
37	30°	375°C	75	25	0
38	30°	375°C	60	40	0
39	30°	375°C	45	55	0
40	30°	375°C	30	70	0
41	30°	375°C	15	85	0
42	30°	375°C	0	100	0
43	30°	375°C	45	45	10
44	30°	375°C	45	35	20
45	30°	375°C	45	25	30
46	30°	375°C	30	60	10
47	30°	375°C	30	50	20
48	30°	375°C	30	40	30
49	30°	375°C	15	75	10
50	30°	375°C	15	65	20
51	30°	375°C	15	55	30

Table 1. Test matrix for natural gas (yellow), hydrogen/natural gas (green), and hydrogen/natural gas/carbon monoxide (blue) lean blowout tests. [gray shaded cases were not tested]

Report Title: Turbine Vanes and Endwalls with Realistic Surface Conditions

Type of Report: UTSR Semi-Annual

Reporting Start Date: July 1, 2005

Reporting End Date: Jan 1, 2006

Principal Investigator: Karen A. Thole, Virginia Polytechnic Institute and State University

Co-Principal Investigator: David G. Bogard, University of Texas-Austin

Report Issue Date: March 6, 2006

DOE Award Number: DE-FC26-02NT41431

UTSR Project Number: Contract Number 03-01-SR110

Submitting Organizations:

VT Experimental and Computational Convection Lab (VTExCCL)
Mechanical Engineering Department
Virginia Tech
Blacksburg, VA 24060
Phone: (540)231-7192
Fax: (540)231-9100

Turbulence and Turbine Cooling Research Lab (TTCRL)
Mechanical Engineering Department
University of Texas
Austin, TX 78712
(512)471-3128
(512)471-8727

Disclaimer

"This report was prepared as an account of work sponsored by an agency of the United States Government. Neither the United States Government nor any agency thereof, nor any of their employees, makes any warranty, express or implied, or assumes any legal liability or responsibility for the accuracy, completeness, or usefulness of any information, apparatus, product, or process disclosed, or represents that its use would not infringe privately owned rights. Reference herein to any specific commercial product, process, or service by trade name, trademark, manufacturer, or otherwise does not necessarily constitute or imply its endorsement, recommendation, or favoring by the United States Government or any agency thereof. The views and opinions of authors expressed herein do not necessarily state or reflect those of the United States Government or any agency thereof."

Abstract

This document reports on the progress of our research program that addresses issues relevant to gas turbine engine service that are directly linked to the part life for turbine airfoils. The focus of our study is to evaluate film cooling performance under realistic operating conditions including surface roughness, cooling hole blockage, particle deposition, erosion, and repeated applications of thermal barrier coatings (TBC). Deposits are formed on the endwall and vane surfaces when the molten contaminants in the mainstream gas are quenched and adhere to the surface. Although experiments are conducted using facilities incorporating simulated first vanes and endwalls, these results will have general applicability in the turbine section. This work is particularly relevant for syngas operations, as well, given the particulates present in the coolant.

Another aspect of the research is concerned with the geometric characteristic of a real turbine endwall that contains a gap (mid-passage gap) in the passage where two adjacent vanes are mated together and at the intersection of the combustor and turbine sections (upstream slot). In addition to being a path for coolant leakage, these gap sizes expand or contract as the turbine goes through operational cycles. To accurately predict turbine component life, it is necessary to quantify the effects of thermal expansion and contraction through the evaluation of the combustor-to-turbine gap leakage on the resulting adiabatic effectiveness levels on the endwall of the first vane.

Results thus far indicate that endwall deposition, film-cooling hole blockage, and TBC spallation have a very dramatic effect on film-cooling effectiveness with the hole blockage causing the most severe reduction in effectiveness. Also, results indicate that deposits formed near the endwall trailing edge film-cooling holes have a more severe effect on film-cooling effectiveness than the deposits formed near the endwall leading edge. Testing of the shallow, transverse trench concept on the vane showed that transverse trench can improve film cooling performance dramatically. Furthermore, with a transverse trench installed, the vane film cooling performance was less susceptible to effects of the obstructions near the coolant holes.

Table of Contents

Executive Summary 1

Project Description 4

Experimental Facilities and Methods 4

Results and Discussion 6

Conclusions 25

References 25

Nomenclature 26

Tables and Figures 28

List of Tables

Table 5.1 Test Matrix for Deposition at the Leading Edge

Table 5.2 Test Matrix for Deposition on Pressure Side

Table 8.1. Completed Tests for Roughness and Obstructions Study

Table 10.1. Experimental program for study of shallow trench configurations with a smooth surface.

List of Figures

Figure 5.1. Illustrates a) leading edge deposition b) deposition along the pressure side of the vane and c) orientation of deposits with respect to the film-cooling row.

Figure 5.2. Contour of adiabatic effectiveness for the baseline case without any deposition with coolant mass flowrates of 0.75 percent through the upstream slot, 0.5 percent through the film-cooling holes, and 0.2 percent through the mid-passage gap.

Figure 5.3. Effectiveness contours comparing the effects of different deposit heights at the leading edge stagnation region with deposit placed upstream of the cooling row.

Figure 5.4. Ratio of laterally averaged effectiveness due to different deposit heights at the upstream location with upstream slot coolant mass flowrates of a) 0.75 percent and b) 0.85 percent

Figure 5.5. Effectiveness contours comparing the effects of different deposit heights at the leading edge stagnation region with deposit placed on either side of the film-cooling row.

Figure 5.6. Augmentation of laterally averaged effectiveness downstream of the leading edge row (marked region in Figure 5.5) due to deposits of different heights placed on either side of the film-cooling row.

Figure 5.7. Effectiveness contours comparing the effect of placing a 0.5D deposit at a) downstream, b) upstream and c) on both sides of the film-cooling row.

Figure 5.8. Augmentation of laterally averaged effectiveness downstream of the leading edge cooling row (marked region in figure 5.7) due to deposits placed at different locations along the cooling row.

Figure 5.9. Effectiveness contours comparing the effect of upstream deposition at the leading edge with upstream slot coolant flow rate of a) 0.75 percent, b) 0.85 percent, and c) 1.0 percent.

Figure 5.10. Adiabatic effectiveness laterally averaged pitchwise downstream of the leading edge cooling row (marked region in figure 5.9) with upstream deposition.

Figure 5.11. Effectiveness contours comparing the effect of downstream deposition at the leading edge with upstream slot coolant flow rate of a) 0.75 percent, b) 0.85 percent, and c) 1.0 percent.

Figure 5.12. Adiabatic effectiveness laterally averaged pitchwise downstream of the leading edge cooling row (marked region in figure 5.11) with downstream deposition.

Figure 5.13. Effectiveness contours comparing the effect of deposition on either side of the cooling row at the leading edge with upstream slot coolant flow rate of a) 0.75 percent, b) 0.85 percent, and c) 1.0 percent.

Figure 5.14. Adiabatic effectiveness laterally averaged pitchwise downstream of the leading edge cooling row (marked region in figure 5.13) with deposition on both sides of the cooling row.

Figure 5.15. Effectiveness contours comparing the effect of downstream deposition at the leading edge with upstream slot coolant flow rate of a) 0.75 percent, b) 0.85 percent, and c) 1.0 percent.

Figure 5.16. Effectiveness contours comparing the effect of upstream deposition at the leading edge with upstream slot coolant flow rate of a) 0.75 percent, b) 0.85 percent, and c) 1.0 percent.

Figure 5.17. Effectiveness contours comparing the effect of deposition on either side of the cooling row at the leading edge with upstream slot coolant flow rate of a) 0.75 percent, b) 0.85 percent, and c) 1.0 percent.
Figure 5.18. . Effectiveness contours comparing the effect of downstream deposition at the leading edge with upstream slot coolant flow rate of a) 0.75 percent, b) 0.85 percent, and c) 1.0 percent.

Figure 5.19. . Effectiveness contours comparing the effect of upstream deposition at the leading edge with upstream slot coolant flow rate of a) 0.75 percent, b) 0.85 percent, and c) 1.0 percent.

Figure 5.20. Effectiveness contours comparing the effect of deposition on either side of the cooling row at the leading edge with upstream slot coolant flow rate of a) 0.75 percent, b) 0.85 percent, and c) 1.0 percent.

Figure 5.42. Adiabatic effectiveness contours with 0.8D deposition upstream of row 2 film-cooling holes with coolant mass flowrates of a) 0.5 percent and b) 0.9 percent.

Figure 5.21. Effectiveness contours showing the effect of deposition at the leading edge between the stagnation regions of the two vanes for deposit heights of a) 0.5D, b) 0.8D, and c) 1.2D.

Figure 5.22. Effectiveness contours showing the effect of 1.2D deposition at the leading edge with deposit placed at a) downstream, b) upstream, and c) on both sides of the cooling row.

Figure 5.23. Effectiveness contours showing the effect of deposition along the pressure side with deposit placed at a) downstream, b) upstream, and c) on both sides of the cooling rows.

Figure 5.24. Adiabatic effectiveness laterally averaged streamwise along the pressure side cooling rows (marked region) with deposition at downstream, upstream, and on both sides of the cooling rows.

Figure 5.25. Adiabatic effectiveness contours with 0.8D deposition along the pressure side film-cooling holes with film-cooling flowrates of a) 0.5 percent, b) 0.75 percent, and c) 0.9 percent.

Figure 5.26. Change in adiabatic effectiveness levels along streamlines S1 and S2 (refer Figure 5.2) for deposits on both sides of the cooling rows.

Figure 5.27. Adiabatic effectiveness contours showing the effect of sequentially increasing the number of row deposits from row 1 to row 4 along the pressure side film-cooling holes.

Figure 5.28. Change in adiabatic effectiveness levels along streamlines S1 and S2 (refer Figure 5.2) caused by sequential increment of deposits from row 1 to row 4.

Figure 5.29. Adiabatic effectiveness contours showing the effect of single row deposits along the pressure side film-cooling holes.

Figure 5.30. Change in adiabatic effectiveness levels along streamlines S1 and S2 (refer Figure 5.2) caused by single row deposition from row 1 to row4.

Figure 5.31. Adiabatic effectiveness contours showing the effect of single row deposits along the pressure side film-cooling holes for a film-cooling mass flowrate of 0.9 percent.

Figure 5.32. Adiabatic effectiveness contours showing the effect of multiple row deposits along the pressure side film-cooling holes for a film-cooling mass flowrate of 0.75 percent.

Figure 5.33. Adiabatic effectiveness contours showing the effect of multiple row deposits along the pressure side film-cooling holes for a film-cooling mass flowrate of 0.9 percent.

Figure 5.34. Adiabatic effectiveness contours with 0.8D deposition downstream of row 1 film-cooling holes with coolant mass flowrates of a) 0.5 percent, b) 0.75 percent, and c) 0.9 percent.
Figure 5.35. Adiabatic effectiveness contours with 0.8D deposition downstream of row 2 film-cooling holes with coolant mass flowrates of a) 0.5 percent and b) 0.9 percent.

Figure 5.36. Adiabatic effectiveness contours with 0.8D deposition downstream of row 3 film-cooling holes with coolant mass flowrates of a) 0.5 percent and b) 0.9 percent.

Figure 5.37. Adiabatic effectiveness contours with 0.8D deposition downstream of row 4 film-cooling holes with coolant mass flowrates of a) 0.5 percent and b) 0.9 percent.

Figure 5.38. Adiabatic effectiveness contours with 0.8D deposition downstream of row 1 and 2 film-cooling holes with coolant mass flowrates of a) 0.5 percent, b) 0.75 percent and c) 0.9 percent.

Figure 5.39. Adiabatic effectiveness contours with 0.8D deposition downstream of row 1, 2 and 3 film-cooling holes with coolant mass flowrates of a) 0.5 percent, b) 0.75 percent and c) 0.9 percent.

Figure 5.40. Adiabatic effectiveness contours with 0.8D deposition downstream of all four rows of film-cooling holes with coolant mass flowrates of a) 0.5 percent, b) 0.75 percent and c) 0.9 percent.

Figure 5.41. Adiabatic effectiveness contours with 0.8D deposition upstream of row 1 film-cooling holes with coolant mass flowrates of a) 0.5 percent, b) 0.75 percent, and c) 0.9 percent.

Figure 5.43. Adiabatic effectiveness contours with 0.8D deposition upstream of row 3 film-cooling holes with coolant mass flowrates of a) 0.5 percent and b) 0.9 percent.

Figure 5.44. Adiabatic effectiveness contours with 0.8D deposition upstream of row 4 film-cooling holes with coolant mass flowrates of a) 0.5 percent and b) 0.9 percent.

Figure 5.45. Adiabatic effectiveness contours with 0.8D deposition upstream of row 1 and 2 film-cooling holes with coolant mass flowrates of a) 0.5 percent, b) 0.75percent and c) 0.9 percent.

Figure 5.46. Adiabatic effectiveness contours with 0.8D deposition upstream of row 1, 2, and 3 film-cooling holes with coolant mass flowrates of a) 0.5 percent, b) 0.75 percent and c) 0.9 percent.

Figure 5.47. Adiabatic effectiveness contours with 0.8D deposition upstream of all four rows of film-cooling holes with coolant mass flowrates of a) 0.5 percent, b) 0.75 percent and c) 0.9 percent.

Figure 6.1. Illustration showing a) the present film-cooling hole geometry and b) film-cooling holes placed in transverse slots to be tested.

Figure 6.2. Illustration of placing deposits at a) downstream, b) upstream, and c) on both sides of a transverse slot geometry.

Figure 8.1. Representative in-test repeatability test for the baseline case at a blowing ratio of M = 0.7.

Figure 8.2. Representative test-to-test repeatability test for the baseline case.

Figure 8.3. Spatially averaged effectiveness plot of the baseline case and the baseline case with the addition of roughness.

Figure 8.4. Laterally averaged effectiveness plot of the baseline case and the baseline case with a rough wall.

Figure 9.1. Schematic of Shape #2 obstruction places upstream and downstream of the coolant hole.

Figure 9.2. Laterally averaged effectiveness plot of the baseline case demonstrating the similar performance for low and high mainstream turbulence.

Figure 9.3. Laterally averaged effectiveness plot of the baseline case and the baseline case with upstream obstructions.

Figure 9.4. Laterally averaged effectiveness plot of the baseline case and the baseline case with the addition of downstream obstructions.

Figure 9.5. Effectiveness contours of the smooth baseline case (top) and the smooth baseline case with downstream obstructions (bottom) at M=0.6.

Figure 9.6. Laterally averaged effectiveness plot of the baseline case and the baseline case with the addition of upstream and downstream obstructions.

Figure 9.7. Spatially averaged effectiveness plot of the baseline case with and without obstructions.

Figure 9.8. Spatially averaged effectiveness plot of the baseline case with a rough wall and the baseline case with the addition of obstructions on a rough wall.

Figure 10.1. Schematic of test vane.

Figure 10.2. Baseline axial hole configuration.

Figure 10.3. Coordinate origin for trench configurations.

Figure 10.4. Schematic of shallow trench configurations.

Figure 10.5. Comparison of laterally averaged adiabatic effectiveness for all trench configurations tested, M = 1.0, Tu_∞ = 1.0%

Figure 10.6 (a) Spatial adiabatic effectiveness distribution for baseline axial holes, M = 1.0, Tu = 1.0%

Figure 10.6 (b) Spatial adiabatic effectiveness distribution for Configuration 2, M = 1.0, Tu = 1.0%

Figure 10.6 (c) Spatial adiabatic effectiveness distribution for Configuration 3, M = 1.0, Tu = 1.0%

Figure 10.6 (d) Spatial adiabatic effectiveness distribution for Configuration 4, M = 1.0, Tu = 1.0%

Figure 10.6 (e) Spatial adiabatic effectiveness distribution for Configuration 5, M = 1.0, Tu = 1.0%

Figure 10.6 (f) Spatial adiabatic effectiveness distribution for Configuration 6, M = 1.0, Tu = 1.0%

Figure 10.6 (g) Spatial adiabatic effectiveness distribution for Configuration 7, M = 1.0, Tu = 1.0%

Figure 10.6 (h) Spatial adiabatic effectiveness distribution for Configuration 8, M = 1.0, Tu = 1.0%

Figure 10.6 (i) Spatial adiabatic effectiveness distribution for Configuration 9, M = 1.0, Tu = 1.0%

Figure 10.6 (j) Spatial adiabatic effectiveness distribution for Configuration 2\10, M = 1.0, Tu = 1.0%

Figure 10.7. Laterally averaged adiabatic effectiveness for axial holes embedded in the narrow trench configuration, p/d = 2.8, and Tu = 3.9%

Figure 10.8. Laterally averaged adiabatic effectiveness for axial holes embedded in a narrow trench configuration, p/d = 8, Tu = 1.0%

Figure 10.9. Spatially averaged adiabatic effectiveness (x/d = 0 to 25) for low and high mainstream turbulence levels.

Figure 10.10. Spatial adiabatic effectiveness distribution for narrow trench configuration, (a) M = 0.4 and (b) M = 1.95.

Figure 10.11. Comparison adiabatic effectiveness at density ratios of DR = 1.3 and 15 using the narrow trench configuration, Tu = 3.9%.

Figure 10.12. Comparison of spatially averaged adiabatic effectiveness for narrow and wide trench configurations (Configurations 2 and 10). For reference, the baseline axial hole configuration is also presented.

Figure 10.13. Comparison of baseline axial hole and narrow trench configurations, Tu = 3.9%

Figure 10.14. Lateral profiles at x/d = 2, with M = 1.0, Tu = 1.0% for (a) axial holes and (b) narrow trench configurations.

Figure 10.15. Comparison of the narrow trench configuration to shaped hole configurations.

Figure 10.16. Laterally averaged effectiveness plot of the narrow transverse trench case and the narrow transverse trench case with a rough wall.

Figure 11.1. Spatially averaged effectiveness for a rough surface with a narrow transverse trench without and with obstructions.

Figure 11.2. Spatially averaged effectiveness plot of the baseline case with obstructions on a rough wall and the narrow transverse trench case with obstructions on a rough wall.

Figure 11.3. Laterally averaged effectiveness plot of the narrow transverse trench case and the narrow transverse trench case with the addition of upstream obstructions.

Figure 11.4. Laterally averaged effectiveness plot of the narrow transverse trench case and the narrow transverse trench case with the addition of downstream obstructions.

Figure 11.5. Laterally averaged effectiveness plot of the narrow transverse trench case and the narrow transverse trench case with the addition of upstream + downstream obstructions.

Figure 11.6. Laterally averaged effectiveness plot of the baseline case with upstream obstructions and the narrow transverse trench case with upstream obstructions.

Figure 11.7. Laterally averaged effectiveness plot of the baseline case with downstream obstructions and the narrow transverse trench case with downstream obstructions.

Figure 11.8. Laterally averaged effectiveness plot of the baseline case with upstream + downstream obstructions and the narrow transverse trench case with upstream + downstream obstructions.

Executive Summary

Task 1 Planning Meetings.

Task is ongoing between Virginia Tech and the University of Texas when necessary.

Task 2 Determination of Appropriate Simulation of Hole Distortion.

Based on the interactions between Virginia Tech, UT-Austin and our Industrial Partners a test matrix was designed to simulate endwall deposition, film-cooling hole blockage and TBC spallation

Summary of Results for Specific Tasks at Virginia Tech

Task 3 Modify previous test configuration and conduct endwall cooling performance tests – with holes, upstream and passage gutter flows

Completed and previously reported

Task 4 Simulate a rough endwall and conduct cooling performance tests

Completed and previously reported

Task 5 Simulate blocked film-cooling holes on a rough endwall and conduct cooling performance tests

Tests were carried out to simulate a distorted endwall condition with: surface depositions at the leading edge and along the pressure side, film-cooling hole blockage at the leading edge, and TBC spallation. A total of 130 tests were carried out to study the effect of endwall distortion on film-cooling. Tests were carried out for three different deposition heights and three different flow rates through the upstream slot and film-cooling holes by keeping the mass flowrate through the mid-passage constant. Previously reported results indicate that these distortions dramatically decrease the film-cooling effectiveness, with hole blockage causing the most severe effect on cooling effectiveness. Along the pressure side, deposition upstream of film-cooling holes caused a higher degradation that downstream deposition. Results also indicate that depositions near the trailing edge of the endwall cause a greater degradation of film-cooling than deposits at the leading edge.

Task 6 Measure cooling performance with a rough endwall and cooling holes placed in the upstream and passage gutter

In the previous report, tests were carried out to quantify the effects of thermal expansion and contraction of the combustor-to-turbine gap. This task was completed by studying the effect of upstream slot width on the endwall cooling effectiveness. Tests were also carried out to study the effect of coolant leakage through the mid-passage gap on endwall effectiveness. Further tests to study cooling performance will be carried out by placing film-cooling holes in transverse slots in the upstream slot location and also on the endwall. Adiabatic effectiveness, flowfield, and thermal field

measurements will be carried out for this geometry. Also, based on our discussions with our industrial partners it was concluded that measurement of heat transfer coefficients on a rough and smooth endwall surface and also along the mid-passage gap will help better understand the effect of surface roughness on turbine part life.

Task 7 **Measure cooling performance with a rough endwall and partially blocked cooling holes placed in the upstream and passage gutter**

Previous results indicated that partially blocking film-cooling holes on the endwall resulted in severely degrading the cooling effectiveness levels. Based on those results it is speculated that partially blocking film-cooling holes placed in transverse slots will lower the effectiveness levels and hence these tests will not be repeated for the transverse slot geometry.

Summary of Results for Specific Tasks at the University of Texas

Task 8 **Roughness effects on film cooling over full vane**

Surface roughness effects on the film cooling performance on the downstream part of the suction side of a vane were studied. These tests complemented previous studies of the surface roughness effects on film cooling adiabatic effectiveness on forward part of the suction side and the pressure side of the vane. Results from measurements following the second row of holes on the suction side of the vane showed a significant degradation of adiabatic effectiveness at blowing ratios for which maximum performance was obtained.

Task 9 **Film cooling performance with distorted coolant holes**

Further measurements of the effects of obstructions on film cooling performance were completed. For these studies we examined effects of obstruction upstream, downstream, and both upstream and downstream of the second row of holes on the suction side of the vane. These tests were conducted with smooth and rough surfaces and with low and high mainstream turbulence levels. In all cases, obstructions upstream of the coolant holes caused a significant degradation film effectiveness, but obstructions downstream of the coolant holes in some cases caused an increase in film effectiveness.

Task 10 **Effect of a transverse trench on film cooling performance**

Nine different configurations for shallow, transverse trenches were tested to determine whether these trenches would improve film effectiveness. Three of the nine configurations were found to cause significant improvements in film effectiveness, particularly at high blowing ratios. The common characteristic of the high performance trenches was location of the downstream edge of the trench at the immediate edge of the coolant holes. The optimum narrow trench configuration was found to have performance similar to shaped holes.

Task 11 Effect of a transverse trench on film cooling with distorted holes

The optimum transverse trench was tested with obstructions upstream, downstream, and both upstream and downstream of the second row of holes on the suction side of the vane. These tests were conducted with smooth and rough surfaces and with low and high mainstream turbulence levels. The tests showed that although obstructions still degraded the film effectiveness, the level of degradation was much less with the trench installed.

Industrial Contact

Pratt & Whitney visited Virginia Tech twice during the past six months and Dr. Karen Thole visited SIEMENS as part of industry interaction. Dr. David Bogard reviewed the results of the study of the transverse trench with representatives of General Electric Global Research.

Project Description

Given the huge number of sustained operational hours required for industrial turbines, two important issues are part life and overall engine performance. Engine performance is highly dependent on the turbine and, in particular, airfoil life. Over time, airfoil roughness and film-cooling hole blockage on the airfoil and endwall, which are due to combinations of particle deposition and repeated TBC applications, can lead to reduced engine performance. While there have been numerous film-cooling and roughness studies in laboratory environments, there has been a lack of studies in which realistic coolant hole distortions have been simulated. Moreover, there have been no reported studies on a film-cooled endwall surface with roughness. These roughness and blockage effects are very important to understand, particularly when trying to assess film cooling performance for an extensive component life.

In the proposed research program, we are investigating the potential of using slots overlying the coolant holes to improve film cooling performance, or at least to alleviate the degradation of film cooling performance when the surface becomes contaminated with depositions of foreign material. For the realistic surface conditions that we are proposing to study here, the slots may have the additional benefit of alleviating the effects of hole contamination. Furthermore, for the endwall, inherent interface gaps in the endwall might be modified to operate as coolant-fed slots in the wall. These possibilities will be investigated in the proposed research program.

Experimental Facilities and Methods

Two existing large-scale, linear vane cascades were used for this research and have been described in detail in previous reports. Studies on the vane endwall are being conducted at Virginia Tech, and studies on the vane itself are being conducted at the University of Texas. Both facilities incorporate linear cascades with the same large scale (9x) vane geometry, and have the capability of generating high mainstream turbulence of varying levels and length scales. The spatial detail obtained with these large scale facilities is crucial for showing the physical characteristics of coolant jet interactions and dispersion, and for validation of CFD predictions. Numerous studies of film cooling performance on the turbine vane and secondary flow effects on the endwall heat transfer, which have been completed in these facilities over the past several of years, serve as benchmark baselines for evaluating the changes in performance caused by the realistic surface

conditions. Particular emphasis is placed on detailed velocity field and thermal field measurements. Infrared imaging of the surface temperatures is the primary means of quantifying effects on the surface heat load and film cooling performance on the vane and endwall.

Modifications to the endwall geometry were made for Virginia Tech studies to include a gutter passage, in the mid-passage between the two vanes, and the provision for a rough endwall. To simulate the effects of changing upstream slot areas, provisions were made to adjust the flow area of the upstream slot. To simulate roughness, large sheets of sandpaper were cut with the contour of the vane with provisions for the film-cooling holes. The sandpaper was attached to the endwall surface with double sided tape. To simulate the deposition, erosion, and blockage, the endwall sandpaper was modified accordingly.

For the surface roughness studies on the simulated vane, adiabatic effectiveness and heat transfer coefficient measurements were made using techniques described in previous reports. Thermal field measurements will be made downstream of the pressure side cooling holes on the endwall in the next reporting period. A special thermocouple probe made of 1-mil thermocouple wire will be used for these measurements. Because of the very large temperature gradients at the exit of the coolant holes, very small thermocouple wires are needed to minimize conduction errors. This probe was shown to have negligible conduction error in a previous study in the UT laboratory (Terrell, 2004).

Results and Discussion

This section of the report discusses the results that have been achieved thus far in the project. This section is organized with respect to the various tasks that were initially proposed for the project.

Specific Tasks at Virginia Tech

Task 2. Determination of appropriate simulation of hole distortion

Completed and previously reported.

Task 3. Modify previous test configuration and conduct endwall cooling performance tests – with holes, upstream and passage gutter flows

Completed and previously reported.

Task 4. Simulate a rough endwall and conduct cooling performance tests

Completed and previously reported.

Task 5. Simulate blocked film-cooling holes on a rough endwall and conduct cooling performance tests

In the previous report (Jan-July05) the effects of varying the deposit height downstream of a cooling row at the leading edge stagnation region was discussed. Results of film-cooling hole blockage and TBC spallation at the leading edge region were also reported. This report primarily focuses on a detailed study of deposition at different locations along the leading edge film-cooling rows and also along the pressure side cooling rows as shown in Figure 5.1a-b. Deposits of varying heights were placed downstream (previously reported), upstream and on both sides of the cooling rows (refer Table 5.1). Both sides refer to placing deposits both downstream and upstream of the cooling hole rows. Figure 5.1c shows the placement of deposits with respect to the cooling rows. All results were compared to a baseline case shown in Figure 5.2. The baseline test was carried out without any deposits for nominal coolant flowrates of 0.75 percent through the upstream slot, 0.5 percent through the film-cooling holes, and 0.2 percent through the mid-passage gap.

Effect on Adiabatic Effectiveness due to Deposition along the Leading Edge Cooling Rows

As mentioned previously in the preceding report, results were presented only for the effect on adiabatic effectiveness due to variation in deposit height downstream of a cooling row near the stagnation region. Deposit of heights 0.5D, 0.8D, and 1.2D were tested at three different locations

along a cooling row: downstream, upstream, and both. For the leading edge study deposits were placed near the stagnation region of the vane and also along the cooling rows between the two stagnation location of the vanes (refer Figure 5.1a). For the leading edge study only the upstream slot flow was varied from 0.75 percent to 1.0 percent while maintaining 0.5 percent mass flow through the film-cooling holes and 0.2 percent through the mid-passage gap region. First, results of varying deposit heights on adiabatic effectiveness levels at upstream and both locations will be presented and compared to downstream deposition (previously reported). Second, the results for a 0.5D deposit at different slot flow rates and different locations will be presented. Finally, the results of placing the deposits at the leading edge cooling holes between the stagnation regions of the two vanes will be presented.

Figures 5.3a-c compare the contours of adiabatic effectiveness at the leading edge region with deposits placed upstream of the cooling row. It can be seen that with an increase in deposit height at the upstream location, the overall effectiveness downstream of the cooling row increases. These effects can be further quantified by looking at the lateral average plots shown in Figure 5.4. Effectiveness was laterally averaged across the pitch downstream of the leading edge film-cooling row as shown in Figure 5.3 (boxed region). Figure 5.4 shows the change in laterally averaged adiabatic effectiveness between the deposit cases, relative to the baseline case. Note that the values greater than one are enhancements in effectiveness levels and less than one are reductions in effectiveness levels. It can be seen that with an increase in deposit height from 0.5D to 0.8D there is a slight increase in overall effectiveness from X/C = -0.05 to X/C = 0.05. A further increase in deposit height to 1.2D increases the effectiveness levels by about 15 percent and adiabatic effectiveness ratio becomes greater than one showing an enhancement in that region. It can be seen that for all deposit heights effectiveness levels are higher between X/C = -.05 to X/C -0.025 and then decreases beyond X/C = -0.025. There is a gradual decrease from X/C > -0.025 due to jet separation caused by higher blowing ratios. A similar phenomenon was seen for higher slot mass flow rate of 0.85 percent. Later in the report it will be shown that increases in upstream slot flow rate have little to no effect on effectiveness levels in the concerned region. An exact explanation for the increase in effectiveness levels with increase in upstream deposit height will become clearer after flowfield measurements are taken at this location.

Figures 5.5a-c compare the contours of adiabatic effectiveness at the leading edge region with deposits placed on both sides of the cooling row. Similar to the downstream deposits

(previously reported), at a deposit of height 0.5D (refer Figure 5.5a) the cooling effectiveness levels were much improved. The reason for this improved cooling is attributed to the fact that the coolant impacts the raised deposit downstream as the jet is slightly separated from the wall for the baseline case. Moreover, it is speculated that a Coanda effect further contributes to the improvement, causing the coolant to move towards the endwall surface. With the increase in deposit height to 0.8D and 1.2D (refer Figure 5.5b-c), the coolant flow stagnates and is then deflected from the surface thereby reducing the cooling effectiveness relative to that of the 0.5D case.

It can be seen from Figure 5.6 that at a deposit height of 0.5D there is an overall enhancement of cooling effectiveness. The initial peak near the exit of the cooling holes is due to the obstruction and collection of the coolant flow caused by the deposit. Though there is decay in the enhancement of cooling effectiveness as the flow proceeds towards the vane-endwall junction it can be clearly seen that a deposit of height 0.5D enhances the overall cooling effectiveness. Figure 5.6 also shows that for deposits of height 0.8D and 1.2D, there is an improvement in effectiveness in the near hole region, but due to jet lift off there is a sudden decrease with reduced cooling relative to the baseline case as the coolant flows towards the vane-endwall junction.

Figures 5.7a-c show the contours of adiabatic effectiveness at downstream, upstream and on both sides of the cooling row for 0.5D deposit. It can be seen that placing deposits on both sides of the cooling row results in a combined effect of upstream and downstream deposition. This can be further quantified by looking at the lateral average plots shown in Figure 5.8, which shows that, the both configuration has higher adiabatic effectiveness levels than the downstream configuration till the stagnation region and then decreases similar to downstream deposition.

As previously reported for downstream deposition , increases in upstream slot flow rate had no effect on adiabatic effectiveness levels downstream of the leading edge cooling row near the stagnation region. Figures 5.9a-c compare the contours of adiabatic effectiveness with deposit placed upstream of the cooling row for different upstream slot flow rates. It can be seen that there is little to no effect on the adiabatic effectiveness levels. Figure 5.10 shows that the laterally averaged adiabatic effectiveness levels for the three slot flowrates are very similar. Figures 5.11-5.14 show similar results for deposits placed downstream and on both sides of the cooling row.

Figures 5.15-5.20 show the contours of adiabatic effectiveness for deposit of heights 0.8D and 1.2D respectively for different slot flow rates and deposit locations. The trends with increase in flow rate and change in deposit location for these deposit heights were found similar to the 0.5D

deposit.

Figures 5.21a-c compare the contour of adiabatic effectiveness for deposits placed along cooling rows between the stagnation regions of the vane, as indicated by the black lines. It can be seen that by placing deposits upstream of the cooling holes there is a localized reduction in effectiveness levels midway along the length of the mid-passage gap (see circled region in Figure 5.21). This effect intensifies with the increase in deposit height and there is higher reduction in effectiveness levels at 1.2D than at 0.8D or 0.5D.

This effect was seen irrespective of the location of the deposit, that is if the deposit was placed at downstream, upstream or on both sides of the cooling row. This can be seen by comparing the contours of adiabatic effectiveness levels in Figure 5.22a-c (see circled regions). It was also observed that the effectiveness levels in this region increased with increase in upstream slot flowrate.

Effects on Adiabatic Effectiveness due to Endwall Deposits on Vane Pressure Side Cooling Holes

In these studies, the effects of single and multiple row depositions along the pressure side on endwall adiabatic effectiveness will be presented. In this region, studies were carried out with a deposit of constant height 0.8D and width 2D. Deposits were placed upstream and downstream of the cooling row as well as at both locations simultaneously (refer table 5.2). First, the effect on multiple row deposition on effectiveness will be presented with a discussion on the behavior of multiple deposits at higher blowing ratios. Second, the effect of sequentially increasing the number of row deposits on adiabatic effectiveness will be discussed. Finally, the results of effect of individual row deposits on cooling effectiveness will be discussed.

During gas turbine operation contaminants in the main flow convects toward the pressure side and adheres on to the endwall. The basis for this study was to understand whether deposits formed in the upstream or downstream locations of the cooling rows has a more detrimental effect on pressure side cooling effectiveness. Deposits were placed on the first four cooling rows in region B as shown in Figure 5.1b. The nominal flowrate was set at 0.75 percent through the upstream slot, 0.5 percent through the film-cooling holes, and 0.2 percent through the mid-passage gap.

Figures 5.23a-c compare the adiabatic effectiveness for a nominal flowrate with deposits downstream, upstream, and on either side of the cooling rows respectively. It was seen that by

placing deposits either on the downstream or upstream of the cooling row there is a reduction in effectiveness. The cooling effectiveness degradation caused by upstream deposit was much higher than the downstream deposit. Figure 5.24 compares the laterally averaged effectiveness along the pressure side cooling rows and it is shown that there is a dramatic decrease in average effectiveness due to deposition. Note that the averaging area and nomenclature are also shown in the box in Figure 5.24. With deposits, the laterally averaged effectiveness mid-way between film-cooling rows is of the order of 30 – 40 percent lower than the baseline case without any deposits.

In comparing the laterally averaged effectiveness for different deposit locations, it is seen from Figure 5.24 that with deposits on either side of the cooling row, the cooling effectiveness deteriorates the most along pressure side. Placing the deposit either at upstream or at both locations simultaneously brings about a similar degradation in cooling effectiveness and it is about 10 percent lower than the degradation caused by placing the deposit downstream. It is concluded that deposits placed upstream of the cooling rows were more instrumental in reducing cooling effectiveness than downstream. By placing the deposits on either side of the cooling row it was found that the coolant flow was channeled towards the endwall junction along the pressure side. Though cooling along the endwall junction improved, it degraded the cooling effectiveness at other regions on the pressure side.

Figures 5.25a-c compare the contours of adiabatic effectiveness for flowrates of 0.5 percent, 0.75 percent, and 0.9 percent through the film-cooling holes for a constant upstream slot flow of 0.75 percent and a mid-passage gap flowrate of 0.2 percent. By placing the deposit on either side of the cooling row it was found that coolant flow gets channeled towards the pressure side endwall junction. However, for the baseline case without deposits as shown in Figure 5.2 the coolant spread in the direction of the mainstream flow.

With the increase in coolant flowrate from 0.5 percent to 0.75 percent there seemed to be an increase in coolant flow along the endwall junction on the pressure side there by improving effectiveness in this region. There seemed to be little or no improvement by further increasing the flowrate to 0.9 percent as shown in Figure 5.25c.

As the coolant jets were directed towards the pressure-surface endwall junction, it was important to quantify the change in adiabatic effectiveness along flow streamlines passing through the cooling holes and also along the pressure-surface endwall junction. Figures 5.26a-b show the variation of adiabatic effectiveness along the flow streamlines at different film-cooling flowrates

with deposits placed on both sides of the cooling rows. Variation in adiabatic effectiveness was measured along two streamlines; S1 and S2 as shown in Figure 5.2. The flow streamlines were computationally predicted at 2 percent span from the endwall surface using FLUENT 6.1.2. Figure 5.26a shows that by placing deposits on both upstream and downstream locations the adiabatic effectiveness levels decreased by about 50 percent along S1 for 0.5 percent (M_{in}=1.5) film-cooling mass flowrate. A similar effect was seen for 0.75 and 0.9 percent flowrate through the film-cooling holes though there was a higher reduction at a mass flowrate of 0.9 percent. The 0.75 and 0.9 percent coolant flowrates corresponded to a global blowing ratio of [k. a.1]=2.2 and [ ]2.7 respectively. The global blowing ratio M_{in} was calculated based on the inlet mainstream velocity U_{in}.

Also, another interesting effect was observed with an increase in mass flowrate through the film-cooling holes. As shown in Figures5.25a-c (see circled region) there is a formation of hot zone mid-way along the length of the mid-passage gap with an increase in film-cooling flowrate from 0.5 percent to 0.9 percent. The reason for this could be that the coolant from the upstream slot becomes obstructed by the high mass flowrate through the leading edge film-cooling holes and thus it fails to reach further downstream into the passage. The flow obstruction from the leading edge cooling holes can be further substantiated by the formation of ripples downstream of the leading edge cooling holes on the suction side. Another possible reason, which could be attributed to this effect, is that higher mass flow rate causes jet liftoff from the endwall surface thereby lowering the overall effectiveness in this region due to film-cooling holes. It is interesting to note that this hot region corresponds to the approximate gap location where flow changes from being ingested into the gap to being ejected from the gap.

A number of tests were carried out to study the effects on adiabatic effectiveness levels caused by the increase in number of deposits along the pressure side cooling holes. This was done by sequentially increasing the number of row deposits from one (1R) to four rows (4R). Figures 5.27a-d compare the contours of adiabatic effectiveness with deposits placed on a single film-cooling row (Figure 5.27a) to four rows (Figure 5.27d). It can be seen that deposit at location 1R has very little effect on the pressure side effectiveness levels, whereas deposit configuration of 2R-4R have a substantial effect on lowering the effectiveness levels downstream of the film-cooling holes. In order to better quantify these effects the ratio of adiabatic effectiveness was plotted along streamlines S1 and S2 as shown in Figure 5.28a-b. Figure 5.28a shows that along S1 with the

increase in the number of row deposits the amount of degradation downstream of the cooling rows increases. The 4R deposits cause the maximum degradation with the 1R deposit causing the least. Figure 5.28b shows that along S2 with the increase in the number of row deposits from 4R to 1R the overall enhancement in effectiveness increases. Also, from Figure 5.28a-b it can be seen that at the location of the deposit, there is a sudden dip in effectiveness levels along S1 showing the degradation and jump in effectiveness levels along S2 which shows an overall enhancement caused by the deposits.

It is important to ascertain the region at which the formation of deposits would deteriorate film-cooling effectiveness along the pressure side. To study these effects tests were carried out by placing individual row deposits from row 1 to row 4 for film-cooling flowrates of 0.5 percent, 0.75 percent, and 0.9 percent for constant flowrates of 0.75 percent through the upstream slot and 0.2 percent through the mid-passage gap.

Figures 5.29a-d compare the adiabatic effectiveness for deposits placed on either side of the film-cooling row from row 1 to row 4 respectively, all at the same cooling flow rates. Comparisons were made for nominal flowrates of 0.75 percent through upstream slot, 0.5 percent through film-cooling hole, and 0.2 percent through mid-passage gap. It can be seen from Figure 5.29a that by placing the deposit on row 1, there was little to no effect on film-cooling downstream of the passage. But by placing the deposits on row 2 to row 4 there was significant degradation in effectiveness levels downstream towards the trailing edge as shown in Figures 5.29b-d. Figure 5.2 shows that without any endwall depositions coolant from row 3 gets attached to row 4 and to each subsequent coolant row as it flows into the passage cascading downstream. But by placing deposits on row 3 the coolant flow separates from the endwall and does not flow into row 4 and hence deteriorates film-cooling effectiveness.

Similar to the previous tests the variation in adiabatic effectiveness was measured along streamlines S1 and S2. Figure 5.30a shows that along S1, maximum amount of degradation occurs at the location where the deposit is placed. Comparing location 1R1-1R4 it can be seen that 1R1 causes the least amount of local degradation of about 20 percent whereas at locations 1R2-1R4 there is a local degradation of about 40 percent. The effectiveness ratio also increases downstream ($s/C > 0.65$) of the individual cooling row with 1R1 causing the least degradation and 1R4 causing the highest degradation. Figure 5.30b shows that along streamline S2 there is a gradual increase in effectiveness at the location where the deposit is placed. Though the effectiveness ratio levels drop

at the downstream locations, there is still an overall enhancement in cooling effectiveness along streamline S2.

Figures 31a-d similar to Figures 29a-d compare the contours of adiabatic effectiveness for single row deposits placed from row 1 to row 4 at a higher film-cooling flow rate of 0.9 percent for the both configuration. Similar to 0.5 percent, deposit along row 4 showed a higher degradation than row 1. Also, for the same deposit configuration Figures 32-33 compare multiple row deposition along the pressure side holes for higher film-cooling flow rates of 0.75 and 0.9 percent respectively.

Figures 34-37 compare single row depositions along pressure side holes with deposits placed downstream of the film-cooling row for a higher film-cooling flow rate of 0.9 percent. Figures 38-40 compare the adiabatic effectiveness contours for downstream deposition for 0.5, 0.75 and 0.9 percent film-cooling flowrates. Similar to the both configuration (deposits on either side of the film-cooling row) it was found that with the increase in the number of row deposits, cooling effectiveness levels degraded downstream of the cooling rows.

Figures 41-44 compare the adiabatic effectiveness contours for single deposit placed upstream of the film-cooling row and Figures 45-47 compare upstream multiple row deposition. It should be noted that though the amount of degradation varied between the downstream, the upstream and the both configurations, the trends in variation of adiabatic effectiveness levels were similar.

Task 6. Measure cooling performance with a rough endwall and cooling holes placed in the upstream and passage gutter

In the previous report the effect of varying the upstream slot width and inducing coolant flow through the mid-passage gap on endwall cooling effectiveness was reported. In the final reporting period from Jan-July 06 tests will be carried out to study the cooling performance by placing film-cooling holes in transverse slots on the endwall and upstream slot location based on the results achieved at UT-Austin. In addition to this, based on our interaction with our industrial partners and to better understand the effect of roughness on endwall cooling, heat transfer coefficients will be measured on a rough endwall surface and along the length of the mid-passage gap.

Figures 6.1a-b illustrates the present cooling hole geometry and the transverse hole geometry that will be tested. Based on a number of tests carried out by UT-Austin for different

transverse slot geometries on a vane surface, the geometry shown in Figure 6.1b was found to show an enhancement in film-cooling effectiveness. These tests will be carried out for film-cooling flow rates of 0.5 percent, 0.75 percent, and 0.9 percent and upstream slot coolant mass flow rates of 0.75 percent, 0.85 percent, and 1.0 percent. For all the tests that will be carried out, the leakage flowrate through the mid-passage gap will be maintained at 0.2 percent as in our previous tests. These tests will also be carried out for different slot depths.

As, previous transverse slot studies [Bunker 2002 and Lu et al. 2005] have shown an improvement in cooling, it is anticipated that similar results will be seen on an endwall. As a result of this it is important to study the effect of surface deposition with the transverse slots as shown in Figure 6.2. Also, thermal field, flowfield, and total pressure loss measurements will be carried out for these studies.

Heat Transfer Coefficient Measurements on the Endwall with Roughness

Heat transfer coefficient measurements will be carried out for the entire endwall; with and without mid-passage gap. Also, tests will be carried out to study the variation of heat transfer coefficients due to endwall surface roughness. Tests will be carried out for different roughness levels and compared with a smooth surface. Measurements will be made by covering the endwall surface with a constant heat flux foil (copper Kapton sheet) which will also simulate a smooth surface. For heat transfer coefficient measurements of a rough surface, sandpaper will be placed on the constant heat flux foil. These tests will be carried out without any film-cooling holes on the endwall surface as the holes tend to cause non-uniformities in heat flux.

Measurements will also be made along the length of the mid-passage gap, as from previous studies we found that there is sufficient hot gas ingestion into the mid-passage gap area. As there are no film-cooling holes in the gap it is important to understand the effect of hot gas ingestion into the gap. In this case, Inconel 600 foil will be used to create a constant heat flux surface along the length of the gap.

Task 7. Measure cooling performance with a rough endwall and partially blocked cooling holes placed in the upstream and passage gutter

From our results reported in the previous period (Jan 05- July 05) it was seen that partial hole blockage resulted in degrading the effectiveness by about 30 percent. It was observed that

blockage typically results in degrading the adiabatic effectiveness levels. As a result these tests will not be repeated for partially blocked film-cooling holes in the upstream slot region.

Task 8. Roughness effects on film cooling over full vane

In the July, 2005 semi-annual report roughness effects on the pressure side of the vane were reported, and previous reports described the effects on the high curvature part of the suction side of the vane. During this reporting period, roughness was placed along the downstream section of the suction side of the vane. In this region the surface curvature was mild and the pressure gradient was small. The effects of this roughness on film cooling performance were conducted on the second row of holes on the suction side located at s/C = 0.367. These tests were conducted on the new suction side hatch created for the transverse trench tests (described in detail in section on Task 10). The row tested had 30° axial holes with a spacing of $p/d = 2.8$.

A number of tests were performed to gain an understanding of what the different effects are due to a rough wall as well as obstructions and how these effects are mitigated by a transverse trench. Tests that included surface roughness, or baseline smooth conditions used for comparison, are tabulated in Tables 8.1. The effects of roughness alone are described in this section, while the effects of hole obstructions and a transverse trench are presented in sections on Tasks 9 and 10, respectively.

Validation of Film Cooling Adiabatic Effectiveness Measurements Accuracy

The principle means for establishing the uncertainty of the adiabatic effectiveness measurements was to determine the precision uncertainty using multiple repeated experiments. Each configuration within each test had a repeated test condition to check for in-test repeatability. A representative sample of this repeatability is shown in Figure 8.1. As Figure 8.1 indicates, in-test repeatability generally resulted in a very small uncertainty, with a statistical analysis providing a level of $\delta\overline{\eta} = \pm 0.0075$ for the laterally averaged adiabatic effectiveness. The in-test uncertainty was used when making comparisons among data obtained within the same test.

Test-to-test repeatability was used to establish the overall uncertainty of adiabatic effectiveness data. This technique is very reliable for establishing the precision uncertainty. Since the bias errors such as conduction losses were corrected within the precision of the measurement, the overall uncertainty of the measurements were dominated the precision uncertainty. Figure 8.2 shows a representative test-to-test repeatability result for the baseline case. Note that the baseline

case for this study is a smooth wall with no transverse trench or obstructions. The measurement uncertainty for all film effectiveness data was $\delta\overline{\eta} = 0.02$.

Effects of Surface Roughness on Film Cooling on Vane Suction Side

Roughness simulation was provided by using 36-grit sand paper which simulates the level of roughness found on typical turbine vanes that have seen extended use (Demling, 2005). For the current study, all rough surface experiments had rough surfaces both upstream and downstream of the second row of coolant holes on the suction side of the vane.

An important aspect of these tests was to understand how roughness performs on the second row of the suction side of the vane. Previous studies in this lab on the suction side were focused on the first row of holes. An overview of film cooling performance with smooth and rough surfaces is presented in terms of spatially averaged adiabatic effectiveness, $\overline{\overline{\eta}}$, in Figure 8.3. For the second row of holes, surface roughness degrades the effectiveness at lower *M*, reducing adiabatic effectiveness by as much as 30%. However, for $M > 0.9$ the effect is reversed and roughness begins to increase the adiabatic effectiveness. This occurs because the roughness mitigates the effects of coolant jet separation which occurs at higher blowing ratios.

More detail of the effect of roughness is evident in the laterally averaged effectiveness, $\overline{\eta}$, distributions presented in Figure 8.4. For $M = 0.4$ and 0.6, there was an approximate 30% degradation in film cooling effectiveness for all positions extending from the hole to 25*d* downstream of the hole. At $M = 1.2$ there was no significant change. These results are similar to the effects of surface roughness on the first row of holes on the suction side previously studied in this lab (Rutledger et al., 2006).

Task 9. Film cooling performance with distorted coolant holes

As reported in the July 2005 report, tests were conducted to determine the effects of obstructions on the suction side of a film-cooled vane using various obstruction shapes. From the study conducted by Demling (2005) and summarized in Demling et al. (2006), it was concluded that of the six shapes tested, Shape #2, which had a sharp leading edge and rounded trailing edge as seen in Figure 9.1, had the largest impact on film effectiveness. Therefore all obstruction tests analyzed in this current study were done with Shape #2 with a height of 1/2d and a base of 1/2d x

1d, and were placed just upstream or downstream of the coolant holes or trench, depending on the case being tested. The effects of obstructions were tested with smooth surfaces and rough surfaces as indicated in the listing of experiments presented in Table 8.1. All experiments were done with approach flow turbulence levels of Tu = 20% and 4%. At the second row of holes the mainstream turbulence levels were reduced to Tu = 3.9% and Tu = 1.0%, of the high and low turbulence levels, respectively. The varying mainstream turbulence levels had little effect on adiabatic effectiveness as shown in Figure 9.2 for the baseline configurations, which is representative of all configurations.

Effects of Obstructions on a Smooth Surface

In order to determine the effect of the obstructions, three configurations were tested: upstream alone, downstream alone, and combined upstream and downstream. Depending on the configuration, the obstructions have varying effects. Figure 9.3 shows the effectiveness results for upstream obstructions versus the baseline. The upstream obstructions caused degradation up to a nominal value of 60%, the worst cases being at low M. This can be attributed to two effects; one being the increase in turbulence generated by the upstream obstructions and the other being the obstructions blocking the flow of the mainstream over the cooling hole so that the mainstream is inhibited from pushing the coolant jets back down to the surface.

For the downstream obstruction case versus the baseline, shown in Figure 9.4, there were some interesting results. Immediately downstream of the coolant holes, the effectiveness was higher over the range of M tested. This can be attributed to the lateral spreading of the coolant as it flows around the obstruction as seen in the contour plot in Figure 9.5. For $M < 0.7$, the rate of decay for the obstruction case was sharp enough to drop the effectiveness below that of the baseline case by $x/d = 5$. For these low M cases, the wake generated by the downstream obstructions cause enough turbulence to disrupt the benefits of the lateral spreading of the coolant. However, for large M, it was found that the obstructions seemed to have increased the cooling effectiveness up to 110% due to this additional turbulence pulling the separated jets back to the surface.

With upstream and downstream obstructions together versus the baseline, the adiabatic effectiveness levels were very similar to the upstream alone results as shown in Figure 9.6. Distributions of $\overline{\overline{\eta}}$ presented in Figure 9.7 shows that the combined upstream and downstream configuration behaves very similar to the upstream alone for low blowing ratios, but results in a

film effectiveness level intermediate between upstream alone and downstream alone for the highest blowing ratio.

Effects of Obstructions on a Rough Surface

The effects of obstructions on film cooling performance when the airfoil surface was rough was similar to the smooth surface results as shown in terms of $\overline{\overline{\eta}}$ in Figure 9.8. The addition of the upstream obstructions to the rough surface baseline caused about 30% degradation, downstream obstructions produced about a 30% increase in adiabatic effectiveness, and the combined upstream and downstream obstructions configuration was very similar to the upstream obstruction alone configuration.

Task 10. Effect of a transverse trench on film cooling performance

A shallow transverse slot was proposed as a configuration that potentially could mitigate the deleterious effects of obstructions around coolant holes, and as a means for protecting the edges of the holes from being blocked by obstructions. Use of a transverse had been proposed by Bunker (2002) as a means of improving film cooling performance by inducing a lateral spreading of the coolant. The concept of using a trench was also investigated earlier by Wang et al. (2000) who measured velocity distributions for various trench configurations.

For our study we modified the test vane to insert a shallow trench at the second row of holes on the suction side. The location of this row of holes is indicated on the schematic shown in Figure 10.1. The second row of holes is located at a position on the vane where the surface curvature was small and the pressure gradient was essentially zero. For these tests the row of holes was modified to have an injection of 30º and a spacing of $p/d = 2.78$, as shown in Figure 10.2. This hole injection angle and spacing between holes are more typical of the most film cooling configurations.

A shallow transverse trench was directly milled into the wall of the test model as shown in Figure 10.3. The trench depth was $S/d = 0.5$. As shown in Figure 10.3, the origin of the x coordinate for the trench configuration was set at trailing edge of the trench. The position is coincident with the origin at the downstream edge of the holes for baseline hole configuration with no trench. Nine trench configurations, designated as number 2-10, were created by using

rectangular and triangular inserts as shown in Figure 10.4. Configuration 1 was the baseline axial hole case, i.e. with no trench.

Evaluation of Various Trench Configurations

Initially, the nine combinations of trench geometries were tested at one blowing ratio and one mainstream turbulence level (M = 1.0, Tu = 1.0%) in order to compare the configurations and decide which configurations warranted in depth testing. Full details of these tests are provided in the M.S. thesis by Scot Waye (2005). The blowing ratio of M = 1.0 because separation occurs for the baseline case at this blowing ratio, and it was hypothesized that the trench would mitigate this separation. The density ratio for this test was DR = 1.3. Results from these tests are shown in terms of laterally averaged adiabatic effectiveness, $\overline{\eta}$, in Figure 10.5. It is immediately obvious that configurations 2, 3, and 4 yields much higher $\overline{\eta}$ values than all the rest. The other configurations seem to be on par with the baseline case, providing little improvement to the adiabatic effectiveness levels. Configurations 2, 3, and 4 have one characteristic in common, each has the rectangular insert situated downstream of the hole. Also, only these configurations had the rectangular insert situated downstream of the hole. Consequently it is evident that edge of trench position right at the downstream edge of the coolant hole is critical for improved performance. Configurations 2, 3, and 4 had values for $\overline{\eta}$ that were 100% higher near the hole and 30% higher downstream for M = 1.0. Another conclusion that can be made is that the downstream insert had much more of an effect on the total cooling of the surface than did the upstream insert. Configuration 2 gave the highest $\overline{\eta}$ values for all x/d locations compared to all the other configurations. This configuration was even 10% better than the other configurations with the rectangular insert downstream.

Spatial distributions of η are presented in Figures 10.6 (a)–(j) for baseline configuration and the nine trench configurations. For the baseline configuration, contours in Figure 10.6 (a) suggest jet separation and reattachment based on the higher peak effectiveness appearing downstream near x/d = 4 where the adiabatic effectiveness is lower immediately after the hole. The spatial distributions of η for configuration 2, shown in Figure 10.6 (b), shows that the trench greatly increased the lateral spread of the coolant resulting in a merging of the jets, although individual jet streaks were still evident. Both configurations 3 and 4 induced similar lateral spreading of the coolant as shown in Figures 10.6 (c) and (d).

Configurations 5, 6, and 7 each had a triangular insert in the downstream section of the trench, and each showed similar η patterns immediately downstream of the trench as shown in

Figures 10.6 (e), (f), and (g). The most noticeable difference between these configurations and the baseline configuration was continuous high η levels immediately downstream of the holes which suggest that the coolant jets have not separated as they did for the baseline case. However, there was essentially no increased lateral spreading, and consequently there was no significant improvement in adiabatic effectiveness.

Configurations 8, 9, and 10 did not have an insert in the downstream section of the slot, so these essentially these were "wide" slots with varying upstream slot geometries. The spatial η distributions for these configurations, shown in Figures 10.6 (h), (i), and (j), show that these wide slot configuration did not induce a lateral spreading of the coolant, and this resulted in the wide slot not being effective for increasing adiabatic effectiveness.

Narrow Trench Configuration

Configuration 2 can also be defined as a narrow trench. The coolant, when ejected, was obstructed by the downstream lip. This helped fill the trench with coolant, before it was ejected out of the trench onto the vane surface. The highest levels of adiabatic effectiveness measured in this current study were those found for configuration 2, or the narrow trench configuration. The dimensions of the trench were s/d = 0.5 and w/d = 2.0, or the length of the axial hole opening (due to the 30° injection angle, the opening was 2d long and 1d wide). This configuration had 10% higher $\overline{\eta}$ than the other configurations with rectangular inserts in the downstream part of the trench, and 30% to 100% higher than the other configurations including the baseline. These results were only for M = 1.0 and low mainstream turbulence, so further testing was carried out to test other blowing ratios as well as high mainstream turbulence. High and low mainstream turbulence levels were examined. Blowing ratios from M = 0.3 to 1.4 were tested for high mainstream turbulence, and M = 0.3 to 1.95 for low turbulence. All data was taken at DR = 1.3 plus a few points were additionally taken at DR =1.5.

Distributions of $\overline{\eta}$ for varying blowing ratios are presented in Figures 10.7 and 10.8 for high and low mainstream turbulence levels, respectively. Immediately apparent is that $\overline{\eta}$ monotonically increased with increasing M, even to blowing ratios of M = 1.95. The variation with blowing ratio is more clearly seen in Figure 10.9 where the spatially averaged adiabatic effectiveness, $\overline{\overline{\eta}}$, is presented as a function of M. This figure shows a strong increase in $\overline{\overline{\eta}}$ from M = 0.3 to 1.0, but essentially a constant level of $\overline{\overline{\eta}}$ for $M > 1.0$.

Also quite evident from Figure 10.9 is that the mainstream turbulence level had no noticeable effect on adiabatic effectiveness when using the narrow trench. Note that the high turbulence of Tu = 3.9% originated from a turbulence level in the mainstream approaching the vane of Tu = 20%, and the low turbulence of Tu = 1.0% originated from an approach mainstream turbulence level of Tu = 4%.

The spatial contour plots of η , presented in Figure 10.10 (a) and (b) for M = 0.4 and 1.95, show that the narrow trench significantly increases coverage at all blowing ratios. For M = 1.0 (Figure 10.6 (b)) and beyond, the spatial η distribution were essentially the same.

All the previously presented experimental results were obtained using a coolant density ratio of DR = 1.3. This was done for practical reasons since it is much easier to maintain frost free conditions in the test section at this lower density ratio. To establish that this lower density ratio provided similar results to what would be obtained at higher density ratio, experiments were conducted with the narrow trench configuration using coolant density ratio of DR = 1.5. Comparisons of the results for DR = 1.3 and DR = 1.5 are shown in Figure 10.11. These results show that there was almost no effect of the density ratio on the $\overline{\eta}$ distributions.

Direct comparisons of the narrow trench and wide trench (Configuration 10) and baseline configuration are shown in Figure 10.12 in terms of $\overline{\overline{\eta}}$ vs M. This figure shows that the narrow trench produced greater average adiabatic effectiveness for all blowing ratios, ranging from a fairly low blowing ratio to very high blowing ratios. The most spectacular increase in adiabatic effectiveness occurred at high blowing ratios, i.e. $M > 1.0$, for which the adiabatic effectiveness for the baseline configuration essentially fell to zero, while the trench configuration still has large levels of adiabatic effectiveness. Since the low levels of adiabatic effectiveness for the baseline configuration at high blowing ratios is due to jet separation, the improvement induced by the trench clearly shows that the trench reduces jet separation. The wide trench configuration performed at much lower level than the narrow trench for all blowing ratios. But at high blowing ratios the wide trench was clearly superior to the baseline configuration, showing some effect on reducing jet separation.

A more detailed comparison between the narrow trench and the baseline configurations is presented in Figure 10.13 where the $\overline{\eta}$ distributions are presented for the Tu = 3.9% case. This figure shows that the greatest distinction between the two configurations is immediately

downstream of the coolant hole exit, i.e. $x/d \geq 0$, where the narrow trench has greatly increased $\overline{\eta}$, presumably due to the greater lateral distribution of coolant.

Further insight into the influence of the trench on the film cooling flow was obtained by measurements of the thermal profiles above the surface. Thermal profiles at a location $2d$ downstream of the trailing edge of the hole are presented in Figure 10.14 for baseline "axial holes" configuration and the narrow trench configuration. The temperature measurements are presented in this figure in terms of the normalized parameter θ defined as follows:

$$\theta = \frac{T - T_\infty}{T_c - T_\infty} \tag{10.1}$$

These thermal profiles showed that the coolant jet was separating for the axial holes at $M = 1.0$, indicated by the peak θ region located off the wall, while the narrow trench thermal profile showed that the coolant was laterally spread and had not separated from the surface.

The narrow trench configuration performed very well compared to the baseline axial holes or the compound hole cases. In fact, it has been suggested that the holes embedded in a transverse trench may be on par with shaped holes (Bunker, 2005). Shaped holes have the benefit of a diffused opening, thus diffusing the coolant along the surface. Adiabatic effectiveness levels for shaped holes are usually better than axial holes, although cost much more to manufacture.

Previous studies have produced data for shaped holes with similar parameters (Saumweber, 2003). Various shaped holes were tested, 14° laterally expanded holes, and full expansion holes (15° forward and 14° laterally expanded). The pitch of the shaped holes was $p/d = 4$, compared to $p/d = 2.8$ for the narrow trench configuration. It should also be noted that the shaped holes were tested on a flat plate. Therefore, the results from the comparison, although given quantitatively, should be viewed partially as qualitative. The two shaped holes are compared to the narrow trench configuration in Figure 10.15 with the round axial holes plotted as a reference. The performance of the axial holes embedded within a narrow transverse trench is clearly comparable to the shaped holes.

Performance of narrow trench configuration with a rough surface

The ideal trench configuration, the narrow trench, was tested with a rough surface to determine the performance of the trench under these conditions. Comparing the rough surface trench case to the smooth surface trench case, shown in Figure 10.16, showed that the trench makes

the adiabatic effectiveness insensitive to roughness. In fact, at low *M*, there was no change in effectiveness with the rough surface. Moreover, at M = 1.2, there was actually a small increase of about 20% for the rough surface case. In this case the added turbulence from the roughness helps bring separated coolant jets back towards the surface.

Task 11 Effect of a transverse trench on film cooling with distorted holes

The goal of this task was to determine whether a shallow transverse trench would mitigate the degradation in film cooling performance due to obstructions around the holes. Experiments were conducted with the optimum narrow trench described in Task 10. The effects of the trench were tested with same Shape #2 obstruction described in Task 9, with a smooth and rough surface, and with low and high mainstream turbulence. All results presented in this section are for the high mainstream turbulence condition.

Effects of Obstructions on a Rough Wall with a Trench

Using a baseline of a rough surface with a narrow trench, the effects of the obstructions on film cooling performance were determined for obstructions positioned upstream alone, downstream alone, and upstream and downstream of the coolant holes. These results are presented in terms of $\overline{\overline{\eta}}$ vs *M* in Figure 11.1. From this plot it can be seen that at low *M*, the degradation is about 20% for all cases with obstructions and as *M* goes up, the degradation goes down. At high *M*, only the upstream case has a significant degradation relative to the rough surface, trench case, again around 20%.

In the worse case scenario, where the surface would exhibit both roughness and obstructions, the transverse trench is definitely beneficial. Figure 11.2 depicts a comparison of $\overline{\overline{\eta}}$ levels configurations with roughness and obstructions, and with and without a trench. For all cases shown, the narrow trench has increased performance over the baseline, and this improvement goes up with increasing *M*. In only one case, the downstream obstruction with *M* = 0.4 case, did the trench have no effect. Maximum improvement occurred for the highest blowing reaching as much as 250% improvement.

Effects of Obstructions on a Smooth Wall with a Trench

An examination of the effects of upstream obstructions on the smooth surface with a narrow trench case can be seen in Figure 11.3. There is a uniform degradation of about 40% across all

blowing ratios, near the hole, but levels of adiabatic effectiveness are similar at $x/d = 25$. Performance with and without downstream obstructions, shown in Figure 11.4, indicate a significant degradation for the lowest blowing ratio of $M = 0.4$, but not for the higher blowing ratios. For both the combined downstream and upstream obstruction cases, shown in Figure 11.5, there was significant degradation for the $M = 0.4$ and 0.6 cases, but no degradation for the $M = 1.2$ case.

To determine if a shallow trench would mitigate the effects of obstructions, smooth test surfaces with obstructions and with and without a shallow trench were tested. These results are presented in Figures 11.6, 11.7, and 11.8, for the configurations with upstream obstructions alone, downstream obstructions alone, and combined upstream and downstream obstructions, respectively. For all cases, at the highest blowing ratio of $M = 1.2$, the trench significantly improved the adiabatic effectiveness. At the lower blowing ratios of $M = 0.4$ and 0.6, the trench generally did had little effect on the performance.

Conclusions

Studies conducted so far indicated that endwall surface deposition, film-cooling hole blockage or TBC spallation generally resulted in reduced endwall cooling effectiveness. A deposit height of 0.5D improved cooling effectiveness when placed downstream of the leading edge cooling rows whereas it reduced the effectiveness levels when placed at the upstream location. Also, at the upstream location effectiveness levels increased with the increase in deposit height from 0.5D to 1.2D though the overall effectiveness was still lower than the baseline case.

Deposits along the pressure side cooling rows resulted in deflecting the coolant towards the pressure side vane endwall junction thereby lowering the effectiveness levels downstream of the cooling rows. It was also found that deposition on the endwall near the trailing edge has a higher degrading effect on cooling effectiveness than deposition at the leading edge.

Further testing of roughness effects on the suction side of the vane showed a significant reduction of the film effectiveness. Also further testing of the effects of obstructions for coolant holes with a shallower injection angle showed that an upstream obstruction significantly reduced film effectiveness. Testing of nine shallow, transverse trench configurations on the vane showed that transverse trench can improve film cooling performance dramatically. Furthermore, with a transverse trench installed, the vane film cooling performance was less susceptible to effects of the obstructions near the coolant holes. The shallow, transverse trench was found to greatly reduce the degradation effects of surface roughness and coolant hole obstructions.

References

Bunker, R. S., 2002, "Film-Cooling Effectiveness Due to Discrete Holes Within a Transverse Surface Slot," GT2002-30178.

Demling, P. D. R., 2005, "The Effects of Obstructions on Film Cooling Effectiveness on the Suction Side of a Gas Turbine Vane." M.S. Thesis, U. of Texas at Austin.

Demling, P. D. R. and Bogard, 2006, "The Effects of Obstructions on Film Cooling Effectiveness on the Suction Side of a Gas Turbine Vane." ASME paper GT2006-90577.

Lu, Y., Nasir, H., and Ekkad, S. V., 2005, "Film Cooling From a Row of Holes Embedded in Transverse Slots," GT2005-68598.

Waye, S.K., 2005, "Film Cooling Effectiveness of Suction Side Axial Holes, Compound Angle Holes, and Axial Holes Embedded within an Overlying Transverse Trench," M.S. Thesis, University of Texas at Austin.

Terrell, E.J., 2004, "A Study of the Convective Heat Transfer through Film Cooling Holes of a Gas Turbine Blade Leading Edge," M.S. Thesis, University of Texas at Austin.

Wang, T., Chintalapati, S., Bunker, R.S., and Lee, C.P., 2000, "Jet Mixing in a Trench," Experimental Thermal and Fluid Science, Vol. 22, pp. 1-17.

Nomenclature

C	true chord of stator vane
C_a	axial chord of stator vane
D, *d*	diameter of film-cooling hole
G	Mid-passage gap width
I	momentum flux ratio, $I = \frac{\rho_s u_s^2}{\rho_\infty U_\infty^2} = \frac{\rho_s (\dot{m}/\rho_s A_s)^2}{\rho_\infty U_\infty^2}$
k_s	equivalent sand grain roughness height
L	length of mid-passage gap
$\dot{m}$	mass flowrate
M	Blowing ratio based on local freestream velocity, $\frac{\rho_j U_j}{\rho_\infty U_\infty}$
M_{in}	blowing ratio based on inlet mainstream velocity
M*	Blowing ratio based on approach velocity, $\frac{\rho_c U_c}{\rho_0 U_0}$
P	vane pitch; hole pitch
P_o or p	total and static pressures
Re_{in}	Reynolds number defined as $Re = CU_{in}/\nu$
R_a	centerline average roughness height
s	distance along vane from flow stagnation
S	span of stator vane
T	temperature
x,y,z	local coordinates
u,v,w	local velocity components
U	velocity global

Greek

θ	non-dimensionalized temperature, $\theta = (T_\infty - T)/(T_\infty - T_c)$
η	adiabatic effectiveness, $\eta = (T_\infty - T_{aw})/(T_\infty - T_c)$
$\overline{\eta}$	laterally averaged effectiveness
ρ	density
ν	kinematic viscosity

Subscripts

aw	adiabatic wall
c	coolant conditions
in	inlet conditions
j	coolant flow through film-cooling holes
s	flow through upstream slot
∞	local freestream conditions

Goals for Next Reporting Period

Virginia Tech Goals

1) Tests will be carried out with perfect and distorted holes placed in the upstream slot and mid-passage gap.
2) Tests will also be carried out to study the effect on endwall film-cooling by imbedding film-cooling holes (on the endwall surface) in transverse slots.
3) Experiments will be conducted to measure the heat transfer coefficients on a rough endwall surface and along the length of the mid-passage gap.
4) The effects of a transverse slot on film cooling performance on the suction side of the vane will be investigated using measurements of adiabatic effectiveness, heat transfer coefficients, thermal fields, and velocity fields.

University of Texas Goals

5) Heat transfer tests will be done with the transverse trench configuration to complement the adiabatic effectiveness tests.
6) Further testing will be done on the effectiveness of a transverse trench in reducing the effects of coolant hole obstructions.

Tables and Figures

Table 5.1 Test Matrix for Deposition at the Leading Edge

Deposition Height	Endwall Roughness	Deposition Location	Film-Cooling flowrate	Upstream Slot flowrate	MP flowrate
0.5D	36 grit	Upstream, Downstream, & Both	0.50 %	0.75 %, 0.85 %, 1.0 %	0.20 %
0.8D	36 grit	Upstream, Downstream, & Both	0.50 %	0.75 %, 0.85 %, 1.0 %	0.20 %
1.2D	36 grit	Upstream, Downstream, & Both	0.50 %	0.75 %, 0.85 %, 1.0%	0.20 %

Table 5.2 Test Matrix for Deposition on Pressure Side

No of Rows	Film-cooling flowrate	Upstream Slot flowrate	MP flowrate	Cooling Row
4	0.5 %,0.75 %,0.9 %	0.75 %	0.2 %	1 to 4
3	0.5 %,0.75 %,0.9 %	0.75 %	0.2 %	1 to 3
2	0.5 %,0.75 %,0.9 %	0.75 %	0.2 %	1 to 2
1	0.5 %,0.75 %,0.9 %	0.75 %	0.2 %	1
1	0.5 %,0.9 %	0.75 %t	0.2 %	2
1	0.5 %t,0.9 %	0.75 %	0.2 %	3
1	0.5 %,0.9 %	0.75 %	0.2 %	4

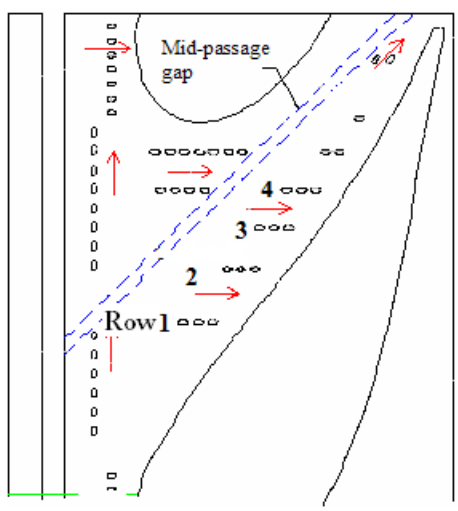

Table 8.1. Completed Tests for Roughness and Obstructions Study

			Obstructions		
Test	**Trench**	**Surface**	**Height**	**Width**	**Configurations**
3	-	Smooth	-	-	-
4	-	Smooth	1d	1d	up+dn/up/dn
5	-	Rough	-	-	-
6	-	Rough	1/2d	1d	up+dn/up/dn
7a	0.5dx2d	Smooth	1/2d	1d	up+dn/up/dn
7b	0.5dx2d	Smooth	-	-	-
8	0.5dx2d	Rough	-	-	-
9	0.5dx2d	Rough	1/2d	1d	up+dn/dn
10a	0.5dx2d	Rough	1/2d	1d	up+dn/up/dn
10b	0.5dx2d	Rough	-	-	-
11a	-	Smooth	1/2d	1d	up+dn/up/dn
11b	-	Smooth	-	-	-

Note: Tests 1 and 2 had problems, also an additional test was run to determine a CC for the rough cases with the trench
Note 2: All tests performed on 2nd row, SS, p/d = 2.8

Table 10.1. Experimental program for study of shallow trench configurations with a smooth surface.

Date	Description	*p/d*	*DR*	*Tu*
6/24/2005	Compound Angle	5.55	1.3	H, L
6/27/2005	Compound Angle	5.55	1.3	H, L
7/12/2005	Baseline	2.775	1.5	H, L
7/13/2005	Baseline	2.775	1.5	H, L
7/19/2005	Various Lip Configurations	2.775	1.3	L
7/27/2005	Wide Trench (WW)	2.775	1.3	L
7/27/2005	Narrow Trench (RR)	2.775	1.3	H, L
7/28/2005	Baseline, WW, RR Hotwire	N/A	N/A	H, L
8/1/2005	Baseline, WW, RR Hotwire	N/A	N/A	H, L
8/2/2005	Wide Trench (WW)	2.775	1.3	H
8/2/2005	Narrow Trench (RR)	2.775	1.5	H
8/2/2005	Baseline	5.55	1.3	H, L
8/2/2005	Baseline	2.775	1.3	H, L
10/12/2005	Narrow Trench Thermal Profiles	2.775	1.2	L
10/13/2005	Narrow Trench Thermal Profiles	2.775	1.2	L
11/4/2005	Baseline Thermal Profiles	2.775	1.2	L

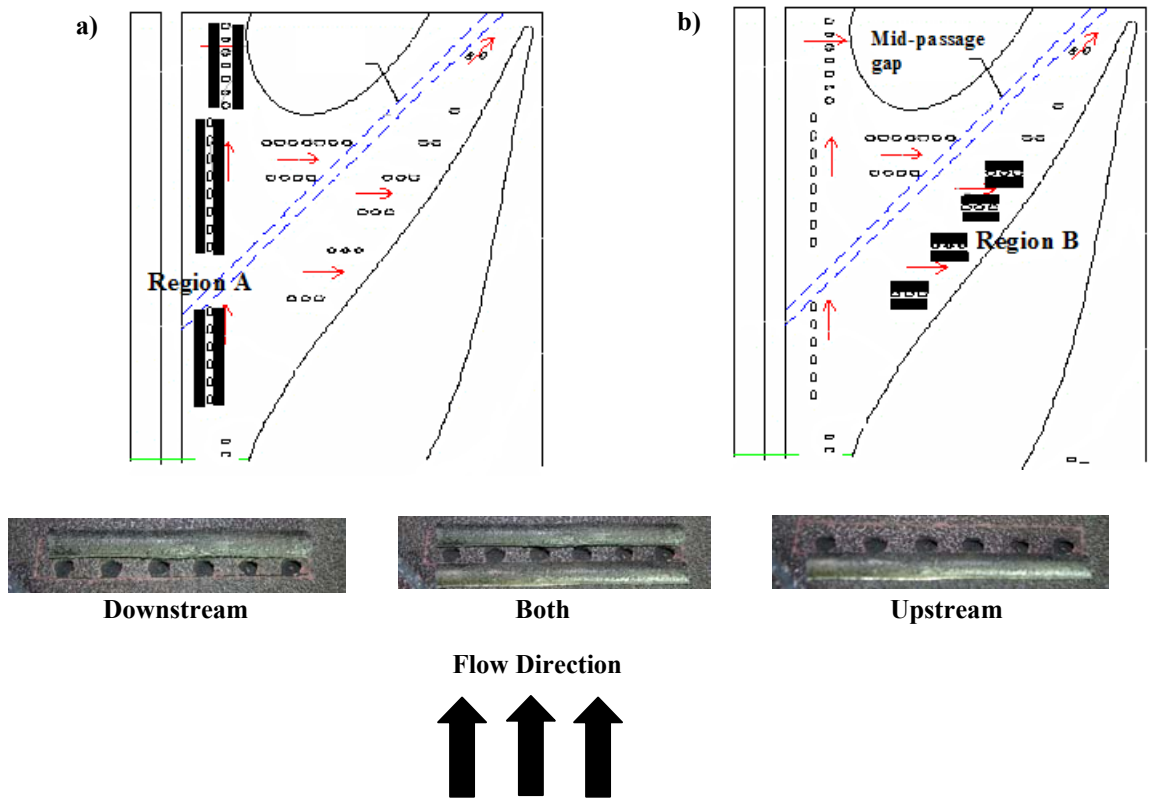

Figure 5.1. Illustrates a) leading edge deposition b) deposition along the pressure side of the vane and c) orientation of deposits with respect to the film-cooling row.

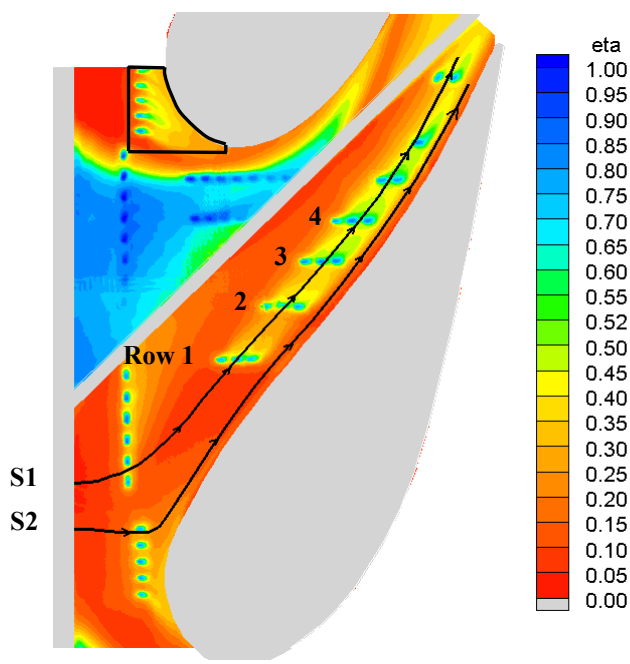

Figure 5.2. Contour of adiabatic effectiveness for the baseline case without any deposition with coolant mass flowrates of 0.75 percent through the upstream slot, 0.5 percent through the film-cooling holes, and 0.2 percent through the mid-passage gap.

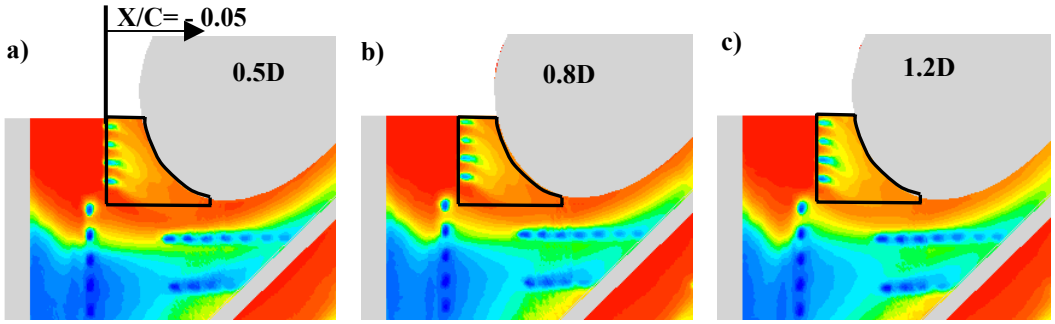

Coolant flowrates	
Upstream slot	0.75%
Film-cooling holes	0.5%
Mid-passage gap	0.2%

Figure 5.3. Effectiveness contours comparing the effects of different deposit heights at the leading edge stagnation region with deposit placed upstream of the cooling row.

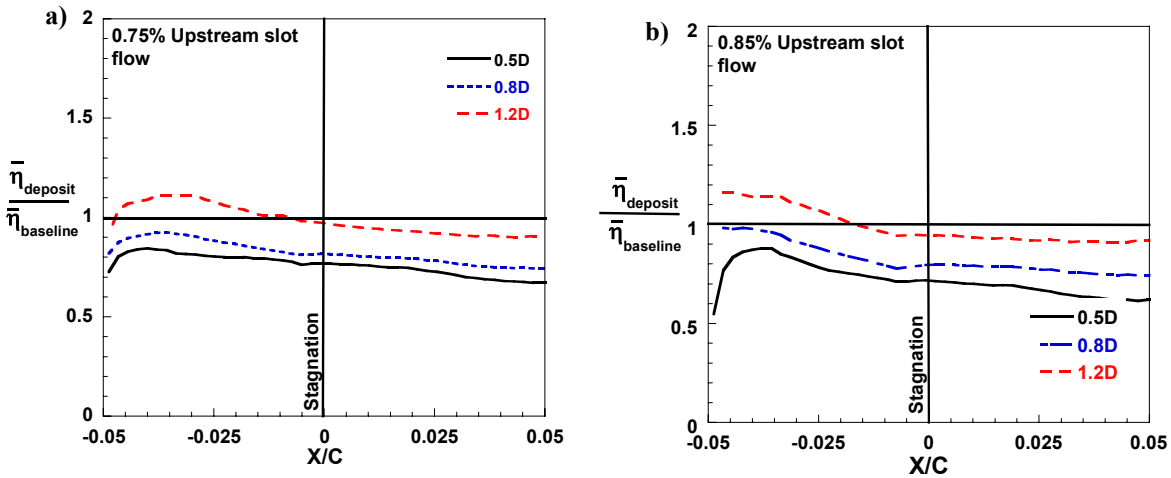

Figure 5.4. Ratio of laterally averaged effectiveness due to different deposit heights at the upstream location with upstream slot coolant mass flowrates of a) 0.75 percent and b) 0.85 percent

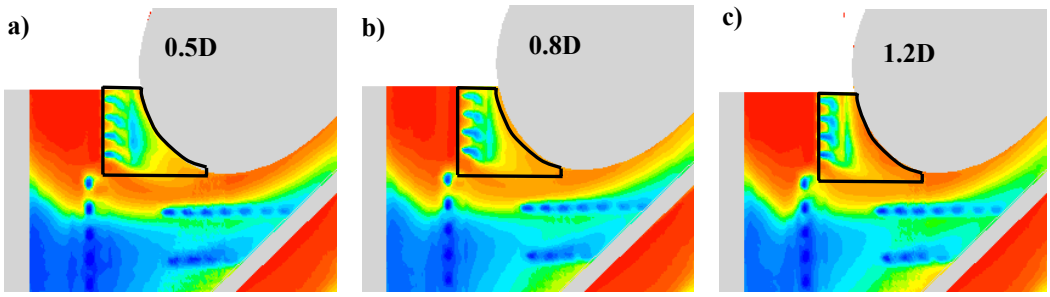

Coolant flowrates	
Upstream slot	0.75%
Film-cooling holes	0.5%
Mid-passage gap	0.2%

Figure 5.5. Effectiveness contours comparing the effects of different deposit heights at the leading edge stagnation region with deposit placed on either side of the film-cooling row.

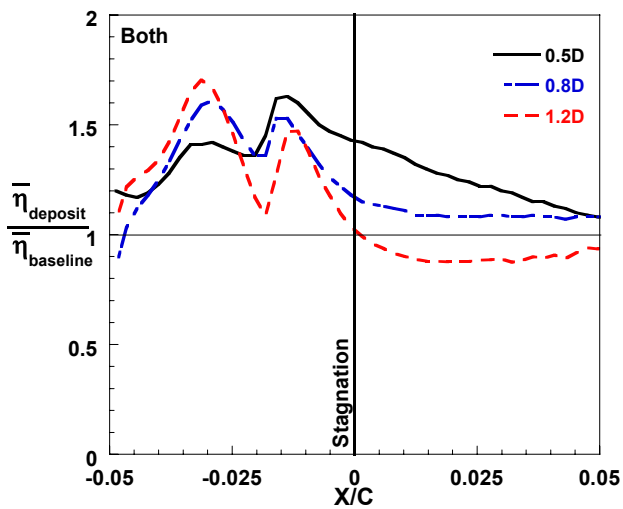

Figure 5.6. Augmentation of laterally averaged effectiveness downstream of the leading edge row (marked region in Figure 5.5) due to deposits of different heights placed on either side of the film-cooling row.

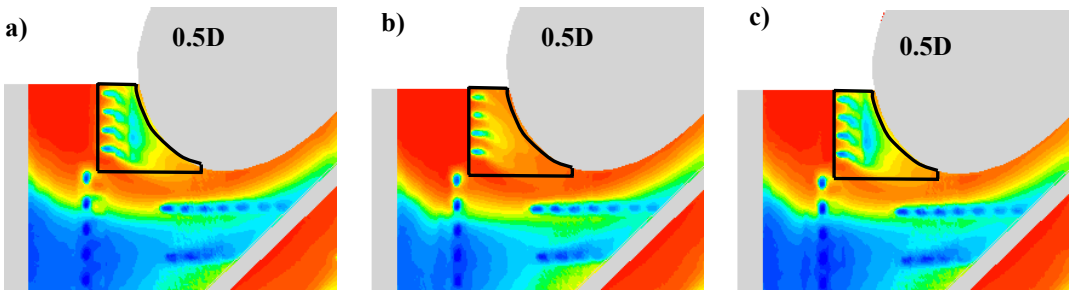

Coolant flowrates	
Upstream slot	0.75%
Film-cooling holes	0.5%
Mid-passage gap	0.2%

Figure 5.7. Effectiveness contours comparing the effect of placing a 0.5D deposit at a) downstream, b) upstream and c) on both sides of the film-cooling row.

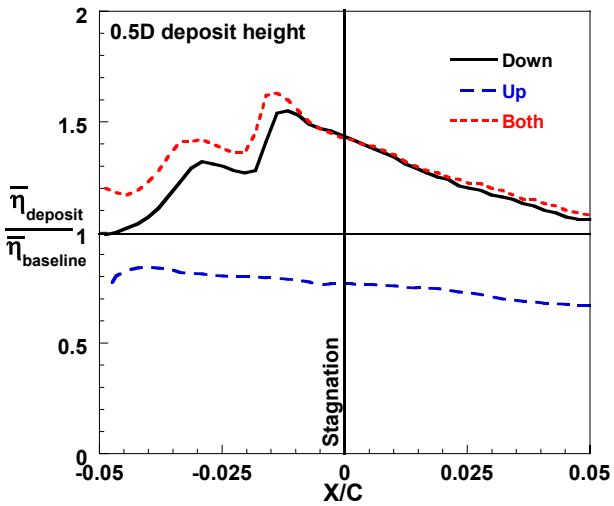

Figure 5.8. Augmentation of laterally averaged effectiveness downstream of the leading edge cooling row (marked region in figure 5.7) due to deposits placed at different locations along the cooling row.

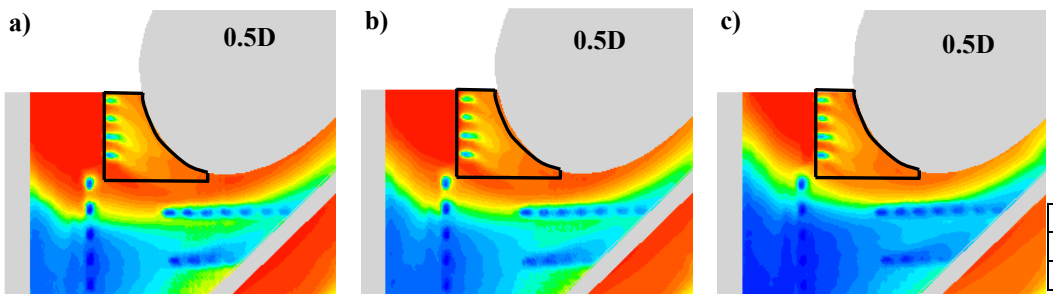

Coolant flowrates	
Film-cooling holes	0.5%
Mid-passage gap	0.2%

Figure 5.9. Effectiveness contours comparing the effect of upstream deposition at the leading edge with upstream slot coolant flow rate of a) 0.75 percent, b) 0.85 percent, and c) 1.0 percent.

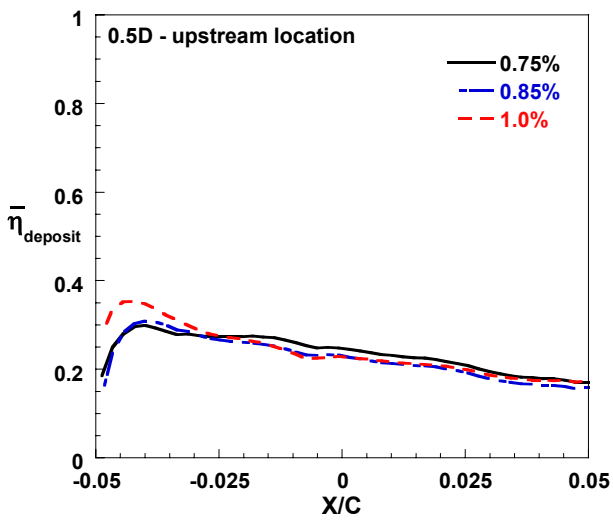

Figure 5.10. Adiabatic effectiveness laterally averaged pitchwise downstream of the leading edge cooling row (marked region in figure 5.9) with upstream deposition.

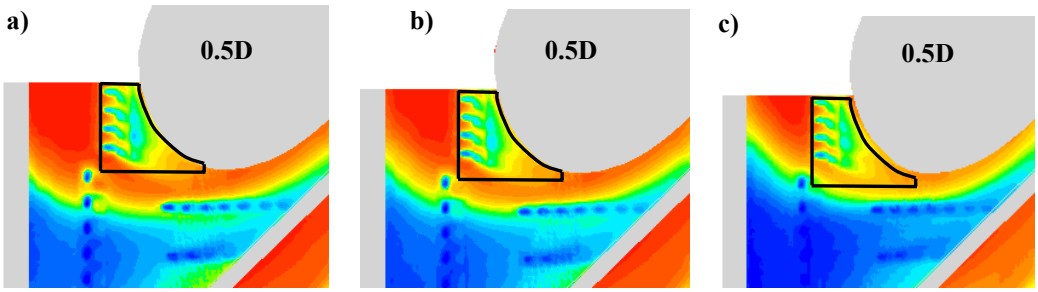

Coolant flowrates	
Film-cooling holes	0.5%
Mid-passage gap	0.2%

Figure 5.11. Effectiveness contours comparing the effect of downstream deposition at the leading edge with upstream slot coolant flow rate of a) 0.75 percent, b) 0.85 percent, and c) 1.0 percent.

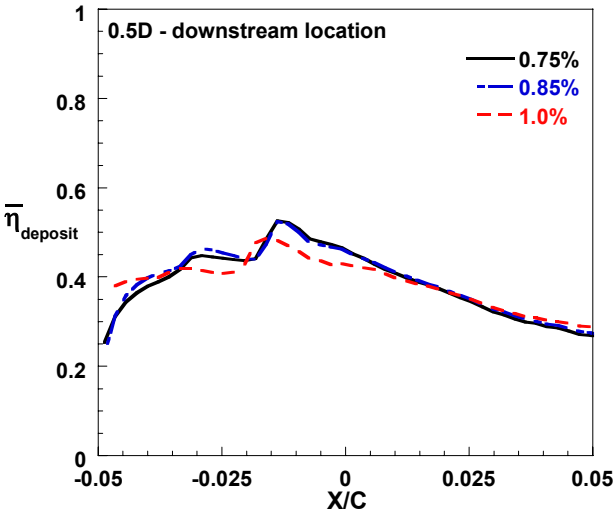

Figure 5.12. Adiabatic effectiveness laterally averaged pitchwise downstream of the leading edge cooling row (marked region in figure 5.11) with downstream deposition.

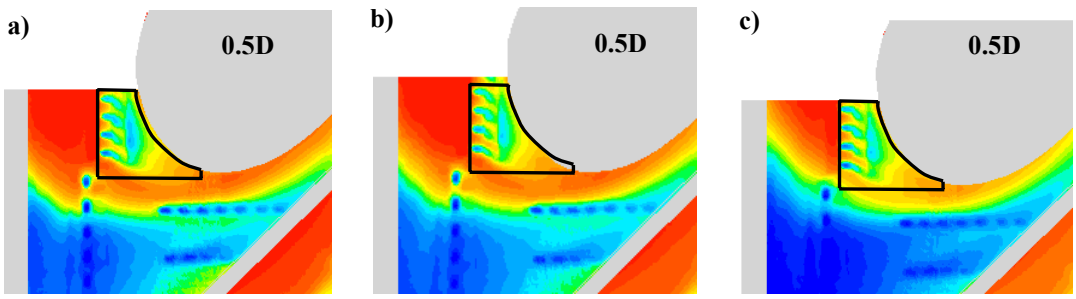

Coolant flowrates	
Film-cooling holes	0.5%
Mid-passage gap	0.2%

Figure 5.13. Effectiveness contours comparing the effect of deposition on either side of the cooling row at the leading edge with upstream slot coolant flow rate of a) 0.75 percent, b) 0.85 percent, and c) 1.0 percent.

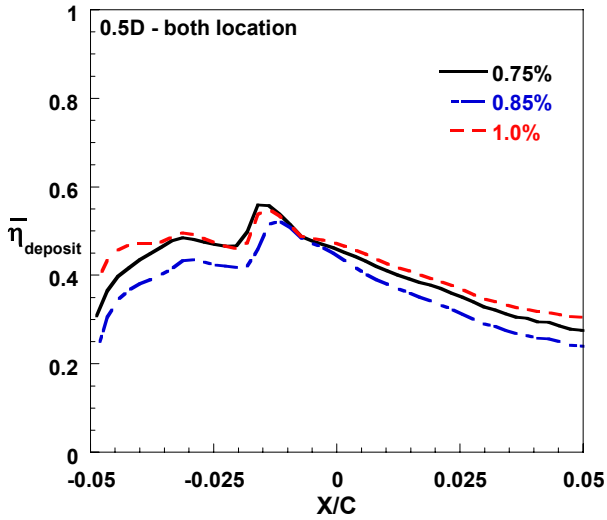

Figure 5.14. Adiabatic effectiveness laterally averaged pitchwise downstream of the leading edge cooling row (marked region in figure 5.13) with deposition on both sides of the cooling row.

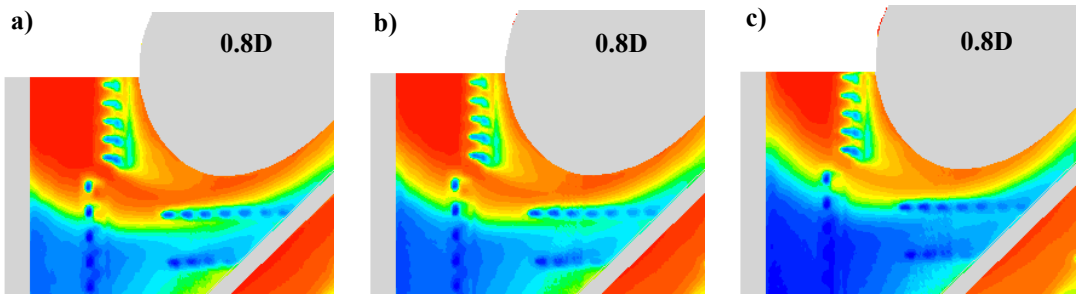

Coolant flowrates	
Film-cooling holes	0.5%
Mid-passage gap	0.2%

Figure 5.15. Effectiveness contours comparing the effect of downstream deposition at the leading edge with upstream slot coolant flow rate of a) 0.75 percent, b) 0.85 percent, and c) 1.0 percent.

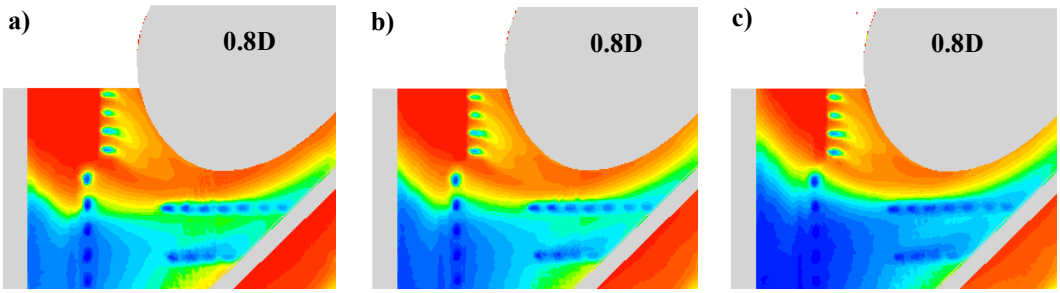

Coolant flowrates	
Film-cooling holes	0.5%
Mid-passage gap	0.2%

Figure 5.16. Effectiveness contours comparing the effect of upstream deposition at the leading edge with upstream slot coolant flow rate of a) 0.75 percent, b) 0.85 percent, and c) 1.0 percent.

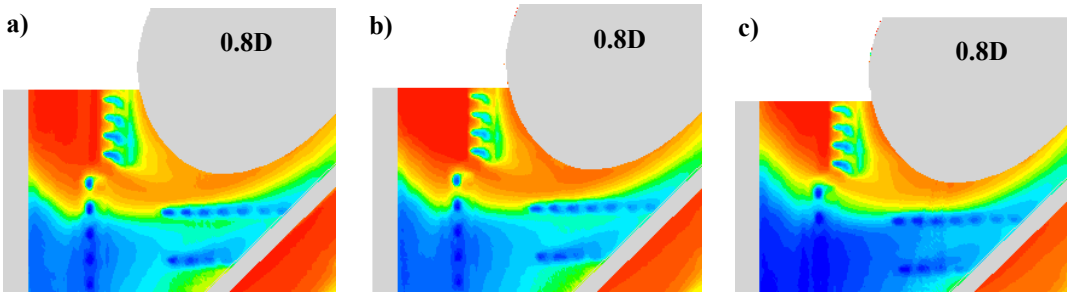

Coolant flowrates	
Film-cooling holes	0.5%
Mid-passage gap	0.2%

Figure 5.17. Effectiveness contours comparing the effect of deposition on either side of the cooling row at the leading edge with upstream slot coolant flow rate of a) 0.75 percent, b) 0.85 percent, and c) 1.0 percent.

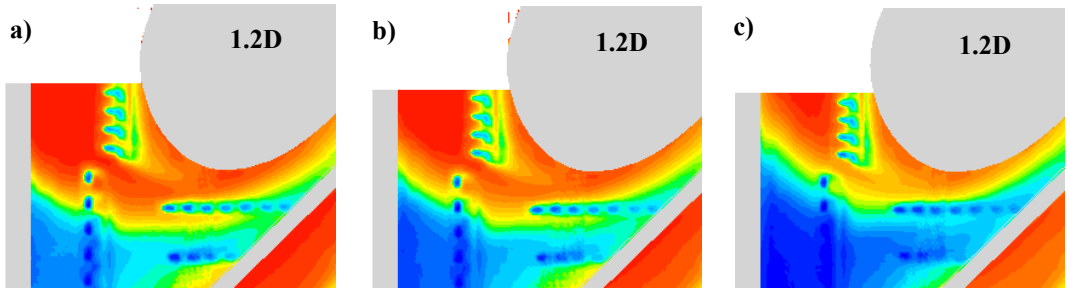

Coolant flowrates	
Film-cooling holes	0.5%
Mid-passage gap	0.2%

Figure 5.18. . Effectiveness contours comparing the effect of downstream deposition at the leading edge with upstream slot coolant flow rate of a) 0.75 percent, b) 0.85 percent, and c) 1.0 percent.

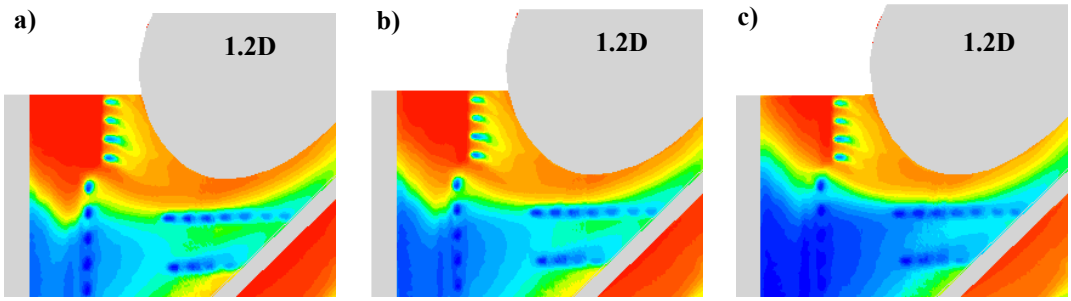

Coolant flowrates	
Film-cooling holes	0.5%
Mid-passage gap	0.2%

Figure 5.19. . Effectiveness contours comparing the effect of upstream deposition at the leading edge with upstream slot coolant flow rate of a) 0.75 percent, b) 0.85 percent, and c) 1.0 percent.

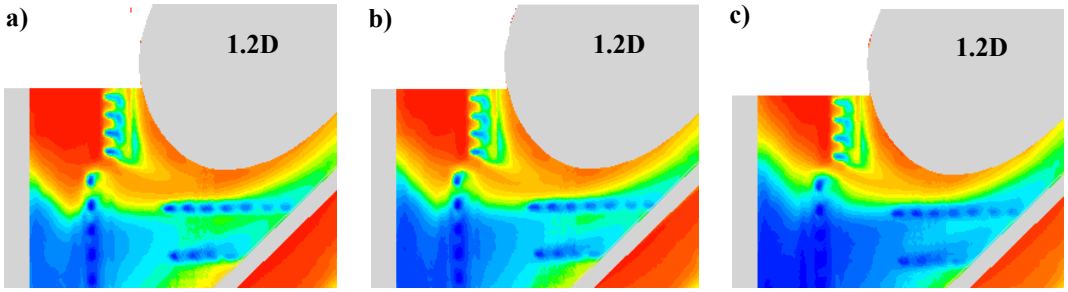

Coolant flowrates	
Film-cooling holes	0.5%
Mid-passage gap	0.2%

Figure 5.20. Effectiveness contours comparing the effect of deposition on either side of the cooling row at the leading edge with upstream slot coolant flow rate of a) 0.75 percent, b) 0.85 percent, and c) 1.0 percent.

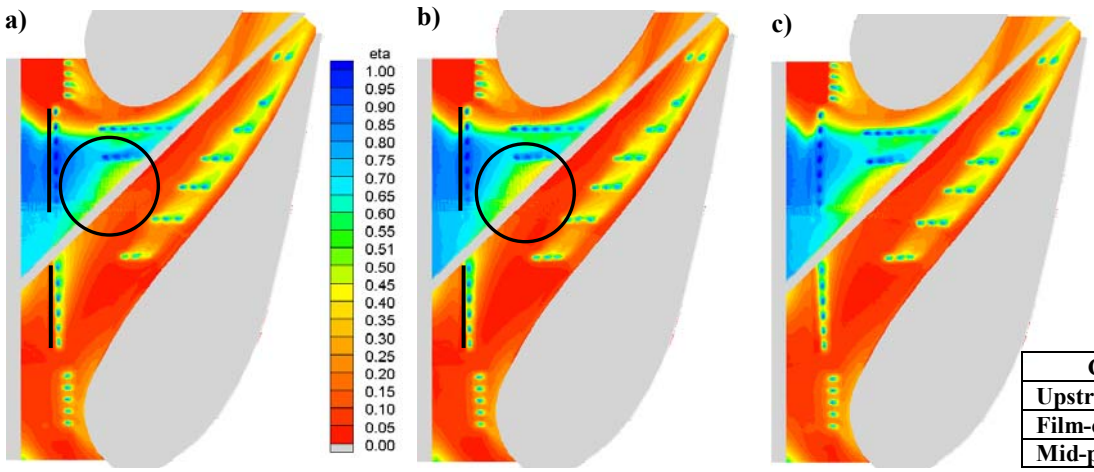

Coolant flowrates	
Upstream slot	0.75%
Film-cooling holes	0.5%
Mid-passage gap	0.2%

Figure 5.21. Effectiveness contours showing the effect of deposition at the leading edge between the stagnation regions of the two vanes for deposit heights of a) 0.5D, b) 0.8D, and c) 1.2D.

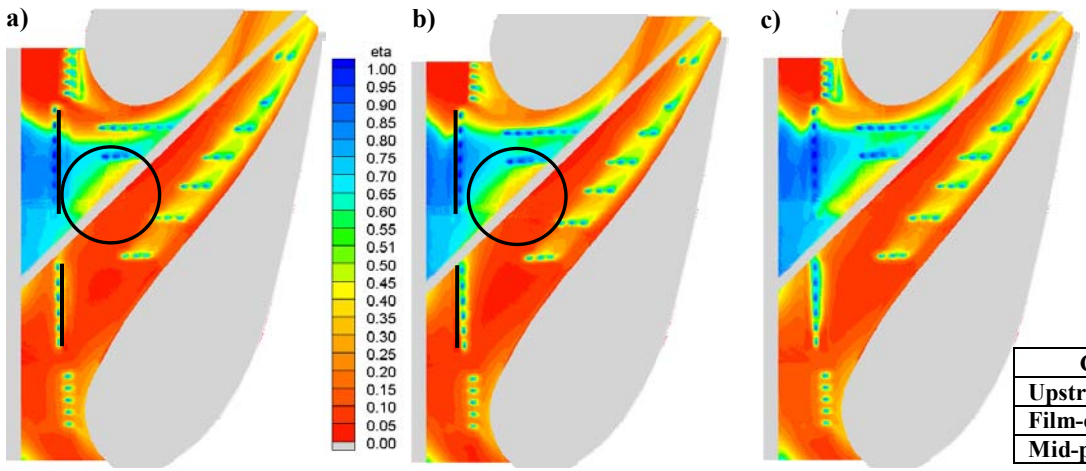

Coolant flowrates	
Upstream slot	0.75%
Film-cooling holes	0.5%
Mid-passage gap	0.2%

Figure 5.22. Effectiveness contours showing the effect of 1.2D deposition at the leading edge with deposit placed at a) downstream, b) upstream, and c) on both sides of the cooling row.

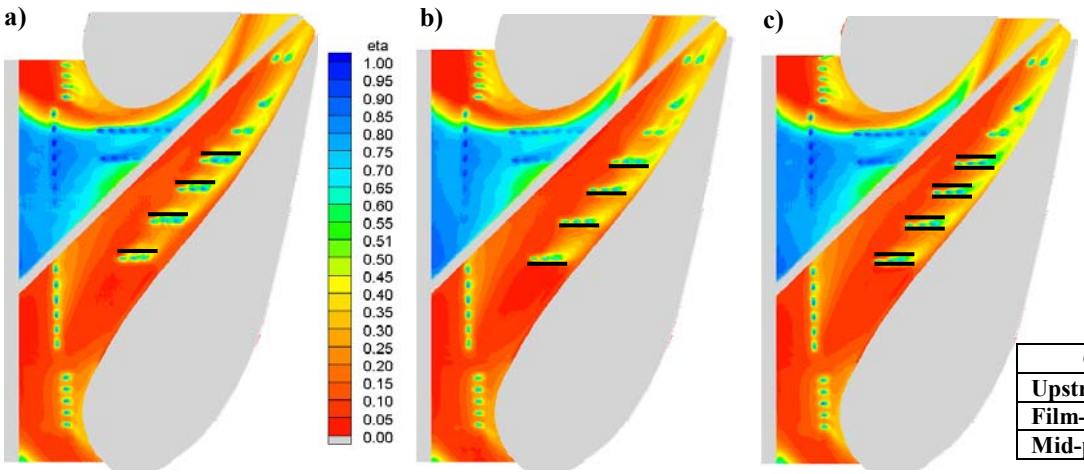

Coolant flowrates	
Upstream slot	0.75%
Film-cooling holes	0.5%
Mid-passage gap	0.2%

Figure 5.23. Effectiveness contours showing the effect of deposition along the pressure side with deposit placed at a) downstream, b) upstream, and c) on both sides of the cooling rows.

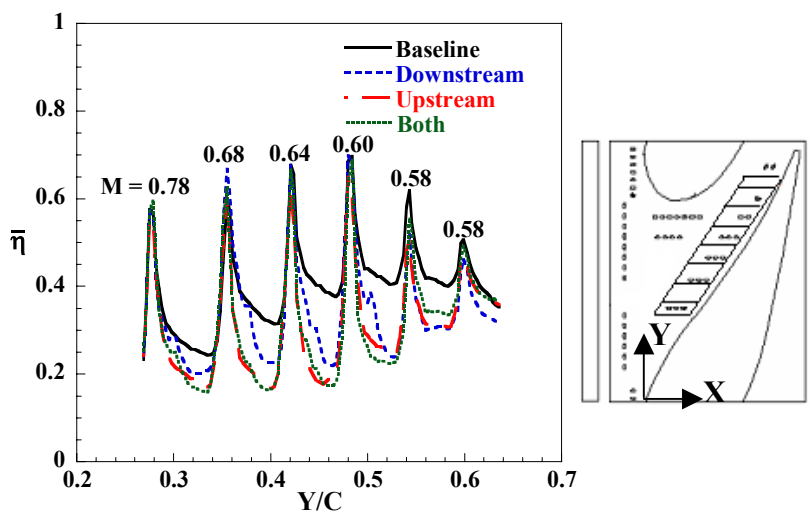

Figure 5.24. Adiabatic effectiveness laterally averaged streamwise along the pressure side cooling rows (marked region) with deposition at downstream, upstream, and on both sides of the cooling rows.

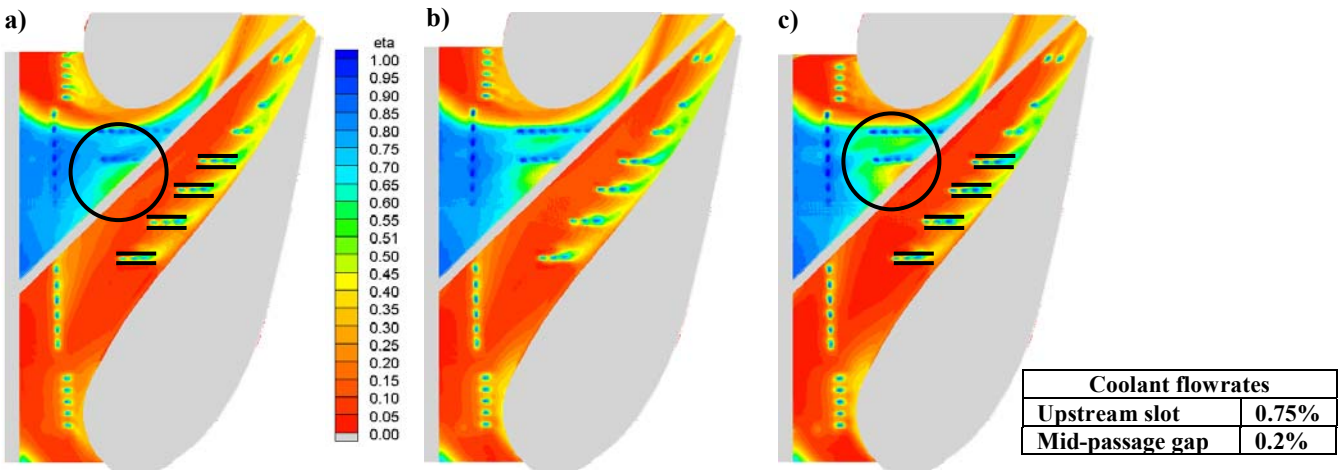

Figure 5.25. Adiabatic effectiveness contours with 0.8D deposition along the pressure side film-cooling holes with film-cooling flowrates of a) 0.5 percent, b) 0.75 percent, and c) 0.9 percent.

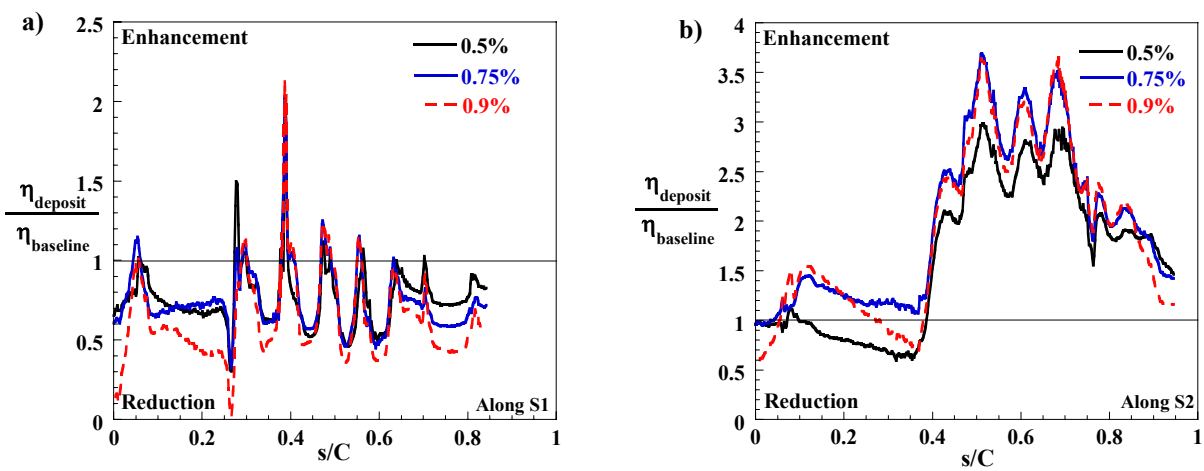

Figure 5.26. Change in adiabatic effectiveness levels along streamlines S1 and S2 (refer Figure 5.2) for deposits on both sides of the cooling rows.

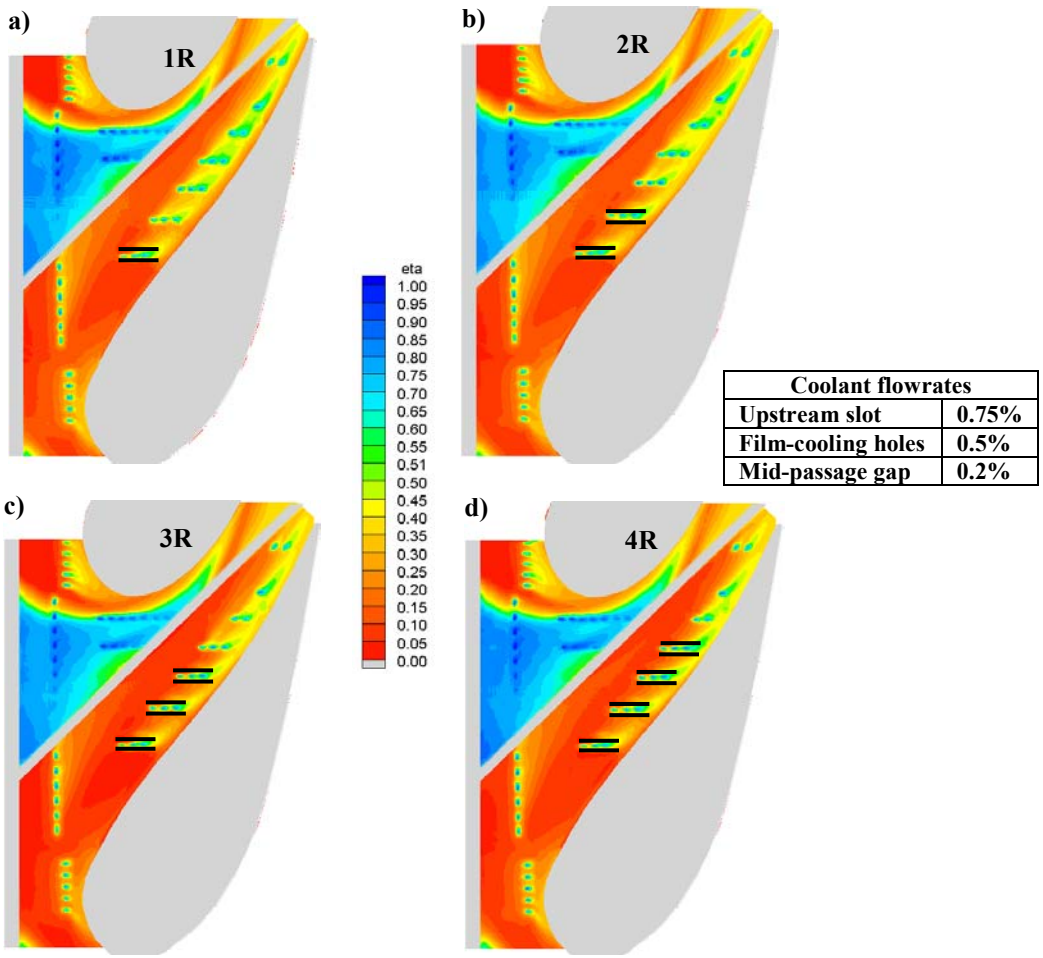

Figure 5.27. Adiabatic effectiveness contours showing the effect of sequentially increasing the number of row deposits from row 1 to row 4 along the pressure side film-cooling holes.

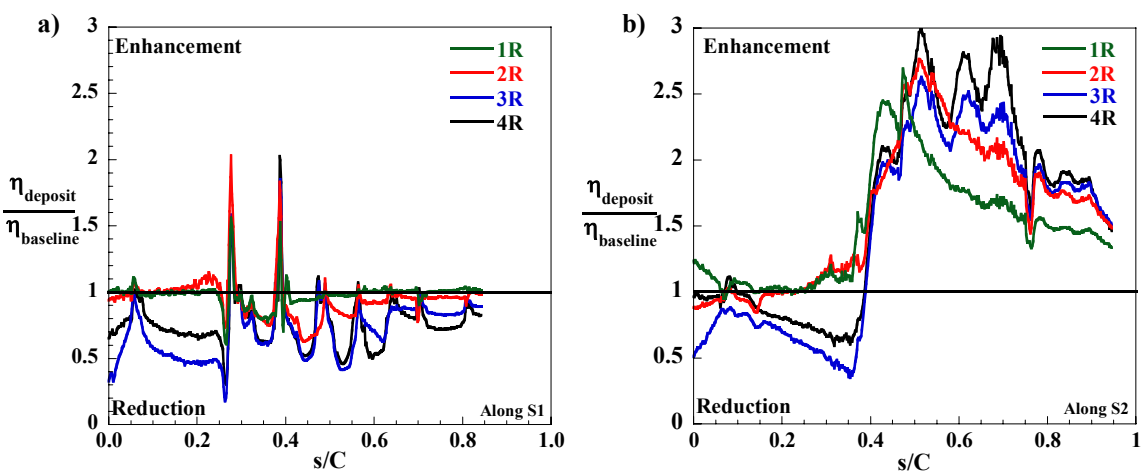

Figure 5.28. Change in adiabatic effectiveness levels along streamlines S1 and S2 (refer Figure 5.2) caused by sequential increment of deposits from row 1 to row 4.

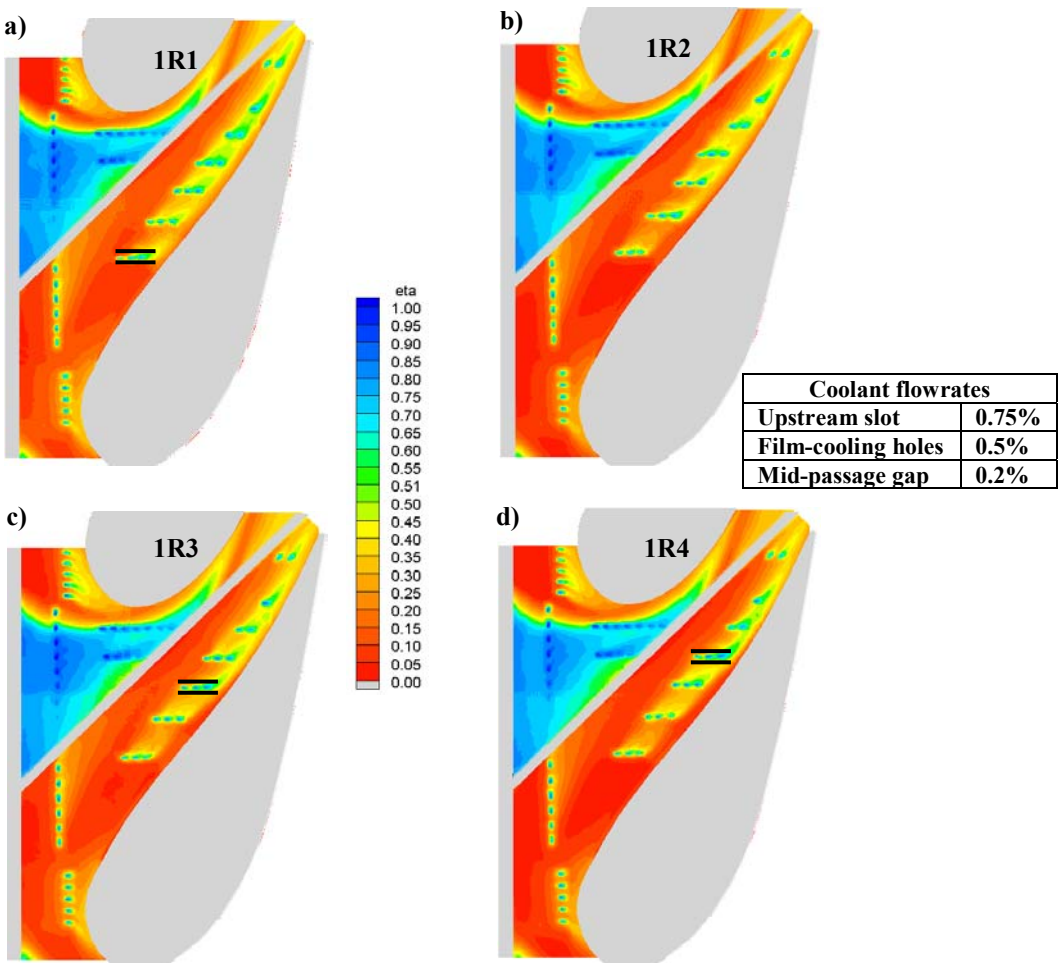

Figure 5.29. Adiabatic effectiveness contours showing the effect of single row deposits along the pressure side film-cooling holes.

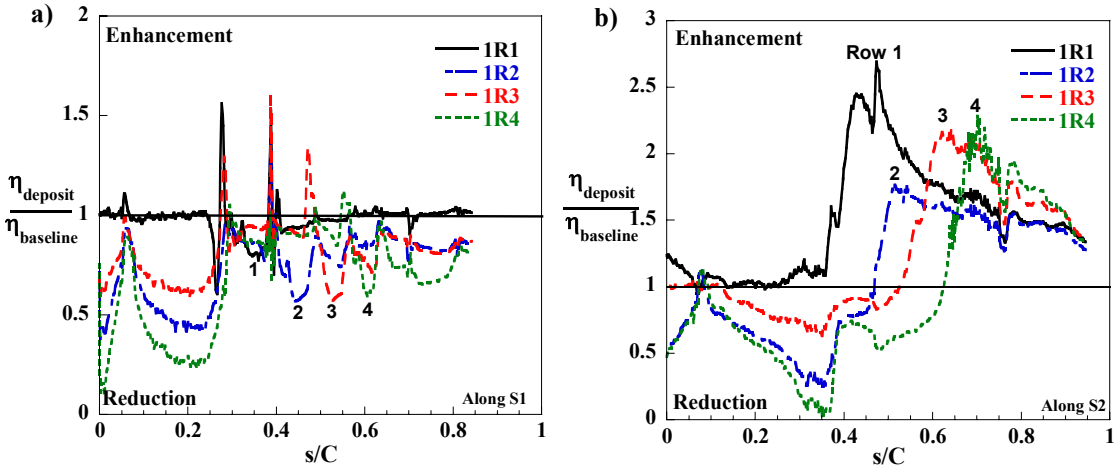

Figure 5.30. Change in adiabatic effectiveness levels along streamlines S1 and S2 (refer Figure 5.2) caused by single row deposition from row 1 to row4.

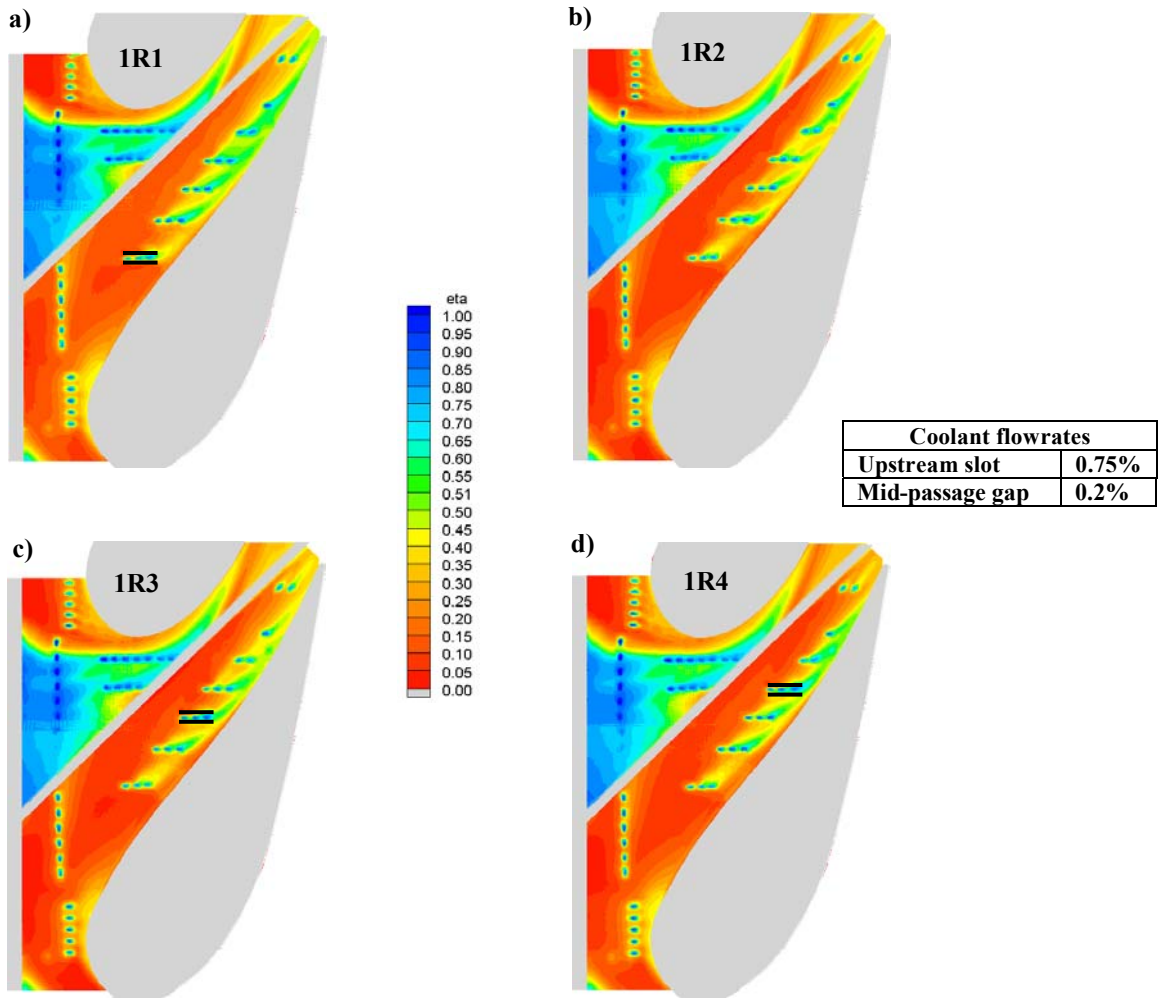

Figure 5.31. Adiabatic effectiveness contours showing the effect of single row deposits along the pressure side film-cooling holes for a film-cooling mass flowrate of 0.9 percent.

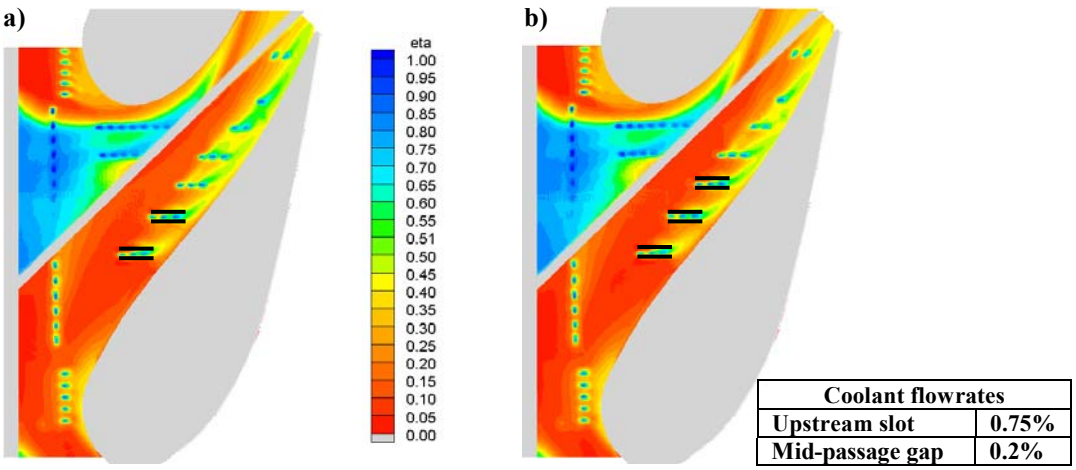

Figure 5.32. Adiabatic effectiveness contours showing the effect of multiple row deposits along the pressure side film-cooling holes for a film-cooling mass flowrate of 0.75 percent.

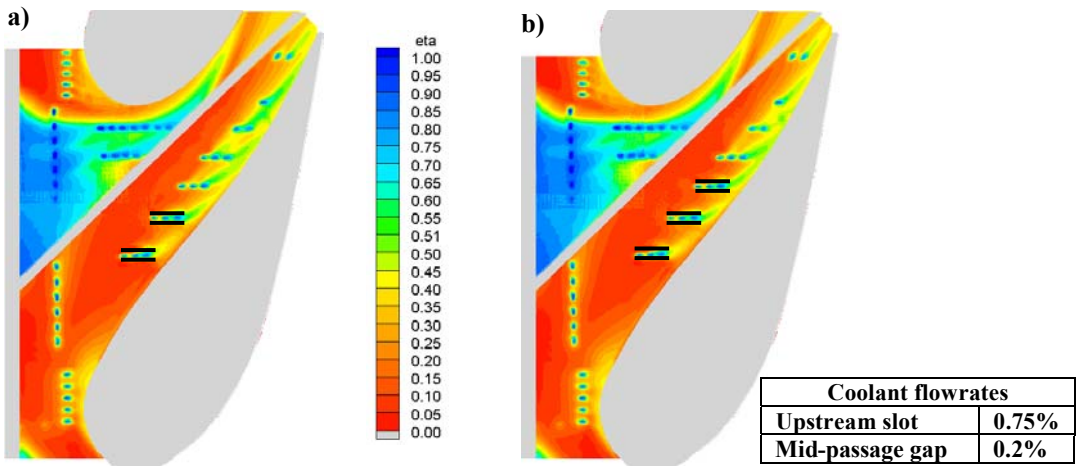

Figure 5.33. Adiabatic effectiveness contours showing the effect of multiple row deposits along the pressure side film-cooling holes for a film-cooling mass flowrate of 0.9 percent.

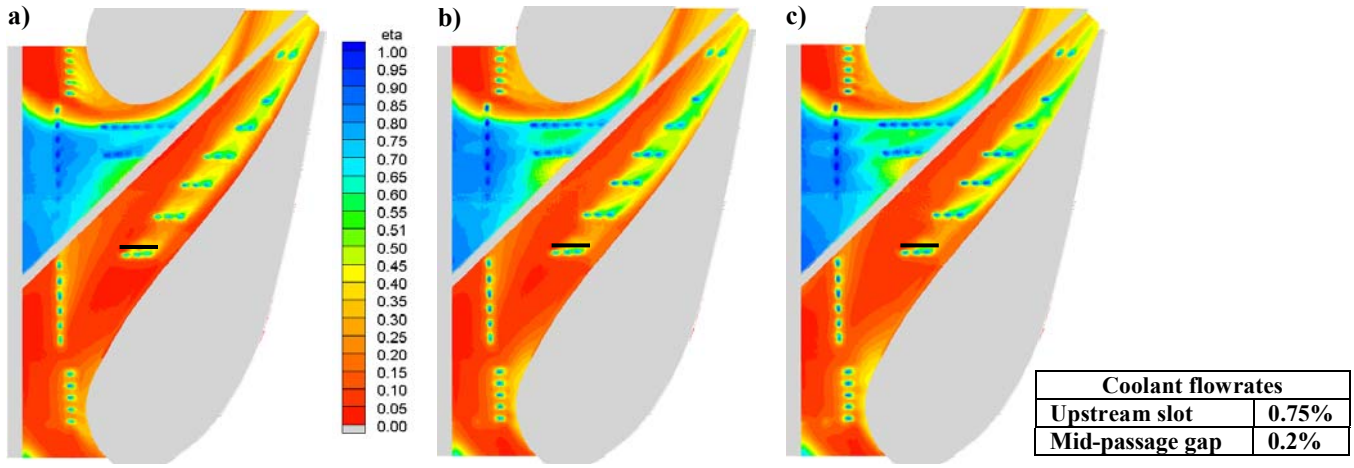

Figure 5.34. Adiabatic effectiveness contours with 0.8D deposition downstream of row 1 film-cooling holes with coolant mass flowrates of a) 0.5 percent, b) 0.75 percent, and c) 0.9 percent.

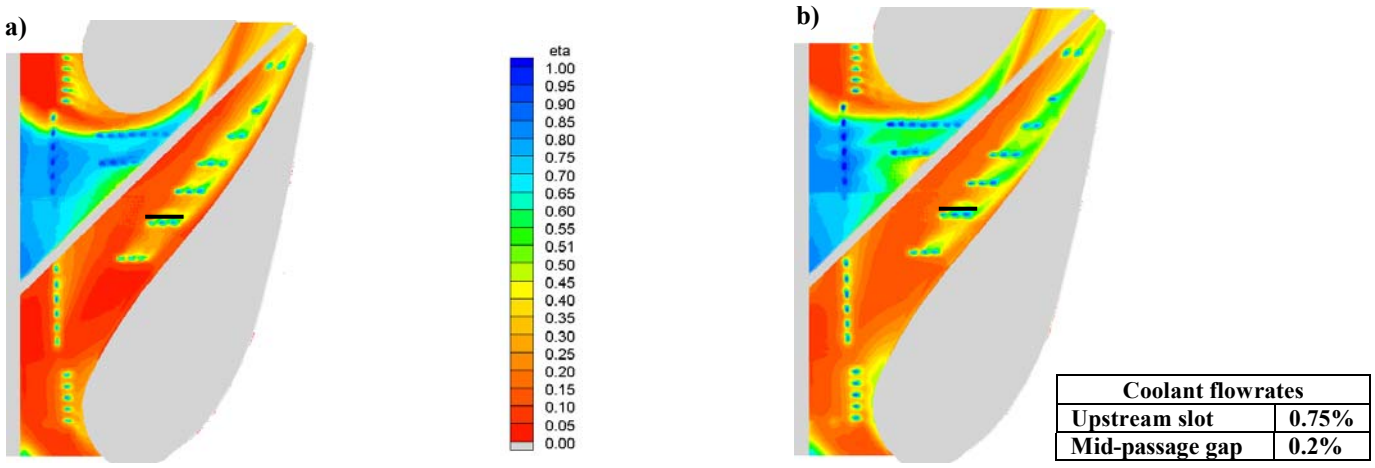

Figure 5.35. Adiabatic effectiveness contours with 0.8D deposition downstream of row 2 film-cooling holes with coolant mass flowrates of a) 0.5 percent and b) 0.9 percent.

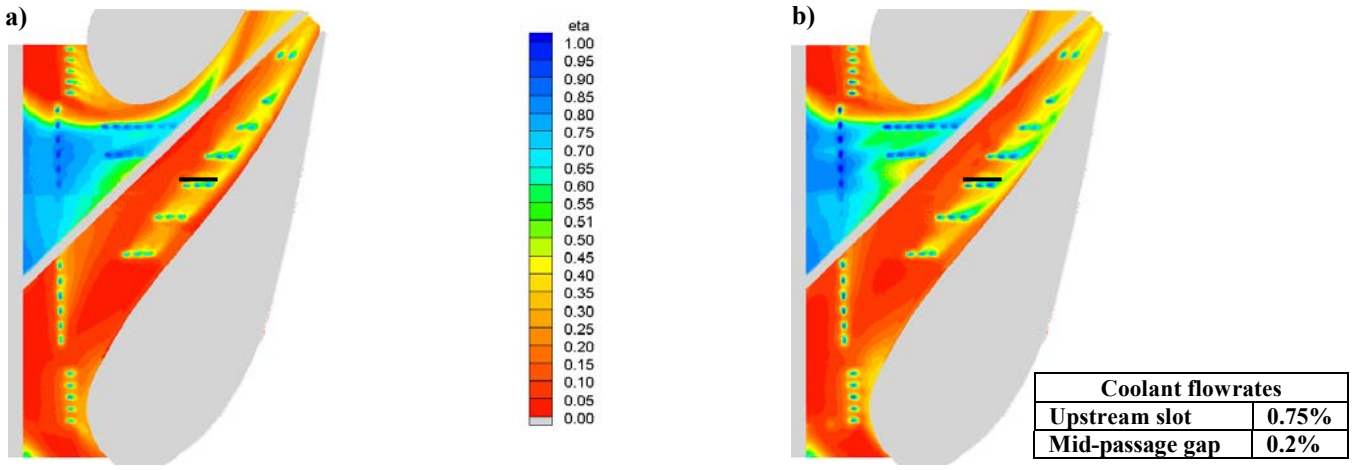

Figure 5.36. Adiabatic effectiveness contours with 0.8D deposition downstream of row 3 film-cooling holes with coolant mass flowrates of a) 0.5 percent and b) 0.9 percent.

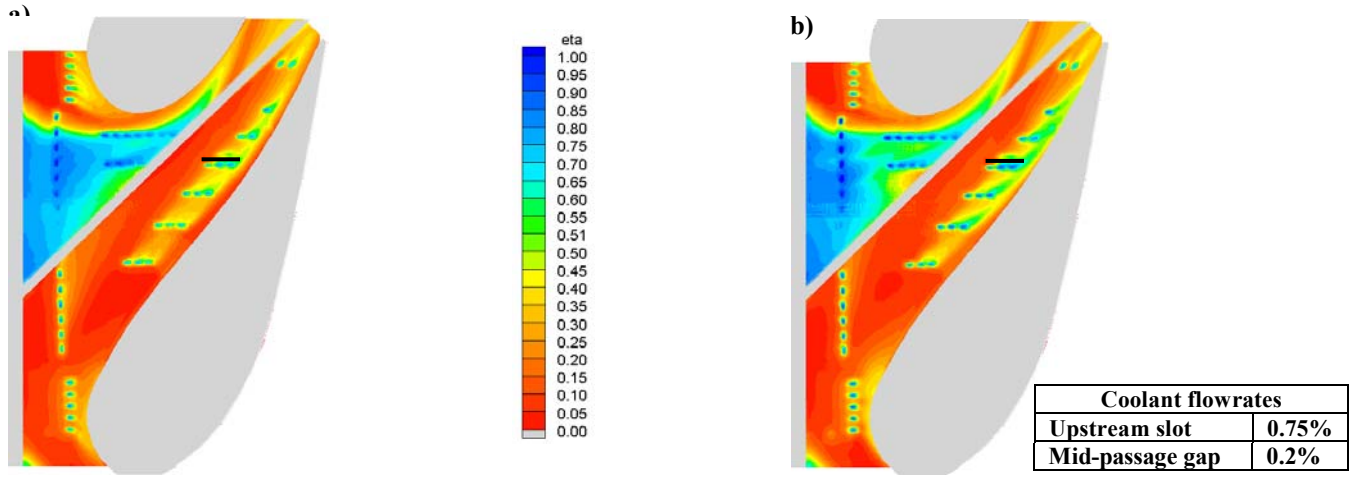

Figure 5.37. Adiabatic effectiveness contours with 0.8D deposition downstream of row 4 film-cooling holes with coolant mass flowrates of a) 0.5 percent and b) 0.9 percent.

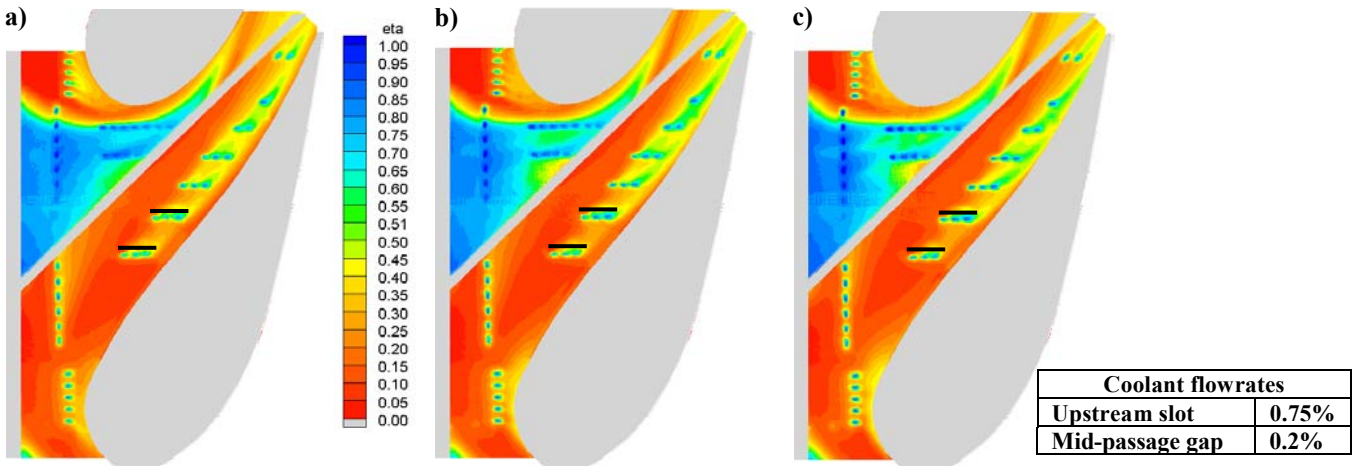

Figure 5.38. Adiabatic effectiveness contours with 0.8D deposition downstream of row 1 and 2 film-cooling holes with coolant mass flowrates of a) 0.5 percent, b) 0.75 percent and c) 0.9 percent.

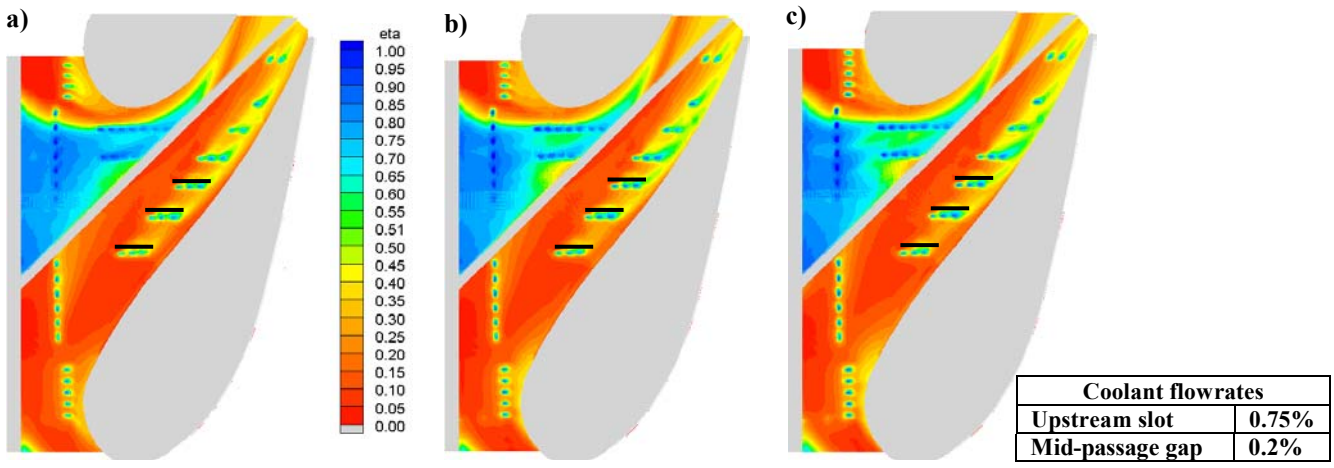

Figure 5.39. Adiabatic effectiveness contours with 0.8D deposition downstream of row 1, 2 and 3 film-cooling holes with coolant mass flowrates of a) 0.5 percent, b) 0.75 percent and c) 0.9 percent.

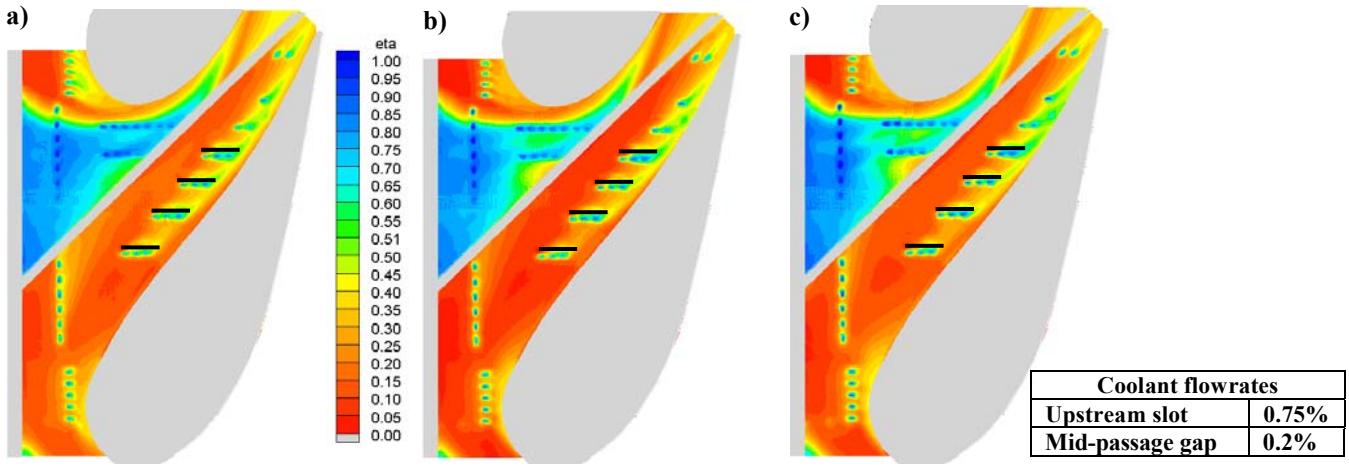

Figure 5.40. Adiabatic effectiveness contours with 0.8D deposition downstream of all four rows of film-cooling holes with coolant mass flowrates of a) 0.5 percent, b) 0.75 percent and c) 0.9 percent.

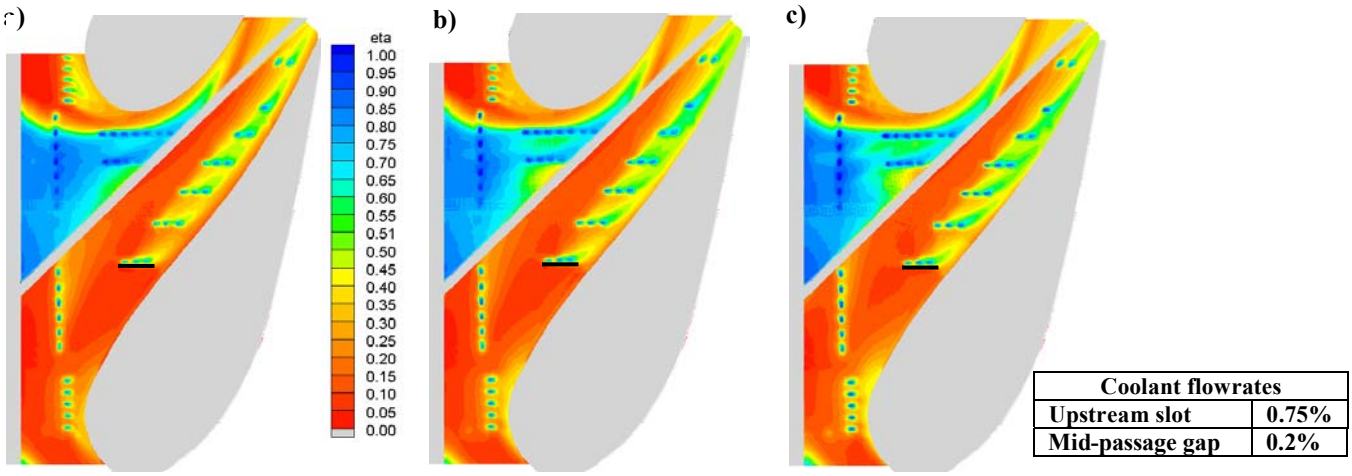

Figure 5.41. Adiabatic effectiveness contours with 0.8D deposition upstream of row 1 film-cooling holes with coolant mass flowrates of a) 0.5 percent, b) 0.75 percent, and c) 0.9 percent.

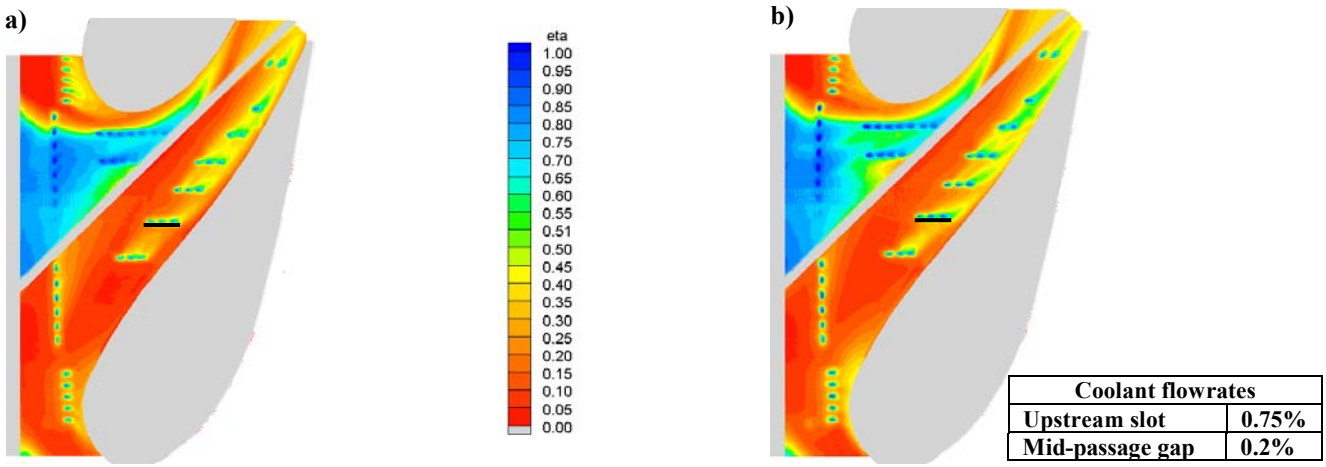

Figure 5.42. Adiabatic effectiveness contours with 0.8D deposition upstream of row 2 film-cooling holes with coolant mass flowrates of a) 0.5 percent and b) 0.9 percent.

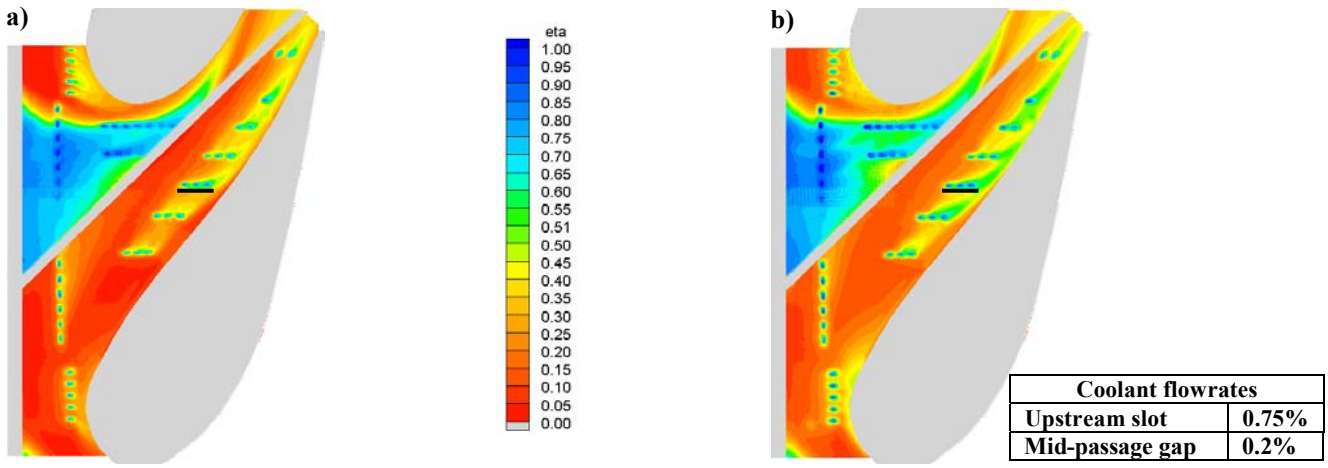

Figure 5.43. Adiabatic effectiveness contours with 0.8D deposition upstream of row 3 film-cooling holes with coolant mass flowrates of a) 0.5 percent and b) 0.9 percent.

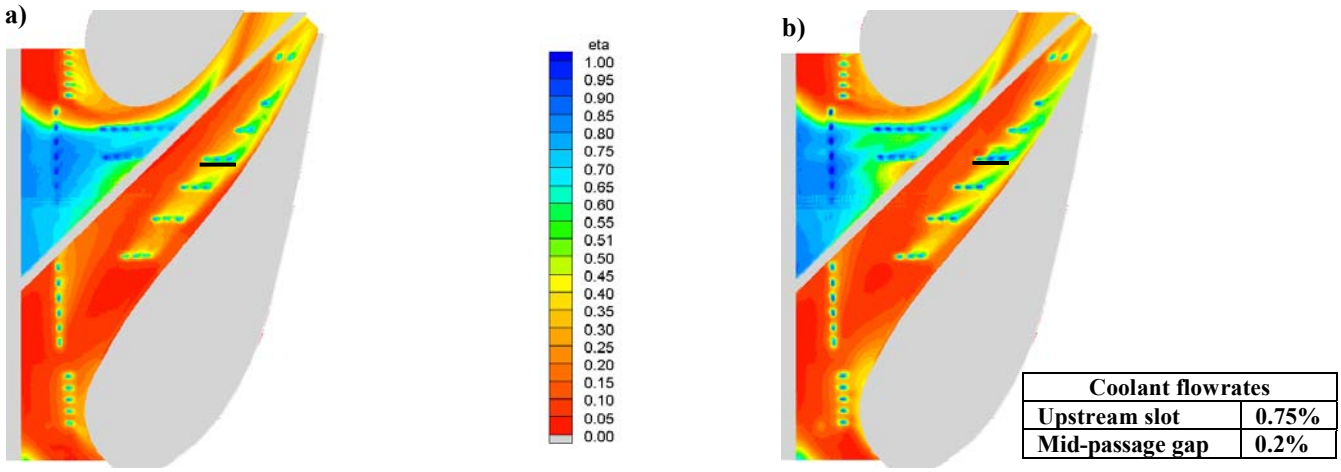

Figure 5.44. Adiabatic effectiveness contours with 0.8D deposition upstream of row 4 film-cooling holes with coolant mass flowrates of a) 0.5 percent and b) 0.9 percent.

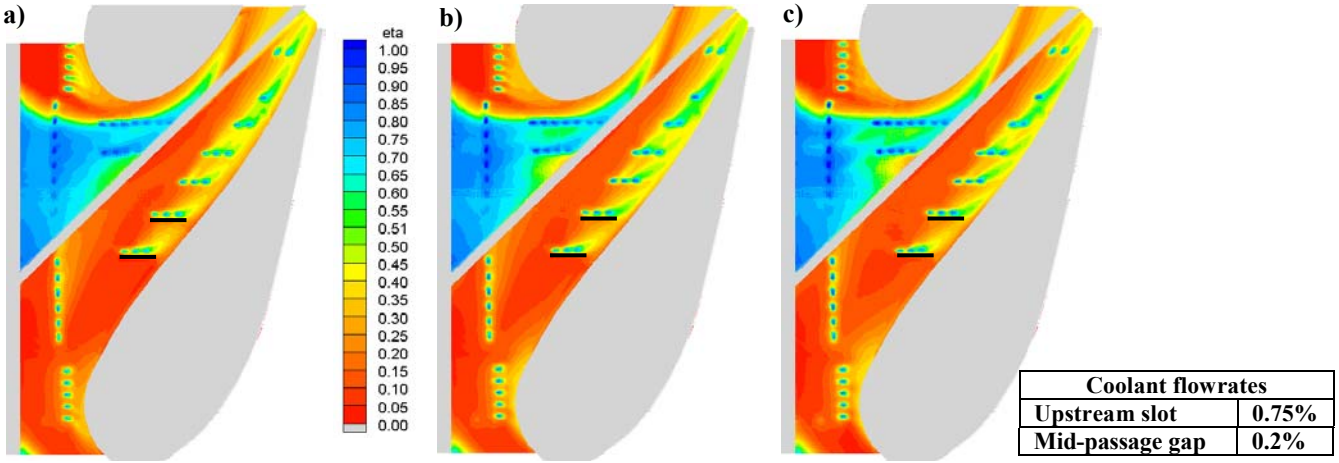

Figure 5.45. Adiabatic effectiveness contours with 0.8D deposition upstream of row 1 and 2 film-cooling holes with coolant mass flowrates of a) 0.5 percent, b) 0.75percent and c) 0.9 percent.

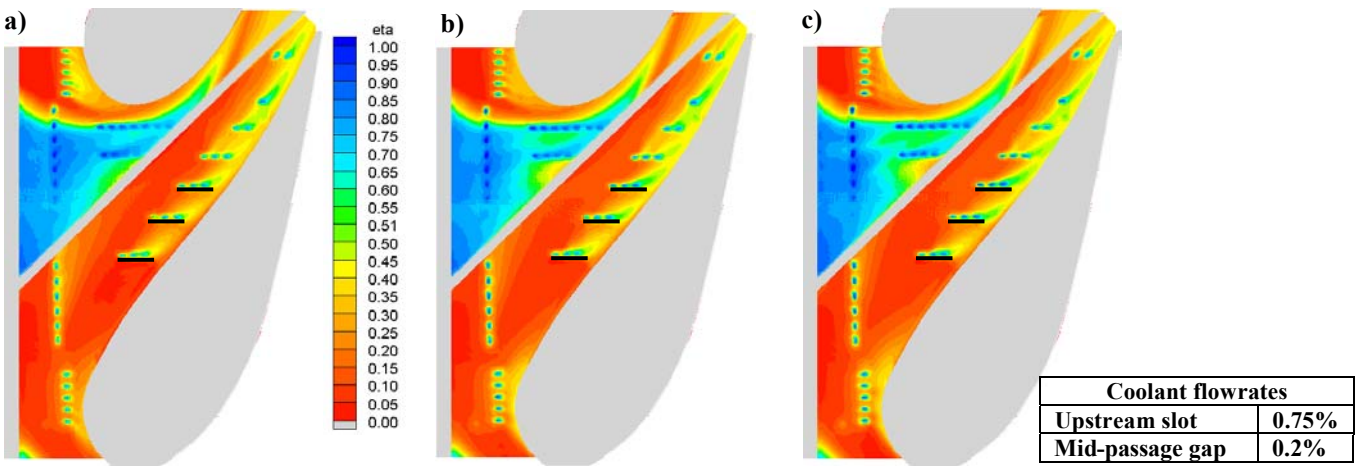

Figure 5.46. Adiabatic effectiveness contours with 0.8D deposition upstream of row 1, 2, and 3 film-cooling holes with coolant mass flowrates of a) 0.5 percent, b) 0.75 percent and c) 0.9 percent.

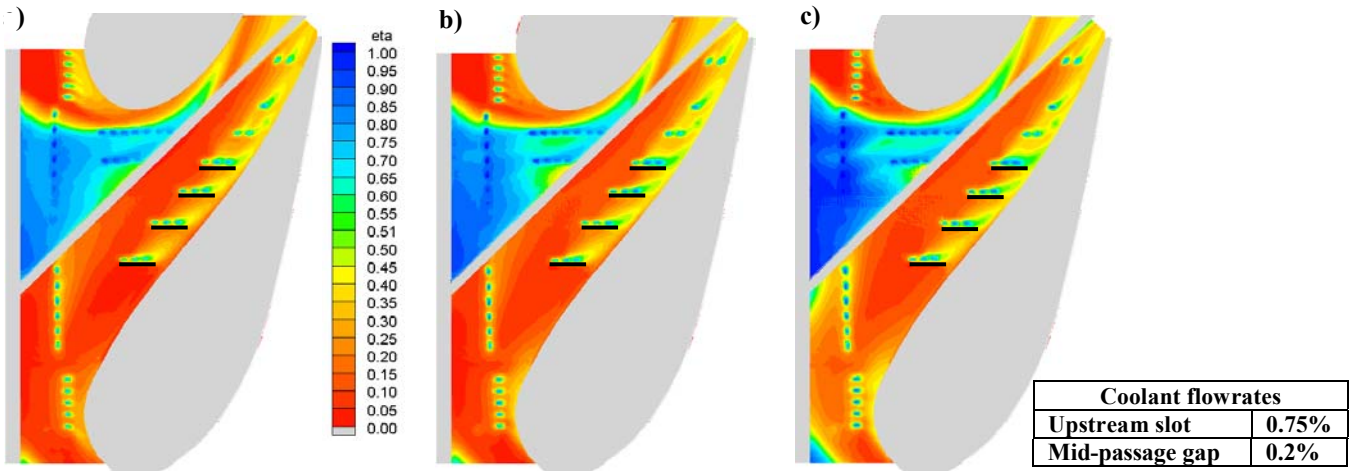

Figure 5.47. Adiabatic effectiveness contours with 0.8D deposition upstream of all four rows of film-cooling holes with coolant mass flowrates of a) 0.5 percent, b) 0.75 percent and c) 0.9 percent.

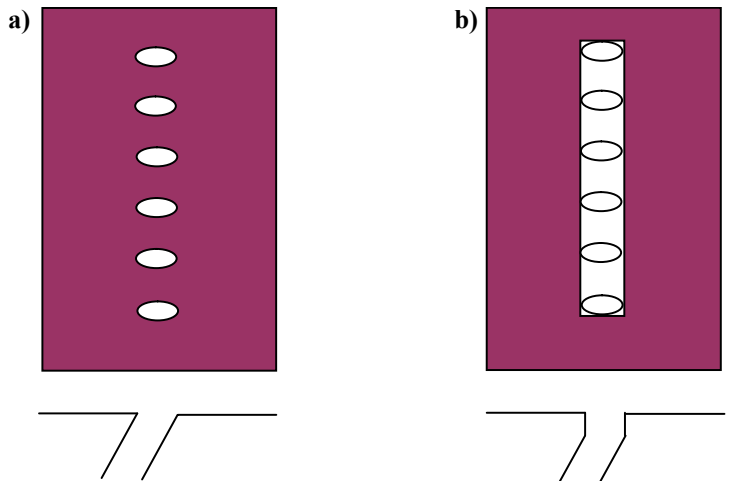

Figure 6.1. Illustration showing a) the present film-cooling hole geometry and b) film-cooling holes placed in transverse slots to be tested.

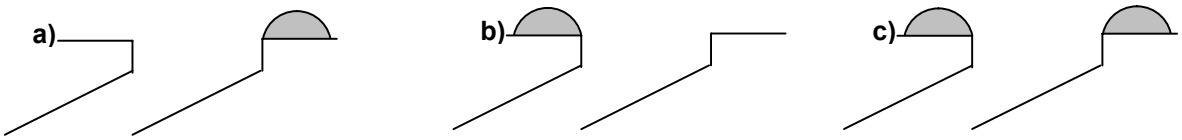

Figure 6.2. Illustration of placing deposits at a) downstream, b) upstream, and c) on both sides of a transverse slot geometry.

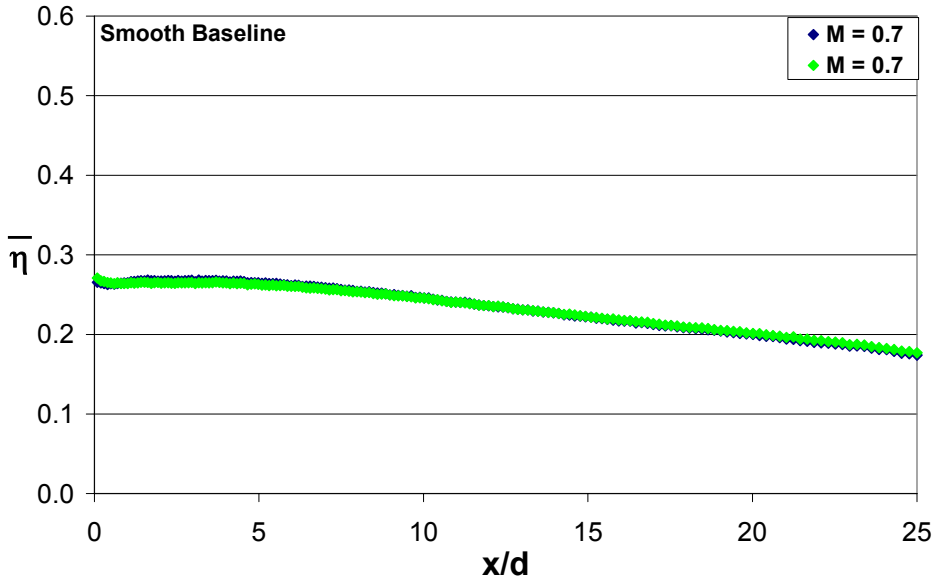

Figure 8.1. Representative in-test repeatability test for the baseline case at a blowing ratio of *M* = 0.7.

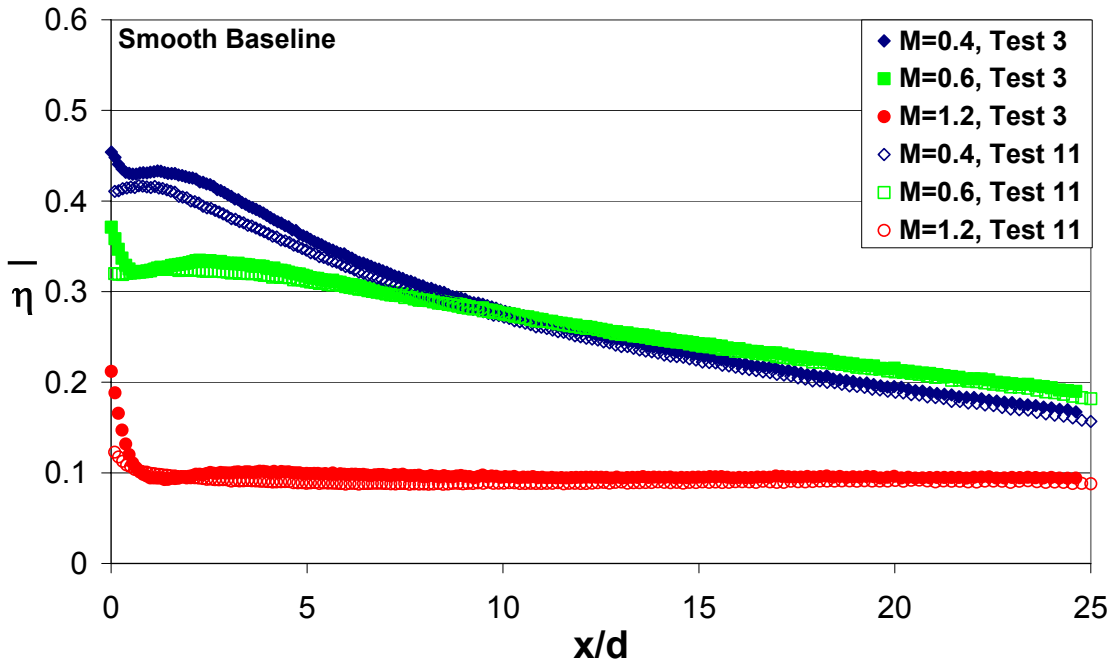

Figure 8.2. Representative test-to-test repeatability test for the baseline case.

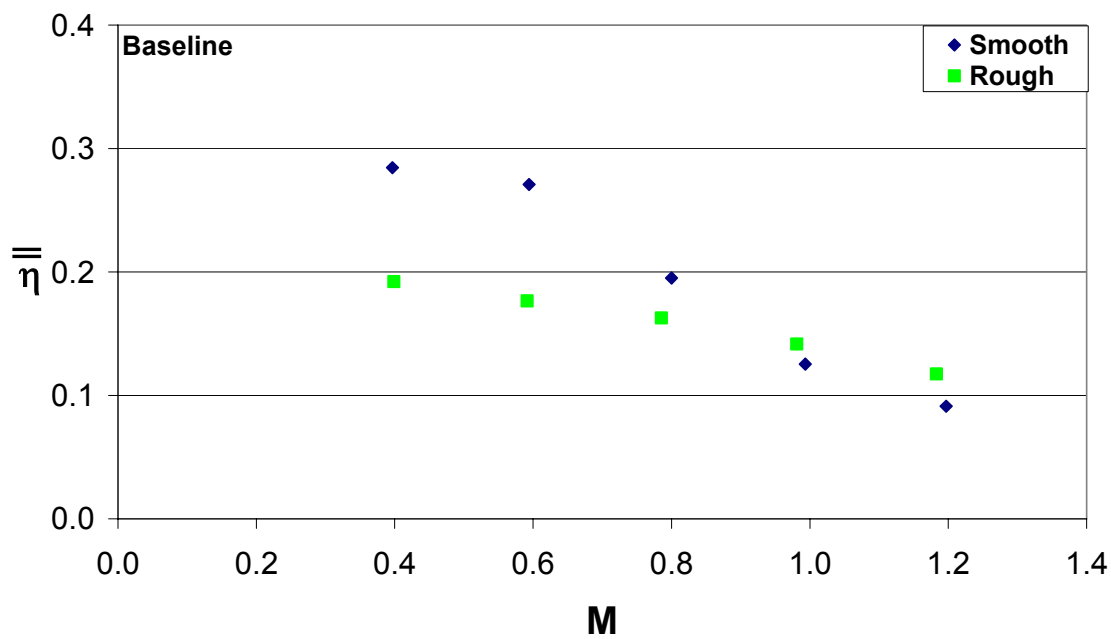

Figure 8.3. Spatially averaged effectiveness plot of the baseline case and the baseline case with the addition of roughness.

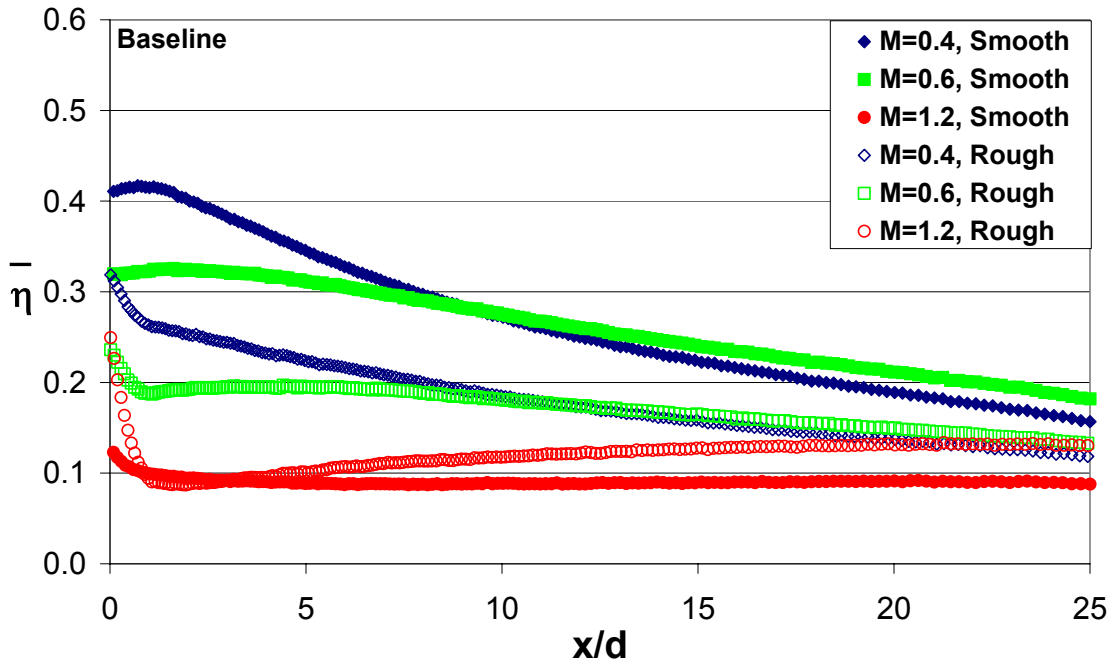

Figure 8.4. Laterally averaged effectiveness plot of the baseline case and the baseline case with a rough wall.

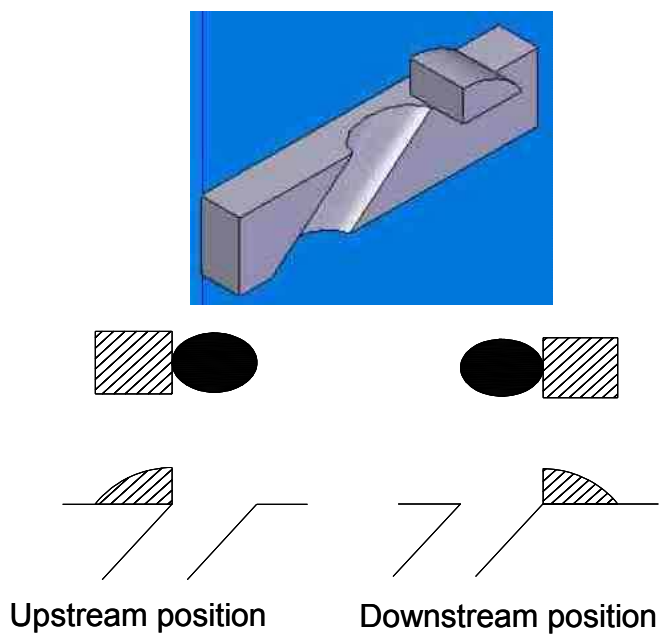

Figure 9.1. Schematic of Shape #2 obstruction places upstream and downstream of the coolant hole.

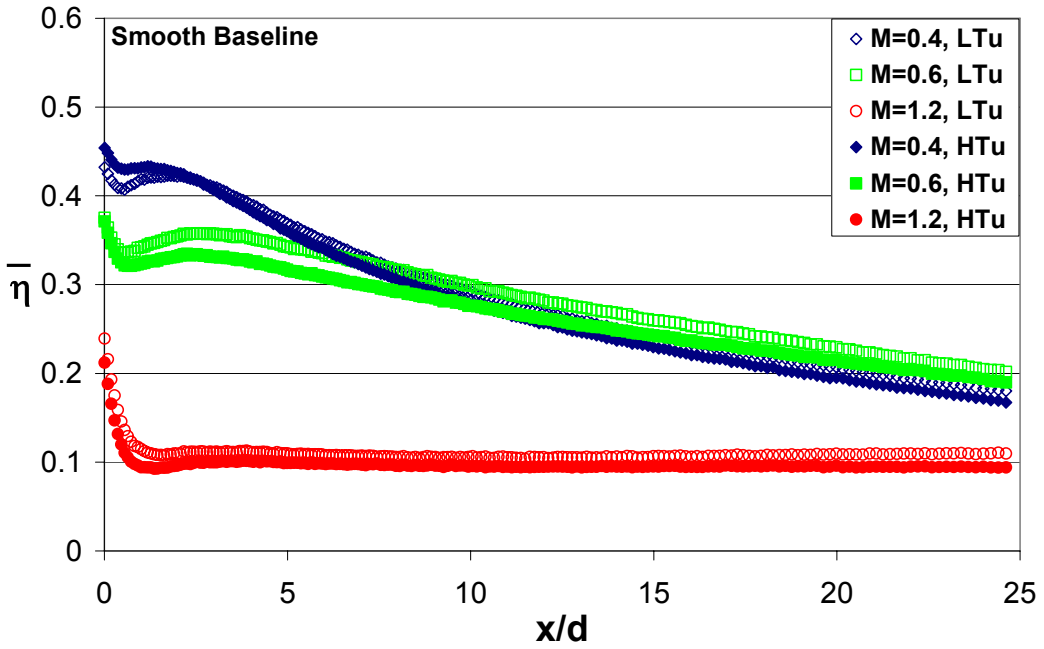

Figure 9.2. Laterally averaged effectiveness plot of the baseline case demonstrating the similar performance for low and high mainstream turbulence.

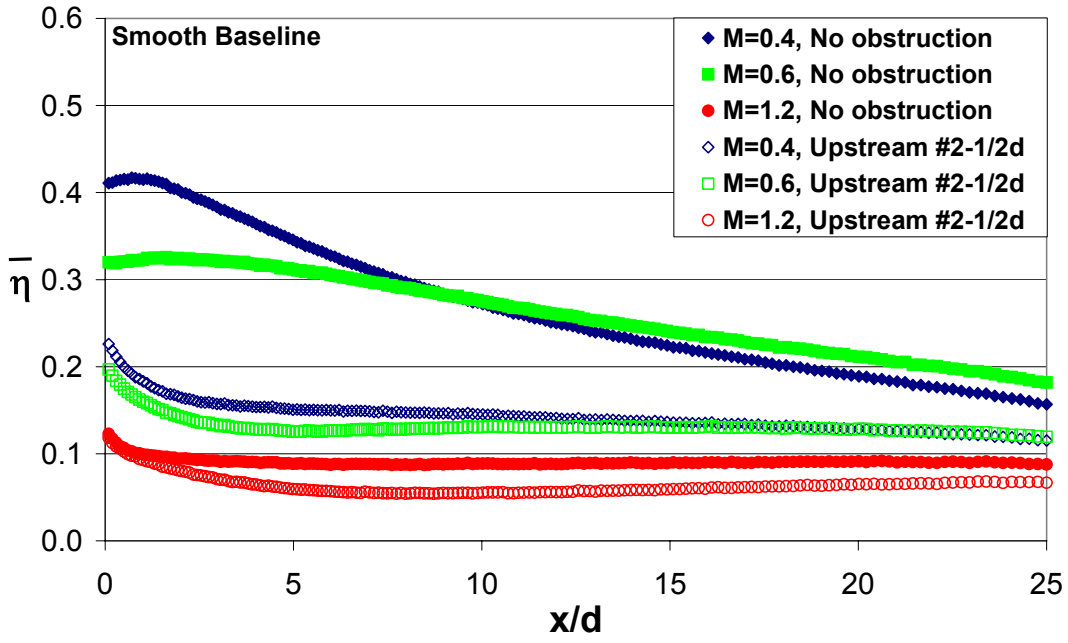

Figure 9.3. Laterally averaged effectiveness plot of the baseline case and the baseline case with upstream obstructions.

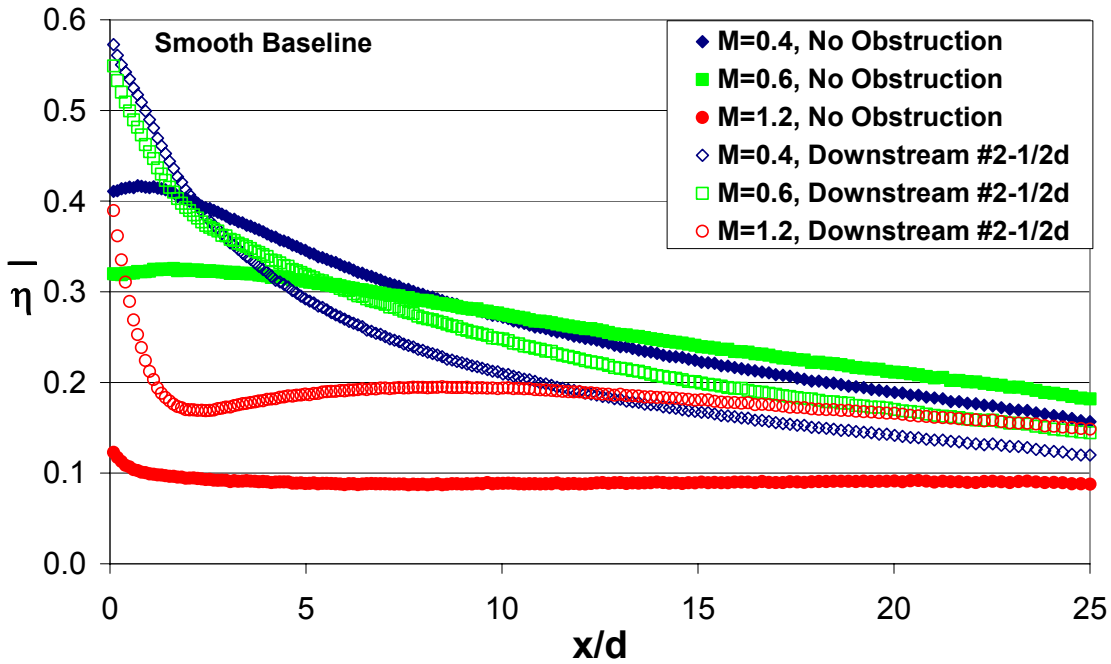

Figure 9.4. Laterally averaged effectiveness plot of the baseline case and the baseline case with the addition of downstream obstructions.

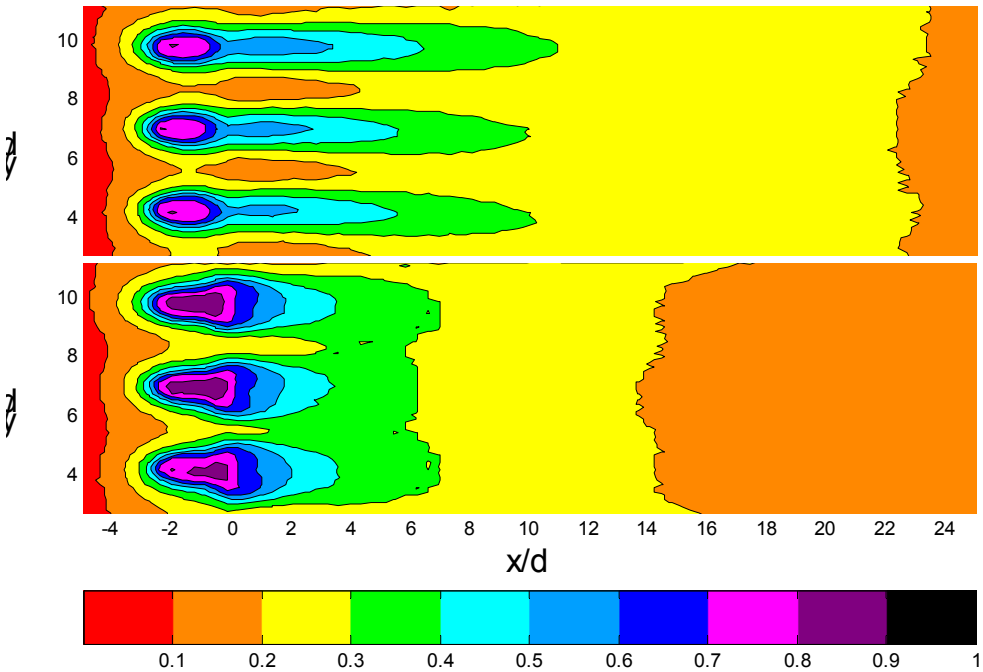

Figure 9.5. Effectiveness contours of the smooth baseline case (top) and the smooth baseline case with downstream obstructions (bottom) at M=0.6.

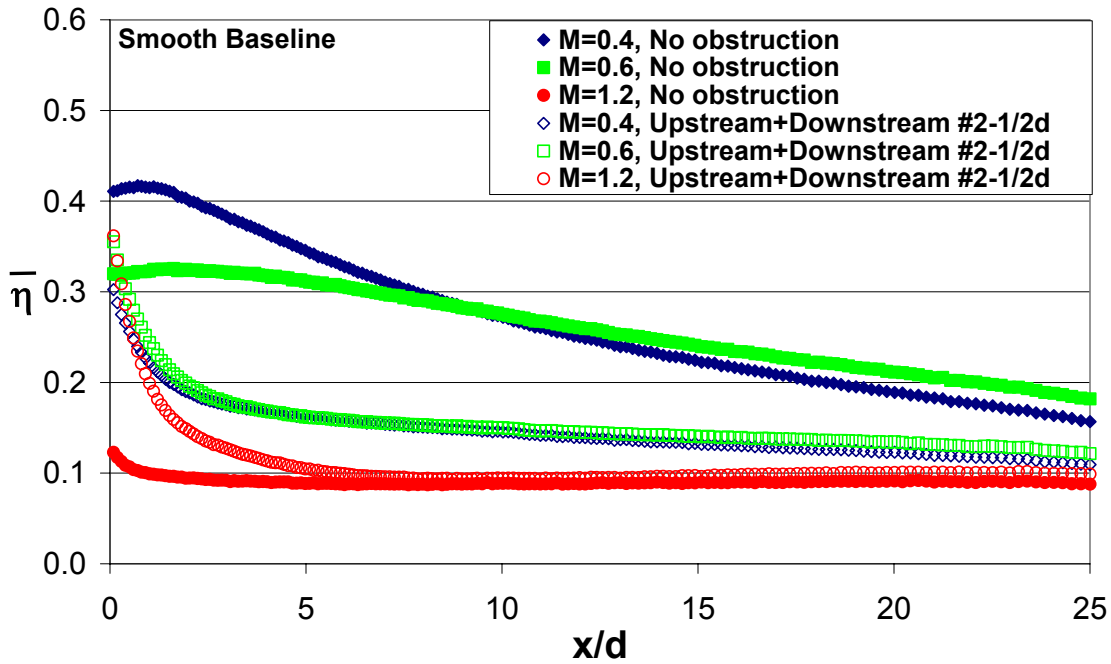

Figure 9.6. Laterally averaged effectiveness plot of the baseline case and the baseline case with the addition of upstream + downstream obstructions.

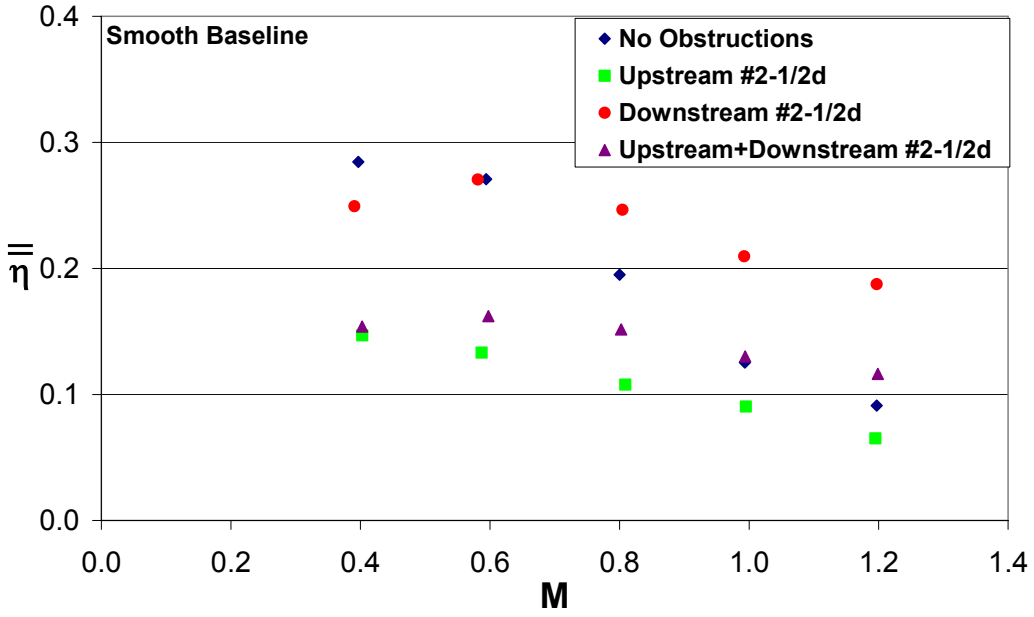

Figure 9.7. Spatially averaged effectiveness plot of the baseline case with and without obstructions.

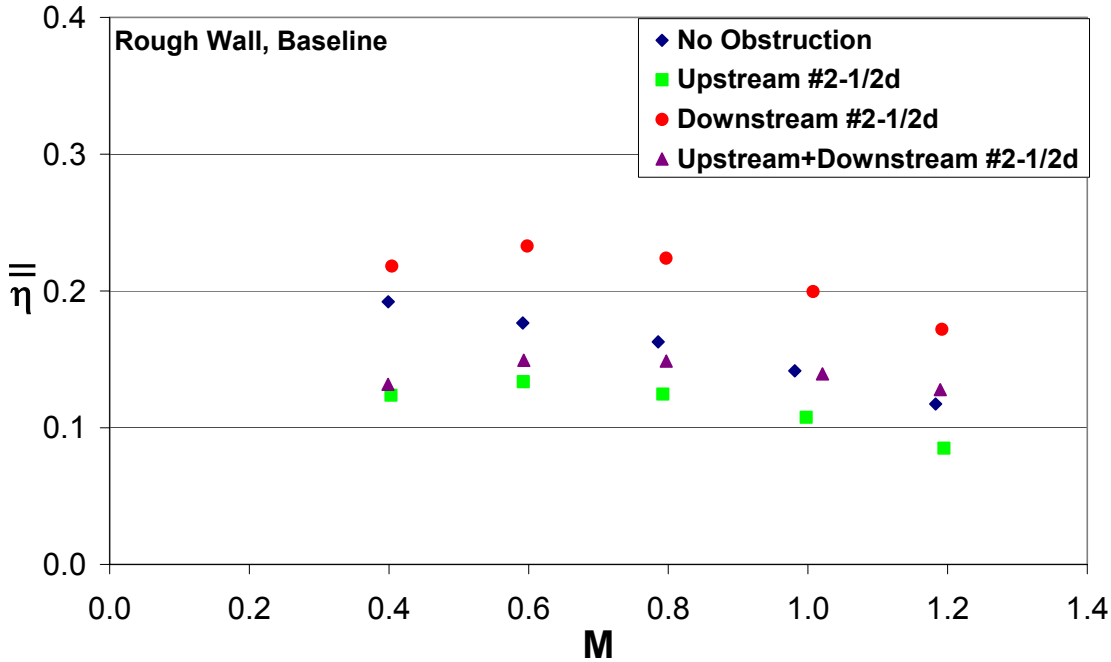

Figure 9.8. Spatially averaged effectiveness plot of the baseline case with a rough wall and the baseline case with the addition of obstructions on a rough wall.

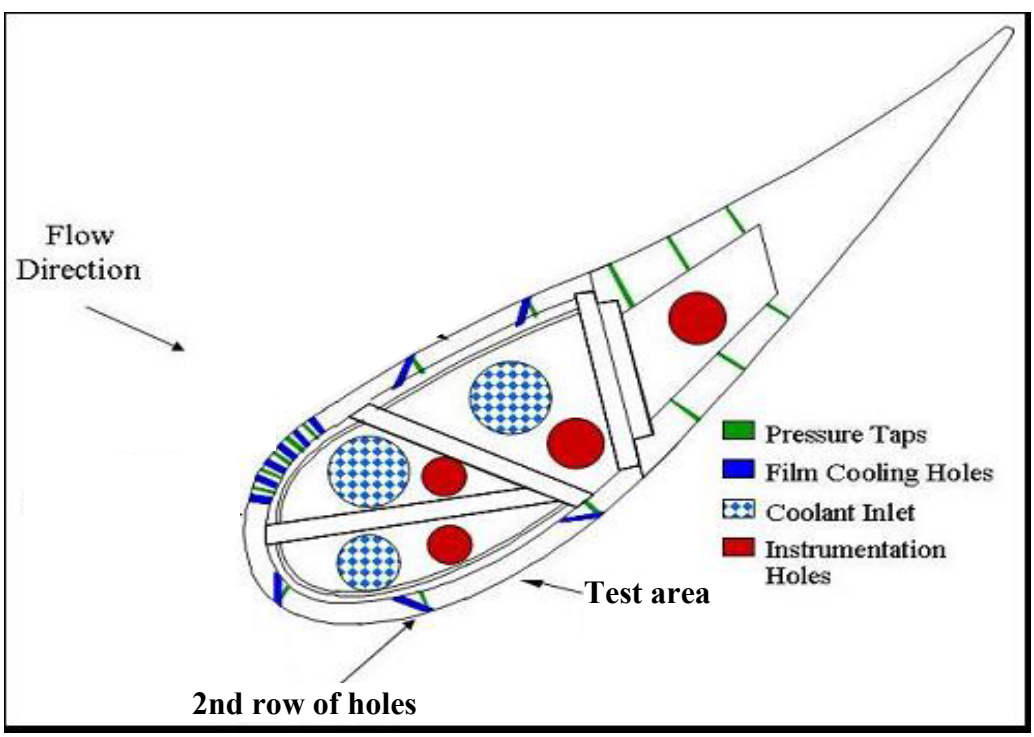

Figure 10.1. Schematic of test vane.

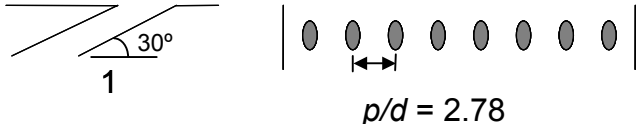

Figure 10.2. Baseline axial hole configuration.

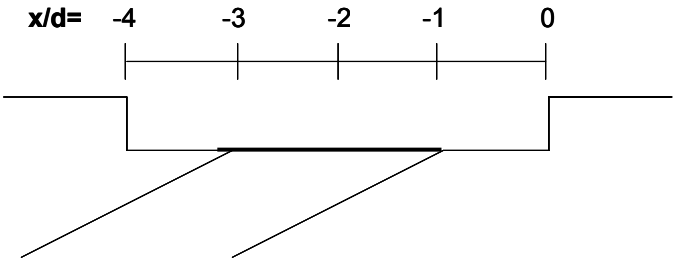

Figure 10.3. Coordinate origin for trench configurations.

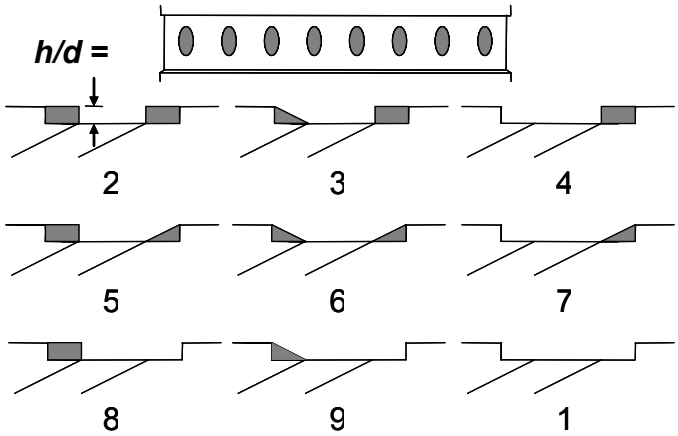

Figure 10.4. Schematic of shallow trench configurations.

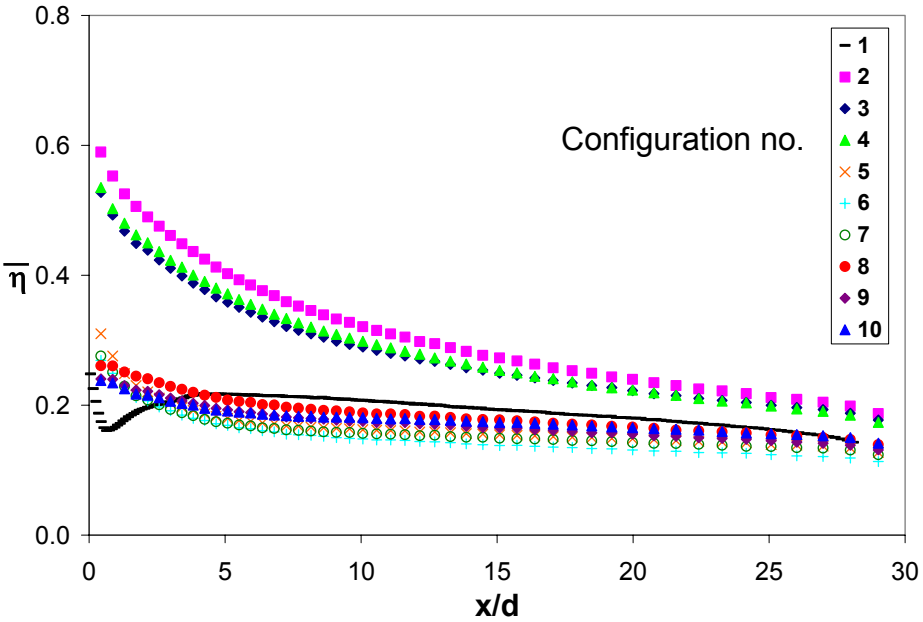

Figure 10.5. Comparison of laterally averaged adiabatic effectiveness for all trench configurations tested, M = 1.0, Tu_∞ = 1.0%

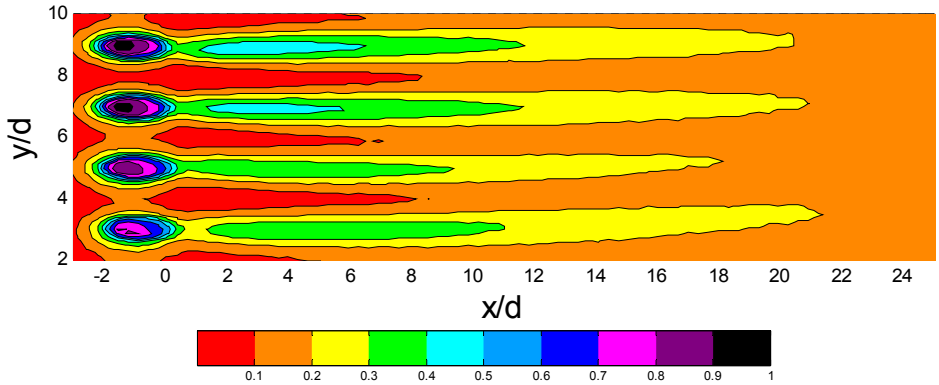

Figure 10.6 (a) Spatial adiabatic effectiveness distribution for baseline axial holes, M = 1.0, Tu = 1.0%

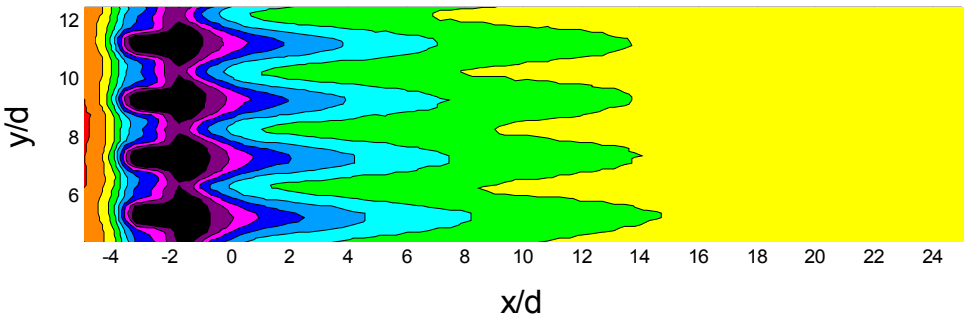

Figure 10.6 (b) Spatial adiabatic effectiveness distribution for Configuration 2, *M* = 1.0, *Tu* = 1.0%

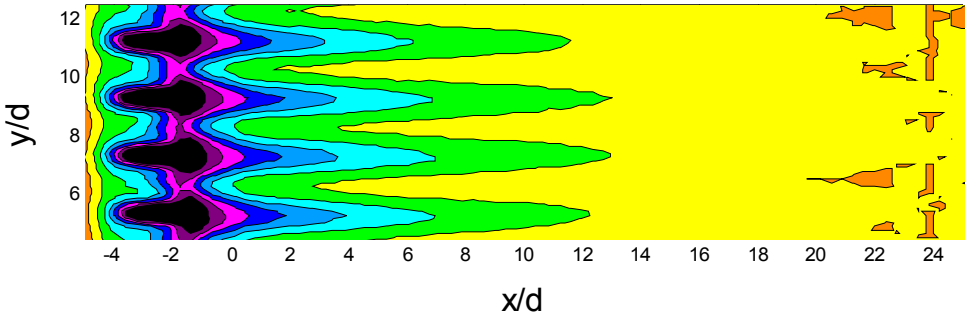

Figure 10.6 (c) Spatial adiabatic effectiveness distribution for Configuration 3, *M* = 1.0, *Tu* = 1.0%

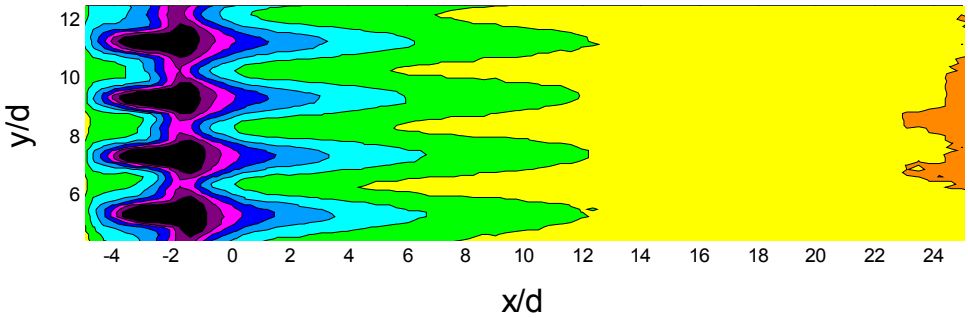

Figure 10.6 (d) Spatial adiabatic effectiveness distribution for Configuration 4, *M* = 1.0, *Tu* = 1.0%

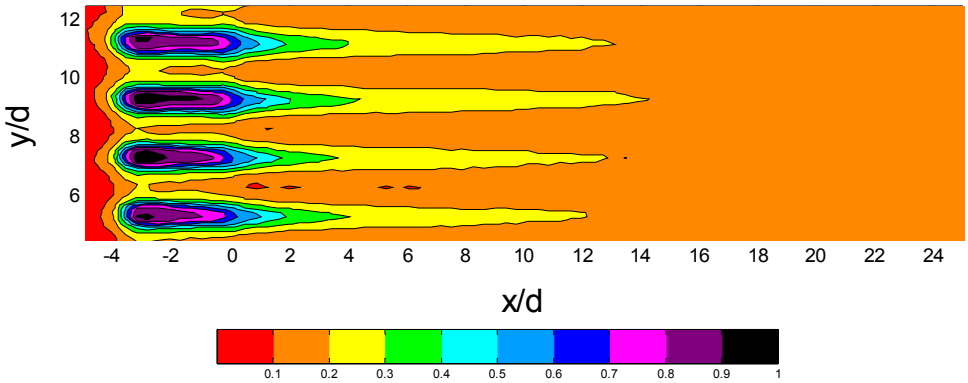

Figure 10.6 (e) Spatial adiabatic effectiveness distribution for Configuration 5, *M* = 1.0, *Tu* = 1.0%

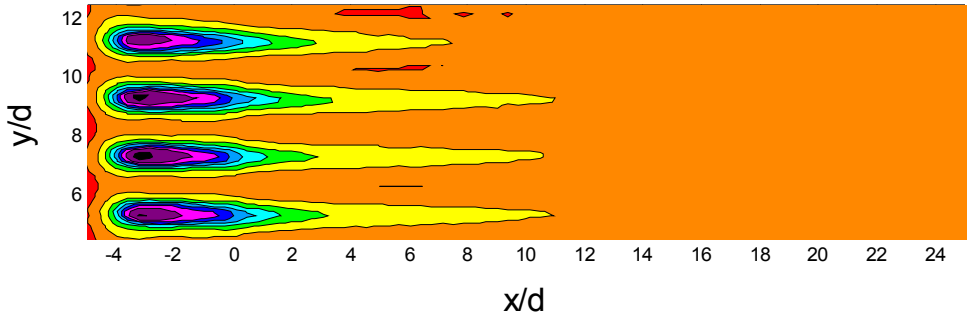

Figure 10.6 (f) Spatial adiabatic effectiveness distribution for Configuration 6, *M* = 1.0, *Tu* = 1.0%

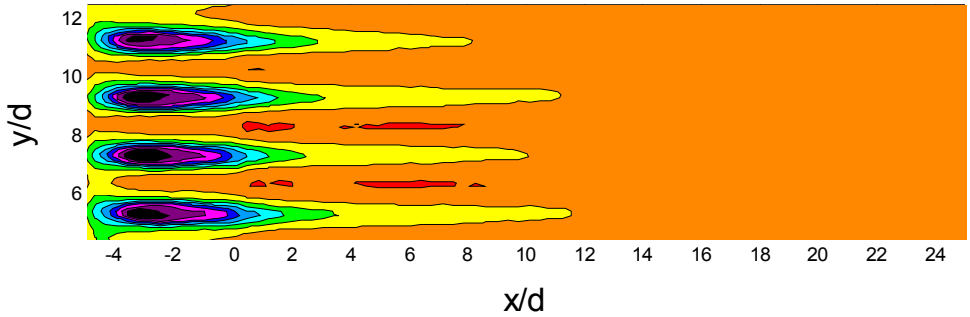

Figure 10.6 (g) Spatial adiabatic effectiveness distribution for Configuration 7, *M* = 1.0, *Tu* = 1.0%

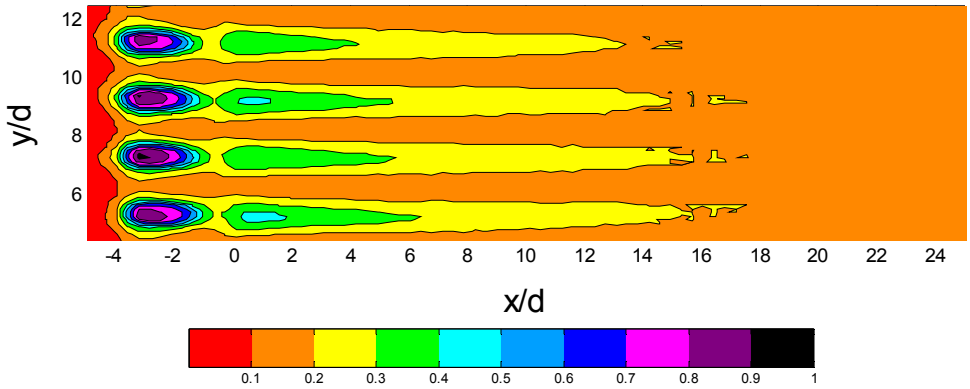

Figure 10.6 (h) Spatial adiabatic effectiveness distribution for Configuration 8, *M* = 1.0, *Tu* = 1.0%

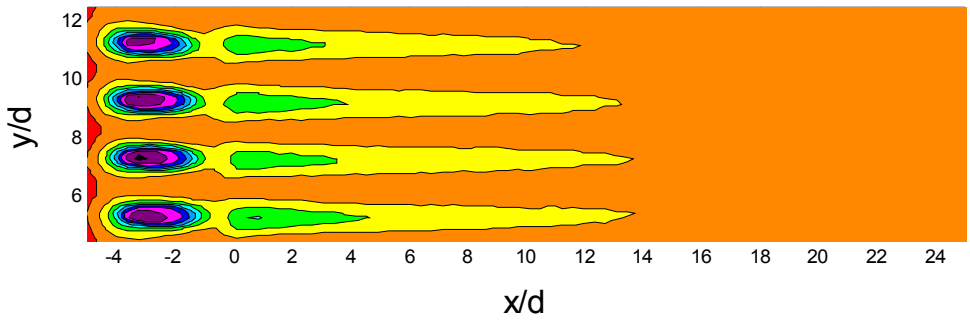

Figure 10.6 (i) Spatial adiabatic effectiveness distribution for Configuration 9, *M* = 1.0, *Tu* = 1.0%

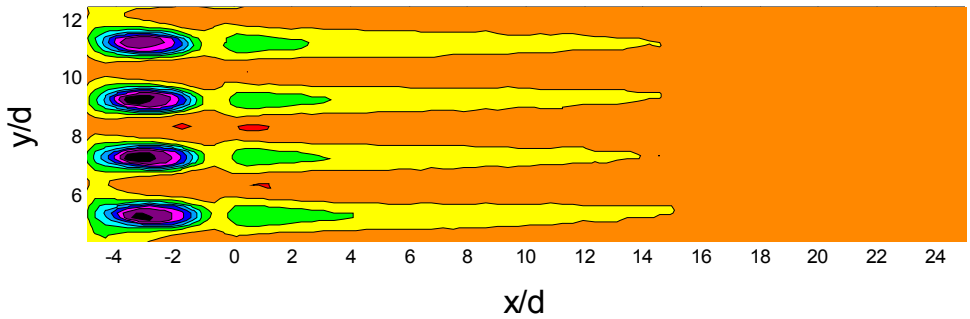

Figure 10.6 (j) Spatial adiabatic effectiveness distribution for Configuration 2\10, *M* = 1.0, *Tu* = 1.0%

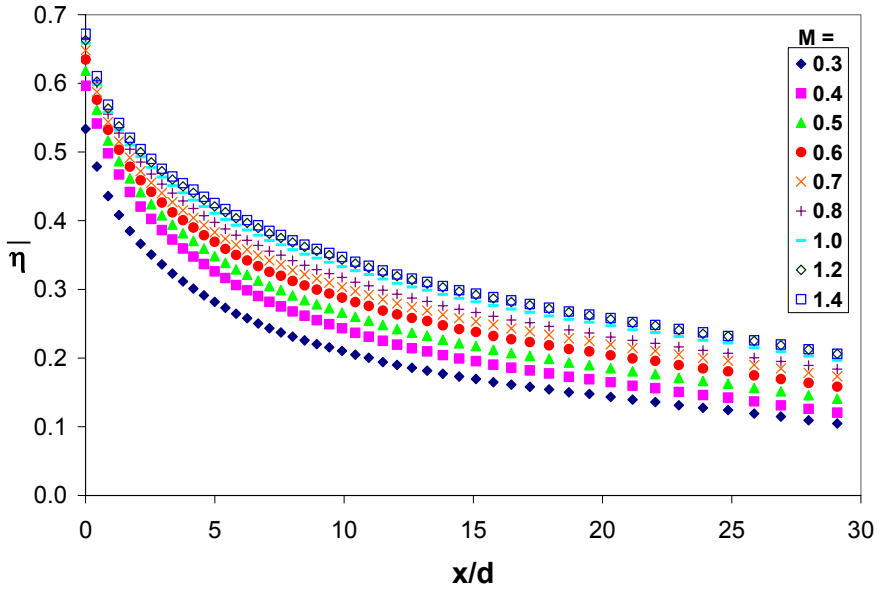

Figure 10.7. Laterally averaged adiabatic effectiveness for axial holes embedded in the narrow trench configuration, *p/d* = 2.8, and *Tu* = 3.9%

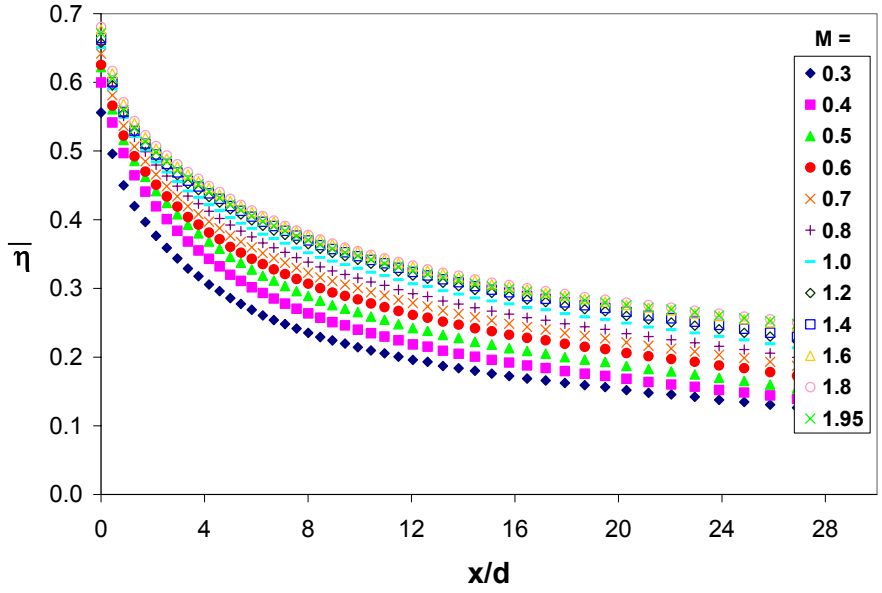

Figure 10.8. Laterally averaged adiabatic effectiveness for axial holes embedded in a narrow trench configuration, *p/d* = 8, *Tu* = 1.0%

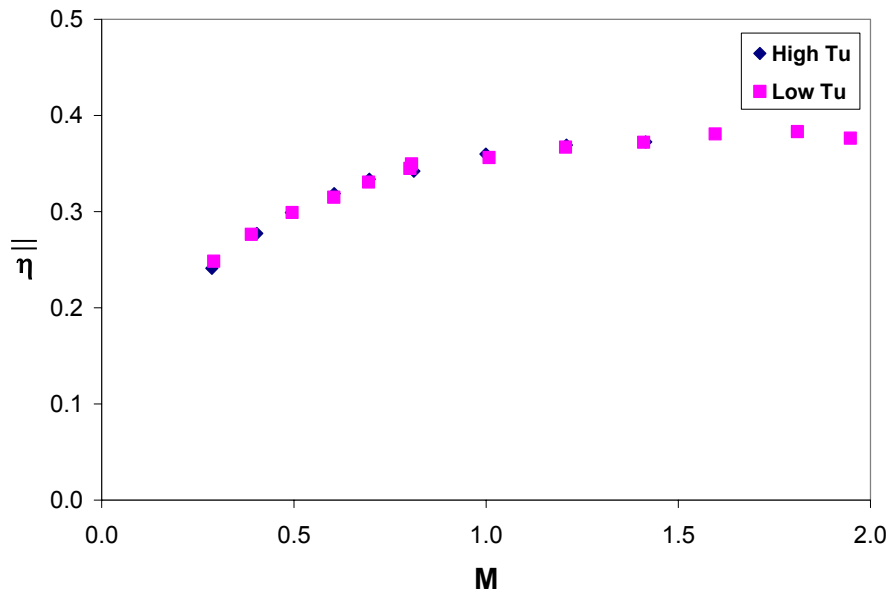

Figure 10.9. Spatially averaged adiabatic effectiveness (x/d = 0 to 25) for low and high mainstream turbulence levels.

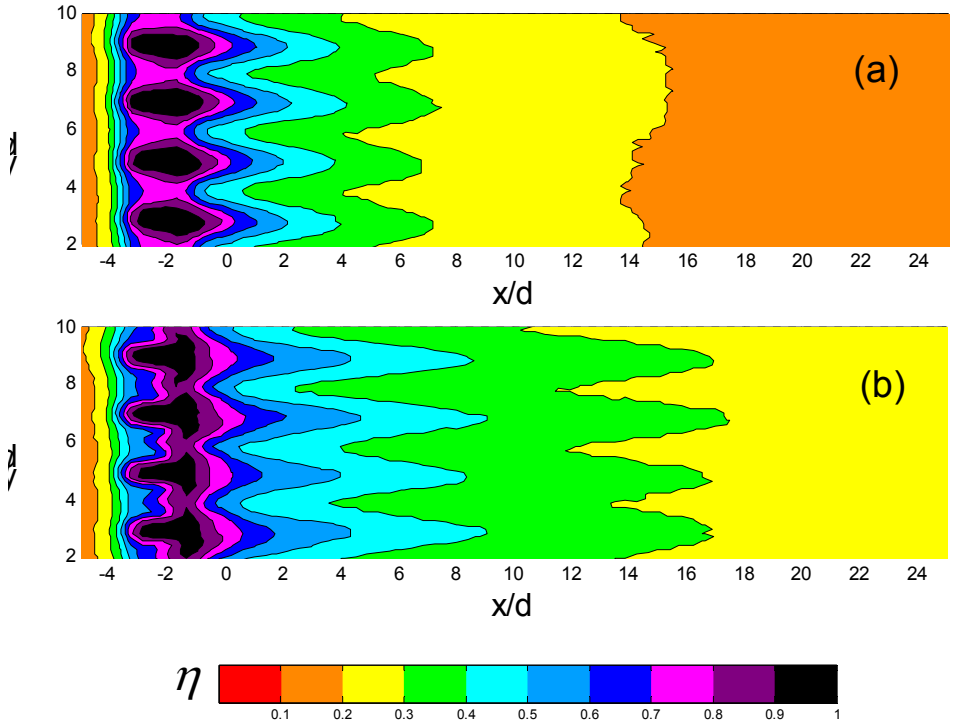

Figure 10.10. Spatial adiabatic effectiveness distribution for narrow trench configuration, (a) *M* = 0.4 and (b) *M* = 1.95.

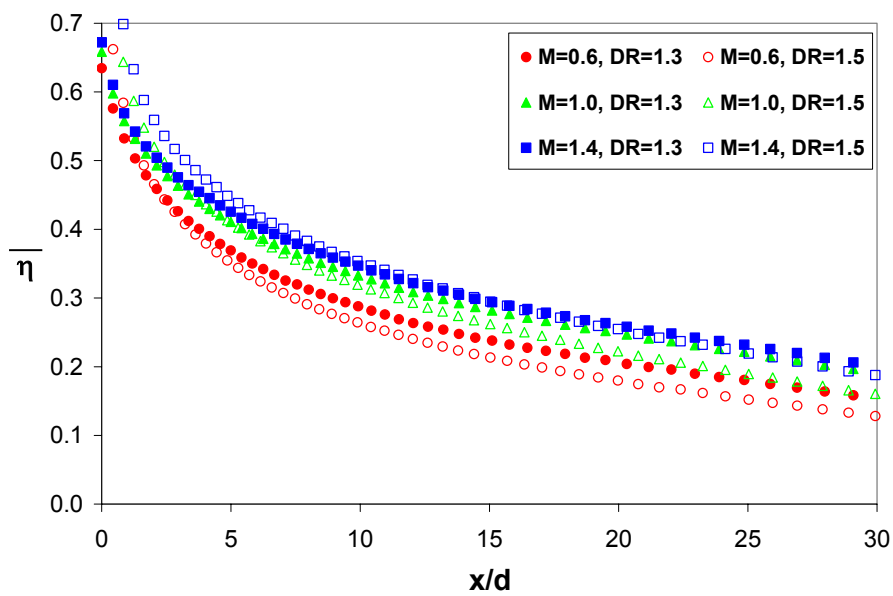

Figure 10.11. Comparison adiabatic effectiveness at density ratios of *DR* = 1.3 and 15 using the narrow trench configuration, *Tu* = 3.9%.

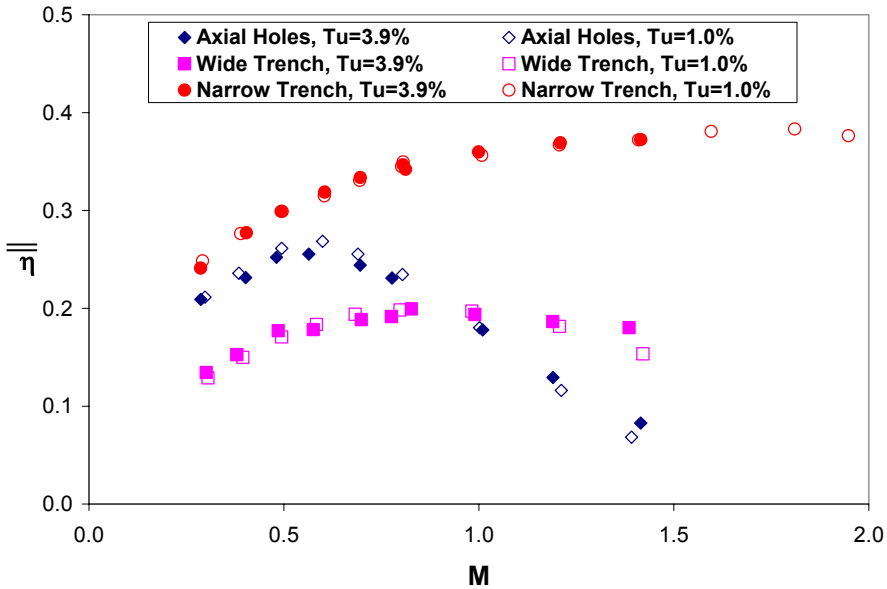

Figure 10.12. Comparison of spatially averaged adiabatic effectiveness for narrow and wide trench configurations (Configurations 2 and 10). For reference, the baseline axial hole configuration is also presented.

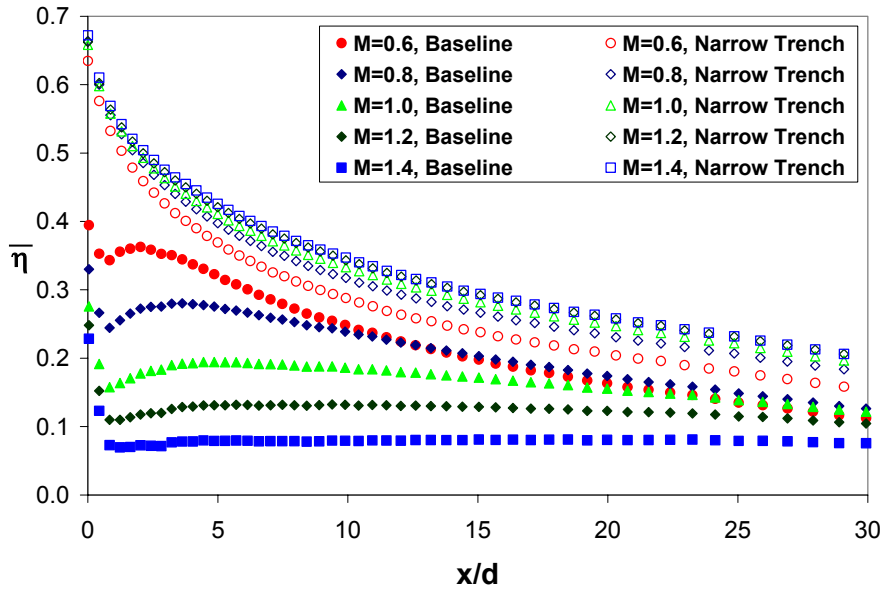

Figure 10.13. Comparison of baseline axial hole and narrow trench configurations, *Tu* = 3.9%

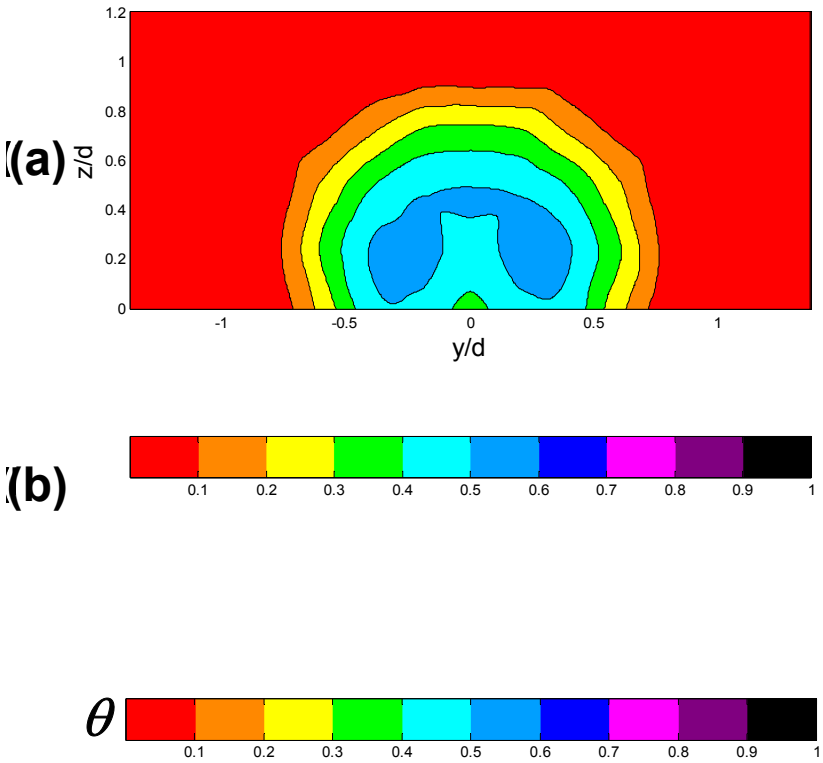

Figure 10.14. Lateral θ profiles at x/d = 2, with M = 1.0, Tu = 1.0% for (a) axial holes and (b) narrow trench configurations.

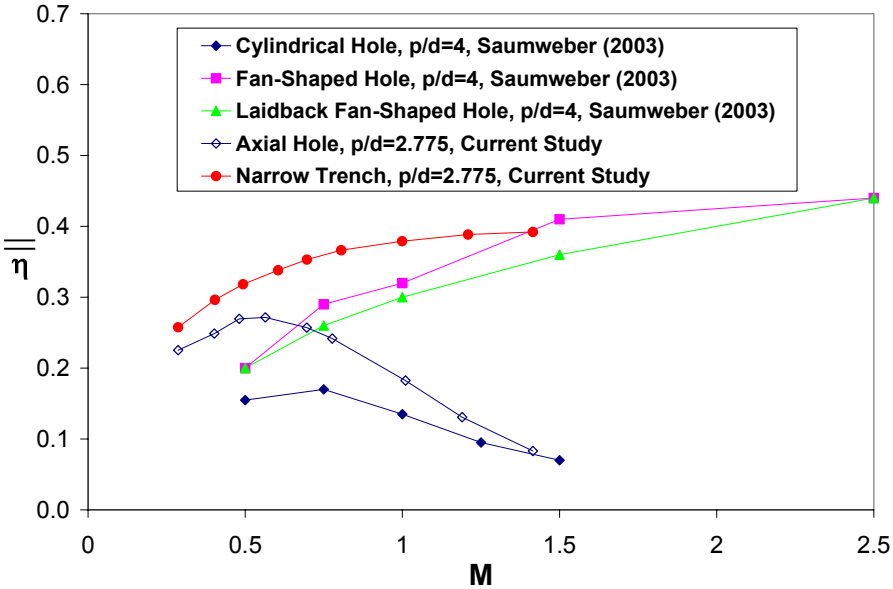

Figure 10.15. Comparison of the narrow trench configuration to shaped hole configurations.

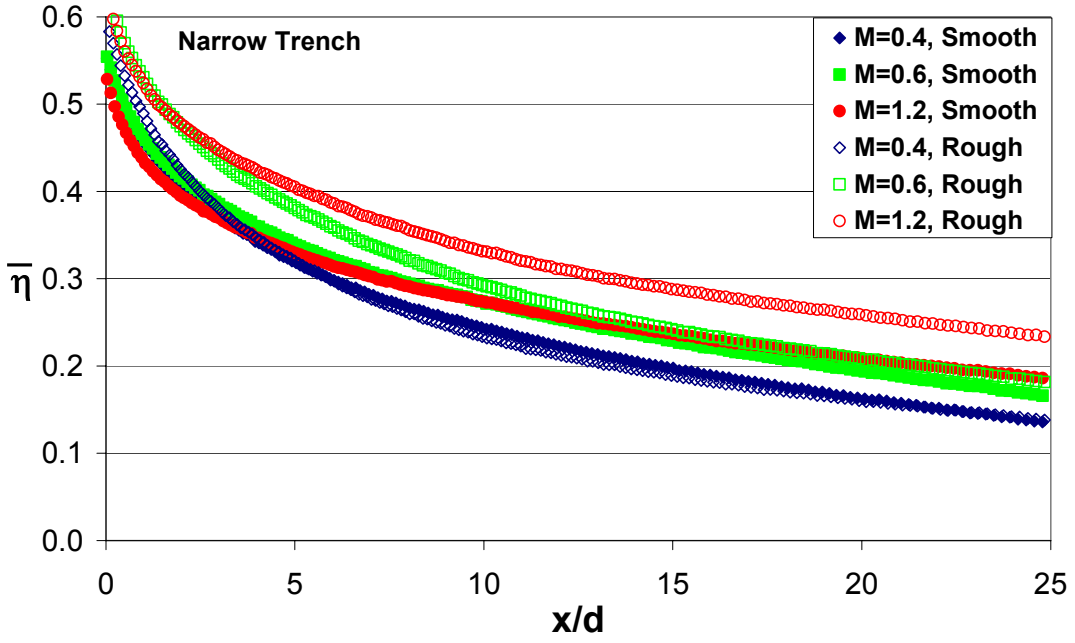

Figure 10.16. Laterally averaged effectiveness plot of the narrow transverse trench case and the narrow transverse trench case with a rough wall.

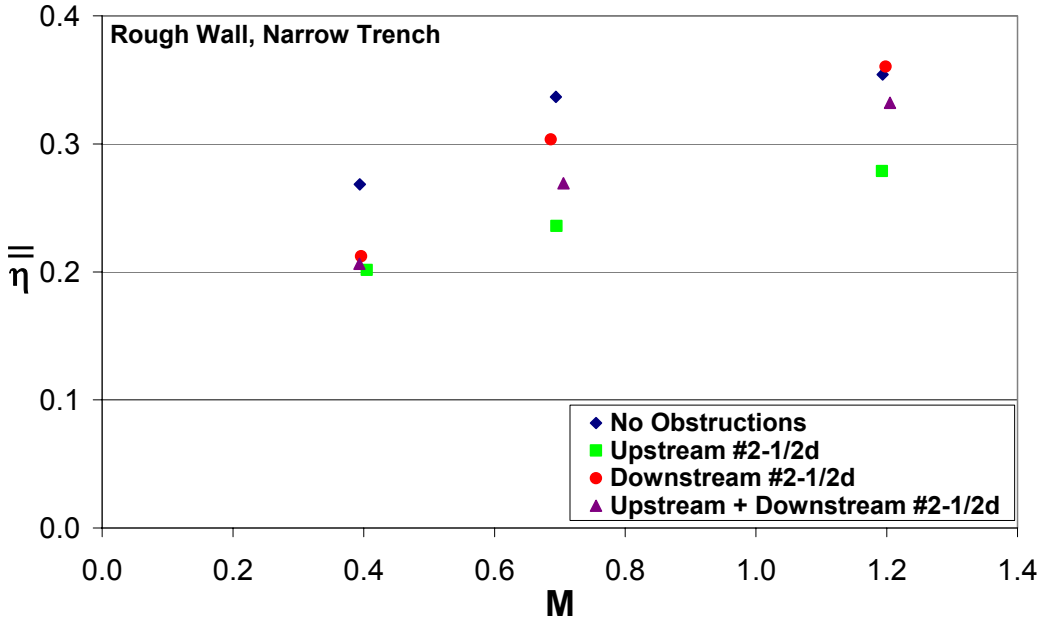

Figure 11.1. Spatially averaged effectiveness for a rough surface with a narrow transverse trench without and with obstructions.

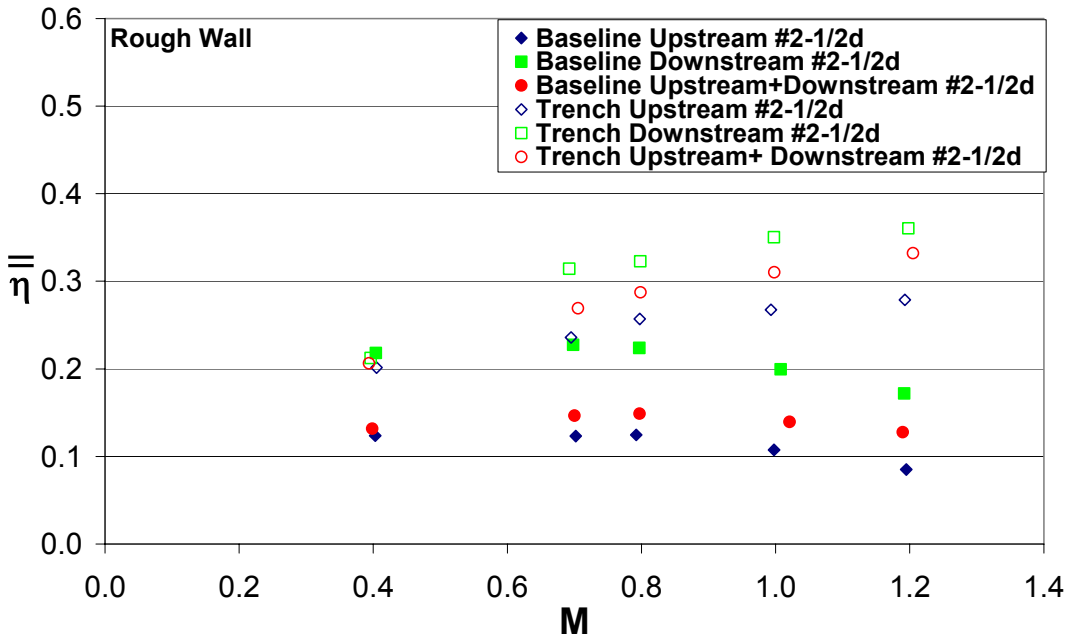

Figure 11.2. Spatially averaged effectiveness plot of the baseline case with obstructions on a rough wall and the narrow transverse trench case with obstructions on a rough wall.

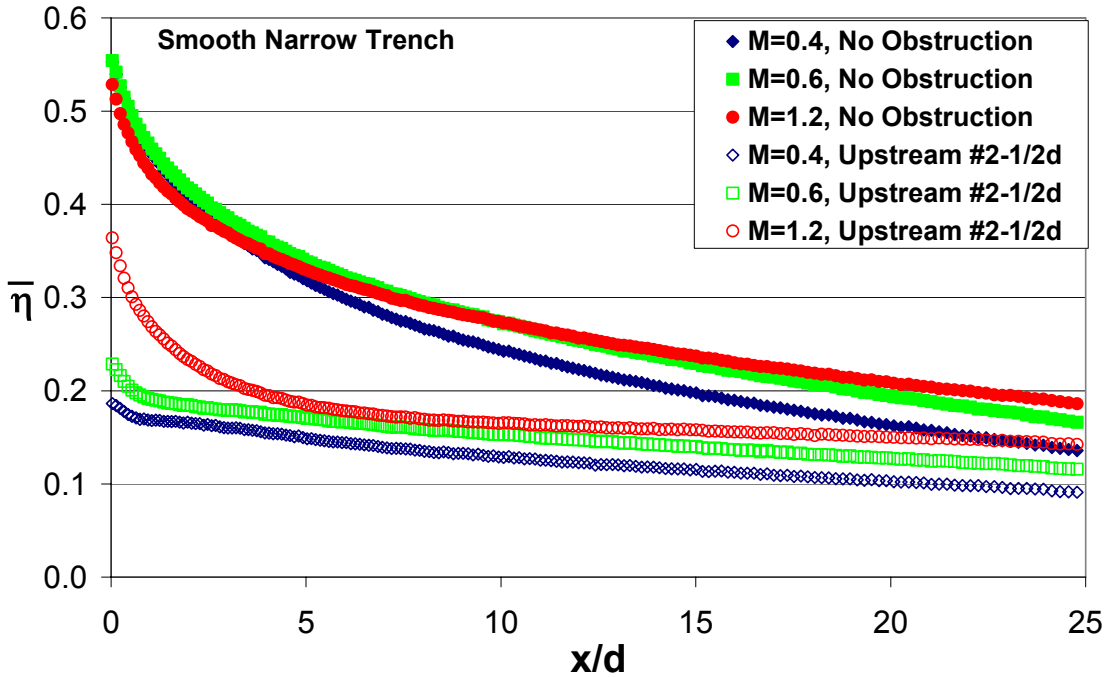

Figure 11.3. Laterally averaged effectiveness plot of the narrow transverse trench case and the narrow transverse trench case with the addition of upstream obstructions.

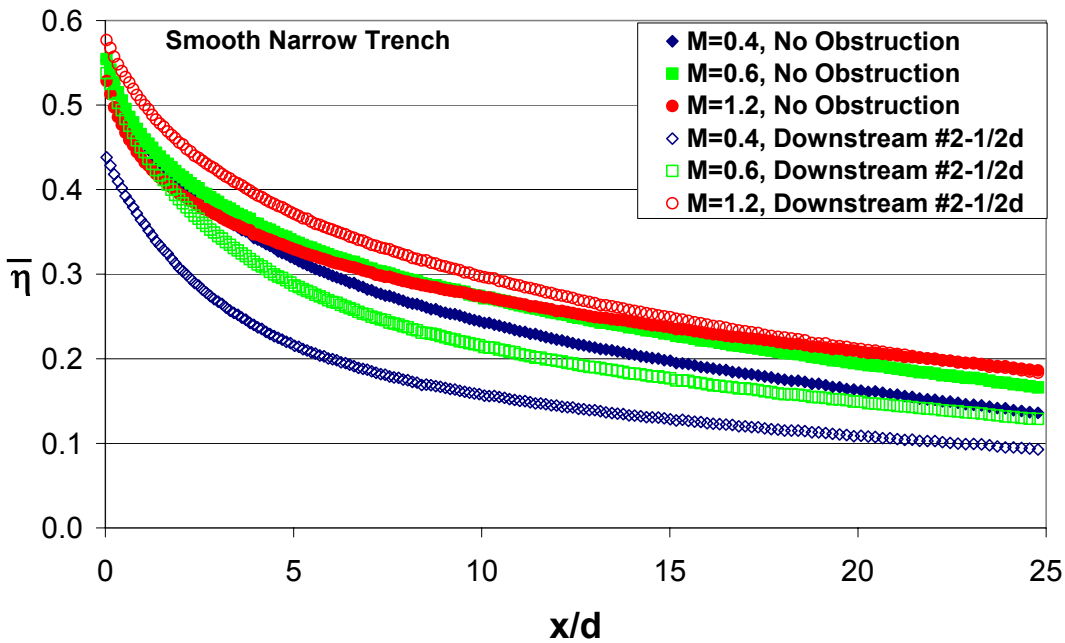

Figure 11.4.
Laterally averaged effectiveness plot of the narrow transverse trench case and the narrow transverse trench case with the addition of downstream obstructions.

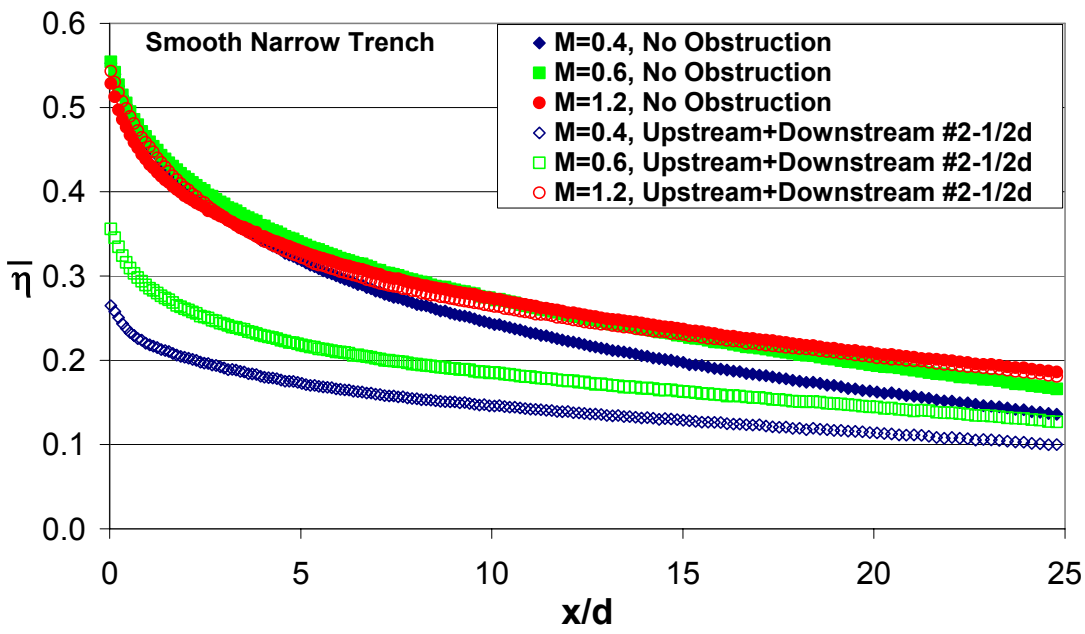

Figure 11.5. Laterally averaged effectiveness plot of the narrow transverse trench case and the narrow transverse trench case with the addition of upstream + downstream obstructions.

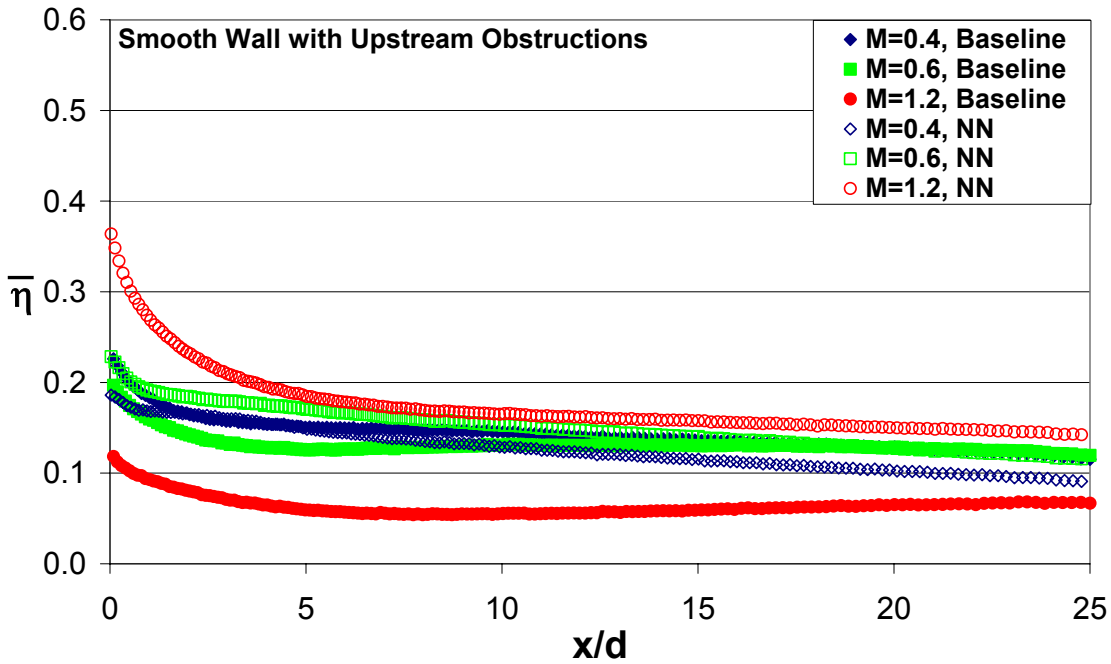

Figure 11.6. Laterally averaged effectiveness plot of the baseline case with upstream obstructions and the narrow transverse trench case with upstream obstructions.

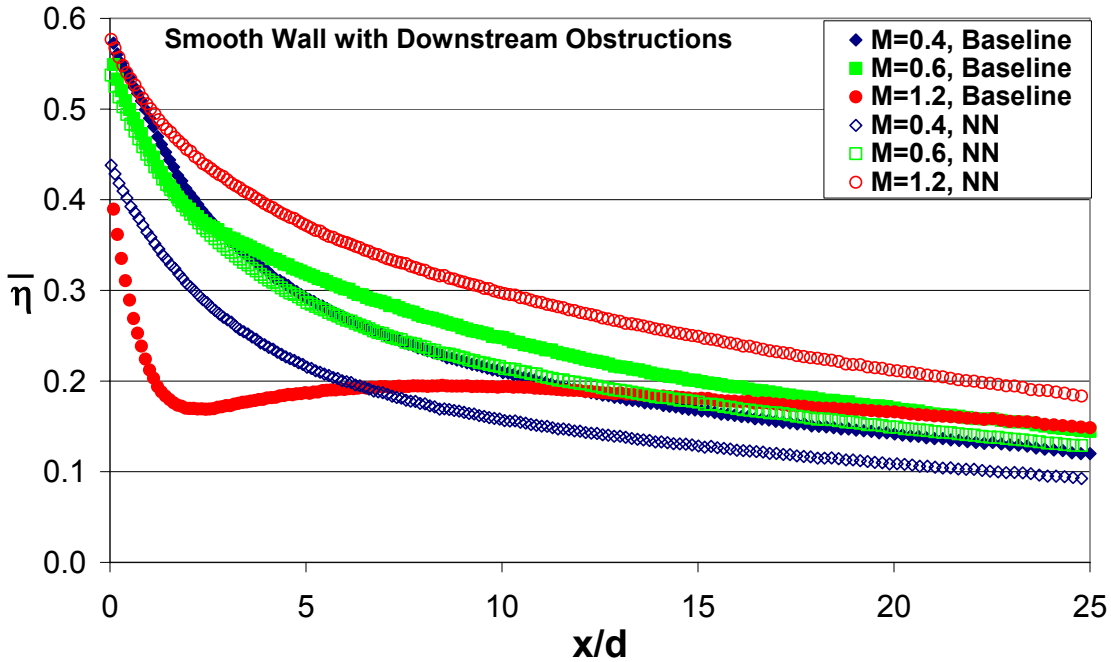

Figure 11.7. Laterally averaged effectiveness plot of the baseline case with downstream obstructions and the narrow transverse trench case with downstream obstructions.

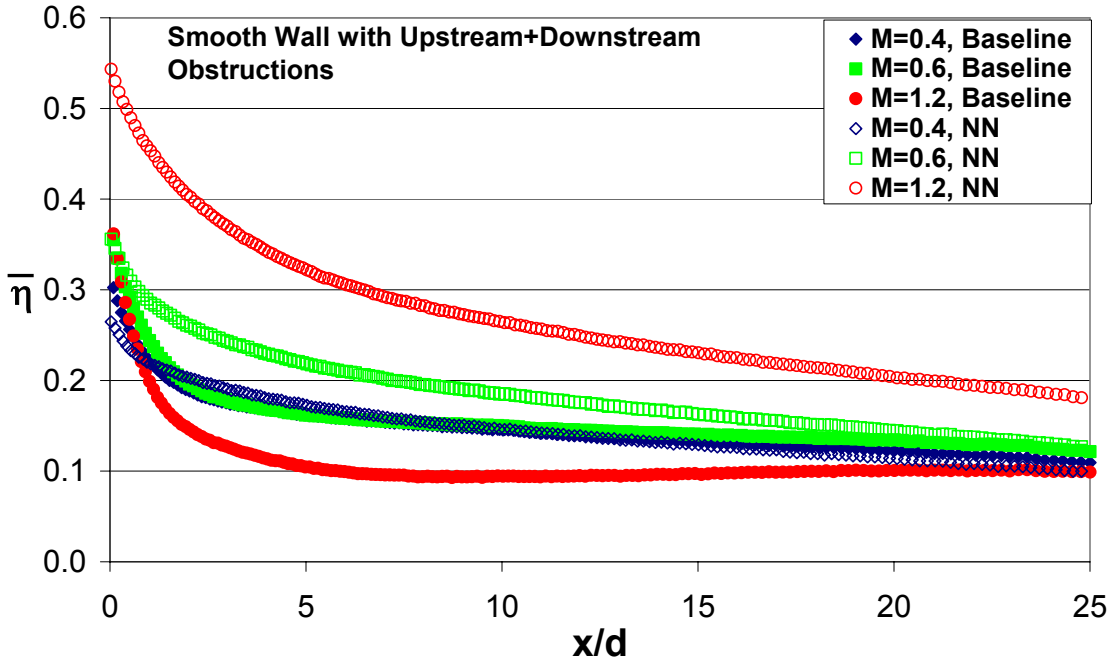

Figure 11.8. Laterally averaged effectiveness plot of the baseline case with upstream + downstream obstructions and the narrow transverse trench case with upstream + downstream obstructions.

Combustion Instability and Blowout Characteristics of Fuel Flexible Combustors

Semi-Annual Report

Reporting Period Start Date: July 31, 2005

Reporting Period End Date: January 1, 2006

Principal Investigators: Tim Lieuwen and Ben Zinn

Date Report was issued February 2, 2006

DOE Award Number 03-01-SR111

School of Aerospace Engineering

Georgia Institute of Technology

Atlanta, GA 30332-0150

DISCLAIMER:

"This report was prepared as an account of work sponsored by an agency of the United States Government. Neither the United States Government nor any agency thereof, nor any of their employees, makes any warranty, express or implied, or assumes any legal liability or responsibility for the accuracy, completeness, or usefulness of any information, apparatus, product, or process disclosed, or represents that its use would not infringe privately owned rights. Reference herein to any specific commercial product, process, or service by trade name, trademark, manufacturer, or otherwise does not necessarily constitute or imply its endorsement, recommendation, or favoring by the United States Government or any agency thereof. The views and opinions of authors expressed herein do not necessarily state or reflect those of the United States Government or any agency thereof."

1. ABSTRACT

Under the High Efficiency Engines and Turbines-University Turbine Research (HEET-UTSR) program, Georgia Institute of Technology is investigating the blowout and combustion instability characteristics of fuel-flexible combustors. Particular attention is given to coal-derived gaseous fuels which are of interest to the HEET program. The program consists of three tasks.

The first task is developing the test matrix that will form the basis for the experiments performed under this program. In support of this effort, we have performed extensive CHEMKIN analyses of such quantities as flame speeds and stretch sensitivities of syngas fuels in order to develop the mixture characteristic information needed to populate the test matrix. We continue to enlarge this database to fit a wider range of fuels and conditions. This database has also been packaged into an easy- to use program that has been circulated to other combustion researchers.

The second and third tasks are measuring the combustor's stability characteristics under self-excited and forced oscillations cases. To date, we have measured the equivalence ratios at lean blow off for a large number of $H_2/CO/CH_4$ mixtures. Data were obtained over a range of fuel compositions at fixed approach or burned flow velocity, reactant temperature, and combustor pressure at several conditions up to 4.4 atm and 470 K inlet reactants temperature. Consistent with prior studies, these results indicate that the percentage of H_2 in the fuel dominates the mixture blowout characteristics. These blowout characteristics can be captured with Damköhler number scalings to predict blowoff equivalence ratios to within 10%. These results can be further improved by incorporating differential diffusion effects, analogous to turbulent flame speed correlations developed for hydrogen containing fuels.

Finally, in cooperation with several other UTSR researchers, the PI led an effort that put together a tutorial paper on fuel variability impacts on combustor operability. The paper is titled "FUEL FLEXIBILITY INFLUENCES ON PREMIXED COMBUSTOR BLOWOUT, FLASHBACK, AUTOIGNITION, AND STABILITY", GT2006-90770.

2. TABLE OF CONTENTS

1. ABSTRACT 3
2. TABLE OF CONTENTS 4
3. LIST OF FIGURES 5
4. EXECUTIVE SUMMARY 6
5. PROJECT DESCRIPTION 8
6. RESULTS 10
7. CONCLUSIONS AND FUTURE WORK 17
8. REFERENCES 18

3. LIST OF FIGURES

Figure 1: Primary color mixing scheme used to denote fuel blend composition..... 11

Figure 3: Damköhler numbers of mixtures at constant approach flow speeds. U_0= 6 m/s, inlet temperature 300 K, pressure 1.7 atm. 13

Figure 4: Predicted blowoff equivalence ratio at Da_B=0.82 with measured equivalence ratio in experiment for blowoff. 14

Figure 5: Damköhler numbers of mixtures based on local equivalence ratio at constant approach flow speeds. U_0= 6 m/s, inlet temperature 300 K, pressure 1.7 atm. 15

Figure 6: Prediction of blowoff equivalence ratio based on local equivalence ratio. U_0= 6 m/s, inlet temperature 300 K, pressure 1.7 atm. 16

4. EXECUTIVE SUMMARY

Under the High Efficiency Engines and Turbines-University Turbine Research (HEET-UTSR) program, Georgia Institute of Technology is investigating the blowout and combustion instability characteristics of fuel-flexible combustors. Particular attention is given to coal-derived gaseous fuels which are of interest to the HEET program. This work is motivated by the fact that the inherent variability in composition and heating value of coal derived and other alternative fuels provides one of the largest barriers towards their usage. This fuel composition variability is of concern because low emissions combustion systems are generally optimized to operate with fuels that meet tight specifications. The objective of this proposed program is to improve the state of the art in understanding and modeling two issues that will be of acute significance in realization of low emissions, fuel-flexible gas turbines: lean blowout and combustion instabilities. Successful completion of this project will benefit the gas turbine and energy industry in several ways. It will remove barriers toward the usage of coal derived gaseous fuels through improved understanding of their combustion characteristics. It will also improve the development of modeling tools needed by OEM's to design fuel-flexible combustion systems. Ultimately, these benefits will increase the air quality and energy security of the USA, by allowing power plants to operate efficiently and with minimal pollution, using a variety of domestic fuel sources.

The program consists of three tasks. The first task is developing the test matrix that will form the basis for the experiments performed under this program. Because of the significant number of independent parameters that need to be examined (e.g., fuel composition, pressure, temperature, premixer design), a systematic effort to develop this test matrix is needed so that the resulting parameter studies are of sufficient breadth and detail, yet still realistic enough in scope to be performed in a university program. In support of this effort, we have performed extensive Chemkin analyses of such quantities as flame speeds and stretch sensitivities of syngas fuels in order to develop the mixture characteristic information needed to populate the test matrix. In addition, we have developed a software utility that utilizes these calculations, determines other basic mixture properties, and has such features as outputting all fuel mixture combinations with a given flame speed, adiabatic flame temperature, or heating value within some given tolerance.

This program has also been distributed to other combustion researchers and has received very favorable feedback for its usefulness.

The second and third tasks are measuring the combustor's stability characteristics under self-excited and forced oscillations cases. We have designed and fabricated a gas-mixing facility that can be used to blend syngas type fuels of arbitrary composition. The blended fuels are burned in a previously developed, high pressure, swirl stabilized combustor that closely resembles typical dry low NOx combustors used by OEM's. So far, lean blow off equivalence ratios of $H_2/CO/CH_4$ mixtures spanning a wide pressure, preheat temperature, and flow velocity range. Consistent with prior studies, these results indicate that the percentage of H_2 in the fuel dominates the mixture blowout characteristics. Significantly, we were able to correlate the blowout limits of these fuels over a very broad fuel range. Physics-based correlations of these data using two blowout mechanisms, well stirred reactor and flame propagation approaches, were evaluated. These blowout characteristics can be captured with Damköhler number scalings to predict blowoff equivalence ratios to within 10%. These results can be further improved by incorporating differential diffusion effects, analogous to turbulent flame speed correlations developed for hydrogen containing fuels. We have also worked to disseminate these results to industrial practitioners who have found this work quite useful.

Finally, in cooperation with several other UTSR researchers, the PI led an effort that put together a tutorial paper on fuel variability impacts on combustor operability. The paper is titled "FUEL FLEXIBILITY INFLUENCES ON PREMIXED COMBUSTOR BLOWOUT, FLASHBACK, AUTOIGNITION, AND STABILITY", GT2006-90770.

5. PROJECT DESCRIPTION

Under the High Efficiency Engines and Turbines-University Turbine Research (HEET-UTSR) program, Georgia Institute of Technology is investigating the blowout and combustion instability characteristics of fuel-flexible combustors. Particular attention is given to coal-derived gaseous fuels which are of interest to the HEET program.

Modern power turbines have the highest operating efficiencies and turn out fewer pollutants than other major combustion energy converting devices[1]. In addition, the low capital costs required to bring a new system online have made them attractive to investors. As a result, gas turbines have become the dominant technology for new power generating capacity in the U.S. and worldwide. These systems have met their aggressive emission targets by operating in a lean, premixed mode of combustion. This mode of burning has significant advantages over its nonpremixed counterpart in achieving low pollutant emissions, particularly in regards to NO_x and soot.[2]

Interest in utilizing the United State's energy resources, as well as concern about energy security have motivated interest in utilizing coal-derived syngas or fuels from other sources, such as biomass, landfill gas, process gas and others. The development of clean coal technologies is particularly compelling given the fact that coal is the United State's most abundant fuel source. Technologies such as integrated gasification combined cycle (IGCC) plants enable the combustion of coal and other solid or liquid fuels, while still maintaining aggressive emissions targets and high efficiency.

The inherent variability in composition and heating value of these fuels provides one of the largest barriers towards their usage, however. Syngas fuels are typically composed primarily of H_2, CO, and N_2, and may also contain smaller amounts of methane (CH_4), O_2, CO_2, and other higher order hydrocarbons.[3] The primary constituents of landfill or sewage gas are typically CH_4 and CO_2.[4] Depending upon the source and particular processing technique, these fuels can have significant ranges in relative composition of these constituents. This variability is a significant problem because state-of-the-art low emission combustion systems are typically optimized to operate with fuels that meet tight fuels specifications.

The objective of this proposed program is to improve the state of the art in understanding and modeling two issues that will be of acute significance in realization of low emissions, fuel-flexible gas turbines: lean blowout and combustion instabilities. Successful completion of this project will benefit the gas turbine and energy industry in several ways. It will remove barriers toward the usage of coal derived gaseous fuels through improved understanding of their combustion characteristics. It will also improve the development of modeling tools needed by OEM's to design fuel-flexible combustion systems. Ultimately, these benefits will increase the air quality and energy security of the USA, by allowing power plants to operate efficiently and with minimal pollution, using a variety of domestic fuel sources.

6. RESULTS

Work during this reporting period, continued work went into developing physics-based correlations of obtained data from this project. These results are detailed below.

Background

Flame stabilization involves competition between the rates of the chemical reactions and the rates of turbulent diffusion of species and energy. While a significant amount of fundamental understanding of flame propagation and stability characteristics of lean, premixed systems has been gained in conventionally fueled, natural gas-air systems[5], little is known about these issues for alternate gaseous fuels, such as syngas or low BTU fuel mixtures. Furthermore, the majority of the fundamental investigations of the combustion characteristics of these synthetic gases are for non-premixed flame configurations[6-10]. Limited studies have been initiated relatively recent to investigate the characteristics of premixed, hydrogen-enriched methane fuels[11-13]. Additional studies are needed, however, to broaden the scope of fuels of interest.

Consider first the factors affecting blowout. Methods for developing blowout correlations using WSR scaling ideas have been studied extensively. Several different theories or physical considerations have been used in past blowout correlation studies, such as those of Zukoski and Marble[14], Spalding[15], Longwell[16], and others[17,18]. As noted by Glassman[19], however, they lead to essentially the same form of the correlation that relates the blowoff limits to a Damköhler number, i.e., ratio of a residence and chemical kinetic time, τ_{res}/τ_{chem}. This ratio is often referred to as a combustor loading parameter. It is possible that the recirculation regions that stabilize many high intensity flames, which may have flamelet properties at most other points along the flame, have distributed reactor-like properties; hence, the success in stirred reactor models in correlating blowout behavior.

When applied to blowoff limits of premixed flames, this chemical time can be estimated as:

$$\tau_{chem} = \alpha / S_L^2 \qquad (1)$$

where S_L and α denote the laminar flame speed and thermal diffusivity, respectively[20,21]. The residence time is generally scaled as d/U_{ref}, where d and U_{ref} denote a characteristic length scale (e.g., a recirculation zone length) and velocity scale, respectively. The Damköhler number is given by:

$$Da = \frac{\tau_{res}}{\tau_{chem}} = \frac{S_L^2 d}{\alpha U_{ref}} \qquad (2)$$

The appropriate reference velocity, U_{ref}, is less clear. Note that U_{ref} need not directly scale with approach flow velocity, U_0, due to the acceleration of the burned gas[20]. Since the burned gas velocity scale is given by $U_b=(T_b/T_0)U_0$, then $U_{ref}=f(U_0, T_b/T_0)$. Similar considerations apply for the recirculation zone scale, d. For this reason, prior workers have often had to measure the recirculation zone length in order to use Eq. (2) (e.g., see Ref. 14).

Experimental Approach

As in previous reports, we represent the mixture composition of $H_2/CO/CH_4$ by its color. Primary colors at the three vertices are used to represent each fuel constituent, where red, yellow, and blue denote H_2, CO, and CH_4, respectively. This is illustrated in the figure below. Unfortunately, Figure 1 will be difficult to interpret if reproduced in grayscale.

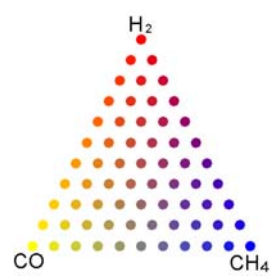

Figure 1: Primary color mixing scheme used to denote fuel blend composition.

The basic test sequence is to operate at uniformly spaced fuel compositions in $H_2/CO/CH_4$ space, such as is depicted in the figure above. At each fuel composition, the mixture

equivalence ratio is adjusted at constant unburned velocity until the mixture blows off. Obtaining this data was complicated by the need to keep the approach flow velocity, combustor pressure, and mixture temperature constant across the range of fuel compositions. As such, fixing the relative fuel compositions required simultaneously adjusting the air and three fuel flow rates in order to keep constant approach flow velocity. In addition, due to variations in mixture burned gas temperature, maintaining a constant combustor pressure required simultaneous adjustment of the back pressure valve. Finally, variations in molar volume of the fuel necessitated adjusting the air temperature in order to maintain a constant reactant temperature. For the data shown in the Results section, the approach flow velocity, pressure, and temperature remains constant to within 2%, 5%, and 20 K of their quoted values.

To clarify, combustor unburned flow velocities are quoted here, which equals the mass flow rate divided by the unburned gas density and combustor area – this is the combustor velocity if there is no flame. It should be emphasized that this is purely a reference velocity, as the actual flow velocities may be different. The burned gas velocity simply equals this velocity multiplied by the theoretical temperature ratio across the flame. The velocity at the premixer exit, relevant for the flashback data, equals the unburned flow velocity multiplied by 18.

It should be emphasized that the manner in which the flame blew off varied with fuel composition. In many cases, the blowoff event occurred abruptly with a small change in fuel composition, although sometimes preceded by slight liftoff of the flame from the burner. Defining the blowoff point was unambiguous in these instances; moreover, the point of blowoff and flame liftoff was nearly identical. This was the case for mixtures composed largely of CH_4 or CO. However, for mixtures with larger than about 60% H_2, the blowoff and liftoff events were quite distinct. Usually, the flame became visibly weaker, lifted off from the holder, and moved progressively downstream with decreases in equivalence ratio before blowing off for good. As such, blowoff is defined here as the point where the flame is no longer visible in the 10.2 cm long optically accessible section of the combustor. This point should be kept in mind when comparing 0-60% H_2 and 60-100% H_2 containing fuels.

Analysis Approach

This section describes the methods used to post-process the data and correlate blowout limits with the parameters identified in the Background section.

Adiabatic flame temperatures were calculated for a given mixture using standard methods. Laminar flame speeds and blowoff residence times were calculated with the PREMIX and AURORA application in CHEMKIN, using the GRI3.0 mechanism. While this mechanism was primarily optimized for methane/air mixtures, good comparisons between its results and measurements have been obtained for a range of H_2/CO mixtures as well[22]. At some lean mixtures where stable flames were observed, we were unable to obtain convergence of the PREMIX results. At all other conditions, we found that the blowoff residence time from the well stirred reactor model and the chemical time estimated from the flame speed using Eq. (1) correlate quite well[23].

Results and Discussion

We consider correlations of the blowoff results. While a variety of other correlations were examined in our prior paper[23], we found Damköhler number correlations based upon the burned gas flow as a reference velocity to work best, using the combustor width, D=0.0508m, as the length scale. The chemical time is the blowoff residence time of a well stirred reactor. A typical result is shown in Figure 2, showing that blowoff occurs at a nearly constant value of Damköhler number, $Da_B \approx 0.82$, for low H_2 (<50%) mixtures. For high H_2 mixtures, Da_B decreases monotonically due to the significant change of blowoff time. Recall, however, that defining the blowoff point is somewhat ambiguous for H_2 levels greater than 60%.

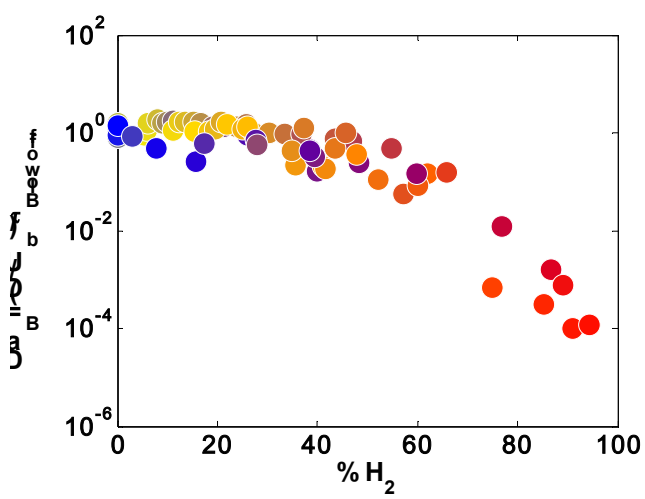

Figure 2: Damköhler numbers of mixtures at constant approach flow speeds. U_0= 6 m/s, inlet temperature 300 K, pressure 1.7 atm.

Nonetheless, assuming a constant value of blowoff Damköhler number as a blowoff prediction tool works reasonably well. Although the blowoff Damköhler number changes by a factor of 100, it should be noted that the underlying change in chemical time corresponds to a change in equivalence ratio of only 0.1. Figure 3 plots the dependence of the predicted equivalence ratio, calculated using CHEMKIN AURORA results to determine what mixture equivalence ratio gives a Da_B=0.82 value, with the actual experimentally measured value. It can be seen that the error is generally less than 0.1, with the RMS error for all points equaling 0.04. Only for the highest H_2 cases is there a clear deviation, as would be expected from Figure 2.

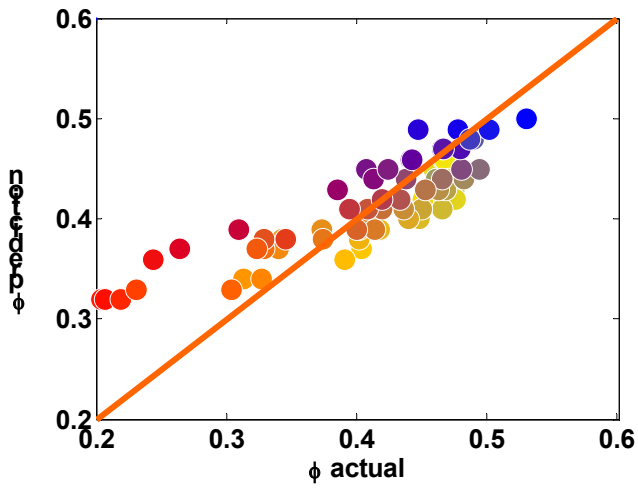

Figure 3: Predicted blowoff equivalence ratio at Da_B=0.82 with measured equivalence ratio in experiment for blowoff.

The change in blowoff *Da* value shown in Figure 2 may be due to preferential diffusion effects, a consideration that has also been used to scale changes in turbulent flame speed of mixtures whose constituents have significant variations in diffusivity. One approach for incorporating these effects is to note that the local equivalence ratio changes along the wrinkled flame, being both higher and lower than the average at different spatial locations. Kido and co-workers[24] suggested correlating mixture turbulent flame speeds by utilizing mixture properties at an adjusted equivalence ratio, equal to the actual value plus some $\Delta\phi$. They suggest the following relation for $\Delta\phi$:

$$\Delta\phi = C * \ln(D_F / D_{OX}) \qquad (3)$$

where D_F and D_{OX} denote the mass diffusivity of fuel and oxygen, respectively, and C is a constant whose value they suggest as 0.3. We found that utilizing a value of C=0.1 gives a nearly constant blowoff Damköhler number for all of our data sets. For example, Figure 4 shows that blowoff occurs at a nearly constant value of local Damköhler number, which is based on local equivalence ratio, in this case Da_B=2.1.

Figure 5 compares the predicted and actual blowoff equivalence ratios, calculated assuming that all mixtures blow off at a constant local Damköhler number, Da_B =2.1, (calculated using the adjusted equivalence ratio). It can be seen that the error is generally less than 0.05, with the RMS error equaling 0.03.

There are a variety of reasons that the remaining scatter could be present, such as inherent noise in the blowoff point. In addition, other more subtle factors, such as reference length and reference flow velocity could easily change somewhat with approach flow velocity.

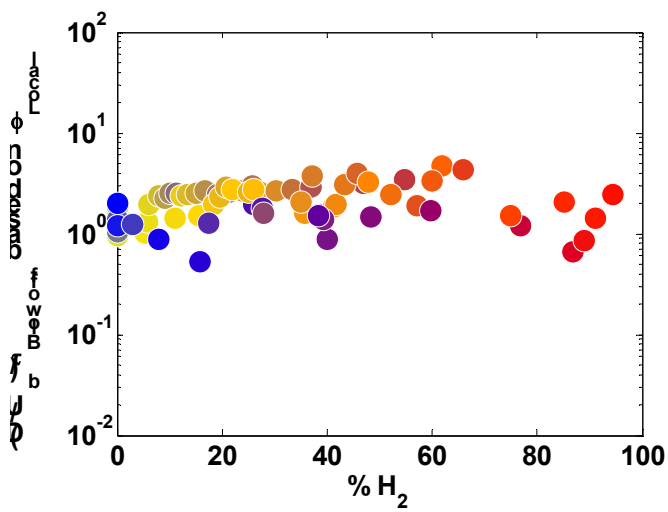

Figure 4: Damköhler numbers of mixtures based on local equivalence ratio at constant approach flow speeds. U_0= 6 m/s, inlet temperature 300 K, pressure 1.7 atm.

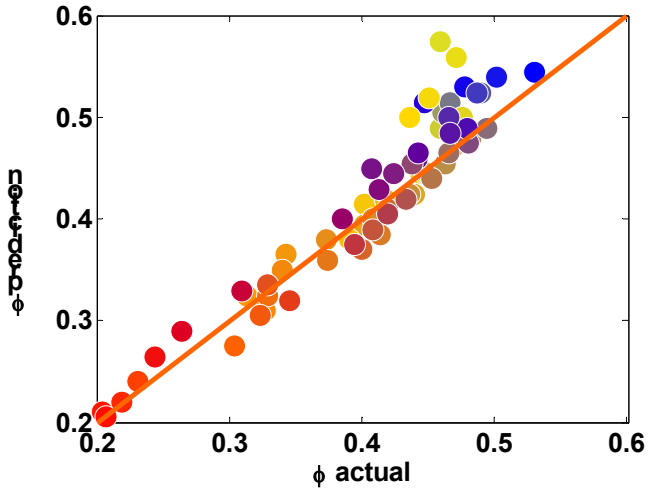

Figure 5: Prediction of blowoff equivalence ratio based on local equivalence ratio. U_0= 6 m/s, inlet temperature 300 K, pressure 1.7 atm.

These results show that if the blowoff equivalence ratio of one fuel is known at a particular condition, the corresponding blowoff point of other fuels can be predicted with an accuracy of ~10% in equivalence ratio.

Test group		Da_B		Da_U	
		$\overline{Da_B}$	RMS of ϕ error	$\overline{Da_U}$	RMS of ϕ error
T =300 K U_0=6 m/s	without Δϕ	0.820	0.043	4.081	0.044
	with Δϕ C=0.1	2.126	0.034	10.814	0.028
T 300 K U_0=4 m/s	without Δϕ	0.350	0.041	1.636	0.042
	with Δϕ C=0.1	1.699	0.030	8.069	0.028
T 458 K U_0=6 m/s	without Δϕ	0.0513	0.027	0.145	0.028
	with Δϕ C=0.1	0.350	0.026	1.041	0.027

Table 1: RMS of predicted equivalence ratio errors of LBO at different working conditions.

7. CONCLUSIONS AND FUTURE WORK

These results show that blowout characteristics can be reasonably captured with classical Damköhler number scalings to predict blowoff equivalence ratios to within 10%. Ongoing work is focusing on further correlations. The next major effort that we are experimentally gearing up for are more detailed characterizations of the dynamic flame blowoff process, and determining the manner in which blowoff phenomenology varies with fuel composition. For this effort, we have duplicated an experimental rig developed at Sandia National Laboratories by Dr. Bob Schefer. We envision performing laser-sheet, high speed imaging of the flame during the blowoff transient at Georgia Tech. From these images, we will select a few test points for more detailed characterization which will be performed at Sandia later in the year.

8. REFERENCES

[1]Langston, Lee, "Gas Turbine Industry Overview", in 2001 IGTI Technology Report and Product Directory, ASME 2001.

[2]Correa, S.M., Power Generation and AeroPropulsion Gas Turbines: From Combustion Science to Combustion Technology, *Twenty Seventh Symposium (International) on Combustion*, The Combustion Institute, Pittsburgh, PA, 1998.

[3]Klimstra, Jacob, Interchangeability of Gaseous Fuels – The Importance of the Wobbe Index, *SAE paper # 861578*, 1986.

[4]King, Steve, The Impact of Natural Gas Composition on Fuel Metering and Engine Operating Characteristics, *SAE paper # 920593*, 1992.

[5]Durbin, M., Ballal, D., "Studies of Lean Blowout in a Step Swirl Combustor," *J. Engr. Gas Turbines and Power*, Vol. 118, 1996.

[6]Barlow, R.S., Fiechtner, G.J., Carter, C.D., Chen, J.Y., "Experiments on the Scalar Structure of Turbulent $CO/H_2/N_2$ Jet Flames," *Comb. Flame*, Vol. 120, 2000.

[7] Correa, S.M., Gulati, A. "Non-premixed Turbulent CO/H_2 flames at local extinction conditions," *Proc. Comb. Inst.* Vol. 22, 1988, pp. 599-606.

[8]Drake, M.C., "Stretched Laminar Flamelet Analysis of Turbulent H2 and $CO/H_2/N_2$ Diffusion Flames," *Proc. Comb. Inst*., Vol. 21, 1986, pp. 1579-1589.

[9]Correa, S.M., Gulati, A., Pope, S.B., "Assessment of a Partial Equilibrium/Monte Carlo Model for Turbulent Syngas Flames," *Comb. Flame*, Vol. 72, 1988, pp. 159-173.

[10]Masri, A. R., Dibble, R. W., "Spontaneous Raman Measurements in Turbulent $CO/H_2/N_2$ Flames Near Extinction," *Proc. Comb. Inst*. Vol. 22, 1988, pp. 607-618.

[11]Maloney, D., "The Simulation Validation Project at NETL," *DOE Report*, 2002.

[12]Schefer, R. W., "Hydrogen Enrichment for Improved Lean Flame Stability," *International Journal of Hydrogen Energy,* 28, 2003, pp. 1131-1141.

[13]Wicksall, D., Agrawal, A., "Effects of Fuel Composition on Flammability Limit of a Lean, Premixed Combustor," *ASME Paper #2001-GT-0007*

[14]Zukoski, E.E., "Afterburners," in *Aerothermodynamics of Gas Turbine and Rocket Propulsion*, G. Oates, Ed., 1997.

[15]Spaulding, D., *Some Fundamentals of Combustion*, Ch. 5, Butterworth Press: London, 1955

[16]Longwell, J., Frost, E., Weiss, M., "Flame Stability in Bluff-Body Recirculation Zones," *Ind. Eng. Chem*., Vol. 45 (8), pp. 1629-1633.

[17]Putnam, A., Jensen, R., "Appplication of Dimensionless Numbers to Flash-back and Other Combustion Phenomena," *Proc. Comb. Inst*., 3rd, 1949, ,pp 89-98

[18]Hoffmann, S., Habisreuther, P., Lenze, B., "Development and Assessment of Correlations for Predicting Stability Limits of Swirling Flames," *Chemical Engineering and Processing*, 33 (1994), pp 393-400

[19]Glassman, I., *Combustion*, Academic Press: New York, 1996.

[20]Plee, S.L, Mellor, A.M., "Characteristic Time Correlation for Lean Blowoff of Bluff Body Stabilized Flames," *Comb. Flame*, 35, 1979, pp. 61-80.

[21] Radhakrishnan, K., Heywood, J., Tabaczynski, R., "Premixed Turbulent Flame Blowoff Velocity Correlation Based on Coherent Structures in Turbulent Flows," *Comb. Flame*, 42, 1981, pp. 19-33.

[22]Natarajan, J., Nandula, S., Lieuwen, T., and Seitzman, J., "Laminar Flame Speeds of Synthetic Gas Fuel Mixtures," *ASME Paper # GT2005-68917.*

[23] Zhang, Q., Noble, D.R., Meyers, A., Xu, K., Lieuwen, T., "Characterization Of Fuel Composition Effects In $H_2/CO/CH_4$ Mixtures Upon Lean Blowout," *ASME Paper # GT2005-689017*

[24]Kido, Hiroyuki, Nakahara, Masaya, "A Model of Turbulent Burning Velocity Taking the Preferential Diffusion Effect into Consideration," *JSME International Journal*, Vol. 41, No.3, 1998, pp. 666-673

CORRELATION OF IGNITION DELAY WITH NATURAL GAS AND IGCC TYPE FUELS

Semi Annual Report

Reporting Period: 07/01/04 – 12/31/04

Scott Samuelsen, Principal Investigator

Vince McDonell, Co-Investigator

Mayumi Greene, Graduate Student Researcher

DOE Award Number: DE-FC26-02NT41431
UTSR Project Number: 03-01-SR112

University of California, Irvine
Irvine, CA 92697-3550
www.ucicl.uci.edu

March 2005

DISCLAIMER

This report was prepared as an account of work sponsored by an agency of the United States Government. Neither the United States Government nor any agency thereof, nor any of their employees, makes any warranty, express or implied, or assumes any legal liability or responsibility for the accuracy, completeness, or usefulness of any information, apparatus, product, or process disclosed, or represents that its use would not infringe privately owned rights. Reference herein to any specific commercial product, process, or service by trade name, trademark, manufacturer, or otherwise does not necessarily constitute or imply its endorsement, recommendation, or favoring by the United States Government or any agency thereof. The views and opinions of authors expressed herein do not necessarily state or reflect those of the United States Government or any agency thereof.

ABSTRACT

Progresses and accomplishments of the ignition delay project at University of California, Irvine Combustion Lab (UCICL) for the duration of 07/01/03 – 06/30/04 will be presented with emphasis on the second semiannual period (01/01/04 – 06/30/04) in this report. Activities during this period include the facility preparation, numerical analysis, and literature reviews. The existing continuous flow reactor and the supporting facility have been modified for this project to achieve conditions that bridge typical flow reactor and shock tube conditions. Details of the facility upgrades will be provided. Concurrently, numerical simulations of autoignition for the various hydrogen and/or carbon monoxide containing fuels were performed using a chemical kinetics code, CHEMKIN. The numerical simulations also include temperature sensitivity analyses. Results of the simulations will be analyzed in regard to differences in the fuel type/composition, and identification/understanding of key reactions. Because the synthetic gases (syngas) associated with the Integrated Gasification Combined Cycle (IGCC) technology is the emphasis of this project, their compositions were reviewed through literature reviews and personal communications. The range of the IGCC syngas will be proposed coinciding with the specific interest in coal gasification and hydrogen production in the U.S.

TABLE OF CONTENTS

ABSTRACT iii

LIST OF FIGURES v

LIST OF TABLES vii

1. EXECUTIVE SUMMARY 1

2. PROJECT DESCRIPTION 3

- 2.1 Gas Turbine Research Need 3
  - 2.1.1 Lean Premixed Combustion 3
  - 2.1.2 Fuel Flexibility 5
- 2.2 Project Approach 5
  - 2.2.1 Experimental Approach 7
  - 2.2.2 Analytical Approach 7
- 2.3 Expected Results and Benefits 8

3. EXPERIMENTAL 9

- 3.1 Continuous Flow Reactor at UCICL 9
  - 3.1.1 Overview 9
  - 3.1.2 Residence Time 12
- 3.2 Upgrades and Modifications 13
  - 3.5.1 Air Heating System 13
  - 3.5.2 Heater Protection 17
  - 3.5.3 Pressure System 18
  - 3.5.4 Fuel Composition Control System 18
- 3.3 Data Acquisition (DAQ) System 20

4. RESULTS AND DISCUSSION 21

- 4.1 CHEMKIN Analysis 21
  - 4.1.1 Reaction Mechanisms 21
- 4.2 Ignition Delay Factorial Study - Design of Experiments 26

5. CONCLUSION 33

REFERENCES 36

LIST OF FIGURES

Figure **1**: UCICL Continuous Flow Reactor with Clam Shell Heaters 10

Figure **2**: Schematic of the Experimental Rig 10

Figure **3**: Insulation Blankets 11

Figure **4**: (a) Venturi Injector, (b) Test Section B 11

Figure **5**: Air Heating System (Total of 72 kW Nominal, 54kW Actual) 14

Figure **6**: Cross-Sectional View of the Air Heating System 15

Figure **7**: Heater Assembly Process 16

Figure **8**: Upstream Flange Layout 16

Figure **9**: Gaseous Fuel Control System for Natural Gas 19

Figure **10**: Comparison of Ignition Delay Predictions using Mueller et al., GRI-Mech3.0, Baulch et al., UCSD, and Davis et al. (H_2/CO/Air, 50% H_2 50% CO, ϕ = 0.6) 24

Figure **11**: Range of Ignition Delay Predictions with Various Mechanisms 25

Figure **12**: Comparison of CHEMKIN Ignition Delay Predictions with the Peschke & Spadaccini Experimental Data: CHEMKIN Simulations Were Performed for 1) 50% H_2 50% CO – Air at ϕ = 0.6 Using Various Mechanisms and 2) Peschke & Spadaccini Baseline Fuel (38.6% H_2 51.1% CO 10.3% CO_2) Using Mueller et al. at the Relevant Peschke & Spadaccini Experimental Conditions. 26

Figure **13**: Ignition Delay Times of UTRC Baseline Fuel: (a) Chemkin Simulation and (b) Experimental Data 28

Figure **14**: Analysis of Variance (ANOVA) Summary for (a) CHEMKIN Simulation Results, and (b) Experimental Data 29

Figure **15**: Pressure (Factor A) – Temperature (Factor B) Interaction at Various Equivalence Ratios. T = 632.90 K (black) and T = 781.20 K (red). 30

Figure **16**: Pressure (Factor A) - Equivalence Ratio (Factor C) Interaction at Various Temperatures. ϕ = 0.23 (black) and ϕ = 0.72 (red). 30

Figure **17**: Variation of the (a) Simulated and (b) Measured Ignition Delay Data from the Resulted Analytical Expressions. 32

LIST OF TABLES

Table **1**: Project Schedule 6

Table **2**: Actual Length of the Test Section 12

Table **3**: Residence Time (sec) of Air at P=21.4 atm (300 psig) for Various Temperatures 13

Table **4**: Currently Available DAQ (National Instruments) Cards 20

Table **6**: Chemical Reaction Mechanisms for Fuels Containing H_2 and/or CO 22

Table **7**: Factors for Design of Experiment Approach..... 27

1. EXECUTIVE SUMMARY

This report summarizes the progress during the third semiannual period (July – December 2004) of the ignition delay project at University of California, Irvine Combustion Lab (UCICL). Detailed progresses during the first year (July 2003 – June 2004) were previously reported [**1, 2**]. Activities during this period mainly consist of the facility preparation, numerical analysis, and literature reviews.

Design and fabrication of the up-graded air heating system (actual capability of 54kW total) was completed during the first year [**1, 2**]. As a part of continuous efforts for the facility preparation, the air heating system has been assembled and is now ready for the final installation to the experimental rig. At the same time, electrical work has progressed in the UCICL high-pressure facility to meet the requirements of the air heating system. The upgrades will allow the facility/rig to reach the targeted maximum temperature and pressure of ~1033 K (1400 ^{o}F) and 18 atm (250 psig), respectively. This expanded capability will facilitate the experiments at the conditions complementing the range achieved by typical flow reactors and shock tubes.

In parallel, efforts evaluating various kinetic mechanisms waere expanded: ignition delay times for a representative IGCC type fuel of 50% H_2 and 50% CO were simulated at various operating conditions using CHEMKIN [**3**]. In addition to the mechanism by Mueller et al. [**4**, **5**], GRI-Mech 3.0 [**6**], and the mechanism by Baulch et al. [**7, 8**], the mechanism by Davis et al. [**9**] and the San Diego Mechanism 2003/08/30 [**10**] were also introduced during this reporting period. Predicted ignition delay times using all the above mechanisms show general agreement in trends. However, the discrepancy among the values predicted by different mechanisms was found to be significant. For example, the ignition delay time at 700 K (800 ^{o}F) simulated by GRI-Mech 3.0 is 684 sec, while the shortest prediction (by San Diego Mechanism 2003/08/30) is 96.6 sec. This discrepancy highlights the importance of having reliable experimental data that allow us to see which mechanism is more representative of actual combustion phenomena for the IGCC type fuels. Other mechanisms for H_2 and/or CO containing fuels are being actively sought and will be added to the numerical tools as they are obtained.

Simulated ignition delay results for 50% H_2 50% CO were also compared with (1) the CHEMKIN results for the baseline fuel (38.6% H_2, 51.1% CO, 10.3% CO_2) of Peschke & Spadaccini [**11**] at their experimental conditions and (2) their experimental data along with the proposed empirical correlation. The CHEMKIN simulation for the Peschke & Spadaccini baseline fuel has the same trend as results for 50% H_2 50% CO. However, discrepancy between the simulated and measured data (or the empirical correlation) was very significant (order of ~5), especially as the temperature apart from 1000 K (1340 ^{o}F). Statistical analyses suggest that strong interactions between pressure and temperature, and pressure and equivalence ratio exist for the experimental data while no such interactions are observed for the simulated data. Currently, the work by Peschke & Spadaccini [**11**] is the only known experimental work for IGCC type fuels. It is evident that ignition delay characteristics should be evaluated with other independent experimental data for more comprehensive analyses. The experimental work at UCICL will serve this role.

Tasks for the next phase of the project include the final integration and temperature characterization of the rig, and experiments using pre-blended IGCC type fuels. Numerical simulations and literature reviews will be continued throughout this project to assist the experimental study. Sensitivity analyses for more extended ranges of operating conditions and fuel compositions, using different mechanisms will be focused to provide kinetics information to understand the ignition delay characteristics observed in the numerical simulations. Together, the experimental results and numerical simulations will be used to provide simplified expressions for ignition delay for IGCC type fuels.

2. PROJECT DESCRIPTION

2.1 Gas Turbine Research Need

This project aims to establish an experimental database of ignition delay times for various fuels at the conditions representative of typical gas turbine operation. In particular, the drive to achieve low emissions with the concomitant requirement to handle fuels of varying composition is requiring more consideration for issues associated with ignition delay. Analytical correlations will be delivered with emphasis on the inclusion of fuel composition. Fuels of interest in this project include Natural Gas (NG) and the range of specific hydrocarbons present within NG, Liquefied Natural Gas (LNG), and fuels containing hydrogen and/or carbon monoxide. Synthetic gas (syngas) produced by the Integrated Gasification Combined Cycle (IGCC) technology, which contains H_2 and CO as main constituents, will be particularly emphasized. In this section, the motivation behind the ignition delay project is described.

2.1.1 Lean Premixed Combustion

Lean premixed combustion is a proven strategy to reduce pollutant emissions. However, the reactive mixture in the premixed combustion system can spontaneously ignite without external ignition sources. This phenomenon, often called autoignition, is a critical safety and reliability issue for advanced low-emission gas turbines.

An example of the most common ignition delay (autoignition time) expressions by Lefebvre et al. [**12**] is shown in Eq. **1**. Incorporating the inversely proportional relationship between the ignition delay and the global reaction rate with the Arrehenius expression of the reaction rate constant, Lefebvre et al. proposed that the ignition delay time τ at the temperature T and pressure P could be expressed as:

$$t \propto \frac{1}{A} \exp\left(\frac{E}{R_u T}\right) [O_2]^{-j} \, [Fuel]^{-m} \; P^{-n} \; T^{-0.5} \quad . \qquad (\mathbf{1})$$

Where A is Arrehenius constant, E is the global activation energy, and R_u is the universal gas constant. Note that concentrations of oxygen and fuel are on volumetric bases to explicitly indicate the pressure effect.

Eq. **1** indicates that ignition delay depends on operating conditions such as pressure, temperature, and equivalence ratio. The advanced gas turbines must be designed based on the autoignition characteristics relevant to their operating conditions.

In addition to the factors stated above, fuel composition is also recognized to have an impact on autoignition behavior. For example, Spadaccini and Colket [**13**] demonstrated that the presence of higher hydrocarbons in NG, a typical fuel of stationary gas turbines, decreases the ignition delay times comparing to that of pure methane. The proposed ignition delay, t is expressed by:

$$t = 1.77 \times 10^{-14} \exp(18693/T) \left[O_2\right]^{-1.05} \left[CH_4\right]^{0.66} \left[HC\right]^{-0.39} . \qquad (\mathbf{2})$$

Where [HC] is the total molar concentration of non-methane hydrocarbons.

Although the resulting expression (Eq. **2**) is significant in terms of accounting for the effect of non-methane hydrocarbons on ignition delay, data at lower-temperature and leaner condition are in need for this higher hydrocarbon effect to be fully applicable to the lean premixed gas turbines [**14**]. In general, studies of the effect of fuel composition are significantly lacking despite the knowledge that different fuel constituents play a role in ignition delay [**15**].

Two research needs for low emission gas turbines are addressed in this project: 1) Experimental ignition delay studies at typical gas turbine operating conditions and 2) the explicit determination of the effect of the fuel composition at conditions of interest. In the current project, the growing needs in fuel flexibility (Section **2.1.2**) suggest priority be given to IGCC type fuels.

2.1.2 Fuel Flexibility

The use of alternative fuels has increasing interest in the energy industry and is being embraced by a society, which continues to have increased recognition of a need for clean energy and relieving the concentrated dependency on petroleum fuels. In the past two decades, stationary gas turbines have achieved significant emissions reductions especially when operated on NG. In light of this focus, it is inevitable that most of the previous autoignition studies for the gas turbine applications focused on methane, the main constituent of NG. In order to meet the increasing needs for alternative fuels, autoignition studies of the relevant fuels at gas turbine conditions are necessary to support the development of the fuel flexible gas turbines technology. In the current project, fuel gas as associated with IGCC plants is of particular interest. As seen in NG, IGCC syngas also varies widely in its compositions. Importance of fuel composition effect on ignition delay must be highlighted here again. This project aims to provide insights to the autoignition characteristics of IGCC syngas at gas turbine conditions as well as experimental data.

2.2 Project Approach

The project is being conducting using both experimental and analytical approaches. The overall project has been divided into four Tasks:

Task 1: At the beginning of the project, the existing facility will be upgraded to simulate various operating conditions (higher operating temperature and pressure) and fuel compositions.

Task 2: In parallel with Task 1, currently available mechanisms for IGCC type fuels (i.e., H_2 and/or CO containing fuels) will be collected and reviewed. Numerical analysis will be performed using the mechanisms. Experiments will be conducted upon completion of Task 1.

Task 3: Data acquired in Task 2 will be analyzed and used to obtain empirical expressions of the ignition delay with emphasis on the effect of the fuel compositions.

Task 4: Finally, the obtained empirical correlations will be verified and refined through iterations of Task 3 and 4.

An updated project schedule is shown in Table **1**. Detail descriptions of the experimental and analytical approaches are provided in the following two sections (**2.2.1**) and (**2.2.2**), respectively.

Table **1**: Project Schedule

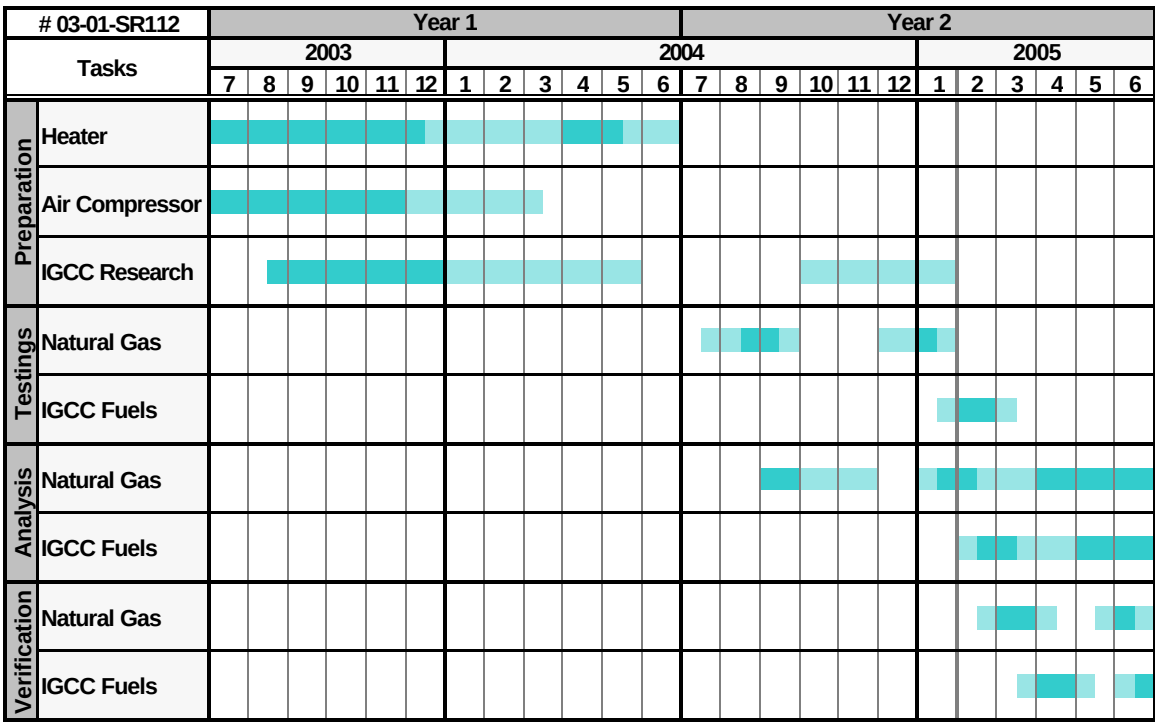

2.2.1 Experimental Approach

The existing continuous flow reactor will be used to measure the ignition delay times for IGCC type fuels of various compositions and conditions. Under Task 1, the experimental facility has been upgraded to increase operating temperature from 922 K (1200 °F) to 1033 K (1400 °F) and pressure from 8 atm (103 psig) to 18 atm (250 psig) to provide a wider range of operating conditions. In order to study the fuel composition effect, various compositions of NG and IGCC syngas will be simulated utilizing the fuel composition control system, which is also being modified. Details of these upgrades will be discussed in Section **3.2**.

Upon completion of Task 1, experiments will be conducted at the designed operating conditions (Task2): Fuel, comprised of carefully controlled mixtures of pure gases selected to simulate the compositions of interest, will be preheated and injected into the separately preheated air stream. Subsequently, the two streams will be mixed through the venturi that is a part of injector and integrated in the flow path. Operating temperature will be controlled carefully throughout the flow path of the combustible fuel/air mixture. Autoignition will be monitored utilizing the thermocouples and photodiodes. Acquired data will be used in the analysis of the ignition delay correlation as well as the validation of the numerical codes.

2.2.2 Analytical Approach

A chemical kinetics codes collection, CHEMKIN, will be utilized throughout the project to provide guidance to the experiments. In the CHEMKIN collection, the AURORA application represents a well-mixed reactor model for both transient and steady state systems [**3**] and thus appropriate for the ignition delay analysis. Chemical reactions that contribute to the ignition delay can also be identified using the sensitivity analysis option in the AURORA application. Under the Tasks 1 and 2, simulation results will be used for hardware design/purchase, evaluations of various chemical reaction mechanisms, and construction of the experimental matrix. CHEMKIN simulations will

also be extensively used to support the iterative analysis-verification process of the empirical expression design under the Tasks 3 and 4. In addition to CHEMKIN, other analytical tools such as Computational Fluid Dynamics (CFD) code may also be used as needed.

2.3 Expected Results and Benefits

The project will deliver benefits to the gas turbine and alternative fuel industries not only upon its completion, but also as it progresses. The facility upgrade in the early stage of this project will extend the capability of a continuous flow reactor to more relevant gas turbine conditions. Incorporating the recognized advantages of the continuous flow reactor, such as relatively easy control over operating conditions and fuel types [**15**], the project will enhance the capability to meet the research needs of industry.

Throughout this project, the IGCC type fuels and various chemical reaction mechanisms for the hydrogen containing fuels will be extensively studied via literature reviews and communication with the industry. It will provide a comprehensive review of many on-going research efforts, which will be a beneficial foundation for current and future studies of fuel flexibility.

Upon the completion of this project, a database for the IGCC synthetic gases will be established as well as complement the existing data for NG. The data can be used to validate the reaction mechanisms. Analytical expressions of ignition delay for the relevant fuels (IGCC syngas, NG, etc) will be proposed with emphasis on the effect of their fuel compositions. The expressions will support the efforts in advancing low-emission technology and the use of alternative fuels.

3. EXPERIMENTAL

The continuous flow reactor (Figure **1)** was fabricated and utilized for the previous research projects at UCICL. The schematic of the experimental rig is shown in Figure **2**. Under the current project, facility upgrades (Task 1) have been undertaken and completed with only final installation of the air heating system to the rig remaining to be accomplished. The upgrades enhance the ability of the facility to reach operating conditions outside of range found in other ignition delay projects using flow reactors and shock tubes. Maximum operating temperature and pressure will be increased from 922 K (1200°F) to ~1033K (1400°F) and 8 atm (103 psig) to 18 atm (250 psig), respectively.

3.1 Continuous Flow Reactor at UCICL

3.1.1 Overview

Because autoignition is a phenomenon that strongly depends on temperature, it is critical to have a great control of operating temperatures in any experimental approaches. At UCICL, operating temperatures are maintained using active (clamshell type tube furnace) and passive (insulation) means to compensate the heat loss over the flow reactor length. For better handling and consistent application of insulation materials, 50.8 mm (2.0 in.) thick insulation blankets (Figure **3**) have been developed for this project. The insulation material is Aluminum Silica, synthetic fiber with the heat transfer coefficient of 5.68 W/m^2-K (1 BTU/hr-ft^2-^oF) per 25.4 mm (1.0 in.) thickness.

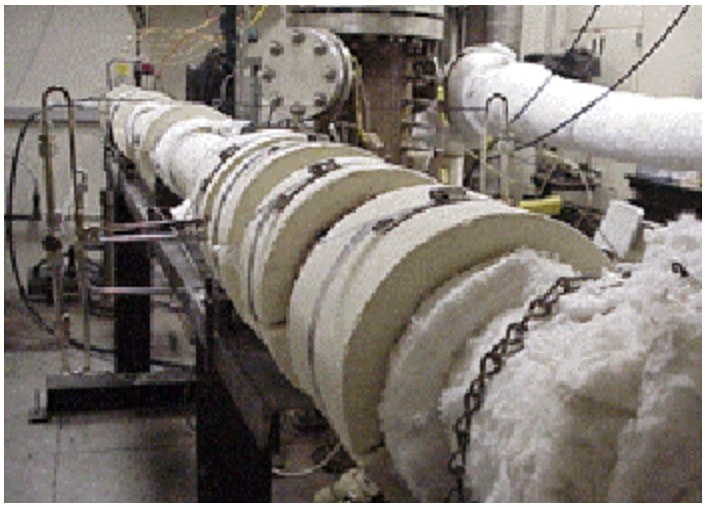

Figure **1**: UCICL Continuous Flow Reactor with Clam Shell Heaters

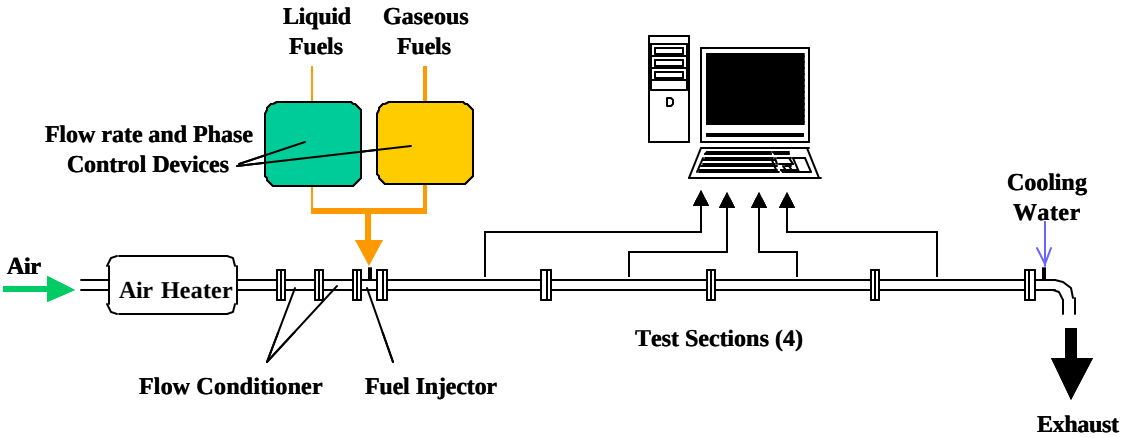

Figure **2**: Schematic of the Experimental Rig

Figure **3**: Insulation Blankets

Individual fuel components will be metered, combined, preheated, injected, and then rapidly mixed with the air stream using a venturi injector (Figure **4** (a)) designed under the previous project [**15**]. The injector is mounted onto the 600 lbs 2” flange. The test section consists of three Test Sections C (0.91m (36”) long each, plain duct) and a Test Section B (0.86m (34”) long, with sensor ports) that is shown in Figure **4** (b). The inside diameter of the experimental rig is 38.1 mm (1.5”). Detailed descriptions of the experimental rig, hardware components, and heat loss compensation were provided in the final report of previous ignition delay study at UCICL [**15**].

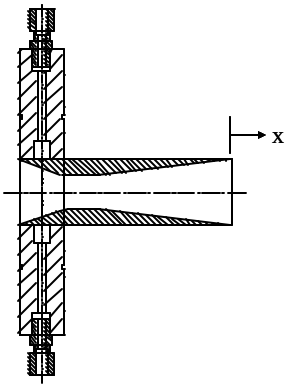

(a)

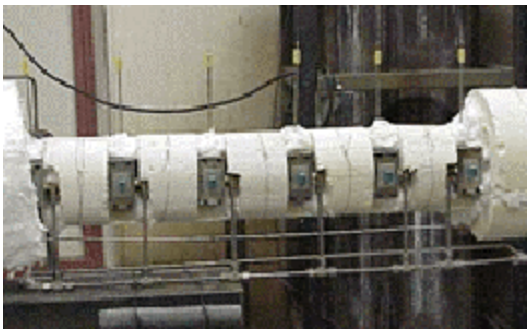

(b)

Figure **4**: (a) Venturi Injector, (b) Test Section B

3.1.2 Residence Time

In order to detect autoignition in the flow reactor, the residence time of a premixed combustible fuel/air mixture must be longer than its ignition delay time. Test Section B (Figure **4** (b)) is typically located at the most downstream of the four test sections. Because photodiodes are mounted to the Test Section B, the clamshell heaters can be installed only to cover the non-sensor sections. As a result, a temperature drop in this sensor test section cannot be avoided despite the heat loss compensation efforts with insulation material. Thus, the valid flow reactor length was defined as the length from the venturi exit to the location of first sensor port in the Test Section B and calculated to be 2.73 m (107.42”). Locations of the components were summarized in Table **2**.

Table **2**: Actual Length of the Test Section

Components		Local Coordinates m (inch)	Components		Local Coordinates m (inch)	Effective Length m (inch)	X Coordinates m (inch)
Venturi Injector	Flange/Duct Inlet	0.00 (0.00)					
	Injection Face	0.01 (0.50)					
	Flange/Duct Exit	0.03 (1.00)					
	---	--- ---	**Test Section C** *[1]	Flange/Duct Inlet	0.00 (0.00)		
	Venturi Exit	0.12 (4.83)		Venturi Exit	0.10 (3.83)	--- ---	0.00 (0.00)
				Flange/Duct Exit	0.91 (36.00)	0.82 (32.17)	0.82 (32.17)
			Test Section C *[1]	Flange/Duct Inlet	0.00 (0.00)		
				Flange/Duct Exit	0.91 (36.00)	0.91 (36.00)	1.73 (68.17)
			Test Section C *[1]	Flange/Duct Inlet	0.00 (0.00)		
				Flange/Duct Exit	0.91 (36.00)	0.91 (36.00)	2.65 (104.17)
			Test Section B	Flange/Duct Inlet	0.00 (0.00)		
				Sensor Port 1	0.08 (3.25)	0.08 (3.25)	**2.73 (107.42)**
				Sensor Port 2	0.22 (8.75)		
				Sensor Port 3	0.36 (14.25)		
				Sensor Port 4	0.50 (19.75)		
				Sensor Port 5	0.64 (25.25)		
				Sensor Port 6	0.78 (30.75)		
				Flange/Duct Exit	0.86 (34.00)		

*[1] *Covered by the clam shell heater*

For an initial evaluation, residence times were calculated for air only at various operating conditions. Sample results at 21.4 atm (300 psig) are shown in Table **3**.

Table **3**: Residence Time (sec) of Air at P=21.4 atm (300 psig) for Various Temperatures

Vdot_air	Residence Time (sec)							
scfm	T=700K (800F)	T=755K (900F)	T=811K (1000F)	T=866K (1100F)	T=922K (1200F)	T=978K (1300F)	T=1033K (1400F)	T=1089K (1500F)
10	5.94	5.50	5.12	4.79	4.50	4.25	4.02	3.82
25	2.37	2.20	2.05	1.92	1.80	1.70	1.61	1.53
50	1.19	1.10	1.02	0.96	0.90	0.85	0.80	0.76
75	0.79	0.73	0.68	0.64	0.60	0.57	0.54	0.51
100	0.59	0.55	0.51	0.48	0.45	0.42	0.40	0.38
150	0.40	0.37	0.34	0.32	0.30	0.28	0.27	0.25

3.2 Upgrades and Modifications

Facility upgrades under Task 1 focused on design/fabrication of a new air heating system while other modifications to the pressure, fuel composition control, and data acquisition systems (Section **3.3**), and the insulation method (Section **3.1.1**) were also executed. In addition, a device for CH_4 (main constituent of natural gas) residence time measurement utilizing a He-Ne laser (3.39 μm) has been developed and will be integrated into the current project.

3.5.1 Air Heating System

In order to achieve the wider range of operating temperatures (maximum temperature ~1033K or 1400°F), the air heating system has been upgraded with the support of an independent research project funded by the California Energy Commission. Three 6kW in-line heaters (total of 18kW) have been replaced with three 24kW in-line

heaters (total of 72kW, 54 kW actual). The newly fabricated and assembled air heating system is shown in Figure **5**. The individual heaters can be staged on/off to accommodate the wide air flow turndown needed for the project. The heaters will also be protected by two fail-safe features. The venturi meter shown in Figure **5** will be utilized to monitor differential pressures as a safety measure to allow shutdown in the event of insufficient airflow through the heaters. Further description of these protective features will be provided in Section **3.5.2**.

Three in-line heaters are housed in a cylindrical pressure vessel (Figure **6**), which has been fabricated utilizing a 12-inch schedule 80 carbon steel pipe. The pressure inside the vessel will be equalized to the pressure inside the air supply lines so that the heaters can be used exceeding their rated pressure limit of 11 atm (150 psig). Air supply lines consist of stainless steel pipes and fittings of schedule 40 or 80. The three heaters merge at downstream in the vessel, which is subsequently mounted onto the flow reactor.

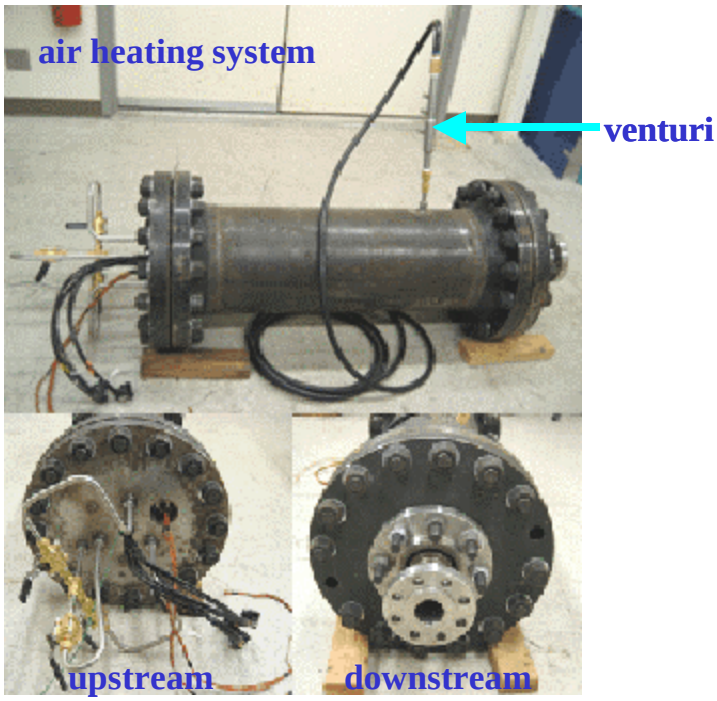

Figure **5**: Air Heating System (Total of 72 kW Nominal, 54kW Actual)

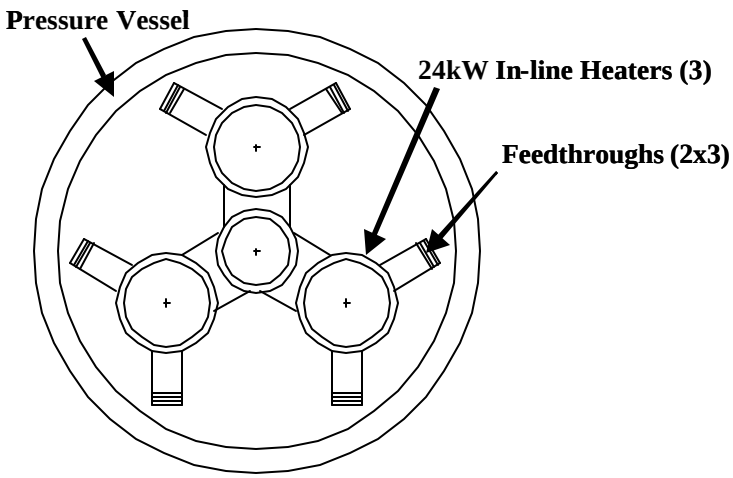

Figure **6**: Cross-Sectional View of the Air Heating System

The assembly process of the air heating system is shown in Figure **7**. Each heater consists of three elements, which are wired in a delta configuration utilizing power distribution blocks for a three-phase operation. Three thermocouples are also mounted near the heater exits to monitor air temperature to prevent overheating. Power supply lines for the heaters and thermocouple wirings are delivered through feedthroughs. The layout of air inlet/outlet and feedthroughs is shown in Figure **8**.

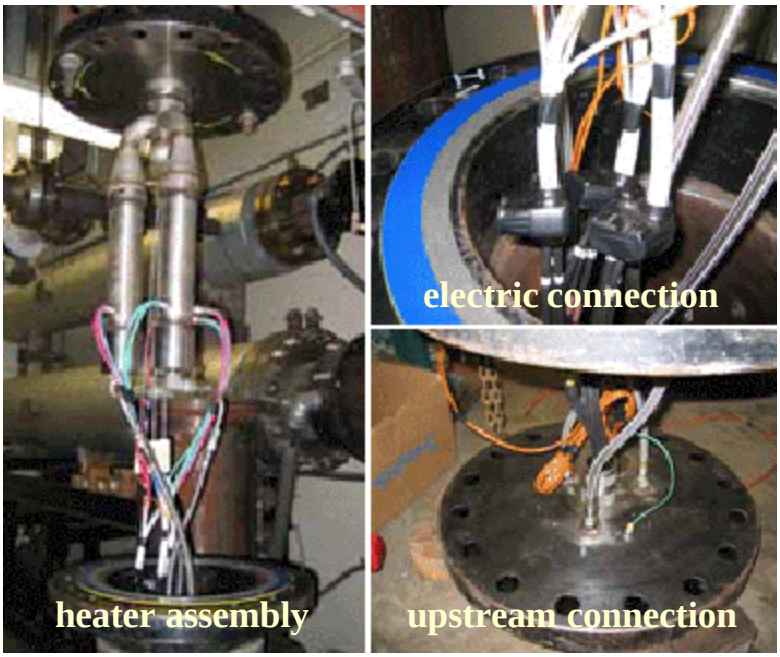

Figure **7**: Heater Assembly Process

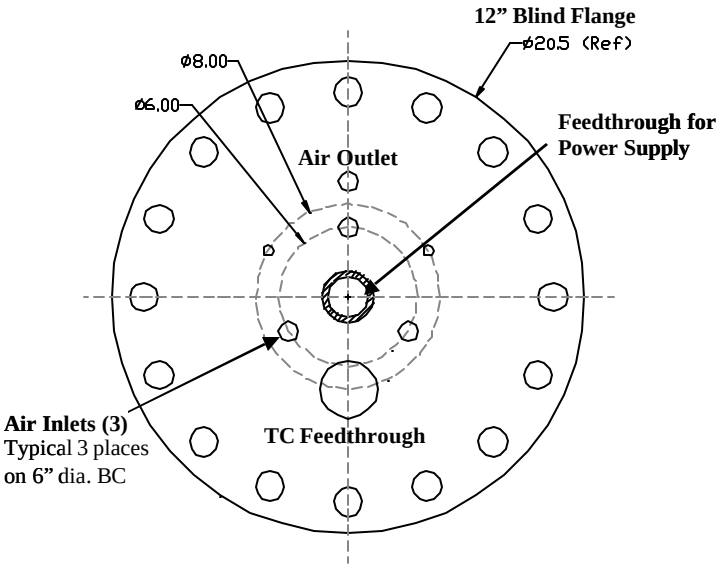

Figure **8**: Upstream Flange Layout

3.5.2 Heater Protection

Air temperatures downstream of the heaters will be monitored utilizing multiple thermocouples and used to maintain the temperature at the set value by the power controller. In addition to this temperature control, air flow rates in the supply line will be monitored to ensure the minimum flow rate preventing overheat of the heaters. At upstream of the pressure vessel, a venturi is installed on the air supply line of 0.5" schedule 40 pipe to enable flow rate measurements. The design calls for β = 0.45 (Eq. **3**)

$$b = \frac{d}{D} \qquad (\mathbf{3})$$

where d is the throat diameter of the venturi and D is the inside diameter of the line. In the present setup, D = 0.622". The discharge coefficient for an ASME conforming venturi, C, is calculated by:

$$C = 0.9975 - \frac{6.53\, b^{0.5}}{R_D^{\;0.5}}\,. \qquad (\mathbf{4})$$

where R_D is the pipe Reynolds number. Eq. **4** can be also expressed as Eq. **5**:

$$C = 0.9975 - \frac{6.53}{\sqrt{R_d}}\,. \qquad (\mathbf{5})$$

where R_d is the Reynolds number at the throat. Thus, a pressure drop can be calculated from:

$$\Delta P = \frac{1}{2r}\left(\frac{\dot{m}_a}{K \cdot A_t}\right)^2 \qquad \text{where} \qquad K = \frac{C}{\sqrt{1 - b^4}} \qquad (\mathbf{6})$$

In Eq. **6**, $\dot{m}_a$ is the actual mass flow rate, ρ is the density of air, and A_t is the throat area of the venturi. Calculating for the designed minimum volumetric flow rate of 10 SCFM, the pressure drop is: ΔP_{min} = 403.68 Pa (1.62 inH_2O). A 43000 series Capsu-Photohelic pressure switch/gage by Dwyer will be used to monitor the differential pressure and turn off the heaters when the pressure drop becomes below ΔP_{min} to protect the heaters from a low flow burnout.

3.5.3 Pressure System

The high-pressure Sullair compressor has been installed. The compressor is capable of the maximum pressure of 25 atm (350 psig) and mass flow rate of 0.29 kg/s (0.63 lb/sec). With this compressor, the attainable pressure will be approximately 18 atm (250 psig), which is a significant improvement from the 8 atm (103 psig) previously available for ignition delay studies at UCICL.

3.5.4 Fuel Composition Control System

Through the previous AGTSR project [**15, 16**], UCICL developed a portable gaseous fuel control system (Figure **9**) capable of blending up to seven gases to simulate flexible NG fuel compositions. Brooks Instrument Mass Flow Controllers (MFCs) of model numbers 5850E, 5851E, and 5853E are used to measure the constituent gases in this system, and controlled by a LabVIEW program.

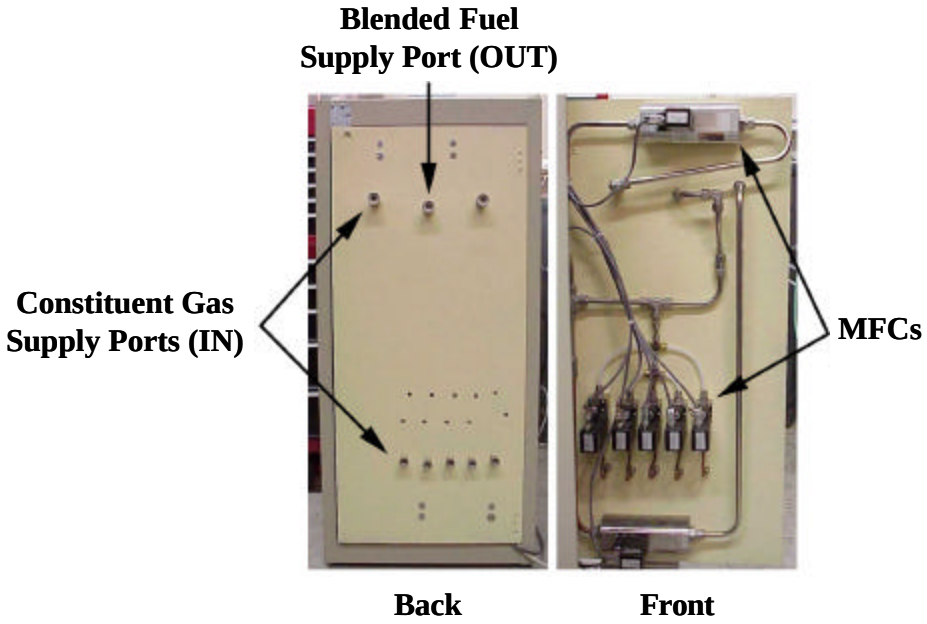

Figure **9**: Gaseous Fuel Control System for Natural Gas

The capability of the existing MFCs has been evaluated with respect to the IGCC syngas constituents, their required flow rates, and compositions. For the experiments with IGCC type fuels at higher pressures, the flow rates of the key constituents (H_2, CO, CO_2, and N_2) are expected to be much higher than the flow rates used in the previous UCICL ignition delay project. Therefore, the resulting large turndown ratios of the constituent flow rates are beyond the capabilities of the existing MFCs and many other commercially available flow rate controllers. Although fuel composition of the IGCC syngas has been reviewed to confront this difficulty (Section **4.2**), the flow rate turndown requirements are still significant. While a series of flow meters present within the laboratory have being calibrated to evaluate their responses, pre-blended IGCC type fuels will be used for preliminary experiments.

3.3 Data Acquisition (DAQ) System

The DAQ needs for this project include the control of air delivery and fuel composition as well as the sampling of the properties (temperature and pressure) of air and air/fuel mixture and sensor signals for ignitions. Sensors used to monitor ignitions are six Type-K thermocouples and six Si photodiodes (Hamamatsu, Type S2386-8K) that are mounted on Test Section B (Figure **4** (b)). Location of the sensor ports are provided in Table **2**. All the DAQ are performed using the code written in National Instruments LabVIEW. The specific data acquisition cards are summarized in Table **4**.

Table **4**: Currently Available DAQ (National Instruments) Cards

DAQ Cards	AO (SE)	AI (SE)	Accessories	Sampling Rate
PCI-6024E	2	16	CD-68LP	200 kS/sec
PCI-MIO-16E-1	2	16	SCXI-1200, 1140, 1304	1.25 MS/sec
PCI-6071E	2	64	SCB-100	1.25 MS/sec
Total	6	96	---	---

The UCICL high-pressure facility is situated on two floors. Previously, this DAQ system was operated using; a flow control system located downstairs, and the experimental rig and fuel composition control system located upstairs. While this worked reasonably well, a lack of time resolution resulted from the LAN system throughput. As a result, a strategy to eliminate this bottleneck was implemented. The current DAQ system has been upgraded to use a single computer downstairs to increase the frequency response of the overall system.

4. RESULTS AND DISCUSSION

Details of the current status and the modifications to date were described in the previous section. In this section, the progresses in numerical simulation (CHEMKIN) and literature reviews are discussed.

4.1 CHEMKIN Analysis

4.1.1 Reaction Mechanisms

Previously, three chemical reaction mechanisms were evaluated and compared: 1) the mechanism by Mueller et al. [**4**, **5**] that involves the H_2/O_2 and $CO/H_2O/O_2$ reactions, 2) the GRI-Mech 3.0 mechanism which is optimized for methane and natural gas [**6**], and 3) the mechanism by Baluch et al. [**7**], compiled by Kaneshige [**8**] of California Technology Institute Explosion Laboratory for their research purpose. Two mechanisms have been added to the evaluation during this reporting period: 4) the first version of Davis et al. [**9**], which is currently being developed and improved, and 5) San Diego Mechanism 2003/08/30 [**10**] developed at the Center for Energy Research of University of California, San Diego. All the mechanisms are summarized in Table **5** as well as the mechanism not yet evaluated - "Hydrogen 2004" developed by Lawrence Livermore National Laboratory (LLNL) [**17**]. Because establishment and improvement of mechanisms is an on-going efforts at many research facilities, evaluations of newly developed or "rediscovered" mechanisms for H_2/CO containing fuels will be continued throughout the current project. In discussions with engine OEMs (Original Equipment Manufacturers) and the generally academic community, the reaction mechanism by Mueller et al. appears to have gained some general acceptance and thus far, has been the primary mechanism utilized for the calculations in the current project.

Table **6**: Chemical Reaction Mechanisms for Fuels Containing H_2 and/or CO

Mechanism	# Species	# Reactions	Notes	Status
Mueller et al.	13	34	can include more elementary reactions	✓
GRI-Mech 3.0	53	325	designed for natural gas combustion	✓
Baulch et al.	42	167	compiled by Kaneshige (1996)	✓
San Diego 2003/08/30	39	173	includes hydrocarbons of C# 1-3	✓
Davis et al.	14	38	version 1 of UD and USC	✓
Hydrogen 2004, LLNL	10	21	does not include CO reactions	not evaluated yet

The AURORA application of the CHEMKIN collection was used to simulate ignition delay times at various operating conditions. Figure **9** summarizes the simulation results for the 50% H_2 50% CO - air mixture at the pressure and equivalence ratio of 15atm and 0.6, respectively. The CHEMKIN default definition of the autoignition time, "the time at which the temperature reaches 400 K higher than the initial value," was employed in this analysis. More accurate definitions (e.g., "at the maximum temperature gradient," and "at the maximum rate of production of OH radicals") were evaluated during the previous ignition delay project at UCICL [**16**]. The default definition has also been confirmed to be sufficiently close to the "time at the maximum temperature gradient" to address the trend of the autoignition characteristics for the relevant fuel (50% H_2 50% CO).

Figure **9** shows that general agreement in trends among the resulted ignition delay times with all the mechanisms. However, Baulch et al. predicts ignition delay significantly longer for the temperature range of 750 K (890 ^{o}F) to 1250 K (1790 ^{o}F) at the simulated condition. Below 750 K (890 ^{o}F), GRI-Mech 3.0 predicts far longer induction period than other mechanisms (Figure **11**). Notice that pre-combustor temperatures of typical gas turbines fall in the range discussed above.

In Figure **12**, the CHEMKIN simulation results are compared with the experimental data of Peschke & Spadaccini [**11**] for their baseline fuel (38.6% H_2, 51.1% CO, 10.3% CO_2) and the CHEMKIN simulations for the same conditions using the

mechanism by Mueller et al. Peschke & Spadaccini proposed the empirical correlation for the ignition delay for the baseline fuel:

$$t\ [O_2]^{0.50}[F]^{0.25} = 1.29\times10^{-7}\exp\left(\frac{3985}{T}\right) \qquad (7)$$

Where τ is an ignition delay time (sec), $[O_2]$ and [F] are the molar concentration (moles/cm^3) of oxygen and fuel, respectively, and T is a temperature (K). This is the only "syngas" ignition delay expression known at UCICL thus far. The simulated data for the Peschke & Spadaccini conditions fall the vicinity of other simulation results for 50% H_2 50% CO, but significantly (by the order of 2 – 5) differ from the experimental data and the empirical correlation except for the narrow temperature range around 1000 K. Temperature range (750 – 1100 K) that Mueller et al. verified own mechanism is also shown as a reference. The discrepancy between CHEMKIN simulation and experimental results is discussed in the next section.

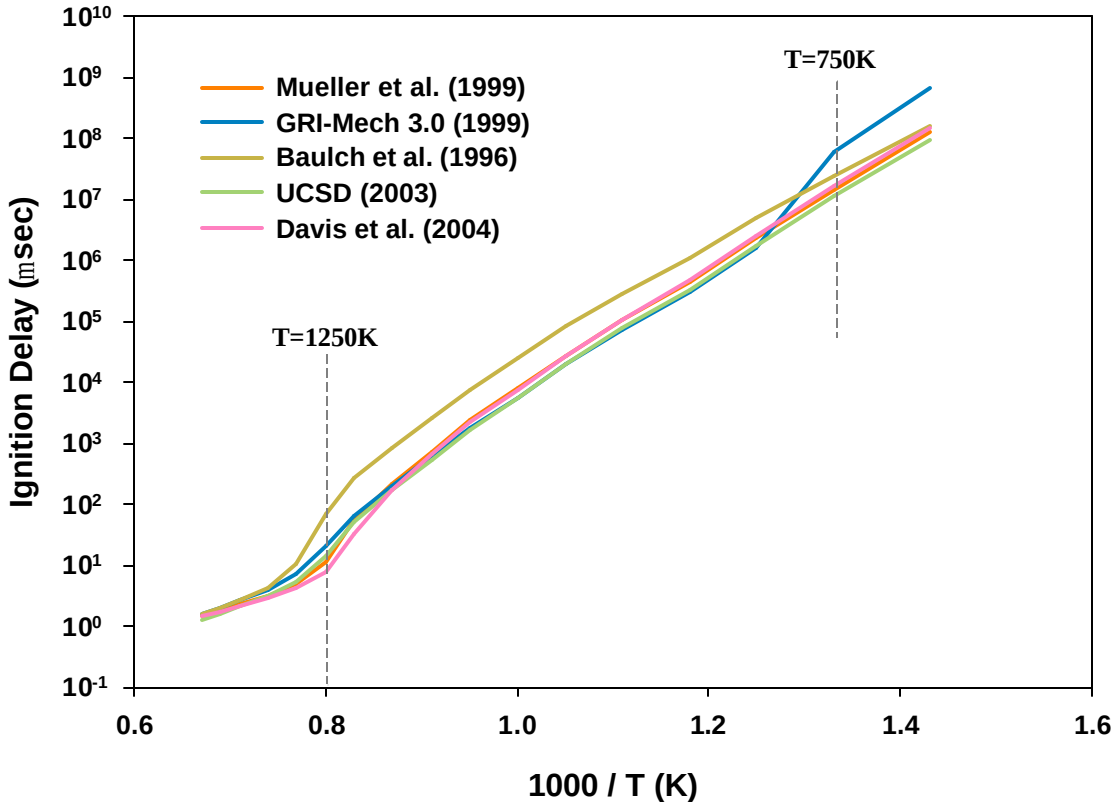

Figure **10**: Comparison of Ignition Delay Predictions using Mueller et al., GRI-Mech3.0, Baulch et al., UCSD, and Davis et al. (H_2/CO/Air, 50% H_2 50% CO, ϕ = 0.6)

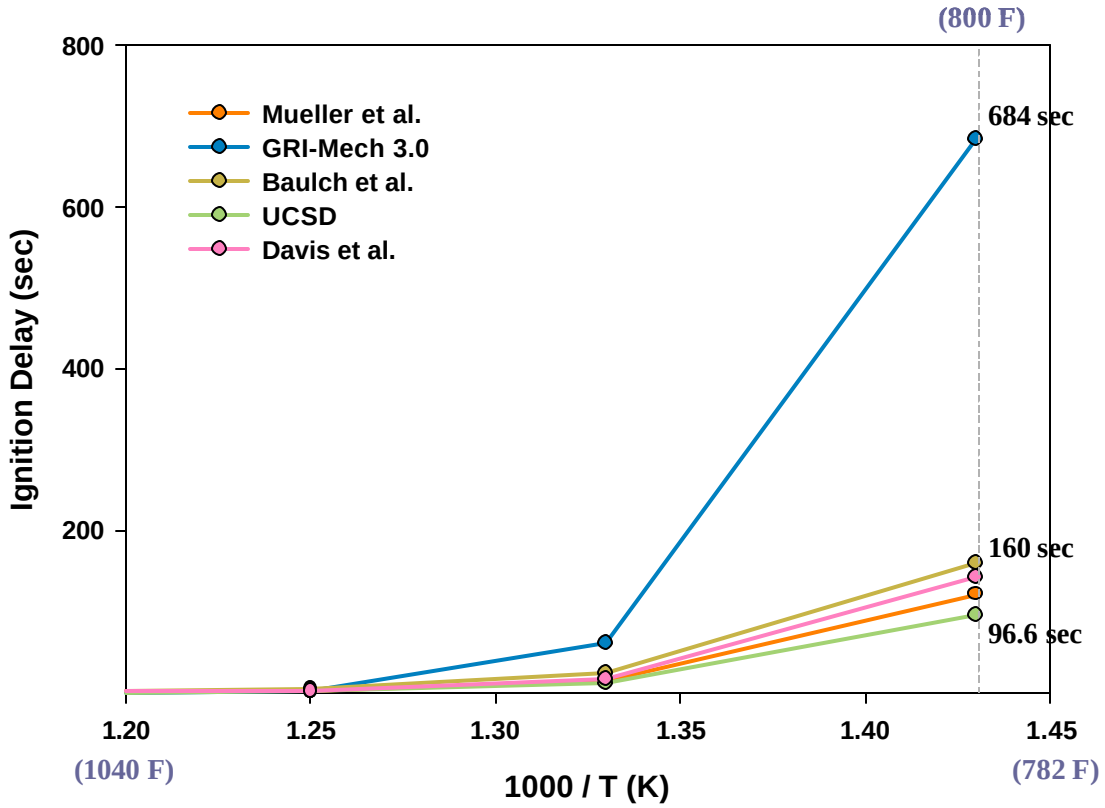

Figure **11**: Range of Ignition Delay Predictions with Various Mechanisms

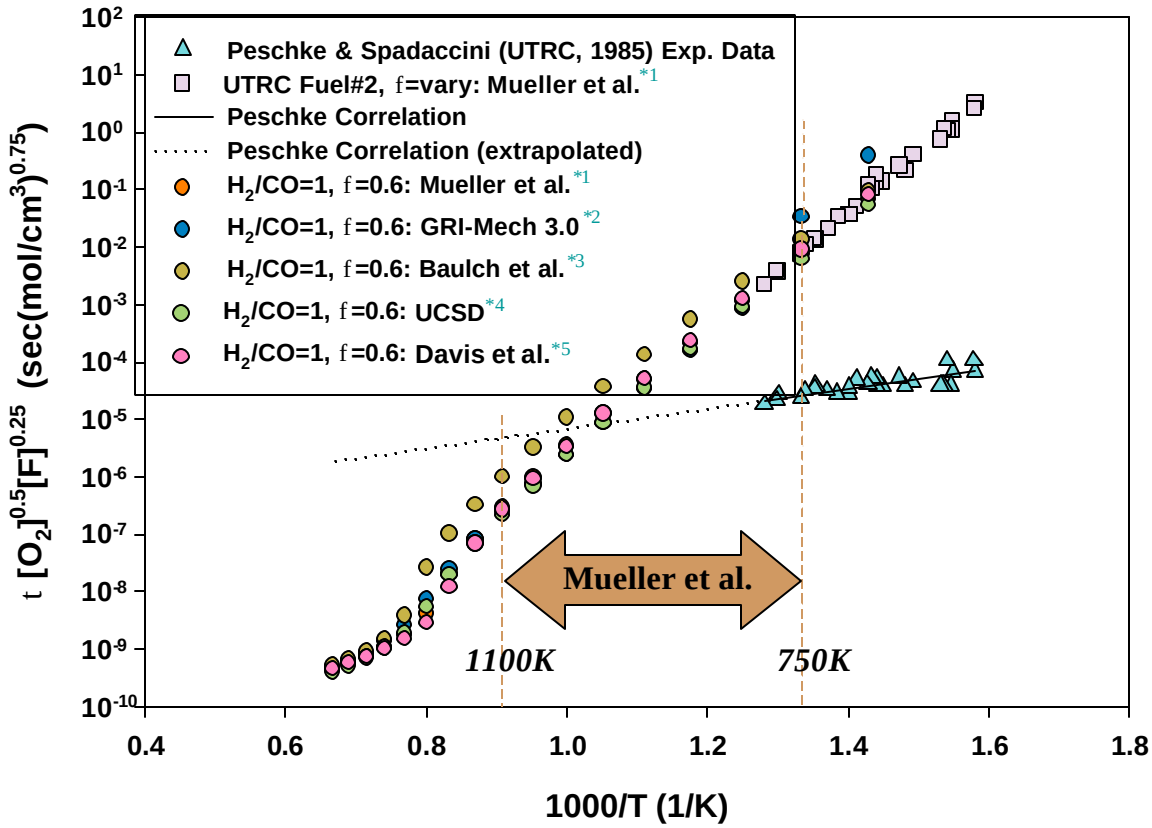

*1 1999, *2 1999, *3 1996, *4 2003, *5 2004

Figure **12**: Comparison of CHEMKIN Ignition Delay Predictions with the Peschke & Spadaccini Experimental Data: CHEMKIN Simulations Were Performed for 1) 50% H_2 50% CO – Air at ϕ = 0.6 Using Various Mechanisms and 2) Peschke & Spadaccini Baseline Fuel (38.6% H_2 51.1% CO 10.3% CO_2) Using Mueller et al. at the Relevant Peschke & Spadaccini Experimental Conditions.

4.2 Ignition Delay Factorial Study - Design of Experiments

Design of Experiments (DoEx), a statistical approach for more effective experiments, was employed to address the discrepancy between the simulated and experimental data illustrated in Figure **12**. Note that the randomness of the data entry was compromised to maintain the run order of original Peschke & Spadaccini [**11**]

experiments. Two-level factorial models were created and analyzed using the Design-Expert software. The factors and their levels (i.e., minimum and maximum limits) are summarized in Table **7**.

Table **7**: Factors for Design of Experiment Approach

Factor	Name	Units	MIN	MAX
A	Pressure	atm	11.9	23
B	Temperature	K	632.9	781.2
C	Equivalence Ratio		0.23	0.72

Figure **13** shows half normal probability plots for (a) the CHEMKIN simulation results and (b) the experimental data. Note that the ignition delay times were transformed using base 10 log. Both simulated and measured ignition delay times are heavily dependent on temperature, which coincides with all the autoignition expressions proposed for various fuels. While no factor interactions are observed for the simulated results, the experimental data show apparent AC and AB interactions with the chances that an effect is due to noise are 0.34% and 1.61%, respectively based on ANOVA (Analysis of Variance, Figure **4(b)**). ANOVAs also suggest that pressure (Factor A) and equivalence ratio (Factor C) have significant effects on the simulation (Figure **13(a)**), but are not significant for the experimental results (Figure **13(b)**).

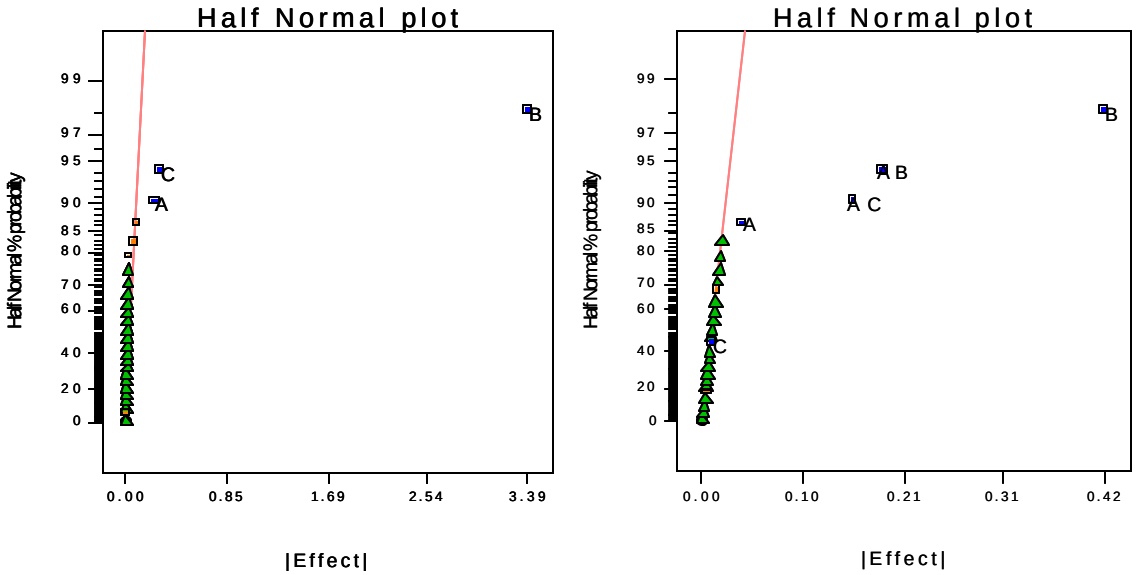

(a) (b)

Figure **13**: Ignition Delay Times of UTRC Baseline Fuel: (a) Chemkin Simulation and (b) Experimental Data

Source	Sum of Squares	DF	Mean Square	F Value	Prob > F	
Model	20.39	3	6.80	1974.95	< 0.0001	significant
A	*0.089*	*1*	*0.089*	*25.97*	*< 0.0001*	
B	*18.62*	*1*	*18.62*	*5412.04*	*< 0.0001*	
C	*0.13*	*1*	*0.13*	*38.11*	*< 0.0001*	
Residual	0.079	23	3.441E-003			
Cor Total	20.47	26				

(a)

Source	Sum of Squares	DF	Mean Square	F Value	Prob > F	
Model	0.42	5	0.084	14.62	< 0.0001	significant
A	*3.546E-003*	*1*	*3.546E-003*	*0.62*	*0.4415*	
B	*0.27*	*1*	*0.27*	*46.32*	*< 0.0001*	
C	*7.907E-003*	*1*	*7.907E-003*	*1.37*	*0.2546*	
AB	*0.063*	*1*	*0.063*	*10.92*	*0.0034*	
AC	*0.039*	*1*	*0.039*	*6.85*	*0.0161*	
Residual	0.12	21	5.762E-003			
Cor Total	0.54	26				

(b)

Figure **14**: Analysis of Variance (ANOVA) Summary for (a) CHEMKIN Simulation Results, and (b) Experimental Data

Interactions AB and AC for the factorial model of the experimental data are shown in Figures **7** and **2**, respectively. In both figures, a black line represents the lower limit of the corresponding factor while a red line represents the higher limit: T = 632.90 K (black) and T = 781.20 K (red) for Figure **7**, and ϕ = 0.23 (black) and ϕ = 0.72 (red) for Figures **2**. For example, at the lower temperature limit, pressure has a slight effect on the ignition delay at the very lean (ϕ = 0.23) condition while the pressure effect becomes

more and more significant as the equivalence ratio increases within the experiment range. On contrary, pressure effect at the higher temperature limit shows the opposite trend.

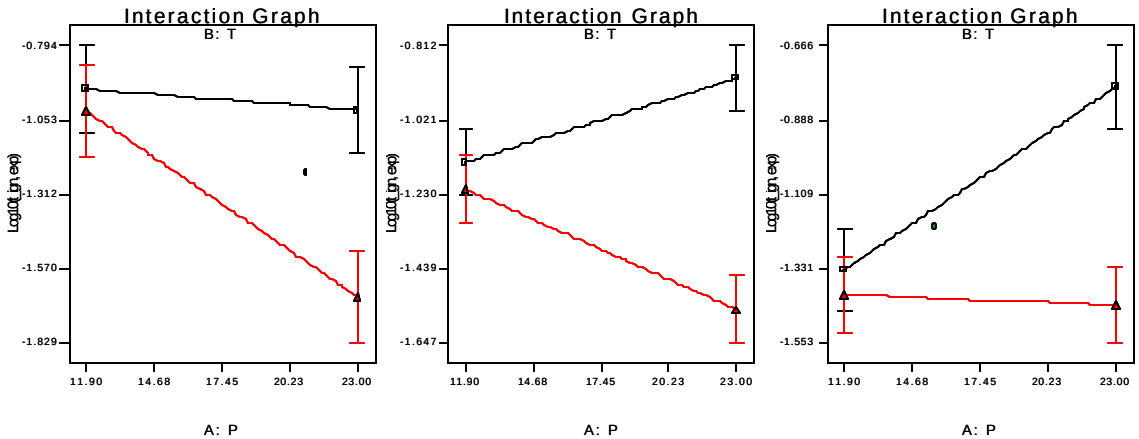

(a) ϕ = 0.23 (b) ϕ = 0.47 (c) ϕ = 0.72

Figure **15**: Pressure (Factor A) – Temperature (Factor B) Interaction at Various Equivalence Ratios. T = 632.90 K (black) and T = 781.20 K (red).

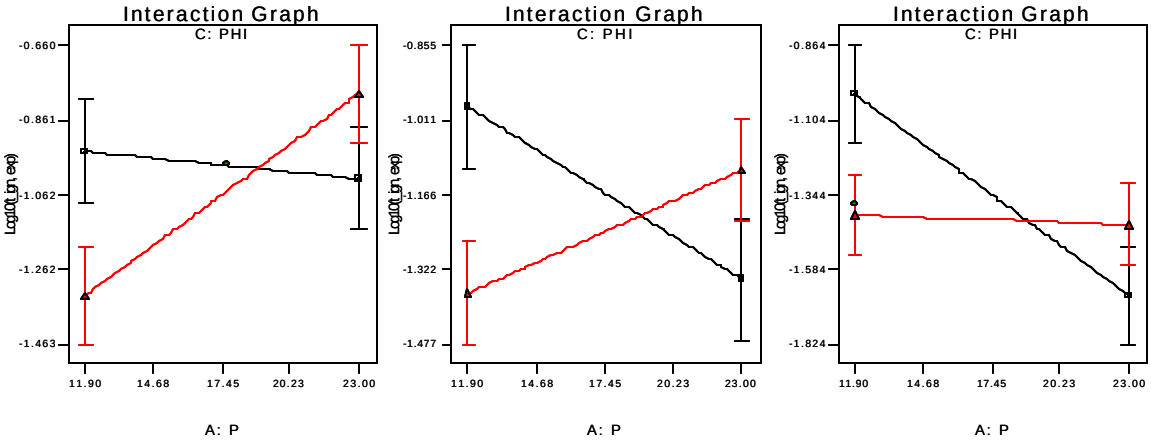

(a) T = 632.90 K (b) T = 709.05 K (c) T = 781.20 K

Figure **16**: Pressure (Factor A) - Equivalence Ratio (Factor C) Interaction at Various Temperatures. ϕ = 0.23 (black) and ϕ = 0.72 (red).

Through the factorial modeling, the expressions for the simulated (Eq. **8**) and measured (Eq. **9**) ignition delay can be obtained in terms of the selected effects (Figure **13**).

Figure **1** illustrates the variations of the actual data, (a) simulated and (b) measured), from the resulted Equations 1 and 2, respectively.

The DoEx analyses shown are solely based on the results of Peschke & Spadaccini [**11**]. Ignition delay characteristics should be evaluated with other independent experimental data for more comprehensive analyses. Our experimental work is essential in this context. The results also raise some concerns in terms of the mechanism behind the observed P-T (AB) and P-ϕ (AC) interactions. If some physical interpretation of these interaction terms can be determined it could help establish the presence (or lack of) any systemic issues with the Peschke & Spadaccini dataset.

$$\log_{10}(t_{ign,simulated}) = +16.98890 - 0.021154 \cdot \mathrm{P} - 0.020140 \cdot \mathrm{T} - 0.63959 \cdot f \qquad (\mathbf{8})$$

$$\begin{aligned}\log_{10}(t_{ign,measured}) = &-2.66723 \\ &+0.18743 \quad *\mathrm{P} \\ &+3.62066\mathrm{E}-003 \quad *\mathrm{T} \\ &-2.13800 \quad *f \\ &-3.47616\mathrm{E}-004 \quad *\mathrm{P}*\mathrm{T} \\ &+0.11317 \quad *\mathrm{P}*f\end{aligned} \qquad (\mathbf{9})$$

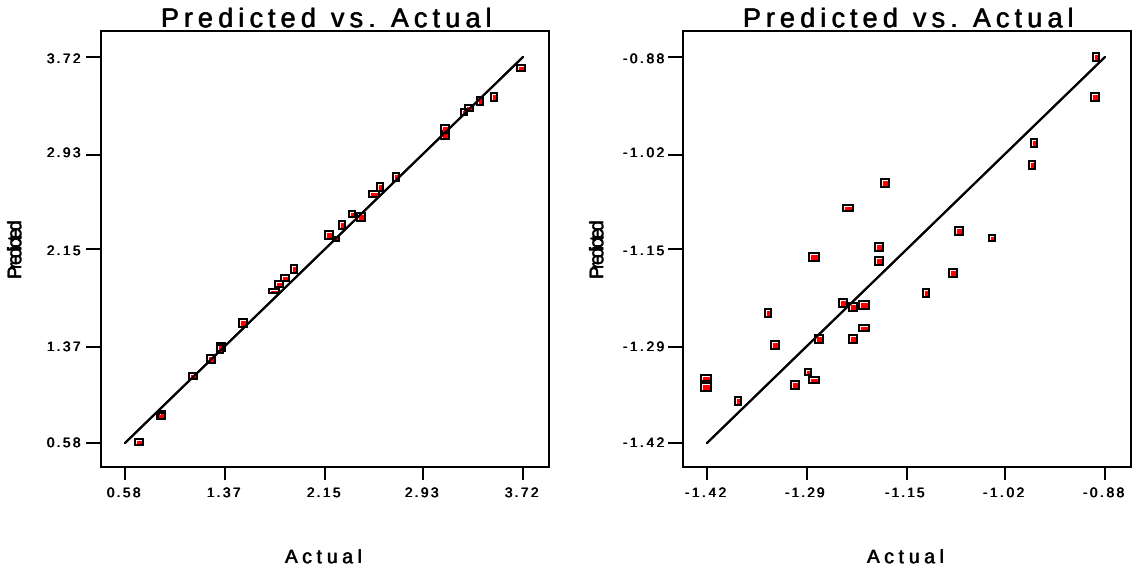

(a) (b)

Figure **17**: Variation of the (a) Simulated and (b) Measured Ignition Delay Data from the Resulted Analytical Expressions.

5. CONCLUSION

Hardware preparation has progressed during this reporting period. The assembly of the air heating system (total of 54kW, actual) has been completed as well as necessary electric preparations in the UCICL high pressure experiment cell. Along with previously reported pressure system upgrade, the UCICL facility is expected to be capable to reach maximum temperature and pressure of ~1033 K (1400 ^{o}F) and 18 atm (250 psig), respectively. Upon the completion of heating system installation and temperature control characterization of the flow reactor, experiments will be conducted with several IGCC type fuels, whose compositions are currently being reviewed.

The UCSD [**10**] and Davis et al. [**9**] reaction mechanisms have been added to our ignition delay simulations for the IGCC type fuel (50% H_2 50% CO) of the equivalence ratio of 0.6 at 15 atm using AURORA application of CHEMKIN. Predicted ignition delay profiles by Mueller et al., GRI-Mech 3.0, Baulch et al., UCSD, and Davis et al. show general agreement. However, The Baulch et al. mechanism and GRI-Mech 3.0 predicted significantly longer ignition delay for the temperature range of 750 – 1250 K (890 – 1790 ^{o}F) and below 750 K (890 ^{o}F), respectively. More detailed comparison is necessary to look into this discrepancy. We note that the Davis et al. [**9**] mechanism used in this analysis is still the first trial version and currently being modified/improved. Other mechanisms for H_2 and/or CO containing fuels will be continuously searched and added to our evaluations.

Significant discrepancy was observed between CHEMKIN simulation results, including simulations at the same conditions as Peschke & Spadaccini [**11**] for their baseline fuel (38.6% H_2, 51.1% CO, 10.3% CO_2), and their experimental data. Statistical approach was taken to address this discrepancy. Temperature was predictably the biggest effect for both predicted and measured data. Pressure and equivalent ratio has small, but significant effects on the simulated data, while their effects were trivial for the experimental results. On the other hand, effects of the interactions between pressure and temperature, and pressure and equivalence ratio were found significant for the

experimental data. Since the only single source of experimental results for IGCC type fuels is available at this point, the interactions cannot be confirmed to be real. Different sets of experimental data, including the current efforts at UCICL, are required to further investigate the autoignition profile of the IGCC type fuels.

REFERENCES

1. Greene, M., Chen, J., McDonell, V., and Samuelsen, S., "Correlation of Ignition Delay with Natural Gas and IGCC Type Fuels," Semi-Annual Report for UTSR Subcontract 03-01-SR112 under DOE NETL Contract DE-FC26-02NT41431, University of California, Irvine Combustion Laboratory, January 2004.

2. Greene, M., Chen, J., McDonell, V., and Samuelsen, S., "Correlation of Ignition Delay with Natural Gas and IGCC Type Fuels," Annual Report for UTSR Subcontract 03-01-SR112 under DOE NETL Contract DE-FC26-02NT41431, University of California, Irvine Combustion Laboratory, July 2004.

3. Kee, R. J., Rupley, F. M., Miller, J. A., Coltrin, M. E., Grcar, J. F., Meeks, E., Moffat, H. K., Lutz, A. E., Dixon-Lewis, G., Smooke, M. D., Warnatz, J., Evans, G. H., Larson, R. S., Mitchell, R. E., Petzold, L. R., Reynolds, W. C., Caracotsios, M., Stewart, W. E., Glarborg, P., Wang, C., Adigun, O., Houf, W. G., Chou, C. P., and Miller, S. F., Chemkin Collection, Release 3.7.1, Reaction Design, Inc., San Diego, CA, 2004.

4. Mueller, M. A., Kim, T. J., Yetter, R. A., Dryer, F. L., "Flow Reactor Studies and Kinetic Modeling of the H_2/O_2 Reaction," *International Journal of Chemical Kinetics*, Vol. 31, 1999, pp. 113-125.

5. Mueller, M. A., Yetter, R. A., and Dryer, F. L., "Flow Reactor Studies and Kinetic Modeling of the $H_2/O_2/NO_X$ and $CO/H_2O/O_2/NO_X$ Reactions," *International Journal of Chemical Kinetics*, Vol. 31, 1999, pp. 705-724.

6. Smith, G. P., Golden, D. M., Frenklach, M., Moriarty, N. W., Eiteneer, B., Goldenberg, M., Bowman, C. T., Hanson, R. K., Song, S., Gardiner, W. C., Jr., Lissianski, V. V., and Qin, Z., http://www.me.berkeley.edu/gri_mech/

7. Baulch, D. L., Cobos, C. J., Cox, R. A., Frank, P., Hayman, G., Just, Th., Kerr, J. A., Murrells, T., Pilling, M. J., Troe, J., Walker, R. W., and Warnatz, J., "Summary Table of Evaluated Kinetic Data for Combustion Modeling: Supplement 1," *Combustion and Flame*, Vol. 98, 1994, pp. 59-79.

8. Akbar, R., Kaneshige, M., Schultz, E., Shepherd, J., "Detonations in H_2-N_2O-CH_4-NH_3-O_2-N_2 Mixtures," Explosion Dynamics Laboratory Report FM97-3, Graduate Aeronautical Laboratories California Institute of Technology (GALCIT), July 1997.

9. Davis, S. G., Joshi, A. V., Wang, H., and Egolfopoulos, F., "An Optimized Kinetic Model of H_2/CO Combustion," 30th International Symposium on Combustion, Chicago, IL, July 25-30, 2004.

10. Williams, F. A., et al., http://maeweb.ucsd.edu/combustion/cermech/

11. Peschke, W. T., and Spadaccini, L. J., "Determination of Autoignition and Flame Speed Characteristics of Coal Gases Having Medium Heating Values," Final Report for AP-4291 Research Project 2357-1, November 1985.

12. Lefebvre, A., Freeman, W., and Cowell, L., "Spontaneous Ignition Delay Characteristics of Hydrocarbon Fuel/Air Mixtures," NASA Contractor Report 175064, 1986.

13. Spadaccini, L. J., and Colket M. B., "Ignition Delay Characteristics of Methane Fuels," *Progress in Energy and Combustion Science*, Vol. 20, 1994, pp. 431-460.

14. Richards, G. A., McMillian, M. M., Gemmen, R. S., Rogers, W. A., and Cully, S. R., "Issues for Low-Emission, Fuel-Flexible Power Systems," *Progress in Energy and Combustion Science*, Vol. 27, 2001, pp. 141-169.

15. Chen, J., Jermakian, V., McDonell, V., Samuelsen, S., "Correlation of Ignition Delay with Fuel Composition and State for Application to Gas Turbine Combustion," Final Report for AGTSR Subcontract 00-01-SR084CS under DOE NETL Contract DE-FC21-92MC29061, University of California, Irvine Combustion Laboratory, January 2003.

16. Chen, J., "Autoignition of Natural Gas Fuels with Ethane and Propane Additives at Low to Intermediate Temperature," Ph. D. Dissertation, University of California, Irvine, 2003.

17. Conaire, M. Ó., Curran, H. J., Simmie, J. M., Pitz, W. J., and Westbrook, C. K., "A Comprehensive Modeling Study of Hydrogen Oxidation," International Journal of Chemical Kinetics, Vol. 36, 2004, pp. 603-622. (UCRL-JC-152569).

Heat Transfer from Rotating Blade Platforms with and without Film Cooling

Semi-Annual Report

Reporting Period
November 1, 2005 – February 28, 2006

Principal Investigators
J.C. Han
M.T. Schobeiri

Report Submitted
March 2006

DOE Award Number
DE-FC26-02NT41431

UTSR Project Number
02-01-SR113

Texas A&M University
Department of Mechanical Engineering
College Station, Texas 77843-3123

DISCLAIMER

This report was prepared as an account of work sponsored by an agency of the United States Government. Neither the United States Government nor any agency thereof, nor any of their employees, makes any warranty, express or implied, or assumes any legal liability or responsibility for the accuracy, completeness, or usefulness of any information, apparatus, product, or process disclosed, or represents that its use would not infringe privately owned rights. Reference herein to any specific commercial product, process, or service by trade name, trademark, manufacturer, or otherwise does not necessarily constitute or imply its endorsement, recommendation, or favoring by the United States Government or any agency thereof. The views and opinions of authors expressed herein do not necessarily state or reflect those of the United States Government or any agency thereof.

ABSTRACT

This project experimentally investigates the heat transfer phenomena on the rotor blade platforms of gas turbine blades. Designers often rely on experimental data gathered from non-rotating models, and in many cases, the non-rotating models inadequately model the flow and heat transfer around the rotating blades. Detailed pressure and heat transfer distributions are gathered on the rotating blade platforms using pressure sensitive and temperature sensitive paints. Detailed film cooling effectiveness distributions are also obtained on rotor platforms with the pressure sensitive paint technique. Miniature five-hole pitot tubes are used to obtain profiles of the mainstream flow through the turbine stage. This experimental data is used to validate numerical simulations, and the numerical predictions are extended to include a wide range of rotor platform configurations and film cooling flow conditions to more closely model actual engine conditions. Film cooling effectiveness measurements have been recorded on the rotating platform using pressure sensitive paint; the film effectiveness has been measured on the rotating platform with coolant from the stator-rotor seal and with coolant from discrete film holes. The measured film cooling effectiveness is significantly lower on the rotating platform, than measured in non-rotating test facilities. The next step for this rotating study is to measure the film cooling effectiveness on the rotating platform with combined coolant from the stator-rotor seal and discrete film holes. A linear five blade cascade is being utilized to study a seal geometry similar to one used in the rotating study, as well as three additional geometries to model more advanced seal configurations. From the cascade studies, it is very clear the film cooling effectiveness on the blade endwall is strongly affected by the passage induced secondary flow. Depending on the amount of coolant used to protect the endwall, a large portion of the passage can be left unprotected. In addition, designers should be cautious when applying flat plate film cooling data to either a rotating or non-rotating platform, as the results may vary significantly due to the passage induced secondary flow.

TABLE OF CONTENTS

DISCLAIMER 2

ABSTRACT 3

EXECUTIVE SUMMARY 9

PROJECT DESCRIPTION 11
- Introduction 11
- Gas Turbine Needs and Project Objectives 18
- Project Tasks 20
  - Task 1 – Rotor Platform Modification and Measurement Technique Development 20
  - Task 2 – Rotor Platforms with Stator-Rotor Seal Ejection 21
  - Task 3 – Rotor Platforms with Stator-Rotor Seal Ejection and Film Cooling Holes 21

EXPERIMENTAL PROCEDURE 23
- Turbine Research Facility 23
- New Turbine Component Design 24
- Pressure Sensitive Paint (PSP) Technique 25
- Temperature Sensitive Paint (TSP) Technique 29

RESULTS AND DISCUSSION 32
- Experimental Rotating Heat Transfer 32
  - Film Cooling Effectiveness from Upstream Slot Cooling 33
  - Film Cooling Effectiveness from Discrete Film Cooling Holes 40
- Flow Measurements and Numerical Predictions 42
  - Interstage Instrumentation 42
  - Aerodynamic Flow Measurement 43
  - Numerical Prediction of the Heat Transfer Coefficients and Film Cooling Effectiveness 44
- Advanced Stator-Rotor Seals in a Five Blade Linear Cascade 58
  - Motivation and Objectives for the Linear Cascade Endwall Study 58
  - Low Speed Wind Tunnel 58
  - Linear Cascade Design 59
  - Platform Cooling Design 60
  - Computational Details 61
  - Film Cooling Effectiveness on the Cascade Endwall 62

FUTURE PLANS 73
- Rotating Heat Transfer 73
- Advanced Stator-Rotor Seals 73

CONCLUSIONS 75

REFERENCES 77

LIST OF FIGURES

Figure 1: Modern Cooled Gas Turbine Blade..... 81

Figure 2: Secondary Flow through a Blade Passage (from Han et al. [1]) 82

Figure 3: Existing Turbine Research Facility 83

Figure 4: Coolant Flow for Film Cooling and Coolant Ejection 84

Figure 5: Detailed Views of Coolant Ejection and Film Coolant Flow Paths 85

Figure 6: Coolant Ejection on the Rotor Blade Platform..... 86

Figure 7: Coolant Ejection and Film Cooling on the Rotor Blade Platform 87

Figure 8: Newly Fabricated Rotor Platform with Stator-Rotor Seal Ejection and Platform Film Cooling Holes 88

Figure 9: Typical Pressure Sensitive Paint Calibration Setup and Calibration Curve..... 89

Figure 10: Modified Engine Housing to Accommodate Viewing of the Rotor Blade Platform with the Required Optical Componenets for PSP and TSP Measurements..... 90

Figure 11: Optical Components Setup for the Model Turbine and PSP..... 91

Figure 12: Viewing Windows for Rotor Platform Measurements..... 92

Figure 13: Film Cooling Effectiveness Distribution on the Rotating Endwall for 2550 rpm..... 93

Figure 14: Velocity Triangles and Relative Inlet and Exit Flow Angles for Design and Off-Design Rotating Speeds 94

Figure 15: Numerical Prediction of Endwall Static Pressure Distribution (kPa) along with Flow Pathlines..... 95

Figure 16: Film Cooling Effectiveness Distribution on the Rotating Endwall for 2000 rpm..... 96

Figure 17: Film Cooling Effectiveness Distribution on the Rotating Endwall for 1500 rpm..... 97

Figure 18: Film Cooling Effectiveness Distribution on the Rotating Endwall for 3000 rpm..... 98

Figure 19: Pitchwise Averaged Film Cooling Effectiveness Distribution along Axial Chord for Different Turbine Rotating Speeds (Mass Flow Ratio Effect) 99

Figure 20: Pitchwise Averaged Film Cooling Effectiveness Distribution along Axial Chord for Different Mass Flow Ratios (Turbine Rotation Speed Effect) 100

Figure 21: Comparison of Pitchwise Average Effectiveness with a Correlation from Goldstein [40] for Different Speeds 101

Figure 22: Film Cooling Effectiveness Distribution From Downstream, Discrete Film Cooling Holes on the Rotating Endwall for 2550 rpm 102

Figure 23: Film Cooling Effectiveness Distribution From Downstream, Discrete Film Cooling Holes on the Rotating Endwall for 2400 rpm 103

Figure 24: Film Cooling Effectiveness Distribution From Downstream, Discrete Film Cooling Holes on the Rotating Endwall for 3000 rpm 104

Figure 25: Pitchwise Averaged Film Cooling Effectiveness Distribution along Axial Chord for Different Turbine Rotating Speeds (Mass Flow Ratio Effect) 105

Figure 26: Radial Distribution of Stator Exit Flow Angle for Varying Rotor Speeds 106

Figure 27: Radial Distribution of Total Pressure Distribution for Varying Rotor Speeds 107

Figure 28: Radial Distribution of Absolute Velocity for Varying Rotor Speeds 108

Figure 29: Prediction of Film Cooling Effectiveness and Heat Transfer Coefficients on Rotating Blade Platform 109

Figure 30: Detailed Grid Distributions Near the Angled Coolant Slot..... 110

Figure 31: Grid Refinement Sutdy for Laterally Averaged Adiabatic Temperature on Rotating Blade Platform 111

Figure 32: Scheme Comparison for Predicted Film Cooling Effectiveness (2550 RPM, MFR = 1.0%)..... 112

Figure 33: Predicted Path of the Coolant From the Rotating Disk onto the Rotating Platform (2550 RPM, MFR = 0.5%) 113

Figure 34: Predicted Pressure Ratio, Streamlines, and Dimensionless Temperature on the Annular Cross-Plane 114

Figure 35: Comparison of the Static Pressure Contours on the Suction Side of the Rotor Blade with and without Purge Flow (2550 rpm, MFR = 1%)..... 115

Figure 36: Comparison of the Total Wall Temperature on the Rotor Platform with and without Purge Flow (2550 rpm, MFR = 1%)..... 116

Figure 37: Comparison of the Adiabatic Film Cooling Effectiveness on the Rotor Platform with Various Rotational Speeds (MFR = 1%) 117

Figure 38: Effect of Rotational Speed on Laterally Averaged Film Cooling Effectiveness (MFR = 1%)..... 118

Figure 39: Predicted Adiabatic Film Cooing Effectiveness on the Rotating Blade Plabrform with Various Coolant Flow Rates 119

Figure 40: Laterally Averaged Adiabatic Cooling Effectiveness Comparison for Various Coolant Flow Rates (2550 RPM) 120

Figure 41: Laterally Averaged Adiabatic Cooling Effectiveness Comparison for Various Rotational Speeds (MFR = 1%)..... 121

Figure 42: Predicted Adiabatic Film Cooling Effectiveness on the Suction Side of the Rotor Blade at Various Rotational Speeds (MFR = 1%)..... 122

Figure 43: Predicted Overall and Adiabatic Heat Transfer Coefficients on the Rotating Platform at Various Time Phases (2550 RPM, MFR = 0.5%) 123

Figure 44: Predicted Overall and Adiabatic Heat Transfer for the Turbine Stage (2550 RPM, MFR = 0.5%) 124

Figure 45: Area Averaged Total / Static Tempeature for Various Stations in the Turbine Stage (2550 RPM) 125

Figure 46: Coolant Path Inside the Rotor Passage for Various Rotational Speeds (MFR = 0.5%, Colored by the Overall Film Cooling Effectiveness) 126

Figure 47: Overall Film Cooling Effectiveness Comparions on the Rotating Blade Platform for Various Time Phases (2550 RPM, MFR = 1.0%) 127

Figure 48: Overview of the Low Speed Wind Tunnel Used to Study Platform Cooling 128

Figure 49: Low Speed Wind Tunnel and Turbine Blade Details..... 129

Figure 50: Platform Film Cooling Configurations..... 130

Figure 51: Computational Grid Used to Numerically Study the Effect of Slot Injection on the Passage Endwall and Turbine Blade..... 131

Figure 52: Measured Film Cooling Effectiveness with Various Slot Injection Rates (Tu = 0.75%) 132

Figure 53: Predicted Mainstream and Coolant Pathlines near the Blade Platform for Upstream Slot Injection Rates of (a) 0.5% and (b) 1.5% 133

Figure 54: Predicted Film Cooling Effectiveness on the Passage Endwall with Various Slot Injection Rates 134

Figure 55: Predicted Film Cooling Effectiveness on the Suction Surface of the Blade with Various Slot Injection Rates 135

Figure 56: Predicted Heat Transfer Coefficients on the Passage Endwall with Various Slot Injection Rates 136

Figure 57: Measured Film Cooling Effectiveness with Various Slot Injection Rates (Tu = 13.4%) 137

Figure 58: Measured Film Cooling Effectiveness with Downstream Discrete Film Cooling.... 138

Figure 59: Measured Film Cooling Effectiveness with Combined Slot Cooling (1%) and Downstream Film Cooling (Tu = 0.75%) 139

Figure 60: Measured Film Cooling Effectiveness with Combined Slot Cooling (2%) and Downstream Film Cooling (Tu = 0.75%) 140

Figure 61: Spanwise Averaged Film Cooling Effectiveness on the Passage Endwall with Upstream Slot Injection 141

Figure 62: Spanwise Averaged Film Cooling Effectiveness on the Passage Endwall Downstream Discrete Film Hole Cooling 142

Figure 63: Spanwise Averaged Film Cooling Effectiveness on the Passage Endwall with Combined Upstream Slot Injection and Downstream Discrete Film Hole Cooling (Tu=0.75%) 143

Figure 64: Comparison of the Spanwise Averaged Film Cooling Effectiveness on the Passage Endwall with Upstream Slot Injection with Correlations for Discrete, Inclined Film Cooling Holes and Tangential Slot Injection over a Flat Plate..... 144

Figure 65: Advanced Platform Film Cooling Configurations 145

EXECUTIVE SUMMARY

This study investigates the flow behavior and heat transfer distributions on rotor blade platforms of gas turbine engines. The experimental and numerical results will provide turbine designers with new rotating blade platform heat transfer and film cooling data which will improve the cooling performances and thermal efficiency of power generation and industrial gas turbine engines. The three year project consists of three tasks in order to provide designers with applicable rotating blade platform cooling data. Task 1 of this project is to redesign and fabricate a new rotor platform to incorporate two coolant flows: stator-rotor ejection and film cooling flow. With Task 2, detailed pressure, heat transfer coefficient, and film cooling effectiveness distributions resulting from coolant ejection from the annular gap between the stator and rotor will be obtained on the rotating blade platform. In Task 3 of the project, detailed rotor blade platform pressure, heat transfer coefficient, and film cooling effectiveness distributions with a typical film cooling hole geometry will be obtained.

The experimental results obtained thus far indicate the film cooling effectiveness on a rotating platform can be significantly lower than the film cooling effectiveness measured in non-rotating test facilities. The blade profile used in the present study is unlike the profile used in most non-rotating studies. The selected profile may alter the behavior of the horseshoe vortices formed at the leading edge of the blade and thus reduce the film cooling effectiveness. This profile, coupled with both the selected seal geometry (injection angle, seal width, coolant blowing ratio) and rotation, lead to reduced film cooling effectiveness on the rotating platform compared to previous non-rotating studies. It has also been observed that the film cooling effectiveness increases as the rotational speed increases. Turbine designers should heed these new experimental results. If blade platforms are cooled using data developed from non-rotating

facilities, the data can tremendously over predict the protection on the rotating platform. This can lead to blades that are not sufficiently protected and premature failure. In addition, at the beginning or end of a cycle, when the engine is not operating at its design speed, the coverage of the film coolant on the platform maybe further reduced, and the functionality of both the turbine components and the engine could be jeopardized.

The film cooling effectiveness and heat transfer coefficients have also been predicted on the rotating blade platform. These predictions give additional insight of the flow around the rotating blades. Currently, the experimental results are being used to verify the numerical prediction, and then the simulations will be extended to consider the heat transfer and cooling on rotating platforms under more advanced conditions (which cannot be achieved in the laboratory).

With an improved understanding of how data obtained on a rotating platform varies from data obtained in more traditional non-rotating facilities, this study can be extended to include more complex configurations in a non-rotating facility. The current cooling configuration is similar to that used in the rotating facility. The measured effectiveness on the non-rotating platform is significantly higher than the effectiveness measured on the rotating platform.

The experimental results from this project will provide turbine designers with detailed heat transfer and film cooling data on the rotating turbine blade platforms. The experimental results will also validate the numerical predictions performed for the blade platforms. From this comprehensive detailed data, engineers will be able to design a more efficient platform geometry with film cooling holes which increase the durability and longevity of the blade platforms. The effective cooling schemes will also save cooling flow. By reducing the cooling flow while effectively cooling the rotating blades, the power output and efficiency of the engine will increase.

PROJECT DESCRIPTION

Introduction

As economies across the world continue to grow, the demand for power also continues to increase. Commercial, industrial, and residential customers have come to expect uninterrupted electrical service required to meet a variety of needs; however, the demand for power is growing faster than the power supply. Meanwhile, the commercial airline industry is facing numerous hurdles while the military is facing new challenges. The common bond between land based power generation and aircraft propulsion is gas turbine engines. With gas turbines also being used for marine propulsion and scores of other specific industrial applications, it is vital that these engines operate efficiently. The efficiency of a gas turbine engine can be increased by raising the temperature of the hot gases at the inlet of the turbine. However, increasing the temperature of the mainstream gas must be done cautiously, as additional problems can develop. The metallic turbine components must be protected in order to survive prolonged exposure to the hot gases. The life of the turbine airfoils can be increased by implementing any of a variety of cooling techniques, as shown in Figure 1. As presented by Han et al. [1], air is extracted from the compressor, and used to cool the airfoils. This coolant air is injected into the hollow airfoils, and circulates through internal cooling passage of the blades and vanes. The coolant is discharged through discrete holes, where it forms a protective film on the outer surface of the airfoil. Figure 2 shows the complex flow around a turbine blade, and this three-dimensional flow can have adverse effects on the film coverage across the airfoils. Many investigations have focused on increasing the heat transfer enhancement within the blades via rib turbulators, jet

impingement, and pin-fins. Also, film cooling has been studied for many years to determine the optimal hole configuration and flow conditions to maximize the protection of the coolant.

With the increasing temperature of the mainstream gases exiting the combustor, the stator vanes and rotor blades must be protected, so they can survive the extreme temperatures. Recently, the blade platform has received renewed attention for an adequate cooling scheme. The vane endwall and the blade platforms comprise a large percentage of the area exposed to the hot mainstream gases. There is a strong potential for "hot spots" to form on the endwalls and platforms. Over this large area it is vital to have accurate heat transfer distributions, so efficient cooling schemes can be developed. The cooling schemes should adequately protect the platforms while minimizing the amount of coolant.

Experimental investigations available in open literature on film cooling and heat transfer on rotating turbine blades and their components are few and far between, primarily due to the difficulty in instrumenting rotating parts. Dring et al. [2] investigated film cooling performance in a low speed rotating facility. A film cooling hole was located on both the pressure and suction sides. They used ammonia and Ozalid paper to qualitatively observe the coolant trace while the quantitative tests were conducted using thermocouples. Their results show that the film coolant had only a small radial displacement, similar to flat plate results, on the suction side. On the pressure side, the film coolant trace had a large radial displacement toward the blade tip. Effectiveness distributions on the blade span for a rotating turbine blade were also provided by Takeishi et al. [3] and Abhari and Epstein [4] using gas chromatography and thin film heat flux gages respectively.

Blair [5] studied the heat transfer on the pressure and suction sides as well as on the hub platform surface for a rotating turbine model. Enhanced heat transfer was observed on the

platform due to the secondary flow effects. Recently, Ahn et al. [6, 7] investigated the film cooling effectiveness on the leading edge of a rotating blade using the PSP technique. The same experimental facility has been used in this paper with a design modification to allow for stator-rotor gap cooling. They studied film cooling due to two row and three row coolant injection on the leading edge at design and off-design rotating conditions. Off-design conditions were found to significantly alter the film coolant traces on the leading edge.

A summary of film cooling effectiveness and heat transfer studies performed on the platforms of stationary cascades follows. Platform film cooling effectiveness investigations have been predominantly performed using cascade vanes. The secondary flow in a turbine passage is very complex and varies based on the blade profile being considered. Langston et al. [8, 9] performed flow measurements to gain insight into this complex secondary flow. They showed at the inlet of the passage, the boundary splits at the leading edge of the blade. A horseshoe vortex forms with one leg on the pressure side of the blade, and the other leg on the suction side of the blade (in the adjacent passage). The pressure side leg of the horseshoe vortex travels from the pressure side of the passage to the suction side; this pressure side leg of the horseshoe vortex becomes known as the passage vortex. This passage vortex will eventually meet the suction side leg of the horseshoe vortex that has remained near the junction of the suction surface and endwall. Goldstein and Spores [10] also studied the flow through a blade passage. They identified multiple "corner" vortices that developed throughout the passage. A pressure side corner vortex develops just downstream of the leading edge, and the vortex carries about one-third of the chord length. Two suction side corner vortices develop along the suction surface in the latter half of the passage. After the passage vortex carries to the suction side of the passage, it lifts from the endwall surface. Below the passage vortex, along the junction where the suction surface meets the endwall, suction side, counter rotating, corner vortices form.

The highly complex, three-dimensional flow has a strong influence on the heat transferred from the mainstream flow to the blade platform. Blair [11] pioneered the study of endwall heat transfer. He found significant variation of the heat transfer coefficient across the passage and downstream to the trailing edge of the vane due to the secondary flow along the endwall. Graziani et al. [12] also reported large variations in the endwall heat transfer coefficients. They showed the heat transfer coefficients on the suction surface of the blade are also influenced by the secondary flow through the passage; however, the heat transfer coefficients on the pressure surface are not affected by the strong secondary flows. Using a mass transfer technique, Goldstein and Spores [10] showed as the boundary layer splits to form the two legs of the horseshoe vortex near the leading edge of the blades, the heat transfer coefficients increase, and the greatest heat transfer enhancement on the endwall occurs near the leading edge. Other variations are present on the endwall due to the path of the passage and corner vortices. In addition near the trailing edge of the blade, the heat transfer coefficients are elevated as the two flows from the two passages meet at the trailing edge. The heat transfer coefficients were also measured on the endwall of a vane passage [13 – 15]. Similar variations were found, as the heat transfer continues to be dominated by the secondary flow. When the effect of freestream turbulence was considered [14, 15], it was found that increasing the turbulence intensity increases the heat transfer coefficients on the passage endwall. However, the effect of the freestream turbulence intensity was minimal near the leading edge and the near the suction surface, where the horseshoe and passage vortices dominate the heat transfer behavior.

With the local areas of high heat transfer identified, film cooling can be implemented on the blade platform to reduce the heat load in these areas. Takieshi et al. [16] obtained heat transfer and film effectiveness distributions on a vane endwall with discrete film cooling holes

placed at three locations in the passage. They found that the effectiveness is very low near the leading edge on the suction side; with the rollup of the horseshoe vortex, the film coolant lifted from the surface, and offered little or no protection. The path of the coolant was also influenced by the passage vortex transporting the coolant from the pressure to the suction side of the passage. Harasgama and Burton [17] used film cooling near the leading edge, just inside the passage, with the film cooling holes located along an iso-Mach line. Although the row of film cooling holes was evenly distributed to span the passage, no coolant reached the pressure side of the passage. The film cooling configuration used by Jabbari et al. [18] consisted of discrete holes placed on the downstream half of the passage. Similar to the upstream design [17], the film cooling effectiveness varied significantly through the passage, with the coolant moving to the suction side of the passage.

Friedrichs et al. [19 – 21] studied the film cooling effectiveness using the ammonia and diazo technique. They found that a simple layout of the film cooling holes throughout the passage can result in areas being over cooled (or under cooled) due to the secondary flow. With their proposed "improved design," the film holes were placed, so the strong secondary flow could be used advantageously. Using the same amount of coolant, they were able to provide improved coolant coverage. Recently, Barizozzi et al. [22] compared the film cooling effectiveness on a passage endwall with cylindrical or fan-shaped film cooling holes. With their cooling designs, they showed that by increasing the blowing ratios, the passage vortex is weakened, and the passage cross flow is reduced; therefore, coolant coverage is more uniform across the passage. Similar to flat plate film cooling, shaped film cooling holes offer better protection than cylindrical holes.

A similarity between the vane endwall and the blade platform is the existence of slot (or gap) upstream of the airfoil leading edge. A gap is commonly in place in the transition from the combustion chamber to the turbine vane (stator). Similarly, a gap exists between the stator and rotor, so the turbine disk can rotate freely. To prevent ingestion of the hot mainstream gases, it is a common practice to inject coolant air through these slots. If this preventive measure is utilized properly, unnecessary discrete film holes can be eliminated, so coolant is not wasted by overcooling areas on the rotating platform. Blair [11] also measured the film cooling effectiveness with upstream injection in his pioneering study; he showed large variations in the film cooling effectiveness over the entire passage due to the strong secondary flow. Roy et al. [23] placed coolant slots upstream of their vane. They showed the heat transfer near the leading edge was reduced due to the secondary air injection. Because the slots were placed directly upstream of the blades, a large area in the center of the passage did not receive adequate film cooling coverage. Slot injection has been the focus of many studies performed at the University of Minnesota [24 – 26]. They found using slots, which span the majority of the passage upstream of their vanes, can provide film coverage over most of the passage to the trailing edge of the vane [24, 25]. They also found that increasing the amount of coolant through the slot can reduce the effect of the secondary flow. In addition, strategically blocking the slot, so the coolant does not exit the slot uniformly provides thermal advantages (and disadvantages) [26].

The heat transfer coefficients and the film cooling effectiveness was measured on endwall of a vane passage with film cooling combined with upstream slot injection by Nicklas [27]. They found that in the upstream region, the film cooling effectiveness was elevated due to the large amount of cooling flow from the slot. However, the effectiveness near the discrete holes located near the center of the passages suffered due to the passage vortex. Liu et al. [28]

used a high volume of discrete holes upstream of their vanes to emulate the effect of upstream slot injection. They determined the film cooling effectiveness was primarily affected by the blowing ratio of the injection; in addition, as the blowing ratio increases, the uniformity of the coverage increases.

The film cooling effectiveness has been measured using pressure sensitive paint by Zhang and Jaiswal [29] and Zhang and Moon [30]. They first measured the effectiveness with two upstream injection geometries: two rows of discrete holes and a single row slot. The effect of a backward facing step was also considered with the discrete hole configuration. They confirmed that increasing the coolant flow can significantly increase the effectiveness, and they reported that the use of a backward step significantly decreases the effectiveness within the passage. Knost and Thole [31] showed that with increased slot flow, the critical areas of the leading edge and pressure side junction can be adequately cooled. Cardwell et al. [32] extended this work to include mid-passage misalignment. With the misalignment that may occur between two adjacent vanes, the film cooling effectiveness is dramatically reduced.

With the secondary flow strongly influencing both the heat transfer coefficients and the film cooling effectiveness on the platform surface, recently, efforts have been directed at mitigating this destructive secondary flow. One method that is gaining popularity is endwall contouring. Han and Goldstein [33] observed that with a fillet around the leading edge of the blade, the horseshoe vortex disappears, and the passage vortex is delayed with elevated turbulence intensity. However, with low freestream turbulence, the strength of the passage vortex is comparable to that in a passage without the fillet. The drawback of the fillet is the increased heat transfer near the leading edge on the pressure side due to the intensified corner vortices.

Gas Turbine Needs and Project Objectives

Most of the turbine blade cooling designs are based on the non-rotating blade and very limited rotating blade data. Based on this type of idealized film cooling heat transfer data, the blade metal temperature prediction can be off by up to 100 to 200°F in certain critical regions of the blade. It is known that blade life can be reduced by half if the blade temperature prediction is off by around 50°F. To overcome the hot spots, the turbine cooling designs need to consume extra amounts of cooling air from the compressor, hurting efficiency and power output. It is clearly an urgent need to have heat transfer and film-cooling data applicable to rotating blades with a generic film-hole geometry at the critical region of the airfoil under realistic engine flow conditions.

Another important issue is the flow parameter in the rotating blade film cooling heat transfer design. The Reynolds number, rotating speed, and Mach number for today's gas turbine engines are much higher than those published in the literature. This creates a challenge for researchers to provide rotating film cooling and heat transfer data for realistic blade film-hole geometry at higher Reynolds number, rotating speed, and Mach number conditions. Few facilities can provide such data. To solve this problem, the computational prediction of flow and heat transfer in rotating film-cooled blades is necessary. It is known that the Fluent commercial code has been validated and used by many researchers through technical publications for turbine blade heat transfer and film cooling predictions. The Fluent commercial code can be used to predict the proposed rotating blade surface heat transfer with film cooling at engine representative flow conditions. The predicted results can be compared with measured data at similar geometric and flow conditions. The prediction can be extended beyond the experimental

conditions. The upgraded CFD-based tool will be the new design trend and will greatly improve the current film cooling heat transfer design.

As mentioned above, there is very limited experimental data available for rotating blade heat transfer and film cooling in the literature. Moreover, there is very limited information available dealing with the turbine platform heat transfer and film cooling under rotating conditions. Therefore, there is a need to study the detailed turbine platform heat transfer and film cooling under engine representative flow and rotating conditions. This investigation provides the designers with new rotating blade platform heat transfer and film cooling data and numerical predictions for improving the cooling performance and thermal efficiency of land-based gas turbines. The objective of the rotating blade platform heat transfer and film-cooling experimental program is to obtain reliable detailed data under land-based gas turbine representative Reynolds and Mach numbers and rotation conditions. In addition, detailed measurements of the mainstream flow will be gathered to show how the mainstream flow is affected by the coolant flows. As a secondary effort, numerical simulations will be preformed to model engines under realistic operating conditions to further understand the heat transfer behavior on the rotating platform. With a better understanding of the flow physics and heat transfer distributions on the rotating blade platforms, it will be possible to reduce the amount of air extracted from the compressor for the purpose of turbine blade cooling. The more effective cooling designs could also result in increased turbine inlet temperatures. The increased temperatures will further enhance the thermal efficiency and power output of the engine. This will dramatically impact the rotor blade cooling design and greatly benefit to the entire land-based gas turbine industry.

Project Tasks

The current project investigates the heat transfer on rotor blade platforms. An existing turbine research facility is used to investigate the rotating blades. The current research turbine facility can be seen in Figure 3. The project consists of three tasks to meet the stated objectives. Detailed pressure distributions, heat transfer coefficient distributions, and film effectiveness distributions will be obtained on the rotor blade platforms with generic cooling geometries as described by the following tasks.

Task 1 – Rotor Platform Modification and Measurement Technique Development

To study cooling techniques commonly employed in gas turbine engines, the existing research facility required modification. The existing facility is incapable of studying the effect of coolant leakage in the seal between the stator and rotor. Therefore, a new rotor platform must be designed and fabricated. This new rotor platform not only incorporates stator-rotor seal ejection, but also has discrete holes for platform film cooling. Figure 4 shows the overall design of the research facility with the two separate coolant flows, and Fig. 5 shows the detailed schematics of the coolant flows to the rotor platform. While the new rotor platform is fabricated, the experimental techniques which are used for the heat transfer and flow measurements are developed. This includes the design and calibration of several miniature five-hole probes that are used for detailed mainstream flow measurements. In addition, the pressure sensitive paint (PSP) and temperature sensitive paint (TSP) techniques are developed. The surface pressure distribution and film cooling effectiveness are measured with PSP; while the surface heat transfer coefficient distributions are determined using the TSP. Also, as a secondary effort, preliminary numerical predictions of pressure, heat transfer coefficient, and film effectiveness distributions are performed.

Task 2 – Rotor Platforms with Stator-Rotor Seal Ejection

The effect of coolant ejection from the annular gap between the stator and rotor on the detailed pressure, heat transfer coefficient, and film cooling effectiveness distributions will be performed as the second task (see Fig. 6). A typical stator-rotor seal geometry is selected based on the suggestion of industrial experts. Detailed pressure distributions on the platform will be measured using PSP for a range of coolant ejection flow conditions. The detailed film cooling effectiveness distributions on the rotating platform will be measured using the PSP technique. The detailed heat transfer coefficient distributions of the platform will be measured using the TSP technique for the same range of rotation and flow conditions. The film cooling effectiveness and heat transfer coefficients will be calculated, and the predictions will be compared to the measured results at similar rotating speeds and coolant ejection rates.

Task 3 – Rotor Platforms with Stator-Rotor Seal Ejection and Film Cooling Holes

The detailed rotor blade platform pressure, heat transfer coefficient, and film cooling effectiveness distributions with a typical film cooling hole geometry will be performed as the final task (see Fig. 7). A typical platform film cooling hole geometry and location is selected based on the advice of industrial experts. In this task detailed pressure distributions on the modified rotating blade platform with the addition of a typical film hole pattern will be measured using the above-mentioned PSP technique. Detailed film cooling effectiveness distributions of the film-cooled rotating platform will be measured by the PSP, and the detailed heat transfer coefficient distributions of the film-cooled rotating platform will also be measured using the TSP technique, for the same range of the blowing and density ratios. As with Task 2, the detailed film cooling effectiveness and heat transfer coefficient distributions of the film-cooled rotating

blade platform will be calculated, and these numerical predictions will be compared to the measured results at the above-mentioned rotational conditions, and blowing and density ratios.

EXPERIMENTAL PROCEDURE

Turbine Research Facility

The experimental investigations have been carried out in a three-stage turbine research facility at the Turbomachinery Performance and Flow Research Laboratory of Texas A&M University. The turbine is the core component of the *TPFL*-research facility designed by Schobeiri [34] in 1997 to address aerodynamics, efficiency, performance and heat transfer issues of high pressure (HP), intermediate pressure (IP), and low pressure (LP) turbine components. Detailed aerodynamic, efficiency, loss and performance measurements were carried out to verify and document the efficiency and performance of a high efficiency 3-D, bowed blade. To compare the results of the investigations reported in [34] with those for 2-D cylindrical blades, detailed measurement were conducted and summarized in the subsequent reports [35] and [36].

To determine the film cooling effectiveness under rotating conditions for leading edge film cooling (Ahn et al. [6, 7]), the turbine rotor was modified to integrate the coolant loop into the downstream section of the hollow turbine shaft and into the cylindrical hub cavity. The same rotor was not compatible with the new geometry which included the circumferential stator-rotor gap which provides for platform cooling. Hence, to perform the research reported in this paper, a further modification of the existing rotor unit did not seem to be feasible. A new rotor incorporating the stator-rotor gap was designed and manufactured.

The overall layout of the test facility is shown in Fig. 3. It consists of a 300HP electric motor connected to a frequency controller which drives the compressor component. A three-stage centrifugal compressor supplies air with a maximum pressure difference of 55kPa and a volume flow rate of $4m^3/s$. The compressor operates in suction mode and its pressure and volume flow rate can be varied by a frequency controller operating between 0 to 66Hz. A pipe with a

transition piece connects the compressor to a Venturi mass flow meter used to measure the mass flow through the turbine component. The exit diffuser serves as a smooth transition piece between the turbine component and the Venturi, which is used for mass flow measurement. The three-stage turbine has an automated data acquisition system for detailed flow measurement at each blade row location. The turbine inlet has an integrated heater that prevents condensation of water from humid air expanding through the turbine during the test. The turbine shaft is connected through a flexible coupling with one end of a high precision torque meter that has a maximum rotational speed of 8500 rpm and a maximum torque rating of 677.9N-m. The other end of the torque meter is coupled via a second flexible coupling with an eddy current low inertia dynamometer with a maximum power capacity of 150kW and a maximum torque of 500Nm.

New Turbine Component Design

A completely new advanced three-stage turbine component as shown in Figs. 4, 5, and 8 was designed to replace the one discussed in [34 – 36] and [6, 7]. In addition to the tasks performed by the old rotor, the new one was designed to operate at high speeds of 8500 rpm close to the transonic range. The first critical speed for vibration for the new rotor at its natural frequency occurs at 6500 rpm. Two independently controlled, concentric coolant loops provide the necessary mass flow for film cooling experiments. The outer loop supplies coolant for film cooling experiments in the blade passage section close to the trailing edge but is not used in this paper. The inner loop coolant jet ejecting from a circumferential gap between the 1st stator and rotor provides for hub platform cooling.

A concentric jet exits this circumferential gap at an angle of 25° into the mainstream (Fig. 5). The maximum normal gap width is designed to be 3mm. However, it can be decreased to up to 0.5mm by translating the entire rotor towards the front bearing. For the current study it was set

to 2.3mm. The axial stator-rotor gap for the 1st stage was measured at 5mm. Similar to the optimization of the trailing edge slot ejection, the reduction of slot width is instrumental in establishing an optimum ejection ratio while keeping the cooling mass flow constant.

The blades attached to the new rotor were taken from the rotor described in [34 – 36] and also used in [6, 7]. They are typical HP-turbine blades used in steam turbines characterized by a relatively thick leading edge portion. This particular blade design allows reducing the total pressure losses due to the adverse off-design incidence changes caused by part-load operation. Thus, these blades are not typical of power generation or aircraft gas turbines. Given the considerable amount of manufacturing expenses that a new set of rotor and stator blades require and the lack of sufficient research funds, it was decided to use the same existing blades to carryout the current research. Although the blade geometry does not represent a typical gas turbine blade geometry, it provides the basic features to extract information relevant to gas turbine design community. These features are (a) stator-rotor unsteady interaction, (b) blade and platform rotation including the relative blade circulation and the exposure of the platform boundary layer to centrifugal and coriolis forces, and (c) the flow acceleration. Except for the last feature (c), none of the above features can be simulated in a cascade investigation.

To ensure that no coolant escapes through the rotary-stationary interfaces, the internal and external loops were sealed with labyrinths. A 24-channel slip-ring is mounted to the rear shaft as shown in Fig. 8 to transfer temperature data from thermocouples from the rotating frame to the data acquisition system.

Pressure Sensitive Paint (PSP) Technique

Data for film cooling effectiveness was obtained by using the PSP technique. PSP is a photo-luminescent material which emits light when excited, with emitted light intensity inversely

proportional to the partial pressure of oxygen. This light intensity can be recorded using a CCD camera and can then be calibrated against the partial pressure of oxygen. Details of using PSP for pressure measurement are given in McLachlan and Bell [37]. The image intensity obtained from PSP by the camera during data acquisition is normalized with a reference image intensity taken under no-flow conditions. Background noise in the optical setup is removed by subtracting the image intensities with the image intensity obtained under no-flow conditions without excitation. The resulting intensity ratio can be converted to pressure ratio using the previously determined calibration curve and can be expressed as:

$$\frac{I_{ref} - I_{blk}}{I - I_{blk}} = f\left(\frac{\left(P_{O_2}\right)_{air}}{\left(P_{O_2}\right)_{ref}}\right) = f\left(P_{ratio}\right) \tag{1}$$

where I denotes the intensity obtained for each pixel and $f\,(P_{ratio})$ is the relation between intensity ratio and pressure ratio obtained after calibrating the PSP.

Calibration for PSP was performed using a vacuum chamber at several known pressures varying from 0 to 1atm with intensity recorded for each pressure setting. The same optical setup was chosen for calibration as well as for data acquisition during the experiments. A schematic of the calibration setup is shown in Fig. 9. PSP is sensitive to temperature with higher temperatures resulting in lower emitted light intensities. Hence, the paint was also calibrated for temperature. It was observed that if the emitted light intensity at a certain temperature was normalized with the reference image intensity taken at the same temperature, the temperature sensitivity can be removed. Hence, during data acquisition, the reference image was acquired immediately after the experiment was completed to avoid errors related to temperature variation. Reference images were acquired after the rotor came to a halt and the temperature change from loaded to stationary condition was small enough to disregard its effect on PSP measurement. Flow and surface

temperatures were monitored by a thermocouple placed 2mm above the surface close to the suction side and by another thermocouple placed underneath the platform surface respectively. The thermocouples were wired through a slip-ring and connected to a microprocessor thermometer with a digital readout.

To obtain film cooling effectiveness, air and nitrogen were used alternately as coolant. Nitrogen which can be assumed to have the same molecular weight as that of air displaces the oxygen molecules on the surface causing a change in the emitted light intensity from PSP. By noting the difference in partial pressure between the air and nitrogen injection cases, the film cooling effectiveness can be determined using the following equation.

$$\eta = \frac{C_{mix} - C_{air}}{C_{N_2} - C_{air}} = \frac{C_{air} - C_{mix}}{C_{air}} = \frac{\left(P_{O_2}\right)_{air} - \left(P_{O_2}\right)_{mix}}{\left(P_{O_2}\right)_{air}} \tag{2}$$

where C_{air}, C_{mix} and C_{N2} are the oxygen concentrations of mainstream air, air/nitrogen mixture and nitrogen on the test surface respectively. The definition of adiabatic film cooling effectiveness is

$$\eta = \frac{T_f - T_m}{T_c - T_m} \tag{3}$$

The accuracy of the PSP technique for measuring film-cooling effectiveness has been compared by Wright et al. [38] on a flat plate with compound angled ejection holes using several measurement techniques such as steady and transient liquid crystal, IR camera and using a foil heater with thermocouples. Results were obtained for a range of blowing ratios and show consistency with each other. Wright et al. [38] found that IR, TSP as well as PSP gave effectiveness results within 15% of each other. Larger uncertainties for heat transfer techniques such as IR and TSP methods were observed due to lateral conduction in the flat plate.

The platform passage under investigation was layered with PSP using an air brush. This coated surface was excited using a strobe light fitted with a narrow bandpass interference filter with an optical wavelength of 520nm. Upon excitation from this green light, the PSP coated surface emitted red light with a wavelength higher than 600nm. A 12-bit scientific grade CCD camera (High speed Sensicam with CCD temperature maintained at –15°C using 2-stage peltier cooler) was used to record images and was fitted with a 35mm lens and a 600nm longpass filter. The filters were chosen to prevent overlap between the wavelength ranges such that the camera blocked the reflected light from the illumination source. A schematic of the optical components setup is depicted in Figs. 10 and 11. The camera and the strobe light were triggered simultaneously from an angular position optical sensor offset to the shaft. By detecting the same angular position, the camera was able to view the same region of interest at every rotation, making it possible to average the image intensities without blurring the information. A minimum exposure time of 18μs was used for image capture from the camera. Estimated rotor movement during image capture at 2550 rpm, for an 18μs exposure time was 1.2mm. A total of 150 TIF images were captured for each experiment with air and nitrogen injection and the pixel intensity for all images was averaged. The image resolution obtained from the camera was 1.5 mm/pixel with each image containing about 500 data points. The relatively low pixel resolution is a consequence of a binning of 8 used on the camera, as the emitted light intensity captured by the camera CCD in such a short exposure time was very low. A computer program was used to convert these pixel intensities into pressure using the calibration curve and then into film cooling effectiveness. The coolant flow rate was set using a rotameter based on prior calculation for the desired mass flow ratio. The coolant was heated to the same temperature as mainstream air (45°C) before injection through the gap.

Uncertainty calculations were performed based on a confidence level of 95% and are based on the uncertainty analysis method of Coleman and Steele [39]. Lower effectiveness magnitudes have higher uncertainties. For an effectiveness magnitude of 0.3, uncertainty was around ±2% while for effectiveness magnitude of 0.07, uncertainty was as high as ±10.3%. This uncertainty is the result of uncertainties in calibration (4%) and image capture (1%). The absolute uncertainty for effectiveness varied from 0.01 to 0.02 units. Thus, relative uncertainties for very low effectiveness magnitudes can be very high (>100% at effectiveness magnitude of 0.01). However, it must be noted that very few data points exist with such high relative uncertainty magnitudes. Uncertainties for the blowing ratios are estimated to be 4%.

Temperature Sensitive Paint (TSP) Technique

Like PSP, temperature sensitive paint (TSP) is also comprised of luminescent molecules suspended in a polymer binder. However, the photophysical process associated with TSP is thermal quenching, rather than oxygen quenching. Unlike with PSP, the polymer binder is not oxygen permeable. Therefore, the luminescence intensity of the TSP is related only to temperature, and is not a function of pressure (unlike the reverse relationship observed with PSP). Like PSP, the luminescent molecules in the TSP must be excited with the absorption of a photon. The molecules return to their ground state with the emission of the photon at a longer wavelength. Increasing the temperature of the luminescent molecules makes the molecules more likely to return to their ground state (releasing the photon through a radiationless process) [38]. Therefore, the emission intensity from molecules at elevated temperatures is lower than the emission of molecules at relatively lower temperatures. This photophysical process is known as thermal quenching.

Similar to the use of PSP, a reference condition is used for the TSP measurements. Typically, the reference condition is set at the room temperature in which the experiments are performed. However, for cryogenic applications, the reference temperature maybe much lower. With the reference condition, and the black image used to eliminate the background intensity from the optical components, the emission intensity is related to the surface temperature as shown in Equation 4.

$$\frac{I(T)-I_b}{I(T)_{ref}-I_b}=f(T) \tag{4}$$

A calibration must be completed to determine the relationship between the emission intensity and the surface temperature. The calibration is completed by attaching a thermocouple to the surface of a copper block. The copper block is coated with the TSP, and positioned between the excitation light and CCD camera. UniCoat TSP from ISSI is sprayed on the copper plate; the same strobe light for excitation and camera used with PSP are now used with TSP. The copper block is heated from room temperature up to 145°F (24 - 63°C). At specific temperatures, the emission intensity is recorded (coupled with black images), so a relationship between the intensity and temperature can be determined.

After completion of the TSP calibration, the TSP can be applied to the rotating blade platform. The experimental setup is identical to the PSP. As the name implies, TSP detects changes in temperature; therefore, this method requires a temperature difference. For this study, TSP is used to measure the steady state surface temperature. The heater fixed to the platform, heats the surface by supplying the surface with uniform heat flux. The unheated film coolant mixes of the mainstream and temperature variations are present on the platform. From the measured surface temperature, mainstream temperature, and power input to the heater, the heat transfer coefficient on the platform can be determined from Equation 5.

$$h = \frac{q''_{in} - q''_{loss}}{T_{wall} - T_{\infty}} \tag{5}$$

During the actual film cooling experiment, only three images are required: black image (no flow, no excitation light), reference image (no flow, with excitation light), and air image (mainstream and coolant flows, with excitation light). With these images, and the calibration data, the adiabatic wall temperature can be determined. If the reference image corresponds to a different temperature than the reference image from the calibration, this must be taken into account. With a temperature being recorded at every pixel in the viewing window, detailed distributions of the film cooling effectiveness can be obtained on the film cooling plate.

RESULTS AND DISCUSSION

Experimental Rotating Heat Transfer

Task one of this project has been completed. Significant modifications were required to the existing turbine research facility. The existing facility was incapable of studying the effect of coolant ejection through the stator-rotor seal and platform film cooling. Therefore, the project began with the design of a new rotor platform. As shown in Fig. 4, modifications of the facility allow two coolant flows to be controlled independently: ejection flow and film cooling flow. Figure 5 shows detailed views of the modified rotor platform. Not only are modifications required for the platform, the rotor shaft required modification for a slip ring. The slip ring will transmit thermocouple and signals to and from the rotating blades. Finally, the housing of the research facility must be modified, so a window can be included. The window will allow the camera to view of the platforms and record images of the PSP and TSP coated surfaces. Design, fabrication, installation, and instrumentation of the modified rotor platform have been completed. Figure 8 shows the newly fabricated rotor platform installed in the existing research facility.

With the fabrication of the new rotor platform, the housing of the existing facility has also been modified. This is due to the required optical access of the instrumented platforms. Figure 9 shows a model of the turbine housing with a window for the required optical components. As described previously, both an excitation light and camera are needed to capture images of the pressure and temperature sensitive paints, and Figure 12 shows the viewing window with the rotor at two different positions to capture images of the rotor platforms with either PSP or TSP.

Data acquisition begins with Task two of this project. Thus far, film cooling effectiveness measurements were performed for four coolant-to-mainstream mass flow ratios of 0.5%, 1.0%,

1.5% and 2.0%. Film cooling data was also obtained for three rotational speeds, 2550 rpm (design condition), 2000 rpm and 1500 rpm (off-design conditions). Total mass flow in the engine was 3.728 kg/s and was ensured to be the same for all three rpm's by adjusting the blower frequency through the frequency controller. The four coolant-to-mainstream mass flow ratios approximately correspond to blowing ratios of 0.12, 0.24, 0.36 and 0.48 respectively. Blowing ratios for each rotating speed differ slightly as the relative mainstream velocity at the rotor inlet changes with the rotating speed.

Film Cooling Effectiveness from Upstream Slot Cooling

Upstream Injection At Design Rotating Condition

Film cooling effectiveness measurements were performed for four coolant-to-mainstream mass flow ratios of 0.5%, 1.0%, 1.5% and 2.0%. Film cooling data was also obtained for three rotational speeds, 2550 rpm (reference condition), 2000 rpm and 1500 rpm. Total mass flow in the engine was 3.73 kg/s and was ensured to be the same for all three rpm's by adjusting the blower frequency through the frequency controller. The four coolant-to-mainstream mass flow ratios approximately correspond to blowing ratios of 0.12, 0.24, 0.36 and 0.48 respectively after assuming that the coolant exits the gap axially. Blowing ratios for each rotating speed differ slightly as the relative mainstream velocity at the rotor inlet changes with the rotating speed.

Variation of rotational speed performed in the [6, 7] showed that the location of the leading edge stagnation line, which yielded symmetric spreading of coolant on the suction and pressure surfaces of the leading edge was at an rpm of 2550. This rotational speed was chosen as the reference rotating condition for the current investigation. The effectiveness results obtained

from using PSP for the reference rotating condition of 2550 rpm are plotted in Fig. 13. The figure shows the contour plots for all four mass flow ratios tested. The contour plots also show the location of the stator-rotor gap upstream of the passage and the path of the mainstream and coolant flow. The effectiveness in the gap, as the coolant escapes through it, could not be recorded as the plexiglass window through which the rotor platform was viewed was not wide enough.

Higher mass flow ratios result in coolant injection with higher momentum. As this momentum increases, it can be observed that the spread of the coolant as well as the effectiveness magnitudes are higher. The injected coolant is at the same density as the mainstream i.e. the coolant to mainstream density ratio is 1. Hence, the injected coolant velocity is higher for higher mass flow ratios. This affects the secondary flow structure in the passage. At lower blowing ratios, the low momentum coolant is not capable of penetrating into the highly vortical secondary flow region on hub platform. It mixes with the main flow where its kinetic energy dissipates, making only a marginal contribution to effectiveness improvement. For the lowest mass flow ratio (MFR = 0.5%), the maximum effectiveness magnitude is less than 0.2

As the mass flow ratio increases, the coolant injection velocity increases due to which the coolant can penetrate the complex secondary flows in the passage resulting in higher effectiveness on the platform. For the highest mass flow ratio of 2%, a region of high effectiveness can be observed near the entrance of the blade passage. The effectiveness from the gap to the beginning of this high effectiveness region is slightly lower. This indicates that the coolant probably detaches itself from the surface as it exits from the gap and then reattaches as it is pushed by the mainstream towards the surface which is marked by the high effectiveness spot (at around 15% of axial chord). Effectiveness magnitudes as high as 0.6 can be observed at this

reattachment spot. Smaller reattachment spots can be observed for MFR = 1.5% too. Thus, as the mass flow ratio increases, the effectiveness magnitude and its spread become larger. The same phenomenon has been recorded by several researchers mentioned earlier with studies for slot film cooling on stationary, flat as well as curved platforms. Common to all blowing ratios investigated is that the suction surface is the location of inception of the effectiveness. Major parameters instrumental in making the suction surface the inception location are: (a) the platform secondary flow, (b) the Coanda effect that helps the injected coolant attach on the suction surface and (c) the coolant injection angle.

The coolant distribution on the platform is predominantly governed by its flow characteristics. A strong pressure gradient exists within the passage from the pressure to the suction side with the static pressure near the pressure side being much higher due to lower mainstream velocities and blade curvature. The coolant traces show slightly higher effectiveness magnitudes towards the suction side near the leading edge. More coolant gets diverted away from the higher pressure stagnation region on the leading edge of the blade and finds its way towards the suction side. Effectiveness magnitudes on the pressure side begin to fade away rapidly as the coolant travels along the axial chord. As the passage vortex moves towards the suction side while gaining strength, it entrains the mainstream on the platform surface damaging the coolant film which results in a sharp drop in effectiveness magnitudes. This sudden drop gives a good indication of the path traced by the passage vortex. Similar coolant spread profiles affected by secondary flows can be observed for stationary platform cooling through slots akin to the current design in turbine as well as vane cascades in the tests conducted by Blair [11].

Upstream Injection At Off-Design Rotating Conditions

At rotational speeds lower than the design speed, the blade flow deflection becomes larger leading to higher specific stage load coefficient and the stagnation region moves towards the pressure side as the flow incidence angle increases as sketched in Fig. 14. At progressively lower rotating speeds, the stagnation line will further move towards the blade pressure side resulting in a higher pressure zone owing to higher flow deflection. The pressure gradient on the platform from the pressure to the suction side gets affected by this shift in the stagnation region due to larger flow incidence angles. Fig. 15 shows the numerical predictions of local static pressures on the platform surface with flow pathlines for 2550 rpm and 2100 rpm. These numerical predictions were performed using the CFD code, FLUENT for the same geometry and flow conditions. About 1.1 million cells were used to grid 1.5 stages of the turbine. A sliding mesh was used to simulate rotation. A Reynolds stress model with a non-equilibrium wall function was used to solve the Reynolds Averaged Navier-Stokes equations. From the figure, the movement of the stagnation region towards the pressure side for lower rpm can be easily discerned. Lower pressure at lower rotating speeds can be observed near the suction side. Fig. 15 also shows the mainstream pathlines near the platform surface. The pathlines for 2100 rpm appear to converge together as the flow gets pushed to the suction side.

The larger gradients in the platform static pressure distribution for lower rotating speeds cause significant movement of the coolant film on the platform surface when it comes from the stator-rotor gap. The local mass flow of coolant from stator-rotor gap depends on the pressure difference between the plenum and the mainstream static pressure. A higher pressure region near the blade pressure side close to the leading edge at lower rotating speeds will result in a smaller pressure difference across the gap as compared to reference condition. This will promote

non-uniform coolant distribution from the stator-rotor gap with the coolant traces re-orienting themselves towards the suction side of the platform. This phenomenon can be clearly observed from data taken for 2000rpm and 1500rpm as shown in Figs. 16 and 17. Both figures include contour plots for 4 different mass flow ratios. More coolant appears to come out from near the suction side of the platform where the pressure difference across the gap from inlet to outlet is larger with the lowest rotational speed of 1500 rpm showing the largest non-uniformity. Thus, the coolant film distribution and hence film cooling effectiveness strongly depends on the pressure distribution on the platform surface. As the blowing ratio increases, the traces get stronger due to the increase in the coolant momentum similar to that observed in Fig. 15.

After comparing Figs. 16 & 17 for lower rotating speeds with Fig. 13 at 2550 rpm (reference speed), it can be observed that the effectiveness magnitudes progressively decrease with lower rpm for the same mass flow ratio. This may be a result of stronger horseshoe vortices close to the suction side owing to the shift in the flow incidence angle at lower rpm. Very low effectiveness levels can be discerned for the lowest blowing ratio, MFR = 0.5% for 1500 rpm as compared to other rpm's. Coolant traces can only be observed locally near the suction side of the blade. The coolant spread for MFR = 2.0% is appreciably larger and some reattachment of coolant can also be observed for 2000 rpm similar to that observed for 2550 rpm. Effectiveness traces on the suction side though are more visible than that for 2550 rpm. Some coolant traces can even be observed close to the trailing edge near the suction side for higher mass flow ratios. For both reference and lower rotating speeds, the region downstream of the throat remains uncooled. Weak traces can be observed in this region for 2550 rpm for MFR = 2.0% near the throat. This region experiences much higher velocities from the accelerating mainstream flow

resulting in high local heat transfer coefficients. The secondary flow vortices in the passage erode the coolant film before it reaches the throat.

The research turbine can also operate at rotational speeds greater than the design speed. Figure 18 shows the measured film cooling effectiveness on the rotating platform operating at 3000 rpm. Although the measured film cooling effectiveness measured at 3000 rpm varies from that measured at 2550 rpm, the variation is less for the higher rotational speed than the lower rotational speeds. Increasing the coolant flowrate increases the coolant coverage area on the rotating platform. As the flowrate increases to 2%, the coolant covers the entire passage; whereas at the other rotational speeds, the pressure side of the passage and the trailing edge region were left unprotected.

In addition to the effect on static pressure distribution and film cooling due to inlet flow incidence angle change with rotational speed, rotation may also affect the coolant flow as it exits the stator-rotor gap. The gap and the disk cavity are bounded by two walls, stator endwall and the rotor platform. The enclosed coolant mass in the disk cavity will rotate with a certain frequency due to the cavity wall shear stress. High shear stresses, caused by relative motion in the circumferential gap, may introduce some swirl in the coolant flow as it exits. Hence, a tangential component may exist in the coolant flow as it exits the stator-rotor gap. This may cause some additional spreading of the coolant which cannot be achieved for film cooling studies in stationary cascades. This might also explain the larger coolant spread with increasing rotational speeds due to a larger tangential velocity component in the coolant as it exits the gap. The determination of the swirl angle as well as the measurement of this tangential velocity component was not the subject of the current paper. However, these are items of high importance along with the inter-stage measurements.

Pitchwise Averaged Film Cooling Effectiveness with Upstream Injection

The film cooling effectiveness results were averaged along the pitchwise direction and the averaged data for all coolant-to-mainstream mass flow ratios and rotational speeds are presented in Fig. 19 along the axial chord. The increase in effectiveness magnitudes with increasing mass flow ratio can be clearly observed from this figure. The averaged plots show a sharp decrease in effectiveness magnitude along the axial chord as indicated earlier with the region beyond x/C_x = 0.6 remaining mostly uncooled with average effectiveness magnitudes below 0.1. The spikes occurring as a result of coolant jet reattachment at MFR = 2.0% for 2550 rpm, 2000 rpm, and 3000 rpm can also be observed. The decrease in effectiveness with lower rotational speeds can also be discerned. Figure 20 shows the same pitchwise averaged film cooling effectiveness results plotted for the four different coolant-to-mainstream mass flow ratios. The impact of turbine rotational speeds on film cooling effectiveness can be clearly perceived from this plot. As rpm increases, the effectiveness magnitudes increase for the same mass flow ratio. Figure 21 shows the average film cooling effectiveness plotted with $x/M_{gap}S$ as the abscissa. The figure compares the data with a correlation from Goldstein [40] for an equivalent two-dimensional slot on a flat stationary surface as given in Eq. 6.

$$\overline{\eta} = \left(1 + 0.249 \cdot \left(x/M_{gap}S\right)^{0.8}\right)^{-1} \tag{6}$$

This correlation works well for $x/M_{gap}S > 10$, where the flow regime is more two-dimensional. For $x/M_{gap}S < 10$, the 3-dimensional flow regime due to mixing of the coolant jet with mainstream results in lower effectiveness than that predicted by the correlation. When compared to current data, for reference rotating condition, it shows relatively good comparison with the correlation at $x/M_{gap}S = 10$ but decays rapidly due to the destructive action of the passage vortex on the coolant film. For lower rotating speeds than reference, more non-uniform

pitchwise effectiveness distribution lowers the average effectiveness value with the data for 1500 rpm showing the largest deviation from the correlation.

Film Cooling Effectiveness from Discrete Film Cooling Holes

As shown in the previous figures, the gas from the stator-rotor seal can adequately protect the upstream half of the blade platform. However, much of the pressure side of the passage, as well as the downstream half of the platform, is not covered by the coolant, and thus left exposed to the hot mainstream gas. To protect these areas of the blade platform, it is necessary to add discrete film cooling holes. The discrete film holes can be used sparingly, as additional coolant is not needed on the upstream half of the blade platform. Taking this into account, nine discrete holes have been added to the rotating platform, as shown in Fig. 7. The film cooling effectiveness can be measured on the rotating platform with PSP. The blowing ratio for the coolant through the discrete film hole is varied from M = 1.0 – 2.0, based on the relative velocity of the mainstream flow at the rotor exit (station 3). In addition, the rotational speed of the turbine is varied to investigate the effect of rotation at design and off-design conditions over a range of blowing ratios. Before combining the upstream slot injection with the discrete film cooling, it is necessary to isolate each flow. Therefore, effectiveness is measured on the platform with only the discrete film cooling holes.

Detailed film cooling effectiveness distributions are shown in Figures 22 – 24. The location of each film hole is denoted by an ellipse drawn on the contour plot. The reader is cautioned that this ellipse does not represent the size of the film cooling holes; ellipses added to the plot are actually much larger than the actual film cooling holes. Due to plotting restrictions,

the ellipses are shown only represent the location of the film holes and not the true size of the holes.

Discrete Film Cooling At Design Rotating Condition

The film cooling effectiveness is measured on the blade platform operating at its design condition of 2550 rpm. At this rotational speed the average blowing ratio for the coolant is varied from 1.0 to 2.0. The detailed film cooling effectiveness distributions for 2550 rpm are shown in Figure 22. At the lowest blowing ratio of 1.0, the coolant traces are undetected. However, when the blowing ratio is increased to 1.25, the coolant from each hole is clearly seen. In general, increasing the blowing ratio increases the film cooling effectiveness on the rotating platform. For traditional, non-rotating, flat plate studies, increasing the blowing ratio begins to reduce the film cooling effectiveness, as the coolant penetrates into the mainstream flow and does not remain attached to the surface. However, on this rotating platform, the highest effectiveness occurs at the highest blowing ratio.

The coolant from the discrete holes is strongly affected by the passage induced secondary flow. Although the discrete holes are positioned to follow in the streamlines of the mainstream flow, the coolant is exits the holes and is carried toward the suction side of the passage. This is similar to the behavior observed for the upstream slot injection.

Discrete Film Cooling At Off-Design Rotating Conditions

Because engines do not operate at their design conditions 100% of the time, it is necessary to investigate how well the blade platform is protected when the engine operates at off-design conditions. Figures 23 and 24 show the measured film cooling effectiveness on the

platform rotating at 2400 rpm and 3000 rpm, respectively. At the off-design condition of 2400 rpm (Fig. 23), the measured film cooling effectiveness is less than at the design condition. Increasing the rotational speed to 3000 (Fig. 24), also yields decreased film cooling effectiveness for all blowing ratios (compared to 2550 rpm). As the engine deviates from its design condition, the film cooling effectiveness is adversely affected.

Pitchwise Averaged Film Cooling Effectiveness with Discrete Film Cooling

The pitchwise averaged film cooling effectiveness for the discrete film cooling holes is shown in Figure 25, and several interesting trends can be seen in the figure. At the design condition of 2550 rpm, the blowing ratio of 2.0 produces the greatest film cooling effectiveness, and this is followed closely by M = 1.5. As the contour plot (Fig. 22) showed, minimal protection is offered by the lowest blowing ratio of M = 1.0.

The trends for the off-design conditions represent the trends that are expected: increasing the blowing ratio, increases the film cooling effectiveness, for both rotational speeds of 2400 rpm and 3000 rpm. Increasing the blowing ratio from 1.25 to 1.5 results in a significant increase in the film cooling effectiveness. However, increasing the blowing ratio beyond 1.5 does not dramatically increase the film cooling effectiveness.

Flow Measurements and Numerical Predictions

Interstage Instrumentation

To achieve a high degree of versatility, the turbine facility has provision for radial aerodynamic measurements at inlet and exit of each blade row and circumferential measurements at 1st stage rotor exit, 2nd stage stator and rotor exit. The turbine was designed with a casing that

incorporated stator rings. It also incorporated three T-rings for sealing the three 90° circumferential traversing slots. The sealed T-rings can move circumferentially inside these slots and effectively prevent the leakage of mass flow through them. Five-hole probes can be mounted on each of the three traversing systems with decoder and encoder for accurate probe positioning. Each of the three circumferential traversing systems has seven axes: 3 axes for radial traverse, 1 axis for circumferential traverse and 3 axes for turning the probes, whenever the flow angle is out of the calibration range. This is particularly true, when the probe is close to the hub or tip. The traverse in the radial direction spans from 1mm below the hub diameter to 1mm above the blade tip.

Aerodynamic Flow Measurement

Aerodynamic flow measurements were performed along the exit of the 1st stage stator to quantify the nature of the mainstream flow ahead of the stator-rotor platform gap. A five-hole probe calibrated for ±20° in pitch and yaw was traversed radially from hub to tip at an interval of 1mm up to 5% of the blade near the hub and tip and 2mm in the central region to obtain accurate pressure, velocity and flow-angle distributions at the stator exit. The precise alignment of the five-hole probe with the direction of flow ensures the accuracy of the data acquired. To enable accurate probe alignment, a stepper motor along with a worm-gear arrangement was used to actively rotate and adjust the five-hole probe inside the turbine. Figures 26 and 27 show the radial distribution of total pressures and absolute velocities for varying turbine speeds. The total pressure distribution for all the three rotor speeds is similar with magnitudes increasing with operating speeds. The effects of the secondary flow at the hub and near the casing are distinctly

seen in the radial velocity distributions for all three rotor speeds. Up to 5% of the flow in the radial direction near the hub and blade tip is affected by the secondary flow.

The absolute velocity (Fig. 28) at the 1st stage stator exit decreases by 3-4m/s as the shaft speed is increased for 1500rpm to 2550rpm. The overall average absolute and relative velocities for all speeds at the exit of the 1st stage stator were measured to be 69.3m/s and 38.8m/s respectively resulting in Mach numbers of 0.2 and 0.11 respectively. The Reynolds number based on the rotor axial chord length and the exit velocity was around 200,000 and the pressure ratio was 1.12 for the first stage. The rotation number corresponding to 2550 rpm, 2000 rpm and 1500 rpm is 0.19, 0.15 and 0.11 respectively. The flow incidence angle change, *i*, relative to the incidence angle at the design operating condition (3000 rpm) shown in Fig. 12, for 2550 rpm, 2000rpm and 1500rpm was determined as 23.2^o, 43.4^o and 54.8^o respectively. This change in incidence angle causes the stagnation line on the blade leading edge to shift towards the pressure side affecting the static pressure distribution on the blade as well as the platform. Consequently, the coolant spread on the platform gets affected with changing rotational speed. The inlet flow conditions thus help to better explain the film cooling effectiveness distributions on the blade platform.

Numerical Prediction of the Heat Transfer Coefficients and Film Cooling Effectiveness

Copmutational Details

The present three-dimensional calculations were carried out for a 1-½ turbine stage, which includes the first-stage stator (stator 1), the first-stage rotor (rotor), and the second-stage stator (stator 2), as shown in Figure 29.

The film coolant enters the disk cavity of the first stage stator and purges through the angled slot in the hub junction between the first-stage stator and the rotor to form a film cooling sheet to protect the rotating platform as shown in Figure 29(a). The portion outlined by blue color is non-rotating, including stator 1, disk cavity of stator 1 and stator 2; while the red color denotes the rotating domain, such as the rotor and its disk cavity. The horizontal width of the slot is 7 mm with 25 degree inclined angle to the rotor platform. The slot length is 16.5 mm and the slot bottom is connected to both the stator 1 and the rotor disk cavity. The length of the disk cavity for stator 1 is 25.4 mm (1 inch), and 12.7 mm (0.5 inch) for the rotor. The height of the disk cavity is 144.8 mm (5.7 inch). Only the rotor platform is film cooled in the present study. The blade height is 63.5 mm (2.5 inch), the root diameter is 558.8 mm (22 inch), and the shroud diameter is 685.8 mm (27 inch). Both the stator and rotor blades are two-dimensional with the same blade profiles in the spanwise direction. To simulate the experimental conditions exactly, it is necessary to use 29 first-stage stator blades, 23 rotor blades and 26 second-stage stator blades with periodic boundary conditions along the circumferential direction. In order to significantly reduce the computer memory and CPU time requirements, it is desirable to use the same number of blades for both the rotor and stators in the 1- ½ turbine stage. This enables us to simulate only one flow passage with periodic boundary conditions in the circumferential direction. Since this paper focuses on the film cooling on the rotor platform, it is reasonable to simplify the turbine stage by using 46 blades for both the first- and second-stage stators while maintaining the correct number of rotor blades as shown in Figure 29(b).

The simulations were performed using the CFD software package Fluent (version 6). The solutions are obtained by solving the compressible Reynolds-Averaged Navier-Stokes (RANS) equations together with a Reynolds stress model (RSM) using a finite volume method to

discretize the continuity, momentum and energy equations. The GAMBIT software with Turbo function was employed to generate the unstructured grids. The computational domain consists of fluid around the stator 1 and its disk cavity, film cooled rotor platform and its disk cavity, and stator 2 with periodic boundary conditions imposed in the circumferential direction as shown in Figure 29. The computational domain is composed entirely of the hexahedral cells, which are more accurate with less numerical diffusion. An interface technique was applied to handle the information exchanged between stators and rotor since the sliding meshes were used for the rotor domain. Relatively coarse grids are used for the majority of the 1-½ turbine stage, while the angled film (purge) slot, the platform of rotor, and the boundary layer of the stator and rotor blades consist of much finer grids for accurate resolution of the film cooling effectiveness and heat transfer. The $y^* = \rho C_\mu^{1/4} k_p^{1/2} y_p / \mu$ value for the non-equilibrium wall function falls between 30 and 100 for most of the regions, where $\boldsymbol{k}$ is the turbulent kinetic energy and the subscript p denotes the near-wall grid point. The geometry and detailed numerical grids around the coolant slot and rotor platform are shown in Figure 30.

Calculations were performed for four different rotating speeds of 2000, 2550, 3000 and 4000 rpm, where the 3000 rpm is the best performance point for the highest turbine efficiency. The inlet total and exit static pressures of the turbine stage are P_{in} = 101,356 Pa and P_{ex} = 85 kPa, respectively, with a pressure ratio of 1.19. At the inlet of the first stage stator, the total temperature (323 K) and turbulence intensity (5%) are specified with an inlet flow angle of 0 degree.

The absolute velocity at the stator 1 inlet is about 30 m/s. A fixed mass flow rate boundary condition is specified at the inlet of the coolant cavity as shown in Figure 1(a), with

temperature 300K and overall mass flow ratios MFR = 0.5%, 1%, and 1.5%, which correspond to blowing ratios of M = 0.12, 0.24 and 0.36, respectively.

Three sets of calculations with different thermal boundary conditions were performed to evaluate the adiabatic film cooling effectiveness (η_{aw}) and the heat transfer coefficient (h). For the calculation of adiabatic film cooling effectiveness $\eta_{aw} = (T_{aw,0}-T_{aw,f})/(T_{aw,0}-T_{tc})$, the turbine inlet total temperature is specified at $T_{t\infty} = 323$ K and the coolant total temperature is $T_{tc} = 300$ K. The adiabatic wall boundary condition is used for the platform and blades to obtain $T_{aw,f}$. It should be noted that $T_{aw,f}$ includes not only the effects of film cooling, but also the temperature change due to turbine work process. In order to determine the true film cooling effectiveness without the complication caused by turbine work process, it is necessary to calculate another adiabatic wall temperature $T_{aw,0}$ for the same blade configurations in the absence film coolant injection. This enables us to isolate the true effect of coolant protection by comparing the temperature differences with and without the presence of purged coolant. For the simulation of heat transfer coefficient, the coolant total temperature is the same as the turbine inlet total temperature 323 K, while the wall temperature is fixed as 300 K to calculate the wall heat flux q_w. The overall heat transfer coefficient is calculated from this formula: $h= q_w/(T_w-T_{t\infty})$, while the adiabatic heat transfer coefficient: $h_{aw}= q_w/(T_w-T_{aw,0})$. It should be noted that the overall coefficient includes the effect of both turbine passage flow and turbine work process, while adiabatic one only includes the passage flow effect, which will be further discussed in the later section.

All calculations were converged to residual levels of the order of 10^{-5}, and to less than 0.1% error in the mass flow rate between the turbine mainstream and coolant inlet and outlet of the computational domain. The selection of the time step in calculating one passing period of the

rotor blade is critical for accurate time-dependent flow predictions. Our previous study shows that the difference between 100 and 200 time steps is below 3%. Therefore, 200 time steps reach the time-step independency, and are used in these simulations. The passing period, T, is defined as the time it takes for the rotor blade to move from one stator to another. The computed results are recorded and analyzed once every 50 time steps (i.e., every 1/4 passing period). To achieve good periodic results, simulations were performed for 10 passing periods and the numerical results were presented at four different time phases with t/T = 9¼, 9½, 9¾, and 10, respectively. The present simulations are computationally intensive since they involve unsteady three-dimensional flow with a sliding rotor mesh. Each simulation was performed using the parallel version of Fluent on two processors, and requires about two weeks of CPU time on the SGI Altix 3700 supercomputer at Texas A&M University. A total of seven simulations were performed to determine the film cooling effectiveness and heat transfer coefficients for the 2000, 2550, 3000 and 4000 rpm, respectively.

Figure 31 shows the predicted laterally averaged $T_{aw,f}$ for the rotating blade platform using two different numerical grids. The coarse grid consists of about 1.1 million elements with 0.3 million cells for the stator-1 domain, 0.5 million cells for the rotor domain, and 0.3 million cells for the stator-2 domain. For the fine grid case, the number of numerical elements for the rotor domain was doubled to about 1 million cells. It is seen from Figure 31 that the maximum change in the laterally averaged $T_{aw,f}$ is less than 0.83 K. In addition to the grid independency study, comparison of 1st order upstream scheme and 2nd order QUICK scheme has been made in Figure 32. The laterally averaged cooling effectiveness shows a small difference between these two schemes in figure 4(a), while unsteady intensity demonstrates a huge difference in Figure 32(b). Because the 1st order upwind scheme inherently has numerical diffusion, and dilutes the

unsteady characters. All the numerical results presented in this paper were obtained based on the find grid with QUICK scheme solutions.

Flow Structure Study

Figure 33 shows a vertical cross section plane and the corresponding streamlines and dimensionless temperature (φ) contours for the film cooled platform with the purged coolant slot. Note that the domain in Figure 33(b) on the right hand side of the white vertical line is rotating, while the left hand side solution domain is non-rotating. Due to the rotating centrifugal force, the fluid in the right hand side of the disk cavity is rotating in counter-clockwise direction and driven radically outward. The centrifugal force pushed (purged) the coolant out of the disk cavity through the inclined coolant slot into the rotor blade passage. It is interesting to note that there is a small circulation region near the slot entrance due to the sharp turn between the disk cavity and the coolant slot. In addition, some mainstream flow was entrained into the coolant slot as seen from the relatively low temperature fluid near the slot exit. It should also be noted that the coolant flow in the slot is highly three-dimensional with significant variations in the circumferential directions.

Besides the flow pattern in the vertical cross plane in Figure 33, an annular (constant radius) cross plane is also shown in Figure 34 to provide a better understanding of the pressure and flow fields for various working conditions. This annular plane is located at 2% of the blade span away from the hub and parallel to the platform. As mentioned earlier, the increasing rotating speed slightly shifts the stagnation point from the pressure side to the suction side direction with a dramatic change in inflow angle. Figure 34(a) compares the pressure ratio ($P_{static,\ local}/P_{\infty,t}$) on the annular cross plane. For the 2000 rpm condition, the high pressure region

was observed on the leading portion of the pressure side due to the flow impingement in that region. The stagnation point gradually shifts from the pressure side to the leading edge direction with increasing rpm to 2550. When the rotating speed was further increased to the 3000 rpm conditions, the high pressure stagnation region was moved to the leading edge of the best performance point. However, the 4000 rpm shifts the stagnation point to the suction side. Figure 34(b) compares the streamlines and dimensionless temperature contours for various rotating speeds. For the 2000 and 2550 rpm condition, the dividing streamline impinges on the pressure side with a positive inflow angle. The coolant from the inclined slot can be clearly detected by the high value dimensionless temperature (φ) near the leading portion. The coolant is pushed away from the blade leading portion suction side by the positive incidence angle flow. For the 3000 rpm condition, the stagnation point shifts to the leading edge of best performance and the coolant is converged near to the blade suction side. However, the coolant does not adhere to the suction side due to the presence of horseshoe vortex along the blade-hub junction. For the 4000 rpm condition, the rotor inlet flow angle switches to negative and the stagnation point is shifted to the suction side. Generally, the streamlines move parallel to the blade pressure side, but converged on the suction side due to the passage vortex. The high value of φ on the rotor trailing portion is not due to the coolant protection. It is, in fact, due to the turbine work process since the adiabatic total temperature decreases significantly along the flow direction.

Figure 35 shows a comparison of the static pressure contours around the rotor blade suction side hub region with and without film cooling. For the non-film-cooled blade shown in Figure 35(a), a low static pressure region is seen on the suction side rotor region. On the other hand, a higher pressure region was observed on the suction side root region for the film-cooled blade shown in Figure 35(b) since the purged coolant from the angled slot was pushed towards

the suction side of the rotor blade. It is also worthwhile to note that the effect of the purged coolant is confined to the root region.

Adiabatic Film Cooling Effectiveness Study

Figure 36 compares the adiabatic total wall temperature on the rotating blade platform with and without film coolant to facilitate a direct evaluation of the true film cooling effectiveness. It is quite clear that the adiabatic wall temperature around the leading edge region is significantly lower for the film cooling case shown in Figure 36(a) as a result of purged coolant protection. In the trailing edge section of the blade passage, however, both blade configurations show a significant decrease in the adiabatic wall temperatures either with or without film coolant protection. As noted earlier, the reduction of the adiabatic total temperature in the trailing edge region is due to the turbine work process rather than the coolant protection.

Figure 37 compares the instantaneous adiabatic cooling effectiveness for various rotating speeds. Generally speaking, the cooling effectiveness decreases along the turbine passage flow due to the mixture with the mainstream flow, and keeps away from the blade suction side because of the horseshoe vortex developing at the leading edge root junction. For the low rpm cases (2000 and 2550 rpm cases), the coolant is pushed away from the suction side due to the positive inlet flow angle of rotor. The difference of effectiveness for the various time phases is not significant, because the rotor-stator interaction is weak for such low rotating speeds; and the wake and turbulence intensity is not strong enough to affect the purged coolant flow distribution on the rotor platform. For the high rpm case (3000 rpm), however, the coolant is pushed towards the blade suction side because of decreasing inlet flow angle. The cooling effectiveness shows a significant difference among various time phases. This maybe attributed to: 1) the high rpm

increases the rotor-stator interaction affect; 2) high turbulence and high wake are introduced by the increasing rpm; and 3) more chaos is produced by the high rotating speed.

Figure 38 compares the laterally averaged cooling effectiveness and unsteady intensity on the rotating platform. The laterally averaged adiabatic cooling effectiveness has been compared in Figure 38(a) for various rotating speeds with MFR=1% (M=0.24). As discussion before, the film cooling decreases along the passage flow direction. Also the effectiveness increases with increasing rpm from 2000, 2550 to 3000, since 3000 rpm is the best performance point. The instantaneous and time averaged adiabatic cooling effectiveness has been plotted in Figure 38(b) for 2500 rpm condition with MFR=1%. Clearly to see that the fluctuation of cooling effectiveness increase from the leading edge to the middle part of the blade, then decreases on the trailing portion. Therefore, it is desirable to quantitatively study the unsteady characteristics of the film cooling effectiveness by defining a cooling effectiveness unsteady intensity $\sqrt{\frac{\Sigma(\eta_i-\bar{\eta})^2}{N}}/\bar{\eta}$ based on a similar concept of root mean square (RMS) of turbulence intensity. Figure 38(c) shows the comparison of cooling effectiveness unsteady intensity for various rotating speeds. Generally, the off-design conditions increase the unsteady intensity. For the 2000 rpm case, the unsteady intensity increases from the leading edge to the peak value of 22% at the location x/Cx of 0.6. With rpm increasing to 2550 rpm, which is more close to the best performance condition, the maxim intensity decreases with the peak value of 15% and locates at the x/Cx of 0.38. When the rpm is further increased to the best performance condition of 3000, the unsteady intensity is further reduced, and the peak value is about 12% with location at x/Cx 0.22. Because the best performance working condition streamlined the passage flow, and thus damped the unsteady fluctuation. The shifting of the intensity peak to the leading portion with increasing rpm is attributed to the changing of inlet flow angle of rotor as shown in figure 34(b).

Figure 39 shows the calculated adiabatic cooling effectiveness for various mass flow ratios (MFRs) for the 2550 rpm condition. The simulation indicates that the film cooling effectiveness, as well as the area of coolant protection, increase with increasing mass flow ratio. All simulations show that the film cooling covers a wide area when existing from the slot, but contracts gradually downstream and adheres to the blade suction side to form a curved triangle region of high effectiveness. In the leading edge portion of the blade passage, the coolant was pushed away from the blade root region by the horseshoe vortex. The experimental results (Fig. 13), however, shows that the film cooling is more uniform in the passage and adheres to the platform leading edge region. In addition, the reattachment of film coolant near the platform leading edge region was also observed in the experiment for the high mass flow ratio (MFR = 1.5%) case.

Figure 40 shows a comparison of the calculated and measured laterally average adiabatic film cooling effectiveness for various mass flow ratios. Except for the leading edge portion, the predictions are in good agreement with the experiment data for the middle and high mass flow ratio cases. The experiment, however, shows some coolant reattachments in the leading edge portion with high film cooling effectiveness, which was not predicted in the present simulations. In addition, the simulation underpredicts the film cooling effectiveness for the MFR=0.5% case.

Figure 41 compares the simulated and measured laterally averaged adiabatic film cooling effectiveness on the rotating blade platform for various rotating speeds. Both the experiment and simulations indicated that the film cooling effectiveness increases with increasing rotating speed. For the 2550 rpm case, the predicted adiabatic film cooling effectiveness is in good agreement with the corresponding measurement except for the leading edge region. However, the film cooling effectiveness is significantly overpredicted for the 2000 rpm case in the leading portion.

Figure 42 shows a comparison of the adiabatic film cooling effectiveness on the blade suction side for various rotating speeds with MFR = 1%. The experimental data on the suction side is not available for comparison at this moment. In general, the coolant jet from the slot gap not only protects the rotating platform, but also benefits the root region of the rotor blade suction side. A high effectiveness strip, extending from the leading edge to the trailing edge, is observed on the suction side. The cooling effectiveness increases with increasing rpm until the 3000 rpm of the best performance condition, then drops significantly for the 4000 rpm of over-design condition.

Heat Transfer Study

Figure 43 compares the overall and adiabatic heat transfer coefficient on the rotating blade platform at various time phases for the 2550 rpm condition with MFR = 0.5%. As mentioned before, the overall heat transfer coefficient is based on the turbine stage inlet total temperature, which is widely used in the industry due to the simple; while the adiabatic heat transfer coefficient is referred to the local adiabatic total temperature, which can isolate the effect of turbine work process. For the both kinds of heat transfer coefficient, a high heat transfer coefficient exists at the rotor leading edge due to the horseshoe vortex. A high heat transfer strip develops on the trailing passage portion because of the passage vortex. In addition, there is a low heat transfer region downstream of the rotor trailing edge due to the low velocity in the wake. The unsteady characteristic of both heat transfer coefficient is explicitly, especially for the overall one.

The adiabatic heat transfer coefficient shows a higher value than the overall one, especially on the trailing passage portion. Because the adiabatic total temperature decreases

along the passage flow direction due to the turbine work process, the driving temperature difference of adiabatic heat transfer coefficient decreases too.

Figure 44 compares the overall and adiabatic heat transfer coefficient for the whole turbine stage. As discussed before, the adiabatic heat transfer coefficient demonstrates a higher value than the overall one because of the turbine work process, especially for the downstream location of the turbine stage, such as rotor and stator 2. Since in that location, the dramatically dropping of the adiabatic total temperature happens, which will be further discussed in the later section. Also for each stator and rotor blade endwalls, the overall and adiabatic heat transfer coefficient increases from the leading edge to the trailing edge, which is confirmed by experiment measurement of Harasgama and Burton [17].

Turbine Work Process Impact on Film Cooling Effectiveness

Figure 45 shows the area averaged total and static temperature at various stations in the 1-1/2 turbine stage. The four station positions have been denoted in Figure 29(a). Turbine is a rotating machine, which extracts the total energy from the hot gas and transfers it into the mechanical energy by the rotating blades. Due to the turbine work process, it is seen that the total energy decreases significantly from station 2 to station 3, where the rotor converts the thermal energy into the mechanical energy. On the other hand, the total energy remains the same across the stators, such as from station 1 to station 2 (position of stator 1), and from station 3 to the station 4 (position of start 2). The static temperature, however, changed significantly for each station, even for the stators. Because the flow is accelerated through the blades to achieve better performance, the difference between the total and static temperature of each station reflects the gas kinetic energy. By comparing the total and static temperatures in Figure 45, it is

desirable to use the total temperature rather than the static temperature as the reference temperature for the study of film cooling effectiveness and heat transfer coefficient since the total temperature is constant across the stators. In view of this, it is useful to define an overall film cooling effectiveness $\eta = (T_{t\infty}-T_{aw,f})/(T_{t\infty}-T_{tc})$ based on the turbine inlet total temperature $T_{t\infty}$ (= 323 K). As noted earlier, the adiabatic wall temperature $T_{aw,f}$ includes not only the temperature change due to film cooling but also the turbine work process. For the overall film cooling effectiveness in the turbine stage shown in Figures 45 and 46, the high cooling effectiveness in the leading portion is due to the coolant protection, while the high value in the trailing portion can be attributed to the low mainstream temperature caused by the turbine work process.

Figure 46 compares the three-dimensional coolant images in the rotor passage for various working conditions. Note that the overall film cooling effectiveness is used for the contour plots in this figure, and the 4000 rpm case is not plotted here due to the small value. For the 2000 rpm condition, the coolant is pushed to the middle of the rotor passage by the positive inflow angle, and looks more concentrated and higher film cooling effectiveness values in comparison with the other working conditions. As the coolant moves downstream, it lifts off the platform and diffuses gradually toward the trailing portion. For the 2550 rpm condition, the coolant trajectory moves to the blade suction side due to the low pressure near the suction side surface. The coolant, however, is not adhered to the leading portion suction side due to the presence of horseshoe vortex along the blade-hub junction. It is also noted that the coolant is pushed away from the pressure side because of the high pressure near the pressure side. For the 3000 rpm condition, the coolant is pushed to the suction side by the increasing inflow angle. Also, the coolant is more dilute with lower overall cooling effectiveness than those observed at the lower

rpm conditions. As noted earlier, the high cooling effectiveness near the trailing edge of the blade passage is attributed to the turbine work extraction.

Figure 47 compares the overall film cooling effectiveness on the rotor blade platform at four time phases for 2550 rpm condition with MFR = 1%. Generally, the difference of cooling effectiveness among the various time phases is not significant in the leading edge portion for this case. The high cooling effectiveness stays outside of the blade leading edge due to the horseshoe vortex, and exists near the suction side due to coolant streamline convergence in the low pressure region. Also as indicated before, the high cooling effectiveness on the trailing portion is not due to the coolant protection. This is because of the turbine work process decreasing the mainstream temperature in the trailing portion, which is strongly influenced by the stator-rotor interaction for various time phases, especially in the rotor wake region.

Advanced Stator-Rotor Seals in a Five Blade Linear Cascade

Motivation and Objectives for the Linear Cascade Endwall Study

Although the primary objective of this study is to obtain detailed pressure, heat transfer coefficient, and film cooling effectiveness distributions on the rotating blade platform, the set of data obtained is rather limited. One stator-rotor seal geometry was chosen based on the advice received from industrial experts, and likewise, one film hole configuration was chosen. In order to investigate additional seal or hole configurations, significant modifications are required to the rotor platform of the rotating facility. In an effort to extend this experimental investigation to include more complex stator-rotor seals, and additional film hole configurations, this study has been extended to a low speed wind tunnel. It is more practical to study multiple geometries in the linear cascade than the rotating facility. With the cascade multiple seal geometries, film cooling hole configurations, and flow parameters can be investigated with relative ease, compared to the rotating facility. Although such work was not initially proposed, the study has been expanded to obtain detailed film cooling effectiveness and heat transfer coefficient distributions on the blade endwall with various seal and film hole geometries.

Low Speed Wind Tunnel

An existing low speed wind tunnel facility was used to study the platform film cooling effectiveness, and schematic of the facility is shown in Figure 48. Modifications were made to the endwall of the wind tunnel that was previously used by Zhang and Han [41]. The open-loop wind tunnel operates in suction with two mesh screens located at the inlet of the wind tunnel. To produce uniform flow entering the cascade, a 4.5:1 contraction nozzle guides the flow to the linear cascade. The test area is 25.4 cm high by 75.0 cm wide, and has a 107.49° turning angle

to match the turning of the five-blade cascade. Head- and tailboards were added to the leading and trailing edges of the inner and outer airfoils to further guide the flow into the cascade. The cascade inlet velocity was maintained at 20 m/s and was set using a variable frequency controller attached to the 15 hp (11.2 kW) blower. The inlet velocity was measured (and continuously monitored) using a pitot tube placed inside the wind tunnel. The mainstream accelerates through the cascade, so the mainstream velocity at the cascade exit is 50 m/s.

The freestream turbulence through the cascade was varied by placing a turbulence grid 30 cm upstream of the cascade. The grid is made of square bars that are 1.3 cm wide, and they are spaced 4.8 cm in both the horizontal and vertical directions. Zhang and Han [41] used hot wire anemometry and showed the inlet turbulence intensity increases from 0.75% (without the grid) to 13.4% with a length scale of 1.4 cm. The turbulence intensity decreases with the flow acceleration through the passage to a level of 5% at the cascade exit.

Linear Cascade Design

Figure 49 shows the typical, advanced, high pressure turbine blade used for this study. The blade, which was scaled up five times, has a 107.49° turning angle with an inlet flow angle of 35° and an outlet flow angle of -72.49°. The chord length of the blade is 22.68 cm and the height of the blade is 25.4 cm. The blade-to-blade spacing at the inlet is 17.01 cm with a throat-to-span ratio of 0.2. The mainstream flow accelerates from 20 m/s at the inlet to 50 m/s at the outlet of the cascade. The inlet flow periodicity and uniformity for the blade design has been measured and reported by Zhang and Han [41]. In addition, the velocity (pressure) distributions along the pressure and suction surfaces of the blades have also been measured. With the turbulence grid placed in the wind tunnel, the freestream turbulence ranges from 13.4% at the

cascade inlet to 5% at the outlet of the cascade, as measured using a hot wire anemometer [41]. The mainstream Reynolds number (based on the inlet velocity and blade chord) is $3.1*10^5$

Platform Cooling Design

To study the film cooling effectiveness on the blade platform, the original smooth platform was altered to include both upstream slot injection and downstream discrete film cooling holes. The upstream slot, shown in Figure 50, covers 1.5 passages. The width of the slot is 0.44 cm wide and is at a 30° angle to the mainstream flow. The length of the slot is 2.54 cm, so the length-to-width ratio (l_s/w) is 5.7. The downstream edge of the slot is aligned with the leading edge of the cascade. Coolant (air or nitrogen) is metered through a square edge, ASME orifice flow meter and piped to a plenum located directly beneath the slot. The plenum is sufficiently large enough to ensure the coolant is uniformly distributed at the exit of the slot. The flow rate of the slot coolant can be varied, so the film cooling effectiveness can be measured over a range of flow rates varying from 0.5% to 2.0% of the mainstream flow.

With the slot expected to provide adequate film coverage over the upstream half of the passage, discrete film cooling holes are only used on the downstream half of the passage. As shown in Fig. 50, the 12 film cooling holes are positioned to approximately follow the blade profile. The holes have a diameter of 0.25 cm, a streamwise angle, θ, of 30° (as with the slot), and the lateral (compound) angle varies to match the blade profile. With a hole length of 2.54 cm, the length-to-diameter ratio (l/d) is 10.2. The coolant (air or nitrogen) is supplied to the film cooling holes via a second plenum located directly beneath the film cooling holes. The coolant flow rate is measured using a volumetric flow meter, and the flow is varied to achieve blowing ratios varying from 0.5 to 2.0 (based on the velocity of the mainstream at the exit of the cascade).

Computational Details

The present three-dimensional calculations were carried out for a cooled endwall, which includes the angled slot and a rotor blade, as shown in Figure 51. Only the angled slot provides film coolant in this numerical study. The blade height is 25.4 cm, and the cord length is 22.68 cm. The rotor blade is two-dimensional with the same blade profile in the span-wise direction, which is exactly the same as the experimental setup mentioned previously. The simulation only considers one flow passage with periodic boundary conditions imposed in the circumferential direction. The slot length is 2.54 cm ($l_s/w = 5.7$), with a 30° angle to the endwall. Calculations are performed at four different injection rates: m_s = 0.5%, 1.0%, 1.5%, and 2.0%. The inlet boundary of the cascade has used the velocity (20 m/s), temperature (300 K), turbulence intensity (1.0%), and the angle (35°). The coolant inlet boundary uses the fixed mass flow rate with a coolant temperature of 350 K and Tu = 0.5%. The cascade outlet boundary condition is specified with the gauge pressure at the outlet equal to zero.

The simulations are performed using the CFD software package Fluent (version 6). The solutions are obtained by solving the incompressible Reynolds-Averaged Navier-Stokes (RANS) equations using a finite volume method to discretize the continuity, momentum and energy equations. The Reynolds stress turbulence model, together with the non-equilibrium wall function have been chosen to solve the turbulent flow. The GAMBIT software with Turbo function was used to generate the unstructured grids, with a fine hexahedral grid clustering around the endwall and the blade boundary layer. The computational domain consists of fluid around the blade and the angled slot with the plenum. The hexahedral cells are used because they are claimed more accurate with less numerical diffusion compared to the tetrahedral cells. Relatively coarse grids are applied for the regions far away from the blade and the endwall to

reduce the computing resources, so approximately 1 million grid points were used for the simulations. For the endwall and blade side, most y* values of the near-wall grids fall between 30-100. All calculations are converged to residual levels on the order of 10^{-5}, and to less than 0.1% error in the mass flow rate between the turbine mainstream and coolant inlet and outlet of the computational domain.

Film Cooling Effectiveness on the Cascade Endwall

The presentation of the results begins with the film cooling effectiveness obtained on the passage endwall with slot injection upstream of the cascade. This includes both experimental and numerical results obtained over a wide range of slot flow rates. The effect of turbulence on this film cooling effectiveness is also experimentally considered. This discussion is followed by the presentation of the film cooling effectiveness measured downstream with coolant only from the downstream discrete holes, including the effects of various blowing ratios and turbulence intensities. The detailed film cooling effectiveness is then obtained for upstream slot injection combined with downstream discrete film cooling. After comparing the detailed film effectiveness distributions for all of these cases, final comparisons will be made using the spanwise averages of the film cooling effectiveness. The slot injection rate is commonly considered as a percentage of the mainstream. However, the blowing ratio (velocity ratio, as coolant and mainstream densities are equal) is also presented as a reference. The slot blowing ratio is based on the mainstream velocity at the inlet of the cascade (20 m/s). The blowing ratio for the downstream film holes is also shown, but because the film cooling holes are located on the downstream half of the passage, the blowing ratio for the discrete holes is based on the exit velocity of the mainstream flow (50 m/s).

Upstream Slot Injection

The detailed film cooling effectiveness was obtained on a single passage with various slot injection rates. Figure 52 shows the detailed effectiveness distribution on the platform with a freestream turbulence intensity of 0.75%. The effect of the blowing ratio is clearly seen comparing Figures 52(a) – 52(d). At the lowest flowrate of 0.5%, the coolant ejection does not cover the entire slot. The coolant is quickly swept from the pressure side of the passage to the suction side. Although the effectiveness approaches the ideal value of unity at the exit of the slot, the effectiveness quickly diminishes, and a large area of the passage is left unprotected. If the injection rate is increased to 1%, the flow from the slot is more uniform. However, the general trend for the effectiveness is the same as with 0.5%: the coolant is carried from the pressure side of the passage to the suction side. The area of protection extends further downstream; however, the downstream half of the passage still does not receive adequate protection. Increasing the injection rate to 1.5% results in more uniform film coverage on the upstream half of the passage. The area of coverage increases, but coverage remains inadequate near the trailing edge of the pressure side. At the maximum flowrate of 2.0%, the effectiveness bands are more uniformly distributed through the entire passage, with the entire passage receiving protection. Zhang and Jaiswal [29] showed similar results for slot injection upstream of a vane. They concluded that at low injection rates (0.5% to 1.5%), the coolant did not reach the pressure side of the passage, and the effectiveness quickly diminished downstream of the slot. However, at high injection rates (2% to 3%), uniform film coverage was measured in the downstream half of the passage with the coverage extending to the trailing edge of the passage [29].

It was noted in previous studies upstream slot injection is an effective tool for weakening the passage vortex. The finding is observed in the present results. At the highest injection rate of 2.0%, the effectiveness distribution is much more uniform than at the lower injection rates of 0.5% and 1.0%. The high momentum coolant disrupts the secondary flow behavior including the horseshoe and passage vortices. However, with the lower momentum coolant flows, the coolant flow is greatly affected by the passage secondary flows.

A sample of pathlines obtained from the predicted flow behavior for the slot and mainstream flows is shown in Figure 53; the pathlines are shown for coolant injection rates of 0.5% and 1.5%. As shown in Fig. 53(a), the coolant exiting the slot (colored red) quickly travels to the suction side of the passage, and the coolant exiting the slot is not evenly distributed over the entire slot. However, as the injection rate increases to 1.5%, the coverage is more uniform, Fig. 53(b) shows the particles are carried from the pressure side of the passage to the suction side. As the particles translate from the pressure to the suction side of the passage, they are also rotating (this can be seen as the ribbon representing the particles twists). This is the effect of the passage vortex gaining strength as it travels across the passage. This figure also shows interesting behavior on the suction side of the blade. The coolant flow lifts from the platform surface, mixes with the mainstream, and travels radially outward, along the suction surface of the blade. Goldstein and Spores [10] observed similar behavior of the passage vortex lifting off the endwall after contacting the suction surface.

The numerical predictions of the film cooling effectiveness on the platform are shown in Figure 54. As noted previously, the computational domain consists of the blade, half the passage on the suction side of the blade, and half the passage on the pressure side of the blade. Therefore, to show a complete passage, the results have been copied and pieced together at the

centerline of the passage. This figure corresponds to the experimental results shown in Fig. 52. The trends that were captured with the experimental data are also captured computationally. The comparison between the experimental and numerical results is very close, with the computations over-predicting the film cooling effectiveness at the higher injection rates. More interesting is the effectiveness predictions on the suction surface of the blade, shown in Figure 55. As shown by the pathlines, the coolant tends to lift off the endwall near the suction surface. These are positive results for film protection on the suction surface. When considering the heat flux distribution around a blade, the leading edge experiences the greatest heat load due to the stagnation of the hot gases. Depending on the specific blade profile, the flow is laminar at the onset along the suction surface. As the flow accelerates, a transition from laminar to turbulent flow occurs, with a spike in the heat transfer coefficients in the transition region. The blade must be adequately protected in this region were the flow transitions from laminar to turbulent. With the coolant from the slot lifting off the surface along the suction side, additional film cooling may not be necessary near the base of the airfoil. The extent of coverage from the slot is dependent on the mainstream flow conditions, the slot injection rate, and the blade profile. However, it is clearly evident from Fig. 55 that additional discrete film cooling holes on the blade surface, could result in wasted coolant, thus reducing the thermal efficiency of the engine.

To give a complete understanding of thermal behavior on the blade platform, the heat transfer coefficients were also predicted. In Figure 56, the heat transfer coefficients are lowest along the pressure side of the passage and highest along the suction side of the passage. At the lower injection rates of 0.5% and 1.0%, the momentum of the slot coolant is not sufficient to alter (or weaken), the secondary flow. Therefore, with the present blade geometry and flow conditions, the heat transfer coefficients rise with the interaction of the mainstream flow and the

coolant due to the passage vortex. However, beyond the injection rate of 1.0%, the heat transfer coefficients begin to decrease. This is attributed to the strong coolant flow effectively weakening the passage vortex. At the higher injection rates the coolant coverage is more uniform, and the heat transfer coefficients decrease along the suction surface. However, the decrease along the suction surface comes at the expense of increased heat transfer on the pressure side of the passage. At m_s = 2.0%, the film coverage is relatively uniform from the pressure side to the suction side of the passage, and the increased film near the pressure side increases the heat transfer coefficients. Though the heat transfer coefficients are elevated near the pressure surface, the severe increase observed along the suction side is not present on the pressure side.

With an understanding of secondary flow on the passage endwall, the effect of an additional complexity on the film cooling effectiveness can be considered. With a turbulence grid added upstream of the cascade, the freestream turbulence intensity at the cascade inlet is raised to 13.4% [41]. Comparing the effectiveness distributions in Figure 57 with those for the freestream turbulence level of 0.75% in Fig. 52, the general trends are the same: increasing the injection rate increases the coverage area and the uniformity of the coverage. For the lowest injection rate of 0.5%, the coverage area extends further downstream with the increased turbulence; although the coverage area increases, the majority of the passage remains unprotected. A significant increase is observed in the protection are with the injection rates of 1.0% and 1.5%. In addition, at 1.5% the shape of the effectiveness contours changes from the low freestream turbulence case. The contours are more uniform across the passage. At 2.0% the uniformity of the effectiveness continues to increase. The passage vortex is weakened with the increased freestream turbulence. The mitigated secondary flow results in better coverage of the slot coolant.

Downstream Discrete Film Cooling

Figure 58 compares the film cooling effectiveness obtained from discrete film holes on the downstream half of the passage with turbulence intensities of 0.75% and 13.4% (measured at the cascade inlet), respectively. The average blowing ratio varies from 0.5 to 2.0 based on the mainstream velocity at the cascade exit. As shown in this figure, increasing the blowing ratio decreases the film cooling effectiveness. At the lowest blowing ratio of 0.5, very distinct film traces are seen from each of the 12 film cooling holes. Increasing the blowing ratio increases the momentum of the jets exiting the holes, the jets blow off the endwall, and the coolant is carried away with the mainstream flow. From flat plate film cooling studies, it is accepted that the optimum blowing ratio occurs between 0.5 and 1.0; increasing the blowing ratio beyond 1.0 for cylindrical holes results in decreased film cooling effectiveness because the coolant does not remain attached to the surface. The strong secondary flow behavior is very clear in Fig. 58(b-i); arrows added to the figure indicate the compound angle of the film cooling hole, designed to follow the blade profile. Regarding the three holes along the pressure side of the passage, the coolant traces follow the discharge angle of the holes. Near the trailing edge of the blades, the passage vortex as already crossed the passage from the pressure side to the suction side of the passage. Therefore, the coolant from these pressure side holes does not significantly deviate from their injection angles. The migration of the passage vortex is clearer with the middle row of film cooling holes. The film traces are altered significantly from the flow direction, and the coolant is pushed to the suction side of the passage. The coolant from the suction side holes covers less area than the other holes. The passage vortex has continued to gain strength, and as shown previously with the upstream slot, the coolant along the suction surface tends to lift off the endwall and attach to the suction surface of the blade due to the growing passage vortex.

The effect of increased turbulence intensity is opposite of the effect observed for the upstream injection. Figure 58 also shows the measured film effectiveness with the turbulence grid in the wind tunnel. The turbulence intensity at the inlet of the cascade is 13.4%, but as the mainstream continues through the passage, the turbulence intensity drops, and near the exit of the cascade, the turbulence intensity is approximately 5% [41]. The effect of blowing ratio with the increased freestream turbulence is the same as the previous case: the blowing ratio of 0.5 offers the best film cooling coverage. However, increasing the freestream turbulence decrease the film effectiveness for all for blowing ratios. At $M_f = 1.0$, the peak effectiveness clearly drops, but the increased turbulence causes the jet to spread, and more area is covered between the holes. At the highest blowing ratio of 2.0, the discrete holes provide coverage for a very small area, and the majority of the area is left unprotected. It is also seen in Fig. 58(b-ii) that the traces from the middle row of jets merge together as the increased turbulence spreads the cooling jets.

Combined Upstream Slot Injection and Downstream Discrete Film Cooling

The detailed film cooling effectiveness is measured on the endwall with upstream slot injection combined with discrete film cooling downstream for a freestream turbulence intensity of 0.75%. Figure 59 shows the film cooling effectiveness distribution on the platform with a slot injection rate of 1.0% and various blowing ratios for the downstream film cooling holes. From Fig. 52(b) a large area of the endwall was left uncooled where the slot coolant did not cover. The discrete film cooling holes obviously increased the effectiveness in the region near the holes, but a large area along the pressure side of the channel remains unprotected. The trends observed in this figure are the same those observed in Fig. 52(a) and Fig. 58. Because the slot coolant is

quickly carried to the suction side of the passage, there is no interaction between the slot coolant and the coolant from the film holes.

Increasing the slot injection rate to 2.0% yields protection throughout the entire passage. Now with the addition of downstream film cooling holes, the two coolants will interact. At the lowest film blowing ratio of 0.5, the peak effectiveness near the film holes is very high, as shown in Figure 60. The peak effectiveness can be as high as 0.81 immediately down stream of the first hole in the middle row. However, when there was not upstream slot injection, the corresponding effectiveness was only 0.67 (an increase of approximately 21%). The increased effectiveness is due to the film accumulation between the slot and film coolants. This effect is less obvious with the other film blowing ratios, as the jets tend to lift off the surface. Although the peak effectiveness is not as significantly affected at the increased blowing ratios, the effectiveness on the downstream half of the passage does increase when compared to the measured effectiveness with only upstream injection. When the downstream film holes are combined with the upstream slot injection, the film coolant begins to cumulate. In addition, without the upstream slot injection, the high momentum downstream coolant readily blows off the surface (Fig 58). However, with the upstream injection, even the high momentum does not lift off as readily, as it is deflected by the slot coolant and remains attached to the passage endwall.

Laterally Averaged Film Cooling Effectiveness

Although valuable insight can be obtained from the detailed distributions, many times spanwise averaged plots offer additional insight and provide clear comparisons for large amounts of data. Figures 61 – 63 make such comparisons of the cases previously discussed. The effectiveness is averaged from the suction side to the pressure side of the passage in the x-

direction, as shown in Fig. 50(a). The effect of the freestream turbulence and injection rate on the effectiveness from the upstream slot injection can be seen in Figure 61. First, increasing the injection rate increases the film cooling effectiveness. At the exit of the slot, the effectiveness of the injection rates of 1.0%, 1.5%, and 2.0% is unity, and the effectiveness gradually decreases. The maximum film cooling effectiveness is only 0.74 (Tu = 0.75%) for m_s = 0.5%. The average is significantly lower because the coolant does not cover the entire passage, as shown in Fig. 54(a). Near the slot ($x/C_{ax} < 0.4$), the level of the film cooling effectiveness for m_s ranging from 1.0 to 2.0 is the same (including Tu = 0.75% and 13.4%). The blowing ratio effect is clearly seen on the downstream half of the channel ($x/C_{ax} > 0.4$), with the effectiveness being proportional to the injection rate. The effect of freestream turbulence is also shown in this figure; as discussed previously, increasing the turbulence intensity increases the film cooling effectiveness because the passage secondary flow is weaken. The combined effect of weakening the secondary flow by increased injection and increased turbulence increases the film cooling effectiveness by a maximum of 20%. The greatest combined effect is seen for m_s = 1.5%, were the film cooling effectiveness is increased by as much as 80%.

The lateral averages for the downstream film cooling holes are shown in Figure 62. The effect of blowing ratio is seen by comparing Figs. 62(a), (b), (c), and (d). For both turbulence intensities, the film cooling effectiveness decreases with increasing blowing ratio. The effect of freestream turbulence is more complicated. In general, increased freestream turbulence decreases the film cooling effectiveness on the platform (as also shown in Fig. 58). This finding varies from studies of film cooled flat plates. For flat plate studies, it has been shown that increasing the freestream turbulence decreases the film cooling effectiveness at low blowing ratios and increases the effectiveness at high blowing ratios. The film cooling effectiveness on

the platform is influenced by both the freestream turbulence intensity and the passage induced secondary flow (passage vortex). Increasing the freestream turbulence increased the effectiveness upstream due to the slot injection. With the turbulence intensity being 13.4% at the inlet of the cascade, the passage vortex was weakened. Near the trailing edge of the passage, where the turbulence intensity is significantly lower (5%) and the passage vortex is weakened, the coolant from the discrete holes can more readily lift off the platform (when compared to the cases without the turbulence grid). Therefore, the effectiveness decreases with increased freestream turbulence due to the combined effect of the freestream turbulence and the passage induced secondary flow.

Figure 63 clearly shows the combined effect of upstream slot injection and downstream discrete film cooling holes. Beginning with the slot injection rate of 1.0%, from the reference case (only upstream slot injection with m_s = 1.0%), the effectiveness drops quickly. However, with the addition of downstream discrete film hole cooling, the film cooling effectiveness increases more than 3 times the amount without the discrete film holes, with the greatest increase coming the with lowest film blowing ratio of $M_f = 0.5$. With the slot injection of 2.0%, the film cooling effectiveness is greater than with 1.0%. The film cooling effectiveness is elevated with the film cooling holes; however, the increase is not as significant as with the injection rate of 1.0%.

When considering the film cooling effectiveness on the passage endwall, there has been a tendency to apply data or correlations obtained from flat plate studies directly to the endwall. Figure 64 illustrates flat plate correlations should be applied to the endwall cautiously. Goldstein [40] gathered experimental data and correlations for the film cooling effectiveness measured downstream of both a slot and discrete film holes. Plotted with the laterally averaged data from

the present study are both a correlation for the effectiveness due to discrete, inclined film cooling holes, and a correlation for tangential slot injection. The film cooling effectiveness of the present study is clearly higher than the accepted correlation for discrete hole film cooling. The coolant exiting a discrete film hole is highly three-dimensional with multiple pairs of vortices. These vortices increase the interaction between the coolant the mainstream flow, and thus reduce the film cooling effectiveness. However, when the coolant exits a full coverage slot, the flow is more two-dimensional, with mixing occurring at the coolant – mainstream interface. The reduced mixing results in better film coverage, and therefore, increased film cooling effectiveness.

The interesting comparison is between the present results and the correlation for tangential slot injection. Near the slot ($x/M_sS < 30$), the current experimental data for slot injection rates of 1%, 1.5%, and 2% collapse together with the established correlation. The injection rate of 0.5% is lower than the correlation because the coolant does not exit the slot uniformly (Fig. 52(a)). Therefore, the lateral average for this lowest injection rate is lower than the other experimental data and the correlation for tangential injection. However, as x/M_sS increases, the current experimental data deviates significantly from the correlation. Beyond $x/M_sS = 22$, the current experimental data is much lower than the established correlation. The contour plots in Fig. 52 clearly show the skewed effectiveness profiles through the passage. Unlike flow over a flat plate, the effectiveness on the passage endwall decreases due to the passage secondary flow. This variation from the tangential slot correlation is seen for both freestream turbulence levels (Figs. 64(a) and (b)).

FUTURE PLANS

Rotating Heat Transfer

Using the pressure sensitive paint technique, the film cooling effectiveness has been measured on the rotating platform with coolant flow from the stator-rotor seal. The effectiveness has also been measured with coolant from discrete film cooling holes. The next step is to measure the film cooling effectiveness on the rotating platform with upstream injection combined with the discrete film holes. With a variety of coolant flow rate combinations, this will provide engineers with detailed film cooling effectiveness distributions under more realistic coolant flow conditions. Following the final film effectiveness measurements, detailed heat transfer coefficient distributions will be obtained on the rotating platform using temperature sensitive paint.

In addition to the experimental work, numerical simulations are also continuing. The experimental results will be used to validate the numerical simulations, and the predictions will be extended to a wider range of flow conditions. The film cooling effectiveness and heat transfer coefficients will be predicted on the rotating platform with separate coolant flow from the stator-rotor seal and discrete film holes, as well as when the coolant flows are combined.

Advanced Stator-Rotor Seals

Parallel experimental work will continue on the five-blade linear cascade. In addition to the fundamental seal geometry that has been considered, more advanced seal configurations will also be studied. As shown in Figure 65, advanced seal that more closely represent advanced stator-rotor seals will be considered. The film cooling effectiveness will measured on the

cascade endwall for each seal configuration. In addition, a second geometry of discrete film cooling holes will be considered and the film cooling effectiveness will be compared to that already measured. With the cascade, not only are the coolant flow rates varied, but the effect of freestream turbulence is also considered.

CONCLUSIONS

Both the experimental and numerical data are vital for engineers to develop more effective platform cooling schemes which will increase platform durability and longevity. The effective cooling schemes will also reduce coolant flow, and ultimately increase power output and thermal efficiency of the engine. To aid designer in developing more effective cooling schemes, detailed film cooling effectiveness distributions have been obtained on both rotating and non-rotating turbine platforms. From the data obtained on the rotating on the rotating blade platform, it was shown that the film cooling effectiveness due to coolant injection from the stator-rotor gap increases with increasing coolant-to-mainstream mass flow ratio. Unlike results that have been obtained in non-rotating facilities, complete coverage of the passage platform cannot be obtained by using coolant injection from the stator-rotor gap. The passage vortex over the platform has an adverse impact on film adherence. If the engine deviates from its design condition the film coolant traces get reoriented more toward the suction side for off-design rotating conditions due to the stagnation region shift towards the pressure side.

Additional film cooling holes are needed to adequately protect the downstream half of the rotating platform. The level of protection offered by these holes is dependant on the rotational speed of the blades and the blowing ratio of the coolant. In general, increasing the blowing ratio of the coolant from M = 1.0 to 2.0 increases the film cooling effectiveness. However, at the off-design conditions, increasing the blowing ratio from 1.5 to 2.0 offers minimal additional protection (compared to the additional coolant that is used).

The film cooling effectiveness has also been predicted on the rotating platform. These preliminary predictions show how the film cooling effectiveness is strongly influenced by the passage induced secondary flow. In addition, the heat transfer coefficients have also been

predicted on the rotating platform. The predictions have identified hot spots that are present on the platform. In addition, the unsteady effect on the film cooling effectiveness and heat transfer coefficients has been shown. Preliminary simulations are underway to calculate the film cooling effectiveness on the rotating platform with both upstream slot coolant and downstream discrete film cooling holes.

The detailed film cooling effectiveness distributions on the rotating platform have a similar trend as those obtained in non-rotating passages. However, the quantitative levels vary significantly. The variation could be the result of different blade profiles use to investigate the film cooling effectiveness. Not only do the blade profiles vary (which will induce different secondary flow patterns), but the geometry of the injection slots are different. With different slot configurations resulting in different blowing ratios, the measured film cooling effectiveness on the two platforms varies. With similar trends, it is worthwhile to extend this rotating study to a non-rotating facility, so more complex cooling configurations can be considered. Experimental results from the current non-rotating facility clearly show how strongly the passage vortex affects the coolant flow through the passage.

The present study provides detailed film cooling data on rotating platforms, which is not openly available for designers. By utilizing these results for film cooling, turbine researchers and designers will be better equipped to implement cooling schemes that adequately protect the turbine components while minimizing coolant consumption. Extending the life of vital components while reducing the amount of cooling air will lead to more efficient and reliable engines.

REFERENCES

[1] Han, J.C., Dutta, S., and Ekkad, S.V., 2000, *Gas Turbine Heat Transfer and Cooling Technology*, Taylor and Francis, New York ,646 pages.

[2] Dring, R. P., Blair, M. F., and Hoslyn, H. D., 1980, "An Experimental Investigation of Film Cooling on a Turbine Rotor Blade," ASME J. of Engineering for Power, 102, pp. 81-87.

[3] Takeishi, M., Aoki, S., Sato, T., and Tsukagoshi, K., 1992, "Film Cooling on a Gas Turbine Rotor Blade," ASME J. of Turbomachinery, 114, pp. 828-834.

[4] Abhari, R.S., and Epstein, A.H., 1994, "An Experimental Study of Film Cooling in a Rotating Transonic Turbine," ASME J. of Turbomachinery, 116, pp. 63-70.

[5] Blair, M.F., 1994, "An Experimental Study of Heat Transfer in a Large-Scale Turbine Rotor Passage," ASME J. of Turbomachinery, 116, pp. 1-13.

[6] Ahn, J., Schobeiri, M.T., Han, J.C., and Moon, H.K., 2004, "Film Cooling Effectiveness on the Leading Edge of a Rotating Turbine Blade," ASME Paper No. IMECE 2004-59852.

[7] Ahn, J., Schobeiri, M.T., Han, J.C., and Moon, H.K., 2004, "Film cooling effectiveness on the leading edge of a rotating Film-Cooled Blade Using Pressure Sensitive Paint," ASME Paper No. GT-2005-68344.

[8] Langston, L.S., Nice, L.M., and Hooper, R.M., 1976, "Three-Dimensional Flow within a Turbine Cascade Passage," ASME Paper No. 76-GT-50.

[9] Langston, L.S., 1980, "Crossflows in a Turbine Cascade Passage," *ASME J. Engineering for Power*, Vol. 102, pp. 866-874.

[10] Goldstein, R.J. and Spores, R.A., 1988, "Turbulent Transport on the Endwall in the Region between Adjacent Turbine Blades." *ASME J. Heat Transfer*, Vol. 110, pp. 862-869.

[11] Blair, M.F., 1974, "An Experimental Study of Heat Transfer and Film Cooling on Large-Scale Turbine Endwall," *ASME J. Heat Transfer*, Vol. 96, pp. 524-529.

[12] Graziani, R.A., Blair, M.F., Taylor, J.R., and Mayle, R.E., 1980, "An Experimental Study of Endwall and Airfoil Surface Heat Transfer in a Large Scale Turbine Blade Cascade," *ASME J. Engineering for Power*, Vol. 102, pp. 257-267.

[13] York, R.E., Hylton, L.D., and Mihelc, M.S., 1984, "An Experimental Investigation of Endwall Heat Transfer and Aerodynamics in a Linear Vane Cascade," *ASME J. Engineering for Gas Turbines and Power*," Vol. 106, pp. 159-167.

[14] Radomsky, R.W. and Thole, K.A., 2000, "High Free-Stream Turbulence Effects on Endwall Heat Transfer for a Gas Turbine Stator Vane," *ASME J. Turbomachinery*, Vol. 122, pp. 299-708.

[15] Kwak, J.S., Lee, J.H., and Han, J.C., 2002, "Heat Transfer and Pressure Distributions on a Gas Turbine Vane End-Wall," Proceedings of the Twelfth International Heat Transfer Conference, pp. 693-698.

[16] Takeishi, K., Matsuura, M., Aoki, S., and Sato, T., 1990, "An Experimental Study of Heat Transfer and Film Cooling on Low Aspect Ratio Turbine Nozzles," *ASME J. Turbomachinery*, Vol. 112, pp. 488-496.

[17] Harasgama, S.P. and Burton, C.S., 1992, "Film Cooling Research on the Endwall of a Turbine Nozzle Guide Vane in a Short Duration Annular Cascade: Part 1 – Experimental Technique and Results," *ASME J. Turbomachinery*, Vol. 114, pp. 734-740.

[18] Jabbari, M.Y., Marston, K.C., Eckert, E.R.G., and Goldstein, R.J., 1996, "Film Cooling of the Gas Turbine Endwall by Discrete-Hole Injection," *ASME J. Turbomachinery*, Vol. 118, pp. 278-284.

[19] Friedrichs, S., Hodson, H.P., and Dawes, W.N., 1996, "Distribution of Film-Cooling Effectiveness on a Turbine Endwall Measured Using the Ammonia and Diazo Technique," *ASME J. Turbomachinery*, Vol. 118, pp. 613-621.

[20] Friedrichs, S., Hodson, H.P., and Dawes, W.N., 1997, "Aerodynamic Aspects of Endwall Film Cooling," *ASME J. Turbomachinery*, Vol. 119, pp. 786-793.

[21] Friedrichs, S., Hodson, H.P., and Dawes, W.N., 1998, "The Design of an Improved Endwall Film Cooling Configuration," ASME Paper No. 98-GT-483.

[22] Barigozzi, G., Benzoni, G., Franchini, G., and Derdichizzi, A., 2005, "Fan-Shaped Hole Effects on the Aero-Thermal Performance of a Film Cooled Endwall," ASME Paper No. GT2005-68544.

[23] Roy, R.P., Squires, K.D., Gerendas, M., Song, S., Howe, W.J., and Ansari, A., 2000, "Flow and Heat Transfer at the Hub Endwall of Inlet Vane Passages – Experiments and Simulations," ASME Paper No. 2000-GT-198.

[24] Burd, S.W., Satterness, C.J., and Simon, T.J., 2000, "Effects of Slot Bleed Injection Over a Contoured End Wall on Nozzle Guide Vane Cooling Performance: Part II – Thermal Measurements," ASME Paper No. 2000-GT-200.

[25] Oke, R., Simon, T., Shih, T., Zhu, B., Lin, Y.L., and Chyu, M., 2001, "Measurements over a Film-Cooled Contoured Endwall with Various Coolant Injection Rates," ASME Paper No. 2001-GT-0140.

[26] Oke, R.A. and Simon, T.W., 2002, "Film Cooling Experiments with Flow Introduced Upstream of a First Stage Nozzle Guide Vane through Slots of Various Geometries," ASME Paper No. GT-2002-30169.

[27] Nicklas, M., 2001, "Film-Cooled Turbine Endwall in a Transonic Flow Filed: Part II – Heat Transfer and Film Cooling Effectiveness," *ASME J. Turbomachinery*, Vol. 123, pp. 720-729.

[28] Liu, G., Liu, S., Zhu, H., Lapworth, B.C., and Forest, A.E., 2004, "Endwall Heat Transfer and Film Cooling Measurements in a Turbine Cascade with Injection Upstream of Leading Edge," *Heat Transfer – Asian Research*, Vol. 33, pp. 141-152.

[29] Zhang, L.J. and Jaiswal, R.S., 2001, "Turbine Nozzle Endwall Film Cooling Study Using Pressure-Sensitive Paint," *ASME J. Turbomachinery*, Vol. 123, pp. 730-735.

[30] Zhang, L.J. and Moon, H.K., 2003, "Turbine Nozzle Endwall Inlet Film Cooling – The Effect of a Backward Facing Step," ASME Paper No. GT2003-38319.

[31] Knost, D.G. and Thole, K.A., 2004, "Adiabatic Effectiveness Measurements of Endwall Film Cooling for a First Stage Vane," ASME Paper No. GT2004-53326.

[32] Cardwell, N.D., Sundaram, N., and Thole, K.A., 2005, "Effects of Mid-Passage Gap, Endwall Misalignment and Roughness on Endwall Film-Cooling," ASME Paper No. GT2005-68900.

[33] Han, S. and Goldstein, R.J., 2005, "Influence of Blade Leading Edge Geometry on Turbine Endwall Heat (Mass) Transfer," ASME Paper No. GT2005-68590.

[34] Schobeiri, M. T., 1999, "Efficiency, Performance and Flow Measurement of Siemens-Westinghouse HP-Turbine Blades, Series 9600 and 5600, Final Report.

[35] Schobeiri, M. T., Gilarranz, J.L, Johansen, E.S., 2000, "Aerodynamic and Performance Studies of a Three Stage High Pressure Research Turbine with 3-D Blades, Design Points and Off-Design Experimental Investigations," 2000-GT-484.

[36] Schobeiri, M.T., Suryanarayanan A., Jermann, C., and Neuenschwander, T., 2004,"A Comparative Aerodynamic and Performance Study of a Three-Stage High Pressure Turbine with 3-D Bowed Blades and Cylindrical Blades," GT-2004-53650.

[37] McLachlan, B., and Bell, J., 1995, "Pressure-Sensitive Paint in Aerodynamic Testing," Exp. Therm. Fluid Sci., **10**, pp. 470–485.

[38] Wright, L.M., Gao, Z., Varvel, T.A., and Han, J.C., 2005, "Assessment of Steady State PSP, TSP and IR Measurement Techniques for Flat Plate Film Cooling," ASME Paper No. HT-2005-72363.

[39] Coleman, H.W., and Steele, W.G., 1989, *Experimentation and Uncertainty Analysis for Engineers*, John Wiley & Sons, New York.

[40] Goldstein, R.G., 1971, "Film Cooling," *Advances in Heat Transfer*, Vol. 7, pp. 321 – 379.

[41] Zhang, L. and Han, J.C., 1994, "Influence of Mainstream Turbulence on Heat Transfer Coefficients from a Gas Turbine Blade," *ASME J. Heat Transfer*, Vol. 116, pp. 896-903.

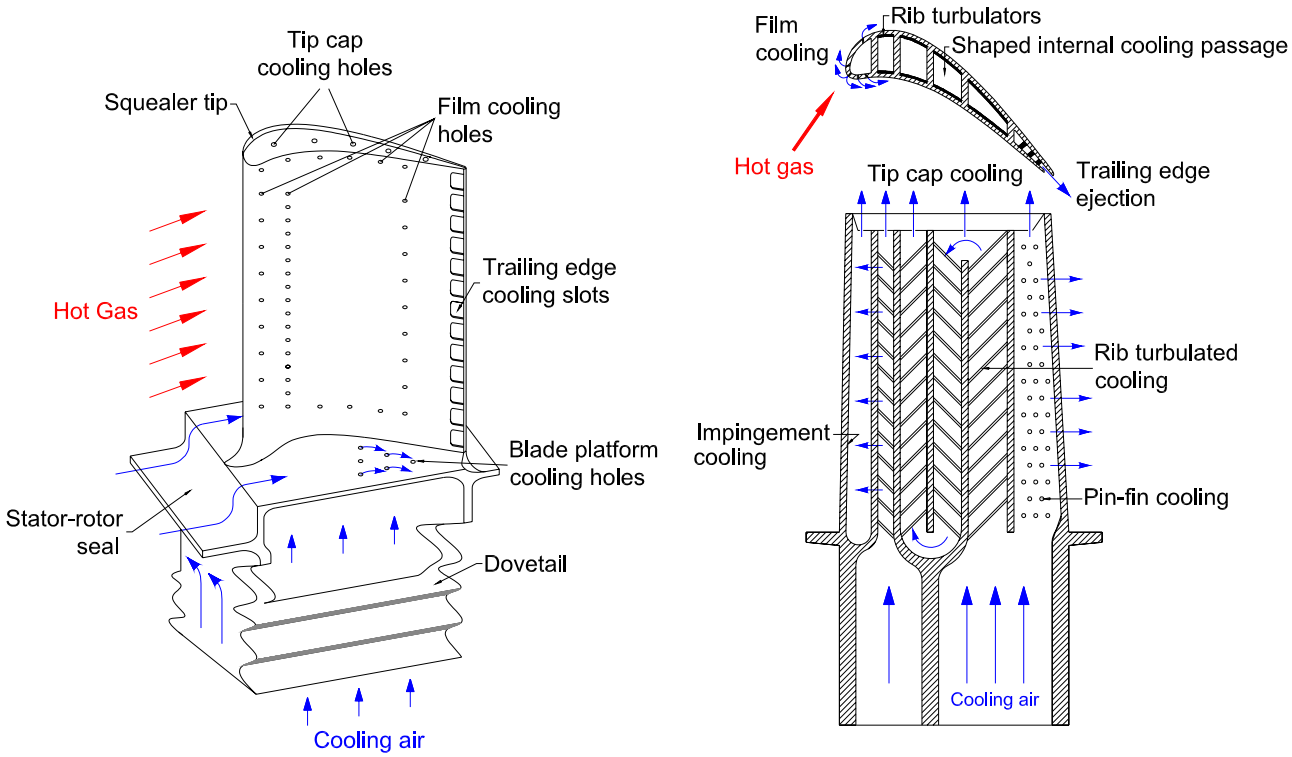

Figure 1: Modern Cooled Gas Turbine Blade

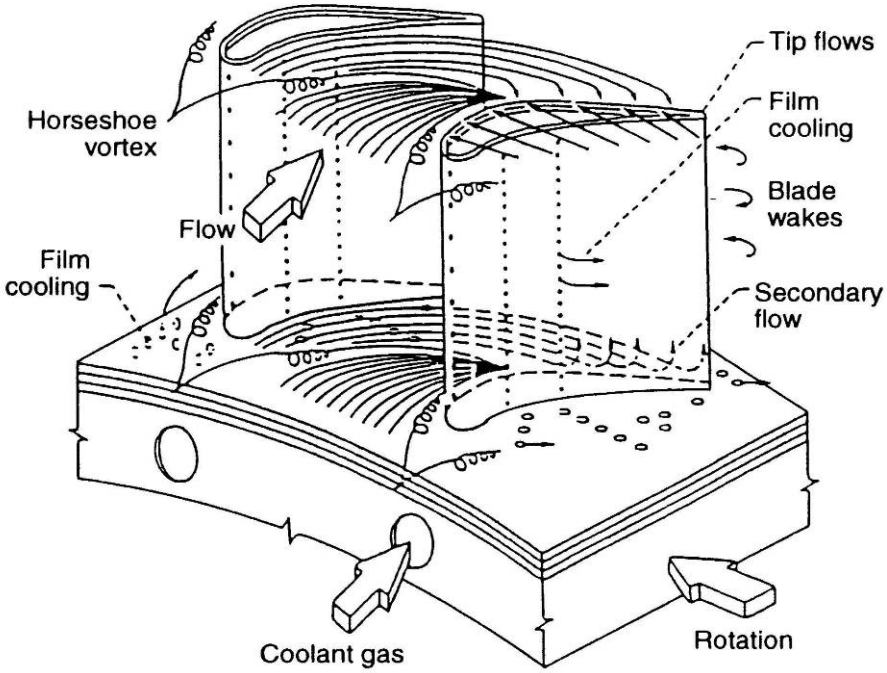

Figure 2: Secondary Flow through a Blade Passage (from Han et al. [1])

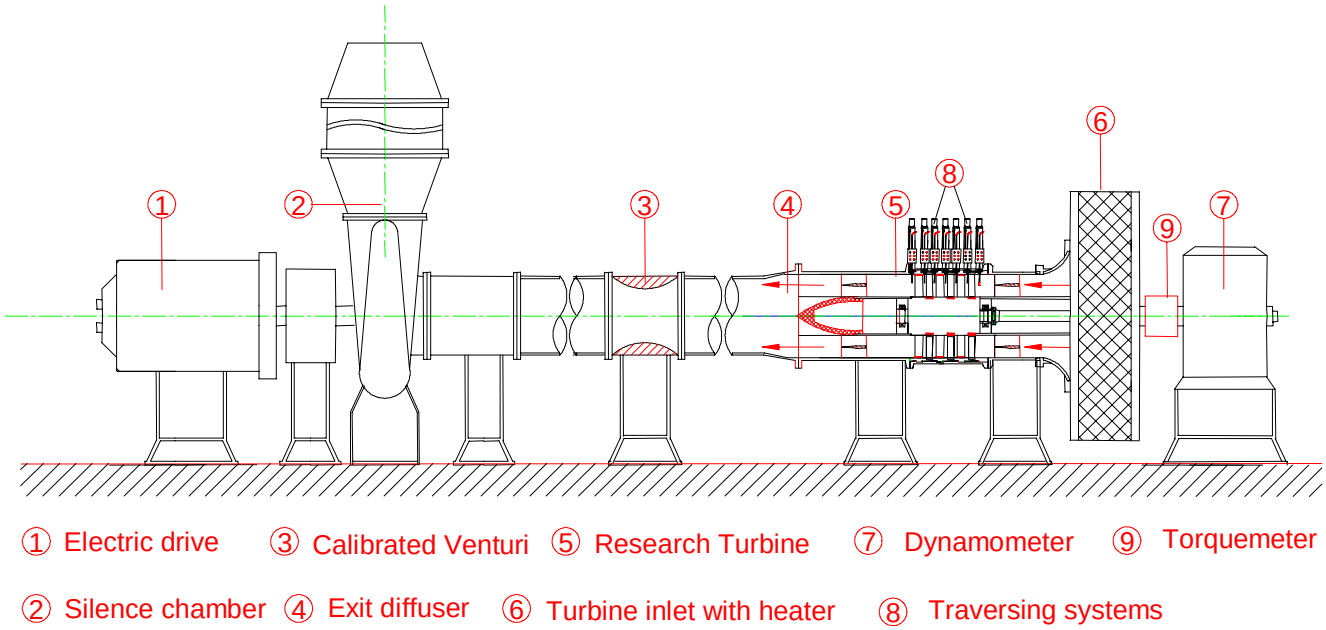

Figure 3: Existing Turbine Research Facility

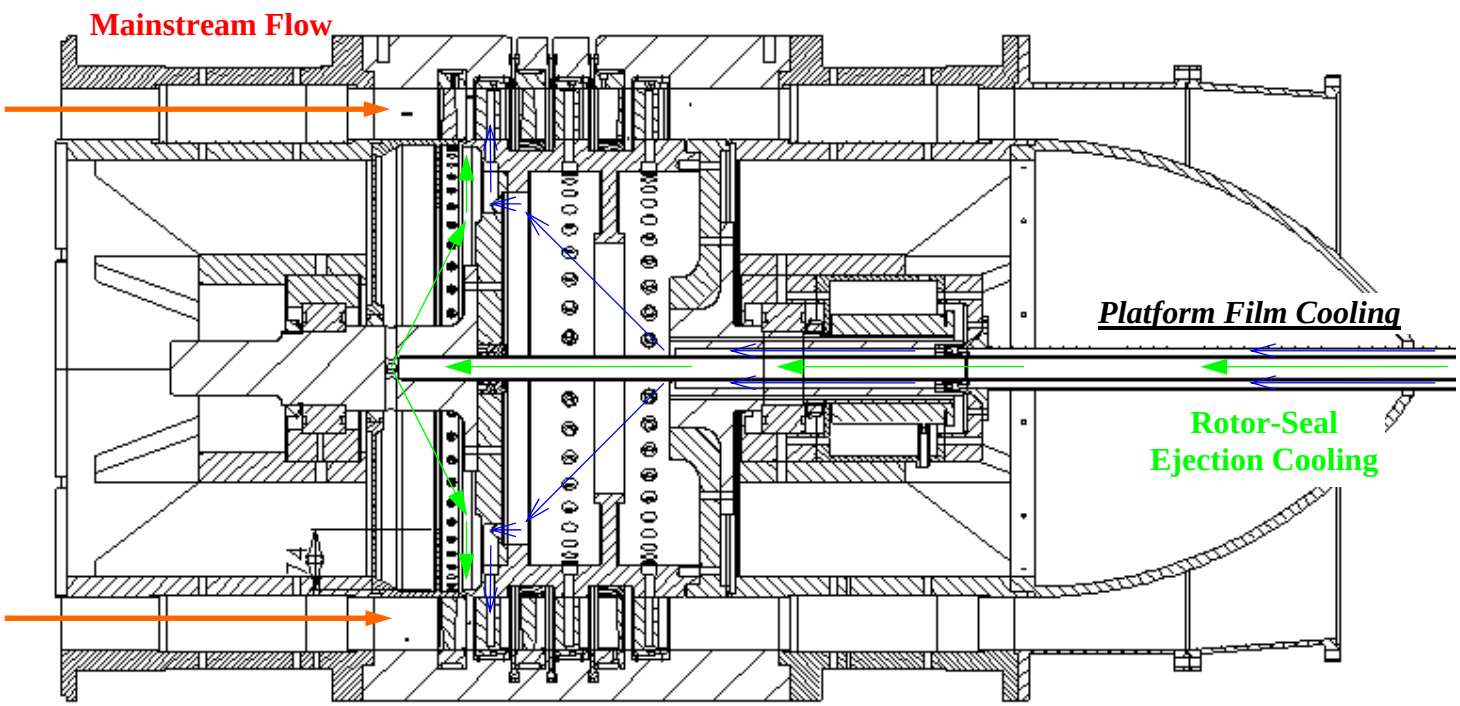

Figure 4: Coolant Flow for Film Cooling and Coolant Ejection

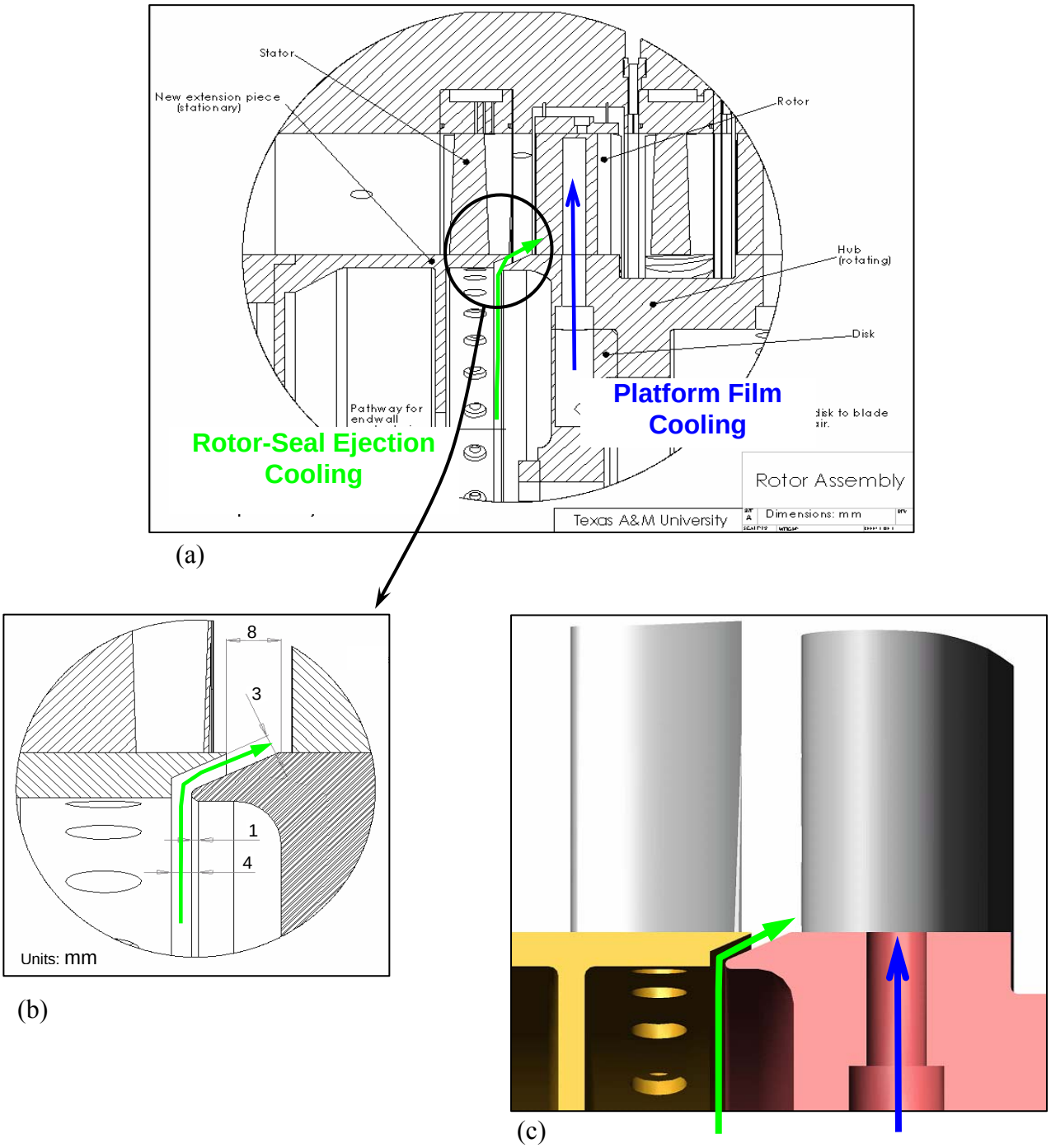

Figure 5: Detailed Views of Coolant Ejection and Film Coolant Flow Paths

(a) Enlarged View of First Stage with Coolant Flows
(b) Detailed View of Stator-Rotor Seal
(c) Solid Model of Stator-Rotor Seal Ejection and Film Coolant Paths

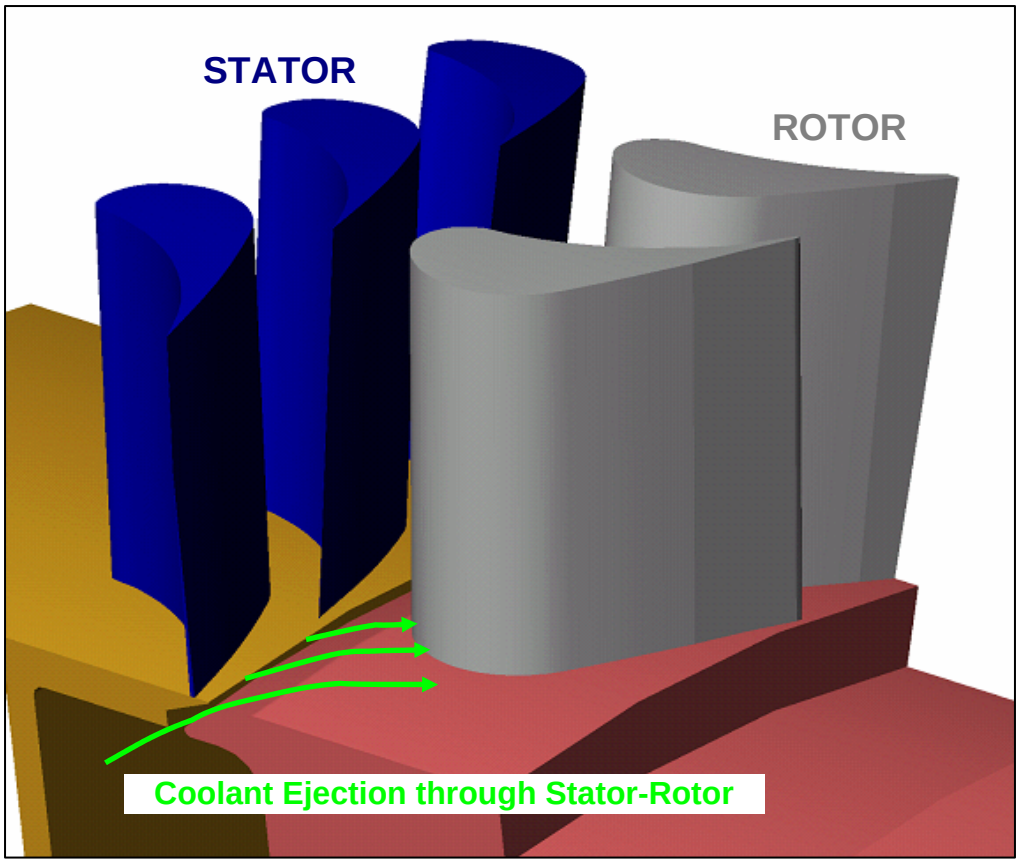

(a)

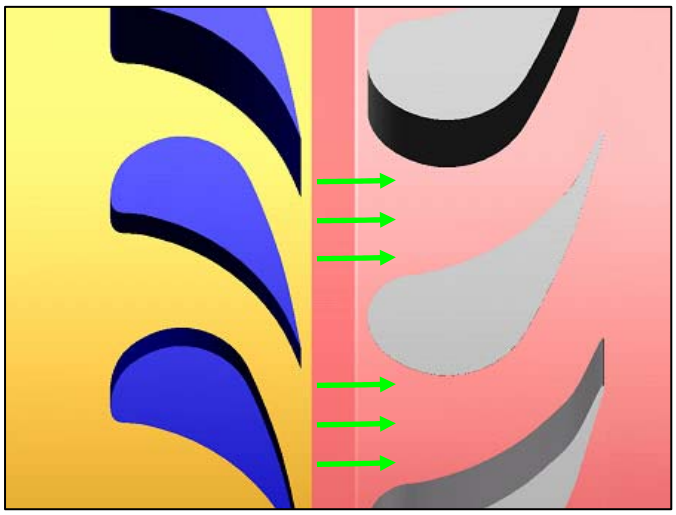

(b)

Figure 6: Coolant Ejection on the Rotor Blade Platform

(a) Three-Dimensional View (One Rotor Blade Removed)
(b) Top View

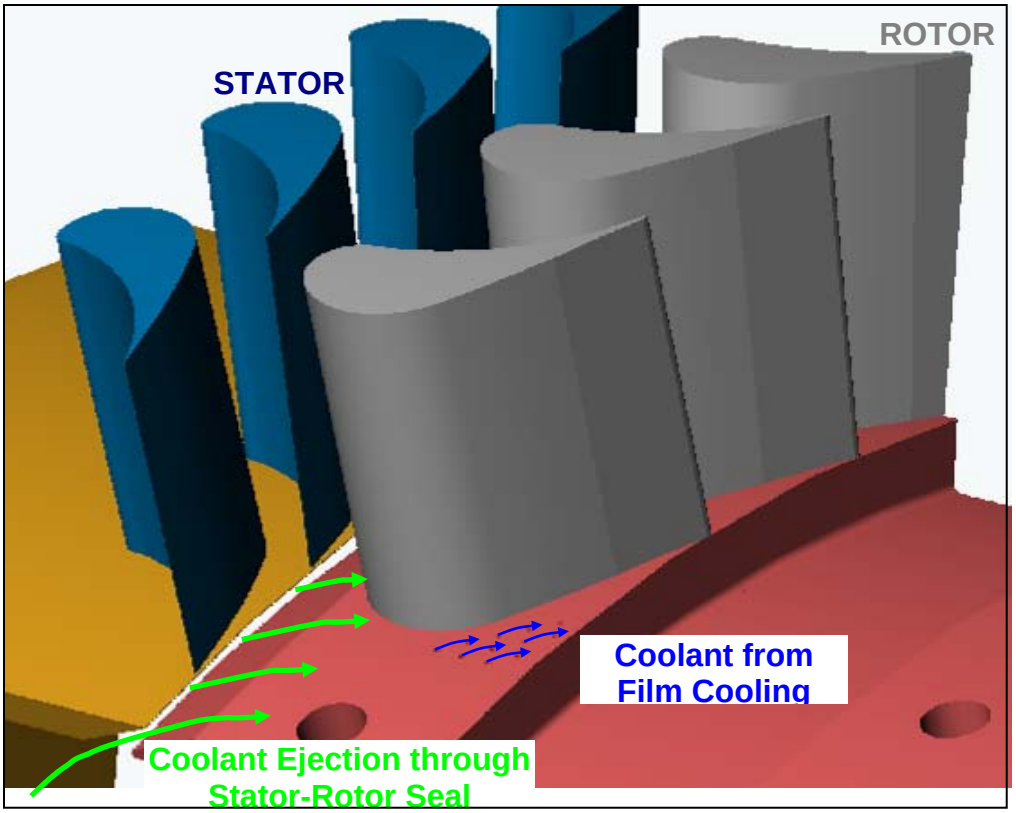

(a)

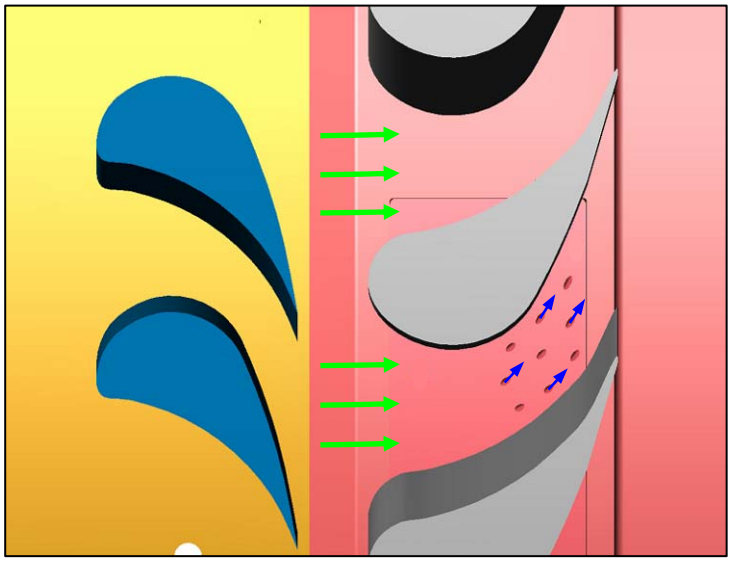

(b)

Figure 7: Coolant Ejection and Film Cooling on the Rotor Blade Platform

(a) Three-Dimensional View (One Rotor Blade Removed to Expose Film Cooling Holes)
(b) Top View

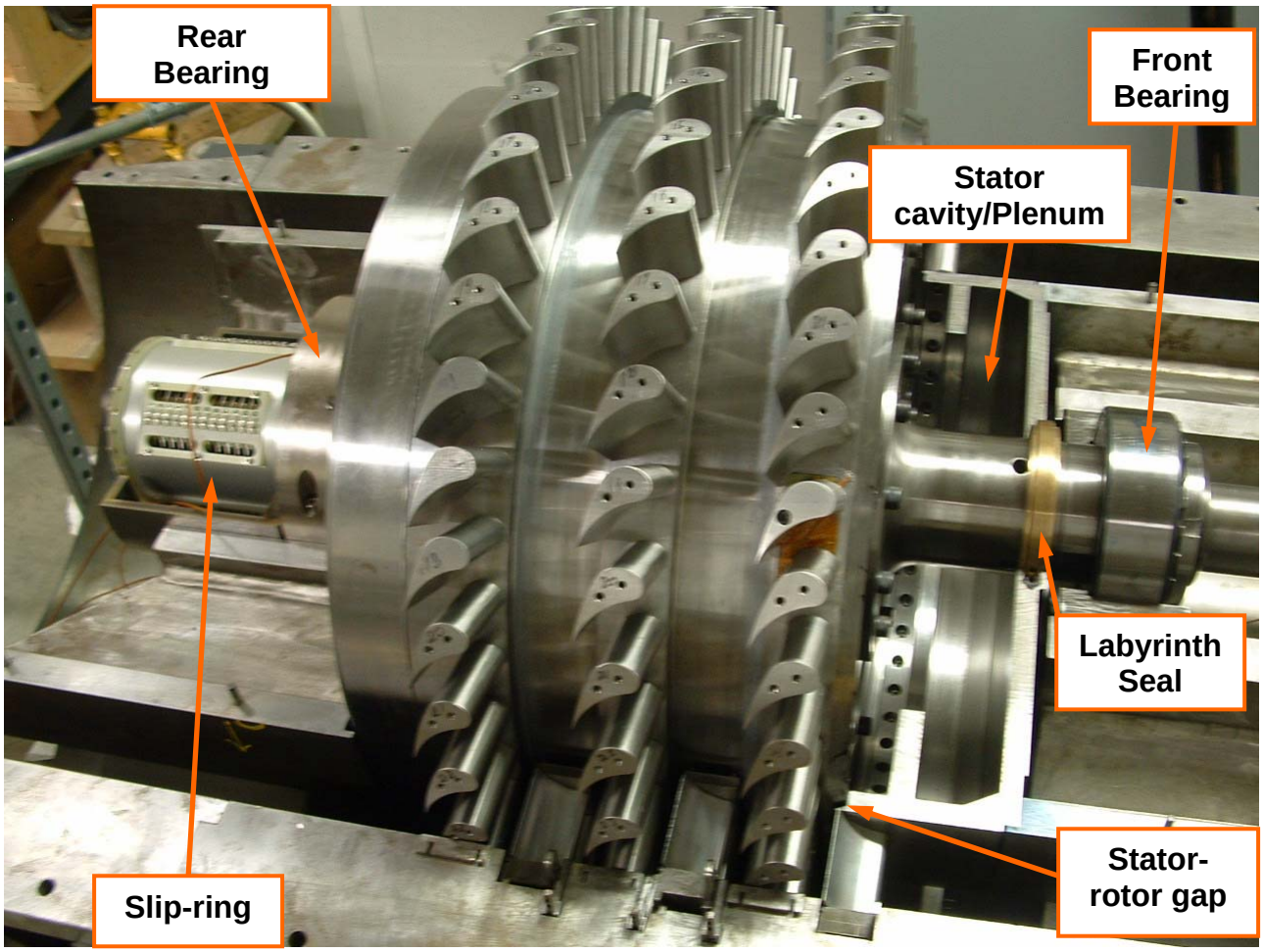

Figure 8: Newly Fabricated Rotor Platform with Stator-Rotor Seal Ejection and Platform Film Cooling Holes

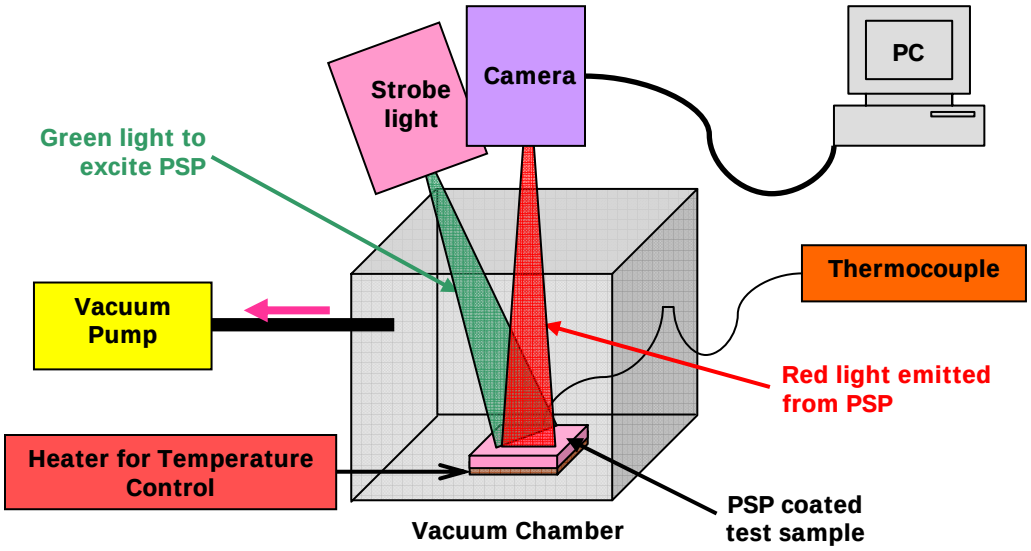

(a)

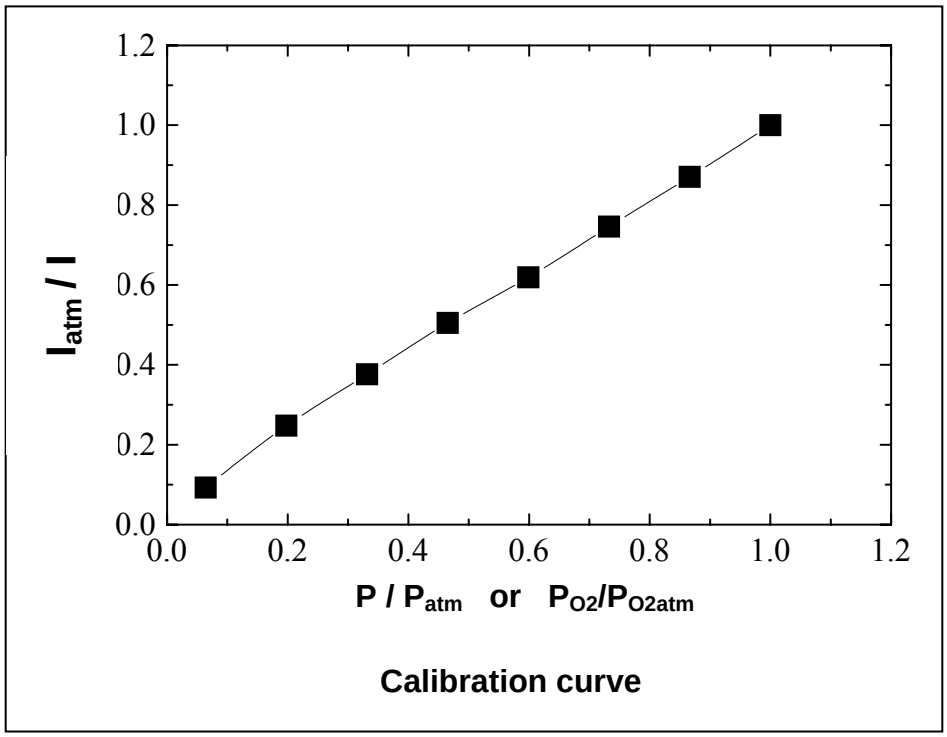

(b)

Figure 9: Typical Pressure Sensitive Paint Calibration Setup and Calibration Curve

(a) PSP Calibration Setup
(b) PSP Calibration Curve

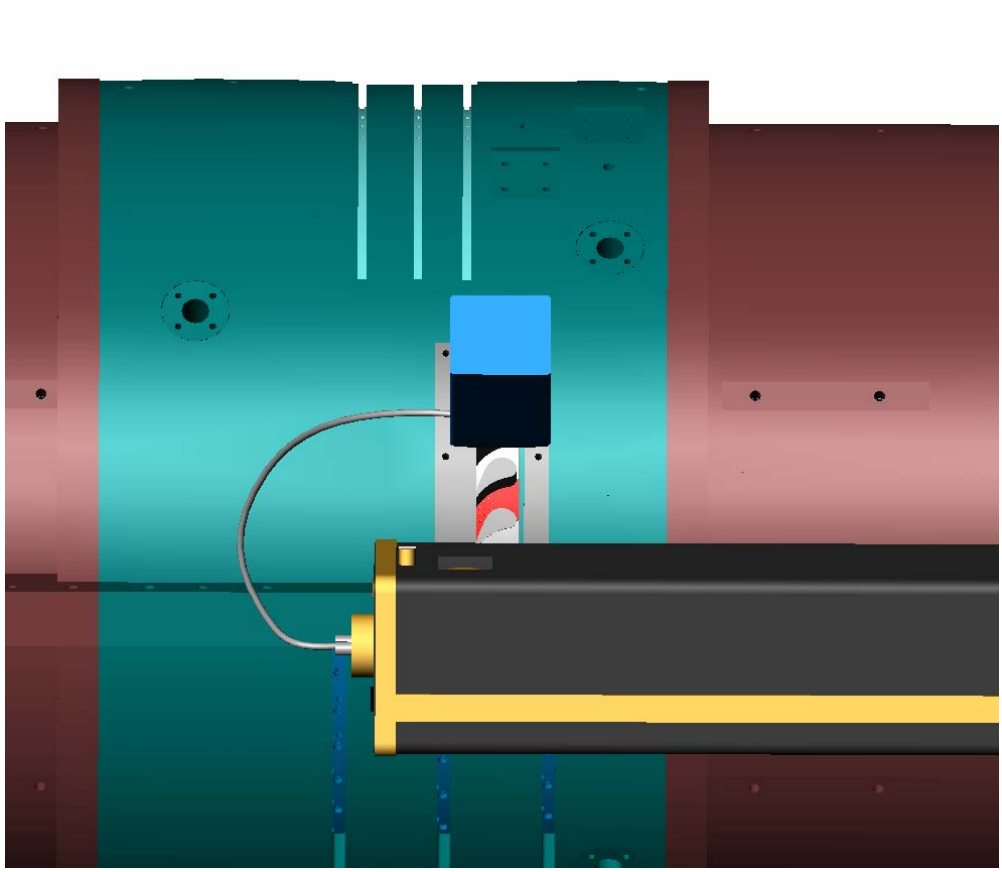

Figure 10: Modified Engine Housing to Accommodate Viewing of the Rotor Blade Platform with the Required Optical Componenets for PSP and TSP Measurements

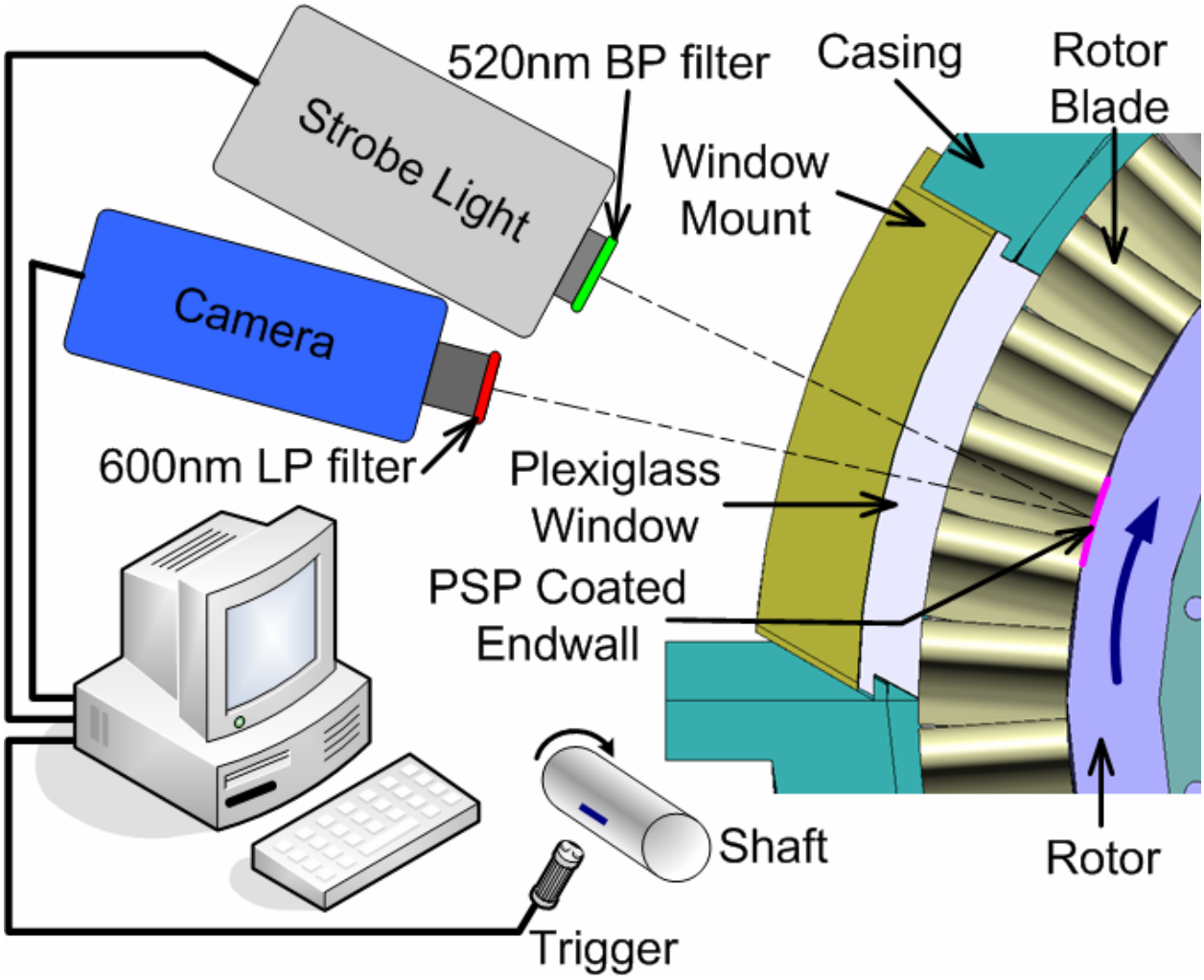

Figure 11: Optical Components Setup for the Model Turbine and PSP

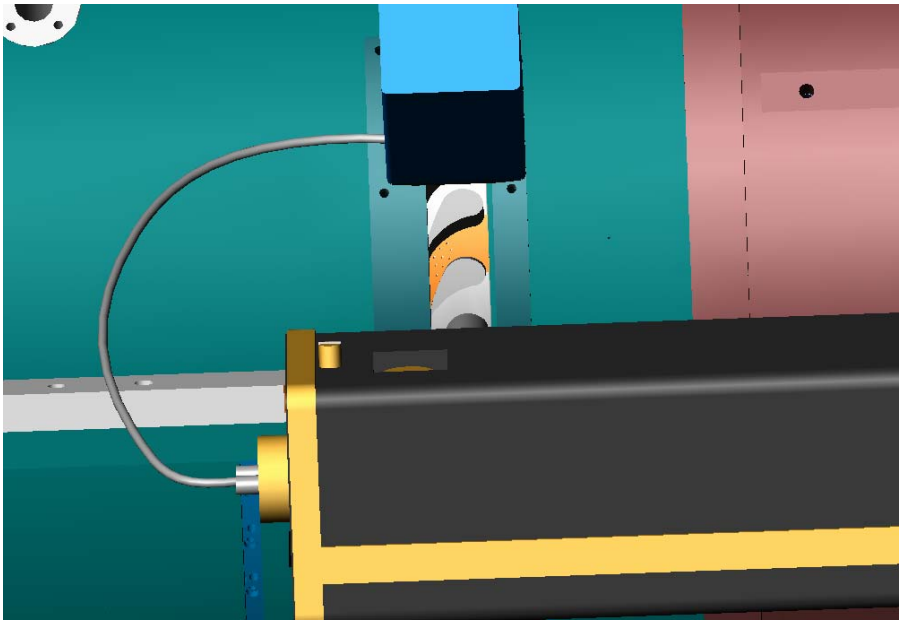

(a)

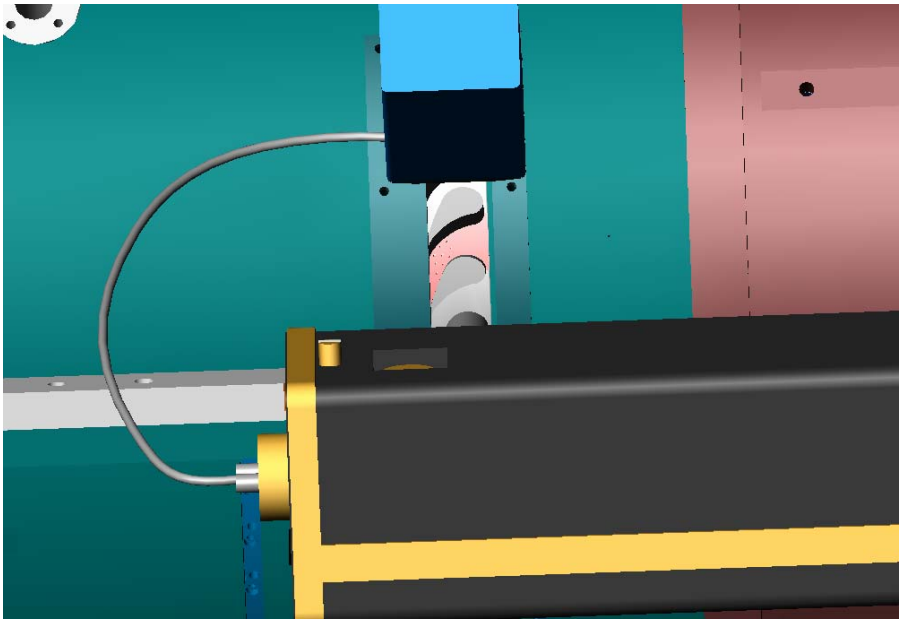

(b)

Figure 12: Viewing Windows for Rotor Platform Measurements

(a) Pressure Sensitive Paint (PSP) Coated Surface
(b) Temperature Sensitive Paint (TSP) Coated Surface

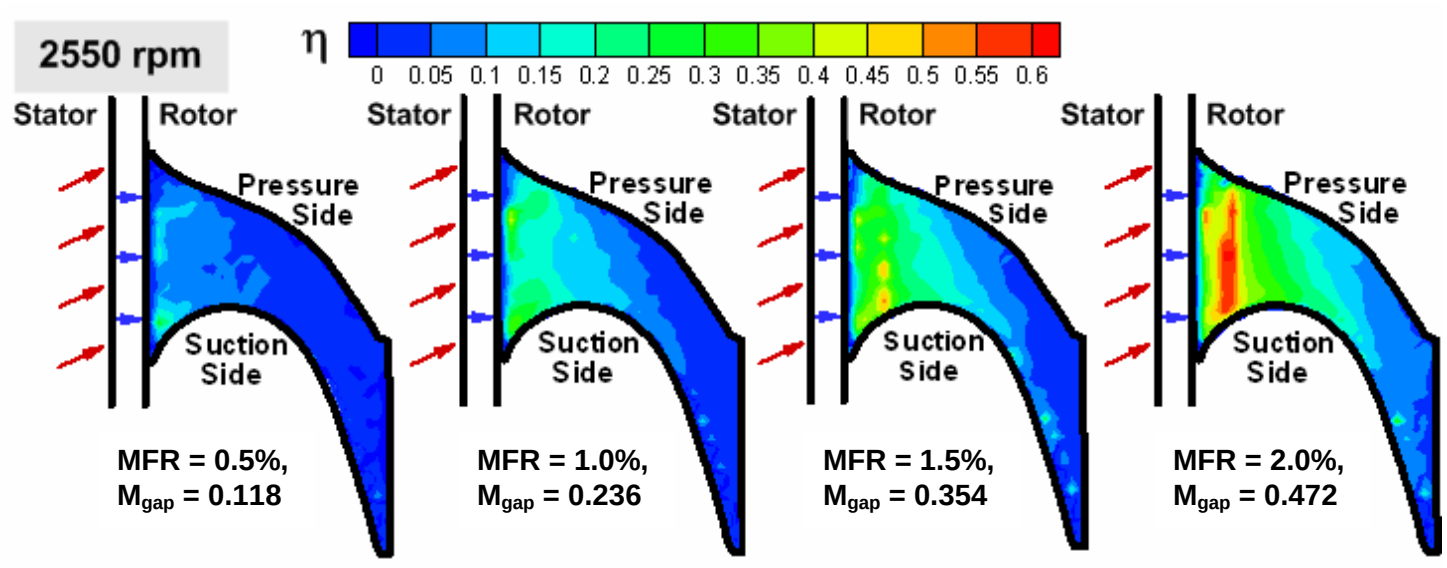

Figure 13: Film Cooling Effectiveness Distribution on the Rotating Endwall for 2550 rpm

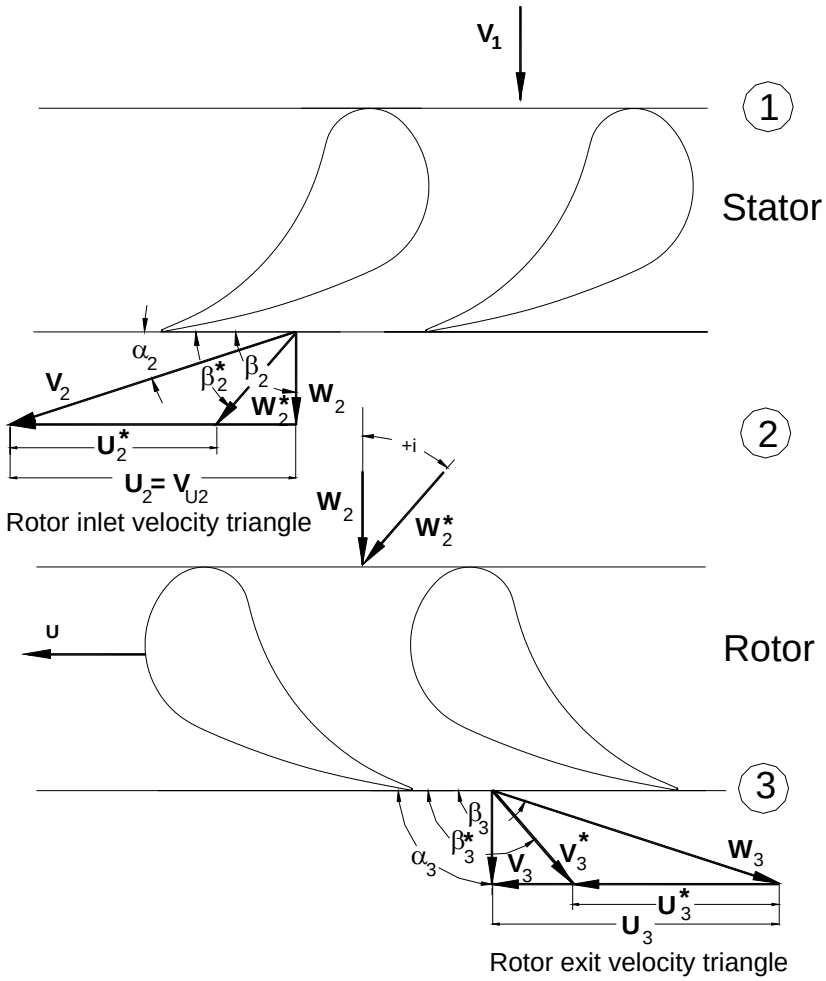

Figure 14: Velocity Triangles and Relative Inlet and Exit Flow Angles for Design and Off-Design Rotating Speeds

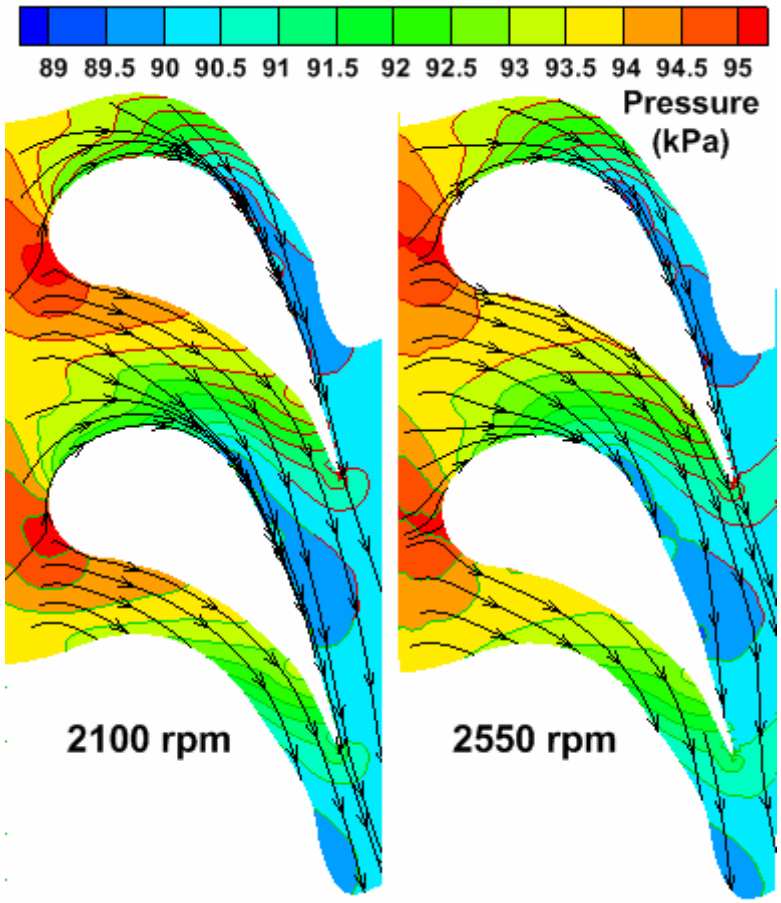

Figure 15: Numerical Prediction of Endwall Static Pressure Distribution (kPa) along with Flow Pathlines

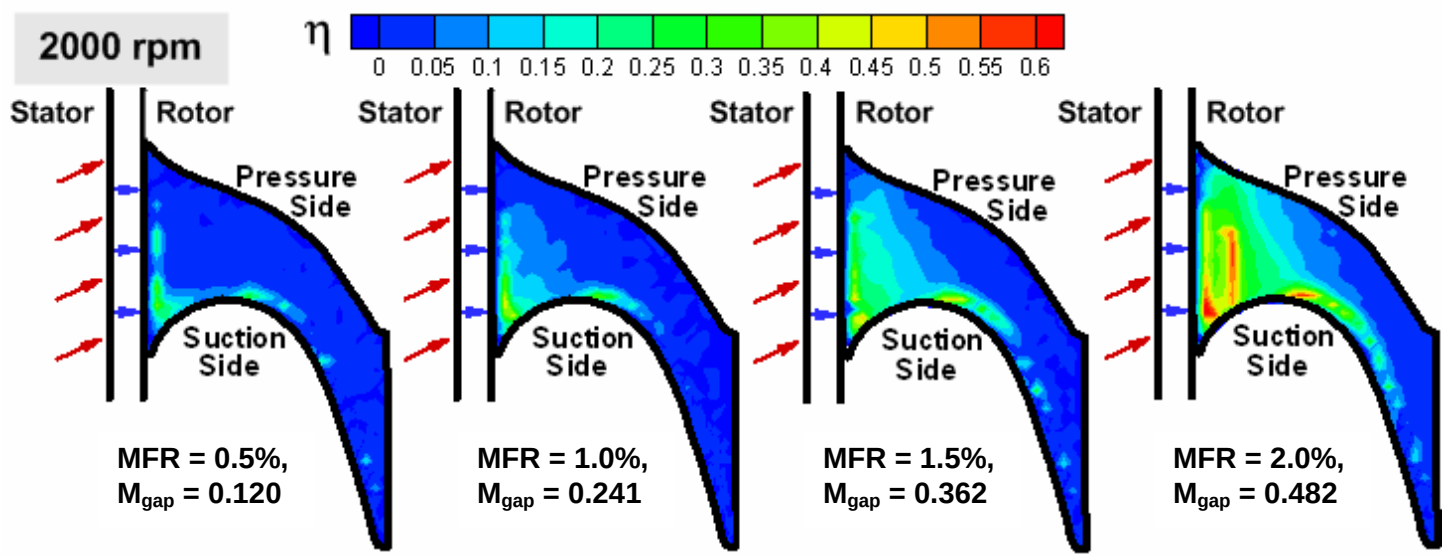

Figure 16: Film Cooling Effectiveness Distribution on the Rotating Endwall for 2000 rpm

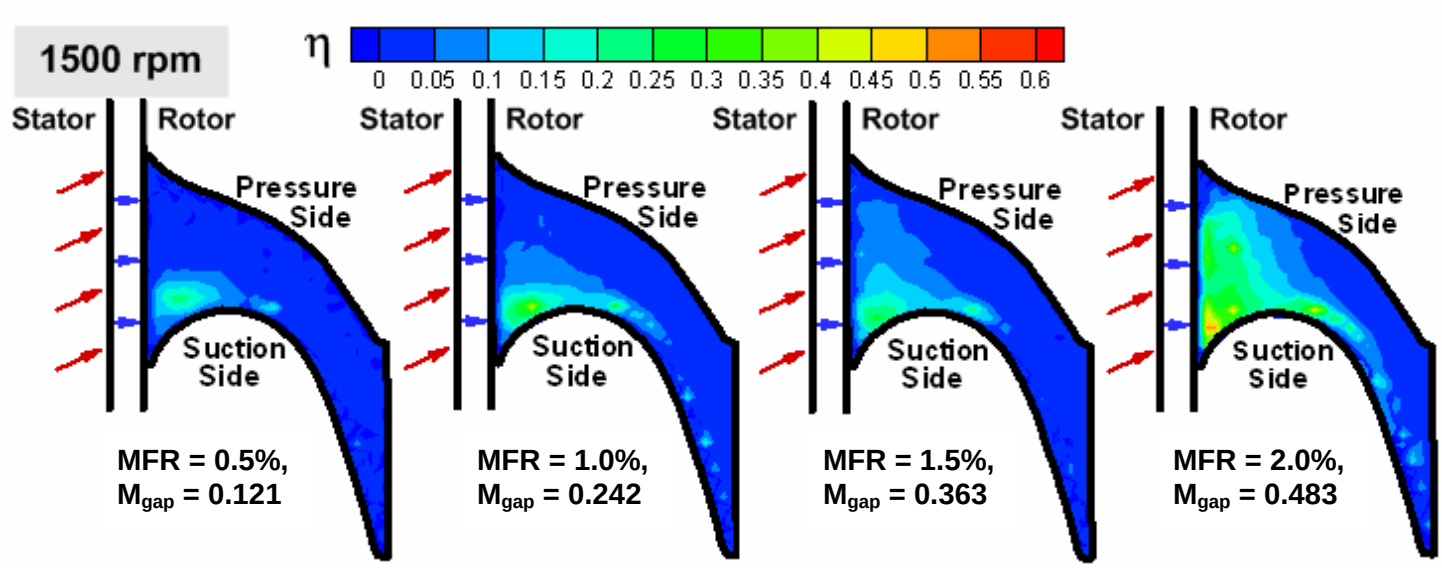

Figure 17: Film Cooling Effectiveness Distribution on the Rotating Endwall for 1500 rpm

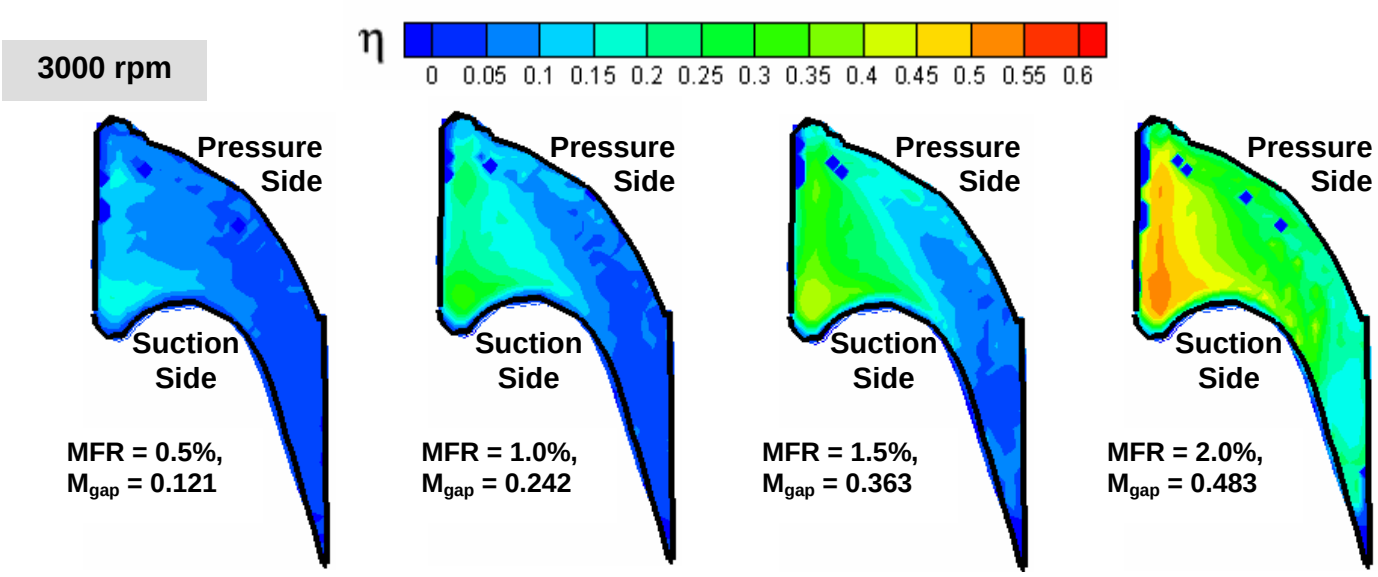

Figure 18: Film Cooling Effectiveness Distribution on the Rotating Endwall for 3000 rpm

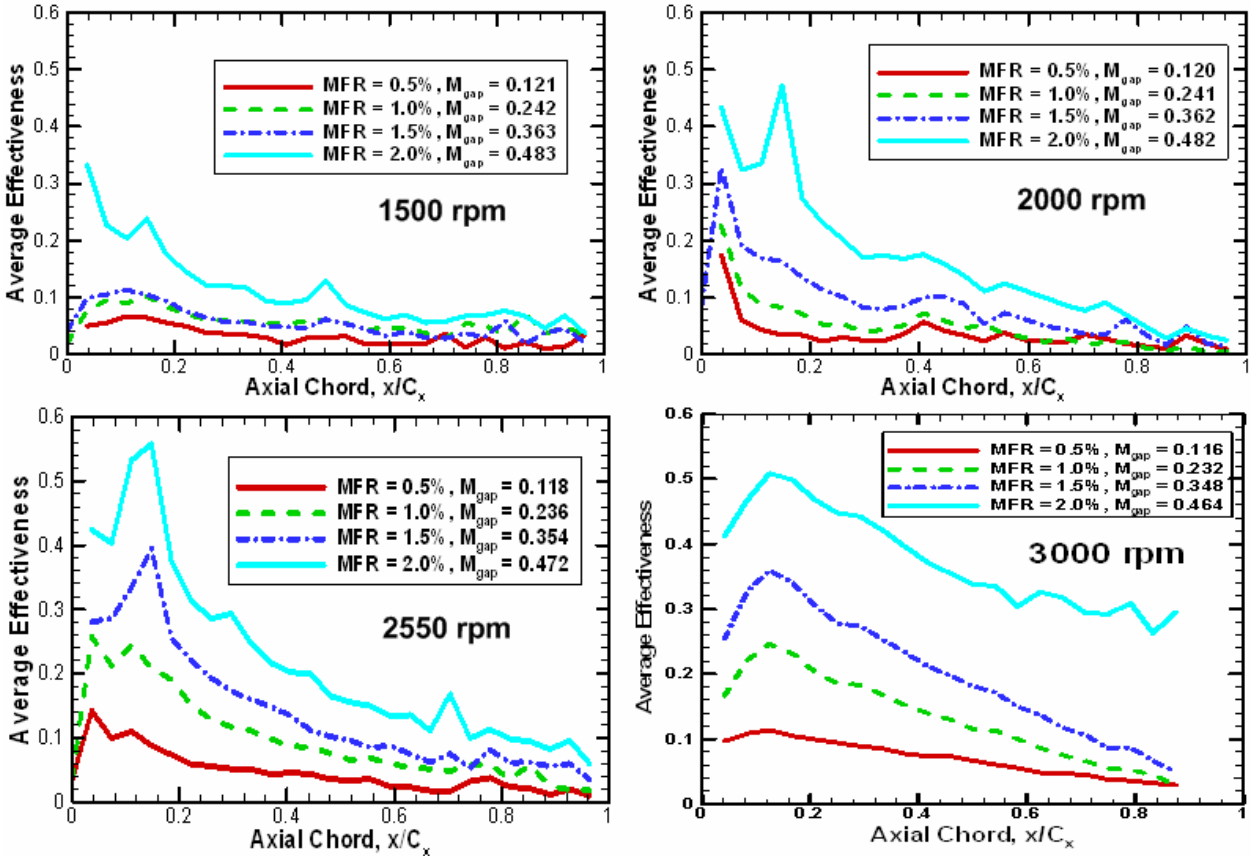

Figure 19: Pitchwise Averaged Film Cooling Effectiveness Distribution along Axial Chord for Different Turbine Rotating Speeds (Mass Flow Ratio Effect)

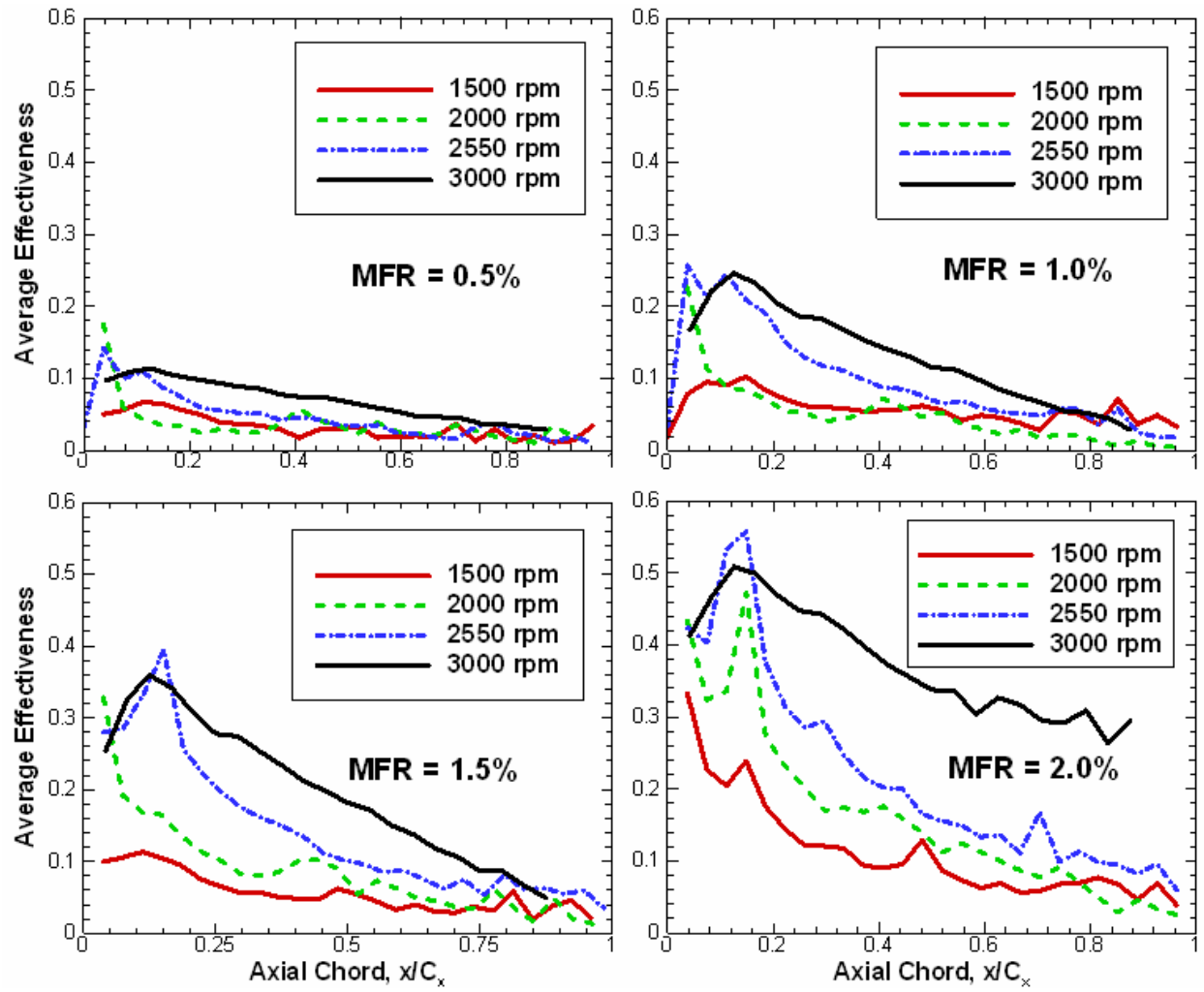

Figure 20: Pitchwise Averaged Film Cooling Effectiveness Distribution along Axial Chord for Different Mass Flow Ratios (Turbine Rotation Speed Effect)

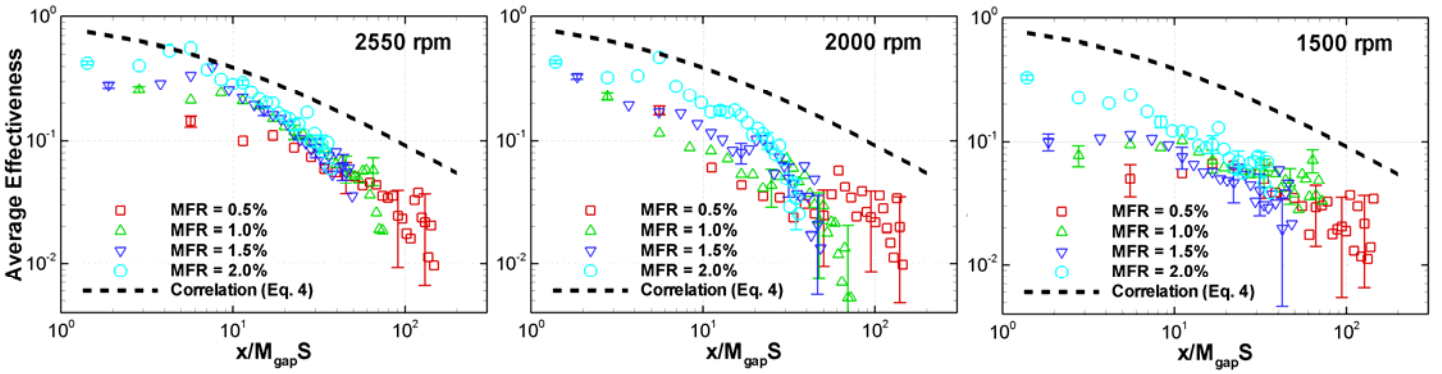

Figure 21: Comparison of Pitchwise Average Effectiveness with a Correlation from Goldstein [40] for Different Speeds

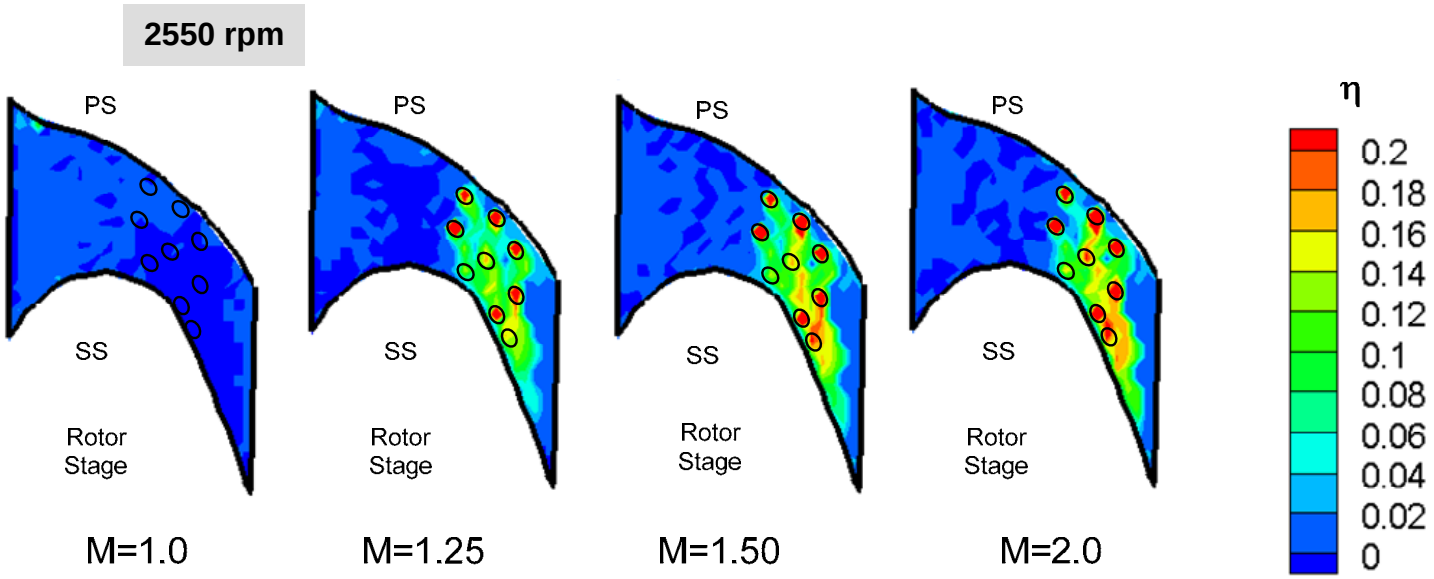

Figure 22: Film Cooling Effectiveness Distribution From Downstream, Discrete Film Cooling Holes on the Rotating Endwall for 2550 rpm

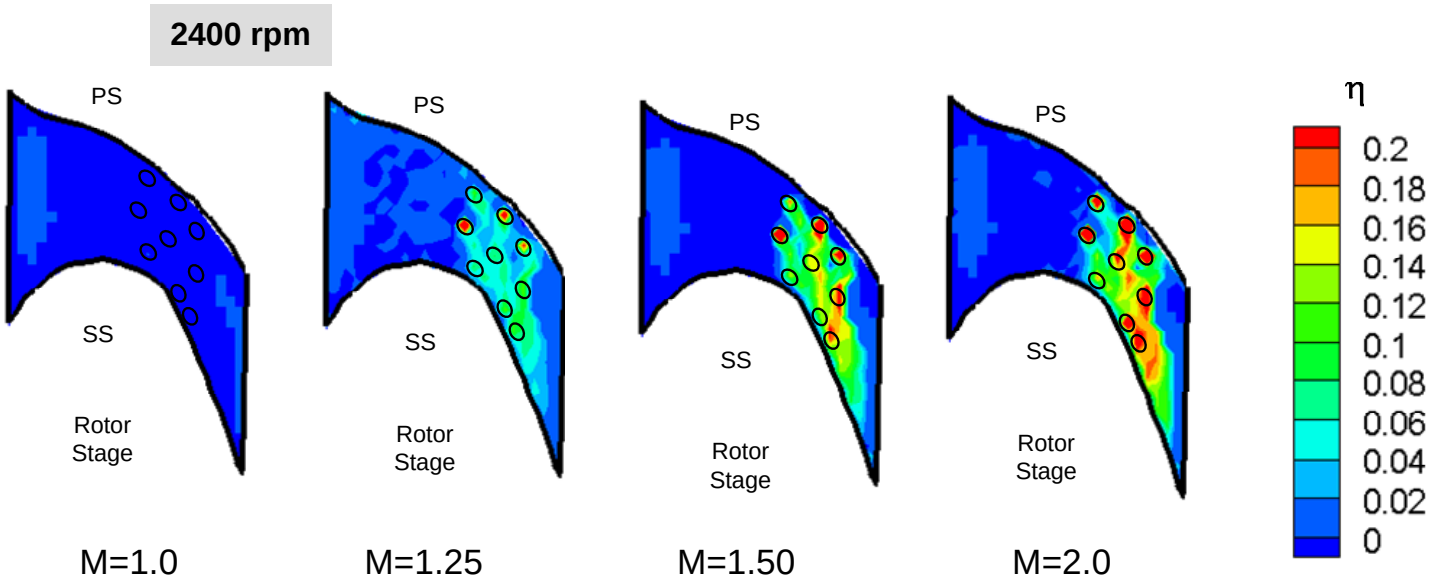

Figure 23: Film Cooling Effectiveness Distribution From Downstream, Discrete Film Cooling Holes on the Rotating Endwall for 2400 rpm

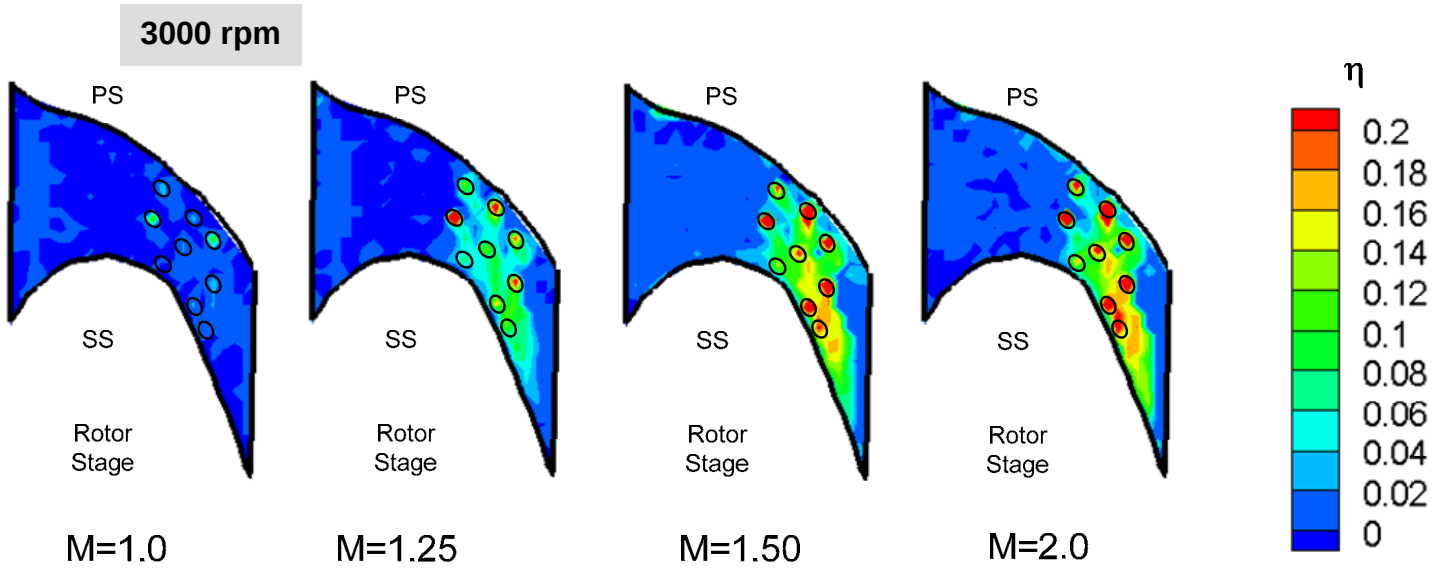

Figure 24: Film Cooling Effectiveness Distribution From Downstream, Discrete Film Cooling Holes on the Rotating Endwall for 3000 rpm

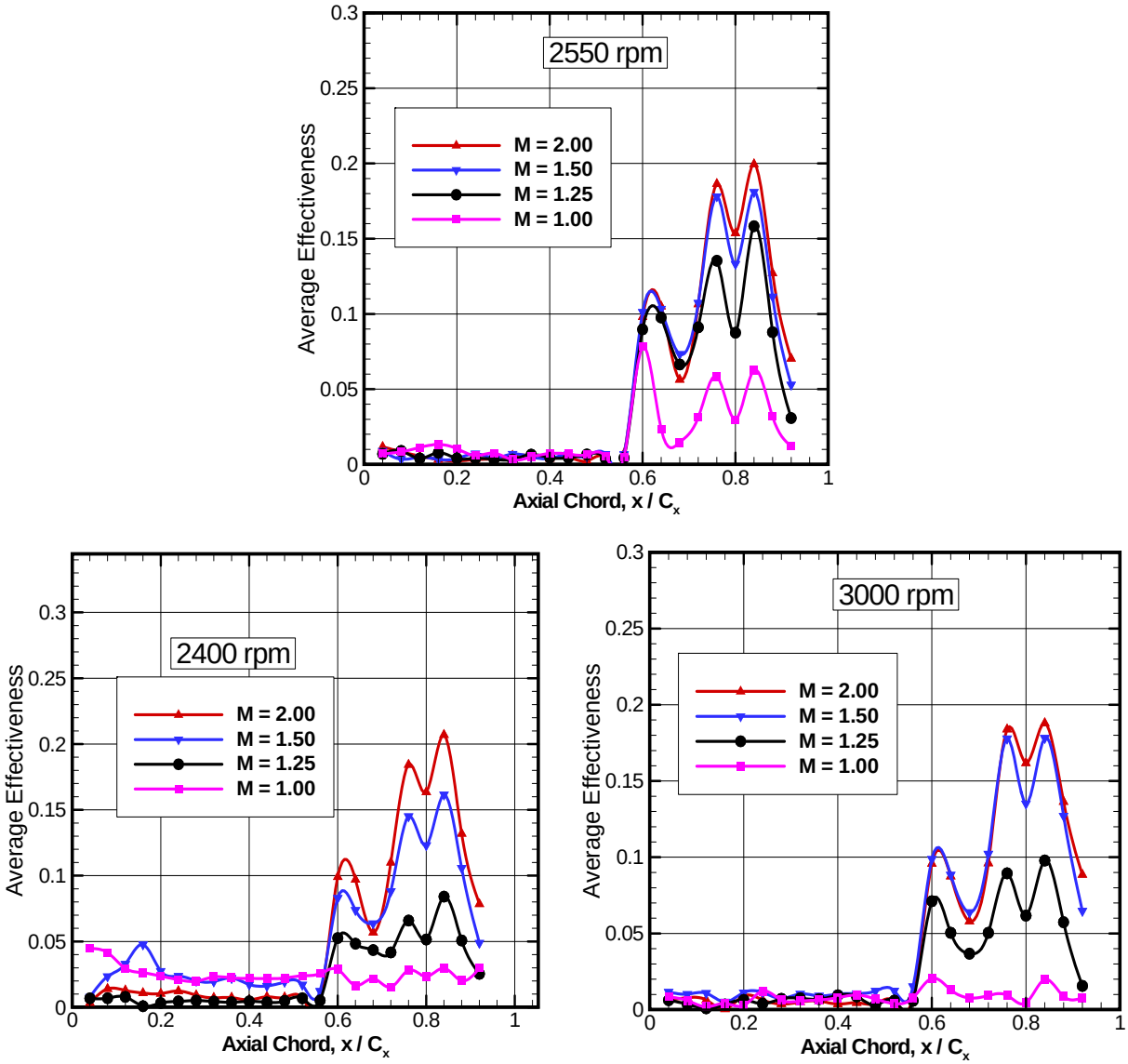

Figure 25: Pitchwise Averaged Film Cooling Effectiveness Distribution along Axial Chord for Different Turbine Rotating Speeds (Mass Flow Ratio Effect)

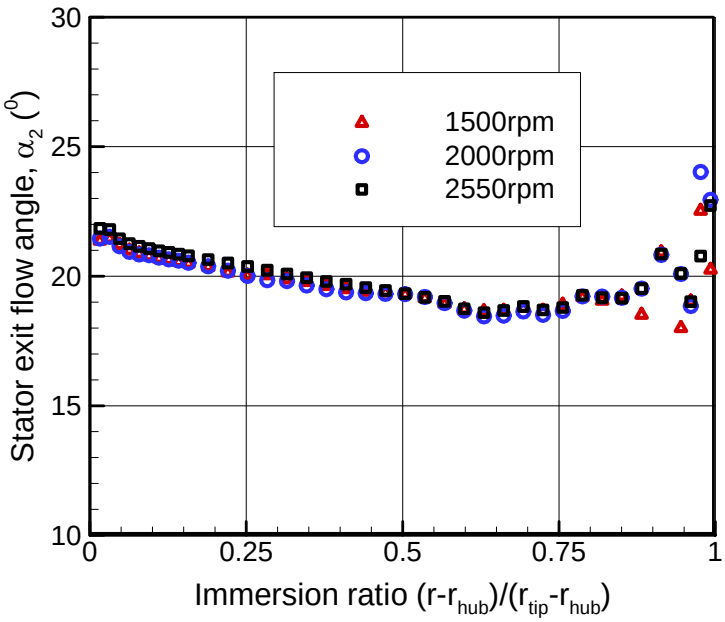

Figure 26: Radial Distribution of Stator Exit Flow Angle for Varying Rotor Speeds

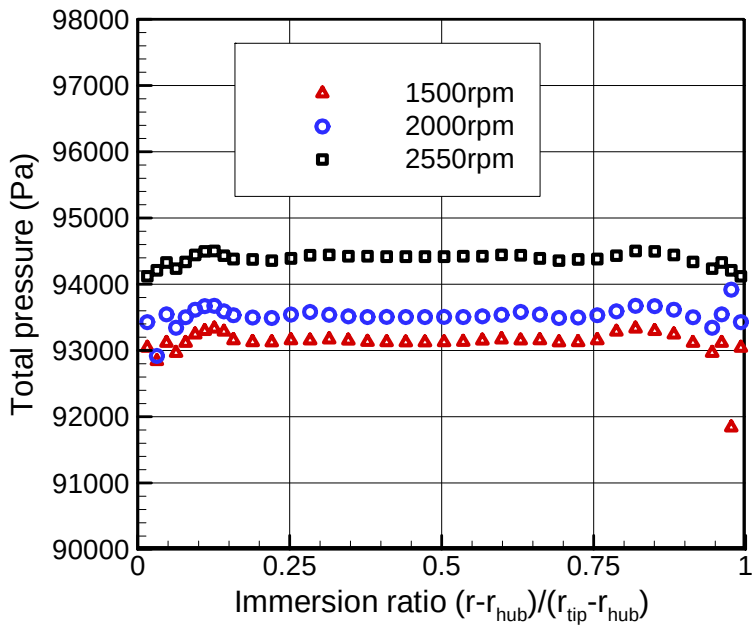

Figure 27: Radial Distribution of Total Pressure Distribution for Varying Rotor Speeds

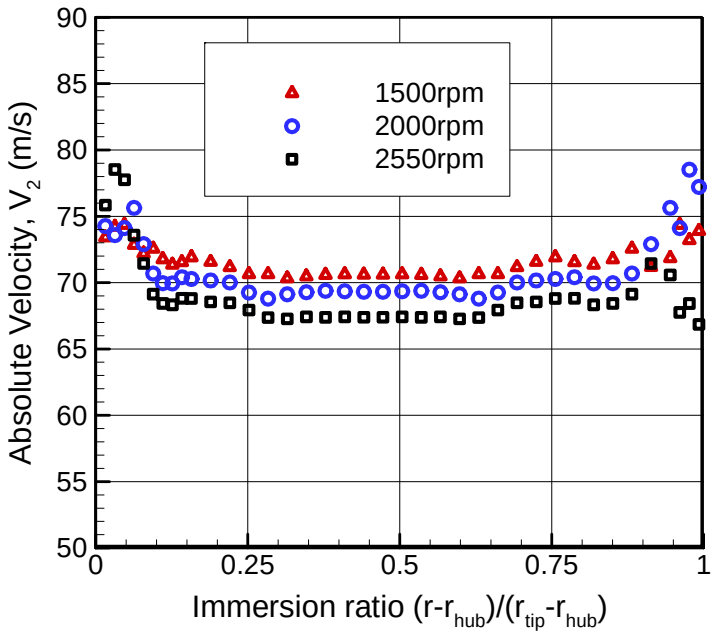

Figure 28: Radial Distribution of Absolute Velocity for Varying Rotor Speeds

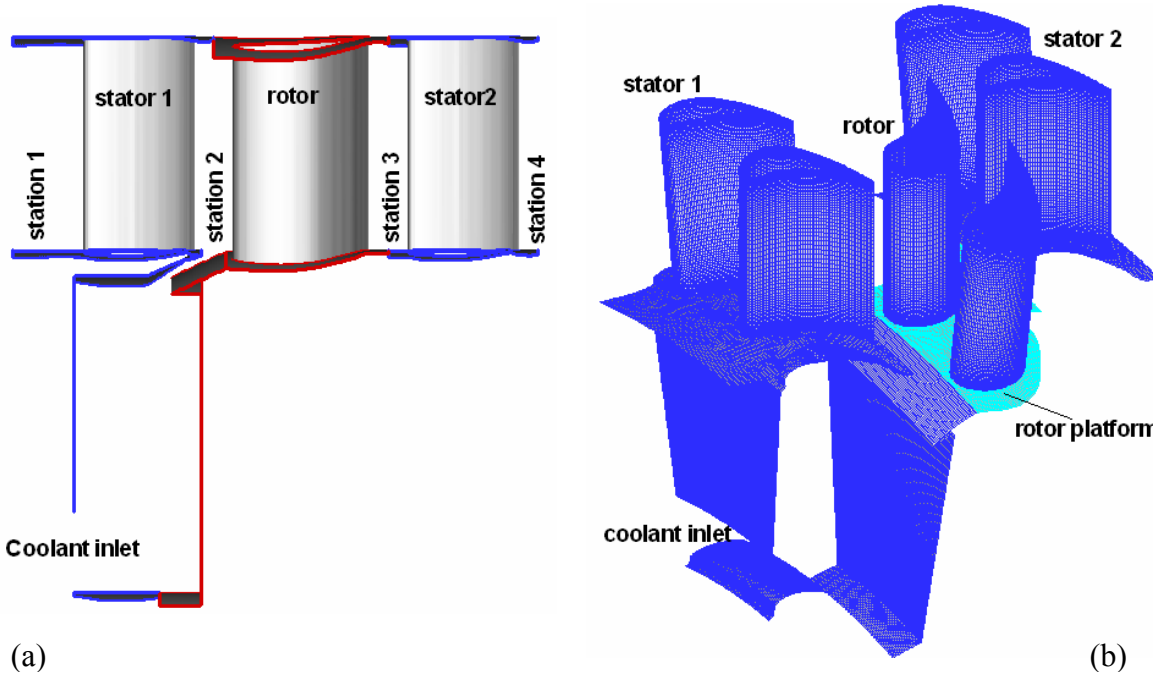

Figure 29: Prediction of Film Cooling Effectiveness and Heat Transfer Coefficients on Rotating Blade Platform

(a) Computational Domain of Platform with Upstream Slot Injection
(b) Numerical Grid

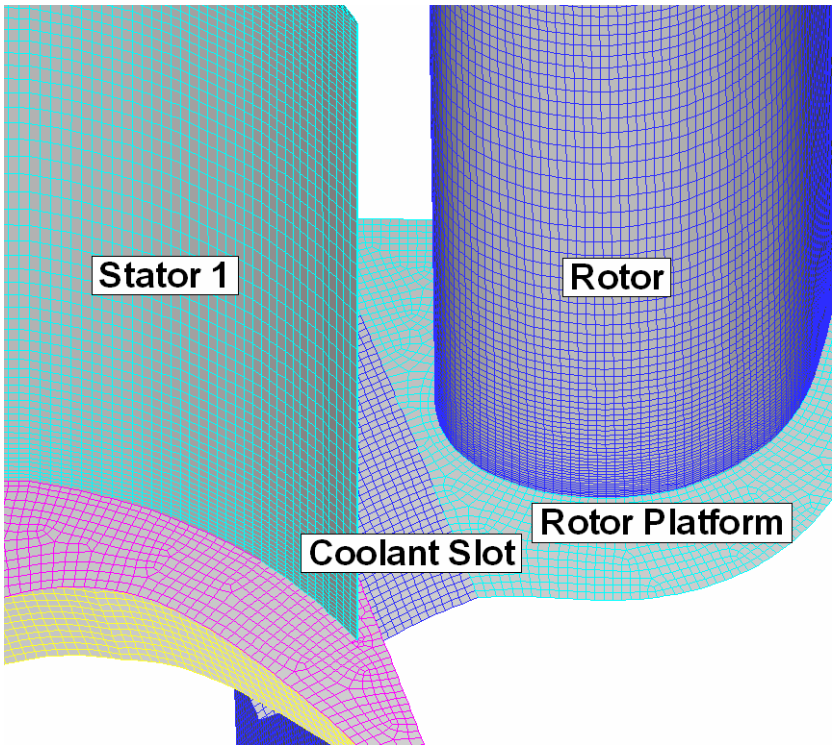

Figure 30: Detailed Grid Distributions Near the Angled Coolant Slot

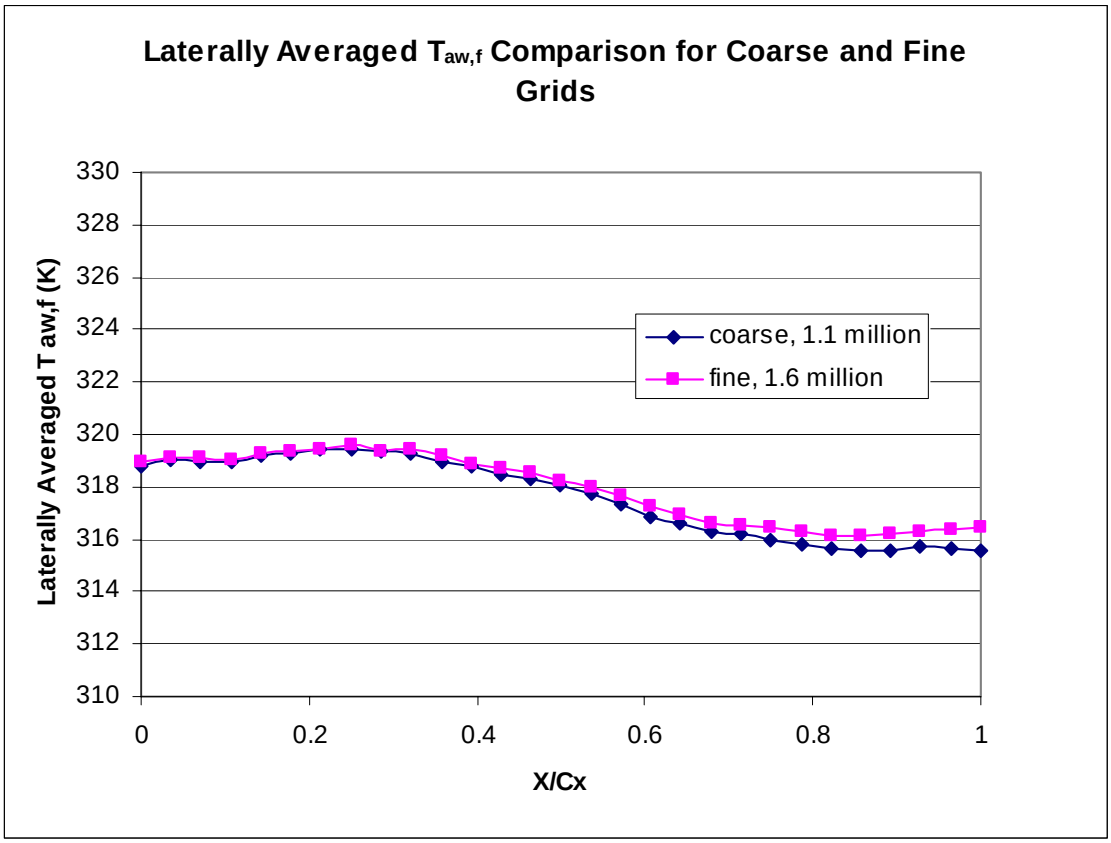

Figure 31: Grid Refinement Sutdy for Laterally Averaged Adiabatic Temperature on Rotating Blade Platform

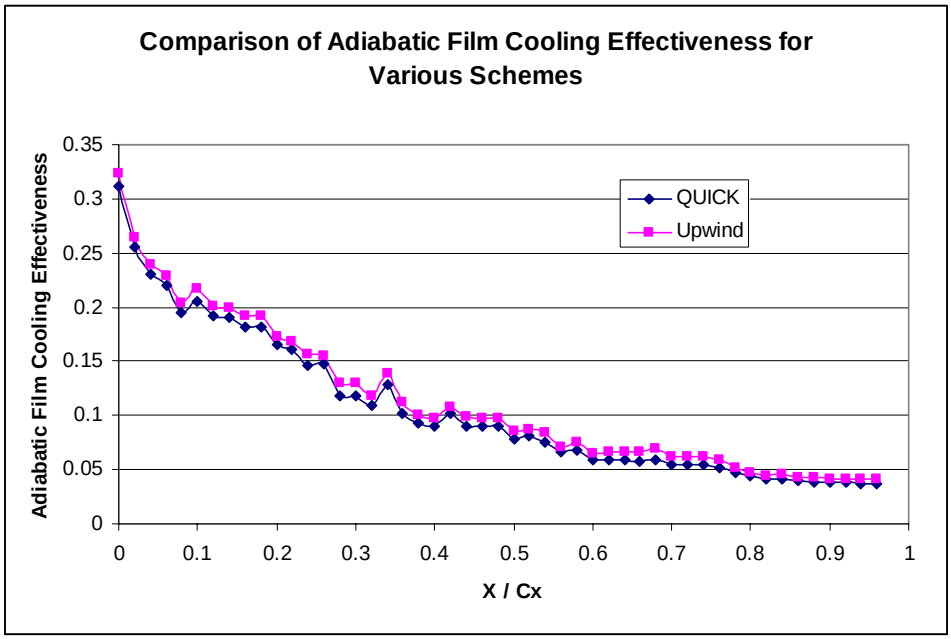

(a)

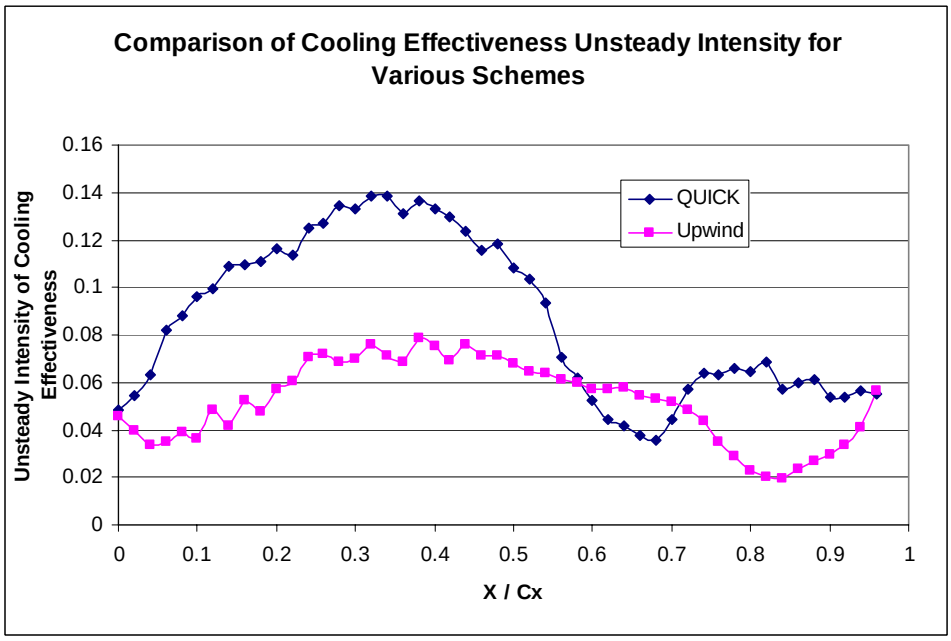

(b)

Figure 32: Scheme Comparison for Predicted Film Cooling Effectiveness (2550 RPM, MFR = 1.0%)

(a) Laterally Averaged Adiabatic Film Cooling Effectiveness
(b) Cooling Effectiveness Unsteady Intensity

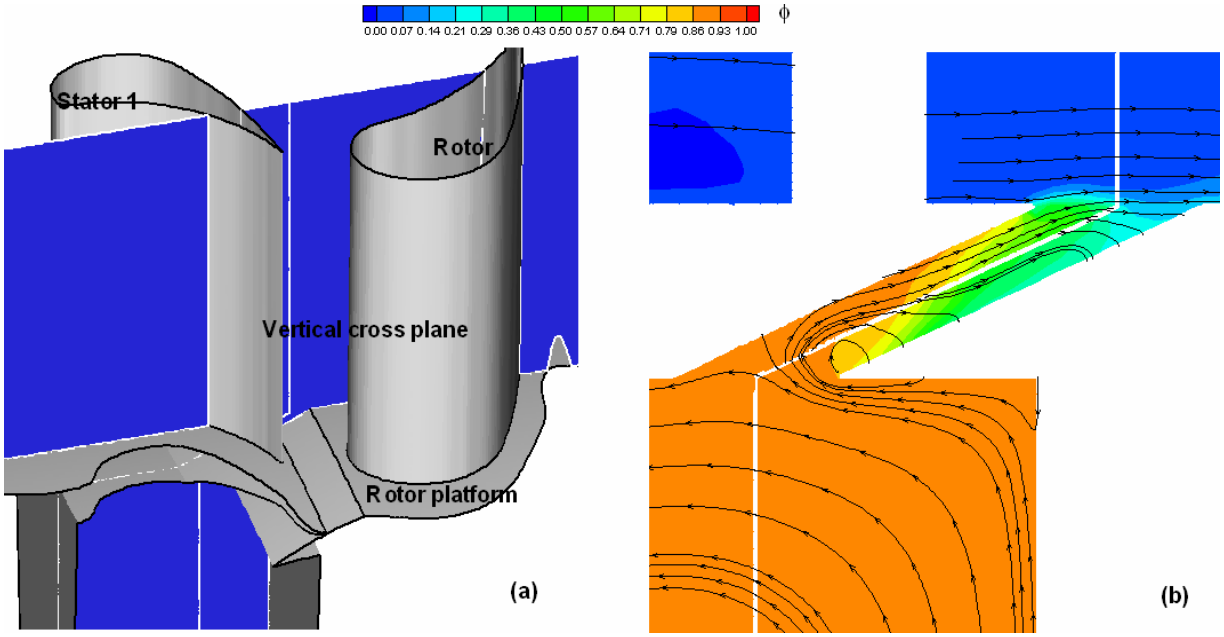

Figure 33: Predicted Path of the Coolant From the Rotating Disk onto the Rotating Platform (2550 RPM, MFR = 0.5%)

(a) Location of Vertical Plane
(b) Dimensionless Temperature Contours and Streamlines

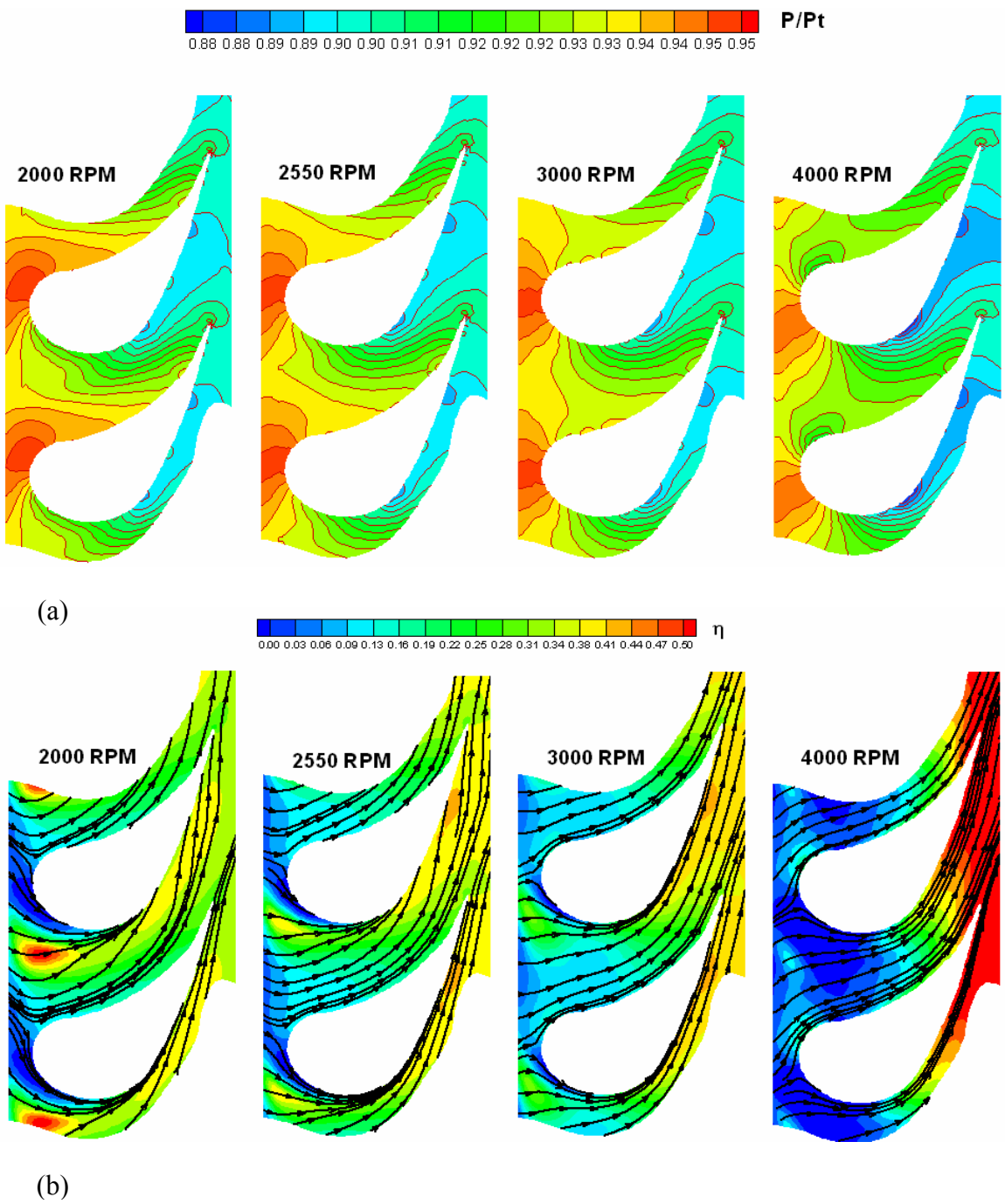

Figure 34: Predicted Pressure Ratio, Streamlines, and Dimensionless Temperature on the Annular Cross-Plane

(a) Pressure Ratio
(b) Streamlines and Dimensionless Temperature Contours

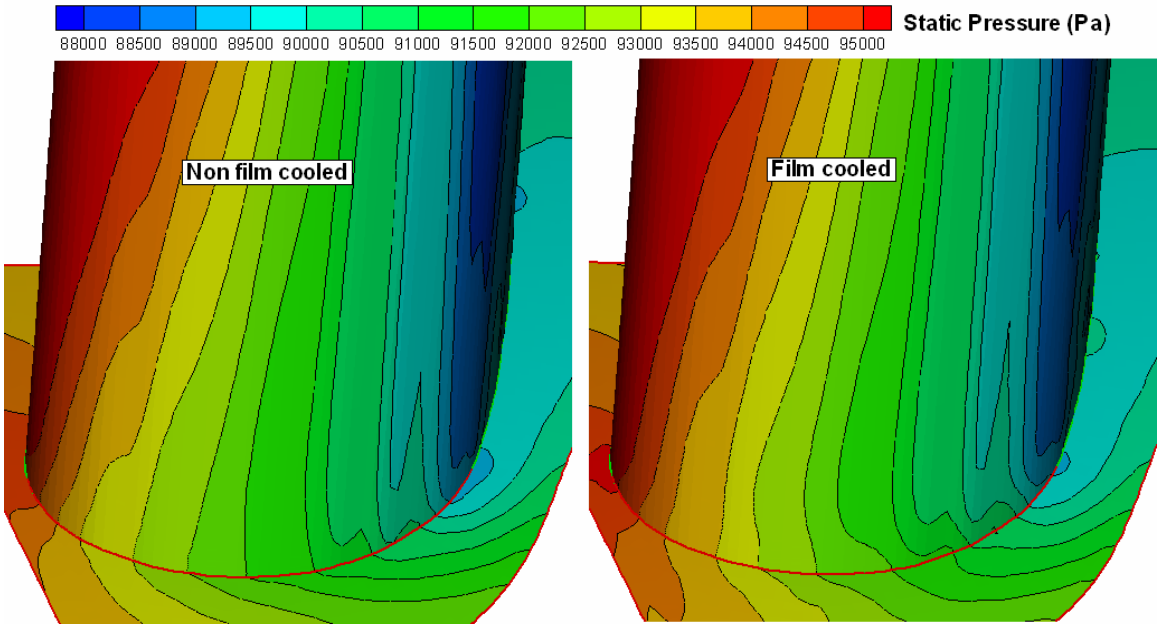

Figure 35: Comparison of the Static Pressure Contours on the Suction Side of the Rotor Blade with and without Purge Flow (2550 rpm, MFR = 1%)

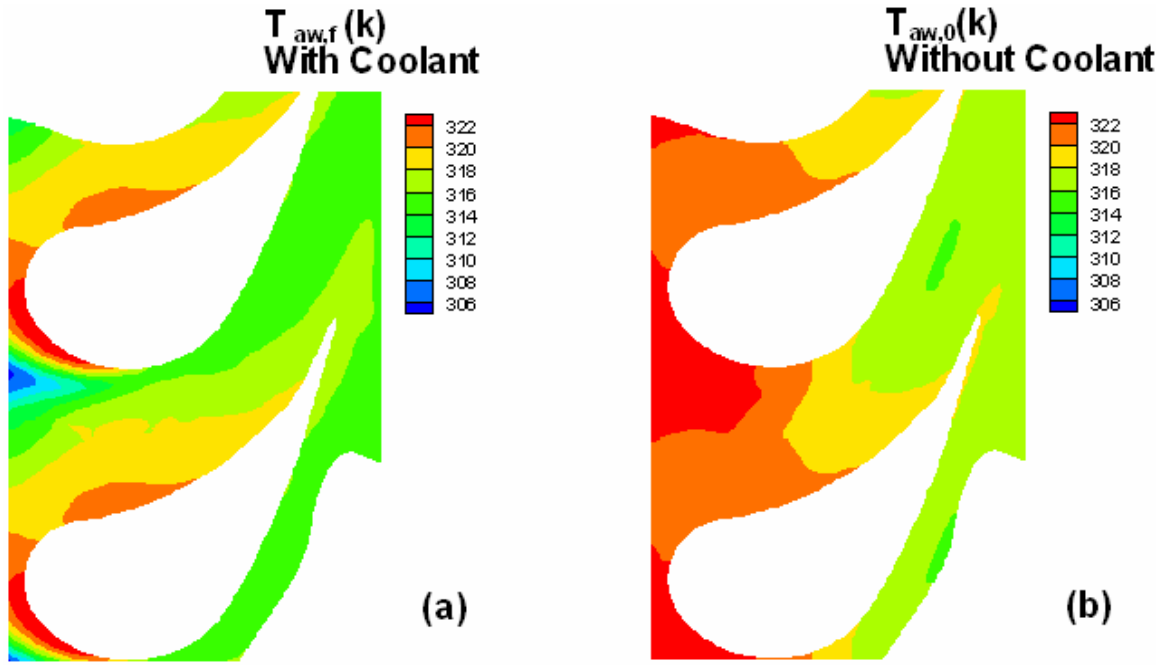

Figure 36: Comparison of the Total Wall Temperature on the Rotor Platform with and without Purge Flow (2550 rpm, MFR = 1%)

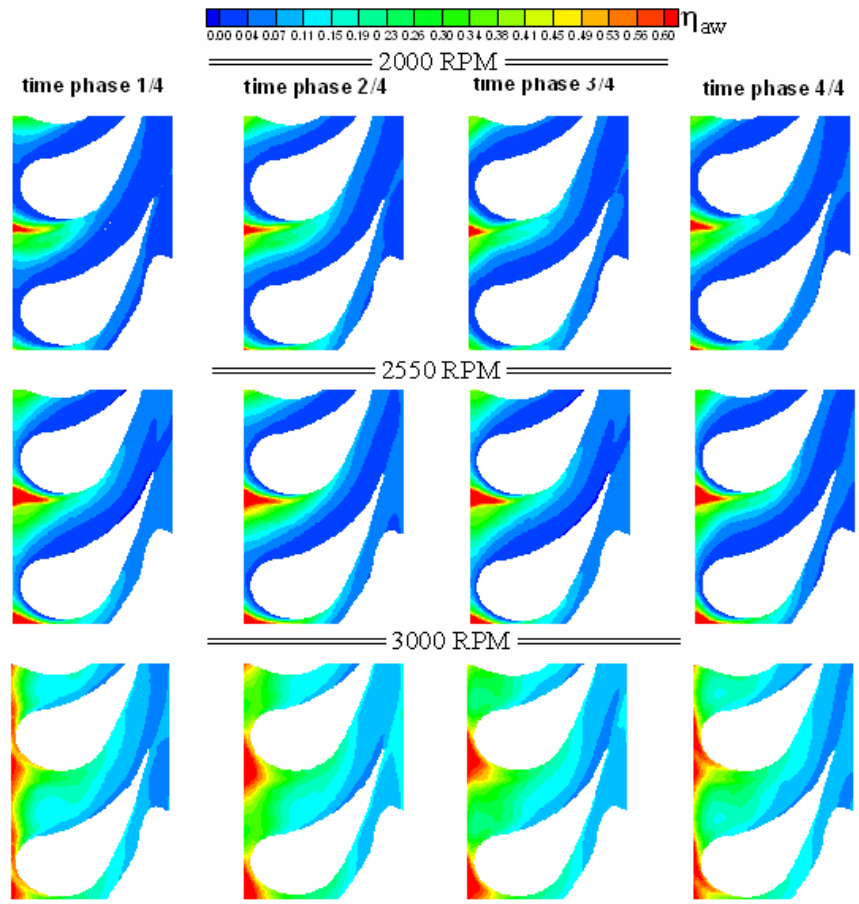

Figure 37: Comparison of the Adiabatic Film Cooling Effectiveness on the Rotor Platform with Various Rotational Speeds (MFR = 1%)

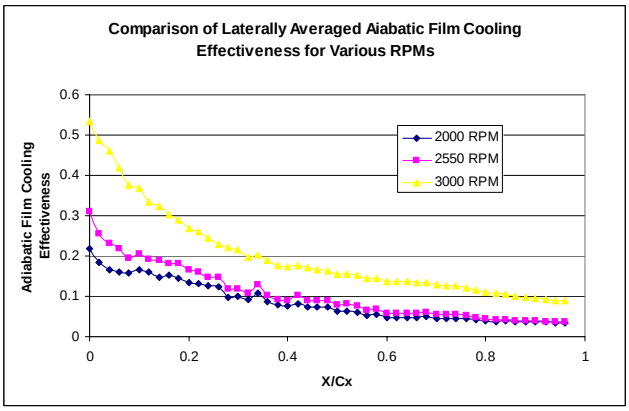

(a)

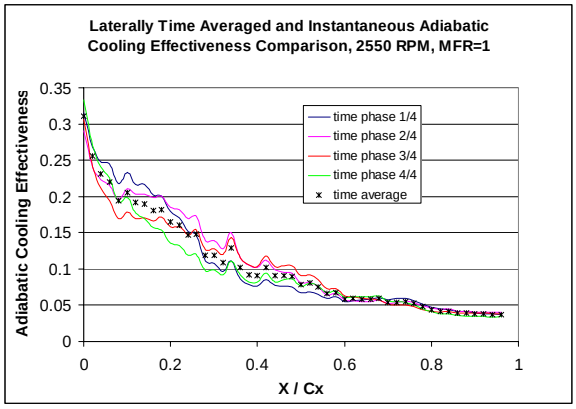

(b)

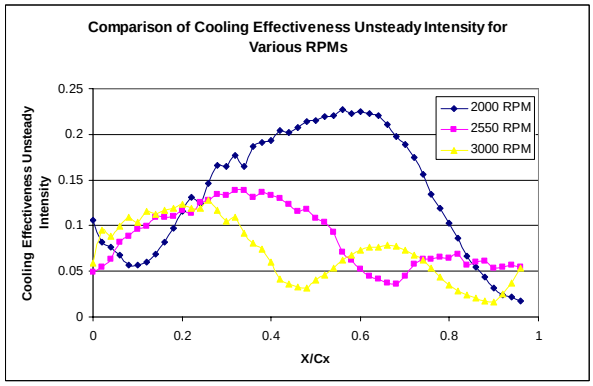

(c)

Figure 38: Effect of Rotational Speed on Laterally Averaged Film Cooling Effectiveness (MFR = 1%)

(a) Laterally Averaged Adiabatic Cooling Effectiveness Comparison at Various Rotational Speeds
(b) Instantaneous and Time Averaged Adiabatic Film Cooling Effectiveness (MFR = 1%, 2550 RPM)
(c) Laterally Averaged Unsteady Intensity at Various Rotational Speeds

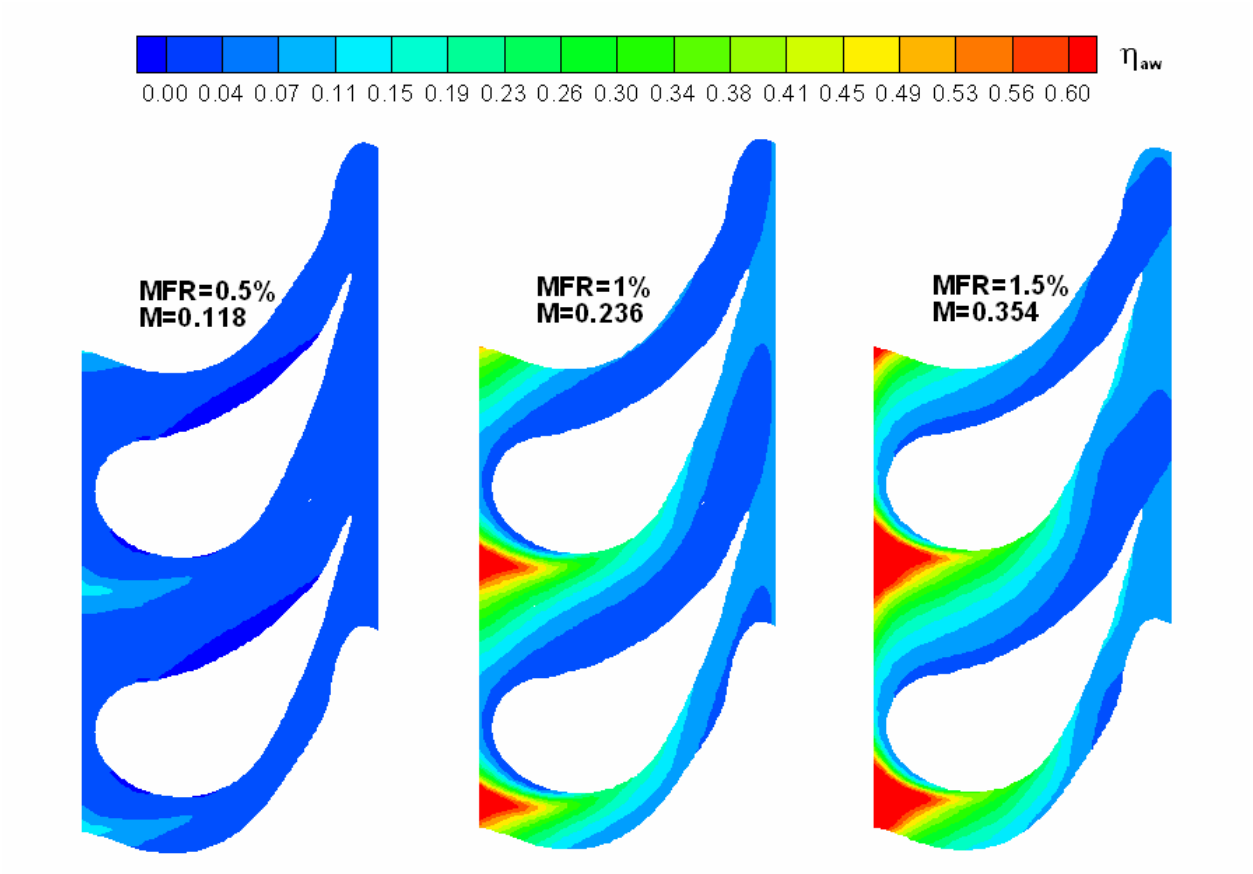

Figure 39: Predicted Adiabatic Film Cooing Effectiveness on the Rotating Blade Plabrform with Various Coolant Flow Rates

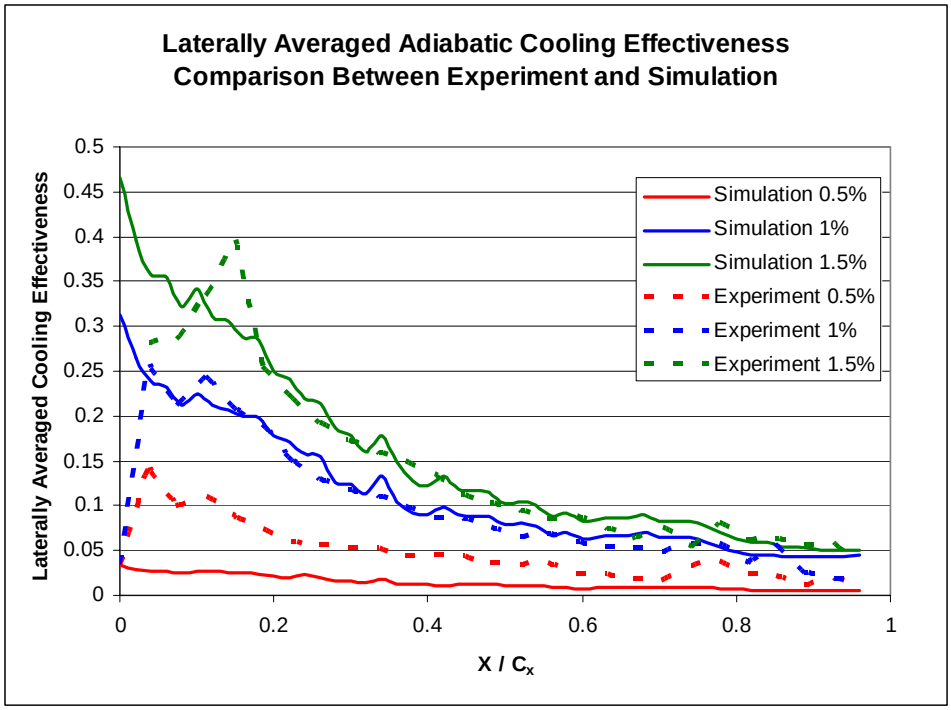

Figure 40: Laterally Averaged Adiabatic Cooling Effectiveness Comparison for Various Coolant Flow Rates (2550 RPM)

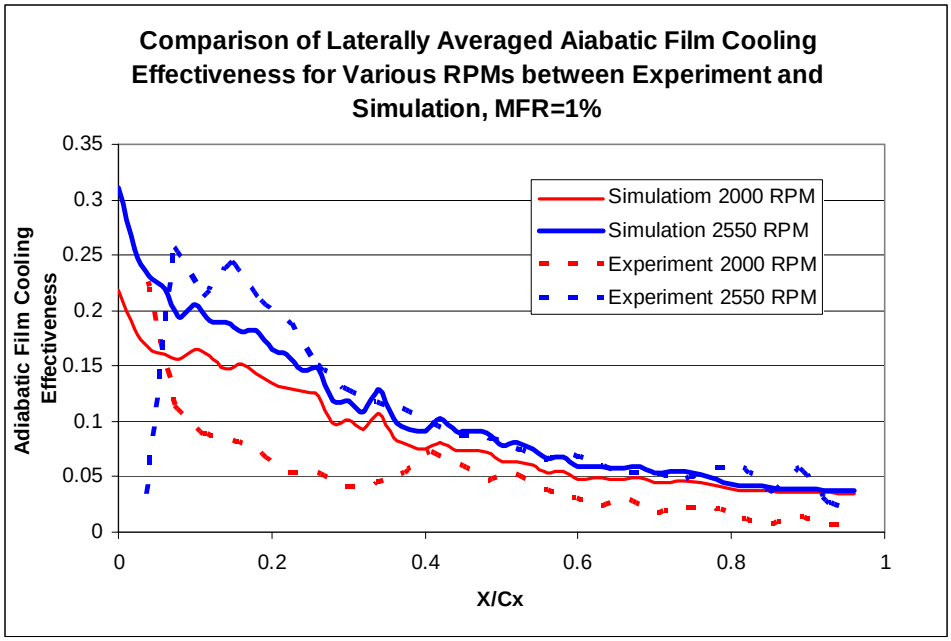

Figure 41: Laterally Averaged Adiabatic Cooling Effectiveness Comparison for Various Rotational Speeds (MFR = 1%)

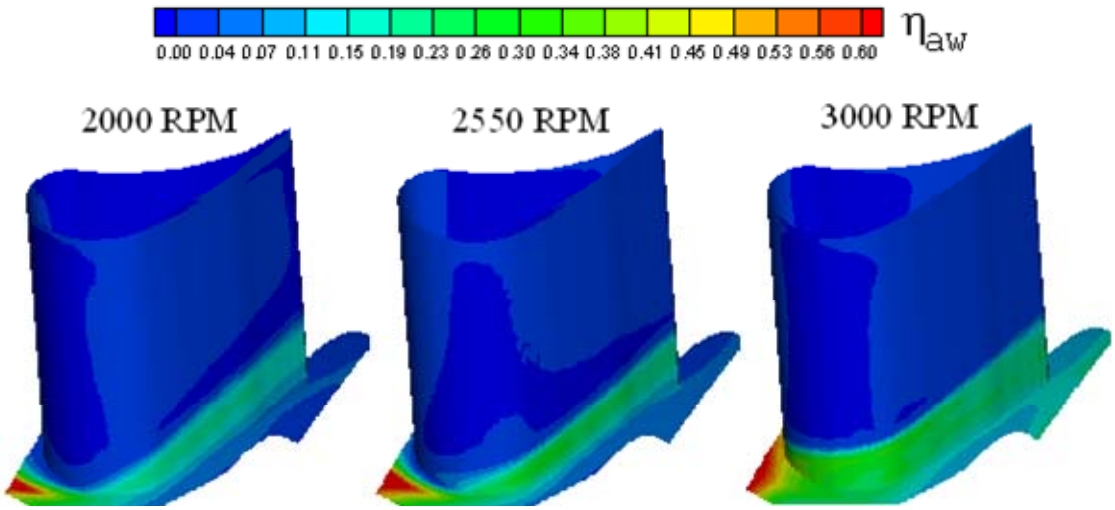

Figure 42: Predicted Adiabatic Film Cooling Effectiveness on the Suction Side of the Rotor Blade at Various Rotational Speeds (MFR = 1%)

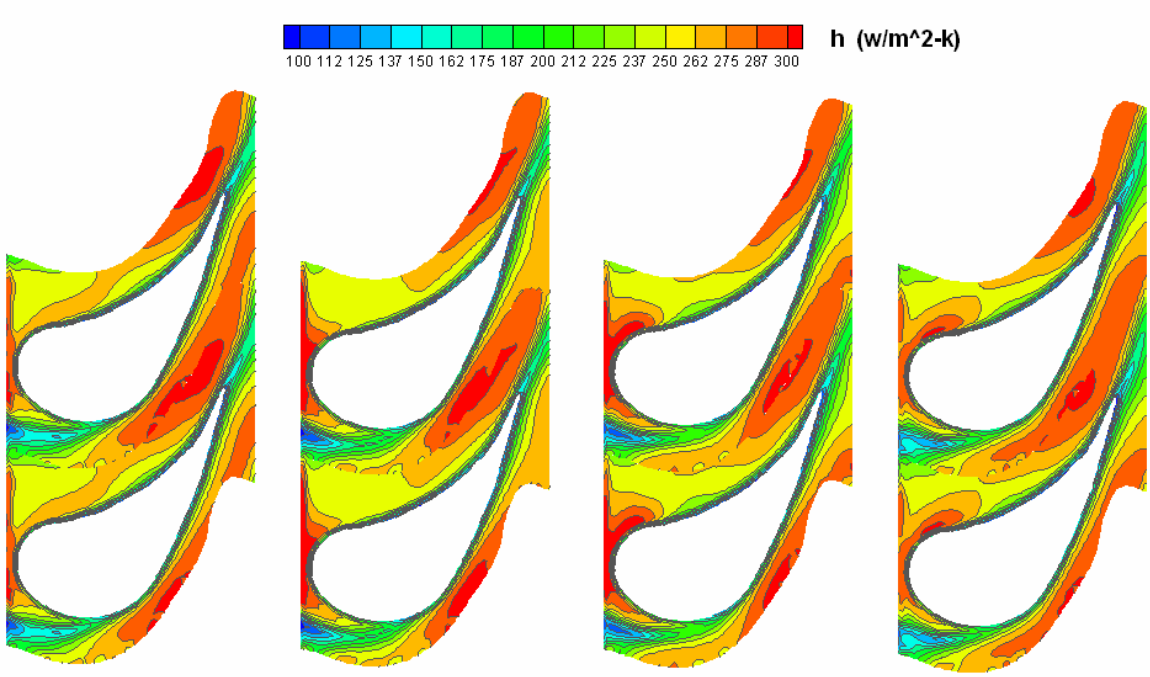

(a)

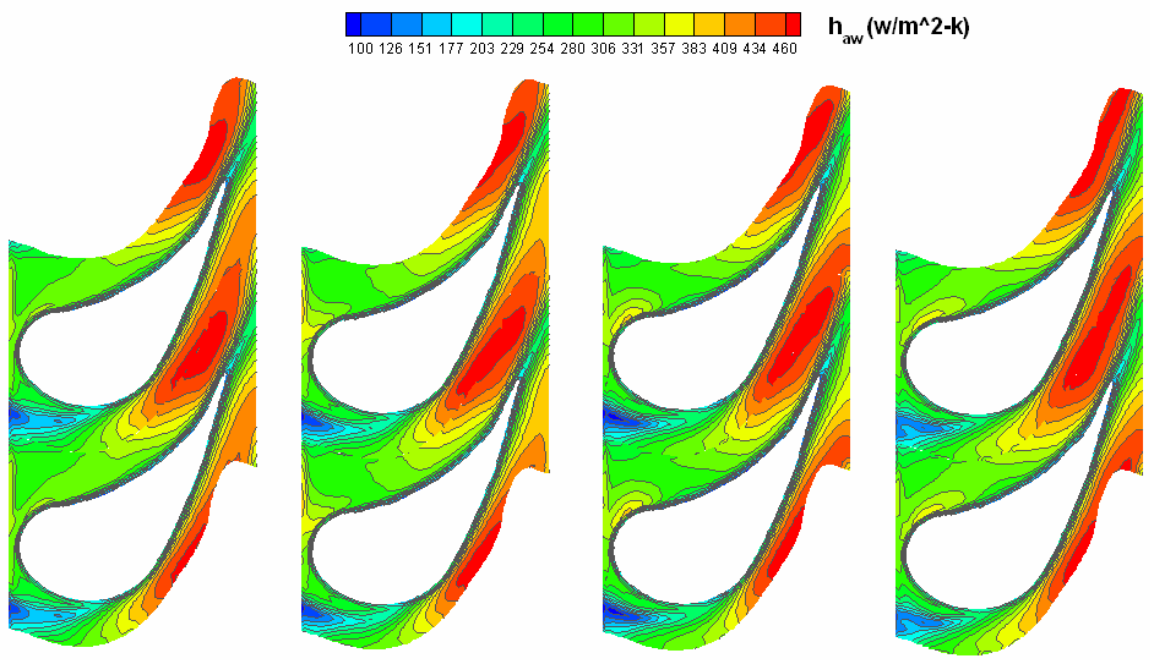

(b)

Figure 43: Predicted Overall and Adiabatic Heat Transfer Coefficients on the Rotating Platform at Various Time Phases (2550 RPM, MFR = 0.5%)

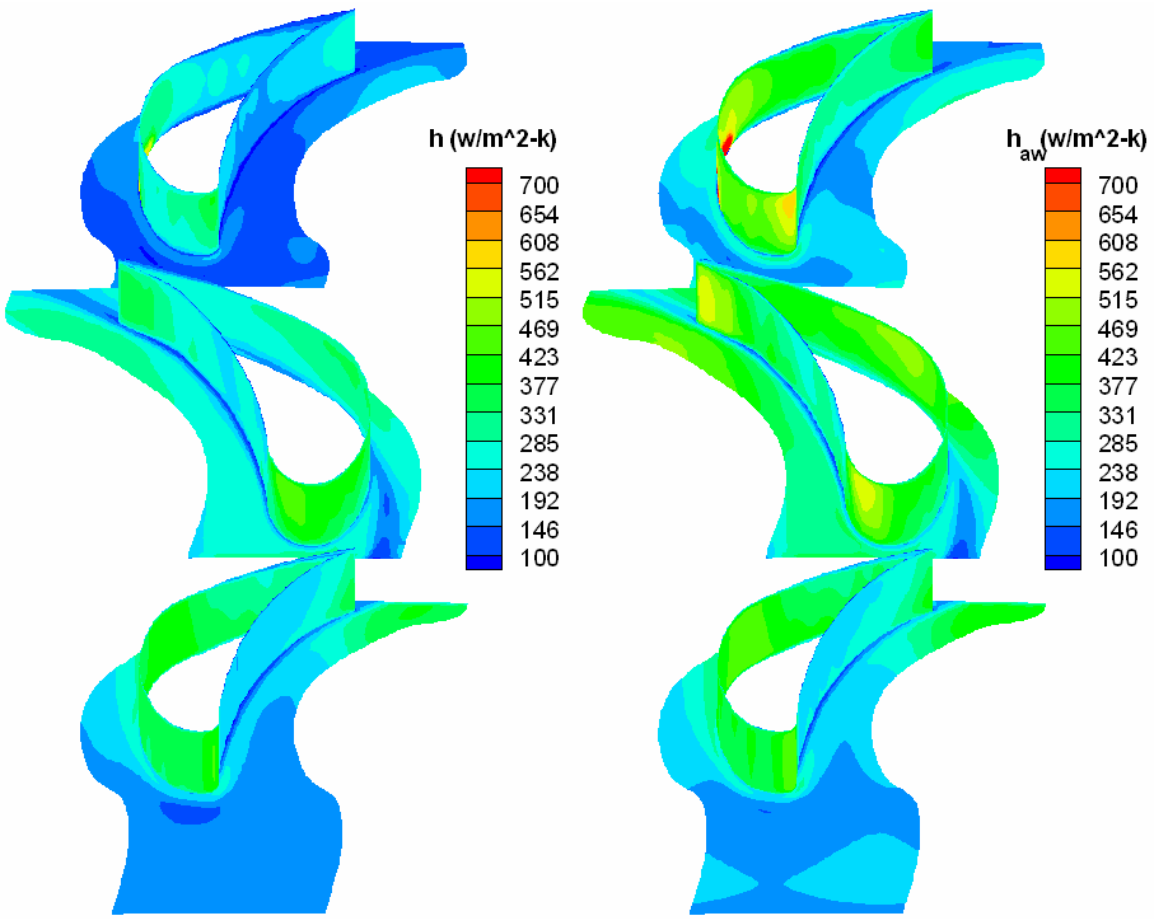

Figure 44: Predicted Overall and Adiabatic Heat Transfer for the Turbine Stage (2550 RPM, MFR = 0.5%)

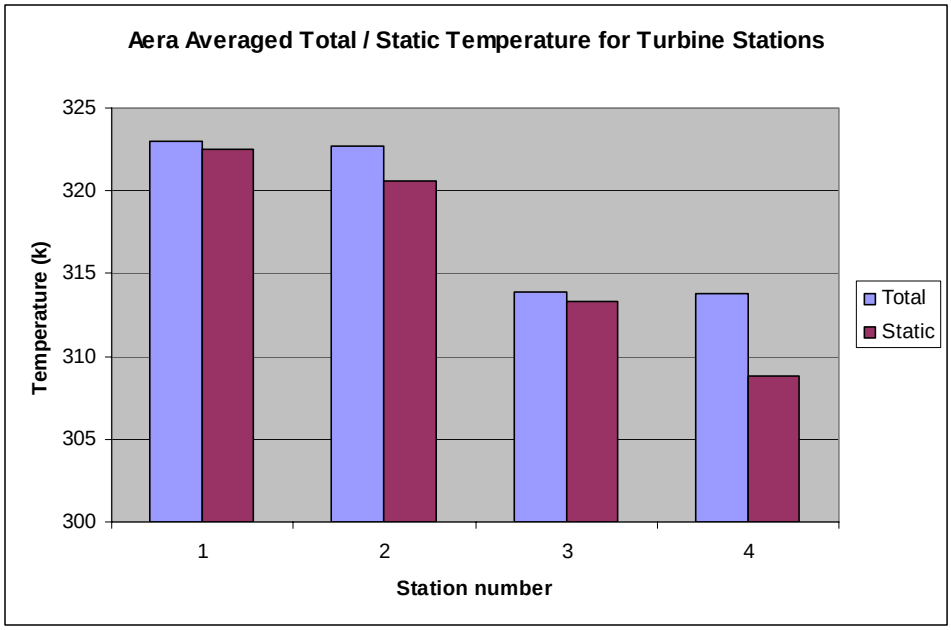

Figure 45: Area Averaged Total / Static Tempeature for Various Stations in the Turbine Stage (2550 RPM)

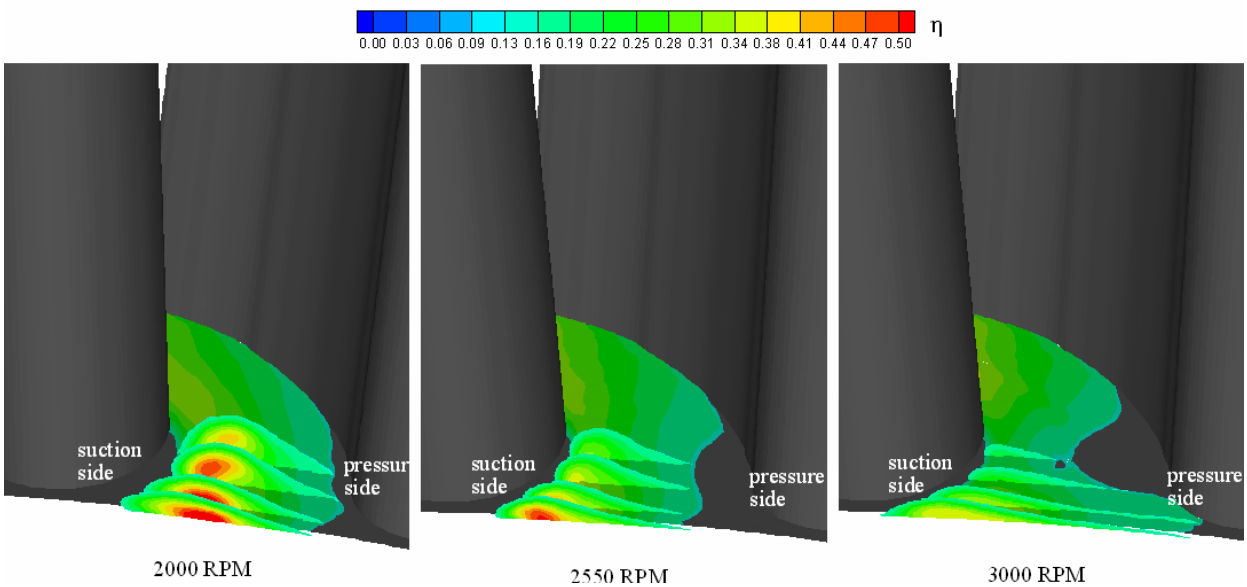

Figure 46: Coolant Path Inside the Rotor Passage for Various Rotational Speeds (MFR = 0.5%, Colored by the Overall Film Cooling Effectiveness)

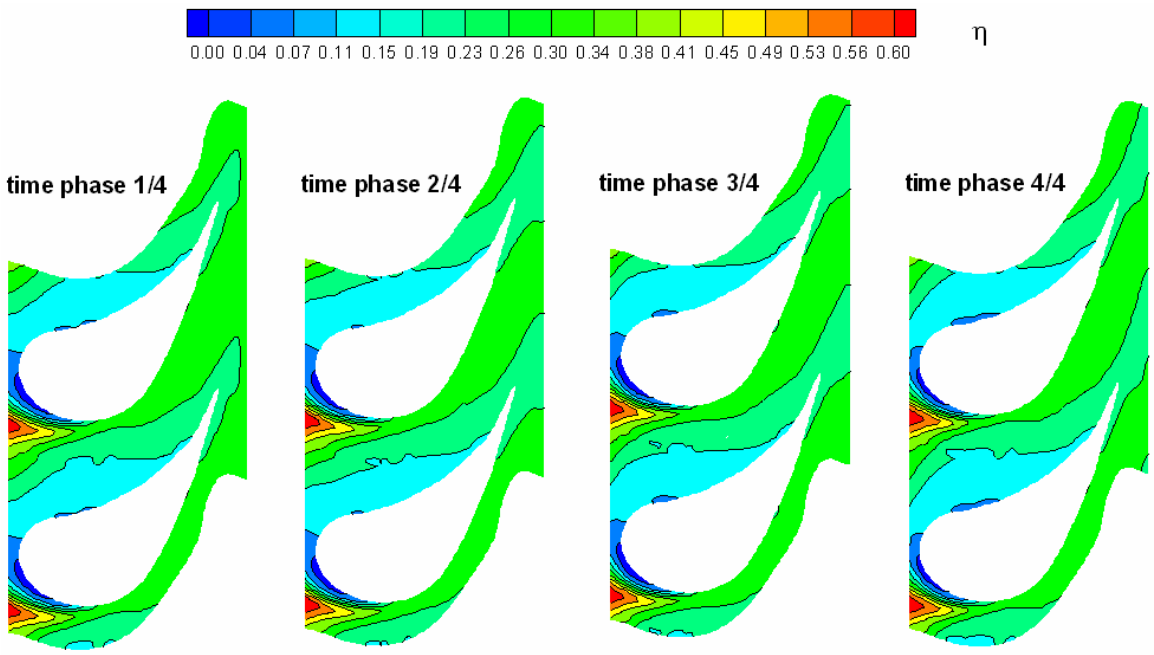

Figure 47: Overall Film Cooling Effectiveness Comparions on the Rotating Blade Platform for Various Time Phases (2550 RPM, MFR = 1.0%)

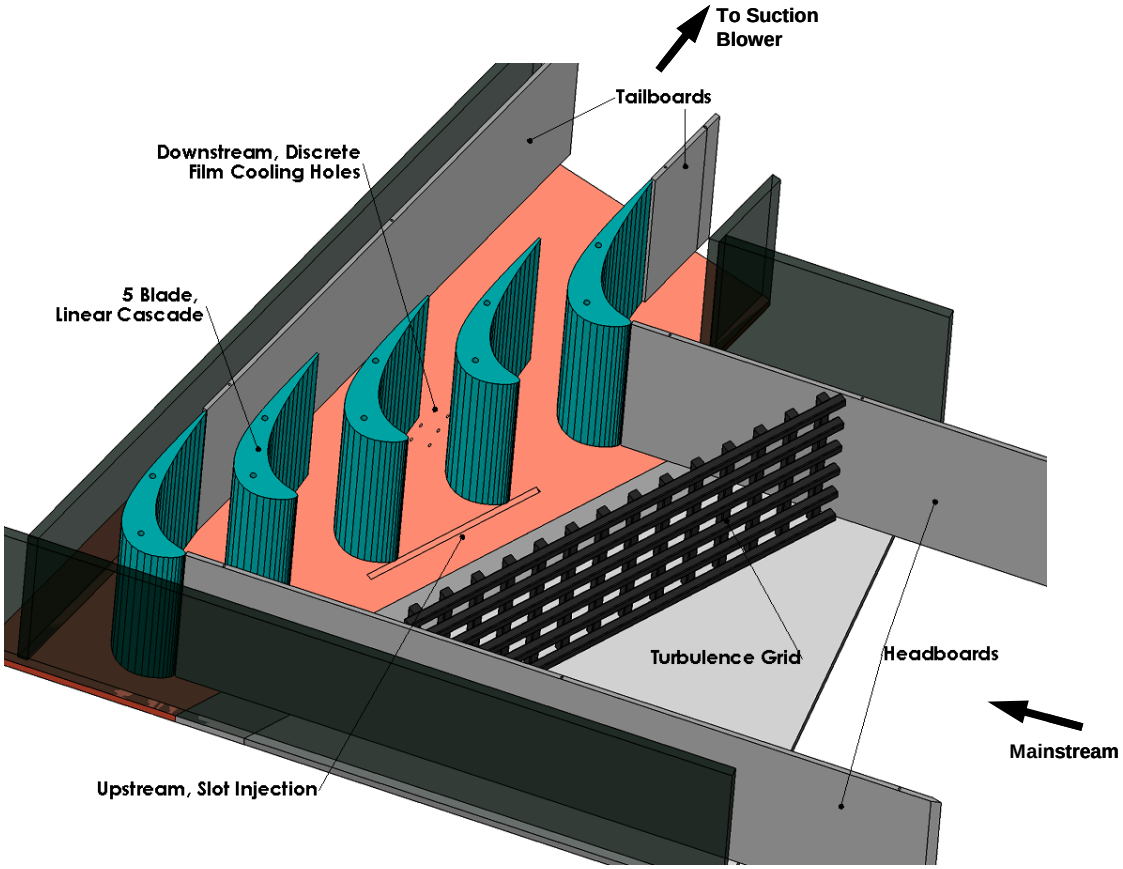

Figure 48: Overview of the Low Speed Wind Tunnel Used to Study Platform Cooling

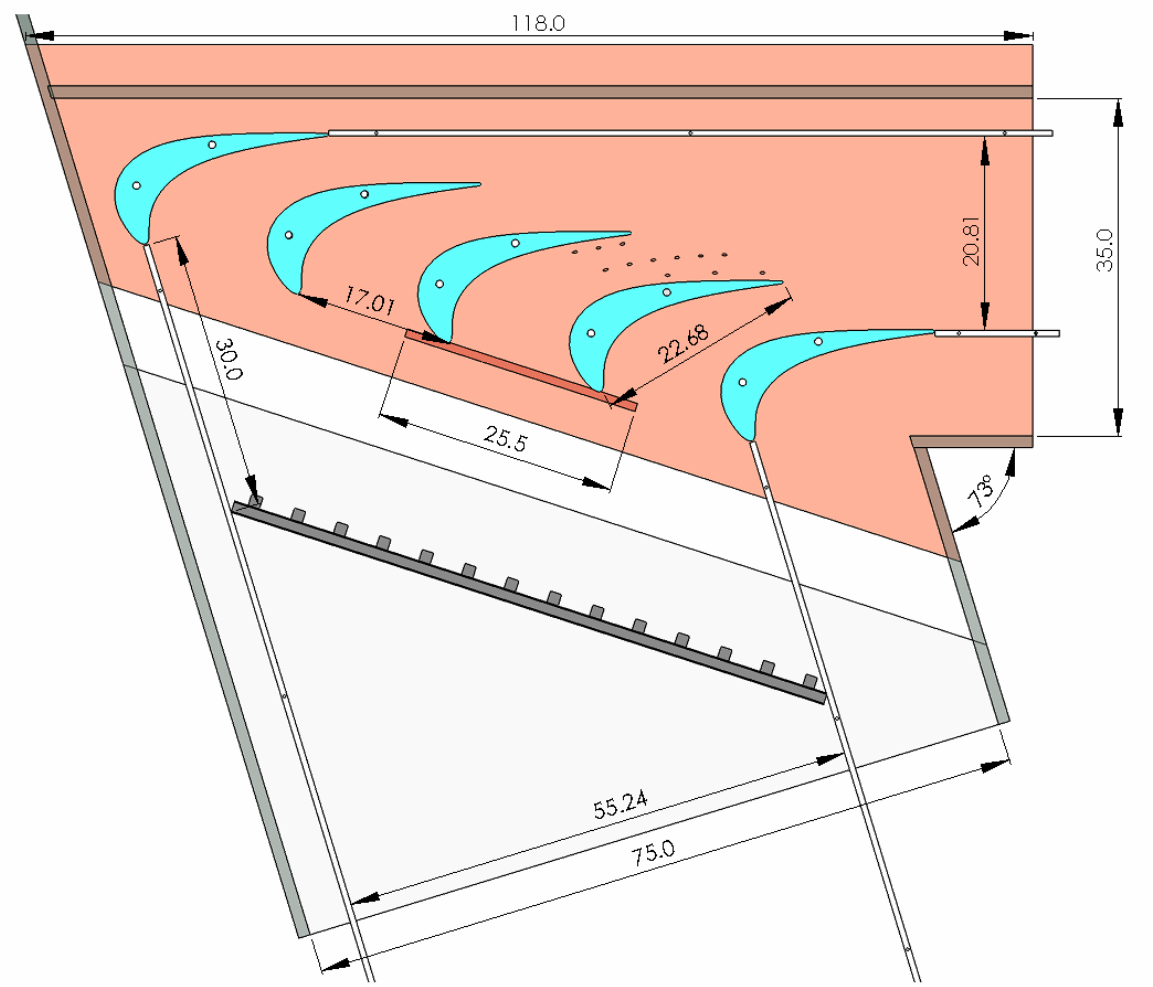

Figure 49: Low Speed Wind Tunnel and Turbine Blade Details

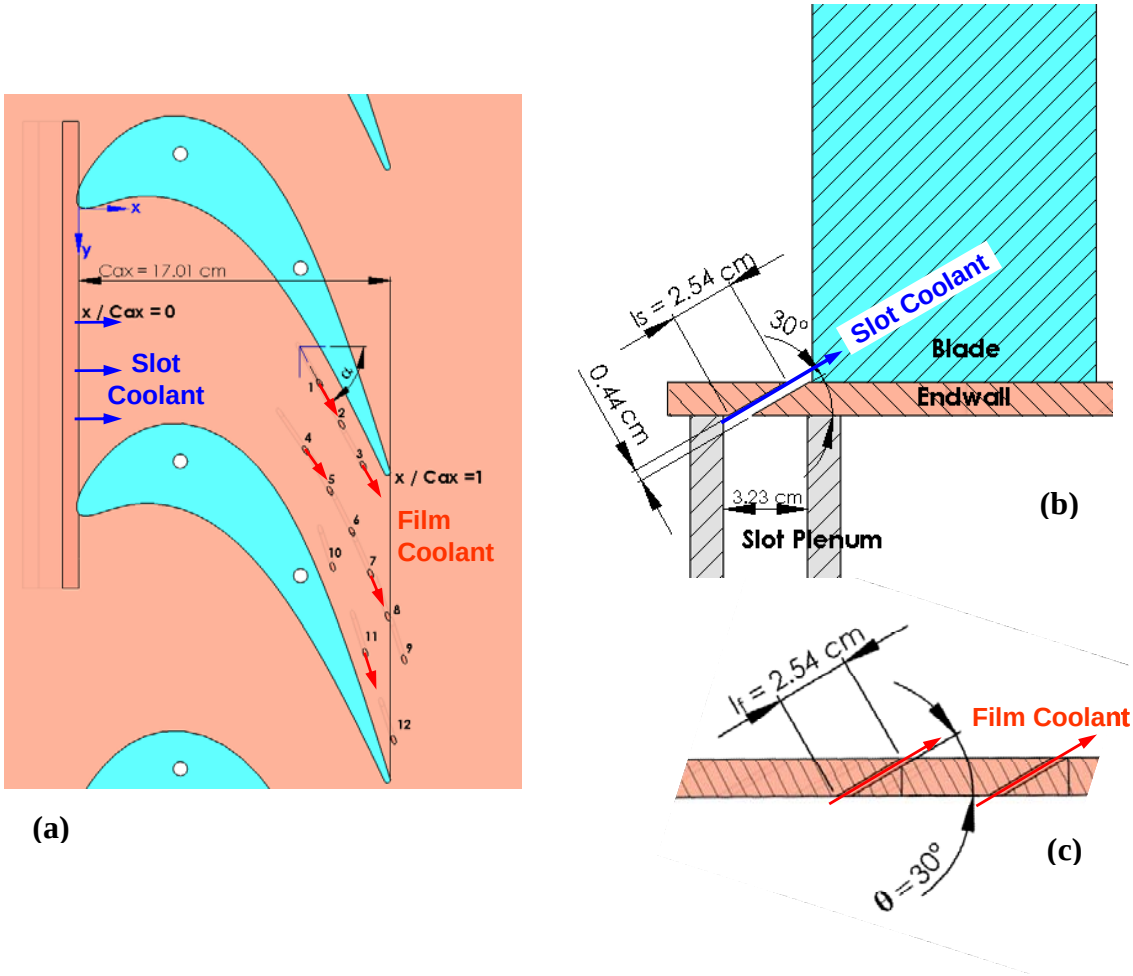

Figure 50: Platform Film Cooling Configurations
(a) Detailed View of Cooled Passage
(b) Upstream Slot Injection Details
(c) Cross-Sectional View of 2 Discrete Film Holes

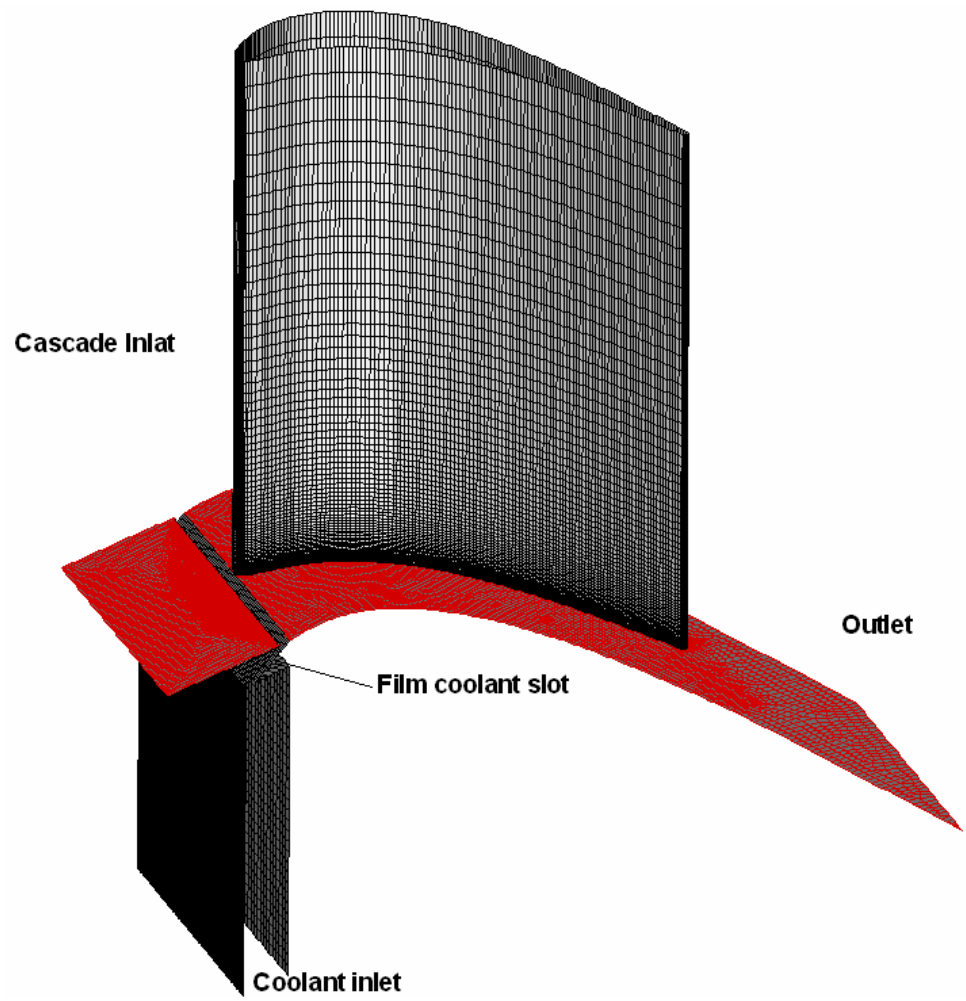

Figure 51: Computational Grid Used to Numerically Study the Effect of Slot Injection on the Passage Endwall and Turbine Blade

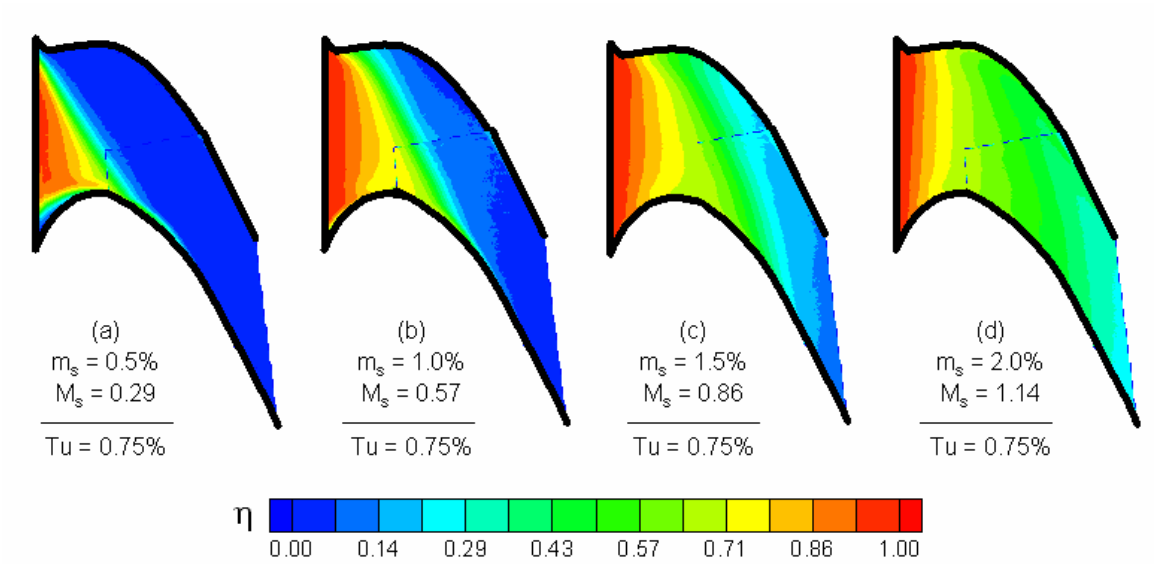

Figure 52: Measured Film Cooling Effectiveness with Various Slot Injection Rates (Tu = 0.75%)

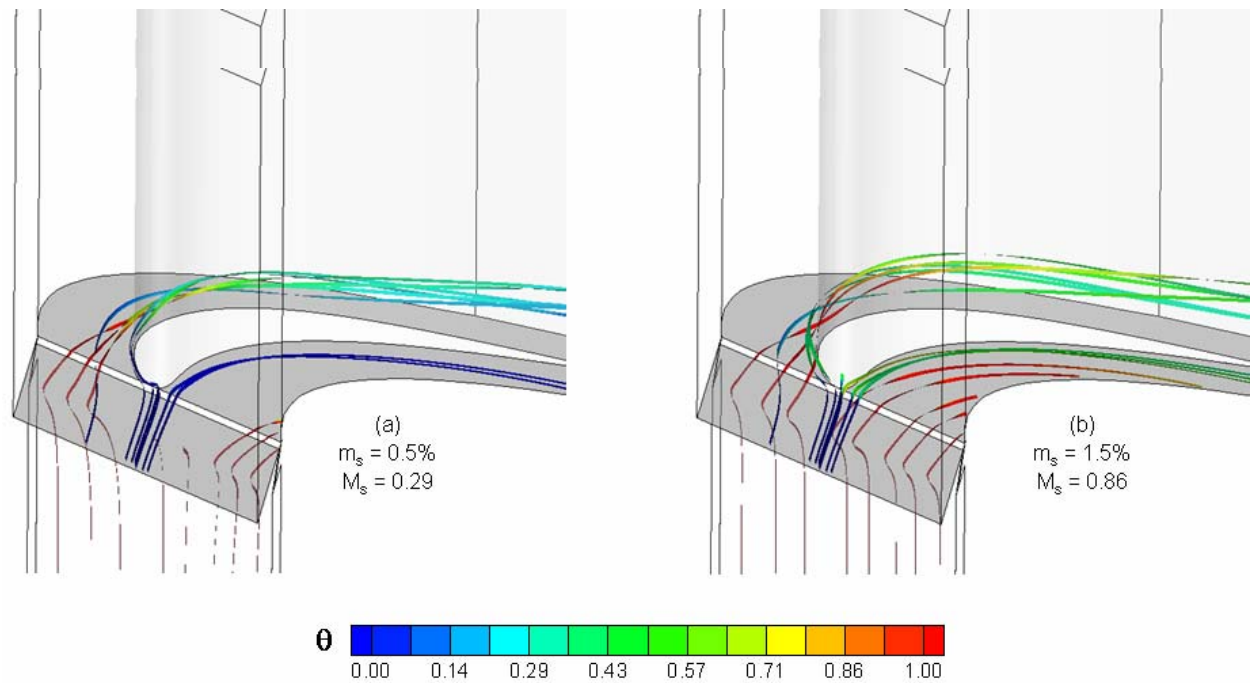

Figure 53: Predicted Mainstream and Coolant Pathlines near the Blade Platform for Upstream Slot Injection Rates of (a) 0.5% and (b) 1.5%
(colored by dimensionless temperature $\theta = (T_m - T) / (T_m - T_s)$)

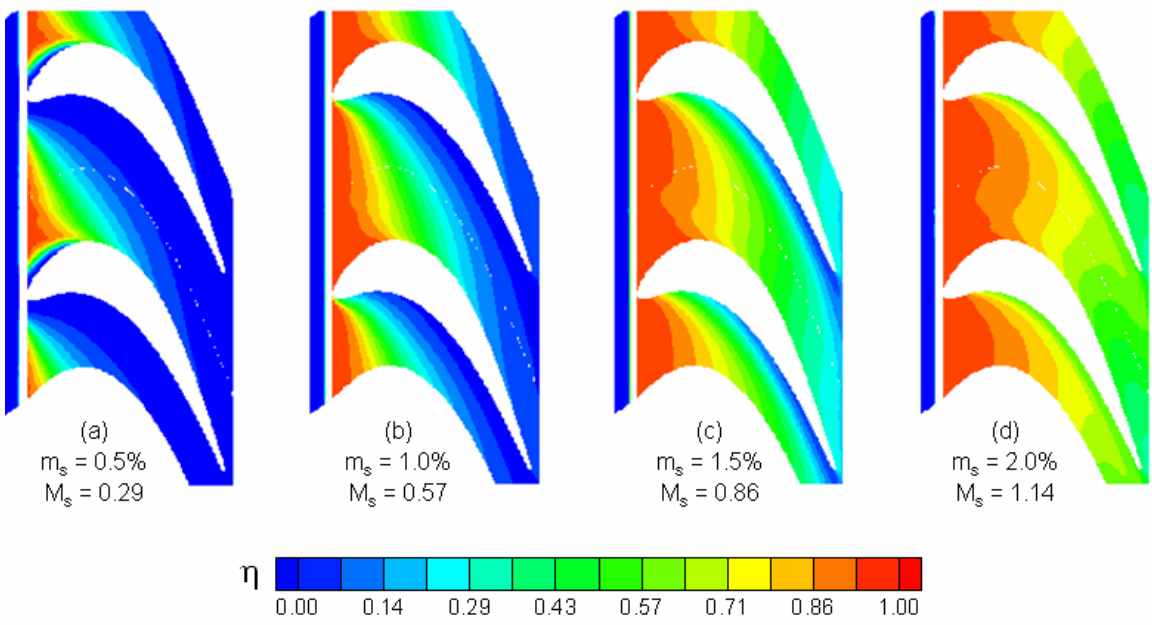

Figure 54: Predicted Film Cooling Effectiveness on the Passage Endwall with Various Slot Injection Rates

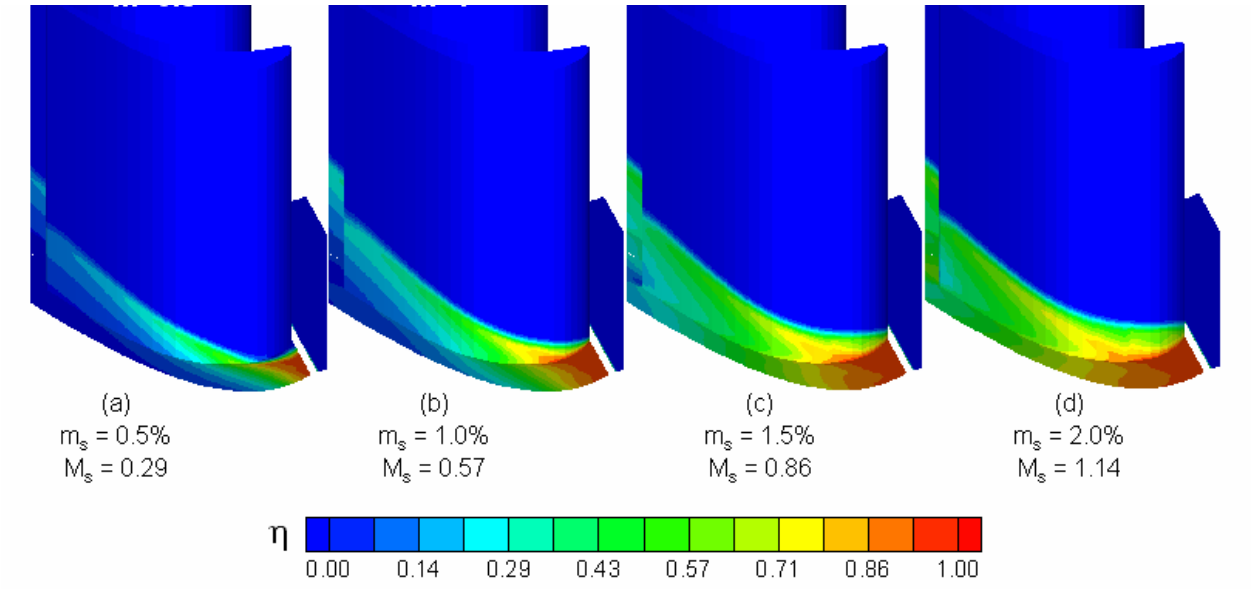

Figure 55: Predicted Film Cooling Effectiveness on the Suction Surface of the Blade with Various Slot Injection Rates

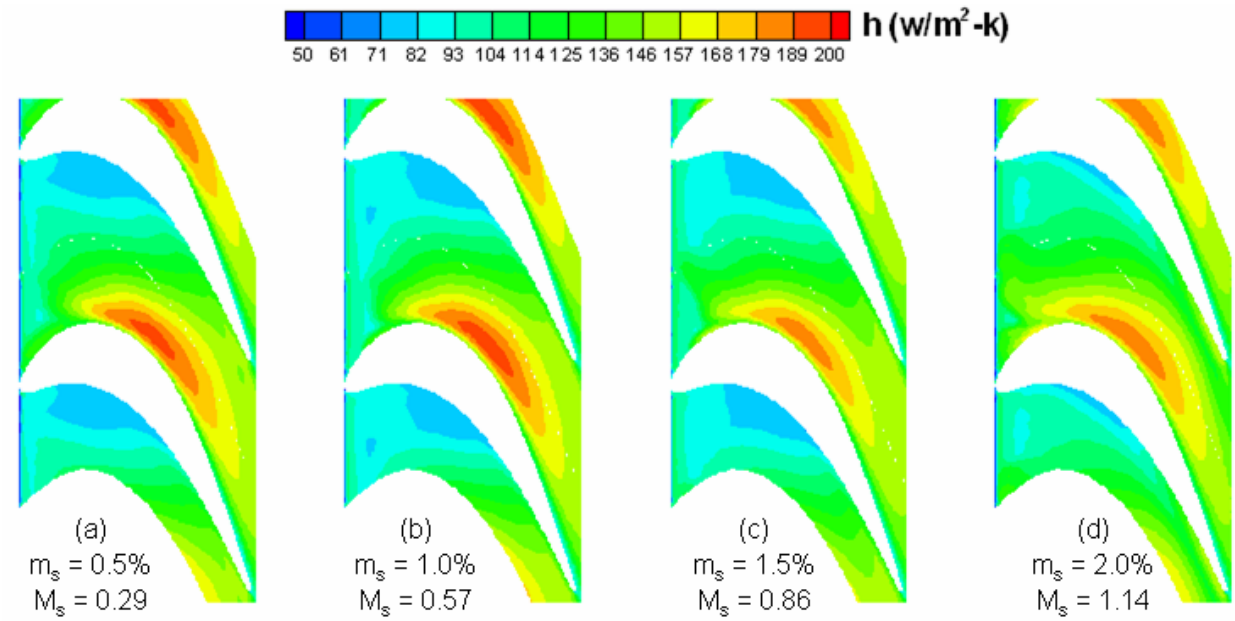

Figure 56: Predicted Heat Transfer Coefficients on the Passage Endwall with Various Slot Injection Rates

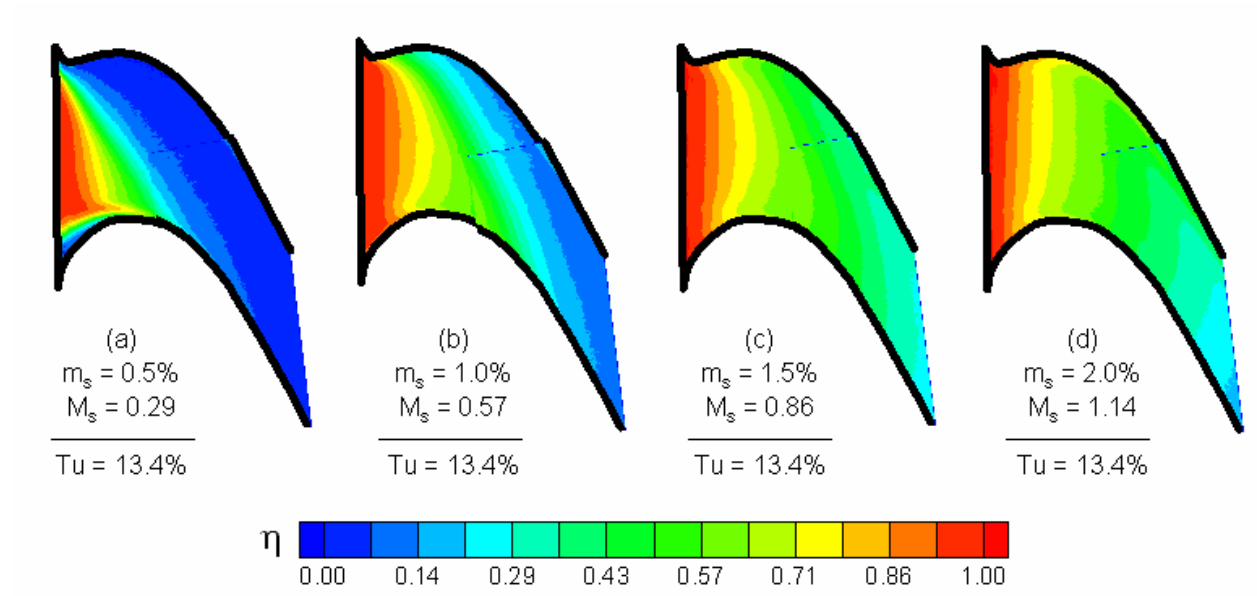

Figure 57: Measured Film Cooling Effectiveness with Various Slot Injection Rates (Tu = 13.4%)

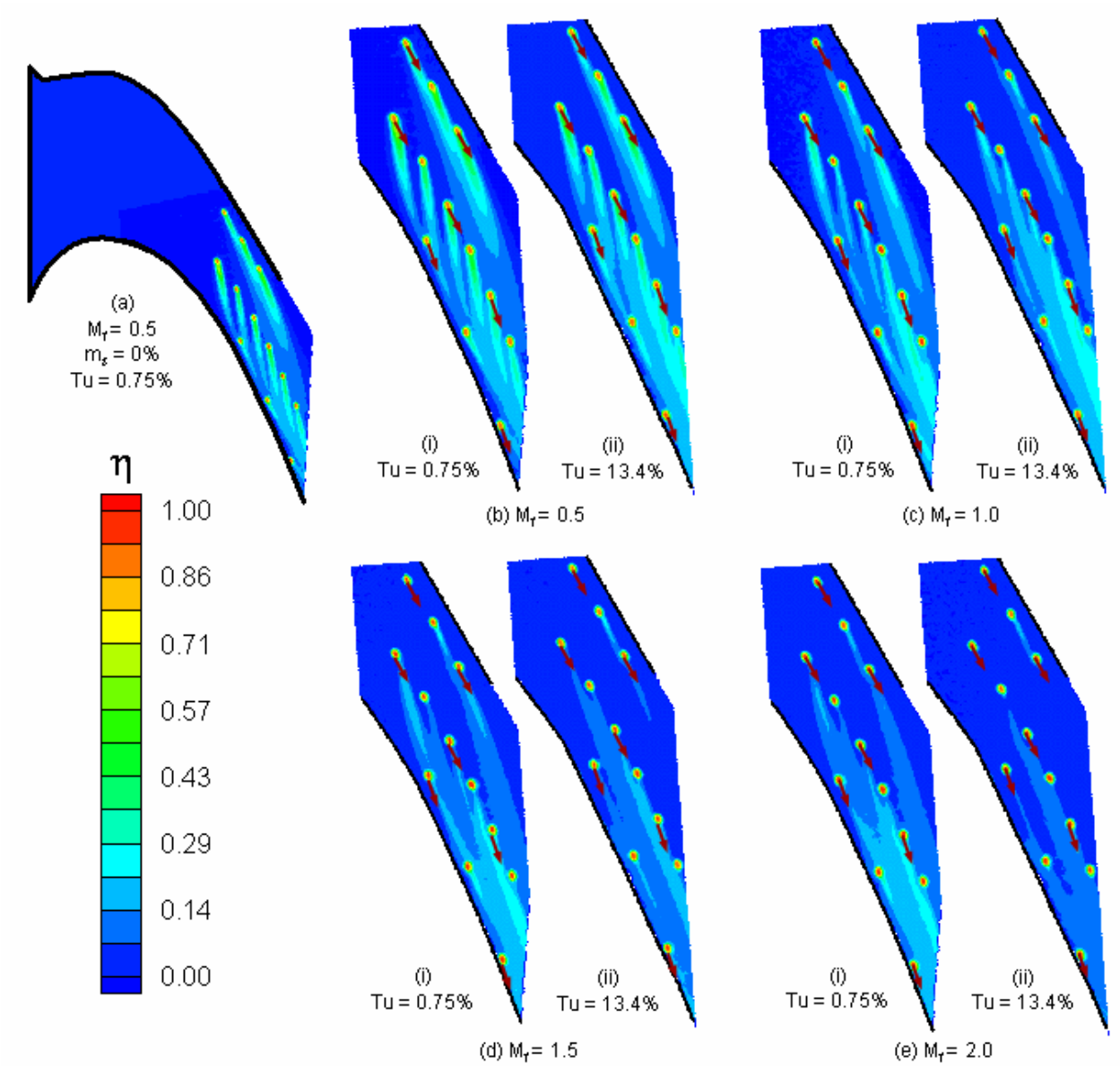

Figure 58: Measured Film Cooling Effectiveness with Downstream Discrete Film Cooling

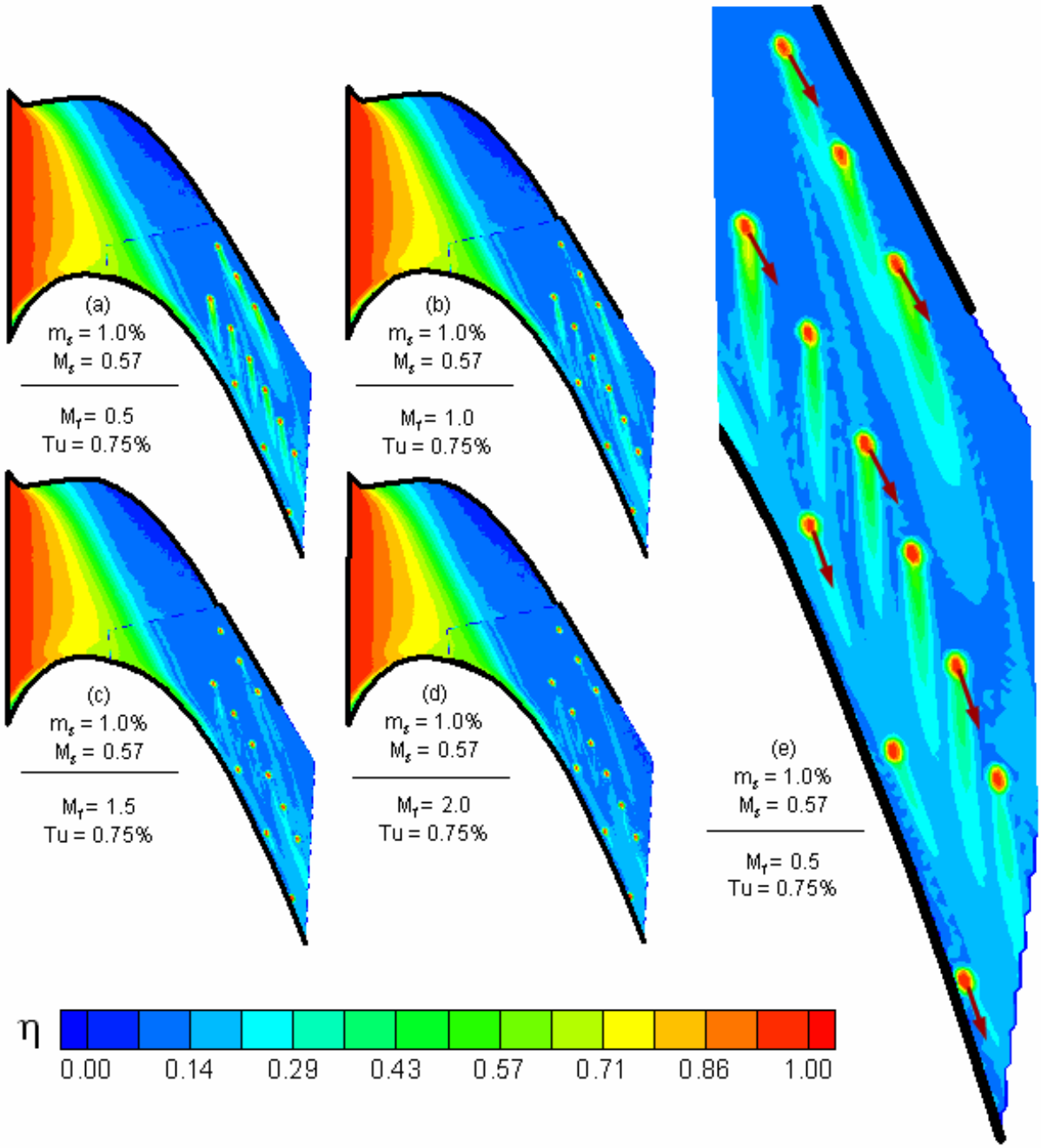

Figure 59: Measured Film Cooling Effectiveness with Combined Slot Cooling (1%) and Downstream Film Cooling (Tu = 0.75%)

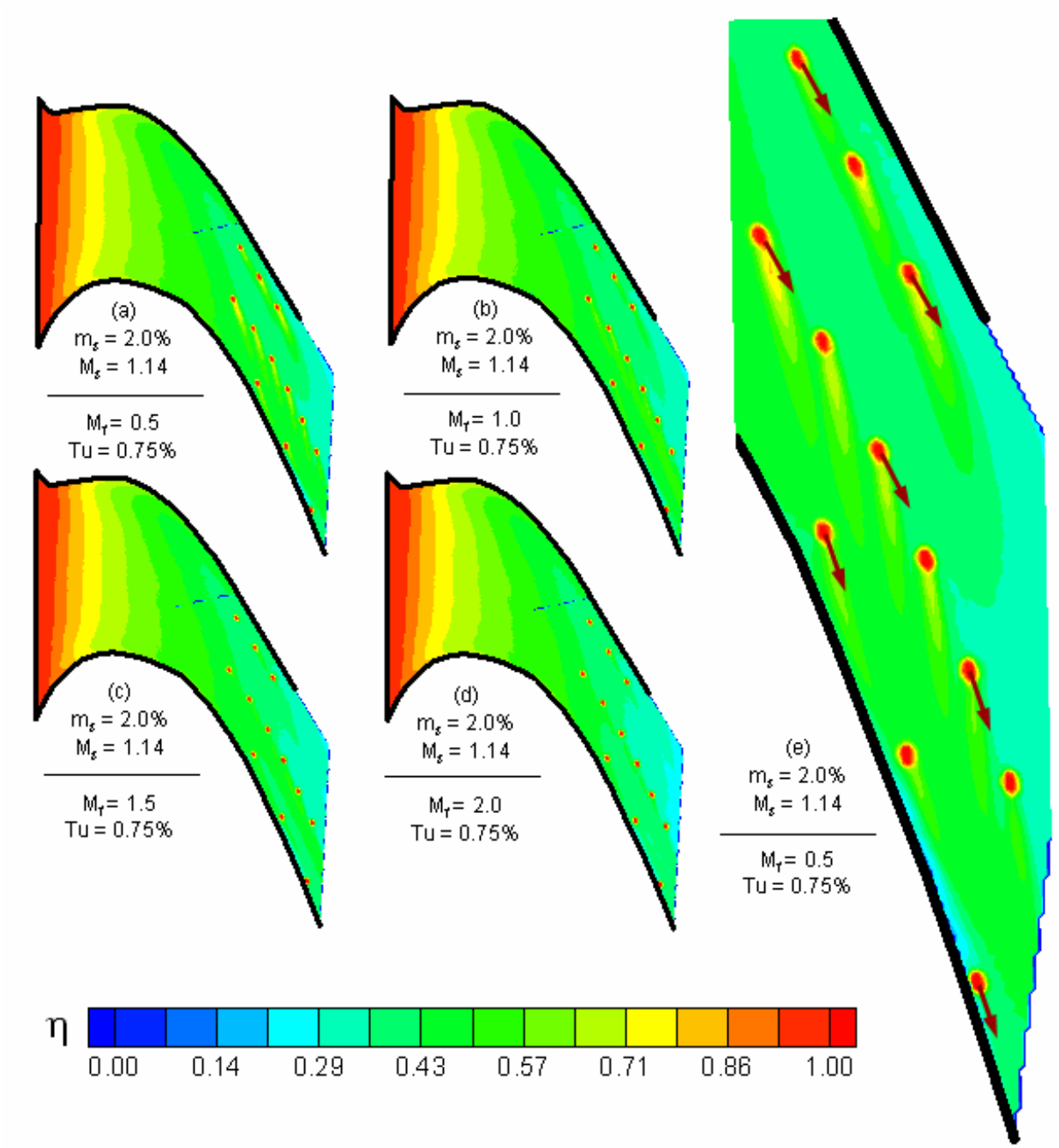

Figure 60: Measured Film Cooling Effectiveness with Combined Slot Cooling (2%) and Downstream Film Cooling (Tu = 0.75%)

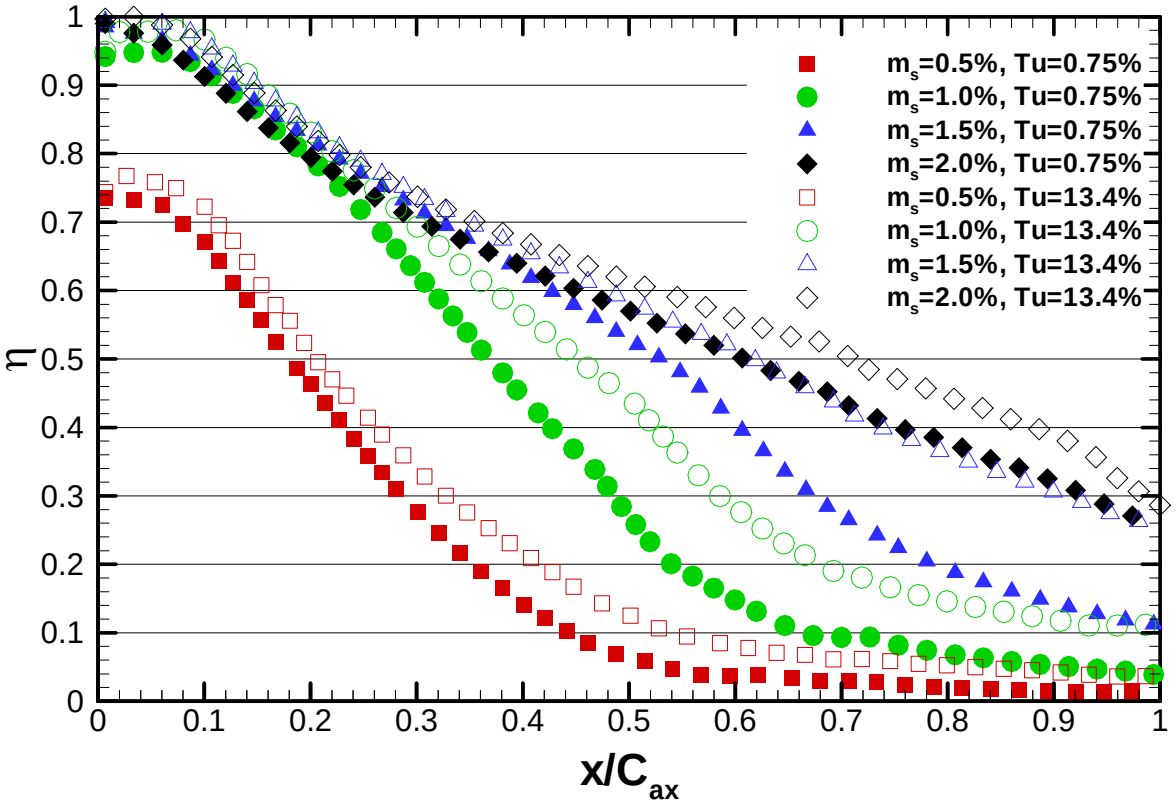

Figure 61: Spanwise Averaged Film Cooling Effectiveness on the Passage Endwall with Upstream Slot Injection

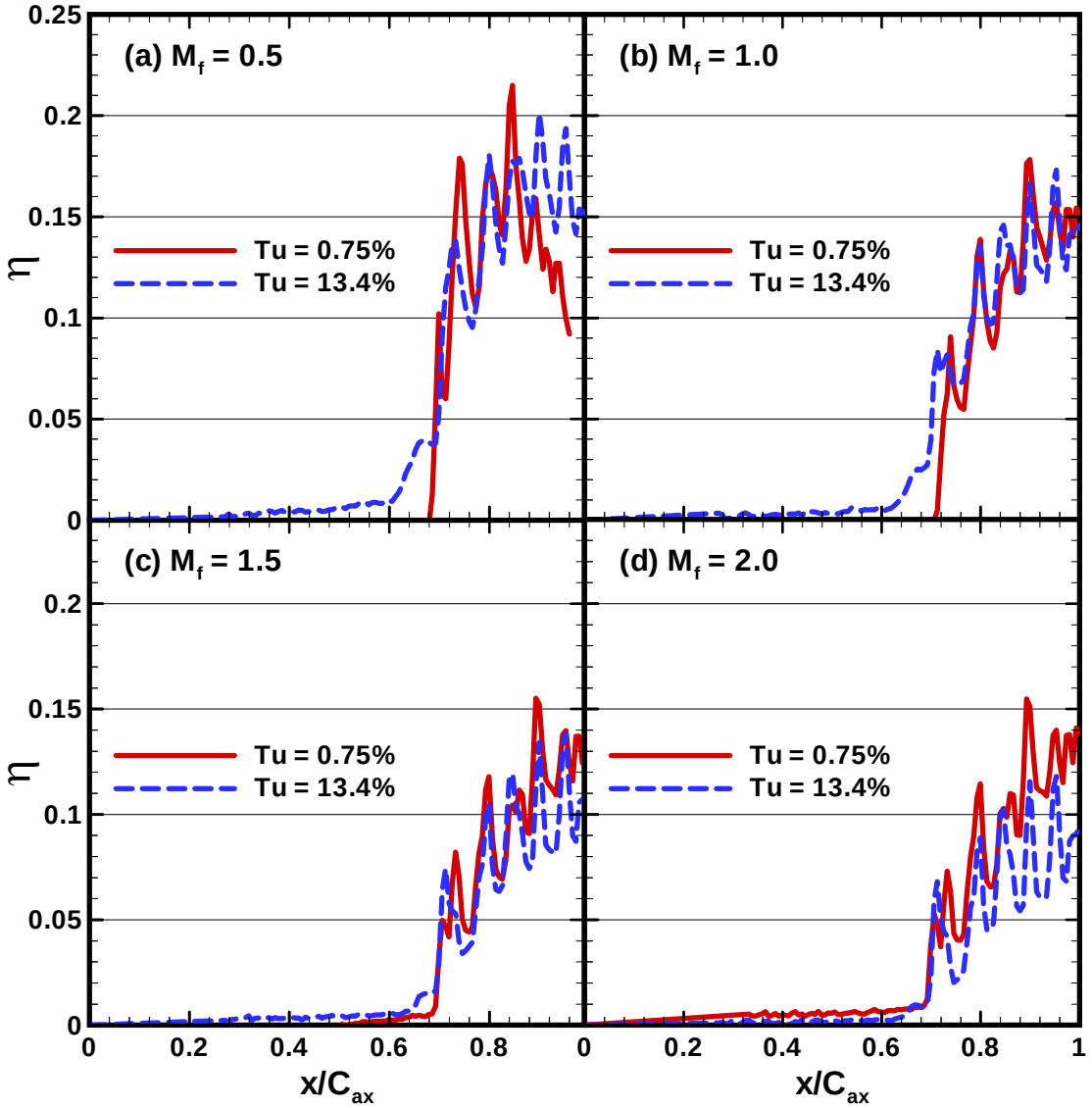

Figure 62: Spanwise Averaged Film Cooling Effectiveness on the Passage Endwall Downstream Discrete Film Hole Cooling

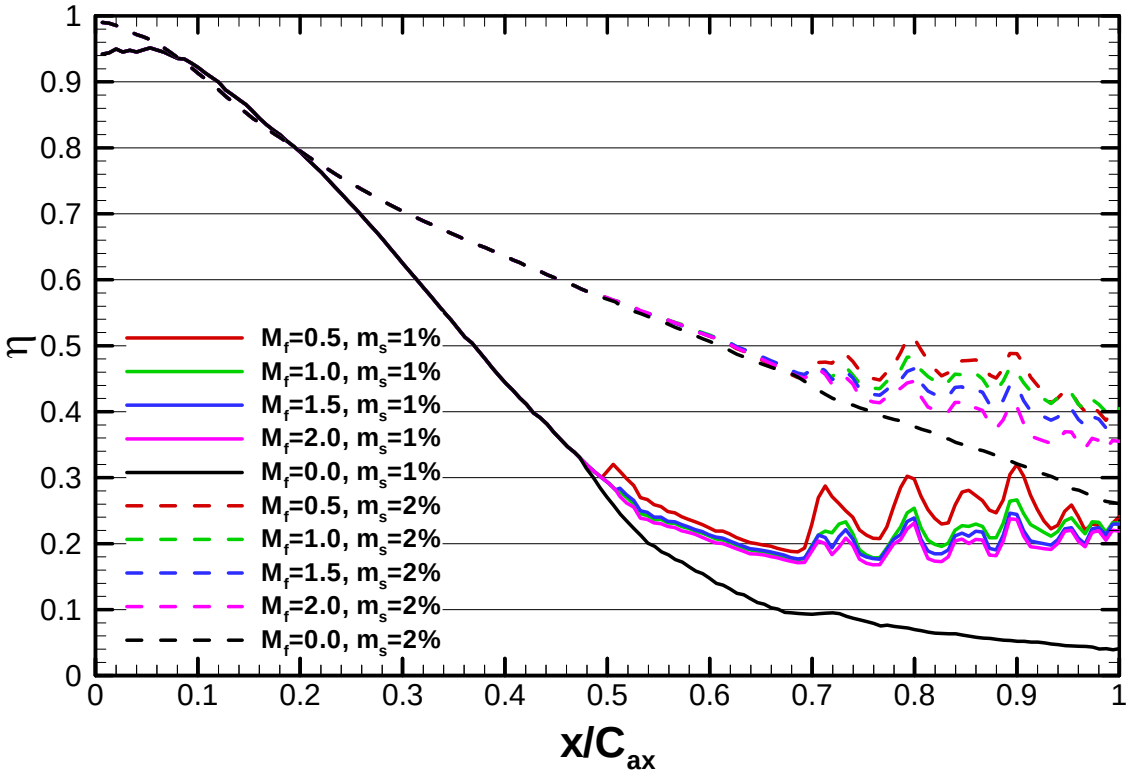

Figure 63: Spanwise Averaged Film Cooling Effectiveness on the Passage Endwall with Combined Upstream Slot Injection and Downstream Discrete Film Hole Cooling (Tu=0.75%)

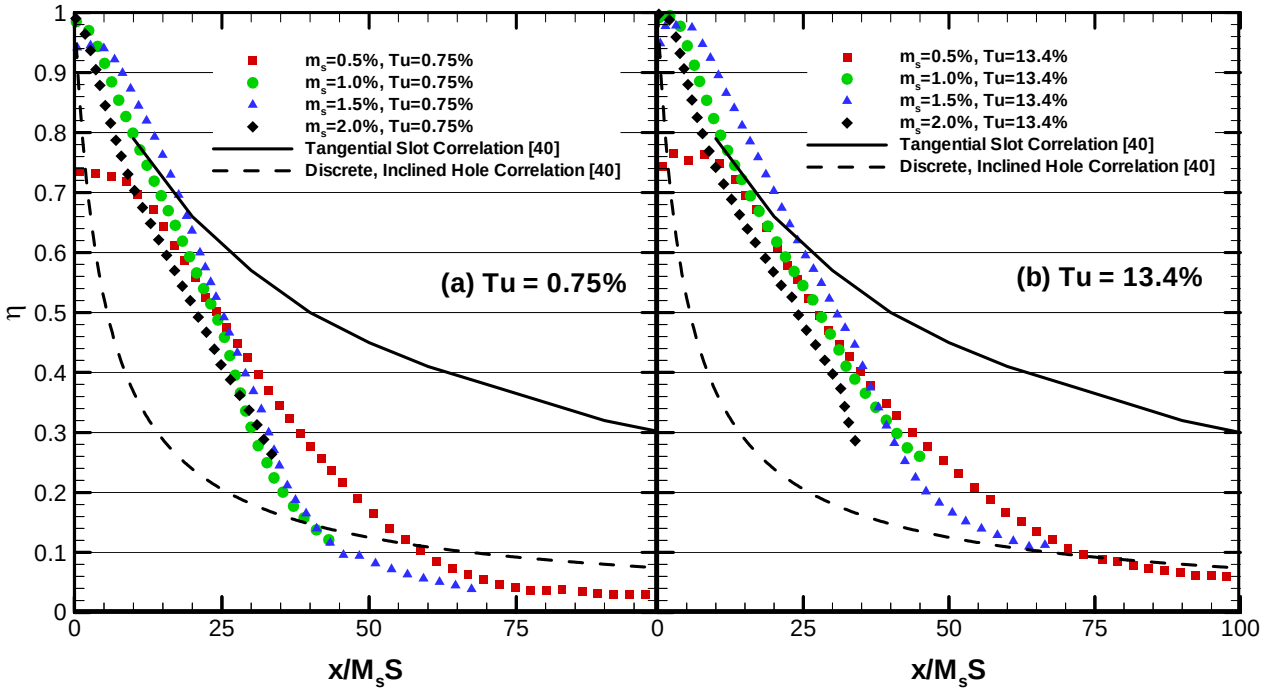

Figure 64: Comparison of the Spanwise Averaged Film Cooling Effectiveness on the Passage Endwall with Upstream Slot Injection with Correlations for Discrete, Inclined Film Cooling Holes and Tangential Slot Injection over a Flat Plate

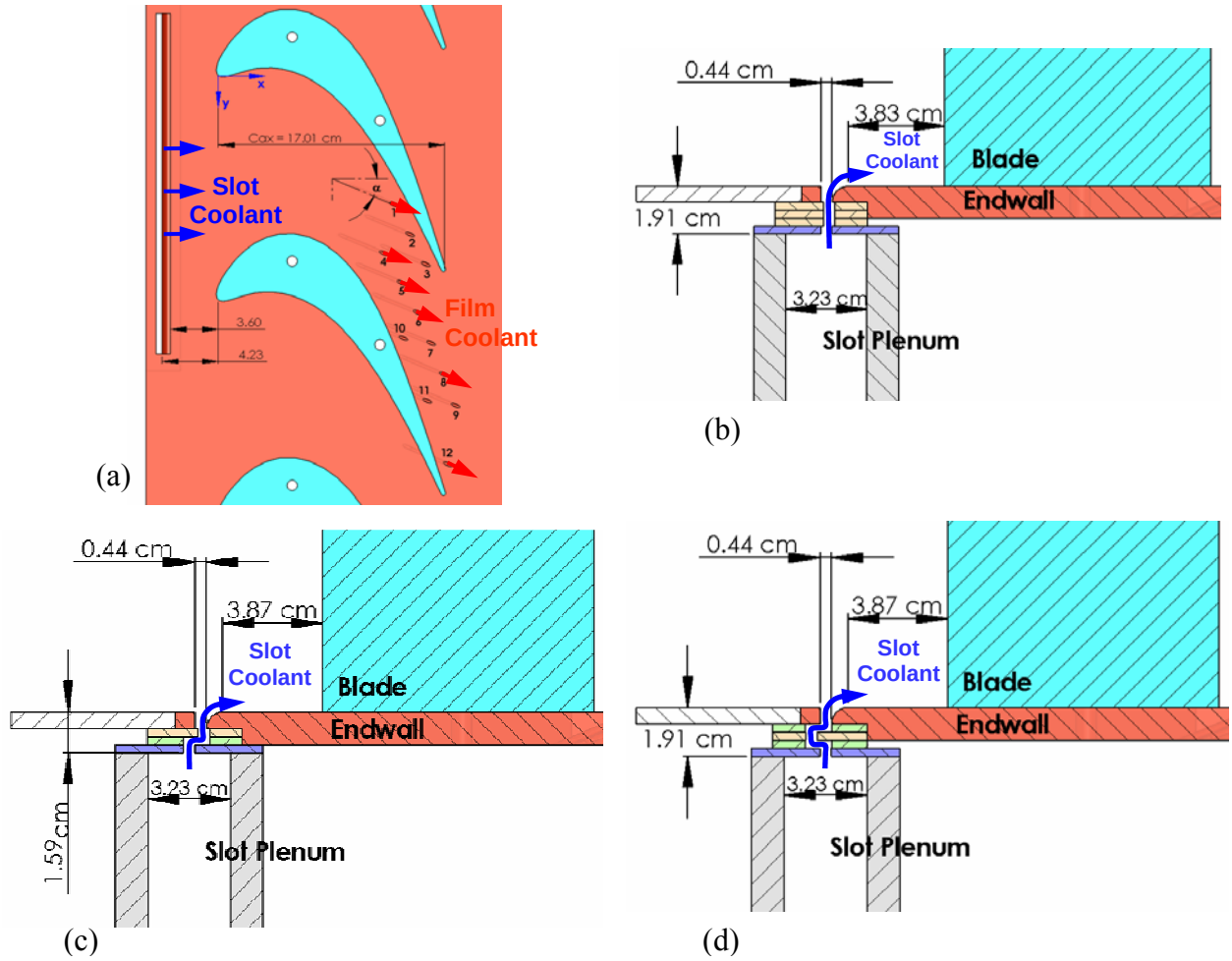

Figure 65: Advanced Platform Film Cooling Configurations
(a) Detailed View of Cooled Passage
(b) Advanced Slot Configuration #1 – Vertical Coolant Injection
(c) Advanced Slot Configuration #2 – Coolant Redirection onto Platform
(d) Advanced Slot Configuration #3 – Labyrinth-like Coolant Flow onto Platform

Combustion Characterization and Modeling of Fuel Blends for Power Generation Gas Turbines

Semi-Annual Report

Start Date: May 1, 2005
End Date: October 31, 2006

Eric L. Petersen (PI)

Issue Date: March 10, 2006

DOE Award Number DE-FC26-02NT41431

UTSR Project Number 04-01-SR114

Mechanical, Materials & Aerospace Engineering
University of Central Florida
PO Box 162450
Orlando, FL 32816

This report was prepared as an account of work sponsored by an agency of the United States Government. Neither the United States Government nor any agency thereof, nor any of their employees, makes any warranty, express or implied, or assumes any legal liability or responsibility for the accuracy, completeness, or usefulness of any information, apparatus, product, or process disclosed, or represents that its use would not infringe privately owned rights. Reference herein to any specific commercial product, process, or service by trade name, trademark, manufacturer, or otherwise does not necessarily constitute or imply its endorsement, recommendation, or favoring by the United States Government or any agency thereof. The views and opinions of authors expressed herein do not necessarily state or reflect those of the United States Government or any agency thereof.

ABSTRACT

To determine gross autoignition behavior for power generation gas turbine engines over a wide range of possible blends, undiluted natural-gas-based mixtures combining CH_4 with C_2H_6, C_3H_8, C_4H_{10}, C_5H_{12}, and H_2 were tested at engine-relevant conditions. The experiments were performed behind reflected shock waves at an average pressure of 20 atm, target temperatures near 800 K, and an equivalence ratio of $\phi = 0.5$. A statistical matrix approach developed in previous papers was employed to cover as wide a range of multiple-fuel blends as possible, resulting in 21 binary and ternary mixtures with methane content in the blends as low as 50% by volume in some mixtures. Both pressure and CH*-emission histories were obtained from the endwall to determine the ignition delay time and the relative strength of the ignition process. Previous work has shown reduced ignition activation energies and similar behavior in the low-temperature, high-pressure regime for higher-order hydrocarbons such as heptane and iso-octane. Similar trends have been obtained in this study for methane-based fuel blends containing higher-order hydrocarbons up to n-pentane, implying a strong reduction in activation energy at lower temperatures and higher pressures. Additionally, for additive levels greater then 25% by volume in the fuel blend, there is little difference between the type of fuel added and the number of carbon atoms in terms of their effect on autoignition time. The results from this study can be directly used for industrial purposes, as validation of potential chemical kinetics mechanisms in this regime, and as a starting point to conduct further studies into the behaviors observed.

Ignition and oxidation characteristics of CO/H_2 fuel blends in air were studied using both experimental and computer simulation methods. Shock-tube experiments were conducted behind reflected shock waves at intermediate temperatures ($890 < T < 1285$ K) and pressures near 1 atm. Emission in the form of chemiluminescence from the hydroxyl radical (OH*) $A^2\Sigma^+ \rightarrow X^2\Pi$ transition near 307 nm was used to monitor reaction progress from which ignition delay times were determined. In addition to the experimental analysis, chemical kinetics modeling was completed to compare existing chemical kinetics mechanisms to the new experimental results. The models were in good agreement with the shock-tube data, especially at higher temperatures, yet there was a tendency for the models to overpredict the ignition delay time at lower temperatures. Subsequently, an ignition delay time sensitivity analysis was completed at higher and lower temperatures to determine reaction rate sensitivities. The results of the sensitivity analysis indicate that the ignition-enhancing reaction $H + O_2 = O + OH$ and hydrogen oxidation kinetics in general were most important regardless of mixture composition or temperature. However, lower-temperature ignition delay time results indicate additional influence from HO_2- and CO-containing reactions. These reactions appear to be the cause of the dramatically longer ignition delay times at the lower temperatures.

TABLE OF CONTENTS

ABSTRACT....3
TABLE OF CONTENTS....4
INTRODUCTION....6
EXECUTIVE SUMMARY....7
PROJECT DESCRIPTION....8
Gas Turbine Research Need....8
Project Experimental and Analytical Approach....8
RESULTS OF FUEL-BLEND TEST MATRIX....11
Background....11
Approach....13
Experiment....14
Results....14
Discussion....18
LEAN CO/H_2/AIR IGNITION....19
Experiment....20
Ignition Delay Time Data....21
Sensitivity Analysis....23
CONCLUSIONS....27
REFERENCES....28

LIST OF GRAPHICAL MATERIALS

TABLES

Table 1 Summary of shock-tube experimental studies with methane-based fuel blends.....12
Table 2 Mixture table with experimental results on the right column.....15
Table 3 Mixtures employed in the CO/H_2 study.....20

FIGURES

Fig. 1 Prediction from the chemical kinetics model of Curran et al. [48] that brackets the limits of the present study.....13
Fig. 2 Endwall pressure and emission traces for Mix 10 under fuel-lean conditions showing strong ignition.....15
Fig. 3 Endwall pressure and emission traces for Mix 6 showing weak ignition.....16
Fig. 4 Results for a 100% CH_4 mixture, $\phi = 0.5$, from 800 to 1400 K from the present study and an earlier study.....16
Fig. 5 CH_4/C_2H_6 Mixtures compared against the high-temperature correlation from Spadaccini and Colket and previous data from Petersen et al.....17
Fig. 6 Plot of all results from Table 2.....17
Fig. 7 Definition of ignition delay time (τ_{ign}) for Mixture 2.....21
Fig. 8 Ignition delay time data and model comparison for Mixture 1 (20% CO – 80% H_2).....22
Fig. 9 Ignition delay time data and model comparison for Mixture 2 (60% CO – 40% H_2).....22
Fig. 10 Ignition delay time data and model comparison for Mixture 3 (80% CO – 20% H_2).....22
Fig. 11 Ignition delay time data and model comparison for Mixture 4 (90% CO – 10% H_2).....22
Fig. 12 Ignition delay time data and model comparison for Mixture 5 (95% CO – 5% H_2).....23
Fig. 13 Normalized ignition delay time sensitivities for Mixture 1 at T = 900 K and P = 1.05 atm.....23
Fig. 14 Normalized ignition delay time sensitivities for Mix 1, T = 1250 K , P = 1.05 atm.....25
Fig. 15 Normalized ignition delay time sensitivities: Mix 5, T = 900K and P = 1.1 atm.....25
Fig. 16 Normalized ignition delay time sensitivities: Mixture 5, T = 1250 K and P = 1.1 atm.....26

INTRODUCTION

With the necessity for clean, efficient electric power generation in all parts of the world, the need to manufacture stationary gas turbine engines with the ability to operate on a wide range of fuel compositions is crucial. Hence, fuel flexibility as a goal for gas turbine combustors is very important and is the topic of the current project. A good example is syngas, which contains significant but often varying levels of H_2, CO, and H_2O. Mixtures of natural gas containing significant levels of hydrocarbons and H_2 will also have significantly varied compositions, depending on the location and application of the blend. Such wide variations in fuel composition often produce wide variations in the chemical behavior of the fuels, not only in terms of their overall energy content but also in important design and performance parameters such as reactivity and flame speed.

Of primary concern, ultimately, is how fuel variability impacts the operation of a stationary gas turbine. For example, the flame speed of the fuel-oxidizer mixture in the combustor relates to its flashback or blowoff tendencies. Likewise, the fuel reactivity, often expressed in terms of its autoignition delay time, has a direct impact on the performance and stability of a given combustor design. Assuming a gas turbine designer or field engineer is aware of the flashback and ignition limitations of a given combustor, a determination as to whether or not a certain fuel will behave adequately in that particular combustor can be made if that fuel's flame speed and ignition characteristics were known *a priori*. However, very little if any fundamental flame speed and ignition data are available for uncommon fuel mixtures such as those mentioned above, much less at realistic engine pressures and concentrations.

A three-year project is underway in which UCF and its collaborators, Flow Parametrics and The Aerospace Corporation, are generating data and models on the combustion characteristics of various fuel blends at gas turbine operating conditions. Presented in this report are the results of the second 6 months of the project, covering the time frame from Nov. 1, 2004 through April 30, 2005. Following the Executive Summary is an overview of the project and the seven specific tasks to be performed. Details on the progress made during this second semi-annual reporting period are provided in the bulk of this report and are divided according to the research topic. Specifically, the topics covered in this report are: 1) the ignition of methane blends; 2) kinetics of the OH* diagnostic; 3) shock-tube tailoring for autoignition times; 4) the flame speed experiments; and, 5) miscellaneous shock-tube measurements, with emphasis on ethane ignition tests.

EXECUTIVE SUMMARY

Most of the shock-tube ignition experiments performed during this time period focused on CO/H_2 blends at fuel-lean conditions. Ignition temperatures ranged from 900 – 1360 K, and pressures ranged from 0.9 – 2.9 atm. CO/H_2 splits of 60/40 and 40/60% were tested first, followed by several other blends and higher pressures later in the reporting period; these data will be analyzed and presented in the next semiannual report. Such ignition data provide engineers with a database of combustion characteristics that are needed when fuel flexibility is a concern, particularly with regard to syngas-based fuels. Two state-of-the-art CO/H_2 kinetics mechanisms were compared to the data, and improvements are needed at the higher pressures and lower temperatures. Engineers will be able to utilize the improved chemical kinetics mechanisms for predicting the effects of syngas fuels on combustor designs at realistic conditions. Such kinetic information will help prevent or predict flashback, autoignition, emissions levels, and possibly combustion instability.

A significant portion of the experimental effort in this program is devoted to addressing the specific problem of autoignition in the premixed lines of gas turbines utilizing exotic fuel blends. To this end, a design of experiments (DOE) approach has been undertaken to efficiently cover the wide range of possible mixture combinations within a realistic time frame. Analyses were performed that produced a balanced, 41-blend matrix of experiments covering multiple combinations of methane mixed with hydrogen, ethane, propane, butane, and pentane. Theses blends will be tested in a tailored shock tube at a temperature of 800 K and a pressure near 18 atm to determine their autoignition times at this T and P combination. Further DOE analyses resulted in an even smaller, 21-test matrix that should produce results equivalent to the larger matrix. The experiments will be performed during the next reporting period. The data obtained from the autoignition experiments will provide engineers with a matrix of results covering the entire scope of possible fuel blends, and from the results they will be able to assess whether or not that particular combination ignites at 18 atm, 800 K within a time frame of ten milliseconds, a typical residence time for premixed circuits. Additional matrices were also formulated to support the other fuel-flexibility experiments in this program.

Much progress was also made on the numerical modeling aspect of the program, the intent of which is to provide a numerical injector/burner testbed in which to test the effects of fuel flexibility on the burner flow field and emissions. Flow modeling combined with reacting chemistry effects provide engineers with a valuable tool that bridges that gap between the fundamental kinetics data generated in the present effort and the reacting, turbulent flow fields of an actual gas turbine combustor. Progress during this reporting period centered on the identification of a model geometry and test data for initial model validation and a series of numerical experiments testing the temporal behavior of the numerical model when applied to classical flame propagation in a premixed fuel and air environment. For the corresponding flame growth experiments, the detail design of the high-pressure flame speed measurement experiment was performed. The data from this device will be unique in both the fuel blends tested and the high-pressure conditions utilized.

PROJECT DESCRIPTION

GAS TURBINE RESEARCH NEED

For several years now, natural gas has been widely used as a fuel for stationary power generation gas turbine engines [1]. Although composed primarily of methane, natural gases can contain from a few percent up to as much as 18% of other gases, depending on the international source [2]. These natural gas impurities are usually higher-order hydrocarbons such as ethane and propane. Composition variations in native and foreign natural gases can cause changes in the combustion chemistry, emissions formation, and stability, among other concerns [3-5].

However, in the near future, power generation gas turbines may be required to burn ever more exotic gaseous fuel blends in addition to indigenous natural gas. Typical fuel blends can include potentially high concentrations (> 10%) of hydrogen and even larger concentrations of hydrocarbons than what are common in natural gases. In addition to changes in the heating value of the fuel blends, significant changes in the ignition chemistry occur when gases such as H_2 and C_2H_6 are added to methane. According to previous studies, even a few percent of higher-order hydrocarbons can greatly accelerate the ignition process of a methane-based fuel [2]. Even larger changes in the combustion chemistry may then occur if the methane-based fuel were to contain significant levels of hydrogen or hydrocarbons. Such chemical effects can have dramatic impacts on existing gas turbine combustors designed to operate on natural gases typical of those found, for example, in the United States. These concerns are complicated by the fact that few data exist on the fundamental effects of fuel composition variation at the fuel/air mixture ratios, temperatures, and pressures of interest to the designers of power generation gas turbines.

With these issues and concerns in mind, the authors are conducting a research program to study ignition delay times, flame speeds, and related chemical kinetics over a wide range of fuel composition, mixture stoichiometry, temperature, and pressure. ***This program will provide data related to fuel flexibility issues, allowing gas turbine designers and field engineers to predict the effects of fuel flexibility on the likelihood of autoignition in premixed regions, flashback, combustor efficiency, emissions, and combustion instability.*** Provided in the next section is an outline of the research effort.

PROJECT EXPERIMENTAL AND ANALYTICAL APPROACH

This 3-year effort is divided into seven experimental and analytical tasks, outlined as follows.

<u>Task 1 – Test Matrix and Literature Search</u>

Since the objective of the experiments is to provide critical flame speed and ignition data as quickly as possible to impact gas turbine designers and field engineers, a Design of Experiments (DOE) approach will be taken. In a DOE test matrix, specific ranges of multiple test variables are chosen using readily available statistical procedures to devise a test matrix that covers the entire breadth of the variables without testing every possible combination of variable levels. Matrices will be developed for the various fuel-blend experiments, with emphasis on the autoignition experiments and the flame speed experiments. In parallel with the DOE selection phase, a comprehensive literature search will be conducted covering the main facets of the program.

Task 2 – Autoignition Measurements

Ignition delay times for the range of mixtures and conditions defined in Task 1 will be measured in Task 2. These experiments involve primarily the shock-tube facilities and related diagnostics. The early focus of this task will be on conditions of most interest to the gas turbine community: fuel lean fuel/air mixtures at elevated pressures. These tests will form the bulk of the experiments during the first two years of the effort. Both methane-based fuel blends and syngas (CO/H_2) fuel blends will be studied.

Task 3 – Flame Speed Measurements

A new flame speed apparatus is being built at UCF to measure the flame speed of gas turbine fuel blends at elevated pressures. The test apparatus includes a spherical (or large cylindrical), stainless steel chamber with two quartz windows to provide optical access. The combustible mixture is ignited at the center of the vessel using electrodes. Measurements involve observing the flames using schlieren motion picture photography in conjunction with a high-speed digital camera to yield an exposure time less than 1 millisecond. The key parameter to be measured is the one dimensional radial propagation velocity of the spherical flame front relative to the unburned mixture, or dr/dt.

Task 4 – Chemical Kinetics Modeling

This task supports and is conducted in parallel with each of the other tasks and forms a critical link between the experimental efforts (Tasks 2,3,6 and 7) and the CFD modeling effort (Task 5). In addition, Task 4 will produce combustion chemistry models that can be used for calculations beyond those that can be performed using empirical correlations obtained in Tasks 2 and 3. This effort will produce two types of models: 1) a full mechanism (or mechanisms) containing hundreds of possible reactions between dozens of molecules in the reaction zone, and 2) reduced mechanisms containing perhaps only dozens of reactions for use in the CFD models. Both types of mechanisms will rely heavily on both existing hydrocarbon-based kinetics models and the data obtained in the proposed effort.

Task 5 – CFD Modeling Effort

This task is being performed by Flow Parametrics and consists of three stages, leading towards the use of finite-rate kinetics for simulations of combustors with emphasis on fuel flexibility. During Year 1, computations of model combustors using established heat release models for synthetic fuels will be performed and compared with available data or design system results. The dynamics of a propagating flame will be emphasized (as in the flame speed experiments). During Year 2, new and improved finite-rate kinetics models for the selected fuel blends will be implemented and compared to the model combustor results. During Year 3, final calibration of the reduced chemical kinetics models within the combustion CFD flow solver will be completed, and demonstration simulations on production or research hardware will be performed. These simulations will be compared with available experimental data and/or design system performance predictions.

Task 6 – NOx Measurements

This task involves a series of quantitative measurements of NOx species such as NO_2 and NO as well as CO for a representative range of syngas and other gas turbine fuel mixtures. Following

an approach similar to that used in Tasks 2 and 3, fuel and parameter combinations from the fuel-blend matrices determined in Task 1 will be explored at realistic temperatures and pressures in the Aerospace and UCF facilities. From the proposed NOx measurements, we will be able to compare the NOx-producing tendencies of the complete range of fuels and conditions defined in Task 1. Likely fuel combinations that are more or less likely to produce NOx will be identified, and empirical correlations will be determined if possible. This task also involves the use of the CFD model under Task 5 to explore the effects of fuel flexibility on NOx production in typical gas turbine configurations using realistic flow rates.

Task 7 – Mechanism Validation Measurements

True validation of any chemical kinetics mechanism for use in gas turbine-related calculations cannot come from comparisons with ignition and flame speed data alone, but from a combination of these and other fundamental data such as species concentration measurements. This task therefore is concerned with acquiring the necessary data from shock-tube experiments. Most of the measurements in Task 7 will be performed using a combination of emission and laser absorption diagnostics. Although the species targeted will depend somewhat on the diagnostics set up in the laboratory from other projects, we anticipate that OH, CO, CH, CH_4, and H_2O can be studied. Typically, such measurements are performed in a chemically well-behaved environment, namely in mixtures with a higher level of dilution. The resulting data will be used to validate the chemical kinetics mechanism(s) over a wider range of ϕ, temperature, and pressure than the initial ignition experiments in Task 2.

RESULTS OF FUEL-BLEND TEST MATRIX (Task 2)

Natural gas is a popular fuel for power generation gas turbines and for some forms of transportation [1], but the need for fuel-flexible engines operating on alternative sources such as landfill gas, LNG tail gas, process gas, and synthetic fuels places a strain on engines originally designed with natural gas in mind [6,7]. Although natural gas consists of mainly methane, its specific make-up can change drastically depending on the geographical location and the season in which it is obtained [6,8,9]. In comparison, the composition of alternative fuels, even those based on natural gas, can have significantly lower volumetric percentages of CH_4. For example, biomass and raw natural gas can have as little as 20-30% methane [6]. The impurities are usually higher-order hydrocarbons from C_2 to C_5, CO, and H_2. The hydrogen might also be artificially added to lower the flammability limit to obtain extremely low emissions. Changes in gas supply are believed to lead to issues with the operation of appliances, turbines, compressor engines, and industrial burners tuned for very low emissions. Variations in existing gas composition have required, for example, turbine engine retuning. Other interchangeability concerns are efficiency, emissions, autoignition, stability, and combustion chemistry [7,10,11].

Former experiments by the authors and others have shown that the effect of higher-order hydrocarbon addition on the ignition behavior of methane-based fuel blends can be drastic in the high-temperature regime ($T > 1300$ K), where the main effect of the hydrocarbon addition is the reduction in ignition delay time of the fuel blend [8,12]. For example, since power gas turbines premix their fuel and oxidizer prior to entering the main combustion zone, there has been a growing concern of the fuel mixture pre-igniting before reaching the combustor, herein referred to as autoignition [12,13]. Although there are suspected differences between autoignition in a steady-flow mixing circuit and a completely premixed system [6,14], fundamental ignition times based on premixed gases at controlled temperatures and pressures, such as in shock tubes, are useful as they place a lower bound on the chemical time scales.

With the above issues and concerns in mind, a research program is underway in the authors' laboratory to study ignition delay times and related chemical kinetics over a wide range of stoichiometry, pressure, and temperature. Since the scope of possible fuel-blend combinations is extremely broad, it is prudent to conduct a gross study that covers a wide fuel-blend parameter space. Such a study would help to identify trends and mixture combinations for more detailed research [13]. To provide timely benefit to the engine community, the current paper focuses on the ignition behavior of lean ($\phi = 0.5$) fuel-air mixtures, pressures around 20 atm, and a target temperature of 800 K, typical conditions at the upper limit of a gas turbine pre-mixer.

Presented first is a background section discussing existing literature on natural gas and fuel blends under similar conditions, followed by the experimental methodology and a short description of the shock tube used in this study. The results are presented in a table and with several plots showing the non-linear behavior of these mixtures in the low-temperature regime.

BACKGROUND

Natural gas consists mainly of methane, which has been studied extensively over the past few decades starting as early as 1963. An excellent summary of the experimental work up to 1994 is given by Spadaccini and Colket [8], including, among others, work by Higgin and Williams [15]

and Seery and Bowman [16]. Most of these studies were conducted under low-pressure (1 atm) conditions. Subsequent high-pressure investigations covered pressures up to 480 atm [17-21].

Analytical studies and modeling were done in the early seventies by Seery and Bowman [16] and later by Spadacinni and Colket [8] and Hunter et al. [22]. Most of the previous modeling and experimental results led to the development of GRI-Mech 2.1 [23] and later GRI-Mech 3.0. [24]. These two mechanisms are able to predict the methane chemistry under high-temperature, low-pressure conditions very well. Modeling at intermediate temperatures and higher pressures was done by Petersen et al. [25], using their mostly fuel-rich data [19]. Li and Williams subsequently created a methane reaction mechanism that covers temperatures from 1000 to 2000 K and pressures up to 150 atm [26]. Huang et al. modified the mechanism of Petersen et al. for IC engine conditions [21].

There has been a considerable amount of research done on the effect of fuel additives on the ignition behavior of methane under a variety of conditions using shock tubes, flow tubes, and jet-stirred reactors. A selected summary of work found by the authors is presented in Table 1. The effect of butane on methane-based fuel blends was studied as early as 1969 by Higgin and Willams [15]. Crossly et al. studied the effect of higher-order hydrocarbons (C_2H_6-C_5H_{12}) with methane relative to propulsion devices [27], and natural gas-based mixtures were investigated in several shock-tube studies [8,9,12,28-32]. Note that most of these studies were conducted in the high-temperature regime, and none at the temperature of interest herein (800 K). The effect of hydrogen on the ignition behavior of methane has also been investigated [12,33,34], and the effect of acetylene was investigated by Krishnan et al. [35].

Table 1. Summary of shock-tube experimental studies with methane-based fuel blends (add 4 to the reference numbers for corresponding numbers of this report).

Authors	Ref.	Additives*	Temp (K)	Press (atm)	ϕ
Higgin & Williams (1969)	[10]	C_4	1800-2500	0.2-0.4	0.5
Crossley et al. (1972)	[22]	C_2-C_5	1400-2000	0.2	1
Eubank et al. (1981)	[23]	C_2-C_4	1200-1850	4	0.2-0.4
Zellner et al. (1983)	[24]	C_2-C_4	1400-2000	3	0.2
Krishnan et al. (1983)	[30]	C_2H_2	1700-1900	1-4	0.5-2
Spadaccini & Colket (1984)	[2]	C_2-C_4	1300-2000	3-15	0.45-1.25
Cheng & Oppenheim (1984)	[28]	H_2	800-2400	1-3	0.5-1.25
Frenklach & Bornside (1984)	[25]	C_3	1300-1600	2.5	1
Goy et al. (2001)	[51]	C_2-C_3	900-1600	5-40	0.5-1
Lamoureux & Paillard (2002)	[3]	C_2-C_3	1485-1900	3-13	0.5-2
Bakali et al. (2004)	[26]	C_2-C_6	1300-1800	0.1	0.75-1.5
Huang & Bushe (2005)	[27]	C_2-C_3	900-1400	16-40	1
Petersen et al. (2005)	[6]	C_2-C_3, H_2	1200-2000	1-25	0.5

* Specifies carbon content of appropriate alkane unless specified otherwise.

Besides shock tubes, jet-stirred reactors, flow tubes, and model combustors have been used to study combustion behavior of natural gas and related fuel blends. Examples include: Cowell and Lefebvre [36], Tan et al. [37], Flores et al. [9,10], Bakali et al. [31], and Daguat and Dayma [38].

Several kinetics mechanisms were created to predict the behavior of natural gas fuel blends. Westbrook modeled the ignition of methane and ethane fuel blends [39], and further analyses were done by Krishnan et al. [35], Zellner et al. [29], Frenklach and Bornside [30], Gardiner et al. [40], Lamoureux and Paillard [9], Huang and Bushe [32], and Petersen et al. [41].

Other autoignition studies at elevated pressures covered mainly large, higher-order hydrocarbons (heptane, and octane, etc.) as related to spark ignition (SI) engines, such as the work by Ciezki and Adomeit [42], Fieweger et al. [43], Herzler et al. [44,45] and Zhukov et al. [46]. Although these studies investigated different fuels, they were done using similar experimental techniques as employed here.

APPROACH

As mentioned above, few if any ignition studies exist at the conditions of interest herein (800 K, 20 atm) and for lean, methane/hydrocarbon fuel blends with significant percentages of additive. Additionally, most studies that have considered methane-based fuel blends pertain to binary fuel blends rather than mixtures of several fuel components. The fuel blends of interest to the present study include methane mixed with up to 50% of H_2, C_2H_6, C_3H_8, C_4H_{10}, and C_5H_{12} in any number of possible configurations. To completely cover such a wide parameter space would require hundreds of blends, even if the possible levels were constrained.

Therefore, the authors turned to a statistical design of experiments approach to select the proper mixtures for a gross ignition study. Complete details on the matrix development are presented elsewhere [13,47]. Briefly, a 21-mixture matrix of binary and ternary fuel blends was formulated for studying the effects of mixture composition. Chemical kinetics modeling was used to guide the selection and to verify that the reduced matrix properly captures the chemistry trends. This L21 matrix forms the basis for the mixtures listed in Table 2. The methodology of the present experiments was to test each of the blends at typical gas turbine conditions, specifically $\phi = 0.5$, 800 K, and ~20 atm.

Chemical kinetics modeling can be used to estimate the expected behavior of the fuel blends. Figure 1 shows the results for the fuels that bound this study, 100% CH_4 and 100% n-pentane, over a range of temperatures above and below 800 K. The calculations were done using the chemical kinetics mechanism of Curran et al. [48] and the shock subroutine of the chemkin package [49]. It must be noted that the Curran et al. model was designed for pressures up to 45 atm and temperatures from 550-1700 K but was developed for iso-octane ignition and not

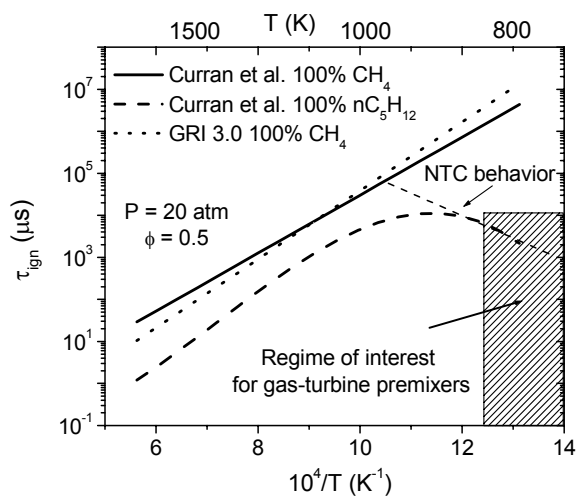

Fig. 1 Prediction from the chemical kinetics model of Curran et al. [48] that brackets the limits of the present study: 100% methane and 100% n-pentane in air. Both are for 20 atm and $\phi = 0.5$

necessarily for methane. It was chosen because it shows some of the low-temperature, high-pressure behavior expected of higher-order hydrocarbons, it contains the species in the target fuel blends, and because no suitable chemical kinetics mechanism currently exists that covers the mixtures and conditions of this study.

It can be seen in Fig. 1 that the 100% n-C_5H_{12}-air mixture (ϕ = 0.5) shows strong negative temperature coefficient (NTC) behavior at low temperatures and 20 atm. For 100% CH_4 blends, the model is similar to GRI-Mech 3.0. As shown, the NTC-like behavior leads to autoignition times well within the range of premixer residence times. Conversely, the kinetics model estimates ignition times for the 100% methane-air mixture (ϕ = 0.5) that are considerably longer than premixer residence times. It should be pointed out, however, that the methane chemistry in the Curran et al. [48] kinetics model—and most kinetics models—are based on existing data. Hence, the trend in activation energy at lower temperatures is predicted to be the same as that at higher temperatures. Nonetheless, the two predicted curves show qualitatively the upper and lower bounds to expect from the L21 matrix.

EXPERIMENT

Petersen et al. [50] provide a comprehensive description of the shock-tube facility, but a brief description follows. The helium-driven shock tube has a 16.2-cm-Dia, 10.7-m-length driven section and a 7.62-cm-Dia, 3.5-m-length driver section capable of reflected-shock pressures of 100 atm. Pre-scored aluminum diaphragms (3 mm) were employed to achieve the target test pressure of ~20 atm. A PCB 134A piezoelectric pressure transducer was used for qualitative endwall pressure readings since the post-shock pressure is determined by using the incident-shock speed [50].

Since the calculated post-shock temperature is most sensitive to the incident-shock speed [51], it is therefore important that potential shock attenuation is accounted for. A total of five pressure transducers (PCB 113A) in combination with 4 counters are used to provide 4 velocity measurements, allowing for linear extrapolation of the incident shock speed to the endwall. For an experiment at 800 K, the estimated uncertainty is less than 10 K [50].

Ignition delay time was observed from the endwall by monitoring the CH^* chemiluminescence through a 430±5 nm bandpass filter with a Hamamatsu 1P21 Photomultiplier tube (PMT) in a homemade housing. Endwall measurements were used since this is believed to give the true ignition delay time without undesired gas dynamic effects [19,30,52,53]. Extended test times were obtained by creating driver-gas mixtures of He and CO_2. This technique is capable of creating test times > 12 ms in the authors' facility [54]. These driver-gas mixtures were produced by filling first the CO_2 and then the He directly into the driver tube from an axially central location. This simple approach provided adequate mixing and highly repeatable experiments.

RESULTS

Table 2 presents the mixtures and the results of each experiment (except for Mix 12 from the original L21 matrix [47]). Although the initial interest was the ignition behavior at just 800 K, several additional experiments were performed at higher temperatures, as reflected in Table 2, resulting in a total of 25 experiments. Argon was used as the "air" bath gas (in lieu of N_2). It has

been shown in previous experiments that methane ignition results using either N_2 or Ar as the diluent are indistinguishable [9,19,25].

Table 2 Mixture table with experimental results on the right column. The basic L21 mixture matrix is from de Vries and Petersen [47]. The numbers for each fuel species represent the fraction of that fuel in the blend. Each mixture was mixed with O_2-Ar "air" at $\phi = 0.5$.

L21	T(K)	P(atm)	CH_4	C_2H_6	C_3H_8	C_4H_{10}	C_5H_{12}	H_2	tign (ms)
1	849	20.1	1.000	0	0	0	0	0	7.00
1	1107	20.2	1.000	0	0	0	0	0	2.35
2	811	20.3	0.750	0.250	0	0	0	0	7.72
3	817	20.2	0.751	0	0.249	0	0	0	10.79
3	1100	20.3	0.751	0	0.249	0	0	0	1.45
4	881	18.7	0.750	0	0	0.250	0	0	5.07
4	976	18.5	0.750	0	0	0.250	0	0	4.24
5	876	15.7	0.750	0	0	0	0.250	0	5.42
5	925	18.2	0.750	0	0	0	0.250	0.000	4.58
6	816	20.7	0.750	0	0	0	0	0.250	8.10
7	827	19.7	0.500	0.500	0	0	0	0	9.69
8	815	20.5	0.500	0.250	0.250	0	0	0	6.92
9	792	18.4	0.493	0.257	0	0.250	0	0	11.96
10	794	20.8	0.497	0.255	0	0	0.248	0	7.90
11	802	20.6	0.500	0.251	0	0	0	0.249	7.80
13	797	20.3	0.498	0.000	0.251	0.251	0	0	9.32
14	791	20.8	0.497	0	0.256	0	0.248	0	8.36
15	786	20.0	0.489	0	0.252	0	0	0.259	8.58
16	914	18.1	0.500	0	0	0.500	0	0	4.00
17	807	20.1	0.500	0	0	0.251	0.250	0	5.34
18	797	18.7	0.501	0	0	0.245	0	0.254	10.38
19	934	15.5	0.500	0	0	0	0.500	0	3.69
19	803	19.2	0.500	0	0	0	0.500	0	6.04
20	798	20.0	0.505	0	0	0	0.248	0.248	5.98
21	803	20.1	0.503	0	0	0	0	0.497	7.70

Figure 2 shows pressure and emission plots for an experiment with a $CH_4/C_2H_6/C_5H_{12}$ mixture. The relatively wide inner diameter of the driven section (16.2 cm) made it possible to create long test times (> 8 ms) without significant boundary-layer effects as reflected in the relatively flat trace until ignition. Ignition delay time is defined as the time between the shock arrival and the rapid onset of emission and is shown in Fig. 2. However, not every mixture tested showed strong ignition as seen in Fig. 2 and as demonstrated in many other high-concentration shock-tube experiments [19,43-46]. For example, Fig. 3 shows pressure and

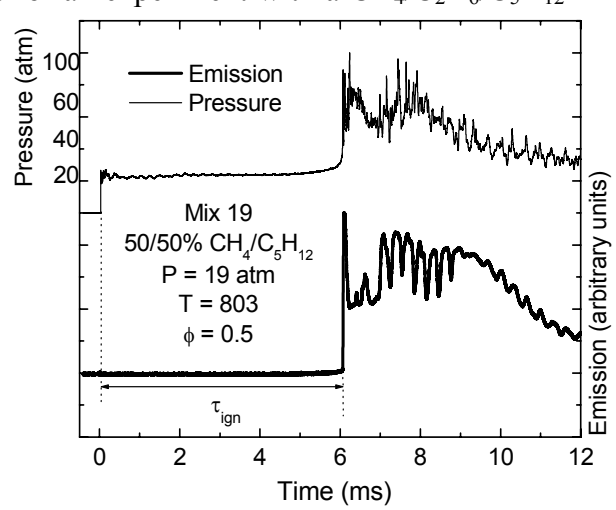

Fig. 2 Endwall pressure and emission traces for Mix 10 under fuel-lean conditions showing strong ignition.

emission traces of a 75/25% mixture of CH_4 /H_2 where ignition takes place more gradually, as in weak ignition. The way τ_{ign} is defined in this case is shown in Fig. 3. Only 100% CH_4 (Mix 1) and the mixture given in Fig. 3 showed weak ignition; the data for all the other mixtures looked similar to the one shown in Fig. 2.

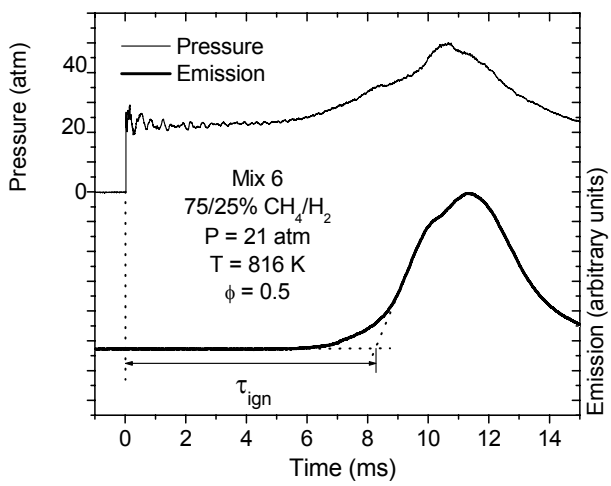

Fig. 3 Endwall pressure and emission traces for Mix 6 showing weak ignition.

Figure 4 presents the 100% CH_4 experimental results combined with results obtained earlier by the authors [12]. Also shown is the correlation by Li and Williams [26], GRI-Mech 3.0, and the results from Goy et al. [55]. There are two interesting observations that can be made from Fig. 4. First, the new data (open squares) have a much smaller ignition time than would have been expected from extrapolating the high-temperature data (solid squares). Second, the low-temperature results seem to merge well with the data obtained previously by the authors [12] around 1200 K, but there is an obvious shift in activation energy. However, the correlation from Li and Williams and the prediction of GRI-Mech 3.0 diverge away from the data with decreasing temperatures as also seen in the model predictions in Fig. 1. Again, these results are not unexpected since the methane models are based on higher-temperature data. The experimental results from Goy et al. [55] presented in the open triangles show qualitatively the same trend as the data obtained herein but are lower by a factor of three and follow a much lower activation energy slope.

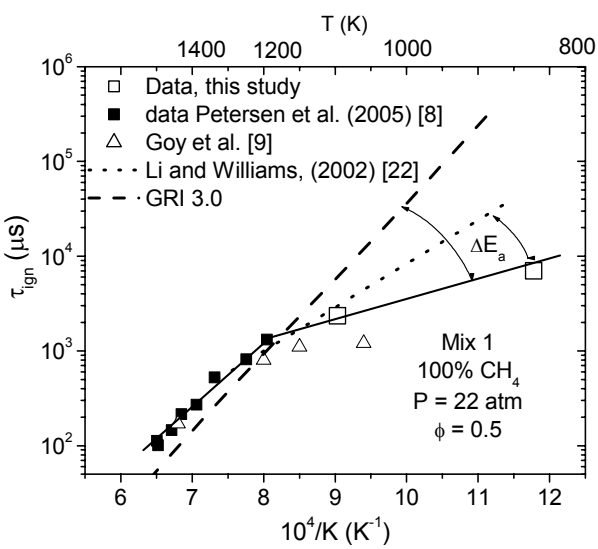

Fig. 4 Results for a 100% CH_4 mixture, ϕ = 0.5, from 800 to 1400 K from the present study and an earlier study [12]. Comparison is also made with the correlation of Li and Williams [26] and GRI-Mech 3.0 [24].

Figure 5 shows mixtures with methane and ethane. Mixtures 2 and 7 from Table 2 are presented together with data obtained previously for higher-temperature CH_4/C_2H_6 blends [12]. The same effect as seen in Fig. 4 can be seen in Fig. 5, where there is a significant drop in activation energy at lower temperatures. The results are compared against the correlation given by Spadaccini and Colket [8]. As mentioned above, the lack of data in the low-temperature regime causes the correlation to overpredict ignition times at lower temperatures, but it shows good agreement with the data obtained by the authors at higher temperatures [12].

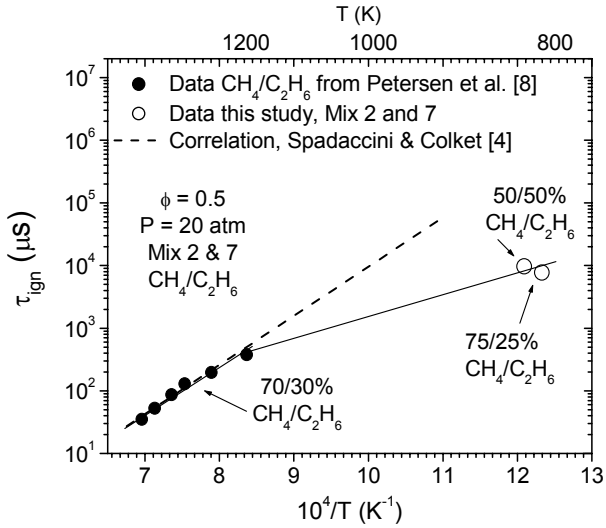

Fig. 5 CH_4/C_2H_6 Mixtures compared against the high-temperature correlation from Spadaccini and Colket [8] and previous data from Petersen et al. [12].

Figure 6 contains the results for all mixtures. For comparison reasons, the earlier-obtained 100% CH_4 data are also included [12]. Since specific hydrocarbons did not seem to have a great impact in this low-temperature regime, Fig. 6 has the mixtures divided by quantity of additive. All mixtures with 75% methane (Mix 2-6) and all 50% CH_4 mixtures (Mix 7-21) are presented with open and closed circles, respectively. It seems that the amount and type of additive have marginal effects on the low-temperature ignition condition of these mixtures. Arguably, there is even little difference between 100% CH_4 and 50% CH_4 in this temperature and pressure regime.

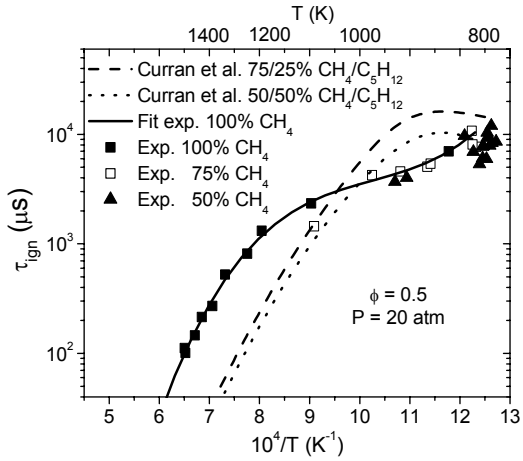

Fig. 6 Plot of all results from Table 2. Also included are the high-temperature methane experiments obtained earlier [12] and the results of a chemical kinetics model [48]. Open circles are 75% CH_4 blends, and the solid circles are 50% CH_4 blends.

DISCUSSION

As intended, the L21 matrix experiments provided an overall glimpse into the ignition behavior of methane/HC blends covering alkanes through n-pentane and relatively large levels of additive (50%). The focus on a particular combination of stoichiometry ($\phi = 0.5$), temperature (800 K), and pressure (~ 20 atm) benefits a specific application: gas turbine engines employing premixing. Perhaps more importantly, the results of this study bring to light several issues worthy of further study: 1) the ignition of completely premixed methane/air mixtures at elevated pressures may be shorter than previously expected; 2) for the levels of HC addition herein, 25-50% of the blend, there is little effect relative to each other and to the ignition of pure methane; 3) for the range of higher-order HC's utilized, there is little difference between C_2 hydrocarbons and C_5 hydrocarbons on methane/HC ignition near 800 K and 20 atm; and, 4) the chemical kinetics modeling of methane-based fuel blends requires improvement in this critical, practical regime.

Regarding the relative order of magnitude and the lower activation energy of fuel-blend ignition at higher pressures and lower temperatures near 800 K, such results are not surprising to the authors in light of the NTC and similar behavior observed in higher-order hydrocarbons (Fig. 1). To illustrate this point further, calculations using the chemical kinetics model of Curran et al. [48] for typical mixtures from Table 2 are plotted in Fig. 6 along with the experimental data. Although the model may require improvement in the methane chemistry, it does indicate that NTC-like behavior is likely for fuel blends with 50% or even 25% methane. Additionally, the accelerating effect of hydrocarbons and even hydrogen on CH_4 ignition and oxidation at higher temperatures ($T > 1100$ K) [12] is not evident in this study. Further exploration of the full temperature, pressure, and blending effects of likely fuels and stoichiometries is therefore warranted but is beyond the scope of this paper.

It should also be noted that the only similar study conducted with methane/HC fuel blends at low temperatures (900-1300 K) and elevated pressures was that conducted by Goy et al. [55], who showed very similar trends, albeit with 3—5 times faster ignition. In their shock-tube study, they also observed independence on HC content and lower ignition times for pure methane oxidation than previously expected. However, Goy et al. added caution to their data since they believed their ignition times could have been impacted by nonideal effects. In the present experiments, such effects are reduced because of the larger tube diameter and the well-characterized gas dynamics within. In a recent study by Huang and Bushe [32], similarly low ignition delay times for practical methane-based mixtures were seen at elevated pressures, with ignition times on the order of 1—10 ms. In fact, ignition times below 1 ms near 800 K for hydrocarbon-air ignition are not unusual at higher pressures and lower temperatures [43-46]. Nonetheless, further study is required to fully understand the differences beginning to emerge between shock-tube experiments at elevated temperature and pressure and available flow reactor data [36].

LEAN CO/H_2/AIR IGNITION (Task 2)

In recent years, the United States has developed an interest in establishing a hydrogen economy due, in large part, to the need for alternatives to hydrocarbon fuels. A candidate fuel for power-generation gas turbines is synthesis gas, or syngas, that is produced during the coal gasification process. Syngas is mainly composed of CO and H_2, with minor amounts of N_2, CO_2, CH_4, and H_2O. Unlike common hydrocarbon fuels such as methane, propane, and kerosene, CO/H_2 oxidation has not been well characterized, especially for shock-tube and ignition delay time data. Hence, there is an increasing need for combustion chemistry data for CO/H_2 fuel combinations for a range of mixture compositions, temperatures and pressures. Such data are especially critical because the implementation of syngas varies greatly throughout the world [56].

Early investigations of CO/H_2 oxidation sought to discover the reaction rates of CO/O_2 with minimal H_2 [57]. In particular, Sulzmann and coworkers used a shock tube to examine the rapid formation of CO_2 during the induction period behind incident shock waves. Subsequently, additional shock-tube investigations were completed in a similar manner, and more reaction rates were characterized for the $CO/H_2/O_2$ system [58-60]. After studying the exponential growth zone for nearly a decade, researchers turned to the study of the entire reaction history with the knowledge that reaction rates determined solely from induction-period data were seemingly incorrect [61]. Interest was again renewed in the $CO/H_2/O_2$ system when proper kinetics data were needed to validate simultaneous research of the kinetics of higher-order hydrocarbon systems [62,63]. During these experiments, data were collected over a range of temperatures to validate mechanisms for a broad range of experimental conditions. Simultaneously, kinetics modeling was applied to such systems and became another avenue to explore reaction rates and allowed for comparison of the theoretical results with experimental results [62,64-73].

Most notable in recent years was the work done by Mueller et al. [74] and Davis et al. [75] to formulate new CO/H_2 kinetics models using updated reaction rates. The work done by Mueller et al. [74] used both an experimental and modeling approach to properly formulate a chemical kinetics model to accurately describe H_2/O_2 and $CO/H_2O/O_2$ combustion in the presence of NO and NO_2. A flow reactor was used to conduct experiments over considerable temperature (750-1100 K) and pressure ranges (0.5-14.0 atm). Their kinetics model is comprehensive, drawing from numerous sources and it models reactions in their given temperature and pressure ranges quite well; however, new rate parameters for important reactions such as $H + O_2 + M = HO_2 + M$ have since been resolved, and therefore a new updated mechanism was needed. Davis et al. [75] conducted their analysis in a similar manner to Mueller et al. [74] and used optimized reaction rates in their model along with a revision of the enthalpy of formation of OH. The result was an improved mechanism that describes the oxidation of H_2 and CO in the presence of small concentrations of NO and NO_2 at temperatures and pressures between 750 - 1100 K and 0.4 – 14.0 atm.

It is important to note, however, that the Mueller et al. [74] mechanism was not formulated for, or compared with, ignition delay time data. In addition, their mechanism did not aim to monitor the reaction progress of OH, a key species formed during the combustion process. Davis et al. [75] formulated their model for ignition purposes using available shock-tube $CO/H_2/Ar$ data. However, the reflected-shock data used for validation was obtained for temperatures above 2000 K. Data obtained in this high-temperature region are known to possess different kinetic

characteristics than those obtained for temperatures between 900 K and 1300 K. Therefore, to provide much needed ignition and oxidation data for the power-generation industry, new experimental data concerning ignition delay times must be compiled to compare results with current CO/H_2 chemical kinetics mechanisms for validation and mechanism enhancement to include regimes such as are encountered in gas turbine power-generation environments.

The current research presents ignition delay time data for several different fuel-lean ($\phi = 0.5$) CO/H_2/Air mixtures for temperatures between ($890 < T < 1285$ K) and pressures near 1 atm. Note that the mixtures investigated in the present study were undiluted fuel-air mixtures, where ignition data in the CO/H_2 system are scarce. The following sections of this paper include a discussion of the shock-tube facility used to conduct the CO/H_2/Air fuel mixture experiments. Subsequently, the ignition delay time results are presented and compared to several current chemical kinetics mechanisms. In addition, an ignition delay time sensitivity analysis is included to determine which reaction rate coefficients have the most effect on ignition times.

EXPERIMENT

All experiments were conducted using the shock-tube facility described by Petersen et al. [76] The shock tube is constructed of stainless steel, and the tube's helium-driven driver section is 3.5 meters in length and 7.62 cm in diameter. The driven section is 10.7 meters in length with a 16.2-cm inner diameter. All experiments were performed behind the reflected shock wave, and reaction progress was monitored by emission from the hydroxyl radical $A^2\Sigma^+ \rightarrow X^2\Pi$ transition (i.e., OH* chemiluminescence). A CaF_2 optical port located on the endwall of the shock tube allowed for non-intrusive optical access, and a Hamamatsu 1P21 photomultiplier tube (PMT) fitted with a narrow-band filter centered at 310 ± 5 nm collected the ultraviolet emission. A PCB 134A pressure transducer was located at the endwall, and five fast-response (< 1 μs) PCB 113A pressure transducers and four Fluke model PM6666 time-interval counters monitored the incident-shock speed at four different axial locations along the shock tube. The data acquisition system includes a Pentium computer and two CS512 computer oscilloscope boards from Gage Applied Sciences, which results in a total of four channels at a speed of 5 MHz per channel with 12-bit resolution. Further details of the shock-tube facility are reported elsewhere [76].

A complete list of all CO/H_2/Air mixtures is provided in Table 3. All mixtures were fuel lean with a fuel/air equivalence ratio of $\phi = 0.5$ and pre-mixed in tanks before being filled into the driven section of the shock tube. Figure 7 shows typical pressure and emission traces and defines ignition delay time as measured from the endwall location. The pressure signal indicated time zero, and the reaction profile was used to determine when ignition had occurred. In all experiments, ignition was clearly defined by the onset of OH* emission through the endwall window. Evidence of ignition was also observed in the corresponding pressure increase, but use of the pressure trace for ignition time tends to be less reliable than the emission trace due to the poorer S/N ratio of endwall pressure measurements (Fig. 7), particularly when the ignition occurs within a few hundred microseconds of reflected-shock passage. In addition, test temperatures behind

Table 3 Mixtures employed in the CO/H_2 study

Mixture	Blend	X_{CO}	X_{H2}	X_{O2}	X_{N2}
1	20/80% CO/H_2	0.035	0.139	0.174	0.652
2	60/40% CO/H_2	0.104	0.07	0.174	0.651
3	80/20% CO/H_2	0.14	0.035	0.174	0.651
4	90/10% CO/H_2	0.156	0.017	0.175	0.652
5	95/5% CO/H_2	0.165	0.009	0.174	0.652

the reflected shock wave were determined from the incident-shock speed using the standard 1-D shock-tube relations and the Sandia thermodynamic database [77].

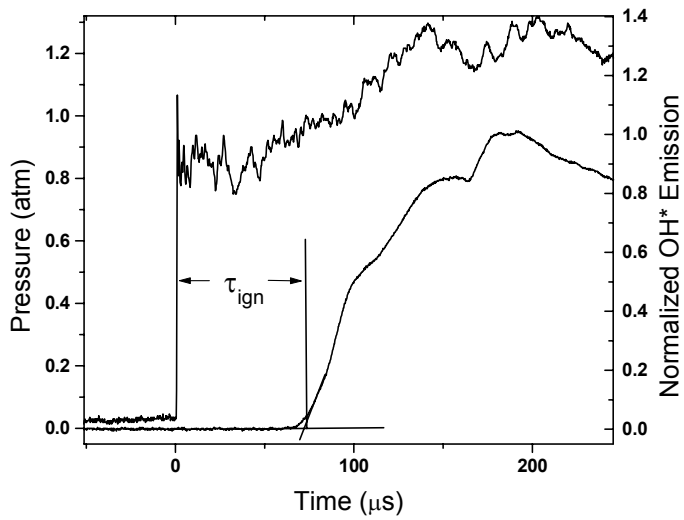

Fig. 7 Definition of ignition delay time (τ_{ign}) for Mixture 2, 1113 K, 1.081 atm.

The following sections contain two types of analysis. The first compares ignition delay time data obtained in this study with those predicted by three different chemical kinetics mechanisms, Davis et al. [75] with updated reactions and reaction rates obtained through personal communication with the author, Mueller et al., [74] and GRI-Mech 3.0 [78]. The second includes an ignition delay time sensitivity analysis that determined which reactions had the largest influence on ignition for both lower (900 K) and higher (1250 K) temperatures.

IGNITION DELAY TIME DATA

As mentioned previously, experimental data were collected for a range of reflected-shock temperatures (890 K < T< 1285 K) with pressures near one atmosphere for the mixtures listed in Table 3. For the model comparison, each of the three mechanisms was employed using the same mixture compositions, temperatures and average pressures as the experimental conditions; however, OH was used to indicate when ignition had occurred. For such high-concentration, exothermic mixtures, it is not necessary to add an OH* mechanism such as Hall et al. [79] to the models mentioned above because the induction times obtained from OH and OH* (and most other species) are identical. Hence, ignition from either OH or OH* is indistinguishable as defined herein when obtained from the chemical kinetics model. Figures 8 through 12 display the results of this analysis on Arrhenius plots.

It is evident that the Davis et al. [75] mechanism most accurately models the oxidation of CO/H_2 combustion for the entire temperature and pressure regime. However, the Mueller et al. [74] mechanism is also in very good agreement with the experimental data, especially at higher temperatures. The GRI-Mech 3.0 mechanism [78] is perhaps the least effective at modeling the behavior of CO/H_2 oxidation, although it nonetheless captures the primary temperature trends.

This result is not unexpected since GRI-Mech 3.0 was designed for higher-temperature oxidation and is largely a methane oxidation mechanism. All three mechanisms model the shift in temperature dependence between 1100 K and 1000 K quite well. This shift in temperature dependence is due to the well-known chain termination kinetics near the second explosion limit of the hydrogen system, as described more fully below. Although all three mechanisms capture the change in activation energy from low to high temperature, both the Mueller et al. and the GRI-Mech 3.0 mechanisms overpredict the experimental data at temperatures below 1000 K, and the Davis et al. [75] mechanism begins to overpredict the experimental data at temperatures below 950 K, as can be seen in Figs. 2 and 4. To more precisely model the oxidation and ignition of CO/H_2 for both high- and low-temperature regimes in the future, an ignition delay time sensitivity analysis was conducted to learn which reactions are most dominant at higher (1250 K) and lower (900 K) temperatures.

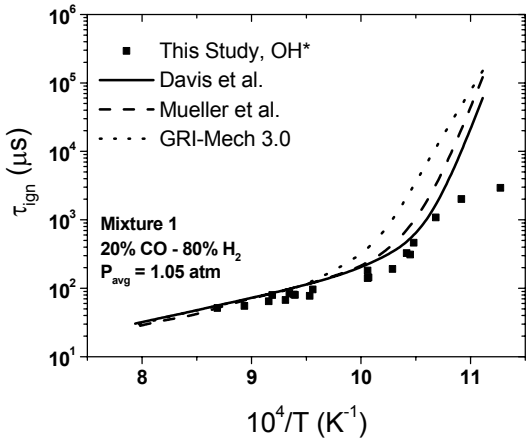

Fig. 8 Ignition delay time data and model comparison for Mixture 1 (20% CO – 80% H_2)

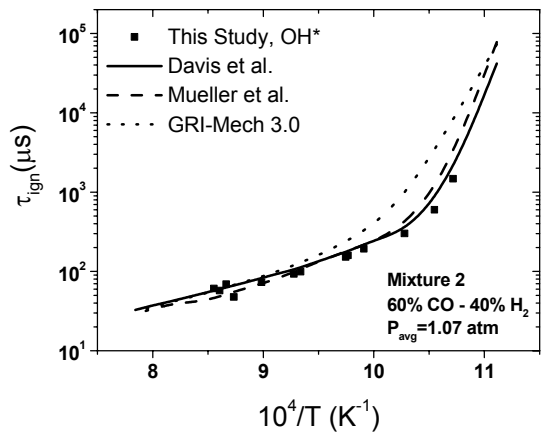

Fig. 9 Ignition delay time data and model comparison for Mixture 2 (60% CO – 40% H_2)

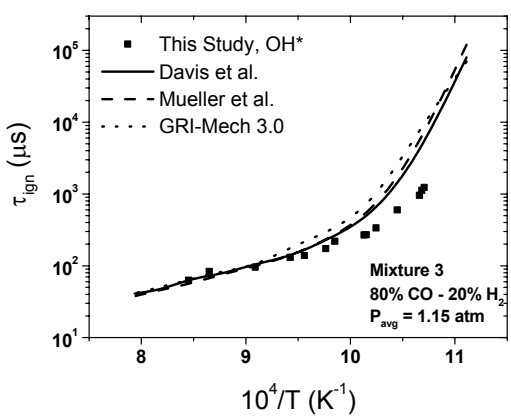

Fig. 10 Ignition delay time data and model comparison for Mixture 3 (80% CO – 20% H_2)

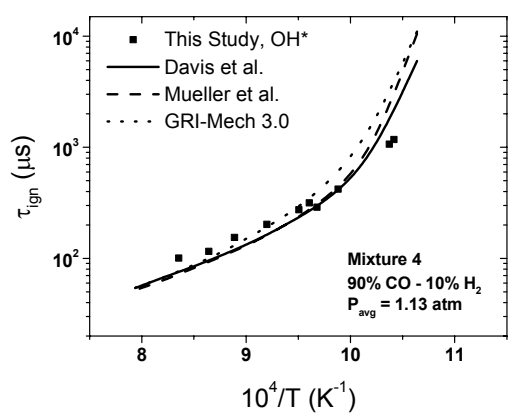

Fig. 11 Ignition delay time data and model comparison for Mixture 4 (90% CO – 10% H_2)

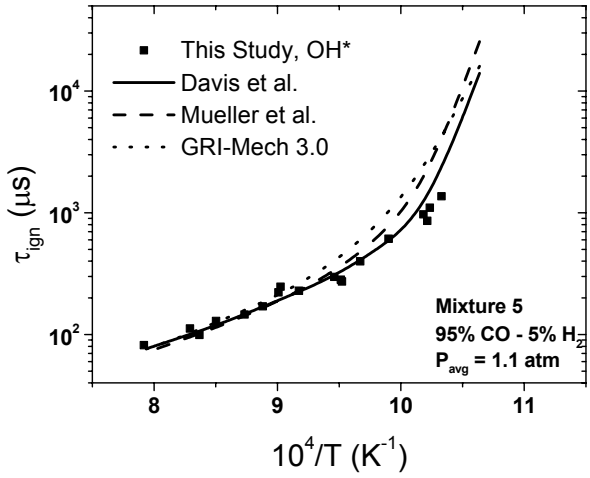

Fig. 12 Ignition delay time data and model comparison for Mixture 5 (95% CO – 5% H_2)

SENSITIVITY ANALYSIS

Using the *Shock* module in the Chemkin Collection [80] software package, an ignition delay time sensitivity analysis was conducted for Mixture 1 (20% CO and 80% H_2) and Mixture 5 (95% CO and 5% H_2) for both lower (900 K) and higher (1250 K) temperatures using the Davis et al. [75] mechanism. Mixtures 1 and 5 were chosen for analysis based on their mixture composition. It was deemed important to study the ignition sensitivity of CO/H_2 mixtures for two opposite fuel compositions to determine which reactions dominate the ignition behavior when the mixture is either composed primarily of H_2 or CO.

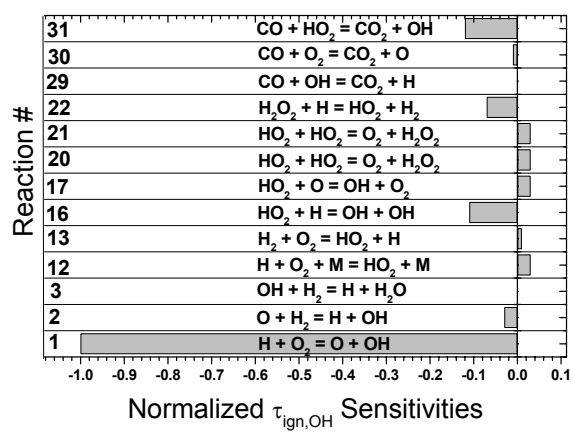

Fig. 13 Normalized ignition delay time sensitivities for Mixture 1 at T = 900 K and P = 1.05 atm

Due to the fact that the Davis et al. [75] mechanism predicted the experimental data most accurately, it was chosen to be used in the sensitivity analysis. Using the OH concentration profile for each reaction i, the ignition delay time, $\tau_{ign,OH}$, was calculated for reaction rates of $1/2k_i$ and $2k_i$. Subsequently, the ignition delay time sensitivity was defined as:

$$sensitivity = \left(\tau\big|_{2k_i} - \tau\big|_{(1/2)k_i}\right) \Big/ \tau\big|_{k_i} \tag{1}$$

where a negative value for sensitivity indicates faster ignition. Results for each mixture and temperature were then normalized by the largest sensitivity value. Sensitivity values below 0.01

were neglected for Mixture 1 and those below 0.02 were neglected for Mixture 5. Results for the τ_{ign} sensitivity are presented in Figs. 13-16.

It is apparent from Figs. 13-16 that the reaction

$$H + O_2 = O + OH \tag{R1}$$

has the largest influence on the ignition delay time for the entire range of mixtures and test conditions herein. Although this important chain branching reaction has a large influence on the overall system kinetics, other reactions also affect ignition characteristics, depending on temperature and level of hydrogen content.

For Mixture 1 (20% CO and 80% H_2) at lower temperatures (900 K, Fig. 7), there are three reactions with influential sensitivity values that are working to speed up ignition in addition to R1, each involving HO_2:

$$HO_2 + H = OH + OH \tag{R16}$$

$$H_2O_2 + H = HO_2 + H_2 \tag{R22}$$

$$CO + HO_2 = CO_2 + OH \tag{R31}$$

Although these three reactions have relatively large individual responses to changes in reaction rate and are the result of increased levels of HO_2 at lower temperatures, the ignition delay time plots indicate that τ_{ign} slows down at lower temperatures. The increase in ignition delay time at lower temperatures can be attributed to HO_2 recombination via R20/R21, the termination reaction R17, and HO_2 formation via R12.

$$HO_2 + HO_2 = O_2 + H_2O_2 \tag{R20/R21}$$

$$HO_2 + O = OH + O_2 \tag{R17}$$

$$H + O_2 + M = HO_2 + M \tag{R12}$$

Conversely, at higher temperature (1250 K, Fig. 14) for the same mixture, the sensitivity analysis indicates that chain propagating and branching reactions are dominant (i.e., R1, R2, R3, R13, and to a lesser extent R29), which all work to speed up ignition.

$$O + H_2 = H + OH \tag{R2}$$

$$OH + H_2 = H + H_2O \tag{R3}$$

$$H_2 + O_2 = HO_2 + H \tag{R13}$$

$$CO + OH = CO_2 + H \qquad (R29)$$

Note that at the higher temperature for this mixture containing primarily hydrogen (Mixture 1), the above four reactions have mostly minor impacts on ignition when compared to R1.

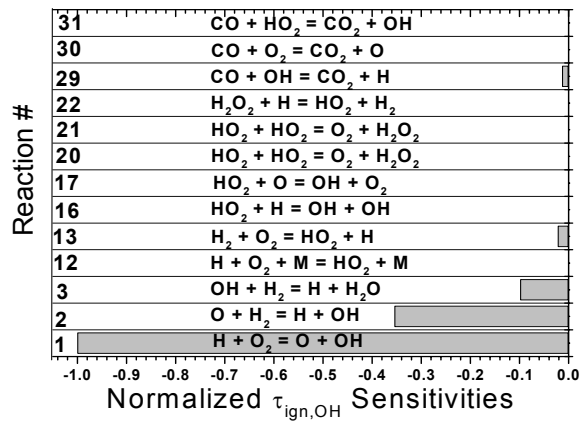

Fig. 14 Normalized ignition delay time sensitivities for Mix 1, T = 1250 K , P = 1.05 atm

On the other hand, Mixture 5 with only a marginal amount of H_2 (95% CO and 5% H_2) had many more reactions influencing ignition than Mixture 1 (Fig. 15). Therefore, as mentioned above, instead of neglecting sensitivities below 0.01, those below 0.02 were neglected. Overall, the τ_{ign} sensitivity analysis for Mixture 5 at lower temperature (900 K) indicated the same dominant H_2/O_2 reactions as the lower-temperature Mixture 1 case described above. However, although the reactions were similar, Mixture 5 reactions showed a much larger response to changes in reaction rate than Mixture 1 (for example, R1 was by far the most sensitive reaction for Mixture 1, with minimal changes in sensitivity for the other ignition-enhancing reactions R16 and R31). For Mixture 5 at 900 K, R1, R2, R16, and R31 all have significant impacts on ignition. Most notably, the CO + HO_2 reaction (R31) becomes a primary ignition promoter at lower temperatures for higher levels of CO in the initial mixture. As mentioned above for Mixture 1 at similar conditions and evident in Figs. 8 and 12, the ignition delay time of Mixture 5 at 900 K is dramatically increased.

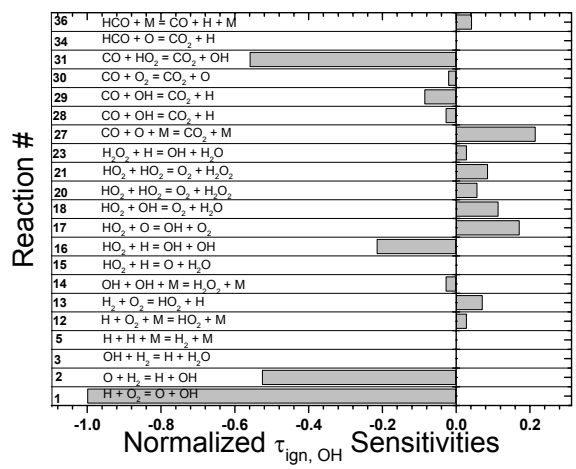

Fig. 15 Normalized ignition delay time sensitivities: Mix 5, T = 900K and P = 1.1 atm

Although the ignition-enhancing reactions had large sensitivity values, several key inhibiting reactions are contributing to the slow ignition trend at lower temperatures. In fact, the reactions contributing most to the slowing down of ignition in this lower-temperature region include the HO_2-containing reactions R17, R18, R20/21 and the CO_2 formation reaction R27.

$$HO_2 + OH = O_2 + H_2O \qquad (R18)$$

$$CO + O + M = CO_2 + M \qquad (R27)$$

It should be noted that although the ignition kinetics are still dominated by the H_2 oxidation system, reactions involving CO become more important for this mostly CO-containing mixture (Mixture 5), for example R27, R29, and R31 than was seen in the mixtures with more H_2.

The Mixture 5 higher-temperature (1250 K) ignition delay time sensitivity results (Fig. 16) show a much weaker effect of HO_2- and CO-containing reactions, as expected, with large sensitivities for R1 and R2. Also, the sensitivity of reaction 31 is almost completely diminished and is replaced by the CO oxidation reaction,

$$CO + O_2 = CO_2 + OH \tag{R30}$$

Additionally, the propagation reaction

$$OH + H_2 = H + H_2O \tag{R3}$$

becomes important at higher temperatures and contributes H radicals that then react with O_2 to form OH and O (i.e., R1). The large number of radicals that are formed for higher-temperature CO/H_2 combustion catalyze ignition.

The focus of the current research was to first obtain ignition delay time data for a range of temperatures at 1 atmosphere and provide a comparison to current chemical kinetics mechanisms. Research currently in progress is aimed at providing data at realistic gas-turbine operating environments (i.e., high temperature and high pressure). Additionally, these future data will serve to again validate and improve CO/H_2 chemical kinetics mechanisms. It is anticipated that the discrepancy between model and experiment at lower temperatures, where HO_2 chemistry becomes important, will be magnified at higher pressures.

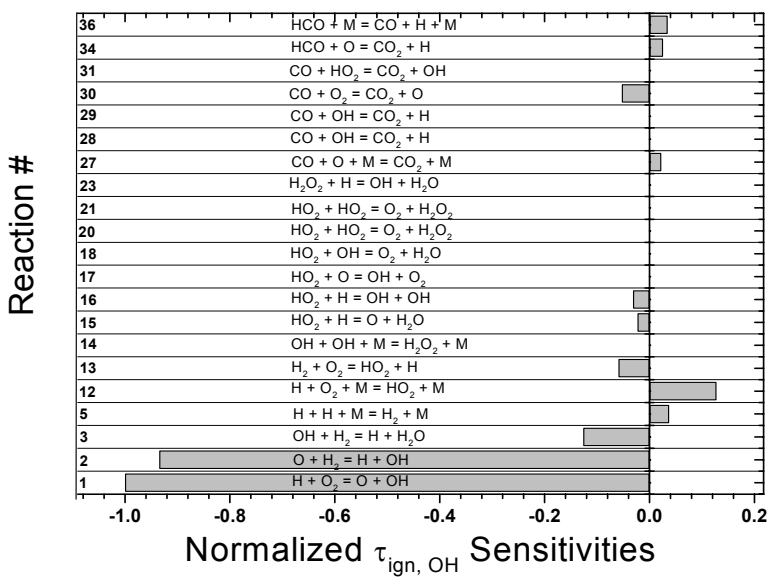

Fig. 16 Normalized ignition delay time sensitivities: Mixture 5, T = 1250 K and P = 1.1 atm

CONCLUSIONS

Experiments related to the use of syngas-based fuels in gas turbines continued during this 6-month reporting, focusing mainly on lower-pressure conditions. Several CO/H_2 blends mixed with air at lean (ϕ = 0.5) equivalence ratios were shock heated to determine their ignition behavior over a range of temperatures from 900 to 1360 K at pressures greater than 3 atm. ***The results of these experiments indicate weaknesses in the CO/H_2 mechanism at lower temperature (and by implication, higher pressures). High-pressure experiments are ongoing during the next reporting period.***

Regarding data on methane-based fuel blends, experiments were performed at typical gas turbine premixer conditions of 18 atm and 800 K to determine whether or not each mixture will ignite within a 10-ms test time—a typical residence time for gas turbine premixers. Blends contained binary and ternary mixtures of methane with hydrogen, ethane, propane, butane, and pentane. The test matrix developed in previous reporting periods was utilized to obtain as much information over a wide range of blends as possible. ***An important result is that all mixtures demonstrated either weak or strong ignition within 10 ms.***

REFERENCES

[1] Lefebvre, A. H., 1999, *Gas Turbine Combustion*, 2nd Ed, Taylor & Francis, Philadelphia PA.

[2] Spadaccini, L. J. and Colket, M. B. III, 1994, "Ignition Delay Characteristics of Methane Fuels," *Progress in Energy and Combustion Science*, Vol. 20, pp. 431-460.

[3] Naber, J. D., Siebers, D. L., Di Julio, S. S., and Westbrook, C. K., 1994, "Effects of Natural Gas Composition on Ignition Delay under Diesel Conditions," *Combustion and Flame*, Vol. 99, pp. 192-200.

[4] Flores, R. M., Miyasato, M. M., McDonell, V. G., and Samuelsen, G. S., 2001, "Response of a Model Gas Turbine Combustor to Variation in Gaseous Fuel Composition," *Journal of Engineering for Gas Turbines and Power*, Vol. 123, pp. 824-831.

[5] Flores, R. M., McDonell, V. G., and Samuelsen, G. S., 2003, "Impact of Ethane and Propane Variation in Natural Gas on Performance of a Model Gas Turbine Combustor," *Journal of Engineering for Gas Turbines and Power*, Vol. 125, pp. 701-708.

[6] Richards, G. A., McMillian, M. M., Gemmen, R. S., Rogers, W. A., Cully, S. R., *Prog. Energy Comb. Sci.* 27 (2001) 141-169.

[7] Lieuwen, T., McDonell, V., Petersen, E., Santavicca, D., ASME Paper GT2006-90770 (2006).

[8] L.J. Spadaccini, M.B. Colket, *Prog. Energy Combust. Sci*. 20 (1994) 431-460.

[9] N. Lamoureux, C.-E. Paillard, *Shock Waves* 13 (2003) 57-68.

[10] R.M. Flores, M.M. Miyasato, V.G. McDonell, G.S. Samuelsen, *J. Eng. Gas Turb. Power* 123 (2001) 824-831.

[11] R.M. Flores, V.G. McDonell, G.S. Samuelsen, *J. Eng. Gas Turb. Power* 125 (2003) 701-708.

[12] E.L. Petersen, J.M. Hall, S.D. Smith, J. de Vries, A. Amadio, M.W. Crofton, ASME Paper GT2005-68517 (2005).

[13] Petersen, E., de Vries, J., AIAA Paper 2005-1165 (2005).

[14] Bi, H., Agrawal, A. K., *Combust. Flame* 113 (1998) 289-302.

[15] R.M.R. Higgin, A. Williams, *Proc. Combust. Inst.* 12 (1969) 579-590.

[16] D.J. Seery C.T. Bowman, *Combust. Flame* 14 (1970) 37-48.

[17] T. Tsuboi, H. Wagner, *Proc. Combust. Inst.* 15 (1974) 883-890.

[18] E.L. Petersen, M. Röhrig, D.F. Davidson, R.K. Hanson, C.T. Bowman, *Proc. Combust. Inst.* 26 (1996) 799-806.

[19] E.L. Petersen, D.F. Davidson, R.K. Hanson*, J. Propul. Power* 15 (1999) 82-91.

[20] V.P. Zhukov, V.A. Sechenov, A.Yu. Starikovskii, *Combust. Explo. Shock+* 39 (5) (2003) 487-495.

[21] J. Huang, P.G. Hill, W.K. Bushe, S.R. Munshi, *Combust. Flame* 136 (2004) 25-42.

[22] T.R. Hunter, H. Wang, T.A. Litzinger, M. Frenklach, *Combust. Flame* 97 (1994) 201-224.

[23] M. Frenklach, H. Wang, M. Goldenberg, G.P. Smith, D.M Golden, C.T. Bowman, R.K. Hanson, W.C. Gardiner, V. Lissianski, *GRI topical report,* Report No. GRI-95/0058.

[24] G.P. Smith, D.M. Golden, m. Frenklach, N.W. Moriarty, B. Eiteneer, M. Goldenberg, C.T. Bowman, R.K. Hanson, S. Song, W.C. Gardiner, V.V. Lissianski, Z. Qin, GRI-Mech 3.0, http://www.me.Berkeley.edu/gri-mech/

[25] E.L. Petersen, D.F. Davidson, R.K. Hanson, *Combust. Flame* 117 (1999) 272-290.

[26] S.C. Li, F.A. Williams, J. *Eng. Gas Turb. Power* 124 (2002) 471-480.

[27] R.W. Crossley, E.A. Dorko, K. Scheller, A. Burcat, *Combust. Flame* 19 (1972) 373-378.

[28] C.S. Eubank, M.J. Rabinowitz, W.C. Gardiner, R.F. Zellner, *Proc. Combust. Insti.* 18 (1981) 1767-1774.

[29] R. Zellner, K.J. Niemitz, J. Warnatz, W.C. Gardiner, C.S. Eubank, J.M. Simmie, *Prog. Aeronautics Astronautic* 80 (1983) 252-272.

[30] M. Frenklach, D.F. Bornside, *Combust. Flame* 56 (1984) 1-27.

[31] A.El. Bakali, P. Dagaut, L. Plillier, P. Desgroux, J.-F. Pauwels, A. Rida, P. Meunier, *Combust. Flame* 137 (2004) 109-128.

[32] J. Huang, W.K. Bushe, *Combust. Flame*, in press (2005).

[33] R.K. Cheng, A.K. Oppenheim, *Combust. Flame* 58 (1984) 125-139.

[34] R. Sierens, E. Rosseel, *J. Eng. Gas Turb. Power* 122 (2000) 135-140.

[35] K.S. Krishnan, R. Ravikumar, K.A. Bhaskaran, *Combust. Flame* 49 (1983) 41-50.

[36] Cowell, L. H., Lefebvre, A. H., SAE Paper 860068 (1986).

[37] Y. Tan, P. Dagaut, M. Cathonnet, J.C. Boettner, *Proc. Combust. Inst.* 25 (1994) 1563-1569.

[38] P. Dagaut, G. Dayma, *Combust. Flame* 143 (2005) 135-137.

[39] C.K. Westbrook, *Combust. Sci. Technol.* 20 (1979) 5-17.

[40] W.C. Gardiner, V.V. Lissianski, V.M. Zamanski, *Proc. Shock Wave Symp. (Int), 19* (1993) 155-160.

[41]Petersen, E. L., Kalitan, D. M., Simmons, S., Bourque, G., Curran, H. J., Simmie, J. M., These Proceedings, submitted (2006).

[42] H.K. Ciezki, G. Adomeit, *Combust. Flame* 93 (1993) 421-433.

[43] K. Fieweger, R. Blumenthal, G. Adomeit, *Combust. Flame* 109 (1997) 599-619.

[44] J. Herzler, L. Jerig, P. Roth, *Combust. Sci. Technol.* 176 (2004) 1627-1637.

[45] J. Herzler, L. Jerig, P. Roth, *Proc. Combust. Inst.* 30 (2005) 1147-1153.

[46] V.P. Zhukov, V.A. Sechenov, A.Yu. Starikovskii, *Combust Flame* 140 (2005) 196-2003.

[47] de Vries, J., Petersen, E., ASME Paper IMECE2005-1165 (2005).

[48] H.J. Curran, P. Gaffuri, W.J. Pitz, C.K. Westbrook, *Combust. Flame* 129 (2002) 253-280.

[49] Kee, R. J., Rupley, F. M., Miller, J. A., Coltrin, M. E., Grcar, J. F., Meeks, E., Moffat, H. K., Lutz, A. E., Dixon-Lewis, G., Smooke, M. D., Warnatz, J., Evans, G. H., Larson, R. S., Mitchell, R. E., Petzold, L. R., Reynolds, W. C., Caracotsios, M., Stewart, W. E., Glarborg, P., Wang, C., Adigun, O., *Chemkin Collection*, Release 3.6, Reaction Design, Inc., San Diego, CA (2000).

[50] E.L. Petersen, M.J.A. Rickard, M.W. Crofton, E.D. Abbey, M.J. Traum, D.M Kalitan, *Meas. Sci. Technol.* 16 (2005) 1716-1729.

[51] A.G. Gaydon, I.R. Hurle, *The Shock Tube in High Temperature Physics,* Reinhold, New York, 1963.

[52] Kalitan, D. M., Hall, J. M., Petersen, E. L., *J. Prop. Power* 21 (2005) 1045-1056.

[53] Davidson, D. F., Hanson, R. K., *Int. J. Chem. Kinet.* 36 (2004) 510-523.

[54] A.R. Amadio, Crofton, M. W., E.L. Petersen, *Shock Waves,* in press (2006).

[55] Goy, C. J., Moran, A. J., Thomas, G. O., ASME Paper 2001-GT-0051 (2001).

[56] Richards, G. A., McMillian, M. M., Gemmens, R. S., Rogers, W. A., and Cully, S. R., "Issues for Low-Emission, Fuel-Flexible Power Systems," *Progress in Energy and Combustion Science*, Vol. 27, 2001, pp. 141-169.

[57] Sulzmann, K. G. P., Myers, B. F., and Bartle, E. R., "CO Oxidation. I. Induction Period Preceding CO_2 Formation in Shock-Heated CO-O_2-Ar Mixtures," *Journal of Chemical Physics*, Vol 42, No. 11, 1965, pp. 3969-3979.

[58] Myers, B. F., Sulzmann, K. G. P., and Bartle, E. R., "Oxidation of CO. II. Influence of H_2 on the Induction Period Preceding Rapid CO_2 Formation in Shock-Heated CO-O_2-Ar Mixtures," *Journal of Chemical Physics,* Vol. 43, No. 4, 1965, pp. 1220-1228.

[59] Brabbs, T. A., Belles, F. E., and Brokaw, R. S., "Shock-Tube Measurements of Specific Reaction Rates in Branched-Chain H_2-CO-O_2 Systems," *Proceedings of the Combustion Institute*, Vol 13. 1970, pp. 129-136.

[60] Gardiner, W. C., McFarland, M., Morinaga, K., Takeyama, T., and Walker, B. F., "Initiation Rate for Shock-Heated Hydrogen-Oxygen-Carbon Monoxide-Argon Mixtures as Determined by OH Induction Time Measurements," *Journal of Physical Chemistry,* Vol. 75, No. 10, 1971, pp. 1504-1509.

[61] Gardiner, W. C., Mallard, W. G., McFarland, M., Morinaga, K., Owen, J. H., Rawlins, W. T., Takeyama, T., and Walker, B. F., "Elementary Reaction Rates From Post-Induction-Period Profiles in Shock-Initiated Combustion," *Proceedings of the Combustion Institute* Vol. 14,1972, pp. 61-75.

[62] Dean, A. M., Steiner, D. C., and Wang, E. E., "A Shock Tube Study of the $H_2/O_2/CO/Ar$ and $H_2/N_2O/CO/Ar$ Systems: Measurement of the Rate Constant for $H+N_2O=N_2+OH^*$," *Combustion and Flame*, Vol. 32, 1978, pp. 73-83.

[63] Slack, M., and Grillo, A., "High Temperature Rate Coefficient Measurements of CO+O Chemiluminescence," *Combustion and Flame,* Vol. 59, 1985, pp. 189-196.

[64] Cherian, M. A., Rhodes, P., Simpson, R. J., and Dixon-Lewis, G., "Kinetic Modelling of the Oxidation of Carbon Monoxide in Flames," *Proceedings of the Combustion Institute*, Vol. 18, 1980, pp. 385-396.

[65] Warnatz, J., "The Structure of Laminar Alkane-, Alkene-, and Acetylene Flames," *Proceedings of the Combustion Institute*, Vol. 18, 1980, pp. 369-384.

[66] Westbrook, C. K., and Dryer, F. L., "Chemical Kinetics and Modeling of Combustion Processes," *Proceedings of the Combustion Institute*, Vol. 18, 1980, pp. 749-764.

[67] Pitz, W. J., Westbrook, C. K., Proscia, W. M., and Dryer, F. L., "A Comprehensive Chemical Kinetic Reaction Mechanism for the Oxidation of N-Butane," *Proceedings of the Combustion Institute*, Vol. 20, 1984, pp. 831-843.

[68] Von Elbe, G., and Lewis, B., "Free-Radical Reactions in Glow and Explosion of Carbon Monoxide-Oxygen Mixtures," *Combustion and Flame,* Vol. 63, 1986, pp. 135-150.

[69] Mass, U., and Warnatz, J., "Ignition Processes in Carbon-Monoxide-Hydrogen-Oxygen Mixtures," *Proceedings of the Combustion Institute*, Vol. 22, 1988, pp. 1695-1704.

[70] Chung, S. H., and Williams, F. A., "Asymptotic Structure and Extinction of CO-H_2 Diffusion Flames with Reduced Kinetic Mechanisms," *Combustion and Flame,* Vol. 82, 1990, pp. 389-410.

[71] Yetter, R. A., Dryer, F. L., and Rabitz, H., "A Comprehensive Reaction Mechanism for Carbon Monoxide/Hydrogen/Oxygen Kinetics," *Combustion Science and Technology,* Vol. 79, 1991, pp. 97-128.

[72] Trevino, C., and Solorio, F., "Asymptotic Analysis of the High-Temperature Ignition of $CO/H_2/O_2$ Mixtures," *Combustion and Flame,* Vol. 86, 1991, pp. 285-295.

[73] Cho, S., and Niksa, S., "Elementary Reaction Models and Correlations for Burning Velocities of Multicomponent Organic Fuel Mixtures," *Combustion and Flame,* Vol. 101, 1995, pp. 411-427.

[74] Mueller, M. A., Yetter, R. A., and Dryer, F. L., "Flow Reactor Studies and Kinetic Modeling of the $H_2/O_2/NO_x$ and $CO/H_2O/O_2/NO_x$ Reactions," *International Journal of Chemical Kinetics*, Vol. 31, 1999, pp. 705-724.

[75] Davis, S. G., Joshi, A. V., Wang, H., and Egolfopoulos, F., "An Optimized Kinetic Model of H_2/CO Combustion," *Proceedings of the Combustion Institute,* Vol. 30, 2005, pp. 1283-1292.

[76] Petersen, E. L., Rickard, M. J. A., Crofton, M. W., Abbey, E. D., Traum, M. J., and Kalitan, D. M., "A Facility for Gas-and Condensed–Phase Measurements Behind Shock Waves," *Measurement Science and Technology*, Vol. 16, 2005, in press.

[77] Kee, R. J., Rupley, F. M., and Miller, J. A., "The Chemkin Thermodynamic Database," SAND87-8251B, Sandia National Laboratory, March 1990.

[78] Smith, G. P., Golden, D. M., Frenklach, M., Moriarty, N. W., Eiteneer, B., Goldenberg, M., Bowman, C. T., Hanson, R. K., Song, S., Gardiner, W. C., Lissianski, V. V., and Qin, Z., GRI-Mech 3.0, http://www.me.berkeley.edu/gri-mech/

[79] Hall, J. M., and Petersen, E. L., "Kinetics of OH Chemiluminescence in the Presence of Hydrocarbons," AIAA Paper 2004-4164, July, 2004.

[80] Kee, R. J., Rupley, F. M., Miller, J. A., Coltrin, M. E., Grcar, J. F., Meeks, E., Moffat, H. K., Lutz, A. E., Dixon-Lewis, G., Smooke, M. D., Warnatz, J., Evans, G. H., Larson, R. S., Mitchell, R. E., Petzold, L. R., Reynolds, W. C., Caracotsios, M., Stewart, W. E., Glarborg, P.,

Wang, C., Adigun, O., *Chemkin Collection*, Release 4.0, Reaction Design, Inc., San Diego, CA, 2004.

EFFECTS OF COATING BLOCKAGE AND DEPOSITS ON FILM COOLING EFFECTIVENESS AND HEAT TRANSFER

Semi-Annual Report
August 1 2005 - January 31, 2006

Minking K. Chyu
Department of Mechanical Engineering
University of Pittsburgh
Pittsburgh, PA 15261
(412) 624-9784
mkchyu@engr.pitt.edu

Tom I-P. Shih
Department of Aerospace Engineering
Iowa State University
2271 Howe Hall, Rm 1200
Ames, IA 50011-2271
(515) 294-6241
tomshih@iastate.edu

January 31, 2006

DOE Award Number - DE-FC21-02NT41431
UTSR Project Number - 04-01-SR115

Department of Mechanical Engineering
University of Pittsburgh
Pittsburgh, PA 15261

Department of Aerospace Engineering
Iowa State University
2271 Howe Hall, Rm 1200
Ames, IA 50011-2271

DISCLAIMER – This report was prepared as an account of work sponsored by an agency of the United States Government. Neither the United States Government nor any agency thereof, nor any of their employees, makes any warranty, express or implied, or assumes any legal liability or responsibility for the accuracy, completeness, or usefulness of any information, apparatus, product, or process disclosed, or represents that its use would not infringe privately owned rights. Reference herein to any specific commercial product, process, or service by trade name, trademark, manufacturer, or otherwise does not necessarily constitute or imply its endorsement, recommendation, or favoring by the United States Government or any agency thereof. The views and opinions of authors expressed herein do not necessarily state or reflect those of the United States Government or any agency thereof.

ABSTRACT

This report describes the progress over the first six months of year 2 of this three-year UTSR research project. The project is concerned with the effects of coating partial blockage and surface deposits on film cooling performance. The research is a joint pursuit of experiment and computational simulation. Progress has been made during this second phase of the program in exploring new film cooling design concepts for better performance. On the computational front, FLUENT code is being used to develop and study three new design concepts for film cooling to increase adiabatic effectiveness. Experimentally, progress has been made on two fronts. First, a new test system that is capable of accommodating a wider test range for hole-blockage study is established. Second, the experiment to explore the effects of surface deposits near film cooling holes is being developed. Key focus of this aspect of research is to potentially control TBC deposit profile for better film cooling performance. All tasks are on schedule and consistent with the original proposal. Both computational and experimental results will be reported in the annual report and presented in the UTSR workshop.

TABLE OF CONTENTS

Cover Page …… 1
Disclaimer …… 2
Abstract …… 3
Executive Summary …… 5
Project Description …… 6
Results and Discussion …… 6
    Experimental …… 6
    Computational …… 8
Conclusion …… 13

EXECUTIVE SUMMARY

The main objective of this DOE UTSR project is to use a coordinated experimental and computational approach to systematically explore the transport processes associated with film-hole partial blockage and surface deposits on the film cooling performance for both round (unshaped) and shaped film holes. Spatially-resolved film effectiveness and heat transfer coefficient for all the test cases will be acquired using a IR transient technique. The objective on the computational front is to develop optimal practice guidelines for CFD simulations of film cooling affected by partial blockage and realistic surface roughness. The experimental database will serve as a reference for validating the CFD simulation. The CFD efforts will complementarily provide important transport insight that is otherwise unattainable by experiments. The collective information gained from this research could further provide guidelines for advanced film cooling strategies, which includes modifying and optimizing hole shapes, better fuel filtration, and improved maintenance scheduling as well as specific clean-up procedures for future turbine engines.

PROJECT DESCRIPTION

This University Turbine System Research program is a combined effort of experiment and numerical computation for studying the transport phenomena related to the effects of blockage and surface deposits around film cooling holes. The primary goal of this research is to provide the turbine manufacturers with fundamental insight that can impact the future design of film cooling. The research team consists of participants from two universities: University of Pittsburgh (Pitt) and Iowa State University (ISU). The Pitt portion of the combined program is an experimental investigation of the film cooling performance affected by blockage and surface deposits. The specific tasks are to perform detailed measurements of surface heat transfer coefficient and film effectiveness. The experimental work at Pitt is coordinated with the computational effort at ISU. The research focus at ISU is to perform CFD simulation of transport phenomena and providing guidelines for improved designs in film cooling. Validation of computational models will use the heat transfer and flow data obtained from the experimental aspect of the program. On the other hand, information gained from the computation will provide the experiment with more detailed insight in data interpretation. This will eventually aid the selection of optimal test geometry and parameters.

RESULTS AND DISCUSSION

Experimental

YEAR 2
TASK
Effects of discrete deposits on film cooling
Effectiveness (η) and heat transfer (h) measurements – round hole and shaped holes with deposits, various flow conditions
Explore new design concepts

Table above shows the proposed tasks and schedule for Year 2. One of the major accomplishments in the first six months of Year 2 is to design and fabricate test rigs for exploring new film cooling design concepts and those for studying the effect of discrete surface deposits. Two new film cooling design concepts have been proposed according to the computational results. One is film cooling hole upstream ramp, the other is flow-aligned blockers, as illustrated in Figure 1 and 2, respectively.

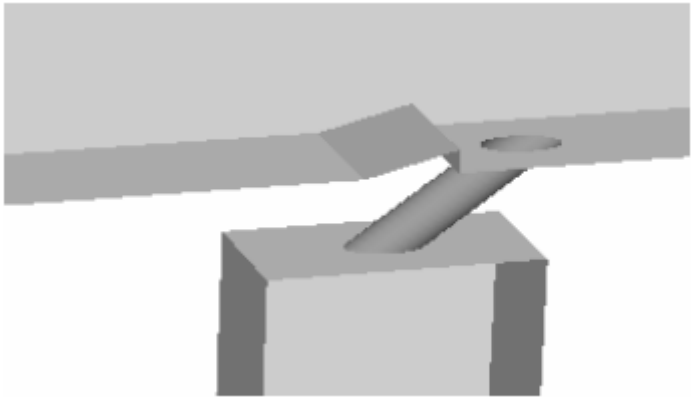

Figure 1 Schematic of a ramp upstream of a film cooling hole

Figure 2 Schematic of blockers downstream of a film-cooling hole

The obvious advantage of these new concepts is that they can be easily implemented by TBC coating, without much extra manufacturing effort. Figure 3 and 4 shows key geometrical parameters.

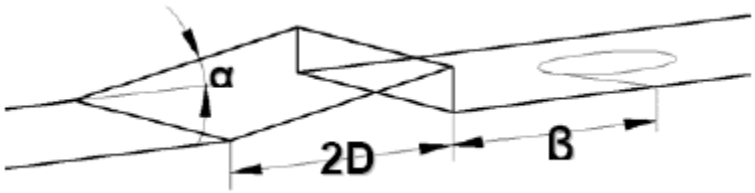

Figure 3 Schematic of the upstream design parameter

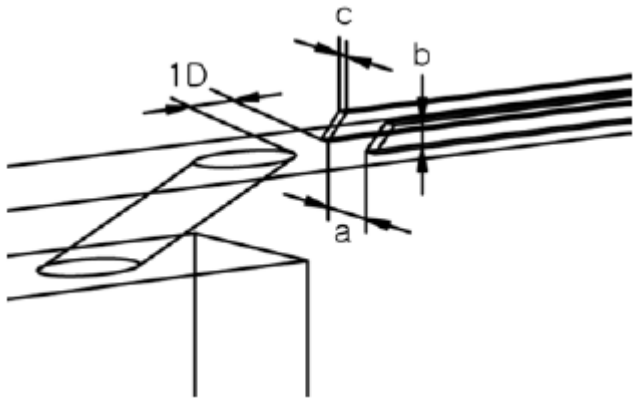

Figure 4 Schematic of generic blocker design parameters

The specific tasks accomplished during this six-months reporting period are:

- Design and fabrication of the test rigs for experimental study of the two new film cooling design concepts.
- Design and fabrication of the test rigs for experimental study of the effect of discrete surface deposits on film cooling.
- Improvement of the test system for higher Reynolds number (up to 200,000 for main flow).

Over the next six months, most of the effort will be devoted to acquiring film cooling data for the two new film cooling design concepts and exploring the effects of partial blockage under high Reynolds number and the effects of discrete surface deposits. The specific tasks to be explored are:

- Film cooling experimental data (both heat transfer coefficient and film cooling effectiveness) for the two new film cooling design concepts
- Effects of partial film-hole blockage on film cooling effectiveness and heat transfer coefficient for single circular round hole for high Reynolds number
- Effects of partial film-hole blockage on film cooling effectiveness and heat transfer coefficient for single shaped hole for high Reynolds number
- Effects of discrete surface deposits on film cooling effectiveness and heat transfer coefficient for single circular round hole
- Effects of discrete surface deposits on film cooling effectiveness and heat transfer coefficient for single shaped hole
- Comparison with corresponding computational results and exploring significant insight

Computational

To provide the design guideline for the experimental study described above, the two new film cooling design concepts (upstream ramp and flow-aligned bumper) have been numerically examined by simulation using Fluent-UNS code.

Upstream Ramp

Figure 5 illustrates the increase in film cooling effectiveness for the concept involving upstream ramp.

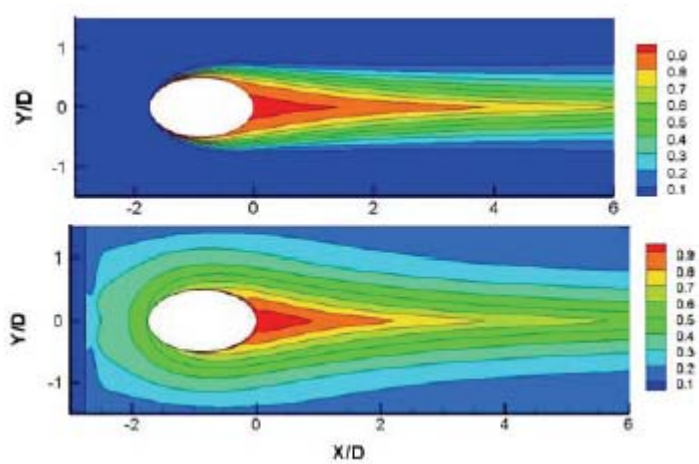

Figure 5 Adiabatic effectiveness on the flat plate about the film-cooling hole. Top: No ramp. Bottom: With ramp

The effects of the following parameters were investigated: □, angle of the ramp (8.5°, 14°), □, distance between the backward-facing step of the ramp and the film cooling hole (0.5D, D), and M, blowing ratio (0.36, 0.49, 0.56, 0.98).

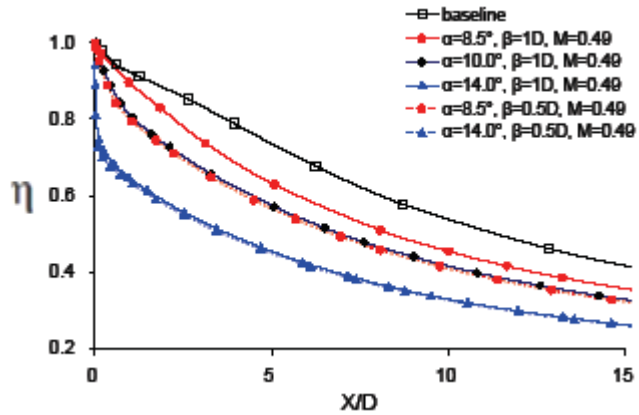

(a)

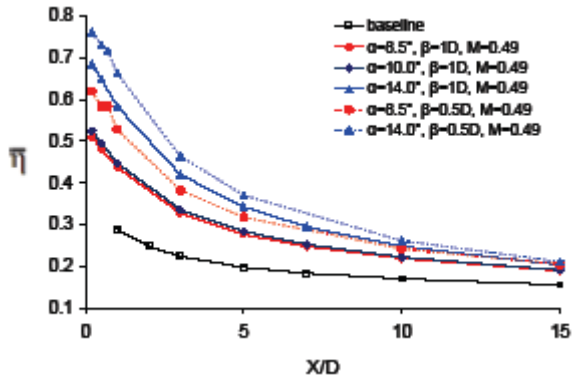

(b)

Figure 6 Adiabatic effectiveness with and without ramp
(a) Centerline adiabatic effectiveness. (b) Laterally averaged adiabatic effectiveness

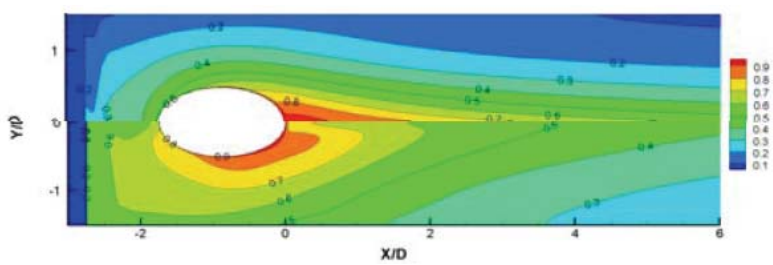

Figure 7 Adiabatic effectiveness for β = D and M = 0.49. Top: α = 8.5°. Bottom: α = 14°

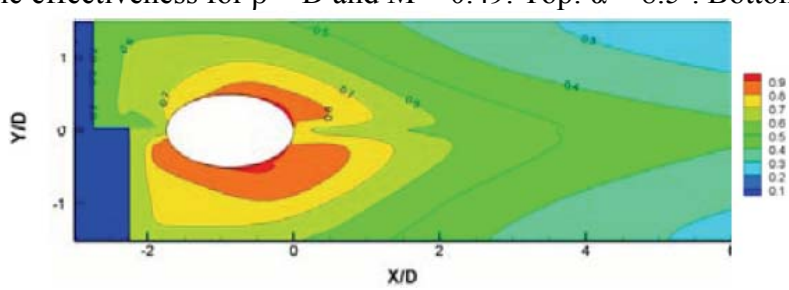

Figure 8 Adiabatic effectiveness for α = 14° and M = 0.49. Top: β = D. Bottom: β = 0.5D.

Figures 6 to 8 show the effects of ramp angle and distance from backward-facing step of the ramp to the film cooling hole. These numerical results lead to following observations. First, increasing the ramp angle (and hence the height of the backward-facing step), the higher is the adiabatic effectiveness, at least for the two angles studied. Second, placing the ramp 0.5D upstream gave higher adiabatic effectiveness than placing it 1D upstream. Evident is that placing a ramp upstream of a row of film-cooling holes increases adiabatic effectiveness significantly. The laterally averaged adiabatic effectiveness with ramp can improve at least 100% higher than that without the ramp.

Figure 9 shows the effects of blowing ratio on adiabatic effectiveness. From this figure, it can be seen that adiabatic effectiveness can decrease if the blowing ratio is too high or too low. Thus, the optimal angle of the ramp or the height of the backward-facing step depends on the blowing ratio. For a ramp with $\alpha = 8.5^{o}$ that is located at $\beta = D$ upstream of the film-cooling hole, blowing ratio around 0.5 maximizes the film cooling performance.

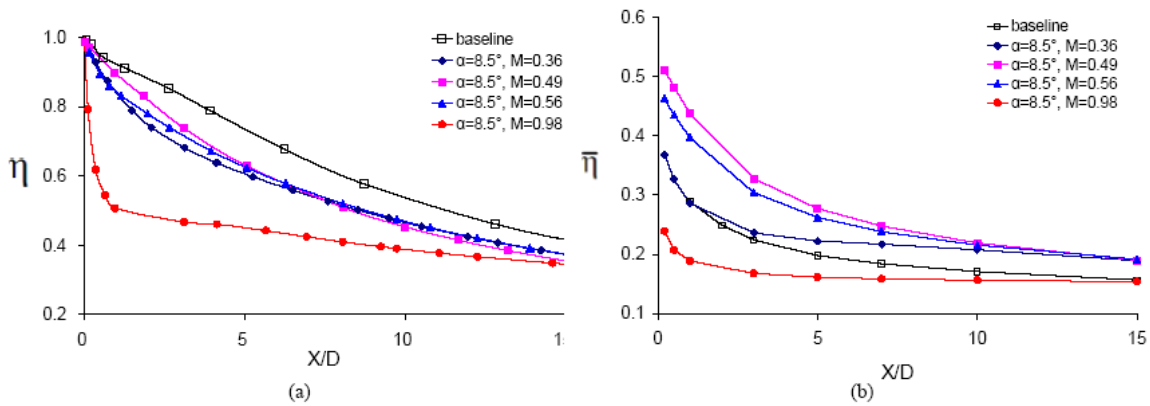

Figure 9 Adiabatic effectiveness as a function of blowing ratio for a given ramp ($\alpha = 8.5^{o}$, β= D). (a) Centerline adiabatic effectiveness. (b) Laterally averaged adiabatic effectiveness.

Flow-aligned Blockers

The computational investigation of the usefulness of flow-aligned blockers in increasing film cooling effectiveness includes the effects of height of the blocker (0.2D, 0.4D, 0.8D), thickness of the blocker (D/20, D/10, D/5), and spacing between the pair of blockers (0.8D, 1.0D, 1.2D), where D is the diameter of the film-cooling hole. Table 1 summarizes the parameter for each computational run.

Table 1 Summary of computational run

Run No.	a	b	c
1	a1 = 0.8D	b1 = 0.2D	c1 = D/20
2	a1	b2 = 0.4D	c2 = D/10
3	a2 = D	b3 = 0.6D	c3 = D/5
4	a2	b1	c2
5	a3 = 1.2D	b2	c3
6	a3	b3	c1

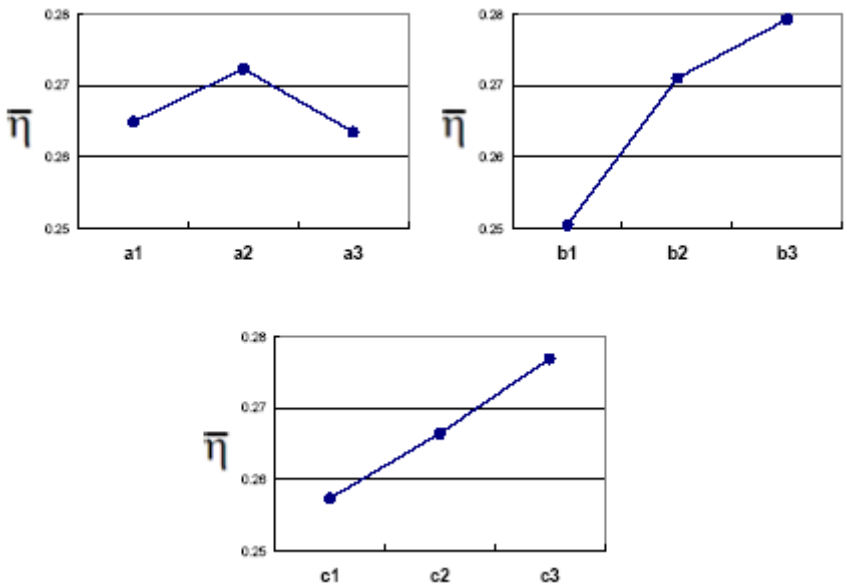

Figure 10 Effects of a, b, and c on average adiabatic effective

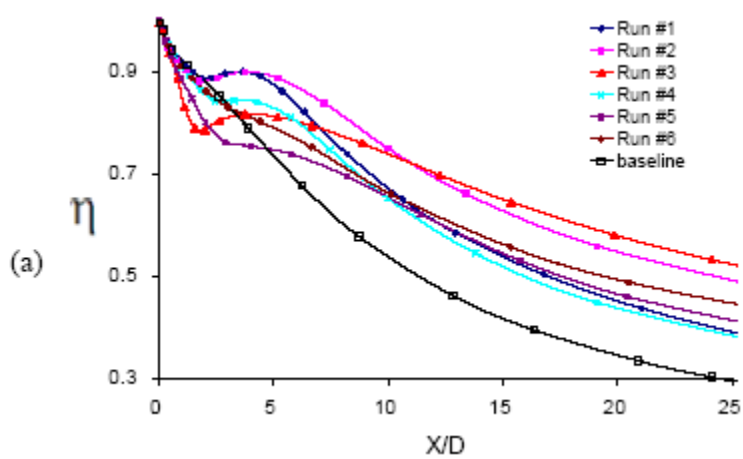

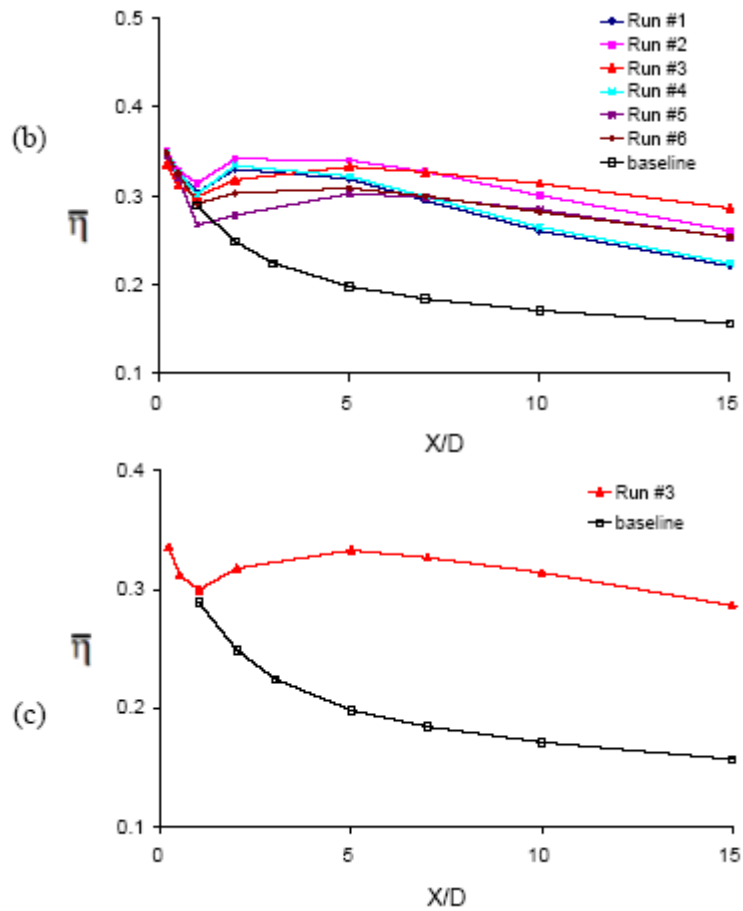

Figure 11 Adiabatic effectiveness with and without blockers (M =0.51). (a) Centerline adiabatic effectiveness for all 6 runs in Table 1. (b) Laterally averaged adiabatic effectiveness for all six runs in Table 1. (c) Laterally averaged adiabatic effectiveness for the optimal blocker, run 3 in Table 1.

Figure 10 shows the average adiabatic effectiveness (i.e., averaged over the entire surface) for all the runs. From this figure, it can be seen that the averaged adiabatic effectiveness is highest when a = a2 = D, b= b3 = 0.6D, and c = c3 = D/5, which corresponds to run number 3 in Table 1. Thus, for the range of the parameters studied, the optimal design is to have the pair of blockers to be spaced D apart and that each blocker should have a height of 0.6D and a thickness of D/5. Figure 10 also shows that D may indeed be near optimum for the spacing between the blockers. However, optimum values for the height and thickness of the blocker remain unclear since the effects of these two parameters remained monotonic in the range studied. It is anticipated that the optimal height is related to the blowing ratio, and the optimal thickness of each blocker is related to the spacing between film-cooling holes since there is a region between film cooling holes that are unprotected by film cooling. Thus, a true optimal design even for the simple design considered here requires further study. Figure 11 gives the centerline and the laterally averaged adiabatic effectiveness for the six runs in Table 1. From this figure, it can readily be seen that all six runs show that "blockers" greatly improve laterally averaged adiabatic effectiveness. For the "optimal" case studied (run 3), Figure 11(c) shows the blockers to maintain the laterally averaged adiabatic effectiveness at nearly the highest levels from D to 15D

downstream of the film cooling hole. At 15D downstream of the film cooling hole, blockers improved laterally averaged adiabatic effectiveness by about a factor of two, which is quite significant. Thus, flow-aligned blockers are indeed useful in improving the utility of film cooling.

The effects of blowing ratio M were also studied. Figure 12 shows the result. It can be seen that even with a blowing ratio of M = 0.37, laterally averaged adiabatic effectiveness is still quite respectable when there are blockers. With a lower blowing ratio, the cooling flow rate is less and so the wrap-around about the blockers is reduced. When the blowing ratio increases to M = 0.65, the laterally averaged adiabatic effectiveness improves further. With higher blowing ratio, more of the coolant spills over and around the blockers.

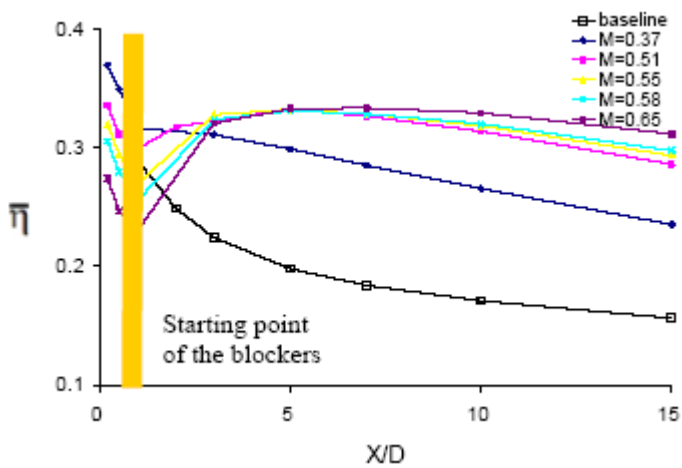

Figure 12 Laterally averaged adiabatic effectiveness for several blowing ratios. Baseline has blowing ratio of 0.5.

In summary, computational results obtained indicate that blockers are very promising in improving film cooling performance. For the blockers studied, the laterally averaged adiabatic effectiveness at 15D downstream of the film-cooling hole is as high as that at 1D downstream.

CONCLUSIONS

Built on the accomplishments made in the first year, reasonable progress in both experimental and computational fronts has been made during the first reporting period of Year 2. Two new film cooling concepts are presented, with extensive parametric computational studies completed. The computational results not only reveal significant promises for improved film cooling performance but also provide the experiment with important design guidelines. On the other hand, design and fabrication of the test rigs for experimental investigation of these innovations are completed. New experimental data will be obtained during the second half of the Year 2. Both detailed computational and experimental results will be presented in the year-end annual report and next UTSR workshop.

INVESTIGATION OF MATERIALS PERFORMANCES IN HIGH MOISTURE ENVIRONMENTS INCLUDING CORROSIVE CONTAMINANTS TYPICAL OF THOSE ARISING BY USING ALTERNATE FUELS IN GAS TURBINES

Semi Annual Report
1 August 2005 – 31 January 2006

Principal Investigators
Gerald H. Meier (ghmeier@engr.pitt.edu)
Frederick S. Pettit (pettit@engr.pitt.edu)

Report Date: February 21, 2006

DOE Award: DE-FC26 02NT41431
UTSR Project: 04 01 SR 116

Submitted by:
Department of Materials Science and Engineering
848 Benedum Hall
University of Pittsburgh
Pittsburgh, PA 15261

DISCLAIMER

"This report was prepared as an account of work sponsored by an agency of the United States Government. Neither the United States Government nor any agency thereof, nor any of their employees, makes any warranty, express or implied, or assumes any legal liability or responsibility for the accuracy, completeness, or usefulness of any information, apparatus, product, or process disclosed, or represents that its use would not infringe privately owned rights. Reference herein to any specific commercial product, process, or service by trade name, trademark, manufacturer, or otherwise does not necessarily constitute or imply its endorsement, recommendation, or favoring by the United States Government or any agency thereof. The views and opinions of authors expressed herein do not necessarily state or reflect those of the United States Government or any agency thereof."

ABSTRACT

This report covers the period from 1 August 2005 through 31 January 2006. It describes the work that was performed to determine the test conditions to be used in the remainder of this program. Based upon the results that were obtained it was decided that subsequent testing of specimens should consist of CaO deposits and exposure at 950°C in air containing water vapor at 0.1atm. Specimens of Rene′ N5, GTD111 and IN738, as well as these alloys with coatings of platinum aluminide, CoNiCrAlY and NiCrAlY, are now being tested and their performances compared using the above described conditions.

TABLE OF CONTENTS

			Page
Abstract			3
Lists of Graphical Materials			5
1.0	Introduction		7
	1.1	Background	7
		1.1.1 Hot Corrosion Induced by Na_2SO_4 and $NaVO_3$	7
		1.1.2 CMAS	8
		1.1.3 Ash Deposits From Fuels	8
		1.1.4 The Effects of Water Vapor on the Oxidation of Alloys	9
		1.1.5 Objectives	10
2.0	Executive Summary		11
3.0	Project Description		12
4.0	Results and Discussion		14
	4.1	Task I	14
	4.2	Task II	15
		4.2.1 Results Obtained For Platinum Aluminide Coatings on Rene′ N5 Exposed at 1150°C in Dry and Wet Air	16
		4.2.2 Results Obtained For Platinum Aluminide Coatings on Rene′ N5 Exposed at 950°C in Dry and Wet Air	18
		4.2.3 Results Obtained For Platinum Aluminide Coatings on Rene′ N5 Exposed at 750°C in Air Containing SO_3	22
		4.2.4 Results Obtained for Platinum Aluminide Coatings On GTD111 Exposed at 950°C	22
		4.2.5 Results Obtained for the CoNiCrAlY Coating on GTD111 Exposed at 950°C	24
		4.2.6 Results Obtained for the CoNiCrAlY Coating on GTD111 Exposed at 750°C in a Gas Mixture Containing SO_3	24
		4.2.7 Selection of Test Conditions for Testing in Tasks III and IV	26
	4.3	Tasks III Comparison of Alloys and Coatings	26
	4.4	Tasks IV Determine Moisture/Contaminant Limits	26
	4.5	Tasks V and VI	26
5.0	Conclusion		27
6.0	References		27

LISTS OF GRAPHICAL MATERIALS

List of figures

.

Figure 1. Schematic flow diagram for the present program

Figure 2. Time line of tasks.

Figure 3. Scanning electron micrograph showing the platinum modified aluminide coating on GTD111.

Figure 4. Scanning electron micrograph showing the platinum modified aluminide coating on Rene′ N5.

Figure 5. (a) Scanning electron micrograph showing the CoNiCrAlY coating on GTD111.
(b) The bright and dark regions represent α phase (aluminum depleted CoNiCrAlY) and β phase (aluminum rich CoNiCrAlY), respectively. Black particles are Aluminum oxides.

Figure 6. Schematic diagram showing the apparatus to cyclically oxidize coupon specimens in gases with defined and controlled amounts of deposits and water vapor in air at a total pressure of 1 atm.

Figure 7. Weight change versus time measurements for cyclic oxidation at 1150°C of platinum aluminide coatings on Rene′ N5 (a) in dry air and (b) in wet air.

Figure 8. Scanning electron micrographs of platinum aluminide coatings on Rene′ N5 exposed at 1150°C after 40 hours in dry air.

Figure 9. Scanning electron micrographs of platinum aluminide coatings on Rene′ N5 exposed at 1150°C after 100 hours in wet air.

Figure 10. Weight change versus time measurements for platinum aluminide coatings on Rene′ N5 exposed at 950°C for 200 hours (a) in dry and (b) in wet air.

Figure 11. Scanning electron micrographs of platinum aluminide coatings on Rene′ N5 exposed at 950°C after 200 hours in dry air.

Figure 12. Scanning electron micrographs of platinum aluminide coatings on Rene′ N5 exposed at 950°C after 200 hours in wet air.

Figure 13. (a) Weight change versus time measurements for exposed specimens of platinum aluminide coatings on Rene′ N5 at 750°C in a gas mixture with SO_3. (b) Stereographic micrograph of platinum aluminide coated Rene′ N5 sample with Na_2SO_4 deposit after 180 hours exposure at 750°C in dry air containing 1000 ppm SO_2.

Figure 14. Scanning electron micrographs of exposed specimens of platinum aluminide coatings on Rene′ N5 with Na_2SO_4 deposit at 750°C in a gas mixture with SO_3 after 180 hours. Figures show (a) low temperature hot corrosion and (b) severely degraded coating.

Figure 15. Scanning electron micrographs of platinum aluminide coatings on Rene′ N5 after 180 hours of exposure at 750°C in air with SO_3. These specimens exhibited very little attack except in the case of the specimen with Na_2SO_4 deposit.

Figure 16. Weight change versus time measurements for the cyclic oxidation at 950°C of GTD111 with platinum aluminide coatings with different deposits (a) for 200 hours in dry and (b) for 100 hours in wet air.

Figure 17. Scanning electron micrographs of platinum aluminide coatings on GTD111 exposed at 950°C after 80 hours in dry air.

Figure 18. Scanning electron micrographs of platinum aluminide coatings on GTD111 exposed at 950°C after 80 hours in wet air.

Figure 19. Weight change versus time measurements for CoNiCrAlY coatings on GTD111 during cyclic oxidation at 950°C (a) for 200 hours in dry and (b) for 100 hours in wet air.

Figure 20. Scanning electron micrographs of CoNiCrAlY coatings on GTD111 exposed at 950°C after 20 hours in dry air.

Figure 21. Scanning electron micrographs of CoNiCrAlY coatings on GTD111 exposed at 950°C after 80 hours in wet air.

List of Tables

Table 1. Alloy Compositions

1.0 INTRODUCTION

1.1 Background

When gas turbines use alternate fuels, ash from the fuels can deposit on turbine hardware. This deposited ash can cause substantial corrosion of turbine hardware which may have significantly different characteristics than Type I and Type II hot corrosion. This program is directed at investigating and understanding the corrosion of materials induced by ash deposits typical of that from use of alternate fuels. The added complication of high moisture environments is also considered.

1.1.1 Hot Corrosion Induced by Na_2SO_4 or $NaVO_3$

The accumulation of airborne contaminants which deposit on hot surfaces in gas turbines has always been a point of concern due to degradation of engine performance resulting from blockage of flow paths and cooling holes, as well as due to accelerated corrosion of alloys and coatings induced by the deposits. This program is concerned with the latter problem, namely, the deposit-induced accelerated corrosion of alloys and coatings. In examining the deposit-induced accelerated corrosion of alloys, an important question is, what is the deposit? The answer to this question, of course, depends upon the operating conditions of the gas turbine, in particular, the turbine inlet temperature, the quality of the fuel and the characteristics of the intake air. Over the past three quarters of a century a number of examples of deposit induced accelerated corrosion have been documented.[1-3] These examples are described briefly in the following.

Whenever fuels with high impurity contents of elements such as S, Na, V, are used in gas turbines, deposits of Na_2SO_4 or $NaVO_3$ may be formed on turbine blades and vanes. When the hardware surface temperatures are between about 800° and 950°C (above 950°C these deposits are not present in significant quantities), the Na_2SO_4 can cause high temperature hot corrosion, Type I hot corrosion. The mechanisms for this type of hot corrosion are well documented in the literature and are often encountered in aircraft gas turbines.[4] If the deposits are $NaVO_3$, sulfides are not present in the alloy, as is the case for Na_2SO_4 deposits, but corrosion is excessive.[5]

If sea salt is ingested in the intake air, NaCl may be deposited on turbine hardware, and the chlorine in the deposit can preferentially remove aluminum from alloys and coatings causing a degradation microstructure consisting of numerous pores.

In the case of gas turbines used for propulsion of marine vehicles, sea salt is often present in the ingested air, and the fuel is often not of the quality of that used in aircraft gas turbines. Also, the operating temperatures are not usually as high as in aircraft gas turbines. As a result of such conditions, degradation of turbine hardware can occur via what is called low temperature hot corrosion, or Type II hot corrosion.[6] In this type of hot corrosion sulfides are often not present in the alloy adjacent to the corrosion products, however, some alloys, especially those rich in nickel, can have substantial sulfide formation.[7] To induce this type of hot corrosion, in addition to Na_2SO_4 deposits, SO_3 must be present in the gas phase at partial pressures in the range 10^{-3}-10^{-5} atms. Type II hot corrosion takes place at temperatures between 650 and 800°C. If the fuels contain vanadium, hot corrosion attack due to $NaVO_3$ deposits can also occur in this temperature range.

1.1.2 CMAS

At times aircraft gas turbines can ingest dust from runways. Also, dust can be ingested when aircraft fly near volcano eruptions or over desert regions. This dust can accumulate on turbine hardware and cause corrosion. These deposits are usually composed of calcium-magnesium-aluminum-silicates (CMAS) with melting points around 1100°C.[8] These deposits can cause degradation of thermal barrier coatings (TBCs). Upon cooling to ambient temperatures, the CMAS on the surface and in the TBC solidifies with an effective modulus significantly larger than that of the porous TBC structure. This stiffer layer can have enough stored energy in it to debond from the rest of the TBC layer. Once debonding occurs, the newly exposed surface of the TBC can be infiltrated by subsequent CMAS deposits, with the process repeating itself until unacceptable amounts or all of the TBC thickness is removed. There is not much data in the literature describing the effect of CMAS on the corrosion of alloys and metallic coatings.

1.1.3 Ash Deposits from Fuels

When fuels are used in gas turbines that have been derived from coal, or other practicable sources, ash can be formed on turbine hardware which can cause corrosion.[9] It is the inorganic matter in fuels that leads to problems with corrosion and deposits.[10] The composition of the ash is difficult to describe precisely. In most coals about 95% of all of the mineral matter is made up of kaolinite ($Al_2O_3 \cdot 2SiO_2 \cdot 2H_2O$), pyrites ($FeS_2$) and calcite ($CaCO_3$).[10] In tests performed using 2 to 3 ppmw ash particulate in the combustion stream, more deposition and corrosion was observed at a gas temperature of 1260°C compared to 1093°C.[9] This corrosion differed from Type I hot corrosion and involved calcium.

Both physical and chemical factors play roles in the formation of deposits. Deposits accumulate on surfaces by at least four physical processes:[10] molecular diffusion, Brownian motion, turbulent diffusion and inertial impact. Although particles of ash may arrive at a surface by physical transport, the accumulation of the ash to form substantial deposits will depend upon the adherence of particle to particle. When the particle to particle adherence is strong ash will continue to build up into thick layers. The sintering characteristics of the ash are affected by many factors but the composition, temperature, and the time the particles are in contact with each other on a heat receiving surface are the most important factors. Depending upon such factors a transition temperature can exist above which increased deposition occurs.

The influence of deposits of CaO, $CaSO_4$ and MgO on the oxidation behavior of a number of Cr_2O_3-forming and Al_2O_3-forming alloys has been investigated over the temperature range 850° to 1050°.[11] Deposits of CaO were observed to accelerate the degradation of Cr_2O_3-forming alloys in oxygen or air by two mechanisms, namely accelerated CrO_3 evaporation over the entire range studied and liquid formation by reaction between CaO and Cr_2O_3 at temperatures above 1000°C which resulted in catastrophic corrosion. The corrosion of Al_2O_3-forming alloys that developed transient Cr_2O_3 was also substantially increased by the CaO deposit. Deposits of $CaSO_4$ did not cause any accelerated corrosion. Deposits of MgO caused increased evaporation of CrO_3, but not any corrosion due to the formation of liquid phases containing MgO.

1.1.4 The Effects of Water Vapor on the Oxidation of Alloys

The effect of water vapor on the oxidation of a number of Cr_2O_3-forming and Al_2O_3-forming alloys has been investigated in a previous program funded by the South Carolina Energy Research and Development Center.[12] The results from this investigation showed that water vapor caused the oxidation resistance of Cr_2O_3-forming and Al_2O_3-forming alloys to be decreased. Water vapor affected the oxidation resistances of these alloys by causing the oxide scales to crack and spall more severely. This increase in spalling of the oxide scales occurred because water vapor decreased the interfacial toughness of the oxide-alloy interface. Water vapor also adversely affected the selective oxidation in the alloys that were Al_2O_3 formers. This adverse effect on selective oxidation was observed in nickel base superalloys rather than coatings on such superalloys. The selective oxidation of aluminum in the nickel base superalloy was adversely affected by water vapor since it caused more transient oxidation during the development of Al_2O_3 scales on these alloys.

The effects of water vapor on the oxidation of a variety of alloys including superalloys has been studied in a number of investigations.[13-23] The effects of water vapor depend upon the alloy and the experimental conditions. Water vapor has been found to affect the high temperature oxidation of alloys in the following ways through the following mechanisms:

- The presence of water vapor permits a H_2-H_2O mixture to be formed in voids which facilitates a rapid inward transport of oxygen across the pores via dissociative gas transport (an oxidation-reduction process).[13-14]
- Water vapor can affect the plasticity of oxide scales. Some investigators propose that the plasticity of oxide scales is decreased and, consequently, the spalling of scales is increased[15]. Other investigators have proposed that plasticity of oxide scales is increased[16] with increased oxidation rates or improved adherence.[16]
- The presence of water vapor adversely affects the selective oxidation of elements such as aluminum and chromium from iron-base alloys.[17] It has also been found that water vapor affects the selective oxidation of aluminum from TiAl.[18]
- Water vapor can affect transport through oxides such as SiO_2 by causing the network structure to be changed.[19]
- Water vapor can cause the vaporization of some oxides to be increased because of the formation of hydrated species with high vapor pressures.[20-22]
- Water vapor causes the concentration of proton defects in oxide scales to be increased which can influence defect-dependent properties such as high temperature creep and diffusion.[23,24]

The effects of water vapor on hot corrosion processes, and on mixed gas corrosion (e.g., in SO_2-O_2-SO_3 gas mixtures), have not been examined but, in view of the results obtained from oxidation experiments, water vapor can be expected to influence these more complex high temperature corrosion processes.

1.1.5. Objectives

The objectives of this program are to conduct experiments, whereby the oxidation degradation of selected materials are documented in high moisture gas environments and in such environments but with corrosive contaminants on specimens typical of deposits that are encountered in use of alternate fuels in gas turbines. More specifically, the goals are to perform laboratory cyclic and isothermal oxidation tests in a gas environment of air with water vapor and in the same gas environment but with deposits arising from using alternate fuels to achieve the following:

1. Develop a fundamental understanding of the degradation processes in moisture environments and in such environments where the specimens have deposits which are typical of deposits that will be encountered from alternate fuels.
2. Attempt to describe how moisture/contaminant levels and temperature affect the corrosion processes.
3. Determine the alloy compositions and coatings that are most resistant to corrosion induced by deposits from alternate fuels.
4. Compare and describe the failure mechanisms of state-of-the-art TBCs and one CMC operating with conventional fuels and with alternate fuels.

2.0 EXECUTIVE SUMMARY

Much of the previous materials development for power generating gas turbines has been performed with natural gas as the fuel of choice. More recently, the need for fuel flexibility has caused alternate fuels such as syngas to be considered for use in gas turbines. Preliminary testing with a variety of alternative fuels has shown increased deposition of ash as well as highly aggressive corrosion of turbine materials that was more severe in the presence of moisture. This program is directed at investigating the corrosion induced by ash deposition and moisture from use of alternative fuels. The alloys and coatings to be studied are typical of those used in current power generating gas turbines, as well as those that may be used in advanced systems. This project has the following five objectives:

- Develop a fundamental understanding of the degradation processes in moisture environments and in such environments where the specimens have deposits which are typical of deposits that will be encountered from the use of alternate fuels.
- Attempt to describe how moisture/contaminant levels and temperature affect the corrosion processes.
- Determine the alloy compositions and coatings that are most resistant to corrosion induced by deposits from alternate fuels.
- Compare and describe the failure mechanisms of state-of-the-art TBCs operating with conventional fuels and with alternate fuels.
- Compare the degradation of a ceramic matrix composite (CMC) under conditions typical of gas turbines using conventional fuels and environments containing water vapor and contaminants representative of turbines using alternate fuels.

To achieve these objectives, the alloys GTD111, IN738 and Rene′ N5 as well as these alloys coated with CoNiCrAlY, NiCrAlY and a platinum aluminide, are being exposed to conditions relevant to corrosion induced using alternative fuels. The test conditions representative of deposits from use of alternative fuels have been selected by testing GTD111 with CoNiCrAlY and platinum aluminide coatings, and N5 with a platinum aluminide coating, at 750°, 950° and 1150°C in a variety of environments with deposits of CaO, $CaSO_4$ and Na_2SO_4.

Based upon results from these tests it has been determined that testing at 750°C is not appropriate because the conditions used at 750°C induced low temperature, type II, hot corrosion in the case of Na_2SO_4 deposits. The other deposits did not cause a substantial amount of degradation. At 1150°C severe attack was observed for all deposits. This temperature caused so much attack that it would be difficult to rank the behavior of the different alloys and coatings. At 950°C attack was induced by all of the deposits but it was more severe in the case of CaO deposits. It has been decided to use CaO deposits in wet air at 950°C to compare the resistances of the alloys and coatings to deposit induced degradation as may occur in gas turbines using syngas (Task III). The effects of water vapor on the degradation induced by CaO will be investigated in Task IV where different water vapor pressures and CaO contaminant levels will be studied using specimens of GTD111 and GTD111 with a CoNiCrAlY coating.

The current results show that all three deposits can cause attack of alloys and coatings on alloys. In view of these results, while the ranking of the various alloys and coatings in regard to resistance to attack is being done with CaO deposits, the effects of deposits such as Na_2SO_4 and $CaSO_4$, as well as iron oxide deposits, will also be investigated in more detail during the next six months of this program.

3.0 PROJECT DESCRIPTION

This program is directed at achieving the goals that were described in the previous section. This program consists of six tasks which are schematically presented in Figure 1. The timeline for these tasks is presented in Figure 2. Task I is concerned with the selection and preparation of alloys and coatings to be investigated in this program. Task II is concerned with identifying the test conditions that are most realistic for examining the degradation of alloys and coatings in moist-contaminant environments. Task III involves testing a number of alloys and coatings at one temperature and deposit conditions in moist air. The resistance of these materials to the moisture-contaminant induced corrosion will be described and compared. Task IV is directed at determining moisture-contaminant limits for the attack of the alloys and coatings used in this program. Task V is directed at comparing the degradation of state-of-the-art TBCs under the conditions selected in Task II. Finally, Task VI will examine the degradation of a CMC using conditions determined in Task II.

This program involves the University of Pittsburgh, Praxair Surface Technologies, Howmet, Inc and GE Power Systems. The oxidation and deposit-induced corrosion experiments are being performed at the University of Pittsburgh. The alloys, some of the coated alloys and the CMC are being provided by GE Energy. Some coatings and TBCs are being prepared by Praxair and Howmet.

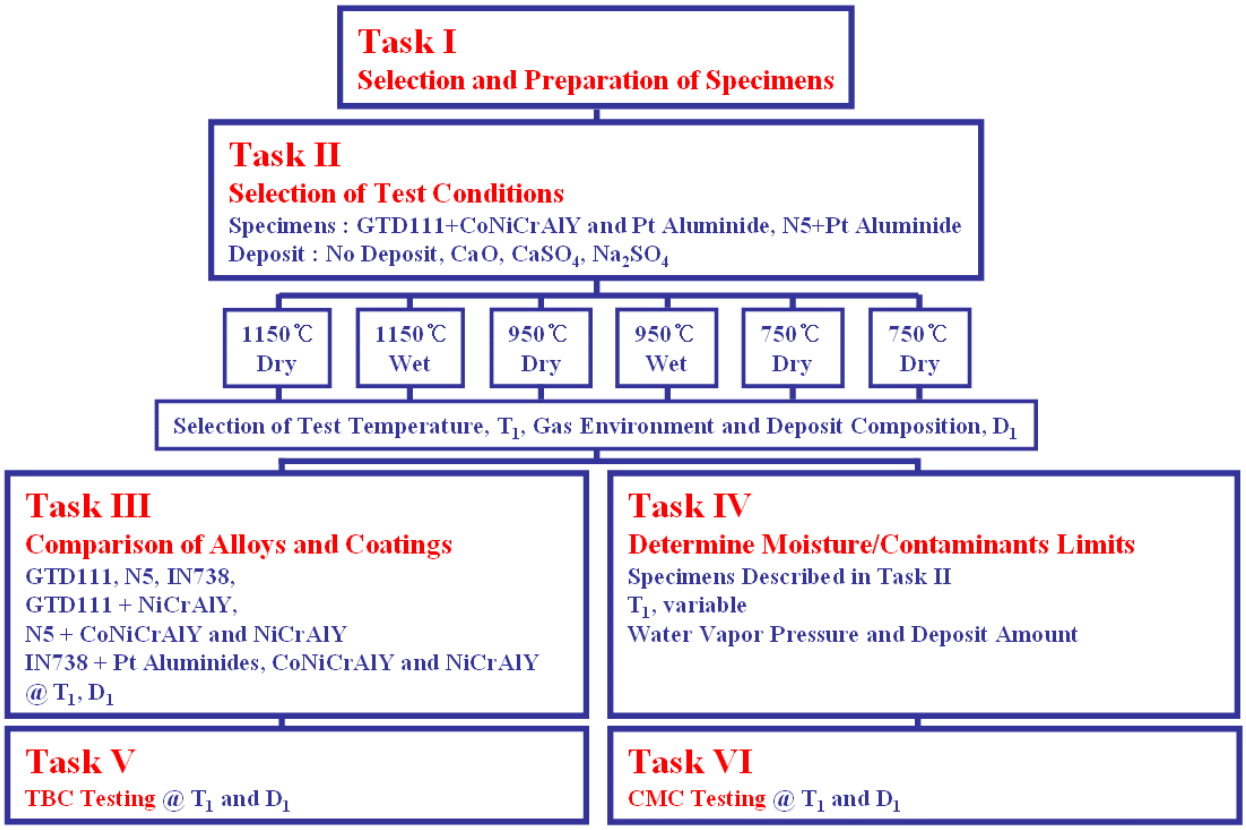

Figure 1. Schematic flow diagram for the present program.

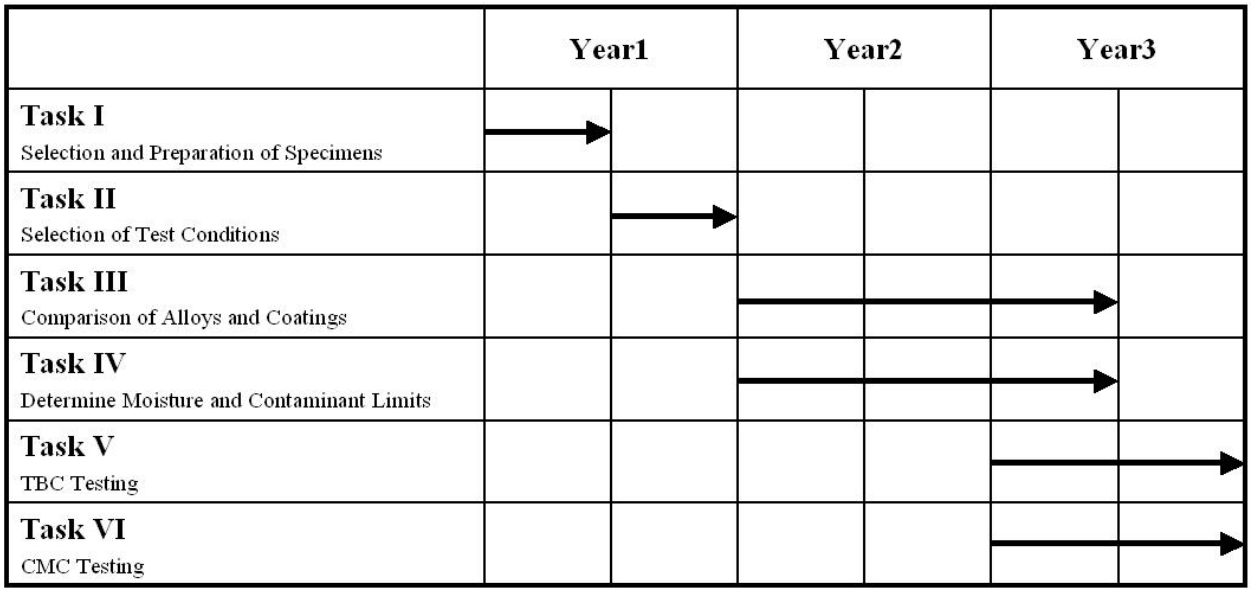

Figure 2. Time line of tasks.

4.0 RESULTS AND DISCUSSION

The results obtained and progress made in this program will be presented in terms of the six tasks that have been described in the previous section.

4.1 Task I: Selection and Preparation of Alloys and Coatings to be Studied in This Program

The alloys being studied in this program are GTD111, Rene′ N5 and IN738. The alloy GTD111 was selected because it is used in current industrial gas turbines. The alloy Rene′ N5 is to be used in advanced gas turbines. The alloy IN738 is looked upon as an alloy that has some resistance to Na_2SO_4-induced hot corrosion attack. Rene′ N5 is a single crystal alloy and an α-Al_2O_3-former. IN738 is a polycrystalline alloy and a chromia-former. GTD111 is a directionally solidified alloy and is also a chromia-former. The compositions of these alloys are presented in the following table.

Table 1. Alloy Compositions*

Alloy	Ni	Cr	Al	Co	Ta	W	Mo	Ti	B	Hf	Re
IN738	Bal.	16	3.4	8.5	1.7	2.6	1.7	3.4	.01	---	---
Rene′ N5 (SC)	Bal.	7	6.2	7.5	6.5	6.0	0.2	---	---	0.1	3.0
GTD111 (DS)	Bal.	14	3.0	9.5	2.8	3.8	1.5	4.9	.01	---	---

The results obtained from the prior oxidation studies in wet and dry air[12] definitely show that coatings should be investigated in the current program. In this program CoNiCrAlY (Co-32Ni-22Cr-10Al-0.3Y*), NiCrAlY (Ni-22Cr-10Al-0.3Y) and a platinum-modified aluminide coating are being investigated. All three of these coatings should provide resistance to cyclic oxidation in wet environments. CoNiCrAlY and NiCrAlY coatings are used in some current power generating gas turbines. Platinum aluminides are mainly used in aircraft gas turbines, however a substantial amount of data is available for the degradation of these coatings in moist and dry air. In this program the platinum modified aluminide coating is included because it is believed to be necessary to have an aluminide coating for comparison with the MCrAlY coatings.

As can be seen in Figure 1, the coating-alloy systems being investigated in Task II are GTD111 with a CoNiCrAlY coating, GTD111 with a platinum-modified aluminide coating, and N5 with a platinum-modified aluminide coating. Ingots of GTD111 and N5 have been obtained from GE Power Systems. Coupon specimens (1.5cm x 1cm x 0.3cm) of GTD111 and Rene′ N5 have been cut from these specimens. Platinum-modified aluminide coatings (MDC-150L) have been applied to the GTD111 and Rene′ N5 specimens, Figures 3 and 4. Some of the GTD111 specimens have had the aluminide coating removed from one side by polishing. A CoNiCrAlY coating (Co-32Ni-22Cr-10Al-0.3Y) has been applied to these GTD111 specimens by using HVOF (polished side only) at GE Power Systems, Figure 5. This coating consists of two metallic phases. It also contains alumina inclusions.

* Unless indicated otherwise all compositions are presented in weight percent.

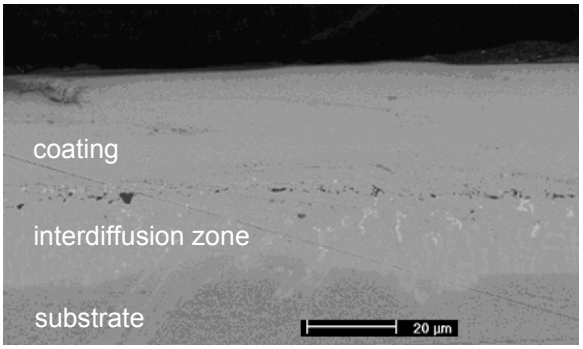

Figure 3. Scanning electron micrograph showing the platinum modified aluminide coating on GTD111.

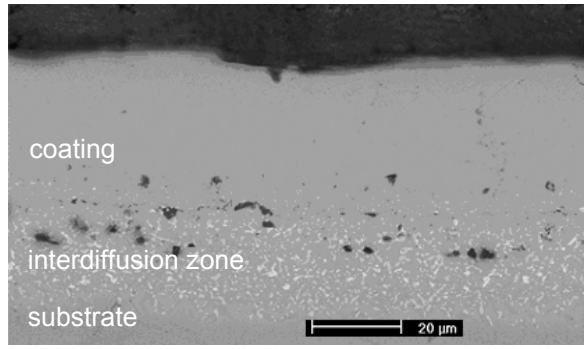

Figure 4. Scanning electron micrograph showing the platinum modified aluminide coating on Rene′ N5.

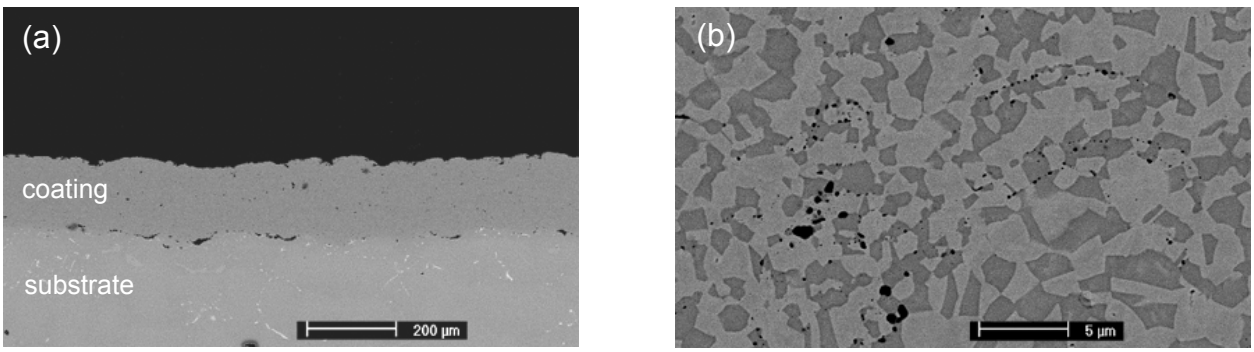

Figure 5. (a) Scanning electron micrograph showing the CoNiCrAlY coating on GTD111.
(b) The bright and dark regions represent α phase (aluminum depleted CoNiCrAlY) and β phase (aluminum rich CoNiCrAlY), respectively. Black particles are Aluminum oxides.

4.2 Task II: Selection of Test Conditions

The objective of Task II is to determine the test conditions to be used for evaluating materials in the remainder of this program. In this task three temperatures have been examined, namely 750°, 950° and 1150°C. Three deposits are considered, in particular Na_2SO_4, CaO and $CaSO_4$. The environments consist of wet and dry air, but some testing is being done in air containing 1000 ppm SO_2 at 750°C. This gas mixture establishes a SO_3 pressure of about 10^{-5} atm. These conditions have been selected based upon the best available information for gas turbines operating with syngas as a fuel. The experiments are being performed in the apparatus shown in Figure 6.

As discussed in a previous semi-annual report,[25] in order to learn more in regard to relevant testing conditions, some deposits from turbine hardware using syngas produced from petroleum coke and a turbine blade used in a gas turbine burning syngas have been examined. The results from these analyses showed that iron oxides were in the deposits along with possibly FeS_2. The turbine blade exhibited a significant amount of erosion on the leading edge. While these results are important, they do not indicate that the test conditions that have been used in

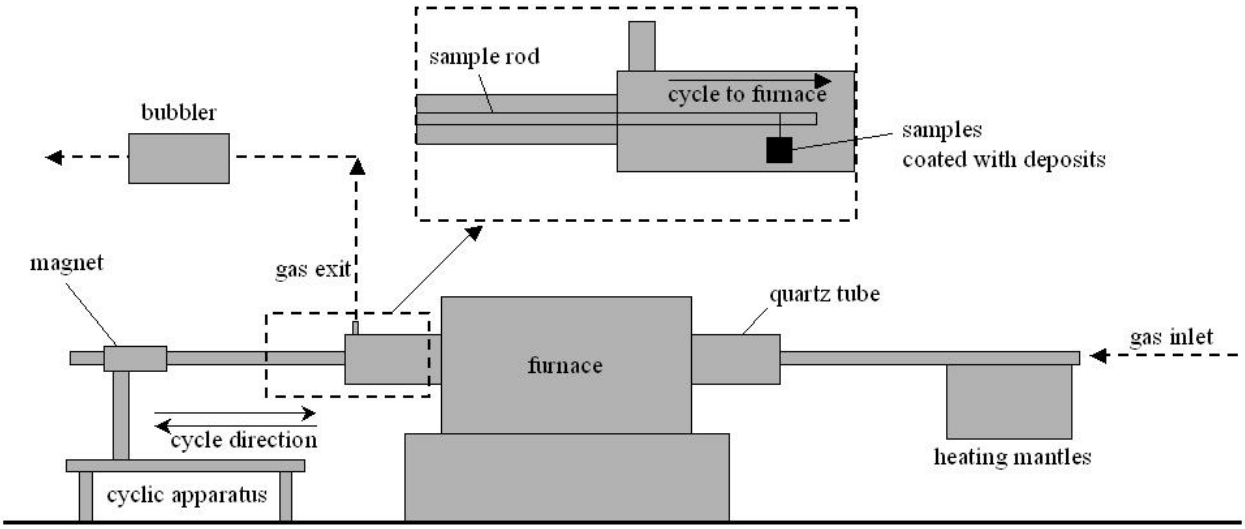

Figure 6. Schematic diagram showing the apparatus to cyclically oxidize coupon specimens in gases with defined and controlled amounts of deposits and water vapor in air at a total pressure of 1 atm.

Task II are inappropriate. However, as will be discussed subsequently in this report, it may be necessary to perform testing with additional deposits.

In order to have a defined surface condition for all test specimens, all specimens were grit blasted at 30 psi for 45 minutes using 20 μm α-Al_2O_3 particles. This provided a surface roughness (Ra) of 2 μm. After grit blasting, the specimens were rinsed in water in an ultrasonic bath and 0.5-1 mg/cm^2 of Na_2SO_4, CaO or $CaSO_4$ was deposited on the specimens using an air spray of aqueous solutions containing these materials. Duplicate specimens were exposed and specimens with no deposit, Na_2SO_4, CaO and $CaSO_4$ deposits were tested concurrently in the same cyclic oxidation (45 minutes hot, 15 minutes cold zone) test apparatus. The weight change of the specimens was determined after every 20 cycles. Prior to these measurements the specimens were washed in warm water to remove the deposits. After the weight change measurements the deposits were applied once again.

4.2.1 Results Obtained For Platinum Aluminide Coatings on Rene′ N5 Exposed at 1150°C in Dry and Wet Air

Weight change versus time measurements for cyclic oxidation at 1150°C of platinum aluminide coatings on Rene′ N5 are presented in Figure 7. The weight changes for CaO deposits in both wet and dry air are larger than those for the other deposits. Scanning electron micrographs of the exposed specimens in dry and wet air are presented in Figures 8 and 9, respectively. In dry air the CaO deposits have caused more degradation than the other deposits, Figure 8. This attack induced by the CaO results in localized areas of preferential attack (arrow, Figure 8) and the coating thickness has been reduced. A protective oxide has been developed on the coatings with the other deposits as well as on the coating with no deposit, however this latter specimen does exhibit a scale with rather large variations in thickness, Figure 8.

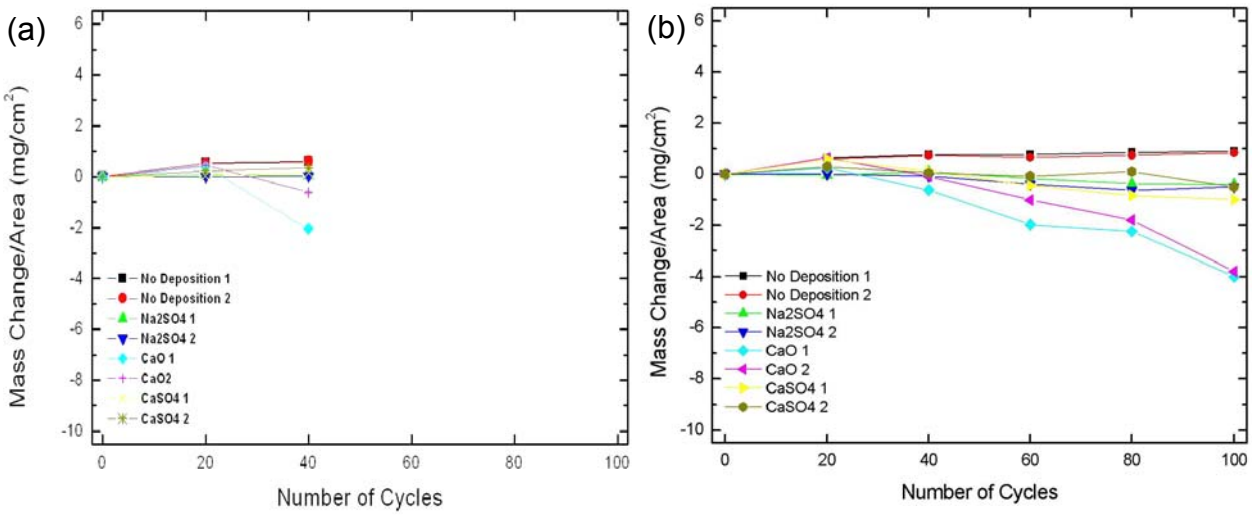

Figure 7. Weight change versus time measurements for cyclic oxidation at 1150°C of platinum aluminide coatings on Rene′ N5 (a) in dry air and (b) in wet air.

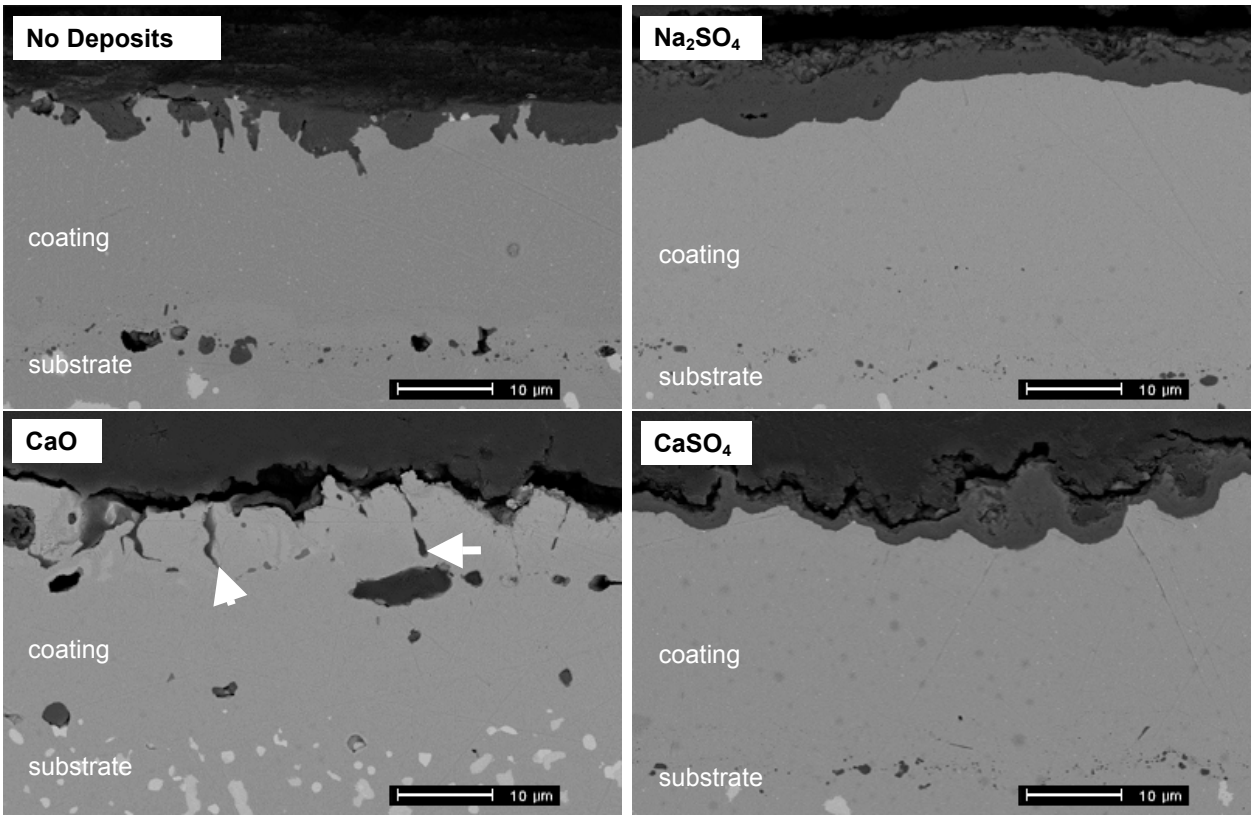

Figure 8. Scanning electron micrographs of platinum aluminide coatings on Rene′ N5 exposed at 1150°C after 40 hours in dry air.

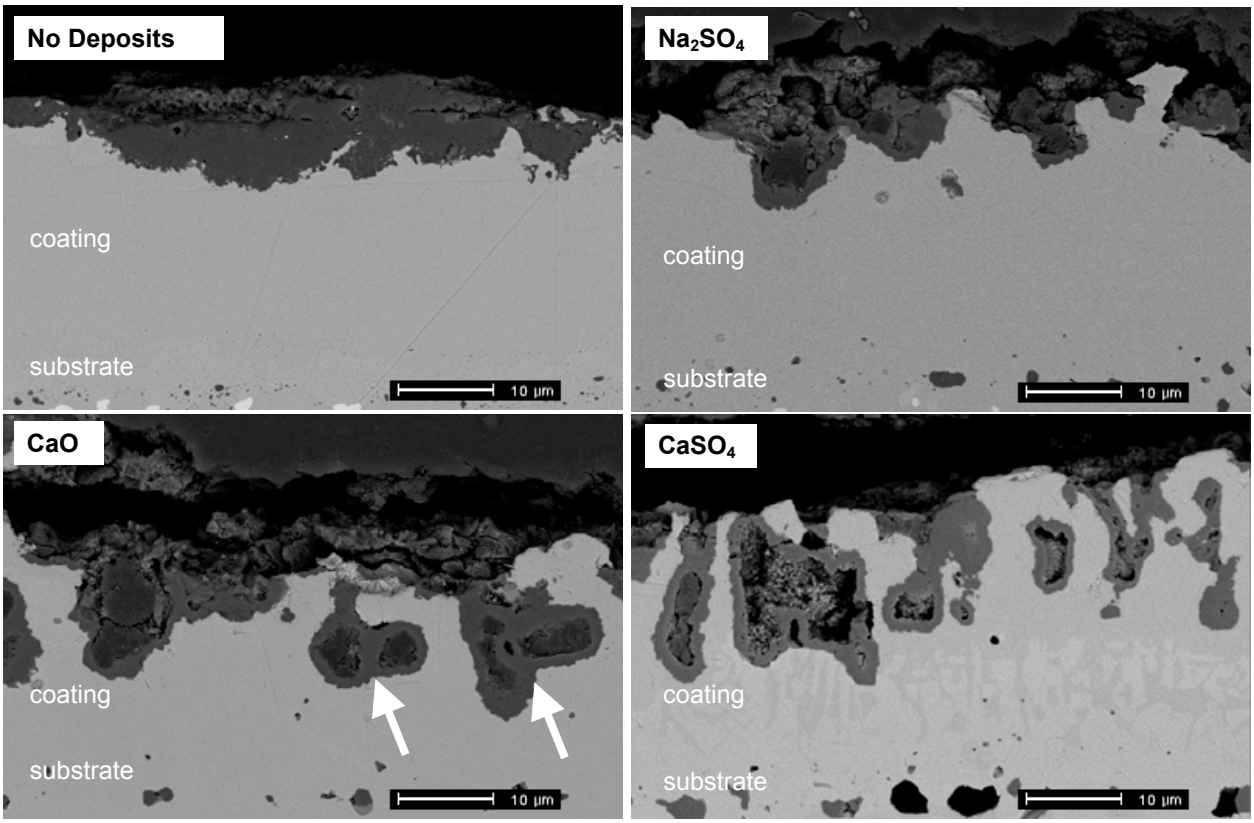

Figure 9. Scanning electron micrographs of platinum aluminide coatings on Rene′ N5 exposed at 1150°C after 100 hours in wet air.

Scanning electron micrographs of the coatings exposed at 1150°C in wet air are presented in Figure 9. As in the case of dry air the CaO deposit has caused more attack, Figure 9. The coating with this deposit has protrusions (arrows) that extend almost to the substrate. The Na_2SO_4 and $CaSO_4$ deposits have also caused degradation where the attack is more severe with the $CaSO_4$ deposits and the attack consists of protrusions extending into the coating as in the case of the CaO deposits.

4.2.2 Results Obtained for Platinum Aluminide Coatings on Rene′ N5 Exposed at 950°C in Dry and Wet Air

Weight change versus time measurements for exposed specimens at 950°C of platinum aluminide coatings on Rene′ N5 are presented in Figure 10. Substantial weight changes are evident for the specimens with CaO deposits in both wet and dry air. Cross-sections of these exposed specimens are presented in Figures 11 and 12. Substantial attack is evident on the coatings with deposits, but the most severe degradation has occurred with the specimens with CaO deposits. In the case of the coatings with this deposit, more attack is evident in wet air.

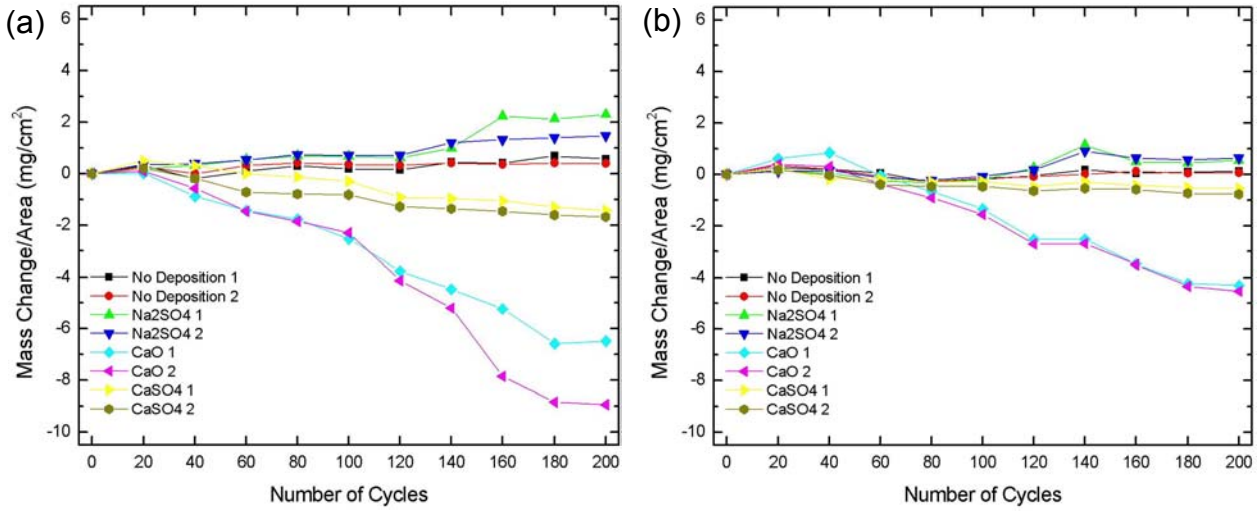

Figure 10. Weight change versus time measurements for platinum aluminide coatings on Rene′ N5 exposed at 950°C for 200 hours (a) in dry and (b) in wet air.

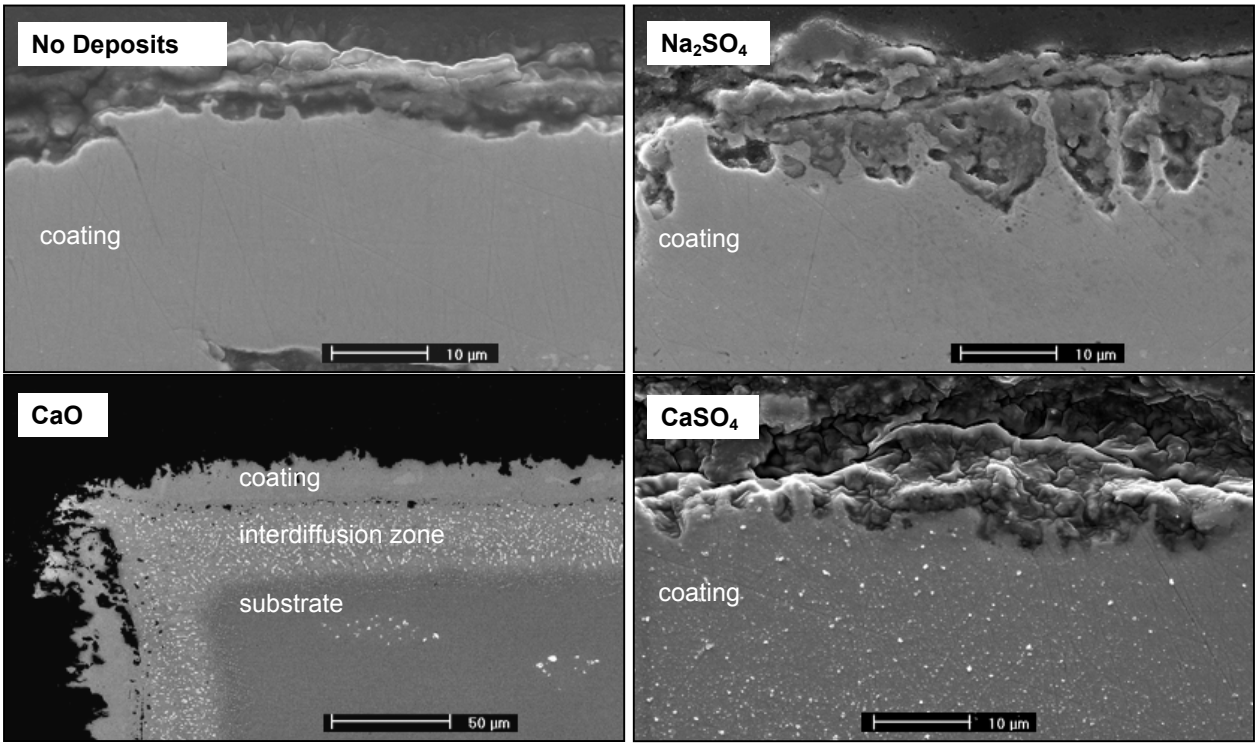

Figure 11. Scanning electron micrographs of platinum aluminide coatings on Rene′ N5 exposed at 950°C after 200 hours in dry air.

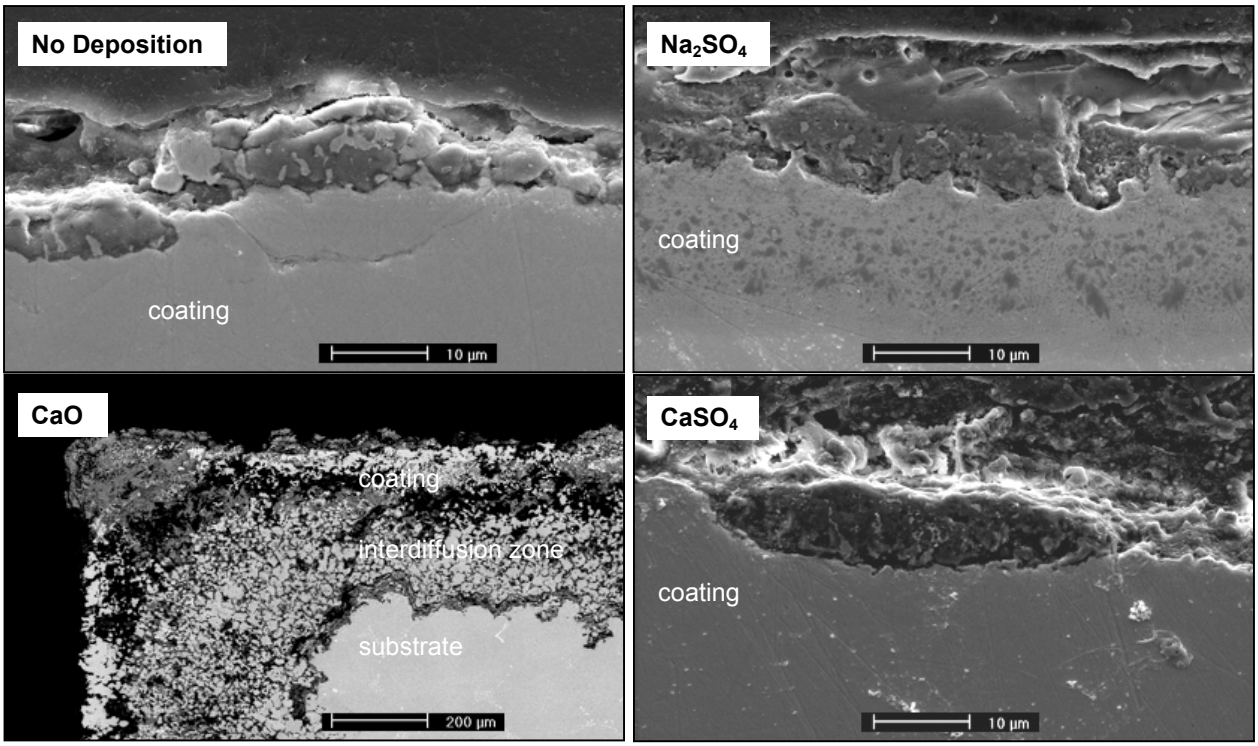

Figure 12. Scanning electron micrographs of platinum aluminide coatings on Rene′ N5 exposed at 950°C after 200 hours in wet air.

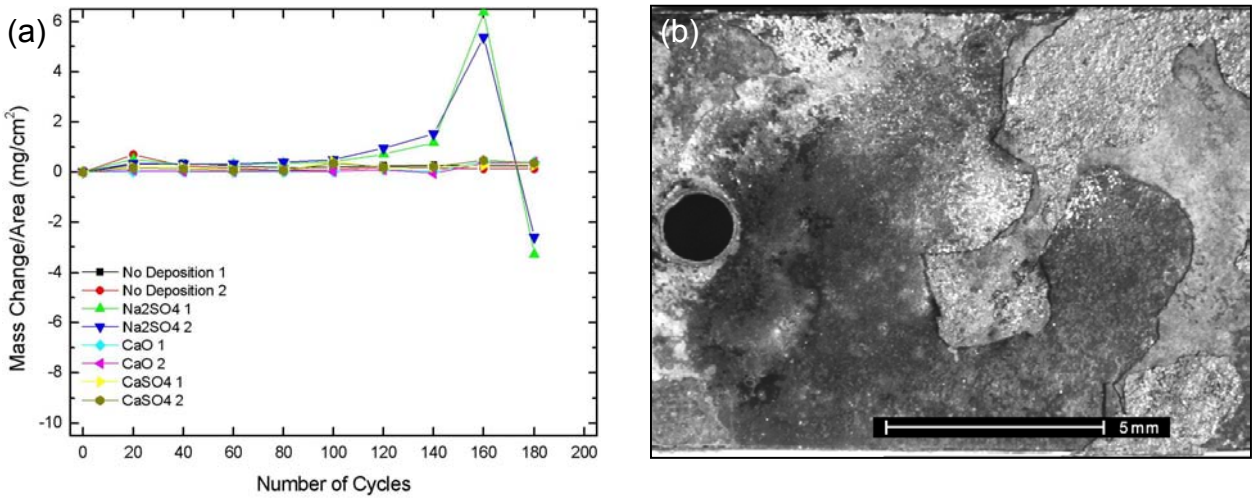

Figure 13. (a) Weight change versus time measurements for exposed specimens of platinum aluminide coatings on Rene′ N5 at 750°C in a gas mixture with SO_3. (b) Stereographic micrograph of platinum aluminide coated Rene′ N5 sample with Na_2SO_4 deposit after 180 hours exposure at 750°C in dry air containing 1000 ppm SO_2.

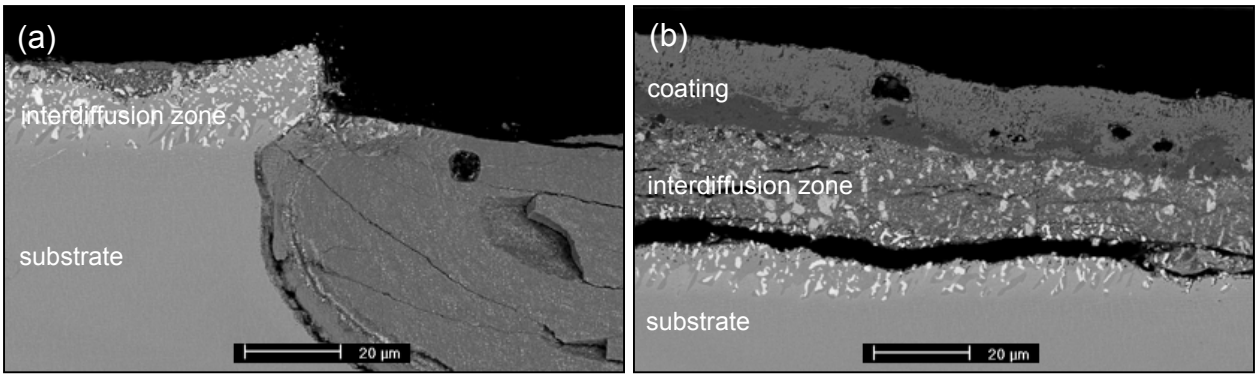

Figure 14. Scanning electron micrographs of exposed specimens of platinum aluminide coatings on Rene′ N5 with Na_2SO_4 deposit at 750°C in a gas mixture with SO_3 after 180 hours. Figures show (a) low temperature hot corrosion and (b) severely degraded coating.

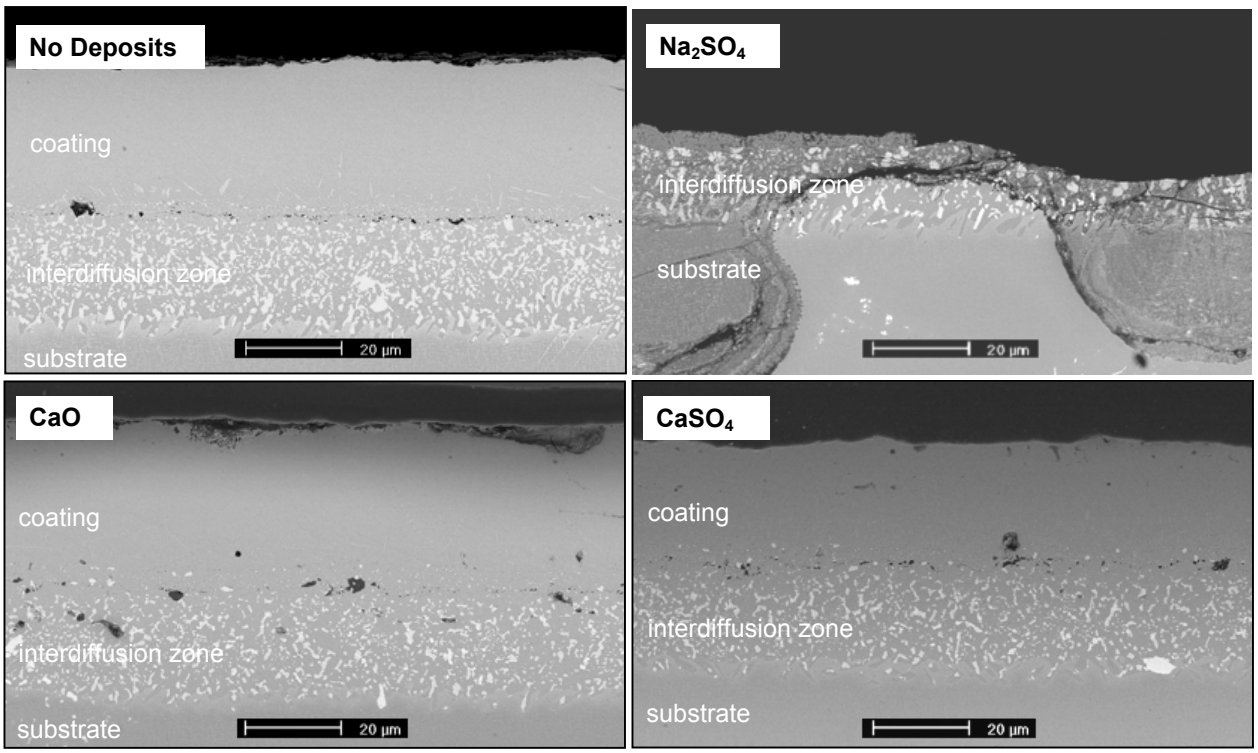

Figure 15. Scanning electron micrographs of platinum aluminide coatings on Rene′ N5 after 180 hours of exposure at 750°C in air with SO_3. These specimens exhibited very little attack except in the case of the specimen with Na_2SO_4 deposit.

4.2.3 Results Obtained for Platinum Aluminide Coatings on Rene′ N5 Exposed at 750°C in a Gas Mixture with SO_3

Weight change versus time measurements for platinum aluminide coatings on Rene′ N5 after exposure at 750°C in a gas mixture with SO_3 are presented in Figure 13 (a). The weight change for the Na_2SO_4 deposits suggest attack induced by the Na_2SO_4 deposit. The coating with this deposit formed a substantial amount of scale that spalled, Figure 13 (b). This attack was so severe that the coating had been completely penetrated and the substrate had been attacked, Figure 14. Metallographic examination of the other coated specimens showed very little attack, Figure 15, but some slight attack was evident on the coating that had a deposit of CaO.

4.2.4 Results Obtained For Platinum Aluminide Coatings on GTD111 Exposed at 950°C

Weight change versus time data for the cyclic oxidation at 950°C of GTD111 with platinum aluminide coatings are presented in Figure 16. The weight changes are not large and seem to be greater for dry compared to wet conditions. However, all weight change data must be used in close comparison with metallographic examination of the exposed specimens. Scanning electron micrographs of the specimens exposed in dry air after 80 hours of exposure are presented in Figure 17. Considering that these specimens have been exposed for only 80 hours at 950°C, the attack of the coatings with all of the deposits is substantial. The attack is most severe in the case of the CaO deposits where the coating has been completely removed. However a substantial amount of attack has also occurred on the coating with a Na_2SO_4 deposit. Less attack is evident on the specimen with the $CaSO_4$ deposit.

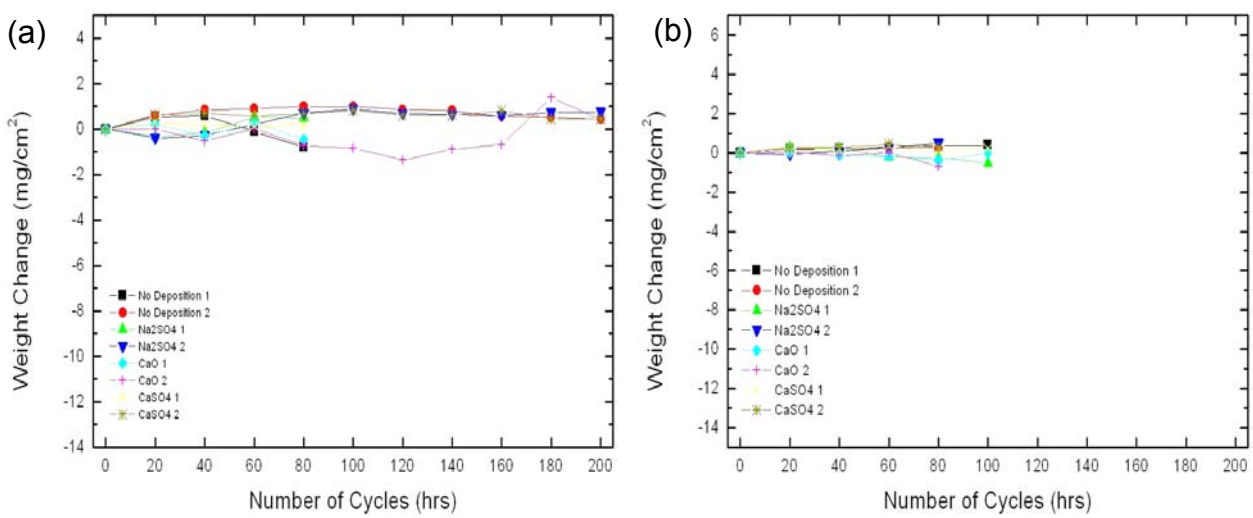

Figure 16. Weight change versus time measurements for the cyclic oxidation at 950°C of GTD111 with platinum aluminide coatings with different deposits (a) for 200 hours in dry and (b) for 100 hours in wet air.

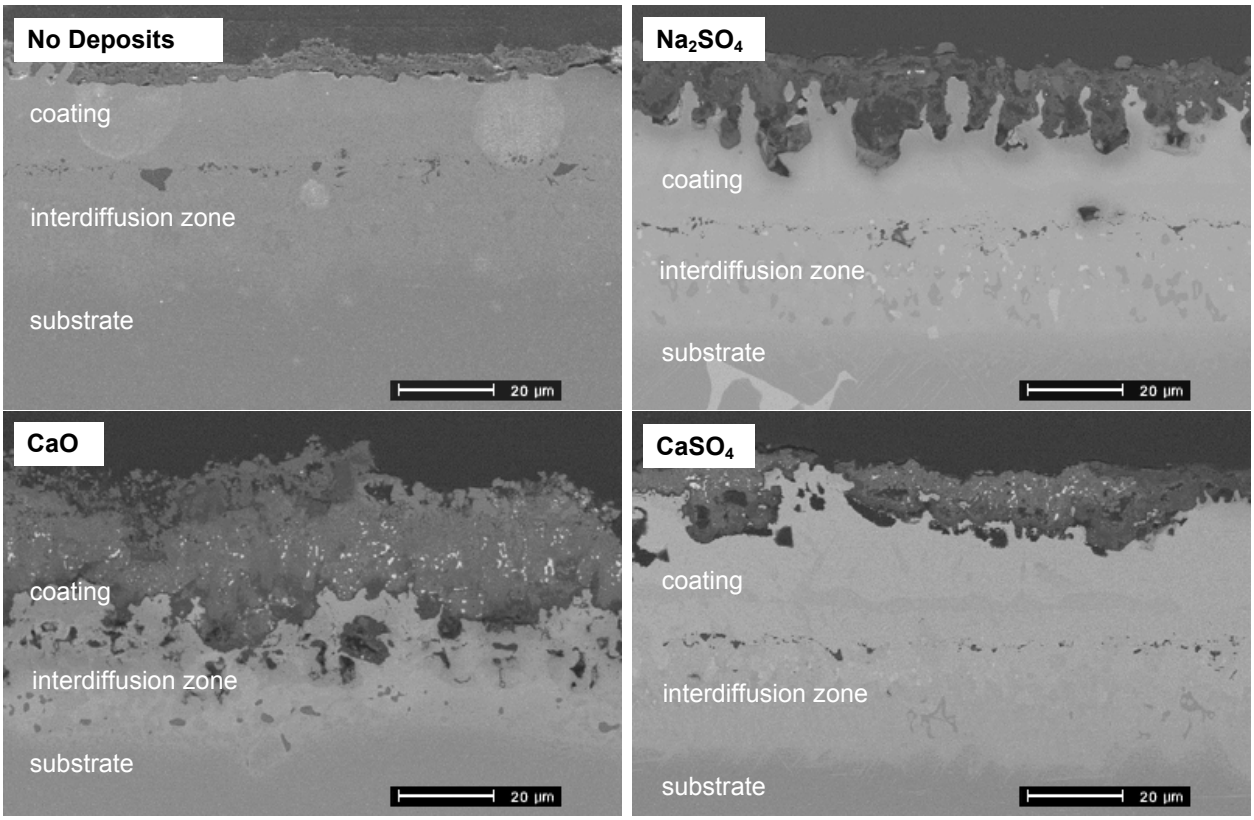

Figure 17. Scanning electron micrographs of platinum aluminide coatings on GTD111 exposed at 950°C after 80 hours in dry air.

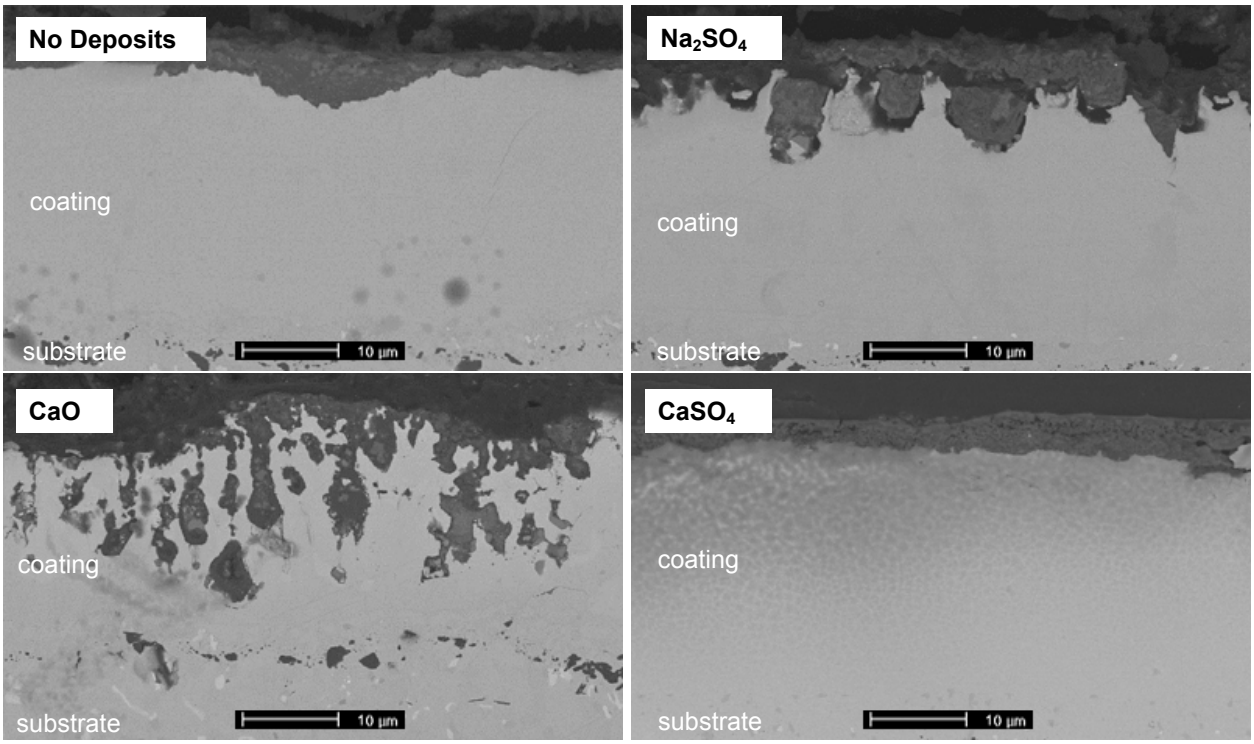

Figure 18. Scanning electron micrographs of platinum aluminide coatings on GTD111 exposed at 950°C after 80 hours in wet air.

Scanning electron micrographs of the specimens that were exposed in wet air at 950°C are presented in Figure 18. The attack may not be as severe as that observed in dry air but in the case of the CaO deposits it is substantial. There is also a significant amount of attack in the case of the Na_2SO_4 deposit.

4.2.5 Results Obtained For The CoNiCrAlY Coating on GTD111 Exposed at 950°C

Weight change versus time measurements for CoNiCrAlY coatings on GTD111 during cyclic oxidation at 950°C are presented in Figure 19. The attack induced by both CaO and Na_2SO_4 deposits has caused rather large weight losses in dry air, but there is not a substantial difference in any of the samples in wet air. Since the attack of the coatings induced by the deposits has been large, cross-sections for metallographic examination of specimens have been made after shorter exposure times, namely, 20 hours for the dry and 80 hours for the wet exposures. The metallographic results obtained in dry air are presented in Figure 20. The attack is not excessive but significant attack is evident for the CaO and $CaSO_4$ deposits in that continuous alumina scales are not present on the specimens. The metallographic results obtained in wet air after 80 hrs of exposure are presented in Figure 21. Significant attack is evident on all of the specimens with deposits. This attack is not excessive but it is clear that continuous alumina scales are no longer present on the surfaces of the coatings exposed to the deposits.

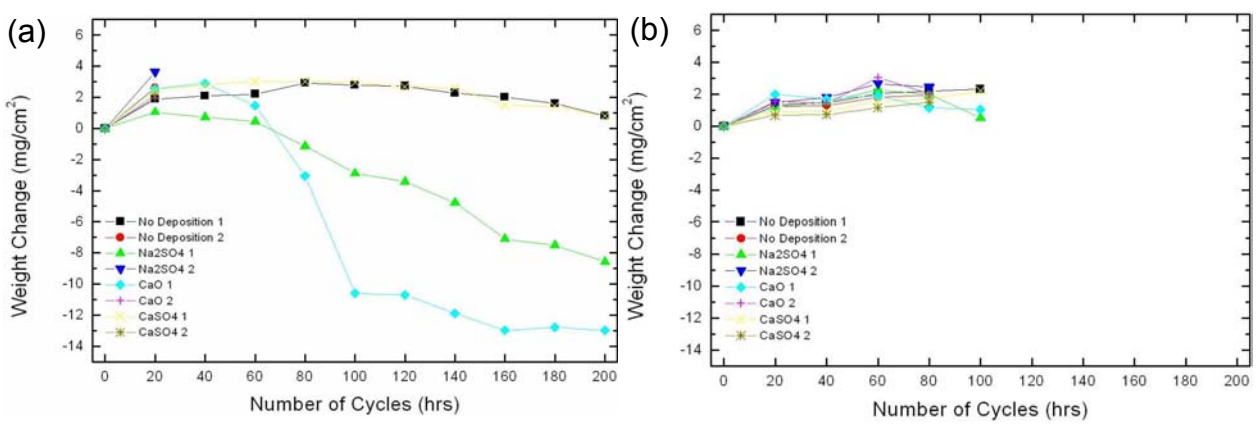

Figure 19. Weight change versus time measurements for CoNiCrAlY coatings on GTD111 during cyclic oxidation at 950°C (a) for 200 hours in dry and (b) for 100 hours in wet air.

4.2.6 Results Obtained for the CoNiCrAlY Coating on GTD111 Exposed at 750°C in a Gas Mixture Containing SO_3

The results obtained for the CoCrAlY coatings exposed to low temperature hot corrosion conditions were similar to those obtained for the platinum aluminide coatings on Rene′ N5 when exposed to similar test conditions. The Na_2SO_4 deposit caused severe degradation of the coatings whereas the other deposits did not cause any significant attack.

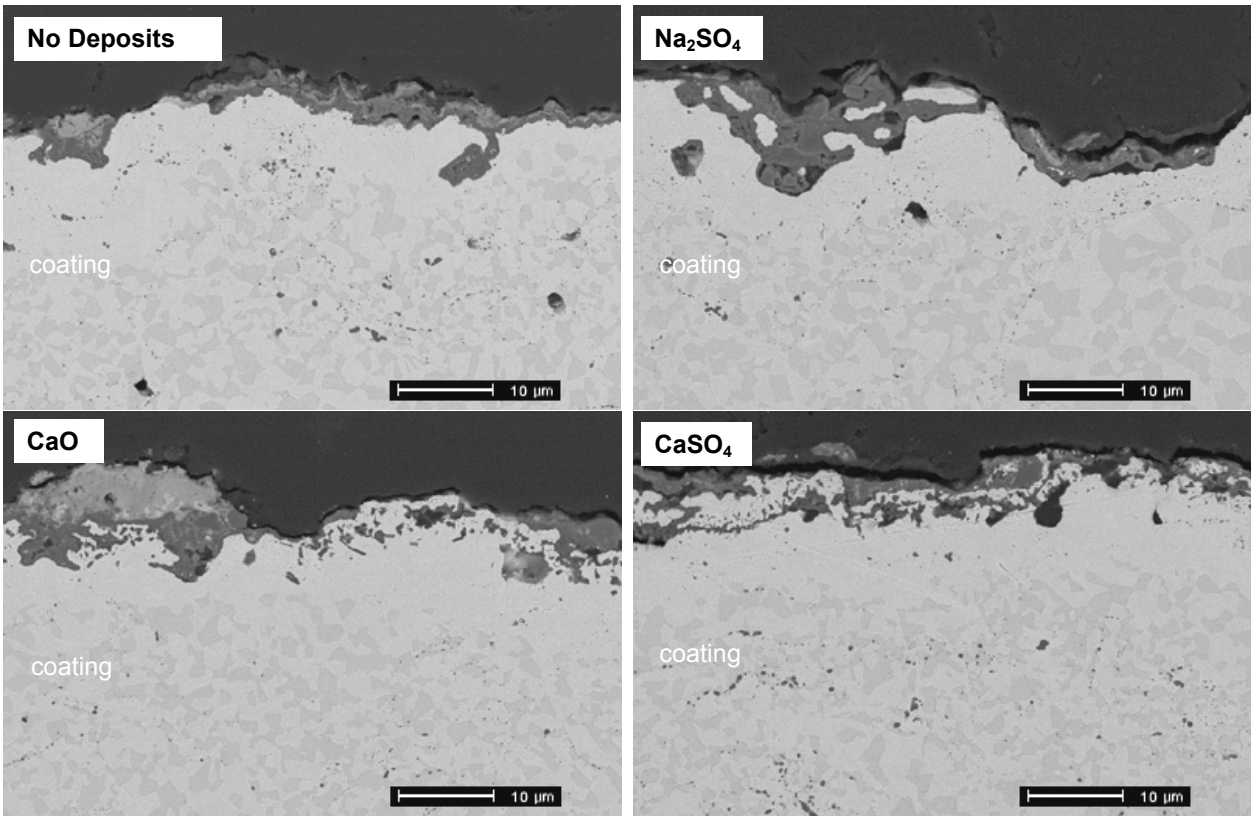

Figure 20. Scanning electron micrographs of CoNiCrAlY coatings on GTD111 exposed at 950°C after 20 hours in dry air.

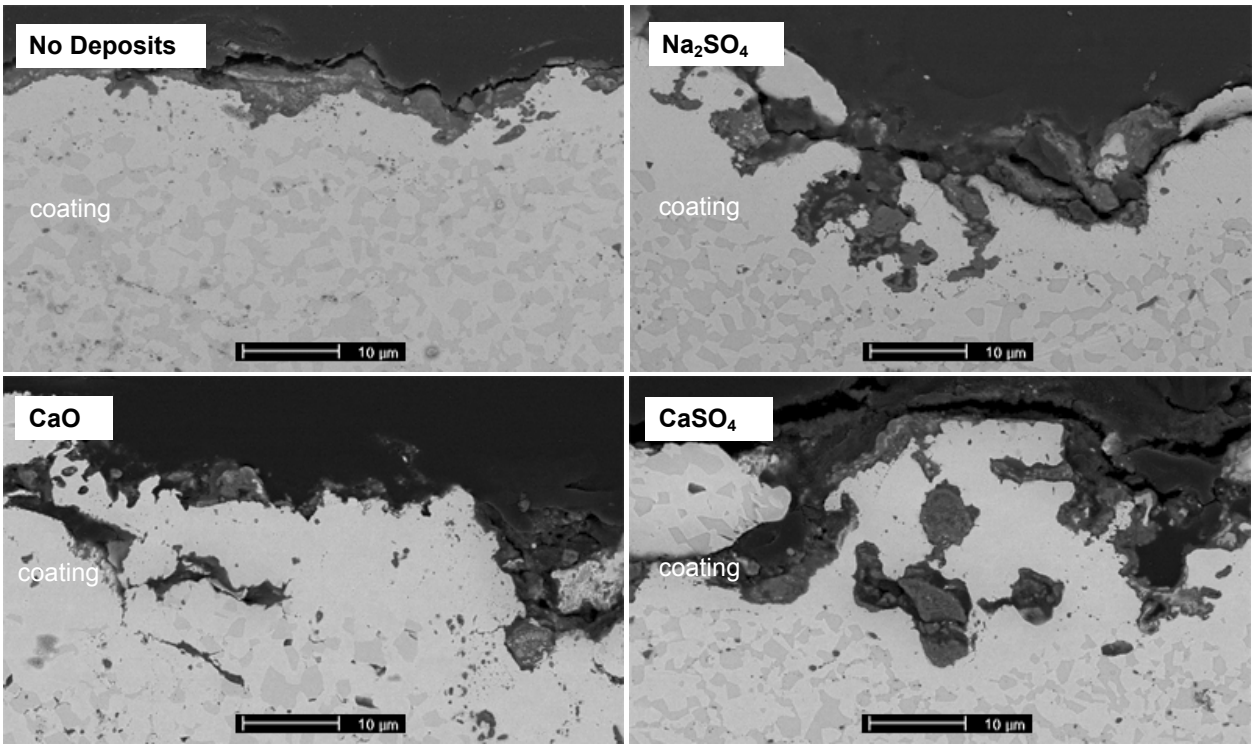

Figure 21. Scanning electron micrographs of CoNiCrAlY coatings on GTD111 exposed at 950°C after 80 hours in wet air.

4.2.7 Selection of Test Conditions For Testing in Tasks III and IV

Based upon the results that have been obtained from the cyclic oxidation tests performed at 1150°C, 950°C and 750°C using deposits of CaO, Na_2SO_4 and $CaSO_4$, it is clear that coating degradation has occurred with all of the deposits at 950° and 1150°C. At 750°C the attack was induced by Na_2SO_4 only. The results obtained at 750°C show that the attack is that of low temperature hot corrosion and such conditions should not be used for the testing to be performed in Task III where the resistance of alloys and coatings on alloys are to be compared.

The testing that was performed at 1150°C showed that CaO deposits caused more attack than deposits of Na_2SO_4 or $CaSO_4$. However the amount of degradation was severe due to the high temperature and it is believed that the testing in Task III should not be at this temperature.

The testing at 950°C showed that all of the deposits caused increased degradation compared to the coatings with no deposits, but the CaO deposits caused the most severe degradation. CaO deposits will be used to compare the behavior of the alloys and coatings in Task III. In most cases the degradation induced by deposits was usually more severe in wet air compared to dry air, but in a few cases the specimens exposed in dry air showed comparable attack to that in wet air. The tests to be performed in Task III will consist of CaO deposits in wet air at 950°C. The effects of water vapor on the degradation process are being examined in detail in Task IV where moisture-CaO contaminant limits are being investigated.

4.3 Tasks III Comparison of Alloys and Coatings

Task III involves testing under one set of conditions to compare the behavior of N5, GTD111, IN738 and coatings on these alloys to deposit induced corrosion. Such tests are now being initiated at 950°C using CaO deposits in wet air.

4.4 Tasks IV Determine Moisture/Contaminant Limits

The purpose of this task is to determine the effects of contaminant amount and water vapor pressure on the deposit-induced degradation. Testing to examine contaminant-moisture limits are now being initiated. These tests will be performed with CaO deposits at 950°C. The initial testing will use specimens of GTD111 and GTD111 with a CoNiCrAlY coating. The water vapor pressure will be fixed at three levels, namely, 0.05, 0.10 and 0.15 atmospheres. The amount of deposit will be varied by using four specimens, all four specimens will have 0.5-1 mg/cm^2 of deposit initially, after 20 hrs 0.5-1 mg/cm^2 will be deposited on three of the specimens and testing will be performed for another 20 hrs using all four specimens. This process will be continued where two specimens will have deposits added after 40 hours, and one specimen after 60 hours. The tests will be concluded after 80 hours and the attack will be compared for the four specimens.

4.5 Tasks V and VI

These two tasks involve tests using TBCs (Task V) and a CMC (Task VI) to investigate the effects of deposit-induced degradation. Testing using such specimens are to be initiated in year 3 of this program. The TBCs and CMC to be used in these tests have been discussed with GE Energy and specimen preparation is in progress.

5.0 CONCLUSION

Based upon the results in Task II, it has been decided to use CaO deposits at 950°C in Tasks III and Task IV. It is quite apparent that CaO deposits cause more attack than $CaSO_4$ and Na_2SO_4 deposits. Nevertheless, Na_2SO_4 and $CaSO_4$ do cause degradation at 950° and 1150°C. Efforts will be made over the next 6 months to attempt to describe in a quantitative manner the mechanism by which CaO deposits cause degradation of the alloys and coatings being studied in this program. As progress is made, it will also be attempted to compare degradation mechanisms for CaO, Na_2SO_4 and $CaSO_4$. At present it appears all the deposits that have been examined react with the alumina and chromia scales that develop on these alloys in such a way that these scales are converted to products that spall and generally are less protective compared to the uncontaminated scales. In view of such effects, it is worthwhile to examine the effects of other deposits that may form during gas turbine operation. Iron oxide deposits are frequently observed on turbine hardware.

6.0 REFERENCES

1. F.S. Pettit and C.S. Giggins, Hot Corrosion, Chapter 12, Superalloys II, C.T. Sims, N.S.Stoloff and W.C. Hagel, eds; John Wiley & Sons, New York (1987).
2. J. Stringer, Ann. Rev. Mat. Sci. 7, 477 (1976).
3. R.A. Rapp, Hot Corrosion of Materials, pp. 291-329, in Selected Topics in High Temperatures Chemistry, O. Johnannesen and A. Anderson, eds; Elsevier, New York (1989).
4. N.S. Bornstein and M.A. DeCrescente, Met. Trans., 2, 2875 (1971).
5. B.M. Warnes, The Influence of Vanadium on the Sodium Sulfate Induced Hot Corrosion of Thermal Barrier Coating Materials, PhD Dissertation, University of Pittsburgh (1990).
6. K.L. Luthra, Met. Trans., 13A, 1647, 1843 (1982).
7. R.H. Barkalow and G.W. Goward, in High Temperature Corrosion, R.A. Rapp, ed; NACE 6, Houston, TX (1983).
8. M.P. Borom, C.A. Johnson and L.A. Peluso, Surface and Coatings Technology, 86-87, 116 (1996).
9. R.R. Wenglarz, "Turbine Flow Path Issues for Syngas and Other Alternate Fuels", Impact of Alternative Fuels on Turbine Materials, Materials Workshop III, DOE, University of Connecticut, October 14-16, 2002.
10. W.T. Reed, External Corrosion and Deposits, American Elsevier Publishing Co., Inc., New York, NY (1971).
11. K.T. Chiang, G.H. Meier and R.R. Perkins, J. Materials for Energy Systems, 6, 71-86 (1984).
12. G.H. Meier and F.S. Pettit, "Interaction of Steam/Air Mixtures with Turbine Airfoil Alloys and Coatings", Subcontract No. 99-01-SR077, South Carolina Energy Research and Development Center, Clemson, SC.
13. A. Rahmel and J. Tobolski, Corros. Sci., 5, 33 (1965).
14. C.W. Tuck, M. Odgers, and K. Sachs, Corros. Sci., 9, 271 (1969).
15. R.L. McCarron and J.W. Shulz, "The Effects of Water Vapor on the Oxidation Behavior of Some Heat Resistant Alloys", Proc. Of Symposium on High Temperature Gas-Metal Reactions in Mixed Environments, AIME, New York, 1973, p. 360.
16. H. Bouaouine, F. Armanet, and C. Coddet, International Congress on Metallic Corrosion, Toronto, Canada, 1989, p. 379.
17. I. Kvernes, M. Oliveira, and P. Kofstad, Corros. Sci., 17, 237 (1977).

18. R. Kremer and W. Auer, Materials and Corrosion, 48, 35 (1997).
19. E.A. Irene, J. Electrochem. Soc., 121, 1613 (1974).
20. J.F. Cullinan, "The Oxidation of Carbon-Carbon Composites between 300°C and 900°C in Oxygen and Oxygen/Water Vapor Atmospheres", MS Thesis, University of Pittsburgh, 1989.
21. E.J. Oplia and R.E. Hann, J. Amer. Ceram. Soc., 80, 197 (1997).
22. J.L. Smialek, R.C. Robinson, E.J. Opika, D.S. Fox and N.S. Jacobson, Adv. Composite Mater., 8, 33 (1999).
23. A.J. Sedriks, "Corrosion of Stainless Steels", 2nd Edition, John Wiley and Sons, Inc., New York, 1996.
24. P. Kofstad, in Microscopy of Oxidation, M.J. Bennett and G.W. Lorimer, eds., The Institute of Metals, London, 1991, p. 2.
25. G.H. Meier and F.S. Pettit, Investigation of Materials Performances in High Moisture Environments Including Corrosive Contaminants Typical of Those Arising by Using Alternate Fuels in Gas Turbines, Semi-Annual Report, February 28, 2005, UTSR Project 04 01 SR 116.

Autoignition Studies of Syngas and Hydrogen (SGH) Fuels

Semi-Annual Report
For
August 1, 2005 to January 31, 2006

R. J. Santoro, Principal Investigator

March 2006

DOE Award No. DE-FC26-02NT41431
UTSR Project No. 05-01-SR117
Clemson University Research Foundation
South Carolina Institute for Energy Studies
Clemson, South Carolina 29634-5181

Department of Mechanical and Nuclear Engineering
The Pennsylvania State University
University Park, PA 16802

DISCLAIMER

This report was prepared as an account of work sponsored by an agency of the United States Government. Neither the United States Government nor any agency thereof, nor any of their employees, makes any warranty, express or implied, or assumes any legal liability or responsibility for the accuracy, completeness, or usefulness of any information, apparatus, product, or process disclosed, or represents that its use would not infringe privately owned rights. Reference herein to any specific commercial product, process, or service by trade name, trademark, manufacturer, or otherwise does not necessarily constitute or imply its endorsement, recommendation, or favoring by the United States Government or any agency thereof. The views and opinions of authors expressed herein do not necessarily state or reflect those of the United States Government or any agency thereof.

ABSTRACT

During this first six-month reporting period, a thorough analytical investigation has been carried out to document the existing H_2/O_2 and $H_2/CO/O_2$ mechanisms and to predict the autoignition times for the range of experimental conditions that will be investigated. The autoignition times for the experimental test conditions have been predicted over a range of pressure (up to 3.04 MPa (441 psia)), temperature (up to 1000 K (1800 R), fuel (H_2 and syngas [$CO + 3H_2$]) and equivalence ratio ($0.3 \leq \phi \leq 1$). These predictions indicate that the experimental flow reactor needs to be designed such that air/fuel mixture temperatures of 800-900 K can be realized. Based on these predictions, the design and fabrication of the high pressure high temperature flow reactor is underway. The existing 280 kW electric heater can heat the air flow to approximately 800 K. However, due to the relatively high heat capacity of the fuel (mainly due to hydrogen), the air/fuel mixture temperature will be reduced significantly if the fuel is introduced at ambient temperature. Currently, the experimental effort is concentrating on design strategies for exacting the required air/fuel mixture temperature. It is expected that the flow reactor will be operational within the next reporting period.

TABLE OF CONTENTS

Disclaimer 2

Abstract 3

List of Figures 5

List of Tables 5

Introduction 6

Executive Summary 7

- Summary of Progress 7
  - Task 1 – Experimental Effort 7
  - Task 2 – Analytical Effort 8
- Industrial Interactions 8

Project Description 9

Experimental 10

Results and Discussion 12

- Experimental Effort 12
- Analytical Effort 12
  - H_2/O_2 Mechanisms - CHEMKIN™ Simulations 12
  - CO/O_2 Mechanisms - CHEMKIN™ Simulations 13
  - $H_2/CO/O_2$ Mechanisms - CHEMKIN™ Simulations 16
  - CHEMKIN™ Simulations for Current Experimental Conditions 17

Conclusions 19

References 21

LIST OF FIGURES

Fig. 1. Schematic of flow reactor. 10

Fig. 2. Flow reactor hydrogen mole fraction versus residence time. P = 1.59 MPa (230.9 psia.), T=914 K (1645 R). 13

Fig. 3. Species profiles for the H_2/O_2 reaction (0.95%H_2 + 0.49%O_2). P = 0.31 MPa (44.4 psia), T=934 K (1681 R). 14

Fig. 4. Temperature profile for the H_2/O_2 reaction (0.95%H_2 + 0.49%O_2). P = 0.31 MPa (44.4 psia), T=934 K (1681 R). 14

Fig. 5. Mean CO mole fraction profiles for $CO/H_2O/O_2$ mixtures. P = 0.101 MPa (14.7 psia), T=952 K (1714 R). 15

Fig. 6. Mean CO mole fraction profiles for $CO/H_2O/O_2$ mixtures. P = 0.101 MPa (14.7 psia), T=943 K (1697 R). 16

Fig. 7. Autoignition delay for a H_2/CO/Air mixture [CO + 3H_2]. ϕ = 1 and 0.5; P = 0.106, 0.304, 1.01 and 3.04 MPa (15.4, 44.1, 147 and 441 psia); Wang and Dryer mechanisms. 17

Fig. 8. Autoignition time versus temperature for the experimental fuel composition and pressure conditions. Predictions use the Dryer mechanism. ϕ = 1.0. 18

Fig. 9. Autoignition time versus temperature for the experimental fuel composition and pressure conditions. Predictions use the Dryer mechanism. ϕ = 0.3. 19

LIST OF TABLES

Table 1. Conditions for the H_2/O_2 CHEMKIN^{TM} simulations. 13

Table 2. Conditions for the CO/O_2 CHEMKIN^{TM} simulations. 15

Table 3. Conditions for the $H_2/CO/O_2$ CHEMKIN^{TM} simulations. 17

INTRODUCTION

The renewed interest in coal-based integrated gasification combined cycle (IGCC) plants is due to the desire for greater fuel supply flexibility and the large known resources of coal in the United States. Current Department of Energy plans strive for efficient, environmentally clean IGCC technologies that can provide both electrical generation and hydrogen production capabilities. Combustion of syngas produced from the coal gasification process, as well as a broader range of syngas and hydrogen (SGH) fuels, has been identified as a key technology area. From an operations standpoint, to meet gas turbine fuel demand requirements, the fuel composition will vary as a function of the gasifier operating levels. Clearly, this introduces new challenges to gas turbine technology since fundamental characteristics of SGH fuels related to autoignition, flashback and blowout are presently not available. This three year effort will systematically examine autoignition phenomena related to SGH fuels at the high pressure, temperature and flow velocity conditions representative of actual gas turbine operating conditions.

The autoignition phenomenon involves a series of spontaneous physical and chemical processes that usually overlap and eventually lead to the ignition of the mixture within a time period referred to as the ignition delay time. For unmixed gaseous fuel and air, the autoignition process involves mixing with concurrent chemical kinetic reactions that lead to a rapid release of energy. The characteristic times for mixing and chemical reaction processes can vary widely for different combustion devices due to differences in initial equivalence ratio, pressure, temperature and flow velocity. Thus, care must be exercised as one utilizes autoignition data obtained under different experimental conditions. Ignition delay is usually characterized using either shock tubes or high-temperature and high-pressure flow reactors. For shock tube studies, the reactants are usually premixed and the near-instantaneous arrival of the shock wave imposes the high-temperature, high-pressure test conditions. Here, mixing effects are absent and the ignition delay time is dominated by energy release processes due to chemical kinetics. In contrast, for flow reactor studies, the fuel and oxidizer are typically introduced separately and mixing times can be a significant fraction of the overall ignition delay time. Consequently, measurements made in these different devices can lead to differing ignition delay times.

The objective of the current work which was initiated six months earlier is to experimentally characterize autoignition of syngas and SGH fuels at high pressures and high temperatures typical of lean premixed gas turbine engine conditions. For gas turbine engines, the temperature and pressure regime of interest usually extends to pressures and temperatures up to nominally 3 MPa and 1000 K, respectively. Since these conditions can readily be matched by flow reactors but not by shock tubes, the experimental research effort on characterizing autoignition for SGH fuels is planned to be carried out in a constant-diameter, variable-length flow reactor.

EXECUTIVE SUMMARY

Project Title: Autoignition Studies of Syngas and Hydrogen (SGH) Fuels

DOE Award Number: DOE Award No. DE-FC26-02NT41431

UTSR Project Number: UTSR Project No. 05-01-SR117

Principal Investigator: Robert J. Santoro

Telephone: (814)863-1285 Fax: (814)865-3389 E-mail rjs2@psu.edu

Summary of Progress

The objective of the current research effort is to parametrically determine the autoignition delay time for CO/H_2 (SGH fuels) as function of CO concentration, equivalence ratio, pressure and temperature. This phase of the proposed effort will be completed during the first two years of the three-year research program. In the third year of research (if funding is provided), the effect of water concentration on autoignition will be determined using mixtures of $CO/H_2/H_2O$. Measurements will be obtained for operating pressures up to 3.0 MPa and typical air mass flow rates of 0.5 kg/s.

Since syngas and SGH fuels have varying concentrations of CO, H_2, H_2O. CO_2 and other gases depending on the specific conditions used in producing these fuels, the research effort has the objective of providing a fundamental set of data on autoignition under well characterized concentration conditions that represent rapidly mixed conditions. Actual gas turbine engines will be characterized by less well controlled mixing processes and will have fuel/air equivalence (mixture fraction) variations. Thus, the present study aims to provide a basis set of autoignition times that can be universally applied to a broad range of injectors and premixing approaches in which operating conditions vary over the range of conditions measured in this study. The experimental phase of this research effort is complemented with an analytical effort.

Task 1 – Experimental Effort

The experimental effort to date has focused on the design and fabrication of the high-pressure high-temperature flow reactor. Initial analytical studies described here indicate that mixed air/fuel (hydrogen to syngas) temperatures need to be in excess of 800 K (possibly as high as 900 K) for the mixtures to autoignite within the length of the reactor (approximately 1.8 m). The existing 280 kW electric heater can heat the air flow to approximately 800 K. However, due to the relatively high heat

capacity of the fuel (mainly due to hydrogen), the air/fuel mixture temperature will be reduced significantly if the fuel is introduced at ambient temperature. Clearly, the options available are to either heat the air to higher temperatures, heat the fuel, or a combination of both. Currently, the experimental effort is concentrating on design strategies for exacting the required air/fuel mixture temperature. Since the goal of the experimental studies is to obtain measurements up to 3.04 MPa (441 psia), commercial off-the-shelf heaters are not available for heating the fuel before injection into the flow reactor. The current design philosophy is geared towards the design of a high-pressure high-temperature heat exchanger that uses the afterburner products to heat the fuel to the necessary 800-900 K range in a regenerative manner. It is expected that the flow reactor will be operational within the next reporting period.

Task 2 – Analytical Effort

During this first six-month reporting period, a thorough analytical investigation has been carried out to document the existing H_2/O_2 and $H_2/CO/O_2$ mechanisms and to predict the autoignition times for the range of experimental conditions that will be investigated. The analytical investigation has been baselined with existing data. Based on this initial verification of the model, the autoignition times for the experimental test conditions have been predicted over a range of pressure (up to 3.04 MPa (441 psia)), temperature (up to 1000 K (1800 R), fuel (H_2 and syngas [$CO + 3H_2$]) and equivalence ratio ($0.3 \leq \phi \leq 1$). These predictions indicate that the experimental flow reactor needs to be designed such that air/fuel mixture temperatures of 800-900 K can be realized. The possible need for such high temperatures has made the design of the flow reactor considerably more complicated, although as discussed earlier, the design is tractable.

Industrial Interactions

The principal investigator has interacted with Dr. Med Colket III of United Technologies Research Center to draw on his experience in autoignition and analysis of detailed chemical kinetic models for a wide variety of combustion systems.

PROJECT DESCRIPTION

Interest in greater fuel supply flexibility and the large known resources of coal in the United States have resulted in renewed interest in coal-based integrated gasification combined cycle (IGCC) plants. Current plans for the FutureGen Program under support from the Department of Energy strive for efficient, environmentally clean IGCC technologies that can generate electricity and also produce hydrogen. One of the challenging key technology areas involves the combustion of syngas produced from the coal gasification process as well as a broader range of syngas and hydrogen (SGH) fuels that may contain higher amounts of hydrogen than typically found in coal gasification product steams.

An additional challenge from an operating perspective is that the fuel composition will vary as a function of the gasifier operating levels to meet gas turbine fuel demand requirements. Thus, absence of a relatively well characterized fuel, such as natural gas, for operation will introduce new challenges to gas turbine technologies for which fundamental information on fuel characteristics related particularly to autoigniton, flashback and blowout is presently not available. The present research effort is aimed at examining the problems of autoignition phenomena related to syngas and hydrogen (SGH) fuels at pressures, temperatures and flow velocities representative of actual gas turbines operating conditions.

For the experimental phase of the research effort, autoignition of SGH fuels will be systematically investigated over a range of CO concentrations in a high-pressure (up to 3.04 MPa (441 psia)) high-temperature (800-900 K (1440-1620 R)) flow reactor. The initial two years of the proposed program will investigate CO/H_2 mixtures from pure syngas [$CO+3H_2$] to pure H_2. The experimental effort in the first year will bracket the problem through experimentation of pure syngas and pure H_2 as a function of equivalence ratio. Based on these results, the second year's effort will first identify three or four other CO concentrations in the fuel for additional characterization. If the effort is extended to the third year, fuels comprising of $CO/H_2/H_2O$ will be investigated for their autoignition characteristics. For the investigation in the latter year, a H_2/O_2/air preburner that supplies H_2O vapor (and air) in required proportions to the in-situ produced CO/H_2 fuel mixtures will be utilized.

Using the extensive data base developed during the study, the ignition delay time will be modeled using both the global ignition delay time approach as well as a detailed chemical kinetic reaction rate mechanism appropriate for the CO/H_2/Air and $CO/H_2/H_2O$/Air systems. These systems represent two of the most thoroughly studied in combustion in terms of detailed chemical kinetic results with much of the existing data incorporated into regularly utilized models such as GRIMECH using the CHEMKIN™ solver [1] . However, there is little data available for the pressure and temperature range to be studied in the current effort. Thus, the current research will provide a critical test for these models regarding their applicability to syngas, SGH and even pure hydrogen at operating conditions for gas turbine systems.

EXPERIMENTAL

The SGH fuels autoignition characterization experiments will be conducted at the Cryogenic Combustion Laboratory at Penn State where high pressure and high temperature experiments utilizing hydrogen fuel are routinely carried out in a safe manner. The flow reactor to be used for the experiments is currently being designed and fabricated based on initial autoignition time predictions for the range of experimental conditions, and is based on the design used by Spadaccini and TeVelde [2]. A simple schematic of the flow reactor is shown in Fig. 1. Air flow at a maximum flowrate of 2.5 kg/s is supplied from two blowdown tanks to an electric resistance-type air heater that can heat 0.5 kg/s of air to a maximum temperature of 800 K. The heated air then flows through a flow straightener section and subsequently mixes with the fuel in the mixer section. The mixed fuel-air mixture then flows through a constant-diameter variable-length instrumented test section and then through a flow nozzle and diffuser section before being burned in an afterburner.

The flowpath including the fuel injector is designed to minimize the possibility of recirculation zones since the presence of any recirculation can cloud the interpretation of data [2]. For autoignition studies, the gaseous fuel injector also needs to be designed to provide rapid mixing without creating

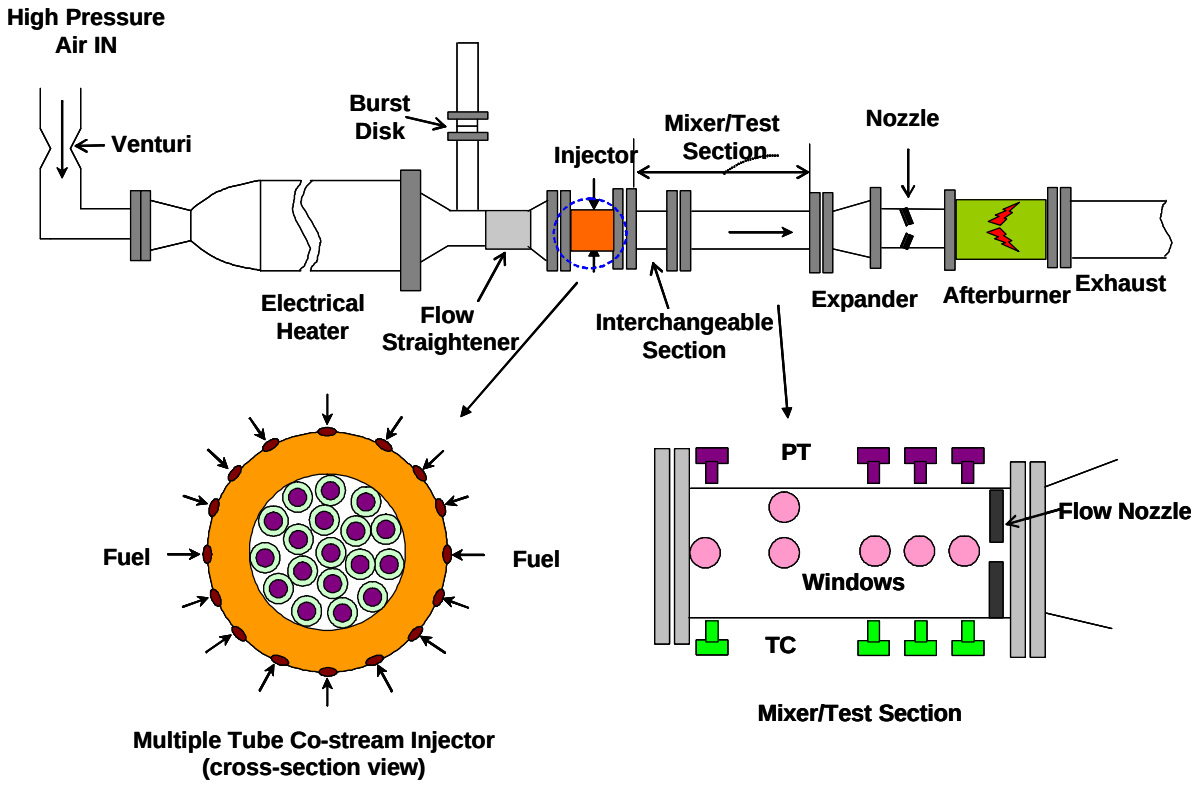

Fig. 1. Schematic of flow reactor.

wakes and recirculation zones. A distributed strut type fuel injector with aerodynamic surfaces or a design that features multiple fuel injection locations is currently being considered to mix the fuel and air streams within a short distance from the injection point.

The variable-length test section (maximum length of 1.83 m (6 ft)) with a circular cross section (diameter of 43 mm (1.7 in.)) will feature limited optical access for laser diode line-of-sight CO absorption measurements as well as flame and chemiluminesce detection at the downstream location. The optical access ports will be designed such that the internal geometry is smooth. The test section will also be instrumented with pressure transducers and an axial array of thermocouples. Such measurements are necessary to document the conditions at which autoignition occurs.

The experimental definition has focused on the design and fabrication of the high pressure high temperature flow reactor. Initial analytical studies described later indicate that mixed air/fuel (hydrogen to syngas) temperatures need to be in excess of 800 K (possibly as high as 900 K) for the mixtures to autoignite within the length of the reactor. The existing 280 kW electric heater can heat the the air flow to approximately 800 K. However, due to the relatively high heat capacity of the fuel (mainly due to hydrogen), the air/fuel mixture temperature will be reduced significantly if the fuel is introduced at ambient temperature. Clearly, the options available are to either heat the air to higher temperatures, heat the fuel, or a combination of both. Currently, the experimental effort is concentrating on design strategies for exacting the required air/fuel mixture temperature. Since the goal of the experimental studies is to obtain measurements up to 3.04 MPa (441 psia), commercial off-the-shelf heaters are not available for heating the fuel before injection into the flow reactor. The current design philosophy is geared towards the design of a high-pressure high-temperature heat exchanger (not shown in Fig. 1) that uses the afterburner exhaust to heat the fuel to the necessary 800-900 K range in a regenerative manner.

RESULTS AND DISCUSSION

Experimental Effort

During this first reporting period, focus has been on the design and fabrication of the flow reactor as discussed in the experimental section earlier. Based on the analytical modeling results presented in the next sub-section, the flow reactor needs to be designed to operate at higher temperatures (up to possibly 900 K) than initially envisioned at the maximum pressure condition (3.04 MPa (441 psia)). Achieving these conditions requires heating the fuel independently, and currently a heat exchanger that uses the afterburner products to heat the fuel to the required inlet temperature is being considered. It is expected that the flow reactor will be operational within the next reporting period.

Analytical Effort

For the analytical phase of the program, various H_2/O_2, CO/O_2 and $H_2/CO/O_2$ mechanisms have been investigated using the CHEMKIN™ program [1]. Calculations have been compared to available experimental results to verify the accuracy of the models. Finally, predictions for the range of flow conditions that will be covered for the experiments under this research program have been completed. In this sub-section, these calculations/comparisons are summarized.

H_2/O_2 Mechanisms - CHEMKIN™ Simulations

Three H_2/O_2 mechanisms from recent papers have been studied. These are the Dryer [3], Westbrook [4] and Wang [5] mechanisms. The first two of these mechanisms have 19 reactions, whereas the Wang mechanism includes the $HO_2 + H = O + H_2O$ reaction (which is not well characterized). Each mechanism was studied over the 600-1100 K temperature range. As these models allow incorporation of pressure-dependant reaction rate constants, results were obtained for different pressure conditions. Two fall-off curve expressions, viz. Lindemann-Hinshelwood and Troe (in. Ref. [6]), were used for the pressure dependant rate constants [7]:

To study the accuracy of these mechanisms, simulations were carried out at the conditions corresponding to two experiments [4, 8]. The test conditions are presented in Table 1. The closed homogeneous batch reactor model was used and the problem was solved by constraining pressure and solving the energy equation. The thermodynamics data files used in the computations are from the authors of the mechanisms used in these studies. Results for the first simulation (**S1**) are plotted in Fig. 2, and results for the second simulation (**S2**) in Figs. 3 and 4. Note that model predictions were shifted in time to match with the experimental results at 50% fuel consumption.

Table 1. Conditions for the H_2/O_2 CHEMKIN™ simulations.

Simulation	P	T_{init}	f	Experimental Data
S1	1.59 MPa	914 K	0.27 and 1	O'Connaire, Curran, Simmie, Pitz, and Westbrook, 2004 [4]. *Figure 28, p. 34.*
S2	0.306 MPa	934 K	0.97	Mueller, Kim, Yetter and Dryer, 1999 [8]. *Figure 4, p. 118.*

The three tested models (Dryer [3], Westbrook [4] and Wang [5] (optimized/not-optimized)) agree fairly well with the experimental data for the two presented simulations. The Dryer model [3] seems to be the most accurate for the second case. Note that the discrepancies observed for the final temperature in Fig. 4 is due to the fact that the model used does not take heat losses into account (i.e. an adiabatic reactor assumption was made for the modelling cases).

CO/O_2 Mechanisms - CHEMKIN™ Simulations

Three CO/O_2 mechanisms from recent papers have been studied. These are the Wang [5], Mueller [9] and Dryer [10] mechanisms. Note that the third mechanism is a C1 mechanism by Dryer [10] which was adapted from a CH_3OH Mechanism [11] with some important revisions done by the author in 2004 (Optimization of the reactions $CO + OH = CO_2 + H$ and $HCO + M = H + CO + M$ to fit the literature experimental results, OH heat of formation adjusted to 8.91 kcal/mol following the works of Ruscic et al. [12].)

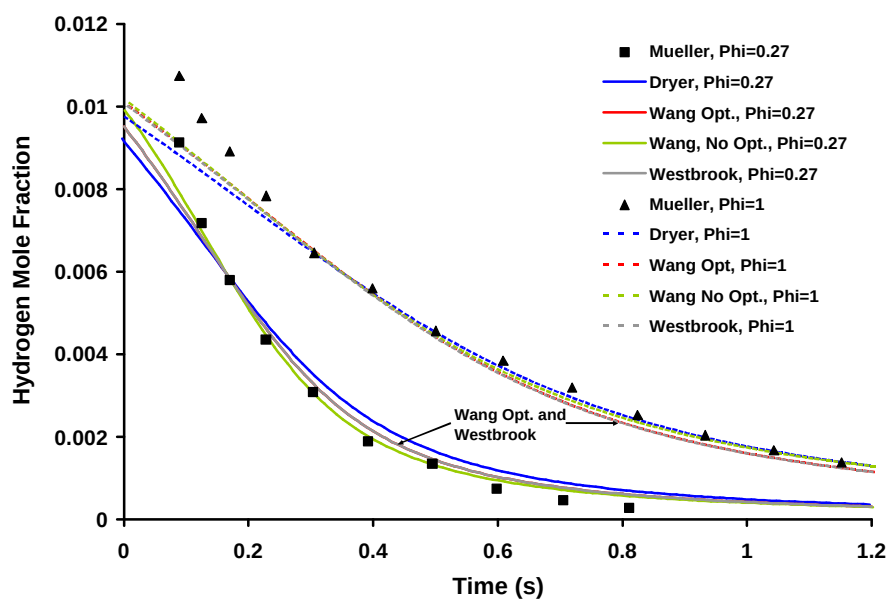

Fig. 2. Flow reactor hydrogen mole fraction versus residence time. P = 1.59 MPa (230.9 psia), T=914 K (1645 R).

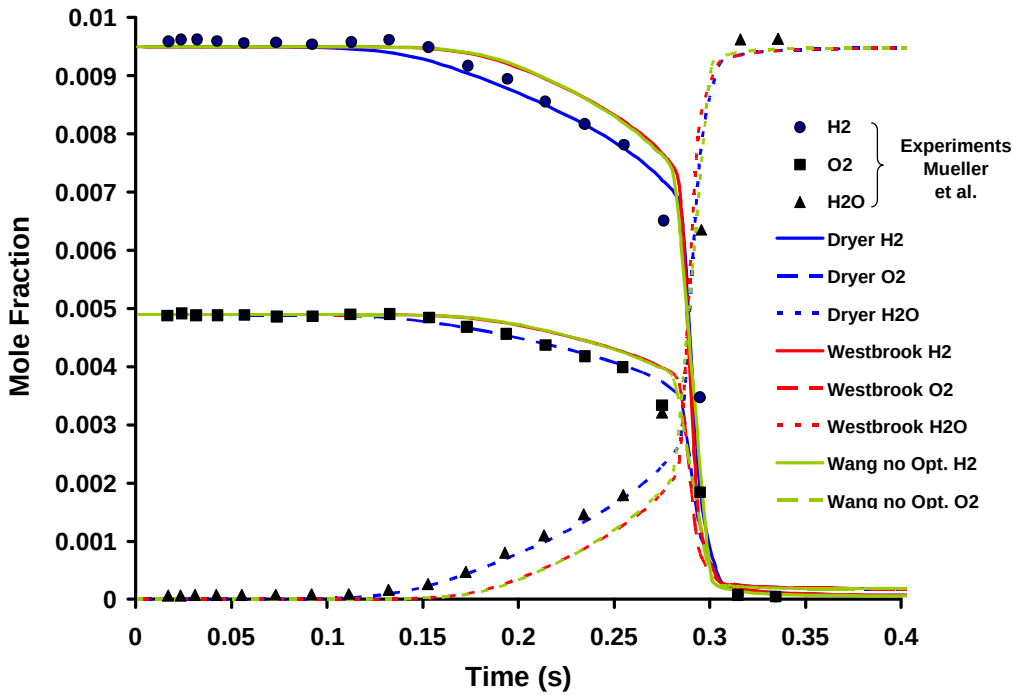

Fig. 3. Species profiles for the H_2/O_2 reaction ($0.95\%H_2 + 0.49\%O_2$). P = 0.31 MPa (44.4 psia), T=934 K (1681 R).

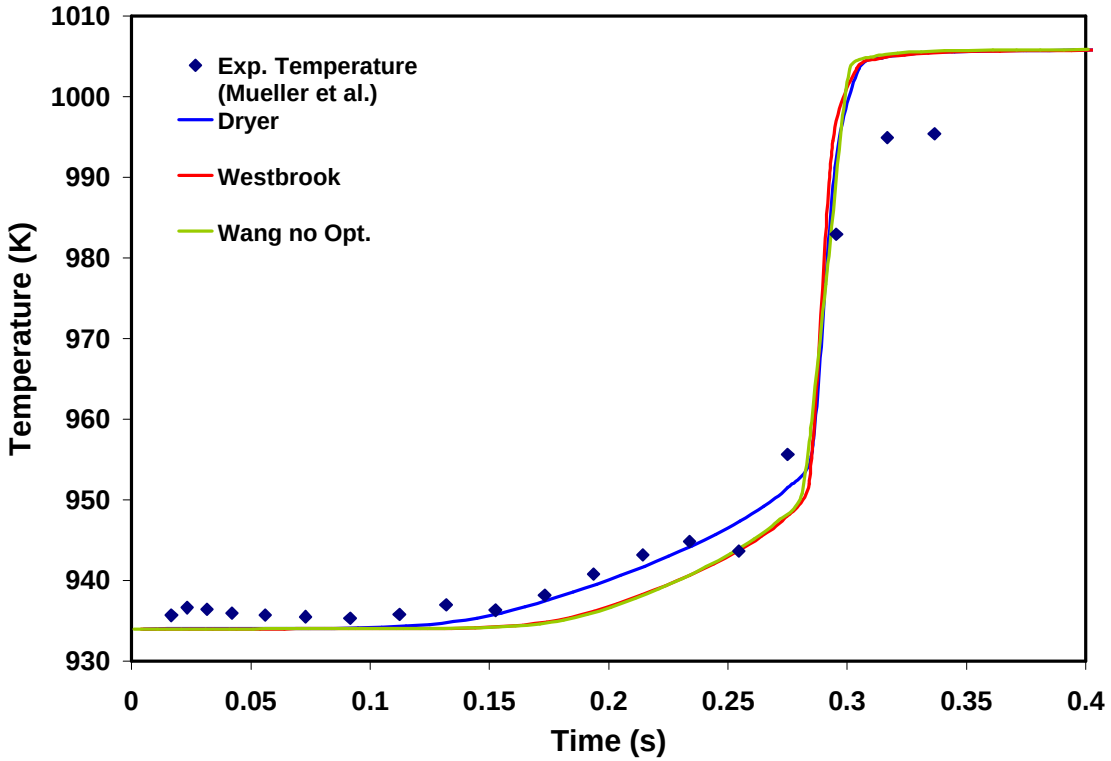

Fig. 4. Temperature profile for the H_2/O_2 reaction ($0.95\%H_2 + 0.49\%O_2$). P = 0.31 MPa (44.4 psia), T=934 K (1681 R).

Table 2. Conditions for the CO/O_2 CHEMKIN™ simulations.

Simulations	P	T_{init}	f	Experimental Data
S3	0.101 MPa	917 K	1.03	Yetter, Dryer and Rabitz, 1991 [13]. *Figure 10, p. 138.*
S4		932 K	1.02	
S5		943 K	1.02	
S6		952 K	1.02	

For all mechanisms, the rate constants were studied over the 600-1100 K temperature range. These three mechanisms differ in the number of reactions included in the model. The Wang [5] model has 10 reactions, the Mueller [9] model has 9 reactions (the reaction $HCO + O = CO_2 + H$ is not used), and finally, the Dryer [10] model has 13 reactions (the following reactions are added: $HCO + HO_2 = CO_2 + OH + H$, $HCO + HCO = H_2 + CO + CO$, $HCO + HCO = CH_2O + CO$). However, the three mechanisms have many rate constant expressions in common. Differences between the rate constants are due to different selected sources, with the Wang mechanism using the most recent ones.

To study the accuracy of these mechanisms, simulations were carried out at four temperature conditions corresponding to an experiment conducted by Yetter et al. [13]. The test conditions are presented in Table 2. The closed homogeneous batch reactor model was used and the problem was solved by constraining pressure and solving the energy equation. The thermodynamics data files computed are

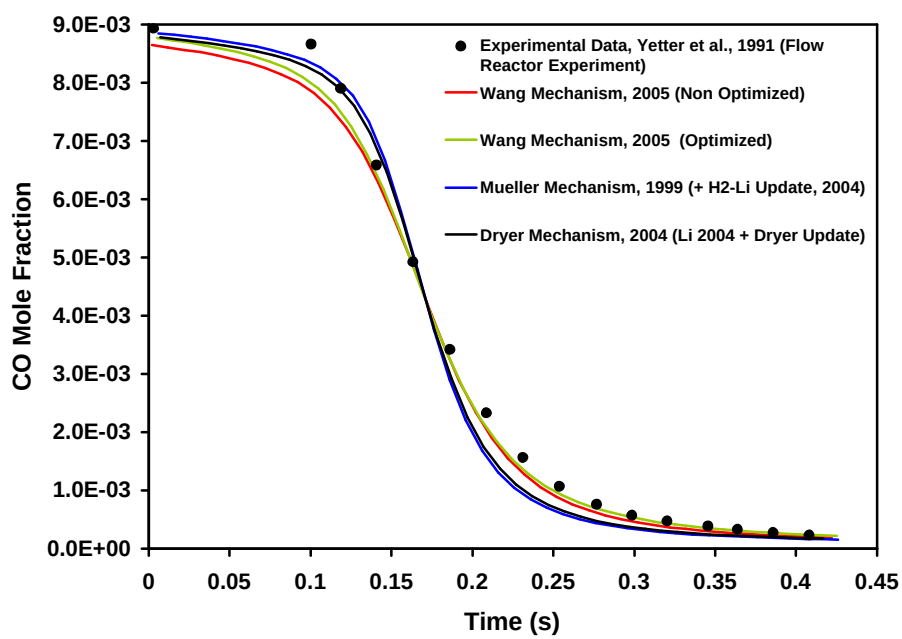

Fig. 5. Mean CO mole fraction profiles for $CO/H_2O/O_2$ mixtures. P = 0.101 MPa (14.7 psia), T=952 K (1714 R).

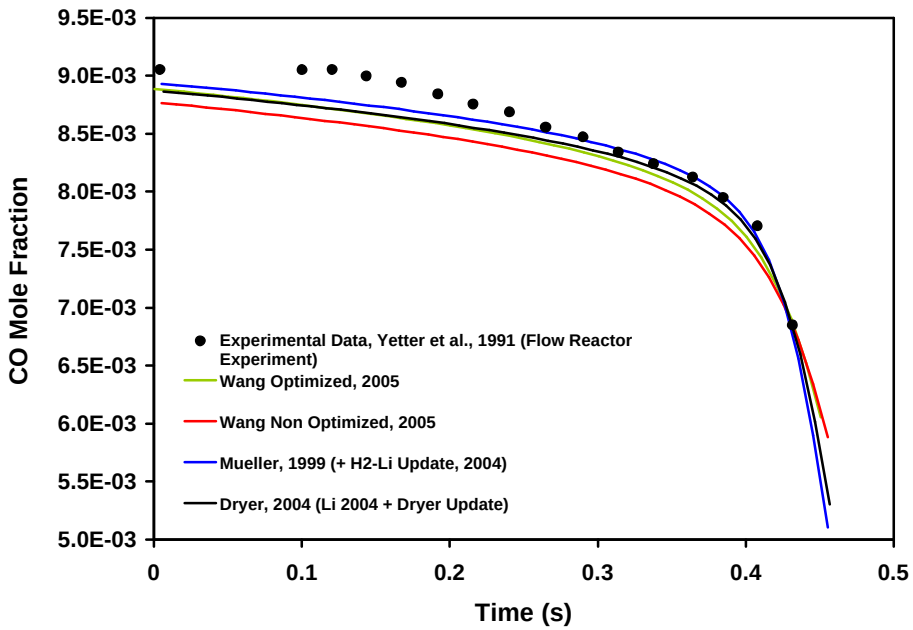

Fig. 6. Mean CO mole fraction profiles for $CO/H_2O/O_2$ mixtures. P = 0.101 MPa (14.7 psia), T=943 K (1697 R).

from the different authors. Representative results are presented in Figs. 5 and 6. Note that as with the H_2/O_2 simulations, model predictions were shifted in time to agree with the experimental data at the point of 50% fuel consumption. These comparisons show that all three mechanisms are very good in predicting the experimental data. For the **S6** case, both Wang mechanisms (trial and optimized) predict a slower CO consumption after 0.15 s, and are therefore closer to the experimental results. In interpreting the results shown in Fig. 6, note that the experimental data covers just the early part of CO consumption, and consequently doesn't allow a 50% fuel consumption time-shifting.

$H_2/CO/O_2$ Mechanisms - CHEMKIN™ Simulations

Two $H_2/CO/O_2$ mechanisms have been studied. These are the Wang mechanism from Davis et al. [5], and the Dryer mechanism composed of the H_2/O_2 mechanism of Li et al. [3] and the updated C1 mechanism adapted from Held and Dryer [11]. To study the accuracy of these two mechanisms, 44 simulations were carried out at the conditions reported in a shock tube experiment [14]. The test conditions are summarized in Table 3. The Perfectly Stirred Reactor model was used and the problem was solved constraining pressure and solving the energy equation. The thermodynamics data files computed are from the different authors. The results of these calculations are presented in Fig. 7.

Table 3. Conditions for the $H_2/CO/O_2$ CHEMKIN™ simulations.

Simulations	P	T_{init}	f	Experimental Data
S7	0.106 MPa	From 800 K to 1000 K	0.5	Kalitan, D. M. and Petersen, E. L. [14]. *Figure 2, p. 3.*
	0.304 MPa		0.5	
	1.01 MPa		0.5 and 1	
	3.04 MPa		0.5 and 1	

The two models used for the simulations give near-identical results. Note that for the selected range of temperature (800 K < T < 1000 K) and pressure (0.106 MPa < P < 3.04 MPa) conditions, ignition delays ranged from 227 μs to 12.5 s. While the ignition time seems to decrease with increasing pressure at lower temperature, the trend at higher temperature is more complex.

CHEMKIN™ Simulations for Current Experimental Conditions

The parameter space for the autoignition experiments that will be conducted under this program is as follows. The pressure range will be from 1.01 to 3.04 MPa, the fuel will be varied from pure H_2 to $CO + 3H_2$, and the equivalence ratio from 1.0 to 0.3. The flow reactor length from the fuel injection

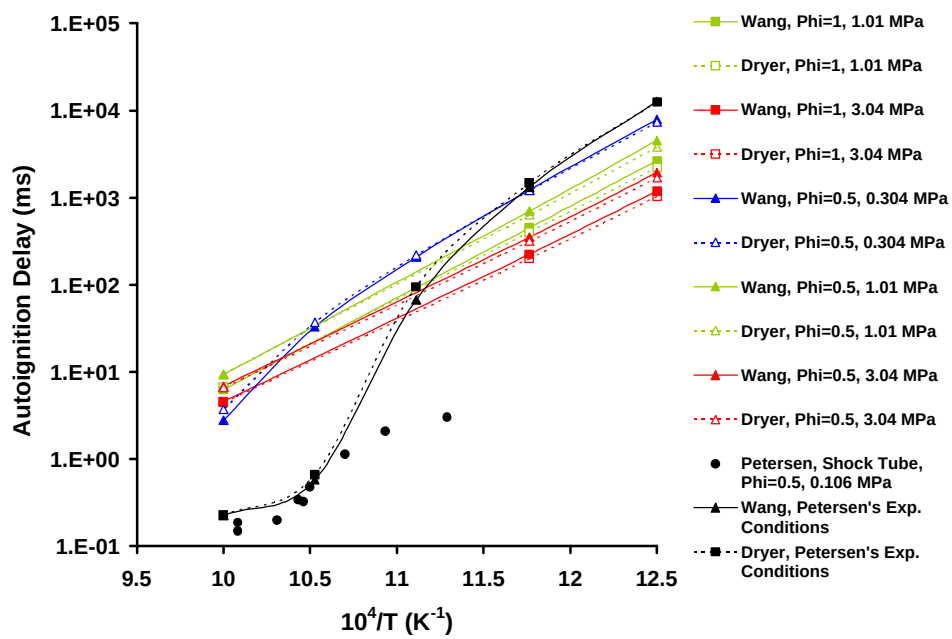

Fig. 7. Autoignition delay for a $H_2/CO/Air$ mixture (fuel is $[CO + 3H_2]$). $\phi = 1$ and 0.5; P = 0.106, 0.304, 1.01 and 3.04 MPa (15.4, 44.1, 147 and 441 psia); Wang and Dryer mechanisms.

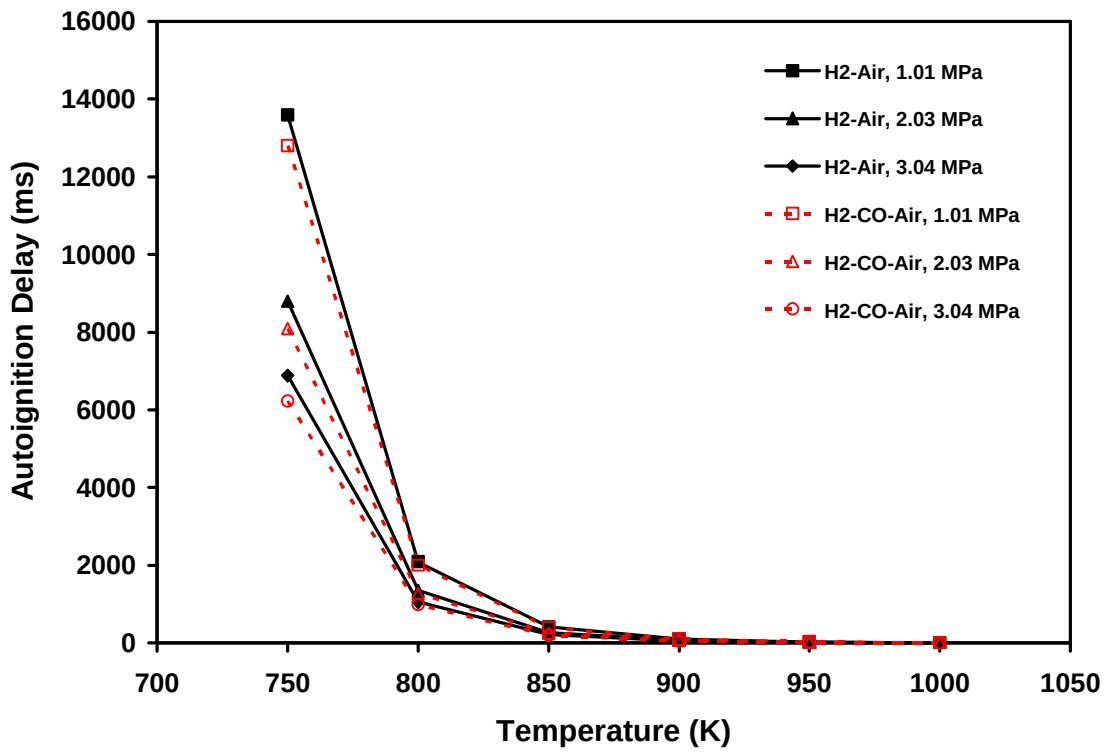

Fig. 8. Autoignition time versus temperature for the experimental fuel composition and pressure conditions. Predictions use the Dryer mechanism. $\phi = 1.0$.

location to the nozzle will at the maximum length be 1.83 m (6 ft). The flow reactor is being designed such that the autoignition time is defined as the ratio of the reactor length and the mixed gas velocity. Consequently, initial calculations to estimate the autoignition time needs to be made in order to set the mixed gas velocity such that autoignition is possible within the length of the reactor.

In this vein, the autoignition times as a function of temperature were calculated using CHEMKIN™ [1] for the Dryer model [10] described earlier for the range of pressure, fuel composition, and equivalence ratio conditions that will be investigated. The results of these calculations are contrasted in Figs. 8 and 9 for equivalence ratios of 1.0 and 0.3, respectively. If these calculations correctly predict the autoignition times at these elevated pressure conditions where data is sparse, it is clear that for the fixed maximum length flow reactor, the mixed gas temperatures need to be in excess of 800 K, in order to study flows with characteristic velocities of meters per second to tens of meters per second. These autoginition time predictions are being used to help in the design of the flow reactor.

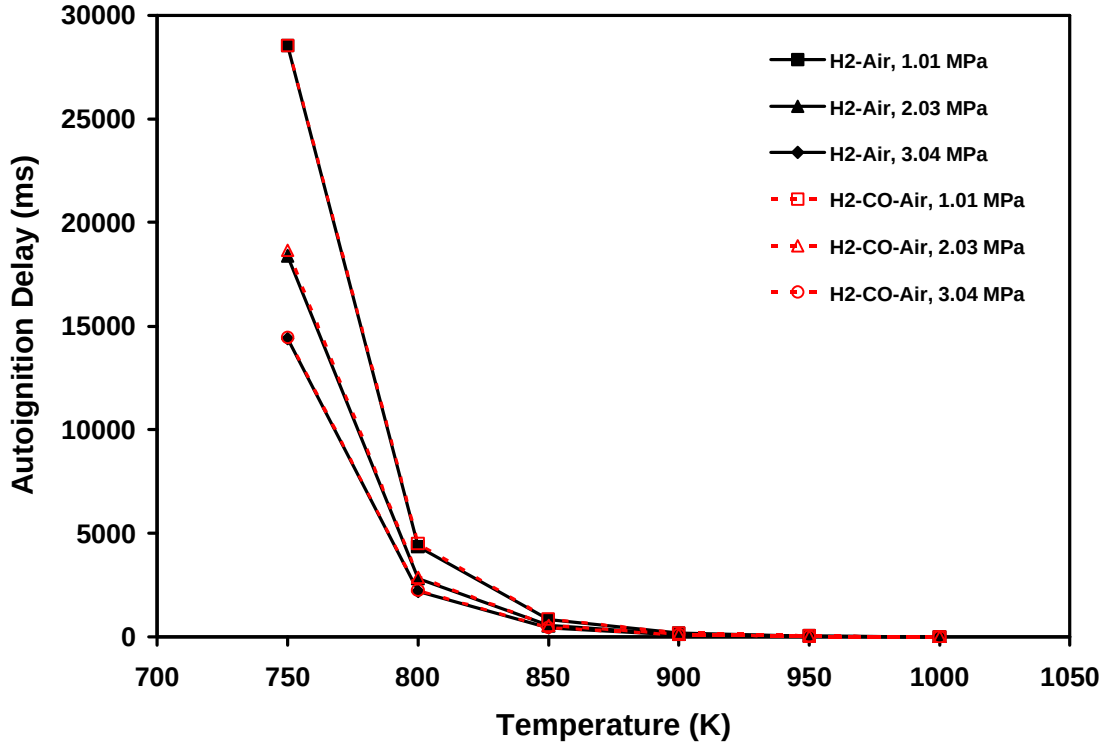

Fig. 9. Autoignition time versus temperature for the experimental fuel composition and pressure conditions. Predictions use the Dryer mechanism. $\phi = 0.3$.

CONCLUSIONS

The predictions of autoignition times for the range of operating conditions to be experimentally studied under this program indicate that the air/fuel mixed temperature needs to be in excess of 800 K for flow velocities of interest (order of 10 m/s). Based on this higher temperature requirement, the flow reactor is being designed and fabricated to function at pressures up to 3.06 MPa (450 psia). The overall thermal management of the experimental rig which currently includes a 280 kW air heater capable of delivering air temperatures up to 800 K has to be augmented with a heating source for the fuel. Currently, the design philosophy is to heat the fuel with an in-house designed heat exchanger that utilizes the afterburner products to heat the fuel higher than 800 K.

With respect to current lean-premixed gas turbine technology needs, the results to date from our research highlights the importance of obtaining data in the pressure and temperature range of the present studies. The modeling results indicate that below approximately 850 K for the pressure range of interest to gas turbines, relatively long autoignition times are expected. However from the limited data available from shock tube studies, measurements show large deviations from the modeling predictions at

temperatures below 950 K (see Fig. 7). If this trend extends to lower temperatures more typical of lean-premixed gas turbine inlet conditions under study in the present work, the results will have a major impact on the design of the fuel/air mixing section of the gas turbine inlet section. Autoignition time is a key parameter for design of the premixing section of lean-premixed gas turbines as it defines the maximum time available for mixing and transport of the fuel/air mixture to the combustor. This in turns limits the compression ratio and efficiency of the gas turbine, which are critical to competitive energy production for gas turbine manufacturers.

REFERENCES

[1] Kee, R. J., Rupley, F. M., Meeks, E., and Miller, J. A.,"CHEMKIN-III: A FORTRAN Chemical Kinetics Package for the Analysis of Gas-Phase Chemical and Plasma Kinetics," Sandia National Laboratories Report No. SAND-96-8216, Livermore, CA, 1996.

[2] Spadaccini, L. J. and TeVelde, J. A., "Autoignition Characteristics of Aircraft-Type Fuels," *Comb. and Flame*, Vol. 46, 1982, pp. 283-300.

[3] Li, J., Zhao, Z., Kazakov, A., and Dryer, F.L., "An Updated Comprehensive Kinetic Model of Hydrogen Combustion", *Int. J. Chem. Kinetics*, Vol. 36, 2004, pp. 566-575.

[4] O'Conaire, M., Curran, H. J., Simmie, J. M., Pitz, W. J., and Westbrook, C. K., "A Comprehensive Modeling Study of Hydrogen Oxidation", *Int. J. Chem. Kinetics*, Vol. 36, 2004, pp. 603-622.

[5] Davis, S. G., Joshi, A. V., Wang, H., and Egolffopoulos, F., "An Optimized Kinetic Model of H_2/CO Combustion", *Proceeding of the Combustion Institute*, Vol. 30, 2005, pp. 1283-1292.

[6] Gardiner, W. C., "Gas-Phase Combustion Chemistry", Springer-Verlag New York, 2000.

[7] Gardiner, W. C., "Rates and Mechanisms of Chemical Reactions", Physical Chemistry Monograph Series edited by Walter Kauzmann, Princeton University, 1979.

[8] Mueller, M. A., Kim, T. J., Yetter, R. A., and Dryer, F. L., "Flow Reactor Studies and Kinetic Modeling of the H_2/O_2 Reaction", *Int. J. Chem. Kinetics*, Vol. 31, 1999, pp. 113-125.

[9] Mueller, M. A., Yetter, R. A., Dryer, F. L., "Flow Reactor Studies and Kinetic Modeling of the H_2/O_2/NOx and CO/H_2O/O_2/NOx Reactions", *Int. J. Chem. Kinetics*, Vol. 31, 1999, pp. 705-724.

[10] Dryer, F. L., Personal Communication, 2005.

[11] Held, T. J., and Dryer, F. L., "A Comprehensive Mechanism for Methanol Oxidation", *Int. J. Chem. Kinetics*, Vol. 30, 1998, pp. 777-867.

[12] Ruscic, B., Wagner, A. F., Harding, L. B., Asher, R. L., Feller, D., Dixon, D. A., Peterson, K. A., Song, Y., Qian, X., Ng, C-Y, Liu, J., Chen, W., and Schwenke, D. W., "On the Enthalpy of Formation of Hydroxyl Radical and Gas-Phase Bond Dissociation Energies of Water and Hydroxyl", *J. of Phys. Chem.*, Vol. 106, 2002, pp. 2727–2747.

[13] Yetter, R. A., Dryer, F. L., and Rabitz, H., "Flow Reactor Studies of Carbon Monoxide/Hydrogen/Oxygen Kinetics", *Combust. Sci. and Tech.*, Vol. 79, 1991, pp. 129-140.

[14] Kalitan, D. M., and Petersen, E. L., "Ignition and Oxidation of Lean CO/H_2 Fuel Blends in Air", 41st AIAA/ASME/SAE/ASEE Joint Propulsion Conference & Exhibit, Tucson, Arizona, July 2005.

Degradation of Thermal Barrier Coatings with Syngas Combustion: Testing by Hyperbaric Advanced Development Environmental Simulator and Characterization by Advanced Electron Microscopy

Report Type:	Semi-Annual No. 1
Reporting Period Start Date:	August 1, 2005
Reporting Period End Date:	January 31, 2006

Principal Investigators:	Yongho Sohn, Vimal H. Desai
Affiliation:	Advanced Materials Processing and Analysis Center and Mechanical, Materials and Aerospace Engineering University of Central Florida Orlando, FL 32816-2455

Date Issued:	February 28, 2006
DOE Award Number:	DE-FC26-02NT41431
UTSR Project Number:	02-01-SR118

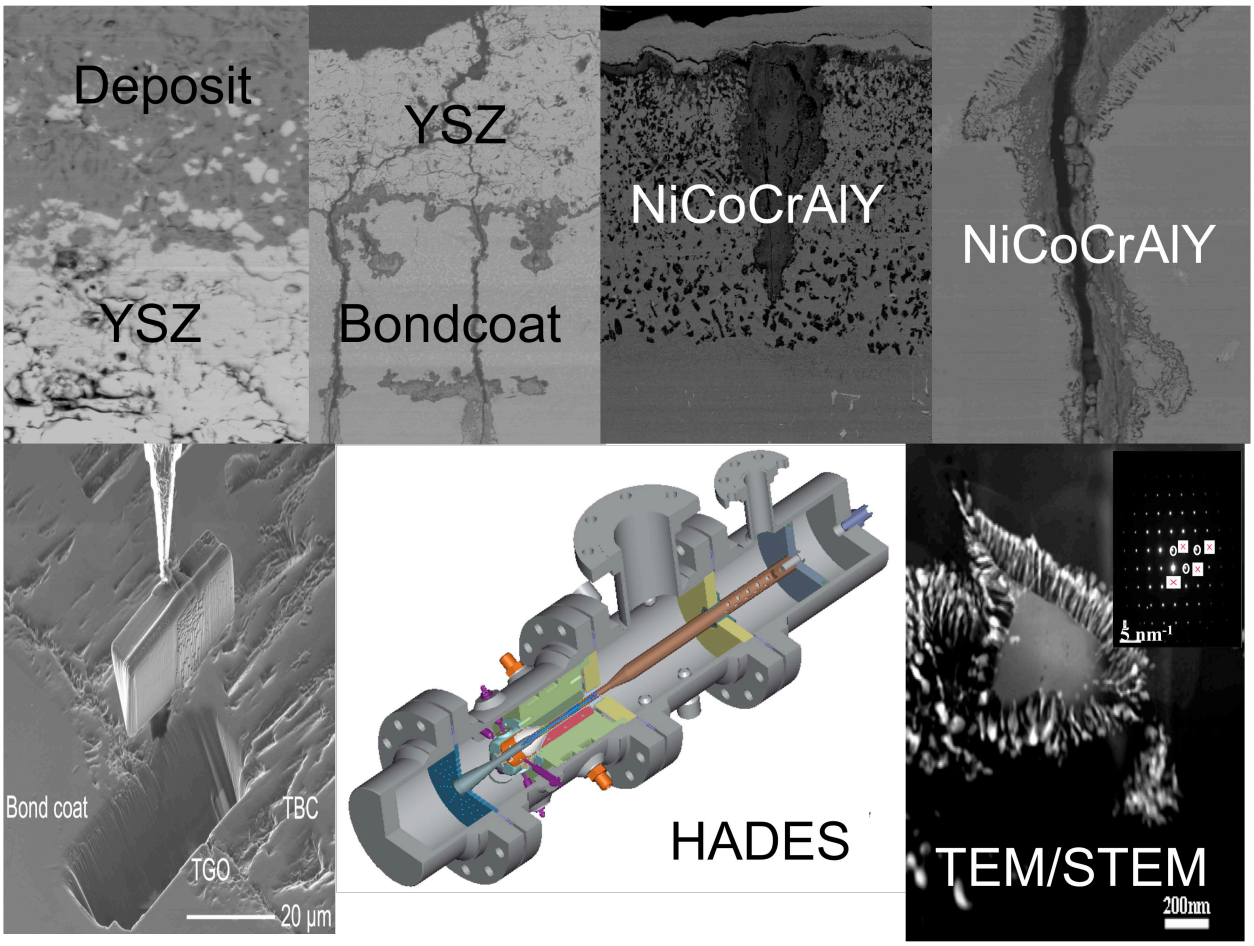

DISCLAIMER

This report was prepared as an account of work sponsored by an agency of the United States Government. Neither the United States Government nor any agency thereof, nor any of their employees, makes any warranty, express or implied, or assumes any legal liability or responsibility for the accuracy, completeness, or usefulness of any information, apparatus, product, or process disclosed, or represents that its use would not infringe privately owned rights. Reference herein to any specific commercial product, process, or service by trade name, trademark, manufacturer, or otherwise does not necessarily constitute or imply its endorsement, recommendation, or favoring by the United States Government or any agency thereof. The views and opinions of authors expressed herein do not necessarily state or reflect those of the United States Government or any agency thereof.

ABSTRACT

The understanding of materials science and engineering that will allow turbine power plant fuel flexibility, and increase the efficiency as well as reliability, availability, and maintainability, with low emissions and life cycle costs is the primary objective of this study. This program is designed to examine the degradation mechanisms of TBCs in a realistic syngas combustion environment using Hyperbaric Advanced Development Environmental Simulator (HADES) built by Florida Turbine Technologies (FTT), Inc., and advanced microstructural analysis techniques including field-emission scanning electron microscope (FESEM), x-ray diffraction (XRD), focused ion beam (FIB) with in-situ lift-out (INLO), transmission electron microscope (TEM), and scanning TEM (STEM). Emphasis is given to the phase identification (i.e., crystallography and compositions) of deposits and their penetration/reaction products as well as reaction products from gaseous contaminations, related to TBC degradation. Critical materials information, such as deposit solubility, eutectic composition, and reaction/hot corrosion rates in the light of TBC constituents will be provided from the selected in-laboratory thermodynamic/kinetics experiment/modeling in addition to HADES testing.

This first semiannual report summarizes results from the first six-month period during which preliminary characterization of TBC degradation was carried out using TBC- and MCrAlY-coated blades that were employed in turbines with syngas combustion. Observations made provided first look at mechanisms of degradations, and information necessary to devise plans for critical laboratory-controlled experiments. Initial consultation regarding HADES was carried out between PIs at UCF and FTT for a discussion on status of HADES and specification of TBCs.

TABLE OF CONTENTS

	Page
DISCLAIMER	**ii**
ABSTRACT	**iii**
TABLE OF CONTENTS	**iv**
LIST OF FIGURES	**v**
LIST OF TABLES	**ix**
I. INTRODUCTION	**1**
II. EXECUTIVE SUMMARY	**10**
III. PROJECT DESCRIPTION	**12**
IV. EXPERIMENTAL	**13**
IV.1. Preliminary Characterization of Syngas Degraded Coatings	**13**
IV.2. Furnace Isothermal Oxidation of Thermal Barrier Coatings	**13**
IV.3. Testing of TBCs using HADES	**13**
IV.4. Microstructural Characterization	**13**
IV.5. Identification of Degradation Mechanisms for TBCs in Syngas Environment	**14**
V. RESULTS AND DISCUSSION	**15**
V.1. Preliminary Characterization of Syngas Degradation	**15**
V.1.1. Air Plasma Sprayed Thermal Barrier Coatings	**15**
V.1.2. Stand-Alone NiCoCrAlY Coatings	**18**
V.2. Status of HADES and In-Laboratory Experiments	**19**
V.2.1. Current Status of HADES at FTT	**19**
V.2.2. In-Laboratory Experimental Plan	**19**
VI. CONCULSION	**21**
VII. RESEARCH PLAN FOR THE NEXT REPORTING PERIOD	**22**
REFERENCES	**23**

LIST OF FIGURES

No.	Title	Page
1	Schematics of FFT HADES: (a) conceptual configuration of the rig; (b) isometric cutaway of the rig; and (c) isometric cutaway of the test specimen section.	3
2	Sequential ion beam images from TEM specimen preparation of TBCs by focused ion beam (FIB) in-situ lift out (INLO) technique: (a) Pt wire is deposited at a site of specific interest; (b) focused ion milling is carried out to create a wedge-shaped specimen, (c) specimen is welded to a micromanipulator, and (d) lifted out, (e) specimen is welded to a TEM grid, and (f) thinned further for TEM analysis.	6
3	Bright field TEM micrograph of intact EB-PVD TBC specimen after 645, 10-hour thermal cycles at 1038°C (1900°F). Extensive decohesion at or near the YSZ/TGO interface was observed [19].	6
4	Transverse TEM/STEM analysis of "oxide-stringers" within the TGO of NiCoCrAlY bond coat: (a) Bright field TEM micrograph of TGO; (b) Bright field TEM micrograph of the Y-rich "oxide-stringer"; (c) HAADF micrograph of the Y-rich "oxide-stringer" indicating eutectoid reaction microstructure; (d) SAD pattern of Y-rich "oxide-stringer" indexed to Y_2O_3; (e) SAD pattern of TGO indexed to Al_2O_3; (f) SAD pattern (unidentified yet) of the white regions in (c).	7
5	Flowchart of the tasks proposed in this program.	8
6	Program schedule according to the specified tasks.	9
7	Internal oxidation damage after TBC spallation: (a) internal oxidation through the bond coat; (b) deposit/bond coat reaction microstructure; (c) penetration deeply into the superalloy substrate; (d) Fe-rich deposits on TGO scalled after TBC spallation.	16
8	Degradation of the YSZ top coat in the form of: (a) YSZ spallation; (b) deposit penetration through YSZ; (c) deposit; (d) YSZ dissolution.	17
9	(a, c) Secondary and (b,d,) backscatter electron micrographs of sulfides and TGO scale observed from the top surface of the stand-alone NiCoCrAlY coatings.	18
10	Internal oxidation of stand-alone NiCoCrAlY coatings in the form of pitting and selective oxidation of Al-rich b-NiAl solid solution.	19

LIST OF FIGURES (Continued)

No.	Title	Page
11	(a) APS YSZ coatings deposited on dissolvable/evaporatable substrate. (b) Free standing YSZ coatings.	20

LIST OF TABLES

No.	Title	Page
1	Comparison of testing conditions for TBC degradation.	3
2	Typical bulk gas compositions (mole% - dry basis) of syngas to be employed for TBC testing at Dakota Gasification Company site.	4
3	Types of commercial production TBCs employed in this program.	13
4	Operating parameter of HADES rig testing of TBCs using syngas combustion.	13

I. INTRODUCTION

The main driver of technology development in modern turbines for energy generation is to increase turbine power plant fuel flexibility and efficiency as well as reliability, availability, and maintainability, with low emissions and life cycle costs. Critical tasks to achieve this objective include the development of turbine technologies that enable low-cost and environmentally acceptable use of its large reserves of coal and operation at high turbine inlet temperature for efficient energy production with reduced emissions. Inevitably, turbines need advanced hot section components and coatings that can tolerate higher operating temperature while being significantly more resistant to the contaminations that erode, corrode, and deposits. The development of advanced TBCs that can tolerate the more aggressive combustion byproducts, while still enable high turbine inlet temperatures, increased power output, and power plant efficiency is highly warranted [1,2].

This program is designed to provide, for the first time, investigation on the mechanism of TBC degradation in syngas combustion environment by using Hyperbaric Advanced Development Environmental Simulator (HADES) that will be build by Florida Turbine Technologies (FTT) Inc. The use of HADES provides realistic test conditions and real time monitoring/controlling of high temperature, high pressure, temperature gradient, erosion, and turbine operation from real syngas combustion. These offer a significant advantage over furnace or burner-rig testing, which requires several assumptions (e.g., effects of total and partial pressures, deposit constituents, gas or oxide constituents, etc.). State-of-the-art characterization techniques such as FIB INLO and TEM/STEM will be employed to identify deposit constituents and hot corrosion reactions to understand the mode and mechanisms of TBC degradation in realistic syngas combustion environment. Use of FIB-INLO and TEM/STEM will enable detailed identification of phase constituents of deposits, penetrants and reaction products, thus providing the exact mechanisms for degradation of TBCs in syngas combustion environment. Critical materials information, such as deposit solubility and eutectic composition, reaction/hot corrosion rates in the light of TBC constituents will be provided from the selected in-laboratory thermodynamic/kinetics experiment/modeling in addition to HADES testing.

Hot Corrosion in Thermal Barrier Coatings

Application of TBCs in syngas combustion environment presents a unique challenge to understand the mode and mechanisms of degradation. It is generally known that the degradation via hot corrosion of ZrO_2-based TBCs becomes a problem when low quality fuels containing appreciable levels of Sulfur, and especially Vanadium, are used [1-5]. The contaminants containing Sulfur, Vanadium and Chlorine such as H_2S, SO_3, V, and HCl have been documented by a recent analysis of syngas [6]. These contaminants, in gaseous form and/or oxidized form (i.e., oxide deposition) are expected to react with ceramic topcoat, destabilize the phase constituents and degrade the integrity of TBCs. For example, for Y_2O_3 stabilized ZrO_2 (YSZ) TBCs in Vanadium-containing environment at high temperature, Kvernes [7], Hamilton and Nagelbert [8] as well as Hertl [9] have reported the tetragonal to (monoclinic+cubic) destabilization of YSZ as:

$$ZrO_2(Y_2O_3) + V_2O_5 \rightarrow ZrO_2 \text{ (monoclinic+cubic)} + 2YVO_4$$

The same reaction leading to degradation of YSZ TBCs has been reported in the presence of phosphorous (i.e., reaction with oxidized P_2O_5) [10]. Based on the argument of thermodynamics, Jones [11] has reported the additional reaction of:

$$ZrO_2(Y_2O_3) + P_2O_5 \rightarrow ZrP_2O_7 + Y_2O_3$$

Although not reported, similar reactions with oxidized Arsenic (As_2O_5) from ArH_3, and Antimony (Sn_2O_5) based on their electronic structure and acidity.

While the effects of Berylium, Chromium, Mercury, Selenium have not been reported, a significant levels of these contaminants would lead to reaction with YSZ that would lead to phase destabilization and formation of deleterious reaction products.

Although YSZ tends to resist sulfur degradation in the presence of SO_3, reaction of Y_2O_3 with SO_3 in the presence of Na_2SO_4 can give a rise to destabilization of YSZ as reported by Pettit and Barkalow [12]:

$$ZrO_2(Y_2O_3) + 3SO_3\ (+Na_2SO_4) \rightarrow ZrO_2\ \text{(monoclinic)} + Y_2(SO_4)_3\ \text{(in } Na_2SO_4 \text{ solution)}$$

It should be noted that most of the previous investigations for TBC hot corrosion employed furnace or burner-rig testings that lack realistic high pressure. The effects of pressure in the case of hot corrosion may significantly influence the reaction of gaseous species (e.g., oxidation, hot corrosion and reaction with YSZ) and hence the degradation mechanisms of TBCs.

In addition, other condensed phases including molten salts that pass through the syngas cleanup system have not been identified and the degradation mechanism associated with these unknown condensed phases is an unexplored area of study for materials scientists and engineers. Strangman [13,14] have reported that the deposition of molten sulfate salts and glassy CMAS (calcia magnesia alumina silicate) dust onto porous TBCs can significantly reduce the durability. In an recent review, Bose and Strangman [15] discussed that the reaction to destabilize YSZ was usually not the life-limiting effect. The more immediate effect has been reported as the penetration of these deposits into the porous YSZ and subsequent thermo-mechanical damage. Considering that the identity of deposits has not been studied in the syngas combustion environment, the use of syngas combustion in HADES with realistic turbine environment will provide valuable information to understand the degradation mechanisms of TBCs and to develop TBCs with superior environmental resistance.

Hyperbaric Advanced Development Environmental Simulator (HADES)

HADES is a test rig, being built by FTT, to examine materials and coatings degradation in syngas combustion environment. As presented in Figure 1, FTT HADES consists of high pressure compressor, syngas combustor, 6-inch long hot zone for specimen testing, exhaust chamber with cooler and silencer. Test section of HADES accommodates tubular specimens (0.5” in diameter with a 0.0375” wall thickness and 6” long) of TBCs, metallurgical coatings and

superalloys. During testing, specimens are exposed to realistic engine conditions as presented in Table I, using the approximate gas composition presented in Table II for combustion.

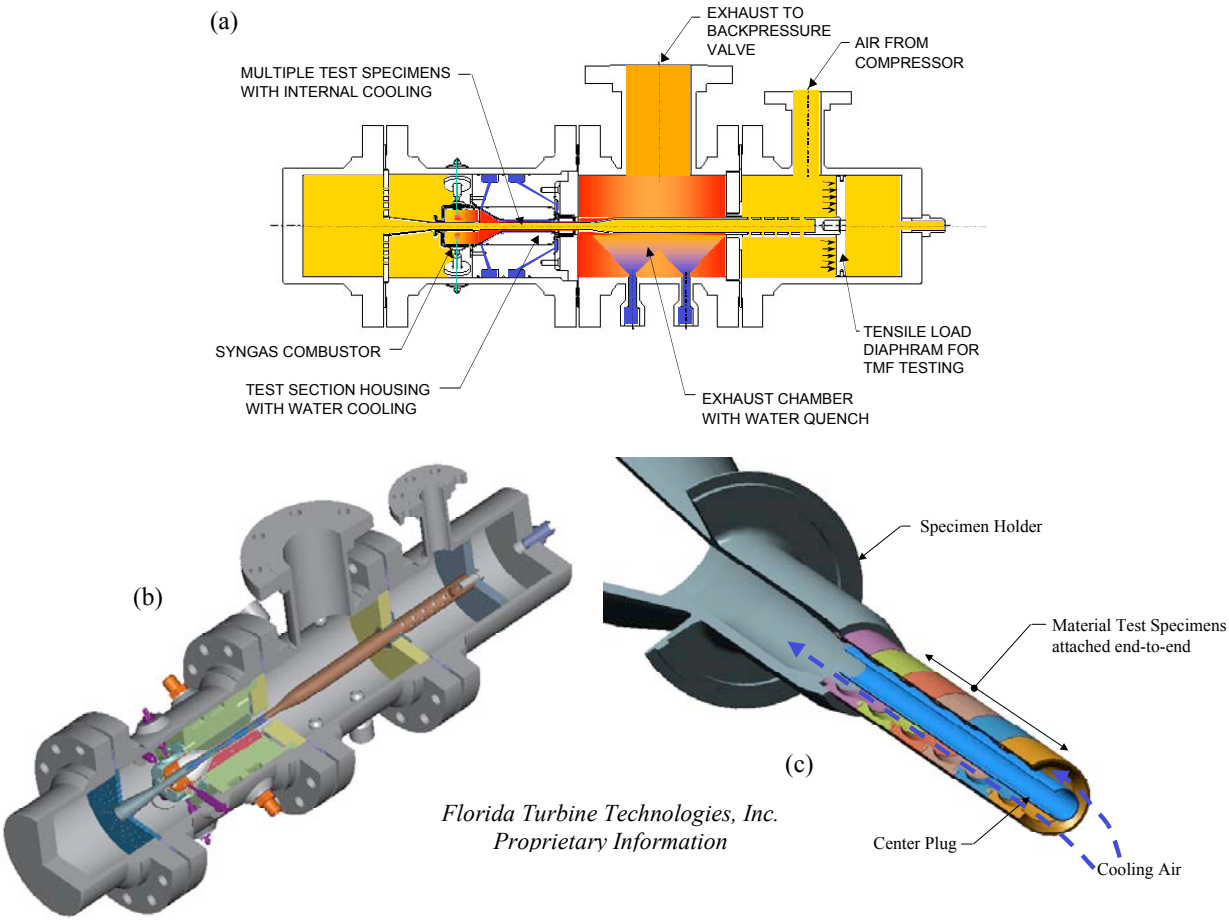

Figure 1. Schematics of FFT HADES: (a) conceptual configuration of the rig; (b) isometric cutaway of the rig; and (c) isometric cutaway of the test specimen section.

Table I. Comparison of testing conditions for TBC degradation.

Factors Related to TBC Failure	Engine Test	FTT HADES	Burner Rig	WaltzMills Plasma Rig	NASA Laser Rig
High Pressure	Yes	Yes	No	No	No
High Temperature	Yes	Yes	Yes	Yes	Yes
Temperature Gradient	Yes	Yes	Partial	Yes	Yes
Thermal Cycling	Yes	Yes	Yes	Yes	Yes
High Velocity Flow Erosion	Yes	Yes	Partial	No	No
Syngas Contaminants	Yes	Yes	Yes	No	No
Axial Fatigue Loading	Yes	Yes	No	No	Unknown

Table II. Typical bulk gas compositions (mole% - dry basis) of syngas to be employed for TBC testing at Dakota Gasification Company site [16].

Bulk Gas Compound	Raw Gas	Shifted Gas	Rectisol Syngas	Product Syngas
Hydrogen	38.60	42.75	62.16	3.1
CO_2	32.4	36.7	0.37	1.4
H_2S	0.72	0.47	ND	ND
O_2/Ar	0.16	0.17	0.20	0.5
Nitrogen	0.02	0.02	0.02	0.1
Methane	11.9	10.9	16.7	94.9
CO	15.4	8.2	20.5	0.01
C_2 + Hydrocarbons	0.81	0.79	0.05	ND
Specific Gravity	0.7546	0.7457	0.3432	0.5562
Compressibility	0.9990	0.9990	0.9999	-
Dry BTU	315	295	438	970
Molecular Weight	21.92	21.66	10.02	16.3
Organic Nitrogen Compound	~100 ppm	~10 ppm	< 1 ppm	ND
Organic Sulfur Compound	200~300 ppm	100~150 ppm	24 ppb	ND

Note: ND refers to Non-Detectable. Does not include trace contaminants analysis.

Current estimates of operating conditions and testing capabilities of FTT HADES satisfy the design point set forth by U.S. DoE and includes TBC surface temperature of 1250°C (2282°F), combustor exit temperature of 1650°C (3000°F), gas pressure of 370 psi, and coolant temperature of 412°C (775°F). The rig will also be equipped with real time monitoring/controlling capabilities including TBC spallation detection through heat flux sensoring.

Microstructural Analysis of TBC Degradation in Syngas Combustion Environment

In addition to pioneering TBC test with syngas combustion in realistic engine conditions, advanced microstructural analysis to understand degradation mechanisms will be carried out using state-of-the-art characterization techniques in this program. This is a step over any previous investigation that relied solely, at best, on qualitative, correlation based on resolution limited XRD and SEM with EDS. Advances in understanding of TBC degradation/hot corrosion in syngas environment require advanced characterization techniques that will exactly identify the phase constituents (both crystallography and composition) at atomic-scale and their microstructural evolution in contact with TBCs. To that end, this program offers, in addition to conventional tools such as XRD, FESEM/EDS, an advantage of microstructural analysis by TEM/STEM with specimen preparation by FIB-INLO. Using these advanced techniques, a site-specific observation of microstructure and identification of phase constituents can be carried out easily for identification of deposits and hot corrosion reaction products that arise from trace contaminants of syngas environment using analytical techniques of TEM/STEM.

FIB prepares a large (20 μm x 20 μm) and uniformly thin (<100 nm) TEM specimens for TEM microstructural analysis. In FIB, gallium (Ga) ions, wetted at a sharp tungsten tip are accelerated through a vacuum column, and section (i.e., mill) materials at lateral resolutions up to 5 nm. The milled specimen is lifted out after being welded to an in-situ probe (INLO). The process of FIB INLO technique is illustrated in Figure 2 with ion beam generated secondary electron images collected during the actual TEM specimen preparation of TBCs. The use of FIB-INLO has been successful in preparing delicate specimens such as heavily oxidized/damaged TBCs as shown in Figure 3. Although the current preparation has been focused on YSZ/TGO/bond coat interfaces [17-19], FIB-INLO process for syngas degradation of TBCs, including near YSZ surface will not pose any difficulties, if not easier. Details of the TEM specimen preparation process by FIB-INLO have been published elsewhere [17-19].

Upon successful completion of TEM specimen preparation by FIB-INLO, syngas degradation of TBCs will be carefully characterized by TEM/STEM. An FEI/Tecnai F30 TEM/STEM system operating at 300 KeV with analytical techniques such as high angle annular dark field (HAADF), STEM imaging that gives compositional contrast (i.e., analogous to backscatter electron images), selected area diffraction (SAD), convergent beam electron diffraction (CBED), fast-Fourier transformed (FFT) diffractograms, nano-spot EDS (n-EDS), and electron energy loss spectroscopy (EELS) will be employed to identify the phase constituents of deposits and reaction products that are critical in understanding the mechanisms of TBC degradation in syngas combustion environment. Identification of the phase constituents would involve accurate determination of crystal structures, compositions, and electron-state. The advanced microstructural analysis using TEM/STEM via FIB-INLO is a progress over any previous investigation that relied solely, at best, on qualitative correlation based on resolution limited XRD, SEM with EDS. Figure 4 represents a typical example illustrating the advantage of TEM/STEM investigation made possible by FIB-INLO [19]. Recently, research effort at UCF, made possible through UTSR No. 02-01-SR103 identified the exact phase constituents of so-called "oxide stringers" in the thermally grown oxide (TGO) from NiCoCrAlY bond coat, including those at the interface, leading to a conclusion that Y_2O_3 oxide stringers grow by eutectoid reaction through grain boundary diffusion of Y^{3+} ions in the Al_2O_3 matrix [20].

Anticipated Public Benefits

The evaluation of TBCs in syngas combustion environment using HADES proposed in this program will help develop IGCC power generation technologies; leading to less expensive and more reliable energy sources, and reduce U.S. dependence on foreign resources. Development of reliable and durable TBCs for IGCC based on decrease fuel cost will increase the performance efficiency of turbines by 2.2%, equivalent to CO_2 emission reduction by 300 million tons per year per unit and operational savings of 6.3% (assuming 40/60 split in fuel/capital cost).

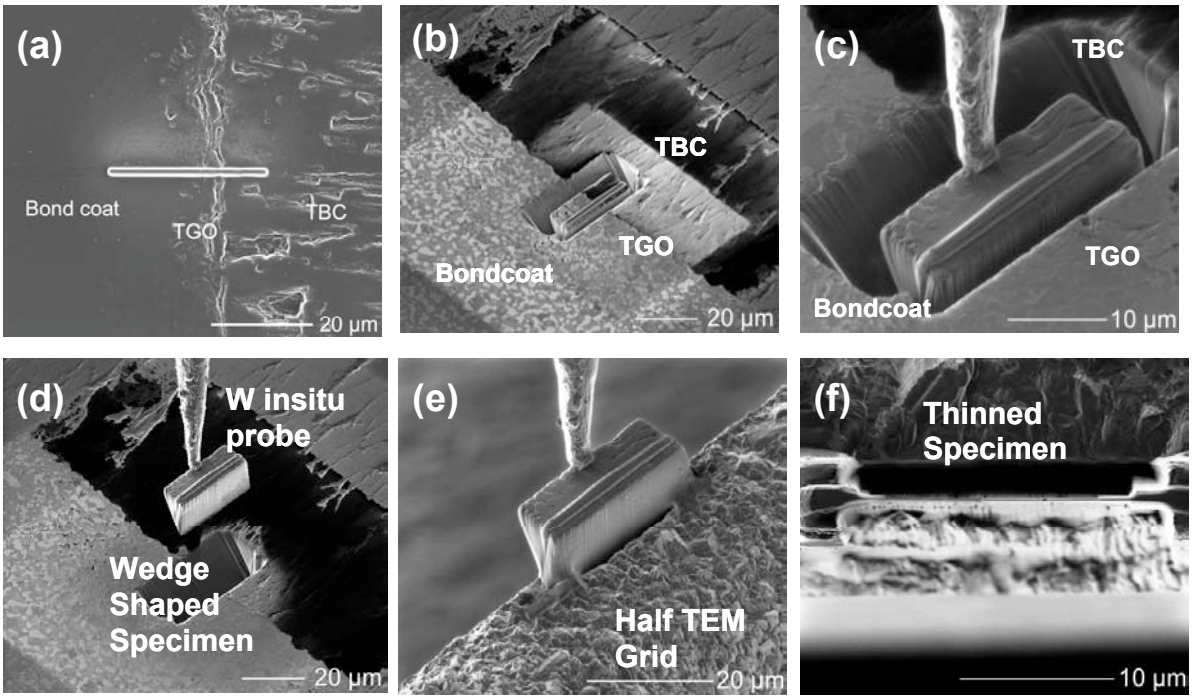

Figure 2. Sequential ion beam images from TEM specimen preparation of TBCs by focused ion beam (FIB) in-situ lift out (INLO) technique: (a) Pt wire is deposited at a site of specific interest; (b) focused ion milling is carried out to create a wedge-shaped specimen, (c) specimen is welded to a micromanipulator, and (d) lifted out, (e) specimen is welded to a TEM grid, and (f) thinned further for TEM analysis.

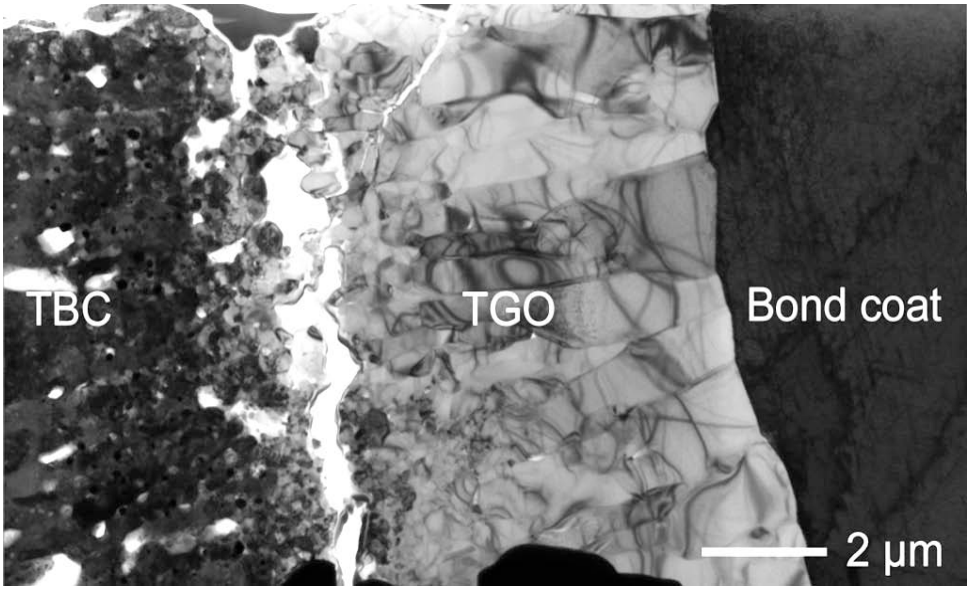

Figure 3. Bright field TEM micrograph of intact EB-PVD TBC specimen after 645, 10-hour thermal cycles at 1038°C (1900°F). Extensive decohesion at or near the YSZ/TGO interface was observed [19].

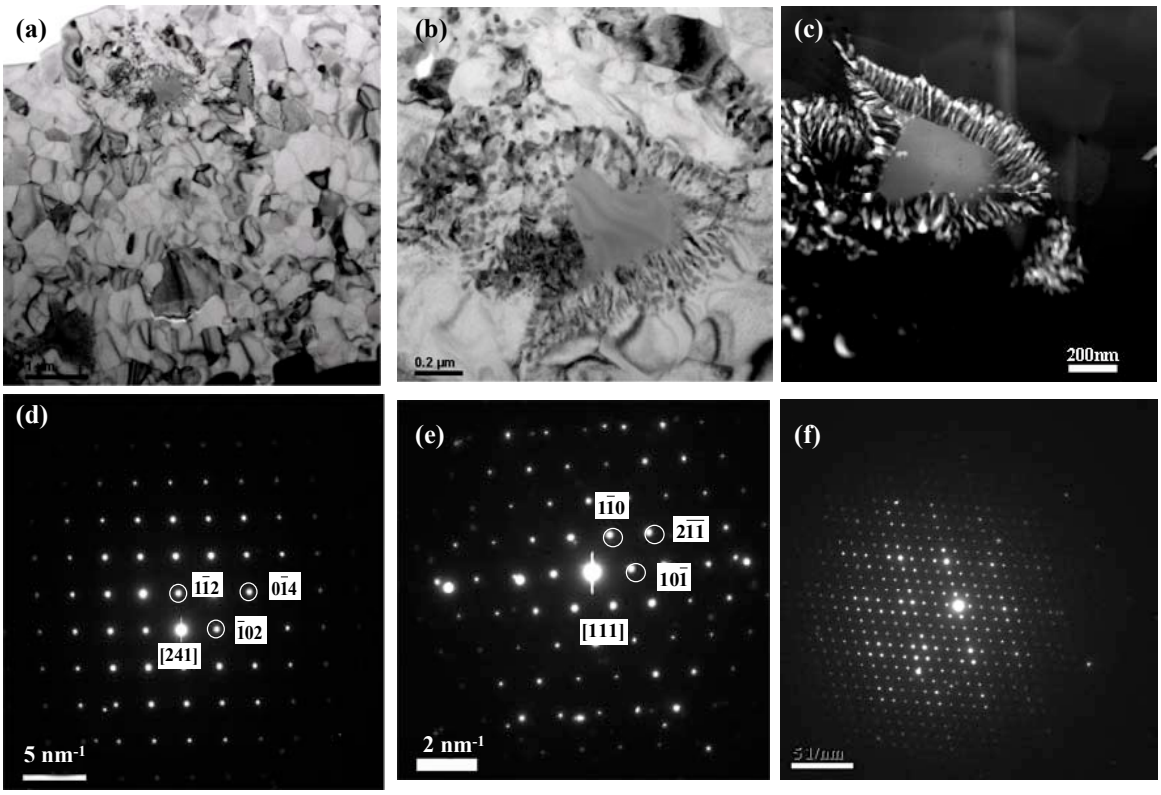

Figure 4. Transverse TEM/STEM analysis of "oxide-stringers" within the TGO of NiCoCrAlY bond coat: (a) Bright field TEM micrograph of TGO; (b) Bright field TEM micrograph of the Y-rich "oxide-stringer"; (c) HAADF micrograph of the Y-rich "oxide-stringer" indicating eutectoid reaction microstructure; (d) SAD pattern of Y-rich "oxide-stringer" indexed to Y_2O_3; (e) SAD pattern of TGO indexed to Al_2O_3; (f) SAD pattern (unidentified yet) of the white regions in (c).

Objectives

The overall objective of the proposed research program is to understand the degradation mechanisms of thermal barrier coatings in syngas combustion environment using advanced microstructural analytical techniques. The findings of the program will provide, for the first time, degradation modes and mechanisms of TBCs that lead to failure, with realistic syngas turbine conditions. TBC tests will be carried out in high pressure, high temperature, temperature gradient and syngas combustion environment using HADES rig designed and built by FTT. APS, DVC and EB-PVD TBC specimens, according to the required specification need of HADES, will be provided by industrial partners. Materials characterization will be carried out using state-of-the-art electron microscopy that includes FESEM, FIB-INLO, TEM/STEM. In order to achieve the overall objective of this program, the following goals have been set forth:

- Degradation testing of APS, EB-PVD and DVC TBCs in air and in syngas combustion environment:
  - Baseline furnace isothermal testing in air.
  - HADES testing with syngas combustion.
- Identification and characterization of the degradation using advanced characterization techniques such as FESEM, FIB-INLO, TEM and STEM:

- Deposits identification.
- Penetration/reaction/degradation characterization

- Development of fundamental understanding of the difference in degradation behavior of TBCs in air and syngas:
  - Identify degradation (e.g., hot corrosion) mechanisms (e.g., YSZ destabilization, deposit penetration and reaction, etc.).
  - Generate critical materials data (e.g., solubility, eutectic compositions and degradation kinetics for realistic turbine environment).
  - Provide feasible approaches to improve resistance against TBC degradation in syngas combustion environment.
- Transfer to industrial partners, the attained knowledge on TBC degradation in syngas combustion environment.
- Provide two pairs of student research teams, with interdisciplinary team-based research activities in collaboration with industrial partners.

To achieve specific goals and the overall objective of this program, six tasks have been defined with corresponding schedule as presented in Figure 5. Task I involves furnace isothermal testing of six types of commercial production TBCs at 1150°C (2100°F) and 1050°C (1920°F) for 10, 100 and 400 hours. The results of this simple task serve as a baseline to be compared to the syngas testing. Task II involves testing of the six types of TBCs using HADES rig in syngas combustion with the same TBC surface temperature and test duration. All tested TBC specimens will be characterized with respect to degradation and microstructural development using advanced characterization techniques as task III. Coupled with extensive literature review and selected in-laboratory experiments, characterization and modeling, detailed mechanisms of TBC degradation in syngas combustion environment will be determined as task IV. In addition, feasible approaches (e.g., chemistry, processing, overlay coating, etc.) for improving the resistance of TBCs in syngas combustion environment will be recommended based on conclusions of this program. Findings and understanding from this program will be frequently communicated with industrial partners for efficient technology/knowledge transfer as task V. A flow chart associated with specific tasks is presented in Figure 5.

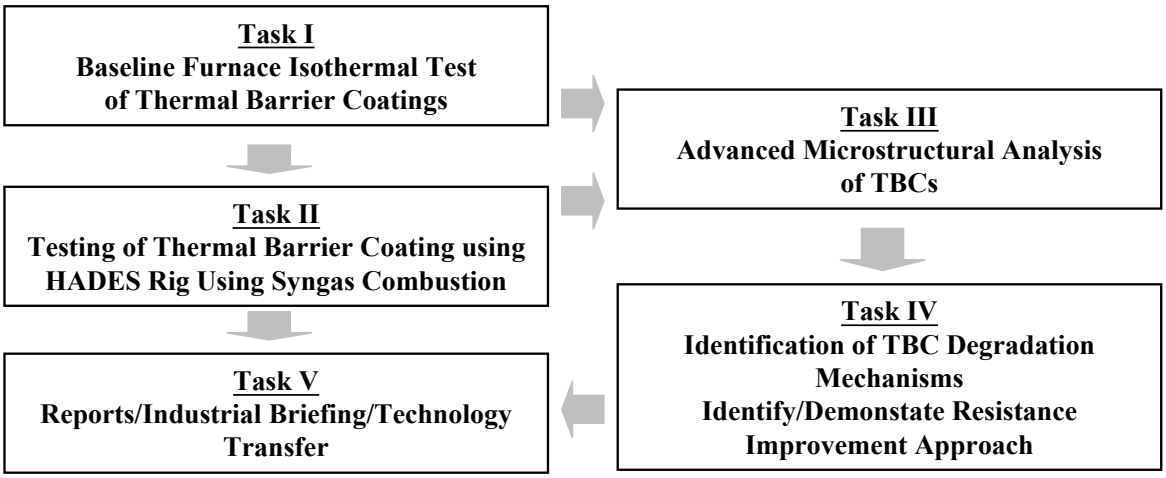

Figure 5. Flowchart of the tasks proposed in this program.

In achieving the overall objective of this program and specific deliverables, the individual tasks, previously described will be carried out according to the schedule shown in Figure 6.

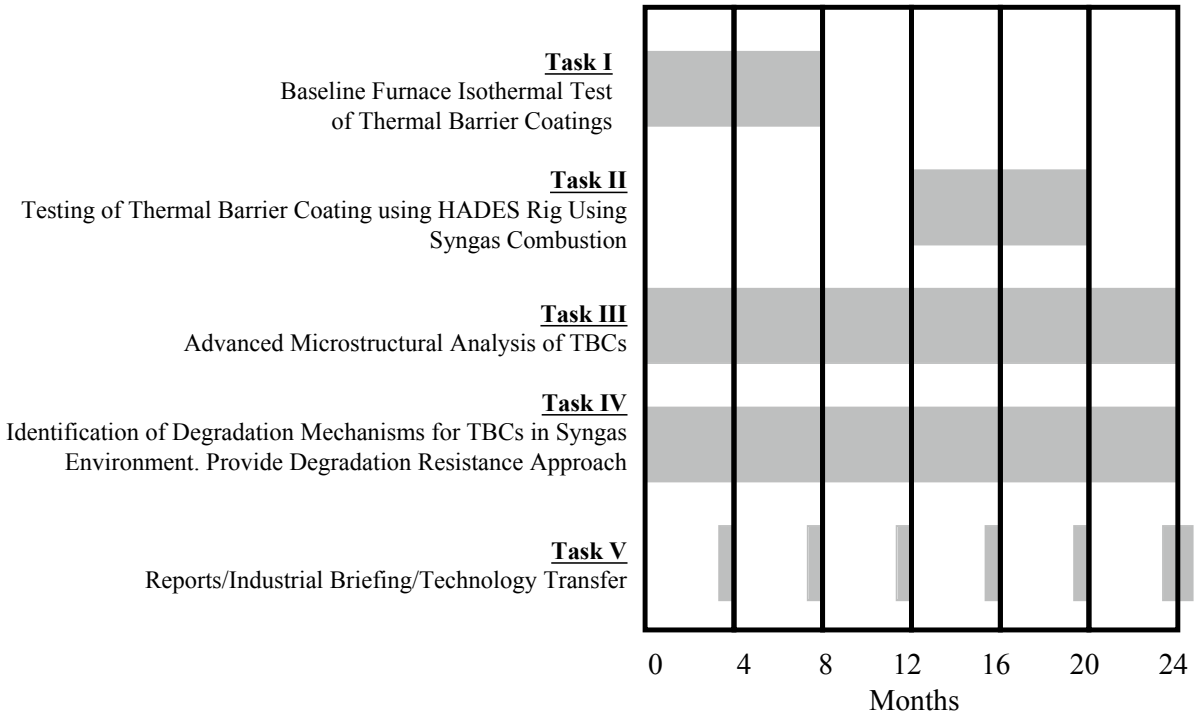

Figure 6. Program schedule according to the specified tasks.

II. EXECUTIVE SUMMARY

Project Title: **Degradation of Thermal Barrier Coatings with Syngas Combustion: Testing by Hyperbaric Advanced Development Environmental Simulator and Characterization by Advanced Electron Microscopy**

Identifiers: **DOE DE-FC26-02NT41431 and UTSR No. 02-01-SR118**

PIs: **Yongho Sohn and Vimal H. Desai**
Affiliation: **Advanced Materials Processing and Analysis Center and Mechanical, Materials and Aerospace Engineering University of Central Florida Orlando, FL 32816-2455**

Reporting Period: **August 1, 2005 ~ July 31, 2007**
Date Issued: **February 28, 2006**

This program examines the degradation mechanisms of TBCs in a realistic syngas combustion environment using advanced microstructural analysis techniques. The findings of the program will provide degradation modes and mechanisms of TBCs that lead to failure in realistic syngas turbine conditions that includes high pressure, high temperature, temperature gradient, syngas combustion contaminants, and high velocity flow erosion using Hyperbaric Advanced Development Environmental Simulator (HADES). Materials characterization will be carried out using state-of-the-art electron microscopy that includes field-emission scanning electron microscope (FESEM), x-ray diffraction (XRD), focused ion beam (FIB) with in-situ lift-out (INLO), transmission electron microscope (TEM), and scanning TEM (STEM). Emphasis will be given to the phase identification (i.e., crystallography and compositions) of deposits and their penetration/reaction products as well as reaction products from gaseous contaminations. Critical materials information, such as deposit solubility, eutectic composition, and reaction/hot corrosion rates in the light of TBC constituents will be provided from the selected in-laboratory thermodynamic/kinetics experiment/modeling in addition to HADES testing.

During the first reporting period, the following tasks were successfully carried out according to the proposed schedule:

- **Preliminary characterization of TBC degradation using TBC- and MCrAlY-coated blades that were employed in turbines with syngas combustion.**
  - **Identified deposits containing Fe, Si, Al, Ca, Mg, Na, K, S.**
  - **Significant presence of spinel-structured and other oxides.**
  - **Penetration into, and dissolution of the YSZ coatings.**
  - **Internal sulfidation and oxidation of NiCoCrAlY either as bond coats and stand-alone coating.**
- **Development of detailed laboratory-controlled experimental plan:**

- **Use of free-standing APS YSZ coatings produced at UCF's Thermal Spray Facility (UCF-TSF) and NiCoCrAlY powders.**
- **Compositional and temperature variation**
  - **0.5, 1, and 10 mM of Na_2SO_4, V_2O_5, $NaVO_3$, P_2O_5, Na_2SO_4 + 5%V_2O_5**
  - **950°, 1050° and 1150°C for 10 and 30 hours.**

- **Initial consultation regarding HADES among PIs at UCF and FTT for a discussion on status of HADES and specification of TBC.**
  - **Delay in development of HADES was reported by FTT, and hence specification of TBC samples has not been finalized.**
  - **HADES testing, "according to the original plan," will not begin until August, 2007.**

In the second reporting period (February 1, 2006 ~ July 31, 2006), preliminary characterization of "syngas-blades" will be completed using TEM/STEM using FIB-INLO to determine the exact composition and structure of hot-corrosion (e.g., reaction) products. In addition, in-laboratory experiments will commence. PIs at FTT will be continuously consulted for the development status of HADES.

III. PROJECT DESCRIPTION

This University Turbine Systems Research (UTSR) program is designed to examine the degradation mechanisms of TBCs in a realistic syngas combustion environment using Hyperbaric Advanced Development Environmental Simulator (HADES) and advanced microstructural analysis techniques including field-emission scanning electron microscope (FESEM), x-ray diffraction (XRD), focused ion beam (FIB) with in-situ lift-out (INLO), transmission electron microscope (TEM), and scanning TEM (STEM). Emphasis is given to the phase identification (i.e., crystallography and compositions) of deposits and their penetration/reaction products as well as reaction products from gaseous contaminations. Critical materials information, such as deposit solubility, eutectic composition, and reaction/hot corrosion rates in the light of TBC constituents will be provided from the selected in-laboratory thermodynamic/kinetics experiment/modeling in addition to HADES testing.

In addition, this program is designed to harvest two graduate and two undergraduate students with strong background in TBCs and other engineering issues related to goals and challenges defined by U.S. DOE. This program is primarily carried out by two graduate students, Mr. Biao Yuan and Mr. Prabakar Mohan, and two undergraduate students, Miss Monica Hopkins and Mr. Michael Thompson. Miss Hopkins is committed to continue her activities in this program as a graduate student, starting fall of 2006. Additional assistance and collaboration for FIB-INLO and TEM/STEM are provided by Miss Jing Liu, a Ph.D. candidate and an Amelia Earhart Fellow.

IV. EXPERIMENTAL

IV.1. Preliminary Characterization of Syngas Degraded Coatings

TBC- and NiCoCrAlY-coated blades from turbines operated under syngas combustion were supplied by industrial partners for preliminary microstructural characterization. Based on characterization techniques described in section IV.4, these blades are being characterized.

IV.2. Furnace Isothermal Test of Thermal Barrier Coatings

Tubular specimens (0.5" diameter, 0.0375" wall thickness and 6" long) coated with TBCs will be supplied by industrial partners of this program. TBCs will be fabricated with current commercial processing practices. Details of the specimen specifications are presented in Table III. These TBC specimens will be subjected to furnace isothermal test using Blue/Lindberg 3-zone high temperature tube furnace at 1150°C (2100°F) and 1050°C (1920°F) for 10, 100 and 400 hours. The results of the microstructural analysis (task III) of the oxidized specimens will serve as a baseline and be compared to the results of syngas testing of TBCs (task II). This task will also introduce and train graduate students about benefits, failure mechanisms, and characterization techniques of TBCs.

Table III. Types of commercial production TBCs employed in this program.

TBC Type	**Topcoat Chemistry and Processing**	**Bond coat Chemistry and Processing**	**Superalloy Substrate**
I	YSZ; APS	MCrAlY; APS	Ni/Co-base Superalloys
II	YSZ; DVC	MCrAlY; VPS	
III	YSZ; EB-PVD	(Ni,Pt)Al; CVD	

IV.3. Testing of Thermal Barrier Coating using HADES Rig Using Syngas Combustion

Tubular specimens (0.5" diameter, 0.0375" wall thickness and 6" long) coated with TBCs according to Table III will be supplied by industrial partners of this program. TBC specimens will be subjected to HADES rig testing of syngas combustion using the operating parameters presented in Table IV. The degradation of TBCs as a function of microstructural variation, including the size, shape and amount of porosity would be examined.

Table IV. Operating parameter of HADES rig testing of TBCs using syngas combustion.

Parameter	**High Temperature Testing**	**Low Temperature Testing**
TBC Surface Temperature	1150°C (2100°F)	1050°C (1920°F)
Combustor Exit Temperature	Up to 1650°C (3000°F)	Up to 1650°C (3000°F)
Gas Pressure	Up to 350 psi	Up to 350 psi
Coolant Temperature	~ 412°C (775°F)	~ 412°C (775°F)
Mechanical Loading	None	None
Test Duration	10, 100 and 400 hours	10, 100 and 400 hours

IV.4. Microstructural Characterization

All air- and syngas-tested TBC specimens will be characterized using advanced microstructural analysis techniques. Aforementioned, this task will employ state-of-the-art characterization techniques including FESEM with EDS, XRD, XPS, AES, EPMA, FIB-INLO, and TEM/STEM equipped with nano-EDS, SAD, HAADF, FFTD, EELS, PEELS. During the characterization, emphasis will be given to the identification of surface deposits and understanding of contaminant-induced reaction/degradation mechanisms in syngas combustion environment. Environment-induced reaction of YSZ (e.g., destabilization) and penetration of deposits will be quantitatively understood in terms of fundamentals of thermodynamics and kinetics.

IV.5. Identification of Degradation Mechanisms for TBCs in Syngas Environment

Results from microstructural analysis coupled with extensive literature review and selected in-laboratory experiments/modeling will be compiled to provide degradation mechanisms of TBCs in syngas combustion environment. Based on results of HADES tests and microstructural analysis, selected experimental investigation will be designed and carried out to quantitatively examine and understand the materials thermodynamics (e.g., phase stability/equilibrium) and kinetics (e.g., rates of reaction/diffusion/penetration) related to TBC degradation in syngas environment. Additional modeling effort (e.g., ThermoCalc) can be carried out to refine the understanding of these fundamentals of TBC degradation. Results and correlation observed will be reported to industrial partners for suggestions and criticisms. Conclusions drawn from this collaborative effort will elucidate degradation mechanisms for TBCs and form a sound basis for identifying feasible approaches (e.g., chemistry, processing, overlay coating, etc.) for improving the resistance of TBCs in syngas combustion environment.

V. RESULTS AND DISCUSSION

V.1. Preliminary Characterization of Syngas Degradation

V.1.1. Air Plasma Sprayed Thermal Barrier Coatings

A turbine blade coated with TBC was supplied by an industrial partner to assist the effort to understand the syngas degradation of TBCs. While the specification of TBC, turbine blade and operating condition remains proprietary, this specimen provide the first look at syngas degraded TBC. Visually, localized damage and spallation of TBCs was observed along with "red" iron oxides on the remaining TBC surface. The blade was sectioned with slow speed Isomet Buehler using diamond wafering blade, mounted in Epo-Thin low viscosity epoxy, and metallographically polished down to 0.25 μm.

In regions where TBCs had spalled, a significant local-internal oxidation was observed as presented in Figure 7. This penetration attack through the length of the bond coat extended into the superalloy substrate as shown in Figures 7(a) and 7(c). The interface between internal oxidation and bond coat revealed a distinctive microstructure (e.g., euctectoid or eutectic) as seen in Figure 7(b). Additional deposits on top of the TGO scale were observed without any indication of TGO/deposit interaction as shown in Figure 7(d).

In regions where TBC is still adherent, several distinctive degradation modes were observed as shown in Figure 8. Clearly, deposits arising from fuel contaminates (a) spalled, (b) penetrated, (c) deposited, and (d) dissolved the YSZ topcoat. While the observed spallation in Figure 8(a) and penetration in Figure 8(b) may be a result (rather than the cause) of other types of damage (such as nearby spallation, foreign object damage, and erosion), microstructural features observed in Figures 8(c) and 8(d) warrants a further examination by TEM/STEM in order to understand reaction mechanism between the YSZ and deposits. This analysis will also identify the composition and crystal structure of deposits and destabilization, if any, of the YSZ coating.

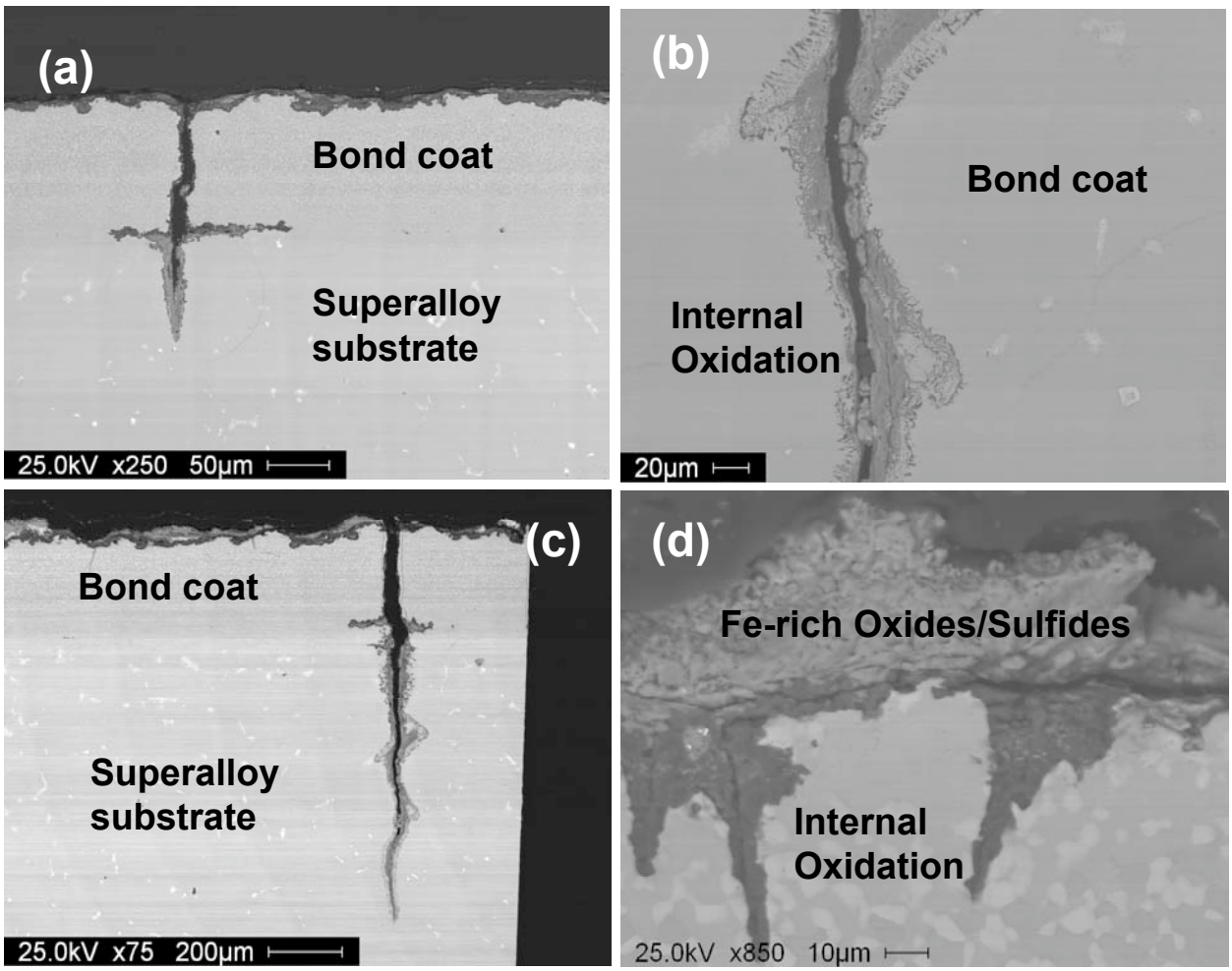

Figure 7. Internal oxidation damage after TBC spallation: (a) internal oxidation through the bond coat; (b) deposit/bond coat reaction microstructure; (c) penetration deeply into the superalloy substrate; (d) Fe-rich deposits on TGO scalled after TBC spallation.

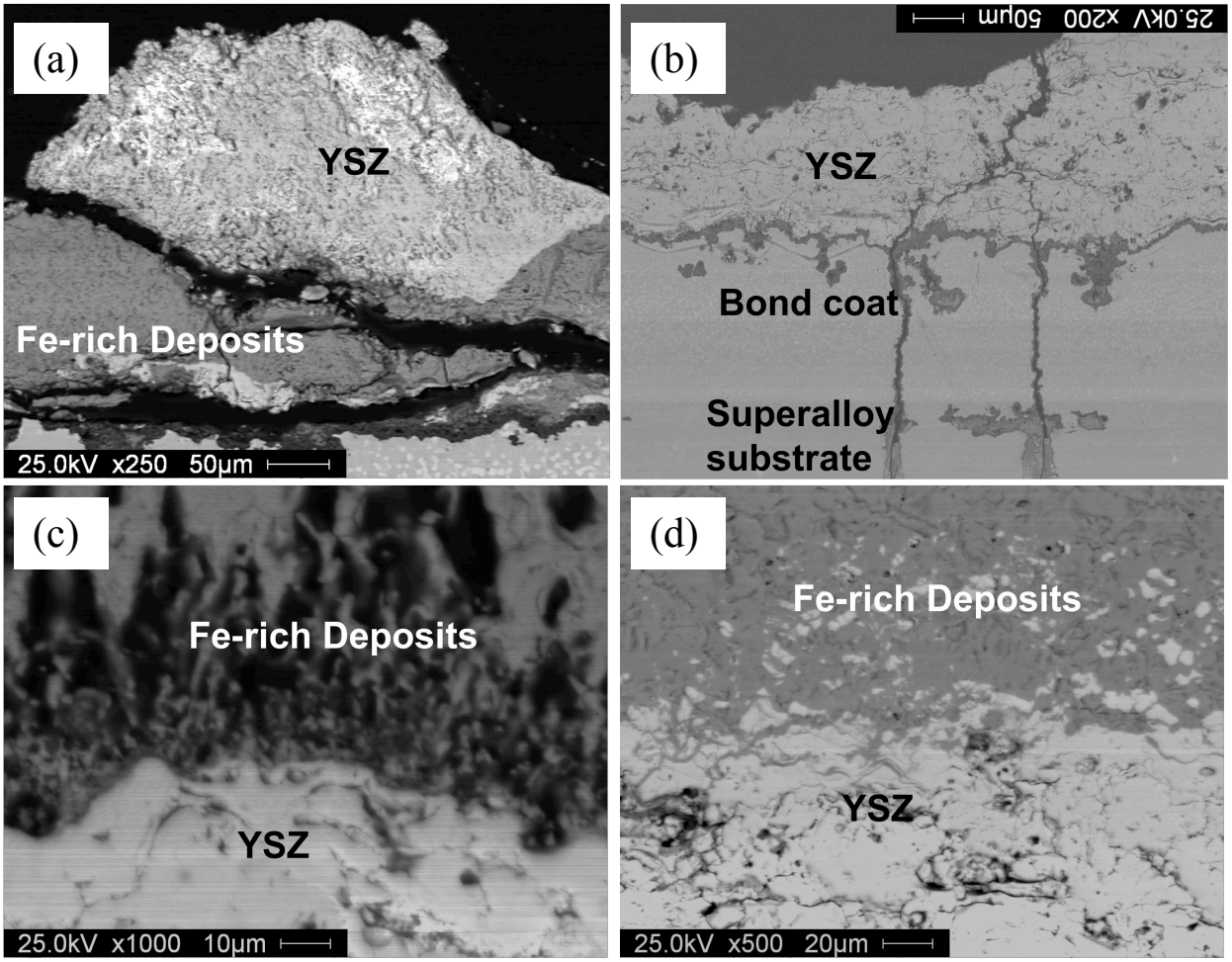

Figure 8. Degradation of the YSZ top coat in the form of: (a) YSZ spallation; (b) deposit penetration through YSZ; (c) deposit; (d) YSZ dissolution.

V.1.2. Stand-Alone NiCoCrAlY Coatings

Another turbine blade coated with stand-alone NiCoCrAlY was supplied by an industrial partner to assist thte effort to understand the syngas degradation of NiCoCrAlY coatings. While the specification of coatings, turbine blade and operating condition remains proprietary, this specimen provided the first look at syngas degraded stand-alone NiCoCrAlY coatings. Visually, localized damage was observed as "roughened" surface. The blade was sectioned with slow speed Isomet Buehler using diamond wafering blade, mounted in Epo-Thin low viscosity epoxy, and metallographically polished down to 0.25 μm.

On the top surface that appeared "roughened," abnormality in TGO scale was observed as presented in Figure 9. This abnormality was determined to be predominantly NiS based on preliminary EDS analysis. While this protruding sulfide feature was not captured on the cross-section, a significant internal oxidation in the form of pitting and selective internal oxidation of β-NiAl solid solution phase was observed as shown in Figure 10. This selective internal oxidation indicates the oxygen solubility in the NiCoCrAlY has changed drastically due to its interaction with fuel-contaminants, and β-phase with higher Al activity has oxidized selectively. Presence of mechanical damage such as craze-crack may accelerate this damage process.

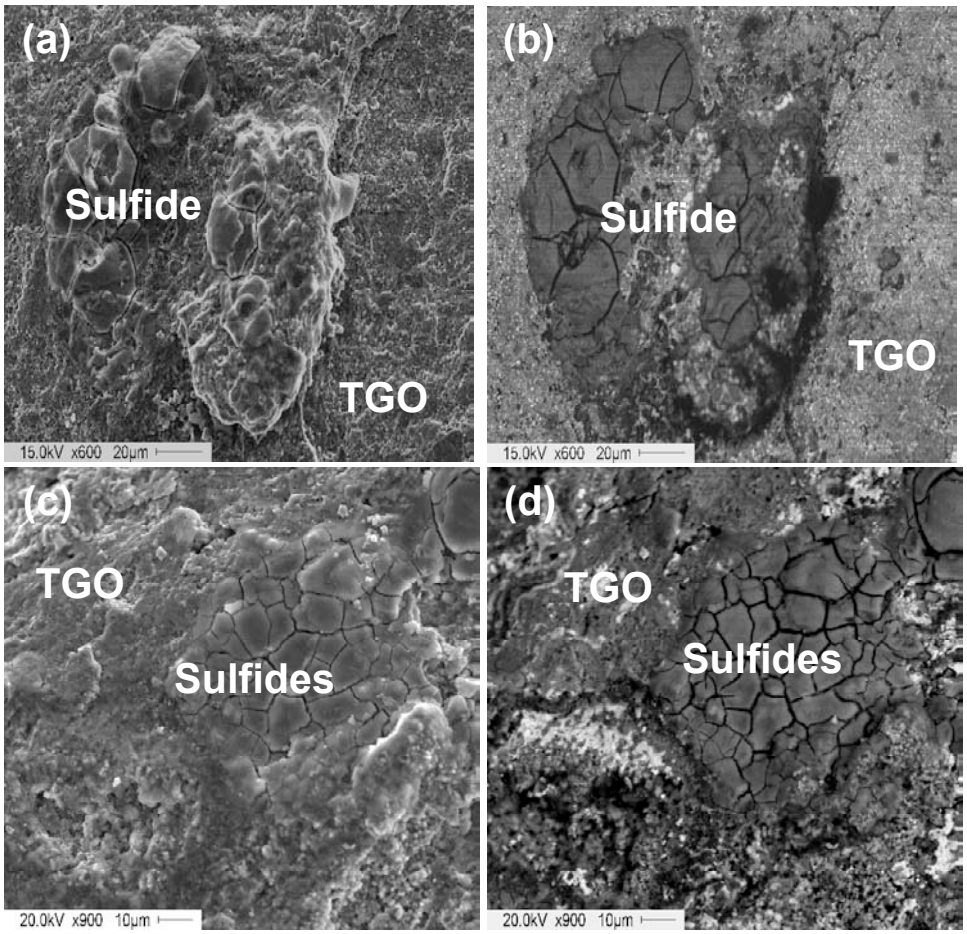

Figure 9. (a, c) Secondary and (b,d,) backscatter electron micrographs of sulfides and TGO scale observed from the top surface of the stand-alone NiCoCrAlY coatings.

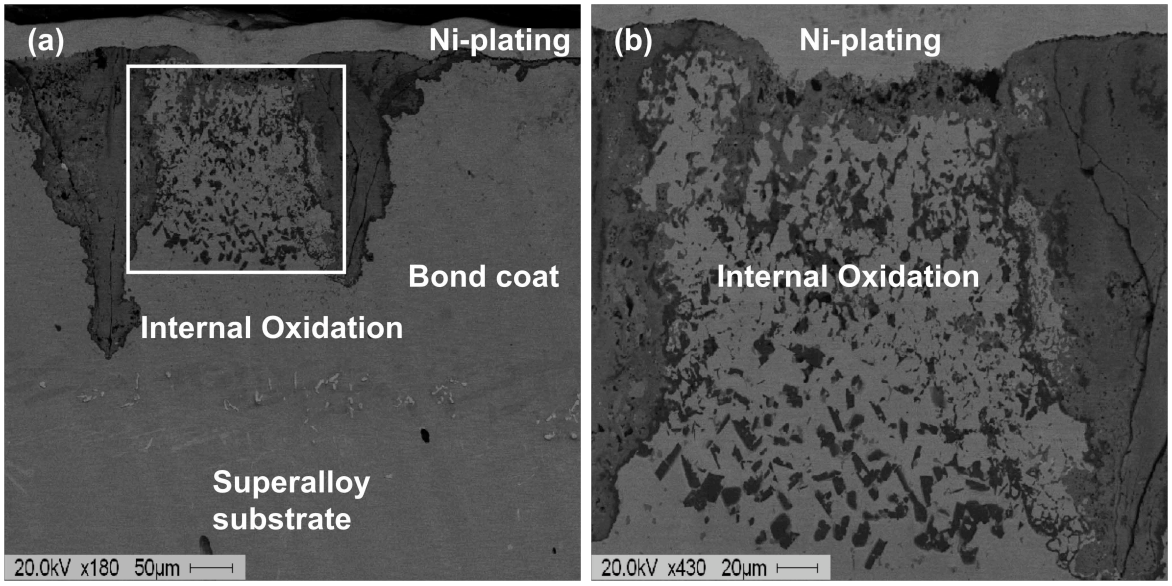

Figure 10. Internal oxidation of stand-alone NiCoCrAlY coatings in the form of pitting and selective oxidation of Al-rich β-NiAl solid solution.

V.2. Status of HADES and In-Laboratory Experiments

V.2.1. Current Status of HADES at FTT

Due to a non-technical difficulty, FTT has reported some delay in development of HADES. During the kick-off meeting among the UCF and FTT PIs, the test rig was reported as "fully manufactured" although its initial testing and operation is being delayed. Since this program, according to the schedule presented in Figure 7, does not require the use of HADES until its second year, PIs have agreed that TBC specification to industrial partners should be on-hold until successful demonstration of HADES is complete.

V.2.2. In-Laboratory Experimental Plan

Based on preliminary characterization of syngas degraded TBCs and NiCoCrAlY coatings, the following experimental plan was devised to provide a fundamental understanding of degradation mechanisms and kinetics. This laboratory testing will employ free-standing APS YSZ coatings produced at UCF's Thermal Spray Facility (UCF-TSF) and NiCoCrAlY powders.

- Contaminants in the form of Na_2SO_4, V_2O_5, $NaVO_3$, P_2O_5, Na_2SO_4 + 5%V_2O_5
- Concentration of 0.5, 1, and 10 mM.
- Isothermal reaction temperature at 950°, 1050° and 1150°C.
- Isothermal reaction duration for 10 and 30 hours.

The APS TBCs produced on dissolvable/evaporatable substrates are presented in Figure 12(a). By dissolving/evaporating the substrate, free standing APS YSZ coatings were obtained as shown in Figure 12(b). For NiCoCrAlY coatings, powders will be mixed in with contaminants and reacted as described above. These specimens will be examined before and after hot-corrosion experiments using XRD, SEM/EDS and TEM/STEM using FIB-INLO.

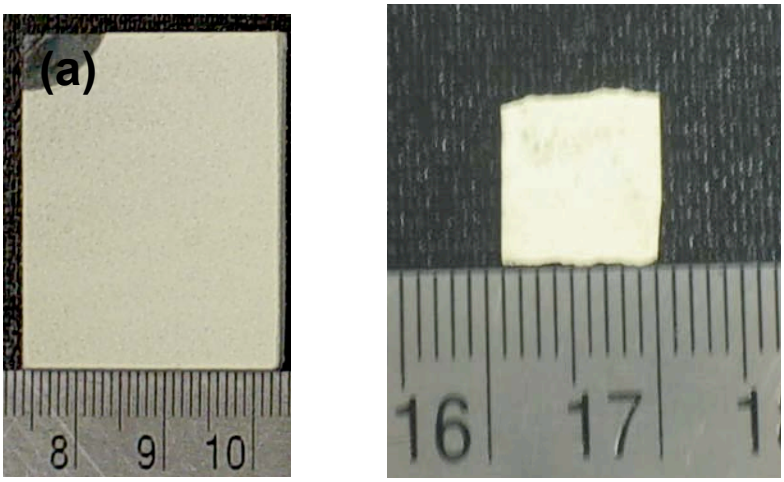

(a) (b)

Figure 12. (a) APS YSZ coatings deposited on dissolvable/evaporatable substrate. (b) Free standing YSZ coatings.

VI. CONCLUSION

This program seeks to provide an understanding for the mechanism of TBC degradation in syngas combustion environment by using Hyperbaric Advanced Development Environmental Simulator (HADES). The use of HADES provides realistic test conditions and real time monitoring/controlling of high temperature, high pressure, temperature gradient, erosion, and turbine operation from real syngas combustion. These offer a significant advantage over furnace or burner-rig testing, which requires several assumptions (e.g., effects of total and partial pressures, deposit constituents, gas or oxide constituents, etc.). State-of-the-art characterization techniques such as FIB INLO and TEM/STEM will be employed to identify deposit constituents and hot corrosion reactions to understand the mode and mechanisms of TBC degradation in realistic syngas combustion environment. Use of FIB-INLO and TEM/STEM will enable detailed identification of phase constituents of deposits, penetrants and reaction products, thus providing the exact mechanisms for degradation of TBCs in syngas combustion environment. Critical materials information, such as deposit solubility and eutectic composition, reaction/hot corrosion rates in the light of TBC constituents will be provided from the selected in-laboratory thermodynamic/kinetics experiment/modeling in addition to HADES testing.

During the first reporting period, preliminary characterizations were carried out on syngas degradation using TBC- and MCrAlY-coated blades that were employed in turbines with syngas combustion. Localized failure of TBCs and NiCoCrAlY coatings were observed visually. Microscopically, deposits containing Fe, Si, Al, Ca, Mg, Na, K, S were identified. These deposits arising from fuel contaminants penetrated and/or dissolved the YSZ coatings. Internal oxidation of NiCoCrAlY either in bond coats and stand-alone coating was observed along with selective internal oxidation of Al-rich β-NiAl solid solution. Based on these observations, a detailed plan for critical laboratory-controlled experiments was devised. This experiment will use free-standing APS YSZ coatings produced at UCF's Thermal Spray Facility (UCF-TSF) and NiCoCrAlY powders. Fuel contaminants in the form of Na_2SO_4, V_2O_5, $NaVO_3$, P_2O_5, Na_2SO_4 + 5%V_2O_5 with concentrations of 0.5, 1, and 10 mM will be reacted at 950°, 1050° and 1150°C for 10 and 30 hours.

In addition, PIs at UCF and FTT had a consultation meeting for a discussion on status of HADES and specification of TBC. FTT has reported a delay in development of HADES, and hence specification of TBC samples has not been decided. No alternative plan has been devised since HADES testing, according to the experimental plan, will not begin until August, 2007.

VII. RESEARCH PLAN FOR THE NEXT REPORTING PERIOD

In the second reporting period (February 1, 2006 ~ July 31, 2006), preliminary characterization of "syngas-blades" will be completed using TEM/STEM using FIB-INLO to determine the exact composition and structure of hot-corrosion (e.g., reaction) products. In addition, in-laboratory experiments as devised will commence. PIs at FTT will be continuously consulted for the development status of HADES. An alternative testing method/site may be solicited.

REFERENCES

1. Materials and Practices to Improve Resistance to Fuel Derived Environmental Damage in Land- and Sea-Based Turbines, ed. D. Olson, G. Edwards, P. Bollinger, A. Lasseigne, G. Atkins, EPRI, Palo Alto, CA, CSM, Golden, CO, ONR, Arlington, VA, DOE, Oak Ridge, TN, 2003.
2. University Turbine Systems Research Request for Proposal No. UTSR 04-01, South Carolina Institute for Energy Studies, Clemson University, Clemson, SC, 2004.
3. R.L. Jones, in Metallurgical and Ceramic Protective Coatings, ed. K.H. Stern, Chapman and Hall, London, p. 194.
4. R.L. Jones, C.E. Williams, S.R. Jones, *J. Electrochem. Soc.*, 133 (1986) 227.
5. R.L. Jones, *High Temp. Mater.*, 6 (1988) 187.
6. A. Wang, Poison Resistant Catalyst Development and Testing: A Report Prepared for U.S. DoE by Air Products and Chemicals, Inc., 1997.
7. I. Kvernes, J.K. Solberg, K.E. Lillerud, in Procd. First Conf. Adv. Mater. Altern. Fuel Capab. Dir. Fired Heat Engines, ed. J.W. Fairbanks, J. Stringer, U.S. DoE, 1979, p. 367.
8. J.C. Hamilton, A.S. Nagelberg, *J. Amer. Ceram. Soc*., 67 (1984) 686.
9. W. Hertl, *J. Appl. Phys*., 63 (1988) 5514.
10. S.C. Singhal, R.J. Bratton, *Trans. ASME J. Engng. Power*, 102 (1980) 770.
11. R.L. Jones, *Mater. High Temp*., 9 (1991) 228.
12. R.H. Barkalow, F.S. Pettit, in Procd. in Procd. First Conf. Adv. Mater. Altern. Fuel Capab. Dir. Fired Heat Engines, ed. J.W. Fairbanks, J. Stringer, U.S. DoE, 1979, p. 704.
13. T.E. Strangman, J.L. Schienle, Trans. AIME *J. Engng. Power*, 112 (1990) 531.
14. T.E. Strangman, J. Neumann, A. Liu, Thermal Barrier Coatings Life-Prediction Model Development – Final Report, NASA CR-179648, 1987.
15. S. Bose, T.E. Strangman, in Materials and Practices to Improve Resistance to Fuel Derived Environmental Damage in Land- and Sea-Based Turbines, ed. D. Olson, G. Edwards, P. Bollinger, A. Lasseigne, G. Atkins, EPRI, Palo Alto, CA, CSM, Golden, CO, ONR, Arlington, VA, DOE, Oak Ridge, TN, 2003.
16. Prepared by Dakota Gasification Company, 2003.
17. S. Laxman, B. Franke, B.W. Kempshall, Y.H. Sohn, L.A. Giannuzzi, K.S. Murphy, Surf. Coat. Technol., 177-8 (2004) 121.
18. A.J. Burns, R. Subramanian, B.W. Kempshall, Y.H. Sohn, Surf. Coat. Technol., 177-8 (2004) 89.
19. B.W. Kempshall, S.K. Jha, Y.H. Sohn, R.R. Vanfleet, J. Kimmel, Thin Solid Films, in Press, 2004.
20. J. Liu, Y.H. Sohn, Unpublished research.

Semi-Annual Report – UTSR Project SR-119

Titled

Aero Losses, Heat Transfer, Discharge Coefficients for Different Vane Trailing Edge Cooling Technologies for Syngas Fired Turbines

Period of Performance

1 August 2005 through 31 January 2006

Prepared by:

Dr. Forrest Ames, Principal Investigator, Mr. Jake Johnson, Mr. Nathan Fiala
Mechanical Engineering Department, University of North Dakota
P O Box 8359, Grand Forks, North Dakota 58202-8359
Phone: (701) 777-2095, Fax: (701) 731-2271, Email: forrest_ames@mail.und.nodak.edu

and

Dr. Phil Ligrani, Principal Investigator, Dr. Qiang Zhang, Mr. Vijay Krishnan
Mechanical Engineering, University of Utah
Salt Lake City, Utah 84112-9208
Phone: (801) 581-4240, Fax: (801) 585-9826, Email: ligrani@mech.utah.edu

February 24, 2006

DOE Award Number: DE-FC26-02NT41431

UTSR Project Number 04-01-SR119

DISCLAIMER* -- The Disclaimer must follow the title page, and must contain the following paragraph:

"This report was prepared as an account of work sponsored by an agency of the United States Government. Neither the United States Government nor any agency thereof, nor any of their employees, makes any warranty, express or implied, or assumes any legal liability or responsibility for the accuracy, completeness, or usefulness of any information, apparatus, product, or process disclosed, or represents that its use would not infringe privately owned rights. Reference herein to any specific commercial product, process, or service by trade name, trademark, manufacturer, or otherwise does not necessarily constitute or imply its endorsement, recommendation, or favoring by the United States Government or any agency thereof. The views and opinions of authors expressed herein do not necessarily state or reflect those of the United States Government or any agency thereof."

ABSTRACT

This initial semi-annual report documents the research progress by the University of North Dakota and the University of Utah during the first six months of UTSR Project 04-01 SR-119, "Aero Losses, Heat Transfer, Discharge Coefficients for Different Vane Trailing Edge Cooling Technologies for Syngas Fired Turbines." The present project has been structured to acquire technology, which will provide gas turbine designers the means to assess competing trailing edge cooling configurations for a syngas environment.

In this initial semi-annual report, the progress made over the initial period of performance has been presented. The focus at both the University of North Dakota and the University of Utah has been to specify the initial trailing edge geometries, ready the cascade facilities for measurements and acquire the initial measurements on the base and gill slot geometries. The University of North Dakota has recently competed the aerodynamic loss measurements for the gill slot geometry over a range of turbulence levels, Reynolds numbers, and discharge flow boundary conditions. The University of North Dakota is currently readying the facilities for internal heat transfer measurements on the gill slot geometry's trapezoidal pin fin array and on vane external heat transfer measurements. The University of Utah has completed extensive modifications of its cascade facility for this project and has begun taking the initial measurements of exit losses for the base vane. In the next six months, both Universities plan to complete aero-loss, heat transfer, and discharge coefficient measurements for the gill slot geometry. At the same time, efforts will be made to develop the other three geometries for vane trailing edge cooling. Currently, the project milestones have been met or exceeded by the research team at the University of North Dakota and the University of Utah.

TABLE OF CONTENTS

Abstract 3

List of Figures and Tables 5

Introduction 7

Executive Summary 7

Project Description 8

Experimental 9

University of North Dakota 10

University of Utah 14

Overall test section and airfoil design, including design of components for optical access of vane surfaces. 14

Construction and assembly of the test section and test airfoils, including components for optical access of vane surfaces. 16

Preparation of the University of Utah Transonic Wind Tunnel for installation of the test sections and for experimental testing. 18

Development of experimental techniques for measurement of vane Mach number and static pressure distributions, aero losses, heat transfer, discharge coefficients, and film cooling effectiveness. 18

Results and Discussion 20

University of North Dakota 20

University of Utah 23

Measurement of aero loss experimental data for a solid airfoil with no film cooling. 23

Expected Results for the Next Six Months 25

Conclusions and Summary 25

LIST OF FIGURES AND TABLES

Figure 1. Comparison of compressible and incompressible vane geometries showing periodic boundaries of the calculation domain. 10

Figure 2. Comparison of calculated compressible and incompressible pressure distributions. 11

Figure 3. Comparison between calculated and measured pressure distributions for incompressible vane. 11

Figure 4. Total pressure loss contours (Omega) and secondary velocities, base vane, Re_C = 2,000,000, low turbulence, taken at ¼ axial chord downstream. 12

Figure 5. Total pressure loss contours (Omega) and secondary velocities, base vane, Re_C = 2,000,000, aero-combustor turbulence, taken at ¼ axial chord downstream. 12

Figure 6. Gill slot geometry for UND's incompressible base vane showing pressure tap locations and pin fin array location. 13

Figure 7. Cascade test section employed for the present investigation (UoU). 14

Figure 8. Airfoil components for the gill slot injection configuration. 15

Figure 9. Airfoil components. 15

Figure. 10. Design details for gill slot injection. 15

Figure 11. Design details for the pressure side vane trailing edge. 15

Figure 12. Details of airfoil gill slot injection configuration design. 16

Figure 13. Photograph of constructed cascade components. 16

Figure 14. Cast vane airfoil with aluminum mold. 16

Figure 15. Airfoil with injection holes. 17

Figure 16. Pressure side part of airfoil. 17

Figure 17. Airfoil with machined holes to locate the pin fins. 17

Figure 18. Airfoil with low solidity pin fin array installed. 17

Figure 19. Completed airfoil with cut-away view of pin fin assembly. 17

Figure 20. U of Utah Transonic Wind Tunnel with installed injection system components. 18

Figure 21. Vane surface Mach number distributions. 18

Figure 22. Airfoil pressure tap locations. 19

Figure 23. Enlarged cut-away view of airfoil segment to measure external heat transfer coefficients. 19

Figure 24. Heater placement on the airfoil with the gill slot injection configuration. 19

Figure 25. Airfoil with surface heater installed for surface heat transfer coefficient measurements. 19

Figure 26. Total pressure loss contours (Omega) and secondary velocities, gill slot vane, full design discharge, Re_C = 2,000,000, low turbulence, taken at ½ axial chord downstream. 20

Figure 27. Total pressure loss contours (Omega) and secondary velocities, gill slot vane, full design discharge, Re_C = 2,000,000, low turbulence, taken at ½ axial chord downstream. 21

Figure 28. Aerodynamic loss data measured one axial chord length downstream of the vane with no film cooling. (a) Total pressure loss coefficient distribution. (b) Normalized Mach number distribution. (c) Normalized kinetic energy distribution. 24

Table 1. Summary of base vane exit losses and flow angle taken at a range of Reynolds numbers and turbulence levels and at two axial positions downstream. 22

Table 2. Summary of gill slot exit losses and flow angle taken at a range of Reynolds numbers and turbulence levels and at two axial positions downstream. 23

Introduction

The present investigation has been structured to acquire the technology, which will allow a gas turbine designer to develop trailing edge cooling configurations for a syngas environment. The design of trailing edge cooling schemes must balance many competing tradeoffs. These tradeoffs include minimizing aerodynamic losses and the resulting flow blockage, providing sufficient internal and external cooling to control peak and average metal temperatures, and developing a design that will not clog and that can be readily manufactured. The present study has the added complication that involves developing the technology for trailing edge designs relevant to the syngas environment. Although the experience with syngas fired gas turbines is limited and the technology used to generate and clean syngas fuel is evolving current evidence suggests that the syngas environment with have significant levels of particulates and impurities. The particulate and impurity levels are expected to result in greater than normal deposition, erosion, and corrosion of turbine airfoil surfaces. The resulting surface degradation will adversely affect surface roughness causing an increased boundary layer free-stream interaction. Surface roughness is known to cause early transition and increase heat transfer rates across the turbulent boundary layer when the roughness features are larger than the sublayer. Roughness has been found to have an even larger impact on aerodynamic losses. Deposition of particulates has the potential to clog cooling discharge holes and produce an adverse effect on trailing edge cooling levels.

Executive Summary

This semiannual report presents the experimental progress for the first six months of this project to characterize the aerodynamic and heat transfer performance for competing vane trailing edge designs for a syngas fueled gas turbine. In the initial six months we have specified the trailing edge geometries of the gill slot and letterbox configurations based on feedback from our industrial heat transfer points of contact. The high speed transient flow facility at the University of Utah has been extensively modified to accept the industry representative vanes, they have begun construction of these new test airfoils, and have initialed tests with the base or uncooled vane configuration. At the University of North Dakota, aerodynamic loss measurements have been made on both the base vane and the gill slot geometry and we are currently preparing for internal heat transfer measurements for the pin fin array as well as external heat transfer measurements for the gill slot.

The present project has been designed to provide accurate data external and internal heat transfer and aerodynamic loss data on each of the cooling configurations so designers can objectively compare the tradeoffs in life and performance for each competing design. At the University of North Dakota we have completed aero-dynamic loss measurements for both the base vane and the gill slot configuration. These measurements included pressure distribution over the vane surface for all conditions, not only over the external surface but also through the pin fin array for the full range of flow rates tested. Measurements were taken at Reynolds numbers ranging from 500,000 to 2,000,000 based on chord exit Reynolds number, for low, grid, and simulated aero-combustor turbulence, and for design and half design flow rates. Our back to back comparisons between our base vane geometry and our gill slot geometry with blowing will provide designers with objective information on the incremental aerodynamic cost of the gill slot cooling design. Turbine vane rows are used to meter the gas flow through the turbine and thus match work between the turbine and compressor. Consequently, information about the blockage developed by a given scheme is critical its successful implementation in an engine. These aerodynamic loss measurements have also included the influence of turbulence on losses and wake development. Turbulence is known to have an influence on boundary layer development, secondary flows and wake profile development. Current aerodynamic loss measurements have not only shown the distribution of

exit losses, but they have also documented turning angle distribution. The wake width and total pressure loss deficit have a significant impact on the impulse the turbine rotor sees from the wake. Aerodynamic designers often adapt the design inlet angle of camber of blades to improve performance. Detailed information on turning angle and exit loss information can offer an opportunity to improve turbine performance.

The present semi-annual report provides summaries of activities and accomplishments at the University of Utah for the following topic areas. (1) Overall test section and airfoil design, including design of components for optical access of vane surfaces. (2) Construction and assembly of the test section and test airfoils, including components for optical access of vane surfaces. (3) Preparation of the University of Utah Transonic Wind Tunnel for installation of the test sections and for experimental testing. (4) Development of experimental techniques for measurement of vane Mach number and static pressure distributions, aero losses, heat transfer, discharge coefficients, and film cooling effectiveness. (5) Measurement of aero loss experimental data for a solid airfoil with no film cooling. The high speed aerodynamic loss measurements acquired at the University of Utah will document compressible flow effects such as shock losses. The detailed aero-performance measurements acquired at the University of North Dakota combined high speed measurements at the University of Utah taken at overlapping conditions are expected to present aero-designers with a complete picture of the aerodynamic impact of the different cooling designs at relevant range of conditions.

The investigative team is pleased to report that we are ahead of schedule in more than one area. At the University of Utah, work has been initiated to characterize roughness on components from a range of industrial gas turbines (task 1). Currently, the external geometries for the base vanes and the vanes with the four external cooling schemes have been specified after discussion with industry (task 2). Additionally, both UND and UoU have begun the process of modifying their existing cascade facilities to conduct the current research program (task 2). Also, construction of the base vanes is complete and construction has begun on the externally cooled vanes (task 2). Although measurements were not scheduled to begin until the third quarter, aerodynamic loss and pressure distributions have already begun on the base vane and the gill slot (task 3 and 4). Activities to assess internal heat transfer are also underway. The pin fin array that will be used on the gill slot and letterbox designs has been constructed and a bench scale heat transfer rig is currently being built (task 6).

Project Description

The overall objective of the three year study is to experimentally investigate heat transfer and aerodynamic tradeoffs of four competing trailing edge cooling designs: the gill slot, the letterbox, pressure side holes, and the covered trailing edge. This experimental assessment will include an evaluation of the aerodynamic performance, external heat transfer performance, internal cooling performance, and cooling configuration discharge coefficients. Each test will be run with a smooth external surface as well as with the simulated roughness of a syngas fueled turbine. The vane aerodynamics of each design will be compared with the aerodynamics of the base vane design without any cooling discharge features. Full three dimensional exit surveys will be acquired at two axial spacings and at two coolant flow rates to assess both profile and endwall losses of each cooling configuration in the low speed cascade and the University of North Dakota (UND). In order to asses the effects of Mach number, profile losses will be acquired at transonic Mach numbers in the compressible cascade at the University of Utah (UoU). Both cascades will be run over an overlapping range of chord exit Reynolds numbers. In addition, both cascades will be run at low turbulence and grid turbulence conditions. In addition, the UND cascade will be run with an aerocombustor turbulence condition.

External heat transfer levels will also be documented experimentally for the base vane and the four trailing edge cooling configurations. Additionally, internal heat transfer levels flow

discharge coefficients will be acquired for three separate internal cooling configurations. External heat transfer measurements will include both external heat transfer rates and an experimental assessment of any film cooling effectiveness on the external surface due to the coolant discharge. External measurements will be made for both surface conditions (smooth and syngas roughened), for all three turbulence conditions, over the full range of Reynolds numbers, and for design and reduced cooling flows. Internal heat transfer levels will be acquired over a full range of the expected Reynolds numbers for the vane tests. This resulting comprehensive data base is expected to supply trailing edge cooling scheme designers with the information needed to assess the tradeoffs of the different trailing edge configurations.

Experimental Approach

The measurements for this study will be conducted using a "fully" or conventionally loaded vane. The large-scale, low-speed cascade facility at the U. of North Dakota, and the high Mach number facility at the U. of Utah are being engaged to conduct these experiments. The two cascades, run at low and transonic Mach numbers, require two different geometries to achieve the same loading profile. The large scale low speed cascade can be run at steady state allowing for detailed 3D exit surveys and greater detail in internal and external heat transfer and pressure distribution investigations. The high speed facility allows the investigation to look at aerodynamic issues related to engine relevant Mach numbers. A comparison of the two geometries is shown in Figure 1. (These two geometries were graciously provided by turbine aero-dynamics and heat transfer group at Rolls Royce.) The resulting calculated compressible (Mach = 0.8) and incompressible (Mach = 0.2) pressure profiles are compared in Figure 2 showing closely agreeing loading distributions. Figure 3 shows a comparison between the measured and predicted pressure distributions for the incompressible vane, both are presented at a Mach number close to 0.2. The comparison shows the very close agreement between the experimental base vane pressure distribution and the Fluent calculation. This close agreement provides confidence that the midline aerodynamics developed by the linear cascade are consistent with the 2-D blade to blade aerodynamics.

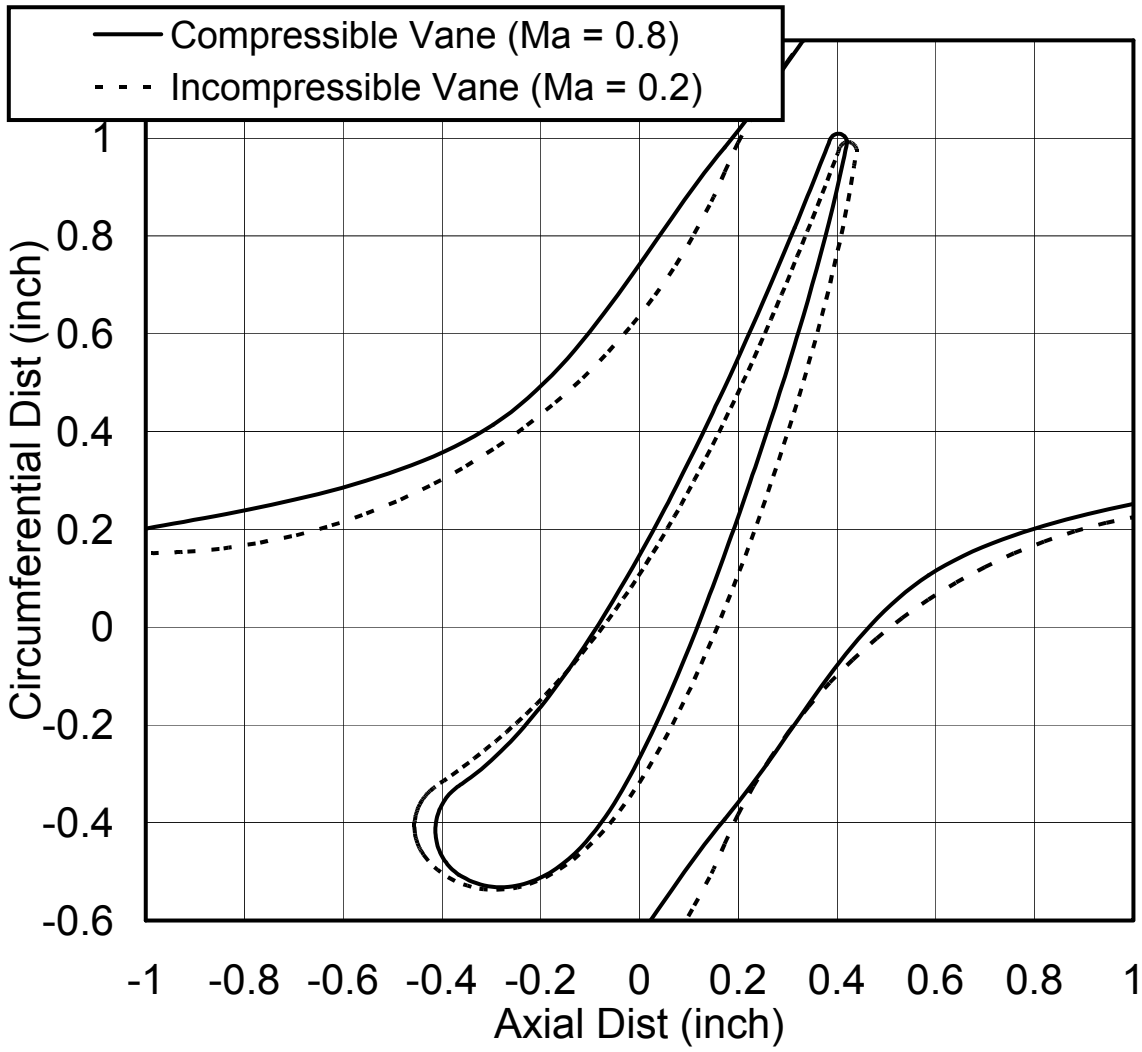

Figure 1. Comparison of compressible and incompressible vane geometries showing periodic boundaries of the calculation domain.

Aerodynamic loss, surface pressure distributions, external heat transfer, adiabatic effectiveness, and trailing edge discharge coefficients will be acquired at both facilities. The facilities will be run over an overlapping range of chord exit Reynolds numbers, at low and elevated turbulence levels, and at design and partial coolant discharge flow rates. The large scale of the University of North Dakota will allow acquiring a greater level of detail, while the compressible measurements at the University of Utah will capture the specific aerodynamic issues dealing with the transonic flow regime. An example of the aerodynamic detail developed by exit surveys is shown in Figures 4 and 5 which present contours of total pressure loss coefficients for the base vane at low turbulence (0.7%) and aero-combustor (13.5%) turbulence.

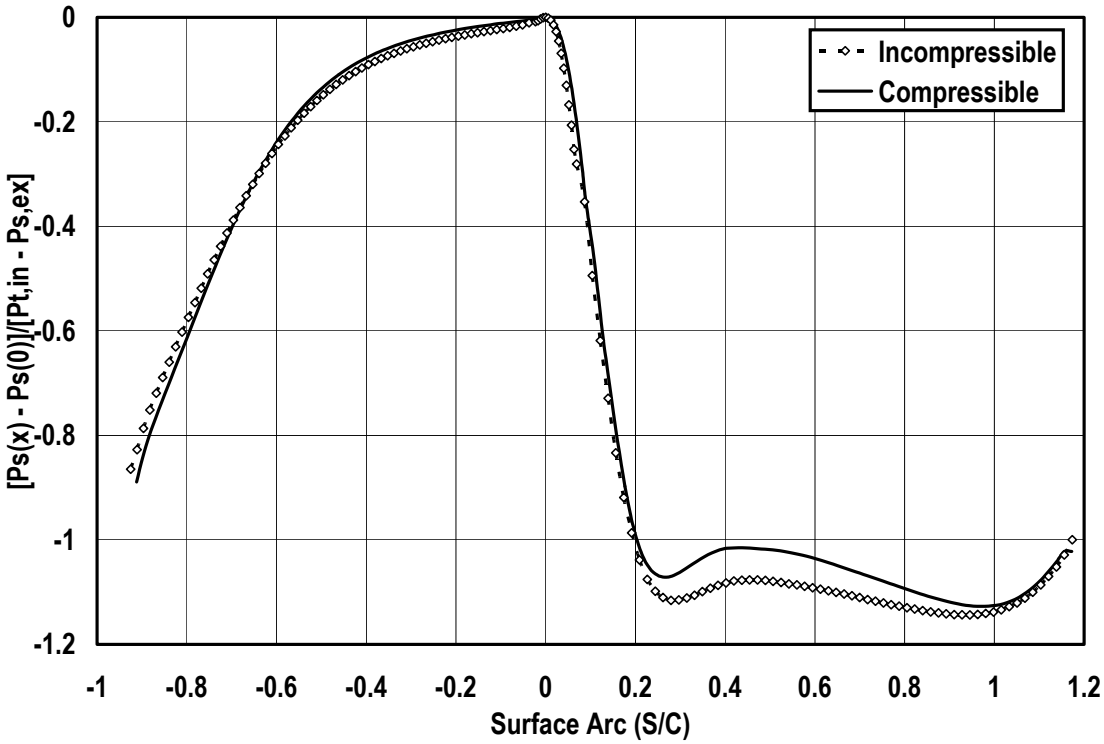

Figure 2. Comparison of calculated compressible and incompressible pressure distributions.

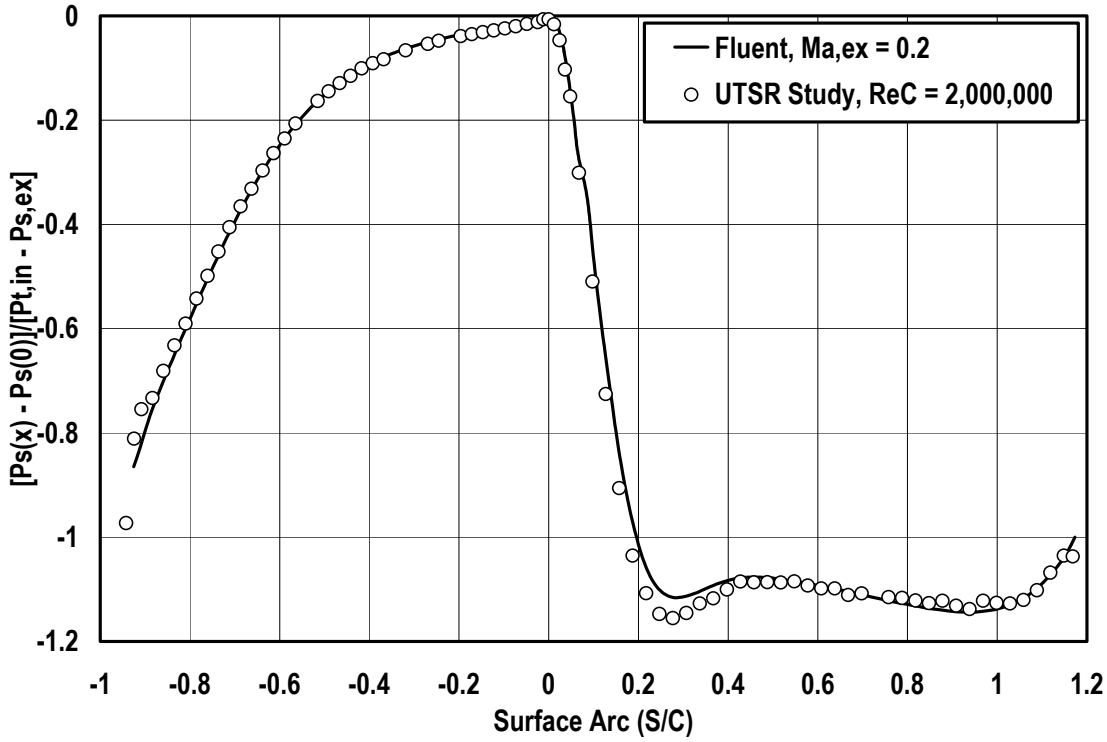

Figure 3. Comparison between calculated and measured pressure distributions for incompressible vane.

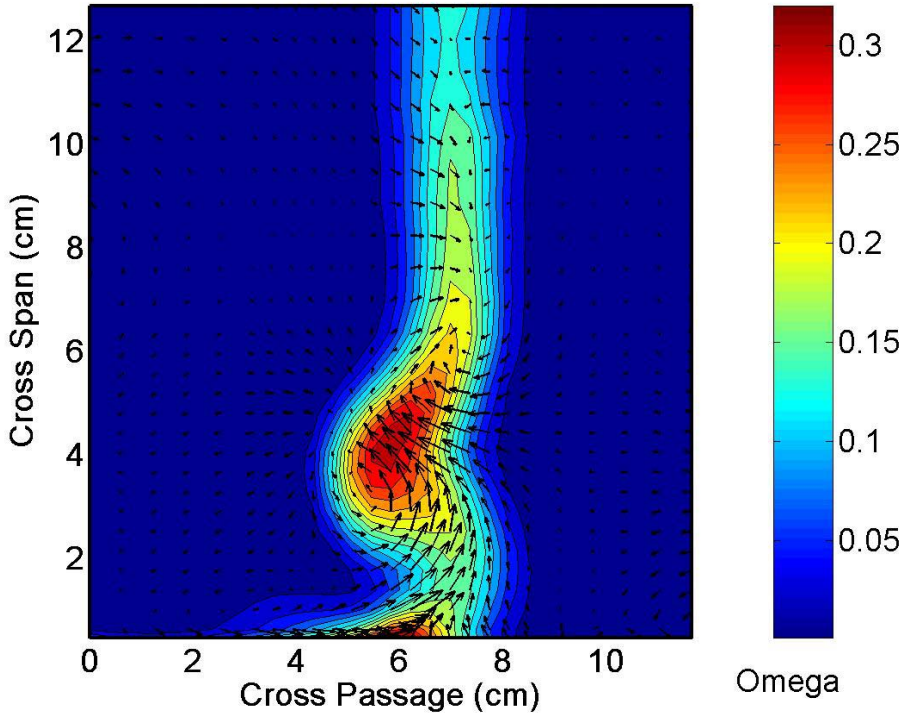

Figure 4. Total pressure loss contours (Omega) and secondary velocities, base vane, Re_C = 2,000,000, low turbulence, taken at ¼ axial chord downstream.

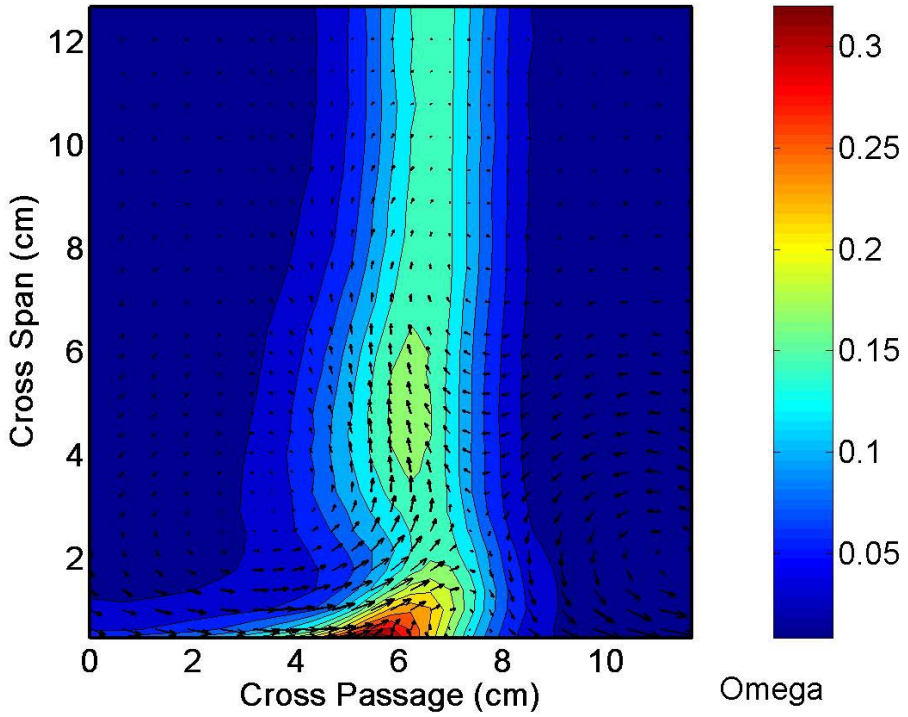

Figure 5. Total pressure loss contours (Omega) and secondary velocities, base vane, Re_C = 2,000,000, aero-combustor turbulence, taken at ¼ axial chord downstream.

The initial geometry being investigated will be the gill slot. This geometry has been developed in the envelope of the base vane configurations. The gill slot geometry for UND's incompressible base vane is shown in Figure 6. The scaling for UND's base vane and gill slot vane is 11 times. The dimensions of the large-scale cascade vane are shown below. The locations of the pressure taps are displayed in the figure along with the location of the gill slot and the five row pin fin array that is located upstream of the discharge from the slot. The aerodynamic vane used for the gill slot measurements has been cast and all aerodynamic measurements have been taken and are briefly documented in the results section of this report.

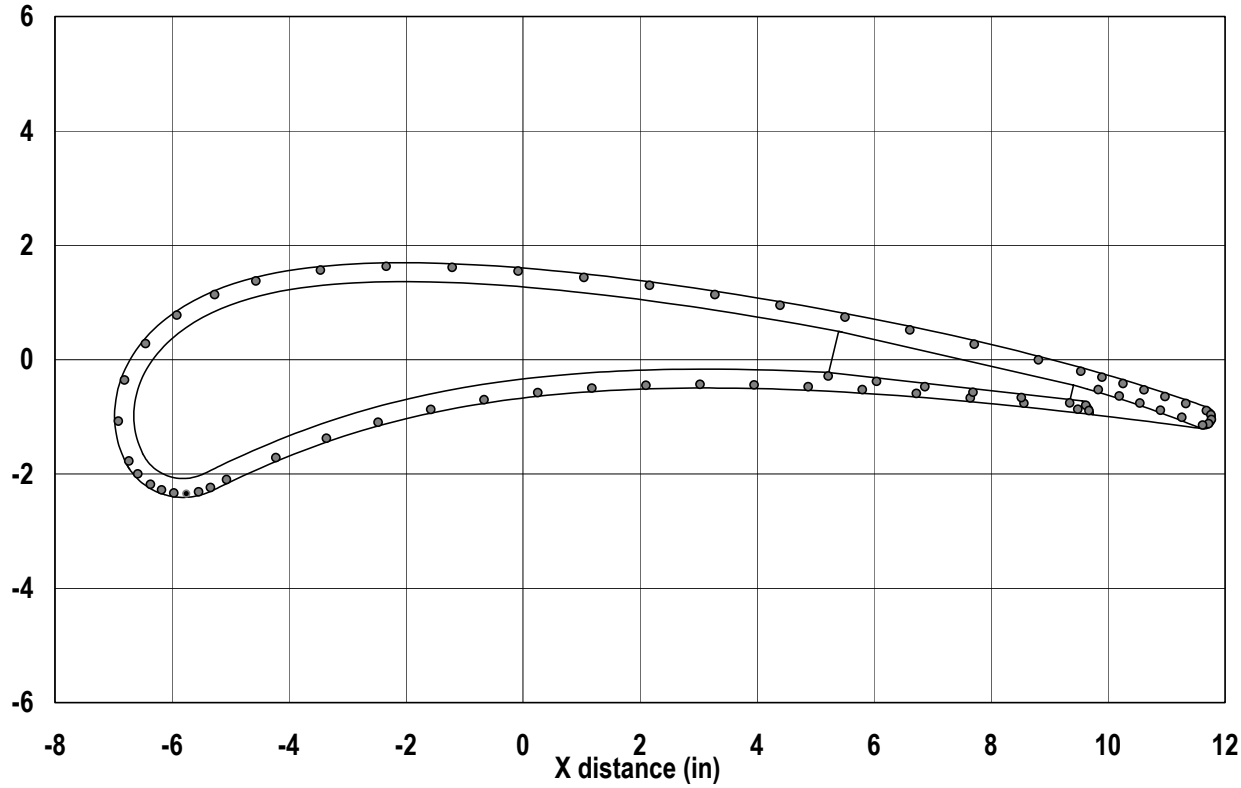

Figure 6. Gill slot geometry for UND's incompressible base vane showing pressure tap locations and pin fin array location.

The gill slot vane for the heat transfer measurements is currently being fabricated and fine wire thermocouples have been placed in locations similar to the locations of the pressure tubing. However, the junctions of the thermocouples have been located against the surface of the epoxy vane wall. This heat transfer vane will use the constant heat flux technique and the foil will be wrapped from the exit of the gill slot on the inner wall of the suction surface, around the trailing edge and over the suction surface and leading edge and will terminate at the trailing edge of the gill slot. This measurement technique will allow us to document heat transfer downstream from the gill slot ejection and around the trailing edge of the vane. The adiabatic effectiveness of the surface will also be determined with this vane. However, internal heat transfer measurements will be taken in a bench scale internal heat transfer experiment. The trailing edge pin fin array has been manufactured and the internal heat transfer experiment is currently being set up for acquisition of internal heat transfer and pressure drop data.

Experimental Approach, University of Utah. The present section provides summaries of experimental approach activities and accomplishments for the following topic areas. (1) Overall test section and airfoil design, including design of components for optical access of vane surfaces. (2) Construction and assembly of the test section and test airfoils, including components for optical access of vane surfaces. (3) Preparation of the University of Utah Transonic Wind Tunnel for installation of the test sections and for experimental testing. (4) Development of experimental techniques for measurement of vane Mach number and static pressure distributions, aero losses, heat transfer, discharge coefficients, and film cooling effectiveness.

(1) Overall test section and airfoil design, including design of components for optical access of vane surfaces. The vane cascade, on which the present investigation is based, has the following characteristics: axial chord C_x = 0.83328 inches, true chord C = 1.64018 inches, pitch = 1.37 inches, turning angle = 73°, and pitch to axial chord ratio = 1.6441. To design the cascade test section used in the present investigation, vane coordinates are scaled by a factor of 1.83. The vane cascade test section employed within the present investigation then has the following characteristics: axial chord C_x = 1.5249 inches, true chord C = 3.0015 inches, pitch = 2.5 inches, turning angle = 73°, and pitch to axial chord ratio = 1.6395. A schematic diagram of the cascade test section is shown in Figure 7. The design includes provision to allow optical access of the vane surfaces.

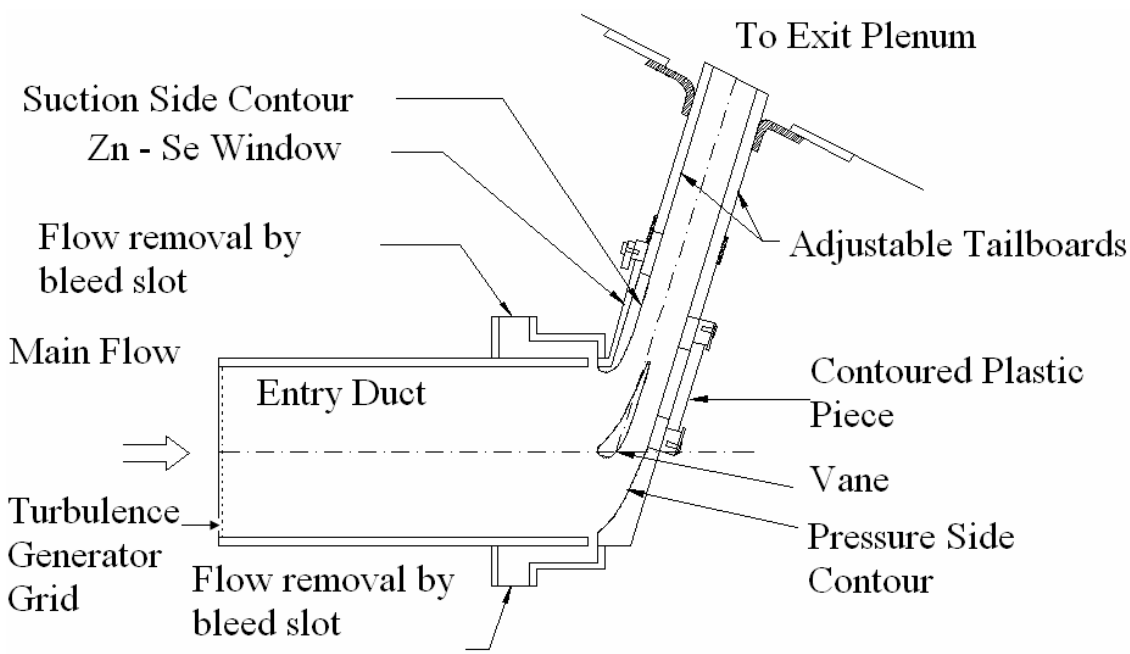

Figure 7. Cascade test section employed for the present investigation (UoU).

The overall design of the airfoil with the gill slot injection configuration is shown in Figures 8-14. Trailing edge sections of the airfoil are interchangeable to allow installation of the other injection arrangements, including the covered trailing edge, letterbox ejection, and pressure-side holes configurations. Note that the pin fin array covers the entire span of the internal trailing edge passage for the gill slot injection configuration.

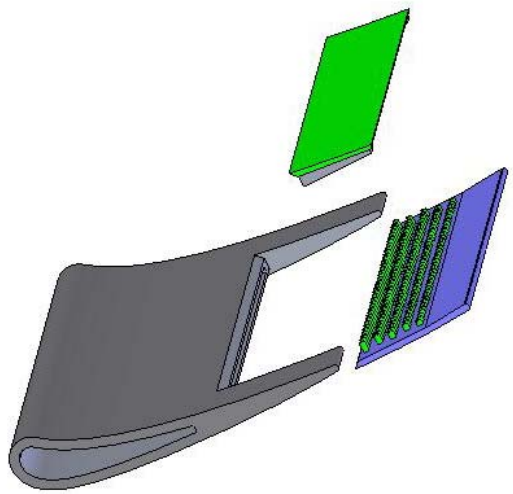

Figure 8. Airfoil components for the gill slot injection configuration.

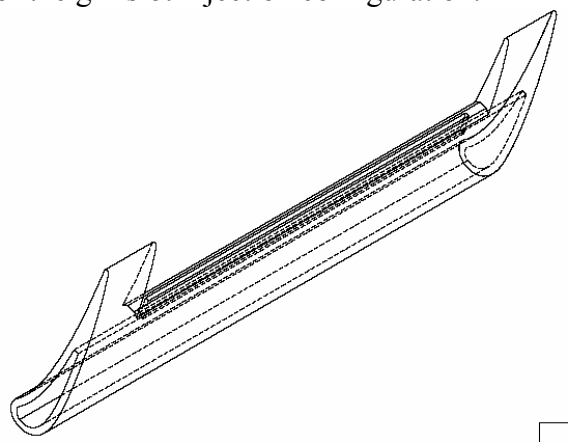

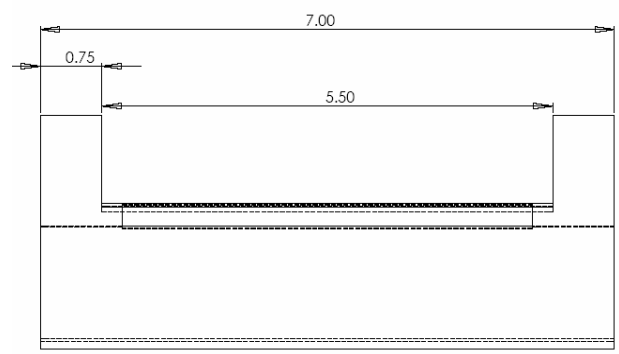

Figure 9. Airfoil components.

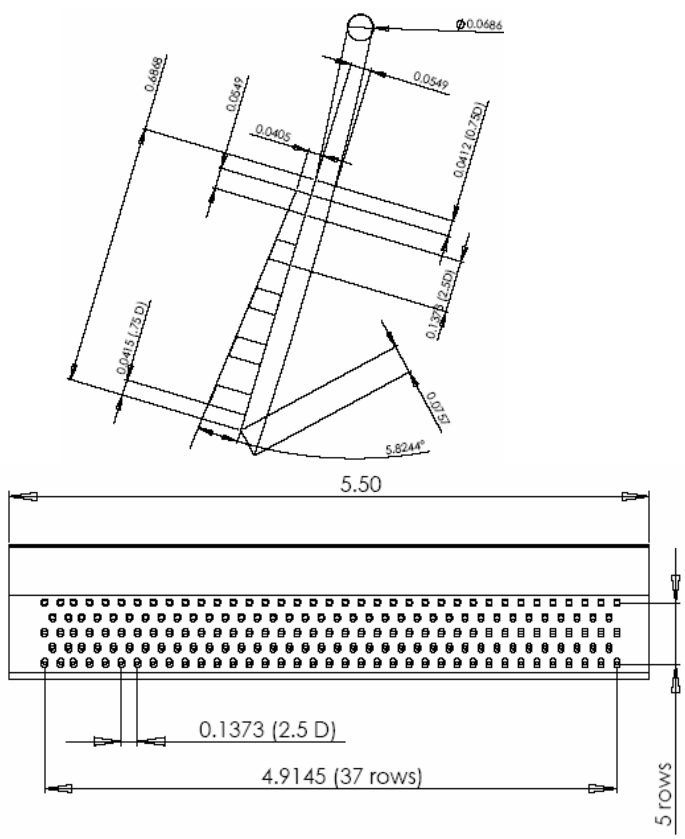

Fig. 10. Design details for gill slot injection

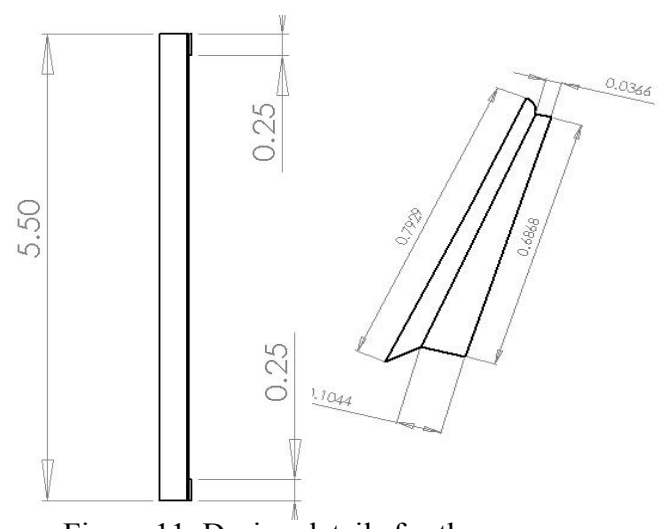

Figure 11. Design details for the pressure side vane trailing edge.

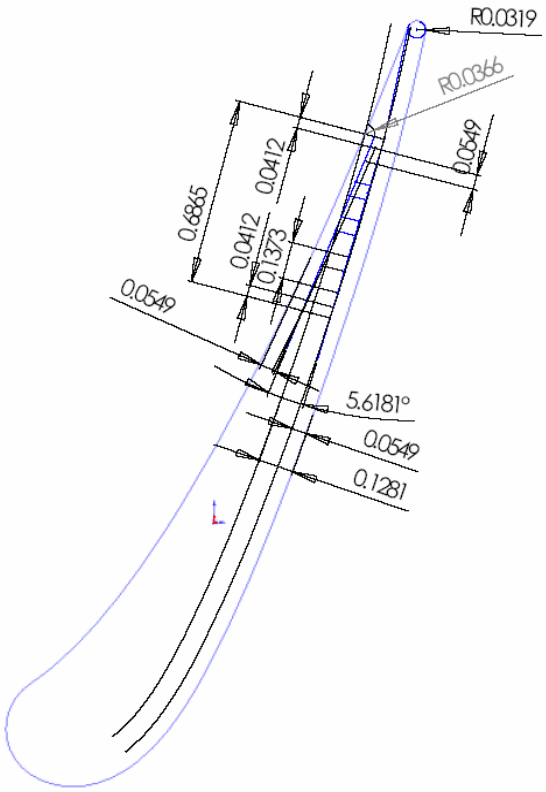

Figure 12. Details of airfoil gill slot injection configuration design.

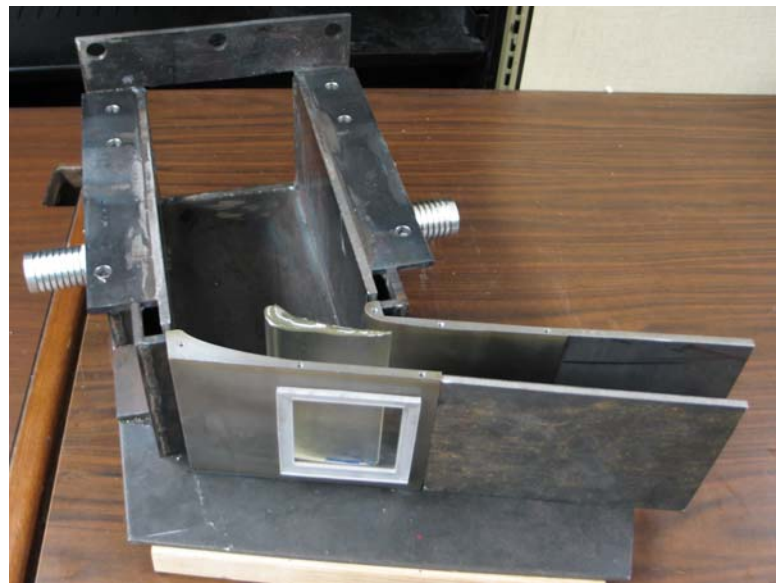

Figure 13. Photograph of constructed cascade components.

<u>(2) Construction and assembly of the test section and test airfoils, including components for optical access of vane surfaces.</u> Figure 13 shows a photograph of constructed cascade components. Parts are constructed of aluminum and welded together. The cascade test section is to be covered by a polycarbonate plate to allow viewing of the test section. Note that the gill slot-vanes employed consist of three parts, as shown in Figures 8, 9, and 11: base part, trailing edge suction side part (with pin fins), and trailing edge pressure side part. The airfoil used in the test section is made of epoxy, and is made by casting the epoxy in an aluminum mold, as shown in Figure 14. Different cascade airfoils are then machined to accommodate different trailing edge configurations.

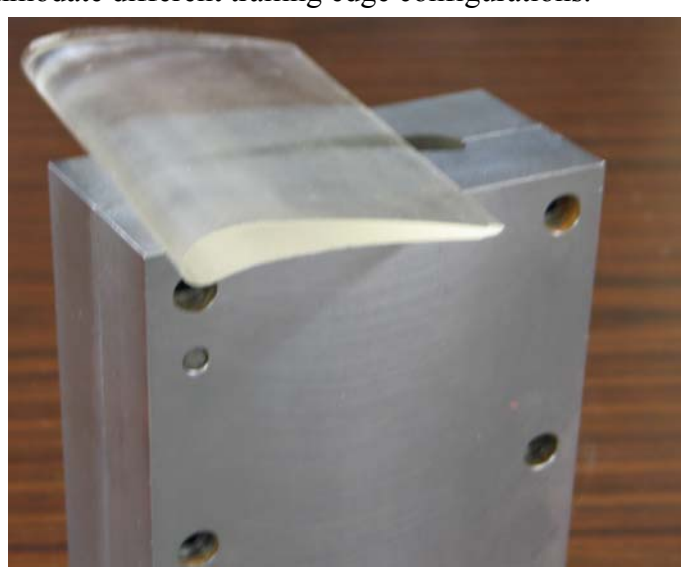

Figure 14. Cast vane airfoil with aluminum mold.

The airfoil with the gill slot injection configuration is to be fabricated using the following procedures, which are illustrated in Figures 21-25. (1) The solid airfoil is obtained from the mold. (2) Internal passages are cut and drilled to provide passages for the injection system. (3) The trialing edge of the airfoil pressure side is machined to produce indentations to mount the pin fins. (4) The pressure side part of the airfoil trailing edge is machined. (5) Teflon rods of diameter 0.055" are cut and fitted into the internal airfoil components. (6) The cut pin fins are then fastened into respective marked locations of the airfoil. (7) The pressure side part is then fitted to airfoil containing pin fins to complete the airfoil with the gill slot injection configuration.

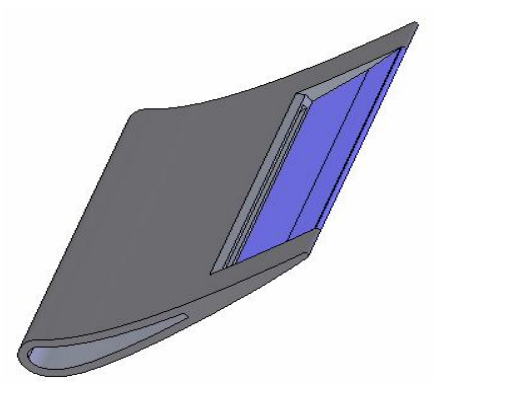

Figure 15. Airfoil with injection holes.

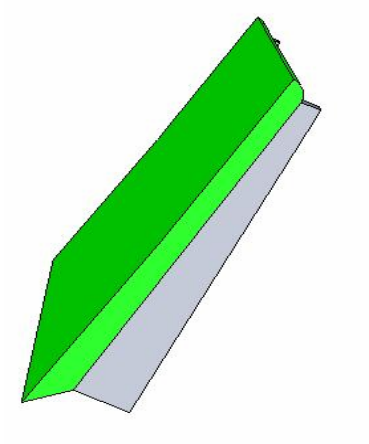

Figure 16. Pressure side part of airfoil.

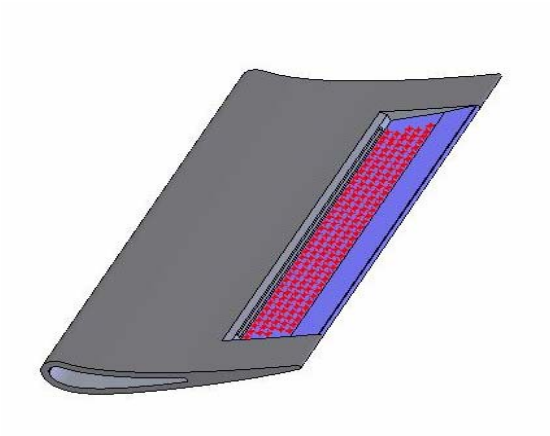

Figure 17. Airfoil with machined holes to locate the pin fins.

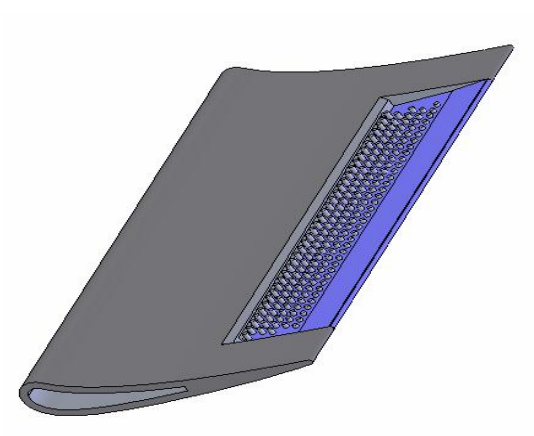

Figure 18. Airfoil with low solidity pin fin array installed.

Figure 19. Completed airfoil with cut-away view of pin fin assembly.

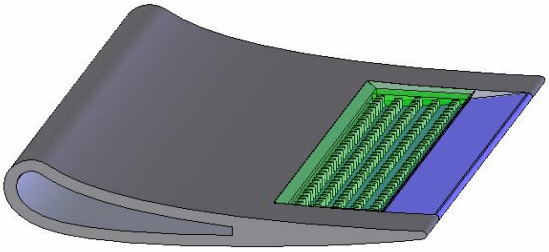

(3) Preparation of the University of Utah Transonic Wind Tunnel for installation of the test sections and for experimental testing. The test section of the University of Utah Transonic Wind Tunnel is under preparation for testing, including assembly of all test section and injection components. Figure 20 shows a photograph of the facility.

Figure 20, U of Utah Transonic Wind Tunnel with installed injection system components.

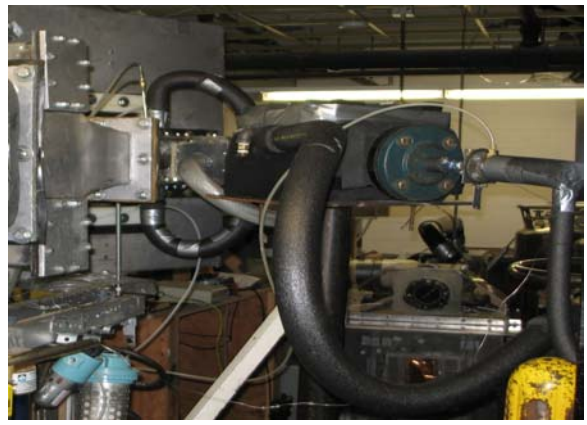

(4) Development of experimental techniques for measurement of vane Mach number and static pressure distributions, aero losses, heat transfer, discharge coefficients, and film cooling effectiveness. The required vane surface Mach number distribution is shown in Figure 21. The airfoil pressure tap locations used to measure this distribution are shown in Figure 22. An enlarged cut-away view of airfoil segment to measure external heat transfer coefficients is shown in Figure 23. Figure 24 then shows the heater placement on the airfoil with the gill slot injection configuration. An airfoil with a surface heater installed for surface heat transfer coefficient measurements (from another investigation) is shown in Figure 25. Such flexible etched foil heaters are encapsulated with a thin layer of Kapton, with a total thickness of 0.003 inches, and are available from Electrofilm Corp. Omega Engineering Inc. thermocouples are then placed under the heater layer. Note that the surface of the epoxy airfoil will be indented and machined to accommodate the thickness of the thin heater so that changes to the surface contour are negligible.

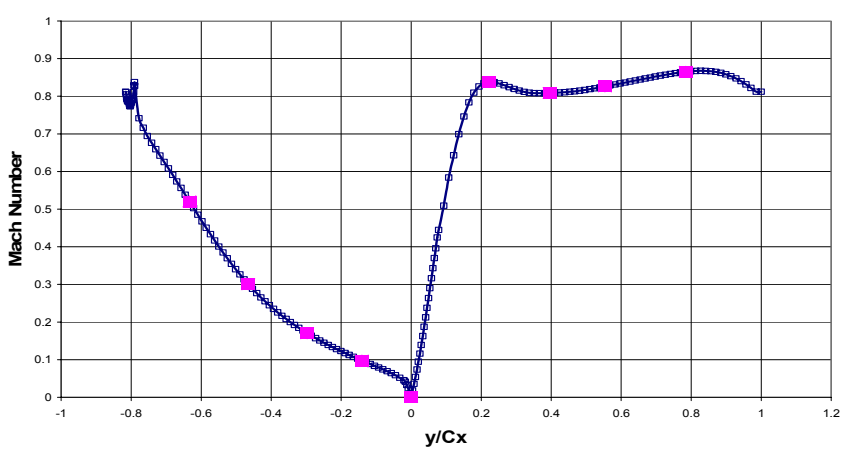

Figure 21. Vane surface Mach number distributions.

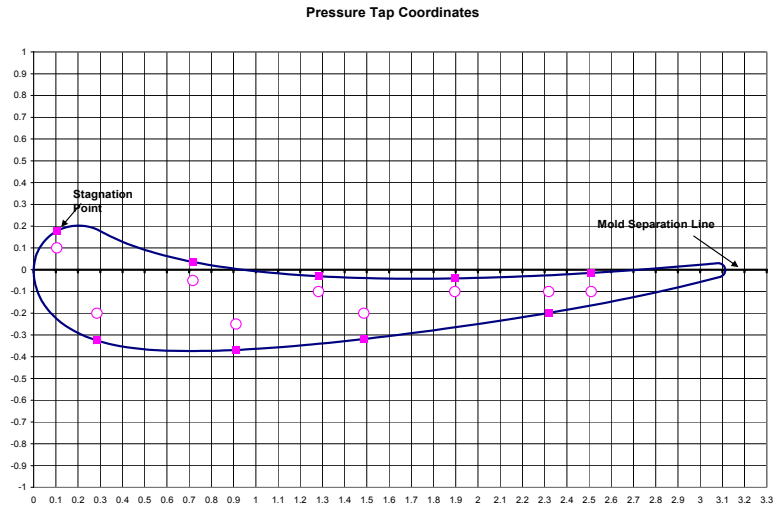

Figure 22. Airfoil pressure tap locations.

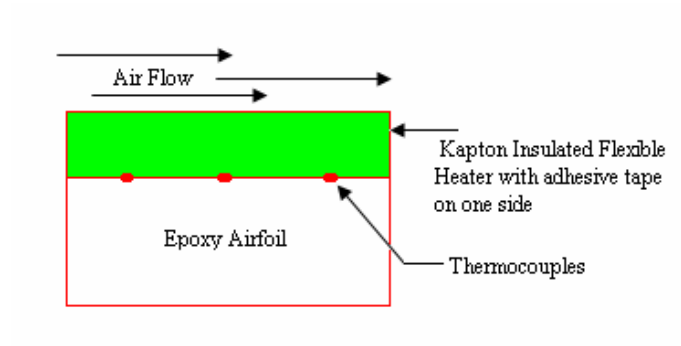

Figure 23. Enlarged cut-away view of airfoil segment to measure external heat transfer coefficients.

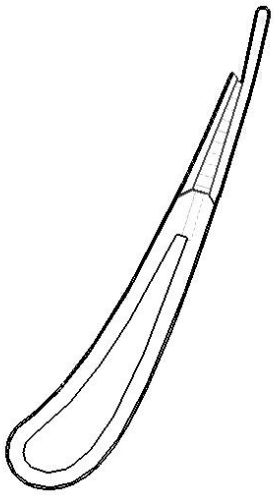

Figure 24. Heater placement on the airfoil with the gill slot injection configuration.

Figure 25. Airfoil with surface heater installed for surface heat transfer coefficient measurements.

Experimental Results

Aerodynamic loss measurements and pressure distributions have been acquired at the University of North Dakota for both the base vane and for the gill slot vane. (It should be noted that the University of North Dakota has used the current vane geometry in a previous study and was consequently in position to immediately commence the base vane measurements.) These measurements have been acquired over a range of chord exit Reynolds numbers (500,000 to 2,000,000), turbulence conditions (low, Tu = 0.7%, grid, Tu = 8.4%, and aero-combustor, Tu = 13.5%), and at two downstream exit locations (¼ and ½ axial chord). Additionally, the gill slot has been run at both design and half flow conditions. An example of the aerodynamic detail developed by exit surveys is shown in Figures 26 and 27 which show contours of total pressure loss coefficients for the base vane at low turbulence (0.7%) and aerocombustor (13.5%) turbulence. These measurements were taken at ½ axial chord downstream from the vane trailing edge and at full design gill slot injection. A comprehensive summary of the results of the exit surveys are tabulated in Table 1 (base vane) and Table 2 (gill slot). These measurements show the systematic influence of turbulence level, Reynolds number effects, and the influence of the gill slot geometry with injection. A paper has been submitted to Turbo Expo 2006 (ASME Paper No. GT2006-90168) detailing the results of the base vane aerodynamic measurements.

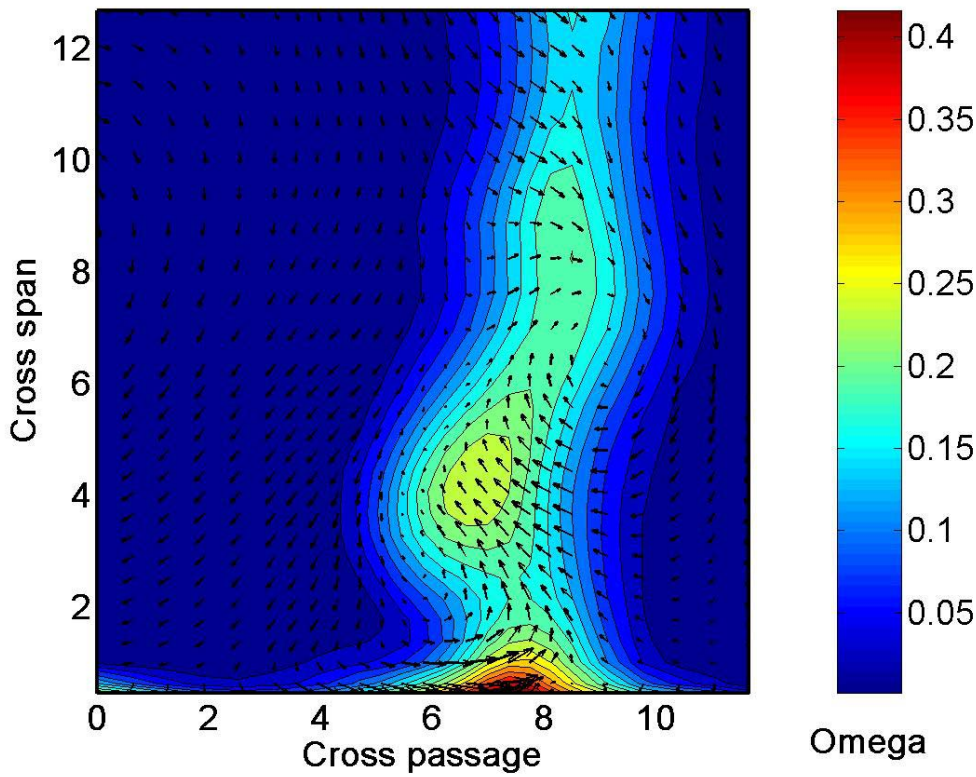

Figure 26. Total pressure loss contours (Omega) and secondary velocities, gill slot vane, full design discharge, Re_C = 2,000,000, low turbulence, taken at ½ axial chord downstream.

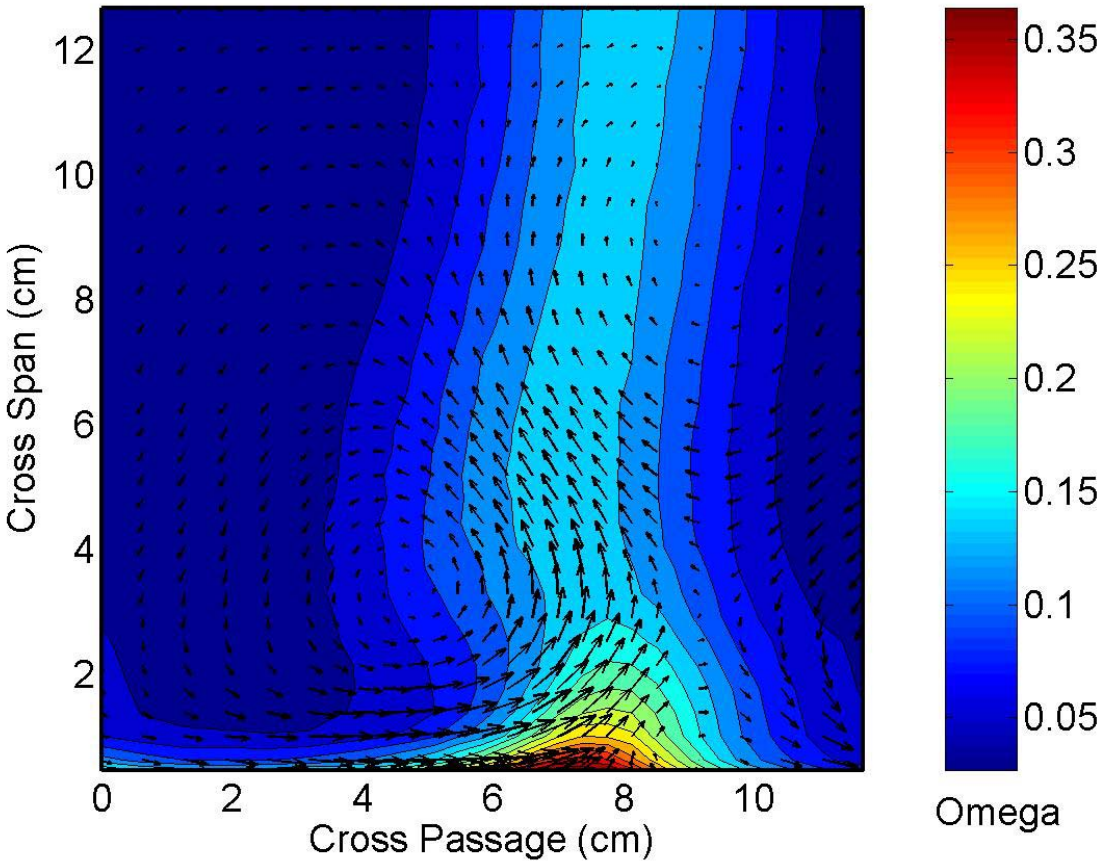

Figure 27. Total pressure loss contours (Omega) and secondary velocities, gill slot vane, full design discharge, Re_C = 2,000,000, low turbulence, taken at ½ axial chord downstream.

Table 1 presents a summary of the total pressure loss measurements taken for the base vane at downstream distances from the trailing edge of ¼ and ½ axial chord. The measurements were acquired at Reynolds numbers of 500,000, 1,000,000, and 2,000,000 for turbulence conditions of low turbulence (0.7%), aero-combustor turbulence (13.5%) and grid turbulence (8%). In addition to the true chord Reynolds numbers based on exit condition, the table presents the inlet total temperature and pressure. The exit velocity and Mach number are also presented and are based on the inlet total pressure and exit static pressures. The mass averaged total pressure loss coefficients (Ω) for one full circumferential spacing and from endwall to midspan comprising 675 individual data points are provided as are the mass averaged loss coefficients at midspan. Additionally, the mass averaged turning angle, based on both the full survey and for midspan, is also detailed in Table 1. General observations show that losses decrease with increasing Reynolds number, increase with increasing turbulence level, and increase with downstream mixing. One of the drivers producing increased losses at higher turbulence levels was the fact that the boundary layers on the vane were laminar at low turbulence levels. At the lowest Reynolds number, we actually had flow separating on the suction surface at the low turbulence condition. This caused increased midspan and full surface losses for this condition.

1/4 Cax	Aero-Combustor			Low Turbulence			Grid Turbulence		
File:	exsvac53	exsvac13	exsvac23	exsvlt53	exsvlt13	exsvlt23	exsvgt53	exsvgt13	exsvgt23
Re_{Cex}	504125	1005268	1955006	498541	1010700	1988775	493910	990667	1968858
Tt,in (K)	294.6	301.3	302.5	297.3	294.2	299.8	300.3	303.5	301.8
Pt,in (Pa)	98340	98541	100321	98365	97935	97922	100064	101278	99446
V_{ex} (m/s)	16.55	34.53	68.46	16.63	33.48	70.43	16.48	33.52	69.34
Ma_{ex}	0.0481	0.0992	0.1956	0.0481	0.0973	0.2021	0.0474	0.0959	0.1983
Ω (Full)	0.0607	0.0564	0.0521	0.0444	0.0369	0.0356	0.0472	0.0453	0.0446
Ω (Midline)	0.0494	0.0475	0.0429	0.0501	0.0251	0.0228	0.0326	0.0333	0.0311
B (Full)	72.91	73.50	73.47	73.30	73.32	73.38	73.30	73.58	73.38
B (Midline)	72.57	73.18	73.26	73.27	73.59	73.54	73.27	73.52	73.49
1/2 Cax	Aero-Combustor			Low Turbulence			Grid Turbulence		
File:	exsvac52	exsvac1	exsvac22	exsvlt5	exsvlt1	exsvlt2	exsvgt52	exsvgt12	exsvgt22
Re_{Cex}	511810	999290	1960947	511475	978582	2006766	507293	992146	1988973
Tt,in (K)	293.4	300.0	302.3	296.6	300.6	300.9	293.3	300.5	299.1072
Pt,in (Pa)	99628	99320	101224	97515	97761	100116	97938	99875	98874.7
V_{ex} (m/s)	16.46	33.79	67.94	17.14	33.73	69.87	16.59	33.45	69.37785
Ma_{ex}	0.0479	0.0972	0.1942	0.0496	0.0970	0.2002	0.0483	0.0962	0.199329
Ω (Full)	0.0706	0.0675	0.0653	0.0530	0.0442	0.0465	0.0593	0.0558	0.0552
Ω (Midline)	0.0553	0.0522	0.0534	0.0583	0.0247	0.0271	0.0382	0.0370	0.0374
B (Full)	73.64	73.97	74.16	73.63	73.80	73.81	73.86	74.29	74.25
B (Midline)	73.29	73.67	74.02	73.60	74.09	73.99	73.85	74.20	74.37

Table 1. Summary of base vane exit losses and flow angle taken at a range of Reynolds numbers and turbulence levels and at two axial positions downstream.

Table 2 presents a summary of the total pressure loss measurements taken for the gill slot vane at full design flow and downstream distances from the trailing edge of ¼ and ½ axial chord. The measurements were acquired at the same Reynolds numbers and turbulence conditions as the base vane. Similar to Table 1, Table 2 tabulates the true chord Reynolds numbers inlet total temperature and pressure, and the exit velocity and Mach number. The mass averaged total pressure loss coefficients (Ω) and turning angle are also presented for both the full surveys and for the midspan surveys. The table also documents the gill slot mass flow rate, the orifice temperature and pressure drop and the atmospheric pressure the test was run at. General observations show that the gill slot adds roughly 1.3% to the full survey exit losses for a condition. Otherwise, gill slot vane loss trends are quite similar to base vane trends. Table 2 is only a partial presentation of results. Results were also acquired for many of the conditions in Table 2 for half flow. Much of the differences were minor due to tradeoffs between increased momentum with increased flow rates and possible influence on the extent of gill slot separation losses.

The aerodynamic tests of the gill slot vane also included vane surface pressure distributions and pressure distributions across the pin. These results have not been presented in this report but are expected to be documented with the gill slot exit losses in a future technical paper.

1/4 Cax	Aero-Combustor			Low Turbulence			Grid Turbulence		
File:	exsvglac53	exsvglac13	exsvglac23	exsvgllt53	exsvgllt13	exsvgllt23	exsvglgt53	exsvglgt13	exsvglgt23
Re_{Cex}	505107	998691	2006273	502785	1002688	2001287	499192	997661	1987008
Tt,in (K)	288.2	293.5	296.4	290.8	289.9	295.4	288.2	294.4	294.7
Pt,in (Pa)	99406	100015	100767	99990	100530	102326	99852	99712	101448
V_{ex} (m/s)	15.77	32.25	67.45	15.85	31.49	65.74	15.52	32.48	65.56
Ma_{ex}	0.0463	0.0938	0.1947	0.0464	0.0922	0.1901	0.0456	0.0943	0.1898
Ω (Full)	0.0764	0.0668	0.0632	0.0620	0.0485	0.0458	0.0670	0.0582	0.0547
Ω (Midline)	0.0655	0.0576	0.0550	0.0655	0.0367	0.0327	0.0540	0.0454	0.0428
B (Full)	73.17	73.67	73.76	73.29	73.56	73.58	73.44	73.65	73.57
B (Midline)	72.96	73.47	73.65	73.14	73.97	74.06	73.48	73.73	73.91
M,dot (kg/s)	0.0135	0.0272	0.0545	0.0134	0.0271	0.0541	0.0135	0.0270	0.0537
T_{orf} (K)	288.5	305.1	286.7	290.3	292.0	290.8	289.7	287.1	290.4
ΔP_{orf} (Pa)	72.9	311.8	1162.7	71.6	293.3	1148.0	72.1	289.7	1136.3
P,atm (Pa)	99310.7	99615.4	99107.5	99886.3	100123.3	100326.5	99750.8	99310.7	99818.6

1/2 Cax	Aero-Combustor			Low Turbulence			Grid Turbulence		
File:	exsvglac52	exsvglac12	exsvglac22	exsvgllt52	exsvgllt12	exsvgllt22	exsvglgt52	exsvglgt12	exsvglgt22
Re_{Cex}	497985	977478	1996901	509880	990322	2004865	482180	1002435	1989548
Tt,in (K)	289.6	295.1	296.4	291.9	294.6	294.5	298.2	295.1	294.1
Pt,in (Pa)	97618	97076	98908	97889	98612	99739	99465	99040	100200
V_{ex} (m/s)	15.97	32.83	68.45	16.54	32.64	67.32	15.98	33.01	66.25
Ma_{ex}	0.0468	0.0953	0.1976	0.0483	0.0948	0.1950	0.0462	0.0958	0.1920
Ω (Full)	0.0864	0.0795	0.0774	0.0722	0.0601	0.0578	0.0727	0.0693	0.0679
Ω (Midline)	0.0701	0.0657	0.0669	0.0759	0.0417	0.0393	0.0519	0.0494	0.0513
B (Full)	73.35	73.91	74.09	73.36	73.84	73.84	73.25	73.80	73.87
B (Midline)	73.26	73.71	73.97	73.33	74.09	74.32	73.33	73.95	74.15
M,dot (kg/s)	0.0138	0.0318	0.0543	0.0135	0.0267	0.0542	0.0135	0.0274	0.0545
T_{orf} (K)	289.5	299.5	289.7	304.6	306.6	295.6	291.0	305.0	296.1
ΔP_{orf} (Pa)	77.9	427.4	1188.6	77.6	305.4	1196.3	73.6	319.7	1185.3
P,atm (Pa)	97516.1	97075.9	97245.2	97787.0	98193.3	98057.9	98882.5	98230.2	98531.9

Table 2. Summary of gill slot exit losses and flow angle taken at a range of Reynolds numbers and turbulence levels and at two axial positions downstream.

Measurement of aero loss experimental data for a solid airfoil with no film cooling. Measurements of aero loss experimental data for a solid airfoil with no film cooling have been taken at the University of Utah and are documented below. Overall, the investigation considers the following experimental arrangements: (i) baseline condition (solid airfoil), (ii) covered trailing edge, (iii) letterbox ejection, (iv) gill slot, and (v) pressure-side holes. In this report, attention is focused primarily on the gill slot configuration.

Examples of aerodynamic loss data obtained with a solid airfoil with no film cooling holes are shown in Figure 28a (total pressure loss coefficient distribution), Figure 28b (normalized Mach number distribution), and Figure 28c (normalized kinetic energy distribution). These data are measured one axial chord length downstream of the vane airfoil with the freestream Mach number distribution shown in Figure 15.

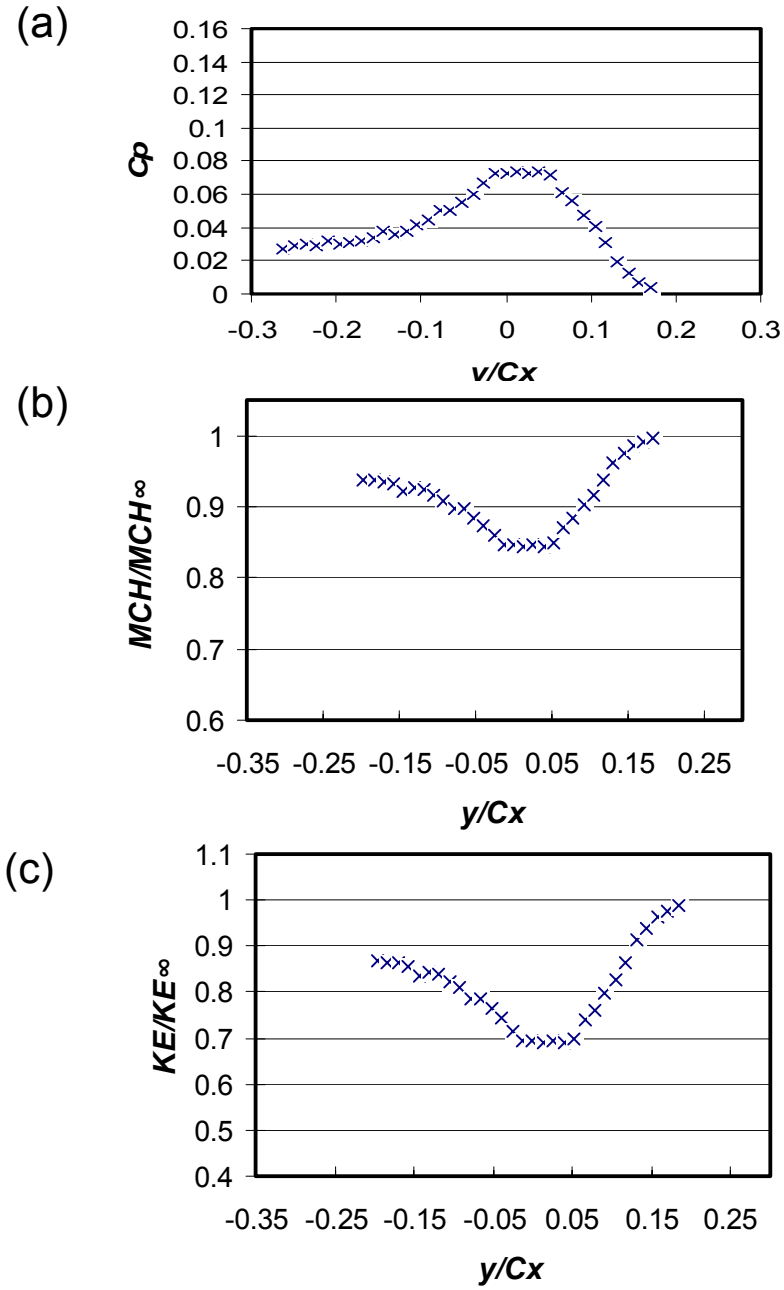

Figure 28. Aerodynamic loss data measured one axial chord length downstream of the vane with no film cooling. (a) Total pressure loss coefficient distribution. (b) Normalized Mach number distribution. (c) Normalized kinetic energy distribution.

Expected Results for the Next Six Months

The results expected in the next six months will include some very useful measurements for heat transfer designers. Under task 1, we expect to continue documenting and updating current information regarding surface roughness and cooling blockage in syngas fired gas turbines. In addition we expect to develop strategies to produce representative surface roughness on aerodynamic and heat transfer airfoils. Under task 2, all facility modifications are expected to be complete and work will continue in fabrication aerodynamic and heat transfer vanes for the four trailing edge geometries. Under task 3, we expect to be well underway acquiring pressure distributions and discharge Cd's for the four trailing edge geometries. At the University of North Dakota we have recently completed pressure distributions and discharge coefficient measurements for the gill slot geometry. Under task 4, aerodynamic measurements are expected to be completed for the gill slot geometry (smooth surface) and are expected to be progressing on the other geometries. At the University of North Dakota, exit loss measurements were recently completed for the gill slot geometry and we are now preparing for gill slot vane heat transfer measurements. Under task 5, the initiation of heat transfer measurements were not initially scheduled for the first year. However, from an investigative standpoint, progressing through an initial set of measurements through heat transfer measurements is more cohesive and gill slot heat transfer measurements are expected to be acquired in the next six months at both universities. Under task 6 we expect to complete internal heat transfer measurements for the low solidity pin fin array and begin preparations for fabricating and acquiring heat transfer and pressure drop measurements for the high solidity pin fin array. Under task 7 we are currently planning to acquire adiabatic film cooling effectiveness measurements for the gill slot in the next six months. Both teams are currently progressing very will with the planned research and fully expect to stay on schedule over the next six months.

Conclusions and Summary

UTSR Project SR-119, "Aero Losses, Heat Transfer, Discharge Coefficients for Different Vane Trailing Edge Cooling Technologies for Syngas Fired Turbines," is currently on track to meet planned goals. In the first six months of this project the teams at the University of North Dakota and the University of Utah are both making good progress and have generated results that are consistent with the original GANT timeline. The team at the University of North Dakota has recently completed aerodynamic testing of the gill slot configuration and is currently progressing rapidly toward making internal and external heat transfer measurements for the configuration. The combination of aerodynamic loss, external heat transfer, and external heat transfer data will provide designers critical information to objectively consider alternative trailing edge cooling designs. The team at the University of Utah has completed extensive facility modifications for the current program. They have acquired pressure distributions and aerodynamic loss measurements for the base vane, which are critical in providing a baseline to the actively cooled trailing edge configurations. They are progressing rapidly with the fabrication and testing of the gill slot configuration. UTSR Project SR-119 is on track and already generating useful information for trailing edge configuration design. Concurrently, we

are developing a database on the influence of syngas on component surface roughness and cooling flow blockage for future application in this project.

Deposition of Alternative (Syngas) Fuels on Turbine Blades with Film Cooling

1 Aug 2005 to 31 Jan 2006
Semi-Annual Report

Principal Investigator: Dr. Jeffrey Bons
Report Issue Date: 28 February 2006
DOE Award Number: DE-FC26-02NT41431
UTSR Project Number: 05-01-SR120

Submitting Organization: Brigham Young University
435 CTB, PO Box 24201, Provo, UT 84602-4201

Co-Investigators
Dr. Thomas Fletcher, Brigham Young University

DISCLAIMER

This report was prepared as an account of work sponsored by an agency of the United States Government. Neither the United States Government nor any agency thereof, nor any of their employees, makes any warranty, express or implied, or assumes any legal liability or responsibility for the accuracy, completeness, or usefulness of any information, apparatus, product, or process disclosed, or represents that its use would not infringe privately owned rights. Reference herein to any specific commercial product, process, or service by trade name, trademark, manufacturer, or otherwise does not necessarily constitute or imply its endorsement, recommendation, or favoring by the United States Government or any agency thereof. The views and opinions of authors expressed herein do not necessarily state or reflect those of the United States Government or any agency thereof.

ABSTRACT

This report documents work completed during the first six month period of a three year research effort into turbine deposition from synfuels. The objective of this effort is to document deposition on turbine hardware from the combustion of synfuels that are or could be used in the power generation industry and evaluate the influence of these deposits on turbine cooling. During this period, significant progress was achieved as documented in this report. Contacts were formed with various industry partners for the donation of hardware and solicitation was made for comments on the redesign of the deposition facility. The redesign will allow for backside cooling (and eventual film cooling) of turbine coupons in the deposition facility. Construction of the redesigned coupon holder has already commenced. Various ash particulate sources were also identified and specimens were prepared for later use. Finally, a test apparatus has been constructed for measuring the thermal resistance of TBC and deposit coated coupons. Preliminary testing is underway to determine the accuracy of this apparatus.

TABLE OF CONTENTS

Page	Section
1	Title Page
3	Abstract
4	Table of Contents
5	Executive Summary
6	Full Progress Report
6	Project Description
8	Experimental Method
10	Results and Discussion
14	Conclusion
14	References

EXECUTIVE SUMMARY

Power generation industry goals for higher turbine inlet temperatures (and thus higher efficiencies) and greater fuel flexibility may well be on a collision course. Little is known about the effect of corrosive elements in coal and biomass fuels at the high (1400C) turbine inlet temperatures of modern gas turbines. Studies conducted with coal-based fuels in the 1980's, at gas temperatures below 1150C, showed that corrosive deposition is strongly dependent on temperature. There is a critical need for fundamental experimental studies to determine the magnitude of deposition, erosion, and corrosion for the application of alternative fuels in modern gas turbines. This assessment must include an evaluation of the effect of deposition on thermal barrier coatings and advanced cooling schemes – two of the technologies that have permitted the substantial increases in firing temperatures.

This research program addresses all three of these critical turbine operability and maintainability issues in three phases. In Phase 1, deposition studies will be conducted in an accelerated turbine deposition facility at Brigham Young University to document the influence of temperature on deposition, erosion, and corrosion from syngas fuels. BYU's accelerated turbine deposition facility is capable of matching both the impact velocity and gas temperature of modern industrial turbines. Arrangements are in place with industrial contacts at GE, Solar, Praxair, and Siemens to make available modern turbine materials and coatings as targets for this study. Once syngas deposits are formed on the target, various analyses will be conducted, including: surface mapping, roughness assessment, deposit thermal conductivity measurement, and elemental decomposition with corrosion assessment.

Phase 1 of the proposed research will also explore the possibility of sub-cooling the turbine surface to mitigate deposition. This will be accomplished by cooling the backside of the target coupon, similar to internal convection cooling in a turbine blade.

Phase 2 will evaluate the influence of deposit formation on film cooling flows. This study will be accomplished in the same turbine deposition facility by injecting coolant from film holes in the target coupon.

Phase 3 (optional) will involve wind tunnel testing of scaled models of the deposit-laden film holes for flow and heat transfer assessments. A 3-D PIV system and IR camera will be used to gather 3-dimensional velocity data as well as surface heat transfer and film effectiveness.

With this aggressive research program, DOE and industry will gain valuable insights into factors affecting the safe, efficient operation of modern industrial turbines with alternative fuels. Findings will also be used to help establish maintenance guidelines and gas cleanup specifications for IGCC plants. Ultimately, this will reduce the time and cost to certify and commercialize modern gas turbines operating with syngas fuels.

This report documents work completed during the first six month period of this three year research effort. Activities during this period have primarily been focused on forming the research team and consulting with industry for test facility redesign, candidate fuels, and hardware donations. Construction of the redesigned coupon holder has commenced and preliminary testing is underway with the deposit thermal resistance measurement apparatus.

FULL PROGRESS REPORT

PROJECT DESCRIPTION:

Gas Turbine Research Need: Turbine inlet temperatures for large power generation gas turbines have been steadily increasing over the last several decades due to significant advances in materials and cooling technologies. By incorporating these critical advancements, the H-class combined cycle machines are expected to operate at up to 1425°C. While this higher combustor exit temperature translates directly to higher cycle efficiency, it does not bode well for the severe operating environment of turbine materials. At the same time, political and economic pressures are pushing utilities to consider fuel flexibility. Limited natural gas resources necessitate the integration of more plentiful sources of coal and biomass into the fuel reserve for gas turbines. Compared to "clean" burning natural gas, these alternative fuels have higher concentrations of trace elements and ash that present significant corrosion challenges to turbine operation.

Coal utilization introduces S, Al, Fe, Ca, and various alkali metals (e.g. Na, K) to the gas turbine, while biomass has lower sulfur content than coal, but has higher concentrations of Ca, Mg, Cl, and K. The concentrations and sizes of these compounds that actually reach the turbine surfaces depend on the combustion and gas-cleanup processes. If combustion products arrive at the turbine blade surface in the liquid (or vapor) phase, it is likely that they will deposit (or condense) there and accelerate material corrosion. A number of studies conducted in the 1970's and 1980's (before the dominant use of natural gas in gas turbines) showed that corrosive deposition is strongly dependent on temperature. Depending on the syngas fuel employed, the threshold temperature for deposition varied from 900°C – 1100°C. Above this threshold, studies showed up to an order of magnitude increase in deposition rates. Since those tests were conducted, several key technologies (e.g. thermal barrier coatings, advanced cooling schemes, and single crystal blades) have permitted substantial increases in firing temperatures. The compatibility of these advances with ash-bearing syngas fuels has yet to be assessed. Clearly, there is a critical need for fundamental experimental studies to determine the magnitude of deposition, erosion, and corrosion for the application of alternative fuels in modern gas turbines.

In addition, limited experimental evidence suggests that by sub-cooling turbine components, deposition may be mitigated. Additional studies are necessary to determine necessary cooling levels for adequate protection from syngas deposits. Finally, film cooling flows provide a cool air stream at the turbine surface that may influence local deposition as molten combustion products cool and harden near the film cooling hole. Such deposition in and around the film cooling hole could significantly impede the flow of critical coolant to the blade surface. These effects must be adequately evaluated and modeled to provide turbine operators with the tools they need to assess the in-service health of cooled turbine components.

Project Experimental and Analytical Approach: This research effort addresses all three of these critical turbine operability and maintainability issues in three phases. In Phase 1, deposition studies will be conducted in an accelerated turbine deposition facility at Brigham Young University to document the influence of temperature on deposition, erosion, and corrosion from syngas fuels. This facility is part of BYU's Advanced Combustion Engineering Research Center (ACERC), a laboratory founded in 1987 by the National Science Foundation. With active contracts totaling approximately $1.5 million/year, the center encompasses research on combustion, mineral matter transformation, deposition, and corrosion in power systems fired by

coal, biomass, black liquor, oil shale, petroleum coke, and natural gas. Rather than simulate the syngas gasification and cleanup process, this research will be conducted by seeding a natural gas combustor with coal and biomass products of combustion and accelerating them onto target turbine materials. Combustion byproducts from two of the reactors within ACERC (one for coal and one for biomass) will be collected, analyzed, and ground down to a mass-mean 10 μm diameter solid particulate for use in the accelerated turbine deposition facility. By performing experiments in this controlled laboratory environment the individual effects of corrosive elements can be properly evaluated. BYU's accelerated turbine deposition facility is capable of matching both the impact velocity and gas temperature of modern industrial turbines. Arrangements are in place with industrial contacts at GE, Solar, Praxair, and Siemens to make available modern turbine materials and coatings as targets for this study. Once syngas deposits are formed on the target, various analyses will be conducted, including: surface mapping, roughness assessment, deposit thermal conductivity measurement, and elemental decomposition with corrosion assessment. Elemental analyses will employ existing BYU diagnostic equipment including: scanning electron microscopy, inductively-coupled plasma with atomic absorption, and x-ray analysis for quantitative analysis of deposits.

Phase 1 of the proposed research will also explore the possibility of sub-cooling the turbine surface to mitigate deposition. This will be accomplished by cooling the backside of the target coupon, similar to internal convection cooling in a turbine blade. Similar post-exposure analyses will be conducted to evaluate both the extent of turbine damage and changes in depositing constituents with surface temperature.

The 2nd phase will evaluate the influence of deposit formation on film cooling flows. This study will be accomplished in the same turbine deposition facility by injecting coolant from film holes in the target coupon. Sections of turbine blades with cooling holes will be solicited for this effort so that the coolant hole geometry is representative of current practice. Deposits in and around cooling holes will be measured and analyzed as before.

During the optional 3rd year of the research program, scaled models of the deposit-laden film holes will be installed in a low-speed wind tunnel at BYU for flow and heat transfer assessments. A 3-D PIV system and IR camera will be used to gather 3-dimensional velocity data as well as surface heat transfer and film effectiveness. The data density available from these sophisticated diagnostics will provide an important database for CFD validation. This phase will also consider the effects of TBC residue left in film holes during the plasma-spray application process since it is likely that this residue bears resemblance to deposits formed during turbine operation.

<u>Expected Results/Benefits:</u> With this aggressive research program, DOE and industry will gain valuable insights into factors affecting the safe, efficient operation of modern industrial turbines with alternative fuels. Findings will also be used to help establish maintenance guidelines and gas cleanup specifications for IGCC plants. Ultimately, this will reduce the time and cost to certify and commercialize modern gas turbines operating with syngas fuels.

EXPERIMENTAL METHOD

Turbine Accelerated Deposition Facility (TADF):

A natural gas burner has recently been commissioned for accelerated turbine deposition studies in the Advanced Combustion Engineering Research Center (ACERC) at BYU (Figure 1). The combustor burns natural gas in a facility capable of mass flow rates up to 1000 slpm. With an exit contraction from 30.5 cm to 1.6 cm diameter, the exit flow from the combustor can exceed 350 m/s. A target holder positioned at the combustor exit is used to expose turbine material coupons to the hot exhaust gases at various impingement angles. The entire hot section of the combustor facility is manufactured from Inconel 601, capable of steady state operation up to 1250°C. Though the pressure at the target coupon is not that of a gas turbine (it is atmospheric pressure), by matching both the velocity and temperature of the exhaust gases, deposition mechanisms similar to those found in an actual engine can be simulated.

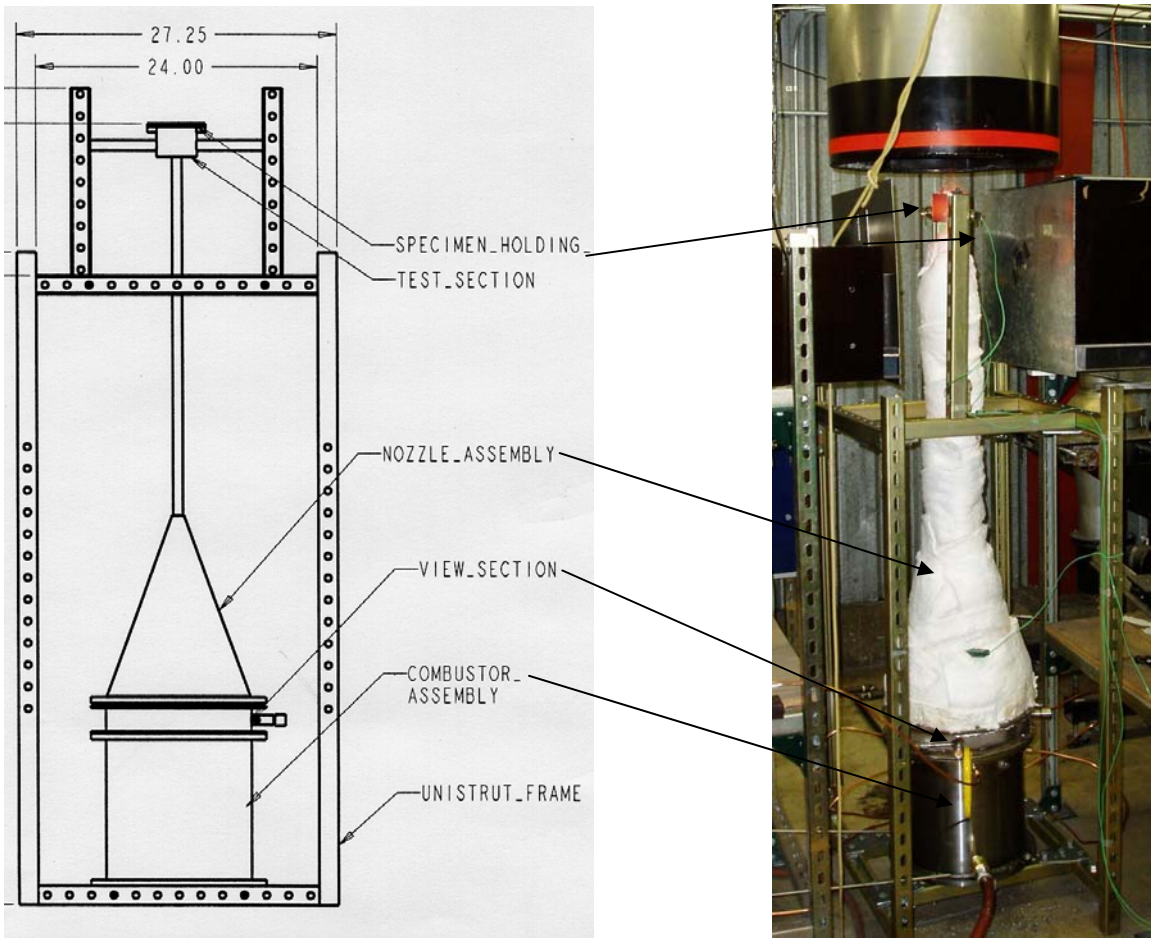

Figure 1: BYU Accelerated Turbine Deposition Facility: schematic and photograph. Photo taken while operating at 1150C (note glowing Inconel test section).

Since the fuel is methane mixed with filtered high pressure air, deposits are created by seeding the combustor with selected particulates using an automated particle feed system. The feeder allows controlled rates of fine, dry particulates (powders) to be added to the hot section

and accelerated in the combustor exit. A 1.2 m long exhaust pipe is provided to insure thermal and velocity equilibrium of the particulate with the gas stream.

Wenglarz and Wright (2002) describe various experiments where particulate concentration and service time seemed to tradeoff between each other. Turbines exhibited large deposits or could even be driven to failure either by high particle loading at low service time or low particle loading for long periods. This suggests that the net particulate throughput is a key parameter for proper deposit simulation. Therefore, the time to produce a surface deposit can be reduced considerably by increasing the concentration of particulate. Since operating a university research facility for a typical 8,000 hour plant operating year is impractical, deposits are instead generated during short one to eight hour tests. Particle feed rates are selected to match the net throughput of particulate.

Tests conducted recently using airborne particulates serve as a validation of this accelerated testing procedure (Jensen et al., 2004). Seed particles from Air Filter Testing Laboratories, Inc. were selected to match the typical particulate size (mass mean particle size of 15 μm with half of the particles less than 5 μm) and chemistry found in the urban atmosphere. Tests with this particulate were conducted for a combustor exit temperature of 1150°C and a Mach number of 0.3. Several 4-hour tests were completed at loadings from 60 to 280 ppmw. This is the same net particulate as 10,000 hrs of operation at 0.024 to 0.061 ppmw, which are typical values for filtered intake air. The test coupons were standard Ni-based alloy with various coating treatments donated from industry. The conclusion of Jensen et al.'s study was that deposits generated in the TADF were similar in deposit structure, surface topography, and thickness to those found on in-service turbine hardware. Since all of these features have a direct influence on heat transfer, deposits generated in this accelerated facility are suitable for assessing the impact of deposition on turbine performance.

The TADF specimen holder is being modified for this study to allow coupon backside cooling and eventually film cooling to the front of the test coupon. Research is being conducted by converting the products of combustion from coal and biomass reactors into fine powders in the 5 μm range.

Deposit Thermal Resistance Measurement Apparatus:

Coupons will also be tested in BYU's thermal resistance measurement apparatus (Figure 2) which is under construction. This will allow an assessment of the degradation of the insulation provided by the TBC when deposits penetrate the surface. The thermal resistance measurement is performed using a flat-flame burner to introduce a stable surface heat flux to the test coupon. The backside surface temperature is measured with an embedded thermocouple while the temperature of the deposit surface is measured with an infrared camera. A heat flux sensor sandwiched between the test coupon and a backside water coolant jet allows the thermal resistance of the coupon to be estimated. Comparing this to a pre-test measurement permits the assessment of the change in thermal resistance due to the deposition process.

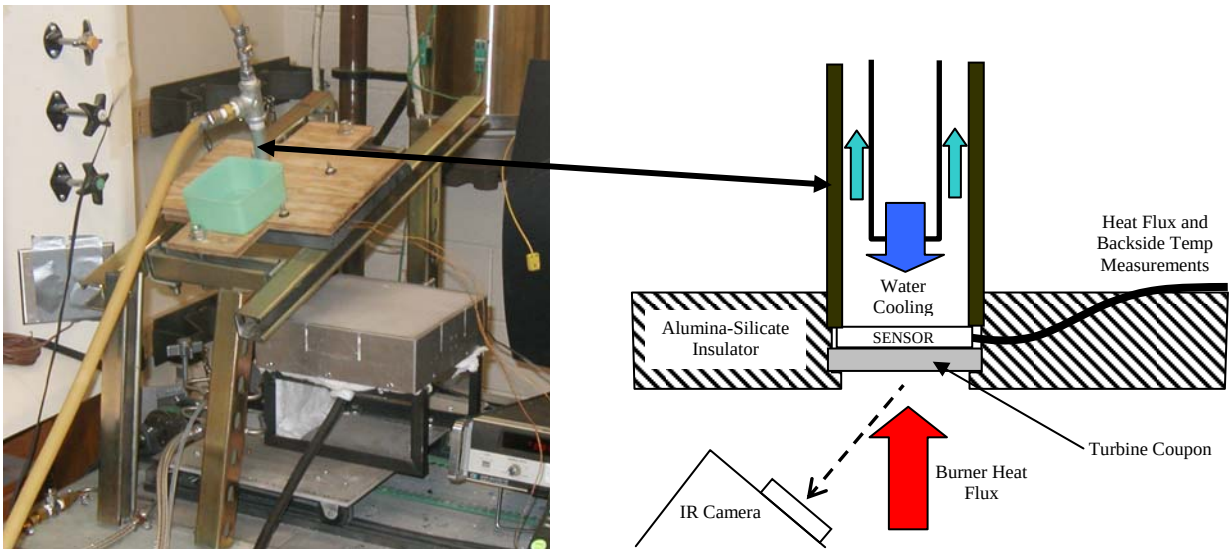

Figure 2: Digital photograph and schematic of BYU's deposit thermal resistance measurement apparatus.

RESULTS AND DISCUSSION

Research Team Formed: With the initiation of the current research effort in August 2005, two graduate (full-time) and three undergraduate (part-time) students were hired to assist with the project. The graduate students (1 MS and 1 PhD) are from the Mechanical and Chemical Engineering Departments, respectively.

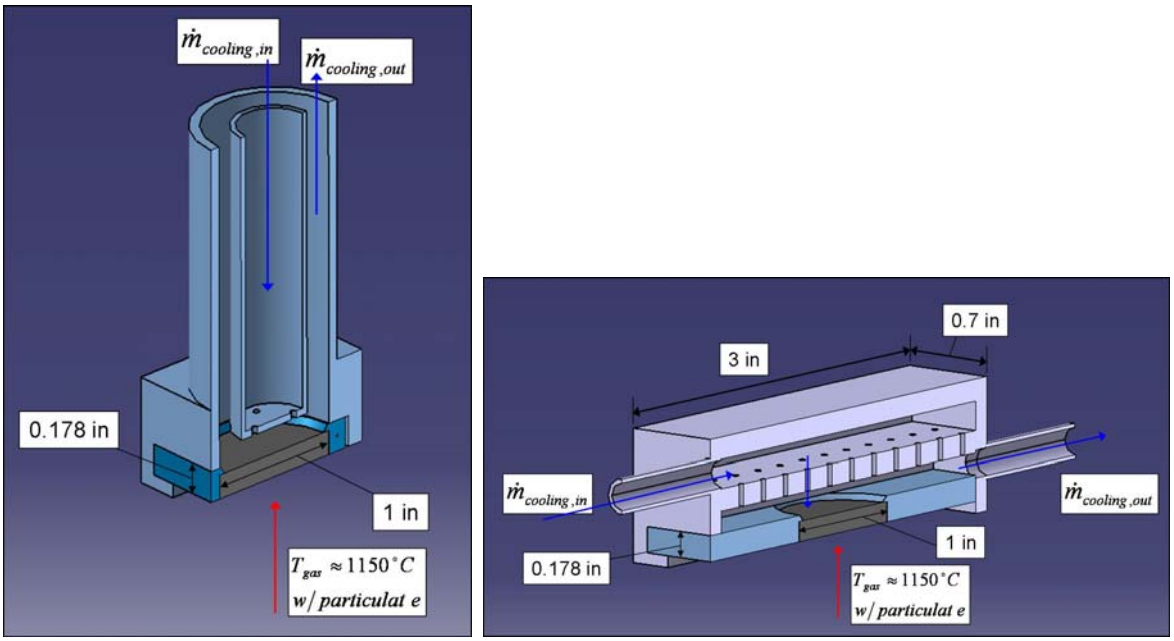

(a) Stagnation Cooled Concept (b) Crossflow Concept

Figure 3: Design concepts for TADF test coupon holder redesign with backside cooling.

TADF Redesign for Backside Cooling: The objective of the specimen holder redesign is to be able to simulate the appropriate thermal gradient through the turbine sample during deposition testing. With their low thermal conductivity (~1 W/mK), TBCs typically experience front to backside temperature differences of 50-100ºC, depending on coating composition and thickness. Figure 3 shows two concepts that were developed to provide this capability in the TADF test fixture. The 1" diameter test coupon is shown in dark olive color, sandwiched between the impinging hot gas (with particles) on the bottom and the coolant chamber above. The coolant chamber design is intended to simulate the internal cooling passages found in the leading edge region of a modern vane or rotor. Concept (a) relies on impinging flow exclusively while concept (b) allows for some cross flow as well. After discussion with engineers at Siemens and GE, concept (a) was selected for the current design. Construction is underway. The design will allow for backside coupon temperature measurement using surface contact thermocouples or optical means. Also, the mass flow of coolant will be measured during testing using an in-line mass flow meter. The redesigned coupon holder is expected to be operational shortly.

Turbine Hardware Donations: Turbine test coupons have been solicited from all members of the UTSR industrial review board. Thus far, coupons have been donated by GE, Praxair, and Siemens. Industry support has been exceptional in this regard. Work is continuing with all other participants. Because we receive hardware donations from multiple companies, the results that we obtain are always presented without reference to the specific source company. This means that the public does not know if the coupon we tested was from GE, Pratt, Siemens, Praxair, or Solar (all have donated parts in the past). However, if any company would like specific data on their donated coupons made available for internal purposes – this can be provided.

Particulate Collection and Preparation: Five different particulate samples have been used to date in the TADF: Arizona dust, coal ash, petcoke ash, straw ash, and sawdust ash. Since the focus of this study is synfuel deposition, the ash compounds will be used. Industry input is still being solicited as to the most relevant compositions of ash that should be studied, but at this point the main focus is coal ash.

The ash compounds were collected from various sources. Coal and petcoke samples were obtained externally, while the biomass samples were prepared locally using facilities in BYU's Advanced Combustion Engineering Research Center (ACERC). Subbituminous coal fly ash was obtained from an operating power plant, while the petcoke ash is boiler slag obtained from a combined cycle gas turbine power plant operating with a blend of 55% petcoke and 45% coal. Straw ash was produced in a two-step process. First, raw material was partially burned to eliminate volatiles. Second, the partially burned ash was placed in a programmable furnace and cycled through a standard ashing process. This same two step process was repeated to generate sawdust ash. A standard kitchen wheat grinder set on the finest setting was used to grind the ash particles to the size needed for testing.

Since the objective of the study is to simulate ash that could be entrained by the flow leading to the turbine, the particles must be small enough to navigate the various gas cleanup systems. Filtration systems in modern gas turbine powerplants are designed to remove all particles with diameters greater than 10 μm and a majority of particles larger than 1 μm. Measurements of particle size distributions from properly functioning advanced filtration systems indicate mass mean diameters (MMD) of order 1 μm, even for hot gas clean-up. With inadequate or degraded

filtration, these levels can be exceeded. Thus the target mass mean particle diameter for this study is less than 10 μm.

After grinding, the size of each ash sample is determined using a laser-based Coulter Counter. The ash is suspended in distilled water and dispersed through the Coulter Counter feed system with the use of a sonicator and/or small amounts of liquid detergent. When illuminated by the laser beam, the particles scatter light in patterns according to their size. This scattered light is detected using photodetectors and converted to the particle distributions. Coulter Counter results from previous deposition studies are presented as mass mean diameters in Table 1. With the exception of the petcoke sample, the mass mean diameters are all between 10-20 μm, with a significant portion of each sample under 10 μm. Because this size distribution exceeds the desired range (<5μm), subsequent testing has demonstrated the capability to grind coal ash to a mass mean diameter of 4 μm. This should be adequate for the testing outlined in the current study.

Table 1: Ash particle summary statistics: size, density, and average elemental composition.

	Coal	Petcoke	Straw	Sawdust
Mass mean diameter (μm)	13.3	33.0	17.6	19.7
Median diameter (μm)	10.6	28.5	15.1	11.8
Bulk density (g/cc)	0.99	1.45	0.84	0.48
Apparent density (g/cc)	1.98	2.90	1.68	0.96
Element	Weight %	Weigh t %	Weight %	Weigh t %
Na	6.9	4.3	1.7	5.9
Mg	3.6	2.2	2.54	12.4
Al	17.8	14.5	1.8	5.1
Si	47.4	38.3	48.4	11.6
P	1.6	0.0	3.4	2.2
S	1.8	1.0	3.0	1.3
Cl	0.0	0.0	2.8	0.0
K	2.6	2.5	23.4	10.7
Ca	8.7	7.5	7.8	42.9
Ti	1.6	0.8	0.0	1.3
V	0.0	3.4	0.0	0.0
Cr	0.0	0.0	0.0	0.0
Mn	0.0	0.0	0.0	4.5
Fe	6.4	22.9	5.0	1.0
Ni	0.0	0.9	0.0	0.0

Following the Coulter Counter measurement, ash samples are placed inside a FEIXL30 environmental scanning electron microscope (ESEM) to obtain qualitative validation of the particle size and shape. Figure 4 shows typical ESEM images from the coal ash sample, which appear mostly spherical in shape. The bulk density of each ash sample was measured in a graduated cylinder, and the apparent density (mass per particle exterior volume) was calculated using an estimated packing factor of 0.5 (see Table 1).

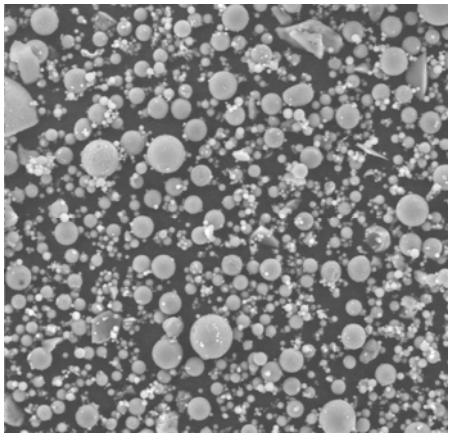

Figure 4: ESEM images of coal ash after processing. Image is approximately 150 x 150μm.

X-ray spectroscopy was used to determine the composition of the four types of ash while they were in the ESEM. An EDAX Phoenix Spectrometer with super ultra-thin window was used to obtain elements down to an atomic number of carbon. The elemental compositions of the four types of ash, as determined by the x-ray analysis, are given in Table 1. Values of 0.0 indicate levels below the background noise level of the spectrometer. An independent elemental analysis was conducted on the four ash samples by ALS Chemex using inductively coupled plasma atomic emission spectroscopy (ICP-AES). The results identified the same elements as the x-ray spectrometer in approximately the same weight percentages, though the ICP-AES analysis of the bulk ash showed 15-20% greater silicon content compared to the x-ray measurements which were spot measurements. Also, the ICP-AES is unable to measure vanadium.

Thermal Resistance Measurement:

A new Chemical Engineering PhD student was hired to continue development of the apparatus for making thermal conductivity measurements. Previous students have attempted measurements, but have obtained low values of thermal conductivities, even for pure metal coupons. The cause for the inaccuracies in the thermal conductivity measurement is currently under investigation.

One of the possible causes was the interference of the post-flame gases with the infrared camera signal. CO_2 and H_2O have significant infrared absorption bands, and hence it was thought that these gases may be causing an inaccurate temperature measurement. An experiment was therefore performed to measure the temperature of a hot plate using the infrared camera, where the post-flame gases from the flat-flame burner were initially not present and then were placed in the path of the camera. The hot plate was slowly ramped from 166°C to 312°C, and then cooled slowly. The results shown in Figure 5 indicate that the post-flame gases from the flame did not significantly influence the temperature measurement. Other causes for the inaccuracies in this approach for thermal conductivity measurements will be investigated in the coming quarter.

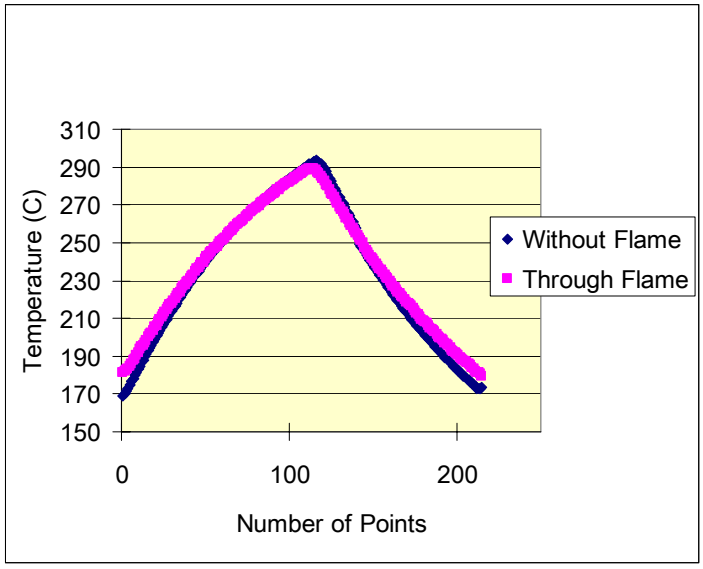

Figure 5. Measurement of the surface temperature of a hot plate using the infrared camera, with and without the presence of the post-flame gases from the flat flame burner.

CONCLUSIONS:

In conclusion, results from the first six months of this deposition study are very promising. Industrial participation is excellent and the student research team has been formed and is fully engaged. The study will investigate the deposition of synfuel contaminants on turbine components. By using hardware donated from industry, the relevancy of the laboratory simulations is insured. Because they are performed in a controlled environment, these deposition studies should provide the framework for semi-empirical deposition and material degradation models. This will in turn provide the engine community with the tools necessary to establish maintenance guidelines and gas cleanup specifications for IGCC plants.

REFERENCES:

Jensen, J.W., Squire, S.W., Bons, J.P., and Fletcher, T.H., "Simulated Land-Based Turbine Deposits Generated In An Accelerated Deposition Facility". *ASME Journal of Turbomachinery*. Vol. 127, pp. 462-470, July 2005.

Wenglarz, R.A., and Wright, I.G., "Alternate Fuels for Land-Based Turbines," published in proceedings of the "Workshop on Materials and Practices to Improve Resistance to Fuel Derived Environmental Damage in Land-and Sea-Based Turbines", October 22-24, 2002, Colorado School of Mines, Golden, Colorado.

Fundamental Studies in Syngas Premixed Combustion Dynamics

Semi-annual report

Reporting Period:
August 2005 to February 2006

Principal Investigator:
Ahmed F. Ghoniem

co-PI:
Anuradha Annaswamy

Students:
Raymond Speth, graduate student, lead researcher and instrumentations
Murat Altay, graduate student, measurements
Jacqueline O'Connor, undergraduate student, designer
Dagfinn Snarheim, visiting graduate student, controls

Report Date:
March, 2006

DOE Award Number:
DE-FC26-02NT41431

UTSR Project Number:
05-01-SR121

Submitting Organization:
Massachusetts Institute of Technology
77 Massachusetts Ave
Cambridge, MA 02139

Disclaimer:

This report was prepared as an account of work sponsored by an agency of the United States Government. Neither the United States Government nor any agency thereof, nor any of their employees, makes any warranty, express or implied, or assumes any legal liability or responsibility for the accuracy, completeness, or usefulness of any information, apparatus, product, or process disclosed, or represents that its use would not infringe privately owned rights. Reference herein to any specific commercial product, process, or service by trade name, trademark, manufacturer, or otherwise does not necessarily constitute or imply its endorsement, recommendation, or favoring by the United States Government or any agency thereof. The views and opinions of authors expressed herein do not necessarily state or reflect those of the United States Government or any agency thereof.

Abstract:

The objectives of this effort are to develop a fundamental understanding of syngas combustion dynamics in cases when flames are stabilized in recirculating flows behind sudden expansions and in swirl stabilized flows. Combustion of syngas differs fundamentally from that of other complex hydrocarbon for a number of reasons, including the short combustion time delay, the high hydrogen content, and the high flame speed. We will construct stability maps of premixed syngas combustion in terms of the Reynolds number-equivalence ratio coordinates for step and swirl stabilized combustors, for different gas compositions and inlet conditions. The focus of the experiments will be on the lean limit and the associated dynamics observed as the equivalence ratio is reduced and the flow velocity is increased, and how the gas composition and other factors affect the blowout limits of the combustor. During the first six months of the effort, Sept 05-March 06, we have been modifying our step-stabilized combustor to run on syngas, developing a matrix of tests to characterize the dynamics of syngas combustion, and designing the swirl-stabilized combustor which will replace the current step-stabilized one. During the next six months, we will run the test matrix, develop stability maps for the combustor, define the dynamics mechanisms and develop descriptive models, build the new swirl stabilized combustor, and examine its operating envelope. We will continue to develop our diagnostics capability to allow for more detailed examination of the underlying dynamics mechanisms of both combustors.

Table of Contents

Executive Summary 5
Project Description 5
Experimental 6
Combustor Modifications 6
Planned Experiments 6
Swirl-stabilized combustor design 8
Results and Discussion 9
Conclusion 9

List of Figures

Figure 1: Fuel supply system for syngas combustor. 10
Figure 2: Swirl stabilized combustor design. 11

Executive Summary

The objectives of this effort are to develop a fundamental understanding of syngas combustion dynamics in cases when flames are stabilized in recirculating flows behind sudden expansions and in swirl stabilized flows. For this purpose, syngas with different mixture compositions and at different inlet combustor temperature will be used in two types of combustors, a planar combustor and an axisymmetric combustor. Stability maps, optical diagnostics of the time dependent flame shape and heat release profiles, and other mechanistic characteristics will be recorded. The insight gained from these experiments will be used to suggest different variations on the flame stabilizations environments aimed at passively stabilizing the flames. Other more advanced probing techniques that may be necessary for this purpose, such as PIV, are currently being investigated.

In the first six months of the project, we have:

(i) rebuilt the planar combustor experiments to enable the use of syngas as a fuel, including the design of upstream fuel preparation section for arbitrary mixture composition and inlet temperature;
(ii) designed and began fabricating the new axisymmetric swirl stabilized combustor, with flexible modular construction and optically accessible test section;
(iii) acquired a new data acquisition system; and
(iv) approached vendors to assess the state of the art of PIV systems.

During the next six months, we plan to

(i) obtain all the data required to accurately describe the instability mechanisms under different operating conditions;
(ii) develop the stability maps for the planar combustor;
(iii) install and "shake-down" the new swirl stabilized combustor;
(iv) experiment with passive stabilization techniques; and
(v) demo the PIV systems.

Project Description

Syngas, produced by burning coal in pure oxygen and steam in high pressure gasifiers, has been proposed as the fuel of choice for modern high efficiency low emission combined cycles power plant, in which gas turbine engines are used as topping cycles that take advantage of high temperature combustion products to improve the overall efficiency of the power plant. Incorporating technologies to filter out turbine-corroding gases from the gasifier products, and delivering clean syngas to the gas turbine combustor, enables the use of syngas in gas turbines. The sequestration of carbon dioxide, following the production of steam for the bottoming cycle, makes this plant environmentally ideal.

Combustion of syngas differs fundamentally from that of other complex hydrocarbon for a number of reasons, including the short combustion time delay, the high hydrogen content, and the high flame speed. The latter endows syngas combustion with extra resistance to extinction under highly turbulent conditions, which can lead to interesting opportunities but may also exasperate the dynamics. The objective of this study is to investigate experimentally the fundamental properties of syngas combustion over a wide range of conditions. Data and models necessary for the design of stable, efficient and clean combustors for gas turbine engines running on syngas will be obtained, and insight into the mechanisms governing the stability limits and the ensuing dynamics will be investigated, with the goal of proposing solutions that lead to efficient, clean and stable burning at high temperatures and high efficiency. Innovative solution for stabilizing combustion at lean and ultra lean conditions will be demonstrated in the laboratory, as well as abstracted in design guidelines.

We will construct stability maps of premixed syngas combustion in terms of the Reynolds number-equivalence ratio coordinates for step and swirl stabilized combustors, for different gas compositions and inlet conditions. The focus of the experiments will be on the lean limit and the associated dynamics observed as the equivalence ratio is reduced and the flow velocity is increased, and how the gas composition and other factors affect the blowout limits of the combustor. Mechanisms and precursors of dynamics, and the relationship between the dynamics and the blowout limits will be investigated using extensive, spatially resolved non-intrusive measurements, and modeling analysis. Besides the static stability limits measured in the experiments, dynamics associated with unstable operation will be categorized under different operating conditions. The experimental measurements will be used to suggest means of modifying the stabilization zone so as to improve the stability limits, passively, and without impacting other performance metrics such as emission and efficiency. Modeling of flame propagation in syngas mixtures will be used to support the analysis of the experimental data.

Experimental Effort

Over the last six months, we have been modifying our combustor to run on syngas and designing the swirl-stabilized combustor which will replace the current step-stabilized one. We have prepared a matrix of tests which bridge our previous research on propane in the step stabilized environment to the new syngas-based system. We have completed a preliminary design for a new swirl-stabilized combustor which will be installed alongside the current combustor.

Combustor Modifications

Starting in the fall we undertook a detailed survey of or laboratory equipment and identified the components that we felt needed to be upgraded or replaced. As a result of

this process, we purchased a new computer and data acquisition system which improved our data acquisition capabilities and centralized control of laboratory hardware. Two inoperable flow meters were also repaired and recalibrated.

In preparation for operating the combustor with syngas, we designed a new fuel supply system that allows the combustor to operate on CO/H2 mixtures of variable composition. A diagram of the new fuel delivery system is shown in Figure 1. The hardware was ordered in November, but because of delays in the purchasing process we are still working on installing the new fuel system. We have also purchased air heaters for both the main and secondary (slot) air lines, which will allow us to operate at inlet temperatures of up to 1000 K, with independent control of the temperature of each air supply.

In addition, we have been examining the prospects of using time-resolved particle imaging velocimetry (PIV) to complement our existing diagnostic tools. A PIV system would improve our ability to characterize combustor dynamics and would assist in validating predictive analytical and numerical models. We are currently involved in discussions with several PIV system vendors to determine a system that will meet our needs at a reasonable cost.

Planned Experiments

The objective of the initial set of experiments is determining the stable and unstable operating regions of syngas combustion at different mixture compositions and operating conditions in the current backward-facing step stabilized combustor. The stability characteristics of the combustion will be quantified by measuring the overall sound pressure level, CH* chemiluminescence and by capturing the images of the flame. In addition to stability characteristics we will measure NO_x and CO emissions for each test that we run. Previous experiments on lean premixed propane-air combustion demonstrated that the instability of the combustor is mainly governed by the hydrodynamics of the flow, which is characterized by the Reynolds number. The equivalence ratio oscillations are also shown to affect the combustor stability characteristics. The effect of equivalence ratio oscillations will be eliminated by locating the fuel bar upstream of the choke plate. The mean equivalence ratio of the flow and the inlet air temperature affect the combustion dynamics and therefore are also critical for combustion instability. The most important impact of the mean equivalence ratio and the inlet temperature is affecting the burning velocity of the flame which has significant impact on flame-vortex interaction mechanism as observed in the earlier numerical studies.

Reynolds number is defined in terms of the mean flow velocity and the step height. By keeping the Reynolds number, equivalence ratio and inlet air temperature constant we will vary the syngas composition and investigate the stability characteristics. Table 1 illustrates typical set of parameters that we propose to run the combustor. Reynolds number, equivalence ratio and inlet temperature are 5000, 0.5 and 25˚C, respectively.

Table 1: Test matrix for Re=5000, – =0.5, 25˚C

Syngas Composition (Molar)	Air flow rate (g/s)	H_2 flow rate (g/s)	CO flow rate (g/s)
All H_2	14.45	0.211	0
20% CO, 80% H_2	13.92	0.162	0.568
40% CO, 60% H_2	13.44	0.117	1.096
50% CO, 50% H_2	13.20	0.096	1.347
60% CO, 40% H_2	12.98	0.076	1.589
80% CO, 20% H_2	12.56	0.037	2.048
All CO	12.16	0	2.480

Using the same set of syngas compositions as in Table 1, the experiments will be repeated for various Reynolds numbers, equivalence ratios and inlet air temperatures. The Reynolds number will be varied from 4000 to 10000 with 1000 increments; the equivalence ratio will be varied from 0.3 to 0.6 with 0.05 increments; and finally the air inlet temperature will be varied from 25˚C to 700˚C with 100˚C increments.

After completing these set of experiments we will investigate the impact of air/air+hydrogen injection from a slot in the cross-stream direction near the location of the step. These tests will be performed at the operating parameters which showed significant combustion instability. The overall sound pressure level, CH* chemiluminescence and flame images will be investigated while varying the air and hydrogen flow rate from the slot. Typical ranges of the air and hydrogen flow rates are $0 < \dot{m}_{jet,air} \leq 5$ g/s and, $0 < \dot{m}_{jet,H2} \leq 9$ mg/s, respectively. Moreover, we will vary the temperature of the jet in the range $25^oC \leq T_{jet} \leq 700^oC$ and explore its effect as well.

By the time these tests are completed, the axisymmetric, swirl-stabilized combustor will be ready and similar set of experiments will be repeated.

Swirl-stabilized combustor design

In an effort to examine flows similar to those in industrial gas turbines, we have designed a swirl stabilized combustor for further research of combustion instabilities and the effects of syngas in combustion processes. The design of this new combustor was completed in three steps. First, we researched current academic swirl stabilized combustor facilities in order to get a feeling for the type of research and size of combustor in the field. The second step was a preliminary design phase in which we calculated the general specifications for the combustor. Finally, we are currently wrapping up the detailed design phase, in which the particulars of the design are being ironed out.

After reading several papers addressing the experimental results of swirl stabilized combustion research, we contacted several schools, including Penn State, Georgia Tech,

Stanford, and University of Cincinnati, in order to see the types of combustors being operated in academia. The schools were very eager to provide helpful information in areas such as swirler design and combustor geometry. This information gave us one basis on which to design our new combustor.

The second step in the process was to size the combustor and decide on a geometry. Due to the current air and fuel systems, the fluid flow rates were relatively fixed. The initial sizing, including expansion ratio and combustor length, was based off the current backwards stepping combustor now being operated in the lab. The overall geometry was decided using the input from the various labs we contacted. Geometries such as a square, cylindrical, and even octagonal expansion section were discussed. The largest consideration was the visual access to the flame. For this reason, we decided on a cylindrical expansion section made entirely of quartz.

The most important part of the design, though, was the swirler design. Some basic figures, such as the number of blades and the angles of incidence, were taken from the advice from other labs. In the current design there are 8 swirl blades. The swirler section is modular and so a swirler with either a 30 degree, 45 degree, or 60 degree angle of incidence can be inserted. The subsequent swirl numbers are 0.404, 0.7, and 1.212, respectively. The design of this system also came from theory described in Gas Turbine Combustion by Arthur Lefebvre.

The final part of the design phase is currently in its last stages. The design has been modeled in Solidworks and is shown in Figure 2. Details such as gaskets, igniter placement, and interfaces are being sorted out with the help of this design tool. Most of the parts are being ordered from vendors such as McMaster-Carr, and the machined parts will be manufactured by MIT's Central Machine Shop.

In order to have the baseline experiment running as soon as possible, the combustor was designed with modularity in mind. As the experiment space grows and the need for more variables arises, new pieces can be manufactured or ordered and inserted without great disturbance to the setup.

Results and Discussion

So far the effort has focused on preparing the existing combustor for test using syngas as a fuel and on designing a new sworl stabilized combustor. This is on target as stated in our proposal. The next six months will fosuc on collecting large data sets from the step stabilized ocmbustors, analysis of the data to define the stability envelope of this combustor and determine the dynamics mechanisms, build and install the new swirl stabilized combustor, and acquire more diagnostics tools. The annual report will document all these data.

We are on target to achieve all the objectives defined in our proposal according to the timeline promised in the proposal.

Conclusion

The experimental work that constitutes the primary effort of this work is on target. We have also added two more tasks to enhance our capability and add more value to the overall effort;

1. We are examining existing PIV systems offered by different vendors, and play to purchase one in the next few months. While the complexity of the dynamics can be investigated using our existing optical and point wise data collection methods, we feel that interrogating the system using planwise diagnostics will be extremely helpful in defining the fundamental mechanisms and suggesting approaches to suppressing or mitigating the dynamics. We sill be seeking funds for this purpose whenever the opportunity arises.
2. We have planned a parallel modeling efforts to use our numerical codes that simulate the flow and cmbustion in the step stabilized combustor to shed the light on the combustion dynamics mechanisms in this combustor. This work is funded through other sources and hence adds value to the UTSR programs without adding expense. We will report on this effort in the annual report.

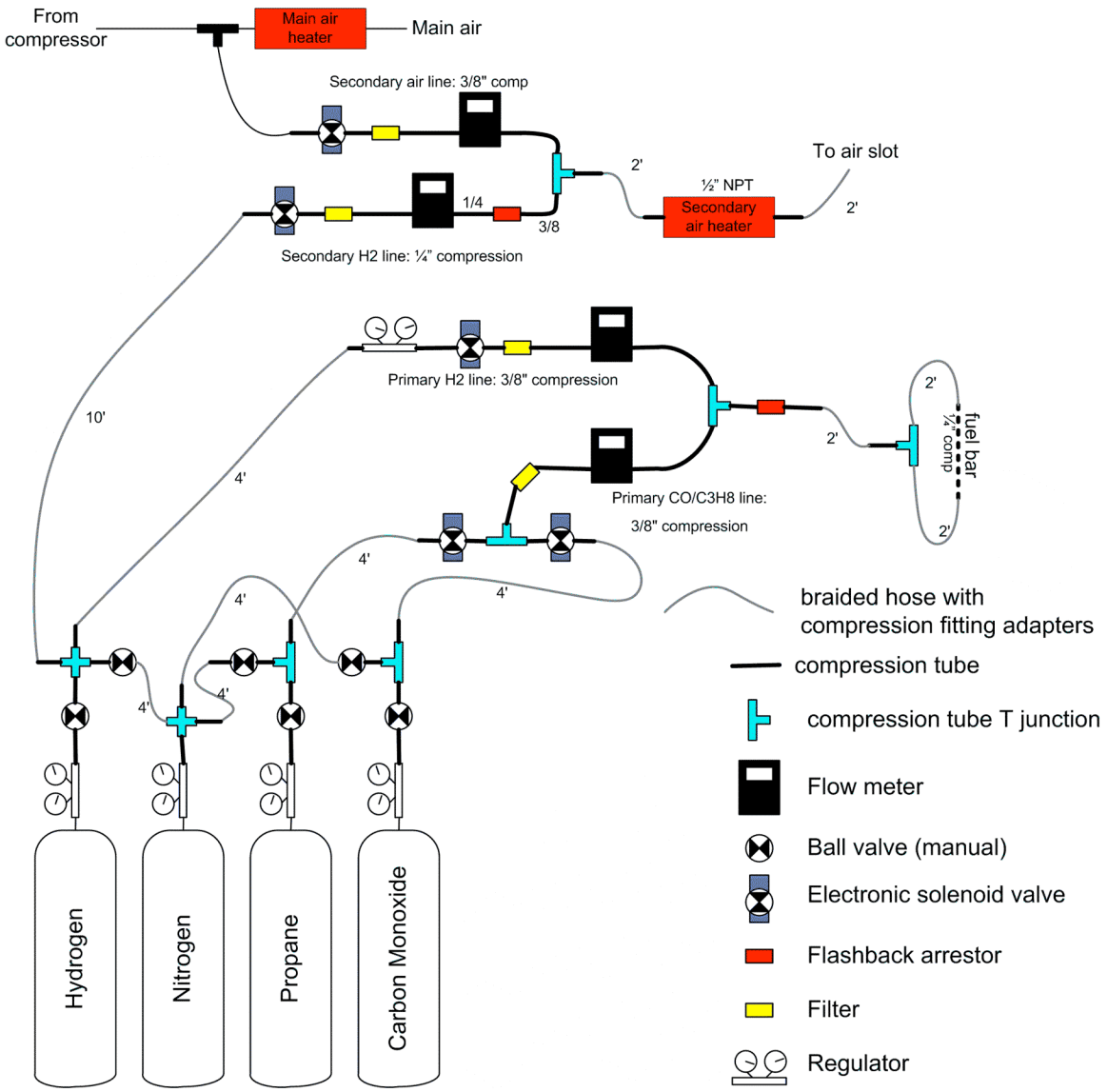

Error! Bookmark not defined.Error! Bookmark not defined.Figure 1: Fuel supply system for syngas combustor.

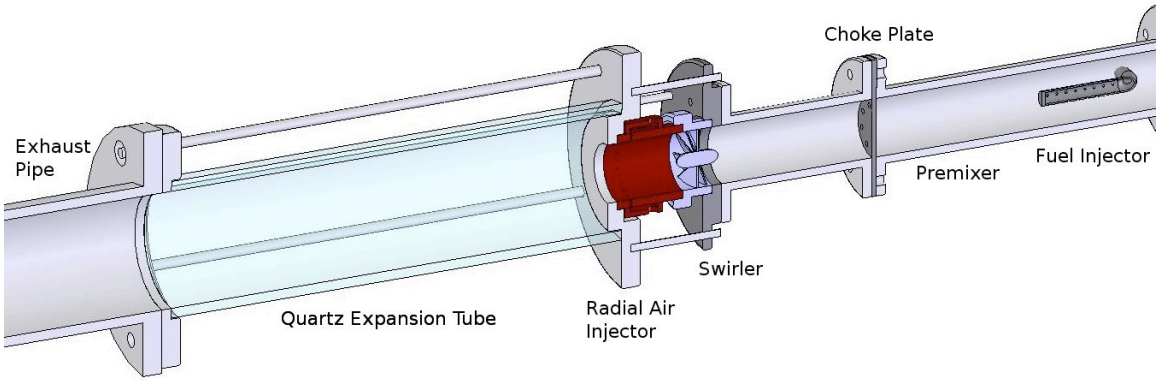

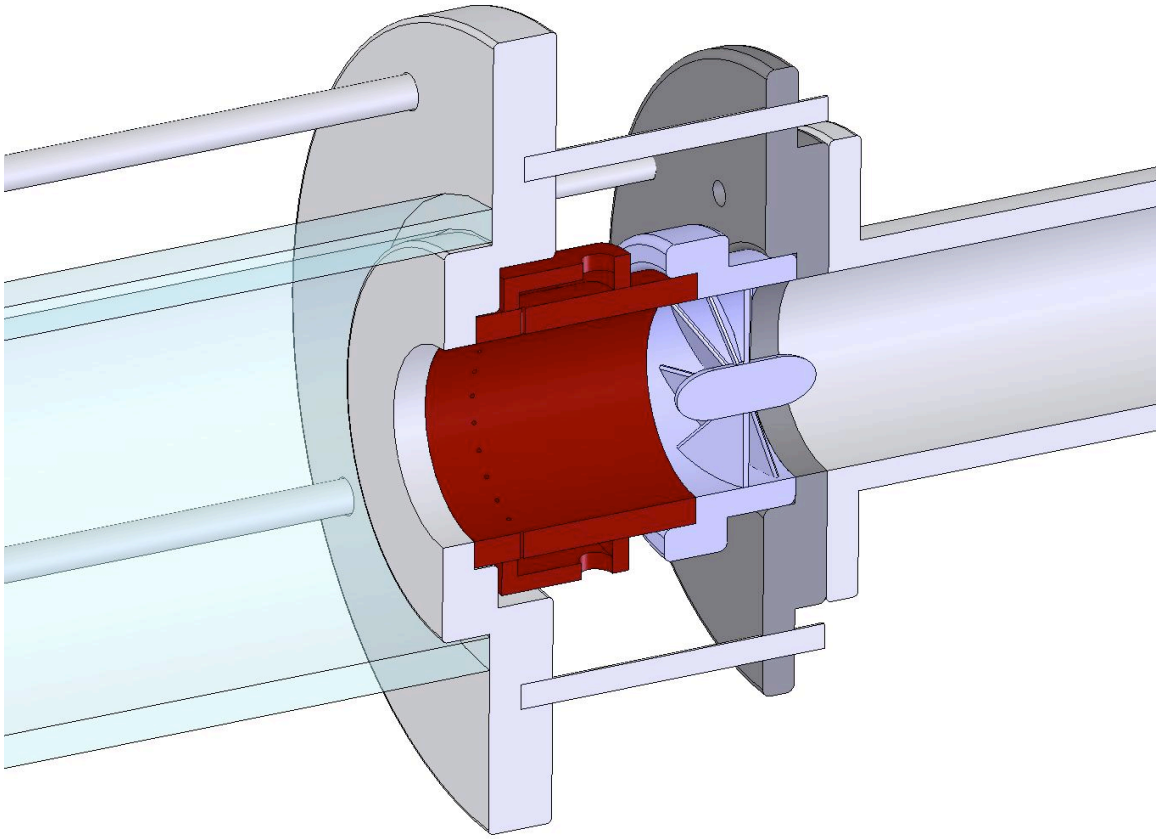

Error! Bookmark not defined.Figure 2: Swirl stabilized combustor design.

ATTACHMENT

Monthly Exception Reports for Year 2005

(January through September 2005, after which the DOE indicated reports were no longer needed)

REPORT FOR JANUARY

Completed Tasks

Peer Review Workshop: The Madren Conference Center has notified SCIES that the auditorium is not available for the first planned day of the Peer Review Workshop. Consequently the Peer Review Workshop and IRB Meeting have been shifted one day later. The date of the IRB Meeting is now Tuesday, October 18 and the Workshop dates are Wednesday, October 19 to noon on Friday, October 21. A workshop announcement with the revised dates will be sent in February to persons on the Workshop distribution list.

UTSR Web Site Development: SCIES is developing a new procedure to continually update the UTSR web site. The UTSR Final Report to the DOE for period September 1992-June 2003 was reviewed with the idea of posting sections of it on the SCIES
Web site, such that it is a living document, updated periodically to show results from 1992 to the most recent update. Draft sections were written for both research and outreach activities with much of the updated information to be included in a format such that the information can be directly incorporated into later major reports to the DOE.

Facilitation Training: All members of the SCIES staff participated in a two-day training course on facilitating effective decision making meetings. The course was taught in the context of the goals and activities of the upcoming Peer Review Workshop, and the instructor provided specific suggestions on enhancing the results from the workshop breakout sessions. This training was timely as SCIES prepares for the next Peer Review Workshop, which will have breakout sessions on growing the UTSR Program.

RFP for 2005: SCIES continues to develop research topics for the next RFP of the UTSR Program, starting from a SCIES list modified by the DOE and then sent to the IRB companies, more than 100 UTSR universities, and Geo Richards for comments. This month the topic list was again modified according to two interactions with Geo Richards in the combustion area and input from GE that resulted in an additional aero/heat transfer topic and input from Siemens Westinghouse that resulted in an additional materials topic and an expansion of another materials topic. The result is four topics in each of the combustion and materials areas and two topics in the area of aero/heat transfer. The topic list has been sent to the DOE for approval to be included in the next UTSR RFP. Later, Siemens Westinghouse provided to SCIES a list of specifications for maximum allowable levels of various elements in the fuel ash for alternate fuels. The specifications can provide some guidance on contaminants to consider in UTSR projects. Most of the contaminant limits were established from experience with oil derived fuels (residual and

crude oils) but limits are also included on Fe and Ni carbonyls based on experience from operating syngas turbines in Europe.

SCIES continues to seek important information to define UTSR research topics and test conditions for future UTSR projects (e.g., composition/particle size distributions of syngas contaminants, nature of materials degradation in syngas turbines, and the contaminants that caused the degradation). Even if not available before the next RFP, this information can be provided to the PI's of the projects awarded from the RFP to better focus and define their research.

Third Stage Blade from SCIES Visit to Syngas Plant: SCIES previously visited the Wabash River IGCC plant to identify syngas turbine issues that might be addressed by research in the UTSR Program. The turbine had experienced a damaging third stage blade failure and Cinergy requested an analysis of a blade to determine if the syngas fuel contributed to the failure. SCIES discussed the request with the DOE, which has now approved funds for the analysis by South West Research Institute (SWRI) through a DOE contract with EPRI.

SCIES sent the blade to SWRI and analyses have started. SWRI requested the operation history and EPRI requested information related to whether observed sulfidation of the blade detected by SWRI might have resulted from the startup fuel or inlet air. SCIES obtained and provided information to SWRI and EPRI in response to their questions.

Responses to Requests:

- SCIES agreed to review proposals submitted to the University Coal Research (UCR) program in the area of combustion kinetics for syngas turbines and completed the Non-Disclosure/Conflict of Interest form required by the DOE.
- An updated Fact Sheet on the UTSR Program was provided to the DOE in the specified format.
- Responding to a request by Mary Anne Alvin, who is working for a DOE on-site contractor, SCIES provided a CD from the most recent UTSR Workshop and information on the US-UK collaborative materials projects.
- SCIES sent to Irwin Stambler, editor of Gas Turbine World (GTW), a proceedings CD from the most recent UTSR Workshop and a copy of the UTSR Project Fact Sheet Booklet from the workshop, for a possible article in GTW.

Press Release: A final copy of a press release was produced which coverers the Academic Advisory Board (AAB) and the appointment of Rick Huntington as Liaison to the AAB from the IRB. The press release was displayed on the ClemsoNews web location.

AAB Meeting: A meeting of the AAB was held at ExxonMobil's research facility in Fairfax, VA. A SCIES presentation was prepared jointly with Jeff Abboud of the Gas Turbine Association. SCIES' portion (delivered by phone with Power Point slides on site) was on accomplishments since the outreach presentation at the Peer Review Workshop last fall, the

outreach objectives for 2005, and suggestions of where the AAB can help outreach activities. Jeff Abboud covered how the AAB might work with GTA. The meeting should benefit integrating the AAB into UTSR work for Outreach.

Sharing Proposals with Other Agencies: From discussions with NSF, it is clear that organization is not in a position to undertake initiatives in working with UTSR that would require new funding, in the near term at least. One collaborative approach may be for SCIES to share summaries of the proposals with NSF for projects that the UTSR deems worthwhile but lacks the funding to pursue. NETL could write letters of endorsement for those proposals. Then, depending on the interest of the PI, the project could be proposed to NSF or other government agencies. This could be announced as part of the next solicitation.

Presentations and Publications

Invited Paper: SCIES has started to produce a paper on turbine deposition to be included with a series of invited survey papers on turbine technologies to be published in a special issue of the AIAA Journal of Propulsion and Power.

Key Milestone Update

There are no milestone modifications this month.

Discussion Topics

None.

Significant Accomplishments – Success Story

Ingersoll Rand Energy Systems and Capstone Turbines have agreed to join the IRB as Associate Members (non voting). These are the first microturbine manufacturers to participate on the IRB and were encouraged to join by the Energy Efficiency and Renewable Energy (EERE) part of DOE. SCIES provided input to the DOE for a possible Secretary of Energy's Weekly Report describing the benefits of this interagency participation in the UTSR Program. SCIES also notified potential applicants to the Fellowship Program that the two new companies are part of the IRB and will be hosting Fellows in 2005.

Site Visits

No site visits occurred or were planned with high level corporate or government officials this month.

Travel

None.

REPORT FOR FEBRUARY

Completed Tasks

Peer Review Workshop/IRB Meeting: The CY 05 IRB Meeting will be held Monday, October 17 and the Peer Review Workshop will be held Tuesday, October 18 to about noon on Thursday, October 20 on the Clemson campus, Madren Center. The sessions on first day of the Peer Review Workshop will be presented in a ballroom at the Madren Center and the remaining general sessions will be presented in the Bell South auditorium.

RFP for 2005: SCIES continues to develop research topics for the next RFP of the UTSR Program, starting from a SCIES list modified by the DOE and then sent to the IRB companies, more than 100 UTSR universities, and Geo Richards for comments. Additional combustion topic recommendations were received this month from Siemens Westinghouse that were consistent with the list already developed.

A remaining issue is aero/heat transfer topics. Several topics suggested by SCIES were not approved because the DOE considers particulate effects and deposition to not be issues. Through discussions with Karen Thole, it was decided that Western Carolina University has not yet demonstrated sufficient capabilities to measure cooling hole blockage so it was decided to not include a topic in this area.

DOE Special Requests: SCIES responded to special requests from the DOE:

- Chuck Alsup asked SCIES to contact materials experts in the SCIES database to request volunteers to review SBIR proposals in the area of novel turbine coatings that can withstand higher turbine firing temperatures. The DOE received more than five volunteers from this request.
- Bruce Utz requested a year 2006 technical milestone for the UTSR Program, which was provided to him. The milestone concerns data and correlations that characterize blowout of fuel flexible combustors.
- Responding to a request from Ron Harp, SCIES reviewed five proposals submitted to the University Coal Research (UCR) program in the area of combustion kinetics for syngas turbines.

Annual Report: Work started on the 2003 Annual Report for the UTSR Program.

US-UK Collaborative Project in Syngas and Alternate Fuels: Resulting from a recommendation by SCIES, one of several US-UK collaborative projects being developed involves using an existing Cranfield University (UK) facility to simulate turbine flow path conditions for tests of materials and turbine protection approaches for syngas turbines. SCIES has been assigned as the lead for the US portion of this collaborative project. Of particular importance will be tests at the higher gas temperatures being considered for next generation syngas turbines to meet the DOE IGCC efficiency objectives.

This month SCIES enlisted Siemens Westinghouse (SW) into the US-UK project. SW has agreed to contribute specimens and data analyses efforts. SCIES forwarded specimen drawings so that

SW can fabricate materials specimens for the tests. SCIES identified materials (alloy and coating) and test conditions (e.g., temperatures) for the tests, requested materials recommendations from Udaya Rao at NETL, and also received recommendations on materials from SW. SCIES coordinated the syngas turbine materials candidates with Bill Ellingson at Argonne National Labs, who is US lead on another thermal barrier coatings (TBC) project in the US-UK collaboration. The candidate materials list for both the syngas turbine project and the TBC project now include thicker TBC of interest to the DOE for increasing the performance of future turbines for operation with syngas and hydrogen (SGH) fuels. Information was also provided to Ellingson on UTSR research and a professor contact that could benefit his project.

Wabash River Syngas Turbine: SCIES previously visited the Wabash River IGCC plant and obtained deposits and spalled TBC from a turbine inspection. Samples of deposits and spalled TBC were previously provided to two UTSR projects (at BYU and University of Pittsburgh) and to ORNL for analyses. Initial results from an ORNL analysis were sent by SCIES to BYU this month.

STAC Project: Based on over 15 years alternate fuels experience in the gas turbine industry, SCIES has been providing turbine flow path protection technology assistance to enhance UTSR university capabilities. One such effort was participation with Brigham Young University (a UTSR university) in a State Technologies Advancement Collaborative (STAC) proposal. A goal of the project was evaluation of deposition under conditions of current turbines operating with syngas and future turbines operating at the higher inlet temperatures planned in the DOE Turbine Program.

The awards from the STAC solicitation were announced and the SCIES/BYU proposal was not selected.

ORNL Project: At the request of ORNL, SCIES provided comments and input to a Field Work proposal submitted to the DOE that addresses materials for turbines operated with syngas and hydrogen fuels. The proposed ORNL project includes SCIES participation.

New IRB Member: Clean Energy Systems has decided to join the IRB and will be eligible to receive a Fellow in 2005.

UTSR Fellowships for 2005: Siemens Westinghouse will support three UTSR fellows from their own funds. These Fellows are in addition to the two DOE-paid Fellows that they will receive. This will be beneficial for the UTSR Program, as more of the applicants will receive placements.

Debbie Haught of EERE has provided $35K funding for three UTSR Fellows in 2005. Two will be for the Fellows for Capstone Turbines and Ingersoll Rand Energy Systems. The third, at Debbie's suggestion, will be for work related to UTC Power, which operates a separate business from P&W and packages microturbines with heating /cooling systems.

UTSR Information on IGTI Website: IGTI has posted a notice on their website promoting the UTSR Program with a link to the SCIES website. This is part of an agreement with Kevin

Gaffney of IGTI for cooperative promotion of each organization. The UTSR notice is located just after the IGTI posting of the Turbo Expo '05.

Annual Joint Meeting of ASERTTI / NASEO: SCIES participation in this meeting provided leads on identifying the benefits of the US gas turbine industry and the usefulness of the UTSR: 1) Study of the Impact of the US gas Turbine Industry. Henry Habicht, member of the National Committee on Energy Policy, provided recommendations to Congress on needed energy legislation. As described by Habicht, the committee contains no members of Congress but does contain members who have non-partisan credibility in the energy field. Their recommendations included a need to develop the economic impact of energy policy on different industries. SCIES asked Habicht to recommend someone capable of determining the impact of the US gas turbine industry on GDP and employment. Habicht recommended two possibilities, and Professor Lester Lave of Carnegie Mellon University (same Congressional district as NETL- Pittsburgh) has been approached by SCIES. Professor Lave is interested in conducting the study. SCIES is working with him on a description of what he could do and a cost estimate.

2) Usefulness of UTSR in Providing Engineers to the Gas Turbine Industry. Another speaker was Karen Harbert, DOE Asst. Secretary for Policy & International Affairs. She expressed a concern over the declining numbers of nuclear power engineers and petroleum engineers. The number of universities graduating nuclear engineering degrees has declined to 5 or less and the DOE started partnerships with 15 universities to change this situation. SCIES approached Ms. Harbert after her talk, described the UTSR Program and confirmed with her that her office addresses the supply of engineers relevant to US energy needs. SCIES asked if we could work with her office to do an assessment of the contribution that UTSR is making to enhance the supply of gas turbine engineers. She agreed to work with us. An email has been sent to her explaining the need for the help from her office.

AAB Meeting and Action Items: SCIES participated in a conference call with Karen Thole and Tim Lieuwen to review the conclusions and recommendations that the AAB had developed in their meeting of 1/28/05 at ExxonMobil. SCIES is now working on several items that require action or approval.

Presentations and Publications

Invited Paper: SCIES completed a draft paper on turbine deposition to be included with a series of invited survey papers on turbine technologies to be published in a special issue of the AIAA Journal of Propulsion and Power. The draft was sent to the DOE and permission was given to proceed with publication.

Articles for Gas Turbine World: SCIES provided Irwin Stambler, editor for Gas Turbine World, information for two possible future articles in that publication. One article being considered is a description of the 2004 Peer Review Workshop. A second article being considered is a description of research at University of Connecticut to develop thicker TBC coatings for improved thermal insulation of turbine components.

Key Milestone Update

There are no milestone modifications this month.

Discussion Topics

None.

Significant Accomplishments – Success Story

Under the University Turbine Systems Research (UTSR) program, a Virginia Tech (VT) project (SR110) is evaluating performance of film cooling for conditions of surface roughness and cooling hole blockage, such as due to deposition and repeated application of thermal barrier coatings. Another focus of the research is effects on film cooling of end wall gaps between adjacent vanes and at the intersection between the combustor sections and first stage vane segments. The research identified a specific gap design configuration between adjacent parts that provides more favorable cooling effects (compared to other designs) from flows passing through the gap between the parts. Experiments using obstructions representing deposits adjacent to cooling holes suggest that, in most cases, film-cooling effectiveness is more sensitive to downstream obstructions (deposits) than upstream obstructions (deposits). Small obstructions have little affect for a cooling hole blowing ratio of 0.4, but obstructions larger than 25% of the cooling hole diameter obliterate the cooling jet and significantly affect cooling performance.

Significance: The VT project is evaluating effects on film cooling performance for turbine passage end walls under roughness and deposit conditions representative of those in syngas turbines. The project has also identified a configuration for end wall gaps between adjacent hot section parts that provides more favorable cooling benefits from gap flows than other configurations, which could aid turbine engineers in the design of end wall gaps.

Site Visits

No site visits occurred or were planned with high level corporate or government officials this month.

Travel

Bill Day traveled to the joint ASERTTI/NASEO meeting in Washington, DC.

REPORT FOR MARCH

Completed Tasks

Peer Review Workshop: Principal investigators (PI's) of active UTSR projects scheduled to end before October were contacted by email to inquire if they would consider requesting a no-cost schedule extension for their projects to at least the end of October, 2005. This would enable them to cover, under their current contract, efforts to prepare, travel, and present their projects at the UTSR Peer Review Workshop in the third week of October of this year. Some PI's responded with requests for no-cost extensions. Others have not yet responded and there remain several projects scheduled to end before the next workshop.

Annual Report: The 2003 Annual Report for the UTSR Program was submitted to the DOE.

UTSR Technical Milestones: A description was written on UTSR program achievements concerning the following 2004 technical milestone:

Develop turbine combustor design data to aid flashback and instability design challenges

The milestone achievements will be included in the 2004 Annual Report for the UTSR Program to be provided to the DOE in April.

UTSR Research Topics: SCIES received input from Rich Dennis and Bruce Utz on university research topics for the UTSR Program. Based on additional DOE information concerning the direction of the Turbine Program, SCIES sent two new aero/heat transfer topics for DOE consideration and comments were received. SCIES also provided comments to the DOE concerning oxy fuel high temperature turbine systems that are being considered.

A meeting at NETL has been set for September 30 to develop university RFP topics. A 3-hour facilitated session will develop research topics with maximum relevance to the FE Turbine Program. Representation will be included from EERE and possibly NSF. Ahead of the meeting SCIES will solicit input from the IRB and Performing Member Universities.

UTSR Proposal Ranking Approach: In response to DOE comments, SCIES described its practice of using the average of the IRB company rankings for each proposal rather than averaging the numerical scores to alleviate most of the possible ways that a company might use to overweight the proposal they like the most or undermine a proposal that might benefit a competitor. Each company is allocated a score of 1 for the proposal they like the best, a 2 for their second choice, etc., down to a score of n (where n is the number of proposals being evaluated) for the proposal they like the least. So each company is allowed the same scoring weight and there is no incentive for a company to attempt to overweight their proposal evaluations, for example, by giving a score of 100 to their top proposal and a zero score to all of the others. Again in response to DOE comments, SCIES addressed effects of setting scores above or below which reviewers would be required to provide a written justification. Many reviewers, although wanting to do a good job, would provide maximum and minimum score just within the limits in order to not spend the extra time for justifications.

RFP for 2005: The available UTSR budget over the five-year program supports a fixed number of multi-year university project awards. The much higher than average yearly number of projects that have been awarded in the first two years of the program (10 in the first year and 9 in the second year) has resulted in fewer projects than average that can be awarded in later years. Budget evaluations this month showed insufficient funding for new project awards in 2006 due to budget requirements for the UTSR projects awarded to date and five projects to be awarded in 2005. Consequently, a UTSR RFP will not be released in 2005.

Placement of 2005 Fellows Nears Completion: Fellows have been placed for the IRB Voting Members (2 each) and for the following Associate Members (1 each): BP, Capstone, Clean Energy Systems, I-R, RAMGEN, and Woodward. SCIES is awaiting confirmation of acceptances from Parker and PCI. Cinergy, EPRI, ExxonMobil, Premcor, and Southern Company have decided not to receive a Fellow in 2005.

DOE Special Requests:

Research Accomplishments: SCIES responded to a request from the Tom George for a description of UTSR research accomplishments. Discussion of eleven major accomplishments from university research projects was provided to the DOE along with a listing of big picture benefits of the UTSR program that go beyond the specific output of the research projects.

White Paper on Fellowship Program: Based on a request from Bruce Utz, SCIES developed a white paper on the Fellowship Program, describing benefits of the program to government, industry and the universities, with a schedule chart and description of the steps in the annual Fellow placement process.

UTSR Poster: At Rich Dennis' request SCIES has provided graphics representing 7 of our more successful projects. The poster is being configured to highlight technical accomplishments. NETL plans to use the poster at Turbo Expo in June, where they have rented a booth. SCIES will also use the poster in its presentation site at Turbo.

EERE Turbine Goals: In response to a request from Tom George SCIES provided EERE's turbine program goals, obtained from Debbie Haught. There is not a formal document stating EERE's turbine goals. The turbine is considered one of several tools to achieve the broader goals of Distributed Energy (DE), so the turbine goals are aggregated with the DE goals. A way to understand the turbine goals is see page 11-13, "Budget in Brief" describing the DE budget at the web site: http://www.eere.energy.gov/office_eere/budget.html. Haught's work specifically concerning gas turbines includes 1) Ceramics (for combustor and turbine components) 2) Environmental Barrier Coatings (to protect the ceramics from erosion /corrosion) and 3) Low emission combustion technology.

US-UK Collaborative Project in Syngas and Alternate Fuels: Resulting from a recommendation by SCIES, one of several US-UK collaborative projects being developed involves using an existing Cranfield University (UK) facility to simulate turbine flow path conditions for tests of materials and turbine protection approaches for syngas turbines. SCIES has been assigned as the lead for the US portion of this collaborative project. Of particular

importance will be tests at the higher gas temperatures being considered for next generation syngas turbines to meet the DOE IGCC efficiency objectives.
At SCIES request, Siemens Westinghouse (SW) provided input on syngas composition along with test conditions for the US-UK project, including gas temperatures and specimen surface temperatures representative of syngas turbines. Additional information on syngas impurity concentration, composition and particle size distribution was requested from SW. Coordination on the syngas turbine materials candidates continued with UK participants and the US lead on another thermal barrier coatings (TBC) project in the US-UK collaboration. SCIES contacted EPRI concerning participating in the US-UK syngas turbine materials project and contributing to the cost for Cranfield operation of their facility to conduct the tests of US interest under syngas turbine conditions.

Wabash River Syngas Turbine: SCIES previously visited the Cinergy Wabash River IGCC plant and obtained deposits and spalled TBC from a turbine inspection and a turbine blade that had operated during third stage rotor blade failure. Through SCIES interactions with the DOE, funding has been provided for analyses of the blade by Southwest Research Institute to determine if operation with syngas contributed to the blade failure. SCIES updated Cinergy on the status of the blade analyses. Initial analyses have shown limited deposits on the blade and significantly higher than typical oxidation levels compared to natural gas operation. Iron, arsenic, sodium and sulfur were present in the deposits.

ORNL Project: At the request of ORNL, a budget was provided for SCIES participation in a Field Work project submitted by ORNL to the DOE that addresses materials for turbine operation with syngas and hydrogen fuels.

EPRI Survey: SCIES responded to an EPRI email survey seeking input on development needs for their Advanced Coal Generation Research, Development, and Demonstration Augmentation Plan. Backup information related to the survey response was also provided.

Natural Gas Interchangeability Forum: The Gas Turbine Association hosted the forum to address the issue of variability in the properties of natural gas, which is affecting all sizes of gas turbines with impacts of reliability and the ability to meet emissions requirements. The agenda and links to the presentations can be found at the following website: www.advocatesinc.com/gta**.**

UTSR Website Updated: A substantial update to the UTSR website has been made which includes a historic view of the UTSR Program from its inception to the present.
Information relating to publications, professor and student participation, and collaborations with gas turbine related entities now appears for each project that has been supported by the UTSR Program. The new website also houses information about the 108 Performing Member Universities. The website address is: http://www.clemson.edu/scies/UTSR/index.htm

Presentations and Publications

Invited Paper: Because of length limitations, SCIES shortened a draft contribution on turbine deposition to be included with a series of invited survey papers on turbine technologies to be

published in a special issue of the AIAA Journal of Propulsion and Power. The shortened draft was sent to Professor Hamed at the University of Cincinnati to be incorporated with her and Professor Tabakoff's contributions into the survey article on turbine erosion and deposition.

ASME Engineering Education Symposium: An abstract of a paper describing the Fellowship Program has been accepted for the ASME Mechanical Engineering Education Symposium in November 2005.

Key Milestone Update

There are no milestone modifications this month.

Discussion Topics

None.

Significant Accomplishments – Success Story

RAMGEN has rejoined the IRB as an Associate Member (non voting). RAMGEN is the sixth organization to join the IRB in 2005. This brings the number of IRB Associate Members to 13, in addition to the 5 Voting Members. SCIES has notified applicants to the Fellowship Program that the new companies are part of the IRB for possible assignment in 2005.

Site Visits

No site visits occurred or were planned with high level corporate or government officials this month.

Travel

None.

REPORT FOR APRIL

COMPLETED TASKS

ANNUAL REPORT: The 2004 Annual Report for the UTSR Program was submitted to the DOE. The report included a description of UTSR program achievements concerning the following 2004 technical milestone:

Develop turbine combustor design data to aid flashback and instability design challenges.

RFP FOR 2005: Budget evaluations have shown insufficient funding for new project awards in 2006 due to mortgage requirements for the much higher than average yearly number of UTSR projects that have been awarded in the first two years of the program. Consequently, contact persons at the 108 Performing Universities were notified that a UTSR RFP will not be released in 2005. SCIES also informed Karen Thole, Chair of the UTSR Academic Advisory Board that an RFP will not be issued in 2005.

FACT SHEET: SCIES provided to the DOE an updated Fact Sheet for the UTSR Program.

NOTIFICATION OF DOE RFP: In early April, SCIES informed all members of the UTSR Industrial Review Board that the DOE has just released a Turbine Program funding opportunity. A link to the internet address describing the solicitation was provided.

DOE SPECIAL REQUESTS:

Reviewers for Proposals. At the request of Tom George, SCIES identified and contacted seven potential reviewers of proposals to be submitted in response to the DOE RFP "Enabling Turbine Technologies for High-Hydrogen Fuels". Two SCIES personnel are also being considered as reviewers.

UTSR Contributions to SGH Turbines. At the request of Tom George, SCIES updated and provided to the DOE summaries of 22 current UTSR projects and 5 short listed projects for 2005 award with additional statements on how they contribute directly or indirectly to the advancement of SGH turbines.

Outstanding UTSR Projects. At the request of Tom George, SCIES provided results and discussion of sixteen outstanding UTSR technical accomplishments and identified the best of those in each of the three major technology areas (combustion, materials, and aero/heat transfer). Professors believed to have good contacts with the gas turbine industry and who might be familiar with benefits to industry of their research were also identified.

Test Rig. At the request of Tom George, SCIES commented on whether a planned turbine test rig at NASA Glenn could be of benefit to participants in the DOE Turbine Program.

Poster Developed at NETL. At the request of Tom George, SCIES worked with Drew Barries at NETL to provide inputs for a poster on the UTSR Program. Several sets of project

descriptions and graphics were provided, including descriptions of benefits to industry. The poster is intended for use by NETL, both in-house and externally. The timing was of poster development was beneficial for use by SCIES at Turbo Expo.

Handout Developed for Turbo Expo. At the request of Tom George, SCIES developed a handout to replace the UTSR Fact Sheet, focusing on program technical output. The cover, derived from the Fact Sheet, highlights benefits to industry from the top projects, then all of the active and pending research projects are summarized, followed by a summary of the Fellowship Program including its benefits to government, industry and universities.

Paper Developed Highlighting Benefits of UTSR to Professors and Vise-Versa. At the request of Tom George, this paper will initiate a campaign of monthly communications with the universities to enable the professors to be ambassadors for the UTSR Program. UTSR advantages to the professors will be part of the SCIES presentation at Turbo Expo, along with a set of benefits for IRB member companies.

Industry Benefits of UTSR Projects. At the request of Tom George an effort is underway to obtain information from PI's on where the results of their research are being used by industry. Several PI's have responded with information that SCIES used to develop a two-slide description of UTSR benefits. The information is also being incorporated into charts for the presentation at Turbo Expo.

US-UK COLLABORATIVE PROJECT IN SYNGAS AND ALTERNATE FUELS: SCIES has been assigned as the lead for the US portion of US-UK collaborative project that uses an existing Cranfield University (UK) facility to simulate turbine flow path conditions for tests of materials and turbine protection approaches for syngas turbines. Of particular importance will be tests at the higher gas temperatures being considered for next generation syngas turbines to meet the DOE IGCC efficiency objectives.

Test Matrix. This month SCIES identified a test matrix for the syngas materials tests. This included test section flow velocity, test gas temperatures representative of current and future syngas turbines, amount of syngas ash to be injected into the flow stream, and the need to inject steam or water to replicate the high water vapor levels in syngas turbines compared to conventional fuels. The test matrix was sent to Canfield to verify their facility can accommodate the specified test parameters.

Syngas Impurity Composition. Efforts continued to define the composition and levels of impurities in syngas to establish the environments for the materials tests. A request to GE resulted in receipt of two reports from their DOE program, “Enabling Technology for Monitoring/Predicting GT Health and Performance”. These reports have provided data on impurities in syngas measured immediately upstream of the combustors of the turbine at the Tampa Electric IGCC plant. The DOE also provided a table of syngas impurities from measurements at University of North Dakota EERC syngas plant and the Eastman Kingsport syngas plant.

Syngas Ash for Tests. A student on one of the UTSR projects has obtained syngas ash for the project through a relative recently retired from a position at a US IGCC plants. SCIES requested information on that contact so that a request could be made for syngas ash captured by a filter located immediately upstream of the turbine combustors. The request would be for sufficient quantities for not only the two 1000 hr tests in the UK-US project (about 400 lbs) but also for UTSR projects conducting research on syngas turbine corrosion and deposition. Use of this material for UTSR deposition and corrosion tests and the US-UK tests would provide data that can be correlated among the projects and with turbine experience at the IGCC plant.

Turbine Deposition/Erosion Model. For the purpose of interpreting test data, SCIES adapted for use on a personal computer a model previously developed for main frame computer predictions of erosion and deposition in turbines operating with alternate fuels. Using first stage flow path geometries and conditions for a representative syngas turbine, the model will be used (after further adapted to use data from the Cranfield facility) in the US-UK project to estimate turbine maintenance intervals associated with deposition/erosion, along with potential benefits of alternate levels of syngas cleanup.

Report and Presentation. SCIES started the report on US activities for the first year of the syngas turbine materials task of the US-UK collaboration. A presentation on this task was also started for the upcoming US-UK Workshop in Knoxville in early May.

EPRI CONTACT: SCIES previously provided comments for an EPRI email survey seeking input on development needs for their Advanced Coal Generation Research, Development, and Demonstration Augmentation Plan. In response, Jeffrey Phillips, Project Manager, Future Coal Generation Options at EPRI contacted SCIES to request a visit. He expressed interest in UTSR syngas-related work for gas turbines and in SCIES in general. EPRI's new president has announced that one of his goals is to improve relations with universities doing research relevant to the electric power industry. The motivation for this is partly due to the aging of EPRI's work force and the need to start grooming their replacements now. A visit by EPRI has been tentatively scheduled for May.

UNLV TO JOIN UTSR: Eric Sandgren, a PI who had been at Virginia Commonwealth University, has moved to the University of Nevada at Los Vegas (UNLV) as Dean of Engineering. SCIES contacted him to ask if he would be willing to join UTSR, to which he has agreed. This will be the first Performing Member University in Nevada, and brings the total number to 41 of states represented by Performing Member Universities.

IGTI TO PROVIDE BOOTH FOR SCIES AT TURBO EXPO: Part of the cooperative agreement between SCIES and IGTI for mutual promotion is booth presence at Turbo Expo. The original idea was for SCIES to share a booth with Oak Ridge National Lab, but IGTI then offered a separate booth for SCIES. IGTI has also agreed to make posters for the UTSR Program from the electronic version that was developed at NETL.

SEARCH CAPABILITY ADDED TO THE SCIES WEBSITE: This capability makes it easier to obtain information about the UTSR Program from the website, for example, project information if someone knows the PI's name but not the project number.

PRESENTATIONS AND PUBLICATIONS

ASME ENGINEERING EDUCATION SYMPOSIUM: A paper describing the Fellowship Program has been written and will be submitted for the ASME Mechanical Engineering Education Symposium in November 2005.

GAS TURBINE WORLD ARTICLE ON THE SHORT COURSE: SCIES provided additional input to GTW, and the article will be in the issue to be distributed at Turbo Expo. This gives excellent publicity to the AAB and the work that they did in putting on the course. SCIES will have reprints of the article at Turbo Expo.

KEY MILESTONE UPDATE

There are no milestone modifications this month.

DISCUSSION TOPICS

None.

SIGNIFICANT ACCOMPLISHMENTS – SUCCESS STORY

Under the University Turbine Systems Research (UTSR) program, a Brigham Young University (BYU) project (SR104) is measuring surface roughness on airfoils that have operated in turbines, measuring surface roughness on specimens from deposition tests using ash from coal and other alternate fuels, and conducting experiments and computations to determine surface roughness effects on flow shear stress and heat transfer for cooled surfaces.

Significance: Surface roughness of turbine airfoils affects both aerodynamic performance and cooling effectiveness. The experimental and computational roughness characteristics determined in this project are correlated with roughness characteristics from turbine components that have experienced service. Consequently, the verified semi-empirical roughness evolution models to be incorporated into computational codes in the project should provide the gas turbine community with useful predictive capabilities for airfoil aerodynamic and cooling design for operation with conventional and alternate fuels such as coal syngas.

SITE VISITS

No site visits occurred or were planned with high level corporate or government officials this month.

TRAVEL

None.

REPORT FOR MAY

COMPLETED TASKS

IRB MEETING: As a part of preparation for the IRB Meeting in October, SCIES provided to the DOE background information concerning the possible increased IRB membership fees, which have not changed since 1992. The information summarized the corporate membership fees for the Semiconductor Research Corporation that provides university research management consortia benefits to its corporate members.

SBIR SOLICITATION RECOMMENDATION: For an upcoming Small Business Innovative Research (SBIR) solicitation, SCIES recommended a topic with supporting discussion on instrumentation that can detect contaminants in syngas fuels more effectively than that currently available. Benefits of this instrumentation were described and specific quantities to be measured (gaseous, and condensed phase compound chemistry and condensed phase size distributions) were specified.

SCIES NEWSLETTER: Two articles related to the UTSR were written for the next SCIES Newsletter. The first describes progress from UTSR Projects in development of data and evaluations to aid in turbine combustor flashback and instability design. This article is based on the 2005 technical milestone for the UTSR project. Subjects in the second article included expansion of the IRB, 2005 Fellowship placements, the cooperation agreement between SCIES and IGTI, and the latest Gas Turbine World article.

UTSR AT TURBO EXPO: As reported last month, IGTI agreed to provide a booth at the annual Turbo Expo conference and to provide a venue for two presentations on the UTSR Program. This month the AAB responded to our request for help in providing coverage for the booth. Karen Thole (VA Tech), Tim Lieuwen (GA Tech), Vince McDonnell (UC Irvine) and Eric Jordan (UCONN) will be helping. Yong-Ho Sohn (UCF) will be out of the country but offered a graduate student (Balaji Jayaraj) who will be helping. Handouts at the booth include a new brochure on the benefits of the UTSR program to the universities, industry and government, a newly designed Fact Sheet which includes all active and pending projects and summaries of major success stories and a reprint of the Gas Turbine World article on the Turbine Short Course which was developed and presented by the AAB.

Also, IGTI is making posters for use at the presentation venue and the booth, using the electronic version that was developed by NETL and SCIES.

UTSR FELLOWSHIP PLACEMENTS: A total of 20 Fellows were placed from 12 universities at 13 companies, up from 15 Fellows last year.

AAB WRITES RESPONSE TO WALL STREET JOURNAL ARTICLE: The response was directed to an article that appeared on May 2, 2005 in the Wall Street Journal entitled New Energy Chief Seeks To Improve Technology Edge. The response urged DOE to adequately fund university research in gas turbines in order to maintain the supply of trained graduates and included the point "The downward trend over the past decade of research funding in turbine

systems has resulted in many academic institutions de-emphasizing this area in their curriculum and in their support for associated research."

IGTI ANNUAL GAS TURBINE OVERVIEW INCLUDES IGCC: At SCIES' request Lee Langston, the Editor of the Journal of Engineering for Gas Turbines and Power, included IGCC's in his article on the gas turbine industry, which covers both aircraft engines and land based gas turbines. Lee's "Gas Turbine Overview" is published annually by IGTI.

US-UK COLLABORATIVE PROJECT IN SYNGAS AND ALTERNATE FUELS: SCIES has been assigned as the US lead for a US-UK collaborative project that uses an existing Cranfield University (UK) facility to simulate turbine flow path conditions for tests of materials and turbine protection approaches for syngas turbines. Of particular importance will be tests at the higher gas temperatures being considered for next generation syngas turbines to meet the DOE IGCC efficiency objectives.

SCIES prepared a draft report on US activities for the first year of the syngas turbine materials task of the US-UK collaboration. This report was sent to the other members of the US team on the task (Siemens Westinghouse, Oak Ridge National Labs, and DOE (Udaya Rao)) for review. SCIES also prepared a presentation on this task for the US-UK Workshop in Knoxville in early May.

Prior to the Workshop, numerous interactions by email between US and UK representatives were used to identify candidate coatings and alloys for the tests, test gas temperatures, specimen surface temperatures, test section mass flow and velocity and capabilities of the Cranfield facility to inject steam and syngas contaminants representative of those experienced by the turbine flow path at IGCC plants. These interactions continued during and following the Workshop. Numerous interactions are needed to take advantage of the ability of the facility to test a wide range of materials and coatings at various surface temperatures for the two1000 hr tests of US interest under syngas turbine conditions and the two 1000 hr tests of UK primary interest under conditions of turbines operating with biomass and low grade oil derived fuels. The US and UK each have available 52 specimen slots for each of the tests. At SCIES request, some of the specimens will be exposed at conditions of European IGCC turbines so corrosion and deposition results from the tests test can be correlated with European syngas turbine experience. Specimens of materials previously tested at the Cranfield facility under natural gas turbine conditions will also be included so that materials performance under natural gas turbine conditions can be compared to that under syngas turbine conditions. Interactions between US and UK participants also coordinated activities with other materials tasks in the US-UK program. These included the TBC Task that is concerned with thicker, higher performance TBCs of DOE interest and the Standardization Task that is concerned with establishing specimen preparation and post-test analyses standards to compare results from the Cranfield rig tests with results from laboratory tests in other Tasks of the US-UK program.

EPRI VISIT: SCIES previously provided comments for an EPRI email survey seeking input on research and development needs for their Advanced Coal Generation Research, Development, and Demonstration Augmentation Plan. In response, Jeffrey Phillips, Project Manager, Future Coal Generation Options at EPRI, contacted SCIES to request a visit. He visited SCIES on May

18. SCIES provided an overview of IGCC related research in the UTSR Program. Phillips summarized EPRI's "CoalFleet for Tomorrow" initiative and the CoalFleet R&D augmentation plan being developed by representatives of the utility industry. SCIES and he then brainstormed on potential ideas for IGCC new R&D, including candidates for CoalFleet Phase 2 funding. Specific areas of concern expressed by Phillips were the phenomena causing de-rating turbine firing temperatures for operation on syngas, the reliability/availability disadvantages of "F class" combined cycles, and prospects that these issues may be even more significant for future advanced gas turbines.

The visit by EPRI provided useful input for UTSR research topics, since Phillips described results to date by the CoalFleet committee on needed IGCC research, particularly from the perspective of the utility industry. Another benefit was that Phillips has requested (from Tampa Electric) ash captured by a filter immediately upstream of the syngas turbine from the IGCC plant for injection into the flow stream in the UK-US project. He is also exploring CoalFleet providing funding to reimburse Cranfield University for two long-term tests in the US-UK project of US interest, since CoalFleet has identified higher turbine inlet temperatures (to be evaluated in the US-UK project) as a high priority issue for next generation syngas turbines.

ORNL PROJECT: At the request of ORNL, SCIES submitted a proposal to participate in a Field Work project that addresses materials for turbine operation with syngas and hydrogen fuels.

SYNERGY AMONG PROJECTS: Involvement of SCIES in other activities such as the UK-US Project and the proposed ORNL project has and will continue to provide important benefits to the UTSR Program, particularly in identifying needed research for SGH turbines and defining input conditions for analyses and experiments in UTSR projects, which requires information that does not exist or is not in the open literature. For example, contacts this month related to the US-UK project have provided information from three additional sources (including European syngas turbine sources) on impurities in syngas and effects of those impurities on turbine materials. Participation in the ORNL program will enable SCIES to obtain additional information from syngas plants and specify input to thermal chemical analyses at ORNL that will calculate the chemical composition (compounds, not just elements) and concentration of the impurities (and water vapor) in the turbine flow path of syngas turbines resulting from combustion of syngas. This information is needed as input information for UTSR projects. UTSR research, such as on-going materials projects at the University of Pittsburgh and the University of Connecticut, cannot provide realistic evaluations of turbine coatings and alloys unless the materials environments in syngas turbines are known and replicated in their laboratory experiments. UTSR aero/heat transfer projects cannot provide realistic results unless the properties of the syngas combustion projects are know and represented in project analyses and experiments.

PRESENTATIONS AND PUBLICATIONS

Invited Paper: SCIES has incorporated its draft contribution on turbine deposition into the contribution on turbine erosion provided by the University of Cincinnati for a paper to be included with a series of invited survey papers on turbine technologies to be published in a special issue of the AIAA Journal of Propulsion and Power.

Reviews of Two Gas Turbine World Articles: One review was on a combined cycle fed by hydrogen and oxygen from an earlier Westinghouse study. It is not clear whether this approach is a good idea since it has not been evaluated on a coal pile to busbar basis as has IGCC.

The other was article on GE's study of improvements that they could make to their 7FA-based IGCC plants. This was quite impressive. The efficiency gain from 40.5% to 43.0% amounts to a reduction of 5.8% in heat rate, which not only reduces the cost of coal per kWh but reduces the size of the gasification and cleanup equipment, which helps reduce $/kW. And the output gains of up to 25% from the same physical size gas turbine also decreases $/kW considerably. Importantly, these improvements can be achieved in the near term (2006) which means that the can be realized in the next set of orders of IGCC plants and thus be demonstrated relatively soon. The high specific cost ($/kW) of IGCC plants has been the principal problem holding back their more widespread deployment. These near term improvements should be significant in improving the situation.

KEY MILESTONE UPDATE

There are no milestone modifications this month.

DISCUSSION TOPICS

None.

SIGNIFICANT ACCOMPLISHMENTS – SUCCESS STORY

Under the University Turbine Systems Research (UTSR) program, a University of Central Florida (UCF) project (SR103) is evaluating and comparing two non-destructive evaluation (NDE) techniques (photostimulated luminescence spectroscopy and electrochemical impedance spectroscopy) for thermal barrier coatings (TBCs). A range of microstructural analytical techniques is also being developed and used to better understand failure mechanisms of TBCs and develop/refine NDE techniques. These evaluation approaches are being applied to five types of TBCs tested under high temperature thermal cycle conditions and analyzed at 10%, 50% and 70% lifetimes.

Significance: TBCs, originally developed for aircraft turbines with relatively frequent maintenance intervals, have needed durability improvements for the much longer life requirements of land-based turbines. The testing and analyses in this program of a range of TBC types with a wide variety of NDE and analyses techniques is developing a comprehensive set of data and knowledge concerning the fundamental science of thermo-kinetics and thermo-mechanics as a basis for improving TBC durability and reliability.

SITE VISITS

The EPRI visit by Jeffrey Phillips to SCIES is described earlier in this report.

TRAVEL

None.

REPORT FOR JUNE

COMPLETED TASKS

SHORT COURSES: SCIES has discussed with Karen Thole, Chair of the AAB the development of additional short courses and where / how they might be offered. The AAB has compiled a preliminary list of possible short courses, 5 each in Combustion, Materials and AHT and 3 in Sensors & Diagnostics. This will be discussed in a conference call with AAB members and SCIES in late July.

UTSR AT TURBO EXPO: IGTI provided the booth, Heritage State venue for presentations and poster (from the electronic version developed with NETL) that were planned, and three professors and one graduate student helped provide coverage at the booth. There was worthwhile traffic at the booth, with three companies and one university indicating a possible interest in joining the program, and generally increasing the visibility of the program to the gas turbine community. SCIES and Karen Thole of the AAB made presentations on the program at the Heritage Stage.

AWARDS FOR 2006: At the request of Phil Anderson, chairman of the IRB, SCIES provided UTSR budget information indicating that funding is insufficient for new UTSR project awards in 2006. Phil Anderson arranged a teleconference call in late June involving the IRB companies to provide them a better understanding of the UTSR funding situation. Prior to the teleconference, the DOE informed Anderson that the UTSR planning budget for FY06 and FY07 is $2.5 million for each year.

COALFLEET WORKSHOP: In May, Jeffrey Phillips, Project Manager, Future Coal Generation Options at EPRI, visited SCIES and summarized EPRI's "CoalFleet for Tomorrow" initiative and the CoalFleet R&D augmentation plan being developed by representatives of the utility industry. The CoalFleet working group is identifying needed R&D projects for IGCC plants, including candidates for CoalFleet Phase 2 funding.

This month SCIES received an invitation from Jeffrey Phillips to attend the EPRI CoalFleet for Tomorrow Workshop at Kingsport, TN in late July. He indicated that attendance will provide an opportunity for SCIES to be exposed to IGCC technology concerns of utilities and thereby help guide future UTSR research. Phillips also invited SCIES to provide an overview presentation on the UTSR Program to the members of the CoalFleet working group and to discuss the planned syngas turbine materials tests in Task 3 of US-UK Collaborative Program. This will enable the working group to consider providing under CoalFleet the remaining funding needed for Task 3. The funding is needed to reimburse Cranfield about 80 K UK pounds for conducting the two long term Task 3 tests under coal syngas turbine conditions of US interest.

INFORMATION PACKAGE ON UTSR SENT TO ALL PERFORMING MEMBER UNIVERSITIES: Following the Turbo Expo conference a package of information was sent to the PI's / Points of Contact at all 108 Performing Member Universities. It consisted of the package of materials handed out at the SCIES booth with a cover letter explaining that this

information may be useful in promoting interest in the program, both internally at your university and with potential other member universities or companies that they may contact.

EVALUATION OF PROPOSALS TO THE TURBINE PROGRAM SOLICITATION: SCIES is participating in the reviews of proposals in topic areas 1, 2A, 2B and 3A, including 19 proposals in all. Write-ups of strengths, weaknesses and funding recommendations were done as well as participation in the three consensus meetings that have taken place so far.

INFORMATION PACKAGES SENT TO DR. ROZELLE: Phone conversations were held with Dr. Peter Rozelle of DOE Headquarters by SCIES and by Karen Thole at SCIES' request, to acquaint him with the UTSR Program. Information packages were sent following the conversations.

SYNGAS IMPURITIES: UTSR research, such as on-going materials projects at the University of Pittsburgh and the University of Connecticut, cannot provide realistic evaluations of turbine coatings and alloys unless the materials environments in syngas turbines are known and replicated in their laboratory experiments. UTSR aero/heat transfer projects cannot provide realistic results unless the properties of the syngas combustion projects are know and represented in project analyses and experiments. To obtain information on syngas composition (including impurities), SCIES requested and received from GE two reports from a DOE project "Enabling Technology for Monitoring and Predicting Gas Turbine Performance in Coal IGCC Powerplants". One of the reports provides syngas chemistry and impurity composition measured immediately upstream of the turbine at the Tampa Electric IGCC Plant. This information will not only help define more representative laboratory test environments for UTSR projects but was also provided this month to the Oak Ridge National Laboratory (ORNL) for their DOE Field Work project that addresses materials for turbine operation with syngas and hydrogen fuels.

ORNL PROJECT: SCIES previously submitted a proposal ORNL to participate in their ORNL Field Work project that addresses materials for turbine operation with syngas and hydrogen fuels, but was informed this month that SCIES participation has been prevented by the DOE. A discussion was sent to Rich Dennis explaining benefits to the UTSR and DOE from SCIES participation. In summary:

- SCIES involvement in the ORNL project (and the US-UK project) would help provide information previously not available on environments in syngas turbine flow paths and thereby enhance the relevancy of UTSR research.

- An additional benefit for the DOE of SCIES participation in the ORNL project would be application to syngas turbines of expertise (developed over 15 years at gas turbine companies) related to determining gas cleanup requirements for turbines operating with alternate fuels. Better syngas impurity specifications developed through SCIES participation in the ORNL project could enable identification of sufficient but no more than necessary cleanup for acceptable turbine life.

REPORTS FOR IRB REVIEW: SCIES sent to the IRB companies a CD with semi-annual reports received from the on-going UTSR research projects over the previous six months. Forms to evaluate the project reports were also provided to the IRB.

PRESENTATIONS AND PUBLICATIONS

GAS TURBINE WORLD TO HIGHLIGHT UTSR PROGRAM IN REPORT ON TURBO EXPO: In the next issue of GTW there will be a write-up on the keynote session at Turbo Expo. At the end of the write-up, referring to the retired President of GE Aircraft Engines and Chair of the keynote session,

"…..Brian Rowe in closing the keynote session, stressed that the industry needs more engineers going into the gas turbine field. For years now, the U.S. Dept. of Energy has helped recruit and develop gas turbine engineers through its University Turbine Systems Research program.

NETL program recruits top gas turbine engineers
DOE also sponsors a gas turbine industrial fellowship program each year that is funded by the National Energy Technology Laboratory and gas turbine companies.

In collaboration with universities and the industry, the program is designed to identify and recruit top engineering students for gas turbine research and development projects.

Typically, university engineering seniors and graduate students spend 10-12 weeks working for gas turbine companies assigned to R&D under the guidance and oversight of a senior engineering manager.

Historically over 70% of the university participants choose gas turbine engineering as their profession and end up being hired by the company as a full-time engineers and researchers.

The fellowship program is administered for NETL by the South Carolina Institute for Energy Studies. SCIES presented a technical paper at the IGTI conference and also had an exhibit manned by several university professors who participate in gas turbine research and development programs."

TURBINE EROSION AND DEPOSITION PAPER: A paper, "Erosion and Deposition in Turbomachinery", with coauthors from the University of Cincinnati and SCIES was submitted this month to the AIAA Journal of Propulsion and Power for a special issue that will review gas turbine technologies. A draft of the deposition portion of the paper was sent to Eric Jordan at the University of Connecticut, who is interested in expanding his expertise to the area of turbine deposition.

2005 SUBCONTRACTS ARE IN INITIAL STAGES OF PROCESSING: The 5 universities and PI's are Penn State / Robert Santoro, U. of Central Fla. / Yongho Sohn, U. of North Dakota / Forrest Ames, BYU / Jeffrey Bons and MIT / Ahmed Ghoniem. Before actual awards can be made, each PI has to fill out a new version of the NEPA Questionnaire which went from 3 to 18/20 pages from last year. Three NEPA's have been returned to SCIES and are now with DOE for approval. Two PI's are still working on theirs and will get forwarded as soon as we receive them.

KEY MILESTONE UPDATE

There are no milestone modifications this month.

DISCUSSION TOPICS

None.

SIGNIFICANT ACCOMPLISHMENTS – SUCCESS STORY

Under the University Turbine Systems Research (UTSR) program, a University of Minnesota (UM) project (SR096) is evaluating contouring of the end wall of transition passages between the turbine combustor and first stage stator vanes for improved end wall cooling and reduced aerodynamic losses in the passage. Cascade tests and computational codes are also being used to identify the aerodynamic and cooling effects of factors such as leakage flows, misalignments that produce steps in the flow boundary, and the slash face gap in the platforms between adjacent vanes.

The project evaluations showed that convex curvature of the end wall stabilizes the boundary layer and reduces the strength of secondary passage flows, thereby reducing aerodynamic losses. Flow leakage through the slash face produced the largest effect (up to 20%) on passage losses of the other passage features that were evaluated. Next in importance is a step in the transition section gap, where a step up on the contoured end wall resulted in a decrease in passage losses.

Significance: The UM project is evaluating effects on aerodynamic performance of transition passage features. The data and analyses will provide turbine engineers with information and data to improve transition passage designs for increased engine performance.

SITE VISITS

None.

TRAVEL

Bill Day attended the Turbo Expo conference in Reno, NV.

REPORT FOR JULY

COMPLETED TASKS

SHORT COURSES: SCIES has worked with Karen Thole, Chair of the AAB, in the development of additional short courses and where / how they might be offered. The AAB has compiled a preliminary list of possible short courses, 5 each in Combustion, Materials and AHT and 3 in Sensors & Diagnostics. During a conference call between SCIES, Karen and Yongho Sohn of UCF it was decided to recommend offering the courses on site at the companies or other organizations that agree to have them presented. The host would pay for the travel cost of the presenter plus a stipend that would be split between an honorarium for the presenter and a fund which SCIES would administer that would provide for AAB expenses such as travel to meetings. This method of offering the short courses will be discussed at the upcoming IRB meeting.

UTSR PEER REVIEW WORKSHOP: A draft agenda to include with registration materials for the UTSR Peer Review Workshop was prepared, provided to the DOE for comments and finalized. Workshop registration fees were also established along with a plan that SCIES will offer reimbursement up to $1500 to cover workshop registration and travel expenses to up to 10 professors not participating in active UTSR projects. SCIES will ask interested professors to send a letter of request describing benefits of their attending the Workshop. They might also participate in the poster session to describe their current non-UTSR funded research. SCIES will select among those applying for registration/travel reimbursement. SCIES will send workshop registration information to the UTSR community in early August.

SCIES PARTICIPATES IN THE REVIEW OF PROPOSALS IN RESPONSE TO THE TURBINE PROGRAM SOLICITATION: A total of 19 proposals were reviewed, comments were written up, consensus meetings were attended by phone, and consensus reports reviewed and commented on.

US-UK COLLABORATIVE PROJECT IN SYNGAS TURBINE MATERIALS: SCIES has been assigned as the US lead for a US-UK collaborative project that uses an existing Cranfield University (UK) facility to simulate turbine flow path conditions for tests of materials and turbine protection approaches for syngas turbines. Of particular importance will be tests at the higher gas temperatures being considered for next generation syngas turbines to meet the DOE IGCC efficiency objectives.

SCIES prepared a summary and brief overview Power Point presentation describing the materials tests under syngas turbine conditions. Technical information in response to questions was also provided to Siemens Westinghouse, which is participating in the project.

E-MAIL SENT TO UTSR ACADEMIC COMMUNITY REQUESTING INDUSTRY BENEFITS INFORMATION: The e-mail contained as examples of what we are looking for, three charts that were developed for the Turbo Expo conference in Reno, showing benefits to industry from three UTSR projects, and asking that PI's prepare similar charts for their projects. This also served to inform both non contracted Performing Member Universities and IRB members of the successes that can be achieved from the program.

PRESENTATIONS AND PUBLICATIONS

COALFLEET WORKSHOP: EPRI is organizing the CoalFleet R&D augmentation plan with

participation by representatives of the utility industry. The CoalFleet working group is identifying needed R&D projects for IGCC plants (and advanced PC boiler plants), including candidates for CoalFleet Phase 2 funding.

At the invitation from Jeffrey Phillips, EPRI Project Manager for Advanced Coal Generation, SCIES attended the EPRI CoalFleet for Tomorrow Workshop at Kingsport, TN in late July. Attendance provided an opportunity for SCIES to be exposed to IGCC technology concerns of utilities and thereby help guide future UTSR research. The following top three IGCC technical issues were determined by vote of workshop participants:

1) reduction of syngas cooler deposition and plugging
2) improvement of gasifier liner refractory life
3) materials/coatings for IGCC turbines, especially at higher inlet temperatures

All three top IGCC technical issues involve materials degradation and deposition, erosion and corrosion of components.

SCIES also provided an overview presentation to the members of the CoalFleet working group on planned syngas turbine materials tests in the US-UK Collaborative program. SCIES requested that the working group consider providing under CoalFleet the remaining funding needed for the project. The funding is needed to reimburse Cranfield about 80 K UK pounds for conducting the two long term (1000 hr) tests of US interest under coal syngas turbine conditions. Eighty percent of the participants in the working group session voted yes to the question on CoalFleet support of the tests in the US-UK Program.

TURBINE HANDBOOK SECTION ON UTSR COMPLETED: The section of the DOE Turbine Handbook which describes the UTSR Program was completed and sent to both DOE and Gas Turbine World. GTW plans to make an article about this section in a future issue. SCIES worked with GTW in providing supplemental information to help with the article.

DOE UTSR PROJECT REVIEW SCHEDULED FOR AUG. 23: The review will be held for Pete Rozelle at Virginia Tech, hosted by Karen Thole. SCIES and Karen will make presentations on the UTSR Program. In preparation for this, several additional slides describing Industry Benefits of the more notable UTSR projects have been prepared, working with the PI's.

ASME PAPER ACCEPTED: The paper, titled "University Turbine Systems Research: An Innovative Approach to Graduate Education", will be presented at the ASME International ME Congress and Exposition in November in Orlando.

KEY MILESTONE UPDATE

The UTSR milestones for the 3rd and 4th quarters of DOE FY 2005 were initially focused around the preparation of a UTSR solicitation and the selection of proposals for award. Since funding was later determined to be insufficient for UTSR awards in 2006, the DOE agreed to the following milestones:

For the 3rd Qtr, -- "Review and update recent UTSR accomplishments"

For the 4th Qtr, -- "Complete program plans for UTSR Conference in FY06".

DISCUSSION TOPICS

None.

SIGNIFICANT ACCOMPLISHMENTS - SUCCESS STORY

Under the University Turbine Systems Research (UTSR) program, a Georgia Tech (GT) project (SR095) is conducting experiments and analyses to evaluate pressure oscillations in turbine combustors. The project has characterized combustion process non-linearities that determine the amplitude of instabilities, developed and validated models of turbulent flame/acoustic wave interactions that occur during screeching instabilities, and has shown practical control approaches for preventing instabilities. Two promising instability control approaches have been demonstrated in the project. The first provides open loop control of combustion instabilities by fuel injection rate modulation at non-resonant frequencies. The second approach demonstrated inhibition of instabilities by adjusting the inner and outer swirler air flow ratio for a combustor fuel injector.

Significance: Results from the GT project are providing the gas turbine industry with improved understanding and methods of control of the processes that cause combustion instabilities that have resulted in removal of turbines from service due to excess noise and structural damage.

TRAVEL

Rich Wenglarz attended the CoalFleet Workshop at Kingsport, TN on July 27 and 28.

REPORT FOR AUGUST

COMPLETED TASKS

CONTINUATION REQUEST: Work started on the UTSR Continuation Request for 2006. Draft sections on both Research and Outreach activities have been written.

UTSR MILESTONES: At the request of DOE (Chuck Alsup), SCIES provided the following suggested UTSR Milestones for FY 2006:

Oct.-Dec.: Execute UTSR Peer Review Workshop
Jan.-Mar.: SGH turbine research needs defined/topics for UTSR RFP completed.
Apr.-Jun.: Release UTSR RFP
Jul.- Sep.: Complete plans for UTSR Peer Review Workshop in FY07.

SHORT COURSES: SCIES has worked with Karen Thole, Chair of the AAB, in the development of additional short courses and where / how they might be offered. The AAB has compiled a preliminary list of possible short courses, 5 each in Combustion, Materials and AHT and 3 in Sensors & Diagnostics. Each tutorial could be offered as a 3-hour interactive lecture to (a) refresh the underpinning/fundamental science, (b) review the current status and issues, as well as survey emerging concepts and technologies related to modern turbine engineering, and (c) present case studies potentially related to on-going UTSR programs. The AAB proposal is to offer the tutorials offered at the site of interest for $2,000 (50% as instructor honorarium and 50% as indirect cost to AAB) plus travel expenses. The indirect cost to AAB will be used to expand and support future activities of AAB. This proposal for offering the short courses will be discussed at the upcoming IRB meeting,

2005 UTSR PEER REVIEW WORKSHOP: The workshop draft agenda prepared by SCIES was modified according to DOE comments. The DOE agreed to a SCIES suggestion of offering reimbursement up to $1500 to cover workshop registration and travel expenses to a maximum of 10 professors not participating in active UTSR projects. SCIES forwarded an invitation to apply for the travel grants from Dr. Karen Thole, Academic Advisory Board Chair for the UTSR Program. The invitation was sent to the more than 100 UTSR Performing Member Universities and also offered the opportunity for applicants to present a poster on their research at the workshop. Eight applications for workshop travel/registration grants were received by the end of August.

SCIES contacted the Principal Investigators (PI's) of the 21 ongoing UTSR projects and sent them workshop presentation guidelines along with the format for project Fact Sheets. Each project Fact Sheet will be included in a booklet which will be provided to the workshop participants. Instructions were also provided describing how to send their presentations to SCIES before the workshop via the internet. The PI's of the 5 newly awarded UTSR projects in 2005 were also notified and provided guidelines for their poster displays at the workshop along with the Fact Sheet format.

SCIES sent by email the workshop invitations to the UTSR community for on line access to workshop information and registration.

IRB MEETING: The IRB Meeting for 2005 is scheduled for October 17, the day before the start of the Peer Review Workshop. SCIES contacted Phil Anderson, Chair of the IRB and suggested the following possible items for discussion (other topics may be added closer to the meeting date):

a) Summary of UTSR finances and future outlook

b) IRB Outreach support

c) Request from Karen Thole to discuss with the IRB the short courses developed by the AAB

d) The following list of 5 items previously discussed and any new items that might be brought to the table.

1)....Voting member and associate member fees to the IRB have been constant since UTSR program inception in 1992. Should an increase in dues occur? If yes to what level should dues be increased?
2).....The associate member base of the IRB now includes 12 companies. Should the associate members have a voting position on the Board? If yes how many votes? Right now the associates pay approximately one third voting member fees so should they get 4 votes (12 divided by 3) ?
3) .....Can/should the IRB via the board chair function for UTSR as GTA functions for the entire turbine industry? That is, speaking before legislative bodies in favor of UTSR.
4) ....Should the AAB receive financial support for expenses? If so what should be covered, what budget should be established and supported from what pot of money?
5) ....Do we need to establish a standard procedure for determining UTSR value to the IRB? Another group does this by assigning a dollar value to Fellows hired by there company and to the research that is done by the consortium project by project. The sum results in a return which then can be used to determine a ROI.

SCIES also asked whether a half day should be planned for the IRB Meeting, considering short listing of university proposals is not needed because an RFP was not released this year due to insufficient funding. Phil Anderson agreed to a half day IRB meeting on the afternoon of October 17.

UTSR PROJECT AWARDS: Four of the five new 2005 UTSR projects were awarded in August. The 5 universities and PI's are Penn State / Robert Santoro, U. of Central Fla. / Yongho Sohn, U. of North Dakota / Forrest Ames, BYU / Jeffrey Bons and MIT / Ahmed Ghoniem. The MIT project negotiations have not yet been completed but the subcontract award should be placed in early September.

ESTIMATING THE MONETARY VALUE OF UTSR PROJECTS: SCIES has begun working with several universities to estimate the monetary value of the benefits from UTSR projects. The first project being evaluated is by UCONN, Maury Gell PI, #091 which produced a 4:1

improvement in the Spallation life of thermal barrier coatings of the EBPVD type (electron beam physical vapor deposition). GE and Siemens responded to our inquiries that they don't use EBPVD type of TBC's but use air plasma spray instead due to lower cost. Discussions are underway with P&W and Rolls Royce. Work has been started with Brigham Young, Jeffrey Bons PI, #104 on improved maintenance intervals, and with VA Tech, Karen Thole PI, #110 on the increased heat transfer to vanes and endwalls with realistic surface conditions.

INTERACTIONS WITH CINERGY: Cinergy is considering the construction of a second IGCC power plant and has contacted SCIES and discussed several related items:

Analysis of Failed Third stage Blade. Resulting from two visits to the Cinergy Wabash River IGCC plant, SCIES obtained a third stage blade that had operated in the syngas turbine and facilitated its analysis at Southwest Research Institute through an EPRI contract with the DOE. Cinergy contacted SCIES and requested information on the analysis of a failed third stage blade from that turbine which is also being evaluated. SCIES contacted Southwest Research Institute and requested an update on the analyses status for Cinergy.

Trapped Vortex Combustion. Cinergy asked for information on a Ramgen trapped vortex project described in an article authored by Rob Steele in the July/August issue of Turbomachinery International. SCIES contacted Dr. Steele and arranged for him to contact Cinergy concerning Ramgen projects related to IGCC power plants.

EPRI CoalFleet Workshop. SCIES informed Harold Stocker of Cinergy about the main IGCC technical issues identified at the CoalFleet workshop, including syngas turbine materials corrosion, erosion and deposition.

UK-US Project. SCIES informed Harold Stocker about the UK-US Fossil Energy Materials Collaboration, described UK-US Syngas Turbine Materials Test project for which SCIES is the US lead, and discussed the possibility of Cinergy participating in the Collaboration. Cinergy is considering that possibility, which would require some contribution to the project efforts. SCIES asked Cinergy about providing ash from filter immediately upstream of the turbine at the Wabash River plant for tests in the UK-US project.

INTERACTIONS WITH ORNL: SCIES provided ORNL (Ian Wright) information obtained from presentations and discussions with participants at the CoalFleet Workshop that should be useful for the ORNL program with the DOE to evaluate effects of syngas operation on turbine hot section components.

INTERACTIONS WITH EPRI: At EPRI (Jeffrey Phillips) request, SCIES provided comments on technical feasibility and issues for a pressurized pulverized coal combustion (PPCC) system being tested on a pilot scale in Europe. The system includes a pressurized coal combustor that provides expansion gases (after hot gas cleanup to remove particulate and alkali) to a gas turbine operating in a combined cycle power block.

TURBINE TIP CLEARANCE: SCIES responded to a request from DOE to provide information on the feasibility of small turbine tip clearances, on the order of 5 mils (0.005 inches) for a small

gas turbine. SCIES consulted an expert in the field and found that 15 mils is as small as they get, in aircraft engines and similar size industrial gas turbines – with the latest active clearance control technology. It is not realistic to count on achieving smaller clearances.

MONTANA STATE HAS JOINED UTSR: This adds a new geographic area to our coverage, the first in Montana.

PRESENTATIONS AND PUBLICATIONS

TURBINE EROSION AND DEPOSITION PAPER: A paper, "Erosion and Deposition in Turbomachinery", with coauthors from the University of Cincinnati and SCIES was accepted this month for publication in a special issue of the AIAA Journal of Propulsion and Power that will review gas turbine technologies. The authors were informed that the paper will also be published in a book that will contain review articles on gas turbine technologies. The paper was modified according to reviewer comments and SCIES provided an abstract for the publications.

ASME PAPER FOR TURBO EXPO 06: The abstract for a paper "University Turbine Systems Research Program: A Partnership between Government, Universities and Industry" has been accepted.

CHARTS ON THE BENEFITS OF UTSR PROJECTS: With good responsiveness from a number of universities SCIES prepared a set of single slide project descriptions as part of a presentation planned at VA Tech with Karen Thole to Pete Rozelle on the UTSR Program. Although Rozelle needed to cancel the event, the charts will be useful in future presentations; they include graphics and brief descriptions of the benefits of the projects.

SIGNIFICANT ACCOMPLISHMENTS - SUCCESS STORY

Under the University Turbine Systems Research (UTSR) program, a Louisiana State University (LSU) project (SR098) is evaluating the potential benefits of contouring the end walls of turbine airfoil passages and the using airfoil fillet shaping to control secondary flows and heat transfer to end walls. Experiments and analyses to date have defined an end wall contour that reduces airfoil passage total pressure losses and end wall heat transfer coefficients compared to a baseline case.

Significance: The LSU project is providing turbine engineers with data and analyses for improved strategies to improve aerodynamic efficiency of turbine airfoil passages and reducing the heat load to passage end walls. The resulting designs offer the potential for lower end wall cooling air requirements, with resulting improved fuel efficiency and improved reliability of gas turbines.

KEY MILESTONE UPDATE

There are no milestone modifications this month.

TRAVEL

No travel during August.

REPORT FOR SEPTEMBER

COMPLETED TASKS

CONTINUATION REQUEST: The UTSR Continuation Request for 2006 was completed and submitted to the DOE/NETL on September 19.

2005 UTSR PEER REVIEW WORKSHOP: SCIES will provide reimbursement up to $1500 to cover workshop registration and travel expenses to professors not participating in active UTSR projects. A total of nine applications were received and all were awarded workshop travel/ registration grants

SCIES previously contacted Principal Investigators (PI's) of UTSR projects and provided them guidelines for presentations, posters and Fact Sheets. The remaining speakers were contacted this month and details were worked out concerning their presentations. SCIES interacted with Doug Straub and provided guidelines concerning a possible poster on DOE syngas and hydrogen fuel turbine research.

Meetings at SCIES developed detailed plans and procedures for facilitating the breakout sessions of the "Managing UTSR Growth" forum at the workshop. Because of the large number of people registered (more than 80), the number of breakout sessions was increased to four. The university and industry participants will be randomly assigned to three breakout sessions with government participants assigned to the fourth breakout session.

An email was sent to workshop registrants reminding them of the "Managing UTSR Growth" forum and asking them to give thought to the topic of UTSR growth prior to the workshop.

As part of an agreement with IGTI under which IGTI provided a booth for SCIES at Turbo Expo in Reno, SCIES will provide a table for IGTI to have a representative distribute literature on IGTI at the UTSR Peer Review Workshop III.

UTSR FACT SHEET: The Fact Sheet for the UTSR Program was updated and provided to the DOE.

UNLV JOINS UTSR: University of Nevada Las Vegas has joined the UTSR Program, bringing the total university membership to 110. The Dean of Engineering, Eric Sandgren, was a former UTSR PI when he was at Virginia Commonwealth University. Nevada adds another state to our representation, which now totals 42 states.

IRB MEETING: The IRB Meeting for 2005 is scheduled for October 17, the day before the start of the Peer Review Workshop. A final decision was made to start the IRB meeting at noon and ending at approximately 5 pm. An evening IRB dinner will follow.

COST BENEFIT ANALYSIS OF UTSR PROJECTS: SCIES has begun working with universities to estimate the monetary value of the benefits from UTSR projects. The first project being evaluated is by UCONN, Maury Gell PI, #091 which produced a 4:1 improvement in the

Spallation life of thermal barrier coatings of the EBPVD type (electron beam physical vapor deposition). GE and Siemens responded to our inquiries that they don't use EBPVD type of TBC's but use air plasma spray instead due to lower cost. P&W and Rolls Royce have said that they will provide estimates. Work has been started with Brigham Young, Jeffrey Bons PI, #104 on improved maintenance intervals, and with VA Tech, Karen Thole PI, #110 on the increased heat transfer to vanes and endwalls with realistic surface conditions. A draft preliminary report has been written for NETL management on this effort, and a presentation has been prepared for the IRB meeting describing the help needed from IRB member companies in this effort.

SGH TURBINE RESEARCH DEFINITION: An upcoming activity is identification of research topics for the next RFP of the UTSR program. Topic selection and UTSR research would benefit from a better definition of the flow path environments and issues for SGH turbines. Accordingly, there is a need to define syngas ash impurity compositions and effects of syngas combustion products on the turbine hot section so that the UTSR projects can produce the proper environments for their laboratory tests and address the appropriate issues.

SCIES previously had discussed the needed information for the UTSR at the EPRI CoalFleet Workshop with Mark Hornick, from Tampa Electric which operates one of the few IGCC plants in the US. This month SCIES contacted Hornick by email and requested information on syngas composition (including impurities), particle size distributions, along with effects of syngas combustion products on hot section components.

SCIES found data from Japanese turbine materials tests (up to 350 hrs in duration) in an actual syngas combustion environment using a small scale Texaco type, oxygen blown gasifier using a hot gas cleanup system. Materials losses are described and there is information on syngas composition (including trace ash elements). Unfortunately, the highest gas temperatures (1920 F) in the materials test section were significantly lower than those entering current syngas turbines and consequently did not produce some of the molten phases (and resulting corrosion and deposition) that would be expected at higher turbine temperatures. Even so, most of the turbine materials experienced accelerated rates of corrosion. (up to 100 microns in 350 hr)

COLLABORATION WITH ORNL: SCIES has been interacting with Oak Ridge National Labs (ORNL) in areas mutually beneficial to their DOE materials project and the UTSR project. ORNL will be conducting thermo-chemical analyses to calculate the composition of species (including trace compounds) in the flow path of SGH turbines. This information will be useful input to materials and aero/heat transfer projects. SCIES is working with ORNL in suggesting analyses beneficial to both programs (effects of turbine inlet temperature and variations in syngas ash chemistry) and attempting to obtain information needed for ORNL to conduct the thermo-chemical analyses. For example, SCIES provided ORNL a typical residence time bounding chemical reactions in the turbine hot section and, through a UTSR contact, a typical combustor residence time. A typical value is 20-25 milliseconds for the combustion process to the exit of combustor transition section (first stator inlet) and approximately 10 milliseconds in the expander from first stator inlet to final rotor exit (at near atmospheric pressure).
SCIES has requested input fuel, air and steam/nitrogen flows to a syngas turbine combustor from one of the IRB companies. SCIES also requested the name of a contact person to obtain syngas ash samples captured by a filter immediately upstream of the turbine at an IGCC plant for ORNL

chemical analyses. SCIES provided information to ORNL from DOE project reporting data on syngas trace element vapor and particulate composition and levels measured at an IGCC plant.

UK-US PROJECT: Task 3 in the UK-US Collaboration in Energy R&D for Fossil Energy Materials will test turbine materials under conditions of current IGCC turbines and higher temperature conditions of future turbines operating with syngas. Since IGCC turbines experience higher rates of flow path degradation than the same model machines operated with natural gas, the goals of the tests are to identify superior materials and improved flow path protection approaches for current and future syngas turbines. As US lead for Task 3, SCIES has been coordinating US technical activities and has been responsible for definition of the turbine flow path environments to be replicated in the tests and obtaining samples of syngas ash for analyses and injection in the tests. Since UTSR materials and aero/heat transfer projects also require identification and replication of syngas turbine flow path environments for their experiments, SCIES participation in the UK-US project benefits the UTSR program.

Agreement has been reached between US and UK participants on test materials, coatings, surface temperatures, and gas temperatures. Siemens (US) has fabricated most of the test specimens and will start their coating in October. SCIES contacted Cranfield University (where the tests will be conducted) to determine their progress in providing the desired test flow velocity and to ask for an updated schedule for the tests which will start in 2006. SCIES contacted all US participants (Siemens (US), ORNL, DOE (Udaya Rao)) to provide their input to the Task 3 semi-annual report and presentation for the upcoming UK-US Workshop on October 20 and 21. SCIES has started the report and presentation slides but will not be able to attend the UK-US Workshop because of conflict with the dates of the UTSR Peer Review Workshop.

SCIES contacted Jeffrey Phillips of EPRI concerning their participation in Task 3 and contributing funds (80 thousand UK pounds) for the two long term tests under syngas turbine conditions at Cranfield. He responded that the EPRI CoalFleet group has endorsed the idea of providing co-funding and is in the process of trying to line up the funds.

PRESENTATIONS AND PUBLICATIONS

TURBINE EROSION AND DEPOSITION PAPER: AIAA has decided on a publication date for the paper, “Erosion and Deposition in Turbomachinery”, with coauthors from the University of Cincinnati and SCIES. The paper will appear in the January 2006 special issue "Turbine Science and Technology" of the AIAA Journal of Propulsion and Power.

ASME PAPER FOR TURBO EXPO 06: The draft for a paper “University Turbine Systems Research Program: A Partnership between Government, Universities and Industry” has been completed and submitted to ASME.

TURBINE HANDBOOK SECTION ON THE UTSR PROGRAM: SCIES submitted to Cassie Clifton a section of the DOE Turbine Handbook on the UTSR Program.

COST BENEFIT ANALYSIS: As reported above, a draft preliminary report was written on the cost benefit analysis that is underway for the UTSR Program. In a related move, we are posting

the single slide project descriptions which show the benefits to industry, of 16 of the most notable projects, see http://www.clemson.edu/scies/UTSR/examples.htm . This is intended to make it easier for the IRB companies to help with the cost – benefit analysis of UTSR projects.

OUTSIDE PUBLICATIONS RELEVANT TO UTSR: SCIES provided NETL management and FE HQ, copies of articles in Business Week and Power Engineering on IGCC, which may be helpful in program planning.

SIGNIFICANT ACCOMPLISHMENTS - SUCCESS STORY

Under a University Turbine Systems Research (UTSR) program, a Virginia Tech (VT) project (SR100) is evaluating various computer simulation algorithms to predict the complex flows and heat transfer for internal cooling channels of turbine airfoils. The project has established that the Large Eddy Simulation (LES) approach can be used for robust, repeatable, and accurate predictions of heat transfer in ribbed cooling channels, such as used in gas turbines. LES has been successfully applied for the first time to develop the detained flow and heat transfer at the entrance and within a 180 degree bend. Detached eddy simulations (DES) were for the first time applied to predict heat transfer in a ribbed channel and shows favorable comparisons with LES but at a much lower computation cost.

The computational advancements achieved in this project have been recognized in an article appearing in the Fall 2004 issue of ACCESS, the publication of the National Center for Supercomputer Applications.

Significance: The VT project is analyzing, developing, and verifying advanced computational techniques for use in improving the cooling design of turbine airfoils. The project has enabled new advances in prediction technology for internal cooling flows. This technology should result in more cost effective design of more efficient cooling of turbines, with corresponding benefits in turbine efficiency and power.

KEY MILESTONE UPDATE

There are no milestone modifications this month.

TRAVEL

No travel during September.